ECTI-CON 2007

Proceedings of the 2007 Electrical Engineering/Electronics, Computer, Telecommunications and Information Technology (ECTI) International Conference

Wednesday May 9 – Saturday May 12, 2007

Mae Fah Luang University, Chiang Rai, Thailand

Organized by

Electrical Engineering/Electronics, Computer, Telecommunications and Information Technology (ECTI) Association

ECTI-CON 2007

Proceedings of the 2007 Electrical Engineering/Electronics, Computer, Telecommunications and Information Technology (ECTI) International Conference

Wednesday, May 9 – Saturday May 12, 2007

Mae Fah Luang University, Chiang Rai, Thailand

Organized by

Electrical Engineering/Electronics, Computer, Telecommunications and Information Technology (ECTI) Association

Steering Committee
Sawasd Tantaratana, Chair (07)
Pansak Siriruchatapong (07)
Wanlop Surakampontorn (07)
Sinchai Kamolphiwong (07)
Weerapant Musigasarn (07)
Somsak Choomchuay (07)
Jun-ichi Takada (08)
Kazushi Nakano (08)
Saykhong Saynasine (08)
Athikom Roeksabutr (08)
Prabhas Chongsatitwattana (08)
Monai Krairiksh (08) Secretary

Technical Advisory Committee
Akinori Nishihara, (TIT, Japan)
Hara Shinji (U. of Tokyo, Japan)
Luigi Benedicenti, (U. of Regina, Canada)
Rolf H. Jansen (Aachen U., Germany)
Narong Yoothanom (SPU)

Local Advisory Committee
Vanchai Sirichana (MFLU)
Ted Tesprateep (MFLU)

General Chair
Wanlop Surakampontorn (KMITL)

Vice Chairs
Kosin Chamnongthai (KMUTT)
Jitkasem Ngamnil (MUT)
Apirat Siritaratiwai (KKU)

Technical Program Chair
Chaiwut Chat-uthai (KMITL)

Technical Program Co-Chairs
Tiparatana Wongcharoen (BU)
Songphol Kanjanachuchai (CU)
Itsda Boonyaroonate (KMUTT)
Vara Varavithya (KMITNB)
Apichan Kanjanavapastit (MUT)
Keattisak Sripimanwat (NECTEC)

Special Session Chairs
Chuwong Phongcharoenpanich (KMITL)
Raungrong Suleesathira (KMUTT)

Local Arrangement Chairs
Preecha Upayokin (MFLU)
Thongchai Yooyativong (MFLU)
Damrong Amorndechaphon (NU-PYO)
Werachate Khan-ngenn (KMITL)

Publication Chairs
Denchai Worasawate (KU)
Teratam Bunyagul (KMITNB)
Daranee Hormdee (KKU)

Publicity Chairs
Danai Torrungrueng (ASUT)
Phongsak Keeratiwintakorn (KMITNB)

Exhibition Chairs
Chalie Charoenlarpnopparut (SIIT)
Wanida Kan-argart (KKU)
Chiranut Sa-ngiamsak (KKU)

Finance Chairs
Banlue Srisuchinwong (SIIT)
Rujipan Sampanna (BU)

General Secretaries
Prayoot Akkaraekthalin (KMITNB)
Vutipong Areekul (KU)

Table of Contents

Message from Steering Committee Chair

Message from General Chair

Message from Technical Program Chair

List of Reviewers

Symposium Schedule at a Glance

ECTI-CON 2007 Session Schedule

Keynote Speech

Technical Program Contents

Technical Papers

Author Index

Message from Chair of Steering Comittee

The first two ECTI-CON's were held in Pattaya, Cholburi. The Steering Committee then had a policy to reach out to researchers in all part s of Thailand. Consequently, the third ECTI-CON was held in Ubon Ratchatani last year. This year the fourth ECTI-CON is scheduled for Chiang Rai on the beautiful campus of Mae Fah Luang University.

Chiang Rai is the northernmost province of Thailand, which is located within the renowned Golden Triangle area where Myanmar, Laos, and Thailand converge, also known as the gateway to Myanmar, Laos, and Southern China. Chiang Rai has a lot of attractions including magnificent mountain sceneries, historic sites, and ethnic villages, as well as several hill tribes who maintain fascinating lifestyles. These are some reasons for choosing Chiang Rai as the venue of ECTI-CON this year. However, the main reason is to initiate a research gateway to this region and motivate researchers in this area to become more active in future ECTI-CON's.

On behalf of the Steering Committee of ECTI-CON, I would like to express my sincere gratitude to all of ECTI-CON 2007 organizing committee members and staff for their excellent work and to the authors from around the world for sharing their results by their presentations and discussions. It is hoped that the participants will enjoy not only the technical aspects of the conference, but also the banquet, food, and culture of northern Thailand. Next year, ECTI-CON will move its venue to Krabi, a beautiful province in the southern part of Thailand. I look forward to seeing all of you at ECTI-CON 2007 and again at ECTI-CON 2008 next year.

Sawasd Tantaratana
ECTI-CON 2007 Steering Committee Chair

Message from General Chair

On behave of the Organizing Committee; it is my great pleasure to cordially welcome all the participants to the 2007 Electrical/Electronics, Computer, Telecommunications, and Information Technology Conference (ECTI-CON 2007). This year the conference is the fourth annual conference in the series and is held in the northern part of Thailand, at Mae Fah Luang University, Chiang Rai province, on May 9-12, 2007. As one of the major activities of the ECTI Association, the ECTI-CON international conference aims annually to provide as a forum to bring together researchers to discuss and exchange of original works, new ideas and new recent advances in the areas.

The success of this conference is due to the sponsor from the National Electronics and Computer Technology Center (NECTEC) of Thailand, and the Western Digital Thailand. The technical collaborations are provided by the IEEE MTT/AP/ED Thailand Chapter, the IEEE CAS Thailand Chapter, the IEEE ComSoc Thailand Chapter, the IEEE LEOS Thailand Chapter and the IEEE Thailand Section. I also would like to express my sincere appreciation for the effort, hard work and significant contributions by the Organizing Committee members, especially the Vice Chair: Assoc. Prof. Dr. Kosin Chamnongthai, the General Secretaries: Assoc. Prof. Dr. Prayoot Akkaraekthalin and Assoc. Prof. Dr. Vuthipong Areekul, the Technical Program Chair: Assoc Prof. Dr. Chaiwut Chat-uthai. The valuable contributions from the authors that submitted technical papers for review, the technical program committee members, the speakers, and the session chairs and the attendees are also gratefully acknowledged.

As you can notice, the ECTI Association tends to organize the ECTI-CON conference at a new place each year. This means that some inconveniences may occur during the arranging of the conference. The Organizing Committee Members will do our best to solve and to make sure that you participate in the conference with pleasure. Finally, we do hope that you will find a good opportunity to meet, to exchange ideas and to make research contacts and collaboration, which are the objectives of the conference too.

Wanlop Surakampontorn
ECTI-CON 2007 General Chairman
President of the ECTI Association

Message from Technical Program Chair

We cordially welcome you to the 4th annual international conference ECTI-CON 2007 held during May 9-12, 2007 in Chiang Rai, farthest north province and intersection of three reigns (Thailand, Myanmar and Laos).

Following the successful conferences of ECTI-CON 2004, 2005 and 2006, ECTI-CON 2007 continuously aims to provide a forum for academic and industrial researchers in the area of Electrical Engineering, Electronics, Computer, Telecommunications and Information Technology to discuss and exchange up-to-date information. The conference received overwhelming response which is apparent from the over 400 papers submitted by researchers around the world. After a careful and rigorous review process, 318 quality papers from 12 countries were accepted. For the reason of topic diversity, this conference provides the presentations of regular papers into 66 sessions of ten parallel rooms. In addition, the invited papers of interesting issues will be also presented in 4 special sessions.

For the ECTI-CON 2007 opening ceremony, we honorably invite Prof. Dr. Akira Taguchi from the Musashi Institute of Technology, Japan, Prof. Dr. Shuzhi Sam Ge from the National University of Singapore, and Dr. Pansak Siriruchatapong, the director of National Electronics and Computer Technology Center (NECTEC), Thailand to be the keynote speakers. At the present, Prof. Akira Taguchi serves the chair of Nonlinear Signal and Image Processing Board (IEEE, EURASIP). Professor Shuzhi Sam Ge is the head of Social Robotics Lab, Interactive and Digital Media Institute, and the director of Edutainment Robotics Lab, Department of Electrical and Computer Engineering. Subsequently at conference banquet in the evening, the best paper awards which were judged by the executive referees will be presented to the authors.

The Organizing Committee and colleagues who have been working behind-the-scenes deserve special mention. In particular, I would like to single out the Technical Program Co-Chairs and Publicity Chairs for their hard work and sincerity. Finally, I would like to say thanks to all honorable keynote speakers, authors, reviewers, session chairpersons, participants and other people for their support, and wish all of you a successful and stimulating meeting and a pleasant stay in Mae Fah Luang University, home to the culture of Lanna.

Chaiwut Chat-uthai
ECTI-CON 2007 Technical Program Chair

List of Reviewers

We would like to express special thanks to the following individual and anonymous reviewers for their effort in the review process of ECTI-CON 2007:

Akinori Nishihara
Amorntep Jirattitichareon
Anuwat Jangwanitlert
Apichan Kanjanavapastit
Apirat Siritaratiwat
Apisak Worapishet
Arporn Teeramongkonrasmee
Athikom Roeksabutr
Boonchai Techaumnat
Boonsong Sutapun
Chaiwut Chat-uthai
Chaiyachet Saivichit
Chanchai Laohapengsang
Chanin Bunlaksananusorn
Chaodit Aswakul
Chiranut Sa-ngiamsak
Chokchai Sangdao
Chumphol Krootkaew
Chutham Sawigun
Chuwong Phongcharoenpanich
Danai Torrungrueng
Denchai Worasawate
Ekachai Leelarasmee
Issarachai Ngamroo
Itsda Boonyaroonate
Jatuporn Chinrungrueng
Keattisak Sripimanwat
Kittipong Tonmitr
Kohji Higuchi
Mitchai Chongcheawchamnan
Monai Krairiksh
Nalin Sidahao
Narumol Kiatwarin
Nipon Theera-Umpon
Nisachon Tangsangiumvisai
Pakorn Kaewtrakulpong
Panuthat Boonpramuk
Paramin Sangwongngam
Parnjit Damrongkulkamjorn
Pasu Kaewplang
Pathomthat Chiradeja
Peng Hin Lee
Phaophak Sirisuk
Phongsak Keeratiwintakorn
Prabhas Chongstitvatana
Prayoot Akkaraekthalin
Ravee Phromloungsri
Saliltip Sinthusonthishat
Samphan Pampichai
Sanpachai Huvanandana
Sansanee Auephanwiriyakul
Santi Asawasripongtorn
Sanya Mitaim
Saowaluck Kaewkamnerd
Saowapak Sotthivirat
Siriroj Sirisukprasert
Somboon Sangwongwanich
Sompob Polmai
Somsak Choomchuay
Somying Thainimit
Songphol Kanjanachuchai
Supakorn Siddhichai
Supat Kittiratsatcha
Surapan Airphaiboon
Suree Pumrin
Tanee Demeechai
Taworn Benjanarasuth
Teerasit Kasetkasem
Thumrongrat Amornraksa
Tiparatana Wongcharoen
Toshiaki Kondo
Vutipong Areekul
Wanlop Surakampontorn
Worapong Tangsrirat
Yoshikazu Miyanaga

Symposium Schedule at a Glance

Wednesday, May 9, 2007

14:30-17:00	Registration at Wangcome Hotel
18:00-22:00	Welcome Party at Wangcome Hotel

Thursday, May 10, 2007

07:30-08:30	Registration at Mae Fah Luang University
08:30-09:00	Open Ceremony
09:00-09:40	Keynote Speech: "*Where Thailand should go for ECTI Research in the next Decade: NECTEC Strategy*" by Dr. Pansak Siriruchatapong, National Electronics and Computer Technology Center (NECTEC), Thailand
09:40-10:20	Keynote Speech: "*Restoration of the Lost Information by Sampling and Quantization"* by Dr. Akira Taguchi, Musashi Institute of Technology, Japan
10:20-10:50	Coffee Break
10:50-12:10	Technical Sessions
12:10-13:00	Lunch Break
13:00-15:00	Technical Sessions
15:00-15:20	Coffee Break
15:20-17:00	Technical Sessions
17:15-17:55	Keynote Speech: "Social Robotics: Integrating Advances in Engineering and Computer Science" by Dr. Shuzhi Sam Ge, National University of Singapore, Singapore
18:30-22:00	Conference Banquet at Mae Fah Luang University

Friday, May 11, 2007

08:30-10:10	Technical Sessions
10:10-10:30	Coffee Break
10:30-12:10	Technical Sessions
12:10-13:00	Lunch Break
13:00-15:00	Technical Sessions
15:00-15:20	Coffee Break
15:20-17:00	Technical Sessions
17:00-18:00	Closing Ceremony

ECTI-CON 2007 Session Schedule

Time	Wednesday, May 9 th, 2007									
14:30-17:00	Registration at Wangcome Hotel									
18:00-22:00	Reception Party at Wangcome Hotel									
Time	**Thursday, May 10 th, 2007**									
7:30-8:30	Registration at Mae Fah Luang University									
8:30-9:00	Opening Ceremony									
9:00-9:40	Keynote Speech: "Where Thailand should go for ECTI Research in the next Decade: NECTEC Strategy" by Dr. Pansak Siriruchatapong, National Electronics and Computer Technology Center (NECTEC), Thailand									
9:40-10:20	Keynote Speech: "Restoration of the Lost Information by Sampling and Quantization" by Dr. Akira Taguchi, Musashi Institute of Technology, Japan									
	Break (10:20-10:50)									
Time	**Session**	**TAM1-1**	**TAM1-2**	**TAM1-3**	**TAM1-4**	**TAM1-5**	**TAM1-6**	**TAM1-7**	**TAM1-8**	**TAM1-9**	**TAM1-10**
	Name	Microwave Technology 1	Processors	CMOS Technology	High Voltage Engineering 1	Optical Communications	Power Electronics 1	Antenna Applications	Integrated Circuits	Image Technology	DSP/Coding
	Chair	Denchai Worasawate (KU)	Prabhas Chongsatitwattana (CU)	Songphol Kanjanachuchai (CU)	Thanapong Suwanasri (KMITNB)	Athikom Roeksabutr (MUT)	Viboon Chunkag (KMITNB)	Sompol Kosulvit (KMITL)	Chiranut Sa-ngiamsak (KKU)	Akira Taguchi (Musashi Tech)	Takao Onoye (Osaka U)
10:50-11:10		TAM1-1-1	TAM1-2-1	TAM1-3-1	TAM1-4-1	TAM1-5-1	TAM1-6-1	TAM1-7-1	TAM1-8-1	TAM1-9-1	TAM1-10-1
11:10-11:30		TAM1-1-2	TAM1-2-2	TAM1-3-2	TAM1-4-2	TAM1-5-2	TAM1-6-2	TAM1-7-2	TAM1-8-2	TAM1-9-2	TAM1-10-2
11:30-11:50		TAM1-1-3	TAM1-2-3	TAM1-3-3	TAM1-4-3	TAM1-5-3	TAM1-6-3	TAM1-7-3	TAM1-8-3	TAM1-9-3	TAM1-10-3
11:50-12:10		TAM1-1-4	TAM1-2-4	TAM1-3-4	TAM1-4-4	TAM1-5-4	TAM1-6-4	TAM1-7-4	TAM1-8-4	TAM1-9-4	TAM1-10-4
	Lunch Break (12:10-13:00)										
Time	**Session**	**TPM1-1**	**TPM1-2**	**TPM1-3**	**TPM1-4**	**TPM1-5**	**TPM1-6**	**TPM1-7**	**TPM1-8**	**TPM1-9**	**TPM1-10**
	Name	Microwave Technology 2	Oscillator Circuits	Mobile Communication Technology	Power Systems 1	Communication Networks	Power Electronics 2	Image Processing 1	Control Engineering 1	Software Engineering and Applications	Network Systems
	Chair	Tuptim Angkaew (CU)	Apinan Thanachaynont (KMITL)	Zia Nadir (Sultan Qaboos U)	Natthaphob Nimpitiwan (BU)	Chalie Charoenlarpnop-parut (SIIT)	Itsada Boonyaroonate (KMUTT)	Rachada Kangkachandra (TU)	Kazushi Nakano (U Electro-Comm)	Prabhas Chongsatitwattana (CU)	Phongsak Keeratiwintakorn (KMITNB)
13:00-13:20		TPM1-1-1	TPM1-2-1	TPM1-3-1	TPM1-4-1	TPM1-5-1	TPM1-6-1	TPM1-7-1	TPM1-8-1	TPM1-9-1	TPM1-10-1
13:20-13:40		TPM1-1-2	TPM1-2-2	TPM1-3-2	TPM1-4-2	TPM1-5-2	TPM1-6-2	TPM1-7-2	TPM1-8-2	TPM1-9-2	TPM1-10-2
13:40-14:00		TPM1-1-3	TPM1-2-3	TPM1-3-3	TPM1-4-3	TPM1-5-3	TPM1-6-3	TPM1-7-3	TPM1-8-3	TPM1-9-3	TPM1-10-3
14:00-14:20		TPM1-1-4	TPM1-2-4	TPM1-3-4	TPM1-4-4	TPM1-5-4	TPM1-6-4	TPM1-7-4	TPM1-8-4	TPM1-9-4	TPM1-10-4
14:20-14:40		TPM1-1-5	TPM1-2-5	TPM1-3-5	TPM1-4-5		TPM1-6-5	TPM1-7-5	TPM1-8-5	TPM1-9-5	TPM1-10-5
14:40-15:00			TPM1-2-6	TPM1-3-6	TPM1-4-6		TPM1-6-6	TPM1-7-6	TPM1-8-6		TPM1-10-6
	Break (15:00-15:20)										
Time	**Session**	**TPM2-1**	**TPM2-2**	**TPM2-3**	**TPM2-4**	**TPM2-5**	**TPM2-6**	**TPM2-7**	**TPM2-8**	**TPM2-9**	**TPM2-10**
	Name	Antennas and Propagations	Filter Technology	Pattern Recognition and Others	High Voltage Engineering 2	Communication Systems 2	Power Electronics 3	Speech And Acoustic Technology	Control Engineering 2	Simulation and Modelling	SS: Microwave and Antennas 1
	Chair	Danai Torrungrueng (Asian U)	Worapong Tangsrirat (KMITL)	Kosin Chamnongthai (KMUTT)	Kittipong Tanmitr (KKU)	Usana Tuntoolavest (KU)	Itsada Boonyaroonate (KMUTT)	Rachada Kangkachandra (TU)	Pramin Artrit (KKU)	Nachol Chaiyaratana (KMITNB)	Jun-ichi Takada (Tokyo Tech)
15:20-15:40		TPM2-1-1	TPM2-2-1	TPM2-3-1	TPM2-4-1	TPM2-5-1	TPM2-6-1	TPM2-7-1	TPM2-8-1	TPM2-9-1	TPM2-10-1
15:40-16:00		TPM2-1-2	TPM2-2-2	TPM2-3-2	TPM2-4-2	TPM2-5-2	TPM2-6-2	TPM2-7-2	TPM2-8-2	TPM2-9-2	TPM2-10-2
16:00-16:20		TPM2-1-3	TPM2-2-3	TPM2-3-3	TPM2-4-3	TPM2-5-3	TPM2-6-3	TPM2-7-3	TPM2-8-3	TPM2-9-3	TPM2-10-3
16:20-16:40		TPM2-1-4	TPM2-2-4	TPM2-3-4	TPM2-4-4	TPM2-5-4	TPM2-6-4	TPM2-7-4	TPM2-8-4	TPM2-9-4	TPM2-10-4
16:40-17:00			TPM2-2-5	TPM2-3-5	TPM2-4-5		TPM2-6-5	TPM2-7-5	TPM2-8-5	TPM2-9-5	TPM2-10-5
17:15-17:45	Keynote Speech: "Social Robotics: Integrating Advances in Engineering and Computer Science" by Dr. Shuzhi Sam Ge, National University of Singapore, Singapore										
18:30-22:00	Conference Banquet at Mae Fah Luang University										

ECTI-CON 2007 Session Schedule (continued)

Friday, May 11 th, 2007											
Time	**Session**	**FAM1-1**	**FAM1-2**	**FAM1-3**	**FAM1-4**	**FAM1-5**	**FAM1-6**	**FAM1-7**	**FAM1-8**	**FAM1-9**	**FAM1-10**
	Name	Power Line Comm./ RFID	Analog Circuits 1	Electrical Analysis	Power Systems 2	Mobile Communication Networks	Digital Signal Processing 1	Material Technology	Information Technology 1	Microwave Devices	SS: Microwave and Antennas 2
	Chair	Chalie Charoenlarpnopparut (SIIT)	Banlue Srisuchinwong (SIIT)	Werachate Khan-ngenn (KMITL)	Ekarin Vasanasong (MUT)	Phongsak Keeratiwintakorn (KMITNB)	Tanee Demeechai (MUT)	Chanchana Thanachaynont (MTEC)	Tong Srikhacha (TOT)	Jaruek Jantree (RMUTSB)	Rangsan Wongsan (SUT)
08:30-08:50		FAM1-1-1	FAM1-2-1	FAM1-3-1	FAM1-4-1	FAM1-5-1	FAM1-6-1	FAM1-7-1	FAM1-8-1	FAM1-9-1	FAM1-10-1
08:50-09:10		FAM1-1-2	FAM1-2-2	FAM1-3-2	FAM1-4-2	FAM1-5-2	FAM1-6-2	FAM1-7-2	FAM1-8-2	FAM1-9-2	FAM1-10-2
09:10-09:30		FAM1-1-3	FAM1-2-3	FAM1-3-3	FAM1-4-3	FAM1-5-3	FAM1-6-3	FAM1-7-3	FAM1-8-3	FAM1-9-3	FAM1-10-3
09:30-09:50		FAM1-1-4	FAM1-2-4	FAM1-3-4	FAM1-4-4	FAM1-5-4	FAM1-6-4	FAM1-7-4	FAM1-8-4	FAM1-9-4	FAM1-10-4
09:50-10:10		FAM1-1-5	FAM1-2-5	FAM1-3-5		FAM1-5-5		FAM1-7-5	FAM1-8-5	FAM1-9-5	FAM1-10-5
	Break (10:10-10:30)										
Time	**Session**	**FAM2-1**	**FAM2-2**	**FAM2-3**	**FAM2-4**	**FAM2-5**	**FAM2-6**	**FAM2-7**	**FAM2-8**	**FAM2-9**	**FAM2-10**
	Name	Modulation and Channel Analysis	Analog Circuits 2	Electronic Devices	Electric Machinery	UWB Channels	Image Processing 2	Biological EE	Digital Signal Processing 3	Medical Engineering and Applications	SS: Electrical Power
	Chair	Keattisak Sripimanwat (NECTEC)	Banlue Srisuchinwong (SIIT)	Boonying Charoen (KKU)	Ekarin Vasanasong (MUT)	Sathaporn Promwong (KMITL)	Manas Sangworasil (KMITL)	Werapon Jiracharit (KMUTT)	K.R. Rao (UTA)	Nachol Chaiyaratana (KMITNB)	Natthaphob Nimpitiwan (BU)
10:30-10:50		FAM2-1-1	FAM2-2-1	FAM2-3-1	FAM2-4-1	FAM2-5-1	FAM2-6-1	FAM2-7-1	FAM2-8-1	FAM2-9-1	FAM2-10-1
10:50-11:10		FAM2-1-2	FAM2-2-2	FAM2-3-2	FAM2-4-2	FAM2-5-2	FAM2-6-2	FAM2-7-2	FAM2-8-2	FAM2-9-2	FAM2-10-2
11:10-11:30		FAM2-1-3	FAM2-2-3	FAM2-3-3	FAM2-4-3	FAM2-5-3	FAM2-6-3	FAM2-7-3	FAM2-8-3	FAM2-9-3	FAM2-10-3
11:30-11:50		FAM2-1-4	FAM2-2-4	FAM2-3-4	FAM2-4-4	FAM2-5-4	FAM2-6-4	FAM2-7-4	FAM2-8-4	FAM2-9-4	FAM2-10-4
11:50-12:10		FAM2-1-5	FAM2-2-5	FAM2-3-5	FAM2-4-5	FAM2-5-5	FAM2-6-5	FAM2-7-5	FAM2-8-5		
	Lunch Break (12:10-13:00)										
Time	**Session**	**FPM1-1**	**FPM1-2**	**FPM1-3**	**FPM1-4**	**FPM1-5**	**FPM1-6**	**FPM1-7**	**FPM1-8**	**FPM1-9**	**FPM1-10**
	Name	Communication Systems	Electronic Circuits	Control Engineering 3	Power Systems 3	UWB Technology	Biometric	Microelectronics	Information Technology 2	Data Mining and Knowledge	SS: Hard Disk Drives
	Chair	Tanee Demeechai (MUT)	Boonying Charoen (KKU)	Wudhichai Assawinchaichote (KMUTT)	Surachai Limyingcharoen (KKU)	Revee Phromloungsri (MUT)	Somying Thainimit (KU)	Songphol Kanjanachuchai (CU)	Tong Srikhacha (TOT)	Raymond Greenlaw (Armstrong U)	Kamon Jirasereeamornkul (KMUTT)
13:00-13:20		FPM1-1-1	FPM1-2-1	FPM1-3-1	FPM1-4-1	FPM1-5-1	FPM1-6-1	FPM1-7-1	FPM1-8-1	FPM1-9-1	FPM1-10-1
13:20-13:40		FPM1-1-2	FPM1-2-2	FPM1-3-2	FPM1-4-2	FPM1-5-2	FPM1-6-2	FPM1-7-2	FPM1-8-2	FPM1-9-2	FPM1-10-2
13:40-14:00		FPM1-1-3	FPM1-2-3	FPM1-3-3	FPM1-4-3	FPM1-5-3	FPM1-6-3	FPM1-7-3	FPM1-8-3	FPM1-9-3	FPM1-10-3
14:00-14:20		FPM1-1-4	FPM1-2-4	FPM1-3-4	FPM1-4-4	FPM1-5-4	FPM1-6-4	FPM1-7-4	FPM1-8-4	FPM1-9-4	FPM1-10-4
14:20-14:40		FPM1-1-5	FPM1-2-5	FPM1-3-5	FPM1-4-5	FPM1-5-5	FPM1-6-5	FPM1-7-5	FPM1-8-5	FPM1-9-5	FPM1-10-5
14:40-15:00		FPM1-1-6	FPM1-2-6	FPM1-3-6	FPM1-4-6	FPM1-5-6	FPM1-6-6	FPM1-7-6	FPM1-8-6	FPM1-9-6	FPM1-10-6
	Break (15:00-15:20)										
Time	**Session**	**FPM2-1**	**FPM2-2**	**FPM2-3**	**FPM2-4**	**FPM2-5**	**FPM2-6**				
	Name	Antenna Technology	Medical Technology	General EE	Power Systems 4	Communication Technology	Image Processing 3				
	Chair	Chuwong Phongcharoenpanich (KMITL)	Supawadee Swatdiponphallop (KKU)	Punnarumol Temdee (MFLU)	Teratam Bunyagul (KMITNB)	Keattisak Sripimanwat (NECTEC)	Vutipong Areekul (KU)				
15:20-15:40		FPM2-1-1	FPM2-2-1	FPM2-3-1	FPM2-4-1	FPM2-5-1	FPM2-6-1				
15:40-16:00		FPM2-1-2	FPM2-2-2	FPM2-3-2	FPM2-4-2	FPM2-5-2	FPM2-6-2				
16:00-16:20		FPM2-1-3	FPM2-2-3	FPM2-3-3	FPM2-4-3	FPM2-5-3	FPM2-6-3				
16:20-16:40		FPM2-1-4	FPM2-2-4	FPM2-3-4	FPM2-4-4	FPM2-5-4	FPM2-6-4				
16:40-17:00		FPM2-1-5	FPM2-2-5		FPM2-4-5	FPM2-5-5					
End of Conference											

Keynote Speech

Where Thailand should go for ECTI Research in the next Decade: NECTEC Strategy

Dr. Pansak Siriruchatapong

Predicting and forecasting the technology and its impact is a dangerous business. But how the new technologies will emerge is quite clear. For whichever particular technology that can create impact in this near future, its evolution will most likely come from the converging of multiple technologies.

In the next decade, global issues will emphasize on health, energy, and environment. Technologies that will address them must be multidisciplinary and integrated. In the past decade, IT related technologies were major players on the emerging technology fields. IT had made impacts to humanity, putting us on the information explosion age. While IT reach-ability and impacts vary from region to region, undeniably, they are profound. Coming of age, IT will become a driver for convergence of others.

Among many, NBIC (Nano-Bio-Info-Cogno) has been often mentioned and expected to form a powerful convergence. How will it impact the world? Where will Thailand stand on this new land? Will it create new opportunities for us? Will it help solve some of our problems? What are the resources and infrastructure and strategies that will make us ready? These will be partially addressed.

NECTEC, as a member of NSTDA and a national research center specialized in Electronics, Computers, Telecommunication and IT, must prepare for this coming trend. We reformed our organization, and founded 3 new platform technology programs focusing in Sensor, Securities, and Knowledge Engineering. Our strategy will strongly emphasize working with alliances; create common research infrastructure, and sharing visions and intellects to put Thailand on world technology map.

PANSAK SIRIRUCHATAPONG

Date of birth: 25 August 1955

Current position : Director National Electronics and Computer Technology Center (NECTEC)

Office : National Electronics and Computer Technology Center
National Science and Technology Development Agency
Ministry of Science and Technology
112 Thailand Science Park, Phahon Yothin Rd.,
Klong 1, Klong Luang, Pathumthani 12120
Tel : 662 564 6900 ext. 2001 Fax : 662 564 6893

Email : Pansak.siriruchatapong@nectec.or.th **Website :** www.nectec.or.th

Education :

- 1977 Bachelor of Engineering (Electrical) 2nd Class Honors Kasetsart University
- 1979 Master of Engineering (Electrical) Kasetsart University
- 1981 DEA. (Electronics) INPG. ENSERG. FRANCE
- 1984 D.ING INPG. ENSERG. FRANCE

Work Experience :

- 1977 - 1997 Lecturer at Electrical Department, Faculty of Engineering, Kasetsart University
- 1984 - 1993 Special Instructor, Technology promotion association (Thai - Japan)
- 1989 - 1993 Assistance of head of electrical, Faculty of Engineering, Kasetsart University
- 1989 - 1991 Electrical Committee, The Engineering Institute of Thailand under H.M. The King's Patronage
- 1990 - 1995 Board Member of Electronics Association of Thailand
- 1992 - 1995 Electronics Committee, Development, Ministry of Labor
- 1994 - 1995 Assistance Dean of Reserch, Faculty of Engineering, Kasetsart University
- 1994 - 1995 Board of Inventions Member, Kasetsart University
- 1997 - 1998 Board Member of Communication Authority of Thailand
- Board of Measuring Equipment Member, Thai - Japan Technology Advancement Association
- 1993 - Present Special.Lecture, Kasetsart University
- 1993 - Present Deputy Director National Electronics and Computer Technology
- 1998 - Present Board Chairman, Special Project Fund
- 2002 - Present Board Member, National Research Council
- 2002 - Present Board Member, Bangkok Airport System Administration and Information Technology
- 2002 - Present Board Member, Government Computer Budget
- 2002 - Present President of Thai Embedded Systems Association (TESA)
- 2002 - Present Deputy Chairman, Computer Quality Certification Project
- 2003 - Present Managing Director, Government Information Technology Services
- 2004 - Present Chairman, Intellectual Copyrights Policy
- 2004 - Present Advisor, Nectec Newsletter 2004
- 2004 - Present Advisory Committee, Vehicle Electronics Development Research Project

Reserch :

- Video Member for Black / White Television Transmission, 1986, Faculty of Engineering,Kasetsart University
- 2D Histogram Processing System for Television Video, 1987, Faculty of Engineering, Kasetsart University
- Talking Clock, 1988, Faculty of Engineering, Kasetsart University
- Wire - Cut Machine, 1990, Faculty of Engineering, Kasetsart University
- RPM Meter, Programmable Counter, Timer, 1989, Faculty of Engineering, Kasetsart University, N.R Machinery Co, Ltd.
- Voice Memory Address Controller Circuit Design, 1990, Microelectronics Project, Thai - Australia
- 32 Bit Microcomputer Prototype, 1990 - 1992, National Electronics Technology and Computers, Taworn Computer Co.
- Engineering Workstation (Sun SPARC), 1993, National Electronics Technology an Computers, Taworn Computer Co.
- SMD and MLB Technology Development, 1991 - 1993, Network Institute Project, Kasetsart University, National Electronics, Technology and Computers
- Video Sensor Mango Sorter, 1991, National Agriculture Machinery Center, Kasetsart University
- Motorcycle - Petro Engine RPM Meter, 1991, Community Development Project, Faculty of Engineering, Kasetsart University
- Car Speedometer and Distance Meter, 1992, Community Development Project, Faculty of Engineering, Kasetsart University
- Induction Heat Metal Oven for Gem Stones, 1993 - 1995, National Research Council
- Video Memory Card for Microcomputer, 1991, Research Institute, Kasetsart University
- High Speed RPM Meter, 1993, Computer Technology Research Lab, National Electronics Technology and computers
- Telephone Use Counter Version 1, 1994, Computer Technology Research Lab, National Electronics Technology and Computers
- CNC Controller for Automatic Machines, 1997 - Present, Computer Technology Research Lab, National Electronics Technology and Computers
- Talking Bus, 1998, Computer Technology Research Lab, National Electronics Technology and Computers
- Microcomputer Research and Development Center Establishment Project, 1996 - Present, National Electronics Technology and Computers
- Microcomputer Technology Forum for CMOS 1.25 um from IMEC, 1996 - Present, Thai - Belgium
- MATIC (Manufacturing Technology supported by Advanced and integrated Information system through international Cooperation) Project, 1996 - 1998, Joint Project CICC Japan and Computer Technology Research Lab, National Electronics Technology and Computers
- Printed Circuit Technology Development Project, 1997, National Electronics Technology and Computers

Keynote Speech

Restoration of the Lost Information by Sampling and Quantization

Akira Taguchi

Department of Biomedical Engineering,
Musashi Institute of Technology
1-28-1 Tamazutsumi, Setagaya-ku, Tokyo 158-8557, Japan

I. INTRODUCTION

Digital image/video signals are obtained by sampling and quantization of analog signals. It is necessary for sampling to restrict its bandwidth. The resolution of amplitude of signals is restricted by quantization. The signal information is restricted by the Analog to Digital conversion [1]. In this paper, we introduce restoration of the lost information by sampling and quantization.

The restoration problem of the lost information by sampling is equal to the enlargement method of digital image. It is necessary to predict or estimate the unknown higher-frequency components that generate in the enlargement process. In general, enlargement of the digital image is also carried out by the interpolation. However, it is impossible for these methods to predict the unknown high-frequency components.

We have proposed two kinds of image enlargement methods with predicting the unknown high-frequency components. First method is based on the Laplacian pyramid representation [2]-[4],[6],[7]. In this method, we gave the procedures which, can be estimated the unknown high resolution Laplacian image of the arbitrary size. Another enlargement method is the interpolation with warping of the coordinate point and biasing of signal amplitude [8]. We introduce two methods in this paper.

The resolution of amplitude of signals corresponds to the bit-length of signals. The bit-length expansion technique is necessity for the high-quality display such as the liquid crystal display (LCD) and the plasma display. Moreover, bit-length expansion is also necessary for low-bit length images, which are observed the pseudo-contour. We have proposed a bit-length expansion technique from M gray levels to N=(3(M-1)+1) gray levels. This bit-length expansion method is also introduced in this paper.

II. THE RESTORATION OF THE LOST INFORMATION BY SAMPLING (1) - Image Enlargement Method based on Laplacian Pyramid Representation -

II-1. The Laplacian Pyramid Representation[9]

The Gaussian and Laplacian pyramid representations are described in [9]. The Gaussian pyramid consists of low-frequency components image sequences $\{G_0, G_1,..., G_N\}$. G_{n+1} is derived by

$$\overline{G}_{n+1} = W * G_n \tag{1}$$

$$G_{n+1} = DS(\overline{G}_{n+1}) \tag{2}$$

where $*$ shows the convolution operator. W is the Gaussian filter for image compression and $DS(\bullet)$ denotes the down sampling operation.

The Laplacian image L_n, which is consisted of high-frequency components, is calculated as

$$L_n = G_n - EXPAND(G_{n+1}) \tag{3}$$

$$EXPAND(G_{n+1}) = 4 \times (W * G^0{}_{n+1}) \tag{4}$$

$G^0{}_{n+1}$ is the image obtained by interpolating 0s (up-sampling) into G_{n+1}. The size is the same as G_n. The width of G_{n+1} is twice as G_n.

II-2. The Arbitrary Scale Enlargement Method Based on the Laplacian Pyramid Representation

We show an example of the Laplacian pyramid by using the one dimension step signal G_0 as Fig.1. From Fig.1, a position on the edge of the step signal is observed as ZCs in the same position in Laplacian component of each layer. However, the slope of the low layer Laplacian component in the neighborhood of ZCs is steeper than that of the high layer. Therefore, we can estimate the low layer (high resolution) Laplacian component L_n by making the slope near the ZCs of the high layer (low resolution) Laplacian component steeper. Thus, an unknown high-resolution Laplacian signal L_{-1} can be estimated by using the low resolution Laplacian signal L_0. Then, an unknown high-resolution signal G_{-1} is estimated as

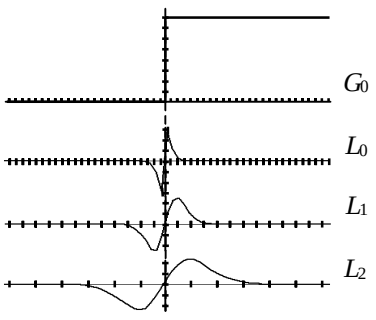

Fig.1 Laplacian pyramid of a step signal.

$$G_{-1} = L_{-1} + EXPAND(G_0) \tag{5}$$

In order to realize the arbitrary scale enlargement, we generalize the relation of the Eq.(5) as

$$G_r = L_r + (EXPAND)_r(G_0) \qquad (r < 0) \tag{6}$$

where G_r and L_r are non-integer layer of the Gaussian and Laplacian components respectively. The width of G_r image is the 2^{-r} times size of G_0 image.

II-3. The Arbitrary Scale Enlargement Method

We explain the arbitrary scale enlargement method according to the idea shown in II-2.

First, we denote how to calculate $(EXPAND)_r(G_0)$ (= $\tilde{G}_r$) of the Eq.(6). The $\tilde{G}_r$ can get from the interpolation of the Gaussian function $W(x)$.

$$W(x) = \frac{1}{2\sqrt{\rho\pi}} e^{-\frac{x^2}{\rho}} \qquad (\rho = 16/9\pi) \tag{7}$$

Then, the signal value $\tilde{g}_r(j)$ (j=1, 2, 3,..., ($M\times 2^{-r}$)) of the $\tilde{G}_r$ can be calculated from the signal value $g_0(i)$ (i=1, 2, 3,..., M) of the G_0 by using the Eqs.(8)~(10).

$$\tilde{g}_r(j) = \sum_{n=-2}^{2} W_r(n) \cdot g_0\left(\mathrm{int}\left(\frac{j}{2^{-r}} \right) + n \right) \tag{8}$$

$$W_r(n) = \frac{3}{8} e^{-\frac{9\pi}{16}(\Delta k + n)^2} \tag{9}$$

$$\Delta k = \mathrm{int}\left(\frac{j}{2^{-r}} \right) - \left(\frac{j}{2^{-r}} \right) \tag{10}$$

Next, we extend Greenspan's method to the arbitrary scale enlargement method.

(Step 1)

$(EXPAND)_r(L_0)$ (= $\tilde{L}_r$) is calculated from the low resolution Laplacian component L_0 by using the Gaussian interpolation $W_r(n)$. L_0 is calculated by Eqs.(1)~(3).

(Step 2)

$\bar{L}_r(j)$ is given by

$$\bar{l}_r(j) = \begin{cases} T & if \;\; T \le \alpha \tilde{l}_r(j) \\ \alpha\, \tilde{l}_r(j) & if \;\; -T < \tilde{l}_r(j) < T \\ -T & if \;\; \alpha \tilde{l}_r(j) \le -T \end{cases} \tag{11}$$

where T is the threshold and α is a constant which must be pre-determined.

(Step3)

The estimated high resolution Laplacian $\hat{L}_r$ is created by using the $\bar{L}_r$ as follows

$$\hat{L}_r = \bar{L}_r - W_r * \bar{L}_r \tag{12}$$

The estimated $\hat{L}_r$ added to the expanded version of G_0 makes the G_r (see in Eq.(6)).

II-4. Decision of the Parameters

It is necessary to decide the suitable parameters T and α. In order to decide two parameters, we use five images with 256×256 pixels and 8bits. We assume the size of 256×256 as G_0 and the scaling down image corresponding to the enlargement rate (S=1/2^{-r} times (r < 0)) as G_{-r}. The optimal parameters are defined as parameters, which are given the minimum mean square error (MSE) between the G_0 image and the estimated $\hat{G}_0$ image from the G_{-r} image. G_{-r} image are obtained by Gaussian filtering and down sampling process.

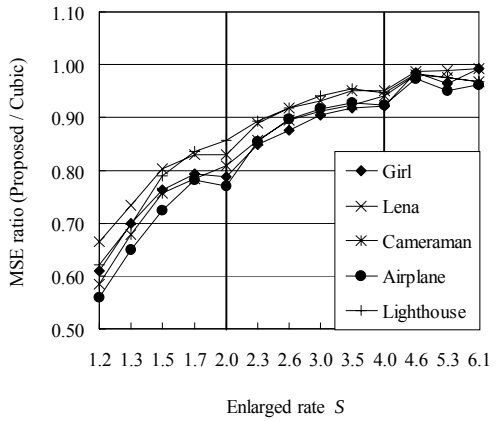

Fig. 2 The decision of scale range.

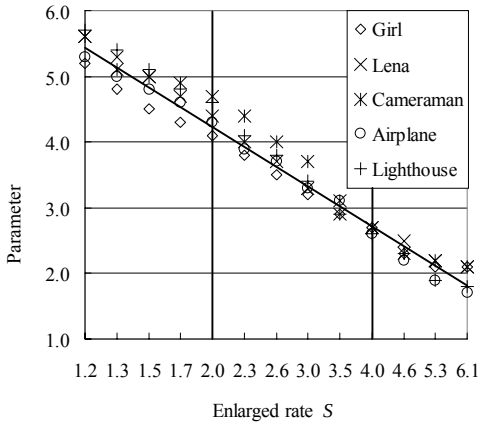

Fig. 3 The suitable α of seven images.

First, we compare our method to the Cubic interpolation (see in Fig. 2). From Fig.2, the proposed method is superior to the Cubic interpolation, not more than 6 times enlarging.

Next, we decided threshold T and parameter α. From Fig.1, the amplitude of the Laplacian component of all layers are almost same one another. The thresholding parameter T is decided as 45 by the experimental results. On the other hand, the parameter α is important to make steeper the slope near the neighborhood of ZCs. The relations between α and the enlargement rate S for five images were shown in Fig.3. Thus, we can derive the relation between α and the enlargement rate S as

$$\alpha = -0.714S + 5.833 \qquad (1 < S \le 6) \tag{13}$$

We compare the proposed arbitrary scale enlargement method to the several methods as follows.

(a) Proposed: The proposed method
(b) Cubic: Cubic interpolation
(c) Hybrid: Hybrid method[7]+Scaling down with the Gaussian filter
(d) Greenspan: Greenspan method[4]+Scaling down with the Gaussian filter

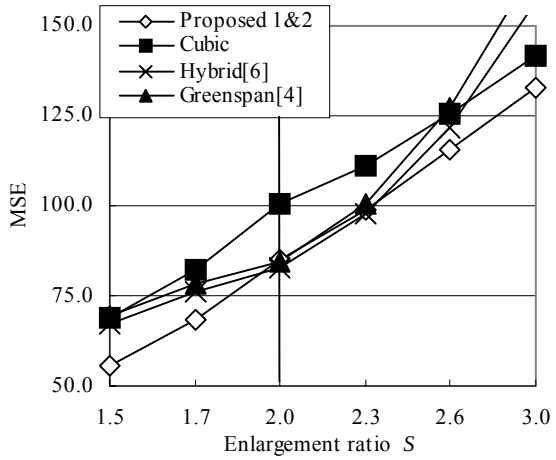

Fig.4 The performance of the proposed method (Lena).

We compare with the five methods concretely by using "Lena". The proposed method is equal to the "Hybrid" and the "Greenspan" for twice enlarging, but that is excellent in all other enlargement rate.

III. THE RESTORATION OF THE LOST INFORMATION BY SAMPLING (2)
- Digital Image Interpolation with Warping of Coordinate Point and Biasing of Signal Amplitude -

III-1. Interpolation with warping of signal amplitude

We present the warping method in order to create the peaks, it is impossible for the conventional method. We consider the one-dimensional (1-D) case. In the case of two-dimensional image we use one-dimensional method by sequential row-wise and column-wise.

Figure 5 shows the concept of the warping technique for signal amplitude, example for the twice size enlarging. The bilinear interpolation result shows the dashed line in Fig.1. When the peak exists between x_k and x_{k+1}, the bilinear interpolation result is smaller than the ideal result. In order to create the peaks, we add the small value to the result of bilinear interpolation.

Let $f(x_k)$ be the value at point x_k. The interpolated point x is located between x_k and x_{k+1}. The distance between x and x_k or x_{k+1} is given by $s = x - x_k$ or $1 - s = x_{k+1} - x$ ($0 \le s \le 1$). The bilinear interpolation result is calculated by

$$\hat{f}(x) = (1-s)\cdot f(x_k) + s \cdot f(x_{k+1}). \tag{14}$$

When twice size enlarging, $s = 0.5$ because x is the center of x_k and x_{k+1}.

It is necessary for creating the peaks to increase or decrease of the value of the result of bilinear interpolation. Let $\bar{f}(x)$ be the result of the proposed interpolation with warping the amplitude as

$$\bar{f}(x) = \hat{f}(x) + l \cdot B. \tag{15}$$

where l is constant and B is defined by

$$B = \frac{C}{2} + \frac{C}{2}\cdot(A-1) \times \mathrm{sgn}\left[\{f(x_{k+1}) - f(x_{k-1})\} \times \{f(x_{k+2}) - f(x_k)\}\right] \tag{16}$$

$$A = \frac{\left|f(x_{k+1}) - f(x_{k-1})\right| - \left|f(x_{k+2}) - f(x_k)\right|}{L-1} \tag{17}$$

$$C = \mathrm{sgn}\left[f(x_k) - f(x_{k-1})\right]\cdot|C| \tag{18}$$

$$|C| = \min\left[s\cdot\left|f(x_k) - f(x_{k-1})\right|, (1-s)\cdot\left|f(x_{k+2}) - f(x_{k+1})\right|\right] \tag{19}$$

where $L = 256$ for 8bits luminance images, $\mathrm{sgn}[\bullet]$ and $\min[\bullet]$ are the sign function and the minimum operation, respectively.

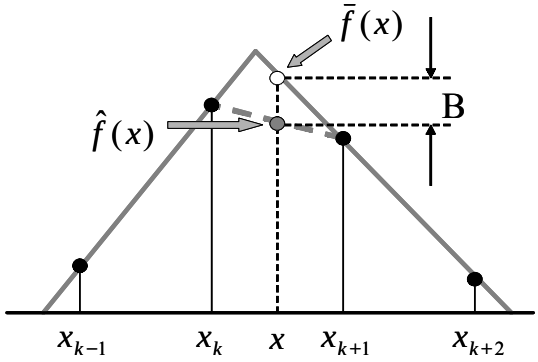

Fig.5 Interpolation with warping of signal amplitude

III-2. Interpolation with warping of coordinate point

In this section, first we explain about the warping method of. Then, we combine the method of section III-1 and the warping method.

In the warping method of [5], s' is used in (14) in place of s. s' is defined by

$$s' = s - kAs(s-1) \tag{20}$$

where k is the parameter which controls the intensity of the warping. "A" is given by Eq.(17). $A = 0$ indicates symmetry. Positive value indicates that the edge is more homogeneous on the right side (see Fig.6), and the pixel to be interpolated belongs to the right objects. Hence pixels on the same side should affect more strongly the interpolated value: accordingly, it should be $s' > s$ if

$A > 0$. The opposite holds if $A < 0$.

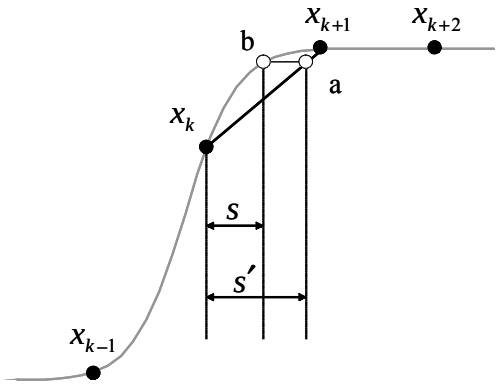

Fig.6 Interpolation with warping of coordinate point

III-3. Interpolation with warping and biasing

We would like to combine the warping method and the biasing method. This procedure is very simple. First, we calculate the warped coordinate points by using Eq.(20). Next, we calculated the biasing of signal amplitude after replacing s with s' in Eqs (16)-(19).

Table 1 Comparing the performance of each methods

(a) Two times enlargement

MSE	Bilinear	Cubic	CW [5]	Proposed (opt.)	Proposed (fix.)
Lena	84.2	73.8	70.7	68.1	68.7
Cameraman	199.6	175.2	168.1	162.9	163.2
Boat	78.7	66.9	62.4	61.4	61.6
Lighthouse	296.5	271.8	268.6	258.9	260.1
Girl	36.3	29.5	30.6	28.0	28.1
Text	173.1	144.0	136.4	129.6	130.9
Airplane	140.7	119.1	115.7	109.3	109.4

(b) Four times enlargement

MSE	Bilinear	Cubic	CW [5]	Proposed (opt.)	Proposed (fix.)
Lena	197.9	178.3	176.7	170.9	171.8
Cameraman	455.1	418.5	410.9	405.2	405.2
Boat	226.9	198.4	205.7	189.8	191.4
Lighthouse	553.5	522.3	516.5	509.8	510.5
Girl	112.7	98.0	100.8	96.5	96.9
Text	496.6	423.5	412.3	397.7	399.8
Airplane	378.8	343.7	345.0	337.2	337.6

III-4. Decision of Parameters

It is necessary to decide the parameter l of Eq.(15) and k of Eq. (20). We derive two parameters based on the mean square error (MSE). We use five images same as Section II. The size of original images is 256×256, we get the $1/2$ size images by low-pass filtering and down sampling, also get the $1/4$ size images. We expand these images to the original size, and calculate MSEs between original image and expanded image for various k or l. We can derive that $k = 2 \sim 4$ and $l = 0.3 \sim 0.7$ are suitable for all test images. Consequently, we can decide $k = 3.0$ and $l = 0.5$ based on MSE. These values of two parameters are robust for a lot of images, since these values are center of suitable regions.

We add new images two images for simulation. Table 1 shows MSEs of the proposed method of $k = 3.0$ and $l = 0.5$ (Proposed(fix.)), the proposed method of optimal parameters (Proposed(opt.)), the method of [5] (CW), the bilinear interpolation (Bilinear) and the cubic interpolation (Cubic). Proposed(fix.) and Proposed(opt.) are same performance on MSE for scaling 2 times or 4 times. This result indicates that the Proposed(fix.) is more effecting than CW and Cubic.

IV. THE RESTORATION OF THE LOST INFORMATION BY QUANTIZATION

IV-1. Procedures of our method

Bit-length of digital images is decided by the quantization. Thus, the resolution of signal amplitude is decided by the quantization. The bit-length expansion technique is necessity for the high-quality display such as the liquid crystal display (LCD) and the plasma display. Moreover, the bit-length expansion technique is also necessary for low-bit length images, which are observed the pseudo-contour. However, strictly speaking, it is impossible to expansion of the bit-length for digital signal.

We have proposed a bit-length expansion method from M gray levels to N=(3(M-1)+1) gray levels. This operation means that two gray-levels are introduced between existing levels. The bit-length expansion method results in the estimation problem of an error image between an M gray level's image and an N gray level's image. The error image is three values pattern image. If the difference between the existing level and the inserted new level is defined as Δ, the N level image is obtained by adding +Δ, 0 or -Δ to the M level image.

The procedures of the three values' error image as follow:

(Step 1)

In order to get the pseudo analog image, M gray level's image is processed by plural ε-filters with various window lengths.

(Step 2)

The pseudo analog image is quantized in N levels and M levels. The difference of two images is the estimated error. If the width of the filter window is small, the error of +Δ and -Δ cannot be calculated in a smooth change part of the background. On the other hand, it is necessary to preserve the signal edge/detail, we should choose the estimated error with small window length at edge/detail region. Thus, we combine the error signals, which are estimated by various window lengths.

(Step 3)

The estimated error is larger than +Δ, we change this value into +Δ. The estimated error is smaller than –Δ, we change this value into –Δ. As a result, the three value error

images are obtained. We add this error image to the M gray level's image.

The block diagram of our method is shown in Fig.7

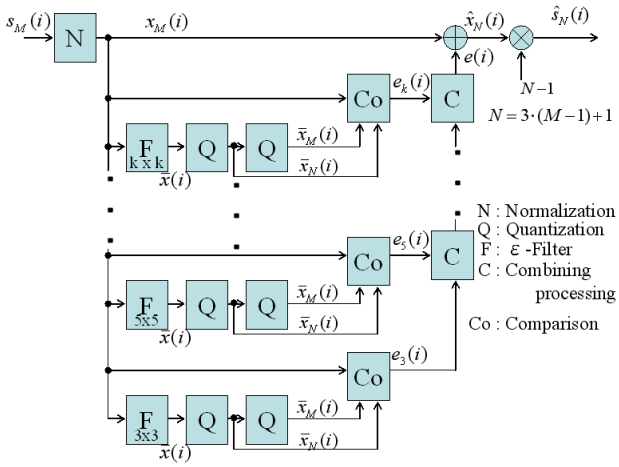

Fig.7 Block diagram of the proposed method

IV-1. Examples

We show a simulation result of our method.

Figure 8(a) shows a Pepper, which is a color image with 4 bit for each component. We make marks in Fig.8(a). We can observe pseudo-contour at the making positions. We apply our method to this image and get the result of Fig.8(b). The pseudo-contour is removed by our method.

V. CONCLUSIONS

In this paper, we introduce restoration methods of the lost information by the analog to digital conversion (ADC). The ADC consists two operations. One is the sampling the other is the quantization.

We explain the enlarging method based on Laplacian pyramid and Warping & Biasing for the restoration of lost information by sampling.

Furthermore, a bit-length expansion method also introduced. We show that the method can remove pseudo-contours of low bit images.

REFERENCES

[1] M. Takagi and A. Shimoda. Image analysis handbook. University of Tokyo Press, pp.441-444, 1991. (in Japanese)

[2] E. Shinbori and M. Takagi. High-quality image enlargement by Gerchberg-Papoulis iteration using DCT. Trans IEICE, vol.J76-D-II, pp.1932-1940, Sept. 1993. (in Japanese)

[3] A. Tanaka, H. Imai, M. Miyakoshi and A. Date. Enlargement of digital image using multiresolution analysis. Trans IEICE, vol.J76-D-II, no.5, pp.819-825, May 1996. (in Japanese)

[4] H. Greenspan, C.H. Anderson and S. Akber. Image enhancement by nonliner extrapolation in frequency space. IEEE Trans. on Image processing, Vol.9, No.6, pp1035-1048, June 2000.

[5] G. Ramponi, "Warped Distance for Space-Variant Linear Image Interpolation," IEEE Trans. Image Processing, vol.8, pp. 629-639, May 1999.

[6] D. Sekiwa, A. Taguchi and Y. Murata. Enlargement of digital image based on Laplacian pyramid by using neural networks. Electronics and Communications in Japan, PART 3, Script a Technical, Vol.82, No.1, pp.1499-1508, January 1999.

[7] Y. Takahashi and A. Taguchi. An enlargement method of digital image based on Laplacian pyramid representation. SPIE vol.3961 (Nonlinear Image Processing XI), pp.163-169, 2000.

[8] A. Shimura, A. Taguchi: "Super-Resolution Digital Image Interpolation with Warping of Coordinate Point and Biasing of Signal Amplitude," Proc. of 12th European Signal Processing Conference (EURASIP), CD-ROM, 2004.

[9] P.J. Burt and E.A. Adelson. The Laplacian pyramid as a compact image code. IEEE Trans Commun., vol.COM-31, pp.532-540, 1983.

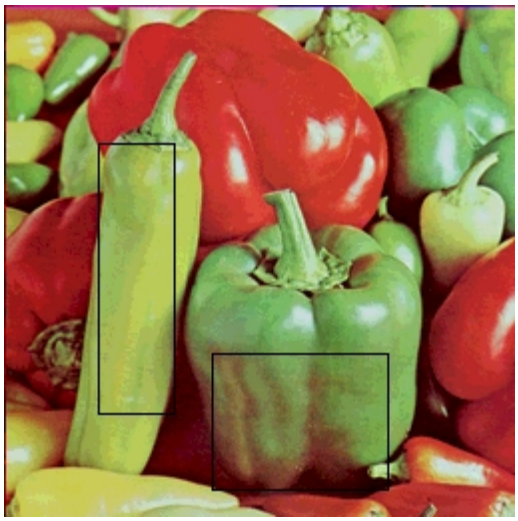

(a) Original image (RGB: 16 levels)

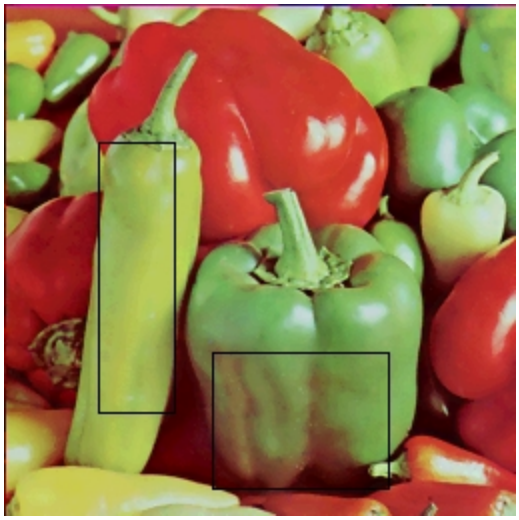

(b) Result of our method (RGB: 46 levels)

Fig.8 Bit-length expansion result

Akira Taguchi received B.E., M.E., and D.E., degrees in electrical engineering from Keio University, Yokohama, Japan, in 1984, 1986, and 1989, respectively. In 1989, he joined the Department of Electrical and Electronic Engineering at Musashi Institute of Technology, Tokyo, Japan. Since 2001 he has been a Professor of Musashi Institute of Technology. From 1993 to 1994 he was on leave from Musashi Institute of Technology as a Visiting Researcher in the Signal Processing Laboratory, Tampere University of Technology, Tampere, Finland. His research interest is in the area of image/video signal processing and color signal processing. He is a member of the IEEE and IEICE. Dr. Taguchi was an Editor of the IEICE Transactions on Fundamentals of Electronics, Communications and Computer Sciences during 2001-2004 and served as the Technical Program Chair of the 2003 International Symposium on Intelligent Signal Processing and Communication Systems and the 2005 International Workshop on Nonlinear Signal and Image Processing. He serves the Chair of Nonlinear Signal and Image Processing Board (IEEE, EURASIP).

Keynote Speech

Social Robotics: Integrating Advances in Engineering and Computer Science

Shuzhi Sam Ge
Edutainment Robotics Laboratory, Dept of Electrical & Computer Engineering, and
Social Robotics Laboratory, Interactive Digital Media Institute
National University of Singapore
Singapore 117576
Tel: (+65) 6516 6821, Fax: (+65) 6779 1103
Email: elegesz@nus.edu.sg

***Abstract*— With the rapid advancement of technology, robots could now be easily equipped with the state of art computing, electronics and communications technologies, with the potential to act as intelligent companions and with important applications in the education, entertainment, games and healthcare industries. The integration of all these technologies is the first step to realizing social robots – robots which will walk amongst humans, playing out their assigned roles whilst interacting with humans in a humanistic way. Social robots can have definite roles and tasks, such as educators, cleaners or guides, with a profound impact on human daily life. This advanced class of robots, just as we humans do, is made up of a complex array of interconnected modules – electronics (inner physical workings), sensing, planning and cognition, and finally, intelligence, interaction and communications. This paper provides an overview of each of these individual aspects, and how advanced technology in these areas can be integrated to form a social robot that can meld seamlessly into the human society.**

***Index Terms*— Social Robots, Machine Intelligence, Human-Robot Interaction, Ubiquitous Robotics**

I. Introduction

Humans are highly adaptive creatures, capable of perceiving the social context of their environment and based on complex sensing and reasoning abilities, adapt and interact with other like agents in their surroundings. Even in cases where a human is transplanted into an entirely different culture where the social norms differ completely from what he/she is used to, adaptation and cultural integration can occur in a short time span. In a world where we envision robots to be an integral part of the social landscape and a competent player amongst humans, we would expect robots to do the same. It is crucial that social robots understand, respond appropriately, and even adapt their behavior based on the cues from human partners and their own understanding of the social environment they are situated within.

A robot that is capable of such advanced functions and complex participation in the workings of the human society term is said to be "sociable" [1]. The ability of a "sociable" robot is to participate pro-actively with the human players in its surroundings, and to meet the humans' expectations of how an able player within their social environment should act. It basically requires the robot to possess an internal understanding and adaptable social model of human society.

There are several core, indispensable modules in the making of a social robot, where the key technical contributions from the fields of electrical/electronic engineering and the computer sciences play crucial roles in shaping its capabilities. Electronic components are getting smaller and smaller, enabling miniaturization of complex circuitry and lower power consumption in robots, and vastly increasing the mobility of robots. Coupled with sophisticated sensing, planning and interaction mechanisms, robots are able to perceive the environment and the humans, direct/focus their attention and gather pertinent information, as well as interact with other agents (humans and other robots) via an understanding of hand gestures and other behavioral cues. Artificial intelligence modules, utilizing the diverse amount of information gathered, as well as interacting with other behavioral modules, allows the social robot to make informed decisions and act in a decidedly 'natural' way. The effective integration of these advanced multi-disciplinary technologies is the main goal at the Edutainment Robotics Laboratory (ERL), Department of Electrical & Computer Engineering, and at the Social Robotics Laboratory (SRL), Interactive Digital Media Institute (IDMI), National University of Singapore (NUS).

These thrusts enable the development of human-centric social robots that adapt dynamically to human intentions, emotions, and needs, and bridge the gap between the three spaces: human space, physical space and information space. The incursion of robots into our everyday lives is unavoidable, and in most cases becoming indispensable. They are not only simple aids and replacements for human activities (vacuuming and cleaning), robots are used in many cases to enrich our lives, for adults and children alike.

Successful research and development in the area of social robots has important implications in several aspects of human society. Social robots, equipped with high level artificial intelligence and adaptive behaviors, can act as capable companions to users from diverse age groups, e.g., as babysitters, personal assistants, and even provide companionship to combat loneliness. In addition to fulfilling the role of an able companion, intelligent social robots can also act as a conduit for bridging the distance between users, where emotions and gestures can be transmitted and manifested on the social robots on either

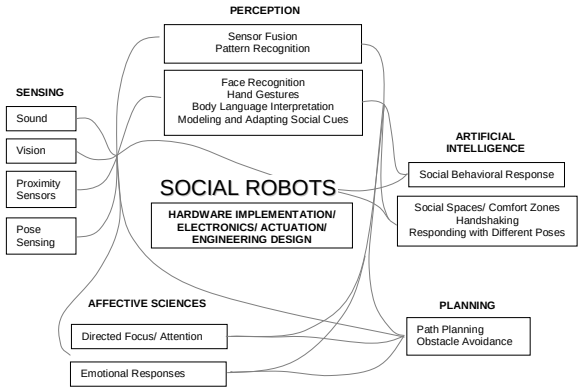

Fig. 1. Overview of the core technologies involved in Social Robotics.

end with humanistic robots serving as realistic personifications of loved ones.

Currently available 'social robots' are clearly inadequate in terms of interactivity, intelligence, mobility and social skills to successfully fulfil the tasks highlighted above. There have been many recent forays by many into the area of social robotics with some commercial examples including the Sony AIBO and QRIO, Hasbro Furby, NEC's PaPeRo, Ugobe's Pleo and WowWee's Robosapien, Robopet, Roboraptor and Chimpanzee, and iRobot's Roomba and Scooba. In addition to social robots developed in the commercial world, many research institutes and universities have been carrying out extensive research and development in the area of social robotics. Examples of sociable robots developed in research institutes and universities include museum guide robots Sage [2], RHINO [3] and Jinny [4], Massachusetts Institute of Technology (MIT) Media Lab's Kismet [5], Leonardo and Huggable [6], CMU's Vikia and Royal Institute of Technology's CERO [7]. A comprehensive survey was conducted on socially interactive robots in [8], where a number of issues pertaining to socially interactive robots were studied.

In this paper, we briefly review the latest advances in the core technologies (as shown in Fig. 1) that form the backbone of social robotics, and also provide an overview of how the field and related technologies are set to evolve in the near future. In the following sections, we first examine the sensing and perception aspects of social robots, followed by advanced planning mechanisms, and finally affective sciences and social behavior generation, as well as decision making and artificial intelligence, for effective interaction with humans.

II. Robot Sensing: Sound and Vision

Sound and visual sensing are crucial for humans, and that is also the case for social robots. These sensing capabilities allow the gathering of crucial information required for navigation, planning and other higher cognitive processes like decision making. Effective sound and vision localization allows robots to focus their attention on pertinent objects/elements within their environment much like how humans act.

A. Sound Localization

Sound localization is a listener's ability to identify the location of a detected sound or the methods in acoustical engineering simulate the placement of an auditory cue in a virtual 3D space. It has attracted much attention in the literature [9]–[19] owing to the wide applications including robot perception [20], human-machine interfaces [21], handicappers' aids [22], [23] and some military applications [24]. Due to the importance of sound localization, it has been greatly explored. Related works can fall into following categories in terms of sensors:

1) Smart audio sensors: Psychoacoustic studies on humans have provided us with information about the cues to locate sound sources, namely, Interaural Time Differences (ITD), Interaural Intensity Differences (IID) and spectrum [25]–[29]. To mimic human dimensional hearing, a neuromorphic microphone was proposed by making use of biologically-based monaural spectrum cues [30]. This microphone relied on a specially shaped reflecting structure - a parabola simulating the pinna's curved surface and a sound source can be located in the front half plane by using echo-time processing. Based on the analysis of biological sound localization systems (such as the barn owl, bats, etc), neural networks have been successfully used to locate sound sources with relative azimuth [10]. In [31] and [32], a simplified model of the auditory system for human beings was developed, which consisted of a three-microphone set and several banks of band-pass filters. Zero-crossing was used to detect the arrival temporal disparities and the histogram mapping method was introduced to localize multiple sound sources in the azimuth direction.

2) Microphone arrays [33]–[36]:

- Relative sound localization
  It focuses on sound localization with respect to the reference frame attached to the microphone arrays. It can be classified into three categories, namely, localization based on beamformer, signal correlation matrix and time difference of arrival (TDOA) [37] respectively. The first is similar to that of radar and can be achieved using beamformer-based energy scans [38], [39], by which output power of a steered-beamformer should be maximized. The second makes use of high resolution spatio-spectral correlation matrix derived from signal received by sensors. TDOA-based localization covers the receptive environment of interest, instead of "focalization", based on high resolution TDOA estimation. Related techniques of relative sound localization include triangulation [24], Least-Square (LS) approach [40], Maximum likelihood technique [41], sensor fusion [42] and so forth.
- Global sound localization
  Global sound localization is similar to Simultaneous Localization and Mapping (SLAM) in the research domain of map building and robotics. It focuses on the source localization with respect to the global reference frame. It consists of two main issues, namely, the relative source localization with respect to the microphone array and the

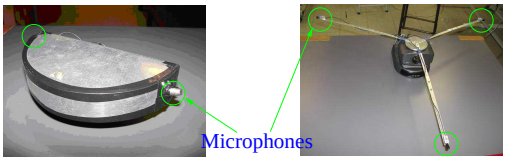

Fig. 2. Microphone sets

localization of microphone array itself with respect to the global reference frame. The latter can be referred to as inverse sound localization problem [43] and has significant impact on the overall sound localization.

B. Localization with Microphone Sets

It is well known that 4 microphones are required for 3D sound localization [11]. However, to further streamline the design and implementation of accurate localization systems on social robots that should be highly mobile, we seek to investigate and improve an implementation using fewer than 4 microphones.

To this end, we have shown that adequate localization can be done with a two-microphone set and a three-microphone set, as shown in Figure 2. A three-microphone set is shown in the right picture of Figure 2. These microphones form a Y-shaped frame whereby all the nodes are connected to a common point. It has been shown that this configuration can be used to estimate azimuth and elevation of a sound source simultaneously.

This technique developed at the SRL and ERL has been successfully applied for sound localization by robots, as well as localization by virtual avatars of robots within the virtual space. As the name specifies, the played music provides spatial feeling for listeners with earphones. Figure 3(a) shows an artificial virtual robotic head which can hear 3D sound in space. Figure 3(b) shows its implementation to an interactive teddy bear, which is able to estimate the direction of a radio receiver and respond appropriately to the aural stimulation.

(a) Sound Localization by a Robot's Avatar in Virtual Space

(b) Teddy bear locating a radio receiver

Fig. 3. Sound Localization in both Physical and Virtual Worlds.

C. Vision-based Interaction

With the rapid developments in the fields of sensing technologies and robotics, there is an increasing need to employ intelligent robots [44] with a friendly human-machine interface

Fig. 4. Human Detection by a Social Robot for Attention Focusing

in a human environment for the purpose of surveillance, monitoring, services and so forth. This necessitates an intelligent visual perception system to robustly detect and identify human beings with a variable background, motivating the investigation of visual human detection using multiple cameras.

Without a prior knowledge and constraints on the background, it is difficult to detect human beings using a monocular camera [45], [46]. Methods employing the use of a monocular camera requires knowledge of the scene's background. This can be achieved by having a stationary camera or a model of the background [47]–[49]. Face detection techniques [50], [51] dispense with this requirement, but is only applicable to frontal views of humans. On the other hand, stereo-vision systems is able to provide depth or scale information to the detection of human beings in a clustered environment, and it enables the spatial object segmentation and also brings about the challenges, e.g., distinguishing humans from human-like objects, in the realization of human detection as a result of this new piece of information. With the advantages of stereo vision, and given that humans, ourselves, utilize such a technique, it is natural to develop robust stereo vision techniques that will give this capability to social robots. Coupled with infrared thermal imaging [52]–[56], the capabilities of social robots can far exceed that of humans, and be valuable aids for a wide range of applications. This is indeed one of the key research thrusts of the Edutainment Robotics and Social Robotics Laboratories, fusing stereo and infrared vision and integrating these visual systems onto a mobile robot (as shown in Fig. 4) to achieve more reliable human detection and identification for social robots. The robot prototype is able to detect humans, estimate the relative direction and distance of him/her, and follow him/her at a comfortable distance.

III. Affective Sciences

A. Human-Robot Interaction

The emotion exchanges and interaction is one of the most important and necessary characteristics of the social robotics. This is also called the affective sciences – the scientific study of emotion. Amongst humans, emotions are conveyed through facial expressions, audio cues, hand and body gestures. Likewise, it is an important factor in the determining the level and type of interactions that occur between a robot and a human. The capacity to emote, and respond to emotes, further

improves the robots ability to engage in fruitful interactions with the human user.

B. Facial Emotion Recognition System

A key component of emotions, and one that social robots must be capable of, is the ability for facial/emotion recognition. It is the first step in synthesizing the aspect of empathy within robots. The ability to mimic human facial expressions lays the foundation for establishing a meaningful nonverbal communication between humans and robots. Facial expression analysis originates from Darwin in the 19th century when he proposed the concept of universal facial expressions in Man and animals [57]. Recently, research on facial recognition and expressing emotions in robots has received much attention since this is the most straightforward and efficient way for the research on affective science of robotics. In 1978, Ekman and Friesen developed the facial action coding system (FACS) for analyzing and synthesizing facial expression based on action units (AU) which describe basic facial movements [58]. In [59]–[61], target oriented approaches were used to infer the human emotion and classify the facial expression from one single image containing one typical facial expression. For facial expression classification, gesture oriented methods [62], [63], using temporal information from a sequence of facial expression motion images, can be employed

Facial expression is a dynamic process, how to fully make use of the dynamic information can be critical to the recognition result. There is a growing that the temporal information is a critical factor in the interpretation of facial expressions [64]. In [65], independent component analysis, optical flow estimation and Gabor wavelet representation methods were used and a 95.5% average recognition rate was achieved.

At the ERL and SRL, we have developed both off-line training method and real-time classifier for facial/emotion recognition system, which are then integrated into the interactive robot platforms for testing and further development. This emotion recognition system is used to identify the emotion of the human, which supporting the nonverbal emotion communication between humans and robots. The objective of the emotion recognition system is for human emotion understanding and intelligent human-robot interface. Our system is based on both the deformation and motion information. The framework of our recognition system is shown in below figure. It starts with the facial image acquisition and ends with 3D facial expression animation.

IV. Robot Navigation: Obstacle Avoidance & Path Planning

Sociable robots, by their nature, is required to work amongst, and in close proximity to humans. Due to the dynamic nature of the working environment and the severe consequences of a human-robot collision, an advanced dynamic obstacle avoidance and path planning system is a prerequisite for all mobile sociable robots.

The potential field method is commonly used for autonomous mobile robot path planning [66]–[80]. The basic concept of the potential field method is to fill the robot's workspace with an artificial potential field in which the robot is attracted to its target position and is repulsed away from the obstacles [66]. This method is particularly attractive because of its elegant mathematical analysis and simplicity. To solve the problem of motion planning in a dynamic environment where the obstacles are moving, one approach is to include time as one of the dimensions of the model world and thus the moving obstacles can be regarded as stationary in the extended world [81]–[83]. Accordingly, the dynamic motion planning problem is reduced to motion planning in stationary environments. Another approach was proposed in [74] and [75] which extended the potential field method to the problems of moving obstacle avoidance by constructing repulsive potential functions which take into account the velocity information. In [75], velocity information of the robot and the obstacle are exploited for better obstacle avoidance.

Global sensor-based planning approaches [84]–[86] build a global world model based on sensory information and use it for path planning. By mapping the entire (accessible) environment, the global approaches can somewhat solve the basic path planning problem which implies the property of "global convergence" of path planning. In contrast, the local sensor-based path planning approaches use local sensory information in a purely reactive fashion. These methods include the potential field methods [66], [67], [71], [87], [88], behavior-based systems [89], [90] and fuzzy logic approaches [91]. Bug algorithms and their variants, combine local planning with global information to solve the problem of a point mobile automaton moving amidst unknown obstacles of arbitrary shape [92]–[95].

As a step towards greater autonomy and robustness in obstacle avoidance, a potential field method has been developed at the ERL, for motion planning of a mobile robot in a dynamic environment where the target and obstacles are moving can be used [88]. This approach does not require that the trajectories of the obstacles to be known a priori.

In addition, an "Instant Goal" approach has been developed in ERL and SRL [96] [97] which allows a physical robot equipped with a rangefinder to follow an obstacle of arbitrary shape. The "Instant Goal" is a local target specially designed for action planning based on sensory input. The Instant Goal Driven method was first presented in [96] where instant goals are generated at each time instant for behavior-based navigation. In [97], the proposed approach allows the robot to move forward along the boundary of an obstacle without collision in obstacle cluttered environments. To facilitate realtime planning, a vector representation, which saves greatly on memory space, is used to represent the local environment sensed by a rangefinder. The search range for each Instant Goal is restricted to a certain scope determined by previous status and current range data input such that the boundary following is performed in the desired direction. The concepts of "safe path" and "passage" are used to distinguish the "disturbing" obstacles from the desired one such that Instant Goals are able to be determined under any complex obstacle condition.

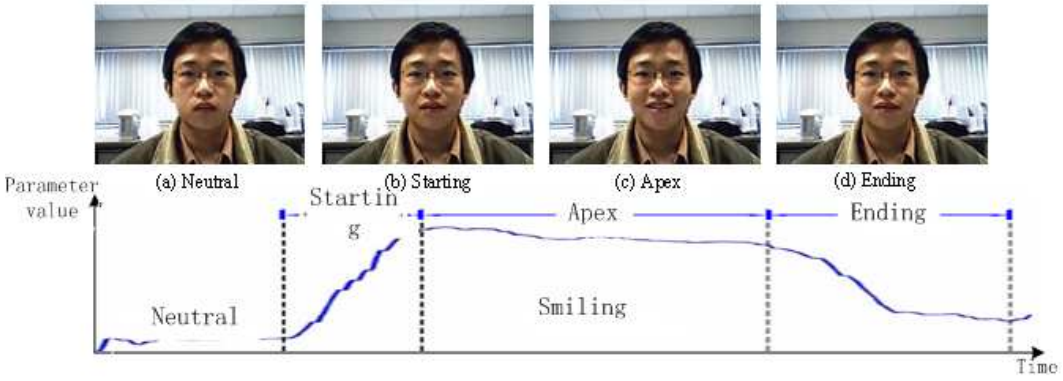

Fig. 5. Emotion Recognition Module at the Edutainment Robotics Laboratory, NUS

Based on the boundary following function, a practical convergent path planner is presented for navigation of a mobile robot without first building a global map of the environment. It uses a Bug-like strategy to switch between the two motion modes in order to achieve global convergence of path planning. A special leave condition is proposed for the robot to decide whether it should leave the currently followed obstacle and switch back to move toward the goal. Rather than assuming the robot is able to follow an obstacle, the path planner is based on the Instant Goal approach, which does not require a range sensor to have a perfect sensing ability. Different from subgoals in the work of [98] which are simply set to be near the polygon vertices in a polygon environment, path planning is accomplished through reaching a series of Instant Goals leading the robot to follow an obstacle in the desired direction in a complex, obstacle cluttered environment.

The potential field method developed in ERL and SRL, combined with robust, convergent approaches, such as the Instant Goal method and modified boundary following [96], [97], the social robot will be able to navigate successfully and safely in dynamic, cluttered environments.

V. Robot Communications

A. Handshaking with Robots

Although not a universal form of greeting, hand shaking is still recognized as one of the most commonly used greeting in the world today and it is commonly associated with the demonstration of good will between the two parties.

In recent years, research in the replication of handshaking behaviors in robots has attracted the attention of roboticists worldwide. In [99], coordinated movements of humans and robots in the act of handshaking is studied. During handshaking between humans, the motions between the humans become coordinated naturally without a master leading and a slave following the motions. As such, there is a need for synchronized motions within handshaking in order for a realistic replication of human handshaking in human-robot interactions. To achieve synchronized handshaking, neural oscillators were used in [99], where human-robot motions are synchronized by feeding the external force applied on the robotic arm into the neural oscillators and adapted. In [100], emotionally acceptable motions for human-robot handshaking, through experimental observations of human handshaking, were proposed and investigated . It has been noted that within human society, handshaking is commonly initiated by party in higher social standings whereas it is not appropriate for those of lower social standings initiate handshaking. Similarly, in human-robot interactions, handshaking should be initiated by humans and not the robot. Although similar comments where made in [100] on the need for robots to respond to an offered handshake from humans and not initiate the handshaking, the procedures used to detect an offered handshake are not clearly detailed.

Fig. 6. Handshaking implemented in a robotic bear.

In our research at the ERL and SRL, we focus on the implementation of a recognition system to accurately interpret the human's intention to offer a handshake and respond to the offer, mimicking the socially accepted behavior associated with the initiation handshaking (as shown in Fig. 6). Additional considerations include the continuation and termination of the handshaking process. In general, handshaking is ended when one party disengages. In implementing this behavior

into human-robot handshaking, we have to first consider the scenario when the human initiates the termination. In this case, once the robot senses that the human has disengaged, the robot will have to stop its hand motions. In an alternative scenario, when the human does not disengage, the robot has to realize that the handshaking has continued for too long and has become unnatural. To indicate that the robot wishes to stop the handshaking, the robot will have to stop the hand motions.

B. Hand Gestures

Hand gestures and behavioral cues are one of the basic mechanisms humans use for conveying their messages. Such a mechanism via gestures have been shown to be a viable form of communication without requiring speech, for instance through sign language. Even with the inclusion of verbal dialogue, body gestures exhibited by individuals also provide vital information about the emotional state and attitudes of an individual. For instance, huge animated movements usually signal a state of excitement or anger, while a dismissive wave of the hand indicates a non-committal state of mind.

A hand gesture identification system, can further improve the robot's level of interactivity and social pro-activity, by being able to identify the hand gestures made by the human. It will also allow communication via sign language, and further emphasizes the diverse role of a social robot in the human society that caters for everyone. Aside from formal sign language, such a system can be made to recognize body language and informal hand signs. A common initiation of handshaking in human interactions is the extending of an open palm. The vision system can differentiate and recognize the open palm. Once an extended open palm is detected, the robot will move its hand towards the palm. Proximity sensors installed at the sides of the robot's hands coupled with a vision system will be required to accurately move the robot's hand near the human's hand to start the handshaking.

C. Social Spaces and Comfort Zones

Apart from direct verbal exchanges and other directly perceivable interaction mechanisms like hand gestures and facial expressions, a fundamental regulator of human social behavior in human-human interactions is the perception of social spaces. There have been extensive studies in psychology and the social sciences about its role in human societies, and how human behavior, attitudes, responses and relationships are influenced by it [101]. The concept of social spaces varies according to a number of factors such as cultural norms, relationships between specific individuals, and social scenarios.

The first step designers of social robots have to take is to synthesize understanding of social cues in human societies. An understanding of the concept of social spaces and synthesis of appropriate behavioral responses are crucial elements. There have been a number of studies conducted regarding the quantitative demarcation of spatial zones based on human-human relationships [102]. Preliminary studies that draw parallels between the human-human and human-machine relationships have also been conducted [103]. These studies also indicate

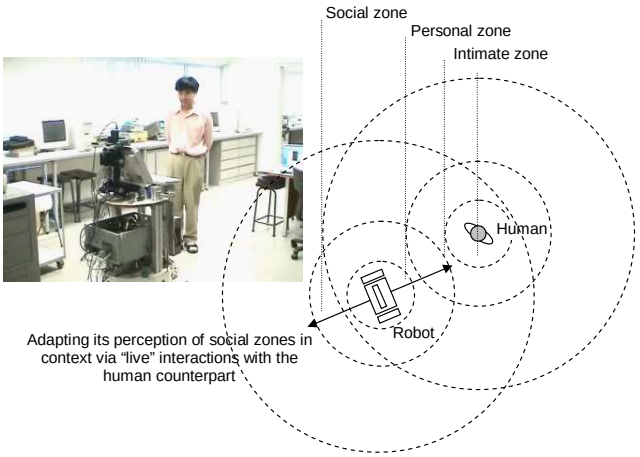

Fig. 7. Social distances and adaptation of the perceived comfort zones between a robot and a human user.

that the gap between social distances adopted for human-human and human-computer interactions narrows based on the perception of the robot's role in society – from merely "socially evocative" to being "sociable" [1]. It also indicates the presence of a continuous feedback loop between the human user and the robot, mediated by human expectations and robot behaviors. Human expectations and the level of acceptance of robots in the social landscape are altered based on how a social robot behaves and how well it reacts to fundamental social cues such as social spaces.

A robot that can respect the comfort zone and social space of each individual human in its surroundings, and eventually learn and adapt its own social space according to the evolution of its personal relationship with these individuals, would find it easier to be recognized as a member of mainstream society. As a move towards "sociable" robots, the issue of social spaces applied to human-robot interactions should be examined in further detail. Simple behavioral responses that enable the robots to keep a predetermined distance from human users, although necessary, is not sufficient for social interactions. The robots have to adapt and learn of the social context it is situated in, and must also be able to infer the level of social relationships between themselves and the human users. Consider the situation where a robot starts interacting with a human user. It first gives the user the priority of determining the comfortable interaction distance, through a series of observations of the distance the user maintains between them. If a user repeatedly backs away from the robot during their interactions, the robot adaptively increases the distance it maintains from the user, and vice versa, as shown in Fig. 7. As with human-human interactions, it is obvious that interaction distances are larger in more formal contexts, where participants are less familiar with each other, and also during interactions between people of differing social statuses. This applies also to human-robot interactions. Through other cognitive modules implemented on the social robot, such as vision and machine intelligence, the robot continually adapts

its model of the social environment as it continues interaction with different people, perhaps gradually closing the interaction distance (through constant feedback/ observations of the human counterpart) as the personal relationship with specific individuals evolve over time.

VI. Decision Making & Computational Intelligence

At one of the highest rungs of the cognitive ladder for socially adept robots is the ability to manipulate, organize and reason about available information, and from there, make relevant operational plans that conform to the abstract objectives of complex missions/tasks demanded of the robots. Overall, this topic is also of interest to engineers/researchers [104] and philosophers [105]–[107] because of the potential impact high level robot cognition have on the moral and ethical fabric of society.

Technical research in this area is thus devoted to the study of the mechanisms that are involved in the decision making process of robots. It ranges from tools for improving the efficiency of computationally intensive processes, to deliberation and planning protocols for the accomplishment of tasks.

In the near future where social robots are integral part of the social landscape, it is inevitable that each will be required to interact with other (humans/artificial) entities around it. The advancement of technology in robotics, control, computer science and communications, has made possible, the deployment of large teams of mobile robots in real life scenarios. This leads to research in Multi-Agent Systems (sometimes referred to as Distributed Artificial Intelligence) [108], consisting of huge numbers of interacting agents, linked together in complex networks. Such agents manifest themselves in the form of virtual robots, humans and embodied mobile robots. Specifically, technical issues involve robust and adaptive task allocation and behavior generation in robotic systems [109]–[111], and scheduling and rescheduling [112] mechanisms. This is a major research thrust at the Social Robotics Laboratory.

Much work can still be done in this area, where the major challenge is the synthesis of an unprecedented level of intelligence in social robots that goes beyond mere user predefined state changes, a level of cognition that mirrors the human decision making process. Open problems still exists in the fields of decision optimization, neural networks and fuzzy logic, and many more.

VII. Conclusions and Future Work

As we look ahead, it seems clear that social robots will play an ever larger role in our world, working for and in cooperation with humans. Social robots will assist in health care, rehabilitation, and therapy. Social robots will work in close proximity to humans, serving as tour guides, office assistants, and household staff. Social robots will engage and entertain. Central to the success of social robots will be close and effective interaction between humans and robots. There is still much that can be done in each of these modules, which involves scientists and researchers from all disciplines of engineering and computer science. We have, in this paper, provided a general review of the core technologies critical to the development of social robots, and also a holistic view of the system and how individual modules (from sensing to perception to cognition and planning) support and augment each other in the overall scheme of things.

References

[1] C. Breazeal, "Toward Sociable Robots," *Robotics and Autonomous Systems*, vol. 42, pp. 167–175, 2003.

[2] I. R. Nourbakhsh, J. Bobenage, S. Grange, R. Lutz, R. Meyer, and A. Soto, "An affective mobile robot educator with a full-time job," *Artificial Intelligence*, vol. 114, no. 1-2, pp. 95–124, 1999.

[3] W. Burgard, A. Cremers, D. Fox, D. Hähnel, G. Lakemeyer, D. Schulz, W. Steiner, and S. Thrun, "The interactive museum tour-guide robot," in *Proceedings of the Fifteenth National Conference on Artificial Intelligence*, Madison, Wisconsin, 1998, pp. 11–18.

[4] G. Kim, W. Chung, K.-R. Kim, M. Kim, S. Han, and R. H. Shinn, "The autonomous tour-guide robot jinny," in *Proceedings of the IEEE/RSJ International Conference on Intelligent Robots and Systems*, vol. 4, Sendai, Japan, Oct 2004, pp. 3450–3455.

[5] C. L. Breazeal, *Designing Sociable Robots*. Cambridge: The MIT Press, 2002.

[6] W. D. Stiehl and C. Breazeal, "A sensitive skin for robotic companions featuring temperature, force, and electric field sensors," in *Proceedings of the IEEE/RSJ International Conference on Intelligent Robots and Systems*, Beijing, China, Oct 2006, pp. 1952–1959.

[7] K. Severinson-Eklundh, A. Green, and H. Hüttenrauch, "Social and collaborative aspects of interaction with a service robot," *Robotics and Autonomous Systems*, vol. 42, pp. 223–234, 2003.

[8] T. Fong, I. Nourbakhsh, and K. Dautenhahn, "A survey of socially interactive robots," *Robotics and Autonomous Systems*, vol. 42, pp. 143–166, 2003.

[9] A. Mahajan and M. Walworth, "3D position sensing using the differences in the time of flights from a wave source to various receivers," *IEEE Transactions on Robotics and Automation*, vol. 17, no. 1, pp. 91–94, 2001.

[10] M. Rucci, G. M. Edelman, and J. Wray, "Adaptation of orienting behavior: From the barn owl to a robotic system," *IEEE Transactions on Robotics and Automation*, vol. 15, no. 1, pp. 96–110, 1999.

[11] J. Y. Weng and K. Y. Guentchev, "Three-dimensional sound localization from a compact noncoplanar array of microphones using tree-based learning," *Journal of the Acoustical Society of America*, vol. 110, no. 1, pp. 310–323, 2001.

[12] S. L. Gay and J. Benesty, *Acoustic signal processing for telecommunication*. Boston: Kluwer Academic, 2000.

[13] D. Nandy and J. Ben-Arie, "Estimating the azimuth of a sound source from the binaural spectral amplitude," *IEEE Transactions on Speech and Audio Processing*, vol. 4, no. 1, pp. 45–55, January 1996.

[14] G. Arslan and F. A. Sakarya, "A unified neural-network-based speaker localization technique," *IEEE Transactions on Neural Networks*, vol. 11, no. 4, pp. 997–1002, July 2000.

[15] K. W. Lo and B. G. Ferguson, "Broadband passive acoustic technique for target motion parameter estimation," *IEEE Transactions on Aerospace and Electronic Systems*, vol. 36, no. 1, pp. 163 – 175, January 2000.

[16] H. C. Schau and A. Z. Robinson, "Passive source localization employing intersecting spherical surfaces from time-of-arrival differences," *IEEE Transactions on Acoustics, Speech, and Signal Processing*, vol. ASSP-35, no. 8, pp. 1223–1225, August 1987.

[17] Q. H. Wang, T. Ivanov, and P. Arari, "Acoustic robot navigation using distributed microphone arrays," *Information Fusion*, vol. 5, no. 2, pp. 131–140, June 2004.

[18] J. Tabrikian and H. Messer, "Three-dimensional source localization in a waveguide," *IEEE Transactions on Signal Processing*, vol. 44, no. 1, pp. 1 – 13, January 1996.

[19] F. Rojas, C. G. Puntonet, M. Rodr$mb\acute{o}xi$guez-Álvarez, I. Rojas, and R. Martín-Clemente, "Blind source separation in post-nonlinear mixtures using competitive learning, simulated annealing, and a genetic algorithm," *IEEE Transactions on Systems, Man and Cybernatics - Part C: Applications and Reviews*, vol. 34, no. 4, pp. 407–416, November 2004.

[20] J. Huang, T. Supaongprapa, I. Terakura, N. Ohnishi, and N. Sugie, "Mobile robot and sound localization," in *Proceedings of the IEEE/RSJ International Conference on Intelligent Robots and Systems*, vol. 2, Grenoble, France, September 7-11 1997, pp. 683–689.

[21] H. Buchner and W. Kellermann, "An acoustic human-machine interface with multi-channel sound reproduction," in *Proceedings of IEEE Fourth Workshop on Multimedia Signal Processing*, Cannes, France, October 3-5, 2001 2001, pp. 359 –364.

[22] J. G. Desloge, W. Rabinowitz, and P. Zurek, "Microphone-array hearing aids with binaural output - part 1 : Fixed-processing systems," *IEEE Transactions on Speech and Audio Processing*, vol. 5, no. 6, pp. 529 –542, 1997.

[23] D. Welker, J. Greenberg, J. Desloge, and P. Zurek, "Microphone-array hearing aids with binaural output. ii. a two-microphone adaptive system," *IEEE Transactions on Speech and Audio Processing*, vol. 5, no. 6, pp. 543 –551, 1997.

[24] B. G. Ferguson, L. G. Criswick, and K. W. Lo, "Locating far-field impulsive sound sources in air by triangulation," *Journal of the Acoustical Society of America*, vol. 111, no. 1, pp. 104–116, 2002.

[25] D. T. Blackstock, *Fundamentals of Physical Acoustics*. New York: Wiley, 2000.

[26] P. R. Cook, *Music, Cognition, and Computerized Sound,- An Introduction to Psychoacoustics*. Cambridge, Massachusetts: The MIT Press, 1999.

[27] S. Handel, *Listening-An Introduction to the Perception of Auditory Events*. Cambridge, Masachusetts: The MIT Press, 1989.

[28] B. G. Shinn-Cunningham, S. Santarelli, and N. Kopco, "Tori of confusion: Binaural localization cues for sources within reach of a listener," *Journal of the Acoustical Society of America*, vol. 107, no. 3, pp. 1627–1636, 2000.

[29] M. Morimoto, "The contribution of two ears to the perception of vertical angle in sagittal planes," *Journal of the Acoustical Society of America*, vol. 109, no. 4, pp. 1596–1603, 2001.

[30] C. J. Pu, J. Harris, and J. C. Principe, "A neuromorphic microphone for sound localization," in *Proceedings of IEEE International Conference on Systems, Man, and Cybernetics, Computational Cybernetics and Simulation*, vol. 2, Orlando, USA, October 1997, pp. 1469 –1474.

[31] J. Huang, N. Ohnishi, and N. Sugie, "A biomimetic system for localization and separation of multiple sound sources," *IEEE Transactions on Instrumentation and Measurement*, vol. 44, pp. 733–738, 1995.

[32] ——, "Sound localization in reverberant environment based on the model of the precedence effect," *IEEE Transactions on Instrumentation and Measurement*, vol. 46, pp. 842–846, 1997.

[33] M. Brandstein and D. Ward, *Microphone Arrays - Signal Processing Techniques and Applications*. New York: Springer, 2001.

[34] B. G. Ferguson and K. W. Lo, "Passive ranging errors due to multipath distortion of deterministic transient signals with application to the localization of small arms fire," *Journal of the Acoustical Society of America*, vol. 111, no. 1, pp. 117–128, 2002.

[35] S. Gazor and Y. Grenier, "Criteria for positioning of sensors for a microphone array," *IEEE Transactions on Speech and Audio Processing*, vol. 3, no. 4, pp. 294 – 303, July 1995.

[36] M. S. Brandstein, J. E. Adcock, and H. F. Silverman, "A closed-from location estimator for use with room environment microphone arrays," *IEEE Transactions on Speech and Audio Processing*, vol. 5, no. 1, pp. 45–50, January 1997.

[37] M. S. Brandstein, "A framework for speech source localization using sensor arrays," Ph.D. dissertation, Brown University, May 1995.

[38] V. Katkovnik and A. B. Gershman, "A local polynomial approximation based beamforming for source localization and tracking in nonstationary environments," *IEEE Signal Processing Letters*, vol. 7, no. 1, pp. 3–5, January 2000.

[39] Sofiéne, S. Gazor, and Y. Grenier, "An algorithm for multisource beamforming and multitarget tracking," *IEEE Transactions on Signal Processing*, vol. 44, no. 6, pp. 1512–1522, June 1996.

[40] Y. T. Huang, J. Benesty, G. W. Elko, and R. M. Mersereau, "Real-time passive source localizatin: A practical linear-correction least-squares approach," *IEEE Transaction on Speech and Audio Processing*, vol. 9, no. 8, pp. 943–956, November 2001.

[41] J. C. Chen, R. E. Hudson, and K. Yao, "Maximum-likelihood sound localization and unknown sensor location estimation for wideband signals in the near-field," *IEEE Transactions on Signal Processing*, vol. 50, no. 8, pp. 1843–1854, August 2002.

[42] J. Chen, L. Jiang, and W. Ser, "A framework for speaker tracking using microphone array and camera," in *Proceedings of 5th International Conference on Signal Processing*, vol. 2, Beijing, China, 21-25 Aug 2000, pp. 1384 –1387.

[43] P. Aarabi, "Self-localization dynamic microphone arrays," *IEEE Transactions on Systems, Man and Cybernatics - Part C: Applications and Reviews*, vol. 32, no. 4, pp. 474–484, November 2002.

[44] S. S. Ge and C. H. Fua, "Queues and artificial potential trenches for multi-robot formations," *IEEE Transactions on Robotics*, vol. 21, no. 4, pp. 646–656, August 2005.

[45] A. Mohan, C. Papageorgiou, and T. Poggio, "Example-based object detection in images by components," *IEEE Transactions on Pattern Analysis and Machine Intelligence*, vol. 23, no. 4, pp. 349–361, April 2001.

[46] I. Haritaoglu, D. Harwood, and L. S. Davis, "W^4: Real-time surveillance of people and their activities," *IEEE Transcations on Pattern Analysis and Machine Intelligence*, vol. 22, no. 8, pp. 809–830, August 2000.

[47] D. M. Gavrila, "The visual analysis of human movement: A survey," *Computer Vision and Image Understanding*, vol. 73, no. 1, pp. 82–98, 1999.

[48] C. R. Wren, A. Azarbayejani, T. Darrell, and A. P. Pentland, "Pfinder: Real-time tracking of the human body," *IEEE Transcations on Pattern Analysis and Machine Intelligence*, vol. 19, no. 7, pp. 780–785, July 1997.

[49] S. J. McKenna, S. Jabri, Z. Duric, and A. Rosenfeld, "Tracking groups of people," *Computer Vision and Image Understanding*, vol. 80, 42-56 2000.

[50] B.-L. Zhang, H. Zhang, and S. S. Ge, "Face recognition by applying wavelet subband representation and kernel associative memory," *IEEE Transactions on Neural Networks*, vol. 15, no. 1, pp. 166 – 177, January 2004.

[51] R. L. Hsu, M. Abdei-Mottaleb, and A. K. Jain, "Face dectetion in color images," *IEEE Transactions on Pattern Analysis and Machine Intelligence*, vol. 24, no. 5, pp. 696–706, May 2002.

[52] N. Kakuta, S. Yokoyama, and K. Mabuchi, "Human thermal models for evaluating infrared images," *IEEE Engineering in Medicine and Biology Magazine*, vol. 21, no. 6, pp. 65–72, november-December 2002.

[53] N. Nanadhakumar and J. L. Aggarwal, "Integrated analysis of thermal and visual images for scene interpretation," *IEEE Transcations on Pattern Analysis and Machine Intelligence*, vol. 10, no. 4, pp. 469–480, July 1988.

[54] W. L. Chan, A. T. P. So, and L. L. Lai, "Three-dimensional thermal imaging for power equipment monitoring," *IEE Proceedings - Generation, Transmission and Distribution*, vol. 147, no. 6, pp. 355 – 360, 2000.

[55] X. P. V. Maldague, *Infrared Methodlogy and Technology*, ser. Nondestructive Testing Monographs and Tracts, W. J. McGonnagle, Ed. Switzerland: Gordon and Breach Sicence Publishers, 1994, vol. 7.

[56] M. M. Trivedi, S. Y. Cheng, E. M. C. Childers, and S. J. Krotosky, "Occupant posture analysis with stereo and thermal infrared video: Algorithms and experimental evaluation," *IEEE Transations on Vehicular Technology*, vol. 53, no. 6, pp. 1698–1712, November 2004.

[57] C. Darwin, *The Expression of the Emotions in Man and Animals*. Albemarle Street, London: John Murray, 1872.

[58] P. Ekman and W. Friesen, *Facial Action Coding System: A Technique for the Mea-surement of Facial Movement*. Palo Alto, California, USA: Consulting Psychologists Press, 1978.

[59] A. Young and H. E. Ellis, *Handbook of Research on Face Processing*. North-Holland,Amsterdam: Elsevier Science Publishers B.V., 1989.

[60] C. Padgett and G. Cottrell, "Representing Face Images for Classifying Emotions," vol. 9, 1997.

[61] C. Padgett, G. Cottrell, and B. Adolps, "Categorical perception in facial emotion classification," *Proc. Cognitive Science Conf.*, vol. 18, pp. 249–253, 1996.

[62] Y. Yacoob and L. Davis, "Recognizing Human Facial Expressions from Long Image Sequences using Optical Flow," *IEEE Trans. Pattern Analysis and Machine Intelligence*, vol. 18, pp. 636–642, June 1996.

[63] T. Otsuka and J. Ohya, "Recognition of facial expressions using HMM with contin-uous output probabilities," *Proc. 5th IEEE Int. Workshop on Robot and HumanCommunication RO-MAN*, pp. 323–328, 1996.

[64] C. E. Izard, "Facial expressions and the regulation of emotions,"

Journal of Personalityand Social Psychology, vol. 58, no. 3, pp. 487–498, 1990.
[65] G. Donato, M. S. Bartlett, J. C. Hager, P. Ekman, and T. J. Sejnowski, "Classifying Facial Actions," *IEEE Transactions on Pattern Analysis and Machine Intelligence*, vol. 21, no. 10, pp. 974–989, 1999.
[66] J. C. Latombe, *Robot Motion Planning*. London: Kluwer Academic Publishers, 1991.
[67] J. Borenstein and Y. Koren, "Real-time obstacle avoidance for fast mobile robots," *IEEE Transactions on Systems, Man and Cybernetics*, vol. 19, no. 5, pp. 1179–1187, 1989.
[68] ——, "The vector field histogram - fast obstacle avoidance for mobile robots," *IEEE Transactions on Robotics and Automation*, vol. 7, no. 3, pp. 278–288, 1991.
[69] J. H. Chuang and N. Ahuja, "An analytically tractable potential field model of free space and its application in obstacle avoidance," *IEEE Transactions on Systems, Man, and Cybernetics, Part B: Cybernetics*, vol. 28, no. 5, pp. 729–736, 1998.
[70] E. Rimon and D. E. Koditschek, "Exact robot navigation using artificial potential functions," *IEEE Transactions on Robotics and Automation*, vol. 8, no. 5, pp. 501–518, 1992.
[71] O. Khatib, "Real-time obstacle avoidance for manipulators and mobile robots," *The International Journal of Robotics Research*, vol. 5, no. 1, pp. 90–98, 1986.
[72] E. Rimon, "Exact robot navigation using artificial potential functions," Ph.D. dissertation, Yale University, 1990.
[73] J. O. Kim and P. K. Khosla, "Real-time obstacle avoidance using harmonic potential functions," *IEEE Transactions on Robotics and Automation*, vol. 8, no. 3, pp. 338–349, 1992.
[74] N. Y. Ko and B. H. Lee, "Avoidability measure in moving obstacle avoidance problem and its use for robot motion planning," in *Proceedings of the IEEE/RSJ International Conference on Intelligent Robots and Systems*, vol. 3, Osaka, Japan, 1996, pp. 1296–1303.
[75] B. Hussien, "Robot path planning and obstacle avoidance by means of potential function method," Ph.D. dissertation, University of Missouri-Columbia, 1989.
[76] P. Khosla and R. Volpe, "Superquadric artificial potentials for obstacle avoidance and approach," in *IEEE International Conference on Robotics and Automation*, vol. 3, Pittsburgh, PA, 1988, pp. 1778–1784.
[77] P. Veelaert and W. Bogaerts, "Ultrasonic potential field sensor for obstacle avoidance," *IEEE Transactions on Robotics and Automation*, vol. 15, no. 4, pp. 774–779, 1999.
[78] C. W. Warren, "Global path planning using artificial potential fields," in *IEEE International Conference on Robotics and Automation*, vol. 1, Scottsdale, AZ, 1989, pp. 316–321.
[79] ——, "Multiple robot path coordination using artificial potential fields," in *IEEE International Conference on Robotics and Automation*, vol. 1, Cincinnati, OH, 1990, pp. 500–505.
[80] J. F. Canny and M. C. Lin, "An opportunistic global path planner," in *IEEE International Conference on Robotics and Automation*, vol. 3, Cincinnati, OH, 1990, pp. 1554–1559.
[81] K. Fujimura and H. Samet, "A hierarchical strategy for path planning among moving obstacles," *IEEE Transactions on Robotics and Automation*, vol. 5, no. 1, pp. 61–69, 1989.
[82] C. L. Shih and T. Lee, "A unified approach for robot motion planning withmoving polyhedral obstacles," *IEEE Transactions on Systems, Man and Cybernetics*, vol. 20, no. 4, pp. 903–915, 1990.
[83] R. A. Conn and M. Kam, "Robot motion planning on n-dimensional star worlds among moving obstacles," *IEEE Transactions on Robotics and Automation*, vol. 14, no. 2, pp. 320–325, 1998.
[84] A. Stentz, "Optimal and efficient path planning for partially-known environments," in *Proceedings of the IEEE International Conference on Robotics and Automation*, vol. 4, May 1994, pp. 3310–3317.
[85] H. Choset and J. Burdick, "Sensor based planning, part ii: Incremental construction of the generalized voronoi graph," in *Proceedings of the IEEE International Conference on Robotics and Automation*, vol. 2, May 1995, pp. 1643–1648.
[86] V. Lumelsky and A. A. Stepanov, "Sensor-based exploration: The hierarchical generalized voronoi graph," *The International Journal of Robotics Research*, vol. 19, no. 2, pp. 96–125, 2000.
[87] Y. Koren and J. Borenstein, "Potential field methods and their inherent limitations for mobile robot navigation," in *Proceedings of the IEEE International Conference on Robotics and Automation*, vol. 2, Apr 1991, pp. 1398–1404.
[88] S. S. Ge and Y. J. Cui, "Dynamic motion planning for mobile robots using potential field method," *Autonomous Robots*, vol. 13, no. 3, pp. 207–222, 2002.
[89] R. A. Brooks, "A robust layered control system for a mobile robot," *IEEE Journal of of Robotics and Automation*, vol. 2, no. 1, pp. 14–23, 1986.
[90] R. C. Arkin, "Motor-schema-based mobile robot navigation," *The International Journal of Robotics Research*, vol. 8, no. 4, pp. 92–112, 1989.
[91] H. R. Beom and H. S. Cho, "A sensor-based navigation for a mobile robot using fuzzy logic and reinforcement learning," *IEEE Transactions on Systems, Man and Cybernetics*, vol. 25, no. 3, pp. 464–477, 1995.
[92] V. Lumelsky and A. A. Stepanov, "Path-planning strategies for a point mobile automaton moving amidst unknown obstacles of arbitrary shape," *Algorithmica*, vol. 2, pp. 403–430, 1987.
[93] V. Lumelsky and T. Skewis, "Incorporating range sensing in the robot navigation function," *IEEE Transactions on Systems, Man, and Cybernetics*, vol. 20, no. 5, pp. 1058–1069, 1990.
[94] I. Kamon and E. Rivlin, "Sensory-based motion planning with global proofs," *IEEE Transactions on Robotics and Automation*, vol. 13, no. 6, pp. 814–822, 1997.
[95] I. Kamon, E. Rimon, and E. Rivlin, "Tangentbug: A range-sensor-based navigation algorithm," *The International Journal of Robotics Research*, vol. 17, no. 9, pp. 934–953, 1998.
[96] S. S. Ge, Y. J. Cui, and C. Zhang, "Instant-goal-driven methods for behavior-based mobile robot navigation," in *Proceedings of IEEE International Symposium on Intelligent Control*, Oct 2003, pp. 269–274.
[97] S. S. Ge, X. C. Lai, and A. A. Mamun, "Boundary following and globally convergent path planning using instant goals," *IEEE Transactions on Systems, Man, and Cybernetics, Part B: Cybernetics*, vol. 35, no. 2, pp. 1–15, 2005.
[98] B. H. Krogh and D. Feng, "Dynamic generation of subgoals for autonomous mobile robots using local feedback information," *IEEE Transation on Automatic Control*, vol. 34, no. 5, pp. 483–493, 1989.
[99] T. Kasuga and M. Hashimoto, "Human-robot handshaking using neural oscillators," in *IEEE International Conference on Robotics and Automation*, Barcelona, Spain, 2005, pp. 3802–3807.
[100] M. Jindai, T. Watanabe, S. Shibata, and T. Yamamoto, "Development of a handshake robot system for embodied interaction with humans," in *IEEE International Workshop on Robots and Human Interactive Communication*, Hatfield, UK, 2006, pp. 710–715.
[101] E. T. Hall, *The Hidden Dimension: Man's Use of Space in Public and Private*. London, UK: The Bodley Head Ltd, 1966.
[102] D. Lambert, *Body Language*. Harper Collins, 2004.
[103] M. L. Walters, K. Dautenhahn, R. te Boekhorst, K. L. Koay, C. Kaouri, S. Woods, C. Nehaniv, D. Lee, and I. Werry, "The Influence of Subjects' Personality Traits on Predicting Comfortable Human-Robot Approach Distances," *Proceedings of COGSCI 2005 Workshop*, pp. 29–37, July 2005.
[104] B. M. O'Connell, "Anticipating Ethics," *Proc. IEEE International Symposium on Electronics and the Environment*, pp. 48–52, 8-11 May 2006.
[105] D. C. Dennett, *Consciousness Explained*. Boston: Little Brown and Co., 1991.
[106] D. J. Chalmers, "Facing Up to the Problem of Consciousness," *Journal of Consciousness Studies*, vol. 2, pp. 200–219, 1995.
[107] J. Searle, "Minds, Brains, and Programs," *Behavioral and Brain Sciences*, vol. 3, pp. 417–458, 1980.
[108] K. P. Sycara, "Multiagent systems," *AI Magazine*, vol. 10, no. 2, pp. 79–93, 1998.
[109] L. E. Parker, "ALLIANCE: An Architecture for Fault Tolerant Multirobot Cooperation," *IEEE Transactions on Robotics and Automation*, vol. 14, no. 2, pp. 220–240, April 1998.
[110] B. P. Gerkey and M. J. Matarić, "Sold!: Auction Methods for Multirobot Coordination," *IEEE Transactions on Robotics and Automation*, vol. 18, no. 5, pp. 758–768, October 2002.
[111] C. Fua and S. S. Ge, "COBOS: Cooperative Back-Off Adaptive Scheme for Multi-Robot Task Allocation," *IEEE Transactions on Robotics*, vol. 21, no. 6, pp. 1168–1178, December 2005.
[112] G. E. Vieira, J. W. Herrmann, and E. Lin, "Rescheduling Manufacturing Systems: A Framework of Strategies, Policies, and Methods," *Journal of Scheduling*, vol. 6, pp. 39–62, 2003.

Shuzhi Sam Ge

Professor, IEEE Fellow, PhD, DIC, BSc, PEng

Director, Edutainment Robotics Lab, Department of Electrical & Computer Engineering, and Head, Social Robotics Lab, Interactive Digital Media Institute The National University of Singapore
Singapore 117576 Tel: (+65) 6516 6821, Fax: (+65) 6779 1103

E-mail: elegesz@nus.edu.sg , http://vlab.ee.nus.edu.sg/~sge

Professor Shuzhi Sam Ge is Head of Social Robotics Lab, Interactive and Digital Media Institute, and the Director of Edutainment Robotics Lab, Department of Electrical and Computer Engineering, the National University of Singapore. He received his PhD degree and DIC from the Imperial College, London, and BSc degree from Beijing University of Aeronautics & Astronautics. He has published a number of books, over 300 scientific journal and international conference papers, given invited talks/plenary speeches, managed/completed a number of projects of impact, and delivered many working systems and prototyping to industry and funding agencies, the inventor of 3 patents and the 4th one on Interactive e-Book Authoring System filed for PCT. Dr. Ge has received the highest accolades from his University, from Singapore, from China, and from USA. He was the recipient of the 1999 National Technology Award, Singapore; 2001 Young Research Award, NUS; 2002 inaugural Temasek Young Investigator Award, DSTA; 2004 NSF Outstanding Overseas Young Researcher Award, China; and 2006 IEEE Fellowship, USA. In his 2002 inaugural Temasek Young Investigator Award on intelligent control of unmanned vehicles, he delivered many more deliverables in prototypes and software packages to DSTA across sensor fusion, decision making, path planning, and intelligent control.

He serves on the Board of Governors, IEEE Control Systems Society (CSS), as elected member from 2007 to 2009, Chairman of the Technical Committee of Intelligent Control, IEEE CSS since 2005, Dr Ge served as Chairman of IEEE Singapore SMC Chapter (2003), and Chairman of IEEE Singapore R&A Chapter (2004, 2005). Dr Ge served as the founder and General Chair of IEEE Conference on Robotics, Automation & Mechatronics, and IEEE Conference on Cybernetics & Intelligent Systems in 2004, and the Chair of the Steering Committee for the two conferences in Bangkok, 2006. He served/serves as an Associate Editor for a number of flagship journals, Book Editor for Taylor & Francis Automation and Control Engineering Series.

He is the Chairman and founding Director of Personal E-Motion Pte Ltd in delivering interactive digital multimedia authoring platforms and multimedia digital books generation and delivering systems for education and e-publishing.

Technical Paper

Circuit and Systems

Control Engineering

Electrical Power Engineering

Other Related Fields

Communication Systems

Signal Processing

Computer and Information

Table of Contents

10:50 AM - 12:10 AM — **Session TAM1-3** — **Thursday,10 May 2007**

CMOS Technology

Chairperson : Songphol Kanjanachuchai ,Chulalongkorn University

TAM1-3-1 **10:50 AM** — **High Frequency, High Precision CMOS Half-Wave Rectifier** — **1**
Montree Kumngern, Kobchai Dejhan
Engineering and Research Center for Communication and Information Technology, King Mongkut's Institute of Technology Ladkrabang, Bangkok, Thailand

TAM1-3-2 **11:10 AM** — **A Modified CMOS Differential-Pair-Based Triangular-and-Trapezoidal to-Sine** — **5**
Kanitpong Pengwon, Ekachai Leelarasmee
Electrical Engineering Department, Chulalongkorn University, Bangkok, Thailand

TAM1-3-3 **11:30 AM** — **A Design of CMOS Class-AB Differential Log-Companding Amplifier** — **9**
Kobkaew Opasjumruskit[1], Apisak Worapishet[2], Ekachai Leelarasamee[1]
[1]IC Design and Application Research Laboratory (IDAR), Department of Electrical Engineering, Chulalongkorn University, Thailand
[2]Mahanakorn Microelectronics Research Centre (MMRC), Mahanakorn University of Technology, Thailand

TAM1-3-4 **11:50 AM** — **A Novel Structure of Wide-Swing CMOS Voltage Buffer** — **13**
Chutham Sawigun, Jirayuth Mahattanakul
Department of Electronic Engineering, Faculty of Engineering, Mahanakorn University of Technology, Bangkok, Thailand

10:50 AM - 12:10 AM — **Session TAM1-8** — **Thursday,10 May 2007**

Integrated Circuits

Chairperson : Chiranut Sa-ngiamsak, Khon Kean University

TAM1-8-1 **10:50 AM** — **A Compact Low Voltage CMOS Four-Quadrant Analog Multiplier** — **17**
N. Kiatwarin[1], W. Ngamkham[2], W. Kiranon[1]
[1]Department of Telecommunication Engineering, Faculty of Engineering, King Mongkut's Institute of Technology Ladkrabang, Thailand
[2]Department of Control and Instrumentation Engineering Mahanakorn University of Technology, Bangkok, Thailand

TAM1-8-2 **11:10 AM** — **Verifying Various Generation of Random Number Sequence on Wave-Pipelined PRNG** — **21**
Tomoaki Sato, Kazuhira Kikuchi, Masa-aki Fukase
Hirosaki University, Bunkyo-cho 3 Hirosaki, Aomori, Japan

TAM1-8-3 **11:30 AM** — **Asynchronous System Bus Enhancement by Interrupt and DMA Technique** — **25**
Sufian Sudeng, Arthit Thongtak
Digital System Engineering Laboratory (DSEL), Department of Computer Engineering, Chulalongkorn University, Bangkok, Thailand

TAM1-8-4 **11:50 AM** — **CMOS compatible Ion Sensitive Field Effect Transistor with Silicon Nitride Membrane for pH Measurement System** — **29**
W. Bunjongpru, O. Trithaveesak, K. Sowsuwan, W. Jeamsaksiri, C. Hruanun, A. Poyai
Thai Microelectronics Center (TMEC), Chachoengsao, Thailand

1:00 PM - 3:00 PM | **Session TPM1-2** | **Thursday,10 May 2007**

Oscillator Circuits

Chairperson : Apinan Thanachaynont, King Mongkut's Institute of Technology Ladkrabang

TPM1-2-1 **1:00 PM** — **Current Tunable Quadrature Oscillator Using Only CCCDBAs and Grounded Capacitors** — **32**

Sumaytee Pisitchalermpong, Danucha Prasertsom, Thanawat Piyatat,
Worapong Tangsrirat, Wanlop Surakampontorn
Research Center for Communication and Information Technology (ReCCIT),
King Mongkut's Institute of Technology Ladkrabang, Bangkok, Thailand

TPM1-2-2 **1:20 PM** — **Implementation of a Chua's Chaotic Oscillator Using "Roughly-Cubic-Like" Nonlinearity** — **36**

Banlue Srisuchinwong, Wimol San-Um
Sirindhorn International Institute of Technology,
Thammasat University, Bangkadi Campus, Pathumtani, Thailand

TPM1-2-3 **1:40 PM** — **Improved Implementation of Sprott's Chaotic Oscillators Based on Current-Feedback Op Amps** — **38**

Banlue Srisuchinwong, Chun-Hung Liou
Sirindhorn International Institute of Technology,
Thammasat University, Bangkadi Campus, Pathumtani, Thailand

TPM1-2-4 **2:00 PM** — **Multiphase Oscillator using Operational Transconductance Amplifiers** — **41**

Montree Kumngern[1], Montri Somdunyakanok[2], Pipat Prommee[1], Kobchai Dejhan[1]
[1]Research Center for Communication and Information Technology,
King Mongkut's Institute of Technology Ladkrabang, Bangkok, Thailand
[2]Electrical Engineering Department, Siam University, Bangkok, Thailand

TPM1-2-5 **2:20 PM** — **Dual-mode Multiphase Sinusoidal Oscillator using CDBAs** — **45**

D. Pulsub, W. Surakampontorn
King Mongkut's Institute of Technology Ladkrabang, Bangkok, Thailand

TPM1-2-5 **2:40 PM** — **A CMOS-based Electronically and Linearly Tunable Quadrature Oscillator** — **49**

Khanittha Kaewdang[1], Wanlop Surakampontorn[2]
[1]Department of Electrical and Electronics Engineering, Faculty of Engineering,
Ubon Rajathanee University, Ubon Rajathanee, Thailand
[2]Research Center for Communication and Information Technology (ReCCIT),
King Mongkut's Institute of Technology Ladkrabang, Bangkok, Thailand

3:20 PM - 5:00 PM | **Session TPM2-2** | **Thursday,10 May 2007**

Filter Technology

Chairperson : Worapong Tangsrirat, King Mongkut's Institute of Technology Ladkrabang

TPM2-2-1 **3:20 PM** — **Cascadable Three-Input Single-Output Current-Mode Universal Filter Using CDBAs** — **53**

Visawa Sawangarom[1], Teerasilapa Dumawipata[2],
Worapong Tangsrirat[1], Wanlop Surakampontorn[1]
[1]Research Center for Communication and Information Technology (ReCCIT),
King Mongkut's Institute of Technology Ladkrabang, Bangkok, Thailand
[2]Department of Industrial Electrical Technology (IET), Faculty of Engineering,
King Mongkut's Institute of Technology North Bandkok, Bangkok, Thailand

TPM2-2-2	**Minimum Devices Active-only Current-mode Universal Filter**	**57**
3:40 PM	Pipat Prommee, Montri Somdunyakanok, Montree Kumngern, Kobchai Dejhan *Research Center for Communication and Information Technology (ReCCIT)* *King Mongkut's Institute of Technology Ladkrabang, Bangkok, Thailand*	
TPM2-2-3	**A Systematic Design of Electronically Tunable Ladder Filters Employing DO-OTAs**	**61**
4:00 PM	Winai Jaikla[1], Montree Siripruchyanun[2] [1]*Electric and Electronic Program, Faculty of Industrial Technology,* *Suan Sunandha Rajabhat University, Bangkok, Thailand* [2]*Department of Teacher Training in Electrical Engineering,* *King Mongkut's Institute of Technology North Bangkok, Bangkok, Thailand*	
TPM2-2-4	**A Novel Current-Mode Alternative Topology for Realization of Universal Filter and**	**65**
4:20 PM	**Quadrature Oscillator** Winai Jaikla [1,] Montree Siripruchyanun [2] [1]*Electric and Electronic Program, Faculty of Industrial Technology,* *Suan Sunandha Rajabhat University, Bangkok, Thailand* [2]*Department of Teacher Training in Electrical Engineering,* *King Mongkut's Institute of Technology North Bangkok, Bangkok, Thailand*	
TPM2-2-5	**3 Input/ 2 Output Current-Mode Universal Biquad Filter Using Single DO-CCCDTA**	**69**
4:40 PM	Winai Jaikla[1], Montree Siripruchyanun[2] [1]*Electric and Electronic Program, Faculty of Industrial Technology,* *Suan Sunandha Rajabhat University, Bangkok, Thailand* [2]*Department of Teacher Training in Electrical Engineering,* *King Mongkut's Institute of Technology North Bangkok, Bangkok, Thailand*	
8:30 AM - 10.10 AM	**Session FAM1-2**	**Friday, 11 May 2007**
	Analog Circuits 1 Chairperson : Banlue Srisuchinwong, Sirindhorn International Institute of Technology	
FAM1-2-1	**Fast Analysis of Analog Design Trade-offs via Geometric Programming**	**73**
8:30 AM	Theerachet Soorapanth *National Electronics and Computer Technology Center, Bangkok, Thailand*	
FAM1-2-2	**A Current-Mode Square-Rooting Circuit Using Negative Feedback Technique**	**77**
8:50 AM	Ittipong Chaisayun *South-East Asia University, Bangkok, Thailand*	
FAM1-2-3	**Application of A Fourier Centroid Shift Method for Estimation of Ultrasonic**	**81**
9:10 AM	**Attenuation Coefficients** M. Lohakan[1,2], N. Pueiam[1], S. Boonsang[1], C. Pintavirooj[1] [1]*Research Center for Communication and Information Technology (ReCCIT), Department of Electronics* *King Mongkut's Institute of Technology Ladkrabang, Bangkok, Thailand* [2]*Department of Teacher Training in Electrical Engineering,* *King Mongkut's Institute of Technology North Bangkok, Bangkok, Thailand*	

FAM1-2-4	**A Compact Class-AB CMOS Variable Gain Amplifier**	**85**
9:30 AM	Phanumas Khumsat[1], s Apinunt Thanachayanont[2], Siraporn Sakphrom[2] *[1]Department of Electrical Engineering,* *Faculty of Engineering, Prince of Songkhla University, Hat-Yai, Thailand* *[2]Research Center of Communications and Information Technology,* *King Mongkut's Institute of Technology Ladkrabang , Bangkok, Thailand*	
FAM1-2-5	**Realization of Current Conveyors-based Floating Simulators Employing Grounded**	**89**
9:50 AM	**Passive Elements** Winai Jaikla[1,] Montree Siripruchyanun[2] *[1]Electric and Electronic Program, Faculty of Industrial Technology,* *Suan Sunandha Rajabhat University, Bangkok, Thailand* *[2]Department of Teacher Training in Electrical Engineering,* *King Mongkut's Institute of Technology North Bangkok, Bangkok, Thailand*	
8:30 AM - 10:10 AM	**Session FAM1-3** **Electrical Analysis**	**Friday, 11 May 2007**
	Chairperson : Werachate Khan-ngenn, King Mongkut's Institute of Technology Ladkrabang	
FAM1-3-1	**A Simplified Active Input EMI Filter of Common-mode Voltage Cancellation for**	**93**
8:30 AM	**Induction Motor Drive** C. Khun[1], V. Tarateeraseth[2], W. Khan-ngern[1], Masaaki Kando[3] *[1]Research Center for Communications and Information Technology (ReCCIT),* *King Mongkut's Institute of Technology Ladkrabang, Bangkok, Thailand* *[2]Faculty of Engineering, Srinakharinwirot University, Nakornnayok, Thailand* *[3]Department of Electrical and Electric Engineer, Tokai University, Japan*	
FAM1-3-2	**The Comparison of the Input Impedance Measurement of SMPS between**	**97**
8:50 AM	**the Resonance Method and the Insertion Loss Method** K. Kiatgamjorn[1], V. Tarateeraseth[2], W. Khan-ngern[1] *[1]Research Center for Communications and Information Technology (ReCCIT),* *King Mongkut's Institute of Technology Ladkrabang, Bangkok, Thailand* *[2]Faculty of Engineering, Srinakharinwirot University, Nakornnayok, Thailand*	
FAM1-3-3	**Trade-off between EMI Separator and RF Current Probe for Conducted EMI Testing**	**101**
9:10 AM	D. Sakulhirirak[1], V. Tarateeraseth[2], W. Khan-ngern[1], N. Yoothanom[3] *[1]Research Center for Communications and Information Technology (ReCCIT),* *King Mongkut's Institute of Technology Ladkrabang, Bangkok, Thailand* *[2]Faculty of Engineering, Srinakharinwirot University, Nakornnayok, Thailand* *[3]Sripatum University, Faculty of Engineering, Bangkok, Thailand*	
FAM1-3-4	**The Relation of Critical Current Negative Resistance and External Magnetic Field in**	**105**
9:30 AM	**GdBa2Cu3O7-x Superconducting Material** Wisit Wongsuttitum[1], Wisut Titiroongruang[1], Masamori Iida[2] *[1]Electronics Research Center, King Mongkut's Institute of Technology Ladkrabang, Thailand* *[2]Tokai University Junior College, Tokyo, Japan*	
FAM1-3-5	**Implementation of Electrical Capacitance Tomography using Analytical**	**109**
9:50 AM	**Sensitivity Maps** Denchai Worasawate, Phuwaphat Klongpramong *Kasetsart Advanced RF and ElectromagNetics Laboratory,* *Department of Electrical Engineering, Kasetsart University, Bangkok, Thailand*	

10:30 AM - 12:10 AM **Session FAM2-2** **Friday, 11 May 2007**

Analog Circuits 2

Chairperson : Banlue Srisuchinwong , Sirindhorn International Institute of Technology

FAM2-2-1 **Composite Four-Terminal Floating Nullor with Variable Voltage and Current Gains** **113**
10:30 AM
Jirawat Hirunporm[1], Sumalee Unhavanich[2], Worapong Tangsrirat[1],
Wanlop Surakampontorn[1]
[1]*Research Center for Communication and Information Technology (ReCCIT),*
King Mongkut's Institute of Technology Ladkrabang, Ladkrabang, Thailand
[2]*Department of Industrial Electrical Technology (IET),*
King Mongkut's Institute of Technology North Bangkok, Bangkok, Thailand

FAM2-2-2 **Current-mode Universal Biquad Including Minimum Component Count Circuits** **117**
10:50 AM
Pratya Mongkolwai, Tattaya Pukkalanun, Worapng Tangsrirat
Research Center for Communication and Information Technology (ReCCIT),
King Mongkut's Institute of Technology Ladkrabang, Bangkok, Thailand

FAM2-2-3 **A Study of Adaptive Forward Error Control in Audio Communication using Smooth** **121**
11:10 AM **Method**
Phichet Moungnoul, Kornhathai Klappong, Wiphada Inkiew, Somyot Junnapiya
Research Center for Communication and Information Technology (ReCCIT),
King Mongkut's Institute of Technology Ladkrabang, Bangkok, Thailand

FAM2-2-4 **Rectangular Wave Delta Modulation Buck Regulator for Voltage Regulator Modules** **125**
11:30 AM
J. Ngarmnil, K. Sooksood
Department of Electronic Engineering, Faculty of Engineering,
Mahanakorn University of Technology, Bangkok, Thailand

FAM2-2-5 **Dual Input All-Pass Networks Using MO-OTA and its Application** **129**
11:50 AM
Pipat Prommee[1], Krit Angkeaw[2], Jirasak Chanwutitum[2], Kobchai Dejhan[1]
[1]*Research Center for Communication and Information Technology (ReCCIT),*
King Mongkut's Institute of Technology Ladkrabang, Bangkok, Thailand
[2]*Industrial Electrical Technology Department, Faculty of Engineering,*
King Mongkut's Institute of Technology North Bangkok, Bangkok, Thailand

10:30 AM - 12:10 AM **Session FAM2-3** **Friday, 11 May 2007**

Electronic Devices

Chairperson : Boonying Charoen, Khon Kean University

FAM2-3-1 **A Physics-Based InP/InGaAs SHBT Model for SPICE simulation** **133**
10:30 AM
Suchat Osaklang[1], Chiranut Sangiamsak[2]
[1]*Graduate School, Department of Electrical Engineering,*
Khon Kaen University, Thailand
[2]*Department of Electrical Engineering,*
Khon Kaen University, Thailand

FAM2-3-2	**Devices Design, Fabrication and Characterizations of 0.8 µm CMOS Technology**	**137**
10:50 AM	A. Ruangphanit[1], N. Phongphanchantra [1,2], P. Meesapawong[1], C. Hruanan[1], S. Niemcharoen[2], R.Muanghlua[2] *[1]Thai MicroElectronics Center(TMEC), National Electronics and Computer Technology Center ,Chachoengsao, Thailand* *[2]Electronics Research Center, King Mongkut's Institute of Technology Ladkrabang Lampratue District, Thailand*	
FAM2-3-3	**Characteristics of GaAs-based Phototransistors after high-power operation**	**141**
11:10 AM	N. Thudsalingkarnsakul, S. Thainoi, S. Kanjanachuchai *Semiconductor Device Research Laboratory, Department of Electrical Engineering, Chulalongkorn University, Bangkok, Thailand*	
FAM2-3-4	**CMOS Digital-to-Analog Converter**	**145**
11:30 AM	Pipat Prommee[1], Krit Angkeaw[1], Kobchai Dejhan[1], Montri Somdunyakanok[2], Jirasak Chanwutitum[3] *[1]Research Center for Communication and Information Technology(ReCCIT), King Mongkut's Institute of Technology Ladkrabang, Bangkok, Thailand* *[2]Faculty of Engineering, Siam University, Bangkok, Thailand.* *[3]Industrial Electrical Technology Department, Faculty of Engineering, King Mongkut's Institute of Technology North Bangkok, Bangkok, Thailand*	
FAM2-3-5	**Degradation Characteristics of Blue Light-Emitting Diodes under Accelerated DC**	**149**
11:50 AM	**Aging Process** T. Limwongse, S. Thainoi, S. Kanjanachuchai *Semiconductor Device Research Laboratory, Department of Electrical Engineering, Faculty of Engineering, Chulalongkorn University, Bangkok, Thailand*	

1:00 PM - 3:00 PM — **Session FPM1-2** — **Friday, 11 May 2007**

Electronic Circuits

Chairperson : Boonying Charoen, Khon Kean University

FAM1-2-1	**FPGA Implementation of Acoustic Echo Canceller with Low Resource Utilization**	**153**
1:00 PM	Sompop Janyavilas[1], Ekaroon Piluck[2], Phaophak Sirisuk[3], Monai Krairiksh[1] *[1]Research Center for Communications and Information Technology (ReCCIT), King Mongkut's Institute of Technology Ladkrabang, Bangkok, Thailand* *[2]Department of Electronic Engineering, Mahanakorn University of Technology, Bangkok, Thailand* *[3]Department of Computer Engineering Mahanakorn University of Technology, Bangkok, Thailand*	
FAM1-2-2	**Analog Nonlinear Circuits Based On the Voltage Level Shift Buffer**	**157**
1:20 PM	Ittipong Chaisayun[1], Kobchai Dejhan[2] *[1]South-East Asia University Bangkok, Thailand* *[2]King Mongkut's Institute of Technology Ladkrabang Ladkrabang, Bangkok, Thailand*	
FAM1-2-3	**Quantitative Estimation of Ultrasonic Attenuation Coefficients in A Solid Immersed**	**161**
1:40 PM	**Case with Multinarrow Band Technique** M. Lohakan[1,2], N. Pueiam[1], S. Boonsang[1], C. Pintavirooj[1] *[1]Research Center for Communication and Information Technology (ReCCIT), Department of Electronics, King Mongkut's Institute of Technology Ladkrabang, Thailand* *[2]Department of Teacher Training in Electrical Engineering, King Mongkut's Institute of Technology North Bangkok, Bangkok, Thailand*	

FAM1-2-4	**High-Value Floating Controlled Resistor**	**165**
2:00 PM	Wirote Jongchanachavawat, Montree Kumngern, Kobchai Dejhan *Research Center for Communication and Information Technology (ReCCIT),* *King Mongkut's Institute of Technology Ladkrabang, Bangkok, Thailand*	
FAM1-2-5	**A Fully-Swing Adiabatic Circuit for Low Power Applications**	**168**
2:20 PM	Rungruang Sangpratheep, Kasin Vichienchom *King Mongkut's Integrated Circuits Lab (KMICL), Department of Electronics,* *King Mongkut's Institute of Technology Ladkrabang, Bangkok, Thailand*	
FAM1-2-6	**Effect of Resonances on Shielding Effectiveness in Enclosure with Apertures**	**172**
2:40 PM	P. Dangkham[1], P. Sujintanarat[1], S. Chaichana[1], K. Aunchaleevarapan[2], P. Teekaput[1] *[1]Faculty of Engineering, Chulalongkorn University, Bangkok, Thailand* *[2]Electrical and Electronic Products Testing Center, NECTEC, NSTDA,* *King Mongkut's Institute of Technology Ladkrabang, Bangkok, Thailand*	
1:00 PM - 3:00 PM	**Session FPM1-7**	**Friday, 11 May 2007**
	Microelectronics	
	Chairperson : Songphol Kanjanachuchai, Chulalongkorn University	
FPM1-7-1	**Quartz Crystal Microbalance Humidity Sensor using Electrospun PANI Sensing Layer**	**176**
1:00 PM	K. Jaruwongrungsee[1], A. Tuantranont[1], Y. Wanna[2], A. Wisitsoraat[1], T. Lomas[1] *[1]Nanoelectronics and MEMS Laboratory, National Electronics,* *Computer Technology Center Thailand Science Park, Pathumthani, Thailand* *[2]National Nanotechnology Center, Pathumthani, Thailand*	
FPM1-7-2	**Optical Gas Sensor Array Based on Metallo-Phthalocyanines and Metallo-Porphyrins**	**180**
1:20 PM	Sureeporn Uttiya[1], Teerakiat Kerdcharoen[1], Paisarn Daungjak Na Ayutthaya[2], Worawan Bhanthumnavin[3], Radchada Buntem[4], Sirapat Pratontep[5] *[1]Center of Nanoscience and Nanotechnology, Department of Physics,Faculty of Science,* *Mahidol University, Bangkok, Thailand* *[2]Institute of Science, Walailak University, Nakorn Srithammarat, Thailand* *[3]Department of Chemistry, Faculty of Science, Chulalongkorn University, Bangkok, Thailand* *[4]Department of Chemistry, Faculty of Science, Silpakorn University, Nakorn Pathom, Thailand* *[5]National Nanotechnology Center, National Science and Technology Development Agency,* *Thailand Science Park, Pathumthani, Thailand*	
FPM1-7-3	**Symmetrical Wheatstone MEMS Cantilever Sensors with On-chip Resistors for**	**184**
1:40 PM	**Temperature Feedback** Adisorn Tuantranont, K. Jaruwongrungsee, T. Lomas, A. Jomphoak, A. Wisitsoraat *Nanoelectronics and MEMS Laboratory, National Electronics and Computer Technology Center,* *Thailand Science Park, Pathumthani, Thailand*	
FPM1-7-4	**Fabrication and Characterization of Polydimethylsiloxane (PDMS) Microfluidic**	**187**
2:00 PM	**Channels** Thitima Maturos, Tanom Lomas, Adisorn Tuantranont, Anurat Wisitsora-at *Nanoelectronics and MEMS Laboratory, National Electronics and Computer Technology Center,* *Thailand Science Park, Pathumthani, Thailand*	

FPM1-7-5	**Gas Sensing Characterization of Ion-Assisted Ebeam Evaporated TiO2 Thin Films**	**191**
2:20 PM	**with Nanometer Scale Thickness**	
	A. Wisitsoraat[1], C. Promjuntuk[2], V. Patthanasettakul[1], A. Tuantranont[1]	
	[1]Nanoelectronics and MEMS Laboratory,	
	National Electronics and Computer Technology Center (NECTEC), Thailand	
	[2]Department of Physics, Faculty of Sciences and Technology,	
	Nakhonratchasima Rajabhat University, Nakhonratchasima, Thailand	
FPM1-7-6	**Maskless Etching of Microfabricated Structures with Low-Power Focused Ion Beam**	**194**
2:40 PM	Peerasak Chantngarm	
	Department of Electronics and Telecommunication Engineering,	
	Pathumwan Institute of Technology, Bangkok, Thailand	
1:00 PM - 3:00 PM	**Session TPM1-8**	**Thursday,10 May 2007**
	Control Emgineering 1	
	Chairperson : Chairperson : Kazushi Nakano, The University of Electro-Communications	
TPM1-8-1	**Fuzzy Control for Robot Manipulator Based on Geometric Error**	**198**
1:00 PM	Heydar Toossian Shandiz, Khalil Syahlooei	
	Shahrood University of Technology, Electrical Engineering Faculty, Shahrood, Iran	
TPM1-8-2	**Fuzzy Logic Based Embedded Controller for Control System Education**	**202**
1:20 PM	N. Jasungnuen, P. Janchaichanakun, P.Koseeyaporn	
	Department of Teacher Training in Electrical Engineering,	
	King Mongkut's Institute of Technology North Bangkok, Bangkok, Thailand	
TPM1-8-3	**Electromagnetic Flux Density Controlled by Fuzzy Logic Method**	**205**
1:40 PM	Satean Tunyasrirut, Santi Wangnipparnto	
	Faculty of Engineering, Pathumwan Institute of Technology, Pathumwan, Bangkok, Thailand	
TPM1-8-4	**Fuzzy I-PD Controller for Two-Link Robot Manipulator**	**209**
2:00 PM	Wicharn Chatrattanawuth[1], Songmoung Nundrakwang[1], Taworn Benjanarasuth[1],	
	Jongkol Ngamwiwit[1], Noriyuki Komine[2]	
	[1]Research Center for Communication and Information Technology (ReCCIT),	
	King Mongkut's Institute of Technology Ladkrabang, Bangkok, Thailand	
	[2]School of Information Science and Technology, Tokai University, Kanagawa, Japan	
TPM1-8-5	**A New Modal of Variable Air Volume Diffuser for Thermal Comfort based on**	**213**
2:20 PM	**Fuzzy Logic Control**	
	Yingrak Auttawaitkul[1], Veerapol Monyakul[2], Apichit Therdyothin[1]	
	[1]School of Energy, Environment and Materials,	
	King Mongkut's University of Technology Thonburi, Bangkok, Thailand	
	[2]National Science and Technology Development Agency (NSTDA),Thailand	
TPM1-8-6	**Simultaneous Perturbation Approach to Neural Control of a Flexible System**	**217**
2:40 PM	Jorge Ivan Medina Martinez[1], Kazushi Nakano[1], Umerujan Sawut[2]	
	[1]The University of Electro-Communications, Chofu-ga-oka, Chofu, Tokyo, Japan	
	[2]Nikki Co., Ltd., Kamiechi, Atsugi, Kanagawa, Japan	

3:20 PM - 5:00 PM | **Session TPM2-8** | **Thursday,10 May 2007**

Control Engineering 2

Chairperson : Pramin Artrit, Khon Kean University

TPM2-8-1 **Design of PID Controllers via Genetic Algorithm for Benchmark Systems** **221**
3:20 PM
C. Thammarat, P. Sukserm, D. Puangdownreong
Department of Electrical Engineering, Faculty of Engineering,
South-East Asia University, Bangkok, Thailand

TPM2-8-2 **A Design Method for Modified PID Controllers for Time-delay Plants and Their** **225**
3:40 PM **Application**
Kou Yamada, Takaaki Hagiwara, Yosuke Shimizu
Department of Mechanical System Engineering, Gunma Universitym, Kiryu, Gunma, Japan

TPM2-8-3 **DC Motor Identification and Tuning PID Controller Using Particle Swarm** **229**
Optimization
4:00 PM
Poomyos Payakkawan[1], Poj Tangamchit[1], Saravuth Pothiya[2]
[1]Department of Control System and Instrumentation Engineering,
King Mongkut's University of Technology Thonburi, Bangkok, Thailand
[2]Department of Electrical Engineering, North Eastern University, Khon Kaen, Thailand

TPM2-8-4 **Simplified PI Controller for Two-Inertia System** **233**
4:20 PM
Peerapon Pattanavijit[1], Songmoung Nundrakwang[1], Taworn Benjanarasuth[1],
Jongkol Ngamwiwit[1], Noriyuki Komine[2]
[1]Research Center for Communication and Information Technology (ReCCIT),
King Mongkut's Institute of Technology Ladkrabang, Bangkok, Thailand
[2]School of Information Science and Technology, Tokai University, Kanagawa, Japan

TPM2-8-5 **Hybrid PD - Sliding Mode Controller Designed for Inverted Pendulum System** **237**
4:40 PM
Samatthachai Panya[1], Jongkol Ngamwiwit[1], Taworn Benjanarasuth[1],
Songmoung Nundrakwang[1], Noriyuki Komine[2]
[1]Research Center for Communication and Information Technology (ReCCIT),
King Mongkut's Institute of Technology Ladkrabang, Bangkok, Thailand
[2]School of Information Science and Technology, Tokai University, Kanagawa, Japan

1:00 PM - 2:40 PM | **Session FPM1-3** | **Friday,11 May 2007**

Control Engineering 3

Chairperson : Wudhichai Assawinchaichote, King Mongkut's University of Technology Thonburi

FPM1-3-1 **Control Strategies of Doubly Fed Induction Generator of Wind Turbine for Maximum** **241**
1:00 PM **Active Power with Minimum Copper Losses**
Bunlung Neammanee, Somporn Sirisumrannukul
Department of Electrical Engineering, Faculty of Engineering,
King Mongkut's Institute of Technology North Bangkok, Bangkok, Thailand

FPM1-3-2 **Soft-Switching Single-Phase Inverter for Small Grid-Connected PV Systems** **245**
1:20 PM
D. Amorndechaphon[1], S. Premrudeepreechacharn[2], K. Chamnongthai[3]
[1]Department of Electrical Engineering, Naresuan University Phayao Campus, Phayao, Thailand
[2]Department of Electrical Engineering, Chiangmai University, Chiangmai, Thailand
[3]Department of Electronics and Communication Engineering,
King Mongkut's University of Technology Thonburi, Bangkok, Thailand

FPM1-3-3	**Control and Implementation of Line Side Converter for Doubly Fed Induction**	**249**
1:40 PM	**Generator of Wind Turbine**	
	Watee Sudmee, Bunlung Neammanee	
	Department of Electrical Engineering, Faculty of Engineering,	
	King Mongkut's Institute of Technology North Bangkok, Bangkok, Thailand	
FPM1-3-4	**Thermal Conductivity Tester**	**253**
2:00 PM	Santi Wangnipparnto, Tianchai Suksri	
	Faculty of Engineering, Pathumwan Institute of Technology, Bangkok, Thailand	
FPM1-3-5	**An Enhanced Adaptive Voltage Control in Gas Tungsten Arc Welding**	**257**
2:20 PM	Poolsak Koseepaporn	
	Department of Teacher Training in Electrical Engineering, Faculty of Technical Education,	
	King Mongkut's Institute of Technology North Bangkok, Bangkok, Thailand	
FPM1-3-6	**Robust Hα Fuzzy Control Design for Nonlinear Two-Time scale System with**	
2:40 PM	**Markovian Jumps based on LMI Approach**	
	Wudhichai Assawinchaichote[1], Sing Kiong Nguang[2]	
	[1]King Mongkut's University of Technology Thonburi, Bangkok, Thailand	
	[2]The Department of Electrical and Computer	
	Engineering, The University of Auckland	

10:50 AM - 12:10 AM	**Session TAM1-4**	**Thursday,10 May 2007**
	High Voltage Engineering 1	
	Chairperson : Thanapong Suwanasri, King Mongkut's Institute of Technology North Bangkok	
TAM1-4-1	**Study Effect of Different Shape of Rod-rod Gaps on Positive DC**	**261**
10:50 AM	T. Boonwern, S. Chotigo	
	Department of Electrical Engineering, Faculty of Engineering,	
	King Mongkut's University of Technology Thonburi, Bangkok, Thailand	
TAM1-4-2	**A Preliminary Study of Dissipation Factor (tan δ) in Dielectric of Cables Produced in**	**265**
11:10 AM	**Thailand**	
	A. Aurairatch, S. Kleesuwan	
	Department of Electrical Engineering, Faculty of Engineering,	
	King Mongkut's Institute of Technology North Bangkok, Bangkok, Thailand	
TAM1-4-3	**Partial Discharge Measurement for High Voltage Cable Terminators Using Air**	**269**
11:30 AM	**Compression**	
	P. Apiratikul[1], P. Boonchiam[1], B. Plangklang[1], T. Suwanasri[2]	
	[1]Department of Electrical Engineering,	
	Rajamangala University of Technology Thanyaburi, Pathumthani, Thailand	
	[2]The Sirindhorn International Thai-German Graduate School of Engineering,	
	King Mongkut's Institute of Technology North Bangkok, Bangkok, Thailand	
TAM1-4-4	**Development and Construction of Dielectric Heating Machine**	**273**
11:50 AM	Prasit Chanmontree, Ekarin Vasanasong	
	Department of Electrical Power Engineering,	
	Mahanakorn University of Technology, Bangkok, Thailand	

10:50 AM - 12:10 AM **Session TAM1-6** **Thursday,10 May 2007**

Power Electronics 1

Chairperson : Viboon Chunkag, , King Mongkut's Institute of Technology North Bangkok

TAM1-6-1 **Performance Comparison between Average-Value and Instantaneous-Value Voltage** **277**
10:50 AM **Controls of a Single-Phase AC Chopper**
E. Sugprajun, S. Polmai
Department of Electrical Engineering, Faculty of Engineering,
King Mongkut's Institute of Technology Ladkrabang, Bangkok, Thailand

TAM1-6-2 **Power Electronics-Based Fuel Cell Emulator** **281**
11:10 AM
Siriroj Sirisukprasert, Trin Saengsuwan
Department of Electrical Engineering, The Faculty of Engineering,
Kasetsart University, Bangkok, Thailand

TAM1-6-3 **The Comparative Study and Design Guidelines of a High Frequency Transformer for** **285**
11:30 AM **Improving Cross Regulation in Multiple-Output Flyback Converters**
Pairote Sangampai, Kusumal Chalermyanont, Anuwat Prasertsit, Surapon Theinmontri
Prince of Songkla University, Faculty of Engineering, Songkla, Thailand

TAM1-6-4 **Analysis and Design of Portable AC Power-pack with Full-bridge Series-loaded** **289**
11:50 AM **Resonant Converter**
Karun Wanthong, Viboon Chunkag
Department of Electrical Engineering, Faculty of Engineering,
King Mongkut's Institute of Technology North Bangkok, Bangkok, Thailand

1:00 PM - 3:00 PM **Session TPM1-4** **Thursday,10 May 2007**

Power Systems 1

Chairperson : Natthaphob Nimpitiwan, Bangkok University

TPM1-4-1 **Particle Swarm Optimization for Optimal DG Placement in Distribution System** **293**
1:00 PM
W. Krueasuk, W. Chankaipol, S. Hintamai, K. Chayakulkheeree
Power System and Electrical Energy Research Group,
Department of Electrical Engineering, Sripatum University, Bangkok, Thailand

TPM1-4-2 **A Graph Theory Approach in Reliability Improvement of a Radial Distribution System** **297**
1:20 PM **with PV Grid-Connected Systems**
P. Sritakaew[1], A. Sangswang[2]
[1]*Department of Electrical Engineering, Faculty of Engineering,*
Rajamangala University of Technology Lanna Chiangrai, Chiangrai, Thailand
[2]*Department of Electrical Engineering, Faculty of Engineering,*
King Mongkut's University of Technology Thonburi, Bangkok, Thailand

TPM1-4-3 **Analysis of AC Losses in Superconducting Transmission Line** **301**
1:40 PM
T. Satiramatekul
Department of Computer Engineering, Kasetsart University, Kamphaengsaen Campus, Thailand

TPM1-4-4 **Power Quality Improvement by Use of a New Topology of Fault Current Limiter** **305**
2:00 PM
Seyed Hossein Hosseini[1], M. Abapour[2], M. Tarafdar Hagh[2]
[1]*Electrical Engineering Department, Islamic Azad University of Bonab, Bonab, Iran*
[2]*Faculty of Electric & Electronic Engineering, University of Tabriz, Tabriz, Iran*

TPM1-4-5 **2:20 PM**	**Genetic Algorithm Application for DSP-Based Maximum Power Point Tracking in PV Generation System** Somsak Senapukdee, Ekarin Vasanasong *Department of Electrical Power Engineering,* *Mahanakorn University of Technology, Bangkok, Thailand*	**309**
TPM1-4-6 **2:40 PM**	**Adaptive Characteristic of Mho Distance Relay for Compensation of the Phase to Phase Fault Resistance** D. Surachet, T. Saengsuwan *Department of Electrical Engineering, Kasetsart University, Bangkok, Thailand*	**313**

1:00 PM - 3:00 PM **Session TPM1-6** **Thursday,10 May 2007**

Power Electronics 2

Chairperson : Itsada Boonyaroonate, King Mongkut's University of Technology Thonburi

TPM1-6-1 **1:00 PM**	**A Novel Control Method of a Switched-Capacitor AC-DC Converter for Small Power Applications** Kei Eguchi[1], Hongbing Zhu[2], Ichirou Oota[3], Shinya Terada[4], Fumio Ueno[4] *[1]Faculty of Education, Shizuoka University, Shizuoka, Japan* *[2]Department of Computer Science,* *Hiroshima Kokusai Gakuin University, Nakano Aki-ku, Hiroshima, Japan* *[3]Department of Information and Communication,* *Kumamoto National College of Technology, Kumamoto-ken, Japan* *[4]Department of Electrical System and Computer Engineering,* *Sojo University, Ikeda, Kumamoto, Japan*	**317**
TPM1-6-2 **1:20 PM**	**Approximate 2DOF Digital Control for DC-DC Converter with Additional Zeros** Eiji Takegami[1], Kohji Higuchi[2], Kazushi Nakno[2], Satoshi Tomioka[1], Kazushi Watanbe[1] *[1]DENSEI-LAMBDA K.K., Togawa, Settaya, Nagaoka, Japan* *[2]Department of Electronic Engineering,* *University of Electro-Communications, Chofu, Tokyo, Japan*	**321**
TPM1-6-3 **1:40 PM**	**New Automatic Multi-Stage Bumpless Mode Switching Digital Control for PWM Power Amplifier using Load Estimation** Ryosuke Okazaki[1], Koji Matsushita[2], Kohji Higuchi[1], Kazushi Nakano[1], Tatsuyoshi Kajikawa[1], Fumiho Chino[2] *[1]Department of Electronic Engineering,* *The University of Electro-Communications, Chofu, Tokyo, Japan* *[2]NF Corporation, Tunashimahigashi,Kohoku-ku, Yokohama, Japan*	**325**
TPM1-6-4 **2:00 PM**	**A Quasi-Constant Frequency Hysteretic Current-Programmed Converters with Control of Bifurcation** Noppadol Khaehintung[1], Chaiboon Kangsajian[1], Phaophak Sirisuk[2] *[1]Department of Control and Instrumentation Engineering,* *Mahanakorn University of Technology, Bangkok, Thailand* *[2]Department of Computer Engineering, Mahanakorn University of Technology, Thailand*	**329**

TPM1-6-5	**The Adaptive P&O Algorithm with a Hysteretic Current-mode Converter for**	**333**
2:20 PM	**a Solar-powered Battery Charger**	
	Noppadol Khaehintung[1], Phaophak Sirisuk[2]	
	[1]Department of Control and Instrumentation Engineering,	
	Mahanakorn University of Technology, Bangkok, Thailand	
	[2]Department of Computer Engineering,	
	Mahanakorn University of Technology, Bangkok, Thailand	
TPM1-6-6	**Proposal for Simple Repetitive Controllers**	**337**
2:40 PM	Kou Yamada, Hiroshi Takenaga, Yusuke Saitou, Keiji Satoh	
	Department of Mechanical System Engineering, Gunma University, Kiryu, Gunma Japan	
3:20 PM - 5:00 PM	**Session TPM2-4**	**Thursday,10 May 2007**
	High Voltage Engineering 2	
	Chairperson : Kittipong Tanmitr, Khon Kaen University	
TPM2-4-1	**Dielectric Investigation of Fresh Fruits**	**341**
3:20 PM	K. Tonmitr, A. Kaewrawang, S. Swatdiponphallop, A. Suksri,	
	A. Siritaratiwat, P.Bursri	
	Department of Electrical Engineering, Khon Kaen University, Khon Kaen, Thailand	
TPM2-4-2	**Construction of A 100 kV Capacitive Voltage Divider**	**345**
3:40 PM	J.Sarasook, S. Chotigo, B.Puengsiri	
	Department of Electrical Engineering, Faculty of Engineering,	
	King Mongkut's University of Technology Thonburi, Bangkok, Thailand	
TPM2-4-3	**The Hydrophobic of Polymeric Insulator under Industrial Dust Pollution and**	**349**
4:00 PM	**A Comparison with Artificial Pollution**	
	Apisit Chaisaengsukkul, Norasage Pattanadech, Siriwat Potivejkul	
	Electrical Engineering Department, Faculty of Engineering,	
	King Mongkut's Institute of Technology Ladkrabang, Bangkok, Thailand	
TPM2-4-4	**A Comparison of Corona Inception Phenomena between Porcelain and Polymeric**	**353**
4:20 PM	**Insulators under Dust Pollution in Thailand**	
	Apisit Chaisaengsukkul, Siriwat Potivejkul, Norasage Pattanadech	
	Electrical Engineering Department, Faculty of Engineering,	
	King Mongkut's Institute of Technology Ladkrabang, Bangkok, Thailand	
TPM2-4-5	**Modulation Circuit for VLF Transformer**	**357**
4:40 PM	S. Chotigo, S. Seesanga	
	Department of Electrical Engineering, Faculty of Engineering,	
	King Mongkut's University of Technology Thonburi, Bangkok, Thailand	
3:20 PM - 5:00 PM	**Session TPM2-6**	**Thursday,10 May 2007**
	Power Electronics 3	
	Chairperson : Itsada Boonyaroonate, King Mongkut's University of Technology Thonburi	
TPM2-6-1	**The Challenges of Near-Future EMC Facility**	**361**
3:20 PM	Vichate Ungvichian	
	EMI Lab., Florida Atlantic University, Boca Raton, Florida	

TPM2-6-2 **3:40 PM**	**Development of an FPGA-Based Gate Signal Generator for a Flying-Capacitor Inverter** S. Khummanee, S.Polmai *Department of Electrical Engineering, Faculty of Engineering,* *King Mongkut's Institute of Technology Ladkrabang , Bangkok, Thailand*	**366**
TPM2-6-3 **4:00 PM**	**Comparison Between Phase- and Level-shifted PWM Schemes for Flying Capacitor Multilevel Inverter** S. Ketsakoon, S. Polmai *Department of Electrical Engineering, Faculty of Engineering,* *King Mongkut's Institute of Technology Ladkrabang , Bangkok, Thailand*	**370**
TPM2-6-4 **4:20 PM**	**A New Online Control Method for Multicell Converter Based on Duty Cycle Control** Seyed Hossein Hosseini[1], M. Almaleki[2] [1]*Department Electrical Engineering, Islamic Azad University of Bonab, Bonab, Iran,* [2]*Faculty of Electric & Electronic Engineering, University of Tabriz, Tabriz, Iran*	**374**
TPM2-6-5 **4:40 PM**	**A High-Frequency Induction Cooker using Quasi-resonant Converter** Saichol Chudjuarjeen[1], Chayant Kumpai[2] [1]*Department of electrical engineering, Rajamangala University of Technology Krungthep, Rajamangala University of Technology Krungthep, Bangkok, Thailand* [2]*Department of electrical engineering, King Mongkut's University of Technology Thonburi, King Mongkut's University of Technology Thonburi, Bangkok, Thailand*	**378**

8:30 AM - 9:50 AM **Session FAM1-4** **Friday,11 May 2007**

Power Systems 2

Chairperson : Ekarin Vasanasong, Mahanakorn University of Technology

FAM1-4-1 **8:30 AM**	**New Method in Nonlinear State Estimation Single Machine Infinite Bus** Heydar Toossian Shandiz, Ahmad Hajipoor *Shahrood University of Technology, 7 Th Tir Square, Shahrood, Iran*	**382**
FAM1-4-2 **8:50 AM**	**Assessment of Reliability Worth in Distribution Systems with Substation Originated Outage by Sequential Monte Carlo Simulation** Somchai Songsiri, Somporn Sirisumrannukul *Department of Electrical Engineering, Faculty of Engineering,* *King Mongkut's Institute of Technology North Bangkok, Bangkok, Thailand*	**386**
FAM1-4-3 **9:10 AM**	**Detailed Analysis of Load Voltage Compensation** Paisan Boonchiam[1], Nadarajah Mithulananthan[2] [1]*Department of Electrical Engineering,* *Rajamangala University of Technology Thanyaburi, Pathumthani, Thailand* [2]*Energy Field of Study, Asian Institute of Technology, Thailand*	**390**
FAM1-4-4 **9:30 AM**	**A New Voltage dip and Grid Unbalance Detection Method for Distribution Static Synchronous Compensator Application** Thip Manmek[1], Chathura P. Mudannayake[2], Colin Grantham[2] [1]*Department of Control and Instrumentation Engineering,* *Mahanakorn University of Technology, Bangkok, Thailand* [2]*School of Electrical Engineering and Telecommunication,* *The University of New South Wales, Sydney, Australia*	**394**

10:30 AM - 12:10 AM **Session FAM2-4** **Friday,11 May 2007**

Electric Machinery

Chairperson : Ekarin Vasanasong, Mahanakorn University of Technology

FAM2-4-1 **Starting Jerk Reduction for Switched Reluctance Motors Using Initial Rotor Position** **398**
10:30 AM **Estimation Method**
P. Jitkreeyarn[1, 2], K. Tungpimolrut[1], P. Nakmahachalasint[2]
[1]*National Electronics and Computer Technology Center, Thailand Science Park, Pathumthani, Thailand*
[2]*Faculty of Engineering, Thammasat University, Pathumthani, Thailand*

FAM2-4-2 **Linear Model of a Switched Reluctance Machine using Flux Tube Analysis** **402**
10:50 AM C. Boonkham, S. Kittiratsatcha
Department of Electrical Engineering, Faculty of Engineering, King Mongkut's Institute of Technology Ladkrabang, Bangkok, Thailand

FAM2-4-3 **Field Efficiency Estimation Technique for Inverter-Fed Induction Motor** **406**
11:10 AM T.Phumiphak[1] , C. Chat-uthai[2]
[1]*Department of Electrical Power Engineering, Mahanakorn University of Technology, Bangkok, Thailand*
[2]*Department of Electrical Engineering, King Mongkut's Institute of Technology Ladkrabang, Bangkok, Thailand*

FAM2-4-4 **Design of Economical Small Transformer Base on Temperature Rise Evaluation** **410**
11:30 AM T.Phophongviwat[1], C. Chat-uthai[2]
[1]*Department of Electrical Power Engineering, Mahanakorn University of Technology, Bangkok, Thailand*
[2]*Department of Electrical Engineering, King Mongkut's Institute of Technology Ladkrabang, Bangkok, Thailand*

FAM2-4-5 **Steady State and Dynamic Behaviors of Doubly Fed Induction Machines in Wind** **414**
11:50 AM **Energy Conversion Systems**
S. Wangsathitwong[1], S. Sirisumrannukul[1], S. Chatratana[2], W. Deleroi[3]
[1]*King Mongkut's Institute of Technology North Bangkok, Bangkok, Thailand*
[2]*Technology Management Center, National Science and Technology Development Agency, Thailand Science Park, Phatumthani, Thailand*
[3]*B-4728 Corsostraße 3, Hergenrath, Belgium*

10:30 AM - 11:50 AM **Session FAM2-10** **Friday,11 May 2007**

SS : Electrical Power

Chairperson : Natthaphob Nimpitiwan, Bangkok University

FAM2-10-1 **Design of Power Transformer Winding Fault Model using PSCAD/EMTDC** **418**
10:30 AM Dusit Uthitsunthorn, Teratam Bunyagul
Department of Electrical Engineering, Faculty of Engineering, King Mongkut's Institute of Technology North Bangkok, Bangkok, Thailand

FAM2-10-2 **10:50 AM**	**A study of Efficiency Improvement Tracking Algorithm for Maximum Power Point Tracking of Photovoltaic System** Chamnan. Ratsame[1], Tanes. Tanitteeapan[1], Sirichai. Thepa[2], Narong. Mungkung[1], Itsda Boonyaroonate[3] *[1]Department of Electrical Technology Education,* *[2]Division of Energy Technology,* *[3]Department of Electrical Engineering,* *King Mongkut 's University of Technology Thonburi, Bangkok, Thailand*	**422**
FAM2-10-3 **11:10 AM**	**Vibration Signal Analysis for Condition Monitoring of High Voltage Circuit Breakers** T. Suwanasri[1], N. Charbkeaw[2], T. Bunyagul[2] *[1]The Sirindhorn International Thai-German Graduate School of Engineering* *King Mongkut's Institute of Technology North Bangkok, Bangkok, Thailand* *[2]Electrical Engineering Department, Faculty of Engineering* *King Mongkut's Institute of Technology North Bangkok, Bangkok, Thailand*	**426**
FAM2-10-4 **11:30 AM**	**Generator Participating Factors for Sensitivity Analysis in a Deregulated Electricity Supply Industry** C. Adsoongnoen[1], T. Suwanasri[2] *[1]Department of Electrical and Computer Engineering, Faculty of Engineering,* *Naresuan University Phitsanulok, Thailand* *[2]The Sirindhorn International Thai-German Graduate School of Engineering,* *King Mongkut's Institute of Technology North Bangkok, Bangkok, Thailand*	**430**

1:00PM - 3:00PM	**Session FPM1-4** **Power Systems 3** Chairperson : Surachai Limyingcharoen, Khon Kaen University	**Friday,11 May 2007**
FPM1-4-1 **1:00 PM**	**A Network Topology Processor for Accurate Power System State Estimation** Warayut Kampeerawat[1], Surachai Limyingcharoen[2], Anupap Meesomboon[2] *[1]Graduate School, Department of Electrical Engineering, Khon Kaen University, Thailand* *[2]Department of Electrical Engineering, Khon Kaen University, Thailand*	**434**
FPM1-4-2 **1:20 PM**	**Topology Error Detection by Using Fast Approximate Power Flow with Power Transfer Distribution Factors (PTDFs)** Warayut Kampeerawat[1], Anupap Meesomboon[2] *[1]Graduate School, Department of Electrical Engineering, Khon Kaen University, Thailand* *[2]Department of Electrical Engineering, Khon Kaen University, Thailand*	**438**
FPM1-4-3 **1:40 PM**	**Ant Colony Optimization to Solve the Economic Dispatch Problem with Nonsmooth Cost Functions** Phakhapong Thanitakul, Yuttapoom Chernklang, Wisut Somsamai, Saravuth Pothiya *Department of Electrical Engineering, North Eastern University, Khon Kaen, Thailand*	**442**
FPM1-4-4 **2:00 PM**	**Relevant Factors for Failure Rate Estimation of Overhead Distribution Feeders** N. Teera-achariyakul, D. Rerkpreedapong *Department of Electrical Engineering, Kasetsart University, Bangkok, Thailand*	**446**

FPM1-4-5 **2:20 PM**	**Congestion Management in a Hybrid Pool and Bilateral Market** Komson Daroj[1], Bundhit Eua-Arporn[2] *Department of Electrical Engineering, Faculty of Engineering,* *[1]Ubonratchathani University ,Ubonratchathani, Thailand* *[2]Chulalongkorn University ,Bangkok, Thailand*	**450**
FPM1-4-6 **2:40 PM**	**Fault Diagnosis in Transmission Systems for Alarm Processing by Fuzzy Relation and Fault Tree Analysis** Radomboon Taksana, Somporn Sirisumrannukul *Department of Electrical Engineering, Faculty of Engineering,* *King Mongkut's Institute of Technology North Bangkok, Bangkok, Thailand*	**454**

3:20 PM - 5:00 PM — **Session FPM2-4** — **Friday,11 May 2007**

Power Systems 4

Chairperson : Teratam Bunyagul, King Mongkut's Institute of Technology North Bangkok

FPM2-4-1 **3:20 PM**	**Analysis of Substation Ground Grid for Ground Potential Rise Effect Reduction in Two-Layer Soil** A. Puttarach, N. Chakpitak , T. Kasirawat, C. Pongsriwat *ChiangMai University , ChiangMai, Thailand*	**458**
FPM2-4-2 **3:40 PM**	**Design of Automatic Generation Control Using the Method of Inequalities** Raksanai Nidhiritdhikrai, Suchin Arunsawatwong, Bundhit Eua-arporn *Department of Electrical Engineering, Faculty of Engineering,* *Chulalongkorn University, Bangkok, Thailand*	**462**
FPM2-4-3 **4:00 PM**	**Optimal Feeder Routing in Distribution System with Demand Uncertainty** S. Wattanasophona[1], B. Eua-Arpornb[2] *[1]Department of Electrical Engineering, Faculty of Engineering,* *Dhurakij Pundit University, Bangkok, Thailand* *[2]Department of Electrical Engineering, Chulalongkorn University, Bangkok, Thailand*	**466**
FPM2-4-4 **4:20 PM**	**Optimal Capacitor Banks Placement and N-1 Contingency Improvement Using Excels Solver: Case of Laos PDR.** S. Hungsasutra, A.Suksri, J. Triyangkulsri, M. Vonglokham *Department of Electrical Engineering, Faculty of Engineering,* *Khon Kaen University, Khon Kaen, Thailand*	**470**
FPM2-4-5 **4:40 PM**	**Voltage Sag Compensation Capability by Parallel Type Compensator with Series Inductor** Sumate Naetiladdanon *Department of Electrical Engineering* *King Mongkut's University of Technology Thonburi, Bangkok, Thailand*	**474**

8:30 AM - 10:10 AM	Session FAM1-7	Friday,11 May 2007

Material Technology

Chairperson : Chanchana Thanachaynont, National Metal and Materials Technology Center

FAM1-7-1 **8:30 AM**	**Application of Nanoporous Silicon for Visible Light Photodetector** N. Atiwongsangthong, S. Niemcharoen, K. Sato, W. Titiroongruang *Electronics Research Center, Faculty of Engineering,* *King Mongkut's Institute of Technology Ladkrabang, Bangkok, Thailand*	**478**
FAM1-7-2 **8:50 AM**	**Computational Molecular Modeling and Simulation of Functionalized Carbon Nanotubes** Chatchawal Wongchoosuk[1], Sriprajak Krongsuk[2], Teerakiat Kerdcharoen[1,3] [1]*Department of Physics and Center of Nanoscience and Nanotechnology, Mahidol University, Bangkok, Thailand* [2]*Department of Physics, Khon Kaen University, Khon Kaen, Thailand* [3]*Networked Laboratory of Nanodevice Engineering, National Nanotechnology Center, Pathumthani, Thailand*	**482**
FAM1-7-3 **9:10 AM**	**The Electronic and Energetic Properties of Linearly Fused Single-walled Carbon Nanotubes by Pentagon-Heptagon Pair Defects** Md.Shafiqzzaman[1], Anurak Udomvech[1,2], Teerakiat Kerdcharoen[1] [1]*Department of Physics and Center of Nanoscience and Nanotechnology, Mahidol University, Bangkok, Thailand* [2]*Department of Physics, Thaksin University, Songkhla, Thailand*	**485**
FAM1-7-4 **9:30 AM**	**Optical Profiling on Lateral Spreading of Space-Charge-Region Metal-Semiconductor-Metal Structures** S.Khunkhao[1], A.Thaworn[1], S.Somdetsakun[1], S.Nuanloy[1], S.Korchareon[2], S. Niemcharoen[2] [1]*Department of Electrical engineering, Sripatum University, Bangkok, Thailand* [2]*Electronics Research Center, Faculty of Engineering, King Mongkut's Institute of Technology Ladkrabang, Bangkok, Thailand*	**489**
FAM1-7-5 **9:50 AM**	**Influences of Fabrication Process on Aggregation of Conjugated Polymer in Thin Films and its Roles on the Performance of Plastic Solar Cells** Kasin Kasemsuwan[1], Chanchana Thanachayanont[2], Rakchart Traiphol[3], Teerakiat Kerdcharoen[1] [1]*Department of Physics and Center of Nanoscience and Nanotechnology, Mahidol University, Thailand* [2]*National Metal and Materials Technology Center, Thailand* [3]*Department of Chemistry, Faculty of Science, Naresuan University, Thailand*	**493**

10:30 AM - 12:10 AM | **Session FAM2-7** | **Friday,11 May 2007**

Biologocal EE

Chairperson : Werapon Jiracharit, King Mongkut's University of Technology Thonburi

FAM2-7-1 **Application of an Electronic Nose for Body Odor Recognition: Opportunity and Problem** **497**
10:30 AM
Sanchai Harnsoongnoen[1], Mario Lutz[2], Neti Waranuch[3], Adisorn Tuantranont[4], Teerakiat Kerdcharoen[2]
[1]Department of Physics, Faculty of Science, Mahasarakham University, Mahasarakham, Thailand
[2]Department of Physics and Center of Nanoscience and Nanotechnology, Faculty of Science, Mahidol University, Bangkok, Thailand
[3]Cosmetics and Natural Products Research Center, Faculty of Pharmaceutical Sciences, Naresuan University, Phitsanuloke, Thailand
[4]Nanoelectronic and MEMS Lab, National Electronic and Computer Technology Center, Pathumthani, Thailand

FAM2-7-2 **Lighting System for Growth Enhancement of Thai Orchids** **501**
10:50 AM
Phanumas Khumsat, Kamplon Panprayoon
Department of Electrical Engineering, Prince of Songkla Univesity, Hat-Yai, Thailand

FAM2-7-3 **Electronic Nose System for Orange Juice Freshness Quality Control** **505**
11:10 AM
Wattanasit Pimpao[1, 2], Assawapong Sappat[1], Teerakiat Kerdcharoen[3], Manas Sangworasil[2]
[1]Nanoelectronics and MEMS Laboratory, National Electronics and Computer Technology Center (NECTEC), Thailand Science Park, Pathumthani, Thailand
[2]Department of Electronics, Faculty of Engineering, King Mongkut's Institute of Technology Ladkrabang, Bangkok, Thailand
[3]Department of Physics, Center of Nanoscience and Nanotechnology, Faculty of Science, Mahidol University, Bangkok, Thailand

FAM2-7-4 **A Wireless Heart Rate Monitor for Fitness Exercise Researches Using 2.4 GHz RF Transceivers** **509**
11:30 AM
W. Siwaprapakorn[1], B. Charoen[2]
[1]Graduate School, Faculty of Engineering, Khon Kaen University, Thailand
[2]Department of Electrical Engineering, Faculty of Engineering, Khon Kaen University, Thailand

FAM2-7-5 **An Algorithm of 3D Objects Connection for Dental Bridge Design** **513**
11:50 AM
Teeraporn Kusalanukhun, Chanjira Sinthanayothin, Wichit Tharanon
Advanced Dental Technology Center (ADTEC), National Science and Technology Development Agency (NSTDA), Thailand Science Park, Pathumthani, Thailand

1:00 PM - 3:00 PM | **Session FPM1-6** | **Friday,11 May 2007**

Biometric

Chairperson : Somying Thainimit, Kasetsart University

FPM1-6-1 **Adaptive Thresholding for Iris Recognition** **517**
1:00 PM
Peeranat Thoonsaengngam, Somying Thainimit
Kasetsart Signal and Image Processing Laboratory (KSIP Lab), Department of Electrical Engineering, Kasetsart University, Bangkok, Thailand

FPM1-6-2	**On-Line Signature Verification Based on Time-Frequency Characteristics**	**521**
1:20 PM	**of Barycenter Trajectory**	
	P.Thumwarin[1], N.Suthithummathat[1], T.Matsuura[2]	
	[1]Research Center for Communications and Information Technology,	
	King Mongkut's Institute of Technology Ladkrabang, Bangkok, Thailand	
	[2]Faculty of Information Technology and Electronics, Tokai University, Japan	
FPM1-6-3	**Signature Identification Using Linear Predictive Code Coefficients and Neural Network**	**525**
1:40 PM	T. Wijitpornchai, J. Koseeyaporn, P. Wardkein	
	Department of Telecommunication Engineering, Faculty of Engineering,	
	King Mongkut's Institute of Technology Ladkrabang, Bangkok, Thailand	
FPM1-6-4	**Generalized N-Tuple Machine on Signature Verification**	**529**
2:00 PM	Phongsan Nunsuk, Yuttana Kitjaidure	
	King Mongkut's Institute of Technology Ladkrabang, Bangkok, Thailand.	
FPM1-6-5	**Detection Segment Retinal Blood Vessel of Anatomical Structures in Retinal Image**	**533**
2:20 PM	Chaichana Thanapong[1], Sookpotharom Supot[1,2], Turmchokkasam Sirichai[2],	
	Pintavirooj Chuchart[1], Sangworasil Manas[1,2]	
	[1]Faculty of Engineering, Computer Research and Service Center,	
	King Mongkut's Institute of Technology Landkrabang, Bangkok, Thailand	
	[2]School of Engineering, Bangkok University, Pathumtani, Thailand	
FPM1-6-6	**Identification of Carcinoma in Situ from Segmented Squamous Cervical Cells**	**537**
2:40 PM	C. Aupayagoson, W. Chiracharit, K. Chamnongthai	
	Department of Electronic and Telecommunication Engineering,	
	King Mongkut's University of Technology Thonburi, Bangkok, Thailand	

1:00 PM - 3:00 PM	**Session FPM1-10**	**Friday,11 May 2007**
	SS : Hard Disk Drives	
	Chairperson : Kamon Jirasereeamornkul, King Mongkut's University of Technology Thonburi	
FPM1-10-1	**Effect of D.C. Field-Induced Breakdown on GMR Heads at Slider-Bar Level**	**541**
1:00 PM	A. Siritaratiwat [1,2], N. Suwannata[2], C. Sukprong [2]	
	[1]Industrial/University Cooperative Research Center in HDD Component,	
	Khon Kaen University, Khon Kaen, Thailand	
	[2]Department of Electrical Engineering, Khon Kaen University, Khon Kaen, Thailand	
FPM1-10-2	**A Study of RFID-Electromagnetic Field Effect on Recording Heads in Writing Process**	**545**
1:20 PM	A. Pratoomthip[1,2], C. Sa-ngiamsak[2], A. Siritaratiwat[2]	
	[1]Graduate school, Khon Kaen University, Thailand	
	[2]Department of Electrical Engineering, Khon Kaen University, Thailand	
FPM1-10-3	**The Effect of Head Protrusion on Recording Field for Perpendicular Recording System**	**549**
1:40 PM	D. Tongsomporn[1], A. Siritaratiwat [2], N. Afzulpurkar[3], B. Bargmann[4]	
	[1]Microelectronics Field of Study, Asian Institute of Technology, Thailand	
	[2]KKU-Seagate Cooperation Research Laboratory, Department of Electrical Engineering,	
	Khon Kaen University, Thailand	
	[3]School of Engineering and Technology, Asian Institute of Technology, Thailand	
	[4]Seagate Technology (Thailand) Co., Ltd., Nakorn Ratchasima, Thailand	

FPM1-10-4	**Design of High-Rate Modified Array Codes for Magnetic Recording System**	**553**
2:00 PM	W. Singhaudom, S. Noppanakeepong, P. Suphithi *Research Center for Communications and Information Technology (ReCCIT),* *I/U CRC in Data Storage Technology and Applications,* *King Mongkut's Institute of Technology Ladkrabang, Bankok, Thailand*	
FPM1-10-5	**Subblock Encoder Design of Modified Array-Based Low-Density Parity-Check Codes**	**557**
2:20 PM	P. Leekul[1], S. Chivapreecha[1], K. Sripimanwat[2], P. Supnithi[1] [1]*Research Center for Communications and Information Technology,* *I/U CRC in Data Storage Technology and Applications,* *King Mongkut's Institute of Technology Ladkrabang, Bangkok, Thailand* [2]*National Electronics and Computer Technology (NECTEC),* *Thailand Science Park, Patumthani, Thailand*	
FPM1-10-6	**Timing Recovery in Magnetic Recording Systems**	**561**
2:40 PM	Piya Kovintavewat *Faculty of Science and Technology,* *Nakhon Pathom Rajabhat University, Nakhon Pathom, Thailand*	
3:20 PM - 5:00 AM	**Session FPM2-2**	**Friday,11 May 2007**
	Medical Technology Chairperson : Supawadee Swatdiponphallop, Khon Kaen University	
FPM2-2-1	**ECG Classification Using Fisher's Discriminant and Fuzzy c-mean**	**565**
3:20 PM	Sayan Rakbanjong, Yuttana Kitjaidure *King Mongkut's Institute of Technology Ladkrabang, Bangkok, Thailand*	
FPM2-2-2	**ECG Data Compression by Wavelet-Based Average Beat Subtraction (WABS)**	**569**
3:40 PM	S. Pathoumvanh[1], S. Airphaiboon[1], M. Sangworasil[1], K. Hamamoto[2] [1]*Research Center for Communications and Information Technology (ReCCIT),* *King Mongkut's Institute of Technology Ladkrabang, Bangkok, Thailand* [2]*Tokai University, Information Media Technology Department, Kanagawa, Japan*	
FPM2-2-3	**Classification of Muscular Contraction Using EMG Topological Mapping**	**573**
4:00 PM	D. Sueaseenak[1,3], T. Chanwimalueang[1], K. Wong-ek[2], N. Laoopugsin[3], C. Pintavirooj[1] [1]*Research Center for Communication and Information Technology (ReCCIT),* *Department of Electronics, King Mongkut's Institute of Technology Ladkrabang, Bangkok, Thailand* [2]*Department of Medical Technology, Faculty of Applied Health Science,* *Thammasat University, Pratumthanee, Thailand* [3]*Faculty of Medicine, Srinakharinwirot University, Nakorn Nayok, Thailand*	
FPM2-2-4	**An Automatic Classification of Microcalcification Clusters Using Shape and**	**577**
4:20 PM	**Distribution Features** W. Chiracharit *Department of Electronic and Telecommunication Engineering,* *King Mongkut's University of Technology Thonburi, Bangkok, Thailand*	
FPM2-2-5	**3D Shape-Recovery System Based on Photographic Tomography with Flexible Camera**	**581**
4:40 PM	**Orientation** P. Greesuradej, S. Gimjumpa, M. Sangworasil, C. Pintavirooj *Research Center for Communications and Technology (ReCCIT),* *King Mongkut's Institute of Technology Ladkrabang, Bangkok, Thailand*	

3:20 PM - 4:40 PM | **Session FPM2-3** | **Friday,11 May 2007**

General EE

Chairperson : Punnarumol Temdee, Mae Fah Luang University

FPM2-3-1	**Production Planning and Scheduling Approach in a Supply Chain**	**585**
3:20 PM	R. Masuchun *Faculty of Engineering, King Mongkut's Institute of Technology Ladkrabang, Bangkok, Thailand*	
FPM2-3-2	**Distributed Context Aware System for Travel Time Estimation Based on**	**589**
3:40 PM	**Cellular Probes in Metropolitan Environment** Panraphee Raphiphan[1], Arkady Zaslavsky[1], Wasan Pattara-Atikom[2], Passakon Prathombutr[2] [1]*Caufield School of Information Technology, Monash University, Caulfield East, Australia* [2]*National Electronics and Computer Technology Center,* *Thailand Science Park, Pathumthani, Thailand*	
FPM2-3-3	**Ontology Development: An Integrated Engineering Approach**	**593**
4:00 PM	Paola Di Maio *School of Information Technology, Mae Fah Luang University, Chiang Rai, Thailand*	
FPM2-3-4	**A Satellite Collision Analysis During Orbit Deployment**	**597**
4:20 PM	Manop Aorpimai, Peerawat Artitthang *Department of Control and Instrumentation Engineering,* *Mahanakorn University of Technology, Bangkok, Thailand*	

High Frequency, High Precision CMOS Half-Wave Rectifier

Montree Kumngern and Kobchai Dejhan
Faculty of Engineering and Research Center for Communication and Information Technology,
King Mongkut's Institute of Technology Ladkrabang, Bangkok 10520, Thailand
Tel: 66-2326-4238, 66-2326-4242, Fax: 66-2326-4554,
E-mail: montree_kumngern@yahoo.com, kobchai@telecom.kmitl.ac.th

***Abstract*–In this paper, a high frequency and high precision CMOS half-wave rectifier circuit with positive and negative outputs is presented. The proposed circuit consists of a voltage-to-current converter, a precision current-mode rectifier with operating in class-AB, and two current-to-voltage converters. A voltage input signal is changed into a current signal by the voltage-to-current converter. The class-AB current mode rectifiers rectify these current signals, resulting in positive and negative half-wave current signals that are converted to positive and negative half-wave voltage signals by the current-to-voltage converters. The circuit exhibits low component counts, high frequency operation, good temperature stability and suitable of IC fabrication. The simulation results are used to verify the performance of the proposed circuit. Simulated rectifier performance with standard 0.5μm CMOS technology using ±1.2V supply voltage shows the proposed half-wave rectifier circuit provides an operating frequency more than 250MHz and excellent temperature stability.**

I. INTRODUCTION

Precision rectifier is one of important nonlinear circuits extensively used in wattmeter, AC voltmeter, RF demodulator, function fitting, triangular-wave frequency doubling, error measurements and RMS to DC conversions. Usually, a rectifier can be realized by using diodes but diode rectifier is limited by the threshold voltage of diodes. As a result diode-only rectifiers are used in only those applications in which the precision in the range of threshold voltage is insignificant, such as RF demodulators and DC voltage supply rectifiers. To overcome this problem is based on the use of operational amplifiers (op-amps), diodes, and resistors [1]-[4]. However, the classical problem with conventional precision rectifiers based on op-amps and diodes is that during the non-conduction/conduction transition of the diodes the op-amps must recover with a finite small-signal dv/dt (slew-rate) resulting in significant distortion during the zero crossing of the input signal. Moreover, op-amps-based precision rectifier circuits are limited to a frequency performance well below the gain-bandwidth product (GBW) of op-amps [5]. This problem was improved by designing the rectifier circuit by the use of the current rectifying techniques [5]-[11]. The current conveyors-based current-mode rectifier circuits were presented in [5]-[7] enjoy the high precision. However, the proposed circuits require a floating resistor and grounded resistors, which is not ideal for IC implementation and some of these have problem about temperature stability [5],[6]. In [7] was realized a current-mode rectifier circuit based on the use of one current conveyor and bipolar transistors operating in class-B, this circuit is a realization that enjoys the high precision rectifier. However, the two grounded resistors are used and the high frequency performance is limited in this scheme. In [8]-[9] proposed the current-mode CMOS rectifier circuits operating in class-AB. This technique requires the signal current to be greater than four times of the bias current to avoid the square-law error of MOS transistors. However, the circuit features wide-band capability. Recently, a dual output CMOS half-wave rectifier circuit has been proposed in [10]. This circuit composed of two sections. The first is rectifier circuit uses the V-I converter to change the input voltage into currents, the diodes to rectify the currents, and the I-V converters to change the rectified currents into the output voltage. Second is the bias voltage source circuit, it used the diodes bias voltages to clad the output voltage excursion during the zero crossings. The advantages of this circuit are: (i) all of MOS transistors are used, thus the circuit suitable for IC fabrication, (ii) employs a ±1.2V supply voltage and provides an operating frequencies up to 100MHz, and (iii) high accuracy and good temperature stability by using the bias voltage source circuit. In [11] proposed a rectifier circuit by using all MOS transistors suitable for IC fabrication and high operating frequency up to 200MHz.

In this paper, a high frequency CMOS half-wave rectifier circuit is presented. The proposed circuit consists of a voltage-to-current converter, a current-mode precision rectifier with operating in class-AB to support the high frequency operation, and two current-to-voltage converters. In particular, the proposed half-wave rectifier circuit has the following features:

- The proposed rectifier uses 31 MOS transistors whereas the proposed rectifier in [10] uses 44 MOS transistors; hence when the rectifier circuits are fabricated, the proposed rectifier will be used small area of chip than the previous rectifier.
- The proposed rectifier using supply voltage about ±1.2V is equal to the rectifier circuit in [10]. However, the proposed rectifier provides an operating frequency more than 250MHz, whereas in [10] identified by authors is 100MHz (simulated results with 0.5μm CMOS model obtained though MIETEC).
- The proposed half-wave rectifier provides excellent temperature stability without compensation circuit.

II. CIRCUIT REALZATION

The proposed CMOS half-wave rectifier circuit realization scheme consisting of three main components: the V-I converter, the current-mode rectifiers, and the I-V converters, as shown in Fig. 1. The V-I converter is composed of negative-type CCII (CCII-) (M1-M17) and input resistor R_{in} (MR1-MR2), the precision current rectifier is current mirrors (MC1-MC4) and current sources and (I_1-I_5), and I-V converters are composed of resistors R_{o1} (MR3-MR4) and R_{o2} (MR5-MR6). The operation of the half-wave rectifier circuit is as follows. When the input voltage V_{in} is applied into the circuit, it is converted to current i_z by negative-type CCII (CCII-) and a grounded resistor R_{in}. The grounded resistors can be implemented by two matched MOS transistors are diode-connected [12]. In Fig. 1(b), assume MR1 and MR2 operating in saturation region and have the same characteristics. The resistance value of MOS resistor of Fig. 1(b) can be expressed as [12]:

$$R = \frac{1}{2K(V_{DD} - V_{TH})} \tag{1}$$

where $K=\mu_O C_{OX}(W/L)$, V_{TH}=threshold voltage, V_{DD}=-V_{SS}=supply voltage, μ_O is the carrier mobility, C_{OX} is the gate capacitance per unit area, W and L are the channel width and length, respectively. Therefore the current i_z can be written as

$$i_z = \frac{V_{in}}{R_{in}} \tag{2}$$

The MOS transistor MD2 and the current source I_1 generate a constant voltages V_A, and the MOS transistor MD4 and the current source I_2 generate constant voltages V_B to provide bias voltage for MOS transistors MD1 and MD3, respectively. The constant voltage V_A and V_B should be fairly close to the threshold voltage of MOS transistors MD2 and MD4, respectively, to obtain precision results, and cause them to operating in class-AB. CM1 and CM2 is applied by the current sources I_3 and I_4, respectively, which ensures that two current mirrors are on all the times to the improving frequency response and overall system linearity. When i_z>0, this current is fed through MD1 and then is reflected by CM1 to the output current of CM1 as I_{o1} (+i_z). In addition, when i_z<0, this current is fed through MD3 and then is reflected by CM2 to the output current of CM2 as I_{o2} (+i_z). The relations between the input current, i_z, and the output current of CM1 as I_{o1}, and the output current of CM2 as I_{o2} can be expressed as

$$i > 0; I_{o1} = +i_z + I_5 \tag{3}$$
$$i < 0; I_{o2} = +i_z + I_6 \tag{4}$$

Since the constant current sources, I_5 and I_6, compensate the offset currents, I_3+I_1 and I_4+I_2, respectively, from (4) and (4), the currents I_{o1} and I_{o2} can be rewritten as

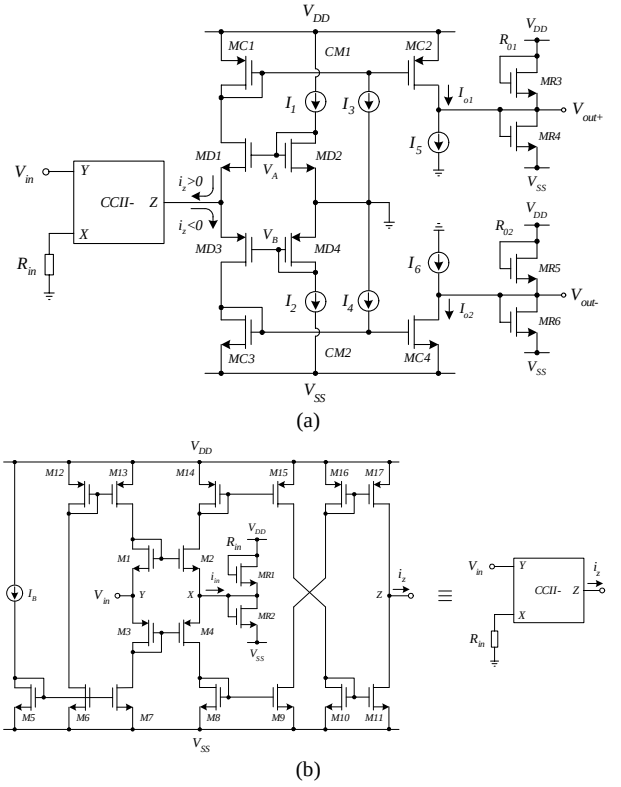

Fig. 1. (a) Proposed half-wave rectifier circuit, (b) a voltage to current converter circuit using CCII- and MOS resistor.

Since the constant current sources, I_5 and I_6, compensate the offset currents, I_3+I_1 and I_4+I_2, respectively, from (4) and (4), the currents I_{o1} and I_{o2} can be rewritten as

$$i > 0; I_{o1} = +i_z \tag{5}$$
$$i < 0; I_{o2} = +i_z \tag{6}$$

Suppose R_{o1}=R_{o2}=R_{in}, with the use of the closely matched MR1 to MR6, we can write the relations between V_{in}, and V_{out+} as

$$V_{in} > 0; V_{out+} = V_{in} \tag{7}$$
$$V_{in} < 0; V_{out+} = 0 \tag{8}$$

and the relations between V_{in}, and V_{out}- as

$$V_{in} > 0; V_{out-} = 0 \tag{9}$$
$$V_{in} < 0; V_{out-} = V_{in} \tag{10}$$

This means that the proposed rectifier can be operated as positive and negative half-wave rectifier into a single circuit.

III. SIMULATION RESULTS

In order to test the ideal designed, the scheme of dual output half-wave rectifier of Fig. 1 has been simulated using PSPICE simulation program. For the circuit simulation, the 0.5μm CMOS model obtained though MIETEC as listed in [10] is used. The aspect ratios (W/L) of MOS transistors are: 10μm/0.6μm for M1-M2, M5-

M11, MD1-MD2, MC3-MC4; 40µm/0.6µm for M3-M4, M12-M17; 30µm/0.6µm for MD3-MD4, MC1-MC2; 4µm/0.6µm for MR1-MR2; 2µm/0.6µm for MR3-MR6. The supply voltage used is ±1.2V. The current sources I_B=50µA, I_1=I_2=5µA, and I_3=I_4=100µA. The first test applied an input signal of amplitude 200mV peak and frequencies100MHz and 250MHz. The results of these tests are shown in figures 2 and 3, respectively. As is evident, satisfied half-wave rectified signals are produced at all two frequencies. This is as a direct result of the operation of the class-AB and the fast action of the voltage-to-current converter using the CCII. The amplitude errors between the input and output signals in figure 3 results from the decrease of the gain of the proposed rectifier for the operation at high frequency. It can correct by increase the value of R_{o1} and R_{o2}.

Several solutions to improve the poor temperature characteristic have been proposed. The good temperature stability can be achieved. However, it is causes of few problems such as use of many transistors [10], the precision decreasing at the high frequency [13], and the solving technique only suitable for bipolar technology [14]. To demonstrate the temperature performance of proposed circuit of Fig. 1, we simulate the proposed circuit in Fig. 1 at the frequency of 100MHz by changing temperatures form 50°C to 100°.

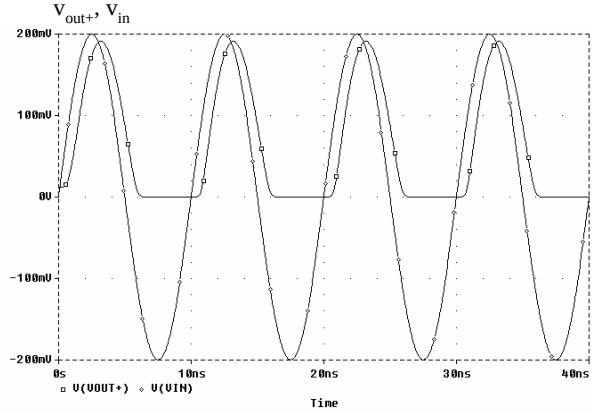

(a)

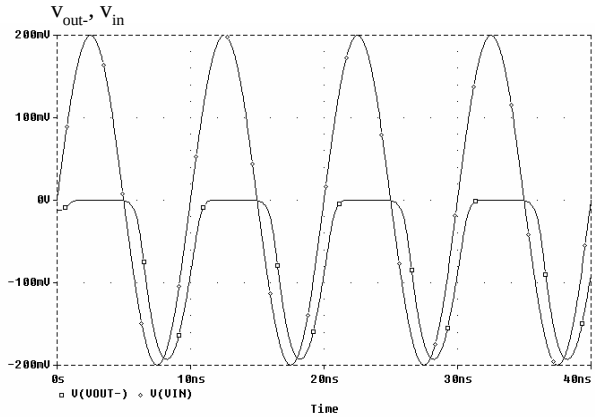

(b)

Fig. 2. Operation of half-wave rectifier at the input signal frequency 100MHz: (a) the input and positive half-wave output V_{out+} and (b) the input and negative half-wave output V_{out-}.

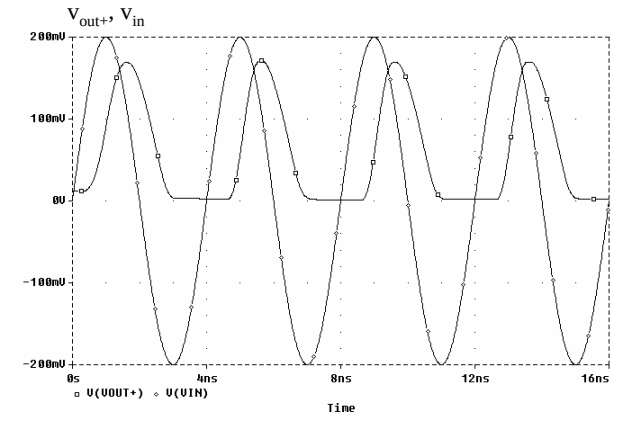

(a)

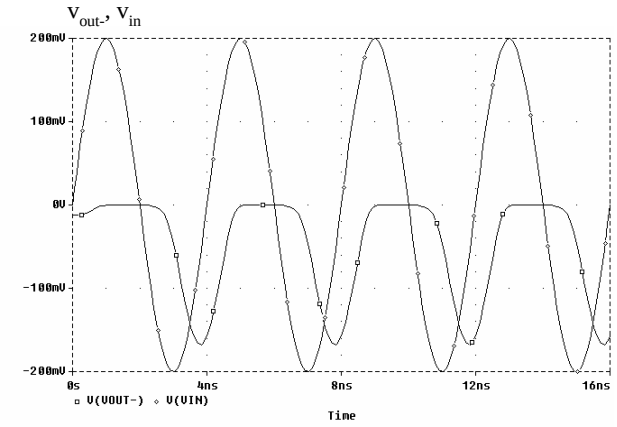

(b)

Fig. 3. Operation of half-wave rectifier at the input signal frequency 250MHz: (a) the input and positive half-wave output V_{out+} and (b) the input and negative half-wave output V_{out-}.

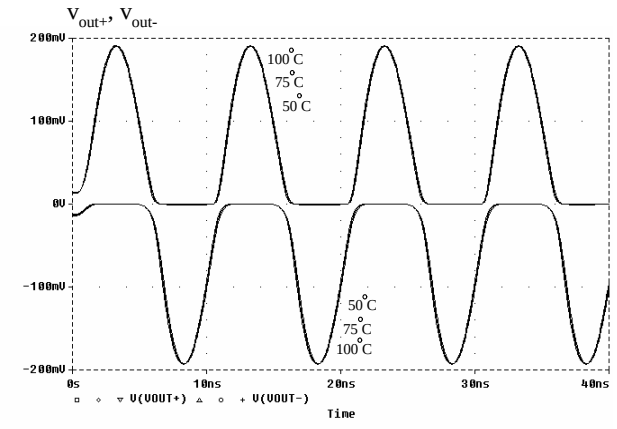

Fig. 4. Output wave forms at different temperature at the input signal frequency 100MHz.

Fig. 4 shows the output waveforms of the proposed rectifier at temperature of 50°C, 75°C, and 100°C. In Fig. 4, it can see that the proposed circuit very temperature stable without the compensation technique. In [8], [9] recommended that the class-AB technique requires the signal current to be greater than four times of the bias current to avoid the square-law error of MOS transistors.

This limitation can be corrected by setting the quiescent currents. The changing of the quiescent currents is directly proportional to the zero crossing. To demonstrate this point, we simulate the proposed rectifier in Fig. 1 again. Fig. 5(a) shown the operation of half-wave rectifier at the bias currents I_1=I_2=1µA and the input signal frequency 100MHz for 25mV_{peak}, (a) the input and output V_{out+}, (b) the input and output V_{out-}. Note that the precision and frequency range parameters of proposed rectifier can be controlled. Two parameters dependence on the setting of the quiescent currents, $I_1$and I_2, The low quiescent current may limit the high frequency capability of the proposed rectifier. In this case may be is an advantage for application. When we want to application in high precision system, the precision rectifier can be given. Again, if we want to application in high frequency system, the frequency range can be controlled.

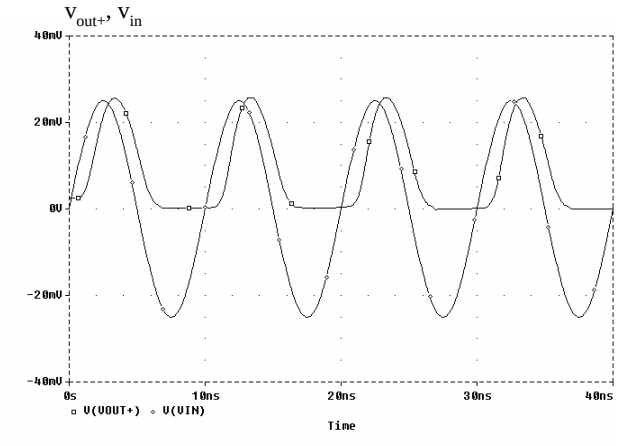

(a)

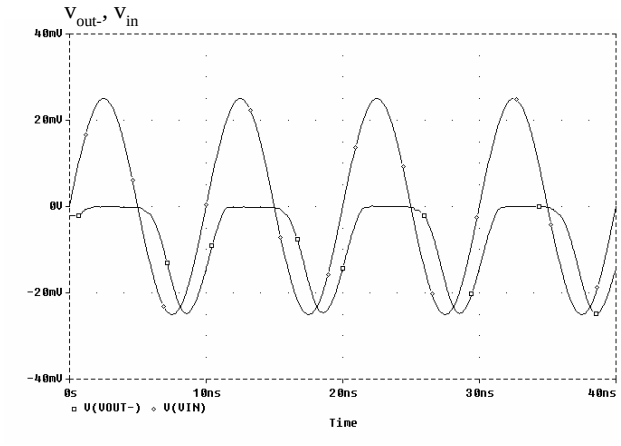

(b)

Fig. 5. Operation of half-wave rectifier at the bias current I_1=I_2=1µA and the input signal frequency 100MHz for 25mV_{peak}, (a) the input and output V_{out+}, (b) the input and output V_{out-}.

IV. CONCLUSIONS

A high frequency and high precision CMOS half-wave rectifier circuit was presented. The proposed circuit have distinguish in used of a negative-type CCII, current mirrors, and current sources and its combine a positive half-wave rectifier, a negative half-wave rectifier into single circuit. Although, the proposed rectifier is based on previously reported circuit conveyor rectifier but with the different circuit structure, the proposed half-wave rectifier yields features superior to the previously proposed current conveyor rectifier in view of the voltage employed, the power consumption, the number of devices, the operating frequency, and the temperature stability. The configuration described is very suitable for integrated circuit implementation in both bipolar and CMOS technology. The performance of the proposed circuit is confirmed from PSPICE simulation results.

REFERENCES

[1] J. Peyton and V. Walsh, *Analog electronics with op amps: a source book of practical circuits*, Cambridge University Press, New York, 1993.

[2] R. G. Irvine, *Operational amplifier characteristics and applications*. Prentice Hall International, New Jersey, 1994.

[3] Z. Wang, "Full-wave precision rectification that is performed in current domain and very suitable for CMOS implementation," *IEEE Transaction on Circuit and Systems-I*, vol. 39, pp. 456-462, 1992.

[4] S. J. G. Gift, "A high-performance full-wave rectifier circuit," *International Journal of Electronics*, vol. 89, pp. 467-476, 2000.

[5] C. Toumazou, F. J. Lidgey, and S. Chattong, "High frequency current conveyor precision full-wave rectifier," *Electronics Letters*, vol. 30, pp. 745-746, 1994.

[6] A. Khan, M. Abou El-Ela, and M. A. Al-Turaigi, "Current-mode precision rectification," *International Journal of Electronics*, vol. 79, pp. 853-859, 1995.

[7] A. Monpapassorn, K. Dejhan, and F. Cheevasuvit, "A full-wave rectifier using a current conveyor and current mirrors," *International Journal of Electronics*, vol. 88, pp. 751-758, 2001.

[8] V. Surakumpontorn and V. Riewruja, "Integrable CMOS sinusoidal frequency doubler and full-wave rectifier," *International Journal of Electronics*, vol. 73, pp. 627-632, 1992.

[9] V. Riewruja and R. Guntapong, "A low-voltage wide-band CMOS precision full-wave rectifier," *International Journal of Electronics*, vol. 89, pp. 467-476, 2002.

[10] A Monpapassorn, K. Dejhan, and F. Cheevasuvit, CMOS dual output current mode half-wave rectifier," *International Journal of Electronics*, vol. 88, pp. 1073-1084, 2001.

[11] M. Kumngern and K. Dejhan, "High frequency and high precision CMOS full-wave rectifier," *International Journal of Electronics*, vol. 93, pp. 185-199, 2006.

[12] Z. Wang, "2-MOSFET transistor with extremely low distortion for output reaching supply voltage," *Electronics Letters*, vol. 26, pp. 951-952, 1990.

[13] K. Hayatleh, S. Porta and F.J. Lidgey, "Temperature independent current conveyor." *Electronics Letters*, vol. 30, pp. 2091-2093, 1994.

[14] D. Stiurca, "Truly temperature independent current conveyor precision rectifier." *Electronics Letters*, vol. 31, pp. 1302-1303, 1995.

A Modified CMOS Differential-Pair-Based Triangular-and-Trapezoidal-to-Sine Converter

Kanitpong Pengwon[1] and Ekachai Leelarasmee[2]
Electrical Engineering Department, Chulalongkorn University
459 Phaya-thai Road
Patumwan, Bangkok 10330 Thailand
Email: [1]kanitp@eng.cmu.ac.th, [2]ekachai.l@chula.ac.th

***Abstract* - To simplify structure of a sinusoidal generator without serious performance degradation is one of major challenges in circuit design. An extremely simplified architecture triangular-and-trapezoidal-to-sine converter is presented. Curve of output signal, generated by the converter, is also low sensitive to temperature. Results from HSPICE simulations show that the approximated signal with a total harmonic content of 0.54 percent and an SFDR of –46 dBc at 1 kHz is achieved. The SDFR of output signal is adequate to be used in instrumentation systems.**

I. INTRODUCTION

Sinusoidal-function generators have been used in widely ranges of applications such as in modern communication module, instrument and motor control application. For communication applications, a waveform with -60 dBc of SFDR or better is acceptable while only -40 dBc one is required for instrument applications [2]. Many techniques to realize sinusoidal waveforms have been reported. Most of them, such as [1], [3] and [6], are based on nonlinear or picewise-linear approximations because it is difficult to directly generate a sinusoidal waveform.

Fig. 1 shows the general structure of sinusoidal generators that is divided into two parts. The first part is a signal generator, which is controlled by other circuits. The generator could employ triangular and trapezoidal function generators that are basic building blocks, [5]. The signals are fed to the second part called a converter. It converts linear signals to sinusoidal signals using nonlinear approximations. The study adopts this architecture to realize sinusoidal waveform. This paper reports the modification of the design of the converter structure, based on MOS differential pair amplifiers. The purposed circuits are based on n-well CMOS technology that provide isolated n-well PMOS transistor, which is useful to eliminate the body effect.

II. NONLINEAR FUNCTIONS

A set of nonlinear functions, whose domain and range are $\{x|\ 0 \le x \le 1\}$, is used to approximate an ideal sinusoidal function in the 1st quadrant. These functions are defined in (1) as shown in Fig. 2 (a).

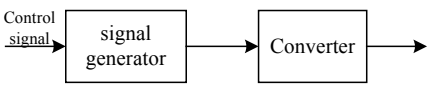

Fig. 1. General structure of sinusoidal generators

On the specified domain, the first function that is always lower than the sine function is named *the inner function* or $f_I(x)$. The second function is always larger than the sine function, so it is called the outer function or $f_O(x)$. These properties of the two functions are averaged and this average results in the average function denoted by $f_A(x)$. Since it is very close to the sine function, the error between the average and sine functions can be observed and shown in Fig. 2 (b).

A triangular-and-trapezoidal-to-sine converter (TTSC) is employed to generate the average function. The TTSC inputs, generated by amplifiers whose details are not reported in this paper, consist of two triangular waveforms (v_A and v_B), two trapezoidal waveforms (v_M and v_N) and constant voltage reference (V_{REF}). The amplifiers provide four input waveforms, derived from a triangular waveform denoted by v_{PH}. The signals are expressed in (2) that shown in Fig. 4.

$$\begin{aligned} f_I &= x\sqrt{2-x^2} \\ f_O &= x(2-x) \\ f_A &= (f_I + f_O)/2 \\ f_S(x) &= \sin(\pi/2\, x) \end{aligned} \tag{1}$$

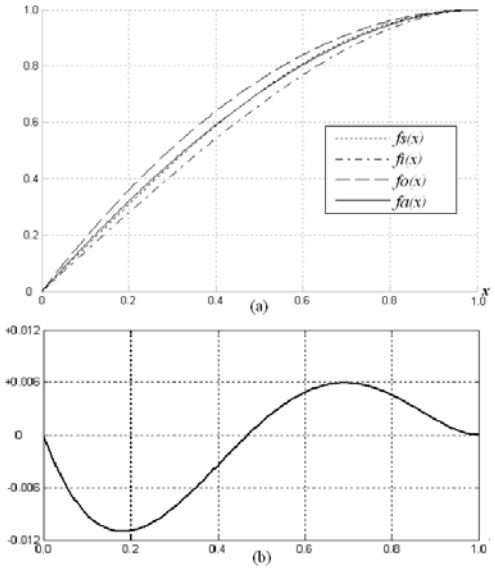

Fig. 2. (a) Nonlinear functions (b) $f_S(x) - f_A(x)$

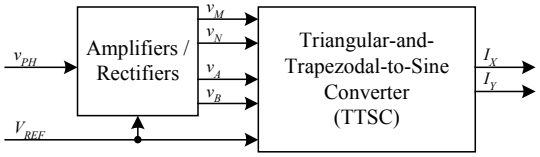

Fig. 3. Block diagram

$$
\begin{aligned}
v_A &= \frac{d_{AB}}{2V_{PH-PK}} v_{PH} + V_{CM} \\
v_B &= \frac{-d_{AB}}{2V_{PH-PK}} v_{PH} + V_{CM} \\
v_M &= \min\left\{ \frac{d_{MN}}{V_{PH-PK}} v_{PH} + d_{MN},\ d_{MN} \right\} \\
v_N &= \min\left\{ -\frac{d_{MN}}{V_{PH-PK}} v_{PH} + d_{MN},\ d_{MN} \right\}
\end{aligned}
\tag{2}
$$

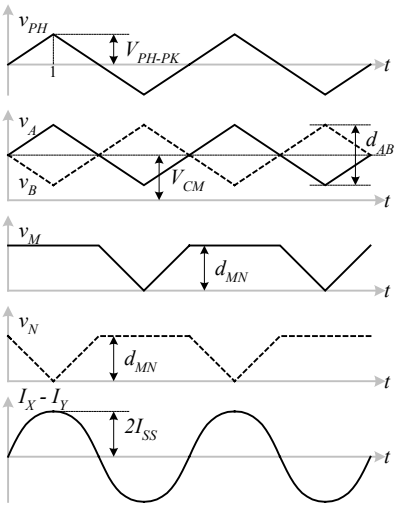

Fig. 4. Input and output signals of TTSC

Fig. 5 shows more details of the TTSC block diagram. The $(v_A - v_B)$ is a differential signal whose common-mode voltage denoted by V_{CM}. The v_A and v_B are fed directly into the inner function generator, while v_M and v_N are pre-compensated before being fed into the outer function generator. Finally, outputs of the two generators are summed and divided by 2 in order to achieve the average function. Dividing the summation by 2 is not necessary because the curve of the final output $(I_X - I_Y)$, which is two times of the average function, is also close to a sine function.

III. Practical Design

There are three kinds of building block circuits used to construct the TTSC, shown in Fig. 5. The inner function generator employs a differential pair amplifier. Secondly, the outer function generator composes of two MOS transistors. The two MOS transistors can be considered as a very basic differential amplifier without a current tail. The third circuit is a threshold-voltage compensated circuit denoted by THVC.

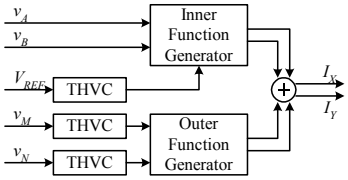

Fig. 5. Structure of TTSC

A. Square Law Based Functions

In order to generate the inner function, v_A and v_B are fed at the inputs of a differential pair amplifier, shown in Fig. 6 (a). According to Razavi [4], given that the second order effects are neglected, the description of a relation between $(v_A - v_B)$ and $(i_A - i_B)$ using square law model as shown in (3) can be achieved based on the assumption that two NMOS transistors, M_A and M_B, are identical match and in a saturated region.

$$
(i_A - i_B) = k_{AB}(v_A - v_B)\sqrt{\frac{2I_{SS}}{k_{AB}} - (v_A - v_B)^2} \tag{3}
$$

where

$k_{AB} = \frac{1}{2}\mu C_{ox}(W/L)_{AB}$

$(W/L)_{AB}$ aspect ratio of M_A and M_B

When v_A is more highly positive enough than v_B, it causes M_B to turn off. As a result, M_A drains the entire current. In this condition, $(i_A - i_B)$ equals to I_{SS}. We define a minimum value of $|vA - vB|$ that can put the circuit into the condition, as d_{AB}. The proper value of d_{AB} is expressed in (4).

$$
d_{AB} = \sqrt{I_{SS}/k_{AB}} \tag{4}
$$

From Fig. 4, $(v_A - v_B)$ equals to d_{AB} when t = 1. Equation (5) which is a normalized function is derived from (4) and (3) which is divided by I_{SS}.

$$
\frac{(i_A - i_B)}{I_{SS}} = t\sqrt{2 - t^2} \tag{5}
$$

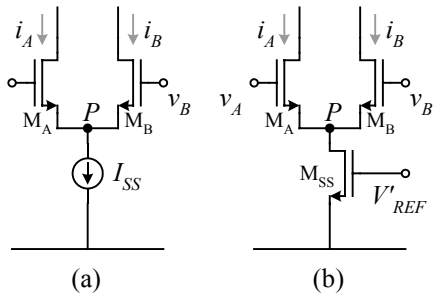

Fig. 6. A differential pair amplifier with (a) an ideal current source (b) an NMOS as bias current

Sweeping $(v_A - v_B)$ over the proper range of $\pm d_{AB}$ brings the achievement of the inner function in (5). Unfortunately, if temperature increases, k_{AB} will considerably decrease while d_{AB} remains constant. The output cannot reach I_{SS} while input

reaches its maximum d_{AB}. This causes a *pointed distortion*, shown in Fig 7. On the other hand, when temperature decreases, k_{AB} considerably increases. The output reaches I_{ss} while the input is lower than d_{AB}. This causes another kind of distortion, called *clipped distortion* [1].

To eliminate temperature dependency, M_{SS} is used as bias current instead of an ideal current source I_{SS}, shown in Fig. 6 (b). The ratio of M_A and M_{SS} aspect-ratio is given by $(W/L)_{AB} = F_1(W/L)_{SS}$. The override voltage of M_{SS} is $V'_{REF} - V_{TH}$ and V_P is high enough to put M_{SS} in saturated region. Because the value of V_P tracks V_{CM}, the minimum value of V_{CM} should agree with the expression in (7) in order to ensure that M_{SS} is in saturated region. Then the proper value of d_{AB} is redefined as (6).

$$d_{AB} = (V'_{REF} - V_{TH}) \Big/ \sqrt{F_1} \tag{6}$$

$$V_{CM} \geq \left(1 + 1\Big/\sqrt{2F_1}\right)(V'_{REF} - V_{TH}) + V_{TH} \tag{7}$$

The right-hand side of (6) remains sensitive to temperature because V_{TH} also depends on temperature. However, (6) is more practical than (4) because k_{AB} is more sensitive to temperature than V_{TH}, reported in [2]. V_{TH} effect can be compensated with a THVC circuit, shown below.

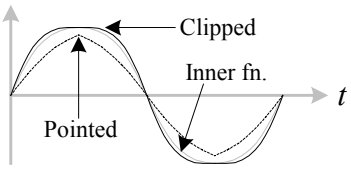

Fig. 7. Distortions due to change of k_{AB}

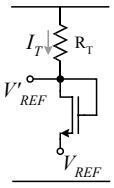

Figure 8. A threshold voltage compensated circuit

$$\frac{\sqrt{V_{DD} - V'_{REF}}}{V'_{REF} - V_{REF} - V_{TH}} = \sqrt{\tfrac{1}{2}\mu C_{ox}(W/L)_T R_T} \tag{8}$$

The expression in (8) is achieved from applying Ohm's law and square law to the circuit shown in Fig. 8. Enlarging the right-hand side of (8) makes V'_{REF} close to $V_{REF} + V_{TH}$. Then the value of term $(W/L)_T R_T$ should be large. Again, the proper value of d_{AB} is redefined as (9).

$$d_{AB} = V_{REF} \Big/ \sqrt{F_1} \tag{9}$$

From (9), the proper input range becomes temperature independent. From (5), by replacing I_{SS} with $k_{SS}V^2_{REF}$, the inner function becomes (10). Although the function's amplitude depends on k_{SS} whose temperature-dependency is very high, the function's curve is not changed.

$$\frac{(i_A - i_B)}{k_{SS}V^2_{REF}} = t\sqrt{2 - t^2} \tag{10}$$

Let's revisit the expression of the outer function in (1). In order to achieve the outer function, $x(2\text{-}x)$, negative, shift and mirror operations are requested to perform on a basic square function, x^2. As a result, the outer function generator circuit is nothing more than two identical match NMOS transistors whose characteristics obey the square law, shown in Fig. 9 (a). The gate terminals of two NMOS transistors: M_M and M_N, are driven by threshold voltage compensated signals, v'_M and v'_N. The effective override voltages are v_M and v_N, respectively. The maximum current, created by M_M and M_N, must equal the current generated by M_{SS} in the inner function generator. This gives an expression, shown in (11). And the ratio of $M_{M,N}$ and M_{SS} aspect-ratio is given by $(W/L)_{MN} = F_2(W/L)_{SS}$. Then the relation between d_{NM} and V_{REF} is expressed in (12).

$$k_{MN}d^2_{MN} = k_{SS}V^2_{REF} \tag{11}$$

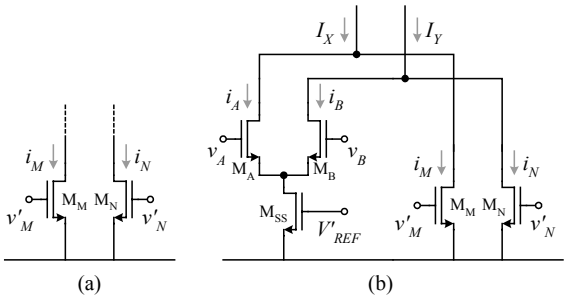

Fig. 9 (a) A differential amplifier without a current tail
(b) a combination of the inner and outer function generators

$$d_{MN} = V_{REF} \Big/ \sqrt{F_2} \tag{12}$$

$$i_M - i_N = k_{MN}v^2_M - k_{MN}v^2_N \tag{13}$$

From Fig. 4, on the range $0 \leq t \leq 1$, v_M is constant and equals d_{MN} while v_N changes with a negative slope, $-d_{MN}$. Thus, v_N can be written in term of t, shown below.

$$v_N(t) = d_{MN} - d_{MN}t \tag{14}$$

From (11) and (14), (13) is rearranged to achieve the outer function, expressed in (15). Like the inner function, amplitude of the outer function is also proportional to k_{SS}, but its curve is not. If constant in amplitude is request, the output can be multiplied by a current which is inverse proportional to mobility, purposed in [2].

To achieve the final output of TTSC, the outputs of the two generators are connected to each other, shown in Fig. 9 (b). $I_X = i_A + i_M$ and $I_Y = i_B + i_N$, then the final output is defined in a

differential term of (I_X – I_Y), shown in (16). A normalized function of the averaged function is derived from (10), (15) and (16) divided by $k_{SS}V^2_{REF}$, shown in (17).

$$\frac{(i_M - i_N)}{k_{SS}V_{REF}^2} = 1-(1-t)^2 = t(2-t) \quad (15)$$

$$I_X - I_Y = (i_A - i_B) + (i_M - i_N) \quad (16)$$

$$\frac{I_X - I_Y}{k_{SS}V_{REF}^2} = t\sqrt{2-t^2} + t(2-t) \quad (17)$$

B. Second-Order Effects

All functions derived previously are based on square law model. Two second-order effects are neglected in the previous analysis. They are short-channel and body effects. The volume of short-channel effect can be indicated by λ-parameter. The λ in a short-channel transistor is larger than in a long-channel transistor. In order to make the effects less significant, long-channel transistors should be used in the design.

For another effect, the body effect is not significant in the operation of the differential pair amplifier, although the source terminals of M_A and M_B are not connected to V_{SS}. The different voltage between bulk and source terminals causes an increase in threshold voltage. If common-mode voltage of differential input is high enough, the increase in threshold voltage can be neglected, as shown in (7). The body effect causes significant effects in operation of M_M, M_N and M_{SS}. These transistors are driven by compensated voltages, which are outputs of THVC circuits. Including the body effect, output voltage of THVC circuit, shown in Fig. 8, can be expressed in (18).

$$V'_i = V_i + V_{TH0} + \gamma\left(\sqrt{2\phi_{FB} - V_i} - \sqrt{2\phi_{FB}}\right) + \sqrt{\frac{2I_T}{\mu C_{ox}(W/L)_T}} \quad (18)$$

where V_{TH0} is threshold voltage without the body effect.

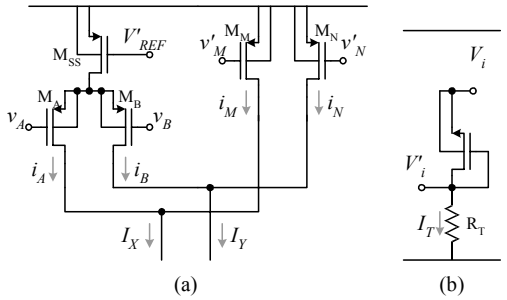

Fig. 10. A PMOS version of (a) TTSC (b) THVC

Errors in compensation are the 3rd and the last term of the right-hand side in (18). The value of the last term is very small because $(W/L)_T$ is large. The 3rd term is the body effect that can be completely removed by connecting the bulk terminal to its own source terminal. The bulk-source connection in NMOS is not allowed in general CMOS process. PMOS transistors are employed instead of NMOS transistors, as shown in Fig. 10. Each PMOS is also located in an isolated n-well to minimize the body effect.

IV. Simulation Results

A 0.18-micron n-well CMOS technology is used to model the test circuit, implemented with PMOS as shown in Fig. 10, for HSPICE simulating. Fig. 11 shows output curve in the temperature range of 0 to 100 °C, and Table I indicates that output with better than – 40 dBc of SFDR is achieved on the temperature range of 0 to 75 °C.

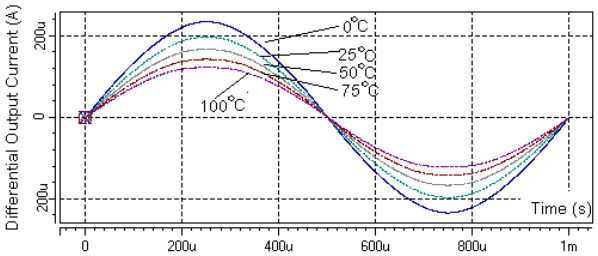

Fig. 11. Output signals in various temperature conditions

TABLE I
HSPICE Simulation Results

Temperature (°C)	THD (%)	SFDR (dBc)	20*log(a_N/a_1)		
			a_3	a_5	a_7
0	0. 878	-43.8	-44.6	-43.8	-61.2
25	0. 538	-46.4	-58.3	-46.4	-53.5
50	0. 616	-47.2	-47.2	-51.0	-49.3
75	1.089	-40.0	-40.0	-67.2	-46.9
100	1.729	-35.7	-35.7	-53.2	-45.3

V. Conclusion

The design of CMOS nonlinear circuits for sinusoidal function approximations and a threshold voltage compensated circuit reported in this paper. These circuits are non-complicated CMOS circuits. They are fed by triangular and trapezoidal waveform in order to convert the input signal to a sinusoidal waveform. The HSPICE simulations show that the circuits generate a sinusoidal waveform with total harmonic content of 0.538 percent and SFDR = – 46.4 dBc at 1 kHz, at the room temperature 25 °C. The purposed architecture provides a moderate level of performance which is needed in some instrumentation systems.

References

[1] J.W. Fattaruso and R. G. Meyer, "Triangle to sine wave conversion with MOS technology," *IEEE J. Solid-State Circuits*, vol. SC-20, no. 2, pp. 623–631, Apr. 1985.

[2] C.-H. Lee and H.-J. Park, "All-CMOS temperature-independent current reference," *Electon. Lett.*, vol. 32, pp. 1280–1281, Jul. 1996.

[3] A. McEwan and S. Collins, "Direct Digital-Frequency Synthesis by Analog Interpolation," *IEEE Trans. Circuits Syst. II*, vol. 53, pp. 1294–1298, Nov. 2006.

[4] B. Razavi, *Design of Analog CMOS Integrated Circuits.* McGraw-Hill, Singapore, 2001, page 108.

[5] M. Kachare, J. Ramírez-Angulo, R. G. Carvajal and A. J. López-Martín, "New Low-Voltage Fully Programmable CMOS Triangular/Trapezoidal Function Generator Circuit," *IEEE Trans. Circuits Syst. I*, vol. 52, pp. 2033–2042, Oct. 2005.

[6] Intersil, "ICL8038 Precision Waveform Generator/Voltage Controlled Oscillator," Data Sheet, April 2001.

A Design of CMOS Class-AB Differential Log-Companding Amplifier

Kobkaew Opasjumruskit[1] , Apisak Worapishet[2]and Ekachai Leelarasamee[3]
[1,3]IC Design and Application Research Laboratory (IDAR),
Department of Electrical Engineering, Faculty of Engineering, Chulalongkorn University, Thailand
[2]Mahanakorn Microelectronics Research Centre (MMRC), Mahanakorn University of Technology, Thailand
email : *kobkaew.o@digital.ee.eng.chula.ac.th, apisak@mut.ac.th ,ekachai.l@chula.ac.th*

Abstract – This paper presents a new low-voltage and low-power amplifier based on the class-AB differential log-companding technique. The circuit has been designed using a 0.25 μm CMOS process. The proposed amplifier consumes less than 3.2 μW from 0.6 V supply voltage at the maximum input current. The CMRR of this circuit is 35.76 dB; thus, it has very high performance in eliminating the common mode signal. The presented technique can be applied to many applications, such as filter, reference voltage, rectifier, etc.

I. INTRODUCTION

The main purposes in developing a better amplifier for hearing aid chips are shrinking its area, reducing power consumption and improving noise rejection. A previous hearing-aid amplifier [1] was designed based on the log-companding technique using CMOS technology [1], allowing its operation at 1 V. This design utilizes a class-A amplifier which consumes large amount of power at zero input. A class-AB integrator [2], which is also based on the log-companding technique, is proposed to reduce the power consumption. This circuit generates positive and negative voltages from a single input, and then passes them through a non-linear processing. The results are used to generate a single-ended output. Since the input and the output are both single-ended, this circuit is differential only in the non-linear processing section. In this work, a truly differential class-AB amplifier is developed by exploiting complementary NMOS and PMOS transistors. The quiescent current flowing through PMOS is reused in NMOS, thus this amplifier can consume lower power. Because of the class-AB operation, the proposed amplifier can handle larger input compared to the amplifier in [1]. Moreover, the differential structure improves common mode signal rejection. The proposed technique is suitable for portable application where the power is limited and the supply voltage is as low as 0.6 V.

II. DESIGN PRINCIPLES

A. Log-Companding Technique

The signal in the current form (I-domain) is compressed into the voltage form (V-domain) by a compressor. Then, the compressed signal V_{in} is processed by a non-linear function. Finally, the processed signal V_{out} is expanded back to the I-domain by an expander. From the I-domain point-of-view, the overall process is a linear function. The block diagram of this technique is shown in Fig. 1. The compression in this technique helps lowering the supply voltage required for the non-linear processing section. The log-companding technique can be used with many types of transistors, such as BJT and CMOS. To use a CMOS transistor in a log-companding circuit, the transistor must be operated in the subthreshold region that gives exactly the logarithmic compression and exponential expansion.

B. MOS characteristics in the subthreshold region

MOS transistors can operate in 3 main regions corresponding to the voltage between gate and source of the transistor (V_{gs}) comparing with the threshold voltage (V_{TO}). If $V_{gs} << V_{TO}$, this region is called *Weak Inversion* (or Subthreshold). On the other hand, if $V_{gs} >> V_{TO}$ this region is called *Strong Inversion* which further categorized into saturation region and triode region. Elsewhere, the region that V_{gs} is close to V_{TO} is called *Moderate Inversion*. MOS that operates in the subthreshold region has logarithmic characteristic. Equation of NMOS that operates in the subthreshold region from EKV model [3] is shown in eq. (1)

$$I_{DN} = I_{SN} \exp\left[\frac{V_{GB} - V_{TON}}{n_N U_t}\right]\left(\exp\left[-\frac{V_{SB}}{U_t}\right] - \exp\left[-\frac{V_{DB}}{U_t}\right]\right) \quad (1)$$

$$V_{SB,DB} >> \frac{V_{GB} - V_{TO}}{n} \text{ and } I_S = 2n\beta U_t^2$$

Whereas I_{Sx} is the specific current, $ß_x$ is the current multiplier, n_x is the subthreshold slope, U_t is the thermal potential and V_{TOx} is the threshold voltage. The *x* in the subscript can be N or P denoting parameters of NMOS and PMOS respectively or omitted in case of generic parameters that share between NMOS and PMOS

For PMOS, the equation is shown in eq. (2).

$$I_{DP} = -I_{SP} \exp\left[\frac{-V_{GB} - V_{TOP}}{n_P U_t}\right]\left(\exp\left[\frac{V_{SB}}{U_t}\right] - \exp\left[\frac{V_{DB}}{U_t}\right]\right) \quad (2)$$

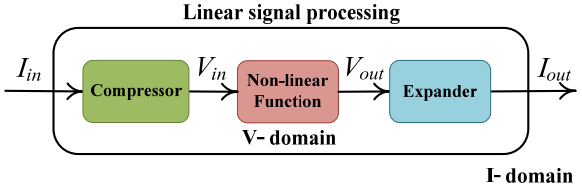

Fig. 1. Log-companding signal processing

For a CMOS model used in this work, we used BSIM3 level 49 [5] which gives V_{TON} of approximately 0.5V and PMOS's V_{TOP} of approximately 0.6V.

III. Proposed Circuit and Analysis

The proposed class-AB differential amplifier based on log-companding technique consists of the compressor to logarithmically compress the input currents into voltages and the expander to convert these voltages exponentially back into the output currents. The amplifier's gain can be controlled by adjusting V_{SB} of NMOS and PMOS in the compressor.

A. Compressor

The compressor circuit is shown in Fig. 2(a). It is sufficient to consider only half of the circuit because of the symmetry. If parameters n, I_S, $|V_{TO}|$ and $|V_{SB}|$ between NMOS and PMOS are equal, I_{ip} can be separated into I_{p1} and I_{n1} as shown in eq. (3).

$$I_{ip} = I_{N1} + I_{P1}$$
$$I_{ip} = I_{SS}\exp\left[\frac{V_{ip}}{nU_t}\right] - I_{SS}\exp\left[\frac{-V_{ip}}{nU_t}\right] \quad (3)$$

Where $$I_{SS} = I_S \exp\left[\frac{-V_{TO} - n|V_{SB}|}{nU_t}\right]$$

Rearranging the above equation, V_{ip} can be expressed in term of I_{ip} as shown in eq.(4)

$$V_{ip} = nU_t \sinh^{-1}\left[\frac{I_{ip}}{2I_{SS}}\right] \quad (4)$$

In general, n, I_S, $|V_{TO}|$ and $|V_{SB}|$ of NMOS and PMOS may not be identical. Difference in coefficient and exponent of I_{p1} and I_{n1} yields implicit function of V_{ip}; thus, it is difficult to write V_{ip} in term of I_{in} ($V_{ip} = f(kI_{in})$, k is arbitrary constant) directly. However, we can still expand V_{ip} and V_{in} using both NMOS expander and PMOS expander. This can be shown straightforward that even in the case of unmatched NMOS and PMOS parameters, the proposed expander still operate correctly.

B. Expander

The basic expander is shown in Fig. 2(b). This circuit expands V_{ip} and V_{in} exponentially into I_{op} and I_{on} respectively. The equation of the basic expander is shown in eq. (5) and (6).

$$I_{op} = I_N \exp\left[\frac{V_{ip}}{n_N U_t}\right] + I_P \exp\left[\frac{-V_{ip}}{n_P U_t}\right] \quad (5)$$

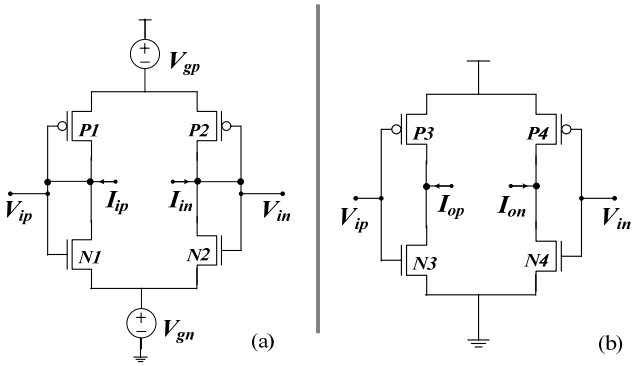

Fig. 2. (a)The proposed class-AB compressor (b) The basic expander

$$I_{on} = -I_P \exp\left[\frac{-V_{in}}{n_P U_t}\right] - I_N \exp\left[\frac{V_{in}}{n_N U_t}\right] \quad (6)$$

Where $I_N = I_{SN}\exp\left[\frac{-V_{TON}}{n_N U_t}\right]$ and $I_P = -I_{SP}\exp\left[\frac{-V_{TOP}+V_{DD}}{n_P U_t}\right]$

The basic expander's equation can be rewritten as $I_{op} = g(V_{ip})$ whereas $g(x)$ is the inverse function of $f(x)$. When we combine the compressor in Fig. 2(a) and the basic expander in Fig. 2(b) together to make a basic class-AB amplifier, the amplifier's transfer function is $I_{op} = g\,(f\,(k \bullet I_{ip})) = k \bullet I_{ip}$. The transfer function is obtained by substituting V_{ip} in eq. (5) with the term in eq. (4). In general case, the transfer function is still valid even V_{ip} is an implicit function of I_{ip} (the proof is beyond the scope of this paper). Choosing $V_{gp} = V_{gn} = V_{gain}$ simplifies the transfer function of the amplifier which is shown in eq. (7).

$$\frac{I_{op} - I_{on}}{I_{ip} - I_{in}} = \exp\left(\frac{V_{gain}}{U_t}\right) \quad (7)$$

From the equation, the gain of this amplifier can be varied by changing the value V_{gain}. Although the basic expander exhibits a good performance in cancelling the effect of I_N, I_P, n_N and n_P, this circuit cannot eliminate the common mode noise from the input. To solve this problem, we need to construct a true differential expander.

C. Amplifier

Based on the basic idea in [6], the proposed differential expander is shown in Fig. 3. This circuit proposes better common mode noise rejection.

The circuit expands V_{ip} and V_{in} exponentially into differential output currents. V_{ip} is expanded exponentially by N3, N4, P3 and P4, while expanding V_{in} is done by N5, N6, P5 and P6. A current expanded from V_{in} by N6 is copied to subtract with a current expanded from V_{ip} by N4 to

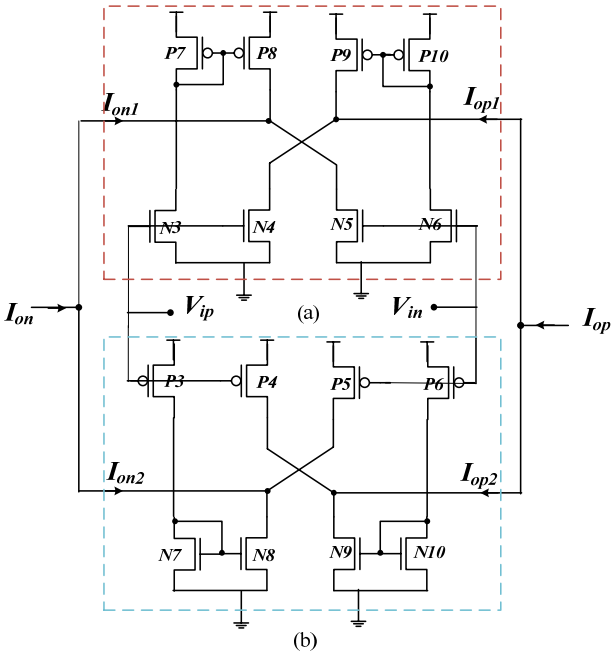

Fig. 3. Proposed (a) NMOS expander (b) PMOS expander

generate I_{op1}. The same is true for an expanded current from P6 and P4 subtracting each other to generate I_{op2}. Finally, I_{op1} and I_{op2} are combined to generate I_{op}. An equation of I_{op} is shown in eq. (8). I_{on} is generated in the same way with an equation shown in eq. (9).

$$I_{op} = I_N\left(\exp\left[V_{ip}/\left(n_N U_t\right)\right] - \exp\left[V_{in}/\left(n_N U_t\right)\right]\right) + I_P\left(\exp\left[-V_{in}/\left(n_P U_t\right)\right] - \exp\left[-V_{ip}/\left(n_P U_t\right)\right]\right) \quad (8)$$

$$I_{on} = I_N\left(\exp\left[V_{in}/\left(n_N U_t\right)\right] - \exp\left[V_{ip}/\left(n_N U_t\right)\right]\right) + I_P\left(\exp\left[-V_{ip}/\left(n_P U_t\right)\right] - \exp\left[-V_{in}/\left(n_P U_t\right)\right]\right) \quad (9)$$

When I_{ip} increases positively, according to the operation of the compressor, it increases V_{ip} and decreases V_{in}. Then, the expander gives an increased I_{op} and a decreased I_{on} creating differential output currents. In common mode operation, a matched change in V_{ip} and V_{in} makes no change to I_{op} and I_{on} because changed in expanded currents are cancelled internally. Therefore, this expander can reject common mode input.

To construct the amplifier based on the diagram shown in Fig. 1, we combine the class-AB compressor and the differential expander together. The proposed amplifier's gain can be controlled by adjusting V_{gain} in the compressor. Based on the calculation, the gain of this amplifier is 2 times larger than in eq. (7) because of the differential operation. This technique not only reduces the required supply voltage of the compressor but also decreases the number of CMOS used in the class-AB compressor from ref. [2]. Moreover, the differential expander exhibits better common mode rejection capability.

IV. Simulation Results

To prove that the proposed compressor can compress the signal logarithmically, the current $I_{ip} = -I_{in}$ are fed into the circuit and the output V_{ip} and V_{in} are plotted. From Fig. 4 and Fig. 5, the V_{ip} and V_{in} are plotting with I_{ip} in linear and logarithmic scale respectively. Notice that V_{ip} and V_{in} make straight line in the logarithmic scale. Moreover, the proposed expander can also expand V_{ip} and V_{in} exponentially. Fig. 6 and Fig. 7 show the variation of I_{op} and $|I_{on}|$ with respect to V_{ip} in linear and logarithmic scale of the output current respectively. Also remarked that logarithmic values of I_{op} and $|I_{on}|$ are proportional to V_{ip}.

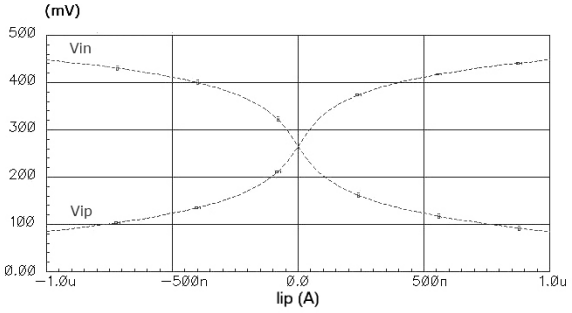

Fig. 4 Variation of V_{ip} and V_{in} respect to I_{ip} in linear scale

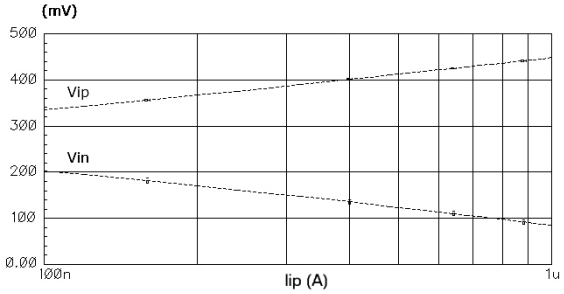

Fig. 5. Variation of V_{ip} and V_{in} respect to I_{ip} in logarithmic scale

The proposed amplifier should have a transfer function 2 times larger than in eq. (7). The simulated result in Fig. 8 shows that the amplifier is operating as expected, except for a minute offset current in I_{op} and I_{on} which will be cancelled automatically by the differential output scheme.

Parameters of MOS used in the proposed amplifier are shown in TABLE I. We can see that the circuit draws very low current at DC state from TABLE II. There are offset currents in I_{op} and I_{on} due to bias currents which affect the linearity of the amplifier's gain. This makes the result slightly differ from what we expected. Nevertheless, the proposed circuit has differential output that can finally eliminate the offset value in the output current. As mentioned in the previous section, the gain of this amplifier is affected by the value of V_{gain}. The gain of amplifier respect to V_{gain} is shown in Fig. 9.

TABLE I Parameters of Transistors Used in the Proposed Circuit

Name	P1-P6	N1-N6	P7-P10	N7-N10
W/L (μm)	3/0.3	3/0.3	30/0.3	30/0.3

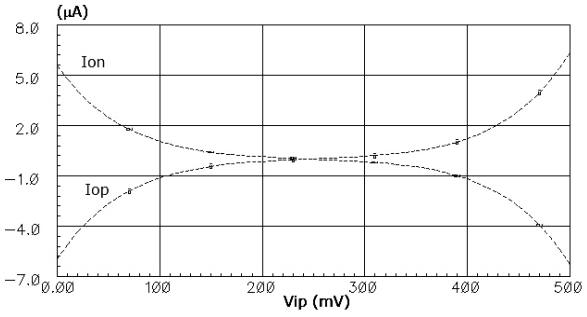

Fig. 6 Variation of I_{op} and I_{on} in linear scale respect to V_{ip}

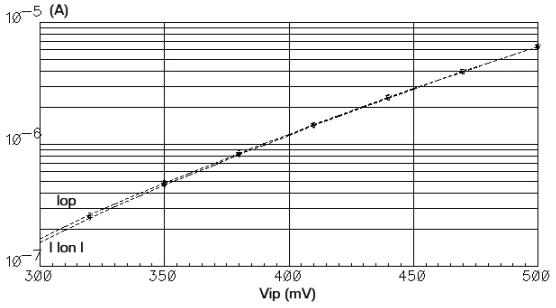

Fig. 7. Variation of I_{op} and $|I_{on}|$ in logarithmic scale respect to V_{ip}

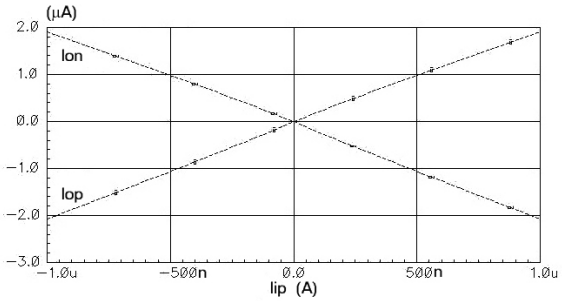

Fig. 8 Shows output currents varied with the input current

The linearity of the proposed circuit is defined by THD (Total Harmonic Distortion). From the simulation result shown in Fig. 10, THD of the proposed circuit is 0.55% and CMRR is 35.76 dB from 1μA sinusoidal input. The frequency range of the circuit is up to 200 kHz which is satisfactory for audio application. The small signal gain from frequency analysis shown in Fig. 11 is approximately 2.02. Because of the differential structure, this circuit has very high performance in eliminating the common mode input. Moreover, the power consumption of the circuit is 291nW while the circuit operates in quiescent state. At the maximum input state the circuit consumes 3.16 μW from 0.6 V supply voltage. The summary of the proposed amplifier's performance is shown in TABLE III.

TABLE II QUIESCENT VALUE OF THE CIRCUIT

Name	$\|I_d\|$ (nA)	$\|V_{GS}\|$(mV)	Name	$\|I_d\|$ (nA)	$\|V_{GS}\|$(mV)
P1-P2	25.94	327.6	N1-N2	25.94	272.4
P3,P6	29.50	327.6	N3,N6	31.82	272.4
P4,P5	29.79	327.6	N4,N5	29.37	272.4

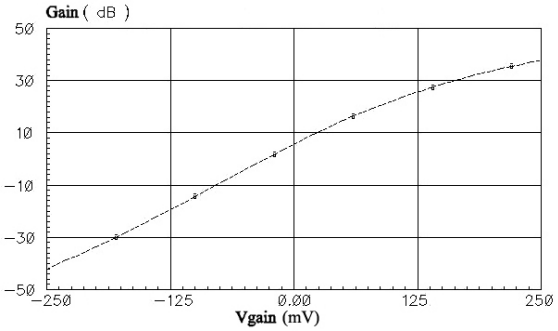

Fig. 9. Gain Variation of the proposed amplifier respect to V_{gain}

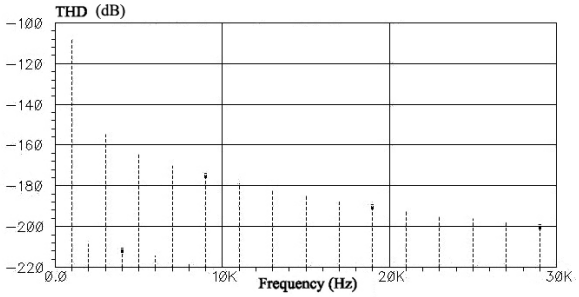

Fig. 10. THD analysis of the proposed amplifier

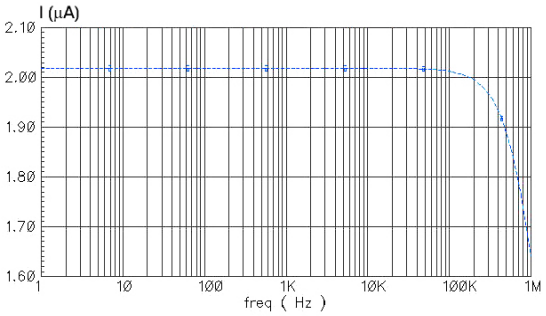

Fig. 11. Frequency Response of the proposed amplifier

TABLE III SUMMARY OF THE PROPOSED CIRCUIT'S PERFORMANCE

Name	Value	Condition
Voltage Supply	0.6 V	-
Gain	-40 to 38 dB	-
Input Range	-1 to 1 μA	-
Max. Input Frequency	200 kHz	-
Power	3.16 μW	Vgain=0, Maximum Input
%THD	0.55 %	Maximum Input
CMRR	35.76 dB	Maximum Input

V. CONCLUSION AND FUTURE WORK

Log-companding technique can reduce circuit's supply voltage value. Moreover, class-AB and differential technique are used to decrease total power consumption and eliminate common mode noise. In this work, the circuit is operated well with 0.6 V supply voltage. The total power consumption is 3.16422 μW. The amplifier gain can be varied from -40 dB to 38 dB, the THD of the circuit is 0.55%, and the CMRR of the proposed amplifier is 35.76 dB. These techniques can be used in many others applications. The future work is to design a log-companding filter based on these techniques.

REFERENCES

[1] Francisco Serra-Graells, Jose L. Huertas, Adoracion Rueda; "Low-Voltage Cmos Log Companding Analog Design" , Kluwer Academic Pub, June 2003

[2] Redondo, X.; Serra-Graells, F.; "1 V compact class-AB CMOS log filters" Circuits and Systems, 2005. ISCAS 2005. IEEE International Symposium on 23-26 May 2005 Page(s):2000 - 2003 Vol. 3

[3] G.A.S. Machado, C.C. Enz, and M. Bucher; "Estimating key parameters in the EKV MOST model for analogue design and simulation," proc. of IEEE ISCAS'95.

[4] G.Giustolisi, G.Palumbo, M.Criscione, and F.Cutri, "A low-voltage low-power voltage reference based on subthreshold MOSFET"; *IEEE J. Solid-State Circuits*, vol.38, no.1, pp. 151-154, Jan.2003

[5] Y.Cheng and C.Hu, *MOSFET Modeling & BSIM3 User's Guide*. New York: Kluwer, 1999

[6] Khumsat, P.; Worapishet, A." High-gain current amplifiers for low-power MOSFET-C filters";Circuits and Systems, 2006. ISCAS 2006. Proceedings. 2006 IEEE International Symposium on 21-24 May 2006 Page(s):4 pp.

A Novel Structure of Wide-Swing CMOS Voltage Buffer

Chutham Sawigun and Jirayuth Mahattanakul
Department of Electronic Engineering, Faculty of Engineering
Mahanakorn University of Technology, Bangkok, THAILAND
Email: chotharn@mut.ac.th, jirayut@mut.ac.th

Abstract— **This paper presents a novel structure of wide-swing CMOS voltage buffer, which is based on the flipped voltage follower. When compared with the previously established buffer based on the same principle, the proposed circuit is less complex and consumes less power while attaining wide bandwidth and high slew-rate. Simulated results of the proposed buffer using a 0.35μm CMOS process are provided.**

I. INTRODUCTION

Analog voltage buffers or voltage followers can be found in various analog applications such as current conveyors [1], current feedback amplifiers [2], output stages of power amplifiers and line drivers [3], and analog filter realizations [4]. In order to drive large capacitive loads with high speed and attain high signal-to-noise ratios, analog buffers must provide an output current and voltage swing range which is as high as possible. To meet these requirements, a fast, unity-gain class-AB amplifier circuit with rail-to-rail signal capability is required. Combining the class-AB operation and rail-to-rail signal swing usually requires a complicated biasing circuit to extend the common-mode input range of the buffer [5]. Unfortunately, this increases the buffer complexity and power consumption.

In this paper, we describe a compact, class-AB CMOS analog buffer with rail-to-rail signal capability, which dispenses with the requirement for a complicated biasing circuit. The circuit employs the complementary class-AB differential transconductor proposed in [6] and its common-mode input range limitation is solved by inserting level shifters into the local feedback path of the transconductor. Although, this technique is similar to the voltage buffer proposed in [7], our approach avoids the complicated biasing circuit required in [7] to stabilize the circuit DC operating points when the input signal goes either excessively high or low. As a result, the overall buffer complexity and quiescent power consumption are reduced, while still attaining rail-to-rail signal swing and high driving ability.

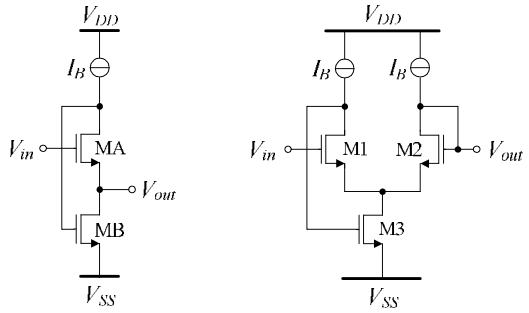

Figure1. (a) Flipped voltage follower. (b) Buffer without level shifting.

The remaining sections of the paper are organized as follows. Section II provides an overview of previous works in analog rail-to-rail buffer design and Section III presents the proposed circuit. Simulated results using parameters for a 0.35μm CMOS process are presented in Section IV and conclusions suitably drawn in Section V.

II. PREVIOUS BUFFERS

A. Flipped Voltage Follower

Fig. 1a shows the high accuracy buffer which is called "flipped voltage follower" by the fact that a bias current I_B is injected to drain instead of source terminals of MA. Compared with the traditional source follower circuit, following behavior of the circuit in Fig.1a is far better because the drain current of MA is regulated by constant current source resulting in constant gate-source voltage as well. Moreover a very large loop gain provided by common source circuit MB, which is embedded in a local negative feedback loop of the circuit, forcing a small signal output resistance of this circuit to be very low [9] and the feedback mechanism can be simplify by a feedback block diagram shown in Fig 2, where g_{mi} is a small signal transconductance gain of each transistor and r_{ds} is a drain-source resistance and r_B is an output resistance of the

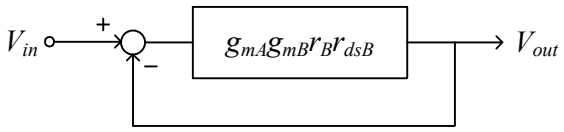

Figure 2. Feedback block diagram of the flipped voltage follower.

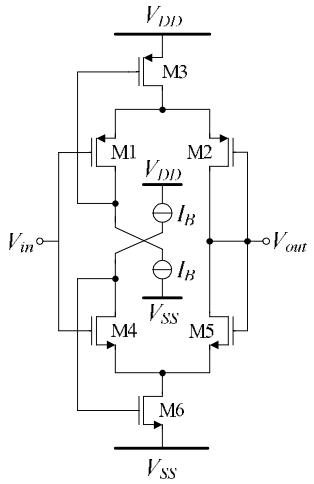

Figure 3. Class-AB buffer in [6].

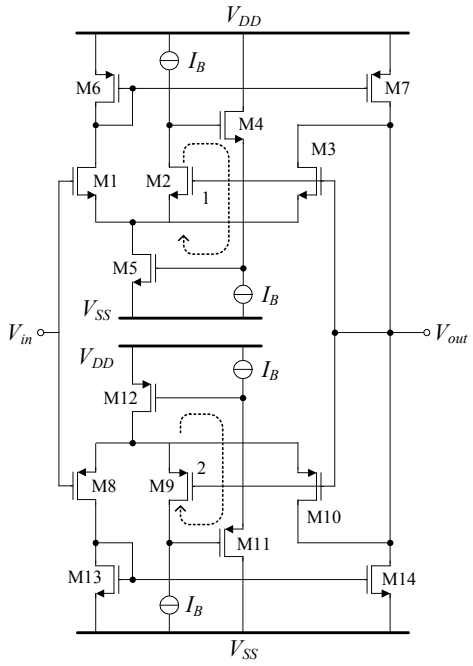

Figure 4. Proposed rail-to-rail buffer.

current source I_B. To compensate for a DC level shifting between input and output voltages of the circuit in Fig.1a, the circuit in Fig.1b is employed. This circuit operates as a single stage amplifier connected in unity gain feedback scheme which also maintains equality between input and output voltages by a large loop gain of a global feedback path. When large signal characteristics are considered, it can be seen that both circuits in Figs. 1a and 1b can maximally push current to load by I_B, whereas pull currents can be much higher.

To fulfill the asymmetrical output currents of both circuits, a buffer circuit providing fully class-AB characteristic is proposed in [6] and shown in Fig.3. It is simply realized by stacking the circuit in Fig. 1b in a complementary fashion. The circuit is compact and has very low quiescent power consumption given by

$$P = 3I_B\left(V_{DD} - V_{SS}\right). \tag{1}$$

Moreover, it provides a class-AB output current suitable for large capacitive loads but its signal swing is limited by the circuit topology itself. An attempt to extend signal swing of the buffer has been done in [7]. Although, however, the signal swing is successfully enhanced, the overall circuit is bulky and required almost quadrupling of power consumption of the buffer in Fig.3.

III. PROPOSED CIRCUIT

Fig. 4 shows the proposed rail-to-rail CMOS analog buffer. The circuit can be divided into two parts; the upper circuit consisting of devices M1-M7 and the lower circuit of devices M8-M14. Each of these sub-circuits resembles a single-stage class-AB amplifier. The purpose of level shifters, M4-M5 and M11-M12 are to provide negative feedback loops (1 and 2), thereby extending the input common-mode range [7].

By virtue of the negative feedback around loops 1 and 2, the impedances at the source terminals of M2 and M9 are forced to be very low. As a result, the gate-source voltages of M2 (V_{GS2}) and M9 (V_{SG9}) are kept nearly constant, causing the current at the circuit output node to feature class-AB behavior [9]. Considering the circuit in Fig. 3 without M3 and M10 we can see that it may properly operate as a unity-gain amplifier or voltage buffer. However, when the input voltage (V_{in}) goes low or high and exceeds the following range:

$$V_{SS} + \left(V_{eff5} + V_{eff2} + V_{Tn}\right) \le V_{in} \le V_{DD} - \left(V_{eff12} + V_{eff9} + \left|V_{Tp}\right|\right) \tag{2}$$

where V_{eff} is the effective or saturation voltage, V_{Tn} and V_{Tp} are the threshold voltages of n and p channel devices respectively, either the upper or the lower sub-circuit will be forced out of the active region. As a result, there will be no DC current to support the output branch of the rest of the circuit, leading to inevitable shut down of the entire buffer circuit.

Here, the main objective of inserting M3 and M10 into the circuit in Fig. 4 is to widen its input range, i.e., to be higher than (2). Since the gate-source voltages of M3 and M10 are respectively copied from M2 and M9, their current conducting behavior will be similar and controlled by V_{in}. Devices M3 and M10 function as controlled constant current sources and stabilize the DC current of the output branch devices M7 and M14. The DC stabilizing mechanism will be considered next.

First consider the case when $V_{in} = 0$. By virtue of the negative feedback from the output node (V_{out}) to the inverting input terminals (gate terminals of M2, M3, M9 and M10), the input and output voltages are forced to be identical, i.e., $V_{in} = V_{out} = 0$. At this point, both the upper (M1-M5) and lower (M8-M12) input pairs are biased in the active region, and the drain currents of M1 and M8 (both equal to I_B) are copied to the output branches via the current mirrors M6-M7 and M13-M14. Also, M3 and M10 are active with drain currents of $I_{D3} = I_{D10} = I_B$. In this situation, we can see that no DC operating problem occurs because the drain current of M7 (I_{D7}) is fully absorbed by a drain current of M14 (I_{D14}) and the total current consumption is $8I_B$ then static power consumption of this circuit can be calculated as

$$P = 8I_B\left(V_{DD} - V_{SS}\right), \tag{3}$$

showing that this circuit consumes less power than the buffer in [7]. Interestingly, M3 and M10 may appear to be redundant. Although true when $V_{in} = 0$, for $V_{in} \neq 0$, M3 and M10 play a significant role as discussed next.

When a positive V_{in} is applied and reaches the upper limit of (2), M12 will be forced to enter the triode region. If V_{in} goes higher than this limit, I_{D12} will be reduced and M8-M10 will be pushed out of the active region, eventually resulting in zero drain current in M8-M10 and M13-M14. However, the upper sub-circuit will still continue to work properly because I_{D7} can be fully absorbed by I_{D3} (even if M14 is already turned-off). In the reverse situation, i.e., when V_{in} goes more negative than the lower limit of (2), the lower sub-circuit will be fully functional, whereas the upper sub-circuit will be turned off. Thus, we can find that the input range of the buffer is extended from (2) to be

$$V_{DD} - \left(V_{eff11} + V_{eff12} + 3\left|V_{Tp}\right|\right) \le V_{in} \le V_{SS} + \left(V_{eff4} + V_{eff5} + V_{Tn}\right). \tag{4}$$

Hence, by appropriate choice of the voltage supply rails and effective voltages in (4), we can achieve rail-to-rail capability. To show the compactness of the proposed circuit a component of the proposed buffer, excluding bias circuits, is summarized in Table 1.

Table1: List of Components and Current Consumption of the proposed circuit.

Parameter	Fig.3
Transistor count	14
Current sources	4
Current consumption	$8I_B$

Table2: Transistor Dimensions.
(channel length L = 1μm for all transistors)

Transistor	W [μm]
M1-M3	20
M4	0.6
M5	10
M6-M10	60
M11	1.8
M12	30
M13-M14	20

Table3: Performance Summary.

Circuit performance	Value
Bandwidth	6.8MHz
Slew rate: positive, negative	61.3V/μs, 68.2V/μs
THD@1.4V_p, 100KHz	-42dB
Static power consumption	282 μW

IV. SIMULTION RESULTS

The circuit in Fig.4 was simulated using SPICE with parameters for a 0.35 μm CMOS process ($V_{Tn} \cong 0.55$V and $V_{Tp} \cong -0.71$V). The transistor dimensions are listed in Table 2. Capacitive load of 10pF were used, and the supply voltage ($V_{DD} = -V_{SS}$) and bias current I_B were set to 1.5V and 10μA, respectively.

The DC characteristic of the buffer circuits is shown in Fig.5. The tracking behavior, between the input and output voltages is shown in Fig.5a, and the offset error is shown in Fig.5b. It can thus be seen that the output voltages of the proposed buffer follow the input voltage for almost the entire range of the voltage supply and the offset of the proposed buffer is very low.

The operating speed of the proposed buffer was evaluated by applying a 1.4V, 2 MHz square signal at the input. The transient response is depicted in Fig. 6 showing that the step response of the proposed buffer is faster than 60V/μs.

The circuit linearity was evaluated by simulated total harmonic distortion (THD) with a 100 kHz sinusoidal input voltage with varying amplitude. The result is shown in Fig. 7 where it can be seen that less than -40_{dB}THD of the proposed buffer is achieved for amplitudes in excess of 1.4V. Finally, for a 10pF load, the buffer exhibited a bandwidth of 6.8 MHz and details of other simulated parameters are summarized in Table 3.

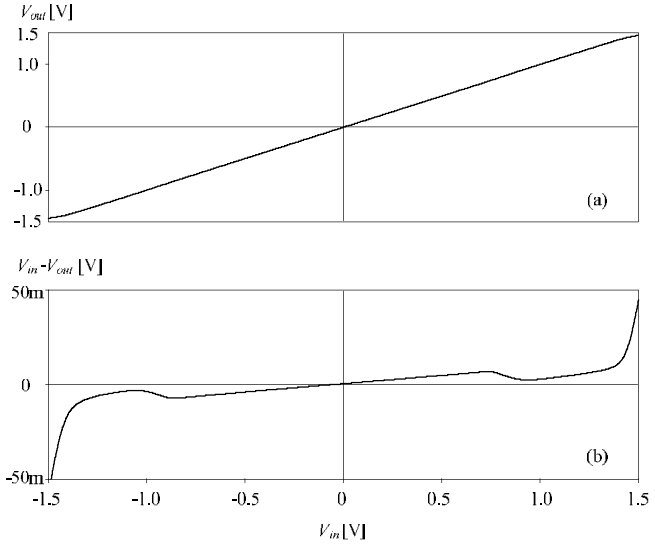

Figure 5. DC characteristic of the proposed buffer
(a) input-output tracking behavior (b) voltage error.

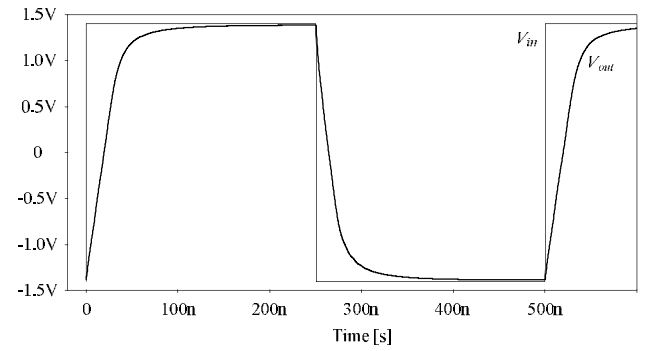

Figure 6. Transient response of the proposed buffer.

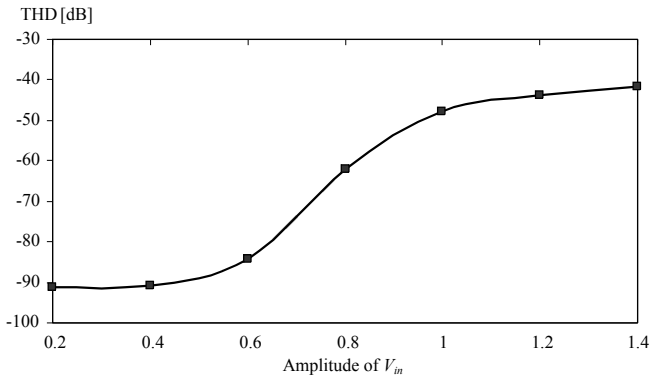

Figure 7. Simulated total harmonic distortion.

V. CONCLUSION

A novel compact structure of the high-performance class-AB CMOS analog voltage buffer has been presented. The proposed buffer combines high driving capability and rail-to-rail signal swing. The circuit complexity and quiescent power consumption of the proposed circuit are lower compared with a previously reported buffer based on the same principle. Simulated results have been provided to show the performance of the circuit.

ACKNOWLEDGMENT

The authors would like to thank A. Demosthenous, for invaluable suggestions and discussions. His kind help creating this paper is highly appreciated.

REFERENCES

[1] A. S. Sedra and K. C. Smith, "A Second Generation Current Conveyor and its Applications," *IEEE Trans Circuit Theory*, vol. CT-17, pp. 132-134, 1970.

[2] F. J. Lidgey and K. Hayatleh, "Current Feedback Operational Amplifiers and Applications," *Electronics & Communication Journal*, pp. 178-182, Aug.1997.

[3] N. P. Ramachandran, H. Dinc and A. I. Karsilayan, "A 3.3 V CMOS Adaptive Analog Video Line Driver With Low Distortion Performance," *IEEE J. Solid-State circuits*, vol.38, no.6, pp. 1051-1058, Jun 2003.

[4] K. Salama, "Continuous time universal filters using unity gain cells," *Int. J. Electron. Commun*, no.2, pp. 1-4, 2002.

[5] C. H. Lin and M. Ismail, "A low voltage rail to rail class-AB input/output op-amp with slew rate and settling enhancement ," *IEEE ISCAS'98*, vol. 1, pp. 448-451, Monterey, California, May 1998.

[6] A. Torralba, R. G. Cavajal, J. Galan, and J. Ramirez angulo, "Compact low-power high slew rate CMOS buffer for large capacitive loads," *Electronics letters*, vol. 38, no. 10, pp. 1348-1349, October 2002.

[7] J. M. Carrillo, R. G. Cavajal, A. Tarralba, and J. F. Duque Carrillo, "Rail to rail low-power high slew rate CMOS analog buffer," *Electronics letters*, vol. 40, pp. 843-844, July 2004.

[8] V. Peluso, P. Vancorenland, A. Marques, M. Steyaert and W. Sansen, "900mW low power delta sigma A/D converter with 77-dB dynamic range," *IEEE J. of Solid-State Circuits*, vol.33, no.12, pp.1887-1897, Dec. 1998.

[9] R. G. Cavarjal, J. Ramirez Angulo, A. J. Lopez Martin A. Torralba , J. A. Gomez Galan, A. Corlosena, F. M. Chavero, "The flipped volltage follower: a useful cell for low-voltage low-power circuit design," *IEEE Trans. on Cir. and Syst. I: regular paper*, vol.52, no.7, 2005, pp. 1276–1291.

A Compact Low Voltage CMOS Four-Quadrant Analog Multiplier

N. Kiatwarin*, W. Ngamkham** and W. Kiranon*

* Department of Telecommunication Engineering, Faculty of Engineering,
King Mongkut's Institute of Technology Ladkrabang, THAILAND
Tel: (662) 9883655 Ext. 239, Email: narumol@mut.ac.th

**Department of Control and Instrumentation Engineering
Mahanakorn University of Technology
51 Chuem Samphan Rd. Nong-Chok Bangkok 10530, THAILAND
Tel: (662) 9883655 Ext. 239, Email: wanaya@mut.ac.th

***Abstract*-In this paper, a compact low-voltage CMOS four-quadrant analog multiplier is proposed. The proposed circuit is obtained by rearranging circuit topology of a recently reported multiplier which is unpractical since the circuit topology itself needs an ideal voltage reference to form a multiplication function. By doing so, the ideal voltage reference is no longer required leading to achieve a new multiplier circuit with real compactness. Simulated results using PSPICE for 0.35μm CMOS process show that main performances of the proposed multiplier, including linearity, bandwidth and power consumption, are successfully improved.**

I. INTRODUCTION

Analog multipliers are found in many applications such as modulator, frequency doublers, absolute value circuit, and etc. These applications are required to operate in low voltage environment for improving their power efficiency and incorporating with mixed signal systems to be used in portable applications [1]. A number of circuit techniques for realizing a CMOS analog multiplier had been collected and systematically evaluated by G. Han and E. Sanchez-Sinencio [2].

According to [2], there are several means to realize a four quadrant analog multiplier and it is also suggested by [3] that using saturated MOSFET in strong inversion is more practical than any other means. Recently, based on a square-law relation of saturated MOSFET, various compact multiplier architectures which are constituted by a circuit cell called a "flipped voltage follower: FVF" [4], have been chronologically proposed in [5]-[8]. Most of them feature wide input range, high operating frequency and low power consumption which are resulted from excellent manipulations of the square-law function in high compactness structures.

Focusing on the latest version in [8], which is seemed to be the most compact circuit, it is found that the overall multiplier circuit can not be called compact since it requires an extra voltage reference connected between the resistive loads. To generate the extra voltage reference, more power consumption and circuit complexity are unavoidable.

In this paper, we propose a new multiplier circuit which is based on a similar technique to [8] but an arrangement of the circuit in transistor level is improved such that the extra voltage reference becomes redundant and can be eliminated. We then obtain a four quadrant analog multiplier with real compact structure. Therefore, some circuit performances of the proposed multiplier are successfully improved. In order to validate the circuit performances, the proposed multiplier has been simulated in PSPICE by using model parameter for 0.35 micron CMOS process. The results show that bandwidth, linearity and power consumption of the proposed circuit are better than those of the circuit in [8].

The remaining of this paper is organized in the following sections, a basic concept for realizing the analog multiplier is introduced in Section II. Next, a modification of square rooting circuit used to form an analog multiplier is described in Section III. The proposed multiplier circuit is illustrated in Section IV. In addition, simulated results of the proposed multiplier and conclusion are presented in Section V and VI, respectively.

II. BASIC CONCEPT

Realizing a proposed analog multiplier and the multiplier in [8] is based on a similar approach showing in Fig. 1. It comprises a pair of common source amplifier (M1 and M2), which acts as input transistors to provide output currents in term of squaring functions of input voltages (V_1 and V_2), and two identical voltage controlled square root blocks which operate as non-linear cancellation paths. Injecting the output currents of the input transistors into the square root blocks, a differential output current of the overall circuit will become a multiplication function of two input signals V_{12} and V_{34}. More detail of mathematical analysis using square-law relation of saturated MOSFET in strong inversion will be shown in the paragraph below.

Assuming the MOSFET M1 and M2 are biased in active region and neglecting channel length modulation effect, the current I_A and I_B can be respectively found as

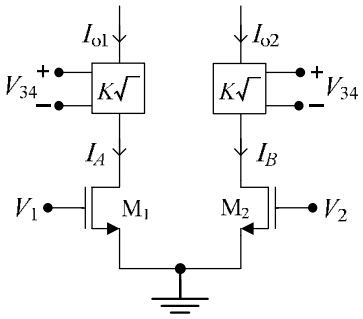

Figure 1. Basic concept for realizing a four quadrant analog multiplier.

$$I_A = \beta_n (V_1 - V_{tn})^2 \tag{1}$$

and

$$I_B = \beta_n (V_2 - V_{tn})^2 , \tag{2}$$

where $\beta_n = 0.5\mu_n C_{ox}(W/L)$ is a transconductance parameter of each MOSFET and V_{tn} is the threshold voltage of NMOS transistor.

From (1) and (2), the relationship between the current I_A and I_B and the differential input voltage $V_{12} = V_1 - V_2$ can be given by

$$\sqrt{I_A} - \sqrt{I_B} = V_{12}\sqrt{\beta_n} \tag{3}$$

The drain currents I_A and I_B are fed into the square root blocks controlled by V_{34}, results in

$$I_{out} = I_{o1} - I_{o2} = KV_{34}\left(\sqrt{I_A} - \sqrt{I_B}\right) \tag{4}$$

where K is the gain of the square root blocks.

Substituting (3) into (4), yields

$$I_{out} = K\sqrt{\beta_n} V_{12} V_{34} \tag{5}$$

It can be seen that an output current appeared in (5) is in form of a multiplication function between two input signals V_{12} and V_{34}.

Based on this approach, both linear transconductor [9] and four-quadrant analog multiplier [10] have been proposed. Unfortunately, the early works in [9] and [10] require more than 3V for supply voltage which is not sufficiently low for modern analog design. Subsequently, a new square rooting circuit operated under 1.5V single supply was proposed in [11] which can be applied as a compact four quadrant analog multiplier as well [8]. However, the multiplier in [8] is not practical since it requires an ideal voltage reference to create the multiplication function.

In the next section, the improved square root circuit which is more suitable for realizing an analog multiplier will be described.

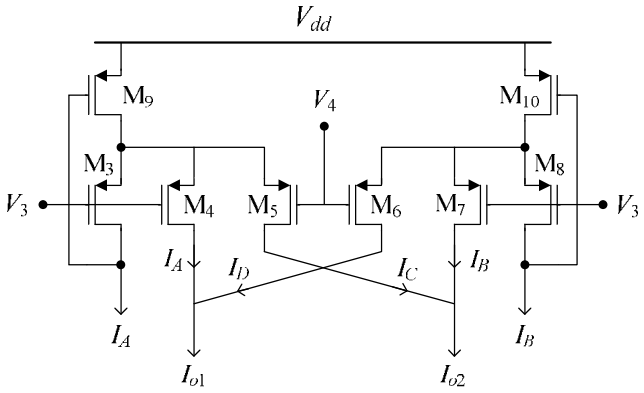

Figure 2. The proposed square rooting circuit.

III. SQUARE ROOTING CIRCUIT

A proposed square rooting circuit which is improved from [11] is shown in Fig.2. Using square-law relation of saturated MOSFET in strong inversion and setting M3-M8 to be identical, the currents I_C and I_D are found to be

$$I_C = \beta_p \left(V_{34} + \sqrt{\frac{I_A}{\beta_p}} \right)^2 \tag{6}$$

and

$$I_D = \beta_p \left(V_{34} + \sqrt{\frac{I_B}{\beta_p}} \right)^2 , \tag{7}$$

where $\beta_p = 0.5\mu_p C_{ox}(W/L)$ is a transconductance parameter of each PMOS transistor and $V_{34} = V_3 - V_4$ is a differential control voltage.

Considering (6) and (7) in conjunction with the fact that $I_A + I_D = I_{o1}$ and $I_B + I_C = I_{o2}$ leading to

$$I_{o1} = \beta_p V_{34}^2 + 2V_{34}\sqrt{\beta_p}\sqrt{I_A} + I_A + I_B \tag{8}$$

and

$$I_{o2} = \beta_p V_{34}^2 + 2V_{34}\sqrt{\beta_p}\sqrt{I_B} + I_A + I_B \tag{9}$$

Subtracting (8) and (9), results in

$$I_{out} = I_{o1} - I_{o2} = 2V_{34}\sqrt{\beta_p}\left(\sqrt{I_A} - \sqrt{I_B}\right) \tag{10}$$

It is obvious that the output current of the improved square root circuit is a function of a square root of I_A and I_B and its gain can be adjusted by the voltage V_{34} and transconductance parameter β_p .

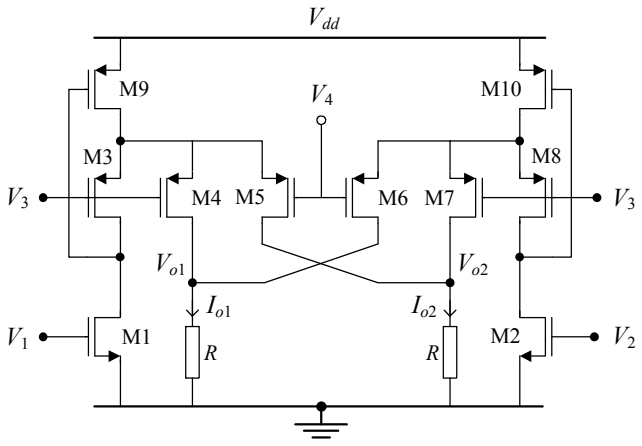

Figure 3. The proposed four quadrant analog multiplier circuit.

IV. Proposed Multiplier Circuit

Fig.3 shows the proposed multiplier circuit which is constituted by substituting the square rooting circuit in Fig. 2 into the square root blocks of Fig.1. Focusing on the differential output voltage we have found that

$$V_{out} = V_{o1} - V_{o2} = R\left(I_{o1} - I_{o2}\right), \tag{11}$$

Substituting (10) into (11), differential output voltage can be found as

$$V_{out} = 2RV_{34}\sqrt{\beta_p}\left(\sqrt{I_A} - \sqrt{I_B}\right) \tag{12}$$

Finally, substituting (3) into (12) yields

$$V_{out} = 2R\sqrt{\beta_n\beta_p}V_{12}V_{34} \tag{13}$$

Now, we have an output offset-free four quadrant analog multiplier and its gain can be adjusted by the load resistor R and the dimensions of each MOSFET.

V. Simulation Results

The multiplier circuit in Fig. 3 was designed and simulated by using PSPICE for 0.35 micron CMOS process parameter with main parameters $V_{tn} \cong 0.51$ and $V_{tp} \cong -0.66$. The input voltage V_{12} and V_{34} are set to be balance with common mode voltages of $V_{C1} = 1$V and $V_{C2} = 0.2$V, respectively and supply voltage V_{DD} is set at 1.8V. Transistor dimensions are listed in Table 1. Trying to avoid channel length modulation and short channel effects, the channel lengths of all transistors are set to be two times longer than 0.35 micron. The load resistors R are chosen to be 2.5 kΩ. At the quiescent point, power consumption of the proposed multiplier is 165 μW.

Fig. 4 shows simulated DC transfer characteristics of the proposed multiplier, when V_{12} was swept continuously from -0.4V to 0.4V while V_{34} was varied from -0.4V to 0.4V with 0.1V step size. It can be observed that the linear range of V_{12} is approximately ±0.4V.

Transient response of the multiplier operated as amplitude modulator is shown in Fig. 5. A 0.4V, 25 kHz sinusoidal carrier signal V_{12} shown in Fig. 5(a) was multiplied by a 0.4V, 1 kHz sinusoidal modulating signal V_{34} shown in Fig. 5(b). A resulting waveform is shown in Fig. 5(c).

Frequency response of the multiplier for various gains was set by sweeping V_{34} from 0.1V to 0.4V with 0.1V step size as the same condition of DC sweep and the results show in Fig. 6 demonstrating that bandwidth of the proposed circuit is higher than 110 MHz for all gains.

Circuit linearity is examined by simulated total harmonic distortion (THD), when V_{34} was fixed at 0.4V and applying various amplitudes of 25 kHz sinusoidal V_{12}. The result is displayed in Fig. 7 that less than 0.6% THD is achieved for V_{12} amplitude about 0.4V.

Comparative results of the simulated performances between this work and [8] are shown in table II.

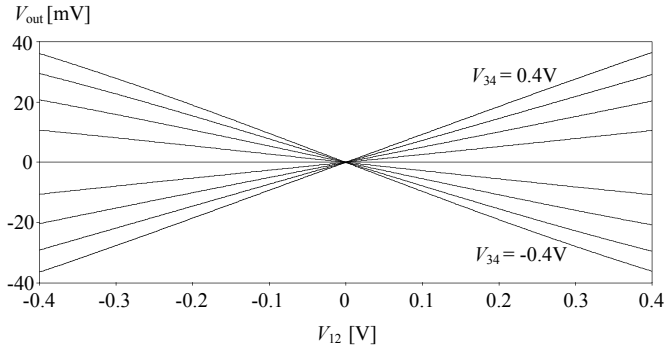

Figure 4. DC transfer characteristics.

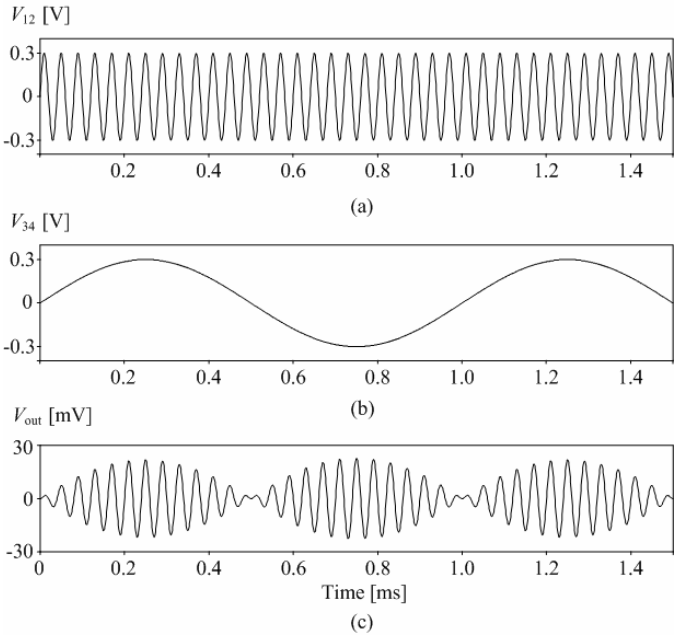

Figure 5. Output waveforms
(a) V_{12} sinusoidal carrier signal (b) V_{34} sinusoidal modulating signal
(c) Output waveform of amplitude modulator

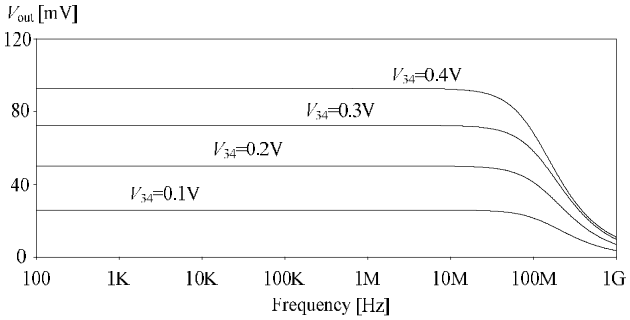

Figure 6. Frequency response.

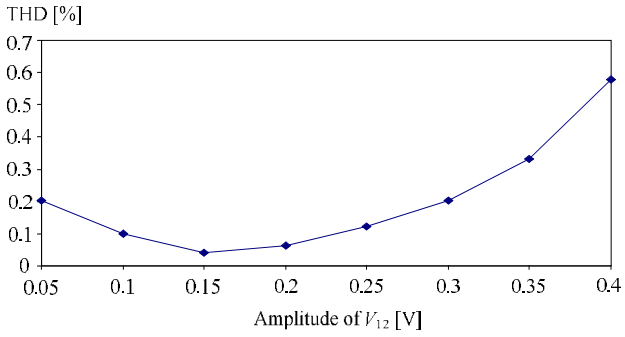

Figure 7. Simulated total harmonic distortion.

TABLE I
TRANSISTOR DIMENSION

Transistor	*W* [μm]	*L* [μm]
M1-M2	1	1
M3-M8	3.5	1
M9-M10	40	1

TABLE II
Comparison of simulated characteristics between the proposed multiplier and the multiplier in [8]

Multiplier characteristic	Proposed	Ref. [8]
Power consumption [μW]	165	200
THD [%] *	≅ 0.6	≅ 0.8
-3 dB Bandwidth [MHz]	>110	>10
Total physical area [μm]^{2} **	103	672

* V_{34} was fixed at 0.4V and V_{12} is a 25 kHz sinusoidal signal with amplitude of 0.4V
** roughly estimated from transistor dimensions

VI. CONCLUSION

A new square rooting circuit can be used for realizing a CMOS four-quadrant analog multiplier has been presented. The resulting multiplier circuit is improved to be more compact than the previous work. The extra voltage reference is not required for the proposed circuit. As a result, the proposed multiplier provides high bandwidth, high linearity and low static power consumption. Simulation results are given to verify the multiplier circuit performances.

ACKNOWLEDGMENT

The authors would like to thank C. Sawigun for useful suggestion and discussion.

REFERENCES

[1] S. Yan and E. Sanchez-Sinencio, "Low Voltage Analog Circuit Design Techniques: A Tutorial," *IEICE Trans. Analog Integrated Circuits and Systems*, vol. E00-A, no. 2, pp. 1-8, Feb. 2000.

[2] G. Han and E. Sanchez-Sinencio, "CMOS Transconductance Multipliers: A Tutorial," *IEEE Trans. Circuits Syst. II*, vol. 45, no. 12, pp. 1550-1563, Dec. 1998.

[3] B. Maundy and M. Maini, "A Comparison of Three Multiplier Based on the V_{gs}^{2} Technique for Low-Voltage Applications," *IEEE Trans. Circuits Syst. I*, vol. 50, no. 7, pp. 937-940, Jul. 2003.

[4] R. G. Cavajal, J. Ramirez-Angulo, A. J. Lopez Matin, A. Torralba, J. A. Gomez Galan, A. Carlosena, and F. M. Chavero, "The flipped voltage follower: a useful cell for low-voltage low-power circuit design," *IEEE Trans. Circuits Syst. I*, 2005, 52,(7), pp. 1276-1291.

[5] J. Ramirez-Angulo, R.G. Carvajal, and J. Martinnez-Heredia, "1.4V supply, wide swing, high-frequency CMOS analogue multiplier with high current efficiency," *Proc IEEE ISCAS*, May 2000, Geneva Switzerland, Vol. V, pp. 553-536.

[6] A. Demosthenous, and M. Panovic, "Low voltage MOS linear transconductor/squarer and four-quadrant multiplier for analog VLSI," *IEEE Trans on Cir. and Syst. I: Regular paper*, vol. 52, no. 9, pp. 1721-1731, 2005.

[7] C. Sawigun, and J. Mahattanakul, "A low voltage CMOS linear transconductor suitable for analog multiplier application," *Proc. IEEE ISCAS'06*, pp. 1543-1546, KOS, Greece, 2006.

[8] C. Sawigun and A. Demosthenous, "Compact low voltage CMOS four quadrant analog multiplier," *Electronics Letters*, vol. 39, no. 25, pp. 1771-1772 , Sep. 2006.

[9] J. Mahattanakul and C. Toumazou, "Independent control of transconductance gain and input linear range in a MOS linear transconductance amplifier," *Electronics Letters*, vol. 32, no. 18, pp. 1629-1630 , Aug. 1996.

[10] A. Hyogo, Y. Fukutomi and K. Sekine, "Low voltage four quadrant analog multiplier using square-root circuit based on CMOS pair," *Proc. of IEEE ISCAS'99*, pp. II 274-277, 1999.

[11] C. Sawigun, N. Kiatwarin and W. Ngamkham, "A low voltage MOS linear transconductor with constant input linear range," *ECTI 2006*, vol. 1, pp. 167-170, Ubon Ratchathani, Thailand, 2006.

Verifying Various Generation of Random Number Sequence on Wave-Pipelined PRNG

Tomoaki Sato, Kazuhira Kikuchi, and Masa-aki Fukase
Hirosaki University
Bunkyo-cho 3
Hirosaki, Aomori 036-8561 JAPAN

***Abstract*- A circuit design by using wave-pipeline technology is very useful to achieve a high-speed and low-power circuit. Wave-pipelined PRNG (Pseudo-Random Number Generator) has not only these features but also the function to change the order of the pseudo-random number sequence easily by changing an operation clock frequency of the output register. However, the function has not yet so far verified. Thus, it is verified in this paper by the gate-level simulation for wave-pipelined PRNG added to output registers.**

I. INTRODUCTION

A strong cipher is needed for an embedded device including a mobile phone or PDA connected with the Internet [1]. In addition, the embedded device requires a circuit operating with high-speed and low-power consumption. Wave-pipelined PRNG (Pseudo-Random Number Generator) [2] is one of the circuits that can satisfy these demands.

Wave-pipeline technique that enables a pipeline operation without using a register [3]-[5] is very useful to achieve a circuit operating with high-speed and low-power consumption [6]. Nevertheless, wave-pipeline technique applied up to now has been limited to only combination logical circuits. Thus, we have exploited wave-pipelined LFSR (Linier Feedback Shift Register) [7], [8]. Wave-pipelined PRNG is composed of LFSR.

We have evaluated wave-pipelined PRNG in view of performance, operation speed, and power consumption. We have also found that wave-pipelined PRNG is able to generate various random number sequences easily by controlling the operation clock frequency [9]. However, the generation has not so far verified.

This paper presents the verification of random number generation by wave-pipelined PRNG. We add output registers to wave-pipelined PRNG and verify the output value of registers by gate-level simulation. As a result, wave-pipelined PRNG is shown that various random number sequences easily generated.

II. WAVE-PIPELINE TECHNIQUE

Not only high clock frequency but also low power dissipation can be obtained at the same time by wave-pipelining [3]-[5]. It exploits high throughput combinational logic blocks in which as many as data are launched unless they conflict. Although wave-pipelining was attempted to the entire region of a processor, it was viewed pessimistically because it requires removing general registers as well as pipeline registers from processors. It seems hard to eliminate general registers playing fundamental roles in sequential circuits. The insufficient power of CAD tools so far developed is another reason why wave-pipelines have been applied out of processors.

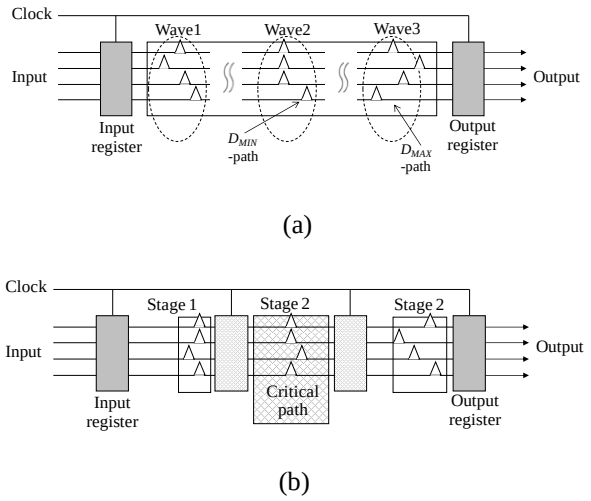

Figure 1. Synchronization of pipelines. (a) Wave-pipeline. (b) Conventional pipeline

Accordingly, design and evaluation methods for wave-pipelines have not yet established well compared with those for conventional pipelines. Mostly wave-pipelines have been so far applied to simple unifunctional circuits such as adders, multi-pliers, counters, and DRAM. Regarding multifunctional wave-pipelines, a wave-pipelined ALU has recently appeared [10]-[13].

Then, a microprocessor developed by using wave-pipelines in part appeared [14]. It is 14-segment ULTRASPARC-III whose second and third instruction fetch segments have been wave-pipelined. Another example is an asynchronous wave-pipeline, though it is not compatible with conventional processors. Wave-pipelined LFSR that is a sequential circuit had not been achieved [2].

The signal path of combinational circuit is uneven of delay time. The most high-speed signal in one group in a clock has the possibility to collide with the slow signal in just before clock. The problem was solved to wave-pipelined combinational circuit shown in Figure 1 (a) by the delay time of all signal paths is brought close at the delay time of critical path.

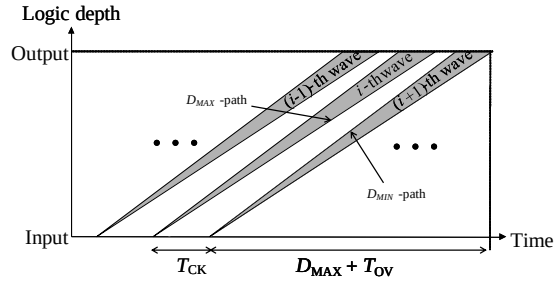

Figure 2. Wave model of Figure 1 (a)

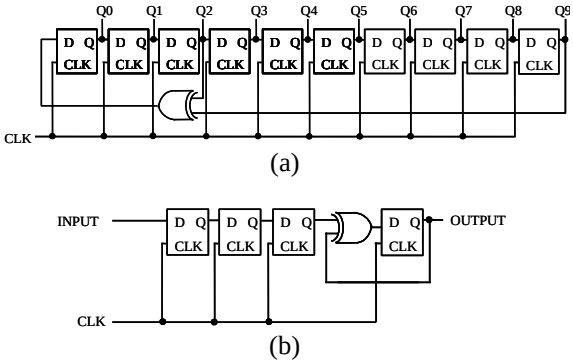

Figure 3. Conventional LFSR. (a) PRNG. (b) CRC

The relation between the clock cycle and delays is obtained as follows [4].

$$T_{CK} > (D_{MAX} - D_{MIN}) + T_{OV}. \qquad (1)$$

Here,

T_{CK}: Clock cycle time

T_{OV}: Overhead time

From Eq. (1), $D_{MAX} - D_{MIN}$ should be close to 0 as much as possible in order to obtain minimum T_{ck}. One of solution to satisfy this requirement can be conceived from Figure 2 that shows relation between time and logical depth.

TABLE I
DEVELOPMENT ENVIRONMENT

Function	Name	Vendor
Microprocessor Main Memory	Celeron 2.4GHz 512 Mbytes	Intel
Operating System	Windows 2000 Professional	Microsoft
Development Software	Quartus II Version 5.1	Altera
CPLD Device	MAX7000S EPM7128LC84-15	Altera
Power Estimator	MAX Power Calculator Spreadsheet Version 1.2	Altera

III. WAVE-PIPELINED PRNG

A. *Wave-pipelined LFSR*

A LFSR circuit includes all circuit that multiplied return by shift register in some arithmetic circuit as shown in Figure 3 [2]. A PRNG of Figure 3 (a) and a CRC Circuit of Figure 3 (b) are a LFSR circuit. CRC-32 used for Ethernet hardware is composed of 32 registers, and initial value of WEP that is encryption of wireless LAN uses PRNG composed of 24 registers.

The use of a lot of registers is a cause of the increase of power consumption with a clock. Because the use of a wireless LAN is indispensable in a mobile computing, the CRC processing circuit and the WEP processing circuit become indispensable. Therefore, power consumption is increased in using it.

B. *Design of Wave-pipelined PRNG*

Table I shows development environment, and Figure 4 shows the logic circuit of conventional PRNG and Wave-pipelined PRNG. Wave-pipeline technique should adjust delay time by the methods other than the use of a register. Here, we adjust delay time by using buffers.

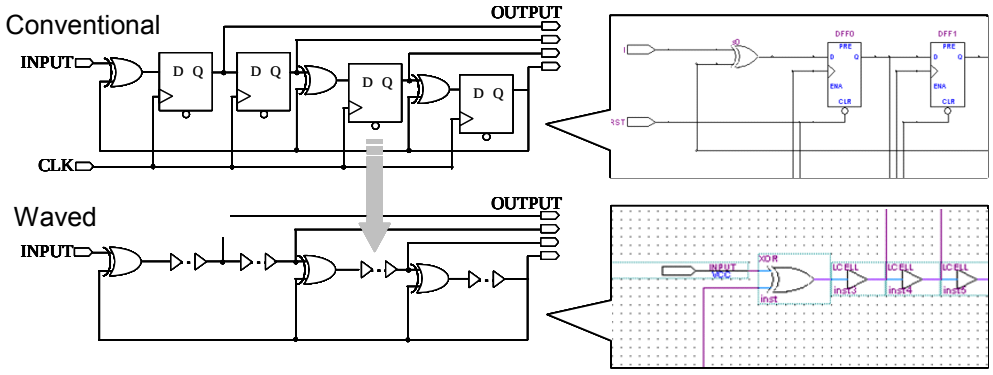

Figure 4. The logic circuit of conventional PRNG and Wave-pipelined PRNG.

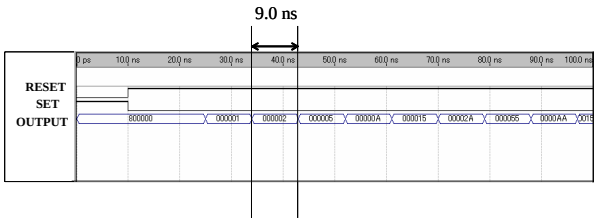

Figure 5. Gate-level simulation result of 24-bit waved-PRNG.

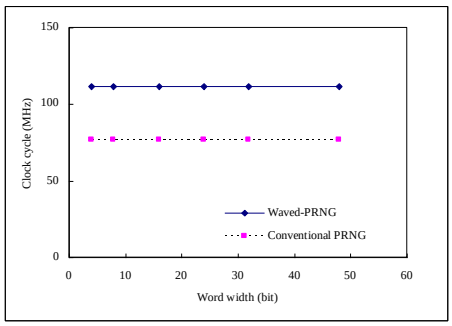

Figure 6. Operation speed of waved-PRNG circuit vs. conventional PRNG circuit.

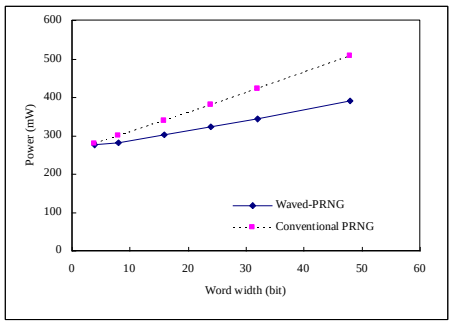

Figure 7. Power consumption of waved-PRNG circuit vs. conventional PRNG circuit.

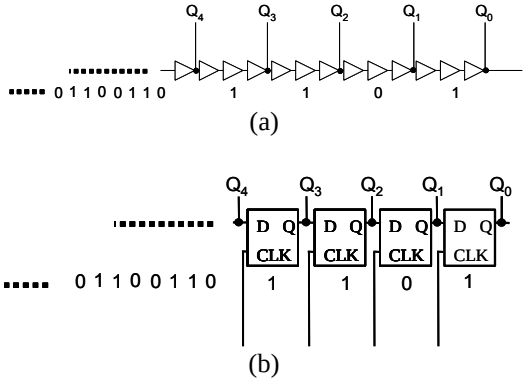

Figure 8. PRNG operation. (a) Wave-pipelined PRNG circuit. (b) Conventional PRNG circuit.

C. Evaluation of operation clock speed and power consumption

We have evaluated Wave-pipelined PRNG by using the development environment in Table I. Figure 5 shows the gate-level simulation result of 24-bit Wave-pipelined PRNG. According to the result of gate-level simulation, it shows that the 24-bit Wave-pipelined PRNG circuit operates normally without using a register and by 111.1 MHz.

Figure 6 shows the evaluation result of operation speed of conventional PRNG circuit and Wave-pipelined PRNG circuit. Figure 7 shows the evaluation result of power consumption of them. According to Figure 6 and Figure 7, Wave-pipelined PRNG circuit is unities high-speed and low-power consumption operation. Plotting word width of Figure 6 and Figure 7 are 4, 8, 16, 24, 32, and 48 bits respectively.

IV. VERIFYING RANDOM NUMBER SEQUENCES

We discuss that the Wave-pipelined PRNG circuit generates various random number sequences by controlling the operation clock frequency. As shown in Figure 8 (a), the Wave-pipelined PRNG generates random numbers. Figure 9 shows output when the operation clock speed is reduced by half and 1/3. There is a definite relation between clock frequency and random output. This does not hold for

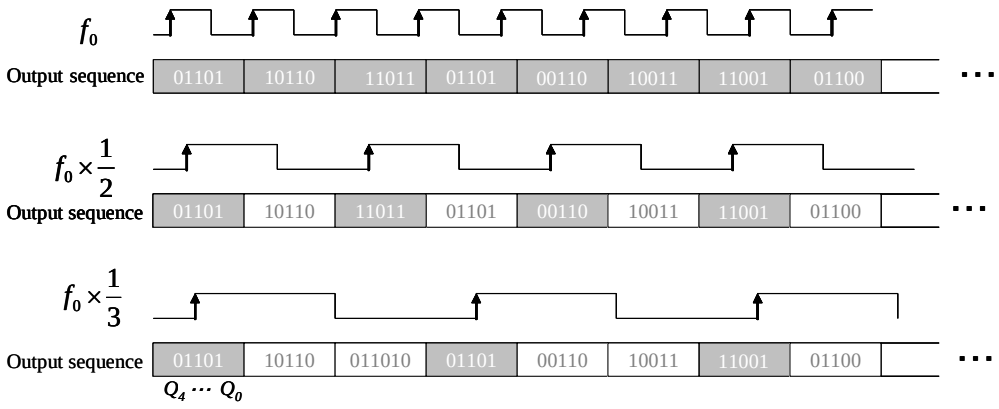

Figure 9. Output values of Figure 8 (a).

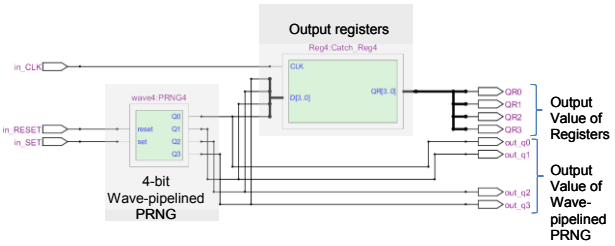

Figure 10. Wave-pipelined PRNG with output registers.

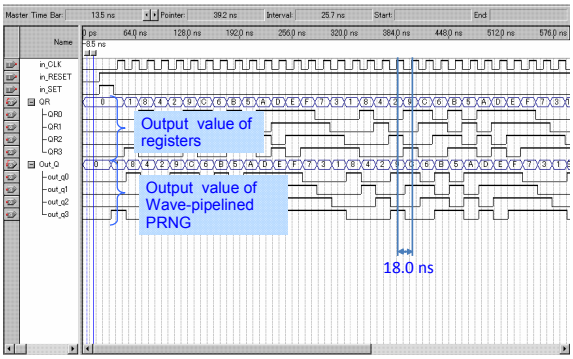

(a)

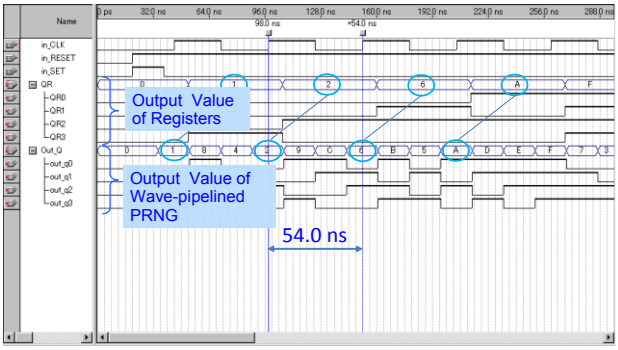

(b)

Figure 11. The simulation result of Figure 10. (a) 55.6MHz operation. (b) 18.5MHz operation.

conventional PRNG as is explained in Figure 8 (b).

Because we did not add Wave-pipelined PRNG to output registers, we were not able to confirm the operation of Figure 9. Therefore, output registers are added to Wave-pipelined PRNG as shown in Figure 10.

A. Verifying by gate-level simulation

The circuit is evaluated by the gate level simulation using the development environment of Table I. Figure 11 is shown the simulation result of Figure 10. Figure 11 (a) shows that 55.6 MHz operation is the same as the operation speed of Wave-pipelined PRNG. Figure 11 (b) shows that 18.5 MHz operation is 1/3 at the operation speed of Wave-pipelined PRNG. The reason why the circuit of Figure 10 is slower than the result of Figure 6 is to use output registers.

The result of Figure 11 (b) shows Wave-pipelined PRNG generates various random number sequences by controlling the operation clock frequency. When conventional PRNG circuit is used, the generation of various random number sequences needs the circuit that uses a lot of registers.

V. CONCLUDING REMARKS

We have described in this paper generating various number sequences by controlling the operation clock frequency of output registers of wave-pipelined PRNG. The function has been verified by the gate level simulation. Additionally, wave-pipelined PRNG has the feature that operates by high-speed and low-power consumption. Wave-pipelined PRNG makes it possible to design a strong cipher that operates by high-speed and low-power consumption.

REFERENCES

[1] M. Fukase, H. Takeda, and T. Sato, "Hardware/Software Co-Design of a Secure Ubiquitous System," Lecture Notes in Artificial Intelligence, 2007 (To be published).

[2] T. Sato, R. Sakuma, D. Miyamori, and M. Fukase, "High-Speed and Low-Power LFSR by Wave-Pipelining," Proc. of CCCT, Vol. III, pp. 396-401, 2004.

[3] L. Cotton, "Maximum rate pipelining systems," Procs. AFIPS Spring Joint Computer Conference, pp. 581-586, 1969.

[4] F. Klass and M. J. Flynn, "COMPARATIVE STUDIES OF PIPELINED CIRCUITS," Stanford University Technical Report, No. CSL-TR-93-579, July 1993.

[5] W. P. Burleson, M. Ciesielski, F. Klass, and W. Liu, "Wave-Pipelining: A Tutorial and Research Survey," IEEE Trans. on Very Large Scale Integration (VLSI) Systems, Vol. 6, No. 3, pp. 464-474, Sept. 1998.

[6] M. Fukase, T. Sato, R. Egawa, and T. Nakamura, "A Wave-Pipelined Biprocessor Achieving Remarkable Compatibility between Low Power and High Speed," Proc. of 10th NASA Symposium on VLSI Design, pp. 8.3.1-8.3.8, Mar. 2002.

[7] D. Miyamori, R. Sakuma, T. Sato, and M. Fukase, "The Evaluation of Wave-Pipelined CRC," 2003 Joint Convention Record, the Hokkaido chapters of the Institutes of Electrical and Information Engineers, pp. 349, 2006.

[8] T. Sato, R. Sakuma, D. Miyamori, and M. Fukase, "Hardware Security-Embedded Wireless LAN Processor," Proc. of ECTI-CON 2006, Vol. II, pp 839-842, 2006.

[9] T. Sato, K. Kikuchi, and M. Fulase, "A PRNG Circuit on PLD with Feature of Low-Power, High-Speed, and Various Generation of Random Number Sequence," Proc. of IEEE TENCON 2006, pp. CA2.1.1-CA2.1.4, 2006.

[10] T. Sato, M. Fukase, and T. Nakamura, "Performance analysis of a wave-pipelined ALU," Technical Report of IEICE, CPSY 2000, Vol. 100, No. 20, pp. 1-6, 2000.

[11] M. Fukase, T. Sato, R. Egawa, and T. Nakamura, "Scaling up of Wave Pipelines," THE FOURTEENTH INTERNATIONAL CONFERENCE ON VLSI DESIGN, Jun. 2000.

[12] M. Fukase, T. Sato, R. Egawa, and T. Nakamura, "Breakthrough of Superscalar Processors by Multifunctional Wave-Pipelines," Proc. of 9th NASA Symposium on VLSI Design, pp. 6.3.1-6.3.17, Nov. 2000.

[13] M. Fukase, T. Sato, R. Egawa, and T. Nakamura, "Designing a Wave-Pipelined Vector Processor," Proc. of the Tenth Workshop on Synthesis and System Integration of Mixed Technologies, pp. 351-356, Oct. 2001.

[14] Tim Horel and Gary Lauterbach, "UltraSPARC-III: Designing Third-Generation 64-Bit Performance," IEEE Micro, Vol. 19, No. 3, pp. 73-85, 1999.

Asynchronous System Bus Enhancement by Interrupt and DMA Technique

Sufian Sudeng and Arthit Thongtak
Digital System Engineering Laboratory (DSEL), Department of Computer Engineering,
Faculty of Engineering, Chulalongkorn University
254 Phyathai Road, Pathumwan, Bangkok, Thailand 10330
Tel: +66-2-218-6956, Fax: +66-2-218-6955
E-mail: Sufian.S@Student.chula.ac.th, Arthit@cp.eng.chula.ac.th

***Abstract*- This paper proposes a procedure to enhance an asynchronous system bus. The designed bus is incorporated with synchronizing operation between synchronous components and asynchronous ones. Interrupt and DMA technique are chosen for bus capability enhancement.. The prominent point of this work is to take an interrupt and DMA technique assembled with asynchronous system bus. The designed system bus is described in HDL language. The experiments can show the concurrent processing between asynchronous processor execution and DMA transfer operation.**

I. INTRODUCTION

Asynchronous circuits are well known for last decade because of the clock skew avoided. The clock skew occurs when the global clock used to synchronize their operation which can not be distributed to the entire system at the same frequency [1]. It is a major problem cause the system may malfunction. It is very hard to avoid this problem when high speed circuits' transfer needed. As a result, it limits the speed of synchronous circuits. Asynchronous circuits do not use global clock, circuits respond to signal transitions at any time, and outputs can be sent instantly after the operation completion. More outstanding shot of the asynchronous circuit over synchronous circuits is high speed operation because it is not limited by the slowest part of circuits. Low power consumption due to signal transitions are made only when necessary [2].

Causes of complex circuits' design of asynchronous circuit produce some limitation to the design to be large system. Which operate with asynchrony operation, some asynchronous circuits design like processor, there emerge limitation to enhance the design to be large system. It also serious when propagation needed, like connecting an asynchronous processor with multiple peripherals, because memory and I/O module on a present time operate with clock [6], It's a choice if be able to compromise some element that operate with clock to work together with asynchronous circuits, bus enhancement and communicating between synchronous and asynchronous circuits are main purpose of this paper.

DMA design is splash to five working state, compose of registers to store intermediate data, adder/subtracted to count up and down of write and read addresses, the DMA design is capable to work with our asynchronous system bus as well by add stretchable interfacing [6]between bus and DMA module.

Asynchronous processor architecture, control unit, and instruction has modified for interrupt and DMA capability.

Part of paper start with introduction to background of asynchronous system bus design and explain the design of interrupt and DMA, and follow with full system simulation and provide some future work on the final section.

II. ASYNCHRONOUS SYSTEM BUS OVERVIEW

The bus designs are Multiplex. There are data and address transition on the same lines. 8-bit with dual-rail encoded, transition by 4-phase signaling transition protocol[4]. The processes are start with design each component and group them together.

A. Bus components [8]

a. Bus Interface

Bus interface is design to interface with asynchronous processor. Due to the multiplex bus design, bus interface also handshake with bus controller to control the sequence of data, address or spacer transition.

b. Bus Driver

Bus Driver act like an on/off switch to enable/disable transition signal on the bus. Design with tri-state buffer and C-element (the element that produce output 1 when all of input are 1, produce out 0 when all of input are 0, Otherwise its hold previous state)

c. Bus lines

On account of high impedance state of Tri-state buffer, there were making some problem for asynchronous circuits. Need to improve to be zero value when it's high impedance by added weak inverter to each line on the bus.

d. Bus Receiver

This component use to receive data from bus signal and catch all signals before transfer to the destination, Design with C-element

e. Bus Controller

Design with STG (Signal Transition Graph), use to control the synchronization on the bus, due to multiplexing, its responsible to control the sequence of data, address, and spacer transition.

III. INTERRUPT DESIGN

The processor instruction that use in this system has 16-bit length instruction set, by load instruction from ROM to IR register. When 16-bit instruction load in to IR register, IR register response to separate instruction in to two types, *opcode* and *operand*, opcode is load to control unit section, the operand is load to general purpose register or accumulator follow on instruction type [5, 7]. The modification, benefit to generate ***virtual instruction*** that occur during interrupt even, When interrupt instruction has occurred, a virtual instruction has generate by external signal and load to IR register.

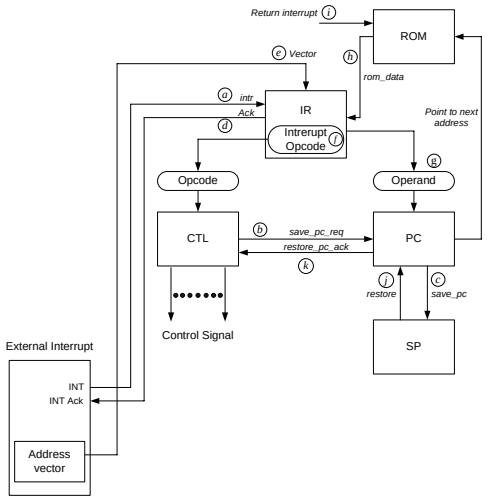

Figure 1. Interrupt Instruction in Asynchronous Processor design

From figure 1 illustrate transaction sequence of an interrupt operation.

a. Interrupt signal asserted
b. Control unit tell pc register to save current pointer
c. Save PC to SP register
d. Interrupt acknowledge asserted
e. Address vector load to IR register
f. Interrupt opcode is generated
g. Load new PC value
h. PC point to interrupt service routine, ROM data load to IR
i. Instruction meets RETI command (return interrupt).
j. RETI command produces SP register to restore value to PC.
k. PC restore acknowledge to control unit
l. Process normal instruction

The processor work on following sequences, First step load instruction that point by PC to IR register, and process base on type of instruction. When EI flags is disable, interrupt is not respond until finish instruction execution of previous instruction EI is enable, if interrupt signal occur by assert *intr* signal by external device, the IR register release ROM connection and produce it self instruction call *virtual instruction* , this instruction is valid for interrupt instruction and separate instruction to two piece, opcode and operand. Opcode is responsible to save / restore signal to pc register , operand is first address that keep an interrupt service routine, when PC register receive save signal from control unit it save current pointer to SP register and jump to next address that produce by virtual opcode.

IV. DMA DESIGN

The Asynchronous processor is a master device on the asynchronous system bus, that it is able to initiate read and write transfers to all devices on the bus. The DMA controller is slave device, which is only able to response to read or write requests. The DMA controller is required to initiate read and write transfers to memory and also other I/O on the bus, DMA controller also required to be a master device

As there will be more than on asynchronous bus master in the system, the asynchronous system bus specification required the presence of a bus arbiter. The bus arbiter selects which master is to have right to the bus at any one instant in time. An arbiter also exits for the asynchronous processor. Initially the DMA controller is programmed by asynchronous processor. This information is stored in internal DMA registers. Include following information: base address for transfer source, base address in memory to where the data is transferred and size of data transfer. The DMA controller also be slave on the asynchronous system bus in order the asynchronous processor access these registers

A. DMA Function

The DMA controller waits for *dma_req* line to assert and take over the asynchronous system bus from asynchronous processor. It checks its internal registers to obtained details of the transfer. The DMA controller read data from the source, store it in internal buffer, and then write it out to the memory, until the transfer is complete. The DMA controller then release usage of asynchronous system bus and activate the IRQ line in order to indicate the asynchronous processor that transfer was complete. If any time the asynchronous processor requires usage of asynchronous system bus it is able to take priority over the DMA controller. The DMA controller check it has control of the bus at each stage, if it does not the controller wait for the bus become available, the asynchronous processor has finished using the bus

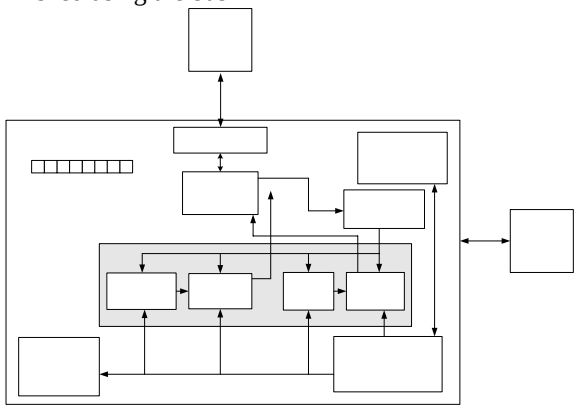

Figure 2. DMA controller architecture

B. DMA Architecture

The internal architecture is very closely based on the classic DMA controller that shown of figure 2, the architecture proposed of the DMA controller split into above functional units. The most complex of these units is timing and control unit, which consist of a large state machine which described in the diagram on the figure 3. The address decoder derives clock enable signal and present 8-bit registers which store details of the transfers.

C. DMA state machine

The most complex part of DMA controller is state machine as shown figure 3

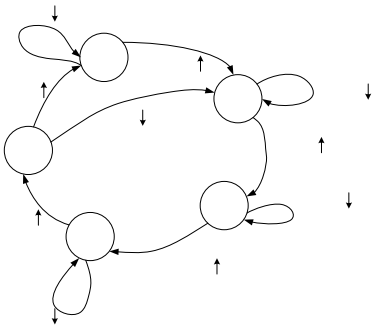

Figure 3. DMA state machine

S0 – Initial State
S1 –DMA Programmed & Ack_to_I/O
S2 – Check status of I/O device
S3 – Reset R/W signals
S4 – Terminal Check

D. Transaction flow

The DMA transaction following on this sequence

a. I/O Module assert *DMA_req* signal
b. DMA assert *Hold* signal to processor
c. Processor assert *Hold_ack* signal to DMA (processor program base address to DMA base register and count register [ST command]).
d. DMA assert *DMA_ack* signal to I/O Module
e. I/O Module assert Device_ready to DMA (transfer type is set by I/O Module (Read or Write)
f. DMA transfer (read or write transaction occur)
g. DMA assert *TC* signal indicate zero value of count register
h. DMA interrupts to processor for complete transaction

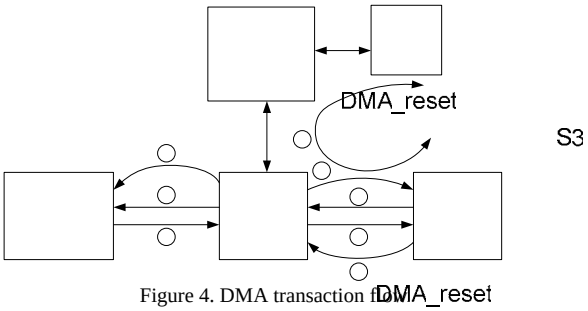

Figure 4. DMA transaction flow

V. SYNCHRONOUS AND ASYNCHRONOUS INTERFACING

This part is design to communicate between synchronous and asynchronous section, design with stretchable clock [6].

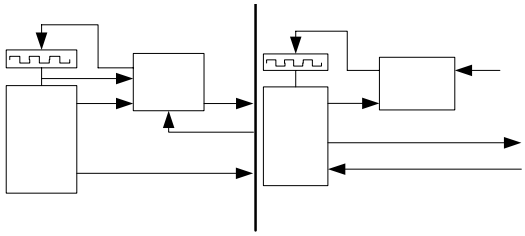

Figure 5. Stretchable clock for read (a) and write (b) interfacing

The clock control is generated using the handshaking signals and the internal state of the synchronous region, a block has either a read port or a write port. Read port provides data for an external element while a write port receive data into the module. In a 4-phase protocol, each module must receive two asynchronous transitions to complete a cycle. Each synchronous module must go through to two clock cycles to allow for two possible stretch signals.

VI. SIMULATION RESULT

The system is design with VHDL description language [3] separately on each component and simulates each component for correct signal behavior and functional. Then combined those together to form a full system as shown on figure 6 .after that experimental simulation are shown.

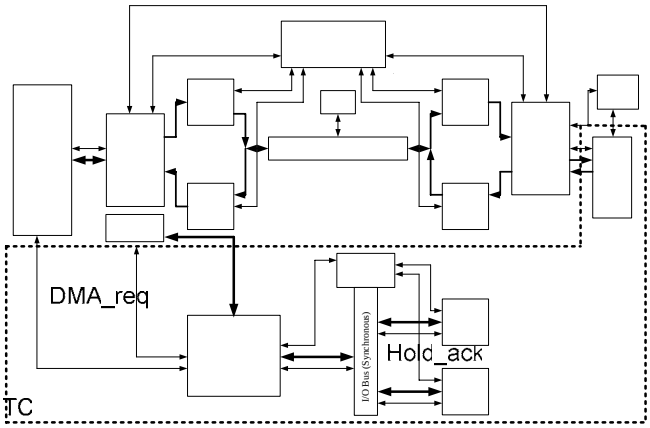

Figure 6. Simulation Environment

Simulation Program

```
            ORG     0000H
            LD      A,#39H  ; A = 39H
            ST      A,R0    ; R0 = 39H
            LD      A,#24H  ; A = 24H
            ST      A,R1    ; R1 = 24H
Device_ready AND    A,#14H  ; A= 04H
            LD      A,#C8H  ; A = C8H
            ADD     A,R0    ; A = 01H, CARRY = 1
            ST      A,R1    ; R1 = 01H
```

```
OR      A,R0     ; A = 39H
OR      A,#B7H ; A = BFH
LD      A,#13H  ; A = 13H
ST      A,@R1   ; M(01) = 13H
LD      A,#00H  ; A=00H
INTR :
LD      A,#01H   ; A=01H
ST      A,@1FFH ; DMA_Base = 01H
LD      A,#0AH  ; A=0AH
ST      A,@2FFH ; DMA_Count = 0AH
RETI
END
```

The bold lists on simulation program are shown on waveform diagram.

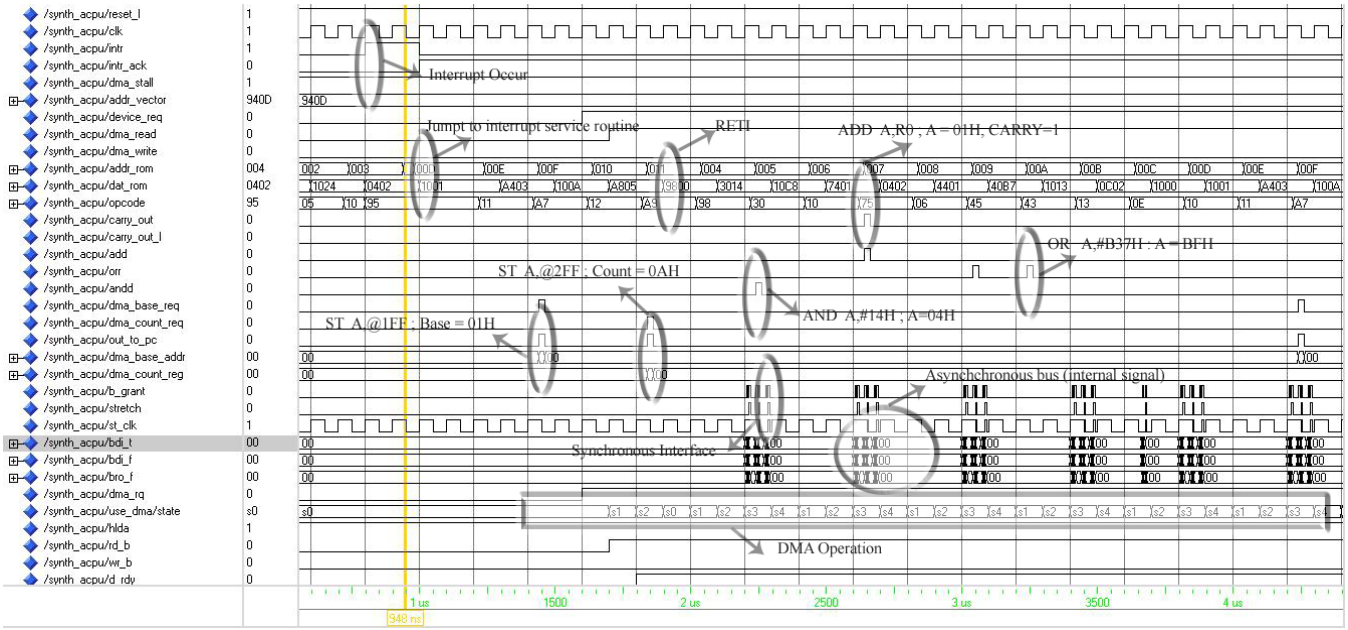

Figure 7. Experimental Simulation Result

VII. Conclusion And Future Work

This paper proposes a technique to enhance an asynchronous system bus [8]. Introduce synchronization procedure between synchronous and asynchronous circuits. Interrupt and DMA technique are chosen for bus enhanced, DMA is design with state diagram, and connect with two input/output buffers, I/O arbitration controlled, The system work as follows, interrupt signal from I/O module assert to tell processor release the bus, when processor release it, operation begin by DMA controller concurrently with processor execution. For future work, improve the system to interface with present I/O devices, such as USB, LCD character screen or serial port interfacing, PS/2 mouse/keyboard, VGA and etc. moreover, modify DMA controller to be asynchrony operation.

Acknowledgment

The research is supported by TJTTP-OECF (Thailand - Japan Technology Transfer Project – Japanese Overseas Economic Cooperation Fund)

References

[1] Davis. A, Nowick.S.M “An Introduction to Asynchronous Circuit Design” , 1997

[2] S.Hauck. “Asynchronous Design Methhodologies : An Overview”. Proceedings of the IEEE. vol.83. No.1. pp.69-93, January 1995.

[3] J.Bhasker. “*A VHDL Primer*”. Prentice-Hall, Inc., 1992. ISBN 0-13-952987-X.

[4] Molina, P.A.; Cheung, P.Y.K ,“A Quasi Delay-Insensitive Bus Proposal for Asynchronous Systems” Proceedings Third International Symposium on Advanced Research in Asynchronous Circuits and Systms, 1997 Pages:129-139

[5] T.Nanya., Y.Ueno., H.Kagotani., M.Kuwako., A.Takamura. TITAC : Design of a Quasi-Delay-Insensitive Microprocessor. IEEE Design & Test of Computers., Vol.11., No.2, pp.50-63, Summer 1994.

[6] Bormann, D.S.; Molina, P.A.; Cheung, P.Y.K, “Combining asynchronous and synchronous circuits using stretchable clocks” IEEE Colloquium on Design and Test of Asynchronous Systems, 28 Feb 1996,pp.4/1-4/8

[7] P.Ruangsilsap. “Design of 8-bit scalable-delay-insensitive microprocessor using FPGA”. Master thesis, Chlalongkorn University, Bangkok, Thailand, 2001

[8] S.Sudeng, A.Thongtak:” A Design of System Bus for Asynchronous Circuits” International Technical Conference in Circuits/Systems Computer and Communication (ITC-CSCC2006), Pang Suan Kaew hotel, Chiangmai, Thailand on July 10-13, 2006

CMOS compatible Ion Sensitive Field Effect Transistor with Silicon Nitride Membrane for pH Measurement System

W. Bunjongpru, O. Trithaveesak, K. Sowsuwan, W. Jeamsaksiri, C. Hruanun, and A. Poyai
Thai Microelectronics Center (TMEC)
51/4 Moo1, Suwintawong road, Wangtakien district, Amphur Muang, Chachoengsao
Thailand 24000

***Abstract*- Two main parts are necessary to implement a prototype of pH measurement system: pH sensor and interface unit. The pH sensors, based on Ion Sensitive Field Effect Transistor (ISFET), are designed and then fabricated used 6-inch silicon wafers by conventional CMOS process. As ion sensitive membrane, all transistors have 50nm high quality silicon nitride thin film which was deposited on 10nm silicon dioxide. The sensitivity of sensors is found in the range of 40-55 mV/pH. The interface unit supplies the sensor with a constant current and voltage. The pH value is identified from the output voltage of the circuit. From the results, the system can be used for measuring the pH values in the range of 4-10 with a resolution of 0.1 pH.**

I. INTRODUCTION

Monitoring of pH value is beneficial for the agriculture and environment fields. The conventional pH sensors are in a form of the glass electrode. Such sensors have many disadvantages, the size and maintenance of electrode, the reaction time, for examples. An alternative pH sensor was introduced by Bergveld [1]. In stead of glass electrode, the sensor is a solid state device, known as Ion Sensitive Field Effect Transistor (ISFET). Principally the ISFET is very similar to Metal Oxide Semiconductor Field Effect Transistor (MOSFET). Fig.1 shows the schematic of MOSFET compared to ISFET. In stead of the gate on the isolator in case of MOSFET, the gate of ISFET, called reference electrode, float in the electrolyte and the insulator, as know as Ion Sensitive Membrane (ISM), contacts directly to the solution. the surface potential changes with the pH value of the solution, this results in changes of the threshold voltage V_T of the ISFET. In the conventional CMOS process two insulators can be used as ISM: silicon dioxide and silicon nitride. Due to the more stability and shorter response time [2,3], silicon nitride is used in the studies. By combining with CMOS technology process, the sensors can be fabricated in mass production and the membrane dimension can be reduced to an area of a few thousand of square microns.

In the implementation of pH meter, a read out circuit is connected to the sensors. So the accuracy of the system depends not only on the properties of the sensors but also on interface unit. Fig. 2 shows the read out circuit, which is used for the prototype [4]. The circuit is designed to apply constant both drain-source current I_{DS} and drain-source voltage V_{DS} to the sensors. The operation point can be adjusted individually by R_1 and R_2 respectively. From the output voltage V_O the pH value is derived from the calibration in standard buffers.

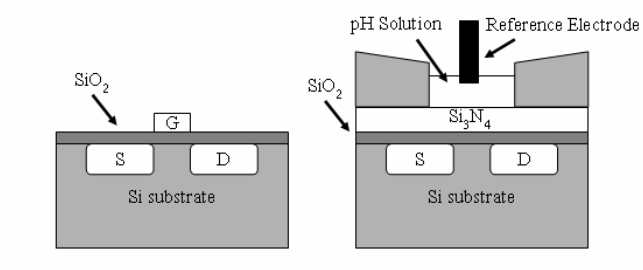

Figure 1. (a) MOSFET has a gate dielectric deposited on top of insulator membrane while (b) ISFEET does not have gate directly deposited on top of the dielectric.

The following parts of the paper will start from the experiments, the electrical characterization and finally the conclusion.

II. EXPERIMENTS

The design and fabrication of ISFET on 6-inch silicon wafers are described in detail elsewhere [5,6]. After the fabrication process is finished, the wafer is diced into individual units. The diced sensor is then glued on a prepared print circuit board and bond wired to metal pads. For encapsulation, negative photoresist SU8-100 is spreaded on the metal parts and the edge of Si substrate. Finally the sensor is cured at 85^{O}C for 30 min and then exposed in UV light 5 min.

The electrical characterization began with the measurement of gate leakage I_G, drain current I_D and source current I_S in the pH7-standard solution using HP 4156B. The purpose of the leakage current measurements is to check the quality of the sensors. By measuring a constant voltage V_{DS} of 0.3 V is applied between source and drain. Between gate and ground the voltage V_G is varied from 0 to 2 V in steps of 0.1 V and the I_S, I_D and I_G are recorded.

Three pH buffers are used for characterization of sensitivity. It begins with the measurement of pH4 solution. Like the leakage current characterization a constant V_{DS} of 0.3 V is applied with variation of V_G from 0 V to 2 V. Before measuring in the next solutions, pH7 and pH10, the sample is then rinsed with deionized water and dried with paper wiper.

The sensitivity is calculated from the shift of V_G at the same I_D with respect to the change in pH values.

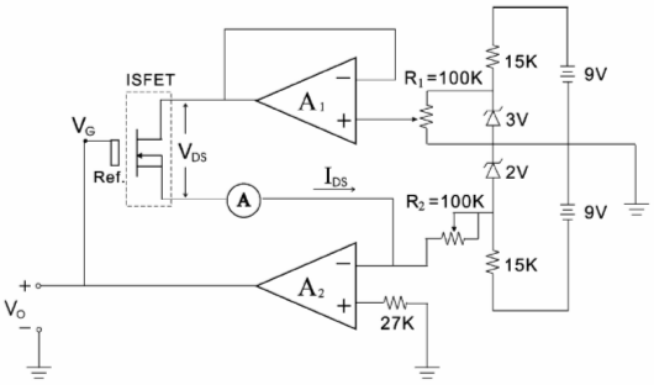

Figure 2. Interface circuit applies both constant V_{DS} and I_{DS} to sensor.

For the implementation of the pH meter, the response time and the memory effect are also studied here. It corresponds to the reliability of the system. In order to characterize the sensor, the sensor is connected with an interface circuit. At the operation point the circuit supplies V_{DS} of 0.3 V and I_{DS} of 10 μA and the V_O were recorded for the period of 3 minutes with the following steps: pH 4, 7, 10, 7 and 4. Furthermore, the sensor is immersed in pH 7 for 10 hours to reveal long time drift behavior.

III. RESULTS AND DISCUSSION

A. Sensors characterization

1. Leakage current measurement

Fig. 3 shows the current response of a sensor with a gate length (L) of 4000 μm and a gate width W of 10 μm by the leakage current measurement. Very low gate leakage current (less than 50 pA at V_G 2 V) is achieved, hence the other curves, I_D and I_S, are not affected from the leakage current and virtually symmetrical about the V_G axis. From the result it indicates that the sample has the ISFET properties, good encapsulated and can be used for the further characterization.

2. Sensitivity

In Fig. 4 the currents of ISFET with L = 10 μm and W = 3200 μm is illustrated. In different buffers, I_{DS} are separated obviously due to the threshold voltage drift. The drift is caused by ion-sensitive of the electrode-liquid-oxide interfaces [7][8]. The sensitivity is specified from the varying of V_G at the same I_{DS} in different pH buffers. From the sample in Fig. 4 the sensitivity varies linearly with 55 mV/pH at 10 μA. Various ISFETs are characterized and the range of sensitivity is 40-50 mV/pH under the same bias condition.

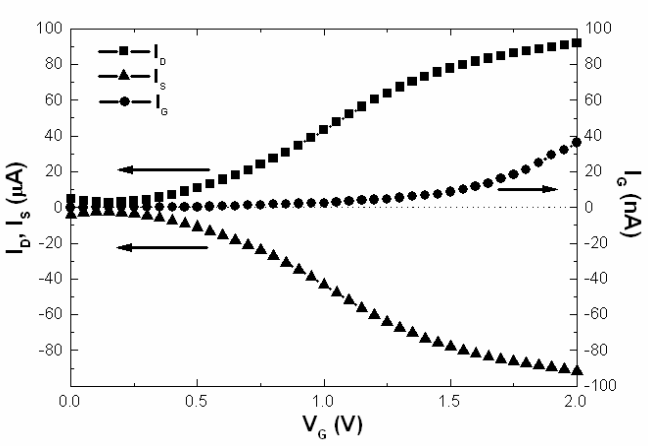

Figure 3 Result of a leakage current measurement at VDS=0.3V, and sweep VG from 0 to 2 V in steps of 100mV.

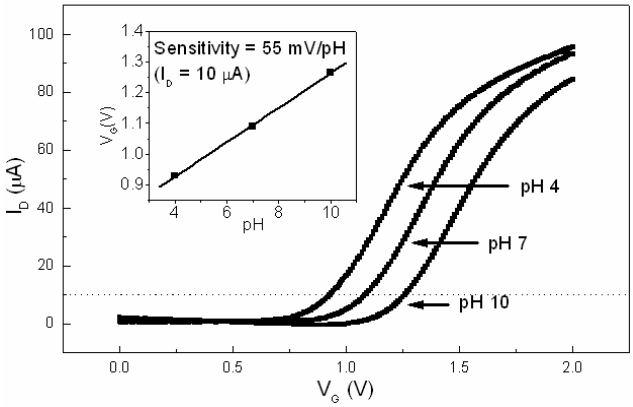

Figure 4 I_D curves in different pH buffers and inset shows the sensitivity of the ISFET.

B. Sensors characterization

1. Memory effect

At operating point, the interface circuit is set to supply a constant current I_{DS} of 10 μA and voltage V_{DS} of 0.3 V. In order to characterize the ISFET, the ISFET is immersed in the following buffers; pH4, 7, 10, 7, and 4, respectively. Fig. 5 illustrates the output voltage V_O of a sample with L = 10 μA and W = 4000 μA. Whatever solution into which the ISFET is immersed , V_O reaches stable value after immersing for a few seconds. This indicates fast response time of the sensors. From the same measurement the accuracy of the sensor can be also defined. The inset of Fig. 5 shows the response of the sensor as function of different pH values. A small voltage drift can be observed only. The discussions of the hysteresis behavior is detailed by Bousse *et al.*[9]. This very small drift corresponds to the high accuracy of the sensors. From the plot the sample shows a voltage drift of 5 mV at pH 4. By the

sensitivity of 50 mV/pH the drift corresponds to the measurement accuracy of 0.1 pH.

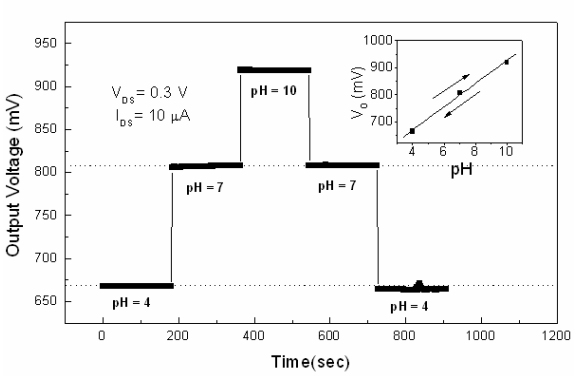

Figure 5 V_O of the interface circuit in different buffers and the inset shows V_O-pH behavior of the ISFET.

2. Drift behavior

Fig. 6 shows the 10 hours record of V_O in pH 7. From the fitting line the voltage drifts with the rate of 1 mV/h. Compared to the accuracy of the sensors, the long time drift behavior can be neglected by the measurement.

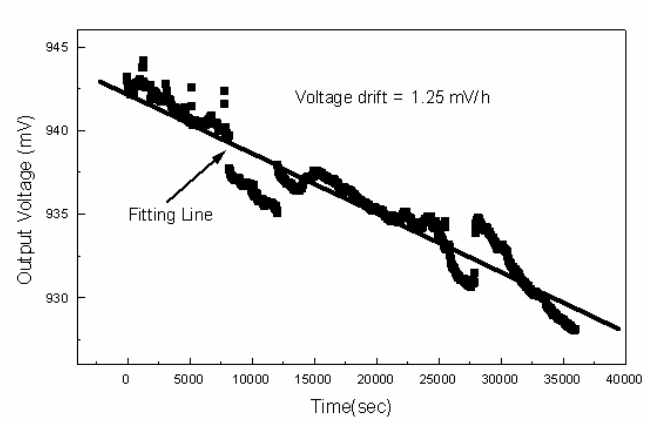

Figure 6 V_O as the function of time in pH7 buffer

IV. Conclusion

The ISFET were fabricated by CMOS compatible process. From the characterization the sensitivity of pH sensors is 40-50 mV/pH. In the prototype implementation, constant I_{DS} of 10 μA and a constant V_{DS} of 0.3 V are supplied to the sensors. The system shows the measurement accuracy of 0.1 pH. The long time drift behavior is negligible.

Acknowledgment

The authors would like to thank TMEC pilot line for processing the devices and MEMS and Nanotechnology group at National Electronics and Computer Technology Center for the access to the bond wire tool

References

[1] P. Bergveld, "Development of an ion-sensitive solid-state device for neurophysiological measurement," *IEEE Transactions on Electron devices*, Vol. BME-17(1), pp. 59-63, 1970

[2] P. Bergveld, "Development, operation, and application of the Ion-Sensitive Field Effect Transistor as a tool for electrophysiology," *IEEE Trans. Biomed. Eng*., Vol. BME-19(5), pp. 342-351, 1972

[3] P. Bergveld, "Future applications of ISFETs," *Sensor and Actuators B*, Vol. 4, pp. 125-133, 1991

[4] S.-S. Jan, J.-L. Chiang, Y.-C. Chen, J.-C. Chou and C.-C. Cheng, "Characteristics of the hydrogen ion-sensitive field effect transistors with sol–gel-derived lead titanate gate," *Chimica Acta*, vol. 469(2), pp. 205-216, 2002.

[5] W. Jeamsaksiri, W. Bunjongpru, N. Atthi, K. Upracoat, C. Hruanun, and A. Poyai "Truely CMOS compatible Nitride membrane ISFET design, fabrication, testing, and market considerations," *Proc. of The 1st International Conference On Applied Science*, pp. 578-583, 2006.

[6] W. Bunjongpru, W. Jeamsaksiri, K. Upracoat, O. Trithaveesak, C. Hruanun, and A. Poyai, "Fabrication and electrical characterization Hydrogen ion-sensitive field effect transistor," *Proc.of The 29th Electrical Engineering Conference Thailand Volume 2*, pp. 677-680, 2006.

[7] L. Bousse, N.F. de Rooij and P. Bergveld, "Operation of chemically sensitive field effect sensors as a function of the insulator-electrolyte interface," *IEEE Transactions on Electron Devices*, Vol. ED-30 (10), pp. 1263-1270, 1983.

[8] S.D. Moss, C.C. Thomson and J. Janata, "Hydrogen, calcium, and potassium ion sensitive FET transducers: A preliminary report," *IEEE Transactions on Biomedical Engineerin*, vol. 25(1), pp. 49-54, 1978.

[9] L. Bousse S. Mostarshed, B. van der Schoot and N.F. de Rooi, "Comparison of the hysteresis of Ta_2O_5 and Si_3N_4 pH-sensing insulators," *Sens. Actuator B*, Vol. 17(2), pp. 157-164, 1994.

Current Tunable Quadrature Oscillator Using Only CCCDBAs and Grounded Capacitors

Sumaytee Pisitchalermpong Danucha Prasertsom Thanawat Piyatat

Worapong Tangsrirat Wanlop Surakampontorn

Faculty of Engineering and
Research Center for Communication and Information Technology (ReCCIT),
King Mongkut's Institute of Technology Ladkrabang (KMITL),
Ladkrabang, Bangkok 10520, Thailand
E-mail : *S.pisitchalermpong@hotmail.com , ktworapo@kmitl.ac.th*

***Abstract*- An electronically tunable quadrature oscillator using only two current-controlled current differencing buffered amplifiers (CCCDBAs) and two ground capacitors without external passive resistor is proposed. The outputs of two sinusoidal waveforms with 90° phase difference are available from the configuration. The oscillation condition and the oscillation frequency ω_o of the proposed oscillator circuit are tunable by electronically through controlling the external dc bias currents of the CCCDBAs. The simulation results with PSPICE are used to verify the theory.**

I. INTRODUCTION

The quadrature sinusoidal oscillator plays an essential electronic circuit, because it can produce two sinusoidal outputs of identical frequency but of 90° phase shift, as for example in telecommunications for quadrature mixers and single-sideband generators [1] or for measurement purposes in vector generator or selective voltmeters [2]. Therefore, quadrature oscillators are widely used in many communications, signal processing and instrumentation systems. Many quadrature oscillator circuits have been reported in [3]-[11]. Note that these earlier quadrature oscillators in [3]-[7] produced voltage-mode signals, whereas the ones in [8]-[11] generated current-mode signals.

Since an introduction of the current differencing buffered amplifier (CDBA) in 1999, it has been acknowledged to be a versatile active building block in designing analog circuits [12]. The CDBA can be considered as a collection of current-mode and voltage-mode unity gain amplifiers, it thus offers large dynamic range and wide bandwidth similar to its current-mode counterparts such as a second-generation current conveyor (CCII) and a current feedback amplifier (CFA) [13]. Numerous CDBA-based applications have been reported by various researchers [13]-[17]. The CDBA is also useful for sinusoidal oscillator design [18]-[19]. Ozcan *et al.* introduced six CDBA-based sinusoidal oscillator circuits that each consists of one CDBA, three resistors and two floating capacitors. However, the oscillation conditions and oscillation frequencies of these oscillators cannot be independently controllable. Moreover, these sinusoidal oscillators use floating capacitors, which is not suitable for integration [20]. In 2002, Horng proposed a new technique for implementing a quadrature oscillator circuit that consists of two CDBAs, four resistors and two grounded capacitors. Its oscillation condition and oscillation frequency can independently controllable. However, this configuration still uses a large number of passive resistors. On the other hand, by recently introducing the current-controlled current differencing buffered amplifier (CCCDBA) [21], it allows the design of analog circuits with electronically tunable circuit parameters, while offering all the advantages of the conventional CDBA. Also considering the absence of the external resistors in circuit realizations, the CCCDBA-based circuits seem to be good choices to use for the realization of IC oscillator circuits…

In this paper, proposed an electronically tunable quadrature oscillator using only two CCCDBAs and two grounded capacitors without external passive resistor requirement is proposed. The proposed oscillator circuit provides two sinusoidal signals with 90 phase difference. The oscillation condition and the oscillation frequency ω_o of the proposed oscillator circuit are tunable by electronically through controlling the external dc bias current. The circuit also displays low passive and active sensitivities. The employment of only grounded capacitors is a very attractive feature for monolithic integrated circuit technology [20].

II. CURRENT-CONTROLLED CURRENT DIFFERENCING BUFFERED AMPLIFIER (CCCDBA)

The circuit representation and the equivalent circuit of the CCCDBA are shown in Fig.1, where p and n are input and w and z are output terminals. The CCCDBA is defined by the flowing matrix equation [21].

$$\begin{bmatrix} v_p \\ v_n \\ i_z \\ v_w \end{bmatrix} = \begin{bmatrix} 0 & 0 & R_p & 0 \\ 0 & 0 & 0 & R_n \\ 0 & 0 & 1 & -1 \\ 1 & 0 & 0 & 0 \end{bmatrix} \begin{bmatrix} v_z \\ i_z \\ i_p \\ i_n \end{bmatrix} \quad (1)$$

where R_p and R_n are respectively the parasitic resistances at the terminals p and n of the CCCDBA. A possible bipolar realization of the CCCDBA is shown in Fig.2. In this case, the resistances R_p and R_n can be given by

$$R_p \cong R_n = \frac{V_T}{2I_o} \qquad (2)$$

where V_T is the thermal voltage that is equal to 26 mV at room temperature. Equation (2) shows that it is possible to tune the values of R_p and R_n by means of an external dc bias current I_O.

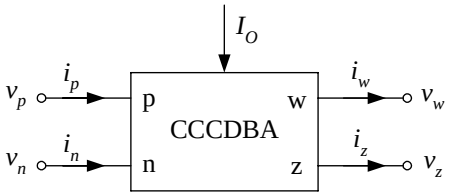

(a)

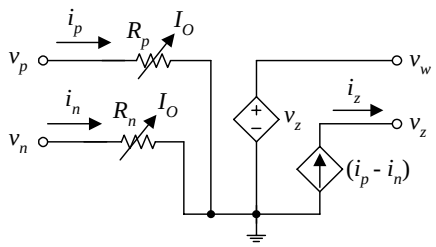

(b)

Fig.1 The CCCDBA

(a) circuit symbol (b) equivalent circuit

III. PROPOSED CONFIGURATION

Fig.3 shows the proposed electronically tunable quadrature oscillator using CCCDBAs as active elements. The oscillator circuit employs only two CCCDBAs and two grounded capacitors without passive resistor requirement, which is ideal for integration [20]. Circuit analysis yields the characteristic equation of the circuit as follows :

$$s^2 + \left(\frac{1}{R_{p2}} - \frac{1}{R_{p1}}\right)\frac{s}{C_1} + \left(\frac{1}{R_{n1}R_{p2}C_1C_2}\right) = 0 \qquad (3)$$

where R_{pi} and R_{ni} denote the parasitic resistances R_p and R_n of the i-th CCCDBA (i = 1, 2), respectively. Thus, the oscillation condition and the oscillation frequency (ω_o) obtained from the proposed circuit are given by :

$$R_{p1} = R_{p2} \qquad (4)$$

and

$$\omega_o = \frac{1}{\sqrt{R_{n1}R_{p2}C_1C_2}} \qquad (5)$$

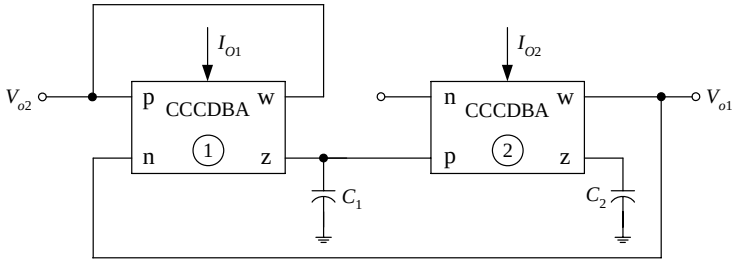

Fig.3 Proposed electronically tunable quadrature oscillator using CCCDBAs.

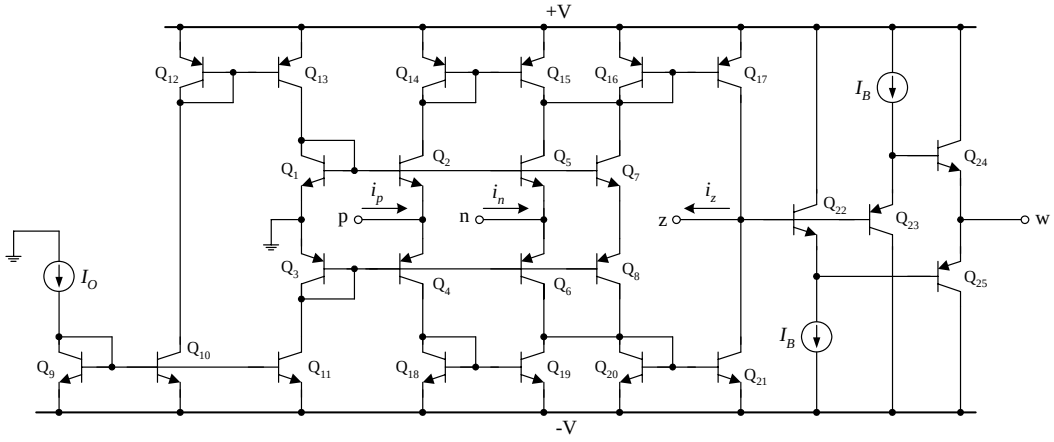

Fig.2 Bipolar realization of the CCCDBA.

Furthermore, if we setting $I_{O1} = I_{O2} = I_O$ and $C_1 = C_2 = C$, then the proposed oscillator circuit of Fig.2 can be controlled to oscillate at the oscillation frequency of

$$f_o = \frac{\omega_o}{2\pi} = \frac{I_O}{\pi V_T C} \tag{6}$$

It is clearly seen from equation (6) that the oscillation frequency of the proposed circuit can be controlled electronically by linearly adjusting the bias current I_O. It is also to be noted that the ω_o is temperature sensitive, the temperature compensation scheme is essential under varying environmental conditions [22]. Moreover, owing to the output impedance at the terminal w of the CCCDBA is very small, the output signal V_{o1} and V_{o2} can be directly connected to the next stage.

From Fig.3, the two quadrature outputs V_{o2} and V_{o1} can be expressed as:

$$\frac{V_{o2}}{V_{o1}} = sC_2R_{p2} \tag{7}$$

Therefore, the phase difference (ϕ) between V_{o2} and V_{o1} is equal to

$$\phi = 90^\circ \tag{8}$$

which guarantees that the voltages V_{o2} and V_{o1} are to be quadrature outputs.

IV. Effects of The CCCDBA Non-idealities

By taking into consideration of the non-ideal CCCDBAs, the relationship of the terminal currents and voltages given with equation (1) can be rewritten as :

$$\begin{bmatrix} v_p \\ v_n \\ i_z \\ v_w \end{bmatrix} = \begin{bmatrix} 0 & 0 & R_p & 0 \\ 0 & 0 & 0 & R_n \\ 0 & 0 & \alpha_p & -\alpha_n \\ \beta & 0 & 0 & 0 \end{bmatrix} \cdot \begin{bmatrix} v_z \\ i_z \\ i_p \\ i_n \end{bmatrix} \tag{9}$$

where $\alpha_p = 1\text{-}\varepsilon_p$, ε_p ($\varepsilon_p << 1$) is the current tracking error from p terminal to z terminal, $\alpha_n = 1\text{-}\varepsilon_n$, ε_n ($\varepsilon_n << 1$) is the current tracking error from n terminal to z terminal, and $\beta = 1\text{-}\varepsilon_v$, ε_v ($\varepsilon_v << 1$) is the voltage tracking error from z terminal to w terminal of the CCCDBA, respectively. Re-analysis the circuit configuration of Fig.3, the non-ideal characteristic equation becomes :

$$s^2 + \left(\frac{1}{R_{p2}} - \frac{\beta_1\alpha_{p1}}{R_{p1}}\right)\frac{s}{C_1} + \left(\frac{\beta_1\beta_2\alpha_{n1}\alpha_{p2}}{R_{n1}R_{p2}C_1C_2}\right) = 0 \tag{10}$$

where α_{pi} , α_{ni} and β_i are the parameters α_p, α_n and β of the i-th CCCDBA, respectively. In this case, the modified oscillation condition and oscillation frequency (ω_{on}) can be rewritten as :

$$R_{p1} = \beta_1\alpha_{p1}R_{p2} \tag{11}$$

and

$$\omega_{on} = \sqrt{\frac{\beta_1\beta_2\alpha_{n1}\alpha_{p2}}{R_{n1}R_{p2}C_1C_2}} \tag{12}$$

It may be pointed out from equations (11) and (12) that the modified oscillation condition and ω_{on} due to the CCCDBA non-idealities will be slightly changed from the ideal case. Moreover, from equation (12), the passive and active sensitivities of this circuit are calculated as :

$$S^{\omega_{on}}_{C_1,C_2} = -\frac{1}{2} \tag{13}$$

$$S^{\omega_{on}}_{R_{n1},R_{p2}} = -\frac{1}{2} \tag{14}$$

and

$$S^{\omega_{on}}_{\beta_1,\beta_2,\alpha_{n1},\alpha_{p2}} = \frac{1}{2} \tag{15}$$

All which are less than 0.5 in magnitude.

V. Simulation Results

The proposed quadrature oscillator in Fig.3 has been simulated by PSPICE to verify the given theoretical analysis. In the simulations, the AT&T ALA400-CBIC-R parameter was used [23]. The power supply voltages were selected as ±V = ±3 V. As an example, the values of capacitors are equal to $C_1 = C_2 = C = 0.01$ μF and bias currents I_B and $I_O = I_{O1} = I_{O2}$ are approximately 500 μA and 200 μA, respectively. This setting was designed to obtain the oscillation frequency f_o at 245 kHz. Fig.4(a) shows the simulated quadrature output waveforms V_{o1} and V_{o2} of the proposed CCCDBA-based quadrature oscillator of Fig.3, where the oscillation frequency f_o is measured to be 216 kHz. Fig.4(b) shows the simulated frequency spectrums of the quadrature outputs V_{o1} and V_{o2}.

The total harmonic distortion (THD) for the designed frequency has been analyzed, and it has also been observed that the THD is approximated to 7.590% for all the quadrature outputs. The results of the total harmonics distortion analysis are summarized in Table 1.

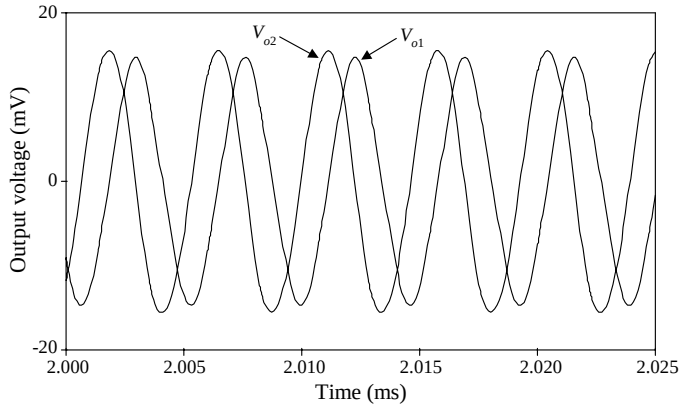

(a)

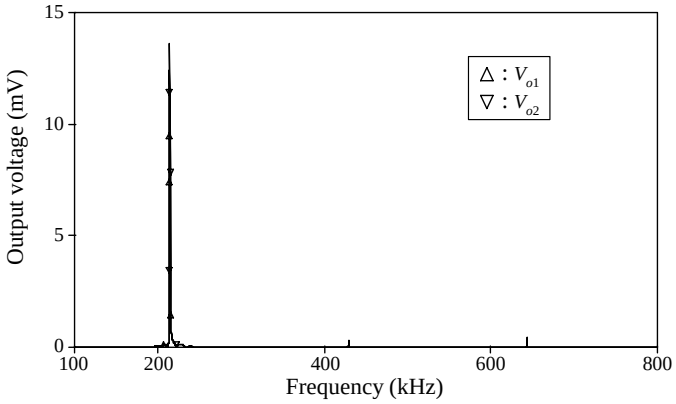

(b)

Fig.4 Simulation results of the quadrature outputs V_{o1} and V_{o2} of the proposed oscillator.
(a) output waveforms (b) output spectrums.

Table 1: Total Harmonic distortion analysis

Harmonic no.	Frequency (Hz)	Fourier component	Normalized component	Phase (Deg)	Normalized Phase
1	2.449E+05	1.455E-02	1.000E+00	-8.345E+01	0.000E+00
2	4.897E+05	1.032E-03	7.096E-02	-5.776E+01	1.091E+02
3	7.346E+05	3.150E-04	2.165E-02	-2.875E+01	2.216E+02
4	9.794E+05	1.957E-04	1.345E-02	-3.317E+01	3.006E+02
5	1.224E+06	1.317E-04	9.056E-03	-2.180E+01	3.954E+02
DC component = 1.051418E-02					
Total harmonic distortion = 7.594297E+00 PERCENT					

VI. CONCLUSIONS

A new quadrature sinusoidal oscillator employing only two CCCDBAs and grounded capacitors has also been proposed. The proposed quadrature oscillator circuit offers the following advantages ; (i) two quadrature sinusoidal output waveforms of 90° phase shift are obtained simultaneously; (ii) it provides low output impedance ; (iii) the oscillation condition and the oscillation frequency are controllable electronically; (iv) using only grounded capacitors for its realization, which is suitable for integration; (v) low passive and active sensitivities.

ACKNOWLEDGMENT

This work is founded by the Thailand Research Fund (TRF), under the Senior Research Scholar Program, grant number RTA4680003.

REFERENCES

[1] P. Horowitz, and W. Hill, *The Art of Electronics*, Cambridge, U.K., Cambridge University Press, p.291, 1991.
[2] U. Tietze, and C. Schenk, *Electronic Circuits : Design and Applications*, Berlin, Germany, Springer, pp.795-796, 1991.
[3] R. Holzel, "A simple wide-band sine wave quadrature oscillator", *IEEE Trans. Instrum. Meas.*, vol.42, pp.758-760, 1993.
[4] M.T. Ahmed, I. A. Khan and N. Minhaj, "On transconductance-C quadrature oscillators", *Int. J. Electron*., vol.83, pp.201-207, 1997.
[5] A.M. Soliman, 'Synthesis of grounded capacitor and grounded resistor oscillators", *J. Franklin Institute*, vol.336, pp.735-746, 1999.
[6] I.A. Khan and S. Khwaja, "An integrable Gm-C quadrature oscillator", *Int. J. Electron*., vol.87, pp.1353-1357, 2000.
[7] J.W. Horng, C.L. Hou, C.M. Chang, W.Y. Chung, H.W. Tang and Y.H. Wen, "Quadrature oscillator using CCIIs", *Int. J. Electron*., vol.92, pp.21-31, 2005.
[8] J.J Chen, C.C. Chen, H.W. Tsao, and S.I. Liu, "Current-mode oscillator using single current follower", *Electron. Lett.*, vol.27, pp.2056-2059, 1991.
[9] M.T. Abuelma'atti, "Grounded capacitor current-mode oscillator using single current follower", *IEEE Trans. Circuits Syst.-I : Fundamental Theory and Applications*, vol.39, pp.1018-1020, 1992.
[10] S. Minaei and O. Cicekoglu, "New current-mode integrator, all-pass section and quadrature oscillator using only active elements", *1st IEEE Int. Conf. Circuits and Systems for Communications*, pp.70-73, 2002.
[11] J. W. Horng, "Current-mode quadrature oscillator with grounded capacitors and resistors using two DVCCs", *IEICE Trans. Fundamentals*, vol.E86-A, pp.2152-2154, 2003.
[12] C. Acar and S.Ozoguz, "A new versatile building block : current differencing buffered amplifier suitable for analog signal processing filters", *Microelectron. J.*, vol.30, pp.157-160, 1999.
[13] S. Ozoguz, A. Toker, and C. Acar, "Current-mode continuous-time fully integrator universal filter using CDBAs", *Electron. Lett.*, vol.35, pp. 97-98, 1999.
[14] C. Acar and H. Sedef, "Realization of nth-order current transfer function using current differencing buffered amplifiers", *Int. J. Electron.*, vol.90, pp.277-283, 2003.
[15] W. Tangsrirat, W. Surakampontorn, and N. Fujii, "Realization of leapfrog filters using current differential buffered amplifiers", *IEICE Trans. Fundamental*, vol.E86-A, pp.318-326, 2003.
[16] A. U. Keskin, "Voltage-mode high-Q band-pass filters and oscillators employing single CDBA and minimum number of components", *Int. J. Electron.*, vol.92, pp.479-487, 2005.
[17] A. U. Keskin, and E. Hancioglu, "Current-mode multifunction filter using two CDBAs", *Int. J. Electron. Commu. (AEUE)*, vol.59, pp.495-498, 2005.
[18] S. Ozcan, A. Toker, C. Acar, H. Kuntman and O. Cicekoglu, "Single resistance-controlled sinusoidal oscillator employing current differencing buffered amplifier", *Microelectron. J.*, vol.31, pp.169-174, 2000.
[19] J. W. Horng, "Current Differencing buffered amplifiers based single resistance controlled quadrature oscillator employing grounded capacitors", *IEICE Trans. Fundamental*, vol.E85-A, pp.1416-1419, 2002.
[20] M. Bhusan and R. W. Newcomb, "Grounding of capacitors in integrated circuits", *Electron. Lett.*, vol.3, pp.148-149, 1967.
[21] S. Maheshwari, and I. A. Khan, "Current-controlled current differencing buffered amplifier implementation and applications", *Active and Passive Elec. Comp.*, vol.4, pp. 219-227, 2004.
[22] W. Surakampontorn, V. Riewruja, K. Kumwachara and C. Fongsamut, "Temperature compensation of translinear current conveyor and OTA", *Electron. Lett.*, vol.34, pp.707-709, 1998).
[23] D.R. Frey, "Log-domain filter : an approach to current-mode filtering", *IEE Proceedings, Pt. G.*, vol.140, pp.406-416, 1993.

Implementation of a Chua's Chaotic Oscillator Using "Roughly-Cubic-Like" Nonlinearity

Banlue Srisuchinwong and Wimol San-Um
Sirindhorn International Institute of Technology, Thammasat University, Bangkadi Campus,
131 Moo 5, Tiwanont Road, Muang, PaThum Tani, 12000, Thailand, banlue@siit.tu.ac.th

***Abstract*— Implementation of a Chua's chaotic oscillator is proposed using roughly-cubic-like nonlinear resistor. A simple current mirror and a single-ended differential pair shape a grounded nonlinear resistor and exhibit roughly cubic-like voltage-current characteristics. A simulated trajectory of the double-scroll chaotic attractor is demonstrated.**

I. INTRODUCTION

Over the past two decades chaotic oscillators [1-3] have received increasing interest as a useful tool not only for investigation of nonlinear phenomena, bifurcation and chaos, but also for a variety of applications such as synchronizations, control [4] and chaos-based communications systems [5]. Chua's circuit [3] is one of the best-known chaotic oscillators using a nonlinearity known as a (piecewise-linear) "Chua Diode". Several techniques including the "cublic" nonlinearity [6] or "cubic-like" nonlinearity [7, 8] have alternatively been proposed to replace the Chua diode.

In this paper, an implementation of the Chua's chaotic oscillator is presented using roughly-cubic-like nonlinearity. A single-ended differential pair and a simple current mirror are combined to form a compact four-transistor grounded nonlinear resistor that exhibit roughly cubic-like voltage-current characteristics. The circuit develops the double-scroll chaotic attractor.

II. CIRCUIT IMPLEMENTATION

Figure 1 shows the proposed Chua's chaotic oscillator using a roughly-cubic-like nonlinear resistor R_N. Inductor L1, capacitors C1 and C2 form parts of the Chua's circuit. A single-ended differential pair (M1, M2), a simple current mirror (M3, M4) and a current source I1 form the nonlinear resistor R_N. For simplicity, let the effects of the channel length modulation of transistors be neglected. Let v_x and i_x be the input voltage and input current to R_N, i.e. $R_N = v_x / i_x$ at the gate of M1. A routine small-signal analysis suggests that $i_x = -2i_d$ where $i_d \cong g_{m1}v_x / 2$ and g_{m1} is the transconductance of transistor M1 or M2. Consequently, for a small-signal operation, R_N exhibits a negative resistance i.e.

$$R_N \cong -\frac{1}{g_{m1}} \tag{1}$$

For a large signal operation, R_N can be distored in a nonlinear fashion because of the nonlinearity of the MOS transistors or eventually may enter into saturation.

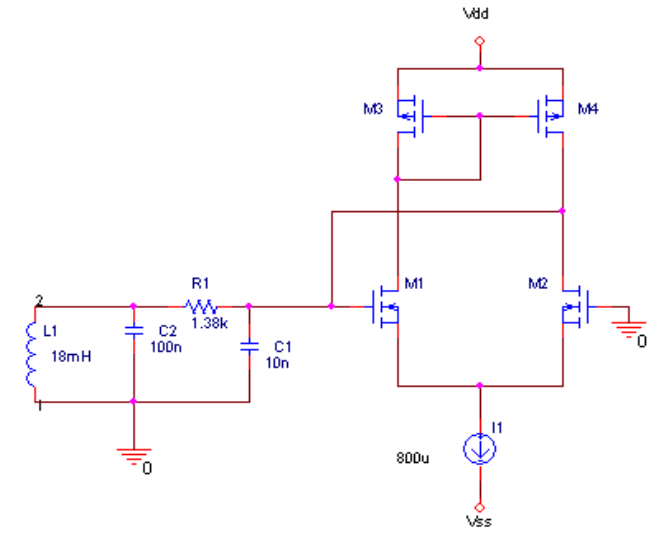

Figure 1 Chua's circuit using roughly-cubic-like nonlinearity.

III. SIMULATION RESULTS

The performances of the circuits shown in Fig. 1 have been simulated through Pspice using models IRF150 and M2N6849 for NMOS and PMOS transistors, respectively. The aspect ratio of all transistors are W/L = (100 μm)/(2 μm) and the threshold voltage of the NMOS V_{TH} = 2.831 V. The values of I1 = 800 μA, L1 = 18 mH, C1 = 10 nF, C2 = 100 nF, R1 = 1.38 kΩ. The gate-source DC voltage of M1 and M2 is V_{GS1} = 3.71 V. Consequently, $g_{m1} = I1/(V_{GS1}-V_{TH}) = 910.12\ \mu\Omega^{-1}$ and, for the small-signal analysis, the calculated value of R_N = –1.09 kΩ.

Figure 2 shows the simulated voltage-current characteristics of the nonlinear resistance R_N where v_x in the x axis is between -5 V to 5 V and i_x in the y axis is between -800 μA to 800 μA. For the small-signal analysis, the measured value of $R_N = v_x / i_x$ = (–40 mV)/(35 μA) = –1.14 kΩ and is consistent with the calculated value. It can be seen from Fig. 2 that, for the small signal operation, the negative resistance R_N is evident through the negative slope whilst, for the large signal operation, R_N exhibits nonlinearity. The curve of R_N shown in Fig. 2 looks like a roughly coarse version of a "cubic-like" voltage-current characteristics and hence the name "roughly-

cubic-like" nonlinearity. For purposes of comparison, a simulated example of a "cubic-like" voltage-current characteristics is shown in Fig. 3. Fig. 4 depicts the simulated trajectory of the double-scroll chaotic attractor developed in Fig. 1 in the $V_{C1} - V_{C2}$ plane where V_{C1} and V_{C2} are the voltages across the capacitors C1 and C2, repectively.

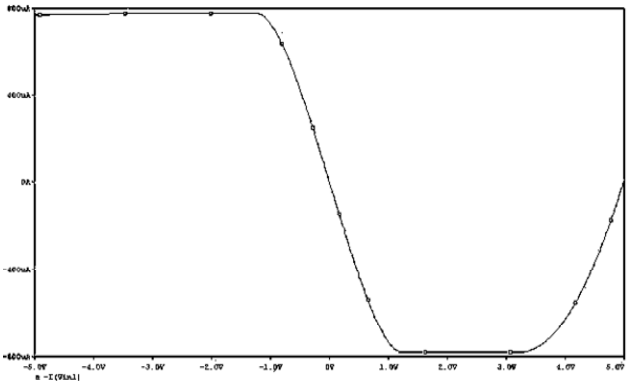

Figure 2 Voltage-current characteristics of R_N looks like a roughly coarse version of the "cubic-like" characteristics.

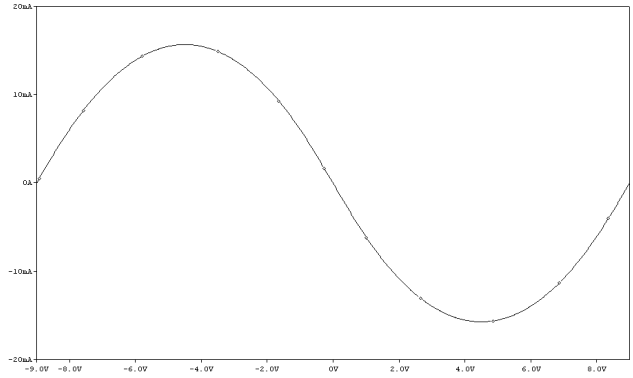

Figure 3 An example of a "cubic-like" voltage-current characteristics

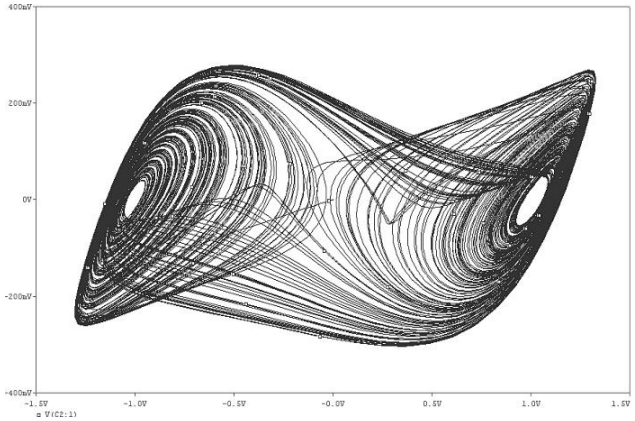

Figure 4 A simulated trajectory of the double-scroll chaotic attractor developed in Fig. 1

IV. CONCLUSIONS

Implementation of a Chua's chaotic oscillator has been presented using the roughly "cubic-like" voltage-current nonlinearity. The combination of a single-ended differential pair and a simple current mirror with a feedback has enabled a roughly cubic-like nonlinear resistor. The simulated double-scroll chaotic attractor has been demonstrated.

ACKNOWLEDGMENTS

Authors are grateful to Mr. Chun-Hung Liou for his useful assistant.

REFERENCES

[1] Special issue on chaos in nonlinear electronic circuits, Part A : Tutorials and Reviews, IEEE Transactions on Circuits and Systems 40(10), 1993.

[2] Delgado-Restituto, M. and Rodriguez-Vazquez, A. (2002), "Integrated Chaos Generators", Proceedings of the IEEE, vol. 90, No. 5, May, 2002, pp. 747-767.

[3] Chen, G. and Ueta T. ed., Chaos in Circuits and Systems, World Scientific, Singapore, 2002.

[4] Special issue on chaos synchronization, control, and applications, IEEE Transactions on Circuits and Systems 44(10), 1997.

[5] Mandal, S. and Banerjee, S., "Analysis and CMOS Implementation of a Chaos-Based Communication System," IEEE Trans. Circuits and Systems – Part I 51(9), Sep. 2004, pp. 1708-1722.

[6] Zhong, G.Q., "Implementation of Chua's Circuit with a Cubic Nonlinearity", IEEE Trans. Circuits and Systems-1, 41(12), 1994, pp. 934-941.

[7] Eltawil, A.M. and Elwakil, A.S., "Low-Voltage Chaotic Oscillator With an Approximate Cubic Nonlinearity," Int. J. Electron. Commun. (AEUE), 53(3), 1999, pp. 11-17.

[8] Donoghue, K.O., Kennedy, M.P. and Forbes, P., "A Fast and Simple Implementation of Chua's Oscillator using a "Cubic-Like" Chua diode," Proceedings of the 2005 European Conference on Circuit Theory and Design, 2005.

Improved Implementation of Sprott's Chaotic Oscillators Based on Current-Feedback Op Amps

Banlue Srisuchinwong and Chun-Hung Liou
Sirindhorn International Institute of Technology, Thammasat University, Bangkadi Campus,
131 Moo 5, Tiwanont Road, Muang, PaThum Tani, 12000, Thailand, banlue@siit.tu.ac.th

***Abstract*- Improved implementation of Sprott's chaotic oscillators based on current-feedback op amps (CFOAs) is proposed. A Sprott's jerk function and four different types of nonlinear components are implemented using the attractively high-frequency features of the CFOAs operating in both voltage and current modes. Four trajectories of the chaotic attractors are demonstrated. The chaotic spectrums are easily scaled and extended to higher frequencies by a factor of 277 to 380**

I. INTRODUCTION

Over the past two decades there has been increasing interest in the study of chaotic oscillators [1-3]. Chaotic oscillators are useful tools not only for investigation of nonlinear phenomena, bifurcation and chaos, but also for a variety of applications such as synchronizations, control [4] and chaos-based communications systems [5]. Chua's circuit [3] is one of the best-known chaotic circuits but is difficult to scale to arbitrary frequencies because of the inductor with its frequency-dependent resistive losses [6] although inductorless versions of Chua's circuit have been possible [7]. Three reactive components (capacitors or inductors) and a nonlinear component are typically required for chaos systems with continuous flows so that the Kirchhoff representation of the circuit contains three first-order ordinary differential equations (ODEs).

Recently, Sprott [6] has alternatively proposed chaotic oscillators based on a single third-order ODE in a simple form of $d^3x/dt^3 = F(d^2x/dt^2, dx/dt, x)$ called a "jerk function" (time derivative of acceleration). One of the Sprott's jerk functions in a general form is [6]

$$\frac{\partial^3 x}{\partial t^3} + A\frac{\partial^2 x}{\partial t^2} + \frac{\partial x}{\partial t} = G(x) \tag{1}$$

where G(x) is a nonlinear function and A = 0.6. The most straightforward implementation involves three successive active integrators to generate d^2x/dt^2, dx/dt and x from d^3x/dt^3 coupled with a nonlinear element G(x) and feeds it back to d^3x/dt^3. Although Sprott's chaotic oscillators [6] based on (1) can be easily constructed using operational amplifiers (op amps) and be easily scaled to different frequencies, the operation has been somewhat delicate and the circuit has exhibited hysteresis because of the finite gain-bandwidth product and slew rates of the op amps [6, 8]. This problem has been circumvented by operating at a lower frequency of around 1.59 kHz [6, 8].

In this paper, high frequency implementation of Sprott's chaotic oscillators is presented using current-feedback op amps (CFOAs). The CFOAs are currently recognized as versatile alternatives to the traditional op amps for their excellent performance in bandwidth and slew rates [9].

II. CIRCUIT IMPLEMENTATION

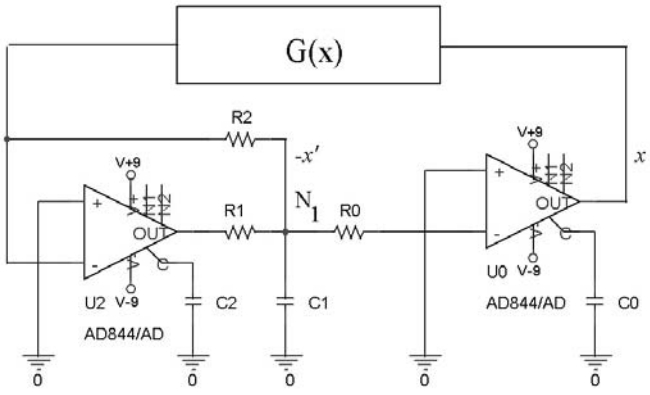

Figure 1. High frequency implementation of Sprott's chaotic oscillator using CFOAs and each of G(x) shown in Figure. 2.

Fig. 1, shows the high frequency implementation of the Sprott's chaotic oscillator based on CFOAs. The nonlinear components G(x) [6] can be implemented using CFOAs as shown in each of the system in Figs. 2(a) to 2(d) where related parameters are also listed. In Fig. 1, the CFOA U_0 forms an integrator U_0 where the zero-dB crossing (ZdB) frequency $\omega_0 = 1/\tau_0$ and $\tau_0 = R_0C_0$. The CFOA U_2 forms another integrator U_2 where the ZdB frequency $\omega_2 = 1/\tau_2$ and $\tau_2 = R_2C_2$. An expected integrator between U_0 and U_1 is replaced by a simpler passive RC filter. A routine analysis in Fig. 1 reveals that the resulting jerk function at node N_1 is

$$\begin{aligned} K_3\frac{\partial^3 x}{\partial t^3} + K_2\frac{\partial^2 x}{\partial t^2} + K_1\frac{\partial x}{\partial t} &= G(x) \\ K_3 &= \frac{\tau_0\tau_X\tau_2 R_1}{R_X R_2} \\ K_2 &= \frac{\tau_0\tau_2}{R_2}\left(1+\frac{R_1}{R_X}\right) \\ K_1 &= \frac{\tau_0}{R_2} \end{aligned} \tag{2}$$

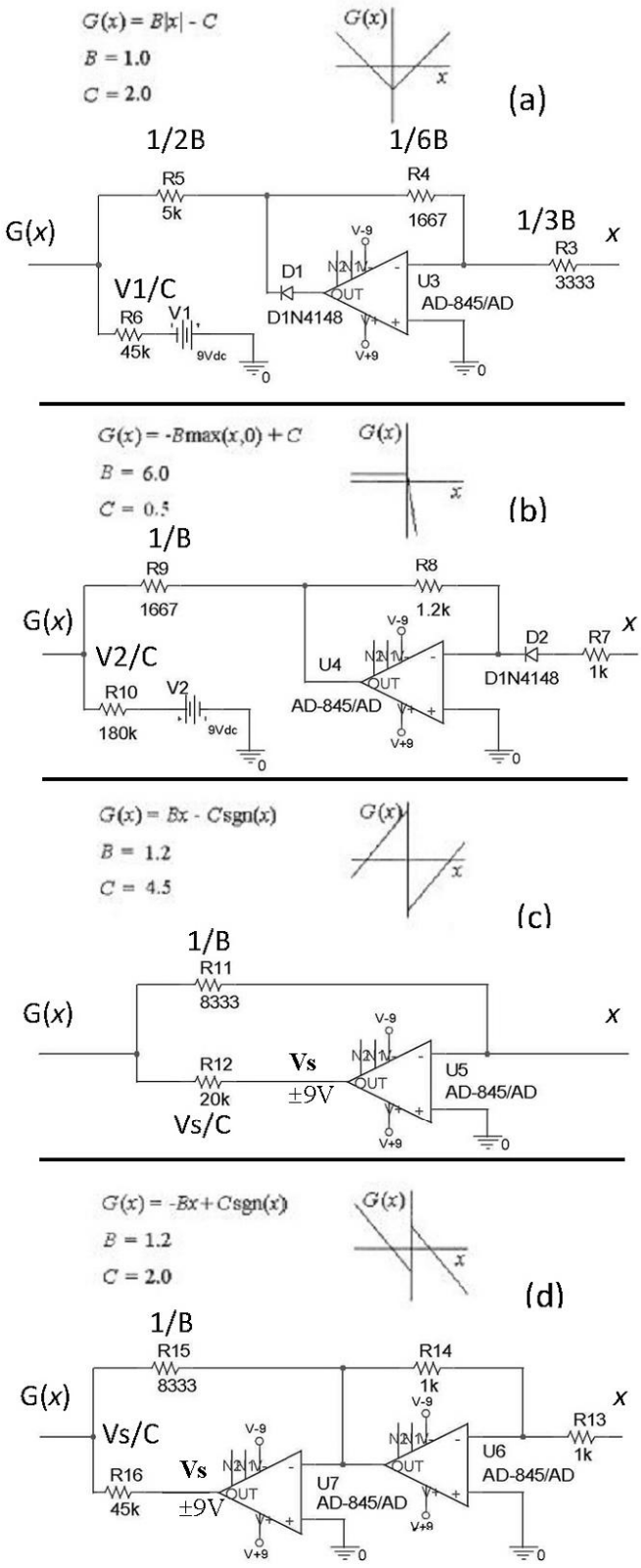

Figure 2. Nonlinear components G(*x*) using CFOAs.

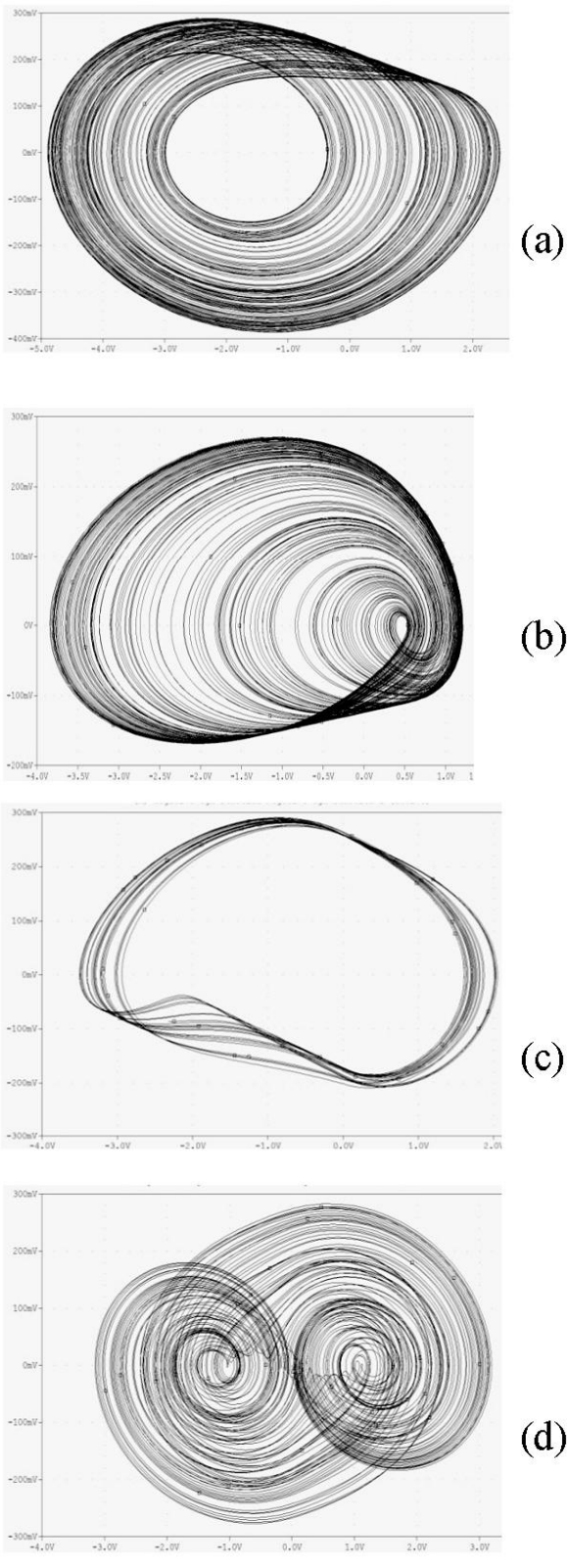

Figure 3. Chaotic attractors produced by Fig.1 using each of the nonlinear components G(x) shown in Fig. 2.

where $\tau_1 = R_1C_1$, $R_X = (R_0R_2)/(R_0+R_2)$, and $\tau_X = R_XC_1$. As (1) = (2), therefore $K_1 = 1$, $K_2 = A = 0.6$ and $K_3 = 1$. For simplicity, let $R_2 = R_1 = R_0 = R_T$. Consequently, $C_2 = A/(3R_T)$, $C_1 = 3/(AR_T)$ and $C_0 = R_2/R_0 = 1$. Table I summarizes the calculated values of the capacitors for $R_T = 1\ \Omega$ and also, with slight modification or scaling, the practical values of the capacitors for $R_T = 1\ k\Omega$.

TABLE I
Calculated and practical values of resistors and capacitors.

Components (Fig. 1)	Calculated Values	Practical Values	
		G(x) in Figs. 2(a), (b), (d)	G(x) in Fig. 2(c)
C_0	1	0.01 µF	0.5 µF
C_1	3/A	0.50 µF	25.0 µF
C_2	A/3	0.02 µF	1.00 µF
R_0	1	1 kΩ	1 kΩ
R_1	1	1 kΩ	1 kΩ
R_2	1	1 kΩ	1 kΩ

III. SIMULATION RESULTS

The performances of the circuits shown in Figs. 1 and 2 have been simulated through Pspice. Models AD844/AD and AD-845/AD are CFOAs with and without current feedback terminal, respectively. By using the practical values shown in Table I, the simulated trajectories of the chaotic attractors in the x-(dx/dt) plane are shown in Figs. 3(a)-3(d) for each of the nonlinear components G(x) shown in Figs. 2(a)-2(d), respectively. In Table I, the practical values of capacitors C_0, C_1, C_2 may be scaled down until the simulated chaotic attractors shown in Fig. 3 corrupt at which point Table II records the minimum values of such capacitors for each G(x) shown in Fig. 2 whilst maintaining the value of $R_0 = R_1 = R_2 = 1\ k\Omega$. Consequently, the operating frequency f_S where the chaotic spectrum is centered will be maximum as shown in Table II.

Table II
Minimum values of capacitors and the corresponding maximum operating frequencies f_S.

G(x)	Types	C_2 (F)	C_1 (F)	C_0 (F)	f_S (Hz)	$\frac{f_S(CFOAs)}{f_S(OAs)}$
Fig. 2(a)	OAs	0.02 u	0.50 u	0.01 u	1.49 k	365
	CFOAs	0.05 n	1.25 n	25.0 p	544 k	
Fig. 2(b)	OAs	2.00 n	50.0 n	1.00 n	14.6 k	277
	CFOAs	5.00 p	125.0 p	2.50 p	4.05 M	
Fig. 2(c)	OAs	1.00 u	25.0 u	0.50 u	24.49	380
	CFOAs	2.50 n	62.5 n	1.25 n	9.33 k	
Fig. 2(d)	OAs	0.01 u	0.25 u	5.00 n	3.81 k	317
	CFOA	25.0 p	625.0 p	12.5 p	1.21 M	

As an example in Table II where G(x) is shown in Fig. 2(d), Fig. 4 shows the corresponding output voltage waveform x and the chaotic frequency spectrum (dBm) centered around f_S = 1.21 MHz. The latter is obtained through the fast fourier transform of x. For purposes of comparisons, Table II also includes the minimum values of the capacitors and the resulting frequency f_S for the similar cases using op amps (OAs). It can be seen from Table II that the proposed implementation using CFOAs enables higher f_S by a factor of 277 to 380.

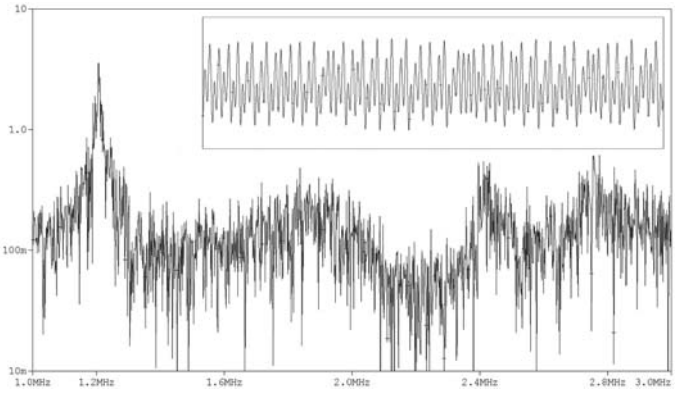

Figure 4. An example of the output voltage waveform and the chaotic spectrum (dBm) centered around 1.21 MHz indicated in Table II.

IV. CONCLUSIONS

High frequency implementation of Sprott's chaotic oscillators has been presented using CFOAs. The Sprott's jerk function and four different types of nonlinear components have been implemented using CFOAs. Four trajectories of the chaotic attractors have been illustrated. The operating frequencies are easily scaled and extended by a factor of 277 to 380.

ACKNOWLEDGMENTS

Authors are grateful to Mr Wimol San-Um who brings the topics of chaotic oscillators to the authors' attentions.

REFERENCES

[1] Special issue on chaos in nonlinear electronic circuits, Part A : Tutorials and Reviews, IEEE Transactions on Circuits and Systems 40(10), 1993.
[2] Delgado-Restituto, M. and Rodriguez-Vazquez, A. (2002), "Integrated Chaos Generators", Proceedings of the IEEE, vol. 90, No. 5, May, 2002, pp. 747-767.
[3] Chen, G. and Ueta T. ed., Chaos in Circuits and Systems, World Scientific, Singapore, 2002.
[4] Special issue on chaos synchronization, control, and applications, IEEE Transactions on Circuits and Systems 44(10), 1997.
[5] Mandal, S. and Banerjee, S., "Analysis and CMOS Implementation of a Chaos-Based Communication System," IEEE Trans. Circuits and Systems – Part I 51(9), Sep. 2004, pp. 1708-1722.
[6] Sprott, J.C. "A New Class of Chaotic Circuits,", Physics Letters A, 266, 2000, pp. 19-23.
[7] Morgul, O. "Inductorless realization of chua oscillator," Electron. Lett. 31(17),1995,pp.1403-1404.
[8] Sprott, J.C. "Simple Chaotic Systems and Circuits," Am. J. Phys. 68(8), Auguest, 2000, pp. 758-763.
[9] Elwakel, A.S. and Kennedy, M.P. "Improved Implementation of Chua's Chaotic Oscillator Using Current-Feedback Op Amp," IEEE Trans. Circuits and Systems, Part I, 47(1), 2000, pp. 76-79.

Whereas, previous CCCII-based MSO scheme is only suitable for bipolar technology and not guarantee generate the sinusoidal at the high frequency. Therefore, the proposed MSO has more flexibility for IC implementation and dealing with the applications than the previous CCCII-based MSO.

II. CIRCUIT DESCRIPTIONS

Fig. 1 shows the symbol of the multiple-output OTA. An ideal OTA is a finite bandwidth voltage-controlled current source, with an infinite input and output impedance. The output currents of the ideal multiple-output OTA is given by

$$I_o = \pm g_m (V_+ - V_-) \tag{1}$$

where g_m is the transconductance gain, I_o the output current, V_+ and V_- is the non-inverting and inverting input voltages, respectively. For the case of OTA implemented with MOS transistors operating in saturation, the transconductance (g_m) is proportional to $(I_{abc})^{1/2}$ and it implemented with bipolar transistors, the g_m is directly proportional to I_{abc}.

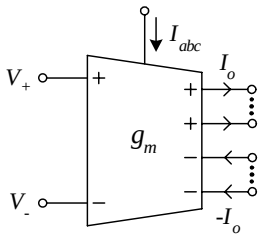

Fig. 1. Circuit symbol of the multiple-output OTA.

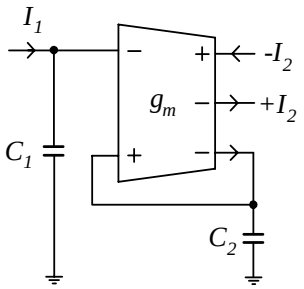

Fig. 2. Basic building block of the proposed multiphase oscillator.

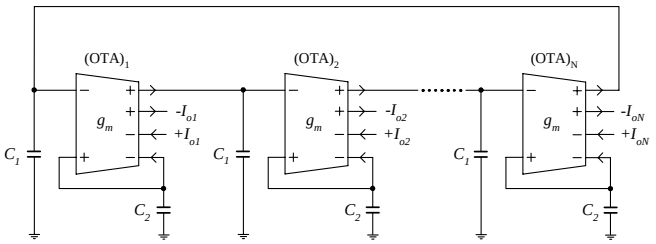

Fig. 3. Generalized circuit for realizing multiphase oscillator.

Fig. 2 shows the basic block of the proposed multiphase oscillator circuit. It consists of a multiple-output OTA and two grounded capacitors. The transfer functions between the output and input terminal of the circuit in Fig. 2 can be given by

$$\frac{I_2}{I_1} = \frac{\pm C_2/C_1}{1 + s(C_2/g_m)} \tag{2}$$

Based on Fig. 2, the generated circuit for realizing an MSO is shown in Fig. 3. Assuming that all OTA in Fig. 3 are identical, by using (1) the loop again can be expressed as

$$L(s) = \left(\frac{-(C_2/C_1)}{1 + s(C_2/g_m)} \right)^N \tag{3}$$

According to the Barkhausen criterion, the condition for the proposed circuit to provide sinusoidal oscillation of frequency is

$$\left(\frac{-(C_2/C_1)}{1 + s(C_2/g_m)} \right)^N_{S=j\omega_o} = 1 \tag{4}$$

or

$$\left(1 + j\omega_o (C_1/g_m)\right)^N + (-1)^{N+1} (C_2/C_1)^N = 0 \tag{5}$$

By expanding (5), it is show that (5) would have a solution only if the value of N is odd ($N \geq 3$). By equating the imaginary and real parts to zero, respectively, the frequency of oscillation (FO) and the condition of oscillation (CO) can be expressed as

FO
$$\omega_o = \frac{g_m}{C_2} \tan\left(\frac{\pi}{n}\right) \tag{6}$$

CO
$$\frac{C_2}{C_1} \geq \left(1 + \tan^2\left(\frac{\pi}{n}\right)\right)^{1/2} \tag{7}$$

From (6) and (7), the FO and CO of a three-phase sinusoidal oscillator (N=3) can be given as

$$\frac{C_2}{C_1} \geq 2 \tag{8}$$

and

$$f_o = \frac{\sqrt{3} g_m}{2\pi C_2} \tag{9}$$

The frequency of oscillation and the condition of oscillation for realizing N-phase sinusoidal oscillator, equal in amplitude and equally spaced in phase, are summarized in Table. From Fig. 3, the use of multiple output-OTA provides an inverted of the output current. Thus, there are $2n$=6, 10, 14 even-phase available output currents. Therefore, the MSO circuit of Fig. 3 can generate both odd-number and even-number of phase by a single circuit. From (8) and (9), the frequency of oscillation and the condition of oscillation can be orthogonally controllable. The oscillation condition can be adjusted the capacitor C_1 and the frequency condition can be tuned by electronically the transconductance g_m through the bias current. The high frequency oscillation can be obtained without the effect of OTA bandwidth in term of oscillation condition. Since the output impedance of the OTA is very high, the MSO current

outputs can be directly connected to the next stage without the using additional current followers. The active and passive sensitivities of proposed MSO circuit have low, approximately -1 to 1.

CONDITION AND FREQUENCY OF OSCILLATION OF MULTIPHASE SINUSOIDAL OSCILLATOR.

Number of phase (N)	Condition of oscillation	Frequency of oscillation (ω_o)
3	$C_2=2C_1$	$1.732g_m/C_2$
5	$C_2=1.237C_1$	$0.728g_m/C_2$
7	$C_2=1.11C_1$	$0.482g_m/C_2$
9	$C_2=1.063C_1$	$0.364g_m/C_2$

III. SIMULATION RESULT

To the theoretical analysis of the proposed multiphase sinusoidal oscillator, a CMOS design example has been simulated through PSPICE simulation program. The PSPICE model parameters for NMOS and PMOS transistor are standard 0.5μm CMOS process of MOSIS. The multiple-output plus/minus OTA schematic is modified from well know single-ended OTA structure [19]-[20], as shown in Fig. 4. It consists of a source-coupled pair with identical MOS devices (M1-M2) operating in the saturation region [19] where the output current is replicated using the current mirrors. The MOS transistors aspect ratios are: 20μm/2μm for M1, M2; 40μm/2μm for M3-M6, M9-M10, M13-M14, M17-M18; and 46μm/2μm for M7-M8, M11-M12, M15-M16, M19-M20. The power supply is V_{DD}=-V_{SS} =2.5V. Fig. 5 presents the simulation results of proposed MSO circuit with C_1=10pF, C_2=20.12pF, I_{abc}=250μA (g_m=0.371mS) for N=3 where C_2 was designed to be larger than 2 times of C_1 to ensure the oscillation will start. Fig. 6 shows sinusoidal waveform for six phases.

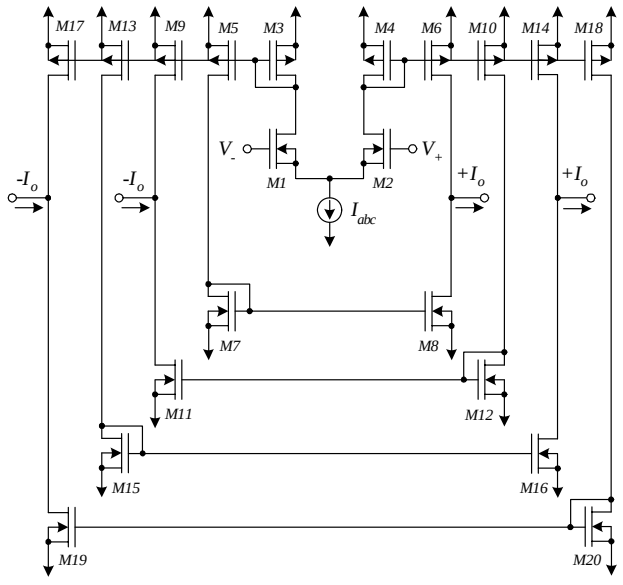

Fig. 4. CMOS multiple-output OTA implementation used in simulation.

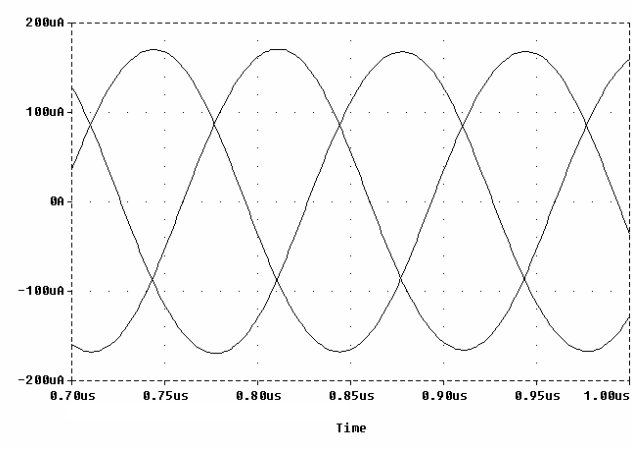

Fig. 5. The simulated output waveform of three phase oscillator of Fig. 3.

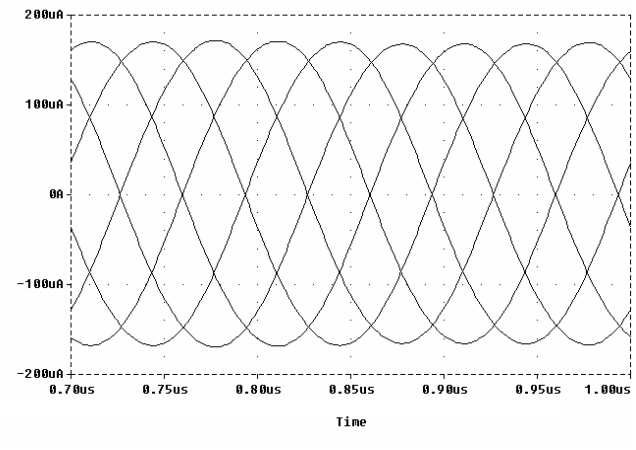

Fig. 6. Simulated output waveform of six phase oscillator of Fig. 3.

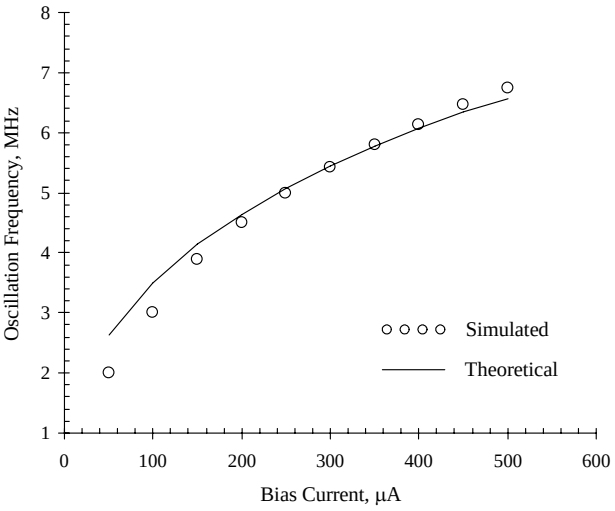

Fig. 7. Variation of the oscillation frequency with the bias current.

Fig. 7 presents the simulation results of oscillation frequency of Fig. 3 by varying the value of the bias current I_{abc} (i.e. 50μA to 500μA or equal g_m from 0.1928mS to 0.48mS) with C_1=10pF and C_2=20.12pF. The relationship between C_2 and oscillation frequency is shown in Fig. 8, which C_1 is varied by C_2 on (8). It shows that the proposed

MSO can be generated the frequency high up to 10MHz according with theoretical. The circuit be generated the frequency higher than 10MHz but the simulation results not confirm with theory, this error cause from the parasitic capacitor of OTA. Finally, Fig. 9 shows the output currents against varied bias current I_{abc}.

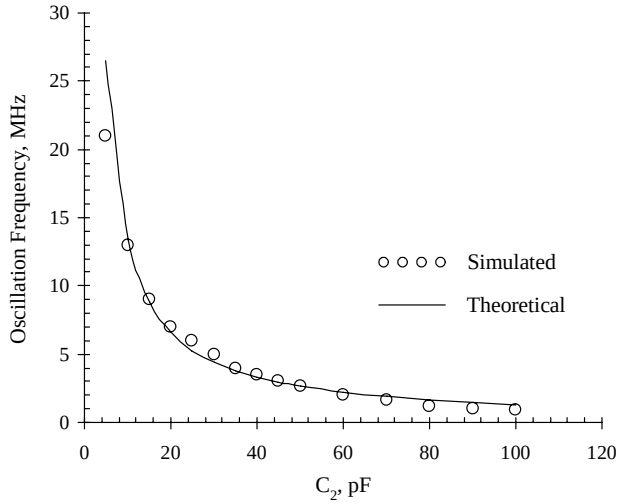

Fig. 8. Variation of the oscillation frequency with capacitor C_2.

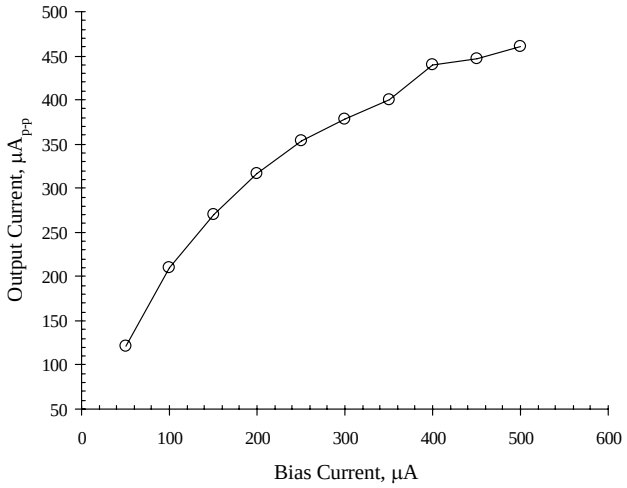

Fig. 9. Output currents of proposed multiphase sinusoidal oscillator again varying bias current with C_1=10pF and C_2=20.12pF.

IV. CONCLUSIONS

In this paper, a new electronically tunable MSO circuit has been presented. The proposed MSO circuit has a simple configuration which uses a multiple-output OTA and two grounded capacitors per section. The MSO circuit can be configured to provide an odd-number of equal-amplitude equally special in-phase output current. The frequency and condition of oscillation are independent controlled. The proposed MSO enjoys simple structure, an electronically tunable and suitable for IC implementation as both CMOS and bipolar technologies. Simulation results, which confirm the theoretical analysis, are obtained.

REFERENCES

[1] E. Sanchez-Sinecio, J. Ramirez-Angulo, B. Linares-Barranco and A. Rodriguez-vazquez, "Operational transconductance amplifier-based non-linear function syntheses," *IEEE Journal of Solid-State Circuits*, vol. 24, pp. 1576-1586, 1989.

[2] A. Rodriguez-Vazquez, B. Linares-Barranco, J. L. Huertas and E. Sanchez-Sinencio, "On the design of voltage-controlled sinusoidal oscillators using OTA's," *IEEE Transactions on Circuits and Systems*, vol. 37, pp. 198-211, 1990.

[3] I. A. Khan, M. T. Ahmed and N. Minhaj, "Tunable OTA-based multiphase sinusoidal oscillators," *International Journal of Electronics*, vol. 72, pp. 443-450, 1992.

[4] J. Wu, "Current-mode high-order OTA-C filters," *International Journal of Electronics*, vol. 78, pp. 1119-1126, 1994.

[5] T. Tsukutani, M. Ishida, S. Tsuiki and Y. Kukui, "Versatile current-mode biquad filter using multiple current output OTAs," *International Journal of Electronics*, vol. 80, pp. 533-541, 1996.

[6] Y. Sun and J. K. Fidler, "Structure generation and design of multiple loop feedback OTA-grounded capacitor filter," *IEEE Transaction on Circuits and Systems*, vol. 44, pp. 1-11, 1997.

[7] P. Prommee and K. Dejhan, "An integrable electronic-controlled quadrature sinusoidal oscillator using CMOS operational transconductance amplifier," *International Journal of Electronics*, vol. 89, pp. 365-379, 2002.

[8] B. Z. Kaplan and S. T. Bachar, "A versatile voltage controlled three phase oscillator," *IEEE Transaction on Industrial Electronics and Control Instrumentation*, vol. 26, pp. 192-195, 1979.

[9] A. Rahman and S. E. Haque, "A simple three-phase variable-frequency oscillation," *International Journal of Electronics*, vol. 53, pp. 83-89, 1982.

[10] V. P. Ramamurti and B. Ramaswami, "A novel three-phase reference sinewave generator for PWM inverter," *IEEE Transactions on Industrial Electronics*, vol. 29, pp. 235-240, 1982.

[11] W. B. Mikhael and S. Tu, "Continuous and switched-capacitor multiphase oscillators," *IEEE Transactions on Circuits and Systems*, vol. 31, pp. 280-293, 1984.

[12] C. Hou and B. Shen, "Second-generation current conveyor-based multiphase sinusoidal oscillators," *International Journal of Electronics*, vol. 78, pp. 317-325, 1995.

[13] D.–S. Wu, S.–I. Liu, Y.–S. Hwang and Y.–P. Wu, "Multiphase sinusoidal oscillator using second-generation current conveyors," *International Journal of Electronics*, vol. 78, pp. 645-651, 1995.

[14] D.–S. Wu, S.–I. Liu, Y.–S. Hwang and Y.–P. Wu, "Multiphase sinusoidal oscillator using the CFOA pole," *IEE Proceeding on Circuits, Devices and Systems*, vol. 142, pp. 37-40, 1995.

[15] S. J. G. Gift, "Multiphase sinusoidal oscillator system using operational amplifiers," *International Journal of Electronics*, vol. 83, pp. 61-67, 1997.

[16] S. J. G. Gift, "Multiphase sinusoidal oscillator using inverting-mode operational amplifiers", *IEEE Transactions on Instrumentation and Measurement*, vol. 47, pp. 986-991, 1998.

[17] M. T. Abuelma'atti and M. A. Al-Qahani, "A new current-controlled multiphase sinusoidal oscillator using translinear current conveyor," *IEEE Transactions on Circuits and Systems-II: Analog and Digital Signal Processing*, vol. 45, pp. 881-885, 1998.

[18] M. Bhusan and R.W. Newcomb, "Grounding of capacitors in integrated circuits", *Electronics Letters*, vol. 3, pp. 148-149, 1967.

[19] M. Tan and R. Schaumann, "Simulation general LC-ladder filters for monolithic realizations with only transconductance elements and grounded capacitors", *IEEE Transaction on Circuits and Systems*, vol. 36, pp. 299-307, 1989.

[20] S. Szczepanski, A. Wyazynski, and R. Schaumann, "High linear voltage-controlled CMOS transconductances", *IEEE Transaction on Circuits and Systems*, vol. 40, pp. 258-262, 1993.

Dual-mode Multiphase Sinusoidal Oscillator using CDBAs

D. Pulsub and W. Surakampontorn
Faculty of Engineering, King Mongkut's Institute of Technology Ladkrabang (KMITL),
Ladkrabang, Bangkok 10520, THAILAND E-mail: tump555@hotmail.com, kswanlop@kmitl.ac.th

***Abstract*- This paper describes a multiphase sinusoidal oscillator based on the use of Current Differencing Buffered Amplifiers (CDBAs). The proposed oscillator provides output signals both in voltage and current forms simultaneously. It comprises *N* cascaded lossy integrators and an inverter, and generates *N*+1 sinusoidal signals with 180°/*N* phase difference. The SPICE simulation results obtained using AD844 macro model are given to confirm the theoretical analysis.**

I. INTRODUCTION

The wide use of the multiphase sinusoidal oscillators (MSOs) in power controllers, communication system and signal processing [1-5] have stimulated the development of the MSOs. Voltage-mode operational amplifiers (op-amps) are widely used for realizing the multiphase sinusoidal waveforms [6] due to their commercial availability. However, circuit synthesis techniques in current domain using current conveyors [7], current followers [8] and operational transductance amplifiers [9] have gained substantial interests. The main advantages of processing signal in current form are wide bandwidth, high slew rate and independent gain realization without a constant gain–bandwidth product constraint.

Recently, a new active building block named as a current differencing buffered amplifier (CDBA) has been introduced [10]. Since the CDBA consists of a unity-gain differential amplifier and a unity-gain voltage amplifier, a high frequency operation and less parasitic can be expected. The MSO based on CDBAs has been reported in the literature [11], however it can produce only sinusoidal voltage output. This paper presents a CDBAs based MSO circuit, which is possible to provide output sinusoidal signals in both voltage and current forms simultaneously. The oscillator structure is constructed by cascading of *N* stages current domain lossy integrators and a current inverter. Consequently, the *N*+1 outputs with 180°/*N* phase difference are available.

II. CIRCUIT DESCRIPTION

The circuit symbol of the CDBA is shown in Fig. 1, where *p* and *n* are the input terminals, *z* and *w* are the output terminals. Its current and voltage characteristics can be described by the following relations [1-2]

$$v_p = 0\,,\quad v_n = 0\,,\quad i_z = i_p - i_n \quad \text{and} \quad v_w = v_z \qquad (1)$$

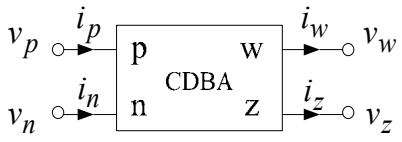

Figure 1. Circuit symbol of CDBA Put units in parentheses.

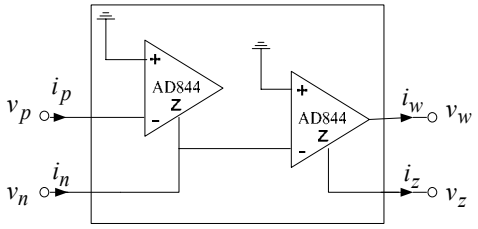

Figure 2. Circuit implementation of CDBA using two CFOAs (AD844).

According to Eq. (1), an output current at the *z*-terminal i_z follows the difference of input currents through the *p*-terminal and n-terminal. Then, the output current is converted into an output voltage v_w through an impedance connected at the terminal *z*. Although there are numerous techniques to realize the CDBAs, a popular one is obtained by using two commercially available CFOAs, AD844 [12], as shown in Fig. 2 [13]. Fig. 3 shows a general block diagram of the MSO for *N*+1 phase sinusoidal oscillator. It is constructed by cascading *N* stages of current domain lossy integrators and a current inverter. The output current $I_{o,N}$ of the last stage is fed back to the first stage through the current inverter. Therefore, the transfer function between I_i and $I_{o,N}$ can be written as:

$$\frac{I_{o,N}}{I_i} = \left(\frac{K}{1+Ts}\right)^N = -1, \qquad (2)$$

where *K* is DC current gain of each stage and system time constant *(T)* is $1/\omega_c$, when ω_c is the internal-pole of the lossy integrator. By expanding Eq. (2), the characteristic equation is obtained as

$$(1+Ts)^N + (-1)^{N+1} K^N = 0 \qquad (3)$$

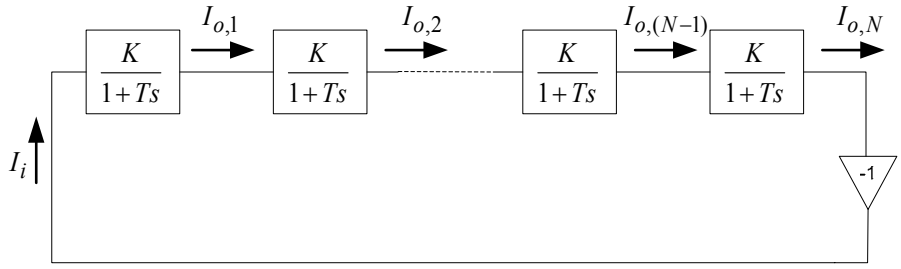

Figure 3. General block diagram of the multiphase oscillator

By replacing $s = j\omega_0$, into Eq. (3), we can find the oscillation frequency and oscillation condition. It can be proved that this equation will give a realistic solution only for $N \geq 3$. To solve for K and ω_0, the real and imaginary parts of Eq. (3) are set to zero. In case of $N = 3$, Eq. (3) yields

$$(1 + j\omega_0 T)^3 + K^3 = 0 , \quad (4)$$

hence,

$$1 - 3\omega_0^2 T^2 + K^3 = 0 , \quad (5)$$

and

$$3j\omega_0 T - j\omega_0^3 T^3 = 0 \quad (6)$$

where ω_0 is the oscillation angular frequency. The oscillation frequency f_0 of this case is obtained by solving equation (6) as

$$f_0 = \frac{\sqrt{3}}{2\pi T} . \quad (7)$$

Substituting Eq. (7) into (5) will give the oscillation condition that is $K = 2$. The conditions of the MSO for the others N can be obtained in a similar way and will result in the MSO with $N + 1$ outputs. Each output is equal in amplitude and has phase shift by 180°/N.

III. Proposed CDBA-Base Multiphase Sinusoidal Oscillator

According to the block diagram representation of the MSO shown in Fig. 3, the system consists of two repeated sub-blocks such: current domain lossy integrator and current inverter. In this work, two new sub-blocks using the CDBA are introduced in Fig. 4. To perform lossy integrator function , the proposed sub-block consisting of one CDBA, three resistors and one capacitor is show in fig. 4(a). The current transfer function I_o/I_i can be written as

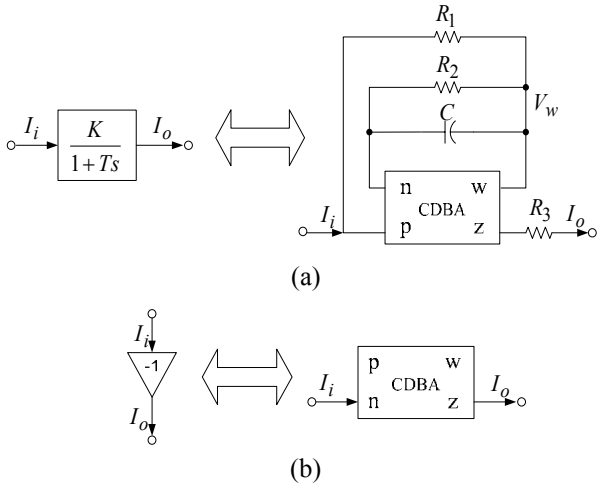

Figure 4. Sub-blocks and their realization using CDBAs
(a) current domain lossy integrator (b) current inverter

$$\frac{I_o}{I_i} = \frac{K}{1+Ts} = \frac{\left(\frac{R_1 R_2}{R_1 R_2 + R_1 R_3 - R_2 R_3}\right)}{1 + sC\left(\frac{R_1 R_2 R_3}{R_1 R_2 + R_1 R_3 - R_2 R_3}\right)} . \quad (8)$$

For simplicity sake, the current inverter is designed using the CDBA as shown in figure 4(b). From Eq. (1), when the input current at terminal p is absent, the current transfer function (I_o/I_i) is obtained equal -1.

By substituting our proposed sub-circuits into the general block diagram of the MSO in fig. 3, the complete circuit of the CDBA-based MSO for $N = 3$, which has 60° phase difference, can be obtained as shown in fig. 5. Since our proposed structure exploits an advantage of having both voltage and current outputs of the CDBA, the resulting MSO will be able to produce the sinusoidal signals in voltage and current forms simultaneously. This gives a potential to apply this circuit in wider range of applications. The current and voltage transfer function between each lossy integrator stage are equivalent and can be directly represented use by Eq. (8). For the sake of

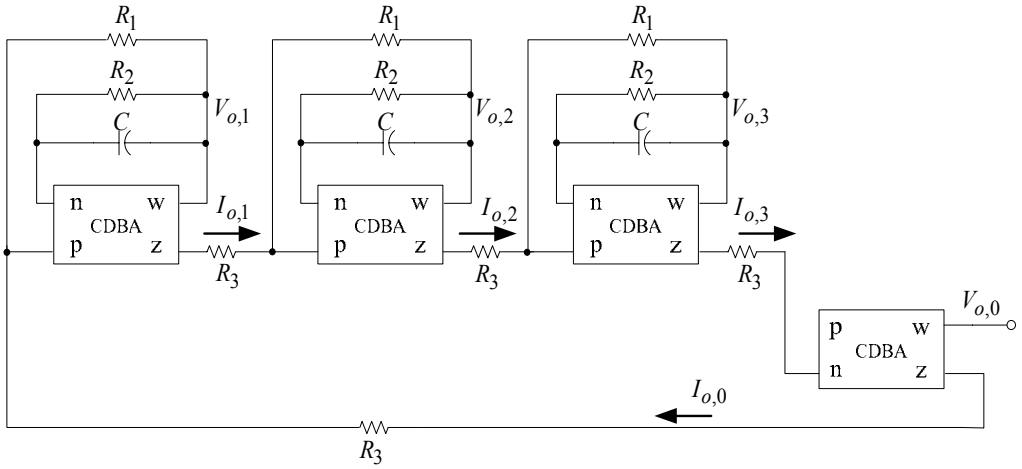

Figure 5. Proposed CDBAs-base multiphase sinusoidal oscillator, which can generate 4 outputs current and 4 outputs voltage different phase sinusoidal both voltage and current signal output each shifted in phase by 60°

design, let us select the circuit components such that $R_1 = R_3$. Therefore, the current and voltage transfer function are

$$\frac{I_{o,N}}{I_{o,N-1}} = \frac{V_{o,N}}{V_{o,N-1}} = \frac{K}{1+Ts} = \frac{(R_2/R_3)}{1+sCR_2} \quad . \quad (9)$$

The oscillation conditions and the oscillation frequency solving from Eq. (4) of this circuit are

$$K = \frac{R_2}{R_3} \quad , \quad (10)$$

$$f_o = \frac{\sqrt{3}}{2\pi R_2 C}. \quad (11)$$

As already determined in the previous section, the oscillation condition is satisfied when $K = 2$ or $R_2 = 2R_3$. It should be noted that, the output voltages are ready to be used since they appear at the voltage output ports of the CDBAs. However, the current outputs need additional ports to duplicate the desired signals to the next stage. This configuration is easily implemented by employing multi-output current mirrors in many customed design CDBAs available both Bipolar and CMOS technology [14 -15].

IV. Simulation Results

Simulation results of the proposed circuit as depicted in Fig. 5 are obtained using the PSPICE circuit simulator with ±18V supply voltage. To verify the proposed circuit, the dual-mode MSO is designed at 27.6 kHz oscillation frequency. Hence, the capacitor and resistors are calculated by using Eq. (10) and (11), that are C = 1nF, $R_1 = R_3$ = 5 kΩ and R_2 = 10 kΩ. The CDBA was constructed using two AD844 as shown in Fig. 2. In fact, there are non-zero impedances at the

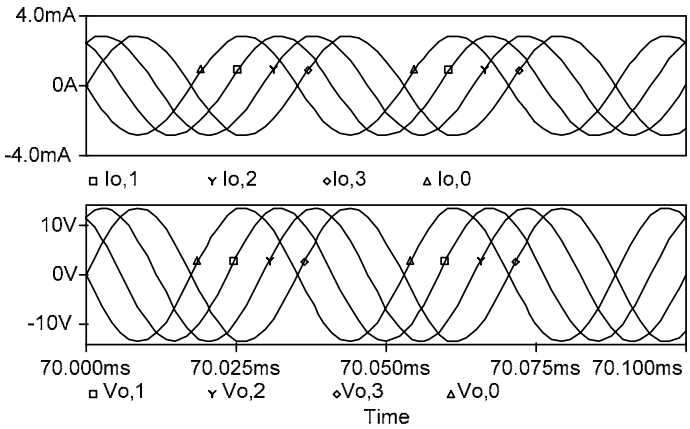

Figure 6. The simulated output voltage ($V_{o,0}$, $V_{o,1}$, $V_{o,2}$, $V_{o,3}$) and output current ($I_{o,0}$, $I_{o,1}$, $I_{o,2}$, $I_{o,3}$) over time at frequency of 28kHz

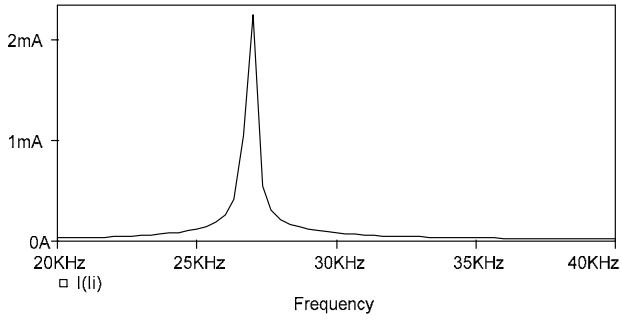

Figure 7. Frequency spectrum of the waveform in Fig. 6.

input ports, p and n, that cause the current transfer error and hence resulting in an oscillation condition violation ($K < 2$). In order to compensate this error, the resistor R_1 and R_3 have to be reduced to satisfy the oscillation condition ($K > 2$). In this case, $R_1 = R_3$ = 4.7 kΩ is selected and K = 2.087 is obtained. The simulated oscillation frequency of 28 kHz is

observed and its output voltages ($V_{o,0}$, $V_{o,1}$, $V_{o,2}$, $V_{o,3}$) and output currents ($I_{o,0}$, $I_{o,1}$, $I_{o,2}$, $I_{o,3}$) over time are shown in Fig. 6. The outputs have equal amplitude of 13.3 V and 2.83 mA for voltage and current signals, respectively. Fig. 7 shows frequency spectrum of the output current signal, which has the total harmonic distortion (THD) about 1.19 %. Note that the oscillation frequency is slightly higher than the calculation. This can be explained by considering Eq. (5). It can be seen that increasing K will also make ω_0 higher.

TABLE I
FREQUENCY, AND CURRENT PHASE WHEN VARYING THE OSCILLATION FREQUENCY

Parameters: C, $f_{expected}$	Oscillation frequency	Phase comparison		
		$I_{o,0}$ - $I_{o,1}$	$I_{o,0}$ - $I_{o,2}$	$I_{o,0}$ - $I_{o,3}$
C = 0.1 nF, f_e = 276 kHz	266 kHz	59.38°	118.13°	179.7°
C = 1 nF, f_e = 27.6 kHz	28 kHz	59.86°	119.98°	179.8°
C = 10 nF, f_e = 2.76 kHz	2.8 kHz	59.66°	119.87°	179.79°
C = 0.1 uF, f_e = 276 Hz	280 Hz	59.68°	120°	180°
C = 1 uF, f_e = 27.6 Hz	28 Hz	59.67°	119.97°	180°

The simulation results when varying the capacitor C to 0.1 nF, 1 nF, 10nF, 0.1uF and 1uF, are summarizable in TABLE I. The expected oscillation frequency, the simulated oscillation frequency and the phase difference of the output currents $I_{o,1}$, $I_{o,2}$, $I_{o,3}$ with respect to $I_{o,0}$ are given. For the frequency of 28 kHz and lower, the frequency error and phase shift error of less than 1.82 % and 1.7 % are observed, respectively. These errors are larger at higher frequency due to the limitation of the employed AD844. Therefore, for the high frequency applications, a high performance CDBAs either implemented in CMOS or Bipolar technology should be properly designed to overcome this problem. Fig. 8 shows simulation results of the MSOs for N = 4 at frequency 28 kHz.

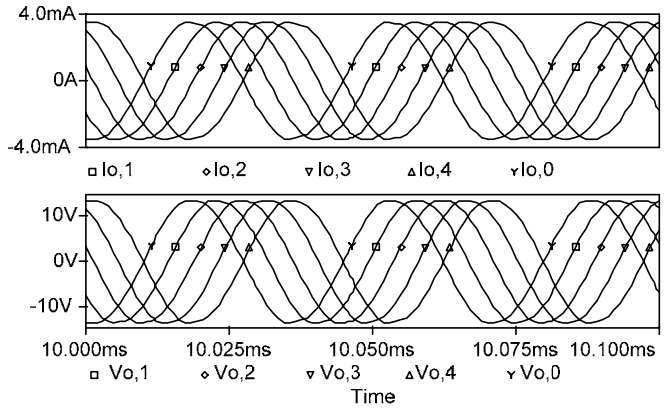

Figure 8. The output voltages ($V_{o,0}$,$V_{o,1}$,$V_{o,2}$,$V_{o,3}$) and output currents ($I_{o,0}$,$I_{o,1}$,$I_{o,2}$,$I_{o,3}$) over time at frequency 28 kHz.

The output voltage ($V_{o,0}$, $V_{o,1}$, $V_{o,2}$, $V_{o,3}$, $V_{o,4}$) and output current ($I_{o,0}$, $I_{o,1}$, $I_{o,2}$, $I_{o,3}$, $I_{o,4}$) have equal amplitude of 13.3 V and 3.5 mA, respectively.

V. CONCLUSION

A new multiphase sinusoidal oscillator based on CDBAs is proposed. The proposed circuit can generate sinusoidal waveforms of both voltage and current signals in the same circuit, so it can be applied in both voltage mode and current mode applications. The circuit can realize N+1 difference phase sinusoidal output signals by using N cascaded lossy integrators and an inverter. This circuit possesses another advantage of that the oscillation condition can be always realized from resistor ratio for every chosen oscillation frequency. The simulation results confirm the theoretical conclusions very well.

REFERENCES

[1] A. Rahman and S. E. Haque, "A simple three-phase variable-frequency oscillator," *Int. J. Electron*., vol. 53, pp. 83–89, July 1982.

[2] V. P. Ramamurti and B. Ramaswami, "A novel three-phase reference sinewave generator for PWM invertors," *IEEE Trans. Ind. Electron*., vol. IE-29, pp. 235–240, Aug. 1982.

[3] R. Rabinovici, B. Z. Kaplan, and D. Yardeni, "Fundamental topologies of three-phase LC resonators and their applications for oscillators," *Proc. Inst. Elect. Eng.,* vol. 140, pt. G, pp. 148–154, June 1993.

[4] W. B. Mikhael and S. Tu, "Continuous and switched-capacitor multiphase oscillators," *IEEE Trans. Circuits Syst*., vol. CAS-31, pp. 280–293, Mar. 1984.

[5] B. Z. Kaplan and S. T. Bachar, "A versatile voltage controlled three phase oscillator," *IEEE Trans. Ind. Electron. Contr. Instrum*., vol. IECI-26, pp. 192–195, Aug. 1979.

[6] J.Stephan and G.Gift, "Multiphase sinusoidal system using operational amplifiers", *International Journal of Electronics*, vol.83, no.1, pp.61- 67, 1997.

[7] M.T.Abuelma, atti and M.A AI'Quahatani, "Low component second generation current conveyor-based multiphase sinusoidal oscillator", *International Journal of Electronics*, vo1.84, no.1, pp.45-52, 1998.

[8] D. Prasertsom, T. Pukkalanun, W. tangsrirat "Realization of current-mode multiphase sinusoidal oscillator based on current followers", *The 21st international Technical Conference on Circuit/Systems, Computers and communications*, pp.105-108,2006.

[9] M.T. Abuelma'atti and M.A Ai'Quahatani, "New current controlled multiphase sinusoidal oscillator using translinear current conveyors", *IEEE Trans.Circuit & Sys*., vol.72, pp.443-450,1992.

[10] C. Acar, and S. Ozoguz, "A new build block: current differencing buffered amplifier", *Microelectronics journal*, 30, pp.157-160, 1999.

[11] K. Klahan, W. Tangsrirat and W.Surakampontorn, "Realization of multiphase sinusoidal oscillator using CDBAs", *IEEE Asia pacific on conference on Circuits and Systems*, Dec. 6-9, 2004.

[12] AD844 Data Sheet (1992).

[13] J.A Svoboda, l.Mcgory and S. Webb, "Applications of a commercially available current convoyer", *Int. J. Electron*,' vol. CAS-23, pp.166-169, 1976Science,1989

[14] V. Sawangarom, W. Tangsrirat, W. Surakampontorn, "NPN-based current differencing buffered amplifier and its application" , *SICE-ICASE*,'Otc.18-21,2006

[15] K. Klahan, W. Tangsrirat and W. Surakampontorn, "A low voltage CMOS current differencing buffered amplifier", *EECON-26*,'pp.1337-1340

A. An Electronically and linearly tunable CMOS OTA (EOTA)

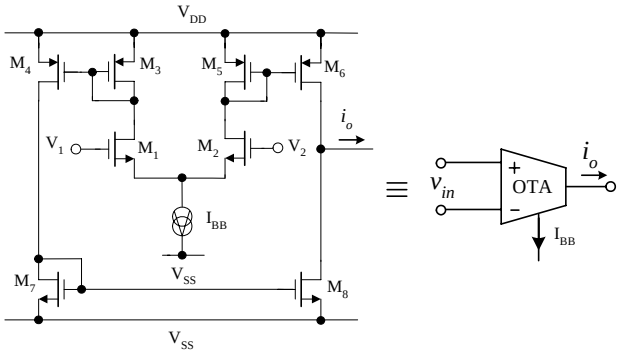

Figure 1 A balanced CMOS OTA

Figure 1 shows a balanced single-output CMOS OTA, which is formed by MOS coupled pair and current mirrors, where V_{in} is the differential input voltage (V_{in}=V_1-V_2), i_o is the output current and I_{BB} is the bias current. Let us assume that M_1 and M_2 are perfectly matched and the current mirrors have unity current gain. By using equation (1), the differential output current of the circuit in Figure 1 can be given by

$$i_o = i_2 - i_1 = \sqrt{2I_{BB}K}\cdot V_{in}\cdot\sqrt{1-\frac{KV_{in}^2}{2I_{BB}}}, \quad for -\sqrt{\frac{I_{BB}}{K}} \le V_{in} \le \sqrt{\frac{I_{BB}}{K}} \qquad (2)$$

The transconductance gain (g_m) of the MOS coupled pair can be derived by taking the derivative of (2) with respect to V_{in}, yielding

$$g_m = \left.\frac{di_o}{dV_{in}}\right|_{V_{in}=0} = \sqrt{2I_{BB}K}, \quad for -\sqrt{\frac{I_{BB}}{K}} \le V_{in} \le \sqrt{\frac{I_{BB}}{K}} \qquad (3)$$

A CMOS-based electronically and linearly tunable OTA, called as an EOTA [10], that realized by using three OTAs the circuit diagram shown in figure 1.

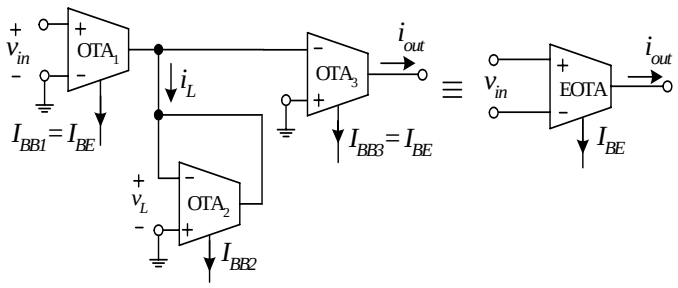

Figure2. An electronically and linearly tunable CMOS OTA (EOTA)

The OTA_1 converts a differential input signal voltage $v_{in} = v_1 - v_2$ into a signal current i_L to flow into an active resistor R_L, formed by the OTA_2, where $Z_L = 1/g_{m2}$ and gm_2 represents the transconductance gain of the OTA_2. Since the current signal $i_L = g_{m1}V_{in}$, the voltage drop across the active resistor (OTA_2) becomes

$$v_L = i_L Z_L = g_{m1}v_{in}\cdot\frac{1}{g_{m2}} \qquad (4)$$

The OTA_3 will convert the voltage v_L, with the transconductance gain of g_{m3}, into the output current i_{out} as

$$i_{out} = g_{m3}v_L \qquad (5)$$

From equations (4) and (5), the current i_{out} can be rewritten as

$$i_{out} = \frac{g_{m1}g_{m3}}{g_{m2}}v_{in} \qquad (6)$$

Since $g_{m1} = \sqrt{2I_{BB1}K_1}$, $g_{m2} = \sqrt{2I_{BB2}K_2}$ and $g_{m3} = \sqrt{2I_{BB3}K_3}$, if we set I_{BB1}=I_{BB3}=I_{BE}, then from equation (6) we obtain

$$i_{out} = \frac{2I_{BE}\sqrt{K_1K_3}}{\sqrt{2I_{BB2}K_2}}V_{in} = g_{mT}v_{in} \qquad (7)$$

where g_{mT} represents the transconductance gain of the proposed EOTA and can be expressed as

$$g_{mT} = 2I_{BE}K_T \qquad (8)$$

and $K_T = \sqrt{K_1K_3/2I_{BB2}K_2}$, which can usually be kept to constant. The equation (8) clearly indicted that the transconductance gain of the proposed EOTA can be electronically and linearly tuned by the bias current I_{BE}.

B. The proposed electronically and linearly tunable sinusoidal quadrature oscillator

The proposed electronically tunable sinusoidal quadrature oscillator is constructed by using EOTAs and OTAs

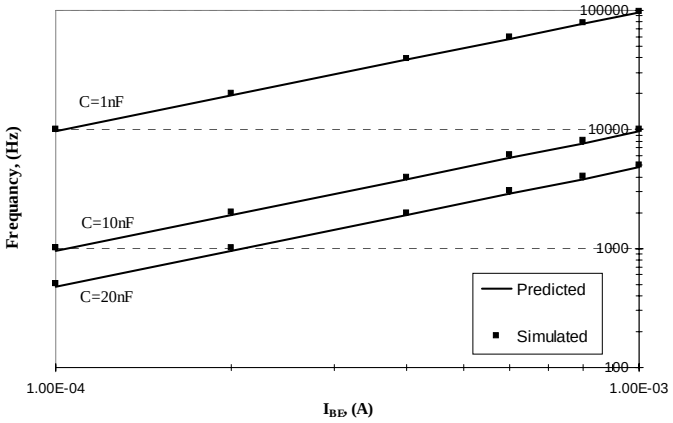

Figure 5. Frequency tunable range of the oscillator

Figure 5 demonstrates the oscillation frequency that tunable with respect to the dc bias-current $I_{BE1}=I_{BE2}=I_{BE}$, where the bias current is varied from 100μA to 1000μA. and for the cases of C= 20nF, C=10nF and C=1nF, respectively. The figure shows that, for the cases of C= 20nF, C=10nF and C=1nF, the oscillation are in the frequency ranges of 500 Hz to 5 kHz, 1 kHz to 10 kHz and 10 kHz to 98 kHz, respectively, with the error of less that 5%. This result demonstrates that the maximum frequencies up to 98 kHz is achieved by reducing the capacitance values ($C_1=C_2=C=1nF$).

IV. CONCLUSIONS

A design of CMOS-based electronically tunable quadrature oscillator has been proposed. The oscillator is realize by using two EOTAs, two OTAs and two grounded capacitors which is suitable for implementing in CMOS integrated form. Its oscillation frequency can be electronically and linearly tuned for a wide range by the transconductance gain without affecting the oscillation condition and the capability of operation at high frequencies. Simulation results have been employed to demonstrate the performances of the proposed oscillator.

REFERENCES

[1] M.T. Abuelma'atti, "Two new integrator active OTA-based voltage (current) controlled oscillator", *International Journal of Electronics*, Vol.66, 1989, pp.135–138.

[2] B. Linaress-Barranco, A. Rodriguez-Vazquez, E., Sanchez-Sinencio, and J.L. Huertas, "CMOS OTA-C high frequency sinusoidal oscillators", *IEEE Journal of Solid-State Circuits*, Vol.26, 1989, pp.160–165.

[3] M.T. Ahmed, I.A. Khan, and N. Minhaj, "On transconductance-C quadrature oscillator", *International Journal of Electronics*, Vol.83, 1997, pp.201–207.

[4] I.A. Khan and S. Khwaja, "An integrable gm-C quadrature oscillator", *International Journal of Electronics*, Vol.87, 2000, pp.1353–1357.

[5] B. Srisuchinwong, "Fully balanced current-tunable sinusoidal quadrature oscillator", *International Journal of Electronics*, Vol.87, 2000, pp.547–556.

[6] Sen-Iuan Liu and Tu-Hung Liao, "Current-mode quadrature sinusoidal oscillator using single FTFN", *International Journal of Electronics*, Vol.81, 1996, pp.171–175.

[7] B. Linaress-Barranco, A. Rodriguez-Vazquez, E. Sanchez-Sinencio, and J.L. Huertas, "10 MHz CMOS OTA-C voltage controlled quadrature oscillators", *Electronics Letters*, Vol.25, 1989, pp.765–767.

[8] Michael P. Flynn and Sverre U. Lidholm, "A 1.2-um CMOS Current-Controlled Oscillator", *IEEE J. of Solid-State Circuits*, Vol. 27, no.7, 1992, pp.982-987.

[9] Antonio J. Lopez-Martin and A. Carlosena, "A tunable CMOS square-root domain oscillator", IEEE Symposium on Circuits and Systems, Geneva, Switzerland, 2000, pp.V-573-V-576.

[10] K. Kaewdang, W. Tangsrirat and W. Surakampontorn, "An Electronically and Linearly Tunable CMOS OTA," *The 2004 International Technical Conference On Circuits/Systems,Computers and Communications (ITC CSCC 2004)*, Sendai, Japan, 2004, pp. 6A3L-1-1--6A3L-1-4.

[11] K. Kumwachara and W. Surakampontorn, "An Integrable Temperature-Insensitive gm-RC Quadrature Oscillator" *International Journal of Electronics*, Vol. 90, no.9, 2003, pp. 599 - 605.

[12] H. O Elwan, A. M. Soliman, "Low-Voltage Low-Power CMOS Current Conveyors," *IEEE Trans. Circuits and Systems* 44 (1997) 828-835.

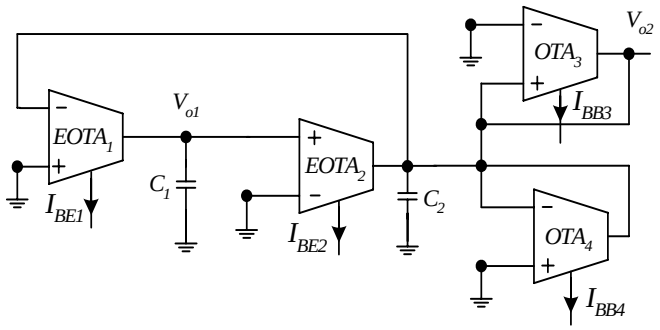

Figure 3. The proposed electronically and linearly tunable sinusoidal quadrature oscillator

The g_m-C quadrature oscillator based on the use of EOTAs is shown in Fig.3. The quadrature oscillator circuit diagram is similar to the bipolar-based quadrature oscillator circuit of the reference 11. The basic building blocks of the oscillators consist of two integrators cascaded in a loop; an inverting integrator (EOTA and C_1) and a non-inverting integrator ($EOTA_2$ and C_2). It should be noted that a regenerative circuit made by the balance CMOS OTA, OTA_3 and OTA_4, are included in order to place the poles in the right-half complex plane so that the circuit is unstable and self-starting, from equation (7), the characteristic equation of the oscillator can be express as

$$s^2 - s\left(\frac{g_{m3} - g_{m4}}{C_2}\right) + \frac{g_{mT1}g_{mT2}}{C_1C_2} = 0 \qquad (9)$$

Therefore, in order to initially locate the poles inside the right-half complex frequency plane to assure self-starting operation, the condition for the oscillation can be start as

$$g_{m3} - g_{m4} \geq \varepsilon \qquad (10)$$

or

$$\sqrt{I_{BB3}} - \sqrt{I_{BB4}} \geq \varepsilon \qquad (11)$$

where ε is a small positive number. The oscillating frequency is

$$\omega_0 = \sqrt{\frac{g_{mT1}g_{mT2}}{C_1C_2}} \qquad (12)$$

Where $g_{mT1}=2I_{BE1}K_T$ and $g_{mT2}=2I_{BE2}K_T$. For simplicity, if we set $C_1=C_2=C$ and $g_{m1}=g_{m2}=2I_{BE}K_T$, the frequency of oscillation can be given by

$$\omega_0 = \frac{g_{mT}}{C} = \frac{2I_BK_T}{C} \qquad (13)$$

It is obvious from (12) and (13) that the oscillation frequency can be tuned without disturbing the oscillation. Moreover, the frequency of oscillation ω_0 can be linearly controlled by adjust the dc bias current $I_{BE1}=I_{BE2}=I_{BE}$.

III. Simulation Results

The performance of the proposed electronically and linearly tunable sinusoidal quadrature oscillator of figure3 was verified through the use of PSPICE simulation results. All the balanced CMOS OTA and EOTAs were simulated by using CMOS transistor parameters of the SCN2 level 2 of MOSIS [12]. The dimensions of transistors M_1 and M_2 are W=50μm and L=10μm. The dimensions of the transistor M_3-M_8 are W=100μm and L=10μm. The power supply voltage were set to V_{DD} = -V_{SS} = ± 5V.

Figure 4 shows the results obtained from the electronically and linearly tunable quadrature oscillator circuit of figure 3 in the case of $C_1=C_2=C$=20nF. $I_{BE1}=I_{BE2}=I_{BE}$=1mA, I_{BE3}=1mA, I_{BE4}=995μA, with $\varepsilon = \sqrt{2I_{BE3}K_3} - \sqrt{2I_{BE4}K_4}$ =1.26μA. The simulated oscillation frequency with quadrature outputs of equal magnitude of about 5 kHz is achieved. The circuit provides the oscillation frequency with the error of less than 5%, since the predicted oscillation frequency from the equation (13) is about 4.8 kHz.

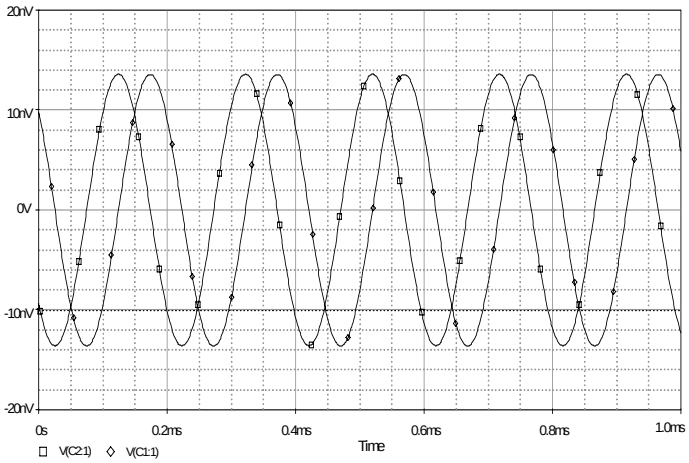

Figure 4. Simulation results of the gm-C quadrature oscillator

Cascadable Three-Input Single-Output Current-Mode Universal Filter Using CDBAs

Visawa Sawangarom* Teerasilapa Dumawipata** Worapong Tangsrirat* Wanlop Surakampontorn*

* Faculty of Engineering and Research Center for Communication and Information Technology (ReCCIT),
King Mongkut's Institute of Technology Ladkrabang (KMITL),
Ladkrabang, Bangkok 10520, THAILAND

** Department of Industrial Electrical Technology (IET), Faculty of Engineering,
King Mongkut's Institute of Technology North-Bandkok (KMITNB),
Bandsue, Bangkok 10800, THAILAND

E-mail : visawa.sawangarom@gmail.com , ktworapo@kmitl.ac.th

***Abstract*-This paper presents the three-input single-output current-mode universal filter using three current differencing buffered amplifiers (CDBAs), two resistors, and two grounded capacitors. By properly selecting the input signals, the filter can realize five standard biquadratic functions, i.e. lowpass, bandpass, highpass, bandstop and allpass current responses from the same circuit topology. The natural frequency ω_o and the bandwidth *BW* are independently controllable. No critical matching condition is required for realizing all the filter responses, and all the incremental parameter sensitivities are also low. The performances of the proposed circuit are confirmed by PSPICE simulations.**

Keywords:current differencing buffered amplifier (CDBA), universal filter.

I. INTRODUCTION

In recent years, a new active building block, which is called a current differencing buffered amplifier (CDBA), has received much attention. Many applications in active filter design based on CDBA were reported in the literature [1]-[9]. They have been demonstrated that the CDBA is a versatile active building block for voltage- and current-mode signal processing applications. Despite the fact that the current-mode filter with multiple-input and single-output terminals concerning CDBA's is now available. To the best of our knowledges, only one work proposes a current-mode Kerwin-Huelsman-Newcomb (KHN) biquad circuit using three CDBAs and eight passive elements [8]. Actually, the number of the passive elements employed in this filter realization is rather high. Moreover, the filter does not exhibit a high output impedance, which cannot be cascaded to the next stage directly. Although a cascadble CDBA-based current-mode filter has been proposed recently [9], it requires an additional CDBA and component matching conditions for realizing a highpass response. Therefore, a few applications on the cascadable multiple-input single-output (MISO) current-mode universal filter using CDBAs as active components are available.

In this paper, the CDBA-based MISO current-mode universal biquadratic filter is proposed to show versatility of CDBA in current-mode operation. The proposed circuit configuration with three input and single output terminals employs only three CDBAs, two virtually grounded resistors and two grounded capacitors, which provides the advantage of an integrated circuit (IC) implementation [10]-[11]. The filter can realize five standard biquadratic filtering functions, i.e., lowpass (LP), bandpass (BP), highpass (HP), bandstop (BS) and allpass (AP) from the same configuration by properly selecting the input signals. The circuit also provide the low-impedance inputs and high impedance output which is no problem for the input signal current source and easily cascadable to the next stage without needing additional buffers. For the realization of all the filter responses, no critical component matching condition is required, and both active and passive sensitivities are low. PSPICE simulation results are used to verify the performances of the proposed circuit.

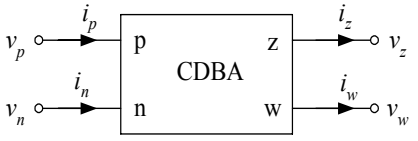

Figure 1. Electrical circuit symbol of the CDBA

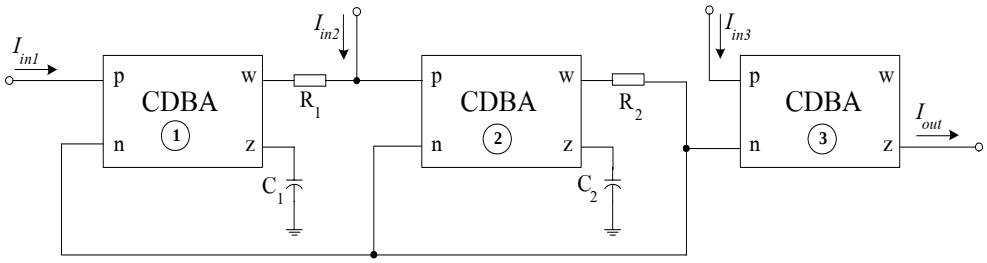

Figure 2. Proposed cascadable TISO current-mode universal filter employing CDBAs

II. CIRCUIT DESCRIPTION

An electrical circuit symbol of the CDBA is shown in Fig.1, where p and n are input terminals, and z and w are output terminals. The characteristic equation of this device can be expressed by the following matrix equation.

$$\begin{bmatrix} i_z \\ v_w \\ v_p \\ v_n \end{bmatrix} = \begin{bmatrix} 0 & 0 & 1 & -1 \\ 1 & 0 & 0 & 0 \\ 0 & 0 & 0 & 0 \\ 0 & 0 & 0 & 0 \end{bmatrix} \cdot \begin{bmatrix} v_z \\ i_w \\ i_p \\ i_n \end{bmatrix} \qquad (1)$$

According to above equation, the difference of the input currents i_p and i_n at the terminals p and n, respectively, is converted to the output voltage v_w at the terminal w through an impedance connected at the terminal z. It can be further inferred that the terminal impedances of the p and n terminals are internally grounded.

Fig.2 illustrates the proposed three-input single-output (TISO) cascadable current-mode universal filter, which consists of only three CDBA, two resistors and two grounded capacitors. Since all the capacitors are grounded, thus the circuit is beneficial to an IC implementation [10]-[11]. By routine circuit analysis based on equation (1), the current transfer function of the proposed CDBA-based filter can be given by :

$$I_{out} = \frac{D(s)I_{in3} - sR_1C_1I_{in2} - I_{in1}}{D(s)} \qquad (2)$$

where $D(s) = s^2 3R_1R_2C_1C_2 + sR_1C_1 + 1$.

According to equation (2), if the magnitudes of the input current I_{in1}, I_{in2} and I_{in3} are chosen as table I, then all the standard biquad filtering functions can be obtained. This means that the proposed filter can realize five standard types of the biquadratic filtering functions without any component matching condition requirements.

TABLE I
The I_{in1}, I_{in2} and I_{in3} values for each filter function

Function type	I_{in1}	I_{in2}	I_{in3}
LP	I_{in}	0	0
HP	I_{in}	I_{in}	I_{in}
BP	0	I_{in}	0
BS	0	I_{in}	I_{in}
AP	0	$2I_{in}$	I_{in}

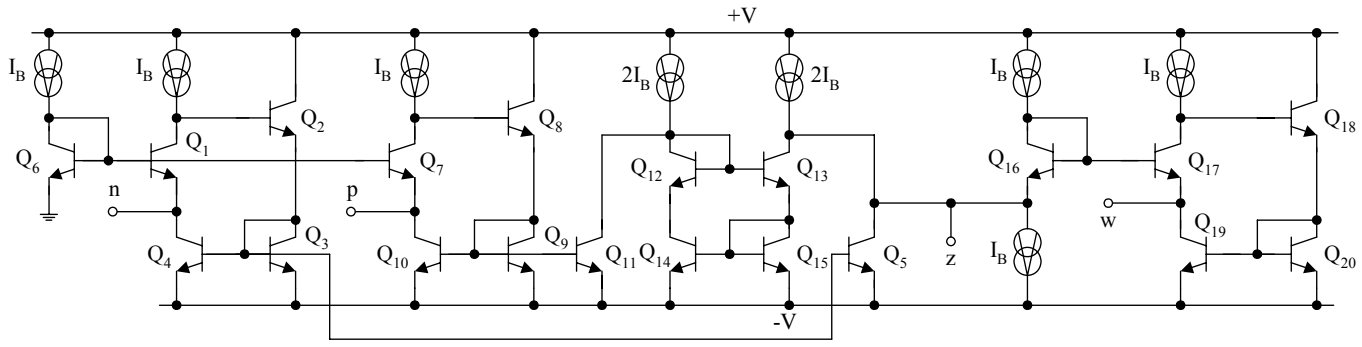

Figure 3. Schematic bipolar implementation of CDBA used in simulations [4].

The natural frequency ω_o and the bandwidth BW of the proposed filter are found to be

$$\omega_0 = \sqrt{\frac{1}{3R_1R_2C_1C_2}} \tag{3}$$

and

$$BW = \frac{1}{3R_2C_2} \tag{4}$$

From equations (3) and (4), it can readily be shown that the ω_o for all the filter responses can be adjusted by controlling the resistor R_1 and/or the capacitor C_1 without disturbing the parameter BW. Therefore, the filter parameters ω_o and BW are independently controllable.

III. Non-Ideal Considerations

The effects of CDBA non-idealities on the filter performance have been now considered in this section. By taking into consideration of the non-ideal CDBAs, the relationship of the terminal currents and voltages given with equation (1) can be rewritten as :

$$\begin{bmatrix} i_z \\ v_w \\ v_p \\ v_n \end{bmatrix} = \begin{bmatrix} 0 & 0 & \alpha_p & -\alpha_n \\ \beta & 0 & 0 & 0 \\ 0 & 0 & 0 & 0 \\ 0 & 0 & 0 & 0 \end{bmatrix} \cdot \begin{bmatrix} v_z \\ i_w \\ i_p \\ i_n \end{bmatrix} \tag{5}$$

where α_p = 1 - ε_p and ε_p ($|\varepsilon_p| << 1$) denotes the current-tracking error from p terminal to z terminal, α_n = 1 - ε_n and ε_n ($|\varepsilon_n| << 1$) represents the current-tracking error from n terminal to z terminal, and β = 1 - ε_v and ε_v ($|\varepsilon_v| << 1$) is the voltage-tracking error from z terminal to w terminal of the CDBA. Therefore, considering into account the factors due to the non-idealities of the CDBA given in equation (5), the modified current transfer functions of the proposed filter can be expressed as :

$$I_{out} = \frac{(\alpha_{p3}D_n(s))I_{in3} - (sR_1C_1\alpha_{p2}\alpha_{p3}\beta_2)I_{in2} - (\alpha_{p1}\alpha_{p2}\alpha_{p3}\beta_1\beta_2)I_{in1}}{D_n(s)} \tag{6}$$

where $D_n(s) = s^2 3R_1R_2C_1C_2 + sR_1C_1\alpha_{n2}\beta_2 + \alpha_{n1}\alpha_{p2}\beta_1\beta_2$,

and α_{pi} , α_{ni} and β_i are the parameters α_p, α_n and β of the i-th CDBA (i = 1, 2, 3), respectively. In this case, the modified parameters ω_o and BW are given by :

$$\omega_0 = \sqrt{\frac{\alpha_{n1}\alpha_{p2}\beta_1\beta_2}{3R_1R_2C_1C_2}} \tag{7}$$

and

$$BW = \frac{\alpha_{n2}\beta_2}{3R_2C_2} \tag{8}$$

The incremental passive and active sensitivities are calculated as:

$$S^{\omega_0}_{R_1,R_2,C_1,C_2} = -S^{\omega_0}_{\alpha_{n1},\alpha_{p2},\beta_1,\beta_2} = -\frac{1}{2} \tag{9}$$

$$S^{\omega_0}_{\alpha_{p1},\alpha_{n2},\alpha_{p3},\alpha_{n3}} = 0 \tag{10}$$

$$S^{BW}_{R_2,C_2} = -S^{BW}_{\alpha_{n2},\beta_2} = -1 \tag{11}$$

and

$$S^{BW}_{R_1,C_1} = S^{BW}_{\alpha_{p1},\alpha_{n1},\alpha_{p2},\alpha_{p3},\alpha_{n3},\beta_1} = 0 \tag{12}$$

It is clearly observed from equations (9)-(12) that the absolute value of all ω_o and BW sensitivities with respect to α_{pi}, α_{ni} and β_i are within unity. Thus, the proposed filter exhibits a low sensitivity performance.

IV. Simulation Results

To confirm the theoretical analysis, the characteristics of the proposed filter in Fig.2 have been simulated with PSPICE program. For this purpose, PSPICE circuit simulations were performed with AT&T ALA 400-CBIC-R [12] process parameters for a bipolar CDBA realization shown in Fig.3 [4]. The DC supply voltages were chosen as ±1V and the DC bias current was I_B = 100 μA.

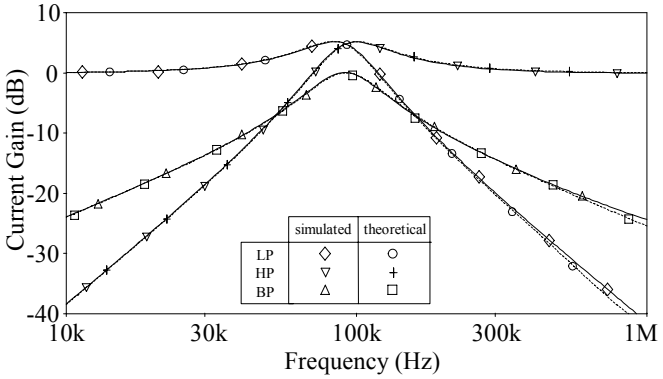

Figure 4. Simulated frequency responses of the proposed CDBA-based universal filter of Figure 2.

Fig.4 shows the simulated frequency responses of the proposed CDBA-based TISO current-mode universal filter with $R_1 = R_2 = 1$ kΩ and $C_1 = C_2 = 1$ nF. This setting leads to obtain the filter responses with $f_o = \omega_o/2\pi \cong$ 91.88 kHz. It was found from the simulation results that the frequency deviation is 0.78%. These results are found to be in good agreement with the critical values. Fig.5 and Fig.6 show the simulated frequency response and the theoretical behavior of the gain and phase characteristics of the AP and BS filters at $f_o \cong$ 91.88 kHz, which agree very well with the presented theory. It can be observed from all figures that the proposed filter performs all the standard biquadratic filtering functions well.

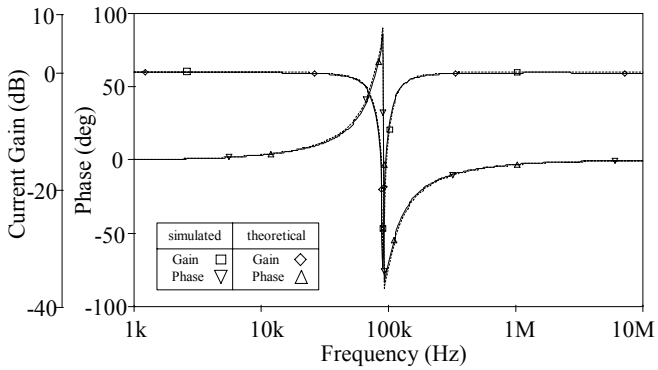

Figure 5. Gain and phase characteristics of the BS filter.

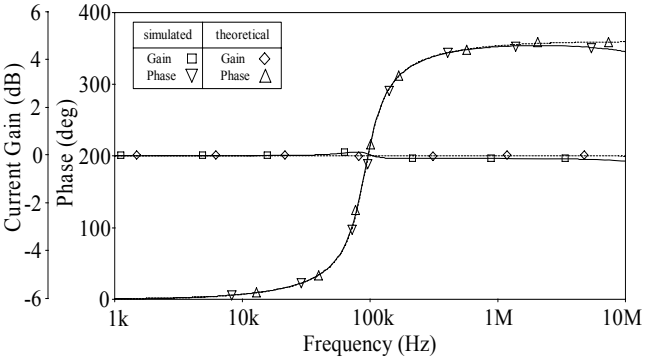

Figure 6. Gain and phase characteristics of the AP filter.

V. CONCLUSION

This paper presents a TISO current-mode multifunction biquadratic filter using only three CDBAs, two resistors and two grounded capacitors, which is very suitable for IC implementation. The proposed filter can realize the LP, HP, BP, BS and AP filter responses all at the high impedance output terminal, which allows easy cascading in current-mode operation. The filter also requires no component matching conditions and has low passive and active sensitivities. An orthogonal control between the natural frequency ω_o and the parameter BW is achieved.

ACKNOWLEDGEMENTS

This work is funded by the Thailand Research Fund (TRF) under the Senior Research Scholar Program, grant number RTA4680003.

REFERENCES

[1] C. Acar, and S. Ozoguz, "A new versatile building block: current differencing buffered amplifier", *Microelectronics Journal* , Vol.30, pp.157-160, 1999.

[2] K. N. Salama, and A. M. Soliman, "Voltage mode Kerwin-Huelsman-Newcomb circuit using CDBAs." *Journal of RF- Engineering and Telecommunications*, Vol.54, No.3-4, pp.90-93, March.-April.2000.

[3] H. Sedef, and C. Acar, "On the realization of voltage- mode filters using CDBA." *Journal of RF-Engineering and Telecommunications*, Vol.54, No.9-10, pp.198-202, 2000.

[4] V. Sawangarom, W. Tangsrirat and W. Surakampontorn, "NPN-based current differencing buffered amplifer and its application", *SICE-ICASE International Joint Conference*, BAXCO(Busan Exhibition & Convention Center), Busan, KOREA, pp.5766-5769, October 18-21, 2006.

[5] C. Acar, and H. Sedef, "Realization of nth-order current transfer function using current differencing buffered amplifiers," *International Journal of Electronics*, Vol.90, No.4, pp.277-283, 2003.

[6] A. U. Keskin, "Cascade approach for the realization of high order voltage-mode filters using single CDBA-based first and second sections", *Journal of RF-Engineering and Telecommunications*, Vol.58, No.7-8, pp.188-194, 2004.

[7] A. U. Keskin, "Voltage-mode high-Q band-pass filters and oscillators employing single CDBA and minimum number of components", *International Journal of Electronics*, Vol.92, No.8, pp.479-487, 2005.

[8] A. Toker, S. Ozoguz and C. Acar, "Current-mode KHN-equivalent biquad using CDBAs", *Electronics Letters*, Vol.35, No.20, pp.1682-1683, 1999.

[9] S. Ozcan, H. Kuntman, and O. Cicekoglu, "Cascadble current mode multipurpose filters employing current differencing buffered amplifier (CDBA)", *International Journal of Electronics and Communications (AEU)*, Vol.56, pp.67-72, 2002.

[10] M. Bhusan, and R. W. Newcomb, "Grounding of capacitors in integrated circuits", *Electronics Letters*, Vol.3, No.4, pp.148-149, 1967.

[11] K. Pal, and R. Singh, "Inductorless current conveyor allpass filter using grounded capacitors", *Electronics Letters*, Vol.18, No.20, pp.47, 1982.

[12] D.R. Frey, "Log-domain filtering : an approach to current mode filtering ", *Proc.IEE*, pt-G, Vol. 140, No.6, pp.406-416, 1993.

Minimum Devices Active-only Current-mode Universal Filter

Pipat Prommee, Montri Somdunyakanok, Montree Kumngern and Kobchai Dejhan
Faculty of Engineering and Research Center for Communication and Information Technology
King Mongkut's Institute of Technology Ladkrabang, Bangkok 10520, Thailand
Email: pipat@telecom.kmitl.ac.th, monsom@siamu.com

***Abstract*— An active-only devices current-mode universal filter using the biquadratic transfer function is proposed. The proposed circuit is realized focusing on the minimized active-only components count without external passive elements. The different kinds of filter function as low-pass, high-pass, band-pass and band-reject response can be obtained without changing circuit topology. The proposed circuit is realized by using 4 MOS transistors, 2 OTAs, and 2 OPAMPs. The parameters ω_P can be electronically tuned through simply adjusting the transconductance gains of the OTAs or supply voltage of electronic resistors. The Q_P can be tuned in both concepts, changing of their components and the transconductance gain. The simulation results are given by PSpice.**

I. INTRODUCTION

The high performance active filters have been received much attention. In filter circuit design, current-mode filters are becoming popular, since they have many advantages compared with their voltage-mode counterparts. Design of current-mode filters employing active devices such as current followers (CFs) [1], second generation current conveyors (CCIIs) [2] and operational transconductance amplifiers (OTAs) [3,4]. The transfer function biquadratic filter is a basic principle for synthesized is filter circuit to obtain efficiency especially universal filter, and the principle for auxiliary create to filter with integrator based on a synthesized [13]. The open-loop gain of operational amplifier, OA is known well in term of Gain-Bandwidth, GBW. While to obtain using OTA, therefore can be implemented by filter circuit. The same with a high frequency and they have been introduced in the literatures. The current-mode operations were proposed in recent literatures [5-7]. The voltage-mode operations were proposed in recent literatures [8-9]. Although, many active elements are employed but they have very advantages in high-frequency and further integration.

This paper focuses on the synthesized of universal filter using active-only devices. The proposed circuit is realized by using MOS transistors, OAs, and OTAs. The objective on the design is current-mode of evation based on biquadratic function using only active elements without any external passive elements in recent literatures [5-9]. The minimization of active elements and electronically is tunable a core of this paper.

Consider in previous of current-mode active-only filter in recent literatures [5-6], which using 2 OAs and 3 OTAs. The ω_P is tuned by an OTA which in term of square-root function. The linear controlled can not be achieved and complicate in the practical. Another filter [7], the ω_P is tuned with linear controlled has been achieved but the many components are used, 2 OAs, 5 OTAs, that is not suitable for the compactness ICs fabrication. This paper proposed only using 2 OAs, 2 OTAs and 4 MOS transistors for circuit implementation. The achieved circuit can be electronically tuned by either transconductance gains of OTA and electronic resistor for the ω_P parameter. The proposed circuit can be also physically and electronically tuned by changing of transistor aspect ratio for Q_P parameter without effect to the ω_P parameter.

II. THEORY AND PRINCIPLE

The 2 integrators-loop principles have been introduced in recent literatures [12]. The block diagram has been shown in Fig.1 and transfer function can be expressed in (1) as follows

$$\frac{V_2(s)}{V_1(s)} = \frac{sB_2}{s^2 + sB_2k_1 + B_1B_2k_0} \tag{1}$$

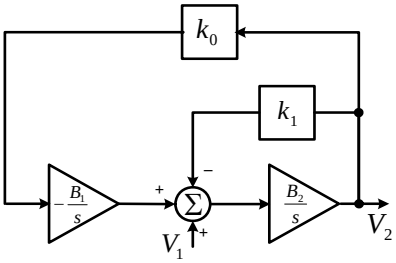

Fig.1 The 2 Integrators-loop block diagram

The comparison of (1) and characteristic equation (2)

$$D(s) = s^2 + s\frac{\omega_P}{Q_P} + \omega_P^2 \tag{2}$$

The parameters ω_P and Q_P can be expressed as

$$\omega_P = \sqrt{B_1B_2k_0} \text{ and } Q_P = \frac{1}{k_1}\sqrt{\frac{B_1B_2k_0}{B_2}} \tag{3}$$

A. Voltage-Gain Circuit

The voltage-gain circuit [10] which used in this paper consists of an OTA and an electronic resistor as show in Fig.2. The transresistance of the electronic resistor circuit can be expressed in (4)

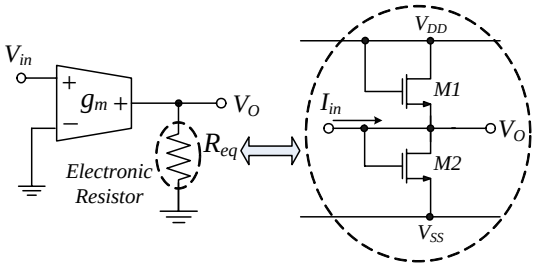

Fig.2 The voltage-gain circuit [10]

$$R_{eq} = \frac{V_O}{I_{in}} = \frac{L}{2\mu C_{OX} W\left(V_{DD} - V_T\right)} \tag{4}$$

The voltage gain of Fig.2 can be obtained to

$$\frac{V_O}{V_{in}} = g_m R_{eq} \tag{5}$$

B. Opamp as a lossless integrator

Consider the open-loop GBW of OA [6], as shown in Fig.3 can be expressed the transfer function as a lossless integrator as (6)

$$A(s) = \frac{B_i}{s} \quad (i = 1, 2) \tag{6}$$

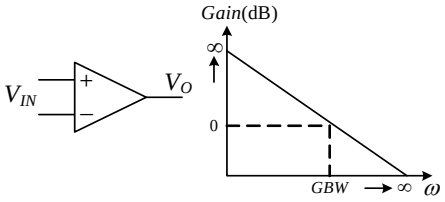

Fig.3 The OA and frequency response, ω_P

C. Current-mode Universal Filter Realization

The proposed filter are realized by using the above methods as shown in Fig.4

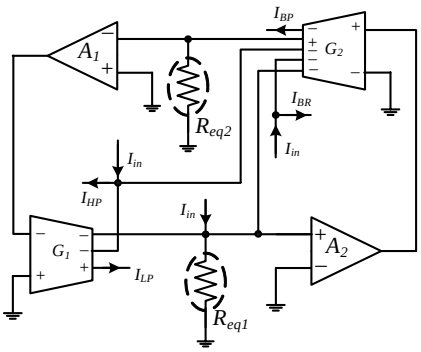

Fig.4-1 The first implementation of proposed current-mode universal filter

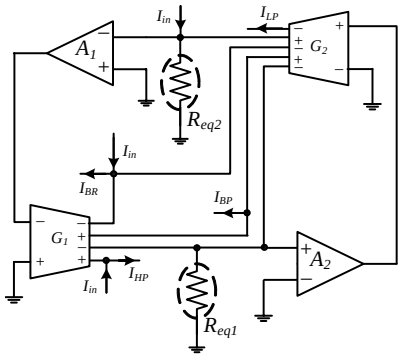

Fig.4-2 The second implementation of proposed current-mode universal filter

From Fig.4-1and 4-2, the different transfer functions are illustrated in (7) – (10)

$$\frac{I_{LP}}{I_{in}} = \frac{R_{eq1}R_{eq2}B_1B_2g_1g_2}{D(s)} \tag{7}$$

$$\frac{I_{HP}}{I_{in}} = \frac{s^2}{D(s)} \tag{8}$$

$$\frac{I_{BR}}{I_{in}} = \frac{s^2 + R_{eq1}R_{eq2}B_1B_2g_1g_2}{D(s)} \tag{9}$$

$$\frac{I_{BPa}}{I_{in}} = \frac{sR_{eq1}B_2g_2}{D(s)} \quad ; \text{ for Fig.4-1} \tag{10a}$$

and

$$\frac{I_{BPb}}{I_{in}} = \frac{sR_{eq2}B_1g_1}{D(s)} \quad ; \text{ for Fig.4-2} \tag{10b}$$

where $D(s) = s^2 + sR_{eq1}B_2g_2 + R_{eq1}R_{eq2}B_1B_2g_1g_2$ (11a)

and $D(s) = s^2 + sR_{eq2}B_1g_1 + R_{eq1}R_{eq2}B_1B_2g_1g_2$ (11b)

Eq.(11a) and (11b) are obtained for Fig.4-1 and 4-2, respectively. The concerning parameters ω_P and Q_P are become

$$\omega_P = \sqrt{R_{eq1}R_{eq2}B_1B_2g_1g_2} \tag{12}$$

$$Q_{Pa} = \sqrt{\frac{R_{eq2}B_1g_1}{R_{eq1}B_2g_2}} \quad ; \text{ for Fig.4-1} \tag{13a}$$

and

$$Q_{Pb} = \sqrt{\frac{R_{eq1}B_2g_2}{R_{eq2}B_1g_1}} \quad ; \text{ for Fig.4-2} \tag{13b}$$

The parameter g_i represents for the transconductance of OTA (i) and R_{eqi} represents for the electronic resistors (i) Generally, B_i is OAs open-loop GBW, are identical suppose that (B_1=B_2=B), the quality factor is unity (Q_P =1), From (12) and (13), the ω_P can be electronically tuned by giving simply parameters as ($g_1 = g_2 = g$) and ($R_{eq1} = R_{eq2} = R_{eq}$). From (12), The frequency response parameter can be will become is also obtained $\omega_P = R_{eq}Bg$.

Therefore, the frequency response can be linearly tuned by 2 approaches, through the transconductance gain of OTA or the electronic resistors from (4) and (13). The parameter Q_P is distinguished for flexible to adjust in electronically and physically.

For $Q_P > 1$, first method the physically tuned can be obtained by ratio adjusting of (R_{eq1}, R_{eq2}) while ($g_1 = g_2 = g$), another method can be tuned by the transconductance gain g_1 and g_2 while ($R_{eq1} = R_{eq2} = R_{eq}$). However, Q_P achievement by ratio adjusting of (R_{eq1}, R_{eq2}) or (g_1, g_2) have to perform in the properly rule otherwise that may effect to the ω_P. The properly adjusting rule of (g_1, g_2) can be described below

$$g_1 g_2 = A \qquad \text{or} \qquad g_1 = \frac{A}{g_2} \tag{14}$$

From (13), the parameters are given as ($R_{eq1} = R_{eq2}$) and ($B_1 = B_2$). The parameter Q_P in (13) can be obtained by setting of g_1 and g_2 as follows

$$Q_{Pa} = \sqrt{\frac{g_1}{A/g_1}} = \frac{g_1}{\sqrt{A}} = \frac{\sqrt{A}}{g_2} \tag{15a}$$

$$Q_{Pb} = \sqrt{\frac{A/g_1}{g_1}} = \frac{\sqrt{A}}{g_1} = \frac{g_2}{\sqrt{A}} \tag{15b}$$

III. SENSITIVITY

The other filter performances can be considered by its sensitivities. The performance with respect to active elements according to the frequency response $S_x^{\omega_P}$ and quality factor $S_x^{Q_P}$, while x is active elements. The achieved sensitivities can be as follows: $S^{\omega_P}_{g_1,g_2,R_{eq1},R_{eq2},B_1,B_2}$ and $S^{Q_P}_{g_1,R_{eq2},B_2}$ are 0.5 and $S^{Q_P}_{g_2,R_{eq1},B_1}$ = -0.5, respectively.

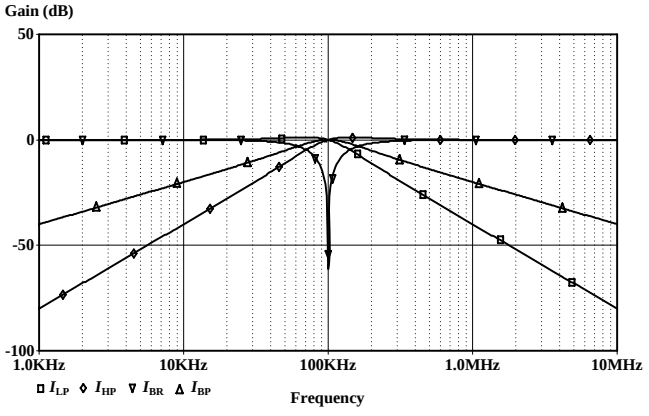

Fig.5 Proposed filter characteristic while power supply of R_{eq} are ± 5 Volt

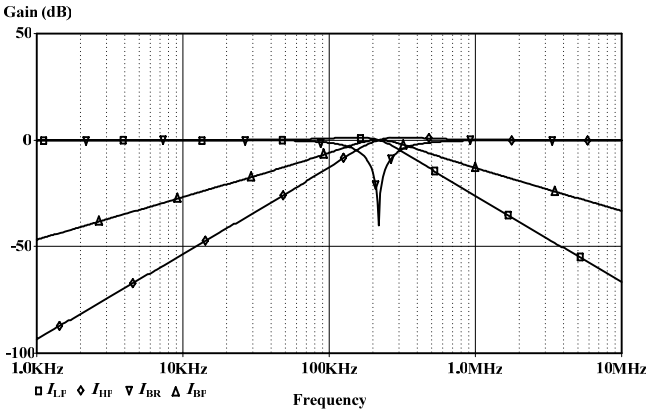

Fig.6 Proposed filter characteristic while power supply of R_{eq} are ± 1 Volt

IV. SIMULATION RESULTS

The proposed universal filter can be confirmed its performances and characteristics by PSpice. The T14Y MOSIS 0.25 μm CMOS model has been employed, V_{TN} = 0.42 volts and $\mu_N C_{OX}$ = 250.1048$\mu A/V^2$ for the electronic resistors. The OA and OTA use the macro model [11] of LF351 and CA3080, respectively. The ± 5 volts power supply is used for the electronic resistors. The transistor aspect ratio (W/L) used for electronic resistors (R_{eq1}, R_{eq2}) are defined for the Q_P adjustment according to (4) and (13).

The electronically controlled ω_P can be confirmed by adjusting power supply of R_{eq} shows in Fig.5 and Fig.6. The characteristic of universal filter as shows in Fig.4 with Q_P = 1. The following equipment parameters can be defined (W/L) = ($1\mu m/1\mu m$) for the electronic resistors $R_{eq1} = R_{eq2}$ = 2.63 $k\Omega$, open-loop GBW of OAs are about 4 MHz or $B_1 = B_2$ = 25.37x10^6 rad/s, power supply of R_{eq} are ± 5 volts and ± 1 volts, respectively. The frequency response ω_P are shown about 100 kHz and 220 kHz. The electronically controlled ω_P by adjusting the supply voltage of electronic resistors or transconductance gain 2 OTAs are confirmed according to the theory above.

TABLE I. THE DIFFERENT Q_P ADJUSTED BY $R_{eq\,1}$, $R_{eq\,2}$ AND g_1, g_2

Q_P	$g_1 = g_2 = 9.42\mu s$		R_{eq1}=R_{eq2}=($1\mu m/1\mu m$)	
	R_{eq1} (W/L)	R_{eq2} (W/L)	g_1	g_2
1	$(1\mu m/1\mu m)$	$(1\mu m/1\mu m)$	$9.42\mu s$	$9.42\mu s$
2	$(2\mu m/1\mu m)$	$(.5\mu m/1\mu m)$	$18.84\mu s$	$4.71\mu s$
4	$(4\mu m/1\mu m)$	$(.25\mu m/1\mu m)$	$37.68\mu s$	$2.35\mu s$
8	$(8\mu m/1\mu m)$	$(.12\mu m/1\mu m)$	$75.36\mu s$	$1.17\mu s$
16	$(16\mu m/1\mu m)$	$(.06\mu m/1\mu m)$	$150.7\mu s$	$0.59\mu s$

Consider (15), the adjusting of Q_P without effect to ω_P by simulation results of universal filter. The ω_P is defined at 100*kHz* while Q_P is varied as 1, 2, 4, 8 and 16, respectively. Firstly, The parameters (g_1=g_2=g) are defined. The adjustment resistor R_{eq1} and R_{eq2} can be adjusting of by (W/L) as table I. The secondly method is based on the setting of (R_{eq1} = R_{eq2} = R_{eq}) and transconductance gain of OTA, g_1, g_2 are adjusted electronically according to table I.

The simulation results in term of BPF and BRF with the different Q_P in table I, are shown in Fig.7 and 8 respectively. The adjusting parameter Q_P without effect to its ω_P can be observed. The frequency response when Q_P increased has a few errors because the error of electronic resistor that is a channel length modulation effects: λ (L=1μm). The ω_P and its magnitude are quite stable while Q_P is varied according to the theory above.

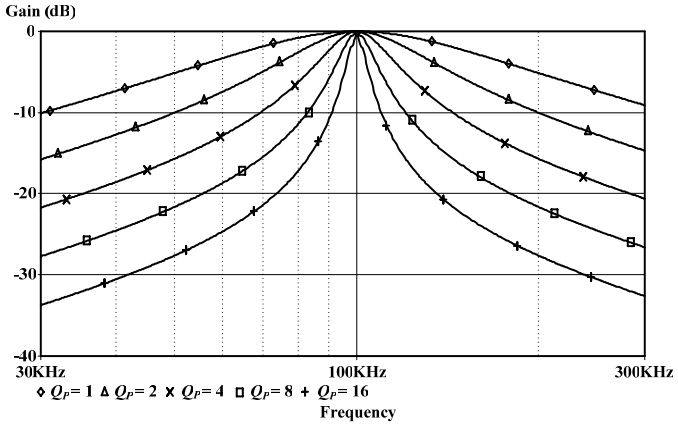

Fig.7 Proposed BPF output with varying Q_P by 1-16

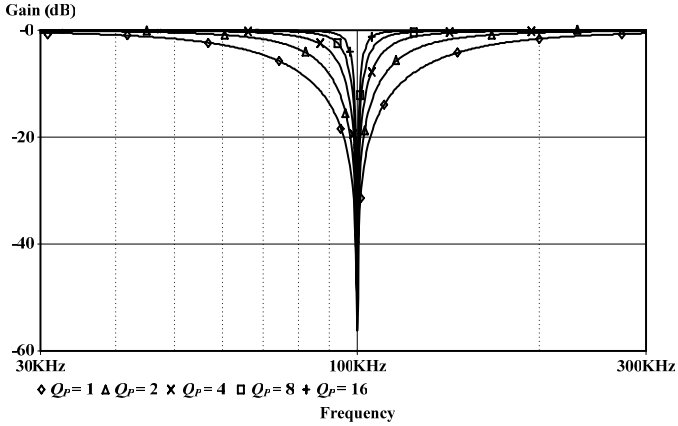

Fig.8 Proposed BRF output with varying Q_P by 1-16

V. CONCLUSION

This paper described a minimum active-only devices current-mode universal filter without external passive elements. In this paper, the high-frequency applications and further ICs technology are suitable. The proposed filter realization is operated based on 2 integrators-loop principles. The ω_P can be electronically tuned through the transconductance or supply of devices. The proposed circuit comprised 2 OTAs, 2 OAs, and 4 MOS transistors that met the minimum devices target. The pole frequency response is given by open-loop GBW of OA corporated with the transconductance gain. The adjustable Q_P can be obtained without effect to ω_P.

REFERENCES

[1] S. I. Liu, J. J. Chen, Y. S. Hwang, "New Current mode Biquad filters using current follower," *IEEE Trans. Circuits Syst*., vol. 42, pp.380-383, July 1995.

[2] E. O. Gunes, A Toker and S. Ozoguz, "Insensitive current-mode universal filter with minimum component using dual-output current conveyors," *Electron. Lett*., vol. 35, pp.524-525, April 1999.

[3] C. Chang, "New multifunction OTA-C biquads," *IEEE Trans. Circuits and Syst*., vol. 47, pp.1235-1238, 2000.

[4] C. Chang and S. Pai, "Universal current-mode OTA-C biquad with the minimum components," *IEEE Trans. Circuits and Syst*., vol. 46, pp.820-824, 1999.

[5] T. Tsukutani, M. Ishida, S. Tsuiki, and Y. Fukui, "Current-mode biquad without passive elements," *Electron. Lett*., vol. 32, pp.197-198, Feb. 1996.

[6] T. Tsukutani, M. Higashimura, Y. Sumi and Y. Fukui, "Electronically tunable current-mode active only biquad filter," *Int. J. Electron.*, vol. 87, pp.307-314, 2000.

[7] M. T. Abuelma' Atti and H. A Alzaher, "Universal three input and one output current-mode filter without external passive elements, *Electron. Lett*., vol. 33, pp.281-283, Feb. 1997.

[8] T. Tsukutani, M. Higashimura, N. Takahashi, Y. Sumi and Y. Fukui, "Novel voltage-mode biquad using only active divices,"*Int.J.Electron.*, vol. 88, pp.339-346, 2001.

[9] T. Tsukutani, M. Higashimura, Y. Sumi and Y. Fukui, "Voltage-mode active only biquad," *Int. J. Electron*., vol. 87, pp.1435-1442, 2000.

[10] P. Prommee and K. Dejhan, "An integrable electronic-controlled quadrature sinusoidal oscillator using CMOS operational transconductance amplifier," *Int. J. Electron*., vol. 89, pp.365-379, 2002.

[11] J. Wu, "Current-mode high-order OTA-C filter," *Int. J. Electron*., vol. 76, pp.1115-1120, 1994.

[12] E. Sanchez-sinnencio, R. L Geiger and H. Nevarez-Lozano, "Generation of Continous-Time Two Integrator Loop OTA filter structures," *IEEE Trans. Circuits and Syst*., vol. 35, pp.936-946, Aug. 1988.

[13] W. J. Kerwin, L. P. Huelsman, and R. W. Newcomb, "State-variable synthesis for insensitive integrated circuit transfer function," *IEEE Trans. Solid-state Circuits*, vol. SC-2, pp.87-92, 1967.

A Systematic Design of Electronically Tunable Ladder Filters Employing DO-OTAs

Winai Jaikla* and Montree Siripruchyanun**
*Electric and Electronic Program, Faculty of Industrial Technology,
Suan Sunandha Rajabhat University, Dusit, Bangkok, 10300, THAILAND Email: jnai2004@yahoo.com
**Department of Teacher Training in Electrical Engineering, Faculty of Technical Education,
King Mongkut's Institute of Technology North Bangkok, Bangkok, 10800, THAILAND Email: mts@kmitnb.ac.th

***Abstract*-A systematic design of continuous-time current-mode ladder filter using Dual-Output OTAs (DO-OTAs) is resented. The proposed technique is based on leapfrog simulation of RLC ladder filter using only DO-OTAs and grounded capacitors that lead to simple structure, easy to design and suitable for IC fabrication. A fifth-order Chebyshev low-pass filter and a sixth-order Chebyshev band-pass filter which retain a minimum requirement of passive elements and have an advantage of electronically tunable will be introduced. The feasibility of realization strategy is confirmed through PSPICE circuit simulations.**

I. INTRODUCTION

Double terminated passive RLC ladder filters are well known on having an inherent advantage over active filter in terms of their sensitivity to component tolerances. There are several methods to extract this benefit from the prototype passive filter using the opamp-based RC-active and OTA-C-based circuits [1]. The leapfrog structure seems to receive more popular sine it shares the entire low sensitivity characteristic and low component spread of the precedent RLC filter. Traditionally, the simulation is based on modeling all circuit equations as voltage signals [1]. Recently, current-mode signal processing has been received substantial consideration owing to its higher performance properties. Consequently, many suggestions of current-mode leapfrog ladder filter had been published employing OTAs [2] and CCIIs [3] as the active building blocks. However, all of them are established from simulating the operation of the ladder by mean of realizing the transfer function, which require a lot of active and passive elements and sometime the sensitivity may not necessitate being low. The implementation of leapfrog filter using current differential buffered amplifies or CDBAs has been proposed [4], which can perform high frequency and low voltage supply operation. This scheme can simplify the signal flow graph of leapfrog filter and then realize each circuit element one by one, hence the low sensitivity basis is promised. Unfortunately, several floating resistors are required for voltage to current conversion and the utilized frequency is exactly fixed by determined passive elements.

This paper follows the idea of realizing the voltage-current relationships of each element corresponding to the prototype RLC, filters one by one. OTA is chosen to function as a V-to-I converter cell regenerating all voltage parameter into current form because it is a commercially available component. This proposed scheme possesses many advantages. Firstly, the structure is very simple and easy to design. No any external resistor is required, which can save the area in case of fabricating in a silicon chip. Moreover, the center frequency can be tuned electronically by adjusting the bias current of OTAs. This will be useful in redeeming when the values of passive devices are deviated; including changing the system's characteristic is also very comfortable.

This work is organized as follows. Firstly, the Dual-output Operational Transconductance Amplifier will be introduced. The simulated elements, which are grounded resistance simulator, grounded/floating inductance simulators and floating capacitance simulator, are included in Section II. The filter design methodology will be given in Section III. Section IV shows the simulation results. They compare the results of filter synthesis from simulated and ideal elements.

II. PRINCIPLE OF OPERATION

A. The Dual-Output Operational Transconductance Amplifier (DO-OTA)

Since the proposed circuits are based on DO-OTAs, a brief review of the DO-OTA is given in this section. An ideal DO-OTA has infinite input and output impedances. Output current of the DO-OTA is given by

$$I_{O+} = -I_{O-} = g_m(V_1 - V_2)\,. \tag{1}$$

Where g_m is the transconductance parameter of an OTA. For a bipolar OTA, the transconductance gain can be expressed by

$$g_m = \frac{I_B}{2V_T}\,. \tag{2}$$

Where I_B and V_T are bias current and thermal voltage, respectively. The symbol of the DO-OTA is shown in Fig. 1.

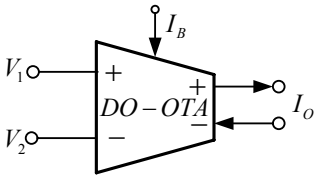

Figure 1. Circuit symbol of DO-OTA

B. Grounded Resistance simulator

The OTA-based grounded resistance simulator is shown in Fig. 2 [5]. From routine analyzing the circuit in Fig. 2, we will get the equivalent grounded resistance as

$$R_{eq} = \frac{1}{g_m} = \frac{2V_T}{I_B}. \quad (3)$$

From Eq. (3), the resistance value is controlled by adjusting I_B.

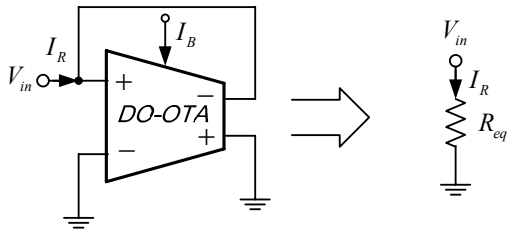

Figure 2. Grounded resistance simulator

C. Grounded Inductance Simulator

Fig. 3 depicts the proposed grounded inductance simulator [6]. Considering the circuit in Fig. 3 and using OTA properties in Section A, we will receive

$$Z_L = \frac{V_{in}}{I_L} = \frac{sC}{g_{m1}g_{m2}}. \quad (4)$$

From Eq. (4), it is obvious that the circuit shown in Fig. 2 simulates a grounded inductance with a value

$$L_{eq} = \frac{C}{g_{m1}g_{m2}} = \frac{4V_T^2 C}{I_{B1}I_{B2}}. \quad (5)$$

It can be clearly seen from Eq. (5) that the inductance value L_{eq} can be adjusted electronically by either I_{B1} or I_{B2}.

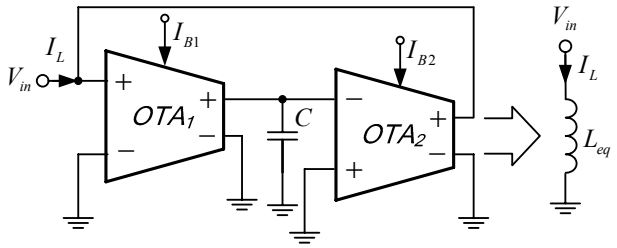

Figure 3. Grounded inductance simulator

D. Floating Inductance Simulator

Fig. 4 depicts the proposed floating inductance simulator, where I_{B1} and I_{B2} are input bias currents of the OTA_1 an OTA_2, respectively.

Considering the circuit in Fig. 4 and using the OTA properties in section A, we will receive

$$Z_L = \frac{V_1 - V_2}{I_L} = \frac{sC}{g_{m1}g_{m2}}. \quad (6)$$

From Eq. (6), it is obvious that the circuit shown in Fig. 4 simulates a floating inductance with a value

$$L_{eq} = \frac{C}{g_{m1}g_{m2}} = \frac{4V_T^2 C}{I_{B1}I_{B2}}. \quad (7)$$

It can be clearly seen from Eq. (7) that the inductance value L_{eq} can be adjusted electronically by either I_{B1} or I_{B2}.

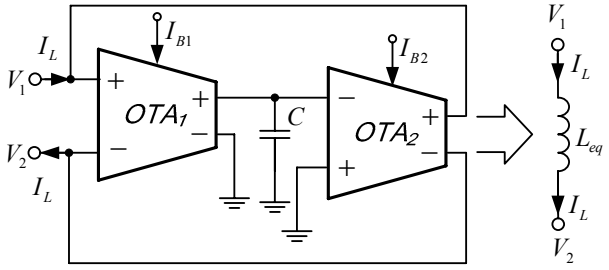

Figure 4. Floating inductance simulator

E. Floating Capacitance Simulator

Fig. 5 depicts the floating capacitance multiplier originated from a grounded capacitor [7]. Considering the circuit in Fig. 5 and using OTA properties in Section A, we will receive the input impedance as

$$Z_C = \frac{V_1 - V_2}{I_C} = \frac{g_{m3}g_{m4}}{sCg_{m1}g_{m2}}. \quad (8)$$

From Eq. (8), it is clearly seen that the circuit can provide the floating capacitor with a value

$$C_{eq} = \frac{I_{B1}I_{B2}}{I_{B3}I_{B4}}C. \quad (9)$$

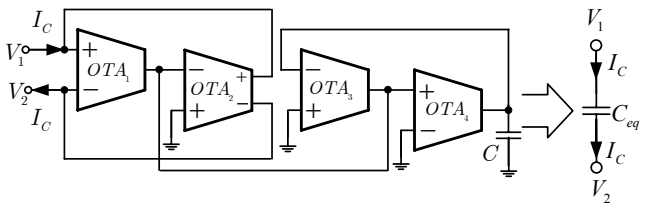

Figure 5. Floating capacitance simulator

From Eq. (9), we found that, if the connected capacitor is free from temperature, the capacitive value is ideally temperature-insensitive and can be adjusted by any input bias

currents. Then the capacitive value, with adjusting by input bias currents, is very widely tuned. For example, the minimum input bias current can be as low as nano-ampere range while the maximum input bias current can be as high as milli-ampere range.

III. Filter Design Methodology

A current-mode fifth-order low-pass RLC ladder filter shown in Fig. 6 is adopted as an example. It comprises the minimum requirement of DO-OTAs and capacitors. There is no obligation of any external resistor, even the terminated resistor, *Rs* and *Ro*; are also implemented using DO-OTA (in Section B). Not only the attempt to eliminate the passive components, it is the necessary for tuning pole frequency feature. Furthermore, this composition has several high impedance outputs, which allow to be easily cascaded without any additional matching circuits.

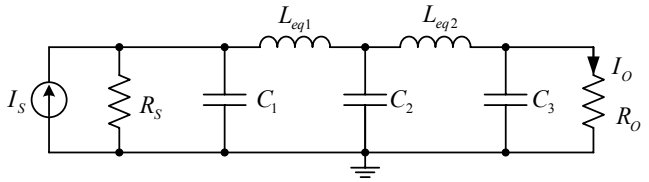

Figure 6. Current-mode fifth-order Chebyshev low-pass RLC ladder filter

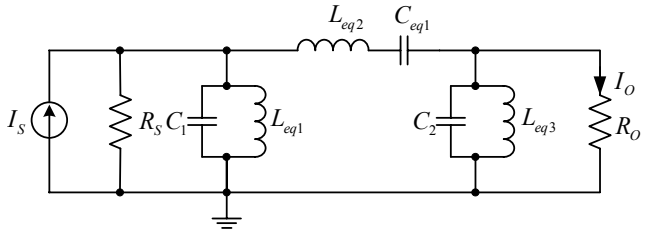

Figure 7. Current-mode sixth-order RLC band-pass filter

In addition, deriving the RLC ladder band-pass filter with this procedure is also possible. Consider a current-mode sixth-order band-pass filter in Fig. 7. In this case, the floating and grounded R, L and C branches can be realized using the basic block as shown in Section II.

IV. Simulation Results

To prove the performances of the proposed principle, the PSPICE simulation program was used for the examination. The PNP and NPN transistors employed in the proposed circuit were simulated by respectively using the parameters of the PR200N and NR200N bipolar transistors of ALA400 transistor array from AT&T [8] with ±2.5V supply voltages and all bias currents I_B were set to be 100μA, except that the I_B of grounded resistances *Rs* and *Ro* were set to be 200μA to obtain resistance value of *276*Ω. Fig. 8 depicts schematic description of the DO-OTA used in the simulations.

To show the frequency domain performance of the current-mode fifth-order Chebyshev low-pass RLC ladder filter in Fig. 6, it was simulated with PSPICE program. $C_1=C_2=C_3=10\mu F$ and $C_{Leq1}= C_{Leq2}=1nF$ are chosen to obtain inductance value of *328μH*. The simulated frequency responses of the ideal and simulated low-pass ladder filter are compared in Fig. 9. The result is very close to ideal filter implemented from the practical passive elements. Tuning ability is also simulated and shown in Fig. 10 by varying bias current to 50μA 100μA and 150μA. It is found that the pole frequency can be tuned by the input bias current.

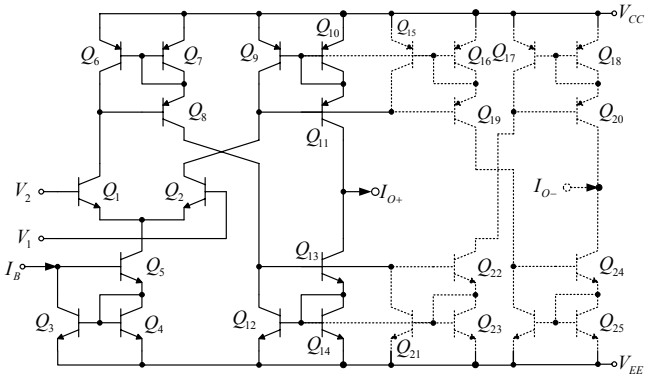

Figure 8. Internal construction of the DO-OTA

Furthermore, $C_1=C_2=10\mu F$, $C_{Leq1}= C_{Leq2}= C_{Leq3}=1nF$ and $C_{Ceq1}=10\mu F$ are taken to obtain inductance and capacitance of *328μH* and *10μF*, respectively. Comparison of the ideal and simulated current-mode sixth-order RLC band-pass filter responses is depicted in Fig. 11. In addition, center frequencies can be adjusted by varying the input bias current of the DO-OTAs, as shown the results in Fig 12.

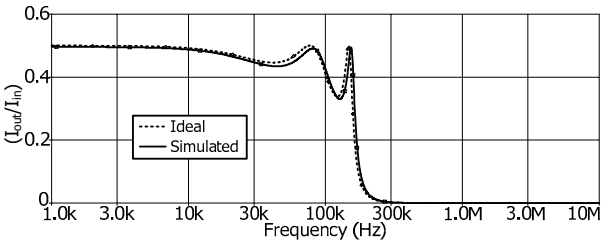

Figure 9. Compared results of current-mode fifth-order Chebyshev low-pass RLC ladder filter

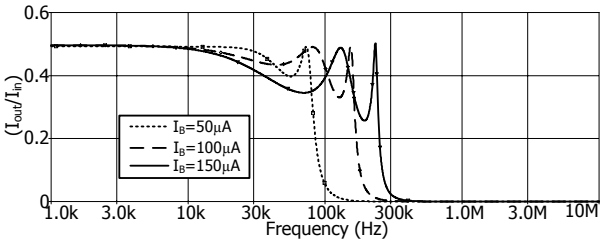

Figure 10. Results for cut-off frequency tunability of the simulated low-pass RLC ladder filter

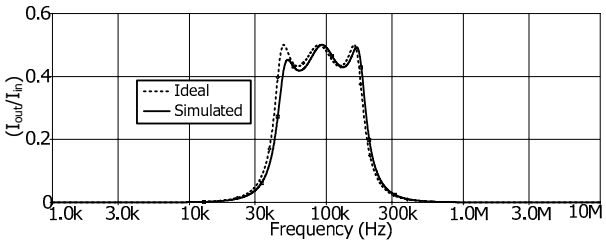

Figure 11. Compared results of current-mode fifth-order Chebyshev band-pass RLC ladder filter

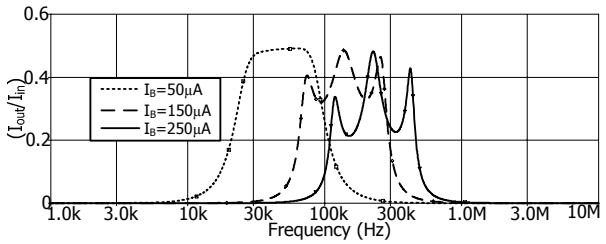

Figure 12. Results for center frequency tunability of the simulated band-pass RLC ladder filter

CONCLUSIONS

A design of RLC ladder filters using simulated elements (resistors, inductors and capacitors) based on the Dual-Output Operational Transconductance Amplifiers (DO-OTAs) has been described. The design strategy is very simple and requires the minimum passive components. The pole or center frequency can be tuned electronically by controlling the bias currents of DO-OTAs, which is very helpful in compensating unmatched components as well as varying the characteristic without changing any device. Fifth-order Chebyshev low-pass filter and sixth-order Chebyshev band-pass filter are derived as examples. Actually, the simulated elements can be applied in any filter functions. The PSPICE simulation results give a good agreement with the theoretical expectations.

REFERENCES

[1] R. Schaumann, and M.E. Van Valkenberg, *Design of Analog Filters*, Oxford University Press, New York, 2001.

[2] J. Ramirez-Angulo. and E. Sinchez-Sinencio "High Frequency Compensated Current-Mode Ladder Filters Using Multiple Output OTAs." *IEEE Trans. Circuirs Sysr.II,* vol. 41.no. 9,pp. 581-586, Sep. 1994.

[3] Y.S. Hwang, P.T. Hung W. Chen and S.I. Liu, "Systematic Generation of Current-Mode Linear Transformation Filters Based on Multiple Output CCIIs," *J. Analog Integrated Circuit and Signal Proc*., vol. 32. pp. 123.134, Aug. 2002.

[4] W. Tangsrirat. N. Fujii. and W. Surakampontorn, "Current-mode leapfrog ladder filters using CDBAs," *Proc. Inter. Symp. Circuits Systems*, pp.V57-V60. 2002.

[5] V. Springl, W. Jaikla and M. Siripruchyanun, "Floating positive/negative resistance simulators employing single dual-output OTA", *Proc. Inter. Symp. on Communications and Information Technologies 2006 (ISCIT 2006)*, Bangkok, Thailand, 18-20 October 2006.

[6] W. Jaikla and M. Siripruchyanun, "Floating positive and negative inductance simulators based on OTAs", *Proc. Inter. Symp. on Communications and Information Technologies 2006 (ISCIT 2006)*, Bangkok, Thailand, 18-20 October 2006.

[7] W. Jaikla and M. Siripruchyanun, "An electronically controllable capacitance multiplier with temperature compensation," *Proc. Inter. Symp. on Communications and Information Technologies 2006 (ISCIT 2006)*, Bangkok, Thailand, 18-20 October 2006.

[8] D. R. Frey "Log-domain filtering: an approach to current-mode filtering," *IEE Proc. Circuit Devices Syst.,* vol. 140, no. 406-416, 1993.

A Novel Current-Mode Alternative Topology for Realization of Universal Filter and Quadrature Oscillator

Winai Jaikla * and Montree Siripruchyanun **
* Electric and Electronic Program, Faculty of Industrial Technology,
Suan Sunandha Rajabhat University, Dusit, Bangkok, 10300, THAILAND Email: jnai2004@yahoo.com
** Department of Teacher Training in Electrical Engineering, Faculty of Technical Education,
King Mongkut's Institute of Technology North Bangkok, Bangkok, 10800, THAILAND Email: mts@kmitnb.ac.th

***Abstract*- In this article, a new topology which can function both as quadrature oscillator and universal biquad filter is introduced. Working as quadrature oscillator, the oscillation condition and oscillation frequency can be adjusted independently. Functioning as universal biquad filter, it can provide 3 standard functions (Highpass, Lowpass, Bandpass), the quality factor and cutoff frequency can be tuned orthogonally. It comprises 2 voltage to current converters, 2 grounded capacitors, 1 positive grounded and 1 negative grounded resistors. The proposed topology can work as either quadrature oscillator or biquad filter without changing circuit topology. In addition, it can provide output signal both in current-mode and voltage-mode simultaneously. The current-mode universal filter and quadrature oscillator using OTAs being active elements as an example are proposed to shown the usefulness of proposed topology and the PSPICE simulation results are depicted. The given results agree well with the theoretical anticipations.**

***Index Terms*- universal filter, OTA, current-mode, quadrature oscillator, topology**

I. INTRODUCTION

An oscillator and a filter are 2 basic important building blocks which are frequently employed. A quadrature oscillator is widely used because the circuit provides two sinusoids with 90^{o} phase difference, as for example in telecommunications for quadrature mixers and single-sideband generators or for measurement purposes in vector generators or selective voltmeters. Therefore, the quadrature oscillator constitutes an important unit in many communication and instrumentation systems [1-5]. In similar, nowadays, the applications and advantages in the realization of various active transfer functions, called as universal biquad filters, have received considerable attention. A universal filter may be used in phase locked loop FM stereo demodulators, touch tone telephone and crossover networks used in three-way high fidelity loudspeakers [6].

In the last decade, there has been much effort to reduce the supply voltage of analog systems. This is due to the command for portable and battery-powered equipment. Since a low-voltage operating circuit becomes necessary, the current–mode technique is ideally suited for this purpose more than the voltage-mode one. Presently, there is a growing interest in synthesizing the current-mode circuits because of more their potential advantages such as larger dynamic range, higher signal bandwidth, greater linearity, simpler circuitry and lower power consumption [7-8].

The purpose of this paper is to introduce a new topology to implement current-mode universal biquad filter and quadrature oscillator. The features of proposed topology are that:

- It can work as universal filter and quadrature oscillator without changing the circuit topology.
- When it works as universal filter, it can provide 3 functions (lowpass, highpass and bandpass) in the same time. In addition, the natural frequency can be adjusted independently from the quality factor.
- When it works as quadrature oscillator, the proposed topology can provide quadrature sinusoidal signals in both voltage-mode and current-mode simultaneously. Moreover, the oscillation condition can be adjusted independently from the oscillation frequency.
- The topology requires only grounded capacitors (beneficial to an IC implementation [9]).
- It can be implemented by employing any active building blocks to serve as voltage to current converters and positive/negative resistors, such as current conveyor, Operational Transconductance Amplifier (OTA), current feedback op-amp, etc.

Due to commercial availability, the bipolar OTAs are used as the main active elements to be an example and to investigate the performances of proposed topology. The PSPICE simulation results are also shown, which are in correspondence with the theoretical analysis.

II. PROPOSED TOPOLOGY

A. Proposed topology as a current-mode universal filter

The block diagram of the proposed topology is shown in Fig. 1. It consists of inverting/non-inverting voltage-to-current converters, positive/negative grounded resistors and two grounded capacitors. Straightforwardly analyzing the block diagram in Fig.1, the transfer functions at different terminals of this network can be obtained as

$$\frac{I_{HP}}{I_{in}} = \frac{s^2}{s^2 + s\frac{1}{C_1}\left(\frac{1}{R_1} - \frac{1}{R_2}\right) + \frac{K_1K_2}{C_1C_2}}, \quad (1)$$

$$\frac{I_{BP}}{I_{in}} = \frac{sK_1/C_1}{s^2 + s\frac{1}{C_1}\left(\frac{1}{R_1} - \frac{1}{R_2}\right) + \frac{K_1K_2}{C_1C_2}}, \quad (2)$$

$$\frac{I_{LP}}{I_{in}} = \frac{K_1K_2/C_1C_2}{s^2 + s\frac{1}{C_1}\left(\frac{1}{R_1} - \frac{1}{R_2}\right) + \frac{K_1K_2}{C_1C_2}}. \quad (3)$$

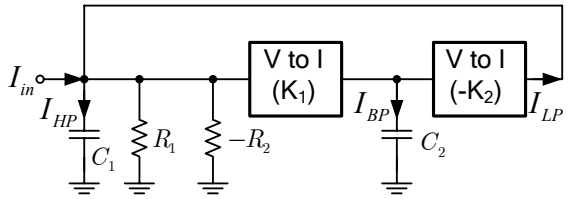

Figure 1. Proposed circuit topology

From Eqns. (1)-(3), the natural frequency ω_0 and quality factor Q_0 of each filter response can be expressed as

$$\omega_0 = \sqrt{\frac{K_1K_2}{C_1C_2}}, \quad (4)$$

and

$$Q_0 = \omega_0 \frac{C_1}{1/R_1 - 1/R_2}. \quad (5)$$

From Eqns. (4) and (5), it can be seen that the quality factor can be adjusted by varying R_1 or R_2 without affecting the natural frequency. On the other hand, the natural frequency can be adjusted by varying K_1, K_2, C_1 or C_2. Thus bandwidth (BW) is given by

$$BW = \frac{\omega_0}{Q_0} = \frac{1/R_1 - 1/R_2}{C_1}. \quad (6)$$

We found that the bandwidth can be controlled by R_1, R_2 or C_1. Moreover, the quality factor can be much high by controlling $1/R_2$ to be much less than $1/R_1$.

B. Topology Sensitivities

The sensitivities of the proposed topology are low and can be found as

$$S_{K_1}^{\omega_0} = S_{K_2}^{\omega_0} = \frac{1}{2};\ S_{C_1}^{\omega_0} = S_{C_2}^{\omega_0} = -\frac{1}{2}, \quad (7)$$

$$S_{K_1}^{Q_0} = S_{K_2}^{Q_0} = \frac{1}{2};\ S_{C_1}^{Q_0} = \frac{1}{2};\ S_{C_2}^{Q_0} = -\frac{1}{2}, \quad (8)$$

$$S_{R_1}^{Q_0} = \frac{1}{1-(R_1/R_2)};\ S_{R_2}^{Q_0} = -\frac{1}{(R_2/R_1)-1}, \quad (9)$$

and

$$S_{R_1}^{BW} = \frac{1}{1-(R_1/R_2)};\ S_{R_2}^{BW} = -\frac{1}{(R_2/R_1)-1}. \quad (10)$$

C. Proposed topology as a quadrature oscillator

If no input current applied to the topology as shown in Fig. 2, system characteristic equation can be expressed as

$$s^2 + s\frac{1}{C_1}\left(\frac{1}{R_1} - \frac{1}{R_2}\right) + \frac{K_1K_2}{C_1C_2} = 0. \quad (11)$$

From Eqn. (11), it can obviously seen that the proposed topology can be set to be an oscillator if

$$R_1 = R_2. \quad (12)$$

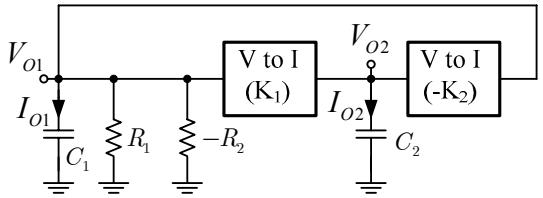

Figure 2. Proposed quadrature oscillator

Eqn. (12) is called as condition of oscillation, then the characteristic equation of the system is changed to

$$s^2 + \frac{K_1K_2}{C_1C_2} = 0. \quad (13)$$

From Eqn. (13), the oscillation frequency of this system can be obtained as

$$\omega_0 = \sqrt{\frac{K_1K_2}{C_1C_2}}. \quad (14)$$

It can be seen, from Eqns. (12) and (14), that the oscillation condition can be adjusted independently from the oscillation frequency by varying R_1 or R_2, while the oscillation frequency can be adjusted by varying K_1, K_2, C_1 or C_2.

Furthermore, the quadrature sinusoidal signals can be obtained both in current-mode and voltage-mode at I_{O1} and I_{O2} or V_{O1} and V_{O2} of Fig. 2, respectively, with the same time.

III. Application Examples

A. Current-Mode Universal Filter Using OTAs

Fig. 3 demonstrates the circuit scheme of the current-mode universal filter using OTAs. The OTAs are employed as voltage to current converters and positive/negative resistance simulators. The depicted bias currents I_{B1}, I_{B2}, I_{B3} and I_{B4} are the input bias currents of OTA1, OTA2, OTA3 and OTA4, respectively. From routine analysis, the following current transfer functions are obtained

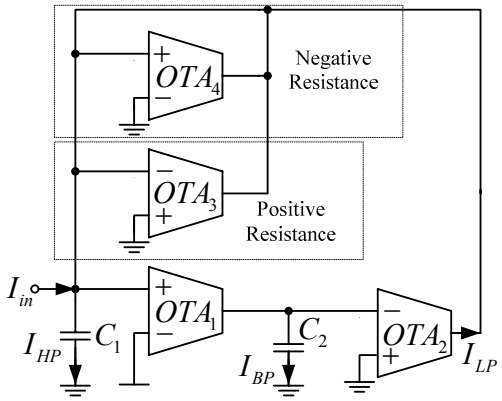

Figure 3. Current-mode universal filter using OTAs

$$\frac{I_{HP}}{I_{in}} = \frac{s^2}{s^2 + s\frac{1}{C_1}(g_{m3} - g_{m4}) + \frac{g_{m1}g_{m2}}{C_1C_2}}, \tag{15}$$

$$\frac{I_{BP}}{I_{in}} = \frac{sg_{m1}/C_1}{s^2 + s\frac{1}{C_1}(g_{m3} - g_{m4}) + \frac{g_{m1}g_{m2}}{C_1C_2}}, \tag{16}$$

$$\frac{I_{LP}}{I_{in}} = \frac{g_{m1}g_{m2}/C_1C_2}{s^2 + s\frac{1}{C_1}(g_{m3} - g_{m4}) + \frac{g_{m1}g_{m2}}{C_1C_2}}. \tag{17}$$

From Eqns. (15), (16) and (17), the parameters ω_0 and Q_0 can be expressed as

$$\omega_0 = \sqrt{\frac{g_{m1}g_{m2}}{C_1C_2}}, \tag{18}$$

and

$$Q_0 = \omega_0 \frac{C_1}{(g_{m3} - g_{m4})}. \tag{19}$$

Where $g_{mi} = I_{Bi} / 2V_T$. V_T is the thermal voltage. For simple consideration, and we assign that $I_{B1} = I_{B2} = I_B$ and $C_1 = C_2 = C$, it yields

$$\omega_0 = \frac{I_B}{2V_TC}, \tag{20}$$

and

$$Q_0 = \frac{I_B}{I_{B3} - I_{B4}}. \tag{21}$$

From Eqns. (20) and (21), it should be observed that the quality factor can be adjusted independently from the natural frequency, as explained in section *II.B*, by varying I_{B3} or I_{B4}. In addition, the natural frequency can be adjusted by I_B or C. Thus bandwidth (BW) is given by

$$BW = \frac{\omega_0}{Q_0} = \frac{I_{B3} - I_{B4}}{2V_TC}. \tag{22}$$

In the same view, the bandwidth can be linearly tuned by I_{B3}. Another advantage of the proposed circuit is that the high Q_0 circuit can be obtained by setting I_{B4} close to I_{B3}, which differs from conventional universal filters in such that the maximum Q_0 is limited by component values.

B. Circuit Sensitivities due to element variations

The sensitivities of the OTAs-based circuit are low and can be found as

$$S_{g_{m1}}^{\omega_0} = S_{g_{m2}}^{\omega_0} = \frac{1}{2};\ S_{C_1}^{\omega_0} = S_{C_2}^{\omega_0} = -\frac{1}{2}, \tag{23}$$

$$S_{g_{m1}}^{Q_0} = S_{g_{m2}}^{Q_0} = \frac{1}{2};\ S_{C_1}^{Q_0} = \frac{1}{2};\ S_{C_2}^{Q_0} = -\frac{1}{2}, \tag{24}$$

$$S_{g_{m3}}^{Q_0} = \frac{1}{1-(g_{m4}/g_{m3})};\ S_{g_{m4}}^{Q_0} = -\frac{1}{(g_{m3}/g_{m4})-1}, \tag{25}$$

and

$$S_{g_{m3}}^{BW} = \frac{1}{1-(g_{m4}/g_{m3})};\ S_{g_{m4}}^{BW} = -\frac{1}{(g_{m3}/g_{m4})-1}. \tag{26}$$

C. Quadrature Oscillator Using OTAs

If no input current applied to the circuit in Fig. 3 as shown in Fig. 4, system characteristic equation can be expressed as

$$s^2 + s\frac{1}{C_1}(g_{m3} - g_{m4}) + \frac{g_{m1}g_{m2}}{C_1C_2} = 0. \tag{27}$$

From Eqn. (27), it can obviously seen that the proposed circuit can be set to be an oscillator if

$$g_{m3} = g_{m4}. \tag{28}$$

Eqn. (28) is called as condition of oscillation, this is achieved by $I_{B3} = I_{B4}$, then the characteristic equation of the system becomes

$$s^2 + \frac{g_{m1}g_{m2}}{C_1C_2} = 0. \tag{29}$$

From Eqn. (29), the oscillation frequency of this system can be obtained as

$$\omega_0 = \sqrt{\frac{g_{m1}g_{m2}}{C_1C_2}}. \tag{30}$$

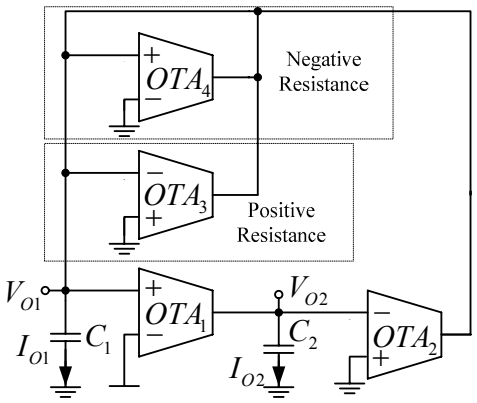

Figure 4. Quadrature oscillator using OTAs

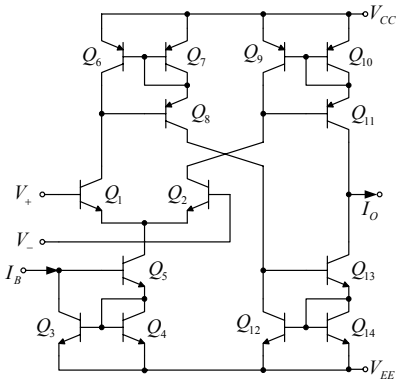

Figure 5. Internal construction of OTA

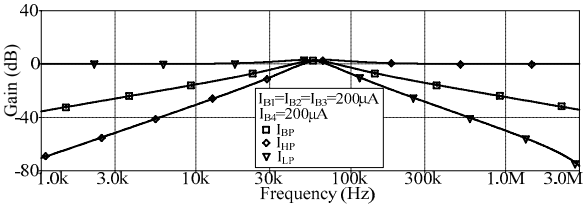

Figure 6. Gain responses of universal filter

D. Simulation Results

To prove the performances of the proposed circuits, the PSPICE simulation program was used for the examination. The PNP and NPN transistors employed in the proposed circuits were simulated by respectively using the parameters of the PR200N and NR200N bipolar transistors of ALA400 transistor array from AT&T [10]. Fig. 5 depicts schematic description of the OTA used in the simulations. All OTAs were biased with ±2V power supplies and $C_1 = C_2 = 10nF$. The results shown in Fig. 6 are the gain responses of the universal filter obtained from Fig. 3. There are clearly seen that the universal filter circuit can provide low-pass, high-pass and band-pass functions, simultaneously.

Fig. 7 display gain responses of bandpass, with different I_{B4} values. They are shown that the quality factor can be adjusted by the input bias current I_{B4} as depicted in Eqn. (21) without affecting the natural frequency. Figs. 8 and 9 show the responses when operation as quadrature oscillator. The maximum oscillation frequency is about 11.23MHz.

IV. CONCLUSIONS

The new circuit topology has been presented. The advantages of the proposed topology are that: it can function both as quadrature oscillator and current-mode universal filter (lowpass, highpass and bandpass) without changing a circuit topology: when it works as the universal filter, the quality factor and the natural frequency can be orthogonally controlled by using input bias currents of the OTAs, this is easily modified to use in control systems using a microcontroller [7]: when it functions as quadrature oscillator, its oscillation condition and oscillation frequency can be adjusted independently. To investigate and verify the performances of proposed topology, the current-mode universal filter and quadrature oscillator based on OTAs have been proposed. The PSPICE simulation results are well agreed with the theoretical anticipations.

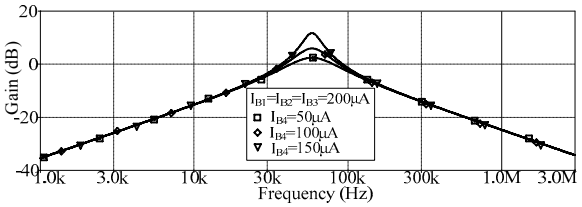

Figure 7. Bandpass responses at different values of I_{B4}

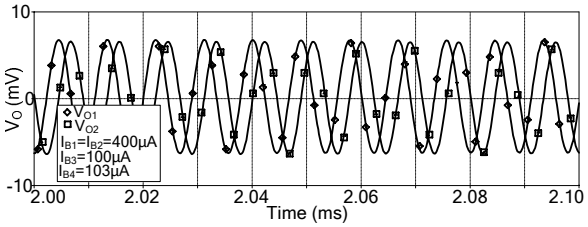

Figure 8. Transient responses in voltage-mode outpuyt signals

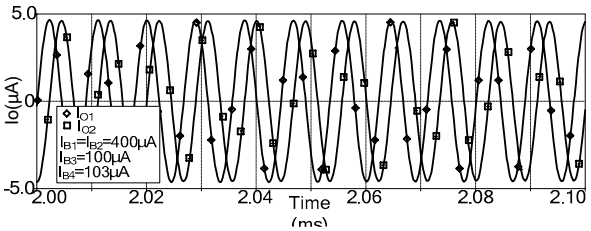

Figure 9. Transient responses in current-mode output signals

REFERENCES

[1] A. S. Sedra and K. C. Smith Microelectronic circuits, 5rd ed., Florida: Holt, Rinehart and Winston, 2003.

[2] I. A. Khan and S. Khawaja, "An integrable gm-C quadrature oscillator". *Int. J. Electronics*, vol. 87 no.1, pp. 1353-1357, 2000.

[3] R. Holzel. "A simple wide-band sine wave quadrature oscillator. *IEEE Trans. on Instru & Meas*., vol. 42, no.3, pp. 758-760, 1993.

[4] M. T. Ahmed, I. A. Khan and N. Minhaj. "On transconductance-C quadrature oscillators," *Int. J. Electronics,* vol. 83, no. 2 pp. 201-207, 1997.

[5] A. M. Soliman. "Synthesis of grounded capacitor and grounded resistor oscillators," *J. Franklin Inst.*, vol. 336, pp. 735-746, 1999.

[6] M. A. Ibrahim, S. Minaei and H. A. Kuntman. "A 22.5 MHz current-mode KHN-biquad using differential voltage current conveyor and grounded passive elements". *Int. J. Electron. Commun. (AEU)*, vol. 59, pp. 311-318, 2005.

[7] C. Toumazou, F. J. Lidgey and D. G. Haigh. Analogue IC design: the current-mode approach, London: Peter Peregrinus, 1990.

[8] C. S. Hilas and Tn. Laopoulos. "Circuit design: a study on voltage-mode to current-mode conversion technique," *Proceedings of MELECON '96*, Bari, Italy, May 1996, pp. 1309-1312.

[9] J. W. Horng, "Current-conveyors based allpass filters and quadrature oscillators employing grounded capacitors and resistors," *Computers and Electrical Engineering*, vol. 31, pp. 81-92, 2005.

[10] D. R. Frey, "Log-domain filtering: an approach to current-mode filtering," *IEE Proc. Circuit Devices Syst.*, vol. 140, pp. 406-416, 1993.

3 Input/ 2 Output Current-Mode Universal Biquad Filter Using Single DO-CCCDTA

Winai Jaikla* and Montree Siripruchyanun**
*Electric and Electronic Program, Faculty of Industrial Technology,
Suan Sunandha Rajabhat University, Dusit, Bangkok, 10300, THAILAND Email: jnai2004@yahoo.com
**Department of Teacher Training in Electrical Engineering, Faculty of Technical Education,
King Mongkut's Institute of Technology North Bangkok, Bangkok, 10800, THAILAND Email: mts@kmitnb.ac.th

***Abstract*- This article presents a three-input two-output current-mode universal biquadratic filter performing completely standard functions: low-pass, high-pass, band-pass, band-reject and all-pass functions, based on Dual-Output Current Controlled Current Differencing Transconductance Amplifier (DO-CCCDTA). The features of the circuit are that: the quality factor and pole frequency can be tuned orthogonally via the input bias currents: the circuit description is very simple, consisting of merely one DO-CCCDTA, one voltage buffer and 2 grounded capacitors. Additionally, each function response can be selected by suitably selecting input signals in digital method. Without any external resistors and using only grounded elements, the proposed circuit is very suitable to further develop into an integrated circuit. The PSPICE simulation results are depicted. The given results agree well with the theoretical anticipation. The maximum power consumption is approximately 1.81mW at ±1.5V power supply voltages.**

***Index Terms*- biquadratic filter, DO-CCCDTA, current-mode**

I. INTRODUCTION

In electrical engineering works, as well-known, an analog filter is an important block and widely used for continuous-time signal processing. It can be found in many fields: for instance, communication, measurement and instrumentation, and control systems [1-2]. One of most popular analog filters is a universal biquadratic filter since it can provide several functions. Nowadays, a universal filter working in current-mode has being been more popular than voltage-mode one. Since the last decade, on the other hand, there has been much effort to reduce the supply voltage of analog systems. This is due to the command for portable and battery-powered equipment. Since a low-voltage operating circuit becomes necessary, the current–mode technique is ideally suited for this purpose. Actually, a circuit using the current-mode technique has many other advantages: for example, larger dynamic range, higher bandwidth, greater linearity, simpler circuitry and lower power consumption [3-4].

The literature surveys show that a large number of circuit realizations for current-mode universal filters have been reported [5-19]. Unfortunately, these reported circuits suffer from one or more of following weaknesses

a) excessive use of the active and/or passive elements and require changing circuit topologies to achieve several functions [5-9]
b) lack of electronic adjustability [6-13], [16]
c) the outputs of the filter responses are not in high output impedance [18-19]
d) use of floating capacitor, which is not convenient to further fabricate in IC [6-13]
e) cannot provide completely standard functions [5, 7-8, 10-12, 15-16]

This work is arranged to propose a new three-input two-output current-mode universal biquadratic filter, emphasizing on use of DO-CCCDTA. The features of proposed circuit are that: the proposed universal filter can provide completely standard functions without changing circuit topology by appropriately selecting the input signals in digital method: the circuit description is very simple, it consists of one DO-CCCDTA and 2 grounded capacitors, which is suitable for fabricating in monolithic chip: the filter does not require any external resistor and passive parameter matching conditions. In addition, the quality factor and pole frequency can be tuned orthogonally via the input bias currents. The performances of proposed circuit are illustrated by PSPICE simulations, they show good agreement as mentioned.

II. PRINCIPLE OF OPERATION

A. The Dual-Output Current Controlled Current Differencing Transconductance Amplifier (DO-CCCDTA)

Since the proposed circuit is based on DO-CCCDTA, a brief review of DO-CCCDTA is given in this section. Basically, the DO-CCCDTA is composed of translinear element, mixed loops and complementary current mirrors. Generally, the DO-CCCDTA properties are similar to the conventional CDTA, except that input voltages of DO-CCCDTA are not zero and the DO-CCCDTA has finite input resistances R_p and R_n at the p and n input terminals, respectively. These parasitic resistances are equal and can be controlled by the bias current I_{B1} as shown in the following equation

$$\begin{bmatrix} V_p \\ V_n \\ I_{z11,12} \\ I_{x11,12} \\ I_{x2} \end{bmatrix} = \begin{bmatrix} R_p & 0 & 0 & 0 & 0 \\ 0 & R_n & 0 & 0 & 0 \\ 1 & -1 & 0 & 0 & 0 \\ 0 & 0 & 0 & -g_{m1} & 0 \\ 0 & 0 & 0 & 0 & g_{m2} \end{bmatrix} \begin{bmatrix} I_p \\ I_n \\ V_x \\ V_{z1} \\ V_{z1} \end{bmatrix}. \quad (1)$$

Where $$R_p = R_n = \frac{V_T}{2I_{B1}}, \quad (2)$$

$$g_{m1} = \frac{I_{B2}}{2V_T}, \quad (3)$$

and $$g_{m2} = \frac{I_{B3}}{2V_T}. \quad (4)$$

Where g_m is the transconductance gain of the CCCDTA and V_T is the thermal voltage. The symbol and the equivalent circuit of the CCCDTA are illustrated in Fig. 1(a) and (b), respectively.

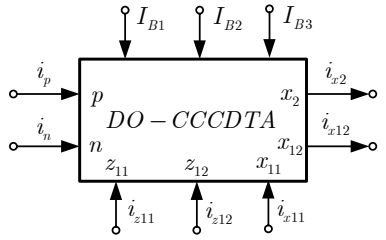

(a)

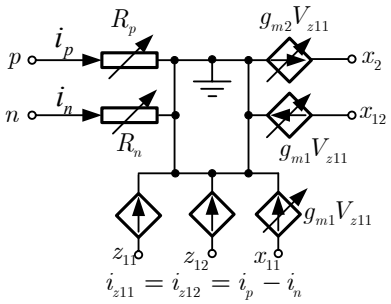

(b)

Figure 1. DO-CCCDTA (a) Symbol (b) Equivalent circuit

B. Proposed universal biquad filter

The proposed current-mode universal biquad filter is shown in Fig. 2. From routine analyzing the circuit in Fig. 2, we will get the output currents as

$$I_{O1} = \frac{1}{D(s)}\left[g_{m1}I_{in1} - sC_2R_pg_{m1}I_{in2} + D(s)I_{in3}\right], \quad (5)$$

and $$I_{O2} = \frac{1}{D(s)}\left(g_{m2}I_{in1} - sC_2R_pg_{m2}I_{in2}\right). \quad (6)$$

Where $D(s) = s^2C_1C_2R_p + sC_2R_pg_{m1} + g_{m2}$. From Eqs. (5) and (6), the magnitudes of input currents; I_{in1}, I_{in2} and I_{in3} are chosen as Table. 1 by digital method to obtain a standard function of the 2nd–order network. From Eq. (5), the pole frequency (ω_0) and quality factor (Q_0) of each filter response can be expressed as

$$\omega_0 = \sqrt{\frac{g_{m2}}{C_1C_2R_p}}, \quad (7)$$

and $$Q_0 = \frac{C_1}{g_{m1}}\sqrt{\frac{g_{m2}}{C_1C_2R_p}}. \quad (8)$$

For simple consideration, if we set $C_1 = C_2 = C$ and $I_{B1} = I_{B3} = I_B$, Eqs. (7) and (8) are subsequently modified to

$$\omega_0 = \frac{I_B}{CV_T}, \quad (9)$$

and $$Q_0 = \frac{2I_B}{I_{B2}}. \quad (10)$$

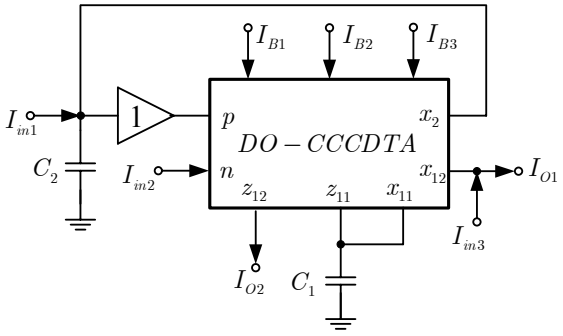

Figure 2. Proposed current-mode universal filter

TABLE I
The I_{in1}, I_{in2} and I_{in3} values for each filter function response

Filter Responses		Input		
I_{O1}	I_{O2}	I_{in1}	I_{in2}	I_{in3}
-	LP	1	0	0
HP	-	-1	1	1
BP	-	0	1	0
BR	-	0	1	1
AP	-	0	2	1

It is obviously found that, from Eqns. (9) and (10), the quality factor can be adjusted by I_{B2} without affecting the pole frequency. Reversely, the pole frequency can be controlled via I_B. In addition, bandwidth (*BW*) of the system can be expressed by

$$BW = \frac{\omega_0}{Q_0} = \frac{I_{B2}}{2CV_T}. \quad (11)$$

We found that the bandwidth can be linearly controlled by I_{B2}. Moreover, the quality factor can be much high by controlling I_{B2} to be much less than I_B. This differs from the conventional current-controlled universal filters in such that they use an input bias current to control the quality factor. However, it has a limited value of current in the circuits, the quality factor is then restricted.

C. Sensitivities

The sensitivities of the proposed circuit are low and can be found as

$$S_{I_B}^{\omega_0} = 1;\ S_C^{\omega_0} = -1, \quad (12)$$

and $$S_{I_B}^{Q_0} = 1;\ S_{I_{B3}}^{Q_0} = -1. \quad (13)$$

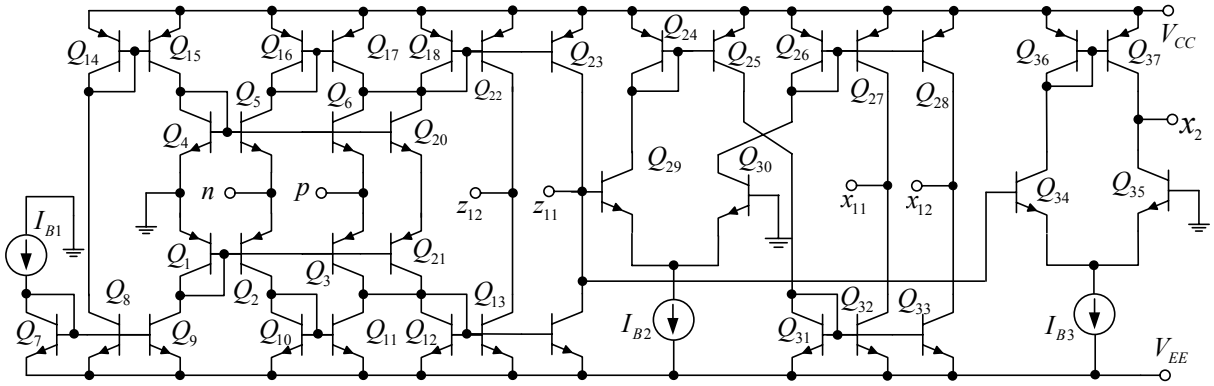

Figure 3. Internal construction of DO-CCCDTA

D. Non-ideal case

For non-ideal case, the I_z and I_x of DO-CCCDTA can be respectively characterized by

$$I_{z11} = \alpha_{p1} I_p - \alpha_{n1} I_n , \quad (14)$$

$$I_{z12} = \alpha_{p2} I_p - \alpha_{n2} I_n , \quad (15)$$

$$I_{x11} = \beta_{11} g_m V_{z11} , \quad (16)$$

$$I_{x12} = \beta_{12} g_m V_{z11} , \quad (16)$$

and

$$I_{x2} = \beta_2 g_m V_{z11} . \quad (18)$$

Where α_p, α_n and β are transferred error values deviated from one. In the case of non-ideal consideration, reanalyzing the proposed filter circuit in Fig. 2 yields the denominator as

$$D(s) = s^2 C_1 C_2 R_p + s C_2 R_p g_{m1} \beta_{11} + g_{m2} \alpha_{p1} \beta_2 . \quad (19)$$

In this case, the ω_0, Q_0 and BW are changed to

$$\omega_0 = \sqrt{\frac{\alpha_{p11} \beta_2 g_{m2}}{C_1 C_2 R_p}} , \quad (20)$$

$$Q_0 = \frac{C_1}{\beta_{12} g_{m1}} \sqrt{\frac{\alpha_{p1} \beta_2 g_{m2}}{C_1 C_2 R_p}} , \quad (21)$$

and

$$BW = \frac{\omega_0}{Q_0} = \frac{\beta_{12} g_{m1}}{C_1} . \quad (22)$$

Eqs. (20)-(22) degrade the performances of proposed filter at high frequency applications in such restricted frequency response and temperature dependence because of the parasitic elements of active device used in the circuit.

Actually, if careful design technique is employed to design the CCCDTA, these deviations are very small and can be ignored**.**

III. SIMULATION RESULTS

To prove the performances of the proposed circuit, the PSPICE simulation program was used for the examination. The PNP and NPN transistors employed in the proposed circuit were simulated by respectively using the parameters of the PR200N and NR200N bipolar transistors of ALA400 transistor array from AT&T [20]. The voltage buffer was used as an ideal voltage buffer. Fig. 3 depicts schematic description of the DO-CCCDTA used in the simulations.

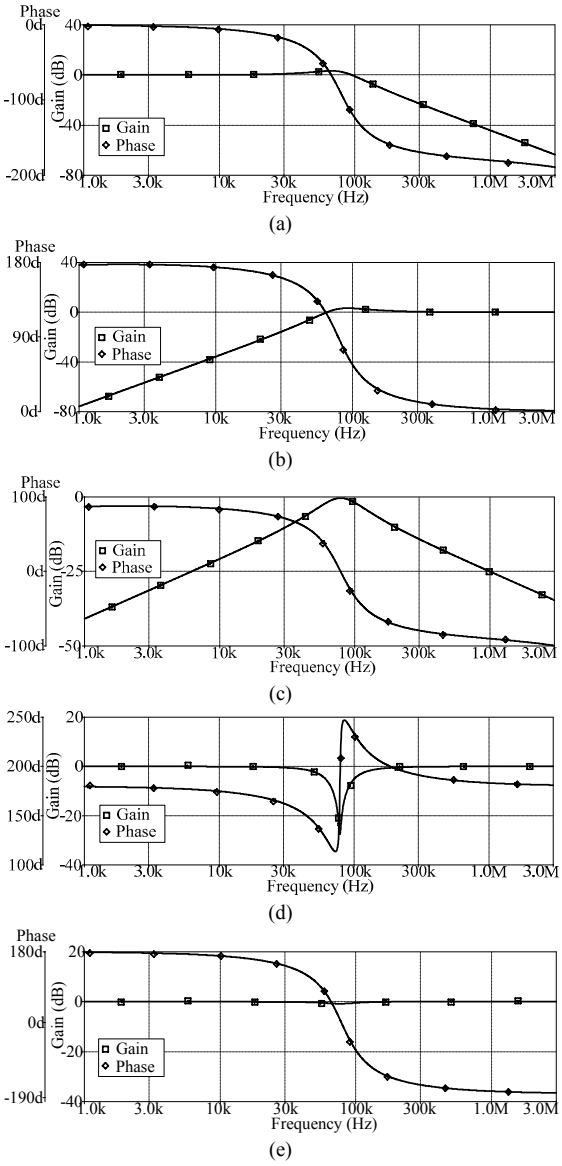

Figure 4. Frequency responses for different functions

The circuit was biased with ±1.5V supply voltages and $C_1 = C_2 = 10nF$. The results shown in Fig. 4 are the gain and phase responses of the proposed biquad filter obtained from Fig. 2 with different functions as shown Table 1, where I_{B1}, I_{B2} and I_{B3} are equal to $50\mu A$, $200\mu A$ and $200\mu A$, respectively. There are clearly seen that the proposed biquad filter can provide low-pass, high-pass, band-pass, band-reject and all-pass functions dependent on selection as shown in Table 1, without modifying major circuit topology.

Fig. 5 displays gain responses of band-pass function with different I_{B2} values. It is obviously shown that the bandwidths of the responses can be linearly adjusted by the input bias current I_{B2} as depicted in Eq. (10) without affecting the pole frequency. Similarly, the results in Fig. 6 are phase responses of all-pass function. It confirms the performances of proposed filter in such controllability of the quality factor via I_{B2} without affecting the pole frequency as well. Maximum power consumption is about 1.81mW.

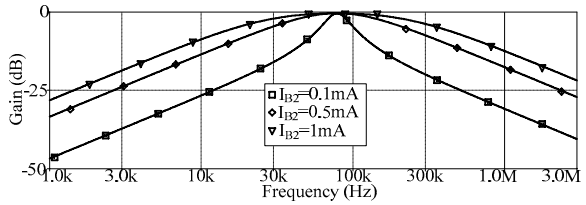

Figure 5. Bandwidth variation of band-pass function for different I_{B2}

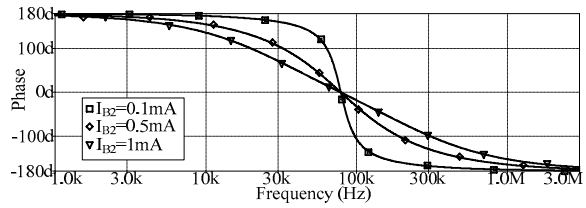

Figure 6. Phase responses of all-pass function for different I_{B2}

IV. CONCLUSIONS

The current-mode universal biquadratic filter based on DO-CCCDTA has been presented. The advantages of the proposed circuit are that: it performs low-pass, high-pass, band-pass, band-reject and all-pass functions with two outputs depending on an appropriately selecting of three input signals: the quality factor and pole frequency can be tuned orthogonally via the input bias currents, this is easily modified to use in control systems using a microcontroller [3]. The circuit description comprises only one DO-CCCDTA and 2 grounded capacitors cooperating with one voltage buffer. With mentioned features, it is very suitable to realize the proposed circuit in a monolithic chip for use in battery-powered, portable electronic equipments such as wireless communication system devices.

REFERENCES

[1] A. S. Sedra, and K. C. Smith, *Microelectronic circuits*, 5rd ed., Florida: Holt, Rinehart and Winston, 2003.

[2] M. A. Ibrahim, S. Minaei, and H. A. Kuntman, "A 22.5 MHz current-mode KHN-biquad using differential voltage current conveyor and grounded passive elements," *Int. J. Electron. Commun. (AEU)*, vol. 59, pp. 311-318, 2005.

[3] C. Toumazou., F. J. Lidgey, and D. G. Haigh, *Analogue IC design: the current-mode approach*, London: Peter Peregrinus, 1990.

[4] D. R. Bhaskar, V. K. Sharma, M, Monis, and S. M. I. Rizvi, "New curren-mode universal biquad filter," *Microelectronics Journal*, vol. 30, pp. 837-839, 1999.

[5] N. A. Shah nad M. A. Malik, "Voltage/current-mode universal filter using FTFN and CFA," *Analog Integrated Circuits and Signal Processing*, vol. 45, pp. 197-203, 2005.

[6] C. M. Chang, T. S. Liao, T. Y. Yu, E. S. Lin, C. H. Teng, and C. L. Hou, "Novel universal current-mode filters using unity-gain cells," *Int. J. Electronics*, vol.86, pp. 929-932, 2001.

[7] H. Y. Wang and C. T. Lee, "Versatile insensitive current-mode universal biquad implementation using current conveyors," *IEEE Trans. on. Circuits and Systems II*, vol. 48, pp. 409-413, April 2005.

[8] R. K. Sharma and R. Senani, "Universal current-mode biquad using a single CFOA," *Int. J. Electronics*, vol. 91, pp. 175-183, March 2004.

[9] S. H. Tu, C. M. Chang, and K. P. Liao, "Novel versatile insensitive universal current-mode biquad employing two second-generation current conveyors," *Int. J. Electronics*, vol. 89, pp. 897-903, 2002.

[10] N. A. Shah and M. A. Malink, "High impedance voltage and current-mode multifunction filters," *Int. J. Electron. Commun. (AEU)*, vol. 59, pp. 262-266, 2005.

[11] M. Sagbas and K. Fidanboylu, "Electronically tunable current-mode second-order universal filter using minimum elements," *Elec. Letters*, vol. 40, pp. 2-4, January 2004.

[12] J. Wu and e. I. El-masry, "Universal voltage and current-mode OTAs based biquads," *Int. J. Electronics*, vol. 85, pp. 553-560, 1998.

[13] J. W. Horng, "Current-conveyors based allpass filters and quadrature oscillators employing grounded capacitors and resistors," *Computers and Electrical Engineering*, vol. 31, pp. 81-92, 2005.

[14] M. Bhusan, R. W. Newcomb, "Grounding of capacitors in integrated circuits," *Elec. Letters*, vol. 3, pp.148-149, 1967.

[15] N. Pandey, S. K. Paul, A. Bhattacharyya, and S. B. Jain, "A novel current controlled current mode universal filter: SITO approach," *IEICE Electronics Express*, vol. 2, 451-457, 2005.

[16] R. Senani, V. K. Singh, A. K. Singh, and D. R. Bhaskar, "Novel electronically controllable current-mode universal biquad filter," *IEICE Electronics Express*, vol1, 410-415, 2004.

[17] Y. Maruyama, A. Hyogo, and K. Sekine, "A digitally programmable CMOS biquad filter using current-mode integrators," *IEICE trans. on fundamentals*, vol. E85-A, no. 2, pp. 316-323, 2002.

[18] S. Celma, J. Sabadell and P. Martinez, "Universal filter using unity-gain cells," *Elec. Letters,* 31, pp. 1817–1818, 1995.

[19] R. M. Weng, J. R. Lai and M. H. Lee, "New universal biquad filters using only two unity-gain cells," *Int. J. Electronics*, vol. 87, pp. 57–61, 2000

[20] D. R. Frey, "Log-domain filtering: an approach to current-mode filtering," *IEE Proc. Circuit Devices Syst.*, vol. 140, pp. 406-416, 1993.

Fast Analysis of Analog Design Trade-offs via Geometric Programming

Theerachet Soorapanth
National Electronics and Computer Technology Center, Bangkok, Thailand
Email: theerachet.soorapanth@nectec.or.th

***Abstract*-This paper concerns a method for solving a variety of analog design trade-off problems, which is based on formulating the problem as a geometric program (GP). These nonlinear, constrained optimization problem can be transformed to convex optimization problems, and then solved (globally) very efficiently. Designers can analyze quantitatively trade-offs among different specifications as well as construct trade-off curves very quickly owing to the efficiency of the method.**

I. INTRODUCTION

Most analog design problems deals with how to size a circuit appropriately to achieve a set of specifications subject to various constraints while spending the least amount of resources such as power consumption, for instance. This scenario allows one to formulate such problem as a constrained optimization problem. The variables are often the sizes of transistors and other circuit components as well as biasing conditions. It is also possible to include other design variables such as threshold voltage, supply voltage, and oxide thickness. The choice of design variables determines various top-level circuit objectives, such as the total area of the circuit, the total power it consumes, its bandwidth and other objectives such as noise tolerance, robustness to process and environment parameter variations, and so on. These objectives can be very complex functions of the design variables. In addition, there are many constraints that must be satisfied. There are many approaches to circuit sizing, including heuristics, and methods based on circuit simulation coupled to a generic numerical optimization.

This paper focuses on a particular approach, in which the sizing problem is modeled (at least approximately) as a geometric program (GP), a special type of mathematical optimization. Fortunately, majority of analog circuit sizing problems can be directly (if not, approximately) casted as GP problems. Over the years, the efficient algorithms, such as an interior-point method, to solve such problems have been developed. GPs with tens of thousands of variables and hundreds of thousands of constraints can be reliable solved in minutes, on a personal computer. In addition, since GP is a type of convex optimization, the achieved solution (if feasible) is guaranteed to be globally optimal.

II. GEOMETRIC PROGRAMMING

GP-based circuit optimization is not new; it has been used for digital circuits since the 1980s. In [1], a method was proposed for transistor and wire sizing based on Elmore delay, that was later found to be a GP. Other digital circuit design problems, that can be formulated as GPs, can be found in, e.g. [2,3,4]. Recently, GP has been introduced to solve analog and mixed-signal circuit problems [5,6].

A geometric program is an optimization problem of the form

$$\begin{array}{lll} \text{minimize} & f_0(x) & \\ \text{subject to} & f_i(x) \le 1, & i=1,\ldots,m \\ & g_i(x) = 1, & i=1,\ldots,p \\ & x_i > 0, & i=1,\ldots,n \end{array} \tag{1}$$

where $f_0,\ldots,f_m$ are posynomial functions and $g_1,\ldots,g_p$ are monomial functions. Posynomial function has the form

$$f(x_1,\ldots,x_n) = \sum_{k=1}^{t} c_k x_1^{\alpha_{1k}} x_2^{\alpha_{2k}} \ldots x_n^{\alpha_{nk}} \tag{2}$$

where $c_j \ge 0$ and α_{ij} is real. When there is only one term in the sum, f is called a monomial function. A geometric program can be reformulated as a convex optimization problem by changing variables and considering the logs of the function involved. We define new variables $y_i = \log x_i$ and take the logarithm of a posynomial f to get

$$h(y) = \log f(e^{y_1},\ldots,e^{y_n}) = \log\left(\sum_{k=1}^{t} e^{\alpha_k^T y + b_k}\right) \tag{3}$$

where $\alpha_k^T = [\alpha_{1k} \cdots \alpha_{nk}]$ and $b_k = \log c_k$. It can be shown that h is a convex function of the variable y. Similar transformation can be made to the equality constraint function g. The convexity property guarantees the problem's solution (if feasible) is globally optimal. In addition, the problem can be solved using a very efficient interior-point method [7].

III. CIRCUIT MODELING FOR GP

For circuit problem to be solved by GP, each design equations must be modeled (or approximated) by posynomial/monomial functions. Fortunately, majority of

circuit design equations can be modeled as such. For instance, the following long-channel MOS device equation

$$I_D = \frac{1}{2} K_p W L^{-1} (V_{GS} - V_T)^2 \tag{4}$$

can be considered as a monomial function of transistor width W, transistor length L, and overdrive voltage $V_{GS} - V_T$. Similarly, the transconductance equation can be written in monomial form as

$$g_m(W, L, I_D) = \left(2K_p\right)^{1/2} W^{1/2} L^{-1/2} I_D^{1/2} \tag{5}$$

In addition to device equations, constraint on device operating condition can be modeled by a monomial as well. For instance, the constraint for an MOS to be in saturation, $V_{GS} - V_T \le V_{DS,\min}$, can be written in monomial form as

$$\left(\sqrt{\frac{2}{K_p}} \frac{1}{\left(V_{DS,\min} + V_T\right)}\right) I_D^{1/2} L^{1/2} W^{-1/2} \le 1 \tag{6}$$

Submicron short-channel devices can also be modeled with a posynomial by performing a SPICE-simulation-based posynomial function fitting over large ranges of length, width, and bias currents.

IV. Example: An Op-Amp Design

As an example, we will apply the GP method to the design of a common analog circuit building block, an operational amplifier. There are several op-amp architectures. We will consider a two-stage architecture as shown in Fig. 1. Other op-amp architectures can be applied as well, but this particular architecture is chosen for its design simplicity and good achieved performance.

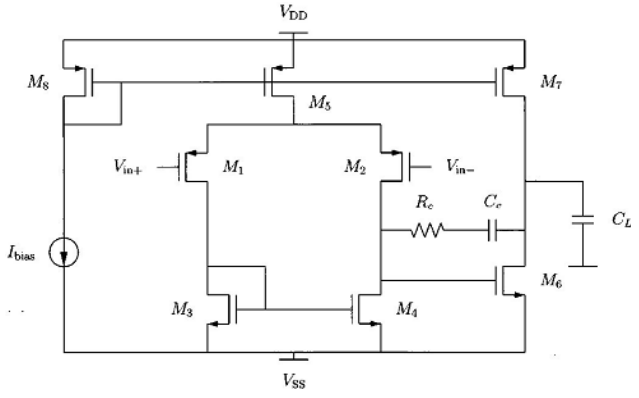

Figure 1. Two-stage op-amp architecture.

To set up the op-amp design problem for GP, we have to consider a variety of performance measures and constraints, which must be formulated in GP-compatible forms. The design variables are the transistor sizes (width and length), the value of the passive components (capacitors and resistors), and the value of the bias currents and bias voltages. For this particular two-stage op-amp, there are nineteen design variables. The constraints in the design of this op-amp are summarized as follows

- Symmetry and matching: $M_1 = M_2$, $M_3 = M_4$
- Limit on device sizes: $W \ge W_{\min}$, $L \ge L_{\min}$
- Limit on chip area: $A \le A_{\max}$
- Systematic input offset voltage
- Current ratio equalities: $I_{M5} \propto I_{M8}$, $I_{M7} \propto I_{M8}$, $I_{M1} \propto I_{M5}$
- Bias conditions: $V_{GS} - V_T \le V_{DS}$
- Gate overdrive voltage: $V_{GS} - V_T \ge V_{OD,\min}$
- Limit on power consumption: $P \le P_{\max}$
- Open-loop DC gain
- Unity-gain bandwidth
- Phase-margin
- Slew-rate
- Common-mode rejection ratio
- Power-supply rejection ratio
- Input-referred noise

In total, there are forty-six constraints, both inequalities and equalities expressed by posynomials and monomials, respectively, according to (1). The objectives of the design can vary depending on the specifications.

V. Design Implementations

The op-amp design has been implemented in C language for GP optimization. We choose a 0.8-μm CMOS technology and specify the design objective to be unity-gain bandwidth maximization. The results are shown in Table 1 and 2.

The first column in Table 1 identifies the performance measures; the second gives the specification. The third column shows the performance of the design obtained from GP optimization. The fourth column shows the value of the specification as simulated by SPECTRE from our optimal design (Fig. 2).

We can see that both GP calculation and SPECTRE simulation achieve or exceed all of the required specifications. Note that some of the constraints are loose, some are tight. Tight constraints include power consumption, phase margin, and input-referred noise, for instance. This suggests that there are some trade-offs among these performance measures, which will be further explored in the next section.

The computer time required for the design is two seconds owing to the efficiency of the interior-point algorithm.

The optimal design parameters found are shown in Table 2.

TABLE 1
DESIGN SPECIFICATIONS AND ACHIEVED PERFORMANCE

Performance Measure	Specification	Optimal (GP calculation)	Optimal (SPECTRE simulation)
Device length (μm)	≥ 0.8	0.8 (min)	0.8 (min)
Device width (μm)	≥ 2.0	2.0 (min)	2.0 (min)
Area (μm^2)	≤ 10000	7283	7283
Capacitance size (pF)	0.1 ≤ C ≤ 2000	2.68	2.68
Load capacitance (pF)	3	3	3
Common-mode input range (V)	includes 0.5Vdd	includes 0.5Vdd	[0,0.77]Vdd
Output voltage range (V)	[0.1,0.9]Vdd	[0.028,0.91]Vdd	[0.02,0.94]Vdd
Power (mW)	≤ 5	5	4.9
DC gain (dB)	≥ 80	89.4	95.5
Unity-gain BW (MHz)	≥ 80	90.1	123
Phase margin (°)	≥ 60	60	72
Slew rate (V/μs)	≥ 10	87.2	49
CMRR (dB)	≥ 60	92.6	99
Neg. PSRR (dB)	≥ 80	98.5	104.5
Pos. PSRR (dB)	≥ 80	118.5	125.5
Input-referred noise, @1KHz (nV/√Hz)	≤ 300	300	274

TABLE 2
OPTIMAL DESIGN FOR DESIGN EXAMPLE

Variable	Optimal value
W1=W2	225.3 μm
W3=W4	109.5 μm
W5	57.5 μm
W6	557.9 μm
W7	146.6 μm
W8	2 μm
L1=L2	0.8 μm
L3=L4	0.8 μm
L5	0.8 μm
L6	0.8 μm
L7	0.8 μm
L8	0.8 μm
Cc	2.68 pF
Rc	94.3 ohm
Ibias	9.1 μA

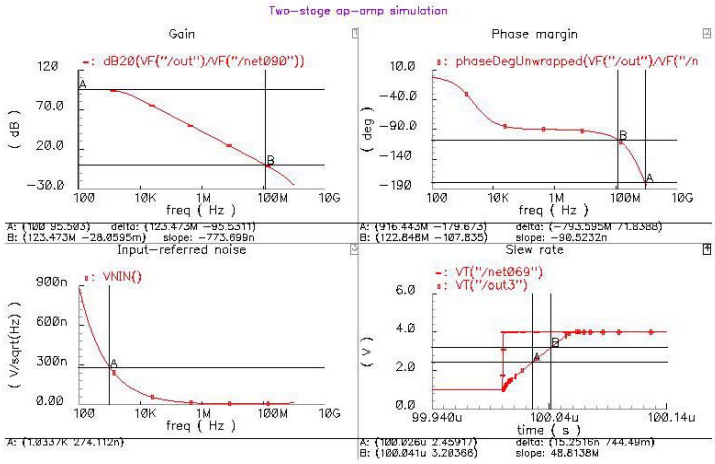

Figure 2. SPECTRE simulation plots.

TABLE 3
ACHIEVED PERFORMANCE FOR DIFFERENT DESIGN OBJECTIVES

Performance Measure	Specification	Design Objective			
		Max. UGBW	Max. DC gain	Min. noise	Min. power
Device length (μm)	≥ 0.8	0.8 (min)	0.8 (min)	0.8 (min)	0.8 (min)
Device width (μm)	≥ 2.0	2.0 (min)	2.0 (min)	2.0 (min)	2.0 (min)
Area (μm^2)	≤ 10000	7283	9162	10000	7218
Capacitance size (pF)	0.1 ≤ C ≤ 2000	2.68	2.7	3.86	2.68
Load capacitance (pF)	3	3	3	3	3
Common-mode input range (V)	includes 0.5Vdd	includes 0.5Vdd	includes 0.5Vdd	includes 0.5Vdd	includes 0.5Vdd
Output voltage range (V)	[0.1,0.9]Vdd	[0.028,0.91]Vdd	[0.018,0.9]Vdd	[0.026,0.904]Vdd	[0.024,0.908]Vdd
Power (mW)	≤ 5	5	5	5	***3.9***
DC gain (dB)	≥ 80	89.4	***95.8***	91.7	91.5
Unity-gain BW (MHz)	≥ 80	***90.1***	80	80	80
Phase margin (°)	≥ 60	60	60	60	60
Slew rate (V/μs)	≥ 10	87.2	53.5	61.4	68.5
CMRR (dB)	≥ 60	92.6	99.1	95	94.7
Neg. PSRR (dB)	≥ 80	98.5	105	100.9	100.6
Pos. PSRR (dB)	≥ 80	118.5	124.9	120.8	120.6
Input-referred noise, @1KHz (nV/√Hz)	≤ 300	300	244.7	***209***	300

VI. Trade-Off Analysis

We can consider trade-offs among design specifications by running GP optimization with four different objectives as follows

- Maximizing unity-gain bandwidth
- Maximizing DC gain
- Minimizing input-referred noise
- Minimizing power consumption

Keeping the constraints unchanged, the optimization results are compared in Table 3. The results indicate clear trade-offs among gain, noise, unity-gain bandwidth, and power consumption. For instance, if higher DC gain is desired, the optimal design possesses lower unity-gain bandwidth. If lower input-referred noise is preferred, larger chip area would be required to accommodate larger device sizes. Finally, if low power is favored, the smallest allowed bandwidth and maximum allowed noise level result. Also, it is interesting to note that some constraints, e.g. phase margin specification, remain tight regardless of design objectives. This suggests that all four previously-mentioned performance measures become worsen with higher phase margin requirement.

Since the computation time for each optimization takes merely two seconds, we can explore various design trade-offs very quickly. Besides changing design objectives, we can construct trade-off curves, like Fig. 3, by repeatedly solving the design problem while varying one of the specifications. Within a matter of minutes, we can sweep out the globally optimal trade-off curve between competing objectives (with the others fixed). Designers can determine which specifications are more critical or relaxed.

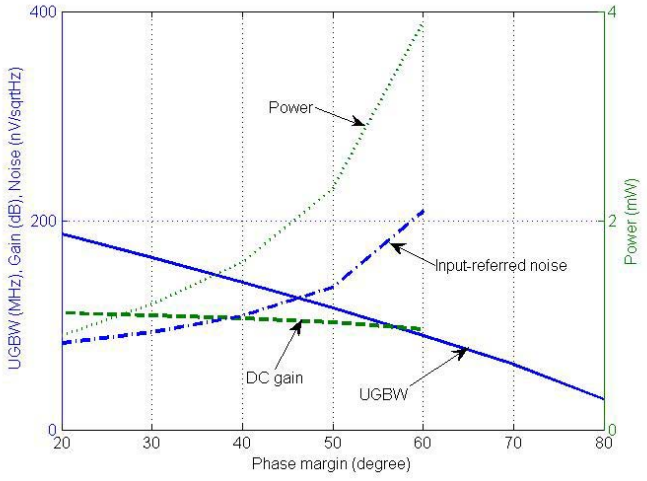

Figure 3. Trade-off curves between optimal unity-gain bandwidth, DC gain, input-referred noise and power consumption, all versus phase margins.

VII. Conclusions

We have shown how geometric programming can be used to design analog circuits such as op-amps. The method is very fast and efficient, can handle a wide variety of constraints and provide *globally optimal* design. This allows designers to spend more time on exploring different circuit architectures rather than wasting time on optimizing a particular design which may end up with a *locally optimal* solution. Trade-off analysis can be performed very quickly thanks to the efficiency of the GP algorithm.

References

[1] J. Fishburn, and A. Dunlop, "TILOS: A posynomial programming approach to transistor sizing," *IEEE International Conference on Computer-Aided Design (ICCAD-85) Digest of Technical Papers,* pp. 326-328, 1985.

[2] C. Chu and D. Wong, "Closed form solutions to simultaneous buffer insertion/sizing and wire sizing," *ACM Transactions on Design Automation of Electronic Systems*, 6(3), pp.343-371, 2001.

[3] D. Patil, Y. Yun, S.-J. Kim, S. Boyd, and M. Horowitz, "A new method for robust design of digital circuits," *International Symposium on Quality Electronic Design (ISQED) Digest of Technical Papers,* 2005.

[4] W. Chen, C.-T. Hseih, and M. Pedran, "Simultaneous gate sizing and placement," *IEEE Transactions on Computer-Aided Design of Integrated Circuits and Systems,* 19(2),pp.206-214, Feb. 2000.

[5] M. Hershenson, S. Mohan, S. Boyd, and T. Lee, "Optimization of inductor circuits via geometric programming," *Proceedings of 36th Design Automation Conference,* pp.994-998, Jun. 1999.

[6] M. Hershenson, "Design of pipeline analog-to-digital converters via geometric programming," *Proceedings of IEEE/ACM International Conference on Computer-Aided Design,* pp.317-324, Nov. 2002.

[7] K. Kortanek, X. Xu, and Y. Ye, "An infeasible interior-point algorithm for solving primal and dual geometric programs," *Math Programming,* 76, pp.155-181, 1996.

A Current-Mode Square-Rooting Circuit Using Negative Feedback Technique

Ittipong Chaisayun
South-East Asia University
Bangkok 10160,THAILAND, Email:ittipong@sau.ac.th

***Abstact*-In this paper, a square-rooting circuit operating in current mode is proposed. The negative feedback technique is used to realize the proposed circuit. This circuit uses only fourteen CMOS transistors and requests no current source, and moreover it can operate at low voltage supply. Simulation results are carried out by using PSpice. Experimental results by using CD 4007 transistor arrays are shown to confirm the operation.**

I. INTRODUCTION

A square-rooting circuit is a useful building block used in neural networks applications, measurement and instrumentation. For example it can be used to compute the Euclidean distance between two vectors[1], or to calculate the r.m.s. value of an arbitrary waveform[2]. In the past, square-rooting circuit was proposed by using operational amplifiers(op-amp) and bipolar junction transistors[3]. This approach provides the logarithmic principle to realize a square-rooting function. However the frequency performance is limited by the bandwidth of an op-amp. Then, the square-rooting circuit[4] has been proposed by bipolar junction transistors(BJT) in translinear configuration which is suitable for implementing in monolithic integrated circuit form. After that the voltage-mode square-rooting circuits[5-6] and the current-mode square-rooting circuits[7-8] based on CMOS transistors have been reported. In recent years, current-mode analogue signal processing circuit techniques have received wide attention due to the high accuracy, the wide signal bandwidth and the simplicity of implementing signal operations such as addition, subtraction and multiplication[4]. However, the current-mode square-rooting circuit is less involved, so this paper proposes a current-mode square-rooting circuit. The current-mode square-rooting circuit[7] is realized by using the back gate of CMOS biased in weak inversion. Even it uses low voltage supply and only nine transistors, but it has more error about 20%. The current-mode square-rooting circuit[8] is realized by a class AB configuration. Although it achieves a wide dynamic rang and a wide-band capability, but it uses more components (sixteen transistors and three current sources). The novel higher precision current-mode square-root circuit[9] has been reported recently. Although it has high precision, but it uses more devices (twenty-six transistors). In this paper, the current-mode square-rooting circuit is realized by using negative feedback on current squaring circuit. It has low error and uses only fourteen transistors and no current source.

II. PRINCIPLE OF OPERATION

A. *Principle of The Square-Rooting Circuit*

The block diagram in Fig. 1 consists of a squaring circuit, a current-differencing amplifier (CDA) and an NMOS transistor.

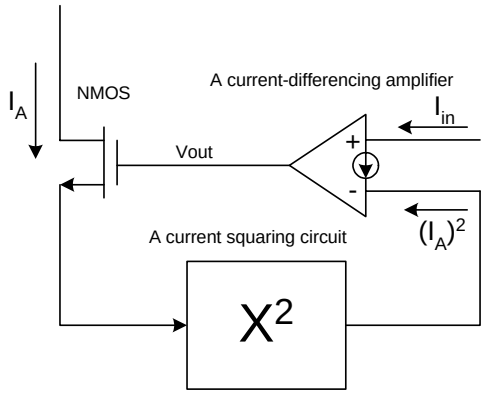

Fig. 1. Block diagram of the proposed circuit

The operation of the block diagram can be explained as: the current-differencing amplifier will convert difference of I_A^2 and I_{in} to be the single ended output voltage V_{out} , and V_{out} will control I_A by the NMOS transistor. Then I_A is fed to the input of the squaring circuit, and its output is I_A^2 which is fed to the inverting input of CDA. Consider feedback loop on the CDA. It is negative feedback. Effect of negative feedback on CDA forces the current at inverting input equating the current at noninverting input or it can be written as $I_A^2 = I_{in}$. In another word, the effect of negative feedback on CDA is that I_A^2 tracks I_{in}. Assume I_A is the output current and I_{in} is the input current. Relationship of I_A to I_{in} can be rewritten

$$I_A = \sqrt{I_{in}} \qquad (1)$$

In this research, all NMOS transistors operate in saturation region, and the drain current can be expressed as follows

$$I_D = \frac{K}{2}(V_{GS} - V_T)^2 ; V_{GS} > V_T, V_{DS} > V_{GS} - V_T \qquad (2)$$

Where $K(= \mu C_{ox} \frac{W}{L})$ is the transconductance, V_T is the threshold voltage, V_{DS} is the drain-to-source voltage, and V_{GS} is the gate-to-source voltage.

B. *Squaring Cell*

The squaring circuit[9] is shown in Fig. 2.

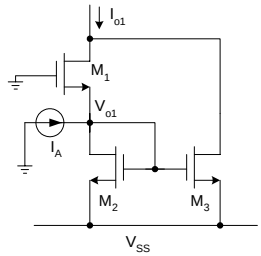

Fig.2. The squaring cell.

In Fig. 2., I_A is the input current, V_{O1} is the input voltage and I_{o1} is the output current. Relation of the drain current to input current can be written as

$$I_A = I_{D2} - I_{D1} \tag{3}$$

Using (2), V_{O1} can be written as

$$V_{O1} = \frac{I_A}{2K(-V_{SS} - 2V_T)} + \frac{V_{SS}}{2} \tag{4}$$

The output current I_{o1} can be written as

$$I_{O1} = I_{D1} + I_{D3} \tag{5}$$

Using (2) and (4), it obtains

$$I_{o1} = 2K\left(\left(\frac{I_A}{2K(-V_{SS} - 2V_T)}\right)^2 + \left(V_T + \frac{V_{SS}}{2}\right)^2\right) \tag{6}$$

It should notice that I_{o1} is squaring of I_A

C. *A Square-Rooting Circuit*

The simple square-rooting circuit can be realized from the current squarer formed by M_1 -M_3 and two current mirrors shown in Fig. 3

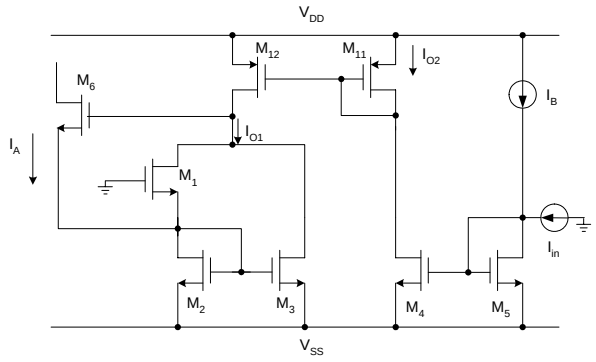

Fig.3. The simple square-rooting circuit.

The basic current-differencing amplifier makes use of a PMOS current mirror. The ratio of the PMOS current mirror consisting M_{11} and M_{12} is equal to 1:1, and The ratio of the NMOS current mirror consisting M_4 and M_5 is also equal to 1:1. I_A is input current of squaring circuit and also is output current of square-rooting circuit, I_{o1} is output current of the squaring circuit, and I_{o2} is sum of I_{in} and I_B. The CDA converts difference of I_{o1} and I_{o2} to be the voltage fed to gate terminal of M_6. The effect of negative feedback on CDA regulates the equilibrium of I_{o1} and I_{o2}

$$I_{o1} = I_{o2} \tag{7}$$

Using (6), it can be rewritten as

$$2K\left(\left(\frac{I_A}{2K(-V_{SS} - 2V_T)}\right)^2 + \left(V_T + \frac{V_{SS}}{2}\right)^2\right) = I_{in} + I_B \tag{8}$$

Define $$I_B = 2K\left(V_T + \frac{V_{SS}}{2}\right)^2 \tag{9}$$

The relation of I_A to I_{in} is

$$I_A = 2K(-V_{SS} - 2V_T)\sqrt{\frac{I_{in}}{2K}} \tag{10}$$

It should notice that I_A is square rooting of I_{in}. To design the circuit with no current sources and no grounded circuit node, the simple square-rooting circuit is improved as Fig. 4. The transistors M_7-M_{10} is used to generate I_B and the ratio of the current mirror consisting M_9 and M_{10} is equal to 1:2. In Fig. 4, the relation of I_o to I_{in} is

$$I_o = 2K(V_A - 2V_T)\sqrt{\frac{I_{in}}{2K}} \tag{11}$$

Where $$V_A = \frac{\left[V_{DD} - |V_{TP}| + V_{TN}\sqrt{\frac{K_N}{K_P}}\right]}{1 + \sqrt{\frac{K_N}{4K_P}}} \tag{12}$$

Defing $K = K_N$ and $V_T = V_{TN}$ are the transconductance and the threshold voltage of NMOS transistor respectively, and K_P and V_{TP} are the transconductance and the threshold voltage of PMOS transistor respectively. Remark M_1 and M_8 should be placed in separate well to eliminate body effect.

D. *Input Range*

Consider the circuit in Fig. 3 when $I_{in} = 0$, it find that $I_{D1} = \frac{I_B}{2}$ and $I_A = 0$. Then when $I_{in} > 0$, it find that

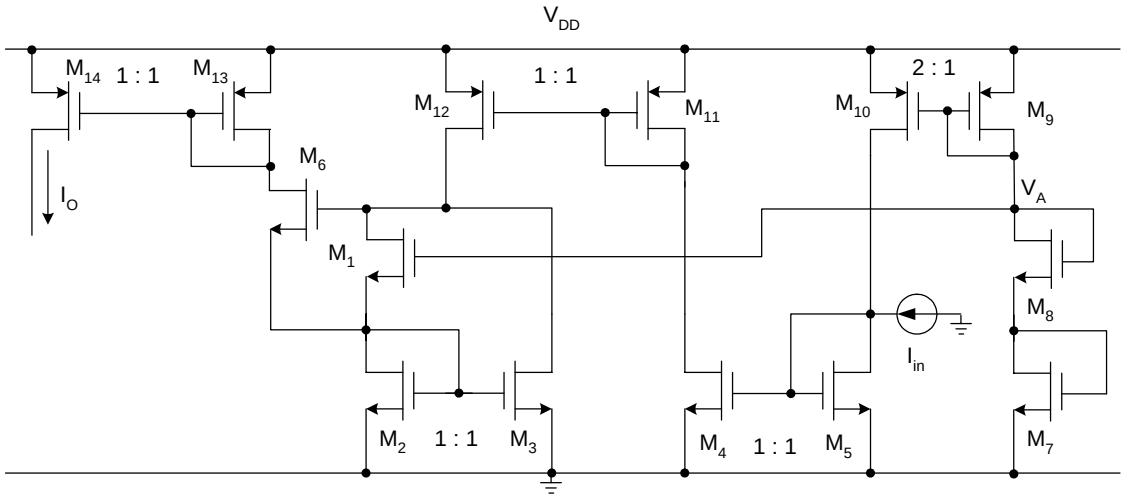

Fig.4. The completed square-rooting circuit.

$I_{D1} < \frac{I_B}{2}$ and $I_A > 0$. Where $I_{in(MAX)}$ or maximum input current, it find that $I_{D1} = 0$ and $I_{A(MAX)}$ or maximum output current is

$$I_{A(MAX)} = \frac{I_B}{2} \tag{13}$$

Using (9) and (10), the input range can be written as

$$0 < I_{in} < \frac{K(2V_T + V_{SS})^2}{8} \tag{14}$$

Consider the circuit in Fig. 4. The input range can be derived by using the same way as the circuit in Fig. 3, and it can be expressed as

$$0 < I_{in} < \frac{K(2V_T - V_A)^2}{8} \tag{15}$$

III. RESULTS

The simulation results have been done by PSpice using transistor model of MOSIS with level 3. The W/L ratio of NMOS transistors M_1 to M_8 is equal to 3μm/3μm, the W/L ratio of PMOS transistor M_9 is equal to 100μm/5μm, and the W/L ratio of others is equal to 200μm/5μm. The voltage supply is set to V_{DD} = 3 volts. The dc transfer characteristics of the proposed circuit is demonstrated in Fig. 5 when i_i is varied from 0_A to 25μA compared to ideal curve($= \frac{\sqrt{V_i}}{135}$). Fig. 6 shows relative error of Fig. 5. (%error=$\left|\frac{X_i - X_s}{X_i}\right| \times 100$ %, X_i is ideal value, X_s is simulated value) Fig. 7 shows the output current when i_i is triangular wave of peak amplitude 20μA.

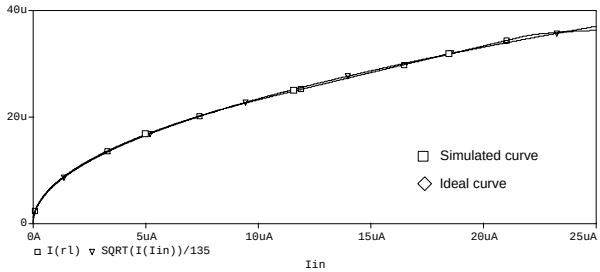

Fig. 5. The dc transfer characteristic of circuit in Fig. 4 compares with ideal curve ($= \frac{\sqrt{I_{in}}}{135}$)

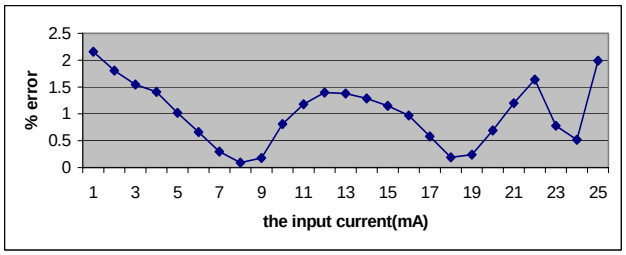

Fig. 6. the relative error of the result in Fig.5 .

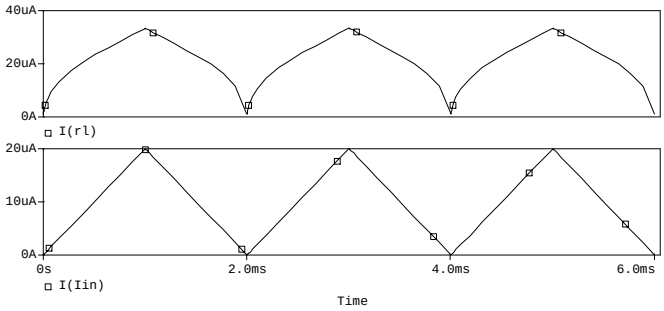

Fig. 7. Triangular wave response of circuit in Fig. 4
Upper trace output, lower trace input

The average of relative error of Fig. 6 is 1.007%. It is important to observe the no circuit node is connected to ground, so this circuit can operate on both a single supply and dual supplies.

The proposed circuit is tested experimentally by using commercial CMOS transistor arrays (CD4007) and the input current is constructed by the linear voltage to current conversion [11]. The voltage supply is set to V_{DD}=6.6 Volts. Fig. 8 shows the dc transfer characteristic when I_i is varied from 0_A to 300μA compared to ideal curve ($=0.2+\frac{\sqrt{i_i}}{1.7}$). Fig. 9 shows the output voltage waveform when I_i is triangular wave of peak amplitude 300μA at 10 kHz frequency and it accords to simulation results in Fig. 7.

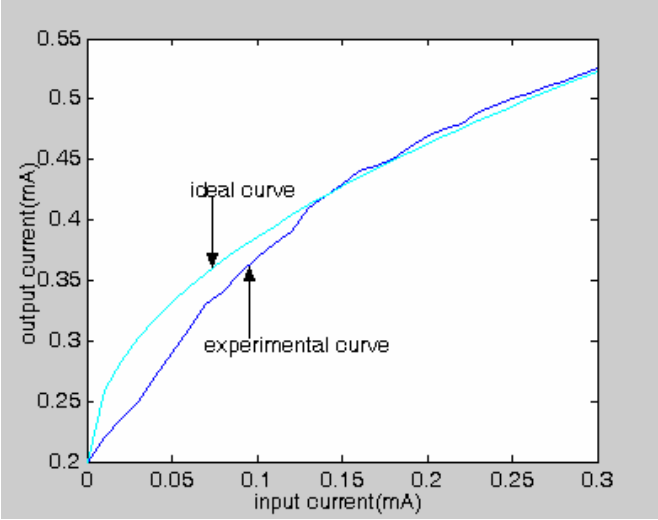

Fig. 8. The dc transfer characteristic

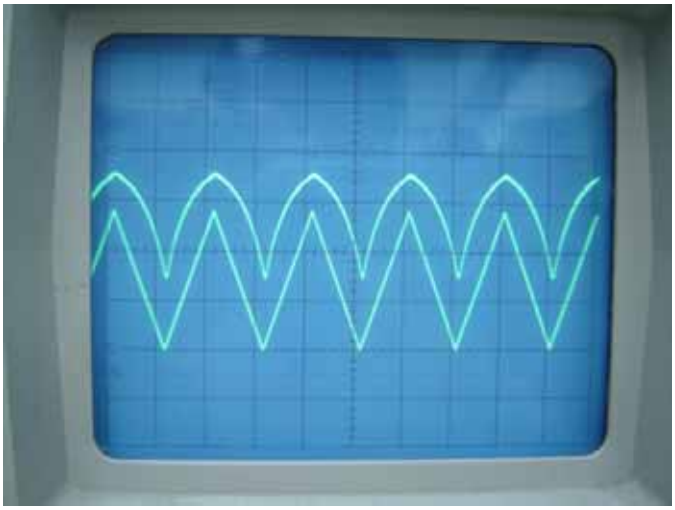

Fig. 9. The output waveform (upper trace) when I_i is triangular wave (lower trace)

Note that the output current of experimental result has dc offset current about 0.2 mA, it may occur from the mismatch problem of devices.

IV. CONCLUSION

A new square-rooting circuit has been presented in this paper. The realization method is based on the principle of negative feedback. This circuit can operate under low voltage supply, so it can be applied widely and is suitable for implementation in CMOS integrated circuit form. Simulation results are carried out by PSpice program. They find that the circuit can operate at 3_V voltage supply, the current input range is 20μA, the relative error is 1.007%, and the current output range is 35μA. Experimental results agree with simulated results.

REFERENCES

[1] T. Kohonen, "Self-Organization and Associative Menory," Springer-Verlag, Berlin, pp.119-157, 1988.

[2] O. E. Doebelin, "Measurement systems: Application and Design," New york, Mcgraw Hill.

[3] J. Millman and A. Grabel,"Microelectronics," New york, Mcgraw Hill.

[4] C. Toumazou, F.J. lidgey and D.G. Haigh, "Analogue IC Design : the current-mode Approach," london, UK, Peter Peregrinus.

[5] I. M. Filanovsky, and H. P. Baltes, "Simple CMOS analog square-rooting and squaring circuits,"IEEE Trans. Circuits Syst., vol.39, pp.312-315, 1992.

[6] K. Dejhan, C. Soonyeekan, P. Prommee and F. Cheevasuvit, "An MOSFET square-rooting circuit," Proc. of ROVPIA'96, pp.597-601, Malaysia, 1996.

[7] M. Vander Gevel and J.C. Kuenen, "$\sqrt{x}$ circuit based on a novel,back-gate using multiplier," Electronics letters, vol.30, pp.183-184,1994.

[8] V. Riewruja, K. Anutahirunrat and W. Surakampontorn, "A class AB CMOS square-rooting circuit," Int. J. Electronics, vol. 85, no. 1 pp. 55-60, 1998.

[9] K. Bult and H. Wallinga. "A class of analog CMOS circuits based on the square-law characteristic of an MOS transistor in saturation," IEEE J. Solid-State Circuits. Vol. SC-22. No. 3, pp. 357-365, 1987.

[10] S. Menekay, R.C Tarcan, H. Kuntman, "a novel higher precision current-mode square-root circuit," Proc. of 2006 IEEE 14th Signal Processing and Communications Applications, pp.1-4, 2006

[11] R. Mancini, Edition in Chief, "Op-Amp for Everyone ; Design Reference", Texas Instrument, 2nd edition, 2003.

TABLE I
LONGITUDINAL VELOCITY OF MATERIAL

Material	Longitudinal Velocity (*c*) (mm /μs)
Aluminum	6.350
Brass	4.430
Copper	4.700
Plexiglas	2.680
Stainless	5.610
Steel	5.940
Water	1.494

B. Ultrasonic Signal Simulation

Ultrasonic signal can be modeled by gaussian function in Figure 2 and sine wave in Figure 3. $e(t)$ may be expressed in (2). F_0 is transducer center frequency. t is time. σ^2 is variance of gaussian function. t_0 is position of scatters in time domain. Figure 4 shows $e(t)$ at t_0 =2 μs. $h(t)$ is an impulse response of a scatter function used to convolute with $e(t)$ as described in (3).

$$e(t) = \exp[-2\pi^2\sigma^2(t-t_0)^2]\sin(2\pi F_0 t) \quad (2)$$

$$s(t) = e(t) * h(t) \quad (3)$$

For a medium of scatters, the echo signal $s(t)$ can be modeled in frequency domain as follows:

$$s(t) = e(t) * h(t) = \sum_M e(t) * h_a^2(M,t) * h_d(M,t) \quad (4)$$

where $h(t)$ is impulse response of scatters that relate to (5) and (6) in frequency domain. h_a^2 is the two ways impulse response of attenuation of a scatter in position M and $H_a^2(M,f)$ is frequency domain of h_a^2. $2Z$ is the total distance traveled by the ultrasound wave. $h_d(M,t)$ is a set of impulses in time domain that relate to position M in frequency domain as shown in (8). β is attenuation coefficient, which is estimated from FCS.

$$S(f) = E(f) \cdot H(f) \quad (5)$$

$$S(f) = \sum_M E(f) \cdot H_a^2(M,f) \cdot H_d(M,f) \quad (6)$$

$$H_a^2(M,f) = e^{-2Z\beta f} \quad (7)$$

$$H_d(M,f) = \delta(Z) \quad (8)$$

h_d is the scattering impulse function simulated by Dirac function. The position Z of a scatter is determined with function of object modeled. In this paper, two positions of Dirac function are utilized according to experimental system.

$$h_d(f,Z) = \delta(Z) \quad (9)$$

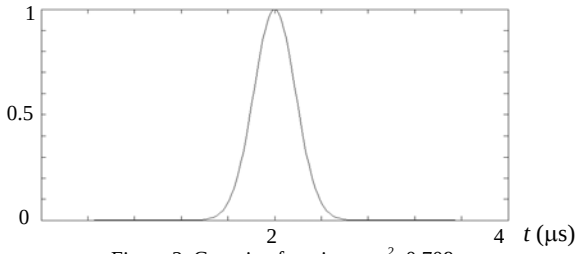

Figure 2. Gaussian function at σ^2=0.709

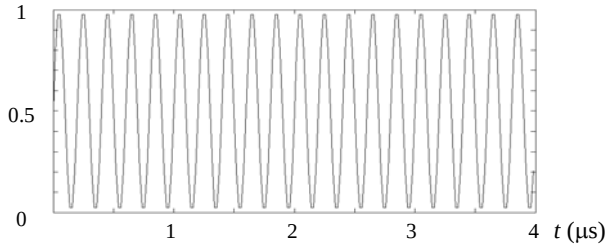

Figure 3. Sine wave at 5 MHz

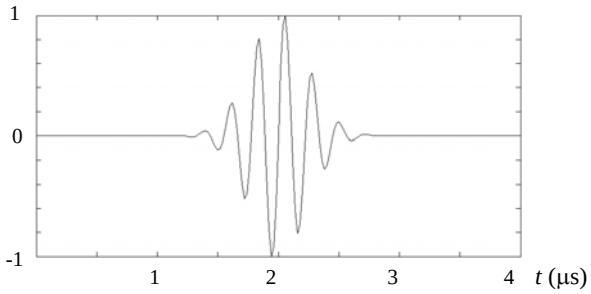

Figure 4. $e(t)$ function

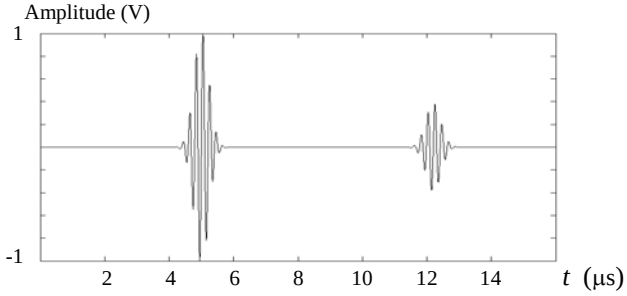

Figure 5. Ultrasonic simulation signal

TABLE II
ATTENUATION OF TISSUE AT 1 MHZ [5]

Tissue	Characteristic Impedance $\rho_0 c$ (10^6Ns/m^3)	Attenuation at 1 MHz (dB/cm)
Blood	1-62	0.2
Spleen	1-6	0.4
Liver	1-65	0.7
Fat	1-38	0.8
Brain	1-60	0.8
Muscle	1.65-1.74	1.5-2.5
Bone	3.2-7.4	11
Lung	0.26-0.46	40
(Water)	1.49	0.002

III. Fourier Centroid Shift Method

FCS is one of strategies in Fourier statistics method that depends on the spectral moment estimation. The spectral centroid $f_c(\tau_i)$ at spectral amplitude $|S(f)|$ as expressed in (10).

$$f_{c(\tau_i)} = \frac{m_1(\tau_i)}{m_0(\tau_i)} \tag{10}$$

m_j is moment of order j defined by (11). τ_i is position of the window on the echo line.

$$m_{j(\tau_i)} = \int_{-\infty}^{+\infty} f^j \cdot S(\tau_i, f) \cdot df \tag{11}$$

With the classical assumption of linear with frequency attenuation, $\alpha(f)$ is attenuation expressed in dB/cm and β is the attenuation coefficient expressed in dB/cmMHz. The relation between $\alpha(f)$ and β can be described in (12).

$$\alpha(f) = \beta \cdot f \tag{12}$$

An estimation of attenuation coefficient can be obtained by (13). σ^2 is variance of spectrum that can be calculated by (14). Additionally, the moment order 0 to 2 is used to obtain σ^2. C is ultrasonic longitudinal velocity. Equation (15) expresses unit conversion from Neper to dB.

$$\beta = \frac{-8.68}{C\sigma^2(\tau)} \cdot \frac{df_c}{d\tau} \tag{13}$$

$$\sigma^2(\tau_i) = \frac{m_2(\tau_i)}{m_0(\tau_i)} - \left(\frac{m_1(\tau_i)}{m_0(\tau_i)}\right)^2 \tag{14}$$

$$\beta\,[\text{dB/cmMHz}] = 8.68 \cdot \beta\,[\text{Neper/cmMHz}] \tag{15}$$

IV. Numerical Simulation

According to ultrasonic transducer, 5 MHz of center frequency is selected to simulate ultrasonic signal with attenuation coefficient of brass = 0.50dB/cmMHz [6] as shown in Figure (6). The difference of time corresponds to Z=2.5 cm at c=4.430 mm/μs as described in Table I.

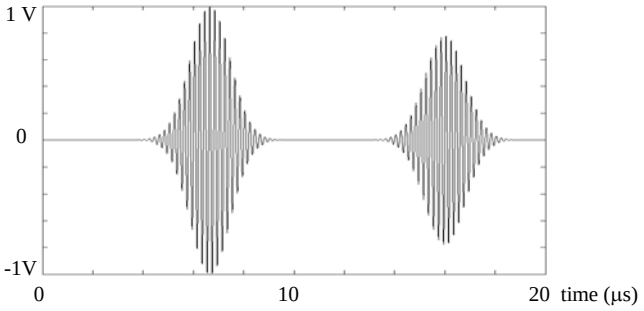

Figure 6. Simulation of Ultrasonic signal at 5 MHz

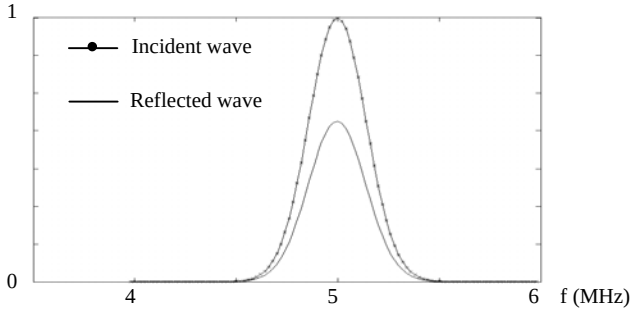

Figure 7. Spectrum of incident wave and reflected wave

From Figure 7, the attenuation coefficient is solved to verify the FCS that described in previous section. The result of β in simulation is 0.50 dB/cmMHz same as [6]. Additionally, other β value at 1 MHz and 5 MHz are tested as shown in Table IV.

TABLE IV

Attenuation Coefficients computed by Simulated Signal

β (dB/cmMHz)	Fourier Centroid Shift Method	
	1 MHz	5 MHz
0.1	0.1124	0.1001
0.3	0.3032	0.2998
0.5	0.5004	0.4997
0.7	0.7000	0.6995
1.0	1.0000	0.9993
1.5	1.5000	1.4989
2.0	2.0000	1.9986
3.0	3.0000	2.9978

TABLE V

Error of Attenuation Coefficients computed by Simulated Signal

β (dB/cmMHz)	Error (%)	
	1 MHz	5 MHz
0.1	12.4000	0.1000
0.3	1.0667	0.0667
0.5	0.0800	0.0600
0.7	0.0000	0.0714
1.0	0.0000	0.0700
1.5	0.0000	0.0733
2.0	0.0000	0.0700
3.0	0.0000	0.0733

$$\text{Error (\%)} = \frac{\left|\beta_{theory} - \beta_{estimation}\right|}{\beta_{theory}} \cdot 100 \tag{15}$$

V. Experimental Validation

TABLE III

Instrument and Device used in Experimentation

Instrument/Device	Model
Pulse Generator	Panamatrics: Model500PR
Digital Scope	Tektronix: TDS3012
Ultrasonic Transducer	Panamatrics: Model V309

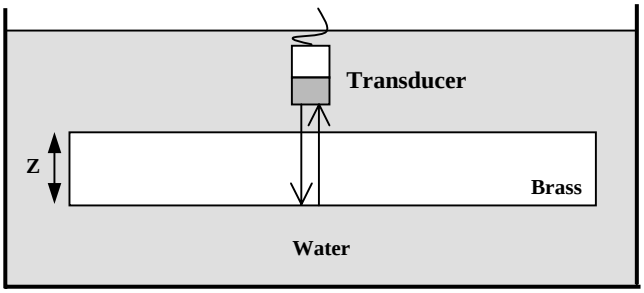

Figure 8. Ultrasonic simulation signal

The experimentation is built up as shown in Figure 8. The metal, brass, is immersed in Plexiglas water tank. Furthermore, the ultrasonic transducer is located at the top of water tank and linked to digital oscilloscope. The instruments and devices as shown in Table III are setup to obtain an ultrasonic signal. Ultrasonic pulse generator and transducer are selected in same manufacturer, Panamatrics. The reflection mode is selected to measure the ultrasonic signal. The echo signal from transducer is digitized with digital oscilloscope and sent as a digital data set to personal computer by GPIB cable. The ultrasonic signal, $s(t)$, is digitized with a sampling interval $\Delta t = 1/F_s$ (F_s is the sampling frequency = 500 MHz), in 10,000 samples. Figure 9 displays a captured signal. The digitized data is computed to obtain β by FCS algorithm. The peaks of spectrum at 5 MHz correspond to transducer center frequency used. The spectrum of measured signal is displayed in Figure 10. So, β of measured signal is 0.4415 dB/cmMHz. The error calculated by (15) of β between simulation and experimentation is approximately 11%.

VI. Conclusion

A FCS method for estimation of ultrasonic attenuation coefficients has been developed. The FCS algorithm is tested by ultrasonic simulation signal. The method has been established on the basis of spectrum in frequency domain that is used to calculate the echoes from the front and back surfaces of the immersed metal. To validate the model, the experimentation has been setup. The 5MHz ultrasonic transducer and brass are selected and immersed in Plexiglas water tank. The data is acquired and computed by FCS algorithm. The result show that β from simulated signal is 0.50 dB/cmMHz while β from experimentation is 0.4415 dB/cmMHz. The error is around 11% because this work omits the ultrasonic diffraction phenomenon. However, the result in simulation and experimentation is satisfied. To reduce an error, the Lommel diffraction correction method [7] will be compensated in future work.

Acknowledgement

This work was sponsored by NSTDA and TRF funding contract no. F-31-206-22-02 and MRG4980072 respectively.

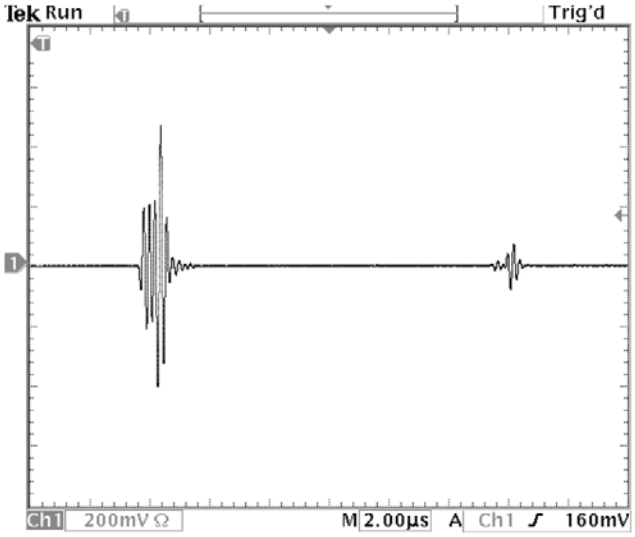

Figure 9.Captrued signal from brass at transducer center frequency=5MHz

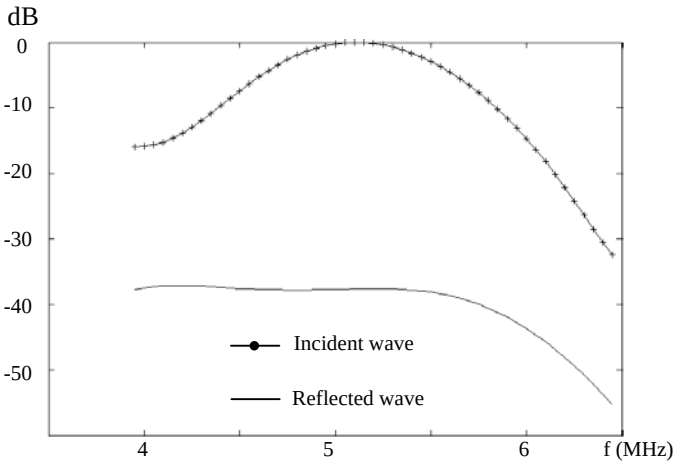

Figure 10. Normalized spectrum of measured signal

References

[1] Ping Wu, Tadeusz Stepinski, "Quantitative estimation of ultrasonic attenuation in a solid in the immersion case with correction of diffraction effects," *Ultrasonics*, Elsevier,38, pp.481-485, 2000.

[2] T. Baldeweck, P. Laugier, A. Herment, G. Berger, "Application of Autoregressive Spectral Analysis for Ultrasound Attenuation Estimation Interest in Highly Attenuating Medium," *IEEE Transactions on Ferroelectrics and frequency control*, 42, pp.99-110, 1995.

[3] Celine Fournier, S. Lori Bridal, Alain Coron, Pascal Laugier, "Optimization of Attenuation Estimation in Reflection for In Vivo Human Dermis Characterization at 20 MHz," *IEEE Transactions on Ferroelectrics and frequency control*, 50, pp.408-418, 2003.

[4] Valery Roberjot, S. Lori Bridal, Pascal Laugier, Genevieve Berger, "Absolute Backscatter Coefficient over a Wide Range for Frequencies in a Tissue-Mimicking Phantom Containing Two Populations of Scatters," *IEEE Transactions on Ferroelectrics and frequency control*, 43, pp.970-978, 1996.

[5] Heinrich Kuttruff., "Ultrasonics Fundamentals and Applications," *ELSEVIER Applied Science*, 1991.

[6] V. R. Singh and Ashok Kumar (1995): "Development of A Focused Ultrasonic Transducer with Increased Efficiency," *Proceedings of IEEE-EMBS*, pp.4.47-4.48, 1995.

[7] S. Boonsang and R J Dewhurst, "Pulsed Photoacoustic signal characterization incorporating near- and far-field diffraction effects,"*Meas. Sci. Technol.*, vol 16, pp. 885-899, 2005.

A Compact Class-AB CMOS Variable Gain Amplifier

Phanumas Khumsat
Department of Electrical Engineering
Faculty of Engineering, Prince of Songkhla University
Hat-Yai, Thailand 90112
e-mail: phanumas.k@psu.ac.th

Apinunt Thanachayanont and Siraporn Sakphrom
Faculty of Engineering and Research Center of
Communications and Information Technology
King Mongkut's Institute of Technology Ladkrabang
Ladkrabang, Bangkok, Thailand 10520
e-mail: ktapinun@kmitl.ac.th, yungying_ee@yahoo.com

Abstract— **A compact class-AB variable gain amplifier has been proposed. The amplifier structure is based on two-stage architecture comprising a linear transconductor cascaded by a current amplifier-based feedback transimpedance amplifier. The major advantage of such VGA circuit is its ability to offer a good degree of signal linearity without sacrificing the original advantages of its predecessor on both aspects of the power consumption and circuit complexity. Superiority of the proposed VGA has been confirmed by circuit simulation employing 0.18μm standard CMOS technology in designing a 50-MHz VGA under 1V supply voltage draining static power consumption less than 60μW.**

I. INTRODUCTION

Variable gain amplifier (VGA) is an important building block that is used to maximize the dynamic range of the overall system in many applications [1], [2], [3], In communication receiver, VGA is typically employed in a feedback loop to realize an automatic gain control (AGC), to provide constant signal power to baseband analog-to-digital converter (ADC) for unpredictable received signal strengths. The voltage gain of the VGA is controlled by the AGC loop, and a linear-indB gain control characteristic is usually desired to obtain constant settling time of the AGC loop [4]. In addition, VGA is generally required to maintain high linearity and low noise over the entire bandwidth and gain range. It is also important that the bandwidth of the amplifier remains constant when the voltage gain is varied and this can be obtained by employing current-mode techniques [5].

In portable communication devices, VGA, as well as other circuits, are required to operate with low power supply voltage and low power consumption. As the process technologies develop, the maximum allowable supply voltage will scale down. It is inevitable that most low power integrated circuits will have to operate with power supply voltages between 1 V to 1.5 V. It is very challenging to design a VGA with high linearity and wide bandwidth with low supply voltage and low power consumption.

Recently, a compact low supply voltage and low power consumption VGA in [6] has been designed to achieve high linearity and wide bandwidth with acceptable power dissipation. However, since its operation is limited at class-A amplifier, signal swing is small compared to class-AB amplifier. This paper presents an improved VGA to the circuit in [6]. It will be shown that the proposed circuit operates in class-AB manner outperforms its predecessor (class-A), especially, in terms of signal swing and linearity while maintaining the same static power consumption and silicon area.

II. TWO-STAGE CURRENT-MODE VARIABLE GAIN AMPLIFIER

The recently proposed VGA in [6], [7] has shown its versatility and potential to operate at low supply voltage, low power consumption with high bandwidth while maintaining good degree of dynamic range and occupying small silicon area. This VGA's architecture is presented in Fig. 1a, which is a cascade of a linear transconductor cascaded and a linear transimpedance amplifier with shunt-feedback resistors (Rf). This allows constant bandwidth when varying the voltage gain. The voltage gain of the VGA circuit is the product of the transconductance gain (Gm) and the transimpedance gain (R_m). The transimpedance gain is given by

$$R_m = -\left(\frac{R_f A_i - R_{in}}{1 + A_i}\right) \tag{1}$$

where Rin and Ai, respectively, are the input resistance and the current gain of the current amplifier. Note that, when Ai >> 1, we have $R_m \approx -R_f$. There a linear Gm and a high-gain current amplifier are required to realize a high-linearity VGA.

The proposed VGA circuit realization in CMOS is also depicted in Fig. 1b. The circuit is very compact; it however possesses a major limitation at which the output current signal

This work has been financially supported by Thailand Research Fund (under grant no. RSA4680027).

swing is restricted by constant current sources, i.e. the VGA operates in a class-A manner. This would prohibit the VGA to achieve a rail-to-rail output voltage swing.

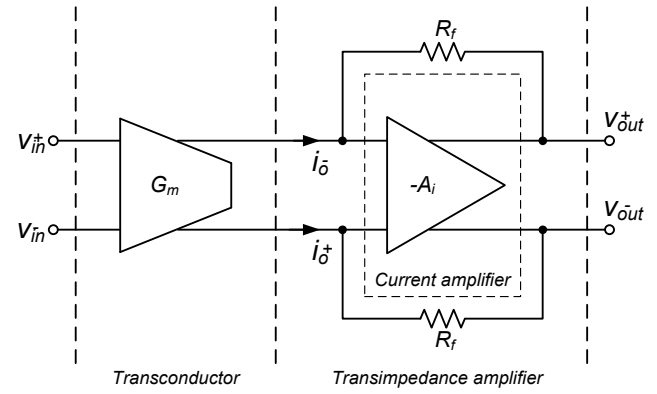

(a)

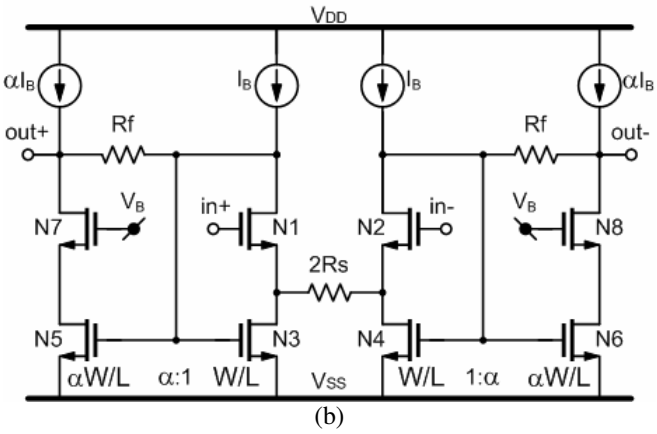

(b)

Fig. 1 VGA proposed in [6], [7] (a) architecture (b) circuit realisation with CMOS.

III. PROPOSED CLASS-AB VARIABLE GAIN AMPLIFIER

An improved VGA based on the architecture of Fig. 1a is presented in Fig. 2. The transconductor stage (N1 – N2, Rs) utilizes source degeneration technique without any constant current sources in order to maximum transconductance/bias current efficiency and minimize supply voltage and noise [8]. Despite these advantages, such structure possesses a serious drawback in being unable to reject common-mode signal. The second stage mirror-based current amplifier (P1 – P6, N3 – N6) resolves this problem by employing feedforward technique that allows differential signals to be constructively combined while on the other hand cancel a common-mode signal [9, 10]. This current amplifier combined with feedback resistors Rs form a transimpedance amplifier necessary for current-to-voltage conversion. Moreover, such output stage also provides a class-AB operation allowing larger signal swing compared to its predecessor presented in [6], [7]. Thus the major advantage of such VGA circuit is its ability to offer excellent signal linearity without sacrificing the original advantages on both aspects of the power consumption and circuit complexity.

A small-signal transconductance of the first stage is simply expressed as

$$G_m = \frac{g_m}{1 + g_m R_S + sR_S C_{gs}} \tag{2}$$

where gm and Cgs are respectively transconductance and gate-source capacitance of N1 and N2. The amplifier differential current gain A_i and input resistance R_{in} have been analysed to be

$$A_i = \frac{g_{mx}}{(g_{mi} + sC_x)}\left(1 + \frac{g_{my}}{g_{my} + sC_y}\right) \tag{3}$$

and

$$R_{in} = \frac{1}{g_{mi} + sC_x} \tag{4}$$

where g_{mi}, g_{mx} and g_{my} are transconductance of P1 – P2, P3 – P6 and N3 – N6 respectively. The parameters C_x and C_y are equivalent total capacitance (referred to ground) at gates of P1 (P2) and N3 (N4) whose values are mainly contributed from gate-source capacitance. At low frequency, since $g_{mx} = g_{mi}(\alpha/2)$, thus Ai of Fig. 2 equals to α, which is the same as what obtained from the original circuit in Fig. 1b. Thus, by substituting (3) and (4) into (1), a small-signal transimpedance gain could be obtained to be

$$R_m = -\frac{\alpha\left[2R_f - \frac{1}{g_{mx}} + s\frac{C_y}{g_{my}}\left(R_f - \frac{1}{g_{mx}}\right)\right]}{2\left[1 + \alpha + s\left(\frac{C_y}{g_{my}}\left(1 + \frac{\alpha}{2}\right) + \frac{C_x}{g_{mi}}\right) + s^2\frac{C_x C_y}{g_{mi} g_{my}}\right]} \tag{5}$$

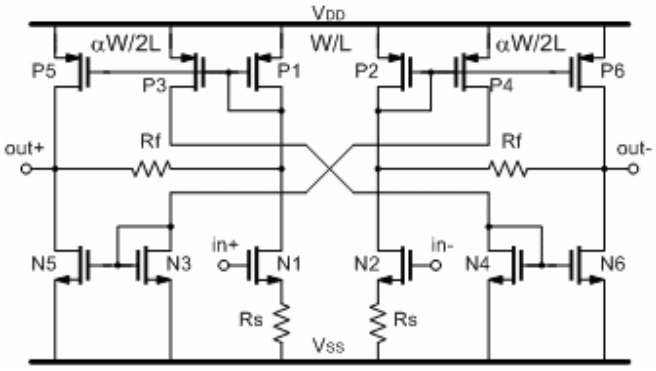

Fig. 2 Improved VGA based on the structure in Fig. 1a with class-AB output stage and signal feedforward topology.

The feedback resistor Rf is selected to set a voltage gain range whereas a source degeneration resistor Rs is tuned to vary the amplifier gain. The minimum value of Rs sets the maximum gain for a specific gain range (as previously set by Rf) and it also defines the maximum static current consumed by the VGA. The similar technique proposed in [8] can be used to tune the grounded resistor Rs.

IV. SIMULATION RESULTS

The improved VGA circuit was designed to operate with a single 1V power supply voltage. The circuit was simulated by using Spectre employing a 0.18-µm standard CMOS technology where device threshold voltages were 0.49V and -0.46V for NMOS and PMOS respectively. With $\alpha = 5$, transistor sizing of the VGA circuit in Fig. 2 is listed in Table I. The minimum value of Rs is chosen to be 500 Ohms to ensure a maximum current consumption not exceeding 60µA for a bandwidth over 50MHz.

Table I: Transistor sizing within the VGA operating under a 1V supply voltage.

Transistors	W/L (um/um)
N1 – N2	1.5/0.18
P1 – P2	10/0.5
P3 – P6	25/0.5
N3 – N6	5/0.5

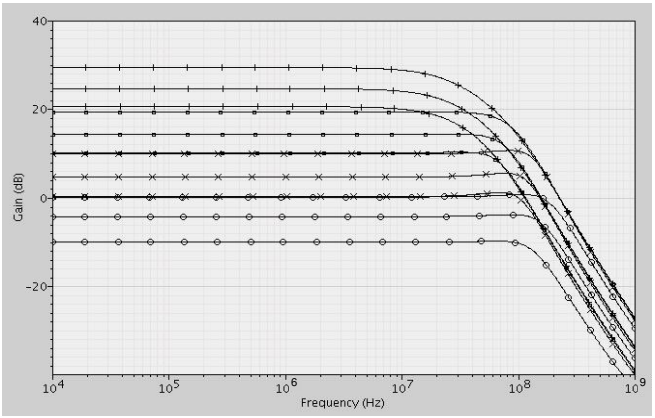

Fig. 3 Frequency response of the VGA where Rf: 500kΩ, 150kΩ, 50kΩ, 15kΩ and Rs: 500Ω – 15kΩ.

It is vital to see how the proposed VGA perform compared to the original VGA circuit of [6], [7] using the same design process. The proposed VGA and its counterpart class-A circuit have been designed under the same power supply voltage of 1V with identical static power and occupy same silicon area. By using a periodic steady-state analysis within Cadence IC design platform, Fig. 4 show simulated output signal swing and total harmonic distortion (THD) compared between two VGA circuits at the same voltage gain of 20dB where we can see that the linearity improvement of over 13dB can be achieved. The THD improvement at various gain values for differential output amplitude of -10dBVp at 1MHz and at other frequencies are depicted in Fig. 5. Other performances are summarized in Table II indicating that the proposed VGA is more superior specifically in terms of linearity.

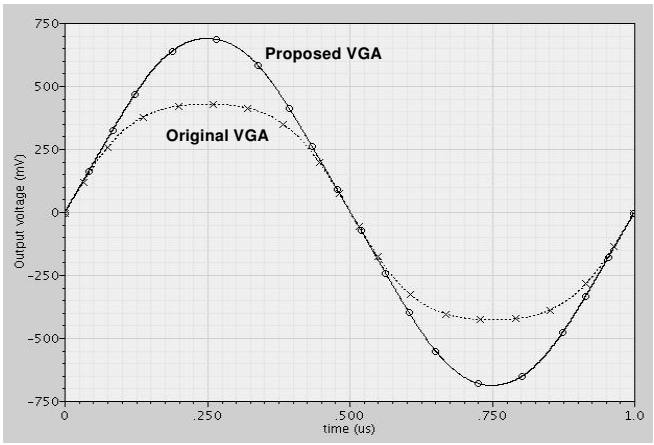

(a)

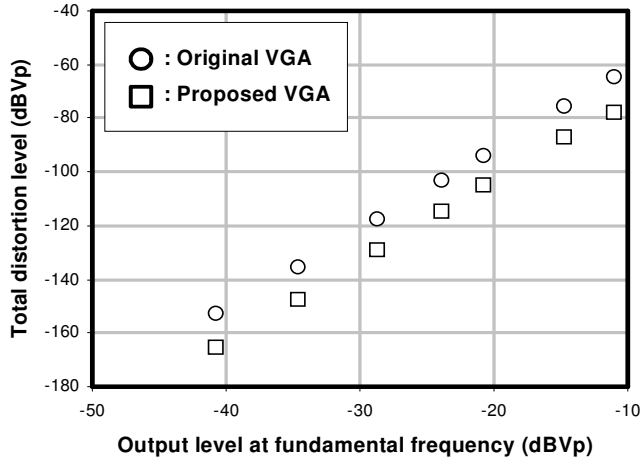

(b)

Fig. 4 Distortion comparison with voltage gain of 20dB at 1MHz (a) output signal swing and (b) THD vs input ampitude.

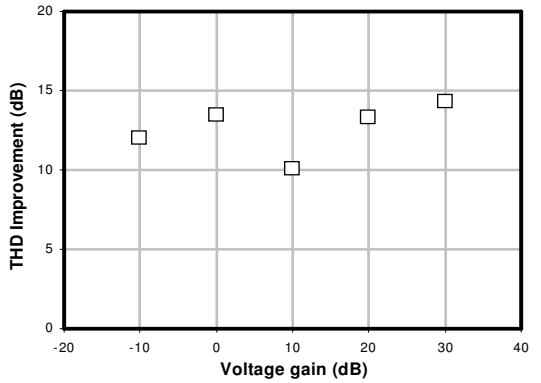

(a)

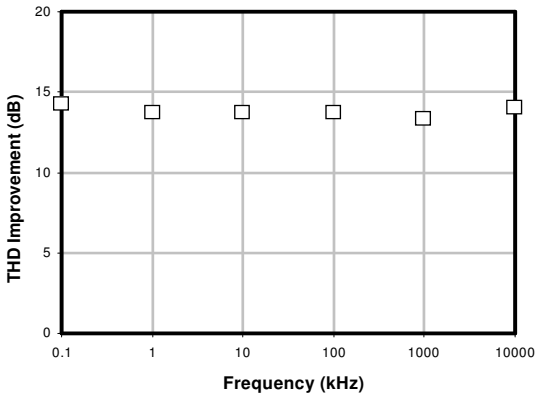

(b)

Fig. 5 THD improvement vs (a) gain at 1MHz, and (b) frequency for gain = 20dB (for output level at -10dBVp in both cases).

Table II: VGA performance comparison.

Parameters	This work	Circuit in [11]
Supply voltage	1V	
Technology	0.18μm CMOS (V_{TP} = -0.46V, V_{TN} = 0.49V)	
Power consumtion (static)	≤ 60μW	60μW
Bandwidth	~ 50MHz	~ 50MHz
Input-referred noise (gain = 20dB)	8.0×10^{-8} V^2	9.4×10^{-8} V^2
Differential output signal swing for -40dB THD	0.76Vp	0.33Vp
THD improvement	> 13dB	-
Gain range at constant bandwidth	25dB	23dB

V. CONCLUSION

A compact class-AB variable gain amplifier has been proposed. The amplifier structure is based on two-stage architecture comprising a linear transconductor cascaded by a current amplifier-based feedback transimpedance amplifier. The major advantage of such VGA circuit is its ability to offer a good degree of signal linearity without sacrificing the original advantages of its predecessor on both aspects of the power consumption and circuit complexity. Superiority of the proposed VGA has been confirmed by circuit simulation employing 0.18μm standard CMOS technology in designing a 50MHz VGA under 1V supply voltage draining static power consumption less than 60μW.

ACKNOWLEDGEMENT

Financial support from Thailand Research Fund (under grant no. RSA 4680027) is gratefully acknowledged. The authors would like to thank A. Worapishet for sharing his views on feedforward techniques.

REFERENCES

[1] W. A. Serdijn, A. C. Van der Woerd, J. Davidse, and A. H. M. Van Roermund, "A low-voltage low-power fully integratable automatic gain control for hearing instruments," IEEE J. Solid-State Circuits, Vol. 29, pp. 943-946, Aug 1994.

[2] R. Harijani, "A low-power CMOS VGA for 50 Mb/s Disk Drive Read Channels," IEEE Trans. on Circuits and Systems-II: Analog and Digital Signal Processing, Vol. 42, no. 6, pp. 370-376, June 1995.

[3] G. S. Sahota and C.J Persico, "High Dynamic Range Variable Gain Amplifier for CDMA Wireless Application," in Proc. 1997 IEEE International Solid-State Circuits Conference, pp. 374-375, 1997.

[4] J. J. F. Rijns, "CMOS Low-Distortion High-Frequency Variable-Gain Amplifier," IEEE Trans. on Solid-State Circuits, Vol. 31, no. 7, pp. 1029-1034, July 1996.

[5] K. Phang, D. A. Johns, "A 1 V 1 mW CMOS Front-End with On-chip Dynamic Gate Biasing for a 75Mb/s Optical Receiver," IEEE Int. Solid-Stage Circuits Conference, pp. 218-220, 2001.

[6] A. Thanachayanont and P. Naktongkul, "Low-voltage wideband compact CMOS variable gain amplifier," *Electronics Letters*, vol. 41 No. 2, January 2005.

[7] P. Naktongkul and A. Thanachayanont, "1.5-V 900uW 40-dB CMOS variable gain amplifier," Proceedings of 2006 IEEE International Symposium on Circuits and Systems, May 2006.

[8] F. Behbahani, W. Tan, A. Karimi-Sanjaani, A. Roithmeier, and A. A. Abidi, "A Broad-Band Tunable CMOS Channel-Select Filter for a Low-IF Wireless Receiver," *IEEE Journal of Solid-State Circuits*, vol. 35, pp. 476-489, April 2000.

[9] S. Rabii and B. A. Wooley, "A 1.8-V Digital-Audio Sigma-Delta Modulator in 0.8-μm CMOS," *IEEE Journal of Solid-State Circuits*, vol. 32, pp. 783-796 , June 1997.

[10] P. Khumsat and A. Worapishet, "Compact Two-Stage Class-AB CMOS OTA for Low-Voltage Filtering Applications," *IEICE Transactions on Electronics*, Vol. E90-C, No. 2, pp. 543-546, February 2007.

Realization of Current Conveyors-based Floating Simulator Employing Grounded Passive Elements

Winai Jaikla* and Montree Siripruchyanun**
*Electric and Electronic Program, Faculty of Industrial Technology,
Suan Sunandha Rajabhat University, Dusit, Bangkok, 10300, THAILAND Email: jnai2004@yahoo.com
**Department of Teacher Training in Electrical Engineering, Faculty of Technical Education,
King Mongkut's Institute of Technology North Bangkok, Bangkok, 10800, THAILAND Email: mts@kmitnb.ac.th

***Abstract*- A novel circuit for realizing floating inductance, floating capacitance, floating frequency dependent negative resistance (FDNR) and grounded to floating admittance converter depending on the passive component selection is proposed in this paper. The proposed simulator employs second-generation current conveyors (CCIIs), differential voltage current conveyor (DVCC) and only grounded passive elements. The non-ideal current and voltage gains as well as parasitic impedance effects on the proposed circuit are investigated. Also, simulation results using PSPICE program are given for the introduced floating simulator to verify the theory and to exhibit the performances of the circuit.**

***Index Terms*- CCII, Capacitor, DVCC, FDNR, Inductor.**

I. INTRODUCTION

Recently, a simulated immittance has become a standard research topic since it can be applied in areas like oscillator design, active filters and cancellation of parasitic elements [1]. The advent of integrated circuits has encouraged the design of synthetic inductances, which can be used instead of the bulky inductors in passive filters. Although it is difficult to implement inductors and floating capacitors in the integrated circuits, several published circuits [2-15] employing different high-performance active building blocks. The circuits given in [2–7] can realize floating inductor employing a grounded capacitor but the circuits [3–6] can realize floating FDNR employing floating capacitors, at least one of two capacitors is floating, which is not convenient to further fabricate in IC. Also, some circuits introduced in the literature can realize floating FDNR [10–15] and some of the circuits reported in the literature can realize floating capacitor [8-9]. The proposed circuit in [7] needs for passive element matching

As a result, a circuit for the simulation of a floating inductance, capacitance, FDNR and grounded to floating admittance converter depending on the passive element choice is presented. The proposed circuit consists of CCIIs and DVCC as active components. In addition, the proposed circuit employs two to three grounded resistors and one to two grounded capacitors as passive components. The circuit can realize a lossless floating inductance and capacitance, and can convert the grounded admittance into the corresponding floating admittance without changing the original topology. Furthermore, the effects of non-ideal gains on the proposed simulator are considered. The PSPICE simulation results are also shown, which are in correspondence with the theoretical analysis.

II. PRINCIPLE AND OPERATION

A. The Differential Voltage Current Conveyor (DVCC)

The DVCC, whose electrical symbol and equivalent circuit are shown in Fig. 1, is a four-terminal network with the terminal ideal characteristics described by following equation

$$\begin{bmatrix} V_X \\ I_{Y1} \\ I_{Y2} \\ I_Z \end{bmatrix} = \begin{bmatrix} 0 & 1 & -1 & 0 \\ 0 & 0 & 0 & 0 \\ 0 & 0 & 0 & 0 \\ 1 & 0 & 0 & 0 \end{bmatrix} \begin{bmatrix} I_X \\ V_{Y1} \\ V_{Y2} \\ V_Z \end{bmatrix}. \quad (1)$$

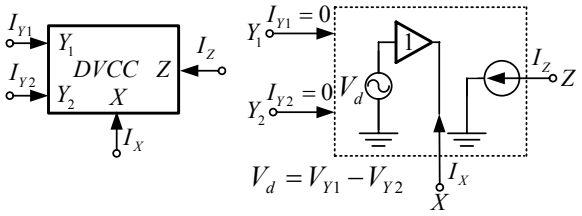

Figure 1. The DVCC (a) Symbol (b) Equivalent circuit

B. The Second Generation Current Conveyor (CCII)

The characteristics of ideal CCII are represented by the following hybrid matrix

$$\begin{bmatrix} I_Y \\ V_X \\ I_Z \end{bmatrix} = \begin{bmatrix} 0 & 0 & 0 \\ 1 & 0 & 0 \\ 0 & \pm 1 & 0 \end{bmatrix} \begin{bmatrix} V_Y \\ I_X \\ V_Z \end{bmatrix}. \quad (2)$$

The symbol and the equivalent circuit of the CCCII are illustrated in Fig. 2(a) and (b), respectively.

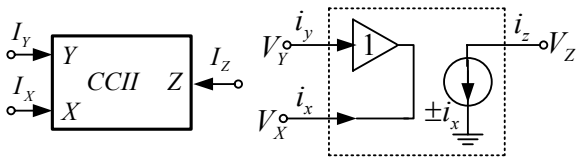

Figure 2. The CCII (a) Symbol (b) Equivalent circuit

C. Proposed floating simulator

The proposed floating simulator is shown in Fig. 3. Straightforwardly analyzing circuit in Fig. 3, it gives the following short circuit admittance matrix

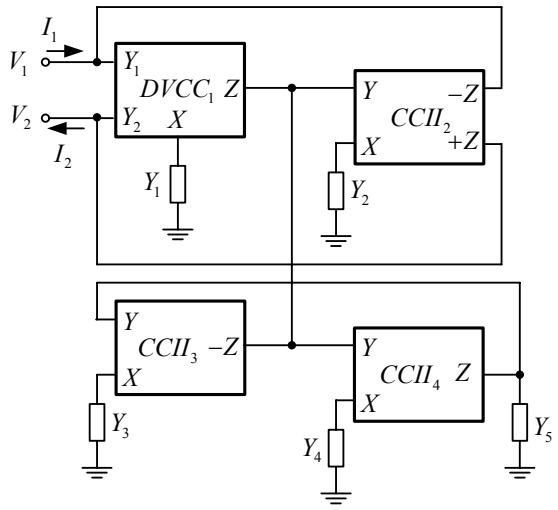

Figure 3. Proposed floating simulator

$$[Y]=\frac{Y_1Y_2Y_5}{Y_3Y_4}\begin{bmatrix}1 & -1\\ -1 & 1\end{bmatrix}. \tag{3}$$

For the proposed circuit, the following passive elements are chosen to achieve floating inductance, capacitance, FDNR and admittance converter, as following explained.

a) If $Y_1=sC_1, Y_2=G_2, Y_3=G_3, Y_4=G_4$ and $Y_5=G_5$ are taken for the circuit in Fig.1, the short circuit admittance matrix of the floating capacitance simulator is obtained as

$$[Y_C]=\frac{sC_1G_2G_5}{G_3G_4}\begin{bmatrix}1 & -1\\ -1 & 1\end{bmatrix}=sC_{eq}\begin{bmatrix}1 & -1\\ -1 & 1\end{bmatrix}. \tag{4}$$

Hence, $C_{eq}=C_1G_2G_5/G_3G_4$.

b) If $Y_1=G_1, Y_2=sC_2, Y_3=G_3, Y_4=G_4$ and $Y_5=G_5$ are chosen, the short circuit admittance matrix of the floating capacitance simulator is found to be

$$[Y_C]=\frac{sC_2G_1G_5}{G_3G_4}\begin{bmatrix}1 & -1\\ -1 & 1\end{bmatrix}=sC_{eq}\begin{bmatrix}1 & -1\\ -1 & 1\end{bmatrix}. \tag{5}$$

Hence, $C_{eq}=C_2G_1G_5/G_3G_4$.

c) If $Y_1=G_1, Y_2=G_2, Y_3=sC_3, Y_4=G_4$ and $Y_5=G_5$ are obtained, the short circuit admittance matrix of the floating inductance simulator is found to be

$$[Y_L]=\frac{G_1G_2G_5}{sC_3G_4}\begin{bmatrix}1 & -1\\ -1 & 1\end{bmatrix}=\frac{1}{sL_{eq}}\begin{bmatrix}1 & -1\\ -1 & 1\end{bmatrix}. \tag{6}$$

Hence, $L_{eq}=C_3G_4/G_1G_2G_5$.

d) If $Y_1=G_1, Y_2=G_2, Y_3=G_3, Y_4=sC_4$ and $Y_5=G_5$ are achieved, the short circuit admittance matrix of the floating inductance simulator is found to be

$$[Y_L]=\frac{G_1G_2G_5}{sC_4G_3}\begin{bmatrix}1 & -1\\ -1 & 1\end{bmatrix}=\frac{1}{sL_{eq}}\begin{bmatrix}1 & -1\\ -1 & 1\end{bmatrix}. \tag{7}$$

Hence, $L_{eq}=C_4G_3/G_1G_2G_5$.

e) If $Y_1=G_1, Y_2=G_2, Y_3=G_3, Y_4=G_4$ and $Y_5=y(s)$ are taken, the short circuit admittance matrix of grounded to floating admittance converter is calculated as

$$[Y_C]=\frac{G_1G_2}{G_3G_4}y(s)\begin{bmatrix}1 & -1\\ -1 & 1\end{bmatrix}=ay(s)\begin{bmatrix}1 & -1\\ -1 & 1\end{bmatrix}. \tag{8}$$

Thus, $a=G_1G_2/G_3G_4$ is defined as a multiplier, and $y(s)$ is the grounded admittance.

f) If $Y_1=sC_1, Y_2=sC_2, Y_3=G_3, Y_4=G_4$ and $Y_5=G_5$ are taken, the short circuit admittance matrix of the FDNR is found to be

$$[Y_D]=\frac{s^2C_1C_2G_5}{G_4G_3}\begin{bmatrix}1 & -1\\ -1 & 1\end{bmatrix}=s^2D_d\begin{bmatrix}1 & -1\\ -1 & 1\end{bmatrix}. \tag{9}$$

Consequently, $D_d=C_1C_2G_5/G_4G_3$ is obtained. As the frequency increases, the absolute value of negative resistance decreases.

g) If $Y_1=G_1, Y_2=G_2, Y_3=sC_3, Y_4=sC_4$ and $Y_5=G_5$ are taken, the short circuit admittance matrix of the FDNR is found to be

$$[Y_D]=\frac{G_1G_2G_5}{s^2C_4C_3}\begin{bmatrix}1 & -1\\ -1 & 1\end{bmatrix}=\frac{D_i}{s^2}\begin{bmatrix}1 & -1\\ -1 & 1\end{bmatrix}. \tag{10}$$

Consequently, $D_i=G_1G_2G_5/C_4C_3$ is obtained. As the frequency increases, the absolute value of negative resistance also increases.

D. Non-ideal case

For non-ideal case, the DVCC can be respectively characterized with the following equations

$$I_{Y11}=I_{Y12}=0, \tag{11a}$$
$$V_X=\beta_{11}V_{Y1}-\beta_{12}V_{Y2}, \tag{11b}$$
$$I_Z=\alpha I_X, \tag{11c}$$

While then non-idea of CCII can be respectively presented with the following equations

$$I_Y=0, \tag{12a}$$
$$V_X=\beta V_Y, \tag{12b}$$
$$I_Z=\alpha I_X, \tag{12c}$$
$$I_{Z-}=-\gamma I_X. \tag{12d}$$

α and γ are the frequency dependent current gains besides β_i is the frequency dependent voltage gain. These gains are ideally equal to unity. In practice, they depend on the frequency of operation, temperature and transistor parameters of the DVCC and CCII.

In the case of non-idea, the short matrix in Eq. (3) is converted to

$$[Y]=\frac{Y_1Y_2Y_5}{Y_3Y_4}\frac{\alpha_1\beta_2}{\alpha_3\alpha_4\beta_3\beta_4}\begin{bmatrix}\gamma_2\beta_{11} & -\gamma_2\beta_{12}\\ -\alpha_2\beta_{11} & \alpha_2\beta_{12}\end{bmatrix}. \quad (13)$$

If parasitic resistances (R_X in series ideally equal to zero, $R_Y=1/G_Y$ and $R_Z=1/G_Z$ in parallel ideally equal to infinity) and parasitic capacitances (C_Y and C_Z in parallel ideally equal to zero) affecting the impedance of the circuit in Fig. 3 are considered, the following equations are obtained

- Second port is grounded

$$Z_{in1}=\frac{V_1}{I_1}=\frac{1}{sC_{Y11}+G_{Y11}}//Z_L. \quad (14)$$

Hence,

$$Z_L=\frac{(sC_A+G_A)+\left(\frac{1}{sC_B+Y_5+G_B}\right)\left(\frac{Y_4}{1+R_{X4}Y_4}\right)\left(\frac{Y_3}{1+R_{X3}Y_3}\right)}{\left(\frac{Y_1}{1+R_{X1}Y_1}\right)\left(\frac{Y_2}{1+R_{X2}Y_2}\right)}. \quad (15)$$

Where $C_A=C_{Y2}+C_{Y4}+C_{Z1}+C_{Z3}$,
$G_A=G_{Y2}+G_{Y4}+G_{Z1}+G_{Z3}$, $C_B=C_{Y3}+C_{Z4}$ and
$G_B=G_{Y3}+G_{Z4}$.

- First port is grounded

$$Z_{in2}=\frac{V_2}{I_2}=\frac{1}{sC_{Y12}+G_{Y12}}//Z_L. \quad (16)$$

Also, if $Z_{P1}=1/(sC_{Y11}+G_{Y11})$ and $Z_{P2}=1/(sC_{Y12}+G_{Y12})$ are defined, the short circuit admittance matrix in Eq. (3) turns to

$$[Y]=\begin{bmatrix}\frac{1}{Z_{p1}//Z_L} & -\frac{1}{Z_L}\\ -\frac{1}{Z_L} & \frac{1}{Z_{p2}//Z_L}\end{bmatrix}. \quad (17)$$

Note that the term $1/(sC_{Y11}+G_{Y11})$ and $1/(sC_{Y12}+G_{Y12})$ in Eqs. (14) and (16) are effected at very high frequency. There are also high and low frequency limitations depending on the passive element selection.

If $Y_1=G_1, Y_2=G_2, Y_3=sC_3, Y_4=sC_4$ and $Y_5=G_5$ are taken for the circuit in Fig.1 as the case d), the first developed circuit has limitations at low frequencies due to terms $1+R_{X3}sC_3$, $1+R_{X4}sC_4$, $s(C_{Y2}+C_{Y4}+C_{Z1}+C_{Z3})+G_{Y2}+G_{Y4}+G_{Z1}+G_{Z3}$ and $s(C_{Y3}+C_{Z4})+G_5+G_{Y3}+G_{Z4}$ as given in Eq.(15) thus the limit at low frequencies is found as

$$f\gg\frac{1}{2\pi}\max\left(\frac{G_{Y2}+G_{Y4}+G_{Z1}+G_{Z3}}{C_{Y2}+C_{Y4}+C_{Z1}+C_{Z3}},\frac{G_5+G_{Y3}+G_{Z4}}{C_{Y3}+C_{Z4}},\frac{1}{C_3R_{X3}},\frac{1}{C_4R_{X4}}\right). \quad (18)$$

As it is seen from Eqn. (18), C_3 and C_4 should be chosen large in order to decrease the limit at low frequencies.

If $Y_1=sC_1, Y_2=sC_2, Y_3=G_3, Y_4=G_4$ and $Y_5=sC_5$ are taken for the circuit in Fig.1, the circuit has limitations at high frequencies due to terms $1+R_{X1}sC_1, 1+R_{X2}sC_2$ $s(C_{Y2}+C_{Y4}+C_{Z1}+C_{Z3})+G_{Y2}+G_{Y4}+G_{Z1}+G_{Z3}$ and $s(C_{Y3}+C_{Z4}+C_5)+G_{Y3}+G_{Z4}$ as given in Eq. (15) thus the limit at high frequencies is found as

$$f\ll\frac{1}{2\pi}\min\left(\frac{G_{Y2}+G_{Y4}+G_{Z1}+G_{Z3}}{C_{Y2}+C_{Y4}+C_{Z1}+C_{Z3}},\frac{G_{Y3}+G_{Z4}}{C_5+C_{Y3}+C_{Z4}},\frac{1}{C_1R_{X1}},\frac{1}{C_2R_{X2}}\right). \quad (19)$$

As seen from Eq. (19), C_1, C_2 and C_5 should be chosen as small as possible in order to increase the high frequency performance.

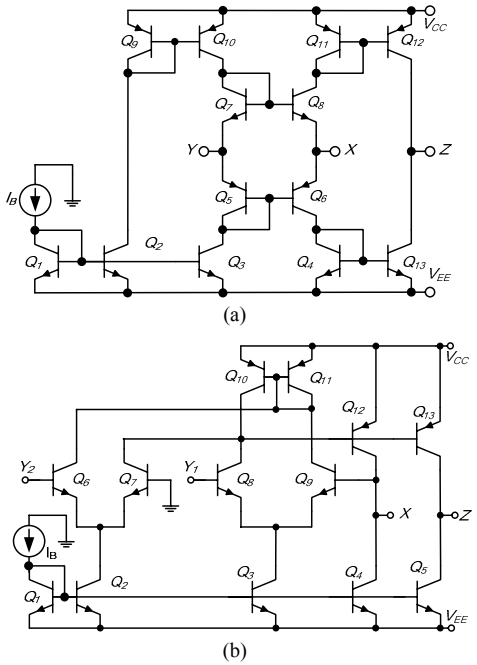

(a)

(b)

Figure 4. Internal construction of (a) CCII (b) DVCC

III. Simulation Results

To prove the performances of the proposed circuit, the PSPICE simulation program was used for the examination. The PNP and NPN transistors employed in the proposed circuit were simulated by respectively using the parameters of the PR200N and NR200N bipolar transistors of ALA400 transistor array from AT&T [16] with ±1.5V supply voltages and $I_B=200\mu A$. Fig. 4 depicts schematic descriptions of the CCII and DVCC used in the simulations. Phase and magnitude responses for the impedances of the proposed circuit in Fig. 3 are given in Fig. 5 where the second port of the floating inductor is grounded. There can be seen that, in case of (a) and (b), the useful frequency ranges are about 1kHz to 3MHz and approximately 10kHz to 1MHz, in case of (c) and (d).

In order to show the frequency domain performance of the proposed circuit, the second-order band-pass filter example in

Fig. 6 was simulated with PSPICE program. $G_1=G_2=G_4=G_5=1mS$ and $C_3=1nF$ are chosen to obtain inductance value of $1mH$. Furthermore, $G_2=G_3=G_4=G_5=1mS$ and $C_1=1nF$ are taken to obtain capacitance of $1nF$. Both of the ideal and simulated bandpass (V_o/V_{in}) filter responses is depicted in Fig. 7. The maximum power dissipation is about 20.09mW.

IV. CONCLUSION

A novel circuit which can simulate floating inductance, floating capacitance, floating admittance and floating FDNR employing CCIIs and DVCC has been proposed. The presented circuit requires no critical component matching constraints, and employs only grounded passive components so it is easy to fabricate the proposed circuit in a fully integrated circuit technology. Under non-ideal considerations, the presented circuit is still lossless synthetic inductor or capacitor. The simulation results agree well with the theoretical calculations.

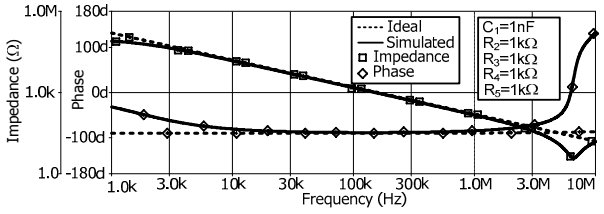

(a) Capacitance simulator (case a)

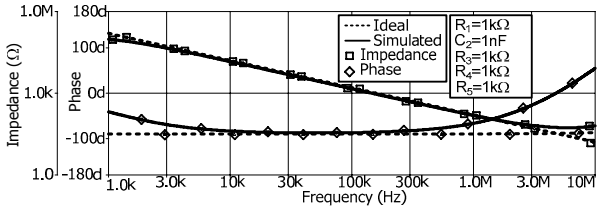

(b) Capacitance simulator (case b)

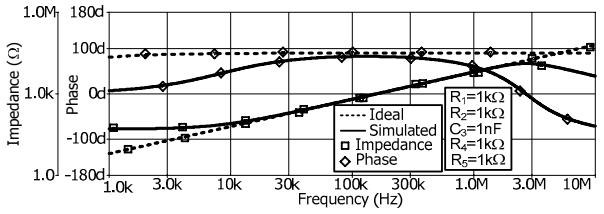

(c) Inductance simulator (case c)

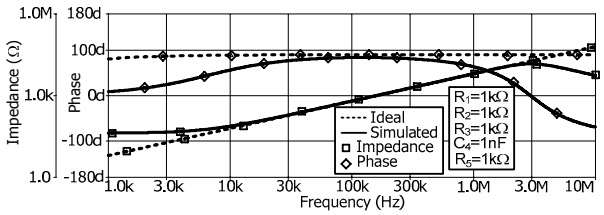

(d) Inductance simulator (case d)

Figure 5. Phases and impedances of the proposed circuit when the second port is grounded

REFERENCES

[1] G. Ferri and N.C. Guerrini, Low-Voltage Low-Power CMOS Current Conveyors. Kluwer Academic Publishers, London, 2003.

[2] E. Yuce, S. Minaei, and O. Cicekoglu, "Resistorless floating immittance function simulators employing current controlled conveyors and a grounded capacitor." *Electrical Engineering,* vol.88, pp. 519–525, 2006.

[3] E. Yuce, O. Cicekoglu, and S. Minaei, "Novel floating inductance and FDNR simulators employing CCII+s." *Journal of Circuits, Systems and Computers*, vol. 15, no. 1, pp. 75–81, 2006.

[4] E. Yuce, O. Cicekoglu, and S. Minaei, "CCII-based grounded to floating immittance converter and a floating inductance simulator." *Analog Integrated Circuits and Signal Processing,* vol. 46, no. 3, pp. 287–291, 2006.

[5] S. Minaei, E. Yuce, and O. Cicekoglu, "A versatile active circuit for realizing floating inductance, capacitance, FDNR and admittance converter." *Analog Integrated Circuits and Signal Processing*, vol. 47, no. 2, pp. 199–202, 2006.

[6] E. Yuce, "On the implementation of the floating simulators employing a single active device." *Accepted for Publication in International Journal of Electronics and Communications (AEU)*, 2006.

[7] E. Yuce, "Floating inductance, FDNR and capacitance simulation circuit employing only grounded passive elements." *International Journal of Electronics*, vol. 93, no. 10, pp. 679-688, 2006.

[8] K. Pal, "New inductance and capacitor floatation schemes using current conveyors." *Electronics Letters*, vol. 17, pp. 807–808, 1981.

[9] M.T. Abuelma'atti and N.A. Tasadduq, "Electronically tunable capacitance multiplier and frequency-dependent negative resistance simulator using the current-controlled current conveyor." *Microelectronics Journal*, vol. 30, pp. 869–873, 1999.

[10] R. Senani, "Floating ideal FDNR using only two current conveyors." *Electronics Letters*, vol. 20, no. 5, pp. 205–206, 1984.

[11] M. Higashimura and Y. Fukui, "New lossless tunable floating FDNR simulation using two current conveyors and an INIC." *Electronics Letters,* vol. 23, no. 10, pp. 629–630, 1987.

[12] M. Higashimura and Y. Fukui, "Novel lossless tunable floating FDNR simulation using two current conveyors and a buffer." *Electronics Letters*, vol. 22, no. 18, pp. 938–939, 1986.

[13] S. Nandi, P.B. Jana, and R. Nandi, "Floating ideal FDNR using current conveyors." *Electronics Letters*, vol. 19, no. 7, pp. 251–252, 1983.

[14] S. Nandi, P.B. Jana, and R. Nandi, "Novel floating ideal tunable FDNR simulation using current conveyors." *IEEE Transactions on Circuits and Systems*, vol. CAS-31, no. 4, pp. 402–403, 1984.

[15] H. Sedef and C. Acar, "A new floating FDNR circuit using differential voltage current conveyors." International Journal of Electronics and Communications (AEU), vol. 54, no. 5, pp. 297–301, 2000.

[16] D. R. Frey "Log-domain filtering: an approach to current-mode filtering," *IEE Proc. Circuit Devices Syst.,* vol. 140, no. 406-416, 1993.

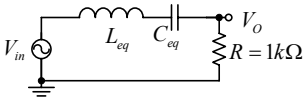

Figure 6. A bandpass filter example

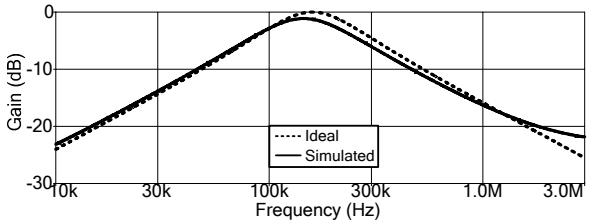

Figure 7. Both of the ideal and simulated responses of the filter in Fig. 6.

A Simplified Active Input EMI Filter of Common-mode Voltage Cancellation for Induction Motor Drive

C. Khun*, V. Tarateeraseth**, W. Khan-ngern*, Masaaki Kando***
*Research Center for Communications and Information Technology, Faculty of Engineering,
King Mongkut's Institute of Technology Ladkrabang, Bangkok, Thailand.
** Faculty of Engineering, Srinakharinwirot University, Ongkharak, Thailand.
***Department of Electrical and Electric Engineer, Tokai University, Japan

***Abstract*— This paper presents the application of the active and passive electromagnetic interference (EMI) filters in order to solve practical problems and improve the passive EMI filter performance. First, the basic active filter topologies are discussed and the basis of discussion is based on an equivalent circuit model, which includes the possible combinations of the desirable attributes. Next, a simplified active input EMI filter (AIEF) is proposed, and a large common-mode (CM) inductor of passive EMI filter is replaced by small passive components and an active circuit. A prototype of AIEF verifies the effectiveness and validity with an induction motor drive and ac motor. The CM noise is analyzed using high-frequency (HF) current probe. Finally, the proposed circuit effectiveness is verified by experimental results.**

I. INTRODUCTION

Nowadays, the broader use of power electronic based loads (rectifiers, inverter, motor control systems, etc) has led to a growth of power pollution and conducted electromagnetic emissions also have been produced because of the nonlinear voltage or current characteristics of these loads. So that, there are many researches on passive EMI filters have been done. But the size, cost and performance of EMI filter components are also important considerations in power application. With this reason, there have recently many articles of active common-mode or current ripple cancellation provides alternative approaches to the problem [1-6].

The high-speed switching devices such as IGBT's have enabled to increase a carrier frequency of voltage-source of PWM inverters, thus leading to much better operating characteristics. However, high-speed switching can accompany the serious problems from a steep change in voltage or current such as: ground current escaping to earth through stray capacitors inside motors, conducted and radiated EMI and bearing current and shaft voltage [5, 6]. Consequently, many practical forms of active cancellation circuits have been reported in recently with the same operation. The general topologies of possible active EMI filters have been introduced in [3]. The nullification process was established to classify the basic noise cancellation methods and the insertion loss analysis of active EMI filters are introduced in [4]. They mainly focused on active filters that mitigate the common-mode EMI caused by a switched mode power supply.

In this paper, a simplified active input EMI filter is introduced in order to mitigate the conducted common-mode EMI. It can provide the sufficient attenuation under the limited LC products. The PWM inverter fed ac motor drive system included motors, ac drive system (front-end single-phase diode-bridge rectifier and PWM inverter system) leads, and other possible units that are using to develop a complete motor system. The analysis and experimental results is given, respectively.

II. BASIC ANALYSIS OF ACTIVE FILTER

Generalized topologies are identified by grouping combinations of passive elements with ideal active elements to construct filter varying complexity. A typical passive EMI filter and configuration is shown in Fig. 1 and consisted of CM choke, C_y capacitors, DM choke and C_x capacitor. A good performance filter normally has a CM choke with few mH and CM capacitors are limited by safety considerations for ground leakage current that can calculate by equation (1).

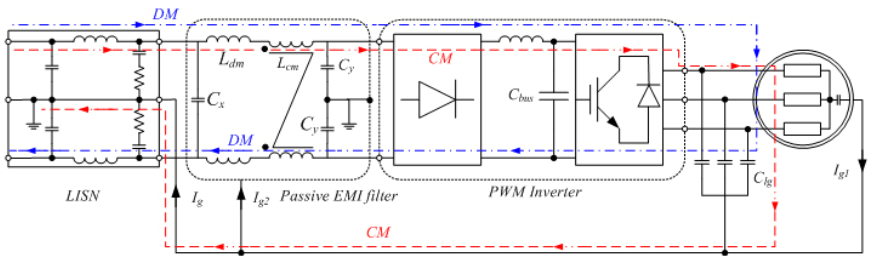

Figure 1. Typical passive EMI filter and PWM inverter system configuration.

The DM choke has lower value (typically < 1 mH) and sometime is used by the few percent leakage inductance of CM choke.

$$C_y = \frac{I_{leakage}}{2\pi \times f \times 115 \times V} \quad (1)$$

where: $I_{leakage}$ is the ground leakage current, V is ac line voltage, f is power line frequency that generally is equal to 50 or 60 Hz [7].

Reference [3] have been analyzed the feedback prototype of active filters as shown in Fig. 2 and their insertion losses (ILs) are summarizes as illustrated in Table I, where internal impedances of detecting and compensating unit are ignored as assumed in ideal case.

As shown in Fig. 2 the noise signal at receiver can be a noise voltage or current, and the compensating signal by active filter can be a voltage or current. Z_s represents the impedance of a noise receiver where one evaluates the noise power due to the noise source i_n. Z_n is an internal impedance of the noise source i_n. The insertion loss is defined as:

$$IL = \frac{v_{s,wo}}{v_{s,w}}. \quad (2)$$

where $v_{s,wo}$ is the receiver's voltage without and any filter installed and $v_{s,w}$ is the receiver's voltage with filter installed.

III. Proposed Active Input EMI Filter Design

The input filter can be an additional passive filter, which gives additional insertion loss as maintained in [2, 4]. So that, a small passive EMI filter is designed to reduce conducted EMI noise where is over the capability of active filter. Fig. 3 illustrates the application of the proposed active EMI filter designed with voltage detecting and voltage compensating (type IV). In the previous active common-mode filter [5, 6], the push-pull amplifier is used the dc voltage, which is supplied to the inverter, to power the active circuit. But in this work, the active input EMI filter is comprised of a common-mode choke with an auxiliary winding, a push-pull type emitter follower circuit using two complementary transistors T_1 (C3230) and T_2 (A1276) as shown in Fig. 3. The emitter follower is supplied from a separate source V_d. The high input impedance is used to minimize the value of C_1, for common-mode voltage detection. The coupling capacitors C_c connected to ac input lines of the system, it is possible to construct a separate input filter stage.

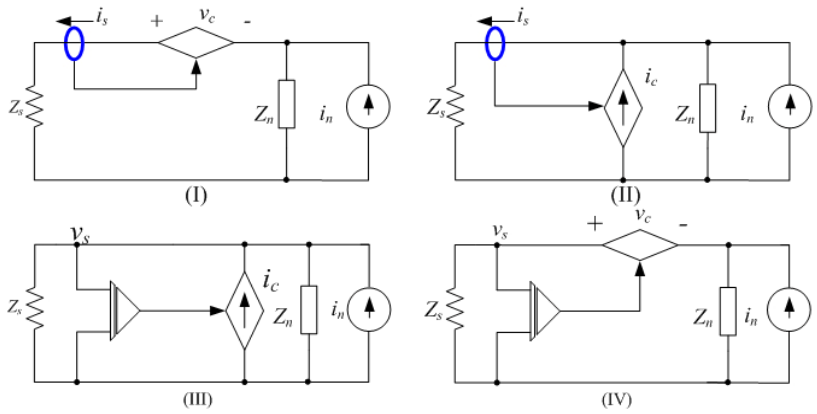

Figure 2. Feedback-type active filters [3]. (I) Current detecting and voltage conpensating, type I. (II) current detecting and current compensating, type II. (III) voltage detecting and current compensating, type III. (IV) voltage detecting and voltage compensating, type IV.

TABLE I
INSERTION LOSS OF FEEDBACK TYPE ACTIVE FILTER IN FIG. 3 [3]

Type	Insertion Loss (IL)	Amplifier gain	Condition for maximum IL
Type I	$1+\frac{A_1}{z_s+z_n}$	Trans-impedance $v_c = -A_1 \cdot i_s$	$A_1 >> z_s + z_n$
Type II	$1+\frac{z_n}{z_s+z_n} \cdot A_2$	Current gain $i_c = -A_2 \cdot i_s$	$z_n >> z_s$
Type III	$1+\frac{A_3}{z_s \parallel z_n}$	Trans-admittance $i_c = -A_3 \cdot v_s$	$A_3 >> z_s \parallel z_n$
Type IV	$1+\frac{z_s}{z_s+z_n} \cdot A_4$	Voltage gain $v_c = -A_4 \cdot v_s$	$z_s >> z_n$

A. *Selection of* C_1

The ceramic capacitors C_1 placed at the inverter input terminals of the inverter. Indeed, the resistors can be used to replace the capacitors C_1. However, there are not attractive because the resistors add more power losses to the system due to the flowing of the normal-mode currents.

The C_1 selection must be based on the maximum current that can be drawn from the main source to the inverter. If a large value of C_1 is chosen, the inverter power devices can be subjected to excessively high current pulse (capacitor charging current). Therefore, these capacitors should be selected as small as possible. The inverter for adjust speed drive is operated with the nominal current 6.4 A, and fed by a single-phase ac input system. Assuming that the inverter's switches are turned on within 500 ns, the maximum value of C_1 for 240 V is expressed:

$$6.4 = \frac{240}{500 \times 10^{-9}} \cdot C_{1,\max} \tag{3}$$

Hence, $C_{1,\max} \approx 15$ nF.

In the test setup, C_1 = 390 pF is selected as shown in Fig. 3 to get high input impedance for CM voltage detection.

B. *Complementary Transistors*

The complementary transistors use in [5, 6] are the high frequency and high voltage devices. It is quite difficult to find and expensive. In this paper, the low voltage complementary transistors are proposed because they are the commercially available for cost optimization. The transistors used in the practical implementation are A1276 and C3230. The characteristic of the both transistors are described in the table II.

TABLE II
THE COMPLEMENTARY TRANSISTORS CHARACTERISTIC

	V_{CBO} [V]	V_{CEO} [V]	I_C(dc) [A]	P_C [W]	H_{FE}
C3230-NPN	30	30	3	10	70
A1276-PNP	-30	-30	-3	10	70

C. *Separated DC Power Supply*

In the test setup, the separate 15 Vdc power supply is realized by a single-phase rectifier supplying the two capacitors C_0 connect in series. This power supply is applied to power the active circuitry. In order to remove the dc components, the capacitors C_0 are connected as illustrated in Fig.3. The small capacitance of C_0 makes the large variation of the neutral point potential V_0 [5]. Thus, C_0 is chosen as a value large enough to reduce the voltage variation. In the practical work, the capacitor of 2.2 µF is selected for C_0.

D. *CM Transformer*

In this case, the CM transformer is the same as a conventional CM choke of passive EMI filter, except for connecting a tightly coupled additional winding (auxiliary winding) to the output of the emitter follower and it applies the detecting CM voltage to the CM transformer. The two primary windings of CM transformer with the same polarity are connected between LISN and inverter input plug. Then the polarity of the compensating voltage V_c is opposite to the CM voltage generated by the inverter. Because of the CM transformer played in role of CM choke of passive EMI filter, so the value of L_{cm} should be a few mH. In the test setup, L_{cm} = 3 mH is selected within 1:1:1 winding ratio.

IV. SYSTEM CONFIGURATION AND EXPERIMENTAL RESULTS

In this section, the conducted EMI measurements have been setup: LISN 10A, high frequency current probe 10 kHz to 250 MHz bandwidth, an inverter motor drive, ac motor and EMC spectrum analyzer.

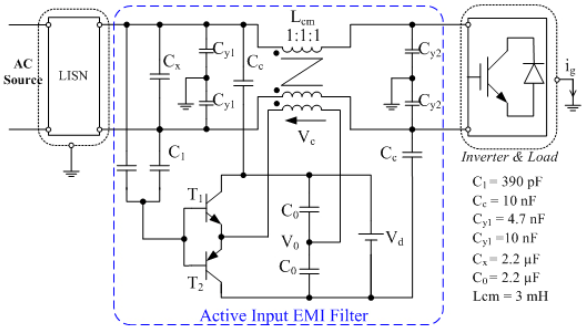

Figure 3. Configuration of experiemental system

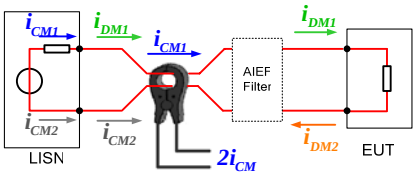

Figure 4. Common-mode EMI measurement.

The operation without load and with load is presented with the completed configuration shown in Fig. 3. An induction motor (1/2 hp, 220/380 V, 2.0/1.15 A, 50/60 Hz) is used as a load of the PWM inverter. The input filter circuit is implemented separate from PWM inverter circuit. A single-phase LISN 10 A is used to provide the stable source impedance at the high frequency while the high frequency current probe is also connected to EMC spectrum analyzer to observe CM noise as shown in Fig. 4. Because of using current probe to measure CM noise, the received results from current probe are equal to $2I_{CM}$ [7]. The CM current or voltage attenuation can be calculated from equations (4) and (5).

$$A_{dB} = \left|2I_{CM}\right|_{dB} - 6\,\text{dB} \tag{4}$$

$$V_{dB} = \left|2V_{CM}\right|_{dB} - 6\,\text{dB}. \tag{5}$$

where $\left|2I_{CM}\right|_{dB}$ and $\left|2V_{CM}\right|_{dB}$ are CM current and voltage measured using high frequency current probe, respectively.

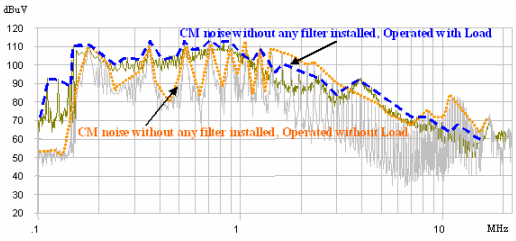

Figure 5. CM noise spectrum without any filter installed

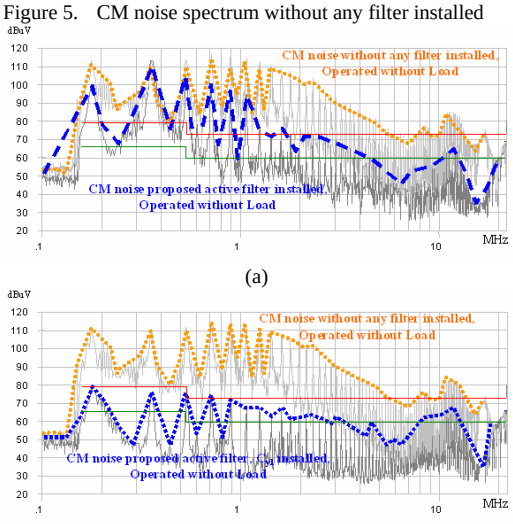

(a)

(b)

Figure 6. Measured CM noise while the proposed AIEF installed in case of operation without load. (a) uninstalled C_{y1}, C_{y2}. (b) installed C_{y1}, C_{y2}.

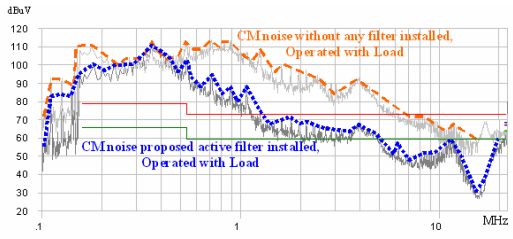

(a)

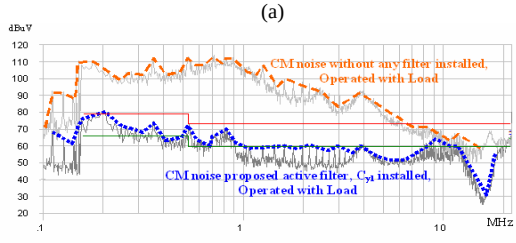

(b)

Figure 7. Measured CM noise while the proposed AIEF installed in case of operation full load. (a) uninstalled C_{y1}, C_{y2}. (b) installed C_{y1}, C_{y2}.

The conducted EMI noise is composed of CM and DM noise. Both of them are separated, but DM is not discussed in this article with assumption that some appropriate DM components are installed for each design stage. The CM spectrum of the system without any EMI filter of both operations is shown in Fig. 5, and the conducted EMI spectrum of the both operations when the proposed AIEF is installed in the system demonstrated in Fig. 6. The experimental results of both operations are shown in Figs. 6 and 7.

V. Discussion

According to the measuring results above, it can be discussed as follows:

1). In case of the operation without load, the result is given about 35 dB of the IL at 1.5 MHz to 15 MHz when the proposed AIEF is installed, but it cannot comply with the limit-line at low frequency from 150 kHz to 1.5 MHz as shown in Fig. 6(a). When the C_{y1} and C_{y2} is installed, it adds more attenuation at low frequency up to 35 dB of the IL from 150 kHz to 3 MHz and 20 dB from 3 MHz to 20 MHz as shown in Fig. 6(b), respectively.

2). When the motor is run within full load, the result is given about 20 dB of the IL at the high frequency from 600 kHz until 15 MHz as shown in Fig. 7(a). While the C_{y1} and C_{y2} is installed, it gains about 40 dB of the IL at 150 kHz to 4 MHz and 20 dB of the IL from 4 MHz to 8 MHz. It can comply with the limit-line whole the specified frequency range as shown in Fig. 7(b).

As the results, the proposed AIEF can work as active CM voltage canceller and passive EMI filter that can comply with EN 55022 class A conducted.

VI. Conculsion

This paper presents a simplified active input EMI filter based on the CM voltage detecting and voltage compensation technique. This proposed AIEF is reliable to suppress CM voltages generated by PWM inverter using low voltage complementary transistors as the push-pull amplifier. The experimental results of two operated conditions, no load and full load of induction motor, are demonstrated the effectiveness of this AIEF using HF current probe over the frequency range 150 kHz to 30 MHz.

References

[1] Wenjie Chen, Xu Yang, Zhaoan Wang, "An Active Filtering Technique for Improving Passive Filter Low-Frequency Performance," *IEEE. Trans. Electromagnetic Compatibility*. vol. 48, pp. 172-177, February 2006.

[2] Y. C. Son, S. K. Sul, "A Novel Active Common-mode EMI Filter for PWM Inverter," in *Proc. APEC 2002*, vol. 1, pp. 545-549, March 2002.

[3] Y. C. Son, S. K. Sul, "Generalization of active filters for EMI reduction and harmonic compensation," *IEEE Trans. Industrial Applications.*, vol. 42, pp. 545-551, April 2006.

[4] N. K. Poon, J. C. P. Lui, C. K. Tse, "Techniques for Input Ripple Current Cancellation: Classification and Implementation," *IEEE Trans. Power Electron.*, vol. 15, no. 6, pp. 1144-1152, Nov 2000.

[5] S. Ogasawara, H. Ayano, H. Akagi, "An Active Circuit for Cancellation of Common-mode Voltage Generated by a PWM Inverter," *IEEE Trans. Power Electron.*, vol. 13, pp. 835-841, Sept. 1998.

[6] I. Takahashi, A. Ogata, H. Kanazawa, A. Hiruma, "Active EMI Filter for Switching Noise of High Frequency Inverters," in *Conf. Rec. IEEE PCC-Nagaoka'97*, pp. 331-334, 1997.

[7] Mark J. Nave, Power Line Filter Design for Switched-Mode Power Supplies. Van Nostrand, 1991, pp. 105-151.

The Comparison of the Input Impedance Measurement of SMPS between the Resonance Method and the Insertion Loss Method

K. Kiatgamjorn[1], V. Tarateeraseth[2], W. Khan-ngern[1]

[1]King Mongkut's Institute of Technology Ladkrabang (KMITL),
Research Center for Communications and Information Technology (ReCCIT),
Faculty of Engineering, Bangkok, Thailand, E-mail: kkveerac@kmitl.ac.th
[2]Srinakharinwirot University, Faculty of Engineering, Ongkharak, Thailand, E-mail: vuttipon@swu.ac.th

***Abstract*- This paper addresses the comparison of the input impedance measurement between the resonance method and the insertion loss method. The result of the input impedance from the measurement can be used to effectively design the EMI filter or to analyze the stability problem of the system when EMI filter is connected.**

I. INTRODUCTION

The input impedance of the switched mode power supplies (SMPS) is essential in its power line electromagnetic interference (EMI) filter design, and when ignored, the system may be not meet EMI regulation. To meet EMI regulation, the EMI filters are one of the most popular applied by industries to suppress EMI problems. According to, the EMI filter performance depends not only on itself. But the selections of the appropriate EMI filter components are also importance to designs EMI filter. The input impedance characteristic (Z_{in}) of the SMPS is a key parameter to design the EMI filter effectively. However, it should be noted that the transfer function of the system is effected when the EMI filter is inserted into the system. Therefore, the stability issue may be occurred.

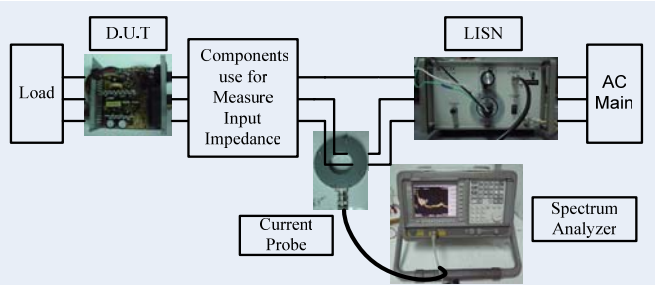

Figure 1. The input impedance measurement setup of SMPS.

There are many paper is presented the method to measure the input impedance of SMPS [1], [2] and [3]. This paper is focused on the measurement of the input impedance of the SMPS and comparison between the resonance method and the insertion loss (IL) method. Two methods to measure the input impedance use the same equipments: the spectrum analyzer and the current probe.The input impedance of SMPS measurement setup is shown in Fig. 1.

Schneider [1] proposed the resonance method to measure the input impedance. This method assumes the SMPS is a Norton circuit with reactive source impedance and employs the quality factor (Q) to solve the input impedance.

Shih [2] proposed the insertion loss method to address the input impedance of SMPS and verified the experimental results by mathmatical expression.

II. THE INPUT IMPEDANCE OF SMPS

The three wires system (line, neutral and ground) can be separated as common mode and differential mode. The impedance between the shorted line-neutral terminals and the ground terminal, is defined as a common mode input impedance. While the differential mode input impedance is the impedance between line terminal and neutral terminal. The common mode input impedance and the differential mode input impedance diagrams of SMPS are showed in Fig. 2 (a) and (b), respectively.

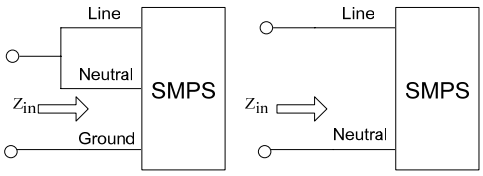

Figure 2. Definition of input impedance
(a) common mode (b) differential mode.

A. *The Input Impedance Measurement Using the Insertion Loss Method*

The input impedance characteristic (Z_{in}) of SMPS can be fined out by insertion loss method. The insertion loss is defined as a ratio of voltages across R_{LISN} before and after the filter element is inserted. The definition of insertion loss is expressed in equation (1).

$$IL = 20 \log \left(\frac{V_{LISN}\ without\ filter}{V_{LISN}\ with\ filter}\right) \quad (1)$$

Figs. 3 - 4 show the conducted emission model and deriving $|Z_{in}|$ by the insertion loss method, respectively.

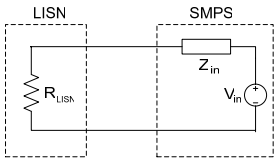

Figure 3. The conducted emission model.

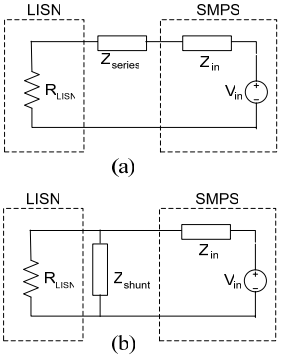

Figure 4. $|Z_{in}|$ by the insertion loss method.

(a) Z_{series} is inserted for common mode input impedance measurement.

(b) Z_{shunt} is inserted for differential mode input impedance measurement.

By the insertion loss method can be separated for two cases. In the first case, the Z_{series} is added with the condition that $|Z_{in}| \gg R_{LISN}$ and $|Z_{series}| \gg |Z_{in}|$. This assumption only uses for measuring common mode input impedance.

$$IL = \frac{\frac{R_{LISN}}{R_{LISN}+Z_{in}} \times V_{in}}{\frac{R_{load}}{R_{LISN}+Z_{in}+Z_{series}} \times V_{in}}$$

$$= 1 + \frac{Z_{series}}{R_{LISN}+Z_{in}}$$

$$\approx 1 + \frac{Z_{series}}{Z_{in}}$$

Since $|IL|$ is normally much greater than 1, then

$$|Z_{in}| \approx \frac{|Z_{series}|}{|IL|} \quad (2)$$

In the case 2, $|Z_{in}| \ll R_{LISN}$ assuming by added a shunt component with $|Z_{shunt}| \ll |Z_{in}|$, the insertion loss can be simplified as follows:

$$IL = \frac{\frac{R_{LISN}}{R_{LISN}+Z_{in}} \times V_{in}}{\frac{R_{LISN} // Z_{shunt}}{R_{LISN} // Z_{shunt}+Z_{in}} \times V_{in}}$$

$$= 1 + \frac{R_{LISN} // Z_{in}}{Z_{shunt}}$$

$$\approx 1 + \frac{Z_{in}}{Z_{shunt}}$$

Similar to the first case $|Z_{in}|$ can be approximated by

$$|Z_{in}| \approx |Z_{shunt}| \times |IL| \quad (3)$$

B. The Input Impedance Measurement Using the Resonance Method

Common mode emission is caused by parasitic capacitance to chassis. The charging and discharging of insulator capacitance are the culprit for common mode electromagnetic interference (EMI). Differential mode emission is generated by diode reverse-recovery phenomena. The resonance of conducted EMI can be determined the input impedance of SMPS by assuming that the SMPS is a Norton circuit with reactive impedance as shown in Fig. 5. First, the Norton current source can be obtained by shorts circuit at the load side. Second, the resistive and capacitive impedance of SMPS can be achieved by resonating the load side with added inductor, and the Q of source may be found at the single frequency. The Q of the circuit is defined as

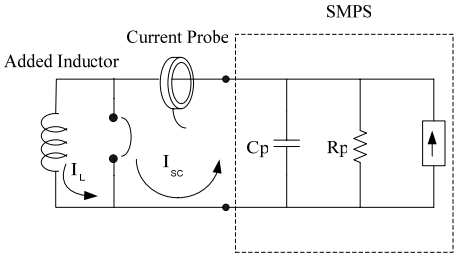

Figure 5. The schematic of resonance method.

$$Q = \frac{I_1}{I_{sc}} \quad (4)$$

Where I_1 is the current when adding the inductor at the load side.

I_{sc} is the short circuit current.

The input resistance of SMPS as shown in equation (5)

$$R = Q\omega L \quad (5)$$

Then, the input capacitance as shown in equation (6)

$$C = \frac{Q}{\omega R} \qquad (6).$$

III. *Test Setup and Experimental Results*

The device under test (DUT) 250 W power supply, input: 200–240 VAC, 3.5 A, output 15 VDC, 3.4 A.

Fig. 6 (a) shows the test setup for common mode input impedance measurement of SMPS by the insertion loss method while Fig. 6 (b) shows the test setup for differential mode input impedance of SMPS by the insertion loss method, respectively [1].

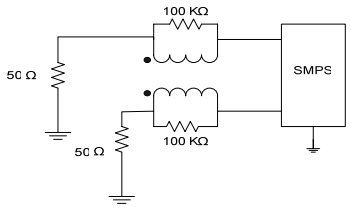

(a)

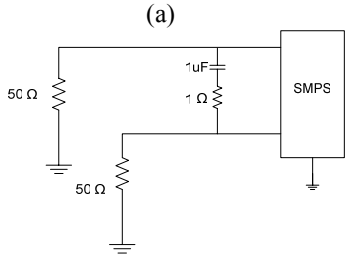

(b)

Figure 6. The test setup of the insertion loss method.
(a) The common mode input impedance measurement.
(b) The differential mode input impedance measurement.

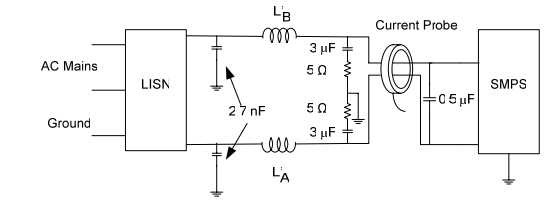

(a)

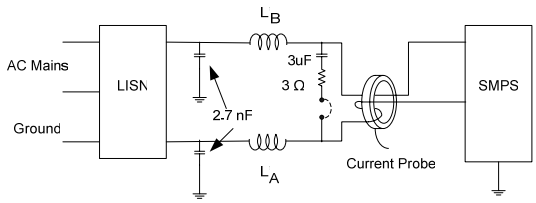

(b)

Figure 7. The setup of the resonance method.
(a) Common mode input impedance measurement.
(b) Differential mode input impedance measurement.

To measure the common mode input impedance of SMPS by the insertion loss method two the common mode choke "Z_{series}" is added two 50 Ω resistors are shown as a equivalent resistor (R_{LISN}) of Line Impedance Stabilization Network (LISN) are paralleled (25 Ω). The common mode input impedance of SMPS are derived by equation (2).

Similarly, the case of the differential mode input impedance of SMPS adds the parallel "Z_{shunt}" to SMPS. The Z_{shunt} is the series combination of a 1 Ω resistor and 1 μF capacitor.

Fig. 7. shows the setup of the resonance method. Fig. 7 (a) shows the common mode setup and Fig. 7 (b) shows the differential mode setup.

The experimental results of C_p and R_p for common mode and differential mode are shown in Figs. 8-9. In Fig. 8 is the derivation of resonance method for common mode input impedance of SMPS (C_p and R_p), by equations (4)-(6). The average of R_{pCM} is 46 kΩ, C_{pCM} is 0.71 nF.

Fig 9 is the derivation of resonance method for differential mode input impedance of SMPS (diode "on") and the average of R_{pDM} and C_{pDM} are 320 kΩ and 0.1 nF, respectively.

The R_p and C_p of the differential mode input impedance is the high source impedance, that is the characteristics of diode reverse-recovery-generated EMI and the low source impedance component is more correctly modeled as a series RL circuit. Its values ranged from 0.5 to 1 μH and 0.5 Ω [4]. Fig. 11 shows the correct differential mode input impedance model.

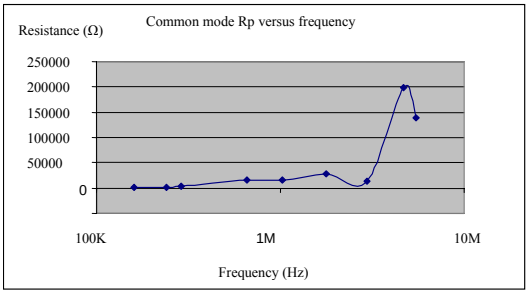

(a)

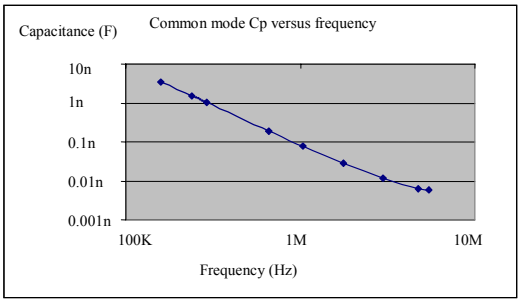

(b)

Figure 8. Common mode input impedance of SMPS by resonance method.
(a) The common mode parallel resistor (R_{pCM}) of SMPS.
(b) The common mode parallel capacitor (C_{pCM}) of SMPS.

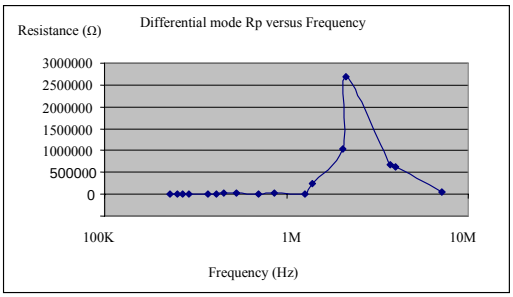

(a)

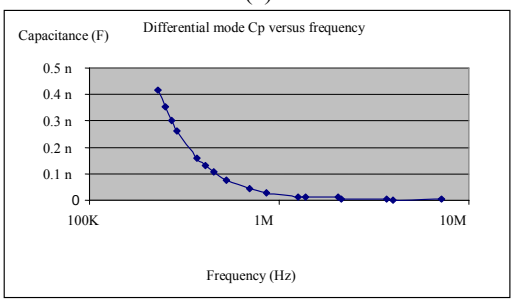

(b)

Figure 9. Differential mode input impedance of SMPS by resonance method.

(a) The differential mode parallel resistor (R_{pDM}) of SMPS

(b) The differential mode parallel capacitor (C_{pDM}) of SMPS.

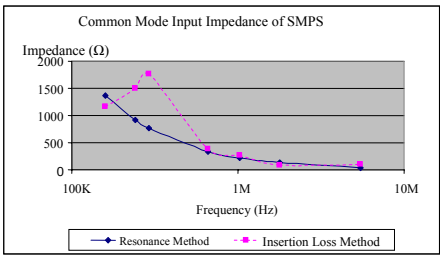

(a)

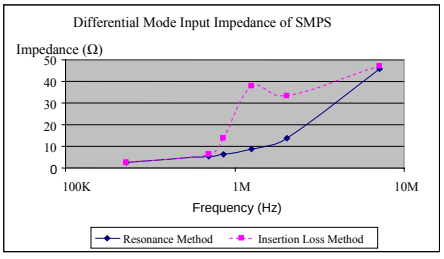

(b)

Figure 10. The comparison of the input impedance of SMPS.
(a) The common mode comparison.
(b) The differential mode comparison.

The input impedance using the resonance method (R_{pCM}, C_{pCM}, R_{pDM} and C_{pDM}) is plotted as a bold line shown in Fig. 10. For the insertion loss method, the attenuation for each frequency (150 kHz-30 MHz) is measured, then calculating the Z_{in} of the SMPS as a dash line shown in Fig. 10 (a). The differential mode input impedance comparison between the resonance method and the insertion loss method is shown in Fig. 10 (b). The differential mode input impedance of SMPS has the low value both the resonance method and the insertion loss method. The input impedance values are in the same results about 300 kHz-900 kHz and different after 1 MHz. The common mode input impedance of SMPS has the low value both the resonance method and the insertion loss method. The input impedance values are different before 900 kHz and in the same results about 900 kHz–10 MHz.

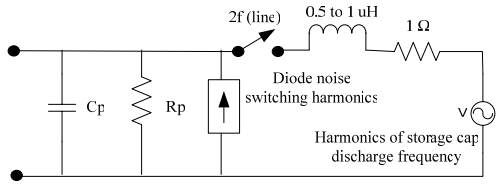

Figure 8. The correct differential mode input impedance model

IV. Conclusion

The insertion loss method and the resonance method are verified to be the simple and effective choice to measure the characteristic of the input impedance of SMPS. The phase of the input impedance can be found by Hilbert transform [5]. For the insertion loss method may be found the input impedance as the voltage source series with input impedance while the resonance method may be found the input impedance as the current source paralleled with the input impedance.

The experimental results are in the same trend in some frequency range of input impedance values, both common mode and differential mode. The insertion loss method, the input impedance values are calculated by attenuation of the EMI of SMPS, which can use these data to calculate the input impedance of SMPS at all frequency range (150 kHz – 30 MHz).

In the other hand, for the resonance method, the input impedance (R_p and C_p) is calculated and averaged the values from 150 kHz-30 MHz. The high source impedance (diode "off") can calculate by equations (4) - (6) However, the low source impedance (diode "on") as the series RL circuit must be selected from 0.5 to 1 µH and roughly 0.5 Ω that makes the error of the differential mode input impedance of SMPS.

References

[1] Dan Y. Chen, "Measurement of Noise Source Impedance of Off-Line Converters," *IEEE Trans.Power Electron.*,vol. 15, Sep 2000, pp 820-825.

[2] L.M. Schneider, "Noise source equivalent circuit model for off-line converters and its use in input filter design," in Proc.IEEE EMC'83 Symposium, 1983, pp. 167-175.

[3] K.Y. See, J Deng, "Measurement of noise source impedance of SMPS using a two probes approach," *IEEE Trans.Power Electron.*,vol. 19, Issue 3, May 2004, pp 862-868.

[4] M. Nave, *Power Line Filter Design for Switched Mode Power Supplies.* New York: Van Nostrand.1991, pp. 102-110.

[5] F.M. Tesche, "On the use of the Hilbert transform for processing measure CW data," *IEEE Trans. Electromag. Compat.*, vol.34, Aug 1992, pp 259-266.

Trade-off between EMI Separator and RF Current Probe for Conducted EMI Testing

D. Sakulhirirak[1], V. Tarateeraseth[2], W. Khan-ngern[1], and N. Yoothanom[3]

[1]Research Center for Communications and Information Technology (ReCCIT),
Faculty of Engineering, King Mongkut's Institute of Technology Ladkrabang (KMITL), Bangkok, Thailand.
[2]Srinakharinwirot University, Faculty of Engineering, Ongkharak, Thailand.
[3]Sripatum University, Faculty of Engineering, Bangkok, Thailand.
E-mail: s8060210@kmitl.ac.th[1], vuttipon@swu.ac.th[2], kkveerac@kmitl.ac.th[1], nyt@spu.ac.th[3]

Abstract-This paper presents the trade-off between EMI separator and the RF current probe for conducted EMI measurement. EMI toolkit is used as a noise source for investigating effects from differential-mode (DM) and common-mode (CM). Paul-Hardin noise separation network or EMI separator is used as a benchmark to compare with the RF current probe. The conducted electromagnetic interference between RF current probe and EMI separator is compared by the experiment. Finally, the trade-off between two measurement methods is verified by both theoretical and experimental results.

I. INTRODUCTION

Electromagnetic Compatibility (EMC) is an electronic system which is able to function compatibly with other electronic systems and not produce or be susceptible to interference with its environment [1]. The interference can be divided widely into two groups: conducted and radiated interferences. In this paper, the conducted emission is emphasized and mentioned to separate noise components (Differential-Mode: DM and Common-Mode: CM) for electromagnetic environment. It is very useful to know noise components in every interested circuit [2]. Generally, there are two methods, often used for separating noise components. The first method is a classical measurement using radio frequency current probe (RF current probe). The second method is measurement CM and DM by using separating devices such as CM/DM discrimination network [3], Paul-Hardin noise separation network [4] and noise separator [5] etc. However, all separation networks in this paper are called as the EMI separator.

The Equipment Under Test (EUT) in this paper is EMI toolkit, used for conducted EMI studying in terms of theory and practice. Fig. 1 shows outside of EMI toolkit. Boost converter is a main part which generates EMI. In addition, a lot of study functions are combined in the toolkit and it can be selected functional operation such as self-resonant frequency (SRF) of the passive components, reverse recovery time of diodes, switching frequencies, and gate drive control [6].

To understand noise behaviors in a boost converter, Fig. 1 can be rewritten to Fig. 2 which includes Line Impedance Stabilization Network (LISN) schematic and two 50 Ω terminators. These terminators are connected to the RF output ports of LISN when measuring by RF current probe but when using Paul-Hardin network these terminators are input impedance of the network. V_P and V_N stand for phase and neutral voltage signal, respectively. C_S is a parasitic capacitance caused by MOSFET (Q) between drain and frame ground via its heat-sink.

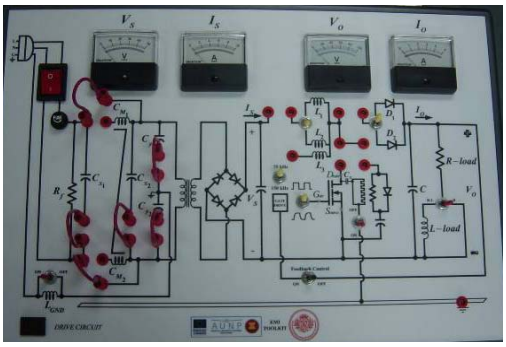

Figure 1. Top view of EMI toolkit configuration.

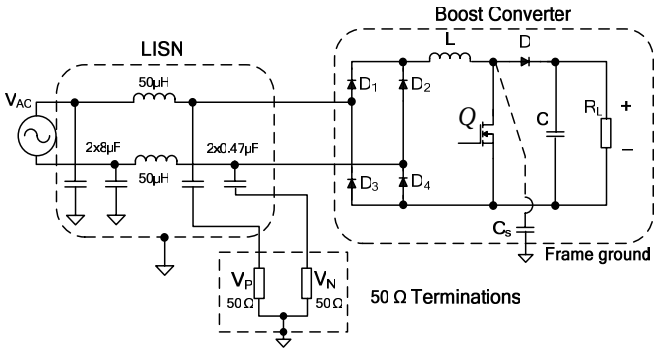

Figure 2. Schematic of LISN and boost converter under consideration.

II. CONDUCTED EMI MEASUREMENTS: RF CURRENT PROBE AND EMI SEPARATOR CONCEPTS

Conducted EMI emission is measured using a LISN as a 50 Ω impedance. The DM noise current (I_{DM}) flows out from line and returns via neutral while the CM noise current (I_{CM}) flows out from line and neutral and returns via ground wire as shown in Fig. 3 Eqns. (1)-(3) are line, neutral and ground current and Eqns. (4)-(5) are line and neutral voltages, respectively [7].

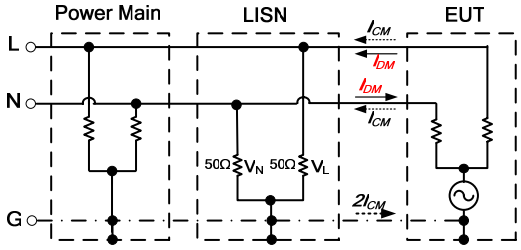

Figure 3. DM and CM currents from LISN.

$$I_{Line} = I_{CM} + I_{DM} \quad (1)$$

$$I_{Neutral} = I_{CM} - I_{DM} \quad (2)$$

$$I_{Ground} = 2 \cdot I_{CM} \quad (3)$$

$$V_{Line} = 50 \cdot (I_{CM} + I_{DM}) \quad (4)$$

$$V_{Neutral} = 50 \cdot (I_{CM} - I_{DM}) \quad (5)$$

A. *RF Current Probe*

RF current probe is a clamp-on RF current transformer designed for use with EMI Test Receivers/Spectrum Analyzers, or with any similar instrument having a 50 Ω input impedance, to determine the intensity of RF current present in an electrical conductor or group of conductors [7]. Fig. 4 shows the RF current probe within bandwidth 10 kHz - 250 MHz. The maximum primary current from DC - 400 Hz is up to 100 A and the transfer impedance (Z_T) is 5 Ω [8]. The performance of the RF current probe may be expressed in terms of sensor transfer impedance: Eqn. (6). Where V_{out} is the voltage developed across a 50 Ω termination on the output and I_{cond} is the current flowing through the conductor being measured. The probe transfer impedance is often expressed in terms of dB which can be calculated the measured current from Eqn. (7) [9].

(a) Top view (b) Side view

Figure 4. Toroidal RF current probe.

$$Z_T = \frac{V_{out}}{I_{cond}} \quad (6)$$

$$I_{cond}(dB\mu A) = V_{out}(dB\mu V) - Z(dB) \quad (7)$$

B. *EMI separator*

Many papers have been discussed and proposed EMI separators [3-5], [10-11]. They can be separated roughly in two groups based on magnitude of output signal, single and double output noise. Moreover, in group of double output [4] has no guarantee that it can be used representative of RF current probe.

Fig. 5 shows the Paul-Hardin noise separation network schematic. There are two important elements; two wideband transformers (1:1 ratio) and single-pole-double-throw (SPDT) switch, which operate simultaneously [7].

The line-ground voltage (V_{LG}) and neutral-ground voltage (V_{NG}) are connected to EMI separator, using Eqns. (8) and (9) for voltage across switch at A and B position respectively.

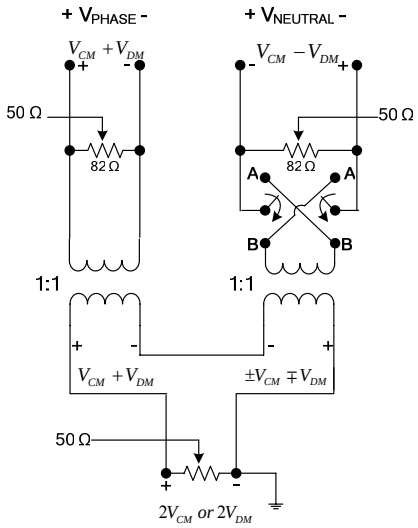

Figure 5. Paul-Hardin noise separation network schematic.

$$|V_{LG} - V_{NG}| = |V_{CM} + V_{DM}| - |V_{CM} - V_{DM}| = |2V_{DM}| \quad (8)$$

$$|V_{LG} + V_{NG}| = |V_{CM} + V_{DM}| + |V_{CM} - V_{DM}| = |2V_{CM}| \quad (9)$$

$$\text{or } |2V_{DM}| = |V_{LG} - V_{NG}| = 50 \cdot |2I_{DM}| \quad (10)$$

$$|2V_{CM}| = |V_{LG} + V_{NG}| = 50 \cdot |2I_{CM}| \quad (11)$$

The output is $|V_{LG} - V_{NG}|$ for $2V_{DM}$ defined by Eqn. (8) and $|V_{LG} + V_{NG}|$ for $2V_{CM}$ defined by Eqn. (9) and lastly, leakage between the DM and CM at the output should be small because noise measurement between the DM and CM must be guaranteed small interference [5]. The impedance of two inputs are 50 Ω within 20 percent tolerance according to CISPR 16-1 standard because both of them have to connected with LISNs. The CM output impedance of network is very closed to 50 Ω (in range 45 Ω – 50 Ω at 150 kHz – 30MHz) but for DM output impedance is nearly 20% tolerance from 50 Ω (35 Ω – 50 Ω) as shown in Fig. 7. The performance of EMI separator can be described in term of rejection attenuation value of both modes; some papers call "CM/DM rejection ratio" [2], [10] as shown in Fig. 8.

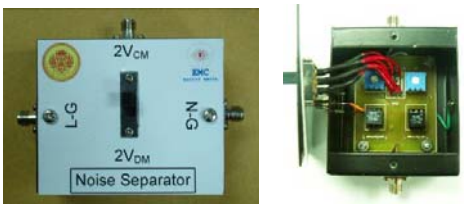

(a) Outside (b) Inside

Figure 6. Paul-Hardin noise separation network.

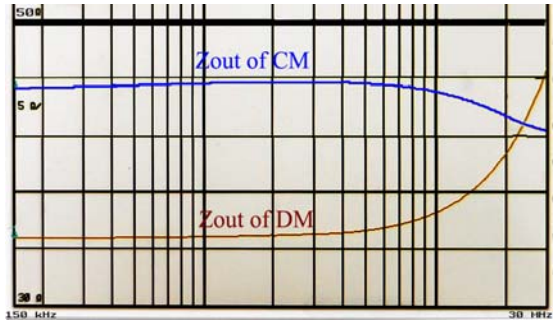

Figure 7. CM and DM output impedance of EMI separator.

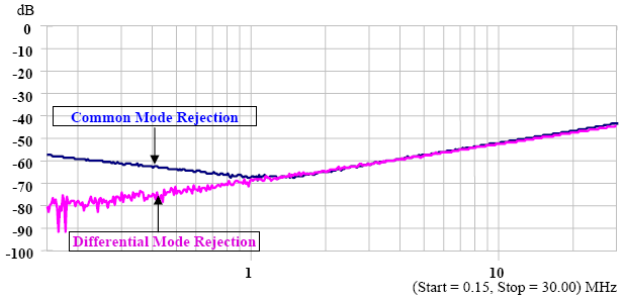

Figure 8. CM and DM rejection.

III. Measurement Methods

A. RF Current Probe Measurement

Figs. 9 (a)-(b) show basically method to measure DM and CM noise, respectively. However, the measured results of DM and CM are double ($2I_{DM}$ and $2I_{CM}$) caused by sum of current vectors in same direction. The current probe is usually clamped between the EUT and the LISN as near as possible. In some EMC standard current probes, such as the DEF STAN 59-41 DCE01, have to away 5 cm from the LISN connection on the power lead [7].

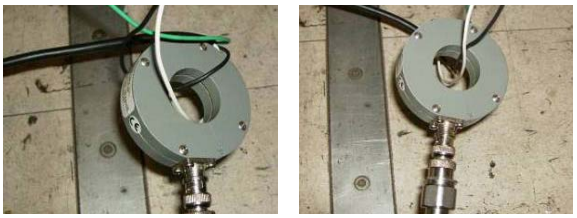

(a) Measured 2DM noise (b) Measured 2CM noise

Figure 9. RF Current probe measurement method.

B. EMI separator Measurement

The second method to measure DM and CM noise components are displayed in Fig. 10. LISN-1 couples voltage from line-ground while LISN-2 couples voltage from neutral-ground. Output of separator is connected with 50 Ω terminal of spectrum analyzer. In addition, coaxial cables (50 Ω) with BNC connector are connected with two RF output terminals of LISNs for coupling line-ground and neutral-ground signal simultaneously.

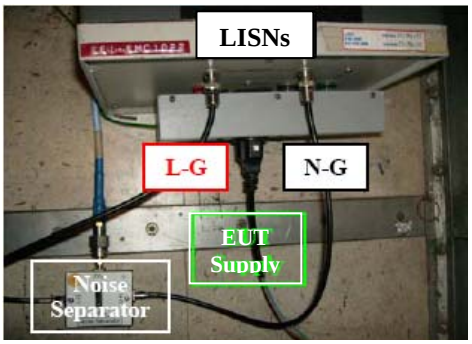

Figure 10. EMI separator measurement method.

IV. Experimental Results

In this section, noise floor between the RF current probe and EMI separator are measured first for using as reference levels. There are three noise floors: RF current probe, CM EMI separation and DM EMI separation which are the same level of noise floors about 25 dB.

Measured results of $2V_{CM}$ and $2V_{DM}$ are divided into three sections by comparison results between RF current probe and EMI separator. Firstly, noise source is measured without filter components this is a full noise condition as shown in Figs. 11-12. Secondly, adding two X-capacitors between line and neutral, 0.47 µF, as shown in Figs. 13-14, which show DM and CM comparing between RF current probe and EMI separator with and without filter components. A dash line prefers to EMI measured result when filter components are added in the circuit. Finally, two Y-capacitors are added across line-ground and neutral-ground, 0.2 µF, as shown in Figs. 15-16.

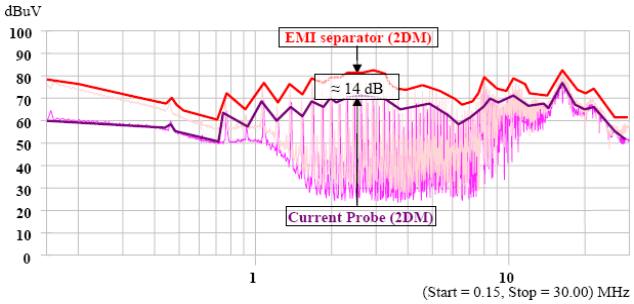

Figure 11. The comparison of $2V_{DM}$ between RF current probe and EMI separator.

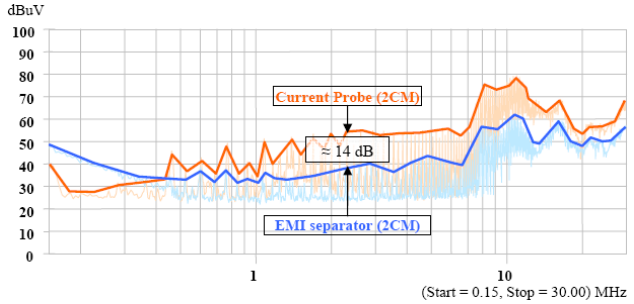

Figure 12. The comparison of $2V_{CM}$ between RF current probe and EMI separator.

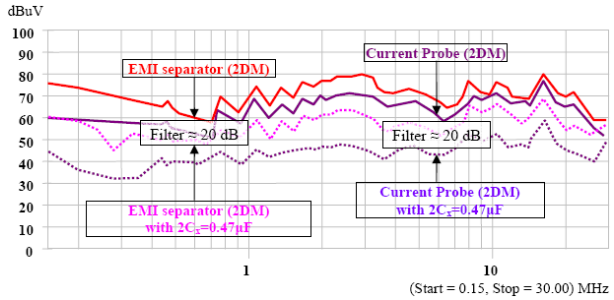

Figure 13. The comparison of $2V_{DM}$ when adding C_x filter between RF current probe and EMI separator.

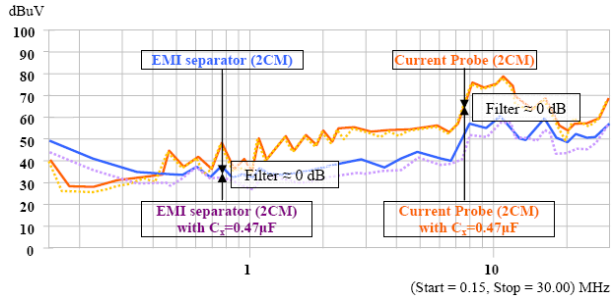

Figure 14. The comparison of $2V_{CM}$ when adding C_x filter between RF current probe and EMI separator.

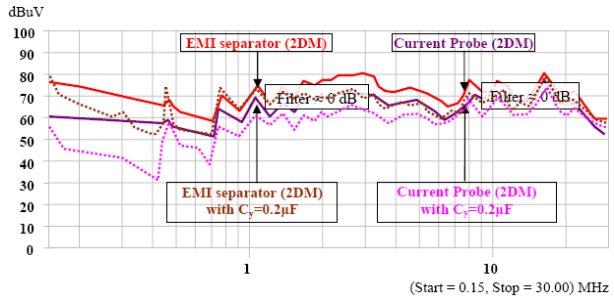

Figure 15 The comparison of $2V_{DM}$ when adding C_y filter results between RF current probe and EMI separator.

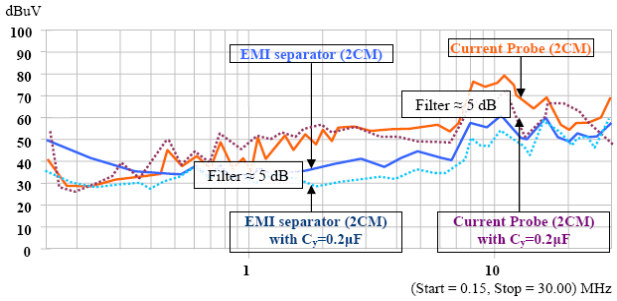

Figure 16 The comparison of $2V_{CM}$ when adding C_y filter results between RF current probe and EMI separator.

V. Analysis

From Eqn. (6), the transfer impedance of the current probe (Z_T) is 5 Ω and the measured current I_{cond} is represented by $2I_{DM}$ or $2I_{CM}$ as follows;

$$V_{out(CM)} = (5)\cdot(2I_{CM}) \text{ and } V_{out(DM)} = (5)\cdot(2I_{DM}) \qquad (12)$$

Where $V_{out(CM)}$ and $V_{out(DM)}$ are common mode and differential mode output voltage measured by RF current probe respectively.

Then, multiplication Eqn. (12) by two to compare with Eqns. (10)-(11) and inverting them to dB values using logarithm function.

The compared results show the different value between using RF current probe and EMI separator about 13.98 dB.

The experimental results as shown in Figs. 11-12, can be realized by the theoretical expression as mention. Fig. 13 shows the performance of X capacitor filters. The DM EMI is decreased about 20 dB while the CM EMI has a little changed as shown in Fig. 14 and the difference between RF current probe and EMI separator still about 14 dB. Figs. 15-16 show EMI results which are mitigated by Y capacitors. The performance of C_y can suppress noise about 5 dB for common mode and nearly 0 dB for differential mode

VI. Conclusions

The separation of conducted EMI measurement, measured by RF current probe and EMI separator, is compared. The attenuation value between RF current probe and EMI separator is about 14 dB, realized by the theoretical and experimental results. The performance of EMI separator has been realized using the convenient EUT as EMI toolkit. However, it should be noted that the EMI separator, which is low cost, can be used at low-medium power level because the saturation of wideband transformer while the RF current probe can be covered the high level.

References

[1] Clayton R. Paul, Introduction to Electromagnetic Compatibility. Wiley-Interscience, A John Wiley & Sons, Inc., publication, 1992.

[2] Ting Guo, Dan Y. Chen and Fred C. Lee "Separation of the Common-Mode-and Differential-Mode-Conducted EMI Noise", IEEE Trans. Power Electron, vol. 11, no. 3, pp. 480-488, 1996.

[3] See Kye Yak "Network for EMI", Electronic Letter, vol. 35, no. 17, pp. 1446-1447, 19th Aug 1999.

[4] Clayton R. Paul and Keith B. Hardin "Diagnosis and Reduction of Conducted Noise Emissions", IEEE Trans. on Electromagnetic Compatibility, vol. 30, no. 4, pp. 553-560, Nov 1988.

[5] Shou Wang, Fred. C Lee and Willem Gerhardus Odendaal. "Characterization Evaluation, and Design of Noise Separator for Conducted EMI Noise Diagnosis", IEEE Trans. on Power Electronics, vol. 20, no. 4, pp. 974–982, July 2005.

[6] Werachet Khan-ngern, Vuttipon Tarateeraseth. "Self-learning EMC Toolkit for Electronic and Electrical Engineers", ICEMC Conf. on EMC on Education, July 2005, session 3C-1.

[7] V. Prasad Kodali, Engineering Electromagnetic Compatibility. The Institute of Electrical and Electronics Engineers, Inc., New York, 2001.

[8] Fischer Custom Communications, Inc. (2004). Instrumentation: Available:http://www.fischercc.com/instframe.html [Online].

[9] David Morgan, A handbook for EMC testing and measurement. Wiley-Interscience, Short Run Press Ltd., Exeter, 1994.

[10] Marco Chiadó Caponet and Francesco Profumo "Devices for the Separation of the Common and Differential Mode Noise: Design and Realization", Applied Power Electronics Conference and Exposition (APEC) Seventeenth Annual IEEE, vol. 1, pp. 100-105, March 2002.

[11] Mark J. Nave "A Novel Differential Mode Rejection Network for Conducted Emissions Diagnostics", IEEE National Symposium on Electromagnetic Compatibility, pp. 223–227, May 1989.

II. EXPERIMENTAL

Ceramic sample of Gd 1:2:3 were prepared by conventional powder processing from high-purity oxides and carbonates, calcining at 930°C, the powder were pressed into pellets with a pressure of 1 ton/cm^2 .The pellets were sintered at 900°C, 920°C, 925°C, 930°C, 935°C, 940°C, 945°C, 950°C, 955°C, 960°C, 965°C and 970°C for 10 hours.

We had experimentally investigated the following effect of external magnetic field on current-voltage characteristics and magnitude of negative resistances. The current-voltage characteristics were measured by the four probe technique with indium electrodes at 77 K. The magnetic field is applied to samples perpendicular with the direction of current flow.

III. EXPERIMENTAL RESULTS

A. The Optimum condition of critical current for the occurrence of negative resistance

From Fig. 2 shown the relationship between sintering temperature and critical current (I_C). It's found that, the highest I_C is 2.2 A at sintering temperature 930°C. At the highest I_C sample must be applied external magnetic field (B_{EXT}) higher than the low I_C sample, to destroy the superconducting state. However the negative resistance could not be observed at this highest I_C. But negative resistance obviously occurred as I_C is reduced from maximum point.

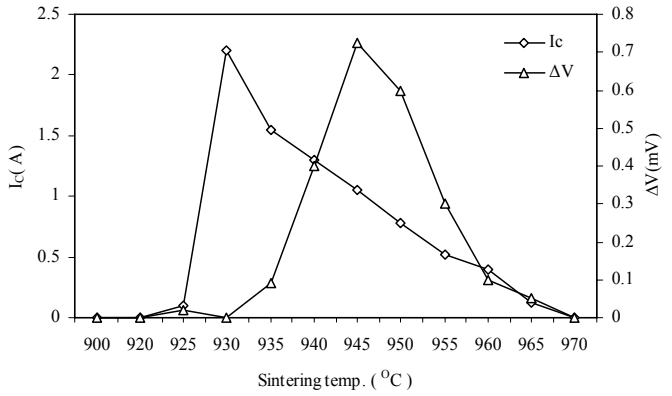

Figure 2. The plot of I_C, ΔV vs sintering temperature

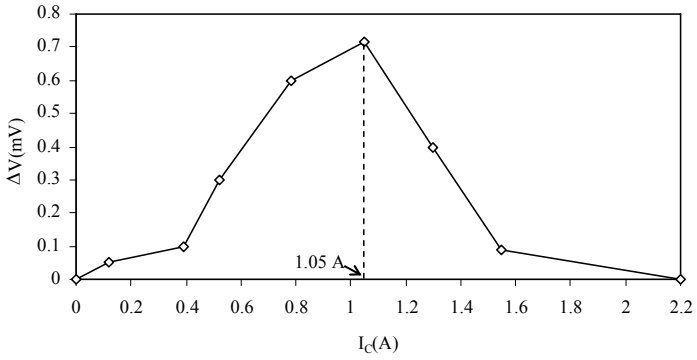

Figure 3. Dependence of ΔV on I_C

The maximum magnitude of difference voltage(ΔV) is obtained at I_C = 1.05 A. ΔV will be to zero while I_C is decreased to zero as shown in Fig. 2 and Fig. 3. Thus, it can be seen that the negative resistance phenomena is apparently found in the range of low I_C.

B. The effect of magnetic field on magnitude of negative resistance

The influences of B_{EXT} on the magnitude of differential voltage (ΔV) are studied. Sample used here show the various values of critical currents which are 1.55A, 1.3A, 1.05A, 0.78A, 0.52A, 0.39A and 0.12A respectively. Current-voltage relations and the dependences of ΔV on B_{EXT} are shown in Fig.4. It's found that the magnitude of ΔV depends on B_{EXT} [4]. For example, for the sample with I_C = 1.05 A, when we applied B_{EXT} from 0 to 0.2 mT, ΔV was increased. However if applied B_{EXT} exceeded 0.2 mT, then ΔV was decreased continuously. The maximum ΔV (ΔV_{MAX}) was obtained at 1.4 mV.

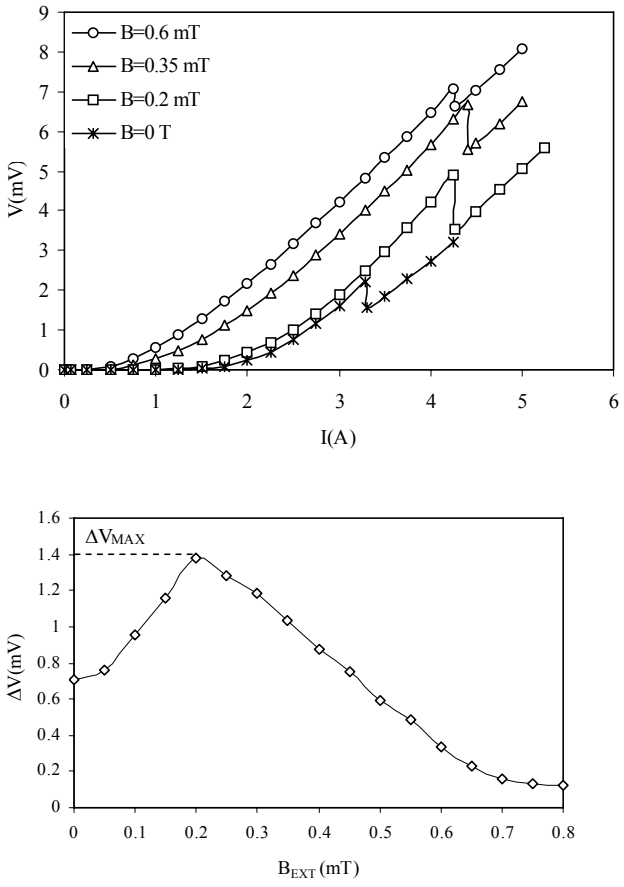

Figure 4. The effect of B_{EXT} on samples with various I_C

Fig. 5 shows ΔV versus B_{EXT} relations obtained from sample with various critical current. It is found from Fig. 6 that the sample with I_C = 1.05 A shows the highest value of ΔV_{MAX} comparing with other I_C samples.

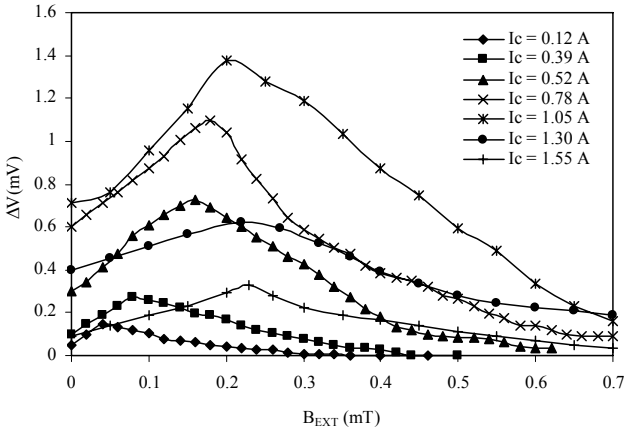

Figure 5. The plot of ΔV vs B_{EXT} at various I_C

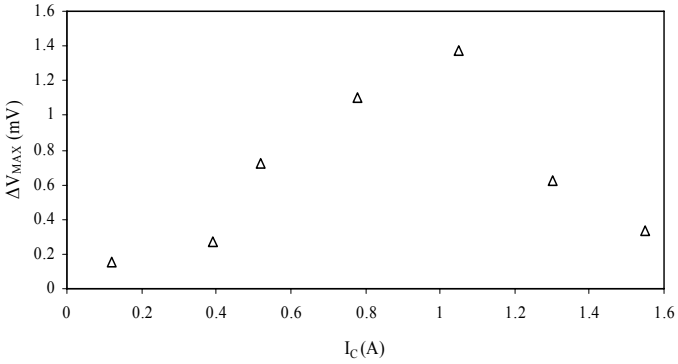

Figure 6. The relationship between ΔV_{MAX} and I_C

IV. DISCUSSIONS

The experiment al results can be explained by the macrostructure model of Gd-Ba-Cu-O. Since the high-I_C sample exhibits superconducting state more completely than the low-I_C sample, then the connection of weak point region must be stronger than the low-I_C sample as shown in Fig. 7.

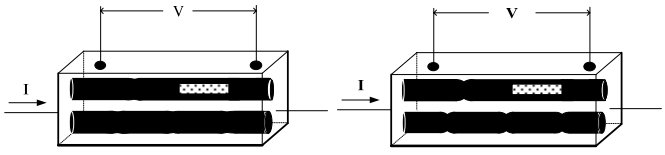

a) Sample with I_C = 2.2 A b) Sample with I_C = 1.55 A

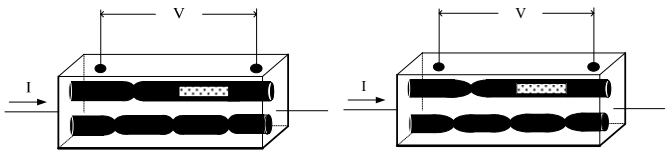

c) Sample with I_C = 1.05 A d) Sample with I_C = 0.52 A

Figure 7. Illustration of a macrostructure model at various I_C

From Fig. 8, when the applied current (I) is equal to (or less than) its critical current(I_C) value, both sides of the sample are connected by the superconduction parts. Then, the resistance of sample does not appear. But when $I>I_C$, superconduction part will be cut-off, because weak point region is destroyed. The resistance appears in this condition. Because the volume of upper destroyed parts are less than lower destroyed parts, all current will flow over the upper part only. Then, the small voltage drop will appear across the upper part. When the current reaches I_N, the upper superconduction part, where has magnetic substance, is destroyed. Thus, overall cut-off region of the upper part is more than lower part. The resistance of upper part increases quickly. Then all current flows to lower part, which has low resistance. Therefore, the voltage drop across sample decreases immediately. This phenomenon is called Negative-resistance. The magnitude of differential voltage (ΔV) is about 0.71 mV.

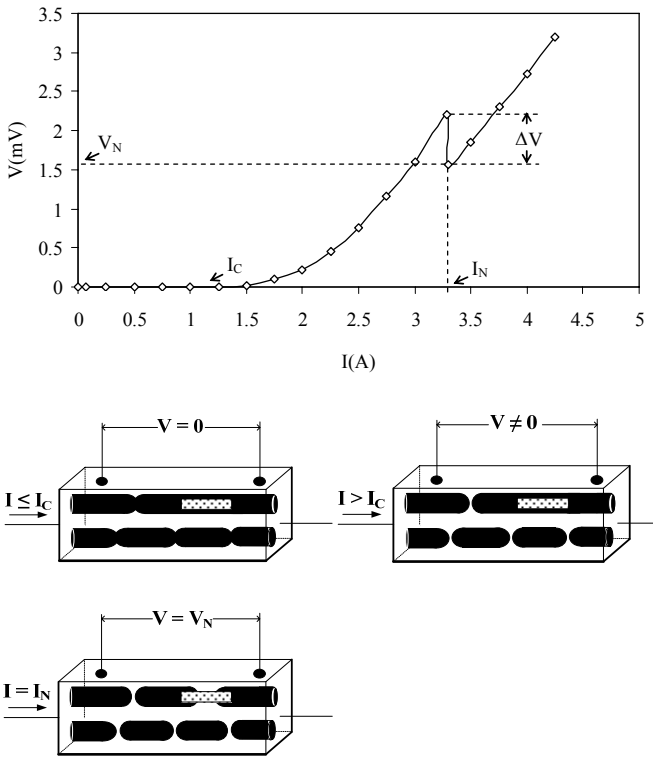

Figure 8. Illustration of current-voltage characteristics of sample with I_C = 1.05 A

We will consider the effect of B_{EXT} on ΔV as follows. In the case of the sample showing I_C=1.55A, ΔV was increased by B_{EXT} in the range of 0 ~ 0.23 mT, as shown in Fig. 5. This phenomenon can be explained by considering the macrostructure model as shown in Fig. 9 a). Since the cut-off region which has magnetic substance, was broadened by B_{EXT}, ΔV increases, that is, current path changes from the upper high resistance path to the lower low resistance path. When the external magnetic flux B_{EXT} exceeds 0.23 mT, ΔV was decreased. Since B_{EXT} also destroys partially the lower superconduction part as shown in Fig. 9 a), the difference of electrical resistance between the upper path and the lower path became small. Then, ΔV decreases. For sample I_C = 1.05 A, when B_{EXT} = 0.2 mT, the highest ΔV is obtained. Consequently, the cut-off region, containing magnetic substance, is broadened until magnetic substance is uncovered completely.

In the case of sample showing I_C = 0.52 A, when B_{EXT} = 0.16 mT, ΔV_{MAX} is obtained. Due to the cut-off region, which has magnetic substance, is broadened until magnetic substance is uncovered completely. Nevertheless, B_{EXT} will also destroy partially the lower part similarly as shown in Fig. 9c). Then, ΔV_{MAX} in this case less than the sample with I_C = 1.05 A as shown in Fig. 6.

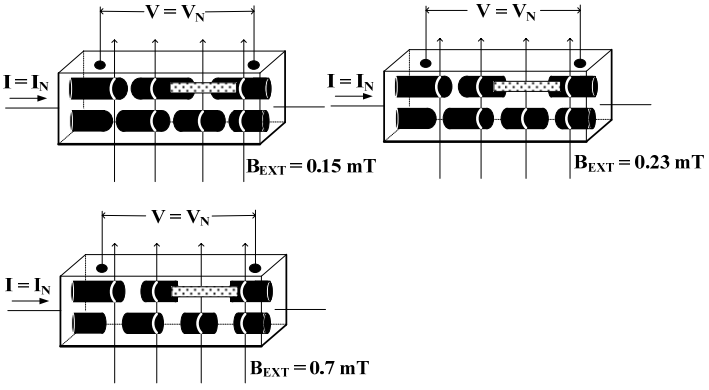

a) Sample with I_C = 1.55 A

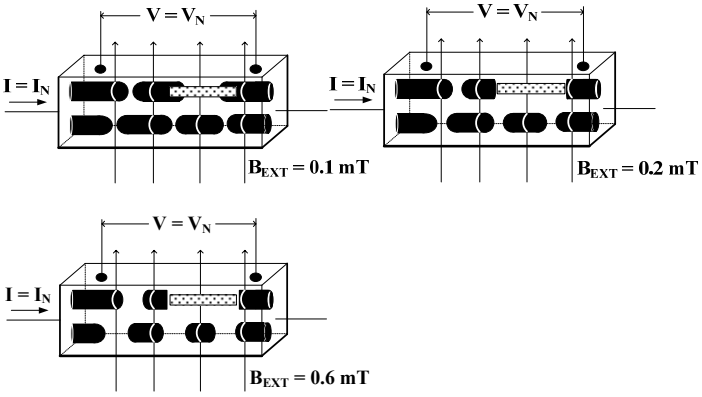

b) Sample with I_C = 1.05 A

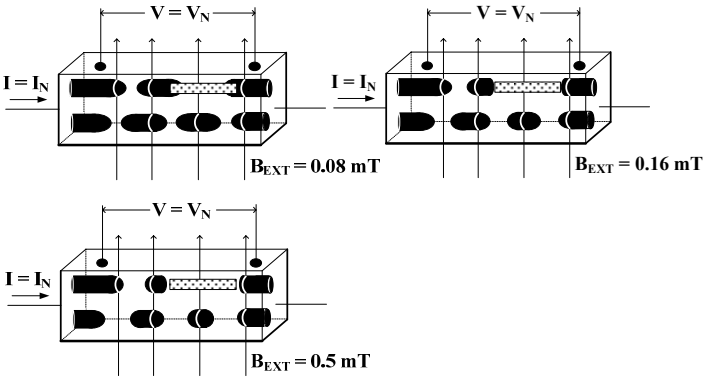

c) Sample with I_C = 0.52 A

Figure 9. Illustration of a macrostructure model at various applied magnetic field

V. CONCLUSIONS

From the investigation of Current and Voltage characteristics in $GdBa_2Cu_3O_{7-x}$ superconducting ceramic material, it's found that the negative resistance phenomenon is apparently found in range of low critical current. Moreover, the magnitude of differential voltage (ΔV) depends on external magnetic field and critical current. The largest differential voltage ΔV_{MAX} is obtained by the employment of suitable B_{EXT}. Moreover, the occurrence of ΔV_{MAX} in the high-I_C sample must be applied B_{EXT} higher than the low-I_C sample.

Some experimental results can be quite explained by the macrostructure model of $GdBa_2Cu_3O_{7-x}$ superconducting ceramic materials.

ACKNOWLEDGMENT

We are indebted to A. Keawcharoen and, C. Suriyaamaranont for technical assistance

REFERENCES

[1] W. Wongsuttitum, W. Titiroongruang, "Macrostructure Model of Gd-Ba-Cu-O Superconducting Ceramic Materials," *Proc. Of Thailand's 24th Electrical Engineering Conference*, (2001), pp. 992- 997

[2] W. Titiroongruang, Y. Akiba, S. Supadech, T. Kurosu and M. Iida, "Macrostructure Model of Y-Ba-Cu-O System," *Proceeding of Faculty of Engineering, Tokai University*. (1991) 17, pp. 7-13.

[3] Y. Akiba, W. Titiroongruang, T. Kurosu, M. Iida and T. Nakamura, "Electromagnetic Memory Effect in Superconductivity Y-Ba-Cu-O System," *Oyo Butsuri* 58 No. 1 (1989) 151. [in Japanese]

[4] W. Wongsuttitum, R. Piyananjaratsri, W. Titiroongruang and M. Iida, "The Effect of The External Magnetic Field on Negative Resistance Phenomena of $GdBa_2Cu_3O_{7-x}$ Superconducting Ceramic Materials," *KMITL SCIENCE JOURNAL*, Vol. 6, No.1 , pp. 169-175, Jan-Apr 2006.

Implementation of Electrical Capacitance Tomography using Analytical Sensitivity Maps

Denchai Worasawate and Phuwaphat Klongpramong
Kasetsart Advanced RF and ElectromagNetics Laboratory
Department of Electrical Engineering, Kasetsart University, Bangkok 10900, Thailand
fengdcw@ku.ac.th, http://karen.ee.ku.ac.th/

***Abstract*- This paper presents an analytical method to compute a sensitivity map for the electrical capacitance tomography (ECT). These analytical equations are obtained by assuming that the gaps between each electrode around a circular cylindrical sensor are infinitely small. With this assumption, the potential on the boundary of the cylindrical sensor is known. Laplace's equation can be analytically solved and the analytical equations for the sensitivity maps are obtained. The sensitivity maps for the consecutive electrodes are excluded from the image reconstruction equation because its singularities. The reconstructed images using proposed sensitivity maps are presented. It shows acceptable results but it does not have enough resolutions to separate two close objects.**

I. INTRODUCTION

Nondestructive imaging of moisture inside objects particularly in fruits is an important issue. This paper uses the electrical capacitance tomography to monitor moisture in sample objects. The most important part of image reconstruction algorithm is to compute the sensitivity map. The sensitivity map was computed using a finite-element-method (FEM) in [1]. The sensitivity map for a pair of electrodes at a specific location inside the sensor is defined as the change of capacitance between the pair as a result of the change of permittivity in that particular location. It is a time-consuming to compute the sensitivity map for each pair of electrodes at every location. The new definition of the sensitivity map for a pair of electrodes at a specific location proposed by [2] is the dot-product of the electric field produced by applying high potential at one of the pair electrodes and the electric field produced by applying high potential at the other one of the pair electrodes at a particular location. The sensitivity map in [2] was computed using a finite difference-method (FDM). The results in [1]–[2] were done using numerical methods in both the sensitivity map calculation and the capacitance measurement. This paper presents an analytical method to compute the sensitivity maps instead of a numerical method. The ECT system is implemented. The sensor is built using a polyvinyl chloride (PVC) pipe and the capacitances are physically measured. Good reconstructed images of sample objects are obtained.

II. SENSOR STRUCTURE

Fig. 1 shows the top view of the constructed ECT sensor. The sensor consists of 6 electrodes which are fabricated from a flexible thin substrate. The dimensions of each electrode are shown in Fig. 2. Only the middle plate is used as an electrode. The top and bottom plates are a system ground and used to confine electric field in the middle region.

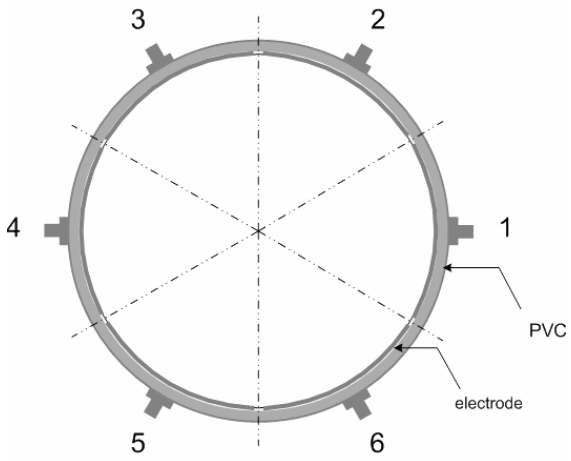

Figure 1. Top view of the circular cylindrical ECT sensor.

III. SENSITIVITY MAP CALCULATION

This paper computes the sensitivity map using the definition in [2]. The expression of the sensitivity map for a pair of electrodes at a specific location inside the sensor is given by

$$S_{ij} = -\int_{P(x,y)} \frac{\mathbf{E}_i}{V_{oi}} \cdot \frac{\mathbf{E}_j}{V_{oj}} dx'dy' \qquad (1)$$

where $\mathbf{E}_i$ is the electric field inside the sensor when the i^{th} electrode is applied with potential V_{oi}. $\mathbf{E}_j$ is the electric field inside the sensor when the j^{th} electrode is applied with potential V_{oj} and $P(x,y)$ is the region where (x,y) is its center. Using the assumption that the gap between each electrode is infinitely small, the potential inside the sensor is given by

$$V_i(r,\phi) = \sum_{m=1}^{\infty} \frac{2V_{oi}}{m\pi b^m} \sin\left(\frac{m\pi}{6}\right) r^m \cos\left(m\left(\phi - \frac{\pi(i-1)}{3}\right)\right) + \frac{V_{oi}}{6} \qquad (2)$$

where V_i is the potential inside the sensor when the i^{th} electrode is applied with potential V_{oi}. The variables r and ϕ

are the cylindrical coordinate of the potential point. They can be transformed to the Cartesian coordinate systems using simple equations. After the expression for the potential is obtained, the expression of the electric field, $\mathbf{E}$, is derived by using $\mathbf{E} = -\nabla V$. The expression is given by

$$E_{ri} = -\sum_{m=1}^{\infty} \frac{2V_{oi}}{\pi b^m} \sin\left(\frac{m\pi}{6}\right) \cos\left(m\left(\phi - \frac{(i-1)\pi}{3}\right)\right) r^{(m-1)} \quad (3)$$

$$E_{\phi i} = -\sum_{m=1}^{\infty} \frac{2V_{oi}}{\pi b^m} \sin\left(\frac{m\pi}{6}\right) \sin\left(m\left(\phi - \frac{(i-1)\pi}{3}\right)\right) r^{(m-1)} \quad (4)$$

where E_{ri} and $E_{\phi i}$ are the radial and the phi–components of the electric field respectively.

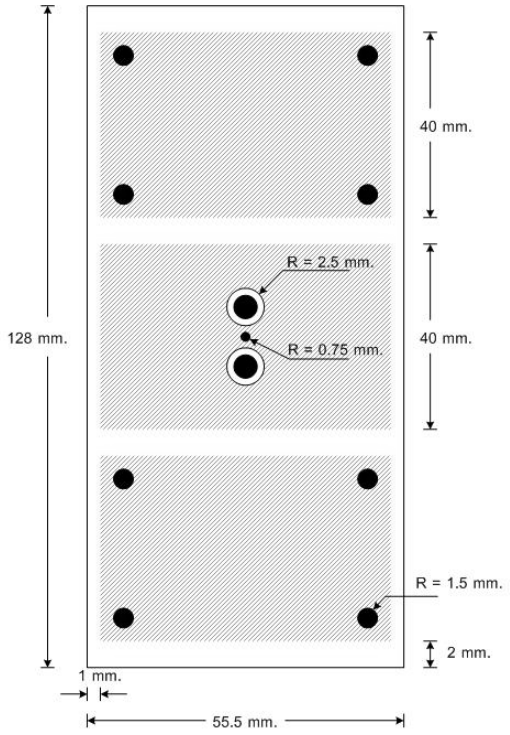

Figure 2. Dimensions of each electrode.

Using the approximation that $P(x, y)$ is so small such that the electric field in the area is almost constant and the applied potential for each electrode is one, (1) can be rewritten as

$$S_{ij} = -\left(E_{ri}E_{rj} + E_{\phi i}E_{\phi j}\right)\Delta s_{(x,y)} \quad (5)$$

where $\Delta s_{(x,y)}$ is the area of $P(x, y)$ and (3) and (4) are used for the radial and the phi–components of the electric field respectively. Fig. 3 shows the surface plot of the sensitivity map between the 1st electrode and the 2nd electrode, S_{12}. Fig. 4 shows the surface plot of the sensitivity map between the 1st electrode and the 3rd electrode, S_{13}. Fig. 5 shows the surface plot of the sensitivity map between the 1st electrode and the 4th electrode, S_{14}. The surface plot of S_{ij} where $i = j \pm 1$ is similar to the one for S_{12}. The surface plot of S_{ij} where $i = j \pm 2$ is similar to the one for S_{13}. The surface plot of S_{ij} where $i = j \pm 3$ is similar to the one for S_{14}. The radius of the sensor is 5.5 cm. Because of the singularity of the electric field in the area close to the electrodes, large errors of the sensitivity maps computation is observed. The sensitivity maps for the middle area with the radius of 4cm are used and shown in Figs. 3–5. The images outside this area are not computed.

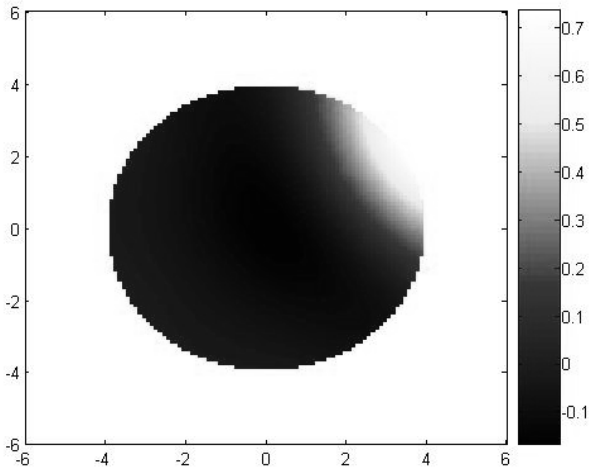

Figure 3. Sensitivity map between the 1st electrode and the 2nd electrode.

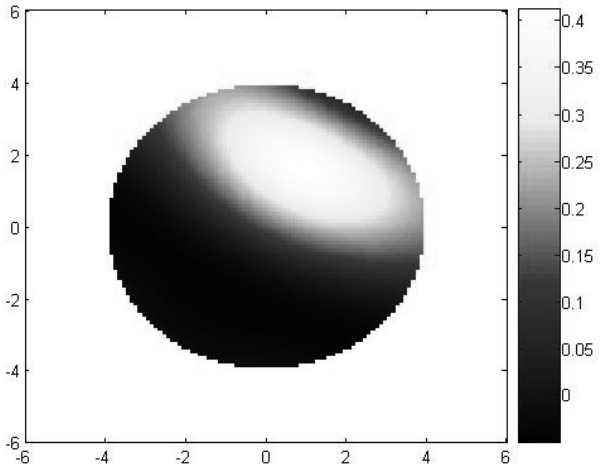

Figure 4. Sensitivity map between the 1st electrode and the 3rd electrode.

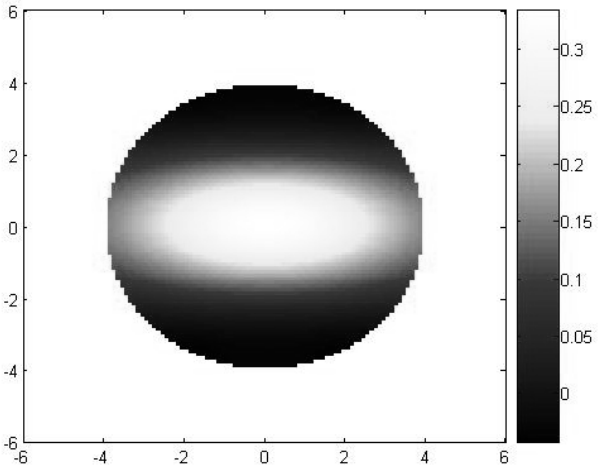

Figure 5. Sensitivity map between the 1st electrode and the 4th electrode.

IV. Image Reconstruction Technique

The image reconstruction technique used in this paper is the linear-back-projection (LBP) which is the simplest reconstruction technique. The gray level of the pixel having (x, y) as its center is given by [1]–[2]

$$G(x,y) = \frac{\sum_i \sum_j C_{ij}^* S_{ij}(x,y)}{\sum_i \sum_j S_{ij}(x,y)} \tag{6}$$

where C_{ij}^* is the normalized capacitance between the i^{th} electrode and the j^{th} electrode given by

$$C_{ij}^* = \frac{C_{ij}^{mea} - C_{ij}^{air}}{C_{ij}^{air}} \tag{7}$$

where the superscript *mea* indicates that the capacitor is measured when the sensor is filled with a sample object. The superscript *air* indicates that the capacitor is measured when the sensor is filled with air. Only the cases for *i* greater *j* are included in (6) since $C_{ij}^* = C_{ji}^*$. Due to the limitation of electrode fabrication process, the gap between each electrode is not identical. This gives a large contribution to the capacitance measurement error. In sensitivity map calculation, infinitely small gap is assumed. This causes singularities in the sensitivity maps for the consecutive electrodes. Because of these reasons, the error of the sensitivity maps for the consecutive electrodes or $i = j + 1$ is large. Because of this problem, the cases for $i = j + 1$ are not included in (6). There are only 9 terms included in each summation in (6).

V. Experimental Results

Three different sample object arrangements are used for the experiments. Each object is a water filled PVC container. The capacitance is measured using the UTI evaluation board from Smartec BV [3] shown in Fig. 6. Figs. 7–9 show the arrangements of sample objects and its reconstructed images.

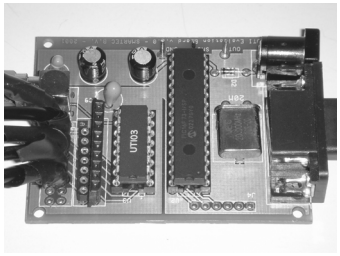

Figure 6. UTI evaluation board from Smartec BV.

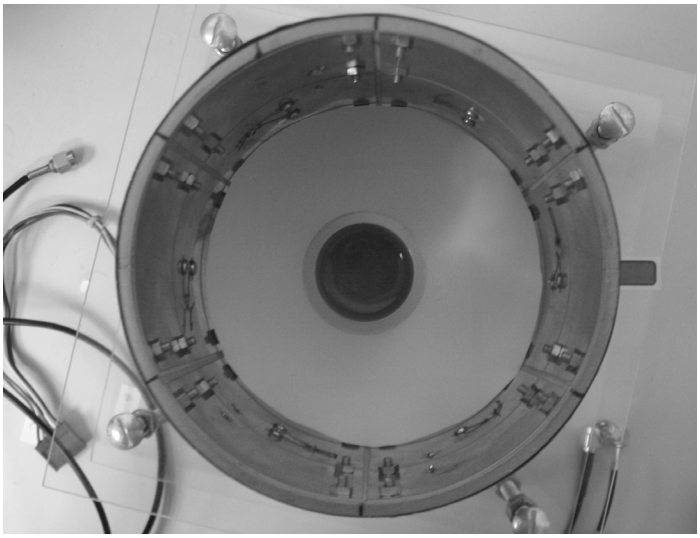

(a)

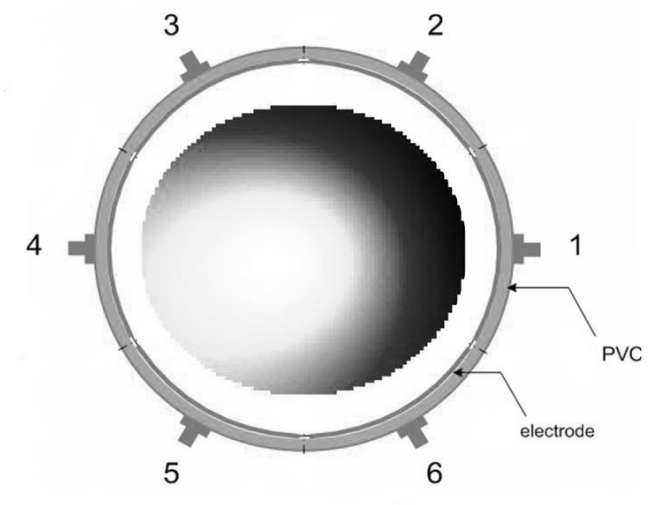

(b)

Figure 7. Case I: (a) arrangement of sample object, (b) reconstructed image.

VI. Conclusions

The results show that the reconstructed images give sizes and locations information of the sample objects. Fig. 9 shows that the reconstructed image does not have enough resolutions to separate two close objects. Increasing the number of the electrodes could improve the resolutions but it could raise the measurement error since the capacitance values would be smaller. The results serve the objective of this paper which is to implement the ECT system and show the idea of using analytical equations for the sensitivity maps instead of using the time-consuming numerical method such as FEM or FDM.

Acknowledgment

Authors would like to thank Amorndech Puttipipatkhachorn, a faculty member of the department of food engineering at Kasetsart University, Kamphaeng Saen Campus, for his useful discussion and his UTI evaluation board leading to this paper. Authors would also like to thank Susunpas Sthianrapapong and Pornprom Lerdpatshareekul for their initial work of building the sensor.

References

[1] T. Loser, R. Wajman and D. Mewes, "Electrical capacitance tomography: image reconstruction along electrical field lines," *Inst. of Phy. Pub.—Measure. Sci. and Technol.*, no. 12, pp. 1–9, 2001.

[2] W. Q.Yang and S. Liu, "Electrical capacitance tomography with a square sensor," *Electron. Lett.*, vol. 35, no. 4, pp. 295–296, 1999.

[3] Smartec BV. INTERFACE Evaluation Kit. [Online]. Available: http://www.smartec.nl/interface_utikit.htm. [Accessed Jan. 30, 2007].

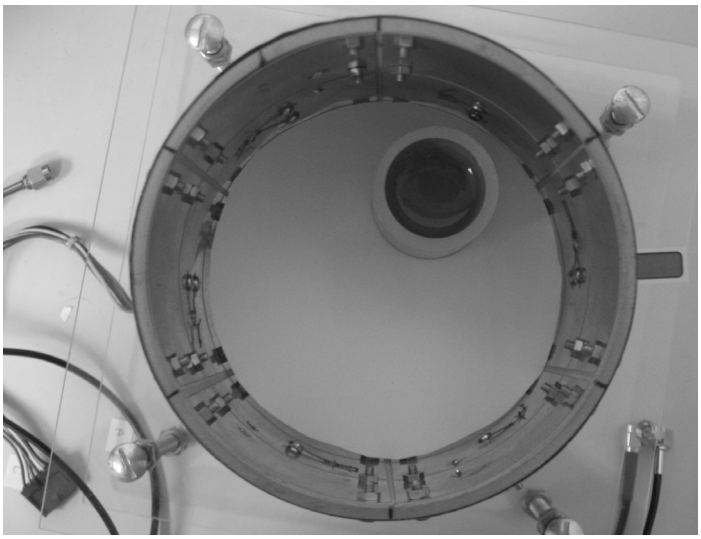

(a)

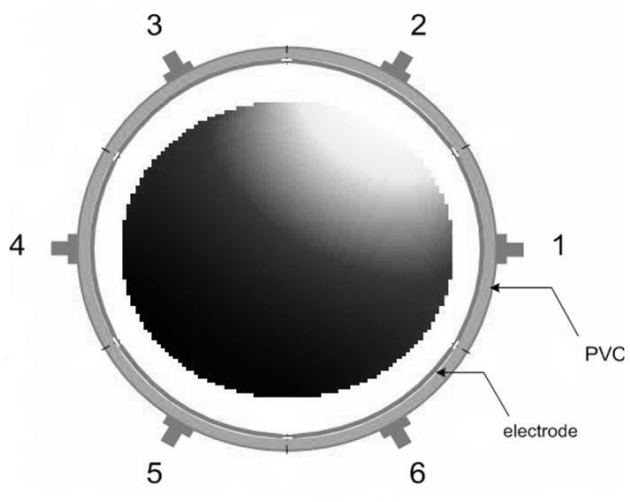

(b)

Figure 8. Case II: (a) arrangement of sample object, (b) reconstructed image.

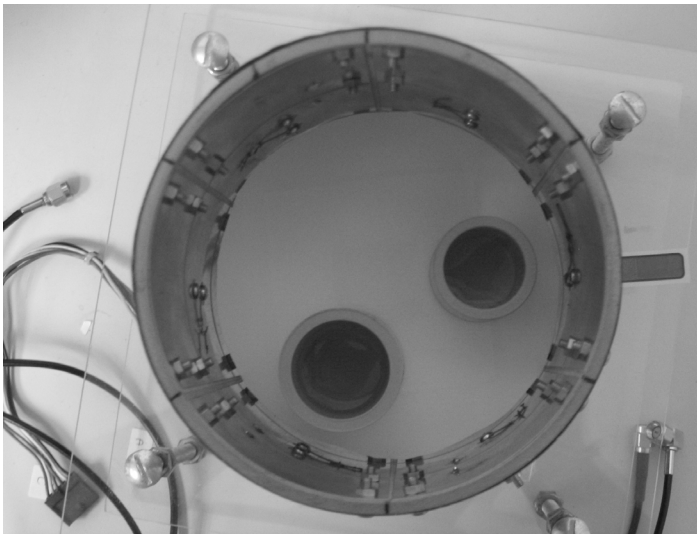

(a)

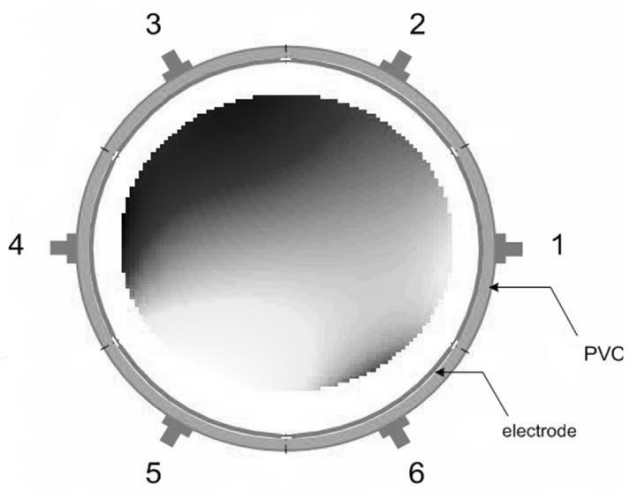

(b)

Figure 9. Case III: (a) arrangement of sample object, (b) reconstructed image.

Composite Four-Terminal Floating Nullor with Variable Voltage and Current Gains

Jirawat Hirunporm* Sumalee Unhavanich** Worapong Tangsrirat* Wanlop Surakampontorn*

* Faculty of Engineering and Research Center for Communication and Information Technology (ReCCIT),
King Mongkut's Institute of Technology Ladkrabang (KMITL),
Ladkrabang, Bangkok 10520, THAILAND

** Department of Industrial Electrical Technology (IET), Faculty of Engineering,
King Mongkut's Institute of Technology North-Bandkok (KMITNB),
Bandsue, Bangkok 10800, THAILAND

E-mail : *s8060506@kmitl.ac.th , ktworapo@kmitl.ac.th*

***Abstract*- A design technique for the practical implementation of a variable four-terminal floating nullor (FTFN) is presented, which contains three operational mirrored amplifiers (OMAs) and four grounded resistors. The proposed FTFN provides tunable both voltage-gain and current-gain with constant bandwidth property by varying the value of a single grounded resistor. PSPICE simulation results that agree with the theoretical analysis are obtained by modeling a variable-gain FTFN using commercial AD844 ICs.**

I. INTRODUCTION

At present, current-mode circuits have been receiving significant attention owing to its advantage over the voltage-mode, particularly for higher frequency of operation and simpler filtering structure [1]. Recently, the applications and advantages in the realization of transfer functions using four-terminal floating nullors (FTFNs) have received considerably attention. The designs of current-mode circuits employing FTFN as active devices such as amplifiers [2], current-mode filters [3-4], sinusoidal oscillators [5-6] and floating immittances [7], have been developed in the literature. Some previous-mentioned topologies have been demonstrated that an FTFN is a more flexible and all-round building block than an operational amplifier and a current conveyor [2],[4]. This is due to the fact that the nullor model of FTFN, the nullator and the norator, are isolated from each other, which is more flexible in active network synthesis. Moreover, the FTFN-based structures also provide a number of potential advantages, such as, complete absence of passive component-matching requirement, minimum number of employed passive elements. In addition, the FTFN whose the gain can be independently tuned seems to be more attractive, flexible and suitable for design and implementation of the frequency selective systems, such as, biquads, oscillator and so forth. Although some tunable FTFNs have been recently reported [8-9], they can variable only current-gain between i_w and i_z. There are no circuit realization based on tunable FTFN that can variable both voltage-gain and current-gain.

The aim of this paper is to propose a circuit technique for the practical implementation of the FTFN with variable voltage and current gains. The circuit realization uses only three operational mirrored amplifiers (OMAs) and four grounded resistors. The proposed tunable FTFN offers independently variable dc voltage and current gains while remaining a constant bandwidth. Moreover, it is interesting to show that the dc gains of the circuit can be tuned by adjusting grounded resistors without effecting the useful bandwidth. The performances of the proposed variable-gain FTFN using a commercial AD844 ICs are given with the simulation results, which will show that the characteristics of the resulting circuit become tunable.

II. CIRCUIT DESCRIPTION

An FTFN has the potential of being an extremely versatile analog active building block. It is a four-terminal active device with two input terminals (y, x) and two output terminals (w, z), whose circuit representation is shown in Fig.1. The terminal characteristics of the FTFN can be defined by means of the following relationship.

$$i_y = i_x = 0 \quad , \quad v_x = \beta . v_y \quad \text{and} \quad i_z = \pm \alpha . i_w \qquad (1)$$

where β = 1-ε, ($|\varepsilon| << 1$), and ε denotes the voltage tracking error, and α = 1-δ, ($|\delta| << 1$), and δ represents the current tracking error of an FTFN. The sign "+" is applied for the positive FTFN (FTFN+), whereas the sign "–" uses for the opposite polarity case, represented the negative FTFN (FTFN-). For an ideal FTFN, the voltage and current tracking error are equal to zero, i.e., $\varepsilon = \delta = 0$, or $\beta = \alpha = 1$. The usefulness of the FTFN can be extended if equation (1) is implemented in such a way that the voltage and current transfer ratios can be varied, in which case a more generalized tunable FTFN should be investigated.

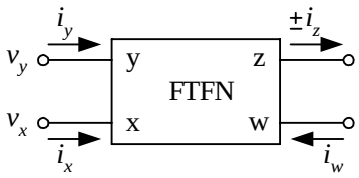

Figure 1 : Symbol of an FTFN

Fig.2 shows the circuit implementation and representation of the OMAs. The negative OMA (OMA-) comprising an op-amp and two pairs of current mirrors as shown in Fig.2(a) is a more general and flexible device owing to it can be equivalent to an ideal nullor or FTFN+ [1-2], whereas the other type of OMA which requires only one pairs of current mirrors is named the positive OMA (OMA+) and is shown in Fig.2(b). Therefore, it can be concluded from Fig.2 that the port characteristics of the OMA can be characterized as :

$$v_2 = v_1 \quad , \quad i_1 = i_2 = 0 \quad \text{and} \quad i_4 = i_3 \qquad (2)$$

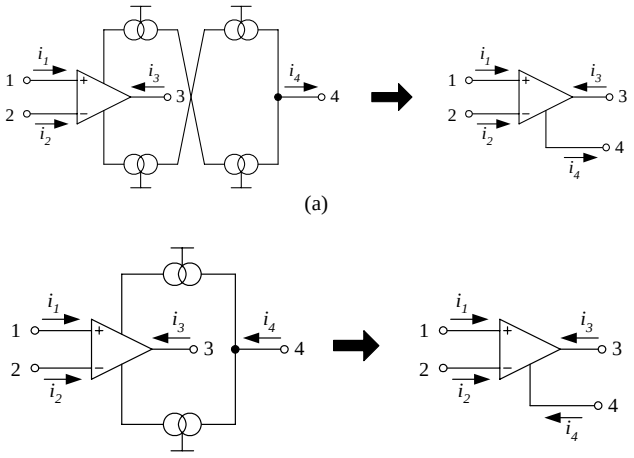

(a)

(b)

Figure 2 : Possible implementation of OMAs
(a) negative OMA (OMA-) (b) positive OMA (OMA+)

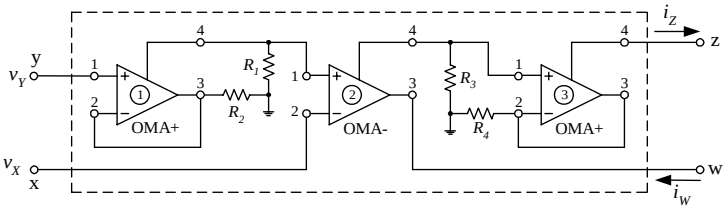

(a)

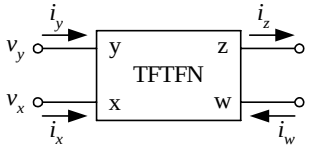

(b)

Figure 3 : Proposed tunable FTFN (TFTFN)
(a) circuit implementation (b) its symbol

The proposed tunable FTFN with arbitrary voltage-gain and current-gain, named TFTFN, is shown in Fig.3. It mainly consists of three OMAs and four grounded resistors. A detail analysis results that the voltage-current characteristics of this device can be defined by :

$$i_y = i_x = 0 \quad , \quad v_x = \left(\frac{R_1}{R_2}\right) v_y \quad \text{and} \quad i_z = \left(\frac{R_3}{R_4}\right) i_w \qquad (3)$$

Also note that the proposed TFTFN of Fig.3 is more flexible, which can be varied the voltage-gain and the current-gain through the ratio of two grounded resistors. Furthermore, if the 3rd positive OMA (OMA+) of Fig.3(a) is used instead with the negative OMA (OMA-), then the variable-gain FTFN- will also be obtained.

III. Performance Analysis

One important issue that must to be taken into account is the non-idealities of each OMA on the frequency dependent performance. Fig.4 shows the macro-model of the OMA, where β and α denote the non-ideal voltage- and current gains of the OMA. By applying the model from Fig.4 into the sub-circuit between OMA1 and OMA2 of Fig.3(a), routine analysis obtains that

$$\frac{v_X}{v_Y} = \left(\frac{\beta_1\beta_2\alpha_3 R_A}{R_2}\right)\left(\frac{1}{1+sR_AC_A}\right) \qquad (4)$$

where $R_A = R_1 // R_y // R_z$, $C_A = C_y + C_z$ and β_i and α_i are the voltage gain and current gain of the OMAi (i = 1, 2, 3). Typically, the values of R_y and R_z are too large and can also approximate to R_y , $R_z >> R_1$, then equation (4) can be rewritten as :

$$\frac{v_X}{v_Y} \cong \left(\frac{\beta_1\beta_2\alpha_3 R_1}{R_2}\right)\left(\frac{1}{1+sR_1C_A}\right) \qquad (5)$$

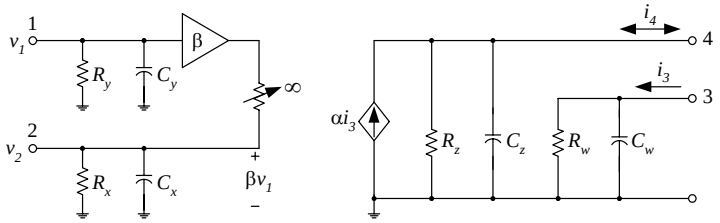

Figure 4 : Macro model for non-ideal OMA

According to equation (5), the dc voltage gain, β_{dc}, and the high-frequency dominant pole between the port y and the port x, ω_{pv}, can respectively be given by

$$\beta_{dc} = \frac{\beta_1\beta_2\alpha_3 R_1}{R_2} \tag{6}$$

and $$\omega_{pv} = 2\pi f_{pv} = \frac{1}{R_1 C_A} = \frac{1}{R_1(C_y + C_z)} \tag{7}$$

It can easily be noted from equations (6) and (7) that the dominant pole frequency can be adjusted by tuning the value of the resistor R_1, while the dc voltage-gain of this circuit can be adjusted through the resistor R_2 without affecting the bandwidth property. For example, if R_1 = 5 kΩ, C_y = 2 pF and C_z = 4.5 pF, then this pole frequency will locate at 4.89 MHz. This means that the dc voltage-gain of the proposed TFTFN can be independently varied without changing the useful bandwidth.

In the same way as above, the transfer characteristic between the currents i_Z and i_W can be considered by applying the model from Fig.4 into the sub-circuits formed of OMA2 and OMA3 of Fig.3(a). Reanalysis gives the relations :

$$\frac{i_z}{i_w} = \left[\frac{\beta_3\alpha_2\alpha_3 R_m R_z}{R_n(R_z + R_L)}\right]\left[\frac{1}{(1+sR_mC_A)(1+sR_LC_z)}\right] \tag{8}$$

where $R_m = R_3 // R_y // R_z$, $R_n = R_4 // R_x$ and R_L is the load resistance connected to the port z. Since R_3 and R_4 are very small, comparable to those resistances, i.e., R_y , $R_z >> R_3$, $R_x >> R_4$. Thus equation (8) can be reduced to :

$$\frac{i_z}{i_w} = \left[\frac{\beta_3\alpha_2\alpha_3 R_3}{R_4}\right]\left[\frac{1}{(1+sR_3C_A)(1+sR_LC_z)}\right] \tag{9}$$

if we choose $R_3 >> R_L$, then the above equation becomes :

$$\frac{i_z}{i_w} = \left[\frac{\beta_3\alpha_2\alpha_3 R_3}{R_4}\right]\left[\frac{1}{(1+sR_3C_i)}\right] \tag{10}$$

Hence, the dc current-gain, α_{dc}, and the high-frequency dominant pole between the port w and the port z, ω_{pi}, are

$$\alpha_{dc} = \frac{\beta_3\alpha_2\alpha_3 R_3}{R_4} \tag{11}$$

and $$\omega_{pi} = 2\pi f_{pi} = \frac{1}{R_3 C_A} = \frac{1}{R_3(C_y + C_z)} \tag{12}$$

From equations (11) and (12), R_3 should be selected so as to meet the desired bandwidth, whereas R_4 can be modified to change the gain without disturbing the bandwidth. Similarly, if R_3 = 5 kΩ, C_y = 2 pF and C_z = 4.5 pF, then this pole frequency is also located at 4.89 MHz. It also concludes that the dc current-gain of the proposed TFTFN can be independently controlled without changing the useful bandwidth.

IV. Simulation Results

The performances of the proposed variable-gain FTFN of Fig.3 have been simulated with PSPICE using an OMA, which consists of AD844 transimpedance op-amps as shown in Fig.5 [6]. The simulation was performed using macro-model of the AD844 IC shown in Fig.6 [12].

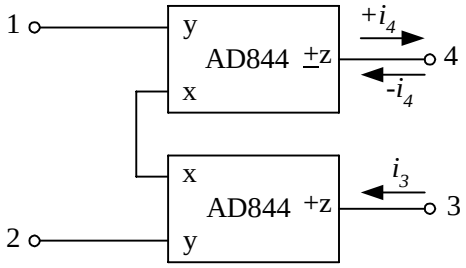

Figure 5 : Realization of OMA± with commercial available AD844 ICs

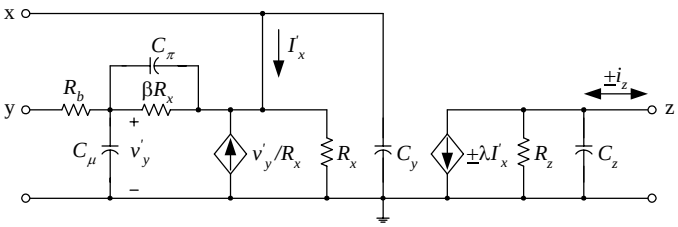

Figure 6 : Small signal equivalent circuit for the AD844 transimpedance amplifier [12] : R_b = 300 Ω, R_x = 50 Ω, βR_x = 20 kΩ, R_z = 2 MΩ, C_μ = 2 pF, C_π = 26 pF, C_x = 2 pF and C_z = 4.5 pF

Fig.7 shows the voltage frequency responses, v_x / v_y , when R_1 = 5 kΩ and R_2 is changed to 5 kΩ, 2.5 kΩ, 1 kΩ and 0.5 kΩ, which corresponds to the dc voltage gain β = 1, 2, 5 and 10, respectively.

The ac current responses of the proposed TFTFN for R_3 = 5 kΩ are shown in Fig.8. From the simulated frequency responses in Figs.7 and 8, it is evidenced in both cases that the useful bandwidth is nearly constant with respect to the variation of the voltage-gain or the current-gain of the proposed TFTFN, which are well confirmed the theoretical analysis.

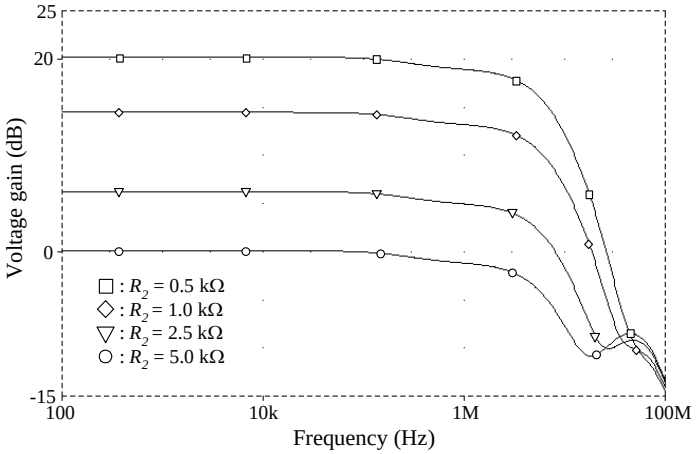

Figure 7 : Voltage transfer characteristics of the proposed tunable FTFN for R_1 = 5 kΩ

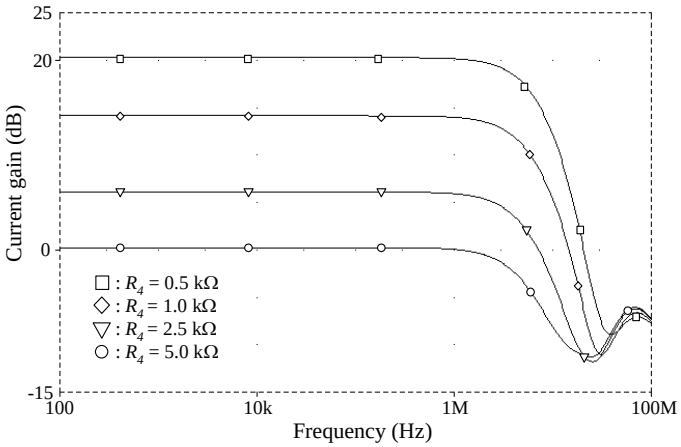

Figure 8 : Current transfer characteristics of the proposed tunable FTFN for R_3 = 5 kΩ

V. Further Applications

Finally, the proposed FTFN with variable-gain can be applied for implementing active filters with electronic control of the important circuit parameters, such as, the natural angular frequency ω_o, the quality factor (Q-factor) and the absolute bandwidth. Moreover, oscillator with electronic control of the frequency and the condition of oscillators can also be realized. But it is not demonstrated in this paper, because of some applications employing this device have been recently reported in references [7-11].

VI. Conclusions

In this paper, a circuit configuration for an FTFN with variable voltage- and current-gains is proposed in order to simplify the representation of different building block in the ideal case. The proposed tunable FTFN employs only three OMAs and four grounded resistors, and offers constant bandwidth, whereas both the dc voltage- and current-gains can be independently controlled through a single grounded resistor. PSPICE simulation results obtained from an implementation with the AD844 transimpedance op-amp have been demonstrated that its performance is quite satisfactory for discrete high-frequency circuit designs, such as, biquads, oscillators and so forth.

Acknowledgment

This work is funded by the Thailand Research Fund (TRF) through the Senior Research Scholar Program; grant number RTA4680003.

References

[1] B. Wilson, "Recent development in current conveyors and current mode circuits", *IEE Proceedings*, vol.137, Pt. G., pp.63-77, 1990.

[2] J.H. Huijsing, "Operational floating amplifier", *IEE Proceedings*, vol.137, Pt. G., pp.131-136, 1990.

[3] M.T. Abuelma'atti and H.A. Al-zaher, "Universal two-input two-output current-mode active biquad using FTFNs", *International Journal of Electronics*, vol.86, pp.181-188, 1999.

[4] M. Higashimura, "Realization of current-mode transfer function using four-terminal floating nullor", *Electronic Letters*, vol.27, pp.170-171, 1991.

[5] D.R. Bhaskar, "Single resistance controlled sinusoidal oscillator using single FTFN", *Electronic Letters*, vol.35, pp.190, 1999.

[6] S.I. Liu, "Single-resistance-controlled sinusoidal oscillator using two FTFNs", *Electronic Letters*, vol.33, pp.1185-1186, 1997.

[7] R. Senani, "A novel application of four-terminal floating nullors", *Proceedings of the IEEE*, vol.75, pp.1544-1546, 1987.

[8] W. Tangsrirat, S. Unhavanich, T. Dumawipata and W.Surakampontorn, "FTFN with variable current gain", *Proceedings of TENCON 2001*, Singapore, pp.209-212, August 19-21, 2001.

[9] J. Hirunporm, W. Tangsrirat and W. Surakampontorn, "Electronically tunable multiple-output FTFN and its applications", *Proceedings of ECTI-CON 2006*, Thailand, pp.805-808, May 10-13, 2006.

[10] J. Hirunporm, W. Tangsrirat and W. Surakampontorn, "Current-controlled current-mode biquadratic filter using tunable multiple-output FTFNs", *Proceedings of The 2006 International Conference on Circuits/Systems, Computers and Communications (ITC-CSCC 2006)*, Thailand, pp.705-708, July 10-13, 2006.

[11] J. Hirunporm, T. Pukkalanun and W. Tangsrirat, "Current-controlled current-mode biquadratic filter with two inputs and three outputs using multiple-output FTFNs", *Proceedings of International Joint Conference 2006 (SICE-ICCAS 2006)*, Korea, pp.5691-5694, October 18-21, 2006.

[12] E. Bruun and O.H. Olesen, "Conveyor implementation of generic current mode circuits", *International Journal of Electronics*, vol.73, no.1, pp.129-140, 1992.

transfer function of the proposed filter in Fig.3 can be given by :

$$I_{o1} = -\left[\frac{g_{m1}g_{m2}}{D(s)}\right] I_1 \qquad (3)$$

and

$$I_{o2} = \left[\frac{D(s)I_2 - (sC_2 g_{m1})I_1}{D(s)}\right] \qquad (4)$$

where $D(s) = (s^2C_1C_2 + sC_2g_{m1} + g_{m1}g_{m2})$ (5)

and g_{mi} denotes g_m of the i-th MO-OTA (i = 1, 2).

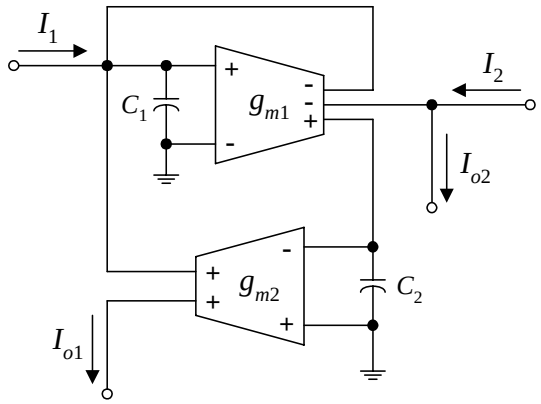

Fig.3 : Proposed TITO current-mode universal filter employing only MO-OTAs and grounded capacitors

From equations (3)-(5), it can be seen that :

1) a LP function is realized with $I_1 = I_{in}$, $I_2 = 0$ and $I_{o1} = I_{out}$.
2) a BP function is realized with $I_1 = I_{in}$, $I_2 = 0$ and $I_{o2} = I_{out}$.
3) a BS function is realized with $I_1 = I_2 = I_{in}$ and $I_{o2} = I_{out}$.
4) a AP function is realized with $I_1/2 = I_2 = I_{in}$ and $I_{o2} = I_{out}$.
5) a HP function is realized with $I_1 = I_2 = I_{in}$ and $I_{o1} + I_{o2} = I_{out}$.

Thus, the proposed TITO filter can realize all the five standard types of the biquadratic filtering functions from the same circuit configuration. Note also that the circuit needs no inverting-type current input signal for realizing any biquadratic functions. As seen from the proposed circuit configuration, it employs only grounded passive elements especially grounded capacitors and there are no critical component-matching conditions or cancellation constraints in the design, thus the circuit is very suitable for fully IC technology.

Also from equations (3)-(5), the filter parameters ω_o and ω_o/Q are given by :

$$\omega_o = \sqrt{\frac{g_{m1}g_{m2}}{C_1C_2}} \qquad (6)$$

and

$$\frac{\omega_o}{Q} = \frac{g_{m1}}{C_1} \qquad (7)$$

It can be seen from above expressions that the ω_o for all the filter responses can electronically be tuned by varying g_{m2} and/or C_2 without affecting the parameter ω_o/Q.

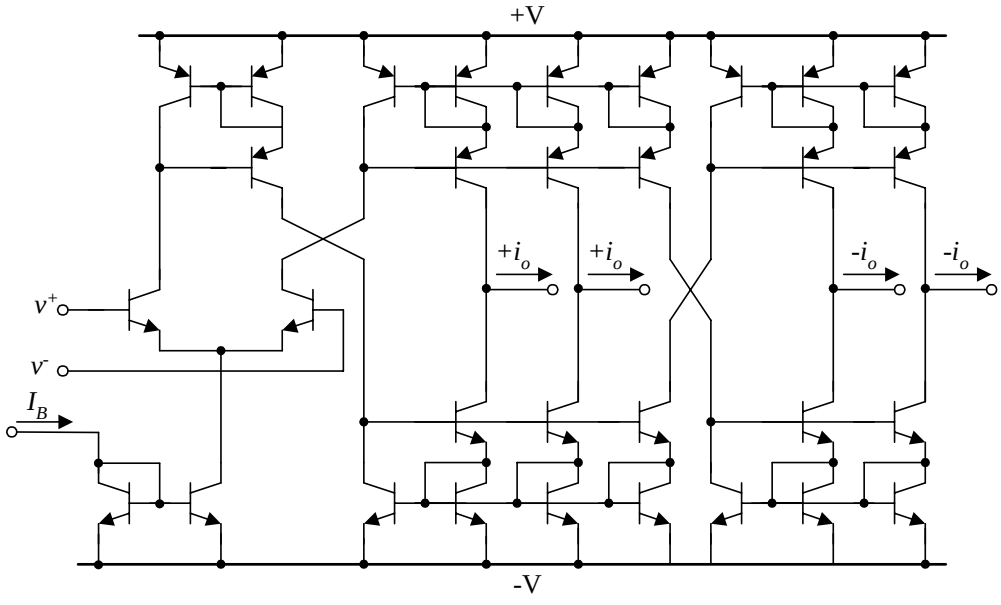

Fig.2 : Circuit diagram of an ordinary MO-OTA

Moreover, the ω_o and ω_o/Q sensitivities can be given by

$$S_{g_{m1}}^{\omega_o} = S_{g_{m2}}^{\omega_o} = \frac{1}{2} \tag{8}$$

$$S_{C_1}^{\omega_o} = S_{C_2}^{\omega_o} = -\frac{1}{2} \tag{9}$$

and

$$S_{g_{m1}}^{\omega_o/Q} = S_{C_1}^{\omega_o/Q} = 1 \tag{10}$$

All the active and passive sensitivities are not more than unity in magnitude.

III. Non-ideal Study

The circuit model of the non-ideal MO-OTA can be shown in Fig.4, where G_i and G_o are the parasitic input and output conductances, and C_i and C_o are the parasitic input and output capacitances, respectively. Therefore, re-analysis the proposed filter of Fig.3 by taking into account the non-idealities of the MO-OTA, the denominator polynomial of the non-ideal transfer function can be rewritten as :

$$D(s)=s^2C_1C_2+s[C_2(g_{m1}+G_{i1})+(C_1G_{i2})]+[g_{m1}g_{m2}+(g_{m1}+G_{i1})G_{i2}] \tag{11}$$

where G_{ik} represents the parasitic input conductance of the k-th MO-OTA.

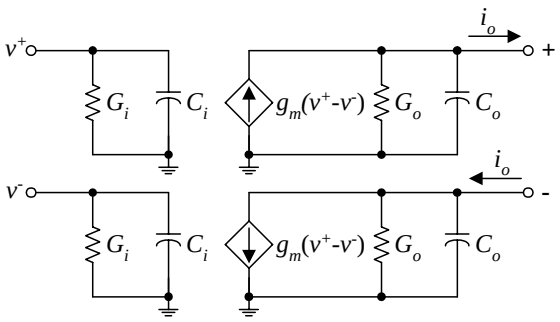

Fig.4 : Circuit model of the non-ideal MO-OTA operating in linear region

In this case, the modified parameters ω_o and ω_o/Q are calculated as

$$\omega_o = \sqrt{\frac{g_{m1}g_{m2}+(g_{m1}+G_{i1})G_{i2}}{C_1C_2}} \tag{12}$$

and

$$\frac{\omega_o}{Q} = \left(\frac{g_{m1}+G_{i1}}{C_1}\right)+\left(\frac{G_{i2}}{C_2}\right) \tag{13}$$

From these relations, the active sensitivities can be found as

$$S_{G_{i1}}^{\omega_o} = \frac{1}{2}\sqrt{\frac{G_{i1}G_{i2}}{g_{m1}g_{m2}+(g_{m1}+G_{i1})G_{i2}}} < \frac{1}{2} \tag{14}$$

$$S_{G_{i2}}^{\omega_o} = \frac{1}{2}\sqrt{\frac{(g_{m1}+G_{i1})G_{i2}}{g_{m1}g_{m2}+(g_{m1}+G_{i1})G_{i2}}} < \frac{1}{2} \tag{15}$$

$$S_{G_{i1}}^{\omega_o/Q} = \frac{1}{2}\left[\frac{G_{i1}C_2}{C_2(g_{m1}+G_{i1})+C_1G_{i2}}\right] < \frac{1}{2} \tag{16}$$

and

$$S_{G_{i2}}^{\omega_o/Q} = \frac{1}{2}\left[\frac{G_{i2}C_1}{C_2(g_{m1}+G_{i1})+C_1G_{i2}}\right] < \frac{1}{2} \tag{17}$$

It can easily be observed from equations (14)-(17) that the entire active sensitivities are still less than 0.5 in magnitude. Thus, the proposed filter structure displays a low sensitivity performance.

IV. Simulation Results

To verify the theoretical prediction, the characteristics of the proposed current-mode universal filter of Fig.3 have been simulated with PSPICE program. The MO-OTA is simulated using the bipolar structure given in Fig.2 with DC supply voltages of ±3V. The transistors model parameters are taken from the PR100N (PNP) and NP100N (NPN) of the bipolar arrays ALA400 from AT&T [8].

Fig.5 shows the simulated frequency responses of the LP, BP and HP filter functions of the proposed circuit in Fig.3. In simulations, equal bias current values of I_{B1} = I_{B2} = 100 μA, and capacitance values of C_1 = C_2 = 1 nF were chosen to obtain $f_o = \omega_o/2\pi \cong 318$ kHz and Q = 1. With the same setting, the gain and phase responses of the BS and AP filters are also given in Figs.6 and 7, respectively. All the simulation results agree quite well with the theory.

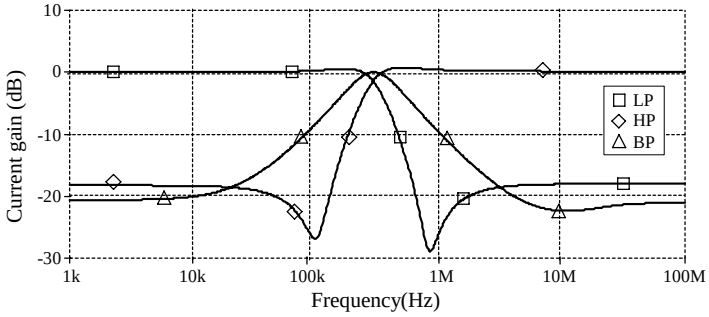

Fig.5 : LP, BP and HP current responses of the proposed current-mode universal filter in Fig.3.

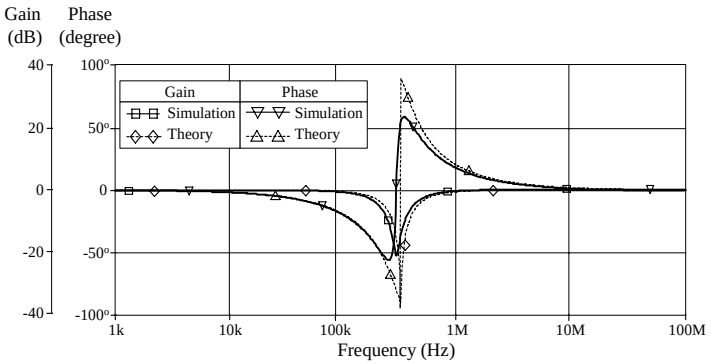

Fig.6 : BS current response of the proposed current-mode filter.

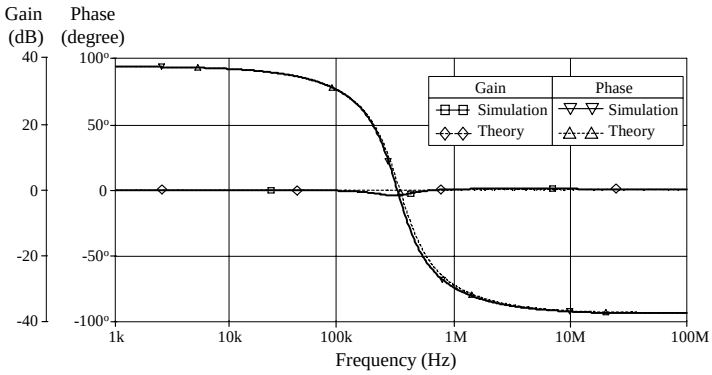

Fig.7 : AP current response of the proposed current-mode filter.

V. CONCLUSIONS

In this paper, a two-input two-output current-mode universal biquadratic filter that employs a minimum number of active and passive components has been described. The configuration consists of only two MO-OTAs and two grounded capacitors, which is advantageous from IC fabrication. The proposed filter can realize all the five standard biquadratic filter functions without any matching conditions. The filter parameters ω_o and ω_o/Q are tuned electronically and independently, and all the passive and active sensitivities are low.

ACKNOWLEDGMENT

This work is funded by the Thailand Research Fund (TRF) through the Senior Research Scholar Program; grant number RTA4680003.

REFERENCES

[1] J. Wu, "Current-mode high-order OTA-C filters", *International Journal of Electronics*, vol.76, pp.1115-1120, 1994.

[2] T. Tsukutani, M. Ishida, S. Tsuiki and Y. Fukui, "Versatile current-mode biquad filter using multiple current output OTAs", *International Journal of Electronics*, vol.80, pp.533-541, 1996.

[3] Y. Sun and J. K. Fidler, "Design of current-mode multiple output OTA and capacitor filters", *International Journal of Electronics*, vol.81, pp.95-99, 1996.

[4] J. Wu and E. I. El-Masry, "Current-mode band-pass ladder filters using OTAs", *International Journal of Electronics*", vol.85, pp.61-70, 1998.

[5] C. M. Chang and S. K. Pai, "Universal current-mode OTA-C biquad with the minimum components", *IEEE Transaction on Circuits and Systems-I: Fundamental Theory and Applications*, vol.47, pp.1235-1238, 2000.

[6] M. Bhusan and R. W. Newcomb, "Grounding of capacitors in integrated circuits", Electronics Letters, vol.3, pp.148-149, 1967.

[7] K. Pal and R. Singh, "Inductorless current conveyor allpass filter using grounded capacitors", Electronics Letters, vol.18, p.47, 1982.

[8] D. R. Frey, "Log-domain filtering : an approach to current-mode filtering", *IEE Proceedings Part G, Circuits, Devices and Systems*, vol.140, pp.406-416, 1993.

A Study of Adaptive Forward Error Control in Audio Communication using Smooth Method

Phichet Moungnoul, Kornhathai Klappong, Wiphada Inkiew and Somyot Junnapiya
Faculty of Engineering and Research Center for Communication and Information Technology
King Mongkut's Institute of Technology Ladkrabang, Chalongkrung Road, Bangkok, 10520, Thailand
E-mail: {phichet,somyot}@telecom.kmitl.ac.th,s46064125@kmitl.ac.th

***Abstract*-This paper studies the adaptive FEC control algorithms to improve control the amount of redundancy. The recently adaptive FEC "CNR algorithm" considers the history of packet loss in the network before changing the amount of redundancy and does not waste time. The performance of the CNR algorithm is used for simulation model. The smoothing parameter is varied in order to adapt and changed the characteristics of time series from the packet loss. Result shows the adaptive error control algorithm can decrease the loss rate by using a variability smoothing factor to appropriate network condition.**

I. INTRODUCTION

The motivation for transporting audio stream over IP networks potential is cost savings to achievable by eliminating or bypass the circuit-switched telephony infrastructure. The conversation quality between the sender and the receiver in the Internet telephony system is depends on specific impairments such as packet loss, delay, jitter, etc., which related to the characteristic of packet network. A number of techniques dealing with packet loss problems exist for application that exchange real-time voice [2].

Packet loss causes degradation in the quality of audio transmission applications. Forward Error Correction (FEC) methods which add redundant information to audio packets can be used to minimize the effects of packet loss. While these methods can reduce the effects of packet loss, they increase the amount of bandwidth used by an audio stream [9].

Most of audio transmission applications use UDP as the transport layer protocol. The Real-time Transport Protocol (RTP) [4] is used to provide additional functionality including sequence numbers and time stamps. The Real Time Control Protocol (RTCP) is used to return receiver statistics (e.g., the number of packets detected as lost) to the sender. RTCP packets are sent every 5 seconds by a receiver to a sender and consume very little bandwidth. IP networks are inherently best effort networks with variable packet delays and loss. While audio traffic can tolerate some amount of packet loss, a packet loss rate greater than 5% is considered harmful to the audio quality [8]. The amount of packet loss rate that can be tolerated depends on the nature of the encoding algorithm and on the sampling rate of the audio stream. Changing the IP infrastructure to support guaranteed bandwidth sessions would allow for effective transport of audio streams. Changing the Internet infrastructure is a difficult proposition, hence the interest in application level techniques for compensating for packet delay jitter and loss. Algorithms using Forward Error Correction (FEC) methods have been developed to compensate for packet loss.

However, existing methods which used media specific FEC technique can not forecast a network performance in advance. The drawback of this algorithm is in part of increasing combination number (number which specific the pattern of a redundant copy of packet) [7].

Using a currently loss report to make a decision for a transmission rate that suited for the next loss situation has not always accurate. Because of the loss rate in the next interval may not be rated to the previous intervals.

The single exponential smoothing (SES) technique is a simple and pragmatic approach to forecasting, whereby the forecast is constructed from the exponentially weighted average of pass observation [5]. If the packet loss prediction use bounded adaptive smoothing constant from the forecast loss rate in the next interval. The loss rate will be a predictable variation sequence of the number as time series (time series of packet loss), more correctly and less error in case of significant time series average changing [1].

In this paper, to study the media specific FEC-based algorithm based on increasing the combination number. The adaptive FEC control algorithm developed in [11] (the "CNR algorithm") is studied and significant improvements are evaluated. Also, Redundant Codec Combination Selection (RCCS) algorithm uses smoothing factor to calculate the reward and penalty at selecting combination [8]. Both RCCS and CNR are FEC-based error control mechanisms that the amount of redundancy is controlled by the network loss rate. This paper is to develop mechanism that attempts to eliminate or at least minimize the impact of packet loss and end-to-end delay on the quality of the audio delivered to the destinations. Analyze the effect of the variability parameters that use in process of each algorithm for improve audio transmission in the future.

This paper is organized as follows. Section II reviews the adaptive error recovery algorithms which use media specific FEC-based technique and smoothed loss scheme. Section III and IV are the experiment setup and experimental result respectively. Finally, section V presents the conclusions.

II. RECOVERY ALGORITHM WITH SMOOTHED LOSS

A. RCCS Algorithm

Myoung-Kyoung Ji[8] proposed new adaptive FEC-based algorithm, called RCCS algorithm using loss and delay in order to improve the internet telephony. They used smoothing factor for update the reward and the penalty of current combination, as in equation (1) and equation (2).

$$R_i = \alpha(L_b / L_a) + (1-\alpha)R_{i-1} \quad (1)$$

$$P_i = \alpha(D_a / D_b) + (1-\alpha)P_{i-1} \quad (2)$$

This algorithm has 3 steps: the first step updates the reward and the penalty of current combination. The second step is the procedure that selects the combination whose estimate of loss rate within the maximum and minimum threshold. The last is selects the combination that exceeds the maximum of end-to-end delay.

B. CNR Algorithm

Centre for Network Research (CNR) algorithm [11] is the media specific FEC-based algorithm. Improves the Bolot (1996) [6] algorithm by increasing the combination number of audio redundancy by one (1) in each period. This will reduce waste time from CNR algorithm chooses G.723.1 codec, because it is the most widely-used audio codec in the IP Telephony system and it has low bit rate enough (6.3 kbps) [11]. Besides, it is better than encoding each audio unit two times with high and low bit rate codec. The CNR algorithm requires the Real-time Transport Control Protocol (RTCP) packet including packet loss rate before and after the reconstruction at the receiver. Whenever the RTCP packet is received, the reward value (the L_a and L_b ratio) of current combination R_c using the loss information in the packet is calculated such as equation (3) in Figure 1.

```
For each receiver report packet received do
1.Update reward of the current combination
  //Let Rc stands for reward of the current combination
                    Rc = Lb/La                          (3)
2. Calculate the percentage of packets lost
   before reconstruction, Lb
   Lb = Number of packets lost before
        reconstruction / Number of
        packets expected
3. Calculate the percentage of packets lost
   after reconstruction, La
   La = Lb / Reward associated with current
        combination number
4. If (La > HIGH) then
     new_combination = MAX_COMBINATION
     For i =1 to MAX_COMBINATION
       Lai = Lb / reward of combination #i
       If (Lai <= HIGH) then
         new_combination = i
         exit for loop
     combination = new_combination
5. If (La < LOW)for N times then
     Decrement combination
```

Figure 1. The pseudo code of the CNR algorithm

C. Proposed Method

Base on our research, the CNR algorithm can uses the exponential smoothing method to calculate the reward value in the next interval. The reward value in a previous interval will be used to decide which combination number should be adjusted.

We added the adjustment smoothing constant which was developed by Trigg and Leach [3] in the CNR algorithm to calculate reward value for unpredictable variation sequences of the number via time series method, as in Figure 2.

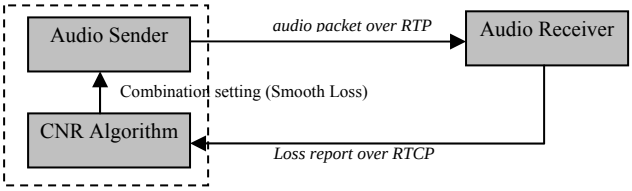

Figure 2. Mechanism to smoothing loss report

The smoothing value can obtain by the following equation. [10]

$$S_t = \alpha X_t + (1-\alpha)S_{t-1}(X) \quad (4)$$

Where S_t represents for smoothed value at time t with $0<\alpha<1$ is a smoothing factor.

Change the reward calculation (R_c) by including smoothing factor in reward formula following equation (4) by equation (5), like reward calculation in RCCS algorithm.

$$R_c = \alpha(L_b / L_a) + (1-\alpha)R_{i-1} \quad (5)$$

III. EXPERIMENT SETUP

This experiment simulated the CNR algorithm which included the adaptation logic of smoothing factor using NS-2 program [13] used a network simulator.

The topology of the simulation model is shown in Figure 3. All links are drop tail links. Most of them have 10 Mbps capacity and 1ms delay except the bottleneck link between N2 and N3 which has 2 Mbps capacity and 50 ms delay.

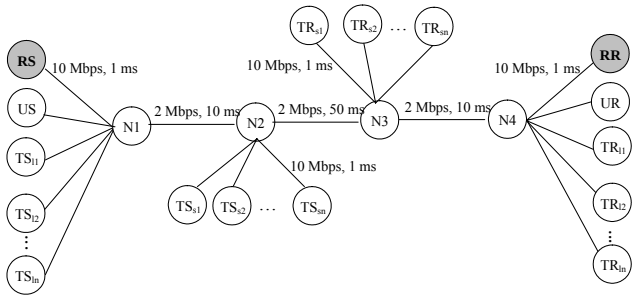

Figure 3. The topology of simulation model

The audio packets was sent from the sender (node RS) to the receiver (node RR) via the Real-time Transport Protocol (RTP) in every 30 milliseconds. RR sends the receiver report every five (5) seconds to RS. There were other nodes that sent the Transmission Control Protocol (TCP) and User Datagram Protocol (UDP) traffics. Each session was repeated by adding the smoothing factor by 0.1 until it is 0.98. The whole experiment would be repeated in each level of the loss model.

IV. Experimental Result

The performance of the recovery algorithm can be evaluated from many important parameters. Table I shows some statistics from NS-2 trace files in network. All average parameters were calculated from N1 source and N2 destination node. The packet size was 24 bytes. The audio traffic started to send a packet at 0.1 second and stopped at 1200 seconds.

The results shows that is used 0.2 as smoothing constant in the unloaded traffic situation, the receiver (RR) would receives amount of packets greater than smoothing constant at 0.98.

TABLE I
SIMULATION RESULTS FROM NS-2 TRACE FILE

Parameters	α = 0.2	α = 0.98
No. period that L_a>high threshold	19	16
Received Packets	528,500	516,505
Average Throughput (kbps)	1,882.86	1,871.72
Average Delay (ms)	7.82829	7.68629
Average Jitter1(ms)	71.018	78.1758

Figure 4 shows the comparison of different traffic congestion. It also shows that smoothing constant of 0.2 can be used in the unloaded traffic to have better amount of the received packets. And for the better result in the loaded and congested traffics, recommended adjusting the smoothing constant is 0.98.

Using the CNR to compare with RCCS mechanism for simulated the topology in the loaded traffic network, the results shown in Figure the effect of higher smoothing factor is better for adaptive error control mechanism than the lower value, as Figure 5.

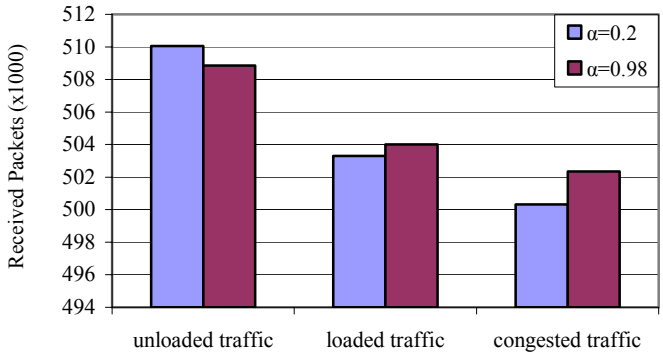

Figure 4. The received packets in different traffic congestion

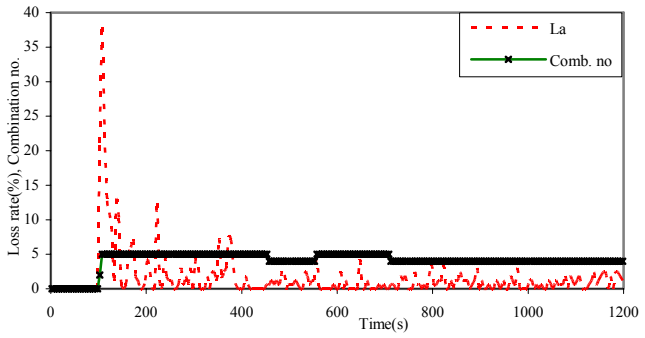

Figure 5. Behavior of loss rate when reward value follows equation (3)

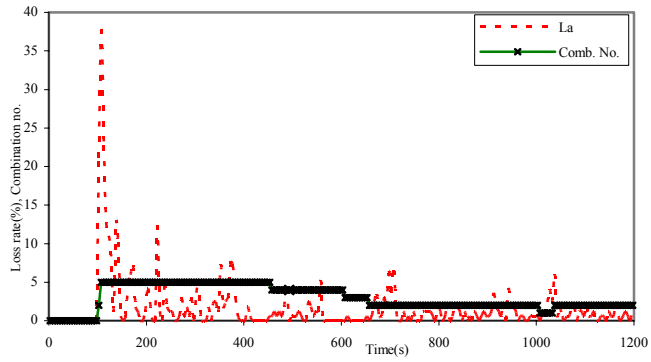

Figure 6. Behavior of loss rate when reward value follows equation (5)

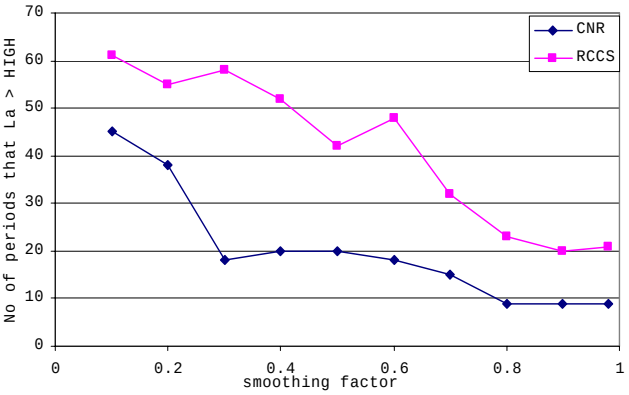

Figure 7. L_a when smoothing factor is 0.1 until 0.98 in unload traffic

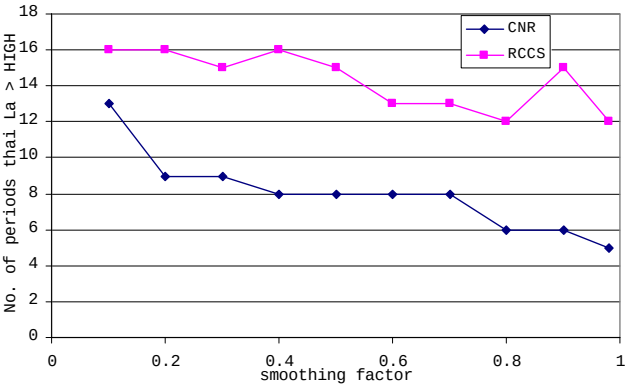

Figure 8. L_a when smoothing factor is 0.1 until 0.98 in loaded traffic

We observed from running the CNR algorithm the behavior perform follow Figure 5-8 that after changing the combination number of loaded and unloaded traffic, these two behaviors use the same value of smoothing factor, which was 0.98. However, when we adjusted a situation of network by using a smoothing factor of 0.2 in the unloaded traffic behavior and calculated the reward value (R), the results showed that the loss rate was not greater than the high threshold (5%) and not lower than the low threshold (1%). Moreover, the combination number of communication transmission was decreased. Consequently, the redundant packets were decrease. The receiver and the sender would have a better quality of communication in exchanging the real time voice.

V. CONCLUSION

In this paper, introduce an adaptive parameter exponential smoothing method to solve the drawback of the media specific FEC algorithm in part of increasing combination number. The CNR algorithm performs well when varying smooth parameter at low value (0.2) in unloaded traffic and better performance when set this parameter at high value (0.98) in loaded or congested traffic. The suited redundant information of audio packets can be adjusted to appropriate network in advance. Therefore, the adaptive recovery algorithm can apply the smooth method to recovery mechanism in order to obtain more available utilized bandwidth.

REFERENCES

[1] B. Piyatamrong P. Piyakhun., "Smooth loss with variability smoothing factor to increase bandwidth utilization," *PACRIM 2001*, Vol.2, 26 -28 August, Victoria, B.C., Canada, 2001, pp. 493 – 494.

[2] C. Perkins, O. Hodson, and V. Hardman, "A Survey of Packet Loss Recovery Techniques for Streaming Audio," *IEEE Networ*k, Vol. 12, No. 5, September-October 1998, pp. 40 – 48.

[3] Douglas C. Montgomery, Lynwood A. Johnson, John S. Gardiner, *Forecasting & Time series Analysis 2nd Edition*, McGraw-Hill, Inc., 1990.

[4] H. Schulzrinne, S. Casner, R. Fredrick and V. Jacobson, "RTP: A Transport Protocol for Real-Time Applications," Internet Engineering Task Force, RFC 1889, January 1996

[5] James W. Taylor, "Smooth Transition Exponential Smoothing," Journal of Forecasting, 2004, Vol. 23, pp. 385-394

[6] J-C. Bolot, A.V Garcia, "Control mechanisms for packet audio in the Internet," *Proc. IEEE INFOCOM '96*, April 1996, pp.232-239.

[7] J-C Bolot, S. Fosse-Parisis and D. Towsely, "Adaptive FEC-Based Error Control for Internet Telephony," *Proceedings of IEEE INFORCOM*, Vol. 3, 1999, pp.1453-1460.

[8] M. Ji, S. Lee, T. Choi, S. Park, J. Hang, K. Chung, "Selecting an audio redundancy codec combination for error control in Internet telephony," *ICPADS 2001*. Proceeding. Eighth International Conference on 26-29 June 2001, pp. 645-649.

[9] N. Jayant and S. W. Christensen, "Effects of Packet Losses in Waveform Coded Speech and Improvements due to an Odd-Even Sample-Interpolation Procedure," *IEEE Transactions on Communications*, Vol. COM-29, No. 2, February 1981,pp. 101 - 109,

[10] Robert G. Brown, *Smoothing, Forecasting and Prediction of Discrete Time Series.* Prentice-Hall, Inc., 1963.

[11] S.Chuaywong, S. Kamolphiwong,T. Kamolphiwong, "Performance Enhancement of FEC Mechanism for IP Telephony," *Proceeding of the 2005 ECTI*, vol.2, Cholburi, Thailand, May. 2005, pp. 697-700.

[12] V. Kumar, M. Korpi and S. Sengoodan, *IP Telephony with H.323*, Wiley, United State of America, 2001.

[13] The Network Simulator, NS-2, "http://www.isi.edu /nsnam/ns/"

Rectangular Wave Delta Modulation Buck Regulator for Voltage Regulator Modules

J. Ngarmnil and K. Sooksood
Department of Electronic Engineering, Faculty of Engineering,
Mahanakorn University of Technology, Bangkok, 10530, Thailand
Email: jitkasam@mut.ac.th, ksooksood@ieee.org

***Abstract*-This paper describes design of rectangular wave delta modulation (RWDM) buck regulator for voltage regulator modules (VRM). This regulator does not require clock generator as PWM regulators do. It has simple and compact circuit; it consumes less chip area. Hence, it is suitable for VRM application. The proposed regulator was simulated by HSpice simulation program using AMIS 0.5 µm CMOS parameters to verify the concept. It shows very fast transient response and 70.55% maximum efficiency. Moreover, the proposed buck regulator can easily be integrated onto a monolithic chip.**

I. INTRODUCTION

Buck regulators have seen increasing popularity in their utilization in the voltage regulator modules (VRM) for modern microprocessor system. To decrease power consumption and increase the speed, the microprocessors will operate at significantly low voltage and high current. A VRM is used to deliver highly accurate supply voltage regulation and high output current to the microprocessors.

Conventional buck regulators in VRM use pulse width modulation (PWM) signal to control on and off duration of switches in order to supply the input voltage to load. The switching is done at constant frequency and on time of the switch is adjusted to control the average output voltage. There are many control techniques both in analog and digital can be used to make PWM signal to control buck regulators [1-2]. However, to obtain high performance and efficiency of the regulators, a larger chip area and complexity are required to facilitate the required high performance control circuitries such as amplifier, saw-tooth generator, oscillator, A/D converter and an embedded controller in fully digital control. Function of the wave generator circuit is always critical under modern low voltage environment and having power supply variations from battery operation. Then a robust wave generator, which always comes with a high cost, will be needed. As a result, a high performance PWM-based regulator becomes expensive for a practical implementation.

RWDM principle is also another attractive technique that can be used in high performance DC-DC converters because the RWDM output signal is pulse like PWM but fewer devices are required in the control circuitries. RWDM principle is firstly applied to switching power converter system in an inverter [3]. It shows an excellent low order harmonic attenuation. Recently, the RWDM control approach has been applied and successfully implemented onto a class-D audio amplifier [4-5] of which 92% maximum power efficiency has been achieved. In scenario of efficiency, ease of control, simple and compact structure, the RWDM is seen as another promising technique to be implemented in the control loop of a buck converter. This paper presents a new RWDM-based buck regulator scheme having four advantages. First, the triangular wave generator or oscillator is not required. Second, the integrator of the RWDM loop is reduced since the actual output voltage, which is essentially proportional to the switching rectangular wave, can be used instead. Third, the switching frequency is variable. Then, the power loss is low at low load current [6]. Finally, it provides faster transient response than V^2 control method [7]. The proposed architecture is verified through HSpice simulation program.

This work has been supported by a grant from Shell Centennial Education Fund.

II. RWDM PRINCIPLE

The RWDM principle is shown in Fig. 1 [8]. Conceptually, RWDM is similar to PWM except that the input signal $V_R(t)$ is compared with the feedback signal $V_e(t)$, which is essentially the integrated signal of RWDM by integrator. Then, $V_e(t)$ can track the amplitudes of $V_R(t)$ within the ΔV hysteresis boundary. From Fig. 1, the frequency of RWDM signal can be given by

$$f = \frac{1}{T^+ + T^-} = 1 \Big/ \left(\frac{\Delta V}{m^+ - x'(t)} + \frac{\Delta V}{m^- + x'(t)} \right) \qquad (1)$$

where m^+ and m^- denote the slopes of the rising and falling

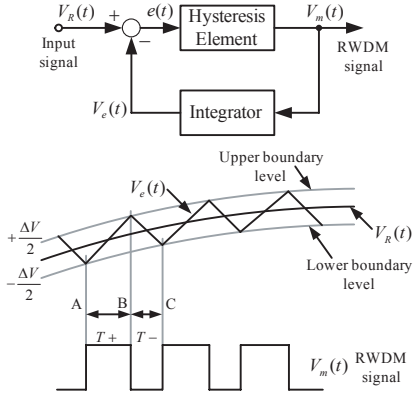

Figure 1. RWDM principle

curve of the feedback signal $V_e(t)$, respectively. $x'(t)$ is the average slope of the input signal $V_R(t)$ and ΔV is the tracking boundary corresponding to the magnitude of the hysteresis loop which is controlled directly by the trip voltage of the comparator. m^+ and m^- are also controlled by the time constant of the integrator in the feedback path. Derived in Eq. (1), the frequency of RWDM output signal is variable frequency. The frequency is a function of hysteresis boundary and slopes of both input and feedback signal.

Based on the principle, RWDM controller is simple for implementation. RWDM-based converters can then be integrated with less area consumption than conventional PWM converters. Considering Eq. (1), it can notice that the slope of the input signal $x'(t)$ of the RWDM loop is normally small in the application of switching regulator as compared to m^+ and m^-. Then, the variation of the switching frequency is not too broad and can be a predictable parameter.

The RWDM-based buck regulator is illustrated in Fig. 2. It is noted that the preliminary integrator in the RWDM loop is cancelled out of the circuit, while the integration of RWDM signal is taken from the output voltage of error amplifier node. However, this is double integral signal because a buck regulator is always second order system.

III. Buck Regulator Analysis and Design

The steady state analysis and design of RWDM-based buck regulator is discussed in this section. Fig. 3 demonstrates the ideal waveforms of output voltage and inductor current used for calculation. The proposed buck regulator is designed to meet a following specification for VRM: V_{in} = 12 V, V_{out} = 1.5 V ±1%, and I_{out} = 20 A. The inductor L is 0.9 µH, output capacitor C is 3300 µF and load resistor is 75 mΩ.

A. On-Time Interval

During MP is closed and MN is opened (t_{on}). It is obviously seen that, this is a second order system with DC forced response. The differential equation of the output voltage is

$$\frac{d^2}{dt^2}v_{out} + \frac{d}{dt}\frac{v_{out}}{R_L C} + \frac{v_{out}}{LC} = \frac{V_{in}}{LC}. \quad (2)$$

The t_{on} can be straightforward analyzed by solving second order differential equation of the output voltage under the initial condition of $v_{out}(0) = V_{out}$ and $i_L(0) = I_{L\min}$. The t_{on} is the time that $v_{out}(t) = V_{out}$. Calculating Eq. (2) yields t_{on} = 0.343 µs.

B. Off-Time Interval

The off-time interval (t_{off}) is taken during MP is opened and MN is closed. This is a second-order system with zero forced response. Thus, the differential equation of the output voltage is

$$\frac{d^2}{dt^2}v_{out} + \frac{d}{dt}\frac{v_{out}}{R_L C} + \frac{v_{out}}{LC} = 0. \quad (3)$$

Similar to the t_{on}, the t_{off} can be determined by solving Eq. (3) under the initial condition of $v_{out}(0) = V_{out}$ and $i_L(0) = I_{L\max}$. The t_{off} is the time that $v_{out}(t) = V_{out}$. Calculating Eq. (3) yields t_{off} = 2.4 µs.

C. Switching Frequency

From the above analysis, it can be observed that the time intervals are a function of L, C, load resistance, input voltage and output voltage level. Then, the switching frequency is varied as a function of these values and directly obtained from

$$f = \frac{1}{t_{on} + t_{off}} = 364.564\,\text{kHz}. \quad (4)$$

D. RWDM Signal Slopes

Referring to Eq. (1), the frequency of the RWDM signal depends on signals' slope. The input signal of the RWDM is the regulated output voltage and the feedback signal is the PI-controller output voltage. The rising and falling slope of the regulated output voltage can be approximated as follow:

$$S_R = \frac{\Delta V_{out}}{t_{on}} = 87463.56\,\text{V/s} \quad (5)$$

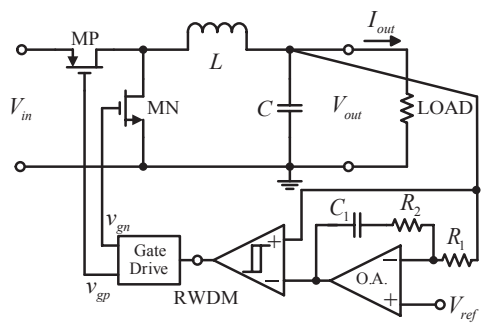

Figure 2. RWDM buck regulator

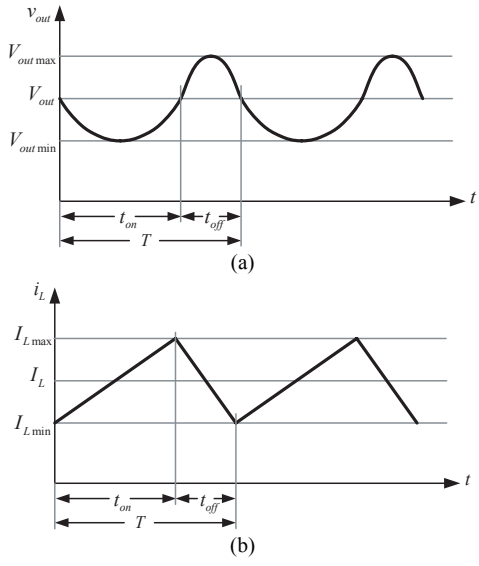

Figure 3. Ideal waveforms, (a) output voltage and (b) inductor current

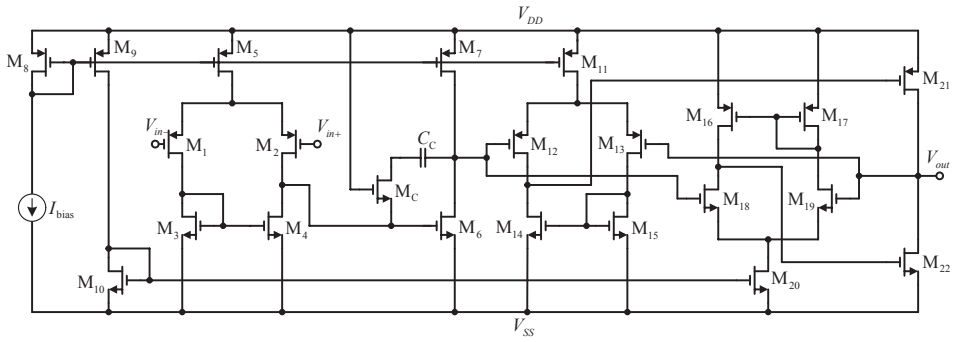

Figure 4. CMOS operational amplifier

$$S_F = \frac{\Delta V_{out}}{t_{off}} = 12500\ \text{V/s} \tag{6}$$

where S_R and S_F are the slopes of rising and falling curve, respectively. ΔV_{out} is a desired output ripple. The feedback signal slopes (m^+ for rising and m^- for falling curve) are obtained by multiplying slopes of the regulated output voltage with error amplifier gain. Error amplifier is designed using PI-controller with the gain of 50 and the integrating time of 1 ns. Thus, m^+ = 4373177.843 V/s and m^- = 625000 V/s.

E. Hysteresis Boundary

The average slope of the regulated output voltage is much smaller than feedback signal slopes. Then, the $x'(t)$ in Eq. (1) can be neglected as

$$f = \frac{m^+ m^-}{\Delta V\left(m^+ + m^-\right)}. \tag{7}$$

Substituting known value (f, m^+, and m^-) into the Eq. (7), the hysteresis boundary of the RWDM loop can then be obtained as ΔV = 1.5 V.

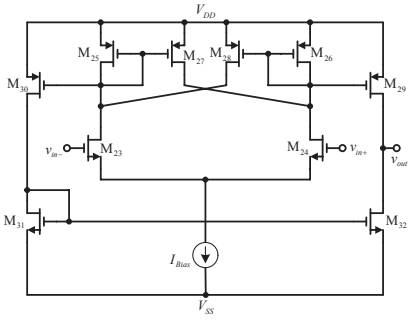

Figure 5. CMOS hysteresis comparator

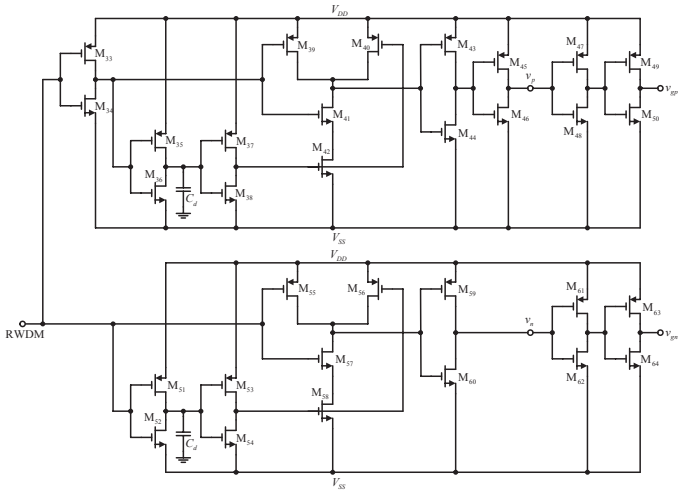

Figure 6. CMOS gate driver with dead time

IV. Simulation Results

The proposed buck regulator has been verified through HSpice using AMIS 0.5 μm CMOS parameters. The PMOS switch (MP) with W/L = 600 mm/1 μm and the NMOS switch (MN) with W/L = 200 mm/1 μm were employed. They showed 0.01 Ω on resistance. The parameter of a 0.9 μH MVR series Coilcraft inductor was used. It had 1.72 mΩ of dc resistance. The output capacitor was 3300 μF with 3 mΩ ESR. The CMOS opamp with class-AB output buffer was used as illustrated in Fig. 4. The simple CMOS hysteresis comparator in Fig. 5 was also utilized. The gate driver was design using CMOS inverter chains [9] with 100 ns dead time, demonstrated in Fig. 6. The control circuitries were biased with regulator input voltage and I_{bias} = 50 μA. The transistors aspect ratios and component values are listed in Table 1. The simulation results of the output voltage are shown in Fig. 7 and 8. The output voltage has maximum ripple of 11.8 mV and switching frequency of 407.554 kHz at 20-A output current.

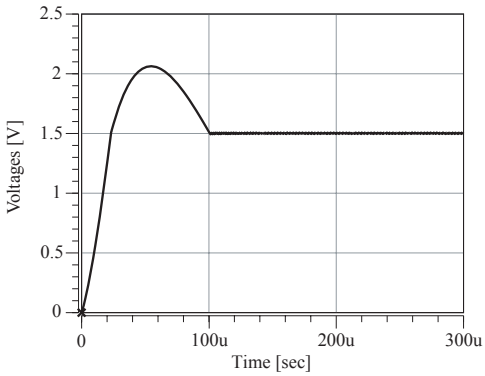

Figure 7. Simulated output voltage

Fig. 9 exhibits the regulated output voltage and current when output current is stepped from 10-A to 20-A. It can be seen that the RWDM buck regulator provides very fast transient response (approximately 1.5 μs). In addition, the switching frequency only depends on output current, but the output voltage level and ripple are not affected.

Finally, the power efficiency as a function of output current at V_{in} = 12 V and V_{out} = 1.5 V is illustrated in Fig. 10. It shows maximum power efficiency of 70.55% at 10-A output current. The power efficiency of the designed RWDM buck regulator is not too high, because the employed CMOS process is improper for high power operation. To improve power efficiency, the external discrete power MOSFET should be used as switches.

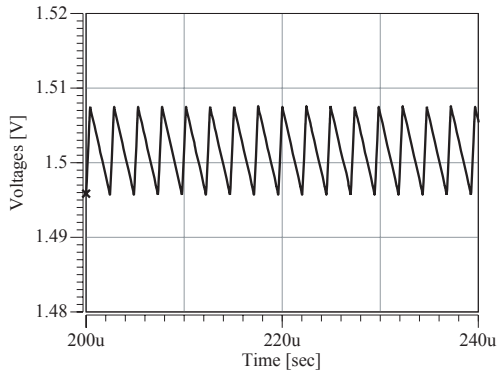

Figure 8. Simulated output ripple

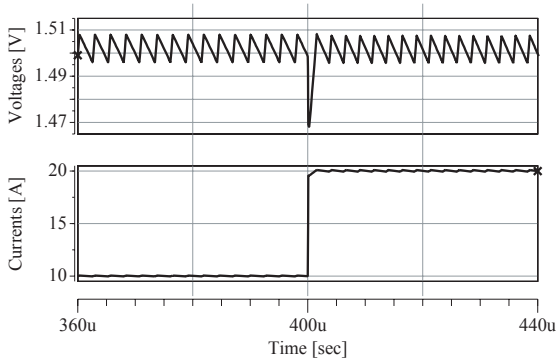

Figure 9. Regulated output voltage when output current is stepped

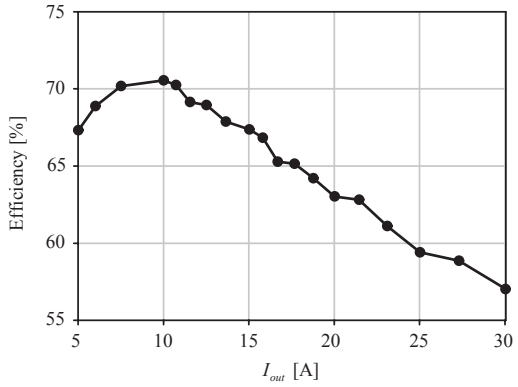

Figure 10. Power efficiency versus output current

V. Conclusion

The analysis and design of RWDM-based buck regulator for VRM is presented in this paper. It has simple circuit and can be easily integrated onto monolithic chip. Furthermore, the proposed regulator provides very fast transient response, which suitable for VRM applications. The HSpice simulation results are included to confirm the theory. They agree well with the theoretical calculations. They show 1.5 μs transient response and 70.55% maximum power efficiency.

References

[1] R. W. Erickson, and D. Maksimović, *Fundamentals of Power Electronics*, 2nd ed., Massachusetts: Kluwer Academic Publishers, 2001, ch. 1.

[2] S. Maniktala, *Switching Power Supply Design & Optimization*, New York: McGraw-Hill, 2004, ch. 3.

[3] P. D. Ziogas, "The delta modulation technique in static PWM inverters," *IEEE Trans. Ind. Appl.*, vol. 17, no. 2, pp. 199-204, 1981.

[4] K. Nandhasri, J. Ngarmnil, and K. Moolpho, "A 2.8V RWDM class-D power amplifier using an FGMOS comparator," *Proc. IEEE ISCAS 2002*, vol.5, pp. 261-264, 2002.

[5] S. C. Li, V. C. Lin, K. Nandhasri, and J. Ngarmnil, "New high efficiency 2.5V/0.45W RWDM class-D audio amplifier for portable consumer electronics," *IEEE Trans. Circuits Syst. I, Reg. Papers*, vol. 52, no. 9, pp. 1767-1774, 2005.

[6] B. Arbetter, R. Erickson, and D. Maksimović, "DC-DC converter design for battery-operated systems," *Proc. IEEE PESC 95*, vol. 1, pp.103-109, 1995.

[7] D. Goder and W. R. Pelletier, "V^2 architecture provides ultra-fast transient response in switch mode power supplies," *Proc. HFPC 96*, pp.19-23, 1996.

[8] R. Steele, *Delta Modulation Systems*, London: Pentech Press, 1975, ch. 6.

[9] A. J. Stratakos, S. R. Sanders, and R. W. Broderson, "A low-voltage CMOS DC-DC converter for a portable battery-operated system," *Proc. IEEE PESC 94*, vol. 1, pp. 619-626, 1994.

TABLE I
TRANSISTORS ASPECT RATIOS AND COMPONENT VALUES

Components	Dimension
M1-M2	20 μm/2 μm
M3-M4	38 μm/2 μm
M5, M8, M9, M10, M11	6.9 μm/1 μm
M6	152 μm/2 μm
M7	28 μm/2 μm
Mc	1.5 μm/2 μm
M12, M13, M16, M17	22 μm/2 μm
M14, M15, M18, M19	22 μm/1 μm
M20	40 μm/1 μm
M21	600 μm/0.5 μm
M22	400 μm/0.5 μm
M23-M24	25.5 μm/1 μm
M25-M26, M29-M30	28.5 μm/2 μm
M27-M28	29 μm/1 μm
M31-M32	6 μm/1 μm
M33, M35, M37, M43, M45, M51, M53, M59	5 μm/2 μm
M34, M36, M38, M44, M46, M52, M54, M60	10 μm/2 μm
M39-M40, M55-M56	10 μm/1 μm
M41-M42, M57-M58	20 μm/1 μm
M47, M49, M61, M63	100 μm/1 μm
M48, M50, M62, M64	50 μm/1 μm
C_c	0.15 pF
C_d	100 pF

Dual Input All-Pass Networks Using MO-OTA and its Application

Pipat Prommee[1], Krit Angkeaw[2], Jirasak Chanwutitum[2], and Kobchai Dejhan[1]
[1]Faculty of Engineering and Research Center for Communication and Information Technology
King Mongkut's Institute of Technology Ladkrabang, Bangkok 10520, Thailand
Tel: +66-2326-4238, +66-2326-4242, Fax: +66-2326-4554
[2]Industrial Electrical Technology Department, Faculty of Engineering
King Mongkut's Institute of Technology North Bangkok, Bangkok 10800, Thailand
Email: pipat@telecom.kmitl.ac.th

***Abstract*— This paper presents a realization of grounded passive elements first order all-pass networks using a multiple-output operational transconductance amplifier (MO-OTA) and three grounded passive elements. The proposed circuit is operated in current-mode for the good benefit as well as high output impedance and cascadability. Therefore, it can be directly employed as a subsystem of monolithic circuit without additional matching circuits. Furthermore, a new quadrature oscillator is presented as an application for confirmed the theory and realistic practically. The PSpice simulation results verifying of theoretical are also included.**

I. INTRODUCTION

Current mode signal processing circuits have recently demonstrated many advantages over their voltage mode counterparts including increased bandwidth, higher dynamic range and better suitability for operation in reduced supply environment [1]. In many papers, current mode circuits are presented by using CCII based [2]-[4]. Unfortunately, CCII does not have a differential input. The OTA is a familiar device for voltage-mode and current-mode applications. The OTA provides a highly linear electronic tunability and a wide frequency range. Moreover, OTA-based circuits require no resistors and therefore, are suitable for monolithic implementation and small die area [5]-[6]. The MO-OTA has been proposed in previous paper [7]. From the strong points, due to many output of OTA, the MO-OTA has more flexible to use in term of a modern analog signal processing as well.

The previously presented all-pass filter topologies employing conventional OPAMP [8-9] that ensure the low bandwidth and voltage-mode are achieved. The FTFN [10], Current Differencing Buffer Amplifier (CDBA) [11] and CCII [2]-[4] are also introduced but some of these reports suffer from floating passive components. The floating components are trade-off in the practical realizations, parasitic capacitances, bandwidth restrictions, complicated adjustment. The floating node passive devices have to avoid in the design for minimized the error reasons.

This paper presents the design of all grounded passive elements all-pass network using one MO-OTA and three grounded passive elements. The presented topologies can be designed by using both in CMOS or bipolar technology. The circuits comprise phase lead and phase lag Moreover, current gain can be adjust by a transconductance (gm) through I_{abc}. The simple construction and low voltage are proposed that suitable for further IC fabrication.

II. THEORY AND PRINCIPLE

The OTA is a simple device that has been found in many recently reports. The benefit of OTA is a voltage and current mode realization can be done with a simple structure. The tunable characteristic is a strong excellent point for the future applications. The single output OTA is a conventional device that might be has some restrictions on the design. The modification of OTA can be eliminated that restrictions by extended the output port namely a multiple-output OTA (MO-OTA).

A. Multiple-output operational transconductance amplifier

The OTA has input as voltage and current output. The simple structure of the well-known OTA, having used only four transistors and current source. Figure 1 shows the symbol of MO-OTA. The output current of MO-OTA yields

$$I_o = \pm g_m (V_+ - V_-) \qquad (1)$$

The transconductance g_m is variable by bias current I_{abc}. Note that the transconductance base on CMOS and bipolar technology are equal to $(\beta I_{abc}/4)^{1/2}$ and $I_{abc}/2V_T$ respectively. A possible implementation of OTA using multiple output operation transconductance amplifiers was proposed [12].

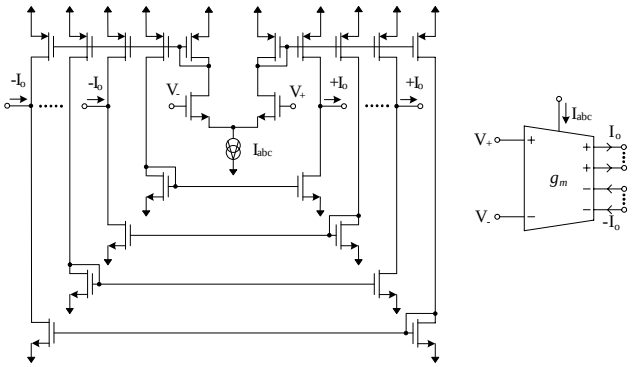

Fig.1. (a) CMOS MO-OTA structure and (b) symbol

The transconductance of above CMOS OTA can be expressed as:

$$g_m = \sqrt{\frac{\beta I_{abc}}{4}} = \sqrt{\frac{\mu C_{OX} W I_{abc}}{4L}} \qquad (2)$$

The realization of the proposed all-pass network filter using OTA is show in Fig.2. The circuit comprises one MO-OTA, 2 grounded resistors and a grounded capacitor. From this point of view, the proposed structure is simpler than the other existing all-pass realizations [2]-[4]. In Fig.2(a) and Fig.2(b), the all-pass transfer functions are realized as eq.3 and eq.4 respectively.

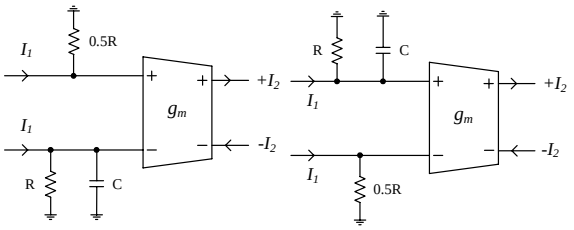

Fig.2. Proposed Allpass Filter Networks

$$\frac{I_2}{I_1} = \pm K\left(\frac{sCR-1}{sCR+1}\right) \qquad (3)$$

$$\frac{I_2}{I_1} = \pm K\left(\frac{1-sCR}{1+sCR}\right) \qquad (4)$$

Gain (K) is a constant and defined as

$$K = \frac{g_m R}{2} \qquad (5)$$

From Eq.(3), the phase shift are varying between 180° to 0° while (4), the phase shift are varying between 0° to -180°. The pole frequency (ω_o) can be expressed as

$$\omega_o = \frac{1}{RC} \qquad (6)$$

The passive sensitivities can be obtained as

$$S_R^{\omega_O} = S_C^{\omega_O} = -1 \qquad (7)$$

In Fig. 2, it can see that the output impedance of the circuit is very high due to the OTA current output; hence it can be directly interconnection with load or any current mode circuits without the buffer circuit. The output current gain can be adjusted by gm through the bias current I_{abc}.

The circuit model of a non-ideal OTA operating in saturation region is shown in figure 3, where C_i is the input capacitance, C_O is the output capacitance and G_O is the output conductance. Generally G_O is less than g_m. The proposed circuits in figure 2(a) and 2(b) can be express in term of high frequency as eq(8) and eq(9), respectively.

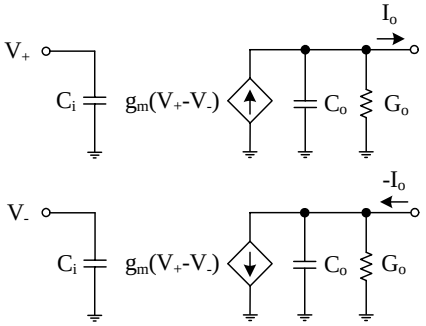

Fig.3. Circuit model for non-ideal case of the MO-OTA

$$\frac{I_2}{I_1} = \pm K\left(\frac{sR(C+2C_i)-1}{(sRC+1)(0.5sRC_i+1)}\right) \qquad (8)$$

$$\frac{I_2}{I_1} = \pm K\left(\frac{1+sR(C+2C_i)}{(1+sRC)(1+0.5sRC_i)}\right) \qquad (9)$$

From (8)-(9) imply that the parasitic capacitances affect to the poles and zeros of the transfer function at the high frequency.

III. Quadrature Oscillator Application

The quadrature oscillator based on all-pass network is shown in Fig. 4. The circuit consists of phase-lead and phase-lag all-pass network configurations in Figs. 2(a) and (b). In Fig. 4, the circuit can be oscillated due to the loop-gain is unity, the transfer function can be expressed as

$$T_1(s)T_2(s) = K_1K_2\left(\frac{1-sC_2R_2}{1+sC_2R_2}\right)\left(\frac{sC_1R_1-1}{sC_1R_1+1}\right) = 1 \qquad (10)$$

Where the constants are $K_1=g_{m1}R_1/2$ and $K_2=g_{m2}R_2/2$, loop-gain is unity independent with the any transconductances , g_{mi}. The phase of first all-pass network is written as

$$\phi(\omega) = -2\tan^{-1}(\omega\tau_1),\ \tau_1 = C_1R_1 \qquad (11)$$

Likewise, the phase of second all-pass network is

$$\phi(\omega) = 180 - 2\tan^{-1}(\omega\tau_2),\ \tau_2 = C_2R_2 \qquad (12)$$

The frequency of oscillation can be given as

$$\omega = \frac{1}{\sqrt{\tau_1 \tau_2}} \qquad (13a)$$

or

$$\omega = \frac{1}{\sqrt{C_1 C_2 R_1 R_2}} \qquad (13b)$$

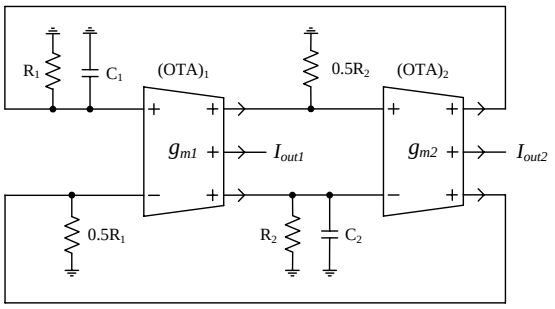

Fig. 4. The quadrature oscillator using proposed all-pass networks

From (13), the oscillation frequency is depended on passive elements, R_1, R_2, C_1 and C_2. The components are defined identically as $R_1=R_2=R$ and $C_1=C_2=C$. The oscillation frequency is actually becomes

$$\omega = \frac{1}{\sqrt{CR}} \qquad (14)$$

IV. Simulation Results

In order to confirm the validity of the proposed circuits, PSpice simulation was carried out. The parameters used in simulation are 0.5µm CMOS model obtained through MIETEC as listed in table 1. The W/L parameters of MOS transistors are assumed of 20µm/1µm for NMOS and 60µm/1µm for PMOS. The supplied voltages are V_{DD} = -V_{SS} = 1.5 V. The corner frequency of 15.9 kHz are obtained with such passive elements setting as R=10kΩ and C=10nF. The simulation results are illustrated for the current transfer function characteristic in Fig.6 (a) and Fig.6 (b). The characteristics represent for the phase response of phase-lead and phase-lag all-pass filter, respectively. It can be observed that the circuits provide a bandwidth for a several MHz. From Fig.6, the effective of parasitic capacitances at output of OTA are taken in order to the high frequency according to eq. (8) and (9).

The application of proposed all-pass networks is a quadrature oscillator as shown in Fig.4. The simulation result of proposed oscillator application has shown in Fig. 7. The 2 outputs can be obtained for a quadrature behavior. The phase different is about 90° according with the theoretical. The waveform of the quadrature oscillator are in the assuming conditions, $g_{m1}=g_{m2}$=200µs, $R_1=R_2$=10kΩ and $C_1=C_2$=0.01µF. The oscillation frequency can be obtained ensure that are in agreement with the above theoretical about 16 kHz.

TABLE 1. PARAMETER USED IN SIMULATION

```
.MODEL  NMOS  LEVEL=3  UO=460.5  TOX=1.0E-8  TPG=1
VTO=+0.62  JS=1.08E-6  XJ=0.15U  RS=417  RSH=2.73
LD=0.04U VMAX=130E3 NSUB=1.71E17 PB=0.761 ETA=0.00
THETA=0.129   PHI=0.905   GAMMA=0.69   KAPPA=0.10
CJ=76.4E-5   MJ=0.357   CJSW=5.68E-10   MJSW=0.302
CGSO=1.38E-10      CGDO=1.38E-10      CGBO=3.45E-10
KF=3.07E-28 AF=1 WD=+0.11U DELTA=+0.42 NFS=1.2E11
DELL=0U LIS=2 ISTMP=10 TT=0.1E-9

.MODEL PMOS LEVEL=3 UO=100 TOX=1.0E-8 TPG=1 VTO=-
0.58 JS=0.38E-6 XJ=0.10U RS=886 RSH=1.81 LD=0.03U
VMAX=113E3     NSUB=2.08E17     PB=0.911     ETA=00
THETA=0.120 PHI=0.905 GAMMA=0.76 KAPPA=2 CJ=85E-5
MJ=0.429  CJSW=4.67E-10  MJSW=0.631  CGSO=1.38E-10
CGDO=1.38E-10   CGBO=3.45E-10   KF=1.08E-29   AF=1
WD=+0.14U  DELTA=0.81  NFS=0.52E11  DELL=0U  LIS=2
ISTMP=10 TT=0.1E-9
```

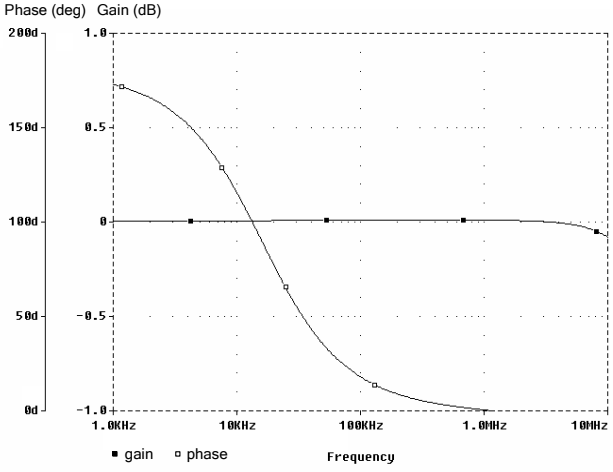

Fig .6 (a) The phase response of filter topology in Fig.2(a)

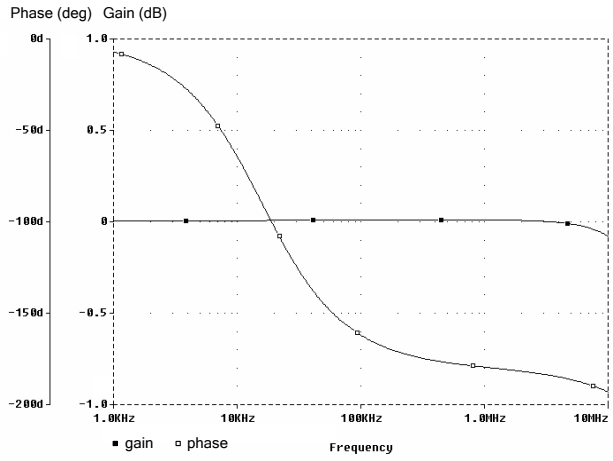

Fig .6(b) The phase response of filter topology in Fig.2(b)

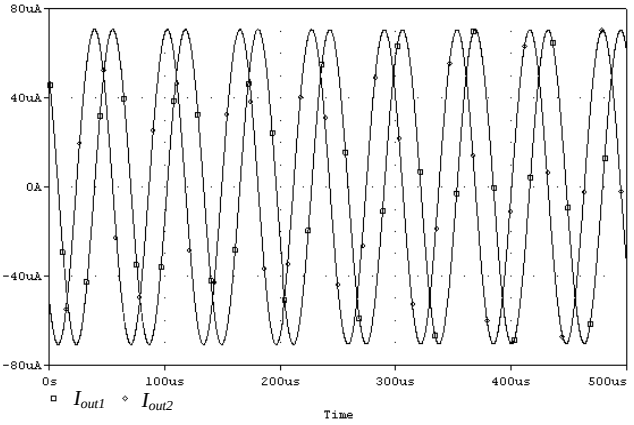

Fig. 7. Output waveform of quadrature oscillator in Fig. 4

V. CONCLUSION

The dual input multiple-output OTA all-pass filter topologies with all grounded passive elements are presented. The phase-lead and phase-lag can be simply modification with a few passive components changed. The proposed topologies does not limit for the implementation in bipolar or CMOS technology. The proposed circuits tried to use the MOS transistors for OTA realization. The output current can be applied to next circuit without the any matching devices. The cascadable topology is a benefit of proposed current mode schemes. The cascade of proposed both types can be obtained a quadrature oscillator as an application. Due to the minimized component, decreasing components can be done by the electronic resistors [13] that implemented from only 2 MOS transistors. The oscillator will used only 2 capacitors for the passive elements. The filter and oscillator simulation results are obtained a good agreement with the theories suitable for further IC fabrication.

REFERENCES

[1] C. Toumazou, C. Lidgey, and D. G. Haigh, Analogue IC design: the current mode approach, Peter peregrinus ltd., 1990.

[2] M. Higashimura and Y. Fukui, "Realization of current mode all-pass networks using a current conveyor," *IEEE Trans. Circuits and Syst.*, vol. 37, pp. 660-661, 1990.

[3] A. M. Soliman, "Generation of current conveyor based all-pass filters from op-amp based circuits," *IEEE Trans. Circuits and Syst*., *II*, vol. 44, pp. 324-330, 1997.

[4] O. Cicekoglu, H. Kuntman, and S. Berk, "All-pass using a single current conveyor," *Int. J. Electron.*, vol. 86, pp. 947-955, 1999.

[5] E. Sanchez-Sinencio, J. Ramirez-Angulo, B. Linares-Barranco, and A. Rodriguez-Vazquez, "Operational transconductance amplifier-based nonlinear function syntheses," *IEEE J. Solid-State Circuit*, vol. 24, no. 6, pp. 1576-1586, 1989.

[6] A. Rodriguez-Vazquez, B. Linares-Barranco, J. L. Huertas, and E. Sanchez-Sinencio "On the design of voltage-controlled sinusoidal oscillators using OTAs," *IEEE Trans. Circuits and Syst*., vol. 37, pp. 197-211, 1990.

[7] J. Ramirez-Angulo, and E. Sanchez-Sinencio, "High-frequency compensated current-mode ladder filter using multiple output OTAs," *IEEE Trans. Circuits and Syst., II*, vol. 49, pp. 581-586, 1994.

[8] J. V. Vosper, "Synthesis of first-order active-R allpass networks and their application in sinusoidal oscillator design," *Electron. Lett*., vol. 27, pp. 53-55, 1991.

[9] R. Holzel, "A simple wide-band sine wave quadrature oscillator," *IEEE Trans. Instrum. Meas.*, vol. 42, pp. 758-760, 1993.

[10] M. Higashimura, "Current-mode allpass filter using FTFN with grounded capacitor," *Electron. Lett*., vol. 27, pp. 1182-1183, 1991.

[11] A. Toker, S. Ozoguz, O. Cicekoglu, and C. Acar, "Current-mode all-pass filters using current differencing buffered amplifier and a new high-Q bandpass filter configuration," *IEEE Trans. Circuits and Syst*., *II*, vol. 47, pp. 949-954, 2000.

[12] C.-C. Hsu and W.-S. Feng, "Structural design of current-mode biquad filters," *Int. J. Electron.*, vol. 88, pp. 41-51, 2001.

[13] Z. Wang, "2-MOSFET transistors with extremely low distortion for output reaching supply voltage," *Electron. Lett.*, vol. 26, pp. 951-952, 1990.

PDF-XCHANGE Click to buy NOW! www.docu-track.com

A Physics-Based InP/InGaAs SHBT Model for SPICE simulation

Suchat Osaklang [1] and Chiranut Sa-ngiamsak [2]
[1] Graduate School, Department of Electrical Engineering, Faculty of Engineering, KKU, Thailand
[2] Department of Electrical Engineering, Faculty of Engineering, KKU, Thailand
Email: g4880070@eestud.kku.ac.th and chiranut@kku.ac.th

***Abstract*- A physics-based, large-signal SPICE model for an abrupt-junction uniform-base InP/InGaAs SHBT is reported. This work was developed from the physics-based model for AlGaAs/GaAs SHBT. The SPICE parameters for this model are directly and automatically calculated from the transistor profile. A specific InP/InGaAs SHBT was studied. The simulations of the IV characteristics were compared with the measurements. The results show a good agreement between this work and the measurements. The comparison between the DC characteristics of InP-based HBT and of GaAs-based HBT demonstrates better suitability of this model to InP-based HBT due to the reduction of a deviation of the V_{CE} offset voltage (ΔV_{CE} offset). That of InP-based and GaAs-based SHBTS are ~0.16V and ~0.30 V, respectively.**

I. Introduction

Full-custom IC design is usually carried out by first choosing an IC manufacturing technology and then circuit development is conducted until it reaches satisfactory. This conventional IC design has the restriction upon the choices of transistor technologies and its profile. This restriction became an inspiration for a newly proposed way to design ICs. This new approached is called "Physical ICs Design" [1]. "Physical IC Design" offers a door of opportunity for circuit designers to modify and to investigate the impacts of changes of a transistor profile upon circuit performance. The new idea requires a physics-based transistor model which can provide a monitoring tool for electrical effects resulted from changes in transistor profile. This physics-based transistor model was initially begun with AlGaAs/GaAs Single Heterojunction Bipolar Transistors (SHBTs). Lately, due to an immerging of new III-V semiconductors such as InP-based HBTs casts a light into this research by reapplying the physics-based model for AlGaAs/GaAs SHBTs into InP-based HBTs. For high-speed ICs designs, InP-based HBTs are generally favorable comparing with GaAs-based HBTs because InP-based HBTs show the superior in microwave characteristics. Hence InP-based HBTs become an excellent candidate for high-speed and high-frequency applications [2].

Consequencely, the purpose of this work is to investigate the possibility for reapplying the Physical ICs design principle designed for AlGaAs/GaAs SHBTs to InP-based SHBTs. The set of SPICE parameters is directly calculated from the given profile. An accuracy of this model was verified by comparing the simulations with the measurements.

List of Symbols

D_{pE}	Hole diffusivity at emitter ($cm^{-3}\ s^{-1}$)
$\Delta Ec, \Delta Ev$	Conduction and valence band discontinuities (eV)
$\Delta En, \Delta Ep$	Electron and hole back barrier heighs (eV)
Eg_B, Eg_E	Band-gap energy at the base and the emitter (eV)
$\hbar$	Planck's constant divided by 2π (J-s)
J_C, J_E	Collector and emitter current density (A/cm^2)
L_E	Diffusion length of hole at emitter (cm)
k	Boltzmann's constant $(=1.38\times10^{-23}\ J/K)$
m_n^*	Electron effective mass at emitter (in unit of m_0)
$\overline{n}_{B0}$	Electron density at thermal equilibrium (cm^{-3})
n_{in}, n_{ip}	Intrinsic carrier density at the emitter and the base (cm^{-3})
N_B, N_E	Doping density at the base and the emitter layers (cm^{-3})
$\overline{p}_E$	Equilibrium hole concentration in emitter (cm^{-3})
q	Electron charge $(=1.6\times10^{-19}C)$
T	Absolute temperature (K)
V_{bi}	Built-in voltage (V)
V_{bc}	Applied voltage across the B-C junction (V)
V_{be}	Voltage across the B-E junction (V)
V_T	Thermal voltage $(=kT/q)$ (V)
V_{TnE}, V_{TpE}	Electron and hole thermal velocity at the emitter (cm/s)
W_E	Emitter layer thickness (cm)
Xne, Xpe	Depletion region at the emitter and the base (cm)
γ_n	Tunneling factor
$\varepsilon_B, \varepsilon_E$	Dielectric constant of the base and the emitter layers
χ_B, χ_E	Electron affinity of the base and the emitter (eV)

II. Device Structure

Table 1 shows a doping profile of an InP/InGaAs SHBT grown by MOVPE (Metal Organic Vapor Phase Epitaxy). This profiled is obtained from Topaloglu S. [3] and the electrical properties for this device are referred to [4] and [5].

Table 1
Transistor profile of InP/InGaAs SHBT
for the emitter area (A_E) of 1x15 μm^2 [3]

Emitter-cap	n++ InGaAs	1E19cm-3	100nm
Emitter contact	n++ InP	1E19cm-3	50nm
Emitter	n+ InP	2E17cm-3	50nm
Base	p++ InGaAs	3E19cm-3	50nm
Collector	n- InGaAs	1E17cm-3	600nm
Stop Etch	InP		10nm
Subcollector	n++ InGaAs	8E18cm-3	300nm
Buffer	InP		50nm
S.I InP Substrate			

PDF-XCHANGE Click to buy NOW! www.docu-track.com

III. HBT MODEL

A. *Abrupt-Junction Uniform-Base HBTs model*

This work focuses on a large-signal InP/InGaAs HBT model [6] for the case of an abrupt-junction uniform-base structure only. The specific AlGaAs/GaAs SHBTs model development for "physical IC design" was proposed by Sa-ngiamsak C. [1]. The report of Sa-ngiamsak C. shows a good agreement between the I-V characteristic of the simulations and the measurements; Her work becomes an initiation for this work to investigating on reapplying this model to an InP/InGaAs SHBT due to its superior properties over GaAs/AlGaAs HBTs.

Reapplying the existing model of GaAs/AlGaAs HBTs to InP-based HBTs is not a straight forward task. The following investigations have to be carried out:

1. Linearity of electron back barrier high(ΔE_n)
2. Linearity of hole back barrier high(ΔE_p)
3. Effects of tunneling factor (γ_n)

The details and reasons for this condition checkout are thoroughly explained in [1] and [6]

B. *Voltage dependency parameters of an InP/InGaAs HBTs model*

According to [1], [6] and [7], the SPICE-based HBT model can be represented by using the Ebers-Moll (E-M) BJT model when Aij parameters are constant only.

The emitter and the collector currents for the E-M BJT model are written as:

$$J_E = -A_{11}\left(e^{qV_{be}/kT}-1\right)+A_{12}\left(e^{qV_{bc}/kT}-1\right)$$
$$J_C = A_{21}\left(e^{qV_{be}/kT}-1\right)-A_{22}\left(e^{qV_{bc}/kT}-1\right) \quad (1)$$

Reapplying the E-M model to represent a SHBT cannot be directly accomplished due to the Aij parameter for SHBTs are not constant.

For example, the A_{11} parameter of a SHBT is shown below:

$$A_{11} = \frac{u_n y_n \bar{n}_{B0}}{1+\frac{u_n y_n}{z_n}} + \frac{J_{PE}}{R_E}\cosh\left(\frac{W_E}{L_E}\right) \quad (2)$$

where $J_{PE} = qD_{pE}\bar{p}_E / L_E \sinh(W_E / L_E)$ and

$R_E = 1+\left(J_{pE} / qV_{TpE}\bar{p}_E\right)\exp\left(-\Delta Ep / kT\right)\cosh(W_E / L_E)$ [7]

The first and the second terms reflect the electron and the hole currents, respectively. The first term of A_{11} can be simplified as: $\bar{n}_{B0} Z_n$ where $u_n y_n / z_n >> 1$ in case of an abrupt junction [6] and $z_n = qv_{TnE}\gamma_n e^{-\Delta E_n / kT}$. Moreover, the electron back barrier height (ΔE_n), the hole back barrier height (ΔE_p) and tunneling factor (γ_n) are all a voltage dependency parameter Overcoming this matter, if the $\gamma_n e^{-\Delta E_n / kT}$ term of an InP/InGaAs SHBT can be proven as an exponential, then there is a possibility to define this term in a single diode equation.

The investigation of the linearity of the electron and hole back barrier height are shown in Fig.1 & Fig.2.

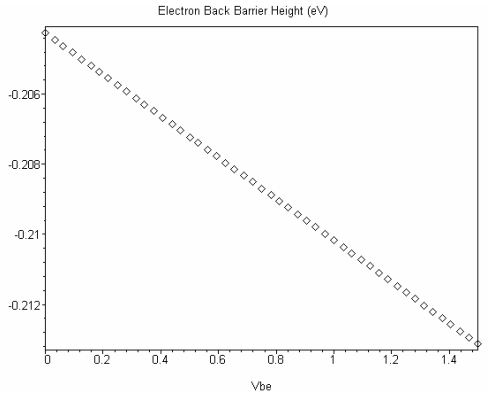

Fig. 1 Electron back barrier height in the emitter-base junction of InP/InGaAs HBTs.

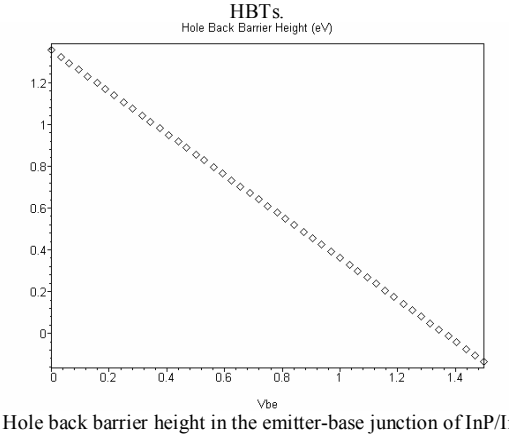

Fig. 2 Hole back barrier height in the emitter-base junction of InP/InGaAs HBTs

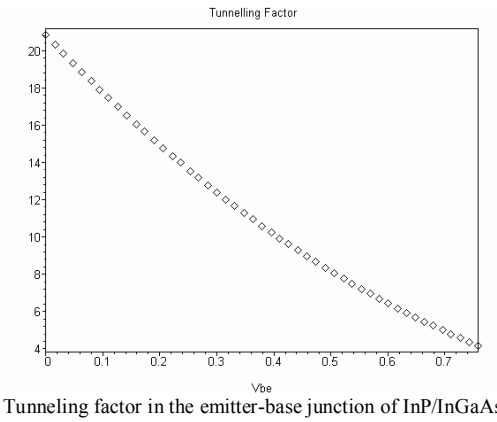

Fig. 3 Tunneling factor in the emitter-base junction of InP/InGaAs HBTs

PDF-XCHANGE Click to buy NOW! www.docu-track.com

Fig.1 demonstrates that the simulation result of the relation between ΔE_n and a bias voltage (V_{be}) is linear and so that of ΔE_p and V_{be} as shown in Fig.2. Hence, the $e^{-\Delta E_n / kT}$ term located in z_n parameter can be expressed in a diode-like format and merging the effects of ΔE_n into the E-M model in Eq.(1).

Regarding the characteristic of the tunneling factor (γ_n) shown in Fig.3, it depicts that the tunneling factor for the case of an InP/InGaAs HBT possessed an exponential relation with the bias voltage (V_{be}). So that, the $\gamma_n e^{-\Delta E_n / kT}$ terms in z_n can be exponentially expressed. In conclusion, $A_{ij}\left(e^{qV_{be}/kT}-1\right)$ and $A_{ij}\left(e^{qV_{bc}/kT}-1\right)$ of Eq.(1) can be defined in a single diode equation.

C. *Verification of Assumptions in the Model*

The assumption of $(u_n y_n / z_n)+1 \approx (u_n y_n / z_n)$ which was applied to Eq.(1) is proven in Fig.4

Fig.4 is a plot of $(u_n y_n / z_n)$ of the InP/InGaAs SHBT profile shown in Table 1. This figure clearly demonstrates that $(u_n y_n / z_n) >> 1$ for the normal mode operation range of V_{be} (0.4-1.0 Volt).

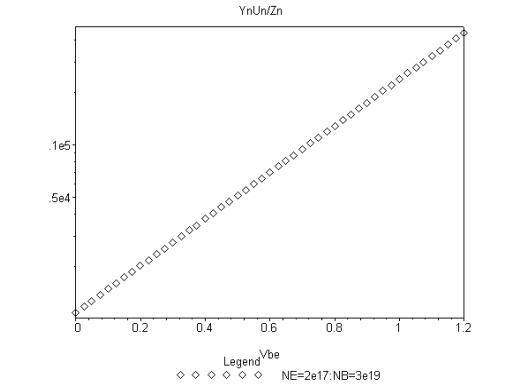

Fig. 4 The estimation result of $u_n y_n / z_n$ term in case of InP/InGaAs SHBT, for the doping profile listed in Table 1

An exponential expression of the voltage-dependent term $\left(\gamma_n e^{-\Delta E_n / kT}\right)$ describes the carrier transport across a heterojunction. The $\gamma_n e^{-\Delta E_n / kT}$ term which consists of physics-based equations of the device is fitted to $A^* e^{-V_{be}/SVt}$ where A^* and S are constant. The results of the best fit for the InP-based SHBT profile given in Table 1 are show in Fig.5. The best-fit parameters (A^* and S) for a range of doping concentration were calculated and listed in Table 2.

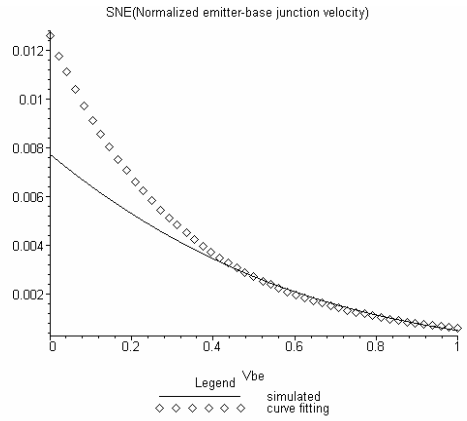

Fig. 5 The product $\gamma_n e^{-\Delta E_n / kT}$: comparison of the result from computation and the best-fit, over the bias range 0.4-1.0 V. for the uniform-base InP/InGaAs SHBT

Table 2
Fitting parameter of InP/InGaAs SHBT with different doping profile

N_E (cm^{-3})	N_B (cm^{-3})	A^*	S
1×10^{17}	1×10^{19}	0.006099	13.766864
2×10^{17}	1×10^{19}	0.022011	9.697101
2×10^{17}	3×10^{19}	0.012584	12.540796

IV. Results and Discussions

This section presents the comparisons of the DC characteristic obtained from the simulation and the measurements [3] of the InP/InGaAs SHBT profile given in Table 1. The simulation results were generated by using PSpice where the list of the calculated SPICE parameters is in Table 3. The simulation results (dashed-lines) and the measurements (solid-lines) are depicted in Fig.6.

Table 3
SPICE parameters of InP/InGaAs SHBT [6]

SPICE parameter	Value
β_f	49.485
β_r	0.0228
I_s	3.069E-22
I_{se}	8.56E-28
I_{sc}	1.476E-28
N_f	1.0866
N_r	1
N_e	1
N_c	1
R_e	0.86
R_b	18.5
R_c	4.4

PDF-XCHANGE Click to buy NOW! www.docu-track.com

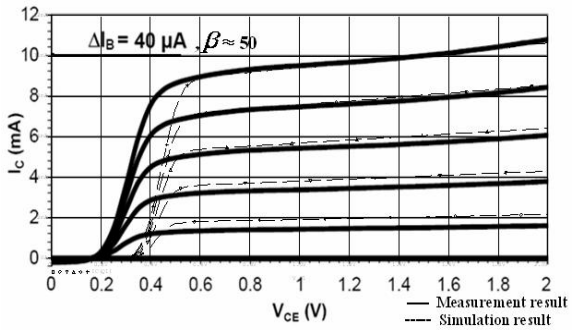

Fig. 6 Comparison of the DC characteristics between measurements (solid-lines) and simulations (dashed-lines)of the InP/InGaAs SHBT

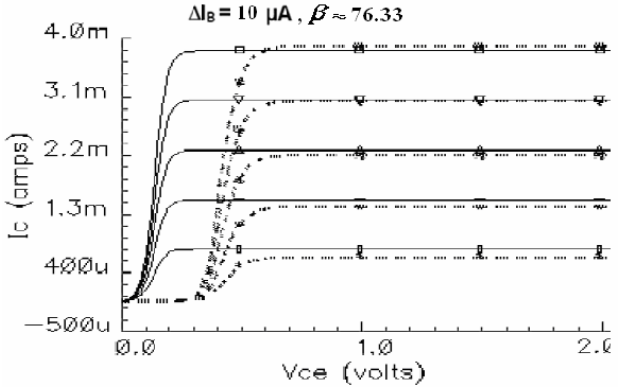

Fig. 7 Comparison of the DC characteristics between measurements(dashed-lines) and simulations (solid-lines) of the AlGaAs/GaAs HBTs where [1]

Fig.6 demonstrates a nice agreement of extending this model into InP/InGaAs SHBT devices. However, the deviation increases with smaller I_b due to the influence of the surface recombination effect being ignored at the low-level injection of carrier into emitter-base heterojunction [8].

Moreover, this model is proven to be more suitable to InP/InGaAs SHBT devices than AlGaAs/GaAs SHBT due to a smaller deviation of the V_{CE} offset voltage between the simulations and the measurements. The comparison of this figure between InP/InGaAs SHBTs (Fig.6) AlGaAs/GaAs SHBTs (Fig.7) listed in Table 4.

Table 4
Deviation of the offset voltage between the simulations and measurements of InP/InGaAs HBT vs AlGaAs/GaAs HBT

ΔV_{CE} offset	
InP/InGaAs SHBTs (Fig.6)	AlGaAs/GaAs SHBTs (Fig.7)
~0.16 V	~ 0.30 V

V. Conclusion

The extension of the physics-based HBT model for AlGaAs/GaAs HBTs has been successfully applied to InP-based HBTs. The set of SPICE parameters for a given transistor profile was calculated; and the accuracy of this approach was verified by comparing the simulations with the measurements of the specified transistor for the case of an abrupt-junction uniform-base InP/InGaAs SHBTs. The results show a good agreement in DC characteristics and an improvement in the reduction of an error regarding to knee voltage. This work can benefit to further study on the finding of a suitable InP-based SHBT profile for a specific-purpose integrated circuits which is the core of "physical ICs design" approach.

Acknowledgement

We gratefully acknowledge the financial support from the KKU's Graduate Research Fund Academic Year 2006.

Appendix: Electron and hole back barrier heights ($\Delta E_n, \Delta Ep$) [1]

From the energy band diagram of a heterojunction is shown

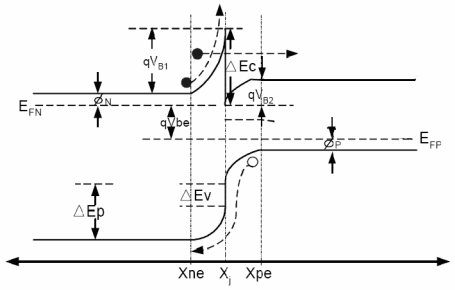

Fig.A1 Energy band diagram of an abrupt-junction and graded base HBT

The electron barrier height (ΔE_n) of an abrupt heterojunction is given by

$$\Delta E_n = qV_{B2} - \Delta Ec \qquad \text{(A1)}$$

where $qV_{B2} = \frac{qN_B}{2\varepsilon_B} Xpe'$, $Xpe = \sqrt{\frac{2N_E\varepsilon_E\varepsilon_B(Vbi - Vbe)}{qN_B(N_E\varepsilon_E + N_B\varepsilon_B)}}$,

$$\Delta Ec = \chi_B - \chi_E,\ Vbi = \Delta Ec - \frac{Eg_E}{2} + \frac{Eg_B}{2} + \frac{kT}{q}\left(\frac{N_E N_B}{n_{in} n_{ip}}\right).$$

The hole barrier height (ΔE_p) is defined as a level of energy which holes need to travel from the heterojunction to the emitter area. The function of the hole barrier height is given by

$$\Delta E_p = qV_{B1} - \Delta Ev \qquad \text{(A2)}$$

where $qV_{B1} = \frac{qN_E}{2\varepsilon_E} Xne'$, $Xne = \sqrt{\frac{2N_B\varepsilon_E\varepsilon_B(Vbi - Vbe)}{qN_E(N_E\varepsilon_E + N_B\varepsilon_B)}}$,

$$\Delta Ev = \Delta Eg - \Delta Ec$$

Reference

[1] Sa-ngiamsak C., "Physical Modelling and Optimizaton of the HBT Profile in an HBT/FET op-amp for Switched-Capacitor Circuits", Ph.D. Thesis, UMIST, UK, 2004.

[2] Esame O. et al., "Performance comparison of state-of-art HBT based on AlGaAs/GaAs, Si/SiGe, and InGaAs/InP", Microelectronics Journal, vol.35, p901-908, June. 2004.

[3] Topaloglu S., "Process Technology High Speed InP Based Heterojunction Bipolar Transistors", Ph.D. thesis, University Duisburg Essen, Germany, 2006.

[4] Lopez-Gonzalez J.M. et al., "Numerical Modeling of Abrupt InP/InGaAs HBTs" Solid-St Electron, vol.39, no.4, pp. 523-5 27,1996.

[5] Palankovski V. and Quay R., "Analysis and Simulation of Heterostructure Devices", Springer-Verlag Wein, N.Y., 2004.

[6] Feng J.J.X. et al., "A Physics-Based HBT SPICE Model for Large-Signal Applications", IEEE Trans. Electron Device, vol. 42, no.1, Jan. 1995.

[7] Ho S.C.M. et al., "The Effect of Base Grading on the Gain and High-Frequency Performance of AlGaAs/GaAs HBTs, IEEE Trans. Electron Device, vol.36, no.10, Oct. 1989.

[8] Searles S. and Pulfrey D. L. "An Analysis of Space-Charge-Region Recombination in HBTs", IEEE Trans. Electron Device, vol.41, no.4, April, 1989.

Devices Design, Fabrication and Characterizations of 0.8 μm CMOS Technology

A. Ruangphanit[1], N. Phongphanchantra [1,2], P. Meesapawong[1], C. Hruanan[1], S. Niemcharoen[2] and R.Muanghlua[2]
[1]Thai MicroElectronics Center(TMEC), National Electronics and Computer Technology Center 51/4 Moo 1, Wang takien District, Amphur Muang Chachoengsao, Chachoengsao 24000 Thailand.
[2] Electronics Research Center, Faculty of Engineering, King Mongkut's Institute of Technology Ladkrabang Lampratue District, Ladkrabang , Bangkok 10250 Thailand.

***Abstract*-This paper describes the concept, design and characterizations of 0.8 CMOS for technology development at Thai Microelectronics Center (TMEC). Both NMOS and PMOS have been designed form concept and using the process simulation software TSUPREM-4 and device simulation software MEDICI. Device design emphasis for example threshold voltage, off state leakage current, punchthrough voltage and Drain Induced Barrier Lowering (DIBL) effect have been seriously investigation to improve the device performance. Furthermore, the sensitivity of following parameters such as N-well dose and energy, voltage threshold adjust(VTA) dose and energy, gate oxide thickness and gate length variation have been determined. Extraction of devices model have been done on test chip. Based on measurements results, the I-V characteristics of MOSFET and Voltage Transfer Characteristics (VTC) of a testing inverter were present.**

I. INTRODUCTION

TMEC have been developed the 0.8 μm CMOS technology fabrication. Some parameters such as threshold voltage, off state leakage current, punchthrough voltage, and subthreshold behaviors should be carried out and determined. TSUPREM-4 and MEDICI are used to simulate that act as a guide line. In this paper, the design, fabrication and device characterization of 0.8 CMOS technology were proposed

II. DEVICE DESIGN

Twin well process is used for NMOS and PMOS independently. The N-well and the P-well were fabricated by phosphorus with dose of 3.6×10^{12} cm^{-2} and boron implantation with dose of 6×10^{11} cm^{-2}. For its dose, N-well and P-well doping concentration were approximately 3.0×10^{16} cm^{-3} and 1.0×10^{16} respectively. Both well are done on p type substrate 5 ohm-cm. of resistance .In order to minimize the complexity of fabrication process, n^+ polysilicon is fabricated for gate electrode. A boron ion implantation for threshold voltages adjust in a channel was implemented in order to match the threshold voltage of the NMOS and PMOS device, as require in the modern CMOS technology process. As a result, a surface channel and a buried channel are formed in NMOS and PMOS respectively. The magnitudes of threshold voltage depend on various parameters in channel doping implants simulated by MEDICI shown in Fig.1. In order to get the threshold voltage $|V_{TH}|\cong$ 1.0 V for NMOS and PMOS, the N-well implantation dose must be 4.5×10^{12} cm^{-2} and the boron implantation dose must be more than 9.0×10^{11} cm^{-2}. Fig.2 shown the threshold voltage of both MOSFET versus gate length and oxide thickness also. The threshold voltage is change rapidly as the gate length is less than 0.6 μm. The low threshold voltage is designed to improve the output current. The Anti-punchthrough implantation of NMOS is used for punchthrough suppression. The energy is 50 KeV. So that the channel peak concentration is approximately the S/D junction depth to reduce the lateral widening of depletion region at the drain end and prevents the Drain Induced Barrier Lowering (DIBL) effect also.

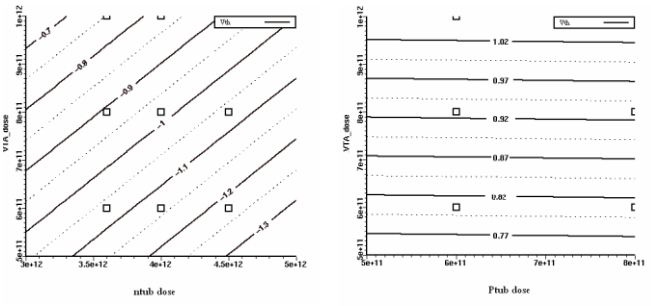

(a) (b)

Fig.1. Simulated threshold voltage of NMOS and PMOS versus (a) N-well implantation dose and VTA implantation dose and (b) P-well implantation dose and VTA implantation dose

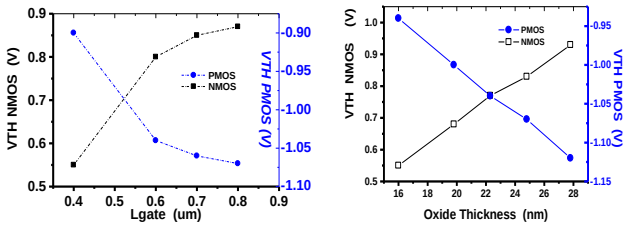

(a) (b)

Fig.2. Simulated threshold voltage of NMOS and PMOS versus (a) gate length and (b) oxide thickness

For isolation, the field oxide thickness is 650 nm .The field threshold voltage which is more than 15 V for supply operation under the thick field oxide is designed. The N-field implantation beneath the field oxide is implanted for increasing the field threshold voltage. However, the bird's break encroachment must be controlled in order to affect the source/drain formation. Besides this effect, the bird's beak encroachment into the active area must be determined in order to know the minimum design gate width which has an

enough active area will be form. To reduce the hot carrier, phosphorus with 6×10^{13} cm^{-2} and boron with 1×10^{13} cm^{-2} is implemented to form the lightly doped drain (LDD) of NMOS and PMOS structure. As and BF_2 are implemented to produce source/drain to achieve 54 Ω/sq for n^+ and 65 Ω/sq for p^+ source/drain. From simulation results, the S/D junction depth was 0.3 and 0.5 μm for NMOS and PMOS and the effective channel length was approximately 0.6 μm of both MOSFET also. The shallow junction will be improved the subthreshold swing to 80 mV/dec and minimized the Drain Induced Barrier Lowering(DIBL) effect.

III. Process Fabrication

Twin well process are fabricated for NMOS and PMOS independently. The N-well and the P-well were implemented by phosphorus with dose of 3.6×10^{12} cm^{-2} and boron implantation with dose of 6×10^{11} cm^{-2}. For its dose, N-well and P-well doping concentration were approximately 3.0×10^{16} and 1.0×10^{16} cm^{-3} respectively. Both tubs are done on p type substrate 5 ohm-cm. In order to minimize the complexity of fabrication process, n^+ polysilicon is fabricated for gate electrode. A self align n^+ polysilicon gate was 350 nm in thickness and gate oxide was 25 nm in thickness. A boron ion implantation for threshold voltage adjusts in a channel was implemented in order to match the threshold voltage of the NMOS and PMOS device, as require in the modern CMOS technology process. As and BF_2 are implemented to produce source/drain to achieve 54 Ω/sq for n^+ and 65 Ω/sq for p^+ source/drain. The 350 nm polysilicon is grown on gate oxide and used phosphorus implanattion to form n^+ polysilicon gate. After NMOS and PMOS LDD implantation, the sidewall is formed and the following S/D implantations are done. The annealing process 900°C, 30 min is done to activate impurity and maintain the impurity doping profile. After front end process, the oxide, SOG and oxide dielectric layer is deposited and reflow at 750 °C. The contact windows are opened and 30/80 of Ti/TiN are deposited and follow by metal1,TiN deposition and patterning. After an IMD layer is deposited follow by the via, windows are opened. The metal 2 and TiN are deposited and patterned. The next deposition layer is nitride to act as a passivation layer. After passivation layer, the pad window is opened to measure.

IV. Device Characterization

Measurement and extraction of a testing device are tested on a test chip. Some performance such as threshold voltage, saturation drain current, leakage current and punchthrough voltage have been determined. All I-V characteristics measurements have been done at the room temperature. The measurement system is consisted of probe station cascade ALESSI REL6100 model, semiconductor parameter analyzer HP4156B, Precision LCR meter HP 4184A, low leakage switch E5250A and ICS software for measurement through PC computer as a controller. The device parameters with N-well dose of 3.6×10^{12} cm^{-2} and VTA with dose of 9×10^{11} cm^{-2} are illustrated in table I

TABLE I
DEVICE PARAMETERS

Parameter	NMOS	PMOS	Units
Threshold Voltage	0.77	-0.68	V
Body Factor	0.6	0.64	$V^{1/2}$
Process Transconductance	74.6	26.3	$\mu A/V^2$
Effective Channel Length	0.57	0.78	μm
Width Encroachment	0.18	0.2	μm
Punch Through Voltage	12	-13	V
Leakage Current	1	1.5	pA/μm
Maximum Drain Current	328	148	μA/μm
Poly Field Threshold	10	-12	V

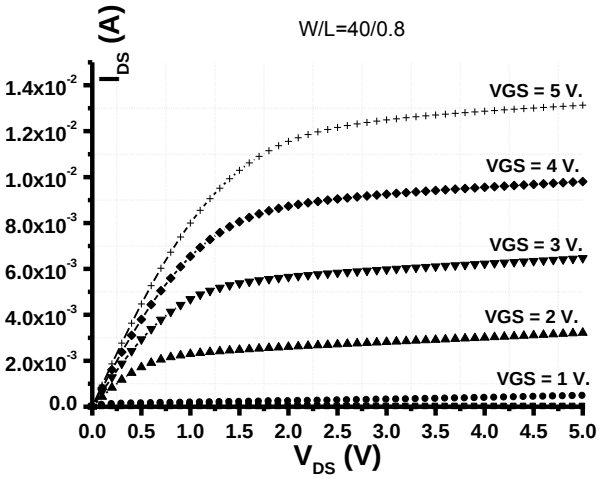

Fig.3. Measured I_{DS} &V_{DS} of NMOS with different V_{GS} (0→5 V, 1V./step)

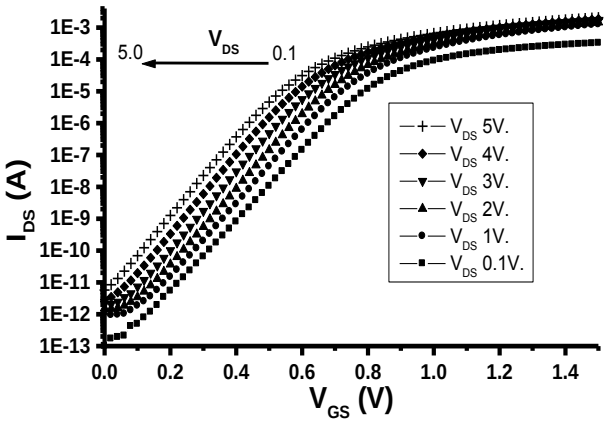

Fig.4. Measured Log I_{DS} &V_{GS} of NMOS with different V_{DS} (1./step)

Fig.3 shows the I_{DS}&V_{DS} characteristics of NMOS. The saturation current per width of NMOS and PMOS is 328 and 148 μA/μm respectively. Fig.4 shows the I_{DS}&V_{GS} characteristics of NMOS as the gate voltage V_{GS} is sweep from 0V to 1.5 V at different drain voltage V_{DS} and grounded

source and substrate together. The off stage current is in order of pA/μm for both.

The subthreshold swing is measured and compared with simulation results. The measured subthreshold swing is approximately 100mV/dec for both. The measured curve indicated that there was no punchthrough effected on a testing device same as the simulation results. The punchthrough effect is measured on I_{DS}&V_{DS} curve by sweep the drain voltage from 0 V to 20 V and ground gate and source terminal. The punchthrough voltage detected at drain current of 1nA/μm [1] is 12 V for NMOS and -13 V for PMOS.

The DIBL effect is observed by a shift of threshold voltage as a function of drain voltage The threshold voltage measurement for testing device is performed by measuring a set of I_{DS}&V_{DS} with increasing V_{DS} value as a parameter. The gate voltage at which the drain current of 0.1μA/μm is claim the threshold voltage. The measured DIBL is 40mV/V and 50 mV/V of NMOS and PMOS respectively. Since the buried channel PMOS, then more leakage current flow.

Based on the spice model level 3, the extraction model parameter was done on the testing device with the W/L ratio 40/40, 40/0.8 and 0.8/40 of value. Fig.5 show the measurement and simulation I-V curve for 40/0.8 NMOS device. It can be seen that the prediction model does not fit well with experiment. This may be because of limitations in spice model level 3.

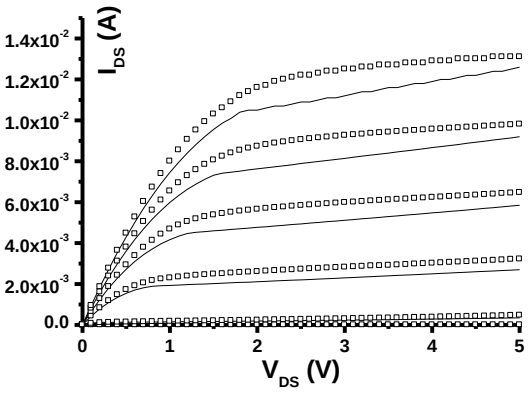

Fig.5. comparison between measurement (square symbol) and simulation (straight line)I-V characteristics of NMOS with dimension 40/0.8 .the drain bias is sweep from 0 to 5 V.(0.1V/step) and the gate voltage is step from 0 to 5V, (1V/step)

For a basic circuit testing, we test the basic CMOS inverter with a difference size of PMOS to compare with NMOS. The minimum dimension W/L of NMOS is designed at 1.6/0.8. The Voltage Transfer Characteristics (VTC) of a testing CMOS inverter show in Fig.6. The supply drain current I_{DD} versus input voltage Vin for CMOS inverter show in Fig.7. The maximum supply drain current is 130 μA at the midway of input voltage and the maximum power dissipation is a function of supply voltage.

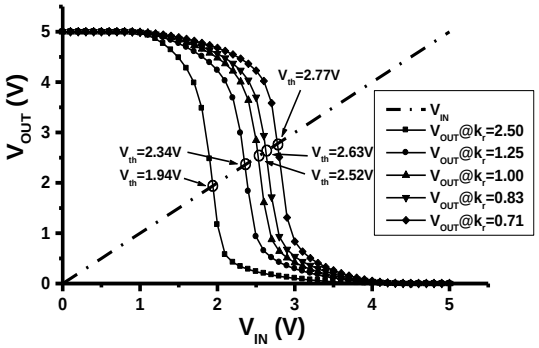

Fig.6. Measured Voltage Transfer Characteristics of a CMOS inverter with K_r as a parameter (K_r=2.5[$(W/L)_n/(W/L)_p$])

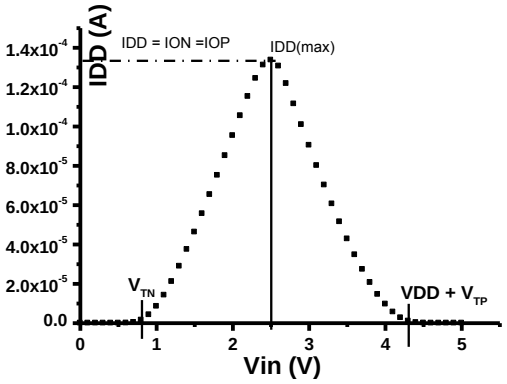

Fig.7. Measured CMOS supply drain current at K_r = 1.0

V. CONCLUSION

The 0.8 CMOS technology fabrication have been designed and developed at Thai Micro Electronics Center. A single Voltage Threshold Adjust (VTA), Anti Punthrough (APT) process and n^+ polysilicon gate electrode are fabricated to minimize the complexity of fabrication process can be achieved. The I-V curve show that the MOSFET is a good turn off rate in subthreshold region and no punchthrough problems. Surface DIBL investigation shows no surface leakage current. Using an inverter for a basic circuit testing, The VTC shows a good curve at Kr = 1.0.

ACKNOWLEDGEMENT

The authors would like to thank all TMEC's staff for device fabrication.

REFERENCES

[1] S. Wolf, Silicon Processing for the VLSI Era, vol. 3. California Lattice Press, 1995, pp.205-311.

[2] J.Y. Chen, CMOS devices and Technology for VLSI . New jersy, Prentice-Hall.Inc., 1990.
[3] K.M. Cham and S.Y. Chiang, "Device Design for the Submicrometer P-channel FET with n+ Polysilicon gate," *IEEE Tran Electron Devicesl.*, vol ED-31, pp. 964, July 1984.
[4] A.E. Schmitz and J.Y. Cheng, "Design and Fabrication of Subhalf-Micrometer CMOS Transistor," *IEEE Tran Electron Devicesl.*, vol ED-33, no 1, pp. 148, January 1986.
[5] A.E. Schmitz and J.Y. Cheng, "Twin Tub III r," *IEEE Tran Electron Devicesl.*, vol ED-33, no 1, pp. 148, January 1986.
.

Characteristics of GaAs-based Phototransistors After High-Power Operation

N. Thudsalingkarnsakul, S. Thainoi and S. Kanjanachuchai
Semiconductor Device Research Laboratory, Department of Electrical Engineering
Faculty of Engineering, Chulalongkorn University, Phayathai Road
Bangkok 10330, Thailand

***Abstract*-A commercial phototransistor (SG-105F) with a rated power of 50 mW has been subject to high-power operation (at 300 mW). Its electrical and optical characteristics before and after 24, 48 and 72 hours of high-power operation are analyzed. The output electrical characteristics (I_C-V_{CE}) and the sensitivity (I_C/I_{LED} ratio) show degradation behaviors which correlate well with the optical measurements. The photocurrent-wavelength plot indicates that the intrinsic properties of the material do not change while the reduction in the peak photocurrent values, together with the electrical results, positively identifies increased contact resistance as the source of the device's degradation.**

I. INTRODUCTION

Phototransistors are widely used in many applications; for examples, in floppy disk drives and in toll booths. After several years of operation, the phototransistors may lose their sensitivities and may malfunction as a result. The purpose of this paper is to subject a sample phototransistor to high-power operation and study the degradations in electrical and optical characteristics.

The high-power operation or high-current injection is an attempt to simulate long-term operation of the device under normal biasing conditions and thus can be thought of as an accelerated DC aging process [1, 2].

The main function of phototransistors is to detect light, or photons. The structure of phototransistors is the same as a typical bipolar junction transistor (BJT) which consists of an emitter (E), a base (B) and a collector (C). Only the E and C terminals are available; the base is exposed to the environment via a transparent capping material. Photon can travel through the capping material and be absorbed by the base, generating free carriers which can move under an externally applied electric field (V_{CE}, for example). The output from the phototransistor is the collector current (I_C) whose magnitude depends on the biasing circuit and the wavelength and the intensity of the input light.

The phototransistor under test will be characterized electrically and optically before and after being subject to high-power operation. The electrical measurements will examine how much output (I_C) can be obtained for a fixed input light, while the optical measurements will determine the range of wavelengths to which the device is sensitive.

The organization of the paper is as follows: the experimental procedures will be given in Section II, followed by results and discussions in Section III and the conclusion in Section IV

II. EXPERIMENT

The device under test is a commercially available phototransistor (SG-105F) manufactured by Kodenshi. The SG-105F is a reflection-based device that consists of an infrared light-emitting diode (LED) placed next to an npn GaAs-based phototransistor.

The LED emits light at a peak wavelength of 940 nm. The sensitivity of phototransistor can be measured from the I_C/I_{LED} ratio. Given a constant I_{LED}, the higher the output current I_C the more sensitive the device to the input light. The I_C/I_{LED} ratio will be used extensively in the analysis in the next section.

The electrical measurements set-up is shown in Fig. 1. The LED is fed with a constant current of I_{LED} = 40mA by a power supply, Advantest TR6143. The light is reflected off a mirror towards the phototransistor which is biased at a constant voltage of V_{CE} = 5V, while the collector current I_C is simultaneously measured (by a Pico-ammeter, HP4140B). This set-up is considered a normal operating condition.

In the high-power operating mode (to simulate long-term operation), the power dissipation at the phototransistor is set well above the rated output power of 50mW. The phototransistor is thus operated at 300mW (I_C = 20mA, V_{CE} = 15V) when subject to high-power operation. Due to the small package of the SG-105F, the LED which comes with it does not provide sufficient light to drive the phototransistor to 300mW. Consequently, the high-power operation is carried out using a separate LED (TOIR – 50b94bCEa manufactured by OASIS) which can output high intensity light at the wavelength of interest.

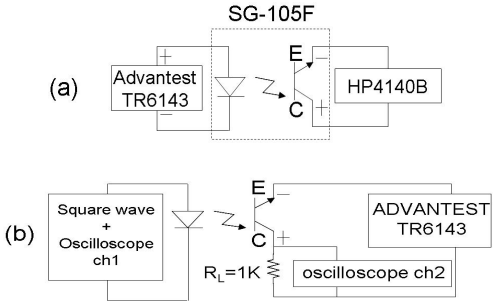

Fig. 1. Electrical set-up for (a) normal and high-power operation (b) response time measurement.

Another important electrical measurement which can be used to study the phototransistor is the response time measurement whose set-up is shown in Fig. 1(b). The purpose of this measurement is to determine the dynamical characteristics of the phototransistor, mainly to measure the rise time (t_r) and the fall time (t_f). In order to do so, the input (LED) is fed with a 500Hz, $4V_{p-p}$ square wave. The LED thus generates light at the same frequency; the phototransistor correspondingly detects the LED light. The phototransistor is connected in series to a 1-kΩ resistor is order to study the rising and falling edges of the output current I_C using an oscilloscope. The time response of the output (I_C), however, lacks those of the input (I_{LED}), giving rise to non-abrupt changes in the rising and falling edges.

The rise and fall times depend mainly on the *RC* time constant and thus are a good indicator of physical changes of the device, whether intrinsic or extrinsic. All electrical measurements are carried out in the dark, with only intended light from a relevant LED.

The optical measurement serves to illustrate the range of wavelengths of light to which the phototransistors can respond. The set-up shown in Fig. 2 makes use of a wavelength filter (the spex 1000M monochromator) which at one end receives a broad spectrum light from a tungsten lamp and at the other end outputs a monochromatic light of wavelength set by internal gratings. The monochromatic output light is then shone onto the phototransistor which is biased at V_{CE} = 5V. The resulting current is simultaneously measured by a digital multimeter (Keithley 485). The monochromator can be programmed to scan from one wavelength to another at a specified wavelength step. The resolution of the scanning mechanism is better than 1 Å and when coupled with the current readout (from Keithley 485) can provide a high-resolution photocurrent response of any photo device, including phototransistors.

III. RESULTS AND DISCUSSIONS

The phototransistor's characteristics, both electrical and optical, are measured before and after high-power operations; the latter is measured in intervals: at 24, 48 and 72 hours of operation. The following results thus comprise a set of four curves corresponding to 0, 24, 48 and 72 hours of high-power operations.

The output electrical characteristic (I_C-V_{CE}) of the phototransistor is shown in Fig. 3. All curves are measured at a constant input light, I_{LED} = 40mA. It is clear from the figure that after each high-power operation, the resultant output degrades. For example, the output current I_C at V_{CE} = 10V reduces from 0.275 mA to 0.267, 0.250 and 0.241 mA after 24, 48 and 72 hours of high-power operations, or over 12% after 3 days .

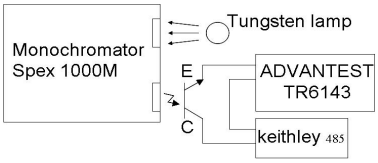

Fig. 2. Set-up for photocurrent measurement

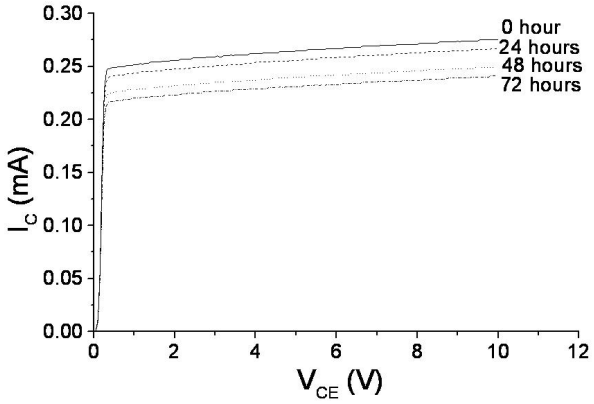

Fig. 3. Output electrical characteristic (I_C-V_{CE}) of the phototransistor before and after being subject to high-power operation for 24, 48 and 72 hours. I_{LED} = 40mA for all curves.

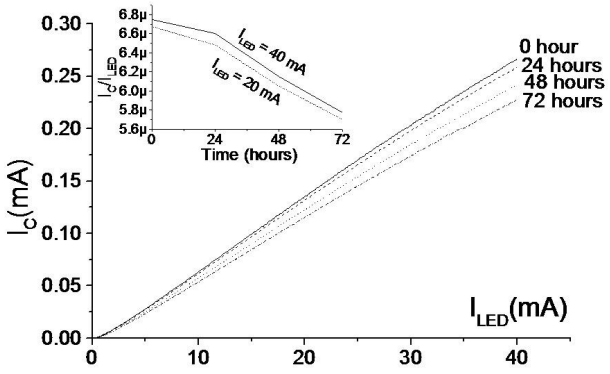

Fig. 4. The I_C-I_{LED} plot and (inset) the I_C/I_{LED} ratio vs time plot of phototransistor before and after being subject to high-power operation for 24, 48 and 72 hours. V_{CE} = 10V for all curves.

The I_C-I_{LED} plot shown in Fig. 4 further supports the above results. It can be seen in Fig. 4 that for all I_{LED}'s, the longer the high-power operation, the further reduction in the output current I_C. This fact is made more obvious in the I_C/I_{LED} plot shown in the inset of Fig. 4 which shows the reduction in the I_C/I_{LED} ratio as a function of the number of hours of high-power operation.

In order to understand the underlying mechanism(s) that cause the degradation in sensitivity of the phototransistor it is important to examine the factors that influence the I_C/I_{LED} ratio. Since the LED light is kept constant for all tests, the carriers thus get generated in the base by the same amount. The I_C/I_{LED} ratio can thus be interpreted as the I_C/I_B ratio whose value is given by [3]:

$$\beta = \frac{I_C}{I_B} \cong \frac{\tau_n}{\tau_t} \qquad (1)$$

where τ_n is the electron recombination lifetime in the base and τ_t is the transit time across the neutral base width W_b. The reduction in β can thus be explained by the reduction in τ_n, or the increase in τ_t, or the combination both. The reduction in

τ_n, however, can be discarded due to the fact that τ_n is a material parameter which depends on impurity concentration, and is unlikely to change during tests. The increase in τ_t is thus a more likely cause for the reduction in β.

The value of τ_t can be shown to be related to the neutral base width W_b according to [3]:

$$\tau_t = \frac{W_b^2}{2D} \tag{2}$$

where D is the diffusion coefficient which, in turn, depends on the carrier mobility μ in the base according to the Einstein's relationship:

$$\frac{D}{\mu} = \frac{kT}{q} \tag{3}$$

where k is the Boltzmann's constant, T is the temperature, and q is the electronic charge. Therefore, the value of D is also unlikely to change during tests due to the fact that the mobility, which depends on the doping concentration, is not affected by high-power operation. The increase in τ_t can thus only be explained by the increase in W_b.

The neutral base width W_b depends on the depletion regions at the emitter junction (a) and the collector junction (b) according to the relationship:

$$W_b = W - a - b \tag{4}$$

where W is the metallurgical base width, see Fig. 5 for visual representation of W, W_b, a and b. The variations in either a or b, or both, can thus have an impact on W_b, and, in turn, on τ_t and β.

It has been found that high-power operation of semiconductor devices can increase contact resistances to the outside world due to electromigration or degraded metal/semiconductor interface [4]. The operation at 300mW in our case in much higher than the rated 50mW which the device can adequately dissipate. The heat can thus build up throughout the device, affecting all contacts and can degrade (increase) contact resistance. The small-signal equivalent circuit of the BJT shown in Fig. 5(b) shows that at a constant V_{CE}, the increase in emitter contact resistance (r_e) and the collector contact resistance (r_c) will affect the voltages dropped across the emitter and collector junctions, respectively. The voltage drops result in the reduction in a and b because the depletion width x of a p-n junction depends on the voltage drop V across it according to:

$$x = \left\{ \frac{2\varepsilon_s \varepsilon_0 V}{q} \left(\frac{1}{N_a} + \frac{1}{N_d} \right) \right\}^{\frac{1}{2}} \tag{5}$$

where ε_s is the relative permittivity of the semiconductor, ε_0 is the permittivity of vacuum, and N_a and N_d are the acceptor and donor concentrations of the p- and n-side of the junction, respectively.

The increase in contact resistances r_e and r_c thus results in the reduction in voltage drops across the emitter and collector junctions which, according to (5), decrease a and b. Consequently, W_b increases, due to (4), which increases τ_t, due to (2), and ultimately decreases β, due to (1).

The increase in contact resistance as the cause of reduced sensitivity is further supported by the response time measurements. Table 1 summarizes the rise and fall times of the phototransistor before and after 24, 48 and 72 hours of high-power operation. While the rise time increases by approximately 4%, the fall time increases by a greater percentage of 8%. The combined 12% increase in rise and fall times very well reflects the similar reductions in the output current in Fig. 3 and the I_C/I_{LED} ratio in Fig. 4.

The electrical characterizations above suggest that after long-term operation at high-power condition (300mW), only contact resistances increase while basic material parameters do not change. If this is the case, the absorption/emission characteristics of the phototransistor should reflect this.

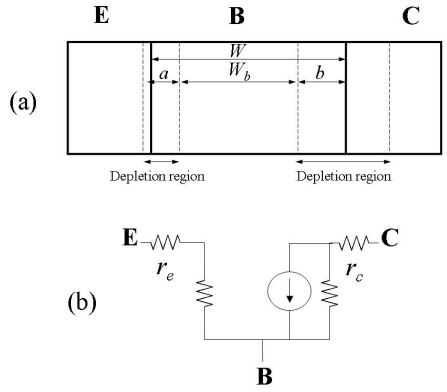

Fig. 5. (a) Cross section and (b) small-signal equivalent circuit of a BJT

TABLE I
Measured rise and fall times of the phototransistor before and after 24, 48 and 72 hours of high-power operation.

duration of high-power operation (hrs)	t_r (μsec)	t_f (μsec)
0	50	48
24	50	48
48	52	52
72	52	52

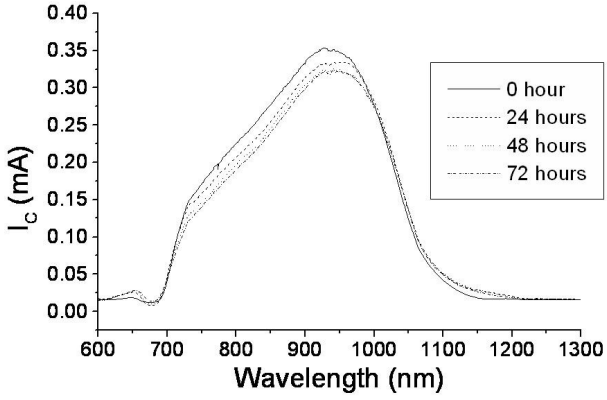

Fig. 6. The photocurrent plot of the phototransistor before and after being subject to high-power operation for 24, 48 and 72 hours. V_{CE} = 5V for all curves.

The photocurrent as a function of wavelength is shown in Fig. 6 for the phototransistor before and after high-power operations.

It can be seen that for all conditions, the device's optical characteristics remain virtually the same: the two peaks (at 730- and 940nm) and the full-width-at-half-maxima (FWHM = 274nm) of the normalized curves (not shown) are the same. Further examination of the peak absorption at 730- and 940-nm wavelengths shows that the reduction in I_C is approximately 12%.

The fact that the peak positions and the FWHM do not change implies that the intrinsic properties of the device (thus the material) are not affected. The reduced peak, however, can be explained by the increase in contact resistances, r_c and r_e, which results in reduced in voltages dropped across the emitter and collector junctions, in good agreement with the electrical results.

IV. CONCLUSION

In summary, a commercially available phototransistor has been subject to high-power operations (300mW as opposed to the nominal, rated power of 50mW) and its electrical and optical characteristics studied. It is found that the device's electrical and optical behaviors are degraded in the same way: the electrical sensitivity reduced by approximately 12%, and the optical responses around the sensitivity peaks are reduced by approximately 12%. The dynamic behaviors also indicate an increase of rise and fall times by the same amount. The resulting electrical and optical degradations have been explained in terms of increased contact resistances, while the intrinsic properties of the device remain unchanged.

ACKNOWLEDGMENT

N. Thudsalingkarnsakul acknowledges scholarships from Thailand Graduate Institute of Science and Technology (TGIST).

REFERENCES

[1] M. G. Adlerstein and J. M. Gering, "Current Induced Degradation in GaAs HBT's", *IEEE Transactions on Electron Device,* vol. 47, no. 2, February 2000, pp. 434-439.

[2] B. Surridge and J. Law, "Accelerated Reliability Testing of InGaP/GaAs HBTs", GaAs MANTECH Conference, April 8-11, 2002, San Diego, California.

[3] B G.Streetman and S. Banergy, *Solid state electronic devices* 5th Ed, 2000, Prentice Hall, Inc., pp.129, 167, 328, 368.

[4] S. P. Hau-Riegea and C. V. Thompsonb "Electromigration saturation in a simple interconnect tree" *Journal of Applied Physics*, vol 88, number 5, 1 September 2000, pp.2382-2385.

CMOS Digital-to-Analog Converter

Pipat Prommee[1], Krit Angkeaw[1], Kobchai Dejhan[1], Montri Somdunyakanok[2] and Jirasak Chanwutitum[3]
[1]Faculty of Engineering and Research Center for Communication and Information Technology
King Mongkut's Institute of Technology Ladkrabang, Bangkok 10520, Thailand
Tel: +66-2326-4238, +66-2326-4242, Fax: +66-2326-4554
[2]Faculty of Engineering, Siam University, Bangkok 10160, Thailand.
Tel: +66-2457-0068 Fax: +66-2457-3982
[3]Industrial Electrical Technology Department, Faculty of Engineering
King Mongkut's Institute of Technology North Bangkok, Bangkok 10800, Thailand
Email: pipat@telecom.kmitl.ac.th

***Abstract*— This paper presents a CMOS Digital-to-Analog Converter (D/A) Circuit. The voltage clipping circuit building blocks based on minimum circuit and electronic resistor are deployed. The proposed circuit uses a worth of current-mode signal processing for minimized circuitry. The clipping circuit can be obtained the current output according to its voltage output and the electronic resistor. The clipping voltage output is achieved by input clipping voltage and input voltage relations. The D/A currents output can be simply obtained by summing of their currents. The direct connection method and n-bits expandable without any restrictions can be obtained that is an advantage of current-mode approach. The integrity analog output can be obtained either current or voltage. The simulation results are performed by PSpice based on MOSIS CMOS process 0.25µm. The analog integrity output can be obtained.**

I. INTRODUCTION

In analogue signal processing [1], [3], digital-to-analog converter (D/A) is an important part for interpret a digital word to an analog signal. The familiar OPAMP D/As [2] have been found in very long time ago such as linear combination and 2-2R ladder [4], [5]. The complicated resistors design has been found and slow response behavior cause of the OPAMP bandwidth.

The clipping circuit based on OPAMP and zener diode has been introduced [4-6] that operates in voltage-mode. The clipping voltages are set by each zener diode across voltage. The mention clipping circuit is not practical because zener diodes are complicated to find out. The OPAMP-based is used a large die area in fabrication and the frequency response is also limited by its gain-bandwidth (GBW).

This paper is focused on the components reduction and without the resistor. This paper describes a CMOS D/A based on voltage-clipping circuit. The voltage clipping circuit is modified by a minimum circuit [8]. The current mirrors and electronic resistors have been added for obtained a current output. The D/A circuit is constructed by n-clipping circuits for n-bits digital signal. The reference voltage can be simply adjusted by a particular voltage weighting assignment. The number of digital bit inputs can be flexible increased and decreased without changing of the topology that is a benefit of proposed D/A. The output current is quite accurate according to the input signal and clipping reference voltage. The expected analog signal output can be obtained either in current or voltage.

II. THEORY AND PRINCIPLE

The proposed circuit is constructed by n-parts of clipping circuit. The CMOS transistors are realized for a clipping circuit. The minimum circuit and electronic resistor are deployed for obtained the current output.

A. Shunt-Feedback Buffer Circuit

Fig. 1 shows shunt-feedback buffer circuit [7]. It contains the 2 current sources and 3 transistors. The transistor M_1 is using for supply its source voltage, M_2 using for supply current at node V_O and M_3 is done for output current. All transistors are operated in saturation region. So, the voltage output can be written as follows :

$$V_O = V_C - \sqrt{\frac{I_1}{k_N}} - V_{TN} \qquad (1)$$

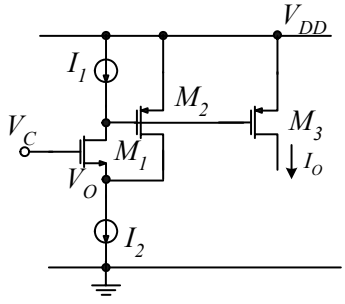

Fig. 1 The Shunt-Feedback Buffer Circuit

The output current I_O equals I_2-I_1 obtaining from current mirror M_3. However, the bias I_1 can be cancelled by symmetry scheme because I_1 is constant, while the transistors of both sides must be identical. The current source I_1 is a drain current of M_1 and I_2 is a total current source of circuit. While input voltage (V_C) is applied in gate of M_1, source voltage is appeared. The enough current should be supplied in case of load connected at node V_O. Thus, M_2 and I_2 are deployed to supply such current.

B. Minimum Circuit

The minimum circuit [8] as shown in fig.2 can be realized by the 2 shunt-feedback buffer circuits with a swapping of bias transistor M_2 and I_2. Suppose that, the input section 1 and 2 are perfectly matched. The transistor M_{51} and M_{52} will operate according to which the gate voltage input is lower. The source voltages (V_{OUT}) are connected together that take care the current output by the negative current sources M_{81}, M_{82}.and positive current source I_2. The output voltage is appeared according to the V_{IN1} and V_{IN2} that can be written as:

$$V_{OUT} = V_{\min}\Big|_{V_{IN1},V_{IN2}} \tag{2}$$

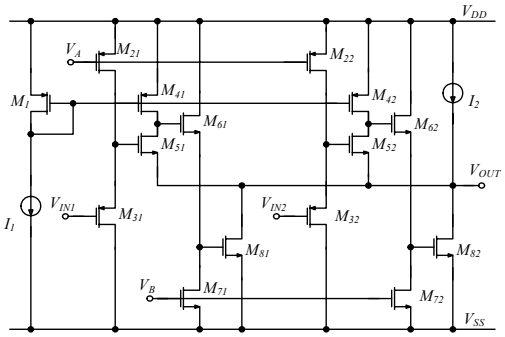

Fig.2 CMOS Minimum Circuit

C. MOS Electronic Resistor

The MOS electronic resistor circuit [9] as shown in Fig.3 has been introduced in 1990. This electronic resistor circuit is performed as a grounded resistor. The resistance can be adjusted by its supply voltage and its aspect ratio (*W/L*). The transresistance of the electronic resistor circuit can be expressed in Eq.(3).

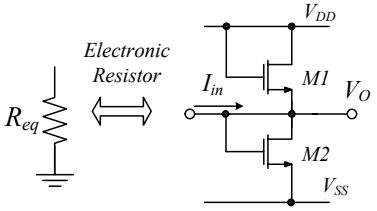

Fig.3 MOS Electronic Resistor Circuit

$$R_{eq} = \frac{V_O}{I_{in}} = \frac{L}{2\mu C_{OX} W\left(V_{DD} - V_T\right)} \tag{3}$$

D. Clipping Circuit

For clipping building block, the above minimum circuit and electronic resistor are deployed. The clipping voltage input is applied in a particular port and V_{in} is applied in the rest port as shown in Fig.4. The transistors M_9 and M_{10} are connected as an electronic resistor. The resistor current based on the clipping and input voltage conveyed to the output by the current mirrors M_{81} - M_{84}. The simplify building block can be described in fig. 5. The current output of clipping circuit according to the input, clipping voltage and electronic resistor can be expressed as:

$$I_{OUT} = \frac{V_{\min}}{R_{eq}}\Big|_{V_{IN1},V_{CLIP}} \tag{4}$$

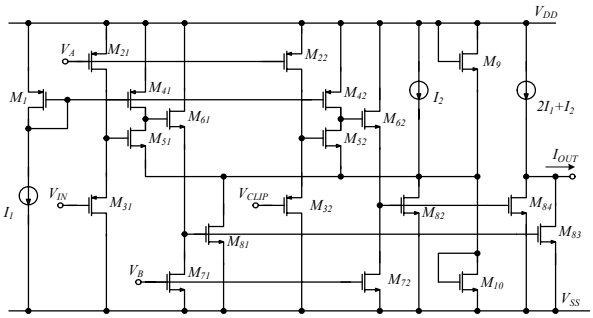

Fig.4 Complete Clipping Circuit

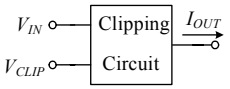

Fig. 5 Simplify Clipping Circuit Building Block

III. DIGITAL-TO-ANALOG CONVERTER

The D/A is a useful building block and found in analog signal processing area. The variety mix-signal processing integrated circuits can be processed in digital or analog approaches. Although, the analog can be process perhaps a digital process can be also well done. The natural signal input always analog that should be convert to digital for taking some process and finalized output in analog again. So the A/D and D/A are very important parts to carry out this point.

The CMOS D/A has been reported [10] that used CMOS based diode connection for clipped a signal. That circuit was worked seem to be a rectifier function. The low-output impedance is a problem of current mode that giving the errors when the summation current outputs are connected.

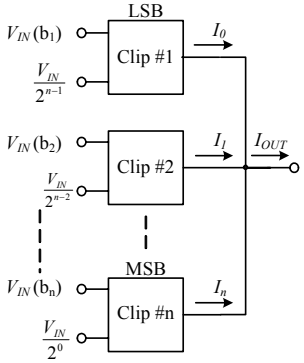

Fig.6 The D/A Block Diagram

The proposed D/A scheme has been shown in fig.6 using connection of n-stages clipping circuits. The current output can be obtained by the summing of several clipping circuit outputs. Each signal output is controlled by particular data digital bit input (0 or 1) that applied by V_{in}. The current output

is weighted by the clipping voltage according to the bit significant.

The summation of their current can be simply direct connection cause of worth in current-mode processing. From the current-mode approach, the data bit inputs enjoy more expandable without any restriction. The voltage output can be also easily obtained using R_L connected. The b_1 and b_n are least significant bit (LSB) and most significant bit (MSB), respectively. The current output of D/A can be obtained as:

$$I_O = \frac{V_{IN}}{R_{eq}}\left(\frac{b_1}{2^{n-1}} + \frac{b_2}{2^{n-2}} + ... + \frac{b_n}{2^0}\right) \qquad (5)$$

or

$$I_O = \frac{V_{IN}}{R_{eq}}\sum_{i=1}^{n}\frac{b_i}{2^{n-i}} \qquad (6)$$

From Eq. (6), the linear combination algorithm can be seen without the complicate resistor design. The full-scale current output is given by all bits set to '1'. Supposed that n is approach to infinite. The current output will become:

$$I_O\big|_{fs} \to \frac{2V_{IN}}{R_{eq}}; \quad (n \to \infty) \qquad (7)$$

The only LSB is '1' that the output can be obtained to

$$I_O\big|_{1LSB} \to \frac{V_{IN}}{2^{n-1}R_{eq}} \qquad (8)$$

IV. Simulation Results

The proposed D/A in fig.6 can be assumed for 4 bits by identical 4-stages of clipping circuit. The performances have been confirmed by PSpice. The level 3 model T14Y MOSIS 0.25µm with the following parameters, V_{TN} = 0.42V, V_{TP} = -0.55V, $\mu_N C_{OX}$ = 250.1048$\mu A/V^2$ and $\mu_P C_{OX}$ = 51.94153. $\mu A/V^2$ is assumed. The aspect ratio of transistors is shown in table 1 and CMOS model is listed in table 2

TABLE 1. THE ASPECT RATIO OF TRANSISTORS

Transistors	W/L($\mu m/\mu m$)
M_{2i}, M_{3i}, M_{5i}-M_{7i}	2/0.5
M_{8i}	30/0.5
M_1, M_{4i}	10/0.5
M_9, M_{10}	0.5/0.5

The bias currents, I_1 and I_2 equal to 21.4µA and 100µA, respectively. The bias voltages, V_A and V_B are 0.9 Volts. The supply voltage, ±1.5 volts is used. The voltage reference of various clipping circuit are given in the rule of Eq. (5). The minimum circuit carries out the input range of 0.5 volts for V_{IN}. The clipping reference voltages of LSB to MSB are achieved as 0.0625, 0.125, 0.25 and 0.5, respectively.

TABLE 2. MOSIS LEVEL 3 MODEL 0.25µm

```
.MODEL NMOS1 NMOS (LEVEL=3 TOX=5.7E-9 NSUB=1E17
+GAMMA=0.4317311 PHI=0.7 VTO=0.4238252 DELTA=0
+UO=425.6466519 ETA=0 THETA=0.1754054 KP=2.501048E-4
+VMAX=8.287851E4 KAPPA=0.1686779 RSH=4.062439E-3
+NFS=1E12 TPG=1 XJ=3E-7 LD=3.162278E-11
+WD=1.232881E-8 CGDO=6.2E-10 CGSO=6.2E-10 CGBO=1E-10
+CJ=1.81211E-3 PB=0.5 MJ=0.3282553 CJSW=5.341337E-10
+MJSW=0.5)
.MODEL PMOS1 PMOS (LEVEL=3 TOX=5.7E-9 NSUB=1E17
+GAMMA=0.6348369 PHI=0.7 VTO=-0.5536085 DELTA=0
+UO=250 ETA=0 THETA=0.1573195 KP=5.194153E-5
+VMAX=2.295325E5 KAPPA=0.7448494 RSH=30.0776952
+NFS=1E12 TPG=-1 XJ=2E-7 LD=9.968346E-13
+WD=5.475113E-9 CGDO=6.66E-10 CGSO=6.66E-10
+CGBO=1E-10 CJ=1.893569E-3 PB=0.9906013 MJ=0.4664287
+CJSW=3.625544E-10 MJSW=0.5)
```

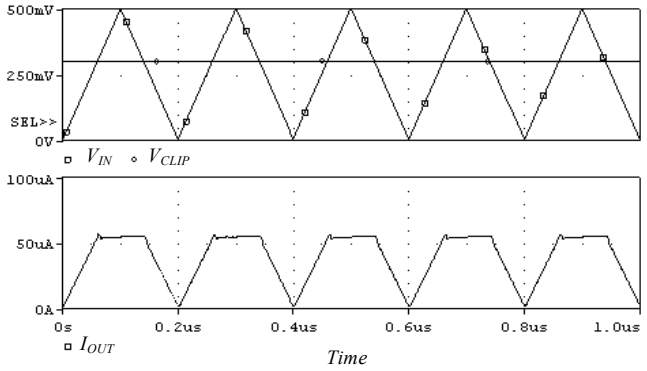

Fig.7 The current output of clipping circuit in fig. 4

The electronic resistors that used in this paper are performed by M_9 and M_{10} with aspect ratio in table.1. The resistance can be obtained about 5kΩ. The clipping performance can be confirmed by applying saw-tooth signal of 0.5 $V_{p\text{-}p}$ with 0.25 volts offset for V_{IN} and clipping voltage is set at 0.3 volts. The current output can be obtained the accurate clipping as shown in fig. 7.

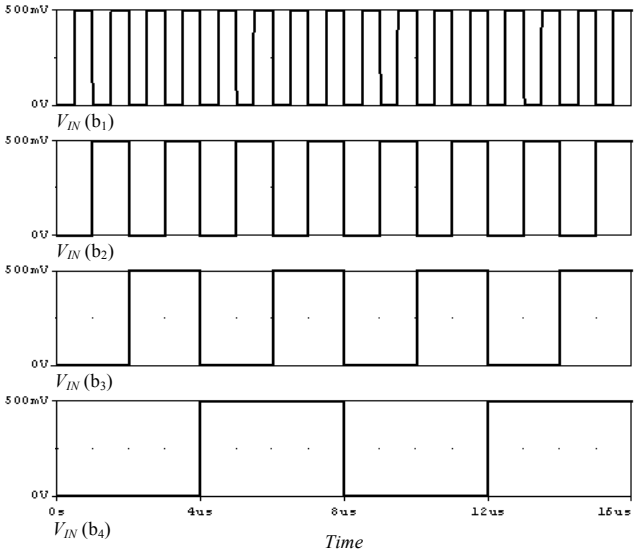

Fig.8 Digital input signal for proposed 4 bits D/A

The 4 bits D/A performance can be simulated by giving the data input as different consecutive pulses trains as shown

in fig. 8. The sampling frequency of digital input is supposed at 1 MHz.

The full scale current output due to 4 bits inputs can be roughly calculated using Eq. (7) about 187.5μA. The 1LSB current output using Eq. (8) can be also found about 12.5μA. The simulation results are confirmed the current outputs are in agreement with the calculation about 172.64μA and 12.22μA for full scale and 1LSB current output, respectively. The output signal that seems to be a ramp signal can be obtained in fig. 9.

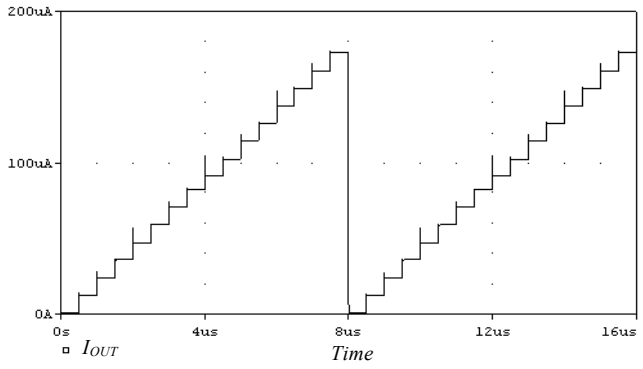

Fig.9 Analog output current of proposed D/A

For voltage output, the 5kΩ resistor is connected to the output port of proposed D/A circuit. The full scale voltage output due to 4 bits inputs can be roughly calculated using Eq. (7) about 937.5mV The 1LSB current output using Eq. (8) can be also found about 62.5mV. The simulation results are confirmed the current outputs are in agreement with the calculation about 784.52mV and 53.54mV for full scale and 1LSB voltage output, respectively. The output signal that seems to be a ramp signal can be obtained in fig. 10. The achieved output voltage has some error due to the load resistance connection.

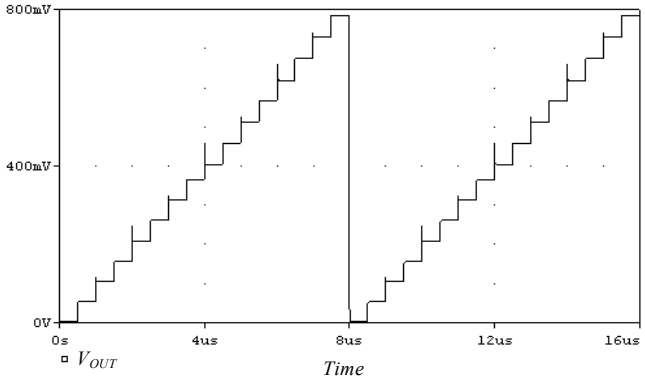

Fig.10 Analog output voltage of proposed D/A while R_L= 5kΩ connected

V. CONCLUSION

The CMOS Digital-to-Analog Converter (D/A) Circuit based on clipping circuits is proposed. The signal of proposed circuit is processed in current-mode for minimized a circuitry. The minimum circuit and electronic resistor are implemented for a clipping circuit. The current output of D/A can be simply obtained by summing of their clipping current outputs. This algorithm can be flexibly increased and decreased the number of digital bits input. The reference voltage can be simply calculated by basic mathematical. The analog output can be obtained either current or voltage.

REFERENCES

[1] D. Johns, and K. Martin, "*Analog integrated circuit design*," New York: John Wiley & Sons, 1997.

[2] W. D. Stanley, "*Operational amplifiers with linear integrated circuits*," USA, Macmillan College, 1994.

[3] C. Toumazou, F. J. Lidgey and D. G. Haigh, "*Analogue IC design: the current mode approach*," Peter peregrinus ltd.1990.

[4] Karadimas, D.S.; Mavridis, D.N.; Efstathiou, K.A.; "A digitally calibrated R-2R ladder architecture for high performance digital-to-analog converters," ISCAS.2006 21-24 May 2006

[5] M. P. Kennedy, "On the robustness of R-2R ladder DAC's, "*IEEE Trans. Circuits & Syst. II*," vol. 47, Feb. 2000.

[6] T. L. Floyd, Basic operational amplifiers and linear integrated circuits. USA: 1994.

[7] T. R. Visawanathan, "CMOS Transconductance Element," *Proc. IEEE* , Vol.74(1), pp.222-224, 1986.

[8] K. Angkeaw, M. Somdunyakanok, P. Prommee, M. Kumngern, K. Dejhan, and J. Chanwutitum, "CMOS Low-voltage Max/Min circuits and its application," *Proc. of ECTI-CON 2006*, Ubon-Ratchathani, Thailand, May 10-13, 2006.

[9] Z. Wang, "2-MOSFET Transistors with Extremely low distortion for output reaching supply voltage," *Electron. Lett.*, Vol.26, pp.951-952., June 1990.

[10] A.Monpapassorn S. Maitreechit and S. Sonanta "A CMOS Positive Current Clipping and A New D/A Converter Application*," KKU Engineering Journal*, Vol. 31(2), pp.201-213, April-June 2004.

Degradation Characteristics of Blue Light-Emitting Diodes under Accelerated DC Aging Process

T. Limwongse, S. Thainoi, and S. Kanjanachuchai
Semiconductor Device Research Laboratory, Department of Electrical Engineering
Faculty of Engineering, Chulalongkorn University, Phayathai Road
Bangkok 10330, Thailand

***Abstract*-Blue light-emitting diodes (LEDs) have been subject to high-current DC aging process at room temperature in order to study its degradation characteristics by electrical and optical characterizations. Electrical measurements show that after each cycle of aging, the diode's ideality factor increases at all forward bias levels. The reverse saturation current also increases after each aging process. Optical measurements show that although the peak wavelength of the diode remains almost constant at 468nm, its full-width-at-half-maximum (FWHM) value broadens from 27nm to 34nm after 24-hr of aging, and nearly saturate at 39nm after 48 hours. The peak wavelength intensity also decreases steadily with time. We attribute the LED's degradation to the creation (or activation) of defect levels inside the band gap. These levels provide pathways for non-radiative recombination, resulting in dimmed LEDs under forward bias. They also contribute to generation current under reverse bias.**

I. INTRODUCTION

Blue light-emitting diodes (LEDs) are widely used in general electrical appliances and electronic devices such as function panels in cars and keypads light in mobile phones. In general, LEDs are finding more lighting and signaling applications as they are more efficient than other light sources. Because of growing usage, LED characteristics must be fully understood. When used in commercial applications, warranties are usually given against LED malfunction. For manufacturers or system designers to be confident of the warranty period, it is important to subject blue LEDs of interest to accelerated DC aging and study the electrical and optical properties of the LEDs before and after aging.

The blue LED under test is a commercially available, InGaN-based high-brightness blue LED. The LED is well encapsulated under blue cover and its rated nominal working parameters are 20mA of forward injection current, and 3.2-3.9V of forward voltage under the ambient temperature at 25^{o}C. For the reverse bias region, the maximum bias should not exceed -5V in order to avoid damage to the LED. At normal forward bias operation, the peak wavelength is 464nm and the full-width-at-half-maximum (FWHM) is 23nm.

It is generally known that long-term operation of diodes degrades their electrical and optical characteristics: LEDs become dimmer and consume more power with time. It usually takes a long time for such degradation to be noticeable. In order to simulate the aging process in a controlled environment, all the LEDs used in this study are subjected to accelerated DC aging where power larger than the rated value is intentionally supplied to the LEDs. Since the power supplied is larger than the amount that the packaging can dissipate, the heat builds up inside the device and accelerates the degradation mechanisms. With proper DC bias and power supplied, it is possible to subject the LEDs to one day under test which has a theoretical equivalence of one year of continuous operation at the rated conditions. Care must be taken, however, for LEDs can easily be damaged in the event of sudden change of device temperature. By studying the LED characteristics before and after accelerated DC tests, it is possible to estimate the LED's lifetime which has important implications for warranty periods.

The LED's characteristics of interest are optical and electrical performances before and after the aging process. What follows in the remaining of the paper will show how the electrical and optical characteristics are degraded, and what are the causes and consequences of the degradation. The structure of the paper is as follows: the experimental procedures including the electrical and optical measurement set-ups will be given next in Section II. This is followed by Section III where the results are shown and discussions are given, followed by the conclusion in Section IV.

II. EXPERIMENT

The structure of the blue LED under test is shown in Fig. 1. The device is grown on a sapphire substrate starting from n-type contact layer (n-GaN), InGaN active layer, p-AlGaN emitter and p-GaN as the top contact layer. The device is subjected to the accelerated DC aging process shown in Fig. 2. For each cycle of the process, the LED's electrical and optical characteristics are measured using the set-ups shown in Figs. 3 and 4, respectively.

The schematic flow diagram in Fig. 2 describes how the LED is subjected to tests and measurements. The LED is measured before (0 hour) and after each of the three 24-hour aging cycles (24, 48 and 72 hours). A computer program has been written to control a power supply (Advantest TR6143) in such a way that only dissipated power needs be input. The program will automatically adjust the current and voltage to match the power required. The program has a ramp-up and down features to prevent sudden temperature change of the device. The program is set to supply the required power (500mW) for 24 hours before being terminated. Afterwards, the LED's electrical and optical characteristics are measured

and the LED is further subjected to the same aging process until it is aged by 72 hours, which corresponds to approximately 3 years of operation at the nominally rated conditions.

The electrical measurement set-up shown in Fig. 3 consists of a control personal computer (PC) which is connected to a power supply via a general-purpose interface bus (GPIB). The power supply is either a HP 4140 or Advantest TR6143, depending on the required current/power used in measurement or for aging process. In either case, the power supply outputs a current (I) and measures the voltage (V), or vice versa. Each data point (I,V) can be subsequently read back by the PC via GPIB.

The optical measurement set-up shown in Fig. 4 consists of a monochromator, a photomultiplier and a digital multimeter (DMM). The PC is used to adjust the grating of the manochromator so that only selected wavelength can go through it. The filtered light is subsequently detected at the other end by a photomultiplier whose output is measured by the DMM and read back by the PC. The control value (λ required) and the result read back (volt, corresponding to light intensity) are then used to plot the optical characteristic.

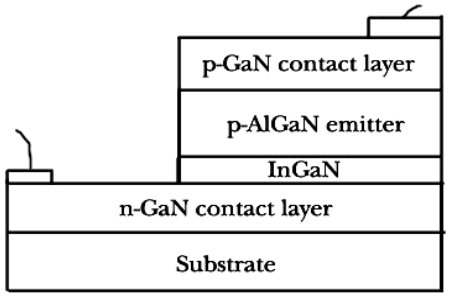

Fig. 1. Structure of the device.

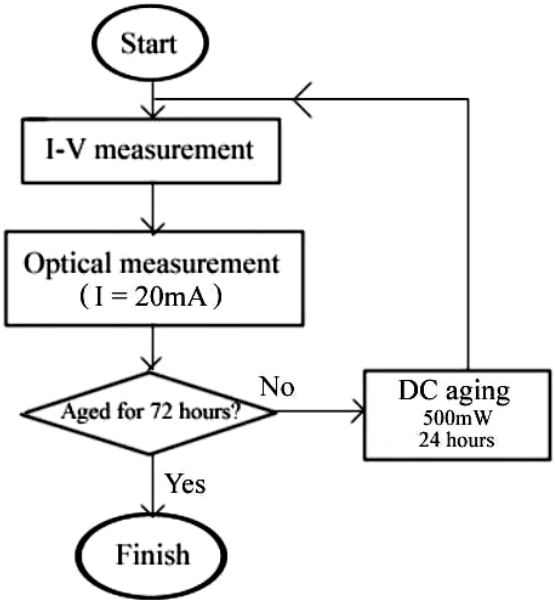

Fig. 2. Flow diagram of the accelerated DC aging process.

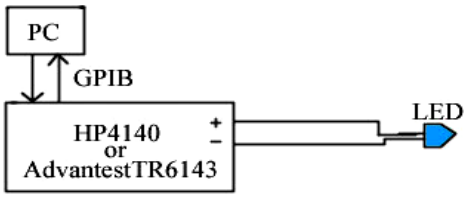

Fig. 3. The electrical measurement set-up.

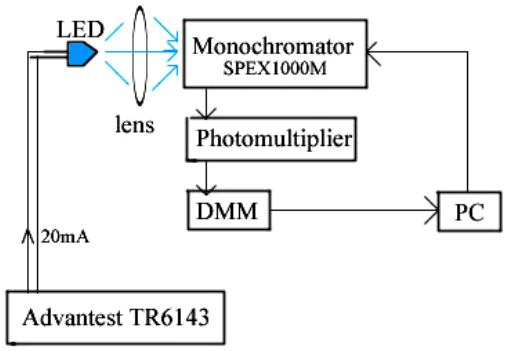

Fig. 4. The optical measurement set-up.

III. RESULTS AND DISCUSSIONS

The electrical characteristic of the LED in Fig. 5 shows the current-voltage (I-V) of the diode before and after being aged at 500mW for 24, 48 and 72 hours. The semi-logarithmic plot shows that the electrical characteristics of the diode's forward and reverse biases are significantly affected, most notably after the first 24 hours of aging. The inset of Fig. 5 shows that the reverse saturation current of the LED increases with the aging time, indicating that there may be physical changes in the active area of the LED.

The reverse saturation current is associated with generation centres in the semiconductor band gap. The centres may be inactive as grown, but become active after prolonged usage.

These mid-gap centers can also become active at forward bias conditions where they are effective as recombination centers. This is evident in Fig. 6 which shows the plot of ideality factor as a function of forward bias for two conditions: new and 24-hour aged LEDs. The ideality factor η can be determined from the relationship [3]:

$$I = I_0(\exp(qV/\eta\, k_B\, T)-1) \qquad (1)$$

where I is the current, V is the voltage, I_0 is the reverse saturation current, q is the electronic charge, k_B is the Boltzmann constant, and T is the temperature.

The ideality factor depends on relative contribution of diffusion and recombination currents. The value of η approaches 1 if all current components are diffusion currents, and reaches 2 when recombination current dominates [2,3]. Fig. 6 shows that the ideality factor η increases for all bias levels [1]. Ideality factor even greater than 2 is possible if the quasi-Fermi levels splitting is less than bias voltage and the recombination spreads out over a wide region [5].

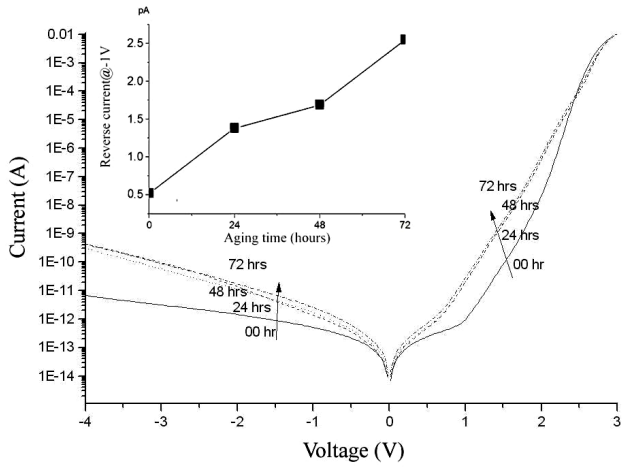

Fig. 5. The current-voltage (I-V) characteristics of the blue LED before and after being aged at 500mW for 24, 48 and 72 hours.

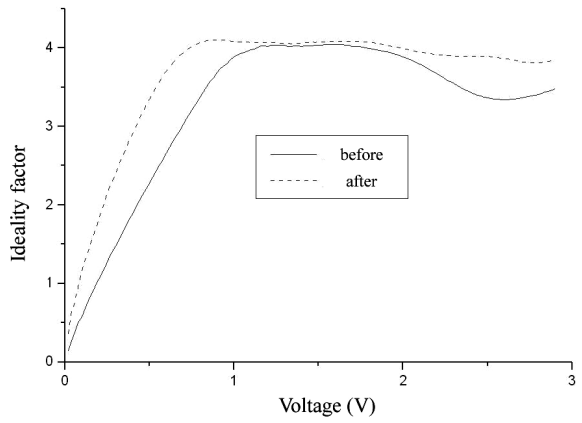

Fig. 6. Ideality factor of the LED before and after being aged at 500mW for 24 hours.

The optical characteristic of the LED is shown in Fig. 7. The intensity of light output from the LED when it is forward biased at the rated current (20mA) is shown before and after being aged at 500mW for 24, 48 and 72 hours. The inset shows the relative peak intensity and FWHM values of each aged cycle.

The optical results show that the peak wavelengths stay almost constant at the rated value of 465 nm while the intensity at the peak wavelength reduces significantly, most notably between the first and the second aged cycles (i.e between 24 and 48 hours). The FWHM values which indicate the "purity" of the color that the eyes perceive also degrade after each aging cycle. The reduced intensity results in dimmer LEDs after long-term operation while the broadened FWHM contributes to the change in color that human eyes perceive.

The fact that the electrical characteristic undergo a critical change after 24 hours of aging while the optical characteristic undergo a critical change between 24 and 48 hours of aging is indicative that different mechanisms may be responsible for electrical and optical degradations However, it has been suggested that defects in recombination region may be responsible for both types of degradations [4].

In order to explain our results, and in agreement with the mechanism suggested by Cao [4], we propose a simple model to illustrate why the reverse current increases and the emission efficiency decreases after each aged cycle.

Fig. 8 shows a plot of (upper) energy-wave vector (E-k) diagram and (lower) energy-distance diagrams across a p-n junction in the case of (left panels) new and (right) aged LEDs. A mid-gap energy level (E_r) is shown only for the aged LEDs. The existence of E_r in the E-k diagram means that carrier recombination can occur via indirect recombination, which results in heat or phonons. E_r in the energy-distance diagram shows that it can function as an effective generation center under reverse bias conditions [3], resulting in increased reverse current as shown by the comparatively larger arrow in Fig. 8.

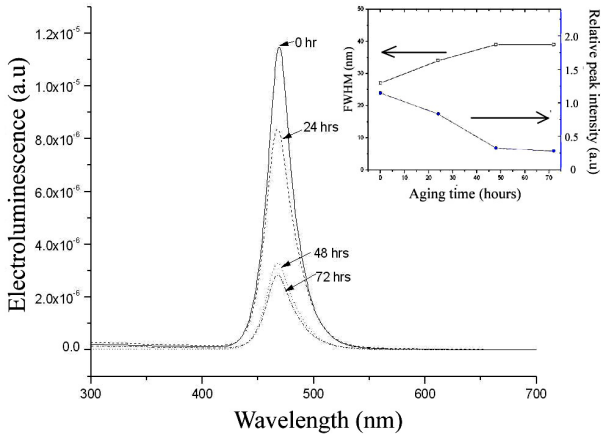

Fig. 7. Optical emission from the LED before and after being aged at 500mW for 24, 48 and 72 hours. The inset shows the peak wavelength and FWHM of each cycle.

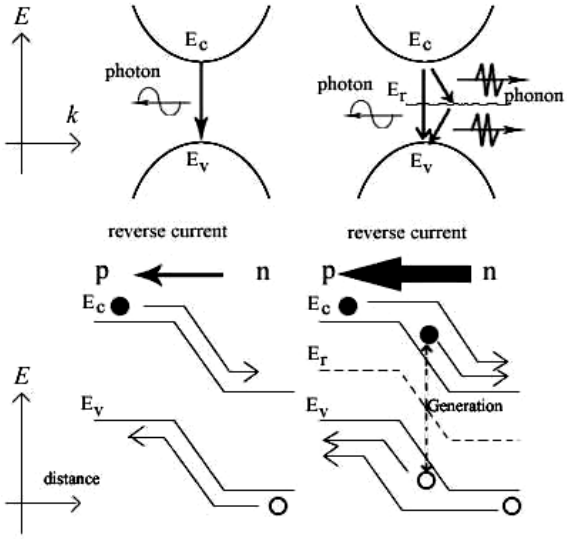

Fig 8. Energy-wave vector (upper) and energy-distance across a p-n junction (lower) of new (left) and aged (right) LEDs.

IV. CONCLUSION

In conclusion, commercially available blue LEDs have been subject to accelerated DC aging process and their electrical and optical characteristics are measured. It is found that both characteristics are degraded after each aging cycle: the ideality factor and the reverse saturation current in *I-V* characteristics increase while the peak wavelength intensity in the electroluminescence characteristic decreases. We attribute the degraded characteristics to the formation (or activation) of mid-gap energy levels which can effectively function as non-radiative recombination centres in the forward-biased mode, and generation centres in the reverse-biased mode.

ACKNOWLEDGMENT

T. Limwongse acknowledges scholarship from Thailand Graduate Institute of Science and Technology (TGIST). The LEDs in this work (HP HLMP-HB57) are supplied by VITA EMTECH Co., Ltd.

REFERENCES

[1] G. Meneghesso, S. Levada, R. Pierobon, "Degradation mechanism of GaN-based LEDs after accelerated DC current aging,"*International Electron Devices Meeting, 2002. IEDM '02,* pp. 103 - 106

[2] V. Wittipahl, Y. Y. Lui, D. S. H. Chan, "A Degradation Monitor for the Light Output of LEDs based on Cathodoluminsecence Signal and Junction Ideality Factor," *Reliability Physics Symposium, 1996. 34th Annual Proceedings., IEEE,* pp. 188-194.

[3] B. G. Streetman, S. Banerjee, "*Solid State Electronic devices 5th edition*. Prentice Hall, pp 214-218.

[4] X. A. Cao, P. M. Sandvik, S. F. LeBoeuf, S. D. Arthur, "Defect generation in InGaN/GaN light-emitting diodes under forward and reverse electrical stresses," *Microelectronics Reliability,* Volume 43, Number 12 (2003), pp. 1987-1991.

[5] P. A. Beck, J. H. Nickel, P. G. Hartwell, "High Current Density in uc-Si PECVD Diodes for Low Temperture Application," *HPL-2004-63, MRS Spring Proceedings 2004.*

FPGA Implementation of Acoustic Echo Canceller with Low Resource Utilization

Sompop Janyavilas[1], Ekaroon Piluck[2], Phaophak Sirisuk[3] and Monai Krairiksh[1]
[1]Faculty of Engineering and Research Center for Communications and Information Technology,
King Mongkut's Institute of Technology Ladkrabang, Bangkok 10520, Thailand.
Tel: 66-2-7373000 Ext. 3327, Fax: 66-2-7392429
[2]Department of Electronic Engineering
[3]Department of Computer Engineering
Mahanakorn University of Technology, Bangkok 10530, Thailand
Phone : 0 2988 3666 Fax : 0 2988 4040 Email : phaophak@mut.ac.th

***Abstract*- This paper presents FPGA implementation of an Acoustic Echo Canceller (AEC) for teleconferencing systems. For AEC adaptation, a Normalized Least Mean Square (NLMS) algorithm is employed. Two circuit techniques, namely Distributed Arithmetic (DA) and Multiply and Accumulation (MAC), are utilized to improve resource utilization in the proposed AEC. Synthesis of the AEC is achieved via VHDL language. Simulations are presented to confirm functionalities of AEC and investigate performance of FPGA implementation.**

I. INTRODUCTION

In a teleconferencing system, the coupling between loudspeakers and microphones usually results in many undesirable properties [1]. To overcome the difficulties, it is well accepted that an Acoustic Echo Canceller (AEC) is required. Operation of AEC is illustrated in Fig. 1. Essentially, the adaptive filter endeavors to model the room characteristics possibly using an FIR filter. Attempts have been made towards implementation of AEC using several techniques including FPGA, see e.g. [2], [3]. However, most existing works do not address the issue of optimal implementation.

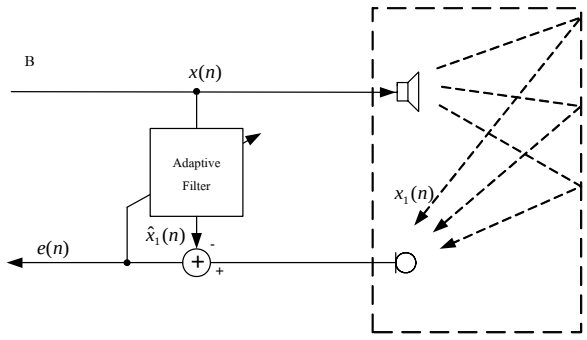

Figure 1 AEC Block Diagram

This paper presents efficient FPGA implementation of AEC using NLMS algorithm. Two circuit techniques, particularly Distributed Arithmetic (DA) and Multiply and Accumulate (MAC) are exploited leading to efficient implementation. The paper is organized as follows. Section 2 reviews NLMS algorithm that is used for AEC adaptation. Section 3 descries method of acoustic echo canceller part structure processor unit in the , Section 4 MAC, Section 5 DA , Section 6 design and implementation, Section 7 the testing , and Conclusion in section 8.

II. NLMS ALGORITHM

An adaptive filter [1] is different from a general filter in that its coefficients are not fixed but rather changed in accordance with signal and environment statistics. Basically, it consists of two parts, i.e. a filter and adaptation. The popular filter structure is FIR filter due to its simplicity. As for the adaptation algorithm, there exist many techniques presented, see e.g. [1] and reference therein. In AEC context, it is accepted that a Normalized Least Mean Square (NLMS) is one of the most appropriate algorithms in terms of tradeoff between performance and computational complexity.

The original Least Mean Square (LMS) algorithm has a limitation in terms of convergence speed. By introducing step-size normalization, NLMS can overcome the problem. In this case, convergence is guaranteed if the step-size

$$0 < \mu < \frac{2}{(p+1)E\{|x(n)|^2\}} \tag{1}$$

where $x(n)$ is the input signal at time n and E{•} denotes expectation operation. From the above equation, the expected input power is estimated by its time average, i.e.

$$\hat{E}\{|x(n)|^2\} = \frac{1}{p+1}\sum_{k=0}^{p}|x(n-k)|^2 \tag{2}$$

Thus convergence is guaranteed if

$$0 < \mu < \frac{2}{\mathbf{x}^H(n)\mathbf{x}(n)} \tag{3}$$

Using Eq. (3), the update equation for NLMS is easily obtained by replacing the LMS step-size with

$$\mu(n) = \frac{\beta}{\mathbf{x}^H(n)\mathbf{x}(n)} = \frac{\beta}{\|\mathbf{x}(n)\|^2} \tag{4}$$

resulting in the following update equation

$$\mathbf{W}(n+1) = \mathbf{W}(n) + \beta \frac{\mathbf{x}^*}{\varepsilon + \|\mathbf{x}(n)\|^2} e(n) \tag{5}$$

where $\mathbf{w}(n)$ and $\mathbf{x}(n)$ denotes the weight and input vector at time n. In addition, $e(n)$ is the error signal and β is the step-size. Note that ε in Eq. (5) is used to avoid numerical instability.

III. Distributed Arithmetic

Basically, distributed arithmetic [4]-[7] is a bit serial computational operation that forms an inner (dot) product of a pair of vectors in a single direct step [4]. The technique significantly reduces hardware complexity [7], as a fundamental MAC operation becomes a simple shift and add operation. Eq. (6) shows DA, which has a similar form to an FIR filter.

$$y(n) = \sum_{k=0}^{N-1} A_k \bullet x_k(n) \tag{6}$$

where A_k is fixed coefficient, x_k is data input, and N is the total number of taps. If each data input x_k is a 2's-complement binary number scaled such that $|x_k| < 1$, then it can be written as

$$x_k = -x_{k0} + \sum_{b=1}^{B-1} \left(x_{kb} \bullet 2^{-b} \right) \tag{7}$$

where B is number of input data, x_{kb} is bit of input value 0 or 1, and x_{k0} is a sign bit of theinput data. By substituting x_k from Eq. (7) into Eq. (6), we obtain

$$y = \sum_{k=0}^{N-1} A_k \left(-x_{k0} + \sum_{b=1}^{B-1} x_{kb} \bullet 2^{-b} \right) \tag{8}$$

Rearranging Eq. (8), we obtain

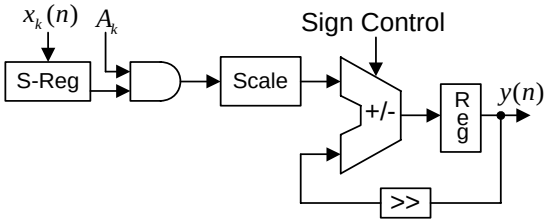

Figure 2 Block diagram of Distributed Arithmetic (1 Tap)

$$y = -\sum_{k=0}^{N-1} x_{k0} A_k + \sum_{b=1}^{B-1} 2^{-b} \left(\sum_{k=0}^{N-1} x_{kb} A_k \right) \tag{9}$$

Explicitly expressing all the product terms under the summation symbols results in the DA equation:

$$\begin{aligned} y = &-\left[\left(x_{00}A_0 + x_{10}A_1 + x_{20}A_2 + \ldots + x_{(N-1)0}A_{N-1} \right) \right] \\ &+ \left[\left(x_{01}A_0 + x_{11}A_1 + x_{21}A_2 + \ldots + x_{(N-1)1}A_{N-1} \right) \right] 2^{-1} \\ &+ \left[\left(x_{02}A_0 + x_{12}A_1 + x_{22}A_2 + \ldots + x_{(N-1)2}A_{N-1} \right) \right] 2^{-2} \\ &\ldots \\ &+ \left[\left(x_{0(B-1)}A_0 + x_{1(B-1)}A_1 + x_{2(B-1)}A_2 + \ldots + x_{(N-1)(B-1)}A_{N-1} \right) \right] 2^{-(B-1)} \end{aligned} \tag{10}$$

Each multiplication of a x_{kb} term and an A_k term is the product of a coefficient word with an input bit. This can be implemented by using an AND gate between each bit of the coefficient word and the input bit. Each scaling factor (2-i) can be implemented by shifting the data to be scaled right i bit. Eq.(10) therefore becomes the summation of the scaled summation of a series of AND gate. This operation could be performed in parallel, or bit-serially, where each clock cycle a single bit from every x_k is multiplied by the corresponding A_k, forming one bracketed term in Eq.(10). These partial products are then accumulated together with the appropriate scaling to produce a final multiplier output. An example of bit-serial multiplication for a single coefficient and input is shown in Fig.2.

IV. MAC Processor

Generally, a relationship between the input $x(n)$ and output $y(n)$ of an FIR filter with the impulse response $h(n)$ is expressed as

$$y(n) = \sum_{k=0}^{N-1} h(k)x(n-k) \tag{11}$$

Implementation of Eq. (11) can be achieved using a multiply-and-accumulate processor (MAC) [8]. Fig. 3 illustrates implementation of a four-tap FIR filter using MAC processor. Its operation is as follows. During cycle 0, the processor multiply the input at time instant n with the first weight stored in ROM. The result then accumulated with the previous regis-

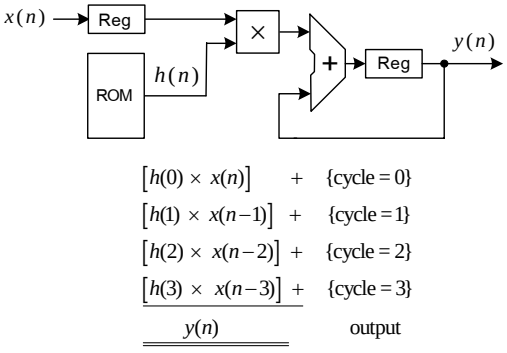

Figure 3 Structure MAC

ter value. Finally, the accumulated is stored in the register.

V. FPGA IMPLEMENTATION OF AEC

Fig. 4 depicts a structure of the proposed AEC. It relies upon DA together with reusable MAC processors. A First-in First-out (FIFO) register is used for realization of a unit-delay. After delay, a Parallel-in-Serial-out (PISO) converts the data from parallel to serial format. Here, the Least Significant Bit (LSB) is shifted first. The data is then fed to COF where it is multiplied with the error forming the coefficients for each tap. Another FIFO is employed in the COF to store the coefficients, which are updated during the next time instant.

The PISO output is also fed to MUX for step-size computation in RAM. The output from RAM is fed to power-of-two circuit that estimates $\|\mathbf{x}(n)\|^2$. The sum of product output for each serial bit is then scaled, shifted to produce the complete output. The last part of circuit aims for MAC reuse control.

TABLE I
AEC SPECIFICATION

Sampling rate of the input signal	16 KHz
Number of taps	256 tap
Number of bits of the input signal	16 bit
Number of bits of the output signal	16 bit

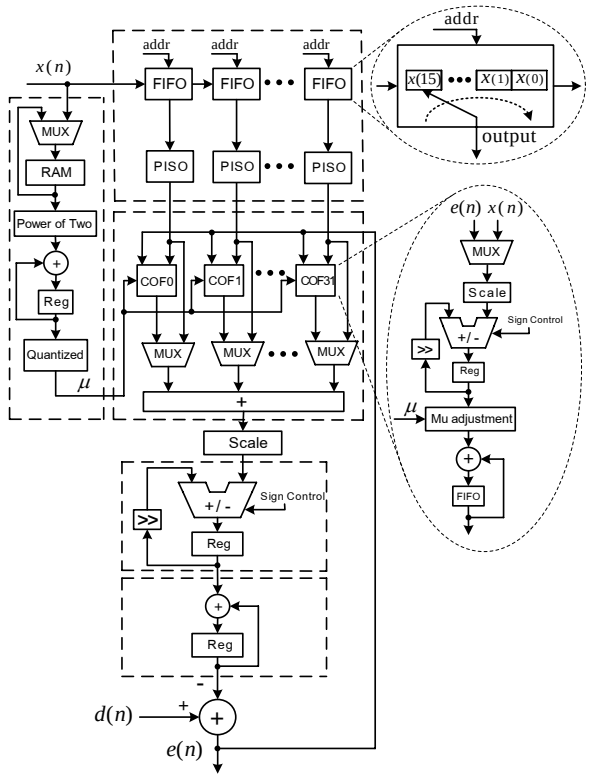

Figure 4 Acoustic Echo Canceller by DA with MAC

VI. RESULTS

The proposed AEC was realized by means of VHDL language. Firstly, simulations were conducted through Xilinx ISE to evaluate performance of the proposed structure. Table I lists the proposed AEC specification, while Table II shows synthesis results on Xilinx XC2VP30FF896-7. It is seen that resource utilization is moderately low. Further reduction of resource utilization can be achieved by reusing MAC processors. A timing diagram of the proposed AEC is illustrated in Fig. 5. The AEC output obtained from simulations was compared with one obtained from MATLAB using fixed-point arithmetic. It was found that the simulation results resembled the MATLAB results confirming AEC functionalities. Next, the proposed AEC is implemented on the Xilinx development tool kits. The input under test was white Gaussian noise with unity variance. Fig. 6 shows the error output of the proposed AEC. Clearly, it is seen that AEC converged after n=2,000 iterations.

TABLE II
SYNTHESIS RESULTYPE

Device utilization summary : 2vp30ff896-7				
Number of Slices:	10482	out of	13696	76%
Number of Slice Flip Flops:	15938	out of	27392	58%
Number of 4 input LUTs:	16634	out of	27392	33%
Number of bonded IOBs:	51	out of	396	12%
Number of BRAMs:	1	out of	136	0%
Number of GCLKs:	5	out of	16	31%

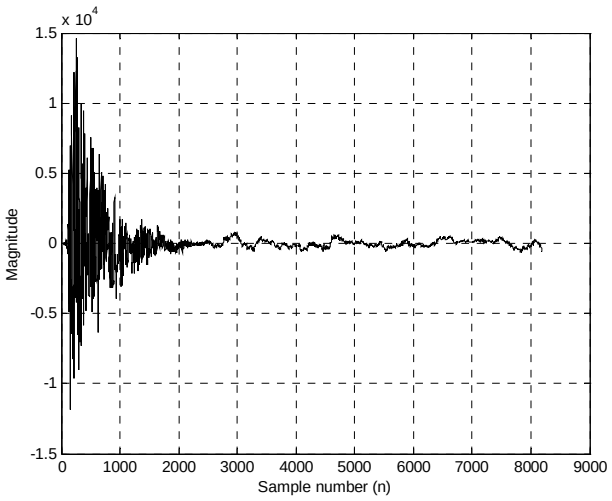

Figure 6 error signal of Adaptive filter with white noise

VII. CONCLUSION

In this paper, FPGA implementation of AEC using NLMS algorithm has been presented. Distributed arithmetic and MAC reusing techniques have been introduced for optimizing resource utilization in the proposed AEC. Simulation and experimental results have demonstrated that AEC can be realized with moderate resource utilization.

REFERENCES

[1] S. Haykin, *Adaptive Filters Theory 3rd ed.*, Prentice-Hall,1996.
[2] E. Hänsler and G. Schmidt, *Acoustic echo and noise control: a practical approach*, John Wiley and Sons, Inc., New Jersey.
[3] P. Eneroth, S. L. Gay, and T. Gänsler, "A Real-Time Implementation of a Stereophonic Acoustic Echo Canceller", *IEEE Transactions on Speech and Audio Processing*, vol. 9, No. 5 pp. 513-523, July 2001.
[4] Sinha and M. Mehendale, "Improving Area Efficiency of FIR Filters Implemented Using Distributed Arithmetic", International Conference on VLSI Design, *VLSI Design'98*, pp. 104-109, 1998.
[5] M. Mehendale and S.D. Sherlekar, *VLSI Synthesis of DSP Kernels: Algorithmic and Architectural Transformations*, Kluwer Academic Publishers, 2001.
[6] R.S.Grove, W. Shang and Q. Li, "A faster distributed arithmetic architecture for FPGAs", *10th ACM Int. Sym. Field Programmable Gate Arrays*, pp. 31-39, CA, 2002.
[7] S. A. White, "Application of distributed arithmetic to digital signal processing: A tutorial review", *IEEE ASSP Magazine*, Vol. 6, no.3, pp. 4-13, July 1989.
[8] P. Kollig, B.M. Al-Hashimi, K.M. Abbott, "FPGA Implementation of High Performance FIR Filter", *IEEE ISCAS'97*, June, 1997.

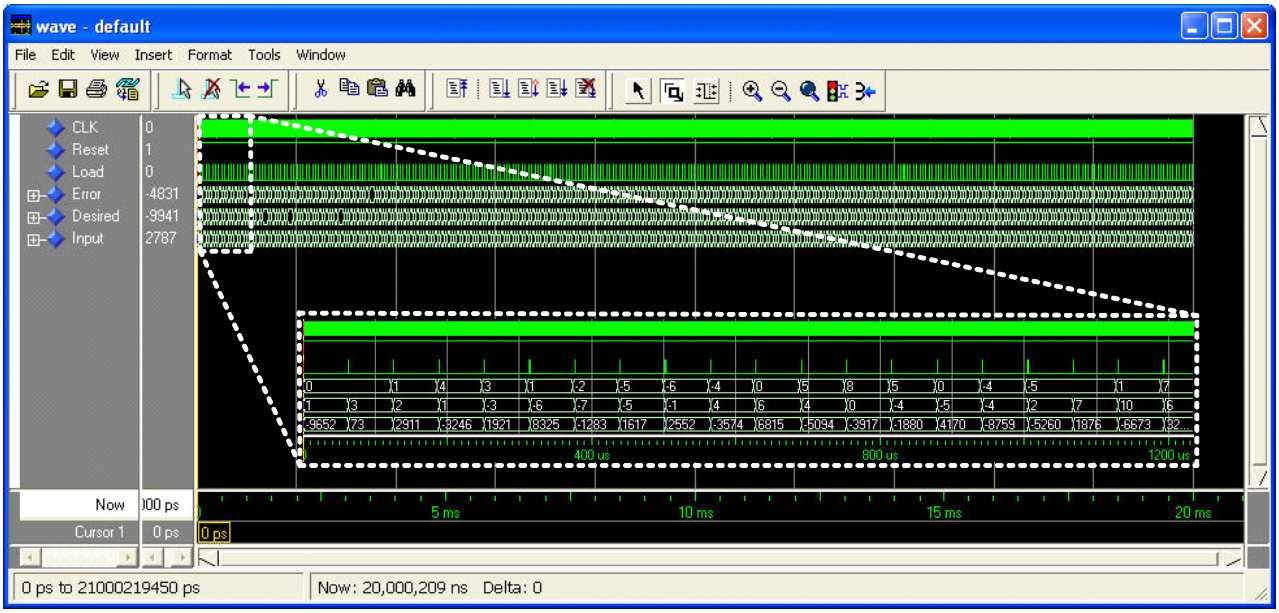

Figure 5 Simulation on Modelsim

Analog nonlinear circuits based on the voltage Level shift buffer

Ittipong Chaisayun and Kobchai Dejhan*
South-East Asia University
Bangkok 10160, THAILAND, Email:ittipong@sau.ac.th
*King Mongkut's Institute of Technology Ladkrabang
Ladkrabang, Bangkok 10520, THAILAND

***Abstact*-This paper describes analog nonlinear integrated circuits operable on low voltage supplies. The paper presents three analog functional circuits as follows: the squarer, square-root, and multiplier. These circuits make use of voltage level shift buffer as fundamental circuit. All circuits have simple structure and do not use many devices. Simulation results are given to show performance of the proposed circuits. Experimental result is done to confirm operation.**

I. INTRODUCTION

Squaring circuit, square-rooting circuit, and multiplier are nonlinear signal processing functions which are very useful in instrumentation, communication, and control systems. Nonlinear circuits were published by using operational amplifier[1] and current conveyor[2]. These circuits were not suitable for implement in integrated circuit form. Then some circuits[3-5] using only CMOS have been proposed. These circuits use many devices and have complex structure. In this paper we propose nonlinear circuits using the voltage level shift buffer, and all circuits have simple structure and do not use many devices. The voltage level shift buffer was applied to transconductor[6], composite transistors[7]and current conveyor[8], so in this paper the voltage level shift buffer is applied to nonlinear circuits. Presently, the power supply voltages for monolithic integrated circuits have been continuously reduced, since the MOS transistor has turned out to be the device most amenable to microstructure downscaling. Analog circuit design intends low voltage circuits, so the circuits in this paper are designed for low voltage supplies.

II. PRINCIPLE OF OPERATION

Assume that all CMOS transistors in this paper operate in saturation region with individual well connected to their source to eliminate the body effect, and the drain current of transistor can be expressed as

$$I_D = K(V_{GS} - V_T)^2 \qquad (1)$$

where K is the transconductance parameter, V_{GS} is the gate-to-source voltage, and V_T is the threshold voltage.

A. *The voltage level shift buffer*

The voltage level shift buffer is performed by shunt-series feedback configuration shown in fig. 1.

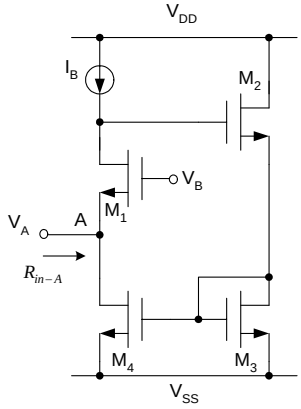

Fig. 1 The voltage level shift buffer

The voltage level shift buffer generates the adjustable voltage source. The relationship of the voltage at the terminal A, V_A, to bias current I_B and the input voltage V_B can be expressed

$$V_A = V_B - \sqrt{\frac{I_B}{K}} - V_T \qquad (2)$$

The equation (2) shows that V_A can be varied by V_B and I_B. Defining $I_B \cong 0$ and $V_B = 0$, so the above equation can be rewritten as

$$V_A = -V_T \qquad (3)$$

The input resistance at terminal A, R_{in-A}, was analyzed in [9] and can be expressed as

$$R_{in-A} = \left(1 + \frac{g_{m2} g_{m4} r_{o1}}{g_{m2} + g_{m3}}\right)^{-1} \cdot \frac{1}{g_{m1}} \qquad (4)$$

where g_{mi} is the transconductance of the transistor M_i, the r_{o1} represents the output resistance of I_B. The equation (4) shows that the circuit has very low input resistance required much for voltage source. The voltage level shift buffer can get the current from other circuit, and it can supply a little current which is less than I_B. The sinking current at terminal A will pass M_4 and effects change of gate terminal voltage of M_4, but V_A constant as long as V_B and I_B constant. The voltage level shift buffer is set to $V_A = -V_T$ for squaring circuit and square-rooting circuit and set to $V_A = V_B - \sqrt{\frac{I_B}{K}} - V_T$ for multiplier.

B. *The squaring circuit*

The squaring circuit shown in fig. 2 consists of a differential amplifier and the voltage level shift buffer.

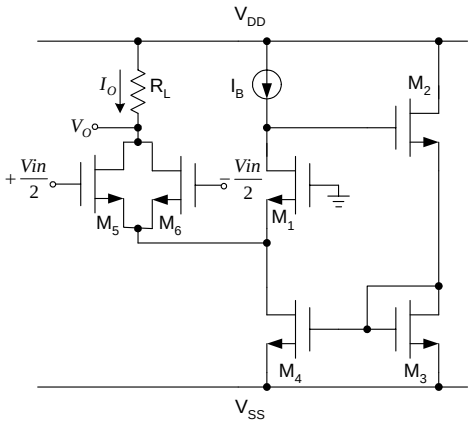

Fig. 2 The squaring circuit

In Fig. 2 the source terminal voltage of both M_5 and M_6 is equal to $-V_T$. The transistors M_5 and M_6 are biased in class B when V_{in} is signal voltage with no dc offset voltage. The relationship of output current I_o to input voltage V_{in} can be expressed as

$$I_o = K\left(\frac{V_{in}}{2}\right)^2 \qquad (5)$$

Note that if V_{in} is positive value, M_5 will turn on (whereas M_6 turn off) and if V_{in} is negative value, M_6 will turn on (whereas M_5 turn off)

C. *The square-rooting circuit*

The square-rooting circuit shown in fig. 3 consists of an MOS transistor and the voltage level shift buffer.

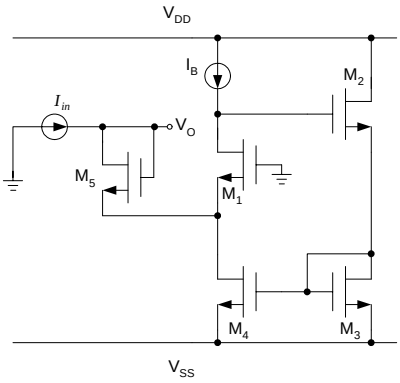

Fig. 3 The square-rooting circuit

The transistor M_5 in fig. 3 is used as a simple current-to-voltage converter. When source terminal voltage of M_5 is equal to $-V_T$. The relationship of input current I_{in} to output voltage V_o can be expressed as

$$V_o = \sqrt{\frac{I_{in}}{K}} \qquad (6)$$

D. *The four- quadrant analog multiplier.*

The core of many MOS four-quadrant analog multipliers which have been proposed thus far is based on the four cross-coupled transistor circuit of fig. 4[5].

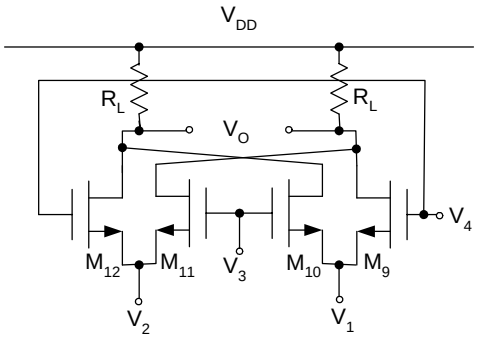

Fig. 4 The core of multiplier

Consider the circuit of Fig. 4, where four transistors are matched and in the saturated mode of operation. Using (1) to each device yields

$$V_o = KR_L(V_3 - V_4)(V_1 - V_2) \qquad (7)$$

To ensure all devices in their saturation region, it requires

$$(V_4, V_3)_{\min} > (V_1, V_2)_{\max} + V_T \qquad (8)$$

To design the multiplier under condition of (8), voltage level shift buffers are used. The proposed multiplier consists of two

voltage level shift buffers and the core of multiplier shown in Fig. 5

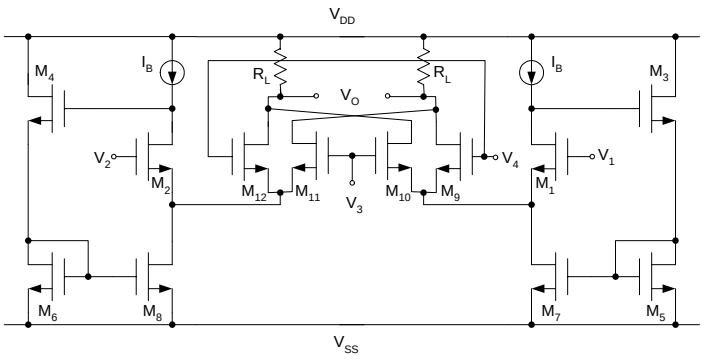

Fig. 5 The four quadrant analog multiplier

The output voltage of the proposed multiplier is the same as (7)

III. RESULTS

To verify the operations of the circuits, the designs were simulated in a 0.25µm T14Y model of MOSIS with level 3. The aspect ratio of transistors is shown in table 1 which likes the aspect ratio of ones in literature [9]. The voltage supplies are set to $V_{DD} = -V_{SS}=1$ volts and load resistors R_L are 10kΩ. Squaring circuit and square-rooting circuit use $I_B = 1\mu A$, and the multiplier circuit uses $I_B = 20\mu A$.

Table 1 W/L ratio of proposed circuits

squaring and Square-rooting circuits		The multiplier circuit	
transistor	W/L(µm/µm)	transistor	W/L(µm/µm)
M_1	10/1	M_1, M_2	200/1
M_2	10/4	M_3, M_4	10/4
M_3	5/2	M_5, M_6	5/2
M_4	15/2	M_7, M_8	15/2
M_5, M_6	10/4	$M_9 - M_{11}$	8/4

The dc transfer characteristic of the squaring circuit is demonstrated in Fig. 6 when V_{in} is varied from -1_V to 1_V compared to expected curve $\left(= \frac{V_{in}^2}{16555}\right)$, and the frequency double in Fig. 7 is done by applying 1_Vp-p, 1MHz-sinusoidal signal to input of the squaring circuit and the output signal accord to the equation as $\sin^2 \omega t = \frac{1}{2}[1 - \cos 2\omega t]$. The dc transfer characteristic of the square-rooting circuit is demonstrated in Fig. 8 when I_{in} is varied from 0_A to 100_µA compared to expected curve $\left(= 65\sqrt{I_{in}}\right)$. The dc transfer characteristics of multiplier are shown in Fig. 9(a) and (b) by alternating the input signal V_{12} and V_{34}.

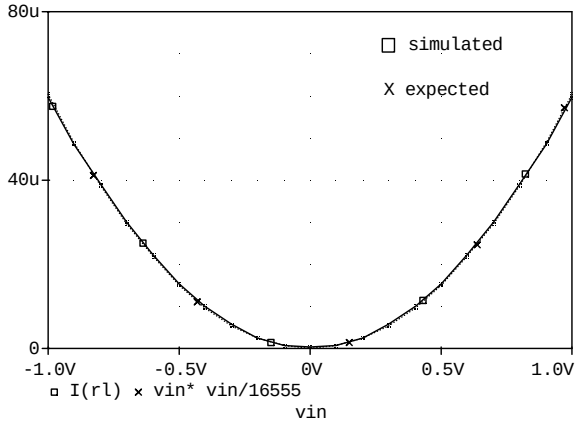

Fig. 6 The dc transfer characteristic of the squaring circuit

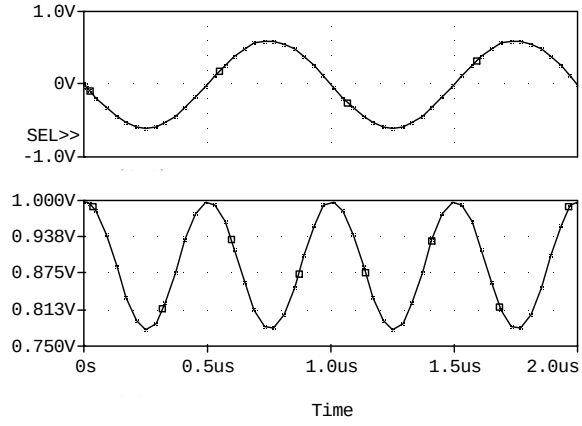

Fig. 7 frequency doublers where input is 500mVp, 1MHz-sinusoidal signal(upper trace) and the output waveform(lower trace)

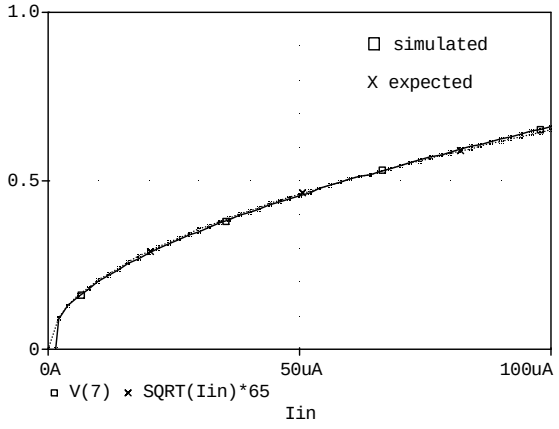

Fig. 8 The dc transfer characteristic of the square-rooting circuit

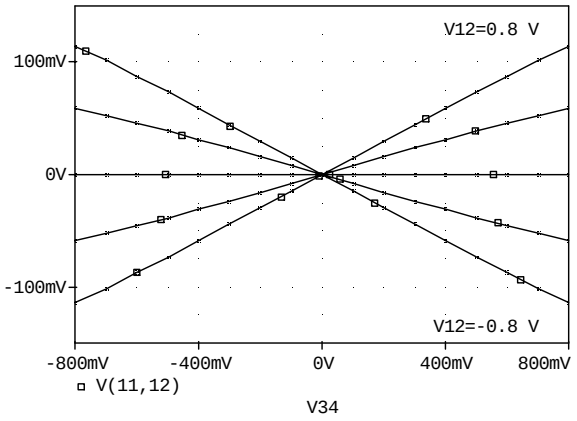

(a)

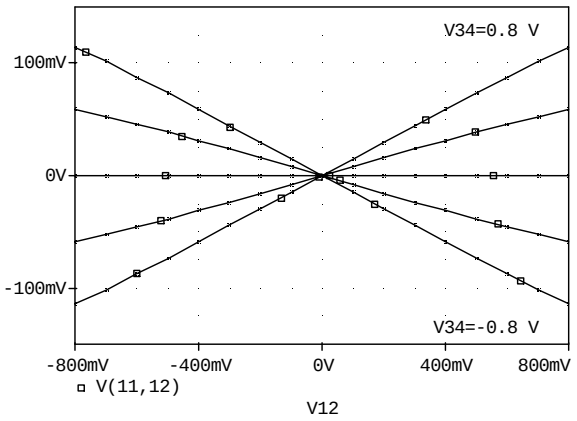

(b)

Fig. 9 The dc-characteristics of multiplier

The relative error of Fig. 6 is 1.1 % within the ±1_V input range (%error=$\left|\frac{X_e - X_s}{X_e}\right| \times 100\,\%$, X_e is expected value, X_s is simulated value). The relative error of Fig. 8 is 1.2 % within the 100μA input range. The total harmonics distortion (THD) of the proposed multiplier is 1.1% (where V_{34} is a $800mV_{P\text{-}P}$ input signal at 1MHz and V_{12} is 0.4_V dc voltage) and 0.8% (where V_{12} is a $800mV_{P\text{-}P}$ input signal at 1MHz and V_{34} is 0.4_V dc voltage). The -3dB bandwidth of multiplier circuit is 16GHz (where V_{34} is ac signal and V_{12} is dc signal) and 142MHz by alternating the input signal V_{12} and V_{34}.

The proposed squaring circuit in Fig. 2 is tested experimentally by using commercial CMOS transistor arrays (CD4007) The voltage supplies were set to V_{DD}=-V_{SS}=4 Volts, the load resistor R_L was 10kΩ . Fig. 10 shows the output voltage waveform when V_i is a $800mV_{P\text{-}P}$, 10 kHz-sinusoidal signal.

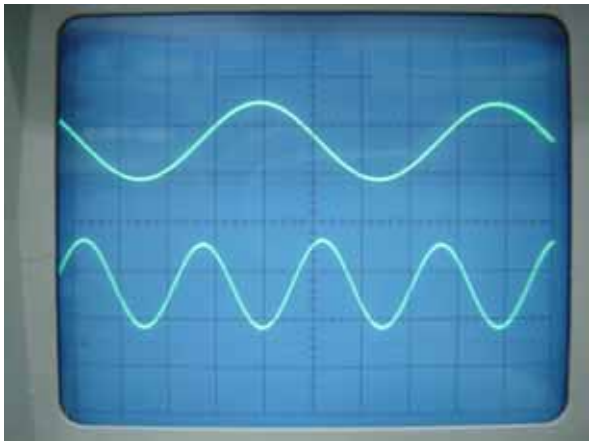

Fig. 10. The output waveform of frequency doublers (lower trace) when input is 800mVp-p,10 kHz-sinusoidal signal (upper trace)Volt/Div=0.5V, Time/Div=20μS.

IV. CONCLUSION

Squaring circuit, square-rooting circuit, and multiplier circuit using a voltage level shift buffer have been presented. The advantages of proposed circuits are simple structure, few devices, wide input range, and low voltage supplies. Simulation results show that all circuit can operate at ±1_V power supplies, the voltage input range of the squarer circuit is wide up ±1_V with 1.1% relative error, the current input range of the square-rooting circuit is about 100_μA with 1.2% relative error, the THD of the multiplier is less than 1.2% for a $800mV_{P\text{-}P}$ input signal at 1MHz fundamental frequency. These circuits are expected to be useful in many analog signal-processing applications.

REFERENCES

[1] I. M. Filanovsky, and H. P. Baltes, "Simple CMOS analog square-rooting and squaring circuits," IEEE Trans. Circuits Syst., vol.39, pp.312-315, 1992.

[2] S. I. Liu, "Square-rooting and vector summation circuits using current conveyors," IEE Proceedings G-Circuits, Devices and Systems, vol.142, pp. 223-226, 1995.

[3] S. I. Liu and C. C. Chang, " A CMOS square-law vector summation circuit," IEEE Trans. Circuits Syst., vol.43, pp.520-523, 1996.

[4] C. Netbut, M. Kumngern, P. Prommee and K. Dejhan, " A versatile vector summation circuit," Proc. of ISCIT 2006, Banngkok, Thailand, Oct. 18-20, 2006.

[5] H.-J. Song and C. K. Kim, "An MOS Four-Quadrant Analog Multiplier Using Simple Two-Input Squaring Circuits with Source Followers," IEEE J. Solid-State Circuits, vol. 25, no. 3, pp. 841-848, June 1990.

[6] S. R. Zarabadi and M. Ismail, "Linear voltage to current converter including feedback network," U.S. Pateent 5317279, May 31, 1994.

[7] A. Hyogo, C. Hwang, M. Ismail and K. Sekine, "LV/LP CMOS square-law composite transistors for analog VLSI applications," IEEJ. 1st Analog VLSI Workshop Proceedings, ECT-97-32, pp. 139-143, May 1997.

[8] O. Oliaei and J. Port, "Compound current conveyor (CCII+andCCII-)," Electron. Lett., vol..33, pp.253-254,Feb, 1997.

[9] E. Ibaragi, A. Hyogo, and K. Sekine, "A Phase Compensation Technique without Capacitors for the CMOS Circuit with a Very Low Impedance Terminal," IEICE Trans. Fundamentals, vol. E83-A, no. 2, Feb. 2000.

TABLE I
LONGITUDINAL VELOCITY OF MATERIAL

Material	Longitudinal Velocity (*c*) (mm /μs)
Aluminum	6.350
Brass	4.430
Copper	4.700
Plexiglas	2.680
Stainless	5.610
Steel	5.940
Water	1.494

B. Ultrasonic Signal Simulation

Ultrasonic signal can be modeled by gaussian function in Figure 2 and sine wave in Figure 3. $e(t)$ may be expressed in (2). F_0 is transducer center frequency. t is time. σ^2 is variance of gaussian function. t_0 is position of scatters in time domain. Figure 4 shows $e(t)$ at t_0 =2 μs. $h(t)$ is an impulse response of a scatter function used to convolute with $e(t)$ as described in (3).

$$e(t) = \exp[-2\pi^2\sigma^2(t-t_0)^2]\sin(2\pi F_0 t) \quad (2)$$

$$s(t) = e(t) * h(t) \quad (3)$$

For a medium of scatters, the echo signal $s(t)$ can be modeled in frequency domain as follows:

$$s(t) = e(t) * h(t) = \sum_M e(t) * h_a^2(M,t) * h_d(M,t) \quad (4)$$

where $h(t)$ is impulse response of scatters that relate to (5) and (6) in frequency domain. h_a^2 is the two ways impulse response of attenuation of a scatter in position M and $H_a^2(M,f)$ is frequency domain of h_a^2. $2Z$ is the total distance traveled by the ultrasound wave. $h_d(M,t)$ is a set of impulses in time domain that relate to position M in frequency domain as shown in (8). β is attenuation coefficient, which is estimated from FCS.

$$S(f) = E(f) \cdot H(f) \quad (5)$$

$$S(f) = \sum_M E(f) \cdot H_a^2(M,f) \cdot H_d(M,f) \quad (6)$$

$$H_a^2(M,f) = e^{-2Z\beta f} \quad (7)$$

$$H_d(M,f) = \delta(Z) \quad (8)$$

h_d is the scattering impulse function simulated by Dirac function. The position Z of a scatter is determined with function of object modeled. In this paper, two positions of Dirac function are utilized according to experimental system.

$$h_d(f,Z) = \delta(Z) \quad (9)$$

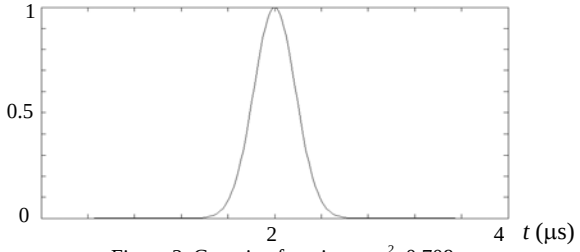

Figure 2. Gaussian function at σ^2=0.709

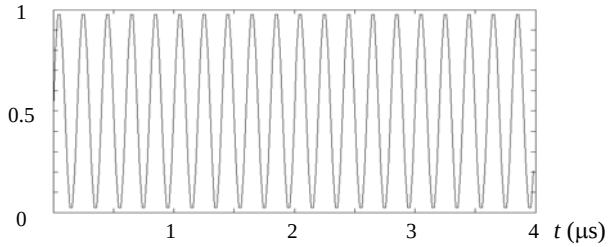

Figure 3. Sine wave at 5 MHz

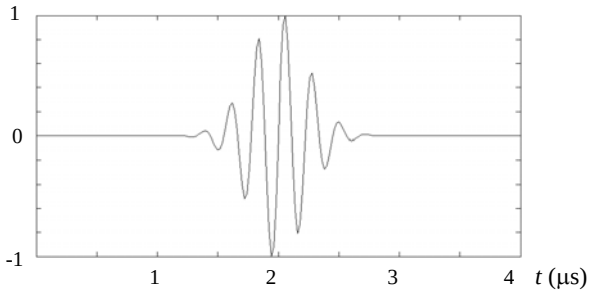

Figure 4. $e(t)$ function

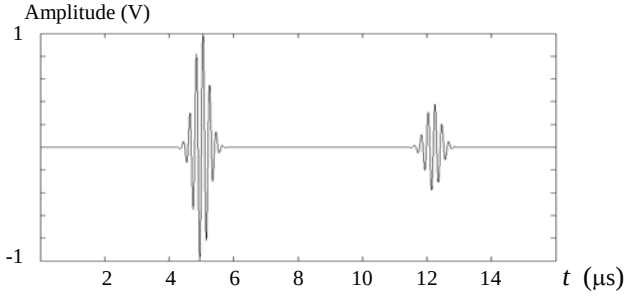

Figure 5. Ultrasonic simulation signal

TABLE II
ATTENUATION OF TISSUE AT 1 MHZ [5]

Tissue	Characteristic Impedance $\rho_0 c$ (10^6Ns/m^3)	Attenuation at 1 MHz (dB/cm)
Blood	1-62	0.2
Spleen	1-6	0.4
Liver	1-65	0.7
Fat	1-38	0.8
Brain	1-60	0.8
Muscle	1.65-1.74	1.5-2.5
Bone	3.2-7.4	11
Lung	0.26-0.46	40
(Water)	1.49	0.002

III. MULTINARROW BAND TECHNIQUE

MNB is one of strategies in Fourier statistics method that depends on the log-spectral estimation. The relation between incident wave and reflected wave in frequency domain can be described in (10).

$$S(f) = E(f) \cdot e^{-2Z\beta f} \quad (10)$$

E(f) is spectrum of incident wave from front surface and *S(f)* is the spectrum of reflected wave from back surface that is attenuated by factor $e^{-2Z\beta f}$ where 2*Z* is the propagation distance in material. With the classical assumption of linear with frequency attenuation, $\alpha(f)$ is attenuation expressed in dB/cm and β is the attenuation coefficient expressed in dB/cmMHz. The relation between $\alpha(f)$ and β can be expressed in (11).

$$\alpha(f) = \beta \cdot f \quad (11)$$

So, the βf in (10) is substituted by $\alpha(f)$ in (11) and get (12).

$$S(f) = E(f) \cdot e^{-2Z\alpha(f)} \quad (12)$$

The process to estimate the attenuation coefficient can be obtained by logarithm of (12) as shown in (13)-(16). Assuming, the sample is homogeneous. The attenuation $\alpha(f)$ may be estimated as a function of frequency from the slope of a linear regression fit to the log decay of spectra. The slope of ultrasonic attenuation coefficient, β, may be calculated via a linear frequency dependence of attenuation curve, $\alpha(f)$, versus frequency as shown in Figure 6. Equation (17) expresses unit conversion from Neper to dB.

$$10\log S(f) = 10\log E(f) - 20Z\alpha(f) \cdot \log e \quad (13)$$

$$10\log S(f) = 10\log E(f) - 20Z\alpha(f) \cdot \frac{1}{\ln 10} \quad (14)$$

$$10\log S(f) - 10\log E(f) = -20Z\alpha(f) \cdot \frac{1}{\ln 10} \quad (15)$$

$$\alpha(f) = \left(\frac{10\log S(f) - 10\log E(f)}{-20Z} \right) \ln 10 \quad (16)$$

$$\beta\,[\text{dB/cmMHz}] = 8.68 \cdot \beta\,[\text{Neper/cmMHz}] \quad (17)$$

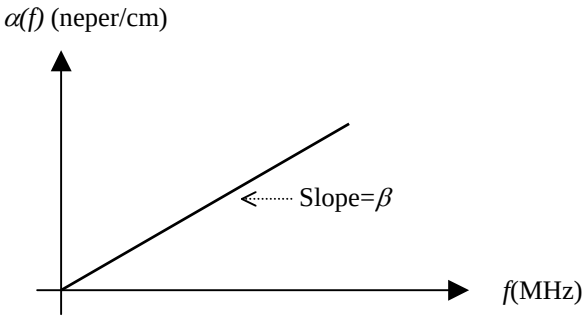

Figure 6. Slope of $\alpha(f)$

IV. NUMERICAL SIMULATION

According to ultrasonic transducer, 5 MHz of center frequency is selected to simulate ultrasonic signal with attenuation coefficient of brass = 0.50dB/cmMHz [6] as shown in Figure (7). The difference of time corresponds to Z=2.5 cm at *c*=4.430 mm/μs as described in Table I.

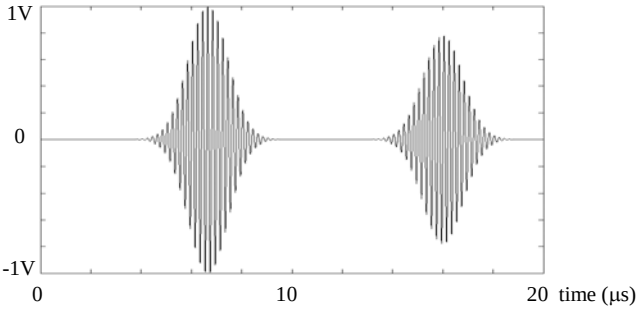

Figure 7. Simulation of Ultrasonic signal at 5 MHz

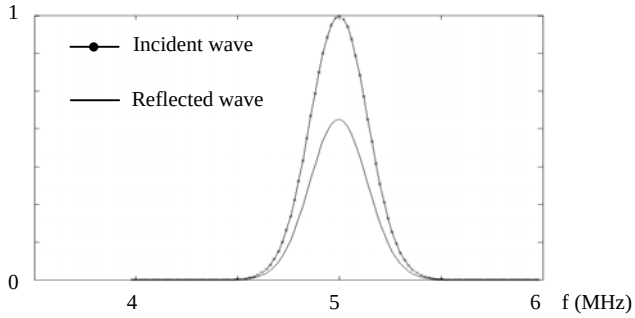

Figure 8. Spectrum of incident wave and reflected wave

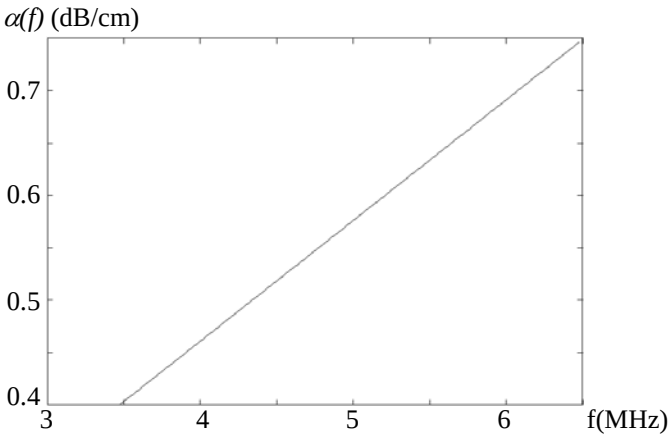

Figure 9. Attenuation versus frequency of simulated signal

From Figure 8, the spectrum of both incident wave and reflected wave is computed. The β in term of $\alpha(f)$ is estimated by (16) and plotted in function of frequency as shown in Figure 9. The slope of Figure 9 is 0.0576 Neper/cmMHz. To convert Neper unit to dB, equation (17) is applied by factor 8.68. Then, the result of the ultrasonic attenuation coefficient of simulated signal is 0.4999 dB/cmMHz. Additionally, other β values at 1 MHz and 5 MHz are tested and verified as shown in Table III.

TABLE III

ATTENUATION COEFFICIENTS COMPUTED BY SIMULATED SIGNAL

β (dB/cmMHz)	MNB		Error (%)	
	1 MHz	5 MHz	1 MHz	5 MHz
0.1	0.1020	0.1000	2.0000	0.0000
0.3	0.3001	0.3000	0.0333	0.0000
0.5	0.5021	0.5000	0.4200	0.0000
0.7	0.7021	0.7000	0.3000	0.0000
1.0	1.0021	1.0000	0.2100	0.0000
1.5	1.5021	1.5001	0.1400	0.0067
2.0	2.0021	2.0001	0.1050	0.0050
3.0	3.0022	3.0001	0.0733	0.0033

V. EXPERIMENTAL VALIDATION

The experimentation is built up as shown in Figure 10. The metal, brass, is immersed in Plexiglas water tank. Furthermore, the ultrasonic transducer is located at the top of water tank and linked to digital oscilloscope. The instruments and devices as shown in Table IV are setup to obtain an ultrasonic signal. Ultrasonic pulse generator and transducer are selected in same manufacturer, Panamatrics. The reflection mode is selected to measure the ultrasonic signal. The echo signal from transducer is digitized with digital oscilloscope and sent as a digital data set to personal computer by GPIB cable. The ultrasonic signal, *s(t)*, is digitized with a sampling interval $\Delta t = 1/F_s$ (F_s is the sampling frequency = 500 MHz), in 10,000 samples. Figure 11 displays a captured signal. The digitized data is computed to obtain β by MNB algorithm. So, β of measured signal is 0.4485 dB/cmMHz. The error calculated by (18) of β between simulation and experimentation is approximately 10.3%.

$$\text{Error (\%)} = \frac{\left|\beta_{theory} - \beta_{estimation}\right|}{\beta_{theory}} \cdot 100 \qquad (18)$$

VI. CONCLUSION

The primary goal of this paper is to establish the quantitative estimation for obtaining the ultrasonic attenuation coefficient in solid immersed in water. The MNB technique is the log-spectral estimation in frequency domain. The β is estimated by a linear frequency dependence of attenuation curve versus frequency. The ultrasonic reflection mode is selected to simulate and measure. The 5 MHz unfocused ultrasonic transducer and brass are selected and immersed in Plexiglas water tank. The data is acquired and computed by MNB algorithm. The result show that β from simulated signal is 0.50 dB/cmMHz while β from experimentation is 0.4485 dB/cmMHz. The error is approximately 10.3% because this work excludes the ultrasonic diffraction effect. However, the result in simulation and experimentation is in agreement with the experimental values To reduce the error, the Lommel diffraction correction method [7] will be compensated in future work.

ACKNOWLEDGEMENT

This paper was supported by NSTDA contract no. F-31-206-22-02 and TRF contract no. MRG4980072.

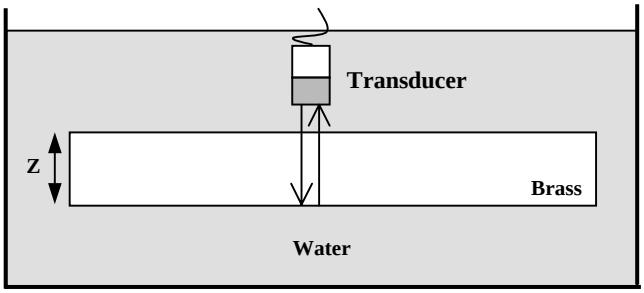

Figure 10. Ultrasonic simulation signal

TABLE IV

INSTRUMENT AND DEVICE USED IN EXPERIMENTATION

Instrument/Device	Model
Pulse Generator	Panamatrics: Model500PR
Digital Scope	Tektronix: TDS3012
Ultrasonic Transducer	Panamatrics: Model V309

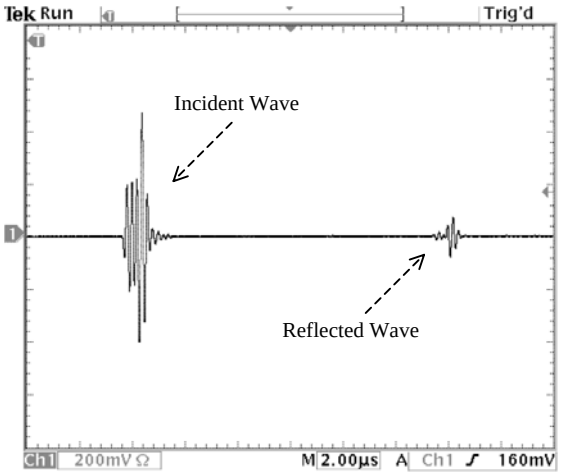

Figure 11.Captrued signal from brass at transducer center frequency=5MHz

REFERENCES

[1] Ping Wu, Tadeusz Stepinski, "Quantitative estimation of ultrasonic attenuation in a solid in the immersion case with correction of diffraction effects," *Ultrasonics,* Elsevier,38, pp.481-485, 2000.

[2] T. Baldeweck, P. Laugier, A. Herment, G. Berger, "Application of Autoregressive Spectral Analysis for Ultrasound Attenuation Estimation Interest in Highly Attenuating Medium," *IEEE Transactions on Ferroelectrics and frequency control*, 42, pp.99-110, 1995.

[3] Celine Fournier, S. Lori Bridal, Alain Coron, Pascal Laugier, "Optimization of Attenuation Estimation in Reflection for In Vivo Human Dermis Characterization at 20 MHz," *IEEE Transactions on Ferroelectrics and frequency control*, 50, pp.408-418, 2003.

[4] Valery Roberjot, S. Lori Bridal, Pascal Laugier, Genevieve Berger, "Absolute Backscatter Coefficient over a Wide Range for Frequencies in a Tissue-Mimicking Phantom Containing Two Populations of Scatters," *IEEE Transactions on Ferroelectrics and frequency control*, 43, pp.970-978, 1996.

[5] Heinrich Kuttruff., "Ultrasonics Fundamentals and Applications," *ELSEVIER Applied Science*, 1991.

[6] V. R. Singh and Ashok Kumar (1995): "Development of A Focused Ultrasonic Transducer with Increased Efficiency," *Proceedings of IEEE-EMBS*, pp.4.47-4.48, 1995.

[7] S. Boonsang and R J Dewhurst, "Pulsed Photoacoustic signal characterization incorporating near- and far-field diffraction effects,"*Meas. Sci. Technol.*, vol 16, pp. 885-899, 2005.

High-Value Floating Controlled Resistor

Wirote Jongchanachavawat, Montree Kumngern, and Kobchai Dejhan
Faculty of Engineering and Research Center for Communication and Information Technology,
King Mongkut's Institute of Technology Ladkrabang, Bangkok 10520, Thailand
Tel: 66-2326-4238, 66-2326-4242, Fax: 66-2326-4554,
E-mail: {jongwirote, montree_kumngern}@yahoo.com, kobchai@telecom.kmitl.ac.th

***Abstract*–In this paper, we propose an electronically tunable high-value floating resistor by using CCCII with controlled output current gain. The very high-value resistor can be easily achieved by increasing the current gain of CCCIIs without changing the circuit configuration. The resistance value can be tuned electronically by bias current or current gain of CCCIIs. The proposed floating resistors were confirmed by using PSpice simulation.**

I. INTRODUCTION

The electronically tunable floating resistor is widely used in analog circuits. The application can be found in telecommunications, electronics and instruments such as active RC filter, oscillators, variable gain amplifiers, voltage or current to frequency converters etc. In VLSI technology, a resistor is formed on silicon wafer. However, resistors of practical values on silicon wafer suffer from limited values, high variability due to process variations and large temperature coefficients. Moreover, its resistance values are not variable. Therefore, they are generally replaced by active resistors. In the past, several electronically tunable resistors have been reported in the literatures with different techniques in literature [1]-[5]. However all of these reports are limited the resistance value. Recently, the high-value floating resistor using CMOS technology was reported in [6] enjoys electronically tunable and it is suitable for integrated circuits fabrication.

In this paper, a high-value electronically tunable floating resistor in bipolar technology has been presented. The proposed circuit bases second-generation current conveyors (CCCIIs) with controlled current gain. Our structure has more flexibility when the resistance value can be tuned by bias current or current gain of CCCIIs.

II. CIRCUIT REALZATION

The symbol of the relatively active element CCCII with controlled current gain is shown in Fig. 1(a), and is characterized by the relationship:

$$\begin{pmatrix} I_Y \\ V_X \\ I_Z \end{pmatrix} = \begin{pmatrix} 0 & 0 & 0 \\ 1 & R_X & 0 \\ 0 & k & 0 \end{pmatrix} \begin{pmatrix} V_Y \\ V_X \\ V_Z \end{pmatrix} \tag{1}$$

The input impedances for the ideal CCCII are infinite at terminal Y and R_X at terminal X, respectively. The terminal Z, that is equivalent to a current generator, possesses infinite output impedance. The schematic implementation for CCCII with current gain, implemented with bipolar technology is shown in Fig. 1(b). The intrinsic resistance R_X can be tuned by the bias current I_o, given by [7]

$$R_X = \frac{V_T}{2I_o} \tag{2}$$

where V_T is the thermal voltage. The current gain k of this current conveyor is determined by the current ratio [8]. The current gain k can be changed by varying I_1 or I_2, expressed as [8]

$$k = \frac{I_1}{I_2} \tag{3}$$

The schematic in Fig. 1(b) is used to realize the high-value floating resistor.

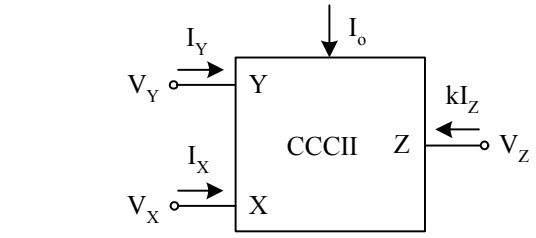

(a)

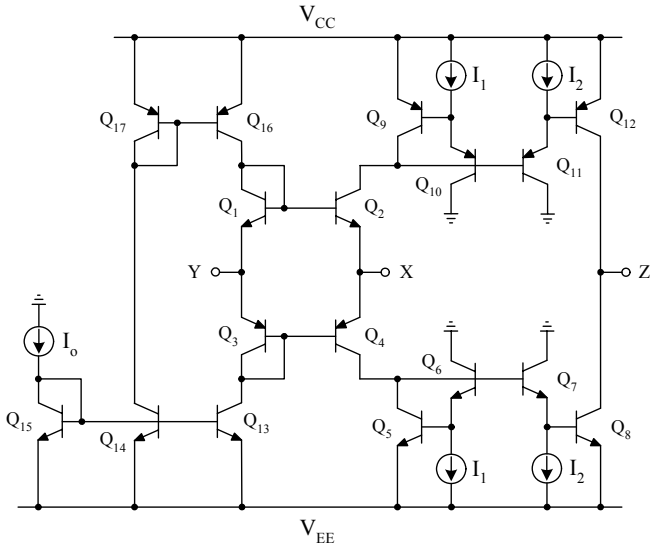

(b)

Fig.1. Bipolar CCCII: (a) symbol and (b) schematic.

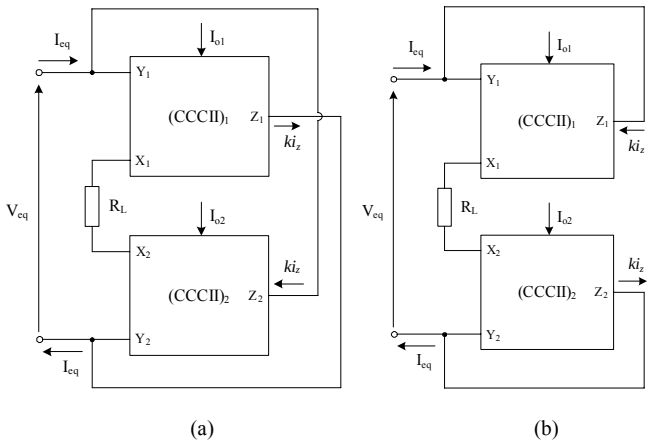

Fig. 2. Symbolic of proposed current controlled floating resistors: (a) positive floating resistor and (b) negative floating resistor.

Fig. 2 shows the proposed high-value current controlled floating resistor. The resistor R_X is an intrinsic resistance in each port X_1 and X_2. The load resistor R_L is connected between X_1 and X_2. The output of each CCCII is constituted by a current gain cell. Therefore, the output current on ports Z_1 and Z_2, they are equal to i_X/k. The outputs Z_1 is connected to Y_2 and Z_2 is connected to Y_1 to be the high-input positive floating resistor impedance as shown in Fig.2(a) or the outputs Z_1 is connected to Y_1 and Z_2 is connected to Y_2 to be the high-input negative floating resistor impedance as shown in Fig.2(b). Its floating resistance value can be given by

$$R_{eq} = \frac{1}{k}\left(2R_X + R_L\right) \tag{4}$$

Using (2)-(3), (4) can be rewritten as

$$R_{eq} = \frac{I_2}{I_1}\left(\frac{V_T}{I_0} + R_L\right) \tag{5}$$

From (5), it notes that the resistance value of proposed resistor can be tuned by bias current I_o. Moreover, the high-value of resistance can be adjusted by current gain ratio through I_1 and I_2. Note that by using CCCII with controlled current gain, resistance value of proposed resistor can be electronically tuned with both the bias current and current gain. Whereas the resistor circuit of Zouaoui-Abouda and Fabre [6] used CCCII with fixed current gain, thus only current bias can be tuned. Hence our structure has more flexibility than the resistor circuit of [6].

III. Simulation Results

The simulations were carried out at 27°C. Using the bipolar transistors NR100N and PR100N [9]. The floating resistor circuits in Fig. 2 are simulated. The DC supply voltage is ±2.5V. The results can be shown as follows. Figs. 3-4 show the variation of resistance of circuit in Fig. 2(a) with the current gain k=10 and R_L=0 and 1kΩ, respectively, against varies the current bias I_o. From Fig 3, the value of resistor decreases from 127 to 4.75kΩ when I_o varies between 2 and 50μA while the value of resistor decreases from 138.5 to 13.7kΩ when I_o varies between 2 and 50μA as shown in Fig. 4. Fig. 5 shows the variation of the negative resistance value of circuit in Fig. 2(b) as a function of I_o. With R_L=0Ω, the value of the resistor decreases from 90.2 to 7.2kΩ when I_o varies between 3 and 50μA. With R_L=1kΩ, the value of the resistor decreases from 104.5 to 16.4kΩ when I_o varies between 3 and 50μA, as shown in Fig. 6. From Figs. 3-6, all simulation results are confirmed with theoretical. Note that the proposed circuit can be provided high-value of resistance close up with theoretical results. To demonstrate the proposed resistor circuit has more flexibility than previous resistor circuit, the circuit in Fig. 2(a) is simulated again. Fig.7 shows the variation of the floating resistance value as a function of the load resistor R_L when I_o is 10μA and current gain is 10. The value of the resistor increases from 40 to 250.2kΩ when R_L varies between 1 and 20kΩ. Fig.8 shows the variation of the floating resistance value resistor as a function of the current gain (k) when I_o is 10μA and R_L=1kΩ. The value of the resistor increases from 7.2 to 92.3kΩ when k varies between 2 and 20.

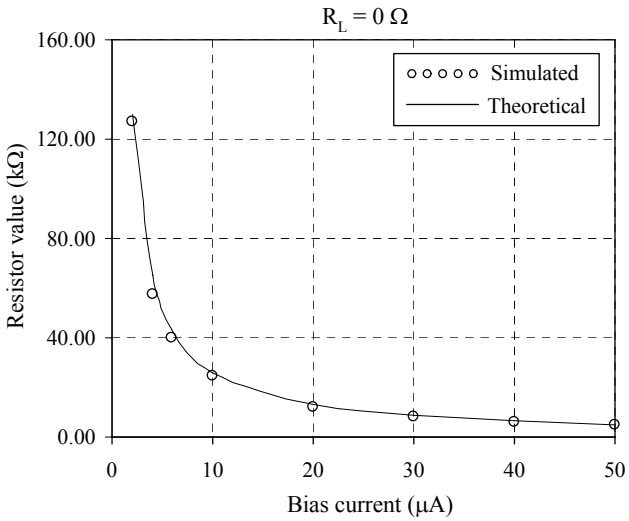

Fig. 3. Variation of positive resistance with DC bias current with R_L=0Ω.

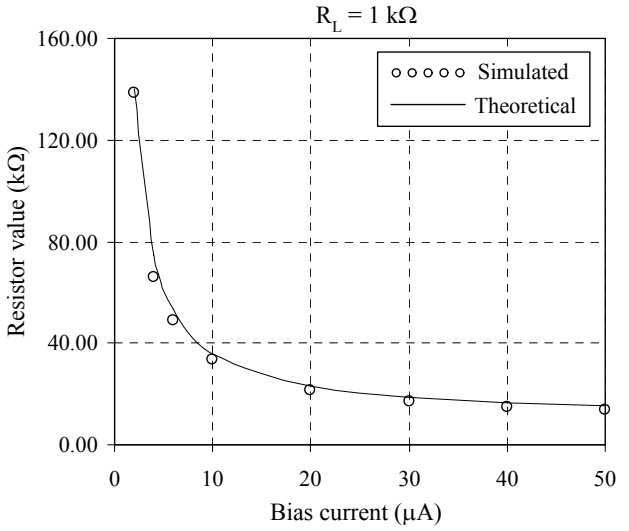

Fig. 4. Variation of positive resistance with DC bias current with R_L=1kΩ.

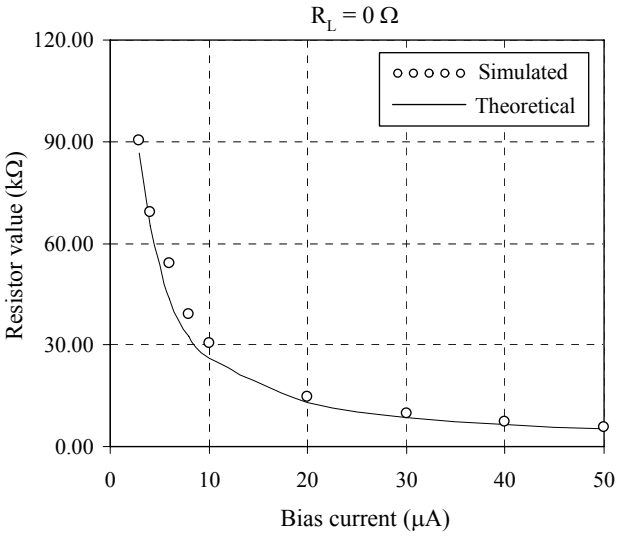

Fig. 5. Variation of negative resistance with DC bias current with R_L=0kΩ.

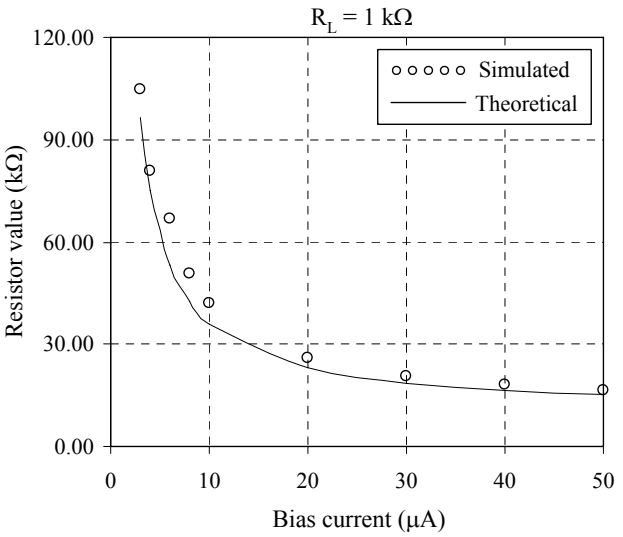

Fig. 6. Variation of negative resistance with DC bias current with R_L=1kΩ.

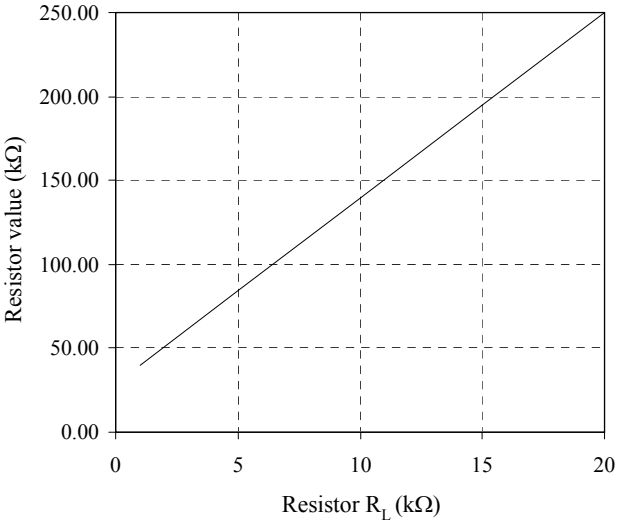

Fig. 7. Variation of resistance with the load resistor R_L.

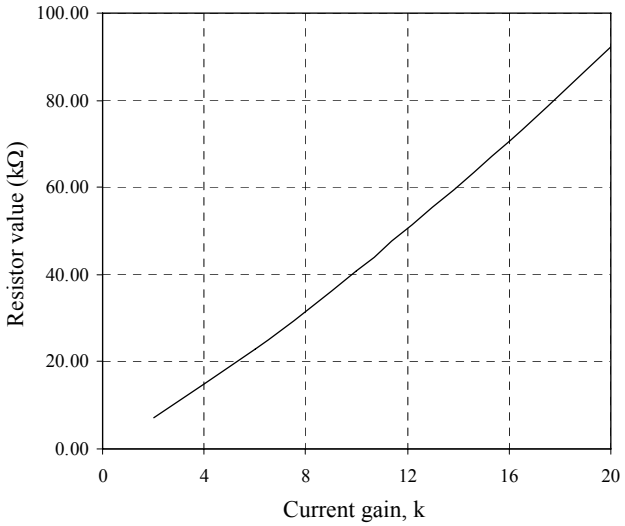

Fig. 8. Variation of resistance with the current gain k.

IV. CONCLUSIONS

A new technique for realizing the floating controlled resistor has been described. The high-value of resistance can be achieved and electronically tuned. It consists of two CCCIIs with controlled current gain, which can be fully integrated in bipolar technology. The resistance value can be electronically tuned by bias current or current gain. Moreover, by using CCCII with controlled current gain, the high-value or low-value range of resistances can be selected by varies the current gain. Simulation results have confirmed the performance of proposed circuits.

REFERENCES

[1] I. A. Khan and M. T. Ahmed, "Realization of tunable floating resistors," *Electronics Letters*, vol.22, pp. 799-800, 1986.

[2] R. Senani, "Realization of linear voltage-controlled resistance in floating forms," *Electronics Letters*, vol.30, pp.1909-1910, 1994.

[3] H. O. Elwan, S. A. Mahamoud, and A. M. Soliman, "CMOS voltage controlled floating resistor," *International Journal of Electronics*, vol.81, pp.471-476, 1996.

[4] G. Wilson and P. K. Chan, "Floating CMOS resistor," *Electronics Letters*, vol. 29, no. 3, pp. 306-307, 1993.

[5] H. Barthelemy and A. Fabre, "A new floating controlled resistance operating in class AB," *IEEE Transactions on Circuit and Systems-I*, vol.47, pp. 67-72, 2000.

[6] H. Zouaoui-Abouda and A. Fabre, "New High-Value Floating Controlled Resistor in CMOS Technology," *IEEE Transactions on Instrumentation and Measurement*, vol.55, pp.1017-1020, 2006.

[7] A. Fabre, O. Saaid, F. Wiest, and C. Boucheron, "High Frequency applications based on a new current controlled conveyor," *IEEE Transaction on Circuit and Systems-I*, vol.43, pp.82-91, 1996.

[8] A. Fabre and N. Mimeche, "Class A/AB second generation current conveyor with controlled current gain," *Electronics Letters*, vol. 43, pp. 82-91, 1996.

[9] D. R. Frey, "Log domain filter: An approach to current mode filtering, *IEE Proceedings Part G of Circuits, Devices and Systems*, vol. 140, pp. 406-416, 1993.

A Fully-Swing Adiabatic Circuit for Low Power Applications

Rungruang Sangpratheep and Kasin Vichienchom
King Mongkut's Integrated Circuits Lab (KMICL)
Department of Electronics, Faculty of Engineering
King Mongkut's Institute of Technology Ladkrabang
Bangkok, Thailand 10520

***Abstract*-This paper presents a fully-swing adiabatic circuit. The proposed circuit can reduce a non-adiabatic loss by completely returning charge at the output node during the recovery phase to the clocked supply. As a result, overall efficiency is improved toward its theoretical limit. In order to confirm its operation, circuit simulations of inverter/buffer chain are performed. Simulation results show that the proposed circuit achieves energy saving as much as 24% compared to 2N-2N2P adiabatic logic implementation at clock rate of 100 MHz.**

I. INTRODUCTION

Power dissipation has been a highly concerned issue in the performance of VLSI circuits. For high-speed digital CMOS circuits, there are several methods to achieve a low power dissipation such as reducing the supply voltage, the voltage swing, the load capacitance, and the switching activity. Although those methods try to minimize the power dissipation, still all of its energy drawn from its dc supply is completely dissipated in the circuit. Alternatively, adiabatic circuits can reduce power dissipation by utilizing ac power supplies to recycle the energy stored in the load capacitance instead of being dissipated in the circuits. Since their operation require slow transition of their ac supply voltage, adiabatic circuits lose their energy efficiency when operate at high frequency. However they still have some advantages over CMOS circuits for applications that do not require very high speed such as portable electronics.

The current adiabatic circuits can be classified as either partially adiabatic or fully adiabatic. In the fully adiabatic circuit, all the charge on the load capacitance is recovered by the power supply while in the partially adiabatic circuit, only some charge is recovered. The examples of the fully adiabatic circuits are Pass Transistor Adiabatic Logic (PAL)[1] and Split Rail Charge Recovery Logic (SCRL)[2]. This types of circuits however are difficult to implement due to its complexity of synchronization between cascading stages which limits its maximum operating speed. In contrast the partial adiabatic circuits can be designed based on a CMOS logic. The popular partially adiabatic families include 2N-2N2P[3], Efficient Charge Recovery Logic (ECRL)[4], Clock Adiabatic Logic (CAL)[5], and True Single Phase Adiabatic Logic (TSEL)[6]. The power supply for adiabatic operation is usually a trapezoidal or sinusoidal voltage source. This supply voltage also acts as a clock. Digital systems with multiple stages/cascades based upon the described adiabatic power clocking scheme usually require four clock phases when using a trapezoidal voltage source and two clock phases when using a sinusoidal voltage sources. The sinusoidal signal also can be considered as an approximation of the trapezoidal waveform with zero hold phase.

Although it is simple to implement and has a rather high operating frequency, the voltage output low of 2N-2N2P is not equal to GND but a threshold of PMOS. We proposed a partially adiabatic circuit based on 2N-2N2P structure which uses two complementary sinusoidal supply clocks. The circuit gives a full swing output while still possesses the advantages of 2N-2N2P. As a result, energy saving are improved. The paper is organized as follows. In Section II, the adiabatic switching and 2N-2N2P are discussed. Section III describes the operation of the proposed circuit. The performance comparisons of 2N-2N2P and the proposed circuit are presented in Section VI. Finally, we draw our conclusion in Section V.

II. ADIABATIC CIRCUITS

The dominant factor in the dissipation of static CMOS logic is the power required to charge capacitive node.

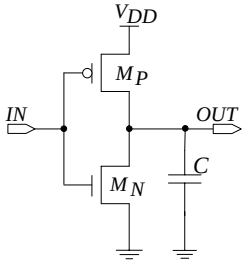

Figure 1. Static CMOS inverter.

In the CMOS inverter of Figure 1, when the output changes to high, the total energy drawn from the power supply is $E= CV^2_{dd}$, where C is the capacitance of the output node and V_{DD} is the supply voltage. Half of this energy is dissipation on the on-resistance R of the device MP, and the other half is stored in the output capacitance. When the output is driven low at a

later cycle, the energy stored in the output capacitor is dissipated on the on-resistance R of the device MN.

A. *Adiabatic Switching Theory*

The principle of adiabatic switching can be explained by its comparison to a simple RC circuit. Figure 2(a) shows current as a function of time during a switching of a static CMOS circuit. A low to high transition at node *out* can be modeled as a charging of load capacitor through a switch and its effective resistance. When the switch is turn on, *C* is charged up to V_{dd}. The current through the resistance decreases exponentially as the time passes. The energy dissipates is equal to $(1/2)CV^2_{dd}$ where V_{dd} is the voltage change at the node *out*. In an adiabatic circuit Figure 2(b), the transition is slowed down by using a time-varying voltage source instead of a static voltage supply. By spreading the transfer of charge to the capacitor over time, the current is greatly reduced. The overall energy dissipation is reduced to $(RC/T)CV^2_{dd}$ [7] if the current flow is maintained constant where *T* is total switching time. Ideally, with *T* approaching infinity, the energy dissipation for a switching will approach zero.

The power supply for adiabatic circuits produces a time-varying periodic signal, or *ac-supply*, that gradually swings between 0V and V_{dd}. The period of this signal is long enough to maintain a small potential drop V_R across the resistor. Alternatively, a simple form of adiabatic charging can also accomplished by using a power supply with a ramp output. Such a signal can be approximated as an oscillating signal from a resonant RLC circuit. The number of phase of *ac-supply* required to control cascaded gates is an important consideration in adiabatic logic design since it affects energy consumption, operating speed, and design complexity.

B. *2N-2N2P adiabatic logic*

The 2N-2N2P is a partially adiabatic circuit, as shown in figure.3. It uses a pair of cross-coupled NMOS(MN1 and MN2) to obtain non-floating output. To cascade 2N-2N2P circuits it needs four-phase *ac-supply*. Note that MP1 and MP2 are used for both charging the output node and return charge to the supply, thus its energy loss per cycle is

$$E = 2\left(\frac{R_P C_L}{T}\right) C_L V_{dd}^2 + C_L V_{tp}^2 \qquad (1)$$

Where C_L is the load capacitance, R_P is the turn-on resistance of PMOS, T is the transition time of the supply, V_{dd} is the peak voltage of the supply, and V_{tp} is threshold voltage of PMOS. In Eq. (1), the first term represent adiabatic energy, which can be reduced by lowering operation frequency and the second term represent non-adiabatic energy loss which is dependent on the load capacitance.

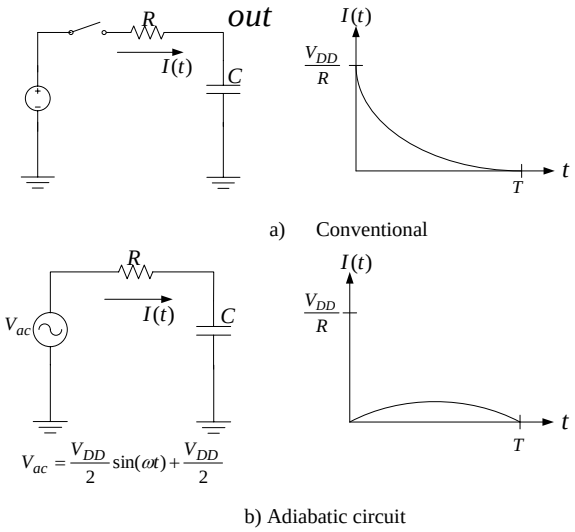

Figure 2. Modeling of the charging process in different circuit.

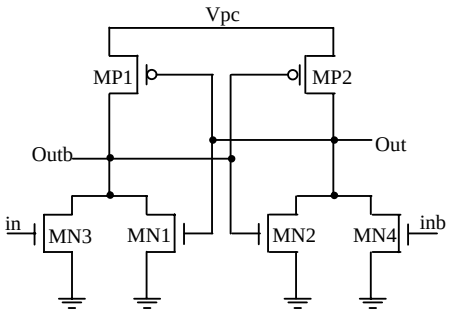

Figure 3. 2N-2N2P adiabatic logic.

III. PROPOSED ADIABATIC LOGIC

The proposed circuit is made up of a 2N-2N2P buffer/inverter and two additional pulse-controlled transistors (MN5, MN6) shown in the Figure 4. Pc and Pcb are the two opposite phases ac supply used for cascading stages as in Figure 5. The operation of the circuit can be explained as follows. While Pc ramps up from GND to V_{dd} if the input IN is high and INb is low, MN3 is turned on and MN4 is turned off. Therefore, the output node OUTb is discharged to ground by MN3. Consequently MP2 turns on. As a result the output node OUT increases as the supply (Pc) rises. When the supply (Pc) ramp down from V_{dd} to GND, the charge previously stored in the load capacitance at the OUT node returns to the supply. Due to the threshold voltage of PMOS, as the supply reaches about a threshold above GND MP1/MP2 stop conducting current. Hence, the output voltage cannot drop to GND. Therefore some of the charge remains in the load capacitance. To prevent this additional NMOS (MN5/MN6) are connected between the output nodes and the supply in the proposed circuit. As a result, when PULSE is high, MN5/MN6 are turned on the remaining charge at output node can be discharged to supply via MN5/MN6. Consequently, the output

voltage can reach GND. Thus, more charge can return to the supply.

The basic proposed circuit buffer/inverter logic gate can be expanded to other complex gates, such as AND/NAND, OR/NOR, and multiplexer, by using NMOS tree to replace MN3 and MN4. Then all these can build up various circuits, for example, adder, counter, and multiplier.

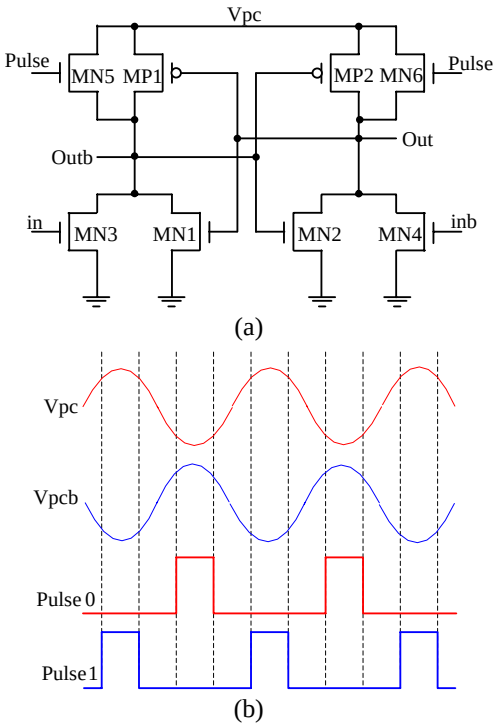

Figure 4. a) The proposed circuit b) Waveform and timing relationship between the supply voltage and pulse signal.

IV. SIMULATION RESULTS

The proposed circuit was simulated using 0.35 μm TSMC CMOS technology. A capacitive load of 20fF is placed at output nodes. The amplitude of sinusoidal power supply is 0.75V. Note that the PULSE signals can be obtained directly from the control signals used in a supply generator circuits. We discuss the result of HSPICE simulation of 4-stage pipeline using two-phase sinusoidal power supply shown in figure.5.

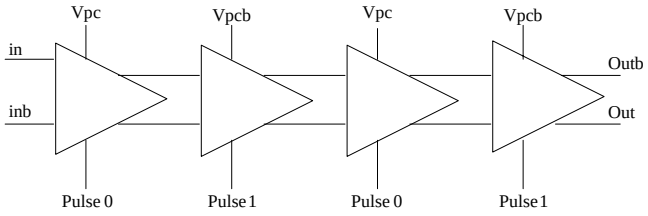

Figure 5. The 4-stage pipeline using two-phase sinusoidal power supply.

Figure 6 shows transient waveforms of the 2N-2N2P and the proposed circuit. In figure 6(a) the output voltages can not reach the ground level. In figure 6(b), when the supply is low and PULSE signal is active the MN5/MN6 are on and both of their output nodes (OUT, OUTb) are pulled to the same voltage level as the supply i.e., GND.

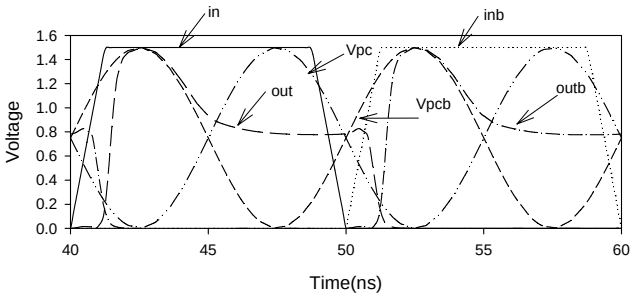

a) the 2N-2N2P circuit

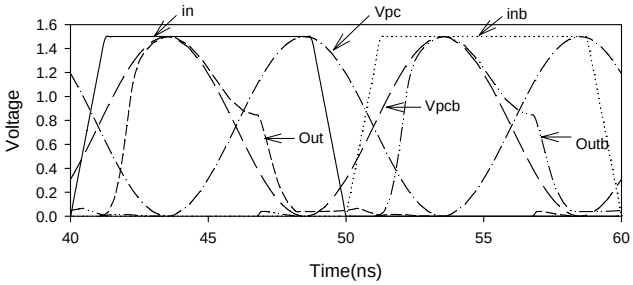

b) the proposed circuit

Figure 6. Transient waveforms of 2N-2N2P and proposed circuits at frequency 100MHz

The Figure 7(a) and 7(b) shows plots of the power dissipation of the circuits at 100MHz. Negative and positive values indicate power flowing into and out of the circuit. Figure 7(c) shows the energy consumption during the transients of 2N-2N2P and proposed circuit. Clearly, the consumed energy of the proposed circuit is smaller than that of the 2N-2N2P circuit. Excluding power consumption used to generate the PULSE signal, the proposed circuit consumes 3.45 pJ, which is 76% of that of the 2N-2N2P (4.5 pJ).

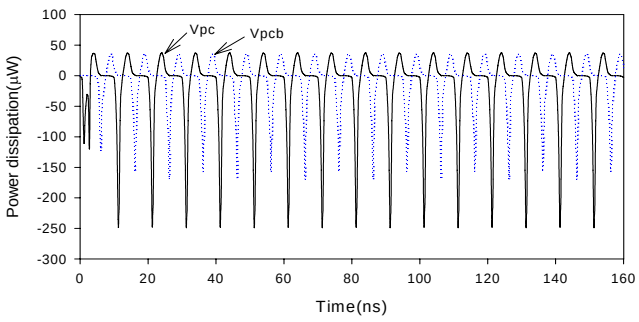

a) Power dissipation of power clocks, Vpc, and Vpcb in 2N-2N2P circuit.

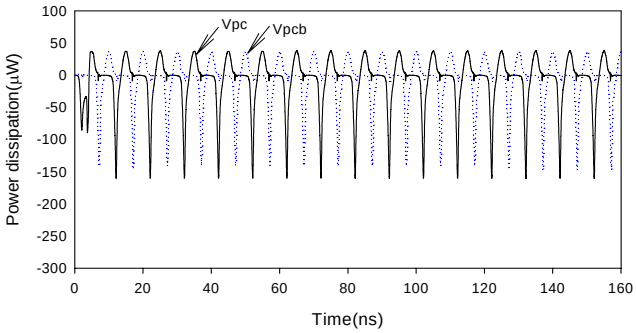

b) Power dissipation of power clocks, Vpc, and Vpcb in proposed circuit

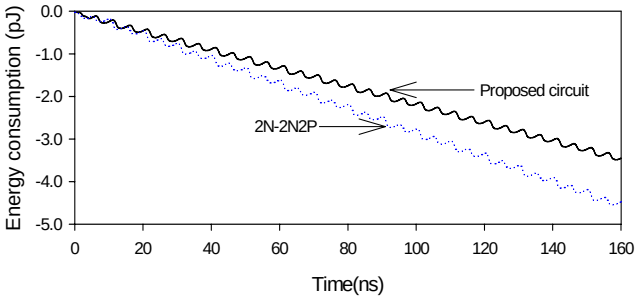

c) Energy profiles

Figure 7. The power profiles of the simulation circuits at 100MHz

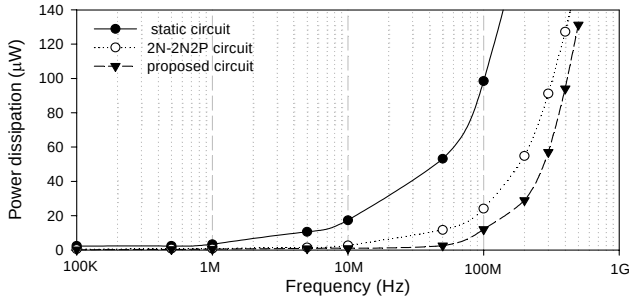

Figure 8. Power dissipation against operating frequency

Figure. 8 shows the power dissipation against the operating frequency of the 2N-2N2P, the proposed circuit, and static circuit at a supply voltage 1.5V ac and dc respectively . At 100MHz, the 2N-2N2P circuit consumes 26 μW, the static circuit consumes 98 μW, and the proposed circuit consumes 19 μW.

The setup of the complete system is shown in Figure. 9. The pulse generator circuit produces two non-overlapsing clocks, *Pulse0* and *Pulse1* from the system clock *Clk*. These two pulses control oscillation frequency of the sinusoidal supply as well as allow outputs of each stages to reach GND

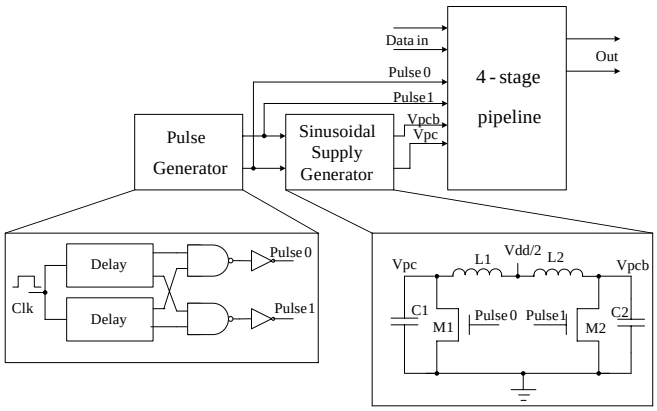

Figure 9. Simulation setup for buffer/inverter chain

V. CONCLUSION

We present a low power adiabatic circuit based on a 2N-2N2P adiabatic circuit. The proposed circuits is able to eliminate the non-adiabatic loss. The simulation results show that at operation frequency of 100MHz the proposed circuit consumed 76% of the energy of a conventional 2N-2N2P adiabatic circuit. The circuit is suitable for the low power applications such as portable devices where speed is not a critical factor.

REFERENCES

[1] V. G. Oklobdzija and D. Maksimovic,"Pass-transistor adiabatic logic using single power-clock supply," *IEEE Trans. Circuits Systems II: Analog Digital Signal Processing.*,vol. 44, pp. 842-846, Oct. 1997

[2] S. G. Younis and T. F. Knight, "Asymptotically Zero Energy Split-Level Charge Recovery Logic," *International Workshop on Low Power Design* , Napa Valley, CA, pp. 177-182

[3] A. Kramer, J.S. Denker, B. Flower, and J. Moroney, "Second-order adiabatic computation with 2N-2P and 2N-2N2P logic circuit," *Int. Symp. Low Power Design*, Dana Point, CA, April 1955, pp. 191-196.

[4] Y. Moon and D. Jeong, "An efficicent charge recovery logic circuit," *IEEE J. Solid State Circuits*, vol. 31, pp.514 -522, Apr. 1996.

[5] D. Maksimovic, V. G. Oklobdzija, B. Nikolic, and K. W. Current, "Clocked CMOS adiabatic logic with integrated single-phase power clock supply," *IEEE Trans. Very Large Scale Integration Syst.*, vol. 8, pp. 460-463, Aug. 2000.

[6] S. Kim and M. C. Papaefthymiou, "True single-phase energy-recovering logic for low-power, high-speed VLSI, in *Proc. Int. Symp. Low-Power Electronics and Design*, Monterey, CA, Aug. 1998, pp. 167-172.

[7] W. C. Athas, L. J. Sevensson, J. G. Koller, N. Tzartzanis, and E. Chou, "A Framework for Practical Low-Power Digital CMOS System Using Adiabatic-Switching Principles," *International Workshop on Low Power Design*, 1994, pp. 189-194.

Effect of Resonances on Shielding Effectiveness in Enclosure with Apertures

P. Dangkham[1], P. Sujintanarat[1], S. Chaichana[1], K. Aunchaleevarapan[2], and P. Teekaput[1]
[1]Faculty of Engineering, Chulalongkorn University, Bangkok, Thailand
[2] Electrical and Electronic Products Testing Center, NECTEC, NSTDA, KMITL Bangkok, Thailand
Email: kraison.aun@ptec.or.th

***Abstract*-This paper presents the effect of resonances in enclosure with apertures. An analytical formulation has been employed for the shielding effectiveness. The factors such as the size and shape of aperture, sum of apertures are important to shielding performance. To improve the shielding, the use of metal piece inside enclosure is studied for removing the lowest resonance frequency. Results show that the place of metal piece can be used to evaluate shielding effectiveness for design purposes.**

I. INTRODUCTION

The shielding enclosure has already been studied many times. It is frequently used to reduce the emission or to improve the immunity of the electronic equipment. Electromagnetic compatibility (EMC) of enclosures of electronic equipment is a key issue that must be taken into account in the early stages of design. The integrity of shielding enclosures is compromised by slots and apertures for heat dissipation, CD-ROMs, I/O cable penetration or other possibilities. These apertures tend to become the coupling route of Electromagnetic Interference (EMI) from interior to outside hence degrade the Shielding Effectiveness (SE) of the enclosure. This parameter is defined as the ratio between the incident field in absence of the shield and the field in the same position when the effect of the enclosure is taken into account, the definition of Electrical Shielding Effectiveness (SE_E) will be as [1]:

$$SE_E = 20log(E_2/E_1) \quad (1)$$

E_1: Electrical field with shielding;
E_2: Electrical field without shielding.

There are two methods to calculate the shielding effectiveness[2], numerical simulation and analytical formulation. For numerical method that have been researched and used to calculate the shielding effectiveness include transmission line matrix (TLM)[6], finite difference time domain[7] (FDTD), method of moments (MoM) and finite element method (FEM)[8]. These methods can model complex structures but often require a relatively large amount of computer memory and computation time to give reasonable accuracy. Although they are good at predicting the shielding of a particular enclosure, it is difficult for designers to use them to investigate the effect of design parameters on SE and SM. For analytical formulation, it provides a much faster calculating shielding effectiveness. Analytical methods include transmission line analogy and circuit theory. A simple a rectangular enclosure with an aperture at one face can be modeled by an equivalent circuit, to predict the shielding effectiveness as a function of the frequency and the size of the aperture. The size of the enclosure is often expressed in units of the wavelength of the radiation, commonly known as the electrical size of the enclosure. The apertures can behave like antennas, and their electrical size can be defined analogously to that of antennas. We employ the analytical formulation[3]. It can be calculated as functions of frequency, aperture dimensions, enclosure dimensions, wall thickness and position within the enclosure. Results show that shielding effectiveness related to the parameters above.

In this work, we present the technique to improve the shielding by metal piece. The enclosures will produce resonance frequencies. These resonances are possible to suppress or remove by resize the enclosure dimensions. While almost enclosures dimensions are fixed, the use of metal piece inside the enclosures is studied for removing the lowest resonance frequency. We found the distance from the back wall of enclosure to the metal piece influence to shielding effectiveness.

II. THEORY

A rectangular enclosure with a rectangular aperture is represented by the equivalent circuit which is shown in Fig. 1. The electric shielding, a distance p from the aperture is obtained from the voltage at point P in the equivalent circuit, while the current at P gives the magnetic shielding. The radiating source is represented by voltage V_0 and impedance $Z_0 \cong 377\,\Omega$ and the enclosure by the shorted waveguide whose characteristic impedance and propagation constant are Z_g and k_g. According to Robinson *et al.*[3], the first process is finding an equivalent impedance for the slot and then using simple transmission line theory to transform all the voltages and impedances to point P.

First, the slot impedance is calculated. The aperture is represented as length of coplanar strip transmission line. For aperture impedance Z_{ap}, it is calculated from the short circuits at the ends of the aperture through a distance $l/2$ to center. This is represented by point A in the equivalent circuit and include a

factor *l/a* to account for the coupling between the aperture and the enclosure. The aperture impedance Z_{ap} is defined in

$$Z_{ap} = \frac{l}{2a} jZ_{0s} \tan\frac{k_0 l}{2} \quad (2)$$

where $k_0 = 2\pi/\lambda$ and Z_{0s} is characteristic impedance which given by Gupta *et al*[5].

According to Robinson *et al.*, to calculate the electric and magnetic shielding effectiveness, it is defined from voltage and current at point *P*, respectively.

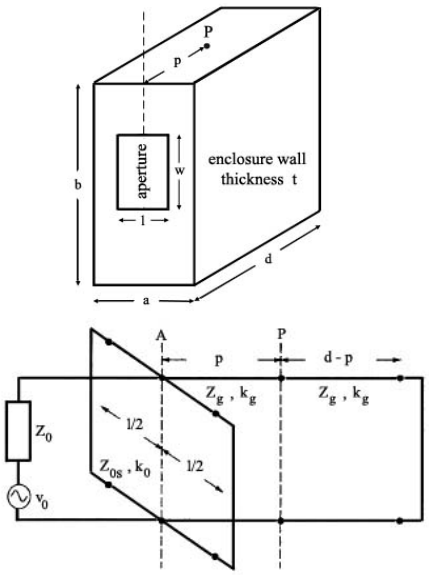

Fig. 1. Rectangular enclosure with aperture and its equivalent circuit.

Here we employ the analytical formulation for calculate the shielding effectiveness in difference parameters to show that the enclosure resonance. We set the enclosure dimension at 20x40x45 cm, aperture sizes are 1x18 cm, 2x9 cm and 3x6 cm, thickness at 0.2 cm and distance from the aperture *p* is 5 cm. All apertures are the same area at 18 cm^2. We will compare the shielding effectiveness with the aperture of different shape. The result is shown in Fig. 2.

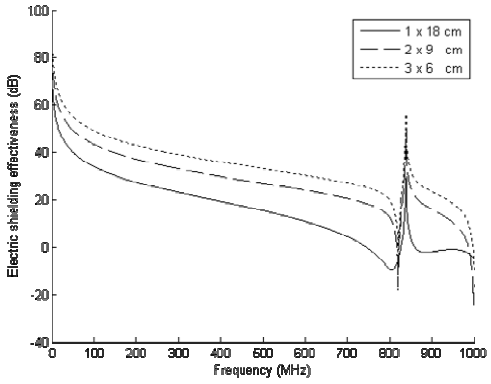

Fig. 2. Calculate SE_E at 5 cm of 20x40x45 cm enclosure with 1x18, 2x9, 3x6 cm apertures.

The calculation shows that the shielding effectiveness of the 3x6 cm aperture is better than 2x9 and 1x18 cm apertures. Shielding effectiveness decrease from low frequencies to high frequencies and resonate at the same point. We concentrate in resonance frequencies, all of them resonate at approximately 800 MHz.

Now we investigate the influence to resonance frequencies by changing the dimension of enclosure. We keep the same aperture size at 2x9 cm and measurement point *p* at 5 cm from aperture, while we change the parameter 'a', 'b' and 'd'. The results are shown below.

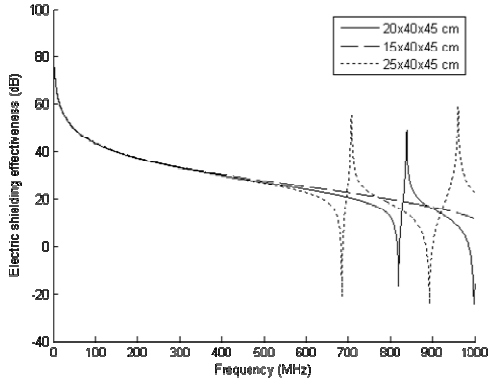

Fig. 3. Calculate SE_E of difference parameter 'a' enclosures.

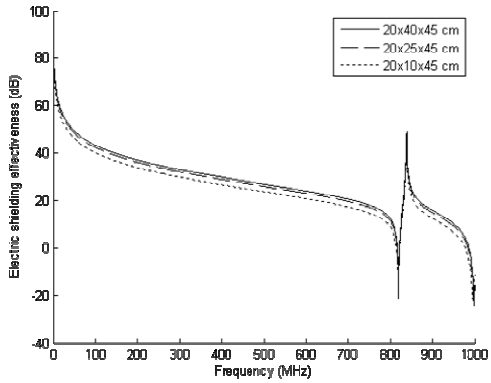

Fig. 4. Calculate SE_E of difference parameter 'b' enclosures.

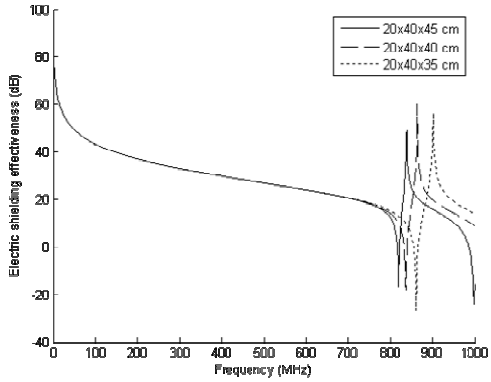

Fig. 5. Calculate SE_E of difference parameter 'd' enclosures.

Fig. 3 shows the results which difference resonance frequencies. For ‘a’ = 20 cm, the resonance is 800 MHz. While we decrease ‘a’ to 15 cm, the resonance frequency has been shifted over 1000 MHz. When ‘a’ is increased to 25 cm, the resonance frequencies are 700 MHz and 900 MHz. In Fig. 4, the resonance frequencies are the same point at approximated value of 800 MHz. The results show difference shielding effectiveness. The 20x40x45 cm enclosure is better than 20x10x45 cm enclosure. Fig. 5 shows the results when we change ‘d’ parameter. We found that while the ‘d’ is decreased, the resonance frequency is increased.

In case of ‘d’, the parameter influences to the resonance frequency. While almost enclosures dimensions are fixed, to resize enclosures is uncomfortable. The use of metal piece inside the enclosures is studied for removing the lowest resonance frequency. It is possible to do that because these resonances will be absorbed by the metal piece inside the enclosure and it is more comfortable than changing enclosure dimension.

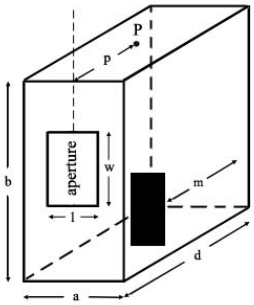

Fig. 6. Measurement set up with a metal piece inside the enclosure.

III. MEASUREMENTS

We set up the 20x40x45 cm aluminium enclosure for test. A rectangular 1x18 cm aperture is placed at the front face of the enclosure. There is a metal piece in the enclosure with the distance *m* from the back wall. Fig. 6 shows a metal piece inside the enclosure. The measurements are performed in a semi anechoic chamber. The experimental equipment are an EMI receiver with Bi-log antenna in the range of 30 MHz – 1000 MHz, signal generator, dipole antenna and ferrite clamps. A signal generator produces frequencies from 30 MHz to 1000 MHz with a step frequency of 10 MHz and 5 V peak-to-peak amplitude. We set the dipole antenna in the box for electromagnetic source. The measurement configuration is shown in Fig. 7.

IV. RESULTS

The shielding effectiveness for the enclosure under study can be observed in Fig. 8 with comparison analytical formulation and measurement. The result shows that for lower frequencies differ from expected. At range of low frequencies from the simulation result and actual measurement are different because

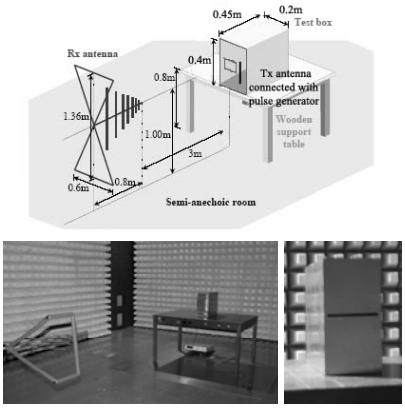

Fig. 7. Configuration of measurement.

the simulation base on free space condition but in actual base on reflection effect which depend on the size and characteristic of the chamber. In frequency range 300 MHz – 1 GHz, the both results are in good agreement. For resonance frequency, both results also agree with an approximated value of 800 MHz.

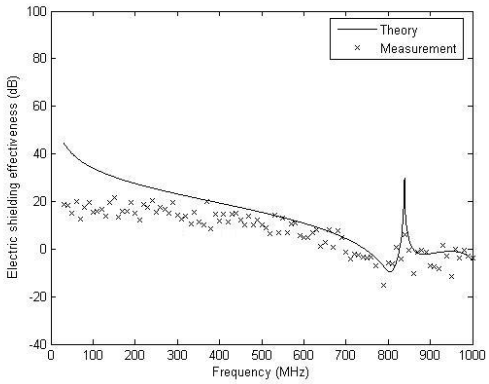

Fig. 8. Shielding effectiveness for enclosure with aperture.

We concentrate in removing the lowest resonance frequency by metal piece inside enclosure. According to Fig. 5, we found the smaller enclosure has higher resonance frequency. Introducing a metal piece as shown in Fig. 6 produces a frequency shift due to the reflection effect. We set up the 10x20x0.2 cm metal piece inside the enclosure with 1x18 cm aperture. The difference distances from back wall *m* are 5, 10 and 15 cm. The result is shown in Fig. 9

For *m* = 5 cm, the resonance frequency is about 820 MHz. When we increase distance to 10 cm, the resonance has been shifted to approximately 870 MHz. The enclosure with metal piece placed at 15 cm produces the resonance about 900 MHz. We found the results are similar from the Fig. 5. In that results show the resonances have been shifted to higher when the enclosure decrease dimension. According to Fig. 9, the increase distance from back wall is like decrease the dimension of the enclosure. The results show the metal piece inside enclosure can be removing the lowest resonance frequency.

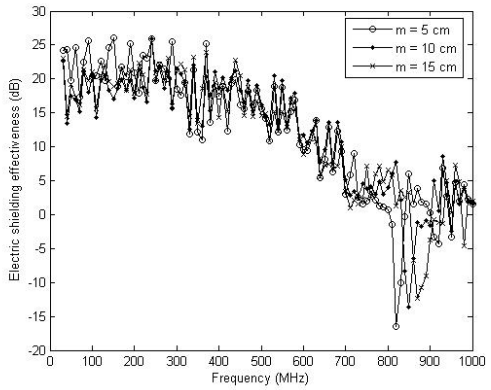

Fig. 9. Shielding effectiveness for enclosure with a metal piece inside.

V. CONCLUSION

In this paper, we propose the improvement of shielding effectiveness. The use of metal piece inside enclosure is studied for removing the lowest resonance frequency. Obtained results point out the metal piece as one of important design parameter. The effect of the placing metal piece is well seen at the resonance. When the distance from the back wall is longer, the resonance frequency will increase. Placing metal piece becomes a partial solution as long as they are designed to remove the lowest resonance frequency. Further investigations in variation of conductivity and orientation of metal piece are still needed.

ACKNOWLEDGMENT

Electrical and Electronic Products Testing Center (PTEC) is gratefully acknowledged for the measurement.

REFERENCES

[1] F.A. Po'ad, M.Z.M Jenu,. C. Christopoulos, D.W.P. Thomas, W.R. Abdullah, K.Yusoff, and B.M. Shariff, "Shielding effectiveness of rectangular metallic enclosures with apertures," *Conference on Applied Electromagnetics*, 20-21 Dec. 2005.

[2] P. Sewell, J.D. Turner, M.P. Robinson, D.W.P. Thomas, T.M. Benson, C. Christopoulos, J.F. Dawson, M.D. Ganley, A.C. Marvin, and S.J. Porter, "Comparison of analytic, numerical and approximate models for shielding effectiveness with measurement," in *Proc. IEE Sci. Meas. Technol.*, vol. 145, no. 2, 1998, pp. 61-66.

[3] M.P. Robinson, T.M. Benson, C. Chistopoulos, J.F. Dawson, M.C. Ganley, A.C. Marvin, S.J. Porter, and D.W.P. Thomas, "Analytical formulation for the shielding effectiveness of enclosures with apertures," *IEEE Transactions on Electromagnetic Compatibility*, vol. 40, August 1998, pp. 240-247.

[4] A.C. Marvin, J.F. Dawson, S. Ward, L. Dawson, J. Clegg, A. Weissenfeld, "A proposed new definition and measurement of the shielding effect of equipment enclosures," *IEEE Transactions on Electromagnetic Compatibility*, vol. 46, no. 3, August 2004, pp. 459-468.

[5] K.C. Gupta, R. Garg, and I.J. Bahl, *MicrostripLines and Slotlines*. Norwood, MA: Artech House, 1979.

[6] C. Christopoulos, *The Transmission Line Modeling Method TLM*. IEEE Press, New York, 1995.

[7] M. Li, J. Nuebel, and J.L. Drewniak, "EMI from airflow aperture arrays in shielding enclosures – Experiments, FDTD and MoM modeling," *IEEE Transactions on Electromagnetic Compatibility*, vol. 42, August 2000, pp. 265-275.

[8] W.P. Carpes Jr., L. Pichon, and A. Razek, "A 3D FEM model for EMC analysis: Coupling of an EM wave with a wire inside a cavity," in *Proc. Int. Symp. Elecromagnetic Fields in Electrical Engineering (ISEF'99)*, Pavia, Italy, Sept. 1999, pp. 57-60.

Figure 1. QCM sensor in the experiments.

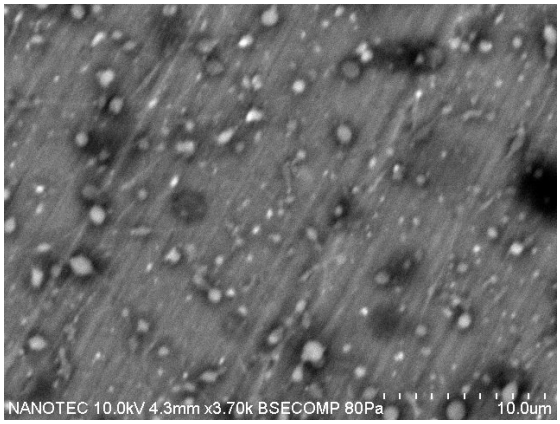

Figure 2. SEM Image of PANI coated QCM electrode surface.

distilled aniline was mixed in a polymerization vessel that was cooled at 0 ℃. In a separate flask, 1 N HCl was combined with ammonium peroxidisulfate and cooled to 0 ℃. Thereafter, the aqueous ammonium persulfate solution was added slowly to the aniline/HCl solution with both solutions being precooled to 0 ℃. The mixture was stirred for about 3.5 h at –5 to 0℃. The desired green emeradine hydrochloride precipitate was extracted by filtration and washed first in water and then in methanol until the filtrate became colorless. The precipitate was then treated in aqueous ammonium hydroxide solution for about 3 h to obtain the powder of polyemradine hydrochloride salt. Next, the green emeradine salt was washed by distill water and filtered until the filtrates were neutral. Finally, the obtained powder was dried in vacuum at 50 ℃ for 48 h and then stored in a vacuum desiccate.

For protonation doping, 2 Molar (M) maleic acid was prepared by adding 236.89 g maleic acid to 1000 ml of distilled water [10]. In order to obtain maleic acid doped polyaniline at mole ratio of 1000:1, 0.35 g of emeradine base was immersed in 2 M maleic acid solution at particular volume of 425.36 ml. The mixture was vigorously stirred and allowed to reach equilibrium for 48 h. The doped powder was filtered and dried at 60 ℃ for 40 h in a vacuum oven. Polyaniline doped powder was dissolved in N-Methylpyrrolidone (NMP) with the ratio of 0.5 g: 10 ml [11].

For the PANI coating process, the electrospinning of PANI solvent is used. The PANI solvent is loaded into electrospin syringe and syringe to QCM substrate distance is approximately 5 cm. The electrospinning was conducted at a high voltage in the range between 10-20 kV. The photograph of a QCM sensor which used in the experiment is shown in Figure 1. It is a low-cost commercial quart crystal resonator with silver electrode. The scanning electron micrograph (SEM) showing the surface morphology of PANI coated electrode is demonstrated in figure 2. It shows that the electrospun surface is covered with mixture of micro and nano particles with diameter less than 2 μm.

IV. EXPERIMENT

The diagram of experimental system is shown in Figure 3. The humidity control system is a sealed high-quality plastic chamber with low humidity absorption. The QCM sensor and the commercial humidity sensor are placed in the chamber at the same level. The data of frequency and humidity are sent to the computer via USB port every second, the frequency output, humidity and temperature will be then recorded in the computer.

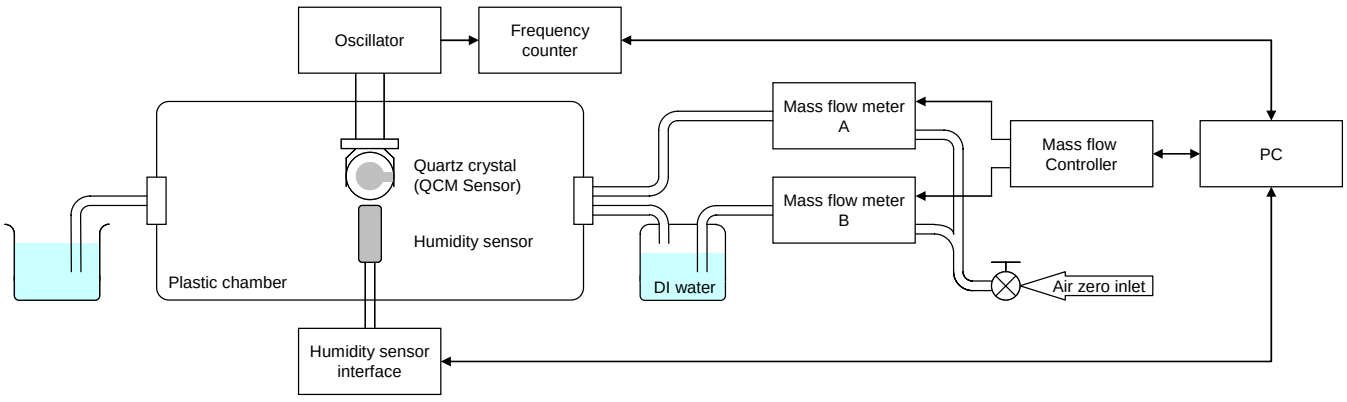

Figure 3. Diagram of data acquisition system.

For the humidity control, water bubbler system is used. Air zero, pure and low humidity air, is split into two lines. The first line is passing through mass flow controller A and directly flown into the chamber. The second one is passing through mass flow controller B and bubbled through deionized water before entering the chamber. Initially, the chamber is filled with air zero flowing at the rate of 1000 sccm. Next, the desired humidity is input into the chamber by turning on the water bubbled air zero at a predetermined flow rate and turning off air zero from mass flow controller A. After the humidity is stabilized and the sensing response is recorded, the humidity is then dislodged by turning off the air zero flowing through the bubbler and restoring the air zero from mass flow controller A. The same procedure is repeated for different humidity by varying water bubbling flow rate.

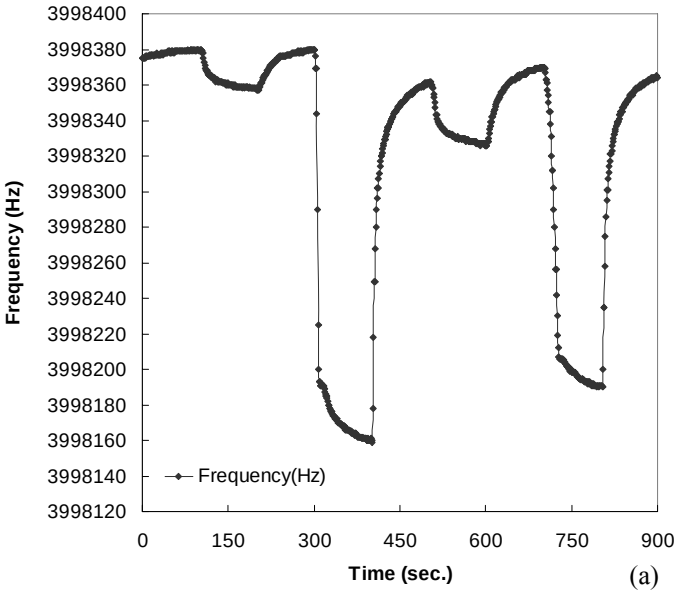

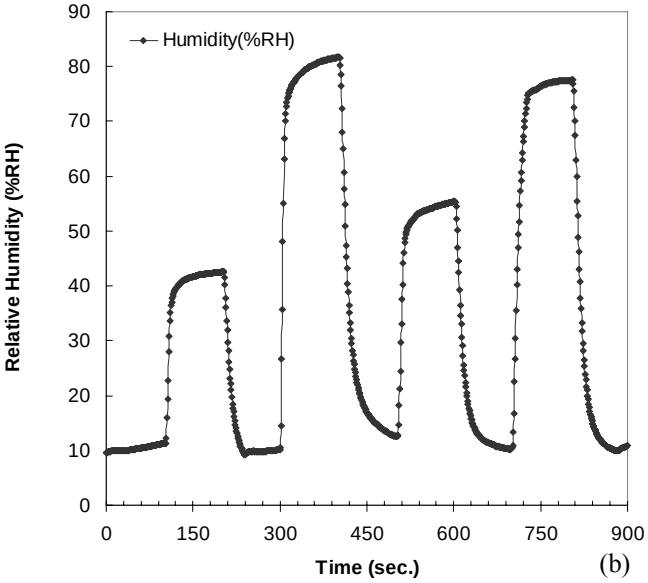

Figure 4. Typical dynamic response of (a) frequency change vs. time of PANI coated QCM humidity sensor and (b) relative humidity measured by the commercial humidity sensor

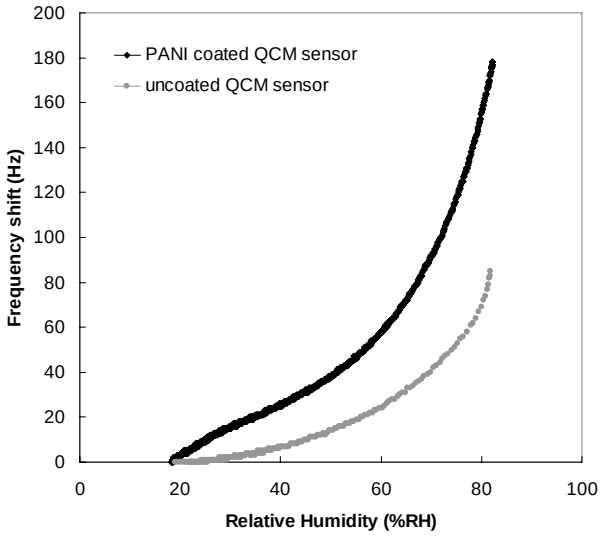

Figure 5. Frequency shift vs. relative humidity at ambient temperature of 21.6°C

V. Results and Discussion

Typical dynamic response of the PANI coated QCM humidity sensor and the corresponding dynamic humidity measured by the commercial humidity sensor are shown in Figure. 4 (a) and (b), respectively. From the figure, it can be seen that the PANI coated sensor can respond well to the controlled relative humidity of 40% to 80%. In addition, it has short response and recovery times. The response time is measured to be between 3 and 10 seconds depending on relative humidity while the recovery time is determined to be between 40 and 200 seconds. The humidity response is found to be stable and reversible over whole range of relative humidity between 20% and 80%.

Figure 5 show the measured results of frequency change of uncoated QCM sensor and PANI coated QCM sensor as a function of relative humidity. It is clear that the frequency shift of QCM sensor at a given humidity is considerably increased after PANI coating. The increase of humidity sensitivity is more that the factor of 2.2 for relative humidity between 20% and 80%. The result confirms that the PANI electrospun thin film considerably increase water vapor absorption.

VI. Conclusion

In conclusion, we have developed a low-cost humidity sensor made by coating a commercial quartz crystal resonator with Polyaniline (PANI) thin film. The electrospinning technique is used to coat the PANI nanometer-scale thin film to the electrode of quartz crystal. From experimental results, it

was found that PANI coating on the QCM electrode is an effective way to improve humidity-sensing characteristic of QCM sensor. The PANI coated sensor has good response to the humidity with short response and recovery times. The humidity-sensitivity of PANI coated QCM sensor is increased by more than factor of 2 compared to uncoated QCM sensor.

REFERENCES

[1] J. Rabe, S. Buttgenbach, J. Schroder, and P. Hauptmann, "Monolithic miniaturized quartz microbalance array and its application to chemical sensor systems for liquids," *IEEE Sensors Journal*, Vol. 3, pp. 361 - 368, August 2003.

[2] Masashi Kikuchi, Katsuya Omori, and Seimei Shiratori, "Quartz Crystal Microbalance (QCM) Sensor for Ammonia Gas using Clay/ Polyelectrolyte Layer-by-Layer Self-Assembly Film," *IEEE Sensors Proceedings 2004*, vol. 2, pp. 718-721, October 2004.

[3] Kosmas Galatsis, Wenmin Qu, and Wojtek Wlodarski, "Quartz crystal microbalance humidity sensor with Porous Electrodes," *Optoelectronic and Microelectronic Materials Devices*, pp. 373-375, 1999.

[4] H. Ito, S. Kakuma, R. Ohba, and K. Noda, "Development of a humidity sensor using quartz crystal microbalance," *SICE Annual Conference 2003*, pp. 1175-1178, August 2003.

[5] Robert B. Towery, Newton C. Fawcett, and Jeffrey A. Evans, "Determination of chloroplast DNA in a cultured soybean line using a QCM biosensor," *IEEE Sensors Journal*, Vol. 4, pp. 489 - 493, August 2004.

[6] Y. Jimenez, R. Fernandez, R. Torres, and A. Arnau, "A contribution to solve the problem of coating properties extraction in quartz crystal microbalance applications," *IEEE Transactions on Ultrasonics, Ferroelectrics, and Frequency Control*, Vol. 53, pp. 1057 - 1072, May 2006.

[7] Narsimha Parvatikar, Shilpa Jain, Syed Khasim, M. Revansiddappa, S.V Bhoraskar, and M.V.N. Ambika Prasad, "Electrical and humidity sensing properties of polyaniline/WO_3 composites", *Sensor and Actuators B*, vol. 114, pp. 599-603, 2006.

[8] S. Jain, et. al, "Humidity sensing with weak acid doped polyaniline and its composites" *Sensor and Actuator B*, vol. 96, 2003, pp124-129.

[9] S.C.K Misra, et. al., "Vacuum-deposited anocrystalline polyaniline thin film sensors for detection of carbon monoxide" *Sensor and Actuator A*, 2004.

[10] J. Sangwarng, "Conductive polymer as gas sensor" Master thesis, The Petroleum and Petrochemical College, Chulalongkorn University, 2001.

[11] Dan Xie, et. al., "Fabrication and characterization of polyaniline-based gas sensor by ultra-thin film technology," *Sensors and Actuator B*, vol. 81, 2002, pp. 158-164.

Optical Gas Sensor Array Based on Metallo-Phthalocyanines and Metallo-Porphyrins

Sureeporn Uttiya[1], Teerakiat Kerdcharoen[2], Paisarn Daungjak Na Ayutthaya[3],
Worawan Bhanthumnavin[4], Radchada Buntem[5], Sirapat Pratontep[6]
[1,2] Center of Nanoscience and Nanotechnology, Department of Physics,
Faculty of Science, Mahidol University, Bangkok 10400, Thailand
[3] Institute of Science, Walailak University, Nakorn Srithammarat 80160, Thailand
[4] Department of Chemistry, Faculty of Science, Chulalongkorn University, Bangkok 10330, Thailand
[5] Department of Chemistry, Faculty of Science, Silpakorn University, Nakorn Pathom 73000, Thailand
[6] National Nanotechnology Center, National Science and Technology Development Agency,
Thailand Science Park, Pathumthani 12120, Thailand

***Abstract*-Electronic nose devices are of increasing interest to the quality control of alcohol and food processing. Optical gas sensors that require low electrical power are in great need to such devices. The zinc (II) -2,9,16,23-tetra-*tert*-butyl-29H,31H-phthalocyanine (ZnTTBPc) and zinc (II) -5,10,15,20-tetraphenyl-porphyrin (ZnTPP) organic thin film sensors have been produced by spin-coating onto glass substrates for detecting specific alcoholic volatile organic compounds (VOCs). Responses of the films to various alcohols and Thai whisky were monitored by optical absorption spectroscopy. The classification of alcohol volatile organic compounds (VOCs) using these fabricated optical gas sensors were obtained by Principle Component Analysis (PCA). The system is able to distinguish ethanol, methanol and Thai whisky. This results are in good agreement with the Density Function Theory (DFT) calculations whereby the interactions of ZnTTBPc and ZnTPP to methanol (MeOH), ethanol (EtOH) and iso-propanol (IPA) have been investigated by using B3LYP/6-31G* method. The presence of zinc atom in the center of both ZnTTBPc and ZnTPP molecules causes an increase of positive NBO charge while the oxygen atom in the alcohol molecules leads to a decrease. NBO charge calculations shows that the interaction of zinc atoms both in ZnTTBPc and ZnTPP with the oxygen atom in alcohol occurs by charge transfer.**

I. INTRODUCTION

Metal-phthalocyanines (MPc) and metal-porphyrins (MP) are organic semiconductor materials with technological importance [1]. The electrical and optical properties of MPc and MP are strongly influenced by electron donor and acceptor with gas [2]. This makes MPc and MP a natural choice of gas detection for VOCs. Examples for their gas sensing applications include lutetium bisphthalocyanine (LuPc) films for detecting VOCs from olive oil or wine [3], Manganese phthalocyanine (MnPc) for detecting trimethylamine as an indication for the freshness of fish [4], Zinc Tetraphenyl porphyrin (ZnTPP) for sensing 4-aminophenyl, which is an environmental contaminant from various industry sectors and from municipal wastewater treatment plants [5]. Responses of MPc and MP opto-chemical gas sensors to organic vapor are presented by the change of some physical properties [1], for example, electrical conductance [6], capacitance, work function, refractive index [7] and optical absorbance [8].

In the present work, we report the fabrication of ZnTTBPc and ZnTPP spin-coated thin films as an alcohol vapor sensing device with the optical absorbance response in the UV-visible spectral range. The absorbance change induced by exposure to various alcohol vapors including Thai whisky has been analyzed by Principle Component Analysis. In addition, quantum mechanical calculations have been conducted in parallel to investigate the interaction of ZnTTBPc and ZnTPP with alcohol molecules (MeOH, EtOH and IPA), in termsof interaction energy, charge transfer and energy gap.

II. QUANTUM MECHANICS COMPUTATIONAL METHOD

Initial structures of ZnTTBPc, ZnTPP, MeOH, EtOH and IPA models were constructed by a molecular mechanics force field program. The optimized geometries were obtained by using the DFT calculation based on B3LYP/6-31G* level. The calculations were performed by using the Gaussian 03 program. The potential interaction energy was calculated by varying the distance between oxygen in OH group of alcohol molecules and zinc atom in the center of ZnTTBPc and ZnTPP molecules.

III. EXPERIMENTAL METHOD

Zinc(II)-2,9,16,23-tetra-*tert*-butyl-29H,31H-phthalocyanine (ZnTTBPc) was obtained from Sigma-Aldrich, while zinc(II)-5,10,15,20-tetraphenylporphyrin (ZnTPP) has been synthesized by our research group using a standard method. ZnTTBPc and ZnTPP thin films were prepared by the spin-coating technique on cleaned glass slides. For ZnTTBPc, its chloroform solution at 0.015 molar concentration was spin-coated onto glass substrates at 1000 rpm for 30 sec. For ZnTPP, the same method was applied for its chloroform solution (0.007 molar). An improvement in the ZnTTBPc sensing properties has been achieved by thermal annealing in a furnace under a

flow argon gas and heated at the heating/cooling rate of 5°C/min until reaching 340°C [9]. The optical absorption spectra of sensor films were recorded at room temperature and at normal incidence in the range of 340-795 nm by Jenway UV-Vis Spectrophotometer.

The alcohol sensing capability of the ZnTTBPc and ZnTPP films has been investigated under dynamic conditions by using a home-built stainless steel chamber with quartz windows for optical measurements. The test was conducted under a flow system at a constant rate of 755 mL/min by using 99.9% nitrogen as both a carrier and a reference gas. The dynamic optical response was monitored by recording the absorbance intensity at fixed interval of 10 min during alcohol exposure and another 10 min during recovery under a nitrogen flow.

IV. Results and Discussion

A. *Quantum Mechanics Calculation*

The quantum mechanics calculations of ZnTTBPc and ZnTPP with different types of alcohols are illustrated in Figure 1. In particular, ZnTTBPc indicated the strongest interaction with methanol and the weakest interaction with iso-propanol, whereas the results for ZnTPP showed intriguingly the opposite. Table 1 compares the interaction energies at the optimized distance, the change in HOMO-LUMO (Energy Gap ; Eg) and the change in the NBO charge of zinc and oxygen atoms. The results indicates a possible charge transfer mechanism for the interaction of ZnTTBPc and ZnTPP with the alcohol molecules. This also suggests a possibility for detectable changes in the optical absorbance in the presence of alcohol vapour flow the alcohols vapour.

TABLE I
CALCULATED INTERACTION ENERGY ; E(kcal/mol) AT THE OPTIMIZED DISTANCE ; D(Å), CHANGE IN HOMO-LUMO ENERGY GAP ; △Eg(meV), CORRESPONDING WAVELENGTH ; λ(nm) AND THE CHANGE IN NBO CHARGE AT ZINC AND OXYGEN ATOMIC SITE ($\times 10^{-3}$a.u.)

Interaction	E	D	$\triangle E_g$	$\triangle\lambda$	Zinc	Oxygen
ZTTBPc-MeOH	7.13	2.50	+13.88	+3.61	+26.89	-41.79
ZnTTBPc-EtOH	5.37	2.63	+ 5.17	+1.35	+19.91	-31.65
ZnTTBPc-IPA	4.18	2.88	+ 3.54	+0.92	+14.01	-25.92
ZnTPP-MeOH	4.49	2.75	-30.75	-4.78	+26.42	-30.67
ZnTPP-EtOH	5.40	2.63	-29.12	-4.52	+24.59	-33.17
ZnTPP-IPA	5.96	2.63	-34.02	-5.29	+27.13	-31.53

(E_g and λ of ZnTTBPc, ZnTPP are 2.18, 2.84 eV and 569.47, 436.62 nm)

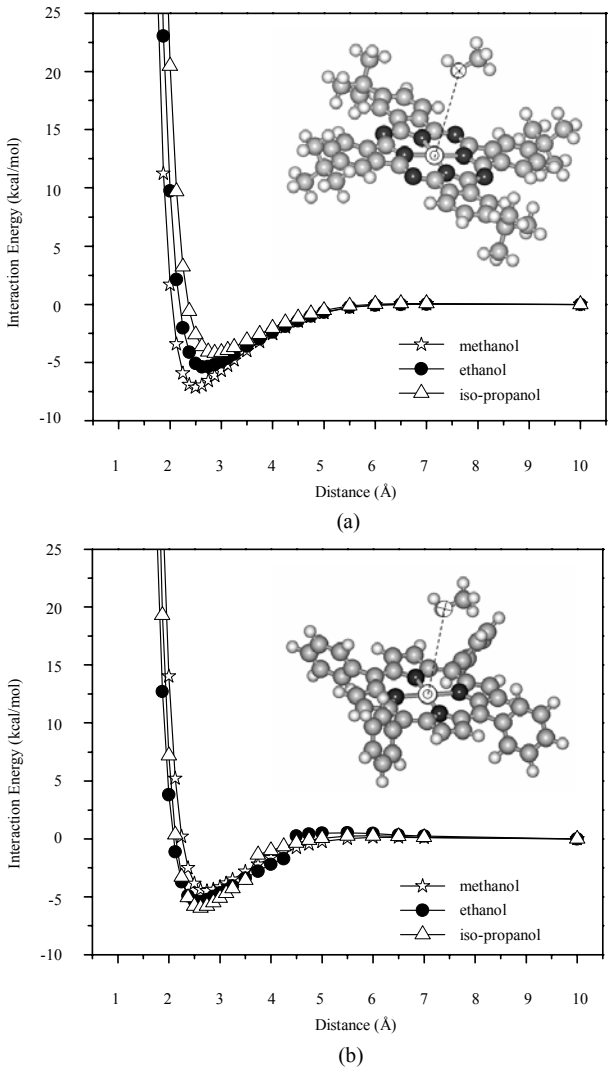

Figure 1. The interaction energy between (a) annealed ZnTTBPc and (b) ZnTPP with alcohols as a function of the intermolecular distance. Inset: (a) ZnTTBPc and (b) ZnTPP (Zn atom) interacting with MeOH (O atom) as shown by the dot line. Representation: Zn-double, N-black, C-grey, H-white and O-cross balls.

B. *Optical Absorption Measurements and Optical Sensing Characteristics*

The ZnTTBPc, ZnTPP spectra are signified by the intense B band at 330, 433 nm and Q band at 621, 551 nm, as shown in Figure 2. The delocalized π-electron system near central metal atom in MPc and MP is an important feature for VOC vapor detection. This comprises a highly polarized electron cloud and weakly bound π-electrons. Thus ZnTTBPc and ZnTPP are a relatively good electron donor. For the interaction mechanism, the electrons are likely to transfer to alcohol molecules, acting as an electron acceptor. This is also supported by the quantum mechanics calculated results.

The results of dynamic response test to alcohol vapors are illustrated in Figure 3, for which the optical absorption spectrum was selectively divided into five intervals, covering

the entire range for observable changes, as R1:340-415, R2:415-565, R3:565-625, R4:625-635 and R5:635-795 nm. The optical absorption response $\Delta A/A_{ZnTTBPc}$ and $\Delta A/A_{ZnTPP}$ for each interval was calculated from $(A-A_0)/A_{ZnTTBPc}$ and $(A-A_0)/A_{ZnTPP}$, where A and A_0 are the area integrals measured during alcohol vapor exposure and during the nitrogen gas flow, respectively, and $A_{ZnTTBPc}$ and A_{ZnTPP} are the initial area integral of ZnTTBPc and ZnTPP.

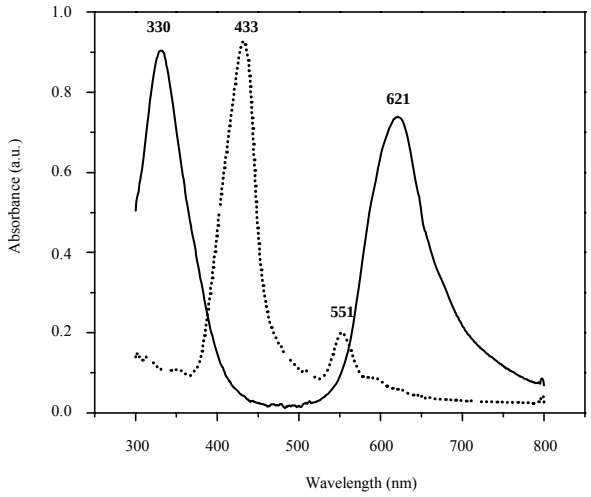

Figure 2. Optical absorption spectra of ZnTTBPc and ZnTPP (dotted line) thin films.

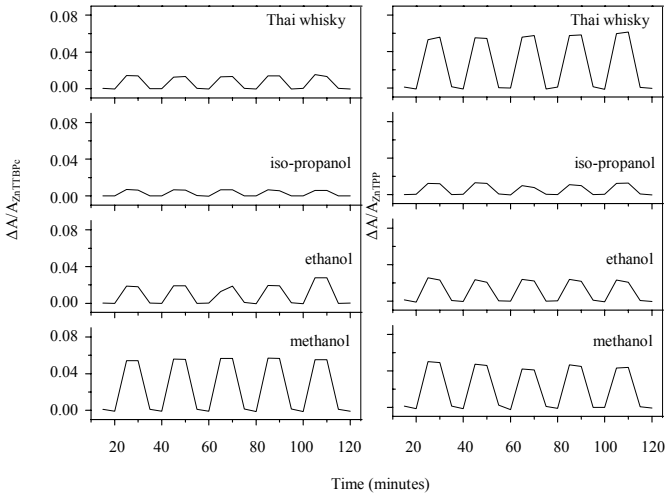

(a) (b)

Figure 3. The typical dynamic responses in the presence of alcohol vapors of (a) ZnTTBPc-R5 and (b) ZnTPP-R3

Figure 4 illustrates a histogram comparing the optical responses of ZnTTBPc and ZnTPP films to alcohols. The average response ΔS was calculated from the average of $S-S_0$ for all observable response pulses, where S is the dynamic sensor signal during alcohol vapor exposure and S_0 is the base sensor signal in nitrogen gas flow.

Overall, the responses of ZnTTBPc films to alcohols produce the strongest response with methanol in R5 (635-795 nm) for ZnTTBPc, whereas for ZnTPP the strongest response was observed in R3 (565-625 nm) for the Thai Wisky. Note that the strongest response for ZnTTBPc corresponds to the Q band at 621 nm for π-π* transitions of phthalocyanine ring [1]. The result is consistent with the expected change in the delocalize π-electron system, in good agreement with the calculations.

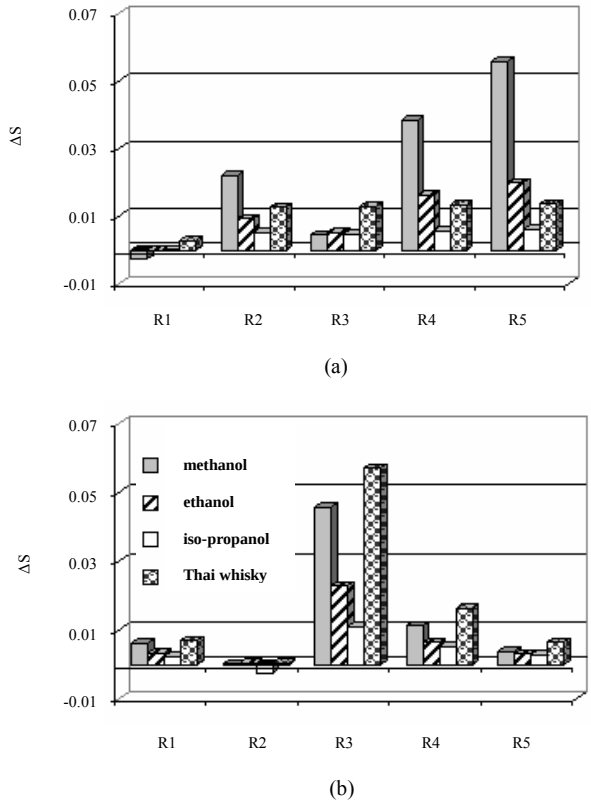

(a)

(b)

Figure 4. The average responses of (a) ZnTTBPc and (b) ZnTPP thin films

C. *Principle Component Analysis*

To evaluate the alcohol identification performance of the sensor array based on phthalocyanines and porphyrins, a simple statistical chemometric technique has been used, namely the Principle Component Analysis (PCA). PCA operates data by reducing abundant information into limited data space dimensions [10]. The data sets for ZnTTBPc and ZnTPP have been analyzed independently by PCA. The principle components were computed iteratively such that the first Principle Component (PC) carried the most variance, hence, information. Figures 5 and 6 show the 3D score plots of PCA analysis for the first three PCs. The results for ZnTTBPc and ZnTPP films evidently illustrate distinctive clustering of the data corresponding to methanol, ethanol and iso-propanol. This suggests that a sensor with only a single type of organic molecules may already be sufficient as an electronic nose [5]. We have also applied our optical gas sensor to test a

commercial brand of Thai whisky. Figure 6 shows the PCA results for the ZnTTBPc sensors, which indicates the Thai whisky is probably closer to ethanol than methanol. The discrepancies may originate from the lower alcoholic percentage in the Thai whisky than the pure ethanol. Further investigations will be required to assess the performance of our optical gas sensors.

V. CONCLUSION

We have demonstrated that ZnTTBPc and ZnTPP thin films can be used as gas sensors, capable of classifying different types of alcohol. The interaction of the sensing molecules with alcohol vapor molecules has been studied by the quantum mechanical calculations, which indicates a charge transfer mechanism between the oxygen atom in alcohol and the central Zn atom in the sensing molecules. The strong sensor signal of methanol is attributed to strong interaction between the sensing molecules and methanol as depicted in Fig. 1 together with higher vapor pressure (30 kPa which is higher than ethanol 9 kPa and iso-propanol 2.4 kPa at 20 ^{o}C). The potential application in the food industry of our gas sensor array has been demonstrated in the classification of the Thai whisky in comparison to ethanol and methanol.

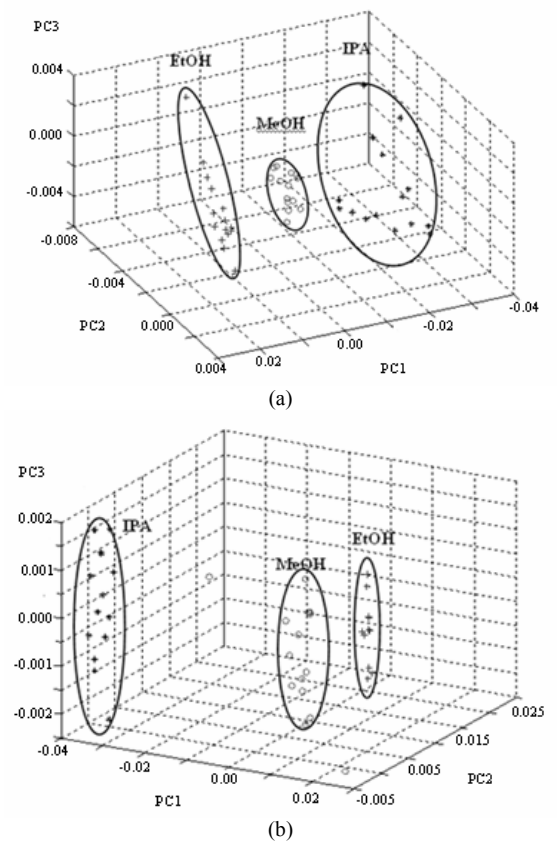

Figure 5. PCA three-dimensional score plot related to the response of the array optical sensors corresponding to (a) ZnTTBPc and (b) ZnTPP thin films

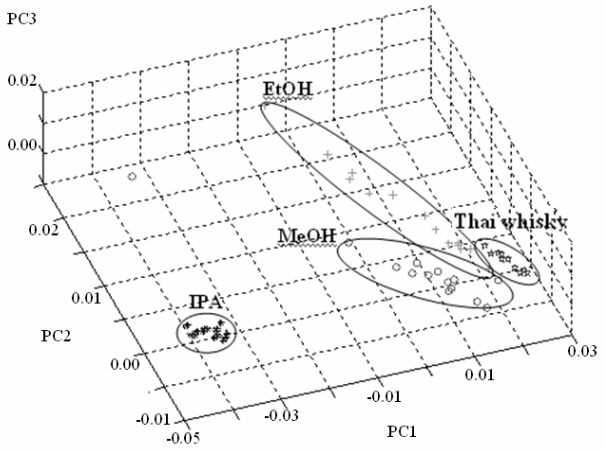

Figure 6. PCA three-dimensional score plot related to the response of the array optical sensors corresponding to ZnTTBPc and ZnTPP thin films

ACKNOWLEDGEMENT

We acknowledge the financial supports by the Thailand Graduate Instituted of Science and Technology (TGIST) scholarship and the National Nanotechnology Center (NANOTEC), the National Science and Technology Development Agency (NSTDA).

REFERENCES

[1] J. Spadavecchia, G. Ciccarella, and R. Rella, "Optical characterization and analysis of the gas/surface adsorption phenomena on phthalocyanines thin films for gas sensing application," *Sens. Actuators B Italy*, vol. 106, pp. 212-220, 2005.

[2] I.L. Emelianov, and V.V. Khatko, "The composite phthalocyanine-based Langmuir-Blodgett films : structural peculiarities and NO-sensitive properties," *Thin Solid Films Belarus*, vol. 354, pp. 237-244, 1999.

[3] M.L. Rodríguez-Méndez, J. Souto, R.D. Saja, J. Martínez, and J.A.D. Saja, "Lutetium bisphthalocyanine thin films as sensors for volatile organic components (VOCs) of aromas," *Sens. Actuators B Spain*, vol. 58, pp. 544-551, 1999.

[4] X. Ma, H. Chen, M. Shi, G. Wu, M. Wang, and J. Huang, "High gas-sensitivity and selectivity of fluorinated zinc phthalocyanine film to some non-oxidizing gases at room temperature," *Thin Solid Films China*, vol. 489, pp. 257-261, 2005.

[5] J. Spadavecchia, R. Rella, P. Siciliano, M.G. Manera, A. Alimelli, R. Paolesse, C. Di Natale, and A.D' Amico, "Optochemical vapour detection using spin coated thin film of ZnTPP," *Sens. Actuators B Italy*, vol. 115, pp. 12-16, 2006.

[6] C. Park, D.H. Yun, S.T. Kim, and Y.W. Park, "Enhancement of the NO_2-sensing capability of copper phthalocyanine by measuring the relative resistance change," *Sens. Actuators B Korea*, vol. 30, pp. 23-27, 1996.

[7] S.N. Alamri, A.A. Joraid, and S.Y. Al-Raqa, "Structural and optical properties of thermally evaporated 1, 4, 8, 11, 15, 18, 22, 25 – octahexyphthalocyanine thin films," *Thin Solid Films Saudi Arabia*, vol. 510, pp. 265-270, July 2006.

[8] Z. Gu, J. Yin, P. Liang, and F. Gan, "Temperature characteristics of optical parameters of phthalocyanine LB films and spin-coated films," *Opt. Mater. China*, vol. 27, pp. 1618-1622, 2005.

[9] S. Uttiya, T. Kerdcharoen, S. Vatanayon, and S. Pratontep, "Effect of structural transformation to the gas sensing properties of Phthalocyanine thin film," *Proceedings of the 3rd International Workshop On Nanophysics and Nanotechnology (3rd IWONN ; Vietnam) Thailand*, pp. 596-597, December 2006.

[10] J. Spadavecchia, G. Ciccarella, R. Rella, S. Capone, and P. Sicilaino, "Metallophthalocyanines thin films in array configuration for electronic optical nose applications," *Sens. Actuators B Italy*, vol. 96, pp. 489-497, 2003.

Symmetrical Wheatstone MEMS Cantilever Sensors with On-chip Resistors for Temperature Feedback

Adisorn Tuantranont, K. Jaruwongrungsee, T. Lomas, A. Jomphoak, A. Wisitsoraat
Nanoelectronics and MEMS Laboratory, National Electronics and Computer Technology Center
112 Thailand Science Park, Pahol Yothin Rd., Klong 1, Klong Luang, Pathumthani 12120 THAILAND
Tel. +66(2)-564-6900 Ext. 2111 Fax. +66(2)-564-6756 Email: adisorn.tuantranont@nectec.or.th

***Abstract*— Microcantilever sensors have been modeled and characterized for biosensor applications. The stress induced on gold surface with polysilicon piezoresistive sensing is demonstrated. In principle, an adsorption of biochemical species on a functionalized surface of the microfabricated cantilever will cause a surface stress and consequently the cantilever bending. The sensing mechanism relies on the piezoresistive properties of the polysilicon wire encapsulated in the beam. The sensitivity of the sensing technique could be measured by external read-out circuit as a balanced Wheatstone bridge configuration. The resistance change output of the cantilever is directly proportional to the amount of bending in the MEMS cantilever. Compensation by resisters on the substrate significantly reduces the temperature dependence.**

I. INTRODUCTION

Microcantilever has been widely used as chemical and biological sensors [1]-[3], atomic force microscopes [4] and data storage devices [5]. The deflection of these cantilever beams apply various techniques same as the techniques for atomic force microscopy AFM technology such as optical reflection, piezoresistive, piezoelectric, capacitive, and electron tunneling [6]. Microcantilever acts as a surface stress sensor which sensitivity of detection based upon the adsorption induced force when a specific biochemical species adsorbed on a functionalized surface of the cantilever beam [7]. These biosensors can be applied as a patient classifier for the presence of various diseases with faster responses, higher accuracy and lower cost.

In this paper, the model and characterization of our microfabricated cantilever have been described. The temperature dependence of microcantilevers has been studied and compensated by symmetric Wheatstone bridge configuration with on-chip resistors.

TABLE I
All dimension of MEMS cantilever beam

Material layer	Wide (μm)	Long (μm)	Thickness (μm)
Nitride	40	100	0.5
Polysilicon	10	400	0.5
Silicon dioxide	40	200	2.5
Gold	40	200	0.5

II. EXPERIMENTAL

A. *Microcantilever Fabrication*

The cantilever-based sensors have been developed with the integrated piezoresistive read-out with the integration of a full and symmetric Wheatstone bridge on chip with two resistors placed on the cantilevers and two resistors on chip as shown in Fig. 1. The piezoresistive cantilever can be functionalized with biochemical materials to perform antigen-antibody reaction or DNA hybridization while the other bare cantilever can be applied as a reference beam, thus there is a possibility to perform differential measurements through the subtraction of signals from two cantilevers. The background noises from thermal drift and fluid turbulence effects were minimized. Commercial available Multi-users MEMS Process (PolyMUMPs) was used to fabricate this device. The cantilever beam comprised of four structural layers, silicon nitride, polysilicon, silicon dioxide and gold. We have previously reported the fabrication process of cantilever beam with piezoresistive read-out [8], which can be operated in gas phase and consisted of a large array of cantilever sensors. The polysilicon wire forms a piezoresistive element that runs down the length of the beam and back. Silicondioxide layer fills the gap between polysilicon and top gold layer. The AFM picture of top gold layer acts as a reactive or adsorption layer was shown in inset of Fig.1.

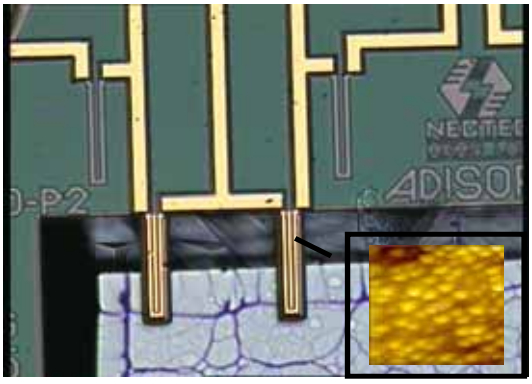

Figure 1. Scanning electron micrograph (SEM) of fabricated cantilever array sensors and gold layer surface.

The beam has a length of 200 micrometers with 40 micrometers width. All layers dimension including thickness was shown in Table I.

B. Device Modeling

This methodology is conducted to analyze the beam deflection due to surface stress after the device was adsorbed by biochemical molecules. The adsorbed layer can attempt to expand or may try to contract know as a compressive surface stress and a tensile surface stress, respectively.

MEMS cantilever is bending due to mechanical force generated by molecular adsorption. Adsorption-induced stress sensors have a sensitivity range based on adsorbed mass which proportional to molecular size. In addition, MEMS cantilever bending is also ideal for liquid-based biosensor applications.

The mechanical design of piezoresistive polysilicon wire encapsulated in MEMS cantilever is optimized for detecting changes in surface stress upon analyzes surface adsorption. The fractional change of resistance ($\triangle R/R$) in a piezoresistive wire is described by the following expression,

$$\frac{\Delta R}{R} = 3\beta\pi_L \frac{(1-v)}{t}\Delta\sigma \qquad (1)$$

where π_L is the piezoresistive coefficient of polysilicon , $\Delta\sigma$ is the difference of the longitudinal stress and the transverse stress, t is the thickness of the cantilever, and β is a factor that is adjusted for the thickness of the piezoresistor. From the above expression, the $\triangle R/R$ ratio is proportional to the stress difference, $\Delta\sigma$ is the stress difference distribution depends on the geometric factors of the layers and the reaction forces between the gold surface and the biochemical molecules. Therefore, maximizing the stress difference in the way of changing the geometric factors can increase the deflection signals.

C. Device Simulation

A piezoresistive simulation is performed using Coventorware. Firstly, the tip deflection was varied from 0 to 4 micrometers to verify the resistance change due to beam deflection. The simulation result of tip deflection shows in inset. The plot of normalized resistance change versus beam tip deflection was shown in Fig. 2. From the simulation, the resistance of the beam has increased about 2% when the tip of the cantilever beam was increasingly deflected of 1 micrometer.

The relationship of resistance change (piezoresistivity) with beam deflection is in linear manner with a constant slope (sensitivity).

D. Characterization (Temperature Dependence)

Microcantilever beam has been tested at room temperature to study the change of piezoresistive by various external temperatures. The Wheastone Bridge with built-in offset and consisting of four identically behaving resistors was shown in Fig. 3, the output signal will vary linearly with supply voltage [9-12].

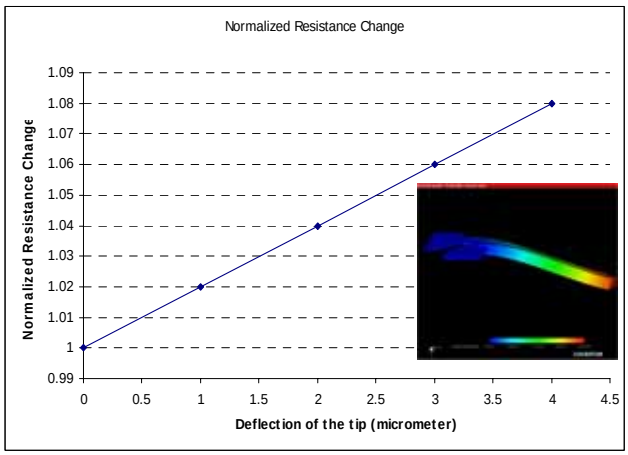

Figure 2. Plot of normalized resistance change in relative with beam deflection.

To characterize temperature dependence, the beam was placed on an adjustable PID hot plate in chamber and varied temperature up to 80 degrees.

The output voltage of uncompensated and compensated beam varied with temperature as shown in Fig. 4. The diagram of amplifier circuit for amplifying the output signal from the Wheatstone bridge was shown in Fig. 5. The four part of low power J-FET OPAMP TL064 are used to be the differential amplifier. Input A and B are connected to Wheatstone bridge output Vo- and Vo+ respectively. Each input signal will buffering by one part of OPAMP and then amplifies with differential amplifier. Voltage gain of this circuit will be controlled by feedback signal from the last OPAMP, we can control it by varies the variable resistor 1MOhm.

From the experimental results, the temperature sensitivity of uncompensated cantilevers is at 28 mV/degree C (Celsius) compared to feedback compensated cantilevers which is less than 0.0015 mV/degree C. From this result, compensation by resisters on the substrate significantly reduces the temperature dependence, therefore this microcantilever sensors can be operated at various temperature ranges and suitable to implement for nano-biosensor applications.

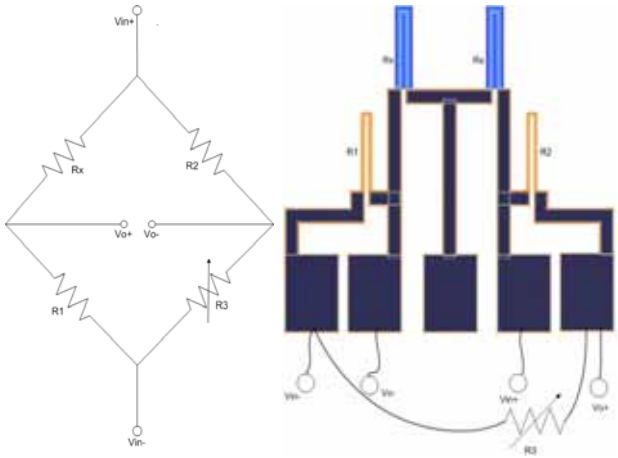

Figure 3. The cantilever beam series act as Wheatstone bridge that fabricated on sensor chip.

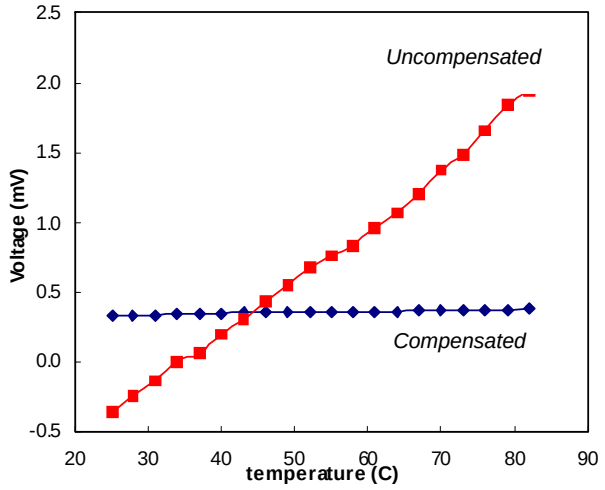

Figure 4. Plot of temperature dependence of cantilever beam non-compensate temperature (A) and compensate temperature (B).

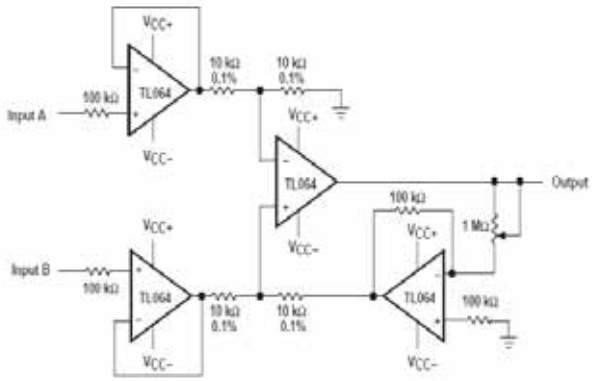

Figure 5. Diagram of amplifier circuit used in the experiment.

III. Conclusion

Microcantilever sensors have been modeled and characterized for biosensor applications. The stress induced on gold surface with polysilicon piezoresistive sensing is demonstrated. In principle, an adsorption of biochemical species on a functionalized surface of the microfabricated cantilever will cause a surface stress and consequently the cantilever bending. The sensing mechanism relies on the piezoresistive properties of the polysilicon wire encapsulated in the beam. The sensitivity of the sensing technique could be measured by external read-out circuit as a balanced Wheatstone bridge configuration. The relationship of resistance change (analogous to piezoresistivity) with beam deflection is in linear manner with a constant slope (analogous to sensitivity). Therefore, the resistance change output of the cantilever is directly proportional to the amount of bending in the MEMS cantilever and can be measured by piezoresistive read-out. Compensation by resisters on the substrate significantly reduces the temperature dependence. The temperature sensitivity is reduced from 28 mV/degree C (Celsius) of uncompensated cantilevers to 0.0015 mV/degree C in case of feedback compensated cantilevers. Therefore this microcantilever sensors can be operated at various temperature ranges and suitable to implement for nano-biosensor applications.

Acknowledgment

This work is supported by National Electronics and Computer Technology Center (NECTEC), National Science and Technology Development Agency (NSTDA).

References

[1] M. Yue, H. Lin, D. E. Dedrick, S. Satyanararayana, A. Majumdar, A.S. Bedekar, J. W. Jenkins, and S. Sundaram, "A 2-D microcantilever array for multiplexed biomolecular analysis," *J. Microelectromechanical Systems*, Vol. 13, no. 2, pp. 290-299, 2004.

[2] F. M. Battiston, J. P. Ramseyer, F. P. Lang, M.K. Baller, C. Gerber, J. K. Gimzewski, E. Meyer, and H. J. Guntherodt, "A chemical sensor based on a microfabricated cantilever array with simultaneous resonance frequency and bending readout," *Sensors and Actuators B* Chemical, vol. 77, pp. 122-131, 2001.

[3] G. Wu, H. Ji, K. Hansen, T. Thundat, R. Datar, R. Cote, M. F. Hagan, A. K. Chakraborty, and A. Majumdar, "Origin of Nanomechanical Cantilever Motion Generated from Biomolecular Interactions," *Proc. Natl. Acad. Sci. USA.*, vol. 98, pp. 1560-1564.

[4] G. Bennig, C. F. Quate, and C. Gerber, "Atomic force microscopes," *Physic Review Letter*, vol. 56, no. 9, pp. 930-933, 1986.

[5] H. Mamin, L. Fan, S. Hoen, and D. Rugar, "Tip-based data storage using micromechanical cantilevers," *Sensors and Actuators A*, vol. 48, pp. 215-219, 1995.

[6] Vo-Dinh, B.M. Cullum, D.L. Stokes, "Nanosensors and Biochips: Frontiers in Biomolecular Diagnostics," *Sensors and Actuators B*, vol. 74, pp. 2-11, 2001

[7] G. Y. Chen, T. Thandat, E. A. Wachter, and R. J. Warmack, "Absorption-induced surface stress and its effects on resonance frequency of microcantilevers," *J. Appl. Phys.*, vol. 77 (8), pp. 3618-3622, 1995.

[8] A. Tuantranont, D. Klaitubtim, and T. Lomas, "Design consideration and finite element modeling of MEMS cantilever for biosensor applications," *Proc. 2005 IEEE-conference on Nanotechnology*, pp. 27-31, 2005.

[9] D. W. Dareing and T. Thandat, "Simulation of adsorption-induced stress of a microcantilever sensor," *J. Appl. Phys.*, vol. 97, pp. 0435261-5, 2005.

[10] A. Boisen, J. Thaysen, H. Jensenius, O. Hansen, "Environmental sensors based on micromachined cantilevers with intergrated read-out," *Ultramicroscopy*, vol. 82, pp. 11-16, 2000.

[11] J. Thaysen, A. Boisen, O. Hansen, S. Bouwstra, "Atomic force microscopy probe with piezoresistive read-out and a highly symmetrical Wheatstone bridge arrangement," *Sensors and Actuators A*, vol. 83, pp. 47-53, 2000.

[12] P. A. Rasmussen, J. Thaysen, O. Hansen, S. C. Eriksen, and A. Boisen, "Optimized cantilever biosensor with piezoresistive read-out," Ultramicroscopy, vol. 97, pp. 371-376, 2003.

Fabrication and Characterization of Polydimethylsiloxane (PDMS) Microfluidic Channels

Thitima Maturos, Tanom Lomas, Adisorn Tuantranont and Anurat Wisitsora-at
Nanoelectronics and MEMS Laboratory, National Electronics and Computer Technology Center,
112 Thailand Science Park, Pahol Yothin Rd., Klong Laung, Pathumthani 12120, Thailand
E-mail: thitima.maturos@nectec.or.th

***Abstract*- Recently, a wide variety of polymeric materials have been widely used to construct micron-sized channels on a glass or silicon chip. In particular, polydimethylsiloxane (PDMS) has been used extensively, because it is robust, optically transparent, nonpolar, and impermeable to aqueous solutions. In addition, it allows the easy, fast, and inexpensive fabrication of devices by using micromolding techniques. The microchannel was formed by complex 2-dimensional (2-D) patterned PDMS layers using microfabrication technique. The micromolding technique was used to fabricate PDMS slabs with micro-sized grooves, and then the completed microchannel was formed by bonding PDMS slab with glass with oxygen plasma treatment. The contact angle and the flow leak test of microchannel are studied under various conditions of oxygen plasma treatment including RF power and treatment time. The proper condition for plasma treatment to achieve optimal surface hydrophilicity and bonding strength is at RF power of 6.8 Watt for 1-5 minute.**

I. INTRODUCTION

Microfluidic systems increasingly gain importance in modern life sciences as well as in diagnostic and therapeutic biomedical engineering and under development to address a variety of medical problems. Key advantages of micro total analysis systems based on microfluidic technology are the promise of small size and the integration of sample handling, measurement functions within a single, automated device and having low mass-production costs.

The most development of these technologies is named "lab-on-a-chip", and is poised to provide chemistry and biochemistry professionals with a powerful new tool. Lab-on-a-chip applications, especially in polymerase chain reaction (PCR) [1-4] and Capillary electrophoresis (CE) [5-8] need a development for microfluidic channel fabrication. Thus microfluidic technology plays the important role because it can make a rapid prototype and reduce the reagent including sample.

Polydimethylsiloxane (PDMS) is one of the materials that widely used as the materials of choice for microfluidic molding due to its easy and low cost fabrication, good optical transparency and easy sealing to other materials etc. In this paper, the molding procedure on silicon wafer, PDMS microchannel fabrication and surface treatment by oxygen plasma are reported. Moreover, surface treatment condition is varied to optimize bonding strength between PDMS and glass substrate. The bonding strength between PDSM structure and glass substrate is examined by the leak test of microfluidic channel.

II. EXPERIMENTAL

Silicon wafer were cleaned in piranha solution (mixture of 1: 4 of 50% H_2O_2 and 97% H_2SO_4) at 120 ^oc for 10 minutes, then carefully rinsed several time in deionized water and dried with gentle stream of air. After that silicon wafer were dehydrated by bake at 150-200 ^oC for 10 minutes. SU-8 photoresist was spin-coated on silicon wafer using a spin coater (Laurell technologies corp. model WS–400A–6NPP), then soft baked to remove all the solvent in the layer. The photoresist coated wafers were exposed using MJB4 mask aligner (SUSS microtec) then post-baked in order to selectively cross-link the exposed portions of the film. The sample was left in the desiccators to cool down slowly at room temperature for more than 13 hours. Finally sample was developed and cleaned with deionized water and isopropyl alcohol, and then it was gently dried with air. Spin speed, exposure time, baked time and developing time were optimized to achieve a smooth surface on mold. SU-8 mold was checked by microscope CX41 (Olympus) and the mold thickness was investigated by surface profiler measurement (Veeco model dektak^3 series).

Fig. 1. PDMS on SU8 master mold

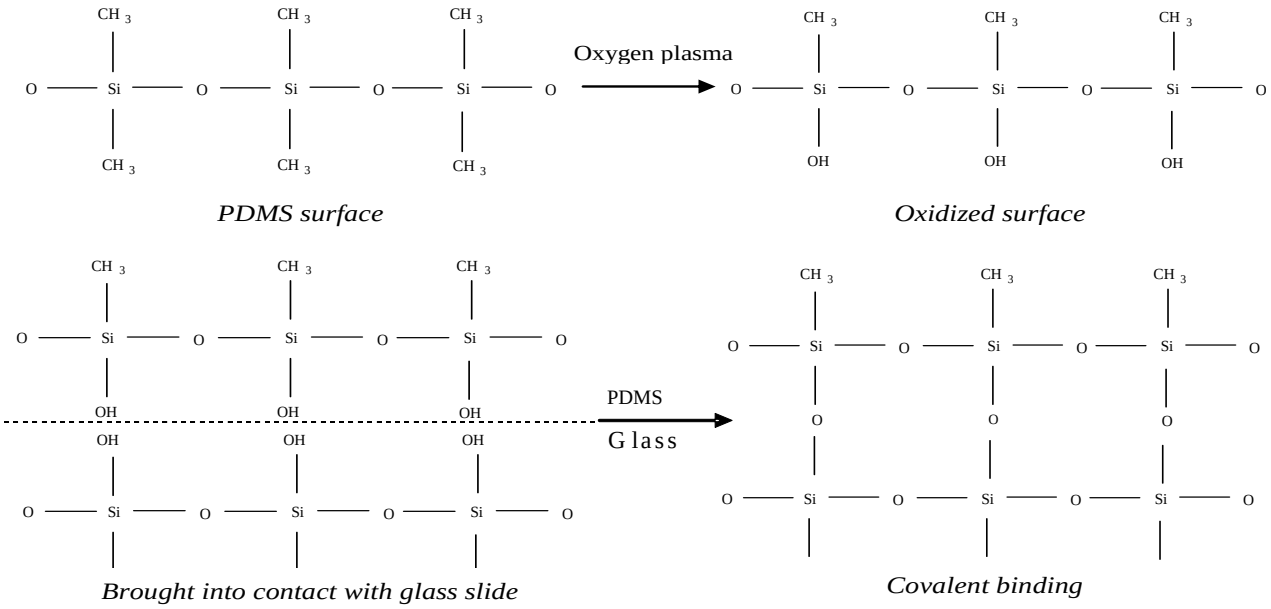

Fig. 2 Binding procedure of the modified surface of PDMS with glass slide.

Sylgard 184 Silicone Elastomer kit (Dow Corning), consisting of PDMS was prepared by mixing the precursors sylgard with a curing agent at a ratio of 10:1 by volume. The prepolymer mixture was degassed at 20-50 mTorr in ambient temperature desiccators with a mechanical vacuum pump for 10 minutes to remove any air bubbles in the mixture. PDMS mixtures were gradually poured onto the SU8 master mold to the height over the depth of designed channels as shown in Fig. 1. After the PDMS is cured at 100 ^{o}C for 30 minutes on a SU-8 mold, the molded polymer samples are peeled.

PDMS and glass slide were treated under oxygen plasma in a commercial plasma system (Harrick scientific corp. model PDC –32 G). The PDMS and glass substrate were then attached together to complete the microchannel. The procedure occurred in binding process of PDMS and glass substrate was shown in Fig.2. Treatment of PDMS in oxygen plasma result in the formation of hydroxyl groups at the surface which is changed to hydrophilic property through a dehydration reaction. Then the hydrophilic PDMS can form covalent bond with glass substrate. In order to find the optimum plasma treatment conditions for PDMS-glass bonding, the RF power and treatment time were varied. Water contact angle measurement and leak test of treated microchannel were conducted for each treatment condition. Contact angle measurements were performed by using contact angle measurement system (Rame'- hart instrument co. model 200). For leak test, deionize water was flown into the microchannel at various flow rates by using micropump (New era pump systems Inc. model NE-1000). The experimental setup for leak test is shown in Fig. 3. The flow rates that cause the leakage of the microchannel were observed.

III. RESULT AND DISCUSSION

The microchannel thickness and profile of microfabricated mold has been characterized by Dektak surface profile. Nice profile and the slight variation of thickness have been observed. The thickness variation may due to the viscosity change of the photoresist during spinning process.

PDMS were treated under oxygen plasma and then taken into contact with glass substrate to complete microchannel structure. For contact angle measurement, PDMS were immersed in methanol for 10 minutes and dried under the compress dry air. The photo of water contact angle of PDMS and PDMS treated under oxygen plasma are shown in Fig. 4. The water contact angle of untreated PDMS is about 117 degree. The water contact angles of PDMS treated versus treatment time at various conditions are shown in Table 1. It can be seen that PDMS surface treated under the low RF power at 6.8 Watt for 1 minute has the lowest contact angle at about 9 degree. For PDMS treated under high RF power of 10.5 Watt, the minimum water contact angle is 10 degree at 10 seconds treatment time. The results indicate that optimum contact angle of PDMS treated by low RF power of 6.8 Watt is better than that treated by high RF power at 10.5 Watt.

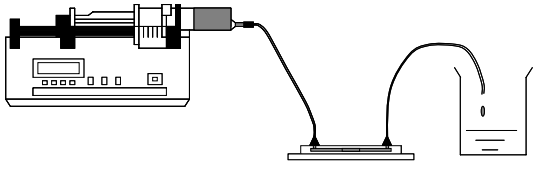

Fig. 3 Schematic of experimental setup for leak test

(a) (b)

Fig. 4 Water contact angle of PDMS treated under RF 6.8 and 10.5 Watt at various times

TABLE I
FLOW RATE THAT CAUSE LEAKAGE OF MICROCHANNEL THAT TREAT UNDER OXYGEN PLASMA

Exposure time (second)	Contact angle (degree)	
	6.8 Watt RF power	10.5 Watt RF power
5	57	13
10	45	10
20	24	12
30	22	16
40	20	16
50	12	20
60	9	22
300	33	48
600	40	65
900	49	79
1200	60	80

The microchannel for the leak test in this experiment consists of chamber, microchannel, inlet and outlet as show in Figure 6. The dimension of microchannel are 2 cm. x 100 µm x 100 µm. and chamber's dimension is 0.4 mm. x 0.9 mm x 100 µm. Leak test of the microchannel were performed by gradually increasing the flow rate of deionized water into microchannel and observed the flow rate that cause the leakage. The result of leak test is shown in Table 2. The microchannel treated at RF power 6.8 Watt for 60 and 300 seconds can endure the flow rate more than 10 ml/min. It can be indicated that the attachment of the low water contact angle of PDMS lead to the good adhesion between glass and PDMS. In contrary, the microchannel treated for a longer time was leaked at a lower flow rate. This can be explained by considering the effect of RF power and treatment time to the bonding strength between PDMS and glass. For PDMS treated under high RF power, the kinetic energy of ion incident on the substrate is high. Thus the siloxane backbone on the PDMS surface should be damaged and consequently reduced the Si-OH available for bonding with glass slide [4]. The effect of plasma treatment time on PDMS has been reported by Owen and Smith [5]. The report mentioned that the long treatment time will lead to the crack of the surface, which results in the poor bonding between glass and PDMS.

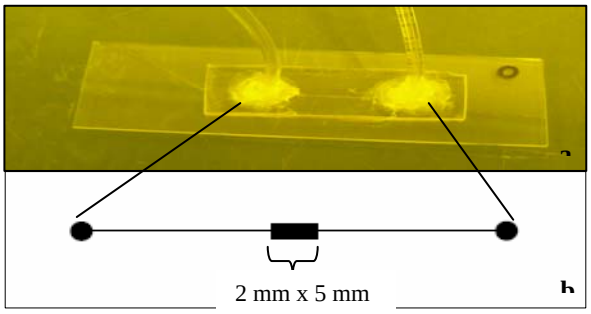

Fig. 6 The microchannel for the leak test (a) PDMS-glass microchannel and (b) micro channel model

TABLE II
FLOW RATE THAT CAUSE LEAKAGE OF MICROCHANNEL THAT TREAT UNDER OXYGEN PLASMA

Exposure time (seconds)	Flow rate that cause leakage (ml/min)	
	6.8 Watt RF power	10.5 Watt RF power
5	8	8
10	9	9.8
20	9	10
30	8.6	4.8
40	8	5
50	10	5.5
60	>10*	9.8
300	>10*	3.2
600	10	1.2
900	2.6	0.9
1200	1.1	1.1

(* Flow rate that causes leakage is out of normal usage range)

IV. CONCLUSION

We have successfully fabricated PDMS based microfluidic channel. PDMS slab with micropatterned grooves is bonded with glass substrate to complete microchannel. The good bonding between PDMS and glass substrate is obtained by treating PDMS and glass surfaces into hydrophilic state in order to provide covalent binding between glass and PDMS. Surface treatment can be done by commercially available oxygen plasma cleaner. The various conditions for oxygen plasma treatment including RF power and treatment time have been studied to optimize surface hydrophilicity and bonding strength. The proper treatment condition for optimize surface hydrophilicity is at RF power of 6.8 Watt for 1 minute or at RF power of 10.5 Watt for 10 seconds. The results indicate that the low contact angle of the treated PDMS surface lead to the good bonding strength between glass and PDMS. The proper treatment condition that leads to the best boding strength of microchannel is treatment at 6.8 Watt for the time between 1 to 5 minutes.

REFERENCE

[1] A. Ranjit Prakash, S. Adamia, V. Sieben, P. Pilarski, and C.J. Backhouse, " Small volume PCR in PDMS biochips with integrated fluid control and vapour barrier", *Sensors and actuators B,* vol. 113, pp. 398-409, 2006

[2] E. T. Lagally, C. A. Emrich and R. A. Mathies, "Full integrated PCR-capillary electrophoresis microsystem for DNA analysis", *Lab on a chip,* vol. 1, pp. 102-107, 2001

[3] J. M. Song, M. S. Yang, and H. T. Kwan, "Development of a novel DNA chip based on a bipolar semiconductor microchip system", *Biosensors and bioelectronics,* vol. 22, pp. 1447-1453, 2007

[4] P. M. Pilarski, S. Adamia , andChristopher J. Backhouse, "An adaptable microvalving system for on-chip polymerase chain reactions", *Journal of immunological methods,* vol. 205, pp. 48-58, 2005

[5] R. Wilke, and S. Buttgenbach, " A micromachined capillary electrophoresis chip with fully intregrated electrodes for separation and electrochemical detection", *Biosensors and Bioelectronics,* vol. 19, pp. 149-153, 2003

[6] R. Wilke and S. Buttgenbach, "A micromachined capillary electrophoresis chip with fully integrated electrodes for separation and electrochemical detection", *Biosensors and bioelectronics,* vol. 19, pp. 149-153, 2003

[7] S. Novakova , S. V.Dycka, A. V. Schepdael, J. Hoogmartens, and Z. Glatz, "Electrophoretically mediated microanalysis", *Journal of Chromatography A,* vol. 1032, pp. 173-184, 2004

[8] T. Pan, R. T. Kelly, M. C. Asplund, and A. T. Wooley, "Fabrication of calcium fluoride capillary electrophoresis microdevices for on-chip infrared detection", *Journal of Chromatography A,* vol. 1027, pp. 231-235, 2004

[9] S. Bhattacharya, A. Datta, J. Berg and S. Gangopadhyay, " Studies on surface wettability of Poly(dimethyl) siloxane (PDMS) and glass under oxygen-plasma treatment and correlation with bond strength", *Journal of microelectromechanical systems,* vol. 14, no. 3, pp. 590-597, 2005

[10] M. J. Owen and P. J. Smith., " Plasma treatment of poly (dimethyl) siloxane", *Journal of Adhesion Science and Technology,* vol. 8, no. 10, pp. 1063-1075, 1994

Gas Sensing Characterization of Ion-Assisted E-Beam Evaporated TiO_2 Thin Films with Nanometer Scale Thickness

A. Wisitsoraat[1], C. Promjuntuk[2], V. Patthanasettakul[1] and A. Tuantranont[1]
[1]Nanoelectronics and MEMS Laboratory,
National Electronics and Computer Technology Center (NECTEC)
112 Thailand Science Park, Pahol Yothin Rd., Klong Laung, Pathumthani 12120
http://www.nectec.or.th/mems, Tel: +662-564-6900 Ext. 2111, Fax: +662-564-6756
Email: anurat.wisitsoraat@nectec.or.th
[2]Department of Physics, Faculty of Sciences and Technology
Nakhonratchasima Rajabhat University, 340 Suranarai Rd., Muang District,
Nakhonratchasima, 30000 Thailand Tel: +664-425-4000 Ext. 1303, Fax+664-427-2939

Abstract- **In this work, we study the effect of nanometer-scale thickness and annealing temperature on gas sensing behaviors of TiO2 nanocrystalline thin films prepared by electron beam evaporation with ion-assisted deposition (IAD). TiO_2 thin film has been prepared with different thicknesses from 30 nm to 100 nm and annealing temperatures upto 400 °C. From structural characterization by X-ray diffraction (XRD) and atomic force microscopy (AFM), the as-deposited TiO_2 thin film has amorphous structure with smooth surface. After annealing above 300 °C, the TiO_2 film becomes polycrystalline anatase structure with increased roughness and porosity. The ethanol-sensing characterization shows that as-deposited film has moderate sensitivity, which is increased with the film thickness and temperature. In addition, TiO_2 thin films annealed at 400 °C exhibit higher sensitivity, which is relatively insensitive to the film thickness and operating temperature. The results suggest that the effective region for gas sensing of TiO_2 thin film is only within a few tens of nanometers from the surface and only very thin film with thickness as small as 30 nm may be sufficient for gas sensing.**

Keywords: **Titanium dioxide, thin film, semiconductor gas sensor, nanometer scale thin film**

I. INTRODUCTION

Semiconductor gas sensors have been widely investigated for gas sensing applications due to their low cost, good performances and easy implementation [1]. The principle of operation consists of a variation of the resistivity of the sensing material when its surface is exposed to different kind of reducing or oxidative gases. Usually, the behavior is based on an n-type electronic conduction, in which the resistance of the sensing layer decreases when exposed to reducing gases, such as CO or hydrocarbons. Transition metal oxides, such as SnO_2, WO_3, ZnO, ITO and TiO_2 have been proposed as candidates for gas detection [2-4]. Titanium dioxide (TiO_2) is a versatile material, which has been used in many applications such as, solar cell, electrical insulution, photocatalytic layer for self-cleaning glass, optical coating for filters and waveguides, etc. For gas sensing applications, TiO_2 is used in anatase phase that has lower resistance and higher sensitivity to gas adsorbents than the rutile phase, which is stable at higher temperature. TiO_2 nanocrystalline thin films are desired because of stable and good gas-sensing characteristics at operating temperature below 400 °C [5-6]. In the last application, it's clearly reported in the literature that the physical and gas-sensing properties of the sensor depends considerably on the method and the condition of the sensitive film preparation [7].

Electron-beam evaporation is one of preferred techniques for thin film gas sensor fabrication because of ease of batch fabrication and ability to form high-quality multilayer thin film structures. In addition, the properties of the thin film material can be manipulated to enhance the gas-sensing characteristics of e-beam evaporated thin film with ion-assisted deposition (IAD). In this work, we prepared TiO_2 nanocrystalline thin film by ion-assisted e-beam evaporated for gas-sensing applications. The gas-sensing performance of ion-assisted electron beam evaporated TiO_2 thin film has been characterized with different thickness in nanometer scale.

II. HELPFUL HINTS

The starting gas sensitive material is an analytical grade titanium oxide (TiO_2) pellets (99.99%). The substrates for thin film coating were (100) silicon wafers and 200 µm-thick Alumina sheets. The gas sensors were then fabricated from a series of thin film deposition using Denton's ion-assisted e-beam evaporator system. The gas sensor fabrication process started with the deposition of chromium (Cr) and gold (Au) interdigitated electrodes on alumina substrates. Chromium and gold layer were then successively e-beam evaporated over the alumina substrates through electroplated-Ni shadow masks having an interdigitated pattern. The thickness of Cr and Au layer were ~200 and ~100 nm, respectively. Next, the TiO_2 layer was evaporated over interdigitated electrode through another electroplate shadow mask with square window pattern aligned to interdigitated area. For this study, the depositions were conducted with different thickness in nanometer scale

Authorized licensed use limited to: Chulalongkorn University. Downloaded on August 10,2010 at 08:39:42 UTC from IEEE Xplore. Restrictions apply.

from 30 nm to 100 nm. The deposition rate, oxygen flow rate, and substrate temperature were ~ 0.2 nm/s, 25 sccm, and 200 °C, respectively. The ion driving voltage and ion flux current are ~400 V and ~0.15 A. The films were then annealed at different temperatures up to 400 °C. The microstructure of the TiO_2 films at different temperature annealing was studied by means of atomic force microscopy (AFM) and X-ray diffraction (XRD). The surface morphology was observed by field emission scanning electron microscopy (FESEM).

For gas sensing measurements, the gas sensors were mounted in a stainless steel gas-testing chamber and the electrode to connect with probe. Inside the chamber there is a heating stage to achieve a certain sensor operating temperature. The gas-sensing experiments were done in the temperature range from 200 to 400 °C. For gas testing, purified air (99.999% Air Zero) and Air containing gas sample were mixed with different ratio and flow with mass flow controller into the testing chamber.

III. UNITS

X-ray diffractograms and AFM images of TiO_2 thin films with 30 nm thick TiO_2 thin film with different annealing temperatures are shown in Fig. 1 and 2, respectively. It can be seen that the as-deposited TiO_2 thin film has amorphous structure with smooth surface. After 2 hour-annealing at 300 °C and 400 °C, the TiO_2 thin film becomes polycrystalline structure with nanometer grain size and anatase phase with (101) preferred orientation [6]. It is interesting that the polycrystalline structure of TiO_2 thin film can be observed by XRD even though the thickness is very small in nanometer scale. In addition, it was found from AFM data that the root mean square (rms) surface roughness of the film increases from 1 nm to 2 nm as the annealing temperature increases up to 400 °C. Furthermore, the film becomes more porous with nanometer pores after annealing above 300 °C.

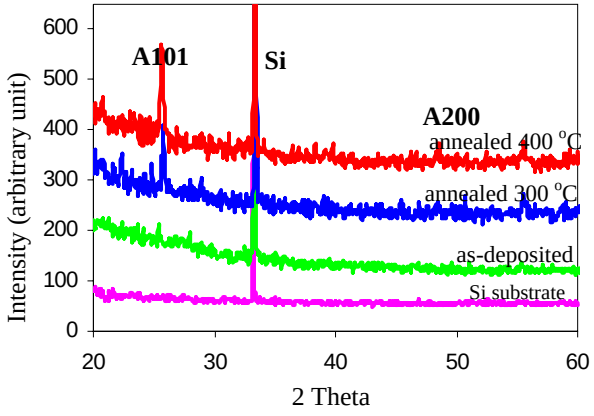

Figure 1. X-ray diffractograms of 30 nm thick TiO_2 thin film with different annealing temperatures.

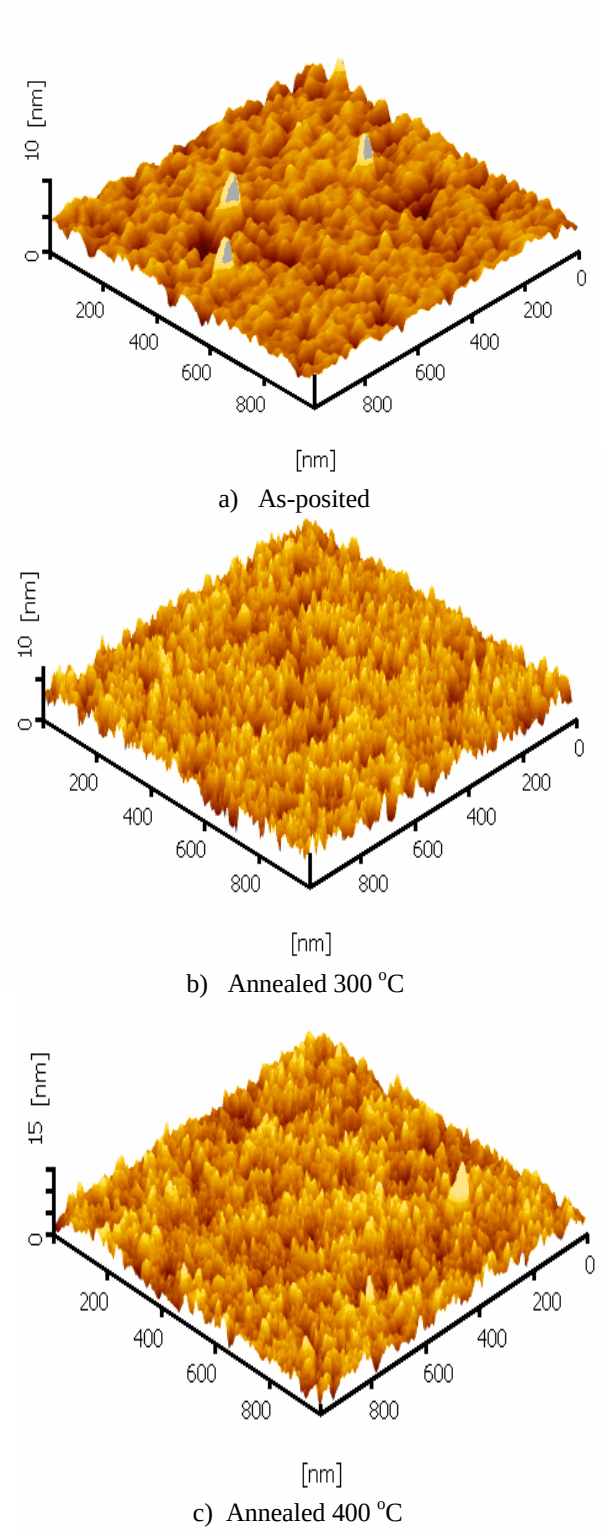

Figure 1. AFM images of TiO_2 thin films with 30 nm thick TiO_2 thin film with different annealing temperatures.

The gas sensing characteristics of the gas sensors are characterized in term of gas-sensing response. The resistance of the TiO_2 thin films was reduced upon the exposure to reducing gas, indicating that it is n-type semiconductor. In

addition, the resistance of the TiO_2 thin films is decreased as thickness and annealing temperature increases. The gas sensing response of n-type semiconductor gas sensor to a reducing gas is normally defined as the ratio of the background resistance to the resistance with gas sample, (R_o/R_g), while the response to an oxidizing gas is defined in the reverse way. The gas-sensing response was calculated time response data and plotted versus various parameters including gas concentration and temperature.

The gas-sensing responses of TiO_2 e-beam evaporated thin films before and after annelaing toward ethanol are shown in Figs. 3 and 4, respectively. It shows that the responses to ethanol of the as-deposited films tend to increase with operating temperatures. In addition, the response is slowly increased with the film thickness. After annealing at 400 ^oC, the response to ethanol of all TiO_2 thin films are improved and become almost independent of the film thickness. Moreover, the effective operating temperature ranges become wider with maximized response at around 350 ^oC.

The improved response after annealing is attributed to the improvement in surface roughness, porosity, and crystallinity of the TiO_2 thin films as is evident from structural characterization. In addition, the observed thickness independence of the response after annealing at sufficiently high temperature suggests that the effective region for gas sensing of TiO_2 thin film is only within a few tens of nanometers from the surface and only very thin film with thickness as small as 30 nm is sufficient for gas sensing. However, the resistivity of very thin film is very high, complicating electrical measurement. It should be noted that the TiO_2 thin films still can sense ethanol at lower operating temperature than 250 ^oC, however the background current is not sensible at these temperature.

IV. CONCLUSION

In conclusion, we study the gas sensing behaviour of TiO_2 thin film prepared by electron beam evaporation with ion-assisted deposition (IAD). TiO_2 thin film has been characterized for structural and gas-sensing characteristics as a function of IAD deposition parameters with thickness in nanometer scale. From structural characterization by X-ray diffraction (XRD) and scanning electron microscope (SEM), the as-deposited TiO_2 thin film has amorphous structure with smooth surface. After annealing at or above 300 °C, the TiO_2 film becomes polycrystalline structure with nanometer grain size and anatase phase with (101) preferred orientation. The experimental results show that 30 nm-thick TiO_2 thin films annealed at 400 °C exhibit high sensitivity to low concentration ethanol in the range of 300 ppm with high response at operating temperature above 250 °C and maximized response at around 350 °C.

REFERENCES

[1] Wisitsoraat, A., Tuantranont, A., Patthanasettakul, V., Lomas, T., and Chindaudom, P. (2005) *Science and Technology of Advanced Materials*. **6,** 261-265.

[2] Tomchenko, A., Harmer, P., Marquis, T., and Allen W. (2003) *Sensors and Actuators B*. **93**, 126-134.

[3] Vaishnav, V.S., Patel, P.D., and Patel, N.G. (2005) *Thin solid Films*. **490**, 94-100.

[4] Ruiz A.M., Sakai, G., Cornet, A., Shimanoe, K., Morante J.R., and Yamazoe N., (2003) *Sensors and Actuators B*. **93**, 509-518.

[5] Tang, H., Prasad, K., Sanjines, R., and Levy, F. (1995) *Sensors and Actuators B*. **26-27**, 71-75.

[6] Rothschild, A., Edelman, F., Komem, Y., and Cosandey, F. (2000), *Sensors and Actuators B*. **67**, 282-289.

[7] Taurino, A.M., Capone, S., Boschetti, A., Toccoli, T., Verucchi, R., Pallaoro, A., Siciliano, P. and Iannotta, S. (2004), *Sensors and Actuators B*.**100**, 177-184.

Maskless Etching of Microfabricated Structures with Low-Power Focused Ion Beam

Peerasak Chantngarm
Department of Electronics and Telecommunication Engineering,
Pathumwan Institute of Technology, Bangkok 10330, Thailand

Abstract - **Characteristics of the structures microfabricated by 20-keV Ga^+ FIB on Si have been investigated with AFM images and photographs from a Nomarski microscope. The images from AFM show redeposition effect inside and near the edges of the holes etched by FIB. The images also show great damages of the as-implanted structures induced by the high current density of FIB. The relationship between the dose of ion beam and the structures fabricated by FIB was studied. The results indicated that the depth of the structures is directly proportional to the dose of the ion beam with sputtering rate of 132 nm/minute, when the beam current is 28 pA. The line width is also directly proportional to the dose, when the implanting time does not reach the critical value. The experimental results revealed the discrepancies between the beam diameter and the width of the microfabricated structures, which is considered to be the results of combined effects from surface charging effects, vibration, and the part of ion beam with weaker intensity.**

I. INTRODUCTION

Nanoelectronics, including Micro-Electro-Mechanical Systems (MEMS) and Nano-Electro-Mechanical Systems (NEMS), has become one of research areas that attracts a lot of attentions. At the same time, the technologies to fabricate nanoscale structures have been developed rapidly. One of key technologies is photolithography; however, there are many difficulties to be resolved to make further progress. Focused ion beam (FIB) is one of alternative technologies for photolithography in some applications [1-2]. With a very small ion beam diameter, about 0.1 μm, FIB is suitable for maskless etching, maskless implantation, and maskless ion-assisted deposition, etc.

In order to properly fabricate devices, it is essential to fully understand the fundamental characteristics of FIB system itself, and of the structures fabricated with FIB. Although conventional microscopy method such as scanning electron microscopy (SEM) is good enough to acquire images showing topography of the microfabricated structures, atomic force microscope (AFM) is known to provide more detailed information for very small structures. With a probe placed very close to the sample, AFM can acquire a detailed image of the sample over a small area by measuring the attractive forces or repulsive forces between the tip and the sample [3]. The forces are then processed by software to show color images on a screen where the color of images represents the friction between a tip and the sample.

In this study, we investigated fundamental characteristics of the structures microfabricated by 20-keV Ga^+ FIB. AFM was used to examine the surface topography and the depth of the etched specimens, which gave us very detailed information. A Nomarski microscope was also used in our experiments to acquire optical images of microfabricated structures. Three experiments have been done with Si in this study. The first experiment is to examine the surface topography of Si after being bombarded with FIB in dot-mode and area-mode. The second experiment is done to find the relationship between the dose and the depth of holes etched by FIB. The last experiment is to find out the correlation between the implanting time and the width of lines.

The rest of the paper is organized as follows. Section II briefly introduces the fundamentals of stopping mechanisms in solids as well as the redeposition effect associated with ion beam etching. Section III describes the experimental procedures, FIB system, and beam diameter which is an important parameter. Section IV discusses the experimental results and we draw out conclusion in section V.

II. THEORY

A. Stopping Mechanisms

When charged particles are implanted into solids, they collide with atoms of the target and lose energy until stop. There are two kinds of stopping mechanisms for ions implanted into targets, nuclear stopping and electronic stopping. The dominant mechanism is determined by the mass and the energy of the accelerated ions, as well as the mass of the target atoms. Generally, when the energy is relatively low, the stopping is dominated by nuclear stopping, the elastic collisions with nuclei or whole atoms which absorb the impact. On the other hand, when the energy is relatively high, the stopping is dominated by electronic stopping, the inelastic collision with bound electrons of the target atoms so that the atoms of target are excited or ionized. Hence, on the assumption that both mechanisms are independent, the energy loss per distance unit could be expressed as follows:

$$-\frac{dE}{dx} = N\left|S_n(E) + S_e(E)\right| \tag{1}$$

where N is the atomic density of the target atoms, $S_n(E)$ and $S_e(E)$ are nuclear-stopping and electronic-stopping cross-sections, respectively. In the case of implanting 20-keV Ga^+ into Si, the major part of energy loss is due to nuclear stopping which contributes to cascade collision and sputtering [4].

B. Redeposition Effect

One characteristic of etching by ion beam is that the etching and the redeposition of nonvolatile etch product species have taken place simultaneously [5]. Hence, the final net sputtering is the result of combined effects between the etching and the redeposition. Other factors that affect the sputtering are the incidence angle of ion beam, the structure of target materials whether it is an amorphous or a crystalline structure, and the orientation of the crystalline structure, etc. Although FIB has much higher beam current density, the similar redeposition effect is expected.

III. Experimental

Three experiments have been done. First, Si was bombarded with FIB in dot-mode and area-mode, and the surface topography was observed with AFM. In dot-mode, standing ion beam was implanted into just one point for 1 minute. In area-mode, ion beam was raster scanned into area of 5x5 μm^2 for 2 minute 23 seconds. The distance between the center of adjacent holes and areas was 10 μm. The beam current was 28 pA. In the second experiment, FIB was used to etch holes on Si with different dwell time: 1 minute, 2 minutes and 3 minutes. The objective is to find out the relationship between dwell time and the depth of holes. The beam current and the distance between adjacent holes are the same as in the first experiment. The third experiment is to find the correlation between implanting time and the line width on Si. The implanting time was 8 and 82 seconds, while the beam current used in this experiment was 33 pA. We used AFM from Seiko model SPA300 to examine the surface topography and to measure the depth of each holes. A Nomarski microscope was used to acquire the optical images in the last experiment. In all experiments, Czochralski (CZ) grown *n*-type Si substrates of (100) orientation were used. The size of substrates was 2x2 cm^2. The FIB system is introduced in subsection A, and the definition of beam diameter used in the experiments is described in subsection B.

A. FIB System

The FIB system used in this study is model EFIB-2000S from Eiko Engineering. The ion source was needle-type liquid metal ion source (LMIS) which provides Ga^+ ions. When an ion beam hits a target, atoms of the target are sputtered off, secondary electrons and ions are emitted, and the primary ions are implanted. Hence, FIB could be used as a scanning ion microscope (SIM) to provide high-contrast images during ion bombardment [6]. Prior to using FIB in each experiment, the ion beam was adjusted to get well-conditioned beam and stable beam current.

B. Beam Diameter

There are several methods to find out a beam diameter, such as the knife-edge method, the $1/e^2$ optical intensity criterion, and the 1/e electric field strength criterion. In reality, the beam diameter of FIB is affected by several factors, such as beam energy, beam current, etc [7]. In our study, instead of measuring the beam diameter directly, we derived the beam diameter from beam energy and beam current based on the specification from the manufacturer. Assuming that the beam energy is 20 keV, when the beam current is 100 pA the beam diameter is about 0.15 μm, and when the beam current is 30 pA the beam diameter is about 0.1 μm [7]. The beam current used in our experiments is around 30 pA. Hence, the beam diameter should be about 0.1 μm by specification. One way to make sure that the beam is focused enough is by viewing the SIM image of a standard sample provided with the FIB system. The standard sample has an Al layer on the top with LATEX particles, which is a type of polymer. Fig. 1 shows the SIM image of LATEX particles, and lines generated by FIB. The diameter of LATEX particles is 1 μm and the width of the line generated by FIB is about 0.2 μm. Once we get the image of the LATEX particles clearly, it means that the beam ion beam is well conditioned. However, it is not unusual that the minimum line width of the structure etched by 0.1-μm-diameter FIB would be larger than 0.1 μm. The wider minimum line width is caused by the part of ion beam with weaker intensity. It is reported that the minimum line width on Si etched with 0.1-μm-diameter FIB could be 0.5 μm [8]. The discrepancies between the beam diameter and the line width would be further discussed in section IV.

IV. Results And Discussion

It is known that ion bombardment causes damages to the targets due to elastic collisions with nuclei of target atoms. With beam current density 10^5 times higher than conventional ion beam [8], it is expected that FIB could cause more damages to the targets. The reason that Ga^+ ions were used in our study is due to the large sputtering yield, as well as the stability and the ability to operate at room temperature of the Ga^+ ions LMIS. Fig. 2 is the AFM images showing the surface topography of Si after ion bombardment with FIB in the first experiment. The diameter of two holes in the middle of Fig. 2(a) is 2 μm and the size of implanted areas in Fig. 2(b) is 5x5 μm^2. From the images, it could be seen that the roughness on the edges of holes in Fig. 2(a) and on the implanted areas in Fig. 2(b) is nonuniform. This phenomenon is considered to be the combined effect of cascade scattering and redeposition effect, which were explained in section II.

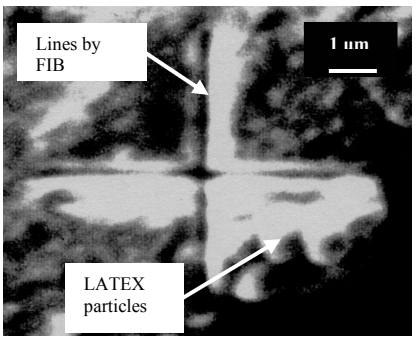

Fig. 1. The SIM image of LATEX particles and lines generated by FIB.

Fig. 3 is the AFM images showing top view and cross section of the holes on Si in the second experiment. The line above holes in the middle of Fig. 3(a) is a reference line to display the cross section of the holes. Here, the holes under the line could be separated into three groups: two on the left, three in the middle, and two on the right. The dwell time for each group is 1 minute, 2 minutes and 3 minutes, respectively. The rough areas near the holes in Fig. 3(a) are the same damages at the implanted areas as in Fig. 2. Two vertical lines in the middle of Fig. 3(b) are also reference lines used to measure the depth of the holes. The cross section in Fig. 3(b) shows some interesting characteristics. First, the feature profile of the holes is not anisotropic, but conical. This is due to the energy distribution profile of ion beam, which has the highest current density at the center, combining with the redepostion effect taking place near the bottom of the holes [9]. Second, the two holes with the shortest dwell time have a two-peak feature profile. This could be explained with the AFM image in Fig. 2(b). When the dwell time is not long enough, the sputtering process is continuing at the surface and the area could be nonuniform. Third, there are two hones at the edges of the holes with the height of left hones directly proportional to the dwell time. These hones are also considered to be the result of redeposition effect. The same effect also caused faceting near the edges of two holes with the longest dwell time. Fourth, the diameter of the holes on the surface of Si substrate is about 2 μm, which is the same for all holes.

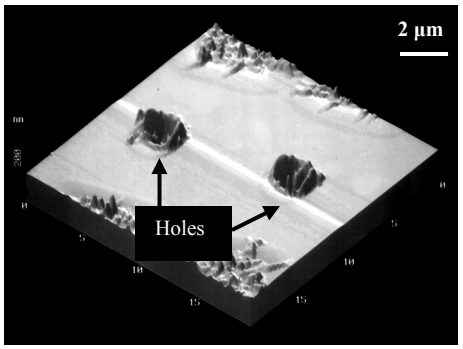

(a)

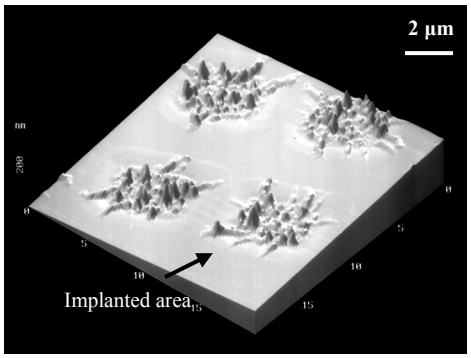

(b)

Fig. 2. AFM images showing FIB ion bombardment results on Si. (a) Two holes with 2μm diameter. (b) Implanted area with size of 5x5 μm^2.

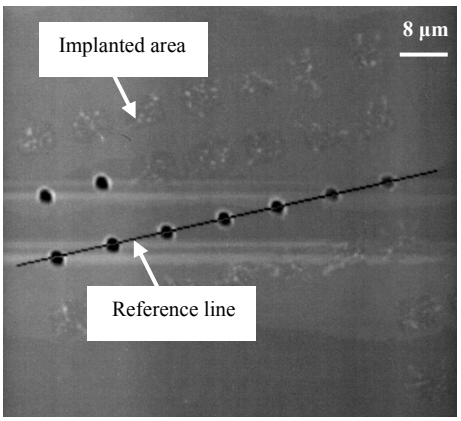

(a)

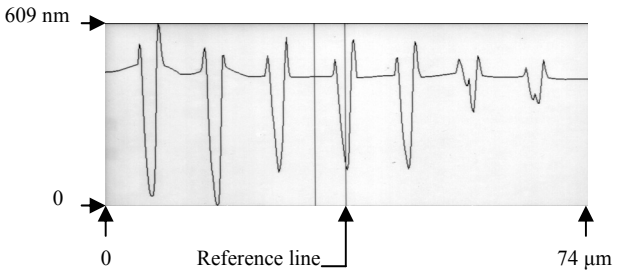

(b)

Fig. 3. Holes examined with AFM. (a) Top view. (b) Cross-sectional view.

Fig. 4 shows the relationship between dose and the depth of holes. The depths of holes were measured by AFM. Dose is used instead of dwell time, because the beam current is hard to precisely control and make it continuously stable. Fig. 4 indicates that the depth of the holes is directly proportional to the dose. This is because when the number of ions bombarded the target increases, the number of target atoms sputtered out also increases. In this case, when the beam current is 28 pA, the sputtering rate of 20-keV Ga^+ FIB ion etching with normal incident angle beam is 132 nm/minute.

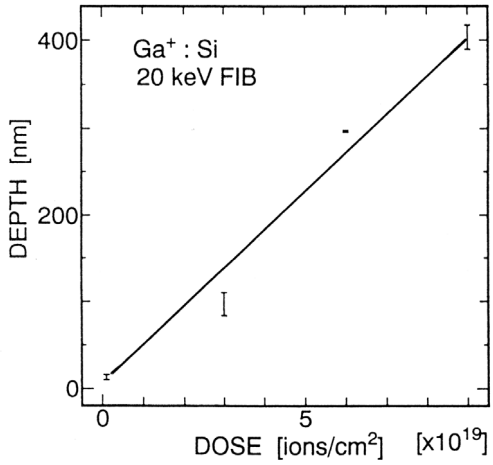

Fig. 4. The relationship between dose and the depth of holes.

In the third experiment, we used FIB to draw lines in vertical and horizontal directions on Si with different implanting time, as shown in Fig. 5. The objective is to find out the correlation between implanting time and line width. When the implanting time is 8 seconds, the line width is 1.3 μm. The line width increased to 2.7 μm, when the implanting time is 82 seconds. The dots in vertical direction are caused by the line-drawing mechanism of the FIB system, which uses a raster scan. Fig. 5(a) shows that the scan mode used in this experiment has large space between lines. With longer implanting time, each dot increases the size and connects to each other; however, the trace of raster scan still remains.

The results from all three experiments show one common issue. The size of pattern on Si is much larger than the beam diameter in specification, 0.1 μm. Although we expected that the size of pattern could be up to 0.5 μm, the results from experiments went beyond that. Hence, we need other explanations in addition to contribution from the part of ion beam with weaker intensity. Here, there are few experimental results that gave us some insight. First, the holes in Fig. 3(a) and the dots in Fig. 5(a) are not complete circles, which could make the beam diameter larger in some directions. This might be the results of beam adjustment or might be the surface charging effect caused by ion bombardment on Si, a low-conductivity material. One way to avoid the surface charging effect is by depositing thin layer of metal on the Si. Second, the line widths in the third experiment increase with the implanting time. There are two possible reasons for this. One is small vibration of the equipment, and the other is the part of ion beam with weaker intensity. In fact, it might be the combined effects of both. Due to small feature size fabricated in our experiment, even small amount of vibration might affect the line width. Third, the diameters are the same for all holes in Fig. 3. This might look contradictory to the previous fact; however, there is an explanation for this. With a few seconds of short implanting time, only the central part of beam could etch the target, so the line width is narrow. When the implanting time also increases, the part of beam with weaker intensity shows accumulated effects on the target, so the line width increases. On the other hand, when the implanting time is long enough to reach the critical value, for example, more than 1 minute for etching a hole, the diameter of the hole does not increase any further. This is because the weaker part of ion beam has already played the role.

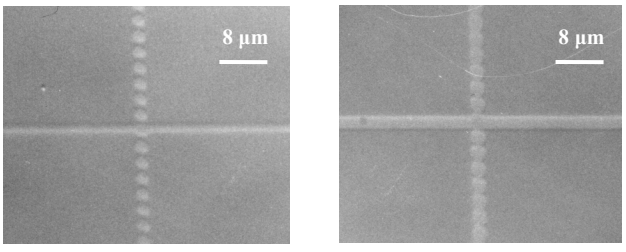

(a) (b)

Fig. 5. Lines drawn on Si with FIB. (a) Implanting time is 8 seconds. (b) Implanting time 82 seconds.

V. Conclusion

Three experiments have been done to investigate the fundamental characteristics of the FIB system and the structures on Si microfabricated with 20-keV Ga^+ FIB. The first experiment is to examine the surface topography of Si after being bombarded with FIB in dot-mode and area-mode. The results show nonuiformity on the implanted area and at the edges of the holes due to the combined effect of cascade scattering and redeposition effect. The second experiment is to find the relationship between dose and the depth of holes etched by FIB, which indicates that the depth is directly proportional to the dose. The results also show the conical shape of the holes, except when the dwell time is not long enough which the bottom of the holes would not be smooth. In addition, there were evidences of redeposition effect causing hones and faceting near the edges of the holes. The last experiment is to find out the correlation between implanting time and the width of lines, which shows that the line width is also directly proportional to the dose. However, further analysis suggests that the line width is directly proportional to the dose only when the implanting time is shorter than the critical value. In other words, the hole diameter and the line width should remain the same beyond the critical value. In addition, our analysis suggests that the discrepancies between the beam diameter and the size of fabricated structure are possibly due to surface charging effect, vibration, and the part of ion beam with weaker intensity. Further studies shall be done on other kinds of materials to confirm the analysis and obtain deeper insight in FIB system and the structures fabricated with FIB.

Acknowledgment

I would like to express my deep appreciation to Prof. H. Matsunami and everyone in Matsunami Laboratory for very fruitful discussions and providing equipments used in this research.

References

[1] J. H. Daniel, D. F. Moore and J. F. Walker, "Focused Ion Beams for Microfabrication," *Eng. Sci Edu. J*. pp. 53-56, April 1998.
[2] J. A. Doherty, B. W. Ward, and E. M. Kellogg, "Focused Ion Beams in Microelectronic Fabrication," *Trans. Components, Hybrids, and Manuf. Technol.*, vol. Chmt-6, no. 3, pp. 329-333, September 1983.
[3] D. Baselt, "The tip-sample interaction in atomic force microscopy and its implications for biological applications," *Ph.D. thesis*, California Institute of Technology, 1993.
[4] H. Ryssel and I. Ruge, *Ion Implantation*, John Wiley & Sons, UK, 1986, pp. 5-12.
[5] R. E. Chapman, "Redeposition: A Factor in Ion-Beam Etching Topography," *J. Mater. Sci.*, vol. 12, no. 6, pp. 1125-1133, June 1977.
[6] J. Melngailis, "Focused Ion Beam Technology and Applications," *J. Vac. Sci. Technol.*B, vol. 5, pp. 469-495, March 1987.
[7] Eiko Engineering, *Focused Ion Beam System User Manual*, 1995.
[8] S. Furukawa, T. Asano, *Fundamental of Ultra Microfabrication (in Japanese)*, Ohm: Japan, 1989, pp. 98-103.
[9] S. M. Sze, *VLSI Technology*, 2nd ed., McGraw-Hill: Singapore, 1988, pp.200-206.

Fuzzy Control for Robot Manipulator Based on Geometric Error

Dr Heydar Toossian Shandiz, Khalil Syahlooei
Shahrood University of Technology, Electrical Engineering Faculty
7 Th Tir Square, P.o.Box 36155-316, Shahrood, IRAN
htshandiz@shahroodut.ac.ir

Abstract- **Inverse solution of robot kinematics has many Answers. In order to have a unique solution using other criteria such as cost function for optimal situation is necessary. The task is more difficult if the assumption of rigid body not acceptable as it is in practical world. In this work a fuzzy controller is proposed to overcome the above mentioned problems. The new part of this work is using geometric error which make implementation of fuzzy controller more efficient than other methods. The result shows rapid convergence in inverse solution of robot kinematics.**

I. INTRODUCTION

Desired trajectory of robot manipulator is usually given in the Cartesian space. Whereas, the controllers are designed in joint space. It means mapping between these two spaces are necessary. This mapping for manipulator, when the joint space is converted to the Cartesian is known as kinematics. The mapping is called inverse kinematics if Cartesian space is mapped to joint space.

There are two difficulties in kinematics mapping, first due to intensive computational complexity because of coupling effects of the robots and the second is obtaining closed form solution of inverse kinematics. Differential relationship which is called Jacobian can be used to avoid solving the closed form kinematics and the inverse kinematics. The Jacobian matrix related the changing in Cartesian position or orientation and changing in joint angle. The following equation shows this relation:

$$dx = J(q).dq \qquad (1)$$

In which x is the Cartesian vector, q is the joint vector and $J(q)$ is Jacobian matrix.

Many industrial robots are like human arm. For moving hand no body solve the complex kinematics or inverse kinematics equation which related position of the links to rotation of the joints. It is the clue which led the researcher to use fuzzy logic and fuzzy controller for robot manipulator.

S. w. Kim and J. J. Lee proposed a solution method in which they have found a rough solution based on gradient method and then refine it by introducing the fuzzy logic through the extension principle [1].

Y. Xu and M. Nechiba use fuzzy method in different way to solve inverse kinematics [2]. These two groups are first researchers who start to use fuzzy method to find a fast solution of inverse kinematics.

M. T. H. Beheshti and A. K. Tehrani based on Kim and Lee work developed an adaptive fuzzy method for a robot with extra degree of freedom. They continue their work by solving the inverse kinematics of redundant robots in an environment with obstacles. Their PD fuzzy controller has been improved by considering distance from singularity points and updating the rule base [3-5].

Y. Xia and J. A Wnag, proposed a dual neural network for solving inverse kinematics differential equations [6].

E. Oyama et all, used a modular neural network to solve inverse kinematics for robot with extra degree of freedom [7].

In this work a new method based on geometrical error and fuzzy logic is proposed. The result is compared with other methods.

II. PROBLEM FORMULATIONS

Figure one shows the two links robot, which is used in this work.

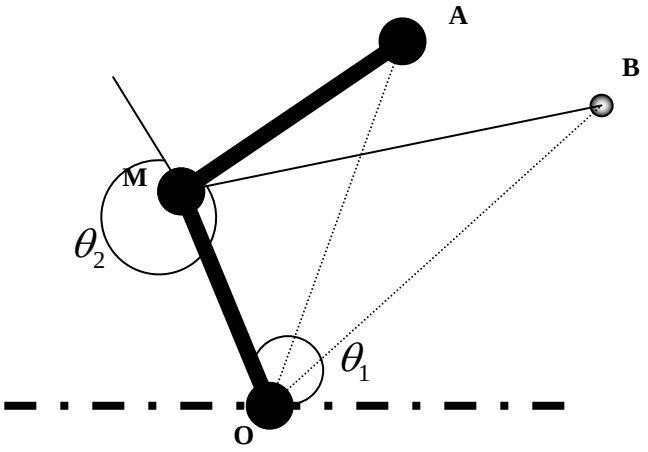

Figure 1. Two links robot

In the figure O is origin of robot, M joints two links, A is the place for actuator, B is the desired target, θ_1 and θ_2 are the joint variable for link one and two, respectively.

There are three errors which are used in this work as follow. First error is actuator error in Cartesian space, which is given by following formula:

$$\varepsilon_0 = \left| x_d(t) - x(t) \right| \quad (2)$$

In which $x_d(t)$ is desired trajectory and $x(t)$ is the position of actuator in time t. It is obvious that the smaller ε_0 means less difference between desired trajectory and real place of actuator. The second error is difference between the length of vector between origin - actuator and origin – target. The following formula explains this error in mathematics language:

$$\varepsilon_1 = \left| OA \right| - \left| OB \right| \quad (3)$$

Where $\varepsilon_1 = 0$ occurs in two situations. First the actuator is in desired place if $\varepsilon_0 = 0$ and the second by changing θ_2 it reaches to the asked position, if $\varepsilon_0 \neq 0$. The following formula shows the amount of this change:

$$\Delta\theta_2 = Arc\tan\left(\frac{AB}{2MA}\right) \quad (4)$$

Third error is difference between the length of vector between point M - actuator and point M – target. The following formula explains this error in mathematics language:

$$\varepsilon_2 = \left| MA \right| - \left| MB \right| \quad (5)$$

Where $\varepsilon_2 = 0$ occurs in two situations: the actuator is in desired place if $\varepsilon_0 = 0$ or the by changing θ_1 it reaches to the asked position, if $\varepsilon_0 \neq 0$. The following formula shows the amount of this change:

$$\Delta\theta_1 = Arc\tan\left(\frac{AB}{2OM}\right) \quad (6)$$

The output of controller increases or decreases the distance between actuator real and desired position.

III. FUZZY CONTROLLER

The basic configuration of fuzzy logic controller (FLC) in figure 2 is used in this work [8]. It has four principle parts as: fuzzification interface, a knowledge base, decision making logic and a defuzzification interface.

Fuzzification interface changes the process output errors ε_1 and ε_2 which are crisp to fuzzy data. It is mapped the inputs data into suitable linguistic values. In other word the input data is viewed as labels of fuzzy set. This is based on membership function.

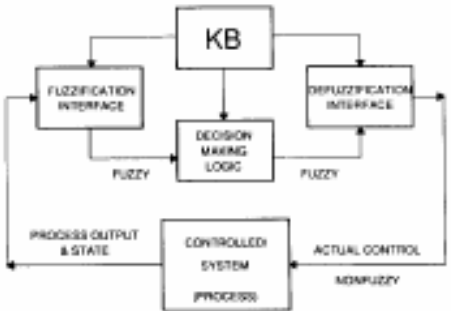

Figure 2. Basic configuration of FLC

Our experience due to simulation and reviewing other researchers work shows the triangular membership function is the best. In this work span of ε_1 is [-4 , 4] and ε_2 is [-6 , 2]. There are 9 levels for each variable as shown in figure 3.

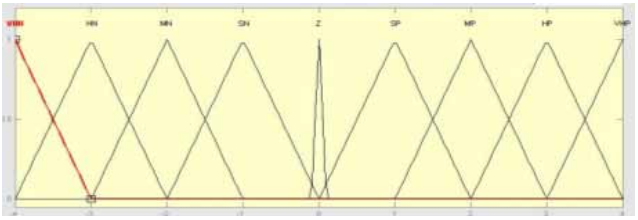

(a)

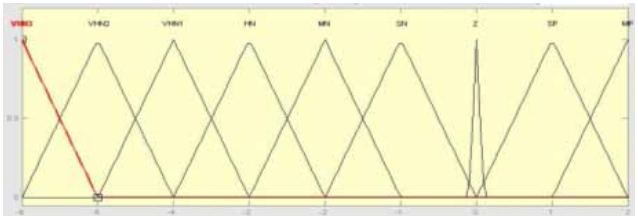

(b)

Figure 3. Membership function of (a) ε_1 and (b) ε_2

The knowledge base consists of a data base and a linguistic or fuzzy control rule base. With conditional statements all output of fuzzification are related to a set of linguistic control rule.
The two control variables which are used in rule base have the membership function as shown in figure 4.
After rejecting the redundant rule the following rules are used in this work.

If (ε_1 Is VHN) then ($\Delta\theta_2$ Is VHP)

If (ε_1 Is HN) then ($\Delta\theta_2$ Is HP)

If (ε_1 Is MN) then ($\Delta\theta_2$ Is MP)

If (ε_1 Is SN) then ($\Delta\theta_2$ Is SP)

If (ε_1 Is Z) then ($\Delta\theta_2$ Is Z)

If (ε_1 Is SP) then ($\Delta\theta_2$ Is SN)

If (ε_1 Is MP) then ($\Delta\theta_2$ Is MN)

If (ε_1 Is HP) then ($\Delta\theta_2$ Is HN)

If (ε_1 Is VHP) then ($\Delta\theta_2$ Is VHN)

If (ε_2 Is VHN3) then ($\Delta\theta_1$ Is VHN3)

If (ε_2 Is VHN2) then ($\Delta\theta_1$ Is VHN2)

If (ε_2 Is VHN1) then ($\Delta\theta_1$ Is VHN1)

If (ε_2 Is HN) then ($\Delta\theta_1$ Is HN)

If (ε_2 Is VHN3) then ($\Delta\theta_1$ Is VHN3)

If (ε_2 Is HN) then ($\Delta\theta_1$ Is VHN3)

If (ε_2 Is MN) then ($\Delta\theta_1$ Is MN)

If (ε_2 Is SN) then ($\Delta\theta_1$ Is SN)

If (ε_2 Is Z) then ($\Delta\theta_1$ Is Z)

If (ε_2 Is SP) then ($\Delta\theta_1$ Is SP)

If (ε_2 Is MP) then ($\Delta\theta_1$ Is MP)

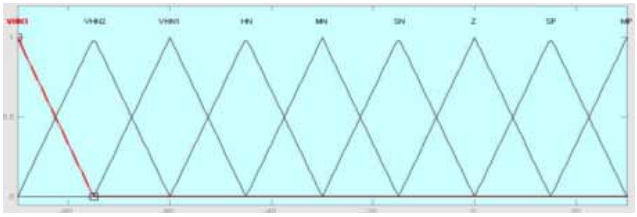

(a)

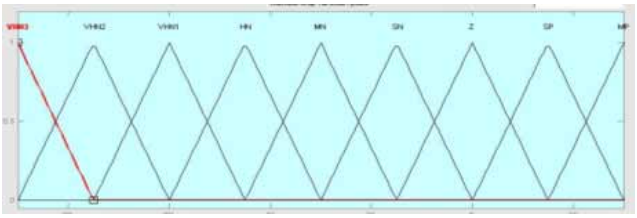

(b)

Figure 4. Membership function of (a) $\Delta\theta_1$ and (b) $\Delta\theta_2$

Decision making logic is a part in FLC which has the capability of simulating human decision making. The decision is in fuzzy form.

The last part is defuzzification part. The task of this part is exactly vice versa of fuzzification part. This part changes the fuzzy value to crisp value. In this work the center of area is used for defuzzification task.

$$\Delta\theta_i = \frac{\sum_{j=1}^{9} \mu_{\Delta\theta_i}(w_j).w_j}{\sum_{j=1}^{9} \mu_{\Delta\theta_i}(w_j)} \qquad i = 1, 2 \tag{6}$$

In which $\mu_{\Delta\theta_i}(w_j)$ is membership function of $\Delta\theta_i$ and w_j is center of jth membership function.

IV. EXPERIMENTAL RESULTS

The robot motion is simulated by using MATLAB. In order to comparing the result of proposed method with other methods sinusoidal input for Cartesian space is used. In this work 2.5 present flexibility for link and joint is considered. Figure 5 shows our result and other researcher results in best situation.

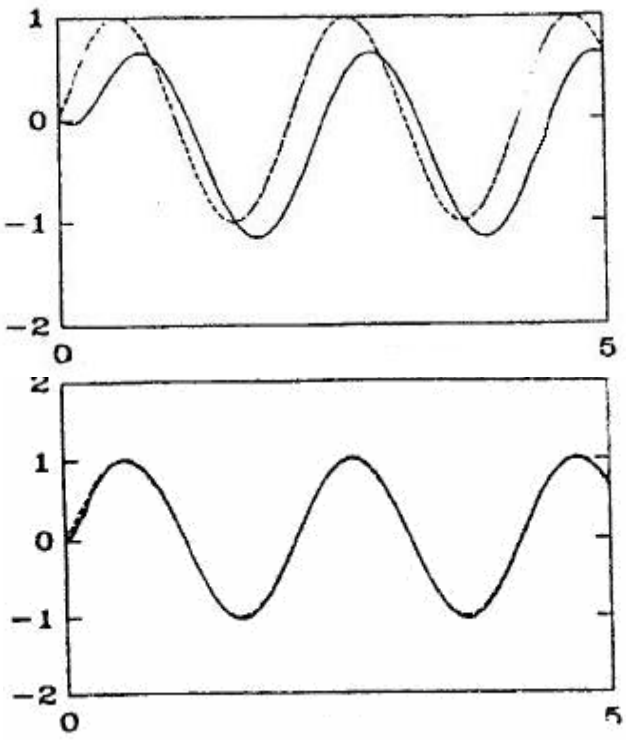

Figure 5. Researcher result (above) our result (below)

V. CONCLUSIONS

As simulation result shows our method is more accurate and faster than other method. In our simulation we considered 2.5 percent flexibility whereas other researchers assume the links and joints are rigid.

REFERENCES

[1] S. W. Kim and J. J. Lee Inverse Kinematics Solution based on Fuzzy Logic for Redundant Manipulators, *IEEE International Conference on Intelligent Robotics and Systems*, pp. 904-910, 1993.

[2] Y. Xu and M. Nechiba, Fuzzy Inverse Kinematics mapping: Rule Generation, Efficiency and Implementation, *IEEE International Conference on Intelligent Robotics and Systems*, pp. 911-918, 1993.

[3] M. T. H. Beheshti and A. K. Tehrani, An adaptive fuzzy algorithm for solving inverse kinematics of redundant robots, *IASTED international conference on intelligent systems and control*, pp. 185-188, 1998.

[4] M. T. H. Beheshti and A. K. Tehrani, Obstacle avoidance for cinematically redundant robots using an adaptive fuzzy logic algorithm, *American Control Conference*, pp. 1371-1375, 1999.

[5] M. T. H. Beheshti and A. K. Tehrani, An optimized adaptive fuzzy inverse kinematics solution for redundant manipulators, *IEEE international symposium on intelligent control*, pp. 924-929, 2003.

[6] Y. Xia and J. A Wnag, dual neural network for kinematics control of redundant robot manipulators, *IEEE Transactions on Systems, Man and Cybernetics-Part B:Cybernetics*, Vol. 31, No. 1, 2001.

[7] E. Oyama et. al, Inverse kinematics learning by modular neural networks with performance prediction networks, *IEEE International Conference on Robotics and Automation*, 2001.

[8] Lee C. C. Fuzzy Logic in Control Systems: Fuzzy Logic Controller, Parts I and II, *IEEE Transactions on Systems, Man and Cybernetics*, Vol. 20, No. 2, 1990.

Fuzzy Logic Based Embedded Controller for Control System Education

N. Jasungnuen, P. Janchaichanakun, and P.Koseeyaporn
Department of Teacher Training in Electrical Engineering
King Mongkut's Institute of Technology North Bangkok, 1518 Bangkok, THAILAND

***Abstract*-This paper presents an education tool of fuzzy logic control in embedded microcomputer applied to an undergraduate control laboratory course. A control script interpreter is implemented on the embedded side allowing flexibility in changing control algorithm so that controller design skill can be achieved in training program. To simplify the usability for undergraduate level, graphic user interface for PC is developed. Therefore, the controller parameters such as membership functions and rule base can be designed with less effort. Communication between PC and embedded module provides transferring information of controller to the embedded side and retrieving the control result from embedded part to the PC for graphically observation. The system model implementation for testing the controller in embedded module is based on operational amplifier circuit. The results show that the implemented software and hardware is suited for control system training.**

***Index Terms*-Embedded microcomputer, fuzzy logic controller.**

I. Introduction and Background

Fuzzy logic, or fuzzy set theory, was fist present by Zedah [1]. Since then, many applications of fuzzy logic have been revealed continuously. Fuzzy logic controller is also widely used especially for imprecise and nonlinear systems [2]. As in academic part, classical control is rather been focused. Mathematical model of the system has to be known in order to design a well-matched controller. On the other hand, mathematical model of the system is not required for designing of fuzzy logic controller. Instead, the well-knowledge of system behavior is needed. In order to allow academic training program to catch up the recent technology, a laboratory tool of fuzzy logic control for DC brushless motor has been introduced [3]. For undergraduate level, migrating knowledge of linear control to the complex approach may have some difficulty. Simplification of the gap between linear and nonlinear control is needed. Another aspect is that the cost of laboratory tool for training program is high. For these reasons, an effortless and low cost training tool is required. As described in [4], one choice of implementing such a low cost computation tool for control system is embedded system. It has the capability that is similar to personal computer (PC). There is one benefit of using embedded module for academic program. Because the embedded system has already been employed in industrial sector, the training program that uses embedded module will make the students get familiar to this kind of technology.

In this paper, an ease-of-use tool for designing of fuzzy logic controller is introduced. A set of training tool for undergraduate control laboratory based on embedded system is implemented.

II. Embedded Microcomputer

Embedded module is compact and low cost. As almost the same capability as PC, embedded module is widely used in manufacturing. Engineering training of embedded module is, therefore, required. The training covers programming and interfacing skill. The embedded module consists of CPU, RAM, and communication ports. The embedded module employed here is the Mity Mite CPU 386XS module, which can be operated under MS-DOS operating system. The program implemented in this embedded module can be achieved by using C++ compiler under DOS operating system. Communication port provides sending and receiving data between PC and embedded module via general SOCKET communication. Fig.1 shows the embedded module applied in this work.

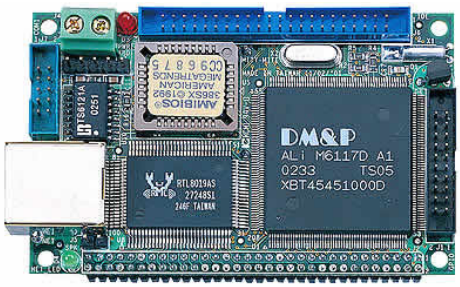

Figure 1. Embedded system module.

III. Fuzzy Logic Controller

Unlike classical control scheme, fuzzy logic control use linguistic terms to represent quantity of the inputs and outputs. In addition, mapping between input and output is another important part. To this, a well understanding between input and output is needed. Fuzzy logic controller is composed of three parts; fuzzification, inference engine, and defuzzification part as can be seen in Fig. 2. Fuzzfication behaves as an interpreter. It interprets the numerical quantity into fuzzy meaning. Fuzzy meaning can be composed of several levels.

Each level, so called fuzzy membership function, may cross the boundary of another fuzzy membership function. Each membership function may be a form of triangle, a trapezoid, or bell shape. For simplicity, triangle is often chosen as

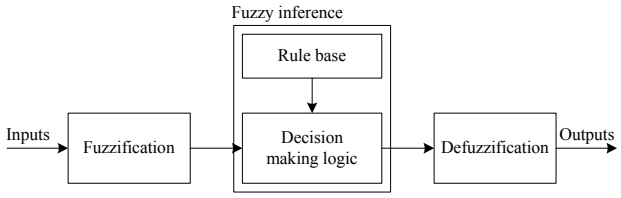

Figure 2. Fuzzy logic controller block diagram

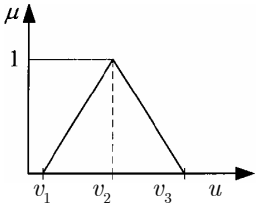

Figure 3. Triangle membership function

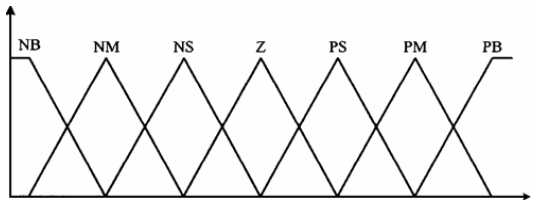

Figure 4. Seven levels of fuzzy membership function.

$$\mu(u_i) = \begin{cases} \dfrac{u_i - v_1}{v_2 - v_1}, & v_1 \le u_i \le v_2 \\ \dfrac{v_3 - u_i}{v_3 - v_2}, & v_2 \le u_i \le v_3 \\ 0, & otherwise. \end{cases} \quad (1)$$

where the graphical view of this function is shown in Fig. 3.

To fuzzify input quantity to linguistic terms, a set of membership function as in Fig. 4 is used. Each membership function represents the fuzzy level of input such as negative big (NB), negative medium (NM), negative small (NS), zero (Z), or positive small (PS). Based on this fuzzy linguistic, fuzzy inference will map the relation between inputs and output linguistic in term of database provided by expert. The evaluation of this process is based on logical decision-making scheme. The database in this inference engine is so called rule-base. The rule-base is typically a text or linguistic format which is in logical form such as "and" or "or" relation. Finally, defuzzification will transfer the linguistic output to the numerical format. The output (u_o) is generally evaluated by averaging of the individual centroid corresponding to their weight as

$$u_o = \frac{\sum_{i=1}^{n} u_i \mu(u_i)}{\sum_{i=1}^{n} \mu(u_i)} \quad (2)$$

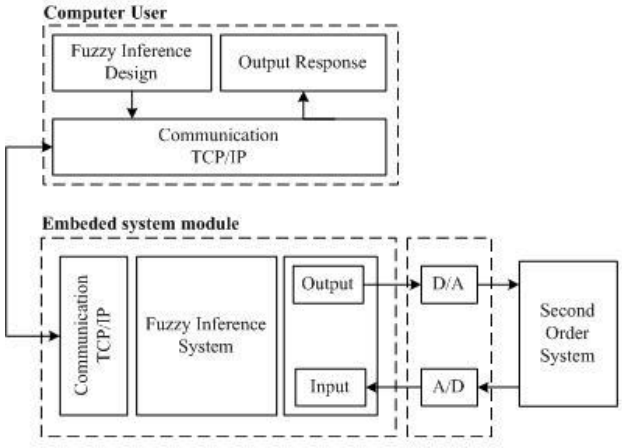

Figure 5. System communication

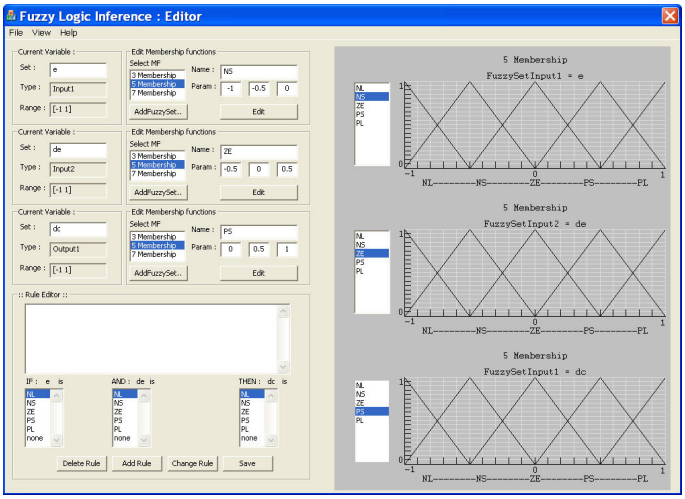

Figure 6. FLC setup window.

IV. Design of System and Program

As shown in Fig. 5, the designed system is composed of three parts, PC program, embedded module, and linear system model in operation amplifier circuit. The PC part allows user to conveniently design FLC. This can be done by providing a Graphic User Interface (GUI) implemented by using Visual C++ compiler as the result shown in Fig. 6. The user can specify number of membership function and the details of the membership function. Rule base can be also added by simply selecting the membership functions at both input and output sides. The results of design FLC can be exported into file and displayed as shown in Fig. 7.

The second part is the embedded module, which receives the information setting of FLC in text format file from PC side where the communication between embedded module and PC is based on SOCKET communication. After the file is loaded into the embedded module, the embedded module is ready to provide the output the system via digital to analog interface as shown in Fig. 8 (right). The systems as shown in Fig. 8 (left) consist of first-, second-, and third-order circuits built from operational amplifiers. The parameters of the system models can be adjusted so that the students can practice different type of system characteristic. An example of system step response

is illustrated in Fig. 9. Additionally, the input and output ports of the embedded system allows user to choose the program to run according the laboratory instruction. The result at the embedded side can be sent back to the PC side so that the user can observe the result graphically as shown in Fig. 10.

V. Experimentation Procedure

The procedure of experiment performing is based on learning objective orientation including controller design and embedded interfacing skill. The students are assigned to adjust controller parameters based on different types of system in actual circuit models. By using the graphical tool described previously, the controller can be designed rapidly resulting in saving time while the understanding is still permitted. The second step is to save the designed result to the embedded module. After that, the module will be ready to plug into the system circuit models. The result of testing of output is then ready to be loaded into the PC side for observing the response. Finally, the discussion and report will be made or more experiment can be performed repeatedly.

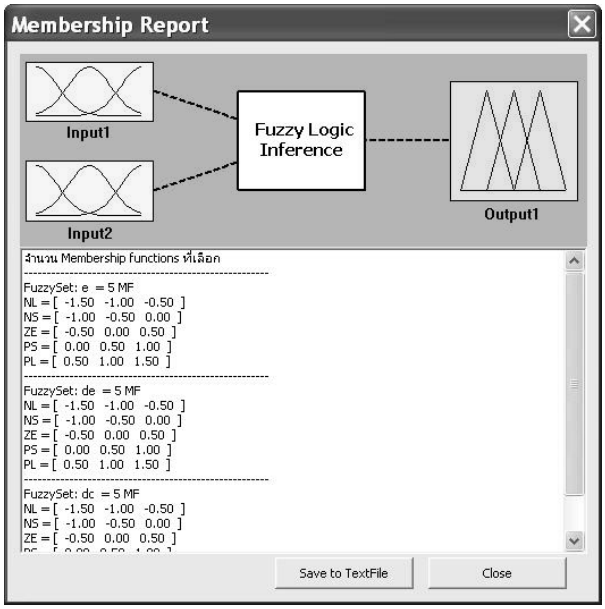

Figure 7. Window showing the results of the designed FLC.

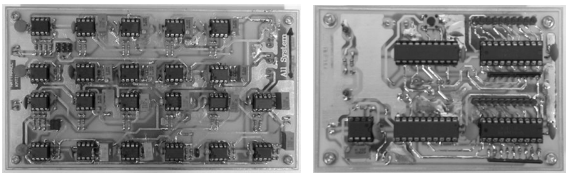

Figure 8. System model (left) and A/D, D/A circuit board (right).

VI. Conclusion

A tool for training of fuzzy logic controller and embedded system is presented. It has the benefit of low cost and effective training tool. The learning objectives cover programming skill, controller design, and embedded application. The students are motivated to link their knowledge of linear control system to the fuzzy type of controller resulting in broader knowledge. The laboratory allows gaining in experience in recent technology. The flexible structure of the embedded system provides higher efficiency in training tool, reusability in different type of controller design training.

References

[1] L. A., Zadeh, "Fuzzy Sets", *Information and control*. New York: Academic, 1965, vol. 8, pp. 338-353.

[2] Xiping Zhang, et al., "Multi-parameter Decision-making in Complex Systems," IEEE International conference on Systems, Man, and Cybernetics, vol. 1, 14-17 Oct. 1996, pp. 99-101.

[3] M.A. Akcayol, A. Cetin and C. Elmas, "An Education Tool for Fuzzy Logic-Controlled BDCM," *IEEE Transaction on Education*, vol. 45, No 1, February, 2002, pp 33-42.

[4] J.S. Freudenberg and b.H. Hrogh, "Industry needs for Embedded Control Education," American Control Conference, OR, USA, Jun. 8, 2005, pp. 4543-4550.

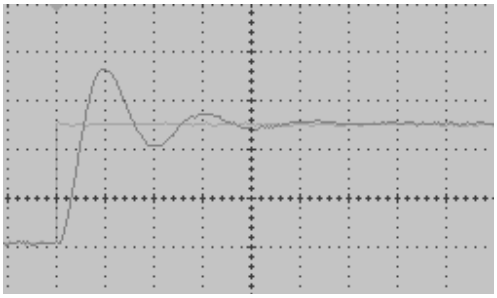

Figure 9. Example of system step response.

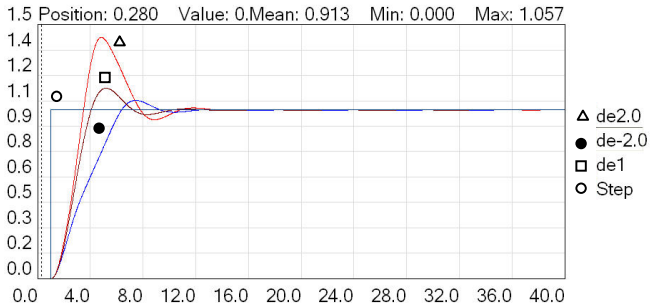

Figure 10. Graphical output on PC side.

Electromagnetic Flux Density Controlled by Fuzzy Logic Method

Satean Tunyasrirut and Santi Wangnipparnto
Faculty of Engineering, Pathumwan Institute of Technology,
833 Ram 1 Rd, Pathumwan, Bangkok, 10330, Thailand.

***Abstract*- This research studies on the electromagnetic flux density controlled by fuzzy logic method as well as to control a working process with the utilization of aISA-A57 interfacing card. Regarding to control a personal computer is used through DOS operational system. Spontaneously, the aISA-A57 card (D/A, A/D & I/O Interfacing Board) with the utilization of Borland C++ 5.0 programming language. From the experiment shown that the design fuzzy logic control at 0-5 volt able to control the electromagnetic flux density in 0-90 millitesla by using the response time less than 0.23 second and has steady error less than ± 3 % of error over all.**

I. INTRODUCTION

Nowadays, the various parameters in the process of industrial are controlled such as temperature, level, and etc. Some process needs to keep the electromagnetic flux for control the position, force, and speed of the equipments such as the motor, solenoid valves, electric train, and etc. The objective of the controller is to maintain a electromagnetic flux set point at a given value and be able to accept new set point values dynamically. The conventional proportional-integral-derivative (PID) is commonly utilized in control, but the parameter of its must be turned by tuning method either in time response of frequency response to meet their required performances[1],[2]. On the other hand, the fuzzy controller is also popularly implemented in many practical industrial automation applications. In this paper presents design and implements the fuuzy logic controller for control electromagnetic flux. The aim of this paper is two-fold. The first is shown the dynamics response of system when changes the step set point and see the steady state errors. The second shown the phenomena effect of the iron powder under the magnetic flux density.

II. THEORY

Magnetic flux density(B)

When a electric current flows through a conductor (copper wire), it generates a magnetic field. Arrangement the conductor on the magnetic materials such as the soft iron as shows in Fig. 1, the magnetic material's atomic parts will align in a certain direction and send the magnetic field is perpendicular to the direction of current flow and its direction is given by the right hand rule. The flux density(B) is given by the flux passing

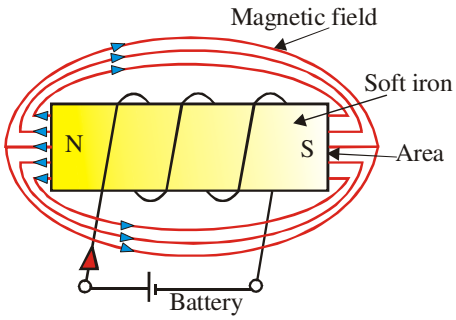

Fig. 1. Magnetic flux density.

per unit area through a place at right angle to the flux as defined as

$$B = \varnothing/A \quad (1)$$

The unit of magnetic flux density is called gauss or Tesla. 1 Tesla is10,000 gauss and using the letter for Flux is "B"

The relationship between B and H may be written

$$B = \mu H = \mu_0 \mu_r H \quad (2)$$

Where: μ_r is the relative permeability of the material. and μ_0 is the magnetic permeability of free space [$4\pi x10^{-7}$ H/m].
H is the field strength at any point within a magnetic field and it is a function of input current so we can control the flux density by adjust the current that passing the conductor.

Fuzzy logic controller

The structure of the proposed magnetic flux control system is shown in Fig. 2.

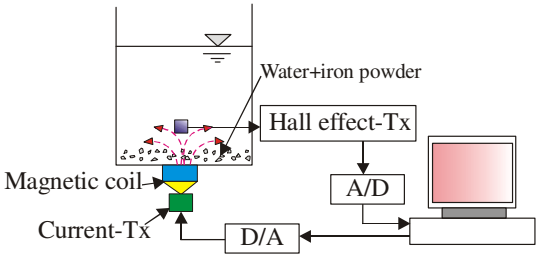

Fig. 2. The proposed magnetic flux system.

The input of fuzzy logic controller is the magnetic flux density error(e) between the set point and the process variable. The fuzzy logic controller consists of fuzzification, fuzzy inference,and defuzzification stages as shown Fig. 3. The number of membership functions for each input variable is designated in five ranges and the names of them are positive large /positive small/zero/negative small/ negative large. The fuzzy controller output has 25 membership functions. The form of all input and output membership functions are selected to be triangle-shaped functions for simplicity. In fuzzification stages, the input variables, the position is converted into fuzzy variables using the membership function as shown in Fig. 4. The linguistic rules of e and ce of temperature are shown in Table 1.

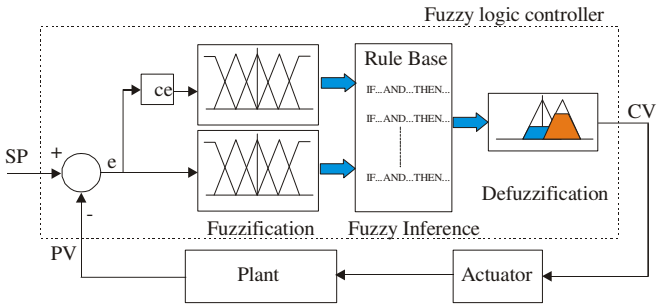

Fig. 3. Block diagram of fuzzy logic controller.

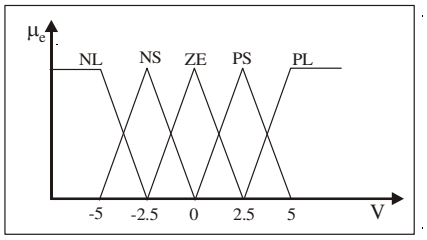

a.)

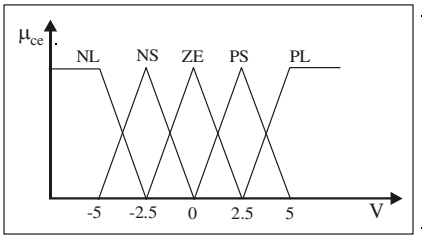

b.)

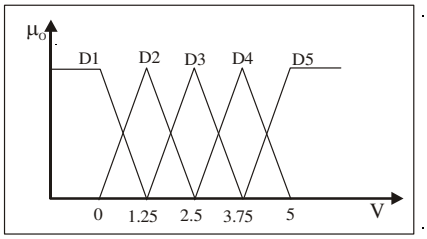

c.)

Fig. 4. Membership function of input and output variables of the magnetic flux density control. .

TABLE 1.
Control rules for input and output variables

ce / e	NL	NS	ZE	PS	PL
NL	D1	D1	D1	D1	D1
NS	D2	D2	D2	D2	D2
ZE	D3	D3	D3	D3	D3
PS	D4	D4	D4	D4	D4
PL	D5	D5	D5	D5	D5

The defuzzificating operation, in this paper, uses the centroid defuzzification method because of its implementation simplicity.

III. EXPERIMENTAL SETUP

The experimental set up consists of the hardware such as personal computer, the aISA-A57 card (D/A, A/D & I/O Interfacing Board), the beaker size 1000 ml that filling the water and the iron powder, hall effect sensor, V to I transmitter, and magnetic flux density generator as shown in Figure 5 and the software programming language using the Borland C++ 5.0. The calibration of the hall effect sensor is shown in Fig. 6.

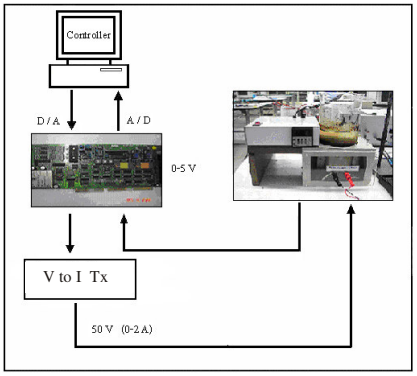

Fig. 5. The experimental setup.

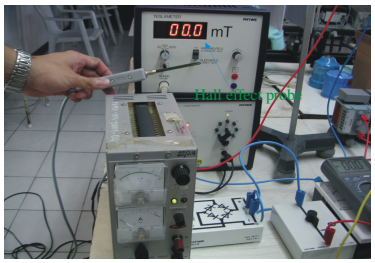

Fig. 6. The calibration of the hall effect sensor setup.

IV. Experimental Results

The experimental results in this paper can be divided in two parts, the first shows performance of the fuzzy logic controller, the second shows the effect of iron power under maagnetic field.

A. Tthe magnetic flux density control by fuzzy logic controller

The responses time and steady state error of the temperature control when changing the step set point from 20mT to 90mT and 90mT to 20mT are shown in Fig. 7. and Figure.8 respectively. The Table 2 shows the responses time and steady state error at another the step set point and found that the response time less than 0.23 second and has steady error less than ± 3 % of error over all.

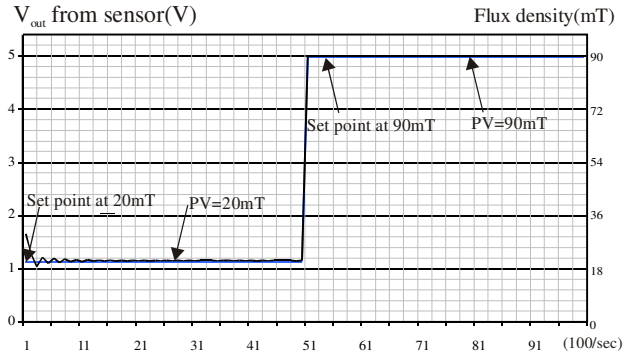

Fig. 7. Changing the step set point from 20mT to 90mT.

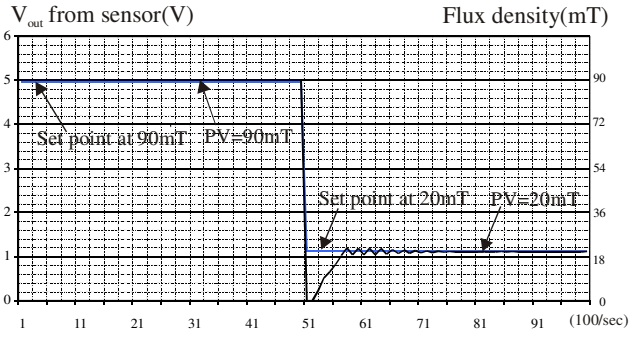

Fig. 8. Changing the step set point from 90mT to 20mT.

TABLE 2.
Performance of the fuzzy logic controller when changing the flux density step set point.

Step set point [mT]	Response time [sec]	Steady state error [%]
20-30	0.23	1
20-40	0.18	0.125
20-50	0.2	0.54
20-60	0.19	1
20-70	0.18	0.17
20-80	0.18	0.112
20-90	0.01	0.02
90-20	0.22	2
90-30	0.2	0.66
90-40	0.2	1
90-50	0.21	1.4
90-60	0.16	1
90-70	0.16	0.28
90-80	0.21	0.375

B. Effect of iron power under maagnetic field.

When applied the maagnetic flux density 90 mT on the iron powder that mixed with the water in the beaker size 1000 ml, we found that the iron powder will extend following the magnetic line and after cut off magnetic flux density, the iron powder will falling to the bottom of the beaker by gravity force, so we can be using this effect to enhancement heat transfer in the beaker.

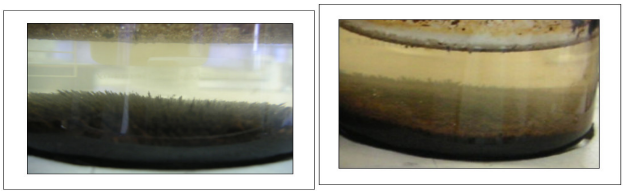

a,) b.)

Fig. 9. The phenomena of iron powder under magnetic field.
a.) has maagnetic flux density b.) no maagnetic flux density

V. Conclusion

The fuzzy logic controller has been proposed control the electromagnetic flux density passing the beaker to the water that mixed the iron powder. It has been shown that when changing the flux density set point, the response time less than 0.23 second and has steady error less than ± 3 % of error over all. The effect of magnetic field force can be done the the magnetic materials movement in the liquid so we can apply its to enhancement heat transfer in the system or another applications.

ACKNOWLEDGMENT

The authors gratefully acknowledge the Mr. Teerawat Maneedang and Mr. Attapon Panyo who testing the experimental apparatus hardly.

REFERENCES

[1] J.G.Ziegler and N.B.Nichols, "Optimum settings for automatic controller," ASME Trans. Vol64, pp.759-768, 1942.

[2] W.K.Ho, C.C. Hang, and J.H.Zhou, "Performance and gain and phase margins of well-known PI Tuning formulas," acceptedfor publication in IEEE Trans. Contr. Syst. Technol., 1995.

[3]..Wangnipparnto, S., Srikwankeaw,P.,and Thong-o, S., "Relative Humidity Controlled by Fuzzy Logic Control", Prince of Songkla university, 8-9 December, pp44, 2004.

Fuzzy I-PD Controller for Two-Link Robot Manipulator

Wicharn Chatrattanawuth[1], Songmoung Nundrakwang[1], Taworn Benjanarasuth[1],
Jongkol Ngamwiwit[1] and Noriyuki Komine[2]
[1] Faculty of Engineering and ReCCIT, King Mongkut's Institute of Technology Ladkrabang, Bangkok, Thailand
(Tel: +662-739-2405, E-mail: knjongko@kmitl.ac.th)
[2] School of Information Science and Technology, Tokai University, Kanagawa, Japan
(Tel: +81-463-58-1211, E-mail: komine@keyaki.cc.u-tokai.ac.jp)

***Abstract*-This paper presents a fuzzy I-PD controller for two-link robot manipulator. The proposed controller consists of a Mamdani fuzzy I and a Mamdani fuzzy PD controller and its parameters are adjusted to make the manipulator follow to desired trajectory. The experimental results in controlling the two-link robot manipulator by using the proposed fuzzy I-PD controller with the same parameters (proportional gain, integral gain and derivative gain) as the conventional I-PD controller are also shown in this paper.**

I. INTRODUCTION

The most well-known and widely used controllers in the industries are the conventional PID-family controllers. The good points of the PID type controllers are the simple in adjusting their parameters to meet the desired control system performances by using the tuning method such as Zeigler-Nichols' (Z-N) tuning formula or coefficient diagram method (CDM) [1-2]. However, when the PID controller is used to control the nonlinear system such as a manipulator system, it is difficult to achieve the desired trajectory, since the manipulator systems contain uncertain components.

Recently, the fuzzy logic controller has been used in control system when the mathematical model of the process is vague or exhibits uncertainties or when PID-family controller can not generate the satisfactory performance [3]. However, due to popularity and simplicity of PID type controller, fuzzy PID-family controllers have been also employed in control system by combining the merits of both controllers.

It is known that I-PD controller has a property to avoid large changes in control signal due to the proportional and derivative actions when there is a sudden change in the reference input. Therefore, a fuzzy I-PD controller, which is the modification of conventional I-PD controller structure, is presented in this paper. Firstly, the conventional I-PD controller is divided into I controller part and PD controller part. After rearranging the structure of I and PD controllers, they will be constructed as a Mamdani fuzzy I controller and a Mamdani fuzzy PD controller. The inputs of Mamdani fuzzy I controller will consist of two inputs, error and change of error, and Mamdani fuzzy PD controller will consist of two inputs, output and change of output. The control signal of the controller is the subtraction value of the output of Mamdani fuzzy I controller and Mamdani fuzzy PD controller. The proposed controller is implemented to control two-link robot manipulator. The experimental results are shown that the parameters of Mamdani fuzzy I-PD controller can be adjusted to make the manipulator follow desired trajectory. The experimental results are also shown by comparing the proposed fuzzy I-PD controller to the conventional I-PD controller where the values of proportional gain, integral gain and derivative gain of fuzzy and conventional controllers are identical.

II. TWO-LINK ROBOT MANIPULATOR

In Fig. 1, when the effect of gravity is negligible, the Lagrange dynamics of the two-link robot manipulator is [4]

$$M(q)\ddot{q} + V(q,\dot{q}) + F(\dot{q}) + \tau_d = \tau \tag{1}$$

where $q, \dot{q}$ and $\ddot{q} \in R^2$ are joint angle, velocity and acceleration vectors, $M(q) \in R^{2x2}$ is the inertia matrix, $V(q,\dot{q}) \in R^2$ is the Coriolis/centripetal torque vector, $F(\dot{q})$ is the friction, τ_d and $\tau \in R^2$ are disturbance and input torque vectors. The term $M(q)$ and $V(q,\dot{q})$ in dynamic equations (1) are given by

$$M(q) = \begin{bmatrix} J_1 + J_2 + 2rC_2 & J_2 + rC_2 \\ J_2 + rC_2 & J_2 \end{bmatrix} \tag{2}$$

and

$$V(q,\dot{q}) = \begin{bmatrix} -rS_2(2\dot{q}_1\dot{q}_2 + \dot{q}_2^2) \\ rS_2\dot{q}_1^2 \end{bmatrix} \tag{3}$$

where $J_1 = I_1 + m_1 a_1^2 + m_2 \ell_1^2$, $J_2 = I_2 + m_2 a_2^2$, $r = m_2 \ell_1 a_2$, $C_2 = \cos q_2$, $S_2 = \sin q_2$ and $q = [q_1 \; q_2]^T$. $F(\dot{q})$ is assumed to be zero.

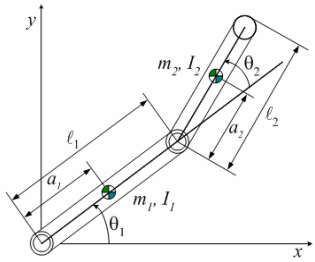

Figure 1. Structure of two-link robot manipulator (top view).

Fig. 2 shows the SCARA type robot manipulator which will be used in the experiments. The mass and the length of robot arms are m_1 = 4.37 kg, m_2 = 1.24 kg, $\ell_1 = \ell_2 = 200$ mm,

$a_1 = 63$ mm and $a_2 = 80$ mm. Maximum torque of the 1st and the 2nd joint are 70 Nm and 15 Nm when the maximum torque commands are produced at ±8 V by 2 channels 24 bits D/A PC interface card. Optical encoders of the 1st joint and the 2nd joint are 614,400 and 507,904 pulse/rev.

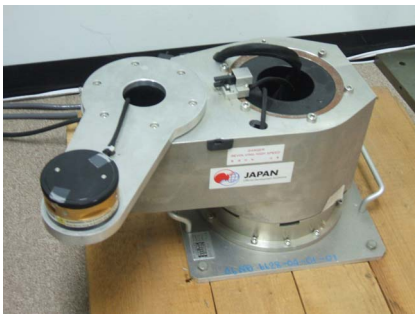

Figure 2. SCARA type robot manipulator.

III. FUZZY I-PD CONTROL SYSTEM

The conventional I-PD controller and fuzzy I-PD control system structure which composes of a Mamdani fuzzy I controller and a Mamdani fuzzy PD controller, will be describe in this section.

A. Conventional I-PD Control System Structure

The conventional I-PD control system which consists of a plant, an integral controller and a PD feedback controller, is shown in Fig. 3. Here, K_i is the integral gain of the integral controller, and K_p and K_d are the proportional gain and derivative gain of the PD controller respectively.

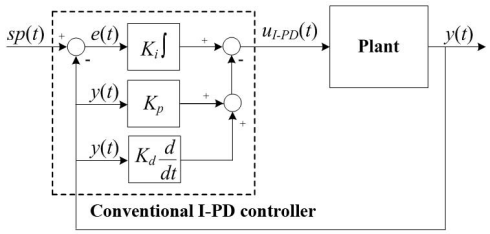

Figure 3. Conventional I-PD control system structure.

The control signal of the conventional I-PD controller of the control system shown in Fig. 3 can be expressed as

$$u_{I-PD}(t) = K_i \int_0^t e(t)dt - K_p y(t) - K_d \frac{dy(t)}{dt} \tag{4}$$

where $e(t)$ is the error signal and $y(t)$ is the output signal of the control system. After rearranging (4), it can be rewritten as

$$u_{I-PD}(t) = u_I(t) - u_{PD}(t) \tag{5}$$

where

$$u_I(t) = K_i \int_0^t e(t)dt \tag{6}$$

and

$$u_{PD}(t) = K_p y(t) + K_d \frac{dy(t)}{dt}. \tag{7}$$

The control signal of the system $u_{I\text{-}PD}(t)$ in (5) can be transformed into discrete time as

$$u_{I-PD}(nT) = u_I(nT) - u_{PD}(nT) \tag{8}$$

where T denotes the sampling time.

B. Fuzzy I-PD Control System Structure

The structure of the fuzzy I-PD control system shown in Fig. 4 consists of a process and a fuzzy I-PD controller which is the modification of the conventional I-PD controller. The control signal of the fuzzy I-PD controller $u_{I\text{-}PD}(nT)$ is the subtraction of Mamdani fuzzy I control signal and Mamdani fuzzy PD control signal.

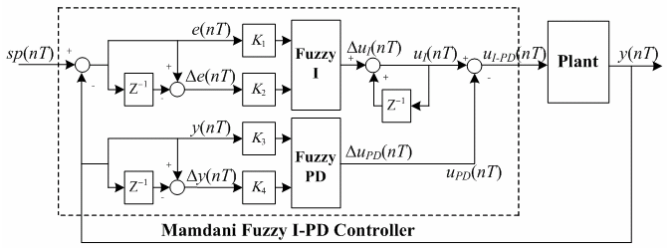

Figure 4. Fuzzy I-PD control system structure.

The output of Mamdani fuzzy I controller $u_I(nT)$ can be computed from (6) by approximating the integral term with the trapezoidal summation. Therefore

$$u_I(nT) = K_1 e(nT) - K_2 \Delta e(nT) + u_I(nT - T) \tag{9}$$

where the error $e(nT) = sp(nT) - y(nT)$, the change of error $\Delta e(nT) = e(nT) - e(nT\text{-}T)$, $K_1 = K_i T$ and $K_2 = K_i T/2$. When the term $K_1 e(nT) - K_2 \Delta e(nT)$ is replaced by $\Delta u_I(nT)$, the new output of Mamdani fuzzy I controller can be obtained as

$$u_I(nT) = \Delta u_I(nT) + u_I(nT - T) \tag{10}$$

where $\Delta u_I(nT)$ is the output change of fuzzy I controller whose inputs are $K_1 e(nT)$ and $K_2 \Delta e(nT)$.

In the same manner, the output of Mamdani fuzzy PD controller $u_{PD}(nT)$ can be directly computed from (7) by approximating the derivative term with two-point difference form. Then

$$u_{PD}(nT) = K_3 y(nT) + K_4 \Delta y(nT) \tag{11}$$

can be obtained, where $y(nT)$ is the output, $\Delta y(nT)$ is the change of output, $K_3 = K_p$ and $K_4 = K_d/T$. Define $\Delta u_{PD}(nT)$ to be $K_3 y(nT) + K_4 \Delta y(nT)$, the new output of Mamdani fuzzy PD controller becomes

$$u_{PD}(nT) = \Delta u_{PD}(nT). \tag{12}$$

IV. FUZZY I-PD CONTROLLER DESIGN

In this section, the Mamdani fuzzy I controller and the Mamdani fuzzy PD controller design will be described. The fuzzification, fuzzy rules and defuzzification are needed for designing the fuzzy controllers.

A. Fuzzification

In fuzzification, $K_1e(nT)$ and $K_2\Delta e(nT)$ are the Mamdani fuzzy I controller inputs and $K_3y(nT)$ and $K_4\Delta y(nT)$ are the Mamdani fuzzy PD controller inputs. Input scaling uses two input membership functions (n : negative and p : positive). Since the fuzzy I and fuzzy PD controllers have similar structure, the membership functions of all inputs are similarly selected with the adjustable constant L as shown in Fig. 5.

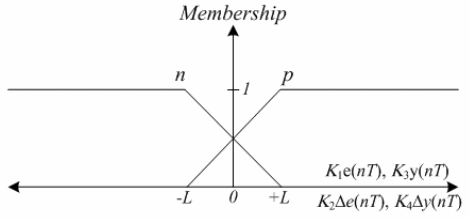

Figure 5. Input membership functions.

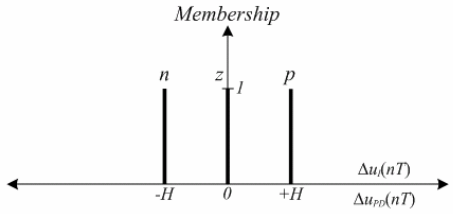

Figure 6. Output membership functions.

B. Fuzzy Rules

The output membership functions for Δu_I and Δu_{PD} are shown in Fig. 6. Three output membership functions are used (n : negative, z : zero and p : positive), where H is the adjustable constant. Based on the input membership functions in fuzzification stage and these output membership functions, the fuzzy control rules for the Mamdani fuzzy I controller are

R^1: IF $K_1e(nT)$ is n & $K_2\Delta e(nT)$ is n THEN $\Delta u_I(nT)$ is n
R^2: IF $K_1e(nT)$ is n & $K_2\Delta e(nT)$ is p THEN $\Delta u_I(nT)$ is z
R^3: IF $K_1e(nT)$ is p & $K_2\Delta e(nT)$ is n THEN $\Delta u_I(nT)$ is z
R^4: IF $K_1e(nT)$ is p & $K_2\Delta e(nT)$ is p THEN $\Delta u_I(nT)$ is p.

Similar rules are also applied for assigning the Mamadani fuzzy PD controller. Hence,

R^1: IF $K_3y(nT)$ is n & $K_4\Delta y(nT)$ is n THEN $\Delta u_{PD}(nT)$ is n
R^2: IF $K_3y(nT)$ is n & $K_4\Delta y(nT)$ is p THEN $\Delta u_{PD}(nT)$ is z
R^3: IF $K_3y(nT)$ is p & $K_4\Delta y(nT)$ is n THEN $\Delta u_{PD}(nT)$ is z
R^4: IF $K_3y(nT)$ is p & $K_4\Delta y(nT)$ is p THEN $\Delta u_{PD}(nT)$ is p.

C. Defuzzification

The centroid defuzzifier is used to calculate the output change $\Delta u_I(nT)$ of the Mamdani fuzzy I controller and $\Delta u_{PD}(nT)$ of the Mamdani fuzzy PD controller. The defuzzification results are respectively obtained from

$$\Delta u_I(nT) = \frac{\sum_{r=1}^{4} \mu_{I_r} \Delta u_{I_r}}{\sum_{r=1}^{4} \mu_{I_r}} \text{ and } \Delta u_{PD}(nT) = \frac{\sum_{r=1}^{4} \mu_{PD_r} \Delta u_{PD_r}}{\sum_{r=1}^{4} \mu_{PD_r}}, \qquad (13)$$

where μ_{I_r} and μ_{PD_r} are the membership values at the r^{th} rule, Δu_{I_r} and Δu_{PD_r} are the singleton outputs at the r^{th} rule.

Fig. 7 and Fig. 8 show the input spaces of Mamdani fuzzy I and Mamdani fuzzy PD controller that can be decomposed into 12 different input spaces (ICs). The results of $\Delta u_I(nT)$ and $\Delta u_{PD}(nT)$ are obtained by applying defuzzification algorithm (13) to each membership area. The expressions of $\Delta u_I(nT)$ and $\Delta u_{PD}(nT)$ in IC1 to IC12 are shown in Table 1.

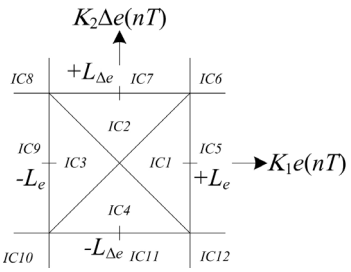

Figure 7. Input spaces of fuzzy I controller.

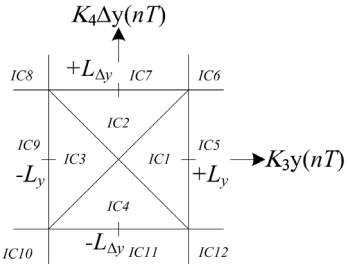

Figure 8. Input spaces of fuzzy PD controller.

TABLE I
IC1 to IC12 for $\Delta u_I(nT)$ and $\Delta u_{PD}(nT)$

IC#	$\Delta u_I(nT)$	$\Delta u_{PD}(nT)$
IC1	$\frac{2HL_{\Delta e}K_1e(nT)+2HL_eK_2\Delta e(nT)}{8L_eL_{\Delta e}-4L_{\Delta e}K_1e(nT)}$	$\frac{2HL_{\Delta y}K_3y(nT)+2HL_yK_4\Delta y(nT)}{8L_yL_{\Delta y}-4L_{\Delta y}K_3y(nT)}$
IC2	$\frac{2HL_{\Delta e}K_1e(nT)+2HL_eK_2\Delta e(nT)}{8L_eL_{\Delta e}-4L_eK_2\Delta e(nT)}$	$\frac{2HL_{\Delta y}K_3y(nT)+2HL_yK_4\Delta y(nT)}{8L_yL_{\Delta y}-4L_yK_4\Delta y(nT)}$
IC3	$\frac{2HL_{\Delta e}K_1e(nT)+2HL_eK_2\Delta e(nT)}{8L_eL_{\Delta e}+4L_{\Delta e}K_1e(nT)}$	$\frac{2HL_{\Delta y}K_3y(nT)+2HL_yK_4\Delta y(nT)}{8L_yL_{\Delta y}+4L_{\Delta y}K_3y(nT)}$
IC4	$\frac{2HL_{\Delta e}K_1e(nT)+2HL_eK_2\Delta e(nT)}{8L_eL_{\Delta e}+4L_eK_2\Delta e(nT)}$	$\frac{2HL_{\Delta y}K_3y(nT)+2HL_yK_4\Delta y(nT)}{8L_yL_{\Delta y}+4L_yK_4\Delta y(nT)}$
IC5	$\frac{HK_2\Delta e(nT)+HL_{\Delta e}}{2L_{\Delta e}}$	$\frac{HK_4\Delta y(nT)+HL_{\Delta y}}{2L_{\Delta y}}$
IC6	H	H
IC7	$\frac{HK_1e(nT)+HL_e}{2L_e}$	$\frac{HK_3y(nT)+HL_y}{2L_y}$
IC8	0	0
IC9	$\frac{HK_2\Delta e(nT)-HL_{\Delta e}}{2L_{\Delta e}}$	$\frac{HK_4\Delta y(nT)-HL_{\Delta y}}{2L_{\Delta y}}$
IC10	$-H$	$-H$
IC11	$\frac{HK_1e(nT)-HL_e}{2L_e}$	$\frac{HK_3y(nT)-HL_y}{2L_y}$
IC12	0	0

V. EXPERIMENTAL RESULTS

In this section, the proposed Mamdani fuzzy I-PD controller is implemented to control the two-link robot manipulator shown Fig. 2 in order to demonstrate the effectiveness of the proposed the controller. In the experiments, the sampling time T is chosen to be 0.001 second.

First, the parameters K_i = 25.0, K_p = 25.0 and K_d = 10.0 of the conventional I-PD controller are found from the CDM tuning method when the stability index $\gamma_2 = 4$ [5] and then they will be used for designing the proposed Mamdani fuzzy I-PD controller as stated in section III. Consequently, the gains for the Mamdani fuzzy I controller are K_1 = 0.025 and K_2 = 0.0125, and for the Mamdani fuzzy PD controller are K_3 = 25.0 and K_4 = 10000, respectively. The adjustable constants for 1st joint are chosen as L_e = 600, $L_{\Delta e}$ = 50000, L_y = 85000, $L_{\Delta y}$ = 85000, $H_{\Delta u_I} = 20400$ and $H_{\Delta u_{PD}} = 11400$. The adjustable constants for 2nd joint are chosen as L_e = 7500, $L_{\Delta e}$ = 500000, L_y = 850000, $L_{\Delta y}$ = 650000, $H_{\Delta u_I} = 14600$ and $H_{\Delta u_{PD}} = 12600$.

The experimental results of the Mamdani fuzzy I-PD and the conventional I-PD control systems are shown in Fig. 9 to Fig. 14. It is seen from Fig. 9 and Fig. 12 that the Mamdani fuzzy I-PD controller can control the robot manipulator rapidly follows the desired cubic polynomial trajectories [6] than the conventional I-PD controller. Both control systems can reach to the desired angular position at 90 degrees without steady-state error as shown in Fig. 10 and Fig. 13 where the smaller error of both links of the Mamdani fuzzy I-PD control system can be noticed. Furthermore, it can be seen that the magnitude of the control signals of the 1st link and the 2nd link of the fuzzy I-PD control system are smaller than the control signals of the conventional I-PD control system as shown in Fig. 11 and Fig. 14. Thus, the effectiveness of the Mamdani fuzzy I-PD controller for the two-link manipulator is confirmed by the experimental results.

VI. CONCLUSIONS

The Mamdani fuzzy I-PD controller has been proposed in this paper and has been implemented to control the angular position of the two-link robot manipulator. The proposed Mamdani fuzzy I-PD controller can control the robot manipulator to rapidly follow the desired trajectories without steady-state error. In conclusion, the proposed controller has the efficiency to handle the robot manipulator.

REFERENCES

[1] J. G Zeigler and N. B. Nichols, "Optimum Settings for Automatic Controllers," *ASME Trans*., vol. 64, pp. 759-768, 1942.

[2] S. Manabe, "Coefficient Diagram Method," *14th IFAC Symposium on Automatic Control in Aerospace*, pp. 199-210, 1998.

[3] H. Ying, *Fuzzy Control and Modeling: Analytical Foundations and Applications*, Institute of Electrical and Electronics Engineers, Inc., 2000.

[4] F.L, Lewis, C.T. Abdallah and D.M. Dawson, *Control of Robot Manipulators,* Macmillan Publishing Company, 1993.

[5] A. Ucar and S.E. Hamamci, "A controller based on coefficient diagram method for the robotic manipulators," *The 7th IEEE International Conference on Electronics, Circuits and Systems,* Jounieh, Lebanon, vol. 2, pp. 777-780, December 17-18, 2000.

[6] R. K. Mittal and I. J. Nagrath, *Robot and Control,* Tata McGraw-Hill Publishing Company Limited, 2003.

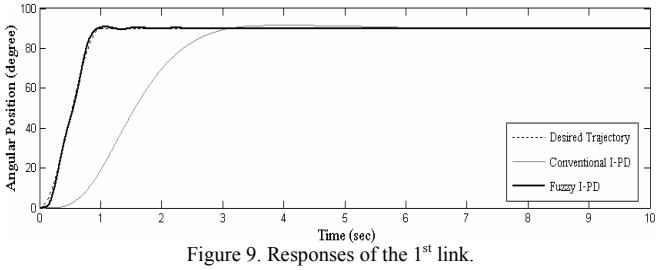

Figure 9. Responses of the 1st link.

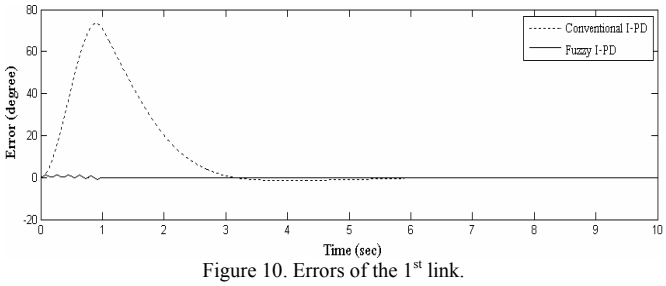

Figure 10. Errors of the 1st link.

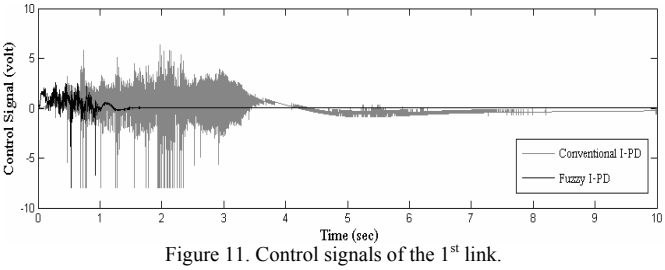

Figure 11. Control signals of the 1st link.

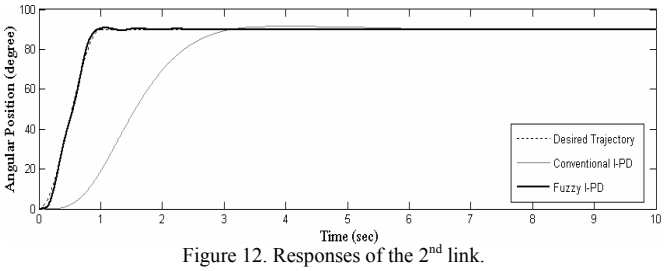

Figure 12. Responses of the 2nd link.

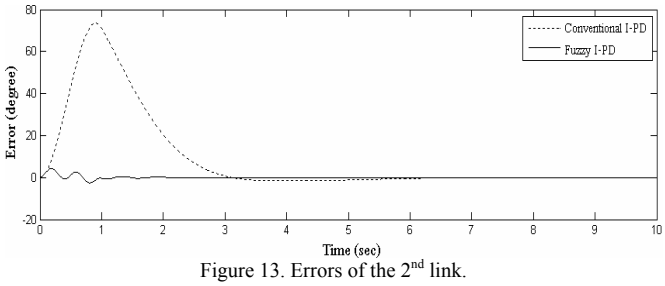

Figure 13. Errors of the 2nd link.

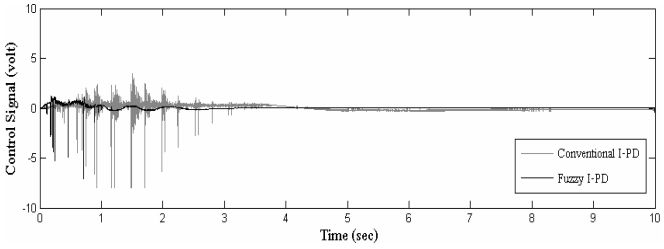

Figure 14. Control signals of the 2nd link.

A new modal of variable air volume diffuser for thermal comfort based on fuzzy logic control

Yingrak Auttawaitkul,Veerapol Monyakul*,Apichit Therdyothin
School of Energy, Environment and Materials,
King Mongkut's University of Technology Thonburi
*National Science and Technology Development Agency (NSTDA),Thailand

***Abstract*- The tower building categories used in the energy breakdown are HVAC, lighting, computers and diverse equipment. The HVAC system has the greatest energy saving potential as it is the major energy consumer. It consumes approximately 64 percent of the total building energy. Good HVAC control in buildings helps reduce energy use and maintain occupant comfort. To this end, there are many design conditions to observe HVAC systems. Such as the heat exchanger, connecting ductwork, damper, mixing air components, and PI, PID, Fuzzy, EMC, QUICK control systems. This paper critically examines indoor climate control technologies. A new modal of variable air volume diffuser can control room air velocity, mixing of supply air and room air for thermal comfort based on fuzzy logic control. Constant air supply and variable air room volume can convert maximum heat from surface 20 percent increase.**

Keywords: HVAC; PMV; Fuzzy control; Diffuser

I. INTRODUCTION

The consumption of energy by heating, ventilating, and air conditioning (HVAC) equipment in industrial and commercial buildings constitutes 50 percent of the world energy consumption [1]. It is impact on the development of new control methodologies for HVAC systems aiming at improving their energy efficiency. The design of HVAC control system capable of maintaining comfort conditions within a thermal space and reduce energy wastes regardless of the thermal loads acting upon the system[2]. Optimal control strategies for time-scheduled operation of heating, ventilating and air conditioning systems are showing the optimal mass flow rates to the zones, air and water supply temperatures[3].

A large number of thermal comfort indices have been set up for the analysis of indoor climates[4,5,6,7]. Such as the new fuzzy PMV calculation does not require an iterative solution and can be easily adjusted depending on the specific thermal sensation of users. The fuzzy PMV is as accurate as Fanger's PMV [8]. The designing duct is the fundamentals for a pressure controlled variable air volume (VAV) system. The flow to each zone is controlled at the diffuser outlet which constant pressure draft [9]. The vortex diffuser is generally assumed with high diffusion performance. The flow pattern in the vicinity of outlet region for vortex diffuser and highly turbulent [10]. This paper present a new modal of variable air volume diffuser. One of equipment design for thermal comfort room. The diffuser can mix air supply and air room subject to relation between air temperature and relative velocity for thermal comfort condition. The motor speed control by v/f drive base on fuzzy logic. The diffuser capable of maintaining comfort conditions both a thermal space and reduce main energy. The diffuser save energy by increase air room velocity before decrease temperature air supply. To decrease temperature HVAC air supply system use more power than use in control speed motor diffuser.

Nomenclature

A	=	Surface Area
EMC	=	Energy Management Control
h	=	Convection heat transfer coefficient
HVAC	=	Heating, Ventilation and Air-Conditioning
PI	=	Proportional, Integral
PID	=	Proportional, Integral and Derivative
PMV	=	Predicted Mean Vote
Q	=	Quantity
Ts	=	Surface temperature
$T\infty$	=	Ambient temperature
V	=	Air velocity
VAV	=	Variable Air Volume
ρ	=	Density

II. METHODOLOGY

A. HVAC System

HVAC system show in Fig.1. It consists of the following components: a heat exchange, a circulating air fan, the thermal space, the chiller providing chilled water to the heat exchanger, connecting ductwork, damper, and mixing air components.

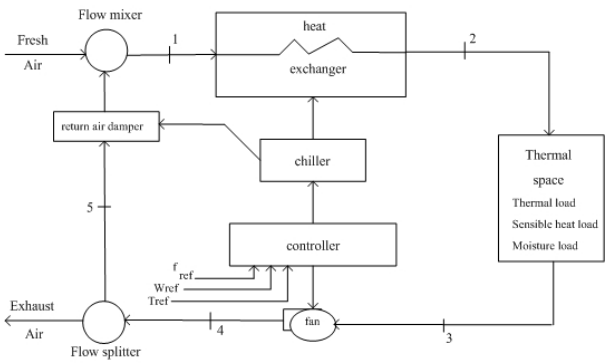

Fig. 1 HVAC system

The basic operation of the system in the cooling mode is as follows:

1. The fresh air is allowed into the system and mixed the recalculated air (number5) at the flow mixed
2. Air mixed at the flow mixer (number1) enters heat exchanger where it gets conditioned. The air entering the heat exchanger is mixed with chilled water from the chilled to get cooled.
3. The air coming out of the heat exchanger is already conditioned to enter the thermal space, and it is called supply air (number2).
4. The supply air enters the thermal space to offset the thermal loads acting upon the system.
5. The air in the thermal space is drawn through a fan (number3), this air gets recalculated and the rest is exhausted from the system.

The controller maintains the heat exchanger temperature, the space temperature the set point. The air flow is to each zone is varied by changing the out lat area of the supply air diffuser, a certain outlet area and static pressure in the branch duct well equal an air flow as shown in Fig.2

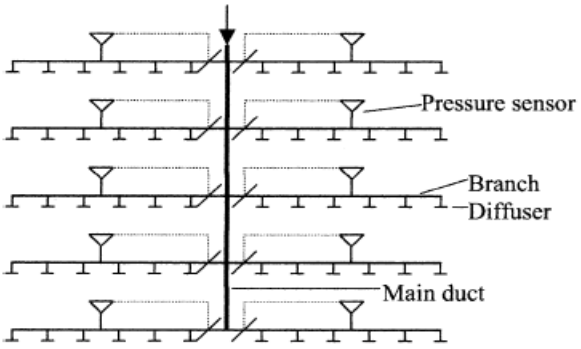

Fig.2 Supply air system with main duct, branches, dampers, pressure sensors

B. Thermal comfort fuzzy system

Fuzzy logic modeling based on the original work of Fanger is used to approximate the human's comfort/discomfort level in a given indoor climate as show in Fig.3. The most common and best understood one is Fanger's 'Predicted Mean Vote' PMV. In 1970, Fanger [4] published a general comfort equation which makes it possible, for any activity level and any clothing insulation, to calculate all combinations of the environmental variables (air temperature, air humidity, mean radiant temperature and relative air velocity) which will create optimal thermal comfort. The PMV index determines whether a given indoor climate is satisfactory or not using a seven-point thermal sensation scale. Fig. 3 summaries the overall process of using the six variables associated with thermal comfort sensation to evaluate the PMV.

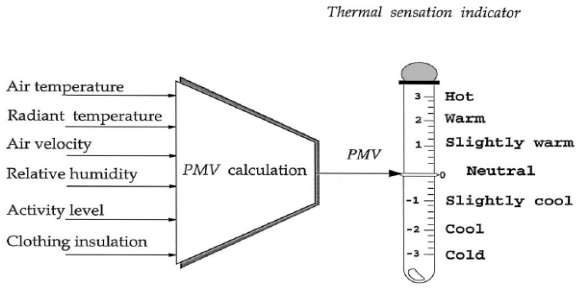

Fig.3 Fanger's PMV and thermal sensation.

On the basis of this analysis, a fuzzy PMV is designed and a general fuzzy rule base is derived to describe the state of human's thermal sensation. For any activity level and any clothing, the fuzzy rule base is able to calculate all combinations of the environmental variables which will create optimal thermal comfort as shown in Fig.4. The new designed thermal sensation index can then be easily used in feedback control.

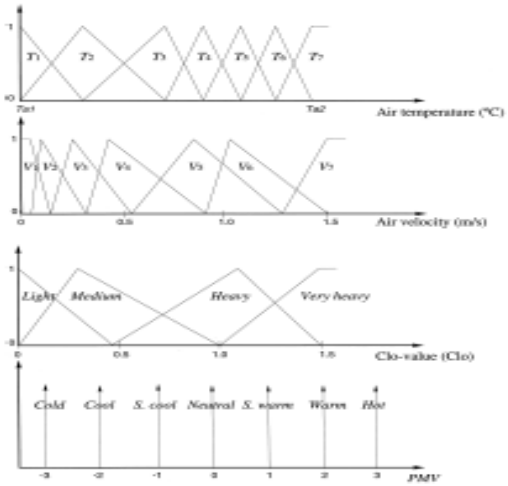

Fig.4 Fuzzy PMV membership functions.

C. Variable air volume diffuser

The variable air volume ceiling diffuser as shown in Fig. 5, has a relatively high entrainment due to the swirl of the exit air,

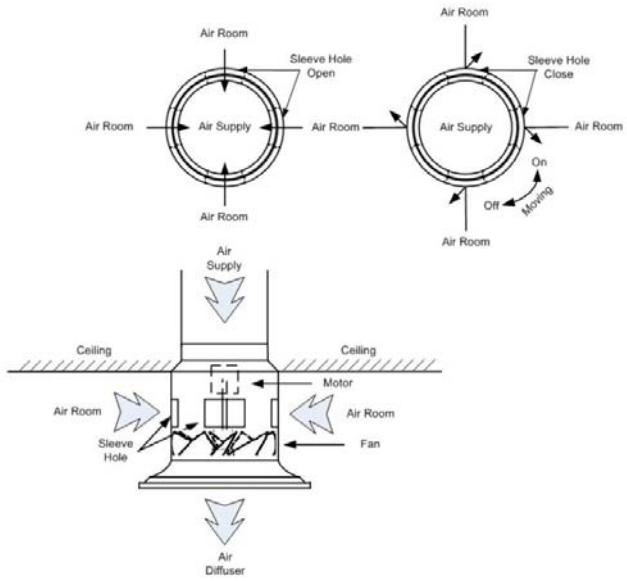

Fig 5. Variable air volume diffuser

which creates a more thorough mixing of supply air and room air than other diffusers. The control of the motor diffuser can be adjusted to the lowest level resulting in a horizontal flow for cooling applications, and to the highest level resulting in a downward flow for heating applications. So the diffuser is a variable outlet load diffuser.

Heat is converted from surface to moving fluid. The temperature gradient is dependent on the rate at which the fluid carries the heat away, a high velocity produces a large temperature gradient, and so on. Thus the temperature gradient at the surface depends on the flow field. To express the overall effect of convection, we use Newton's law of cooling.

$$q = hA\left(T_s - T_\infty\right)$$

The continuity equation below is a statement of conservation of mass. For a system of particles, mass is constant because it can be neither created nor destroyed. In other words, the mass entering the control volume equals mass stored plus mass leaving. For steady flow with no storage of mass.

$$\sum_{in} \rho AV = \sum_{out} \rho AV$$

$$\sum_{in} AV = \sum_{out} AV$$

$$Q_{AirSupply} + 4Q_{AirRoom} = Q_{AirDiffuser}$$

There are fore hole round the diffuser when sleeve move right the hole open and left the hole shut down. The hole round diffuser use for input air round the room when the system increases air quantity.

III. CONTROL SYSTEM

The control system of the variable air volume diffuser is using fuzzy PMV membership functions model The fuzzy PMV model has signal input as clothing set point, room air temperature and air flow rate to start v/f drive for variable speed motor and open or close sleeve hole. shown in Fig,6.

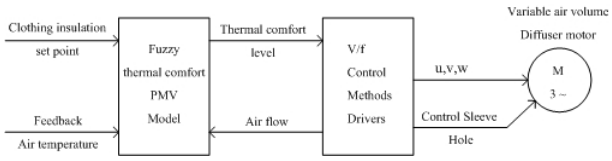

Fig.6 Diffuser motor control loop schematic

In Fig.7 as shown the testing room diagram. It has variable heat load for assume as person activity or sensible heat load.

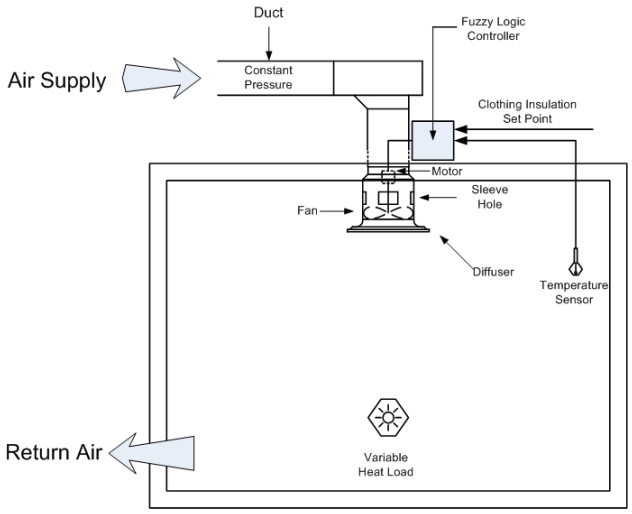

Fig.7 Schematic diagram of the testing room

IV. RESULTS AND CONCLUSION

In this paper, the new modal of variable air volume diffuser for thermal comfort based on fuzzy logic control can help the HVAC systems to maintain the main air supply system. In Fig.8-9 shown that when you have a constant air temperature supply but you want to incrust heat load in the area you can incrust room air velocity. Table 1. shows the testing room thermal comfort result data. The temperature from 22-26°C, load level from 50-70 kcal/m^2hr compare with PMV data.

Load level = 50 kcal/ m^2hr
At 22°C air temperature supply, velocity 0.1m/s
Calculated PMV = -0.33 the thermal sensation is neutral.
At 24°C air temperature supply, velocity 0.2m/s
Calculated PMV = 0.2 the thermal sensation is neutral.
At 26°C air temperature supply, velocity 0.15m/s
Calculated PMV = 0.75 the thermal sensation is slightly warm.

Load level = 60 kcal/ m^2hr
At 22°C air temperature supply, velocity 0.15m/s
Calculated PMV = 0.1 the thermal sensation is neutral.
At 24°C air temperature supply, velocity 1 m/s
Calculated PMV= 0.54 the thermal sensation is slightly warm.
At 26°C air temperature supply, velocity 1.5m/s
Calculated PMV = 0.98 the thermal sensation is warm.

Load level = 70 kcal/ m^2hr
At 22°C air temperature supply, velocity 0.5m/s
Calculated PMV = 0.39 the thermal sensation is neutral.
At 24°C air temperature supply, velocity 1.5 m/s
Calculated PMV= 0.76 the thermal sensation is warm.
At 26°C air temperature supply, velocity 1.5m/s
Calculated PMV = 1.13 the thermal sensation is warm.

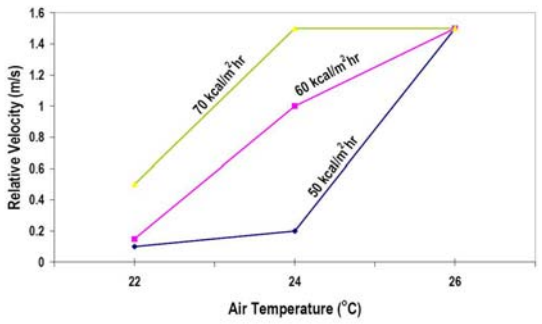

Fig.8 Relation between air temperature and relative velocity for thermal comfort condition

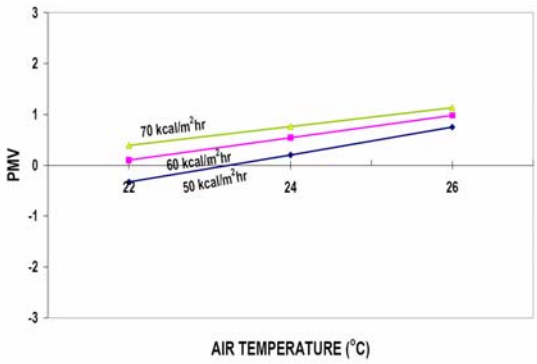

Fig.9 Relation between air temperature and PMV at constant air diffuser

TABLE I
PMV Thermal comfort data

Room temp (°C) \ Load level (kcal/ m^2hr)	50	60	70
22	N	N	N
24	N	SW	W
26	N	W	W

N = Neutral
SW = Slightly warm
W = Warm

REFERENCES

[1] Imbabi, M.S. *Computer Validation of Scale Model Tests for Building Energy Simulation. International Journal of Energy Research*, vol.14,pp. 727-736, 1990.

[2] Betzaida Arguello-serrano and Miguel Velez-Reyes, "*Design of a Nonlinear HVAC Control System with Thermal Load Estimation*", Research sponsored by INDUNIV Research Canter, San Juan, PR 00936,under grant INDUNIV G-93-04.

[3] M. Zaheer-uddin, G.R. Zheng, "*Optimal control of time-scheduled heating, ventilating and air conditioning processes in buildings*", Centre for Building Studies, Concordia University, Montreal, Quebec, Canada H3G 1M8 Received 7 August 1998; accepted 22 March 1999.

[4] P.O. Fanger, "*Thermal Comfort, Analysis and Applications in Environmental Engineering*", McGraw-Hill, 1972.

[5] C.C. Federspiel, "*User-adaptable and minimum-power thermal comfort control*", PhD thesis, MIT, Department of Mechanical Engineering, June 1992.

[6] A.P. Gagge, A.P. Fobelets, L.G. Berglund, "*A standard predictive index of human response to the thermal environment*", ASHRAE Transactions 92 (2B) 1986.709–731.

[7] M. Sherman, "*A simplified model of thermal comfort*", Energy and Buildings 8 (1985) 37–50.

[8] Maher Hamdi, Ge´rard Lachiver), Franc¸ois Michaud, "*A new predictive thermal sensation index of human response*" De´partement de ge´nie e´lectrique et de ge´nie informatique, Uni1ersite´ de Sherbrooke, Sherbrooke, Que´bec, Canada J1K 2R1Received 23 May 1997

[9] Fredrik Engdahl Anders Svensson ,"*Pressure controlled variable air volume system*" Byggnadsfysik-LTH, Physics Building, Lund University, Box 118, Lund 22100, Sweden Received 5 July 2003; received in revised form 8 September 2003

[10] S.C. Hu "*Airflow characteristics in the outlet region of a vortex room air diffuse*r" Department of Air-Conditioning and Refrigeration Engineering, National Taipei University of Technology,1, Section 3, Chung-Hsiao E. Rd, Taipei 106, Taiwan, ROC Received 19 October 2001; received in revised form 25 July 2002; accepted 12 September 2002

Simultaneous Perturbation Approach to Neural Control of a Flexible System

Jorge Ivan Medina Martinez [1], Kazushi Nakano [2] and Umerujan Sawut [3]
[1,2] The University of Electro-Communications, 1-5-1 Chofu-ga-oka, Chofu, Tokyo 182-8585, Japan
email: ivan@francis.ee.uec.ac.jp, nakano@ee.uec.ac.jp
[3] Nikki Co., Ltd., 3029 Kamiechi, Atsugi, Kanagawa 243-0801, Japan
email: umerujan@nikkinet.co.jp

Abstract – **In a direct inverse control scheme, a neural network must learn an inverse system of an objective unknown or uncertain plant. The control scheme described here does not require information about the Jacobian of the plant, because the simultaneous pertrubation–stochastic approximation (SPSA) method estimates the gradient using only values of the error defined by the output of the plant and its desired output. This paper aims to assess the potential of the learning rules using the SPSA method for a neuro-controller (NC) of a flexible arm system. The performance of the proposed NC can be improved in terms of preventing weights from shifting, fast convergence to constant values, and suppressing vibration in the flexible arm. Lastly, the proposed control method is compared with the Smith predictor method.**

Keywords – **Stochastic Approximation, Simultaneous Perturbation, Neuro-Controller, Flexible Arm, Learning Rule, Smith Predictor.**

I. Introduction

Over the past several years, neural networks (NNs) have been increasingly applied to the identification and control of nonlinear systems. Since the NNs usually involve a large number of unknown parameters, it is extremely computation-intensive to evaluate the gradient by varying the parameter at a time, as required in conventional finite difference (FD) approximation method[1],[2]. The simultaneous perturbation (SP) approximation method makes use of a very efficient technique based on simultaneous (random) perturbations in all the parameters and requires only two evaluations of the gradient.

However, if we introduce simultaneous perturbation–stochastic approximation (SPSA) learning rules, there is no need to know the sensitivity function of the unknown or uncertain plant. Even if only using the values of an error function, the learning rules can estimate a gradient of the error function with respect to adjustable parameters[3],[4]. Because of this advantage, this paper proposes a NC which uses the SPSA learning rule for a flexible arm system[5]. The NC learns an inverse system of an objective plant and controls the plant at the same time (see Fig.1).

The NN is then trained by the SPSA learning rule in the closed-loop to provide improved training performance over other standard methods, such as the back-propagation (BP) algorithm. Another major motivation for using SPSA instead of the popular BP algorithm is its excellent convergence property[6]. This paper introduces the SPSA method for stochastic optimization of multivariate systems[7], Next, the SPSA method is compared with other methods for reducing the vibration such as the Smith predictor methods, which are known as common and effective dead-time compensators. It guarantees superior control performance for a system with large time delay if an accurate model of the system is available in advance. Many Smith predictors modified with different structures have been proposed. For comparison with our procedure, the Smith predictor presented by Liang[8] is used, because it gives similar performance for suppressing the vibration to the SPSA method.

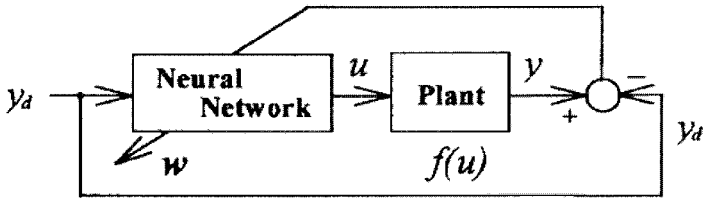

Fig. 1. NC by inverse control scheme: learning rule by SP

II. Stochastic Approximation–Simultaneous Perturbation

One optimization method which has attracted considerable international attention is the simultaneous perturbation–stochastic approximation (SPSA) method. SPSA is especially efficient in high-dimensional problems in terms of providing a good solution for a relatively small number of measurements of the objective function. The essential feature of SPSA, which provides its power and relative ease of use in difficult multivariate optimization problems, is the underlaying gradient approximation which requires only two objective function measurements per iteration regardless of the dimension of the optimization problem. The goal is to minimize a loss function $L(\theta)$, where this is a scalar-valued performance measure and θ is a continuous-valued p-dimensional vector of parameters to be adjusted. The SPSA algorithm works by iterating from an initial guess of the optimal θ, where the iteration process depends on the above-mentioned highly efficient SP approximation to the gradient $g(\theta) = \partial L/\partial\theta$. The optimization problem can be translated into finding the mini-

mum θ^* such that the gradient $g(\theta) = 0$. The general form of SA recursive procedure is given as

$$\hat{\theta}_{k+1} = \hat{\theta}_k - a_k \hat{g}_k(\hat{\theta}_k) \tag{1}$$

where the gain a_k is a positive constant, and $\hat{g}_k(\hat{\theta}_k)$ is the estimate of the gradient $\partial L/\partial\theta = 0$ at the k th iteratition, based on the measurements of the loss function. Under appropriate conditions, the iteration in Eq.(1) converges to θ^* in some stochastic sense[7].

Simultaneous Perturbation (SP): All the elements of $\hat{\theta}_k$ are randomly perturbed together to obtain two measurements of y, but each component of $\hat{g}_k(\hat{\theta}_k)$ is formed from a ratio involving the individual components in the perturbation vector and the difference in the two corresponding measurements. For the two-sided SP, we have

$$\hat{g}_{ki}(\hat{\theta}_k) = \frac{y(\hat{\theta}_k + c_k\Delta_k) - y(\hat{\theta}_k - c_k\Delta_k)}{2c_k\Delta_{ki}} \tag{2}$$

where c_k is a positive scalar and Δ_k is user generated zero-mean random vector satisfying certain regularity conditions, whose i th component is $\Delta_k = [\Delta_{k1}, \Delta_{k2}, \cdots, \Delta_{kp}]^T$ with symmetrically Bernoulli distribuited random variables.

III. Neuro-Conrtoller Via Simultaneous Perturbation

First of all, we define the following perturbation vector c_t which gives small disturbances to all weights:

$$c_t = \left[c_t^1, ..., c_t^n \right]^T \tag{3}$$

where t denotes the number of iterations for updating weights and n denotes the number of weights.

Learning Rule 1: First, we estimate $\partial J/\partial w$. Then, we define the component of the modifying vector of the weight Δw_t as

$$\Delta w_t^i = \frac{J(u(w_t + c_t)) - J(u(w_t))}{c_t^i} \tag{4}$$

Weights of the network are updated in the following manner:

$$w_{t+1} = w_t - \alpha \Delta w_t \tag{5}$$

where α is a positive learning coefficient.

Learning Rule 2: Next, we estimate the first differential coefficient of the unknown plant with respect to the weights of the NN. Then, we define the compobent of the modifying vector of the weight as

$$\Delta w_t^i = e_t \frac{J(u(w_t + c_t)) - J(u(w_t))}{c_t^i} \tag{6}$$

Since the control error e_t can be easily measured, $\partial f/\partial w$ also can be estimated.

IV. Application to Flexible Arm System

In an usual control scheme, we must have an exact model of an objective plant, since controllers are basically designed based on the identified model. We first define the deflection as follows:

$$\mu(x,t) = \sum_{i=1}^{\infty} \phi_i(x) q_i(t) \simeq \sum_{i=1}^{N} \phi_i(x) q_i(t) \tag{7}$$

where ϕ_i is the ith modal function which satisfies boudary conditions described below, and N is the number of vibration modes to be considered in the control, which will be set at 6 in the simulation. The actuator torque $u(t)$ as an input in tuning the arm. In order to derive the state equation from the above equations, we first must determine ϕ_i from the boudary conditions.

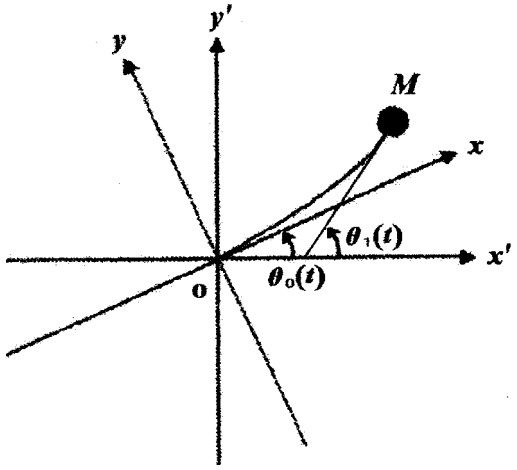

Fig. 2. One-link flexible arm

As well known, the arm is governed by the Euler-Bernoulli equation:

$$EI\frac{\partial^4 \mu(x,t)}{\partial x^4} = -\rho A_b \frac{\partial^2 \mu(x,t)}{\partial t^2} \tag{8}$$

where E is Youg's modulus, I the moment, ρ the density, and A_b the cross section area of the arm. The boundary conditions of Eq.(8) are given by

1) $\mu(0,t) = 0$
2) $\frac{d\mu(0,t)}{dx} = 0$
3) $\frac{d^2\mu(L,t)}{dx^2} = 0$
4) $EI\frac{d^3\mu(L,t)}{dx^3} = -M\frac{d^2\mu(L,t)}{dt^2}$

When taking account into a weight with mass M as shown in Fig. 2. From a certain initial state, we would like to reduce bending at the tip of the flexible arm. For this purpose, we first need a training set for pre-training of the NN. After that, the NN is utilized as a controller of the plant. We next add perturbations at all weights simultaneously. Then, we have a value of the error. By using Eq.(5), we can update all the weights in NC, and repeat this procedure.

Further, six states to control the plant is selected as follows:

$$\bar{x} = \left[\theta_0, \dot{\theta}_0, x_1, \dot{x}_1, \theta_1, \dot{\theta}_1 \right] \tag{9}$$

where θ_0 and $\dot{\theta}_0$ are the angle and angular velocity at the origin, respectively, θ_1 and $\dot{\theta}_1$ are those at the tip, respectively, and x_1 and $\dot{x}_1$ are the x-position and its velocity at the tip, respectively. As seen in Fig. 3, these six states are measurable and neccesary to produce proper command inputs for the NN.

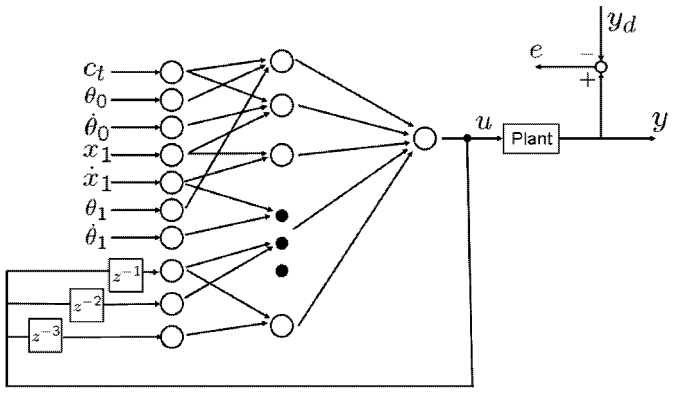

Fig. 3. NC using leaning rules via SPSA

V. Simulation Results

The weights and thresholds of the NNs are randomly initialized $[-1, +1]$. The perturbations used in these simulations are randomly generated in the interval $[-0.01, +0.01]$. The learning coefficient α and the perturbation c are both 0.0002. In this simulation, inputs and outputs of the plant are connected to the time-delay feedforward NN.

If using the learning rule 1 and modifying the weights of every sets of the desired position, we can define the following total error function at the tip position as Eq.(10), and can use the learning rule 1 of Eq.(4) directly:

$$J = \sum_{t=1}^{N_L} (x_{1t} - x_{1dt})^2 + (y_{1t} - y_{1dt})^2 \qquad (10)$$

where (x_1, y_1) and (x_{1dt}, y_{1dt}) denote the measured position and the corresponding desired position at the tip, respectively, and N_L is the total number of learning. That is, the error function is a sum of the squared errors of the desired positions. First, we can measure a series of outputs of the plant for one cycle. We obtain a value of the total error function as a sum of the squared errors at each sampling time. Next, we add the perturbation vector to the weight vector of the NN. Then, the same procedure is repeated. As a result, is obtained a value of the total error function under the perturbation. If using learning rule 2 of Eq.(6), we do not use the total error function like Eq.(10). We have to calculate the follwing modifying quantities of the weights for every sampling time:

$$\Delta w_t^i = (x_{1t} - x_{1dt})\frac{\hat{x}_{1t} - x_{1t}}{c_t^i} + (y_{1t} - y_{1dt})\frac{\hat{y}_{1t} - y_{1t}}{c_t^i} \qquad (11)$$

where ($\hat{x}_1$, $\hat{y}_1$) denotes the position at the tip when adding the perturbation vector to the weights. Once a desired position are applied to the NN, we can measure a position of the arm and calculate the errors (x_{1t} - x_{1dt}) and (y_{1t} - y_{1dt}). In this simulation, we update every sampling time.

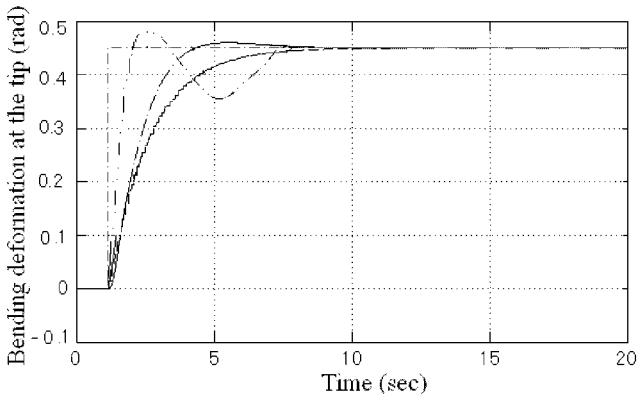

Fig. 4. Bending deformations at tip by SPSA method

Fig. 4 shows typical responses of the system at the tip position to a step-command (dashed-dotted). The dashed-two dotted line shows that using only 100 iterations the response is very poor. Using 25,000 iterations, we found from the dashed-dotted line that the tip moves to the commanded position, and the arm is positioned effectively in about 1.5(sec) from the start. This response is very close to critical damping and there is a very little overshoot. It is possible to increase the rise time at the expense of overshoot by increasing the feedback gains. Using 50,000 iterations, we found from the solid line that the tip position are a little over-damped. The arm is then effectively positioned in about 2.7(sec).

VI. Comparison between SPSA and Smith predictor methods

For comparison of the SPSA with the Smith predictor method, the next simulation is carried out in ordet to reduce the vibration and improve the performance of the system. The Smith predictor method is probabily the most famous method for the control of systems with time delays[8],[9]. Consider a typical feedback control system with time delay θ.

$$\frac{y(s)}{y_d(s)} = \frac{C(s)P_0(s)e^{-\theta s}}{1 + C(s)P_0(s)e^{-\theta s}} \qquad (12)$$

where the system to be controlled is given by $P(s) = P_0(s)e^{-\theta s}$, and the output y is the velocty at the tip and y_d the correponding reference input, which is set at 0. $\hat{P}_0(s)$ and $\hat{P}(s)$ are nominal models of $P_0(s)$ and $P(s)$, respectively. The nominal models can be approximately derived by Eq.(8). Here, only the boundary condition is slightly changed such as

4') $EI\frac{d^3\mu(L,t)}{dx^3} = u(t) = -k_L\frac{d\mu(L,t)}{dt}$

where k_L is a control gain. The boundary controller $C(s)$ combined with $\hat{P}_0(s)$ - $\hat{P}(s)$ is called the Smith predictor, where $\hat{P}_0(s)$ and $\hat{P}(s)$ are nominal models. If assuming the perfect model matching $\hat{P}(s) = P(s)$, we can obtain the

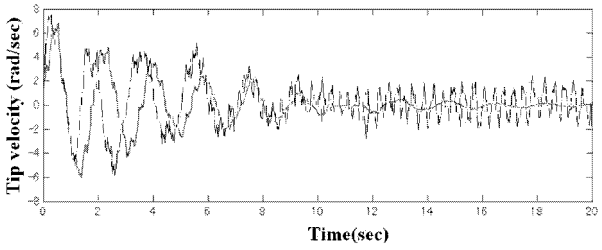

Fig. 5. Tip velocities by SPSA method used 100,000 and 50,000 iterations

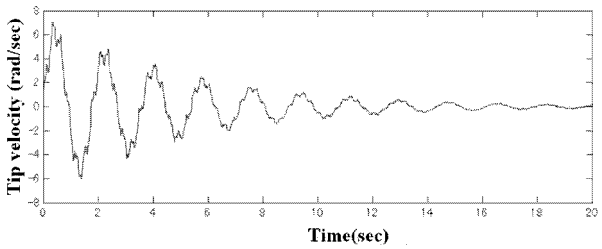

Fig. 6. Tip velocity by Smith predictor method

closed-loop transfer function

$$\frac{y(s)}{y_d(s)} = \frac{C(s)P(s)}{1 + C(s)P_0(s)} \tag{13}$$

Now, it is clear what the underlying idea of the Smith predictor is. In order to attenuate the magnitude of vibration further, we consider to apply the Smith predictor presented by Liang[8]. This version has the best performance among several Smith predictor methods. Therefore, the comparison with SPSA method can give us a better idea about the performance of our method.

The SPSA method is also applied under almost the same conditions as in the previous simulation. The tip velocities of the arm, which is controlled by the SPSA and Smith predictor methods, are shown in Fig. 5 and Fig. 6, respectively. Especially, Fig. 5 includes the two cases of 100,000 (solid) and 50,000 iterations (dashed-dotted) iterations. The latter case cannot suppress vibration even as time goes. However, we can observe that the Smith predictor method and the SPSA mathod with 100,000 iterations gives almost the same response as the Smith method. Therefore, both the methods are very effective in order to attenuate the magnitude of vibration. Generally speaking, the Smith predictor method is easier to be implemented than the SPSA method. However, the SPSA method does not need much infromation on exact model, i.e., the values of physical variables and modal functions.

VII. Conclusions

In this proposal, a direct NC using the SPSA learning rule for an unknown or uncertain plant was introduced and applied to the control of a flexible arm system. The SPSA approach is a very powerful technique which allows an approximation of the gradient and/or the Hessian of a noisy performance criterion, which is computed by effecting simultaneous random perturbations in all the parameters. In the simulation, the deflection was reduced and almost null. In comparison of the performances between iteration numbers of the NN, it was shown that a larger number of iterations reduces the vibration more quickly.

Next, the comparison between the SPSA and Smith predictor methods was shown. The Smith predictor method required less time for suppressing the vibration in the flexible arm than the SPSA method. In the simulation, the magnitudes of both velocity and displacement were very small. The SPSA used 100,000 iterations for obtaining the same suppression as the Smith predictor method. Therefore, the comparison between both methods showed that, while the SPSA method is able to reduce the vibration in this kind of system very well, the Smith predictor method is more effective because the convergence is faster. Nevertheless, the SPSA method is also useful in this kind of unknown or uncertain system.

Although the rigorous proof of the stability of this control scheme is left as a future work, the performance of the SPSA method has been satisfactory in terms of simulations.

References

[1] D. H. Pham and X. Liu, Neural Networks for Identification, Prediction and Control, Springer, 1995.

[2] M. Jabri and B. Flower, "Weight Perturbation - An optimal architecture and learning technique for analog VLSI feedforward and recurrent multilayered networks," IEEE Trans. Neural Networks, vol.3, issue 1, pp.154-157, 1992.

[3] Y. Maeda, H. Hirano, and Y. Kanata, "A learning rule of neural networks via simultaneous perturbation and its hardware implementation," Neural Networks, vol.2, no.2, pp.251-259, 1995.

[4] Y. Maeda and Y. Kanata, "Learning rules for recurrent neural networks using prturbation their application to neuro-control," Trans. Inst. Electr. Eng. Japan, vol.113-C, no.6, pp.402-408, 1993.

[5] H. Tanaka, K. Nakano and U. Sawut, "A two-level sliding-mode approach to position control of flexible arms," SICE Annual Conf. 2002, pp.2796-2800, 2002.

[6] Y. Maeda and R. J. P. de Figueiredo, "Learning rules for neurocontroller via simultaneous perturbation," IEEE Trans. on Neural Networks, vol.8, no.5, pp.1119-1130, 1997.

[7] J. C. Spall, "A stochastic approximation algorithm for large dimensional systems in the Kiefer-Wolfowitz setting," Proc. 27th IEEE Conf. Decision and Contr., pp.1544-1548, 1988.

[8] J. Liang, Y. Q. Chen and B.-Z. Guo, "A new boundary control method for beam equation with delayed boundary measurement using modified Smith predictors," Proc. 42nd IEEE Conf. Decision and Contr., vol.1, pp.809-814, 2003.

[9] W. Zhang and X. Xu, "Analytical design for open loop unstable processes with time delay," Proc. of American Control Conference 1999, vol.3, pp.1822-1826, 1999.

Design of PID Controllers via Genetic Algorithm for Benchmark Systems

C. Thammarat, P. Sukserm, and D. Puangdownreong
Department of Electrical Engineering, Faculty of Engineering,
South-East Asia University, Bangkok, 10160, THAILAND
Email: dp@sau.ac.th

***Abstract*-This paper presents an intelligent method for designing proportional-integral-derivative (PID) controllers using the genetic algorithm (GA), one of the most efficient AI search techniques. The goal is considered heuristic approach and more flexible design method. With its robustness and effectiveness, GA can well perform finding optimum parameters of a PID controller in order to minimize some particular objectives. To evaluate its performance, the proposed method is applied to several benchmark systems for PID control presented by Åström, et al. [1]. Based on the result obtained from a series of simulations, the proposed GA-based PID design method is found to yield satisfactory performance for various designing PID controllers.**

I. INTRODUCTION

The proportional-integral-derivative (PID) control schemes in industrial applications were first introduced in 1939 [2]. Due to ease of use and simple realization, PID controllers have been widely used in most of process control systems over decades. To obtain appropriate controller's parameters, one can proceed with available analytical design methods or tuning rules. Mostly the analytical design methods assume known plant models [3],[4],[5], while the tuning rules assume known process responses [6],[7], and known plant models [8]. Every analytical design method and every tuning rule, however, have some particular conditions concerning to the plant models, such as dead time or transport lag, fast and slow poles, real and complex conjugated zeros and poles, as well as unstable poles, and to the process responses, such as oscillation and shapes. These conditions make the design methods and tuning rules non-general. In 2000, Åström, et al. [1] proposed a collection of systems which are suitable for testing PID controllers. These collected systems are considered benchmark problems for evaluating post-proposed PID controller design method.

Over two decades, artificial intelligent (AI) techniques have been employed for the controller design in industrial control applications, for example: designing of an adaptive PID controller by genetic algorithm (GA) [9], self-tuning PID controller by GA [10], and finite-precision PID controller by GA [11]. GA is efficient to find the global minimum of the search space. In this paper, GA is briefly reviewed and then applied to design PID controllers for benchmark systems proposed by Åström, et al. [1]. This paper consists of five sections. The problem formulation of PID design is described in Section 2. Section 3 gives GA algorithm in brief. The GA-based design of the PID controllers is illustrated in Section 4, while Section 5 provides the conclusions.

II. PROBLEM FORMULATION

In conventional control loop represented by the block diagram in Figure 1, the PID controller receives the error signal, $E(s)$, and generates the control signal, $U(s)$, to regulate the output response, $C(s)$, referred to the input, $R(s)$, where $D(s)$ is disturbance signal, $G_p(s)$ and $G_c(s)$ are the plant and the controller transfer functions, respectively.

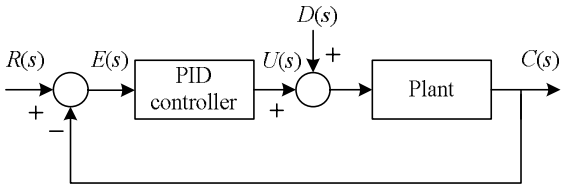

Figure 1. Conventional control loop.

The transfer function of the PID controller is stated in (1), where K_p is proportional gain, K_i is integral gain, and K_d is derivative gain. So, the design problem is simplified to determine the parameters K_p, K_i, and K_d. The closed loop transfer function with PID controller is given in (2).

$$G_c(s) = K_p + \frac{K_i}{s} + K_d s \tag{1}$$

$$\frac{C(s)}{R(s)} = \frac{\left(K_p + \frac{K_i}{s} + K_d s\right) G_p(s)}{1 + \left(K_p + \frac{K_i}{s} + K_d s\right) G_p(s)} \tag{2}$$

$$J = \sum_{t=0}^{T} \left| r(t) - c(t) \right| \tag{3}$$

The use of AI search techniques to design the PID controller can be represented by the block diagram in Figure 2. The cost function, J, sum absolute error (SAE) between $R(s)$ and $C(s)$ as stated in (3), is fed back to the AI tuning block. J is minimized to find the optimum PID controller's parameters that give a satisfactory response. To minimize J, GA method is applied and explained in the next section.

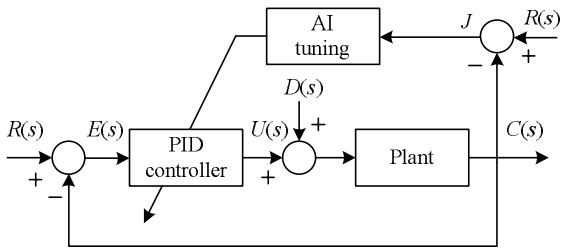

Figure 2. AI-based PID controller design.

III. GENETIC ALGORITHM (GA)

Genetic algorithm (GA) is briefly reviewed in this section. GA is a searching method based on two natural processes, i.e. selection and genetic operation. The search process of GA is similar to the nature evolution of biological creatures in which successive generations of organisms are given birth and raised until they themselves are able to breed. In general, the basic goal of GA is to optimize functions, i.e. fitness and objective functions. GA-based approach differs from other conventional optimization techniques in several ways [12],[13]. Firstly GA works with a coding of the parameter set rather than the parameters themselves. Secondly GA searches from a population of points rather than a single point. Thirdly, GA uses the objective function information, not other auxiliary knowledge. Finally GA uses probabilistic transition rules, not deterministic rules. With these properties, GA is made robust, powerful, and problem-dependent. Algorithms of a simple GA are shown step-by-step as follows.

(1) Random initial populations or chromosomes and set them as a search space.
(2) Evaluate the fitness value of each chromosome via the objective function.
(3) Select some chromosomes giving better fitness value to be parents.
(4) Reproduce new generation (offspring) by genetic operations, i.e. crossover and mutation.
(5) Compute the fitness value of each new chromosome via the objective function.
(6) Replace old chromosomes by new ones and go back to (2).

When the termination criteria are met, GA is stopped. The optimum solution found is the best chromosome in a search space.

IV. GA-BASED DESIGN OF PID CONTROLLER

The GA-based design of the PID controllers is illustrated in this section. Referring to Figure 2, the AI tuning block can be well represented by GA. Then, the parameter tuning process is repeatedly performed in order to minimize J (SAE) stated in (3) until the termination criteria are satisfied. In this work, maximum generation (Max-Gen) of the search process is set as the termination criteria. To evaluate the performance of the proposed design method, the GA-based design of the PID controllers is applied to four benchmark systems suggested by Åström, et al. [1]. Such the systems are difficult to design their PID controllers by conventional design methods or tuning rules.

The desired specification is given in (4), where t_r is rise time, $P.O.$ is percent overshoot, t_s is settling time, E_{ss} is steady state error, $t_{r\text{-}max}$ is maximum rise time allowance, $P.O._{max}$ is maximum percent overshoot allowance, $t_{s\text{-}max}$ is maximum settling time allowance, and $E_{ss\text{-}max}$ is maximum steady state error allowance. They are set as inequality constraints of the optimization. GA is used to obtain K_p, K_i, and K_d of the PID controller. The optimization framework can be defined as (4).

$$\begin{aligned} &\textit{Minimize} && J \\ &\textit{Subject to} && t_r \le t_{r_max},\ P.O. \le P.O._{max}, \\ & && t_s \le t_{s_max},\ E_{ss} \le E_{ss_max} \end{aligned} \tag{4}$$

In GA applied in this work, Max-Gen = 500 is defined as the termination criteria. 40 chromosomes are randomized of which the intervals are heuristically assumed. The chromosomes are selected by the ranking fashion. Crossover and mutation mechanisms are activated at single point with the probability level of 0.8. Replacement could be done on only one chromosome giving better fitness value in each generation.

A. Fourth Order System

The fourth order system as shown in (5) is the first one used to perform the tests. Such the system has four poles whose spacing is determined by parameter α. In this work, α is set as 0.5. The desired specification of this system are given by t_{r_max}=1.0sec, $P.O._{max}$=10.0%, t_{s_max}=2.5sec, and E_{ss_max}=0.00. The parameter ranges to form the search space were given by K_p=K_i=K_d=[0, 10]. After the search process stopped, the PID controller's parameters are successfully obtained. From the search result, the PID controller listed in Table I yields satisfactorily response as shown in Table I. Additionally, the step responses of the fourth order system without and with PID controller are shown in Figure 3, while Figure 4 represents the convergence of J.

$$G_{p1}(s) = \frac{1}{(1+s)(1+\alpha s)(1+\alpha^2 s)(1+\alpha^3 s)} \tag{5}$$

B. Fast and Slow Modes

The system has a fast time constant at T=1sec with a moderate gain and a slow time constant at T=20sec with a large gain as shown in (6). The desired specification of this system is given by t_{r_max}=0.25sec, $P.O._{max}$=10.0%, t_{s_max}=1.5sec, and E_{ss_max}=0.00. The parameter ranges to form the search space were given by K_p=K_i=K_d=[0, 10]. After the search process stopped, the PID controller's parameters are successfully obtained as listed in Table I. The PID controller yields satisfactorily response as also shown in Table I. The step responses of this system without

and with PID controller are shown in Figure 5, and the convergence of J is represented in Figure 6.

$$G_{p2}(s) = \frac{100}{(s+10)^2}\left(\frac{1}{s+1} + \frac{0.5}{s+0.05}\right) \quad (6)$$

C. Oscillatory System

The oscillatory system is expressed in (7), where ω_0 =1 and ζ = 0.1. The desired specification of this system is given by t_{r_max}=2.5sec, $P.O._{max}$=25.0%, t_{s_max}=10.0sec, and E_{ss_max}=0.00. The parameter ranges to form the search space were given by K_p=K_i=K_d=[0, 5]. After the search process stopped, the PID controller's parameters are successfully obtained as listed in Table I. The PID controller yields satisfactorily response as also shown in Table I. The step responses of this system without and with PID controller are shown in Figure 7, and the convergence of J is represented in Figure 8.

$$G_{p3}(s) = \frac{\omega_o^2}{(s+1)(s^2 + 2\zeta\omega_o s + \omega_o^2)} \quad (7)$$

D. Unstable System

The unstable system as stated in (8) is a simple model of an inverted pendulum.The desired specification of this system is given by t_{r_max}=0.1sec, $P.O._{max}$=15.0%, t_{s_max}=0.5sec, and E_{ss_max}=0.00. The parameter ranges to form the search space were given by K_p=[400, 500] and K_i=K_d=[0, 50]. After the search process stopped, the PID controller's parameters are successfully obtained as listed in Table I. The PID controller yields satisfactorily response as also shown in Table I. The step responses of this system without and with PID controller are shown in Figure 9 and, the convergence of J is represented in Figure 10.

$$G_{p4}(s) = \frac{1}{s^2 - 1} \quad (8)$$

V. CONCLUSIONS

The intelligent method for designing PID controllers using GA is proposed in this paper. The proposed method is considered the heuristic approach. It is more flexible than the conventional design methods and tuning rules. The presented method has been evaluated via four benchmark systems. As the results, the appropriated parameters of PID controllers have been successfully obtained, and achieved high satisfactorily responses. The usefulness and flexibility of the proposed intelligent design approach have been confirmed.

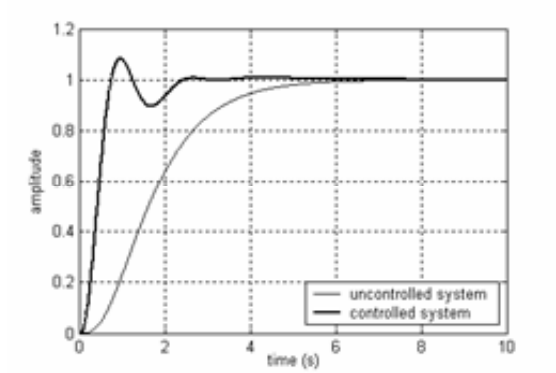

Figure 3. Step responses of the fourth order system.

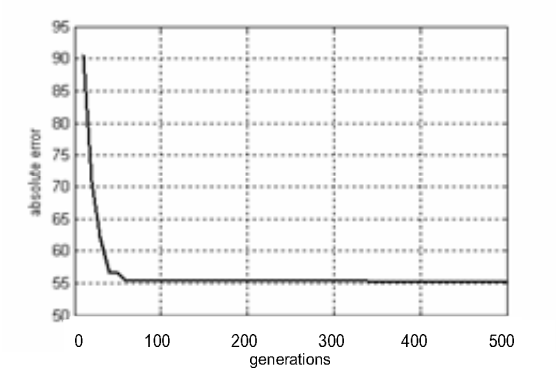

Figure 4. SAE Convergence of the fourth order system.

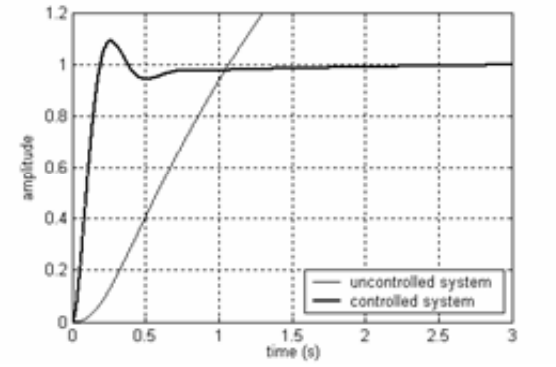

Figure 5. Step responses of fast and slow modes.

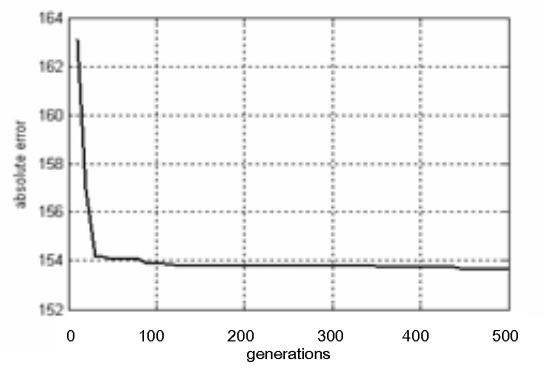

Figure 6. SAE Convergence of fast and slow modes.

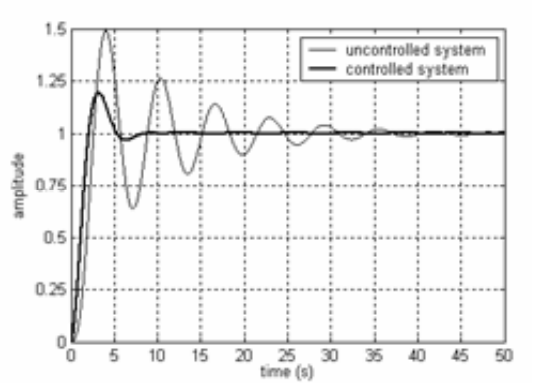

Figure 7. Step responses of the oscillatory system.

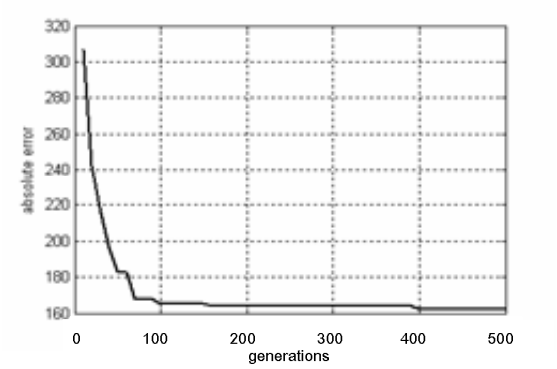

Figure 8. SAE Convergence of the oscillatory system.

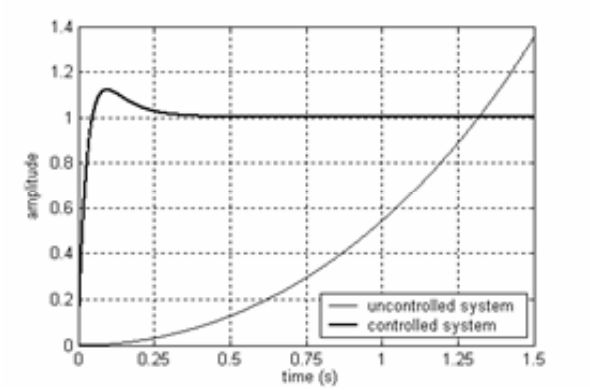

Figure 9. Step responses of unstable system.

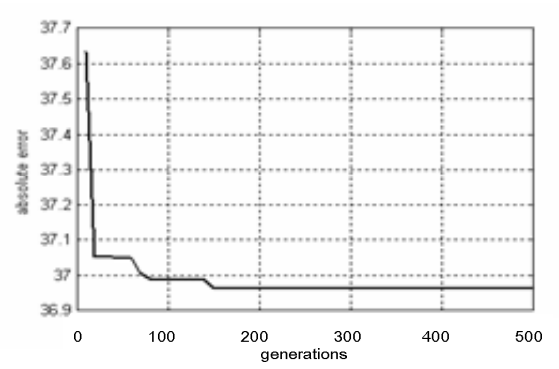

Figure 10. SAE Convergence of the unstable system.

REFERENCES

[1] K. J. Åström and T. Hägglund, "Benchmark Systems for PID Control," *IFAC Digital Control: Past, Present and Future of PID Control*, Terrassa, Spain, pp.165-166, 2000.

[2] S. Bennett, "Development of the PID controller," *IEEE Control System Magazine*, pp.58-65, 1994.

[3] B. J. Kuo, *Automatic Control Systems*, John Wiley & Sons, 2003.

[4] K. Ogata, *Modern Control Engineering*, Prentice-Hall, 2002.

[5] R. C. Dorf, *Modern Control Systems*, Prentice-Hall, 2005.

[6] J. G. Ziegler and N. B. Nichols, "Optimum Settings for Automatic Controllers," *Trans. ASME*, vol. 64, pp.759-768, 1942.

[7] G. H. Cohen and G. A. Coon, "Theoretical Consideration of Retarded Control," *Trans. ASME*, vol. 75, pp.827-834, 1953.

[8] A. O. Dwyer, *Handbook of PI and PID Controller Tuning Rules*, Imperial College Press, 2003.

[9] S. Mehrdad and C. Greg, "An Adaptive PID Controller based on Genetic Algorithm Processor," *Proc. IEE Conf. on Genetic Algorithm in Engineering System*, pp.88-93, 1995.

[10] Y. Mitsukura, T. Yamamoto, and M. Kaneda, "A Design of Self-tuning PID Controller using a Genetic Algorithm," *Proc. American Control Conference*, pp.1361-1365, 1999.

[11] J. F. Whidborne, "A Genetic Algorithm Approach to Design Finite-Precision PID Controller Structures," *Proc. American Control Conference*, pp.4338-4342, 1999.

[12] D. E. Goldberg, *Genetic Algorithm in Search, Optimization, and Machine Learning*, Addison-Wesley Publishing, 1989.

[13] L. Davis, *Handbook of Genetic Algorithms*, International Thomson Publishing, New York, 1991.

TABLE I
LIST OF PID CONTROLLERS AND STEP RESPONSES OBTAINED FROM GA.

Plant	PID controllers			System responses				Cost function, J
	K_p	K_i	K_d	t_r (sec)	$P.O.$(%)	t_s (sec)	E_{ss}	
$G_{p1}(s)$	3.78	2.16	2.32	0.80	8.50	2.20	0.00	55.40
$G_{p2}(s)$	8.33	1.50	1.20	0.22	9.00	1.25	0.00	153.78
$G_{p3}(s)$	0.24	1.21	1.22	2.20	19.50	7.50	0.00	162.44
$G_{p4}(s)$	449.86	45.75	44.83	0.08	12.50	0.38	0.00	36.96

A Design Method for Modified PID Controllers for Time-Delay Plants And Their Application

Kou Yamada, Takaaki Hagiwara and Yosuke Shimizu
Department of Mechanical System Engineering
Gunma University
Kiryu, Gunma 376–8515 Japan
Email: yamada@me.gunma-u.ac.jp

***Abstract*—In this paper, we examine a design method for modified PID (Proportional-Integral-Derivative) controllers for stable or minimum-phase time-delay plants. PID controller structure is the most widely used one in industrial applications. Recently the parametrization of all stabilizing PID controller has been considered. However no method has been published to guarantee the stability of PID control system for any stable or minimum-phase time-delay plants and the admissible sets of P-parameter, I-parameter and D-parameter to guarantee the stability of PID control system are independent from each other. In this paper, we propose a design method for modified PID controllers such that the modified PID controller make the feedback control system for any stable or minimum-phase time-delay plants stable and the admissible sets of P-parameter, I-parameter and D-parameter are independent from each other.**

I. Introduction

PID (Proportional-Integral-Derivative) controller is most widely used controller structure in industrial applications [1–3]. Its structural simplicity and sufficient ability of solving many practical control problems have contributed to this wide acceptance. Several papers on tuning methods for PID parameters have been considered [4–14]. However the method in [4–14] do not guarantee the stability of closed-loop system. The reference in [15–18] propose design methods of PID controllers to guarantee the stability of closed-loop system. However, using the method in [15–18], it is difficult to tune PID parameters to meet control specifications. If admissible sets of PID parameters to guarantee the stability of closed-loop system are obtained, we can easily design stabilizing PID controllers to meet control specifications.

The problem to obtain admissible sets of PID parameters to guarantee the stability of closed-loop system is known as a parametrization problem [3], [19], [20]. If there exists a stabilizing PID controller, the parametrization of all stabilizing PID controller is considered in [3], [19], [20]. However the method in [3], [19], [20] remains a difficulty. The admissible sets of P-parameter, I-parameter and D-parameter in [3], [19], [20] are related each other. That is, if P-parameter is changed, then the admissible sets of I-parameter and D-parameter change. From practical point of view, it is desirable that the admissible sets of P-parameter, I-parameter and D-parameter are independent from each other. Yamada and Moki initially tackle this problem and propose a design method for modified PI controllers for any minimum-phase systems such that the admissible sets of P-parameter and I-parameter are independent from each other [21]. Yamada expand the result in [21] and propose a design method for modified PID controllers for minimum-phase plant such that the admissible sets of P-parameter, I-parameter and D-parameter are independent from each other [22]. For stable plants, a design method for modified PID controllers have been considered in [23]. However, no paper gives a design method for modified PID controllers for any stable or minimum-phase time-delay plants such that the stability of control system is guaranteed and the admissible sets of P-parameter, I-parameter, D-parameter, which guarantee the stability of PID control system are independent from each other.

In this paper, we expand the result in [21–23] and propose a design method for modified PID controllers such that modified PID controller makes the closed-loop system stable for any stable or minimum-phase time-delay plants and the admissible sets of P-parameter, I-parameter and D-parameter to guarantee the stability of closed-loop system are independent from each other.

II. Problem formulation

Consider the closed-loop system in Fig. 1. Here, $G(s)e^{-sT}$

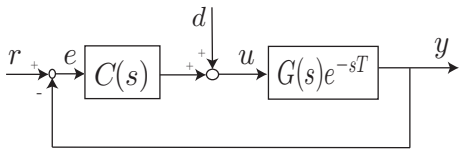

Figure 1. Feedback control system

is the single-input/single-output time-delay plant, $G(s) \in R$ is assumed to be strictly proper and to have no zero on the origin, $T > 0$ is time-delay, $C(s)$ is the controller, $r \in R$ is the reference input, $u \in R$ is the control input, $y \in R$ is the output, $d \in R$ is disturbance and $e \in R$ is the error.

When the controller $C(s)$ has the form written by

$$C(s) = a_P + \frac{a_I}{s} + a_D s, \tag{1}$$

then the controller $C(s)$ is called the PID controller [1], [3], [19], [20], where $a_P \in R$ is the P-parameter, $a_I \in R$ is the I-parameter and $a_D \in R$ is the D-parameter. a_P, a_I and a_D are

settled so that the closed-loop system in Fig. 1 has desirable control characteristics such as steady state characteristic and transient characteristic. For easy explanation, we call $C(s)$ in (1) the conventional PID controller. The transfer function from r to y in Fig. 1 is written by

$$y = \frac{G(s)\left(a_P + \frac{a_I}{s} + a_D s\right)e^{-sT}}{1 + G(s)\left(a_P + \frac{a_I}{s} + a_D s\right)e^{-sT}} r. \tag{2}$$

It is obvious that when a_P, a_I and a_D are settled at random, the stability of the closed-loop system in Fig. 1 does not guaranteed. Using the result in [3], [19], [20], if a stabilizing PID controller $C(s)$ in (1) for $G(s)$ exists, we can design PID controller $C(s)$ in (1) to stabilize the closed-loop system in Fig. 1. That is, the admissible sets of a_P, a_I and a_D to stabilize the closed-loop system in Fig. 1 are obtained in [3], [19], [20]. According to [3], [19], [20], the admissible sets of a_P, a_I and a_D are related each other. That is, if a_P is changed, then the admissible sets of a_I and a_D change. From practical point of view, it is desirable that the admissible sets of a_P, a_I and a_D are independent from each other. Further, generally, the transfer function in (2) has an infinite number of poles. It is difficult to give desirable control characteristics such as input output characteristics and disturbance attenuation characteristics.

The purpose of this paper is to propose a design method for modified PID controllers $C(s)$ in Fig. 1, which have following characteristics.

1) The stability of the closed-loop system in Fig. 1 is guaranteed.
2) The transfer functions from r to y and that from d to y in Fig. 1 have a finite number of poles.
3) The admissible sets of P-parameter a_P, I-parameter a_I and D-parameter a_D to guarantee the stability of closed-loop system in Fig. 1 are independent from each other.
4) The role of P-parameter a_P, I-parameter a_I and D-parameter a_D in the modified PID controller are equivalent to that of the conventional PID controller in (1).

III. The basic idea

In this section, we describe a basic idea to design for modified PID controllers $C(s)$ that have characteristic described in Section II .

In order to design modified PID controllers $C(s)$ that can be applied to any stable or minimum-phase time-delay plants and to make the transfer function from r to y and that from d to y have a finite number of poles, we adopt the parametrization of all stabilizing modified Smith predictors for any stable or minimum-phase time-delay plant in [24]. Using the result in [24], the basic idea to design for modified PID controllers $C(s)$ that have characteristics descibed in Section II . is summarized as follows.

1) When $G(s)$ is stable
According to [24], the parametrization of all stabilizing modified Smith predictor for stable time-delay plants is written by

$$C(s) = \frac{Q(s)}{1 - Q(s)G(s)e^{-sT}}, \tag{3}$$

where $Q(s) \in RH_\infty$ is any function. Using the controller in (3), the transfer function from r to y and that from d to y in Fig. 1 are written by

$$y = Q(s)G(s)e^{-sT}r \tag{4}$$

and

$$y = (1 - Q(s)G(s)e^{-sT})G(s)e^{-sT}d, \tag{5}$$

respectively. From the assumption that $Q(s) \in RH_\infty$, the transfer function in (4) and (5) have a finite number of poles. In addition, it is obvious that the stability of the closed-loop system in Fig. 1 is guaranteed. In order to design the modified PID controllers that have characteristics described in Section II ., the free parameter $Q(s)$ in (3) is settled so that $C(s)$ in (3) has the same characteristics to conventional PID controller $C(s)$ in (1). Therefore, next, we describe the role of conventional PID controller $C(s)$ in (1) in order to clarify the condition that the modified PID controller $C(s)$ must be satisfied. From (1), using $C(s)$, the P-parameter a_P, the I-parameter a_I and the D-parameter a_D are decided by

$$a_P = \lim_{s\to\infty}\left\{-s^2\frac{d}{ds}\left(\frac{1}{s}C(s)\right)\right\}, \tag{6}$$

$$a_I = \lim_{s\to 0}\{sC(s)\} \tag{7}$$

and

$$a_D = \lim_{s\to\infty}\frac{d}{ds}\{C(s)\}, \tag{8}$$

respectively. Therefore, if the controllers $C(s)$ in (3) holds (6), (7) and (8), the role of controller $C(s)$ in (3) is equivalent to that of the conventional PID controller $C(s)$ in (1). That is, we can design stabilizing modified PID controllers such that the role of controllers $C(s)$ in (3) is equivalent to that of the conventional PID controller $C(s)$ in (1).

2) When $G(s)$ is of minimum phase
According to [24], the parametrization of all stabilizing modified Smith predictor for minimum-phase time-delay plants is written by

$$C(s) = \frac{C_f(s)}{1 - C_f(s)G(s)e^{-sT}}, \tag{9}$$

$$C_f(s) = \frac{\bar{G}_u(s)}{G_u(s)}\left(1 + \frac{Q(s)}{G_u(s)}\right), \tag{10}$$

where $Q(s) \in RH_\infty$ is any function, $\bar{G}_u(s) \in \mathcal{U}$ satisfies

$$\bar{G}_u(s_i) = \frac{1}{G_s(s_i)e^{-s_i T}} \quad (i = 1, \ldots, n), \tag{11}$$

n is the number of unstable poles of $G(s)$, $s_i (i = 1, \ldots, n)$ are unstable poles of $G(s)$, $G_s(s)$ is a stable minimum-phase function of $G(s)$, that is, when $G(s)$ is factorized as

$$G(s) = G_u(s)G_s(s), \tag{12}$$

$G_u(s)$ is the unstable biproper minimum-phase function and $G_s(s)$ is the stable minimum-phase function. using the controller in (9), the transfer function from r to y and that from d to y are written by

$$y = \bar{G}_u(s)\left(1 + \frac{Q(s)}{G_u(s)}\right) G_s(s)e^{-sT}r \tag{13}$$

and

$$\begin{aligned} y &= \left\{1 - \bar{G}_u(s)\left(1 + \frac{Q(s)}{G_u(s)}\right)\right. \\ &\quad \left.\cdot G_s(s)e^{-sT}\right\} G(s)e^{-sT}d, \end{aligned} \tag{14}$$

respectively. From $Q(s) \in RH_\infty$, $\bar{G}_u(s) \in \mathcal{U}$, $G_s(s) \in RH_\infty$ and $1/G_u(s) \in RH_\infty$, the transfer function in (13) and (14) have finite number of poles. In addition, it is obvious that the stability of the closed-loop system in Fig. 1 is guaranteed. If the controllers $C(s)$ in (9) holds (6), (7) and (8), the role of controller $C(s)$ in (3) is equivalent to that of the conventional PID controller $C(s)$ in (1). That is, we can design stabilizing modified PID controllers such that the role of controllers $C(s)$ in (9) is equivalent to that of the conventional PID controller $C(s)$ in (1).

IV. Modified PID controller, when $G(s)$ is stable

In this section, we describe a design method for the free parameter $Q(s)$ in (3) to make the controller $C(s)$ in (3) works as a modified PID controller. On account of limited space, we describe a design method of modified PID controller only.

A. Modified PID controller

In this subsection, we mention a design method for modified PID controller $C(s)$ that holds (6), (7) and (8), makes the closed-loop system in Fig. 1 stable and is able to apply to any stable time-delay plant $G(s)e^{-sT}$.

The modified PID controller $C(s)$ satisfying (6), (7) and (8) is written by (3), where

$$Q(s) = \frac{q_0 + q_1 s + q_2 s^2}{\tau_0 + \tau_1 s + \tau_2 s^2} + q_3 s, \tag{15}$$

$$q_0 = \frac{\tau_0}{G(0)}, \tag{16}$$

$$\begin{aligned} q_1 &= \frac{\tau_1}{G(0)} - q_3\tau_0 \\ &\quad - \frac{\tau_0}{G^2(0)}\left\{\frac{1}{a_I} - TG(0) + \frac{d}{ds}\left(G(s)\right)\Big|_{s=0}\right\}, \end{aligned} \tag{17}$$

$$q_2 = \tau_2 a_P \tag{18}$$

and

$$q_3 = a_D, \tag{19}$$

where $\tau_i > 0 \in R (i = 0, 1, 2)$. Since $Q(s)$ in (15) is improper, $Q(s)$ in (15) is not included in RH_∞. In order for $Q(s)$ to be included in RH_∞, (15) is modified as

$$Q(s) = \frac{q_0 + q_1 s + q_2 s^2}{\tau_0 + \tau_1 s + \tau_2 s^2} + \frac{a_D s}{1 + \tau_D s}, \tag{20}$$

where $\tau_D \in R > 0$. From $\tau_D > 0$ in (20), $Q(s)$ in (20) is included in RH_∞. This implies that the controller $C(s)$ in (3) with (20) makes the closed-loop system in Fig. 1 stable for any stable time-delay plant $G(s)e^{-sT}$ independent of a_P, a_I and a_D.

V. Modified PID controller, when $G(s)$ is of minimum-phase

In this section, we describe a design method for the free parameter $Q(s)$ in (10) to make the controller $C(s)$ in (3) works as a modified PID controller. The detail is omitted on account of limited space.

VI. Application for a heat flow experiment

In this section, we show an application for a heat flow experiment to illustrate the effectiveness of the proposed modified PID controller.

The illustrated heat flow experiment is shown in Fig. 2. The heat flow experiment consists of a duct equipped with a

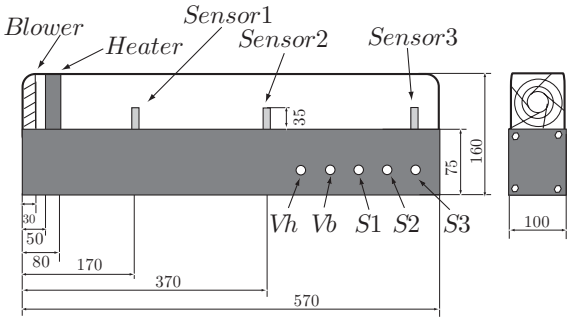

Figure 2. Illustrated heat flow apparatus

heater and a blower at one end and three temperature sensors located along the duct as shown in Fig. 2. V_h and V_b denote the voltage to heater and that to blower, respectively. S_1, S_2 and S_3 are terminals for measurements of temperatures at Sensor 1, Sensor 2 and Sensor 3. We denote T_i a measurements of temperatures at Sensor i.

The problem considered in this section is to design a modified PID controller to make T_3, which is temperature at Sensor 3, $30[\mathrm{deg}]$ steadily. When we settle $V_b = 5[V]$, we find the transfer function from V_h to T_3 which is temperatures at Sensor 3 is written by

$$T_3 = \frac{5.30}{1 + 18.15s}e^{-1.25s}V_h. \tag{21}$$

T_3 and V_h are considered as the output y and the control input u in the control system in Fig. 1, respectively. Then, from (21), $G(s)e^{-sT}$ in Fig. 1 is written by

$$G(s)e^{-sT} = \frac{5.30}{1+18.15s}e^{-1.25s}, \tag{22}$$

where $T = 1.25[\mathrm{sec}]$ and

$$G(s) = \frac{5.30}{1+18.15s}. \tag{23}$$

The reference input r in Fig. 1 is settled by $r(t) = 30[\mathrm{deg}]$.

Since $G(s)$ in (23) is stable, we design a modified PID controllers using the method described in Section IV a_P, a_I and a_D are settled by

$$\begin{cases} a_P &= 4.000 \\ a_I &= 0.140 \\ a_D &= 0.005 \end{cases}. \tag{24}$$

q_0, q_1, q_2 and q_3 are determined by (16), (17), (18) and (19), respectively, where

$$\begin{cases} \tau_0 &= 1 \\ \tau_1 &= 2 \\ \tau_2 &= 1 \end{cases} \tag{25}$$

and τ_D is selected by $\tau_D = 1$. Using above-mentioned parameters, the modified PID controller $C(s)$ is designed by (3) with (20).

Experimental step response of the control system using modified PID controller $C(s)$ is shown in Fig. 3. Figure 3

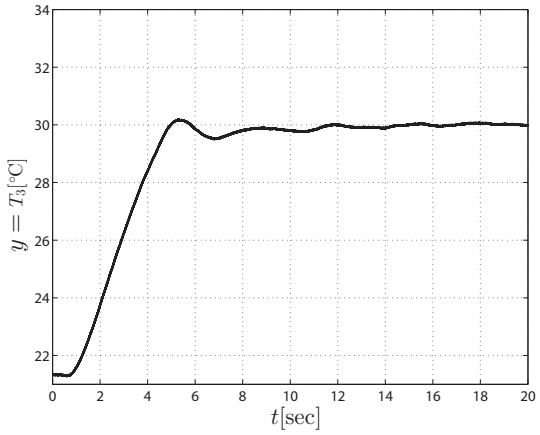

Figure 3. Experimental step response using the modified PID controller

shows that the output $y = T_3$ follows the step reference input $r = 30$ negligible steady state error with high convergence speed comparing to open-loop response.

VII. CONCLUSION

In this paper, we proposed a design method for modified PID controllers such that modified PID controller makes the closed-loop system for any stable or minimum phase time-delay plants asymptotically stable and the admissible sets of P-parameter, I-parameter and D-parameter are independent from each other.

REFERENCES

[1] N. Suda, PID Control, Asakura Shoten, Tokyo, 1992(in Japanese).

[2] K. Astrom and T. Hagglund, PID controllers: Theory design, and tuning, Instrument Society of America, North Carolina, 1995.

[3] A. Datta, M. T. Ho and S. P. Bhattacharyya, Structure and Synthesis of PID Controllers, Springer-Velag, London, 2000.

[4] J.G. Zieglae and N.B. Nicholes, Optimum settings for automatic controllers, *Trans. ASME*, 64, pp.759–768, 1942.

[5] P. Hazebroek and B.L. van der Warden, The Optimal Adjustment of Regulators, *Trans. ASME*, 72, pp.317–332, 1950.

[6] P. Hazebroek and B.L. van der Warden, Theoretical Considerations on the Optimal Adjustment of Regulators, *Trans. ASME*, 72, pp.309–315, 1950.

[7] W.A. Wolf, Controller Setting for Optimum Control, *Trans. ASME*, 73, pp.413–418, 1951.

[8] K.L. Chien, J.A. Hrones and J.B. Reswick, On the Automatic Control of Generalized Passive Systems, *Trans. ASME*, 74, pp.175–185, 1952.

[9] G.H. Cohen and G.A. Coon, Theoretical Consideration of Retaeded Control, *Trans. ASME*, 75, pp.857–834, 1953.

[10] A.M. Lopez, J.A. Miller, C.L. Smith and P.W. Murrill, Tuning Controllers with Error-Integral Criteria, *Instrumentation Technology*, 14, pp.52–62, 1967.

[11] J.A. Miller, A.M. Lopez, C.L. Smith and P.W. Murrill, A Comparison of Controller Tuning Techniques, *Control Engineering*, 14, pp.72–75, 1967.

[12] T. Kitamori, A Method of Control System Design Based upon Partial Knowledge About Controlled process, *Transactions of the Society of Instrument and Control Engineers*, 15-4, pp.549–555, 1979(in Japanese).

[13] T. Kitamori, Design Method for PID Control Systems, *Journal of the Society of the Instrument and Control Engineers*, 19-4, pp.382–391, 1980(in Japanese).

[14] P. Cominos and N. Munro, PID Controllers: Recent Tuning Methods and Design to Specification, *IEE Proceedings*, 149, pp.46–53, 2002.

[15] F. Zheng, Q.G. Wang and T.H. Lee, On the Design of Multivariable PID Controllers via LMI Approach, *Automatica*, 38-3, pp.517–526, 2002.

[16] C. Lin, Q.G. Wang and T.H. Lee, An Improvement on Multivariable PID Controller Design via Iterative LMI Approach, *Automatica*, 40-3, pp.519–525, 2004.

[17] N. Viorel, M. Constantin, A. Dorel and C. Emil, Aspects of Pole Placement Technique in Symmetrical Optimum Method for PID Controller Design, *Preprints of the 16th IFAC World Congress DVD-ROM*, 2005.

[18] K. Tamura and K. Shimizu, Eigenvalue Assignment Method by PID Control for MIMO System, *Transactions of The Institute of Systems, Control and Information Engineers*, 19-5, pp.193-202, 2006(in Japanese).

[19] J. Yang, Parameter Plane Control Design for a Two-tank Chemical Reactor Systems, *Journal of the Franklin Institute*, Vol.331B, pp.61–76, 1994.

[20] M. T. Ho, A. Datta and S. P. Bhattacharyya, "A linear programming characterization of all stabilizing PID controllers", *Proceedings of the American Control Conference 1997*, pp.3922–3928, 1997.

[21] K. Yamada and T. Moki, "A design method for PI control for minimum phase systems", *Intelligent Engineering Systems Through Artificial Neural Networks*, Vol.13, pp.571–576, 2003.

[22] K. Yamada, "Modified PID controllers for minimum phase systems and their practical application", *Proceedings of The 2005 Electrical Engineering/Electronics, Computer, Telecommunication, and Information Technology (ECTI) International Conference*, Vol.II, 2005.

[23] K. Yamada, T. Matsushima and T. Hagiwara: A design method for modified PID controllers for stable plants, Proceedings of the 2006 Electrical Engineering/Electronics, Computer, Telecommunication, and Information Technology (ECTI) International Conference, Vol.I of II, pp.123-126, Ubon Ratchathani, Thailand, 2006.

[24] K. Yamada and N. Matsushima: A design method for Smith predictors for minimum-phase time-delay plants, ECTI Transactions on Computer and Information Technology, 2-2, pp.100-107, 2005.

DC Motor Identification and PID Controller Tuning Using Particle Swarm Optimization

Poomyos Payakkawan[1], Poj Tangamchit[1] and Saravuth Pothiya[2]

[1]Department of Control System and Instrumentation Engineering
King Mongkut's University of Technology Thonburi, Bangkok, Thailand
[2]Department of Electrical Engineering, North Eastern University, Khon Kaen, Thailand
poomyos_khunyai@hotmail.com, ipojchit@kmutt.ac.th.,p_saravuth@hotmail.com

***Abstract*- This paper presents a new technique based on particle swarm optimization (PSO) solving two applications, i.e. identification of a DC motor and tuning PID controller parameters. The identification of a DC motor application, the 2nd order transfer function with time delays is determined by the poles location searching mechanism base on PSO. This application is following: first, time responses of speed are determined by multi-levels step input voltage. Secondly, the noises of time responses are reduced by wavelet soft thresholding. Finally, the noiseless time responses are identified by PSO. The tuning PID controller parameters application, the gains of proportional, integral, and derivative are determined for minimize the integral of time multiplied by absolute error (ITAE) performance criteria by PSO. The simulation results show that the proposed method has effectiveness over Ziegler-Nichols method. This confirms that, the PSO can be efficiently used for system identification and tuning parameters of PID controller.**

Keywords: DC motor, Particle swarm optimization, PID tuning System Identification, Optimization

I. INTRODUCTION

DC motors are widely used in industry for various applications, such as robotics, rolling mills, machine tool, etc. Because of the speed of DC motor is easy to be controlled for the speed-torque curve being almost linear. For the speed control applications, the system identification is a pre-requisite to analysis of a dynamic system and design of an appropriate controller for improving its performance [1,2]. In this paper, a new method based on particle swarm optimization (PSO) to identify more accurate the mathematical model for DC motors is proposed.

During the past decades, the process control techniques in the industry have made great advances. Numerous control methods such as adaptive control, neural control, and fuzzy control have been studied. Among them, the best known is the proportional-integral-derivative (PID) controller, which has been widely used in the industry because of its simple structure and robust performance in a wide range of operating conditions. The Ziegler-Nichols tuning formula is perhaps the best known tuning method [3]. Unfortunately, it has been quite difficult to properly tune the gains of PID controllers because many industrial plants are often burdened with problems such as high order, time delays, and nonlinearities.

To overcome this problem, several heuristic methods have been proposed for tuning parameters of PID controllers. In general, it is often hard to find the optimal or near optimal PID parameters.

Many random search methods, such as simulated annealing (SA), genetic algorithm (GA) [4,5] and tabu search (TS) algorithm and PSO [7], have recently received much interest for achieving high efficiency and searching global optimal solution.

The PSO method, first introduced by Kennedy and Eberhart, is one of the modern heuristic algorithms. It was developed through simulation of a simplified social system, and has been found to be robust in solving continuous nonlinear optimization problems [6]. The PSO technique can generate a high-quality solution within shorter calculation time and stable convergence characteristic than other stochastic methods. Much research is still in progress for proving the potential of the PSO in solving complex problems.

Therefore, this paper, besides demonstrating how to employ the PSO method to identify a DC motor and obtain the optimal PID controller parameters for speed control of DC motor systems.

II. MODELING OF A DC MOTOR AND A PID CONTROLLER

Fig.1 shows a schematic diagram of a dc motor. For constant field, the armature voltage controlled needs to be considered here.

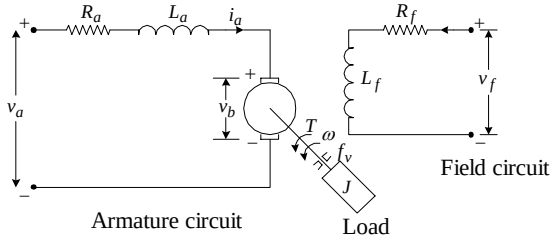

Fig.1. Schematic diagram of a dc motor

A. Mathematical model of a DC motor

Consider the dynamic model of a DC motor given by the following differential equations.

$$T(t) = k_t i_a(t) \quad (1)$$

$$v_b(t) = k_b\omega(t) \quad (2)$$

$$R_a i_a + L_a \frac{di_a(t)}{dt} + k_b\omega(t) = v_a(t) \quad (3)$$

$$T(t) = J\frac{d\omega(t)}{dt} + f_v\omega(t) \quad (4)$$

where, $T(t)$ is motor torque, $i_a(t)$ is armature current, v_b is back emf., $\omega(t)$ is angular velocity, R_a is armature resistance, L_a is armature inductance, $v_a(t)$ is armature voltage, J is moment of inertia, f_v is viscous friction, and k_t, k_b are constants.

Using the Laplace transform, the transfer function from the input voltage, V_a, to the output velocity, W is as follows:

$$G(s) = \frac{W(s)}{V_a(s)} = \frac{k_t}{JL_a s^2 + (JR_a + L_a f)s + R_a f_v + k_t k_b} \quad (5)$$

$$G(s) = \frac{K}{s^2 + as + b} \quad (6)$$

where $K = \frac{k_t}{JL_a}$, $a = \frac{JR_a + L_a f_v}{JL_a}$, and $b = \frac{R_a f_v + k_t k_b}{JL_a}$

Equation (5) is the 2nd order transfer function of a DC motor, If the model is determined using these parameters, it will be complex and will take a long time. Consider equation (5) or (6) again, it consists of two poles and a gain K. The objective of system identification is to determine only the coefficients a, b, and K, which get the time respond equals to the step respond from experiments. This method is an optimization problem, that can be applied to use the PSO

B. PID Controller

The transfer function of a PID controller is

$$u(t) = K_P e(t) + K_I \int_0^t e(t)dt + K_D \frac{de(t)}{dt} \quad (7)$$

where K_P is the proportional gain, K_I is the integral gain, and K_D is the derivative gain.

The variable $e(t)$ represents the tracking error, which is the difference between the desired input value $r(t)$ and the actual output $y(t)$.

The proportional controller K_P will have the effect of reducing the rise time and will reduce, but never eliminate, the steady-state error. An integral control K_I will have the effect of eliminating the steady-state error, but it may make the transient response worse. A derivative control K_D will have the effect of increasing the stability of the system, reducing the overshoot, and improving the transient response.

C. Time delays

Time delays are encounter so frequently in system that they deserve special attention. However, one can be approximated using *Pade' approximation*. In this paper used the 2nd order Pade approximation for approximated the time delays.

$$e^{-Ts} = \frac{1 - Ts/2 + T^2 s^2/12}{1 + Ts/2 + T^2 s^2/12} \quad (8)$$

III. Particle Swarm Optimization

The PSO method is an optimization technique which is motivated by social behaviors of organisms such as fish schooling and bird flocking. PSO provides a population-based search procedure in which individuals called "particles" change their positions (states) with time. In a PSO system, particles fly around in a multidimensional search space. During flight, each particle adjusts its position according to its own experience, and the experience of neighboring particles, making use of the best position encountered by itself and its neighbors. The swarm direction of a particle is defined by the set of particles neighboring the particle and its history experience.

Let x and v denote a particle coordinates (position) and its corresponding flight speed (velocity) in a search space, respectively. Therefore, the i-th particle is represented as $x_i = (x_{i1}, x_{i2}, \mathrm{K}, x_{id})$ in the ***d***-dimensional space. The best previous position of the i-th particle is recorded and represented as $pbest_i = (pbest_{i1}, pbest_{i2}, \mathrm{K}, pbest_{id})$. The index of the best particle among all the particles in the group is represented by the $gbest_d$. The rate of the velocity for particle i is represented as $v_i = (v_{i1}, v_{i2}, \mathrm{K}, v_{id})$. The modified velocity and position of each particle can be calculated using the current velocity and the distance from $pbest_{id}$ to $gbest_{id}$ as shown in the following formulas:

$$v_{id}^{t+1} = w \cdot v_{id}^t + c_1 * rand(\cdot) * \left(pbest_{id} - x_{id}^t\right) + c_2 * rand(\cdot) * \left(gbest_d - x_{id}^t\right) \quad (9)$$

$$x_{id}^{t+1} = x_{id}^t + v_{id}^{t+1},\ i = 1,2,\mathrm{K},n,\ d = 1,2,\mathrm{K},m \quad (10)$$

where n is number of particles in a group; m is number of members in a particle; t is pointer of iterations (generations); w is inertia weight factor; c_1, c_2 are acceleration constants; $rand(\cdot)$ is uniform random value in the range [0,1]; v_i^t is velocity of particle i at iteration t, $V_d^{\min} \le v_{id}^t \le V_d^{\max}$; x_i^t is current position of particle at iteration.

In the above procedures, the parameter $V^{\max}$ determined the resolution, or fitness, with which regions are to be searched between the present position and the target position. In many experiences, $V^{\max}$ was often set at 10–20% of the dynamic range of the variable on each dimension.

The constants c_1 and c_2 represent the weights of the stochastic acceleration terms that pull each particle toward the *pbest* and *gbest* positions. Hence, the acceleration constants c_1 and c_2 were often set to be 2.0 according to past experiences [6]. As originally developed, w often decreases

linearly from about 0.9 to 0.4 during a run. In general, the inertia weight is set according to the following equation:

$$w = w_{\max} - \frac{w_{\max} - w_{\min}}{iter_{\max}} \times iter \qquad (11)$$

where $iter_{\max}$ is the maximum number of iterations and $iter$ is the current number of iterations.

IV. Experiments and Simulation Results

A. Identification DC motor

A 1.1 kW, 220 V, 3000 rpm separately excited DC motor for identification is shown in Fig. 2. Its field current is 0.26 A rated. We applied 40 V to 220 V step input voltage into the DC motor and measured the time response of speed. The test data after reducing noise by wavelet soft thresholding are shown in Fig.3. The aim of identification is to determine the parameters a, b, and K of 2nd order transfer function of the DC motor which get the time response is to match that in the experiment. The performance index is the integral of time multiplied by absolute error (ITAE) between the experiment and the simulation. The ITAE also yields a system with a faster response than other criteria.

$$ITAE = \int_{o}^{t} t\left|f_{ex}(t) - f_{s}(t)\right|dt \qquad (12)$$

where $f_{ex}(t)$ is time response of experiment and $f_s(t)$ is the time response of simulation.

Fig.2 DC motor for identification and speed control

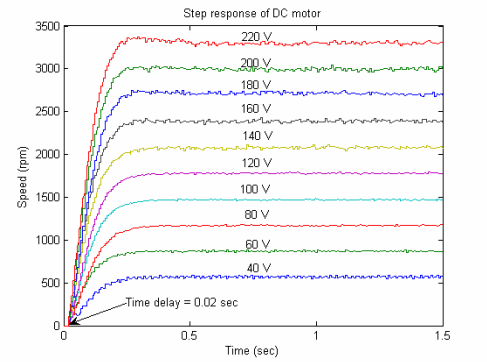

Fig.3 Test data of DC motor

Fig. 4 shows the example for identification in case input voltage is 120 V. After using PSO to identify, the time response of the simulation is nearly matched the time response of the experiment. The error is minimized. For other input voltages,we used the same procedure to identify. The results yield the transfer function for each input voltage as show in Table 1.

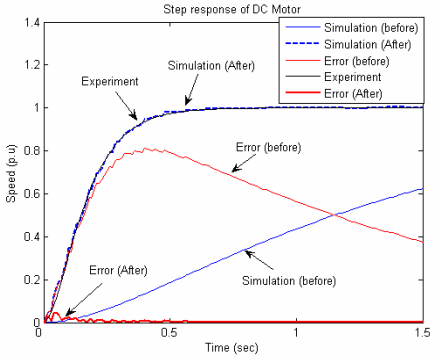

Fig.4 Comparison between experiment and simulation

Table 1 The transfer function of DC motor

Va	G(s)	Va	G(s)
40	$\frac{5632.78}{s^2+43.4s+398.64}$	140	$\frac{6222.45}{s^2+44.3s+433.62}$
60	$\frac{5762.02}{s^2+42.9s+410.4}$	160	$\frac{5860.71}{s^2+40.6s+409.84}$
80	$\frac{5928.01}{s^2+45.3s+416.01}$	180	$\frac{6031.29}{s^2+43.6s+426.24}$
100	$\frac{5826.58}{s^2+44.0s+408.31}$	200	$\frac{6071.60}{s^2+43.9s+420.18}$
120	$\frac{6314.37}{s^2+46.0s+440.64}$	220	$\frac{5855.97}{s^2+44.5s+403.86}$

* Va is input voltage and G(s) represent the transfer function.

The all parameters are represented by interval range.

$$a = [40.6, 46.0],\ b = [398.64, 440.64],\ K = [5632.78, 6314.37]$$

From the experiments, the system have time delays 0.02 sec. The overall transfer function can be compute by averaging the value of all data. Therefore, the overall transfer function with time delays of this DC motor is

$$G(s) = \frac{5950.58}{s^2 + 43.85s + 416.77} . e^{-0.02s} \qquad (13)$$

B. Tuning PID control using PSO

We Used the overall transfer function with time delays of the DC motor is given in equation (13) to design a speed controller based on PID controller using PSO. The objective is finding the parameters of the PID controller to minimize the performance criteria. The performance index used is the integral of time multiplied by absolute error (ITAE). Therefore, the overall transfer function with time delays is

$$G(s) = \frac{2.3802s^2 - 714.0696s + 71406.96}{0.0004s^4 + 0.1375s^3 + 17.4287s^2 + 576.2124s + 5001.24} \quad (14)$$

Table 2 shows the simulation results. In the table, *OS* represents the percent maximum overshoot, t_s stand for the 2 percent settling time, and e_{ss} is the steady state error. Time response is obtained from the process under the control of the PID controller designed using PSO is plotted in Fig.5. The results compare with Ziegler-Nichols method. The controller designed using the proposed method yields better control performance than the Ziegler-Nichols method.

To assess the effectiveness of the optimized PID parameters, the tracking speed input of the whole system, with the standard square wave response as shown in Fig. 6. And then, Fig.7 shows the responses when applied random load.

Table 2 Results obtained by using Ziegler-Nichols and PSO

method	Parameters			Performance		
	k_p	k_i	k_d	t_s	*OS*	e_{ss}
Ziegler-Nichols	0.2536	3.6059	0.0044	0.214	39.34	0
PSO	0.2206	2.1520	0.0063	0.137	12.53	0

*p.u. stand for per unit

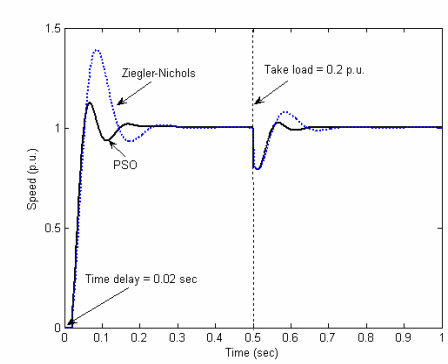

Fig.5 Time response obtained from Ziegler-Nichols and PSO

V. CONCLUSION

The application of PSO in system identification and PID tuning was briefly reviewed in this paper. Therefore, the proposed method has more robust stability and efficiency, and can solve these applications. The experiment confirms the suitability of the proposed method as a high performance control system for the DC motors and tuning PID controller.

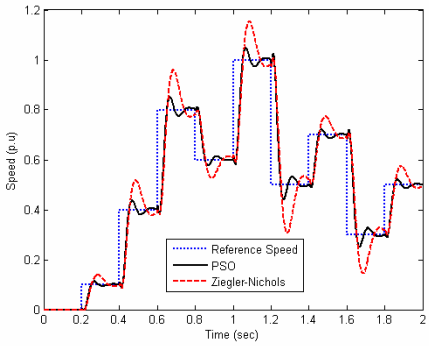

Fig.6 Tracking speed input

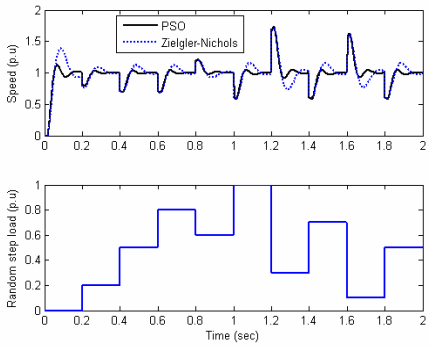

Fig.6 Time response when applied random load

REFERENCES

[1] K. Kristinsson, G.A. Dumont, "System identification and control using genetic algorithm", *IEEE Transaction on System Man and Cybernetics*, Vol. 22, pp. 1033-1046, 1992.

[2] Weixing Lin, Chongguang Jiang, and Jixin Qian, "The Identification of Hammerstein Model Based on PSO with Fuzzy Adaptive Inertia Weight", *Journal of systems Science and Information*, Vol. 3 No. 2, pp. 381-391, 2005.

[3] J.G. Ziegler and N.B. Nichols, "Optimum settling for automatic controllers", Trans. On ASME., vol. 64, 1942, pp. 759-768.

[4] R.A. Krohling and J.P.Rey, "Design of optimal disturbance rejection PID controller using genetic algorithm", *IEEE Trans. Evol. Comput.*, Vol.5, pp. 78-82, Feb. 2001.

[5] A. Visioli, "Optimal tuning of PID controllers for integral and unstable processes", *IEE Proc. Control Theory Appl.*, vol. 148, No. 2, March 2001.

[6] J. Kennedy and R. Eberhart, "Particle swarm optimization", *Proceeding of the 4th IEEE International Conference on Neural Networks*, pp. 1942-1948, 1995.

[7] Zwe-Lee Gaing, "A Particle Swarm Optimization Approach for Optimum Design of PID Controller in AVR System", *IEEE Transactions on Energy Conversion*, Vol. 19, No.2, pp.384-391, 2004.

June 25-28, 2006.

Simplified PI Controller for Two-Inertia System

Peerapon Pattanavijit[1], Songmoung Nundrakwang[1], Taworn Benjanarasuth[1],
Jongkol Ngamwiwit[1] and Noriyuki Komine[2]
[1] Faculty of Engineering and ReCCIT, King Mongkut's Institute of Technology Ladkrabang, Bangkok, Thailand
(Tel: +662-739-2405, E-mail: knjongko@kmitl.ac.th)
[2] School of Information Science and Technology, Tokai University, Kanagawa, Japan
(Tel: +81-463-58-1211, E-mail: komine@keyaki.cc.u-tokai.ac.jp)

***Abstract*- In this paper, a simplified designing method of a PI controller for a higher-order plant by using the concept of plant model reduction and the Coefficient Diagram Method with the less number of stability index γ_i is presented. By ignoring the non-dominant poles of the higher-order plant model, a lower-order plant model is first obtained. Then, the PI controller will be designed for controlling the lower-order plant model by using Coefficient Diagram Method with the appropriate values of stability index in order to achieve the system response without overshoot. Finally, the designed PI controller will be employed to control the original higher-order plant. The proposed controller is implemented to control a two-inertia system. The experimental results show that the PI controller designed from the lower-order plant model is sufficient for controlling the original higher-order plant with acceptable performance.**

I. INTRODUCTION

Since several decades ago, most of industrial processes have employed PID-family controllers due to their simplicity and sufficiency in process control applications. It is reported lately that more than 90% of the industrial controllers used nowadays are PI controllers. However, the parameters of the controller have to be tuned for acceptable responses. The Ziegler-Nichols' tuning formula [1] is the most popular method which is designed to have quarterly decayed overshoot characteristic in the step response but the fine tuning is needed for the practical use to reduce the overshoot in the closed-loop response.

In 1998, a new designing method called Coefficient Diagram Method (CDM) [2] has been proposed. The CDM is an algebraic design algorithm utilizing polynomial form structure. In CDM, the closed-loop characteristic polynomial is designed based on stability index and equivalent time constant, which are used to determine stability and speed of the closed-loop response. Hence, the unknown parameters of the controllers resulting for over-damped response can be obtained accordingly [3-4]. However, it is quite time consuming in designing the parameters of a controller especially for a higher-order plant.

In this paper, the simplified design of a PI controller for higher-order plant using CDM with less number of stability indexes γ_i is presented. By ignoring the non-dominant pole, the higher-order plant model is reduced to be a lower-order plant model. After that, the CDM is used to design the PI controller for controlling the lower-order plant model. Finally, the PI controller designed for the lower-order plant model is employed for controlling the original higher-order plant. In order to check the control capability of this designing method, the simplified PI controller is implemented to control the speed of the two-inertia system.

II. CDM AND PROPOSED CONTROL SYSTEM

The concept of CDM and the rearranged CDM control system structure are described respectively in this section.

A. CDM Concept

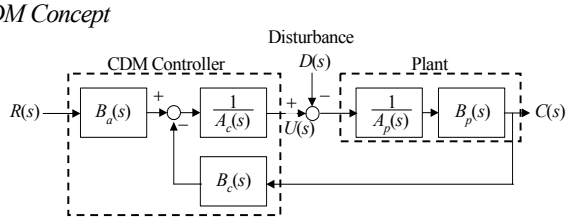

Figure 1. CDM control system structure.

The transfer function of the plant in the polynomial form for each block is

$$A_p(s) = p_k s^k + p_{k-1}s^{k-1} + \ldots + p_0, \tag{1a}$$

$$B_p(s) = q_m s^m + q_{m-1}s^{m-1} + \ldots + q_0, \tag{1b}$$

and the controller polynomials are

$$A_c(s) = l_\lambda s^\lambda + l_{\lambda-1}s^{\lambda-1} + \ldots + l_0, \tag{2a}$$

$$B_c(s) = k_\lambda s^\lambda + k_{\lambda-1}s^{\lambda-1} + \ldots + k_0, \tag{2b}$$

$$B_a(s) = k_0, \tag{2c}$$

where $\lambda < k$ and $m < k$. Hence, the characteristic polynomial of the closed-loop system shown in Fig. 1 can be given as

$$\begin{aligned} P(s) &= A_c(s)A_p(s) + B_c(s)B_p(s) \\ &= \sum_{i=0}^{n} a_i s^i. \end{aligned} \tag{3}$$

Note that it still has unknown controller's parameters to be solved. Based on CDM concept, the performance specification known as stability index γ_i and the equivalent time constant τ are defined by

$$\gamma_i = \frac{a_i^2}{a_{i+1}a_{i-1}}, \tag{4}$$

$$\tau = \frac{a_1}{a_0}, \tag{5}$$

$$\gamma_i^* = \frac{1}{\gamma_{i+1}} + \frac{1}{\gamma_{i-1}} \quad ; \quad \gamma_0, \gamma_n = \infty, \tag{6}$$

where $i = 1,\ldots, n-1$. The equivalent time constant τ is generally selected according to the specified settling time t_s as $t_s = 2.5\tau$ and the standard stability index is recommended to be

$$\gamma_{n-1} = \ldots = \gamma_3 = \gamma_2 = 2, \gamma_1 = 2.5 . \quad (7)$$

From (4) to (6), the coefficient a_i can be written by

$$a_i = a_0 \tau^i \frac{1}{\gamma_{i-1} \cdots \gamma_2^{i-2} \gamma_1^{i-1}} = a_0 \tau^i \prod_{j=1}^{i-1} \frac{1}{\left(\gamma_{i-j}\right)^j} . \quad (8)$$

Consequently, the characteristic polynomial to be employed to design the parameters of a controller is

$$P(s) = a_0 \left[\left\{ \sum_{i=2}^{n} \left(\prod_{j=1}^{i-1} {}^{1}\!/_{\gamma_{i-j}^{j}} \right) (\tau s)^i \right\} + \tau s + 1 \right]. \quad (9)$$

Hence, the parameters of the controller can be obtained by equating the characteristic polynomial in (3) to (9) with the known stability index γ_i and/or the equivalent time constant τ when the mathematical model of the plant is known.

B. Control Systems Structure

For simplicity in design, the original CDM control system structure in Fig. 1 is rearranged to be a rearranged CDM control system structure as shown in Fig. 2.

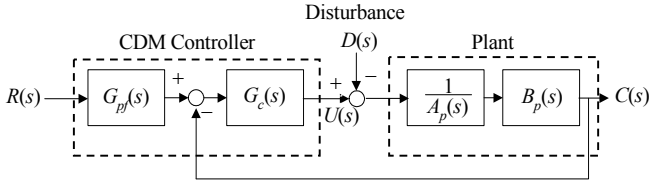

Figure 2. Rearranged CDM control system structure.

The transfer function of controller $G_c(s)$ and the pre-filter $G_{pf}(s)$ of the rearranged control system shown in Fig. 2 are

$$G_c(s) = \frac{B_c(s)}{A_c(s)} \quad (10)$$

and

$$G_{pf}(s) = \frac{B_a(s)}{B_c(s)} . \quad (11)$$

III. Two-Inertia System

The structure of two-inertia system [5] and its block diagram are shown in Fig. 3 and Fig. 4.

Figure 3. Two-inertia system.

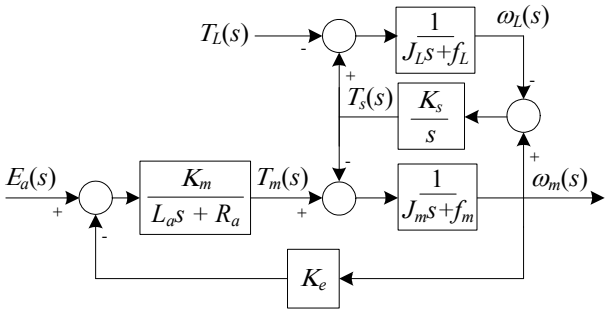

Figure 4. Block diagram of the two-inertia system.

By ignoring the viscous friction of the motor f_m and f_L, the transfer function of the two-inertia system will be

$$G_p(s) = \frac{\omega_m(s)}{E_a(s)} = \frac{a_2 s^2 + a_0}{b_4 s^4 + b_3 s^3 + b_2 s^2 + b_1 s + b_0} \quad (12)$$

where $b_4 = 1$, $b_3 = \frac{R_a}{L_a}$, $b_2 = \frac{K_s L_a (J_m + J_L) + K_m K_e J_L}{J_m J_L L_a}$,

$b_1 = \frac{K_s R_a (J_m + J_L)}{J_m J_L L_a}$, $b_0 = \frac{K_m K_e K_s}{J_m J_L L_a}$, $a_2 = \frac{K_m}{J_m L_a}$, $a_0 = \frac{K_m K_s}{J_m J_L L_a}$

and its parameters are shown in the Table I.

TABLE I
PARAMETER VALUES OF TWO-INERTIA SYSTEM

R_a	Armature resistance	0.25 Ω
L_a	Armature inductance	0.10 *mH*
K_e	Back electromotive force constant	3.85 *v / krpm*
K_m	Motor torque constant	3.2 *N – cm / A*
J_m	Moment of motor inertia	0.8 *kg – cm²*
J_L	Moment of load inertia	0.9 *kg – cm²*
K_s	Torsional stiffness of drive shaft	15 *N – m / rad*

IV. Controller Design

In this section, plant model order reduction, PI controller structure and the controller designing procedure will be described respectively.

A. Plant Model Order Reduction

Consider the *k*-order plant with the transfer function given as

$$G_p(s) = \frac{B_p(s)}{A_p(s)} = \frac{K \prod_{j=1}^{m} (s + z_j)}{\prod_{i=1}^{k} (s + p_i)}; \; k \geq m . \quad (13)$$

Without loss of generality, assuming that the plant contains the non-dominant poles $-p_i$ for $i = 1, 2, \ldots, l$. By ignoring the non-dominant poles, the n-order plant model can then be reduced to a lower-order plant model and its transfer function is

$$\tilde{G}_p(s) = \frac{\tilde{K}\prod_{j=1}^{m}(s+z_j)}{\prod_{i=l+1}^{k}(s+p_i)};\ \tilde{K} = \frac{K}{\prod_{i=1}^{l} p_i};\ k-l \geq m. \quad (14)$$

B. PI Controller Structure

The controller (11) in this paper is the conventional PI controller and its transfer function is

$$G_c(s) = K_p\left(1+\frac{1}{T_i s}\right), \quad (15)$$

where K_p and T_i are the proportional gain and the integral time, respectively. The other form of (15) can also be rewritten as

$$G_c(s) = \frac{B_c(s)}{A_c(s)} = \frac{K_p s + K_i}{s}, \quad (16)$$

where the gain K_p and K_i of (16) can be assigned from the controller design procedure stated in the next sub-section.

C. Controller Design Procedure

The designing steps for the PI controller are as follows:

(1) Find the closed-loop characteristic polynomial of the control system with the lower-order plant model (14) and the PI controller (16).

(2) Choosing the appropriate values of the stability index γ_i and/or the equivalent time constant τ to find the characteristic polynomial such that the over-damped response of the closed-loop system with lower-order plant model including $G_{pf}(s)$ is obtained, where $B_a(s)$ is the coefficient of s^0 of $B_c(s)$.

(3) Find the parameters of the controller by equating the characteristic polynomial obtained in step (2) with the characteristic polynomial obtained in step (1).

(4) Applying the PI controller obtained in step (3) to control the original plant.

V. Experimental Results

The experimental results of the speed control of the two-inertia system using the PI controller obtained from simplified design based on CDM approach will be shown in this section. From the transfer function of the two-inertia system in (12) and the values in Table I, the transfer function from input voltage to the motor speed is given by

$$G_p(s) = \frac{3\times10^4 s^2 + 6.67\times10^7}{s^4 + 2.5\times10^3 s^3 + 1.57\times10^5 s^2 + 8.85\times10^6 s + 2.57\times10^8}.$$

It is the fourth-order system and its open-loop poles are located at s = -39.6, -2436.8, -11.8+j50.2, -11.8-j50.2. The open-loop response of the two-inertia system when applying the input voltage at 5 volts is shown in Fig. 5. It is seen that there is an unsatisfied torsional resonance and must be reduced as much as possible by using a controller.

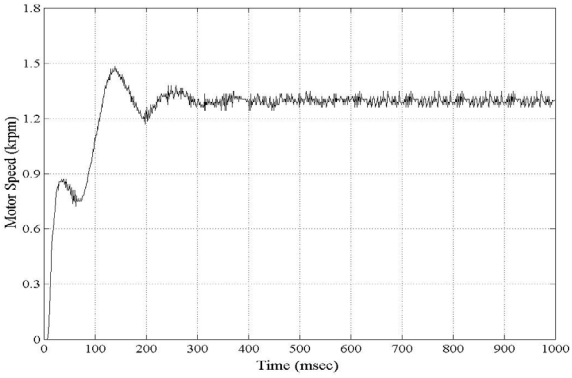

Figure 5. Open-loop step response of two-inertia system.

Since the poles at s = -39.6, -2436.8 are the non-dominant poles, the system is reduced to be a second-order model by ignoring them. Thus, its transfer function can be expressed as

$$\tilde{G}_p(s) = \frac{3\times10^4 s^2 + 6.67\times10^7}{9.65\times10^4 s^2 + 2.28\times10^6 s + 2.57\times10^8}.$$

Based on the controller design procedure stated previously, the parameters K_p and K_i of the PI controller including the equivalent time constant τ of the closed-loop system obtained by using the lower-order plant model with $\gamma_1 = 7$ and $\gamma_2 = 0.5$ are shown in the Table II. Note that the gamma values are chosen to give the positive values of K_p and K_i of the PI controller when the simplified design method is employed. For comparison, the parameters of PI controller and the equivalent time constant τ obtained from the original plant model with $\gamma_1 = 2.5, \gamma_2 = 2, \gamma_3 = 1.34$ and $\gamma_4 = 32.4$ can also be shown in the Table II.

TABLE II
PARAMETERS OF PI CONTROLLERS

Plant Type	K_p	K_i	τ *(msec)*
Original model	0.87	54.08	87
Reduced model	0.41	43.15	88

The PI controller designed from the lower-order plant model is used to control the speed of the two-inertia system at the speed of 1300 rpm. The proposed control system obtained from simplified design method will be compared to the other one using the PI controller obtained by direct design in order to show the effectiveness of the proposed design method. The results will be shown in two aspects. The first aspect is the system performance and the second aspect is the capability of the simplified design PI controller.

A. System Performances

The experimental results in controlling the motor speed of the two-inertia system are shown in Fig. 6. It is seen that the proposed PI controller can control the speed at 1300 rpm without torsional resonance, overshoot and steady-state error. It is also seen that the system response speed quite similar to

the response of the system using PI controller obtained from direct design. This can be seen from the value of equivalent time constant τ obtained from the simplified design shown in the Table II that its value is close to the one obtained from the direct design. The system performances of both control systems are also summarized in Table III.

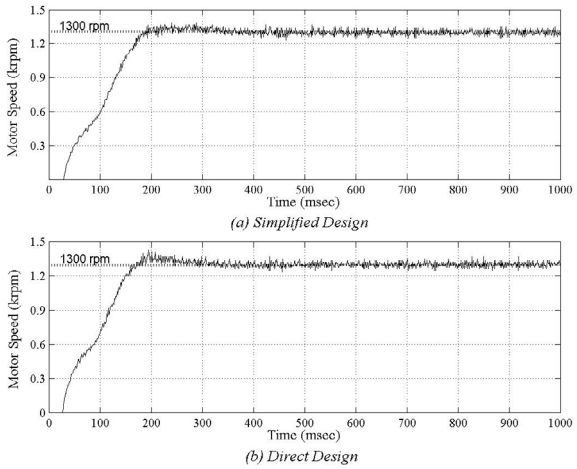

Figure 6. Step responses of control systems at 1300 rpm.

TABLE III
SYSTEM PERFORMANCE AT 1250 RPM.

Design Method	t_r *(msec)*	t_s *(msec)*	P_O *(%)*
Direct	151	292	3.8
Simplified	176	302	2.3

B. Capability of the Simplified Design PI Controller

The capability of the PI controller designed from the lower-order plant model is investigated by retarding the motor reference speed of the control system at 500 msec from 1300 rpm to 800 rpm. Its responses is shown in Fig. 7. From the responses, the motor speed of system using proposed controller can reach to 800 rpm properly and similarly as the control system using the PI controller obtained from direct design.

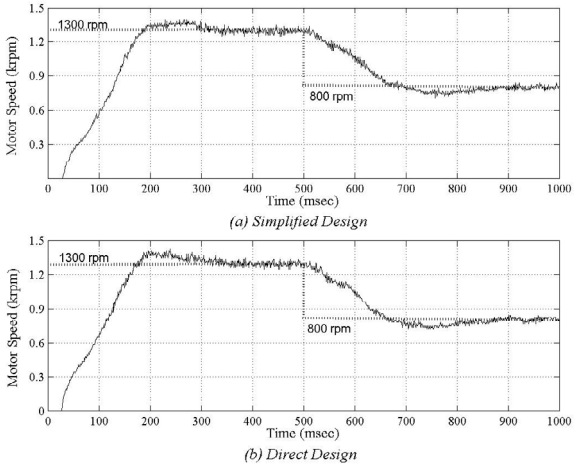

Figure 7. Responses due to speed retard to 800 rpm.

In order to compare the disturbance rejection capability of the simplified design PI controller and the direct design PI controller, the motor reference speed at 1300 rpm and the constant load disturbance entering at 500 msec are considered. It is seen from the Fig. 8 that the proposed control system can reject the effect of the load disturbance and reach to the speed at 1300 rpm without error similarly.

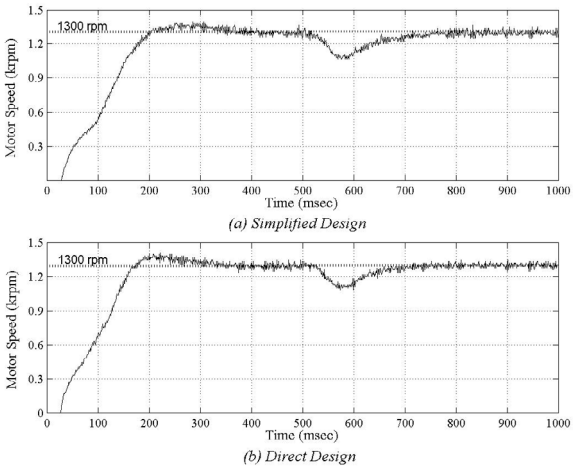

Figure 8. Responses with constant load disturbance.

V. CONCLUSIONS

The simplified design of a PI controller for a higher-order plant by using the CDM concept has been proposed in this paper. The proposed controller is implemented to control the speed of the two-inertia system. Not only the simplicity in designing but the speed of the response can still be improved to meet the desired system performance as well. In addition, the unsatisfied torsional resonance can also be reduced. The effectiveness of this designing method has been confirmed by the experimental results.

REFERENCES

[1] J. G. Ziegler, and N. B. Nichols, "Optimum Settings for Automatic Controllers," *ASME Trans.* 64, pp.759-68, 1942.

[2] S. Manabe, "Coefficient Diagram Method," *Proc. of the 14th IFAC Symposium on Automatic Control in Aerospace*, pp.199-210, 1998.

[3] D. Kumpanya, T. Benjanarasuth, J. Ngamwiwit and N. Komine, "PI Controller Design with Feed forward by CDM for Level Processes," *Proc. of the 2000 IEEE TENCON*, pp. II-65 – II-69, 2000.

[4] S. E. Hamamci, M. Koksal and S. Manabe, "Robust Position Control of a Radar Antenna with the Coefficient Diagram Method*," Proc. of the 4th Asian Control Conference*, pp.1785-1790, 2002.

[5] D. Kumpanya, "Feedforward Controller Design Incorporating PI Controller Designed by Coefficient Diagram Method" Master Thesis, King Mongkut's Institute of Technology Ladkrabang, Bangkok, 2002.

Hybrid PD - Sliding Mode Controller Designed for Inverted Pendulum System

Samatthachai Panya[1], Jongkol Ngamwiwit[1], Taworn Benjanarasuth[1],
Songmoung Nundrakwang[1] and Noriyuki Komine [2]
[1] Faculty of Engineering and ReCCIT, King Mongkut's Institute of Technology Ladkrabang, Bangkok, Thailand
(Tel: +662-739-2405, E-mail: knjongko@kmitl.ac.th)
[2] School of Information Science and Technology, Tokai University, Kanagawa, Japan
(Tel: +81-463-58-1211, E-mail: komine@keyaki.cc.u-tokai.ac.jp)

***Abstract*-The design of hybrid controller consisting of PD controller and sliding mode controller for inverted pendulum system is proposed in this paper. The PD controller is applied for controlling position of the cart to swing up the pendulum from the natural pendent position to around the upright position. The sliding mode controller is utilized for stabilizing the inverted pendulum in the upright position. Root-locus method is applied to tune the PD controller, while the sliding mode controller is designed based on pole placement. The experimental results of the proposed control system are also shown in this paper.**

I. INTRODUCTION

In control area, the inverted pendulums are one of the most commonly studied systems. Many variations of the inverted pendulum often represent different kinds of the robotic arms [1]. The inverted pendulum to be discussed in this paper is an inverted pendulum on cart as depicted in Fig. 1. This inverted pendulum consists of a cart and a pendulum hinged to the cart via a pivot and only the cart is actuated. Swinging up and stabilizing the inverted pendulum have many advantages in theoretical study such as simple structure, nonlinear and uncertain characteristics. Many control methods have been implemented to control the inverted pendulums, for instance, nonlinear control [2], energy-based method [3] and Qubit neural network [4]. Though using these algorithms gives good performance, they are complicated to design and implement.

In this paper, a controller designed by using hybrid PD controller with sliding mode control algorithm to swing up the pendulum from the natural pendent position to around the upright position and to stabilize inverted pendulum in the upright position is proposed. It composes of two parts. The first part is the PD position control and the second part is the sliding mode control. In the first part, a PD controller is employed for swinging up the pendulum from the natural pendent position to around the upright position. The gains of the PD controller are assigned by root-locus method to obtain fast step response with small overshoot. The PD controller controls the motion of the pendulum by moving the cart back and forth within a limited traveling range of the cart. The cart will be controlled to move to the opposite direction when the angular velocity of the pendulum at the stop point of each travel is zero. The cart movement will be repeated to next assigned cart position until the inverted pendulum swings up around the upright position. When this condition is reached, the second part, which is a sliding mode controller, will be switched to stabilize the inverted pendulum. In this paper, this sliding mode controller is designed based on pole placement method. The effectiveness and reliability of the proposed method in actual experiments will be shown.

II. MATHEMATICAL MODEL

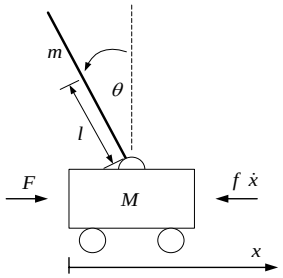

Figure 1. Inverted pendulum on cart.

Fig. 1 shows the structure of the inverted pendulum on cart system where variables θ, x and F denote the pendulum angle (rad), the cart position (m) and the force applied to the cart (N) respectively. The system parameters include the mass of the cart M (kg), the mass of the pendulum m (kg), the distances from the turning center to the center of gravity of the pendulum l (m), and the cart's friction coefficient f (kg/s).

The mathematical model of the inverted pendulum can be computed either by Newton's law or Lagrange's equations with respect to x and θ coordinates. If $x_1 = \theta$, $x_2 = \dot{\theta}$, $x_3 = x$ and $x_4 = \dot{x}$ are selected as state variables and applying force F is denoted by input $u(t)$, the nonlinear state space model of the system can be then obtained as

$$\begin{aligned}
\dot{x}_1 &= x_2 \\
\dot{x}_2 &= \frac{\left(mg \sin x_1 + \dfrac{m \cos x_1 (u - fx_4 - m^2 l x_2^2 \cos x_1 \sin x_1)}{(M+m)} \right)}{\left(\dfrac{4}{3} ml - \dfrac{m^2 l \cos^2 x_1}{(M+m)} \right)} \\
\dot{x}_3 &= x_4 \\
\dot{x}_4 &= \frac{\left(u - fx_1 + \dfrac{3}{4} mg \cos x_1 \sin x_1 - ml x_2^2 \sin x_1 \right)}{(M+m) - \dfrac{3}{4} m \cos^2 x_1}.
\end{aligned} \tag{1}$$

In this case, the input $u(t)$ or the force F is generated by DC motor. The state vector $\mathbf{x}^T(t) = \begin{bmatrix} x_1 & x_2 & x_3 & x_4 \end{bmatrix}^T = \begin{bmatrix} \theta & \dot{\theta} & x & \dot{x} \end{bmatrix}^T$ will be subsequentially used for shortening mathematical notation.

Concerning to the angle of the pendulum, the inverted pendulum system has two distinct equilibrium points. The first one is at the upright position and it is naturally unstable. The other one is at the hanging position and it is stable.

For designing the swinging up PD controller, the model of the inverted pendulum will be linearized at the natural pendent position. Corresponding to this equilibrium point, the control input $u(t)$ and state variables $\mathbf{x}(t)$ are considered at $u_0(t) = 0$ and $\mathbf{x}_0^{\ T}(t) = [\pi \ 0 \ 0 \ 0]^T$. The linear state equations can be obtained as (2)

$$\dot{\mathbf{x}}(t) = \mathbf{A}\mathbf{x}(t) + \mathbf{B}u(t). \tag{2}$$

when

$$\mathbf{A} = \begin{bmatrix} 0 & 1 & 0 & 0 \\ \dfrac{-3(M+m)mg}{4ml(M+m)-3m^2l} & 0 & 0 & \dfrac{3mf}{4ml(M+m)-3m^2l} \\ 0 & 0 & 0 & 1 \\ \dfrac{3mg}{4\left((M+m)-\frac{3}{4}m\right)} & 0 & 0 & \dfrac{-f}{(M+m)-\frac{3}{4}m} \end{bmatrix}, \mathbf{B} = \begin{bmatrix} 0 \\ \dfrac{-3m}{4ml(M+m)-3m^2l} \\ 0 \\ \dfrac{1}{(M+m)-\frac{3}{4}m} \end{bmatrix}.$$

As the main interest of this part is to control the position x of the cart, the following output equation can be given in (3) where $\mathbf{C} = [0 \ 0 \ 1 \ 0]$.

$$y(t) = \mathbf{C}\,\mathbf{x}(t) \tag{3}$$

Nevertheless, in order to design the sliding mode controller for stabilizing the inverted pendulum, the model of the inverted pendulum system is also needed to be linearized at the upright position. The linearization is therefore calculated at $u_0(t) = 0$ and $\mathbf{x}_0^{\ T}(t) = [0 \ 0 \ 0 \ 0]^T$. The resulting linear state equations can be similarly obtained as (2) but with

$$\mathbf{A} = \begin{bmatrix} 0 & 1 & 0 & 0 \\ \dfrac{3(M+m)mg}{4ml(M+m)-3m^2l} & 0 & 0 & \dfrac{-3mf}{4ml(M+m)-3m^2l} \\ 0 & 0 & 0 & 1 \\ \dfrac{3mg}{4\left((M+m)-\frac{3}{4}m\right)} & 0 & 0 & \dfrac{-f}{(M+m)-\frac{3}{4}m} \end{bmatrix}, \mathbf{B} = \begin{bmatrix} 0 \\ \dfrac{3m}{4ml(M+m)-3m^2l} \\ 0 \\ \dfrac{1}{(M+m)-\frac{3}{4}m} \end{bmatrix}.$$

III. HYBRID CONTROL SYSTEM STRUCTURE

The overall structure of the proposed control system is shown in Fig. 2. It is composed of a PD controller and a sliding mode controller. The PD controller is employed to control the inverted pendulum around its upright position while the sliding mode controller is used for stabilizing the inverted pendulum in upright position.

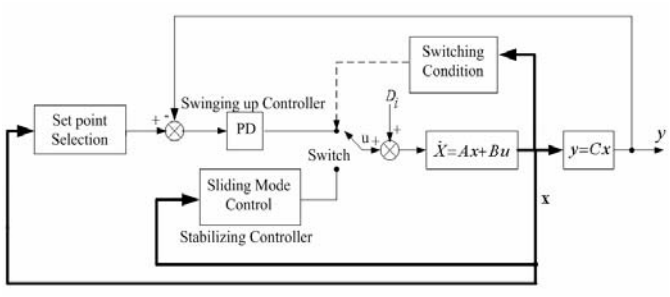

Figure 2. Overall structure of the proposed control system.

A. PD Controller for Position Control

The PD controller is used to control the position of the cart. According to the movement of the cart, the inverted pendulum will be swung up from the natural pendent position to around the upright position. The output command signal $u(t)$ due to the PD controller is given by

$$u(t) = K_p e(t) + K_d \frac{d}{dt} e(t) \tag{4}$$

where K_p is the proportional gain, K_d is the derivative gain and $e(t)$ is the error of the cart position. The PD controller is tuned to achieve fast response without overshoot based on root-locus method. The designed controller will control the cart to move back and forth successively according to the pre-assigned cart position of which the pendulum staying at the natural pendent position is excited. The occurance of back and forth movement of the cart is proceeded when the angular velocity of pendulum is zero until the pendulum can be swung up around the upright position where the sliding mode controller will be switched to stabilize the pendulum.

B. Sliding Mode Controller for Stabilizing

Sliding mode control, often referred as Variable Structure Control, is a high-speed switching feedback control that switches between two values based upon some rule [5], [6]. The control theory uses a high-speed switching law to drive the nonlinear plant's state trajectory onto a specified surface in the state space. This surface is called the "sliding or switching surface". A sliding mode will exist for a system, if in the vicinity of the switching surface the state velocity vector is directed towards the surface. Consider the system

$$\dot{\mathbf{x}}(t) = \mathbf{A}\mathbf{x}(t) + \mathbf{B}[u(t) + f(\mathbf{x},t)] \tag{5}$$

where $\mathbf{x}(t)$ is state vector, $u(t)$ is a scalar control and $f(\mathbf{x},t)$ is a nonlinear perturbation with known upper bound $f_o(\mathbf{x},t)$ with assumption that the sliding surface is chosen [7] as

$$s(\mathbf{x},t) = \mathbf{B}^T\mathbf{x}(t) + z(t). \tag{6}$$

when $z(t)$ is governed by an additional first order dynamic subsystem

$$\dot{z}(t) = -\mathbf{B}^T\mathbf{A}\mathbf{x}(t) - (\mathbf{B}^T\mathbf{B})u_a(t),\ z(0) = -\mathbf{B}^T\mathbf{x}(0). \quad (7)$$

Let the control $u(t)$ in (5) be the discontinuous function

$$u(t) = -M(\mathbf{x},t)sign\ s(\mathbf{x},t), \quad (8)$$

where $M(\mathbf{x},t)$ is the magnitude of the control input $u(t)$. The motion projection on the one-dimensional s-space can be computed by (5), (6) and (7) and it is governed by

$$\dot{s}(\mathbf{x},t) = (\mathbf{B}^T\mathbf{B})(u(t) + f(\mathbf{x},t) - u_a(t)). \quad (9)$$

From (8) and (9), the condition for the existence of a sliding mode $(s\dot{s} < 0)$ is corresponding to

$$M(\mathbf{x},t) \geq |u_a(t)| + f(\mathbf{x},t). \quad (10)$$

The sliding mode arises at the initial instant because $s(0) = 0$. The solution to the algebraic equation $\dot{s}(\mathbf{x},t) = 0$ with respect to $u(t)$ should be substituted into (5) to obtain the sliding mode equation in the plane $s(\mathbf{x},t) = 0$ and it is

$$\dot{\mathbf{x}}(t) = \mathbf{A}\mathbf{x}(t) + \mathbf{B}u_a(t). \quad (11)$$

Therefore if the linear control $u_a(t) = -\mathbf{K}\mathbf{x}(t)$ is designed in compliance with pole-placement method, the system behavior in the presence of an unknown perturbation $f(\mathbf{x},t)$ is described by the linear time-invariant equation (12) with the assigned poles of the system.

$$\dot{\mathbf{x}}(t) = (\mathbf{A} - \mathbf{B}\mathbf{K})\mathbf{x}(t) \quad (12)$$

If the magnitude of control input take only two values M_0 and $-M_0$, the magnitude of control M_0 should satisfy (10), which means that initial conditions and the perturbation should be bounded.

In summary, the steps for designing the sliding mode controller of the inverted pendulum are as

(1) Choose the desired closed-loop poles of the feedback system (12). The linear control $u_a(t) = -\mathbf{K}\mathbf{x}(t)$ is found accordingly by pole placement method.
(2) The dynamic part of the controller (7) is designed and the equation of the discontinuity plane $s = 0$ is found by (6).
(3) The discontinuous control governed by (6), (8) and (10) is designed.

IV. Experimental results

In this section, the proposed hybrid PD-sliding mode controller for swinging up and stabilizing the inverted pendulum on cart will be implemented. The parameter values of the inverted pendulum system are shown in Table 1.

TABLE I
Parameter Values of Inverted Pendulum

M (kg)	m (kg)	l (m)	f (kg/s)
0.642	0.123	0.25	0.165

The linear models of the inverted pendulum on cart (2) can be obtained where

$$\mathbf{A} = \begin{bmatrix} 0 & 1 & 0 & 0 \\ -33.43 & 0 & 0 & 0.74 \\ 0 & 0 & 0 & 1 \\ 1.34 & 0 & 0 & -0.25 \end{bmatrix} \text{ and } \mathbf{B} = \begin{bmatrix} 0 \\ -4.46 \\ 0 \\ 1.49 \end{bmatrix} \quad (13)$$

for equilibrium point at natural pendent position and where

$$\mathbf{A} = \begin{bmatrix} 0 & 1 & 0 & 0 \\ 33.43 & 0 & 0 & -0.74 \\ 0 & 0 & 0 & 1 \\ 1.34 & 0 & 0 & -0.25 \end{bmatrix} \text{ and } \mathbf{B} = \begin{bmatrix} 0 \\ 4.46 \\ 0 \\ 1.49 \end{bmatrix} \quad (14)$$

for equilibrium point at the upright position.

The PD position control can now be designed based on the root-locus method to bring the inverted pendulum up around the upright position as fast as possible. In this case, the dominant poles are chosen at $s = -8 \pm j8.39$ which correspond to 0.5 sec for settling time and 5% for percent overshoot respectively. The desired proportional gain K_p and derivative gain K_d are respectively obtained as 97.205 and 12.54. The sequential travelling positions of cart are assigned to be $10, -16, 17, -17$ and 3.8 cm respectively. Zero angular velocity condition occurred at the stop point of the present position will be used as a criterion for moving the cart to the next assigned position.

For sliding mode controller, system matrix $\mathbf{A}$ and input vector $\mathbf{B}$ in (14) are employed. The gain matrix $\mathbf{K}$ in (12) can be found by assigning the values of percent overshoot and the settling time as 15 % and 5 seconds, respectively. Hence, the closed-loop poles of the inverted pendulum system are at $s = -0.8 \pm j1.324$, -10 and -11. This yields $\mathbf{K} =$ [173.001 27.816 -24.609 -21.792]. The discontinuous control is then derived by assigning the values of $f_0(\mathbf{x},t)$ is 2.

For the experiment with simultaneous control of the inverted pendulum from swinging up control to stabilizing control will be investigated. The initial value of the cart position $\mathbf{x}(0)$ is set at zero and the pendulum angle $\theta(0)$ is at natural pendent position. The stabilizing control will be

switched when the pendulum is around the upright position. The switching condition is selected as $|\theta| < 0.04$ rad and $|\dot{\theta}| < 0.1$ rad/s.

The experimental results obtained from a real machine are shown in Fig. 4 (a), (b) and (c). It is seen from Fig. 4 (a) and (b) that the PD controller can swing pendulum up to around the upright position about 4.42 sec, then the system is switched to stabilizing control mode and it can stabilize the pendulum at its upright position and the cart position at zero. The control input signal for swinging up and stabilizing the inverted pendulum is shown in Fig. 4(c).

V. CONCLUSIONS

The hybrid PD controller with sliding mode control algorithm consists of the PD position control for swinging up the pendulum from the natural pendent position to around the upright position and the sliding mode control for stabilizing the inverted pendulum in its upright position has been proposed in this paper. According to the cooperative tasks of PD and sliding mode controller, the experimental results show that the proposed controller can swing the inverted pendulum to the upright position in a short period of time and the controller has good performance in controlling the cart position and pendulum angle at zero line.

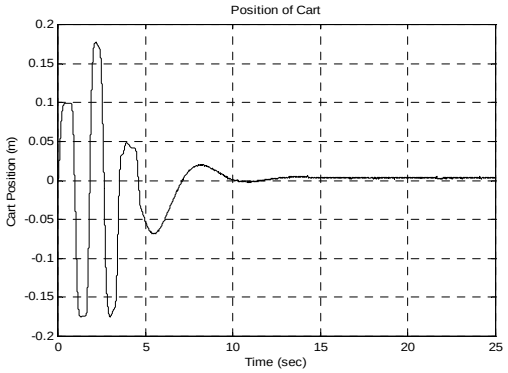

(a) Cart position.

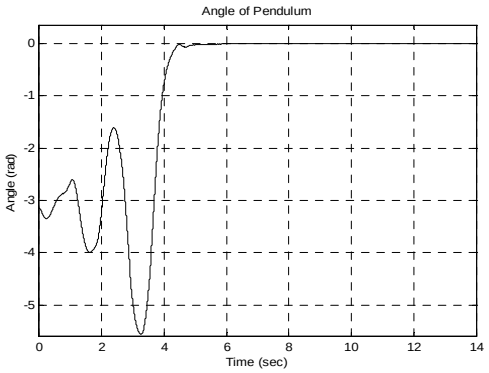

(b) Pendulum angle.

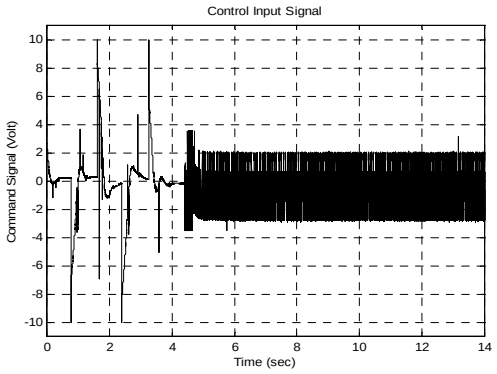

(c) Control input signal.

Figure 4. Experimental results of the inverted pendulum system.

REFERENCES

[1] Chi Youn Chung, Jin Won Lee, Sang Moo Lee and Beom Hee Lee, "Balancing of an Inverted Pendulum with a Redundant Direct-Drive Robot," Proceedings of the 2000 IEEE, International Conference on Robotics & Automation, Sanfrancisco , pp. 3952-3957, April 2000.

[2] W. Torres-Pomales and O.R Gonzalez, "Nonlinear Control of Swing-up Inverted Pendulum," *Proceedings of the 1996 IEEE International Conference on control application*, pp. 259-264, 1996.

[3] K. Yoshida, "Swing-up Control of an Inverted Pendulum by Energy-based Methods," *Proceedings of the American Control Conference*, Vol. 6, pp. 4045-4047, 1999.

[4] N. Kouda, N. Matsui and H. Nishimura, "Control for Swing-up of an Inverted Pendulum using Qubit Neural Network," *Proceedings of the 41st SICE Annual Conference*, Vol. 2, pp. 765-770, 2002.

[5] R.A. DeCarlo, S.H. Zak and G.P. Matthews, "Variable Structure Control of Nonlinear Multivariate Systems: A Tutorial," Proceedings of the IEEE, Vol. 76, No. 3, pp. 212-232, March 1988.

[6] Vadim Utkin, Jurgen Guldner and Jingxin Shi, *Sliding Mode Control in Electromechanical Systems.* TAYLOR & FRANCIS ,1999.

[7] Juergen Ackermann and Vadim Utkin, "Sliding Mode Control Design Based on Ackermann's Formula," IEEE Transaction on Automatic Control, Vol. 43, No. 2, February 1998.

[8] V. Utkin, "Sliding Mode Control Design Principles and Applications to Electric Drives," IEEE Transactions on Industrial Electronics, Vol. 40, no. 1, February 1993.

[9] M.R, Rafimanzelat and M.J. Yazdanpanah, "A Novel Low Chattering Sliding Mode Controller," Proceedings of the IEEE, Vol. 3, pp. 1958-1963, July 2004.

Control Strategies of Doubly Fed Induction Generator of Wind Turbine for Maximum Active Power with Minimum Copper Losses

Bunlung Neammanee and Somporn Sirisumrannukul

Department of Electrical Engineering, Faculty of Engineering
King Mongkut's Institute of Technology North Bangkok
1518 Bangsue, Bangkok 10800, Thailand Phone: 662-913-2500 Ext: 8420, Fax: 662-913-2500 Ext: 8520,
E-mails: bln@kmitnb.ac.th and spss@kmitnb.ac.th

***Abstract*- The doubly fed induction generator (DFIG) is one of the most widely used generator in MW-class wind turbines. It can be controlled through rotor slip recovery with machine and line side converters. The machine side converter is of interest in this paper. The active power flow and the reactive power can be controlled independently. A bi-level control objective is presented in this paper. The first level determines the maximum power from the wind. After the maximum active power is determined, the reactive power can be allocated between the stator and rotor to minimize the copper losses. The decoupled control is simulated by the operation of a DFIG in sub- and supper-synchronous speed. The method can reduce the copper losses, thus improving the efficiency of energy production in the wind conversion system.**

Keywords: *doubly fed induction generator, DFIG control, copper loss minimization, wind turbine control, machine side converter.*

I. INTRODUCTION

The doubly fed induction generator (DFIG) is widely used in wind power generation. A DFIG is a wound rotor induction machine with slip rings attached at the rotor fed by power converters. A DFIG can be controlled by a wide range of rotational speeds through sub- and super-synchronous speed operation. It can regulate active and reactive power flow with the help of machine and line side converters. A DFIG has high stability through a fast active power arrangement to the grid and the size of converters can be reduced about 20 to 30 percent of the rating of the DFIG.

The greatest advantage of the DFIG is that it can be controlled from the rotor through slip power while the stator is being connected directly to the grid. The power converters need to be designed for an improvement of total efficiency because of the avoided converter losses. The major part of the active power is fed into the grid through the stator. The machine side converter supplies a small amount to the grid in super-synchronous mode or it is fed the active power from the grid in sub-synchronous mode through the rotor. However, a DFIG requires slip ring systems, which has a problem on contact erosion. This problem can be solved by using new material contact, such as graphite-union, which has very long endurance [1, 2].

This paper presents control strategies of a DFIG used in a wind turbine system to maximize active power and minimize copper losses. The techniques are based on vector control of a machine side converter. A case study is performed to verify the control performance and copper loss minimization for a wide range of wind speeds.

II. MATHEMATICAL AND CONTROL OPERATION OF DFIG

A. *Control Objectives*

There are two main operating regions of wind turbine control: below rated wind speed and above rated wind speed regions. The control objective in the first region is to track the maximum output power at any wind speeds. In the above-rated wind speed, it is necessary to limit the mechanical power generated by the rotor to a specified value, P_n, of the plant to prevent damage on the turbine by pitch control or stall regulation. Figure 1 shows the optimum control trajectory of wind power which is characterized by power and rotational speed with various wind speed. It can be seen that there exists a range of wind speeds ($\omega_{cut-in} - \omega_{rated}$) that should be used for efficient power conversion from the mechanical wind power to the electrical power. Figure 2 shows the corresponding torque trajectory which gives the output power of Fig. 1.

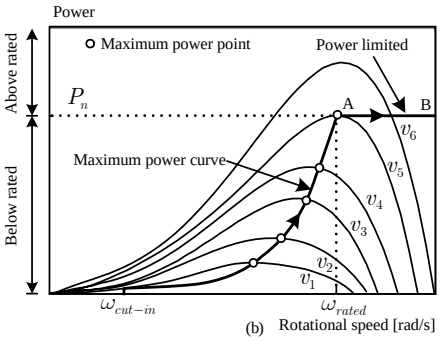

Figure 1. Optimum power trajectory

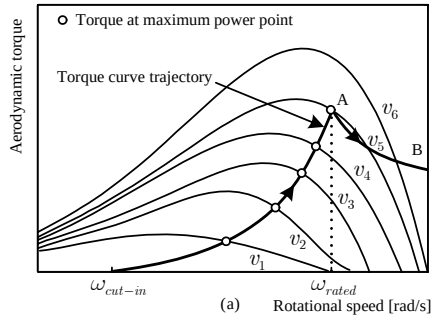

Figure 2. Optimum torque trajectory

Figure 3 shows a schematic diagram of a wind energy conversion system. The stator of the DFIG is directly connected to the grid to supply the active power. In the rotor circuit, there are two voltage-fed PWM converters inserted between the rotor and the grid. The first converter located at line side is used to regulate dc link voltage. There are two modes of operation for this converter. In the first mode called rectifying mode, the DFIG is operated in the sub-synchronous speed to boost voltage. In the second mode called inverting mode, the DFIG is operated in super-synchronous speed. The second converter is located at the machine side connected between the DFIG and the dc link to control the DFIG. This converter supplies and extracts the active power from the rotor when operated in sub- and supper-synchronous speed, respectively.

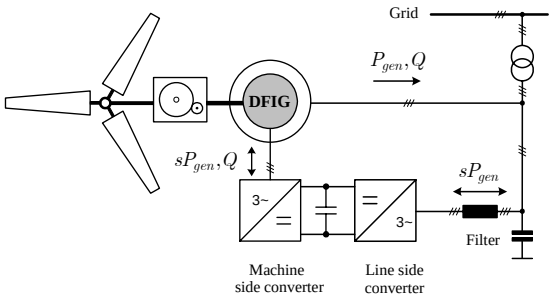

Figure 3. Wind turbine with DFIG vector control system

B. Operating Region

The DFIG generates its output power in sub- and super-synchronous speed with constant voltage and frequency by allowing the machine side converter to supply the rotor frequency at the difference between the rotor and synchronous frequency. When the DFIG is operated at super-synchronous speed (upper part of Fig. 4), the machine side converter supplies the negative sequence to the rotor and therefore the power will flow from both stator and rotor to the grid. When the rotational speed decreases lower than synchronous speed, the machine side converter supplies the reverse sequence and in this case, the power will flow in opposite direction (into the rotor) to prevent the DFIG switching from generator mode to motor-driven mode (lower part of Figure 4). Therefore, the DFIG can generate output power with constant frequency in both speed ranges.

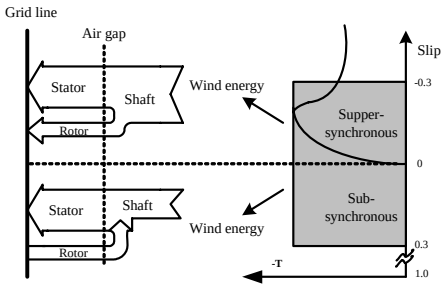

Figure 4. Operating range of DFIG

The optimal operating range of the DFIG should be between $0.7n_S < n < 1.3n_S$ to give the optimal size of converters (30% of the rating). For this reason, converter size is limited and the installed power rating of the wind turbine can be increased only up to 130 % of the rating of the DFIIG. Note that if the operating ranges greater or less than 30 % of synchronous speed, the system requires a larger size of converter that would be uneconomical [3].

C. Vector Control of DFIG

The machine side converter is controlled in a synchronously rotating *d*-, *q*-axis frame, with the *q*-axis oriented along the stator-flux vector position. In this way, a decoupled control between the electrical torque and the rotor excitation current is obtained. The machine side converter provides the actuation, and its controller requires the measurement of the stator and rotor currents, stator voltage and rotor position. Since the stator is connected to the grid, and the influence of the stator resistance is small, the stator magnetizing current i_{ms} can be considered constant. Under stator-flux orientation, the relationship between the torque and the *d*-, *q*- axis voltages, currents and fluxes (all scaled to be numerically equal to the AC per phase values) may be written as [4]:

$$\lambda_S = \lambda_{dS} = L_o i_{mS} = L_S i_{dS} + L_o i_{dR} = \text{constant} \tag{1}$$

$$\lambda_{qS} = L_o i_{qmS} = 0 \tag{2}$$

$$\lambda_{dR} = \frac{L_0^2}{L_S} i_{qmS} + \sigma L_R i_{dR}\,, \quad \lambda_{qR} = \sigma L_R i_{qR} \tag{3}$$

$$v_{dR} = R_R i_{dR} + \sigma L_R \frac{di_{dR}}{dt} - \omega_{slip}\sigma L_R i_{qR} \tag{4}$$

$$v_{qR} = R_R i_{qR} + \sigma L_R \frac{di_{qR}}{dt} + \omega_{slip}(\frac{L_0^2}{L_S} i_{dmS} + \sigma L_R i_{dR}) \tag{5}$$

$$m_M = -3\frac{P}{2} L_m i_{mS} i_{qR} \tag{6}$$

$$\omega_{slip} = \omega_s - \omega_r\,,\ \sigma = 1 - \frac{L_m^2}{L_s L_r} \tag{7}$$

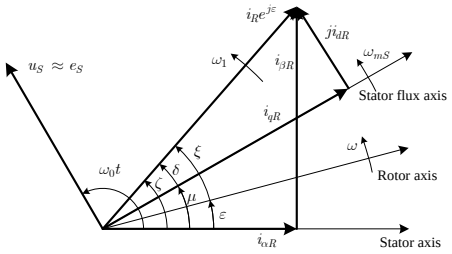

Figure 5. Angular relationships of rotor current vectors in rotor axis, stator flux axis and stator axis

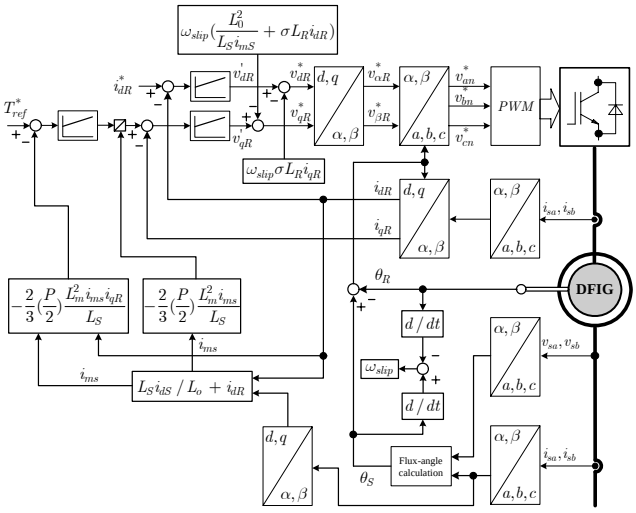

Figure 6. Vector control structure of machine side converter

III. Active and Reactive Power Control with Loss Minimization

A. Active and Reactive Power Control

The stator flux vector is adjusted to be aligned with the *q*-axis. The adjustment of the *d*-axis component of the rotor current controls either the generator torque or the stator side active power of the DFIG. On the other hand, regulating the rotor *d*-axis current component controls directly the stator-side reactive power. Using (1)-(6), the stator active power and reactive power can be obtained as [5-7]

$$P_S = -\frac{3}{2}\frac{L_m}{L_S} v_{qS} i_{qR} \tag{8}$$

$$Q_S = -\frac{3}{2}\frac{L_m}{L_S} v_{qs}(i_{ms} - i_{dR}) \tag{9}$$

where i_{mS} is the magnetizing current

It is noticeable that the stator active power component is proportional to i_{qR} and the stator reactive power component is proportional to i_{dR}. The normal control method is set Q_S equal zero by $i_{dR} = i_{mS}$.

B. Copper Loss Minimization

The output power wind turbine extracted from the wind is shown in (10). The power losses, P_{losses}, are composed of core losses, friction losses and copper losses. The first two losses are constant and therefore only copper losses are focused in this paper. The copper losses, P_{cu}, of DFIG depends on the coil resistances and currents, as described in (11) and (12).

$$P_t = P_S + P_R + P_{losses} \tag{10}$$

$$P_{cu} = P_{cuS} + P_{cuR} \tag{11}$$

where P_{cuS} and P_{cuR} are the stator and rotor copper losses.

$$P_{cu} = \frac{3}{2}(i_{qS}^2 + i_{dS}^2)R_S + \frac{3}{2}(i_{qR}^2 + i_{dR}^2)R_R \tag{12}$$

With $\lambda_S = \lambda_{dS} = L_S i_{dS} + L_o i_{dR}$ and $i_{qS} = -\frac{L_o}{L_S} i_{qR}$, substituting these terms into (12) gives

$$P_{cu} = \frac{3}{2}\left[(-\frac{L_o}{L_S} i_{qR})^2 + (\frac{\lambda_{dS} - L_o i_{dR}}{L_S})^2\right] R_S + \frac{3}{2}(i_{qR}^2 + i_{dR}^2)R_R$$

$$P_{cu} = \frac{3}{2}\left[(-\frac{L_o}{L_S} i_{qR})^2 + \frac{\lambda_{dS}^2}{L_S^2} - 2\frac{\lambda_{dS} L_o i_{dR}}{L_S^2} + \frac{L_o^2 i_{dR}^2}{L_S^2})^2\right] R_S + \frac{3}{2}(i_{qR}^2 + i_{dR}^2)R_R$$

$$P_{cu} = \frac{3}{2}(R_R + \frac{L_o^2}{L_S^2})i_{qR}^2 + \frac{3}{2}\frac{\lambda_{dS}^2}{L_S^2} R_S - 3\frac{L_o}{L_S^2}\lambda_{dS} R_S i_{dR} + \frac{3}{2}(\frac{L_o^2}{L_S^2} R_S + R_R)i_{dR}^2$$

$$P_{cu} = \frac{3}{2}(R_R + \frac{L_o^2}{L_S^2})i_{qR}^2 + \frac{3}{2}\frac{\lambda_{dS}^2}{L_S^2} R_S - 3\frac{L_o}{L_S^2}\lambda_{dS} R_S i_{dR} + \frac{3}{2}(\frac{L_o^2}{L_S^2} R_S + R_R)i_{dR}^2 \tag{13}$$

With constant λ_{dS} and known i_{qR}, the first term of (13) is constant. The copper losses can be minimized by

$$\frac{d}{di_{dR}}[\frac{3}{2}\frac{\lambda_{dS}^2}{L_S^2} R_S - 3\frac{L_o^2}{L_S^2}\lambda_{dS} R_S i_{dR} + \frac{3}{2}(\frac{L_o^2}{L_S^2} R_S + R_R)i_{dR}^2 = 0$$

$$i_{dR} = \frac{\lambda_{dS} R_S L_o}{(R_S L_o^2 + R_R L_S^2)} \tag{14}$$

The value of i_{dR} in (14) is used as the *d*-axis current reference for copper-loss minimization control.

IV. Case Study

The parameters of a DFIG used in this case study is given in the appendix. To verify the control performance of the DFIG and viability of the proposed control scheme, computer simulations are performed using Matlab Simulink.

A. DFIG Operation

The DFIG is initially started with zero stator active power ($i_{qR} = 0$) until t = 250. After that, when the current i_{qR} is stepped up, the DFIG is switched from sub-synchronous speed to super-synchronous speed. Figure 7 a) shows the response for a step change of i_{qR}^* at t = 250 ms with i_{dR}^* constant. Figure 7 b) shows the phase rotor current. Figure 7 c) shows stator voltage and current corresponding to the step current in Figure 7 a). The magnetizing current is initially supplied from both rotor and stator until t = 250 ms. The DFIG generates the active power with a majority part of the magnetizing current from the rotor and some part from the stator to minimize the copper losses. Note that DFIG requires a certain value of reactive power that can be fed from the stator, the rotor or both sides for operation.

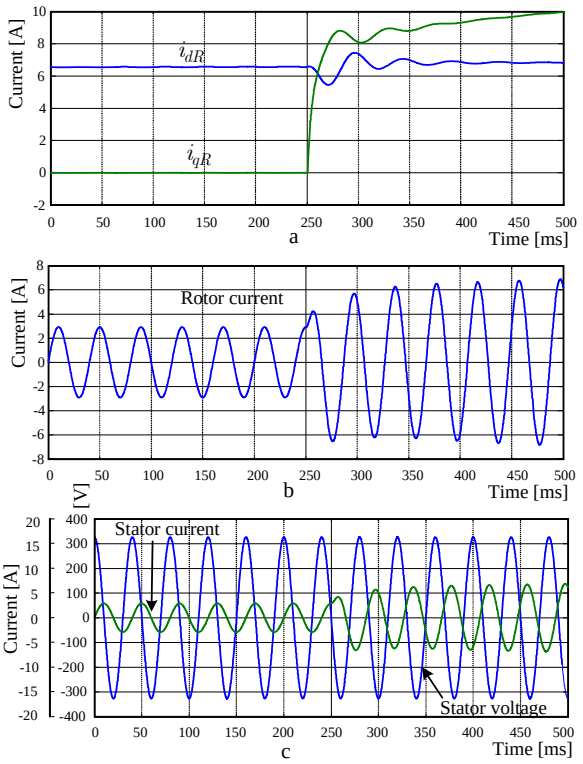

Figure 7. a) *d*- and *q*-axis current, b)rotor current and c)stator current and voltage.

The advantage of the DFIG is a smooth operation through synchronous speed, as can be seen in Fig. 8. The rotor can generate the active power (inverting mode) in the super-synchronous speed. In this case, the DFIG can supply an output power up to 1.3 times of its rating.

B. *Minimization of Copper Loss*

Figure 9 shows the copper losses with various *d*-axis rotor current references and constant torque. It can be seen that there is only one point that yields the minimum copper losses.

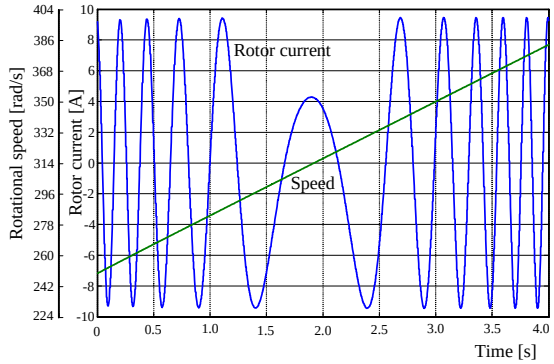

Figure 8. Operation of DFIG through synchronous speed

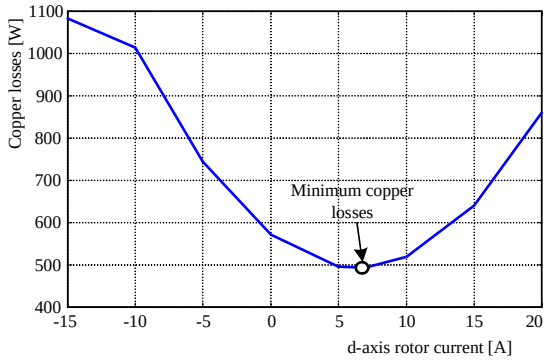

Figure 9. **C**opper losses versus *d*-axis rotor current

C. Efficiency Comparison of Power Losses

Figure 10 compares the efficiency of the copper loss minimization with that of a normal method (i.e., zero stator reactive power). It clearly shows that at low torque (low wind speed), a loss reduction of about 7% can be obtained from the improvement method. For higher torque, the purposed method can decrease a loss by 1-4%.

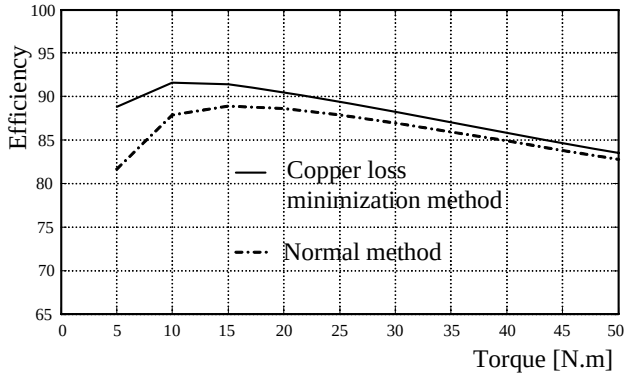

Figure 10. Efficiency with torque variation

V. CONCLUSION

The vector control of machines side converter of DFIG has been described, and the fundamental operational advantages have been verified. The active and reactive power is independently controlled based on *d*- and *q*-axis current, respectively. The main advantages of this control technique are smooth operation through synchronous speed, low distortion current fed to the supply and the ability to control the system power factor. The control objectives are to maximize output power from the wind by *q*-axis rotor current references while minimizing copper losses by *d*-axis rotor current references. The results from a case study show an improvement in the overall efficiency of the DFIG in the wind turbine system, particularly in low torque range (low speed range).

REFERENCES

[1] R. S. Pena, R. J. Cardenas, G. M. Asher and J.C. Clare, "Vector Controlled Induction Machines for Stand-Alone Wind Energy Applications," *IEEE on Industrial Application Conf.*, Vol. 3, 8-12 Oct. 2000, pp. 1409–1415.

[2] W. Hofmann, F. Okafor, "Doubly-Fed Full-Controlled Induction Wind Generator for Optimal Power Utilisation," *IEEE on Power Electronics and Drive Systems*, Vol. 1, No.4, 22-25Oct. 2001, pp. 355–361.

[3] W. Hofmann A. Thieme, "Control of a Double-Fed Induction Generator for Wind-Power Plants," *www.tu-dhemnitz.de/etit/ema/publiken/1998/picm_1.pdf*, pp. 1-8.

[4] Leonhard, W. Control of Electrical Drives, *Springer-Verlag*, third edition, 2001.

[5] Jeong-Ik Jang, Young-Sin Kim and Dong-Choon Lee, "Active and Reactive Power Control of DFIG for Wind Energy Conversion under Unbalance Grid Voltage," *IEEE on IPEMC*, Vol. 3, No.4, 1-6Augt. 2006, pp. 1–5.

[6] R. Pena, J.C. Clare, and G. M. Asher, "Doubly fed induction generator using back-to-back PWM converters and its application to variable speed wind-energy generation," IEE Proc. Electr. Power Appl., Vol. 143, No. 3, May 1996, pp. 231-241.

[7] K. Pierce, "Control Method for Improved Energy Capture Below Rated Power," the 3th *ASME/JSME*, Joint Fluids Engineering Conference, California, 18-23July. 1999, pp. 1–6.

Nomenclature

v_{an}, v_{bn}, v_{cn}	= a, b and c phase voltage
i_{an}, i_{bn}, i_{cn}	= a, b and c phase current
v_{dS}, v_{qS}	= *d*- and *q*-axis stator voltage
i_{dS}, , i_{qS}	= *d*- and *q*-axis stator current
λ_{dS}, λ_{qS}	= *d*- and *q*-axis stator flux
u_{dR} , u_{qR}	= *d*- and *q*-axis rotor voltage
i_{dR} , i_{qR}	= *d*- and *q*-axis rotor current
λ_{dR}, λ_{qR}	= *d*- and *q*-axis rotor flux
ω_S, ω_R, ω_{slip}	= stator, rotor and slip angular speed
n_S	= synchronous speed
L_m, L_S, L_R, L_0	= mutual, stator, rotor inductance
R_S	= per phase stator resistance
R_R	= per phase rotor resistance
P	= pole of machine
m_M	= torque of machine
T^*_{ref}	= reference torque of machine

Appendix

Parameters of DFIG

Power	= 7.5 kW	Stator voltage	= 415 V
Rotor voltage	= 440 V	Rated stator current	= 19 A
Rated rotor current	= 10 A	R_S = 1.06 Ω	
R_R = 0.80 Ω		L_S = 0.2065 H	
L_O = 0.0664 H (refer to rotor)		L_R = 0.0810 H (refer to rotor)	
L_{ext} = 0.0320 H (refer to rotor)		Pole pair = 3	
Rated speed	= 970 rpm	Stator-rotor turn ratio	= 1.7
Stator connection	= delta	Rotor connection	= star

Soft-Switching Single-Phase Inverter for Small Grid-Connected PV Systems

D. Amorndechaphon[1], S. Premrudeepreechacharn[2] and K. Chamnongthai[3]
[1]Department of Electrical Engineering, Naresuan University Phayao Campus, Phayao, 56000 THAILAND
[2]Department of Electrical Engineering, Chiangmai University, Chiangmai, 50200 THAILAND
[3]Department of Electronics and Communication Engineering, King Mongkut's University of Technology Thonburi, Bangkok, 10140 THAILAND

***Abstract*-This paper presents a soft-switching single-phase inverter for small grid-connected photovoltaic system. The proposed inverter is developed from the conventional PWM buck-boost inverter by inserted an auxiliary circuit that is used for achieve the soft-switching conditions without additional current and voltage stresses at switching devices. Theoretical analysis is verified by means of simulation results obtained from a design example rated at 100W. The simulation results show that a smaller switching losses and higher conversion efficiency are obtained by the proposed soft-switching inverter.**

I. INTRODUCTION

Due to the Kyoto agreement on global reduction of greenhouse gas emissions that generated by the burning process from the primary fossil fuels such as coal, oil, natural gas etc.[1] Many renewable energy sources are developed such as solar, wind, biomass and fuel cell. The solar energy is clean and viable source of electricity. It has been used as the main source for electrical loads in rural areas away from the grid or grid-connected in distributed energy production.

In recent years, the conventional buck-boost PWM inverters shown in Fig. 1(a) have been widely used for grid connected PV system [2-3] due to the individual operation and simple control. These systems compose of a PV array, a DC-DC converter and a DC-AC inverter. The DC-DC converter is used to boost the PV voltage to a level higher than the peak of the voltage utility and also responsible for tracking the maximum point of the PV array to fully utilize the PV power. The excessive power from the PV module to the load can be fed to the grid. The balance of power flow is controlled through the inverter. The dc-ac inverter is usually a pulse-width-modulation (PWM) voltage-source inverter, which shapes and inverters the output current. The inverter is also used to act as a high-frequency filter to eliminate the high-frequency component at the inverter output to achieve the low output harmonic distortion and high output power factor.

To minimize the size and weight of overall system, high switching frequency operations are required for inverters. However, high switching causes high switching stresses and switching power losses in the semiconductor devices. In order to solve these problems, resonant converters using zero voltage switching (ZVS) and zero current switching (ZCS) techniques [4] can be used to greatly reduce the switching losses at the expenses of high voltage or current stresses on power switches. For those buck-boost inverters without reactive energy feedback paths, the parasitic reactive energy due to the possible leakage of inductors also imposes transient high voltage, dv/dt or di/dt stresses on switch devices that causes high electromagnetic interference (EMI). Therefore, soft-transition switching techniques such as zero voltage transition (ZVT) and zero current transition (ZCT) [5-6] have been developed to minimize or eliminate both switching losses and stresses, and thus improving converter efficiency.

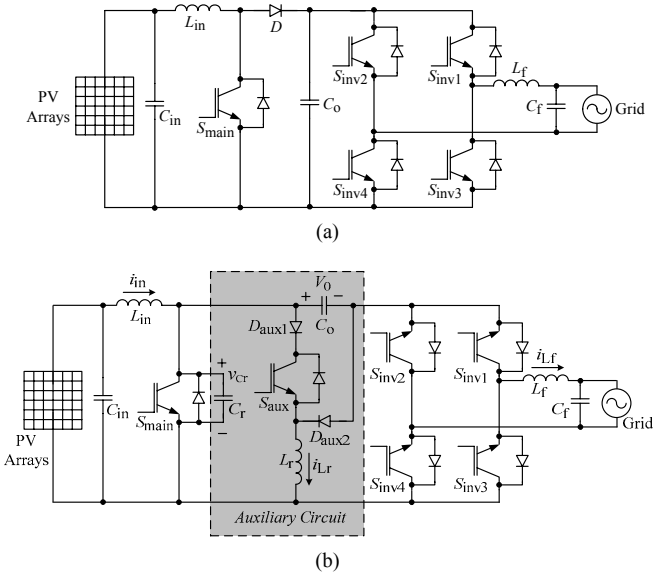

Figure 1. The single-phase inverter for grid-connected PV system
(a) The conventional inverter
(b) The proposed soft-switching inverter

In this paper, a soft-switching single-phase inverter for small grid-connected PV systems shown in figure 1(b) is proposed. This inverter combines the boost PWM dc/dc converter with the buck PWM inverter to a single-stage buck-boost PWM inverter [7]. An auxiliary circuit is used to provide all semiconductor switching devices operate at soft-switching without additional voltage and current stresses.

In the following, the operating principles of the proposed grid-connected PV system will be thoroughly discussed. Simulation results will be given to validate the effectiveness of the fulfilled functions.

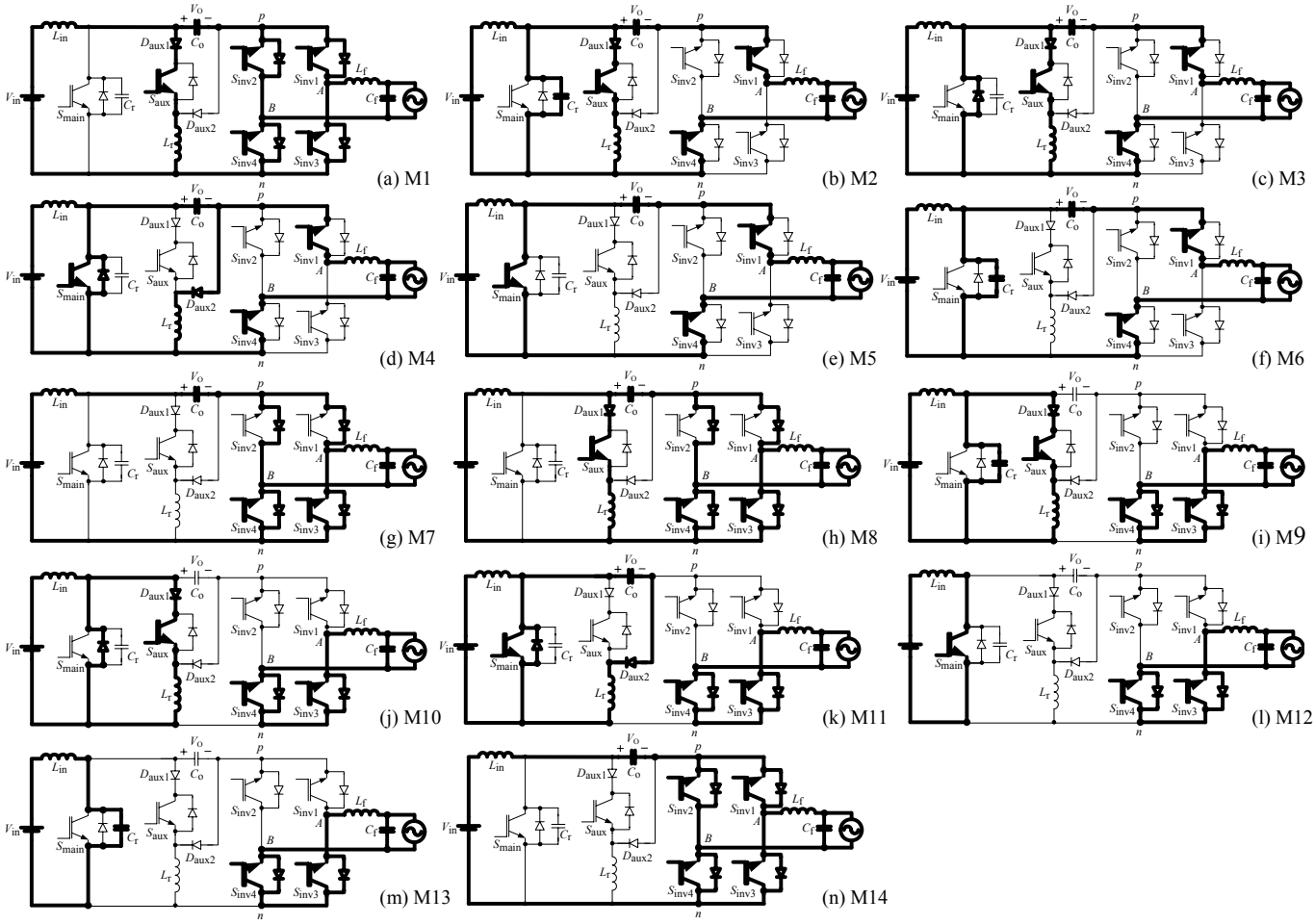

Figure 2. Equivalent circuits for fourteen switching operation modes

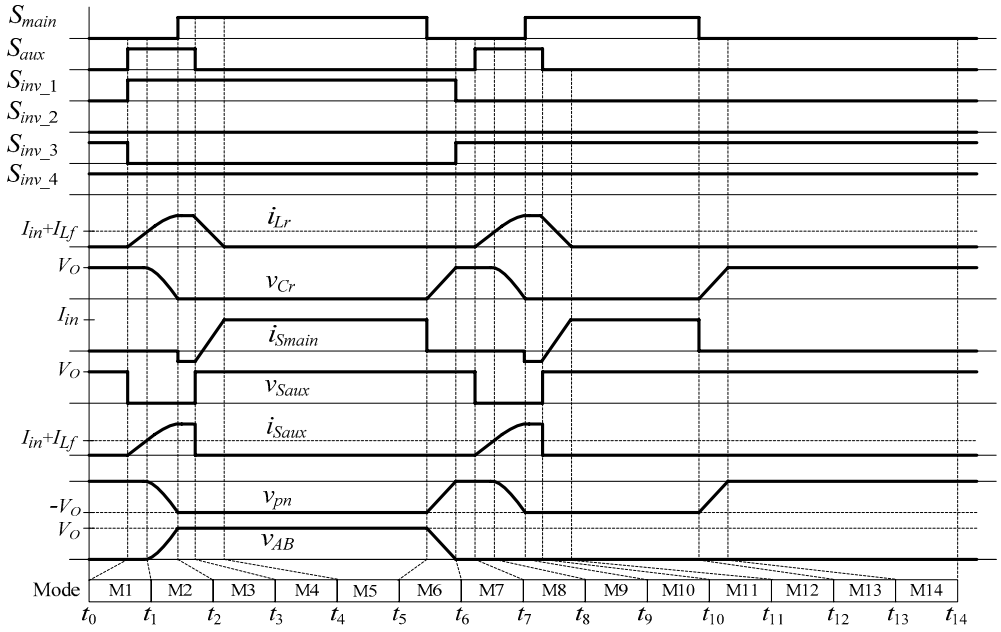

Figure 3. Operating waveforms of the soft-switching single-phase inverter

II. SOFT-SWITCHING SINGLE-PHASE INVERTER

A. Circuit Description

Fig. 1(b) shows a proposed soft-switching single-phase inverter for small grid-connected PV systems. The circuit is composed of three units. The first unit is a PWM dc-dc boost converter which composed of L_{in}, S_{main} and C_o. The second unit is a PWM dc-ac buck inverter which composed of S_{inv1}, S_{inv2}, S_{inv3} and S_{inv4}. The last section is an auxiliary network that provides the soft-switching on the main switch S_{main}. This unit is composed of auxiliary diode D_{aux1}, D_{aux2}, the resonant inductor L_r, the resonant capacitor C_r and auxiliary switch S_{aux}. In the positive (negative) half-cycle of the output voltage $v_0(t)$, the switch S_{inv4} (S_{inv3}) always on, the switch S_{inv1} (S_{inv2}) and switch S_{inv3} (S_{inv4}) perform the inversion function, while the main switch S_{main} performs the dc-dc boost converter function in PWM continuous conduction mode (CCM).

B. Operation of The Proposed Soft-Switching Inverter

Fig. 2 shows the equivalent circuit of the soft-switching single-phase inverter. The operation modes of the inverter circuit are divided into fourteen operation modes from mode 1 to 14 in accordance with operating timing transitions from t_0 to t_{14}. Fig. 3 shows the relevant voltage and current operating waveforms of the soft-switching single-phase inverter.

To simplify the analysis, it is assumed that proposed inverter is operating in steady-state, the input filter capacitors L_{in} is much greater than the resonant inductor L_r and large enough to assume that the input current I_{lin} is constant, the capacitor C_o is large enough to assume that the voltage V_o is constant and no ripple, the resonant voltage of the resonant capacitor C_r is equaled to V_o and the resonant current of the resonant inductor L_r is equal to zero. The operation principle is described in the following.

1) *Mode* 1 [t_0 - t_1]: Prior to $t=t_0$, the switches S_{inv3} and S_{inv4} are turned on, S_{main} and S_{aux} are turned off. The output loop of the inverter is in a freewheeling state. At this time $t=t_0$, S_{aux} can turn on with ZCS, S_{inv1} and S_{inv3} are turned on and off with ZVS, respectively. The resonant inductor current $i_{Lr}(t)$ increases linearly from zero to I_{in} + I_{Lf} that causes the body diodes of inverter switch S_{inv1}-S_{inv4} turn off at $t=t_1$ with ZCS. The resonant current $i_{Lr}(t)$ and resonant voltage $v_{Cr}(t)$ can be respectively described as follows:

$$v_{Cr}(t) = V_0 \tag{1}$$

$$i_{Lr}(t) = \frac{V_0}{L_r} \cdot t \tag{2}$$

2) *Mode* 2 [t_1 – t_2]: At $t=t_0$ a resonance starts through C_r and L_r. Then $v_{Cr}(t)$ decreases from V_0 to zero in a sinusoidal fashion, $i_{Lr}(t)$ increases in a sinusoidal fashion through C_r and L_r.

$$v_{Cr}(t) = V_0 \cdot \cos \omega_n (t - t_1) \tag{3}$$

$$i_{Lr}(t) = I_{in} + \frac{V_0}{Z_n} \cdot \sin \omega_n (t - t_1) \tag{4}$$

where $\omega_n = 1/\sqrt{L_r \cdot C_r}$ and $Z_n = \sqrt{L_r / C_r}$

3) *Mode* 3 [t_2 – t_3]: During this time, a part of the current $i_{Lr}(t)$ freewheels through D_{aux1}, L_r, S_{aux} and body diode of S_{main}. The switch S_{main} can be turned on with ZVS at this time. S_{aux} is turned off at $t=t_3$.

$$v_{Cr}(t) = 0 \tag{5}$$

$$i_{Lr}(t) = I_{in} + \frac{V_0}{Z_n} \tag{6}$$

4) *Mode* 4 [t_3 – t_4]: The auxiliary switch S_{aux} is already turned off at $t=t_3$ then the auxiliary diode D_{aux2} is turned on. The resonant current $i_{Lr}(t)$ is linearly decreased to zero.

$$v_{Cr}(t) = 0 \tag{7}$$

$$i_{Lr}(t) = -\frac{V_0}{L_r} \cdot t + \left(I_{in} + \frac{V_0}{Z_n} \right) \tag{8}$$

5) *Mode* 5 [t_4 – t_5]: The auxiliary circuit is also used to make the dc-link voltage to zero and keep this status for a short switching transition time whenever the inverter switches need to have their status changed. So the switch S_{main} must be temporally turned off at $t=t_5$ for providing soft commutation at inverter switches.

6) *Mode* 6 [t_5 – t_6]: The switch S_{main} is turned off at $t=t_5$ then the resonant voltage $v_{Cr}(t)$ is linearly increased and the dc-link voltage $v_{pn}(t)$ is linearly decreased, respectively. This mode ends when $v_{Cr}(t)$ reaches V_o and $v_{pn}(t)$ is zero at $t=t_6$.

7) *Mode* 7 [t_6 – t_7]: At this time, all body diodes of the inverter switches can be turned on with ZVS. The inverter switch S_{inv1} and S_{inv3} can be turned off and on with ZVS, respectively.

8) *Mode* 8 [t_7 – t_8]: At $t=t_7$, the switch S_{main} will be turned on again to perform continuously the operation of boost converter, so the switch S_{aux} is turned on at this time for providing the ZVS condition for S_{main}.

After $t=t_8$, the inverter circuit acts continuously the freewheeling state. The operation principles of mode 9 to 13 are the same as the mode 2 to 6. The equivalent circuits of mode 9 to 14 are shown in Fig. 2(i) to Fig. 2(n), respectively. At mode 14 the buck inverter acts continuously the freewheeling state. After mode 14 the operation is returned to the first mode.

C. Soft-Switching Condition and Design Equations

In order to achieve soft commutation at ZVS for the main switch, the following constraints should be satisfied. The on time T_{aux} of the auxiliary switch S_{aux} should be as follows:

$$T_{aux} \geq T_1 + T_2 \tag{9}$$

where $$T_1 \equiv t_1 - t_0 = \frac{L_r \cdot I_{in}}{V_0} \quad (10)$$

$$T_2 \equiv t_2 - t_1 = \frac{\pi}{2} \cdot \sqrt{L_r \cdot C_r} \quad (11)$$

The resonant capacitor and inductor is calculated by

$$C_r = \frac{(a-1) \cdot I_{in,\max} \cdot T_{aux}}{\left[\frac{\pi}{2} + \frac{1}{(a-1)}\right] \cdot V_0} \quad (12)$$

$$L_r = \frac{V_0 \cdot T_{aux}}{\left[(a-1)\frac{\pi}{2} + 1\right] \cdot I_{in,\max}} \quad (13)$$

where a is the constant given by $1 \le a \le 1.5$

III. Simulation Results

A 40kHz, 100W, 220V output inverter is designed and simulated using Orcad PSpice simulation. The simulation waveforms shown in Fig. 4 and 5 confirm the soft-switching operation of the both switches in DC-DC converter and DC-AC inverter. The output voltage and current waveform are shown in Fig. 5

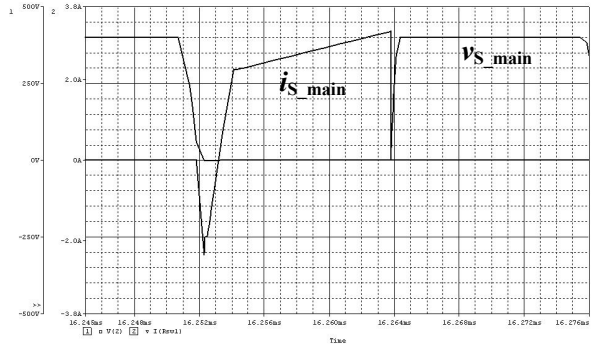

(a)

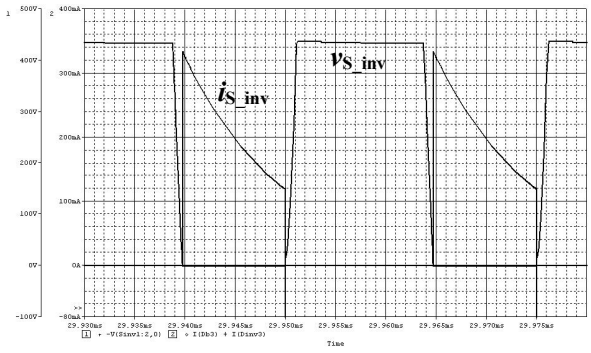

(b)

Figure 4. (a) Voltage and current waveforms of main switch S_{main}
(b) Voltage and current waveforms of inverter switch S_{inv}

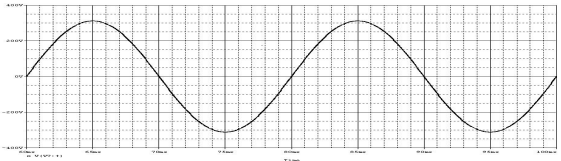

(a)

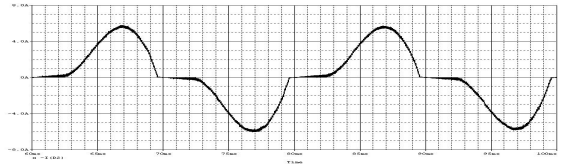

(b)

Figure 5. Simulated output waveform of the proposed inverter
(a) Output voltage (b) Output current

IV. Conclusion

The soft-switching single-phase inverter for small grid-connected PV systems was proposed. The proposed inverter with soft-switching auxiliary circuit was simulated rated at 100W. The simulation results confirmed that the boost switch and inverter switches were operated under soft-switching condition without additional current and voltage stresses.

Acknowledgment

The authors gratefully thank the financial support from Naresuan University Phayao Campus.

References

[1] B. K. Bose, "Energy, environment, and advances in power electronics," *IEEE Trans. on Power Electronics*, vol. 15, pp. 688-701, July 2000.

[2] J. A. Gow and C. D. Manning, "Photovoltaic converter system suitable for use in small scale stand-alone or grid connected applications," *IEE Proceedings on Electric Power Applications*, vol. 147, pp. 535-543, June 2000.

[3] K. Matsui, I. Yamamoto, K. Ando, and T. Kobayashi, "Utility-interactive photovoltaic power conditioning systems with forward converter for domestic applications," *IEE Proceedings on Electric Power Applications*, vol. 147, pp. 199-205, March 2000.

[4] G. Hua and F. C. Lee, "Soft-switching techniques in PWM converter," *IEEE Trans. on Industrial Electronics*, vol. 42, pp. 595-603, December 1995.

[5] G. Hua, C. S. Leu and F. C. Lee, "Novel zero-voltage-transition PWM converters," *IEEE proc. of PESC*, pp. 55-60, 1992.

[6] G. Hua, E. X. Yang, Y. Jiang and F. C. Lee, "Novel zero-current-transition PWM converters," *IEEE Trans. on Power Electronics*, vol. 9, pp. 601-606, Nov. 1994.

[7] C. M. Wang, J. H. Su, J. B. Lio and C. H. Yang, "A novel ZVS-PWM single-stage single-phase AC/DC/AC converter with high power factor," *IEEE proc. of PEDS 2005*, pp. 1051-1055, Nov. 2005.

Control and Implementation of Line Side Converter for Doubly Fed Induction Generator of Wind Turbine

Watee Sudmee and Bunlung Neammanee
Department of Electrical Engineering, Faculty of Engineering
King Mongkut's Institute of Technology North Bangkok
1518 Bang sue, Bangkok 10800, Thailand Phone: 662-913-2500 Ext: 8420, Fax: 662-913-2500 Ext: 8520,
E-mails: te46019@hotmail.com and bln@kmitnb.ac.th

***Abstract*-This paper proposes the design and implementation of line side converter of doubly fed induction generator. The mathematical models of line side converter, axis transformation, decoupling control and phase locked loop control are derived. A vector control system is implemented on a digital signal controller (DSC) with C language to control a 7.5 kW converter to regulate a 550V DC bus. Experiments are set up to test dynamic performance in rectifying and inverting modes of operation. The experimentation results confirm that the system can regulate the DC bus voltage under step load, can bi-directionally control power flow with a constant DC bus voltage, and reduce the line side current with near-unity power factor and low harmonic.**

Keywords: line side converter, decoupling control, vector control, phase locked loop

I. INTRODUCTION

Wind energy has long been recognized as one of the alternative options for electricity production and is gaining increasing importance throughout the world because it is pollution-free, affordable and sustainable. In general, power from a wind turbine highly depends on wind speed (i.e., power increases rapidly with wind speed). Therefore, locating wind generators in a place where wind speed is strong and reasonably constant is an important factor. In addition to such a constraint, operating a wind power plant requires efficient control techniques to extract power from the turbines as much as possible for any input wind speed. In general, a wind turbine is mechanically designed to produce its rated power at a certain wind speed which is referred as rated wind speed.

There are many types of wind generators such as DC generator, synchronous generator and induction generator but the doubly fed induction generator (DFIG) is widely used because it can deliver the active power in both stator and rotor. In addition, a small size of control converters is needed and the active power and reactive power can be independently controlled [1]. The control of a doubly fed induction generator in a wind conversion system uses a machine side converter and a line side converter [2]. The line side converter has two modes of operation: rectifying mode and inverting mode. In the rectifying mode, when the rotational speed of the DFIG is lower than synchronous speed, the rotor consumes the active power from the dc bus voltage, causing a decrease in the dc bus voltage. The line side converter charges the dc bus capacitor to regulate the dc bus voltage. In the inverting mode, when the rotational speed of the DFIG is higher than synchronous speed. The rotor delivers the active power to the dc bus voltage, causing an increase in the dc bus voltage. The line side converter discharges the dc bus capacitor to the grid to regulate the dc bus voltage.

The conversion from single phase and three-phase AC to DC voltage normally uses diode rectifiers, which cause non-sinusoidal line side current. As a result, the line side current contains many harmonic components and causes the difficulty in power factor correction by capacitor banks. For this reason, a new technique is developed to solve the above problem.

This paper proposes the design and construction of a three phase 7.5 kW line side converter. The mathematical models of line side converter, voltage decoupling control, phase locked loop (PLL) and the control block diagram are presented. The converter uses the decoupling control to regulate the DC bus voltage and drive the power converter by space vector PWM. The controller is implemented on a developed DSC board and tested with load to verify control performance.

II. MATHEMATICAL MODEL OF LINE SIDE CONVERTER

Figure 1 shows a three phase line side converter that converts AC voltage to DC voltage by a space vector PWM converter. The per phase voltage equation can be written as in (1)-(3).

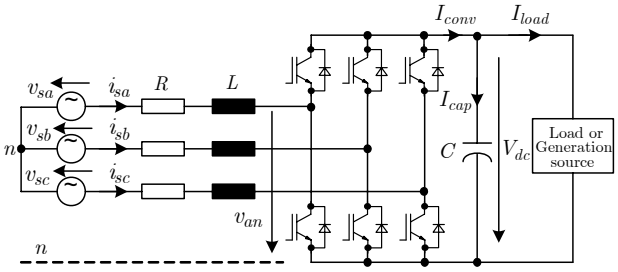

Figure 1. Line side converter

$$v_{sa} = Ri_{sa} + L\frac{di_{sa}}{dt} + v_{an} \quad (1)$$

$$v_{sb} = Ri_{sb} + L\frac{di_{sb}}{dt} + v_{bn} \quad (2)$$

$$v_{sc} = Ri_{sc} + L\frac{di_{sc}}{dt} + v_{cn} \quad (3)$$

Transforming (1)-(3) in three phases in stationary reference frame to two phase synchronous reference frame (*d*-, *q*-axis) gives

$$v_{sd} = (Ls + R)i_{sd} - \omega L i_{sq} + v_{dn} \quad (4)$$

$$v_{sq} = (Ls + R)i_{sq} + \omega L i_{sd} + v_{qn} \quad (5)$$

For the balance three phase,

$$v_{sd} = V_m \quad (6)$$

$$v_{sq} = 0 \quad (7)$$

The converter power, P_{conv}, and current, i_{conv}, can be calculated by (8) and (9) [3].

$$P_{conv} = \frac{3}{2}\left(v_{sd}i_{sd} + v_{sq}i_{sq}\right) \quad (8)$$

$$I_{conv} = \frac{P_{conv}}{V_{dc}^*} = \frac{3}{2}\frac{\left(v_{sd}i_{sd} + v_{sq}i_{sq}\right)}{V_{dc}^*} \quad (9)$$

The capacitor current, I_{cap}, and DC bus voltage, V_{dc}, can be calculated by (10) and (11).

$$I_{cap} = I_{conv} - I_{load} \quad (10)$$

$$V_{dc} = \frac{1}{Cs}\int I_{cap}dt \quad (11)$$

With the transformation of (4)-(11) into s-domain, a block diagram in *d*-, *q*-axis reference frame can be constructed as shown in Fig. 2. It is clear that there is the voltage cross coupling between v_{dn} and v_{qn}. To have independent control of V_{dc}, the coupling voltage should be compensated by a controller [4-5].

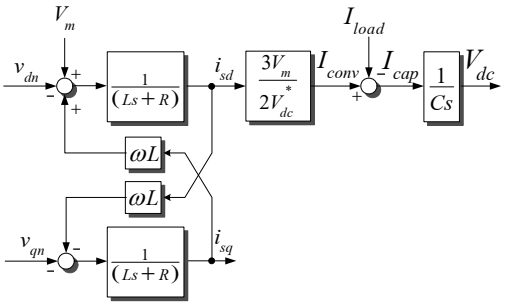

Figure 2. block diagram of line side converter in *d*-, *q*-axis reference frame

III. Control of Line Side Converter

The main control objective is to regulate the DC bus voltage without the voltage cross coupling. To achieve this objective, it is necessary to compensate the coupling components $\omega L i_{sq}$ and $\omega L i_{sd}$ with a PI controller. The control equations are as follows.

$$v_{dn}^* = (K_{pi} + \frac{K_{ii}}{s})(i_{sd}^* - i_{sd}) + \omega L i_{sq} + V_m \quad (11)$$

$$v_{qn}^* = (K_{pi} + \frac{K_{ii}}{s})(i_{sq}^* - i_{sq}) - \omega L i_{sd} \quad (12)$$

If the voltage couplings are compensated, the bus voltage depends only on the current i_{sd}. The PI controller is then used to control the bus voltage by the current i_{sd}. The control equation is shown in (13).

$$i_{sd}^* = (K_{pi} + \frac{K_{ii}}{s})(V_{dc}^* - V_{dc}) \quad (13)$$

With (11)-(13), the line side converter control with a voltage decoupling block diagram can be constructed as in Fig. 3. In the block diagram, the voltage cross coupling is compensated by feeding i_{sd} and i_{sq} with gain ωL. After the voltage is decoupled, the DC bus voltage is controlled by two loops: current and voltage loops. The current i_{sq} does not affect the bus voltage and therefore it is not used. The value of i_{sq} is set to zero.

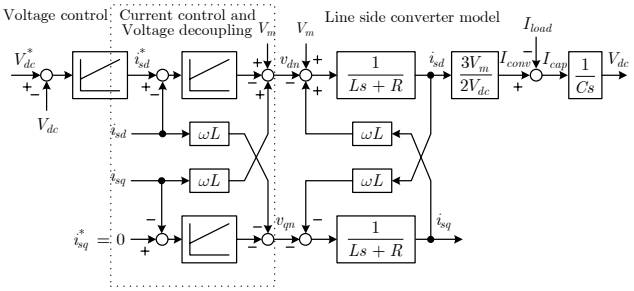

Figure 3. Line side converter with voltage decoupling control

The controller of the line side converter is controlled in *d*-, *q*-axis reference frame. The transformation between three phases and *d*-, *q*-axis requires an angle of phase voltage. A phase locked loop (PLL) to calculate the angle of phase voltage, θ^*, is shown in Fig. 4 [6]. The PLL is composed of voltage transformation, sine and cosine calculation and PI controller. The parameter θ^* in the transformation is obtained by integrating frequency command ω^*. If the frequency is identical to the grid frequency, the voltages v_{sd} and v_{sq} become DC values, depending on the angle θ^*. A PI regulator is used to obtain that value of ω^*, which drives the feedback voltage v_{sq} to the command value v_{sq}^*. The magnitude of the controlled quantity v_{sq} determines the phase difference between the utility voltages and sin(θ^*) or cos(θ^*). This system sets $v_{sq}^* = 0$.

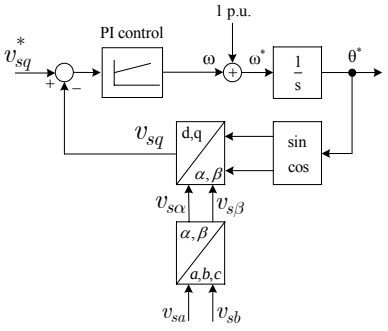

Figure 4. Phase locked loop

IV. Control Block Diagram

The overall control block diagram in Fig. 5 has two main parts. The first part is a power unit consisting of three single phase inductors, a power converter, DC-link capacitors and loads (right hand side). The second part is a control unit consisting of phase lock loop (PLL), axis transformation

(three phase to *d*-, *q*-axis), three PI controllers, axis transformation from *d*-, *q*-axis to a three phase and space vector PWM (left hand side).

To be operated in the rectifying mode, the converter obtains the power from the grid via the three phase inductor used to boost the voltage to the DC bus voltage. The DC output is connected with filter capacitor and loads. The power unit has three current sensors (two for line side and one for DC bus current) and three voltage sensors (two for line side and one for DC bus voltage). When the converter is operated in the inverting mode, the active power in the capacitor is injected via the converter to the grid to regulate the DC bus voltage or vice versa.

The digital signal controller controls the system with two references. One is i_{sq}^* for reactive power control (zero reactive power) and the other is V_{dc}^* for DC bus voltage control (550V). Both references are the inputs of PI controllers. The output of the controller will be changed to *d*-, *q*-axis voltage which is then transformed to three phase voltage. This voltage is converted to drive signal by the SVPWM to control the converter.

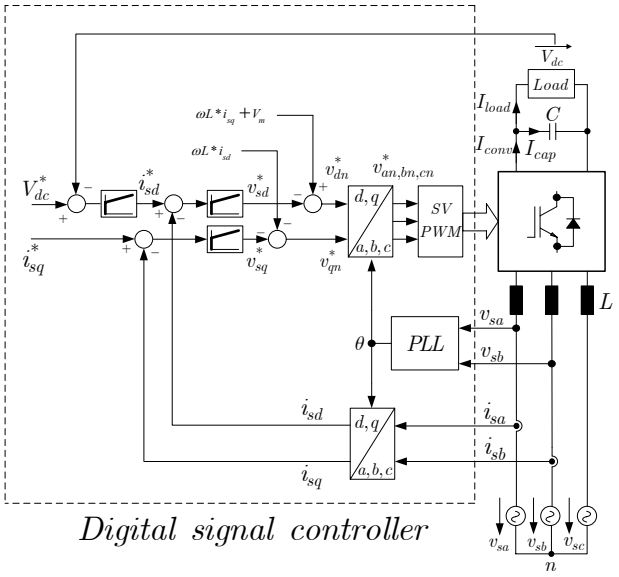

Figure 5. Control block diagram

V. CASE STUDY

A. Experimental Systems

The test system is shown in Fig. 6. The upper right corner of the figure is composed of a three phase 7.5 kW converter, DC link capacitors (925 μF), three single phase inductors (4.5mH), three phase variable voltage transformer, loads, voltage and current sensors. The lower part is composed of a data acquisition system connected to a DSC board, an oscilloscope and a personal computer. The controller board uses a high performance 16 bits dsPIC30f6010 combining the advantage of a high performance 16-bit microcontroller (MCU) and a high computation speed digital signal processors (DSP). The upper left corner is a variable DC voltage supply for tests in the inverting mode. This part can increase the DC voltage higher than the bus voltage to supply the active power in inverting operation.

This system is designed to regulate the DC bus voltage at 550 V and unity power factor with bi-directional power flow. The controller is implemented in the DSC and linked with a personal computer via RS232 port for transferring wind speed data to the DSC board and the other for sending parameters (e.g., $v_{sa}, i_{sb}, i_{sd}, i_{sq}$) to the computer for control verification.

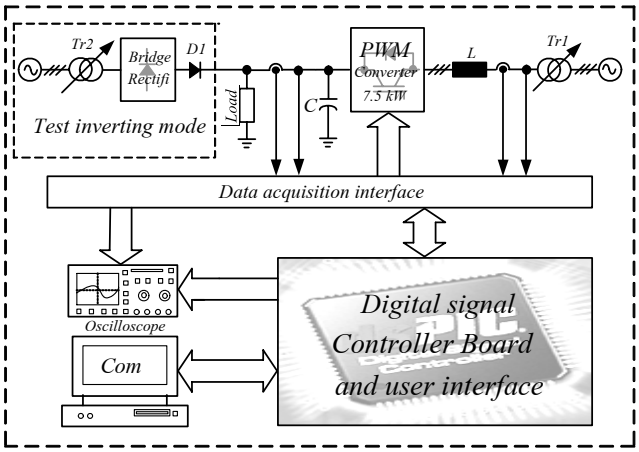

Figure 6. The test system

B. Dynamic Response

Figure 7 shows the DC bus voltage of the line side converter regulated at 550V, $t = 0.2$ seconds (point A). It can be seen that step resistance load causes a reduction in the DC bus voltage. The PI controller then commands to increase current i_{sd} (shown in Figure 8) to regulate the DC bus voltage. It takes 250 milliseconds to reach steady state with an undershoot voltage of 16.36%. At $t = 1.1$ second (point B), the resistance load is removed causing an increase in the DC bus voltage. The PI controller then commands to reduce current i_{sd} (as shown in Figure 8) to regulate the DC bus voltage. It takes 500 milliseconds to reach steady state with an overshoot voltage of 25.24%.

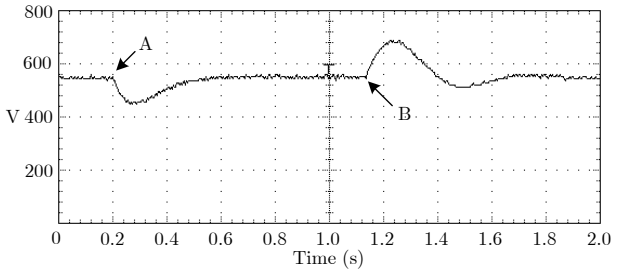

Figure 7. bus voltage with rectifying and inverting mode

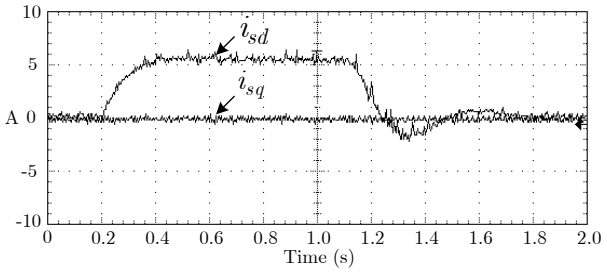

Figure 8. *d*, *q*-axis line current (i_{sd} , i_{sq})

Figure 9 shows the phase voltage v_{sa} and current i_{sa} of the supply side converter when it transits from the rectifying mode to the inverting mode. In the initial state, the system supplies load current and operates in the rectifying mode. After that, the load is suddenly reduced at $t = 10$ seconds, causing the DC bus voltage to increase, and the phase current to reduce to zero and flow to reverse direction. The operating mode is switched to inverting mode with 180° phase shift respect to the phase voltage with a transition time about 120 milliseconds.

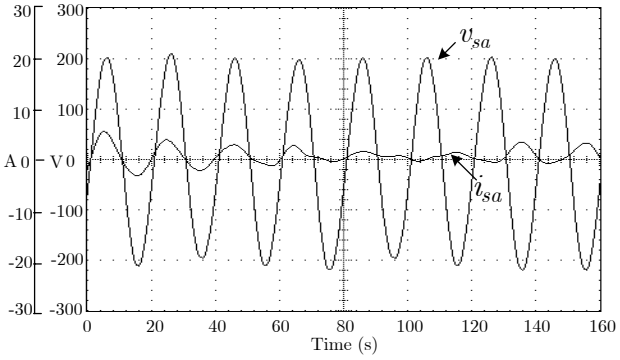

Figure 9. Line voltage, v_{sa} and current, i_{sa}

C. Rectifying and Inverting Mode Operation

Figure 10 shows the phase voltage v_{sa} and current i_{sa} of the supply side in the rectifying mode operation. It is clearly seen that the phase current has a low total harmonic distortion. The phase voltage and current are in phase, and by this mean this converter consumes the only active power from grid. Note that the actual power factor from a measurement is 0.98.

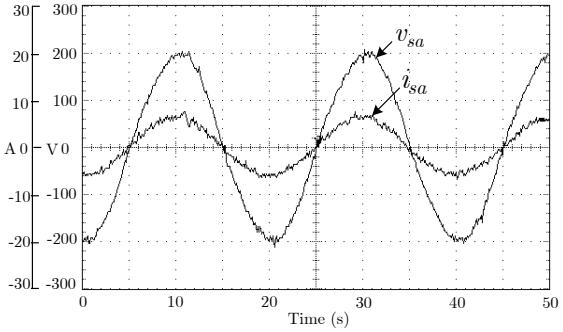

Figure 10. Line voltage, v_{sa} and current, i_{sa} in rectifying mode

Figure 11 shows the phase voltage v_{sa} and current i_{sa} of the supply side in the inverting mode operation. It is clearly seen that phase current has a low total harmonic distortion. The phase voltage and current are 180° out of phase, indicating this converter generates only active power to the grid.

VI. CONCLUSION

The detailed study and implementation of a 7.5 kW, three phase vector control PWM line side converter is presented. The algorithms are implemented on a developed low cost and high performance DSC board. This board also prepares computer interface for data acquisition system. The experimentation results confirm the following advantages of the implemented system. First, the DC bus voltage can be regulated in both rectifying and inverting modes. Second, the system can bi-directional control active power flow with unity power factor. Third, the controller can regulate the DC bus voltage under step load. Finally, this converter is suitable for front end of a doubly fed induction generator in wind turbine systems, power factor correction of the high power inverter and for electronic loads. However, the disadvantages of this system are high overshoot and undershoot voltage, and long setting time. Future work is the improvement of these problems.

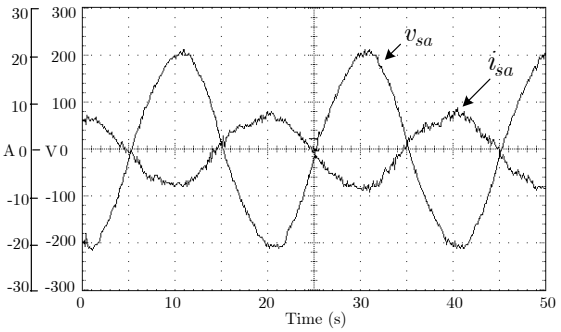

Figure 11. Line voltage, v_{sa} and current, i_{sa} in inverting mode

REFERENCES

[1] Mitsutoshi, Y., and Motoyoshi O., *Active and reactive power control for doubly-fed wound rotor induction generator*, IEE Trans. Power Electron., 1991, 6, (4), pp. 624-629.

[2] R. Pena, J.C. Clare, and G. M. Asher, *Doubly fed induction generator using back-to-back PWM converters and its application to variable speed wind-energy generation*, IEE Proc. Electr. Power Appl., Vol. 143, No. 3, May 1996, pp. 231-241.

[3] Dixon. J.W. and Ooi. B.T., *Indirect current control of a unity power factor sinusoidal boost type three-phase rectifier,* IEEE Trans. on Industrial Electronic, Vol. 35, Issue 4, Nov.1988, pp. 508-515.

[4] R. S. Pena, R. J. Cardenas, J. C. Clare and G.M. Asher, *Control Strategies for Voltage Control of a Boost Type PWM Converter,* IEEE on PESC, Vol. 20, No.4, 17-21 Jun.2001, pp. 730-735.

[5] Lee, D.-C., *Advanced nonlinear control of three-phase PWM rectifiers,"* IEE Proc. on Electric Power Appl., Vol. 147, Issue 5, Sep. 2000, pp. 361-366.

[6] Kaura, V. and Blasko, V., *Operation of a Phase Locked Loop System Under Distorted Utility Condition,* IEEE on Industry Application, Vol. 33, Issue 1, Jan.-Feb1997, pp. 58-63.

Nomenclature

v_{sa}, v_{sb}, v_{sc}	= a, b and c line side phase voltage
i_{sa}, i_{sb}, i_{sc}	= a, b and c line side phase current
v_{sd}, v_{sq}	= *d*, *q*-axis of line side phase voltage
i_{sd}, , i_{sq}	= *d*, *q*-axis of line side phase current
V_m	= peak of phase voltage
V_{dc}	= DC bus voltage
C	= capacitance
L	= per phase inductance
R	= per phase resistance
K_{pi}	= proportional gain
K_{ii}	= integral gain
ω	= radian frequency
θ	= line side phase voltage angle
Tr	= transformer
D	= diode

Thermal Conductivity Tester

Santi Wangnipparnto and Tianchai suksri
Faculty of Engineering, Pathumwan Institute of Technology,
833 Ram 1 rd, Pathumwan, Bangkok, 10330, Thailand.

Abstract- This research has been designed and built the prototype of thermal conductivity tester for appropriate using in Thailand. Temperature ranges 40-60 ^{o}C are controlled by fuzzy logic controller. The four types of material, flat cement asbestos, black glazed mirror, clear mirror, and normal gypsum board are prepared and tested in standard size 100 mm wide, 100 mm long and thickness less than 10 mm. The controller is built by the personal computer, Interface card, and Visual Basic 6.0 program. All equipments are tested in the room where has the temperature range 23-25^{o}C. From the experimental shown that the fuzzy logic controller can be keep the temperature at the set point and has steady state error less than ± 0.5^{o}C. The thermal conductivity (k) value of four materials has the average margin error less than 15.3 % .

I. Introduction

Nowaday everyone interesting the saving energy and the environment in the home, building, and industry. Thermal insulation is the method of preventing heat from escaping a container or from entering the container. In other words, thermal insulation can keep an enclosed area such as a building warm, or it can keep the inside of a container cold. In any location where the effort is to minimize the transfer of heat from one area to another. So the thermal conductivity tester is importance to measuring thermal conductivity (k) of the thermal insulator materials and calculating the heat gain in order to prevent its by adding thickness of insulator or design the new composite insulator materials. For this research is designed and built the prototype of thermal cconductivity tester for using in Thailand.

II. Theory

Thermal conductivity

Thermal conductivity is a property of materials that expresses the heat flux (W/m^2) that will flow through the material if a certain temperature gradient DT (K/m) exists over the material as shows in Fig. 1.

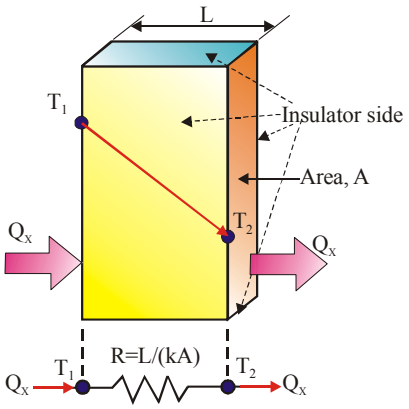

Figure 1. Conduction heat transfer equivalent.

Thermal conductivity is defined as:

$$k = \frac{Q/A}{\Delta T/\Delta L} \qquad (1)$$

where Q is the amount of heat passing through a cross section, A, and causing a temperature difference, ΔT, over a distance of ΔL. Q / A is the heat flux which is causing the thermal gradient, $\Delta T / \Delta L$. The measurement of thermal conductivity, therefore, always involves the measurement of the heat flux and temperature difference. The difficulty of the measurement is always associated with the heat flux measurement. Where the measurement of the heat flux is done directly (for example, by measuring the electrical power going into the heater), the measurement is called absolute.

Fuzzy logic controller

The conventional proportional-integral-derivative(PID) is commonly utilized in controlling the temperature, but the parameters of those controllers must be turned by tuning method[1,2]. On the other hand, the fuzzy logic controller is popularly implemented in many practical industrial automation applications. In this paper, we implement its by control the temperature in the one side of the hot flat plate as show in Fig. 2.

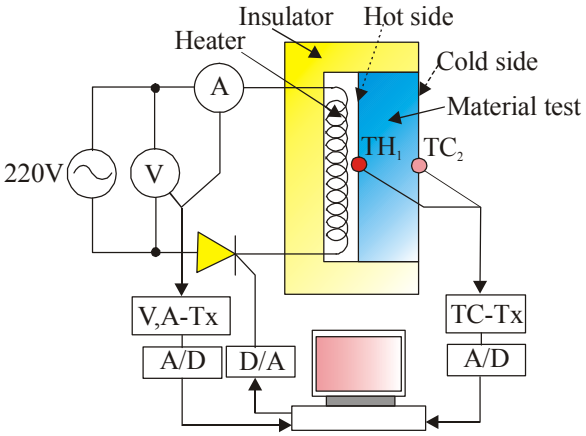

Figure 2. Schematic of thermal conductivity tester.

The input of fuzzy logic controller is the temperature error(e) between the set point and the process or hot plate side variable. The fuzzy logic controller consists of fuzzification, control rule and defuzzification stages as shown in Fig. 3.

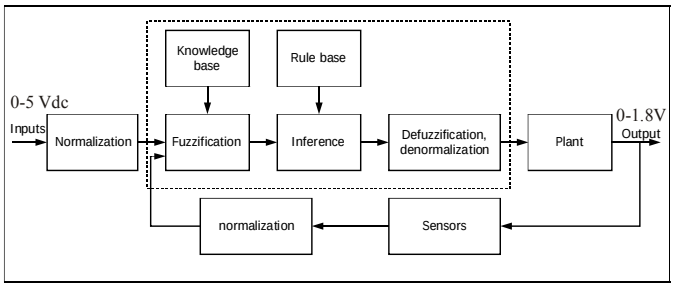

Figure 3. Block diagram of fuzzy logic controller.

Membership function editor is used for expressing input and output variables. The number of membership functions for each input variable is designated in five ranges and the names of its are positive big /positive small/zero/negative small/ negative big. The form of all input and output membership functions are selected to be triangle-shaped functions for simplicity. In fuzzification stages, the input variables, the temperature is converted into fuzzy variables using the membership function as shown in Fig. 4. The linguistic rules of e and ce of temperature are shown in Table 1.

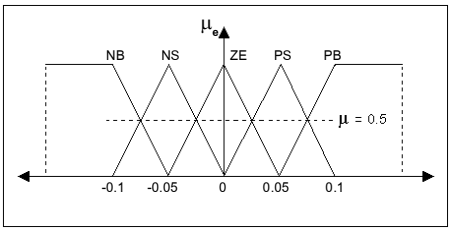

a.)

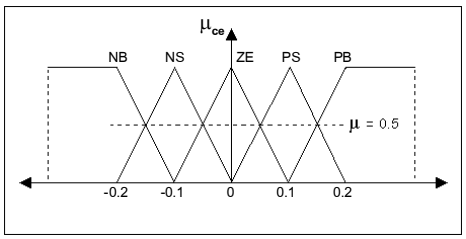

b.)

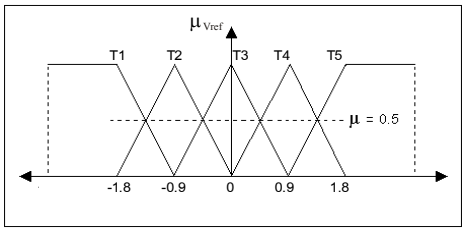

c.)

Figure 4. Membership function of input and output variables of temperature control.

TABLE 1.
Control rules for input and output variables

ce \ e	NB	NS	ZE	PS	PB
NB	T_1	T_1	T_1	T_1	T_1
NS	T_1	T_1	T_2	T_2	T_2
ZE	T_2	T_2	T_3	T_4	T_4
PS	T_4	T_4	T_4	T_5	T_5
PB	T_5	T_5	T_5	T_5	T_5

The defuzzificating operation, in this paper, uses the centroid defuzzification method because of its implementation simplicity.

III. Experimental Setup

The simplified of the thermal conductivity tester can be divided in two parts. The hardware consists of the testing box, personal computer and interface card as shown in Fig. 5. The software consists of the program control and front view of data that built its by Visual Basic 6.0 as shown in Fig. 6.

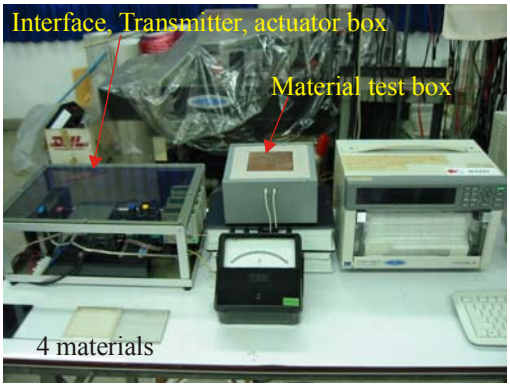

Figure 5. The experimental setup.

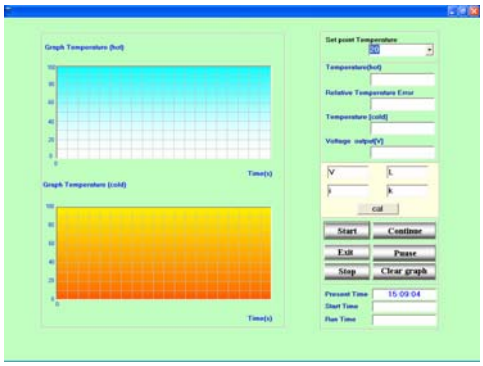

Figure 6 Front view of the thermal conductivity tester.

IV. EXPERIMENTAL RESULTS

The experimental results in this paper can be divided in two parts, the first shows performance of the fuzzy logic controller, the second finds thermal conductivity of four materials which compairing the standard value.

Temperature control by fuzzy logic controller

The hot plate side temperature of material test box is controlled by fuzzy logic controller. The responses time and steady state error of the temperature control when changing the step set point from 30–40°C and 30-60°C are shown in Fig.7 and Fig.8 respectively. From Fig.7 and Fig.8 show that steady state error less than ± 0.5°C and the response time less than 3 minutes.

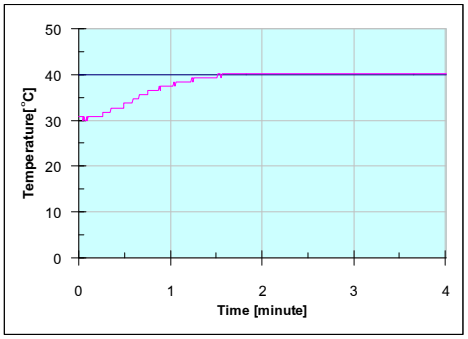

Figure 7. Changing the step set point from 30–40°C.

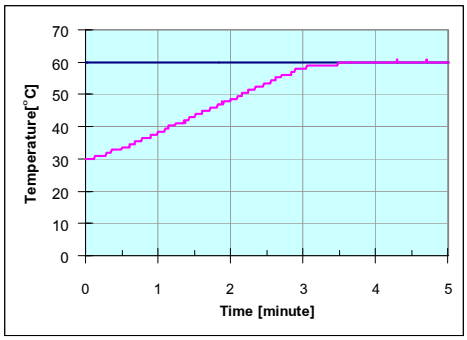

Figure 8. Changing the step set point from 30–60°C.

Thermal conductivity of materials

The four types of material, flat cement asbestos, black glazed mirror, clear mirror, and normal gypsum board are determinded the thermal conductivity by prepairing its in standard size 100 mm wide, 100 mm long and thickness less than 10 mm. Figure 9 shows the thermal conductivity of four materials which compaired the standard value and found that the maximum error occurred at flat cement asbestos about 15.31%.

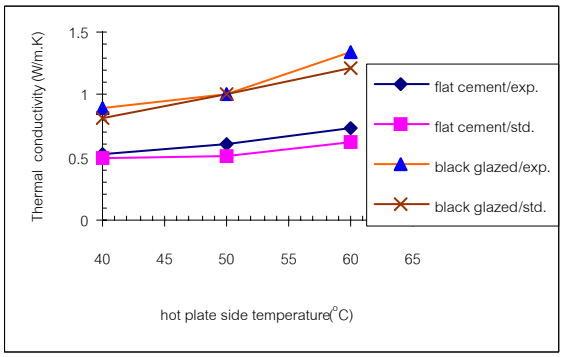

a.)

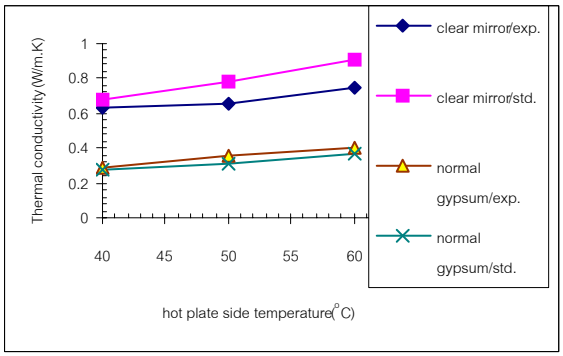

b.)

Figure 9 The thermal conductivity of materials

V. CONCLUSION

The thermal conductivity tester which controlling the hot plate temperature by the fuzzy logic controller has been proposed. It has been shown that the steady state error of the

temperature control less than ± 0.5^{o}C and the response ttime less than 3 minutes.

A good agreement between the thermal conductivity value of all materials that testing by the thermal conductivity tester and the standard value, the flat cement asbestos has the maximum error about 15.31% from the standard value.

ACKNOWLEDGMENT

The authors gratefully acknowledge the Miss Rattana Pooknoi who testing the experimental apparatus hardly.

REFERENCES

[1] J.G.Ziegler and N.B.Nichols, "Optimum settings for automatic controller," ASME Trans. Vol64, pp.759-768, 1942.

[2] W.K.Ho, C.C. Hang, and J.H.Zhou, "Performance and gain and phase margins of well-known PI Tuning formulas," acceptedfor publication in IEEE Trans. Contr. Syst. Technol., 1995.

[3]..Wangnipparnto, S., Srikwankeaw,P.,and Thong-o, S., "Relative Humidity Controlled by Fuzzy Logic Control", Prince of Songkla university, 8-9 December, pp44, 2004.

An Enhanced Adaptive Voltage Control in Gas Tungsten Arc Welding

Poolsak Koseepaporn

Department of Teacher Training in Electrical Engineering
Faculty of Technical Education
King Mongkut's Institute of Technology North Bangkok

***Abstract*-An improvement of the adaptation law of model-based adaptive control scheme is presented in this work. The proposed adaptation modification is designed for an adaptive voltage control in gas tungsten arc welding process. This method can overcome the limitation of persistent excitation of the conventional adaptation; the estimated of unknown parameters would converge to the correct values if the system is persistently excited. For the proposed approach, the true values of unknown parameters are mathematically obtained. As the results, the estimated unknown parameters can be forced to converge to the true values with and without persistent excitation. Therefore, the dynamic performance of the system is improved. The simulation results of the proposed method applied to gas tungsten arc welding process with argon shielding gas model show that the parameter adaptation is improved.**

I. INTRODUCTION

Automatic welding control is widely used for several decades. Servo drive is usually applied to control welding torch moving upward and downward in order to maintain distance from the workpiece which is commonly applied in piping welding based on Gas Tungsten Arc Welding (GTAW). One type of this kind of welding is so called "Automatic Voltage Control (AVC)". As shown in Fig. 1, AVC employs arc voltage, measured from electrode, to maintain arc length at a certain operating electric current. Although AVC is typically working well for automatic welding control, it has some limitation when the system gain has been changed due to welding parameters. It is because system gain varies with the arc length, arc voltage, and arc current as described by Bjorgvinson [1]. In addition, the welding current has to be ramped up and ramped down in order to prevent cracking at the starting and ending point of weld. Therefore, AVC that is designed for constant operating point can not cope with entire welding, especially for those ramped up and ramped down period. Consequently, oscillatory of welding torch will cause some damage at workpiece.

To solve this problem, gain scheduling method [2] has been proposed. However, this technique has a limitation of control method. All of possible welding parameters must be preprogrammed which is time consuming and also requires huge memory to store welding database. Later, an adaptive control method [3] is introduced to eliminate the previous limitation. The designed model-based adaptive controller is able to track the change in welding system gain due to the change in welding current while a fuzzy logic controller is used as a supervisor to monitor and to maintain the arc length stay in safe zone. Although this type of controller can successfully control the welding system, it cannot guarantee that the estimated parameters will converge to the actual unknown values. This is usually occurred if the system is not persistently excited. The reason behind this problem may come from one of these reasons. First, the adaptation gain is not appropriately selected to force the convergence of the estimated parameters to be fast enough within excitation period. Second, the excitation period is too short due to the small change in motion command. For these reasons, the dynamic behavior may not perform well and it requires several tests in order to get the desired dynamic behavior.

This paper presents an improvement of adaptation scheme for overcoming the limitation of persistence excitation. The controller and system equation are used to extract the unknown parameters which will be used to force the adaptive controller to adapt the system parameters to the correct values with and without excitation.

II. ADAPTIVE CONTROLLER DESIGN

To control the position of the welding torch, dc servo motor is widely used. As depicted in Fig. 2, the transfer function of servo motor expresses the relationship between the input motor voltage, $V_m(s)$, and the output arc length, $L_a(s)$. This transfer function is given by

$$G_s(s) = \frac{L_a(s)}{V_m(s)} = \frac{k_s}{s(s+a_s)}, \tag{1}$$

where k_s and a_s are servo gain and servo time constant, respectively. By using the relationship between the arc length and the arc voltage which is $L_a k_a = V_a$, equation (1) can be rewritten in time-domain equation as $\ddot{v}_a + a_s \dot{v}_a = k_s k_a v_m$. By letting $c_1 = (a_s / k_s k_a)$ and $c_2 = (1/k_s k_a)$, this time-domain equation is then

$$c_2 \ddot{v}_a + c_1 \dot{v}_a = v_m. \tag{2}$$

Note that k_a in c_1 and c_2 is a nonlinear function of welding current and arc length. It is, therefore, chosen to be unknown

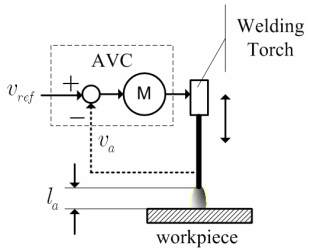

Figure 1. AVC in GTAW system.

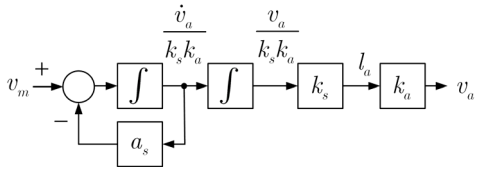

Figure 2. Block diagram of open-loop AVC.

parameters for adaptive system. Let replace the input of motor with a function of proportional-plus-derivative control law as given by

$$v_m = \hat{c}_2 v_m' + \hat{c}_1 \dot{v}_a \,, \tag{3}$$

where $\hat{c}_1$ and $\hat{c}_2$ are the estimated parameters of c_1 and c_2, respectively. In addition, v_m' is chosen as

$$v_m' = \ddot{v}_{ref} + k_v \dot{e} + k_p e \,, \tag{4}$$

where $e = v_{ref} - v_a$ is the error between voltage reference and the measured arc voltage. And k_v and k_p are the derivative and proportional error gain, respectively. By putting (4) into (3) and equating to (2), which is

$$c_2 \ddot{v}_a + c_1 \dot{v}_a = \hat{c}_2 [\ddot{v}_{ref} + k_v \dot{e} + k_p e] + \hat{c}_1 \dot{v}_a \,. \tag{5}$$

By rearranging (5) to be

$$c_2 \ddot{v}_a + (c_1 - \hat{c}_1)\dot{v}_a = \hat{c}_2 \ddot{v}_{ref} + \hat{c}_2 [k_v \dot{e} + k_p e] \,, \tag{6}$$

and subtracting both side by $\hat{c}_2 \ddot{v}_a$, it results in

$$\hat{c}_2 [\ddot{e} + k_v \dot{e} + k_p e] = \tilde{c}_2 \ddot{v}_a + \tilde{c}_2 \dot{v}_a \,, \tag{7}$$

where $\ddot{e} = \ddot{v}_{ref} - \ddot{v}_a$, $\tilde{c}_2 = c_2 - \hat{c}_2$, and $\tilde{c}_1 = c_1 - \hat{c}_1$.
The desired error equation, therefore, is

$$[\ddot{e} + k_v \dot{e} + k_p e] = \hat{c}_2^{-1} [\tilde{c}_2 \ddot{v}_a + \tilde{c}_2 \dot{v}_a] \,. \tag{8}$$

The result shown in (8) implies that if the estimated parameters ($\hat{c}_1$ and $\hat{c}_2$) are perfectly matched to the unknown parameters (c_1 and c_2), the error dynamic will, therefore, converge to zero. Furthermore, the error dynamic will behave upon the chosen k_v and k_p, the derivative and proportional error gain, respectively. Note that the proportional error gain is selected based on the closed-loop stiffness where the derivative gain in chosen upon the desired damping factor.

To derive the parameter estimation equation, the unknown parameters must be extracted from the error equation as

$$\ddot{e} + k_v \dot{e} + k_p e = \hat{c}_2^{-1} \mathbf{W}(\dot{v}_a, \ddot{v}_a)\Phi \,, \tag{9}$$

where

$$\Phi = \begin{bmatrix} c_2 - \hat{c}_2 \\ c_1 - \hat{c}_1 \end{bmatrix} = \begin{bmatrix} \tilde{c}_2 \\ \tilde{c}_1 \end{bmatrix} \text{ and } \mathbf{W}(\dot{v}_a, \ddot{v}_a) = \begin{bmatrix} \ddot{v}_a & \dot{v}_a \end{bmatrix}.$$

Let introduce a filtered servo error signal as

$$\mathbf{E}_1(s) = (s + \psi)\mathbf{E}(s) \,, \tag{10}$$

and substitute to (9) in Laplace transform, then yields

$$\begin{aligned} \mathbf{E}_1(s) &= \frac{s + \psi}{s^2 + k_v s + k_p} \hat{c}_2^{-1} \mathbf{W}\Phi \\ &= \mathbf{H}(s)\hat{c}_2^{-1}\mathbf{W}\Phi \end{aligned} \,, \tag{11}$$

which is corresponding to

$$\begin{aligned} \dot{\mathbf{x}} &= \mathbf{A}\mathbf{x} + \mathbf{B}(\hat{c}_2^{-1}\mathbf{W}\Phi) \\ \mathbf{y} &= \mathbf{C}\mathbf{x} \end{aligned} \,, \tag{12}$$

where $\mathbf{x} = \begin{bmatrix} e & \dot{e} \end{bmatrix}^T$. From the state equation in (12), there exists two positive-definite matrices $\mathbf{P} > \mathbf{0}$ and $\mathbf{Q} > \mathbf{0}$ such that

$$\begin{aligned} \mathbf{A}^T\mathbf{P} + \mathbf{P}\mathbf{A} &= -\mathbf{Q} \\ \mathbf{P}\mathbf{B} &= \mathbf{C}^T \end{aligned} \,. \tag{13}$$

The stability of this system can be obtained by choosing candidate Lyapunov function [4] as

$$\mathbf{V}(\mathbf{x}, \Phi) = \mathbf{x}^T\mathbf{P}\mathbf{x} + \Phi^T\Gamma^{-1}\Phi \,, \tag{14}$$

where $\Gamma = diag(\gamma_1, \gamma_2)$ and γ_i is nonnegative adaptation gain. Hence, the derivative of (14) is

$$\dot{\mathbf{V}}(\mathbf{x}, \Phi) = -\mathbf{x}^T\mathbf{Q}\mathbf{x} + 2\Phi^T(\mathbf{W}^T\hat{c}_2^{-1}e_1 + \Gamma^{-1}\dot{\Phi}). \tag{15}$$

To guarantee the stability of the system, $\dot{\Phi}$ is chosen to be

$$\dot{\Phi} = -\Gamma\mathbf{W}^T\hat{c}_2^{-1}e_1 \,, \tag{16}$$

which gives $\dot{\mathbf{V}}(\mathbf{x}, \Phi) = -\mathbf{x}^T\mathbf{Q}\mathbf{x}$. As can be seen, (16) is therefore the adaptation law for model-based adaptive control.

III. Adaptation Law Modification

From the arc model as shown in Fig. 2, the state after the first integrator gives

$$\frac{1}{k_s k_a}\dot{v}_a = \int v_m dt - \frac{a_s}{k_s k_a} v_a . \tag{17}$$

By rearranging (17) to be

$$\frac{a_s}{k_s k_a} v_a = \int v_m dt - \frac{1}{k_s k_a}\dot{v}_a . \tag{18}$$

Assuming that k_a is constant, the arc length and arc voltage relationship then is $k_a \dot{l}_a \triangleq \dot{v}_a$. Replacing this part to (18), one of unknown parameters can then be written as

$$c_1 = \frac{1}{v_a}\left[\int v_m dt - \frac{1}{k_s}\dot{l}_a\right]. \tag{19}$$

Note that the servo gain (k_s) is assumed to be known which can be obtained at steady state condition. By integrating (2), another unknown parameter can be determined by

$$c_2 = \frac{1}{v_a}\left[\iint v_m dt dt - \int c_1 v_a dt\right]. \tag{20}$$

Based on the adaptation derived from (16), the estimated parameters which are obtained by integration thus are

$$\begin{bmatrix}\hat{c}_1\\ \hat{c}_2\end{bmatrix} = \int \left(\Gamma \mathbf{W}^T \hat{c}_2^{-1} e_1\right) dt . \tag{21}$$

By applying the results from (19) and (20), (21) can be modified such that the estimated parameters converge to the correct values as

$$\begin{bmatrix}\hat{c}_1\\ \hat{c}_2\end{bmatrix} = \int \left(\Gamma \mathbf{W}^T \hat{c}_2^{-1} e_1\right) dt + \int \Phi e^{-\eta|v'_m|} dt , \tag{22}$$

where η is a nonnegative number for adjusting convergence rate. As shown in Fig. 3, the result of the proposed adaptation law can be illustrated in block diagram modified from the conventional adaptive method.

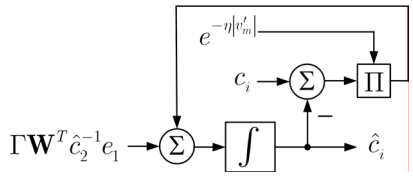

Figure 3. Block diagram of proposed adaptation law.

IV. Simulation Results

This section illustrates the evaluation of the proposed method in the GTAW process. Based on the arc model described in [1], the argon type of shielding gas gives the relation between arc voltage and arc length so called arc sensitivity which as

$$k_v = \frac{dv_a}{dl_a} = \left[0.446 + 0.0029 i_a + e^{-0.073 i_a}\right]. \tag{23}$$

To verify the proposed method, two simulations are introduced. The first simulation demonstrates the dynamic behavior of the system for input step function. The second simulation shows tracking performance when the closed-loop parameters are changed according to the change in arc current set point. The comparison between conventional and the proposed method are provided in both simulations.

Throughout the first simulation, following parameters are set; $k_p = 30$, $k_v = 5$, $a_s = 10$, $k_s = 9$, $\psi = 1.4$, and $\Gamma = diag(0.01, 0.0001)$. In addition, arc current set point is chosen at 100 A, where the reference voltage is a step function from 8 V to 15 V at 5 seconds of time. Result from the first simulation shows that the estimated parameters of the conventional adaptive system could not converge to correct values where the proposed method is able to improve the convergence of the estimated parameters to the actual values as shown in Fig. 4 and 5. As the results, the arc voltage of the proposed method has an improved response compared to the conventional method as illustrated in Fig. 6.

The second simulation demonstrates the behavior of the adaptive systems when the system parameters are changed according to the change of arc current set point varied from 100 A to 5 A as illustrated in Fig. 7. By applying the same set of controller parameters employed in the first simulation, the estimated parameters of the conventional adaptive system cannot be updated to the correct values. In contrast, the estimated parameters of the proposed method can converge to the actual values as shown in Fig. 8. Consequently, the response of the proposed method has a smaller perturbation causing by input current set point as shown in Fig. 9.

V. Conclusions

The higher efficient adaptation law is presented for overcoming the problem of persistence excitation which improves overall dynamic performance of a special type of adaptive system. The unknown welding system parameters can be obtained mathematically resulting in the convergence of the estimated parameters to the true values. For this reason, the proposed adaptive method for GTAW can track the change of system parameters due to the change in arc current set point which is generally to prevent cracking at the starting and ending point of weld. As the results, the dynamic performance of the adaptive system is improved with less effort in finding control parameters.

REFERENCES

[1] Bjorgvinsson, J.B., 1992, "Adaptive Voltage Control in Gas Tungsten Arc Welding," M.S. thesis, Vanderbilt University, Nashville, Tennessee.

[2] Bjorgvinsson, J.B., Cook, G.E., and Andersen., K., "Microprocessor-Based Arc Voltage Control for Gas Tungsten Arc Welding Using Gain Scheduling," IEEE Transactions on Industry Applications, Vol. 29(2), pp. 250-255, 1999.

[3] Koseeyaporn, P., Cook, G.E., and Strauss, A.M., "Adaptive Voltage Control in Fusion Arc Welding," IEEE Transaction on Industry Applications, Vol. 36(5), pp. 1300-13006, 2000.

[4] Craig, J.J., Adaptive Control of Mechanical Manipulators, Addison Wesley, Reading, Massachusetts, 1988.

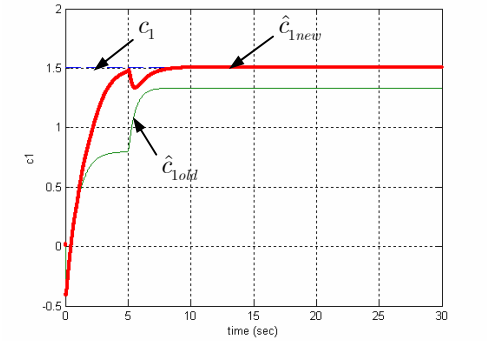

Figure 4. System parameter (c_1), estimated parameter of conventional method ($\hat{c}_{1old}$), and the proposed method ($\hat{c}_{1new}$).

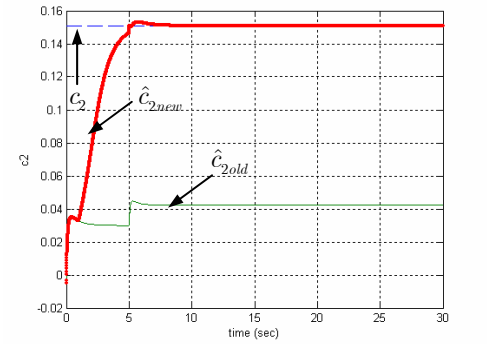

Figure 5. System parameter (c_2), estimated parameter of conventional method ($\hat{c}_{2old}$), and the proposed method ($\hat{c}_{2new}$).

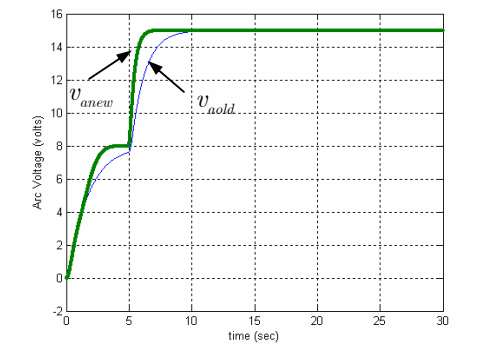

Figure 6. Step input response (8 volts to 12 volts) of conventional method (v_{aold}) and the proposed method (v_{anew}).

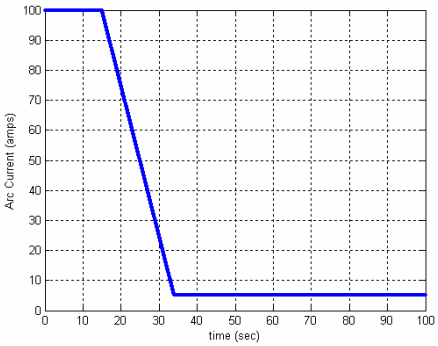

Figure 7. Ramping arc current from 100 A to 5 A.

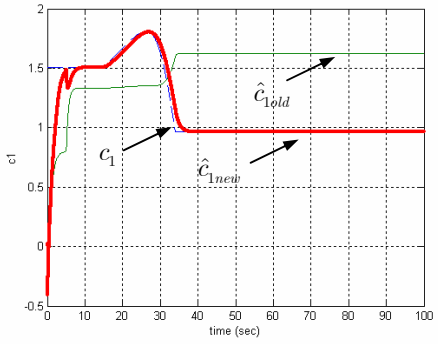

Figure 8. System parameter (c_1), estimated parameter of conventional method ($\hat{c}_{1old}$), and the proposed method ($\hat{c}_{1new}$).

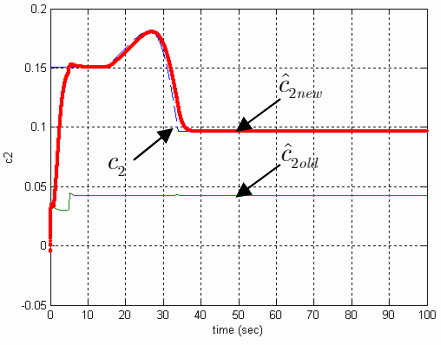

Figure 9. System parameter (c_2), estimated parameter of conventional method ($\hat{c}_{2old}$), and the proposed method ($\hat{c}_{2new}$).

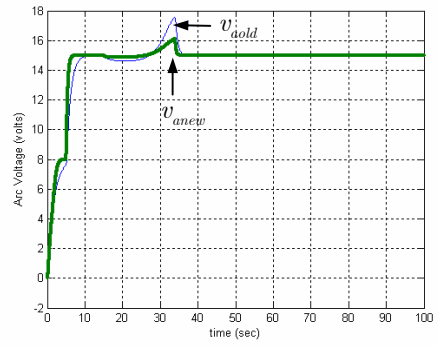

Figure 10. Step input response (8 volts to 12 volts) of conventional method (v_{aold}) and the proposed method (v_{anew}).

Robust $\mathcal{H}_\infty$ Fuzzy Control Design for Nonlinear Two-Time Scale System with Markovian Jumps based on LMI Approach

Wudhichai Assawinchaichote* and Sing Kiong Nguang

***Abstract*— This paper examines the problem of designing a robust $\mathcal{H}_\infty$ state-feedback controller for a class of nonlinear two-time scale systems with Markovian Jumps described by a Takagi-Sugeno (TS) fuzzy model. Based on a linear matrix inequality (LMI) approach, LMI-based sufficient conditions for the uncertain Markovian jump nonlinear two-time scale systems to have an $\mathcal{H}_\infty$ performance are derived. The proposed approach does not involve the separation of states into slow and fast ones and it can be applied not only to standard, but also to nonstandard nonlinear two-time scale systems. A numerical example is provided to illustrate the design developed in this paper.**

I. INTRODUCTION

Markovian jump systems, sometimes called hybrid systems with a state vector, consists of two components; i.e., the state (differential equation) and the mode (Markov process). The Markovian jump system changes abruptly from one mode to another mode caused by some phenomenon such as environmental disturbances, changing subsystem interconnections and fast variations in the operating point of the system plant, etc. The switching between modes is governed by a Markov process with the discrete and finite state space. Over the past few decades, the Markovian jump systems have been extensively studied by many researchers; see [1]-[12]. This is due to the fact that jumping systems have been a subject of the great practical importance.

For the past three decades, singularly perturbed systems have been intensively studied by many researchers; see [12]-[17]. Singularly perturbed systems also known as multiple (two) time-scale dynamic systems normally occur due to the presence of small "parasitic" parameters, typically small time constants, masses, etc. In state space, such systems are commonly modelled using the mathematical framework of singular perturbations, with a small parameter, say ε, determining the degree of separation between the "slow" and "fast" modes of the system. However, it is necessary to note that it is possible to solve the singularly perturbed systems without separating between slow and fast mode subsystems. But the requirement is that the "parasitic" parameters must be large enough. In the case of having very small "parasitic" parameters which normally occur in the description of various physical phenomena, a popular approach adopted to handle these systems is based on the so-called reduction technique. According to this technique the fast variables are replaced by their steady states obtained with "frozen" slow variables and controls, and the slow dynamics is approximated by the corresponding reduced order system. This time-scale is asymptotic, that is, exact in the limit, as the ratio of the speeds of the slow versus the fast dynamics tends to zero.

In the last few years, the research on singularly perturbed systems in the $\mathcal{H}_\infty$ sense has been highly recognized in control area due to the great practical importance. $\mathcal{H}_\infty$-optimal control of singularly perturbed linear systems under either perfect state measurements or imperfect state measurements has been investigated via differential game theoretics approach. Although many researchers have studied the $\mathcal{H}_\infty$ control design of linear singularly perturbed systems for many years, the $\mathcal{H}_\infty$ control design of nonlinear singularly perturbed systems remains as an open research area. This is due to, in general, nonlinear singularly perturbed systems can not be decomposed into slow and fast subsystems.

Recently, a great amount of effort has been made on the design of fuzzy $\mathcal{H}_\infty$ for a class of nonlinear systems which can be represented by a Takagi-Sugeno (TS) fuzzy model; see [18]-[21]. Recent studies [18]-[22] show that a fuzzy model can be used to approximate global behaviors of a highly complex nonlinear system. In this fuzzy model, local dynamics in different state space regions are represented by local linear systems. The overall model of the system is obtained by "blending" of these linear models through nonlinear fuzzy membership functions. Unlike conventional modelling which uses a single model to describe the global behavior of a system, fuzzy modelling is essentially a multi-model approach in which simple sub-models (linear models) are combined to describe the global behavior of the system. Employing the existing fuzzy results [18]-[22] on the singularly perturbed system, one ends up with a family of ill-conditioned linear matrix inequalities resulting from the interaction of slow and fast dynamic modes. In general, ill-conditioned linear matrix inequalities are very difficult to solve.

What we intend to do in this paper is to design a robust $\mathcal{H}_\infty$ fuzzy state-feedback controller for a class of uncertain nonlinear two time-scale dynamic systems with Markovian jumps. First, we approximate this class of uncertain nonlinear two time-scale dynamic systems with Markovian jumps by a Takagi-Sugeno fuzzy model with Markovian jumps. Then based on an LMI approach, we develop a technique for designing a robust $\mathcal{H}_\infty$ fuzzy state-

*Author to whom correspondence should be addressed.

W. Assawinchaichote is with the Department of Electronic and Telecommnunication Engineering, King Mongkut's University of Technology Thonburi, 126 Prachautits Rd., Bangkok 10140, Thailand wudhichai.asa@kmutt.ac.th

S. K. Nguang is with the Department of Electrical and Computer Engineering, The University of Auckland, Private Bag 92019 Auckland, New Zealand

feedback controller such that the $\mathcal{L}_2$-gain of the mapping from the exogenous input noise to the regulated output is less than a prescribed value. To alleviate the ill-conditioned linear matrix inequalities resulting from the interaction of slow and fast dynamic modes, these ill-conditioned LMIs are decomposed into ε-independent LMIs and ε-dependent LMIs. The ε-independent LMIs are not ill-conditioned and the ε-dependent LMIs tend to zero when ε approaches to zero. If ε is sufficiently small, the original ill-conditioned LMIs are solvable if and only if the ε-independent LMIs are solvable. The proposed approach does not involve the separation of states into slow and fast ones, and it can be applied not only to standard, but also to nonstandard two time-scale dynamic systems.

This paper is organized as follows. In Section II, system descriptions and definition are presented. In Section III, based on an LMI approach, we develop a technique for designing a robust $\mathcal{H}_\infty$ fuzzy state-feedback controller such that the $\mathcal{L}_2$-gain of the mapping from the exogenous input noise to the regulated output is less than a prescribed value for the system described in Section II. The validity of this approach is demonstrated by an example from a literature in Section IV. Finally, conclusions are given in Section V.

II. System Descriptions and Definitions

The class of nonlinear uncertain two-time scale systems with Markovian jumps under consideration is described by the following TS fuzzy model with Markovian jumps:

$$\begin{aligned} E_\varepsilon \dot{x}(t) &= \sum_{i=1}^{r} \mu_i(\nu(t))\Big[[A_i(\eta(t)) + \Delta A_i(\eta(t))]x(t) \\ &\quad +[B_{1_i}(\eta(t)) + \Delta B_{1_i}(\eta(t))]w(t) \\ &\quad +[B_{2_i}(\eta(t)) + \Delta B_{2_i}(\eta(t))]u(t)\Big], \;\; x(0) = 0, \\ z(t) &= \sum_{i=1}^{r} \mu_i(\nu(t))\Big[[C_{1_i}(\eta(t)) + \Delta C_{1_i}(\eta(t))]x(t) \\ &\quad +[D_{12_i}(\eta(t)) + \Delta D_{12_i}(\eta(t))]u(t)\Big] \end{aligned} \tag{1}$$

where $E_\varepsilon = \begin{bmatrix} I & 0 \\ 0 & \varepsilon I \end{bmatrix}$, $\varepsilon > 0$ is the singular perturbation parameter, $\nu(t) = [\nu_1(t) \; \cdots \; \nu_\vartheta(t)]$ is the premise variable that may depend on states in many cases, $\mu_i(\nu(t))$ denote the normalized time-varying fuzzy weighting functions for each rule, ϑ is the number of fuzzy sets, $x(t) \in \Re^n$ is the state vector, $u(t) \in \Re^m$ is the input, $w(t) \in \Re^p$ is the disturbance which belongs to $\mathcal{L}_2[0,\infty)$, $z(t) \in \Re^s$ is the controlled output, the matrix functions $A_i(\eta(t))$, $B_{1_i}(\eta(t))$, $B_{2_i}(\eta(t))$, $C_{1_i}(\eta(t))$, $D_{12_i}(\eta(t))$, $\Delta A_i(\eta(t))$, $\Delta B_{1_i}(\eta(t))$, $\Delta B_{2_i}(\eta(t))$, $\Delta C_{1_i}(\eta(t))$ and $\Delta D_{12_i}(\eta(t))$ are of appropriate dimensions. $\{\eta(t))\}$ is a continuous-time discrete-state Markov process taking values in a finite set $\mathcal{S} = \{1, 2, \cdots, s\}$ with transition probability matrix $Pr \triangleq \{P_{\imath k}(t)\}$ given by

$$\begin{aligned} P_{\imath k}(t) &= Pr(\eta(t+\Delta) = k | \eta(t) = \imath) \\ &= \begin{cases} \lambda_{\imath k}\Delta + O(\Delta) & \text{if } \imath \neq k \\ 1 + \lambda_{\imath\imath}\Delta + O(\Delta) & \text{if } \imath = k \end{cases} \end{aligned} \tag{2}$$

where $\Delta > 0$, and $\lim_{\Delta \longrightarrow 0} \frac{O(\Delta)}{\Delta} = 0$. Here $\lambda_{\imath k} \geq 0$ is the transition rate from mode $\imath$ (system operating mode) to mode k ($\imath \neq k$), and

$$\lambda_{\imath\imath} = -\sum_{k=1, k\neq\imath}^{s} \lambda_{\imath k}. \tag{3}$$

For the convenience of notations, we let $\mu_i \triangleq \mu_i(\nu(t))$, $\eta = \eta(t)$, and any matrix $M(\mu, \imath) \triangleq M(\mu, \eta = \imath)$. The matrix functions $\Delta A_i(\eta)$, $\Delta B_{1_i}(\eta)$, $\Delta B_{2_i}(\eta)$, $\Delta C_{1_i}(\eta)$ and $\Delta D_{12_i}(\eta)$ represent the time-varying uncertainties in the system and satisfy the following assumption.

Assumption 1:

$$\begin{aligned} \Delta A_i(\eta) &= F(x(t), \eta, t)H_{1_i}(\eta), \\ \Delta B_{1_i}(\eta) &= F(x(t), \eta, t)H_{2_i}(\eta), \\ \Delta B_{2_i}(\eta) &= F(x(t), \eta, t)H_{3_i}(\eta), \\ \Delta C_{1_i}(\eta) &= F(x(t), \eta, t)H_{4_i}(\eta), \\ \text{and } \; \Delta D_{12_i}(\eta) &= F(x(t), \eta, t)H_{5_i}(\eta), \end{aligned}$$

where $H_{j_i}(\eta), \; j = 1, 2, \cdots, 5$ are known matrices which characterize the structure of the uncertainties. Furthermore, there exists a positive function $\rho(\eta)$ such that the following inequality holds:

$$\|F(x(t), \eta, t)\| \leq \rho(\eta). \tag{4}$$

We recall the following definition.

Definition 1: Suppose γ is a given positive number. A system of the form (1) is said to have the $\mathcal{L}_2$-gain less than or equal to γ if

$$\mathbf{E}\left[\int_0^{T_f} \{z^T(t)z(t) - \gamma^2 w^T(t)w(t)\}\, dt\right] \leq 0, \; x(0) = 0 \tag{5}$$

where $\mathbf{E}[\cdot]$ stands for the mathematical expectation, for all T_f and all $w(t) \in \mathcal{L}_2[0, T_f]$.

Note that for the symmetric block matrices, we use $(*)$ as an ellipsis for terms that are induced by symmetry.

III. Robust $\mathcal{H}_\infty$ Fuzzy State-Feedback Control Design

This section provides the LMI-based solutions to the problem of designing a robust $\mathcal{H}_\infty$ fuzzy state-feedback controller that guarantees the $\mathcal{L}_2$-gain of the mapping from the exogenous input noise to the regulated output to be less than some prescribed value.

First, we consider the following $\mathcal{H}_\infty$ fuzzy state-feedback which is inferred as the weighted average of the local models of the form:

$$u(t) = \sum_{j=1}^{r} \mu_j K_j(\imath)x(t). \tag{6}$$

Then, we describe the problem under our study as follows.

Problem Formulation: Given a prescribed $\mathcal{H}_\infty$ performance $\gamma > 0$, design a robust $\mathcal{H}_\infty$ fuzzy state-feedback controller of the form (6) such that the inequality (5) holds.

Before presenting our first main result, we recall the following lemma.

Lemma 1: Consider the system (1). Given a prescribed $\mathcal{H}_\infty$ performance $\gamma > 0$, for $\imath = 1, 2, \cdots, s$, if there exist matrices $P_\varepsilon(\imath) = P_\varepsilon^T(\imath)$, positive constants $\delta(\imath)$ and matrices $Y_j(\imath)$, $j = 1, 2, \cdots, r$ such that the following ε-dependent linear matrix inequalities hold:

$$P_\varepsilon(\imath) > 0 \tag{7}$$
$$\Psi_{ii}(\imath, \varepsilon) < 0, \quad i = 1, 2, \cdots, r \tag{8}$$
$$\Psi_{ij}(\imath, \varepsilon) + \Psi_{ji}(\imath, \varepsilon) < 0, \quad i < j \leq r \tag{9}$$

where

$$\Psi_{ij}(\imath, \varepsilon) = \begin{pmatrix} \Phi_{ij}(\imath, \varepsilon) & (*)^T & (*)^T & (*)^T \\ \mathcal{R}(\imath)\tilde{B}_{1_i}^T(\imath) & -\gamma\mathcal{R}(\imath) & (*)^T & (*)^T \\ \Upsilon_{ij}(\imath, \varepsilon) & 0 & -\gamma\mathcal{R}(\imath) & (*)^T \\ \mathcal{Z}^T(\imath, \varepsilon) & 0 & 0 & -\mathcal{P}(\imath, \varepsilon) \end{pmatrix} \tag{10}$$

$$\begin{aligned} \Phi_{ij}(\imath, \varepsilon) =& A_i(\imath)E_\varepsilon^{-1}P_\varepsilon(\imath) + E_\varepsilon^{-1}P_\varepsilon(\imath)A_i^T(\imath) \\ &+ B_{2_i}(\imath)Y_j(\imath) + Y_j^T(\imath)B_{2_i}^T(\imath) \\ &+ \lambda_{\imath\imath}E_\varepsilon^{-1}P_\varepsilon(\imath), \end{aligned} \tag{11}$$

$$\Upsilon_{ij}(\imath, \varepsilon) = \tilde{C}_{1_i}(\imath)E_\varepsilon^{-1}P_\varepsilon(\imath) + \tilde{D}_{12_i}(\imath)Y_j(\imath), \tag{12}$$

$$\mathcal{R}(\imath) = \text{diag}\left\{\delta(\imath)I, I, \delta(\imath)I, I\right\}, \tag{13}$$

$$\begin{aligned} \mathcal{Z}(\imath, \varepsilon) =& \Big(\sqrt{\lambda_{\imath 1}}E_\varepsilon^{-1}P_\varepsilon(\imath) \ \cdots \ \sqrt{\lambda_{\imath(\imath-1)}}E_\varepsilon^{-1}P_\varepsilon(\imath) \\ & \sqrt{\lambda_{\imath(\imath+1)}}E_\varepsilon^{-1}P_\varepsilon(\imath) \ \cdots \ \sqrt{\lambda_{\imath s}}E_\varepsilon^{-1}P_\varepsilon(\imath)\Big), \end{aligned} \tag{14}$$

$$\begin{aligned} \mathcal{P}(\imath, \varepsilon) =& \ diag\Big\{E_\varepsilon^{-1}P_\varepsilon(1), \cdots, E_\varepsilon^{-1}P_\varepsilon(\imath-1), \\ & E_\varepsilon^{-1}P_\varepsilon(\imath+1), \cdots, E_\varepsilon^{-1}P_\varepsilon(s)\Big\}, \end{aligned} \tag{15}$$

with

$$\begin{aligned} \tilde{B}_{1_i}(\imath) =& \begin{bmatrix} I & I & I & B_{1_i}(\imath) \end{bmatrix} \\ \tilde{C}_{1_i}(\imath) =& \Big[\gamma\rho(\imath)H_{1_i}^T(\imath) \ \sqrt{2}\aleph(\imath)\rho(\imath)H_{4_i}^T(\imath) \\ & 0 \ \sqrt{2}\aleph(\imath)C_{1_i}^T(\imath)\Big]^T \\ \tilde{D}_{12_i}(\imath) =& \Big[0 \ \sqrt{2}\aleph(\imath)\rho(\imath)H_{5_i}^T(\imath) \\ & \gamma\rho(\imath)H_{3_i}^T(\imath) \ \sqrt{2}\aleph(\imath)D_{12_i}^T(\imath)\Big]^T \\ \aleph(\imath) =& \left(I + \rho^2(\imath)\sum_{i=1}^{r}\sum_{j=1}^{r}\left[\|H_{2_i}^T(\imath)H_{2_j}(\imath)\|\right]\right)^{\frac{1}{2}} \end{aligned}$$

then the inequality (5) holds. Furthermore, a suitable choice of the fuzzy controller is

$$u(t) = \sum_{j=1}^{r}\mu_j K_{\varepsilon_j}(\imath)x(t) \tag{16}$$

where

$$K_{\varepsilon_j}(\imath) = Y_j(\imath)(P_\varepsilon(\imath))^{-1}E_\varepsilon. \tag{17}$$

Proof: The desired result can be carried out by a similar technique used in [23], [24], and [25]. The detail of the proof is omitted for brevity. ■

Remark 1: The linear matrix inequalities given in Lemma 1 becomes ill-conditioned when ε is sufficiently small, which is always the case for the singularly perturbed system. In general, these ill-conditioned linear matrix inequalities are very difficult to solve. Thus, to alleviate these ill-conditioned linear matrix inequalities, we have the following theorem which does not depend on ε. □

Now we are in the position to present our first result.

Theorem 1: Consider the system (1). Given a prescribed $\mathcal{H}_\infty$ performance $\gamma > 0$, for $\imath = 1, 2, \cdots, s$, if there exist matrices $P(\imath)$, positive constants $\delta(\imath)$ and matrices $Y_j(\imath)$, $j = 1, 2, \cdots, r$ such that the following ε-independent linear matrix inequalities hold:

$$EP(\imath) + P(\imath)D > 0 \tag{18}$$
$$\Psi_{ii}(\imath) < 0, \quad i = 1, 2, \cdots, r \tag{19}$$
$$\Psi_{ij}(\imath) + \Psi_{ji}(\imath) < 0, \quad i < j \leq r \tag{20}$$

where $EP(\imath) = P^T(\imath)E$, $P(\imath)D = DP^T(\imath)$, $E = \begin{pmatrix} I & 0 \\ 0 & 0 \end{pmatrix}$, $D = \begin{pmatrix} 0 & 0 \\ 0 & I \end{pmatrix}$,

$$\Psi_{ij}(\imath) = \begin{pmatrix} \Phi_{ij}(\imath) & (*)^T & (*)^T & (*)^T \\ \mathcal{R}(\imath)\tilde{B}_{1_i}^T(\imath) & -\gamma\mathcal{R}(\imath) & (*)^T & (*)^T \\ \Upsilon_{ij}(\imath) & 0 & -\gamma\mathcal{R}(\imath) & (*)^T \\ \mathcal{Z}^T(\imath) & 0 & 0 & -\mathcal{P}(\imath) \end{pmatrix} \tag{21}$$

$$\begin{aligned} \Phi_{ij}(\imath) =& A_i(\imath)P(\imath) + P^T(\imath)A_i^T(\imath) + B_{2_i}(\imath)Y_j(\imath) \\ &+ Y_j^T(\imath)B_{2_i}^T(\imath) + \lambda_{\imath\imath}\tilde{\tilde{P}}(\imath), \end{aligned} \tag{22}$$

$$\Upsilon_{ij}(\imath) = \tilde{C}_{1_i}(\imath)P(\imath) + \tilde{D}_{12_i}(\imath)Y_j(\imath), \tag{23}$$

$$\mathcal{R}(\imath) = \text{diag}\left\{\delta(\imath)I, I, \delta(\imath)I, I\right\}, \tag{24}$$

$$\begin{aligned} \mathcal{Z}(\imath) =& \Big(\sqrt{\lambda_{\imath 1}}\tilde{\tilde{P}}(\imath) \ \cdots \ \sqrt{\lambda_{\imath(\imath-1)}}\tilde{\tilde{P}}(\imath) \\ & \sqrt{\lambda_{\imath(\imath+1)}}\tilde{\tilde{P}}(\imath) \ \cdots \ \sqrt{\lambda_{\imath s}}\tilde{\tilde{P}}(\imath)\Big), \end{aligned} \tag{25}$$

$$\begin{aligned} \mathcal{P}(\imath) =& \ \text{diag}\Big\{\tilde{\tilde{P}}(1), \cdots, \tilde{\tilde{P}}(\imath-1), \\ & \tilde{\tilde{P}}(\imath+1), \cdots, \tilde{\tilde{P}}(s)\Big\}, \end{aligned} \tag{26}$$

$$\tilde{\tilde{P}}(\imath) = \frac{P(\imath) + P^T(\imath)}{2} \tag{27}$$

with

$$\begin{aligned} \tilde{B}_{1_i}(\imath) =& \begin{bmatrix} I & I & I & B_{1_i}(\imath) \end{bmatrix} \\ \tilde{C}_{1_i}(\imath) =& \Big[\gamma\rho(\imath)H_{1_i}^T(\imath) \ \sqrt{2}\aleph(\imath)\rho(\imath)H_{4_i}^T(\imath) \\ & 0 \ \sqrt{2}\aleph(\imath)C_{1_i}^T(\imath)\Big]^T \\ \tilde{D}_{12_i}(\imath) =& \Big[0 \ \sqrt{2}\aleph(\imath)\rho(\imath)H_{5_i}^T(\imath) \\ & \gamma\rho(\imath)H_{3_i}^T(\imath) \ \sqrt{2}\aleph(\imath)D_{12_i}^T(\imath)\Big]^T \end{aligned}$$

$$\aleph(\imath) = \left(I + \rho^2(\imath) \sum_{i=1}^{r} \sum_{j=1}^{r} \left[\| H_{2_i}^T(\imath) H_{2_j}(\imath) \| \right] \right)^{\frac{1}{2}}$$

then there exists a sufficiently small $\hat{\varepsilon} > 0$ such that the inequality (5) holds for $\varepsilon \in (0, \hat{\varepsilon}]$. Furthermore, a suitable choice of the fuzzy controller is

$$u(t) = \sum_{i=1}^{r} \mu_j K_j(\imath) x(t) \tag{28}$$

where

$$K_j(\imath) = Y_j(\imath)(P(\imath))^{-1}. \tag{29}$$

Proof: The detail of the proof is omitted for brevity. ■

IV. Illustrative Example

Consider a modified series dc motor model based on [30] as shown in Fig. 1 which is governed by the following difference equations:

$$\begin{array}{rcl} J\frac{d\tilde{\omega}(t)}{dt} & = & K_m L_f \tilde{i}^2(t) - (D + \Delta D)\tilde{\omega}(t) \\ L\frac{d\tilde{i}(t)}{dt} & = & -R\tilde{i}(t) - K_m L_f \tilde{i}(t)\tilde{\omega}(t) + \tilde{V}(t) \end{array} \tag{30}$$

where $\tilde{\omega}(t) = \omega(t) - \omega_{ref}(t)$ is the deviation of the actual angular velocity from the desired angular velocity, $\tilde{i}(t) = i(t) - i_{ref}(t)$ is the deviation of the actual current from the desired current, $\tilde{V}(t) = V(t) - V_{ref}(t)$ is the deviation of the actual input voltage from the desired input voltage, J is the moment of inertia, K_m is the torque/back emf constant, D is the viscous friction coefficient, and R_a, R_f, L_a and L_f are the armature resistance, the field winding resistance, the armature inductance and the field winding inductance, respectively, with $R \triangleq R_f + R_a$ and $L \triangleq L_f + L_a$. Note that in a typical series-connected dc motor, the condition $L_f \gg L_a$ holds. When one obtains a series-connected dc motor, we have $i(t) = i_a(t) = i_f(t)$. Now let us assume that $|\Delta J| \leq 0.1J$.

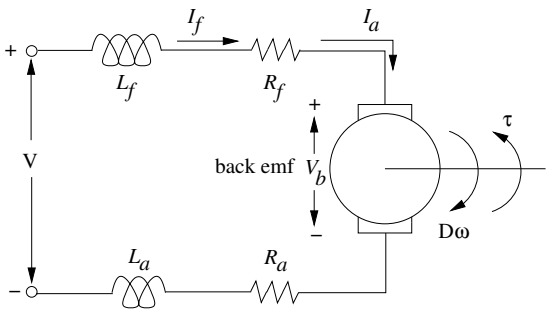

Fig. 1. A modified series dc motor equivalent circuit.

Giving $x_1(t) = \tilde{\omega}(t)$, $x_2(t) = \tilde{i}(t)$ and $u(t) = \tilde{V}(t)$, (30) becomes

$$\begin{bmatrix} \dot{x}_1(t) \\ \varepsilon\dot{x}_2(t) \end{bmatrix} = \begin{bmatrix} -\frac{D}{(J+\Delta J)} & \frac{K_m L_f}{(J+\Delta J)} x_2(t) \\ -K_m L_f x_2(t) & -R \end{bmatrix} \begin{bmatrix} x_1(t) \\ x_2(t) \end{bmatrix} + \begin{bmatrix} 0 \\ 1 \end{bmatrix} u(t) \tag{31}$$

where $\varepsilon = L$ represents a small parasitic parameter. Assume that, the system is aggregated into 3 modes as shown in Table I:

TABLE I
System Terminology.

Mode $\imath$	Moment of Inertia	$J(\imath) \pm \Delta J(\imath)$ (kg·m^2)
1	Small	0.0005 ±10%
2	Normal	0.005 ±10%
3	Large	0.05 ±10%

The transition probability matrix that relates the three operation modes is given as follows:

$$P_{\imath k} = \begin{bmatrix} 0.67 & 0.17 & 0.16 \\ 0.30 & 0.47 & 0.23 \\ 0.26 & 0.10 & 0.64 \end{bmatrix}.$$

The parameters for the system are given as $R = 10\ \Omega$, $L_f = 0.005$ H, $D = 0.05$ N·m/rad/s and $K_m = 1$ N·m/A. Substituting the parameters into (31), we get

$$\begin{array}{rcl} \begin{bmatrix} \dot{x}_1(t) \\ \varepsilon\dot{x}_2(t) \end{bmatrix} & = & \begin{bmatrix} -\frac{0.05}{J(\imath)} & \frac{0.005}{J(\imath)} x_2(t) \\ -0.005 x_2(t) & -10 \end{bmatrix} \begin{bmatrix} x_1(t) \\ x_2(t) \end{bmatrix} \\ & & + \begin{bmatrix} 0 & 0 \\ 0.1 & 0 \end{bmatrix} w(t) + \begin{bmatrix} 0 \\ 1 \end{bmatrix} u(t) \\ & & + \begin{bmatrix} -\frac{0.05}{\Delta J(\imath)} & \frac{0.005}{\Delta J(\imath)} x_2(t) \\ 0 & 0 \end{bmatrix} \begin{bmatrix} x_1(t) \\ x_2(t) \end{bmatrix} \\ z(t) & = & \begin{bmatrix} 1 & 0 \\ 0 & 1 \end{bmatrix} \begin{bmatrix} x_1(t) \\ x_2(t) \end{bmatrix} + \begin{bmatrix} 0 \\ 1 \end{bmatrix} u(t) \end{array} \tag{32}$$

where $x(t) = [x_1^T(t) \quad x_2^T(t)]^T$ is the state variables, $w(t) = [w_1^T(t) \quad w_2^T(t)]^T$ is the disturbance input, $u(t)$ is the controlled input and $z(t)$ is the controlled output.

The control objective is to control the state variable $x_2(t)$ for the range $x_2(t) \in [N_1\ N_2]$. For the sake of simplicity, we will use as few rules as possible. Note that Fig. 2 shows the plot of the membership function represented by

$$M_1(x_2(t)) = \frac{-x_2(t) + N_2}{N_2 - N_1} \quad \text{and} \quad M_2(x_2(t)) = \frac{x_2(t) - N_1}{N_2 - N_1}.$$

Knowing that $x_2(t) \in [N_1\ N_2]$, the nonlinear system (32)

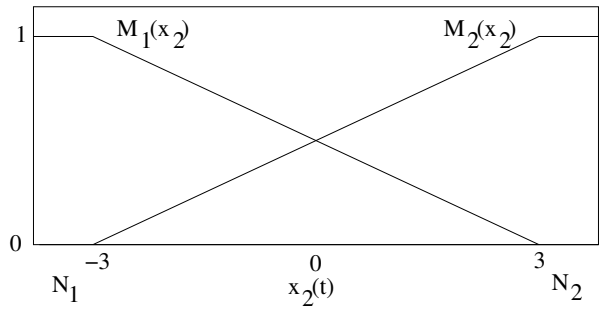

Fig. 2. Membership functions for the two fuzzy set.

can be approximated by the following TS fuzzy model

$$\begin{aligned} E_\varepsilon \dot{x}(t) &= \sum_{i=1}^{r} \mu_i \Big[[A_i(\imath) + \Delta A_i(\imath)]x(t) \\ &\quad + B_{1_i}(\imath)w(t) + B_{2_i}(\imath)u(t) \Big], \quad x(0) = 0, \\ z(t) &= \sum_{i=1}^{r} \mu_i \Big[C_{1_i}(\imath)x(t) + D_{12_i}(\imath)u(t) \Big], \end{aligned}$$

where μ_i is the normalized time-varying fuzzy weighting functions for each rule, $i = 1, 2$, $x(t) = \begin{bmatrix} x_1(t) \\ x_2(t) \end{bmatrix}$, $E_\varepsilon = \begin{bmatrix} 1 & 0 \\ 0 & \varepsilon \end{bmatrix}$, $\Delta A_1(\imath) = F(x(t), \imath, t)H_{1_1}(\imath)$, $\Delta A_2(\imath) = F(x(t), \imath, t)H_{1_2}(\imath)$,

$$A_1(1) = \begin{bmatrix} -100 & 10N_1 \\ -0.005N_1 & -10 \end{bmatrix},$$

$$A_2(1) = \begin{bmatrix} -100 & 10N_2 \\ -0.005N_2 & -10 \end{bmatrix},$$

$$A_1(2) = \begin{bmatrix} -10 & N_1 \\ -0.005N_1 & -10 \end{bmatrix},$$

$$A_2(2) = \begin{bmatrix} -10 & N_2 \\ -0.005N_2 & -10 \end{bmatrix},$$

$$A_1(3) = \begin{bmatrix} -1 & 0.1N_1 \\ -0.005N_1 & -10 \end{bmatrix},$$

$$A_2(3) = \begin{bmatrix} -1 & 0.1N_2 \\ -0.005N_2 & -10 \end{bmatrix},$$

$$B_{1_1}(\imath) = B_{1_2}(\imath) = \begin{bmatrix} 0 & 0 \\ 0.1 & 0 \end{bmatrix},$$

$$B_{2_1}(\imath) = B_{2_2}(\imath) = \begin{bmatrix} 0 \\ 1 \end{bmatrix}, \; C_{1_1}(\imath) = C_{1_2}(\imath) = \begin{bmatrix} 1 & 0 \\ 0 & 1 \end{bmatrix},$$

$$\text{and} \;\; D_{12_1}(\imath) = D_{12_2}(\imath) = \begin{bmatrix} 0 \\ 1 \end{bmatrix},$$

with $\|F(x(t), \imath, t)\| \leq 1$. Then we have

$$H_{1_1}(\imath) = \begin{bmatrix} -\frac{0.05}{J(\imath)} & \frac{0.05}{J(\imath)}N_1 \\ 0 & 0 \end{bmatrix}$$

$$\text{and} \;\; H_{1_2}(\imath) = \begin{bmatrix} -\frac{0.05}{J(\imath)} & \frac{0.05}{J(\imath)}N_2 \\ 0 & 0 \end{bmatrix}.$$

In this simulation, we select $N_1 = -3$ and $N_2 = 3$. Using the LMI optimization algorithm and Theorem 1 with $\varepsilon = 0.005$, $\gamma = 1$ and $\delta(1) = \delta(2) = \delta(3) = 1$, we obtain the results given in Fig. 3, Fig. 4 and Fig. 5.

Remark 2: Employing results given in [18]-[22] and Matlab LMI solver [28], it is easy to realize that when $\varepsilon < 0.005$ for the state-feedback control design, LMIs become ill-conditioned and Matlab LMI solver yields an error message, "Rank Deficient". However, the state-feedback fuzzy controller proposed in this paper guarantee that the inequality (5) holds for the system (32). Fig. 3 shows the result of the changing between modes during the simulation with the initial mode at mode 1 and $\varepsilon = 0.005$. The disturbance input signal, $w(t)$, which was used during simulation is given in Fig. 4. The ratio of the regulated output energy to the disturbance input noise energy obtained by using the $\mathcal{H}_\infty$ fuzzy controller is depicted in Fig. 5. The ratio of the regulated output energy to the disturbance input noise energy tends to a constant value which is about 0.0094. So $\gamma = \sqrt{0.0094} = 0.0970$ which is less than the prescribed value 1. Finally, Table II shows the performance index, γ, for different values of ε. □

V. Conclusion

This paper has investigated the problem of designing a robust $\mathcal{H}_\infty$ state-feedback controller for a class of uncertainty Markovian jump nonlinear two-time scale systems that guarantees the $\mathcal{L}_2$-gain from an exogenous input to a regulated output to be less or equal to a prescribed value. First, we approximate this class of uncertain Markovian jump nonlinear two-time scale systems by a class of uncertain Takagi-Sugeno fuzzy models with Markovian jumps. Then, based on an LMI approach, LMI-based sufficient conditions for the uncertain Markovian jump nonlinear two-time scale systems to have an $\mathcal{H}_\infty$ performance are derived. The proposed approach does not involve the separation of states into slow and fast ones and it can be applied not only to standard, but also to nonstandard nonlinear two-time scale systems. An illustrative example is used to illustrate the effectiveness of the proposed design techniques.

TABLE II

The performance index γ for different values of ε.

	The performance index γ
ε	State-feedback control design
0.005	0.0970
0.10	0.4796
0.30	0.8660
0.40	0.9945
0.41	> 1

References

[1] H. J. Kushner, *Stochastic Stability and Control*, New York: Academic Press, 1967.

[2] E. B. Dynkin, *Markov Process*, Berlin: Springer-Verlag, 1965.

[3] W. M. Wonham, "On a matrix Riccati equation of stochastic control," *SIAM J. Contr.*, vol. 6, pp. 681–697, 1968.

[4] X. Feng, K. A. Loparo, Y. Ji, and H. J. Chizeck, "Stochastic stability properties of jump linear system," *IEEE Tran. Automat. Contr.*, vol. 37, pp. 38–53, 1992.

[5] C. E. de Souza and M. D. Fragoso, "$\mathcal{H}_\infty$ control for linear systems with Markovian jumping parameters," *Control-Theory and Advanced Tech.*, vol. 9, pp. 457–466, 1993.

[6] E. K. Boukas and Z. K. Liu, "Suboptimal design of regulators for jump linear system with time-multiplied quadratic cost," *IEEE Tran. Automat. Contr.*, vol. 46, pp. 944–949, 2001.

[7] E. K. Boukas and H. Yang , "Exponential stabilizability of stochastic systems with Markovian jump parameters," *Automatica*, vol. 35, pp. 1437–1441, 1999.

[8] M. A. Rami and L. Ei Ghaoui, "$\mathcal{H}_\infty$ state-feedback control of jump linear systems," *Proc. Conf. Decision and Contr.*, pp. 951–952, 1995.

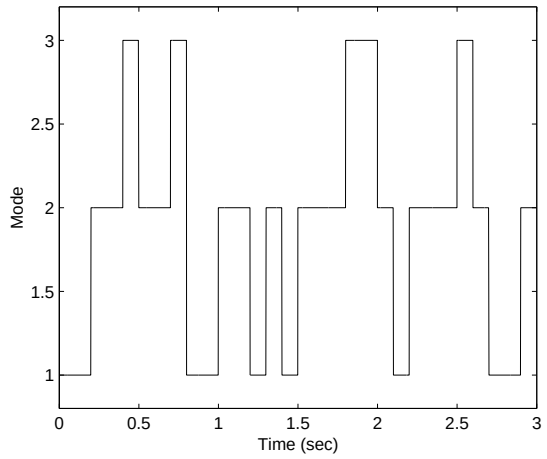

Fig. 3. The result of the changing between modes during the simulation with the initial mode at mode 1.

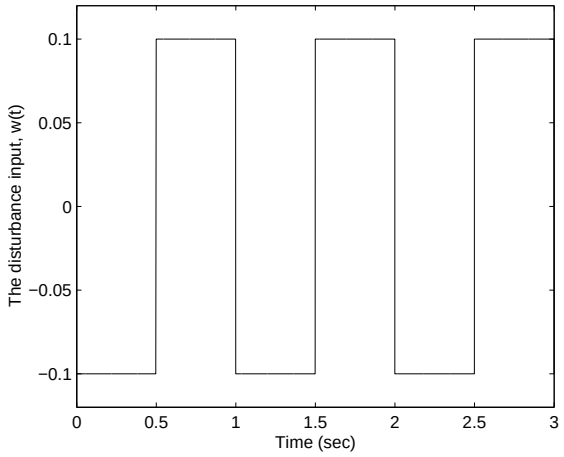

Fig. 4. The disturbance input, $w(t)$.

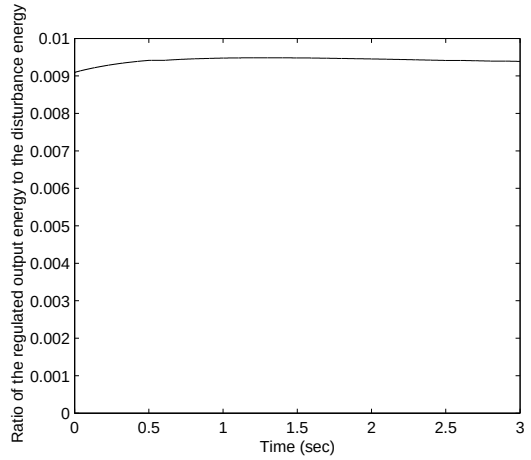

Fig. 5. The ratio of the regulated output energy to the disturbance noise energy, $\left(\frac{\int_0^{T_f} z^T(t)z(t)dt}{\int_0^{T_f} w^T(t)w(t)dt}\right)$ with $\varepsilon = 0.005$.

[9] P. Shi and E. K. Boukas, "$\mathcal{H}_\infty$ control for Markovian jumping linear system with parametric uncertainty," *J. of Opt. Theory and App.*, vol. 95, pp. 75–99, 1997.

[10] K. Benjelloun, E. K. Boukas, and O. L. V. Costa, "$\mathcal{H}_\infty$ control for linear time delay with Markovian jumping parameters," *J. of Opt. Theory and App.*, vol. 105, pp. 73–95, 1997.

[11] E. K. Boukas, Z. K. Liu, and G. X. Liu, "Delay-dependent robust stability and $\mathcal{H}_\infty$ control of jump linear systems with time-delay," *Int. J. of Contr.*, 2001.

[12] V. Dragan, P. Shi, and E. K. Boukas, "Control of singularly perturbed system with Markovian jump parameters: An $\mathcal{H}_\infty$ approach," *Automatica*, vol. 35, pp. 1369–1378, 1999.

[13] Z. Pan and T. Basar, "$\mathcal{H}^\infty$–optimal control for singularly perturbed systems Part I: Perfect state measurements," *Automatica*, vol. 29, pp. 401–423, 1993.

[14] Z. Pan and T. Basar, "$\mathcal{H}^\infty$–optimal control for singularly perturbed systems Part II: Imperfect state measurements," *IEEE Trans. Automat. Contr.*, vol. 39, pp. 280–299, 1994.

[15] E. Fridman, "State-feedback $\mathcal{H}^\infty$ control of nonlinear singularly perturbed systems," *Int. J. Robust Nonlinear Contr.*, vol. 6, pp. 25–45, 2001.

[16] P. Shi and V. Dragan, "Asymptotic $\mathcal{H}_\infty$ control of singularly perturbed system with parametric uncertainties," *IEEE Trans. Automat. Contr.*, vol. 44, pp. 1738–1742, 1999.

[17] P. V. Kokotovic, H. K. Khalil, and J. O'Reilly, *Singular Perturbation Methods in Control: Analysis and Design*, London: Academic Press, 1986.

[18] S. K. Nguang and P. Shi, "$\mathcal{H}_\infty$ fuzzy output feedback control design for nonlinear systems: An LMI approach," *Proc. IEEE Conf. Decision and Contr.*, pp. 4352–4357, 2001.

[19] Z. X. Han and G. Feng, "State-feedback $\mathcal{H}^\infty$ controller design of fuzzy dynamic system using LMI techniques," *Fuzzy-IEEE'98*, pp. 538–544, 1998.

[20] B. S. Chen, C. S. Tseng, and Y. Y. He, "Mixed $\mathcal{H}_2/\mathcal{H}_\infty$ fuzzy output feedback control design for nonlinear dynamic systems: An LMI approach," *IEEE Trans. Fuzzy Syst.*, vol. 8, pp. 249–265, 2000.

[21] K. Tanaka, T. Ikeda, and H. O. Wang, "Robust stabilization of a class of uncertain nonlinear systems via fuzzy control: Quadratic stability, $\mathcal{H}_\infty$ control theory, and linear martix inequality," *IEEE Trans. Fuzzy. Syst.*, vol. 4, pp. 1–13, 1996.

[22] H. O. Wang, K. Tanaka, and M. F. Griffin, "An approach to fuzzy control of nonlinear systems: Stability and design issues," *IEEE Trans. Fuzzy Syst.*, vol. 4, no. 1, pp. 14–23, 1996.

[23] D. P. de Farias, J. C. Geromel, J. B. R. do Val, and O. L. V. Costa, "Output feedback control of Markov jump linear systems in continuous-time," *IEEE Trans. Automat. Contr.*, vol. 45, pp. 944–949, 2000.

[24] S. K. Nguang and P. Shi, "$\mathcal{H}^\infty$ fuzzy output feedback control design for nonlinear systems: An LMI approach ," *IEEE Trans. Fuzzy Syst.*, vol. 11, pp. 331–340, 2003.

[25] S. K. Nguang, "Robust nonlinear $\mathcal{H}_\infty$ output feedback control," *IEEE Trans Automat. Contr.*, vol. 41, pp. 1003–1008, 1996.

[26] W. Assawinchaichote and S. K. Nguang "Fuzzy control design for singularly perturbed nonlinear systems: An LMI approach," *ICAIET*, (Kota Kinabalu, Malaysia), pp. 146–151, 2002.

[27] W. Assawinchaichote and S. K. Nguang, "Fuzzy observer-based controller design for singularly perturbed nonlinear systems: An LMI approach," *Proc. IEEE Conf. Decision and Contr.*, (Las Vegas), pp. 2165–2170, 2002.

[28] P. Gahinet, A. Nemirovski, A.J. Laub, and M. Chilali, *LMI Control Toolbox – For Use with MATLAB*, MA: The MathWorks, Inc., 1995.

[29] S. Boyd, L. El Ghaoui, E. Feron, and V. Balakrishnan, *Linear Matrix Inequalities in Systems and Control Theory*, vol. 15, Philadelphia: SIAM, 1994.

[30] S. Mehta and J. Chiasson, "Nonlinear control of a series dc motor: Theory and experiment," *IEEE Trans. Ind. Electron.*, vol. 45, pp. 134–141, 1998.

Study effect of different shape of rod-rod gaps on Positive DC breakdown

T. BOONWERN and S. CHOTIGO
Department of Electrical Engineering, Faculty of Engineering
King Mongkut's University of Technology Thonburi
126/1 Prachauthit Road, Bangmod, Thungkhru, Bangkok 10140 Thailand.
E-mail:boonwern@hotmail.com

***Abstract*- According to IEC 60-1(1989) [1], the maximum ratio of absolute humidity (h) to the air density factor (δ) which is accepted under DC breakdown in the standard is 13 g/m^3. However, in Thailand, the absolute humidity varies from about 10 g/m^3 to about 26 g/m^3. Therefore, this paper deals with experimental study under positive DC breakdown [2-3] of characteristics of air-gap varied with atmospheric conditions such as temperature and humidity [4-6]. Also, the effect of electrode different shape of rod-rod gaps at humidity between 11-16 g/m^3 was studied. Three different shapes of rod-rod gaps are tested. Rod with tip angles of 15^0 is tested with the gap distance of 2-16 cm. Also, square cut and hemispherical rod with the gap distance of 2-10 cm were used. All test electrodes are made of copper. The breakdown voltage was plotted as a function of the gap distance at different humidity values. Finally, it can be seen that the humidity factor K_h in IEC 60-1[1] is an important factor for the breakdown in the rod-rod gap under DC breakdown**

Keywords: electrode shape, positive DC Breakdown

I. INTRODUCTION

It is well known that humidity in air has considerable influence on flashover voltages of air gaps. The maximum ratio of absolute humidity (h) to the air density factor (δ) which is accepted under DC breakdown in the standard is 13 g/m^3. However, in Thailand, the absolute humidity varies from about 10 g/m^3 to about 26 g/m^3. Therefore, this paper deals with experimental study under positive DC breakdown of characteristics of air-gap varied with atmospheric conditions such as temperature and humidity under positive DC voltage.

II. EXPERIMENTAL SET-UP

A. *Test objects*

Three rod gaps with different shapes at various gap distances were used in this present work as follows:

1) Sharp rod-rod gaps 15^o; electrodes were tested at gap distance of 2, 4, 6, 8, 10, 12, 14, 16 cm. The rods were made of copper with the length of 20 cm. The tip angles of the rods were 15^o.

2) Hemispherical rod-rod gaps; electrodes were tested at gap distance of 2, 4, 6, 8, 10 cm. The rods were made of copper with the length of 20 cm and diameter is 2 cm.

3) Square cut-square cut gaps; electrodes were tested at gap distance of 2, 4, 6, 8, 10 cm. The rods were made of copper with the length of 20 cm with cross section area of 1.2 x 1.2 cm. All rods are shown in Fig.1.

Figure1. Rod electrodes

B. *Experimental Circuit*

The experimental circuit consisted of AC source 220V, variac 0-240V, transformer 220 v/100 kV, diode 150 kV/1.5 A, damping resistor(Rd) 27 kΩ, capacitor 25 nF, water resistance (Rw) 1.4 MΩ, protection sphere gap of 1.5 cm diameter and test gaps as shown in Fig.2.

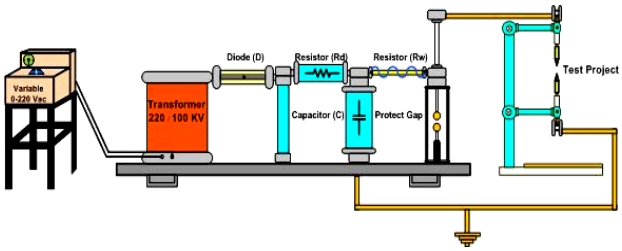

Figure2. Experimental circuit

C *Test Procedures*

$U_{50\%}$ in this present work was obtained by "up and down" method. Each U_{50} value corresponded to applying DC voltage 10 times. Temperature, pressure and relative humidity were also measured.

III. RESULTS

In this work, the results of positive breakdown voltage were separated into two cases. The first case is that the breakdown voltage ($U_{50\%}$) was the actual breakdown voltage obtained from the experiment. The other one was the breakdown voltage corrected with the atmospheric factor (K_t) which is the product of air density factor (δ) and humidity factor (h) as recommended in IEC 60-1[1].

A. Sharp rod-rod gaps 15°; Table I showed the results of breakdown voltage of the sharp rod-rod gaps 15° at 16 g/m^3. The breakdown voltage of the sharp rod-rod gaps 15° without correction and corrected with K_t were plotted as a function of gap length in Fig.3 and 4 respectively. The results showed that the trend of breakdown voltages of sharp rod-rod gaps 15° at different absolute humidities were very similar. Also, it indicated that increase in humidity caused the breakdown voltage higher.

TABLE I

THE BREAKDOWN VOLTAGE OF THE SHARP ROD-ROD GAPS 15° AT 16 G/M^3 WITHOUT CORRECTION AND CORRECTED WITH K_T AT VARIOUS GAP DISTANCES.

Sharp rod - rod gaps 15° at 16 g/m^3				
Gap distance (cm)	$U_{50\%}$ (kV)	$U_{50\%}$ corrected with K_t (kV)	Electric field stress (kV/cm)	
			$E_{50\%}$	$E_{50\%}$ corrected with K_t
2	19.0	18.1	9.5	9.0
4	42.2	40.2	9.0	8.8
6	45.8	43.6	7.6	7.2
8	55.5	52.9	6.9	6.6
10	58.4	55.7	5.8	5.5
12	62.5	59.5	5.2	4.9
14	73.1	69.6	5.2	4.9
16	82.2	78.3	5.1	4.9

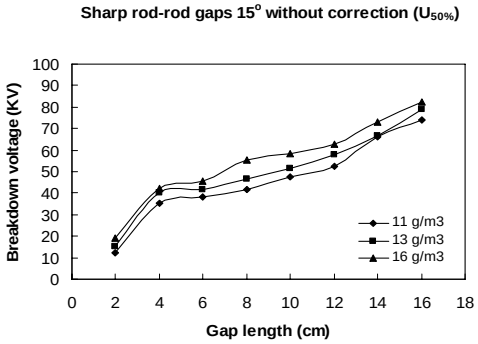

Figure3. Breakdown voltage of the sharp rod-rod gaps 15° without correction as a function of gap length.

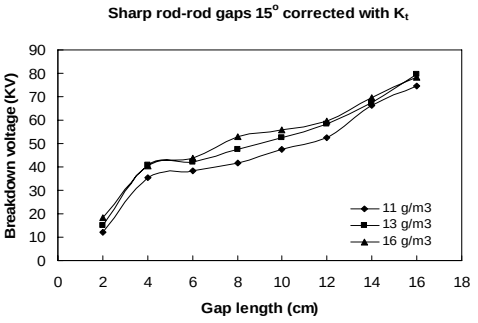

Figure4. Breakdown voltage of the sharp rod-rod gaps 15° corrected with K_t as a function of gap length.

B. Hemispherical rod-rod gaps; Table II showed the results of breakdown voltage of the hemispherical rod-rod gaps at 16 g/m^3. The breakdown voltage of the hemispherical rod-rod gaps without correction and corrected with K_t were plotted as a function of gap length in Fig.5 and 6 respectively. The results showed that the trend of breakdown voltages of hemispherical rod-rod gaps at different absolute humidities were very similar. Also, it indicated that increase in humidity caused the breakdown voltage higher.

TABLE II

THE BREAKDOWN VOLTAGE OF THE HEMISPHERICAL ROD-ROD GAPS AT 16 G/M^3 WITHOUT CORRECTION AND CORRECTED WITH K_T AT VARIOUS GAP DISTANCES.

Hemispherical rod - rod gaps at 16 g/m^3				
Gap distance (cm)	$U_{50\%}$ (kV)	$U_{50\%}$ corrected with K_t (kV)	Electric field stress (kV/cm)	
			$E_{50\%}$	$E_{50\%}$ corrected with K_t
2	57.1	54.4	28.5	27.2
4	64.5	61.5	16.1	15.3
6	73.3	69.8	12.2	11.6
8	76.0	72.4	9.5	9.0
10	80.2	76.4	8.0	7.6

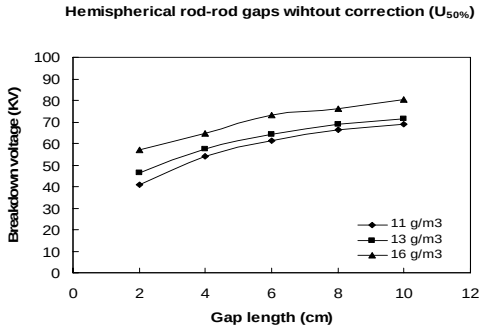

Figure5. Breakdown voltage of the hemispherical rod-rod gaps without correction as a function of gap length.

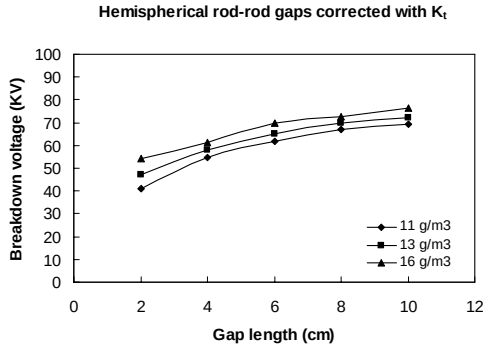

Figure6. Breakdown voltage of the hemispherical rod-rod gaps corrected with K_t as a function of gap length.

C. Square cut-square cut gaps; Table III showed the results of breakdown voltage of the square cut-square cut gaps at 16 g/m^3.The breakdown voltage of the square cut-square cut gaps without correction and corrected with K_t were plotted as a function of gap length in Fig.7 and 8 respectively. The results showed that the trend of breakdown voltages of square cut-square cut gaps at different absolute humidity were very similar. Also, it indicated that increase in humidity caused the breakdown voltage higher.

TABLE III

THE BREAKDOWN VOLTAGE OF THE SQUARE CUT-SQUARE CUT GAPS AT 16 G/M^3 WITHOUT CORRECTION AND CORRECTED WITH K_T AT VARIOUS GAP DISTANCES.

Square cut gaps at 16 g/m^3				
Gap distance (cm)	$U_{50\%}$ (kV)	$U_{50\%}$ corrected with K_t (kV)	Electric field stress (kV/cm)	
			$E_{50\%}$	$E_{50\%}$ corrected with K_t
2	22.4	21.3	11.2	10.6
4	54.1	51.6	11.0	10.4
6	65.2	62.1	10.8	10.3
8	72.6	69.2	9.0	8.6
10	77.3	73.7	7.7	7.3

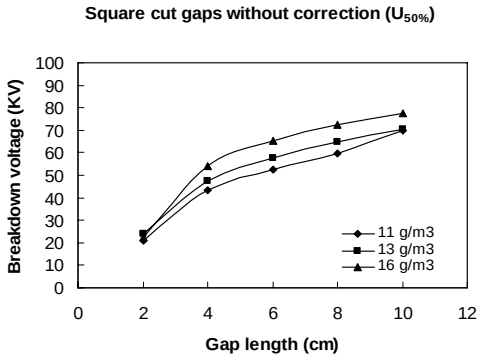

Figure7. Breakdown voltage of the square cut-square cut gaps without correction as a function of gap length.

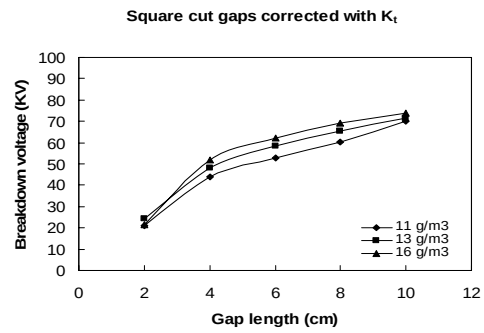

Figure8. Breakdown voltage of the square cut-square cut gaps corrected with K_t as a function of gap length.

E. The electric field stress; the average electric field stress at 16 g/m^3 of the hemispherical rod-rod gaps is higher than that of square cut-square cut gaps and sharp rod-rod gaps 15^o respectively in Table I-III. All values the electric field stress of the rods gaps are shown in Fig.9.

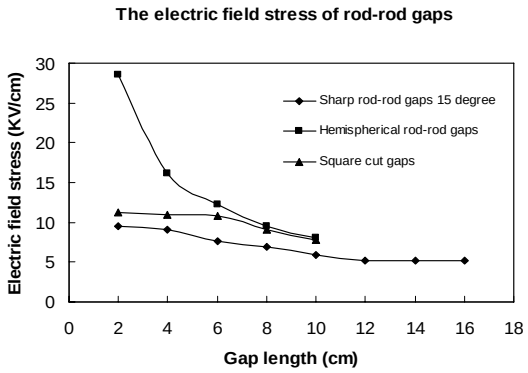

Figure9. The electric field stress of rod-rod gaps with gap length.

IV. DISCUSSIONS

From results in Tables I-III, the breakdown voltage of sharp rod-rod gaps 15^o at 16 g/m^3 less than square cut-square cut gaps and hemispherical rod-rod gaps. From Figure 9, the electric field stress at 16 g/m^3 of hemispherical rod-rod gaps is much higher than that of square cut-square cut and sharp rod-rod gaps 15^o at the gap distance of 2 and 4 cm. This is due to, at gap length of 2 cm and 4 cm, the hemispherical rod-rod gaps has characteristics of uniform field. However, as the gap distance increases to 6, 8 and 10 cm, the effect of the hemispherical tip decreases. This can be seen from its breakdown voltage is close to that of the sharp rod-rod and square cut - square cut gaps. From Tables I-III, it can imply that

- As absolute humidity increases, the breakdown voltage increases.
- The breakdown voltage increases as the gap distance increases.

This was in agreement with S. Chotigo and T. Boonwern [7] which was the results on the rod-rod gap with the tip angles of 30^o, 45^o and 60^o.

However, in this present work h/δ is greater than 13 g/m^3 which is the limit of applying K_h recommended in IEC 60-1. From results in Tables IV and V, %different of $U_{50\%}$ corrected with K_t at 16 g/m^3 and 11 g/m^3 are very high compared to that between 13 g/m^3 and 11 g/m^3. Actually, the value of this breakdown voltage should be closer when it is corrected to the standard condition. This indicates that the atmospheric correction factor K_t recommended in IEC 60-1 is not suitable when h/δ is above 13 g/m^3. It should be noted that the value of h/δ in present work is 16.4, 13.6 and 11.1 g/m^3 when the absolute humidity is 16 g/m^3, 13 g/m^3 and 11 g/m^3

respectively. This may imply that the atmospheric correction factor for rod-rod gaps under positive DC voltage in Thailand has to be found out.

TABLE IV
% DIFFERENCE OF THE BREAKDOWN VOLTAGE CORRECTED WITH K_T AT 13 G/M^3 AND 11G/M^3 OF THE ROD GAPS.

Gap distance (cm)	%difference of $V_{50\%}$ corrected with K_t at 13 g/m^3 and 11 g/m^3		
	Rod 15^o	square cut	hemisphere
2	25.3	15.4	14.5
4	14.3	10.1	6.5
6	9.8	11.2	5.2
8	13.5	8.7	4.3
10	9.9	1.7	3.8

$$\%difference = ((V_{13g/m^3} - V_{11g/m^3}) / V_{11g/m^3}) \times 100$$

TABLE V
% DIFFERENCE OF THE BREAKDOWN VOLTAGE CORRECTED WITH K_T AT 16 G/M^3 AND 11G/M^3 OF THE ROD GAPS.

Gap distance (cm)	%difference of $V_{50\%}$ corrected with K_t at 16 g/m^3 and 11 g/m^3		
	Rod 15^o	square cut	hemisphere
2	49.7	33.3	32.2
4	13.1	17.9	12.7
6	14.0	18.1	13.0
8	26.9	15.2	8.4
10	17.0	4.9	10.0

$$\%difference = ((V_{16g/m^3} - V_{11g/m^3}) / V_{11g/m^3}) \times 100$$

V. CONCLUSION

Three shapes of the rod electrodes were used for investigating the effects of humidity under positive DC voltage. The results can be concluded as follows:

1. The electrode shape has an influence on positive DC breakdown voltage.
2. The breakdown voltage increases as the absolute humidity increases.
3. The breakdown voltage of rod gaps without correction and corrected with K_t increases as the gap distance increases.
4. The electric field stress of hemispherical rod-rod gaps is higher than that of square cut-square cut and sharp rod-rod gaps 15^o
5. The atmospheric correction factor for rod-rod gaps under positive DC voltage recommended by IEC 60-1 is not suitable to apply in Thailand. This can be seen from %difference in Tables IV and V which is really high.

REFERENCES

[1] IEC Publ. 60 High voltage test techniques 1 –1989.
[2] Li Jing, wen Hua, Yao Zhonggan "THE INFLUENCE OF IONS ON ELECTRICAL BREAKDOWN IN AIR" IEEE, 1988.
[3] P.A. Calva, V. del Moral, M.G. Marquez, G.P. Cabrera "New proposal of correction factors for dc voltage" IEEE, 2003.
[4] A. Paul Abraham and B. R. Prabhakar "Effect of Humidity and Temperature on the dc Breakdown of Rod-Rod and Rod-Plane Gap" IEEE Trans. Vol. 27 No. 2, April 1992.
[5] N.L. Allen, M. Boutlendj, R.C. Hughes, H.A. Lightfoot and R.B Neville "Analysis and comparison of rod-plane and rod-rod gaps as direct voltage measurement devices" IEE, Vol 139. No 6, NOVEMBER 1992.
[6] P A Calva Chavarria, A Robledo-Martinez "Effect Of Humidity On DC Breakdown Voltages In Ambient Air At High Altitude" IEEE, October 20-23, 1996.
[7] S. Chotigo and T. Boonwern "Effect of Humidity and Temperature on the DC Breakdown at different tip angles of Rod-Rod Gaps" TENCON, 2006.

A Preliminary Study of Dissipation Factor (tan δ) in Dielectric of Cables Produced in Thailand

A. Aurairatch and S. Kleesuwan
Department of Electrical Engineering, Faculty of Engineering
King Mongkut's Institute of Technology North Bangkok, Bangkok 10800, Thailand
Email: aurirat@gmail.com

***Abstract*–The investigation of the temperature and the voltage influence with dry and wet service conditions of the new and the used XLPE cables produced in Thailand is proposed. This paper also presents the effect of accelerated aging of the cable insulations on changing its dissipation factor (tan δ). During tests, the cables conductor temperature was 20 °C to 100 °C and the electrical field on conductor screen was 6.93 kV to 27.7 kV.**

I. INTRODUCTION

Underground distribution and transmission cable systems are a major investment for electrical utilities. These cables must be highly reliable in order to decrease lost revenues suffered from a premature failure. From a operators point of view, it is of the great importance to be continuously informed of the decrease in electrical strength. Electrical utilities are faced with decisions to maintain, repair, refurbish, or replace their cable systems. In order to make these decisions, the condition of the cable system needs to be determined by knowing [1]:

- How the different components of the system age, i.e. aging factor;
- The system operating conditions;
- How to measure the aging by diagnostics;
- Criteria for "repair, refurbish or replace."

The cause of cable failures stem from electrical, thermal and environmental stresses. Temperature, age, humidity, water content, load and usage all contribute deterioration of underground cable systems. A common cause of cable failures is the wearing and breakdown of the insulation. Insulating materials are dielectrics, which prevent the flow of current when an input voltage is applied. The major insulation used in cables are cross linked polyethylene (XLPE) [2].

The possibility of in situ diagnosis of underground distribution lines has always been actively sought after by utilities across the world. As a matter of fact, an estimation of the remaining useful life of cables in service may prevent high cost, due to unpredicted outages, by replacing them just in time. Also such a possibility of diagnosing cables will increase safety as well as confidence for the crewmen having to work close to the equipment.

Distribution factor measurements base on Schering bridge of XLPE cables produced in Thailand and accelerated aging in the laboratory are presented. Typical distribution XLPE cables have been used for the investigation. The new and the used cables were assembled in the laboratory and were tested such as the main objective measured the dissipation factors of conventional XLPE materials as a function of electric field and temperature. Measurements of the dissipation factor tan δ were performed on 12/20 (24 kV) cable samples in the temperature range 20 °C to 100 °C, up to a maximum voltage of $2U_0$ (27.7 kV).

II. XLPE CABLES

Crosslinked polyethylene (XLPE) cables have been used as power cable insulation for several decades. In the late 1960's to 1970's, XLPE enjoyed tremendous growth in this application, and is still the preferred material [3]. Although the XLPE used today is similar to that developed many years ago, a number of small but progressive modifications have been made to its physical, chemical and electrical properties in order to optimize the performance in medium and high voltage applications.

The physical and electrical properties of XLPE are shown in Table I [4]. The dielectric losses of any high voltage cable are directly proportional to the square of the operating voltage, to the dielectric constant and to the dissipation factor of the insulation.

TABLE I
TYPICAL PROPERTIES OF XLPE CABLE

Physical	**XLPE**
Density, g.cm-3	0.92
Tensile Strength, MPa	19
Elongation, %	500
Modulus of Elasticity, MPa	121
Heat Distortion, %	20
Thermal Conductivity w/m°C at 90 °C	0.27
Electrical	
Dielectric Constant	2.3
Dissipation Factor, % at 23 °C 90 °C	 <0.03 <0.03
Volume Resistivity, Ωm At 23°C	1016
Shout – term AC Breakdown on Miniature Cable, kv/mm	48

III. DISSIPATION FACTOR

The dissipation factor, also called tan δ or loss angle, is a diagnostic method of testing cables to determine the quality of the cable insulation. This is done in order to predict the remaining life expectancy and to prioritize cable replacement.

If the insulation of a cable is free from defects, like water trees, electrical trees, moisture and air pockets, etc, the cable approaches the properties of a perfect capacitor. It is very similar to a parallel plate capacitor with the conductor and the neutral being the two plates separated by the insulation material.

In a perfect capacitor, the voltage and current are phase shifted 90 degrees and the current through the insulation is capacitive. If there are impurities in the insulation, like those mentioned above, the resistance of the insulation will decrease with resulting in an increase of resistive current through the insulation. It is no longer a perfect capacitor. The phase angle between the current and the voltage will be less than 90 degrees, which is indicative of the level of insulation contamination, hence quality/reliability.

Figure 1 is a representation of a cable. The tangent of the angle δ is measured. This will indicate the level of resistance in the insulation. By measuring I_R/I_C, we can determine the quality of the cable insulation. In a perfect cable, the angle would be closed to zero. An increasing angle indicated an increase in the resistive current through the insulation, meaning contamination. If the angle is greater, it will be the worse the cable.

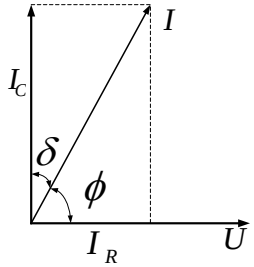

Figure 1. The cable equivalence circuit

If a cable's insulation is perfect, the loss factor (tan δ) will not change as the applied voltage is increased. The capacitance and loss will be similar with 1kv or 10 kV applied to the cable. If the cable has water tree contamination, thus changing the capacitive/resistive nature of the insulation, then the tan δ numbers will be higher at higher voltages. Rather than a flat curve for the loss number versus voltage, the curve will be non linear see the graph in figure 2.

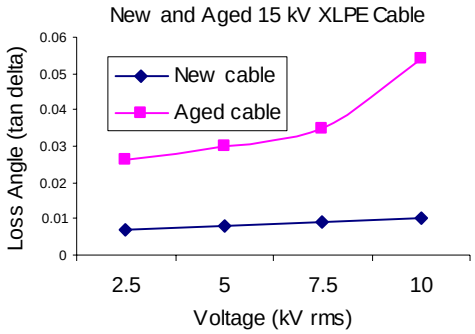

Figure 2. The dissipation factor of the new and the used XLPE cables

Dissipation factor measurements were all preformed at 50 Hz using a Tettex Schering bridge (type 2801) with automatic guard potential regulator [5].

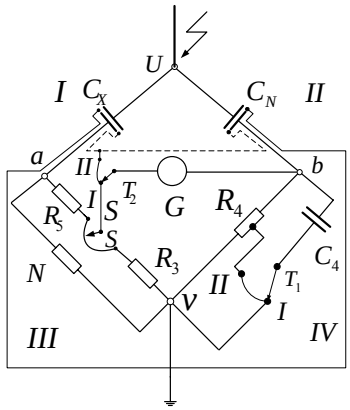

Figure 3. The circuit diagram of the Schering bridge

The Schering bridge involves a measurement carried out in a bridge arrangement, figure 3, comparing the cable samples with a thoroughly loss free standard capacitor, with the capacity and loss factor, tan δ know. The bridge is balanced by setting the resistance, R_4 and R_3 as well as the capacitance C_4 until the indicator on the screen is horizontal. The loss factor is calculated as follows [6-7].

$$\tan\delta = \omega \cdot C_4 \cdot R_4 \qquad (1)$$

IV. EXPERIMENTAL DETAIL

In order to investigate the influence of voltages and temperatures of underground XLPE cables, the new cables, the 5-year used cables and the 10-year used cables were selected. The dissipation factor measurements were all performed on 6 m long, 12/20 (24kV) underground XLPE cable samples with 50 mm^2 stranded copper conductors, all produced by the same cable manufacturer.

The sample of completed cable was heated by cylinder core transformer. The tan δ measured with an alternating voltage of $0.5U_0$, U_0, $1.5U_0$ and $2U_0$ with the temperature of 20°C to 100°C. Figure 4 shows the dissipation factor measuring.

Figure 4. The dissipation factor measuring setup

In order to investigate the influence of moisture, age and time, also studies by others, two cable were selected the new cable and the 10-year used cable. The cables were placed in the cylindrical insulating tank. The water temperature was maintained at 90°C. The voltage of U_0 (13.86 kV AC) was applied conductor to ground continuously during aging. The samples for the evaluation were measured every 100 hours. It is planned to continue the aging time for 1000 hours. In figure 5, the new cable and the 10-year used cable under wet condition were tested.

Figure 5. Cable under wet condition tested.

V. Results and Discussion

A. *Tan δ measurement for the new and the used cable*

The dissipation factor of 12/20 (24 kV) XLPE new cable is shown in figure 6. It is the function of the conductor temperature. The graph shows the dissipation factor is less than 0.8%. At 100°C, the dissipation factor is also less than 0.8%, which accord with the IEC 60502-2 specifications on dissipation factor for conventional XLPE (tan $\delta < 80 \times 10^{-4}$).

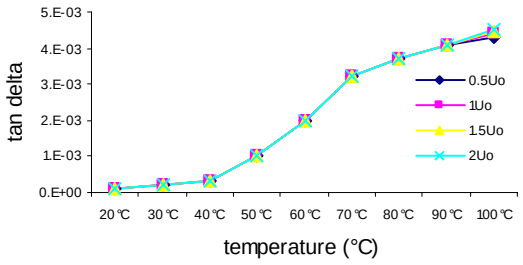

Figure 6. The dissipation factor of 12/20 (24 kV) XLPE new cable

Figure 7 shows a similar pattern with the dissipation factor between 0.43 to 0.45% at 100°C. Power cables rarely operate at above 90°C. The most important parameters are the cable life and the long term stability of the dissipation factor as the cable ages.

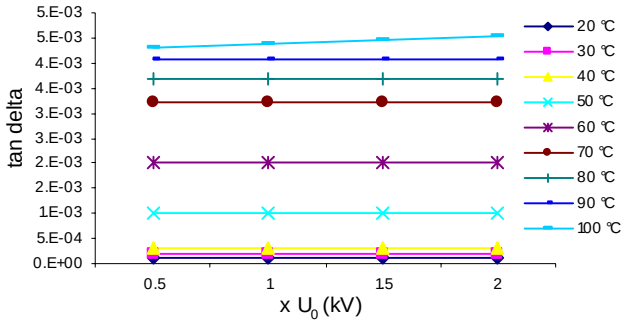

Figure 7. The dissipation factor of 12/20 (24 kV) XLPE new cable

The dissipation factor did not change as the applied voltage was increased. So, a cable's insulation has been perfect.

Figure 8 and 9 show the stability of the dissipation factor for 12/20 (24 kV) 5-year used and 10-year used XLPE cables at 20°C to 100°C temperatures are well.

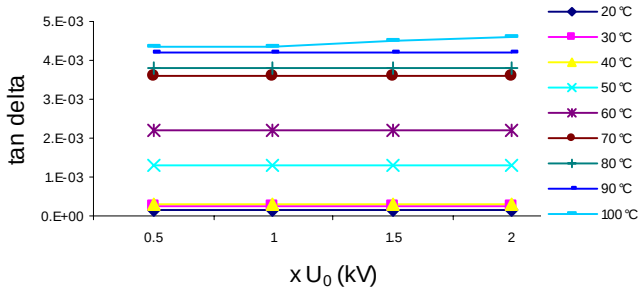

Figure 8. The dissipation factor of 12/20 (24 kV) XLPE 5-year used cable

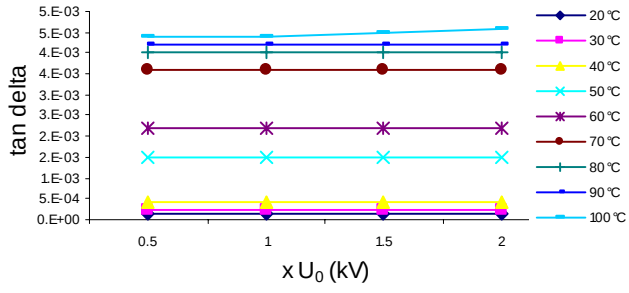

Figure 9. The dissipation factor of 12/20 (24 kV)XLPE 10-year used

B. Cable aging program

The new cable and the 10-year used cable under wet condition tested result for 100 to 400 hours are shown in Figure 10. The tan δ still remains constant after 500 hours. It had a little increase of follow with voltage rise and less than 0.8% that is durable even when the long time tested with the wet condition.

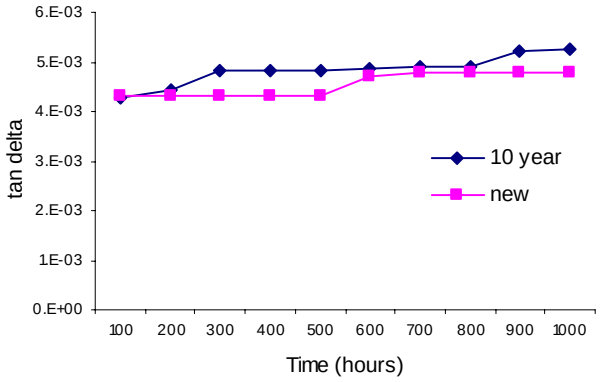

Figure 10. The dissipation factor of 12/20 (24 kV) XLPE new and 10-year used cable under wet condition

At the end of aging period, the cables were removed from the tank and the tan δ was measured. The dissipation factor for this cable is pointed out in figure 11 as functions of conduction temperature.

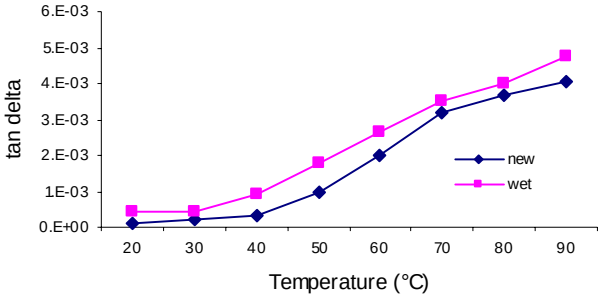

Figure 11. The dissipation factor of 12/20 (24 kV) XLPE new and 10-year used cable under wet condition

This figure presents a comparison of the real valve of the dissipation factor of the new cable and the 10-year used cable (cable aging program) as a function of temperature at a frequency of 50 Hz, 13.86 kV ac. It suggests the new XLPE has a smaller dissipation factor than the 10-year used XLPE.

Figure 12 shows a comparison of the dissipation factor of new cable, 5-year used, 10-year used, new cable wet condition and 10-year used cable wet condition tested as a function of temperature. The tan δ increased lightly following the temperature rise. Except the 10-year use under wet condition tested, it increased immediately following the temperature rise. However, the tan δ of all tests was less than 0.8%.

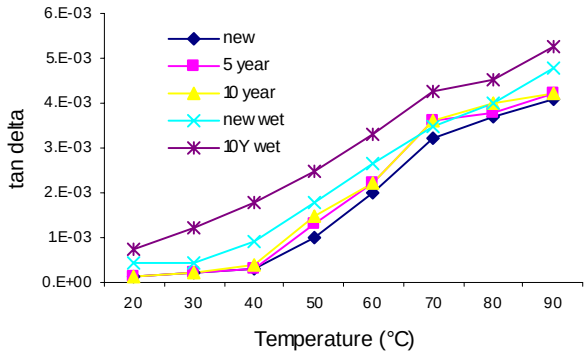

Figure12. The dissipation factor of new cable, 5-year used, 10-year used, new cable wet condition and 10-year used cable wet condition tested

VI. CONCLUSION

If the medium voltage cables, insulated with XLPE, are used in the wet condition after the service time, the tan δ may increase. The probability such a defect is determined by the cable design, the raw materials used, the production process, etc. The results obtained in this investigation have been summarized as follows:

- The tan δ of the XLPE cables has increased follow the temperature rise.
- The influence of moisture, temperature and time affected the increasing of the tan δ of the XLPE cables.
- The XLPE cables with produced in Thailand were durable even those which were in long time used and long time tested, the tan δ did not increased following voltages rise.

REFERENCES

[1] B. Oyegoke, P. Hyvonen, M. Aro, and N. Gao, "Application of Dielectric Response Measurement on Power Cable System," *IEEE Transactions on Dielectrics and Electrical Insulation*, vol. 10, no.5, pp.862–873, October 2003.

[2] S.V. Nikolajevic, "Investigation of Water Effects on Degradation of Crosslinked Polyethylene (XLPE) Insulation," *IEEE Transactions on Power Delivery*, vol.8, no.4, pp. 1682–1688, October 1993.

[3] B.K. Hwang, "A New Water Tree Retardant XLPE" *IEEE Transactions on Power Delivery*, vol.5, no.3, pp. 1617–1627, July 1990.

[4] J.C. Chan, M.D. Hartley, and L.J. Hiivala, "Performance Characteristics of XLPE Versus EPR as Insulation for High Voltage Cables," *IEEE Electrical Insulation Magazine*, vol.9, no.3, pp. 8–12, May/June 1993.

[5] H. Faremo and E. Ildstad, "Water treeing and Dielectric loss of WTR-XLPE Cable Insulation" *IEE Proceedings-A,* vol. 7, no. 2, pp. 393–396, September 1993.

[6] J.A. Williams, *Underground Transmission Systems Reference Book.* Electric Power Research Institute, Inc., U.S.A., 1992.

[7] E. Kuffel and W.S. Zaengl, *High-Voltage Engineering Fundamentals.* Pergamon Press, New York, U.S.A, 1984.

Partial Discharge Measurement for High Voltage Cable Terminators Using Air Compression

P. Apiratikul[1], P. Boonchiam[1], B. Plangklang[1] and T. Suwanasri[2]
[1]Department of Electrical Engineering, Rajamangala University of Technology Thanyaburi
[2]The Sirindhorn International Thai-German Graduate School of Engineering,
King Mongkut's Institute of Technology North Bangkok

Abstract: **This paper presents a partial discharge (PD) measurement for cable terminators of XLPE power cable. The power cable of rated voltage 24 kV and a cross sectional area of 240 mm^2 was used in the experiment. The partial discharge level and dielectric loss are very important factors to indicate the insulation quality of power cable. Therefore, measurement techniques of partial discharge and dielectric loss are required in high voltage applications. This paper proposes a design and construction of a cable terminator by using acrylic tube. Inside of cable connector, the maximum high pressure air can be compressed more than 3 bar. In order to implement the partial discharge and the dielectric loss (tanδ) techniques, the cable terminator has to be tested according to IEC standards No.60502, No.835-3 and No.270. It can be found that the cable terminator testing gives the satisfactory and reasonably accurate results from the measurement techniques. In addition, the cost of construction is much cheaper than a commercial module.**

I. INTRODUCTION

Electrical solid insulations have been used extensively in electrical power devices, particularly in power cables. Most solid insulations are developed from polymeric materials. There are two important electrical characteristics for polymeric insulations, which are the partial discharge level and the dielectric loss (tan δ) [1,2]. It is necessary for cable manufacturers to perform tests on the partial discharge level as well as on the dielectric loss. In order to perform such tests, a cable connector is required [1]. The cable connector is available in the commercial sectors. However, it is difficult for small laboratories to acquire this device due to its price. This paper aims to present a development and a construction of the cable connector using local components available in ASEAN countries. Three types of insulating materials: air, palm oil (vegetable cooking oil) and transformer oil, are used in the connector. Then, the connector is implemented for partial discharge and dielectric loss tests with a power cable.

The rest sections in this paper are organized as follows; Section 2 presents a design and construction of cable terminator. A technique of partial discharge measurement is presented in Section 3 by using partial discharge detector. Section 4 shows a dielectric loss measurement using Schering bridge circuit. Finally, the conclusion and discussion are given in Section 5.

II. CABLE TERMINATOR

When performing partial discharge tests and dielectric loss tests with a cable, outer parts of the cable must be taken off. Next, the conductor of the cable is covered by a terminator and connected to terminals of a transformer, which is a supply for performing partial discharge and dielectric loss tests. The requirement of the cable termination is that the termination needs a sufficient clearance distance between a conductor and a ground part. The inner part of the connector was designed to have a sufficient length to cover all the bare conductor of the cable. The inner part was filled with the insulating medium. The material used for the inner part was acrylic tube so that the inner part was transparent for checking a level of the insulating medium. Solid cylindrical aluminium was connected at the end of the inner part of the connector in order to provide a socket for one terminal from the transformer. The joint between the acrylic tube and the cylindrical aluminium was sealed by using polyester resin in order to reduce the electric stress around the joint, and also protected the leakage of the insulating medium. At the joint between the inner part and the terminal from the transformer, a stress control device in a toroid shape was placed. The outer part of the connector was PVC, and this was a base to support the inner part of the connector. Fig. 1 and Fig. 2 show details of the constructed cable connector while Fig. 3 illustrates an arrangement of the connector for performing cable tests. To reduce the electric stress at the end of the terminator, a toroid is connected to increase the area of cable end terminator as shown in Fig. 3. At the other side of the terminator, the place cover was installed for preventing the air leakage. The pressure gauge is also installed in this cover to indicate the pressure value. Fig. 4 illustrates the set of cable terminator that have already been connected with the power cable inside the shape.

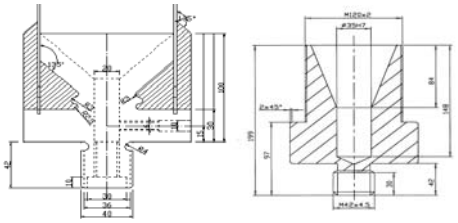

Fig. 1 The joint between the acrylic tube and cylindrical aluminium at the inner part of connector

Fig. 2 Connected terminal of power cable

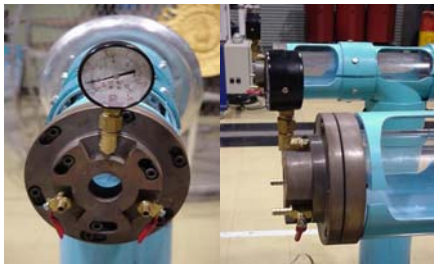

Fig. 3 The place cover and toroid of cable terminator

Fig. 4 A set of cable terminator

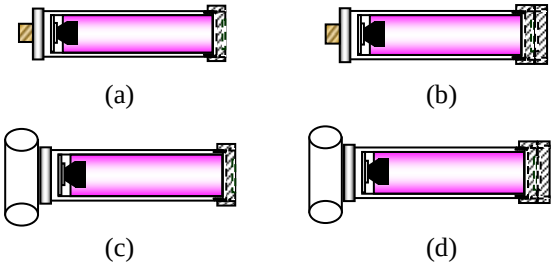

Fig. 5 Each test model of cable terminator

III. Terminator Test Procedure

There are 2 procedures for cable terminator testing, the first is dielectric loss and the second is partial discharge level. Because of no instrument that can directly measure the dielectric loss, the Schering bridge circuit is used to find this value. Two factors can present in this circuit that are capacitance and dissipation factor ($\tan\delta$). The dielectric losses of cable terminator can be found by using Equation (1) as follows:

$$P_d = \omega \cdot C \cdot U^2 \cdot \tan\delta \qquad (1)$$

where, P_d is the dielectric loss in Watt, ω is angular frequency (rad/s), U is tested voltage in kV and $\tan\delta$ is dissipation factor.

Then, a partial discharge level is measured in order to implement the constructed cable terminator. Insulating materials inside the terminator is the controlled-pressure air. Partial discharge tests were performed at the voltage levels of 12 kV and 24 kV. In general standard, the partial discharge level should be less than 5.0 pC [4]. It can be carried out by using the partial discharge detector, PD-TE571, which is calibrated under IEC standard [5].

This paper is classified the terminator into four shapes as follows:
Type A: Cable terminator without a cover and cable connector, Fig. 5(a)
Type B: Cable terminator with cable connector without a cover, Fig. 5(b)
Type C: Cable terminator including toroid, without place cover and cable connector, Fig. 5(c)
Type D: Cable terminator including toroid, with place cover and cable connector, Fig. 5(d)

Table 1: Cable terminator including toroid, without place cover and cable connector, Fig. 5(c)

U_{test} (kV)	f (Hz)	Cx_{test} (pF)	tan δ x 10^{-3}	Dielectric Loss (μW)
12.26	49.80	106.89	1.832	92.421
12.21	49.80	107.74	1.860	93.810
12.24	49.80	107.56	1.847	93.115
24.61	49.90	108.42	1.824	376.085
24.62	49.80	108.60	1.845	381.357
24.44	49.80	109.70	1.886	388.043
24.55	49.83	108.91	1.851	381.828
36.68	49.80	108.42	1.838	841.866
36.68	49.80	108.60	1.847	847.393
36.67	49.80	108.47	1.875	858.741
36.70	49.83	108.49	1.853	849.333

Table 2: Cable terminator including toroid, with place cover and cable connector, Fig. 5(d)

U_{test} (kV)	f (Hz)	Cx_{test} (pF)	tan δ x 10^{-3}	Dielectric Loss (μW)
11.81	49.90	108.50	1.892	89.904
11.81	49.90	108.60	1.845	87.751
11.81	49.90	107.55	1.867	88.827
23.93	49.90	108.80	1.859	363.683
23.92	49.80	108.68	1.875	366.102
23.92	49.80	109.70	1.886	371.706
23.92	49.83	108.34	1.851	367.163
36.59	49.80	109.61	1.827	841.866
36.35	49.80	109.80	1.824	830.932
36.29	49.80	108.47	1.835	823.093
36.35	49.83	108.74	1.853	831.963

Table 1 and table 2 present the test results of cable terminator type C and type D, respectively. They are tested with a standard voltage varied from 12 kV (U_0) to 36 kV. During this process, the power cable was not inserted inside the cable terminator. It can be found that the capacitance value and dissipation factor do not change. This means that the dielectric loss is directly proportion to the input voltage ($P_d \propto U$). Because the dielectric loss of type D is close to type C, the cable terminal with a cover did not produce loss. Therefore, a cover can be installed for testing a cable terminator.

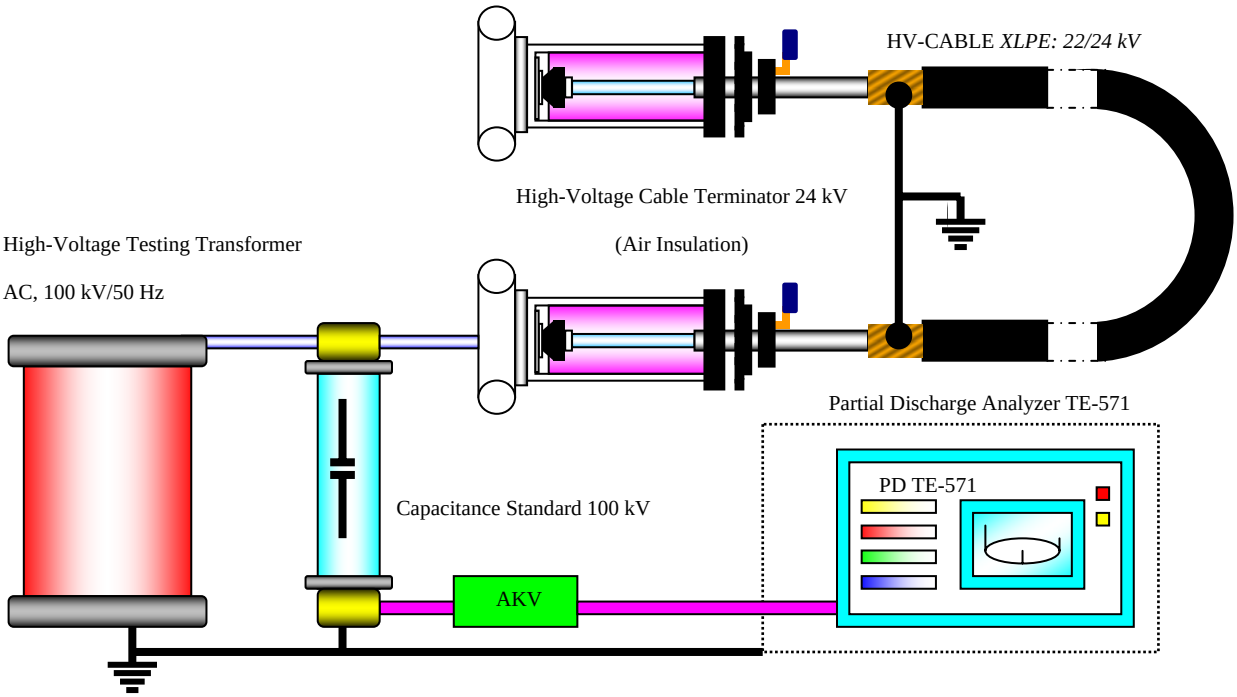

Fig. 6 Test circuit for partial discharge measurement of power cable with compressed air cable terminator

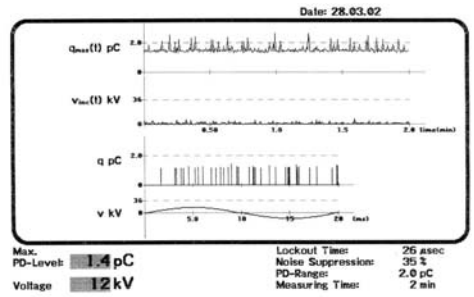

Fig. 7 Partial discharge level of Type D at 12 kV

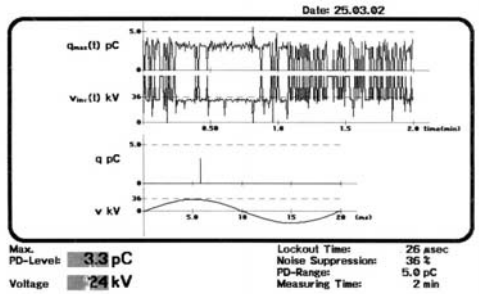

Fig. 8 Partial discharge level of Type D at 24 kV

The partial discharge levels of type-D cable terminator are illustrated in Fig. 7 and Fig. 8. From experiment results, the partial discharge level of type D also depends on input voltage. The partial discharge level in cable terminator can be controlled by the rated voltage at its operation level. The partial discharge is increased when overvoltage or impulse voltage occurred. The protection scheme of voltage must be ensured to protect the cable terminator by design engineers.

IV. Power Cable Procedure

As already mentioned in the previous section, the partial discharge level and dielectric loss depend on the input voltage. In this section, the 240 mm^2 power cable with terminator was tested. The length of power cable is 10 metres. For the terminator tube, the air pressure was controlled within 1 bar to 3 bar. The dielectric loss and partial discharge are carried out by using instrument as described in the previous section. The voltage levels are 12 kV and 24 kV. The dielectric losses of cable are not presented in this section, but they are calculated by using Equation (1). Obviously, it can be noticed that the dielectric loss depends on rated voltage and material inside the tube (power cable). The dielectric loss will be changed according to the variation of the power cable size.

The partial discharge levels are measured by using a test circuit shown in Fig. 6. Fig. 9 to Fig. 11 show partial discharge levels of cable terminator at 1.0 bar, 2.0 bar and 3.0 bar compressed air, respectively. Fig. 12 to Fig. 14 also show partial discharge levels of cable at the same compressed air.

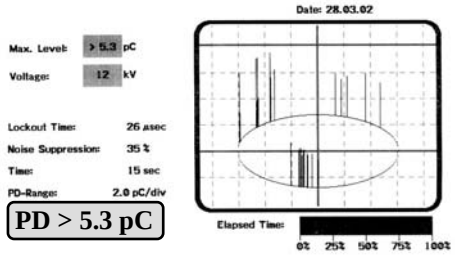

Fig. 9 PD level of terminator with 1.0 bar compressed air and 12 kV rated voltage

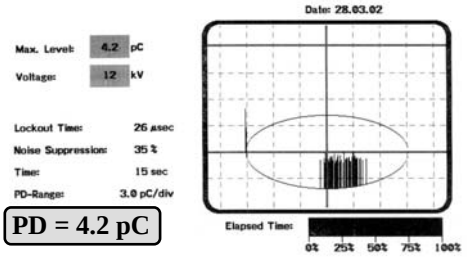

Fig. 10 PD level of terminator with 2.0 bar compressed air and 12 kV rated voltage

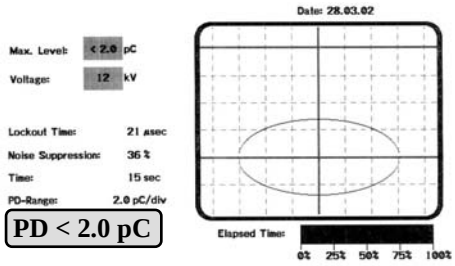

Fig. 11 PD level of terminator with 3.0 bar compressed air and 12 kV rated voltage

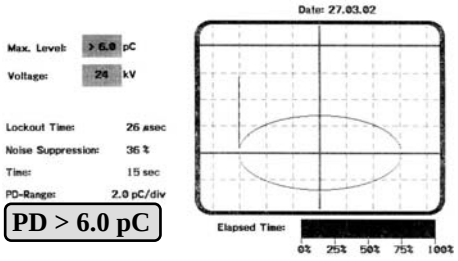

Fig. 12 PD level of terminator with 1.0 bar compressed air and 24 kV rated voltage

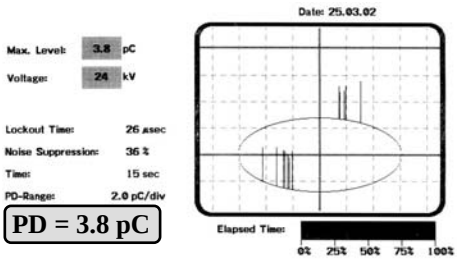

Fig. 13 PD level of terminator with 2.0 bar compressed air and 24 kV rated voltage

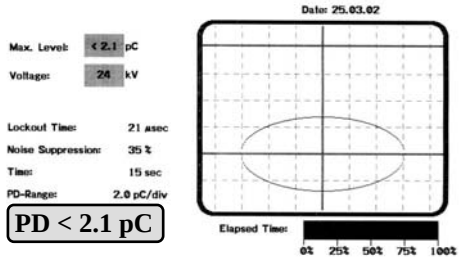

Fig. 14 PD level of terminator with 3.0 bar compressed air and 24 kV rated voltage

The PD level is decreased when the compression of air is increased and it is independent on the voltage rating. As shown in Fig. 11 and Fig. 14, the compression of air is about 3.0 bar. There is no partial discharge value in cable terminator and the PD level is about 2 pC at the different voltage levels. The partial discharge level and dielectric loss given in this paper are primary data for the design engineers before designing of the terminator. Comparing with another material, the using of air as insulation is cheaper than another and simple construction.

V. CONCLUSION

A cable terminator has been constructed and tested with a partial discharge detector and a Schering bridge. Components used in the terminator are available from local suppliers in ASEAN countries. The terminator proposed in this paper has been implemented by partial discharge tests and dielectric loss tests for cable terminator and power cable. The insulating air has been used in the terminator tube. The results obtained from partial discharge tests and dielectric loss tests ensure the use of the developed terminator in the satisfactory level.

REFERENCE

[1] Ahmed, N.; Morel, O.; Srinivas, N., "Partial discharge measurement in transmission-class cable terminations", Transmission and Distribution Conference, 1999 IEEE Volume 1, 11-16 April 1999

[2] Zhu, D.; McGrail, A.J.; Swingler, S.; Auckland, D.W.; Varlow, B.R., "Partial discharge detection in cable termination using acoustic emission techniques and adaptive signal processing", Electrical Insulation, 1994., Conference Record of the 1994 IEEE International Symposium on 5-8 June 1994

[3] I Lupo, G.; Petrarca, C.; Egiziano, L.; Tucci, V.; Vitelli, M., "nterpretation and classification of PD in a HV cryogenic cable termination", Dielectrics and Electrical Insulation, IEEE Transactions on [see also Electrical Insulation, IEEE Transactions on Volume 7, Issue 1, Feb. 2000

[4] Ekberg, M.; Gustafsson, A.; Leijon, M.; Bengtsson, T.; Eriksson, T.; Tornkvist, C.; Johansson, K.; Li Ming, "Recent results in HV measurement techniques", Dielectrics and Electrical Insulation, IEEE Transactions on [see also Electrical Insulation, IEEE Transactions on Volume 2, Issue 5, Oct. 1995

[5] Taylor, N.; Edin, H., "Utilisation of voltage and frequency dependence of stress-grading materials in dielectric diagnostics", Electrical Insulation and Dielectric Phenomena, 2004. CEIDP '04. 2004 Annual Report Conference on 17-20 Oct. 2004

[6] Egiziano, L.; Femia, N.; Garamella, G.; Lupo, G.; Tucci, V., "Characterization of composite organic materials for field stress control of HV cables terminations", Conduction and Breakdown in Solid Dielectrics, 1992., Proceedings of the 4th International Conference on 22-25 June 1992

[7] Barsch, R.; Lambrecht, J.; Pilling, J.; Weichold, J.; Haim, K.D., "The behaviour of medium voltage cable terminations at artificial pollution", Electricity Distribution. Part 1. Contributions. 14th International Conference and Exhibition on (IEE Conf. Publ. No. 438) Volume 3, 2-5 June 1997

[8] Ward, B.H.; Steiner, J.P.; McArdle, K.J., "A new technique for partial discharge testing high voltage polymeric cable in an open environment", Partial Discharge, 1993., International Conference on 28-30 Sep 1993

Development and Construction of Dielectric Heating Machine

Prasit Chanmontree and Ekarin Vasanasong
Department of Electrical Power Engineering, Mahanakorn University of Technology
51 Cheum-Sampan Road, Nongchock, Bangkok 10530 Thailand
Email: pcm@kmitnb.ac.th

***Abstract*- This paper presents the design of Dielectric Heat for gluing wood. Principle of Dielectric Heating is the use of High-Frequency High-Electric field for heating insulating materials by their own dielectric losses. This type of heating has the advantage of being able to heat insulator well, quickly and uniformly. The material to be heated is placed between two electrodes that form a capacitor. The designed Dielectric Heater (DH) employs triode tube 7T84RB for generating frequency at 27 MHz. The DC input voltage is 5 kV. The power output can be adjusted by adjusting coupling capacitor. This technique can replace the phase control for adjusting input voltage supply. The maximum rated output is 4 kW. The test results showed that it can glue two pieces of wood with the same thickness of 0.315 inches with the size of 0.984 inches by 8.66 inches in less than 6 seconds.**

I. INTRODUCTION

Dielectric heating is the use of high-frequency electric fields for heating insulating materials by their own dielectric losses. This type of heating has the advantage of being able to heat good heat insulators quickly and uniformly. The material to be heated must be placed between two electrodes to form a capacitor. The capacitance current flowing through the material generates heat in the material by dielectric loss. The capacitor structure is shown in Fig. 1, with a small rectangular prism of unit cross-sectional area indicated at a location of uniform electric field. The capacitance of this elementary section of the condenser can be calculated from [7]

$$C = \frac{0.225e}{d} \quad pF \tag{1}$$

If the dielectric constant e of the material between the plates is known and the dimensions are given in inches.

When the radio-frequency voltage E is applied across the plates of this condenser, the power absorbed by the rectangular prism is

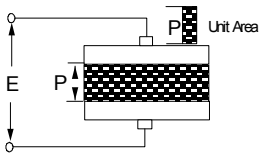

Figure.1 Condenser with dielectric material between plates.

$$P = \left(\frac{E^2}{\sqrt{R^2+X^2}}\right)(\cos q) \quad W \tag{2}$$

Where R and X is ohms are, respectively, the resistive and reactive components of the impedance for this elementary condenser and cos q is the power factor.

Equation (2) can be rewritten in the form of (3) and (4).

$$P = \left(\frac{E^2}{X}\right)\left(\frac{X}{\sqrt{R^2+X^2}}\right)(\cos q) \quad W \tag{3}$$

$$P = \left(\frac{E^2}{X}\right)\left(\sqrt{1-\cos^2 q}\right)(\cos q) \quad W \tag{4}$$

where

$$\frac{X}{\sqrt{R^2+X^2}} = \sin q = \sqrt{1-\cos^2 q} \tag{5}$$

By using the computed value of C from (1), the value of X in this equation for a frequency of f megacycles may be found from $X = \frac{1}{2pfC}$. By substituting this into (4), the equation then can be written as

$$P = \frac{\left(1.415\times10^{-6} feE^2\right)}{d\sqrt{1-\cos^2 q}\,\cos q} \quad W \tag{6}$$

For the power concentration P_c in watts per cubic inch, (6) reduces to

$$P_c = 1.415\times10^{-6} fe\left(E_g\right)^2\sqrt{1-\cos^2 q}\,\cos q \quad W/in.^3 \tag{7}$$

Where E_g is the voltage gradient across the condenser in volts per inch.

In a specific application of dielectric heating, the permissible voltage across the condenser is limited by such factors as configuration of electrodes, dielectric strength, presence of moisture with possible generation of steam, or irregularities in the wood such as knots. Since the power concentration will usually be fixed by oscillator output and volume of material being heated, a helpful revision of (7) is its solution in terms of the voltage gradient E_g as shown in (8) [7]:

$$E_g = 841\left[\frac{P_c}{fe\sqrt{1-\cos^2 q}\,\cos q}\right]^{1/2} \quad V/in. \tag{8}$$

II. MATERIALS AND METHODS

Radio Frequency (RF) heating in industrial (at 13.56 MHz and 27.12 MHz) is an established technique for processing various materials [1, 2]. Applications range from drying of textiles to moisture leveling of biscuits and from the welding of plastics to the heating of woolen bales.

There are two basic technologies characterized the design of equipment in this industry. Self-excited oscillators operated under class C conditions represent of the equipment operating in industry, while the 50 Ω technology employed a crystal oscillator with subsequent amplification through a vacuum amplifier.

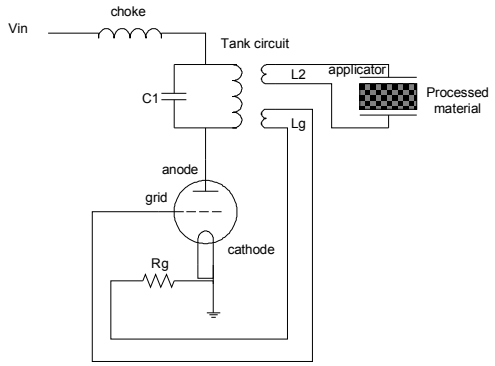

(a) Conventional self-excited oscillators circuit

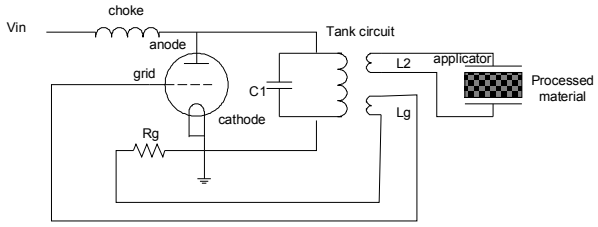

(b) Conventional self-excited oscillators circuit
Figure. 2 Self-excited oscillator circuits

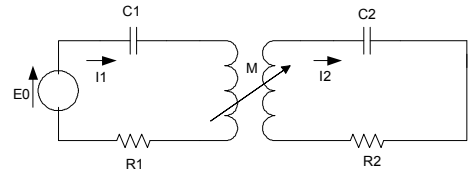

Figure. 3 Equivalent circuit representation of the tank and applicator circuit

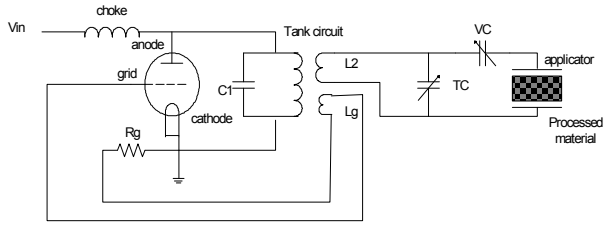

Figure. 4 The proposed self-excited oscillator circuit

This is primarily because of the 50 Ω technology's superior frequency stability. The most commonly arrangement used for dielectric heating installations are the series and shunt fed self-excited tuned anode oscillator circuits as shown in Fig. 2, (a) and (b) respectively. The tank circuits can take the form of either lumped elements as shown in Figure 3 or distributed inductance resonant cavities.

III. Coupling between The Tank and Applicator Circuits

The plate separation of the applicator is varied to enable the applicator and tank circuit resonant frequencies to approach each other so that the state of coupling and matching between the two circuits may be assessed. In this paper only the power coupling efficiency is considered. Therefore the vacuum triode and the associated feedback parts of the circuit can be ignored, reducing the equivalent circuit to that shown in Fig. 3, An ideal sinusoidal voltage source E_0 of frequency $w_0/2p$ excites the coupled resonant circuits. The analysis is carried out for the series tank circuit configuration but a similar treatment would apply to parallel resonant circuits.

The equation (9) and (10) describing the steady-state forced oscillations of the system shown in Fig. 3

$$E_0 = Z_1 I_1 + jMw_0 I_2 \quad (9)$$

$$0 = Z_2 I_2 + jMw_0 I_1 \quad (10)$$

where

$$Z_1 = R_1 + j\left(w_0 L_1 - \frac{1}{w_0 C_1}\right) = R_1 + jX_1 \quad (11)$$

$$Z_2 = R_2 + j\left(w_0 L_2 - \frac{1}{w_0 C_2}\right) = R_2 + jX_2 \quad (12)$$

The suffixes 1 and 2 refer to the tank and applicator circuits, respectively. Solving these equations gives an expression for the primary current I_1

$$I_1 = \frac{E_0}{Z_1 + \frac{M^2 w_0^2}{Z_2}} = \frac{E_0}{Z_{12}} \quad (13)$$

When Z_{12} is the equivalent impedance of the whole system referred to the primary circuit, and is equal to

$$Z_{12} = Z_1 + \frac{M^2 w_0^2}{Z_2} \quad (14)$$

The secondary current is given by

$$I_2 = \frac{-jMw_0 E_0}{Z_1 Z_2 + M^2 w_0^2} = \frac{-jMw_0 E_0}{Z_2 Z_{12}} \quad (15)$$

The circuit is said to be at critical coupling when the following condition is satisfied [14].

$$M^2 w_0^2 = R_1 R_2 \quad (16)$$

At high power level, so it is imperative to ensure that their power transfer efficiency is at its maximum possible value. The input power to the tank circuit is given by

$$P_{in} = \mathrm{Re}\{E_0 I_1^*\} \quad (17)$$

The output power to the load is defined as

$$P_{out} = |I_2|^2 R_2 \quad (18)$$

and the power transfer efficiency h is equal to

$$h = \frac{P_{out}}{P_{in}} = \frac{\left|\frac{Mw_0E_0}{Z_2Z_{12}}\right|^2 R_2}{\mathrm{Re}\{E_0 I_1^*\}} = \frac{1}{1+\frac{R_1\left(R_2^2+X_2^2\right)}{M^2 w_0^2 R_2}} \quad (19)$$

In order to have maximum power transfer efficiency, we need to minimize the following ratio [13].

$$\frac{R_1\left(R_2^2+X_2^2\right)}{M^2 w_0^2 R_2} \quad (20)$$

By differentiating this ratio with respect to w_0 and setting it to zero we obtain the condition for maximum power transfer efficiency as

$$w_0^2 = \frac{w_2^2}{1-\frac{1}{2Q_2^2}} \quad (21)$$

Where w_2 and Q_2 are the angular resonant frequency and Q-factor of the applicator circuit, respectively.

IV. Matching Using The Adjusted by Adjusting Coupling Capacitor

Instead of having a variable inductor inside the generator, our method employed a variable capacitor. This will be series with the load capacitance, given a resultant capacitance which is less than that of the variable one. This resultant capacitance has to tune with the inductance of the coupling coil and the external connecting loads. This method has the advantage that there are no external low loss capacitors which can be damaged, and in principle makes the operation of tuning easier. The test result based on the same mentioned conditions shows that out method can glue two pieces of wood with the same thickness of 0.315 inches with the size of 0.983 inches by 8.66 inches in the time less than 6 seconds. Fig. 5, 6 and 7 shows plate voltage, plate current and grid current of triode tube 7T84RB, respectively. Table I and Table II. The result of gluing wood show that radio frequency heating compared with two hot plate heating.

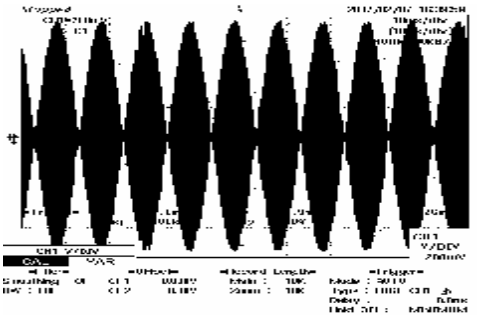

(a) Plate Voltage (V_p)

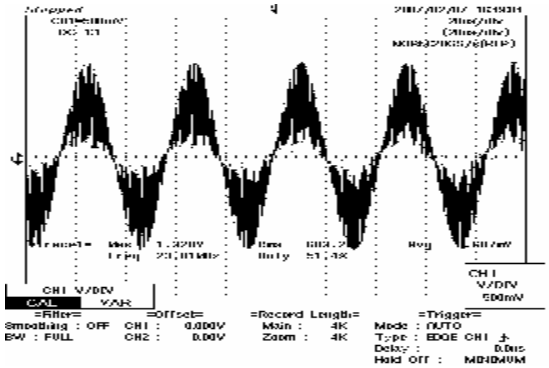

(b) Plate Voltage (V_p)

Figure. 5 Plate Voltage (V_p)

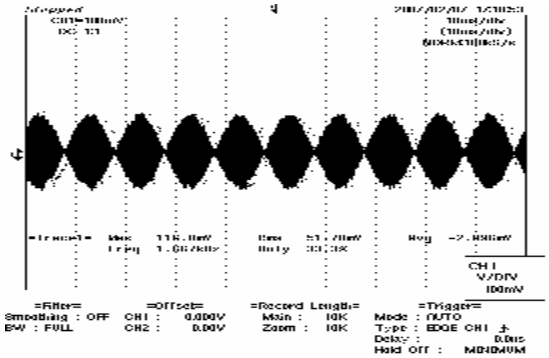

(a) Plate Current (I_p)

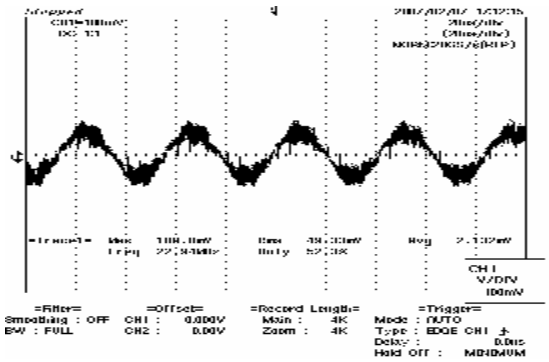

(b) Plate Current (I_p)

Figure.6 Plate Current (I_p)

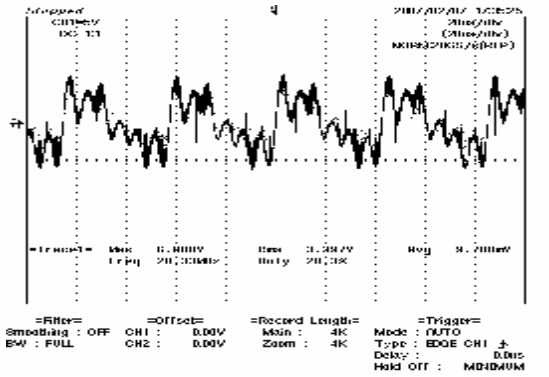

Figure.7 Grid Current (I_g)

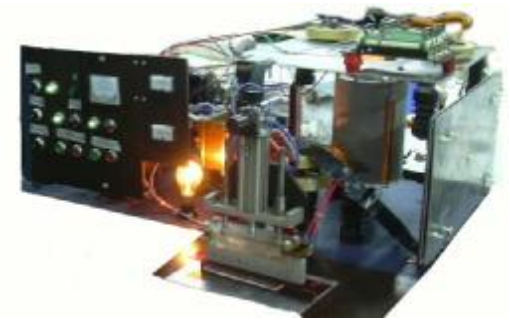

Figure.8 Prototype of Dielectric Heating Machine

Figure.9 Gluing wood processing.

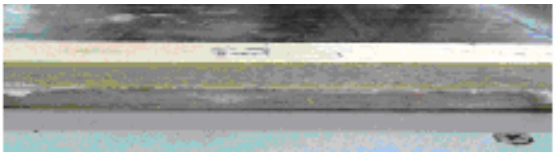

Figure.10 Gluing wood finished.

TABLE I

RESULT OF GLUING WOOD SIZE 0.236 INCHES. 2 PIECES.

Radio Frequency Heating					Two hot plates (2 x 1000 W)	Result
No.	$I_{P(FL)\,(A)}$	I_G (mA)	V_{Load} (V)	Time (per piece)	Time (per piece)	
1-50	0.7	250	1800	6 sec.	3 min.	Glue Completed
51-100	0.8	300	2100	3 sec.		Glue Completed

TABLE II

RESULT OF GLUING WOOD SIZE 0.315 INCHES. 2 PIECES.

Radio Frequency Heating					Two hot plates (2 x 1000 W)	Result
No.	$I_{P(FL)\,(A)}$	I_G (mA)	V_{Load} (V)	Time (per piece)	Time (per piece)	
1-50	0.65	200	1850	11 sec.	4 min.	Glue Completed
51-100	0.75	250	2000	5 sec.		Glue Completed

IV. CONCLUSION

When two hot plates are used, the speed of gluing is determined by the maximum usable plate temperature, that is, the scorch temperature of the wood. It is shown that radio-frequency heating is faster. As the wood section increases in thickness, the argument in favor of radio-frequency heating becomes stronger.

In radio-frequency heating, the central section of the wood is the hottest but for hot-plate gluing the central section is the coolest. Thus if a temperature of say 240 degrees Fahrenheit is needed for gluing in the center of the wood, the remainder of the wood will be at a temperature less than 240 degree, while in two-hot-plate gluing, the remainder of the wood will be at a temperature greater than 240 degrees. Obviously, with lower surface temperatures and shorter heating times, the surface of the wood will not be dried or subjected to surface strains in radio-frequency heating to the extent that occurs in hot-plate heating.

REFERENCES

[1] Neophytou R.I. and A.C. Metaxas, "Computer Simulation of a Radio Frequency Industrial System" ,Journal of Microwave Power and Electromagnetic Energy, vol. 31, pp.251-259, 1996.

[2] Brown, G. H., C. N. Hoyler, "Theory and application of Radio Frequency Heating," D. Van Nostrand Company, Princeton, N.J., 1947.

[3] P. Piyasena and C. Dussault, "Continuous Radio – Frequency Heating of a Model Viscous Solution Influence of a Active Current, Flow Rate, and Salt Content on Temperature Rise," Canadian Biosystem Engineering, vol.45, pp.3.27-3.34, 2003.

[4] Tony Koral, "Radio Frequency Heating and Post-Baking," Biscuit World Issue 4., vol.7, November 2004.

[5] A.C. Metaxas, "The dynamic impedance of radio frequency heating generators," Journal of Microwave Power and Electromagnetic Energy, vol.22, pp.127-136, 1985.

[6] A.C. Metaxas, "Network Analysis on Radio Frequency Prototype Industrial Applicators," Journal of Microwave Power and Electromagnetic Energy, vol.20, pp.197-216, 1985.

[7] H.G.Carlson, "High-frequency Heating," General Electric Company, pp.5-43 - 5-57

[8] R.A. Bierwirth and Cyril N. Hoyler, "Radio – Frequency Heating Applied to Wood Gluing," Proceeding of the Industrial Radio Frequency, pp.529 - 537, October 1943.

[9] A.C. Metaxas and M. Clee, "Coupling and matching of radio frequency industrial applicators," *Power Eng.J.*, vol.22, pp.85 - 93, 1993.

[10] J.-P. Bernard, "A new methodology for the use of radio-frequency in industry," *Microwellen HF Mag.*, vol.15, pp.619 - 620, 1989.

[11] Y. Sun and J.K. Fidler, "Practical consideration of impedance matching network design," in *Proc. 6th Int. Conf. HF Radio Syst. Techn.*, York, U.K., pp.229 - 233, 1994.

[12] A. T. Royley, "The impedance matching of dielectric heating loads to fixed frequency 50 ohm RF generators," Tech. Rep., EA Technol., Chester, U.K., 1992.

[13] Neophytou R.I. and A.C. Metaxas, "Characterisation of radio frequency heating systems in industry using a network analyzer," *IEE Proc.-Sci. Meas. Technol.*, vol. 144, pp.215 - 222, September 1997.

[14] CHAFFEE, E.L., "Theory of thermionic vacuum tubes," McGraw-Hill, chap. 82,1933.

Performance Comparison between Average-Value and Instantaneous-Value Voltage Controls of a Single-Phase AC Chopper

E. Sugprajun and S. Polmai
Department of Electrical Engineering, Faculty of Engineering, King Mongkut's Institute of Technology Ladkrabang
Chalongkrung Road, Ladkrabang, Bangkok 10520, Thailand
E-mail: s8060202@kmitl.ac.th , kpsompob@kmitl.ac.th

***Abstract*-This paper presents experiments and results of two methods for voltage control for a single-phase ac chopper. These methods are average-value voltage control and instantaneous-value voltage control. In average-value control scheme, an instantaneous peak-value of the output voltage is used as the feedback signal and the controller is of the PI type. The instantaneous-value control scheme, previously proposed by the authors, is based on a modified carrier SPWM and instantaneous value voltage and current feedback control system. The purposes of the experiments are to compare the performance of the two methods and to demonstrate the validity of the proposed instantaneous-value voltage control.**

I. INTRODUCTION

Phase controls controlled with thyristors are used for AC power regulation circuits. The output voltage of the circuit is changed by shifting firing angle of the thyristors. As a result, the distortion of the output voltage enlarges, and the circuit requires filters with large capacitance for eliminating the distortion. It also has a disadvantage that the input power factor is low. To overcome these problems, an AC chopper circuit with the pulse-width control is developed. AC chopper has many advantages such as high-quality output voltage with small low-pass filter requirement, fast dynamic response and high input power factor.

In recent works [1], [2], [3], the amplitude of the output voltage is regulated by feedback control of the effective value or instantaneous peak value of the output voltage using PI controller. The controller output, which is a DC signal, is then compared to the sawtooth carrier pulse to make a PWM signal. This method is called here as the average-value voltage control. The advantage of this method is that the control signal is DC so a simple PI controller can be used. Disadvantages of this method are as follows. Owning to the delay in the detection of the effective value or peak value of the output voltage, the feedback controller cannot be designed for fast dynamic response. Otherwise it risks de-stabilizing the closed loop control. Moreover, because the feedback dc signal does not carry the wave-shape quality information of the output voltage, the quality of the output voltage is out of control. When a nonlinear load is connected to the output of the ac chopper, the output voltage becomes distorted.

The author has proposed a novel voltage control for a single-phase ac chopper in [5]. The proposed control method was based on the modified carrier sinusoidal pulse-width modulation and instantaneous value feedback of the output voltage and current signals. This method is called here as the instantaneous-value voltage control. The simulation results confirmed that the proposed method provided very fast dynamic response against both sudden supply voltage and load change. The proposed control method also demonstrated nearly sinusoidal output waveform even under nonlinear load.

In this paper, experiments are carried out on a single-phase ac chopper using both average-value and instantaneous-value voltage controls. The experimental results will be compared to demonstrate the advantages of the proposed instantaneous-value voltage control of the ac chopper. In the following sections the configuration of single-phase ac chopper and methods for voltage control are firstly reviewed. Secondly, the details of the experiment setup are explained. Finally, the experimental results using both control methods are reported and compared.

II. CONFIGURATION OF A SINGLE-PHASE AC CHOPPER

Fig. 1 shows configuration of a single-phase ac chopper for experiments. Typical gate signals of the four switches and the chopped output voltage before filtering are shown in Fig. 2. Let the input supply voltage is defined as follows:

$$v_s = V_m \cos(\omega t), \tag{1}$$

where ω and V_m are the angular frequency and magnitude of the supply voltage, respectively.

The chopped output voltage can be expressed by (2).

$$v_r = DV_m \cos(\omega t) + \sum_{k=1}^{\infty} \frac{V_m \sin kD\pi}{k\pi} \cos(k\omega_s \pm \omega)t, \tag{2}$$

where D and ω_s are the duty ratio and angular switching frequency, respectively. The first term in the right-hand side of (2) is the fundamental component and the second term is the harmonic content distributing around the switching frequency.

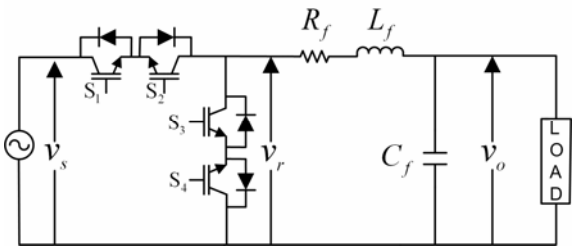

Figure 1. Configuration of a single-phase ac chopper

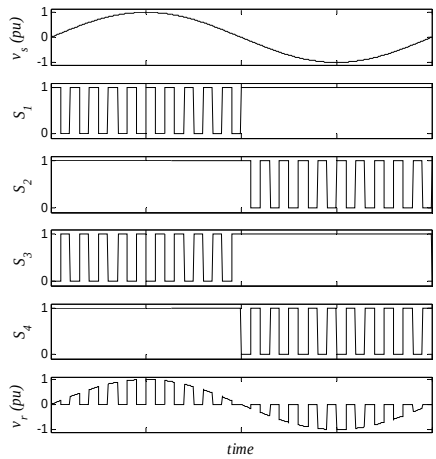

Figure 2. AC chopper waveforms

For a high switching frequency, the harmonic content can be filtered out using appropriated small-size low-pass filter. In steady-state, the filtered output voltage of the ac chopper can be approximately expressed as follows:

$$v_o = DV_m \cos(\omega t - \varphi_1), \tag{3}$$

where φ_1 denotes the fundamental phase delay due to the low-pass filter.

As a result of (3), the amplitude of the output voltage is linearly controlled by the duty ratio of the PWM signal.

III. Controlling of The Output Voltage

A. *Average Value Control Method*

Fig.3 illustrates block diagram for average-value control of the ac chopper. The instantaneous peak value of the output voltage is used as the feedback signal. Calculation of the instantaneous peak value is performed by phase-shifter and multiplier as shown in Fig. 4. The source of the delay of the feedback signal comes from the phase-shifter circuit. The output of the PI controller is used as the modulated signal for the comparator to generate PWM signal.

B. *Instantaneous Value Control Method*

The instantaneous-value voltage control is based on the modified carrier sinusoidal pulse width modulation and

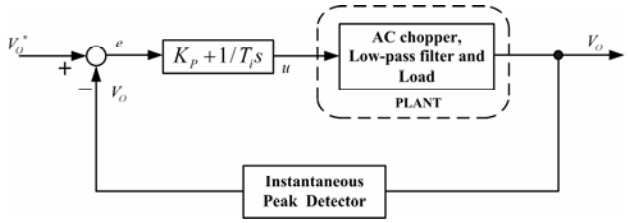

Figure 3. Block diagram for average-value control

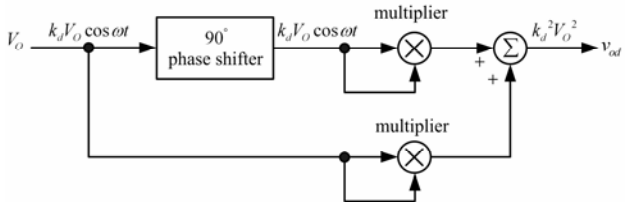

Figure 4. Instantaneous peak detector

instantaneous value feedback of the output voltage and current signals. The modification of the sinusoidal pulsewidth modulator is made at the sawthoot carrier signal generaion. The carrier signal will have its amplitude varying with the instantaneous value of the supply voltage. Fig. 5 illustrates a simplified schematic diagram of the sawtooth carrier pulse generator. This circuit uses a non-inverting integrator in stead of an inverting integrator as in the previously proposed circuit [4], however the principle of operation is the same. The absolute-value of the supply voltage signal is used as the input of the integrator circuit. If the supply voltage is defined by (1), it can be shown as in (4) that the output voltage at t_1+T instant is equal to the amplitude of the supply voltage at t_1+T /2 instant.

$$v_c(t_1 + T) = V_m \cos\omega(t_1 + T/2), \tag{4}$$

where, T is the period of the sawtooth signal. From (4), the amplitude of the sawtooth pulse varies with the amplitude of the T/2-second delayed supply voltage. Because the magnitude of the sawtooth pulse is very low around the zero-crossing of the supply voltage, this could lead to fully-on of the switches and makes it unable to control the output voltage around the zero crossing of the supply voltage. To correct this, small dc voltage is added to the integrator input to increase the slope of the triangle pulse around zero-crossing. The advantage of this circuit is that the output voltage is independent of the supply voltage as long as the duty ratio is less than a unit.

The block diagram of the feedback control of the output voltage is shown in Fig. 6. The plant model of the ac chopper is devired using the state-variable average model method described in [5], where the output current is model as external disturbance. In Fig. 6 the effect of output current is rejected by the feedback of the signal u_{fd} derived from output current. If the parameters of the model match with those of the actual plant the closed loop transfer function of the system becomes

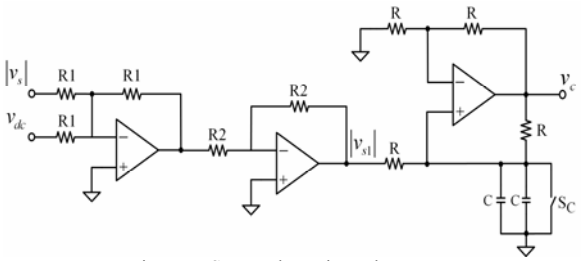

Figure 5. Sawtooth carrier pulse generator

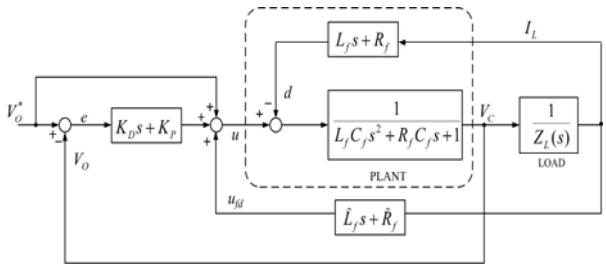

Figure 6. Block diagram for the control system of the output voltage.

$$\frac{V_o(s)}{V_o^*(s)} = \frac{K_D s + K_P + 1}{L_f C_f s^2 + \left(K_D + R_f C_f\right) s + K_P + 1}, \quad (5)$$

where K_D and K_P are the derivative and proportional gain of the PD controller, respectively.

The poles of the closed-loop control system are

$$s_{1,2} = -\zeta\omega_n \pm j\omega_n\sqrt{1-\zeta^2}, \quad (6)$$

where

$$\omega_n = \sqrt{(K_p + 1)/(L_f C_f)}, \quad (7)$$

and

$$\zeta = \frac{1}{2}\left(K_D + R_f C_f\right)\Big/\sqrt{\left(K_P + 1\right) L_f C_f} \quad (8)$$

are the natural frequency and damping factor of the closed-loop system, respectively.

The desired closed-loop control characteristics can be specified by properly selecting the gains K_D and K_P. The absolute value of the controller u and the modified carrier signal v_c is used as the inputs for the comparator to generate PWM signal.

IV. Experimental Results

The experiments have been carried out on the follwing topics; the step response of the referrence signal, the effect of nonlinear load and the effect of sudden supply voltage changes. Both average-value and instantaneous-value voltage control are applied for comparison. The details of the experiment parameters are summarized in Table I.

TABLE I
IMPORTANT PARAMETERS FOR EXPERIMENTS

AC chopper	
Supply voltage	220 V, 50 Hz
Switching frequency	20 kHz
Load-side low-pass filter	
L_f	500 μH
R_f	0.05 Ω
C_f	5 μF
Supply-side filter	
C_s	16 μF
Controller parameters	
K_D	0.00005
K_P	3.6
Conventional PI controller	
K_i	0.005
K_P	0.2
Nonlinear load (Diode rectifier with dc reactor)	
Filter capacitor	2600 μF
Load resistance	18 Ω
DC reactor	15 mH
IGBT	
S1-S4	G20N60B3D, 600V 40A

A. *Step response*

Fig. 7 illustrates the step responses of the ac chopper using the average-value voltage control, Fig. 7(a), and the proposed instantaneous value voltage control, Fig. 7(b), respectively. In the case of instantaneous voltage control the output voltage track in referrence voltage precisely and exhibit only small overshoot while in the case of average value control large overshoot appears at the output voltage.

B. *Effect of nonlinear load*

Fig. 8 illustrates the effect of nonlinear load using both control methods. The output voltage is nearly a sinusoidal wave in the case of the intantaneous value control and it is distorted by the nonlineality of the output current under average value control.

C. *Effect of supply voltage variation*

Fig. 9 shows the results when the supply voltage dipped from 100% to 70%. With the instantaneous value control, the output voltage remained unaltered while with the average value control the output voltage dipped at first and then climbed to the reference value as time passed. Also a large overshoot of the output voltage is observed at the end of voltage dip in the case of average value control.

V. Conclusion

The experiments on average-value and instantaneous-value voltage control of a single-phase ac chopper have been carried out. The purpose of the experiments is to compare the performance of both control schemes. The comparison focus on the four topics including step response, effect of nonlinear load and effect of supply voltage variations. From the experimental results, the proposed instantaneous value voltage control provides improved dynamic response, robustness to the supply variation and less sensitivity to the nonlinear load.

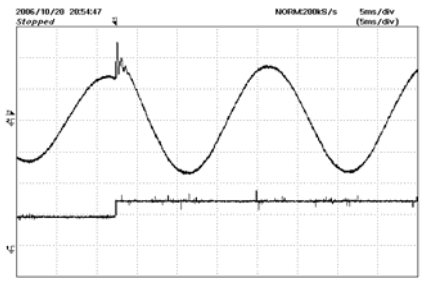

(a) In case of average value control (output voltage, upper trace, 100V/div; reference voltage, lower trace, 5V/div)

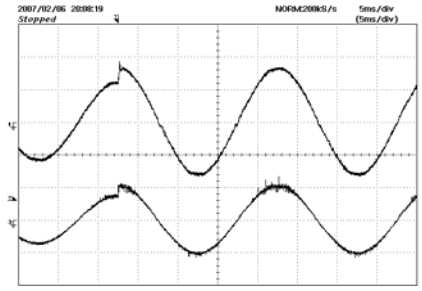

(b) In case of Instantaneous value control (output voltage upper trace, 100V/div; reference voltage, lower trace, 5V/div)

Figure 7. Step response of the ac chopper

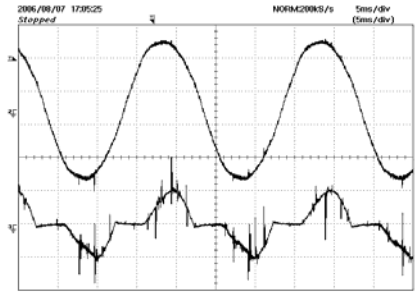

(a) In case of average value control (output voltage: upper trace, 100V/div; load current: lower trace, 1A/div)

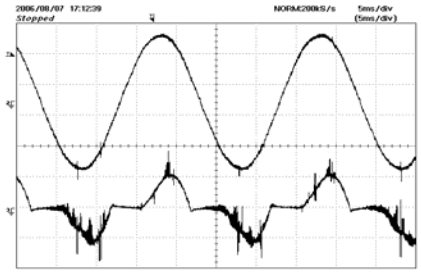

(b). In case of Instantaneous value control (output voltage: upper trace, 100V/div; load current: lower trace, 1A/div)

Figure 8. Effect of nonlinear load

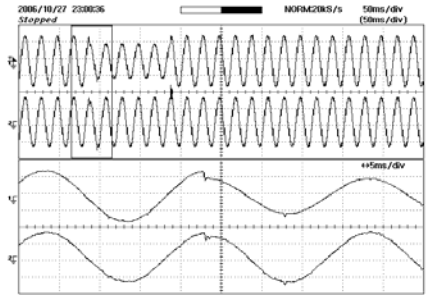

(a) In case of average value control (supply voltage: upper trace, 200V/div; output voltage: lower trace, 100V/div)

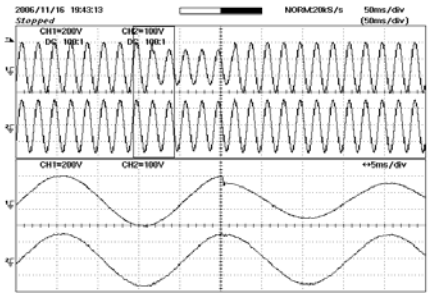

(b).In case of Instantaneous value control (supply voltage: upper trace, 200V/div; output voltage: lower trace, 100V/div)

Figure 9. Effect of supply voltage variation

REFERENCES

[1] B.D. Min and B.H. Kwon, "Novel PWM line conditioner with fast output voltage control", *IEE Proc. Electr. Power Appl.*, Vol. 145, No. 2, March (1998)

[2] H Kwon, G Y Jeong, S H Han, and D H Lee, "Novel line conditioner with voltage up/down capability", *IEEE Trans. Ind .Electron*, vol. 49, pp 1100-1119, October 2002

[3] B.H. Wong, J. H. Youm, and J. H. Choi. "Automatic voltage regulator with fast dynamic speed", *IEE Proc. Electr. Power Appl.*, Vol. 6, No. 2, March (1999)

[4] S. Polmai, "Instantaneous-value voltage control of a single-phase AC chopper", *Proc. International Power Electronics Conference, IPEC-Niigata 2005*, vol. 49, No. 4, (CD-ROM) April 4 – 8, 2005

[5] Andre S. Kislovski, Richard Redl, Nathan O. Sokal, "Dynamic Analysis of Switching-Mode DC/DC Converters", Van Nostarnd Reinhold, NY, 1991

[6] Josep M. Guerrero, Luis Garcia de Vicuna, Jaume Miret, and Jose Matas. "A nonlinear feed-forward control technique for single-phase UPS inverters", *Proc. the IEEE Conference IECON 02*, Vol. 1, pp. 257-261 (2002)

[7] M.J. Ryan; W.E. Brumsickle, and R.D. Lorenz. "Control topology options for single-phase UPS inverters", *IEEE Trans. Industry Applications*, Vol. 33, No. 2, March-April (1997)

Power Electronics-Based Fuel Cell Emulator

Siriroj Sirisukprasert and Trin Saengsuwan
The Department of Electrical Engineering
The Faculty of Engineering, Kasetsart University
50 Phaholyothin Rd., Ladyao, Jatujak
Bangkok, Thailand, 10900.

***Abstract*- This paper proposes a fuel cell emulator used to replace a real fuel cell system during the development stage of a fuel-cell inverter system. The power stage of this new fuel cell emulator consists of a current source converter (buck rectifier) and a dc-to-dc buck converter. With the collaboration of these two power electronics circuits and the controller, the proposed fuel cell emulator provides both an emulated fuel cell response and the high-quality output voltage and current. This research mainly focuses on emulating the behavior of two well-known types of fuel cell systems: Proton Exchange Membrane Fuel Cell (PEMFC) and Solid Oxide Fuel Cells (SOFC). The suggested fuel cell emulator can effectively perform in all three operation regions, i.e. activation, ohmic and concentration. Analysis, modeling and control strategy are presented. The performance of the proposed fuel cell emulation is finally verified by simulation results.**

***Index Terms* – Fuel Cell Simulator, Fuel Cell Inverter.**

I. INTRODUCTION

Today, fuel cell is one of the most promising renewable power sources due to its cleanness, high power density and low emission. Fuel cells can be used as a source of renewable power including transport, portable and residential applications. In addition, the standalone aspect of distributed resource technology makes fuel cells particularly useful in areas not served by a national power grid or where the national grid is unreliable and backup power is required.

Six main types of fuel cells are alkaline, direct methanol, molten carbonate, phosphoric acid, proton exchange membrane (PEM) and solid oxide (SO). Each type has its own advantages for different applications. For example, the most popular fuel cell type for automotive is PEM fuel cell. While, the SO fuel cell is suitable for stationary power source.

The output DC voltage profile of fuel cells depends on the amount of load current and the fuel flow rate. The power conditioning, therefore, is necessary. In general, a fuel cell power supply system consists of a fuel cell stack, a fuel supply system, a power electronic-based inverter and a master controller. The total system performance of the fuel cell system mainly relies on the characteristics of the inverter and a great response of the master controller. Thus, a fine tune process for the system is essential. Moreover, the major cost of the development period of a fuel cell system is the fuel cell stack. Therefore, the objective of this research is to develop a voltage source such that it can properly and efficiently replace a real fuel cell system during this period.

Several attempts to emulate electrical characteristic of fuel cells have been previously made. However, there are some disadvantages. The voltage of the DC link of circuit in [1] is quite high relatively to the output voltage, which can be varied from 20 V to 50 V. This means that the duty cycle for the buck converter is in the range of 0.06 to 0.16. Practically, such low duty cycle lowers the entire system efficiency and introduces an electromagnetic interference problem. In contrast, [2] applied basic electronics components such as bipolar junction transistors, diode and other passive components. The advantage of this kind of circuit is its simplicity. However, the drawback is that the system is inflexible. The circuit must be redesigned when types of fuel cell or operating points are changed. In [3], the system provides very precise fuel cell character. It can be used for various kinds of fuel cell. Nevertheless, the system implementation is somewhat questionable.

This research, therefore, proposes a fuel cell emulator that solves the previous problems. The main advantages of the proposed system are flexibility to provide a wide range of operating point, high efficiency and simplicity in both control stage and power stage.

II. FUEL CELL ELECTRICAL CHARACTERISTICS

To explain the basic characteristics of fuel cells, PEM fuel cell is used as an example. PEM fuel cells basically combine oxygen and hydrogen over a platinum catalyst to produce electrochemical energy. Byproducts of this process are heat and water, which make the fuel cell a clean source. Dash line in Fig. 1 shows the actual voltage-current characteristic of a single cell operating at room temperature and normal air pressure [4]. The variation of voltage for an individual cell is derived from the maximum cell voltage (sometimes called EMF) and the different voltage loss states. Various factors play an important role to the voltage drop in an actual fuel cell that causes the cell voltage to be less than the no load voltage (ideal potential). These losses, which are also called overvoltage, polarization and irreversibility, originate primarily from three sources: a) activation polarization, b) ohmic polarization, and c) concentration (mass transport) polarization.

By using PEM fuel cell as an example, at a given temperature with partial pressure of the reactants and products known, the ideal voltage or no load potential is the maximum voltage that each cell in the stack can produce. For the PEM fuel cell, in general, its ideal terminal voltage can be calculated based on Gibbs free energy, and it is approximately 1.2 V at 25°C, where pure hydrogen and air are used.

This research is supported by The Thailand Research Fund and Commission on Higher Education. Grand no. MRG48-Siriroj Sirisukprasert

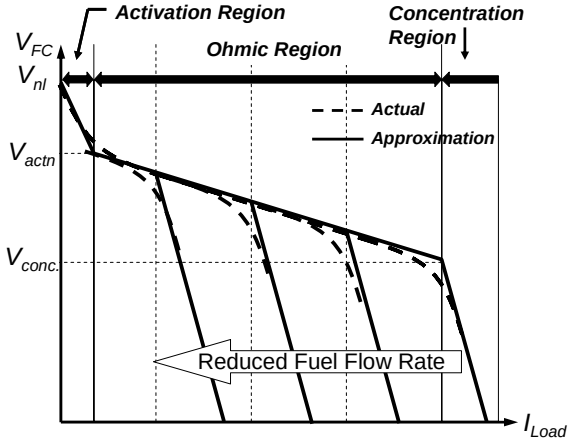

Figure 1. Voltage-Current relationship of PEM fuel cell.

The activation polarization loss is present when the rate of the electrochemical reaction at an electrode surface is controlled by sluggish electrode kinetics. It is dominant at low current density. The higher load current is, the higher activation loss.

With the parasitic resistance of the polymer electrolyte membrane to the ions and the imperfect electrodes, the ohmic polarization loss is present. In this region, the fuel cell terminal voltage linearly decreases with the increasing load.

Concentration polarization (mass transportation) loss relates to the changes in the reactants concentration at the surface area of the electrodes as the fuel is being used. The concentration of the oxidant and the fuel is decreased at various points in the fuel-cell gas channels and is less than the concentration at the inlet value of the stack. This loss becomes significant at higher load currents when the fuel and the oxidant are used at higher rates, while the concentration in the gas channel is a minimum.

The proposed fuel cell emulator follows the actual behavior of a fuel cell by the approximated characteristic (solid line) in Fig. 1. In other words, the proposed system used the solid linear line as a control objective.

III. The Proposed System

The proposed fuel cell emulator system is based on the power electronics technology. The system consists of two main parts: power stage and control stage. As shown in Fig. 2, the power stage receives AC input and then generates a DC output, which can follow the V-I characteristic of fuel cells.

The power stage can be divided into two parts: 1) a three-phase buck rectifier or a three-phase current source inverter (CSI) and 2) a buck converter or a step-down dc-to-dc converter. The three-phase CSI was selected as the input stage of the proposed system because of its high power capability and small ripple DC link. Therefore, a smaller DC link capacitor can be employed. In comparison, a three-phase system can supply three times as much of maximum power and generates three times as less voltage ripple as a single-phase does.

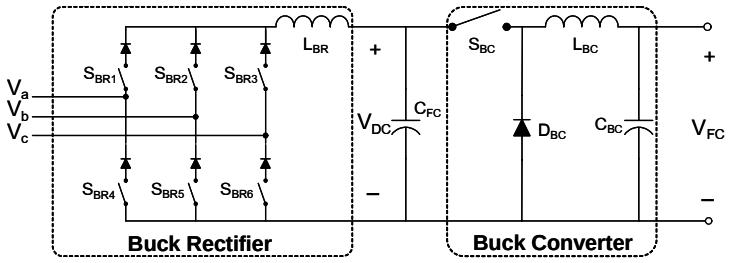

Figure 2. Power stage of the proposed system.

The front end of the proposed power stage is a three-phase buck rectifier. Buck rectifiers converse the three-phase AC voltage to the adjustable DC voltage, which can be varied from 0 V to $0.866 \cdot V_p$, where V_p is peak of the AC input line voltage. Usually, the DC link voltage in this application is set to no-load terminal voltage of fuel cell stack. This buck rectifier comprises 6 main switches (S_{BR1} to S_{BR6}) and 6 series diodes. L_{BR} and C_{FC} are used as a low-pass filter. Main function of the buck rectifier is to emulate the V-I characteristic of fuel cell when flow rate and pressure of fuel (Hydrogen, for example) are changed as shown in Fig 1. The concentration region is where the buck rectifier takes the action. The dynamic characteristic of the output voltage and current can also be emulated by the buck rectifier. Moreover, the very low duty cycle problem in [1] can be solved by using a stepped-down DC link in this stage.

The output end of the power stage for the proposed fuel cell emulator is a buck converter. The function of the buck converter in this system is to generate the output DC voltage consistent with the V-I relationship of a fuel cell stack. The buck converter mainly takes action in both activation and ohmic regions. The buck converter is composed of a main switch, S_{BC}, and free-wheeling diode, D_{BC}. L_{BC} and C_{BC} are used as a low-pass filter.

IV. Power Stage Modeling and Controller Design

The block diagram of the main controller of the proposed system is shown in Fig. 3. At the front end, two line-to-line input voltages are sensed for control synchronization. To control the output DC voltage, the output voltage, V_{FC}, and the output current, i_{Load}, are measured.

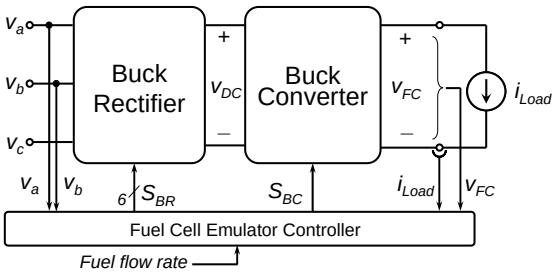

Figure 3. Power stage of the proposed system.

A user command for this system is fuel flow rate, which is a main command of the buck rectifier. The outputs of the controller are switching signals for six switches of the buck rectifier and the switch of the buck converter.

A. Power Stage Modeling

Due to the large output voltage and current variation, the open-loop control is employed for the buck converter. However, to regulate V_{FC}, a closed-loop control on the buck rectifier is used to complete this task instead.

To design the feedback control, the first step is developing a small signal model for the buck rectifier. The following steps are the technique used in this research: 1) developing a switching model 2) developing an average model in abc-coordinates 3) developing an average model in dq0-coordinates and 4) developing a small-signal model in dq0-coordinates. In the dq0 space, the power stage can then be controlled by using the classical linear control theory.

To further simplify the front end controller, the voltage vector in the abc space is arranged to inline with D axis as shown in Fig. 4. By doing so, quadrature components are eliminated. Fig. 5 shows an average model of the proposed power stage. From the average model, the following relationship can be derived:

$$V_{DC} = d_d \cdot V_d. \quad (1)$$

This means that the DC link can be adjusted by varying the direct duty cycle, d_d. From Fig. 5 and (1), the steady-stage transfer function of the proposed power stage is as follows:

$$V_{FC} = d_{BC} \cdot d_d \cdot V_d. \quad (2)$$

B. Controller Design

As shown in Fig. 6, the proposed controller can be divided into 2 parts, i.e. buck converter controller and buck rectifier controller. The controller for buck rectifier is designed in such a way that its control response is much slower than the buck converter.

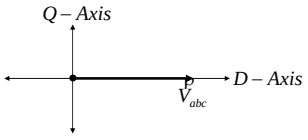

Figure 4. Voltage vector in abc space inline with D axis .

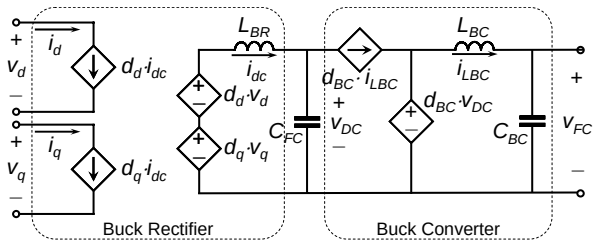

Figure 5. Average model of the proposed power stage.

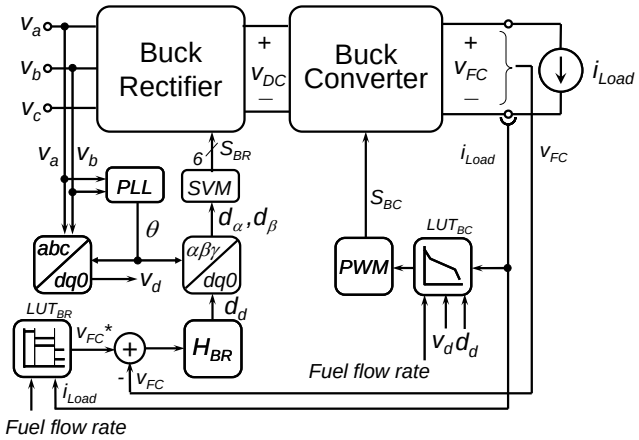

Figure 6. Block diagram of the proposed controller.

The buck converter is working mostly in activation and ohmic regions, while the buck rectifier is working in the concentration region. In the activation and ohmic regions, the duty cycle d_d is kept constant. To avoid control interference between these two loops, the duty cycle d_{BC} maintains unchanged during the concentration region.

As mentioned previously, the buck converter is open-loop controlled. The current, i_{Load}, V_d, d_d and the fuel flow rate command are fed into a look up table, LUT_{BC}. Without the DC link voltage sensor, the DC link can be approximated by multiplying V_d by d_d. The output of LUT_{BC} that is the duty cycle for the buck converter is fed into the pulse width modulation (PWM) to generate the switching signal for the main switch. The estimated technique used in the proposed system is shown by the solid line in Fig. 1. LUT_{BC} contains two linear lines, i.e., one for the activation region and the other one for the ohmic region. In most of fuel cell stacks, the slope of the output voltage in the activation region is higher than that in the ohmic region. As shown in Fig.1, the slope for the activation region can be derived from V_{nl} and V_{actn}, while the slope for ohmic region can be derived from V_{actn} and V_{conc}. The relationship of the voltage and the current in LUT_{BC} depends on the electrochemical characteristics of various fuel cells. Due to the open-loop control, the voltage drop is taken into account and is compensated in LUT_{BC}.

By utilizing dq0 control, two input phase voltages (V_a and V_b) are used as a three-phase synchronous signal. The phase lock loop (PLL) mathematically generates the angle of the input voltage vector, which is used in abc-to-dq0 transformation. Another look up table applied in this control loop is LUT_{BR}. The fuel flow rate command and the load current are the inputs of this look up table. The output of LUT_{BR} is the output voltage command, V_{FC}*. The output voltage command is compared with the feedback output voltage command and the error is compensated by a PI controller (H_{BR}). Later, the command duty cycle, d_d, is derived. By using the inversed transformation matrix, d_d is converted to d_α and d_β. The 0-channel components are all omitted based on the assumption of the balanced three-phase system. The d_a, d_b

and d_c are derived by using a space vector modulation (SVM) for the current source converter.

V. Simulation Results

To verify the performance of the proposed system, the power stage and the controller (shown in Fig. 6) are simulated by a personal computer. The main simulation parameters are shown in table 1. The load is a current source with 2A increment. Voltage-current characteristics used in the simulation are adapted from [3]. The reference V-I characteristic is typical for PEM fuel cells. Four data sets used in the simulation are for the fuel flow rates of 25%, 50%, 75% and 100%. For 100% fuel flow rate, the fuel cell emulator terminal voltage at no load is about 55 V and is about 22 V at full load.

The switching frequency of the buck converter is 30 kHz, which is about three times higher than that of the buck rectifier. To assure the performance of the controller, the bandwidth of control loop for the buck rectifier is about 1 kHz.

TABLE I
Simulation parameters

Parameters	Value
Power Stage	
- Buck rectifier switching frequency	10 kHz
- Buck converter switching frequency	30 kHz
- Input voltage	220 V - 3Φ
Fuel Cell Stack	
- Type of fuel cell stack	PEM
- Maximum power	1.5 kW
- Fuel flow rate (%)	25, 50, 75, 100
- Terminal voltage range	22 V to 55 V
- V-I characteristic	Reference [3]

The simulation results for the fuel flow rates of 25%, 50%, 75% and 100% are shown in Fig.7 to Fig.10, respectively.

VI. Conclusions

The proposed fuel cell emulator is used to replace a real fuel cell system during the development stage of a fuel-cell inverter system. The main advantages of the proposed system are flexibility to provide a wide range of fuel cell characteristics, high efficiency and simplicity in both control stage and power stage. The performance of the proposed fuel cell emulation is finally verified by simulation results. The simulated V-I characteristic is acceptably consistent with the reference characteristics. Now, the prototype of the proposed system is designed and implemented. The complete experimental results will be presented in the next paper.

Acknowledgment

The authors would like to thank Professor Alex Q. Huang at North Carolina State University, USA, for donating the gate driver, Professor Jason Lai at Virginia Tech, USA, for his comments. Thanks to Mr.Wattana Samanjit and Mr.Manoon Boonpramook, EE graduate students at Kasetsart University, Thailand, for their contribution in this research.

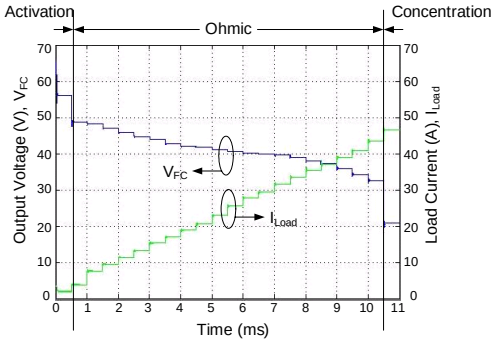

Figure 7. V_{FC} as a function of load current at 100% fuel flow rate.

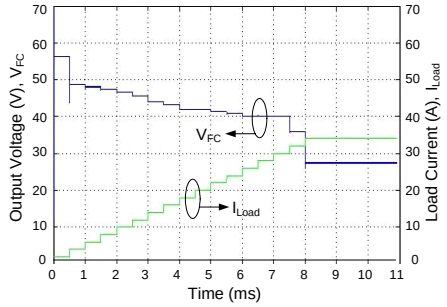

Figure 8. V_{FC} as a function of load current at 75% fuel flow rate.

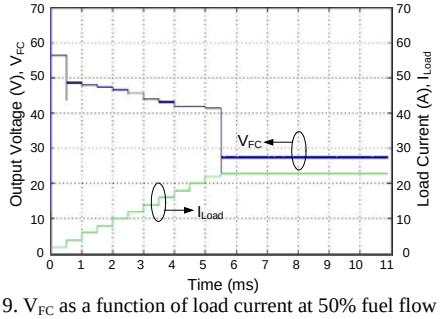

Figure 9. V_{FC} as a function of load current at 50% fuel flow rate.

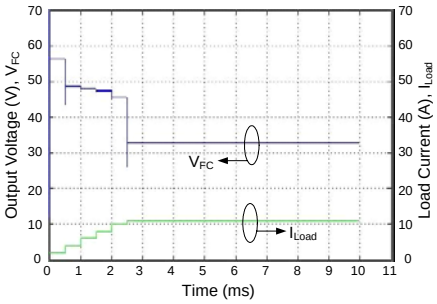

Figure 10. V_{FC} as a function of load current at 25% fuel flow rate.

References

[1] T. W. Lee, S. H. Kim, Y. H. Yoon, S. J. Jang, C. Y. Won, "A 3 kW fuel cell generation system using the fuel cell simulator," in *Proc. IEEE International Symposium on Industrial Electronics*, vol. 2, pp. 833 – 837, 2004.

[2] S. Yuvarajan, Y. Dachuan, "Characteristics and modelling of PEM fuel cells," in *Proc. International Symposium on Circuits and Systems*, vol.5, pp. 880-883m, 2004.

[3] P. Famouri, R. S. Gemmen, "Electrochemical circuit model of a PEM fuel cell," in *Proc. IEEE Power Engineering Society General Meeting*, vol. 3, pp. 1436-1440, 2003.

[4] National Energy Technology Laboratory, "Fuel Cell Hand Book (6th Edition)", Nov. 2002.

The Comparative Study and Design Guidelines of a High Frequency Transformer for Improving Cross Regulation in Multiple-Output Flyback Converters

Pairote Sangampai[1],Kusumal Chalermyanont[2], Anuwat Prasertsit[3], Surapon Theinmontri [4]
Prince of Songkla University, Faculty of Engineering , Thailand
email: Eng_road@hotmail.com, kusumal.c@psu.ac.th, anuwat.p@psu.ac.th, surapon.t@psu.ac.th

Abstract - **The cross regulation in multiple-output flyback converters is affected by leakage inductances of the transformer. The suitable winding arrangements of the transformer will lead to the improved cross regulation. This paper presents the comparative study of the four different winding arrangements in the four winding flyback transformer. The cross regulation model is considered in a form of the resistance matrix that is related to the leakage inductance parameters. The design guidelines for the transformer for improving cross regulation are given based on the experimental results.**

Keywords : Cross regulation , Flyback converters , Leakage inductance

I. Introduction

The multiple-output switching converter is generally used in low power applications for electronic equipments that need different levels of output voltages such as a computer. One of the most favorite used configurations is a multiple-output flyback converter, due to its low component counted, cost-effective structure, and large dynamic range.

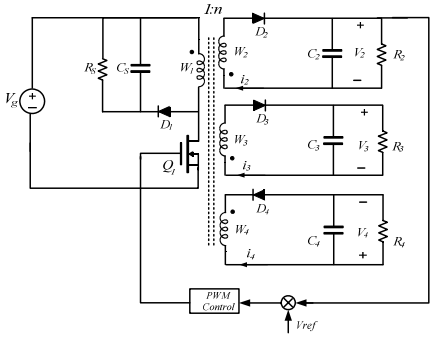

Fig. 1 The Experimental three output flyback converters

Typically, as shown in Fig. 1, the main output voltage of the converter is directly sensed by the feedback network and regulated to the desired value. The auxiliary outputs are not directly regulated, but are fixed with respect to the principle output voltage by the coupling between the transformer windings, which is called cross regulation. The cross regulation analytical models and the methods for improving cross regulation in multiple-output converters are proposed in many forms [2, 3, 4 and 5]. However, it still lacks general sense because they are only considered for one simple magnetics structure. In [6], it presents the effects of several different magnetics structures of the high frequency transformers on cross regulation. It shows that the different magnetic structure of a transformer hardly affects on cross regulation in a multiple-output flyback converter.

In this paper, we present a comparative study and design guidelines of a high frequency transformer to improve cross regulation of a multiple output flyback converter. The winding arrangements are reasonably performed in order to control leakage inductance in such a way to improve cross regulation. The experiments results are illustrated and the transformer design guidelines are concluded to be simple rules to improve cross regulation in multiple-output flyback converter.

II. Analytical model of cross regulation in a multiple flyback converter

a. The Extended Cantilever Model

The behaviors of a multiwinding high frequency transformer can be analyzed using the cantilever model as shown in Fig.2.

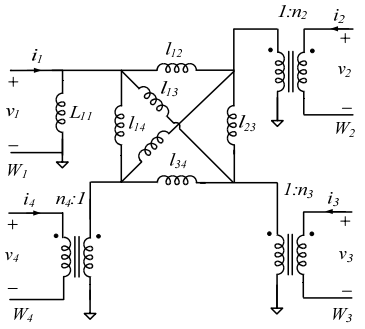

Fig. 2 The Extended cantilever model of four winding Transformer

The extended cantilever model contains *n(n+1)/2* independent parameters including leakage inductance parameters. L_{11} is a self-inductance and l_{jk} is a leakage inductance between winding j[th] and k[th]. All parameters can be directly measured by using a two port technique. For example the effective turn ratio is equal to

$$n_k = \frac{v_k}{v_1} \tag{1}$$

Additionally, the value of leakage inductance parameter l_{jk} is obtained by driving winding W_j with voltage source V_j with all other winding are short-circuited. The current i_k in

winding W_k is measured. The effective leakage inductance l_{jk} is given by

$$l_{jk} = \frac{v_j(s)}{s n_j n_k i_k(s)} \qquad (2)$$

b. The N-port Model

The extended cantilever model is also closely related to *N*-port description of the transformer. The *N*-port model is useful in computer simulation and simple analysis of the multiple-output flyback converter. The primary winding of the *N*-port is modeled as a current controlled Norton equivalent network as illustrated in Fig. 3. The inductance of this port is the primary self-inductance L_{11}. The current controlled current source (CCCS) is equal to the sum of the secondary winding currents. The secondary windings are modeled as voltage controlled Thevenin equivalent networks. Equation (3) is the expression of a series inductance of winding *k*, L_{ok}, which is equal to effective leakage inductance connected to winding *k* as

$$L_{ok} = n_k^2 \left(l_{1k} \| l_{2k} \| \ldots \| l_{(k+1)k} \| l_{(k+1)k} \| \ldots \| l_{Nk} \right) \qquad (3)$$

and the voltage controlled voltage source is given by

$$V_{Tk} = \frac{L_{ok}}{n_k l_{1k}} v_1 + \frac{L_{ok}}{n_1 n_2 l_{2k}} v_2 + \ldots + \frac{L_{ok}}{n_k n_{k-1}} v_{k-1} + \frac{L_{ok}}{n_k n_{k+1} l_{(k+1)k}} v_{k+1} + \ldots + \frac{L_{ok}}{n_k n_N l_{Nk}} v_N \qquad (4)$$

The analysis of the multiple-output flyback converter using the *N*-port model shows that the rate change of the secondary output current i_k is given by

$$\frac{di_k}{dt} = \frac{1}{n_k l_{1k}} v_1 + \frac{1}{n_k n_{k+1} l_{k(k+1)}} v_{k+1} + \ldots + \frac{1}{n_k n_N l_{kN}} v_N - \frac{1}{L_{ok}} v_k \qquad (5)$$

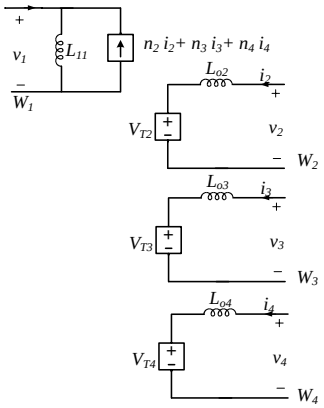

Fig. 3 The four type N-port model

For example, Eq. (6) expresses the rate change of a secondary output current in winding 2 in terms of leakage inductances in the extended cantilever model by

$$\frac{di_2}{dt} = \frac{1}{n_2 l_{12}} v_1 - \frac{1}{L_{o2}} v_2 + \frac{1}{n_2 n_3 l_{23}} v_3 + \frac{1}{n_2 n_3 l_{24}} v_4 \qquad (6)$$

III. The winding arrangements of the high frequency transformers

a. Winding arrangement designs of high frequency transformers

The leakage inductances in the high frequency transformer play important role in the multiple-output flyback converter. Therefore, the control of values of the specific leakage inductances can improve the cross regulation in the converter. As we know, the value of leakage inductance depends on the winding arrangement in the core. Changing position of the winding will change the value of the effective leakage inductance. In this section, the four different top-to-bottom winding arrangements of the four-winding transformer are constructed with the ferrite core of ETD49/25/16 and foil copper winding 1.5 mm thickness as shown in fig. 4(a) - 4(d). The specification input voltage of the converter is 40V. The main output voltage of 5V, and auxiliary output voltage of 12V and -12V. The switching frequency is 100 kHz and a duty ratio of 0.5.

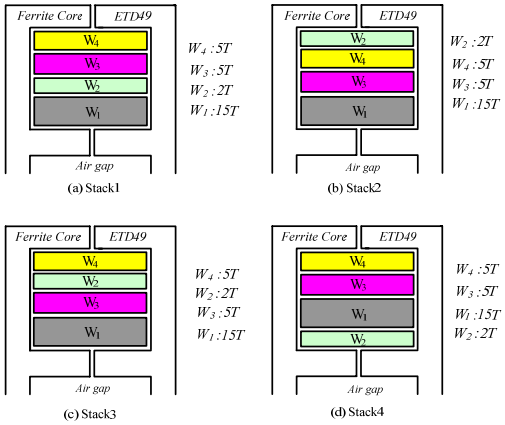

Fig. 4 Experimental winding geometries in flyback transformer

Fig. 5 Experimental high frequency transformers

b. Measurement of Leakage Inductances

Measured leakage inductance values of four winding arrangements are shown in Table 1 using the method mentioned previously. Secondary output current waveforms of the experimental transformers with the main output current I_2 of 3A and auxiliary output currents I_3 and I_4 of 1A are shown in Fig. 6 -9. The slopes of the main output current of

experimental transformers are all positive while the slopes of the auxiliary output currents are all negative.

Table1. Summary of flyback transformer parameter measurements

Inductance parameter	Measure values			
	Stack1	Stack2	Stack3	Stack4
n_2	0.15	0.13	0.15	0.15
n_3	0.3	0.3	0.3	0.3
n_4	0.3	0.3	0.3	0.3
L_{11}	296 μH	312μH	290 μH	294 μH
l_{12}	12 μH	143 μH	64 μH	6 μH
l_{13}	5 μH	3.3 μH	3.2 μH	3 μH
l_{14}	18 μH	11.3μH	16.7μH	9.6 μH
l_{23}	13 μH	35 μH	11 μH	59 μH
l_{24}	37 μH	10.6 μH	12.4 μH	82 μH
l_{34}	3 μH	2.8 μH	6 μH	3 μH

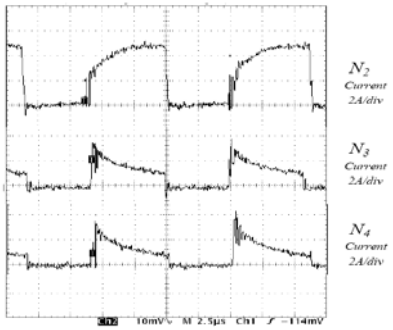

Fig. 6 Experimental waveforms in the high frequency transformer : Stack1 model

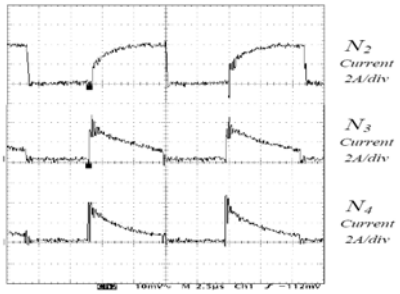

Fig. 7 Experimental waveforms in the high frequency transformer : Stack2 model

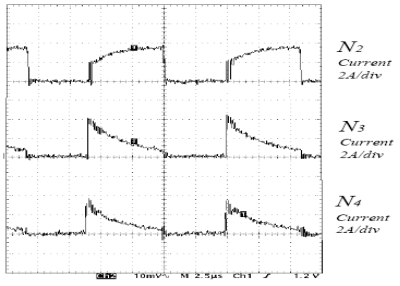

Fig. 8 Experimental waveforms in the high frequency transformer : Stack3 model

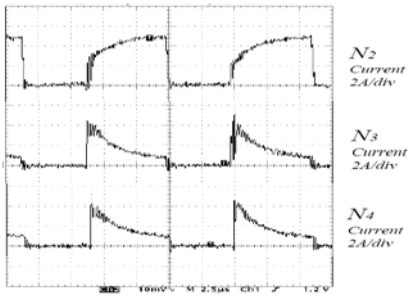

Fig. 9 Experimental waveforms in the high frequency transformer : Stack4 model

The samples of the N-port model and simulation waveforms of the experiment transformers (stack1 model) are illustrated in Fig.10 using and Fig.11.The simulated output current waveforms perfectly agree with the experimental results.

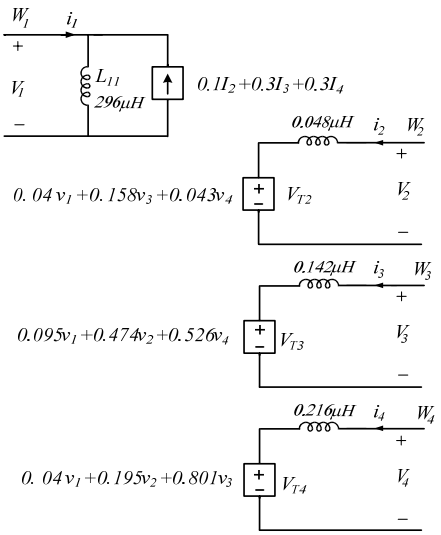

Fig. 10 The *N*-port model of four-winding flyback transformer : Stack1 model

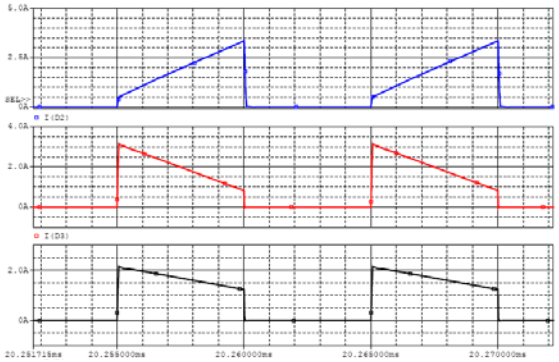

Fig. 11 Simulated waveforms of the *N*-port Model for the flyback converter

IV. The cross regulation results of the experimental transformers in a multiple output flyback converter

Each designed transformer is connected to the experimental three-output flyback converter. The cross regulation is determined by the change of the output voltages of the converter while varying the main output current form 0.5A to 3.5A with keeping other output currents constant at 1A. The expression is in a form of $\Delta\mathbf{V} = -\mathbf{R}\Delta\mathbf{I}$. $\mathbf{R}$ is a resistance matrix model. The converter operates in continuous conduction mode (CCM) for all operating points. Comparatively, Fig. 12 shows the changes of output voltages when varying the main output current of each designed transformer.

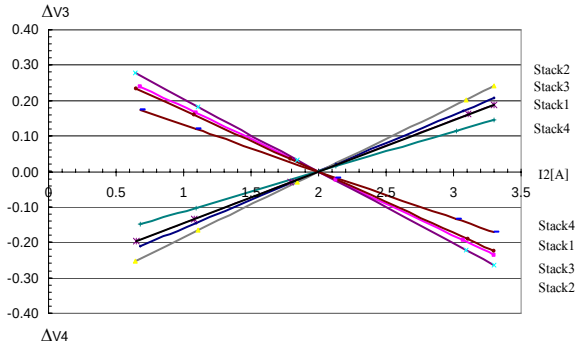

Fig. 12 The comparison of cross regulation in a multiple output flyback converter

The resistance matrix model of each designed transformers can be determined as Eq. (7) – (10).

$$\text{Stack1} = \mathbf{R}_{expriment} = \begin{bmatrix} 0.31 & 0.17 & 0.16 \\ 0.16 & 1.06 & 0.46 \\ -0.18 & -0.52 & -0.95 \end{bmatrix} \Omega \quad (7)$$

$$\text{Stack2} = \mathbf{R}_{expriment} = \begin{bmatrix} 0.33 & 0.16 & 0.16 \\ 0.17 & 0.89 & 0.44 \\ -0.20 & -0.41 & -0.63 \end{bmatrix} \Omega \quad (8)$$

$$\text{Stack3} = \mathbf{R}_{expriment} = \begin{bmatrix} 0.35 & 0.17 & 0.16 \\ 0.15 & 0.95 & 0.41 \\ -0.17 & -0.46 & -0.87 \end{bmatrix} \Omega \quad (9)$$

$$\text{Stack4} = \mathbf{R}_{expriment} = \begin{bmatrix} 0.35 & 0.14 & 0.13 \\ 0.11 & 0.66 & 0.41 \\ -0.12 & -0.21 & -0.79 \end{bmatrix} \Omega \quad (10)$$

The cross regulation in the auxiliary output voltages is considered from non-diagonal elements of the matrix. The small values are required for the improved cross regulation. From experimental results, the designed transformer: Stack 4 is the best among other designs. Since the cross regulation at auxiliary output voltages *V3* and *V4* has been affected by the leakage inductance parameters between windings *W3* and *W4* and the main output winding *W2* (l_{23} and l_{24}). Therefore, controlling the leakage inductance values among those windings will be able to control the cross regulation. In the designed Stack 4, the auxiliary windings are placed away from the main winding. The corresponding leakage inductance values of the designed Stack 4 shown in Table 1 are large results in the small values in non-diagonal elements in the matrix. Hence, based on the experimental results, the transformer design guidelines for improving cross regulation in a multiple-output flyback converter can be given as following:

- The leakage inductances between primary and secondary windings (l_{12} ,l_{13} and l_{14}) should be small to minimize magnetic flux.
- The leakage inductances between secondary and secondary windings (l_{23}, l_{24}, and l_{34}) should be maximized to reduce the effect of magnetic flux between windings when the load changes.
- The main output winding should be positioned near transformers core to reduce the leakage inductance.
- The primary and secondary windings should be in proximity while each secondary windings should be placed away as much as possible.

V.Conclusion

The cross regulation in multiple-output flyback converters is affected by leakage inductances of the transformer. The suitable winding arrangements of the transformer will lead to the improved cross regulation. This paper presents the comparative study of the four different winding arrangements in the four winding flyback transformer. The cross regulation model is considered in a form of the resistance matrix that is related to the leakage inductance parameters. The design guidelines for the transformer for improving cross regulation are given based on the experimental results.

References

[1] Dauhajre, "Modelling and Estimation of Leakage Phenomena in Magnetic Circuits," Ph.D.Thesis, California Institute of Technology, Pasadena, California, April 1986

[2] Erickson and D. Maksimovic, "A Multiple-Winding Magnetics Model Having Directly Measurable Parameters," *IEIE Power Electronics Specialists Conference, May 199*8

[3] Chuanwen Ji,K.Mark Smith,Jr " Cross Regulation in Flyback Converters: Analytic Model ," *IEIE Transactions Power Electronics Conference, 1999*

[4] D. Maksimovic and R. Erickson, "Modeling of Cross Regulation in Multiple-Output Flyback Converters," *IEIE Applied Power Electronics Conference, 1999*

[5] Kusumal Changtong " Magnetic Modeling for improving cross-regulation in multiple output flyback converters" Ph.D. Thesis, University of Colorado at Boulder,1999.

[6] Pairote Sangampai,Kusumal chalermyanont, Anuwat prasertsit and Surapon theinmontri **"** The Study the Effects of High Frequency Transformer Core Types for Improve Cross-Regulation in Multiple-Output Flyback Converters " PSU-Engineering Conference ,Thailand (*PEC 5*), May2007

Analysis and Design of Portable AC Power-pack with Full-bridge Series-loaded Resonant Converter

Karun Wanthong and Viboon Chunkag
Department of Electrical Engineering, Faculty of Engineering,
King Mongkut's Institute of Technology North Bangkok, Bangkok, 10800, Thailand
Phone 0-2913-2500 ext 8503, 2401 Fax 0-2585-7350, E-mail: musekrw@yahoo.com, vck@kmitnb.ac.th

***Abstract*-This research is aimed to design and build a small size, light weight AC power supply. Voltage to frequency converter (VFC) is used to control switching devices of a full-bridge series-loaded resonant converter, which operates in discontinuous conduction mode for reducing switching power losses and also high switching frequency can reduce the size of passive device in the circuit. The proposed approach has been built to deliver sinusoidal AC output voltage at 220 volts 50 Hz with 200 Watts output power.**

Keywords- AC Power pack, Voltage to frequency converter, full-bridge series-loaded resonant converter

I. INTRODUCTION

Normally a DC to AC converter is used for converting DC voltage to AC voltage to supply AC electrical loads. For instance it converts power from a battery (mostly 12 VDC) to standard household AC power (220VAC). The output waveform can be sinusoidal, square, stepped or triangular wave. Pure sinusoidal waveform is the best one, as it is the shape of an (ideal) AC electrical power from utility. The highest-quality inverter must produce the pure sine wave output. This type of output waveform is normally found only in higher-end product.

In this paper, a portable AC Power pack with full bridge series-loaded resonant converter is designed, simulated and built to produce sinusoidal output voltage waveform. The inductor current is controlled to operate in discontinuous conduction mode (DCM), which aims to reduce switching power losses of switching devices in the circuit. Switching frequency is controlled by voltage to frequency converter (VFC) and keeps the highest switching frequency at 100 kHz. The circuit diagram of the system is shown in Fig. 1 [1]-[3].

The power supply was designed to provide 220 V 50 Hz output voltage and 200 W power output. The model was simulated by using Matlab program before implementing in a laboratory.

II. PROPOSED TOPOLOGY

A. Voltage to Frequency Converter

The VFC has become quite popular due to their low cost and can be used in variety of electronic control and measurement systems [4]. VFC compose of an oscillator whose frequency is linearly proportional to control voltage. In the purpose system, it changes an absolute sinusoidal wave to a pulse signal with frequency variation proportional to the amplitude of input voltage. If the input voltage is high, the output frequency is also high and vice versa. The variable-frequency pulse-width can be modified by keeping constant turn on time to suit the operation of the series-load resonant topology. Matlab model of VFC is shown in Fig. 2 the model can be adjusted the turn on time by changing parameter of clock. In the implementation an IC chip number VFC320 is used for designing the VFC. The advantage of this IC is easy to use and convenient for the circuit connection.

B. Discontinuous Mode of Operation

The series load resonant converter which consist of power switching devices Q_1 to Q_4 and series resonant circuit element, L_r and C_r. The circuit is designed to operate in the discontinuous mode. The energy in resonant inductor (L_r) is consumed before the second switching period. There are six stages of operation in one switching cycle as shown in Fig. 3.

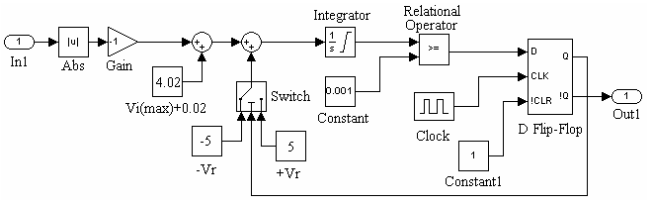

Fig. 2. Matlab model of VFC

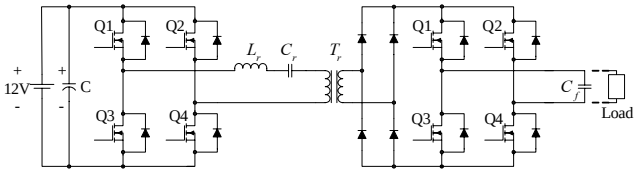

Fig. 1. Circuit schematic of AC power supply

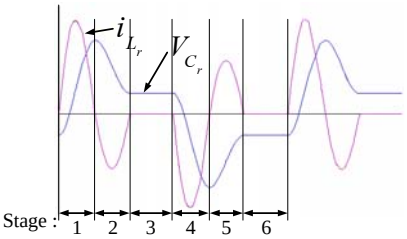

Fig. 3. Switching waveforms for discontinuous mode full-bridge series-loaded resonant converter

In the stage 1 and 2 the switching devices Q1 and Q4 are controlled to be on, and stage 4 and 5 Q2 and Q3 are on. During stage 3 and stage 6, all the switching devices remain off for maintaining the operation is in the discontinuous. The characteristic of this mode leads to zero current switching; so that the switching power losses can be minimized [5].

III. THE MODELING OF ALL SYSTEM

A. Design Switching Frequency and Resonant Frequency

In order to have small size of resonant inductor (L_r) and resonant capacitor (C_r), the resonant frequency and the switching frequency should be high. Choose maximum switching frequency 100 kHz, and turn on time (t_{on}) is $5\,\mu s$. Let assign the resonant frequency time period to 4/3 of the turn on time to guarantee the discontinuous conduction mode, so that resonance frequency is 150 kHz ($6.667\,\mu s$). The relation of switching frequency turn on time and resonant frequency is shown in Fig. 4.

B. Design L_r C_r

The series resonant tank, L_r and C_r are chosen from the well-known equation as in (1)

$$\omega = \frac{1}{\sqrt{L_r C_r}} \quad \text{and} \quad \omega = 2\pi f_r$$

so

$$f_r = \frac{1}{2\pi\sqrt{L_r C_r}} \tag{1}$$

where f_r is resonance frequency, Choose $C_r = 1\mu F$, so that form (1), $L_r = 1.126\mu H$. Use these parameters to make a model for simulation as shown in Fig. 5. The inductor current of the series resonant is

$$i_{Lr}(t) = \frac{V}{Z_O}\sin(\omega t) \tag{2}$$

where $Z_O = \sqrt{\frac{L_r}{C_r}}$

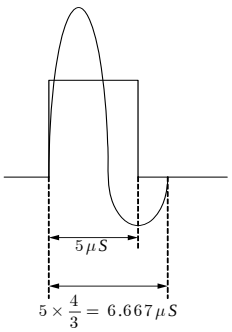

Fig. 4. Resonance frequency

C. AC Power Pack Model

The schematic diagram of AC power supply in Fig. 1, can be built as a model as shown in Fig. 6. The voltage from secondary side of transformer is rectified to be absolute value by bridge rectifier and then convert to be AC signal at the frequency 50 Hz, after that sent to a low pass filter. The first order low pass filter is designed by

$$V_O = \frac{1}{RCS + 1} \tag{3}$$

where $RC = \frac{1}{2\pi f}$

The corner frequency of the filter is selected at 100 Hz, so that RC = 0.0015.

IV. SIMULATION RESULTS

The parameters which have been designed in the section 3 are used in developing simulation model of the proposed AC power supply. The simulated results are discussed below.

A. VFC

The simulated result of the model in Fig. 2 is presented in Fig. 7-8. The absolute sine wave voltage is converted to frequency which proportional to the voltage level.

B. Discontinuous Mode

The current through inductor and voltage cross capacitor of AC power supply (Fig. 5) is shown in Fig. 9. It can be seen that the inductor current is discontinuous.

C. Output Signals

The output of full-bridge block in Fig. 5 which rectified the signal from the secondary side of transformer is converted to absolute value, so that all signals are positive as shown in Fig. 10.

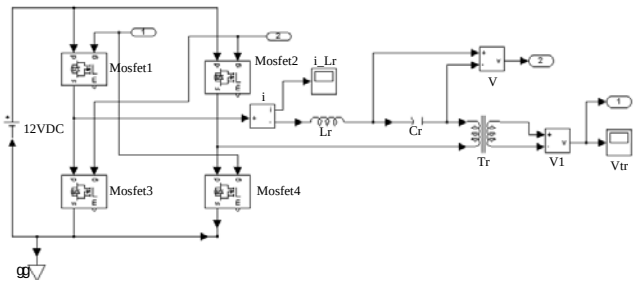

Fig. 5. Matlab model of full-bridge series-loaded resonant converte

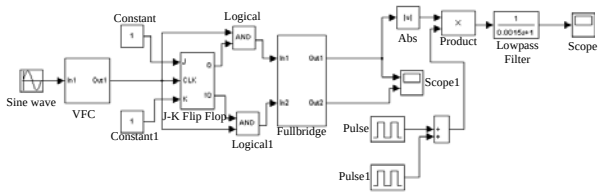

Fig. 6. AC power pack model

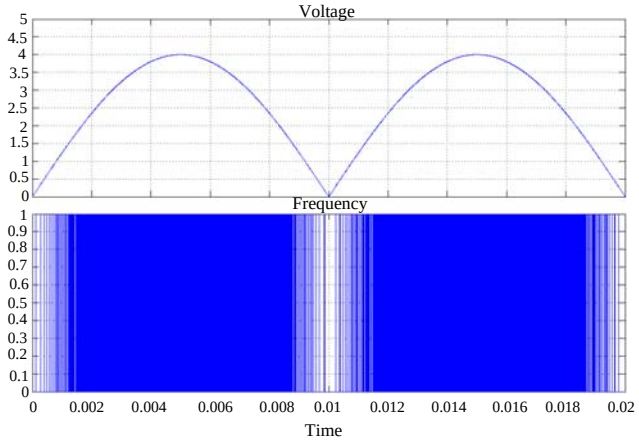

Fig. 7. Signal of VFC

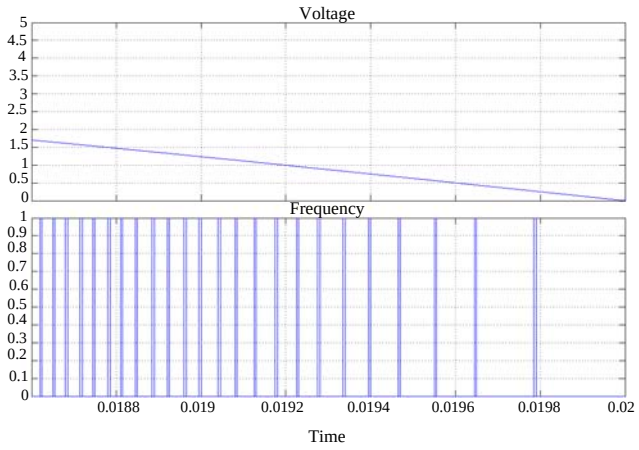

Fig. 8. Zooming in signal of VFC

The signal is brought to phase invert circuit and first order low pass filter. The result is AC output voltage 220 V and frequency 50 Hz, as shown in Fig. 11 and 12 respectively.

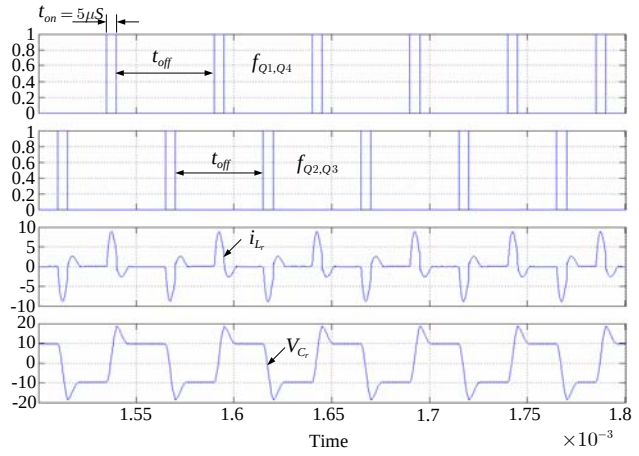

Fig. 9. Waveforms of switching frequency Q_1, Q_4 and Q_2, Q_3 , inductor current, and capacitor voltage

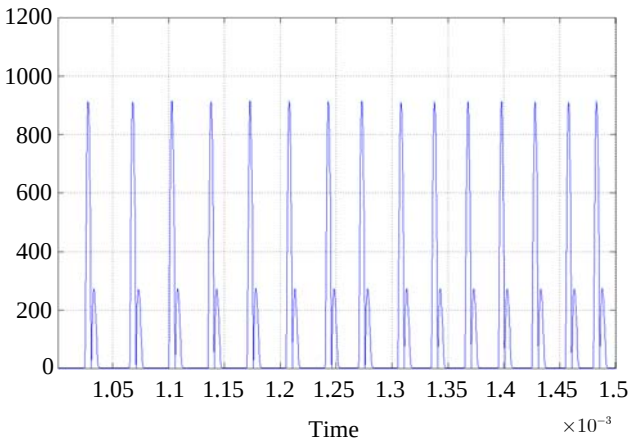

Fig. 10. Signal after pass Abs block

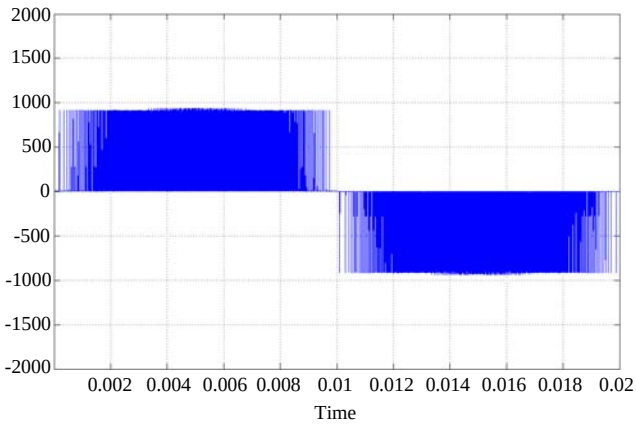

Fig. 11. Signal after pass phase inverse circuit

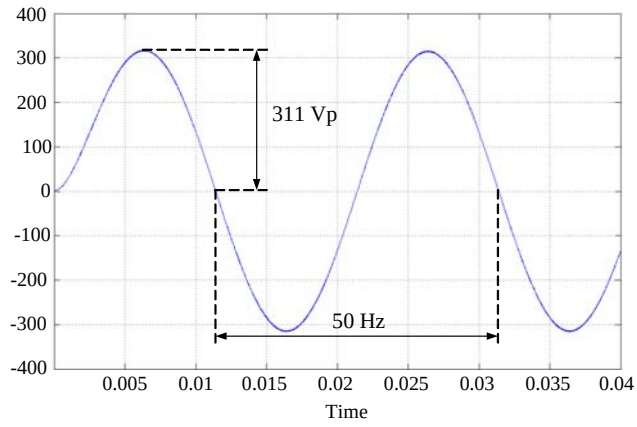

Fig. 12. Signal after pass lowpass filter circuit

V. EXPERIMENTAL RESULTS

The prototype circuit has been built to verify the simulation results. The measurement waveforms are shown in Fig. 13 – 15. The switching control signals is shown in Fig. 13, which indicates that the width of signal is approximately $5\mu S$ as the desired.

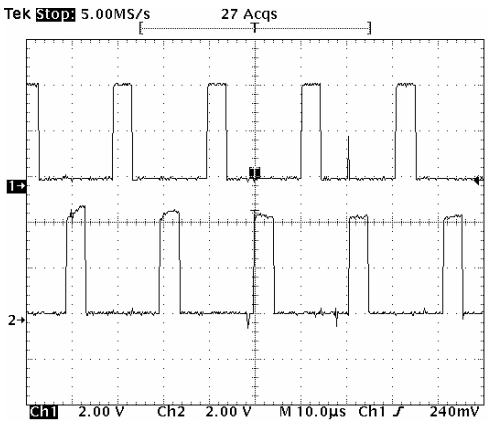

Fig. 13. Waveform of the switching frequency Q_1, Q_4 and Q_2, Q_3

Fig. 14 shows the waveform of the inductor current, and capacitor voltage. The inductor or resonant currents are always discontinuous, and the resonant frequency is also approximately 150 kHz.

Fig. 15 shows the AC output voltage and current when the system supply by a 12 Vdc to a 100 W linear load output. The output voltage and current are sinusoidal. The amplitude of output voltage is $311 V_P$ and frequency 50 Hz. The peak output current is 0.6 A. In Fig. 16 shows step load from 100 W to 200 W

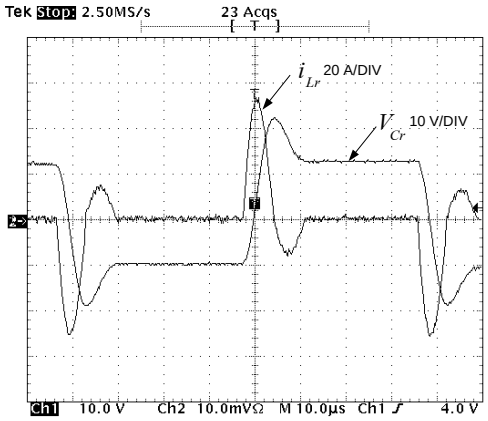

Fig. 14. Waveform of the inductor current, and capacitor voltage

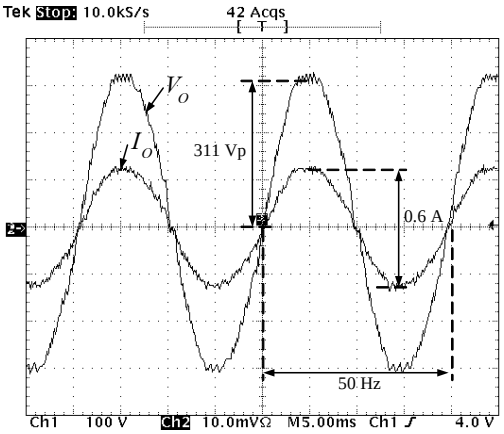

Fig. 15. Waveforms of the output voltage and output current

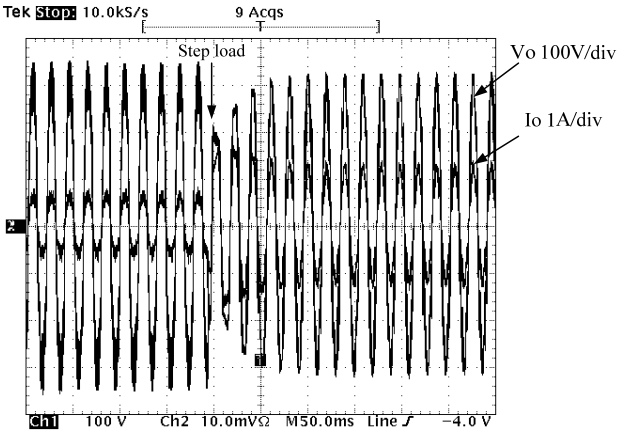

Fig. 16. Step load from 100 W to 200 W

VI. CONCLUSION

The DC-AC converter in this paper is analyzed simulated and built for having a good quality AC output voltage waveform and low power losses. The results show that the sinusoidal AC output voltage waveform can be met. However, it is expecting that after some improvement of design and fabrication, the size and weight of the system shall be small and light as required. By the demand in market, cost and size are important factor for making decision to have a produce.

VII. APPENDIX

The AC power supply (Fig 1) was tested with the following parameters: The DC input voltage V_S =12V, IC VFC320 for VFC circuit, The maximum switching frequency 100 kHz, turn on time (t_{on}) 5 μs , L_r = 0.66 μH , $C_r = 1.7 \mu F$, turn ratio of transformer 6:136, C_f = 0.47 μF /630V, and C = 5000 μF /50V.

ACKNOWLEDGMENT

To my parents, thank you for their love and to my advisor, Assoc.Prof. DR. Viboon Chunkag instilling within me the quest for excellence and providing unlimited support

REFERENCES

[1] S. Simon Ang,"Power-Switching Converters,"1995.
[2] W. Chien-Ming, "A Novel Single-Stage Full-Bridge Buck-Boost Inverter," *IEEE Transactions on power electronic*, vol.19, no.1, pp 150-159, Jan 2004.
[3] H. Ertl, W. Johann Kolar, and C. Franz Zach, "A Novel Multicell DC–AC Converter for Applications in Renewable Energy Systems," *IEEE Transactions on industrial electronic*, vol.49, no 5, Oct 2002.
[4] M Stork, "New $\Sigma - \Delta$ Voltage to Frequency Converter," *The 9th IEEE International conference on electronic circuits and system*, vol.2, pp.631-634, Sept. 2002.
[5] J. Wei, M. Ishida, and T. Hori, "Analysis and Simulation of Series-Resonant High-Frequency AC-Linked DC-AC Converter Realizable by Inverter Modules," *IEEE*, pp. 815-820, 1997

Particle Swarm Optimization for Optimal DG Placement in Distribution System

W. Krueasuk, W. Chankaipol, S. Hintamai and K. Chayakulkheeree
Power System and Electrical Energy Research Group,Department of Electrical Engineering,
Faculty of Engineering Sripatum University, Bangkok, Thailand, E-mail: wichit.kr@spu.ac.th

Abstract—**This paper proposes a particle swarm optimization (PSO) algorithm for optimal placement of distributed generation (DG) in a primary distribution system to minimize the total real power loss. Initially, the algorithm randomly generates the particle positions representing the size and location of DG. Each particle will move from its current position using the velocity and the distance from current best local and global solution reached. The velocity consists of inertia of the particle, memory, and cooperation between particles. Four types of DG are considered and the distribution load flow is used to calculate the exact loss. The results obtained from the 33-bus and 69-bus radial distribution test systems show that the proposed algorithm can perform optimal sites and sizes for each type of DGs with minimum loss compared to other techniques.**

***Index Terms*— Distributed Generation, DG types, Optimal DG size, Particle Swarm Optimization**

NOMENCLATURE

P_i	Net real power injection in bus i.
Q_i	Net reactive power injection in bus i.
R_{ij}	The line resistance between bus i and j.
V_i	The voltage at bus i.
δ_i	The angle at bus i .
$Loss_k$	Distribution loss at section k.
N_{SC}	Total number of sections.
P_L	The real power loss in the system.
P_{DGi}	The real power generation DG at bus i.
P_{Di}	The power demand at bus i.
S^k	Current searching point.
S^{k+1}	Modified searching point.
V^k	Current velocity of agent i.
V^{k+1}	Modified velocity of agent i.
v_{pbest}	Velocity based on pbest.
v_{gbest}	Velocity based on gbest.
n	Number of particles in a group.
m	Number of members in a particle.
$pbest_i$	pbest of agent i.
$gbest_i$	gbest of the group.
ω_i	Weight function for velocity of agent i.
c_i	Weight coefficients for each term.
ω_{min}	The minimum weights.
ω_{max}	The maximum weights.
k	The current iteration.
k_{max}	The maximum iteration.

I. INTRODUCTION

DISTRIBUTED Generation (DG) is a small electric power generator embedded throughout a power system network, providing the electricity locally to customer loads [1]. DG makes use of the latest modern technology which is efficient, reliable, and simple enough so that it can compete with traditional large generators in some areas [2] and [3]. Distributed generation systems can reduce the system loss and defer investment on transmission and distribution expansion. Placement of DGs is an interesting research area due to economical reason. Appropriate size and optimal site are the keys to achieve it [4] and [5].

Many techniques were proposed for distributed generation placement in a primary distribution such as heuristic search [6], power flow algorithm [7] and [8], linear programming [9], genetic algorithm (GA) [10] – [12]. Those researches considered the placement of only one type of a DG which supply only real power (Type 1). However, in [13], the author has presented a new technique, PSO, to determine the optimal sites and sizes of three types multi-DGs to minimize the total real power loss of the distribution systems. They are the DG Type 1, the DG which capable of supplying only reactive power (Type 2), and the DG which capable of supplying real power but consuming proportionately reactive power (Type 3). An additional type of DG (Type 4), the DG that is capable to regulate the terminal bus voltage, is proposed in this paper.

II. PROBLEM FORMULATION

The real power loss reduction in a distribution system is required for efficient power system operation. The loss in the system can be calculated by equation (1) [14], given the system operating condition,

$$P_L = \sum_{i=1}^{n}\sum_{j=1}^{n} A_{ij}(P_iP_j + Q_iQ_j) + B_{ij}(Q_iP_j - P_iQ_j) \quad (1)$$

where,

$$A_{ij} = \frac{R_{ij}\cos(\delta_i - \delta_j)}{V_iV_j}$$

$$B_{ij} = \frac{R_{ij}\sin(\delta_i - \delta_j)}{V_iV_j}$$

The objective of the placement technique is to minimize the total real power loss. Mathematically, the objective function can be written as:

$$\text{Minimize} \qquad P_L = \sum_{k=1}^{N_{SC}} Loss_k \quad (2)$$

Subject to power balance constraints

$$\sum_{i=1}^{N} P_{DGi} = \sum_{i=1}^{N} P_{Di} + P_L \quad (3)$$

voltage constraints: $|V_i|^{\min} \le |V_i| \le |V_i|^{\max}$ (4)

current limits: $|I_{ij}| \le |I_{ij}|^{\max}$ (5)

The DG Type 4 we consider in this case can regulate bus voltage. It will be treated as generator bus in the load flow analysis. Many DG technologies will fit under this category. Real power injected by the DG is found using equation (6) and corresponding reactive power required to support the bus voltage is found by keeping the voltage fixed.

$$P_i = P_{DGi} - P_{Di} = -\frac{1}{A_{ii}}\sum_{\substack{j=1 \\ j\neq i}}^{n}\left(A_{ij}P_j - B_{ij}Q_j\right) \quad (6)$$

III. Particle Swarm Optimization

Particle swarm optimization (PSO) is a population-based optimization method first proposed by Kennedy and Eberhart in 1995, inspired by social behavior of bird flocking or fish schooling [15]. The PSO as an optimization tool provides a population-based search procedure in which individuals called particles change their position (state) with time. In a PSO system, particles fly around in a multidimensional search space. During flight, each particle adjusts its position according to its own experience (This value is called Pbest), and according to the experience of a neighboring particle (This value is called Gbest), made use of the best position encountered by itself and its neighbor (Fig.1).

This modification can be represented by the concept of velocity. Velocity of each agent can be modified by the following equation:

$$v_{id}^{k+1} = \omega v_{id}^{k} + c_1 rand \times \left(pbest_{id} - s_{id}^{k}\right) + c_2 rand \times \left(gbest_d - s_{id}^{k}\right) \quad (7)$$

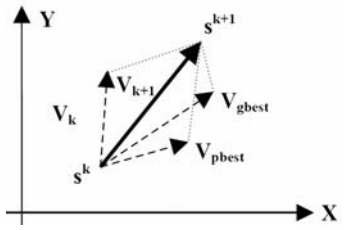

Fig. 1. Concept of a searching point by PSO

Using the above equation, a certain velocity, which gradually gets close to pbest and gbest can be calculated. The current position (searching point in the solution space) can be modified by the following equation:

$$s_{id}^{k+1} = s_{id}^{k} + v_{id}^{k+1}, \quad i = 1, 2, \ldots, n, \quad d = 1, 2, \ldots, m \quad (8)$$

The following weight function is used:

$$\omega_i = \omega_{\max} - \frac{\omega_{\max} - \omega_{\min}}{k_{\max}}.k \quad (9)$$

Appropriate value ranges for C_1 and C_2 are 1 to 2, but 2 is the most appropriate in many cases. Appropriate values for ω_{min} and ω_{max} are 0.4 and 0.9 [16] respectively.

IV. Proposed PSO Methodology

The PSO-based approach for solving the optimal placement of distributed generation problem to minimize the loss, as the flowchart in Fig.2, takes the following steps:

Step 1: Input line and bus data, and bus voltage limits.

Step 2: Calculate the loss using distribution load flow based on backward-forward sweep.

Step 3: Randomly generates an initial population (array) of particles with random positions and velocities on dimensions in the solution space. Set the iteration counter $k = 0$.

Step 4: For each particle if the bus voltage is within the limits, calculate the total loss in equation (1). Otherwise, that particle is infeasible.

Step 5: For each particle, compare its objective value with *the individual best*. If the objective value is lower than *Pbest*, set this value as the current *Pbest*, and record the corresponding particle position.

Step 6: Choose the particle associated with the minimum *individual best Pbest* of all particles, and set the value of this *Pbest* as the current *overall best Gbest.*

Step 7: Update the velocity and position of particle using (7) and (8) respectively.

Step 8: If the iteration number reaches the maximum limit, go to Step 9. Otherwise, set iteration index $k = k + 1$, and go back to Step 4.

Step 9: Print out the optimal solution to the target problem. The best position includes the optimal locations and size of DG or multi-DGs, and the corresponding

fitness value representing the minimum total real power loss.

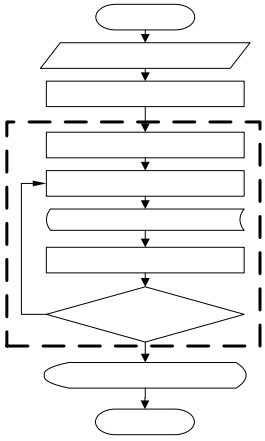

Fig. 2. PSO computational procedure

V. Numerical Results

The distribution test systems are the 33 bus [17] and 69 bus [18] systems. The 33 bus system has 32 sections with the total load 3.72 MW and 2.3 MVar shown in Fig.3 . The original total real power loss and reactive power loss in the system are 221.4346 kW and 150.1784 kVar, respectively. The 69 bus system has 68 Sections with the total load of 3.80 MW and 2.69 MVar, shown in Fig.4 . The original total real and reactive power losses of the system are 230.0372 kW and 104.3791 kvar, respectively. For PSO parameters, population size=200, Maximum generation (k_{max}) = 100. The maximum number of DG is three. The algorithm for solving the test systems is implemented on Matlab7 platform and on 1.6 GHz Pentium, 480-MB of RAM laptop.

The numerical results in Table I shown that the PSO can search the optimal sites and sizes of three DGs, both for 33 bus and 69 bus system, with minimum real power loss compared to the case of load flow analysis without DG about 86.56% and 96.81% respectively. With a DG installed at the same bus, the PSO algorithm can perform lower losses compared to a heuriatic search technique as well.

Table II show the losses when three DGs are installed for the 33 bus and the 69 bus systems compared to the case that without DG. The minimum losses occur when DGs Type 4 are installed. The improvement in the voltage profile after optimally placing the DGs is shown in Fig.5 . Without DG, the bus no. 64 has the lowest voltage of 0.8891 p.u. and the bus voltage has improved to 0.9772 p.u. after installing three type-4 DGs. Moreover, branch currents have reduced and chances of line limit violation have decreased as shown in Fig.6 .

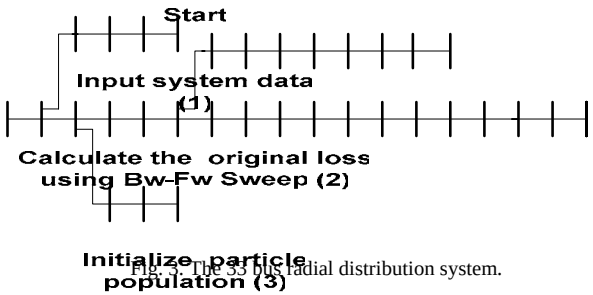

Fig. 3. The 33 bus radial distribution system.

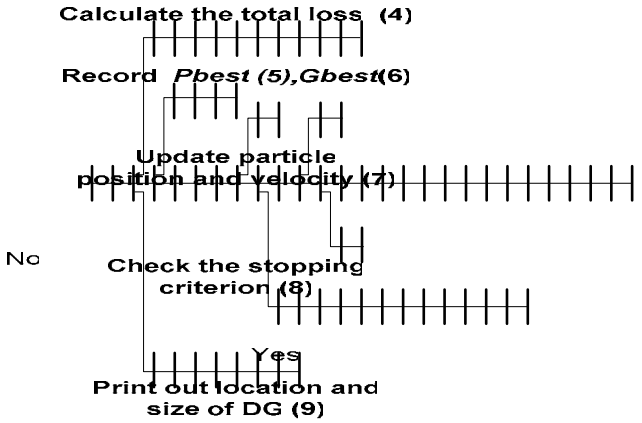

Fig. 4. The 69 bus radial distribution system.

Particle Swarm Optimization

Table I
Optimal DG Placement for DG Type 4

System	Method	Bus No.	DG Size (MW)	Bus No.	DG Size (MW)	Bus No.	DG Size (MW)	Ploss (kW)	Qloss (kvar)	Loss Reduction % Real	Loss Reduction % Reactive
33 bus	Load flow analysis							221.4346	150.1784		
	Heuristic search	12	2.4939					71.3837	57.4205	67.76	61.77
	PSO	12	2.4939					71.3837	57.4205	67.76	61.77
		22	1.1136	27	0.8285			29.8197	21.2726	86.53	85.84
		28	0.1481	22	1.0387	29	0.7598	29.7697	21.3455	86.56	85.79
69 bus	Load flow analysis							230.0372	104.3791		
	Heuristic search	56	1.8071					23.9885	14.9305	89.57	85.70
	PSO	56	1.8074					23.5938	14.6854	89.74	85.93
		56	1.7252	53	0.517			7.3416	8.2134	96.81	92.13
		56	1.7448	4	0.23	55	0.5102	7.3433	8.1907	96.81	92.15

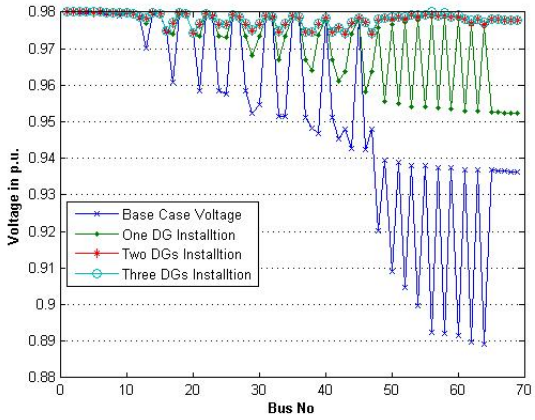

Fig. 5. Bus voltage before and after DGs Installation for DG type-4.

Current in Branch 1 (branch after the root node) has decreased to 0.2516, 0.1963 and 0.1427 p.u. from 0.5008 p.u. after installing one DG , two DGs and three DGs, respectively.

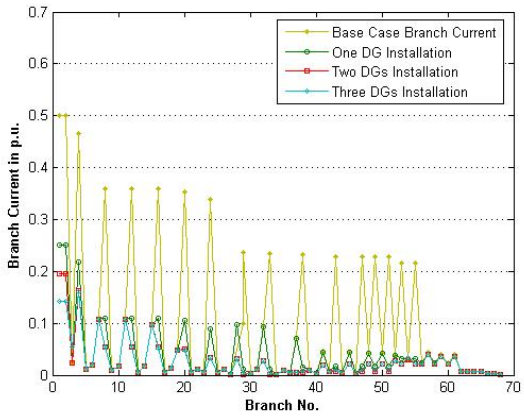

Fig. 6. Branch current before and after DGs Installation for DG type 4

Table II
COMPARISON OF LOSSES WHEN OPTIMAL THREE DGS PLACEMENT USING PSO

Case	P loss (kW)	Q loss (kVar)
For a 33 bus system		
Without DG	221.4346	150.1784
With DGs placement		
- DG Type 1	76.1691	52.9743
- DG Type 2	144.9050	98.7541
- DG Type 3	166.8321	117.0974
- DG Type 4	29.7697	21.3455
For a 69 bus system		
Without DG	230.0372	104.3791
With DGs placement		
- DG Type 1	70.8786	35.6864
- DG Type 2	148.3148	69.1167
- DG Type 3	161.6938	73.9429
- DG Type 4	7.3433	8.1907

VI. CONCLUSION

In this paper, a particle swarm optimization for optimal placement of multi-DGs is efficiently minimizing the total real power loss satisfying transmission line limits and constraints.

The proposed a particle swarm optimization is capable of determining the near global solution. The methodology is fast and accurate in determining the sizes and locations of DGs.

REFERENCES

[1] Thomas Ackermann, GÖran Andersson and Lennart SÖder, "Distributed generation: a definition," Electric Power Systems Research 57, 2001, pp.195-204.

[2] W.El-Khattam, M.M.A.Salama, "Distributed generation technologies, definitions and benefits," Electric Power Systems Research 71, 2004, pp.119-128.

[3] G.Pepermans, J.Driesen, D.Haeseldonckx, R.Belmans, and W.D'haeseleer, "Distributed generation: definitions, benefits and issues," Energy Policy 33, 2005, pp.787-798.

[4] William Rosehart and Ed Nowicki, "Optimal Placement of Distributed Generation," 14th PSCC, Sevilla, 24-28 June 2002.

[5] Caisheng Wang and M. Hashem Nehrir, "Analytical Approaches for Optimal Placement of Distributed Generation Sources in Power Systems," IEEE Transactions on Power Systems, vol.19, no.4, 2004, pp.2068-2076.

[6] Naresh Acharya, Pukar Mahat, and N. Mithulanathan, "An analytical approach for DG allocation in primary distribution network," International Journal of Electrical Power & Energy System, to be published.

[7] N.S. Row, Y.-H Wan. "Optimum location of resources in distributed planning," IEEE Trans. PWRS, 1994, pp.2014-2020.

[8] J.O. K, S.W. Nam, S.K. Park, C. Singh. "Dispersed generation using improved Hereford ranch algorithm," Electric Power System Research, 1998, pp. 47-55.

[9] Andrew Keane and Mark O'Malley, "Optimal Allocation of Embedded Generation on Distribution Networks," IEEE Transactions on Power System, vol.20, no.3, August, 2005, pp.1640-1646.

[10] K.-H. Kim, Y.-J. Lee, S.-B. Rhee, S.-K. Lee, S.-K. You. "Dispersed generator placement using fuzzy-GA in distribution systems," Proc. 2002 IEEE Power Engineering Soc. Summer Meeting, Chicago, IL, July, 2002, pp.1148-1153.

[11] A. Silvestri, A. Berizzi, S. Buonanno. "Distributed generation planning using genetic algorithms," Proc. Int. Conf. on Electric Power Engineering, Power Tech Budapest 99, 1999.

[12] G. Carpinelli, G. Celli, A. Russo. "Distributed generation siting and sizing under uncertainity" Proc. IEEE Porto Power Tech, 2001.

[13] Wichit Krueasuk and Weerakron Ongsakul, "Optimal Placement of Distributed Generation Using Particle Swarm Optimization," Proceedings of the Australasian Universities Power Engineering Conference(AUPEC 2006), Melbourne,Victoria, Australia, 10th -13th December 2006.

[14] I.O. Elgerd. Electric Energy System Theory: an Introduction. McGraw Hill 1971.

[15] Kennedy J and Eberhart R, "Particle Swarm Optimizer," IEEE International Conference on Neural Networks (Perth, Australia), IEEE Service Center Piscataway, NJ, IV, 1995, pp.1942-1948.

[16] Eberhart, R.C. and Shi, Y, "Comparing inertial weights and Constriction factor in particle Swarm optimization," proceeding of the 2000 International Congress on Evaluationing Computation, San Diego, California, IEEE Service Center, Piscataway, NJ, 2000,pp.84-88.

[17] M.A. Kashem, V. Ganapathy, G.B. Jasmon and M.I. Buhari, "A Novel Method for Loss Minimization in Distribution Networks," proceeding of International Conference on Electric Utility Deregulation and Restructuring and Power Technologies, 2000, pp.251-255.

[18] M.E. Baran and F.F. Wu, "Optimal Sizing of Capacitor Placed on Radial Distribution Systems," IEEE Trans,Vol. PWRD-2, 1989, pp.735-743.

A Graph Theory Approach in Reliability Improvement of a Radial Distribution System with PV Grid-Connected Systems

P. Sritakaew
Department of Electrical Engineering, Faculty of Engineering
Rajamangala University of Technology Lanna Chiangrai
Saikhao, Phan, Chiangrai 57120 Thailand

A. Sangswang
Department of Electrical Engineering, Faculty of Engineering
King Mongkut's University of Technology Thonburi
Bangmod, Thungkru, Bangkok 10140 Thailand

***Abstract*-This paper presents a method for reliability improvement of a distribution system by using photovoltaic (PV) grid-connected systems. An experimental setup is prepared to measure the system operating characteristics. The system consists of a PV array and a grid-connected inverter. The measured data are used to investigate the effects of a PV system installation on system reliability. We form an objective function with practical constraints to study distribution system's reliability. A graph theory approach is employed in selecting the installation location. The study has shown that, in an event of a permanent fault follows by a restoration sequence; PV generators can be used to recover system loading capability in the isolated area. This results in less customers with power outage and therefore, better system reliability.**

I. INTRODUCTION

Distribution service reliability is directly related to service interruptions which are caused by events such as storms, accidents and vandalism. The service interruptions can have a profound economic impact on customers. Historically, customers requiring high levels of reliability have depended on equipment such as uninterruptible power supplies and backup generators. Recently, PV systems have received much attention due to major advantages of infinite availability of the prime energy source and no polluted emission. The amount of PV generation is growing rapidly both in size and complexity [1]. This is due to the inherent benefits of the PV systems that can be used as a distributed generation (DG) to the electric utilities. Another advantage of the PV generator is from its close location to the customers which significantly reduces transmission and distribution costs. They can also be used to level the system load curve, improve the voltage profile, reduce line losses and transformer's loading [2]. However, to achieve the mentioned benefits, the PV generators must be of appropriate penetration level and at suitable locations [3]. In practice, its so-called infinite source is a variable energy source. The injected output power to the distribution system varies greatly on the weather conditions of a specific day. There is no guarantee that the mentioned benefits can be fully realized. The operation of the PV grid-connected systems and their responses to disturbances and/or conditions of the power distribution system has increasingly raised concerns, especially in high penetration of PV systems [3]. Regardless of the uncertain characteristics of the generated output power, the PV systems can be used to improve system reliability for radial distribution networks. Extensive research on a reliability evaluation of interconnected power system has been conducted in the past years [4-7]. Considerable efforts in the past have been spent to optimize restoration sequence. The service restoration problem is formulated as a constrained multi-objective optimization problem in [8]. In [5], a switch placement algorithm is proposed along with a distributed generator to improve the distribution system's reliability. With a network reconfiguration through an operation of a tie switch/line, portions of the outage network can receive power from other branches or feeders. By allowing the DGs to support the recovered portions of the system, the amount of customers with power outage can be reduced. Even though, the system reliability may be improved, the voltage and line capacity constraints become important concerns because in a restructured distribution system, lines are usually operated close to the capacity limit, even overloaded.

Unlike other kinds of DGs, when a fault occurs, all PV grid-connected inverters must detect the islanding and stop energizing. From this aspect, a thorough investigation of the PV systems must be performed to assure satisfactory operations. In this paper, we consider issues concerning distribution system's reliability with PV grid-connected systems in the event of faults. A PV grid-connected setup is prepared to experimentally measure the system output characteristics which have effects on the distribution system. The measured data are used in computer simulation to evaluate the distribution system's reliability. A graph theory approach is proposed to select amount and installation locations. A radial distribution system is represented using a tree data structure. The obtained results are compared with a predetermined list method based on loading level.

It should be noted that traditional reliability indices, SAIDI and SAIFI [6], are not appropriate in this work since, they are static indices and, in an event of fault, alternate supply routes are available through a tie line/switch. Therefore customers experiences only momentary interruptions. This paper is organized as follows. Section II describes experimental measurement of PV grid-connected system characteristics.

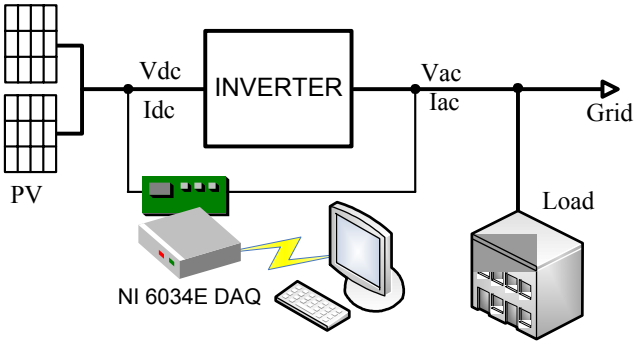

Fig. 1 PV grid-connected system setup

In section III, modeling issues of the PV systems are discussed. Section IV describes the restoration sequence during fault. Section V discusses the reliability improvement issues including problem formulation and proposed search methods. Numerical studies on a test system are given in section VI. Section VII concludes the work.

II. PV Measurement Details

In order to characterize the output of the PV grid-connected system, a measurement setup is prepared. The test system consists of 1.5 kW Amorphous PV array and a 1.7 kW grid-connected inverter from SMA Technologies AG. The system supplies electricity for the building uses consisting of fluorescent lighting, air conditioning units and water pumping. The load is essentially inductive. The system configuration is shown in Fig. 1. Voltage and current measurements on both dc and ac sides are automated using an NI6034E data acquisition (DAQ) card. A program is developed in Labview to calculate necessary values such as power factor, harmonics and frequency. The system automatically records data every minute from 06.00AM to 06.00PM. The inverter's real and reactive powers shown in Fig. 2 are averaged values of the collected data over a month (May 2006). The reactive power is relatively small compared to the real power, especially around noon time. Fig.3 shows the measured voltage and current on the ac side. We note that the measured voltage is the utility's voltage. It is clearly seen that the inverter's real power and current assume similar shape because the voltage varies in a small window except around 10.00 AM where a local heavy load has been turned off.

III. System Modeling

To investigate the power distribution behavior accurately, appropriate models for each of the system components must be employed. The following component modeling is used in the study.

A. PV Grid – Connected System

The majority of the grid-connected inverters produced nowadays are based on the voltage-source inverter with closed-loop current control. In practice, PV modules inject

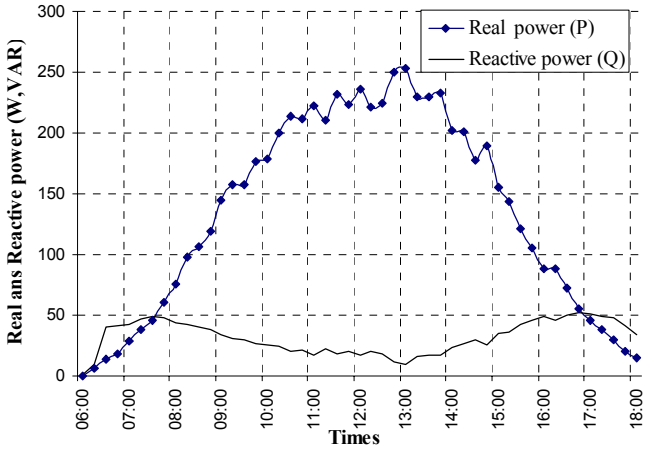

Fig. 2 Output real and reactive powers

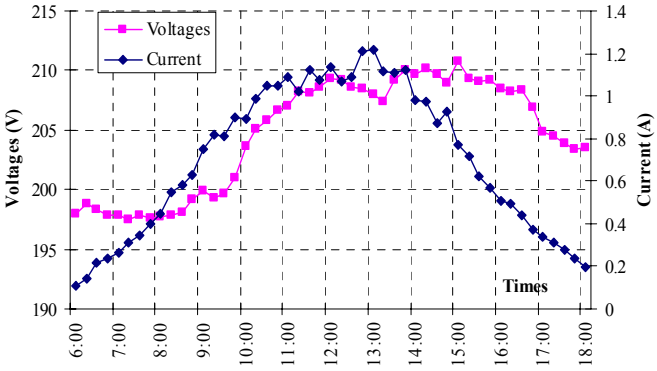

Fig. 3 Inverter's output current and voltage

power to the utility's grid through an inverter with capability of detecting islanding operation. This means that the inverter requires the utility grid voltage for its operation and it cannot operate in an isolated area as other distributed generator because of islanding requirement of the inverter. From the experimental results in section III, a PV grid-connected system has shown to effectively inject active power to the distribution feeder. In addition, its output voltage is governed by the grid voltage. This is reflected by modeling the PV grid-connected systems as PQ loads with negative real power drawn from the distribution system.

B. Lines and Tie Switches

Lines are the predominant branch connections existing in distribution networks. The tie switch's function is to alter network topology in order to provide alternate routes for supplying power to loads when necessary. In this study, standard model admittance matrices for distribution lines and tie switches are used [9]. However, it should be noted that the line charging is not included due to the overall length of the lines.

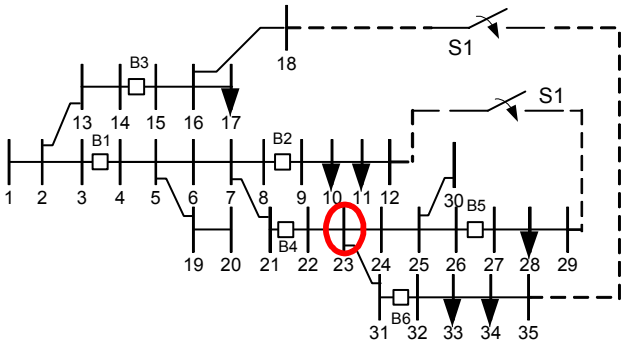

Fig. 4 A typical radial distribution network

C. *Load Models*

For any given amount of real and reactive load at each phase of a bus, three types of representation are used; constant impedance, constant current and constant power loads. In some buses the loads are represented as a linear combination of the three-load types.

IV. Restoration Sequence

A typical radial distribution system consists of distribution lines, transformers, circuit breakers, and manual disconnecting switches. When a fault occurs, protection devices are triggered to clear the fault. The affected area is determined based on the system configuration and protection scheme. The process is illustrated in Fig. 4. It is assumed that the tie lines S1 and S2 are normally open. When a fault occurs on bus 23, the circuit breaker B4 would open to isolate the fault. As a result, customers on buses 28, 33 and 34 experience power outage. This step essentially depends on the setting of protection schemes. Next, a search is performed on the downstream until circuit breakers B5 and B6 are found and the fault can be isolated. With the operations of the tie lines, S1 and S2, the loads on buses 28, 33 and 34 are recovered. In many cases, a tie line may not be able of supplying power to the isolated area. With the PV system installation, the loading level of S1 and S2 can be alleviated and the system can operate under this configuration until the fault is cleared. Therefore, the system reliability is improved. However, with limited availability of the PV systems, the installation locations must carefully be selected.

V. Issues on Reliability Improvement

A. *Problem Formulation*

Our aim in this work is to evaluate the system reliability in the presence of PV grid-connected systems. The objective functions considered are: (1) to minimize the loading level of the tie line, (2) to minimize the system loss and (3) to minimize the number of PV system installations. In summary, the constrained reliability improvement problem using PV system is formulated as follows.

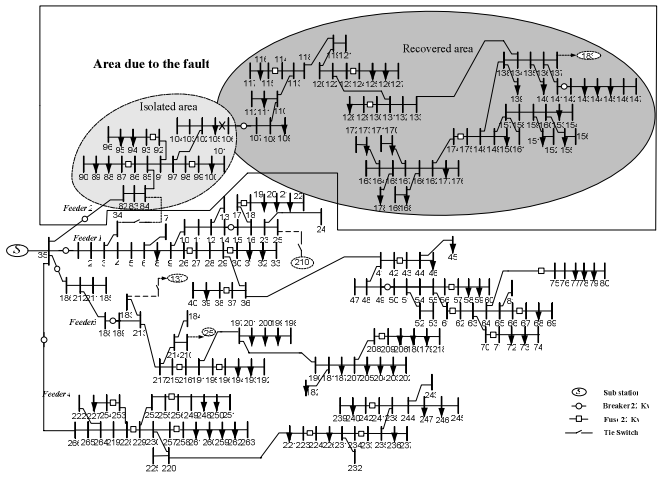

Fig. 5 One-line diagram of the test system

$$\begin{aligned} &\min I_{tie} \\ &\min \sum_{k \in N_L} S_{loss}^{3-\phi} \\ &\min N_{pv} \end{aligned} \tag{1}$$

subject to

$$\begin{cases} V_k^{\min} < \left| V_k^p \right| < V_k^{\max} \\ S_{ik}^{\min} \le S_{ik}^{3-\phi} \le S_{ik}^{\min} \end{cases} \tag{2}$$

where

I_{tie} is the current flows in a tie line

$S_{loss}^{3-\phi}$ is the total system losses

N_{PV} is the number of PV installation

V_k is the voltage at bus k

$S_{ik}^{3-\phi}$ is the complex power flow from bus i to bus k.

B. *Search Methods*

The installation location can be determined using well established graph theory approaches. The following search methods in graph theory are considered.

1) Breadth-first search (BFS) traverses neighboring buses that is, outgoing branches of the bus in the search, before any outgoing branches of the bus. Then for each of those nearest buses, it traverses unexplored neighboring buses, and so on.

2) Depth-first search (DFS) traverses outgoing branches of a bus before processing neighboring buses in the search.

In addition, a list method is also considered where the list is constructed based on the amount of load on each bus, starting from maximum to minimum loading. It is then compared with the results obtained from the above search methods.

VI. Numerical Studies

The test system is a 266-bus radial distribution system of the Provincial Electricity Authority (PEA) of Thailand as shown in Fig. 5. The amount of total system load under

normal operation is 53.60 MW and 33.27 MVar. The system consists of 69 load buses and 2 tie lines (25-210 and 137-183). When a fault occurs on the system, it is isolated by the circuit breaker upstream and the restoration sequence mentioned in section IV is performed. The measured results of the PV systems are scaled up to units of 200 kW and 400 kW, respectively. A fault is assumed to be on the line between bus 105 and 106 and remain fixed. The basic information of the test system during fault is found in Table I. The proposed search methods are used to solve the problem formulated in section V. We note that for the case with no installation of PV systems, the tie carries 620.85A while its ampacity limit is at 600A. To demonstrate the proposed algorithms, each method is compared through the number of PV installations and system loss once the tie line loading is in the limit.

For the case of 200 kW PV systems, the loading list and DFS methods have resulted in the same amount of PV required (5×200 kW) to achieve the tie line limit. However, they provide different installation locations and around 400W difference of loss. The BFS method provide the best result in requiring only (4×200 kW) with similar loss.

We also scale the PV system up to 400 kW each to simulate the situation where a larger PV system is available. The 3 methods result in the same amount of PV required (3×400 kW). It seemed that when the PV is scaled up, the number of PV systems required are the same with relatively close values of loss and tie-line loading even though, the installation locations are different. From the results obtained, the BFS may be a good choice compared to the others. It is also observed that all methods that have been tested provided similar results in terms of installation location. Buses 125, 126 and 127 are often the choices of installation.

TABLE I.
INFORMATION OF THE TEST SYSTEM DURING FAULT

Faults branch	105-106
Load in the recovered area	16.485 MW / 10.215 MVar
Capacity of tie line	600Amp
Number of load buses in recovered area	20
Tie line location	137-183

TABLE II.
THE RESULTS FOR 200 KW INSTALLATIONS

Method	PV installation (kW)	Installation location	System losses (kW)	Tie line loading (A)
		No PV installation	207.65	620.85
BFS	800	126, 127, 109, 173	200.26	596.83
DFS	1000	126 (4 sets) and 127	199.80	596.82
Loading list	1000	125, 126, 153, 145, 151	200.21	596.83

TABLE III.
THE RESULTS INSTALLATION PV 400 KW BY DEPTH FIRST SEARCH

Method	PV installation (kW)	Installation location	System losses (kW)	Tie line loading (A)
		No PV installation	207.65	620.85
BFS	1200	126, 127, 116	198.68	592.05
DFS	1200	126 (2 sets) and 127	198.40	592.05
List	1200	125, 126, 153	198.86	592.05

This can be expected since those buses are heavily loaded buses and they are located at the end of the feeder. The proposed methods can be used in system planning when DGs, especially PV generators, are of interest.

VII. CONCLUSIONS

We investigate the output characteristics of the PV grid-connected system. The measured results are used to examine the issues related to reliability improvement for a radial distribution system. Graph theory approaches, BFS and DFS methods, can be used to improve system reliability. It has been shown that with the action of a tie switch, the system losses and loading level of the tie switch can be reduced with appropriate amount and installation location. The proposed methods have resulted in PV installation at heavily loaded buses and buses located at the end of the feeder.

ACKNOWLEDGMENT

The authors wish to thank the CES Solar Cells Testing Center (CSSC), KMUTT and the Provincial Electricity Authority (PEA), Thailand for their support.

REFERENCES

[1] IEA,"Photovoltaic technology status and prospects ",Japan 2004
[2] D.S. Shugar, "Photovoltaics in the utility distribution system: the evaluation of system and distributed benefits," in proceedings of the 21st Photovoltatic Specialists Conference, vol. 2, pp.836-843,1990.
[3] M. Begovic, A. Pregelj, A. Rohatgi and D. Novosel, "Impact of Renewable Distributed Generation on Power System," in proceedings of the 2001 Conference on System Sciences, 2001.
[4] R.E. Brown and R. Fletcher "Distribution system Reliability Assessment Using Hierarchical Markov Modeling," IEEE Transactions on Power Delivery ,Vol.11, No.4, pp1929-1934, Oct 1996.
[5] Y. Mao and K. N. Miu "Switch placement to improve system Reliability of radial distribution system with distribution," IEEE Trans. Circuits Syst. I, vol. 18, Issue 4 pp.1346-1352, Nov. 2003.
[6] R. Billinton, "Distribution system reliability performance and evaluation,"Elect. Power Energy Syst., vol. 10, no. 3, pp. 190–200, July 1988.
[7] C. Ucak and A. Pahwa, "An analytical approach for step-by-step restoration of distribution systems following extended outages," IEEE Trans. Power Delivery, vol. 9, pp. 1717-1723, July 1994.
[8] K. N. Miu, H.D. Chiang, B. Yuan and G. Darling, "Fast Service Restoration for Large-Scale Distribution Systems with Priority Customers and Constraints," IEEE Trans. Power Systems, vol. 13, No. 3, August 1998.
[9] J.D. Glover and M.S. Sarma, Power system analysis and design, 3rd edition, Brooks/Cole, CA USA, 2002.

Analysis of AC Losses in Superconducting Transmission Line

T. Satiramatekul
Department of Computer Engineering
Faculty of Engineering at Kamphaengsaen
Kasetsart University, Kamphaengsaen Campus
Nakhon Pathom, 73140, Thailand
E-mail: thitipong.s@ku.ac.th

***Abstract*-This paper deals with two-dimensional computation of AC losses in a superconducting transmission line by using a numerical method. For that, we used the finite element method. We observe the effect of the different superconductor models to the evaluation of the instantaneous losses and also the value of the average losses. Moreover, the current density and the magnetic field distributions in the superconducting transmission line will be studied too.**

I. INTRODUCTION

One important characteristic of the superconductors is the absence of the electrical resistivity when the direct current flows through. However, the superconductors generate losses through Joule effect when the alternating current flows through, called Joule losses or AC losses. Even if these losses are relatively small, it is advisable to evaluate them with the precision. The use of superconductors at high critical temperature for transporting the alternating current is now real by using the electrical power transmission lines and the evaluation of losses in proper field is so necessary.

Our objective was to study of the losses in proper field in a superconducting transmission line at high critical temperature. In reality, the characteristic curve of the electrical field E versus the current density J differs rather clearly from that of the theoretical model, called the Bean's model [1]. In order to get a well-behaved curve, the Bean's model is altered by a progressive function [2] [3] and then called the extended Bean's model (Fig. 1).

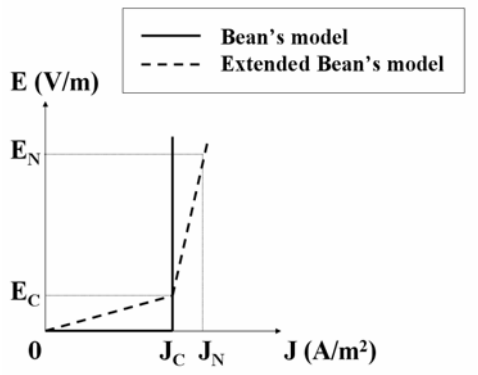

Figure 1. Altering Bean's model to get a well-behaved curve.

Initially, we present a general method for computing the losses in superconducting transmission line described by an extended Bean's model, and then we compare the results of numerical computation of the losses carried out by method presented for different models of extended Bean's model.

II. PROBLEM PRESENTATION

We calculate the losses in a superconducting transmission line, carrying a sinusoidal current of frequency f and of amplitude I_{max}. The characteristics of this transmission line (Fig. 2) are as follows: critical current I_C = 100 A, cross-sectional area S = 22 mm^2, length L = 1 km, inner radius R_i = 4 mm and outer radius R_o = 4.8 mm.

The electromagnetic behavior of the superconductors is dominated by the Maxwell's equations [4]:

$$\nabla \times \vec{E} = -\partial \vec{B} / \partial t \quad (1)$$

$$\nabla \times \vec{B} = \mu_0 \vec{J} \quad (2)$$

$$\nabla \cdot \vec{E} = 0 \quad (3)$$

$$\nabla \cdot \vec{B} = 0 \quad (4)$$

where μ_0 is the permeability of the air and B is the magnetic induction. These equations must be supplemented by the relation equations between B and H (magnetic field), and E and J. For B and H, we have $B = \mu_0 H$. For E and J, we use the extended Bean's model.

Classically, the estimate of the losses is done by using formulas deduced from the Bean's model, well adapted to characterize the superconductors. It is defined by an electrical characteristic $E(J)$ in the form of a step:

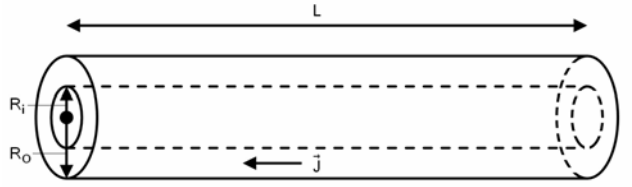

Figure 2. 3D geometry of the superconducting transmission line.

$$E = 0 \quad : \quad 0 \le J \le J_C$$
$$E \neq 0 \quad : \quad J = J_C \tag{5}$$

where J_C is the critical current density.

But for transporting the alternating electrical current at high critical temperature, the real characteristic $E(J)$ differs rather clearly from that of the Bean's model. A more realistic model is obtained by a progressive function of the form:

$$E = \frac{E_C}{J_C} \times J \quad : \quad 0 \le J \le J_C$$
$$E = \frac{(E_N - E_C)}{(J_N - J_C)} \times (J - J_C) + E_C \quad : \quad J_C \le J \le J_N \tag{6}$$

where E_C , E_N and J_N are defined in Fig. 1. These parameters are chosen so that the behavior law $E(J)$ approaches to the experimental characteristic. Let us notice that when E_C approaches to zero and J_N approaches to J_C , we find the Bean's model.

In this model, we are unaware of the one-dimensional aspect of the problem and we suppose that the electrical field and the current density have only one component following the axis of the transmission line, noted respectively E and J. The scalar equation to be solved is written [4]:

$$\partial J / dt = \nabla \cdot \left(\mu_0^{-1} \nabla E\right) = \mu_0^{-1} \nabla^2 E \, . \tag{7}$$

Equation (7) is solved by using the finite element method in space and the Crank-Nicolson method in time. With each step of time, a convex functional is minimized by an iterative procedure of nonlinear Gauss-Seidel. The proposed method takes into account the free boundary in an implicit manner. It seems to be robust and fast to be able to effectively estimate the losses in superconducting transmission line.

The instantaneous losses in Watt can be calculated by using the general formula:

$$p(t) = \int_S jeLds \tag{8}$$

where S is the cross-sectional area.

The Joule losses or AC losses can be directly obtained from the integral of the instantaneous losses over a period of length T of the transport current, we have [5]:

$$P = \frac{1}{T}\int_0^T p(t)dt = \frac{1}{T}\int_0^T \left(\int_S jeLds \right) dt \, . \tag{9}$$

From (9), maybe we can call it the average losses in the superconducting transmission line.

III. Numerical Simulation

The total modeled domain in 2D is shown in Fig. 3. It is composed of the superconductor and the insulator. In this case, we choose to use the air which is a good insulator. Therefore, the transport current flows only in the superconductor. The symmetries of the problem make that only one sixtieth of the domain (six degrees) is modeled. Consequently, the time of calculation is reduced. The transport current is parallel to the axis of the transmission line and varies sinusoidally in time with f = 50 Hz and I_{max} = 20 to 160 A (Fig. 4).

Three different models of the extended Bean's models in Table I are used for calculating the losses. In order to obtain the critical current $I_C \approx 100$ A, the critical current density J_C is set at 4.6×10^6 A/m^2. The values of E_N and J_N are also fixed in order to bound the region for which the material remains superconductive.

IV. Numerical Results

We have realized a series of numerical simulations for a

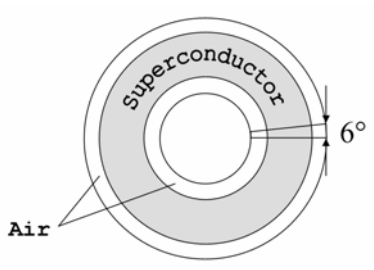

Figure 3. Computational domain in 2D.

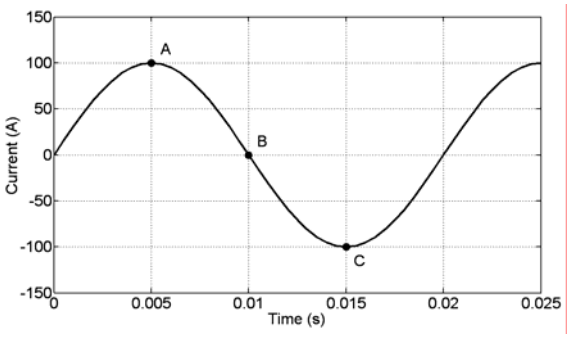

Figure 4. Transport current in superconducting transmission line.

TABLE I
Various Models of Extended Bean's Model

Model	E_C (V/m)	J_C (A/m^2)	E_N (V/m)	J_N (A/m^2)
1	10^{-6}	4.6×10^6	5.3×10^{-4}	5×10^6
2	10^{-5}	4.6×10^6	5.3×10^{-4}	5×10^6
3	10^{-4}	4.6×10^6	5.3×10^{-4}	5×10^6

superconducting transmission line with a transport current as in Fig. 4. Fig. 5 shows the temporal evolution of the Joule losses obtained from three models in Table I for the maximum current equal to 60 A (a), 100 A (b), and 140 A (c). We observe that we obtain coherent values of the losses for the maximum current equal to 140 A which is higher than the critical current ($I_{max} > I_C$). On the other hand, we obtain different values of the losses for the maximum current equal to 60 A which is lower than the critical current ($I_{max} < I_C$).

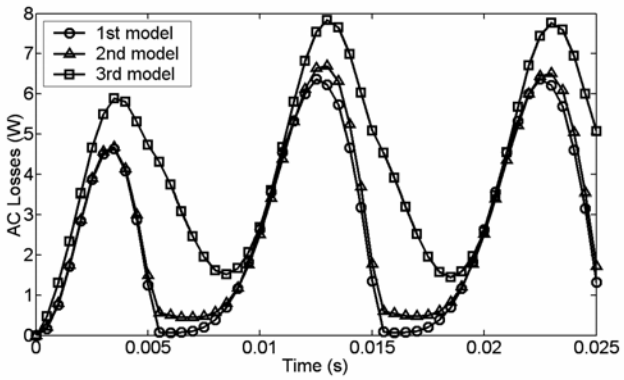

(a) For $I_{max} = 60 < I_C$

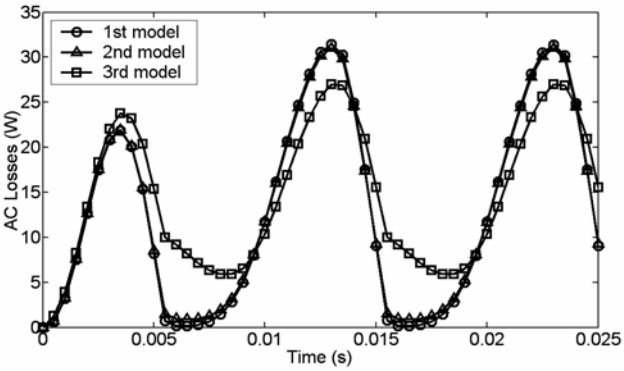

(b) For $I_{max} = 100 = I_C$

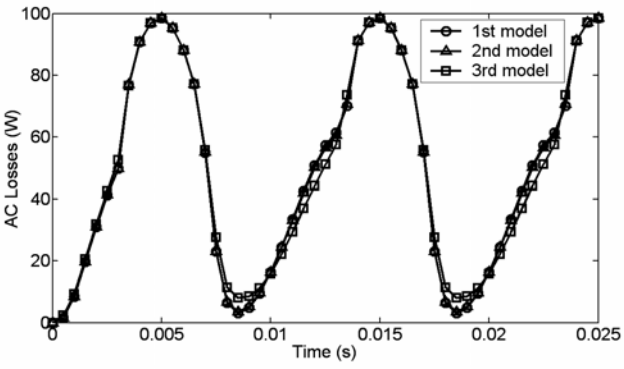

(c) For $I_{max} = 140 > I_C$

Figure 5. Comparison of the instantaneous losses in the superconducting transmission line for the different values of the maximum current.

From the instantaneous losses in Fig. 5, we are able to determine the average losses by using the formula (9). On Fig. 6, we present the evolution of the average losses obtained numerically according to the maximum amplitude of the transport current in the superconducting transmission line. The results obtained show that when the maximum current is higher than the critical current ($I_{max} > I_C$), three models give almost the same results for the values of the average losses. For currents whose maximum amplitude is lower than the critical current ($I_{max} < I_C$), three models give the different values of the average losses.

Fig. 7 illustrates the current density distribution inside the superconducting transmission line at points A (a), B (b), and C (c), respectively as indicated in Fig. 4. These distributions can be described by the critical state model of Bean. The current density distribution can be shown by a shell. At the maximum current (point A), the current density in the superconducting transmission line is equal to the critical current density J_C (Fig. 7(a)). When the current reaches to the minimum value (point C), the current density distribution in the transmission line is the same but the direction of current flows opposed to that of Fig. 7(a) (see Fig. 7(c)). At point B which is intermediate between point A and point C, we find that the transport current is changing its direction. A new shell is created at the outside of the old shell with the transport current circulating in the direction opposed to that of the old shell (Fig. 7(b)).

In Fig. 8 from (a) to (c), we can see the penetration of the magnetic induction inside the superconducting transmission line which progresses well with the rotation whose module is equal to J_C . At point B, we find that the magnetic induction is changing its direction. This is starting from the edge of the superconducting transmission line (Fig. 8(b)).

V. CONCLUSION

Our aim is to calculate the AC losses in a superconducting transmission line. In this paper, we have compared the results of numerical simulations of the instantaneous losses and also

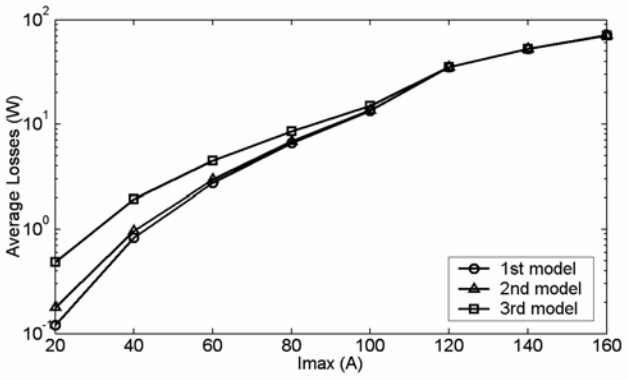

Figure 6. Comparison of the average losses in the transmission line.

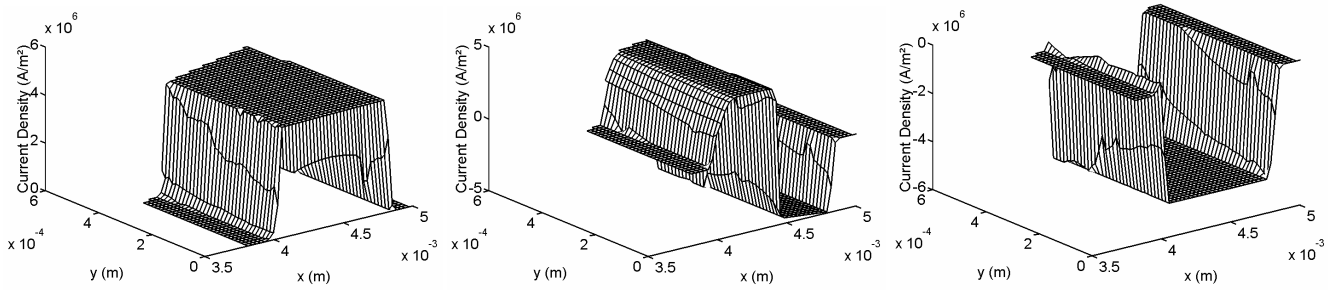

(a) At point A (b) At point B (c) At point C

Figure 7. Current density distribution in the superconducting transmission line at different points in Fig. 4.

of the average losses carried out by the proposed method for different models of the extended Bean's model. These models are modified from the critical state model of Bean.

From the results of numerical simulations, we find that all models give almost the same losses, the instantaneous losses and also the average losses, when the maximum amplitude of the transport current is higher than the critical current of the superconducting transmission line. Furthermore, the distributions of the current density and of the magnetic induction inside the superconducting transmission line show clearly a phenomenon of superconductivity.

The use of superconductors shows the possibility for real applications in the electrical area such as the electrical power transmission lines, the electrical power cables, the electrical machines (motors and generators), or the transformers. So we have to seek for the models of these materials in order to be able to study and analyze all the aspects of them.

REFERENCES

[1] M. Maslouh, F. Bouillault, A. Bossavit, and J.C. Verite, "From Bean's Model to the H-M Characteristic of a Superconductor: Some Numerical Experiments," *IEEE Trans. Appl. Supercond.*, vol. 7, no. 3, pp. 3797-3801, Sep. 1997.

[2] T. Satiramatekul, F. Bouillault, and M. Maslouh, "Modeling of Superconducting Line by the Finite Element Method," *Proc. 2nd Int. Symp. on Communications and Information Technologies*, pp. 217-220, Oct. 2002.

[3] T. Satiramatekul, F. Bouillault, A. Devred, and L. Bottura, "Analytical & Numerical Modelings of Elliptical Superconducting Filament Magnetization," *IEEE Trans. Appl. Supercond.*, vol. 15, no. 2, pp. 3680-3683, June 2005.

[4] T. Satiramatekul, et al., "Study of the Losses in a HT_C Superconducting Tube: Comparison of Methods of Calculation," *Proc. 4th Japanese-Mediterranean Workshop on Applied Electromagnetic Engineering for Magnetic, Superconducting and Nano Materials*, Sep. 2005.

[5] M. Maslouh, F. Bouillault, A. Bossavit, and J.C. Verite, "Numerical Modelling of Superconductor Materials Using an Anisotropic Kim Law," *IEEE Trans. Magn.*, vol. 34, no. 5, pp. 3064-3067, Sep. 1998.

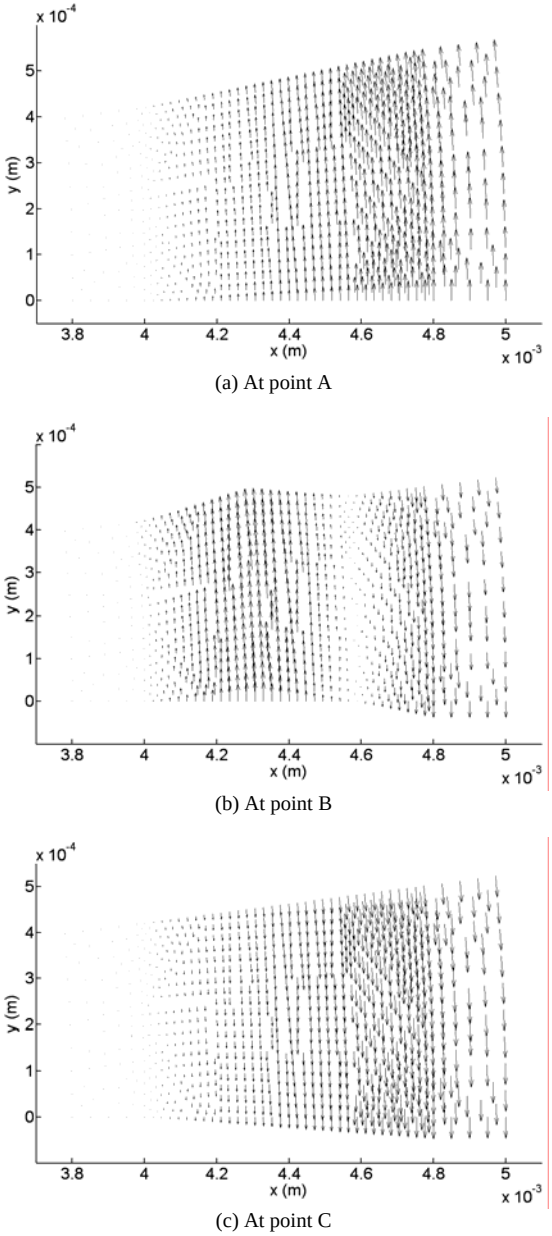

(a) At point A

(b) At point B

(c) At point C

Figure 8. Magnetic induction distribution in the superconducting transmission line at different points in Fig. 4.

Power Quality Improvement by Use of a New Topology of Fault Current Limiter

Seyed Hossein Hosseini[1], M. Abapour [2], M. Tarafdar Hagh [2]

[1]Electrical Engineering Department, Islamic Azad University of Bonab, Bonab, Iran,
(Tel/Fax: +98-411-3300819; Email: hosseini@tabrizu.ac.ir)
[2] Faculty of Electric & Electronic Engineering., University of Tabriz, Tabriz, IRAN

***Abstract*—Short circuit current limitation in distribution utilities can be an effective way to improve power quality, since the expected voltage sag amplitude during faults can be dramatically reduced. In this paper, the analytical analysis of a novel fault current limiter based on DC reactor with using superconductor is presented. Its operation is investigated through computer simulation with ElectroMagnetic Transient Program (EMTP) simulation results based on a model system also show that proposed SFCL are effective for power quality improvement of electric power systems by restraining the fault current.**

I. INTRODUCTION

Voltage sags are a rather old problem in power systems that nowadays are gaining significance due to the growth of sensitive loads. Modern process controls are often sensitive to voltage sags, which may cause significant production outages [1-2]. Universal experience shows that a main reason of voltage sags affecting customers is short circuits on utility's lines, with special reference to the overhead radial distribution ones. Since the voltage sag during the fault is proportional to the short circuit current [3]. An effective fault current limitation by means of a device connected series with the radial feeders will limit the expected voltage sag and improve the system power quality [3]. Also circuit breaker operation in distribution lines causes over voltage in substation and other loads. In this paper a new type of fault current limiter based on DC reactor with using superconductor are presented. In normal operation condition the limiter has no obvious effect on loads. When fault happens, a bypass AC reactor and series resistor will insert the fault line automatically to limit the short circuit current, when the control circuit detects a short circuit fault, the solid state bridge in fault line works as an inverter and is closed as soon as possible. Subsequently the fault current is fully limited by the bypass AC reactor and series resistor. In general this type of SFCL is useful for power quality improvement when fault is occurred in distribution systems.

II. CLASSIFICATION OF VOLTAGE SAGS

Study system in this paper is shown in Fig. 1. A fault on the power system will cause both a dip in voltage magnitude and a shift in phase angle. To predict the magnitude of the voltage sag and the phase angle jump, the simple voltage divider idea proposed in [4] is adopted [5]. A simple model for calculating the resulting voltage, i.e. the voltage magnitude during the sag, can be seen in Fig. 2. This model is based on a voltage divider and it is useful for radial systems and selected from Fig. 1. However, it attends to for describing and explaining the events in a simple and clear way.

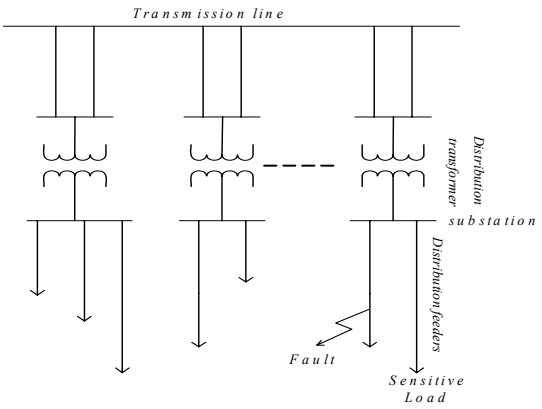

Fig. 1 study system

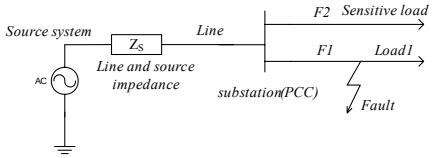

Fig. 2 Simplified diagram of the study system

In this study the load current is not neglected in the simple voltage divider method. Z_S is the source impedance at the PCC. The impedance between PCC and sensitive load define with Z_2, also the impedance between PCC and load1 define with Z_1. It is also necessary to calculate the reactance between the PCC and the fault location. Z_f defined line impedance between the PCC and fault including any fault impedance, if the fault impedance is neglected or included in Z_f. in normal operation the resulting voltage and phase angle will be:

$$Z_N = Z_1 \| Z_2 \quad (1)$$

PCC voltage defines with:

$$\overline{V}_{PCC(N)} = \frac{\overline{Z}_N}{\overline{Z}_S + \overline{Z}_N} \quad (2)$$

$$V_{PCC(N)} = \left| \frac{\overline{Z}_N}{\overline{Z}_S + \overline{Z}_N} \right| \quad (3)$$

$$\varphi_{PCC(N)} = \arctan(\frac{X_N}{R_N}) - \arctan(\frac{X_N + X_S}{R_N + R_S}) \quad (4)$$

where

$Z_1 = R_1 + jX_1$ (Load 1 and F1 impedance)

$Z_2 = R_2 + jX_2$ (sensitive load and F2 impedance)

$\overline{V}_{PCC(N)}$: Voltage phasor at the PCC at normal operation

$V_{PCC(N)}$: Voltage magnitude at the PCC at normal operation

$\varphi_{PCC(N)}$: Phase angle of voltage at the PCC at normal operation

when fault occurs the resulting voltage and phase angle can be expressed by

$$Z_F = Z_2 \| Z_f \quad (5)$$

$$\overline{V}_{PCC(F)} = \frac{\overline{Z}_F}{\overline{Z}_S + \overline{Z}_F} \quad (6)$$

$$V_{PCC(F)} = \left| \frac{\overline{Z}_F}{\overline{Z}_S + \overline{Z}_F} \right| \quad (7)$$

$$\varphi_{PCC(F)} = \arctan(\frac{X_F}{R_F}) - \arctan(\frac{X_F + X_S}{R_F + R_S}) \quad (8)$$

where

$Z_2 = R_2 + jX_2$ (sensitive load and feeder F2 impedance)

$Z_f = R_f + jX_f$ (line impedance between the PCC and fault including any fault impedance in feeder F1)

$\overline{V}_{PCC(F)}$: Voltage phasor at the PCC at normal operation

$V_{PCC(F)}$: Voltage magnitude at the PCC when fault occur

$\varphi_{PCC(F)}$: Phase angle of voltage at the PCC when fault occur

As can be seen from Eq. (8) when fault occur in feeder F2 the changing X_N/R_N ratio and $(X_N+X_S)/(R_N+R_S)$ ratio between causes a phase angle jump at the PCC. This can be referred as the initial phase angle jump. Also fault occurrence causes vital change in Z_N and in result voltage magnitude. In this paper, SFCLs will be added to the power systems to evaluate their effectiveness in reducing the initial phase angle jumps and voltage sag. The SFCL can be used to increase the impedance of the fault by introducing impedance. As the same way it does as a fault current limiter. Then when the SFCL is limiting fault current, therefore it is improve the quality of the supply by mitigating sag.

III. Proposed SFCL Circuit and Its Operation

Proposed topology of fault current limiter is shown in Fig. 3. The circuit consists of two diodes, two thyristor, AC impedance branch and a high-T_C superconducting coil. The system current passes through superconducting coil DC reactor. DC reactor will have no effect on normal operation of system. There would be a forward voltage drop across rectifier diodes V_{DF}, too. During fault condition, the fault current increases and this time varying current passes through DC reactor that increases voltage drop and decreases the fault current magnitude

The fault current will pass through DC reactor for only some milliseconds and then the bridge circuit will retreat from fault circuit.

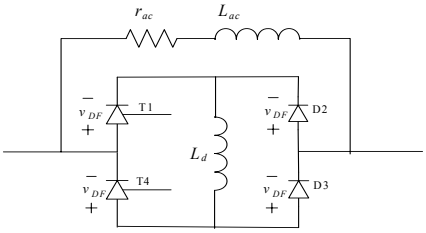

Fig. 3 Circuit diagram of bridge type SFCL

A. Control strategy

There are different control strategies but two types are used mainly in different papers. As a review, these control strategies are presented in this paper.

a) Freewheeling control

At the starting and steady stage of SFCL T1 and T4 are triggered and turned on half cycle at positive and negative phase voltage across zero respectively. In accident, DC reactor retreat from fault circuit and leaving AC reactor and resistor to limit the fault current only. In freewheeling control, remove triggered pulses of thyristor bridge arms T1 and T4. In this way, the bridge circuit will retreat from fault circuit within at most half cycle after the fault is detected, while current on DC reactor run through D2 and D3 to form free-wheeling circuit. The current in DC reactor will be reduced due to energy loss caused by voltage drop on diodes. But voltage drop is very small so that current reduction takes a long time. In this paper we used freewheeling control.

b) Reverse control

In freewheeling control, the current in DC reactor will be reduced due to energy loss caused by voltage drop on diodes. But voltage drop is very small so that current reduction takes a long time. Also if accidents take place many times, current value on DC reactor will rise. For this reasons, this control strategy is not often used.

IV. Analytical Analysis and Simulation Result of Proposed SFCL

In this section analytical analysis of the study system in Fig. 1 to show power system situations in fault condition and SFCL operation for load protection is given. For a fault at the distribution level, for example on F1, SFCL activation on the faulted feeder introduces large limiting impedance between the fault and PCC. The introduced impedance has the effect of isolating the fault from the PCC; hence sensitive loads supplied through the parallel feeder F2 will not feel any significant disturbance due to the fault. In this section for

provide a detailed analysis a similar model to section 2 is used as shown in Fig. 4. The utility voltage is a sinusoidal waveform with angular frequency ω, peak value V.

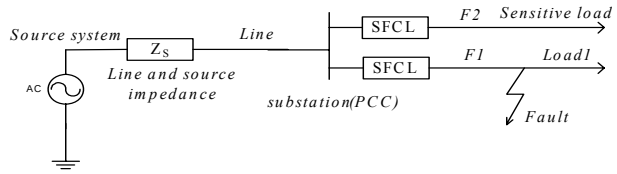

Fig. 4 Simplified diagram of the study system

A. *Time sequence of simulation*

A series of simulations were conducted to analyze the performance of the SFCL.

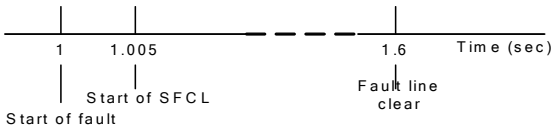

Fig. 5 time sequence of simulation

The short-circuit fault was supposed to occur on the distribution feeder F1 between PCC and load1 as shown in Fig. 4. The Simulation was carried out based on the time sequence as shown in Fig. 5. Remove triggered pulses of thyristor bridge arms T1 and T4 achieved at about 5 (msec) after fault occurrence and the clearance of the fault was supposed to be achieved at about 0.6 (sec) after the occurrence of the fault. Fig. 5 shows the time sequence of simulation.

Study system consists of two distribution feeders originating from the same substation bus. Fault is occurring in feeder F1 where feeder F2 is supplying a sensitive load. In this paper, the SFCLs are placed at the substation end of the distribution feeders, F1 and F2, as shown in Fig. 4. At these sites, the SFCL activation on the faulted feeder will help to keep the bus voltage level at acceptable value. The load is assumed to be a balance R-L load with r_L and L_L as its resistor and inductor, respectively

. Power equipment data are as follow:

Generator: 20 kV, 10 MVA, 1.608 Ω

Transformer: 20 kV/6.6 kV, 10 MVA, 0.0824 pu

Distribution feeder data:

Resistance = 0.220 Ω/km

Reactance = 0.444 Ω/km

Length of F1 = 3 km

Length of F2 = 2 km

Length of Line1 = 10 km

DC inductance of SFCL in faulty line, L_d = 0.1 H

AC inductance of SFCL in faulty line, L_{ac} = 0.1 H

AC resistance of SFCL in faulty line, r_{ac} = 20 Ω

Load data in feeder F1:

Resistance = 20 Ω

Inductance = 0.1 H

Fig. 6 shows the behavior of the distribution bus (PCC) without the SFCL present due to fault applied at time t_0. It shows that PCC voltage of the unlimited system is significantly reduced during the fault and phase angle is jumping. Also Fig. 7 shows the behavior of the distribution bus (PCC) without the SFCL and with uses of circuit breaker. It shows that PCC voltage is a little increased when line1 retreat from test system by circuit breaker operation. Fig. 6 and Fig. 7 are result in simulation analysis. However, when the SFCL is placed into the system, the bus voltage (PCC) is kept practically undisturbed and no dramatic voltage sag is visible. Also the change in phase angle is eliminated. Fig. 8 shows distribution bus (PCC) voltage with using SFCL. It shows that PCC voltage and phase angle of the limited system is kept at acceptable value during the fault and just PCC voltage have little distortion in first half cycle after fault occurrence.

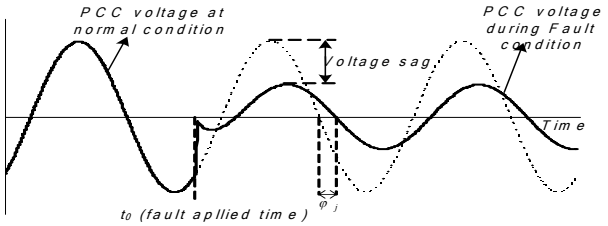

Fig. 6 PCC voltage of the unlimited system

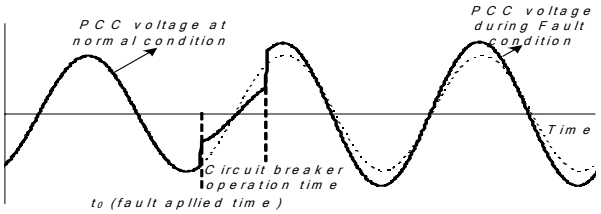

Fig. 7 PCC voltage, protected with circuit breaker

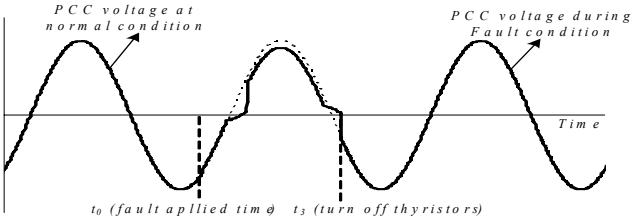

Fig. 8 distribution bus (PCC) voltage with using SFCL

Fig. 9 shows the line and SFCL currents during a fault condition. The fault occurs at $t=t_0$ and the load current begins to increase. As is shown in this figure, before fault condition, the current through inductor is an almost ripple free DC current. The produced voltage across L_d in fault condition has resulted in limiting the fault current as well as distortion of its waveform. The circuit has two modes of operation between t_0 and t_3 before DC reactor retreat from power system (thyristors turn off) as follows:

(a) Charging mode

(b) Discharging mode

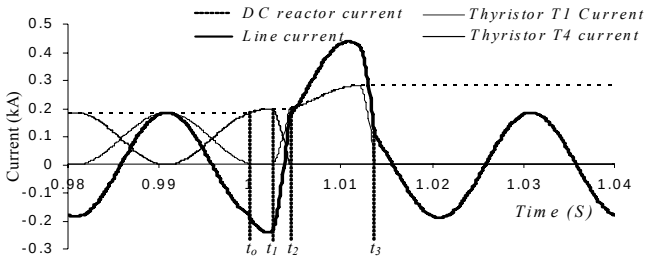

Fig. 9 line and SFCL currents during fault condition

At $t=t_0$ charging mode begins and the line current reaches the inductor current. The operation of SFCL has resulted in fault current limiting between t_0 to t_3. At $t=t_1$ discharging mode starts and it continuous until $t=t_2$. Eq. (10) shows the DC reactor current formula at time interval between t_0 to t_1

$$V\sin(\omega t) = ri_d(t) + \frac{Ldi_d(t)}{dt} + 2V_{DF} \tag{9}$$

$$i_d(t) = e^{-(r/L)(t-t_0)}\left\{i_0 - \frac{V}{z}\sin(\omega t_0 - \varphi) + \frac{2V_{DF}}{r}\right\} + \frac{V}{z}\sin(\omega t - \varphi) - \frac{2V_{DF}}{r} \tag{10}$$

where: $r=r_{SL}+r_F$, $L=L_S+L_d+L_F$, V_{DF} is the forward voltage drop of the diodes that is assumed to be constant, $i_0=i_d(t_0)$, $Z=r+jL\omega$, $Z_F=r_F+jL_F\omega$, $z=|Z|$, $\tan\varphi=\angle Z$ and L_d is the DC reactor inductance. Z_F and Z_S are defined in section (II).

Eq. (12) shows the AC branch of limiter current formula at time interval between t_0 to t_1

$$V\sin(\omega t) = ri_d(t) + \frac{Ldi_d(t)}{dt} \tag{11}$$

$$i_{ac}(t) = e^{-(r/L)(t-t_0)}\left\{i_0 - \frac{V}{z}\sin(\omega t_0 - \varphi)\right\} + \frac{V}{z}\sin(\omega t - \varphi) \tag{12}$$

where: $r=r_{SL}+r_{ac}+r_F$, $L=L_S+L_{ac}+L_F$, , $i_0=i_{ac}(t_0)$, $Z=r+jL\omega$, $Z_F=r_F+jL_F\omega$, $z=|Z|$, $\tan\varphi=\angle Z$ r_{ac} and L_{ac} are the resistance and inductance of ac branch of limiter respectively. Line voltage is given as follows

$$i_L(t) = i_d(t) + i_{ac}(t) \tag{13}$$

At $t=t_2$ thyristor T4 turns off and thyristor T1 conduct DC reactor current. Eq. (14) and Eq. (15) show the line and DC reactor current formula during discharging mode, respectively.

$$i_L(t) = e^{-(r/L)(t-t_1)}\left\{i_1 - \frac{V}{z}\sin(\omega t_1 - \varphi)\right\} + \frac{V}{z}\sin(\omega t - \varphi) \tag{14}$$

$$i_d(t) = i_{d1} - \frac{2V_{DF}}{L_d}(t - t_1) \tag{15}$$

where: $i_1=i_L(t_1)$, $i_{d1}=i_d(t_1)$ $r=r_S+r_F$, $L=L_S+L_F$.

Again at $t=t_2$ charging mode begins and it continues until $t=t_3$. At t_3 thyristor T1 turn off and DC reactor retreat from feeder F1 completely.

In Fig. 10 the effect of using DC reactor in proposed SFCL are considered clearly.

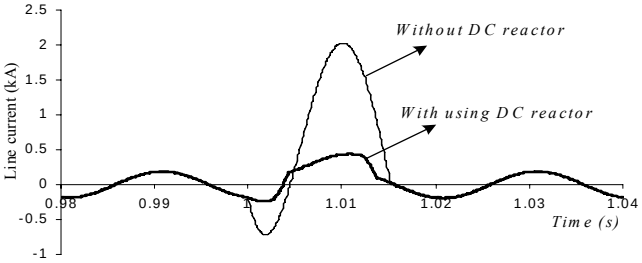

Fig. 10 effect of using DC reactor in proposed SFCL

When DC reactor retreat from feeder F1 at t_3, fault impedance will be equal with Z_1 (load1 and F1 impedance) and we have not any voltage distortion or phase angle jump in PCC as shown in Fig. 8.

V. CONCLUSION

Today the problem of power quality improvement is very real. In this paper a new type of fault current limiter based on DC reactor with using superconductor for power quality improvement are presented. Proposed SFCL is capable of mitigating voltage dips and the associated phase angle jump to acceptable levels for the distribution system considered in this work. However, in order to achieve good voltage dip mitigation (5% to 10% dips), fault currents would need to be reduced to about 2 pu. When fault happens, a bypass AC reactor and series resistor will insert the fault line automatically to limit the short circuit current. Subsequently the fault current is fully limited by the bypass AC reactor and series resistor. In general this type of SFCL is useful for power quality improvement when fault is occurred in distribution systems.

REFERENCES

[1] M.F. McGranaghan, D.R. Mueller, M.J. Samotyj, Voltage sags in industrial systems, IEEE Transactions on Industry Applications (No.2) (March/April 1993) pp. 397–403.

[2] C.J. Melhorn, T.D. Davis, G. Beam, Voltage sags: their impact on the utility and industrial customers, IEEE Transactions on Industry Application (No.3) (May/June 1998) pp. 549–558.

[3] F. Tosato, S. Quaia, Reducing voltage sags through fault current limitation, IEEE Transactions on Power Delivery, (Vol 16), (Jan. 2001) pp. 12-17.

[4] L.E. Conrad, Proposed Chapter 9 for predicting voltage sags (Dips) in revision to IEEE Std. 493, the gold book, IEEE Transactions on Industry Applications (May/June 1994) pp. 805–821.

[5] H. Math, J. Bollen, Fast assessment methods for voltage sags in distribution systems, IEEE Transactions on Industry Applications 32 (No.6) (November/December 1996) pp. 1414–1423.

[6] M.M.R. Ahmed, G.A. Putrus, L. Ran, Power quality improvement using a solid-state fault current limiter, Transmission and Distribution Conference and Exhibition 2002: Asia Pacific. IEEE/PES, (Vol 2), (6-10 Oct. 2002) pp. 1059 – 1064.

Genetic Algorithm Application for DSP-Based Maximum Power Point Tracking in PV Generation System

Somsak Senapukdee and Ekarin Vasanasong
Department of Electrical Power Engineering, Mahanakorn University of Technology
51 Cheum-Sampan Road, Nongchock, Bankok 10530 Thailand
Email: senapukdee@hotmail.com

***Abstract*- This paper presents a maximum power point tracking (MPPT) for photovoltaic (PV) system, which generates signal to control solid-state switch of boost converter. The system controlled by ADMC331 a digital signal processing. The controller tracks maximum power by genetic Algorithm method. Genetic Algorithm is proposed in form of a mathematical model. This is an improved maximum power point tracking system in terms of speed and accuracy.**

I. INTRODUCTION

The people around the world are concerned about conventional sources of energy due to the fossil fuel exhaustion, their prices, and side effects of using fossil fuel. As the cost of fossil based energy is rising and the environmental problem caused by the conventional power generation is observable, renewable energy sources such as PV energy becomes a promising alternative source. Even though, PV energy source is clean, pollution-free and inexhaustible but their installation cost is high and the module efficiency is low therefore the overall system cost can be reduced by using high efficiency power conditioners which, in addition, are designed to extract the maximum possible power form the PV array, called maximum power point tracking (MPPT).

The MPP is effects by irradiation and temperature. They have been many MPPT techniques for PV power generation [1]-[8]. The task of MPPT is to track this MPP regardless of weather or load conditions so that the PV system draws maximum power from the PV system. The MPPT solution is in form of a non-linear dynamic and time-varying system. All algorithms are based on the fact that, looking at the power characteristic, at the left of the MPP the dP/dv > 0, at the right of the dP/dv < 0 and at MPP dP/dv = 0, as show in Fig. 1.

The perturbation and observation method (P&O), which moves the operating point toward the maximum power point by periodically increasing or decreasing the array voltage, is often used in many PV system [1]-[3], that the P&O method works well when the insulation does not vary quickly with time. However, the P&O method fails to quickly track the maximum power points.

The constant voltage (CV) this algorithm makes use of the fact that the MPP voltage changes only slightly with varying

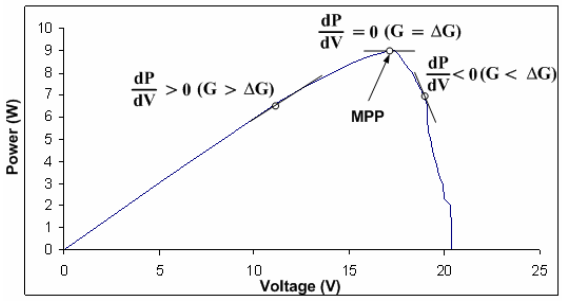

Figure 1. All algorithms are based on the fact that, looking at the power characteristic.

Irradiation [6]-[7], the ratio of VMP/VOC depends on the PV system parameters, but a commonly used value is 76%. In this algorithm the MPPT momentarily sets the PV system current to zero to allow a measurement of the PV system's open circuit voltage. The PV system operating voltage is then set to 76% of this measured value. This operating point is maintained for a set amount of time and then the cycle is repeated. A problem with this algorithm is the available energy is wasted when the load is disconnected form the PV system, also the MPP is not always located at 76% of the PV system's open circuit voltage.

The Incremental conductance method (INC) tracks the maximum power points by comparing the incremental and instantaneous conductance of the PV system [4]-[5], show in Fig. 2. The incremental conductance is estimated by measuring small changes in PV system voltage and current. These small changes may be induced by deliberate control action. A method which improves the INC method and can identify the incremental conductance of the PV system more rapidly than it has been in P&O and CV. Moreover, those search for the maximum operating conditions form the output power and voltage characteristics of PV system techniques are the hill-climbing [8], fuzzy logic control [9], and Artificial Neural Network (ANN) [10].

This paper proposes the implementation of DSP-based MPPT using low-cost low power consumption DSP to control a high efficiency boost-type dc/dc converter while genetic algorithm software has been developed for MPPT with self turning function. The DSP-Based MPPT controller is compared with the INC method to confirm the better results.

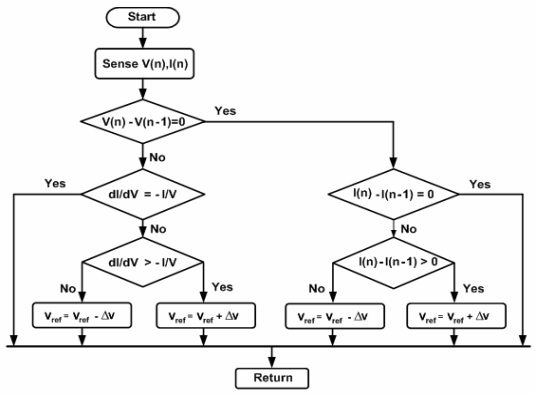

Figure 2. Flowchart INC method of MPPT control.

II. CHARACTERISTICS OF PHOTOVOLTAIC

The amount of the converted PV energy to electrical fluctuates depending on irradiation and temperature, as show in Fig. 3. It is seen that the irradiation charges affect mainly on the PV output current, while the temperature changes affect mainly on the PV output voltage. The intersection of the load-line with the PV system I-V characteristic, for a give irradiation and temperature, determines the operating point. The maximum power production is based on the load-line adjustment under varying atmospheric conditions. The equivalent circuit of the PV system is show in Fig. 4. The traditional I-V characteristic and P-V characteristic of PV system when neglecting the internal shunt resistance, is give by the following equation (1)

$$I_o = I_g - I_{sat}\left\{\exp\left[\frac{q}{AKT}\left(V_o + I_o R_s\right)\right] - 1\right\} \qquad (1)$$

Where I_o and V_o are the output current and output voltage, respectively, I_g is generated current under the irradiation, I_{sat} is the reverse saturation current, q is the electron charge, A is a dimensionless factor, K is the Boltzmann's constant, T is the temperature in (°K), R_s is the series resistance of the cell.

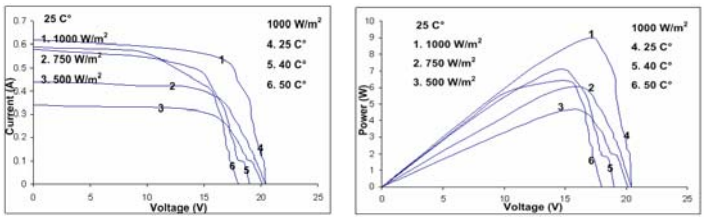

Figure 3. Characteristic of PV system with irradiation and temperature.

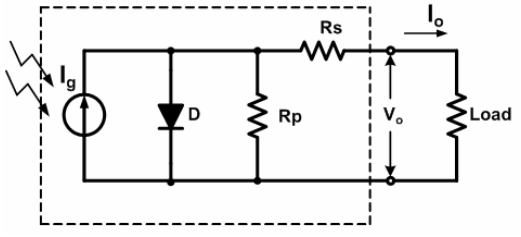

Figure 4. Equivalent circuit of the PV system.

III. BOOST CONVERTER

In a boost regulator the output voltage is greater than the input voltage, depicts a step-up or a PWM boost converter. It consists of dc input voltage source V_S, boost inductor L, controlled switch, diode D, filter capacitor C, and load resister R_L. The boost converter equivalent circuit diagram and its associated theoretical wave forms are show in Fig. 5 and 6, respectively. When the switch is turned on, the current in the boost inductor increases linearly and the diode D is off at that time. When switch turned off, the energy stored in the inductor is released through the diode to the output RC circuit, from which the dc voltage transfer function turns out to be.

$$V_O = \frac{V_S}{(1 - D)} \qquad (2)$$

Where V_O is maximum of the dc component of the output voltage. The output voltage is always greater than the input voltage. The boost converter operates in the continuous conduction mode where $L > L_{min}$

$$L_{min} = \frac{D(1-D)^2 R}{2fs} \qquad (3)$$

The filter capacitor must provide the output dc current to the load. When the diode D is off. The minimum value of the filter capacitance that results in the voltage ripple ΔV_O is give by.

$$\Delta V_O = \frac{V_O D}{RCfs} \qquad (4)$$

Where D is duty cycle at maximum converter output power, ΔV_O is the output voltage peak to peak ripple at maximum power, and fs is switching frequency.

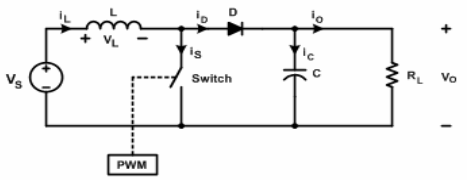

Figure 5. Equivalent circuit diagram of the boost converter.

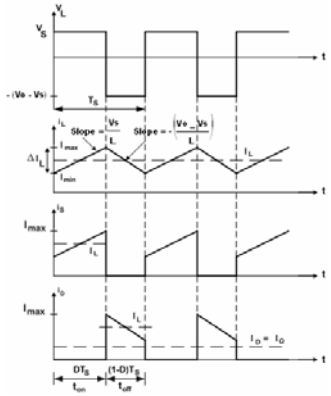

Figure 6. Voltage and current waveforms in a boost converter.

IV. GENETIC ALGORITHM

Genetic algorithms are a part of evolutionary computing, which is a rapidly growing area of artificial intelligence. As you can guess, genetic algorithms are inspired by Darwin's theory about evolution. Genetic algorithms are stochastic search techniques based on the mechanism of natural selection and natural genetics. Genetic algorithms, differing form conventional search techniques, start with an initial set of random solutions called population. Each individual in the population is called a chromosome, a binary bit string. The chromosomes evolve through successive iterations, called generations. During each generation, the chromosomes are evaluated, using some measures of fitness. To create the next generation, new chromosomes, called offspring, are formed by either merging two chromosomes from current generation using a crossover operator or modifying a chromosome using a mutation operator. A new generation is formed by selecting, according to the fitness values, some of the parents and of spring and rejecting others so as to keep the population size constant. Fitter chromosomes have higher probabilities of being selected. After several generations, the algorithm converge to the best chromosome, which hopefully represents the optimum or suboptimal solution to the problem. Structure of genetic algorithm is shown in Fig.7.

1) Generate random population of n chromosomes.
2) Evaluate the fitness f(x) of each chromosome x in the population.
3) Create a new population by repeating following steps until the new population is complete.
   3.1) Select parent chromosomes from a population according to their fitness (roulette wheel selection).
   3.2) With a crossover probability cross over the parents to form a new offspring. If no crossover was performed, offspring is an exact copy of parents.
   3.3) With a mutation probability mutate new offspring at each locus (position in chromosome).
4) Place new offspring in anew population.
5) If the end condition is satisfied, stop, and return the best solution in current population. Go to step 2

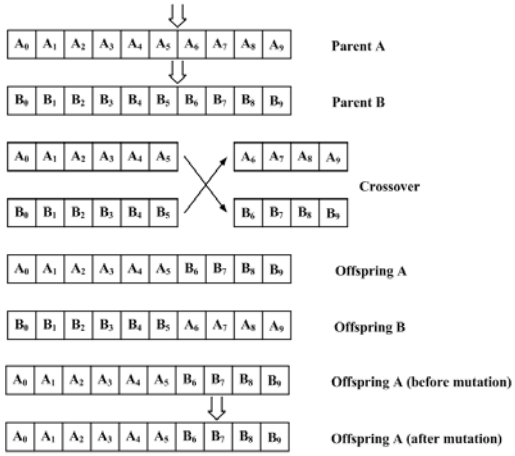

Figure 7. Genetic Algorithm.

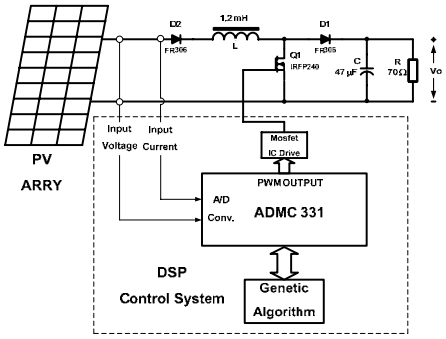

Figure 8. Block diagram DSP-based control MPPT proposed system.

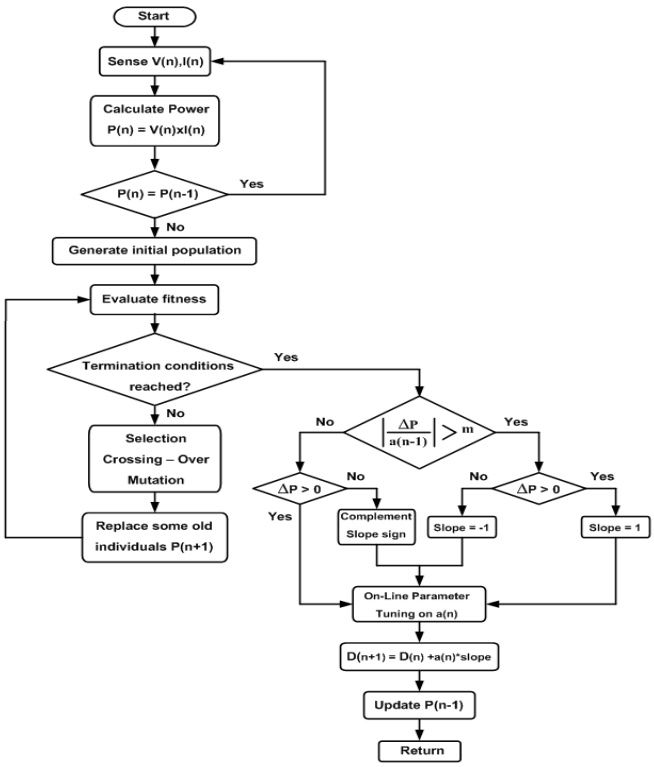

Figure 9. The flowchart of propose MPPT control method.

V. PROPOSED SYSTEM

A block diagram of proposed system is show in Fig. 8. The PV system which is to be used in this paper consists of Solartron Solar Module. Model SP10, P_{max} 10 w, V_{oc} = 21 V, I_{sc} = 0.62 A, V_{mp} = 17.24 V, and I_{mp} = 0.58 A. and DSP-based ADMC331, 26 MIPS, Fix-point 16-bit DSP core.

By using A/D converters, the voltage control which is between 0.3-3 V can be directly measured while current can be using the hall-effect sensor. The flowchart control program is show in Fig. 9, and fitness function for MPPT following in equation 5. Also, it features PWM output with program controlled duty cycle dc/dc boost converter 25 kHz maximum frequency.

$$f(x) = m_i \frac{\Delta P}{\Delta D(n-1)} \tag{5}$$

VI. EXPERIMENTAL RESULT

The MPP of PV system is compared between proposed method and INC method by varying the temperature from 25 °C, 40 °C, and 50 °C and the irradiation from 1000 W/m^2, 750 W/m^2, and 500 W/m^2. The INC used step-size ΔD = 0.02, experimental result, as show in Fig. 10-12, table 1, and 2.

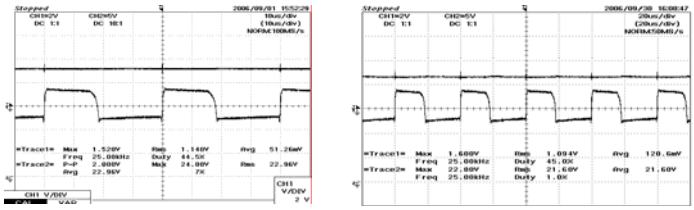

(a) (b)

Figure 10. Constant temperature 50 °C and irradiation 1000 W/m^2 (a) INC method and Vmax = 22.6 V (b) Propose method and Vmax = 22.8 V

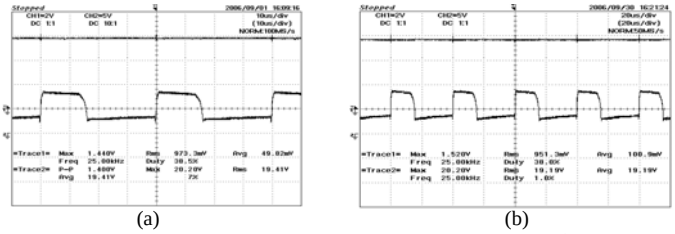

(a) (b)

Figure 11. Constant temperature 50 °C and irradiation 750 W/m^2 (a) INC method and Vmax = 20.2 V (b) Propose method and Vmax = 20.2 V

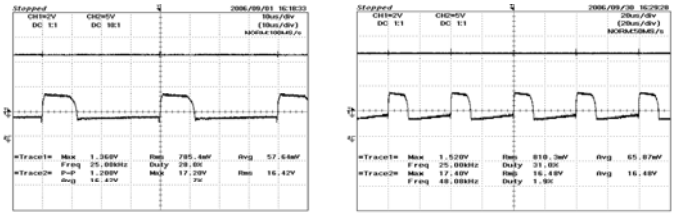

(a) (b)

Figure 12. Constant temperature 50 °C and irradiation 500 W/m^2 (a) INC method and Vmax = 17.2 V (b) Propose method and Vmax = 17.4 V

TABLE I
INCREMENTAL CONDUCTANCE METHOD

W/m^2	T = 25 C°					
	Vmp (V)	Imp (A)	Pin (W)	Vout (V)	Pout (W)	η(%)
1000	17.2	0.53	9.116	24.2	8.366	91.776
750	17.2	0.4	6.880	21.6	6.665	96.877
500	17	0.3	5.100	18.6	4.942	96.908
W/m^2	T = 40 C°					
	Vmp (V)	Imp (A)	Pin (W)	Vout (V)	Pout (W)	η(%)
1000	16.3	0.53	8.639	23.2	7.689	89.005
750	16.3	0.4	6.520	21.2	6.421	98.475
500	15.9	0.29	4.611	17.2	4.226	91.657
W/m^2	T = 50 C°					
	Vmp (V)	Imp (A)	Pin (W)	Vout (V)	Pout (W)	η(%)
1000	15.9	0.49	7.791	22.6	7.297	93.654
750	15.3	0.4	6.120	20.2	5.829	95.247
500	14.6	0.3	4.380	17.2	4.226	96.491

TABLE II
GENETIC ALGORITHM METHOD

W/m^2	T = 25 C°					
	Vmp (V)	Imp (A)	Pin (W)	Vout (V)	Pout (W)	η(%)
1000	17.1	0.53	9.063	24.4	8.505	93.845
750	17.1	0.4	6.840	21.8	6.789	99.256
500	16.9	0.3	5.070	18.59	4.937	97.376
W/m^2	T = 40 C°					
	Vmp (V)	Imp (A)	Pin (W)	Vout (V)	Pout (W)	η(%)
1000	15.9	0.53	8.427	23.4	7.822	92.824
750	15.9	0.4	6.360	21	6.300	99.057
500	15.8	0.29	4.582	17.6	4.425	96.577
W/m^2	T = 50 C°					
	Vmp (V)	Imp (A)	Pin (W)	Vout (V)	Pout (W)	η(%)
1000	15.5	0.5	7.750	22.8	7.426	95.823
750	15	0.4	6.000	20.2	5.829	97.152
500	14.6	0.3	4.380	17.4	4.325	98.748

VII. CONCLUSION

In this paper, the principle of genetic algorithm application has been used to deliver the highest possible power of the load from the PV system. The proposed control algorithm has been showed and compared with the conventional INC. method. The result from the experimental show that the proposed method has better performance of tracking maximum power than the conventional INC. method in term of efficiency.

REFERENCES

[1] D.P. Hohm and M.B. Ropp. "Comparative Study of Maximum Power Point Tracking Algorithms." *Progress in Photovoltaics : Research and Applications*, vol. 11, No. 1, January 2003.

[2] N. Femia, G. Petrone, G. Spagnuolo, and M. Vitelli "Optimization of Perturb and Observe Maximum Power Point Tracking Method." *IEEE Transactions on Power Electronics*. Vol. 20, No. 4, July 2005.

[3] Youngseok Jung, Junghun So, Gwonjong Yu, and Jaeho Choi "Improved Perturbation and Observation Method (IP&O) of MPPT control fpr Photovoltaic Power Systems." Korea Institute of Energy Research, South Korea. pp. 1788-1791. IEEE Transaction. 2005.

[4] Chihchiang Hua, Jongrong Lin, and Chihming shen. "Implementation of DSP-Controlled Photovoltaic System with peak power tracking" IEEE Transactions on Industrial Electronics. Vol. 45, No.1, February 1998.

[5] Eftichiog Koutroulis and Kostas Kalaitzakis. "Development of a Micro controller-based, Photovoltaic maximum power point Tracking control System." IEEE Transactions on Power Electronics. Vol.16, No.1, January 2001

[6] M.A.S.Masoum and H.Dehbonei, " Design, Construction and Testing of a Voltage-Based Maximum Power Point Tracker (VMPPT) for Small Satellite Power Supply ", *Proceedings of the 13th Annual AIAA/USU Conference on Small Satellite*, Satellite, pp. 1 – 12, Utah, USA, 23-26 Aug. 1999.

[7] Mummadi Veerachaey, Tomonobu Senjyu, and Katsumi Uezato "Voltage-Based Maximum Power Point tracking Control of PV System" IEEE Transactions on Aerospace and Electronic Systems. Vol.38, No. 1 JANUARY 2002.

[8] W.Xiao and W.G.Dunford "A Modified Adaptive Hill Climbing MPPT Method for Photovoltaic Power System" Annual IEEE Power Electronics Specialists Conference, 35th, pp. 1957-1963, Aachen, Germany, 2004

[9] M. G. Simoes and N. N. Franceschatti, "Fuzzy optimization based control of a solar array system," Proceedings of the IEEE Electric Power Applications, Vol. 146, No 5, pp. 552 –558, Sao Paulo University, Sept. 1999.

[10] P.E. Goloberg, Genetic Algorithms in Search, optimication, 1994.

[11] Mitsuo Gen and Runweicheng, Genetic Algorithms & Engineering Design, JohnWileg& Sons, 1997.

[12] S.O. Kasap, Principles of Electronic Materials and Devices, MCGRAW-HILL Companies, Inc, 2002.

Adaptive Characteristic of Mho Distance Relay for Compensation of the Phase to Phase Fault Resistance

D. Surachet, and T. Saengsuwan
Electrical Engineering Department Engineering Faculty,
Kasetsart University, Bangkok, Thailand 10900
E-mail: surachetd@hotmail.com , fengtss@ku.ac.th

***Abstract*-This paper presents an adaptive characteristic of mho distance relay for compensation of the phase to phase fault resistance. It has been shown an extend by insert parallelogram which the same as impedance angle of transmission line between *R-X* diagram of mho distance relay. The algolithm of propose system is verified by simulation and results.**

I. INTRODUCTION

Distance relays effectively measure the impedance between the relay location and the fault. If the impedance of the fault is low, the impedance is proportional to the distance from the relay to the fault. For a fault at the remote end of the line, the voltage at the local relay equals the current multiplied by impedance of the line, i.e. *IZ*. Therefore, the ratio of the voltage to the current measured at the relay equals the impedance of the line, *Z*. Since the ratio *V/I* is proportional to the line length between the relay and the fault, the ratio *V/I* is, therefore, a measure of the impedance to the fault. A distance relay is designed to only operate for faults occurring between the relay location and the selected reach point and remain stable for all faults outside this region or zone. In time stepped distance scheme this ensures adequate discrimination for faults that may occur between different line sections.

In this paper, we present an analysis of the adaptive characteristic of *R-X* diagram of mho relay for fault resistance compensation in the phase to phase fault.

II. MHO CHARACTERISTIC

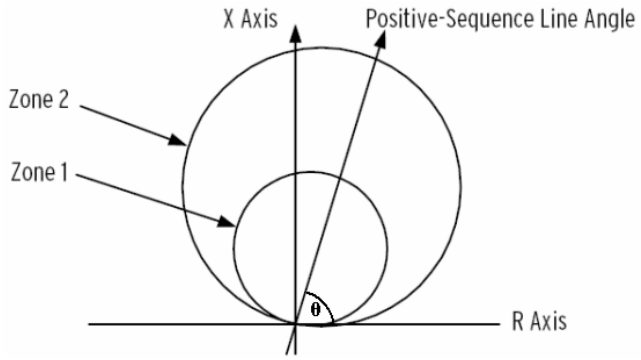

Figure 1. Mho Characteristic

Generally, mho distance relay is used widely in the present that have a circular impedance characteristic. The characteristic is suitable for the phase fault protection and in the case of a low fault resistance. But in the case of high value of fault resistance, the apparent of fault location is outside the zone circle and relay underreaches.

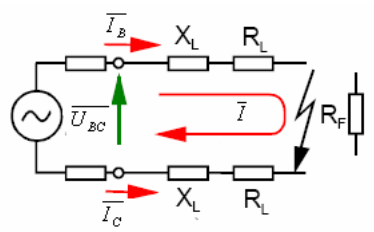

Figure 2. Phase *B-C* short-circuit with a fault resistance (single-ended infeed)

Consider the transmission system as shown in Figure 2, impedance is modified by inclusion of fault resistance, R_F. In the case of phase *B-C* short-circuit, the impedance seen by the faulted phase relay is

$$Z_{BC} = \frac{U_B - U_C}{I_B - I_C} \tag{1}$$

$$U_{BC} = U_B - U_C = 2\left(R_L \cdot I + jX_L \cdot I\right) + R_F I \tag{2}$$

$$I_C = -I_B = I \tag{3}$$

$$Z_{BC} = \frac{2\left(R_L \cdot I + jX_L \cdot I\right) + R_F \cdot I}{2I} = R_L + jX_L + \frac{R_F}{2} \tag{4}$$

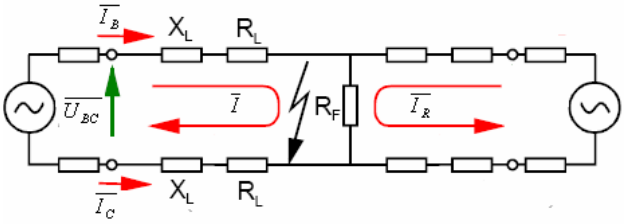

Figure 3. Phase *B-C* short-circuit with fault resistance (infeed from both sides)

Consider the transmission system show in Figure 3, and assume that the fault resistance is equal to R_F. If the contribution to the fault from the remote is I_R, the fault current $I_F=I+I_R$, and the voltage at the relay location is given by

$$U_{BC} = 2\left(R_L \cdot I + jX_L \cdot I\right) + R_F\left(I + I_R\right) \tag{5}$$

$$Z_{BC} = \frac{2\left(R_L \cdot I + jX_L \cdot I\right) + R_F \cdot \left(I + I_R\right)}{2I}$$

$$= R_L + jX_L + \frac{R_F}{2}\left(\frac{I_R}{I} + 1\right) \tag{6}$$

Since I_R may not be in phase with I, the fault resistance may contribute an error to the resistance as well as the reactance of the faulted line segment. This is illustrated in *R-X* diagram in Figure 4. In order to accommodate the resistance in the fault path, it is necessary to shape the trip zone of a distance relay in such a manner that region surrounding the apparent impedance is included inside the zone. It will be seen in this paper that different types of distance relays have different ability of accommodating the fault resistance. It should be remembered that a larger area for the protection zone in *R-X* plane accommodates greater fault path resistance.

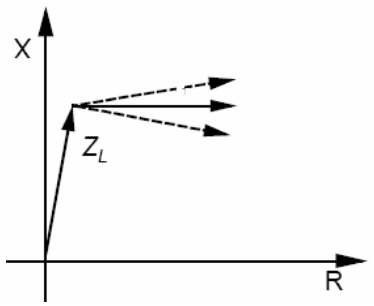

Figure 4. Its effect on the *R-X* diagram

III. Characteristic of Mho Distance Relay in The Case of Non-Adaptive *R-X* Diagram

The simulation of characteristic of mho relay simulate for phase *B-C* short-circuit of IEEE 14 Bus Test Case using the ATP-EMTP program as shown in Figure 5.

The simulation of phase-phase fault without fault resistance (R_F = 0 Ω), there is phase fault and fault location as shown in Figure 5. Assume phase *B-C* short-circuits at the location is about 10% of line length from busbar 1 to 2 or approximate 90% of line length from busbar 2 to 1. The characteristic of mho distance relay for non-adaptive *R-X* diagram is shown in Figure 6 and 7, respectively. All of distance relay setting is 85% of the line length in zone 1 and 120% in zone 2. The simulation result of the propose system with fault resistance 50 Ω (R_F = 50 Ω) is shown in Figure 8 and 9, respectively.

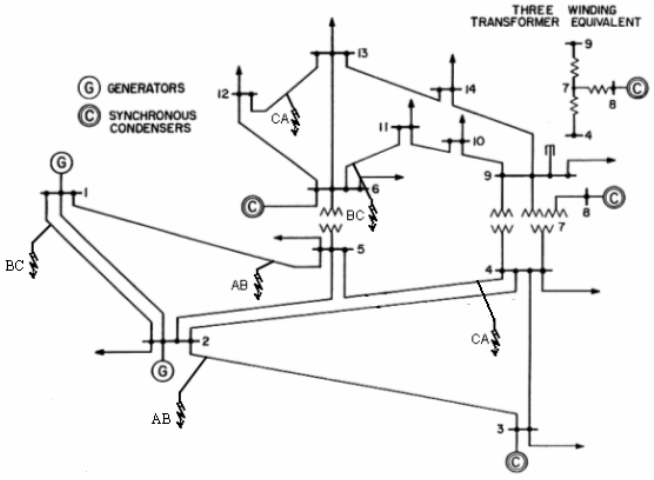

Figure 5. IEEE 14 Bus Test Case for simulation

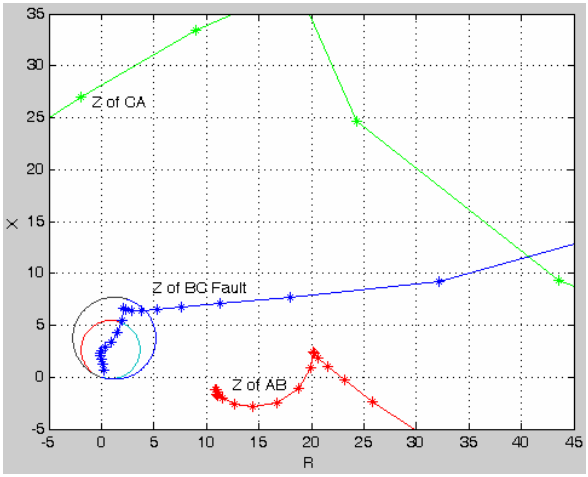

Figure 6. Impedance of fault between phase *B* and *C* (bus1 to bus2) in zone1

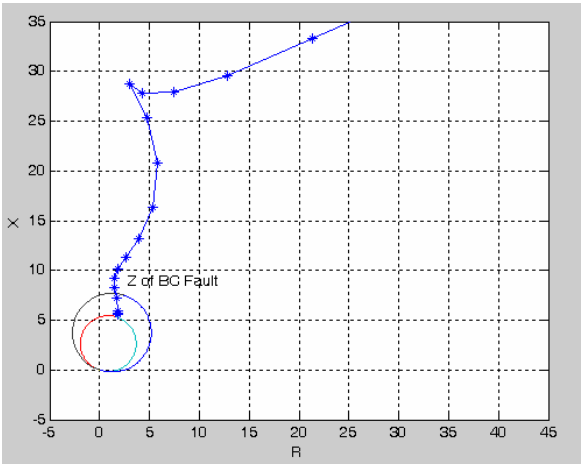

Figure 7. Impedance of fault between phase *B* and *C* (bus2 to bus1) in zone2

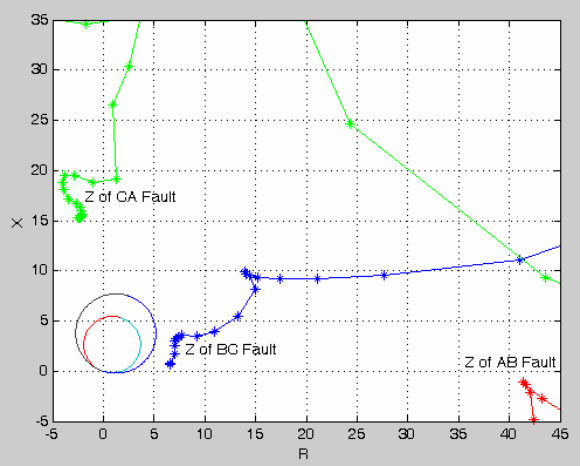

Figure 8. Impedance of fault between phase *B* and *C* (bus1 to bus2) without adaptive characteristic of mho distance relay

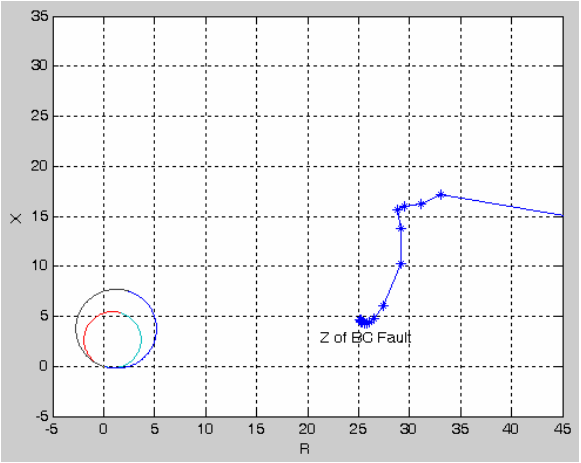

Figure 9. Impedance of fault between phase *B* and *C* (bus2 to bus1) without adaptive characteristic of mho distance relay

IV. Characteristic of Mho Distance Relay in the Case of Adaptive *R-X* Diagram

Fault component of the power system is an uncontrolled parameter which is influenced by many factors, and can be made up of fault arc resistance. The effect of fault resistance at the fault location is generally to reduce the effective reach of distance relay. In this paper presents adaptive characteristic of *R-X* diagram of mho relay for fault resistance compensation in the phase to phase fault. In order to accommodate the resistance in the fault path, it is necessary to shape the trip zone of a distance relay in such a manner that region surrounding the apparent impedance is included inside the zone. It will be seen in this paper that different types of distance relays have differing ability of accommodating the fault resistance. It should be remembered that a larger area for the protection zone in *R-X* plane accommodates greater fault path resistance.

Next, fault phase impedance can be calculated as in (6) with fault resistance of 50 ohms (R_F = 50 Ω) and setting relay for improving characteristic of the mho distance relay which shown in Figure 10 and 11.

The simulation results of all cases are shown in Table 1.

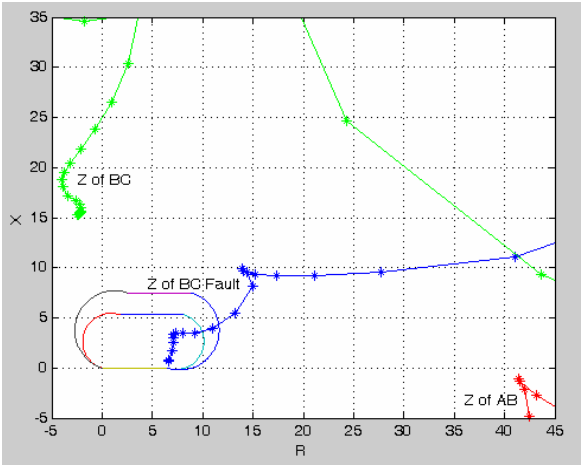

Figure 10. Impedance of fault between phase *B* and *C* (bus1 to bus2) with adaptive characteristic of mho distance relay (zone1)

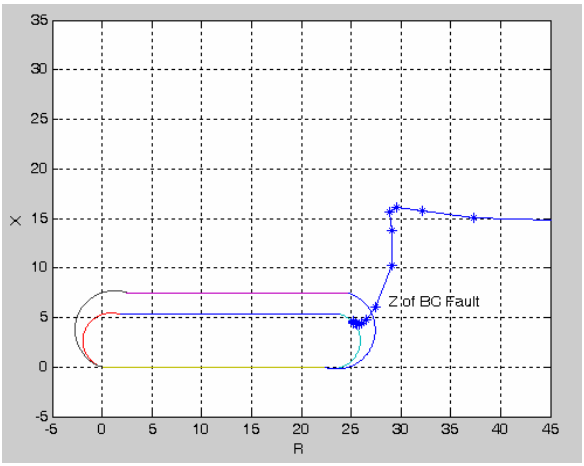

Figure 11. Impedance of fault between phase *B* and *C* (bus2 to bus1) with adaptive characteristic of mho distance relay (zone2)

V. Results

According to IEEE 14 Bus Test Case as shown in Figure 5, contains 31 relays. All the voltages and current at each location are extracted and feeding into the mho distance relay algorithm. In this test all distance relays operate in the conventional three-zone time stepped setting. When the Phase *B-C* short-circuit without fault resistance (R_F = 0 Ω) occurred 10% form busbar 1 on the line between busbus 1 and busbar 2 on circuit 1. Relay-12(circuit 1) operated in zone-one, relay-21(circuit 1), 21(circuit 2), 32, 51 in zone-

two and some in zone-three. At the same condition, when R_F = 50 ohms the mho distance relay does not detect fault between busbar 1 and busbar 2. However, after improve the characteristic of the mho distance relay, it able to correctly detect fault between busbar 1 and busbar 2 inside zone1 and 2, respectively. In another case of distance relay, the simulation results shown in Table 1.

VI. CONCLUSIONS

Adaptive characteristic of mho distance relay by using an extended parallelogram with the same as impedance angle of transmission line between *R-X* diagram of mho distance relay for Compensation of the Phase to Phase Fault Resistance is presented. The proposed system offers the mho distance can extend tripping of zone and correctly tripping circuit breaker.

ACKNOWLEDGMENT

The author would like to express his gratitude to the Graduate School, Kasetsart University, Thailand for providing the financial support for this work.

REFERENCES

[1] V. Cook, "Analysis of Distance Protection", Reseach Studies Press Ltd.,1985.

[2] A. G. Phadake and J. S. Thorp,"Computer Relaying for Power System" Reseach Studies Press Ltd., England, 1988.

[3] Stanley H. Horowitz and Arun G. Phadake, "Power System Relaying" Reseach Studies Press Ltd., England, 1992.

[4] Gerhard Ziegler, "Numerical Distance Protection Principle and Application" Siemens AG., Berlin and Munich, July 1999

[5] T. Saengsuwan, "Modelling of Distance Relays in EMTP" IPST International Conference, Budapest Hungary 1999, pp. 213-217

TABLE I

The Comparasion of The Propose System With and Without Adaptive Charateristic of Mho Distance Relay

Location & Phase of Fault	R_f (Ω)	Relay Response	Adaptive Relay Response
10% from BUS1, *B-C* Fault	0	12c1-z1,21c1,21c2,32,51-z2 and some in z3	-
	25	-	12c1-z1, 21c1-z2
10% from BUS2, *A-B* Fault	0	23-z1,32,42,53-z2 and some in z3	-
	25	-	23-z1, 53-z2
10% from BUS4, *C*-A Fault	0	45-z1,54,15,24,34-z2 and some in z3	-
	25	-	45-z1, 54-z2
10% from BUS5, *A-B* Fault	0	52-z1,25,15-z2 and some in z3	-
	25	-	52-z1, 25-z2
10% from BUS6, *B-C* Fault	0	6_11-z1,11_6,12_6,13_6-z2 and some in z3	-
	25	-	6_11-z1, 11_6-z2
10% from BUS12, *C-A* Fault	0	12_13-z1,13_12,6_12-z2 and some in z3	-
	25	-	12_13-z1,3_12-z2

A Novel Control Method of a Switched-Capacitor AC-DC Converter for Small Power Applications

Kei Eguchi *, Hongbing Zhu †, Ichirou Oota ‡, Shinya Terada § and Fumio Ueno §
* Faculty of Education, Shizuoka University,
Shizuoka, 422-8529 Japan
E-mail: ekeguch@ipc.shizuoka.ac.jp
† Department of Computer Science, Hiroshima Kokusai Gakuin University,
6-20-1 Nakano Aki-ku, Hiroshima 739-0321, Japan
‡ Department of Information and Communication, Kumamoto National College of Technology,
Kumamoto-ken, 861-1102 Japan
§ Department of Electrical System and Computer Engineering, Sojo University,
4-22-1 Ikeda, Kumamoto 860-0082, Japan

***Abstract*— This paper presents a novel control method for a switched-capacitor (SC) AC-DC converter for small power applications. In the proposed method, the capacitors which are not used for electrical charge or discharge in the charge process are connected to an output terminal in parallel. Hence, the converter controlled by the proposed method can improve the properties such as power efficiency and ripple noise. Furthermore, to alleviate the stress to capacitors, the on-resistances of power-switches connected to the ground are controlled to keep a constant voltage in each capacitor. The validity of the proposed method is confirmed by theoretical analyses. The analyses show that the proposed method can improve power efficiency and ripple noise without changing the structure of the converter.**

I. Introduction

In the design of power converters, magnetic elements such as coils, transformers, etc. have been used in most converters. Being distinct from such converters, there is the switched-capacitor (SC) technique which can realize the power converters without magnetic elements. The SC technique has a possibility to implement the converters in an IC form though the power efficiency of SC power converters is inferior to that of the converters using magnetic elements. For this reason, several types of SC power converters have been proposed [1-4]. Among those, aiming at an IC implementation of an AC-DC converter, we focused on an SC AC-DC converter for small power applications.

In the previous studies, Oota realized a series-parallel type SC AC-DC converter [1]. The converter which performs only $1/N$ step-down conversion needs large capacitors, because the capacitors in the converter are charged only once in a half period of an AC input. To solve this problem, Hara et al. proposed a ring-type SC AC-DC converter [3]. Depending on the amplitude of an AC input, the converter controls the ratio of the step-down conversion, $1/P$ $(P \in \{2, 3, \ldots, N\})$, by changing the connections of power-switches at high speed. Thus the size of capacitors can be reduced. However, in the control method [3],[4] of the ring-type power converter, all the capacitors are not used for electrical charge or discharge when $P < N$.

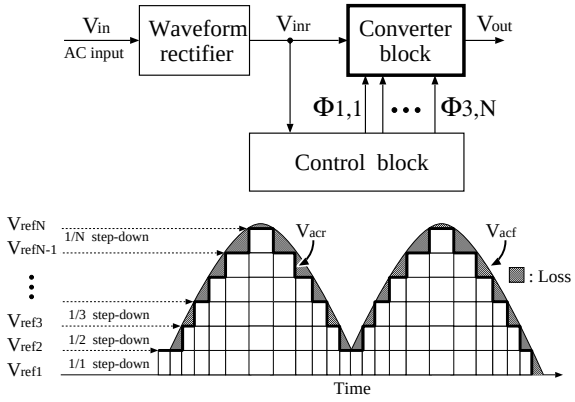

Fig. 1. Architecture of proposed AC-DC converter.

In this paper, a novel control method for an SC AC-DC converter is proposed to improve the properties such as power efficiency and ripple factor. In the proposed method, the capacitors which are not used for electrical charge or discharge in the charge process are connected to an output terminal in parallel. Hence, the converter controlled by the proposed method can improve the circuit properties. Furthermore, to alleviate the stress to capacitors, the on-resistances of power-switches connected to the ground are controlled to keep a constant voltage in each capacitor. The validity of the proposed method is confirmed through theoretical analyses.

II. Circuit Structure

Figure 1 shows the block diagram of the proposed SC AC-DC converter. In this paper, a family of the series-parallel type power converter [1] is used as a converter block [1] . Figure

[1]In the previous studies in [3] and [4], a ring-type power converter is used as the converter block. The ring-type converter needs many switches though it can provide stepped-up/stepped-down voltages. Aiming at the design of a step-down AC-DC converter, we employ a family of the series-parallel type converter. The number of switches for the series-parallel type converter is less than 75 % of that for the ring-type converter.

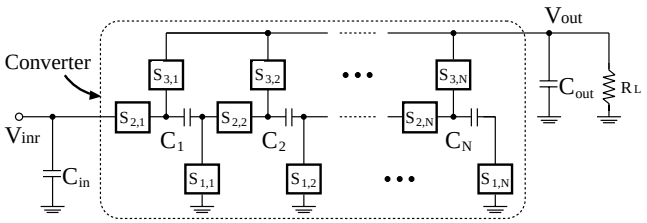

Fig. 2. Detail of converter block.

2 shows the converter block. The power-switches $S_{i,k}$ ($(i = 1, 2, 3)$ and $(k = 1, 2, \ldots, N)$) in Fig.2 are controlled by 2 phase clock pulses $\Phi_{i,k}$.

In the conventional method [3-4], the power-switches are controlled as shown in Fig.3 [2] . That is, all the capacitors are not used for electrical charge and discharge when $P < N$, where P is the number of series-connected capacitors to an input terminal in $State - T1$, N is the total number of capacitors in the converter block, and R_{on} [3] denotes an on-resistance of the power-switch. Figure 4 shows the proposed control method for SC converters. In Fig.4, the instantaneous equivalent circuit in $State - T2$ is omitted to save space, because the circuit in $State - T2$ is the same as Fig.3 (b). As Fig.4 shows, $C_{P+1} \sim C_N$ in Fig.3 (a) are connected to the output terminal. The operation of the converter block is as follows.

Firstly, the the input voltage V_{in} is rectified into a full waveform V_{inr}. In the converter block, V_{inr} is divided equally into N levels by comparators as shown in Fig.1. In the comparators, the reference voltages V_{refP}'s are set to satisfy $|V_{refP} - V_{refP-1}| =$ constant. During $V_{refP-1} < V_{inr} \leq V_{refP}$, the converter block changes the states of switches at the frequency of $1/T$, where the duty factor D of the converter satisfies that $T1 = DT$ and $T2 = (1 - D)T$.

In $State - T1$, depending on the amplitude of V_{inr}, P capacitors are connected in series, and $C_{P+1} \sim C_N$ are connected to the output terminal in parallel when $P < N$ (see Fig.4). In this timing, $S_{1,P} \sim S_{1,N}$, $S_{2,1} \sim S_{2,P}$, and $S_{3,P+1} \sim S_{3,N}$ are On and the other switches are Off, where the on-resistance of $S_{1,P}$, R_{onc} (see in Fig.4), is controlled to charge the voltage of each capacitor to V_{refN}/N. As for SC converters, it is known that the efficiency decreases when the voltage of each capacitor is not constant. Although the energy of the hatched area in Fig.1 becomes a loss, the proposed method enables the following: 1. the capacitors C_k's can be charged in spite of the amplitude of the input voltage, 2. the stress to the capacitors can be alleviated, and 3. the capacitors C_k don't have a dielectric loss.

Next, in $State - T2$, all the capacitors are connected in parallel (see Fig.3 (b)). In this timing, $S_{1,k}$'s and $S_{3,k}$'s are On and $S_{2,k}$'s are Off. By iterating these processes at high speed, the converter provides a DC voltage V_{out}.

[2]In Fig.3, to simplify the theoretical analysis in Sect.3, the resistance R_{on} is connected to the both sides of C_{out}.

[3]To simplify the analysis, the influence of fluctuation of switches is disregarded

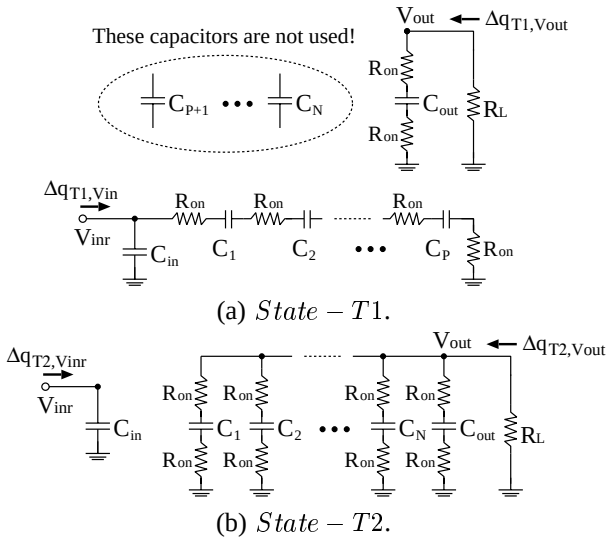

Fig. 3. Instantaneous equivalent circuits for converter using conventional method.

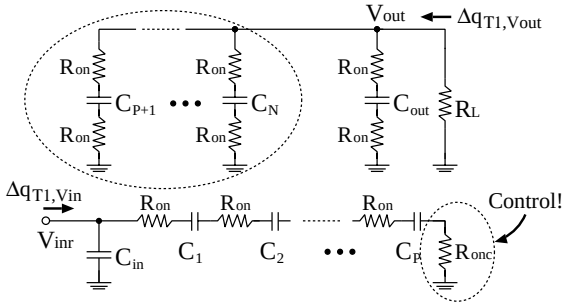

Fig. 4. Instantaneous equivalent circuit for converter using proposed method when $State - T1$.

III. Theoretical Analysis

A. Power Efficiency

Firstly, the equivalent circuit of the SC AC-DC converter by using the proposed method is analyzed. To simplify the theoretical analyses, we assume that the time constant is quite larger than T and parasitic elements are disregarded.

In the steady state, the differential values of the electric charges in C_k satisfy

$$\Delta q_{T1}^k + \Delta q_{T2}^k = 0, \quad (1)$$

where Δq_{T1}^k and Δq_{T2}^k denote the electric charges when $State - T1$ and $State - T2$, respectively. In the case of $T1$, the differential values of the electric charges in the input and the output terminals, $\Delta q_{T1,V_{inr}}$ and $\Delta q_{T1,V_{out}}$, are given by

$$\begin{aligned} \Delta q_{T1,V_{inr}} &= \Delta q_{T1}^{in} + \Delta q_{T1}^1 \\ &\cdots \\ &= \Delta q_{T1}^{in} + \Delta q_{T1}^P, \\ \Delta q_{T1}^1 &= \cdots = \Delta q_{T1}^P, \end{aligned}$$

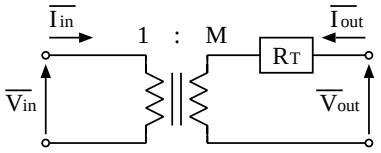

Fig. 5. General equivalent circuit of SC DC-DC converters.

and

$$\Delta q_{T1,V_{out}} = \begin{cases} \Delta q_{T1}^{out} + \sum_{k=P+1}^{N} \Delta q_{T1}^{k} & \text{if } P < N, \\ \Delta q_{T1}^{out} & \text{if } P = N, \end{cases} \quad (2)$$

where P (≥ 2) denotes the number of the series-connected capacitors via $S_{1,P}$ and $S_{2,k}$'s. According to the input V_{inr}, the parameter P is determined as follows:

$$P = \begin{cases} 1 & \text{if } V_{ref1} \leq V_{inr} < V_{ref2}, \\ 2 & \text{if } V_{ref2} \leq V_{inr} < V_{ref3}, \\ & \cdots \\ N & \text{if } V_{refN} \leq V_{inr}. \end{cases} \quad (3)$$

In $State - T1$, to alleviate the stress to capacitors, the on-resistance of $S_{1,P}$ connected to the ground is controlled to keep a constant voltage in each capacitor.

On the other hand, in the case of $State - T2$, $\Delta q_{T2,V_{inr}}$ and $\Delta q_{T2,V_{out}}$ are given by

$$\Delta q_{T2,V_{inr}} = q_{T2}^{in}$$
$$\text{and} \quad \Delta q_{T2,V_{out}} = \sum_{k=1}^{N} \Delta q_{T2}^{k} + \Delta q_{T2}^{out}. \quad (4)$$

During $V_{refP-1} < V_{inr} \leq V_{refP}$, the average currents of the input and the output, $\overline{I_{inr}}$ and $\overline{I_{out}}$, are given by

$$\overline{I_{acr}} = (\Delta q_{T1,V_{inr}} + \Delta q_{T2,V_{inr}})/T$$
$$\text{and} \quad \overline{I_{out}} = (\Delta q_{T1,V_{out}} + \Delta q_{T2,V_{out}})/T. \quad (5)$$

By substituting Eqs.(1), (2), and (4) into Eq.(5), the following equations are derived:

$$T \cdot \overline{I_{inr}} = \Delta q_{T1}^{1}$$
$$\text{and} \quad T \cdot \overline{I_{out}} = \sum_{k=P+1}^{N} \Delta q_{T1}^{k} - \sum_{k=1}^{N} \Delta q_{T1}^{k}. \quad (6)$$

From Eq.(6), the following equation is obtained:

$$\overline{I_{inr}} = -\frac{1}{P}\overline{I_{out}}. \quad (7)$$

As for SC converters, it is known that a general equivalent circuit of SC DC-DC converters [5-6] can be expressed by Fig.5, where M is a ratio of the ideal transformer, and $\overline{V_{in}}$ and $\overline{V_{out}}$ denote an averaged input voltage and an averaged output voltage, respectively. The equivalent circuit of the converter block in Fig.1 can be expressed by using Fig.5 though the circuit of Fig.5 is for the SC DC-DC converters. Because the converter block of Fig.2 can be used also as a DC-DC converter. In Fig.5, the consumed energy W_T is defined by

$$W_T = W_{T1} + W_{T2} \equiv (\frac{\Delta q_{V_{out}}}{T})^2 \cdot R_T \cdot T. \quad (8)$$

Hence, Eq.(8) can be rewritten as

$$W_T = \frac{R_T P^2}{T}(\Delta q_{T1}^{1})^2, \quad (9)$$

because $\Delta q_{V_{out}}$ is expressed by

$$\Delta q_{V_{out}} = \Delta q_{T1,V_{out}} + \Delta q_{T2,V_{out}} = -P\Delta q_{T1}^{1}.$$

Here, from Fig.4 and Fig.3 (b), the consumed energies in $State - T1$ and $State - T1$, W_{T1} and W_{T2}, are given by

$$W_{T1} = PR_{on}T1(\frac{\Delta q_{T1}^{1}}{T1})^2 + 2R_{on}T1\sum_{k=P+1}^{N+1}(\frac{\Delta q_{T1}^{k}}{T1})^2 + R_{onc}T1(\frac{\Delta q_{T1}^{1}}{T1})^2$$
and
$$W_{T2} = 2R_{on}T2\sum_{k=1}^{N+1}(\frac{\Delta q_{T2}^{k}}{T2})^2, \quad (10)$$

respectively. By substituting Eqs.(1), (2), (4),

$$\Delta q_{T1,V_{out}} = \frac{T1}{T}\Delta q_{V_{out}},$$
$$\text{and} \quad \Delta q_{T2,V_{out}} = \frac{T2}{T}\Delta q_{V_{out}}, \quad (11)$$

into Eq.(10), the consumed energy W_T can be derived by

$$W_T = \{\frac{R_{on}P(1+D) + R_{onc}(1-D)}{D(1-D)P^2} + \frac{2R_{on}D}{(N-P+1)(1-D)}\}\frac{P^2}{T}(\Delta q_{T1}^{1})^2. \quad (12)$$

Therefore, from Eqs.(9) and (12), the resistance R_T in Fig.3 can be given by

$$R_T = \frac{R_{on}P(1+D) + R_{onc}(1-D)}{D(1-D)P^2} + \frac{2R_{on}D}{(N-P+1)(1-D)}. \quad (13)$$

The equivalent circuit of Fig.5 can be expressed by the determinant using Kettenmatrix. From Eqs.(7) and (13), the following determinant is obtained:

$$\begin{bmatrix} \overline{V_{inr}} \\ \overline{I_{inr}} \end{bmatrix} = \begin{bmatrix} P & 0 \\ 0 & 1/P \end{bmatrix} \begin{bmatrix} 1 & R_T \\ 0 & 1 \end{bmatrix} \begin{bmatrix} \overline{V_{out}} \\ -\overline{I_{out}} \end{bmatrix}. \quad (14)$$

Hence, the equivalent circuit of the proposed converter can be expressed by the circuit shown in Fig.6. From Fig.6, the

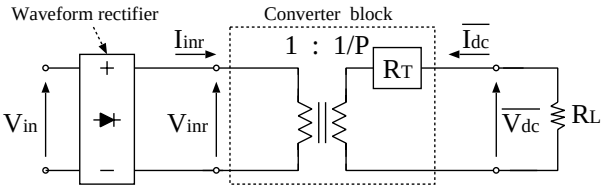

Fig. 6. Equivalent circuit of SC AC-DC converter using proposed control method.

power efficiency [4] is given by

$$\eta = \frac{(P\overline{I_{inr}})^2 R_L}{(P\overline{I_{inr}})^2 R_L + (P\overline{I_{inr}})^2 R_T} = \frac{P^2 R_L}{P^2 R_L + P^2 R_T}. \quad (15)$$

Here, the resistance R_T of the converter using the conventional control method is given by

$$R_T = \frac{R_{on}P(1+D) + R_{onc}(1-D)}{D(1-D)P^2} + \frac{2R_{on}D}{1-D}. \quad (16)$$

As Eqs.(13) and (16) show, the resistance R_T of the proposed method is smaller than that of the conventional method when $P \neq N$. This result means that the converter using the proposed method can improve the power efficiency.

B. Output Ripple Factor

Next, the ripple factor of the proposed converter is analysed. To simplify the analysis, the on-resistance of power-switches are disregarded. In the case of $State-T2$, the output voltage $V_{out,T2}(t)$ of Fig.3 (b) is given by

$$V_{out,T2}(t) = V_{max,T2} \cdot \exp(-\frac{t}{\tau_{T2}}), \quad (17)$$

where $V_{max,T2}$ denotes the output voltage when $V_{out,T2}(0)$ and τ_{T2} is a time constant $(N+1)CR_L$. On the other hand, in the case of $State-T1$, the output voltage $V_{out,T1}(t)$ of Fig.4 is given by

$$V_{out,T1}(t) = V_{out,T2}(T2) \cdot \exp(-\frac{t}{\tau_{T1}}) = V_{max,T2} \cdot \exp(-\frac{T2}{\tau_{T2}}) \cdot \exp(-\frac{t}{\tau_{T1}}), \quad (18)$$

where τ_{T1} is a time constant $(N-P+1)CR_L$. From Eqs.(17) and (18), the output voltage ripple ΔV_{out} and the average output voltage $\overline{V_{out}}$ are derived by

$$\Delta V_{out} = V_{out,T2}(0) - V_{out,T1}(T1) = V_{max,T2}\{1 - \exp(-\frac{T1}{\tau_{T1}} - \frac{T2}{\tau_{T2}})\} \quad (19)$$

[4]In Eq.(15), the energy loss caused by the waveform rectifier and the peripheral circuits such as the pulse generator is disregarded.

and

$$\overline{V_{out}} = \frac{1}{T1}\int_0^{T1} V_{out,T1}(t)dt + \frac{1}{T2}\int_0^{T2} V_{out,T2}(t)dt = V_{max,T2} \cdot [\frac{\tau_{T2}}{T2}\{1 - \exp(-\frac{T2}{\tau_{T2}})\} + \frac{\tau_{T1} \cdot \exp(-\frac{T2}{\tau_{T2}})}{T1}\{1 - \exp(-\frac{T1}{\tau_{T1}})\}], \quad (20)$$

respectively. Then, from Eqs.(19) and (20), the output ripple factor V_{rip} can be expressed by

$$V_{rip} = \frac{\Delta V_{out}}{\overline{V_{out}}} = \frac{1 - \exp(-\frac{T1}{\tau_{T1}} - \frac{T2}{\tau_{T2}})}{DM}, \quad (21)$$

where

$$DM = \frac{\tau_{T2}}{T2}\{1 - \exp(-\frac{T2}{\tau_{T2}})\} + \frac{\tau_{T1} \cdot \exp(-\frac{T2}{\tau_{T2}})}{T1}\{1 - \exp(-\frac{T1}{\tau_{T1}})\}.$$

Here, the difference between the proposed method and the conventional method in the ripple factor is the time constant in $State-T1$. The time constant τ_{T1} for the conventional method is CR_L. Therefore, the time constant τ_{T1} for the proposed method is larger than that for the conventional method when $P \neq N$. Hence, as you can see from Eq.(21), the ripple factor can be reduced by the proposed method.

IV. Conclusion

A novel control method for an SC AC-DC converter has been proposed in this paper. The validity of the proposed method was confirmed by theoretical analyses. The theoretical analyses showed that the proposed method can improve the properties such as power efficiency and ripple noise without changing the structure of the converter.

The IC implementation of the power converter using the proposed control method is left to the future study.

References

[1] I.Oota, F.Ueno, T.Inoue, and H.B.Lian, "Realization and analysis of new switched-capacitor AC-DC converters," *T. IEICE*, Vol.E72, No.12, pp.1292-1298, Dec. 1989

[2] I.Oota, I.Harada, T.Inoue, and F.Ueno, "High efficiency control method of switched-capacitor AC-DC converter," *T. IEICE*, Vol.J76-C-II, No.6, pp.422-431, June 1993

[3] N.Hara, I.Oota, F.Ueno, and I.Harada: "A programmable ring type switched-capacitor AC-DC converter," *Proc. of NOLTA'1999*, vol.1, pp.159-162, 1999

[4] S.Terada, I.Oota, K.Eguchi, and F.Ueno, "A programmable ring type switched-capacitor AC-DC converter," *Proc. of 37th IEEE Power Electronics Specialists Conference*, pp.1884-1887, June 2006

[5] N.Hara, I.Oota, F.Ueno, and T.Inoue, "A new ring type set-up switched-capacitor DC-DC converter with low inrush current at start-up and low current ripple in steady state," *T. IEEJ*, Vol.J81-C-II, No.7, pp.600-612, July 1998

[6] N.Hara, I.Oota, I.Harada, and F.Ueno, "Programmable ring type switched-capacitor DC-DC converters," *T. IEEJ*, Vol.J82-C-II, No.2, pp.56-68, Feb. 1999

Approximate 2DOF Digital Control for DC-DC Converter with Additional Zeros

Eiji TAKEGAMI[1], Kohji HIGUCHI[2], Kazushi NAKANO[3]
Satoshi TOMIOKA[4], Kazushi WATANABE[5]
[1,4,5]DENSEI-LAMBDA K.K., 2701 Togawa, Settaya, Nagaoka 940-1195, Japan
email: e.takegami@densei-lambda.com, s.tomioka@densei-lambda.com
k18.watanabe@densei-lambda.com
[2,3]Dept. of Electronic Engineering, The University of Electro-Communications,
1-5-1 Chofu-ga-oka, Chofu, Tokyo 182-8585, Japan
email: higuchi@ee.uec.ac.jp, nakano@ee.uec.ac.jp

Abstract— **Robust DC-DC converter which can cover extensive load changes and also input voltage changes with one controller is needed. We proposed an aproximate 2DOF digital controller which which realizes the start-up response and dynamic load response independently. The controller makes the control bandwidth wider, and at the same time makes a variation of the output voltage small at sudden changes of loads and the input voltages. In this paper, a new approximate 2DOF digital controller using additinal zeros is proposed. The new controller makes a variation of the output voltage more small at sudden changes of loads and the input voltages. This controller is actually implemented on a DSP and is connected to a DC-DC converter. Experimental studies demonstrate that this type of digital controller can satisfy given severe specifications.**

I. Introduction

In many applications of DC-DC converters, loads cannot be specified in advance, i.e., their amplitudes are suddenly changed from the zero to the maximum rating. Generally, design conditions are changed for each load and then each controller is re-designed. Then, a so-called robust DC-DC converter which can cover such extensive load changes and also input voltage changes with one controller is needed. Then the demand to suppressing output voltage change becomes still severer. The application of the digital controller to DC-DC converter designed by the PID or root locus method etc. has been recently considered[1], [2]. However it is difficult to retain sufficient robustness of DC-DC converters by these techniques. The authors proposed the method of designing a approximate 2-degree-of-freedom (2DOF) controller of DC-DC converter[3]. This controller realized a first-order differential transfer characteristics between equivalent disturbances and an output voltage. In this paper, we propose a new approximate 2DOF digital controller which realise a second-order differential trasfer characteritics. The new controller makes a variation of the output voltage more small at sudden changes of resistive load and the input voltage. This characteristics is realized by introducing an additional zeros into a transfer function between equivalent disturbances and an output. A new DC-DC converter equipped the proposed controller in DSP is actually manufactured. Some simulations and experiments show that this new DC-DC converter can satisfy given severe specifications.

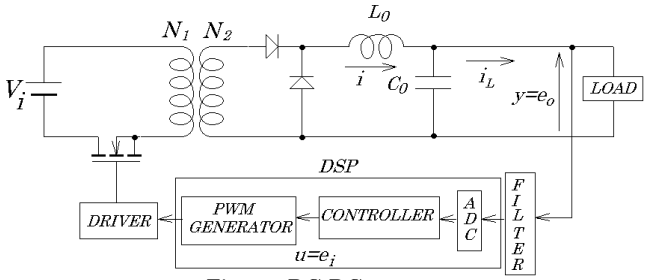

Fig. 1. DC-DC converter

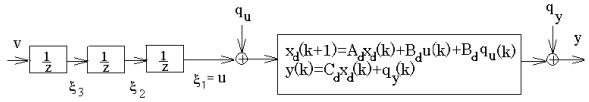

Fig. 2. Controlled object with input dead time $L_d(\leq T)$

II. DC-DC converter

The DC-DC converter as shown in **Fig.1** has been manufactured. We use the DSP(TI TMS320LF2801). This DSP has a built-in AD converter and a PWM switching signal generating part. The switching frequency is set at 400[KHz] and the peak-to-peak amplitude C_m is 125[V]. C_0 is 300[μF] and L_0 is 0.6[μH]. If the frequency of control signal u is smaller enough than that of the carrier, the state equation of the DC-DC converter in Fig.1 except for the controller in DSP can be expressed[**?**] as

$$\begin{cases} \dot{x} = A_c x + B_c u + B_c q_u \\ y = Cx + q_y \end{cases} \tag{1}$$

$$x = \begin{bmatrix} e_o \\ i \end{bmatrix} \quad A_c = \begin{bmatrix} -\frac{1}{C_0 R_L} & \frac{1}{C_0} \\ -\frac{1}{L_0} & -\frac{R_0}{L_0} \end{bmatrix} \quad B_c = \begin{bmatrix} 0 \\ \frac{K_p}{L_0} \end{bmatrix}$$

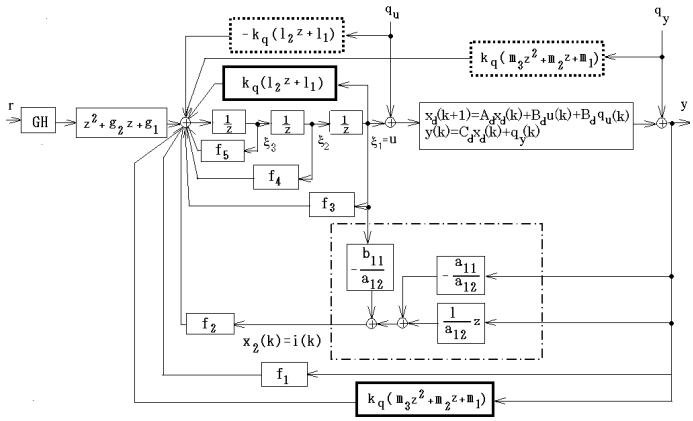

Fig. 3. Feedforward from equivalent disturbances q_u and q_y, and model matching with state feedback

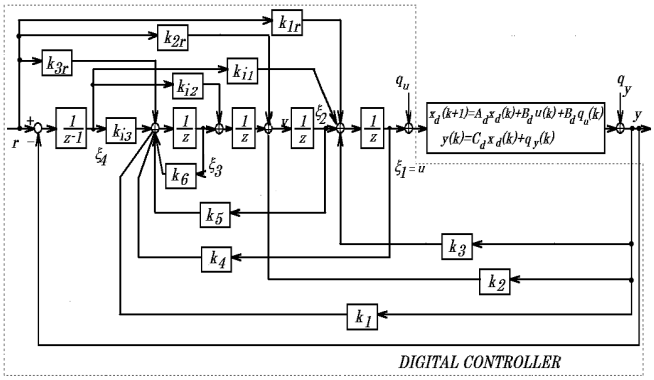

Fig. 4. Approximate 2DOF digital integral type control system

$$C = \begin{bmatrix} 1 & 0 \end{bmatrix} \quad u = e_i \quad y = e_0 \quad K_p = -\frac{V_i N_2}{C_m N_1}$$

and R_0 is the total resistance of coil and ON resistance of FET, etc., and the value is 0.015[Ω]. Then the discrete-time state equation of the system (1) with a zero order hold is expressed as follows :

$$\begin{cases} x_d(k+1) = A_d x_d(k) + B_d u(k) + B_d q_u(k) \\ y(k) = C x_d(k) + q_y(k) \end{cases} \quad (2)$$

$$A_d = \begin{bmatrix} a_{11} & a_{12} \\ a_{21} & a_{22} \end{bmatrix} = e^{A_c T} \quad B_d = \begin{bmatrix} b_{11} \\ b_{21} \end{bmatrix} = \int_0^T e^{A_c \tau} B_c d\tau$$

The DC-DC converter with the following specifications 1-7 is designed and manufactured. Specs 5 and 7 are new ones. These specs are more severe than 50[mV] in references [3].

1. Input voltage V_i is 48[V] and output voltage e_o is 3.3[V].
2. Startup transient reponses are almost the same at resistive load and parallel load of resistance and capacity, where $0.165 \leq R_L < \infty$[Ω] and $0 \leq C_L \leq 200$[μF].
3. The rising time of the startup transient reponse is smaller than 100[μs].
4. Against all the loads of spec.1, an over-shoot is not allowable in the startup transient response.
5. The dynamic load response is smaller than 25[mV] against 10[A] change of load current.
6. The specs. 2, 3, 4 and 5 are satisfied also to change of input voltage of ±20%.
7. Regulation of output voltage is amaller than 25[mV] at the sudden change of input voltage within ±20%.

III. Design method with aditional zeros

A. Addional method of zeros

The following equation is obtained by repeating the difference of the output of eq.(2).

$$Y = O^* x_d(k) + U\bar{u}(k) + U\bar{q}_u + \bar{q}_y \quad (2)$$

$$Y = \begin{bmatrix} y(k) \\ y(k+1) \\ y(k+2) \end{bmatrix} \quad O^* = \begin{bmatrix} C \\ CA_d \\ CA_d^2 \end{bmatrix} \quad U = \begin{bmatrix} 0 & 0 \\ CB_d & 0 \\ CA_dB_d & CB_d \end{bmatrix}$$

$$\bar{u} = \begin{bmatrix} u(k) \\ u(k+1) \end{bmatrix} \quad \bar{q}_u = \begin{bmatrix} q_u(k) \\ q_u(k+1) \end{bmatrix} \quad \bar{q}_y = \begin{bmatrix} q_y(k) \\ q_y(k+1) \\ q_y(k+1) \end{bmatrix}$$

If both sides of eq.(4) are mulutiplied by $\bar{I}_2 = [I_2 \;\; 0]$(I_2 is a 2×2 unit matrix) from the left and solved about x_d, the following equation will be obtained.

$$\begin{aligned} x_d(k) &= (\bar{I}_2 O^*)^{-1} \bar{I}_2 Y - (\bar{I}_2 O^*)^{-1} \bar{I}_2 U \bar{u}(k) \\ &- (\bar{I}_2 O^*)^{-1} \bar{I}_2 U \bar{q}_u - (\bar{I}_2 O^*)^{-1} \bar{I}_2 \bar{q}_y \end{aligned} \quad (3)$$

From eqs.(4) and (5), the following relation is obtained.

$$\begin{aligned} &- (l_2 z + l_1) q_u(k) + (z^2 + m_2 z + m_1) q_y(k) \\ &= (l_2 z + l_1) u(k) + (z^2 + m_2 z + m_1) y(k) \end{aligned} \quad (4)$$

$$\begin{bmatrix} l_1 & l_2 \end{bmatrix} = -(I_3 - O^*(\bar{I}_2 O^*)^{-1} \bar{I}_2) U$$
$$\begin{bmatrix} m_1 & m_2 & m_3 \end{bmatrix} = (I_3 - O^*(\bar{I}_2 O^*)^{-1} \bar{I}_2)$$

The system of Fig.2 is constituted in consideration of a delay time for calculation etc., a estimation of current and a zeros addition. The state equation of Fig.2 can be expressed as

$$\begin{cases} x_{dw}(k+1) = A_{dw} x_{dw}(k) + B_{dw} v(k) \\ y(k) = C_{dw} x_{dw}(k) \end{cases} \quad (5)$$

$$x_{dw}(k) = \begin{bmatrix} x_d(k) \\ \xi_1(k) \\ \xi_2(k) \\ \xi_3(k) \end{bmatrix} \quad A_{dw} = \begin{bmatrix} A_d & B_d & 0 & 0 \\ 0 & 0 & 1 & 0 \\ 0 & 0 & 0 & 1 \\ 0 & 0 & 0 & 0 \end{bmatrix}$$

$$B_{dw} = \begin{bmatrix} 0 \\ 0 \\ 0 \\ 1 \end{bmatrix} \quad C_{dw} = \begin{bmatrix} C & 0 & 0 & 0 \end{bmatrix} \quad \xi_1(k) = u(k)$$

In Fig.3, the parts surrounded by dotted lines are the feedforward coefficients from q_u and q_y and the part surrounded by a chain line is the estimated part of current. From eq.(5), the feedforward of eq.(7) are changed as follws:

$$v(k) = k_q(l_2 z + l_1)u(k) + k_q(z^2 + m_2 z + m_1)y(k) + (z^2 + g_2 z + g_1)r(k) + [f_1\ f_2\ f_3\ f_4\ f_5\ f_6]x_{dw}(k) \quad (6)$$

That is, the parts surrounded by the dotted lines are replaced by the parts surrounded by solid lines from u and y. In Fig.3, the transfer functions between r and y, q_u and y, and q_y and y are as follows:

$$W_{ry}(z) = N_{ry}(z)/D(z) \quad (7)$$
$$W_{q_u y}(z) = N_{q_u y}(z)/D(z) \quad (8)$$
$$W_{q_y y}(z) = N_{q_y y}(z)/D(z) \quad (9)$$

$$\begin{aligned}
N_{ry}(z) &= GH(z^2 + g_1 z + g_0)(b_{11} z + b_{21}a_{12} - a_{22}b_{11}) \\
N_{q_u y}(z) &= N_{qz}N_p \qquad N_{q_y y}(z) = N_{qz}D_p \\
N_p(z) &= b_{11} z + b_{21}a_{12} - a_{22}b_{11} \\
D_p(z) &= z^2 - (a_{11} + a_{22})z + a_{11}a_{22} - a_{21}a_{12} \\
N_{qz} &= (a_{12}z^3 - a_{12}f_5 z^2 + (a_{12}b_{11}k_q - a_{12}f_4)z \\
&- f_3 a_{12} + f_2 b_{11} - a_{12}a_{22}b_{11}k_q + a_{12}^2 b_{21}k_q) \\
D(z) &= z^5 + (-f_5 - a_{22} - a_{11})z^4 + (a_{11}f_5 \\
&+ a_{11}a_{22} - a_{21}a_{12} + a_{22}f_5 - f_4)z^3 \\
&+ (a_{21}a_{12}f_5 - f_3 + a_{11}f_4 - a_{11}a_{22}f_5 \\
&+ a_{22}2f_4)z^2 + (a_{22}f_3 + a_{21}a_{12}f_4 + a_{11}f_3 \\
&- b_{11}f_1 - f_2 b_{21} - a_{11}a_{22}f_4)z + f_2 a_{11}b_{21} \\
&- a_{21}f_2 b_{11} + a_{21}a_{12}f_3 + f_1 a_{22}b_{11} \\
&- f_1 a_{12}b_{21}21 - a_{11}a_{22}f_3
\end{aligned}$$

From $D(z)$, the pole of the overall system can arrange arbitrarily by f_1, f_2, f_3, f_4 and f_5. From $N_{ry}(z)$, two zeros of r-y can arrange arbitrarily by g_0 and g_1. Moreover, from common N_{qz} in $N_{q_z}(s)$ and $N_{q_y y}(s)$, one zeros of $q_u - y$ and $q_y - y$ can be arbitrarily arranged at the same place by k_q. That is, one zeros can be arbitrarily added to W_{Qy}.

B. Design method

First, the transfer function between the reference input r and the output y is specified as follows:

$$W_{ry}(z) = N_H(z)/D_H(z) \quad (10)$$

$$\begin{aligned}
N_H(z) &= (1 + H_1)(1 + H_2)(1 + H_3)(z - n_1)(z - n_2) \\
&\times (z + H_4)(z + H_5) \\
D_H(z) &= (1 - n_1)(1 - n_2)(z + H_1)(z + H_2)(z + H_3) \\
&\times (z + H_4)(z + H_5)
\end{aligned}$$

$[f_1\ f_2\ f_3\ f_4\ f_5]$, $[g_1\ \ g_2]$ and GH are determined so that $W_{ry}(z)$ becomes eq.(16). And the transfer function among the disturbance input q_u, q_y and the output y is specified as follows:

$$W_{q_u y}(z)) = (z - 1)\bar{N}_{qz}N_p/D_H(z) \quad (11)$$
$$W_{q_y y}(z)) = (z - 1)\bar{N}_{qz}D_p/D_H(z) \quad (12)$$

Here the zeros are placed at 1 by setting k_q as the solution of $N_{qz}(1) = 0$. Then k_q becomes as

$$k_q = \frac{-a_{12} + a_{12}f_5 + a_{12}f_4 + f_3 a_{12} - f_2 b_{11}}{a_{12}(b_{11} - a_{22}b_{11} + b_{21}a_{12}} \quad (13)$$

$\bar{N}_{qz}$ is the remaining zeros of N_{qz} which cannot be placed arbitrarily. It shall be specified that the relation of H_1 and H_2, H_3 becomes $|H_1| \gg |Re(H_2)|$, $|H_1| \gg |Re(H_3)|$. Then $W_{ry}(z)$ can be approximated to the following first-order model:

$$W_{ry}(z) \approx W_m(z) = \frac{1 + H_1}{z + H_1} \quad (14)$$

This target characteristics $W_{ry}(z) \approx W_m(z)$ is specified so that it satisfies the specs.3 and 4.

The system added the inverse system and the filter to the system is constituted and an equivalent conversion of is carried out, the approximate 2DOF digital integral-type control systems will be obtained as shown in **Fig.4**. In Fig.4, the transfer function $K(z)$ becomes

$$K(z) = \frac{k_z}{z - 1 + k_z} \quad (15)$$

The transfer functions between $r - y$, $q_u - y$ and $q_y - y$ of the system in Fig.5 are approximated as

$$y \approx \frac{1 + H_1}{z + H_1} r \quad (16)$$
$$y \approx \frac{(z-1)^2}{z - 1 + k_z} \frac{\bar{N}_{qz}N_p}{D_H(z)} q_u y \quad (17)$$
$$y \approx \frac{(z-1)^2}{z - 1 + k_z} \frac{\bar{N}_{qz}D_p}{D_H(z)} q_y y \quad (18)$$

From eqs.(16), (17) and (18), it turns out that the characteristics from r to y can be specified with H_1, and the characteristics from q_u and $q_y y$ to y can be independently specified with k_z. That is, the system in Fig.5 is an approximate 2DOF, and its sensitivity against disturbance becomes lower with the increase of k_z.

In Fig.4, the parameters of the controller are as follows:

$$\begin{aligned}
k_1 &= (f_1 - f_2 a_{11}/a_{12} + k_q(-a_{11}^2 - a_{21}a_{12} + (a_{12}a_{11} \\
&+ a_{12}a_{22})a_{11}/a_{12}) + f_5(-k_q(a_{12}a_{11} \\
&+ a_{12}a_{22})/a_{12} + f_2/a_{12}) + f_5^2 k_q + (f_4 - k_q b_{11})k_) \\
&- GHk_z(g0 + (g1 + f_5)f_5 + f_4 - k_q b_{11})/(1 + H2)
\end{aligned}$$

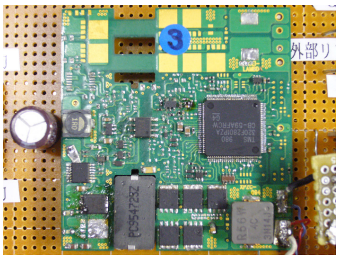

Fig. 5. The manufactured new quarter brick DC-DC converter

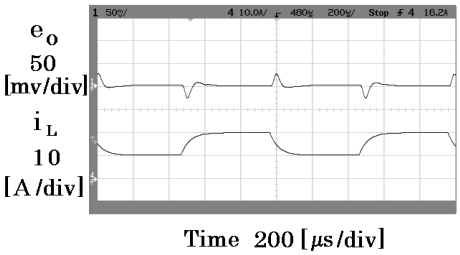

Fig. 6. Experimental result of dynamic load response at resistive load ($R_L = 0.33 \leftrightarrow 0.165[\Omega]$, $C_L = 200[\mu\mathrm{F}]$)

$$
\begin{aligned}
k_2 &= k_q - GHk_z/(1+H2) \quad k_5 = f_4 - k_q b_{11} \quad k_6 = f_5 \\
k_3 &= -k_q(a_{11}a_{12} + a_{12}a_{22})/a_{12} + f_2/a_{12} + f_5 k_q \\
&- (g1 + f_5)GHk_z/(1+H2) \quad k_2 r = (g1 + f_5)GH \\
k_4 &= f_3 - f_2 b_{11}/a_{12} + k_q((a_{12}a_{11} \\
&+ a_{12}a_{22})b_{11}/a_{12} - a_{11}b_{11} - b_{21}a_{12}) \\
k_i 1 &= (g0 + (g1 + f_5)f_5 + f_4 - k_q b_{11})GHk_z \\
k_i 2 &= (g1 + f_5)GHk_z \quad k_i 3 = GHk_z \quad k_1 r = GH \\
k_3 r &= (g0 + (g1 + f_5)f_5 + f_4 - k_{b11})GH \qquad (19)
\end{aligned}
$$

IV. Experimental studies

The sampling period T are set at 2.5[μs] and the input dead time L_d is about $0.999T$[μs]. The nominal value of R_L is 0.33[Ω]. We design a control system so that all the specifications are satisfied. First of all, in order to satisfy the specification on the rising time of startup transient reponse, H_1 and H_4 are specified as

$$
\begin{aligned}
H_1 &= -0.94 \quad H_2 = -0.18 + 0.2i \quad H_3 = -0.18 - 0.2i \\
H_4 &= -0.2 + 0.3i \quad H_5 = -0.2 - 0.3i
\end{aligned}
$$

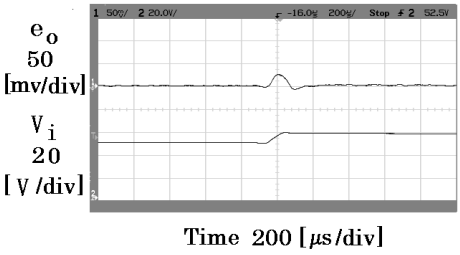

Fig. 7. Experimental result of output reponse at resistive load when input voltage changing suddenly from 48[V] to 58[V]

$$
k_z = 0.17 \quad k_q = -1 \qquad (20)
$$

Then the parameters of controller become as follows:

$$
\begin{aligned}
k_1 &= 1196.4 \quad k_2 = 787.37 \quad k_3 = -1446.4 \\
k_4 &= 0.74539 \; k_5 = 0.45538 \; k_6 = -0.20077 \\
k_{i1} &= -1.9948 \; k_{i2} = 1.6975 \quad k_{i3} = -2.8255 \qquad (21)
\end{aligned}
$$

The manufactured new DC-DC converter built-in DSP is shown in **Fig.5**. This fits in a quarter brick size (37mm x 58mm x 8mm) one. Experimental results when the digital controller with the parameters of eq.(21) is equipping in the DSP shown in **Figs.6** and **Figs.7**. Fig.6 shows the dynamic load response at the resistive load ($R_L = 0.33 \leftrightarrow 0.165[\Omega]$). It turns out that the specification us satisfied. It is checked that almost the same exprimental results as Fig.7 are obtained at the parallel load of resistance ($R_L = 0.33 \leftrightarrow 0.165[\Omega]$) and capacity ($C_L = 200[\mu\mathrm{F}]$). Although the load current changed suddenly from 20 [A] to 10 [A] or reverse, the output voltage change is very small and is suppressed within about 25[mV]. Fig.7 shows the output response at resistive load $R_L = 0.33[\Omega]$ when input voltage changed suddenly from 48[V] to 58[V]. It turns out that the specification us satisfied. It is checked that almost the same exprimental results as Fig.7 are obtained when input voltage changed suddenly from 38[V] to 48[V]. We checked by expriments that all other specifications are satisfied.

V. Conclusion

In this paper, the concept of controller of a DC-DC converter to attain good robustness against extensive load changes and input voltage change was given. The proposed digital controller was implemented on the DSP(TI TMS320LF2801). The new DC-DC converter built-in this DSP was manufactured. It was shown from experiments that a sufficiently robust digital controller is realizable. The characteristics of the dynamic load response and the output response against sudden input voltage change were improved by using the proposed method for approximate 2DOF digital controller with additional zeros. This fact demonstrates the usefulness and practicality of our method. The future work is to design a digital controller robust enough, when (LC+LC) circuits etc. are used as filters for removal of switching and carrier noises.

References

[1] L. Guo, J. Y. Hung, and R. M. Nelms, "Digital controller Design for Buck and Boost Converters Using Root Locus", *IEEE IECON'2003*, 1864/1869 (2003).

[2] H. Guo, Y. Shiroishi and O. Ichinokura, "Digital PI Controller for High Frequency Switching DC/DC Converters Based on FPGA", *IEEE INTELEC'03*, 536/541 (2003).

[3] K. Higuchi, K. Nakano, T.Kajikawa, E.Takegami, S.Tomioka, K.Watanabe, "Robust Control of DC-DC Converter by High-Order Approximate 2-Degree-of-Freedom Digital Controller", *IEEE IECON'2004*, (CD-ROM), 2004.

New Automatic Multi-Stage Bumpless Mode Switching Digital Control for PWM Power Amplifier using Load Estimation

Ryosuke OKAZAKI[1],Koji MATSUSHITA[2], Kohji HIGUCHI[3], Kazushi NAKANO[4]
Tatsuyoshi Kajikawa[5] and Fumiho CHINO[6]
[1,3,4,5]Dept. of Electronic Engineering, The University of Electro-Communications,
1-5-1 Chofu-ga-oka, Chofu, Tokyo 182-8585, Japan
email:okaryo83@francis.ee.uec.ac.jp, higuchi@ee.uec.ac.jp, nakano@ee.uec.ac.jp,
kajikawa@ee.uec.ac.jp
[2,6]NF Corporation, 6-3-20 Tunashimahigashi,Kohoku-ku, Yokohama 223-8508,Japan
email:matsushita-k@nfcorp.co.jp, chino-f@nfcorp.co.jp

Abstract— **In this paper a multi-stage switching type digital controller is proposed for spreading capacitance load range more and improving transient characteristics for inductance load. In the previous proposed controller, the configuration of the controller is the same to all loads. At inductive load, there is a possibility that the transient characteristics may become bad and the specification may not be satisfied. Therefore, a load current is estimated at inductive load, and the controller which also uses load current for feedback is configured. A inductance is estimated and a controller is switched to this controller bumplessly. In order to extend the range of capacitance load, a controller is increased from two stage to three stage, and these are switched to each other bumplessly. A DSP is implemented to this digital controller. It is demonstrated from experiments that the multi-stage switching type digital controller is realizable and the given specifications are satisfied.**

I. Introduction

A Pulse Width Modulation (PWM) switching circuit is used for an electric-power conversion circuit, and a PWM power amplifier which constitutes feedback control systems so that the output voltage supplied to load might be proportional to a reference input is used as an amplifier itself or as a power supply. In many applications loads cannot be specified, i.e., its characteristics are changeable from capacitive to inductive. In addition, its amplitude is also sharply changed from the zero to the maximum rating. Then, a so-called robust PWM power amplifier which can cover such an extensive load change and also direct-current power supply voltage change is needed. We proposed previously the digital controller which uses the bumpless mode switching in order to extend the range of load wider[2]. In this paper a multi-stage switching type digital controller is proposed for spreading capacitance load range more and improving transient characteristics for inductance load. In the previous proposed controller[2], the configuration of the controller is the same to all loads. At inductive load, there is a possibility that the transient characteristics may become bad and the specification may not be satisfied. Therefore, a load current is estimated at inductive load, and the controller which also uses load current for feedback is configured. A inductance is estimated and a controller is switched to this controller bumplessly. In order to extend the range of capacitance load, a controller is increased from two stage to three stage, and these are switched to each other bumplessly. The digital controller with the muliti-stage bumpless mode switching function is actually realized by using DSP. It is demonstrated from experiments that the multi-stage switching type digital controller is realizable and the given larger specifications are satisfied smoothly.

II. PWM power amplifier

The power amplifier as shown in **Fig.1** is being manufactured. The triangular wave double carrier system is adopted as a PWM switching signal generating part. The carrier frequency of triangular waves are $10 - 100$[kHz], and the amplitude c_m is 10[V]. A power amplification part is a full-bridge type chopper circuit, and the voltage of direct-current power-supply E is 150[V]. The LC circuit is a filter for removing carrier and switching noises. The values L_0 and C_0 of LC circuit are determined so that control systems can make their sensitivity to load change low and reduce noise.

If the frequency of input u is smaller enough than that of the carrier, the state equation of the PWM power amplifier at no load and inductive load in **Fig.1** can be expressed from the state equalizing method[1] as follows:

$$\begin{cases} \dot{x} = A_c x + B_c u \\ y = Cx \end{cases} \tag{1}$$

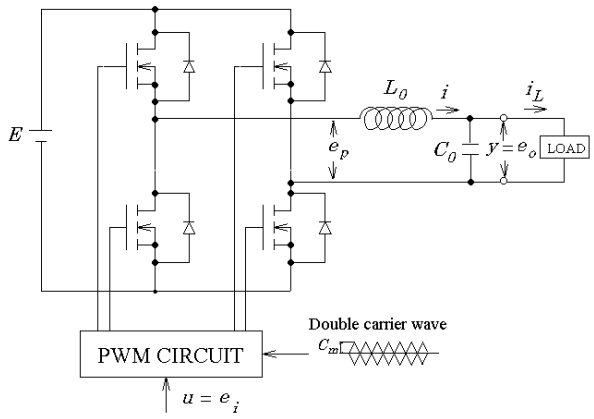

Fig. 1. PWM power amplifier

where at no load

$$x = \begin{bmatrix} e_o \\ i \end{bmatrix} \quad A_c = \begin{bmatrix} 0 & \frac{1}{C_0} \\ -\frac{1}{L_0} & -\frac{R_0}{L_0} \end{bmatrix} \quad B_c = \begin{bmatrix} 0 \\ \frac{K_p}{L_0} \end{bmatrix}$$

$$C = \begin{bmatrix} 1 & 0 \end{bmatrix} \quad u = e_i \quad y = e_0 \quad K_p = -\frac{E}{c_m}$$

and at inductive load

$$x = \begin{bmatrix} e_o \\ i \\ i_L \end{bmatrix} A_c = \begin{bmatrix} 0 & \frac{1}{C_0} & -\frac{1}{C_0} \\ -\frac{1}{L_0} & -\frac{R_0}{L_0} & 0 \\ \frac{1}{L_L} & 0 & \frac{R_{LL}}{L_L} \end{bmatrix} B_c = \begin{bmatrix} 0 \\ \frac{K_p}{L_0} \\ 0 \end{bmatrix}$$

$$C = \begin{bmatrix} 1 & 0 & 0 \end{bmatrix}$$

and R_0 is the total resistance of coil, ON resistance of FET, etc. and R_{LL} is a resistance of inductive load.

When realizing a digital controller by a DSP, a delay time exists between the start point of sampling operation and the output point of control input due to the input computing time and AD/DA conversion times. This delay time is considered to be equivalent to the input dead time which exists in the controlled object.
Then the discrete-state equation of the system with dead time is expressed as follows:

$$\begin{cases} x_d(k+1) = A_d x_d(k) + B_d v(k) \\ y(k) = C_d x_d(k) \end{cases} \tag{2}$$

where

$$x_d = \begin{bmatrix} x \\ \xi \end{bmatrix} \qquad \xi(k) = u(k) \quad C_d = \begin{bmatrix} C & 0 \end{bmatrix}$$

$$A_d = \begin{bmatrix} e^{A_c T} & e^{A_c(T-L_d)} \int_0^{L_d} e^{A_c \tau} B_c d\tau \\ 0 & 0 \end{bmatrix}$$

$$B_d = \begin{bmatrix} \int_0^{T-L_d} e^{A_c \tau} B_c d\tau \\ 1 \end{bmatrix}$$

Now, the power amplifier with the following specifications 1-3 is designed and manufactured by constituting

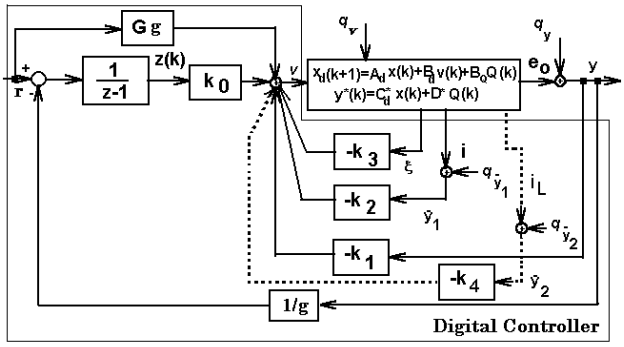

Fig. 2. Approximate 2-degree-of-freedom digital integral type control system

digital control systems to the PWM power amplifier (controlled object) at no load. The range of capacitive load in spec.1 has expanded more than those of our previous results[2].

1. The band-width of control systems is higher than 2[kHz] to each load , i.e., no load, resistance load, capacitive load, parallel load with resistance and capacitive load and inductive load, where $8.8 \leq R_L < \infty[\Omega]$, $0 \leq C_L \leq 100[\mu\text{F}]$, $5 \leq L_L < \infty[\text{mH}]$.
2. Against all the loads of spec.1, an over-shoot is not allowable in a step response.
3. The specs. 1 and 2 are satisfied also to change of the direct-current power supply of $\pm 10\%$.

The approximate 2-degree-of-freedom digital integral-type control systems will be obtained as shown in **Fig.2**. This control system satifies all specifications. In Fig.2, The dashed line including k_4 is a new feedback introduced for current i_L at inductive load.

III. Controller switching method

A. Load estimating method

From eq.(1), the capacitance is computed by the current in the coil and the derivative of output voltage such as

$$C_0 + C_L = \frac{i(t)}{\dot{e}_o(t)} \tag{3}$$

The capacitance can be estimated from eq.(11). In the case of the parallel load of capacitance and resistance, although the amount of feedbacks from $e_o(t)$ is added to $\dot{e}_o(t)$, if it is $\dot{e}_o(t) \gg e_o(t)$, the amount of addition can be ignored and the capacitance estimation can be carried out by eq.(11) even in this case. Eq.(3) can be expressed with discrete approximation as follows:

$$C_0 + C_L = \frac{T(i(k) + i(k-1))}{2(e_o(k) - e_o(k-1))} \tag{4}$$

Here, the current $i(k)$ uses the average value of $t = kT$ and $t = (k-1)T$. Noises, such as a carrier noise and a switching noise, are included in the output voltage of

PWM power amplifier. When the change of output voltage is small, the S/N deteriorates, and it becomes impossible to estimate the capacitance. Therefore, only when the change of output voltage is large, the capacitance can be estimated. When the change is small, the function of holding the previously estimated value is needed.

Next, from eq.(1), the inductance is computed by the output voltage and the derivative of the load current such as

$$L_L = \frac{e_o(t)}{\dot{i}_L(t)} \tag{5}$$

Eq.(5) can be expressed with discrete approximation as follows:

$$L_L = \frac{T(e_o(k) + e_o(k-1))}{2(i_L(k) - i_L(k-1))} \tag{6}$$

Here, the output voltage $e_o(k)$ uses the average value of $t = kT$ and $t = (k-1)T$. Now, the load current i_L is required to compute L_L. Moreover, this load current is required also for load current feedback. A method of estimating load current is used without using a sensor. From eq.(1), the load current is computed by the coil current and the derivative of output voltage such as

$$i_L(t) = i - C_0 \dot{e}_o(t) \tag{7}$$

Eq.(7) can be expressed with discrete approximation as follows:

$$\begin{aligned} i_L(k) &= (i(k) + i(k-1) \\ &- \frac{2C_0}{T}(e_o(k) - e_o(k-1)))/2 \end{aligned} \tag{8}$$

Here, the load current $i_L(k)$ uses the average value of $t = kT$ and $t = (k-1)T$.

Moreover, in order to use the derivatives of e_o and i_L, they have the gain characteristic of 20dB/dec, and have become sensitive to noise. In order to reduce thes influences, the following butterworth low-pass filters are inserted into the estimated values:

$$H(z) = \frac{a_0 z^2 + a_1 z + a_2}{z^2 + b_1 z + b_2} \tag{9}$$

The parameters a_0, a_1, a_2, b_1, b_2 are the suitable values determined that the cutoff frequency of the filters become as about 5[KHz]. Eqs.(4), eq.(6), eq.(8) and eq.(9) are all implemented by DSP.

B. Controller switching method

After estimating of the load current, inductance and capacitance, first it is judged whether there is inductance, next the size of capacitance is judged, and the mode is switched. The switching method using estimated inductance and capacitance is shown in **Fig.3**. About inductance load, it judges whether there is any inductance beyond a certain value, and if it is, it will only switch to mode 4. About capacitance load, when the estimated capacitance value is beyond a certain value , or when it is below, the mode is switched. If the estimated value is changed due to noise etc. when the load capacitance is close to threshold of change, the problem the the mode switches frequently will arise. Therefore, the hysteresis characteristic with mode switchingis established in Fig.3. The widths $TH_1 - TH2$ and $TH_3 - TH_4$ used for hysteresis are sets up so that a change does not arise beyond necessity by experiment. As for the controller, the mode 1 is chosen at the start of DSP execution program. Even when an estimated value exceeds TH_1, it does not switch to the mode 2. Only when it exceeds TH_2, it switches to the mode 2. In the time of being conversely less than TH_1 a switch from the mode 2 to the mode 1 is performed.

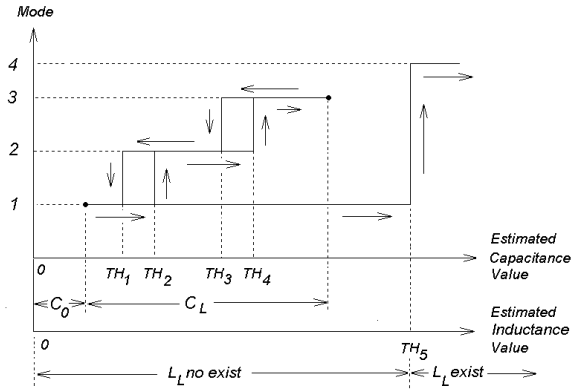

Fig. 3. Mode 1,2,3,4 switching method

C. Bumpless mode switching method

If the control variable is changed rapidly when the controller switches the mode, a bump will arise in an output. In order to suppress the bump, as shown in **Fig.4**, auxiliary feedback functions are implemented by a combination of mode i controller and mode j controller. Here $i = 1, 2, 3, 4$ and $j = 1, 2, 3, 4$ where $i \neq j$. In Fig.4, $X^\star$ is as in $X^\star = [y\ \bar{y_1}\ \xi]$, $k_{fi} = [k_{1i}\ k_{2i}\ k_{3i}]$ (at induccitive load $X^\star = [y\ \bar{y_1}\ \bar{y_2}\ \xi]$, $k_{fi} = [k_{1i}\ k_{2i}\ k_{3i}\ k_{4i}]$) and k_{0i} are the parameters of the mode i controller, $k_{fj} = [k_{1j}\ k_{2j}\ k_{3j}]$ (at induccitive load $k_{fj} = [k_{1j}\ k_{2j}\ k_{3j}\ k_{4j}]$) and k_{0j} is the parameters of the mode j controller. The parameter $k_{si} = 1/k_{0i}$ is the one for the bumpless switching function of the mode i controller and the parameter $k_{sj} = 1/k_{0j}$ is the one for the bumpless switching function of the mode j controller. According to these auxiliary function, at mode j, the control variable V_i of the mode i controller follows the control variable V_j of the controller j, and at mode i V_j follows V_i. Since V_j is mostly in agreement with V_j when

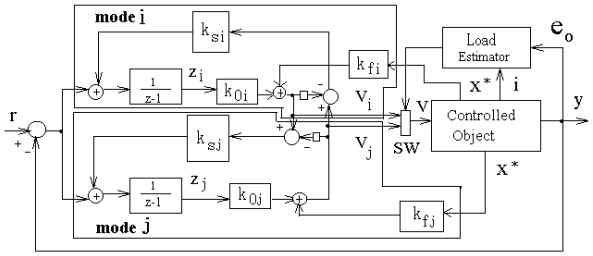

Fig. 4. Bumpless mode switching control system

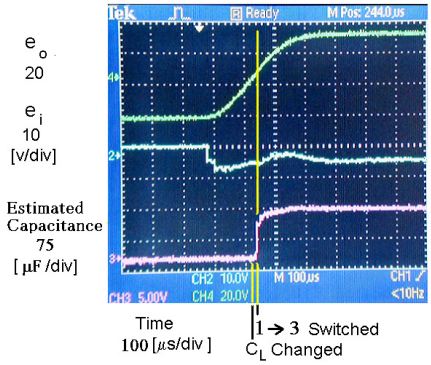

Fig. 5. Experimental result of step response using automatic bumpless switching from mode 1 to mode 2 and to mode 3 according to change of capacitance load from $C_0 + C_L = 0[\mu\text{F}]$ to $C_0 + C_L = 125[\mu\text{F}]$ ($C_0 = 25[\mu\text{F}]$)

the controllers are switched, they will be switched bumplessly. In addition, in Fig.4 the feedforward parameter Gg's are omitted.

IV. Experimental studies

A DSP(TMS320C6416) from Texas Imstruments(TI) is used, which realizes the digital controller in Fig.8. The sampling period T and the carrier frequency f_c are set as 12[μs] and 83.3[kHz], respectively. The input dead time L_d is about 11.9[μs]. At capacitive load the setting value of C_0 is changed. And three controllers which satisfy specifications in the following three kinds of range are designed.

mode 1: $C_0 = 25[\mu\text{F}]$ and $0 \leq C_L \leq 25[\mu\text{F}]$
mode 2: $C_0 = 40[\mu\text{F}]$ and $0 \leq C_L \leq 40[\mu\text{F}]$
mode 3: $C_0 = 60[\mu\text{F}]$ and $0 \leq C_L \leq 65[\mu\text{F}]$

The values of C_0 of mode 2 and 3 are temporary for the design, and the actually used C_0 is 25[μF] in the mode 1. According to actual load capacity, these three controllers are switched as shown in Fig.3. As a result, the capacitance range is as follows and satisfies specification.

$$0 \leq C_L \leq 100[\mu\text{F}] \tag{10}$$

At inductive load the controller (mode 4) using load current feedback is designed.

Experimental results when realizing the digital controller with switchable parameters of Table 2 by using the DSP, and connecting with the controlled object in Fig.1

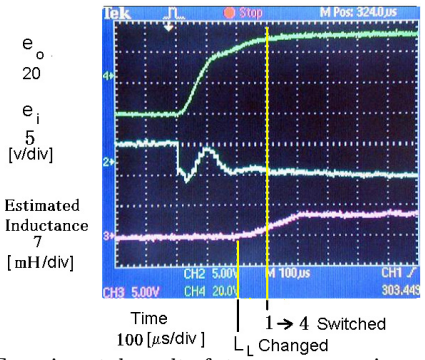

Fig. 6. Experimental result of step response using automatic bumpless switching from mode 1 to mode 4 according to change of inductance load from $L_L = 0[\text{mH}]$ to $L_L = 5[\text{mH}]$ ($C_0 = 25[\mu\text{F}]$)

are shown in **Fig.5** and **Fig.6**. Fig.5 shows the step responses of e_o and e_i and estimated capacitance using the automatic bumpless mode switching from mode 1 to mode 2 and mode 3 at $C_L = 100[\mu\text{F}]$. From Fig.5, it turns out that the parameters of the controller have switched from mode 1 to mode 2 and to mode 3 bumplessly during the transient response and all the specifications are satisfied. This experimental result shows that the bumpless mode switching can spread the range of the value of capacitive load. Fig.6 shows the step responses of e_o and e_i and the estimated inductance using the automatic bumpless mode switching from mode 1 to mode 4 at $L_L = 5[\text{mH}]$. From Fig.6, it turns out that the parameters of the controller have switched from mode 1 to mode 4 bumplessly and the specifications at incuctive load is satisfied.

V. Conclusion

In this paper, the concept of controller with multi-stage bumpless mode switching to attain the robustness to various loads and extensive load changes was given. The digital controller with multi-stage bumpless mode switching was realized by using a DSP implemented to the controlled object(PWM power amplifier which consists of a PWM signal generating part, an electric power conversion part and an LC filter). It is shown from an experiment that a sufficiently robust digital controller is realizable. The range of capacitive load colud be extended and the transient characteristics was improved by performing the multi-stage bumpless mode switching This fact demonstrated the usefulness of our method using the multi-stage bumpless mode switching.

References

[1] H.Fukuda and M.Nakaoka, "State-Vector Feedback Controlled-based 100kHz Carrier PWM Power Conditioning Amplifier and Its High-Precision Current-Tracking Scheme", *IEEE IECON'93*, pp.1105-1110, 1993.

[2] Kohji Higuchi, Kazushi Nakano, Tatsuyoshi Kajikawa, Kuniya Araki and Fumiho Chino, "Robust Digital Control of PWM Power Amplifier by Approximate 2-Degree-of-Freedom System with Bumpless Mode Switching," *Proc.of IEEE CDC-2002*, pp.6248-6253, 2003.

A Quasi-Constant Frequency Hysteretic Current-Programmed Converters with Control of Bifurcation

Noppadol Khaehintung* Chaiboon Kangsajian* Phaophak Sirisuk**

*Dept. of Control and Instrumentation Engineering, Faculty of Engineering, Mahanakorn University of Technology,
**Dept. of Computer Engineering, Faculty of Engineering, Mahanakorn University of Technology,
Bangkok, THAILAND 10530. Email: noppadol@mut.ac.th , chaiboon@mut.ac.th and phaophak@mut.ac.th.

***Abstract*-This paper presents the Quasi-Constant Frequency Hysteretic Current-Programmed Converters (CHCPC) with control of bifurcation. The simple proposed closed-loop control system is realized to regulate the output voltage which away from the first bifurcation. Moreover, by applying simple circuit, this system is maintained to operate at a constant frequency. In spite of nonlinear characteristics and instabilities of the converter, the performance of the closed-loop control system can be considerably improved. The proposed CHPCP can avoid bifurcation phenomena with constant switching frequency. Simulation results show that the technique introduced in this paper gives satisfactory results with the regulating modes in various operating conditions.**

I. INTRODUCTION

As an especially key part of a switching power supply a DC/DC converter is widely used because of the capabilities of chopping and filtering the input voltage through an appropriate switching action, mostly implemented by a Pulse Width Modulation (PWM) circuits, a conventional constant frequency with direct duty ratio control. A current-programmed converter becomes the regulating scheme of choice in DC/DC converter and offers significant improvement over a direct duty ratio control such as automatic overload protection and design flexibility in improving small-signal dynamics [1]. Due to nonlinear characteristics of switching devices employed in the converter, the design of a control scheme for such converter may be difficult because of a rich variety of bifurcation [2].

Recently, the main study of bifurcation and chaos has been observed and analyzed for various kinds of power electronic circuits. In order to guarantee for system stability in most practical situations, the key design problem is the control of bifurcation or chaos control [3] which required stable operation is a period-1. Several researches have focused on the control of bifurcation, especially a Constant clock Frequency Current-mode Boost Converter (CCFCMBC). The work presented in [4], for instance, that uses analog circuit for adjusting variable ramp compensation in a Current-mode Boost Converter (CMBC). Regardless, the technique is restricted to a fixed system component. In order to overcome the previous problem, the sophisticated artificial intelligence controller to optimize a ramp compensation signal has been presented in [5]. However, its structure is generally more complicated and requires relatively high performance processor. Although the gain feedback to control of bifurcation was proposed in [6], Nonetheless, this system was not guarantee the over compensation, lead system to the discontinuous-conduction mode (DCM).

In order to control of bifurcation without the ramp compensation signal, the complicated circuits for implementation of a sliding mode controller (SMC) or a Variable frequency Hysteretic Current-Programmed Converters (VHCPC) for a CMBC has been proposed in [7]. This system, however, is still lacking the unpredictable constant frequency for any given load and the design for automatic closed-loop operation has not been mentioned. Although the quasi-constant frequency with Hysteretic Current-Programmed Converters for CMBC is introduced [8], this system requires current controller not easy to implement in a cost-effectiveness system.

In this paper, in stead of a VHCPC, the proposed Quasi-Constant frequency Hysteretic Current-Programmed Converters (CHCPC) with control of bifurcation of is presented for a CMBC. A simple but very effective control of CMBC is introduced. The performances of the control system are verified using the simulations with various operating conditions. The paper is organized as follows. In Section II, the circuit configuration of a CCFCMBC is described, followed by the proposed control bifurcation using CHCPC in Section III. Simulation results from the control system are given in Section IV. Finally, conclusions are drawn in Section V.

II. THE CMBC CONFIGURATION

A. Circuit Configuration

The CCFCMBC circuit configuration is depicted in Fig. 1. The system consists of a constant DC voltage source, a CMBC and a load. The Proportional plus Integral (PI) current controller is used to regulate the output voltage (v_{out}), accordingly to the desired output voltage (v_{ref}), in spite of the fluctuations in the input voltage (v_{in}) and the changes in load levels (R_{Load}).

In this system, the inductor current, i_L, is chosen as the programming variable which, by comparing with reference current, I_{ref}, from current controller, generates the turning-output signal for switch S. The switch S is turned on by clock pulse signal at time equal to nT and turned off when i_L climbs up to the denoted value I_{ref} and remains in off position until the next cycle as shown in Fig. 2. Typically, the system state equation can be represented by [3]

$$\begin{bmatrix} \dot{v}_{out} \\ \dot{i}_L \end{bmatrix} = \begin{bmatrix} -1/R_{Load}C & q/C \\ -q/L & 0 \end{bmatrix} \begin{bmatrix} v_{out} \\ i_L \end{bmatrix} + \begin{bmatrix} 0 \\ 1/L \end{bmatrix} v_{in}, \quad (1)$$

where q is a switching function which is one during the switch off interval while zero during on interval. To regulate the v_{out}, the PI controller is realized.

B. Nonlinear dynamics of CCFCMBC

In a CCFCMBC, let us define $i_L(n)$ and $i_L(n+1)$ as the inductor current at a $t=nT$ and $t=(n+1)T$, respectively. In steady state condition, the inductor current can be derived from [3] as:

$$i_L(n+1) = I_{ref} + \frac{(v_{in} - v_{out})T}{L} t_n' \quad (2)$$

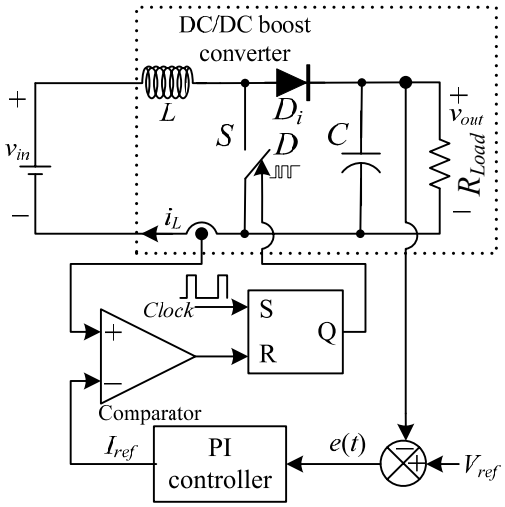

Figure 1. The closed-loop control of CCFCMBC.

and

$$t_n' = T - T\left[\frac{t_n}{T} \bmod 1\right], \tag{3}$$

where T is a clock pulse period and mod(.) is the modulus function. The slope of inductor current can be expressed by inspecting as:

$$\frac{I_{ref} - i_L(n+1)}{(1-D)T} = \frac{v_{out} - v_{in}}{L} \tag{4}$$

and

$$\frac{I_{ref} - i_L(n)}{DT} = \frac{v_{in}}{L} \tag{5}$$

The inductor current shown as solid line in Fig 2 under period-1 operation, which frequency of i_L equal f, can be expressed as:

$$\begin{aligned} i_L(n+1) = &\left(1 - \frac{v_{out}}{v_{in}}\right) i_L(n) \\ &+ \frac{I_{ref} v_{out}}{v_{in}}\left(\frac{v_{out} - v_{in}}{L}\right) T \end{aligned} \tag{6}$$

In order to maintain a stable period-1 operation [3], a CCFCMBC must operate with duty ratio D set below 0.5, so that the criterion of no bifurcation can be achieved. For the CCFCMBC, the equivalent criterion of no bifurcation in terms of I_{ref} using the steady-state equation relating R_{Load} and D is given by:

$$I_{ref} < \frac{v_{in}}{R_{Load}}\left[\frac{DR_{Load}T}{2L} + \frac{1}{(1-D)^2}\right]\Bigg|_{D=0.5} \tag{7}$$

When I_{ref} increases in CCFCMBC, i_L may operate in period-2 until submit the border collision as dot line, and then becomes chaotic as shown in Fig. 2.

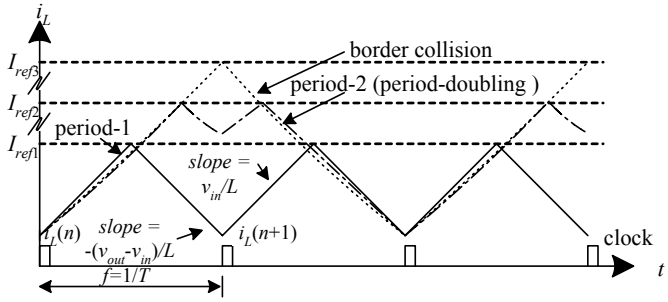

Figure 2. Typical waveform of inductor current i_L in CCFCMBC.

III. THE PROPOSED CHCPC

A. Voltage control loop

In this closed-loop control system I_{ref} is controlled via feedback loop which attempts to keep v_{out} fixed by adjusting I_{ref}. Let us defined the error function $e(t)$ is defined as:

$$e(t) = V_{ref} - v_{out}(t) \tag{8}$$

The output I_{ref} of PI controller can be calculated as:

$$I_{ref}(t) = K_p e(t) + K_i \int e(t)\,dt \tag{9}$$

, where K_p and K_i are PI controller parameters which chosen under system stability but play a role in determining the stability for dynamics response in a small-signal system model [9].

B. Adaptive of a quasi-constant frequency

Due to the disadvantages of a CCFCMBC as described in previous section, the proposed Quasi-Constant frequency Hysteretic Current-Programmed Converters (CHCPC) scheme is shown in Fig. 3, which applying from a variable frequency hysteretic current-programmed control (VHCPC) [7]. For VHCPC, the control signal to the switching converter tries directly to control the inductor current and to control the duty ratio indirectly. The switch S turns on and off by the gap of difference between reference current I_{ref} and inductor current i_L as:

$$\Delta i_L = I_{ref} - i_L(t) \tag{10}$$

The gap of hysteretic current-control ΔI_L is fixed. The switch S is turned off when i_L rises to its peak value determined

$$i_{L\max}(t) = I_{ref} \tag{11}$$

The switch S is turned on when i_L falls to its minimum given as

$$i_{L\min}(t) = I_{ref} - \Delta I_L, \tag{12}$$

where ΔI_L also denotes the ripple inductor current. Typical waveform of VHCPC control is shown in Fig. 4 as dot line. Thus, the switching frequency f for the switch S is given as:

$$f = \frac{v_{in}(t)\left(v_{out}(t) - v_{in}(t)\right)}{L\Delta I_L v_{out}(t)} \tag{13}$$

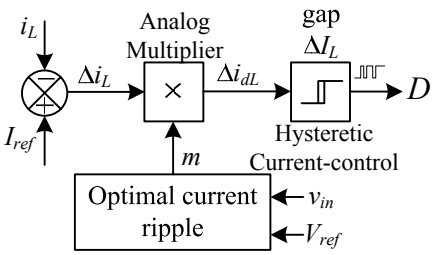

Figure 3. Control inductor current by the proposed CHCPC.

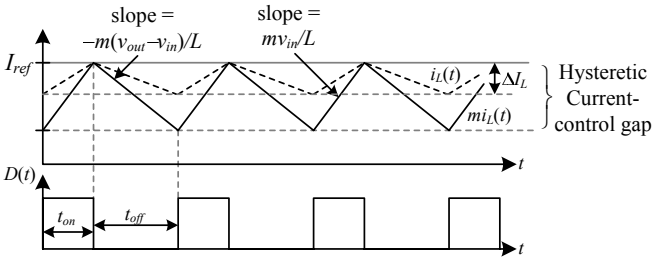

Figure 4. Typical wave forms of VHCPC and CHCPC.

From Fig. 4, it can be found that the switching frequency is varied in VHCPC depended on ΔI_L . Instead of control the switching frequency by adjusting the hysteretic current-control gap, the proposed CHCPC technique can limit the hysteretic current-control gap at the normalized value between 1 and 0 respectively. The control of switching frequency of CHCPC can be varied as shown in Fig.4 in solid-line. The constant switching frequency at steady state response can be obtained by adjusting the ripple current as: as

$$\Delta i_{dL}(t) = m\Delta i_L(t), \tag{14}$$

where m denotes the adjustable inductor current given by

$$m = \frac{V_{ref} L f_d}{v_{in}\left(V_{ref} - v_{in}\right)}, \tag{15}$$

where f_d is the desired switching frequency in this system.

IV. Simulation Results

To evaluate performances of the proposed system, computer simulations were conducted using MATLAB/SIMULINK® [10] as shown in Fig. 5. The CMBC model described in the previous section with the parameters given in Table I was invoked.

The bifurcation diagram [3] for the CCFCMBC is used to study system nonlinear behaviours with the bifurcation parameter I_{ref} (horizontal axis) and I_L (vertical axis). Corresponding to the variation of I_{ref} from 0 to 1A, the sampled i_L is observed and recorded. While R_{Load} is equal to 80Ω, the bifurcation diagram of this system is shown in Fig. 6 (a). In this figure, it can be seen that the period-1 is stable until I_{ref} is equal to 0.18A and 0.36A while v_{in} is fixed at constant values of 3V and 6V, respectively. When changing R_{Load} to 40Ω, this stable point is shifted to i_{ref} of 0.30A and 0.60A as shown in Fig. 6 (b).

The variations of supply voltages and load resistances have been fictitiously set as follows. The supply voltage are denoted constant at 6V and declined to 3V at 0.15s, and the values of load resistance are 80Ω and 40Ω from 0 to 0.4s and 0.4s onwards, respectively. The output voltage converges from the starting point to 10V as desired for all cases. The output voltage v_{out} and inductor current i_L for the CCFCMBC are depicted in Fig. 7.

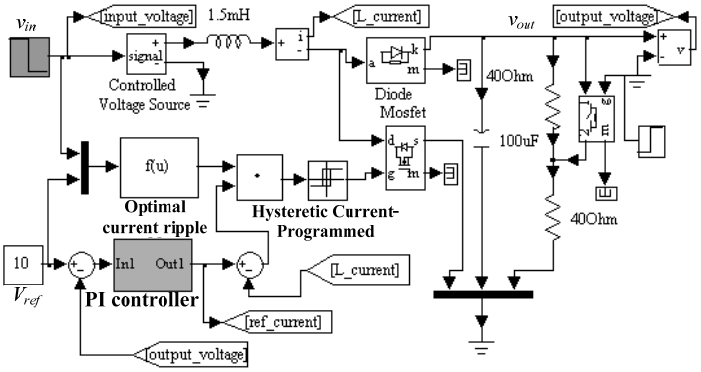

Figure 5. MATLAB/SIMULINK® model of the proposed CHCPC.

TABLE I.
THE CMBC PARAMETERS

Variable	***Definitions***
Inductor (L)	1.5mH
Capacitor (C)	100μF
The desired switching Freq (1/T).	10kHz
Output voltage (v_{out})	10V
Input voltage (v_{in})	3-6V

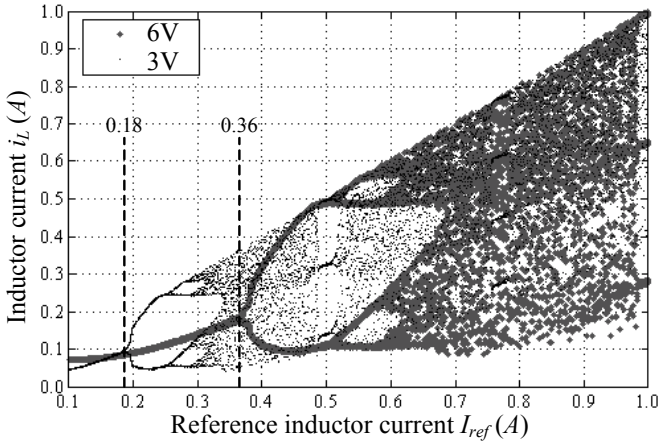

(a) 80Ω R_{Load}.

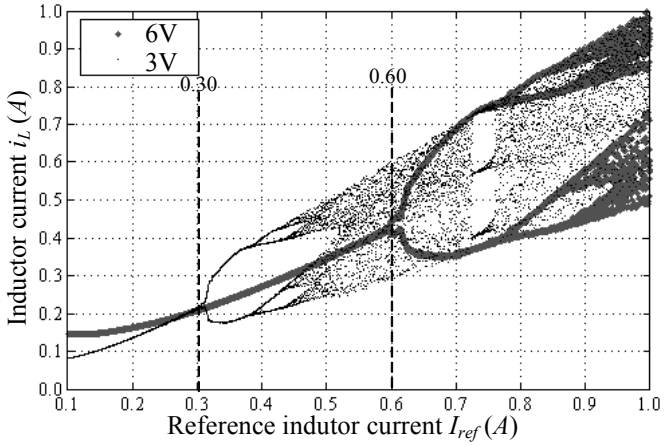

(b) 40Ω R_{Load}.

Figure 6. Bifurcation diagram in (I_{ref},i_L) plane with comparison of input voltage and load change.

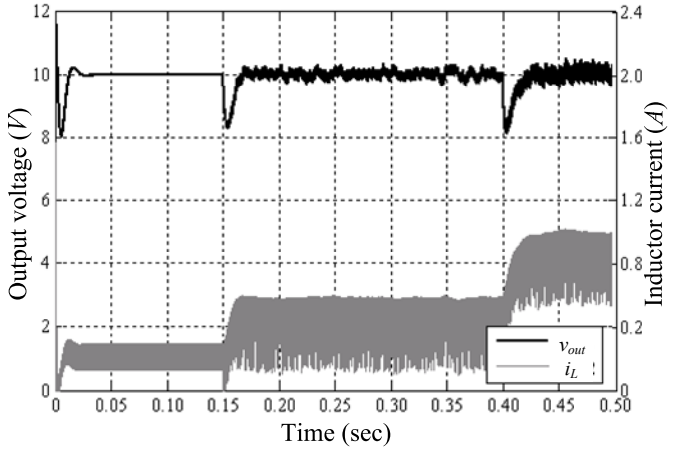

Figure 7. System responses of the CCFCMBC without bifurcation control.

After applying the VHCPC [7] with hysteretic current-control gap constant at 0.16A, the output voltage and inductor current are depicted in Fig 8. This result is confirmed that the VHCPC can compensate effects of the bifurcation phenomena. Generally speaking, the output voltage is not different between VHCPC and CHCPC. Fig 9 shows the result when applying the CMBC to the proposed CHCPC. It can be seen that the proposed CHCPC can maintain the output at period-1 operation for all cases.

In addition, the steady state inductor currents are compared in Fig. 10. The current ripples with R_{Load} of 40Ω, while v_{in} is kept constant at 3V, are 0.46, 0.16 and 0.14A for the CCFCMBC, VHCPC and the proposed CHCPC respectively. However, the frequency of inductor current of CHCPC is keep to control at the desired switching frequency 10kHz. In addition, it is noticeable that, the output voltage and current response between with and without CHCPC are clearly different from CCFCMBC.

V. CONCLUSIONS

In this paper, the Quasi-Constant frequency Hysteretic Current-Programmed Converters (CHPCP) with Control of Bifurcation has been presented. The proposed CHPCP is not only simple but also effective for control of nonlinear characteristics and instabilities of the power converter. The simulation results obviously show that the proposed CHPCP can avoid bifurcation phenomena and system operation at a desired constant switching frequency. Furthermore, the output voltage fluctuation in steady state condition is substantially mitigated. The proposed system is simple but more effective circuit which easy to implement in low cost power system.

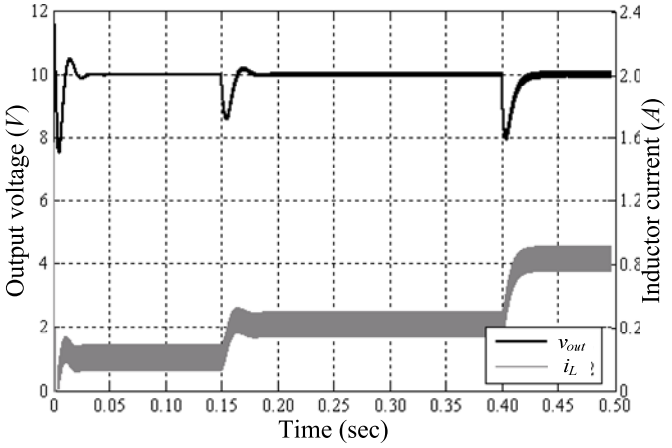

Figure 8. System responses of the VHCPC.

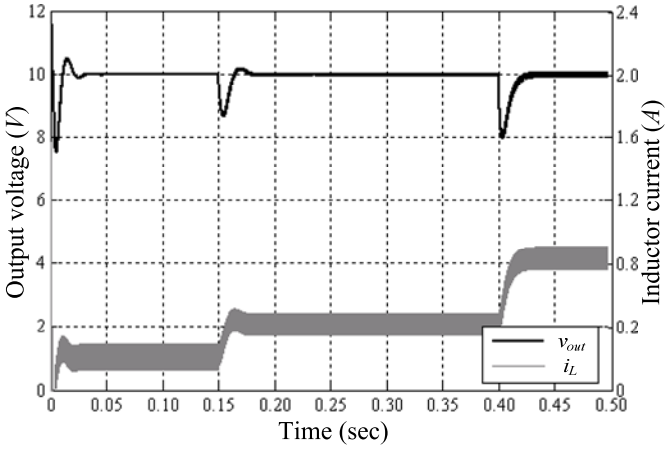

Figure 9. System responses of the proposed CHCPC.

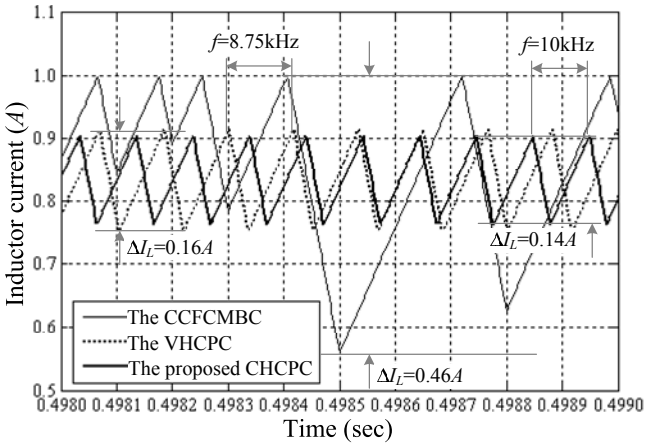

Figure 10. Comparison of steady state inductor currents.

REFERENCES

[1] F. D. Tan and R. D. Middlebrook, "A unified model for current-programmed converters," *IEEE Trans. Power Electronics*, Vol. 10, No. 4 , July, 1995, pp. 397-408.

[2] S. Banerijee and G. C. Verghese, *Nonlinear Phenomena in Power Electronics*, IEEE press, New York, 2001.

[3] M. D. Bernardo, F. Garofalo, L. Glielmo and F. Vasca, "Switchings, Bifurcations, and Chaos in DC-DC Converters," *IEEE Tran. on CAS-I*, Vol. 45, No. 2, 1998, pp. 133–141.

[4] C. K. Tse and Y. M. Lai, "Control Bifurcation in Current-Programmed DC/DC Converters: A reexamination of Slope Compensation," *Proc. IEEE ISCAS's 2000 Conf.*, pp. I-671-674, 2000.

[5] N. Khaehintung, P. Sirisuk and A. Kunakorn, "Control of Bifurcation by Fuzzy Logic Controller for Current-mode Boost Converters," *Proc. IEEE IPEMC's 2006 Conf.*, Vol. 1, pp. 368-372, 2006.

[6] N. Khaehintung, P. Sirisuk and T. Wiangtong, "C Control of Bifurcation for a Current-mode DC/DC Boost Converter by Self-inductor Current Feedback," *Proc. IEEE ISCIT's 2006 Conf.*, pp. W3D-2, 2006.

[7] M. Morel, "Application of slide mode control to a current-mode-controlled boost converter," *Proc. IEEE Ind. Electron. Soc. Conf. (IECON 02)*, Vol. 3, pp. 1824 – 1829, 2002.

[8] X. Yang and Z. A. Wang, "A novel quasiconstant frequency hysteretic current mode control approach," *Proc. IEEE PESC's 2003 Conf.*, Vol. 3, pp. 1147-1150, 2003.

[9] B. Bryantand and M. K. Kazimierczuk, "Open-loop power-stage transfer functions relevant to current-mode control of boost PWM converter operating in CCM," *IEEE Trans. Circuits and Systems-I*, Vol. 52 , No. 10 , Oct, 2005, pp. 2158 – 2164.

[10] http://www.mathworks.com

The Adaptive P&O Algorithm with a Hysteretic Current-mode Converter for a Solar-powered Battery Charger

Noppadol Khaehintung* Phaophak Sirisuk**

*Dept. of Control and Instrumentation Engineering, Faculty of Engineering, Mahanakorn University of Technology,
**Dept. of Computer Engineering, Faculty of Engineering, Mahanakorn University of Technology,
Bangkok, THAILAND 10530. Email: noppadol@mut.ac.th and phaophak@mut.ac.th.

***Abstract*-This paper presents the design of the adaptive Perturbation and Observation (P&O) algorithm with a Hysteretic Current-mode Converter (HCMC) of Maximum Power Point Tracking (MPPT) for a Solar-powered Battery Charger (SPBC). This unit captures solar energy by a solar array and delivers into battery through a boost converter. By slightly modifying the original algorithm, the proposed adaptive P&O algorithm is realized to improve MPPT speed. In addition, the HCMC is employed to improve the stability and dynamic response from a variation of system components. Simulation results with practical parameters show that our proposed MPPT using HCMC outperform the conventional variation of duty ratio for MPPT controller term of accuracy.**

I. INTRODUCTION

As the problem of fossil energy depletion becomes more severe, *photovoltaic* (PV) has received much interest to be used as a secondary energy source to produce the pollution-free energy. The term *photovoltaic* refers to the phenomenon involving the conversion of sunlight into electrical energy via a solar cell [1]. The solar energy is a strong candidate in many countries where a solar power density is relatively high. Under certain temperature and light intensity, there is only single maximum-power point (MPP) in a normal cell. Therefore, maximum power point tracking (MPPT) of the solar cell is essential as far as the system efficiency is concerned.

Several techniques have been proposed in the past decades. Many of them were implemented on digital processor, especially, with a solar-powered battery charging (SPBC) application. They range from conventional methods, such as the Hill-Climbing Method [2] and the Perturbation and Observation Method (P&O) [3], to much more sophisticated artificial intelligent methods, such as Artificial Neural Network (ANN) [2], Fuzzy Logic Control (FLC) [3], Adaptive Neural Fuzzy Inference System (ANFIS) [4]. Comparatively, conventional methods give poorer performances, but they are easier to implement. Artificial Intelligent methods, on the other hand, perform better, but their structures are generally more complicated and require relatively high performance processor. Most importantly, they generally lack the adaptability to deal with time varying environments. The adaptive P&O algorithm was presented and implemented [5] to improve MPPT speed.

Once MPP is determined via MPPT, hardware circuitry is required to move a current operating point of the system to MPP. To this end, DC/DC power converter, which connects PV to any load, is widely employed. The MPPT techniques based on a variation of duty ratio to control switch in a DC/DC boost converter for MPPT were employed [1-5]. The output voltage from the DC/DC converter is achieved by chopping and filtering the input voltage through an appropriate switching action. The variation of duty ratio for MPPT has several disadvantages to use with a DC/DC boost converter such as a variation of circuit parameters [6]. The nonlinear characteristics of the switching devices employed in the converter can lead to a rich variety of bifurcation [7] which compensated by variable ramp compensation. Another current-mode converter is the Hysteretic Current-mode Converter (HCMC) [8] which offers significant improvement over conventional direct duty ratio control such as automatic overload protection and especially design flexibility in improving small-signal dynamics [9].

In this paper, we propose an adaptive P&O Algorithm with a HCMC for an SPBC. Apart from the simplicity adaptive P&O algorithm, the MPPT time response is improved. Moreover, the HCMC merits include good stability suppressing the variation of system components and improving system dynamic response. The remainder of the paper is organized as follows. A typical SPBC system configuration is reviewed in Section II. The proposed MPPT system is addressed in Section III. In Section IV, the simulation results are shown in order to verify the capability of the system. Finally, conclusions are drawn in Section V.

II. SPBC SYSTEM CONFIGURATIONS

A. PV array Characteristic

The characteristic of a solar array can be comprehensively described by its operating curve known as an I-V curve, supplied by manufacturers to represent the solar array behaviors. It shows the relationship between output voltage and current of the solar array at certain light intensity and temperature as depicted in Fig. 1. It can be observed that under a certain light intensity and temperature there is a unique point located at the knee of the I-V curve, at which the maximum power can be generated from the solar array. Thus, a mechanism is required to track those underlying points so that the optimal operation of the overall system can be achieved.

The most commonly used equivalent circuit of a solar cell is shown in Fig. 2. The key equation to the relationship of each parameter, when internal series and shunt resistor are neglected [3], are given by

$$i_s = I_{LG} - I_{os}\left(\exp\left(\frac{v_s q}{AkT}\right) - 1\right), \tag{1}$$

where v_s denotes an output voltage of a solar array, i_s denotes a current of a solar array, A denotes the ideality factor, k is the Boltzman's constant (J/K), T is a cell temperature (K), q denotes an electron charge (C), I_{LG} denotes a light-generated current (A) and I_{os} denotes a cell reverse saturation current (A).

B. The MPPT for the SPBC

The configuration of the SPBC used in this research is shown in Fig. 2. The boost converter circuit used in the battery charging mechanism comprises of one inductor L with a switching device S. The power diode D_1 contributes to preventing the damage due to the reverse flowing current and not discharged from dark current leakage in a system from battery [3]. The capacitor C is large enough to filter

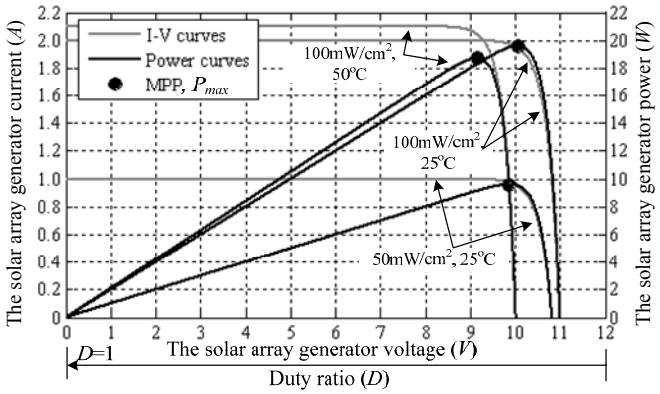

Figure 1. I-V and Power curves under light intensity and temperature.

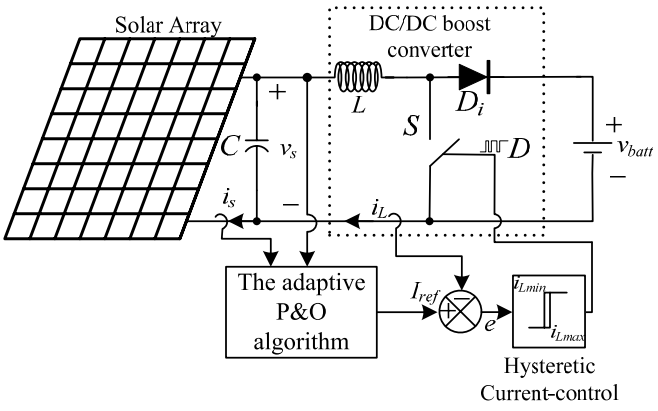

Figure 2. The proposed MPPT for SPBC system.

out the inductor current or to eliminate the pulsating power in this system.

In our design, the controller performs two main functions. First, it determines duty ratio D for the operation of switch S in such a way that the operating point of the solar array can be controlled toward the maximum power point. The controller also has to consistently detect the battery voltage to avoid battery overcharging. When the battery is fully charged, the controller will switch off the switch S. Instead of the direct duty ratio control for the operation of switch S, the HCMC is employed to improve small-signal dynamic response of MPPT system.

C. The SPBC's model

Generally, a power converter can be modeled with a circuit averaging technique [10]. The large-signal model of SPBC operating in continuous-conduction mode (CCM) is depicted in Fig. 3. The small-signal disturbance i_{dpv} and v_{dpv} denote as the output current and voltage of a solar array, v_{dbatt} and d is disturbance output voltage and PWM control signal, respectively. It notes that, I_{pv}, V_{pv}, I_L, D and V_{batt} are the DC components of an output current of a solar array, an output voltage of a solar array, inductor current, duty ratio and battery voltage. These components can be defined as zero in small-signal model. Using Kirchhoff's current and voltage low (KCL and KVL) the system state equations are obtained as:

$$i_{dpv} - C\frac{dv_{pv}}{dt} = i_{dL}\,, \tag{2}$$

$$v_{dpv} - L\frac{di_{dL}}{dt} = (1-D)v_{dbatt} - dV_{batt}\,, \tag{3}$$

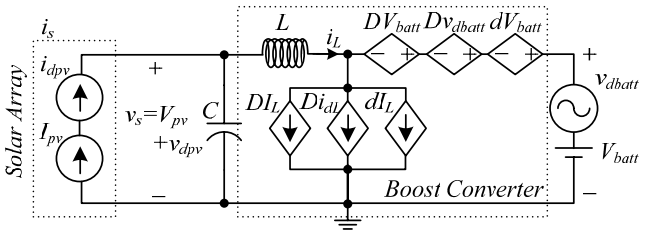

Figure 3. Large-signal model of boost converter operating in CCM.

and [6]

$$i_{dpv} = -Av_{dpv}\,, \tag{4}$$

where $A = (I_{os}q/kT)\exp(v_{dpv}q/kT)$. The duty ratio to output voltage of a solar array transfer function can be found as:

$$\frac{v_{dpv}(s)}{d(s)} = \frac{-V_{batt}/LC}{s^2 + A/C\,s + 1/LC}\,. \tag{5}$$

It can be found that in conversional direct duty ratio control, the capacitance C denotes the different damping or oscillation of v_{dpv} with a perturbation d.

III. The Proposed MPPT System

A. An adaptive P&O

As the name suggests, the P&O algorithm operates by periodically perturbing the control variable and comparing the instantaneous PV output power after perturbation with that before. In an original MPPT controller using P&O method the adjustment of the operating point is achieved by changing the reference voltage of the controller [5]. However, the adjustment can be made through the reference current I_{ref}. The algorithm is summarized in Table I.

Note that $v_s(k)$ and $P(k)$ are output voltage and the power of PV which is calculated from $v_s(k)\times i_s(k)$ at time k, respectively. Besides, $I_{ref.}$ and $\Delta I_{ref.}$ respectively denote reference current and change of reference current. To achieve faster MPPT response and more accurate MPP under dynamic environment, variable perturbation step-size, i.e. ΔI_{ref} can be employed. In fact, ΔI_{ref} can be selected as function of PV power as:

$$\Delta I_{ref}(k) = \alpha\cdot\beta\left|\frac{P(k)-P(k-1)}{v_s(k)-v_s(k-1)}\right|, \tag{6}$$

where α is the constant value to control the movement toward the MPP and the accuracy of convergence for MPPT, β is the sign of step dependent on perturbation direction.

B. Current Control

Due to the disadvantages of a constant variation of duty ratio in a power electronic converter, a Hysteretic Current-mode Control (HCMC) [4] is employed to improve the system dynamic response. In the HCMC, the control signal of the switching converter tries directly to control the inductor current and to control the duty ratio indirectly. The inductor current to input voltage of output voltage of a solar array transfer function can be found as

$$\frac{v_{dpv}(s)}{i_{dL}(s)} = \frac{-1/A}{C/A\,s+1} \tag{7}$$

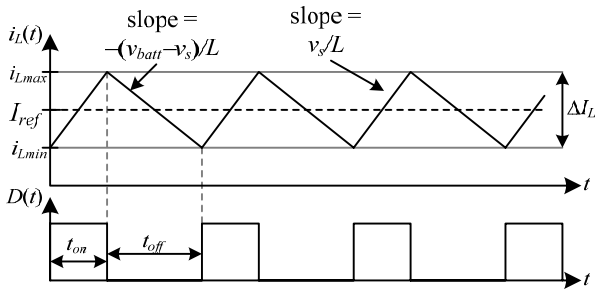

Figure 4. Typical wave forms of HCMC control.

It can be found that when applied the current-mode inductor control, the variation of capacitance C does not effect to the characteristic response of v_{dph}. In the HCMC, the switch S is turned off when i_L rises to its peak value determined by

$$i_{L\max}(t) = I_{ref} + \frac{\Delta I_L}{2}, \tag{8}$$

where I_{ref} is reference current. The switch S is turned on when i_L falls to its minimum given as

$$i_{L\min}(t) = I_{ref} - \frac{\Delta I_L}{2}. \tag{9}$$

The switching frequency f for the switch S is given by

$$\begin{aligned} f &= \frac{1}{t_{on}+t_{off}} \\ &= \frac{v_s(t)\left(v_{batt}(t)-v_s(t)\right)}{L\Delta I_L v_{batt}(t)} \end{aligned} \tag{10}$$

The maximum frequency $f_{\max}$ of the proposed MPPT system can be obtained as

$$f_{\max} = \frac{V_{batt}(t)}{4L\Delta I} \tag{11}$$

IV. Simulation Results

To evaluate performances of the proposed system, computer simulations were conducted using MATLAB/ SIMULINK®[11] with the solar array model described in the previous section as shown in Fig. 5. In addition, the boost converter circuit comprises one inductor (L=1.5mH) with two different capacitors C of 470μF and 4700μF were invoked. Using the solar array whose characteristics described above as shown in Fig. 1, the tracking performance of MPPT obtained from a variation of duty ratio D and the proposed HCMC for MPPT were examined. It should be noted that a sampling time for both algorithms was selected to be 5msec.

In the experiment, the light source was turned on at t = 0 sec under a light intensity of 50mW/cm^2 and temperature of 25^{o}C. The maximum power point at this environment is 9.66W. Fig 6 (a) and (b) show the power tracking results obtained from the variation of D by adaptive P&O algorithm with 470μF and 4700μF capacitors It can be seen that while both power results have the same settling time (t_s) at 0.02sec but the variation of duty ratio reach the steady state within 0.07sec. The performance of MPPT is degraded, however, when C is large. The output voltage of the solar array v_s tends to unstable with ripple (Δv_s) 5% from steady state as show in Fig. 6 (b)

Table I
MPPT Using Modified P&O Method

```
if((P(k) – P(k-1))>0)
    if((v_s(k) – v_s (k-1))>0
        I_ref = I_ref -ΔI_ref;
    else  I_ref = I_ref +Δ I_ref;
    end
 else
    if((v_s(k) – v_s(k-1))>0
        I_ref = I_ref +Δ I_ref;
    else I_ref = I_ref -ΔI_ref;
    end
 end
```

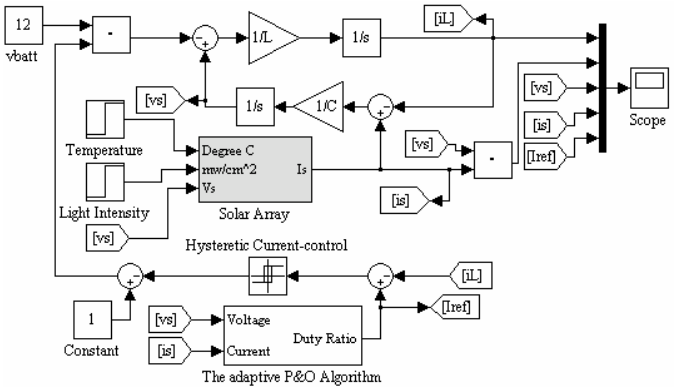

Figure 5. System simulation of MPPT
(Boost Converter, MPPT controller and Battery).

Fig. 7 (a) and (b) show the results of the obtained power from a variation of duty ratio and the proposed HCMC for MPPT. Comparing between Fig 6 (b) and Fig. 7 (b), we can obviously see that the performance of MPPT system is improved. Although the system has the large C, the fluctuated v_s can be mitigated and reached the steady state within 0.3sec.

Practical scenario where light intensity and temperature varies with time were assumed. That is, light intensity was 50 and 100mW/cm^2 from 0 to 0.75sec and 0.75sec onward, respectively. Furthermore, the temperature was 25^{o}C and 50^{o}C from 0 to 1.5sec and 1.5sec onward, respectively. The dynamic environment results in three maximum power points of 9.636W, 19.58W and 18.71W from 0 to 0.75sec, 0.75 to 1.5sec and beyond 1.5sec, respectively. The tracking results from the variation of duty ratio and the proposed HCMC when C is 4700μF are shown in Fig. 8 (a) and (b) respectively. It can be seen clearly that there are smaller power fluctuations in v_s and P during transient and steady state period when using HCMC for MPPT.

V. Conclusions

In this paper, the development an adaptive Perturbation and Observation (P&O) algorithm with a Hysteretic Current-mode Converter (HCMC) for a Solar-powered Battery Charger (SPBC) has been presented. The simulation results obviously show that the proposed adaptive P&O algorithm can give significantly faster tracking speed. Furthermore, the power fluctuation in steady state condition is substantially mitigated by using HCMC comparing with the conventional variation duty ratio control. The proposed system is simple but more effective circuit which is easy to implement in low cost power system.

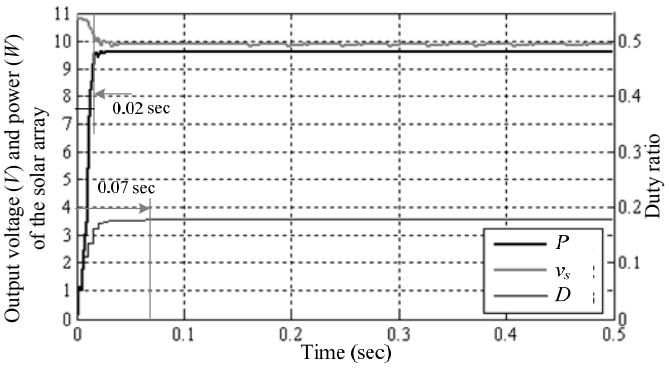

(*a*) C=470μF.

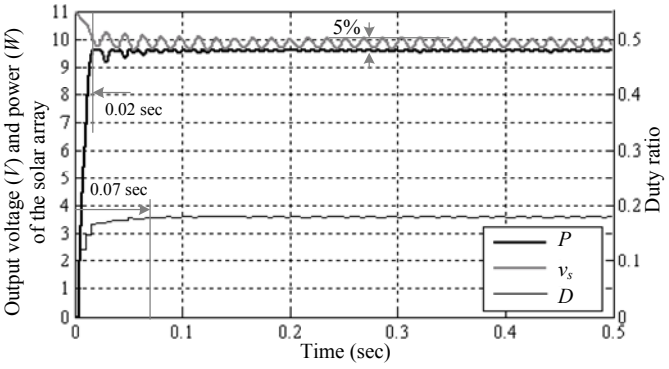

(*b*) C=4700μF.

Figure 6. Tacked power from variation of D.

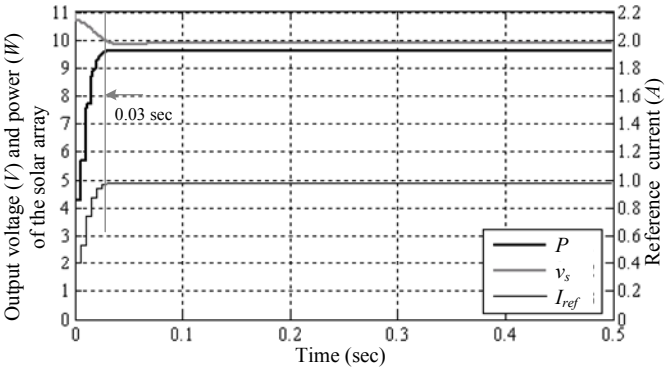

(*a*) C=470μF.

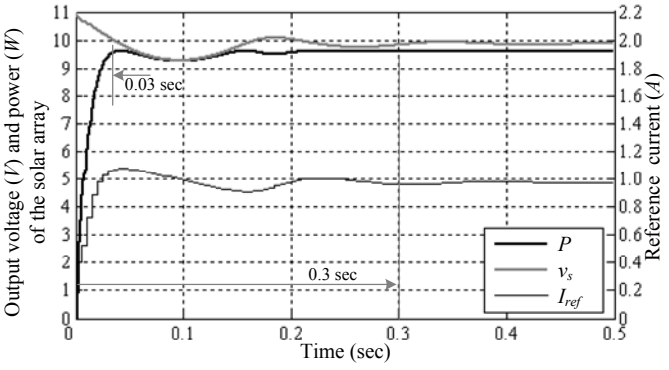

(*b*) C=4700μF.

Figure 7. Tacked power from the proposed MPPT.

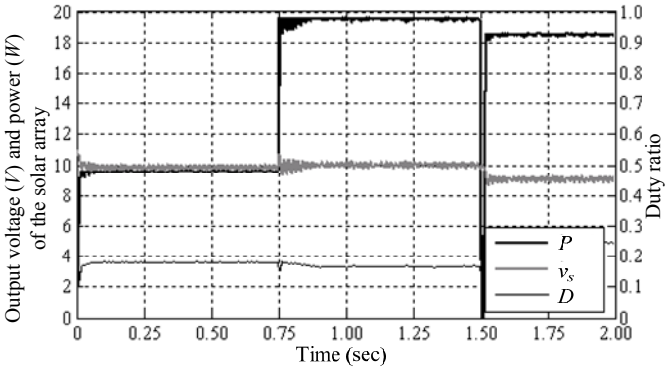

(*a*) A variation of duty ratio.

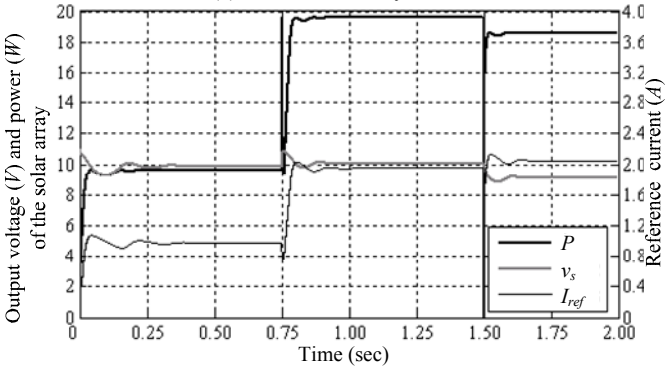

(*b*) The proposed HCMC for MPPT

Figure 8. Tacked power at C=4700μF.

REFERENCES

[1] T. Markvart, *Solar Electricity*, John Wiley & Sons, Chichester, 1994.

[2] P. Petchjatuporn, W. Ngamkham, N. Khaehintung. P. Sirisuk and W. Kiranon, "A Solar-powered Battery Charger with Neural Network Maximum Power Point Tracking Implemented on a Low-Cost PIC-microcontroller," *Proc. of IEEE int. PEDS' 2005*, pp. 507-510, 2005.

[3] N. Khaehintung, K. Pramotung, B. Tuvirat, and P. Sirisuk, "RISC-microcontroller built-in fuzzy logic controller of maximum power point tracking for solar-powered light-flasher applications," *Proc. of int. IECON 2004 Conf.*, pp. 2673-2678, 2005.

[4] N. Khaehintung, P. Sirisuk and W. Kurutach, "A novel ANFIS controller for maximum power point tracking in photovoltaic systems," *Proc. of int. PEDS 2003 Conf.,* Vol. 2, pp. 833-836, Singapore, 2003.

[5] N. Khaehintung, T. Wiangtong and P. Sirisuk, "FPGA Implementation of MPPT Using Variable Step-Size P&O Algorithm for PV Applications," *Proc. of int. ISCIT 2006 Conf.*, pp. W3D-5, 2006.

[6] N. Kasa, T. Iida, and G. MAjumdar, "Robust control for maximum power point tracking in photovoltaic power system," *Proc. of int. PCC 2002 Conf.*, pp. 827 – 832, 2002.

[7] N. Khaehintung, P. Sirisuk and A. Kunakorn, "Simple Current-mode Boost Converters for MPPT in Photovoltaic Systems with Bifurcation Control," *Proc. of int. ECTI 2006*, pp. 737-740, 2006.

[8] L. Yan-Fei and P. C. Sen, "Large-signal modeling of hysteretic current-programmed converters," *IEEE Trans. Power Electronics*, Vol. 11, No. 3 , May, 1996, pp. 423 – 430.

[9] F. D. Tan and R. D. Middlebrook, "A unified model for current-programmed converters," *IEEE Trans. Power Electronics*, Vol. 10, No. 4 , July, 1995, pp. 397-408.

[10] B. Bryantand and M. K. Kazimierczuk, "Open-loop power-stage transfer functions relevant to current-mode control of boost PWM converter operating in CCM," *IEEE Trans. Circuits and Systems-I*, Vol. 52 , No. 10 , Oct, 2005, pp. 2158 – 2164.

[11] http://www.mathworks.com

Proposal for Simple Repetitive Controllers

Kou Yamada, Hiroshi Takenaga, Yusuke Saitou, and Keiji Satoh
Department of Mechanical System Engineering
Gunma University
Kiryu, Gunma 376–8515 Japan
Email: yamada@me.gunma-u.ac.jp

***Abstract*—In this paper, we examine stabilizing simple repetitive controllers. The modified repetitive control system is a type of servomechanism for periodic reference input. Even if the plant does not include time-delay, the transfer function from the reference input to the output of the modified repetitive control system has generally an infinite number of poles. It is difficult to settle the input-output characteristics and the disturbance attenuation characteristics of the modified repetitive control system. From the practical point of view, the input-output characteristics and the disturbance attenuation characteristics of the control systems are required to be settled easily. In order to specify input-output characteristic and the disturbance attenuation characteristic easily, the transfer function from the reference input to the output and that from the disturbance to the output are desirable to have a finite number of poles. In order to specify input-output characteristic easily, we propose simple repetitive control systems such that the transfer function from the reference input to the output and that from the disturbance to the output have a finite number of poles. In addition, the parametrization of all stabilizing simple repetitive controllers is clarified.**

I. Introduction

In this paper, we examine stabilizing simple repetitive controllers. The repetitive control system is a type of servomechanism for periodic reference input. That is, the repetitive control system follows the periodic reference input without steady state error, even if a periodic disturbance or uncertainty exists in the plant [1–10]. It is difficult to design stabilizing controllers for the plant, because the repetitive control system follows any periodic reference input without steady state error is a neutral type of time-delay control system [8]. In order to design a repetitive control system that follows any periodic reference input without steady state error, the plant needs to be biproper [3–8]. However, in practice the plant is strictly proper. Many design methods of repetitive control systems for the strictly proper plants are given by [3–8]. These studies are divided into two types. One uses a low-pass filter [3–7] and the other uses an attenuator [8]. The latter is difficult to design because it uses a state variable time-delay in the repetitive controller [8]. The former has a simple structure and is easily designed. Therefore, the former type of repetitive control system is called the modified repetitive control systems [3–7].

However using the modified repetitive controllers in [3–7], even if the plants does not includes time-delay, the transfer function from the reference input to the output and that from the distrubance to the output have an infinite number of poles. When the transfer function from the reference input to the output and that from the disturbance to the output have an infinite number of poles, it is difficult to specify input-output characteristic and the disturbance attenuation characteristic. From the practical point of view, it is desirable that the input-output characteristic and the disturbance attenuation characteristic are easily specified. In order to specify input-output characteristic and the disturbance attenuation characteristic easily, the transfer function from the reference input to the output and that from the disturbance to the output are desirable to have a finite number of poles. However no paper examines a design method of modified repetitive control systems such that the transfer function from the reference input to the output and that from the disturbance to the output have a finite number of poles. In the following, we call the simple repetitive control systems if the controller works as a modified repetitive controller and the transfer function from the reference input to the output and that from the disturbance to the output have a finite number of poles.

In this paper, we propose simple repetitive control systems such that the controller works as a modified repetitive controller and the transfer function from the reference input to the output and that from the disturbance to the output have a finite number of poles. In addition, the parametrization of all stabilizing simple repetitive controllers is clarified.

II. Simple repetitive control systems and problem formulation

Consider the unity feedback control system given by

$$\begin{cases} y &= G(s)u + d \\ u &= C(s)(r-y) \end{cases}, \tag{1}$$

where $G(s) \in R(s)$ is the plant, $C(s)$ is the controller, $u \in R$ is the control input, $y \in R$ is the output, $d \in R$ is the disturbance and $r \in R$ is the periodic reference input with period $T > 0$ satisfying

$$r(t+T) = r(t) \ \ (\forall t \geq 0). \tag{2}$$

According to [3–7], when the plant $G(s)$ has a periodic disturbance d with period T and an uncertainty, in order for the output y to follow the periodic reference input r with period T with small steady state error, the controller $C(s)$ must be written by

$$C(s) = C_1(s) + C_2(s)C_r(s), \tag{3}$$

where $C_1(s) \in R(s)$, $C_2(s) \neq 0 \in R(s)$. $C_r(s)$ is an internal model for the periodic reference input r with period T and written by

$$C_r(s) = \frac{e^{-sT}}{1 - q(s)e^{-sT}}, \tag{4}$$

where $q(s)$ is a proper low-pass filter satisfying $q(0) = 1$. According to [3–7], if the low-pass filter $q(s)$ satisfy

$$1 - q(j\omega_i) \simeq 0 \quad (i = 0, \ldots, N_{max}), \tag{5}$$

where ω_i is the frequency component of the periodic reference input r written by

$$\omega_i = \frac{2\pi}{T} i \quad (i = 0, \ldots, N_{max}) \tag{6}$$

and N_{max} is the maximum frequency component of the periodic reference input r, then the output y in (1) follows the periodic reference input r with small steady state error. The controller written by (3) is called by the modified repetitive controller [3–7].

Using the modified repetitive controller $C(s)$ in (3), the transfer function from the periodic reference input r to the output y in (1) and that from the disturbance d to the output y in (1) are written as

$$\begin{aligned} \frac{y}{r} &= \frac{C(s)G(s)}{1 + C(s)G(s)} \\ &= \frac{\left\{C_1(s) - (C_1(s)q(s) - C_2(s))e^{-sT}\right\} G(s)}{[1 + C_1(s)G(s) - \{(1 + C_1(s)G(s))q(s) \\ &\qquad -C_2(s)G(s)\} e^{-sT}]} \end{aligned} \tag{7}$$

and

$$\begin{aligned} \frac{y}{d} &= \frac{1}{1 + C(s)G(s)} \\ &= \frac{1 - q(s)e^{-sT}}{[1 + C_1(s)G(s) - \{(1 + C_1(s)G(s))q(s) \\ &\qquad -C_2(s)G(s)\} e^{-sT}]}, \end{aligned} \tag{8}$$

respectively. Generally, the transfer function from the periodic reference input r to the output y in (7) and that from the disturbance d to the output y in (8) have an infinite number of poles. When the transfer function from the periodic reference input r to the output y and that from the disturbance d to the output y have an infinite number of poles, it is difficult to specify the input-output characteristic and the disturbance attenuation characteristic. From the practical point of view, it is desirable that the input-output characteristic and the disturbance attenuation characteristic are easily specified. In order to specify the input-output characteristic and the disturbance attenuation characteristic easily, the transfer function from the periodic reference input r to the output y and that from the disturbance d to the output y are desirable to have a finite number of poles.

From above practical requirement, we propose the concept of the simple repetitive controller as follows:

Definition 1: (simple repetitive controller)
We call the simple repetitive controller, if following expressions hold true:

1) The controller $C(s)$ works as a modified repetitive controller. That is, the controller $C(s)$ is written by (3), where $C_1(s) \in R(s)$, $C_2(s) \neq 0 \in R(s)$, $C_r(s)$ is written by (4) and $q(s) \in R(s)$ satisfies $q(0) = 1$.
2) The controller $C(s)$ makes the transfer function from the periodic reference input r to the output y in (1) and that from the disturbance d to the output y in (1) have a finite number of poles.

The problem considered in this paper is to propose the parametrization of all stabilizing simple repetitive controllers. That is, we find all controllers written by the form in (3) to make the transfer function from the periodic reference input r to the output y in (1) and that from the disturbance d to the output y in (1) be written as

$$y = \left(\bar{G}_{r1}(s) + \bar{G}_{r2}(s)e^{-sT}\right) r \tag{9}$$

and

$$y = \left(\bar{G}_{d1}(s) + \bar{G}_{d2}(s)e^{-sT}\right) d, \tag{10}$$

respectively, where $\bar{G}_{ri}(s) \in RH_\infty (i = 1, 2)$ and $\bar{G}_{di}(s) \in RH_\infty (i = 1, 2)$.

III. The parametrization

The parametrization of all stabilizing simple repetitive controllers is summarized in the following theorem.

Theorem 1: The controller $C(s)$ is a stabilizing simple repetitive controller if and only if $C(s)$ is written by

$$C(s) = \frac{X(s) + D(s)(Q(s) + \bar{Q}(s)e^{-sT})}{Y(s) - N(s)(Q(s) + \bar{Q}(s)e^{-sT})}, \tag{11}$$

where $N(s) \in RH_\infty$ and $D(s) \in RH_\infty$ are coprime factors of $G(s)$ on RH_∞ satisfying

$$G(s) = \frac{N(s)}{D(s)}, \tag{12}$$

$X(s) \in RH_\infty$ and $Y(s) \in RH_\infty$ are any functions satisfying

$$X(s)N(s) + Y(s)D(s) = 1, \tag{13}$$

$Q(s) \in RH_\infty$ and $\bar{Q}(s) \neq 0 \in RH_\infty$ are any functions satisfying

$$\frac{N(0)\bar{Q}(0)}{Y(0) - N(0)Q(0)} = 1. \tag{14}$$

Proof of this theorem requires following lemma.

Lemma 1: Unity feedback control system in (1) is internally stable if and only if $C(s)$ is written by

$$C(s) = \frac{X(s) + D(s)Q(s)}{Y(s) - N(s)Q(s)}, \tag{15}$$

where $N(s) \in RH_\infty$, $D(s) \in RH_\infty$ are coprime factors of $G(s)$ on RH_∞ satisfying (12), $X(s)$ and $Y(s)$ are RH_∞ functions satisfying (13) and $Q(s) \in RH_\infty$ is any function [11].

Using Lemma 1, we shall show the proof of Theorem 1.

Proof: First, the necessity is shown. That is, we show that if the controller $C(s)$ in (3) makes the control system in (1) stable and makes the transfer function from r to y of the control system in (1) have a finite number of poles, then $C(s)$ takes the form (11). From the assumption that the controller $C(s)$ in (3) makes the transfer function from r to y of the control system in (1) have a finite number of poles,

$$\begin{aligned}\frac{C(s)G(s)}{1+C(s)G(s)} \\ = \frac{\left\{C_1(s)-(C_1(s)q(s)-C_2(s))e^{-sT}\right\}G(s)}{\left[1+C_1(s)G(s)-\{(1+C_1(s)G(s))q(s)\right. \\ \left.-C_2(s)G(s)\}e^{-sT}\right]}\end{aligned} \tag{16}$$

has a finite number of poles. This implies that

$$C_2(s)=\frac{(1+C_1(s)G(s))q(s)}{G(s)} \tag{17}$$

is satisfied, that is, $C(s)$ is necessarily

$$C(s)=\frac{C_1(s)G(s)+q(s)e^{-sT}}{G(s)(1-q(s)e^{-sT})}. \tag{18}$$

From the assumption that $C(s)$ in (3) makes the control system in (1) stable, $C(s)G(s)/(1+C(s)G(s))$, $C(s)/(1+C(s)G(s))$, $G(s)/(1+C(s)G(s))$ and $1/(1+C(s)G(s))$ are stable. From simple manipulation and (18), we have

$$\frac{C(s)G(s)}{1+C(s)G(s)}=\frac{C_1(s)G(s)+q(s)e^{-sT}}{1+C_1(s)G(s)}, \tag{19}$$

$$\frac{C(s)}{1+C(s)G(s)}=\frac{C_1(s)G(s)+q(s)e^{-sT}}{(1+C_1(s)G(s))G(s)}, \tag{20}$$

$$\frac{G(s)}{1+C(s)G(s)}=\frac{(1-q(s)e^{-sT})G(s)}{1+C_1(s)G(s)} \tag{21}$$

and

$$\frac{1}{1+C(s)G(s)}=\frac{1-q(s)e^{-sT}}{1+C_1(s)G(s)}. \tag{22}$$

From the assumption that all the transfer functions in (19), (20), (21) and (22) are stable, $C_1(s)G(s)/(1+C_1(s)G(s))$, $C_1(s)/(1+C_1(s)G(s))$, $G(s)/(1+C_1(s)G(s))$ and $1/(1+C_1(s)G(s))$ are stable. This means that $C_1(s)$ is an internally stabilizing controller for $G(s)$. From Lemma 1, $C_1(s)$ must take the form

$$C_1(s)=\frac{X(s)+D(s)Q(s)}{Y(s)-N(s)Q(s)}, \tag{23}$$

where $Q(s)\in RH_\infty$.

From the assumption that the transfer functions in (19) and (22) are stable, $q(s)/(1+C_1(s)G(s))$ is stable. This implies that unstable poles of $q(s)$ is included in that of $C_1(s)$. That is, $q(s)$ is written by

$$q(s)=\frac{\hat{Q}(s)}{Y(s)-N(s)Q(s)}, \tag{24}$$

where $\hat{Q}(s)\neq 0\in RH_\infty$.

Since the transfer function in (20) is stable, $q(s)/\{(1+C_1(s)G(s))G(s)\}$ is stable. From (23) and (24), we have

$$\frac{q(s)}{(1+C_1(s)G(s))\,G(s)}=\frac{D^2(s)\hat{Q}(s)}{N(s)}. \tag{25}$$

From the assumption that $N(s)$ and $D(s)$ are coprime and the transfer function in (25) is stable, $\hat{Q}(s)$ is written by the form

$$\hat{Q}(s)=N(s)\bar{Q}(s), \tag{26}$$

where $\bar{Q}(s)\neq 0\in RH_\infty$. Substituting (17), (23), (24) and (26) for (3), we have (11). In this way, it is shown that if the controller $C(s)$ in (3) makes the control system in (1) stable and makes the transfer function from r to y of the control system in (1) have a finite number of poles, then $C(s)$ is written as (11). In addition, since $q(0)=1$ holds true, from (24) and (26), (14) is satisfied. Thus, the necessity has been shown.

Next, the sufficiency is shown. That is, if $C(s)$ takes the form (11), then the controller $C(s)$ makes the control system in (1) stable, makes the transfer function from r to y of the control system in (1) have a finite number of poles and works as a stabilizing modified repetitive controller. After simple manipulation, we have

$$\begin{aligned}\frac{C(s)G(s)}{1+C(s)G(s)} \\ = \left(X(s)+D(s)Q(s)+D(s)\bar{Q}(s)e^{-sT}\right)N(s),\end{aligned} \tag{27}$$

$$\begin{aligned}\frac{C(s)}{1+C(s)G(s)} \\ = \left(X(s)+D(s)Q(s)+D(s)\bar{Q}(s)e^{-sT}\right)D(s),\end{aligned} \tag{28}$$

$$\begin{aligned}\frac{G(s)}{1+C(s)G(s)} \\ = \left(Y(s)-N(s)Q(s)-N(s)\bar{Q}(s)e^{-sT}\right)N(s)\end{aligned} \tag{29}$$

and

$$\begin{aligned}\frac{1}{1+C(s)G(s)} \\ = \left(Y(s)-N(s)Q(s)-N(s)\bar{Q}(s)e^{-sT}\right)D(s).\end{aligned} \tag{30}$$

Since $X(s)\in RH_\infty$, $Y(s)\in RH_\infty$, $N(s)\in RH_\infty$, $D(s)\in RH_\infty$, $Q(s)\in RH_\infty$ and $\bar{Q}(s)\in RH_\infty$, the transfer functions in (27), (28), (29) and (30) are stable. In addition, from the same reason, the transfer function from r to y of the control system in (1) has a finite number of poles.

Next we show that the controller in (11) works as a modified repetitive controller. The controller in (11) is rewritten by the form in (3), where

$$C_1(s)=\frac{X(s)+D(s)Q(s)}{Y(s)-N(s)Q(s)}, \tag{31}$$

$$C_2(s) = \frac{\bar{Q}(s)}{\left(Y(s) - N(s)Q(s)\right)^2} \tag{32}$$

and

$$q(s) = \frac{N(s)\bar{Q}(s)}{Y(s) - N(s)Q(s)}. \tag{33}$$

From the assumption of $\bar{Q}(s) \neq 0$ and (32), $C_2(s) \neq 0$ holds true. In addition, from (33) and the assumption in (14), $q(0) = 1$ is satisfied. These expressions imply that the controller in (11) works as a modified repetitive controller. Thus, the sufficiency has been shown.

We have thus proved Theorem 1. ■

IV. Numerical example

Consider the problem to obtain the parametrization of all stabilizing simple repetitive controllers for the plant $G(s)$ written by

$$G(s) = \frac{s - 100}{(s+1)(s-1)} \tag{34}$$

that follows the periodic reference input r with period $T = 2[\mathrm{sec}]$.

A pair of coprime factors $N(s) \in RH_\infty$ and $D(s) \in RH_\infty$ of $G(s)$ in (34) satisfying (12) is given by

$$N(s) = \frac{s - 100}{(s+3)(s+2)},\ D(s) = \frac{(s+1)(s-1)}{(s+3)(s+2)}. \tag{35}$$

$X(s) \in RH_\infty$ and $Y(s) \in RH_\infty$ satisfying (13) are derived as

$$X(s) = -\frac{0.7075(s + 1.056)}{(s+3)(s+2)}, Y(s) = \frac{s^2 + 10s + 38.71}{(s+3)(s+2)}. \tag{36}$$

From Theorem 1, the parametrization of all stabilizing simple repetitive controllers for $G(s)$ in (34) is given by (11), where $Q(s) \in RH_\infty$ and $\bar{Q}(s) \in RH_\infty$ are any functions satisfying (14).

In order for the output y to follow the periodic reference input $r = \sin(\pi t)$ with small steady state error, $Q(s)$ and $\bar{Q}(s)$ are settled by

$$Q(s) = \frac{Y(s)}{N_o(s)}\bar{q}_d(s) \tag{37}$$

and

$$\bar{Q}(s) = \frac{Y(s) - N(s)Q(s)}{N_o(s)}\bar{q}_r(s), \tag{38}$$

respectively, where

$$\bar{q}_d(s) = \frac{1}{0.0001s + 1}, \bar{q}_r(s) = \frac{1}{0.0001s + 1}, \tag{39}$$

$$N_i(s) = -\frac{s - 100}{s + 100}, N_o(s) = -\frac{s + 100}{(s+3)(s+2)}. \tag{40}$$

Using above-mentioned parameters, we have the simple repetitive controller. When the designed simple repetitive controller $C(s)$ is used, the response of the output y in (1) for the periodic reference input $r = \sin(\pi t)$ is shown in Fig. 1. Here, the dotted line shows the response of the periodic reference input r and the solid line shows that of the output y. Figure 1 shows that the output y follows the periodic reference input r with small steady state error.

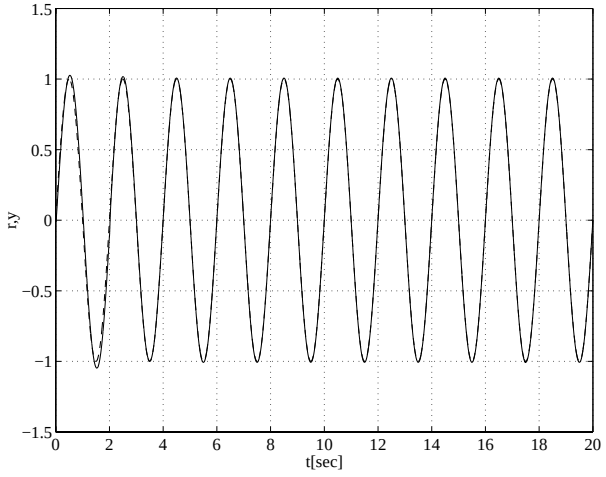

Figure 1. The response of the output y for the periodic reference input $r = \sin(\pi t)$

V. Conclusion

In this paper, we proposed the simple repetitive control systems and the parametrization of all stabilizing simple repetitive controllers.

References

[1] T. Inoue, et al., "High Accuracy Control Magnet Power Supply of Proton Synchrotron in Recurrent Operation", *The Trans. of The Institute of Electrical Engineers of Japan*, Vol.C100, No.7, pp.234-240, 1980.

[2] T. Inoue, S. Iwai and M. Nakano, "High Accuracy Control of Play-Back Servo System", *The Trans. of The Institute of Electrical Engineers of Japan*, Vol.C101, No.4, pp.89-96, 1981.

[3] S. Hara, T. Omata, and M. Nakano, "Stability Condition and Synthesis Methods for Repetitive Control System", *Trans. of the Society of Instrument and Control Engineers*, Vol.22, No.1, pp.36-42, 1986.

[4] S. Hara and Y. Yamamoto, "Stability of Multivariable Repetitive Control Systems - Stability Condition and Class of Stabilizing Controllers", *Trans. of the Society of Instrument and Control Engineers*, Vol.22, No.12, pp.1256-1261, 1986.

[5] Y. Yamamoto and S. Hara, "The Internal Model Principle and Stabilizability of Repetitive Control System", *Trans. of the Society of Instrument and Control Engineers*, Vol.22, No.8, pp.830-834, 1987.

[6] S. Hara, Y. Yamamoto, T. Omata and M. Nakano, "Repetitive Control System: A New Type Servo System for Periodic Exogenous Signals", *IEEE Trans. on Automatic Control*, Vol.AC-33, No.7, pp.659-668, 1988.

[7] T. Omata, S. Hara and M. Nakano, "Nonlinear Repetitive Control with Application to Trajectory Control of Manipulators", *J. of Robotic Systems*, Vol.4, No.5, pp.631-652, 1987.

[8] K. Watanabe and M. Yamatari, "Stabilization of Repetitive Control System-Spectral Decomposition Approach", *Trans. of the Society of Instrument and Control Engineers*, Vol.22, No.5, pp. 535-541, 1986.

[9] M. Ikeda and M. Takano, "Repetitive Control for Systems with Nonzero Relative Degree", *Proc. 29th CDC*, pp. 1667-1672, 1990.

[10] H. Katoh and Y. Funahashi, "A Design Method of Repetitive Controlles", *Trans. of the Society of Instrument and Control Engineers*, Vol.32, No.12, pp.1601-1605, 1996.

[11] M. Vidyasagar, "Control System Synthesis - A factorization approach -", *MIT Press*, 1985.

Dielectric Investigation of Fresh Fruits

K. Tonmitr, A. Kaewrawang, S. Swatdiponphallop, A. Suksri and A. Siritaratiwat and P.Bursri

Department of Electrical Engineering, Faculty of Engineering,
Khon Kaen University, Khon Kaen, 40002, Thailand.
Phone +66-4320-2353, Fax +66-4320-2836, E-mail: *kitton@kku.ac.th*

***Abstract*-The dielectric properties over the frequency range from 20 kHz to 1.5GHz at room temperature approximately 27ºC were measured for liquid sample cut from pineapple, lemon and orange. The dielectric constant and loss-factor data were obtained from the laboratory test for pineapple, lemon and orange. Not only the dielectric loss-factor decreased consistently with the increasing frequency up to 1.5GHz but the aging of fruits also depends on the frequency. The suitable range of frequency for the suitable discrimination is between 50 kHz and 80 kHz.**

Keywords: Dielectric Investigation, Dielectric Spectroscopy, High Frequency, Dielectric, Loss Tangent Factor

I. INTRODUCTION

The dielectric constant is essential information used in the designing capacitors and in other electrical apparatus where a material might be expected to have the capacitance in a circuit. If a material that have high dielectric constant placed into an electric field, the magnitude of that field will reduced the volume of the dielectric. This fact is commonly used to increase the capacitance of a particular capacitor design. The dielectric properties of moist materials can be determined by the electrical methods because of the correlation between molecular structure of material and water content on dielectric permittivity. A method that is used to determine the dielectric properties of fresh material is the use of electromagnetic field. The dielectric properties depends on water content, the frequency of the applied electromagnetic field, the temperature of the material, salts or dissolved iron of water, and the structure of the material[1-5]. The charge particle in the material which differs in molecule structure and composition acts differently in the electromagnetic field. The permittivity measurement determination of agriculture material can be use to determined the stage of freshness of fruits, grain, and seed be fore they are transfer to the customer. The frequency range of 20 MHz to 1.0 GHz is studied due to the ability of the RF analyzer the nondestructive frequency used by most research for RF radio wave to Microwave.

Thailand is one of the agricultural countries that has exported fresh fruits world wide. Nondestructive and destructive methods have been used for an inspection of the quality of fruits. In 1997, permittivity of homogenized macaroni, cheese, and wheat has been measured by S.O. Nelson et al. [6]. In 2001: W. Kongrattanaprasert et al. used force vibration and ultrasonic to classify the maturity of fruits[7]. In 2004, mango and durian inspection have been studied using inverse scattering technique by M.Krairiksh et al. [8]. In this paper, the study concerns with the behavior of dielectric constant, dielectric loss factor and loss tangent of three juices; pineapple, lemon and orange is presented.

II. DIELECTRIC PARAMETERS

A. Dielectric Constant

The dielectric constant is represented as ε_r. It is defined as (1) [9].

$$\varepsilon_r = \frac{\varepsilon_s}{\varepsilon_0} \tag{1}$$

Where

ε_s is the static permittivity of the material

ε_0 is vacuum permittivity

Vacuum permittivity is derived from Maxwell's equations by relating the electric field intensity E to the electric flux density D. In vacuum (free space), The permittivity ε_s is just ε_0, so the dielectric constant is 1.

The relative dielectric constant ε_r can be measured for any static electric fields and described as follows:

First, the capacitance of a test capacitor C_0 is measured with vacuum between its plates. Then, using the same capacitor and distance between its plates, the capacitance C_x with a dielectric between the plates is measured.

The relative dielectric constant can be then calculated as (2)

$$\varepsilon_r = \frac{C_x}{C_0} \tag{2}$$

For time-varying electromagnetic fields, the dielectric constant of materials becomes frequency-dependent and in general it is called permittivity.

B. Permittivity:

Generally, ε is a complex number whose real and imaginary parts depend on frequency as (3).

$$\varepsilon(f) = \varepsilon'(f) - j\varepsilon''(f) \tag{3}$$

Where

ε′(f) = real part (implies electromagnetic stored energy)

ε″(f) = imaginary part (implies electromagnetic loss energy)

If we divide (3) by permittivity of free space (εo = 8.854×10^{-12} F/m), the relative complex permittivity can be written as follows;

$$\varepsilon_r(f) = \varepsilon_r^{/}(f) - j\varepsilon_r^{//}(f) \tag{4}$$

Where

$\varepsilon_r'(f)$ = dielectric constant,

$\varepsilon_r''(f)$ = dielectric loss factor or loss conductivity

$$\varepsilon_r''(f) = \frac{\sigma}{2\pi f \varepsilon_0} \quad (5)$$

Or

$$\sigma = 2\pi f \varepsilon_0 \varepsilon_r''(f) \quad (6)$$

Where

σ = conductivity (S/m),

f = operating electromagnetic frequency (Hz).

The loss tangent of material can be defined as (7):

$$\tan\delta = \frac{\varepsilon''}{\varepsilon'} \quad (7)$$

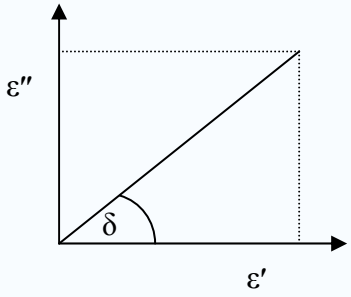

Figure 1.The relative of the loss tangent factor, ε′ and ε″

III. MECHANISMS OF ELECTRICAL POLARIZATION

There are 3 major mechanisms of the electric polarization:

A. Electronic or Optical polarization: the external electric field causes deformation or translation of the electron clouds of atom or molecules within certain media.

B. Atomic or ionic polarization: the electric field causes the atoms or ions of poly-atomic molecules to be displaced relative to each other.

C. Orientational polarization: the electric field causes the reorientation of the permanent dipoles in materials toward the direction of the field.

The peak of absorption loss will occur at resonant frequency, ω_c, that is;

$$\omega_c \tau = 1. \quad (8)$$

Where τ is relaxation time (s).

IV. EXPERIMENTAL LABORATORY

Samples of three different fresh fruit; pineapple, lemon, orange from a local agriculture farm are prepared for the measurements and investigation of the electrical dielectric. The sample fruits are cut in to small pieces of 2*2 cm^2 after picking up from the nearby farm. The sample cuts then are process into liquid form by electric processor. The liquid sample of 150 cm^3 in volume is then kept in a refrigerator at 2 degree Celsius. The liquid samples have water contents greater than 70%.

The electrical equipments are set up in the laboratory. The processes to measure the electrical dielectric of fruits are as follows;

A.The equipment are prepared for the experiment. A Hewlett-Packard network analyzer (model E5061A), a coaxial line cable (RG-58A/U) and a open-ended dielectric probe are used

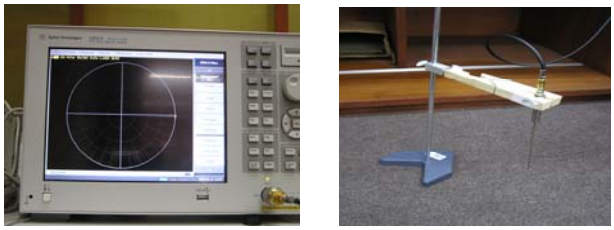

a) b)

Figure 2. Shows the measurement equipments
a) Hewlett-Packard network analyzer model E5061A
b) Dielectric probe

B.The calibration procedure is performed under open-circuit and short circuit test using distilled water at temperature of 25 degree Celsius as standard reference.

a) b)

Figure 3. Shows the probe and glass vessel
a) The calibration probe using distilled water at temperature of 25 degree Celsius as standard reference.
b) The measurement probe for different fruits in a glass vessel

C. Measure the permittivity properties of three different fruits; pineapple ,lemon, and orange on the 1st, 2nd, 3rd, 4th, 5th, 6th and 7th day after picking up from fruit trees at the local agriculture farm.

D. Calculate the permittivity (dielectric constant and loss factor) by using an appropriate 8085 dielectric probe kit software version E100 designed by Agilent technology, USA.

E. Two measurements are obtained from the experiment.

i) The dielectric, loss factor are obtained for three samples of fruits: pineapple, lemon and orange with frequency range from 20 kHz to 1.5GHz at room temperature 27 degree Celsius

ii) The dielectric, loss factor, conductivity of fruit samples are obtained for watermelon with frequency range from 20 kHz to 1.5GHz at temperature 30,50,70,90 degree Celsius.

V. EXPERIMENTAL RESULTS

The results obtained from the experiment conducted in the laboratory are as follows;

A. The dielectric properties of samples from three fruits on the **1st** day with frequency range as table1 are shown in Fig. 4.

TABLE I.

The Data for the Permittivity of All Three Fruits at Temperature of 20 Degree Celsius for Frequencies between 20 kHz,790 MHz and 1.5GHz

f / Fruits	20 MHz		790 MHz		1.5 GHz	
	$\varepsilon_r^{/}$	$\varepsilon_r^{//}$	$\varepsilon_r^{/}$	$\varepsilon_r^{//}$	$\varepsilon_r^{/}$	$\varepsilon_r^{//}$
Pineapple	127.0	225.2	76.3	10.8	74.4	11.3
Lemon	147.1	324.8	76.0	12.5	74.7	11.3
Orange	134.3	253.2	74.4	11.8	72.4	11.7

B. The dielectric properties of samples from three fruits on the **2nd** day with various frequencies are shown in Fig. 5.

C. The conductivity properties of samples from the watermelon with frequency range from 20 kHz to 1.5 kHz at temperature of 30, 50, 70, 90 degree Celsius is shown in Fig. 6.

D. The dielectric constant of watermelon at various frequencies and different temperature is shown in Fig. 7.

E. The dielectric loss factor of watermelon at various frequencies and different temperature is shown in Fig. 8.

VI. CONCLUSIONS

The major conclusions can be drawn from the experimental results as follows;

- The loss tangent, dielectric constant, dielectric loss factor of fruits depend greatly on an electromagnetic frequency. However, these parameters tend to decrease as the frequency of fruits is increased over the interval of 20 MHz-1.5 GHz.
- Over the frequency range 20 – 600 MHz, the dielectric loss factor can be approximated as linear equation.
- The conductivity tends to increase as the frequency and the temperature of fruits is increased.
- The most suitable frequency for the investigation is in the range of 20-100 MHz
- The quality or the degree of freshness of fruits can be determined by the method presented in this paper.

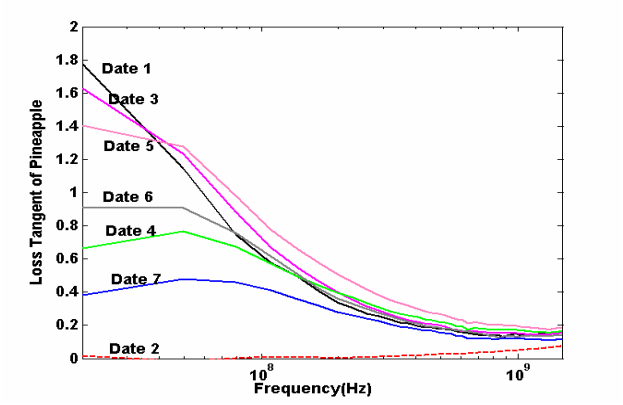

a) Pineapple

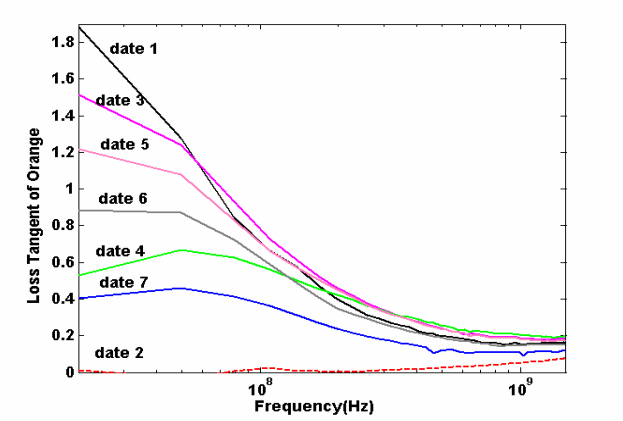

b) Orange

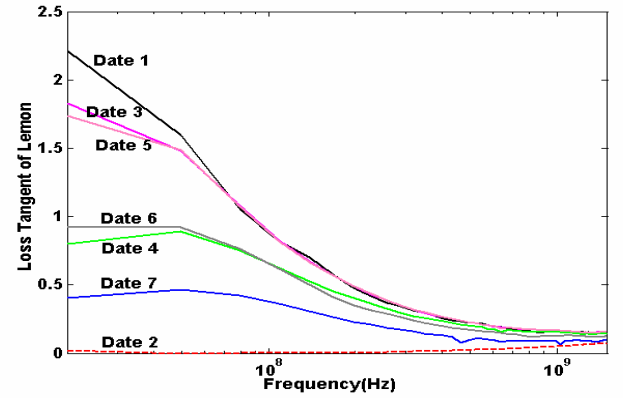

c) Lemon

Figure 4. The variation of the loss tangent properties of samples from three fruits

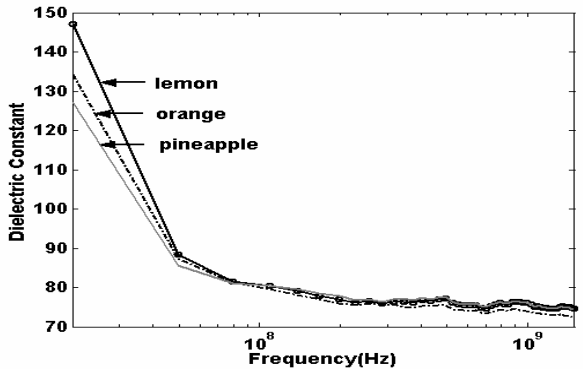

a) Dielectric constant

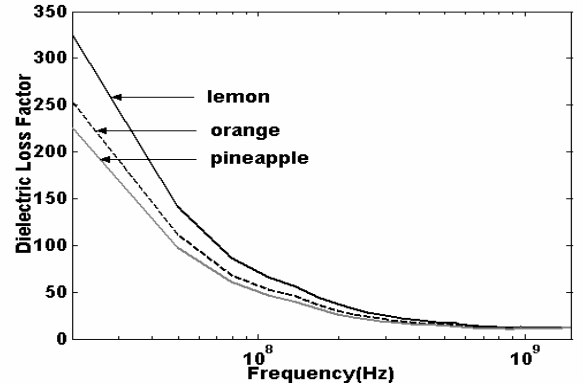

b) Dielectric loss factor, ε_r''

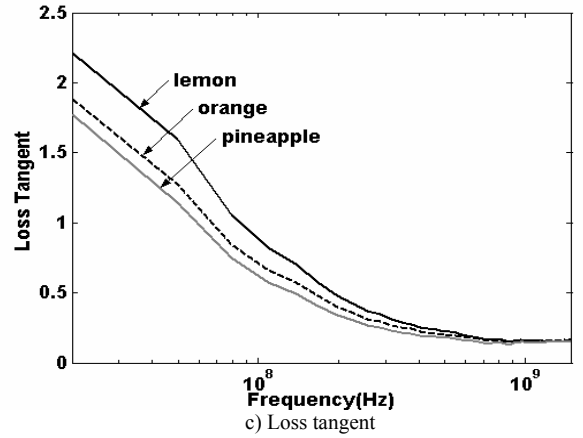

c) Loss tangent

Figure 5. The variation of the dielectric constant, dielectric loss factor, loss tangent properties of samples from three fruits

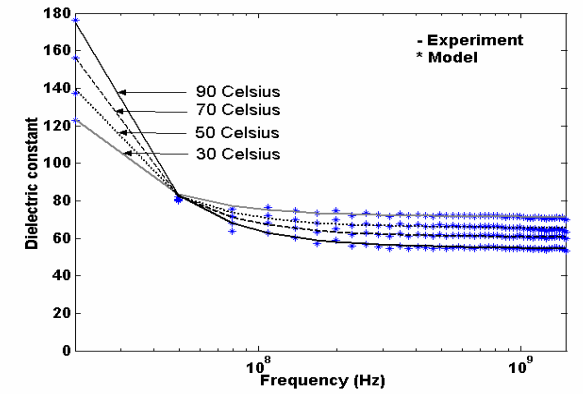

Figure 7. The variation of dielectric constant versus frequency

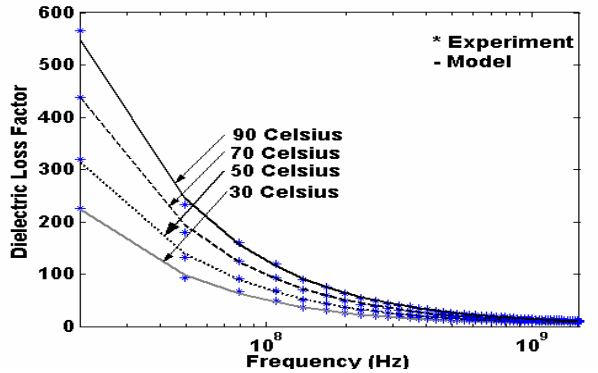

Figure 8. The variation of dielectric loss factor versus frequency

ACKNOWLEDGMENTS

Team researcher wishes to express their thanks to the EMC Laboratory and High Voltage research Laboratory Department of Electrical Engineering, Faculty of Engineering, Khon Kaen University, Thailand for all equipment and partial financial support.

REFERENCES

[1] A.W. Kraszewski, S.O. Nelson, **"**Microwave Permittivity Determination in Agricultural Products**",** 12th Int. Conf. Microwaves and Radar, Vol.4, pp. 230-242**,** May 1998

[2] D. Guan, M. Cheng, Y. Wang, J. Tang, "Dielectric Properties of Mashed Potatoes Relevant to Microwave and Radio-frequency Pasteurization and Sterilization Processes", J. Food Science, Vol.69(Nr.1), pp.E30-E37, 2004

[3] M. Kent, J. Oehlenschlager, S. Mierke-Klemeyer, M. Manthey-Karl, R. Knöchel, F. Daschner and O. Schimmer, "A New Multivariate Approach to the Problem of Fish Quality Estimation", Food Chemistry, Vol.87(4), pp.531-535, Oct. 2004

[4] M. Al-Holy, Y. Wang, J. Tang and B. Rasco, "Dielectric properties of salmon (*Oncorhynchus keta*) and sturgeon (*Acipenser transmontanus*) caviar at radio frequency (RF) and microwave (MW) pasteurization frequencies", J. Food Engineering, Vol.70(4),pp.564-570, Oct. 2005

[5] Kwan Chi Kao, *Dielectric Phenomena in Solids*, Academic Press, USA, 2004

[6] S. O. Nelson and P. G. Bartley, Jr., "Measuring Frequency and Temperature Dependent Permittivities of Food Materials", *IEEE Trans. Instrumentation and Measurement* , Vol.51(4), pp. 589-592.,Aug. 2002

[7] S. Kongrattanapraset, B. Arunrungrusmi, Pungsiri, K. Chamnongthai and M. Okuda, "Nondestructive Maturity Determination of Durian by Force Vibration and Ultrasonic," *Int. J. Uncertainty, Fuzziness and Knowledge Base Systems*, Vol. 9(6), pp.703-719,Dec 2001

[8] M. Krairiksh, A. Mearnchu and C. Phongcharoenpanich. "Nondestructive Measurement for Mango Inspection," *IEEE Int. Sym.Communications and Information Technologies*, Vol.2, pp. 646-649, Oct. 2004

[9] C.A. Balanis, *Advanced Engineering Electromagnetic*, John Wiley & Sons, USA, 1989.

Construction of A 100 kV Capacitive Voltage Divider

J.Sarasook, S. Chotigo and B.Puengsiri
Department of Electrical Engineering, Faculty of Engineering
King Mongkut's University of Technology Thonburi
126/1 Prachauthit Road, Bangmod, Thungkhru Bangkok 10140 Thailand
E-mail: Jassadat@hotmail.com

***Abstract*-This paper represents the design and construction of the 100 kV capacitive voltage divider for alternative voltage measurement. Metallized Polypropylene film capacitors were connected in series circuit as high voltage arm of the voltage divider which was in PVC insulating cylinder. Besides, the same kinds of capacitors were connected in parallel in the brass tube as the low voltage arm. The scale factor of the designed voltage divider is 2000:1. The voltage output of the voltage divider was compared with that obtained from sphere gap calibration in IEC 60-1 [1]. Furthermore, this divider passed the withstand test at 110 kV.**

Key word: Voltage divider, Measuring AC high voltage, High voltage capacitor.

I. INTRODUCTION

At present, production of devices for high voltage in Thailand is quickly developed. Quality examination is necessary for electrical apparatus. The processes followed the processes in national standard. Each examination must use accurate equipment following the standard. In the past, these equipments were ordered from foreign which was more expensive. However, now, electrical high voltage technology in Thailand is high enough to design and construct some equipment using materials in our country which reduces the price a lot. Equipment produced in Thailand has similar quality to the one ordered from foreign. The necessary equipment for high voltage laboratory is voltage divider.

This paper reported the design and construction of capacitive voltage divider, used for measuring AC high voltage up to 100 kV, 50 Hz. The materials used to construct this voltage divider were available in Thailand which had lower price than those ordered from abroad.

II. RELEVANT PRINCIPLES

A High voltage measuring system with voltage divider

High voltage measurement technique uses voltage divider reduced the high voltage to low magnitude as shown in Fig.1. Impedance (Z_1, Z_2) may be resistors or capacitors. Generally, resistive divider is suitable for measuring DC high voltage and capacitive divider is suitable for measuring AC high voltage.

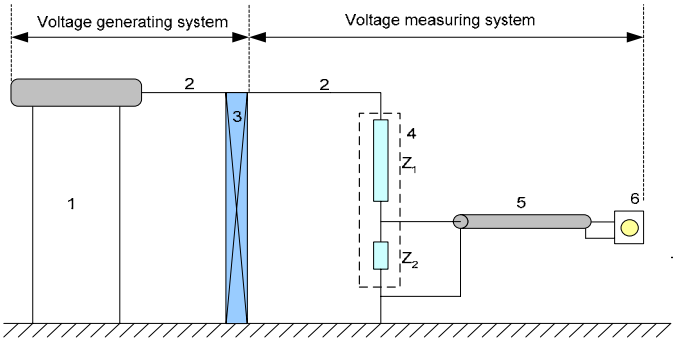

Figure 1. Voltage divider for AC high-voltage measurements

Where

1 = High voltage AC supply
2 = High voltage conductor
3 = Test object
4 = Voltage divider
5 = Measuring cable
6 = Measuring instrument
Z_1 = High voltage arm of voltage divider
Z_2 = Low voltage arm of voltage divider

B. Capacitive voltage divider

Capacitive voltage divider is favorite measurement for AC high voltage. The ratio of V to V2 depended on the values of C_1 and C_2 as expressed in Eq.1.

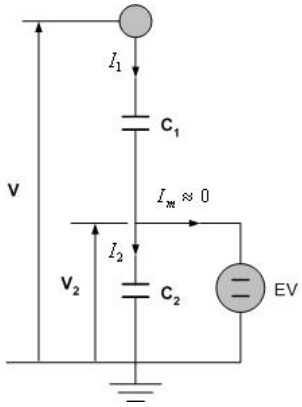

Figure 2. Capacitive voltage divider

$$V = \frac{C_1 + C_2}{C_1} \times V_2 \qquad (1)$$

where

V = High voltage input
V_2 = Low voltage output
C_1 = High voltage capacitance
C_2 = Low voltage capacitance

III. DESIGN OF VOLTAGE DIVIDER

This paper presents the design of 100 kV voltage divider. The designed scale factor is 2,000:1. Detail of design is summarized as follows.

A. Design and construction of 100 kV voltage divider

- High voltage arm

The high voltage arm consists of 100 Metallized Polypropylence Film capacitors, 10 nF/ 2 kV_{DC}, connected in series on acrylic with replace overlap 25 layer, 4 pieces per layer show in Figure 3. The diameter and the length of each capacitor are 10 mm and 32 mm as shown in Figure 4. This high voltage arm can withstand the voltage up to 100 kV with the safety factor of 40%. According to IEC 60-2 [2], the voltage divider must be able to withstand voltage at least 110% of rate for 1 minute. This withstand test is also considered in this present work. The divider is contained in PVC tube which used air insulation, Figure 5.

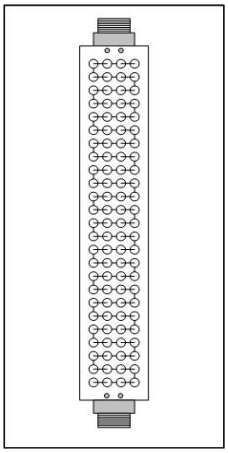

Figure 3. Dimension configuration of high voltage capacitance

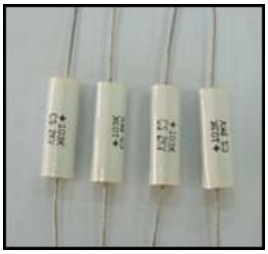

Figure 4. Metallized Polypropylence Film capacitors

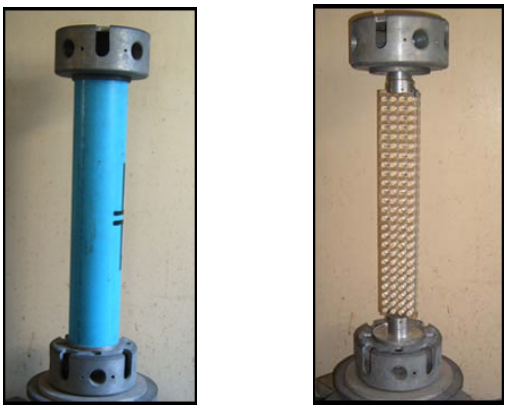

Figure 5. High voltage capacitive configuration

- Low voltage arm

The ratio of voltage at 2,000:1 gives the output voltage (V_2) about 50 V. This low voltage can be measured by the available measuring equipment. Therefore, the low voltage arm consists of two of 100 nF/2 kV_{DC} capacitors connected in parallel as shown in Figure 6. This low voltage arm is contained in brass shield case as seen in Figure 7. The whole set of the capacitive voltage divider is shown in Figure 8.

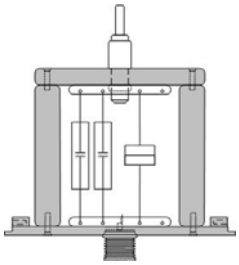

Figure 6. Dimension configuration of low voltage

Figure 7. Low voltage capacitive configuration

Figure 8. Voltage divider rate 100 kV

IV. EXPERIMENTAL RESULTS AND EVALUATION

A. Experimental circuit

The test circuit is shown in Figure 9. It consists of AC voltage source 220 V, variac 0-240 V, transformer 220/100 kV, water resistor (R_W) 1.44 $M\Omega$, Standard sphere diameter 12.5 cm and the designed capacitive voltage divider. 'UP & Down' method is used to find the breakdown voltage (U_{50}) by applying 20 times of AC voltage. The test gap lengths are 0.5, 2, 3.5, 5 cm

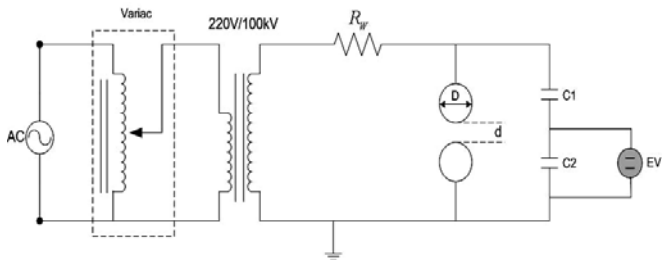

Figure 9. Experimental circuit

B. Comparison with sphere gap calibration

The measuring device needs accuracy and consistency. Therefore, the breakdown voltage (U_{50}) measured from this voltage divider is compared with the voltage obtained by sphere gap calibration following IEC 60-1. Experimental result is shown in Table I.

TABLE I

BREAKDOWN VOLTAGE (U50) OBTAINED FROM DESIGNED VOLTAGE DIVIDER AND SPHERE GAP CALIBRATION.

Gap length (cm)	$U_{50,kd}$ from voltage divider (kVp)	U_{50} from sphere gap calibration (kVp)	%Error
0.5	17.14	16.8	-2.05
2	59.40	59	-0.69
3.5	97.34	97	-0.35
5	128.82	129	0.14

C. Voltage wave shape obtained from voltage divider

Measured output signal of voltage divider may slightly off from sine wave. If wave shape is slightly off sine wave, it may affect the measurement. It may cause higher error. This experimental is referred to IEC 60-1 which assigned $V_P/V_{rms}=\sqrt{2}\pm5\%$ with a frequency in a range 45 to 65 Hz . The output waveform is shown in Fig.10 and Fig 11 which is sinewave with error of -1.12% and frequency of 50.4 Hz. This output waveform is accepted following IEC 60-1.

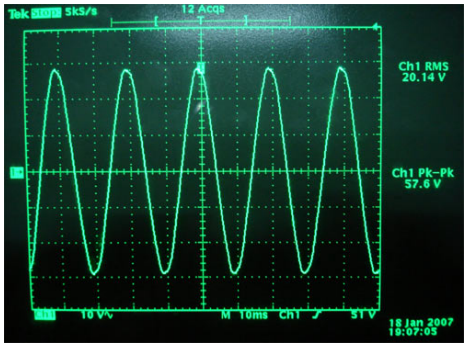

Figure 10. Voltage wave shape of voltage divider

D. AC Withstand voltage test

According to IEC 60-2, the voltage divider must withstand the voltage of 110% of its rating for 1 minute. Therefore, in this present work, the voltage of 111 kV 50 Hz is applied to the voltage divider for 1 minute and then, the divider can withstand this voltage without breakdown. Results are shown in Table 2. This assures that this designed voltage divider is suitable to use at the level of 100 kV.

TABLE II

RESULT OF AC WITHSTAND VOLTAGE TEST.

Rated (kV)	Voltage test (kV)	Time (s)	Voltage with voltage divider correct with k_d (kV)	Error %	Result
100	111.11	60	111.40	0.26	Withstand

V. DISCUSSION

In voltage divider calibration, the instrument used for measuring voltage was multimeter (Amprobe No. 330T). The value measured was RMS value. From results in Table I found that in gap lengths of 2, 3.5, 5 cm, %error was less than 1%, but with the gap length of 0.5 cm, %error was 2.05%. This indicated that this voltage divider can work with a very good accuracy as the breakdown voltage was above 59 kV. While the accuracy of the voltage divider was less as the breakdown voltage was below 20 kV though its error was less than 3% which is the error accepted for sphere gap calibration. This might be due to very low voltage at this gap distance compared to its rating with safety factor of 40%.

VI. CONCLUSION

Design and construction of 100 kV capacitive voltage divider was used for measuring AC high voltage. Materials used in this construction were available in Thailand which its price is much lower than that of materials imported from foreign. The characteristics of the designed voltage divider can be summarized as follows:

1. The maximum error compared to the sphere gap calibration is only 2.05% at the gap distance of 0.5 cm.
2. This voltage divider is tested with AC withstand by applying the 110 kV for 1 minute according to IEC 60-2. The voltage divider can withstand voltage without damage.
3. Output signal of voltage divider is sine wave with the ratio of V_p/V_{rms} less than 5%. This follows IEC 60-1.

Finally, it can be said that this constructed capacitive voltage divider is suitable for use at the level of 100 kV.

REFERENCES

[1] IEC Publication 60-1, "High-Voltage Test Techniques, Part 1: General definition and test requirement", Geneva, 1989

[2] IEC Publication 60-2, ''High-voltage Test Techniques, Part 2: Measuring Systems'', Geneva, 1994.

[3] IEEE Std. 4, ''Standard Techniques for High-Voltage Testing'', IEEE Power Engineering Society, New York, USA, March 1995.

[4] Chaiyaporn Lourtongkum, "Design and Construction of 300 kV Capacitive Voltage Divider for the AC High-Voltage Measurement", Mahanakorn University, EECON, 2546.

The Hydrophobic of Polymeric Insulator under Dust Pollution and A Comparison with Artificial Pollution

Apisit Chaisaengsukkul**, Norasage Pattanadech, Siriwat Potivejkul
Electrical Engineering Dept., Faculty of Engineering, King Mongkut's Institute of Technology Ladkrabang
Bangkok, 10520 Thailand ; E-mail : apisit@cpf.co.th, norasage@yahoo.com

Astract- **This paper presents results of properties of polymeric insulation study, e.g. hydrophobic , ageing which operate influence the electrical characteristic of polymeric insulator etc. when they are subjected by artificial polluted condition compared with natural pollution in Thailand.**

The test results show that hydrophobic property of polymeric insulator under various salinities, i.e. small salinity, medium salinity and high salinity are still relatively remain its property while hydrophobic property under flour dust is partially maintain except the area covered with flour dust. However, hydrophobic property will be lost when it exposed with feed dust and cement dust. It is also found that the insulation resistance of polymeric insulator decreases when it was exposed to polluted condition such as saline solution no matter of any level of salinity, flour dust, animal feed dust or cement dust. When the duration of ageing is prolonged, the insulation resistance trends to be reduced. In addition, the insulation resistance of polymeric insulator under 50 ^{o} C atmospheric is slightly lower than that of 30 ^{o} C.

Keywords: Hydrophobic, polymeric insulator, dust pollution

I. INTRODUCTION

The polymeric insulators are found in many countries in distribution system especially polluted condition such as industrial area where there are many factories generate polluted dust, e.g. cement plant , flour mill etc. In Thailand, they have been used in some areas to solve the problem of flashover which are easily cause to porcelain insulators. Since it is the early stage of using of polymeric insulators and its characteristic needs to be studied to verify whether it is suitable for use or not. The purpose of this paper is to study properties of polymeric insulator such as hydrophobic, ageing under industrial dust pollution generated from factories. As it is known, polymeric insulator has main advantage on its hydrophobic property which can reduce the path of current leakage, in other words, reduce flashover.

II. SAMPLES AND PROCESS OF HYDROPHOBIC VERIFICATION

** The author would like to express thankfulness to Provincial Electricity Authority (PEA); Department of Chemistry, Faculty of Science and High Voltage Engineering Laboratory, Faculty of Engineering , KMITL for their kind support of relevant instrument and equipment.

The pollution process for hydrophobic study can be carried out by preparing twelve specimens from polymeric insulator, then gradually flowing on all specimens with prepared solutions (saline solutions with small salinity, medium salinity and high salinity and solutions with flour dust , animal feed dust and cement dust respectively) two specimens for each type of solutions , let them naturally dry and then sprayed water all over the surface of all specimens to verify hydrophobic property. After that, separated into two group, one to be kept at 30 ◦ C while the other kept at 50 ◦ C. The duration of these specimens under temperature control lasted 8 hour a day and took for five days. After the fifth day, all specimens were sprayed with water to verify hydrophobic and compare with the first day.

Fig. 1. Samples of pollution dusts (from left to right : flour; ,animal feed and cement dust)

III. SAMPLES AND AGEING PROCESS

For ageing study, thirty six specimens from polymeric insulator were prepared, six specimens for each case, there are six cases to be studied : saline solutions (artificial polluted condition) with three salinities : small salinity, medium salinity and high salinity respectively; flour dust, animal feed dust and cement dust collected from factories (natural pollution) . The pollution process for all specimens for ageing study are the same as for hydrophobic study. The specimens for ageing are separated into two group, one group is kept at 30 ◦ C while the other group kept at 50◦ C The duration of specimens to be under temperature

control lasted 8 hours a day and this experiment took place for five days. The insulation resistance of all specimens are measured after completion of temperature control of each day.

To prepare specimens under polluted conditions is referred Solid Layer Method from IEC 507 Standard.

During ageing process, Scanned Electron Microscope (SEM) is also used to monitor insulator surface under various polluted conditions.

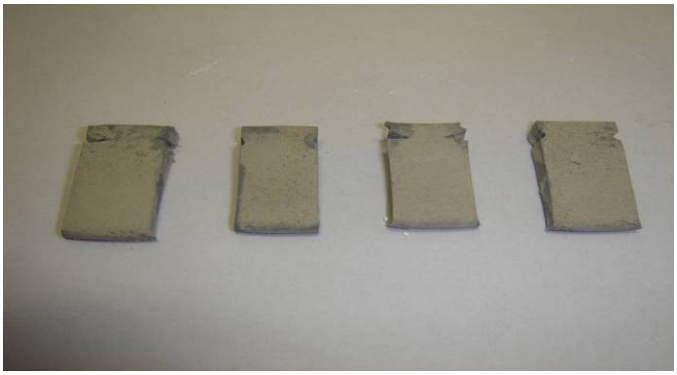

Fig. 2. Specimens for ageing study after pollution process with cement dust

TABLE 1
DATA OF VARIOUS POLLUTED DUST AND SALINE SOLUTIONS

Type of pollution	ESDD (mg /cm^2)	Remark
Saline solutions	0.028	small salinity
Saline solutions	0.102	medium salinity
Saline solutions	0.250	high salinity
Flour	0.041	
Feed	0.662	
Cement	0.106	

IV. TEST RESULTS

From the test results in Fig 3 (a) to (g), it is obvious that hydrophobic property of polymeric insulator under various salinities, i.e. small salinity, medium salinity and high salinity are still relatively remain its property while hydrophobic property under flour dust is partially maintain except the area covered with flour dust. However, hydrophobic property will be totally lost when it exposed with feed dust and cement dust.

In addition, from Fig 4 (a) and (b) it is found that the insulation resistance of polymeric insulator decreases when it was exposed to polluted condition such as saline solutions no matter of any level of salinity, flour dust, animal feed dust or cement dust. When the duration of ageing is prolonged, the insulation resistance trends to be reduced. In addition, the insulation resistance of polymeric insulator at 50 ° C is slightly lower than that of 30 ° C.

(a) Original (HC 1)

(b) Small salinity (HC 2)

(c) Medium salinity (HC 2)

(d) High salinity (HC 2)

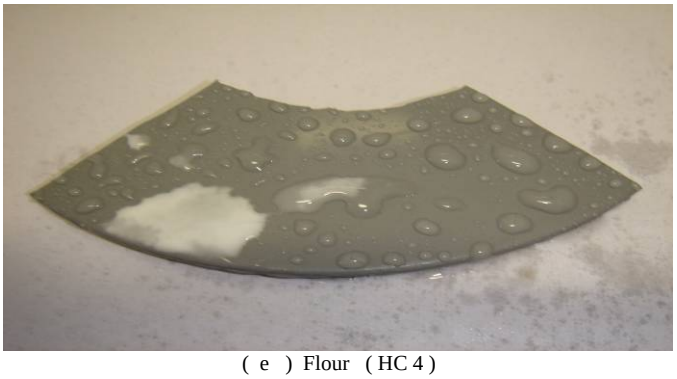

(e) Flour (HC 4)

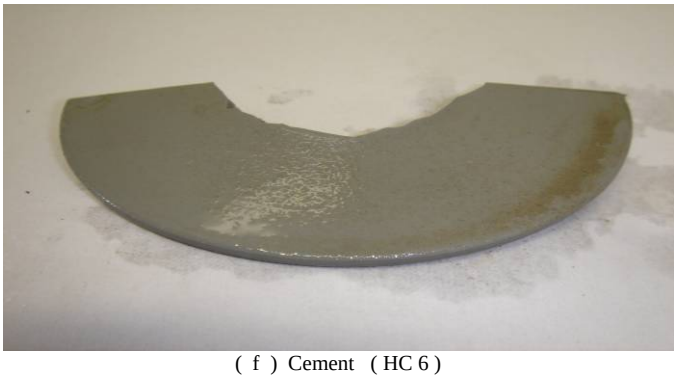

(f) Cement (HC 6)

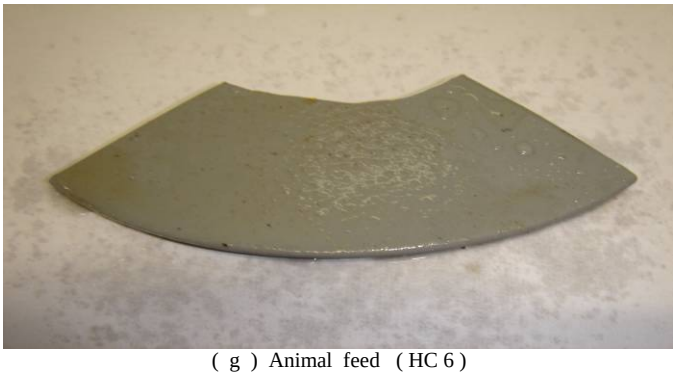

(g) Animal feed (HC 6)

Fig. 3. Hydrophobic property of specimens under various kinds of polluted dust and compared with Hydrophobic Classification Guideline (see Appendix)

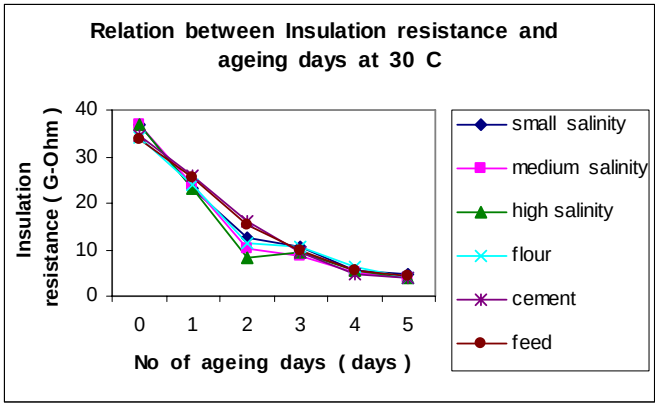

(a)

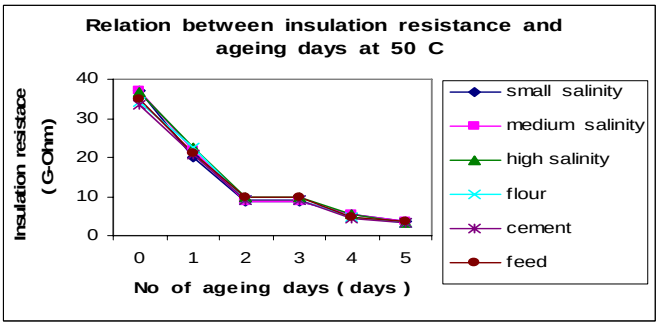

(b)

Fig. 4. Relation between insulation resistance and ageing duration when under temperature control (a) 30 C (b) 50 C

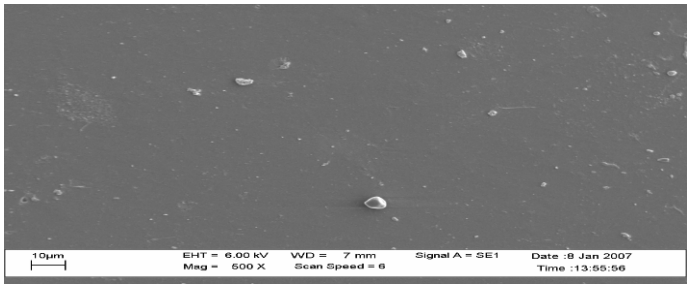

(a) Original

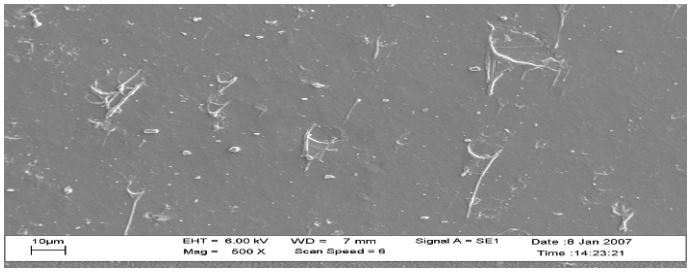

(b) Small salinity

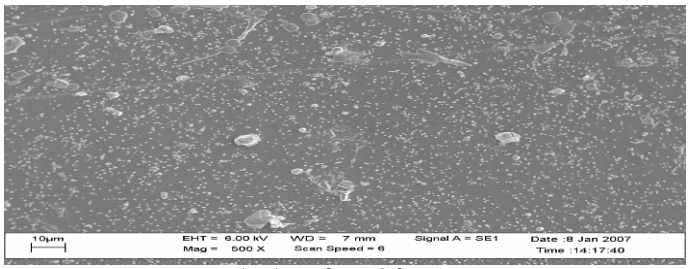

(c) Medium Salinity

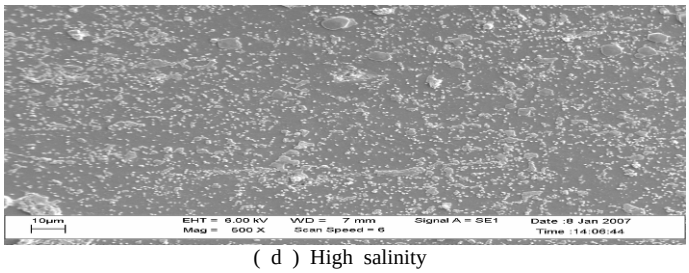

(d) High salinity

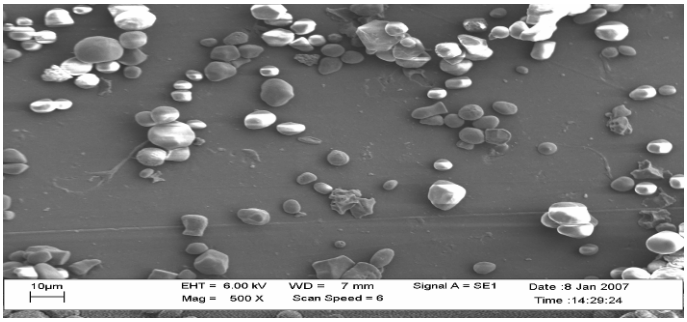

(e) Flour

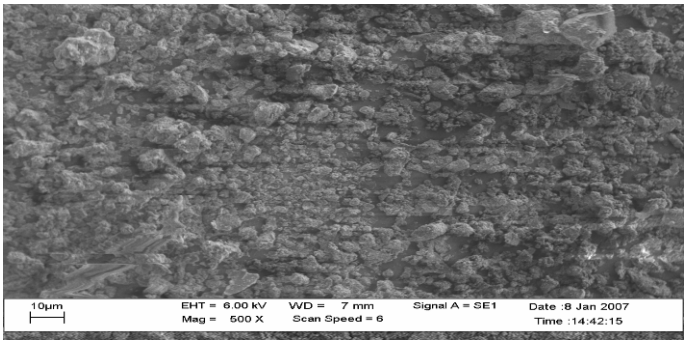

(f) Cement

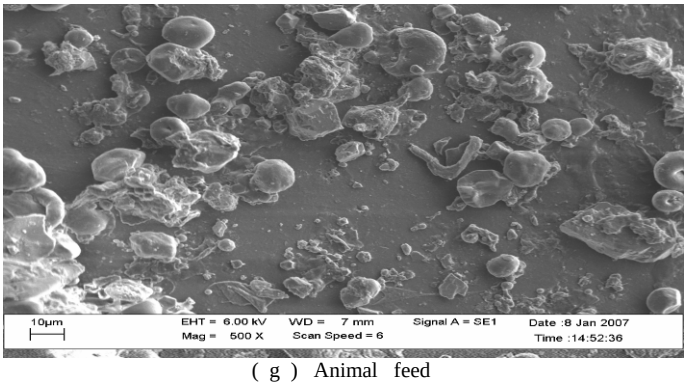

(g) Animal feed

Fig. 5. Illustration of polymeric insulator surface of various Pollutions with magnification of 500 X

V. CONCLUSIONS

Since hydrophobic property of polymeric insulator still relatively maintain when it is under saline solutions and it is partially remain for flour dust except the area that is covered with flour dust. The hydrophobic property of polymeric insulator will be lost when it is under cement dust and animal feed dust. Polymeric insulator is suitable to use for coastal environment while it is unsuitable to use under polluted condition such as cement plant, animal feed factory including flour factory.

When polymeric insulator is under polluted condition, its insulation resistance will be gradually decreased, in such condition, it has the chance to cause flashover to insulator.

ACKNOWLEDGMENT

The author would like to express thankfulness to Provincial Electricity Authority (PEA); Department of Chemistry, Faculty of Science and High Voltage Laboratory, Faculty of Engineering, KMITL for their kind support of relevant instrument and equipment.

REFERENCES

[1] Chris S. Engelbrecht, Ralf Hartings, Senior Member IEEE, Helena Tunell,, Bjorn Engstrom, Harald Janssen and Raimund Hennings , " Pollution Tests for Coastal Conditions on an 800 - kV Composite Bushing ", IEEE Transactions on Power Delivery, Vol. 18, No 3, July 2003, pp. 953 - 959.

[2] Xingliang Jiang, Jianlin Hu, Yu Liang, Lichun Shu, Shujiao Xie, " Pollution Flashover Performance of Short Sample for 750 kV Composite Insulators ", IEEE International Symposium on Electrical Insulation , Indianapolis, USA , September 19-22 , 2004, pp. 312-315

[3] IEC Publ. 507, " Artificial Pollution Tests on High - Voltage Insulators to be Used on A.C. Systems ", Second Edition, 1991-4

[4] D. Devendranath , Pradeep M. Nirgude, G. V. Rao R. S. Shivakumara Aradhya,A.P. Sudheer,N.S. Mohan Rao , Channakeshava , " Investigations on Rain Fog Pollution Test ", IEE High Voltage Engineering Symposium, 22 - 27 August 1999,Conference Publication No. 467 @IEE, 1999, pp. 4.111.S25-4.114.S25

[5] X Wang, S.Yoshimura, " Contamination Performances of Silicone Rubber Subjected to Acid Rain", IEEE Transactions on dielectrics and Electrical Insulation, Voilme 5 No 6 , December 1998, p. 909-916

APPENDIX
Hydrophobic Classification Guideline

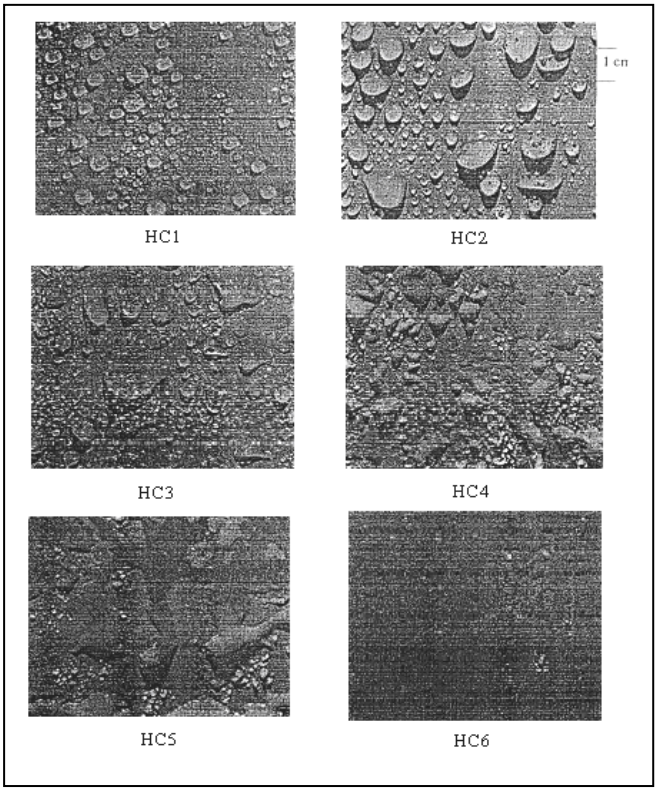

A Comparison of Corona Inception Phenomena between Porcelain and Polymeric Insulators under Dust Pollution in Thailand

Apisit Chaisaengsukkul**, Siriwat Potivejkul, Norasage Pattanadech
Electrical Engineering Dept., Faculty of Engineering, King Mongkut's Institute of Technology Ladkrabang
Bangkok, 10520 Thailand ; E-mail : apisit@cpf.co.th, Kpsiriwa@kmitl.ac.th

Astract- **Porcelain insulators are generally used in distribution system , in some polluted area such as industrial area where there are many factories generated polluted dust, e.g. flour mill , cement plant , animal feed factories etc., polymeric insulators are used to replace porcelain insulators. However, in such polluted condition, it sometimes cause flashover of insulators in power system and as a result, it would impact power system stability. This paper presents results of corona phenomena study on 33 kV system AC insulators under industrially polluted dust , e.g. flour dust, cement dust and animal feed dust collected from factories and compared with kaolin which is artificial pollution.**

The results show that corona inception voltage of porcelain insulators under flour dust, kaolin, feed dust and cement dust are relatively constant when tested pollution levels are increased and corona inception voltage of flour dust and cement dust are higher than that of kaolin and animal feed dust with the increasing of pollution levels.

The corona inception voltage of polymeric insulators under kaolin and feed dust conditions decrease when tested pollution levels are increased while corona inception voltage of polymeric insulator under flour dust and cement dust conditions are relatively constant with the increasing of tested pollution levels.

In addition, corona inception voltage of polymeric insulators under industrial dust, i.e. kaolin, flour dust , animal feed dust and cement dust are higher than that of porcelain insulators.

The leakage current of porcelain insulators under animal feed dust increase when tested pollution levels are increased while leakage current of porcelain insulators under kaolin, flour and cement dust as well as polymeric insulator under various kinds of dust are relatively constant with the increasing of tested pollution levels.

Keywords: polymeric insulator , dust pollution, corona

I. INTRODUCTION

In electrical system particularly distribution system, porcelain insulators are generally used. In some polluted area such as industrial area where there are many factories produced polluted dust, e.g. flour mill , cement plant , animal feed factories etc. , polymeric insulators are widely used to replace porcelain insulators in many countries. However, in such polluted condition, it sometimes cause flashover of insulators in power system and as a result, it would cause power interruption in power system and on the other hands, impact to power system stability.

** The author would like to express thankfulness to Data Entry Co.,Ltd, Faculty of Sceince , KMITL including relevant factories for supporting of equipment and polluted dust.

II. SOLID LAYER METHOD

The simulation of industrial polluted condition can be referred IEC507 standard , this standard recommends Solid Layer Method to verify the insulator being suitable to use under polluted condition. Three porcelain insulators and three polymeric insulators with alternating sheds were provided to carry out the test.

A.. Solid Layer Chamber

Solid layer chamber is fabricated as according to standard requirements. The dimension of chamber is width x length x height = 4.2 x 4.2 x 4.5 m^3 Electric steam generator produces steam from ground level to upwards direction with the rate of approximately 50 g / hr / m^3 The object test is suspended approximately 2.0 m above ground.

(a) Polluted porcelain insulators

(b) Polluted polymeric insulators

Fig. 1. Test objects

B. Solid Layer Preparation

The preparation of solid layer can be done by providing 40 g. Kaolin and 3 g. salt. Then dissolve in the container with 1000 g. water, stir together and fill in jet spray. Spray test objects (porcelain and polymeric insulators) with this solution and let it dry. After test objects naturally dry, carefully collect suspended dust from test objects by using wet brush and dissolve suspended dust in the known quantity water in another container, stir for approximately 2 minutes and then measure its conductivity with conductivity meter and record. The ESDD (Equivalent Salt Deposit Density) can be determined by referring IEC 507 standard. After first ESDD is obtained, the other values of ESDD can be obtained by the procedure mentioned above with appropriate amount of salt as according to tested pollution levels, i.e. 13 and 60 g. etc. The consideration of ESDD in this study focus on three pollution levels , i.e. small contamination, medium contamination and high contamination respectively.

The solid layer including ESDD for other kinds of dust, i.e. flour dust, cement and feed dust can be obtained by repeating steps mentioned in previous paragraph.

Fig. 2 Samples of dust (upper : Kaolin , flour ; lower : cement and feed)

TABLE I
ESDD OF VARIOUS KINDS OF DUST

Pollution level s	ESDD (mg / cm^2)			
	Kaolin	Flour	Feed	Cement
Low	0.033	0.045	0.034	0.037
Medium	0.057	0.13	0.037	0.056
High	0.13	0.36	0.193	0.20

III. TEST PROCEDURE

The test arrangement for solid layer method was set up as shown in Fig. 3. After all equipment including test object (porcelain insulator) with low pollution level of kaolin are set up, the test begins. Test voltage is gradually applied to test object until 19 kV (phase voltage) and then maintain , after that open valve to let steam from steam generator slowly distributes from ground level and flow in upward direction and detect corona phenomena by corona camera. In case no corona occurred, gradually increase voltage level and still detect corona phenomena , the maximum voltage is limited not exceed 55 kV. Then the second specimen of porcelain insulator is taken place. After three specimens of porcelain insulator with low pollution level are tested. The consequential test of three polymeric insulators with low pollution level are carried out. After completion of test for low pollution level of both porcelain and polymeric insulators. Then, porcelain and polymeric insulators with medium pollution level and high pollution level are then provided for the test.

The test is carried out with the same test procedure mentioned above for flour dust, animal feed dust and cement dust respectively. During each test, leakage current is measured and recorded at all applied voltage when corona phenomena occurred. Leakage current can be measured by current transformer with ration 1: 40 and signal is transmitted to digital oscilloscope.

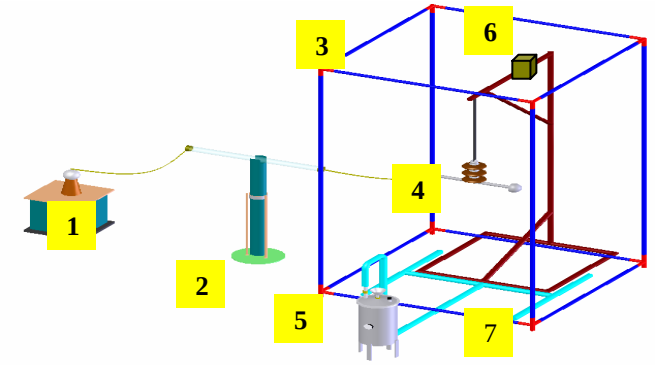

Fig 3 Test arrangement

Where

1. Testing transformer rated 5 kVA , 100 kV
2. Water resistance
3. Test chamber dimension W x L x H = 4.2 x4.2 x 4.5 m^3
4. Test object (porcelain and polymer)
5. Steam generator
6. Current transformer ratio 1: 40
7. Steam distributor

IV. TEST RESULTS

From Fig. 4 (a) for porcelain insulator, corona inception voltage of flour dust, kaolin, feed dust and cement are relatively constant when tested pollution levels are increased and corona inception voltage of flour dust and cement dust are higher than that of kaolin and animal feed dust with the increasing of pollution levels.

From Fig. 4 (b) for polymeric insulator, corona inception voltage of kaolin and animal feed dust decrease when tested pollution levels are increased while corona inception voltage of flour dust and cement dust are relatively constant with the increasing of tested pollution levels.

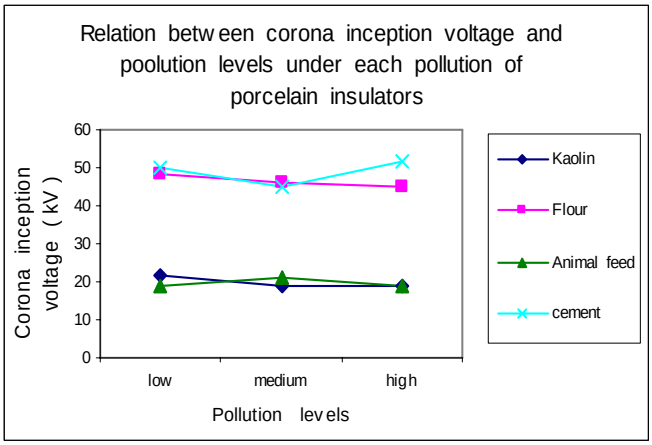

(a)

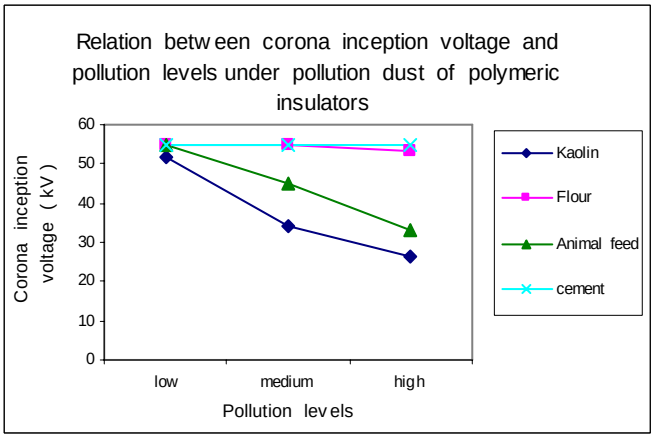

(b)

Fig. 4 Relation between corona inception voltage and pollution levels of each pollution for (a) porcelain insulators and (b) polymeric insulators

From Fig. 5 (a) , for Kaolin , corona inception voltage of porcelain insulators are relatively constant when tested pollution levels are increased while corona inception voltage of polymeric insulators decrease with the increasing of tested pollution levels.

From Fig. 5 (b), for flour dust, corona inception voltage of porcelain insulators and polymeric insulators are relatively constant when tested pollution levels are increased.

From Fig. 5 (c) , for animal feed dust , corona inception voltage of porcelain insulators are relatively constant when tested pollution levels are increased while corona inception voltage of polymeric insulators decrease with the increasing of tested pollution levels.

From Fig. 5 (d) , for cement dust , corona inception voltage of porcelain insulators as well as polymeric insulators are relatively constant when tested pollution levels are increased.

From Fig 5 (a) to (d) , corona inception voltage of polymeric insulators are higher than that of porcelain insulators.

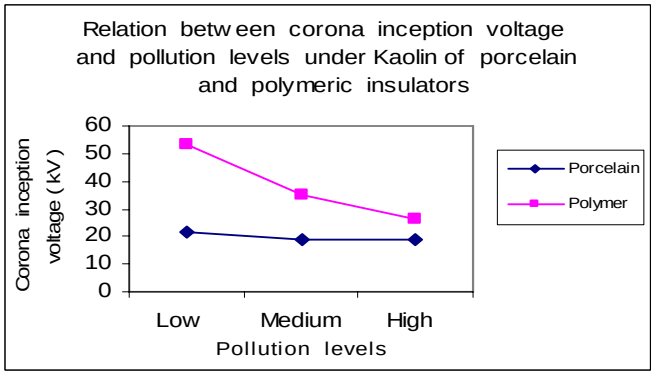

(a) Kaolin

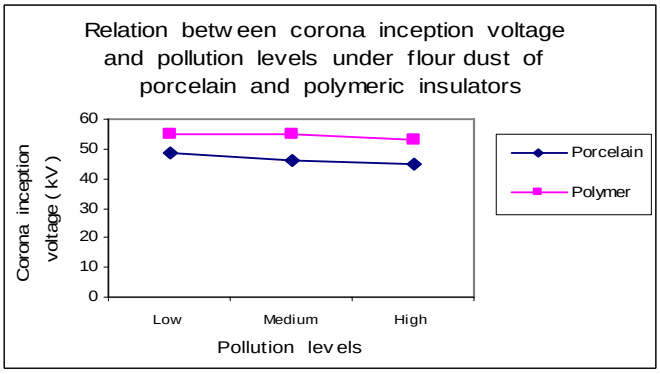

(b) Flour

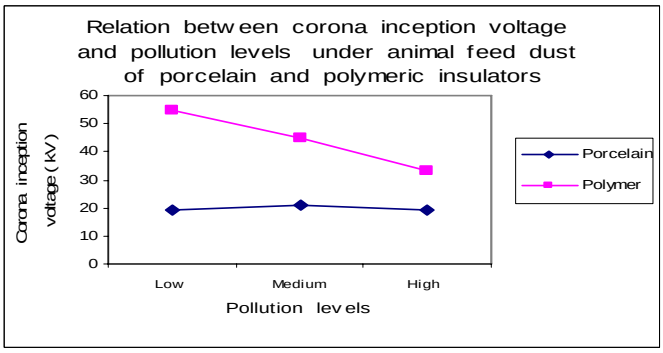

(c) Animal feed

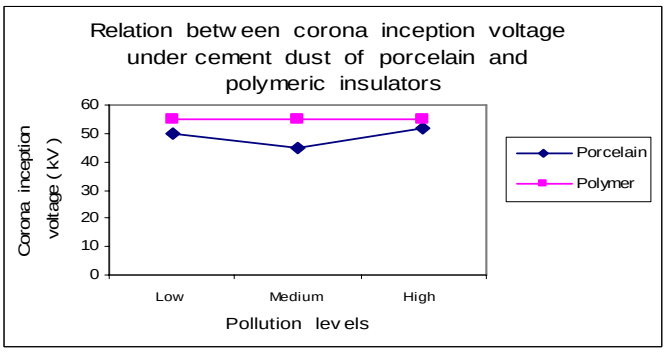

(d) Cement

Fig. 5. Relation between corona inception voltage and various kind of dust for porcelain and polymeric insulators

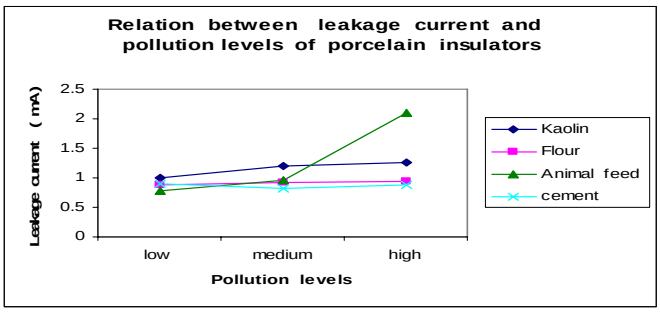

(a)

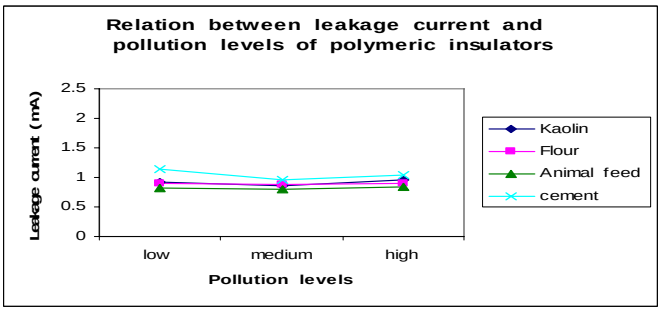

(b)

Fig 6 Relation between leakage current and pollution levels of various kind of dust of (a) porcelain insulators and (b) polymeric insulators

From Fig 6 (a), for porcelain insulator, leakage current of animal feed dust increases when tested pollution levels are increased while leakage current of kaolin, flour and cement dust are relatively constant with the increasing of tested pollution levels.

From Fig 6 (b), for polymeric insulator, leakage current of all various kinds of dust are relatively constant when tested pollution levels are increased.

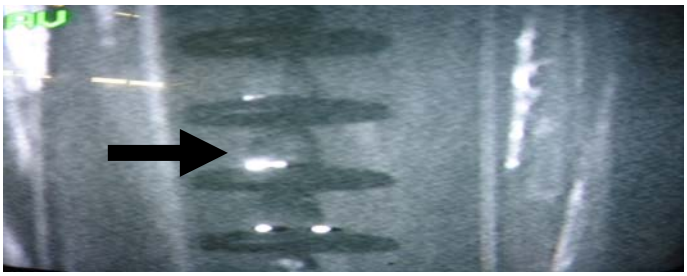

(a)

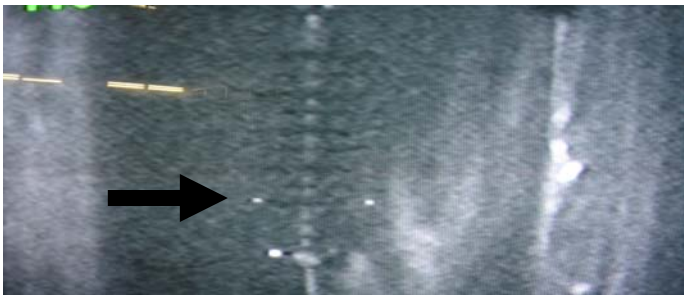

(b)

Fig 7 Corona phenomena of (a) porcelain insulator and (b) polymeric insulator under animal feed dust detected by corona camera (arrow sign indicates corona occurring point)

V. CONCLUSIONS

The corona inception voltage of porcelain insulators under flour dust, kaolin, feed dust and cement are relatively constant when tested pollution levels are increased and corona inception voltage of flour dust and cement dust are higher than that of kaolin and animal feed dust with the increasing of pollution levels.

The corona inception voltage of polymeric insulators under kaolin and feed dust conditions decrease when tested pollution levels are increased while corona inception voltage of polymeric insulator under flour dust and cement dust conditions are relatively constant with the increasing of tested pollution levels.

In addition, corona inception voltage of polymeric insulators under industrial dust, i.e. kaolin, flour dust, animal feed dust and cement dust are higher than that of porcelain insulators.

The leakage current of porcelain insulators under animal feed dust increase when tested pollution levels are increased while leakage current of porcelain insulators under kaolin, flour and cement dust as well as polymeric insulator under various kinds of dust are relatively constant with the increasing of tested pollution levels.

ACKNOWLEDGMENT

The author would like to express thankfulness to Data Entry Co., Ltd; Department of Chemistry, Faculty of Science and High Voltage laboratory, Faculty of Engineering, KMITL including relevant factories for their kind support of concerned test equipment and various polluted dust.

REFERENCES

[1] Stephen A. Sebo, Edgar P. Casale, Jose R. Cedeno, Wibawa Tjokrodiponto and Sheikh A. Akba r, "Review of Features of Fog Chamber at The Ohio State University for Polymer Insulator Evaluation", IEEE Annual Report - Conference on Electrical Insulationand Dielectric Dielectric Phenomena, October 20 - 23, 1996, pp. 443-446

[2] Chris S. Engelbrecht, Ralf Hartings, Senior Member IEEE, Helena Tunell,, Bjorn Engstrom, Harald Janssen and Raimund Hennings, "Pollution Tests for Coastal Conditions on an 800 - kV Composite Bushing", IEEE Transactions on Power Delivery, Vol. 18, No 3, July 2003, pp. 953 - 959.

[3] Xingliang Jiang, Jianlin Hu, Yu Liang, Lichun Shu, Shujiao Xie, "Pollution Flashover Performance of Short Sample for 750 kV Composite Insulators", IEEE International Symposium on Electrical Insulation, Indianapolis, USA, September 19-22, 2004, pp. 312-315

[4] IEC Publ. 507, "Artificial Pollution Tests on High - Voltage Insulators to be Used on A.C. Systems", Second Edition, 1991-4

[5] Wibawa Tjokrodiponto, Stephen A. Sebo, John D. Sakich, Tiebin Zhao, "Simultaneous Electrical and Visual Measurementsof Leakage Currents Along Polymer Insulators in Artificial Pollution Tests", IEEE Preceedings of the 5th International Conference on Properties and Applications of Dielectric Materials, May 25 -30, 1997, Seoul, Korea, pp. 738- 741.

Modulation Circuit for VLF Transformer

S. CHOTIGO and S. SEESANGA
Department of Electrical Engineering, Faculty of Engineering
King Mongkut's University of Technology Thonburi
126/1 Prachauthit Road, Bangmod, Thungkhru, Bangkok 10140 Thailand.
E-mail:samu_eee@yahoo.co.th

***Abstract*-This paper describes a modulation at 0.1 Hz for very low frequency (VLF) transformer. This transformer is used for testing field aged cable. This paper shows a new modulation circuit for VLF transformer by modulation sinusoidal signal with frequency 0.1 Hz and triangular signal frequency 1 kHz. This VLF transformer gives many advantages. First of all, it is not only saves transformer weight but also reduces cost. Secondly, it can be used in diagnostic tests such as partial discharge detection. Thirdly, it is easy to be used at site location. This modulation circuit will be used to construct a VLF transformer to be used in non-destructive testing.**

I. INTRODUCTION

The problem associated with testing field aged cable using DC and AC high voltage test equipment has some disadvantages. The AC high voltage transformer is large, heavy and expensive even with resonant test sets [1]. While testing by DC high voltage needs a very high voltage so it causes some damage on the insulation of the cable. Therefore, the VLF transformer is represented to solve these problems. Typically this equipment produced 0.1 Hz voltage having a sinusoidal waveform. This is not only saves weight and reduces cost but also simplifies its use in diagnostic tests such as partial discharge detection.

TABLE **I**

Suitability of selected waveform in voltage withstand tests

Wave form	Scale of equipment	Water-tree detection capability	Soundness
AC	×	☻	☺
DC	☻	×	×
VLF	☺	☺	☻
SOW	☺	☺	×

☻ : Suitable;

☺ : OK;

×: Unsuitable;

Table 1 shows the results. AC provides high water – tree detection capability. DC test equipment is the most lightweight. In the case of VLF the test equipment can be made lighter and more compact than for AC. Finally, OSW is the equal of VLF in terms of the size of the test equipment and water – tree detection capability.

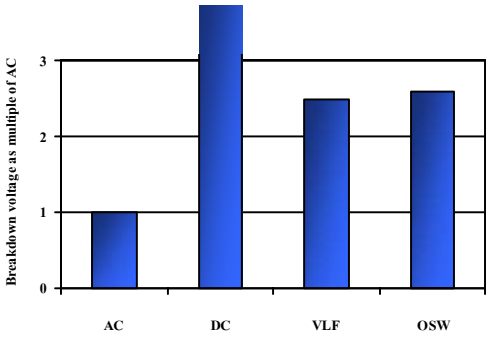

Figure 1. Comparison of AC, DC, VLF and OSW breakdown Voltage during water-tree detection.

Fig.1 shows that comparison of breakdown voltage of cable under AC, DC, very-low frequency (VLF) and oscillating wave (OSW) voltages. This indicates that OSW is the equal of VLF in terms of the size of the test equipment and water-tree detection capability. However. VLF has a better soundness capability. It is therefore concluded that VLF is the most suitable waveform for use in voltage withstands testing of water-tree cable [2].

This paper covers a new modulation circuit for VLF transformer to modulate sinusoidal signal with frequency 0.1 Hz and triangular signal with frequency 1 kHz for VLF transformer.

II. THEORY

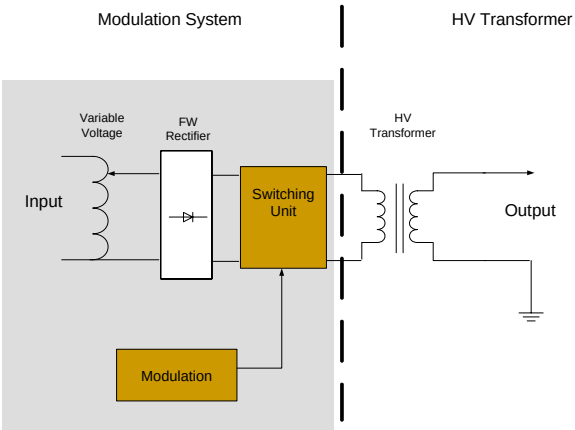

Figure 2. Block Diagram of VLF transformer.

The input power for the system is obtained from a normal 220V 50 Hz source. The input voltage for the rectifier is varied by an autotransformer, then the DC voltage from the rectifier is supplied to the switching unit. The output of this full-wave rectifier is modulated with the desired VLF frequency, 0.1 Hz in this present work. The schematic diagram is shown in Fig.2. Finally, the output voltage from switching unit, which is already AC, is stepped up through the transformer.

The principle of the pulse-width modulation (PWM) circuit. It is the signal lead reference signal (V_{sine}= 0.1 Hz) compared with a carrier of carrier signal (V_{tri}= 1 kHz).

The modulation used full-bridge circuit as a dc-to-ac inverter. One of the full-bridge inverter (square-wave) is unipolar switching scheme [3]. This unipolar switching is chosen for this work to get sinusoid output voltage. Also, it is easy to find the power circuit to drive this inverter.

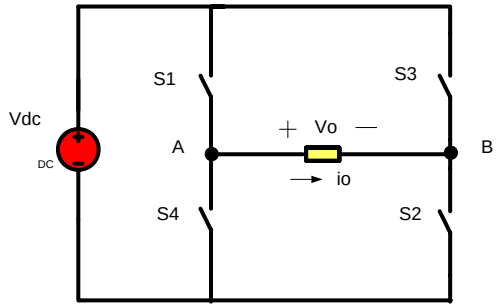

Figure 3. Full-bridge inverter.

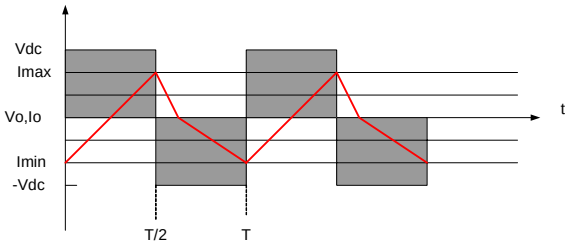

Figure 4. Output voltage and current waveform for PWM operation.

The full-bride inverter circuit is shown in Fig.3. Its output and current waveform are shown in Fig.4. During the first half-cycle, S1, S2 is closed while S3 and S4 is opened. The circuit as shown in Fig.5 (A) will get V_O=V_{dc}. In the next half-cycle, S3, S4 is closed while S1 and S2 is opened. The circuit as shown in Fig. 5(B) will get V_O= -V_{dc}

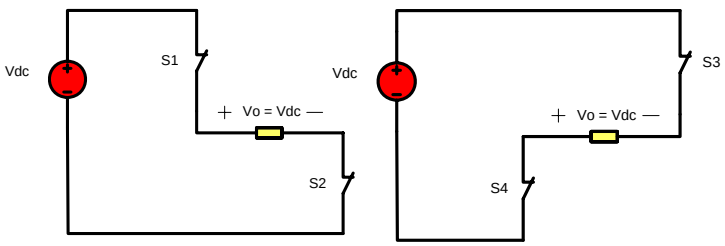

(A) (B)

Figure 5. (A) The first half cycle, (B) The second half cycle.

From in Fig.3 point A and B of the full-bridge inverter are controlled by comparing V_{tri} carrier signal (V_{tri} = 1kHz) with V_{ref} reference signal (V_{sine} = 0.1 Hz) and V_{tri} with - V_{ref}. The waveforms are used to control the switch as follows:

At point A: $V_{ref} > V_{tri}$: S1 on and
$V_{ref} < V_{tri}$: S4 on

At point B: - $V_{ref} > V_{tri}$: S3 on and
- $V_{ref} < V_{tri}$: S2

The PWM signal obtained simulations are showing Fig.6.

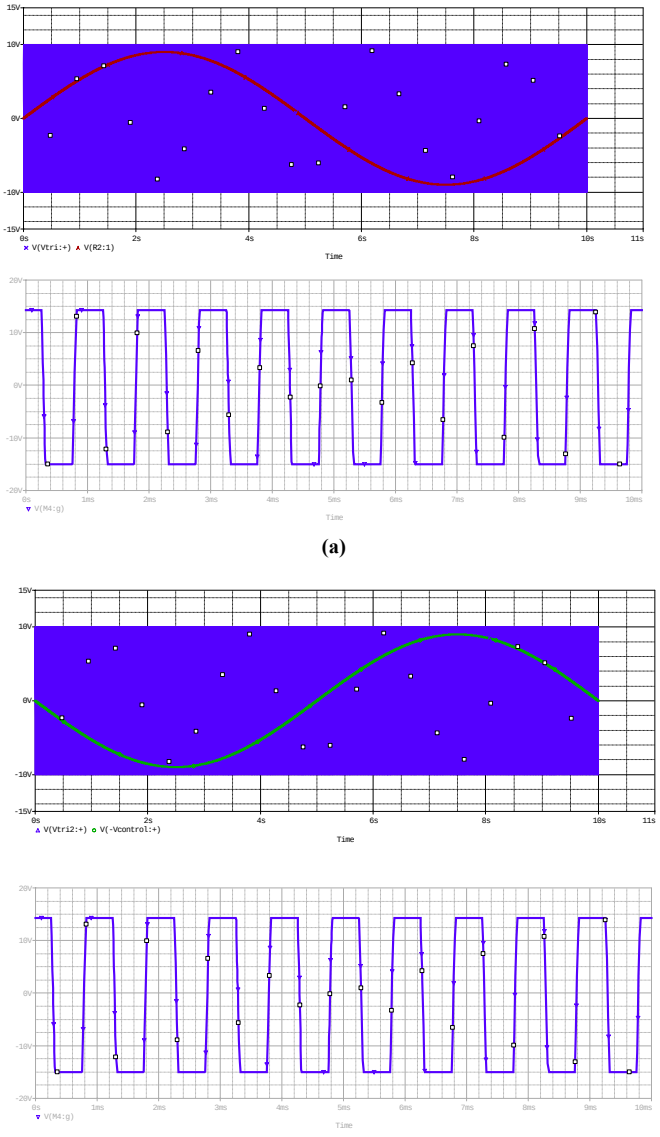

(a)

(b)

Figure 6. PWM signals (a) at point A (b) at point B.

III. EXPERIMENT

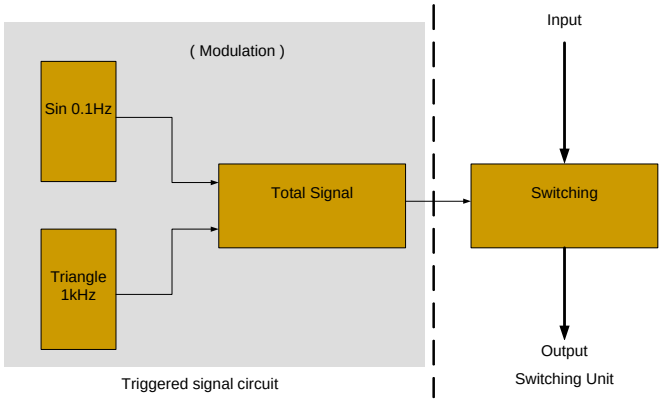

Figure 7. Block Diagram of the Modulation System.

The basic idea of the new modulation circuit is shown in Fig 7. It is used to generate sine wave signal at frequency 0.1 Hz and triangle wave signal at frequency 1 kHz. These two signals, then, are modulated to combine these signals into the total signal. This total signal is used to trig the switching unit

Triggered signal circuit

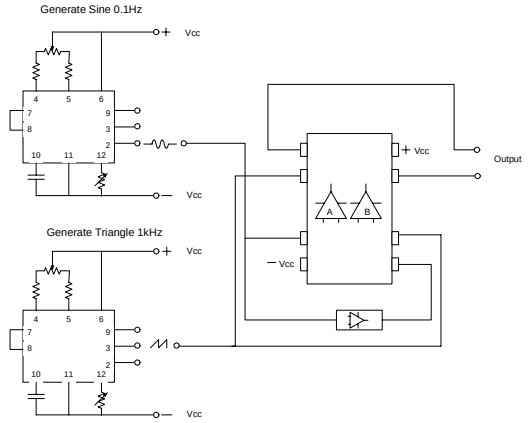

Figure 8. Triggered signal circuit.

The modulation system in Fig. 7 is schematically shown in Fig.8. The output signal is shown in Fig.9.

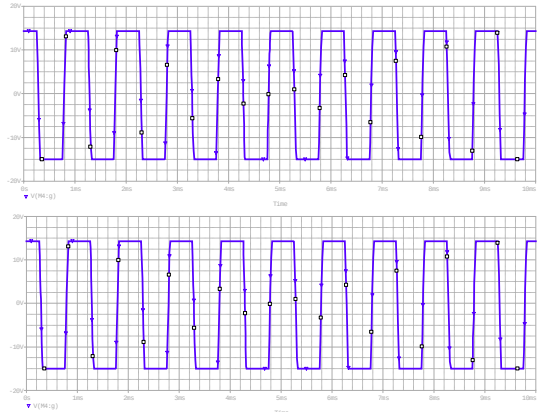

Figure 9. The actual triggered signal.

Switching unit

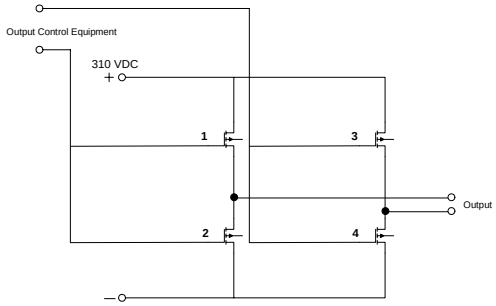

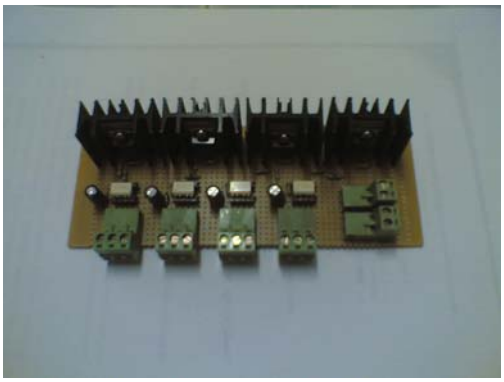

Figure 10. Switching circuit.

The input voltage for the switching circuit is obtained form rectifier which is 310 V_{dc}. The output of this switching circuit is a modulation of a 0.1Hz and 1 kHz carrier waveform at the magnitude of 310Vac. The simulation result is shown in Fig.11. Then, this signal is filtered by the LP filter as shown in Fig. 12.

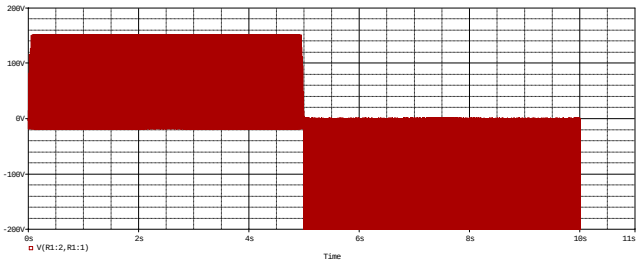

Figure 11. The simulated modulation signal in switching unit.

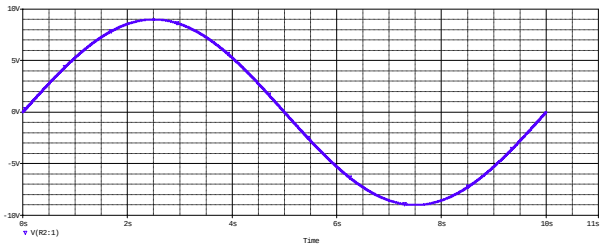

Figure 12. The filtered modulation signal

IV. IC System

Generate Sine 0.1Hz and Triangle 1 kHz

The waveform generator IC in Fig. 8 is capable of producing high accuracy sine, triangular waveform. The frequency can be selected externally from 0.1 Hz to more than 1 kHz.

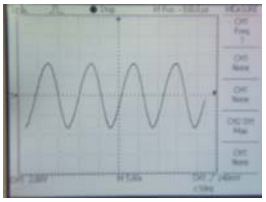

Generated Sine wave 0.1 Hz

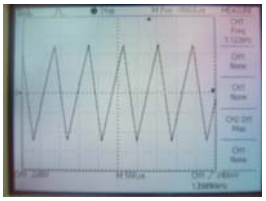

Generate Triangle wave 1 kHz

Total Signal

To combine two signals generated from wave generator IC in Fig.8, two independent, high gains, internality frequency compensated operational amplifiers which a signal power supply over a wide range of voltage are needed. These two Op-Amps should be easily implemented in single power supply systems.

V. Discussion

The utility of the idea discussed above can be shown by illustrating systems that have been designed using these techniques.

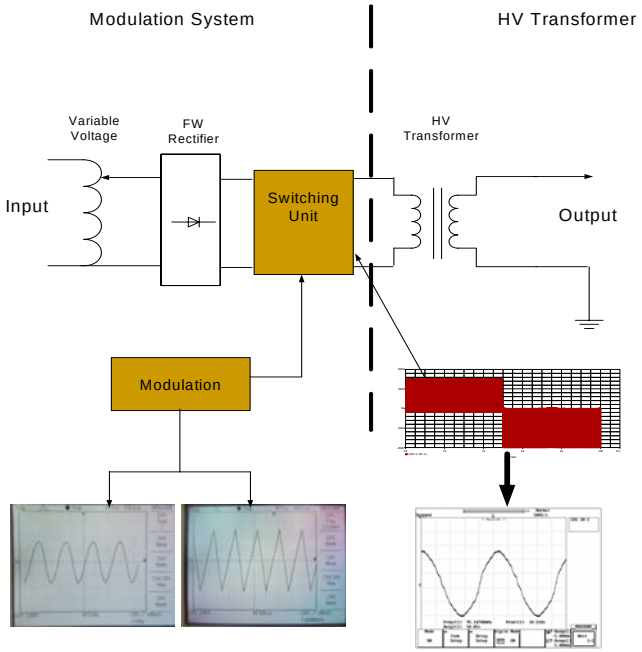

Figure 13. VLF System

When the output signal of the switching unit is filtered by the LP filter, the signal will be 0.1 Hz sine wave signal as shown in Fig.14. The signal can be looked as a sine wave with a frequency of 0.095 Hz.

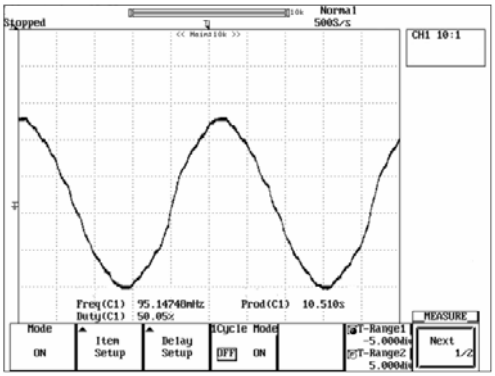

Figure 14. Waveform Produced by Power Equipment after transfer LP filter

VI. Conclusions

The modulation system described in this paper will be used for VLF transformer. This modulation circuit decreases the size of the transformer and reduces cost of the equipment used for withstand test of cables.

VII. Acknowledgment

Thanks for High voltage laboratory, Power Electronic laboratory, especially Mr.Chaiyan Thongsongyod in Department of Electrical Engineering, Faculty of Engineering, KMUTT.

VIII. References

[1] Richard Reid Senior Member High Voltage, Inc. “High Voltage VLF Test Equipment with Sinusoidal Waveform” 0-7803-5515-6/99/$10.00© 1999 IEEE

[2] Katsumi Uchida, Yoichi Kato, Masahiko Nakade, Daisuke Inoue, Hiroyuki Sakakibara and Hideo Tanaka. “Estimating the Remaining Life of Water-Treed XLPE Cable by VLF Voltage Withstand Tests” Furukawa Review, No.20 2001

[3] Mohan, Undeland, Robbins. Power Electronics. 2 nd ed. USA: Prentice-Hall, Inc., 1993.

[4] G.S. Eager, C.Katz, B.Fryszczyn, J. Densley, B.S. Bernstein. “High Voltage VLF Testing of Power Cable” IEEE Transactions on Power Delivery, Vol.12, No.2, April 1997

[5] ดร.สำรวย สังข์สะอาด “วิศวกรรมไฟฟ้าแรงสูง” พิมพ์ครั้งที่ 1 เมษายน 2537 (ฉบับปรับปรุง), ISBN974-92125-5-x

The Challenges of Near-Future EMC Facility

Vichate Ungvichian
EMI Lab., Florida Atlantic University, Boca Raton, Florida, email: ungvich@fau.edu

Abstract -This paper presents the upcoming Electromagnetic compatibility (EMC) requirements and its ripple effect to the EMC evaluation companies. The upper frequency during the EMC evaluation has to cover up to 10 harmonics of the highest operating frequency or 40 GHz, whichever is the lower of the two [1]. Most EMC compliance laboratories are capable of measuring the emissions up to about 5 GHz, which is sufficient for compliance verification for most commercial devices. With the upcoming high-speed digital devices such as Bluetooth, the upper frequency needs to be increased to at least 26 GHz. A challenge lies in the performance of a test site and the sensitivity of a receiving system. A new VSWR technique is proposed to quantify the site. This site validation is very similar to the full-anechoic chamber [2] used in the antenna characterizations [3]. Further discussion will be on the conducted and radiated emissions, the measurement setup and the difficulty in obtaining repeatability.

Keywords: EMC, site evaluation, OATS, Semi-anechoic room, VSWR

I. INTRODUCTION

In the early seventies, Federal Communications Commission (FCC) received many consumers' complaints that the digital devices degraded the sound and picture qualities of their radios and televisions. Performance of amateur radios was also affected. Subsequently, limits at a fixed distance (3, 10, or 30 meters) were introduced to combat the unwanted emissions from several types of devices. According to the FCC Part 15, Subpart B ruling (unintentional emissions), any electronic device employing digital technology and operating 9 kHz clock or higher, must comply with this requirement [4].

In the modern world, digital technology has played a significant part of our daily lives. For example, cell phones, palm tops or PDAs, which use such technology, are present everywhere. The devices have been improved in the past two decades with immense sophistications. Laptop computer operating clock speed has reached 3 GHz and is expected to be even higher. Consumers demand that devices operate longer requiring either better efficiency batteries or lowering system operating voltages. Lithium-ion or Metal Hydride technology has been used in computer or electronic consumer products. However, battery research continues to push for higher performance in terms of storage and recharging time. Fuel cell technology has received more attention in the past decade. The current goal is to use fuel cells as sources of high power supply. But for low consuming power computing devices, Lithium-ion battery is sufficient to supply the power to the units. The computer charger based on the switching power supply (SPS) converts the AC to DC to replenish its energy. The SPS is very noisy in terms of emissions due to the conversion process and it can be used as a conducted noise reference [5].

A commercial product like an SPS must undergo conducted emission evaluations in the typical 150 kHz to 30 MHz frequency range [1, 6-8]. This is an emission generated from the device that directly feeds the unintentional current back to the power grid. If it is strong enough, the emission can interfere with the sensitive devices sharing the same circuit.

A transducer used to monitor the conducted emissions, known as a line-impedance-stabilization network (LISN), provides known load impedance [1] to the device under test (DUT), also filters utility-line noise. The LISN used in this paper operates from 150 kHz to 30 MHz. The LISN has the impedance at 150 kHz around 30 Ω and increases to about 47 Ω from 1 MHz to 30 MHz.

For radiated emissions, normally, the measurements were performed on either an open area test site (OATS) [9] or inside a semi-anechoic chamber. The digital device was placed on an 80-cm wooden table situated above an OATS, and over the metallic ground plane. The minimum conductive ground plane dimensions suitable for selected distance are described in [1]. There should be no large scattering objects or buildings in the vicinity of OATS. For the Semi-anechoic chamber, the absorbing materials are installed on all four walls and the ceiling.

The unintentional radiated emission assessment is another evaluation that the devices have to comply. The emission limits described in the FCC Code of Federal Regulations (CFR) Part 15, Subpart B, are based upon the location of the device to be used, either at a residential or commercial venue. The limit applicable to device for residential use is more stringent than those for a commercial application.

For a low power-transmitting source, the device must comply with the FCC CFR Part 15 Subpart C, Intentional radiator requirements [4]. The discussion of this paper will only be limited to devices operating in the 88-108 MHz FM band. The advertising industry and entertainment industry have low power accessories that allow the consumer to retrofit newly available devices to vehicle. The

modifications stems from direct connect or coupling to the existing aerial antenna. This new category for measurement setup for compliance assessment will be discussed in the subsequent section.

II. CHANGLLENGES

A. *CONDUCTED EMISSIONS*

This aspect of measurement is to determine the voltage level of emission generated by DUT during operation that is transmitted back to the main power utility. As a minimum requirement, the site must have a 2X2 m^2 horizontal ground plane. This is suitable for a floor type of device. An additional 2X2 m^2 vertical ground plane, which is electrically connected with the ground plane along the line where both plates meet, is needed for tabletop device [1, 6]. The LISN bonded to the ground plane is the monitoring junction in which its output port is connected to a receiver, such as a spectrum analyzer.

In most cases, the DUT is easily classified as either floor or tabletop operating device. However, there are many DUTs with unclear classifications. The worse case emission scenario should be the goal of the assessment. But the problem would be how to search for the configuration that will produce the strongest emission and at the same time the results can be reproduced elsewhere, such as at another test laboratory. The conducted evaluation throughout this study has been performed in the shielded enclosure, which has satisfied the site requirements.

As demonstrated, the emissions generated by a SPS used with the laptop computer are setup and measured as tabletop floor. Picture 1 is the tabletop setup and the emission result is depicted in Figure 1. Picture 2 is the floor setup. After moving the cable and the SPS, the emission reading became worse. It can be seen from Figure 2 that very different results are obtained by as much as 10 dB at some frequencies. With the floor setup, stronger emissions on an average can be obtained. The phenomena are due to the mutual coupling between cable and the SPS with the conducting ground plane.

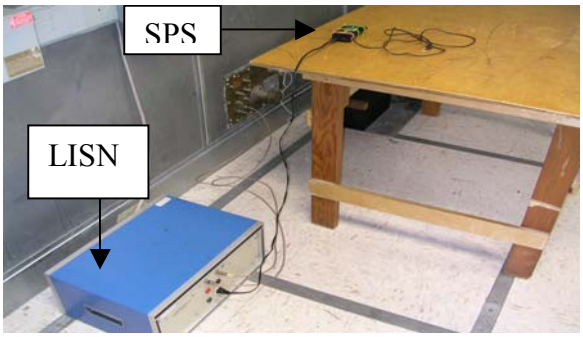

Photograph 1: Laptop SPS on the Table

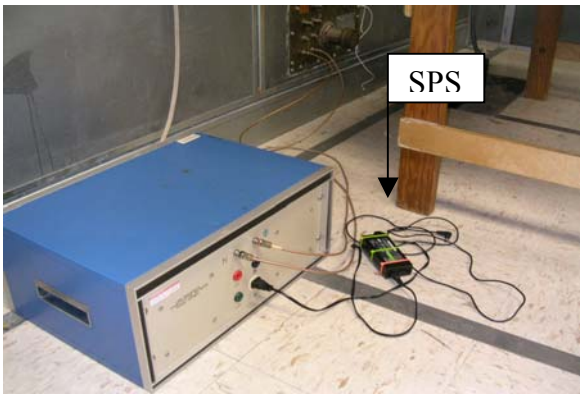

Photograph 2: Laptop SPS on the Floor

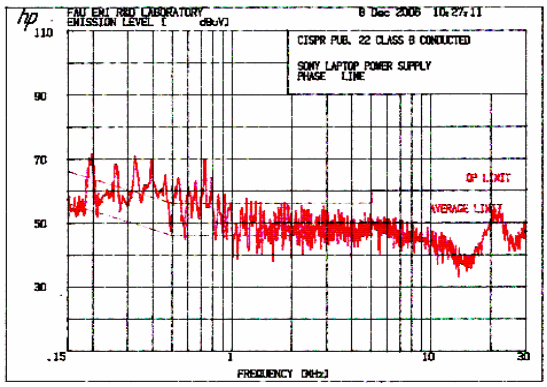

Figure 1: Laptop SPS on the Table

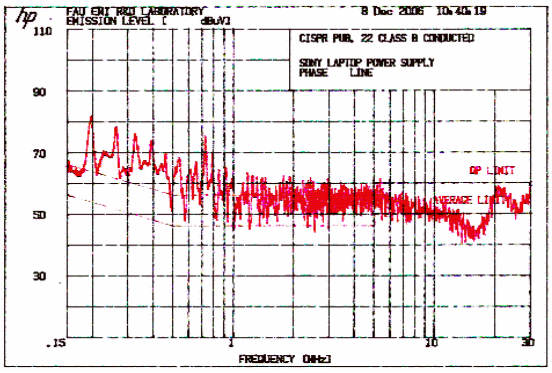

Figure 2: Laptop SPS on the Floor

B. *RADIATED EMISSIONS*

In an attempt to validate the EMC test site beyond the operating frequency of 1 GHz, CISPR has developed a draft CISPR 16-1-4 entitled "Site Evaluation above 1 GHz" [10], which is expected to get an approval sometime this year. The document applies for the site assessment from 1 GHz to 18 GHz. Similar to the current standards, test volume that the DUT occupied is defined as a cylindrical volumetric with radius and the height. The voltage standing wave ratio

(VSWR) is used as a figure of merit in the site performance evaluation. Actually, this approach has been used to assess the classical full-anechoic chamber suitable for antenna pattern and gain measurements. The quieted zone is a common terminology for the RF engineer, which is defined in terms of the amount of amplitude and phase of electric-field ripple on a plane perpendicular to the income wave within a specific area [2-3]. The spherical coordinate system is used in the antenna research. To modify OATS and Semi-anechoic chamber to perform similar to full-anechoic room, the ground plane must be lined with RF absorbing material, to reduce the reflection from the conductive ground. The differences are that the phase information has been ignored and the cylindrical coordinate system is used in the latter. Also the amplitude fluctuation is more relaxed than the full-anechoic room. The lowest height of both transmitting antenna and receiving antenna are 1 meter above the floor. Figures 3-4 depict the cylindrical volume in top view and side view with designated 6 positions at each location [10].

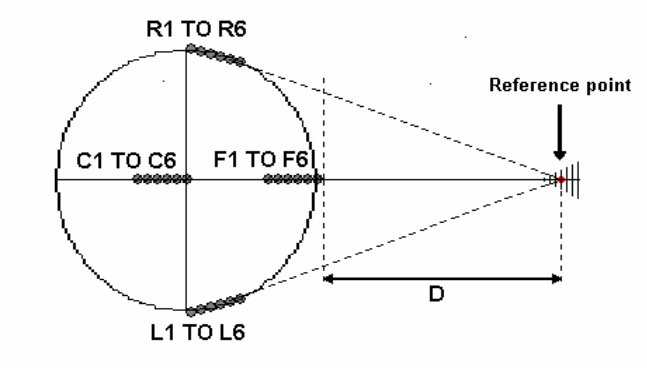

Figure 3: The Volumetric Top View

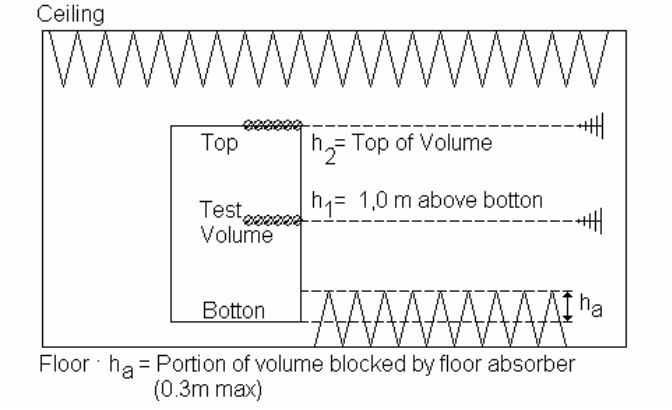

Figure 4: The Side View of VSWR Measuring Positions (Different Height)

There are two VSWR procedures, which are the Standard Site VSWR and Reciprocal Site VSWR. The former is used for OATS and the latter is for Semi-anechoic chamber. The main difference between both procedures is the reversed position between the transmitting antenna and receiving probe. At each location on OATS volume, the measurements will be performed for six predetermined points. The first location (F6, R6, L6 and C6) is the nearest distance, defined in the specification, from the antenna (reference point), see Figures 3-4. The transmitting antenna, which will be subsequently used for normal radiated emissions, is placed at those locations. The distances of 5 locations are the first location (closest to the antenna) plus 2, 10, 18, 30 and 40 cm away from the probe for the subsequent locations. It is important to keep the receiving probe location fixed. The voltage readings are corrected using the distance factor, which is in dB as 20xlog ($D_{actual}/D_{reference}$). After the readings have been corrected for all of the 6 locations and all positions (left, right, front), the site will be acceptable, if the maximum VSWR is ≤ 6 dB across the frequency band. If the top of the volume is ≥ 0.5 m, then the process has to be repeated at this height. However, if the top of the test volume is > 1.5 m, not only will the process have to be repeated, but the additional center position must be included in the assessment. Finally, both horizontal and vertical polarizations must be measured to complete the data set.

The challenges are two folds: 1) the accuracy of distance and six movements along the position as shown in Figures 3 and 4, 2) the receiving signal to process a linear characteristic and maintain 20 dB above the receiver display noise floor.

1) The smallest movement in the order of 2 cm and the broadside aiming of the antenna toward the probe are called for. This may need a laser measuring distance device having ±2 mm accuracy to reduce the measuring uncertainty.
2) The typical probe sensitivity is around 1 V/m. This seems manageable for low GHz. Even with a good amplifier, the transmitting antenna performance and cable loss are stacked up against the required 20 dB signal above the noise floor. The amplifier gain of 30-40 dB can be achieved with current technology. The low-loss cable (TFlex 401) can provide the cable loss of 50 dB/100 ft at 18 GHz. For GHz frequency application, the cable resonance due to the diameter has to be considered. When the operating frequency is above the resonance, the cable no longer possesses only the transverse electromagnetic (TEM) mode, but the multi-modes as well. Hence, the cable loss is quite complicated to determine. The connector is another point of concern. A high quality type N connector without corner bend can handle up to 18 GHz. The 2.9 mm connector may have to be used instead, to extend the upper frequency to 40 GHz. To reduce the distance between the receiving antenna and hence, the cable loss, the

receiving system may have to be placed on a movable cart lined with absorbing material.

C. SEMI-ANECHOIC CHAMBER SHIELDING EFFECTIVENESS

OATS is the simplest site to construct [9]. In the GHz range, the ground plane may not reflect as well, but due to the antenna characteristic, less electric field will illuminate the ground. In addition to having an absorbing material in the area between the receiving antenna and test volume, the ground plays very little role at this frequency range due to the antenna beamwidth. However, for a sweep frequency technique normally employed in EMC test procedure, the ambient has become a major factor in assessing the emissions. But, for a semi-anechoic chamber, the ambient signals will be attenuated from the shielding walls and absorbing materials inside the room. If the existing EMC semi-anechoic room is upgraded to operate beyond 1 GHz, the shielding effectiveness as well as power-line filters must be evaluated. A specification of commonly used EMC filter covers up to 10 GHz. The filters must be either replaced or retrofitted with higher frequency units. Further concern is the room shielding effectiveness in the high GHz frequency. The gaps or slits around the corners or connections between plates may be large in terms of electrical wavelength, and hence they act like apertures. It is recommend that the shielding effectiveness of the room be quantified beyond 1 GHz.

D. SETUP EXPLORATORY

To keep up with new technology, many companies design digital electronic accessories that are retrofitted to the commonly found devices with minimum efforts. The discussion focuses on the radio entertainment industry. For example, the CD player becomes a standard device on late model luxury vehicles. But this is not true for early models; only the AM/FM radio with cassette tape is available in the standard models. When the consumer demands an upgrade, many companies currently offer an external CD player having the coupling mechanism connected to the existing radio antenna as a mean to feed the CD signal directly to the radio RF input. Hence, the original vehicle antenna behaves either in the receiving or transmitting mode. As when the CD signal presents, the vehicle antenna operates in the transmitting mode. The RF leakage may interfere with the proximal vehicles. This RF emission must also comply with the unintentional limit (FCC Part 15 Subpart B) except for the CD intentional frequency (normally in the FM band) where the 250μV/m field strength at 3 m is the limit. Currently, there is no description in the EMC documents [1, 6-8] on how to setup this type of accessory for compliance assessment.

E. EQUIPMENT

An early version of a residential cordless phone, analogue technology operating in the 43-49 MHz with 25channels is used. Later, digital phones operating at 900 MHz, 2.4 GHz and currently 5.8 GHz bands are available. One observation is that for the 2.4 GHz cordless phones, the 10^{th} harmonic (24.0 GHz) is already beyond the intent of the draft CISPR 16-1-4. This is a void at this juncture. For the 5.8 GHz phones, the 10^{th} harmonic is 58.0 GHz, which is over the 40 GHz limits [1]. Hence, only the emission will be evaluated to 40 GHz. Similar to 3.5 GHz phones, the upper limit for compliance testing is 40 GHz. To validate the device compliance, the receiving system [11], including amplifier, cable, connector, antenna, and receiver must be sensitive enough to measure the average electric field of 54 dBμV/m (500 μV/m) at a 3 m distance. This is a challenging task. The system noise floor including noises from the amplifier and receiver is an important factor in determining the system sensitivity. In addition, the receiver noise will increase when the required receiver resolution bandwidth setting is at least 1 MHz [4]. If the amplifier gain is insufficient, then the limit value may be below the noise floor. Obviously, the compliance condition is undetermined.

In the classical antenna characterizations, such as gain or beamwidth, the operating bandwidth is normally in the order of 1 decade. The data collection is done by focusing on a particular frequency at a time. Hence, the resolution can be drastically reduced and the transmitting signal will be higher than the EMC emissions. Therefore, the sensitivity of the receiving system for the antenna area is not an important issue. But for the EMC, the radiated emission covers from 30 MHz to 40 GHz, which is over 3 decades of frequency spans. Several receiving antennas as well as amplifiers must be used in the efforts. One option to overcome the loss is the use of the waveguide system. There is a trade off in the data collecting time due to the waveguide narrow band behavior.

III. CONCLUSIONS

The progress in digital electronics in the last five years has been tremendous. The EMI community must be prepared to upgrade their equipment for the commonly found GHz devices. The EMI test facilities are facing tough challenges in the receiving system sensitivity and bandwidth. Even with the use of the average detector and with preamplifier and the best cable, the compliance limit may be only a few dB above the display noise floor, for the MHz receiver resolution setting. Furthermore, the test site assessment in the GHz range is also a challenge. Very limited documentation suggests the VSWR method can be used for the site evaluation beyond 1 GHz. The interference from other unwanted RF sources are everywhere for OATS; whereas a semi-anechoic chamber with sufficient shielding will eliminate those signals. However, the chamber may be

more difficult to pass the VSWR technique, due to the reflection from chamber walls as well as the floor lined with imperfect absorbing materials.

In the case where the measurement setup does not explicitly describe the setup for a particular device, engineering judgment plays an important decision. Depending upon the conducted emission setup for SPS, either tabletop or floor placement, the reading can be different as much as 10 dB. To be conservative, the worse case value and scenario should be used. Finally, the in situ measurement may still be needed and data should be acceptable if it is impractical to bring the device into the chamber area.

REFERENCES

[1] ANSI C63.4-2001, "American National Standard for Methods of Measurement of Radio-Noise Emissions from Low Voltage Electrical and Electronic Equipment in the range of 9 kHz to 40 GHz", 2001.

[2] Constantine Balanis, "Antenna Theory Analysis and Design", Second Edition, John Wiley, 2005.

[3] IEEE Std 149-1979, "IEEE Standard Test Procedure for Antenna", 1979.

[4] Code of Federal Regulations (CFR), Title 47 - Telecommunication, Part 15 – Radio Frequency Devices, 2006.

[5] Ungvichian, V. and R. Aina, "A Study on Inexpensive Stable Conducted/Radiated Emission Sources Suitable for the EMC Directives", 2006 Int'l RF and Microwave Conference, Putra Jaya, Malaysia, 2006.

[6] CISPR 16, IEC International Electrotechnical Commission, International Special Committee on Radio Interference, "Specification for Radio Disturbance and Immunity Measuring Apparatus and Methods," 2002.

[7] CISPR 22-2003, IEC International Electrotechnical Commission, International Special Committee on Radio Interference "Information Technology Equipment - Radio Disturbance Characteristics - Limits and Methods of Measurement", 2003.

[8] EN55025-2003, "Radio Disturbance Characteristics for the Protection of Receivers Used on Board Vehicles, Boats, and on Devices: Limits and Methods of Measurement", 2003.

[9] ANSI 63.7-1988, "American National Standard Guide for Construction of Open Area Test Sites for Performing Radiated Emission Measurements", 1988.

[10] CISPR 16-1-4, IEC International Electrotechnical Commission, International Special Committee on Radio Interference, "Site Evaluation above 1 GHz", 2006.

[11] CISPR 16-SER, IEC International Electrotechnical Commission, International Special Committee on Radio Interference, "Specification for radio disturbance and immunity measuring apparatus and methods", 2007.

Development of an FPGA-Based Gate Signal Generator for a Flying-Capacitor Inverter

S. Khummanee, S.Polmai
Department of Electrical Engineering, Faculty of Engineering
King Mongkut's Institute of Technology Ladkrabang (KMITL)
Chalongkrung Rd., Ladkrabang, Bangkok THAILAND 10520
E-mail: s7060261@kmitl.ac.th, kpsompob@kmitl.ac.th

***Abstract*- This paper proposes application of FPGA for gate signal generation for a flying-capacitor multilevel inverter. The use of FPGA helps reduce the number of basic logic devices and provides flexibity in design and modification. The design and programming of the FPGA are based on the Quartus II program. The design makes use of Mega Function block diagram already included in QuartusII. This can reduce error and requires no VHDL programming skill. The designed circuit can interface with microprocessor system via 3-bit address bus and 10-bit data bus.**

***Keywords* - FPGA, flying-capacitor multilevel inverter, sinusoidal pulsewidth modulation.**

I. INTRODUCTION

Recently, demand for high power converters for adjustable speed drive for industry, and electric railway system as well as power electronics-based power system devices such as FACT and Custom Power Devices has been increased. These high power converters must capable of handling both high voltage and high current. Connecting several power semiconductor switches in series to increase withstanding voltage level of a composite switch in conventional two-level inverter is not practical due to voltage sharing problem and limited performance. Multilevel inverter technology has emerged as the solution for working with higher voltage level.

Multilevel inverters include an array of power semiconductors and capacitor voltage sources. The output voltage is generated in stepped waveforms. The commutation of the switches permits the addition of the capacitor voltages, which reach high voltage at the output, while the power semiconductors must withstand only reduced voltages [1]. The advantages of multilevel inverter include better electromagnetic compatibility, lower output voltage THD, and higher efficiency due to lower average device switching frequency [2].

Three different topologies have been proposed for multilevel inverters: diode-clamped (neutral-clamped); capacitor-clamped (flying capacitors); and cascaded multicell with separate dc sources. In addition, several modulation and control strategies have been developed or adopted for multilevel inverters including the following: multilevel sinusoidal pulsewidth modulation (PWM), multilevel selective harmonic elimination, and space-vector modulation (SVM) [1].

Sinusoidal pulsewidth modulation (SPWM) technique is commonly used in the two-level inverter and can be applied to multilevel inverter as well. In multilevel sinusoidal puslewidth modulation, multiple carrier signals are used. There are two techniques developed for multicarrier SPWM; phase-shifting carrier and level-shift carrier method [1].

Currently, pulsewidth modulation circuits are included in some of high performance microcontrollers or digital signal processors (DSP). These modulation circuits, however, are designed for use extensively with two-level 6-switch inverters. Multilevel inverters, on the other hand, require larger number of gate signals than those provided with the DPS. If the DPS is used for generating gate signals for multilevel inverter, which can be done by software approach, the burden of the DSP computation increased and results in delay time of the control loop.

This paper proposes application of field programmable gate array (FPGA) for gate signal generation for a five-level flying-capacitor multilevel inverter, which requires 24 gate signals. The design and programming of the FPGA are based on the Quartus II program. The design makes use of Mega Function block diagram already included in Quartus II. This can reduce error and required no VHDL programming skill. The designed circuit is implemented with Altera ACEX1K FPGA and can interface with microprocessor system via 3-bit address bus and 10-bit data bus.

In the following section structure of flying capacitor inverter and multilevel pulsewidth modulation are firstly reviewed. Then the implementation of FPGA for pulsewidth modulation is explained. Finally, the experiment and experimental results are reported.

II. CONFIGURATION OF FIVE-LEVEL FLYING CAPACITOR INVERTER

Fig. 1 illustrates the fundamental building block of a phase–leg of a five-level flying-capacitor inverter. The outermost capacitor is called common DC link capacitor and the other capacitors are called flying capacitors.

The output voltage between point A and 0, i.e. V_{A0} is the result of the summation of the capacitor voltages in series, which can be expresses by

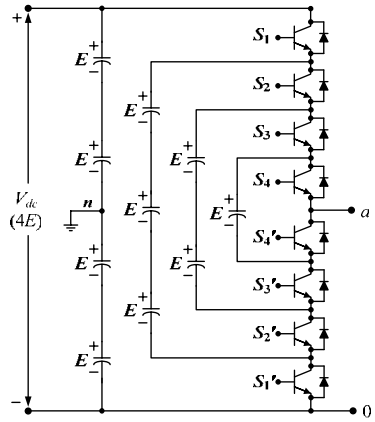

Figure 1. Fundamental building block of a phase-leg of five-level flying-capacitor inverter.

$$V_{A0} = \sum_{i=1}^{m-1} S_i E, \tag{1}$$

$$\text{where, } S_i = \begin{cases} 0 & \text{when switch } i \text{ is "OFF"} \\ 1 & \text{when switch } i \text{ is "ON"} \end{cases}, \tag{2}$$

TABLE I
POSSIBLE SWITCHING STATES OF A FIVE-LEVEL FLYING CAPACITOR INVERTER

Switching states				Output voltage related of capacitor	Inverter phase voltage v_{AN}	C_1	C_2	C_3	C_4
S_1	S_2	S_3	S_4						
1	1	1	1	4*E*	V_{dc}(4*E*)	-	N	N	N
1	1	1	0	4*E* - 1*E*	3*E*	-	N	N	+
1	1	0	1	4*E* - 2*E* + 1*E*		-	N	+	-
1	0	1	1	4*E* - 3*E* + 2*E*		-	+	-	N
0	1	1	1	3*E*		N	-	N	N
1	1	0	0	4*E* - 2*E*	2*E*	-	N	+	N
1	0	1	0	4*E* - 3*E* + 2*E* - 1*E*		-	+	-	+
0	1	1	0	3*E* - 1*E*		N	-	N	+
1	0	0	1	4*E* - 3*E* + 1*E*		-	+	N	-
0	1	0	1	3*E* - 2*E* + 1*E*		N	-	+	-
0	0	1	1	2*E*		N	N	-	N
1	0	0	0	4*E* - 3*E*	1*E*	-	+	N	N
0	1	0	0	3*E* - 2*E*		N	-	+	N
0	0	1	0	2*E* - 1*E*		N	N	-	+
0	0	0	1	1*E*		N	N	N	-
0	0	0	0	0	0	N	N	N	N

Index: 1-sw on, 0-sw off, N-none, + charging mode, - discharging mode

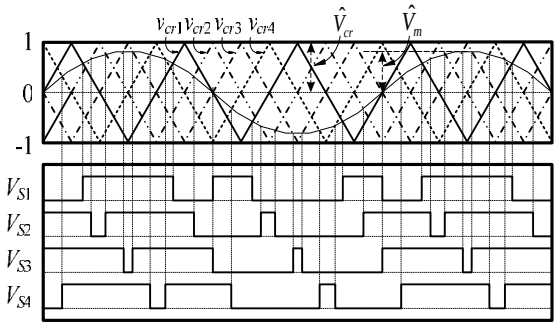

Figure 2. Method for phase-shift carrier pulsewidth modulation.

m is the number of voltage level, S_i is the switching state of the i^{th} switch, and *E* is the voltage across each capacitors, which are assumed to be constant and equal.

In Fig. 1, the voltage across each switch is *E*, and the output voltage could be produced from 0 with the entire switch turning off to 4*E* with the entire switch turning on. Table I summarizes the possible switching state and its corresponding output voltage for the inverter in Fig. 1. In Table I, there are redundant switching states that produce the same output voltage. These redundant states can be utilized for balancing the flying capacitor voltages.

III. MULTILEVEL PULSEWIDTH MODULATION FOR FLYING CAPACITOR MULTILEVEL INVERTER

Two types of multilevel pulsewidth modulation have been developed for multilevel inverter; phase-shifted carrier; and level-shifted carrier technique [3]. Only phase-shifted carrier technique is adopted in this paper. Fig. 2 illustrates the method of phase-shifted carrier pulsewidth modulation. For five-level flying capacitor inverter, four triangular carrier signals with 90-degree phase shifted between each signal are used.

The amplitude modulation index is defined by

$$m_a = \frac{V_m}{V_c}, \ 0 \le m_a \le 1, \tag{3}$$

where, V_m is the amplitude of the modulated signal and V_C is the amplitude of the carrier signal.

The frequency modulation index of the output voltage is given by

$$m_f = \frac{f_c}{f_m} \tag{4}$$

where, f_c is the frequency of the carrier signal and f_m is the frequency of the modulated signal.

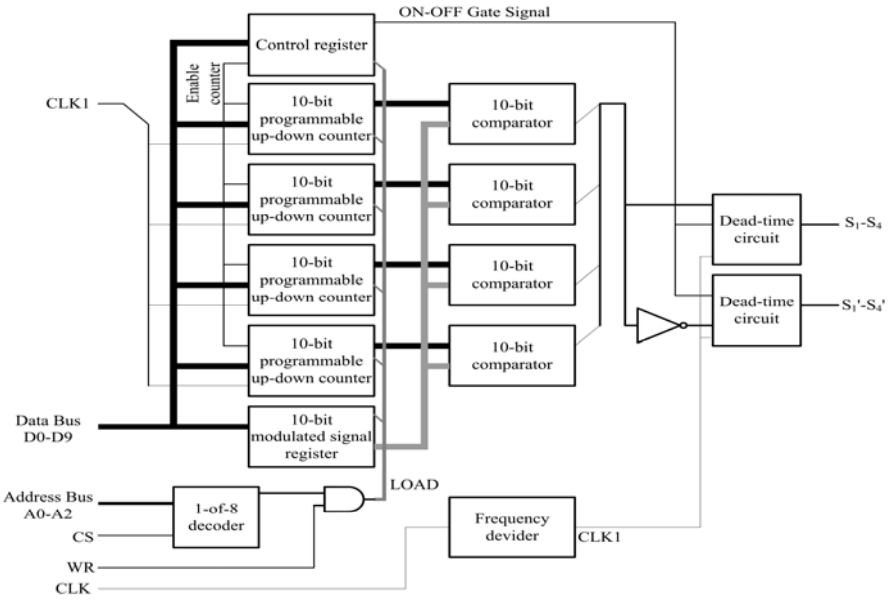

Figure 3. Block diagram of the designed FPGA-based gate signal generator

The device switching frequency is equal to the carrier frequency and the inverter frequency or the output voltage frequency is equal to $(m-1) f_c$.

IV. Implementation of FPGA for Pulsewidth Modulation

A. Block Diagram of Gate Signal Generator

The design and verification of the circuit was done on Quartus II Web Edition. The design makes use of Mega Function block diagram already included in Quartus II. This helps reduce error and requires no VHDL programming skill.

Fig. 3 illustrates block diagram of the modulator for one leg of the inverter. The overall circuit for the inverter generating the total of 24 gate signals includes four up-down counters, three 10-bit modulated signal registers, and twelve 10-bit comparators.

An 18.432 MHz external clock is divided by 12 to make 1.5636 MHz CLK1 signal for the counters and dead-time circuits. Four independent 10-bit up-down counters are used for triangular carrier signal generation. The phase shift between each carrier signal can be programmed by its initial value. In this paper the phase shift between these signals is set to 90 degrees. The frequency of the carrier signal is set to 750Hz. In each sampling, the value of modulated signal will be loaded into the modulated signal register and compared to the carrier signals by 10-bit comparators. The outputs of the comparators are subjected to the dead-time circuit before sending out to the external gate-drive circuits. The dead-time circuit includes four set of D flip-flop in cascade connection. The dead time is equal to four clock signal periods or 2.558 microseconds. The control register controls the operation of the counters and dead-time circuits. To enable or disable the operation of the counter and the dead-time circuit, pre-defined value must be written to this register. Each counter and register has its own address. Access of these devices is controlled by the 1-of-8 decoder.

Figure 4. Picture of FPGA development board

B. FPGA Board

The Altera ACEX1K FPGA is adopted in this paper. Fig. 4 shows the development board. The FPGA features 30,000 typical gates, 1728 logic element, up to 24,576 bit of memory, and independent 171 input-output pins [4]. A blank socket on the top-right of the board is for configuration device storing the design circuit. The stored content will be automatically loaded into the FPGA during power up.

V. Experiment and Results

A prototype three-phase five-level flying capacitor inverter as shown in Fig. 5 has been constructed for experiment. The details of the inverter are given in Table II. A PC equipped

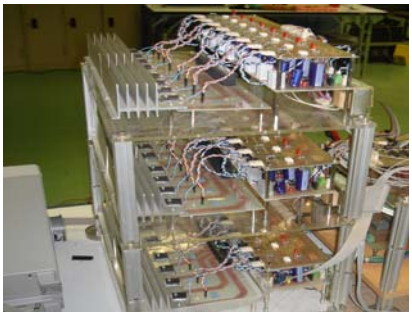

Figure 5. Picture of the prototype five-level flying-capacitor inverter

TABLE II
Parameters of the Prototype Five-Level Flying-Capacitor

DC link capacitor	2.2 mF 450VDC
Flying capacitor	2.2mF 450VDC
DC link voltage	200 V
IGBT	G2BN60B3D (1200V,40 A)
Load	500 W resistive

with a PCI-to-8255 PIO board is used for modulated signal computing. The modulated signals are sent to the FPGA via the PCI-to-8255 PIO board. The modulated signal is computed at a rate of 10,000 samplings per second. The fundamental frequency of the modulated signal is 50Hz.

Fig. 6 shows captured signals during the loading of modulated signals into the modulated signal registers. The figure shows sequentially sending of phase-a, phase-b, and phase-c modulated signals, respectively.

Fig. 7 illustrates captured signals demonstrating the result of the dead-time circuit. The designed value of the dead time is attained.

Fig. 8 shows the captured waveform of the output line-to line voltage. The line-to-line voltage results in 11 voltage levels and agrees well with theoretical results.

VI. Conclusions

For multilevel inverter a larger number of gate signals are required and the software-based gate signal generation is not efficient as it increases computation burden to the DSP or microcontroller. FPGAs are more suitable for this task because all the computations are performed by the dedicated hardware. The application of FPGA for gate signal generation for a five-level flying-capacitor multilevel inverter has been proposed and explained. The experiment has been carried out using prototype laboratory-built inverter and the FPGA-based gate signal generator functioned as designed.

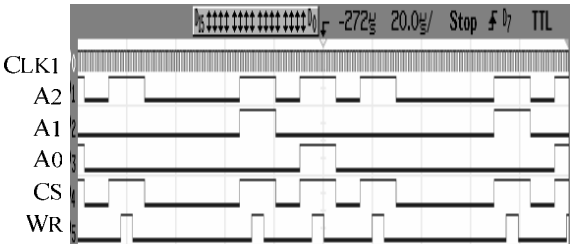

Figure 6. Captured signals during the loading of modulated signals into the modulated signal registers (5V/div, 20 μs/div)

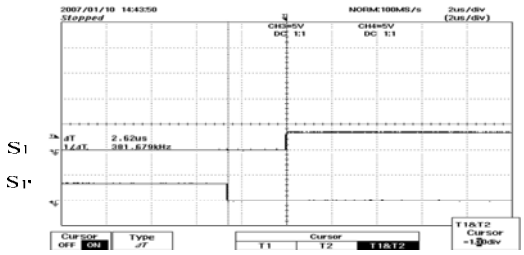

Figure 7. Captured signals demonstrating the result of the dead-time circuit (5V/div, 20 μs/div)

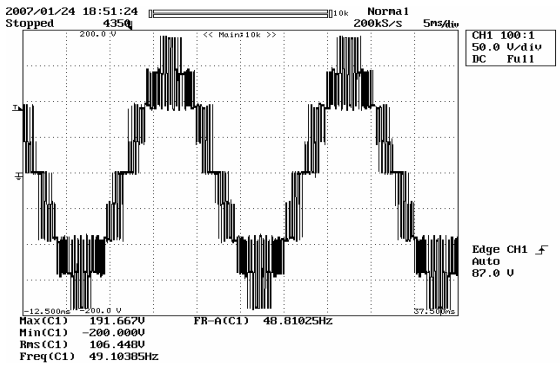

Figure 8. Measured line-to-line output voltage at modulation index 0.9

References

[1] F. Zheng Peng, J. Rodriguez, and J. Sheng Lai ,Multilevel Inverter: A Survey of Topologies, Control and Application, *IEEE Trans. Ind. Applicat*., Vol. 49, No. 4, August 2002.

[2] G. Ebersohm and M.N. Gitau , FPGA-Implemented Carrier based SPWM Multilevel Controller, *IEEE*, pp.1175-1178, 2004

[3] Brendan Peter McGrath and Donald Grahame Holmes, Multicarrier PWM Strategies for Multilevel Inverters., *IEEE transactions on industrial electronics*, vol. 49, no. 4, August 2002

[4] http://www.altera.com

Comparison Between Phase- and Level-shifted PWM Schemes for Flying Capacitor Multilevel Inverter

S. Ketsakoon, S. Polmai
Department of Electrical Engineering, Faculty of Engineering
King Mongkut's Institute of Technology Ladkrabang (KMITL)
Chalongkrung Rd., Ladkrabang, Bangkok THAILAND 10520
E-mail: s7060219@kmitl.ac.th, kpsompob@kmitl.ac.th

***Abstract*-This paper presents the study and comparison of PWM schemes for five-level flying capacitor inverter. The PWM schemes. Included in this study are phase-shifted and level-shifted multi-carrier sinusoidal modulation. The comparison focuses on output voltage THD, capacitor voltage balancing and effect of the dead time. The results of the comparison will be used to aid the design of five-level flying capacitor inverter in the future.**

***Keywords* - Flying-capacitor multilevel inverter, SPWM, total harmonic distortion, energy balance.**

INTRODUCTION

In recent years, industry has begun to demand higher power equipment, which now reaches the megawatt level. Controlled ac drives in the megawatt range are usually connected to the medium-voltage network. Today, it is hard to connect a single power semiconductor switch directly to medium-voltage grids (2.3, 3.3 or 6.9kV). For these reasons, a new family of multilevel inverters has emerged as the solution for working with higher voltage levels [1]-[2].

Today, multilevel inverters are extensively used in high-power applications with medium voltage levels. The field applications include use in motor drive, harmonic elimination and improvement power factor in system and static VAR compensations to system.

Three different topologies have been proposed for multilevel inverters: diode-clamed (neutral-clamped); capacitor-clamed (flying capacitors); and cascaded multi-cell with separated sources. In addition, several modulation and control strategies have been developed or adopted for multilevel inverters including the following: multilevel sinusoidal pulse width modulation (SPWM), multilevel selective harmonic elimination, and space-vector (SVM) [2].

The most attractive features of multilevel inverters are as follows.

- They can generate output voltages with extremely low distortion and lower *dv/dt*.
- They draw input current with very low distortion.
- They can operate with a lower switching frequency.

Table I shows the comparison of the multilevel inverter topologies. In the application that requires energy source, such as adjustable speed drive of ac machines, the dc link energy is normally fed from the ac source via rectifier or converter circuit. Having only single dc link is the benefit in term of reliability and ease of control. Another issue concerning with multilevel inverter is balancing of voltage across each capacitor. Having capability of balancing the capacitor voltage without additional dedicated hardware is preferable. The flying-capacitor and cascade multi-cell inverter utilize the redundant switching states to solve this problem. Owning to the single dc source constraint, the flying-capacitor inverter is selected for this study.

Multilevel sinusoidal pulse-width modulation (SPWM) is investigated in this study. The PWM schemes included in this study are phase-shifted and level-shifted multi-carrier sinusoidal modulation. The investigation focuses on output voltage THD, capacitor voltage balancing and effect of the dead time. The results of the comparison will be used to aid the design of five-level flying-capacitor inverter in the future.

FLYING CAPACITOR INVERTER CIRCUIT

The flying-capacitor inverter Fig. 2 can produce an inverter phase voltage with five voltage levels. When switches S_1, S_2, S_3, and S_4 conduct, the inverter phase voltage v_{AN} is $4E$, which is the voltage at the inverter terminal A with respect to the negative dc bus N. Similarly, with S_1, S_2, and S_3 switched on, $v_{AN} = 3E$. Table II lists all the voltage levels that can be obtained by the six sets of different switching states.

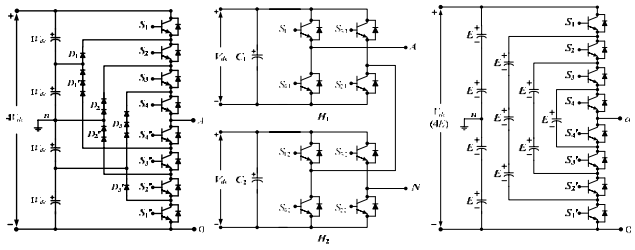

(a) (b) (c)

Figure 1. Multi-level inverter topology. (a) diode-clamped. (b) cascaded-multicell. (c) capacitor-clamped (flying-capacitor).

TABLE I
COMPARISON OF MULTILEVEL INVERTER CIRCUITS TOPOLOGIES

Comparison	Diode-clamped	Cascaded-multicell	Flying capacitor
Common DC link	✓	×	✓
Redundant of switching state.	×	✓	✓
Number of dc capacitors	Few	Few	Many
Isolated voltage dc source	Single	Many	Single

The switching state redundant is a common phenomenon in multilevel converters, which provides a great flexibility for the switching pattern design.

SINUSOIDAL MULTI-CARRIER PULSE-WIDTH MODULATION

Several multi-carrier techniques have been developed to reduce the distortion in multilevel inverters, based on the classical SPWM with triangular carriers [1]. Some methods use carrier disposition and others use phase shifting of multiple carrier signals [3].

A. Phase-shifted Multi-carrier PWM Scheme

Fig. 3 illustrates typical gating signal using phase-shifted multi-carrier PWM for one phase leg of the inverter shown in Fig. 2. In this paper, we choose a number of *m*-voltage levels requires (*m*-1) triangular carriers in one phase with their carriers shifted by an angle given by

$$\theta_{cr} = 360°/(m-1), \quad (1)$$

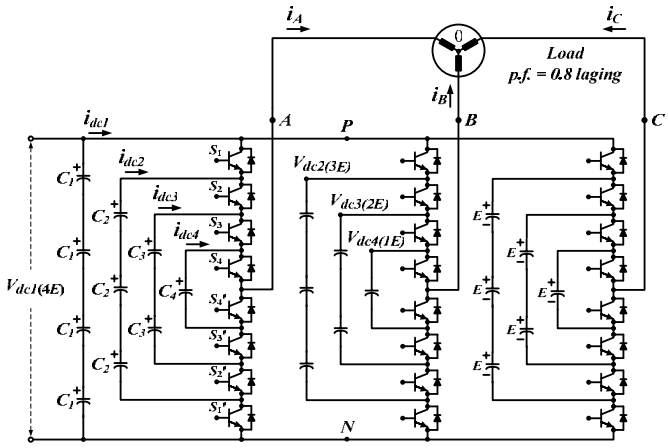

Figure 2. Five-level flying-capacitor inverter.

TABLE II
VOLTAGE LEVEL AND SWITCHING STATE OF A FIVE-LEVEL FLYING-CAPACITOR INVERTER

Switching states				Output voltage related of capacitor	Inverter phase voltage v_{AN}	C_1	C_2	C_3	C_4
S_1	S_2	S_3	S_4						
1	1	1	1	4*E*	V_{dc}(4*E*)	-	N	N	N
1	1	1	0	4*E* - 1*E*	3*E*	-	N	N	+
1	1	0	1	4*E* - 2*E* + 1*E*		-	N	+	-
1	0	1	1	4*E* - 3*E* + 2*E*		-	+	-	N
0	1	1	1	3*E*		N	-	N	N
1	1	0	0	4*E* - 2*E*	2*E*	-	N	+	N
1	0	1	0	4*E* - 3*E* + 2*E* - 1*E*		-	+	-	+
0	1	1	0	3*E* - 1*E*		N	-	N	+
1	0	0	1	4*E* - 3*E* + 1*E*		-	+	N	-
0	1	0	1	3*E* - 2*E* + 1*E*		N	-	+	-
0	0	1	1	2*E*		N	N	-	N
1	0	0	0	4*E* - 3*E*	1*E*	-	+	N	N
0	1	0	0	3*E* - 2*E*		N	-	+	N
0	0	1	0	2*E* - 1*E*		N	N	-	+
0	0	0	1	1*E*		N	N	N	-
0	0	0	0	0	0	N	N	N	N

Index: 1-sw on, 0-sw off, N-none, + charging mode, - discharging mode

B.Level-shifted Multi-carrier PWM Scheme

Fig. 4 illustrates three variation of the level-shifted multi-carrier PWM named (a) in-phase disposition (IPD) where all carriers are in phase, (b) alternative phase opposite disposition (APOD) where all carriers are alternatively in opposite disposition and (c) phase opposite disposition (POD) where all carriers above the zero reference are in phase but in opposition with those below the zero reference. In what follows, only IPD modulation scheme is discussed in detail due to page limitation.

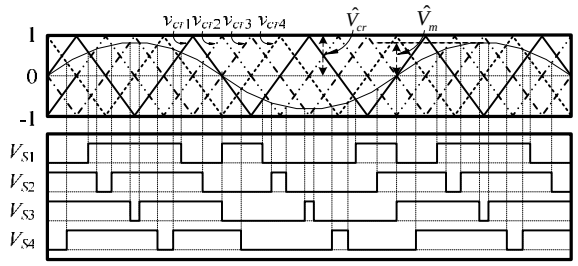

Figure 3. Modified phase-shifted modulation for five-level inverter of one phase-leg.

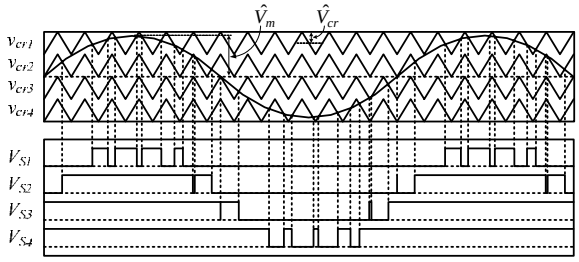

(a) In-Phase Disposition (IPD) .

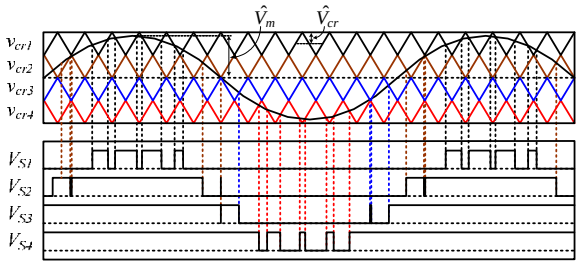

(b) Alternative Phase Opposite Disposition (APOD).

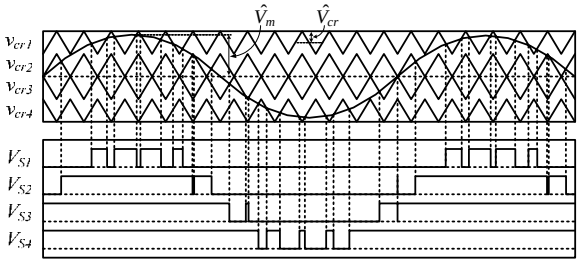

(c) Phase Opposite Disposition (POD).

Figure 4. Level-shifted multi-carrier modulation for five-level inverter.

The phase-shifted PWM scheme have characteristic as follows.

$$m_a = \hat{V}_m / \hat{V}_{cr}, \quad for \quad 0 \le m_a \le 1, \tag{2}$$

$$f_{sw,dev} = f_{cr}, \tag{3}$$

$$f_{sw,inv} = (m\text{-}1) f_{sw,dev}, \tag{4}$$

where

f_m	Fundamental frequency
f_{cr}	Carrier frequency
$f_{sw,dev}$	Frequency switching device
$f_{sw,inv}$	Switching frequency of inverter
m_f	Frequency modulation index (f_{cr} / f_m)
m_a	Modulation index
m	Voltage levels

As stated earlier, the frequency of the dominant harmonic in the inverter output voltage represents the inverter switching $f_{sw,inv}$. Since the dominant harmonics in v_{AN} and v_{AB} distributed around $(m - 1)m_f$.

The level-shifted PWM scheme have characteristic as follows.

$$m_a = \hat{V}_m / \hat{V}_{cr}(m-1), \quad for \quad 0 \le m_a \le 1, \tag{6}$$

$$f_{sw,dev} = f_{cr}/(m\text{-}1), \tag{7}$$

$$f_{sw,inv} = f_{cr}, \tag{8}$$

As stated earlier, the frequency of the dominant harmonic in the inverter output voltage represents the inverter switching $f_{sw,inv}$. Since the dominant harmonics in v_{AN} and v_{AB} distributed around m_f.

SIMULATION RESULT

The simulations comparisons between both schemes are focused on three topics the output voltage THD, capacitor energy balancing and effect of the dead time. To compare the performance of inverter, it is assumed that the average switching frequency of the solid-state devices is the same in both schemes. Table III shows the important parameters used in the simulations.

Fig. 5 shows the simulated waveforms using phase-shift multi-carrier PWM schemes for the inverter operating under the condition of $m_f = 50$, $m_a = 1.0$, $f_m = 60$ Hz, and $f_{cr} = 750$ Hz. As stated earlier, the frequency of the dominant harmonic in the inverter output voltage represents the inverter switching frequency $f_{sw,inv}$. Since the dominant harmonic in v_{AB} in Fig. 5 are distributed around $4m_f$, the inverter switching frequency can be found from $f_{sw,inv} = 4m_f \times f_m = 4f_{sw,dev}$, which is four times the device switching frequency.

Fig. 6 shows the simulated waveforms using IPD multi-carrier PWM schemes for the inverter operating under the condition of $m_f = 50$, $m_a = 1.0$, $f_m = 60$ Hz and $f_{cr} = 3000$ Hz. Although the carrier frequency of 3000 Hz seems high for high-power converters, the average device switching frequency is only 750 Hz.

Fig. 7 shows the THD profile of the line-to-line voltage v_{AB} produced by the phase- and level-shifted modulation schemes. As can be seen from the Figure, the IPD modulation scheme gives the best THD result all over the length of modulation index. The phase-shift and APOD have the same THD characteristic all the range of modulation index. The THD calculation is performed up to 100th order.

TABLE III
INVERTER OPERATING FOLLOWING

Parameter operating	Phase-shifted PWM	Level-shifted modulation
f_m	50 Hz	50 Hz
f_{cr}	750 Hz	3000 Hz
m_f	15	60
$f_{sw,dev}$	750 Hz	750 Hz
$f_{sw,inv}$	3000 Hz	3000 Hz
load	PF = 0.8 *lagging*, 0.414 kVA	

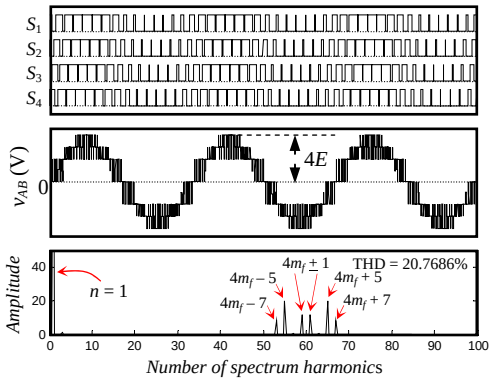

Figure 5. Simulated waveforms for a five-level flying-capacitor inverter with phase-shifted PWM (m_f =15, m_a =1.0, f_m =50 Hz, f_{cr} =750 Hz, and $f_{sw,dev}$ =750 Hz).

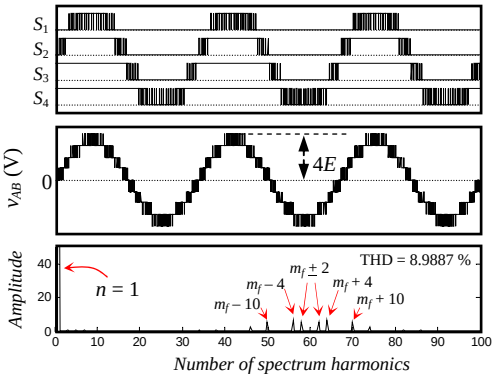

Figure 6. Simulated waveforms for a five-level flying-capacitor inverter with IPD modulation (m_f = 60, m_a = 1.0, f_m = 50 Hz, f_{cr} = 3000 Hz, and $f_{sw,dev}$ = 750 Hz).

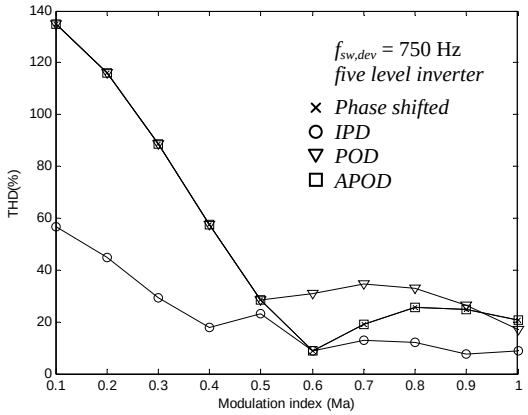

Figure 7. THD profile of v_{AB} produced by the five-level inverter with phase- and level-shifted modulation schemes.

The table IV shows the effect of dead time on THD of the inverter output voltage. The THD increased with the increased dead time but only at a very small fraction.

TABLE IV
PERCENT THD OF V_{AB} AFFECTED BY THE DEAD TIME

		Modulation Index : m_a									
	dead time	0.1	0.2	0.3	0.4	0.5	0.6	0.7	0.8	0.9	1.0
Phase-shifted	1μs	134.97	116.13	88.71	57.60	28.40	8.19	17.98	24.29	23.39	18.92
	2μs	135.10	116.43	89.10	58.01	28.74	8.19	17.79	24.25	23.45	19.01
	4μs	135.36	117.02	89.88	58.84	29.43	8.22	17.41	24.16	23.57	19.20
IPD	1us	55.95	43.67	26.57	12.96	19.78	8.05	9.73	9.61	5.69	7.64
	2μs	56.13	43.85	26.80	13.04	19.58	8.10	9.67	9.69	5.75	7.56
	4μs	56.46	44.24	27.25	13.21	19.19	8.23	9.55	9.82	5.90	7.38
POD	1μs	134.95	116.12	88.70	57.60	28.42	30.08	34.89	34.06	27.49	17.44
	2μs	135.07	116.42	89.09	58.00	28.73	29.96	34.82	34.07	27.60	17.59
	4μs	135.07	116.45	89.06	58.04	28.72	8.25	17.77	24.18	23.41	18.98
APOD	1μs	134.95	116.16	88.67	57.64	28.42	8.25	17.96	24.22	23.34	18.88
	2μs	135.32	117.00	89.87	58.83	29.37	29.71	34.67	34.07	27.80	17.88
	4μs	135.33	117.03	89.83	58.85	29.35	8.28	17.39	24.09	23.53	19.17

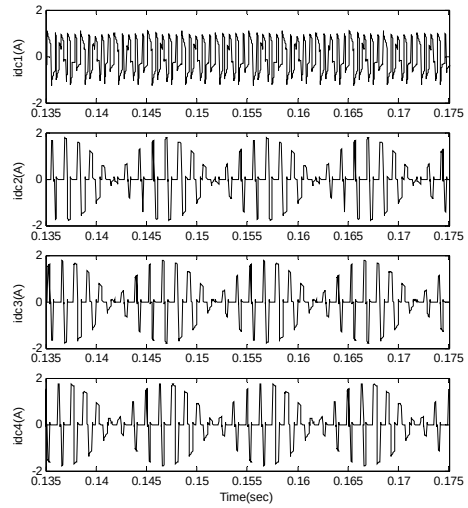

(a) Incase of phase-shifted PWM scheme.

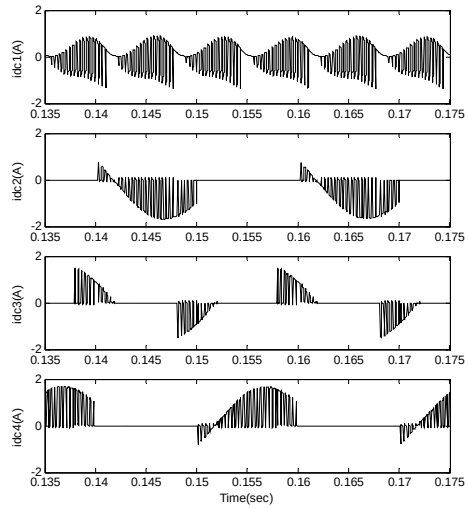

(b) Incase of IPD PWM scheme.

Figure 8. Waveforms of the current flowing through the flying capacitors.

Fig. 8 shows the current flowing through each flying capacitor. In case of phase-shifted PWM scheme the currents flowing in the flying-capacitors are balanced, i.e. the average current is zero. In case of IPD PWM scheme, the currents flowing through the flying-capacitors are not balanced, resulting in a non-zero average current. If no energy source is connected to the flying-capacitor; this would result in uneven level of the output voltage.

CONCLUSION

Simulations of flying-capacitor multilevel inverter have been carried out using phase-shifted and level-shifted PWM schemes. The results of the simulation are compared. The IPD PWM scheme provided the lowest output voltage THD over the range of modulation index. However it could not balance the energy flow of the flying-capacitors and could lead to uneven level of the output voltage. The phase-shifted PWM scheme, while providing a higher output voltage THD, it is capable of balancing the energy flow of the flying-capacitors. Both features, low THD and capacitor energy balancing, could not be attained at the same time by both modulation schemes.

Regarding to the THD performance, IPD PWM scheme will be suitable for adjustable speed-drive application, where full range of modulation is required. Balancing of the capacitor energy under IPD PWM scheme using a technique introduced in [4] as well as other techniques will be reported in the future.

REFERENCES

[1] L. Tolbert, F.-Z. Peng, and T. Habetler, "Multilevel converters for large electric drives," *IEEE Trans. Ind. Applicat.*, vol. 35, pp. 36-44, Jan./Feb. 1999.

[2] F. Zheng Peng, J. Rodriguez, and J. Sheng Lai ,Multilevel Inverter: A Survey of Topologies, Control and Application, *IEEE Trans. Ind. Applicat.*, Vol. 49, No. 4, August 2002.

[3] Bin Wu, *High-Power Converters and ac Drives*, The Institute of Electrical and Electronics Engineerings, Inc., 2006, pp.127-136.

[4] F. Z. Peng and J. S. Lai, "Dynamic performance and control of a static VAR generator using cascade multilevel inverter," *IEEE Trans. Ind. Applicat.*, vol. 33, pp. 748=755, May/June 1997.

A New Online Control Method for Multicell Converter Based on Duty Cycle Control

Seyed Hossein Hosseini[1], M. Almaleki [2]

[1]Electrical Engineering Department, Islamic Azad University of Bonab, Bonab, Iran,
(Tel/Fax: +98-411-3300819; Email: hosseini@tabrizu.ac.ir)
[2] Faculty of Electric & Electronic Engineering., University of Tabriz, Tabriz, IRAN

Abstract— **A new online controller based on duty cycle control is presented. The novel control method is based on optimal control theory. The average model of converter has been used to implement the optimal controller. Also In order to acquire the average model of converter a new solution, based on the step-by-step calculation of state variables in each interval of a switching period, is presented. The approximated discrete model of converter is used to get the average model of inverter. The new proposed algorithm will control the converter's flying capacitor voltage and load current very fast and very precise. By application of this controller, the converter will be capable to track very sharp changes of reference signal. Simulation is performed by using *PSCAD/EMTDC* software.**

Keywords- Multicell converter; optimal controller;

I. INTRODUCTION

MULTICELL Converters are the new generation of high power and high voltage converters, which have been introduced, in the early 1990s. Multicell Converters, make it possible to distribute the voltage constraints among series-connected switches and to improve the output waveforms by increasing the number of levels and switching frequency. An important advantage of this circuit lies in having multiple switching combinations for the same output voltage level then they are flexible for controlling purposes**.** Under certain conditions, a simple open-loop control guarantees natural balancing of the flying voltages. Nevertheless, in this case, the dynamics involved in the balancing transient depend on the impedance of load at the switching frequency. If the impedance at the switching frequency is high (small current harmonic at this frequency) then the natural balancing is very slow and inversely. However to get the best performances, the strict conditions of interleaved patterns will not be obeyed and self-balancing will not be obtained. [1], [2]. Some efficient active control strategies, based on the feedback linearization of the nonlinear state equation of the converter, have been introduced in [2], to control the voltage of flying capacitors and output waveforms. The proposed controller algorithm will result some equations, which are very similar to the relations of the feedback linearization method described in [2]. In this paper a simple online controller is presented that controls the state variables of a Multicell inverter very fast and very precise. The $2\pi/n$ phase shift between firing angle of adjacent cells is neglected in this paper, and The main idea of the novel controller is based on optimal control theory.

II. MODELLING OF MULTICELL CONVERTERS

There are three different mathematical model used to represent a Multicell converter [3].

1) Direct or Instantaneous model
2) Average Model
3) Harmonic Model

The instantaneous model contains state variables of system including voltage of flying capacitors and the current of load inductor for any switching condition. The instantaneous model of a Multicell converter is as below:

$$\dot{V}_{c1} = \dot{X}_1 = \frac{S_2 - S_1}{C} X_2 \tag{1}$$

$$\dot{i}_L = \dot{X}_2 = \frac{S_1 - S_2}{L} X_1 + \frac{S_2 - 0.5}{L} E - \frac{R.X_2}{L} \tag{2}$$

$\boldsymbol{S_1}$ and $\boldsymbol{S_2}$ are the state of the switches and are defined as follow:

$$S_i = \begin{cases} 0 & if \quad S_{id} \quad is \quad conducting \\ 1 & if \quad S_{iu} \quad is \quad conducting \end{cases} \qquad i = 1,2 \tag{3}$$

$$\underline{X}(t) = \begin{bmatrix} X_1(t) \\ X_2(t) \end{bmatrix} \quad , \quad \underline{S}(t) = \begin{bmatrix} S_1(t) \\ S_2(t) \end{bmatrix} \tag{4}$$

By defining the $\boldsymbol{S_i}$ as input controlling signals then the controller must generate such a firing signals with proper duty cycle that the flying capacitor voltages remain at a specified DC voltage level and the waveform of the load current tracks a reference waveform.

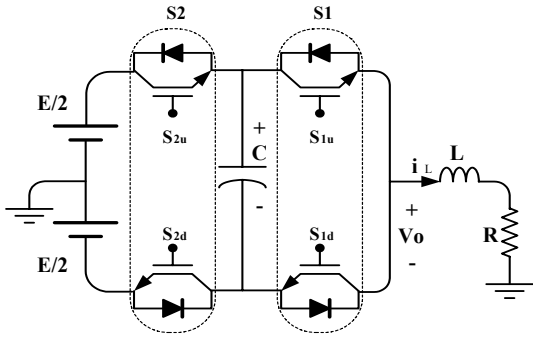

Figure 1. Multicell inverter configuration.

III. PRINCIPLE OF OPERATION OF THE DUTY CYCLE CONTROL METHOD

The main idea of the novel online controller is based on the step-by-step calculation of state variables in each time intervals (fig. 2) within switching periods by using an approximated discrete model of inverter. An approximated discrete model of inverter can be shown as follow:

$$\dot{\underline{X}}(t) = \underline{f}(\underline{X}(t), \underline{S}(t)) \tag{5}$$

$$\underline{X}(t+\Delta t) \approx \underline{X}(t) + \underline{f}(\underline{X}(t), \underline{S}(t)).\Delta t \tag{6}$$

$$\underline{X}([k+1]\Delta t) \approx \underline{X}(k\Delta t) + \underline{f}(\underline{X}(k\Delta t), \underline{S}(k\Delta t)).\Delta t \tag{7}$$

$$\underline{X}(k+1) \approx \underline{X}(k) + \underline{f}(\underline{X}(k), \underline{S}(k)).T \tag{8}$$

For example in the first time interval $kT < t < (k+D_1)T$ with a known value of $\underline{X}(k)$, $\underline{S}(k)$ and using (8) we can calculate the value of $\underline{X}(k+D_1)$ at the end of that time interval. And by successive calculations through entire switching period we can calculate the value of $\underline{X}(k+1)$ as a function of $\underline{X}(k)$, D_1, D_2.

1. $kT < t < (k+D_1)T \quad S_1 = 1 \quad S_2 = 1$

$$\begin{bmatrix} V_c(k+D_1) \\ i_L(k+D_1) \end{bmatrix} = \begin{bmatrix} V_c(k) \\ i_L(k) \end{bmatrix} + \left[\underline{f}(\underline{X}(k), \underline{S}(k)\right] \tag{9}$$

Or

$$\begin{bmatrix} V_c(k+D_1) \\ i_L(k+D_1) \end{bmatrix} = \begin{bmatrix} V_c(k) \\ (1 - RD_1T/L) * i_L(k) + (D_1T/2L) * E \end{bmatrix} \tag{10}$$

2. $(k+D_1)T < t < (k+D_2)T \quad S_1 = 0 \quad S_2 = 1$

$$\begin{bmatrix} V_c(k+D_2) \\ i_L(k+D_2) \end{bmatrix} = \begin{bmatrix} V_c(k+D_1) \\ i_L(k+D_1) \end{bmatrix} + \left[\underline{f}(\underline{X}(k+D_1), \underline{S}(k+D_1)\right] \tag{11}$$

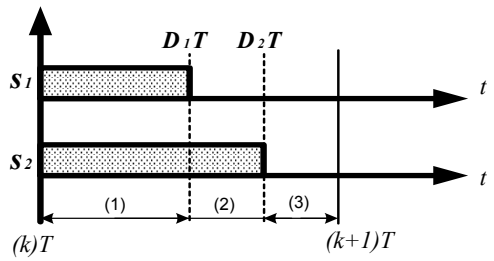

Figure 2. Time intervals created by duty cycles of switches.

$$\begin{bmatrix} V_c(k+D_2) \\ i_L(k+D_2) \end{bmatrix} = \begin{bmatrix} V_c(k) + \dfrac{(D_2 - D_1)T}{C} i_L(k) \\ (1 - \dfrac{RD_2T}{L}) i_L(k) + (\dfrac{(D_1 - D_2)T}{L}) V_c(k) + \dfrac{D_2T}{2L} E \end{bmatrix} \tag{12}$$

We have neglected the T^2, T^3, ... because T is a small number.

3. $(k+D_2)T < t < (1+k)T \quad S_1 = 0 \quad S_2 = 0$

$$\begin{bmatrix} V_c(1+k) \\ i_L(1+k) \end{bmatrix} = \begin{bmatrix} V_c(k+D_2) \\ i_L(k+D_2) \end{bmatrix} + \left[\underline{f}(\underline{X}(k+D_2), \underline{S}(k+D_2)\right] \tag{13}$$

Or

$$\begin{bmatrix} V_c(1+k) \\ i_L(1+k) \end{bmatrix} = \begin{bmatrix} V_c(k) + \dfrac{(D_2 - D_1)T}{C} i_L(k) \\ (1 - \dfrac{RT}{L}) i_L(k) + (\dfrac{(D_1 - D_2)T}{L}) V_c(k) + \dfrac{(D_2 - 0.5)T}{L} E \end{bmatrix} \tag{14}$$

Now we can rearrange (14) as follow:

$$\begin{bmatrix} V_c(1+k) \\ i_L(1+k) \end{bmatrix} = \begin{bmatrix} V_c(k) \\ (1 - \dfrac{RT}{L}) i_L(k) - \dfrac{T}{2L} E \end{bmatrix} + \begin{bmatrix} -\dfrac{T}{C} i_L(k) & \dfrac{T}{C} i_L(k) \\ \dfrac{T}{L} Vc(k) & -\dfrac{T}{L} Vc(k) + \dfrac{TE}{L} \end{bmatrix} \begin{bmatrix} D_1 \\ D_2 \end{bmatrix} \tag{15}$$

As figure 3 shows, in order to minimize J we must hold the following conditions:

$$\text{Minimize } J = \frac{1}{2} \|\underline{X}(k+1) - \underline{ref}(k+1)\|^2 = \theta[X_{k+1}] \tag{16}$$

$$\text{Subjected to: } X_{k+1} = f(X_k, S_k) \tag{17}$$

By defining the *Lagrange* function as follow we must have (18), (19) to guarantee (16):

$$L = \theta[X_{k+1}] + \lambda_{k+1}{}^T (-X_{k+1} + f(X_k, S_k)) \tag{18}$$

$$\frac{\partial L}{\partial X_{k+1}} = 0 \quad \Rightarrow \quad \lambda_{k+1}{}^T = \frac{\partial \theta[X_{k+1}]}{\partial X_{k+1}} \tag{19}$$

$$\frac{\partial L}{\partial S_k} = 0 \quad \Rightarrow \quad \lambda_{k+1}{}^T \frac{\partial f(X_k, S_k)}{\partial S_k} = 0 \tag{20}$$

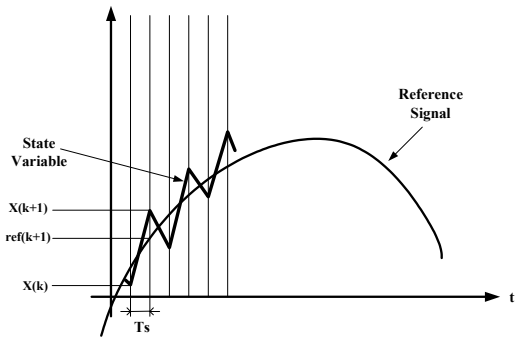

Figure 3. Tracking a reference signal by State Variable.

One apparent answer of the above equation is as follow:

$$\lambda_{k+1}{}^{T} = 0 \qquad \Rightarrow \quad \underline{X(k+1)}=\underline{ref(k+1)} \qquad (21)$$

By using (15), (21) it is possible to calculate the duty cycles.

IV. Simulation Results

By applying the controller to a 2-cell inverter with the following parameters values, the state variable waveforms are derived by using *PSCAD/EMTDC* software.

E=200kV, C=40 μ f, L=5mH, R=12 Ω , T_s=40 μ s

A. Changes in the Load Current reference signal without any changes in the capacitor reference voltage.

At the first section of simulation we will verify the capability of the controller in the tracking the sharp changes only in load current reference signal. The capacitor voltage must remain at the E/2 in order to balance the voltage consideration of the power devices.

Figure 4 shows a typical reference signal. In figure 5 the load current is presented. The ripple of the load current is negligible and controller tracks the sharp changes of the reference signal in a very short time. Also the duty cycles of switches S1, S2 are presented in figure 7. At the steady state condition the duty cycles are equal and have same waveform as the load reference current.

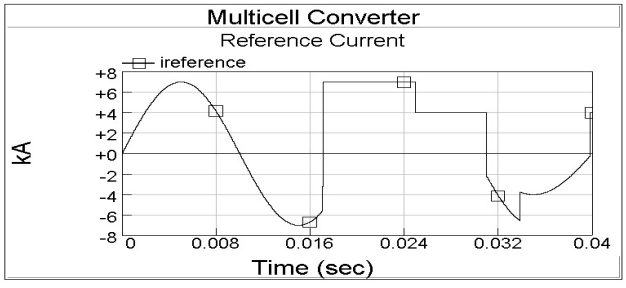

Figure 4. Load Reference Current.

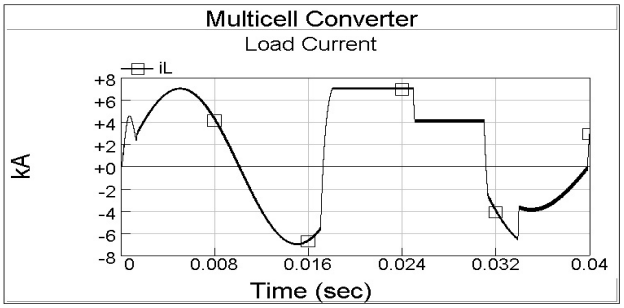

Figure 5. Load Current.

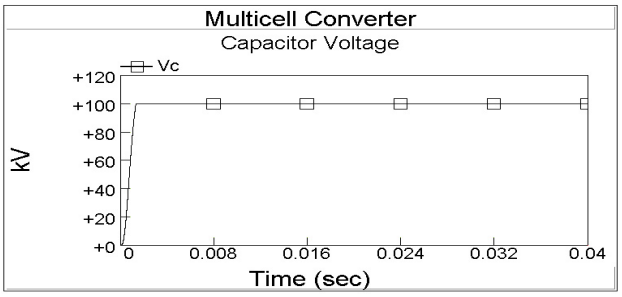

Figure 6. Capacitor Voltage.

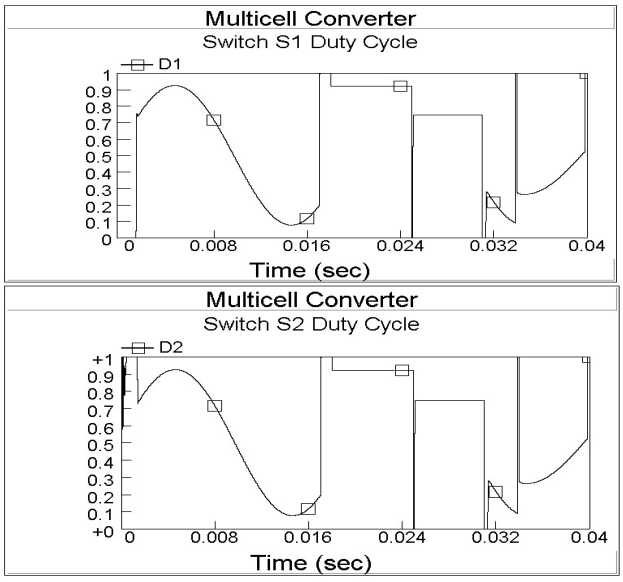

Figure 7. Switches Duty Cycle.

B. Changes in both flying Capacitor reference voltage and load current reference signal.

In this section we will verify the efficiency of the controller under more complex situation. The reference signal changes will apply to the both load current and flying capacitor voltage reference signals.

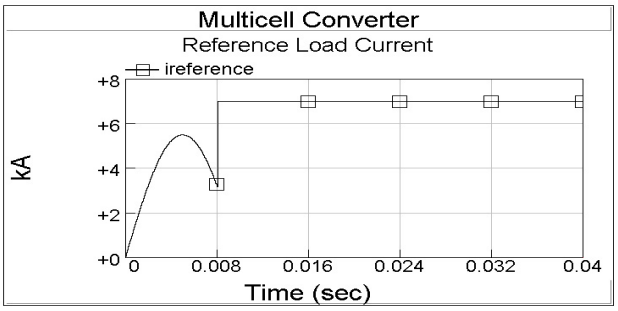

Figure 8. Load Reference Current.

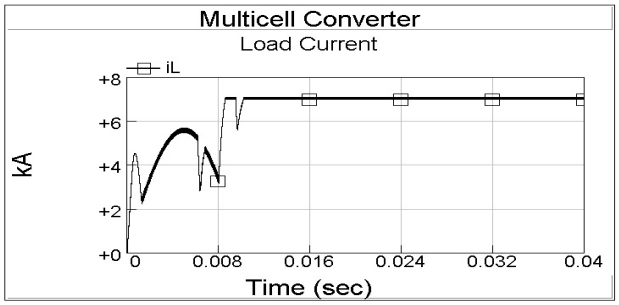

Figure 9. Load Current.

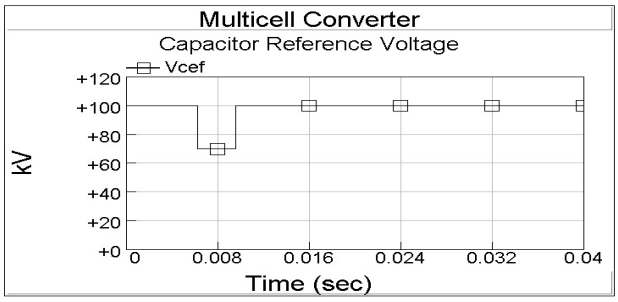

Figure 10. Capacitor ReferenceVoltage.

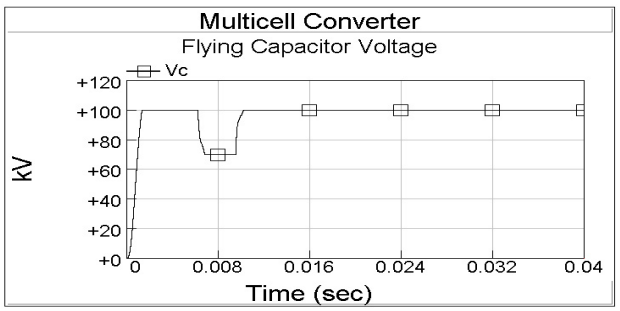

Figure 11. Capacitor Voltage.

It is desired that the state variables track the reference signals. Figures 8-11 prove the efficiency of the controller in tracking the reference signals.

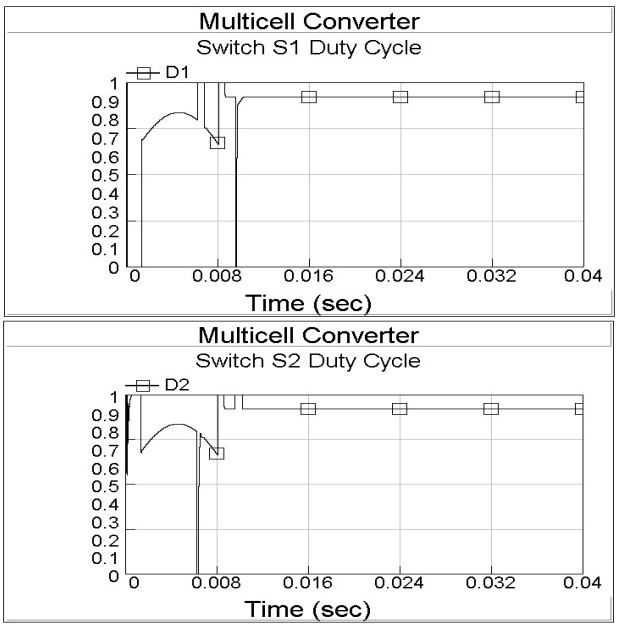

Figure 12. Switches Duty Cycle

V. CONCLUSION

A simple controller is introduced to control the state variables of a Multicell converter. The proposed controller tracks the reference signal changes very fast. Also it has a good response in the presence of the sharp changes in both load current and capacitor voltage reference signals.

REFERENCES

[1] R. Ruelland, G. Gateau, T. A. Meynard, J. Hapiot, "Design of FPGA-Based Emulator for Series Multicell Converters Using Co-Simulation Tools" *IEEE Trans. Power. Electron,*vol. 18, no. 1, January 2003, pp. 455-463.

[2] G. Gateau, M. Fadel, P. Maussion, R. Bensaid, T. A. Meynard, "Multicell Converters: Active Control and Observation of Flying-Capacitor Voltages" *IEEE Trans. Ind. Electron* vol. 49, no.5, October, 2002, pp. 998-1008.

[3] R. H. Wilkinson, T. A. Meynard, H. T. Mouton, "Voltage Unbalance in The Multicell Converter Topology," in Proceedings of the *IEEE Africon 2002*, 0-7803-7570-X/02, pp. 759-764.

[4] T. A. Meynard, H. Foch, P. Thomas, J. Courault, R. Jakob,M. Nahrstaedt, "Multicell Converters: Basic Concepts and Industry Applications" *IEEE Trans. Ind. Electron*, vol., 49, no.5, October, 2002, pp. 955-964.

A High-Frequency Induction Cooker using Quasi-resonant Converter

Saichol Chudjuarjeen[1] and Chayant Kumpai[2]
[1]Department of electrical engineering, Rajamangala University of Technology Krungthep.
[2]Department of electrical engineering, King Mongkut's University of Technology Thonburi.

Abstract-**The paper describes an induction cooker using a quasi-parallel resonant converter. Converter is implemented by using IGBT as its switching. The switching loss is minimized by operating the IGBT in the zero voltage resonance modes. The output power can be adjust by varying the switching frequency of converter. The prototype is rated at approximately 650 W, with operating frequency ranging from 25-31 kHz. It can heat the water about 0.5 liters from room temperature to approximately $100°C$ within 6 minutes with the input power factor about 0.99.**

I. INTRODUCTION

The principles of induction heating are used in various applications such as brazing, surface hardening, forming and annealing. Each application uses different appropriate frequency [3]. The induction cooking is one of many applications for induction heating. It is designed to replace common stove plates. The advantages of induction cooking are the plate stays cool when the vessel is heated and less energy is used for cooking.

Inverter topology commonly used for induction cooking is the half-bridge inverter topologies [4], [6]. But it has some demerit as the half-bridge inverter requires two switching circuit, the overall working process becomes more complicated and the size of the heat sink and PCB should also be larger. In addition, the gate operating circuits must be isolated. Due to the induction cooking is the high cost compared to a conventional stove plate. So the quasi-resonant converter is another choice in induction cooking application because it needs only one switching circuit inside. This enables a relatively smaller design for the heat sink and PCB making the working process simple and its ground of circuit and control circuit can be shared.

This paper describes the quasi-parallel resonant converter for induction cooking application. It operates in zero voltage switching modes. The operation principles of quasi-parallel resonant circuit are investigated and validity is verified by experimental results.

II. PRINCIPLE OF INDUCTION COOKING

The induction coil is connected to a medium- frequency (20-100 kHz) power source producing an alternating magnetic field, which causes eddy currents to occur at the bottom of vessel and these give rise to the heating effect.

Since the spiral current flows at the heating coil side only the bottom of the vessel according to the skin effect, the current value depends on the skin depth as well as on the specific resistance of the vessel material.

Skin depth δ is determined by the vessel-specific resistance ρ , relative magnetic permeability μ_r, and frequency f, as shown in the expression below.

$$\delta = \sqrt{\frac{\rho}{\pi \mu f}} \tag{1}$$

The pan skin resistance R_s is determined by the pan skin depth and specific resistance, as shown in the expression below.

$$R_s = \frac{\rho}{\delta} = \sqrt{\frac{\rho \omega \mu}{2}} \tag{2}$$

The parameter of induction heating load (induction coil and vessel) depend on several variables including the shape of the heating coil, the space between the work-piece and coil, their electrical conductivities and magnetic permeabilities, and the frequency [3].

III. CIRCUIT DESCRIPTION AND OPERATION

The main power circuit features a quasi-resonant converter as in Fig. 1 It consists of full bridge rectifier diode, a bus filter (L1, C1), the IGBT and a diode connected to it in parallel. The resonant circuit is comprised of resonant inductor Lr, and a resonant capacitor Cr.

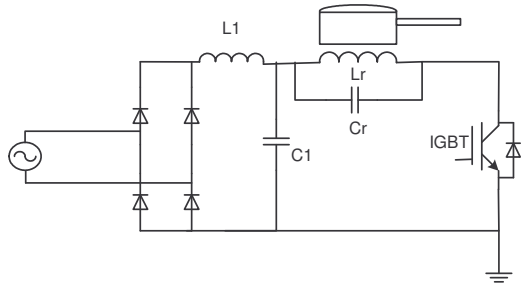

Figure 1. Equivalent circuit of each mode of operation.

A. *Converter operation*

The quasi-resonant converter has four operating modes. The ideal waveform and equivalent circuit of each mode are shown

in Fig. 2 and Fig. 3, respectively. It assumed that all components are ideal. The operations of each mode are explained as following

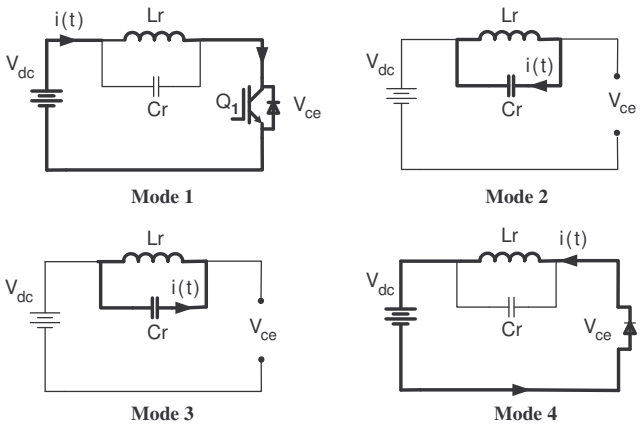

Figure 2. Equivalent circuit of each mode of operation.

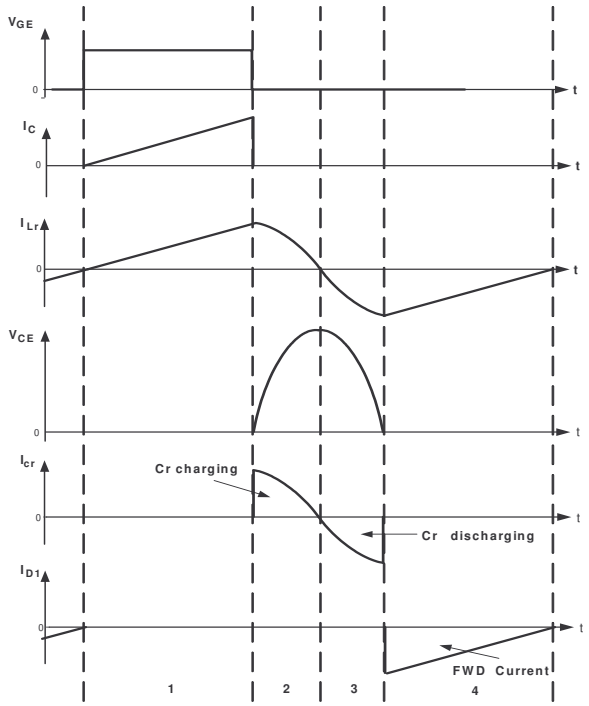

Figure 3. Ideal waveform of quasi-resonant converter.

The operations of each mode are explained as following:

Mode 1: Switch Q_1 is turn on by V_{GE}. Current is biased in the forward direction between the collector and emitter of Q_1. The current flows in the right direction through L_r. The inductor starts to store the energy which makes it possible to do a zero voltage turn-on switching.

Mode 2: when the switch Q_1 is turned off, the current keeps incrementing to reach its maximum at t0. At this point, the energy stored in L_r move to C_r.

Mode 3: Conversely with mode 2. After the current decrease to zero where the voltage S1 reaches its maximum. C_r starts discharging the energy to L_r, which causes the current flowing in inverse to decrement.

Mode 4: In this mode the voltage of L_r converted to polarity and exceeded the voltage at V_{dc}. The current of L_r flows through diode until this current reach the zero.

The used IGBT's is from International rectifier and IRGPH4UD device. The photo coupler TLP250 is used to drive gate of IGBT. To drive the gate of IGBT on at voltage +15 V this is a suitable value to minimize losses. When IGBT is drive off -5V, self-conduction due to external noise is prevented.

B. Filter

The quasi-resonant converter takes the energy from the mains voltage, which is rectified by a full bridge of diodes. A bus filter is designed to allow a big voltage ripple getting a consequence input power factor near to one.

C. Heating coil and load

The coil is a flat pancake with litz wire in order to reduce the losses due to skin effect. The pancake coil is placed underneath a conductive cooking vessel with a thermal insulator between them. The ferrite plates beneath the coil with the work piece (a stainless vessel used for cooking) are intended to obtain a proper shaping of the magnetic field. A thermal insulator is placed underneath stainless vessel to prevent coil damage by heat. The heating coil is air cooled to circulate heat away from it. Fig. 4 represents the equivalent circuit model of the heating coil and stainless vessel. The induction heating load parameters (R_L and L_r) depend on the inverter operating frequency, the position of the load, the distance between the heating coil and vessel. The parameters R_L and L_r are respectively 4.3 Ω and 120 μH. [3]

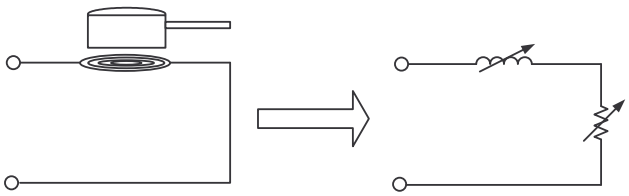

Figure 4. Equivalent circuit model of the heating coil and load.

D. Quasi-resonant Capacitor

The operating frequency is selected at 26 kHz. We can calculate $L_s = 120\,\mu H$ from parameter of induction coil [3].We can select the capacitor which will connect with parallel induction coil for required interval by $C = 1/(\omega^2 Lp) = 0.3\,\mu F$.

IV. Experimental Results

A prototype is built and tested by feeding heat to a stainless vessel which contains water about 0.5 liters. The AC input voltages was 200 V_{rms}. The resonant frequency was about 26.5 kHz. All measured signals are taken at around $100°C$ water temperature.

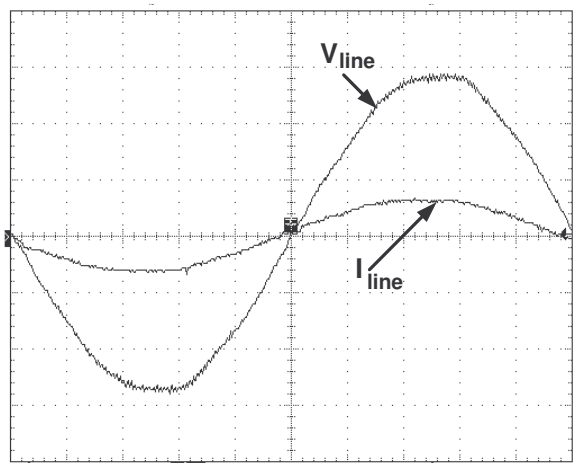

Figure 5. Experimental waveforms of line voltage and line current. (I: 10 A/div, V: 100 V/div and Time: 2ms/div.)

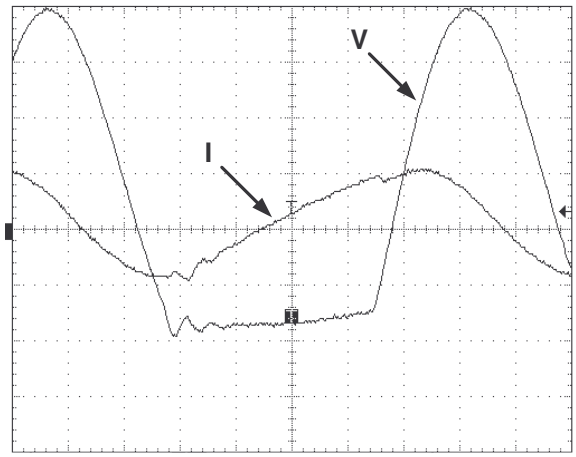

Figure 6. The voltage and current waveform of induction coil. (I: 10 A/div, V: 200 V/div and Time: 5 μs / div.)

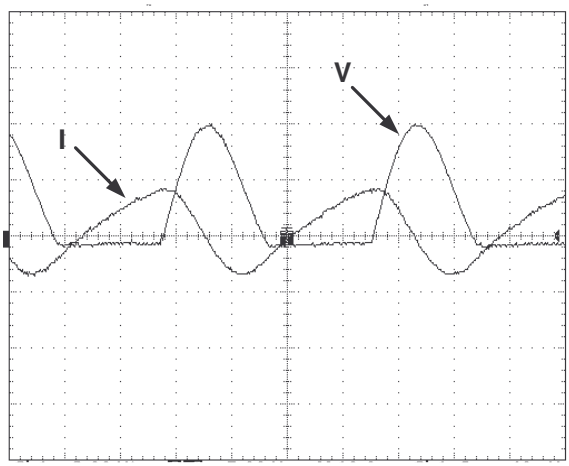

Figure 7. The voltage waveform across IGBT and coil current waveform. (I: 10 A/div, V: 500 V/div and Time: 10 μs / div.)

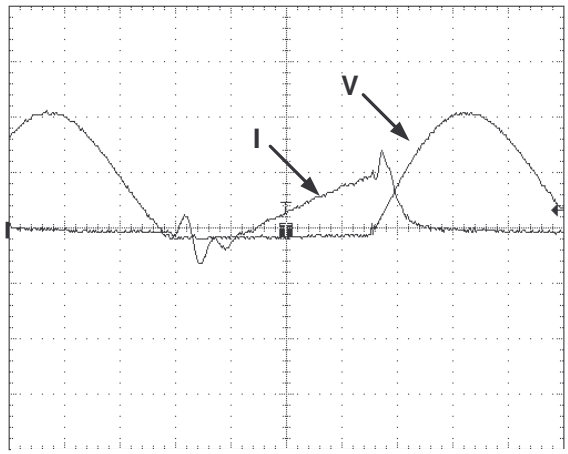

Figure 8. The voltage waveform and current waveform across IGBT. (I: 10 A/div, V: 500 V/div and Time: 5 μs / div.)

The experimental waveforms of line voltage and line current are shown as Fig. 5. The line current is in phase with line voltage without any sign of distortion at zero crossing. Fig. 6 shows the coil voltage and coil current waveforms. Fig. 7 shows the switching voltage across the IGBT and coil current waveform. Fig. 8 shows the voltage waveform and current waveform across IGBT at 25.6 kHz, it obvious that zero-voltage soft-switching and no current spikes. Fig. 9 shows the voltage and current waveform of induction coil where measured at 2 ms/div. Fig. 10 shows the relative graph of input power and operating frequency. The parameters of induction coil are varied by adjust switching frequency. In this reason, input power decreased due to increasing parameters of induction coil.

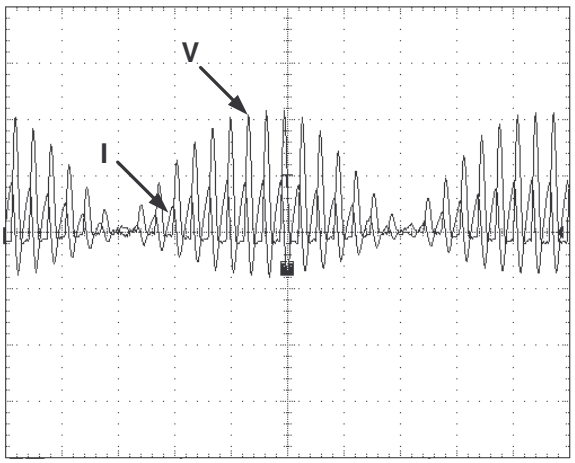

Figure 9. The voltage and current waveform of induction coil where measured in 2 ms/div. (I: 10A/div, V: 500V/div and Time: 2ms/div.)

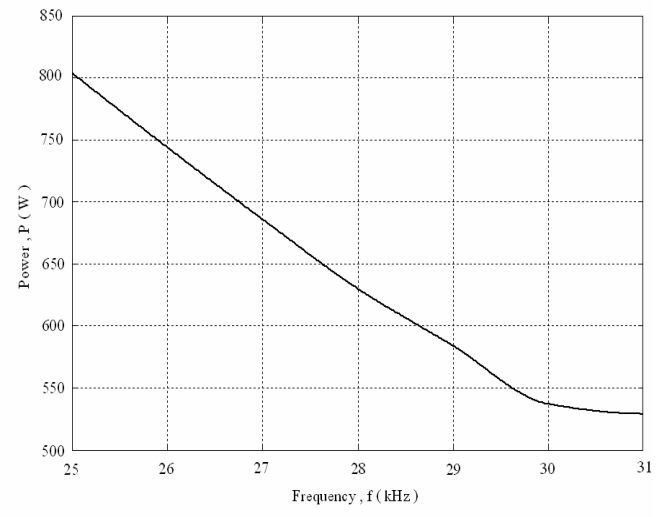

Figure 10. The relative graph of input power and operating frequency

V. CONCLUSION

The induction cooker has been built with quasi-parallel resonant converter. It can heat the water about 0.5 liters which contain in a stainless vessel from room temperature to approximately 100 $^{\circ}C$ within 6 minutes. The switching loss is minimized by operating the IGBT in the zero voltage resonance modes in order to avoid a high current. This converter topology is simple because it has low number of components. But its IGBT switch must withstand high voltage.

REFERENCES

[1] E.J. Davies, J. and Simpson, P., 1979, Induction Heating Handbook, McGraw-Hill, UK.

[2] M. Kamli, S. Yamamoto, and M. Abe, "A 50-150 kHz Half-Bridge Inverter for induction heating Application," *IEEE Transactions on Industrial Electronics,* Vol. 43,February 1996. pp. 163-172

[3] Chudjuarjeen, S., Koompai, C.and Monyakul, "Full-bridge current-fed inverter with automatic frequency control for forging application", *IEEE Power electronics Specialist Conference*, Vol. 4, pp.128-131, Nov. 2004

[4] Viriya, P.; Sittichok, S.; Matsuse, "Analysis of high-frequency induction cooker with variable frequency power control", *IEEE Power electronics Specialist Conference*, Vol. 3, pp.1502-1507, April 2002

[5] C. Chuenwattanapraniti, C. koompai and V. Monyakul,, "Half-Bridge Current Fed Inverter Power Supply for Forging Application," *25th Electrical Engineering Conference*, pp. 97 – 101, 2002

[6] S. Phrommearn, and P. Viriya, "Half-Bridge Current Fed Inverter Power Supply for Forging Application," *26th Electrical Engineering Conference*, pp. 823 – 828, 2003

[7] Dieckerhoff, S, Ruan, M.J, De Doncker, R.W. "Design of an IGBT-based LCL-Resonant Inverter for High-Frequency Induction Heating", *IEEE Conference on Industry Applications,* Vol. 3, pp. 2039 – 2045, Oct.1999

[8] F.P Dawson and P. Jain, "Systems for Induction heating and Melting applications a comparison of load commutated Inverter", *Power Electronics Specialists Conference,* pp.281 – 290, June 1990

New Method in Nonlinear State Estimation Single Machine Infinite Bus

Dr Heydar Toossian Shandiz, Ahmad Hajipoor
Shahrood University of Technology, Electrical Engineering Faculty
7 Th Tir Square, P.o.Box 36155-316, Shahrood, IRAN
htshandiz@shahroodut.ac.ir, hajjipoor@yahoo.com

***Abstract*- Using two new filters in which Jacobian is replaced by divided difference for nonlinear state estimation single machine infinite bus is proposes. Simulation result shows the performance is comparable with extended Kalman filter, which is used normally for on-line assessment of power system dynamic stability of single-machine infinite-bus system.**

I. INTRODUCTION

In a practical power system, not only the state variables can not be measured directly, but also unexpected disturbances and inaccuracy in the system model would prevent the exact prediction of system states. Therefore, the system states should be monitored to ascertain a compliance with the desired operation of the system. In a stochastic system, state estimation provides the necessary feedback to allow reliable control of the system. Modern state estimation algorithms have recently been applied to power systems. Naggar uses an estimation procedure to estimate the asymmetrical components of power system [1]. C. Madtharad et all [2] use a weighted least square estimation technique, which is based on singular value decomposition. Feilat and et all [3] use Kalman filter as a powerful estimation tool to estimate synchronizing and damping torque coefficients in order to determine dynamic stability [4,5]. Miller and Lewis [6] use a linear Kalman filter to estimate dynamic states of the power system [7,8].
In this work, using two new filters as DD1 and DD2 are proposed and tested.

II. PROBLEM FORMULATION

The system under study is shown in Figure 1. The system comprises a steam- generator connected via a tie-line to a large system represented as an infinite bus.

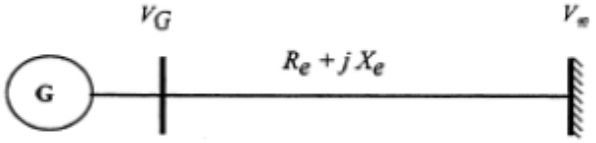

Figure 1. Single machine infinite bus system

For the power system shown in Figure 1, the seventh- order nonlinear dynamic model can be written as follows [9]:

$$\dot{x} = Ax + Bu + N(x)$$

$$y = \begin{bmatrix} x_1 \\ x_2 \\ y_{1q}x_3x_6 + y_{3q}x_3x_7 - y_{1d}x_6x_3 - y_{4d}x_6x_4 - y_{5d}x_6x_5 \end{bmatrix} \quad (1)$$

Where $N(x)$ is the nonlinear term,

$$x = [\delta \;\; \omega \;\; \omega_0\varphi_d \;\; \omega_0\phi_f \;\; \omega_0\phi_D \;\; \omega_0\phi_q \;\; \omega_0\phi_Q]^T$$

is the state vector and

$$u = [T_m \;\; v_f]^T = [u_1 \;\; u_2]^T$$

is the control vector. The relation between fluxes and currents are as follows:

$$\begin{bmatrix} \omega_0\phi_d \\ \omega_0\phi_f \\ \omega_0\phi_D \end{bmatrix} = \begin{bmatrix} -X_d & X_{md} & X_{md} \\ -X_{md} & X_f & X_{md} \\ X_{md} & X_{md} & X_D \end{bmatrix} \begin{bmatrix} i_d \\ i_f \\ i_D \end{bmatrix} \quad (2)$$

and

$$\begin{bmatrix} \omega_0\phi_q \\ \omega_0\phi_Q \end{bmatrix} = \begin{bmatrix} -X_q & X_{mq} \\ X_{mq} & X_Q \end{bmatrix} \begin{bmatrix} i_q \\ i_Q \end{bmatrix} \quad (3)$$

by inversing these two equations we have:

$$\begin{bmatrix} i_d \\ i_f \\ i_D \end{bmatrix} = \begin{bmatrix} y_{1d} & y_{4d} & y_{5d} \\ y_{4d} & y_{2d} & y_{6d} \\ y_{5d} & y_{6d} & y_{3d} \end{bmatrix} \begin{bmatrix} \omega_0\phi_d \\ \omega_0\phi_f \\ \omega_0\phi_D \end{bmatrix} \quad (4)$$

and

$$\begin{bmatrix} i_q \\ i_Q \end{bmatrix} == \begin{bmatrix} y_{1q} & y_{3q} \\ y_{3q} & y_{2q} \end{bmatrix} \begin{bmatrix} \omega_0\phi_q \\ \omega_0\phi_Q \end{bmatrix} \quad (5)$$

In the above equations, the indexes q and Q refer to the quadrature and Damper Q on the q-axis of stator; and, d, D and f refer to the direct, damper D and field exciter on the d-axis of stator, respectively [9].

III. STATE ESTIMATION FOR NONLINEAR SYSTEMS

We have now arrived at the central issue of this note, namely state estimation for nonlinear systems. Two new filters will be suggested that are based on the derived polynomial approximations [10]. The filters are fundamentally different from filters based on Taylor approximations in that the polynomial approximations underlying the new filters take into account the uncertainty on the state estimate. The Taylor approximation underlying conventional filter designs for nonlinear systems, such as The EKF, depends only on the current state estimate and not on its variance. The new filters can generally be implemented more easily as no derivatives are required.

The first filter we shall derive is based on a first-order polynomial approximation. This estimator is a generalized version of the filter presented in [11]. Subsequently, a more accurate filter will be derived that also includes second –order terms. It turns out that this filter has certain similarities with the unscented filter described in [12], [13].

IV. THE DD1 FILTER

In this section a generalized version of the nonlinear state estimation scheme suggested in [11] will be described. The filter is derived by employing the first-order approximation presented in [10]. Basically, this corresponds to the extended Kalman filter (EKF) except that the Jacobian is replaced by divided differences. The state update is therefore the same as in the EKF. The difference is alone found in the update of the various covariance matrices. Generally, they can be implemented more easily. First we will introduce the following four square Cholesky factorization

$$\begin{aligned} Q &= S_v S_v^{\,T} & R &= S_w S_w^{\,T} \\ \overline{P} &= \overline{S}_x \overline{S}_x^{\,T} & \hat{P} &= \hat{S}_x \hat{S}_x^{\,T} \end{aligned} \tag{6}$$

Let the jth column of $\overline{S}_x$ be denoted $\overline{s}_{x,j}$ and vice versa for the other factors. Four matrices containing divided differences are defined by

$$\begin{aligned} S_{x\hat{x}}^{(1)}(k) &= \left\{S_{x\hat{x}}^{(1)}(i,j)\right\} = \{(f_i(\hat{x}_k + h\hat{s}_{x,j}, u_k, \overline{v}_k) \\ &- f_i(\hat{x}_k - h\hat{s}_{x,j}, u_k, \overline{v}_k))/2h\} \end{aligned}$$

$$\begin{aligned} S_{xv}^{(2)}(k) &= \left\{S_{xv}^{(1)}(i,j)\right\} = \{(f_i(\hat{x}_k, u_k, \overline{v}_k + hs_{v,j}) \\ &- f_i(\hat{x}_k, u_k, \overline{v}_k - hs_{v,j})/2h\} \end{aligned}$$

$$\begin{aligned} S_{y\bar{x}}^{(1)}(k) &= \left\{S_{y\bar{x}}^{(1)}(i,j)\right\} = \{(g_i(\overline{x}_k + h\overline{s}_{x,j}, \overline{w}_k) \\ &- g_i(\overline{x}_k - h\overline{s}_{x,j}, \overline{w}_k))/2h\}\} \end{aligned}$$

$$\begin{aligned} S_{yw}^{(1)}(k) &= \left\{S_{x\hat{x}}^{(1)}(i,j)\right\} = \{(g_i(\overline{x}_k, \overline{w}_k + hs_{w,j}) \\ &- g_i(\overline{x}_k, \overline{w}_k - hs_{w,j}))/2h\} \end{aligned} \tag{7}$$

V. THE DD2 FILTER

The DD2 filter obtained by using the estimates of mean and covariance derived in [10]. First we shall define four additional matrices containing divided differences:

$$S_{x\hat{x}}^{(2)}(k) = \left\{ \frac{\sqrt{h^2-1}}{2h^2} \begin{array}{l} (f_i(\hat{x}_k + h\hat{s}_{x,j}, u_k, \overline{v}_k) + \\ f_i(\hat{x}_k - h\hat{s}_{x,j}, u_k, \overline{v}_k) - 2f_i(\hat{x}_k, u_k, \overline{v}_k)) \end{array} \right\}$$

$$S_{xv}^{(2)}(k) = \left\{ \frac{\sqrt{h^2-1}}{2h^2} \begin{array}{l} (f_i(\hat{x}_k, u_k, \overline{v}_k + h\hat{s}_{x,j}) + \\ f_i(\hat{x}_k, u_k, \overline{v}_k - hs_{v,j}) - 2f_i(\hat{x}_k, u_k, \overline{v}_k)) \end{array} \right\}$$

$$S_{y\bar{x}}^{(2)}(k) = \left\{ \frac{\sqrt{h^2-1}}{2h^2} \begin{array}{l} (g_i(\overline{x}_k + h\overline{s}_{x,j}, \overline{w}_k) + \\ g_i(\overline{x}_k - h\overline{s}_{x,j}, \overline{w}_k) - 2g_i(\overline{x}_k, \overline{w}_k)) \end{array} \right\}$$

$$S_{y\bar{x}}^{(2)}(k) = \left\{ \frac{\sqrt{h^2-1}}{2h^2} \begin{array}{l} (g_i(\overline{x}_k, \overline{w}_k + hs_{w,j}) + \\ g_i(\overline{x}_k, \overline{w}_k - hs_{w,j}, \overline{w}_k) - 2g_i(\overline{x}_k, \overline{w}_k)) \end{array} \right\}$$

The priori update proceeding is the same as the DD1 filter.

VI. THE COMPLETE FILTER ALGORITHM

The following procedure outlines the implementation of the new filters.

1. Initialize

$$\overline{x}_0, \overline{P}(0), k = 0.$$

2. Compute

$$\overline{y}_k, S_{y\bar{x}}^{(1)}(k), S_{yw}^{(1)}(k), S_{y\bar{x}}^{(2)}(k), S_{yw}^{(2)}(k)$$

3. Compute P_{xy} according to and determine $S_y(k)$ using Houscholder Triangularization (HT).
4. Solve

$$K_k[\bar{S}_y(k)S_y(k)^T] = P_{xy}$$

for the Kalman gain. Since S_y is square and triangular only forward and back-substitutions are needed: First solve for

$$k' : k'S_y^T = P_{xy}$$

then solve for

$$K_k : K_k S_y = k'.$$

5. A posteriori update of the state estimate

$$\hat{x}_k = \bar{x}_k + K_k(y_k - \bar{y}_k).$$

6. A posteriori update of covariance matrix factor, $\hat{S}_x(k)$, is performed using HT.
7. Determine

$$\bar{x}_{k+1}\ ,\ S_{x\hat{x}}^{(1)}(k+1)\ ,\ S_{xw}^{(1)}(k+1)\ ,\ S_{x\hat{x}}^{(2)}(k+1)\ ,\ S_{xw}^{(2)}(k+1).$$

8. Use HT to compute $\bar{S}_x(k)$
9. $k = k+1$, go to step 2

VII. SIMULATION AND RESULTS

We will compare the performance of the DD1 and DD2 filters with Extended Kalman filter for power system dynamic stability of single-machine infinite-bus system. The state equations are integrated using a fourth – order Runge Kutta method with 200 steps taken between each observation. It is straightforward to implement continues or discrete versions of the DD1 and DD2 filters. We measure δ , ω, T_e and estimate

$$\omega_0\varphi_d\,,\ \omega_0\phi_f\,,\ \omega_0\phi_D,\ \omega_0\phi_q,\ \omega_0\phi_Q$$

in single machine infinite bus system.
To enable a fair comparison of the estimates produced by each of the three filters, the estimations are averaged across a Monte Carlo simulation consisting of 20 runs. Each run is carried out with a different noise sample. The results of the Monte Carlo simulation are shown in Figure 2. Surprisingly, Figure2 shows that the DD2 filter exhibits a performance, which is completely superior to the EKF and the DD1 filter.

VIII. CONCLUSION

In this paper we compare performance of three nonlinear state estimation techniques for estimation of Single Machine Infinite Bus System. The result of simulation demonstrates that the DD2 filter is better than EKF. The implementation is very simple as the filters do not require derivative information and the range of application is wider than for the EKF**.**

REFERENCES

[1] K. M. E1-Naggar, A Fast Method for Identification of Symmetrical Components for Power System Protection, *Electrical Power and Energy Systems* 23 (2001), pp. 813-817.
[2] C. Madtharad, S. Premrudeep, N. Watson, Power System State Estimation Using Singular Value Decomposition, *Electric Power System Research* 00(2003*)*, pp. 1-9.
[3] E. A. Feilat, N. Younan, S. Grzybowski, Estimating the Synchronizing and Damping Torque Coefficients Using Kalman Filtering, *Electric Power System Research* 52(1999), pp. 145-149.
[4] L. Rouco and J. Pereze-Arriaga, Multi-Area Analysis of Small Signal Stability in Large Electric Power Systems by SMA, *IEEE Transactions on Power Systems*, Vol. PWRS-8, No. 3, August 1993, pp. 1257-1265.
[5] Recayi Pecen, Sadrul Ul, Marc Timmerman, Modeling and simulation of a Kalman filter based control scheme for an AC/DC power system, *Electrical Power and Energy Systems* 26 (2004) 173–189.
[6] W. Miller, J. Lewis, Dynamic State Estimation in Power Systems, *IEEE Transactions on Automatic Control*, Vol. AC-16, No. 6, Dec. 1971, pp. 841-846.
[7] R.G. Brown, *Introduction to random Signal Analysis and Kalman Filtering*, John Wiley, New York, 1983.
[8] Adly A. Girgis and T. L. Daniel Hawing, Optimal Estimation of Voltage Phasors and Frequency Deviation using Linear and Non-Linear Kalman Filtering: Theory and Limitations, *IEEE Transactions on Power Apparatus and Systems*, Vol. PAS-103, No. 10, October 1984, pp. 2943-2949.
[9] P.Kundur, *Power System Stability and Control*, McGraw-Hill, Inc., New York, 1994.
[10]. M.Norggrd, N.K. Poulsen and O.Ravn, Advances in Derivative-Free State Estimation for Nonlinear Systems, *IMM-REP*,April 7,2000.
[11]. T.S.Schei, A finite- difference method for linearization in nonlinear estimation algorithms, *Automatica*, 33(11):2051-2058,1997.
[12]. S. J. Julier and J. K. Uhlmann, A general metohod for approximating nonlinear transformations of probability distributations, *Technical report, Robatics Research Group, Department of Engineering Science, University of Oxford*, 1994.
[13]. F. L. Lewis, *Optimal Estimation*, John Wiley & Sons, New York, NY, 1986.

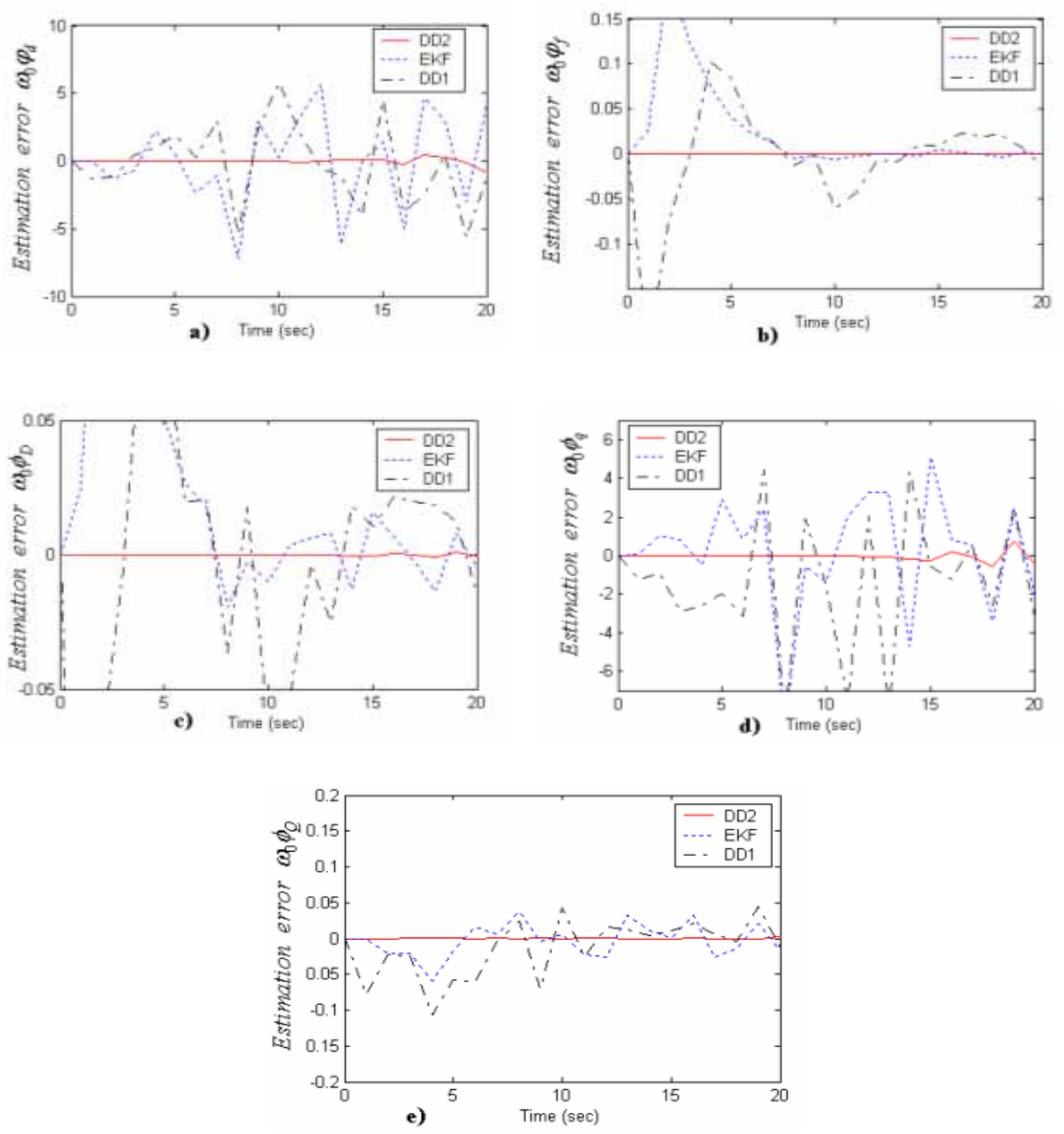

Figure 2. Comparison of DD1, DD2, EKF error in
a) $w_0\varphi_d$, b) $w_0\varphi_f$, c) $w_0\phi_d$, d) $w_0\phi_q$ and e) $w_0\phi_Q$

Assessment of Reliability Worth in Distribution Systems with Substation Originated Outage by Sequential Monte Carlo Simulation

Somchai Songsiri and Somporn Sirisumrannukul

Department of Electrical Engineering, Faculty of Engineering
King Mongkut's Institute of Technology North Bangkok
1518, Pibulsongkram Rd., Bang sue, Bangkok, Thailand
E-mail: somchai.son@pea.co.th, spss@kmitnb.ac.th

***Abstract*- This paper presents a time sequential Monte Carlo simulation approach to distribution reliability worth, taking into account equipment failure originated from substations. Stations, which transfer electrical energy between subtransmission systems and distribution systems, can have significant impact on the overall system reliability of customers. With average disconnected load, outage duration, average interruption cost, reliability worth at the load points can be estimated. The method is illustrated by the Roy Billinton test system with different substation configurations. The study results show that the simulation method can provide reliability worth of load points in terms of expected cost and their probability distributions, and interrupted energy assessment rate.**

Keywords: **Monte Carlo simulation, Reliability worth, Distribution reliability, Substation reliability.**

I. INTRODUCTION

The basic function of a power system is to supply the electrical energy to customers as economically as possible with an acceptable level of reliability [1]. The acceptable level reliability can be quantified in forms of reliability worth. One approach to assess reliability worth is to relate it to the costs or losses incurred by utility customers due to electric supply interruption [2]. The distribution system is an important part of the total electrical supply, as it provides the final connection between bulk transmission system and customers' facilities. It has been reported that more than 80% of all customer interruptions are caused from failed events in the distribution system [3].

In many cases, distribution systems are designed and constructed as radial feeders systems which make them more susceptible to outage in a single event. However, many other systems, although operated as radial systems, can be switched to meshed systems using normally open switches in the event of a system failure [3]. Distribution systems have a set of series components between substations and load points. Therefore, the interruption of load point is not only due to the failure of components in the distribution system but also from those in the substations. Substation configuration can, obviously, have a direct impact on the load points. An appropriate substation configuration can improve the customers' reliability.

A common way to analyze reliability worth is to determine customer costs due to electric power supply interruptions. One convenient way is an interpretation of customer interruption costs in terms of customer damage functions (CDF). The CDF can be determined for given customer types and aggregated to make sector customer damage functions (SCDF), which reflect economic consequences of supply interruption as a function of cost in different groups of customers. The SCDF is normally obtained from customer surveys, the data of which are complied according to major sectors or industrial categories. With the SCDF, outage duration and average disconnected load, customer interruption cost can be evaluated. A useful index known as the interrupted energy assessment rate (IEAR) that relates the reliability indices and the momentary implications of customer supply interruptions can also be obtained.

This paper presents an assessment of reliability worth with substation originated outage using a time sequential Monte Carlo simulation technique. The method represents the random behaviors of system components, such as time to failure, time to repair and switching time by randomly sampling sequences of component states in chronological manner for several periods of time. Each of the component state is superimposed to determine system states for reliability and cost evaluation. The method is demonstrated with the Roy Billinton test system (RBTS) with different substation configurations.

II. MONTE CARLO SIMULATION

Monte Carlo simulation generates historical data for each of the system equipment. The historical data consist of time-to-failure (TTF), time-to-repair (TTR), and time-to-switching (TTS). In this paper, the exponential distribution function is used to represent TTF, TTR and TTS. Given uniformly distributed random numbers U_F, U_R, and U_S, the conversion of TTF, TTR and TTS into the exponential function using the inverse transform method is given in (1)-(3).

$$TTF = -\frac{1}{\lambda}\ln(1-U_F) \tag{1}$$

$$TTR = -\frac{1}{\mu_r}\ln(1-U_R) \tag{2}$$

$$TTS = -\frac{1}{\mu_{sw}}\ln(1 - U_S) \quad (3)$$

where

λ = average failure rate (occ/year)

μ_r = average repair rate (occ/year)

μ_{sw} = average switching rate (occ/year)

The annual expected interruption cost (ECOST) and IEAR of each load point are calculated by the following equations [3]:

$$ECOST_{p,i} = \sum_{j=1}^{N} C_{j,p}(r_j) L_{av,p} \quad (4)$$

$$IEAR_{p,i} = \frac{ECOST_{p,i}}{\sum_{j=1}^{N} L_{av,p} r_j} \quad (5)$$

where

r_j = outage time due to event j

$C_{j,p}$ = cost of interruption for load point p due to event j

N = number of events in each year

$L_{av,p}$ = average connected load at load point p

The simulation process consists of the following steps:

1) Generate three random numbers between 0 and 1 for each component to represent TTF, TTR and TTS.

2) Convert the random numbers to up time, down time and switching time on given TTF, TTR and TTS distributions using (1) – (3).

3) On each year during simulation, the failure of a component defines event j and down time r_j for each load point concerning distribution system failures and substation originated failures.

4) ECOST is calculated for failure events and accumulated for each year. Annual ECOST and IEAR are calculated at the end of each year by (4) and (5).

5) Repeat steps 3) and 4) for a simulation period of 50,000 years.

III. Substation Component Model

Substation reliability evaluation is considered up to second order failure events. The components in the substation to be evaluated consist of busbars, transformers and circuit breakers. All the components can be isolated after failures and can be modeled by the four-state model in Fig. 1 [4].

A. Active failure events (1 – 2 – 3 – 1)

For a failure event that causes the operation of protection and the associated circuit breakers to trip, the failed component can be restored to service only by repair or replacement.

B. Passive failure events (1 – 3 – 1)

For a failure event that does not cause the operation of protection, the failed circuit breaker can be restored to service only by repair or replacement.

The failure mode of the components is defined as follows.

1) Circuit breaker: The circuit breaker failure model is defined for both active and passive failure events.

2) Transformer and busbar: The transformer and busbar failure model is defined only for active failure events.

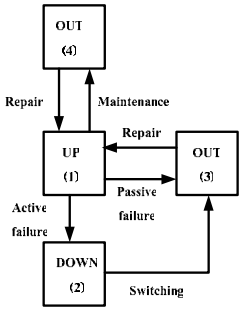

Figure 1. Four-state failure model of substation components.

IV. Substation Configurations and Distribution System

A. Substation Configurations

Four types of substation configurations are considered in this paper: scheme a) single bus configuration without circuit breaker at primary side of transformer (defined at bus 2 of the RBTS), scheme b) breaker-and-a-half configuration, scheme c) ring bus configuration and scheme d) single bus configuration with circuit breaker at primary side of transformer. These four substation configurations are shown in Fig. 2. The recovery of a transformer in the substations is made by repair.

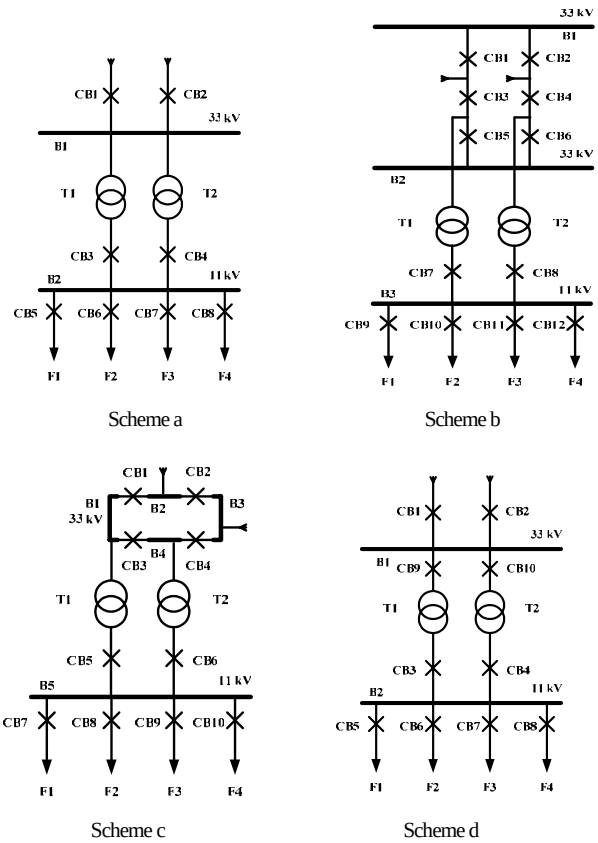

Figure 2. Four different substation configurations.

B. Distribution System

Distribution system at bus 2 of RBTS is employed in this study, as shown in Fig. 3. The reliability data of the components are provided in Table I [5]. The feeders are operated as radial feeders but connected as a mesh through normally open sectionalizing points. The system has disconnecting switches in the main feeders, fuses in each lateral branch and alternative supply at the end of each feeder. The failure of transformer is recovered by replacement.

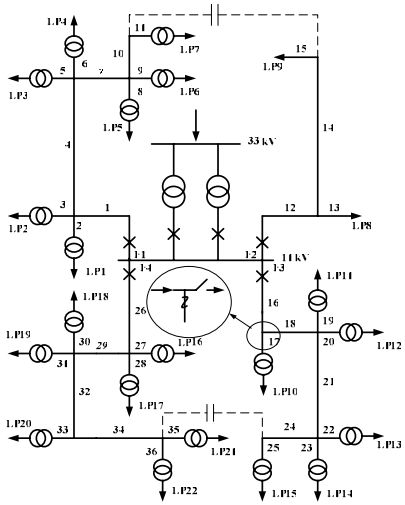

Figure 3. Distribution system at bus 2 of RBTS .

TABLE I
RELIABILITY AND SYSTEM DATA

Component	λ_a	λ_p	r	r_p	s
Transformer					
33/11 kV	0.0150	0.0150	-	15	1.0
11/0.4 kV	0.0150	0.0150	200	10	1.0
Circuit breaker					
33 kV	0.0015	0.0020	4	-	1.0
11 kV	0.0040	0.0060	4	-	1.0
Bus bar					
33 kV	0.0010	0.0010	2	-	1.0
11 kV	0.0010	0.0010	2	-	1.0
Line					
11 kV	0.0650*	0.0650*	5	-	1.0

λ_a = Active failure rate) occ/yr ([*line (occ/km-yr)]

λ_p = Permanent (total) failure rate)occ/yr) [*line (occ/km-yr)]

r, r_p = Repair time and replacement time (hr)

s = Switching time (hr)

C. Customer and Loading Data

The customer and loading data are given in Table II [5]. The customers connected at bus 2 are composed of residential, small industrial, commercial and government customers.

TABLE II
CUSTOMER DATA

Load point (LP)	Cust.type	Average load (MW)	No. of cust. /LP
1,2,3,10,11	Residential	0.535	210
12, 17, 18, 19	Residential	0.450	200
8	Small industrial	1.00	1
9	Small industrial	1.15	1
4, 5, 13, 14, 20, 21	Government	0.566	1
6, 7, 15, 16, 22	Commercial	0.454	10

D. Customer Damage Function

The sector customer damage function (SCDF) of each group of customers is used to calculate customer interruption cost at each load point and is shown in Fig. 4 [2].

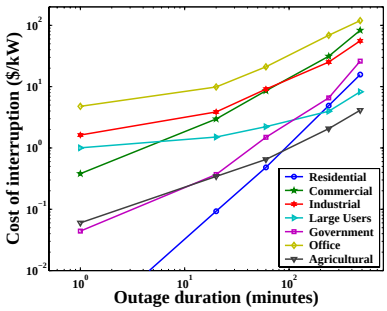

Figure 4. Sector customer damage functions.

RESULTS OF EXPECTED CUSTOMER INTERRUPTION COST AND INTERRUPTED ENERGY ASSESSMENT RATE

The contingency enumeration method is used to estimate ECOST and IEAR [6]. This method considers each outage event in association with the interruption cost data of the customers. A time sequential Monte Carlo simulation is developed to evaluate ECOST and IEAR. Fig. 5 shows the ECOST of the four feeders connected at bus 2 for the four different substation configurations, which are shown in Fig. 2. As can be seen, scheme A is the worst because the failure of a transformer causes the whole substation to be forced outage and the failed transformer needs repairing. Scheme B has the lowest ECOST mainly because it has the highest number of circuit breakers. Although scheme D has only 1 busbar (i.e., no redundancy), its ECOST is slightly higher than that of scheme C, which contains 4 busbars, because of low probability to failure of the busbars and a small amount of repair time (2 hours). A significant difference could be seen if the probability were higher. It is very interesting to note from Fig. 6 that the IEAR of each feeder is quite insensitive to the substation configurations. Fig. 7 illustrates the ECOST of bus 2 for the four different substation configurations. This system ECOST follows the pattern of Fig. 5. The ECOST of load points 1, 9, 14 and 22 for a simulation time of 50,000 years for scheme A is shown Fig. 8. Fig. 9 and 10 show the probability distribution of the ECOST for feeder 1 and bus 2 owing to substation originated outage for the four schemes.

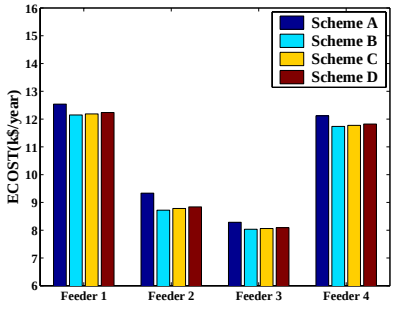

Figure 5. ECOST of feeders at bus 2 in RBTS for four different substation configurations.

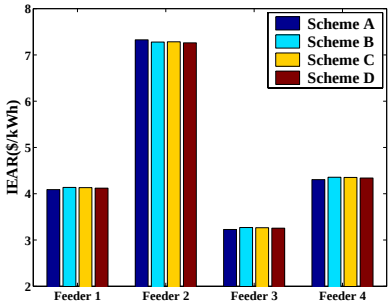

Figure 6. IEAR of feeders at bus 2 in RBTS for four different substation configurations.

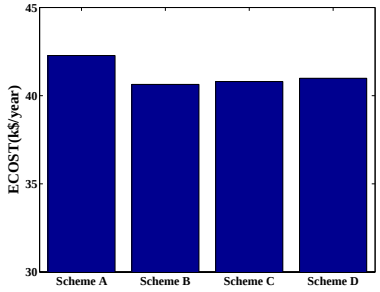

Figure 7. ECOST of bus 2 in RBTS for four different substation configurations.

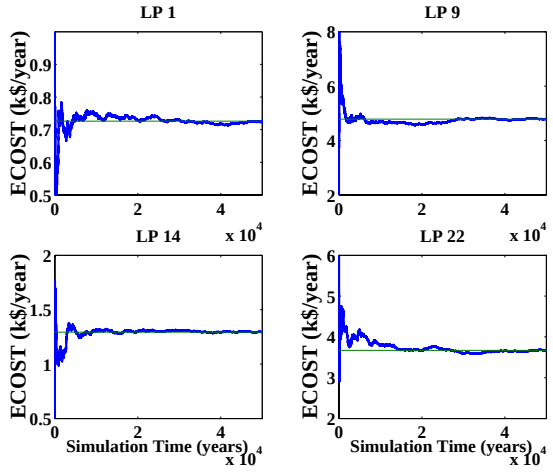

Figure 8. ECOST of load points 1, 9, 14 and 22 as function of simulation time for scheme A.

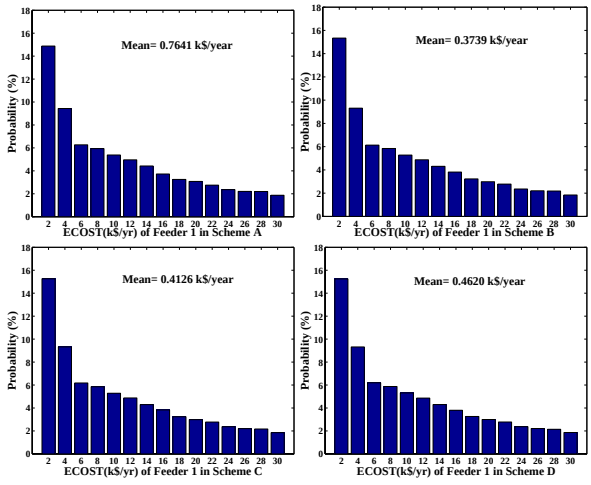

Figure 9. Probability distribution of ECOST for feeder 1 due to substation originated outage.

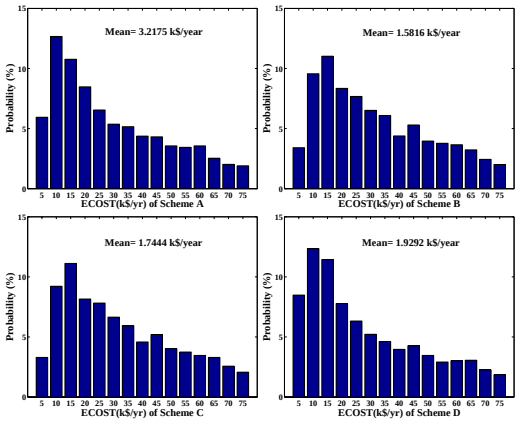

Figure 10. Probability distribution of ECOST due to substation originated outage.

CONCLUSION

This paper presents the application of a sequential Monte Carlo simulation to reliability worth in distribution systems with substation originated outages. The fundamental concept behind this technique is to mimic component behaviors by randomly sampling sequences of component states in chronological manner for several periods of time. The distributions of active or passive failure, switching time and repair time are assumed to be exponentially distributed. Reliability worth at load points are evaluated as expected interruption cost of customers based on the contingency enumeration technique, in which each outage event is taken into consideration in association with the interruption cost data of the customers. The results from a case study show that different substation configurations have different impacts on customers' reliability and therefore their interruption costs. However, a more reliable substation requires more investment cost. Thus, the reliability worth gaining from the substation needs to be justified in conjunction with the additional investment cost for the optimum balance between the utility and customers.

REFERENCES

[1] L. Goel, and Yan Ou, "Reliability Worth Assessment in Radial Distribution Systems using the Monte Carlo simulation technique," *Electric Power Research*, vol. 51, pp. 43-53, 1999.

[2] L. Goel, R. Billinton, and R. Gupta, "Basic Data and Evaluation of Distribution System Reliability Worth," *IEEE Western Canada Conference on Computer, Power and Communication Systems in a Rural Environment*, pp. 271-277, May 1991.

[3] A. A. Chowdhury, and Don O. Koval, "Value-Based Distribution System Reliability Planning," *IEEE Transactions on Industry Applications*, Vol. 34, pp.23-29, 1998.

[4] R. Billinton and G. Lian, "Monte Carlo Approach to Substation Reliability Evaluation," *IEE Proceedings-C*, vol. 140, No. 2, pp. 147-152, March 1993.

[5] R. N. Allan, R. Billinton, I. Sjarief, L. Goel and K. S. So, "A Reliability Test System for Educational Purposes – Basic Distribution System Data and Results," *IEEE Transactions on Power Systems*, Vol. 6, No. 2, pp. 813-820, May 1991.

[6] L. Goel and R. Billinton, "Determination of Reliability Worth for Distribution System Planning," *IEEE Transactions on Power Delivery*, Vol. 9, No. 3, pp. 813-820, July 1994.

[7] Teng-Fa Tsao and Hong-Chan Chang, "Comparative Case Studies for Value-Based Distribution System Reliability Planning," *Electric Power Research*, vol. 68, pp. 229-237, 2004.

Detailed Analysis of Load Voltage Compensation

Paisan Boonchiam[1] and Nadarajah Mithulananthan[2]
[1]Department of Electrical Engineering, Rajamangala University of Technology Thanyaburi, Thailand 12110,
[2]Energy Field of Study, Asian Institute of Technology, Thailand 12120,
E-mail: paisan@rmut.ac.th, mithulan@ait.ac.th

Abstract*—This paper presents the detailed analysis of load voltage compensation for dynamic voltage restorer (DVR) that used for enhancing power quality. DVR is a custom power device used to correct voltage sag (dip) by injecting voltage as well as power into power distribution system. A method of determining the exact amount of voltage injection required to correct a specific voltage reduction with minimum power injection is described. Analytical expressions for both magnitude and angle of the injected voltage are also derived. It has been shown that a voltage reduction and power factor should be analyzed before compensating the voltage. Simulation results show the performance of the proposed analysis though Matlab/simulink tool.

Keywords*—dynamic voltage restorer, power quality, voltage sag, custom power.

I. INTRODUCTION

Voltage sags are now one of the most important power quality problems in the power distribution systems [1]. A voltage sag is a momentary decrease in *rms* ac voltage (0.1 – 0.9 p.u. of the nominal voltage), at the power frequency, of duration from cycles to a few seconds as shows in Fig. 1. Most voltage sags are caused by remote faults, such as single-line-to-ground fault, double line to ground fault on the power distribution system or due to starting of large induction motors and switching of capacitor bank [2].

A dynamic voltage restorer (DVR) is a custom power device capable of protecting sensitive loads against the voltage variations or disturbances [2]. A DVR is a forced commutated voltage source converter (VSC) that injects a dynamically controlled voltage in series with the supply voltage through three single-phase transformers for correcting the load voltage. When the injected voltage is in phase with the supply voltage, the desired voltage correction can be achieved with a minimum voltage injection but it may required a considerable amount of active power injection into the system [3]. When the injected voltage leads the supply voltage, the same correction can be made with a lower value of power injection. When the power injection by the DVR is minimized, the same energy storage can be used for a longer period. Such an operation requires careful determination of injected voltage magnitude and angle, however.

Most papers have had concentrated in the energy storage devices [5]-[8]. They tried to minimize the energy storage by used the optimization techniques or did not use energy storage device by directly connecting the dc-link of VSC to the supply source and used the rectifier converter to change the supply from ac to dc [9]. It made costly when we connected the supply of VSC directly. This paper will propose the DVR that uses the energy storage device. The objective of this paper is to determine the magnitude and angle of the DVR injected voltage so that a given voltage sag can be corrected with minimum active power injection into the system. Analytical expressions for the injected voltage magnitude and angle, in terms of voltage sag and power factor, are also derived.

This paper is organized as follows. Section II discusses the principle operation and equation of DVR. The detail analysis of voltage compensation for DVR is presented by showing the power injection analysis and voltage injection analysis in section III. The simulation results and conclusion are given in section IV and V, Respectively.

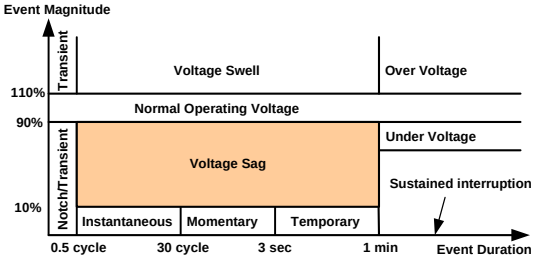

Fig. 1. Voltage Reduction Standard of IEEE Std. 1159-1995.

II. DYNAMIC VOLTAGE RESTORER

DVR is a series-connected device with the grid and case a power disturbance appears, it will inject a power into the grid for mitigating their disturbances, such as voltage sag/swell. In principle, DVR can be installed at any voltage level, but for the low voltage applications, the DVR may be cost-ineffective compared to the uninterruptible power supply (UPS). To be able to mitigate voltage sag, the DVR should be capable of generating and absorbing active and reactive power to/from the grid. Basically, DVR is designed to dynamically inject a voltage V_i into the power system. Figure 2 shows the schematically diagram of a typical DVR used for voltage correction. When the supply voltage V_s changes, the DVR injects a voltage V_i in such a way that the desired load voltage magnitude can be maintained. DVR is simply a VSC that produces an ac output voltage and injects in series with the supply voltage through a transformer. To correct a given voltage sag, not only voltage but also active and/or reactive power injections are needed. The DVR itself is capable of generating the reactive power, but the injected active power must come from the energy storage part of the DVR. Thus minimization of active power injection is essential to increase the lift of the energy storage.

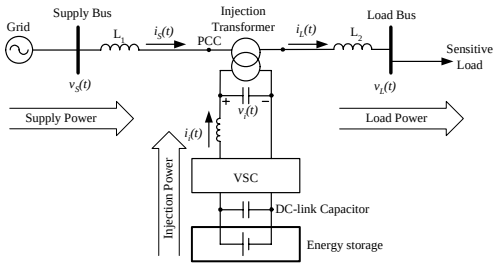

Fig. 2. Schematic diagram of a typical DVR.

III. VOLTAGE COMPENSATING

From Fig. 2, the analysis of voltage compensating can be divided into two parts. First analyzes the injected power and second analyzes the voltage and angle to be the command of VSC in DVR. We can show step by step as the following.

A. *Injected Power Analysis*

The active and the reactive power flow at the load and supply sides of Figure 1 can be written as

$$P_L = V_L I_L \cos\theta_L \quad (1)$$

$$Q_L = V_L I_L \sin\theta_L \quad (2)$$

$$P_S = V_S I_L \cos\theta_S \quad (3)$$

$$Q_S = V_S I_L \sin\theta_S \quad (4)$$

Here θ_L and θ_S are the angle between V_L and I_L and V_S and I_L, respectively. Note that θ_L is the load power factor angle and I_L is the current in both load and source sides. DVR injected active power (P_i) and reactive power (Q_i) are the difference between (1) and (2) and (3) and (4), respectively, and are given by

$$P_i = (P_L - P_S) = V_L I_L \left(\cos\theta_L - \left(\frac{V_S}{V_L}\right)\cos\theta_S \right) \quad (5)$$

$$Q_i = (Q_L - Q_S) = V_L I_L \left(\sin\theta_L - \left(\frac{V_S}{V_L}\right)\sin\theta_S \right) \quad (6)$$

Consider the load voltage magnitude (V_L) and load apparent power ($V_L I_L$) as base quantities. Thus, the injected power in p.u. can be written as

$$P_i = pf_L - V_S \cos\theta_S \quad (7)$$

$$Q_i = \sqrt{1 - pf_L^2} - V_S \sin\theta_S \quad (8)$$

Here $pf = \cos\theta_L$ = load power factor, and V_S is the supply voltage magnitude in p.u. For given values of load power factor and supply voltage magnitude, the injected active power is minimum when:

$$\cos\theta_S = 1 \quad (9)$$

In other words, when $\theta_S = 0$ or V_S and I_L are in phase. Thus, V_L must be lead V_S by the power factor angle θ_L and it can be realized by careful injection of V_i. The main purpose of the DVR is to maintain the desired load voltage magnitude despite a injected voltage of V_i p.u. In this case, the supply voltage magnitude in p.u. can be written as:

$$V_S = (V_L - V_{drop}) \quad (10)$$

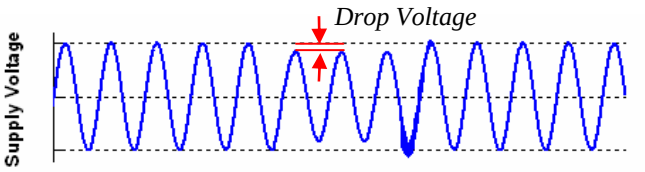

Fig. 3. Definition of voltage drop.

Using equation (5) to (6), the minimum active power $P_i^{\min}$ and reactive power injection $Q_i^{\min}$ of the DVR can be written as

$$P_i^{\min} = V_{drop} - (1 - pf) \quad (11)$$

$$Q_i^{\min} = \sqrt{1 - pf^2} \quad (12)$$

Equation (11) indicates, when $V_{drop} < (1 - pf)$, $P_i^{\min}$ becomes negative and thus the power flows in reverse direction. DVR may not cater to reverse power flow, however. Such a situation can be avoided by adjusting the value of θ_S (instead of zero) so that the power flow becomes zero. The value of θ_S for zero power flow can be obtained from (4) and is given by (13). $Q_i^{\min}$ does not depend on the voltage injection but it depends on the load power factor as given by equation (12) for minimum power injection.

$$\theta_S = \cos^{-1}\left(\frac{pf}{1 - V_{drop}}\right) \quad (13)$$

Figure 4 shows the variation of DVR active power injection against the voltage sag and load power factor. It can be observe, when the voltage drop V_{drop} is less than or equal to ($1\text{-}pf_L$), no active power injection is required to correct the voltage. When V_{drop} exceeds ($1\text{-}pf_L$), the injected power increases linearly with V_{drop}. In this region of voltage drop, the injected power depends on the load factor, and for a given value of V_{drop}, it increase with the increase of load power factor.

Figure 5 presents the variation of injected reactive power against load power factor and Fig. 6 shows the input angle between input voltage and current compare with load power factor and dropped voltage. Note that, the load power factor has effect to the power injection and input phase between voltage and current. If we would like to minimize the energy storage, we need to consider the type of sensitive that we want to protect the systems.

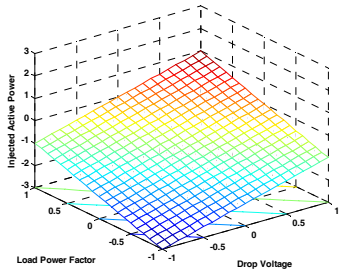

Fig. 4. Variation of DVR active power injection against the dropped voltage.

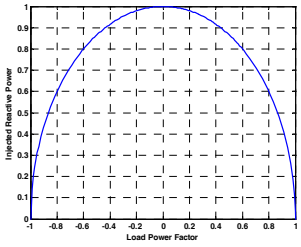

Fig. 5. Variation of DVR reactive power injection against load power factor.

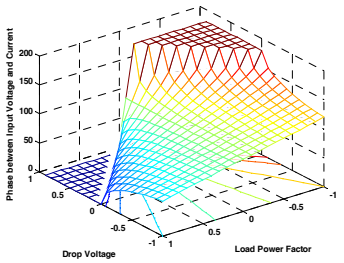

Fig. 6. Variation of the angle of input voltage and current against load power factor and dropped voltage.

B. *Injected Voltage Analysis*

It is demonstrated in the previous section that, when $V_{drop} \le (1-pf)$ the voltage correction can be made without injecting any active but the phase shift between V_S and I_L must be governed by (13). On the other hand, when $V_{drop} > (1-pf)$, injection of active power is required to correct the voltage but its value can be minimized if V_S and I_L are kept in phase. Thus the voltage correction required careful determination of injected voltage so that the desired phase shift (between V_S and I_L) as well as load voltage magnitude can be maintained. The procedure of finding the injected voltage is discussed next.

When $V_{drop} \le (1-pf)$: In this case, the DVR should inject a voltage in such a way that (13) is satisfied as well as the desired load voltage magnitude (1.0 p.u.) is maintained. From Figure 1, the injected voltage V_i can be written as

$$\mathbf{V_i} = \mathbf{V_L} - \mathbf{V_S} \qquad (14)$$

Consider V_S as reference. Thus V_L must have an angle of $(\theta_L - \theta_S)$ to avoid reverse power flow. Note that the angle between V_L and I_L is the power factor angle θ_L. Thus in polar form, (14) can be written as

$$V_i \angle\beta = 1\angle(\theta_L - \theta_S) - (1-V_{drop})\angle 0^\circ \qquad (15)$$

Here V_i and β are the magnitude and angle, respectively, of the injected voltage. After some mathematical manipulations, V_i and β can be expressed as

$$V_i = \sqrt{V_d^2 + 2(1-V_{drop})[1-\cos(\theta_L - \theta_S)]} \qquad (16)$$

$$\beta = \tan^{-1}\left[\frac{\sin(\theta_L - \theta_S)}{\cos(\theta_L - \theta_S) - (1-V_{drop})}\right] \qquad (17)$$

When $V_{drop} > (1-pf)$: In this case, the DVR should inject a voltage in such away that V_S and I_L are kept in phase while maintaining the desired load voltage magnitude. Since V_S is considered as reference, the angle of both V_S and I_L should be zero. To satisfy the power factor angle (between V_L and I_L), however, V_L must lead V_S by θ_L. Thus in phase form, (15) can again be written as

$$V_i \angle\beta = 1\angle\theta_L - (1-V_{drop})\angle 0^\circ \qquad (18)$$

After some mathematical manipulations, the magnitude and angle of the injected voltage can be expressed as

$$\begin{aligned} V_i &= \sqrt{V_{drop}^2 + 2(1-V_{drop})[1-\cos\theta_L]} \\ &= \sqrt{V_{drop}^2 + 2(1-V_{drop})[1-pf]} \end{aligned} \qquad (19)$$

$$\beta = \tan^{-1}\left[\frac{\sin\theta_L}{\cos\theta_L - (1-V_{drop})}\right] = \tan^{-1}\left[\frac{\sqrt{1-pf^2}}{pf - (1-V_{drop})}\right] \qquad (20)$$

The variations of DVR injected voltage magnitude, and angle against the voltage drop are shown in Figure 7-10, respectively. In this region of voltage drop, the injected voltage magnitude increase rapidly with the increase of V_{drop}. When V_{drop} reaches (1-*pf*), the magnitude and angle of the injected voltage become $\sqrt{1-pf^2}$ p.u. and 90°. Note that for

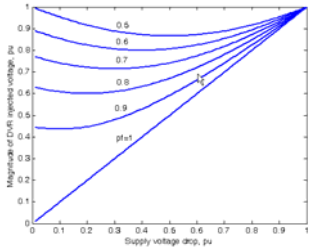

Figure 7. Variation of the magnitude of DVR injected voltage against the voltage drop

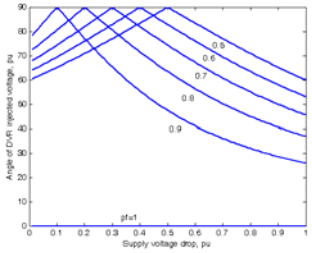

Figure 8. Variation of the angle of DVR injected voltage against the voltage drop.

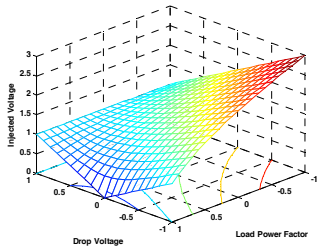

Figure 9. Variation of the magnitude of DVR injected voltage against the voltage drop and power factor.

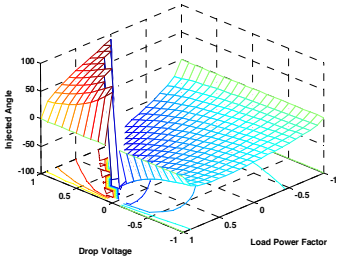

Figure 10. Variation of the magnitude of DVR injected phase against the voltage drop and power factor.

unity power factor, the injected voltage magnitude for V_{drop} = (1-*pf*) is zero and thus its angle is meaningless. In this region, the injected voltage magnitude increases while its angle decreases with the increase of V_{drop}. Finally, when V_{drop} approaches 1 p.u. the entire load power is supplied by the DVR and the injected voltage magnitude and angle become the same as the desired load voltage magnitude and power factor angle, respectively.

IV. Simulation Results

The configuration of the studied system is shown in Figure 1 and the system parameters are given in appendix. The dc/ac inverter used in the DVR is assumed to be a PWM voltage source converter. The total voltage harmonic distortion for 22-kV distribution system cannot be greater than 5.0%. Assuming that the utility source is deal, then the rms value of total harmonics voltage on the primary side of the injection transformer will be 11 kV. suppose the turn ratio of the injection transformer is 7. In practice, the magnitude modulating ratio m_a of the PWM converter used in the DVR my range from 0.0 more than 0.9. The exact value of m_a will depends on the voltage sag depth the DVR attempts to correct, if the filter loading effect is negligible. Figure 11 shows the supply, injected and load voltage when the load power is utility and the balanced voltage sag occurred. And Fig. 12 shows the supply, injected and load voltage when unbalanced voltage sag occurred. It can be observed that when the power factor of load is unity, the DVR can compensate the voltage magnitude and angle by using the minimum energy storage system.

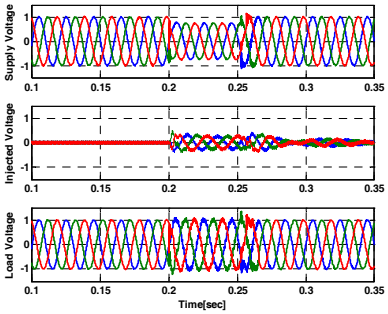

Figure 11. Voltage on supply, injection, and load side.

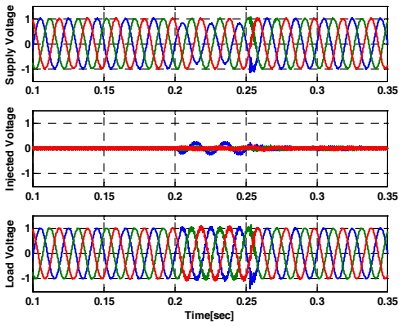

Figure 12. Voltage on supply, injection, and load side.

V. Conclusion

A technique of correcting the voltage drop or sag by a DVR is described in this paper. The expressions for the injected voltage magnitude and angle that minimize the active power injection are also derived. It has been found that a voltage drop of less than or equal to (1-pf) pu can be corrected without drawing any power from the energy storage of the DVR. In this case, only reactive power injection is required to correct the voltage and which can be generated by the DVR. For higher voltage drop, however, both active and reactive power injections are required to correct the voltage. In this case, taking as much power as possible from the energy storage. This can be achieved by maintaining unity power factor at the supply side.

VI. References

[1] Akagi, H., "New trends in active filters for power conditioning," *IEEE Trans. Ind. Applicat.*, vol. 32, pp 1312-1322, Nov./Dec. 1996.

[2] Ghosh,A. and Ledwich,G. (2002). *Power Quality Enhancement using Custom Power Devices.* Kluwer Academic Publishers, United States.

[3] Woodley, N.H, Morgen, L., and Sundaram, A., "Experience with an inverter based dynamic voltage restorer," IEEE Trans. Power Delivery, vol. 14, pp. 1181-1186, 1999.

[4] Choi, S.S., Li, B.H., and Vilathgamuwa, D.M., "Dyanmic voltage restorer with minimum energy injection," IEEE Trans. Power syst., vol.15, pp. 51-57, 2000.

[5] Haque, M.H., "Voltage sag correction by Dynamic Voltage Restorer," IEEE Power Engineering Review,May 2001.

A New Voltage dip and Grid Unbalance Detection Method for Distribution Static Synchronous Compensator Application

Thip Manmek[1], Chathura P. Mudannayake[2], and Colin Grantham[2]
[1]Department of Control and Instrumentation Engineering, Mahanakorn University of Technology, Bangkok, THAILAND
[2]School of Electrical Engineering and Telecommunication, The University of New South Wales, Sydney, AUSTRALIA

***Abstract*- This paper presents the application of the proposed efficient least squares algorithm in power supply voltage dip and unbalance detection for mitigation using a distribution static synchronous compensator (D-STATCOM). The proposed voltage dip detection method is based on an efficient least squares algorithm which offers structural simplicity and less computational complexity. The proposed method is capable of identifying the instantaneous symmetrical components of the fundamental frequency accurately even though the point of common coupling voltage is strongly corrupted by the voltage harmonics. The proposed method extracts detecting the positive- and negative-sequence components and then using those sequence components for generating reference values of current that need to be injected into the point of connection D-STATCOM in order to compensate the voltage errors. The effectiveness of the voltage dip detection method in the D-STATCOM application has been verified by simulation results.**

I. INTRODUCTION

Recently, the distribution static synchronous compensator (D-STATCOM) has been introduced to distribution networks to manage the system reactive power and regulate the voltage at the distribution buses. A D-STATCOM usually consists of a shunt connected voltage source converter (VSC) [1].

The extraction and tracking technique of voltage dip is the core of the D-STATCOM mitigating control strategy. In order to obtain the required information to control the D-STATCOM further processing during voltage unbalance or dip is required and the processed information is required to be updated as fast as possible. Moreover, the choice of techniques for the voltage dip detection is highly dependent on the real-time implementation, the available computational hardware, and the amount of computational effort.

In this paper the voltage dips detection and unbalances detection based on the proposed efficient least squares (ELS) algorithm for using in D-STATCOM applications is introduced. The proposed voltage dip detection system extract the fundamental component and positive and negative-sequence component of the voltage to generate a current reference signal for the D-STATCOM to compensate voltage dips. Simulation results with practical parameter are provided to demonstrate that the proposed balanced and unbalanced voltage dip detection system is an excellent tool for extracting the required information for a D-STATCOM application.

II. VOLTAGE DIP DETECTION BASED ON PROPOSED ELS METHOD

A. Overview of the Proposed Efficient Least Squares Method

The instantaneous voltages waveforms in a three-phase power system can be generally expressed as:

$$v_{Sa}(t) = \sum_{i=1,5,7,\ldots}^{k} V_{Sai}\cos\left(\omega_i t + \beta_{ai}\right) \tag{1}$$

$$v_{Sb}(t) = \sum_{i=1,5,7,\ldots}^{k} V_{Sbi}\cos\left(\omega_i t + \beta_{bi}\right) \tag{2}$$

$$v_{Sc}(t) = \sum_{i=1,5,7,\ldots}^{k} V_{Sci}\cos\left(\omega_i t + \beta_{ci}\right) \tag{3}$$

In which V_{Sai} , V_{Sbi} and V_{Sci} are the unknown magnitude values of the three-phase voltages, and β_{ai} , β_{bi} , and β_{ci} are the unknown phase angles. Subscript $i = 1,5,7,\ldots k$ refers to the fundamental and harmonic components respectively. The symbol ω_i is known angular frequency of the i^{th} harmonic.

The proposed method is used to extract the fundamental component of the three-phase voltages. The discrete-time version of three-phase voltage can be written in matrix notation as

$$y = \mathbf{A}\boldsymbol{x} \tag{4}$$

$\mathbf{A}$ is a complex rotation matrix, $\boldsymbol{x}$ is a complex vector consisting of magnitude and phase angle of the input signal. The vector y is the input signal. The proposed method is based on the conventional least squares algorithm. The aim is to solve the system equations without inverting any matrix with real number elements. The proposed ELS algorithm can calculate harmonic components by simply multiplying each set of input signals by a constant matrix. Consequently, the proposed method is immune to transient distortions and unbalanced conditions. The proposed method is computationally efficient, the size of the matrix is required is only $2 \times L$, since only the fundamental component needs to be identified. The vector $\boldsymbol{x}$ which consists of a complex signal of fundamental and harmonic component can be found using the proposed method as follows:

$$\boldsymbol{x} = \left((\mathbf{R})^{\mathrm{T}}\mathbf{R}\right)^{-1}(\mathbf{R})^{\mathrm{T}} y = \mathbf{C}y \tag{5}$$

where $\mathbf{R} = \begin{bmatrix} H_1^0 & H_{-1}^0 \\ H_1^1 & H_{-1}^1 \\ H_1^2 & H_{-1}^2 \\ \vdots & \vdots \\ H_1^l & H_{-1}^l \end{bmatrix}$

H_1^l is the rotation matrix , ie. $\begin{bmatrix} \cos\omega_1 nT & -\sin\omega_1 nT \\ \sin\omega_1 nT & \cos\omega_1 nT \end{bmatrix}$

L is the number of measured samples,

$\mathbf{C}$ is a constant matrix, ie. $\left(\mathbf{R}^{\mathsf{T}}\mathbf{R}\right)^{-1}\mathbf{R}^{\mathsf{T}}$

B. Voltage Dip Detection Based on Proposed ELS Method

The fundamental component in term of the complex signals can thus be obtained as follows:

$$\begin{bmatrix} v_{Sa1}^{\cos} \\ v_{Sa1}^{\sin} \\ \vdots \\ v_{Sb1}^{\cos} \\ v_{Sb1}^{\sin} \\ \vdots \\ v_{Sc1}^{\cos} \\ v_{Sc1}^{\sin} \end{bmatrix} = \begin{bmatrix} V_{Sa1}\cos\left(\omega_1 t + \beta_{a1}\right) \\ V_{Sa1}\sin\left(\omega_1 t + \beta_{a1}\right) \\ \vdots \\ V_{Sb1}\cos\left(\omega_1 t + \beta_{b1}\right) \\ V_{Sb1}\sin\left(\omega_1 t + \beta_{b1}\right) \\ \vdots \\ V_{Sc1}\cos\left(\omega_1 t + \beta_{c1}\right) \\ V_{Sc1}\sin\left(\omega_1 t + \beta_{c1}\right) \end{bmatrix} = \mathbf{C} \times \begin{bmatrix} v_{Sa}(n) \\ v_{Sa}(n-L+1) \\ \vdots \\ v_{Sb}(n) \\ v_{Sb}(n-L+1) \\ \vdots \\ v_{Sc}(n) \\ v_{Sc}(n-L+1) \end{bmatrix} \tag{6}$$

The fundamental positive- and negative- sequence components are extracted by using equations (7) and (8) respectively.

$$\begin{bmatrix} v_a^+ \\ v_b^+ \\ v_c^+ \end{bmatrix} = \frac{1}{3}\begin{bmatrix} 1 & 0 & -\frac{1}{2} & -\frac{\sqrt{3}}{2} & -\frac{1}{2} & \frac{\sqrt{3}}{2} \\ -\frac{1}{2} & \frac{\sqrt{3}}{2} & 1 & 0 & -\frac{1}{2} & -\frac{\sqrt{3}}{2} \\ -\frac{1}{2} & -\frac{\sqrt{3}}{2} & -\frac{1}{2} & \frac{\sqrt{3}}{2} & 1 & 0 \end{bmatrix}\begin{bmatrix} v_{Sa1}^{\cos} \\ v_{Sa1}^{\sin} \\ v_{Sb1}^{\cos} \\ v_{Sb1}^{\sin} \\ v_{Sc1}^{\cos} \\ v_{Sc1}^{\sin} \end{bmatrix} \tag{7}$$

$$\begin{bmatrix} v_a^- \\ v_b^- \\ v_c^- \end{bmatrix} = \frac{1}{3}\begin{bmatrix} 1 & 0 & -\frac{1}{2} & \frac{\sqrt{3}}{2} & -\frac{1}{2} & -\frac{\sqrt{3}}{2} \\ -\frac{1}{2} & -\frac{\sqrt{3}}{2} & 1 & 0 & -\frac{1}{2} & \frac{\sqrt{3}}{2} \\ -\frac{1}{2} & \frac{\sqrt{3}}{2} & -\frac{1}{2} & -\frac{\sqrt{3}}{2} & 1 & 0 \end{bmatrix}\begin{bmatrix} v_{Sa1}^{\cos} \\ v_{Sa1}^{\sin} \\ v_{Sb1}^{\cos} \\ v_{Sb1}^{\sin} \\ v_{Sc1}^{\cos} \\ v_{Sc1}^{\sin} \end{bmatrix} \tag{8}$$

As may be seen from the (7) and (8), the instantaneous positive- and negative-sequence components can be easily obtained using the instantaneous cosine and sine terms of the proposed ELS algorithm.

The D-STATCOM application that is discussed in the next section uses synchronously rotating reference frame controllers (i.e. $dq-$controllers). Therefore, transformation of the instantaneous positive- and negative- sequence voltage components into the $dq-$axes is required. The transformation of the positive- and negative- sequence components into the $dq-$reference frame is given in (9) and (10) respectively.

The overview of the complete proposed voltage dip detection method is illustrated in Fig. 1. The negative- and positive- sequence components at fundamental frequency are obtained from the instantaneous cosine and sine terms. Then, the $dq-$transformation is carried out to obtain the $d-$ and $q-$components for each sequence.

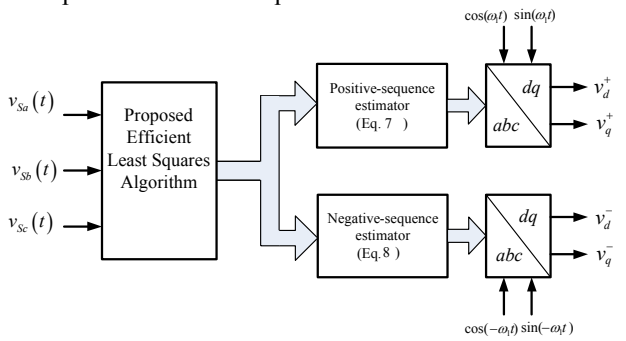

Figure 1 Block diagram of voltage dip detection method based on proposed ELS algorithm.

III. APPLICATION OF PROPOSED VOLTAGE DIP DETECTION METHOD IN D-STATCOM

A. System Configuration

The configuration of the D-STATCOM with the proposed voltage dip detection method is illustrated in Fig.2. The D-STATCOM consists of a three-phase voltage source converter (VSC), a dc-side capacitor C_{dc} with its leakage resistance R_{dc}, and an inductance L_F on the *ac*-side of the converter. The resistance R_F represents the cable resistance of the *ac*-side of the converter. A shunt filter capacitor with capacitance C_F and an inductance L_{tr} that represents transformer leakage inductance are added to the ac- side of the voltage source converter that forms a LCL filter. This filter helps in effectively filtering out the switching ripple in the output voltage waveform. The grid is represented by using an ideal voltage source and impedance. This impedance consists of an inductance L_{line} and a resistance R_{line} which characterizes the transformer and power line respectively. The analysis and design of the D-STATCOM controller are conducted in the rotating reference frame which is synchronized to the voltage vector. The D-STATCOM mitigates the voltage dips by dynamically injecting a current of desired amplitude and phase angle into the grid line. The two inner $dq-$ current regulators in Fig.2 force the converter currents i_{Fd} and i_{Fq} to follow the command currents i_{Fd}^* and i_{Fq}^* respectively. The command i_{Fd}^* to the $d-$axis current loop is obtained by summing the *dc*-link V_{dc}^2 -controller output and $d-$axis component of the reactive power controllers output i_{Cd} . The command i_{Fq}^* is obtained from the $q-$axis component of the reactive power controller output i_{Cq} . The purpose of the outer loop V_{dc}^2 -controller is to regulate the *dc*-link voltage to a required level. The modulation signals m_a , m_b and m_c for the PWM generator are derived from the output of the current controllers.

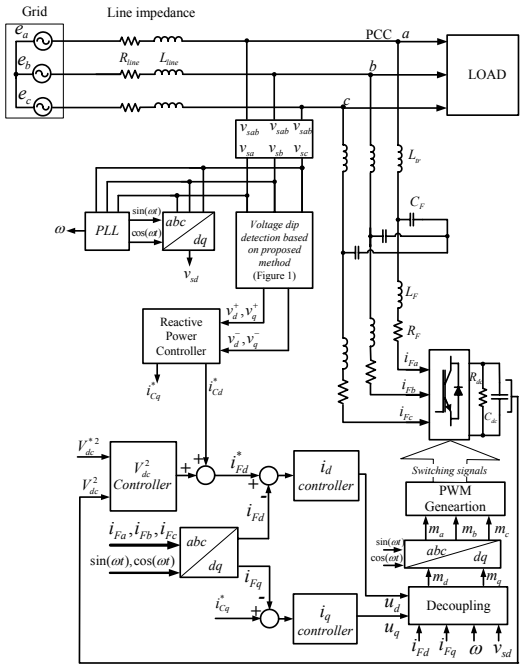

Figure 2 Overall schematic diagram of D-STATCOM with proposed voltage dip detection method.

The decoupling terms are added to the output of the current controllers in order to remove the coupling and are then transformed into the $abc-$ stationary reference frame to obtain the modulation signal for the VSC. The $\sin(\omega_1 t)$ and $\cos(\omega_1 t)$ terms required for the transformation between the $abc-$ and $dq-$ reference fames are obtained via a phase locked loop (PLL) which is synchronized to the fundamental component of the voltage. All of the above are illustrated in Fig. 2.

B. Positive-Negative-Synchronous Reference Frame Controller (Reactive Power Controllers)

In the case of balanced three-phase voltage, the direct transformation of abc voltages into the $d-q$ reference frame will result in dc-quantities. Hence, the D-STATCOM can use a conventional PI-controller to control the injected reactive currents. However, if the grid voltage or the load voltages are unbalanced, a ripple of double the grid frequency will occur in the $d-q$ reference frame. In the case of unbalance three-phase voltages, breaking the voltage signals into positive- and negative- sequence components and then transforming into $d-q$ synchronous reference frame (SRF) results in dc-quantities and these $d-q$ feedback signals allow in control design reactive power control. Transformation of three-phase balance voltages with unity magnitude into the positive- and negative- $d-q$ synchronous reference frame results in dc-quantities with following values.

$$v_d^+ = 1 \text{ pu}\,,\quad v_q^+ = 0 \text{ pu}\,, \text{ and } v_d^- = 0 \text{ pu}\,,\quad v_q^- = 0 \text{ pu}$$

where v_d^+, v_q^+ - dq components of positive-sequence voltage, and v_d^-, v_q^- - dq components of negative-sequence voltage.

The voltage dips (both balanced and unbalanced) in power systems can be corrected by regulating positive- and negative-synchronous dq components to the values corresponding to the balanced case given above. Three controllers are utilized to regulate these dq components of the positive- and negative-sequence voltages as shown in Fig. 3. As shown in Fig. 3 v_d^+ is regulated to 1 pu via i_q^{+*} in the positive-sequence synchronous reference frame. v_d^- and v_q^- are regulated to zero via the i_q^{-*} and i_d^{-*} in the negative-sequence synchronous reference frame. These dq - current components in the positive- and negative- synchronous reference frames are converted into three axes components and added those together to obtain three- phase currents that need to be injected to the line in order to compensate for the voltage dips. These abc current commands are then converted to the positive-sequence synchronous reference frame dq components to generate the current commands (i.e i_{Cd}^* and i_{Cq}^*) for the current controllers. All these are indicated in Fig. 3.

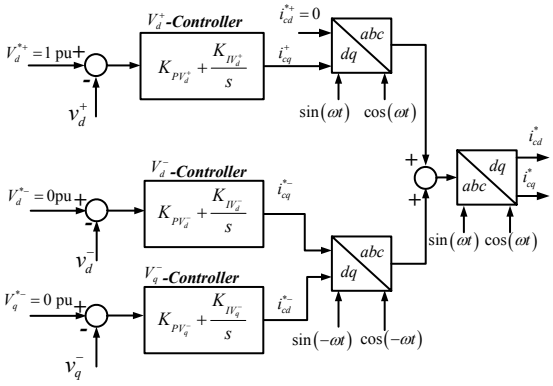

Figure 3 Block scheme of reactive power controller for D-STATCOM.

$$\begin{bmatrix} v_d^+ \\ v_q^+ \end{bmatrix} = \frac{2}{3}\begin{bmatrix} \sin(\omega t) & \frac{1}{2}\left(-\sin(\omega t)-\sqrt{3}\cos(\omega t)\right) & \frac{1}{2}\left(-\sin(\omega t)+\sqrt{3}\cos(\omega t)\right) \\ \cos(\omega t) & \frac{1}{2}\left(-\cos(\omega t)+\sqrt{3}\sin(\omega t)\right) & \frac{1}{2}\left(-\cos(\omega t)-\sqrt{3}\sin(\omega t)\right) \end{bmatrix}\begin{bmatrix} v_{Sa}^+ \\ v_{Sb}^+ \\ v_{Sc}^+ \end{bmatrix} \quad (9)$$

$$\begin{bmatrix} v_d^- \\ v_q^- \end{bmatrix} = \frac{2}{3}\begin{bmatrix} -\sin(\omega t) & \frac{1}{2}\left(\sin(\omega t)-\sqrt{3}\cos(\omega t)\right) & \frac{1}{2}\left(\sin(\omega t)+\sqrt{3}\cos(\omega t)\right) \\ \cos(\omega t) & \frac{1}{2}\left(-\cos(\omega t)-\sqrt{3}\sin(\omega t)\right) & \frac{1}{2}\left(-\cos(\omega t)+\sqrt{3}\sin(\omega t)\right) \end{bmatrix}\begin{bmatrix} v_{Sa}^- \\ v_{Sb}^- \\ v_{Sc}^- \end{bmatrix} \quad (10)$$

where v_d^+ and v_q^+ are the $dq-$ components of the positive-sequence voltage, and

v_d^- and v_q^- are the $dq-$ components of the negative-sequence voltage.

IV. Simulation Results

In this section, the simulation results for the D-STATCOM with the proposed voltage dip detection method will be presented. The configuration of the D-STATCOM system with the proposed ELS algorithm based voltage dip detection that is shown in Fig. 2 is modelled using the MATLAB/SIMULINK software package. The modelling and simulations of the D-STATCOM have been carried out for unbalanced voltage dip. The system has been tested for mitigation of the unbalanced voltage dips. Three-phase grid voltages with 25% voltage dip and 20% amplitude unbalance are shown in Fig. 4 and the corresponding positive- and negative-sequence $dq-$ components are shown in Fig. 5. As shown in Fig. 5, the amplitude of the positive- sequence $d-$ component decreases to 0.75 pu and the $q-$component remains zero. In negative-sequence, the $d-$and $q-$components have amplitudes of 0.08 pu and -0.04 pu respectively during the unbalanced voltage dip. Fig. 6 shows the voltage waveform after compensation by the D-STATCOM with the proposed dip detection method in the case of unbalanced voltage dip. As expected, the PCC voltage is constant at 1 pu before, during and after the voltage dip, apart from the transient at the beginning and at the end of the voltage dip. The error in the voltage waveform is also shown in Fig. 6. As may be seen, the error is very small in the steady-state and the transient errors of less than 0.2 pu appear for short durations.

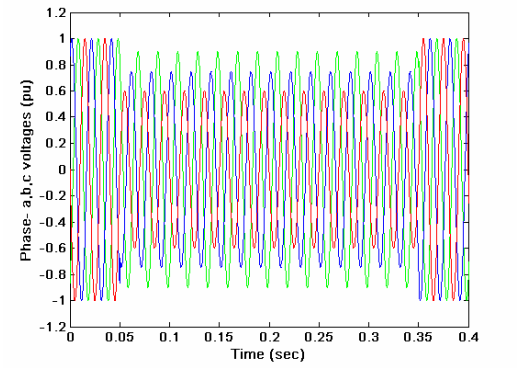

Figure 4 Simulated three-phase grid voltages during unbalanced voltage dip.

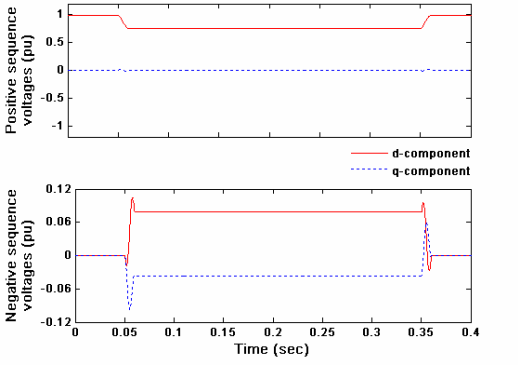

Figure 5 Simulated grid voltages in SRF $dq-$components in case of 25% voltage dip with 20% amplitude unbalance. Top: positive- sequence in positive SRF; bottom: negative-sequence in negative SRF.

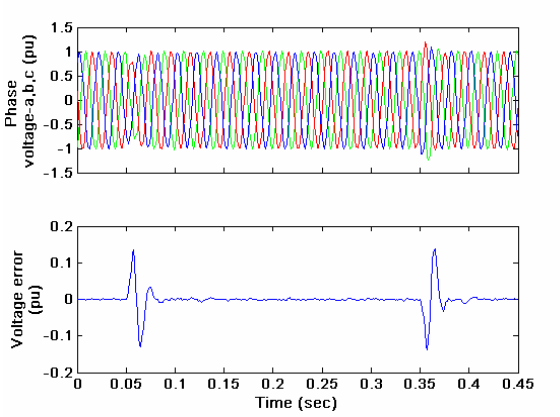

Figure 6 Compensated voltage waveforms at PCC and voltage waveform error in the case of unbalance voltage dip.

V. Conclusions

This paper has shown that the proposed ELS algorithm can be used for voltage dip and unbalanced mitigation in the D-STATCOM. The D-STATCOM consists of positive- and negative-synchronous reference frame controllers that regulate the $dq-$components of the positive and negative voltage to result in balanced three-phase voltages at the point of common coupling. The *dc*-link voltage is regulated to a set value via the $d-$axis current. The synchronous reference frame $dq-$axes current controllers are utilized to force the currents into the grid. The instantaneous positive- and negative- sequence components of the voltages are obtained using the instantaneous cosine and sine terms of the fundamental components of phases -*a*, -*b* and -*c*. The identified positive- and negative-sequence components are then represented in the positive- and negative- synchronous reference frames respectively. These voltage components are regulated to set values that correspond to the three-phase balance voltages in order to mitigate the voltage dips and unbalances. The proposed voltage dip and unbalance detection method allows for extraction of these sequence component within a half fundamental cycle. In addition the proposed method is capable of identifying the voltage dips and unbalances accurately even though the point of common coupling is strongly corrupted by the voltage harmonics. A prototype D-STATCOM system is modelled and simulated using MATLB/SIMULINK. The modelled system is tested for identification and mitigation of the unbalanced voltage dip. Extensive simulation studies showed that the proposed voltage unbalance and dip detection method allows fast and accurate extraction of information that is required for successful operation of the D-STATCOM system.

References

[1] O. C. Montero-Hernandez and P. N. Enjeti, "A fast detection algorithm suitable for mitigation of numerous power quality disturbances," presented at IEEE Industry Applications Conference, 2001.

Starting Jerk Reduction for Switched Reluctance Motors Using Initial Rotor Position Estimation Method

P. Jitkreeyarn[1, 2], K. Tungpimolrut[1], P. Nakmahachalasint[2]
National Electronics and Computer Technology Center[1],
112 Thailand Science Park, Phahon Yothin Rd., Klong 1, Klong Luang, Pathumthani 12120, Thailand
Faculty of Engineering, Thammasat University[2]
Phahon Yothin Rd., Klong 1, Klong Luang, Pathumthani 12120, Thailand

***Abstract*- In this paper a starting jerk reduction method for switched reluctance motors has been proposed. The method is based on an improved initial rotor-position estimation technique at standstill condition. In the propose method, the rotor position is simply estimated using only the phase current data from three current sensors without any priori knowledge of motor parameters. The results from this research have shown reasonable outputs. This could be proved that the purposed method has more accuracy than the previous methods.**

***Index Term*- Reluctance machines, estimation, starting.**

I. INTRODUCTION

With various merits of switched reluctance motors (SRMs), such as rugged low-cost construction, no permanent magnet inside, simple stator and rotor structure, easily cooling system, high reliability and good performance over a wide speed range, have make it a comparable competitor to the other drives and suitable for propulsion systems of the electric vehicle (EV) and hybrid vehicle (HV). Also, its performance can be easily adjusted for various load profile.

For traction drive applications, a high starting torque is required. Therefore, a 3-phase, 6/4 pole (i.e., 6 stator poles, and 4 rotor poles) SRM which has higher inductance ratio is suitable for these applications. In the view point of starting performance, the 6/4 pole SRM which has a large stroke angle may have a poor accelerating characteristic including starting jerk caused by an error on initial rotor position estimation. The oscillation and backward movement from the starting jerk problem are ones of the sensitive problems for EV application.

To solve this problem, incremental encoders, which are much less costly than absolute encoders, are widely used. However, incremental encoders do not have any data at the initial position, thus various estimating methods have been proposed. Most methods are based on complex calculation and machine parameters [1], [2], [3].

In this paper, a simple and more accurate initial rotor position estimation method is proposed, and starting jerk at standstill condition is mainly focused. An incremental encoder is used for the reason of system reliability. The proposed method is analyzed and experimentally investigated on a 1.5 kW 6/4 pole SRM which is designed for small electric vehicles. A Basic principle about the relation between the inductance, winding current and rotor angle at the standstill condition is analytically mentioned. The principle of the proposed method is described, and some information on the test system and its result are shown.

II. BASIC PRINCIPLE

Figure 1 shows the outline of the tested motor at different rotor position. When the rotor rotates into any direction, the inductance of the winding is varied. The relationship between the rotor position and the phase inductance can be drawn as in Figure 2. Under normal running condition and starting condition, the excitation signal for each phase must be properly synchronized to the phase inductance values within torque development zone (i.e., when the inductance profile has a positive slope) in order to generate large positive torque. Therefore, to rotate the motor into the specified direction correctly, the rotor position is required to be known.

For a SRM drive system, even though the widely used incremental encoder can provide the rotor position data, still the rotor position at the initial stage cannot be accessed before the real position has been known. When the motor begins to rotate, some undesirable events could happen, for examples: the motor temporarily rotates into the wrong direction; the motor starts to jerk back and forth before it can run smoothly. The starting jerk problem as shown in Figure 3 and Figure 4 can occur in the situation where the motor with inaccurate initial rotor-position data is attempting to immediately adjust to the true position after the encoder index has been detected. Therefore, a more accurate initial rotor-position estimation technique has been developed in this paper. This improved technique will be described in the next section.

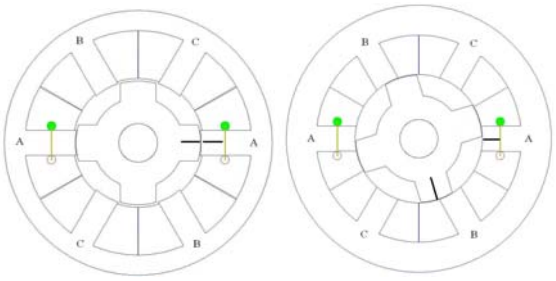

a) Rotor at 0°(aligned position), b) Rotor at 73°

Figure 1. Cross section of a 6/4 pole 3 phase SRM.

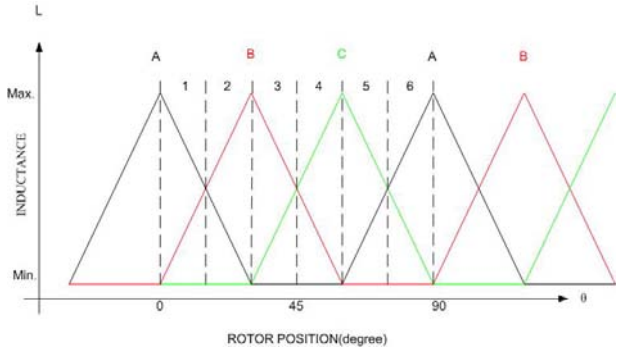

Figure 2. Idealized unsaturated inductance versus the rotor position.

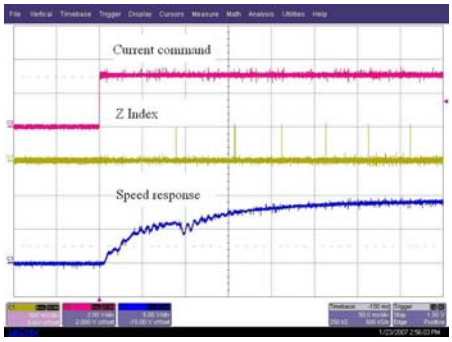

Figure 3. Current command, Z Index and speed response for estimated position = 68°, rotor position = 73° with load 2 Nm.

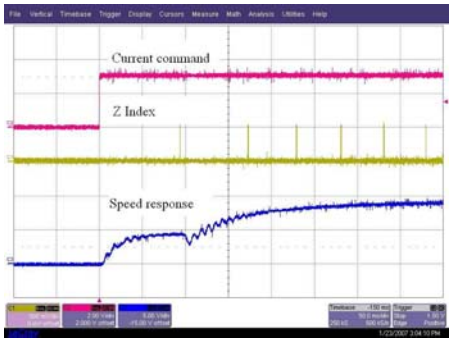

Figure 4. Current command, Z Index and speed response for estimated position = 83°, rotor position = 93° with load 2 Nm.

III. ROTOR POSITION ESTIMATION

A. *Previous methods*

In recent years, several rotor position estimation methods have been studied for SRMs [1]-[5]. In [1], [2] the phase winding at the motor stator is first excited. Then the rotor pole can be aligned in the same direction as the excited stator pole. With this method, the rotor position can be accessed but the rotor has to move. Therefore, there is a possibility that the rotor move to the wrong direction.

In [1], [2], [3] the rotor position estimation method can be done by motor testing. Firstly, the excited voltage has been applied to the stator pole; next the phase current has been measured and calculated for flux linkage. Then the measurement result is compared to the data that has been collected during the motor is working properly.

TABLE I
The relation between the current amplitude and the rotor position

Section No.	Rotor position	Current	Rotor estimation
1	0°<θ<15°	Ia<Ic<Ib	7.5°
1	θ=15°	Ia=Ic<Ib	15°
2	15°<θ<30°	Ic<Ia<Ib	22.5°
2	θ=30°	Ic<Ia=Ib	30°
3	30°<θ<45°	Ic<Ib<Ia	37.5°
3	θ=45°	Ic=Ib<Ia	45°
4	45°<θ<60°	Ib<Ic<Ia	52.5°
4	θ=60°	Ib<Ic=Ia	60°
5	60°<θ<75°	Ib<Ia<Ic	67.5°
5	θ=75°	Ib=Ia<Ic	75°
6	75°≤θ<90°	Ia<Ib<Ic	82.5°
6	θ=90°	Ia<Ib=Ic	90°

Therefore with this method, the necessary data of the motor during the working is needed and this could lead to the mistaken if the voltage period is too small or the measurement instrument is not accurate enough to separate the rotor angles if the voltage period is getting bigger. This also could lead to the undesirable moving of shaft similar to the first method [1], [2], [3].

In [4], [5] the rotor position estimation method is applying the small testing signal and measuring the phase current of the motor. The phase current can estimate the rotor position in some interval and the appropriated phase can be selected for exciting the winding at starting condition. However, this method is only an approximation for the rotor position and is not accurate enough. For applying to the 6/4 pole 3 phase of SRM, the rotor position can be estimated for the interval of 15 degrees only.

Therefore, in order to apply this method in our work, the rotor position could be estimated as in table 1. But the precision was not satisfied and cause the problem in the real application. Therefore the new technique has been developed to solve this kind of problem.

B. *Proposed method*

This estimation method used each phase current data based on the assumptions that the resistive voltage drop is negligible and there is no mutual coupling between two phases, the voltage equation of one SRM phase can be simplified as (1). Using inject the short duration about few hundred microseconds of gate drive signal to each phase simultaneously, each phase winding current will increase as a straight line from zero and have peak value at the end of excitation as shown in Figure 5. The period of the pulse is short enough and do not produce enough torque to move the rotor. That means the relation in (2) is valid and the slope of the current waveform directly depend on the value of V/L.

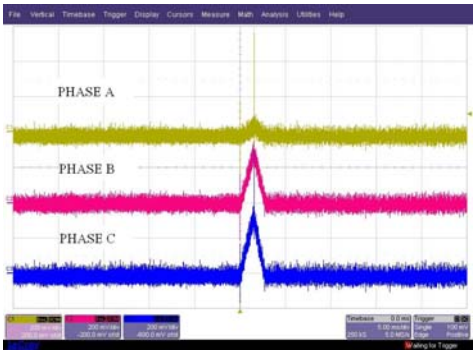

Figure 5. Current from test signal using the proposed method at rotor = 0°.

Where V is the supply voltage and L is the phase inductance, respectively. (1), (2)

$$V = L\frac{di}{dt} \tag{1}$$

$$\Delta i = \frac{V}{L} \times \Delta t \tag{2}$$

Figure 6 indicates the measured winding peak current at every one degree of rotor position. The apply voltage about 600 microsecond is applied and the current is measured by three hall- effect current sensors (HX50-P) and 8-bit A/D converters.

From Figure 6 the current waveform can be also divided in 6 sections similarly to the inductance profile in Figure 2. Each section has one phase that amplitude is nearly zero. The currents in other two phases are used for rotor position calculation in that section. Also, it always has cross section point at 0°, 30°, 60° and 90°. In the proposed method, for example between 15° to 45°, phase C current has minimum value and phase A and B are symmetrical around 30° point. For analysis, the current-profiles are approximated by straight line as shown in Figure 7. The relation between measured current and rotor position can be solved by the following (3).

$$\theta est = 30 + [(Ia - Ib)\frac{\theta base}{(Ia + Ib)}] \tag{3}$$

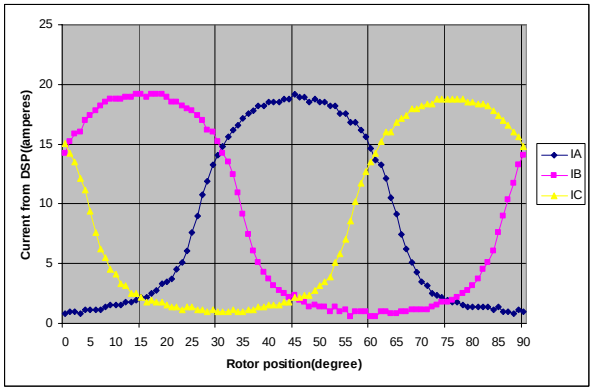

Figure 6. Phase currents obtained from DSP with A/D 8 bits versus the rotor position.

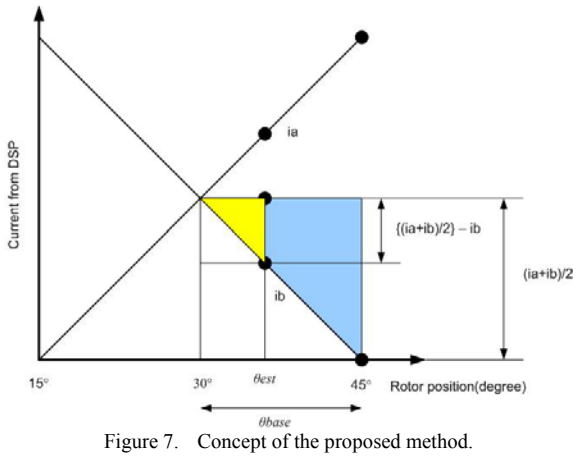

Figure 7. Concept of the proposed method.

Where

θest = Estimate rotor position
Ia = maximum phase current
Ib = second maximum phase current
$\theta base$ = base of section (15°)

It is assumed that the minimum current in each section is very small, therefore its value can be set to zero. With the same concept, the rotor position in the other section can be calculated as below:

Section 1: Rotor position during 0° to 15°, calculate from (4)

$$\theta est = (Ib - Ic)\frac{15}{(Ib + Ic)} \tag{4}$$

Section 2: Rotor position during 16° to 30°, calculate from (5)

$$\theta est = 30 - [(Ib - Ia)\frac{15}{(Ib + Ia)}] \tag{5}$$

Section 3: Rotor position during 31° to 45°, calculate from (6)

$$\theta est = 30 + [(Ia - Ib)\frac{15}{(Ia + Ib)}] \tag{6}$$

Section 4: Rotor position during 46° to 60°, calculate from (7)

$$\theta est = 60 - [(Ia - Ic)\frac{15}{(Ia + Ic)}] \tag{7}$$

Section 5: Rotor position during 61° to 75°, calculate from (8)

$$\theta est = 60 + [(Ic - Ia)\frac{15}{(Ic + Ia)}] \tag{8}$$

And Section 6: Rotor position during 76° to 90°, from (9)

$$\theta est = 90 - [(Ic - Ib)\frac{15}{(Ic + Ib)}] \tag{9}$$

IV. EXPERIMENTAL RESULTS

Figure 8 shows the experiment setup which consists of SRM, torque meter and DC motor. SRM is coupled to the torque meter while the DC motor is used as a load for 2 Nm.

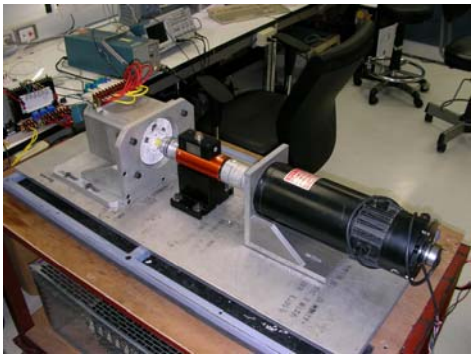

Figure 8. Experimental setup for testing the SRM.

The result of the estimated rotor position using the proposed method is shown and compared to the actual rotor position in Figure 9.

In this experiment, the actual rotor positions were measured after the first index has been detected using an external circuit to detect the rotor position.

Figure 10, 11 show the experimental result by using our technique at the rotor position = 73° and 93° near aligned position with load 2 Nm.

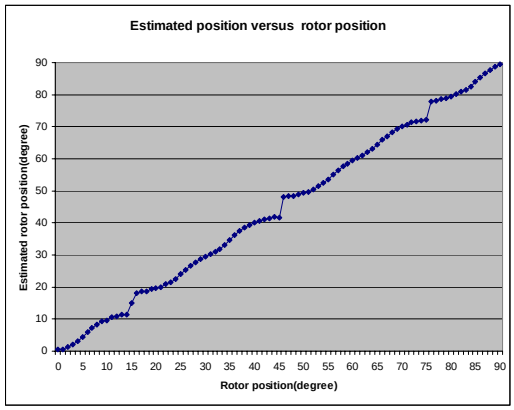

Figure 9. Estimated position versus rotor position.

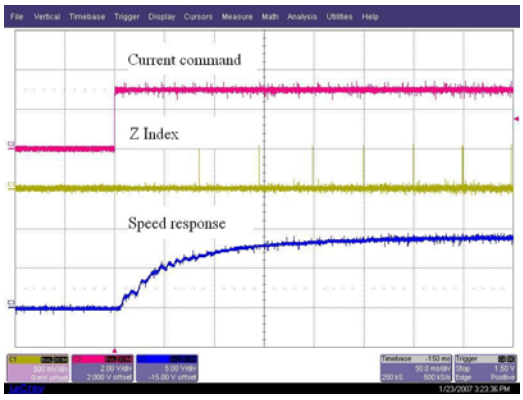

Figure 10. Current command, Z Index and speed response for rotor position estimation from the purposed method at rotor position = 73° with load 2 Nm.

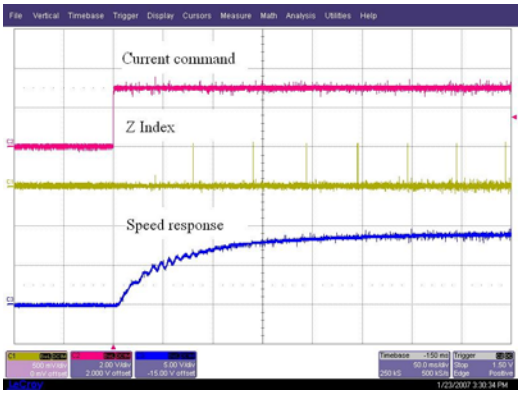

Figure 11. Current command, Z Index and speed response for rotor position estimation from the purposed method at rotor position = 93° with load 2 Nm.

V. CONCLUSIONS

The starting jerk reduction method based on improvement of the initial rotor position method for the SRM had been proposed. The effectiveness of the method is evidently shown by the experimental results. It has been shown that, position errors within 3.5degrees can be achieved whereas the previous method gives position errors within 7.5degrees. Consequently the starting jerk can be significantly reduced. Moreover, the proposed method can be easily implemented using a low-cost DSP without any motor parameter.

REFERENCES

[1] D. Panda, and V. Ramanarayanan, "Accurate Position Estimation in Switched Reluctance Motor With Smooth Starting," Industrial Technology 2000. Proceedings of IEEE International Conference on vol.1, 19-22 Jan 2000.

[2] J. Bu, and L. Xu, "Eliminating Starting Hesitation for Reliable Sensorless Control of Switched Reluctance Motors," IEEE *Trans. Ind. Applicat.*, vol.37 no.1 January/February 2001.

[3] W.D. Harris, J.H. Lang, "A Simple Estimator for Varible-Reluctance Motors," IEEE *Trans. Ind. Applicat.*, vol.26 no.2 , March/April 1990.

[4] H.Gao, F.R. Salmasi., and M. Ehsani, "Sensorless control of SRM at standstill", Applied Power Electronics Conference and Exposition, 2001. APEC 2001. Sixteenth Annual IEEE, vol. 2, 4-8 March 2001.

[5] X. Kai, Z. ionghua, and L. Jianwu, "A New Simple Sensorless Control Method for Switched Reluctance Motor Dives," Electrical Machines and Systems, 2005. ICEMS 2005. Proceedings of the Eighth International Conference on vol. 1, 27-29 Sept.

Linear Model of a Switched Reluctance Machine using Flux Tube Analysis

C. Boonkham , S. Kittiratsatcha
Department of Electrical Engineering, Faculty of Engineering
King Mongkut's Institute of Technology Ladkrabang
Chalongkrung Rd., Ladkrabang, Bangkok THAILAND 10520

***Abstract*- This paper proposes a simple linear model of a switched Reluctance Machine (SRM). The permeability of the core is set to be infinity. The equipotential flux at the air gap is obtained from the Finite Element Analysis (FEA). The approximated permeance or reluctance profile are generated by using flux tube analysis at various rotor positions. The validity of the proposed model is confirmed by the FEA. This linear model is a function of the motor geometry so the designer can choose the estimated sizes of the machine easily.**

I. INTRODUCTION

The magnetic property of the SRM depends on the machine's geometry especially the rotor and the stator poles. They define the characteristic of the pole flux [1]. To design the SRM, if the designer knows the equipotential flux path then the permeance can be calculated [2]. For this paper, the flux tube analysis is used to analyze the permeance profile of the candidate machine. Sine we know the permeance profile or reluctance profile, the magnetizing curve is known and the static torque profile can be estimated. The permeance profile definitely depends on the machine geometry. By developing the linear model, the designer can initially estimate the sizes of the machines. The detail of the design is finally done by the FEA program.

This paper proposes the permeance models at different rotor positions from 0% alignment to 100% alignment with 10% increment. Figure 1 depicts the equipotential flux path obtained from the FEA and the estimated flux path. This estimated flux path is used for the flux tube analysis [3].

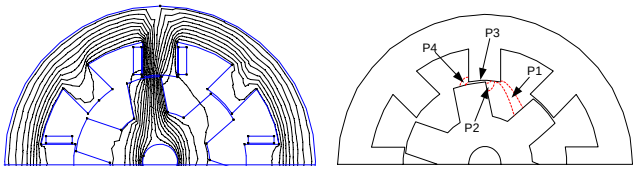

Figure 1. The equipotential flux path (left) obtained from the FEA and the estimated flux path for flux tube analysis (right).

II. FLUX TUBE ANALYSIS

The geometry of the rotor pole defines the inductance profile of the machine. Once the flux paths are known, then the permeance can be calculated. The method used for this calculation is called "flux tube analysis". For this proposal, flux paths are assumed to follow straight line segments as shown in Figure 2 and circular arcs as shown in Figure 3 as an approximation of their actual path. In deriving a model, the permeability of the iron is set to infinity, and saturation effects are neglected, as is fringing flux at the end of the core. A flux tube analysis is performed at different rotor positions from unaligned position to fully aligned position.

A. Straight line section.

Figure 2 shows the straight flux lines flowing from one ferromagnetic surface to another. The permeance is

$$\wp = \mu_0 l \frac{s}{g} \tag{1}$$

where s is the width of a ferromagnetic material, l is the depth of a ferromagnetic material, and g is the air gap between the two ferromagnetic surfaces.

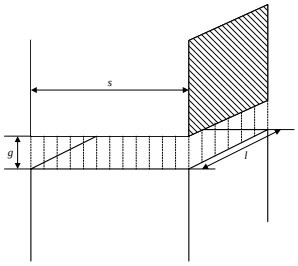

Figure 2. The two ferromagnetic surfaces showing the straight flux path.

B. Circular Arc section.

Figure 3 shows two surfaces that are not parallel and the resulting curved lines that are about a single center point for each equipotential line. The permeance is

$$\wp_3 = \frac{\mu_0 l}{\theta} \ln \frac{x_2}{x_1} \tag{2}$$

where x_1 and x_2 are radii, l is the depth of a ferromagnetic material, and θ is the angle between two ferromagnetic surfaces.

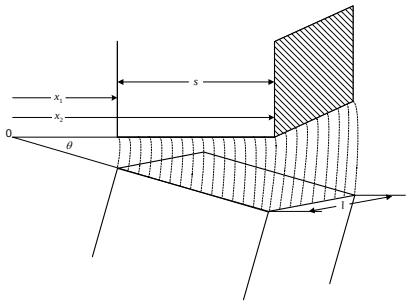

Figure 3. The two ferromagnetic surfaces showing the circular arc flux path.

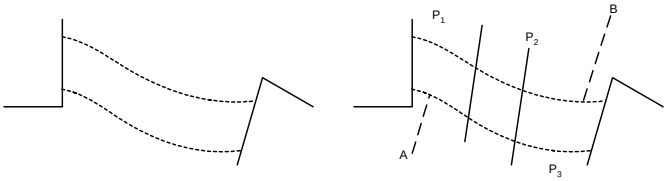

Figure 4. The arbitrary flux path can be divided into 3 basic sections.

For the example shown in Figure 4, the equipotential flux path can be separated into three basic paths. $\wp_1$ is a curved line with a center of rotation at point A. $\wp_2$ is a straight line and $\wp_3$ is a curved line with a center of rotation at point B. The total permeance of Figure 4 is shown as follow:

$$\wp_{total} = \left[\frac{1}{\wp_1} + \frac{1}{\wp_2} + \frac{1}{\wp_3}\right]^{-1} \quad (3)$$

III. Equipotential Flux Path

A finite element analysis program [4] is used to simulate the flux path. The geometry of the candidate machine is shown in Table I. Figure 5 depicts the cross-sectional of the machine in the FEA program. To simulate the linear property of the core, the permeability of the core material is set to be infinity, parameter in the program is set to 10^{12} as shown in Figure 6.

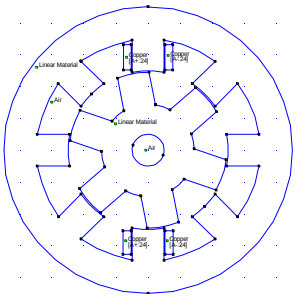

Figure 5. The cross-sectional of the candidate machine.

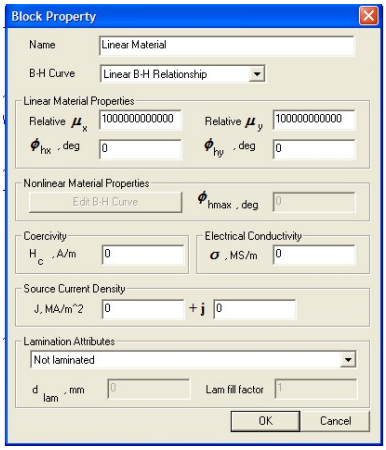

Figure 6. The permeability of the core material is set to 10^{12} in FEA program.

TABLE I
THE DIMENSIONS OF CANIDATE SRM

Stator outer diameter	90.00 mm
Internal stator diameter	34.50 mm
Internal rotor diameter	13.50 mm
Shaft diameter	10.00 mm
Stack length	50.00 mm
Airgap	0.50 mm
Winding turn per pole	24 turns

The results from FEA show the equipotential flux path as depicted in Figure 7. This is used to create the estimated flux path for further analysis.

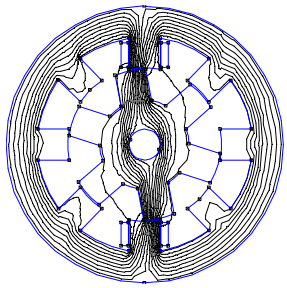

Figure 7. The equipotential flux paths of the exampled rotor position obtained from the FEA program.

IV. Example of the Proposed Method

From the FEA results, the equipotential flux path at different rotor positions is generated. The example is shown in Figure 8. The rest of the rotor positions are shown in the appendix.

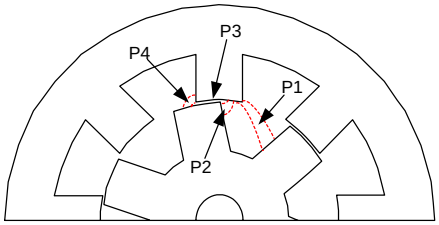

Figure 8. Estimated flux path from the exampled rotor position.

The estimated flux path in Figure 8 is divided into 4 permeance sections. Figure 9 – 12 show the flux path and the parameters for flux tube calculation for each basic section.

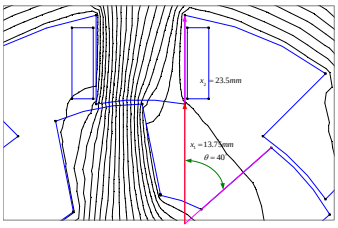

Figure 9. The equipotential flux path of section P1 and its dimension.

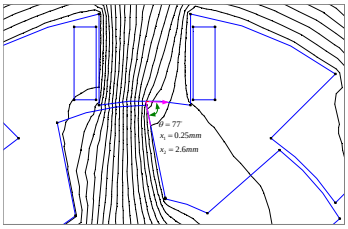

Figure 10. The equipotential flux path of section P2 and its dimension.

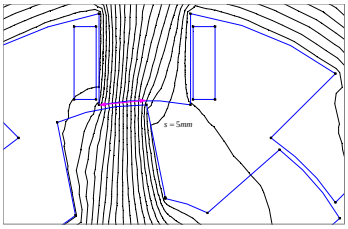

Figure 11. The equipotential flux path of section P3 and its dimension.

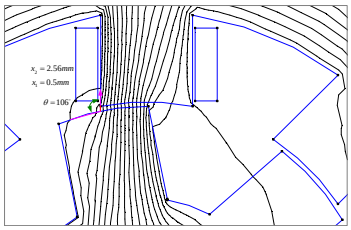

Figure 12. The equipotential flux path of section P4 and its dimension.

Once the permeance of each section is combined, the pole flux is calculated by using Equation 4.

$$\phi = \wp_{total} \times Ni \tag{4}$$

where ϕ is the pole flux, $\wp_{total}$ is the total permeance at considered pole, N is the number of turns and i is the phase current.

From the Figure 13 reveals that the results from FEA and the proposed model are acceptably close. The phase current is set to 1A.

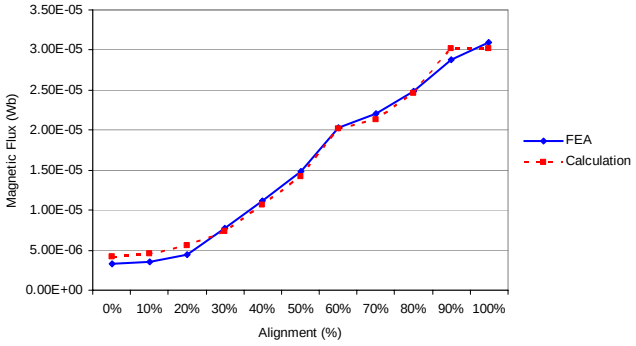

Figure 13. The comparison of the pole flux between FEA and the proposed linear model.

V. CONCLUSION

Flux tube analysis is used to develop a linear model of the SRM. The linear model provides a simple and quick solution of how to determine the machine geometry initially. The results of the proposed model are accurate by comparing with the FEA results. This method can be applied with any numbers of phases of SRM. The non linear model will be discussed in the near future.

REFERENCES

[1] T.J.E. Miller, "Switched Reluctance Motors and Their Control", Hillsboro, OH: Magna Physics Publishing and London: Oxford University., pp. 32-40, Press 1993.

[2] S. Kittiratsatcha, "A Two-Phase Switched Reluctance Motor and Its Drive," *Rensselaer Polytechnic Institute Troy, New York.*, pp. 15-51, August 2002.

[3] J.J. Cathay, "Unidirectional Switched Reluctance Machine," University of Kentucky Research Foundation, September 1992

[4] http://femm.foster-miller.net.

APPENDIX

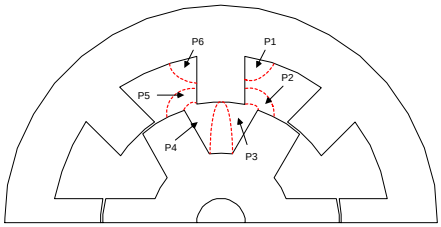

Figure 14. The estimated flux path at 0% alignment.

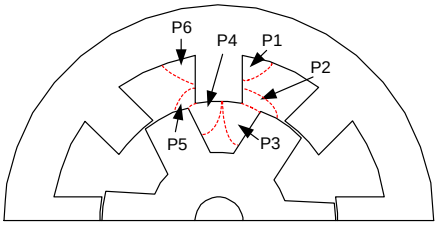

Figure 15. The estimated flux path at 10% alignment.

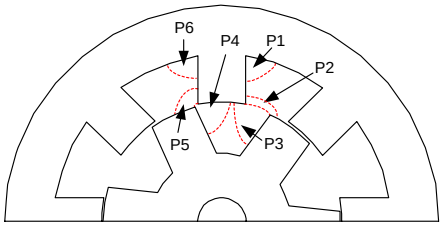

Figure 16. The estimated flux path at 20% alignment.

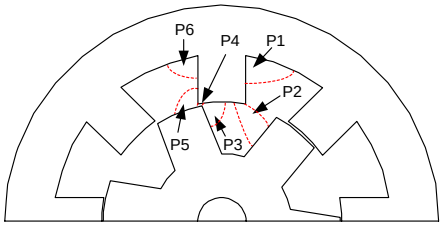

Figure 17. The estimated flux path at 30% alignment.

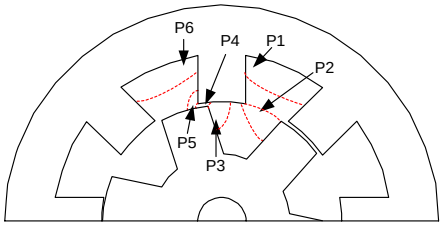

Figure 18. The estimated flux path at 40% alignment.

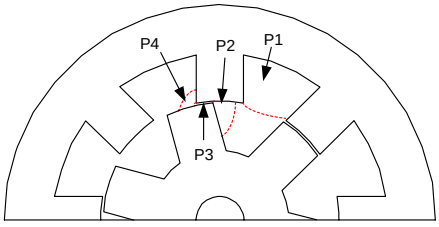

Figure 19. The estimated flux path at 50% alignment.

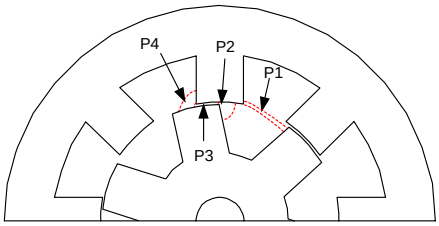

Figure 20. The estimated flux path at 60% alignment.

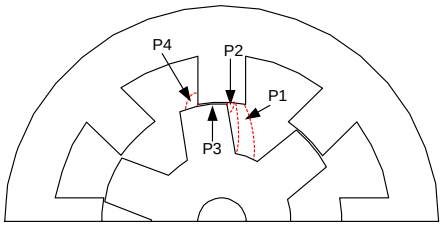

Figure 21. The estimated flux path at 70% alignment.

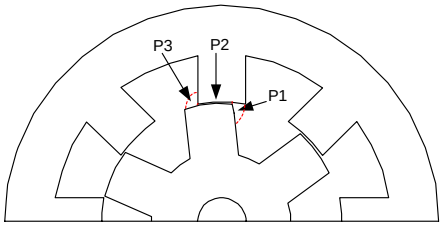

Figure 22. The estimated flux path at 80% alignment.

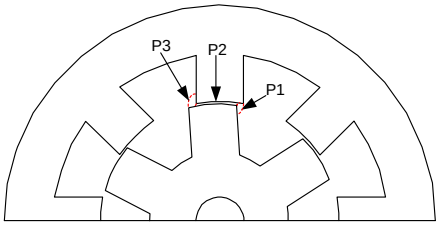

Figure 23. The estimated flux path at 90% alignment.

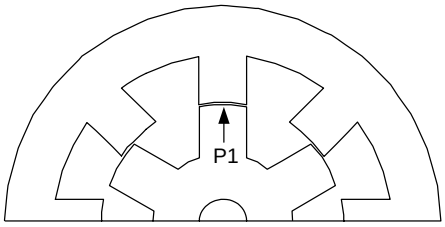

Figure 24. The estimated flux path at 100% alignment.

Field Efficiency Estimation Technique for Inverter-Fed Induction Motor

T. Phumiphak* and C. Chat-uthai**

* Department of Electrical Power Engineering, Faculty of Engineering, Mahanakorn University of Technology, Bangkok 10530, Thailand (e-mail: kcthanaphiwat@yahoo.com)

** Department of Electrical Engineering, Faculty of Engineering, King Mongkut's Institute of Technology Ladkrabang, Bangkok 10520, Thailand (e-mail: kcchaiwu@kmitl.ac.th)

***Abstract*-This paper presents a technique for estimating the field efficiency of inverter-fed induction motor at various operating frequencies and loads using only a set of data from field measurement without the need for measuring output of motor which is highly intrusive task. The field performances of motor such as output power and torque, and efficiency can be estimated by using the measurement data coupled with the use of genetic algorithms based on motor equivalent circuit concept. The 2.2 kW and 5.5 kW three-phase induction motors fed by inverter were tested under operating frequencies of 40, 45, 50 Hz at various loads. The estimated results of proposed technique are presented and then compared to the measured values obtained from laboratory test and found to give a better correlation over a wide range of speeds and loads. This efficiency technique expects to be useful in assisting decisions of replacement of motors in industry because of its acceptable accuracy and non-intrusive operation.**

I. INTRODUCTION

In power system, the largest component of the loads is three-phase induction motors and they are extensively used in industrial and commercial applications. The ac frequency-controlled variable-speed drives have recently shown a growing number of applications in the process industries. The most common configuration is a pulse-width-modulation (PWM) frequency converter. When induction motors are driven by inverters for variable speed, the waveforms become distorted and contain several higher order harmonics. In regard to efficiency considerations, for the motors operating with variable speed, there are two major differences that need to be considered. First, as the cooling fan is attached to the motor shaft, when the operating speed goes down, the fan rotates at lower speed; therefore the air impelled by the fan is then reduced. Secondly, for the motor fed from frequency converter, the core losses change at different operating frequencies affecting the internal losses and temperatures. In addition, current harmonics circulating in the windings produce additional heating.

As far as energy consumption is concerned, reducing induction motor efficiency means that the increase of the induction motor losses. If the rated output of an induction motor is maintained, motor input power will be increased. In other words, when a motor is operating at rated power output with variable speed, the utility has to supply more input power to accomplish the same work. As for the customers, if an induction motor efficiency is reduced (higher total losses), the electricity charge on the customers will be increased. Many research papers have been reported regarding the performance prediction of induction motors under distorted supply systems [1-3]. The predicted performance figures are obtained from the solution of the equivalent circuits whose parameters are different for fundamental and for different harmonics. Some authors have assumed the parameters to be constant irrespective of the presence of harmonic contents in the supply voltage but in practice some of the parameters vary considerably depending upon the order of harmonic. Thus, the predicted performances using such models are quite different from the measurements. Obviously, this is an unacceptable condition.

In this paper, the focus is put on how field efficiency of inverter-fed induction motor can be determined by minimum intrusion. A technique for estimating efficiency of such motor using only a set of accessible data from field measurement without the need for measuring motor output is then proposed. The appropriate value of motor parameters at any operating load (variable speed) can be evaluated by the use of measured data such as frequency, rms voltage, rms current, input power, and speed coupled with the numerical optimization technique called genetic algorithms (GAs) [4]. The GAs are a heuristic technique based on the evolutionary processes similar to natural selection, mutation, and reproduction observed in biological systems that may be used to solve a system of nonlinear equation.

II. INVERTER-FED INDUCTION MOTOR

Induction motor efficiency characterizes the energetic behavior during the conversion of the electrical power in mechanical power. Comparison of motor efficiencies is certainly a valid tool to justify the use of one motor over another. The motor field efficiency is mainly a function of operating output load and speed which is defined as

$$\text{Field Efficiency} = \frac{P_{mechanical}}{P_{electrical}} \cdot 100 \qquad (1)$$

where $P_{mechanical}$ is the output power at motor shaft and $P_{electrical}$ is the electrical power absorbed from supply.

The difference of these two powers is the total operating losses which can be subdivided into the core, windings, and mechanical losses. As stated in [1], the operation of inverter-fed induction motor drive with variable voltage, variable frequency and variable rotational speed has an effect on these operating losses.

The core losses (hysteresis and eddy-current) are highly dependent on frequency and the maximum flux density per pole. For the drive operating in the range of speeds up to the base speed, the maximum flux density is kept constant at different frequencies; therefore the ratio voltage per frequency has to be kept constant. For speeds above the base speed, voltage is constant and frequency is increased. In this range, eddy-current losses become constants, and hysteresis losses reduce slightly with the increase of frequency. Copper losses in windings and rotor bars depend on the rms current squared, and on the resistances. Fundamental frequency current components depend on the motor load, while harmonic components depend on the specific PWM pattern at the operating point, and motor parameters. The effects of current harmonics are mainly two. First, they produce additional vibrations and noise. Secondly these current harmonics produce the extra heating that will affect the steady temperatures reached in the windings. Mechanical losses depend on the operating motor speed, and are related to friction in bearing and windage (rotor blades).

III. FIELD EFFICIENCY ESTIMATION

This paper proposes a non-intrusive technique for estimating the field efficiency of inverter-fed induction motor operating at any load (variable speed) without costly testing procedure. The estimated field efficiency is based on the concept of equivalent circuit parameters [5]. From the equivalent circuit, the motor performances can be defined as follows

$$\mathbf{Z}_1 = R_1 + j\omega L_1 \tag{2}$$

$$\mathbf{Z}_2 = \frac{R_c\, j\omega L_m}{R_c + j\omega L_m} \tag{3}$$

$$\mathbf{Z}_3 = R_{SLL} + j\omega L_2 + \frac{R_2}{s} \tag{4}$$

$$\mathbf{Z}_{total} = \mathbf{Z}_1 + \frac{\mathbf{Z}_2\mathbf{Z}_3}{\mathbf{Z}_2 + \mathbf{Z}_3} \tag{5}$$

the motor power factor can be expressed as

$$PF = \cos\left(\tan^{-1}\left(\frac{\mathrm{Im}(\mathbf{Z}_{total})}{\mathrm{Re}(\mathbf{Z}_{total})}\right)\right) \tag{6}$$

$$\mathbf{I}_1 = \frac{\mathbf{V}_1}{\mathbf{Z}_{total}} \tag{7}$$

$$\text{input power} \quad P_{input} = 3V_1 I_1 (PF) \tag{8}$$

$$\mathbf{I}_2 = \frac{\mathbf{I}_1\mathbf{Z}_2}{\mathbf{Z}_2 + \mathbf{Z}_3} \tag{9}$$

then, the estimated motor performances are obtained from

$$\text{output power} \quad P_{output} = \frac{3I_2^2 R_2 (1-s)}{s} \tag{10}$$

$$\text{output torque} \quad T_{output} = \frac{P_{output}}{\omega_r} \tag{11}$$

$$\text{Efficiency} = \frac{P_{output}}{P_{input}} \cdot 100 \tag{12}$$

where V_1, I_1, R_1 and L_1 denote stator voltage, current, resistance and leakage inductance respectively, I_2, R_2 and L_2 stand for rotor current, resistance and leakage inductance referred to stator respectively, R_c is core loss resistance, L_m is magnetizing inductance, R_{SLL} is the proposed stray load loss parameter [5], s denotes slip and ω denotes angular velocity ($2\pi f$).

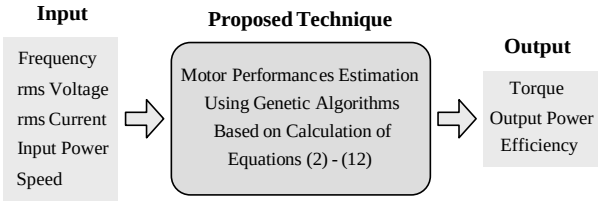

Figure 1. Flowchart of Field Efficiency Estimation

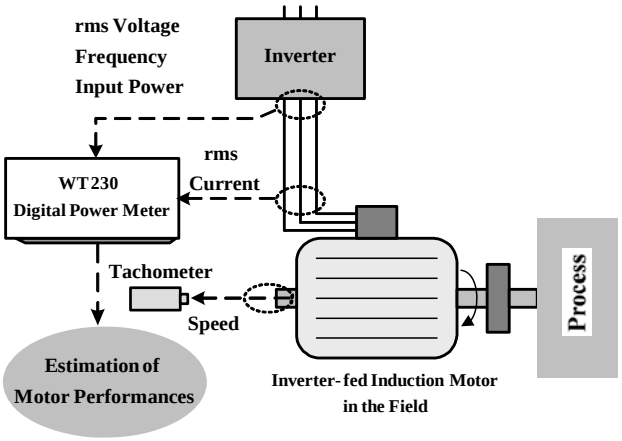

Figure 2. Implementation for Proposed Technique

The appropriate parameters of motor at any condition can be estimated by using a set of measured data coupled with the use of genetic algorithms as shown in Fig. 1. The field data which rely on measuring input frequency, rms voltage (V_1), rms current (I_1), electrical power (P_{input}) and speed of motor are obtained from field measurement as shown in Fig. 2. Then, the motor parameters can be evaluated by using Eq. (7) and (8)

coupled with the GAs in order to minimize the error of Eq. (13).

$$\text{Min.} \quad F_{objective} = \left|\frac{I_{1,cal}}{I_{1,mea}} - 1\right|^2 + \left|\frac{P_{input,cal}}{P_{input,mea}} - 1\right|^2 \qquad (13)$$

where $I_{1,cal}$ and $P_{input,cal}$ are the calculated values using Eq. (7) and (8). $I_{1,mea}$ and $P_{input,mea}$ are the measured values obtained from the operating motor.

IV. EXPERIMENTAL RESULTS

The non-intrusive technique described above was applied to two different sizes of three-phase induction motors. Table 1 shows the nameplate information of the motors. These motors were tested in the laboratory using standard electrical instrumentation. The motors under test were supplied with power from the three-phase inverter (380-480 V, 50/60 Hz, 27.9A, switch frequency 1 kHz, Fuji FRENIC 5000G11, Type FRN7.5G11S-4JE). For input electrical power a three-phase digital power meter (model WT230, Yokogawa) provided data on frequency, voltage, current and power. The values of both voltage and current were measured in mode rms obtained by

$$\sqrt{\frac{1}{T}\int_0^T f(t)^2 dt} \qquad (14)$$

where $f(t)$ denotes input signal (voltage or current) and T is one period of the input signal.

TABEL I
NAMEPLATE INFORMATION OF INDUCTION MOTORS

	2.2 kW (3 hp)	5.5 kW (7.5 hp)
Hz	50	50
V	220/380	220/380
A	8.7/5.0	20.4/11.8
rpm	1420	1430
Pole	4	4

The motors were loaded by a dynamometer with rotating shaft-mounted torque sensor and tachometer for measuring motor output torque and speed. The load test of motors was performed at three different operating frequencies (40, 45 and 50 Hz) under various loads. The load test results (T) of 2.2 kW and 5.5 kW motors were shown in Fig 3 and 4 respectively. To illustrate the use of this proposed technique, assume that an inverter-fed induction motor is operating in the process at a given frequency and load. For example, the 2.2 kW motor is operating at frequency of 40 Hz, the set of data obtained from field measurement is 226.6 V (rms), 5.12 A (rms), 2371 W, 1104.5 rpm as illustrated in Table 2. By using Eq. (13), the appropriate motor parameters under this condition are evaluated and the motor performances can be estimated. The result shows that the estimated (E) output torque and power are 14.56 N-m and 1684.7 W while the actual torque and power obtained from test are 14.86 N-m and 1719.7 W, and the estimated efficiency is 71.06 % while the actual is 72.53 %. From Table 3, the 5.5 kW motor is operating at 45 Hz, the measurement data is 240.3 V, 10.36 A, 5335 W, 1292.6 rpm. The estimated efficiency is 83.46 % while the test is 82.67 %.

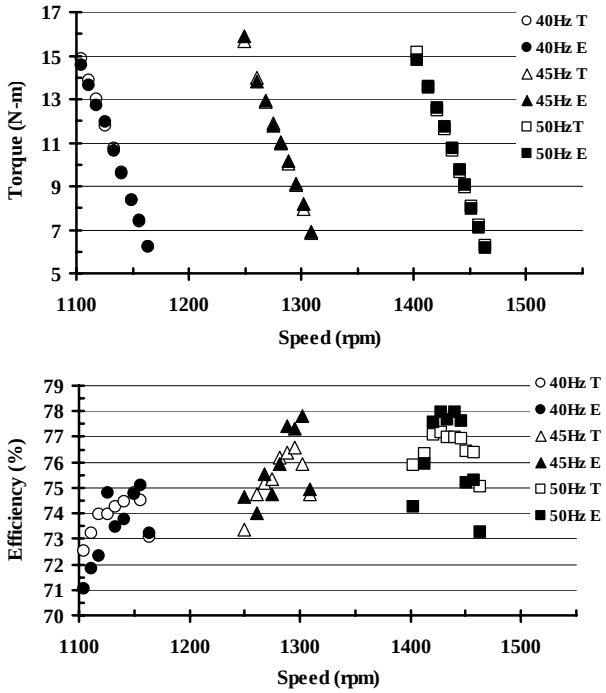

Figure 3. Performances Estimation and Laboratory Test Results of 2.2 kW Motor Versus Speed

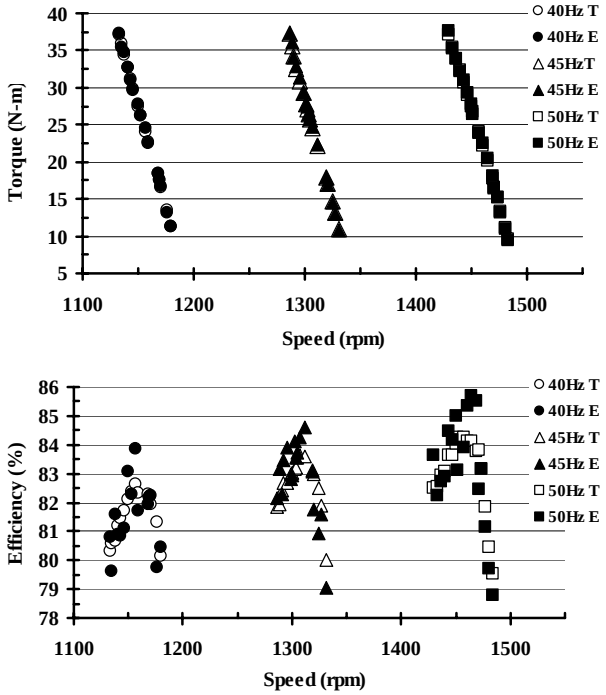

Figure 4. Performances Estimation and Laboratory Test Results of 5.5 kW Motor Versus Speed

TABLE II
EXAMPLE RESULTS OF PERFORMANCES ESTIMATION USING PROPOSED TECHNIQUE FOR 2.2 kW MOTOR

		Fixed Output Power		
Field Measurement		f = **40** Hz	f = **45** Hz	f = **50** Hz
Phase Voltage (V)		226.6	238.2	249.5
Phase Current (A)		5.12	4.56	4.21
Input Power (W)		2371	2278	2250
Speed (rpm)		1104.5	1268.4	1427.5
Performances Estimation E : estimation T : laboratory test				
Output Torque (N-m)	E	14.56	12.95	11.73
	T	14.86	12.89	11.61
Output Power (W)	E	**1684.7**	**1720.8**	**1754.2**
	T	**1719.7**	**1712.9**	**1736.3**
Efficiency (%)	E	71.06	75.54	77.96
	T	72.53	75.19	77.17

		Fixed Output Torque		
Field Measurement		f = **40** Hz	f = **45** Hz	f = **50** Hz
Phase Voltage (V)		226.2	237.8	249.44
Phase Current (A)		4.28	4.29	4.21
Input Power (W)		1883	2110	2250
Speed (rpm)		1125.8	1275.1	1427.5
Performances Estimation E : estimation T : laboratory test				
Output Torque (N-m)	E	**11.94**	**11.81**	**11.73**
	T	**11.81**	**11.90**	**11.61**
Output Power (W)	E	1408.2	1577.6	1754.2
	T	1392.9	1589.6	1736.3
Efficiency (%)	E	74.79	74.77	77.96
	T	73.97	75.34	77.17

TABLE III
EXAMPLE RESULTS OF PERFORMANCES ESTIMATION USING PROPOSED TECHNIQUE FOR 5.5 kW MOTOR

		Fixed Output Power		
Field Measurement		f = **40** Hz	f = **45** Hz	f = **50** Hz
Phase Voltage (V)		228.76	240.3	249.2
Phase Current (A)		11.53	10.36	9.52
Input Power (W)		5486	5335	5264
Speed (rpm)		1133.4	1292.6	1446.9
Performances Estimation E : estimation T : laboratory test				
Output Torque (N-m)	E	37.34	32.88	29.23
	T	37.11	32.57	29.04
Output Power (W)	E	**4433.6**	**4452.5**	**4430.7**
	T	**4406.3**	**4410.5**	**4401.9**
Efficiency (%)	E	80.82	83.46	84.17
	T	80.32	82.67	83.62

		Fixed Output Torque		
Field Measurement		f = **40** Hz	f = **45** Hz	f = **50** Hz
Phase Voltage (V)		228.7	241.0	247.7
Phase Current (A)		11.53	11.63	11.79
Input Power (W)		5486	6124	6737
Speed (rpm)		113.4	1286	1430.1
Performances Estimation E : estimation T : laboratory test				
Output Torque (N-m)	E	**37.34**	**37.34**	**37.62**
	T	**37.11**	**37.20**	**37.10**
Output Power (W)	E	4433.6	5030.6	5636.2
	T	4406.3	5011.7	5558.3
Efficiency (%)	E	80.82	82.15	83.66
	T	80.32	81.84	82.50

Notice that the estimated values in Table 2 and 3 are not much different from the test. For comparison, the example results of torque and efficiency estimations of the motors at any operating frequency and load using this proposed technique are listed with the test data as shown in Fig 3 and 4. It can be observed that the correlation of proposed technique and actual is remarkably good, and the performance results also show the good agreement; many of the errors are obviously less than 2 %. From Fig. 3 and 4 together with Table 2 and 3, it is evident that the efficiency of motors are reduced when they are operating with variable speed under either fixed output power or fixed output torque conditions.

V. CONCLUSION

The proposed non-intrusive technique for estimating field efficiency of inverter-fed induction motor based on field measurement has been described. This technique relies on the available information of measured voltage, current, electrical power and speed of actual motor in the field without conducting motor tests. These field data coupled with the GAs are used for estimating the motor performances. The performance graphs in Fig.3 and 4 clearly illustrate that agreement between the proposed and the actual is good (within 2 %). The attractiveness of this proposed technique is that it is a simple procedure; it is possible to estimate the efficiency of inverter-fed induction motor operated under variable speed at any load in a short time while the motor is in service without the removal of motor. Thus, this non-intrusive technique is suitable for conducting on-site energy audits of motors.

REFERENCES

[1] C. Y. Lee and W. J. Lee, "Effects of Nonsinusoidal Voltage on the Operation Performance of a Three-phase Induction Motor", *IEEE Trans. Energy Con-version*, Vol. 14, No. 2, pp. 193-200, June 1999.

[2] P. K. Sen and H. A. Landa, "Derating of Induction Motor Due to Waveform Distortion", *IEEE Trans. on Industry Applications*, Vol. 26, No. 6, pp. 1102-1107, Nov./Dec. 1990.

[3] V. E. Wagner and et al, "Effects of Harmonics on Equipment", *IEEE Trans. on Power Delivery*, Vol. 8, No. 2, pp. 672-680, April 1993.

[4] Z. Michalewicz, *Genetic Algorithms + Data Struc-tures=Evolution Programs*, 3rd edition., Springer-Verlag Berlin Heidelberg, 1996.

[5] T. Phumiphak and C. Chat-uthai, "An Economical Method for Induction Motor Field Efficiency Estimation for Use in On-site Energy Audit and Management," *Proceedings of 2004 International Conference on Power System Technology, Power-Con 2004*, Singapore, pp. 1–5, November 2004.

Design of Economical Small Transformer Based on Temperature Rise Evaluation

T.Phophongviwat * and C. Chat-uthai**

* Department of Electrical Power Engineering, Faculty of Engineering, Mahanakorn University of Technology, Bangkok 10530, Thailand (e-mail: teerapho@mut.ac.th)

** Department of Electrical Engineering, Faculty of Engineering, King Mongkut's Institute of Technology Ladkrabang, Bangkok 10520, Thailand (e-mail: kcchaiwu@kmitl.ac.th)

***Abstract*-This paper presents a technique for designing small transformers (EI structure) to have minimum cost while at the same time insuring the satisfaction of design constraint (defined temperature rise). The technique is based on an optimization problem which is the minimum cost design using the genetic algorithms (GAs), and coupled with the neural networks for the evaluation of winding temperature rise. Various samples of small low-frequency transformers (less than 240 V and 250 VA) have been designed and tested in order to illustrate how well the appropriate evaluated steady state temperature rise of winding at full-load using this proposed technique match those of the measured values (error less than 5°C). This procedure is suitable for the economical transformer design having the defined winding temperature rise which is considerable flexibility for a particular purpose.**

I. INTRODUCTION

Many computer-aided design procedures relevant to design optimization for small transformers have appeared in the literature [1-3]. As the cost of energy is growing at a high rate, the energy issue has recently resulted in an increase interest in the small transformer efficiency. It is important to consider the economic (low-cost) impact of transformer efficiency (low-loss) on the manufacturer's perspective. For small low-frequency transformers, a standard set of EI structures are often recommended for use in the applications characterized by low operating frequencies and moderate output power. In conventional design, consideration is given to the layout of the core and windings. The laminated core occupies the central space. The windings are wrapped around the core, with the low voltage and high voltage windings. For shell type cores, the core laminations usually come in discrete sizes. They may be fabricated to eliminate waste from stamping from rolled strip, thus the EI cores have specific ratios for their window dimensions and magnetic path sizes [4] as shown in Fig.1. The rms value of sinusoidal source voltage (V) can be expressed in term of frequency (f in hertz), number of turns (N), peak flux density (B in tesla), and effective core cross-sectional area (A_c in m^2) as the relation of volt per turn

Conventional transformer design always starts from determining required frequency, voltage and VA rating, and estimating a number of factors for core and winding arrangement. Such factors are obtained by using values that are generally only known to experienced design engineers [5]. Moreover, this is done while assuming that the flux density, current density (J in A/mm^2), and other electrical or magnetic parameters are fixed. In reality, this design may result in a transformer which does not meet temperature rise requirements. This miserable situation arises because the ultimate design is critically dependent on the electrical and magnetic parameters. For example, a designer may intend to minimize losses or cost or weight of transformer. As a result of these problems, it may imply that transformer design cannot be unique for a given set of ratings and specifications.

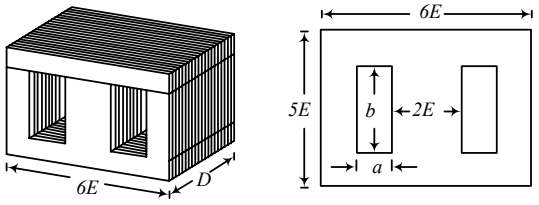

Figure 1. EI Core Geometry and Dimension Ratio (a = E, b = 3E)

$$\frac{V}{N} = \sqrt{2}\,\pi\, f\, B\, A_c\, F_s \tag{1}$$

where F_s denotes the stacking factor and $A_c = 2ED$.

This paper explores the optimal design of low-cost small low-frequency transformers (i.e. how to choose the optimum values for electrical and magnetic parameters) having the constraint of defined temperature rise value. The total cost of transformer (C_t) can be determined by the sum of core cost (C_{core}) and windings cost (C_{cu}) as

$$C_t = C_{core} + C_{cu} = \gamma_{core} W_{core} + \gamma_{cu} W_{cu} \tag{2}$$

where γ_{core} and γ_{cu} denote price of core and winding in Baht per kilogram respectively, W_{core} and W_{cu} are weight of core and winding in kilogram respectively.

The design objective is to minimize the total cost of transformer (C_t) subject to the desired temperature rise value constraint. The flux density (B) and core thickness (D) are set to be the design variables while the core laminations size ($2E$) and current density (J) are the design parameters. This proposed design allows for the exploration in the design of an economical transformer having temperature rise options which is considerable flexibility for a particular application.

II. TEMPERATURE RISE EVALUATION

The losses in a small transformer consist of the core loss (P_{core}) and winding loss (P_{cu}). The core loss at any flux densities below the saturation is a sum of two loss mechanisms; the hysteresis loss and the eddy current loss. The core loss determination employed in this paper is obtained from the interpolation of the test data curves. By definition, P_{cu} in a conductor carrying ac current with a value I_{rms} is

$$P_{cu}(D,B) = \frac{\rho_{cu}\, l_{cu}}{a_{cu}} I_{rms}^2 \tag{3}$$

where ρ_{cu}, l_{cu} and a_{cu} denote the resistivity, effective length and cross-sectional area of conductor respectively. The effective length l_{cu} is estimated by calculating the length of conductor on each layer of the winding, and then summing over all layers, taking into account the increasing diameter of each layer wound around the previous one. The total copper loss is the sum of primary winding and secondary winding losses. To achieve this copper loss practically, hence the effect of temperature rise is then considered in the design in order to improve the accuracy of copper loss calculation.

Consider a body with two parallel faces within which heat is generated uniformly. The two faces extend indefinitely and are exposed to the same ambient temperature. Then, heat is transferred uniformly and equally from both faces. The maximum temperature rise (θ_m) will occur at the midpoint between the two faces as [4]

$$\theta_m = \frac{q_v}{2h_o} L^2 \tag{4}$$

where h_o is coefficient of material thermal conductivity in watt per area-$^\circ$C, L is length between the faces to mid-point of body, and q_v is time rate of heat generation per unit volume. In this work, q_v can be defined by

$$q_v = \frac{P_{cu}(D,B)}{V_{cu}(D,B)} \tag{5}$$

where V_{cu} is winding volume. Note that P_{cu} and V_{cu} are dependent on the design of transformer structure. The average temperature rise through the body is given by

$$\theta_{av} = \frac{2}{3}\theta_m \tag{6}$$

As mentioned above, it is revealed that q_v depends on P_{cu} and V_{cu} , while h_o depends on the material property and exposed coil area of material. Moreover, a coil with laminated structure of several different coefficients of thermal conductivity will have an average coefficient of thermal conductivity normal to laminated structure [4-5]. Thus, it can be seen that the temperature rise is mainly dependent on P_{cu}, V_{cu} and A_{cu} .

In case of winding temperature rise problem, there is no simple relationship among the parameters involved in the solution. In this work, neural networks are proposed to evaluate the appropriate winding temperature rise that results in the design of an economical small transformer. The neural network methodology is a computer information processing system that is capable of sufficiently representing any nonlinear function. The neural network techniques are composed of the elements operating in parallel. The network function is mainly determined by the connections between elements. Generally, the neural networks are trained so that a particular input leads to a specific target output based on a comparison of the output and the target until the network output matches the target. Batch training of a network proceeds by making weight and bias changes based on an entire set (batch) of input vectors [6]. The feed-forward network as shown in Fig. 2 is selected, where **p** is a vector of R input elements, s is number of neurons in layer, **W** is weighting vector, **a** and **b** denote the output vector (temperature rise, Δ_T) and bias vector respectively.

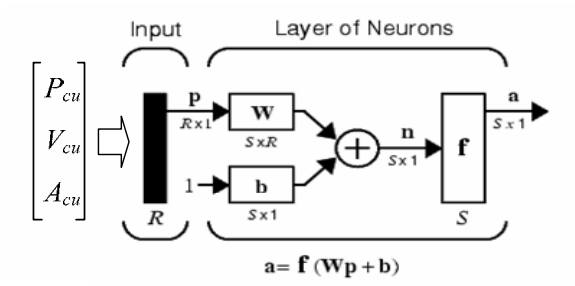

Figure 2. Structure of Feed-forward Network Architecture

Fifteen small transformers having different structures were built and tested. At the training stage, the input elements were defined as P_{cu}, V_{cu} and A_{cu}. The steady state temperature rise data at full-load of the primary and secondary windings were recorded by using analyzing recorder (Yogokawa: AR1100A). Then, the feed- forward network was trained by using those input data (**p** =15) obtained from the laboratory test. Two different rating transformers (TR A and TR B) were designed, built and tested in order to verify this proposed procedure. In this design, the winding temperature rise evaluation using the

TABLE I
DESIGN RESULTS OF TWO TRANSFORMERS
USING TEMPERATURE RISE EVALUATION

	TR A	**TR B**
Rated	24 VA, 220/12 V	220 VA, 220/110 V
$2E$ (mm)	32	44.4
D (mm)	37.5	78
B (tesla)	1	1
Primary (turns)	843	292
Secondary (turns)	46	146
$\Delta_{T,pri}$ ($^\circ$C)	17.84	42.49
$\Delta_{T,sec}$ ($^\circ$C)	15.35	36.44

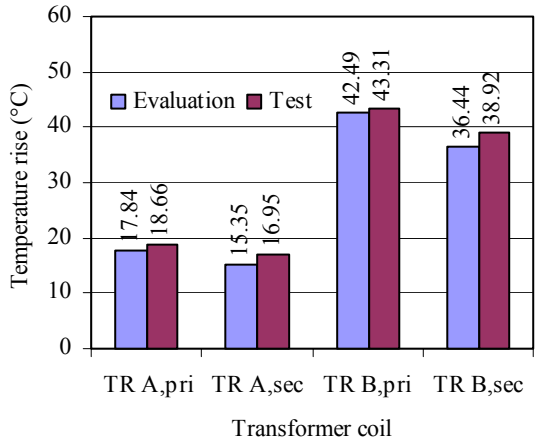

Figure 3. Comparisons of temperature rise evaluation and laboratory test

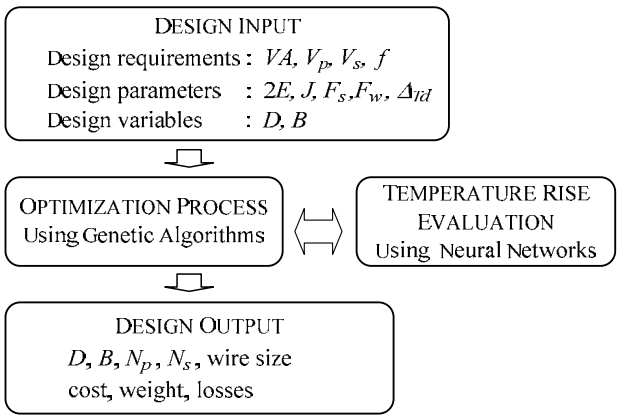

Figure 4. Flow chart of proposed procedure

neural network which has already been trained was implemented using the data of P_{cu}, V_{cu} and A_{cu}. The design results are illustrated in Table 1. The comparisons of winding temperature rise results obtained from the proposed evaluation and laboratory test which show a good agreement are presented in Fig. 3.

III. Design Of Economical Transformer

This section presents the use of optimal design of small transformer. As mentioned above, a designer may intend to minimize total transformer cost for particular purpose. Thus, the determination of optimal transformer parameters can be accomplished more economically with the help of an optimization technique called the genetic algorithms (GAs) [7] coupled with the neural networks for the winding temperature rise evaluation.

The choice of which parameters are fixed and which are free is made by the designer. One approach used previously is to fix the electrical and magnetic parameters and then choose the transformer geometry parameters to minimize cost. An alternate approach is to start with assumed core geometry and then find values for the electrical and magnetic parameters which minimize the design objective. The approach used in this paper, is preferred for practical reasons. First, transformer cores are generally available only in discrete sizes. Second, all core materials saturate at some maximum flux density (B_m). Therefore, the flux density (B) and core thickness (D) are set to be the design variables while the core laminations size ($2E$) and current density (J) are then set to be the design parameters in the optimization process. Note that once the design value for flux density has been settled during the optimization process (GAs), the side constraint of B must always be restricted that $B \le B_m$. Moreover, the updated winding temperature rise using the proposed procedure is also included as shown in Fig. 4.

The optimization task is to minimize the total cost in Eq. (2) subject to temperature rise constraint as follows

$$\textit{Minimize} \qquad C_t(D,B) = C_{core}(D,B) + C_{cu}(D,B) \qquad (7)$$

Subject to

$$\frac{N_p A_p \times N_s A_s}{F_w} - ab \le 0 \qquad (8)$$

$$\Delta_T - \Delta_{Td} \le 0 \qquad (9)$$

where A_p and A_s are conductor cross-sectional area of primary and secondary windings respectively, N_p and N_s are number of turns of primary and secondary windings respectively, F_w denotes window utilization factor of core, Δ_T and Δ_{Td} stand for the value of evaluated and defined temperature rise respectively.

IV. Experimental Results

This section explores the proposed procedure for optimal design of economical small transformers which can help the designer make more intelligent decisions in order to project the production cost of transformer having the temperature rise within desired value. The minimum cost designs with the temperature rise constraint (within 20°C) of two 24 VA, 220/12 V, 50 Hz transformers using different size of S-14 core ($2E$) are implemented. The cost of core and winding are defined as 50 and 400 Baht/kg respectively, and $B \le 1.4$ tesla.

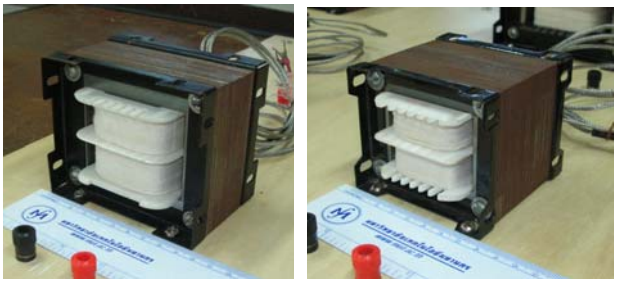

TR C **TR D**

Figure 5. Two prototype transformers (24 VA, 220/12 V) using proposed procedure

TABLE II
DESIGN RESULTS OF TWO ECONOMICAL TRANSFORMERS USING PROPOSED PROCEDURE

	TR C	**TR D**
Rated	24 VA, 220/12 V	24 VA, 220/12 V
$2E$ (mm)	32	25.4
J (A/mm^2)	4	4
D (mm)	39.3	53.1
B (tesla)	0.4663	0.6227
N_p (turns)	1741	1216
N_s (turns)	95	66
Total weight (kg)	1.97	1.66
Total Losses (W)	4.99	4.16
Total cost (Baht)	148.82	121.03
$\Delta_{T,pri}$ ($^\circ$C)	19.21	19.75
$\Delta_{T,sec}$ ($^\circ$C)	18.12	19.08

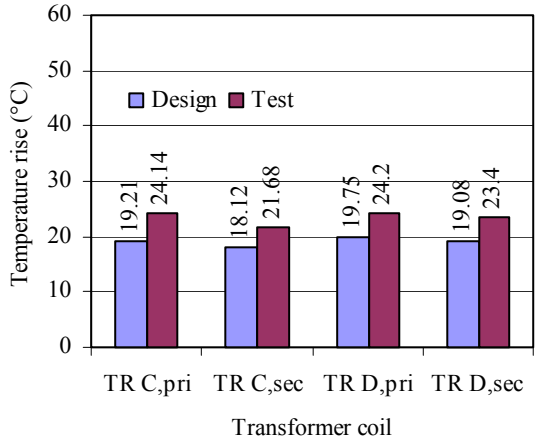

Figure 6. Comparisons of design temperature rise and laboratory test using proposed procedure

The two prototype transformers as shown in Fig. 5 are constructed and the design results are illustrated in Table 2. From Fig. 6, it can be seen that the evaluated values of temperature rise obtained from the design are in agreement with the measured values from test (error less than 5°C).

V. CONCLUSION

The design of economical small transformers using the GAs coupled with neural networks have been presented in which the total cost of transformers were minimized by choosing the flux density and core thickness to be design variables while the core laminations size and current density are set to be the design parameters. In this paper, the proposed temperature rise evaluation procedure is implemented in which the temperature of windings will be updated based on the temperature rise evaluation using neural networks in each iteration. The results of winding temperature rise in Fig. 6 indicate that the differences between evaluated values using this proposed procedure and the measured values from laboratory test are in good agreement (error less than 5°C). The main advantage of this design is that it can be many solutions for the minimum cost design of the same rating transformer having different defined temperature rise values. These solutions can be useful for the use in manufacturers in order to make more intelligent decisions for economical design such as the design of small transformer having low cost with the determination of total losses for the desired efficiency while the temperature rise of windings must be within the insulation class.

REFERENCES

[1] K. D. T. Ngo, R. P. Alley, A. J. Yerman, R. J. Charles, and M. H. Kuo, "Design Issues for the Transformer in a Low-Voltage Power Supply with High Efficiency and High Power Density," *IEEE Transactions on Power Electronics*, vol. 7, no. 3, pp. 592-600, July 1992.

[2] T. H. Pham, S. J. Salon, and S. R. H. Hoole, "Shape Optimization of Windings for Minimum Losses," *IEEE Transactions on Magnetics*, vol. 32, no. 5, pp. 4287-4289, September 1996.

[3] T. Phophongviwat, and C. Chat-uthai, "Minimum Cost Design of Small Low-Loss Transformers, " *in Proc. Tencon 2005*, *IEEE Region 10*, Melbourne, November 2005.

[4] W. M. Flanagan, *Handbook of Transformer Design & Applications*, 2nd edition, McGraw-Hill, 1986.

[5] E. Lowdon, *Practical Transformer Design Hand-book*, 2nd edition, McGraw-Hill, 1989.

[6] M. T. Hagan, H. B. Demuth and M. Beale, *Neural Network Design*, PSW Publishing Company, 1996.

[7] Z. Michalewicz, *Genetic Algorithms + Data Structures=Evolution Programs*, 3rd edition., Springer-Verlag Berlin Heidelberg, 1996.

Steady State and Dynamic Behaviors of Doubly Fed Induction Machines in Wind Energy Conversion Systems

S. Wangsathitwong, S. Sirisumrannukul, S. Chatratana* and W. Deleroi**
King Mongkut's Institute of Technology North Bangkok
1518, Pibulsongkram Rd., Bang sue, Bangkok, Thailand
*Technology Management Center, National Science and Technology Development Agency
111 Thailand Science Park, Paholyothin Rd. Klong 1, Klong Luang, Phatumthani 12120, Thailand
**B-4728 Corsostraße 3, Hergenrath, Belgium
E-mail: ssww@kmitnb.ac.th, spss@kmitnb.ac.th, somchaich@nstda.or.th, werner.deleroi@skynet.be

***Abstract*-This paper presents steady state and dynamic models of doubly fed induction machines operated as generators in wind energy conversion systems. Both models are based on the stator voltage synchronous reference frame. The first model investigates steady state operating point and stability on the torque-slip curve, whereas the second model determines transient response. The operation of DFIG can be categorized into two modes: constant power and maximum power. The objective of the constant power mode is to keep output power at a reference value to avoid disturbance owning to power fluctuation. The objective of the maximum power mode is to extract power from wind energy as much as possible. In this mode, the output power may not be constant depending on wind speed. The mathematical steady state and dynamic models are verified by a case study. The results show that both models provide a good representation of the behavior of DFIG in the two modes of operation.**

NOMENCLATURE

i_{Rd}, i_{Rq}	Rotor current components in d-q axis in stator synchronous reference frame
I_R, I_S	Rotor and stator current phasor
i_{Sd}, i_{Sq}	Stator current components in d-q axis in stator synchronous reference frame
L_0, X_0	Magnetizing inductance and reactance
L_R, X_R	Rotor inductance and reactance
L_S, X_S	Stator inductance and reactance
n_m	Rotor mechanical speed
P	Magnetic poles
P_l	Sum of the stator and rotor losses
P_W	Wind turbine net active power output
P_R, Q_R	Rotor active and reactive power
P_S, Q_S	Stator active and reactive power
R_S, R_R	Stator and rotor winding resistances
s	Slip
T_e, T_m	Electrical and mechanical torque
U_S	RMS stator line-to-neutral voltage
V_R, V_S	Rotor and stator voltage phasor
v_{Rd}, v_{Rq}	Rotor voltage components in d-q axis in stator synchronous reference frame
v_{Sd}, v_{Sq}	Stator voltage components in d-q axis in stator synchronous reference frame
X_{lS}, X_{lR}	Stator and rotor leakage reactance
ϕ	Phase angle of rotor voltage phasor with respect to stator voltage phasor.
ω_0	Stator line voltage frequency
ω_m	Rotor electrical speed
λ	Tip speed ratio

I. INTRODUCTION

The doubly fed induction generator (DFIG) is often used in medium and large wind turbines. The main advantages of these machines are that a small size of converter is required compared to the machine rating and stator active and reactive power with variable speed range can be controlled independently.

The mathematic models of DFIM and a control method were detailed in [1, 2]. In the stator-field-oriented reference frame, stator active power and reactive power can be directly controlled by the quadrature and direct components of the rotor current, respectively. Alternatively, in the stator synchronous reference frame, the stator active and reactive powers are independently controlled by d-q axis of stator current. The steady state performance of DFIG was described in [4].

When connected to the grid, a DFIG can be operated with two modes of operation: maximum and constant output power. In the maximum power mode, the DFIG is operated to extract output power as much as possible, whereas in the constant power mode, the generator is operated to maintain output power at any specified value.

In this paper, both dynamic and steady state models based on the stator voltage oriented reference frame are proposed to investigate both modes of operation. The steady state behavior of DFIG can be effectively investigated by the torque-slip characteristic curve and an operating point on the curve, the dynamic behavior by transient performance. Both two modes are explained and verified by steady state and dynamic models.

II. Doubly Fed Induction Generator Model

The nonlinear voltage equations of DFIG in synchronously rotating reference frame are

$$v_{Sd} = (R_S + L_S \frac{d}{dt}) i_{Sd} - \omega_0 L_S i_{Sq} + L_0 \frac{d}{dt} i_{Rd} - \omega_0 L_0 i_{Rq} \quad (1)$$

$$v_{Sq} = \omega_0 L_S i_{Sd} + (R_S + L_S \frac{d}{dt}) i_{Sq} + \omega_0 L_0 i_{Rd} + L_0 \frac{d}{dt} i_{Rq} \quad (2)$$

$$v_{Rd} = L_0 \frac{d}{dt} i_{Sd} - (\omega_0 - \omega_m) L_0 i_{Sq} + (R_R + L_R \frac{d}{dt}) i_{Rd} - (\omega_0 - \omega_m) L_R i_{Rq} \quad (3)$$

$$v_{Rq} = (\omega_0 - \omega_m) L_0 i_{Sd} + L_0 \frac{d}{dt} i_{Sq} + (\omega_0 - \omega_m) L_R i_{Rd} + (R_R + L_R \frac{d}{dt}) i_{Rq} \quad (4)$$

In this frame, the electrical torque is

$$T_e = \frac{2}{3} \frac{P}{2} L_0 \left(i_{Sq} i_{Rd} - i_{Sd} i_{Rq} \right) \quad (5)$$

When the d-axis of the reference frame aligns to the stator voltage as shown in Fig 1,

$$v_{Sq} = 0$$
$$v_{Sd} = \frac{3}{2} \sqrt{2} U_S$$

In this frame, the stator active power and reactive power can be calculated as in (6) and (7).

$$P_S = \frac{2}{3} v_{Sd} i_{Sd} \quad (6)$$

$$Q_S = -\frac{2}{3} v_{Sd} i_{Sq} \quad (7)$$

For the steady state model, the stator and rotor voltage phasors can be derived from (1) – (4) in terms of reactance.

$$V_S = (R_S + jX_S) I_S + jX_0 I_R \quad (8)$$

$$V_R \angle \phi^o = jsX_0 I_S + (R_R + jsX_R) I_R \quad (9)$$

The electrical torque is given by

$$T_e = \frac{2}{3} \frac{P}{2} \frac{X_0}{\omega_0} \mathrm{Im}(I_S I_R^*) \quad (10)$$

Obviously from (8) - (10), the torque-slip characteristic curve of DFIG at any rotor voltage can be directly determined.

III. Wind Turbine Characteristic

The power converted, $P_{turbine}$, by a wind turbine is related to the power coefficient, C_p, given for a wind speed, V, is

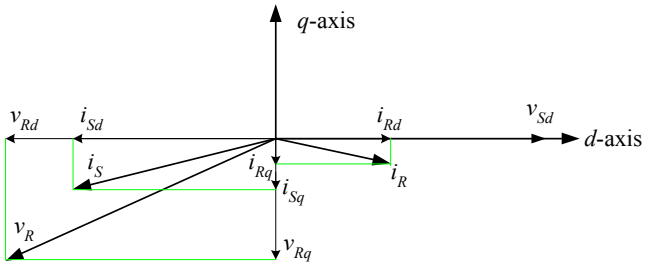

Figure 1. Vector diagram of DFIG in synchronous reference frame.

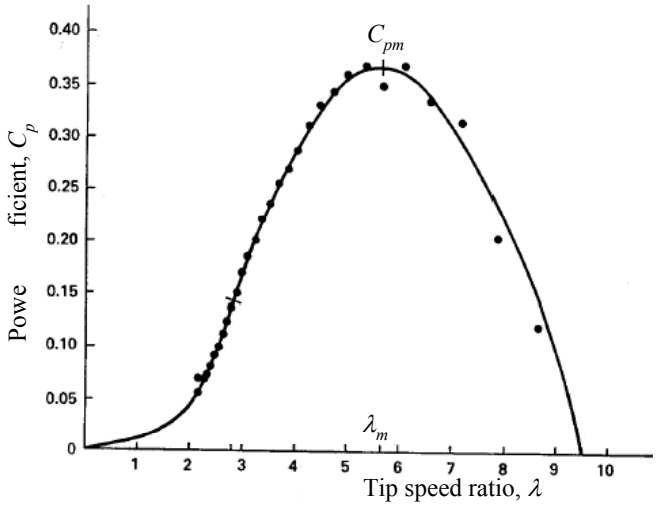

Figure 2. Typical power coefficient versus tip speed ratio curve.

$$P_{turbine} = 0.5 C_p \rho A V^3 \quad (11)$$

where ρ and A are the air density and the swept area by the rotor blades, respectively.

For a variable-speed turbine, the objective is to operate near maximum efficiency, where the resulting maximum power can be expressed by

$$P_{turbine,m} = 0.5 \rho A C_{pm} (R / \lambda_m)^3 \omega^3 \quad (12)$$

where R and ω are the rotor radius measured at the blade tip and the rotation speed of the blade, respectively. The optimum tip speed ratio, λ_m, is defined as a ratio between the rectilinear speed of the blade tip and the wind speed at the maximum power coefficient, as shown in Fig. 2 [5], [6].

It is apparent from (12) and Fig. 2 that as wind speed changes, the rotor speed will change to obtain the maximum power from the wind.

IV. Steady State Behaviors and Torque-slip Curves

As any desired output power, P_W, from the wind turbine, the relation of wind turbine power and electrical power are

$$P_W = P_S + P_R + P_l \quad (13)$$

For small power loss ($P_l \approx 0$), the air gap power is equal to stator power. The stator power and wind turbine output power can then be calculated as a function of slip.

$$P_W \approx (1-s)P_S \quad (14)$$

Therefore, at any given output power, P_W , and reactive power, Q_S, the stator current can be determined from (6) and (7). The rotor current and voltage are found from (8) and (9), respectively. From the calculated rotor voltage, the torque-slip curve can be investigated directly as function of slip.

For examples, the torque-slip curve for various rotor voltages amplitudes and phase angles are shown in Fig. 3 and 4. In Fig. 3 and 4, it can be seen that the pull-out torque depends on the rotor voltage and phase angle. Therefore, at any given torque and speed, the DFIG can be operated in relation to the command by varying the rotor voltage. Likewise, at any fixed given torque, the speed can be varied by controlling the rotor voltage.

V. Verification of Steady State Behavior

For constant output power operation, the stator power is assigned by reference output power as in (15).

$$P_S = P_{ref} /(1-s) \quad (15)$$

Therefore, the rotor voltage can be calculated as described in Section IV for desired P_S and Q_S. When P_{ref} is kept constant at –0.5 p.u. with unity power factor, the result is shown in Fig. 5. The intersection between the electrical torque and torque-slip curve determines an operating point. In this mode of operation, the rotor speed is not constant because the torque is not equal to wind turbine torque. Note that in this mode the output power is nearly constant. Therefore, the rotor speed can be controlled by other methods such as pitch control, stall regulation [7]. For the maximum power mode, an operating point (rotor speed) is determined from the power coefficient curve.

In Fig. 6, the DFIG is assigned to operate at its rated electrical torque, 1 p.u. at slip = -0.4. As can be seen at this point, the operating point is closed to the pull-out torque. Therefore in practice, this point can be avoided for stable operation. In this mode, the rotor speed is constant at steady state when the electrical torque and wind turbine torque are

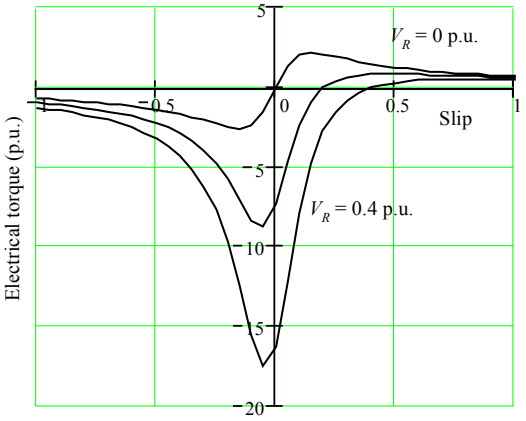

Figure 3. Torque-slip curve as function of V_R = 0, 0.2 and 0.4 p.u. at ϕ = 0.

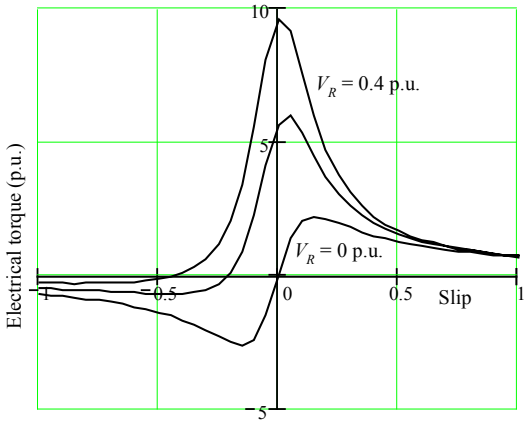

Figure 4. Torque-slip curve as function of v_R = 0, 0.2 and 0.4 p.u at $\phi = \pi$.

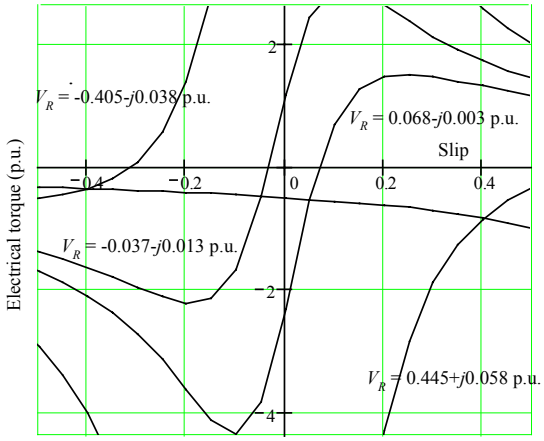

Figure 5. Operating points for constant output power.

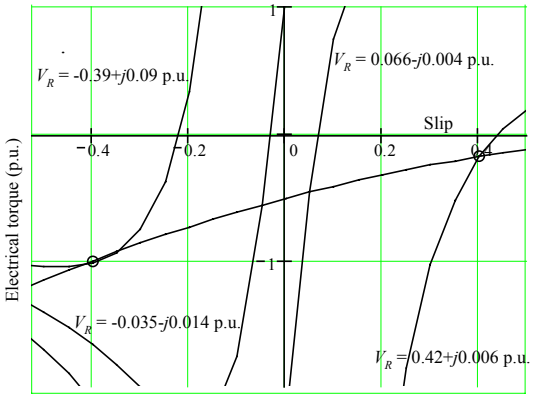

Figure 6. Operating points for maximum output power.

equal. However, if speed command is varied because of inconstant wind speed, the output power will fluctuate.

VI. Verification of Dynamic Behavior

Both modes of operation are verified in a dynamic model simulation to investigate their transient responses and behaviors. In the constant output power operation, a total power of –0.5 p.u is kept constant. while the mechanical torque is varied from –0.4 to –0.6 p.u. The result is shown in Fig. 7 and can be seen that the output power tries to stay constant at –0.5 p.u. or P_{ref} , although the mechanical torque is not constant and fluctuates. However, the rotor speed either increases or decreases depending on which torque is higher. This could lead to DFIG operated in unstable region. For the maximum power operation, the commands for this mode are the desired reactive power and rotor speed that is related to the maximum power coefficient and wind speed.

For the same mechanical torque as in Fig. 7, the results are shown in Fig. 8 and 9. Obviously, the rotor speed response (solid line) is tracked to the speed command (dash line) to keep output power at maximum. When the electrical and mechanical torques are equal, the rotor speed is constant. If the mechanical torque is increased, the electrical torque will reduce to increase the rotor speed until it goes constant at a constant mechanical torque again. The output power of Fig. 9 sees more fluctuation than that of Fig. 7 but can extract more power than the other for the maximum power operation.

VII. Conclusion

Both steady state and dynamic model equations of DFIG are presented based on the stator synchronous frame. In this frame, stator active power and reactive power can be independently controlled by direct and quadrature axis components of stator current, respectively. In the steady state model, the pull-out torque is a complex form represented by a function of rotor voltage. Furthermore, the operating point can be directly seen from the torque-slip curve to determine a steady state stability margin.

DFIG can be operated in two modes of operation: constant power and maximum power. In the first mode, its output power is kept constant at a reference value regardless of input power. In the maximum power operation, the speed command is obtained from the power coefficient-tip speed ratio curve for maximum power extraction. The results reveal that a DFIG can be effectively controlled in both modes of operation.

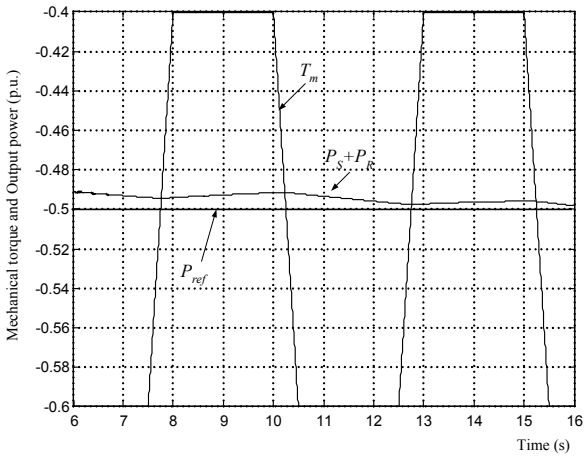

Figure 7. Output power and mechanical torque for constant output power.

References

[1] W.Leonhard, *Control of Electrical Drive*. Berlin German, Springer, 1996.

[2] Y. Tang and L. Xu "A flexible active and reactive power control strategy for a variable speed constant frequency generating system," *IEEE Trans. Power Electron*., vol. 10, no. 4, pp. 472 – 478, July1995.

[3] H. Banakar, C. Luo and B. T. Ooi, "Steady-state stability analysis of doubly-fed induction generators under decouple P-Q control," *IEE Proc.-Electr. Power Appl*, vol. 153, no.2, pp. 300 – 306, March 2006.

[4] M. S. Vicatos and J. A. Tegopoulos, "Steady state analysis of doubly-fed induction generator under synchronous operation," *IEEE Trans. Energy Conversion*, vol. 4, no. 3, pp. 495 – 501, September 1989.

[5] G. L. Johnson, *Wind energy systems*. Electronic Edition, 2001.

[6] A. Tapia, G. Tapia, J. X. Ostolaza and J. R. Saenz, "Modeling and control of a wind turbine driven doubly fed induction generator," *IEEE Trans. Energy Conversion*, vol. 18, no. 2, pp. 194-204, June 2003.

[7] T. Ackerman, *Wind Power in Power System.* John Wiley & Sons, Chichester, 2005.

[8] P. C. Krause, O. Wasynczuk, and S. Sudhoff, *Analysis of electric machinery*. IEEE Press, NJ, 2002.

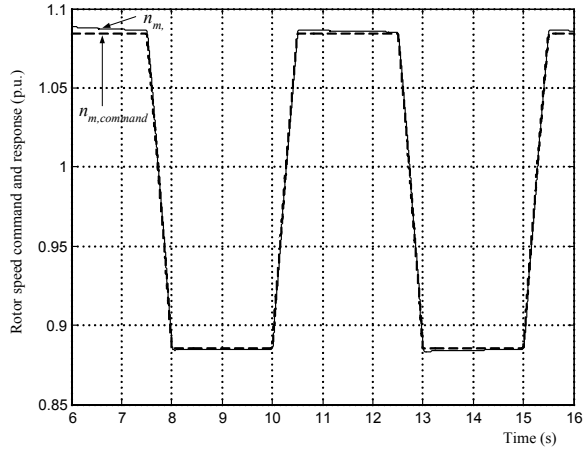

Figure 8. Rotor speed command and response for maximum output power .

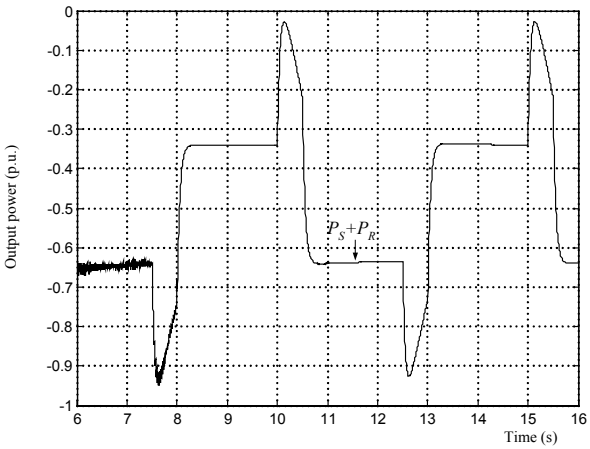

Figure 9. Output power for maximum output power operation operation.

Design of Power Transformer Winding Fault Model using PSCAD/EMTDC

Dusit Uthitsunthorn and Teratam Bunyagul
Department of Electrical Engineering, Faculty of Engineering
King Mongkut's Institute of Technology North Bangkok
1518, Pibulsongkram Rd., Bangsue, Bangkok, Thailand
E-mail: dusitoa@gmail.com, teratam@kmitnb.ac.th

***Abstract*- A power transformer with internal winding faults is designed to study the magnitude of fault current for protecting transformer. There are two types of the winding fault: turn to ground and turn to turn faults. The paper presents the design and results of a power transformer winding faults by using PSCAD/EMTDC program. The simulation results show the magnitude of earth fault current and differential current and the comparison of primary and secondary fault of the transformer.**

Keywords: power transformer, internal fault, winding fault

I. INTRODUCTION

A power transformer is an important equipment on the power system. It is used to step up and down voltage levels on the transmission and distribution system. If a fault occurs in power transformer, the power system will be interrupted for a long time. There are two types of the faults in power transformer: the external fault and the internal fault [1]. The external fault is the outside zone protection of transformer. This causes mechanical stress in transformer winding and increasing temperature in the transformer. Unlike the external fault, the internal fault directly affects on power transformer winding. Faults of power transformer winding consist of turn to ground and turn to turn faults. In the occurrence of the fault, the differential relay must operate to protect power transformer hence decrease cost of the system maintenance [2].

The objective of this paper is to study earth fault current and differential current which occur at the primary and secondary side of a transformer. Therefore, the power transformer with internal faults model is proposed. They are simulated under following conditions:

1. Turn to ground and turn to turn faults at primary winding
2. Turn to ground and turn to turn faults at secondary winding

The models are implemented on PSCAD/EMTDC program.

II. MODEL OF POWER TRANSFORMER

The beginning of the study is to build a model of a three-phase, two winding, six coils transformer which obtains the transformer data from [3]. It starts with inputting the transformer data in BCTRAN's transformer model in ATP/EMTP program to calculate six of the resistance (R) and inductance (L) parameters. A normal transformer has a 6x6 matrix of the R and L parameters as shown in Fig. 1 [9].

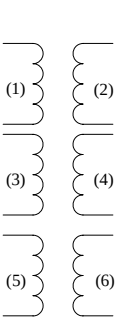

$$[R] = \begin{bmatrix} R_1 & 0 & 0 & 0 & 0 & 0 \\ 0 & R_2 & 0 & 0 & 0 & 0 \\ 0 & 0 & R_3 & 0 & 0 & 0 \\ 0 & 0 & 0 & R_4 & 0 & 0 \\ 0 & 0 & 0 & 0 & R_5 & 0 \\ 0 & 0 & 0 & 0 & 0 & R_6 \end{bmatrix}$$

$$[L] = \begin{bmatrix} L_1 & M_{12} & M_{13} & M_{14} & M_{15} & M_{16} \\ M_{21} & L_2 & M_{23} & M_{24} & M_{25} & M_{26} \\ M_{31} & M_{32} & L_3 & M_{34} & M_{35} & M_{36} \\ M_{41} & M_{42} & M_{43} & L_4 & M_{45} & M_{46} \\ M_{51} & M_{52} & M_{53} & M_{54} & L_5 & M_{56} \\ M_{61} & M_{62} & M_{63} & M_{64} & M_{65} & L_6 \end{bmatrix}$$

Figure 1.. R and L parameters of the 3 phase 2-winding power transformer

Where R_i and L_i is a resistance and self inductance of winding respectively which are represented in diagonal matrices. M_{ij} is the mutual inductance between winding i and j. They are represented in upper and lower matrix.

III. INTERNAL WINDING FAULTS

The internal winding faults occur in two cases. These consist of turn-to-ground and turn-to-turn faults as shown in Fig. 2 [5-8].

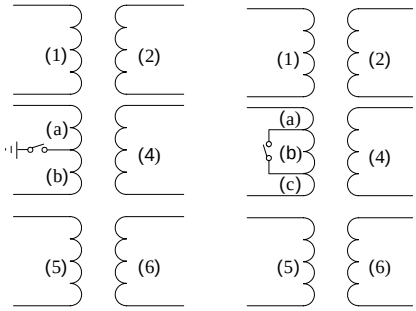

a) turn-to-ground fault b) turn-to-turn fault

Figure 2. Winding faults in power transformer

If a turn-to-ground fault occurs at coil 3 of primary side which is separated into two sub-coil *a* and *b* as shown in Fig. 2a), the matrix of [R] and [L] are modified into 7x7 matrix as shown in Fig 3.

$$[R] = \begin{bmatrix} R_1 & 0 & 0 & 0 & 0 & 0 & 0 \\ 0 & R_2 & 0 & 0 & 0 & 0 & 0 \\ 0 & 0 & R_a & 0 & 0 & 0 & 0 \\ 0 & 0 & 0 & R_b & 0 & 0 & 0 \\ 0 & 0 & 0 & 0 & R_4 & 0 & 0 \\ 0 & 0 & 0 & 0 & 0 & R_5 & 0 \\ 0 & 0 & 0 & 0 & 0 & 0 & R_6 \end{bmatrix}$$

$$[L] = \begin{bmatrix} L_1 & M_{12} & M_{1a} & M_{1b} & M_{14} & M_{15} & M_{16} \\ M_{21} & L_2 & M_{2a} & M_{2b} & M_{24} & M_{25} & M_{26} \\ M_{a1} & M_{a2} & L_a & M_{ab} & M_{a4} & M_{a5} & M_{a6} \\ M_{b1} & M_{b2} & M_{ba} & L_b & M_{b4} & M_{b5} & M_{b6} \\ M_{41} & M_{42} & M_{4a} & M_{4b} & L_4 & M_{45} & M_{46} \\ M_{51} & M_{52} & M_{5a} & M_{5b} & M_{54} & L_5 & M_{56} \\ M_{61} & M_{62} & M_{6a} & M_{6b} & M_{64} & M_{65} & L_6 \end{bmatrix}$$

Figure 3. R and L parameters of the 3 phase 2-winding power transformer

The fault position along the coil is defined by n_a and n_b

Then $n_a + n_b = n_3$

Where n_3 is the number of coil turns

n_a and n_b are the number of sub-coil turns *a* and *b*

Resistance and inductance between sub-coil *a* and *b* are calculated in (1)-(11).

$$R_a = \frac{n_a}{n_3} R_3 \; ; \; R_b = \frac{n_b}{n_3} R_3 \; ; \; k = \frac{n_a}{n_b} \qquad (1)$$

When the variable k is the voltage ratio between sub-coil *a* and *b* which varies with fault position along the coil. This method is to calculate the self and mutual inductance between sub-coil *a* and *b*. Then the method solves the element of fault in terms of L_a, L_b, M_{ab}, M_{ai} and M_{bi} as in (2)-(11).

Consistency $$L_a + 2M_{ab} + L_b = L_3 \qquad (2)$$

Leakage factor $$\sigma_{ab} = 1 - \frac{{M_{ab}}^2}{L_a L_b} \qquad (3)$$

Proportionality $$\frac{L_a}{L_b} = \left(\frac{n_a}{n_b}\right)^2 \qquad (4)$$

The leakage factor between sub-coil is assumed to be zero $(\sigma_{ab} = 0)$. Therefore, L_a, L_b and M_{ab} can be found from (5)-(7).

$$L_a = \frac{L_3}{\frac{1}{k^2} + \frac{2\sqrt{1-\sigma ab}}{k} + 1} \qquad (5)$$

$$L_b = \frac{L_3}{k^2 + 2k\sqrt{1-\sigma ab} + 1} \qquad (6)$$

$$M_{ab} = \frac{L_3\sqrt{1-\sigma ab}}{\left(k + \frac{1}{k}\right) + 2\sqrt{1-\sigma ab}} \qquad (7)$$

The mutual inductance between sub-coil *a* (M_{ai}) and *b* (M_{bi}) in the other coils can be divided to two cases [5].

Case A: the coil i is wound on the same leg as sub-coil *a* and *b*. M_{ai} and M_{bi} can be solved by equation (8)-(9).

$$M_{ai} = M_{3i}\sqrt{\varepsilon}\sqrt{\frac{L_a}{L_3}}\sqrt{1 + \frac{1-\varepsilon}{\varepsilon}\frac{L_3 L_i}{{M_{3i}}^2}} \qquad (8)$$

$$M_{bi} = M_{3i} - M_{ai} \qquad (9)$$

where $\varepsilon = \frac{\sigma_{ai}}{\sigma_{3i}}$

Case B: the coil i is not wound on the same leg as sub-coil *a* and *b*. M_{ai} and M_{bi} can be solved by equation (10)-(11).

$$M_{ai} = M_{ia} = \frac{k}{1+k} M_{3i} \qquad (10)$$

$$M_{bi} = M_{ib} = \frac{1}{1+k} M_{3i} \qquad (11)$$

Fig. 2b) illustrates that the turn-to-turn faults have three sub-coil consist of *a*, *b* and *c*. The [R] and [L] are both 8x8 matrices. The unknown variables in sub-coil *a*, *b* and *c* of turn to turn faults can be calculated by using relations of consistency, leakage factor and proportionality. M_{ab}, M_{ac}, M_{bc}, L_a, L_b and L_c and mutual inductance between sub-coil *a*, *b* and *c* of the other coils can be solved in [5-9].

IV. IMPLEMENTATION

A three-phase two-winding transformer modeled with internal winding faults is implemented on PSCAD/EMTDC program as following steps by using the data of test report obtained from [3].

Step 1: Input the transformer data on short circuit and open circuit test to calculate matrix [R] and ω[L] by BCTRAN. This results in the output file (*.pch file) as shown in Table I. Table I contains elements of [R] and ω[L] without internal winding faults.

Step 2: Calculating the matrix [R] and [L] with internal winding faults and build the model by programming with Fortran in EMTDC as shown in Fig. 4**.**

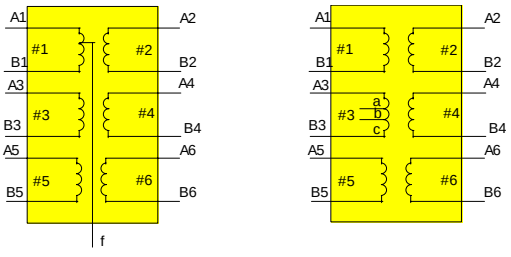

Figure 4. The transformer internal fault model

TABLE I
THE MATRIX [R] , ω[L] FROM BCTRAN *.PCH FILE

Bus	R	ωL
1A	0.39172450050967	301226.10304893
2A	0.01566898002039	60237.573101832 12047.514620366
3B	0.39172450050967	-150140.1272902 -30029.03216127 301226.10304893
4B	0.01566898002039	-30029.03216127 -6005.806432255 60237.573101832 12047.514620366
5C	0.39172450050967	-150140.1272902 -30029.03216127 -150140.1272902 -30029.03216127 301226.10304893
6C	0.01566898002039	-30029.03216127 -6005.806432255 -30029.03216127 -6005.806432255 60237.573101832 12047.514620366

V. SIMULATION RESULT

In this research, the power transformer three-phase two winding 50 MVA 115/23kV 50 Hz Yy0 primary and secondary side, star connected winding with neutral point solidly earthed, was modeled. V_{base} is the transformer voltage. MVA_{base} is 100 MVA

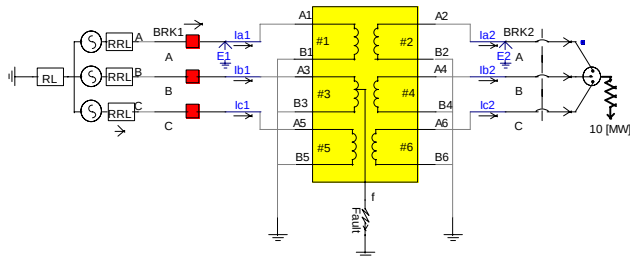

a) The turn to ground fault at primary side Phase B

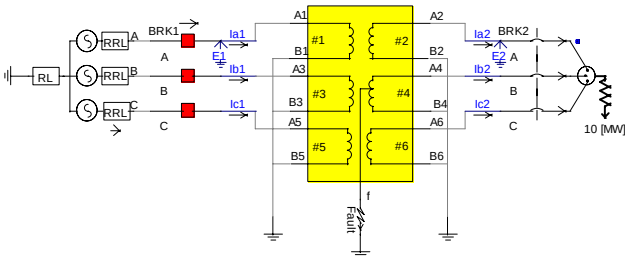

b) The turn to ground fault at secondary side Phase B

Figure 5. The system simulation for turn-to-ground faults

Source: Z_1=0.01192+j0.04378 pu.
Z_0=0.04237+j0.17426 pu.

Fig. 5 shows the models of turn to ground faults at phase B on both sides of the transformer. The fault position will be moved along the winding of transformer which varies between 10% to 90% by starting from terminal to neutral point. The fault current from each fault position is measured to obtain the magnitude. Fig. 6 shows the relation between the magnitude of fault current and distance of turn to ground fault at the winding on the primary side. The fault current rapidly increases when the fault position is close to neutral point. This is because the reactance decreases near the neutral point [1,2].

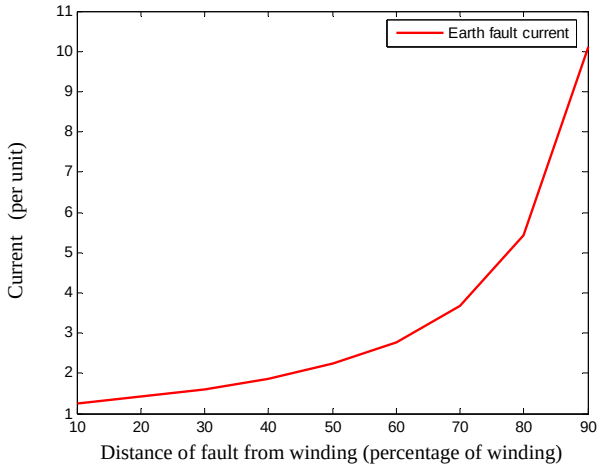

Figure 6. Turn-to-ground fault current on primary side

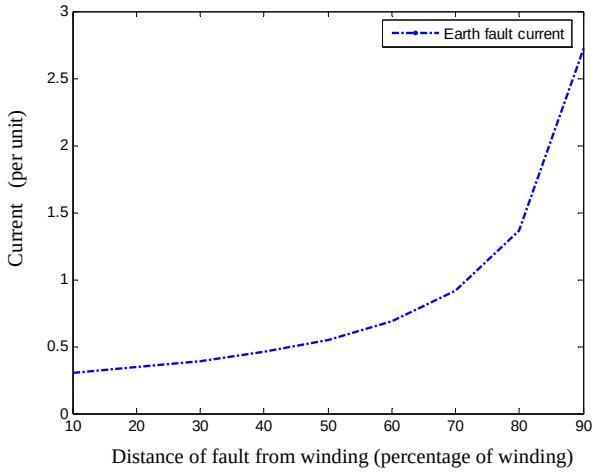

Figure 7. Turn-to-ground fault current on secondary side

Fig. 7 shows the relation between the magnitude of fault current and distance of turn to ground fault at winding on secondary side. The fault current rapidly increases when the fault position is close to neutral point. This is because the reactance decreases near the neutral point [1,2].

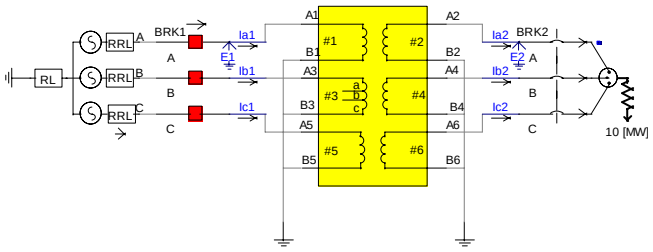

a) The turn to turn fault at primary side Phase B

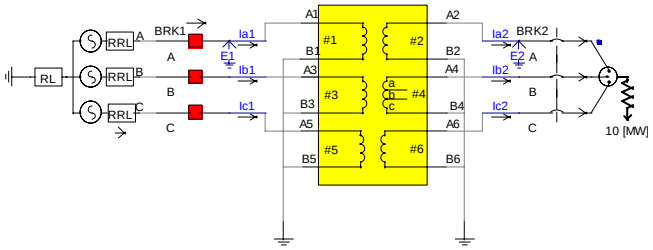

b) The turn to turn fault at secondary side Phase B

Figure 8. The system simulation for turn-to-turn faults

Fig. 8 shows the model of turn to turn faults on both sides of transformer at phase B. The sub-coil *b* is represented turn to turn faults by using midpoint of winding as the reference and expanding to both end of the winding. It will be raised at 10% each step until 90% of winding length. The fault current from each fault positions is measured to obtain the current magnitude.

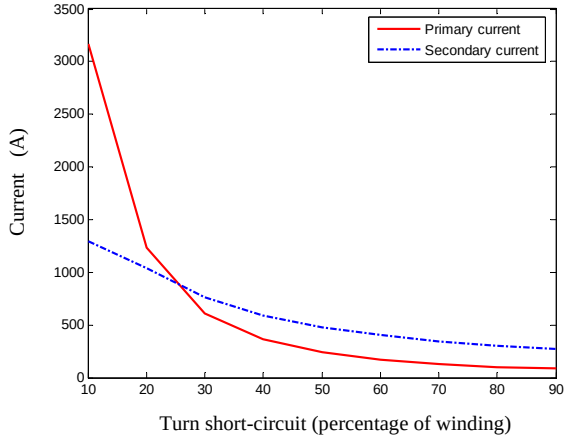

Figure 9. Turn-to-turn fault at primary side

Fig. 9 shows the comparison of the primary and secondary side currents during a turn to turn fault occurred on primary winding. It shows that the terminal fault current rapidly decreases when the range of sub-coil *b* increases. In a few turns of the winding, the primary current is higher than the secondary current. In a greater turns the secondary current is higher than the primary current.

Fig. 10 shows the comparison of the primary and the secondary currents during a turn to turn fault occurred on secondary side winding. The fault current increases proportionally when the range of sub-coil *b* increases [10]. The secondary current has greater slope higher than of the primary current.

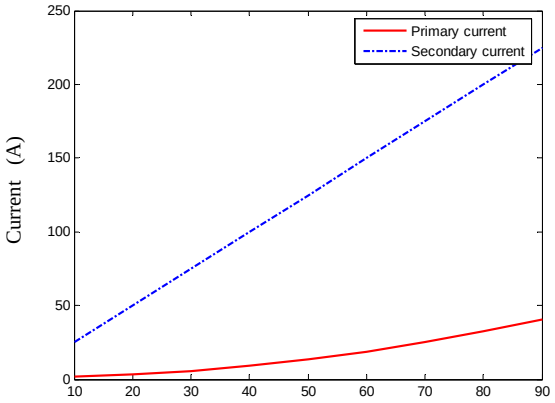

Figure 10. Turn-to-turn fault at secondary side

VI. CONCLUSION

The method of modeling a transformer with internal winding faults is presented. The internal winding faults in a transformer are also studied by PSCAD/EMTDC program in both cases: turn to ground and turn to turn fault. The result indicates that the fault current is higher when fault position close to neutral point in case of turn to ground fault. In case of turn to turn fault at primary side, the difference between the primary and secondary current is slight when compares with the fault at secondary side.

The model provides correct simulation results. This is beneficial to power system protection study. The power transformer winding faults can be modeled then used to test differential relay algorithm.

REFERENCES

[1] GEC Alsthom. “Protective Relay Application Guide”,GEC ALSTHOM Measurement Limited , 1987
[2] Alsthom T&D protection and Control, “Network Protection and Automation Guide”, ALSTOM T&D protection and Control , 1987
[3] ABB Thailand “Test Report no.56039”
[4] Alternative Transients Program (ATP) – Rule Book, Canadian/American EMTP User Group, 1987-1998
[5] Bastard, P.Bertrand, P., and Meunier, M. “A transformer model for winding fault studies”, IEEE Tran.,1994, PWRD-9,(2),pp. 690-699.
[6] Bertrand, P., Devalland, A., and Bastard, P.; “A simulation model for transformer internal faults base for the study of protection and monitoring systems”Electricity Distribution, 1993. CIRED., 12th International Conference on ,17-21 May 1993 Page(s):1.21/1 - 1.21/5 vol.1
[7] Kezunovic, M. and Yong Guo; “Modeling and simulation of the power transformer faults and related protective relay behavior”,Power Delivery, IEEE Transactions on, Volume 15, Issue 1, Jan. 2000 Page(s):44 – 50
[8] B. Kasztenny, M. Kezunovic, and Z. Galijasevic, “A New ATP Add-on for Modeling Internal Faults in Power Transformers American Power Conference”, Chicago, April, 2000.
[9] Aggarwal, R.K. and Mao, P., “Digital simulation of the transient phenomena in high voltage power transformers with particular reference to accurate fault detection”, Simulation '98. International Conference on (Conf. Publ. No. 457), Vol., Iss., 30 Sep-2 Oct 1998, Pages:390-397
[10] Palmer-Buckle, P.,Butler, K.L. and Sarma, N.D.R., “Characteristics of transformer parameters during internal windingfaults based on experimental measurements”, Transmission and Distribution Conference, 1999 IEEE , 11-16 Apr 1999 Volume: 2, On page(s): 882-887 vol.2

A study of Efficiency Improvement Tracking Algorithm for Maximum Power Point Tracking of Photovoltaic system

Chamnan. Ratsame[1], Tanes. Tanitteeapan[1] , Sirichai. Thepa[2] , Narong. Mungkung[1] , Itsda Boonyaroonate[3]
[1] Department of Electrical Technology Education
[2] Division of Energy Technology.
[3] Department of Electrical Engineering
King Mongkut's University of Technology Thonburi
Chamnan.rat @kmutt.ac.th

Abstract **This paper deals with the design and experimental implementation of a maximum power point tracking (MPPT) for photovoltaic system , which is a DC-DC boost converter operating in continuous conduction mode(CCM). The converter is able to draw maximum power from the PV system for a given irradiation level by adjusting the duty cycle of converter. Analytical models are built for the PV system and converter on the basis of the data sheet of manufacturer and the principle of energy conservation. The control technique, implement with a single-chip microcontroller ADMC331, is based on the Hill-climbing / P&O method. From the result obtained it can be concluded that , the MPPT can increase the overall efficiency of the system 87 % under different atmospheric condition.**

Key Words: Photovoltaic, Maximum Power Point Tracking , PI controller, Hill – climbing / Perturbation and Observation Algorithm

I. INTRODUCTION

Photovoltaic(PV) generation assumes increased importance as a renewable source due to advantages such as the absence of fuel cost, little maintenance and no noise and wear due to absence of moving parts. However, Two important factors limit the implementation of photovoltaic systems i.e. high cost and low efficiency in energy conversion. In photovoltaic systems, the PV panel represents 57% of the total cost of the system, and the battery storage system corresponds to 30% of the cost. Other system components such as inverters and maximum power point tracker contribute only with 7% (Hua and Lin, 2003). Due to the high cost of solar cells. Therefore, controlling maximum power point tracking (MPPT) for the photovoltaic system is essential in a PV system. The amount of power generated by a PV system depends on the operating voltage of the array. While a maximum power point (MPP) of PV system varies with solar insulation and temperature. Its V-I and V-P characteristic curves specify a unique operating point at which maximum possible power is delivered. At the MPP, the PV operates at its highest efficiency. Therefore, many methods have been developed to determine MPPT. Three popular tracking methods based on power feedback are widely adopted in PV power systems. They are the perturbation and observation method(P&O) [2], the incremental conductance method (IncCond) [3] and the hill climbing method (HC). Both P&O and InCond are based on the same technology by regulating the PV array's voltage to follow an optimal set point, which represents the voltage of maximum power operating point . This point is continuously tracked and updated to satisfy a simple mathematical equation: dP/dV = 0, where P represents the PV module's output power and V represents the PV voltage., the maximum power points can always be tracked if we keep dP/dV equal to zero., MPP-trackers have been widely implemented with several techniques and power conditioners. In the work developed by Maheshappa et al., the PV array voltage is compared with a constant reference voltage, which corresponds to the PV voltage at the maximum power point, under specific atmospheric conditions, as MPP will depend on the chosen reference. In the work proposed by Medeiros and Antunes, the neural network requires a new training at each change of the system size. The incremental conductance method (Solodovnik et al., 2004) leads to good accuracy in tracking the MPP even under rapidly changing weather, but a digital signal processor (DSP) is necessary in the implementation. Within this text, this work presents the design and experimental implementation of a real time maximum power point tracker for photovoltaic systems. The MPP-tracker proposed in the paper is a study DC-DC converter operating in continuous conduction mode(CCM).The Hill- climbing /P&O algorithm searches the maximum power pint according to irradiation. The algorithm is implemented using microcontroller ADMC 331,whose output signal set the duty cycle of pulse width modulation (PWM) boost converter.

II. Characteristics of Photovoltaic Cell

Fig.1. shows the typical equivalent circuit of PV-cell. The typical I-V output characteristics of PV-cell are represented as following (1).

$$I = I_{ph} - I_{rs} \{e^{q/AKTc}(V+IR_S) - 1\} - (V+IR_S) / R_{sh} \quad (1)$$

Where,

$I_{ph} = \{I_{sc} + K_I (T_C - 25)\}\lambda$, $I_{rs} = [\, T_C / T_r]^3 e^{\{(qE_{gap}/BK)(1/T_r T_C)\}}$

I and V_O : cell output current and voltage
I_{ph} : light generated current
I_{SC} : short circuit current
I_{re} : reverse saturation current
I_{or} : cell saturation current at T_r
TC : cell temperature
T_r = 301.18 ^oK : reference Temperature
q = electron charge
K =1.38e-23 : Boltzmann's constant
K_I = 0.0017 : Temperature coefficient at ISC
Egap : energy gap [eV]
λ : percentage irradiation
R_S : series resistance ,R_{Sh} : shut resistance
A,B : ideality constants

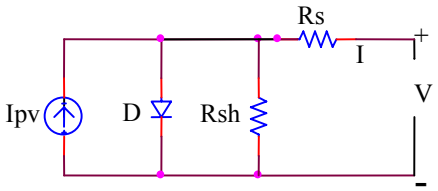

Figure 1. The equivalent model of photovoltaic.

Figure. 2(a) shows the typical I-V and P-V output characteristic curve of PV- module. Fig. 2(b) show the typical P-V output characteristic curves of P-V module in the case that the irradiance is varied.

From Fig.2(b). we know that the output characteristic of PV-module are nonlinear and each curve only has one maximum power point (MPP) . Additionally , the output current of PV- module is mainly affected by irradiation variation , whereas the output voltage of PV-module is mainly affected by temperature variation . therefore, to efficiently use PV-module, in case the atmospheric condition are varied, the maximum power point tracking of PV- module should be implemented.

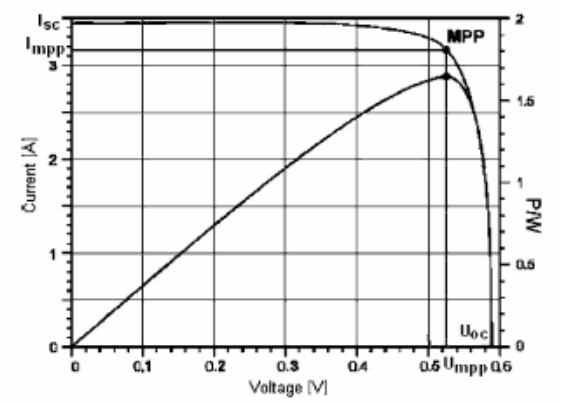

(a) Type characteristic curve

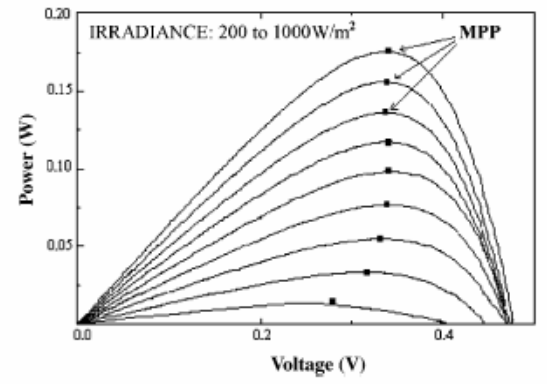

(b) Irradiation variations

Figure 2. The output characteristic curves of PV-cell

III. Boost type DC-DC Converter

In Fig. 3, the schematic of the boost converter power stage is given. It consists of the power switch T, boost inductor L, filter capacitor C, output diode D, and load resistance R. Here, the DC input source voltage Vpv is supplies by PV module. The Boost converter operates in the continuous conduction mode(CCM) where the inductor current flows continuously (i_l>0) are used. When the switch T is in the on state, the current in the boost inductor increases linearly, and at the time, the diode is in off state. When the switch T is turned off, the energy stored in the inductor is released through the diode to the output RC circuit. The pulsating current produced by the switching is smoothed by capacitor filter and DC voltage is provide to the load The boost converter transfer function is obtained by considering its steady state operation . The DC voltage transfer function is

$$\frac{Vout}{V_{PV}} = \frac{1}{1-D} \qquad (2)$$

Assuming a lossless circuit, P_{PV} = Pout

$$V_{out}.I_{out} = V_{PV}.I_{in} = I_{out} / I_{in} = (1- D) \qquad (3)$$

Where V_{PV} and I_{PV} is converter input voltage and current or the output voltage and current of the PV module, respectively, Vout and Iout is the output voltage and current , respectively, and D is the duty ratio of the controllable switch. The boost converter operates in the CCM for L >Lmin Where function is obtained by considering its steady state operation. The DC voltage transfer function is

$$L_{min} = \frac{V_{PV} D}{2\Delta i_L f} \quad (4)$$

Here, f is the switching frequency. And then ,this expression can be to calculated the inductor current ripple value Δi_L such that a given value of inductor is obtained. The minimum value of the filter capacitance that results in voltage ripple is given by

$$C_{min} = \frac{V_{out} D}{2R\Delta v_c f} \quad (5)$$

IV. Characterization of PI controller

PI controllers are in most cases analyzed and tuned in the continuous time domain. The corresponding transfer function is given as following

$$U(S) = K_p\left(1 + \frac{K_I}{K_p} \times \frac{1}{I(S)}\right) \quad (6)$$

Where I and U denote the input error signal and controller's output, s is the Laplace variable and K_p and K_I are the two parameter of the PI controller associated with the proportional (P) and integral (I) part. Equation (6), the transition from the continuous to the discrete time domain entail that the integral operation has to be by Zero order hold (ZOH). Such as can now be shown in the following.

$$U(k+1) = K_p I_{k+1} + K_p\left(\omega_{PI} T_{sample} - 1\right) I_k + I_k \quad (7)$$

Equation (7) , the signal is sampled at the instant k and held constant until the next sampling instant k+1.

V. Maximum Power Point Tracking (MPPT)

Maximum power point tracking means that PV module is always supposed to operate at maximum output voltage rating. A MPPT is a DC/DC converter that sets the PV module to operate at MPP independently of the load. The diagram of the MPP- tracking proposed in this work is shown in Fig.3., Using a power MOSFET is PWM controller, operating with switching frequency equal to 10 KHz. Adjusting the duty cycle of switching. The MPP-tracking control circuit is implemented with microcontroller ADMC 331.

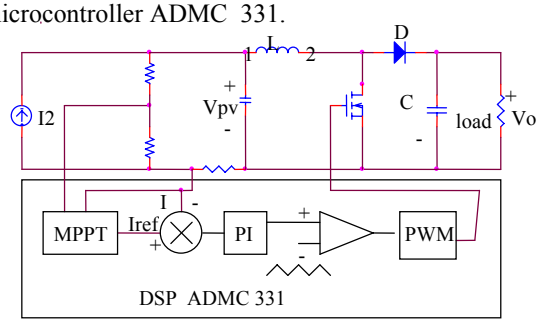

Figure 3. The diagram of the implemented system

VI. Control algorithm

A simple algorithm based on Hill- climbing and Perturbation and observation (P&O) method has been developed for real time track., and then it can fail under rapidly changing atmospheric condition. In the method described in [2], the power converter is controlled using the PV module output power. Figure.4. is based on the calculation of the PV output power and of the power change by sampling voltage and current values. The power change is detected by comparing the present and previous voltage levels, in order to calculate a reference voltage which is used to produce the PWM control signal. The DC/DC converter is driven by a DSP-based controller for fast-response and the overall system stability is improved by including a PI controller which is also used to match the array and reference voltage levels. However, the DSP-based control unit increases the implementation cost of the system.

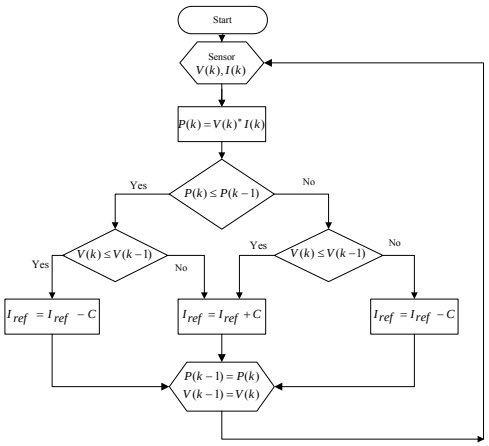

Figure 4. Algorithm flowchart

VII. Experimental Results

The proposed photovoltaic system was implemented using a DSP-based control with microcontroller ADMC 331. The system consists of a nonlinear current source as the power source, the PV-module ,s electrical characteristic ware Voc = 21.6 V, Isc = 3.3 A, IMPP = 3.1 A , VMPP = 17.3 V; there are the manufacturer rated values under standard operating condition., a resistor set as the load is 60 ohmic load. Such as design of inductor and capacitor of DC-DC converter., that the inductor value is calculated as 0.40 mH. The output capacitor value is calculated as 17 µF., Taking into account that the ripple of the PV output current must be less than 2%. The switching frequency is 10 KHz. The simulation was implemented under real time changing irradiation condition. For testing the MPP tracking, the performance of the PV system is studied for a clear sunny day with various radiation level on 15th

January 2007 at King Mongkuk' s University of Technology Thonburi (KMUTT) in Bangkok. All measurements ware recorded by a data logger every 5 second from 10 A.M to 2.30 P.M time. A lot of measurements have been made different sky condition. Figure.5. show of the experiment results gathered using the algorithm. Which refers to different irradiation., As can be observed, the system is stable and operates successfully even in cases of changing atmospheric condition., PV system output power(W) and input power (W) has been plotted, in Fig.6, versus time to show how well the device tracked. Figure.7 has been plotted to show efficiency versus time. Thus , experiment result confirm the method proposed.

VIII. CONCLUSION

The purpose of maximum power tracking is to transfer the maximum available power to the resistance load form the PV system. The MPP- Tracking is a boost converter , The use of microcontroller allows simple modification of the system, controlled by a single chip microcontroller that employs the Hill- climbing / P&O algorithm. Experiment results describe the performance of the designed MPP-tracking . The MPP-tracking increased about 24 % the energy transfer from the PV system to load and the overall efficiency of the MPP-tracking system about 87 % . The results show that proposed MPP- tracking algorithm has successful tracked the MPP in changing illumination condition.

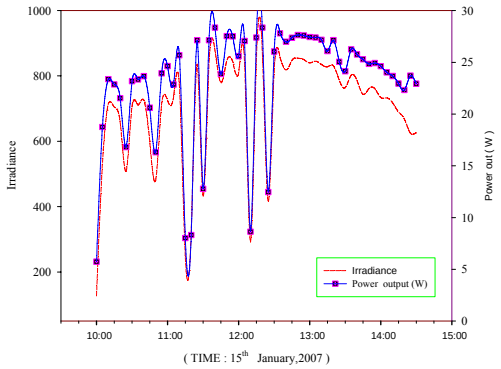

Figure 5. PV output power generation (W) and irradiance (W / m^2) vs. time for a MPPT programmed with the algorithm.

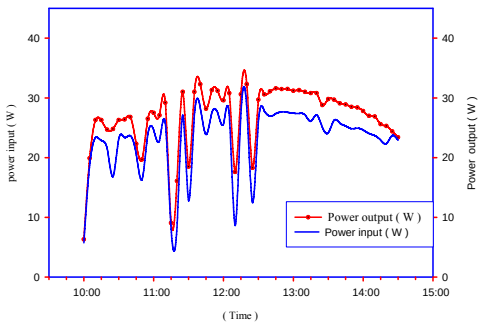

Figure 6. Output power (W) and input power (W) vs. time For a MPPT programmed with the algorithm.

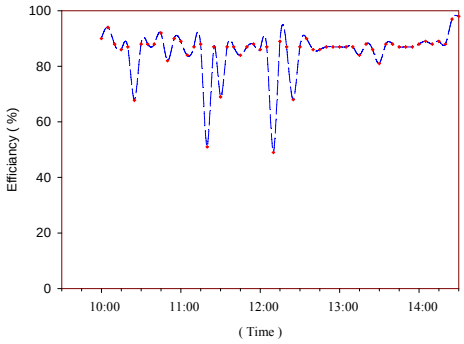

Figure 7. efficiency vs. time for a MPPT programmed with the algorithm.

REFERENCES

[1] Hua and Lin, 2003 C. Hua and J. Lin, An on-line MPPT algorithm for rapidly changing illuminations of solar arrays, *Journal of Renewable Energy* 28 (2003), pp. 1129–1142.

[2] C. Hua, J. Lin, and C. Shen, "Implementation of a DSP- Controlled photovoltaic system with *peak* power tracking", *IEEE Trans Indusl rial Elecfroni*~v~o.l. 45, pp. 99 -107, Feb. 1998

[3] K.H Hussein, I.Muta, T. Hoshino, and M. Osaka, Maximum photovoltaic power tracking: an algorithm for rapidly changing atmospheric conditions", in *IEE Proc. Gemmion. Trammission and Disfribulion.* vol. 142**,** p p . 5 9 4 , Jan. 1995

[4] Medeiros and Antunes, 1998 Medeiros, A., Antunes, F., 1998. A neural network-based real time maximum power tracking controller for grid connected PV system. IEEE-IECON'98, Aachen, Germany, pp. 554–558.

[5] Maheshappa et al., 1998 H.D. Maheshappa, J. Nagaraju and M.V. Krishna Murthy, An improved maximum power point tracker using a step-up converter with current locked loop,*Renewable* Energy 13 (1998) (2), pp. 195–201.

[6] Solodovnik et al., 2004 E.V. Solodovnik, L. Shengyi and R.A. Dougal, Power controller design for maximum power tracking in solar installations, *IEEE Transactions on Power Electronics.* (2004), pp. 1295–1304.

Vibration Signal Analysis for Condition Monitoring of High Voltage Circuit Breakers

T. Suwanasri[1], N. Charbkeaw[2], T. Bunyagul[2]
[1]The Sirindhorn International Thai-German Graduate School of Engineering
[2]Electrical Engineering Department, Faculty of Engineering
King Mongkut's Institute of Technology North Bangkok, Bangkok, 10800, Thailand

***Abstract*- Nowadays, the goals of electrical supply utilities are to reduce equipment failures, to extend service life, to increase equipment reliability and to reduce their related operating and maintenance costs. High voltage circuit breaker is also an important element in the electrical network. In order to determine or to detect the abnormal conditions inside the circuit breakers, the powerful vibration techniques have been proposed for many years. Thus, vibration technique by analyzing the signal in time-frequency-domain was performed in this work under no-load switching operations with a commercially available high-voltage puffer-type circuit breaker without opening its major parts. Vibration of circuit breaker poles and operating mechanism as well as various monitored parameters were recorded under normal and variable operating conditions, which were the variations of auxiliary supply voltage, hydraulic oil pressure and SF_6 gas pressure. After that, a sensitivity of vibration method to the variable operating conditions was evaluated**.

I. INTRODUCTION

Up till now, the preventive maintenance is predominantly used to maintain circuit breakers after specific time interval or after specific number of operations. Even though nowadays, the reliability of the circuit breaker has been continuously improved by various measures in design and construction of the circuit breakers [1], [2], failures still exist and sometimes cause costly consequences. Therefore, maintenance is inevitably needed. However, this task is very costly, time-consuming and sometimes can incorporate unintentional defects due to excessively invasive maintenance.

The condition monitoring and diagnostic tests, especially with non-invasive techniques, have been developed with aiming to facilitate maintenance activity. Some techniques have been developed so far by many researchers, such as measurement of enclosure vibration to detect abnormal contact condition inside GIS [3], development of acoustic analysis by measuring vibration signals of circuit breaker in laboratory and in field test [4], [5], [6]. The idea is that mechanical malfunctions and abnormal behaviors should be detected as changes in the vibration signatures of the circuit breakers.

In this paper, the diagnostic method by analyzing the vibration signatures in time-frequency domain was presented. The tests were performed with a commercial 110kV SF_6 puffer-type circuit breaker, which is a free-standing pole model with 3-pole operating mechanism. At first, the vibration signature was recorded during no-load switching operations under normal operating condition as a reference fingerprint. After that, the signatures under variable auxiliary supply voltage, variable hydraulic oil pressure and SF_6 gas pressure variation were recorded. After comparison with the reference fingerprint, these intentionally variable operating conditions could be detected as changes in the analyzed vibration signatures.

II. EXPERIMENTAL SETUP

This experiment was performed with a 110kV SF_6 puffer-type circuit breaker with hydraulic operating mechanism as shown in Fig. 1 for the experimental setup. The investigation was performed under no-load switching operations. The vibration signals of the free-standing poles and of operating mechanism were recorded under normal and variable operating conditions that could probably occur in service, e.g. variation of control voltage supplied from station service power source or battery from the secondary circuit, SF_6 pressure change due to leakage or over-filling and hydraulic oil pressure change caused by seal and gasket aging.

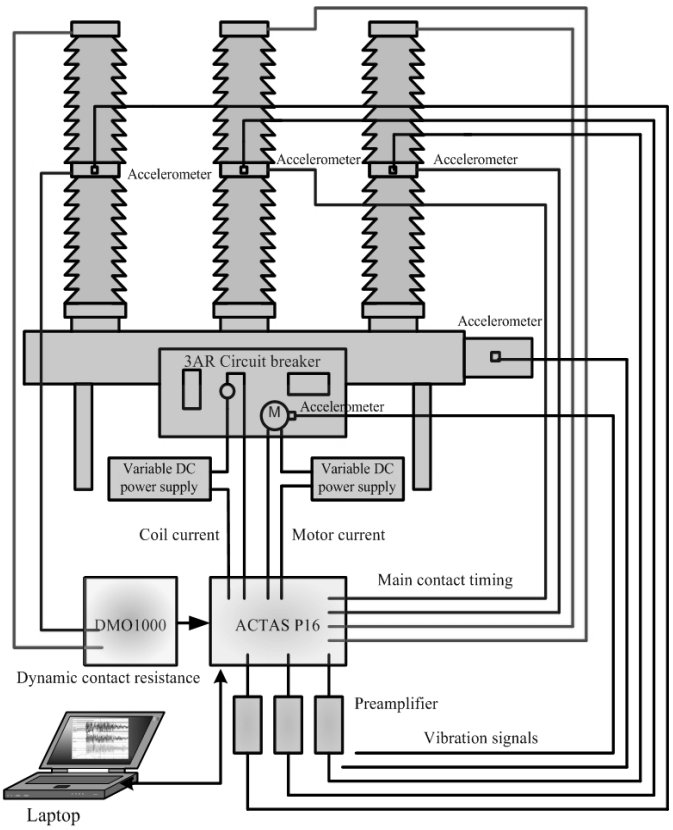

Figure 1. Experimental setup

During each no-load switching operation, other parameters such as close and trip coil current, hydraulic pumping motor current and time, main contact timing, dynamic contact resistance, were also measured as shown in Fig. 2. The measured vibration signatures under normal operating condition were used as a reference base line. The signatures under variable operating conditions summarized in Table I were compared with the reference signature. The tests and measurements were performed in a laboratory because of the readily controlled testing conditions.

The main components of the test system and their details were described as follows:

- A 110kV, 1250A, and 31.5kA puffer-type SF_6 circuit breakers with three-pole-operated hydraulic operating mechanism
- 5 accelerometers type 4501 (B&K) mounted externally at the middle of each pole, hydraulic operating mechanism and pumping motor of the circuit breaker
- 3 preamplifiers type 2626 (B&K) for vibration signal conditioning with optical cable connection to accelerometer
- 1 circuit breaker testing device ACTAS P16[1].
- 1 dynamic contact resistance measurement device DMO1000[1]
- Measurement cables and coaxial cable for serial connection between notebook and measurement device
- 1 notebook as a control unit with ACTAS software program
- 2 variable DC or AC power supply for control circuit and pumping motor
- SF_6 storage and filling unit.

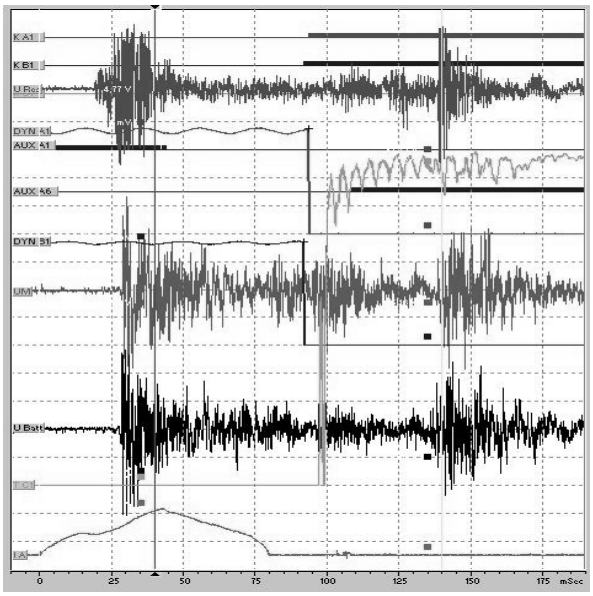

Figure 2. Vibration signals and other measured parameters recorded during closing operation

[1] KoCoS Meßtechnik AG, Südring 42, D-34497 Korbach, Germany

TABLE I
SUMMARY OF TESTING CONDITIONS

Test conditions	Voltage	Oil Pressure (bar)	SF_6 (bar)	Nr. of SW per test
Normal or rated operation	100%	320	6.5	15
Variable supply voltage	115%	320	6.5	15
	70%	320	6.5	15
Variable oil pressure	100%	280	6.5	15
	100%	250	6.5	15
Variable SF_6 pressure	100%	280	8	15
	100%	250	5.5	15

The vibration signals during closing and opening operations were recorded by using accelerometers and a data acquisition system. The vibration measurement consists of the following components:

1. Sensors: The piezoelectric accelerometer is used to measure the vibration signal propagating to the external structure via various parts of the internal mechanism and insulating medium. They were temporarily mounted with adhesive glue on circuit breaker enclosure surface. It produces a charge in proportional to the acceleration (pC/ms^{-2}).
2. Preamplifier and signal conditioner: These devices are needed in order to match the impedance and amplify the signal from accelerometer to reasonable value.
3. Data acquisition: The sampling rate was set at 10kHz. The total record time was set at 200ms for closing operation and 150ms for opening operation.

III. VIBRATION SIGNAL ANALYSIS

A. Circuit breaker's Vibration Signal

Vibration signal monitoring can refer to the movement of moving parts inside circuit breaker. The use of vibration signal can be compared with the hearth beating sound. Doctor can analyze the body health by the rhythm of beating. Like in circuit breaker condition assessment, the circuit breaker conditions can be acquired by vibration signal. Fig. 3 shows example signals of circuit breaker during opening and closing operations.

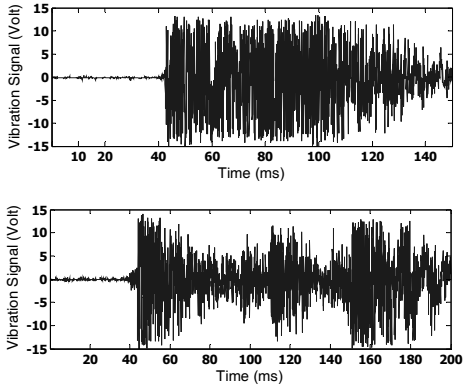

Figure 3. Opening (upper) and closing (lower) vibration signal.

Many sources of acoustic vibration are detected during the closing or opening operation such as the instant of solenoid coins, the impacted of arcing and main contacts. Each source of vibration will generate different vibration signature.

B. Wavelet transform

Wavelet Transform (WT) is a mathematical tool that transforms the signal in time domain to time-frequency domain. Its concept is similar to Short Time Fourier Transform (STFT). The STFT decomposes the original signal to a set of 'sinusoidal signals' with different frequencies. The coefficients of STFT are proportional to the correlation coefficients of the original signal with the unit complex sinusoidal in each frequency.

WT decomposes the original signal to a set of wave like signals, called 'wavelet'. These wavelet signals are the scaled (dilated) and shifted forms of the mother wavelet, as shown in Fig. 4.

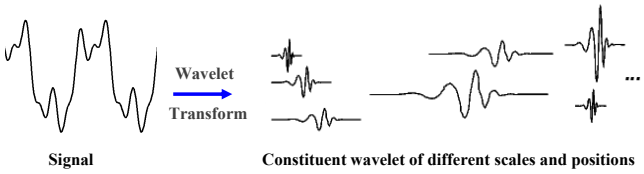

Figure 4. Signal decomposition using wavelet transformation [2]

The WT coefficient can be calculated by using the following expression.

$$C(a,b) = \int_{-\infty}^{\infty} f(t)\frac{1}{\sqrt{a}}\psi(\frac{t-b}{a})\,dt \qquad (1)$$

Where, ψ is the wavelet function and its shape varied by variables **a** (dilation) and **b** (position). Fig. 5 shows the example of the mother wavelet, dilated wavelet (a = 2) and position shifted wavelet (b = 10). The observation can be made that the smaller the dilation means the higher the frequency. The greater the position shifted means the longer the delay.

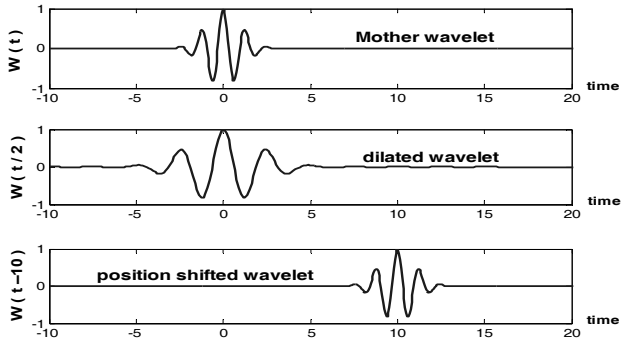

Figure 5. Mother wavelet, dilated wave*let (a=2) and position shifted wavelet (b= 10)*

The great advantage of WT is the ability to decompose the selected frequency component at any time. Therefore it is suitable to analyze instant transient signals. Even a barely visible small discontinuity can still be detected [7].

The event extraction of time domain vibration signal as in Fig. 6 is not easy to perform by human eye, especially opening vibration signal. The Wavelet transform is applied to enhance the event detection. Wavelet transform is a mathematical tool that transforms a signal in time domain to time-frequency domain. For this resource, the complex morlet with 1 bandwidth parameter and 1.5 wavelet center frequencies is selected. Fig. 6 shows the comparison between opening vibration signal and its transformed signal.

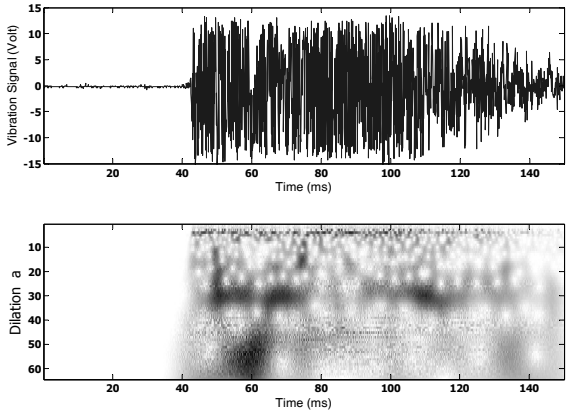

Figure 6. Time domain opening vibration signal (upper) and its wavelet transformed spectrogram (lower)

The wavelet transformed spectrogram in Fig. 6 shows the magnitude of signal in each frequency. At the vertical axis, the higher number of **a** (dilation) refers to the lower frequency signal. The value of horizontal axis is time in millisecond. Moreover, the darker color means the higher magnitude, e.g. the large magnitude low frequency signal (**a**=60) appears at 60ms.

C. Information Extraction from wavelet spectrogram

The wavelet transformed spectrogram contains a lot of information such as moving instant of solenoid armature and its speed, moving instant of moving contact. Fig. 7 shows the wavelet spectrogram of opening operation at normal operation as in table I compared with dynamic resistance (solid line) and delayed solenoid coil current signal (dash line).

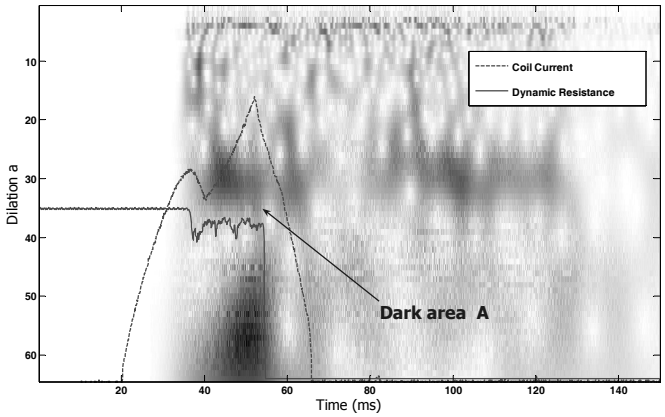

Figure 7. Spectrogram of normal condition closing operation compared with coil current (dash line) and dynamic resistance signal (solid line)

There are a lot of event signatures in the wavelet spectrogram shown in Fig. 7. The starting of shaded area of high frequency scale, at dilation = 1, relates to the starting movement of moving parts. The dark area A at scale of 30 refers to the scratching of arcing contact, and the arcing contact is fully separated at the end of this dark area. This result is confirmed by the comparison with dynamic resistance signal.

IV. RESULTS

A. *Effect of control voltage to vibration signal*

Practically, the dedicate power supply is used to supply the power to every control device including trip circuit. The variation of this control voltage affects to electromechanical mechanism. Fig. 8 shows the comparison between transformed vibration signal of closing operations at 70%, 100% and 115% control voltage.

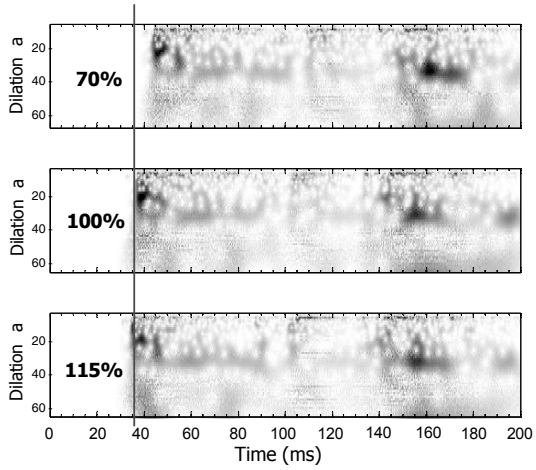

Figure 8. Spectrogram of vibration signal of circuit breaker closing operation which different control voltage

The higher the control voltage, the earlier appearance of the shaded zone of spectrograms occurs. However, the distance between signatures is still similar. Thus, there is no change of contact moving speed.

B. *Effect of hydraulic pressure to vibration signal*

Because the operation of puffer-type circuit break requires extremely high power and high speed, the hydraulic operating mechanism is selected. In the experiment, the hydraulic oil pressure is reduced from 320bar to 280bar and 250bar. The transformed signal is presented in Fig. 9. Each signature shows the same position of starting movement. For the higher hydraulic oil pressure, the faster moving occurs. Therefore, the event signature in this case occurs earlier and the signature becomes shorter, e.g. in Fig. 8, the arcing contact signature of closing operation at 320bar hydraulic oil pressure is much shorter than the others at 280bar and at 250bar.

C. *Effect of SF_6 pressure to vibration signal*

There is no significant effect of SF_6 pressure to the vibration signal. It is not easy to explicitly identify the event signature in the wavelet spectrogram.

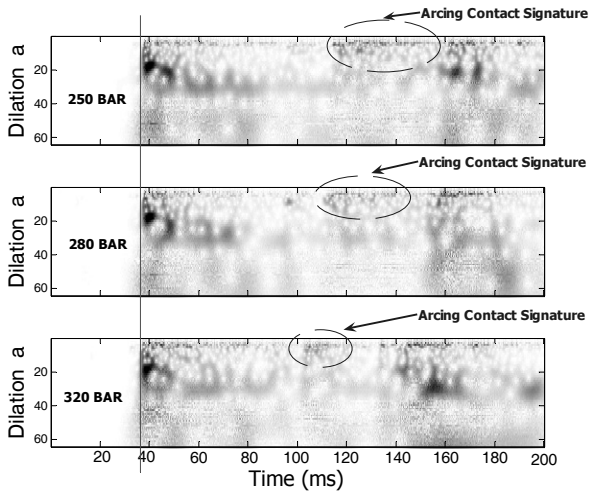

Figure 9. Spectrogram of closing vibration signal which different hydraulic oil pressure

V. CONCLUSION

The vibration signal analysis was performed in this work by using the wavelet transform in order to investigate the sensitivity of this method according to the variations of circuit breaker operating conditions. The variation of auxiliary supply voltage and hydraulic oil pressure results in reasonable changes in the transformed vibration signature. The variation of SF_6 gas pressure can not be detected by this method.

The changes in the transformed vibration signatures according to the variation of its operating conditions have been verified in this work. Thus, this vibration analysis can be used to observe the significant events occurring inside the circuit breaker. Therefore, further development of this method is recommended to use this as circuit breaker diagnostic tool.

ACKNOWLEDGMENT

The author would like to thank SIEMENS AG in Erlangen, Germany and Institute for High Voltage Technology, RWTH Aachen University, Germany for the cooperation and support.

REFERENCES

[1] M. Pflaum, et al., "New aspects of the reliability of high voltage circuit breakers", *Cigre' Session Paper* Ref.13-07, published: 1978.

[2] C. A. Fawdrey, "The application of development and diagnostic techniques to circuit breaker reliability", *Cigre' Session Paper* Ref. 13-02, published: 1978.

[3] Y. Ohshita, A. Hashimoto, Y. Kurosawa, "A diagnostic technique to detect abnormal conditions of contacts measuring vibrations in metal enclosures of gas insulated switchgear", *IEEE transaction on power delivery*, vol. 4, pp. 2090-2094, October 1989.

[4] M. Runde, T. Aurud, L. E. Lundgaard, G. E. Ottessen, K. Faugstad, "Acoustic diagnosis of high voltage circuit breakers", *IEEE transaction on power delivery*, vol 7, no.3, pp 1306-1315, July 1992.

[5] M. Runde, G. E. Ottesen, B. Skyberg, M. Ohlen, "Vibration analysis for diagnostic testing of circuit breakers", *IEEE transaction on power delivery*, vol 11, no.4, pp 1816-1823, October 1996.

[6] T. Suwanasri, A. Schnettler, D. Fricke, A. Noack, "Non-invasive condition monitoring of a high voltage circuit breaker", *XIIIth International Symposium on High Voltage Engineering*, Netherlands, 2003

[7] M. Misiti, Y. Misiti, G. Oppenheim, J. Poggi, "Wavelet Toolbox for Use with MATLAB user guide", *MathWorks, Inc.,1996*

Generator Participating Factors for Sensitivity Analysis in a Deregulated Electricity Supply Industry

C. Adsoongnoen[1] and T. Suwanasri[2]
[1]Department of Electrical and Computer Engineering, Faculty of Engineering
Naresuan University Phitsanulok 65000 Thailand
[2]The Sirindhorn International Thai-German Graduate School of Engineering
King Mongkut's Institute of Technology North Bangkok, Bangkok 10800 Thailand

Abstract- **This paper presents a utilization of generator participating factors for sensitivity analysis in a new electricity environment. In this study, the sensitivity index is referred to the effect of power generation on the use of transmission network facilities. The high sensitivity index means the high usage portion of the network. The generator participating factor is proposed to reduce a strong sensitivity at generation buses by distributing power generations, reducing system loss, and producing high benefit of system-wide usage. The results send incentive signals to generators for power-generation allocation based on system usage. To demonstrate its effectiveness, the proposed method is applied to the IEEE 30-bus system and 118-bus system.**

I. INTRODUCTION

Conventional Electricity Supply Industry (ESI) has been structured as a monopoly business that brings a high price of electricity, less efficiency in operation and management, etc. Therefore, many countries has restructured their ESIs by expecting that the new models will result in the higher efficiency, lower investment including operation and management costs, cheaper electricity price to customers, and higher electricity supply security. In a modern power system as deregulated or partial deregulated structure, the power producers do not have an obligation to serve the electricity. However, they play a roll regarding their costs not only the cost of power generation but also the other costs as transmission charge based on system usage and congestion management. It is important to send the incentive signal to users aiming at utilizing the system-wide facilities. The sensitivity method [1] was proposed to analyze the effects of nodal power injection on the use of transmission facilities. It means that the users with high sensitivity indices use high portions of transmission network. Consequently, the system might not be optimally used and transmission users, both generator and load, might pay high transmission charges. In addition, new participants, who need to install new capacity and find out the suitable location, where the lowest transmission charge is provided, can use the indices as a decision factor. Generator participating factors in [2] was suggested for solving the optimum power flow and finding the minimum cost of power generation [3] in a deregulated ESI.

This paper presents a generator participating factors for sensitivity analysis. The objective of sensitivity method is considered as sending the incentive signal to the generators, while the objectives of the generator participating factors are considered as distributing the power generation agreed by the generation companies in a deregulated environment, reducing system congestion and losses. The IEEE 30-bus system and IEEE 118-bus system are demonstrated for illustration purposes.

II. POWER FLOW MODEL

The problem formulation is originated from power flow analysis by using the decoupled Newton-Raphson method. The power flow model is formulated that power generation at a bus is firstly considered as:

$$P_{G\,i}=P_{Gset\,i}+P_{Gc\,i} \tag{1}$$

where:
i = 1, 2,…, NG, NG+1,…, NB.
$P_{Gi\,max} \geq P_{Gi} \geq P_{Gi\,min}$
$P_{Gc\,i}= \alpha_i \Delta G$
$\Delta G=\Delta P_T$, $\Delta P_T=P_T-P_{T0}$
$\sum \alpha_i = 1.00$

The parameters α_i is the grid's own generator participating factor agreed by the generation companies. Both active and reactive power loads are modeled as function of voltage at the bus. The considered functions are:

$$P_{Li}=P_{Loi}(A_1+A_2V+A_3V^2+A_4V^{ep}) \tag{2}$$

$$Q_{Li}=Q_{Loi}(R_1+R_2V+R_3V^2+R_4V^{eq}) \tag{3}$$

where:
P_{Gi} : p.u. active power generation at bus i
P_{Gseti} : p.u. active power schedule at bus i
P_{Gci} : p.u. active power generation due to primary and secondary controls at bus i
P_T : p.u. active power schedule at tie-line
NG : number of generator connected bus
NB : total number of buses in the system
α_i : participation factor of generator connected to bus i
ΔG : static area control error
P_{Li}, Q_{Li} : actual active and reactive load at bus i
P_{Loi}, Q_{Loi}: scheduled active and reactive load at bus i.
$A_1, A_2, A_3, A_4, R_1, R_2, R_3, R_4, ep, eq$ are constants while $A_1+A_2+A_3+A_4 = 1.0$ and $R_1+R_2+R_3+R_4 = 1.0$.

The power mismatch matrix can be written as:

$$\begin{bmatrix} dP \\ dQ \end{bmatrix} = \begin{bmatrix} Jpd & Jpv \\ Jqd & Jqv \end{bmatrix} \begin{bmatrix} d\delta \\ dV \end{bmatrix} \quad (4)$$

To calculate power flow, bus 1 is assumed as the reference for the purpose of voltage phase angle calculations of the other buses. The decoupled Newton-Raphson iterative solution is used. The example of linear equations for real power can be written as in (5). However, only *Jpd* and *Jqv* are taken into consideration for the power flow calculation.

$$\begin{bmatrix} \Delta P_1 \\ \Delta P_2 \\ \vdots \\ \vdots \\ \Delta P_{NB} \end{bmatrix} = \begin{bmatrix} \frac{\partial P_1}{\partial X} & \frac{\partial P_1}{\partial \delta_2} & \cdots & \frac{\partial P_1}{\partial \delta_{NB}} \\ \frac{\partial P_2}{\partial X} & \frac{\partial P_2}{\partial \delta_2} & \cdots & \frac{\partial P_2}{\partial \delta_{NB}} \\ \vdots & \vdots & \cdots & \vdots \\ \frac{\partial P_{NB}}{\partial X} & \frac{\partial P_{NB}}{\partial \delta_2} & \cdots & \frac{\partial P_{NB}}{\partial \delta_{NB}} \end{bmatrix} \begin{bmatrix} \Delta X \\ \Delta \delta_2 \\ \vdots \\ \Delta \delta_{NB} \end{bmatrix} \quad (5)$$

where:

$$\Delta P^k = P_{specified} - P_{calculated} \quad (6)$$

$$\Delta Q^k = Q_{specified} - Q_{calculated} \quad (7)$$

$$X^{k+1} = X^k + \Delta X \,,\; \delta^{k+1} = \delta^k + \Delta\delta \,,\; V^{k+1} = V^k + \Delta V \quad (8)$$

ΔX is referred to ΔG as unknown. k is iteration of computation. We can solve for ΔX, $\Delta\delta$ and ΔV by iterative process. The power flow solution is used later for sensitivity calculation. The computational procedure is shown in Fig. 1.

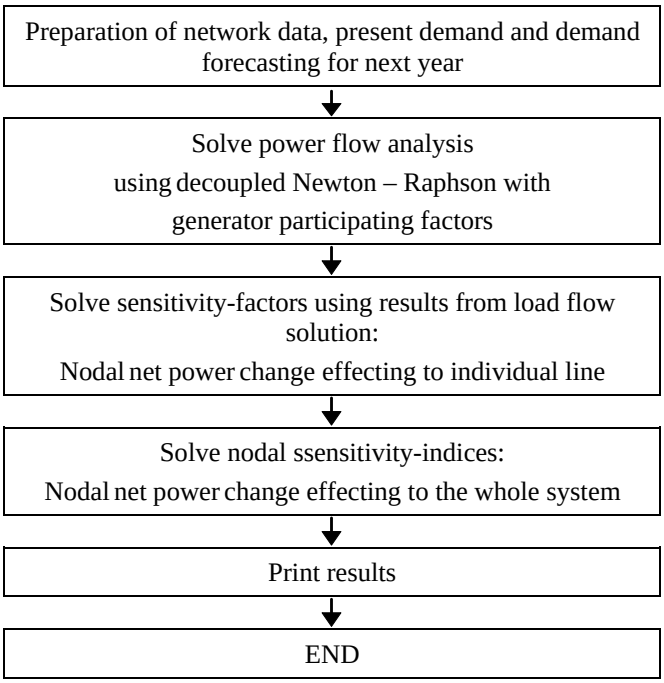

Figure 1. Computational procedure.

III. Sensitivity Indices Calculation

The computation of the sensitivity indices consists of three main steps. Firstly, the sensitivity factors are calculated. They represent an influence of the incremental generation or demand at each bus to the tie-line flows. Secondly, the sensitivity matrix is formed in terms of sensitivity factors. Lastly, the nodal sensitivity indices based on the use of system are determined. These results are used to calculate nodal transmission tariffs.

A. Sensitivity factor calculation

The calculation of sensitivity factors starts from the determination of the Jacobian matrix J which contains the derivatives of the bus power injection with respect to the voltage amounts V_i and angles δ_i of a base load flow case (index 0).

$$J_0 = \begin{bmatrix} J1 & J2 \\ J3 & J4 \end{bmatrix} = \begin{bmatrix} Jpd & Jpv \\ Jqd & Jqv \end{bmatrix}_{(2NBx2NB)} \quad (9)$$

$$J_1 = \begin{bmatrix} \frac{\partial P_1}{\partial X} & \frac{\partial P_1}{\partial \delta_2} & \cdots & \frac{\partial P_1}{\partial \delta_{NB}} \\ \frac{\partial P_2}{\partial X} & \frac{\partial P_2}{\partial \delta_2} & \cdots & \frac{\partial P_2}{\partial \delta_{NB}} \\ \vdots & \vdots & \cdots & \vdots \\ \frac{\partial P_{NB}}{\partial X} & \frac{\partial P_{NB}}{\partial \delta_2} & \cdots & \frac{\partial P_{NB}}{\partial \delta_{NB}} \end{bmatrix}_{(NBxNB)} \quad (10)$$

The matrix J has ($2NB$x$2NB$) dimension as shown in (9) where NB indicates the numbers of buses. To calculate sensitivity factor, the matrix J needs to be inversed. Thus, we get the new matrix L which contains the derivatives of the bus voltage and angle with respect to the bus active power P and reactive power Q injection.

$$L = J^{-1} = \begin{bmatrix} Jpd & Jpv \\ Jqd & Jqv \end{bmatrix}^{-1} = \begin{bmatrix} \frac{\partial \delta}{\delta P} & \frac{\partial \delta}{\delta Q} \\ \frac{\partial V}{\delta P} & \frac{\partial V}{\delta Q} \end{bmatrix} \quad (11)$$

The branch flow equation given in term of voltages and impedances can be written as:

$$S_{i-j} = 3V_i^2 \left(Y_{0ij}^* + Y_{ij}^*\right) - 3V_i V_j^* Y_{ij}^* \quad (12)$$

where Y_{0ij}, Y_{ij} are elements of the π equivalent and *i*, *j* are terminal buses of the considered branch *i-j*. By deriving (12) with respect to V_i, V_j, δ_i and δ_j, the sensitivity factor of line *i-j* due to power injection changes at bus *k* can be determined.

$$K_{i-j,k}^{PP} = \frac{dP_{i-j}}{dP_k} = \frac{\partial P_{i-j}}{\partial \delta_i} \cdot \frac{\partial \delta_i}{\partial P_k} + \frac{\partial P_{i-j}}{\partial \delta_j} \cdot \frac{\partial \delta_j}{\partial P_k} + \frac{\partial P_{i-j}}{\partial V_i} \cdot \frac{\partial V_i}{\partial P_k} + \frac{\partial P_{i-j}}{\partial V_j} \cdot \frac{\partial V_j}{\partial P_k} \quad (13)$$

and

$$K_{i-j,k}^{QP} = \frac{dQ_{i-j}}{dP_k} = \frac{\partial Q_{i-j}}{\partial \delta_i}\cdot\frac{\partial \delta_i}{\partial P_k} + \frac{\partial Q_{i-j}}{\partial \delta_j}\cdot\frac{\partial \delta_j}{\partial P_k} + \frac{\partial Q_{i-j}}{\partial V_i}\cdot\frac{\partial V_i}{\partial P_k} + \frac{\partial Q_{i-j}}{\partial V_j}\cdot\frac{\partial V_j}{\partial P_k} \quad (14)$$

where $\frac{\partial \delta_i}{\partial P_k}, \frac{\partial \delta_j}{\partial P_k}, \frac{\partial V_i}{\partial P_k}, \frac{\partial V_j}{\partial P_k}$ are elements of *L*.

The sensitivity factors can be applied to all branches and affect all buses in the system. The matrix can also be spitted into four sub-matrices by separating active and reactive power as following:

$$[\Delta S_{branch}] = [K][\Delta S_{bus}] \quad (15)$$

$$\begin{bmatrix} \Delta P_{branch} \\ \Delta Q_{branch} \end{bmatrix} = \begin{bmatrix} K^{PP} & K^{PQ} \\ K^{QP} & K^{QQ} \end{bmatrix} \begin{bmatrix} \Delta P_{bus} \\ \Delta Q_{bus} \end{bmatrix} \quad (16)$$

From (16), both incremental active and reactive power flows in any transmission line can be determined. In this paper, only the active and reactive powers influenced by bus real power are considered. It means that the applications of sub-matrix K^{PP} and K^{QP} are applied to form the sensitivity matrix.

B. Sensitivity Matrix and Incremental Flow Calculation

In this step, the sensitivity matrix is performed as shown in Table I. It shows real power sensitivity factors influencing lines L_1 to L_4 due to the power injection of countries A to D. The positive sign of sensitivity factor means that bus power injection increases power flows over the transmission lines. Similarly, the negative sign means that bus power injection reduces power flows over the transmission lines while the zero value means that there is no power injection or absorption to the network at the bus.

Table II presents the net balance injection in MW. T1 represents the time reference (base-case). T2 represents the forecast of the peak bus injection. Then, the expected changes of the flows are calculated based on sensitivity factors in Table I and incremental injection in Table II.

TABLE I
EXAMPLE OF SENSITIVITY MATRIX

Lines / Buses/Nodes	L_1	L_2	L_3	L_4
A	+0.3	+0.2	+0.4	-0.7
B	-0.1	-0.5	-0.3	+0.3
C	+0.5	+0.3	+0.2	-0.1
D	-0.1	-0.3	-0.1	+0.6

TABLE II
NET BALANCES OF SAMPLE NODE (MW)
(+) NET INJECTION, (-) NET ABSORPTION

Nodes / Time	A	B	C	D
T_1 (measured)	+2000	+800	-2300	-500
T_2 (forecasted)	+1300	-200	-1000	-100
Changes	-700	-1000	+1300	+400

For example, the incremental flow on line L1 is equal to (+0.3)x(-700)+(-0.1)x(-1000)+(+0.5)x(+1300)+(-0.1)x(+400) =(-210) + (-100) + (650) + (-40) = 300 MW. The nodes A, B, C, and D cause the incremental flow on L1 as amount of -210, -100, +650, and -40 MW. Similarly, incremental flows in line L2, L3 and L4 can also be determined. The incremental flows are used to calculate the sensitivity indices in the next section.

C. Sensitivity Indices Calculation

To send the correct economic signal based on a system usage and congestion to all users, the sensitivity indices should be determined. The sensitivity index is the nodal factor multiplied with a uniform postage stamp tariff. As a result, the nodal tariffs are computed. The users at each node or country will be charged in the different rates due to their network usages. The nodal sensitivity index is calculated as:

$$SI_k = 1 + \frac{\prod_{i-j} SF_{k,i-j}}{\sum_{k=1}^{n}\left(\prod_{i-j} SF_{k,i-j}\right)} \quad (17)$$

where

$$SF_{i-j,k} = 1 + \frac{\left|\Delta S_{i-j,k}\right|}{\sum_{k=1}^{n}\left|\Delta S_{i-j,k}\right|}\cdot\left|\Delta S_{i-j}\right| \quad (18)$$

SI_k is the sensitivity index at bus *k*. $\left|\Delta S_{i-j,k}\right|$ is the incremental magnitude of power flow of line *i-j* due to the injection change of bus *k*. $\left|\Delta S_{i-j}\right|$ is the total incremental magnitude of complex power of line *i-j*.

IV. SIMULATION RESULTS AND DISCUSSIONS

The IEEE 30-bus system is firstly used as a testing system. It comprises six generation buses and twenty-four lines. To calculate the sensitivity matrix in the year N, load flow data based on the measurement of the base case at the end of the year N-1 and forecasted data of the present year N must be defined. By analyzing the load flow and solving (1)-(16), the sensitivity factors can be calculated. Then, the incremental flow on transmission lines as portions of bus injection is determined. By solving (17)-(18), the sensitivity index of each bus with and without generator participating factor is determined as shown in Table III. However, only generation-buses are demonstrated.

TABLE III
SENSITIVITY INDICES WITH AND WITHOUT GENERATOR PARTICIPATING FACTORS (GPF) FOR THE IEEE 30-BUS SYSTEM

Bus No.	GPF	Sensitivity indices	
		without GPF	with GPF
1	0.2	0.0600990	0.0570269
2	0.2	0.0330780	0.0396866
5	0.2	0.0298085	0.0322901
8	0.0	0.0321596	0.0283024
11	0.2	0.0450555	0.0676295
13	0.2	0.0343001	0.0522836

TABLE IV

LOAD, GENERATION AND SYSTEM LOSSES WITH AND WITHOUT GENERATOR PARTICIPATING FACTORS FOR THE IEEE 30-BUS SYSTEM

(MW)	without GPF	with GPF
Load	233.40	233.40
Power Losses	173.60	48.00
Generation	407.00	281.40

TABLE V

SENSITIVITY INDICES WITH AND WITHOUT GENERATOR PARTICIPATING FACTORS FOR THE IEEE 118-BUS SYSTEM

Bus No.	without GPF		with GPF		
	Pgen (MW)	Indices	GPF	Pgen (MW)	Indices
10	250.0	0.0295	0.1	270.6	0.0260
12	85.0	0.0032	0.1	105.6	0.0035
25	220.0	0.0792	0.1	240.6	0.0511
26	314.0	0.2278	0.0	314.0	0.1602
31	7.0	0.0065	0.0	7.0	0.0079
46	19.0	0.0022	0.0	19.0	0.0030
49	204.0	0.0029	0.0	204.0	0.0039
54	48.0	0.0024	0.0	48.0	0.0033
59	155.0	0.0092	0.0	155.0	0.0119
61	160.0	0.0094	0.0	160.0	0.0124
65	391.0	0.0047	0.0	391.0	0.0068
66	392.0	0.0047	0.1	412.6	0.0067
69	516.4	0.0034	0.1	537.0	0.0042
80	477.0	0.0035	0.1	497.6	0.0045
87	4.0	0.0020	0.0	4.0	0.0027
89	856.3	0.1102	0.1	627.6	0.1100
100	252.0	0.0046	0.1	272.6	0.0042
103	40.0	0.0021	0.1	60.6	0.0027
111	36.0	0.0043	0.1	56.6	0.0039

TABLE VI

LOAD, GENERATION AND SYSTEM LOSSES WITH AND WITHOUT GENERATOR PARTICIPATING FACTORS FOR THE IEEE 118-BUS SYSTEM

(MW)	with GPF	without GPF
Load	3667.99	3668.00
Power Losses	140.91	184.73
Generation	3808.90	3801.21

Consideration without generator participating factors, bus No. 1 is the slack bus. It has a function to generate the electricity supporting the load mismatch. In this case, the slack bus is forced to produce the largest amount of power generation. The sensitivity of this bus as shown in Table III is the highest value as 0.060099 because of its system usage. The other generators show different sensitivity-values. For example, bus No. 5 has 0.0298085 as the lowest value because produce the less net power injection. The other buses can be explained in the same way. The total system loss is 173.60MW as shown in Table IV. Comparing with using generator participating factors, the total power generation is distributed. The power generation and sensitivity index of the slack bus are reduced and while the indices of the other buses are increased due to the participating factors. The system loss is reduced to 48MW. It implies that the factors distribute total power generation to beneficially utilize network facilities and reduce total system loss.

Next, the IEEE 118-bus system is demonstrated as a larger system. It comprises fifty-four generators with nine transformers and hundred seventy-seven lines. Because of a limitation of space, only important generation buses are presented. Thus the summation of sensitivity indices is not equal to one. In this system, the bus No. 89 is represented as the slack bus. The simulation results without using of generator participating factors are used as a reference. The total power loss is equal to 184.73MW. The highest sensitivity index is 0.2278 at the bus No. 26, which is not the slack bus. It can be explained that even through the bus injects low power generation, transmission capacity is increased, which results in capacity loading and congestion problem. This produces high index value. The slack bus has a second highest index as 0.1102. It can be simply described that the high power generation causes high sensitivity because of using high system portion.

With using generator participating factors, bus Nos. 12, 66, 69, 80, and 103 show results as expected, the higher power generation get the higher sensitivity indices. The slack bus is not changed much in sensitivity index value because it still produces a huge amount of electricity comparing to other generators and uses a high portion of the system. However, the system loss is reduced to 140.91MW. Moreover, there are significantly important results of the bus Nos. 10, 25, 100 and 111. They increase power generations by sharing the total generation amount from the slack bus but their sensitivity indices are reduced. It can be explained that by increasing the power generation of these buses, it removes the stress of system usage, capacity loading and congestion. On the other hand, it can be explained that a use of generation participation factor to analyze system sensitivity sends signals based on system usage to optimize power generation and transmission capacity. In additional, the system loss can be also reduced.

V. CONCLUSION

This paper presents a utilization of generator participating factors for sensitivity analyses of bus injections to system. The sensitivity indices send signal regarding the system usage and congestion. The higher sensitivity index means higher usage portion of the network. The generator participating factors are proposed to distribute power generations, remove the stress on sensitivities of the generation buses, make beneficially system usage and reduce transmission loss. The IEEE 30-bus system and 118-bus system are demonstrated.

REFERENCES

[1] C. Adsoongnoen, W. Ongsakul, C. Maurer, and H.-J. Haubrich, "A new transmission pricing approach for the electricity cross-border trade in the ASEAN Power Grid," *European Transactions on Electrical Power*. John Wiley and Sons., in Press

[2] D. Thukaram, K. Parthasarathy, B.S. Iyengar and Tara S. Swamy, "Fast economic dispatch and alleviation of over-voltage under-voltage conditions in a large power system operation," *Sixth National Power System Conference*, NPSC-90, Bombay, India, June 1990.

[3] D. Thukaram, S. Chirarattananon, and K. Chayakulkheeree, "A fast economic dispatch algorithm incorporating generation control and load characteristics, *22nd Electrical Engineering Conference*, Bangkok, Thailand, November 1999.

A Network Topology Processor for Accurate Power System State Estimation

Warayut Kampeerawat[(1)], Surachai Limyingcharoen[(2)], Anupap Meesomboon[(2)]
[(1)] Graduate School, Department of Electrical Engineering, Khon Kaen University, Thailand
[(2)] Department of Electrical Engineering, Khon Kaen University, Thailand

***Abstract* – The state estimation presented in this paper includes a detection step for the possible presence of a topology error. Upon the detection of a possible error, the topology error identification step is invoked to locate its potential location. The suspicious node is then represented by the full bus-section model after which a generalized DC state estimation step capable of identifying the error in the status measurements is applied. This results in an accurate network topology that is used in the subsequent full AC state estimation. The proposed method has been successfully applied to a test system.**

I. INTRODUCTION

Nowadays, state estimation plays an important role in providing the reliable system states from measurements for a power system. The network topology or the information on how the buses and branches of the power system are connected is an important input to the state estimation and is provided by the well-known function called network topology processor.

Conventional network topology processor has the ability to provide system topology by processing the statuses of circuit breakers assuming that they are correct. The resulting system topology is used in later stages of power system analysis, especially state estimation.

When generalized state estimation was proposed in [1], a generalized approach for network topology processing was also proposed as an integral part of the state estimation. By generalized approach, network topology processor is supposed to be able to provide reliable system topology by using a blend of methods to indicate topology error (topology error processing) or to estimate possible topology (topology estimation).

Normally, the conventional state estimation can be performed properly in the environment of gross measurement errors by efficient bad data detection. However, topology errors can have a substantial impact on the results of state estimation. In serious cases, topology error can adversely affect the convergence of state estimation solution [2]. It is therefore desirable for the generalized state estimation to be able to detect not only measurement errors, but also other types of errors, especially topology errors.

Many researchers have proposed ways to carry out the topology error detection as a post-processing or preprocessing step of state estimation [3] and two-stage estimation [4,5]. The generalized state estimation technique is an efficient way to carry out the topology error detection by means of topology estimation [6,7].

The occurrence of topology errors is seldom and not widespread in a practical environment. The full-step and system-wide execution of topology error processing or topology estimation in every pass of state estimation analysis is therefore expensive and unnecessary. Topology error detection based on power transfer distribution factors has been proposed to detect suspected cases affected by topology errors [8,9]. This step is useful to determine whether the full step of topology error processing or topology estimation should be performed or not.

In this paper a generalized approach for network topology processing to provide reliable topology as a preprocessing step of the full ac state estimation for improved accuracy of the estimated states is presented.

II. BACKGROUND

A. Network Topology Processing

Network topology processor (NTP) is a function that determines the system topology from the information on the statuses of circuit breakers. Automatic NTP was first proposed in reference [10]. In a conventional approach, NTP only processes circuit breaker statuses by using graph search technique [10,11], rule-based technique [12], or connectivity matrix technique [13], to provide the system topology that is used in forming the bus admittance matrix (Y_{bus}).

The efficient and simple way for network topology processing is the graph search technique because it avoids calculations and can be applied to any bus configurations.

Topology error will directly affect Y_{bus} that is used in state estimation in terms of the measurement functions of bus injections. The accuracy of state estimation results therefore depends on the system topology obtained from NTP.

In the generalized approach, a process for rejecting topology errors called topology error processing is incorporated in the NTP so that it provides the accurate system topology. Although topology error processing can be performed after state estimation, the use of accurate system topology in state estimation will increase the possibility to provide accurate state estimates without serious problem during the operation.

B. Conventional State Estimation

The state estimation provides the estimates of the power system state variables based on a combination of measurements and virtual measurements. It can be formulated mathematically using the constrained optimization problem:

Minimize $f(z - h(x))$ (1)

Subject to $g(x) = 0$ and $c(x) \le 0$

Where: z is the vector of measurements

x is the vector of state variables

$h(.)$ is the vector functions relating measurements to state variables

$f(.)$ is the objective function

$g(.)$ and $c(.)$ are vectors of functions representing power flow quantities.

In the weighted least-squares method the following quadratic objective function is used:

$$f(z - h(x)) = [z - h(x)]^T W[z - h(x)] \quad (2)$$

Where W is a diagonal matrix of weights (For telemetry, the inverse of measurement variances are normally used as weights)

C. Generalized State Estimation

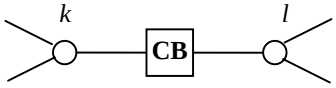

Figure 1. Zero impedance branch or branch of circuit breaker

The generalized state estimation is performed on a model in which part of the network is represented at the physical level, i.e. modeled in terms of bus sections and circuit breakers. This allows the inclusion of measurements made on zero impedance branches or branches of circuit breakers. The conventional states are augmented with new state variables.

The measurements made on zero impedance branches and circuit breakers called pseudo-measurements can be formed by considering the known branch status.

When the branch status is closed:

$$\Delta\theta_{kl} = \theta_k - \theta_l = 0 \quad \text{and} \quad \Delta V_{kl} = V_k - V_l = 0 \quad (3)$$

When the branch status is open :

$$P_{kl} = 0 \quad \text{and} \quad Q_{kl} = 0 \quad (4)$$

The new state variables are the states corresponding to the zero impedance branches or circuit breakers, e.g. power flows and node voltage angles at both ends of the branches.

D. Topology Error

There are 2 types of topology errors.

1. Branch status error:

- Inclusion error: Including a branch outage into the system topology.

- Exclusion error: Excluding an active branch from the system topology.

2. Substation configuration error:

- Bus-split error: Splitting a single bus to multiple electrical nodes.

- Bus-merge error: Merging two bus sections or more into a single electrical node.

III. PROPOSED NETWORK TOPOLOGY PROCESSOR

The proposed NTP consists of main 4 steps:

Step 1. Topology determination: Determine a bus to branch model of the power system.

Step 2. Topology error detection: Check the consistency between the topology and the measurements.

Step 3. Topology error identification: Find the indicator for suspicious area of topology error.

Step 4. Topology estimation: Estimate the statuses of circuit breaker to indicate the possible topology.

The topology error detection step (step 2) has been proposed to detect a suspected case which may be affected by a topology error. This step is useful in determining whether the full step of topology processing should be performed or not. By the approach of two-stage estimation, step 3 and step 4 can be called the first and the second stages of the approach, respectively.

After the system topology is noticed that it may contain a topology error, the topology identification and estimation will be performed consequently and the processing steps may be iteratively repeated for a multiple error case.

A. Topology Determination

For determining system topology the conventional NTP may be applied. The steps in topology determination are:

1. Bus-section processing (substation-level processing): In this step the substation presented in the details of bus-configuration will be changed to electrical nodes by using the statuses of circuit breakers and switching devices.

2. Network connectivity analysis (network-level processing): In this step all electrical nodes will be linked together by transmission lines.

The two popular graph search techniques applied to determine topology are breadth-first search and depth-first search[14]. The breadth-first search is selected to performed topology determination for the proposed NTP because it is a fast and simple way for connectivity analysis.

After all the steps are completed, the resulting network topology will be used to form the bus admittance matrix (Y_{bus}) for later analysis.

B. Topology Error Detection

Power transfer distribution factors (PTDFs) are applied in order to estimate power flow from power injection data. This allows the agreement between the topology and the measurements to be checked [8,9].

The PTDFs are derived from the sensitivities of line flows with respect to bus injections [15]. By assuming that all the per unit bus voltage magnitudes are approximately unity the calculation involves only Y_{bus}:

$$PTDFs(i,k) = conj[(Z_{bus})_{ik} - (Z_{bus})_{jk}] / conj(z_{ij}) \quad (5)$$

The approximated branch power flows can be calculated using:

$$\overline{S}_{branch} \approx PTDFs \times S_{bus} \quad (6)$$

Where i = sending bus , j = receiving bus, k = bus number

$\bar{S}_{branch}$ = a vector of branch power flow
S_{bus} = a vector of bus injection
z_{ij} = the impedance of branch *ij*
Z_{bus} = Bus Impedance Matrix = $(Y_{bus})^{-1}$

When the estimated power flows are obtained, the hypothesis testing is used to decide whether topology is correct or not. The following performance index (*J(r)*) used for the hypothesis testing with chi-square is

$$J(r) = \sum_{i=1}^{N} (r_i^{\,2} / \bar{S}_{branch,i}) \qquad (7)$$

Where: N = the number of power flow measurements
r_i = the residual between the measured and estimated power flows.

C. Topology Error Identification

After the topology error has been detected in the previous step, the specific suspected area will be identified by estimating topology error in terms of the topology index (TI) [16].

For the calculation of the topology index, conventional state estimation will be run to calculate the sensitivity matrix by discarding the accuracy of state variables therefore the less accurate model such as the dc model or fast decouple model may be used.

If the measurements have redundancy, the topology error will directly affect the residuals of all the incidence measurements especially the corresponding node injection [17]. The topology index (TI) used to represent the topology error can be calculated from the equation below:

$$\mathrm{TI} \approx \left(S_{node}^{T} S_{node}\right)^{-1} S_{node}^{T} r \qquad (8)$$

Where S_{node} = Sensitivity Matrix corresponding to node measurements

In the case of a branch status error (exclusion and inclusion error), the two TI values of the two nodes that belong to the error branch often have close values.

In the case of bus configuration error (bus split and merge error), the TI values of the node corresponding to error bus are always the largest and the next largest.

D. Topology Estimation

When the suspicious buses are identified using the hypothesis testing in the previous step, the generalized state estimation will be performed with the expansion of the suspicious buses represented in details to estimate possible statuses of the circuit breakers. To avoid complexity of the state estimation process, only the real power measurements are used in this step [7]. The augment state variables of this step are real power flows through circuit breakers and nodal voltage magnitudes. These state variables are used to indicate the possible corresponding statuses of the circuit breakers.

IV. ILLUSTRATIVE EXAMPLE

The bus-branch model of a 4-bus 4-line test system is shown in Fig.1. The flow measurements of all branches (both ends of the branch), injections and voltage magnitudes of all buses are obtained from power flow calculation with 0.01 MVA power mismatch and then a random error is applied to each measurement. The per-unit values are on the system base of 100MVA.

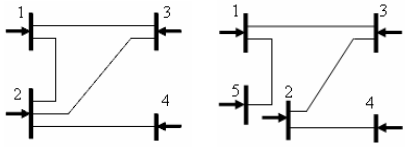

Figure 2. Base Case(A) and Bus split case (B)

For the topology error detection, the number of measurements (N) = 8, thus the threshold of *J(r)* is C = $\chi^2(\alpha, N-1)$=18.5.

For the topology error identification, the standard deviation of the measurements (σ) of 0.01 is used, and the confidence interval α = 0.01. The conventional state estimation with 16 measurements (i.e. bus voltage magnitudes, real power flows at both ends of all branches and real power injections of all buses) is used.

Example 1: Correct topology with normal error of analog measurements

This example is referenced to the power system in the Figures 1, 2 and 3. The real power flow and reactive power flow measurements are used to compare with approximated power flows calculated from the bus injections using the PTDFs. In the cases 4–6, the errors are applied to all the power flows in the percentage of the base MVA.

TABLE 1
TOPOLOGY ERROR DETECTION RESULTS OF EXAMPLE 1

No.	Topology	Measurement	*J(r)*
1	Base case	Base case	5.53
2	Branch 1-3 outage	Error-Free	3.11
3	Bus 2 split	Error-Free	0.47
4	Base case	5% error	23.89
5	Base case	15% error	189.17
6	Base case	20% error	331.11

From the results in table 1, cases 1-3 will pass the test with assumption of correct topology, but case 4-6 will be detected with having a suspicious topology error, thus topology error identification should be invoked for case 4-6. The error of case 4 may be accepted due to slightly difference from threshold.

After topology error identification and estimation of case 4-6, the results will depict that topology is the same as that of previous.

Example 2: Error Topology with normal error of analog measurements

In the case of topology error, the results are shown in Table. 2. Topology error detection determines the presence of a topology error for each case on the criterion that *J(r)* exceeds the threshold (i.e. C > 18.5). After the topology error detection is performed for each suspicious case, the node with the maximum TI is identified as suspicious.

In the case of branch status error (exclusion and inclusion error), the two TI values of the two nodes that belong to the error branch often have close values. The two nodes should thus be considered together in the topology determination step or in a simpler way by reversing the branch status and perform topology detection and identification again.

In the case of bus configuration error (bus split and merge error, Figures 2(B), the TI values of the nodes corresponding the split bus 2 (node 2 and node 5) always have the largest and next largest values. The topology estimation should be performed with the suspicious bus represented in full details.

TABLE 2
TOPOLOGY ERROR DETECTION AND IDENTIFICATION RESULTS OF EXAMPLE 2.

no	topology	measurement	*J(r)*	J(x)	TI max1	TI max 2	node
Exclusion Error							
7	L1-2 outage	Base case	$7x10^4$	$3x10^4$	1.00	0.98	1,2
8	L1-3 outage	Base case	$6x10^4$	7838	0.51	0.47	1,3
Inclusion Error							
9	Base case	L1-2 outage	78	$2x10^5$	9.65	9.24	1,2
10	Base case	L1-3 outage	186	$2x10^4$	1.00	0.94	1,3
Bus-Split Error							
11	Bus split	Base case	$3x10^4$	3276	0.55	0.53	5,2
Bus-Merge Error							
12	Base case	Bus split	118	$5x10^4$	0.80	0.15	2,4

V. CONCLUSIONS

The proposed network topology processor is supposed to be a preprocessing step of the full ac state estimation to provide the reliable topology information for accurate state estimation results. The topology processor consists of two main parts, the first part performing the topology determination which provides the topology information and the second part performing the topology correction which checks and rejects topology errors. In practical environment the topology error is rare and not widespread. In some cases the topology errors do not alter the network configuration therefore their identification is not necessary. The proposed simple error detection by means of the compromise of topology and measurements, and the fast approximation of power flows using PTDFs, is useful for detecting non-serious cases, i.e. the case of acceptable measurement error, to avoid the full steps of the topology processor.

The limitations of the proposed topology processor are :

1. Considerable computational time is needed due to the blends of numerical techniques applied in the topology processor. This may not be suitable for real-time environments.

2. In the some difficult cases (e.g. topology error and gross measurement error occurring at same time, near zero flows in lines, and interacting and conforming measurement errors), the topology correction may be unable to detect and identify the reliable topology information therefore an efficient state estimation and bad data detection may be used to cope with such cases.

3. For the error processing, the measurements are assumed to have redundancy, so the observability analysis is not considered here.

The proposed network topology processor has been successfully applied to simplified test systems and is being extended to apply to more practical and complex systems.

ACKNOWLEDGEMENT

The research reported in this paper was developed with the support of the Electricity Generating Authority of Thailand, Region 2, Khon Kaen.

REFERENCES

[1] O. Alsaç, N. Vempati, B. Stott, and A. Monticelli, "Generalized state estimation," IEEE Trans. on Power Systems, vol.13, no.3, pp. 1069-1075, August 1998.

[2] A. Abur and A. G. Expósito, *Power System State Estimation : Theory and Implementation*, Marcel Dekker , 2004.

[3] M.H. Vuong, S. Lefebvre, and X.D. Do, "A review of methods for topology errors detection," Proc. IEEE PES Transmission and Distribution Conference and Exposition, vol.1, pp. 144-149, September 2003.

[4] A. Monticelli, "Modeling circuit breakers in weighted least squares state estimation," IEEE Trans. on Power Systems, vol. 8, no.3, pp. 1143-1149, August 1993.

[5] A. Abur, H. Kim and M. K. Celik, "Identifying the unknown circuit breaker statuses in power networks," IEEE Trans. on Power Systems, vol.10, no.4, pp. 2029-2037, November 1995.

[6] L. Mili, G. Steeno, F. Dobraca, and D. French, "A robust estimation method for topology error identification," IEEE Trans. on Power Systems, vol. 14, no. 4, pp 1469–1476, November 1999.

[7] N. Vempati, C. Silva, O. Alsaç and B. Stott , "Topology estimation," Proc. IEEE Power Engineering Society General Meeting, vol.1, pp. 806-810, June 2005.

[8] F. L. Alvarado, "State estimation for the detection of market parameter," Proc. IEEE Power Engineering Society Summer Meeting, vol.1, pp. 442-447, July 2001.

[9] S. Lefebvre and J. Prevost, "Topology error detection and identification in network analysis," International Journal of Electrical Power and Energy Systems, vol.28, pp.293-305, 2006.

[10] M. Sasson, S. T. Ehrmann, P. Lynch, and L. S. Van Slyck, "Automatic power system network topology determination," IEEE Trans. on Power App.& Syst., vol. 92, pp. 610-618, Mar./Apr. 1973.

[11] M. Bertran and X. Corbella, "On validation and analysis of a new method for power network connectivity determination," IEEE Trans. on Power App. & Syst., vol. 101, pp. 316-324, 1982.

[12] N. Singh and H. Glavitsch, "Detection and identification of topological errors in on-line power system analysis," IEEE Trans. on Power Systems, vol. 6, no.1, pp. 324–331, February 1991.

[13] F. Goderya, A. Metwally, and O. Mansour, "Fast detection and identification of islands in power network," IEEE Trans. on Power App. & Syst., vol 99, pp. 217-221, Jan/Feb 1980.

[14] A. Bose and K.A. Clements, "Real-time modeling of power networks," Proceedings of IEEE, vol. 75, no. 12, pp.1907-1622, December 1987.

[15] Y. Wallach, *Calculation and Programs For Power System Networks*, Prentice-Hall, 1994.

[16] L. Xu, K. Tomsovic, and A. Bose, "Topology Error Identification using a two-stage DC state estimator," Electric Power Systems Research, vol. 74, pp. 167-175, 2005.

[17] R.L. Lugtu, D.F. Hackett, K.C. Liu, and D.D. Might, "Power system state estimation: detection of topology errors," IEEE Trans. on Power Systems, vol. PAS-99, no.6, pp. 2406–2412, 1980.

Topology Error Detection by Using Fast Approximate Power Flow with Power Transfer Distribution Factors (PTDFs)

Warayut Kampeerawat[(1)], Anupap Meesomboon[(2)]
[(1)] Graduate School, Department of Electrical Engineering, Khon Kaen University, Thailand
[(2)] Department of Electrical Engineering, Khon Kaen University, Thailand

***Abstract* –This paper presents a method of topology error detection using approximate branch power flows calculated from power transfer distribution factors. The correlation between the approximate flow and measurements is used to indicate the presence of possible topology errors. The method has been satisfactorily tested using data from test systems.**

I. INTRODUCTION

Nowadays, state estimation plays an important role in providing the reliable system states from measurements for a power system. The network topology or the information on how the buses and branches of the power system are connected is an important input to the state estimation and is provided by the well-known function called network topology processor.

Conventional network topology processor has the ability to provide system topology by processing the statuses of circuit breakers assuming that they are correct. The resulting system topology is used in later stages of power system analysis, especially state estimation.

When generalized state estimation was proposed in [1], a generalized approach for network topology processing was also proposed as an integral part of the state estimation. By generalized approach, network topology processor is supposed to be able to provide reliable system topology by using a blend of methods to indicate topology error (topology error processing) or to estimate possible topology (topology estimation).

Normally, the conventional state estimation can be performed properly in the environment of gross measurement errors by efficient bad data detection. However, topology errors can have a substantial impact on the results of state estimation. In serious cases, topology error can adversely affect the convergence of state estimation solution [2]. It is therefore desirable for the generalized state estimation to be able to detect not only measurement errors, but also other types of errors, especially topology errors.

Many researchers have proposed ways to carry out the topology error as a post-processing or preprocessing step of state estimation [3] and two-stage estimation [4]. The generalized state estimation technique is an efficient way to carry out the topology error detection by means of topology estimation [5,6].

The occurrence of topology errors is seldom and not widespread in a practical environment. The full-step and system-wide execution of topology error processing or topology estimation in every pass of state estimation analysis is therefore expensive and unnecessary. Topology error detection based on power transfer distribution factors has been proposed to detect suspected cases affected by topology errors [7].

In this paper, topology error detection based on power transfer distribution factors will be simplified and applied to data from the test systems containing typical topology errors. The topology error detection step is useful to determine whether the full step of topology error processing or topology estimation should be performed or not.

II. BACKGROUND

A. *Power Transfer Distribution Factors*

The method of distribution factors is based on the approximate linear behavior of branch flows with bus injections. The Power Transfer Distribution Factors (PTDFs) are derived from the sensitivities of line flows with respect to bus injections [8]. By assuming that all the per unit bus voltage magnitudes are approximately unity the calculation involves only Y_{bus}:

$$PTDFs(i,k) = conj[(Z_{bus})_{ik} - (Z_{bus})_{jk}] / conj(z_{ij}) \quad (1)$$

With the further approximation of DC load flow [9], the following relation results:

$$PTDFs = B^f B^{-1} \quad (2)$$

Where i = sending bus, j = receiving bus
l = branch number, k = bus number
z_{ij} = the impedance of branch ij
Z_{bus} = Bus Impedance Matrix = $(Y_{bus})^{-1}$
B = the matrix of imaginary part of Y_{bus}
B^f = the branch to bus susceptance matrix
Where the admittance of branch ij = g + jb
$B^f_{lk} = b$ *when* $k = i$, $B^f_{lk} = -b$ *when* $k = j$
$B^f_{lk} = 0$ *otherwise*

B. *Topology Error Processing*

Topology Error Processing (TEP) is used to carry out the topology error problem that may occur in the power system network. There are 2 types of topology errors.

1. Branch status error:

- Inclusion error: Including of a branch outage into the system topology.

- Exclusion error: Excluding an active branch from the system topology.

2. Substation (Bus) configuration error:

- Bus-split error: Splitting a single bus to multiple electrical nodes.

- Bus-merge error: Merging two bus sections or more into a single electrical node.

The methods of topology error detection reviewed in [3] have 2 different approaches. The first approach always requires the execution of conventional state estimation and relies on its. Topology error detection will be performed as a post-processing step of state estimation. The alternative approach relies on the consistency check and the critical branch flow discrepancy by using SCADA measurement. The rule-based technique was proposed in [10] for consistency check of the network topology in online power system. This approach is based on many of rules that are suitable for particular systems and therefore practical experiences are needed to set the rules. The approach of critical branch flow discrepancy is the efficient way to detect topology error but it needs the multiple scan of SCADA measurements. The approximated power flow by using PTDFs was proposed in [7] to detect topology error by matching the scenario of topology with the measurement until the lowest residual error is obtained. The matching approach will be more complicated when the system is large and bus configuration errors are presented.

By the approach of topology estimation [5,6], it will be assumed that topology is inaccurate therefore the TEP will be performed by means of topology error identification and estimation. The reliable network topology will be obtained by this approach for later analysis. If the assumption of inaccurate topology is tested and depicted that it is wrong, the full step of topology can be avoided.

III. PROPOSED TOPOLOGY ERROR DETECTION

In this paper the topology error detection is proposed as a preprocessing step of topology error processing (topology error identification and estimation) to detect the suspicious topology error case by using the simple assumption and statistical test. The proposed method consists of main 4 steps as shown in Figure 1:

Step 1. Approximation of power flow by using Power Transfer Distribution Factors (PTDFs)

Step 2. Branch status error detection

Step 3. Bus configuration error detection

Step 4. Hypothesis Testing with Chi-Square

The steps 2-4 have been proposed to detect a suspected case which may be affected by a topology error. This step is useful in determining whether the full step of topology processing should be performed or not. After the system topology is noticed that it may contain a topology error, the topology identification and estimation will be performed consequently and the processing steps may be iteratively repeated for a multiple error case.

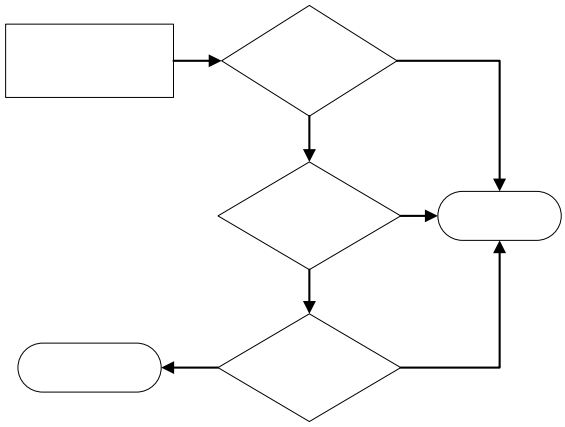

Figure 1. Flow Chart of the Proposed Method

A. Approximate power flow by using Power Transfer Distribution Factors (PTDFs)

Power transfer distribution factors (PTDFs) are applied in order to estimate power flow from power injection data. This allows the agreements between the topology and the measurements to be checked [7,8].

The approximated branch power flows can be calculated using:

$$\overline{S}_{branch} \approx PTDFs \times S_{bus} \quad (3)$$

Where S_{bus} = a vector of bus injection

$\overline{S}_{branch}$ = a vector of branch power flow

B. Branch status error detection

In this step, the agreement between branch status and branch measurement will be checked by the following simple assumptions:

1) When topology information depicts that branch *i* outages, the power flow measurement of branch *i* should be zero or near zero.

2) When the power flow measurement of branch *i* is zero or a very small value, the branch *i* will be suspected that it outages.

To check the assumptions the estimated power flow from the previous step will be used by the following step.

Step 1. Determine the zero threshold which will be used to decide which the power flow should be zero flow (e.g.10^{-5} p.u.)

Step 2. The exclusion error is supposed to be checked in this step by the following condition.

if estimated power of branch *i* = 0, i.e. branch *i* outage, and measured power of branch *i* < threshold then the status of branch *i* is correct.

Step 3. The exclusion error is supposed to be checked in this step by the following condition.

if measured power of branch *i* < threshold and estimated power of branch *i* < threshold then the status of branch *i* is correct.

When some suspicious branch status errors are found, the full step of topology correction will be performed consequently. In the other hand, bus configuration error detection will be performed.

C. *Bus configuration error detection*

In this step, it assumed that when the bus configuration is changed, all power flows corresponding to the bus will be considerably changed correspondingly. Therefore different bus configurations will give the different power flow sets. The correlation between the bus configuration and its corresponding power flows is exploited.

The correlation coefficient (R^2) which represents how two data sets correlate [11] is applied to observe the correlation between the topology information and measurement. The correlation coefficient (R^2) can be calculated by the following equation.

$$R^2 = \frac{\left(\sum_{i=1}^{N}(x_i-\bar{x})(y_i-\bar{y})\right)^2}{\sum_{i=1}^{N}(x_i-\bar{x})^2\sum_{i=1}^{N}(y_i-\bar{y})^2} \quad , \; 0 \le R^2 \le 1 \qquad (4)$$

Where x and y are two data set that have the same number of elements. $\bar{x}$ is the mean value of x and $\bar{y}$ is the mean value of y

The correlation coefficient of the measurements and estimates can be used to represent how well the agreement between measurements and topology is. In the case of branch status error, the correlation coefficient always fail to detect the error therefore the branch status error detection is needed to avoid the failure of topology error detection.

D. *Hypothesis Testing with Chi-Square*

In this step, the hypothesis testing with chi-square [11] will be performed to make sure that the result of the bus configuration error detection is reasonable. The following hypothesis testing is used to decide whether topology is correct or not:

Step1. Define null and alternative hypothesis

H_0 : Topology is erroneous.

H_1 : Topology is correct.

Step2. Calculate the performance index:

$$J(r) = \sum_{i=1}^{N}(r_i^2 / \bar{S}_{branch,i}) \qquad (5)$$

Where: $r_i = S_{branch,i} - \bar{S}_{branch,i}$

N = the number of power flow measurements

Assumption: The residual is assumed to have a normal distribution hence $J(r)$ has the Chi-square distribution.

Step3. if $J(r) \ge C$ then H_0 will be accepted.

if $J(r) < C$ then H_0 will be rejected.

$C = \chi^2(\alpha,\nu)$ where α = confidence interval

ν = degree of freedom = N-1

Because of the inaccurate model used to estimate power flow, the error due to the model will be included in the residual. The threshold should be set to an appropriate value by using C as the minimum and then the threshold can be increased by considering the residual of base case.

IV. ILLUSTRATIVE EXAMPLE

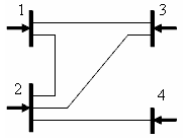

Figure 2. Base Case

The bus-branch model of a 4-bus 4-line test system is shown in Fig.2. The flow measurements of all branches (both ends of the branch), injections and voltage magnitudes of all buses are obtained from power flow calculation with 0.01 MVA power mismatch and then a random error is applied to each measurement. The per-unit values are on the system base of 100MVA.

- For branch status error detection, the zero threshold of 10^{-5} p.u. is used for the zero power flow.
- For bus configuration error detection, the threshold of $R^2 = 0.9$
- For Chi-Square test, the confidence interval $\alpha = 0.01$. 8 measurements (i.e. real and reactive power flows at one end of all branches) is used. The minimum threshold is $C = \chi^2(0.99,7) = 18.5$

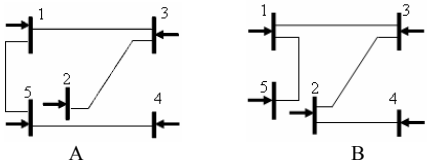

Figure 3. Bus 2 split (configuration A and B)

Example 1: Small test system

This example is referenced to the power system in the Figures 2, 3A and 3B. The real power flow and reactive power flow measurements are used to compare with approximate power flows calculated from the bus injections using the PTDFs.

TABLE 1
TOPOLOGY ERROR DETECTION RESULTS OF EXAMPLE 1

Case	Topology	Measurement	BSE	R^2	J(r)
1.	Fig.1	Base case	-	0.9996	0.55
2.	Fig.1	5 %Error	-	0.9701	23.89
Branch status error					
3.	B 1-2 outage	Base case	B 1-2	0.0245	-
4.	B 2-4 outage	Base case	B 2-4	0.7224	-
5.	Fig.1	B 1-3 outage	B 1-3	0.6523	186
6.	Fig.1	B 2-4 outage	-	0.9984	9.27
Bus configuration error					
7.	Fig.2 (A)	Base case fig.1	-	0.1476	322
8.	Fig.1	Base case Fig.2(B)	-	0.3596	118

From the results in table 1, case 1 will pass the test as having a correct topology. In the case 2, the errors are applied to all the power flows in the percentage of the base MVA, i.e. error is 0.05 p.u. Case 2 will be detected with having a

suspicious topology error or may be accepted if the threshold is adjusted for acceptable measurement error.

In the case of branch status error (case 3-6), the branch with erroneous status will be detected, except for case 6 because the error has no effect on the system.

In the case of bus configuration error (case 7-8), the very low R^2 will depict that the error has a large effect on the system.

Example 2: Topology error detection applied with the larger system

When the larger system is tested, the threshold of topology error detection should be adjusted for each case by considering result of base case.

In table 2 the estimate power flow (real power flow) are compared with the power flow of base case of IEEE test case. From the results, the threshold of R^2 and the Chi-Square test may be selected for the topology error detection e.g. 0.9 and 2C for the threshold, respectively.

TABLE 2.
THE COMPARISON OF ESTIMATED POWER FLOW AND BASE CASE POWER FLOW OF IEEE TEST CASE

Test Case	R^2	$J(r)$	C
IEEE 14 bus	0.9935	56.125	36.19
IEEE 30 bus	0.9951	64.328	63.69
IEEE 57 bus	0.9924	52.063	111.14
IEEE 118 bus	0.9926	349.62	232.67

For large systems, the effect of branch status error will be so little that the R^2 and chi-square test fail. Therefore the branch status error detection must always be performed before the statistical test.

V. COMMENTS

In the practice, the threshold value for the test of the proposed method should be adjusted for accurate results by considering the base case. The most important thing that must be considered for selecting the threshold is the correct topology may be detected that it is error, but the error topology should not be detected that it is correct.

VI. CONCLUSIONS

The topology error detection described above is proposed to be a preprocessing step of the full topology error processing. The topology error detection consists of two main parts, the first part checking the branch status error and the second part checking the bus configuration error. In practical environment the topology error is rare and not widespread. In some cases the topology errors do not alter the network configuration therefore their identification is not necessary. The proposed simple error detection by means of the compromise of topology and measurements, and the fast approximation of power flows using PTDFs, is useful for detecting non-serious cases, i.e. the case of acceptable measurement error, to avoid the full steps of the topology error processing.

The limitations of the proposed topology error detection are:

1. The simple statistical method and assumptions may allow certain types of errors not related to the assumptions to slip through.

2. In the some difficult cases (e.g. topology error and gross measurement error occurring at same time, near zero flows in lines, and interacting and conforming measurement errors), the topology correction may be unable to detect and identify the reliable topology information therefore an efficient topology error processing and bad data detection may be used to cope with such cases.

3. For the error processing with statistical test, the measurements are assumed to have redundancy and the appropriate threshold should be selected for the reliable result.

The proposed topology error detection has been successfully applied to simplified test systems and is being extended to apply to more practical and complex systems.

ACKNOWLEDGEMENT

The research reported in this paper was developed with the support of the Electricity Generating Authority of Thailand, Region 2, Khon Kaen.

REFERENCES

[1] O. Alsaç, N. Vempati, B. Stott, and A. Monticelli, "Generalized state estimation," IEEE Trans. on Power Systems, vol.13, no.3, pp. 1069-1075, August 1998.

[2] A. Abur and A. G. Expósito, *Power System State Estimation : Theory and Implementation*, Marcel Dekker , 2004.

[3] M.H. Vuong, S. Lefebvre, and X.D. Do, "A review of methods for topology errors detection," Proc. IEEE PES Transmission and Distribution Conference and Exposition, vol.1, pp. 144-149, September 2003.

[4] A. Monticelli, "Modeling circuit breakers in weighted least squares state estimation," IEEE Trans. On Power Systems, vol. 8, no.3, pp. 1143-1149, August 1993.

[5] L. Mili, G. Steeno, F. Dobraca, and D. French. "A robust estimation method for topology error identification," IEEE Trans. on Power Systems, vol. 14, no. 4, pp 1469–1476, November 1999.

[6] N. Vempati, C. Silva, O. Alsaç and B. Stott , "Topology estimation," Proc. IEEE Power Engineering Society General Meeting, vol.1, pp. 806-810, June 2005.

[7] S. Lefebvre and J. Prevost, "Topology error detection and identification in network analysis," International journal of Electrical Power and Energy Systems, vol.28, pp.293-305, 2006.

[8] Y. Wallach, *Calculation and Programs For Power System Networks*, Prentice-Hall, 1994.

[9] F. L. Alvarado, "State estimation for the detection of market parameter," Proc. IEEE Power Engineering Society Summer Meeting, vol.1, pp. 442-447, July 2001.

[10] N. Singh and H. Glavitsch, "Detection and identification of topological errors in on-line power system analysis," IEEE Trans. on Power Systems, vol. 6, no.1, pp. 324–331, February 1991.

[11] J. L. Devore, *Probability and Statistics for Engineering and The Sciences*, Duxbury, 2000.

Ant Colony Optimization to Solve the Economic Dispatch Problem with Nonsmooth Cost Functions

Phakhapong Thanitakul, Yuttapoom Chernklang, Wisut Somsamai, and Saravuth Pothiya

Department of Electrical Engineering, North Eastern University, Khon Kaen, Thailand, 40000.
thanitakul_33@hotmail.com, p_saravuth@hotmail.com

***Abstract*- This paper describes a successful adaptation of the ant colony optimization (ACO) approach to solve the economic dispatch (ED) problem in power system. The practical ED problem have nonsmooth cost functions with equality and inequality constraints that make the problem of finding the global or near global optimum difficult. To show its efficiency and effectiveness, ACO is applied to test two ED problems. The first one is ED problem with valve-point loading effects and other one is ED problem considering the multiple fuels. Additionally, the results of ACO are compared with the conventional approaches, such as genetic algorithm (GA), tabu search (TS) algorithm and particle swarm optimization (PSO). The experimental results showed that the proposed ACO approach was indeed capable to obtaining higher quality solution efficiently and computational time.**

Keywords: Ant colony optimization, Economic dispatch problem, Genetic algorithm, Particle swarm optimization, Tabu search algorithm

I. INTRODUCTION

The economic dispatch (ED) problem is one of the optimization problems in power system operation. The objective of ED problem is to schedule the optimal combination of outputs of all generating units to minimize the operating cost while satisfying the load demand and system equality and inequality constraints. Improvements in scheduling of the unit power outputs can lead to significant cost savings.

In the past decades, a number of approaches have been developed for solving this problem using mathematical programming, such as lambda iteration method, gradient method, and linear programming, etc. Unfortunately, the input-output characteristics of modern power generating units are inherently highly nonlinear because of valve-point loading effects, multi-fuel effects, etc. Therefore, they may lead to multiple local minimum points of the cost functions and this makes the problem of finding the global or near global optimum difficult.

Recently, modern heuristic optimization techniques such as simulated annealing (SA) [1], genetic algorithm (GA) [2,3], evolutionary programming (EP) [4,5], Tabu search (TS) algorithm [6], neural network approaches, and particle swarm optimization (PSO) [7,8] have been given much attention by many researches due to their ability to find an almost global optimal solution. From the past literature review, we believed that the ED problem with nonsmooth cost functions not yet applied by ant colony optimization (ACO).

For the last few years, the algorithms inspired by the observation of natural phenomena to help solving combinatorial problems have been increasing interest. One of these algorithms is ACO, which has become a candidate for many optimization applications. The first ACO was introduced by Dorigo [9], which can only be used to solve different combinatorial optimization problem. It was inspired by the behaviors of real ant colonies. In analyzing the behaviors of real ants, it was found that the ants are capable of finding shortest path from food sources to the nest without using cues.

The feasibility study of the ACO is demonstrated for solving the ED problem with nonsmooth cost functions. The results optimized by the ACO are compared to those obtained by the conventional approaches such as GA, TS and PSO in terms of solution quality and computational efficiency.

II. PROBLEM FORMULATION

The objective of ED problem is to find the optimal combination of power generation that minimizes the total generation cost while satisfying an equality constraint and inequality constraints.

A Objective Function

In reality, the objective function of an ED problem has non-differentiable points according to valve-point effects and multiple fuels. Therefore, the objective function should be composed of a set of nonsmooth cost functions.

(i) Nonsmooth cost functions with valve point effects :

To take account for the valve-point effects, sinusoidal functions are added to the quadratic cost functions as follows:

$$F_t = F_i(P_i) = a_i + b_i P_i + c_i P_i^2 + \left| e_i \times \sin(f_i \times (P_i^{\min} - P_i)) \right| \quad (1)$$

where F_t is the total generation cost; F_i is the generation cost function of i^{th} generator is usually expressed as a quadratic polynomial; a_i , b_i , and c_i are the cost coefficients of the i^{th} generator; e_i and f_i are the coefficients of generator reflecting valve-point effects. P_i is the power output of the i^{th} generator and n is the number of generators committed to the operating system.

(ii) Nonsmooth cost functions with multiple fuels:

Generally, a piecewise quadratic function is used to represent the input-output curve of a generator with multiple fuels. The piecewise quadratic function is described as follows:

$$F_i(P_i) = \begin{cases} a_{i1} + b_{i1}P_i + c_{i1}P_i^2 & P_i^{\min} \le P_i \le P_{i1} \\ a_{i2} + b_{i2}P_i + c_{i2}P_i^2 & P_{i1} \le P_i \le P_{i2} \\ \vdots & \vdots \\ a_{ik} + b_{ik}P_i + c_{ik}P_i^2 & P_{ik-1} \le P_i \le P_i^{\max} \end{cases} \quad (2)$$

where a_{ij}, b_{ij}, and c_{ij} are the cost coefficients of generator i for the j^{th} power level.

B) Constraints

(i) Equality constraint

While minimizing the total generation cost, the total generation should be equal to the total system demand plus the transmission network loss. However, the network loss is not considered in this paper for simplicity. This gives the equality constraint

$$\sum_{i=1}^{m} P_i = P_D \quad (3)$$

where P_D is load demand

(ii) Inequality constraint

The generation output of each unit should be between its minimum and maximum limits. That is, the following inequality constraint for each generator should be satisfied

$$P_i^{\min} \le P_i \le P_i^{\max} \quad (4)$$

where $P_i^{\min}$, $P_i^{\max}$: minimum, maximum output of i^{th} generator.

III. Ant Colony Optimization

A) Basic principle of ant colony

ACO is an evolutionary meta-heuristic algorithm based on a graph representation that has been applied successfully to solve various hard combinatorial optimization problems [9]. The main idea of ACO is to model the problem as the search for a minimum cost path in a graph. Artificial ants walk through this graph, looking for good paths. Each ant has a rather simple behavior so that it will typically only find rather poor-quality paths on its own. Better paths are found as the emergent result of the global cooperation among ants in the colony.

B) The ACO algorithm for solving ED problem

To apply the ACO algorithm to solve the ED problem, it is convenient to represent the problem by a graph $G = (N, E)$, where N are the nodes and E is the set of links. Ants cooperate by using indirect form of communication mediated by pheromone they deposit on the links of the graph G while building solutions. For example, 3 units power system as showed in Fig. 1. The ED problem can be represented as a graph of the routes between the nest and food source shown in Fig. 2.

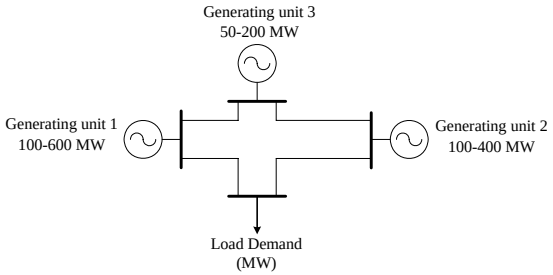

Fig. 1 The power system consists of 3 generating units.

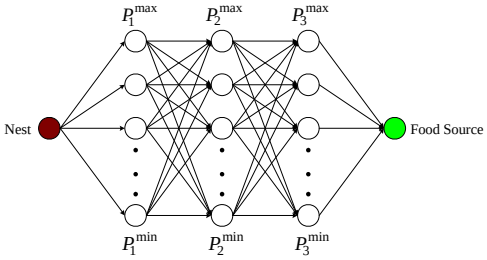

Fig. 2 Routes of ants between nest and food source for ED problem

In this example, each generation output (P_1, P_2, and P_3) is coded by number of nodes depend on resolution. Thus, a large number of nodes, the more accuracy trials are updated only after having constructed a complete path and the solution found. If choose number of node equal to 4,500 for the first generating units yield the resolution is 0.1 MW ($P_1^{\max} - P_1^{\min} = 600 - 150 = 450$ MW)

Informally, the ACO algorithm works as follows: m ants are initially positioned on the node representing the first link. Each ant will construct one possible structure of the entire system. In fact, each ant builds a feasible solution (called a tour) by repeatedly applying a stochastic greedy search, called, *the state transition rule*.

The amount of pheromone is modified by applying the *global updating rule*. Ants are guided, in building their tours, by both heuristic information and by pheromone information. Naturally, a link with a high amount of pheromone is a very desirable choice. The pheromone updating rules are designed so that they tend to give more pheromone to edges, which should be visited by ants.

(i) State Transition Rule

The state transition rule used by the ant colony is given in equation (5). This represents the probability with which ant k selects a link connects node i and node j:

$$p_{ij}^k(t) = \frac{\left[\tau_{ij}(t)\right]^{\alpha}\left[\eta_{ij}(t)\right]^{\beta}}{\sum_{m=1}^{M_i}\left[\tau_{im}(t)\right]^{\alpha}\left[\eta_{im}(t)\right]^{\beta}} \quad (5)$$

where τ_{ij} and η_{ij} are the pheromone intensity and the heuristic information between node i and node j, respectively. α is the relative importance of the trail and β is the relative importance of the heuristic information η_{ij}: The problem specific heuristic information used is:

$$\eta_{ij} = \frac{1}{C_{ij}} \tag{6}$$

where C_{ij} represent the associated cost. That is, the level of link with smaller cost has greater probability to be chosen.

(ii) Global updating rule

During the construction process, no guarantee is given that an ant will construct a feasible solution which obeys the reliability constraint. The unfeasibility of solutions is treated in the pheromone update: the amount of pheromone deposited by an ant is set to a high value if the generated solution is feasible and to a low value if it is infeasible. These values are dependent of the solution quality. Infeasibilities can then be handled by assigning penalties proportional to the amount of reliability violations. In the case of feasible solutions, an additional penalty proportional to the obtained solution is introduced to improve its quality.

Following the above remarks, the trail intensity is updated as follows:

$$\tau_{ij}(new) = \rho\tau_{ij}(old) + \Delta\tau_{ij} \tag{7}$$

ρ is a coefficient such that $(1-\rho)$ represents the evaporation of trail and $\Delta\tau_{ij}$ is:

$$\Delta\tau_{ij} = \sum_{k=1}^{m} \Delta\tau_{ij}^{k} \tag{8}$$

where m is the number of ants and $\Delta\tau_{ij}^{k}$ is given by:

$$\Delta\tau_{ij}^{k} = \begin{cases} Q \cdot penalty_k \cdot C_k & \text{if the } k^{th} \text{ ant chooses level } j \text{ for link } i \\ 0 & \text{otherwise} \end{cases} \tag{9}$$

where Q is a positive number, and $penalty_k$ is defined as follows:

$$penalty_k = \left(\frac{C_k}{C^*}\right)^a \tag{10}$$

C_k is the cost obtained by ant k, C^* is the best obtained solution. Parameter a represents the relative importance of penalties.

IV. Numerical Results

To assess the feasibility of the ACO approach, two cases studies of ED problems with nonsmooth objective function considering valve point effects and multiple fuels.

Each optimization method (GA, TS, PSO, and ACO) was implemented in MatLab®. All the programs were run on a Pentium 4, 2.6 GHz personal microcomputer with 256-MB RAM under Windows XP.

In each case study, 30 independent runs were made for each of the optimization methods, involving 30 differential initial trial solutions for each optimization method.

A) Case studies and simulation results

***Case 1*:** The system contains 13 thermal units of generation with valve-point effects whose characteristics are given in [8]. The load demand is 2,520 MW. In TABLE 1, the best generation powers are obtained by ACO, PSO, TS, and GA. TABLE 2 shows the best, average, worst cost, the standard deviation and computational time achieved by GA, TS, PSO and ACO in 30 runs.

Case 2: The developed ACO has also been applied to the ED problem with 10 generators where the multiple-fuel effects are considered. In this case, the objective function is represented as the piecewise quadratic cost function. The input data and related constraints of the test system are given in [8]. In this case, the total system demand is 2700 MW. In TABLE 3, the best generation powers are obtained by ACO, PSO, TS, and GA. TABLE 4 shows the best, average, worst cost, the standard deviation and computational time achieved by GA, TS, PSO and ACO in 30 runs.

TABLE 1. Best results obtained for case study 1 (13 unit system)

Unit	Po (MW)	Unit	Po (MW)
1	628.32	8	159.72
2	299.06	9	159.72
3	299.17	10	75.47
4	159.73	11	77.33
5	159.73	12	92.10
6	159.73	13	90.59
7	159.73	PT	2520.00
		TC	24169.63

TABLE 2. Convergence results for case study 1 (13 unit system)

Method	Load demand = 2,520 MW				
	Worst	Average	Best	Std.	CPU time
GA	24293.37	24225.24	24183.31	40.10	107.39
TS	24305.81	24305.81	24178.65	29.50	40.32
PSO	24242.57	24194.01	24171.64	20.77	29.10
ACO	24196.74	24179.26	24169.63	7.59	18.26

TABLE 3. Best results obtained for case study 2 (10 unit system)

Unit	Fuel	Po (MW)	Unit	Fuel	Po (MW)
1	2	221.45	6	3	239.11
2	1	211.53	7	1	284.76
3	1	281.62	8	3	240.70
4	3	239.90	9	3	429.61
5	1	276.99	10	1	274.31
				PT	2700
				TC	623.7

TABLE 4. Convergence results for case study 2 (10 unit system)

Method	Load demand = 2,700 MW				
	Worst	Average	Best	Std.	CPU time
GA	626.81	625.75	623.96	1.13	51.42
TS	624.73	624.45	624.05	0.15	16.36
PSO	630.00	624.47	623.81	1.15	7.49
ACO	624.11	623.96	623.83	0.07	5.38

B) Comparison of four Methods

i) Solution Quality:

For 13 units system with valve point effects for 2,520 MW load demand and 10 units system with multiple fuels for 2,700 MW load demand, after performed 30 trials; the best solutions of four methods are given in TABLE 1 and TABLE 3, respectively. The results of proposed ACO method are compared with GA, TS, and PSO in terms of worst, average, best generation cost, the standard deviation, and average computational time are provided in TABLE 2 and TABLE 4, respectively. Obviously, all methods have succeeded in finding the near optimum solution presented in [8] with a high probability always satisfying the equality and inequality constraints.

In order to demonstrate the efficiency of the proposed ACO method, the distribution outlines of the best solution of each trial are considered. Fig. 2 showed the distribution outlines of the best solution of each trial in case 13 units system with valve point effects for 2,520 MW load demand. Almost all generation costs obtained by the ACO method were lower, thus verifying that the ACO method has better quality of solution.

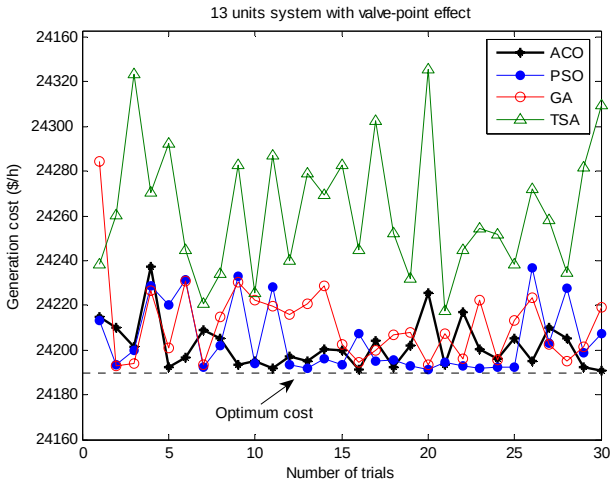

Fig. 2 Distribution of generation cost of four methods (13 unit system)

ii) Computation Efficiency: the convergence characteristics of the proposed MTS method compared with other methods for two case studies. Furthermore, the comparisons of computation time of four methods when applied on three case studies are shown in TABLE 2 and TABLE 4. Obviously, the proposed ACO method has better computation time than other methods for three examples. As seen that, the proposed ACO method converge to optimum solution faster than other methods.

V. Discussion and Conclusions

In this paper, we have successfully employed the proposed ACO method to solve the dynamic ED problem with the valve-point loading effects and multiple fuels. The proposed ACO algorithm has been demonstrated to have superior features, including high-quality solution, stable convergence characteristic, and good computation efficiency. Many nonlinear characteristics of the generator such as valve point effect are considered for practical generator operation in the proposed method. The results show that the proposed method was indeed capable of obtaining higher quality solution efficiently.

In addition, in order to verify it being superior to the GA, TS and PSO method, many performance estimation schemes are performed, such as solution quality and convergence characteristic and computation efficiency.

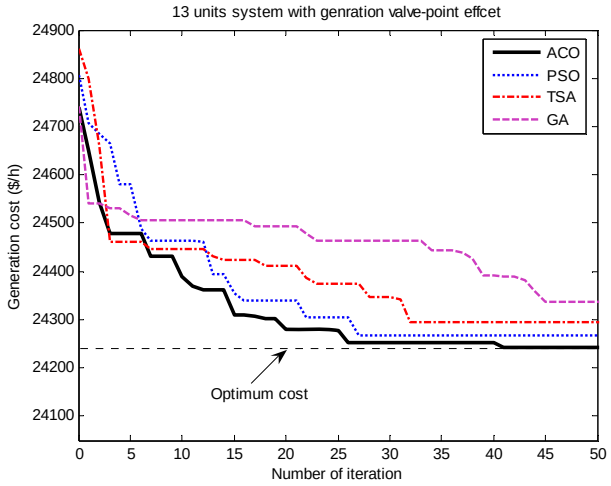

Fig. 9 Convergence curve four methods (13 unit system)

References

[1] K.P. Wang, C.C. Fung. "Simulate Annealing Base Economic Dispatch Algorithm"*IEE. Proc.C.* ,Vol.140 ,No.6., p.507-513, November 1993.

[2] D. C.Walters and G. B. Sheble, "Genetic algorithm solution of economic dispatch with valve point loading," *IEEE Trans. Power Syst.*, vol. 8, pp. 1325–1332, Aug. 1993.

[3] A. Bakirtzis, V. Petridis, and S. Kazarlis, "Genetic algorithm solution to the economic dispatch problem," *Proc. Inst. Elect. Eng.–Gen., Transm. Dist.*, vol. 141, no. 4, pp. 377–382, July 1994.

[4] H.T. Yang, P.C. Yang and C.L. Huang, "Evolution programming based economic dispatch for units with nonsmooth fuel cost functions, " *IEEE Trans. Power Syst.*, vol. 11, no.1, pp. 112–118, Feb. 1996.

[5] N. Sinha, R. Chakrabarti, and P. K. Chattopadhyay, "Evolutionary programming techniques for economic load dispatch," *IEEE Trans. Evol. Comput.*, vol. 7, no. 1, pp. 83–94, Feb. 2003.

[6] Whei-Min Lin, Fu-Sheng Cheng and Ming-Tong Tsay, " An Improved Tabu Search for Economic Dispatch With Multiple Minima", IEEE Transactions on Power System, Vol. 17, No. 1, pp. 108-112, 2002.

[7] T. A. A. Victoire and A. E. Jeyakumar, "Hybrid PSO-SQP for economic dispatch with valve-point effect," *Elect. Power Syst. Res.*, vol. 71, no. 1, pp. 51–59, Sep. 2004.

[8] J.-B. Park, K.-S. Lee, J.-R. Shin, and K. Y. Lee, "A particle swarm optimization for economic dispatch with nonsmooth cost function," *IEEE Trans. Power Syst.*, vol. 20, no. 1, pp. 34–42, Feb. 2005.

[9] Macro Dorigo, Vittorio Maniezzo, Alberto Colorni, "The Ant System :Optimization by a colony of cooperating agents" , IEEE Transactions on systems ,vol.26 No.1 ,pp.1-13 , 1996

Relevant Factors for Failure Rate Estimation of Overhead Distribution Feeders

N. Teera-achariyakul and D. Rerkpreedapong
Department of Electrical Engineering
Kasetsart University, Bangkok 10900 Thailand

***Abstract* – This paper proposes relevant factors that can be used in estimating failure rates of overhead distribution feeders. These relevant factors represent how surrounding features of feeders influence their failure rates. The studied features include tree and cleared-tree areas, types of conductors such as bare and insulated conductors, and types of insulators including line-post and other types. 39 distribution feeders of the Provincial Electricity Authority (PEA) are surveyed to collect required data associated with these features. Once the relevant factors are found, they are used as a multiplier to scale up/down the mean failure rate in estimating the failure rate of an interested feeder. The estimation procedure is illustrated step by step with case studies in the paper.**

I. INTRODUCTION

SAIFI and SAIDI are the most widely used reliability indices that indicate the service quality of electric utilities. In assessing the system reliability, the utilities compute the SAIFI and SAIDI from the past performance by using the historical outage data collected by their operators. However, to predict the level of reliability for the future planning, the SAIFI and SAIDI are normally determined based on the system failure rates.

The failure rates of overhead distribution lines in different areas are varied due to a variety of surrounding conditions and types of equipments installed on utility distribution feeders [5-7]. In this paper, the relevant factors (K) associated with the above features are first introduced, and are developed from collected data including distribution feeder surveys and feeder failure rate database.

Three significant advantages resulted from the relevant factors are as follows: (1) they show an influence of studied surrounding features of feeders as a multiplier to scale up/down the mean failure rate, (2) such scaling factors can be straightforwardly used in estimating an interested failure rate of distribution feeders which locate in different surrounding conditions, and (3) in planning on reliability improvement for feeders with poor failure rates, these relevant factors can be useful for choosing an appropriate maintenance activity to heal the feeder weaknesses.

In this paper, the mean failure rate (λ_M) is first obtained from the Provincial Electricity Authority (PEA) technical report including failure rates of over 2,000 overhead distribution feeders in Thailand [3]. These failure rates are determined from the sustained outages database which contains more than 600,000 events in PEA distribution systems during 2001-2005 [1]. Next, feeder surrounding surveys are conducted on three selected local utilities of the PEA including Saraburi, Bangpakong and Rangsit offices. In section II, the data collected from the surveys, for 39 feeders, contain feeder length, percent of trees along the feeder length, percent of bare and insulated cables used along the feeder length, percent of line-post insulators installed on the feeder, and failure rate of the feeder.

In this research, six different surrounding features of distribution feeders are studied, and the relevant factors of these features are as follows:

(1) Tree factor (K_{tree})
(2) Cleared-tree factor ($K_{cleared}$)
(3) Bare-conductor factor (K_{bare})
(4) Insulated-conductor factor ($K_{insulated}$)
(5) Line-post-insulator factor ($K_{linepost}$)
(6) Other-insulator factor (K_{other})

The above relevant factors are determined in Section III. The estimation formula for feeder failure rates is developed, and the tests with case studies are illustrated in Section IV. Finally, conclusions are given in Section V.

II. FAILURE RATES AND SURROUNDING SURVEYS

A. Mean Failure Rate

The mean failure rate of over 2,000 feeders in Thailand is computed from the sustained outage database of the PEA during 2001-2005. The study of uptime of overhead distribution lines has found that most of feeders have a Weibull distribution [2,4], and the mean failure rate of all feeders is found at 17.38 times per 100 circuit kilometers-year [3], and it is used as the mean failure rate (λ_M) in this paper.

B. Feeder Surrounding Surveys

To analyze the impact of the surrounding features on feeder failure rates, field surveys are conducted on three selected local utilities of the PEA including Saraburi, Bangpakong and Rangsit offices. In TABLE I, the data collected from the surveys, for 39 feeders, contain feeder length, percent of trees along the feeder length, percent of bare and insulated conductors used along the feeder length, percent of line-post insulators installed on the feeder, and failure rate of each feeder.

TABLE I
FEEDER SURROUNDING FEATURES VS. FAILURE RATES
(TIMES/100-CIRCUIT-KILOMETERS-YEAR)

No.	Feeder Length (km.)	Trees (%)	Type of Conductors		Line-Post Insulators (%)	Failure Rate
			Bare (%)	Insulated (%)		
1	1.3	92.31	0.00	100.00	90.00	29.40
2	1.7	100.00	0.00	100.00	90.00	15.88
3	1.9	100.00	0.00	100.00	80.00	17.25
4	2.0	0.00	0.00	100.00	100.00	19.12
5	2.0	100.00	10.00	90.00	90.00	29.74
6	2.2	100.00	0.00	100.00	90.00	28.12
7	2.7	0.00	100.00	0.00	100.00	22.38
8	3.0	0.00	100.00	0.00	100.00	14.46
9	4.0	0.00	100.00	0.00	100.00	21.85
10	5.2	100.00	0.00	100.00	90.00	26.35
11	5.3	5.66	0.00	100.00	80.00	18.28
12	6.3	100.00	44.44	55.56	70.00	15.17
13	7.2	0.00	0.00	100.00	95.00	4.39
14	8.3	100.00	0.00	100.00	80.00	11.26
15	9.2	85.87	0.00	100.00	80.00	11.38
16	9.4	82.98	55.32	44.68	60.00	35.25
17	9.5	26.32	94.74	5.26	80.00	15.26
18	10.6	90.57	0.00	100.00	60.00	11.49
19	10.9	100.00	84.40	15.60	40.00	21.86
20	11.0	100.00	0.00	100.00	100.00	7.72
21	13.7	53.28	59.85	40.15	50.00	6.23
22	14.6	78.08	13.01	86.99	60.00	25.54
23	15.5	64.52	69.68	30.32	60.00	25.16
24	16.2	37.04	39.51	60.49	60.00	13.61
25	17.7	96.61	61.02	38.98	40.00	19.58
26	19.7	44.16	38.58	61.42	70.00	14.35
27	21.2	90.57	12.74	87.26	50.00	4.78
28	21.9	54.34	21.00	79.00	100.00	4.04
29	23.1	35.62	59.23	40.77	70.00	5.93
30	23.3	27.04	21.46	78.54	80.00	17.57
31	29.8	64.77	46.64	53.36	60.00	5.96
32	35.9	69.36	41.78	58.22	60.00	32.39
33	43.2	51.39	40.05	59.95	70.00	19.16
34	47.4	57.81	63.50	36.50	70.00	19.06
35	60.4	55.30	46.19	53.81	60.00	10.33
36	60.7	65.40	71.33	28.67	70.00	6.00
37	66.1	54.61	56.73	43.27	70.00	5.44
38	68.3	48.76	55.05	44.95	60.00	21.16
39	78.7	49.17	38.88	61.12	65.00	7.20

III. RELEVANT FACTORS

From TABLE I, the studied relevant factors are trees, types of feeder conductors, and types of insulators. In more details, the trees associated factors include 2 features, which are tree area and cleared-tree area. Next, the type-of-conductors factors consist of bare-conductor and insulated-conductor (Space Aerial Cable; SAC and Partial Insulated Cable; PIC) features. Finally, the factors regarding types of insulators include two features, which are line-post insulators and the other types of insulators (Pin-type insulators and pin-post-type insulators).

According to the six features as described above, the feeders in TABLE I, which are fit to the feature descriptions, are categorized in TABLE II. The averages (λ_i) of feeder failure rates for each category are also given in TABLE II. The feeders that do not match any categories are highlighted, and they are not included in calculating the average failure rates.

TABLE II
AVERAGE FEEDER FAILURE RATES
(TIMES/100-CIRCUIT-KILOMETERS-YEAR)

	Feature Descriptions		Number of Feeders	Average Failure Rates
FEATURE CATEGORY	Tree	More than 75% of trees along feeders	16	19.42
	Cleared	Less than 25% of trees along feeders	6	16.75
	Bare	Bare conductors installed more than 75% of feeder length	5	19.16
	Insulated	Insulated conductors installed more than 75% of feeder length	17	16.61
	Line post	Line post insulators installed more than 75% on feeder	18	17.47
	Others	Line post insulators are installed less than 40% in feeder	2	20.72

TABLE III
RELEVANT FACTORS

K_{tree}	$K_{cleared}$	K_{bare}	$K_{insulated}$	$K_{linepost}$	K_{other}
1.12	0.96	1.10	0.96	1.01	1.19

The relative factor (K_i) for each feature as shown in TABLE III can be determined from (1)

$$K_i = \frac{\lambda_i}{\lambda_M} \quad (1)$$

where
K_i is the relevant factor due to feature i
λ_i is the average failure rate of feeders in category i
λ_M is the mean failure rate of all PEA feeders.

The relevant factors given in TABLE III illustrate how each surrounding feature influence the failure rate of overhead distribution feeders. The factors that are greater than one generally result in adverse effects on feeder failure rates. For instance, an overhead distribution feeder that utilizes bare conductors is more likely to be faulted by tree and animal contacts. As another example, a feeder placed along the line of growing trees is not safe from contacts between trees and electrical equipments on distribution feeders.

However, when types of insulators are considered, the line-post insulators, which are the best type of insulators, are found the most during the surveys. As a result, the relevant factor $K_{linepost}$ is near one because almost all feeders use line-post insulators as a majority. In addition, the PEA has a plan to replace other types of insulators with the line-post insulators in a little while. Consequently, the relevant factors regarding types of insulators may not be required in the future.

The relevant factors $K_{cleared}$ and $K_{insulated}$ are less than one because they represent the features that decrease the failure rates. For example, a feeder that uses insulated conductors and is located in cleared-tree areas would have a very low rate of power outages.

IV. Failure Rate Estimation

After all relevant factors are determined in Section III, they can be used in estimating the failure rate of an interested feeder using (2).

$$\lambda = \lambda_M \times K_T \tag{2}$$

where

λ is the failure rate of the interested feeder.

λ_M is the mean failure rate of all PEA feeders equal 17.38 times per 100-circuit-km.-year.

K_T is the total relevant factor calculated by (3).

$$K_T = (K_{tree} D_{tree} + K_{cleared} D_{cleared}) \times (K_{bare} D_{bare} + K_{insulated} D_{insulated}) \times (K_{linepost} D_{linepost} + K_{other} D_{other}) \tag{3}$$

where

K_{tree} is the relevant factor for tree-area feature.

$K_{cleared}$ is the relevant factor for cleared-tree-area feature.

K_{bare} is the relevant factor for bare-conductor feature.

$K_{insulated}$ is the relevant factor for insulated-conductor feature.

$K_{linepost}$ is the relevant factor for line-post-insulators feature.

K_{other} is the relevant factor for other-types-insulators feature.

D_{tree} is the ratio of tree-area distance to feeder length.

$D_{cleared}$ is the ratio of cleared-tree-area distance to feeder length.

D_{bare} is the ratio of bare-conductor distance to feeder length.

$D_{insulated}$ is the ratio of insulated-conductor distance to feeder length.

$D_{linepost}$ is the proportion of line-post insulators of feeder.

D_{other} is the proportion of the other types of insulators of feeder.

For example, an overhead distribution feeder in a rural area has a feeder length of 68.3 km. The length of bare conductors used in this feeder is 37.6 km. About 60% of insulators installed in the feeder are line-post insulators. The total length of feeder portions over tree areas is about 33.3 km. The failure rate of such a feeder can be estimated step by step as follows.

Step1. Find D_i i.e. D_{tree}, $D_{cleared}$, D_{bare}, $D_{insulated}$, $D_{linepost}$, and D_{other} (0.49, 0.51, 0.55, 0.45, 0.6 and 0.4 respectively),

Step2. Calculate the total relevant factor K_T by substituting all D_i found from step1 and K_i from TABLE III in (3). So,

$K_T = (1.12\times0.49 + 0.96\times0.51) \times (1.10\times0.55 + 0.96\times0.45) \times (1.01\times0.6 + 1.19\times0.4)$

$= 1.16$

Step3. Estimate the feeder failure rate, λ, by substituting K_T obtained in step2 in (2). So, $\lambda = 17.38\times1.16 = 20.20$ times per 100-circuit-km.-year.

The actual failure rate of this feeder calculated from PEA interruption data during 2001-2005 is 21.16 times per 100-circuit-km.-year. A difference between the estimated failure rate and the actual one is around $|21.16\text{-}20.20| \times 100 / 21.16 = 4.52\%$.

The estimated failure rates of 39 surveyed feeders are plotted to compare with the actual values in Figure 1.

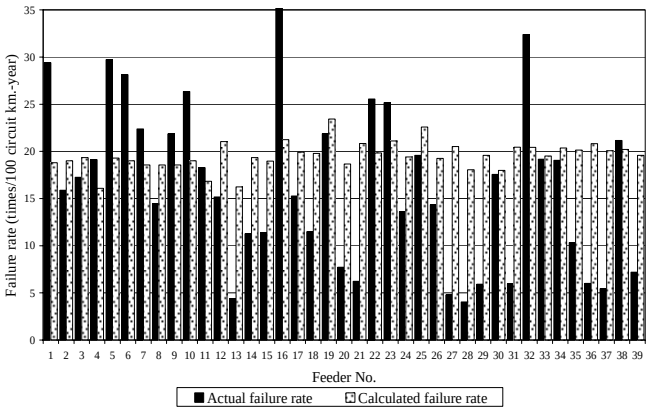

Figure 1. Estimated failure rates vs. actual values of surveyed feeders.

According to the above results, the median of estimation errors is about 30%. It indicates that a few additional relevant factors (animal density, contamination, etc.) besides what presented in this paper may be taken into account for better estimation performance, which could lead to further research. Nevertheless, a worthy advantage of the proposed estimation is that the failure rate of interested feeders can be easily determined without involving any sophisticated mathematical analyses. This estimation method helps electric utilities to approximate their feeder failure rates in no time, when surrounding features of their feeders change in the future.

On reliability improvement using relevant factors, utility engineers can plan to reduce the failure rate of interested feeders to an expected value with an appropriate maintenance activity. For example, an overhead distribution feeder uses 100% of bare conductors (K_{bare} = 1.10). If the bare conductors are totally replaced by insulated conductors ($K_{insulated}$ = 0.96), this maintenance activity will result in a decrease of failure rate by (1.10-0.96)/1.10×100 = 12.7%.

V. CONCLUSIONS

This paper introduces the relevant factors that can be used in estimating failure rate of overhead distribution feeders. These relevant factors represent how surrounding features of overhead feeders influence the failure rates. The studied features include tree and cleared-tree areas, types of conductors such as bare and insulated conductors, and types of insulators including line-post and other types. 39 distribution feeders of the Provincial Electricity Authority (PEA) are surveyed to collect required data associated with these features. Once the relevant factors are found, they are used as a multiplier to scale up/down the mean failure rate in estimating the failure rate of an interested feeder.

The estimation procedure of failure rates are illustrated by case studies. A key advantage of the proposed estimation is its simplicity. Since no sophisticated mathematical analyses are involved, it makes this method practical to be applied by electric utilities. On reliability improvement, an appropriate maintenance activity can be planned to achieve the targeted feeder failure rates using the relevant factors presented in this paper.

REFERENCES

[1] The Provincial Electricity Authority (PEA) of Thailand, "The Interruptions Database (JF.3)", 2001-2005.

[2] A. Kwansawaitham, "Analysis of Distribution Failure Rate of Components in Distribution System of Provincial Electricity Authority, Thailand" (in Thailandese), M.Eng thesis Kasetsart University, 2006, unpublished.

[3] Kasetsart University, "Technical Report on PEA's Distribution System Failure Rate Analysis" (in Thailandese), 2006.

[4] W. Tippachon, A. Kwansawaitham, N. Klairuang, D. Rerkpreedapong, and J. Hokierti, "Failure Analysis of Power Distribution Systems in Thailand", *IEEE-POWERCON2006 Proceedings*, 22-26 Oct 2006, China.

[5] Duane T. Radmer, Paul A. Kuntz, Richard D. Christie, Subrahmanyam S. Venkata, and Robert H. Fletcher, "Predicting Vegetation-Related Failure Rates for Overhead Distribution Feeders" *IEEE Trans. on Power Delivery*, vol.17, No.4, October 2002.

[6] W.F. Horton, S. Goldberg, , C.A. Volkman, "The Failure Rates of Overhead Distribution System Components", *in Proc. 1991 IEEE Power Engineering Society Transmission and Distribution Conf*, pp.713 – 717.

[7] Jong-Fil Moon, Jae-Chul Kim, Hee-Tae Lee; Chang-Ho Park, Sang-Yun Yun, Sang-Seung Lee, "Reliability Evaluation of Distribution System through the Analysis of Time-Varying Failure Rate" *in Proc. 2004 IEEE Power Engineering Society General Meeting* , pp.668 – 673.

Congestion Management in a Hybrid Pool and Bilateral Market

Komson Daroj* and Bundhit Eua-Arporn**
Department of Electrical Engineering, Faculty of Engineering,
*Ubonratchathani University, Phone 045-353367, Fax 045-353333, E–mail: daroj@hotmail.com
**Chulalongkorn University, Phone 02–2186528–31, Fax 02–2186529, E–mail: Bundhit.E@chula.ac.th

***Abstract*- A congestion management (CM) framework for a competitive electricity supply industry is proposed in this paper. The proposed framework manages the congestion separately between power pool and bilateral market. The MVA thermal limit of transmission lines is used associated with various means, i.e. generation re-dispatch, interruptible loads and distributed generations, to relief the congestion. The problem is tested with a 6-bus system and solved by a linear programming.**

I. INTRODUCTION

Trading activity of electric energy under electricity markets can be achieved through power pool and bilateral markets. A power pool is generally defined as a centralized market where preferred bids and offers are cleared under a predefined mechanism [1], which is generally performed to maximize social welfare. On another hand, transactions under bilateral markets are contracted based on agreement between a pair of selling and buying entities [2]. During a normal trade, congestion situation may be occurred. In this circumstance, the system operator (SO) needs a CM methodology, which can be classified into congestion relief and congestion cost allocation procedures. The congestion relief is a procedure of utilizing existing means, i.e. generation re-scheduling and load curtailing, to alleviate the overloaded line. The congestion cost allocation is a methodology of allocating the additional cost from the former procedure to participants in a non-discrimination manner. For a power pool, participants sell/buy electric energy according to their nodal or zonal prices, which is formulated based on a spot pricing theory [3]. Transmission services charges, e.g. transmission loss and congestion cost is normally included in both prices. These prices can be calculated using either the objective functions of minimizing the least square of power deviated from the preferred schedule [4] or minimizing the re-scheduled cost [5]. In contrast, under bilateral markets, a dispatching methodology based on contingency constrained together with a minimum number of transaction adjustments is proposed in [6]. In [7, 8], the North American Electricity Reliability Council (NERC) proposes a transmission loading relief (TLR) procedures for bilateral transaction curtailment. Nevertheless, it is argued in [9, 10] that strictly curtailing according to TLR procedures may lead to an unnecessary curtailment. To allocate the congestion cost among bilateral transactions, a power transfer distribution factor (PTDF) is adopted in this regard [11-12]. These schemes [3-12] are basically developed to suit with desired trading arrangement. Unfortunately, due to the co-existence of difference trading arrangements in the same electricity market, implementation of only one CM methodology may not satisfy the whole participants. Therefore, this paper emphasizes on a methodology to manage congestion under a hybrid of power pool and bilateral activities.

In this paper, a complete CM under a hybrid power pool and bilateral market is proposed. In the proposed framework, congestion relief is firstly performed with an objective function to minimize the re-scheduling cost. Then, this cost is allocated among participants in the pool and bilateral market based on their contributions. For a power pool, the allocated cost is a shadow embedded in a nodal price. In contrast, a PTDF is adopted to allocate this cost among bilateral transactions. Others details will be described in related section.

II. TRANSMISSION LINE THERMAL LIMIT MODEL

In this paper, the MVA flow is used as a thermal model in association with π model of a transmission line as shown in Fig. 1.

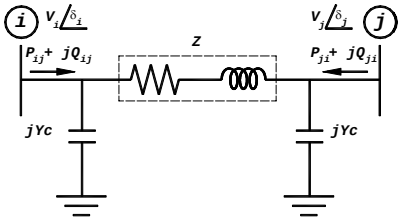

Figure 1 The transmission line model, connected between *bus-i* and *bus-j*

The terms P_{ij} and Q_{ij} are the real and reactive power flowing from *bus-i* $\rightarrow$ *j*, which can be written as (1) and (2) respectively.

$$P_{ij} = V_i V_j Y_{ij} \cos\left(\theta_{ij} - \delta_i + \delta_j\right) - V_i^2 Y_{ij} \cos\theta_{ij} \quad (1)$$

$$Q_{ij} = V_i^2 Y_{ij} \sin\theta_{ij} - V_i^2 Y_c - V_i V_j Y_{ij} \sin\left(\theta_{ij} - \delta_i + \delta_j\right) \quad (2)$$

where V_i, δ_i and V_j, δ_j are the voltage magnitude and angle of *bus-i* and *bus-j* respectively. Y_{ij} and θ_{ij} are the magnitude and angle of elements of bus-admittance matrix at row-*i* and column-*j*, and Y_c is a half of line charging admittance of the line connected between *bus-i* and *bus-j*.

The thermal limit of this line can be represented by apparent power flow in MVA as expressed in (3).

$$P_{ij}^2 + Q_{ij}^2 \le S_{ij}^2 \quad (3)$$

III. Congestion Relief Cost and Procedure

A. Congestion Relief Cost

In case the system operator (SO) dispatches power away from the preferred transactions, reimbursement must be paid to all requested means, which can be described as follow:

- Cost of generation re-dispatching; based on willingness to accept price in case of it is requested to operate away from the preferred value,
- Cost of shedding interruptible load and re-dispatching committed distributed generations, and
- Cost of reactive power from capacitor-banks.

It should be noted that, in case generation is requested to decrease its power it will receive reimbursement less than its bidding price.

B. Congestion Relief Procedure

In our proposed methodology, the congestion relief procedure is formulated in such a way that the congestion relief cost is minimized and all specified constraints are satisfied, which can be described below.

$$Minimize \quad [f]^T [X]$$

$$= \sum_{i \in G,S} C_{G_i} . \Delta P_{G_i} + \sum_{i \in L} C_{L_i} . \Delta P_{L_i} + \sum_{i \in R} C_{R_i} . \Delta Q_{R_i} \quad (4)$$

subject to

$$P_{sch_i} = \sum_{j=1}^{N} P_{ij} \quad (4a)$$

$$Q_{sch_i} = \sum_{j=1}^{N} Q_{ij} \quad (4b)$$

$$S_{ij}^0 + \Delta S_{ij} \le S_{ij}^{max} \quad (4c)$$

$$\sum_{i \in G} \Delta P_{G_i} + \sum_{i \in L} \Delta P_{L_i} + \Delta P_{G_S} = 0 \quad (4d)$$

$$P_{G_i}^{min} \le P_{G_i}^0 + \Delta P_{G_i} \le P_{G_i}^{max} \quad (4e)$$

$$Q_{G_i}^{min} \le Q_{G_i}^0 + \Delta Q_{G_i} \le Q_{G_i}^{max} \quad (4f)$$

$$Q_{R_m}^{min} \le Q_{R_m}^0 + \Delta Q_{R_m} \le Q_{R_m}^{max} \quad (4g)$$

$$V_L^{min} \le V_L^0 + \Delta V_L \le V_L^{max} \quad (4h)$$

where

$[f]$ is a vector of willingness to accept prices of means,

$[X]$ is a row vector of available means,

C_{G_i} is a willingness to accept price of generation at *bus-i*,

C_{L_i} is a bid price of interruptible load at *bus-i*,

C_{R_i} is a reactive power price of capacitor at *bus-i*,

ΔP_{G_i} is the change of generation at *bus-i*,

ΔP_{L_i} is the amount of load curtailment at *bus-i*,

ΔQ_{R_i} is the change of reactive power capacitor at *bus-i*,

ΔV_L is the change of voltage magnitude at load buses.

Subscripts *G*, *L* and *R* represent generation, load and reactive reserve buses respectively, where *N* represents the number of buses. The superscripts *0*, *min* and *max* represent current status, minimum and maximum values of available means respectively.

The objective function of (4) is to minimize the congestion relief cost of available control variables/means as described earlier. Equality constrains of (4a) and (4b) are power flow balance of real and reactive power respectively. Inequality constraint of (4c) is an MVA line flow limit, whereas (4d) is necessary to activate the generation willingness to accept price of a slack bus. Inequalities (4e)-(4g) are traditionally included as acceptable capability limit of control apparatuses, whereas voltage magnitude limit is reflected in (4h).

IV. Congestion Cost Allocation

A. Contributory between Power Pool and Bilateral Markets

Normally, trading volume of power in both power pool and bilateral markets influences to the congested lines. Thus, degree of the contribution between these two markets must be firstly calculated. To cope with nonlinearity of a system, a DC power flow is used, which can be described below.

For a congested line *k*, we assume that a power flow through this line may come from both power pool and bilateral activities, which can be expressed in (5).

$$PF^k = PFPo^k + PFBi^k \quad (5)$$

where

PF^k is a power flow through line *k*,

$PFPo^k$ is a power flow through line *k* from pool market, and

$PFBi^k$ is a power flow through line *k* from bilateral markets.

The term PF^k can be obtained without considering trading arrangement. The terms $PFPo^k$ and $PFBi^k$ can be obtained by treating the trades under bilateral and power pool activities independently.

B. A Nodal Price

A nodal price can be defined as (6).

$$\pi_{p,k} = MCP\left(1 + \frac{\partial F}{\partial p_k}\right) + \rho \frac{\partial H}{\partial p_k} \quad (6)$$

$\pi_{p,k}$ is a nodal price corresponding to the real power injected at *bus-k*; p_k, which can be decomposed into three terms. The first term of (6) is a marginal clearing price; MCP, which is an energy price of buying/selling in a market. The cost of transmission loss that all participants must be paid is the second term. The third term is a congestion charge and it is activated if some transmission line flows are violated. The functions *F* and *H* in general represent a power flow equation

and inequality constraints of a system respectively. The term ρ is a marginal congestion cost.

The term MCP, and marginal clearing quantity (MCQ) can be obtained from a bidding mechanism with objective of social welfare maximization, as shown in Fig. 2.

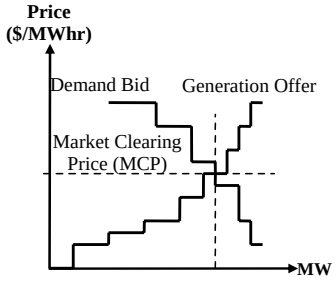

Figure 2 MCP and MCQ of a bidding process

A slack bus is assumed to be a bus of which the last generating unit wins in a bidding process.

C. *Congestion Cost Allocation in a Bilateral Markets*

The term $PFBi^k$ of (5) can be decomposed into (7).

$$PFBi^k = \sum \left(PTDF_{i,j}^k \right) \left(t_{i,j} \right) \quad \forall \quad i \in So, j \in Si \qquad (7)$$

where

$PTDF_{i,j}^k$ is the PTDF of line k for the source at *bus-i* and the sink at *bus-j*, and

$t_{i,j}$ is the amount of power under bilateral contract of source at *bus-i* and sink at *bus-j*.

The terms *So* and *Si* are used to represent source and sink buses of bilateral transactions. Formulation of PTDF can be found in the Appendix.

V. Numerical Results

A. *Test System*

The proposed method is tested with a 6-bus system [13]. Transactions under bilateral markets are shown in Table I.

TABLE I
TRANSACTION UNDER BILATERAL MARKETS

Transaction No.	Generation Bus No.	Load Bus No.	Quantity (MW.)
1	1	4	12
2	1	5	12
3	2	4	12
4	2	6	18
5	3	5	18
6	3	6	18

For simplicity, we assume that loads at buses No. 4, 5 and 6 of 20, 25 and 30 MW are traded in a power pool. According to a bidding mechanism, Generation at buses No. 1, 2 and 3 are selected to dispatch of 16, 20 and 24 MW. In addition generation at bus No. 1 is the last clearing unit with MCP of 10,000 Baht/MW-hr. According to the thereby it is selected to be a slack bus. As a result, power flow result of this transaction can be shown in Fig. 3.

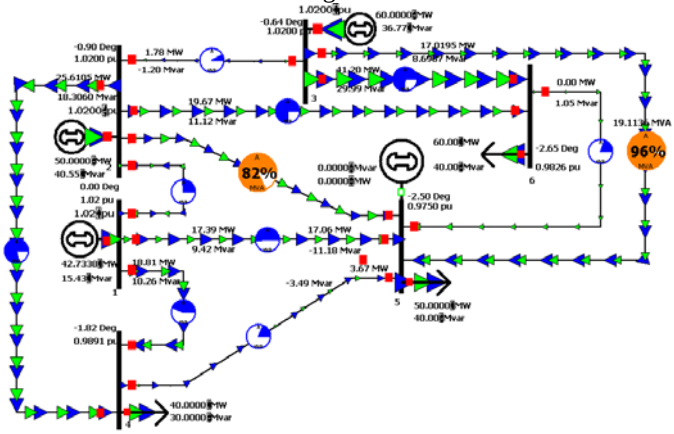

Figure 3 Power flow of a base-case transaction

In practice, entities who can provide means may submit bid to the SO. Then the SO accumulates this information and use them to perform balancing mechanism or congestion management in a spot market. The bidding information is assumed as shown in Table II.

TABLE II
COST OF VARIOUS UTILIZED MEANS WITH THEIR OPERATING LIMIT

No.	Type	Bid Prices (x1000) (Baht/MW-hr or MVar-hr)	Operating Limit Min	Operating Limit Max
1	P_{G_1}	$213.1 + 11.669P_{G_1} + 0.00533P_{G_1}^2$	10	80
2	P_{G_2}	$200.0 + 10.333P_{G_2} + 0.00889P_{G_2}^2$	15	90
3	P_{G_3}	$240.0 + 10.833P_{G_3} + 0.00741P_{G_3}^2$	20	100
4	P_{G_5}	*20*	5	40
5	$L_4\ L_5\ L_6$	*100*	0	10
6	$Q_{R_4}\ Q_{R_5}\ Q_{R_6}$	*100*	0	20

We further assume that close to real time 4 lines are tripped as shown in Fig. 4.

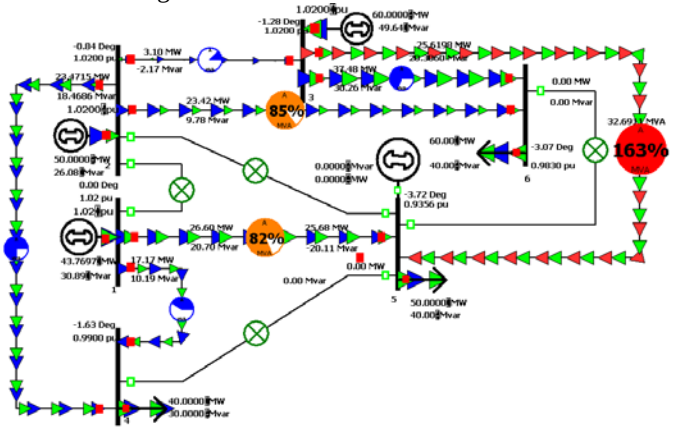

Figure 4 Post-outages power flow result

As a result, 63% overloading occurs at the line connected between buses No. 3 and 5. After the congestion relief procedure is performed, its solution can be shown in Fig. 5.

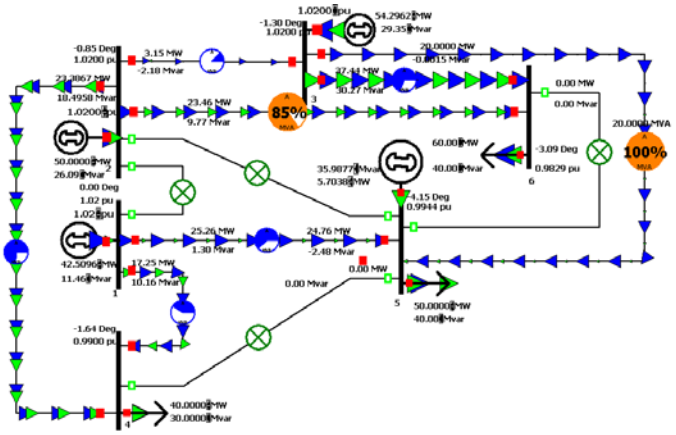

Figure 5 Power flow result after perform the congestion relief procedure

From the method presented in section IV, the minimized congestion cost of Fig. 5 is 127,380 Baht, which is 50,592 and 76,428 Baht responsible by power pool and bilateral markets respectively. The nodal prices of a power pool market are shown in Table III. The congestion cost allocated among bilateral transactions can be shown in Table IV.

TABLE III
COMPONENTS OF NODAL PRICES

BUS NO.	*MCP*	$MCP.\frac{\partial F}{\partial p_k}$	$\rho\frac{\partial H}{\partial p_k}$	NODAL PRICE
1	10,000	0	0	10,000
2	10,000	81	698	10,779
3	10,000	7	1,010	11,017
4	10,000	170	-460	9,710
5	10,000	442	1,289	11,731
6	10,000	202	-911	9,291

TABLE IV
ALLOCATED COST FOR BILATERAL TRANSACTIONS

TRANSACTION NO.	DC PTDF	CONTRIBUTORY DEGREE (%)	ALLOCATED COST (BAHT)
1	-20.07	0	0
2	30.11	19.07	12,146
3	10.04	6.36	4,051
4	-9.12	0	0
5	73.91	70.23	44,729
6	4.56	4.33	2,758

VI. CONCLUSIONS

A CM methodology of a hybrid power pool and bilateral markets is proposed in this paper. A spot pricing theory is used to charge all participants of a power pool. A PTDF is adopted to allocate this cost among bilateral transactions. Various means are considered together with a MVA thermal model. It is tested with a 6-bus system with satisfied results.

REFERENCES

[1] M. Shahidehpour, H. Yamin and Z. Li, "Market Operations in Electric Power Systems," Copyright 2002, John Wiley & Sons Inc.
[2] L. L. Lai, "Power System Restructuring and Deregulation," Copyright 2001, John Wiley & Sons Inc.
[3] F.C. Schweppe, M.C. Caramanis, R.D. Tabors and R.E. Bohn, "Spot Pricing of Electricity (Book)," Copyright 1988, Kluwer Acadamic Publishers.
[4] A. K. David, "Dispatch Methodologies for Open Transmission Systems," *IEEE Transactions on Power Systems, vol. 13, No. 1*, pp. 46-53.
[5] A. Kumar, S. C. Srivastava and S. N. Singh, "A Zonal Congestion Management Approach Using Real and Reactive Power Rescheduling," *IEEE Transactions on Power Systems, vol. 19, No. 1, 2004*, pp. 554-562.
[6] M. I. Alomoush and S. M. Shahidehpour, "Contingency-Constrained Congestion Management with a Minimum Number of Adjustments in Preferred Schedules," *International Journal of Electrical Power & Energy Systems, vol. 22, No. 4, 1999*, pp. 277-290.
[7] NERC Operating Manual, Appendix 9C1-Transmission Loading Relief Procedure, Version 2. [Online]. Available: http://www.nerc.com.
[8] North American Electric Reliability Council (September 1999), Transmission Loading Relief: Possible Improvements and Long-term Solutions, [Online]. Available: http://www.nerc.com.
[9] R. Rajaraman and F. L. Alvarado, "Inefficiencies of NERC's Transmission Loading Relief Procedures," *The Electricity Journal*, vol. *11, No. 8, 1998*, pp. 47-54.
[10] J. W. Bialek, A. Germond and R. Cherkaoui, "Improving NERC Transmission Loading Relief Procedures," *The Electricity Journal*, vol. *13, No. 5, 2000*, pp.11-19.
[11] H. H. Yan, "PTDF and TLR from a power marketer's perspective," *IEEE Power Engineering Summer Meeting 1999, vol. 1*, pp.156-161.
[12] X. Cheng and T. J. Overbye, "PTDF-based power system equivalents," *IEEE Transactions on Power Systems, vol. 20, No. 4, 2005*, pp.1868-1876.
[13] A. J. Wood and B. F. Wollenberg, "Power Generation Operation and Control," 2nd. edition, Copyright 1996, John Wiley & Sons Inc.

APPENDIX

Generation shift factor for *line l* connected between *bus-i* and *bus-j* to changed power at *bus-g* can be shown in (A1).

$$GSF_{l,g} = \frac{1}{x_{ij}}\left[X_{ig} - X_{jg}\right] \qquad \text{(A1)}$$

PTDF of a real power flow through line *l* from transaction of source at *bus-g* and sink at *bus-d* can be expressed as below.

$$PTDF^{l}_{g,d} = GSF_{l,g} - GSF_{l,d} \qquad \text{(A2)}$$

Substitute (A1) into (A2) result in (A3).

$$PTDF^{l}_{g,d} = \frac{1}{x_{ij}}\left[\left(X_{ig} + X_{id}\right) - \left(X_{jg} + X_{jd}\right)\right] \qquad \text{(B9)}$$

Komson Daroj received the B. E., M. E. and Ph.D. degrees in electrical engineering from Chulalongkorn University, Bangkok, Thailand, in 1993, 1999 and 2005 respectively. He joined the Department of Electric Engineering at Sripatum and Ubonratchathani University in 1998 and 2000.
His areas of research are power system operation & control, power system deregulation and power quality.

Bundhit Eua-Arporn received both Bachelor and Master Degrees from Elec. Eng. Dept., Faculty of Engineering, Chulalongkorn University. In 1992, he received Ph.D. degree from Imperial College of Science Technology and Medicine, London, UK. He is currently an associate professor at the Elec. Eng. Dept., and deputy director for Research affair at the Energy Research Institute, Chulalongkorn University

Fault Diagnosis in Transmission Systems for Alarm Processing by Fuzzy Relation and Fault Tree Analysis

Radomboon Taksana and Somporn Sirisumrannukul

Department of Electrical Engineering, Faculty of Engineering
King Mongkut's Institute of Technology North Bangkok
1518, Pibulsongkram Rd., Bang sue, Bangkok, Thailand
E-mail: radomboon.t@egat.co.th, spss@kmitnb.ac.th

Abstract-Fault diagnosis in a transmission system is a process to identify faulted components using the postfault statuses of the protective relays and circuit breakers. However, it is not always easy to do so because the system operator has to quickly analyze a large number of messages and alarms transmitted to the control center to draw a conclusion for which a proper action can be taken to restore the system. Therefore, the system operator needs analysis tools to provide assistance in interpreting the data. This paper proposes a method to solve the problem of locating faults that occur randomly anywhere in transmission systems. The method is based on fuzzy relation that utilizes information on operating time sequences of the actuated relays and tripped circuit breakers, and fault tree that can efficiently handle circuit breaker failure. The method is versatile in that uncertainties, such as protective relay failure, circuit breaker failure are taken into consideration. The method is applied to a 6-bus system. The results show that not only can a fault component be precisely identified but also the problem of loss of alarm data in relays can be solved.

Keyword: Fault diagnosis, Alarm Processing, Expert systems, Fuzzy relation, Fault tree analysis.

I. INTRODUCTION

Every component in a power system is subject to a fault. A fault in a power system must be isolated as quickly as possible because it affects the reliability and security of the system. When a fault occurs, the fault section must be detected and removed from the rest of the system thorough the series of relay and circuit breaker operations [1]. However, the identification of faults is a time consuming and complex task because a large amount of data obtained from monitoring devices needs to be analyzed to ascertain whether the relevant protection schemes responded correctly. Other constraints are some false operations of relay and circuit breakers, inexperienced system operators, and simultaneous faults with different locations. Therefore, a system operator needs analysis tools to provide assistance in interpreting the data and comes with a critical piece of information.

A number of methods have been proposed such as artificial neural network [2]. Of these, the expert system is the most established. For example, Pseudo-relaxation method is a fast iterative learning algorithm combined with neural network to find a solution [3]. However, it is computationally expensive for a large-scale system, and in some cases, it may not converge to a solution. An expert system based on "If-Then-Rule" also has a limitation on designed rule-base that cannot cover all possible situations. In other word, the expert system can perform satisfactorily only for those situations that have been considered during the development of knowledge base. An expert system based on fuzzy relation was proposed in [4]. The paper ranks fault section candidates in terms of the degree of membership and the malfunction or wrong alarm. This method provides more flexibility than conventional expert system methods. However, circuit breaker failure are not taken into account.

This paper proposes a technique for fault identification in transmission systems for alarm processing by fault tree analysis and fuzzy relation. The proposed method is able to deal with circuit breaker failure. The method builds a sagittal diagram for each of the components to represent operating conditions of the relays and circuit breakers during a fault. The degree of membership of is then calculated by fuzzy arithmetic. This degree of membership will be used to determine the maximum likelihood of the fault location. The paper is organized as follows. Section II describes the basic principle for SCADA. Protective systems emphasizing on transmission networks are given in Section III. Sagittal and fuzzy relations are described in Section IV. Section V details fault tree analysis. Section VI shows a case study for a 6-bus power system. Section IV concludes the paper.

II. SCADA SYSTEM IN CONTROL CENTER

SCADA stands for supervisory control and data acquisition. It is used to monitor or to control the system equipment in remote areas. SCADA has a capability of checking the statuses of the system equipment (e.g., relay, circuit breaker) and data (e.g., current, voltage) and reporting them back to the control center. A SCADA system has proven to be efficient and economical for power system operations, making it possible for them to maintain relatively complete knowledge of condition and the portions of the system for which they are responsible [5]. In general, SCADA consists of control center, remote terminal units (RTU) and communicating system. A typical SCADA system in a control power system is shown in Fig. 1.

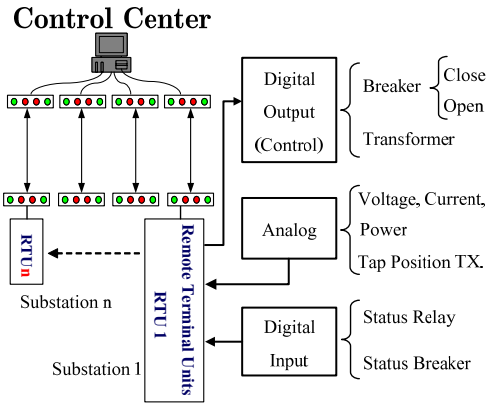

Figure 1. Configuration of SCADA in control center

III. Protection System

The basic function of the relay is to detect a faulted element and remove it, with the help of circuit breaker, from the remaining healthy system as quickly as possible so that as much as the rest of the system is left to continue service and to avoid damage and maintain security or reliability of supply

A protective relay is a device that senses a fault, determines the fault location, and sends tripping command to the proper circuit breaker. A fault may not be cleared if the circuit breaker fails to open or relay malfunctions. In such case, the fault is cleared by backup protection. This situation will not favor the system operator as it makes the data interpretation more difficult to be analyzed to find the fault location.

Differential and distance relays are widely used for the protection of transmission systems because the relays are more effective than overcurrent relays. Differential relays detect abnormal conditions in the area for which they are responsible. They are often used to protect busbars and transformers. Distance relays, in general, protect transmission line in three zones: zone 1 covering 100% of line impedance with instantaneous operation, zone 2 covering 80% with time delay and zone 3 covering 120-150% with time delay.

For example, in Fig. 3 [6] above, CB1 and CB2 are the protection devices of L1. The primary relays are L1AZ1 and L1CZ1 and the backup relays are L1AZ2, L1AZ3, L1CZ2, and LICZ3. When a fault occurs at L1 and is cleared from the system, the alarm messages of CB-01, CB-02, L1AZ1, and L1CZ1 are shown in the control center. If L1CZ1 (Zone 1) fails to operate, L1CZ2, the back-up protection, will respond instead or if L1CZ1 and L1CZ2 do not take any action, the backup protection in Zone 3 will realize that, thus L2BZ3 and L3DZ3 providing the back-up.

IV. Sagittal and Fuzzy Relations

Sagittal diagrams represent the fuzzy relations for power systems and diagnose fault sections using the operation in fuzzy relation [4]. A sagittal diagram has a three set of layers that describe the relationship of fault section (first layer), relay (second layer), and circuit breaker (third layer). In each layer, there are nodes representing the appropriate device. The interconnection between the nodes in each layer is determined from the normal operations of relays and circuit breakers in the occurrence of fault, and the causality is denoted by arrow.

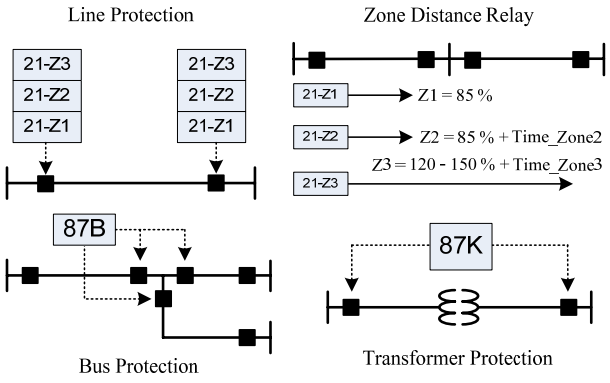

Figure 2. Protection systems

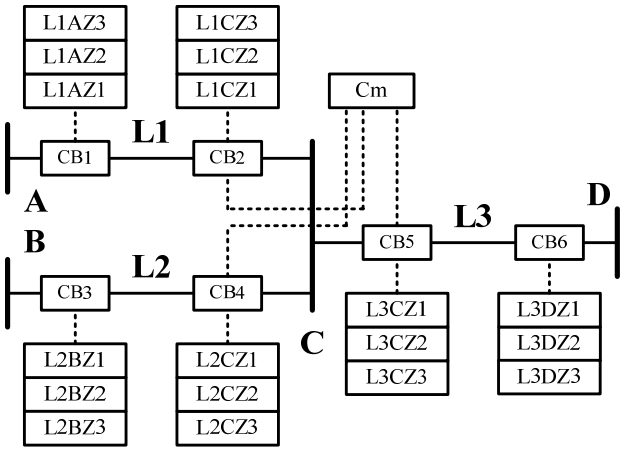

Figure 3. 4-bus power system

For example, the sagittal diagram of L1 is shown in Fig. 4. The label on a line is statistically determined considering the uncertainty of operation and the priority of relays and circuit breakers. The value of a label is between 0 and 1. A label of 0.9 on the line L1AZ1-CB1 indicates that if CB1 operates, a chance of 90% is due to the command from L1AZ1. A label of 0.8 on the line L1-L1AZ1 indicates that if relay L1AZ1 responses, the likelihood of the fault on L1 is 80%. With this method, uncertainty can be taken into account instead of the "If-Then" rule, which can only give the answer "yes (1)" or "no (0)". Note that nodes CB3 and CB6 in the figure will be considered only when CB2 is not tripped as they are served as a backup protection.

The algorithm to find degree of membership for each of the system component from fuzzy relation consists of the following steps.

Step 1: Draw sagittal diagrams of all the devices. For example, there are four sagittal diagrams, L1, L2, L3, and Bus C, for the network in Fig. 3.

Step 2: Find the path that links layer 1, layer 2 and layer 3 in each sagittal diagram. The path is determined from relays

and circuit breakers alarmed. From Fig. 4, path 1 is L1-LICZ1-CB2 and path 2 is L1-L1AZ2-CB1.

Step 3: Calculate the fuzzy relation intersection for each path by

$$i_w(a,b) = 1 - ((1-a)^w + (1-b)^w)^{\frac{1}{w}} \quad (1)$$

Where
a = label on a line connected between layers 1 and 2
b = label on a line connected between layers 2 and 3
w = weight factor of Yager's family of operators [7]

The parameter w is positive number. A weight factor of 3 is used in this paper.

Step 4: Calculate fuzzy union for each sagittal diagram by (2).

$$u_w(a,b) = (a^w + b^w)^{\frac{1}{w}} \quad (2)$$

Step 5: Choose the maximum value of u_w in each sagittal diagram. This value indicates the maximum likelihood of a faulted component.

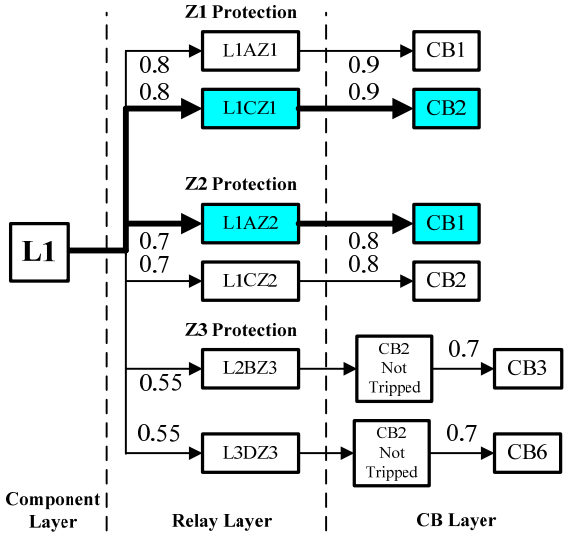

Figure 4. Sagittal diagram of line1

V. Fault Tree Analysis

The event of circuit breaker failure makes it difficult to analyze the faulted component because the backup protection is involved in the investigation. To overcome that problem, this paper introduces fault tree analysis (FTA), which is a top-down approach that utilizes the statuses of the circuit breakers and protective relays as an indicator. The advantage of FTA is that it provides a good, diagrammatic connection of events, as shown in Fig. 5. The symbol ▭ stands for a further-analyzed event and ○ for a terminal event. The connection between events can be represented by the symbols ∩ or ∪. Fig. 5 shows that CB2 fails owing to the following three sub events: the protection of CB2 operates, CB2 closes after receiving command from relay and zone 3 of other transmission lines sees and clears the fault (i.e., L2, L3).

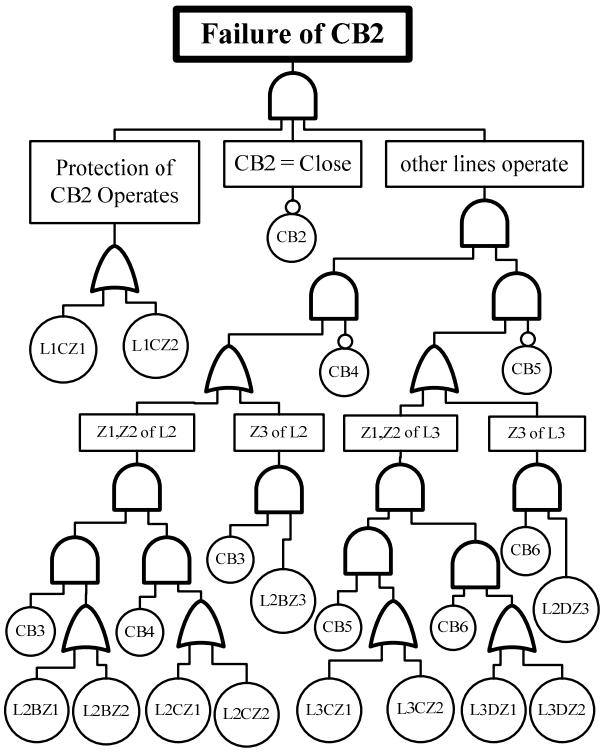

Figure 5. Fault tree analysis for failure of CB2

VI. Case Study

A computer program was developed on MATLAB and tested with a system modified from Fig. 3 by adding buses, and transmission lines to make it more complicated. The test system is shown in Fig. 6, consisting of 6 buses, 7 transmission lines and 14 circuit breakers. Table I shows the input of the case study, which contains 9 scenarios. The scenarios cover various events such as multiple faults, circuit breaker failure and alarm of relay not shown at the control center. The outputs are faulted components and circuit breaker failure. Note that 03 in Table I represents circuit breaker No.3 and 121 represents a distance relay of L1 close to bus 2 in protection zone 1. Table II shows the simulation result for each scenario. It is clearly seen from each scenario that the developed program is able to correctly identify the faulted components and the circuit breaker failure obtained from FTA. The computation time for each scenario is less than 1 second, confirming the efficiency of the method. The diagnosis detail for each scenario is given in Table III. The results of all the scenarios are graphically shown in Fig. 7.

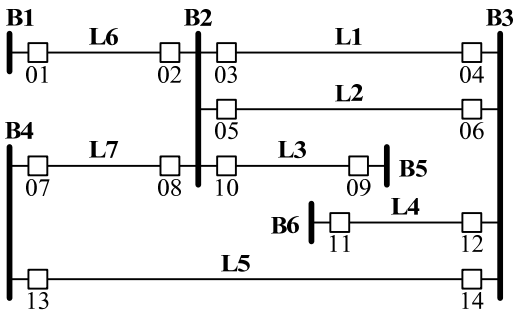

Figure 6. 6-bus test system

TABLE I
INPUT DATA

Scenario	Tripped Circuit Breaker	Responding Relay
1	03, 04	121, 132
2	03, 04, 05, 06	121, 131, 221, 231
3	09, 10, 02, 03, 05, 08	351, 321, B2m
4	09, 10, 02, 03, 05, 08	321, B2m
5	03, 04, 05, 06	121, 221, 231
6	01, 04, 05, 06, 07, 09	121, 131, 221, 231, 353, 613, 743
7	03, 04, 05, 11, 13	121, 131, 221, 463, 543
8	01, 04, 06, 07, 09	121, 131, 233, 321, 351, 613, 743
9	03, 04, 05, 06, 13, 14	131, 221, 531, 541

TABLE II
RESULT OF EACH SCENARIO

Scenario	Possible Faulted Component	CB Failure (searched by FTA)	Faulted Component
1	**L1 = 0.90702**	-	L1
2	**L1 = 0.99785** **L2 = 0.99785**	-	L1, L2
3	**L3 = 0.99785** **B2 = 0.87733**	-	L3, Bus2
4	**B2 = 0.87733** **L3 = 0.79199**	-	Bus2, L3
5	**L2 = 0.99785** **L1 = 0.79199**	-	L2, L1
6	**L2 = 0.99785** **L1 = 0.83000** L3 = 0.53134 L6 = 0.53134 L7 = 0.53134 B2 = 0.53134	**03**	L2, L1
7	**L1 = 0.99785** **L2 = 0.83000** B3 = 0.53134 L4 = 0.42173 L5 = 0.42173	**06**	L1, L2
8	**L1 = 0.83000** **L3 = 0.83000** L2 = 0.53134 L7 = 0.53134 B2 = 0.53134 L6 = 0.42173	**03** **10**	L1, L3
9	**L5 = 0.99780** **L1 = 0.79190** **L2 = 0.79190**	-	L5, L1, L2

TABLE III
DIAGNOSIS DETAIL OF EACH SCENARIO

Scenario	Diagnosis Detail
1	Fault at L1 + failure of Z1 protection of CB04
2	Fault at L1, L2
3	Fault at L3, Bus2
4	Fault at L3, Bus2 + alarm of 351 not shown
5	Fault at L1, L2 + alarm of 131 not shown
6	Fault at L1, L2 + failure of CB03
7	Fault at L1, L2 + failure of CB06 + alarm of 221 not shown
8	Fault at L1, L3 + failure of CB03 + failure of CB10
9	Fault at L1, L2, L5 + alarms of 121 and 231 not shown

VII. CONCLUSION

The main advantage of fuzzy relation and expert system presented in this paper is the reduction of complexity in creating rule base by using the sagittal diagram. The method can efficiently solve the problem of loss of alarm for relays. This paper also introduces fault tree analysis to deal with the problem of circuit breaker failure. The case study performed has shown that a fault location can be precisely identified within a short period of time, indicating a promising result to help the system operator in decision making for real time operation. Future work is the application of the proposed method to a more complex, large-scaled system and to a variety type of relays, for example transformer differential relay, recloser relay and overcurrent relay.

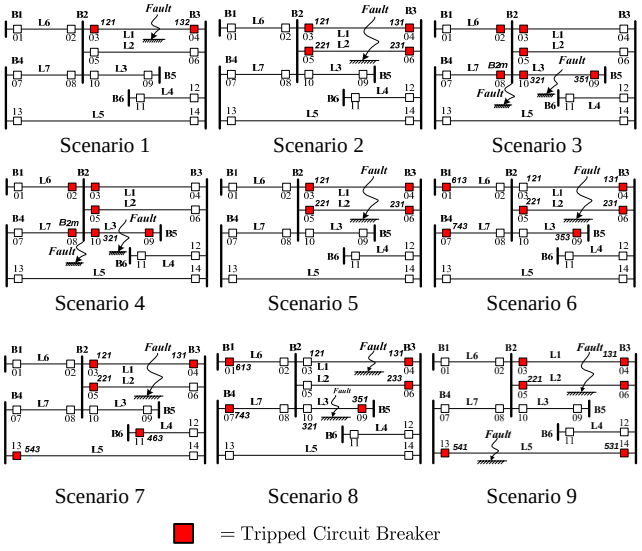

Figure 7. Graphic result of each scenario

REFERENCES

[1] C. Fukui and J. Kawakami, "An Expert System for Fault Section Estimation using Information from Protective Relays and Circuit Breakers," IEEE Transactions on Power Delivery, Vol. PWRD-1, No. 4, pp. 83-90, October 1986.

[2] A.P. Alves da Silva, A.H.F. Insfranan, P.M. da Silveira and G. Lambert-Torres, "Neural Networks for Fault Location in Substations," IEEE Transactions on Power Delivery, Vol. 11, No. 1, pp. 234-239, January 1996.

[3] H. Oh and Suresh C. Kothari, "Adaptation of the Relaxation Method for Learning in Bidirectional Associative Memory," IEEE Transactions on Neural Networks, Vol. 5, No. 4, pp. 576-583, July 1994.

[4] Hyun-Joon Cho and Jong-Keun Park, "An Expert System for Fault Section Diagnosis of Power Systems using Fuzzy Relations," IEEE Transactions on Power Systems, Vol. 12, No. 1, pp. 342-348, Feb 1997.

[5] Robert H. Miller and James H. Malinowski, Power System Operation, Mcgraw-Hill, 1994, 2nd Edn.

[6] Sang-Won Min, Jong-Keun Park, Kwang-Ho Kim, In-Ho Cho and Heung-Jae Lee, "A fuzzy relation based fault section diagnosis method for power systems using operating sequences of protective devices," Power Engineering Society Summer Meeting, 2001, Vol. 2, pp.933-938, 15-19 July 2001.

[7] E.M. Meza, J.C.S. de Souza, M.T. Schilling and M.B. Do Coutto Filho, "Exploring Fuzzy Relations for Alarm Processing and Fault Location in Electrical Power Systems," Power Tech Proceedings, 2001 IEEE Porto, Vol. 3.

Analysis of Substation Ground Grid for Ground Potential Rise Effect Reduction in Two-Layer Soil

A. Puttarach, N. Chakpitak , T. Kasirawat and C. Pongsriwat

***Abstract*--**This paper presents an effects of ground grid and ground rods on grounding performance in a two-layer soil structure with a low resistivity top layer for ground potential rise (GPR) effect reduction. When the grid is completely buried in the low resistivity top layer, its GPR is gradually reduced depend on the buried depth level. On the contrary, when the grid is buried in the high resistivity bottom layer, its GPR is more gradually reduced. A GPR comparison of ground grid with rod and without rod is done, the result shows that the GPR is significantly reduced when the rods are especially applied with the grid in the high resistivity bottom layer.

Index Terms -- **Ground Potential Rise, Resistivity, Ground Rod, Ground Grid, GPR, CDEGS.**

I. Introduction

The effect of fault-produced ground potential rise can directly result in a mistaking operation, damaging of equipment or human safety [1]. Normally, the magnitude of the GPR depends upon such factors as the impedance to ground of the substation grounding system and the fault current [2]. Ground resistivities are also the most important factor to GPR analysis, typically, actual resistivities tests are imperative and should be made within the site to determine the soil layer [3]-[9].

In this paper, from the different characteristic of soil structure particularly in two-layer soil, the influence of variations in depth of ground grid is investigated. Commonly, ground grid buried in top layer or bottom layer of two-layer soil gives distinct result in GPR because of the different of soil resistivities in both layers. Therefore, in this study, the performances of ground grid buried in each layer depth are done to select whose layer is proper to bury. Moreover, consideration of soil layer depth is also the most important in substation ground grid design.

II. Resistivity Measurements

The most frequently used method to determine the soil resistivity depth is the four-point method. Also called *Wenner method* (as shown in Figure 1). The four rods are arranged with the same spacing *a*, five measurements with the spacing a = 2 m, 4, 8, 16 and 32 m are carried out, *b* is the depth of the electrodes in m. For each measurement a current I is injected between the probes C_1 and C_2 and the voltage between P_1 and P_2 is measured [10].

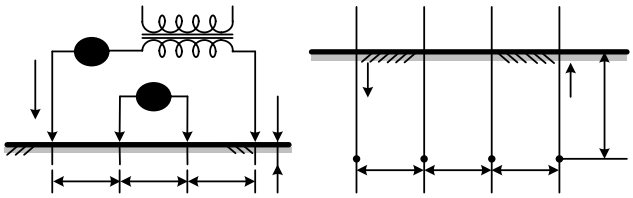

(a) (b)

Fig. 1 (a) Principle diagram of an earthing tester**.**
(b) Current injection into the soil**.**

The resistivity ρ in the terms of the length units in which *a* and *b* are measured is:

$$\rho_a = \frac{4\pi aR}{1+\frac{2a}{\sqrt{a^2+4b^2}}-\frac{a}{\sqrt{a^2+b^2}}} \quad (1)$$

It should be noted that this does not apply to ground rods driven to depth *b*; it applies only to small electrodes buried at depth *b*, with insulated connecting wires. However, in practice, four rods are usually placed in a straight line at intervals *a*, driven to a depth not exceeding 0.1 a. Then we assume *b* = 0 and becomes [2]-[3]:

$$\rho_a = 2\pi aR \quad (2)$$

And gives approximately the average resistivity of the soil to the depth *a*.

III. Two-Layer Soil Apparent Resistivity

A resistivity determination using the Wenner-method (see Figure 2) result in an apparent resistivity which is a function of the electrode separation, *a* In terms of the above parameters the apparent resistivity (ρ_a) can be shown to be:

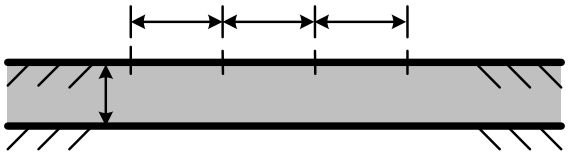

Fig. 2 Two-Layer Earth**.**

A. Puttarach and N. Chakpitak are with Department of Electrical Engineering , Faculty of Engineering , Chiang Mai University, Chiang Mai, 50200 Thailand (e-mail :Arm_Arwut@hotmail.com , nopasit@camt.info).

T. Kasirawat and C.Pongsriwat are with PEA (Provincial Electricity Authority), Chiang Mai, 50000 Thailand (e-mail : tirapong.kas@pea.co.th , chotepong.pon@pea.co.th).

Where

h First layer height.

ρ_1 First layer resistivity, in Ω.m

ρ_2 Deep layer resistivity, in Ω.m

$$\rho_a = \rho_1 \left(1 + 4 \sum_{i=1}^{\infty} \frac{K^n}{\sqrt{1+\left(2n\frac{h}{a}\right)^2}} - \frac{K^n}{\sqrt{4+\left(2n\frac{h}{a}\right)^2}} \right) \quad (3)$$

A two-layer soil model can be represented by an upper layer soil of a finite depth above a lower layer of infinite depth. The abrupt change in resistivity at the boundaries of each soil layer can be described by means of a reflection factor. The reflection factor , K , is defined by Equation(4) [11].

$$K = \frac{\rho_2 - \rho_1}{\rho_2 + \rho_1} \quad (4)$$

IV. CDEGS Model Of Studied System

The grounding grid system of a practical 22 kV substation, in which the ground grid is made from copper, is calculated by virtue of the CDEGS software (Current Distribution Electromagnetic Interference Grounding and Soil Structure Analysis) [12]. The study, supported by Provincial Electricity Authority (PEA), Thailand, is based on grounding grid system of Royal Flora RATCHAPHRUEK substation. The supporting soil resistivity data has been obtained from field tests at the substation. Models of system studied have been presented as follow.

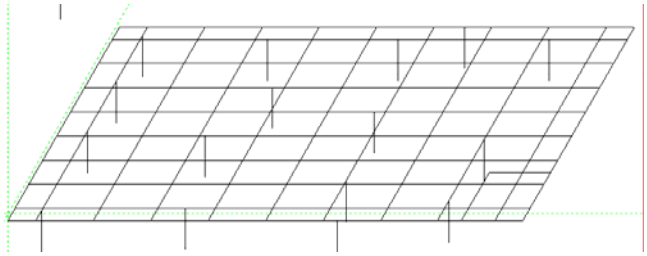

Fig. 3 The grounding grid system of Royal Flora RATCHAPHRUEK substation.

95 mm^2. Hard Drawn Copper Cable.

Exothermic Welding (Graphite Mould).

Copper-Clad Steel Ground Rod.

To study the influence of the soil layer depth in which ground grid is buried to the effect of GPR, ground grid buried at 0.5m below the ground level with 3m rod length is chosen to be the original model in this study , as shown in Figure 3. The following of ground grid characteristics on GPR are investigated:

Case A: Ground grid with constant 3m rod length in variation of soil layer depth, as shown in Figure 4.

Case B: Ground grid without rod in variation of soil layer depth.

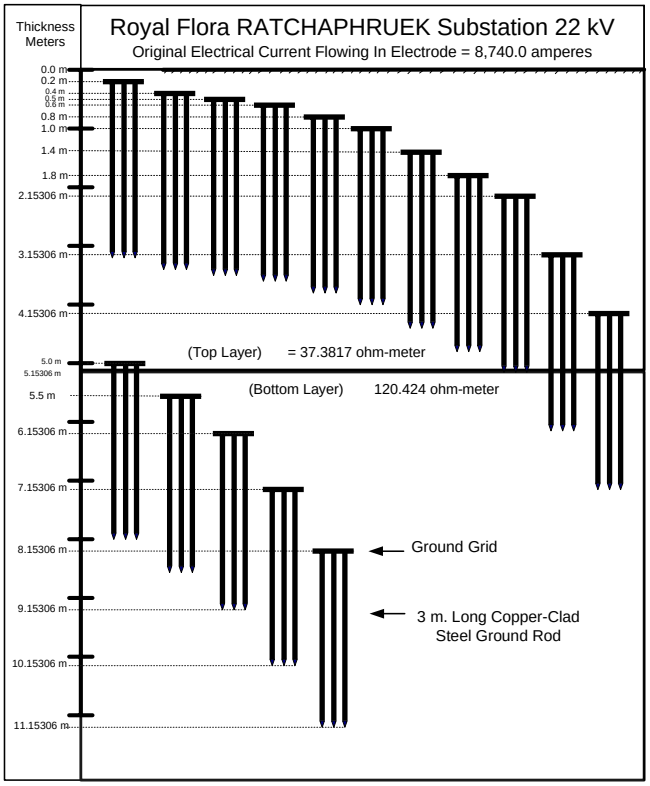

Fig. 4 variation of soil layer depth for ground grid with 3m rod length.

V. Simulation Results

From simulation, the results show the interpreted soil resistivity. Moreover, the ground potential rise of each case is shown. The fault current value 8,740A of PEA fault current report at 22 kV level was utilized in the studies.

A. Soil resistivity results

The resistivities of top and bottom layer are 37.8167 Ohm-m and 120.4224 Ohm-m respectively. The top layer has the resistivity less than the bottom layer (deep layer).

TABLE I

Resistivity of each soil layer (System information summary)

Layer Characteristics				
Layer	Resistivity (Ohm-m)	Thickness (Meters)	Reflection Coefficient(p.u.)	Resistivity Contrast Ratio
Top	37.38167	5.153056	-1.0000	0.37382E-18
Bottom	120.4244	infinite	0.52623	3.2215

Soil layer characteristics were shown in TABLE I, the soil characteristic was interpreted in two-layer model.

The soil resistivity interpretation, which was done by using RESAP module of CDEGS program, is logarithmically manifested in Figure 5.

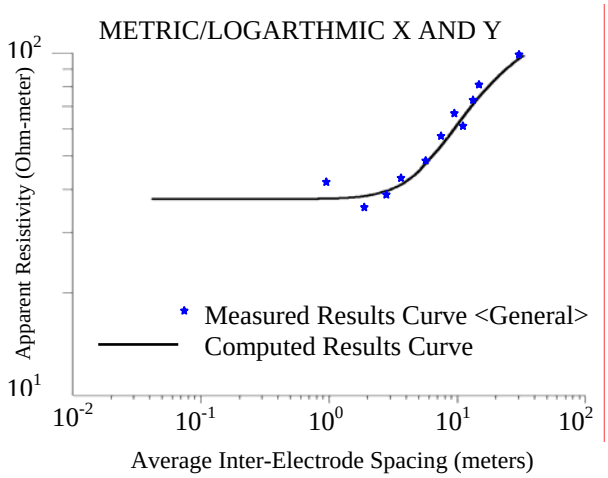

Fig. 5 Soil Resistivity Model.

B. Ground potential rise results

The result of GPR in each case is shown in Table II and the GPR performance in each layer thickness and 3-D of GPR in original case are shown in Figure 6 and 7 respectively

TABLE II
Substation Ground Potential Rise

Layer Thickness (m)	GPR Comparison with Remote Ground (V)		GPR Difference between Point C1 & C2 (V)	
	case A	case B	case A	case B
0.20000	8,494.3	8,504	390.56	440.50
0.40000	8,415.4	8,485	279.06	312.44
0.50000	8,386.0	8,475	223.57	306.82
0.60000	8,359.2	8,463	218.38	240.00
0.80000	8,312.0	8,436	167.71	182.33
1.00000	8,270.6	8,404	125.76	134.82
1.40000	8,200.9	8,345	72.33	76.73
1.80000	8,144.9	8,258	85.29	91.68
2.15306	8,105.0	8,136	87.80	104.34
3.15306	8,039.6	8,981	101.88	116.76
4.15306	8,020.6	8,416	114.91	131.46
5.00000	8,072.4	8,331	129.79	160.16
5.50000	8,889.7	8,082	155.50	167.32
6.15306	8,997.5	8,623	168.55	172.85
7.15306	9,038.3	8,384	337.08	345.69
8.15306	9,026.9	8,232	328.33	335.43

From case A, as soil layer depth of buried ground grid is varied, the results show that soil resistivities of top-layer is lower than the bottom layer and the GPR is continuously reduced along with the increasing of layer thickness until it reach the boundary of this two-layer

From case B, the ground grid with absence of ground rods buried in each soil layer depth is considered. The results show that the value of GPR is not significantly different from case A, noticeably, ground rod can keep the lower value of GPR in both top and bottom layer, especially in bottom layer.

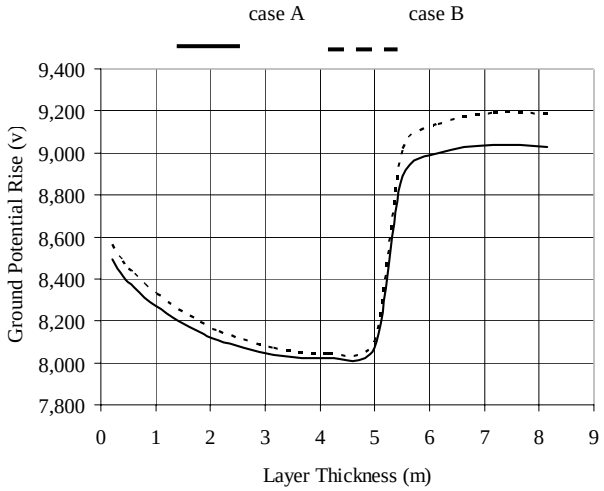

Fig. 6 GPR and layer thickness in each case.

Figure 7 illustrates the GPR of substation comparison with remote ground of ground grid buried in 0.5m depth below the ground plane with 3m rod length. The GPR difference within substation is also compared as seen in Figure 8 between point C1 and C2.

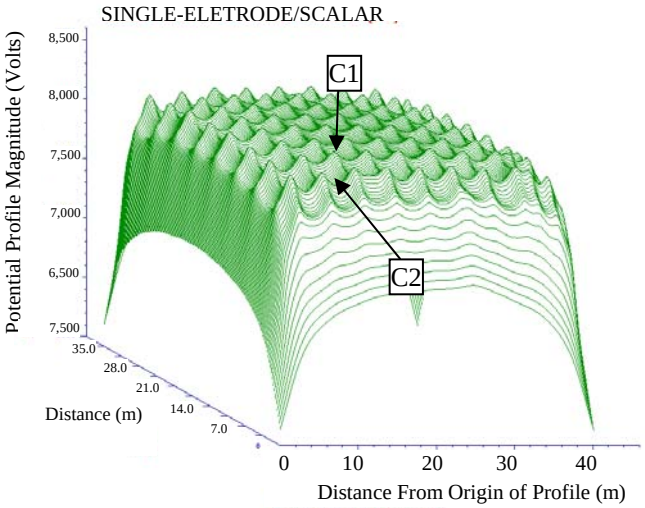

Fig. 7 GPR of ground grid buried in 0.5m depth with 3m rods.

GPR difference between point C1 and C2 was done where C1 is the highest point of GPR and C2 is the lowest point of GPR within substation. The results show that , from case A, at 0.2 m. layer thickness the GPR difference between C1 and C2 is 390.56 V and when the layer thickness increases to 1.4 m. the GPR difference is just decrease to 72.33 V which is the most minimum difference of GPR as shown in Figure 8(a) and 8(b).

When the ground grid buried in the high resistivity bottom layer, the GPR difference strongly increased compared to the ground grid buried in the low resistivity top layer, besides, the results also accord with the GPR which compared to remote ground.

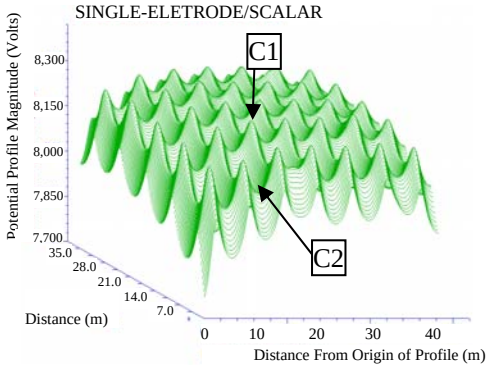

(a) At 0.5m layer thickness.

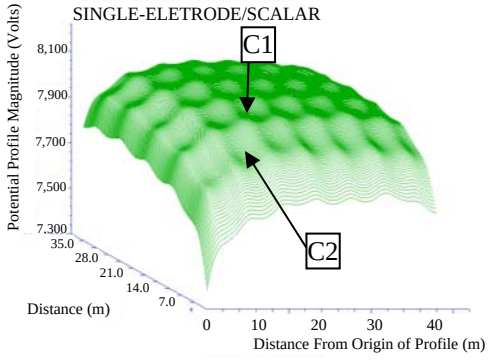

(b) At 1.4m layer thickness.

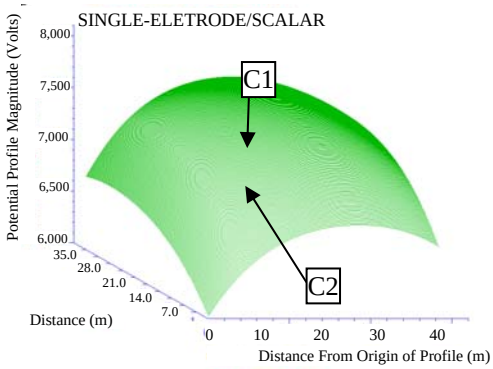

(d) At 6.5m layer thickness.

Fig. 8 GPR Difference between two point within substation.

From the study, ground grid with rod buried in variation of soil layer depth gives outstandingly result in GPR difference reduction within substation and better result of GPR than ground grid without rods.

VI. CONCLUSION

For substation ground grid designs, a factor which should be considered in design phase is the layer of buried ground grid, that is, in case of two-layer soil structure and the top soil resistivities is lower than the bottom soil resistivities, ground grid buried in low resistivities top layer can reduce the GPR more than the ground grid buried in the high resistivities bottom layer. However, the high resistivities of bottom layer does not affect to the reduction of GPR but to the contrary. Finally, the layer thickness of buried ground grid can significantly reduce the GPR difference between two points within substation and bring about the same results with the remote ground GPR comparison.

VII. Reference

[1] C.Pongsriwat, T.Kasirawat and C.Wattanasakpoobal, " Ground Potential Rise Analysis for the damage problem of recloser control unit " , Provincial Electricity Authority Conference of transmission and distribution engineering, PEA, Bangkok, 2005.

[2] *IEEE Guide for safety in AC Substation Grounding, 2000.*

[3] *IEEE Guide for Measuring Earth Resistivity Ground Impedance and Earth Surface Potentialsof a GroundSystem, 1983.*

[4] F. P. Dawalibi and D. Mukhedkar, "Optimum design of substation grounding in two-layer earth structure - Part I, Analytical study", *IEEE Trans. PAS*, Vol.94, No.2, March-April 1975, pp.252-261.

[5] A. P. Meliopoulos, R.P. Webb, and E.B. Joy, "Analysis of grounding systems," *IEEE Trans. PAS*, Vol.100, No.3, March 1981, pp.1039-1048.

[6] F. P. Dawalibi and N. Barbeito, "Measurement and computations of the performance of grounding systems buried in multilayer soils", *IEEE Trans. PWRD*, Vol.6, No.4, October 1991, pp.1483-1490.

[7] J. Ma, F.P.Dawalibi and W.K. Daily, "Analysis of grounding systems in soils with hemispherical layering", *IEEE Trans. PWRD*, Vol.8, No.4, October 1993, pp.1773-1781.

[8] J. Ma and F.P.Dawalibi, "Analysis of grounding systems in soils with cylindrical soil volumes", *IEEE Trans. PWRD*, Vol.15, No.3, July 2000, pp.9133-918.

[9] Research Project of PEA's Ground Grid in Substaion and Grounding in HV and LV Distribution System, Thailand,2006.

[10] F.Kiessling, P.Nefzger, J.F.Nolasco and U.Kaintzyk, Overhead Power Lines, Germany:Dip.-Ing, pp.115-141,2003.

[11] F.Dawalibi and C.J. Blattner "Earth Resistivity Measurement Interpretation Techniques'' *IEEE Transactions on Power Apparatus and Systems*, Vol.pp-103-106,No.2

[12] Engineering Guide a Simple Substation Grounding Grid Analysis, Safe Engineering Services & Technologies, Ltd, 2004,www.sestech.com/Downloads/Engineering HowTo.aspx [15 September 2006].

VIII. BIOGRAPHIES

Arwut Puttarach was born in Chiang Rai. He received his B.Eng, degree in Electrical Engineering from Rajamamgla Institute of Technology Chiang Mai Campus, Thailand, in 2003. He is currently a master degree student in Electrical Engineering, Chiang Mai University, Thailand. His currently interests in power system grounding analysis.

Nopasit Chakpitak received his first degree in Electrical Engineering from Chiang Mai University. His professional career was in Electricity Generating Authority of Thailand between 1989-1994. He has finished his Ph.D in Electrical Engineering in 2003 from the University of Strathclyde Scotland. Now he is a full-time lecturer of department of Electrical Engineering, Chiangmai University.

Tirapong Kasirawat was born in Karbi, Thailand 1963. He received B.Eng (Electrical Engineering) M.Eng (Electrical Engineering) from Chiang Mai University, Thailand, in 1987 and 1995 respectively. Currently, He works with Provincial Electricity Authority, Thailand (PEA North1) and special lecturer of department of Electrical Engineering Chiang Mai University. His research interest includes high-voltage engineering, power quality, and information technology in power system.

Chotepong Pongsriwat was born in Lampang, Thailand 1976. He received B.Eng (Electrical Engineering) , M.S.(Information Technology and Management) and M.Eng (Electrical Engineering) from Chiang Mai University, Thailand, in 1997, 2003, and 2004 respectively. Currently, He works with Provincial Electricity Authority, Thailand (PEA North1). His research interest includes power quality, power system analysis and information technology in power system.

Design of Automatic Generation Control Using the Method of Inequalities

Raksanai Nidhiritdhikrai, Suchin Arunsawatwong and Bundhit Eua-arporn
Department of Electrical Engineering
Faculty of Engineering, Chulalongkorn University
254 Phayathai Road, Bangkok 10330 Thailand.
Emails: raksanai@hotmail.com, suchin.a@chula.ac.th and bundhit.e@chula.ac.th

***Abstract*— This paper describes a new design strategy for a multiarea Automatic Generation Control (AGC) system and a procedure for solving it using the method of inequalities. In this strategy, electricity market constraints are taken into consideration in order to increase technical and economical reliability of the system. The design problem is formulated as a set of inequalities in accordance with the multiobjective nature of the problem. As a result, the design can be carried out in an effective way.**

I. INTRODUCTION

Nowadays, electricity market criteria have significant impact in power system operation. The violation of these criteria should be firstly prevented by a proper design of the AGC controller system taking into account the required criteria as constraints. With this design concept, we can increase technical and economical reliability compliance to the power system.

In the past, methods for designing an AGC controller are generally based on optimal control [1][2][3], fuzzy control [4], and state feedback control concepts. However, the mathematical formulation employed by these methods do not easily enable the designers to fulfil all the design requirement. When the design process has been finished, they need to perform simulations on the obtained system so as to check whether the results satisfies all the design criteria. If the system does not satisfy all the criteria, they have to conduct a trial and error process in redesigning the system again. As a result, the design process can be time-consuming.

The method of inequalities [5] gives rise to a formulation in the form of a set of inequalities that represent all the design requirements. After the design process, provided the formulation is accurate and realistic, the designer can see whether the obtained design satisfies all the requirements without having to perform a number of unnecessary simulations for verification. For this reason, we employ the method of inequalities in designing the AGC system.

II. MATHEMATICAL MODEL OF AGC SYSTEM

In this paper, we consider an interconnected power system with two identical control areas. Each area consists of thermal and hydro power generating units. The block diagrams of the system are shown in Figures 1–4 [6][7][8]. The values of the system parameters are given in Table I.

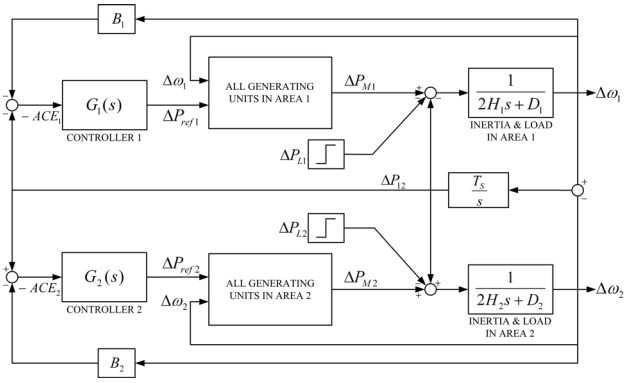

Fig. 1. Two area interconnected AGC model.

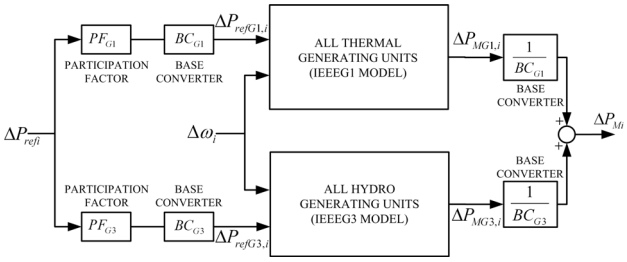

Fig. 2. Model of all generating units of area i.

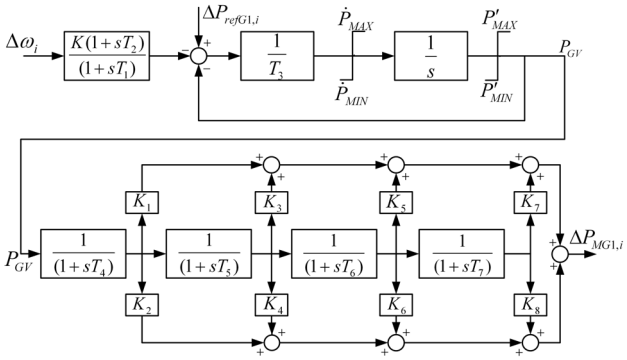

Fig. 3. Thermal generating unit model of area i.

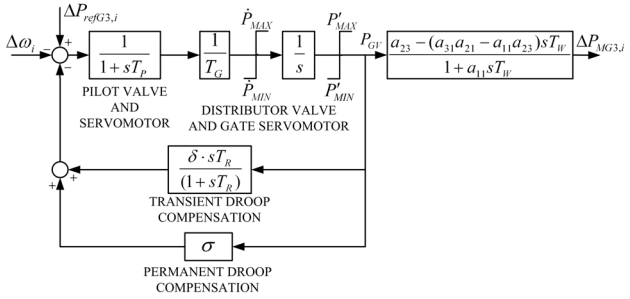

Fig. 4. Hydro generating unit model of area i.

TABLE I
MODEL PARAMETERS

Parameters of all generating unit

$PF_{G1} = 0.75$	$PF_{G3} = 0.25$	$BC_{G1} = 500/400$	$BC_{G3} = 500/70$

Two area AGC parameters

$H_1 = H_2 = 4.1526$	$D_1 = D_2 = 0.9760$	$B_1 = B_2 = 27.3$	$T_s = 2$

IEEEG1 parameters

$K = 20$	$K_1 = 0.3$	$K_2 = 0$	$K_3 = 0.4$
$K_4 = 0$	$K_5 = 0.3$	$K_6 = 0$	$K_7 = 0$
$K_8 = 0$	$T_1 = 0.25$	$T_2 = 0$	$T_3 = 0.1$
$T_4 = 0.3$	$T_5 = 10$	$T_6 = 0.4$	$T_7 = 0$
$\dot{P}_{MIN} = -0.1$	$P_{MIN} = 0$	$\dot{P}_{MAX} = 0.1$	$P_{MAX} = 1$

IEEEG3 parameters

$T_G = 0.2$	$T_P = 0.04$	$T_R = 5$	$T_W = 1$
$a_{11} = 0.5$	$a_{13} = 1$	$a_{21} = 1.5$	$a_{23} = 1$
$\sigma = 0.04$	$\delta = 0.4$	$\dot{P}_{MIN} = -0.1$	$P_{MIN} = 0$
$\dot{P}_{MAX} = 0.1$	$P_{MAX} = 1$		

III. ELECTRICITY MARKETS

Ancillary service [9] generally consists of voltage support, regulation and frequency, energy imbalance, operating reserve and black start capacity services, etc. The energy imbalance service which service balances the interconnection system frequency, called as Direct Frequency Control (DFC). The DFC which is one of the most essential services consists of regulation and load following services.

The primary difference between the regulation and load following service is the time frame of consideration. Regulation service is defined to be the higher frequency of power service following the minute-to-minute load variation, whereas the load following service is intended to follow the lower frequency component of load variation, the time scale of which normally covers period of hours [9].

In this paper, we consider only regulation service as a constraint in the design process of the AGC controller.

A. Regulation Components

In hourly generation scheduling, the boundary between regulation and load following occurs at a frequency with a period length of twice the scheduling period, i.e. two hours [9]. All variation in load with full cycle period less than two hours is considered as part of the regulation service and all variations in load with full cycle periods equal to or greater than two hours are considered as load following service.

A regulation example is shown in Figure 5, comprising total load, smoothed load, and regulation. The regulation component is calculated by using Fourier transforms to decompose

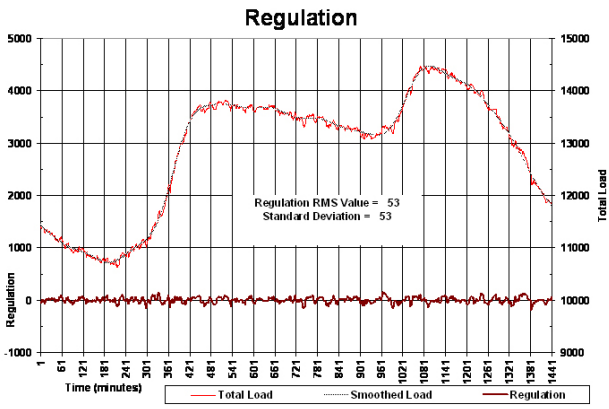

Fig. 5. The regulation component of total load.

the total load into the regulation component and the smoothed load component. With the decomposition in this manner, the regulation component of the load has a net integrated energy of zero. In other words, there is no energy or energy imbalance associated with the regulation component. The root mean square (RMS) value for regulation is also calculated. In this case, since the net integrated energy of the regulation ($\bar{x}$) is zero, then the standard deviation (σ) for regulation has the same value as the RMS. The equations for the standard deviation (σ) and the RMS values can be written as (1) and (2).

$$\sigma^2 = \frac{1}{n}\sum x_i^2 - \bar{x}^2 \tag{1}$$

$$RMS^2 = \sigma^2 + \bar{x}^2 \tag{2}$$

B. Real energy service measurement

The measurement standard presented in [10][11][12] called Control Performance Standard 1 ($CPS1$) uses compliance factor (CF) to measure controller performance of each area. The CF is defined as:

$$CF = \frac{1}{n}\sum \frac{\overline{ACE} * \overline{\Delta F}}{B} \tag{3}$$

where $\overline{ACE}$ is the one minute average ACE and $\overline{\Delta F}$ is average standard error of frequency in one minute. A positive CF means the control area is acting as a burden to the interconnection regulation requirement. On the other hand, a negative CF indicates that the area is supporting the interconnection regulation requirement.

The $CPS1$ is a standard reference for defining capacity and measurement of regulation and load following services. Illiam and Hoffman [10] showed the importance of coincidence between scheduled errors of interconnection systems. Regulation and load following service measurement should use the RMS value combined with coincidence factor as follows:

$$C_{reg}^2 = \frac{1}{n}\sum \overline{\Delta T} * \overline{\Delta F} \tag{4}$$

where $\overline{\Delta T}$ is the schedule error over a of one minute period.

IV. THE METHOD OF INEQUALITIES [5][13]

The method of inequalities [5][13] requires that a design problem be formulated as a set of inequalities:

$$\Phi_i(p) \le C_i, \qquad i = 1, 2, \ldots, m \tag{5}$$

where $p \in \mathbf{R}^n$ is a design parameter, $\Phi_i(p)$ is a real number representing an aspect of the behaviors of the system, and the bound C_i is the maximum tolerable value of $\Phi_i(p)$. Any value of p that satisfies (5) is called a solution of the inequalities (5) and characterizes an acceptable design.

One can solve inequalities (5) either by analytical or numerical method. But, in general, it is necessary and practical to use numerical methods. In this work, an algorithm called the moving boundaries process (MBP) is used to solve inequalities (5). The details of the MBP algorithm can be found in Zakian's original article [5], and also in chapters 1 and 6 of Zakian's recent book [13].

The inequalities (5) include two principal subsets. One is the subset that represents required performance. Whereas constraints have traditionally been represented by inequalities, the representation of desired performance by a set of inequalities is a significant departure from the traditional that requires that performance be represented by a single number $\Phi(p) = \sum_{i=1}^{m} w_i \Phi_i(p)$ (the w_i are weights chosen by the designer), which is to be minimized.

The method of inequalities recognizes that desired performance is appropriately stated by means of several distinct criteria, thus allowling greater insight into the design process.

Over the last thirty years or more, it has been shown that a wide range of practical design problems can be formulated in the form of (5). See [5], [13], [14] and the references therein.

V. AGC CONTROLLER SYSTEM DESIGN

We apply the method of inequalities to the design of a multiarea AGC system. The following assumptions are used in our design formulation.

- We consider only Load Frequency Control (LFC) in the AGC system and discard the coupling effects of automatic voltage regulator.
- Load disturbance, which is demand change, is a step function.
- We consider only small signal dynamic of the system. Therefore, the magnitude of the disturbance is 0.01 p.u.
- We discard the time delay of system.

When a small step disturbance occurs, the AGC system is normally required to fulfil the following objectives.

- Keep frequency deviations $\Delta\omega_i$ equal to zero in steady state.
- Keep the tie-line power flow deviation ΔP_{12} equal to zero in steady state.

According to the concept of tie-line bias control, the area control error in area i (ACE_i) is given by

$$ACE_1 = \Delta P_{12} + B_1 \Delta\omega_1 \tag{6}$$

$$ACE_2 = \Delta P_{21} + B_2 \Delta\omega_2 \tag{7}$$

where B_i is the frequency bias factor in area i. In order that the control system can drive $\Delta\omega_i$ and ΔP_{12} to zero in steady state, it is necessary that the controller employ the integral feedback of ACE_i (see (11) and (13)).

In addition to the above design objectives, we also include some significant electricity market constraints (as described in section III) in the formulation so as to increase the technical and economical reliability of the power system. The details of the design are given below.

A. Design Formulation

Since both areas are identical, it suffices to assume further that only a 0.01 p.u. load disturbance occurs in area 1 (i.e. $\Delta P_{L1} = 0.01$ p.u. and $\Delta P_{L2} = 0$ p.u.). See Figure 1. For the system to have good dynamic responses, it is required that (A) the maximum overshoot (OS), the rise time (T_r) and the settling time (T_s) of the total mechanical power deviation (ΔP_{M1}) are sufficiently small; (B) the maximum values of $|\Delta P_{12}|$, $|\Delta\omega_1|$, $|\Delta\omega_2|$, the total mechanical power deviations of thermal generating unit (IEEEG3 model) in area 1 and 2 ($\Delta P_{MG3,1}$ and $\Delta P_{MG3,2}$) are sufficiently small. The requirement (A) leads to the following design inequalities:

$$\begin{aligned} \Phi_1 &= OS \text{ of } \Delta P_{M1} && \le C_1 \\ \Phi_2 &= T_r \text{ of } \Delta P_{M1} && \le C_2 \\ \Phi_3 &= T_s \text{ of } \Delta P_{M1} && \le C_3 \end{aligned} \tag{8}$$

whereas the requirement (B) leads to

$$\begin{aligned} \Phi_4 &= \max\{|\Delta P_{12}(t)| : t \ge 0\} && \le C_4 \\ \Phi_5 &= \max\{|\Delta\omega_1(t)| : t \ge 0\} && \le C_5 \\ \Phi_6 &= \max\{|\Delta\omega_2(t)| : t \ge 0\} && \le C_6 \\ \Phi_7 &= \max\{\Delta P_{MG3,1}(t) : t \ge 0\} && \le C_7 \\ \Phi_8 &= \max\{\Delta P_{MG3,2}(t) : t \ge 0\} && \le C_8 \end{aligned} \tag{9}$$

In order to increase the system's economical reliability, it is required that (C) the regulation service quality of area 1 (C_{reg1}) and the compliance factor of each area (CF_1 and CF_2) are in the acceptable range described in the market agreement. Since there is no disturbance in area 2, i.e. $C_{reg2} = 0$, we do not consider C_{reg2}. The requirement (C) leads to the following design inequalities.

$$\begin{aligned} \Phi_9 &= C_{reg1} && \le C_9 \\ \Phi_{10} &= CF_1 && \le C_{10} \\ \Phi_{11} &= CF_2 && \le C_{11} \end{aligned} \tag{10}$$

Since the two control areas are identical, the transfer functions of both area controllers (see Figure 1) are chosen to be the same; that is, $G_1(s) = G_2(s)$.

In solving the inequalities given in (8), (9) and (10) for an acceptable design solution, various forms of $G_1(s)$ and $G_2(s)$ are chosen. Usually, it is a common practice to start with $G_1(s)$ and $G_2(s)$ with the least complexity; if a design solution is not found, then a more complex controller structure is used.

B. Numerical Results

First, choose

$$G_1(s) = G_2(s) = \frac{p_1}{s} \tag{11}$$

After a large number of iterations, the MBP cannot locate an acceptable design specified in Table II. An approximate solution can be found by relaxing some design specification in Table II. For example, by letting $C_1 = 0.2$, $C_3 = 41$ sec. and $C_9 = 0.51$, an approximate solution is found.

$$G_1(s) = G_2(s) = \frac{0.10816}{s} \tag{12}$$

where the corresponding values of $\Phi_i(p)$ are given in Table III.

Then, reformulate the design problem by choosing

$$G_1(s) = G_2(s) = \frac{p_1}{s} + p_2 \cdot \left(\frac{s+p_3}{s+p_4}\right) \tag{13}$$

After a number of iterations, the MBP locates a sucessful design given by

$$G_1(s) = G_2(s) = \frac{0.02148}{s} + 0.03997 \cdot \left(\frac{s+1.39888}{s+0.06939}\right) \tag{14}$$

where the corresponding values of $\Phi_i(p)$ are given in Table III and the responses of the system are in Figures 6 and 7.

TABLE II

DESIGN SPECIFICATIONS

$C_1 = 0.1$	$C_2 = 2.5$ sec.	$C_3 = 27$ sec.
$C_4 = 0.0045$ p.u.	$C_5 = 0.0015$ p.u.	$C_6 = 0.0015$ p.u.
$C_7 = 0.0099$ p.u.	$C_8 = 0.0099$ p.u.	$C_9 = 0.3950$
$C_{10} = 6.525 \times 10^{-5}$	$C_{11} = 6.525 \times 10^{-5}$	

TABLE III

DESIGN RESULTS

For AGC with integral controller (12)

$\Phi_1 = 0.19457$	$\Phi_2 = 2.44116$ sec.	$\Phi_3 = 40.7617$ sec.
$\Phi_4 = 0.00450$ p.u.	$\Phi_5 = 0.00125$ p.u.	$\Phi_6 = 0.00076$ p.u.
$\Phi_7 = 0.00923$ p.u.	$\Phi_8 = 0.00289$ p.u.	$\Phi_9 = 0.50881$
$\Phi_{10} = 2.078 \times 10^{-7}$	$\Phi_{11} = 7.254 \times 10^{-9}$	

For AGC with more complex controller (14)

$\Phi_1 = 0.09248$	$\Phi_2 = 2.33385$ sec.	$\Phi_3 = 26.9983$ sec.
$\Phi_4 = 0.00438$ p.u.	$\Phi_5 = 0.00124$ p.u.	$\Phi_6 = 0.00059$ p.u.
$\Phi_7 = 0.00895$ p.u.	$\Phi_8 = 0.00193$ p.u.	$\Phi_9 = 0.39338$
$\Phi_{10} = 5.38 \times 10^{-6}$	$\Phi_{11} = -3.99 \times 10^{-8}$	

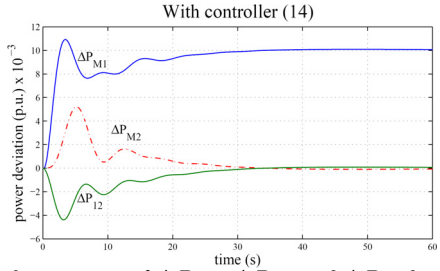

Fig. 6. The responses of ΔP_{M1}, ΔP_{M2} and ΔP_{12} due to ΔP_{L1}.

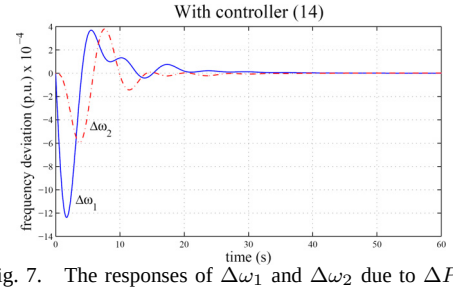

Fig. 7. The responses of $\Delta\omega_1$ and $\Delta\omega_2$ due to ΔP_{L1}.

VI. CONCLUSION

From the numerical results, we can see that the method of inequalities can solve this kind of design problem effectively so that the AGC system can have good dynamic responses and, at the same time, can increase its economical reliability. Furthermore, the advantage of this method is that new design criteria are easily incorporated into the design process in the form of additional inequalities. When the market criteria are changed, it is easy to update the parameters of the AGC controller in order to gain the system reliability. It is worth pointing out here that, by using the method of inequalities, we can choose to design not only the controller parameters but also the parameters in other parts of the power system.

ACKNOWLEDGMENT

The authors would like to gratefully acknowledge Chulalongkorn University graduate scholarship to commemorate the 72^{nd} anniversary of His Majesty King Bhumibol Adulyadej.

REFERENCES

[1] M. Calovič, Linear regulator design for a load and frequency control, *IEEE Transactions on Power Apparatus and Systems*, vol. 91, 1972, pp. 2271–2285.

[2] C. E. Fosha and O. I. Elgerd, The megawatt frequency control problem: A new approach via optimal control theory, *IEEE Transactions on Power Apparatus and Systems*, vol. 89, no. 4, 1970, pp. 563–577.

[3] E. C. Tacker, C. C. Lee, T. W. Reddoch, T. O. Tan, and P. M. Julich, Optimal control of interconnected electric energy systems: A new formulation, *Proceedings of the IEEE*, vol. 60, 1972, pp. 1239–1241.

[4] G. A. Chown and R. C. Hartman, Design and experience with a fuzzy logic controller for Automatic Generation Control (AGC), *IEEE Transactions on Power Systems*, vol. 13, no. 3, August 1998, pp. 965–970.

[5] V. Zakian and U. Al-Naib, Design of dynamical and control systems by the method of inequalities, *Proceedings of the IEE*, vol. 120, no. 11, November 1973: 1421–1427.

[6] P. Kundur, *Power System Stability and Control*, New York: McGraw-Hill, 1994.

[7] H. Saadat, *Power system analysis*, Singapore: McGraw-Hill, 1999.

[8] IEEE Committee Report, Dynamic models for steam and hydro turbines in power system studies, *IEEE Transactions on Power Apparatus and Systems*, November/December 1973, pp. 128–139.

[9] New York Independent System Operator, *NYISO Ancillary services manual*, New York: New York Power Pool, 1999.

[10] H. F. Illian and S. P. Hoffman, *Real Energy Interconnected Operations Services* [Online], Available from: http://www.nerc.com

[11] N. Jaleeli and L. S. VanSlyck, NERCs new control performance standards, *IEEE Transactions on Power Systems*, vol. 14, no. 3, August 1999, pp. 1092–1099.

[12] M. Yao, R. R. Shoults and R. Kelm, AGC Logic based on NERCs new control performance standard and disturbance control standard, *IEEE Transactions on Power Systems*, vol.15, no. 2, May 2000, pp. 852–857.

[13] V. Zakian, ed., *Control Systems Design*, London: Springer, 2005.

[14] V. Zakian, Perspectives on the principle of matching and the method of inequalities, *International Journal of Control*, vol. 65, 1996, pp. 147–175.

Optimal Feeder Routing in Distribution System with Demand Uncertainty

S. Wattanasophon[a] and B. Eua-Arporn[b]
[a] Electrical Engineering Department, Dhurakij Pundit University, Laksi, Bangkok, 10210 Thailand
[b] Electrical Engineering Department, Chulalongkorn University, Payathai, Bangkok, 10330 Thailand

***Abstract*-This paper proposes a method for solving an optimal feeder routing problem. All practical issues, e.g., technical constraints (voltage drop and thermal limits), uncertainty of future demand, and existing infrastructure, etc., are taken into consideration. The proposed method can automatically determine appropriate feeder configuration and does not require prior knowledge of feeder routing candidates. The method integrates planner's experience and optimization process to achieve appropriate practical solutions. Then, the optimal conductor size is selected base on minimum cost with fuzzy cost analysis. The proposed method has been tested with an actual distribution system, from which the results indicate that it can provide satisfactory plans.**

I. INTRODUCTION

Distribution system planning basically involves the optimization of both location and size of a new substation and feeders to meet the requirement of an expected demand while satisfying specified constraints, e.g. substation capacity, feeder thermal capacity, voltage drop, etc.

Optimal distribution system planning is recognized as a very complex problem due to a large number of variables and network configuration candidates, related to the characteristics of the geographical area and the consumer load. Several approaches have been proposed [1-9] to solve distribution system planning problem. Each approach is based on mathematical programming techniques, e.g., linear programming [1, 2], mixed-integer programming [3], non-linear programming [4], dynamic programming [5], quadratic programming [6], and branch and bound algorithm [7, 8]. However, most of the approaches assume that the candidates of feeders routing is known in advance. With this assumption, the problem can be simplified but more appropriate solutions may be neglected.

Since the planning period normally ranges from 5 to 20 years, the demand uncertainty is embedded in the problem. However, in general, intrinsic uncertainty on the future demand is not explicitly considered in solving distribution system planning problems [1-9]. Recently, an extensive application of geographical information systems (GIS), i.e. routes of streets and roads, has enabled the representation of distribution systems in more detail. The distribution planning can be done in a more detailed consideration.

In this paper, a method for the distribution system planning of a radial network of medium voltage (MV) level is presented. To cope with demand uncertainty, a fuzzy number is employed to model the future demand. In addition, heuristic rules by experienced planners will be incorporated to determine feeder path according to actual geographical conditions, e.g. streets, canals, etc., in the planning area. Based on the developed algorithm, the program selects the path and size of conductors, which provide minimum or close to minimum total cost of the system.

II. OPTIMAL FEEDER ROUTING

A. *Objective Function*

The objective of this proposed method is to determine size and configuration of feeders based on the minimum cost. Thus, the problem can be formulated as (1).

$$\text{Min } Cost_{total} = \text{Min } [Cost_{feeder} + Cost_{losses}] \quad (1)$$

where $Cost_{total}$ is the total cost over the planning period,
$Cost_{feeder}$ is the cost of conductor to be installed, and
$Cost_{losses}$ is the cost of expected power loss.

B. *Solving Procedure*

The solving process of the proposed method can be illustrated by the flowchart shown in figure 1.

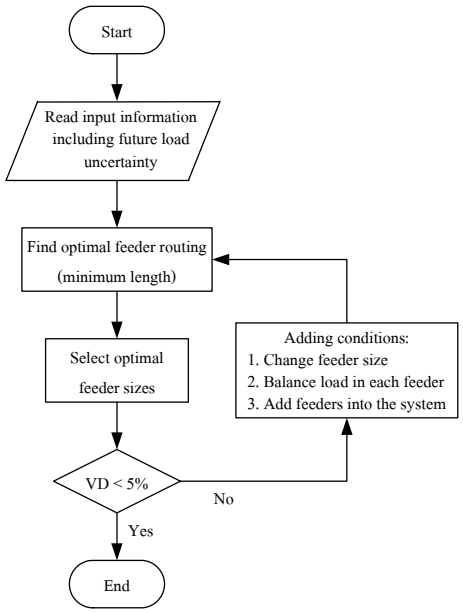

Figure 1. Flowchart of the solving process

This process comprises two solving steps, e.g., determine appropriate routing and select optimal size of feeders.

The process starts from input information, i.e. the location and demand of each load point, the future load growth, and the substation location, etc. Then, feeder routing is determined by the minimum path algorithm with heuristic rules taking into account existing infrastructure, e.g. streets, roads, etc. Then optimal size of the feeder in each branch is selected in the next step.

As a preliminary result, the single-line diagram of the distribution network is obtained, from which system voltage drop is verified. If the voltage drop constraint is violated, a three-step procedure, i.e. 1) adjusting the larger conductor size, 2) balancing load in each feeder, and 3) adding the number of feeder, is applied.

III. FUZZY DEMAND MODEL [10,11]

For considering the demand uncertainty, the fuzzy model is used to represent the future load growth. In this paper, the future load growth is modeled by a triangular fuzzy number, which can be illustrated by figure 2.

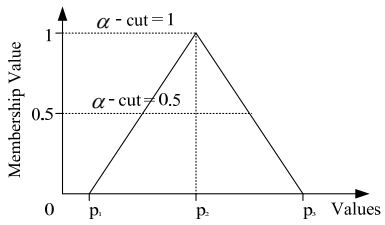

Figure 2. Future load growth model, $\tilde{p} = (p_1, p_2, p_3)$

where p_1 - the minimum plausible load growth value
p_2 - the highest plausible load growth value
p_3 - the maximum plausible load growth value

Base on planner's experiences, the future load growth can be appropriately defined. For example, the planner expected load growth is about 4% but not over 5% and not less than 3%, so the expected load growth can be defined by (3%, 4%, 5%).

This model will be applied with all load points which the load growth value at each load point will depend on the planner's experiences.

IV. THE PROPOSED METHODOLOGY

The proposed method can be divided in two main steps, e.g. determine optimal routing, and select optimal size of feeder. Details of each step can be illustrated below.

A. Optimal Feeder Routing

From the input data, the site and the demand of the medium voltage (MV) substation are known. The objective is to search for an appropriate feeder routing which can save both investment and operation cost subjected to certain constrains.

As the cost of feeder is proportional to its length, the problem may be simplified to minimize feeder length. Minimum path algorithm [9] is used and described below.

The minimum path algorithm:

- Initially, the planner assigns a required number of feeders from the new substation, e.g. two feeders. Then, two sets of nodes are created for each feeder, i.e. connected nodes (A) and unconnected nodes (A′).

A = {substation node}

A′ = {all the load points and road points}

- The distance from any nodes in A′ to the nodes in A is computed and the number of nodes (equal to number of feeders), close to the substation, are removed from set A′ to set A.

- The distance from any nodes in A′ is then compared with the nodes in A. The shortest distance is then sought out. The node with the shortest distance is added to A.

- Repeat above steps until all the load points are in set A and set A′ is an empty set.

In order to present the principles of this step, a system which consists of 130 expected load points as shown in figure 3 is considered, where the geographical information which is presented by ARCVIEW is taken into account. The light line at the back of figure presents the existing road in the study area.

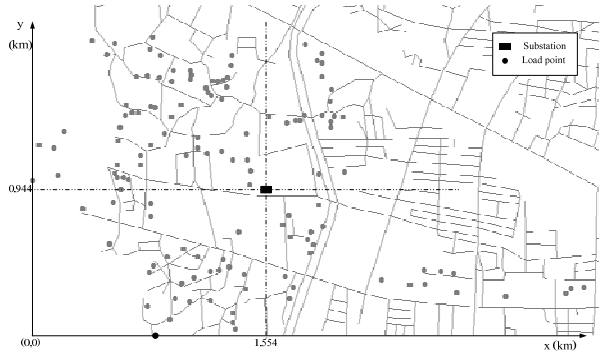

Figure 3. Case study system

Optimal feeder routing will be obtained from this step. If the existing infrastructure is neglected, the main feeder will be connected directly from one load point to another by using the minimum path algorithm.

In case of considering existing infrastructure, we assume that the main feeders should be lined along the existing road. Therefore, the point on the road which is nearest to the defined load point will be considered and use as a candidate for determining the optimal feeder path. The procedure for considering existing road can be described below.

1) The planner firstly defines a maximum allowable length from a load point to an existing road.
2) Distance between a couple of load points and the specified road is considered. If the distance is within the defined value, a lateral line will be connected from that load point to the existing point on the road which is used to be a candidate for determining the main feeder routing.
3) The load points with the distance longer than the defined value will be used to determine the main feeder routing.
4) In case that some load points are connected to very close points on the same road, e.g. within 2 meters, etc.,

they will be set into the same group. In figure 4, there are three load groups.

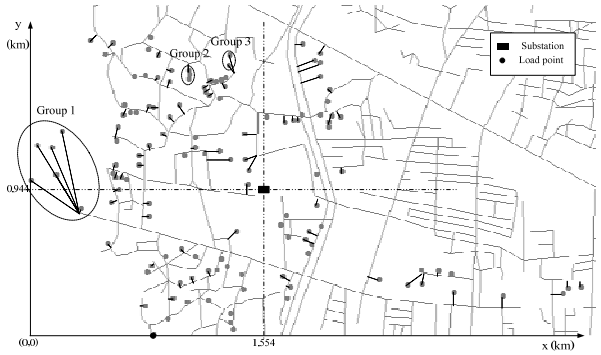

Figure 4. Distance from load points to the nearest road.

5) In each group, all load nodes are connected to each other before being connected to the main feeder using the minimum path algorithm. For example, group1 consists of 6 load points, which are connected to each other using the minimum path algorithm. The result is shown in figure 5. The node which is closest to the specified road is defined as the candidate point of the group.

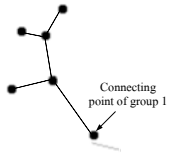

Figure 5. Minimal path in group 1.

In addition each candidate has to strictly comply with the heuristic rules defined below.

Rule 1. If the line has a right of way problem then it is not acceptable.

Rule 2. If the line has high cost passage then it is not acceptable.

Rule 3. If the line pass through an obstacle, i.e. forest, lake, etc., then it is not acceptable.

After using the above process, the optimal feeder routing is determined by using the minimal path algorithm. Then conductor sizes in each branch will be selected as described in the next topic.

B. Selecting Optimal Conductors

Cost function of the conductor is composed of two parts, i.e. *fixed cost* representing capital cost, maintenance and operation (O&M) cost, and *variable cost* representing cost of energy and demand loss. The total cost is obtained by following expression.

$$\tilde{C}_{Total} = C_{fixed} + \tilde{C}_{\text{var}} \cdot L^2 \qquad (2)$$

$$C_{fixed} = \left[\frac{A \cdot i}{[1-(1+i)^{-N}]} + B \right] \times \frac{1}{i}\left[1-(1+i)^{-n}\right] \qquad (3)$$

$$\tilde{C}_{\text{var}} = \left(\frac{8760 \times 10^3 \cdot E \cdot R \cdot L_f}{V^2} \right) \sum_{m=1}^{n} \frac{(1+\tilde{\tau})^{2m}}{(1+i)^m} \qquad (4)$$

where L = Peak Demand flow in conductor (MVA)
A = Investment Cost (Baht)
B = Maintenance & Operation Cost (Baht)
E = Energy Cost of losses (Baht/kWh)
i = Interest rate (%)
L_f = Loss factor, $\left(L_f = 0.3L_d + 0.7L_d^2\right)$
N = Expected life time (years)

An appropriate size of the conductor should be selected in order that the total cost is minimum. Four conductor sizes, of which their details are shown in Table I, are considered.

TABLE I
THE DETAILS OF EACH CONDUCTOR SIZES

Type (mm^2)	Capital Cost (Baths/km)	O & M Cost (Baths/km)	R (Ω/km)	X (Ω/km)
50	102740	1541	0.6895	0.7888
95	131670	1975	0.4005	0.7548
120	168320	2525	0.3158	0.7576
185	241587	3624	0.2250	0.7434

From the cost information in Table I, the fuzzy cost of each conductor size will be obtained by assuming that the loss value of 2 Baht/kWh, 20 years planning period, 30 years life-time, 6% annual interest, and load growth is (4%, 6%, 8%), which is illustrated in figure 6.

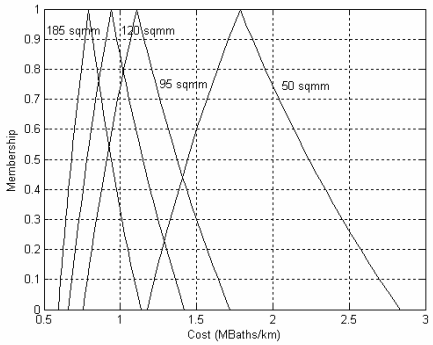

Figure 6. Fuzzy cost of each conductor size at load 2 MW

The fuzzy cost of each conductor size will be compared to find the best option using the center of areas method to convert the fuzzy costs into crisp costs. In figure 6, the 185 sqmm. conductor size is selected because of it provides minimum cost.

Voltage drop is then considered after the above process has been completed. If the voltage drop in the network is within an acceptable limit (5%), the process will be terminated. However, if it violates the limit, one of the following steps must be performed.

- *Adjusting the conductor size*: the conductor in each branch will be adjusted and analyzed.
- *Balancing load in each feeder*: review the load balance in the case of having more than one feeder. If the difference of the aggregated load on each feeder is more than the capacity of lowest load point, the feeder which supplies loads less than other feeders will be forced to connect with more loads, i.e. the nearest load.
- *Adding the number of feeders*: if 1) and 2) have been done and the voltage drop violates the defined limit, the number of feeders should be increased by one more feeder.

This procedure is repeated until the voltage drop is with in the limit.

V. STUDY CASE

The study system is an actual distribution system in Thailand which is shown in figure 3. A 22-kV network is composed of 130 nodes which are divided into two zones. In each zone, a future load growth is differently defined, i.e. (2, 4, 6) % and (1, 3, 5) % respectively. The results of the optimal feeder routing in each case are shown in Table II.

TABLE II
COMPARATIVE RESULTS OF EACH CASE

Case Optimal Routing	Cost of conductor (MBaht)	
	Fuzzy	Expected
I. Ignoring the existing path	(5.268, 6.857, 9.527)	6.946
II. Allowable distance		
- 50 m	(5.625, 7.231, 9.931)	7.322
- 60 m	(5.706, 7.330, 10.059)	7.421
- 70 m	(5.951, 7.660, 10.533)	7.757
- 80 m	(5.880, 7.522, 10.283)	7.615
- 90 m	(5.870, 7.504, 10.251)	7.596
- 100 m	(5.878, 7.511, 10.256)	7.603

From Table II, case I which ignores existing road results in the lowest solution. In case II with the maximum allowable distance from the load point being considered to the existing road of 50 -100 meters is considered. It can be found that the maximum allowable distance of 50 meters provides the lowest cost. The results show that the defined distance does not dictate the conductor cost, however, the geographical characteristics will play an important role in such case.

VI. CONCLUSIONS

The proposed method provides appropriate feeder routing and sizing with consideration of demand uncertainty and existing infrastructure. The future demand uncertainty is considered by representing future load growth with fuzzy model. Moreover the geographic information and heuristic rules are applied in the problem while all technical constraints, i.e., voltage drop, thermal limits are taken into account. This method can be effectively applied in realistic problems, where all the above mentioned constraints are taken into account.

REFERENCES

[1] M. A. Farrag, M. M. El-Metwally, and M. S. El-Bages, "A new model for distribution system planning," *Electrical Power and Energy Systems 21*, pp. 523-531, 1999.

[2] M. Vaziri, K. Tomsovic, and A. Bose, "A directed graph formulation of the multistage distribution expansion problem," *IEEE Trans. PWRD 19*, No. 3, pp. 1335-1341, July 2004.

[3] T. Gonen and I. J. Ramirez-Rosado, "Optimal multi-stage planning of power distribution systems," *IEEE Trans. PWRD 2*, no. 2, pp. 512-519, April 1987.

[4] V. H. Quintana, H. K. Ternraz, and K. W. Hipel, "Two-stage power system distribution planning algorithm," *Proc. IEE*, vol. 140, no. 1, pp. 17-28, January 1993.

[5] J. Partanen, "A modified dynamic programming algorithm for sizing, locating and timing of feeder reinforcements," *IEEE Trans. PWRD 5*, no. 1, pp. 277-283, January 1990.

[6] M. Ponnavaikko, K. S. Prakasa, and S. S. Ventaka, "Distribution system planning through a quadratic mixed integer programming approach," *IEEE Trans. PWRD 2*, no. 4, pp. 1157-1163, October 1987.

[7] I. J. Ramirez-Rozado and T. Gonen, "Pseudodynamic planning for expansion of power distribution systems," *IEEE Trans. on Power Systems*, vol. 6, no. 1, pp. 245-254, February 1991.

[8] M. A. El-Kady, "Computer-aided planning of distribution substation and primary feeder," *IEEE Trans. on Power Apparatus and Systems*, vol. PAS-103, no. 6, pp. 1183-1189, June 1984.

[9] R. Ranjan, B. Venkatesh, and D. Das, "A New Algorithm for Power Distribution System Planning", *Electric Power Systems Research 62*, pp. 55-65, 2002.

[10] C. T. Lin and C. S. George Lee, *Neural Fuzzy Systems: A Neuro-Fuzzy Synergism to intelligent Systems*. New Jersey: Prentice-Hall P T R, 1996.

[11] George, J. KLIR, and Bo Yuan, *Fuzzy Sets and Fuzzy Logic Theory and Applications*. New Jersey: Prentice-Hall, 1995.

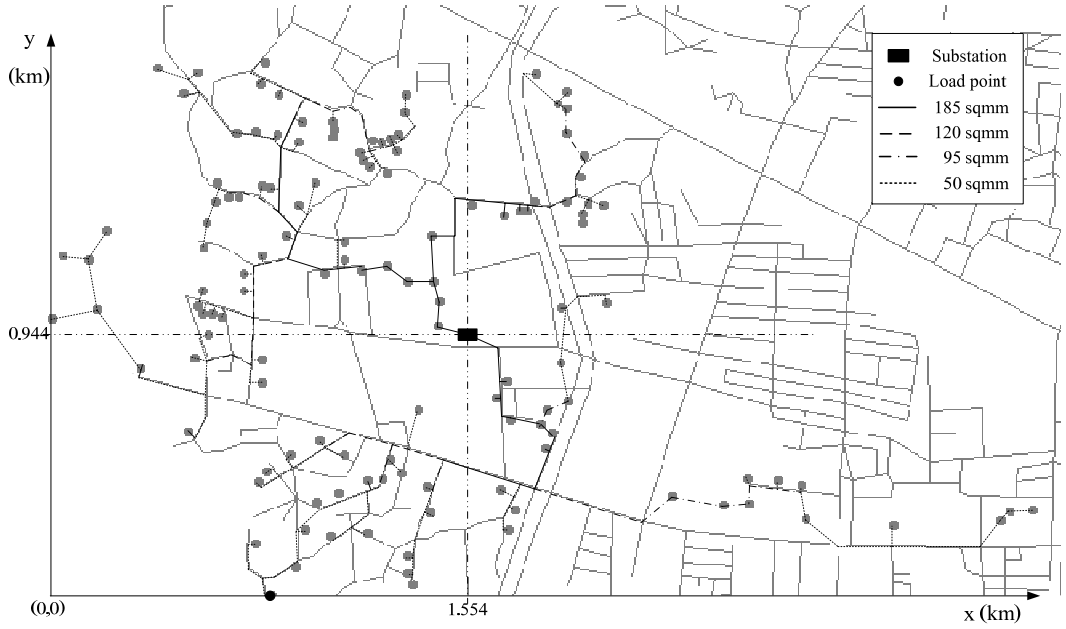

Figure 7. Optimal feeder routing considered the existing way case 50 m.

Optimal capacitor banks placement and N-1 contingency improvement using excels solver: Case of Laos PDR.

S. Hungsasutra, A.Suksri, J. Triyangkulsri and M. Vonglokham
Department of Electrical Engineering, Faculty of Engineering
Khon Kaen University, Khon Kaen, 40002, Thailand
Phone +66-4320-2353, Fax +66-4320-2836, Email: Manothongv@hotmail.com

Abstract- **This paper presents the problems of 115 kV and 22kV transmission network of the Central 1 area in Lao PDR under expected load increase forecasted in the years 2005-2013 and optimizes capacitor banks allocations to maximize the net saving cost resulting from power losses and energy losses reduction. The installation of capacitor banks also reduces equipment's overloading in the system. The problems of the system in the future are shortage of reactive power support, under voltage at various buses, increased transmission losses and the tendency of voltage collapse initiation in the industrial area. This paper studies a simulated system of Lao PDR under a load forecasted in 2005-2013 to determine the susceptibility of the system under increased loading and demonstrates the effectiveness of optimization techniques to allocate capacitor banks at certain buses to mitigate the problems at the minimum investment cost.**

Keywords: Power flow, Voltage profile, capacitor bank, losses reduction

I. INTRODUCTION

At present, power systems are steadily growing and become more complex. Interconnection with neighboring system is necessary for power transfer commitment, reliable and economic operation conditions. Under increased loading, power systems are confronted with many problems such as voltage instability, under voltages and high transmission loss. These problems become a major concern in power system planning and operation.

One of the major problems of the system is insufficient reactive power support under increasing load demand, which results in voltage drop at various buses. Addition capacitor banks must be installed at the candidate buses, in the vicinity of large reactive load, to improve the voltage profile of the system and to reduce the risk of voltage instability problem and to lower transmission loss. The problem concerning adding new capacitor banks to improve the system is referred to as "reactive power allocation problem".

Reactors and capacitor banks have long been utilized as a remedy for voltage problems in power system. Large reactive power surplus or deficiency at light or heavy load conditions, and transmission's equipment overloading, can be overcome with the placement of reactors and capacitor banks at appropriate locations in the network.

A system contingency is defined as a potentially harmful for a steady state operation of an electrical network that can result in possible loss of parts in the network.

This paper addresses to optimize capacitor banks placement by seeking suitable locations and sizes of capacitor banks to maximize net savings and to mitigate the N-1 contingency problem in providing enough electric power of sufficient quality to customers for the proposed system using excel solver.

II. THE LAO PDR SYSTEM

The electricity supply system in Lao PDR comprises four isolating networks as shown in Figure 1. The system is quite small. In the Central-I area, the transmission network encounters many problems such as high system losses, low reliability, and excessive voltage drop during heavy load. Moreover, the active power demands of the Electricity Generating Authority of Thailand (EGAT) forces the surplus active power to of the central I to be less than 20 MW while the central-I has only a 25 MVar capacitor banks [1].

Fig. 1. Service areas in Lao PDR

This paper will focus on the problems of the 115 kV and 22kV transmission network of Central I area in Lao PDR under the forecasted loading.

III. Problem Formulation.

The optimal capacitor placement seeks the optimal locations and sizes of capacitor banks to be placed on the system to maximize the net saving cost resulting from reduction in power losses and energy losses at the minimum investment and installation costs. The optimal capacitor placement problem can be expressed mathematically as follows:

Maximize:

$$J = K_P \Delta P_L + K_E \Delta E_L - C_Q \qquad (1)$$

Subjected to:

1. Power flow analysis. (Equality Constraints).

$$P_{ij} = V_i^2 Y_{ij} \cos(\theta_{ij}) - V_i V_j Y_{ij} \cos(\theta_{ij} - \delta_i + \delta_j)$$
$$Q_{ij} = V_i V_j Y_{ij} \sin(\theta_{ij} - \delta_i + \delta_j) - V_i^2 Y_{ij} \sin(\theta_{ij}) - V_i^2 Y_{sh}$$
$$P_{ji} = V_j^2 Y_{ji} \cos(\theta_{ji}) - V_j V_i Y_{ji} \cos(\theta_{ji} - \delta_j + \delta_i)$$
$$Q_{ji} = V_j V_i Y_{ji} \sin(\theta_{ji} - \delta_j + \delta_i) - V_j^2 Y_{ji} \sin(\theta_{ji}) - V_j^2 Y_{sh}$$
$$P_{Li} - P_{Gi} + \sum_{\substack{j=1 \\ j \neq i}}^{n} Pij = 0 \qquad Q_{Li} - Q_{Gi} - Q_{shi} + \sum_{\substack{j=1 \\ j \neq i}}^{n} Qij = 0$$

2. Inequality Constraints.

$$V_{i\min} \le V_i \le V_{i\max} \qquad V_{j\min} \le V_j \le V_{j\max}$$
$$P_{G_{i\min}} \le P_{G_i} \le P_{G_{i\max}} \qquad Q_{G_{i\min}} \le Q_{G_i} \le Q_{G_{i\max}}$$

The expression for objective function contains several conversion factors to saving in dollars e.g. reduction in power loss(K_P), different in power loss due to the addition of capacitors (ΔP_L); the reduction in energy loss to saving in dollars(K_E); the different in energy loss due to the addition of capacitors(ΔE_L); the total cost of the capacitor banks including installation and maintenance costs(C_Q). The difference in total savings minus the total cost of the capacitor banks yields the net savings dollars resulting from the capacitor placement (1).

The energy loss is calculated by using the load duration curve. It is obtained by subtracting the energy loss after the addition of capacitors from the energy loss of the base case. The reduction in energy loss is multiplied by the factor K_E to obtain its contribution to saving dollars. The reduction in energy loss can be expressed mathematically as follows:

$$\Delta E_L = \Delta P_L \times L_S F \times 8760 \text{ , } L_S F = 0.2LF + 0.8LF^2$$

LF = Total annual energy / (Annual peak load × 8760)

L_sF, LF are loss and annual factors respectively.

IV. Capacitor Banks Allocation by Excel Solver

The processes of optimized capacitor banks allocation with excel solver is shown in Figure 2.

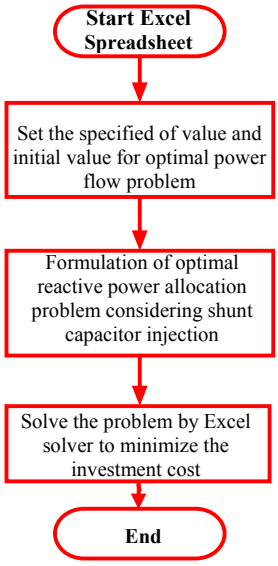

Fig.2. Processes of optimized capacitor bank allocation with excel solver

V. N-1 Contingency Analysis.

The N-1 contingency analysis is a part of reliability assessment of transmission system expansion project. It assesses the ability of the network to provide enough electric power of sufficient quality to connected customers. The process of N-1 contingency analysis using the Excel solver can be illustrated in Figure 3:

Step I. Study the load flow analysis for the existing power system under normal condition

Step II. Analyze the existing power system with increased loading demand requirement following load forecasting results.

Step III. N-1 contingency for all transmission lines in order to find out the weak buses, the transmission losses, and transmission overloading.

Step IV. Solve the problem by indicate weak bus allocate Var source injection and add new transmission's equipment

VI. Results and Discussions.

1. Results of Optimal Capacitors Placement.

The study is carried out on the existing 50-bus ,115/22 kV system of the Central 1 in Lao PDR shown in Figure 4 whose system data are in tables 1,2, and 3. The results of the base case in year 2005 show that the initial MW and MVar losses in the transmission lines are 9.47 MW and 15.58 MVar respectively. The cost of capacitor banks and other associated costs are presented in table 4. The values of the conversion factors K_P and K_E of the objective function were chosen to be $1390/kW per year and $0.031/kWh respectively.

From the simulation results, in case of year 2007 as shown in tables 5 and 6, there are 11 weak buses, three overloading transformers and the system losses is increased from the base case of year 2005. These problems can be improved by additional var sources of 7.5 MVar, 3MVar, 5.5 MVar, 5 MVar, 2.5 MVar and 5MVar at buses 31, 32, 33, 36, 37, 38

respectively and a transformer of 30 MVA must be installed between buses 12(TNL 115kV) and 29(TNL 22kV) to avoid overloading. Similarly, from the year 2008 to 2013 a new var source and transmission's equipment must be installed to improve the voltage profile and avoid transmission's equipment overloading and to reduce transmission losses.

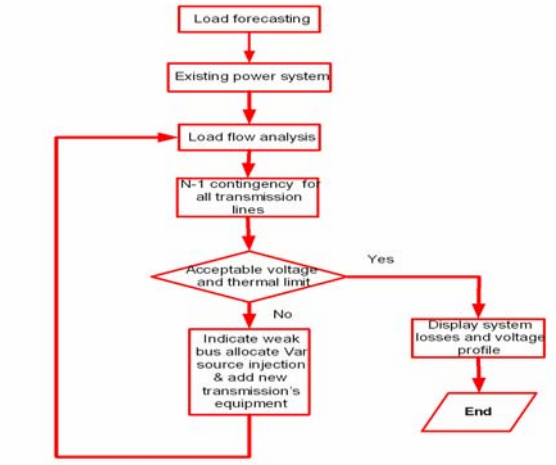

Fig .3. Procedure of N-1 contingency analysis using Excel's solver

TABLE I: EXISTING GENERATOR DATA IN CENTRAL 01 AREA

Bus No	Bus name	Pgen (MW)	Qgen (MVar)	Qmax (MVar)	Qmin (MVar)
01	NNG H1 11kV	15	9	9	-7
02	NNG H2 11 kV	15	0.8	7	-3.8
03	NNG H3 11 kV	40	0.8	26.3	-10
04	NNG H4 11 kV	40	2.2	26.3	-10
05	NNG H5 11 kV	40	9	18.4	-10
06	NLEK H1 11kV	30	4.5	15	-12.8
07	NLEK H2 11 kV	30	4.5	15	-12.8
08	NM3 H1 11 kV	20	1.3	11.7	-6.9
09	NM3 H2 11 kV	20	5.4	11.7	-6.9
47	ND H1 0.4 kV	1	0.7	0.7	-0.5

TABLE II: ENERGY DEMAND CONSUMPTION FORECAST (GWh)

No	Province	2005	2006	2007	2008	2009	2010	2011	2012	2013
1	VTC	693.8	737.8	788.6	838.4	891.3	947.6	949	1000	1054
2	LPB	45.5	51.9	57.8	64	70.5	77.4	81	88	95
3	XYBL	19.8	27.7	36	44.8	54	61.6	80	86	91
4	XKH	3.2	6.7	10.5	14.6	18.8	23.3	39	43	47
5	VTP	164.8	179.9	195.9	211.5	228.5	247.2	263	283	304
6	BLKX	37	44.8	51	55.3	59.6	64.3	89	94	100
7	XSB	3.7	4.4	65.5	321	319	318	316	315	313
	TOTAL	968	1053	1145	1234	1330	1429	1817	1909	2004

TABLE III: SUBSTATIONS PEAK LOAD FORECAST (MW)

Bus No	Bus Name	2005	2006	2007	2008	2009	2010	2011	2012	2013
28	PT	15.0	15.8	16.8	17.7	18.7	19.8	21.0	22.2	23.6
29	TNL	37.8	39.9	42.4	44.8	47.3	49.9	53.0	56.1	59.7
30	KSA	9.6	10.1	10.7	11.3	11.9	12.6	13.4	14.2	15.1
31	NXT	29.3	30.9	32.8	34.6	36.5	38.6	41.0	43.4	46.2
32	TGNE	10.0	10.6	11.2	11.8	12.5	13.2	14.0	14.8	15.8
33	PS	13.2	13.9	14.7	15.5	16.3	17.3	18.6	19.9	21.4
34	BD	0.8	0.8	0.9	0.9	1.0	1.1	1.1	1.2	1.3
35	NH	1.7	1.7	1.8	1.9	2.1	2.2	2.3	2.5	2.7
36	VV	10.4	11.0	11.6	12.2	12.9	13.6	14.7	15.8	16.9
37	XYBL	2.9	3.9	4.9	5.8	6.8	7.5	8.1	8.8	9.4
38	LPB	9.0	9.7	10.3	10.9	11.5	12.2	13.0	13.9	15.0
39	NLEK	0.6	0.7	0.7	0.7	0.8	0.8	0.9	0.9	1.0
40	PKX	6.5	7.0	7.8	8.3	8.9	9.6	10.6	11.3	12.1
41	PSV	1.1	2.0	2.7	3.3	3.9	4.4	5.0	5.5	6.1
42	DNS	-	-	-	-	-	-	-	-	-
43	TTL	15.0	15.8	16.8	17.8	18.7	19.8	21.0	22.3	23.7
44	SSK	20.0	21.1	22.4	23.6	24.9	26.3	28.0	29.6	31.5
45	SPL	-	-	-	-	-	-	-	-	-
50	TLT	7.6	7.9	8.4	8.9	9.4	9.9	10.7	11.4	12.3

TABLE IV:COST DATA FOR CAPACITOR BANK AND EXISTING SIZES

Item	Cost($)
300 kVar bank	$1,500
600 kVar bank	$3,000
900 kVar bank	$4,500
1200 kVar bank	$6,000
5000 kVar bank	$24,941
Installation cost	$1,000
Maintenance cost	$1,000

Bus Name	Capacitor Banks(Mvar)
PHT 22kV	25
TNL 22kV	10
KSA 22kV	10
DNS 22kV	17.5
SPL 22kV	20

TABLE V: IMPROVE VOLTAGE PROFILE BY CAPACITOR INJECTED TO SYSTEM IN THE YEAR 2007 ON BASE 100MVA

Bus No	Bus Name	Before add Cap.Bank Voltage(p.u.)	After added Cap.Bank Voltage(p.u.)	Existing Cap. Banks (MVAR)	New Cap. Banks Installed (MVAR)
21	VV 115kV	0.93800	0.97213	0	0
22	XNG 115kV	0.91806	0.96678	0	0
23	XYBL115kV	0.90876	0.96418	0	0
24	LPB 115kV	0.91273	0.96388	0	0
28	PT 22KV	0.97891	0.98650	25	0
29	TNL 22KV	0.95905	0.96287	20	0
30	KSA 22KV	0.99129	0.98681	10	0
31	NXT 22KV	0.94790	0.96713	0	7.5
32	TGN 22KV	0.93847	0.95712	0	3
33	PS 22KV	0.95133	0.97604	0	5.5
36	VV 22KV	0.91854	0.96514	0	5
37	XYBL 22KV	0.88581	0.95864	0	2.5
38	LPB 22KV	0.89005	0.95928	0	5
42	DNS 22KV	1.00820	1.02041	17.5	0
43	TTL 22KV	0.94395	0.95077	0	0
45	SPL 22KV	0.98257	0.98861	20	0
46	ND 22KV	0.89382	0.96281	0	0
47	ND	0.92582	0.99281	0	0

TABLE VI: TRANSFORMER OVERLOADING IMPROVEMENT IN THE YEAR 2007 BASE ON 100MVA

No	Before Cap. Bank installation					After Cap installation
	From bus	To bus	Rate (MVA)	Loading (MVA)	% Loading	% Loading
1	TNL 115kV	TNL 22kV	30	31.39	104.66	64.64
2	PS 115kV	PS 22kV	16	18.17	113.62	97.32
3	ND 22kV	ND	1.3	1.318	101.42	94.58

Table 7 depicts the results of cost comparison between before and after the implementation of the capacitor banks in the system under increased load demand forecasted in the years 2005-2013.

TABLE VII: COST COMPARESON BETWEEN BEFORE AND AFTER CAPACITOR INSTALLATION ($M)

Year	Before capacitor installation			After capacitor installation			Net revenue
	Total Cost	Loss cost	Cap cost	Total cost	Loss cost	Cap cost	
2005	14.123	14.123	0	13.873	13.772	0.101	0.249
2006	15.490	15.490	0	15.190	15.056	0.134	0.299
2007	16.182	16.182	0	15.510	15.357	0.153	0.672
2008	17.537	17.537	0	16.554	16.366	0.188	0.982
2009	19.113	19.113	0	17.886	17.687	0.199	1.227
2010	22,666	22,666	0	19.110	18.911	0.199	3.555
2011	24.837	24.837	0	21.843	21.490	0.352	2.994
2012	26.792	26.792	0	23.357	23.004	0.352	3.435
2013	36.337	36.337	0	26.124	25.666	0.457	10.213

2. N-1 CONTINGENCY ANALYSIS.

N-1 contingency analysis is an important task for safe operation of electrical energy network .The study of N-1 contingency will be simulated base on 115kV transmission line in year 2007. If the line between bus 10(PHT 115kV) and 11(NNG1 115kV) is tripped out, there will be 14 weak buses, 3 transformers and 1 line overloading. To evade these problems, new var source of 7.5 Mvar, 7.5 MVar, 5.5 MVar, 5 MVar, 2.5 Mvar, 5 Mvar and 15 Mvar must be installed at buses 31, 32, 33, 36, 37, 38, 43 respectively as illustrated in the table 8.

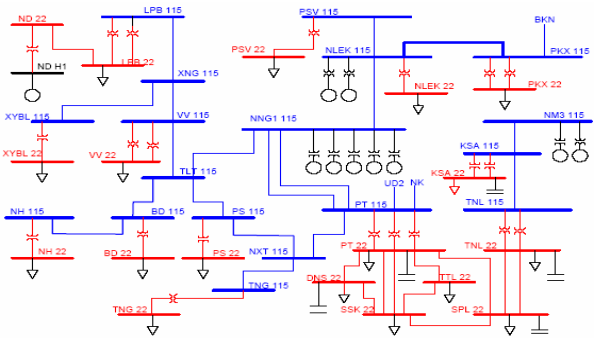

Fig.4. Single line of Central I area Transmission network

TABLE VIII: IMPROVE VOLTAGE PROFILE BY CAPACITOR INJECTED TO SYSTEM WHEN LINE FROM BUS NUMBER 10 TO 11 TRIPPED IN THE YEAR 2007 BASE ON 100MVA

Bus No	Bus Name	Before add Cap.Bank Voltage (p.u.)	After added Cap.Bank Voltage (p.u.)	Existing Cap. Banks (MVAR)	New Cap. Banks Installed (MVAR)
15	NXT 115kV	0.92931	0.96610	0	0
16	TNG 115kV	0.92420	0.96402	0	0
21	VV 115kV	0.93511	0.97152	0	0
22	XNG 115kV	0.91440	0.96613	0	0
23	XYBL115kV	0.90503	0.96352	0	0
24	LPB 115kV	0.90904	0.96323	0	0
28	PT 22KV	0.99672	1.02262	25	0
29	TNL 22KV	0.98034	0.99392	20	0
30	KSA 22KV	1.01048	1.01516	10	0
31	NXT 22KV	0.91897	0.96524	0	7.5
32	TGN 22KV	0.90172	0.96353	0	7.5
33	PS 22KV	0.93863	0.97348	0	5.5
36	VV 22KV	0.91496	0.96450	0	5
37	XYBL 22KV	0.88198	0.95795	0	2.5
38	LPB 22KV	0.88627	0.95859	0	5
42	DNS 22KV	1.00475	1.04094	17.5	0
43	TTL 22KV	0.96203	1.01250	0	15
45	SPL 22KV	1.00186	1.02939	20	0
46	ND 22KV	0.89004	0.96213	0	0
47	ND	0.92216	0.99215	0	0

VI. CONCLUSION

The results of simulation demonstrate that transmission losses, voltage profile and transmission's equipment overloading when load demand increased in the years 2005 - 2013 can be improved by optimize suitable of locations and sizes of capacitor banks to identified weak buses in the Central 1of Lao PDR system in order to maximize the net saving in dollars resulting from reduction in power losses and energy losses, less the investment and installation costs of capacitor banks. In the N-1 contingency analysis, the addition capacitor banks improve the voltage profile of the system. Therefore, transmission equipment's loading can be alleviated.

ACKNOWLEDGMENT

The authors would like to thank advisors for their generous advices for the project and acknowledge the support from The Electricity Generating Authority of Thailand (EGAT).

REFERENCES

[1]. Power development plan 2004-2013, System planning office Development Division, Electric Du Laos.
[2]. John Peschon; Donald W. Bree, JR., and Laszlo P. Hajdu "Optimal Power – Flow Solutions for Power System Planning" Proceedings of the IEEE, VOL. 60, NO, 1 January 1972.
[3]. Hsiao – Dong Chiang, Jin-Cheng Wang, Jainzhong Tong "Optimal Capacitor Placement, Replacement and Control in Large –Scale Unbalanced Distribution Systems: System Modeling and A New Formulation" School of Electrical Engineering Cornell University Ithaca, NY 14853.
[4]. J. L. Bala, Jr., SMIEEE "Optimal capacitor allocation using a distribution – analyzer – recorder" Department of Electrical Engineering Gonzaga University Spokane, WA 99258.
[5]. P.Varilone and G. Carpinelli and A.Abur "Capacitor Placement in Unbalanced Power Systems" 14th PSCC, Sevilla, 24-28 june 2002, Session 03, Paper 2, Page 1.
[6]. H. N. Ng ; M. M. A. Salama and A. Y. Chikhani " Classification of Capacitor Allocation Techniques" IEEE Transactions on power delivery, VOL. 15, No. 1, January 2000.
[7] Maurizo Defanti, Gianpietro, P. Granelli " Optimal Capacitor Placement Using Determistic and Genetic Algorithms" IEEE Transaction on power system, VOL. 15, NO. 3, AUGUST 2000.
[8]. B. O. Philavanh; S. Premrudeepreechacharn and J. Triyangkulsri " Power and Voltage Control of Central 1 Transmission Network in Lao PDR Using Excel's Solver" POWERCON 2004, the Pan Pacific , Singapore November 21-24 , 2004.
[9]. Katia C. Almeida and Roberto Salgado "Optimal Power Flow Solution under Variable Load Condition" IEEE Transactions on Power Systems, VOL. 15, NO. 4, November 2000.
[10]. Miroslav M. Begovic, Branislav Radibratovic, Frank C. Lambert " On multiobjective volt- var optimization in power systems" Proceedings of the 37th Hawaii International Conference on System Sciences- 2004.
[11]. Panagis N. Vovos and Janusz W. Bialek " Optimal placement of reactive power compensation banks for the Maximization of new generation capacity" International Journal of Emerging Electric power Systems Vol. 4[2005], No. 1, Article 1113.
[12]. Dimitrios Semitekos and Nikolaos Avouris "Power system contingency analysis using artificial neural network" Proceedings of the 4th International Workshop on Computer Science and Information Technologies CSIT'2002.

BIOGRAPHIES

Dr. Sumrit Hungsasutra received a bachelor degree in electrical engineering from Khon Kaen university in 1974, MSc. from the university of Manitoba in 1987, Ph.D. from the university of Western Ontario, Canada in 1990. He is currently an assistant professor at the department of electrical engineering Khon Kaen university.

Amnart Suksri graduated with the degree of Master of Science in Electrical Engineering from the University of Manchester, Manchester, UK. At present he is an assistant professor at Khon Kaen University, Khon Kaen, Thailand

Jittipath Triyangkulsri received a B.Eng. in electrical engineering and M.Eng. in electrical and system engineering from Khon Kaen University, Thailand. He is a system dispatcher at Northeastern Dispatching Center, Electricity Generating Authority of Thailand (EGAT).

Manothong VONGLOKHAM received a Bachelor's degree of electrical engineering at Lardkrabang University, Thailand in 1999. He is presently working at IT department in Electrice Du Laos (EDL) and studying Master of electrical engineering at Khon Kaen University.

Voltage Sag Compensation Capability by Parallel Type Compensator with Series Inductor

Sumate Naetiladdanon
Department of Electrical Engineering
King Mongkut's University of Technology Thonburi
126 Pracha Utit Rd. Bangmod, Toongkru, Bangkok 10140 Thailand

***Abstract*- In this paper, the voltage sag compensation capability by parallel type compensator with series inductor is presented. The parallel type compensator injects the current into the system so that the voltage across the series inductor can instantaneously compensate the voltage at the load. The three types of current injection schemes are described and analyzed. The voltage sag compensation capability by parallel type compensator with series inductor is explained and analyzed for each scheme. Simulation results confirmed that voltage sag compensation capability is the function of series inductor and compensator capacity.**

I. INTRODUCTION

Voltage sags are considered as the most dominant and unavoidable power quality problem affecting both utilities and industrial consumers, especially in the term of high costs from lost productivity and downtime. The most effective way to mitigate for voltage sag at the customer level is to apply a voltage sag mitigation equipment at the customer site. Different solutions are currently available for the voltage sag mitigation [1]-[2], where a power electronic converter-based compensator is recognized as an effective mitigating device for its fast compensation capability.

Since voltage sags generally only occur a few times each year at any particular location, a voltage sag compensating device will generally spend most of its time in standby mode. It would be beneficial if the mitigating device can compensate for load as well as voltage sags. The load compensation by the series compensator is not preferable because it will increase the loss for keeping the dc bus voltage constant. The parallel compensator with a static switch can be used for load compensation during normal operation, and compensate a voltage sag during the voltage sag event [3]. However, the compensator must supply load at 100% and the delay from opening the static switch is occurred. The fast voltage sag compensation by parallel type compensator without using the static switch has been presented recently [4]-[6]. The voltage sag compensation is based on injecting the active and reactive power from the parallel type compensator.

This paper shows three different current injection schemes of voltage sag compensation by parallel type compensator with series inductor. The voltage sag compensation capability for these schemes is described. Steady state performances are shown based on simulation results with the various sizes of series inductor and compensator capacity.

II. VOLTAGE SAG COMPENSATION PRINCIPLE

The parallel type compensator with series inductor consists of a voltage source converter (VSC) with an energy storage device in parallel with the load and the inductor in series with the supply voltage, as shown in Fig. 1. A transformer could be used to connect the output of voltage-source converter to the system in parallel. A small capacitor is present on the dc side of the converter where the capacitor voltage is kept constant, by exchanging energy with the energy storage reservoir.

The converter acts as a controllable current source connected in parallel with the load. The parallel compensator can instantaneously compensate voltage sags by regulating the load voltage using the injected current from the converter and the voltage across series inductor bridges the sag. The magnitude of the converter's output ac voltage (i.e. load voltage) is equal to the magnitude of the pre-sag load voltage. The relation of load, line current and injected current can be expressed by

$$\dot{i}_{\mathrm{L}} = \dot{i}_{\mathrm{T}} + \dot{i}_{\mathrm{C}} . \tag{1}$$

And the relation of supply, load and series inductor voltage can be expressed by

$$\dot{v}_{\mathrm{T}} = \dot{v}_{\mathrm{L}} + \dot{v}_{\mathrm{LS}} . \tag{2}$$

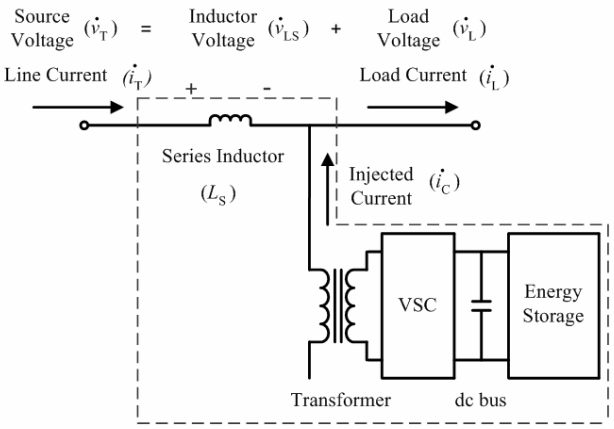

Figure 1. Parallel type compensator with series inductor.

III. CURRENT INJECTION SCHEMES

There are three current injection schemes for voltage sag compensation with different purposes as follows.

A. Phase-invariant current injection scheme

The purpose of this scheme is to protect load voltage from both magnitude and phase disturbances of the supply. The output voltage from the compensator, which is the voltage across the load, will be the same as the pre-sag load voltage ($\dot{V}_{\mathrm{L-pre}}$). The injected current ($\dot{I}_{\mathrm{C}}$) equals to the difference of the load current ($\dot{I}_{\mathrm{L}}$), which equals the pre-sag load current ($\dot{I}_{\mathrm{L-pre}}$), and the during-sag supply current ($\dot{I}_{\mathrm{T}}$) and it can be derived as

$$\left.\begin{aligned} \dot{I}_{\mathrm{L}} &= \dot{I}_{\mathrm{L-pre}} \\ \dot{I}_{\mathrm{C}} &= \dot{I}_{\mathrm{L}} - \dot{I}_{\mathrm{T}} = \dot{I}_{\mathrm{L}} - \frac{\dot{V}_{\mathrm{T}} - \dot{V}_{\mathrm{L}}}{j\omega L_{\mathrm{S}}} \end{aligned}\right\} \tag{3}$$

or

$$I_{\mathrm{C}} e^{j\alpha} = I_{\mathrm{L}} e^{j\varphi} - I_{\mathrm{T}} e^{j\beta} = I_{\mathrm{L}} e^{j\varphi} - \frac{V_{\mathrm{T}} e^{j\theta} - V_{\mathrm{L}} e^{j0}}{\omega L_{\mathrm{S}} e^{j\pi/2}} \tag{4}$$

where φ is the load power factor angle, β is the line current phase angle, α is the injected current phase angle, and θ is the source voltage phase angle by using the pre-sag load voltage as a reference ($\dot{V}_{\mathrm{L}} = \dot{V}_{\mathrm{L-pre}} = V_{\mathrm{L}} e^{j0}$). Fig. 2 illustrates the phasor diagram of the phase-invariant current injection scheme.

B. Minimum energy current injection scheme

The purpose of this scheme is to minimize active power supplied to the load by the compensator. From phase-invariant injection scheme, the injected active power can be expressed by

$$P_{\mathrm{C}} = 3V_{\mathrm{L}}\left(I_{\mathrm{L}}\cos\varphi - I_{\mathrm{T}}\cos(\beta-\gamma)\right) = 3V_{\mathrm{L}}\left(I_{\mathrm{L}}\cos\varphi - \frac{V_{\mathrm{T}}}{\omega L_{\mathrm{S}}}\sin(\theta-\gamma)\right) \tag{5}$$

where γ is the phase angle of the load voltage command, which equals zero in phase-invariant scheme. Note that the sign of γ is negative, if γ is measured by clockwise direction as shown in Fig. 3. The minimum injected active power can be achieved if the difference of θ and γ equals $\pi/2$. However, this could result as the active power absorption from the system in the case of $I_{\mathrm{L}}\cos\varphi \le V_{\mathrm{T}}/(\omega L_{\mathrm{S}})$. Thus, the condition of minimum active power injection can be accomplished by setting γ in (5) to the following angle γ_1 as

$$\gamma_1 = \begin{cases} \theta - \dfrac{\pi}{2} & \text{, when } I_{\mathrm{L}}\cos\varphi > \dfrac{V_{\mathrm{T}}}{\omega L_{\mathrm{S}}} \\ \theta - \sin^{-1}\left(\dfrac{I_{\mathrm{L}}\cos(\varphi)\times\omega L_{\mathrm{S}}}{V_{\mathrm{T}}}\right) & \text{, when } I_{\mathrm{L}}\cos\varphi \le \dfrac{V_{\mathrm{T}}}{\omega L_{\mathrm{S}}} \end{cases} . \tag{6}$$

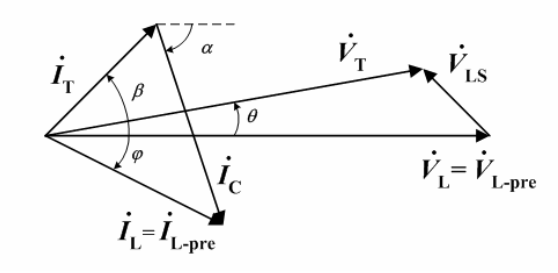

Figure 2. Phasor diagram of phase-invariant injection scheme.

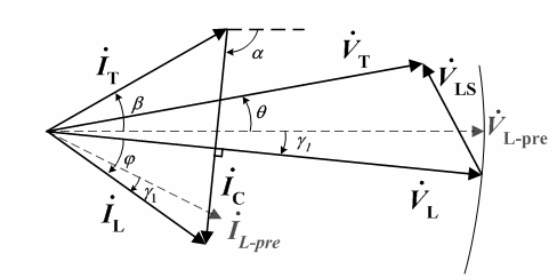

Figure 3. Phasor diagram of minimum energy injection scheme.

Fig. 3 illustrates the phasor diagram of the minimum energy current injection scheme. In a specific case where $I_{\mathrm{L}}\cos\varphi \le V_{\mathrm{T}}/(\omega L_{\mathrm{S}})$, the injected active power can be reduced to zero by setting the injected current phasor to be perpendicular with the load voltage phasor. Because the incoming line must supply active power to the load as much as possible, the incoming line current magnitude will be increased by using this scheme. Instant change of injected current from this scheme might cause the sudden phase angle shift or discontinuity of the load current and voltage during the start-up of injection.

C. Minimum apparent power current injection scheme

The purpose of this scheme is to minimize apparent power supplied to the load by the compensator (i.e. to minimize the compensator's rating). The injected current magnitude can be solved by (3), and the condition of minimum apparent power injection is shown in (7).

$$\frac{\partial I_{\mathrm{C}}}{\partial \gamma} = 0 . \tag{7}$$

Solving equation (7) yields the angle γ as γ_2 which equals by

$$\gamma_2 = \tan^{-1}\left(\frac{Z_{\mathrm{L}}\sin\theta + \omega L_{\mathrm{S}}(\sin\theta\sin\varphi - \cos\theta\cos\varphi)}{Z_{\mathrm{L}}\cos\theta + \omega L_{\mathrm{S}}(\cos\theta\sin\varphi + \sin\theta\cos\varphi)}\right) \tag{8}$$

where Z_{L} is the magnitude of the load impedance. Fig. 4 illustrates the phasor diagram of the minimum apparent power current injection scheme. Instant change of injected current from this scheme might also cause the sudden phase angle shift or discontinuity of the load current and voltage during the start-up of injection.

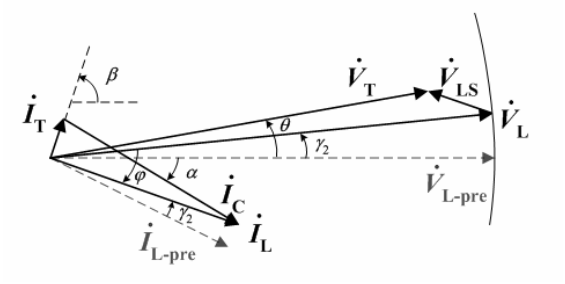

Figure 4. Phasor diagram of minimum apparent power injection scheme

IV. VOLTAGE SAG COMPENSATION CAPABILITY

During the voltage sag compensation, the voltage across series inductor bridges the sag voltage and it can be expressed by

$$\dot{V}_{LS} = j\omega L_S \times \left(\frac{P_T - jQ_T}{\dot{V}_L} \right) = -\frac{\omega L_S Q_T}{\dot{V}_L} - j\frac{\omega L_S P_T}{\dot{V}_L} \tag{9}$$

where P_T is the incoming line active power and Q_T is the incoming line reactive power. The relation of the load, incoming line and injected active power and reactive power can be expressed by

$$\left.\begin{aligned} P_L &= P_T + P_C \\ Q_L &= Q_T + Q_C \end{aligned}\right\}. \tag{10}$$

If $\dot{V}_L = V$+j0 is taken as the reference phasor, the magnitude of the supply voltage during voltage sag compensation can be expressed by

$$\dot{V}_{LS} = j\omega L_S \times \left(\frac{P_T - jQ_T}{\dot{V}_L} \right) = -\frac{\omega L_S Q_T}{\dot{V}_L} - j\frac{\omega L_S P_T}{\dot{V}_L}. \tag{11}$$

If Z_L is the magnitude of load impedance, then $V = Z_L$ x I_L where I_L is the load current magnitude. The supply voltage magnitude during voltage sag compensation can be rewritten as

$$V_T = \sqrt{\left[V - \frac{\omega L_S}{Z_L} \times \frac{Q_T}{S_L} \times V \right]^2 + \left[\frac{\omega L_S}{Z_L} \times \frac{P_T}{S_L} \times V \right]^2} \tag{12}$$

or

$$v = \sqrt{[1 - x \times q]^2 + [x \times p]^2} \tag{13}$$

where S_L is the load apparent power, v is the ratio of incoming line voltage magnitude with the load voltage magnitude, x is the ratio of series inductor's reactance with the load impedance, q is the ratio of incoming line reactive power with the load apparent power and p is the ratio of incoming line active power with the load apparent power. By controlling the incoming line active and reactive power through the injected active and reactive power of the compensator, the compensator can have various current injection schemes to compensate the same voltage sag. Thus, the voltage sag compensation capability of the system is the function of the size of series inductor and the capacity of compensator. Although the large series inductor increases the voltage sag compensation, it causes a poor power factor and voltage drop problem during the normal operation. The power availability at load is also reduced due to the increase of the line impedance as well. The voltage sag compensation capability due to the capacity of compensator can be described according to the current injection schemes as follows.

A. Phase-invariant current injection scheme

The injected active power has been expressed by (5) and the injected reactive power from the converter can be expressed by (14) implying that the voltage sag compensation capability is inversely proportional to the source voltage phase angle θ.

$$Q_C = 3V_L \left(I_L \sin\varphi + \frac{V_L - V_T \cos\theta}{\omega L_S} \right) \tag{14}$$

B. Minimum energy current injection scheme

In a specific case where $I_L \cos\varphi \le V_T/(\omega L_S)$, the injected active power can be zero (P_C = 0). The voltage sag compensation capability in (13) can be rewritten as (15) implying that the voltage sag compensation capability is proportional to the compensator capacity.

$$v = \sqrt{[1 - x \times q]^2 + [x \times \cos\varphi]^2} \tag{15}$$

C. Minimum apparent power current injection scheme

As the compensator capacity can be minimized, the voltage sag compensation capability is maximized by this injection scheme. The condition of maximum voltage compensation is shown in (16). Solving (16) yields the required reactive power and voltage sag compensation capability as shown in (17) and (18) where s_C is the ratio of compensator capacity with the load capacity.

$$\frac{\partial v}{\partial q} = 0 \tag{16}$$

$$q = \frac{s_c}{\sqrt{1 + x^2}} \tag{17}$$

$$v = \sqrt{[1 - xq]^2 + \left[x\left(\cos\varphi - \sqrt{s_C^2 - (\sin\varphi - q)^2} \right) \right]^2} \tag{18}$$

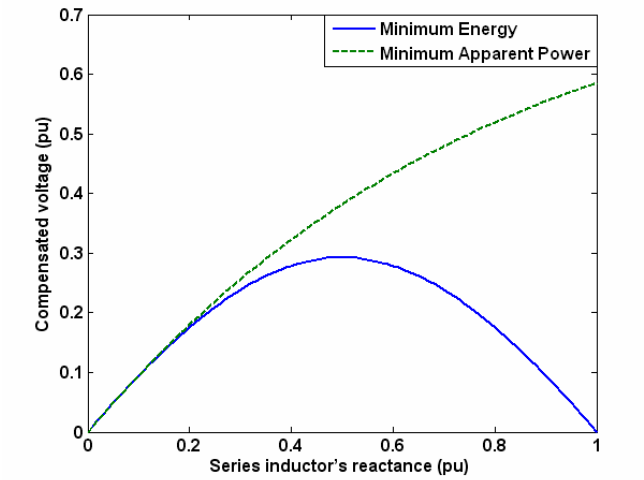

Figure 4. Compensation capability as function of series inductor.

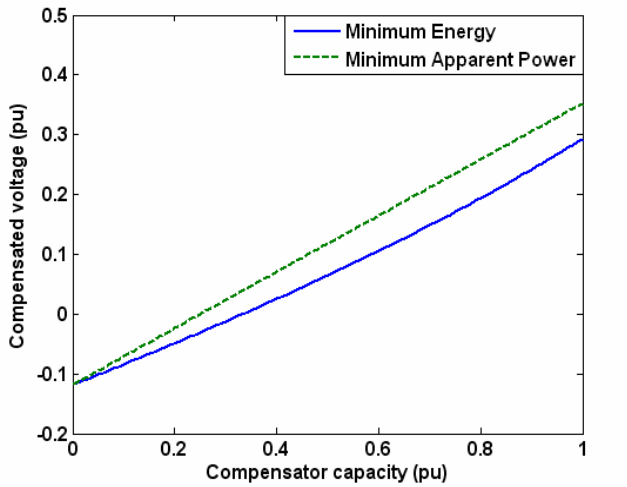

Figure 5. Compensation capability as function of compensator capacity.

V. Simulation Results

The system in Fig. 1 is used to demonstrate the steady state performance of voltage sag compensation capability. It is considered that the pre-sag load voltage magnitude is 1.0 pu and the system load is 1.0 pu with unity power factor, then the incoming line reactive power is the result of the compensator's injected reactive power. Note that the phase-invariant current injection scheme is not considered due to the variation of source voltage phase angle θ.

A. With Fixed Compensator Capacity

The capacity of compensator is considered to be the same as the load capacity, that is S_C = 1.0 pu. The voltage sag compensation capability as the function of series inductor size is shown in Fig. 4 for the minimum energy and minimum apparent power injection scheme. Using the minimum apparent power injection scheme, the compensated voltage can be increased as the series inductor size increases. For the minimum energy injection scheme, the compensated voltage reached its maximum at the series inductor's reactance = 0.5 pu. The reason of that is the injected current phasor must be perpendicular with the load voltage and it is required more reactive power as the series inductor increases beyond the maximum point.

B. With Fixed Series Inductor Size

The series inductor's reactance is considered to be half of the load impedance, that is x = 0.5 pu. The voltage sag compensation capability as the function of compensator capacity is shown in Fig. 5 for the minimum energy and minimum apparent power injection scheme. Using both injection schemes, the compensated voltage can be increased as the compensator capacity increases where the minimum apparent power scheme give a better compensation performance. The negative compensated voltage occurred at the small compensator capacity because the size of series inductor is too big for the compensation.

VI. Conclusion

The steady state performance of the parallel type compensator with a series inductor has been studied in this paper. The voltage sag compensation is based on injecting reactive power in order to regulate the load voltage, and consequently the voltage across series inductor compensates the sag voltage. Three current injection schemes for different purposes are discussed. Simulation results indicated that the voltage sag compensation capability is determined by the size of series inductor, compensator capacity and current injection scheme as well.

References

[1] Math H.J. Bollen, *Understanding Power Quality Problems, Voltage Sags and Interruptions*, IEEE Press Series on Power Engineering, The Institute of Electrical and Electronics Engineers, Inc., New York, 2000.

[2] A. Sannino, M.G. Miller, M.H.J. Bollen, "Overview of voltage sag mitigation," *Proceeding of Power Engineering Society Winter Meeting*, vol. 4, pp. 2872 - 2878, 2000.

[3] J. Lamoree, Le Tang, C. DeWinkel, P. Vinett, "Description of a Micro-SMES system for protection of critical customer facilities," *IEEE Transactions on Power Delivery*, vol. 9, Issue 2, pp. 984 - 991, 1994.

[4] M.H. Haque, "Compensation of distribution system voltage sag by DVR and D-STATCOM," *Proceeding of Power Tech Conference*, vol. 1, 2001.

[5] J. Xiaohua et al., "A 0.3 MJ SMES magnet of a voltage sag compensation system," *IEEE Transactions on Applied Superconductivity*, vol. 14, Issue 2, pp. 717 - 720, 2004.

[6] S. Naetiladdanon, Y. Miura, T.Ise, "Current Injection Control Scheme of Voltage Sag Compensation by Parallel Type Compensator with Series Inductor," *Trans. IEE of Japan,* vol.126-D, No.10, pp. 1382 - 1391, 2006.

Application of Nanoporous Silicon for Visible Light Photodetector

N. ATIWONGSANGTHONG, S. NIEMCHAROEN, K. SATO, W. TITIROONGRUANG
Electronics Research Center, Faculty of Engineering
King Mongkut's Institute of Technology Ladkrabang
Bangkok 10520, Thailand, E-mail: kanarin@kmitl.ac.th

***Abstract*- In this research, we present the study on the application of nanoporous silicon for optoelectronic device which called nanoporous silicon visible light photodetector in this paper. This device was fabricated on nanoporous silicon layer which was formed by electrochemical etching of silicon wafer in hydrofluoric acid solution under various anodization condition such as the resistivity of silicon wafer, current density, concentration of hydrofluoric acid solution and anodization time. The experiment will study on photoresponse and responsetime of nanoporous silicon visible light photodetector which was fabricated on various porosity of nanoporous silicon layer, the photoresponse of device will expand toward the short-wavelength and bandwidth of spectum response will cover visible light. In addition, it is found that responsetime of device increases.**

I. INTRODUCTION

Nanoporous silicon is not a new material. It was observed the first time about its photoluminescence by Canham in 1990 [1]. Although first porous silicon layer had been observed by Ulrich in 1956 [2] and later by Turner but only Canham report about room temperature luminescence beginning significant interest in this material [3]. Later, more detail studies of this film were done by researcher around the world. Because lower cost of a product, possibility of improved performance and optical properties caused that the investigations of luminescence and electrical properties have been made in many laboratories. After the first few years, not only multicolour photoluminescence, but also visible electroluminescence had been reported. Today, the focus of the research has been reported to formatiom, structure and many application of nanoporous silicon such as photovoltaic devices, and light emitting diodes. In this paper, we present results on the study of nanoporous silicon for visible light photodetector.

II. MATERIAL AND METHODS

The nanoporous silicon layer were formed by electrochemical etching of p-type silicon wafers with a resistivity of 10 Ω-cm in hydrofluoric acid solution concentration of 48% for etch times of 20 min which will show in Fig.1. Between anodization using a constant anodic current density of 10, 20 and 40 mA/cm^2. After the electrochemical attack, the samples were rinsed in de-ionized water and blown dry with nitrogen gas. Next step, porosity measurement of nanoporous silicon layer with gravimetric method [4] which calculated using (1) and show in Fig.2.

$$\text{Porosity } \% = \frac{m_1 - m_2}{m_1 - m_3} x100 \qquad (1)$$

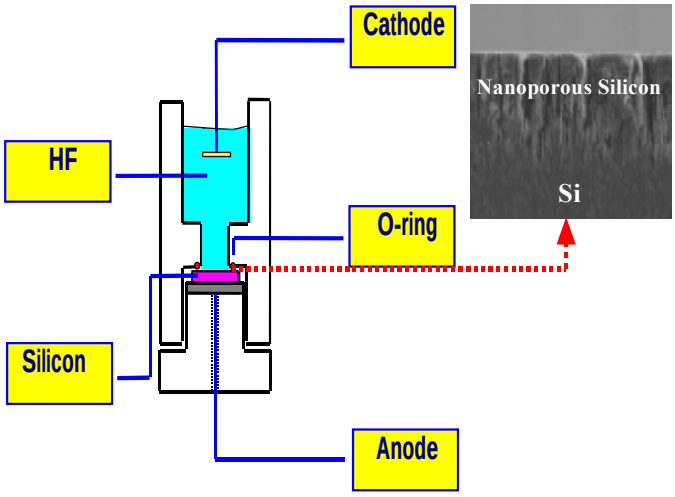

Figure 1. Schematic of electrochemical etching cell for anodization process.

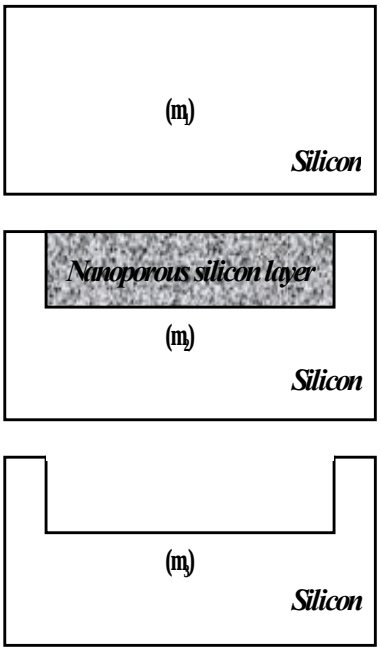

Figure 2. Cross section schematic of silicon wefer in porosity measurement of nanoporous silicon layer with gravimetric method.

Al Schottky contacts were evaporated on top of the nanoporous silicon layer by evaporator in an area of 7x7 mm^2. Show in Fig.3.

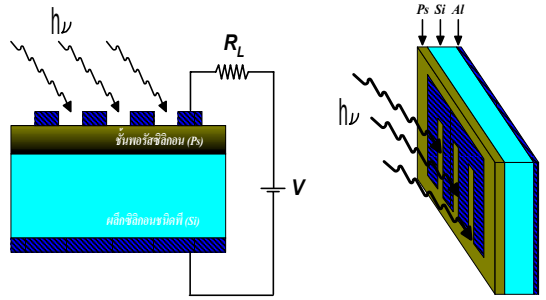

(a)

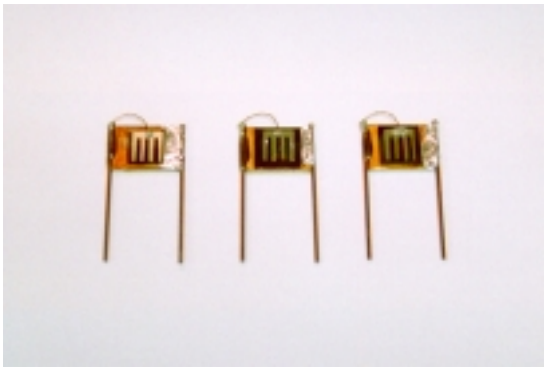

(b)

Figure 3. (a) Schematic and (b) picture of nanoporous silicon visible light photodetector.

Then devices were reverse-biased voltage and illuminated with a 150w halogen lamp for photoresponse measurement at various wavelength in a rang 400-1200 nm by monochomator. Show in Fig.4.

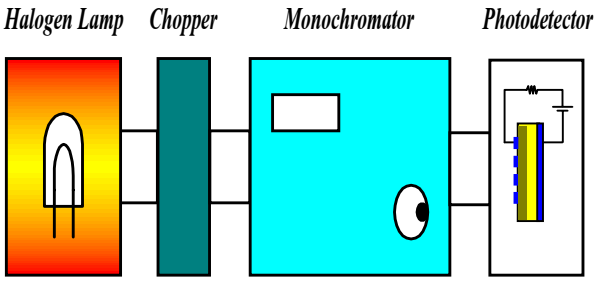

Figure 4. Cross section schematic of silicon wefer in porosity measurement of nanoporous silicon layer with gravimetric method.

After measurement photoresponse, devices were illuminated with red light input from laser diode (LD) at frequency 100 kHz for responsetime measurement of nanoporous silicon photodetector.

III. RESULTS AND DISCUSSION

From the results of porosity measurement of nanoporous silicon layer with gravimetric method. It is found that increasing anodic current density of 10, 20 and 40 mA/cm^2 between anodization have effect to increasing porosity of nanoporous silicon layer with 65%, 70% and 85%, which will show in Fig.5. and Fig.6. respectively.

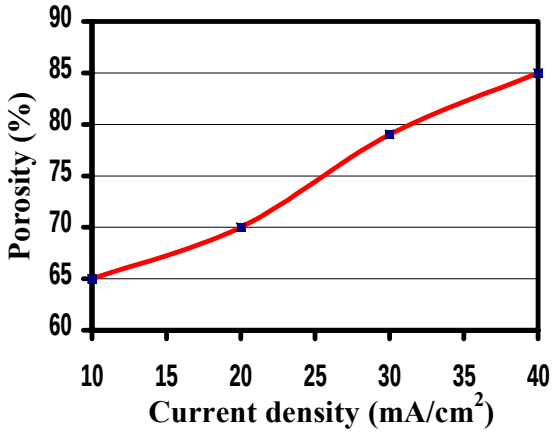

Figure 5. Show the results of porosity measurement with gravimetric method of nanoporous silicon layer which was formed by electrochemical etching under various anodic current density.

(a) 65% porosity

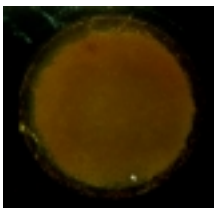

(b) 70% porosity

(c) 85% porosity

Figure 6. Top view of nanoporous silicon were formed by electrochemical etching under anodic current density of (a) 10 mA/cm^2 (b) 20 mA/cm^2 and (c) 40 mA/cm^2 respectively.

And from the results of photoresponse measurement of nanoporous silicon photodetector were reverse-biased voltage and illuminated with a 150w halogen lamp at various wavelength in a rang 400-1200 nm by monochomator which will shown in Fig.7.

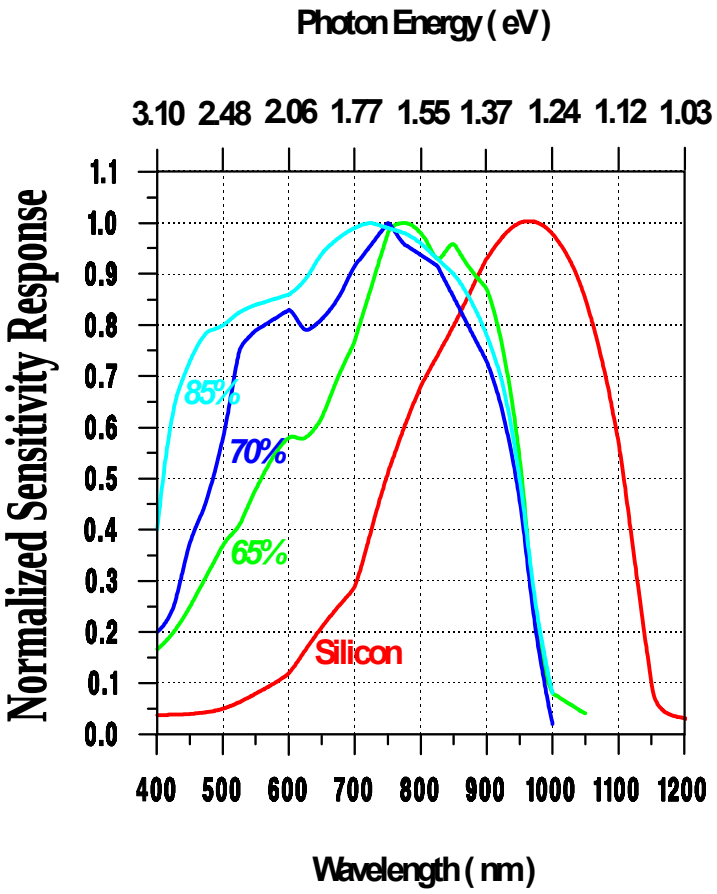

Figure 7. Photoresponse of nanoporous silicon photodetector which was fabricated on nanoporous silicon layer with 65%, 70% and 85% porosity at various wavelength compare with silicon photodiode

It is found that when devices fabricated on higher porosity nanoporous silicon layer, the photoresponse of device will expand toward the short-wavelength and bandwidth of spectrum will cover visible light in a rang 500 to 625 nm. The explanation of this effect, when structure of nanoscale porous silicon decreases which occurs from increasing porosity of nanoporous silicon, the band gab of nanoporous silicon has increase owing to the quantum size effect [5].

From the results of responsetime measurement of nanoporous silicon photodetector which was fabricated on nanoporous silicon layer with 65%, 70% and 85% porosity and it was illuminated with red light input from laser diode (LD) at frequency 100 kHz will show in Fig.8. It is found that when devices fabricated on higher porosity nanoporous silicon layer, the response time of device increases with 2.0 μs, 1.4 μs and 0.8 μs, respectively. This results occurs from increasing of electrical field in space-charge region between Al Schottky contacts and nanoporous silicon layer.

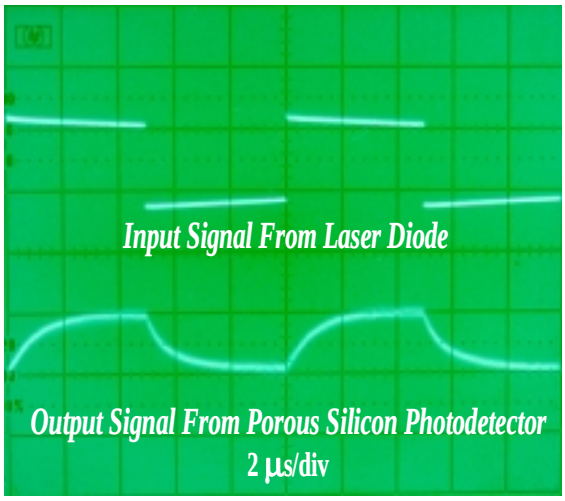

(a)

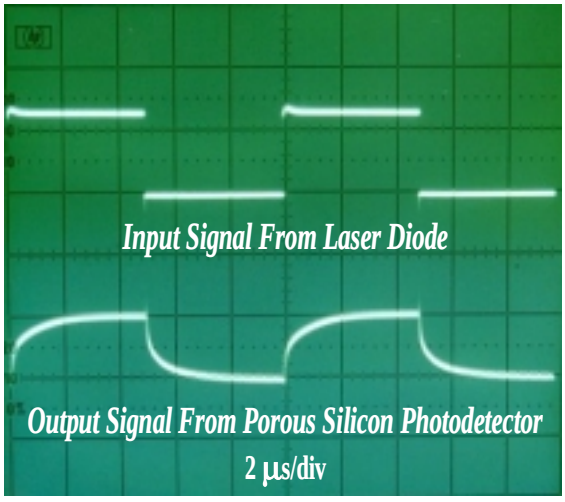

(b)

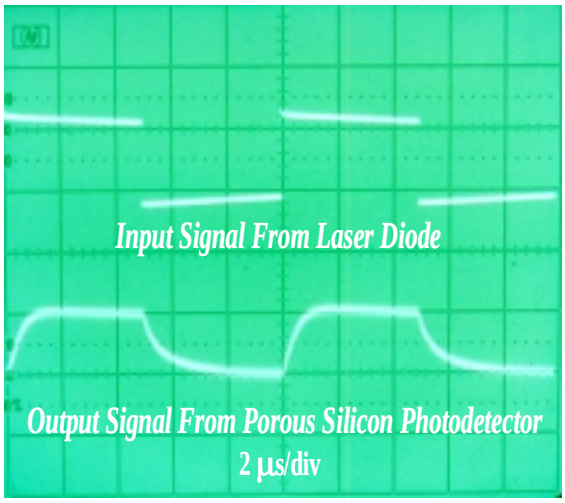

(c)

Figure 8. Responsetime of nanoporous silicon photodetector at fabricated on porous silicon layer with (a) 65% porosity (b) 70% porosity and (c) 85% porosity.

IV. CONCLUSIONS

In this research, we found that the nanoporous silicon layer can fabricate to optoelectronic device such as the nanoporous silicon visible light photodetector. From the results of experiment, the nanoporous silicon photodetector can response to visible light and have bandwidth spectrum cover in a rang 500 to 625 nm. Different with general silicon photodetector that reponse to infrared wavelength. This results occurs from effect of quantum size effect. And it is found that when nanoporous silicon visible light photodetector was fabricated on higher porosity nanoporous silicon layer, the responsetime of device will increases.

References

[1] L.T. Canham, "Silicon quantum wire array fabrication by electrochemical and chemical dissolution of wafers", Appl.Phys.Lett. 57, Issue 10, pp.1046-1048, 1990.

[2] A. Uhlir, "Electrochemical Etching of Silicon in HF Acid", Tech.J., Vol.35, pp.333, 1956.

[3] U. Gosele. and V. Lehmann, Material Chemistry and Physics 40, 253-259, 1995.

[4] R. Herino, G Bomchi, K. Barla and C. Bertrand, "Porosity and pore size distribution of porous silicon", J. Electrochem Soc : Solid State and Tecnology, Vol. 14, No. 8, pp. 1994-2000, 1987.

[5] V. Lehmann and U. Gosele. "Porous silicon formation: Aquantum wire effect", Appl. Phys. Letts., Vol. 58, No. 8, pp. 856-858, 1991.

Computational Molecular Modeling and Simulation of Functionalized Carbon Nanotubes

Chatchawal Wongchoosuk[1], Sriprajak Krongsuk[2], Teerakiat Kerdcharoen[1,3]
[1]Department of Physics and Center of Nanoscience and Nanotechnology, Faculty of Science, Mahidol University, Bangkok 10400
[2]Department of Physics, Faculty of Science, Khon Kaen University, Khon Kaen 40002
[3]Networked Laboratory of Nanodevice Engineering, National Nanotechnology Center, Pathumthani 12120

***Abstract*-In this paper, we have investigated various properties of tubule-end functionalized carbon nanotubes using various computational modeling and simulation techniques. Geometrical and electronic properties of chemically modified carbon nanotubes were studied using semi-empirical method based on AM1 Hamiltonian. The movement of water molecule into the center of model tubes was investigated using first principles density functional theory (DFT) calculation and molecular dynamics (MD) simulation. Hydrogen atom (-H), hydroxyl (-OH) and carboxyl (-COOH) functional groups are chemically adsorbed at the open-end of the nanotubes. The results show that the average C-C bond lengths of all tubes are similar about 1.42 Å and the three model tubes exhibit characteristic of semiconducting material. The movement of water molecule into the tip-modified tubes is easier than that of the pristine tube. The tip-modification can improve hydrophilic behavior of pristine and does not alter electronic and mechanical properties of the carbon nanotube. These findings are in agreement with previous experimental works.**

I. INTRODUCTION

Carbon nanotubes (CNT) were first discovered in 1991 by Iijima [1]. After that discovery, research on CNT reaches a critical mass in many areas of physics and chemistry. Because of its remarkable electronic and mechanical properties, CNT is one of the best candidate materials for use in various industrial applications [2]. However, some properties of the pristine tubes limit their use in many applications. For examples, the pristine tube is not soluble in water or common solvent [3] which hinders chemical approaches and preparation of nanocomposite materials. To overcome this obstacle, several research groups try to add surfactants or hydrophilic groups (i.e., hydroxyl (OH), carboxyl (COOH) and aliphatic amines) to the open ends of the tubes [4,5]. After tip-modification these nanotubes are able to disperse in the common solvents as well. However, the geometrical and electronic properties of the CNT and behavior of tubes in water after tip-modification are yet clearly understood due to difficulty in obtaining experimental data at atomic level. Therefore, computational molecular modeling and simulation approaches have emerged as important tools that can be used to predict atomic structure, geometrical and electronic properties, binding energies, tubes-water interactions, etc. In this paper, we employed quantum mechanics (QM) calculations and molecular dynamics (MD) simulation to study the electronic and structural properties, and the movement of water molecule into the model tubes. The built systems for this study are investigated elaborately and systematically.

II. METHODOLOGY

In this study, we consider the single-walled (9,0) carbon nanotubes with chemically modified edges. The ends of the tubes are capped with hydrogen atoms (-H), hydroxyl (-OH) and carboxyl (-COOH) functional groups, respectively, as shown in Fig. 1. Diameter of the tubes is about 7.0 Å. First of all, we investigate the electronic and structural properties of each tube using semi-empirical quantum calculations based on AM1 Hamiltonian [6] and DFT calculations [7] based on 6-31G* basis set. The AM1 method is good enough for the geometry optimization of the nanotubes [8] and B3LYP/6-31G* level was found to be much more reliable for electronic structures [9].

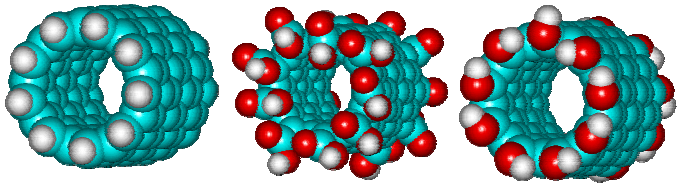

(a) (b) (c)

Figure 1. Geometrical structures of (a) H-SWNT (b) OH-SWNT and (C) COOH-SWNT after optimization by AM1 method

From Fig. 1, these model SWNTs were simulated in the aqueous solution using molecular dynamics technique for studying the water-tubes interaction. The simulations of the model systems have been performed at the constant volume and temperature in a rectangular box containing one SWNT and 871 water molecules. The SWNT is represented by a flexible model based on OPLS force field [10] as well as the SPC water model [11]. The SWNT-water and water-water interactions are represented by a sum of the Lennard-Jones and Coulomb potentials

$$V_{LJ}(r_{ij}) = 4\varepsilon_{ij}\left(\left[\frac{\sigma_{ij}}{r_{ij}}\right]^{12} - \left[\frac{\sigma_{ij}}{r_{ij}}\right]^{6}\right) + \frac{q_i q_j}{r_{ij}} \quad (1)$$

Here, ε and σ are Lennard-Jones parameters, and q_i and q_j represent the charges on atom i and atom j, respectively.

In addition, the results obtained from the MD simulation were verified with the results obtained from ab initio self-consistent field (SCF) calculation also.

III. Results and Discussions

The structural and electronic properties of three different kinds of tip-modified carbon nanotubes are summarized in Table 1. From the Table 1, it indicates that the average C-C bond lengths of all tubes are nearly the same and close to the C-C bond length in the perfect nanotube with sp^2 hybridization (1.42 Å). It means that adsorption of molecules at the tips of the tube does not bring about any structural distortion of the tube whereas adsorption of molecules at the sidewall of tube strongly affect the structure of tube [12], ~1.52 Å of C-C bond length. For electronic properties, energy gaps of the tubes were calculated by using the highest occupied molecular orbital (HOMO) and the lowest unoccupied molecular orbital (LUMO).

$$E_{gap} = LUMO - HOMO \quad (2)$$

The COOH-SWNT has the smallest energy gap while the H-SWNT has the highest one. Such functional groups affect weakly on the energy gap. They help increase an electrical conductivity of the pristine tube. However, if we assume that the energy gap obtained from HOMO and LUMO calculations is equivalent to the band gap concept in solid-state physics, these results would suggest that the SWNTs (9,0) with finite size, which may have or have no modification at the tip of tubes, are small-gap semiconducting tube in which it will become metallic and have no energy gap when the length is long enough [13].

TABLE I
THE AVERAGE C-C BOND-LENGTHS AS OBTAIND FROM GEOMETRY OPTIMIZATION USING AM1 METHOD AND ENERGY GAP OF H-,OH- AND COOH-SWNTS AS CALCULATED FROM B3LYP/6-31G*

System	C-C (Å)	E_{gap}(eV)
H-SWNT	1.417	1.133
OH-SWNT	1.424	1.082
COOH-SWNT	1.424	0.823

After studying fundamental properties of model tubes using QM calculation, the tubes are simulated in water environment containing in the periodic boundary of rectangular box. From this simulation, we calculate radial distribution function (RDF), $g_{x-y}(r)$ and coordination numbers, $n_{x-y}(r)$, from O of the water to center of mass (COM) of tubes, as shown in Fig. 2. The RDF plot of both OH- and COOH-SWNTs is rather similar. It shows one sharp peak of each tube, positioned at 1.89 Å of OH-SWNT and 1.83 Å of COOH-SWNT whereas the RDF plot of H-SWNT does not appear the sharp peak. It indicates that water molecules move close to the center of the tip-modified tube more than the pristine tube. The functionalized groups may ease the entering of water into the hydrophobic tube's interior, in agreement with previous experimental works [4,5].

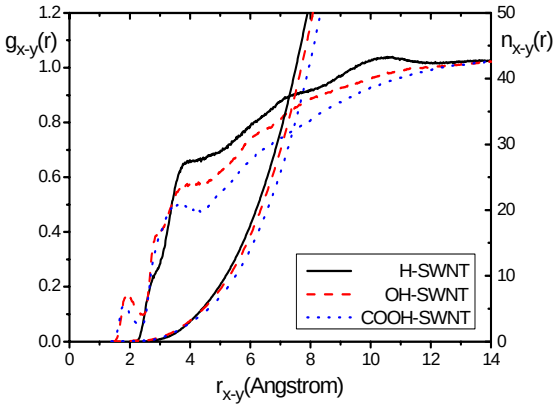

Figure 2. The radial distribution functions, $g_{x-y}(r)$, and corresponding running integration numbers, $n_{x-y}(r)$, from O of the water to COM of H-SWNT, OH-SWNT and COOH-SWNT

To confirm the MD simulation result, interaction between a water molecule and each model tube is calculated by using B3LYP/6-31g* method. For an illustration, the definition of trajectory for a tube interacting with a water molecule is presented in Figure 3. The oxygen atom of a water molecule is moved along the tube axis z, and the hydrogen atoms are symmetrically placed giving the water molecule a fixed orientation.

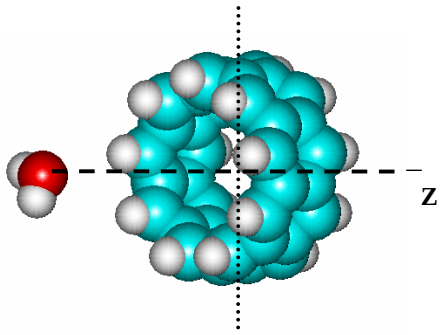

Figure 3. Definition of trajectory for SWNT interacting with a water molecule of fixed orientation at various positions along the tube axis.

In order to evaluate the interactions between these model tubes and the water molecule, the interaction energies are evaluated via (3)

$$E_{int} = E(X\text{-}SWNT/water) - E(X\text{-}SWNT) - E(water) \quad (3)$$

Where E(X-SWNT/water) is the total energy for the model SWNTs plus water molecule (where X= H, OH and COOH), E(X-SWNT) is the total energy of the model tubes and

E(water) is the total energy of the water molecule. In all the analyzed systems, the starting molecules are optimized by using AM1 Method.

Figure 4 shows the interaction energies varying the distances from the O of water molecule to the centers of mass of model tubes. One can be observed that the H-SWNT has a high potential barrier in the range of 2-4 Å from the center of tube and beyond 2 Å, the potential energy barrier is decreasing. It means that water molecule will not move into the center of the tube because the potential barrier height occurs at the tip of tube. In other word, if a water molecule occupy in a tube, it can not go out from the tube's interior. For OH-SWNT, the potential barrier decreases when the water molecule move close to COM of the tube while it experiences a deep potential well when entering the COOH-SWNT from the right side in the given. It indicates that water molecule may enter into the OH-SWNT easier than the COOH-SWNT and the water molecule tend to occupy the position ~ 2-3 Å from COM of COOH-SWNT. The results are in good agreement with the RDF analysis obtained MD simulation above.

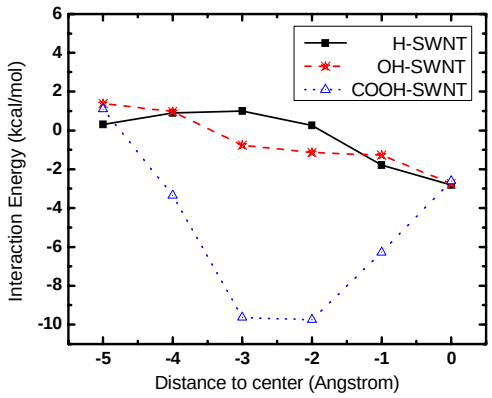

Figure 4. Potential energy surface for the SWNTs interacting with a water molecule of fixed orienta-tion at various positions along the z-tube axis

IV. Conclusions

We have studied the structural and electronic properties in atomically level of chemically modified SWNTs (OH-SWNT and COOH-SWNT) and the pristine SWNT (H-SWNT). Semi-empirical quantum mechanics based on AM1 Hamiltonian and density functional theory (DFT) calculations are employed for such investigations. After modification at the tips of tubes, the C-C bond lengths of all tubes are not different and electrical conductivity of tube increases a little bit. All three model tubes show semiconducting characteristic. For simulations of model tubes in water, the results indicate that water molecules are preferable to move close to the COM of the tip-modified tubes in comparing with the pristine tube. After modification, the water molecules can occupy the hydrophobic tube's interior corresponding to results obtained from the quantum mechanic calculation.

Acknowledgment

This project is financially supported under the "Design and Development of Odor Sensor" project of the National Electronic and Computer Technology Center (NECTEC).

References

[1] S. Iijima, "Helical microtubules of graphitic carbon", *Nature (London)* 354, 1991, pp. 56-58.

[2] M. Terrones, "Science and technology of the twenty-first century: Synthesis, Properties, and Applications of Carbon Nanotubes", *Annu. Rev. Mater. Res. 33*,2003, pp 419–501.

[3] W. A. Scrivens et al., "Potent Solvents for C_{60} and Their Utility for the Rapid Acquisition of ^{13} C NMR Data for Fullerenes", *J. Chem. Soc., Chem. Commun.* 1993, pp 1207-1209.

[4] J.E. Huang, X.H. Li, J.C. Xu and H.L. Li, "Well-dispersed single-walled carbon nanotube/polyaniline composite films", *Carbon,* 41(14), 2003, pp 2731–2736.

[5] D. Tasis, N. Tagmatarchis, V Georgakilas and M.Prato, "Soluble carbon nanotubes", *Chem Eur J* , 9, 2003, pp 4000–4008.

[6] M.J.S. Dewar, E.G. Zoebish, E.F. Healy and J.J.P. Stewart, "AM1: A New General Purpose Quantum Mechanical Molecular Model", *Journal of the American Chemical Society,* 107, 1985, 3902-3909.

[7] Y. Kumeda, Y. Fukuhiro, T. Taketsugu, and T. Hiramo, "Theoretical Study of Nanotube Growth in Terms of Frontier Density Distribution", *Chemical Physics Letters*, 333, 2001, 29-35.

[8] C. Wongchoosuk, A. Udomvech and T. Kerdcharoen, "Open-ended Functionalized Single-walled Carbon Nanotubes: A Quantum Mechanics Study of The Effects of Tubule Length and Functional Groups", *Laos Journal on Applied Science*, Vol.1 No.1 2006, pp 75-81.

[9] W. Koch, and M.C. Holthausen, "A Chemist,s Guide to Density Functional Theory", second ed. Wiley-VCH, Weinheim, 2001.

[10] W.L. Jorgensen, J. Tirado-Rives, "The OPLS [optimized potentials for liquid simulations] potential functions for proteins, energy minimizations for crystals of cyclic peptides and crambin", *J. Am. Chem. Soc.* 110, 1988, pp 1657-1666.

[11] O. Teleman, B. Jonsson, and S. Engstrom, "A molecular dynamics simulation of a water model with intramolecular degrees of freedom", *Mol. Phys.,* 60 (1), 1987, pp 193-203.

[12] H. park, J. Zhao and J.P. Lu, "Distinct properties of single-wall carbon nanotubes with monovalent sidewall additions", *Nanotechnology,* 16, 2005, pp 635-638.

[13] M.S. Dresselhaus, G. Dresselhaus, and R. Saito, "C60 related tubules", *Solid State Communications*, 84, 1992, pp 201-205.

The Electronic and Energetic Properties of Linearly Fused Single-Walled Carbon Nanotubes by Pentagon-Heptagon Pair Defects

Md.Shafiqzzaman[1], Anurak Udomvech[1,2], Teerakiat Kerdcharoen[1]
[1] Department of Physics and Center of Nanoscience and Nanotechnology, Faculty of Science, Mahidol University, Rama 6 Road, Bangkok 10400, Thailand
[2] Department of Physics, Faculty of Science, Thaksin University, Songkhla 90000, Thailand

***Abstract*-The electronic and energetic properties of topological defect of single-walled carbon nanotube junctions (SWCNTJ) have been investigated based on the semi-empirical AM1 Hamiltonian calculation. The geometries of junctions occur at the interface between two zigzag tubes having different helicities and diameters. One segment of the fused nanotube is kept constant by using the (5,0) nanotube, while varying another segment from (6,0) to (10,0). Practically, the junctions are constructed by insertion of pentagon-heptagon pair as a defect into the perfect hexagonal lattice. The study shows that junction geometries of SWCNT are dependent on the variation of diameter and length of carbon nanotubes. The HOMO and LUMO levels exhibited the contradiction of even-odd "quantum size" oscillation of nanotube chiralities, although tubule length increased. The occurrence of decreasing energy gap depends on the relationship between tubes index and their length. The energy of formation linearly changes with the variation in nanotubes diameter but not with the tubule length. The (5,0)//(10,0) SWCNTJ have more stability than other SWCNTJ. The outcome of this study would be of help for collection of information in the field of molecular electronic devices made of carbon nanotubes.**

I. INTRODUCTION

At present, carbon nanotubes [1] are one of the most fascinating materials in the field of nanodevices. The experimental observations have shown that the defects structures are possibly form on the hexagonal network structure of carbon nanotubes [2]. These defects can be typically classified into three groups: topological (introduction of ring types other than hexagons), rehybridization (ability of carbon atom to hybridize between sp^2 and sp^3), and incomplete bonding defects (vacancies, dislocations, etc.).

Two nanotubes fused by topological defect group results in tubular junction having different electronic properties [3] that can be useful for construction of various molecular electronic devices. It was predicted theoretically that two carbon nanotubes with different diameter and helicities can be connected by insertion of a pentagon and heptagon rings on the hexagonal lattice of carbon nanotubes [4,5]. The junction nanotubes can be of two types, i.e. positive curvature and negative curvature, thus depending on the pentagon and heptagon on the sidewall of SWCNTs. Therefore, a single walled carbon nanotube (SWCNT) can be either metallic or semiconducting, depending on its chirality and diameter [6].

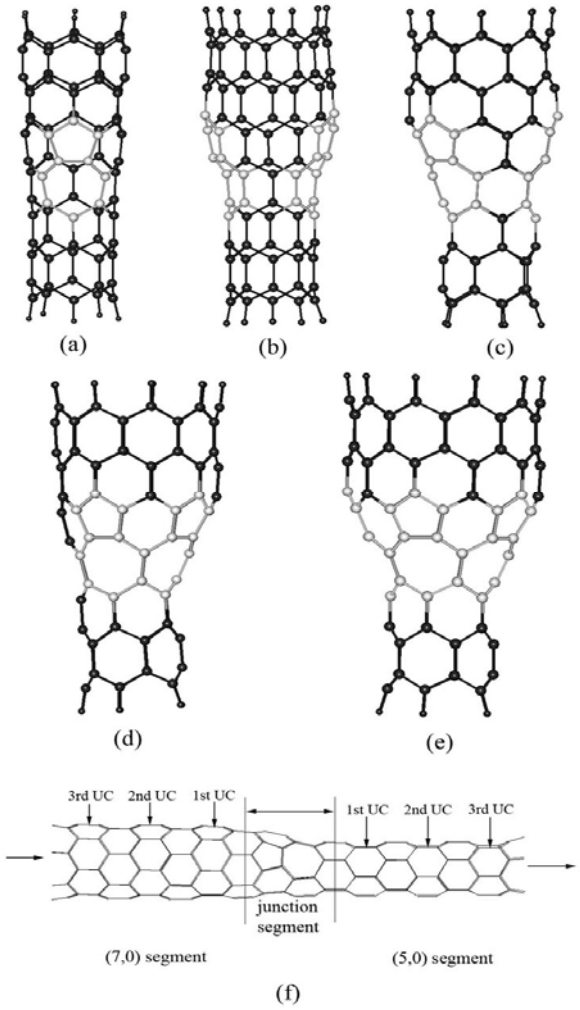

Figure 1. The SWCNTJ models represent the fusing two single walled carbon nanotubes, (a) (5,0)//(6,0) 1UC, (b) (5,0)//(7,0) 1UC, (c) (5,0)//(8,0) 1UC, (d) (5,0)//(9,0) 1UC, and (e) (5,0)//(10,0) 1UC. The variation of tubule length is represent in (f)

Hence, the combination of two segments of SWCNT having different diameters and helicities will lead to different electronic properties of nanotube junction.

In this work, the single-walled carbon nanotube junctions (SWCNTJ) were constructed by fusing two nanotube segments having different diameters (i.e. zigzag (5,0)//(*m*,0)). The different junction geometries of two different diameter SWCNTs are modeled to study the change in electronic structure depending on the variation of tubes diameter and their length by using semi-empirical quantum mechanical calculation. The energies of formation are also investigated the stability of SWCNTJ.

II. Computational Procedures

Two carbon nanotubes with different chiralities and diameters can be fused by inserting a pentagon-heptagon (5/7) pair defect. Different combination of (5/7) pair defects result in different types of junction. In this work, single-walled carbon nanotube junctions (SWCNTJ) are constructed by joining two zigzag (5,0)/(*m*,0) nanotube segments; where *m* is an integer and varies from 6 to 10 (see Fig.1). In this case, the (5,0) segment is kept constant. Creation of various junction structures can be done by inserting various numbers of a (5/7) pair defects into a perfect cylindrical hexagonal lattice around the circumference of SWCNTs. The SWCNTJ of a pentagon and heptagon (5-7) point defect is considered [7]. The junction geometry has constructed by using the "ConTub" web based software [8,9].

The geometries of all SWCNT structure are initially optimized by molecular mechanics (MM3) method. These structures have been used as basis geometries for further optimization by higher-level techniques. The optimized geometries, energetics, and electronic structure of the entire structural variables were obtained from semi-empirical AM1-RHF method. The formation energy of the SWCNTJ is defined as $H_n = -E_{(SWCNTJ)} + E_{(5,0)} + E_{(m,0)} + E_{junction}$, where $E_{(SWCNTJ)}$ is the total energy of SWCNTJ, $E_{(5,0)}$ and $E_{(m,0)}$ are the total energy of each nanotubes segment, and $E_{junction}$ is total energy of junction segment (mean topological (5/7) pair defects structure) and the SWCNT, respectively. All computations were performed by using GAMESS package [10].

III. Results and Discussion

A. Electronic Properties

In the study, the electronic structure versus two parameters, i.e. tube diameter and length, was considered. The HOMO-LUMO energy level was plotted with respect to the varying diameter of (m,0) segments as well as the tube length is increased (see Fig. 2). There is the changing of the numbers of a (5/7) pair defects around the tube circumference. In the diameter variation, it was found that the HOMO and LUMO levels exhibit the contradictory even-odd "quantum size" oscillation, even though the tubule length is increased. For instance, the (5,0)//(7,0) and (5,0)//(9,0) junctions have lower HOMO-LUMO energy than the (5,0)//(6,0), (5,0)//(8,0) and (5,0)//(10,0) pairs. These effects would be useful for design of electronic devices. This is the primary information that should be taken into account when nanoscale devices that made from SWCNTJ are to be constructed. In Fig. 3, the energy gap demonstrates that both tubule diameter and length parameters

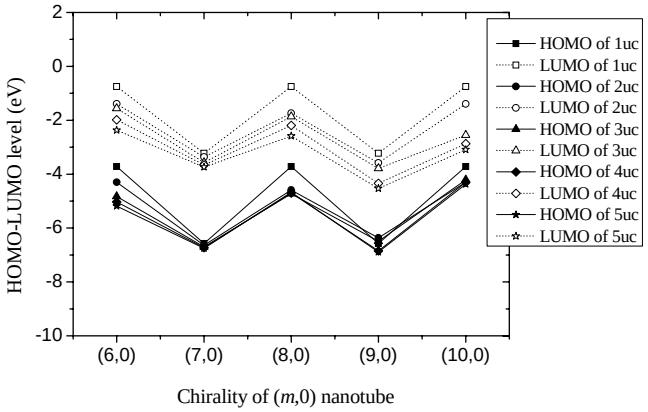

Figure 2. Demonstration of HOMO-LUMO energy levels versus the variation of zigzag nanotube indices.

contribute to the difference in energy gap of SWCNTJ. For instances, the consideration of diameter changed with respect to 1UC (see Fig. 1), it does not show any change in energy gaps. In contrast, the increasing tubule length has a consequence of decreasing energy gap for all tube indices. Especially, the (5,0)//(10,0) junction shows the energy gap decreasing from 2.9 eV to 1.3 eV of 1UC to 5UC, respectively. For other SWCNTJs, even if the tubule length is increased to 5UC, the energy gap is still larger than the (5,0)//(10,0) junction.

The energy gap respects to increasing numbers of unit cell (UC) was plotted in Fig. 4. It exhibits that the energy gap of the (5,0)//(10,0) junction at 5UC is less than the other configurations in conjuction with Fig 3. It must be noted that our prediction is rather rough because the semi-empirical AM1 RHF technique neglects the repulsive interactions and overestimates the frontier energy gap. However, the geometrical parameters obtained from such low-cost method can be transferred to further studies using more accurate methods. Consequently, these results would assist in checking

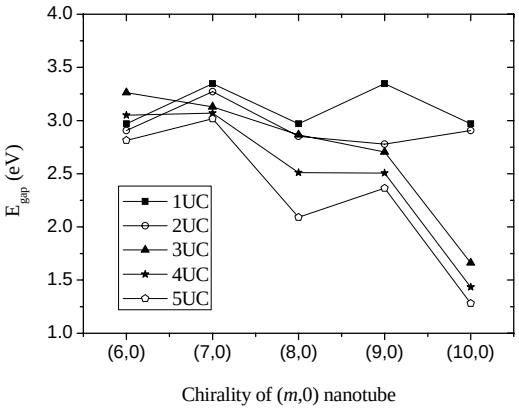

Figure 3. The energy gap (E_{gap}) of SWCNTJ plotted versus tube indices as well as tubule length.

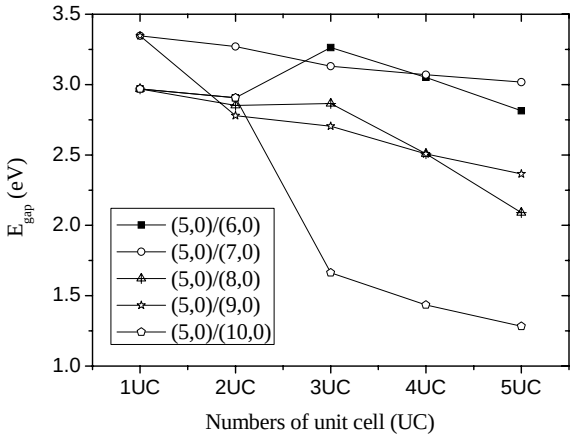

Figure 4. The energy gap (E_{gap}) of various SWCNTJ plotted respect to tubule length.

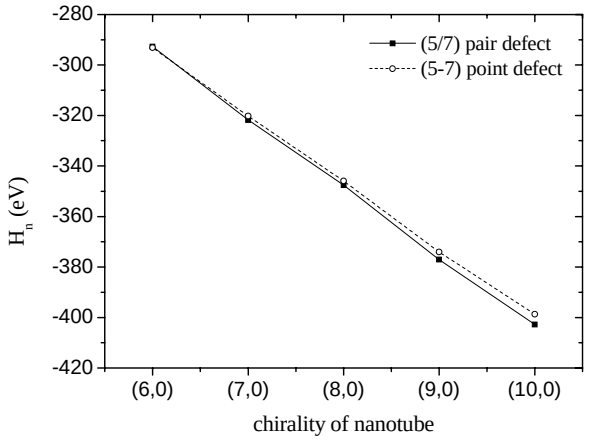

Figure 6. The energy of formation (H_n) of two types SWCNTJ 3UC respects to chiralities of nanotube.

the possibility of making moletronic devices, e.g. molecular rectifier, from the SWCNTJ structures.

B. Formation of SWCNTJ

The energy of formation of our (5/7) pair defect of SWCNTJ structures were plotted in comparison with a (5-7) point defect of SWCNTJ as shown in Fig. 6. A (5-7) point defect junction is shown in Fig 5. It is composed of separated pentagon and heptagon rings on the hexagonal network of

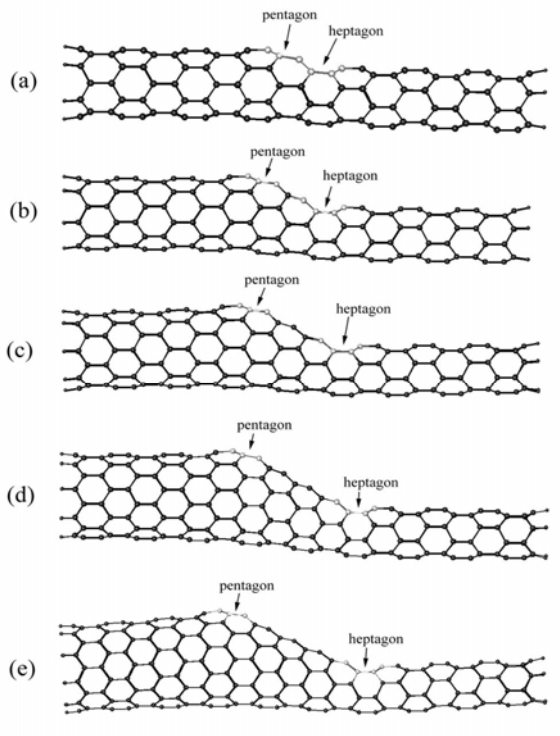

Figure 5. The representation of a (5-7) point defects of SWCNTJ 3UC structures. The models follow (a) (5,0)//(6,0), (b) (5,0)//(7,0), (c) (5,0)//(8,0), (d) (5,0)//(9,0), and (e) (5,0)//(10,0), respectively.

SWCNT that also make two nanotube segments to be connected. The pristine SWCNT of structures follow the same indices of a (5/7) pair defect of 3UC SWCNTJ structures.

The energy of formation as a function of the tube's chiralities reveal that the (5,0)//(10,0) structure is more stable than other ones. The energy of formation for both pair defect and point defect junctions are almost the same, for instances, the pair defect and point defect (5,0)//(10,0) junctions have the energy of formation of 402 eV and 398 eV, respectively. From the variations of tube diameter, i.e. (6, 0) (or ~ 4.75 Å) to (10, 0) (or ~7.92 Å), the energy of formation is decreasing linearly as the diameters of SWCNT are increasing. However, the energy of formation as a function of tubule length is not linearly dependent on the tubule length.

IV. Conclusion

In summary, the results from AM1-RHF calculations have shown that the electronic structure, i.e. HOMO-LUMO energy and energy gap, depends on variation of diameter and length of carbon nanotubes. The HOMO and LUMO levels exhibited the contradiction of even-odd "quantum size" oscillation of nanotube chiralities, although the tubule length is increased. The energy gap that implies metallic or semi-conducting behavior depends on correlation between the tubes indices and tubule length. The energy of formation linearly changes with the variation of nanotubes diameter but not with the tubule length. The (5,0)//(10,0) SWCNTJ have more stable than other SWCNTJ. The outcome of this study would be of help for collection of information in the field of molecular electronic devices made of carbon nanotubes.

Acknowledgment

This project is financially supported by the National Synchrotron Research Center (GRANT1-2548/PS02).

References

[1] S. Iijima, "Helical microtubules of graphitic carbon," *Nature*, vol. 354, pp 56-58, November 1991.

[2] T.W. Ebbesen and T. Takada, "Topological and SP^3 defect structures in nanotubes," *Carbon*, vol. 33, pp.973-978, February 1995.
[3] Z. Yao, H.W.Ch. Postma, L. Balents, and C. Dekker, "Carbon nanotube intramolecular junctions," *Nature*, vol. 402, pp. 273-276, November 1999.
[4] M. Meyyeppan, *Carbon Nanotubes Science and Applications*, CRC Press LLC: Florida, 2005, pp. 54-58.
[5] C. Garau, A. Frotera, D. Quiñonero, A. Costa, P. Ballester, and P.M. Deya, "Structural and energytic features of single-walled carbon nanotubes junctions: a theoretical ab initio study," *Chem. Phys*., vol. 303, pp. 265-270, June 2004.
[6] R. Saito, G. Dresselhaus and M.S. Dresselhaus, *Physical Properties of Carbon Nanotubes*, Imperial College: London, 1999, pp. 59-72.
[7] M. Ouyang, J.-L. Huang, C.L. Cheung, and C.M. Lieber, "Atomically Resolved Single-Walled Carbon Nanotube Intramolecular Junctions," *Science*, vol. 291, pp. 97-100, January 2001
[8] S. Melchor and J.A. Dobado, "CoNTub: An Algorithm for Connecting Two Arbitrary Carbon Nanotubes," *J. Chem. Inf. Comput. Sci.*, vol.44, pp. 1639-1646, April 2004.
[9] Web address: http://www.ugr.es/~gmdm/java/contub/contub.html.
[10] M.W. Schmidt, K.K. Baldridge, J.A. Boatz, S.T. Elbert, M.S. Gordon, J.H. Jensen, S. Koseki, N. Matsunaga, K.A. Nguyen, S.J. Su, T.L. Windus, M. Dupuis, and J.A. Montgomery, "The general atomic and molecular electronic structure system," *J. Comput. Chem.*, vol. 14, pp. 1347-1363, 1993.

Optical profiling on lateral spreading of space-charge-region metal-semiconductor-metal structures

S.Khunkhao [a] A.Thaworn [a] S.Somdetsakun [a] S.Nuanloy [a] S.Korchareon [b] , S. Niemcharoen [b]

Department of Electrical engineering, Faculty of Engineering, Sripatum University, 61 Phahonyothin Road, Saenanikhom, Jatujak, Bangkok 10900, Thailand.Email: Sanya@spu.ac.th

[b] Electronics Research Center, Faculty of Engineering, King Mongkut's Institute of Technology Ladkrabang, Charongkrung Road, Ladkrabang, Bangkok, 10520 Thailand.Email: knsurasa@kmitl.ac.th

***Abstract*-Optical profiling on lateral spreading of space-charge-region properties of Schottky-barrier metal-semiconductor-metal (MSM) structures have been investigated experimentally. Making use of a planar molybdenum/n-type silicon /molybdenum (Mo/n-Si/Mo) MSM structure with a wide electrode separation, one-dimensional (1D) profiling of optical–beam intensity distribution from a helium-neon (He-Ne) laser was carried out. It was also confirmed that, in addition to existing photosensing function, the sensitivity (output photocurrent) of such a structure could be controlled by an applying bias via lateral spreading of the surface space-charge-region (SCR) at the side of the Schottky-junction reverse-biased.**

I. INTRODUCTION

The blocking (Schottky-barrier) metal-semiconductor-metal (MSM) structure is a viable and fundamental device structure in the field of light-wave communication and optical data processing systems. This structure provides several advantages such as wide-band operation, low-noise behaviour [1], ease of integration with other functions on the same chip and so forth [2].

Recently we experimentally confirmed that a planar MSM structure having a wide separation between the two metal electrodes exhibits not only the function of a basic optical sensor but also optical sensitivity field-controllable by the bias applied between the electrodes [4]. In this study, we present the experimental results of one-dimensional (1D) optical-beam profiling properties of an MSM structure as its application[2,3]. To our knowledge, no study has appeared on such an application of planar MSM structures.

II. MODEL OF OPERATION

The essential cross-section of the structure we treat in this study is illustrated schematically in Fig.1. The structure is of single-slit type (not interdigitated), the bird's eye view of which is also inset in Fig.1. Schottky-barrier is formed at each boundary between the metal and the semiconductor. The separation between the electrodes located at both ends is wide enough to leave the undepleted neutral region under the bias we examined. When a bias voltage is applied between the electrodes, one Schottky-junction is reverse-biased and the other junction is forward-biased.

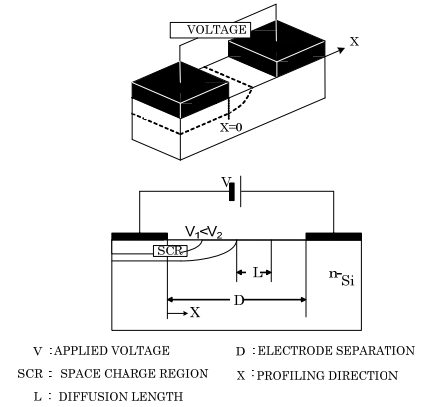

Figure 1. Schematic illustration of an MSM structure, leaving an undepleted region even under a bias.

Such a structure is expected to show lateral spreading of its space-charge-region (SCR) at the Schottky-barrier reverse-biased, the spreading of which is possible to be controlled by bias. According to the simplified model of such a structure, the width of the lateral spreading of the SCR of the Schottky-junction reverse-biased in the direction of profiling is expressed semi-empirically as[4]

$$W(V_a) = \sqrt{\beta(V_0 + V_a)} \qquad (1)$$

where $W(V_a)$ is the width of lateral spreading of the SCR along the surface of the active area at an applied bias V_a, $\beta = 2\varepsilon_s / qN_D$, ε_S is the permittivity of the semiconductor employed, q is the elementary charge, N_D is the impurity concentration and V_0 is the built-in voltage of the Schottky-barrier, respectively. The barrier on the other side is forward-biased and assumed to be nearly flattened for simplicity, although the residual undepleted region might exhibit an appreciable resistance reflecting its wide length. Therefore, when the influence of this resistance is taken into account, the applied bias V_a might be replaced by V_a-IR in (1), where I is the device average current and R is the equivalent series resistance. Thus, the photoinduced current $I_P(V_a)$ is approximately formulated as [4]:

$$I_p(V_a) = \eta[kW(V_a) + L] \qquad (2)$$

where L is the diffusion length of the semiconductor and k means that the SCR is k-times more effective to generate the photocurrent than the residual undepleted region (presumably, larger than unity, and η is the proportionality factor including the effect of quantum efficiency and intensity level of irradiation. As a result, $I_P(V_a)$ is would be an increasing function of applying bias V_a with the dependence on $\sqrt{V_0 + V_a}$ This means that the device structure under consideration is to furnish the field-controllable iris, although the equivalent size as a pixel also increases in the direction of profiling with the bias applied.

III. EXPERIMENTAL

A. Sample description

To make the electrodes of $3\times3\ \mathrm{mm}^2$, molybdenum film working also as barrier metal was deposited onto an n-type silicon wafer by an electron-beam evaporator and was subsequently processed by photolithography lift-off technique. The electrode separation is mainly 2000 μm. The resistivity of the wafer used was $(40\text{-}50)\,\Omega\mathrm{cm}$. This resistivity would provide corresponding donor concentration of some $3\times10^{16}\mathrm{cm}^{-3}$. The height of the Schottky-barrier on both sides was estimated to be $(0.55\text{-}0.65)\,eV$ from the forward current–voltage characteristic[5]. Furthermore, from this value of the barrier-height, the built-in voltage V_0 is deduced to be approximately $0.23\,eV$

B. Optical profiling procedure

Here we examine profiling of the light-beam from a He-Ne laser, the wave length of which is 633nm. The experimental system for profiling was arranged to suppress the influence of the stray light including reflected light from the ambient surfaces of the sample under test. The orientation of the incident light from the light source was tilted a little from the normal line of the active area of the device in the plane perpendicular to the profiling direction. The optical beam was scanned by every 15 μm in the perpendicular orientation of the tilting plane of the beam. Correspondingly, the influence of the tilt of the beam is presumably minimized in 1D direction where we are intending to profile. Spatial intensity distribution of the beam to be detected was assumed to be Gaussian distribution with the radius (2σ) of 480 μm defined at the point of $1/e^2$ its maximum just at the aperture of the light source quoted by the manufacturer [6]. The dispersion angle of the beam from the source is approximately $0.23\,mrad$. To control the light intensity incident onto the sample, a neutral density (ND) filter was utilized. Furthermore, since the electrode separation is wide, no interference of incident light is assumed at the very edge of each electrode.

IV. RESULT AND DISCUSSION

A. 1D-profiling properties

We observed the spatial distribution of detected photocurrent over the whole region between the electrodes, the typical plot of which is shown in Fig. 2.

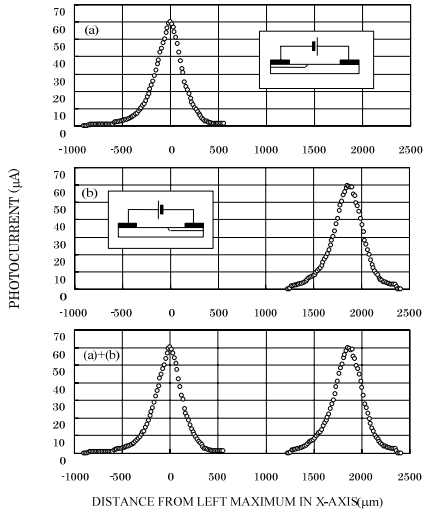

Figure. 2. Spatial distribution of the photocurrent under a constant optical illumination level versus the lateral position of every 15 μm step. Electrode separation is 2000 μm.

The photocurrent was obtained by subtracting the dark current from the current as measured at the same bias. Each peak in the Fig.2(a) and (b) corresponds to the profile when the polarity of applied bias is reversed. From the Fig. (a)+(b), the separation of the two peaks is estimated to be about 1920 μm, which is a little smaller than the electrode separation.

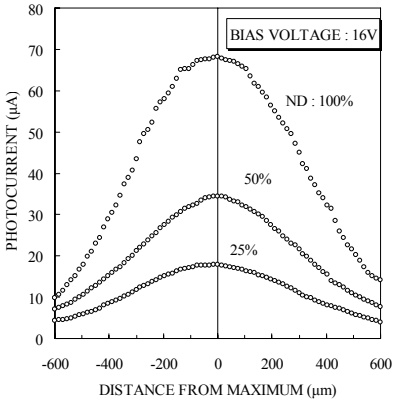

Figure.3. Photocurrent distribution under three different intensities of illumination at $V_a = 16\mathrm{V}$ for the same sample appeared in Fig.2.

It is apparent from these Figures that only the SCR of the junction reverse-biased generates significant photocurrent. On the contrary, the current from the barrier forward-biased on the other side is extremely small and is substantially ignored. Therefore, these two similar peaks must correspond to the photocurrent dominantly from the SCR of respective junction reverse-biased, showing k is larger than unity. Therefore, these results suggest that the region where no detectable photocurrent is observed can be treated to have substantially flat band.

Figure 3 shows the photocurrent versus position relationship for the sample appeared in Fig. 2 under a bias of 16V at the distance of 10cm from the aperture of the light source, taking the intensity of the illumination as a parameter. Here the light intensity was controlled by an ND filter between 25 per cent and 100 per cent of its maximum. One finds that the level of each peak corresponds to the optical intensity level.

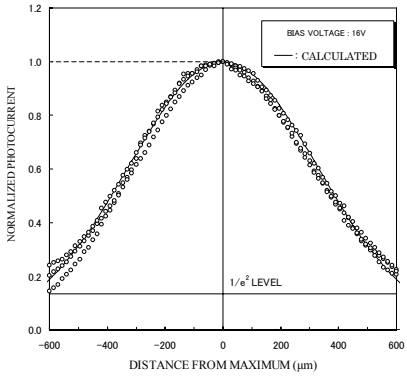

Figure.4. Normalized plot of the spatial current distribution from the data in Fig.3. Solid line represents the calculated Gaussian distribution for reference, taking $2\sigma = 480\mu m$.

Furthermore, the normalized plots from the data in Fig.3 are shown in Fig.4, where the solid line represents the Gaussian curve calculated from the parameters given by the manufacturer of the light source. A good agreement has been obtained between the experimental plots for different illumination levels and the plot theoretically expected. We also performed the profiling at the several different distances from the light source ranging from 10cm to 60cm. The plots given in Fig. 5 are the ones showing the detected current distribution of the beam versus the distance from each maximum.

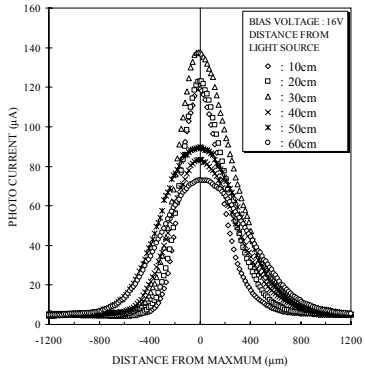

Figure.5. 2σ dependence of the spatial distribution of current on the distance from the light source.

From the data in Fig. 5, halves of normalized curves are replotted in Fig. 6, where the solid lines correspond to the lines calculated respectively. It is found that a good agreement has also been achieved between the experimental and calculated plots. In Fig. 7 is shown the radii of the optical beam experimentally obtained and numerically expected with respect to the distance from the light source for the case $V_a = 16V$. With increasing the distance, the difference between these two plots seems to decrease.

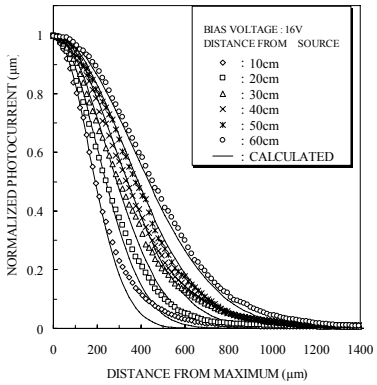

Figure.6. Normalized profiles of currents with respect to the distance from the maximum, where solid lines were calculated, respectively.

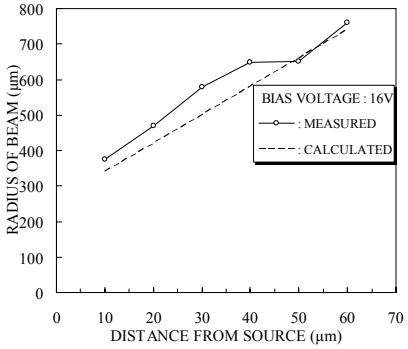

Figure.7. Experimental and calculated radii of the beam versus distance from light source.

This is curious a little. Generally, an increase in the difference between the two plots is expected with increasing the distance from the source.

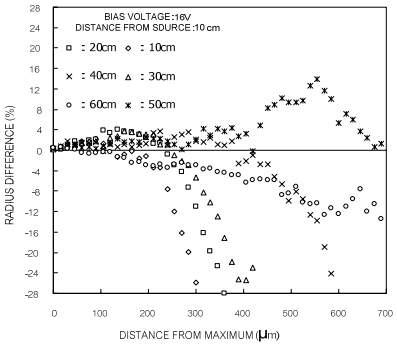

Figure. 8. Dependence of the difference in radii between experimentally observed and calculated on distance from the maximum.

In order to clarify this result further, we plotted in Fig. 8 the dependence of the difference in per cent between the experimental and calculated plots on the distance from the intensity maximum point, where the distance from the source was taken as a parameter. On the contrary, the difference seems to increase more or less with the distance from its maximum. These results observed might be attributed to incompleteness of avoiding the influence of stray light on the measured photocurrents. That is, with increase in the distance from the source, the influence of stray light on the profiling decreases.

B. Field-controllability of profiling

We also carried out profiling by changing the bias voltage. Fig. 9 pictures the experimental plots for V_a=2V, 4V and 16V biases. In Fig.10, the plots normalized at the peak value are shown, where the solid line corresponds the level theoretically expected. Again, a good agreement has been obtained from the view point of the level predicted, while the beam size being substantially unchanged even under the change in the bias applied. As a result, it can be concluded that the planar MSM structure examined can be used as a simple intensity profiler of an optical-beam of this size.

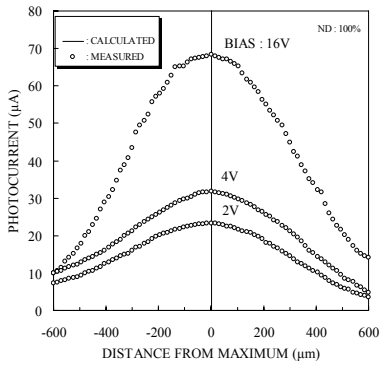

Figure.9. Bias dependence of experimental spatial intensity distribution for $Va = 2V, 4V$ and 16V.

However, it should be in mind that the detected spatial distribution of the current is for the photocurrent essentially given by (2). Therefore, with the increase in bias, the width of the SCR also increases following (1), which means the increase in size of the pixel. We used, in the present experiments, the silicon wafer of the resistivity of (40-50) Ωcm for preparing samples. This resistivity expects the change in the width of the SCR, $W(V_a)$, from 6 μm to 16 μm at most between 2V and 16V. As mentioned earlier, the profiling was carried out changing the relative position by every 15 μm step, which is still larger or approximately equal comparing to the width of the SCR.

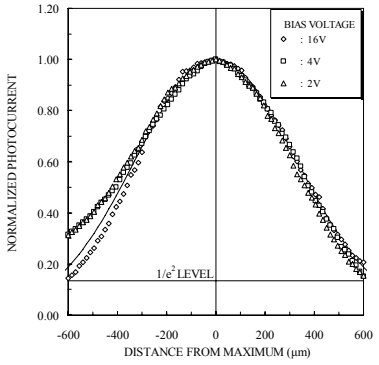

Figure. 10. Profiling normalized at the maximum for the bias V_a=2V,4V and 16V obtained from Fig.9.

Therefore, it can be mentioned that the beam profiling would still be effective. We repeated the similar measurements on the structure having 20 μm electrode separation. In spite that the diffusion length estimated to be 70 μm must be considered in generating photocurrents, no direct evidence of the contribution from the diffusion current was observed. This result might be attributed that the SCR is several times more efficient than the same area within the diffusion length in generating photocurrent [4,5]. Therefore, one can mention that the structure examined in this study is usable as a pixel for 1D optical-beam profiling, having the field-controllable sensitivity. It can also be mentioned that the increase in detected photocurrent is explained by the reflection of the photoexcited current due to the carriers laterally accumulated by spreading of the SCR with an applied bias. It is of interest that the effect of an optical spot position on the performance of MSM structures with no applied bias has been investigated previously [5]. This method, however, utilizes solely the current generation via photoexcitation of carriers like a solar cell. Therefore, the operation mechanism of this structure is essentially different from that of the structure we proposed in the present study.

V. CONCLUSION

As a novel application, a planar MSM (metal-semiconductor-metal) structure has been applied to profiling of the spatial intensity distribution of an optical beam in visible range. The Gaussian intensity distribution of the beam from a He-Ne laser was confirmed experimentally. The MSM structure proposed in this study also exhibits field-controllable sensitivity making use of lateral spreading of the SCR (space-charge-region) at the active surface. The performance of this structure is well explained by the simplified model.

ACKNOWLEDGEMENT

The authors wish to thank Prof.Dr.Kazunori Sato, Assoc.Dr.W. Titiroongruang and S.Niemcharoen of King Mongkut's Institute of Technology for valuable discussions and comments throughout this work. Continuous encouragement of Dr.R.P.Phukkamarn of Sripatum University is deeply appreciated. This work was supported in part by The Thailand Research Fund and Commission on Higher Education (Grant No.MRG5080004)

REFERENCES

[1] Burroughes JH., Rogers DL., Arjavalingam G., Pettit GD.,and Goorsky MS.,1991,*Doping induced bandwidth enhancement in metal-semiconductor-metal photodetectors*,IEEE Photonics Letters;3,657-659

[2] Safwat AME., Lin CK., Kim J., Johnson FG., Johnson WB., Goldsman N., Lee C., 2000, *Investigation of the optical spot position on the performance of metal-semiconductor-metal structures: novel application*. Solid-State Electronics, 44, 2077-2080.

[3] Yuang RH., Shieh JL., Chyi JI., and Chen JS., 1997, *Overall performance improvement in GaAs MSM photodetectors by using recessed-cathode structure*, IEEE Photonics Letters, 9, 226-228

[4] Khunkhao S., Yasumura Y., Kitagawa K., Masui T., and Sato K., 2003, *On laterally spreading of space-charge-region in planar metal-semiconductor-metal structures*. Solid-State Electronics., 47, 1811-1816.

[5] Masui T., Khunkhao S., Kobayashi K., Niemcharoen S., Supadech S., and Sato K., 2003, *Photosensing properties of interdigitated metal-semiconductor-metal structures with undepleted region*, Solid-State Electronics, 47, 1385-1390.

[6] Arafa M., Wohlmuth WA., Fay P., and Adesida I., 1998, *Effect of Diffraction and Interference in Submicron Metal-Semiconductor-Metal Photodetectors*, IEEE Transactions on Electron Devices, ED-45, 62-67.

Influences of Fabrication Process on Aggregation of Conjugated Polymer in Thin Films and its Roles on the Performance of Plastic Solar Cells

Kasin Kasemsuwan[1], Chanchana Thanachayanont[2], Rakchart Traiphol[3], Teerakiat Kerdcharoen[1*]
[1]Department of Physics and Center of Nanoscience and Nanotechnology, Faculty of Science, Mahidol University, Thailand
[2]National Metal and Materials Technology Center, Thailand
[3]Department of Chemistry, Faculty of Science, Naresuan University, Thailand

***Abstract*-.This contribution reports the correlation between conditions of film preparation and magnitude of the interchain aggregation of conjugated polymer, poly[2-methoxy,5-(2′-ethylhexoxy)-1,4-phenylenevinylene] (MEH–PPV). It was found that the extent of interchain aggregation in thin films, prepared by spin casting from solutions, depended on solvents and spinning speed. Uv/vis absorption spectroscopy revealed that the use of polymer solutions in xylene resulted in the films with higher aggregate fraction compared to that of the films made from the solutions in 1,2-dichlorobenzene. The results were consistent with the measurements by atomic force microscopy, which suggested a better chain packing in the smoother films made from solutions in xylene. Increasing spinning speed was also found to promote the interchain aggregation, attributed to the stretching of main chain due to the increase of centrifugal force. The MEH-PPV films fabricated by using different conditions were fabricated into plastic solar cell, constituting of the structure Al/MEH-PPV/PSS:PEDOT/ITO/Glass. The properties of the obtained plastic solar cells were compared to explore the relationship between magnitude of interchain aggregation in thin films and the device performance.**

I. INTRODUCTION

The photovoltaic (PV) cells have become increasingly attractive to scientific community due to their potential as a clean alternative energy source. The disadvantage of the crystalline silicon-base PV mainly arises from the relatively high cost of semiconductor manufacturing. On the other hand, the polymer based PV devices provide several advantages [1]. In addition to the low cost of materials and fabrication process, polymer PV cells also exhibit properties such as mechanical flexibility and durability, which are unachievable from the inorganic counter part [2]. However, fundamental understanding about properties of the conjugated polymers used to fabricate the PV cells is essential for the optimization of its performance. The optical and charge transport properties of the conjugated polymers have been known to depend significantly on conformation of individual chain and the molecular packing in solid state . The extended chain conformation and interchain aggregation of conjugated polymers in thin films promotes charge transport, which in turn is expected to enhance the performance of solar cells [3]. Therefore it is rather important to learn how to control the degree of interchain aggregation in thin films. Since the aggregation requires significant overlapping of multiple conjugated backbones, local chain conformation affects its magnitude significantly [3]. In this study, we explore the relationship between the fabrication processes and degree of interchain aggregation in thin films of the well-known conjugated polymer, poly[2-methoxy, 5-(2′-ethylhexoxy)-1,4-phenylenevinylene] (MEH–PPV). Several studies have demonstrated that the conformation of MEH-PPV varies significantly with local polymer-solvent interactions [3,10]. Therefore, one may utilize this knowledge to adjust the MEH-PPV chains to be in the desired conformation. The films prepared from solutions using different solvents are expected to contain different fraction of aggregates. Since the fabrication process of the PV devices normally uses the spin casting technique to prepare polymeric thin films, the spinning of substrate which unavoidably applies centrifugal force to polymeric chains is also expected to play important role. These two processing parameters are investigated in this study. The performances of PV devices constituting of MEH-PPV with different degree of interchain aggregation are compared to explore its role.

II. METHODOLOGY

The MEH-PPV was synthesized according to the procedure described in literature [4]. Fresh solutions were prepared by dissolving powder sample in solvents, 1,2-dichlorobenzene (DCB) and dimethylbenzene (xylene). All solutions appeared homogeneous. The films for atomic force microscopy (AFM) measurements were prepared by dropping solutions (0.01, 0.05, 0.5 mg/ml) on a freshly cleaned silicon wafer. The cleaning of the silicon wafers were performed by soaking in a warm piranha solution (7:3 v/v mixture of conc. H_2SO_4 and 30% H_2O_2) for about 1 h. The substrate was rinsed several times by deionized water and dried by pressurized N_2 gas. All films were allowed to dry in ambient conditions for over night. The morphologies of thin films were explored by using AFM (SPI3800N Nanoscope II, Seiko Instrument Inc., Japan). The films for UV/vis absorption measurements were prepared by spin casting from solutions with concentrations of 10 and 15 mg/mL onto glass substrate. The spinning speeds were varied from 1,000 to 5,000 rpm. The absorption spectra

of each film were recorded using a Jenway 6405 Uv/vis spectrophotometer. The surface morphologies and thicknesses of spin cast films were measured by AFM.

Structure of photovoltaic solar cells in this study consists of Al/MEH-PPV/PSS:PEDOT/ITO. All devices have area of 1.6×2 cm^2. Thickness of ITO, PSS:PEDOT and Al layers are about 140, 35 and 100 nm, respectively. The thickness of MEH-PPV depends on fabrication conditions (see below). The cleaning of ITO coated on glass substrate was performed by subsequent rinsing and sonicating in deionized water and isopropanol. The substrates were dried with nitrogen gas. It is followed by spin coating a thin layer of poly(3,4-ethylenedioxythiopene)(PEDOT):poly(styrenesul fonate) (PSS) to modify the ITO surfaces. Active layers of these devices were prepared by spin casting MEH-PPV solutions (10 or 15 mg/mL) on PSS: PEDOT/ITO with resistance of 30 Ω/c.m. All films were dried by keeping them in a glove box filled with nitrogen gas for overnight. Finally, the aluminum electrode was evaporated on top of the polymeric film. The current voltage (*I-V*) curves were measured with keithley 4200 semiconductor analyzer.

III. Results and Discussion

In first section, the effects of solvent and spinning speed on the magnitude of interchain aggregation in thin films are explored by utilizing UV/vis absorption spectroscopy. Fig. 1, illustrates the absorption spectra of MEH-PPV films prepared by using different solvents and spinning speeds. All spectra exhibit a maximum absorption at about 490-500 nm with broad red-shift shoulder at about 550 nm. It has been shown that the absorbance at 550 nm corresponds to the concentration of aggregated chains, which require significant interchain stacking, while the absorbance at 490-500 nm represents the fraction of non-aggregated one [5]. It is clear that increasing spinning speed is accompanied by the growth of the red-shift shoulder as shown in Fig. 1a Using different solvents to fabricate the films while spinning speed is kept constant also results in different pattern of absorption spectra. Fig. 1b, shows that the use of xylene solvent provides absorption spectrum with relatively stronger red-shift shoulder. The increase of absorbance at about 550 nm corresponds to the higher fraction of aggregates in the films [5]. We can compare the fraction of aggregates in different films by measuring ratio of absorbance at 550/490 nm. Fig. 2, illustrates this absorbance ratio of different films. It is obvious that the films prepared form solutions in xylene consist of larger fraction of aggregates. The increase of spinning speed from 1,000 to 3,000 rpm also causes a systematic increase of aggregate fraction. Further increasing the spinning speed to 4,000 and 5,000 rpm, however, hardly affects the aggregate fraction.

The effects of solvent on the magnitude of aggregation in thin films are attributed to the different of chain conformation in each solvent. The MEH-PPV chain constitutes of phenyl rings, double bonds and alkoxy side chains, making it virtually a non-polar molecule. Therefore, it is expected that it adopts different conformation in xylene and 1,2-dichlorbenzene, a non-polar and polar solvents, respectively. In fact, study by static light scattering indicates that p-xylene is a moderate solvent for MEH-PPV [6]. In other word, the conformation of MEH-PPV in p-xylene is a random coil. The chain is expected to collapse in the more polar solvent, DCB, due to the unfavorable polymer-solvent interactions. The chain in the more open conformation is expected to promote the aggregation in thin films consistent with other studies [3]. The effects of spinning speed are also expected to arise from the change of local chain conformation during the fabrication process. The spinning of substrate means that the centrifugal force is applied to the polymeric chains. The magnitude of this force increases with spinning speed, which stretches the chain to larger extent. The stretched chains can stack more efficiently, resulting in larger fraction of aggregates in the films.

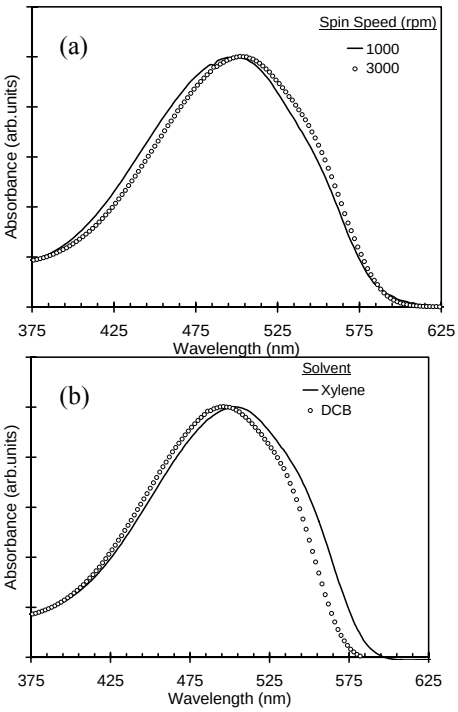

Figure 1. Normalized absorption spectra for MEH-PPV films prepared by using different (a) spin speeds and (b) solvents. The concentration of all solutions was 10 mg/mL. Solvent in (a) is xylene. Spinning speed in (b) is fixed at 4,000 rpm.

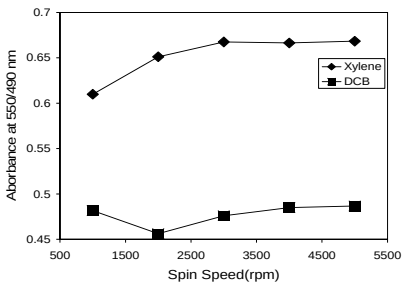

Figure 2. Plot of absorbance at 550 nm relative to 490 nm as a function of spin speed. The films were made from 10 mg/mL MEH-PPV solutions in in DCB and xylene.

The molecular packing of polymers in thin films was further explored by using AFM. The films were prepared by drop casting (i.e. self-assembling) and spin casting. The study of drop cast films provides information of film morphology forming without the perturbation of external forces. Therefore, local polymer-solvents play a major role on the molecular packing into thin film. Fig. 3, illustrates AFM topography images of the MEH-PPV films prepared by the drop casting of 0.05 mg/mL solutions of DCB and xylene. The films obtained by using the two solvents exhibit rather different surface morphologies. Using the solutions of DCB provides rather rough surface with relatively large domains distributing throughout the film. The polymer solution in xylene, on the other hand, yields much smoother film. Study of the films prepared from 0.01 and 0.5 mg/mL solutions provides consistent results. The detection of many polymer droplets in Fig. 3a, corresponds to the unfavorable interactions between DCB solvent and MEH-PPV. The polymeric chains minimize interfacial contact with solvent during the evaporation process by segregation into large domains. For the MEH-PPV chains dispersed in xylene, the magnitude of polymer-polymer interactions and polymer-solvent interactions is comparable (i.e. moderate solvent). Therefore, the formation of polymer droplets is much less in this case. This argument is consistent with the discussion in previous section, suggesting that the MEH-PPV chain is more collapsed in DCB. It is important to note that the number of polymer droplets does not reflect degree of interchain aggregation in thin films. There are other types of interchain association that do not lead to photophysical change of MEH-PPV [3, 5]. The films prepared by spin casting exhibit smoother surfaces as shown in Fig. 4,, However, the film obtained form the solution of DCB still contains more polymeric droplets compared to the film prepared from the solution of xylene.

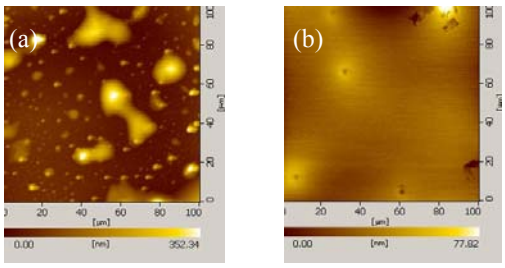

Figure 3. AFM topographic images of drop cast films prepared from 0.05 mg/mL MEH-PPV solutions. Solvents: (a) DCB and (b) xylene

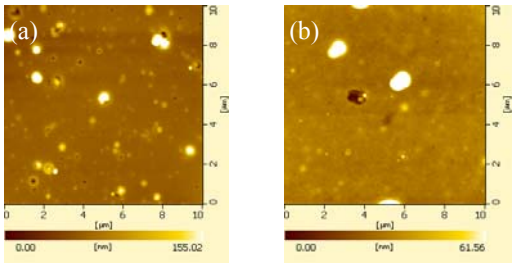

Figure 4. AFM topographic images of spin cast films prepard from 15 mg/mL MEH-PPV solutions. Solvents: (a) DCB and (b) xylene

The relationship between spin speed and thickness of MEH-PPV films are also investigated as shown in Fig. 5,. The film thickness decreases significantly upon increasing spinning speed from 1,000 to 3,000 rpm. Further increasing the spinning speed to 4,000 and 5,000 rpm slightly affects the film thickness, which range from 100 to 800 nm depending on polymer concentration and solvent. The varying of solvent and spinning speed also affects the root mean square surface roughness (RMS) of MEH-PPV films, which is one important parameter controlling the efficiency of the PV devices [8].

The higher surface roughness will give higher efficiency device which may result in a more efficient charge collection at the interface. Cause of the increase of contact area between the polymer film and metal electrode for the film with higher surface roughness [8]. It is known that the diffusion length of charge carrier in organic materials is often only a few nanometer[9] and on those carriers generated near the electrode will be collected and give rise to a photocurrent . Our results found that increasing spinning speed from 1,000 to 5,000 rpm causes the RMS roughness of MEH-PPV films prepared from 15 mg/mL solution of DCB to decreases from 18.61, 18.25, 23.94, 10.63 and 12.76 nm, respectively. The films made from solutions of xylene exhibit similar results. The RMS roughness of the films varies from 4.473, 9.091, 9.347, 2.471 and 10.81 nm upon increasing spinning speed.

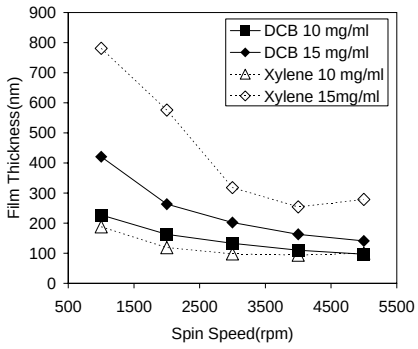

Figure 5. Film thickness of MEH-PPV film under different spin speed with concentration 10, 15 mg/ml from DCB and xylene solution.

The difference of RMS between DCB and xylene are in a range of 98%-969% relative to RMS of xylene. The difference is much. This result indicated that the area between polymer and metal electrode of devices from DCB is higher than xylene. We concluded from morphology study that device performance of the device made from DCB is higher than xylene solution.

Current density J(v) characteristics under dark and illumination modes of device fabricated from DCB and xylene solution concentration 10, 15 mg/ml are shown in Fig. 6 , and Fig. 7,Fig. 8, and Fig. 9 P_{max}, I_{sc} and FF represent maximum power output, short circuit current and fill factor, respectively, as a function of spin speeds. In this case the measured value of I_{sc} and P_{max} show an increase upon the rising spin speed, while not in the case of FF where the its trend is random. P_{max} represents for efficiency of device for this experiment because we did not measure the power incidence of the light source. P_{max} in these devices made from DCB and xylene solutions is

increaseing with the rising spin speed and film thickness but decreasing at the higher speeds of 4000 and 5000 rpm. In general, the optimum film thickness for organic solar cells is 100 nm. In our work, the film thickness for the best device performance made from DCB and xylene are 133, 100 nm with corresponding P_{max} of 0.137 and 0.033 μw, respectively. The higher optimum device performances of the film made from DCB solution is believed to have the larger contact surface area between the metal electrode and the film [8].

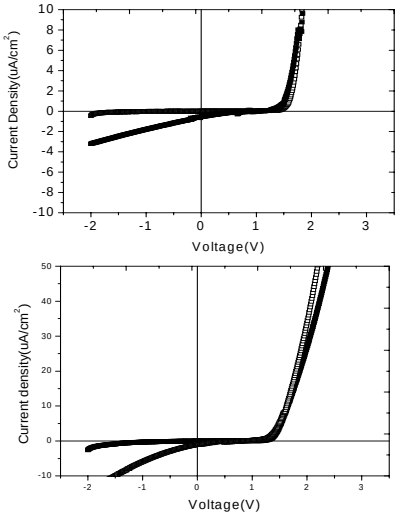

Figure 6. *I-V* characteristic under dark and illumination mode of device made from DCB (upper) and xylene (lower) concentration 15 mg/ml with spin speed 2000 rpm.

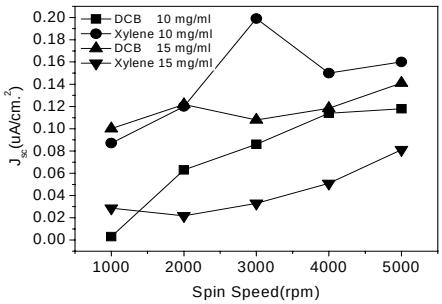

Figure 7. Short circuit current plot as function of spin speed of device made from DCB and xylene with concentration 10, 15 mg/ml.

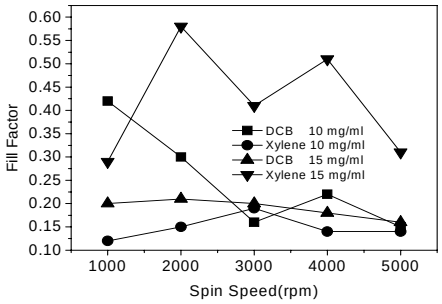

Figure 8. Fill factor plot as function of spin speed of device made from DCB and xylene with concentration 10, 15 mg/ml.

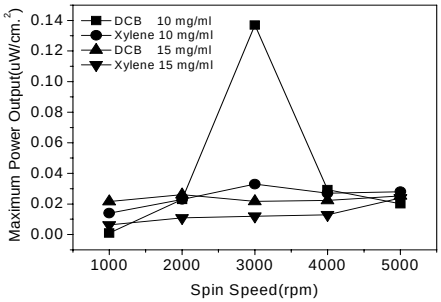

Figure 9. Maximum power out plot as function of spin speed of device made from DCB and xylene with concentration 10, 15 mg/ml.

We concluded that the RMS is an important role for the device efficiency enhancement.

Another factor for device performance is the degree of aggregation as mentioned above. It was found that the degree of aggregation in xylene solution is higher than DCB solution. Although both factors affect the performance of plastic solar cells, the RMS roughness seems to play a major role in the present case.

IV. CONCLUSIONS

We have found evidence that the degree of aggregation in solution of xylene is higher than DCB by Uv/vis and AFM study. The degree of aggregation can be controlled by factors such as spin speed and polymer concentration and choices of solvent. RMS roughness and film thickness is an important factor for optimal device performance.

ACKNOWLEDGMENT

This project is financially supported by the National Metal and Materials Technology Center. K.K. expresses his gratitude to the Thailand Graduate Institute of Science and Technology.

REFERENCES

[1] C. J. Brabec, V. Dyakonov, " Organic photovoltaics : Concept and Realization.", Spinger, Hidelberg, 1993

[2] P. W. M. Blom, M. J. M. de Jong, "Electric field and temperature dependence of the hole mobility in poly(p-phenylenevinylene)." , Phys. Rev. B, 1997, vol. 55, pp. R656-R659,

[3] Schwartz BJ., "Conjugated polymer as molecular materials." Annu. Rev. Phys. Chem., 2003, vol. 54, pp. 141-172

[4] Neef CJ, Ferraris JP, "MEH-PPV improved synthetic procedure and molecular weight control.", Macromolecules, 2000, vol. 33, pp. 2311-2314

[5] Traiphol, R.; Charoenthai, N.; Srikhirin, T.; Kerdcharoen, T.; Osotchan, T.; Maturos, T., "Chain Organization and Photophysics of Conjugated Polymer in Poor Solvents: Aggregates, Agglomerates and Collapsed Coils.", Polymer, 2007, vol. 48, pp. 813-826.

[6] Gettinger CL, Heeger AJ, "A photoluminescence study of poly(phenylene vinylenene) derivative : the effect of intrinsic persistence length."„ J. Chem. Phys., 1994, vol. 101, 1673--1678

[7] Sumpter BG, Kumar P, "Computational study of the structure, dynamics, and photophysical properties of conjugated polymers.", 2005, J. Phys. Chem. B , vol. 109, pp. 7671-7685

[8] Gang Li, Vishal Shrotriya, "Investigation of annealing effects and film thickness dependence of polymer solar cells based on poly(3-hexylthiophene.", J. Appl. Phys., 2005, vol. 98, pp.043704-043708

[9] P. Peumans, S. R. Forrest, "Very-high-efficiency double-heterostructure copper phthalocyanine/C_{60} photovoltaic cells.", Appl. Phys. Lett., 2001, vol. 79, pp. 126-128

Application of an Electronic Nose for Body Odor Recognition: Opportunity and Problems

Sanchai Harnsoongnoen[1], Mario Lutz[2], Neti Waranuch[3], Adisorn Tuantranont[4], Teerakiat Kerdcharoen[2,*]

[1]Department of Physics, Faculty of Science, Mahasarakham University, Mahasarakham 44150
[2]Department of Physics and Center of Nanoscience and Nanotechnology, Faculty of Science, Mahidol University, Bangkok 10400
[3]Cosmetics and Natural Products Research Center, Faculty of Pharmaceutical Sciences, Naresuan University, Phitsanuloke 65000
[4]Nanoelectronic and MEMS Lab, National Electronic and Computer Technology Center, Pathumthani 12120

Abstract **- In this paper, the opportunity and problems of human recognition through detecting body odor by using electronics nose (E-Nose) are presented. The developmental E-Nose system is a symmetrical reference-sample switching unit equipped with activated carbon cleaned air and constant high humidity produced by a humidity generator. An array consists of five metal-oxide gas sensors including humidity and temperature sensors. The measurement circuit uses the voltage divider resistor for each sensor. The principle component analysis method was used for pattern recognition. The sensitivity of the E-Nose system was compared with a human nose, to classify the strength of human body smell that can be mapped to different levels of artificial isovaleric acid normally produced by the human body. It was shown that the system can classify up to 4 levels of intensity. In this setup of air flow switching system and sensor chamber, it is only possible to detect strong human body smell. Also only two sensors have a useful reaction to the odors produced by the human body. To classify different persons it needs more dimensions of data this means more sensors that react. A classification and recognition of different persons with weak or normal body odor will be less efficient with this setup. The use of deodorant and different humidity of the samples disturb the recognition but can be solved by various techniques.**

I. INTRODUCTION

It is well known that humans recognize each other by to observe from the various characteristics of them such as face, voice or gait. The authentication in computer systems has been traditionally based on something that one has (key, magnetic or chip card) or one knows (PIN, password). However, tend to get stolen or lost and passwords are often forgotten or disclosed [1]. To achieve more reliable verification or identification we should use something that really characterizes the given person. Therefore, the biometrics system is proposed which recognizes a person based on a feature vector derived from a specific physiological or behavioral such as a fingerprint or a voice sample [2]. These characteristics are measurable, unique and should not be duplicable. One of the body odors is physical characteristics of human and scientists already have linked a collection of immunity sense with unique human body odor the able individual, and can be used to identify people [3], though this is more often done by dogs [4], However, dogs works only as well as his master and tedious work can lead to unreliability. Thus an ENoses to detect human body odor will be a suitable replacement of dogs [5]. Addition, ENoses sensitive enough to test beer, perfume sample and uncover pollution and disease. Since, an ENoses will be possible to identify persons [6]. From this idea, we interest to research about the body odor recognition and presented in this paper. The main purpose of this study was to identify persons by their body odor an ENoses must be used with opportunity and problems.

The paper is organized as follows: after the introduction presented in section I, the discussion is focused on body odor. Afterwards, the experimental setup is presented on section II and some results are presented on section III. The discussions are presented in IV. Finally, the paper conclusions are presented at section V.

II. EXPERIMENTAL SETUP

The setup is a symmetrical reference-sample switching unit with activated carbon cleaned air and constant high humidity produced by a humidity generator (bottle of water at a specific temperature within the air flow) as shown in Figure 1. The data acquisition is realized by a USB-DAQ-Card National Instruments NI USB-6008 and the measurement program is written in LabView 8.

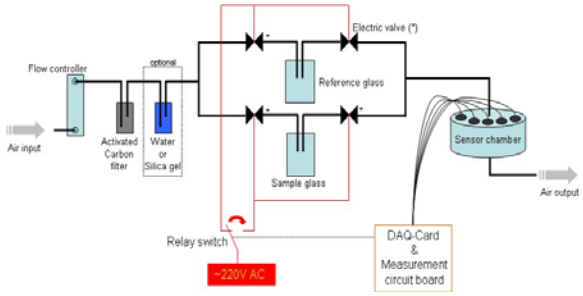

Figure 1 The reference-sample switching unit

It is necessary for this type of measurement to switch between a reference and a sample line. Therefore, four electrically controlled solenoid valves are used for this. Always two solenoid valves are open, the other two are closed. This ensures there is no mixing of the gas from the reference and sample line. It is also possible to remove the sample glass while the reference line is used without disturbance of the gas flow.

One digital output line of the DAQ card controls a "relay for remote" circuit board to switch 220V with a relay for the valves. The solenoid valves models are "Parker VE161-VE" with a magnetic coil "Parker Coil KT09 (220/230V – 9W)". The activated carbon filter remove alcohol, acetone and other aerosols from the air that can disturb the measurement if a pump and normal air of the room is used.

To control the humidity a bottle of water at a specific temperature to get a higher humidity or silica gel to reduce the humidity can be used.

A. Sensors chamber

The sensor chamber consists of a glass cylinder with a Teflon plate on top and bottom to seal the chamber. Both Teflon plates have an inlet or exhaust hole with a screw-in connector for standard plastic pipes. The top plate also holds the sensors and the connector (9-pin RS232) to connect the measurement circuit board. Under the inlet hole there is a small Teflon plate to avoid a laminar air flow from top to bottom. Under this turbulence plate there is a single-chip humidity / temperature sensor mounted. The connectors for this sensor go through the top Teflon plate but the hole is sealed with a special gum. The whole construction is set up on a cylindrical polystyrene stand for better stabilization. As show in Figure 2.

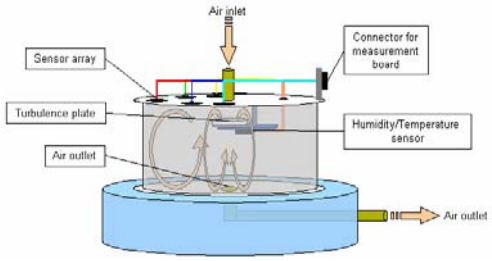

Figure 2 Sensor chamber layout

B. Sensor types

The sensors were chosen for react to body odor show in table I.

Table I: sensor was used choose

Sensor type	Detection of
TGS 813	Combustible gases
TGS 822	Organic solvent vapors
TGS 825	Hydrogen sulfide
TGS 880	Cooking vapors
TGS 2602	Air contaminants

The two possibilities to arrange the sensors for this kind of sensor chamber are first on the top plate and the second on bottom plate. It is easier to connect the sensors to a measurement board if the sensors are located on top plate of the chamber. The sensors are arranged around the air inlet and the turbulence plate will bring the gas to the sensors.

A single-chip Sensirion SHT15 sensor to measure humidity and temperature at the same time is mounted under the turbulence plate so it does not disturb the air flow to the other sensors. The turbulence plate and the SHT15 are mounted with the same screw to a small aluminum holder.

C. Measurement Circuit

The measurement circuit consists only of a voltage divider resistor for each sensor, the RS232 connector, a connector for the power supply and a connector to the DAQ card. The voltage is measured over a variable resistor to adjust a unique resistance for each sensor. The highest sensitivity to small changes of the sensor resistance is reached if the measurement resistor has approximately the same resistance like the sensor resistance with the reference gas / air. To keep the circuit and the connection to the sensors simple and use as less connectors as possible all sensors use the same voltage for the heater and the voltage divider. The connection principle show in figure 3 :

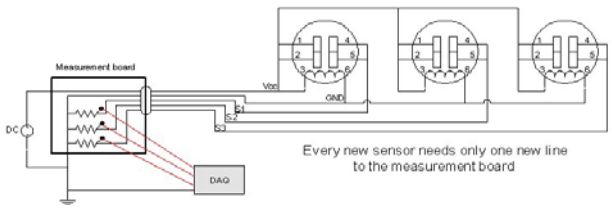

Figure 3 Measurement circuit board and connections

The sensor itself is between pin 1,2 and 4,5. The heater is on pin 3 and 5. The pin layout may differ for different sensor types but the connection principle is the same.

D. Measurement of different levels of artificial body smell

The first experiment it was necessary to find out the sensitivity of the e-nose system, especially the sensors, is comparable with a human nose.

To classify the strength of human body smell it can be compared to different levels of artificial isovaleric acid normally produced by the human body.

The subjective impression of the human nose is in a logarithmic scale and the concentrations of the isovaleric acid levels are also logarithmic to fit the subjective impression. But the sensors work linear and so the results should be recalculated into a logarithmic scale to see a linear slope of the result. A value scale in six steps from 0 to 5 is used to evaluate the intensity of the body odor which show in table II

Table II: the concentration of the isovaleric acid levels

Level	Isovaleric acid / water (ml / L)	Subjective impression
0	0	Nothing
1	0.013	Slight
2	0.053	Definite
3	0.22	Moderate
4	0.87	Strong
5	3.57	Very strong

E. Long-term measurement of armpit smell

The experiment time is 5 days with a sample collection of the armpit smell in the morning after waking up and in the afternoon 8 hours after the sample in the morning. The pad must be in direct contact to the armpit for 10 minutes for each arm and stored into a special sample glass bottles with a screw-on closure. Date and time must be noted on the sample glass bottles. The measurement should done as fast as possible after collection to avoid changes in smell due to bacteria.

The conditions for the person during time of experiment and one day before are:

- have a shower in the evening and in the morning after collecting the sample
- use of deodorant only in the morning after taking a shower and only on the right arm, leave the other untouched
- no alcohol and sex allowed
- no sports before afternoon sample collection
- no strong smelling food (e.g. durian or garlic)
- keep life and activities in same pattern

Each person has to collect the sample by itself.

III. RESULTS

The measurement results of different levels of isovaleric acid show below:

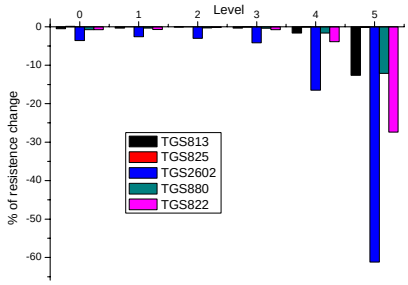

Figure 4 Different levels of isovaleric acid

Figure 4 shows that sensors can be detected on the strong smell (equal to isovaleric acid level 3, 4 and 5) and the highest sensitivity to body odor have sensor TGS822 and TGS2602. Mathematically adjusted results to eliminate the logarithmic scale of the levels by the formula: $Y = \ln(1 - \%R_S)$ which the result shows in figure 5.

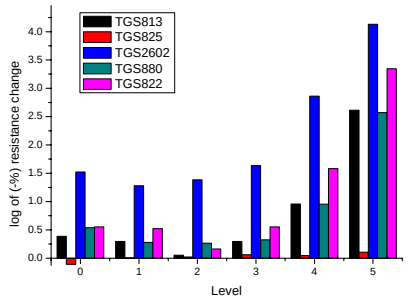

Figure 5 Logarithm of measurement result

The comparison between left and right arm on morning and afternoon (average of 5 days) show in figure 6 and 7, respectively.

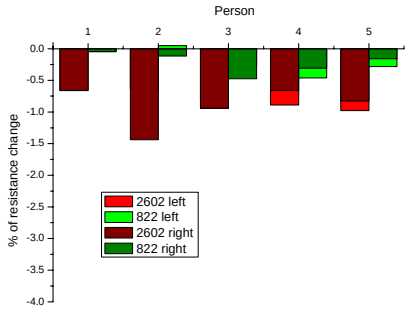

Figure 6 Morning comparison left-right arm

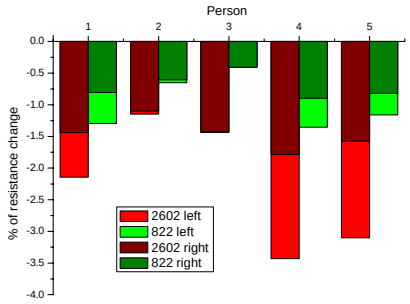

Figure 7 Afternoon comparison left-right arm

In the figure 6 and 7 show that the morning all persons have only a weak smell and there is nearly no difference between right and left arm. For some people a big difference between the left (without deodorant) and right arm (with deodorant) in the afternoon such as person 4 an 5. For person 2 and 3 have a naturally weak smelling. The effect of deodorant can be shown very good. The deodorant reduces the strength of smelling for persons with a strong smell (here in the afternoon).

The principle component analysis (PCA) method is used in this. The analysis result by PCA of: two person (person 4 and 5), afternoon, left and right armpit, over a period of 5 days show in figure 8.

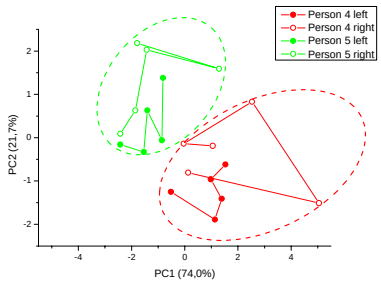

Figure 8 PCA-Graph of 2 different person

IV. DISCUSSION

The results of the isovaleric acid measurements show it is only possible to clearly detect level 4 and 5. Level 3 can be detected if the environmental conditions are very good. Not all sensors are sensitive to the isovaleric acid. The highest sensitivity have sensor TGS822 and TGS2602. The logarithmic scale of the isovaleric acid solution can be eliminated by calculations to show the sensors work linear.

For the human body smell measurements it is only possible to detect strong smells (equal to isovaleric acid level 3, 4 and 5). In the afternoon it is normal for people to have a strong smell if no deodorant is used. In the morning all persons have only a weak smell and there is nearly no difference between right and left arm. The "noise level" is at about 1% of resistance change for sensor TGS822 and 0.5% for sensor TGS2602. Maybe contaminated pipes disturb the measurement. With the PCA it is not easy to classify persons. The data of afternoon of the two persons with the strongest smell can classify these two different persons. If the data contains all persons only these two persons are different and the rest is very similar.

Also the contamination of the plastic pipes is a problem. After measuring a strong sample a weak sample produce a higher sensor response than it should do. Maybe replacing the plastic pipes with Teflon pipes reduces the effect. Also a good cleaning of the system is necessary after a measurement. . It is necessary to test different types of other sensors. The humidity is also a problem because different persons produce different humidity that can change all the time. So the best results can be reached if the background humidity is always nearly equal to the humidity of the sample.

V. CONCLUSION

The present setup is efficient to detect strong human body smell. The capability to recognize and distinguish weak body odor is yet to be explored. In this setup, only two sensors are effective to the odors produced by the human body. To classify different persons it needs more dimensions of data this means more sensors that response. A classification and recognition of different persons with weak or normal body odor is the scope of future development as well as the use of different deodorant.

ACKNOWLEDGMENT

This project is financially supported by National Electronic and Computer Technology Center (NECTEC).

REFERENCES

[1] Z. Riha and V. Matyas, "Biometric Authentication System," FI MU report series, FIMU-RS-2000-08.

[2] S. Prabhakar, S. Pankanti, and A. K. Jain, "Biometric recognition: Security and Privacy Concerns," IEEE Security & Privacy, March/April 2003, pp. 33-42.

[3] K. Delac and M. Grgic, "A Survey of Biometric Recognition Methods," 46th International Symposium Electronics in Marine, ELMAR-2004, 16-18 June, Croatia: pp.184-193.

[4] Wikipedia.org/Body odor, 2007. http://en.wikipedia.org/wiki/Body_odor

[5] A.W. Teo, H.K. Garg, and S. Puthusserypady, "Detection of Humans Buried in Rubble: An Electronic Nose to Detect Human Body Odor," Proceeding of the second joint EMBS/BMES Conference Houston, Tx, USA, October 23-26, 2002, pp. 1811-1812.

[6] Z. Korotkaya "Biometric Person Authentication: Odor," available at http://www.it.lut.fi/kurssit/03-04/010970000/seminars/Korotkaya.pdf

Lighting System for Growth Enhancement of Thai Orchids

Phanumas Khumsat and Kamplon Panprayoon
Department of Electrical Engineering,
Faculty of Engineering, Prince of Songkla Univesity, Hat-Yai, Thailand 90112
E-mail: phanumas.k@psu.ac.th

Abstract— **Lighting system has been designed for enhancing orchid growth rate. Light sources have been implemented from low-cost red (λ~640nm) and blue (λ~470nm) light emitting diodes. Optical sensing and feedback techniques with active-RC lag compensator have been deployed to maintain photon flux density to the desired values 4.9 μmol m^{-2} s^{-1} and 14 μmol m^{-2} s^{-1} for blue and red lighting conditions regardless of ambient luminous condition or changes in LED output over time and temperature fluctuation. Experimental results clearly show that the orchid baby seedlings subjected to additional red and blue lights outgrow those cultivated under normal lighting condition.**

I. INTRODUCTION

It has been widely known that plants' basic need for light reside within three spectral ranges responsible for photosynthesis, phototropism and photomorphogenesis, respectively. Photosynthesis requires light in the vicinity of the absorption peaks of chlorophylls a and b (at 662 nm and 642 nm, respectively), which are the most important photosynthetic pigments. Phototropic processes, which control motion of plant organs in response to light and ensure optimization of biophysical and biochemical reactions, are triggered by light with wavelengths in the range of 400–500 nm. Finally, plant morphogenesis, encompassing processes such as shooting, pigment synthesis and healthy plant development, depends on far-red radiation in the range of ~ 730–735 nm.

For many decades, many researchers around the world have been carried out to investigate how light spectrum affect plants' growth rates and their properties based on plant's photobiology (photosynthesis, photomorphogenesis and phototropism) [1-8]. To the best of authors' knowledge, not much research has focused on cultivation of Thai orchid under various or combination of light spectrum. Thailand's export values of orchids each year exceed USD 30 million thanks to the plants' unique beauty and originalities. Techniques that help enhance orchid's growth rate and productivity would be truly beneficial to the orchid industry. The techniques may open huge possibility of commercial indoor plantation under a well-controlled environment which is no longer season dependent. The products can be continuously supplied throughout the year and satisfactorily serve for high market demand. This study presents preliminary results on how light at particular wavelength affects orchid growth. The findings presented here might change the way orchid farmers grow their plants more effectively and profitably.

II. LIGHTING SYSTEM DESIGN

Schematic of the lighting system is illustrated in Fig. 1 where a current source comprising PMOS M1 (IRF9540) and Rs is switched at the base of PNP Q1 (TIP2955) by pulse trains coming from a pulse generator to provide an appropriate amount of current to clusters of light emitting diodes (LEDs) via improved-Wilson current mirrors Q2-Q5 (one current mirror per cluster containing five LEDs). LEDs are particularly well suited for plant growth, as opposed to fluorescent or incandescent lamps, as they have an extraordinary life (about 100,000 hours), require little maintenance, and radiate little amount of heat. The pulse is generated by PIC microcontroller 16F877A (with additional circuitry for adjusting logic level from 0-5V to 0-12V) where frequency (10Hz – 100kHz) and duty cycle (0% – 100%) can be independently varied. The maximum current supplied to the LEDs can be adjusted by selecting suitable degenerate resistor Rs and gate voltage of PMOS M1 as given by (assuming that this happens when the pulse logic is low and M1 is in a saturate strong-inversion mode and Q1 is switched on to allow drain current of M1 to flow into the current mirror at the bottom)

$$I_{\max} = \frac{1}{R_S}\left(V_{CC} - |V_{TP}| - V_G + \frac{1}{R_S\beta}\right) + \frac{1}{R_S^2\beta}\sqrt{1 + 2R_S\beta\left(V_{CC} - |V_{TP}| - V_G\right)} \quad (1)$$

where V_{TP} and V_G are threshold voltage and gate voltage of M1. The parameter β being a PMOS device constant and it is approximated to be 2 for IRF9540 (extrapolated from datasheet).

The Red LED is of LTL2R3SEK model which is made with AlInGaP technology and it emits visible red light with a dominant wavelength of 640nm. The blue LED is of TOL-50aUBdCEa-ETB6 made from AlGaN/GaN rendering blue light with peak wavelength of 470nm.

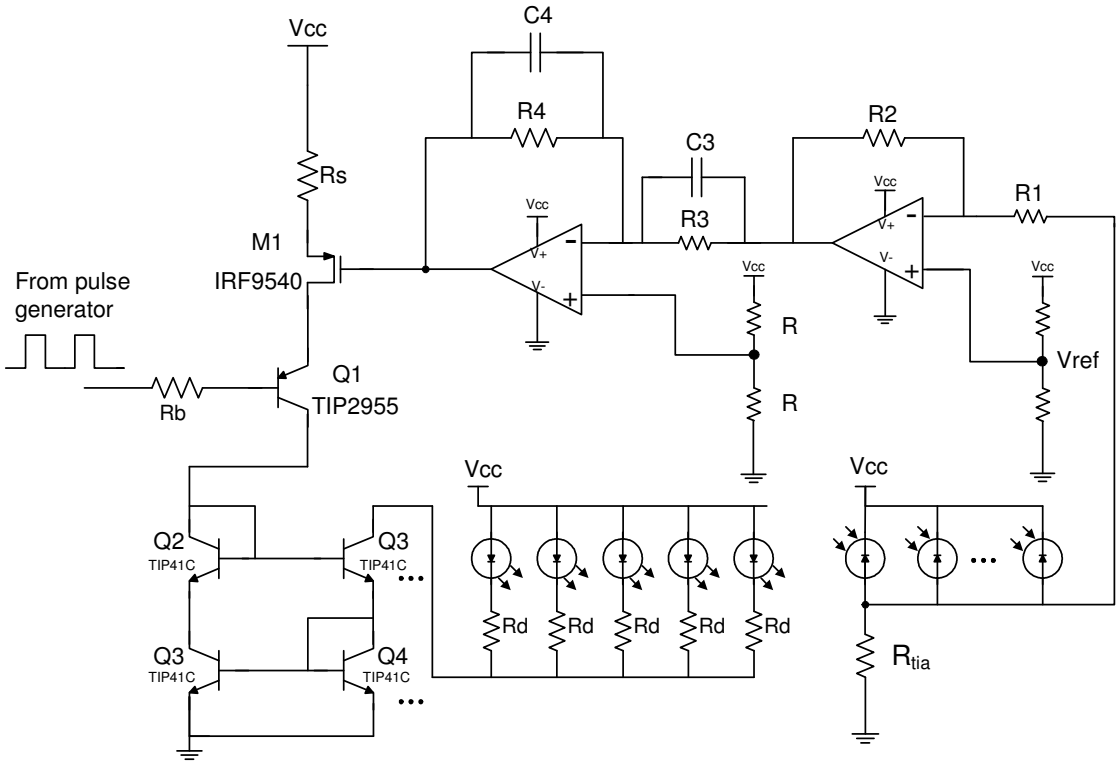

Fig. 1 Schematic of the orchid lighting circuitry.

To maintain photon flux density at desired level, a feedback loop is employed to adaptively vary gate voltage of M1 in order to encounter variation of ambient light. The output light intensity is sensed by an array of Silicon PIN photodiode (model SFH203) and the resulting voltage is compared with Vref (set at Vcc/2 = 6V) by the first amplifier. The amplifier's output voltage is then fed to a lag compensator implemented from a single opamp, R3, R4, and C3, C4 and its corresponding s-domain characteristic is simply described by

$$T(s) = -\frac{C_3}{C_4}\frac{\left(s+\frac{1}{R_3C_3}\right)}{\left(s+\frac{1}{R_4C_4}\right)} \qquad (2)$$

where $R_4C_4 > R_3C_3$. The operational amplifiers employed for this system are LF353N and they have been designed so that their nominal DC input and output voltages are at Vcc/2 = 6V.

With 1kHz pulse and 50% duty cycle, the resistor R_{tia} is selected to maintain photon flux density at 4.9×10^{-6} mol m^{-2} s^{-1} and 1.4×10^{-5} mol m^{-2} s^{-1} for blue and red lighting conditions respectively while each of both type of LEDs draws average current of 70mA from 12V supply. The design component values are listed in Table 1.

Fig. 2 confirms proper functionality of the light intensity stabilizing feedback loop where the voltage at the photodiodes' anodes can be successfully maintained at 6V despite the ambient light has been subjected to significant change (extra light source controlled by 10-Hz pulse has been employed to imitate ambient light fluctuation).

Table 1: Design parameters

Parameters	Red Lighting	Blue Lighting
Rb	1 kΩ	
Rs	5 Ω	
Rd	100 Ω	
Rtia	500 kΩ	1000 kΩ
R1	10 kΩ	
R2	100 kΩ	
R3	10 kΩ	
R4	100 kΩ	
C3	10 nF	
C4	10 nF	
R	10 kΩ	

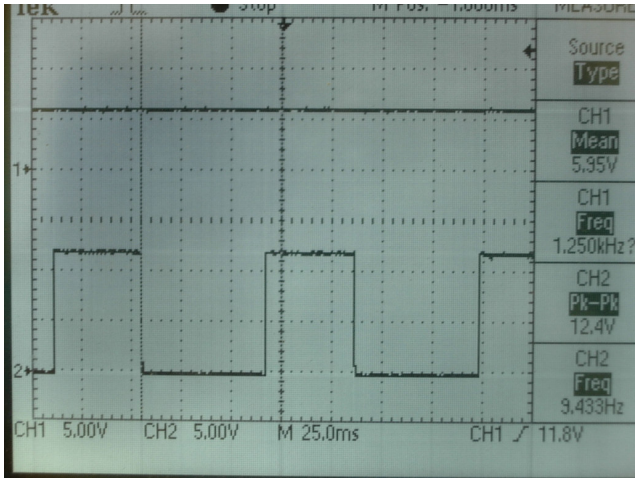

Fig. 2 Oscilloscope captures a stabilised voltage at 6V (top) at photodiode's anodes compared to the circuit without feedback (bottom).

III. EXPERIMENTAL RESULTS

The experiment setup is as shown in Fig. 3. It is important to note that the experiment has not been carried out inside a dark room. This is because we expect orchid farmers to employ this system within a usual growing environment. The main purpose is to see whether *additional* blue and red lighting can help improve orchid development compare to typical lighting condition. Orchid species under study is Rhybchostylis gigantean (or 'Red Elephant' in local name). Exposure period is between 6hr to 18hr with twenty baby seedling samples for each lighting condition (red, blue, normal).

From photographic comparison in Fig. 4, it can be seen that the seedlings subjected to blue and red light outperform those under normal lighting condition in various aspects including leaf area, number of leaves, root size, number of roots as numerically charted in Fig. 5.

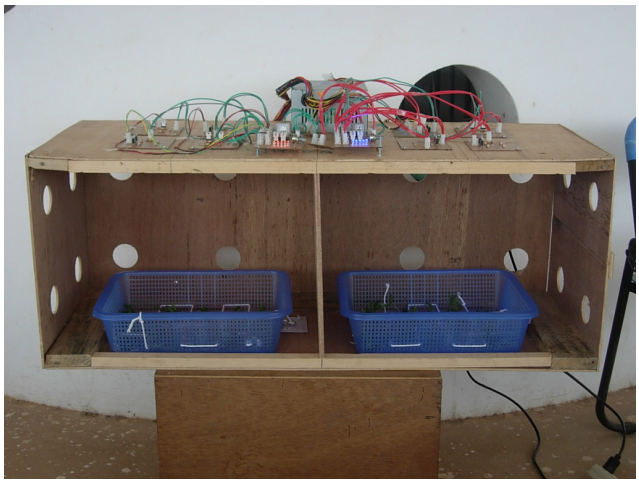

Fig. 3 Photograph of the experiment setting for red and blue lighting exposure regimes.

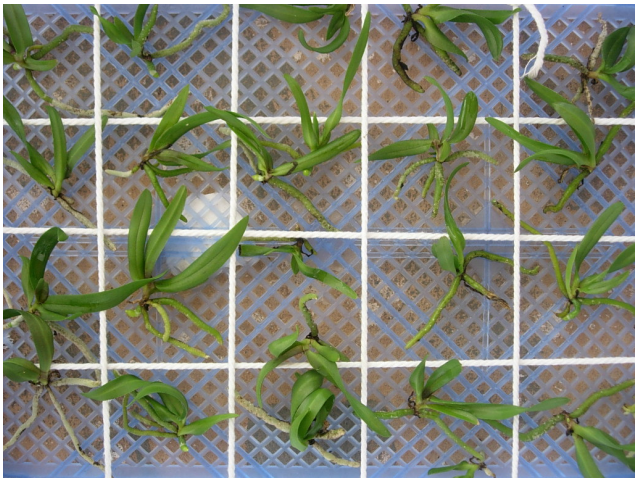

(a) Red

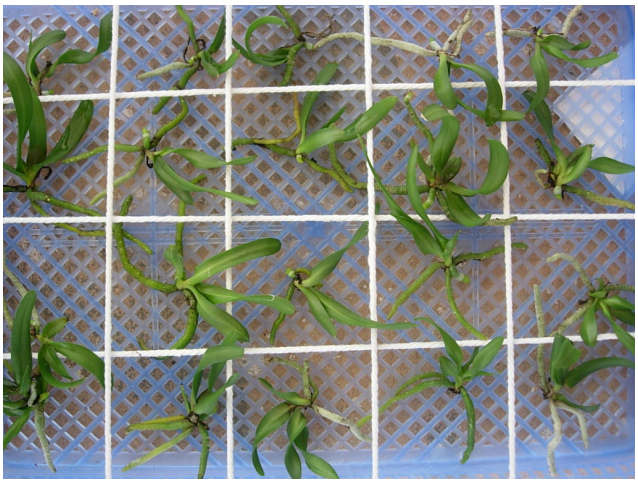

(b) Blue

(c) Normal lighting

Fig. 4 Comparison of orchid seedling development under different light exposures after two months.

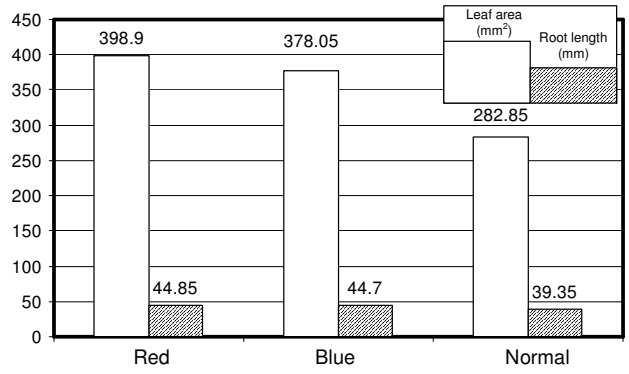

(a) Leaf area, root length

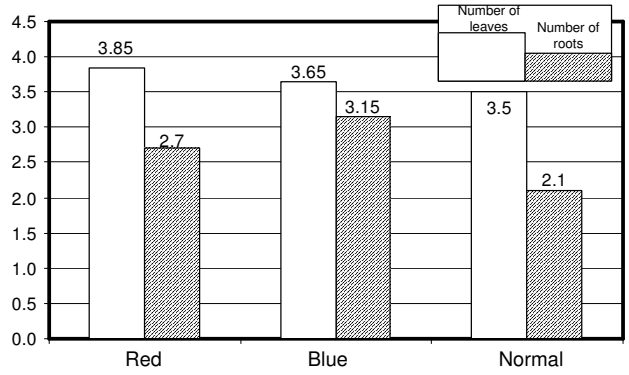

(b) Number of leaves, number of roots

Fig. 5 Orchid dimension comparison (average over 20 samples).

IV. CONCLUSION AND FUTURE WORKS

Lighting system has been designed for enhancing orchid growth rate. Optical sensing and feedback techniques with opamp-RC lag compensator have been deployed to stabilise photon flux density to the desired values taking into account ambient lighting fluctuations, LED properties that drift with temperature or time. Preliminary experimental results clearly show that the orchid baby seedlings with additional red and blue lighting exposure outgrow those cultivated under normal lighting condition. Due its modularity of the implemented building blocks, the system can be straightforwardly expanded for the purpose of mass production. Future work should include investigation on different species of orchids at various stages of its life. Multiple wavelength sources (red, green, blue and infrared) could be combined to produce specific spectrum requirement for the experimental purpose in order to figure out the optimum light mixture for particular species of orchid. It is also of great interest to not only foster plant growth, but to *control* plant growth. The supplementation of specific wavebands or skewing of overall spectrum may help modulate the progression of plant development events. The possibility that combinatorial light regimes may help to optimize growth and control developmental transitions makes the presented concept particularly attractive to the design of controlled environments targeted to plant production for aesthetic applications, or applications relevant to human nutrition. If spectral quality alone can delay or hasten the floral transition it may have profound effects on modulating the delivery of nursery goods or perhaps affect the availability of consumable produce in a finite, controlled environment.

REFERENCES

[1] H. A. Borthwich, S. B. Hendricks, M. W. Parker, E. H. Toole, V. K. Toole, "A Reversible photoreaction controlling seed germination," Proc. Natl. Acad. Sci. USA 38: 662-666.

[2] T. Kitamura, "PHOTO ESSAY: Red LEDS for Green Groceries," IEEE Spectrum, vol. 42, issue 4, April 2005, pp: 22-23.

[3] G. Tamulaitis, P. Duchovskis, Z. Bliznikas, K. Breive, R. Ulinskaite, A. Brazaityte, A. Novickovas, and A. Zukauskas, "High-power light-emitting diode based facility for plant cultivation," Journal of Physics D: Applied Physics, vol. 38, pp.3182-3187, 2005.

[4] K. M. Folta, L. L. Koss, R. McMorrow, H.-H. Kim, J. D. Kenitz, R. Wheeler, and J. C. Sager, "Design and fabrication of adjustable red-green-blue LED light arrays for plant research" BMC Plant Biology, 5:17, 2005.

[5] Sun-Ja Kim, Eun-Joo Hahn, Jeong-Wook Heo and Kee-Yoeup Paek, "Effects of LEDs on net photosynthetic rate, growth and leaf stomata of chrysanthemum plantlets in vitro," Scientia Horticulturae, Vol. 101, Issues 1-2 , 3 May 2004, Pages 143-151.

[6] B. M. Parks, "The Red Side of Photomorphogenesis," Plant Physiology, December 2003, Vol. 133, pp. 1437-1444.

[7] P. J. Aphalo, "Light signals and the growth and development of plants – a gentle introduction," available at http:// www.cc.jyu.fi/~aphalo/old_pages/pdf/notes1.pdf

[8] W. Fang, R. Jao, D. H. Lee, "Artificial Lighting Apparatus for Young Plants Using Light Emitting Diodes as Light Source," United State Patent, Patent No. US 6,554,450 B2, Apr. 2003.

Electronic Nose System for Orange Juice Freshness Quality Control

Wattanasit Pimpao[1, 2], Assawapong Sappat[1], Teerakiat Kerdcharoen[3], Manas Sangworasil[2]
Anurat wisitsoraat[1], and Adisorn Tuantranont[1]
[1]Nanoelectronics and MEMS Laboratory,
National Electronics and Computer Technology Center (NECTEC)
112 Thailand Science Park, Phahol Yothin Rd., Klong Laung, Pathumthani 12120
http://www.nectec.or.th/mems, Tel: +662-564-6900 Ext. 2109, Fax: +662-564-6756
Email: wattanasit.pimpao@nectec.or.th
[2]Department of Electronics, Faculty of Engineering
King Mongkut 's Institute of Technology Ladkrabang Bangkok 10520, Thailand
[3]Department of Physics, Center of Nanoscience and Nanotechnology, Faculty of Science
Mahidol University, Rama 6 Road, Bangkok 10400, Thailand

***Abstract*- In this work, we have developed a gas sensor array for effective odor monitoring, measuring, recognizing and analyzing systems. The odor sensing system consists of four main components: gas flow system, gas sensor array circuit, microcontroller, and computation. The system is made compact and portable by suitable electronic design. Several small commercial gas sensors and simple voltage-divider sensing circuit are employed. A low cost microcontroller system is designed to process time-multiplexed sensor signals, calculate gas concentration, generate output to the computer, and analyze gas concentration. Principal Components Analysis (PCA) technique is used to investigate relationships between the individual points in the data set. The system has been tested toward orange juice odor. It has been able to recognize and distinguish different odors of fresh and rotten orange juice with satisfactory accuracy.**

I. INTRODUCTION

Recently, the demand of various gas sensing applications including alcohol driver testing, environmental monitoring, and agricultural product's odor testing have been considerably increased. Thus, effective monitoring and controlling systems for detection and quantification of various gases or vapors have gained much attention. Analytical instruments such as gas chromatography /spectroscopy, which provide precise analysis, are time consuming, expensive, and non-portable. Semiconductor gas sensor is among the most widely used commercial gas sensors due to their low cost, high sensitivity, fast response, and simple electronic interface. However, a single gas sensor cannot be used to identify the specific gas and determine the corresponding concentration because it has limited gas sensing selectivity. The concept of gas sensor array has been proposed for effective gas monitoring, measuring, recognizing and analyzing systems and a number of such systems have been developed. In this work, we have developed an electronic nose with compact electronic design comprising only one microcontroller that generates a basic function to implement Principal Component Analysis (PCA) with the commercial complier. Principal Components Analysis (PCA) technique is used to investigate relationships between the individual points in the data set. In this case, we have developed e-nose system particularly for agricultural product testing. It can be used to distinguish odors between fresh orange juice and ripe orange juice. The objectives of this application are to improve the quality of fruit products of Thailand and utilize a new technology to reduce the farmer problem in the future.

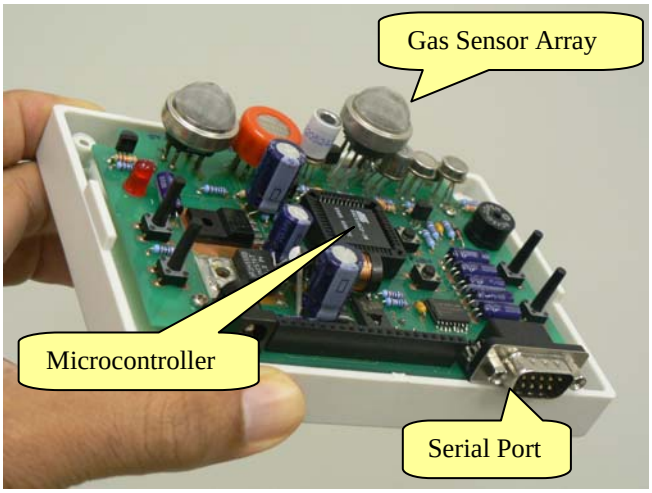

Figure 1. Photograph of an Electronic Nose System.

II. GAS SENSOR OPERATING PRINCIPLE AND CHARACTERISTICS

A. General

Gas sensor is generally operated based on a change of its electrical characteristics as a result of gas interaction with the sensing element. Semiconductor gas sensors utilizing the transduction of a chemical reaction between the gas species and semiconductor materials into electrical resistance change are the most widely used commercial gas sensors.

Semiconductor gas sensor is typically a resistor made of metal oxide materials that is sensitive to different target gases. The common sensing materials are SnO_2, WO_3, etc., typically containing a wide variety of dopants or catalysts to enhance

gas-sensing sensitivity and selectivity. In addition to gas sensing material, there must be a built-in heater to heat the gas sensor to operating temperature between 200 and 400 °C. The heating element is usually made of Pt thin film or NiCr wire.

B. Sensing Circuit

The resistance of the gas sensor is measured through a simple voltage divider circuit given by.

$$R_S = \frac{V_{CC} + V_{RL}}{V_{RL}} \quad (1)$$

where V_{RL} is the voltage across of the load resistor, R_L, and V_{CC} is the supplied voltage.

The gas sensor is heated to a fixed operating temperature, which is typically 300-350 °C by the V_{CC} heating voltage. The heating voltage is controlled by on-off mechanism to maintain a constant temperature.

C. Calibration

The characteristics of commercial semiconductor gas sensor are largely varied depending on material and fabrication process. Due to base line drift behavior of these sensors, their characteristic is characterized in term of relative resistance change, which is known as sensitivity. Gas-sensing sensitivity, S, of a semiconductor gas sensor is normally defined as the ratio of resistance with no gas sample to that with gas sample:

$$S = \frac{R_S}{R_O}, \quad (2)$$

where R_S is the resistance with gas sample and R_O is reference sensor resistance at a given gas concentration. The sensitivity strongly depends on gas concentration and operating temperature of the sensor.

D. Algorithms

A microcontroller is used to process sensor signal, calculate gas concentration, and generate output to computer. The algorithms for microcontroller software have 2 modes. First, the controller is initialized by waiting for 10 seconds to let the sensor be heated to its operating temperature. During the calibration mode, the microcontroller calculates the input resistance, maps the results to the known input concentration, and stores the calibrated data into the sensor's characteristic table. In the normal operating mode, the microcontroller continuously samples and reads output voltage, V_{RL}, from sensing circuit via Analog-to-Digital Converter (ADC). The ADC has multiple channels so that it can be connected to multiple sensing circuits for various sensors and the microcontroller can time-multiplex different sensor input signals by simple periodic addressing. Software programmed in the controller then performs calculation to convert the voltage into resistance, sensitivity, and gas concentration. The gas concentration is determined from calibration table. The final data set output are secured and convert into a protocol message send to computer serial port with computer interface unit. The computer analyzes data set using PCA technique in order to recognize odor. The calculated results are displayed on the PCA graph with the odor group.

III. GAS SENSOR ARRAY

A single gas sensor cannot be used to identify the specific gas and determine the corresponding concentration because it has limited gas sensing selectivity. The gas sensor array is the array of difference type of gas sensors. Each sensor is highly responsive to different a target gas while each sensor has lower response to other gases. At a result, it can provide the identified output characteristics of each odor similar to the human nose. The list of commercial gas sensors in the array is shown in TABLE I.

TABLE I
LIST OF GAS SENSOR IN THE ARRAY

No	Sensor	Target Gas
1	TGS2620	Alcohol
2	TGS825	Hydrogen Sulfide
3	TGS826	Ammonia
4	MQ3	Alcohol
5	MiCS2710	Nitrogen Dioxide

IV. GAS FLOW SYSTEM

The main structure of gas flow system is shown in Figure 2. First, sample air is entered into this system by a pump whose flow rate is controlled by a mass flow controller in order to obtain more accurate detection. In the next progress, air sample flows directly into the filters that consist of 2 parts, activated carbon filter to clean the air and water/silica gel to provide the steady humidity. After that, purified air will be drained into reference gas or sample gas chambers by 2 different valves controlled by an electronic selector to prevent surplus gas return. As valve1 and valve2 are opened, the purified air is passing through the reference gas chamber and then into the mixing chamber. On the other hands, if valve3 and valve4 are opened, process will be the same. During these steps, Valve1 and valve3 will be closed to block returning air. In the last progress, the reference gas or sample gas will flow into the mixing chamber that consists of many types of gas sensors for monitoring, measuring, and analyzing signals fed from sensors.

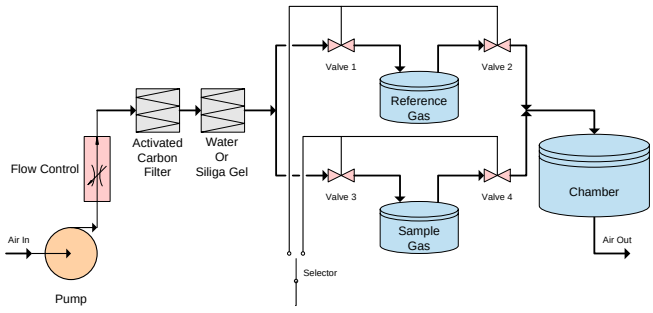

Figure 2. Diagram of a gas flow system.

V. Principal Component Analysis (PCA)

Principal Component Analysis is a useful statistical technique for applications in various fields, such as face recognition, image compression, and pattern recognition for data of high dimension such as odor. Statistic is based around the idea to analyze them in terms of the relationships between the individual points in a big set of data.

The mean X used to indicate the average value of each data set. It does not tell us a lot about the data except for a scale of data. The spread of data is difference. The standard deviation (s) of a data set is a measurement of how spread out the data is. Variance (s^2) is simply the standard deviation squared and almost qualitatively identical to the standard deviation.

$$s = \sqrt{\frac{\sum_{i=1}^{n}\left(X_i - \overline{X}\right)^2}{(n-1)}} \tag{3}$$

The two measures are purely 1-dimensional. In contrast, covariance is always a measure between 2-dimensions.

$$\mathrm{cov}(X,Y) = \frac{\sum_{i=1}^{n}\left(X_i - \overline{X}\right)\left(Y_i - \overline{Y}\right)}{(n-1)} \tag{4}$$

If we have a data set more than 2-dimensions, a higher dimension measure is defined by

$$C^{n\times n} = \left(c_{i,j}, c_{i,j} = \mathrm{cov}\left(Dim_i, Dim_j\right)\right) \tag{5}$$

Where $C^{n\times m}$ is a matrix with n rows and m columns, and Dim_x is the x^{th} dimension. This matrix consists of the relationships between the data sets. We shall look at eigenvectors and eigenvalues of a given matrix. These are rather important, as tell us useful information about our data. Eigenvectors appear as diagonal dotted line on the plot. It provides information about the patterns in the data while eigenvalues are the ones that pointed down the middle of the data. It is the most significant relationship between the data dimensions.

The PCA process consists of five main steps. The first step is data acquisition. In this case, gas concentration data set is read from each sensor via ADC and the data is stored in 2-D array versus sampling time. Subsequently, data for each sensor is subtracted by their mean values and covariance matrix of the subtracted data is computed. The eigenvectors and eigenvalues of the covariance matrix are then calculated. Finally, the principle components are chosen and featuring vectors are formed.

VI. Experimental

During the start-up period when the power has just been applied to the sensor and system, the sensor is heating up and not stable for operation. The stable waiting time must be determined to notify the user that the sensor is ready for operation. In general, the gas sensor characteristic will enter a stable period after applying heating power for ~ 5 seconds.

The electronic nose system was then tested for fresh and rotten orange juice vapor detection by standard flow through technique. Synthetic air is bubbled through that odor solution in water with a flow rate of 0.5 liter/min and flow through the gas sensors. The sensor output is continuously calculated to obtain gas concentration and sent to the computer by the microcontroller. Typical dynamic response of gas sensing measurement toward fresh and rotten orange juice vapor obtained from the mobile gas-sensing system is shown in Figure 3 and Figure 4. From the typical dynamic response, the difference in data set between fresh and ripe orange juice odor cannot be noticed. To identify the difference, the data sets are analyzed by Principal Component Analysis technique. Figure 5 demonstrated the corresponding results from PCA analysis. The results show that the data from fresh and rotten orange juice can be effectively identified by PCA because two data sets can be completely separated in the PCA domain.

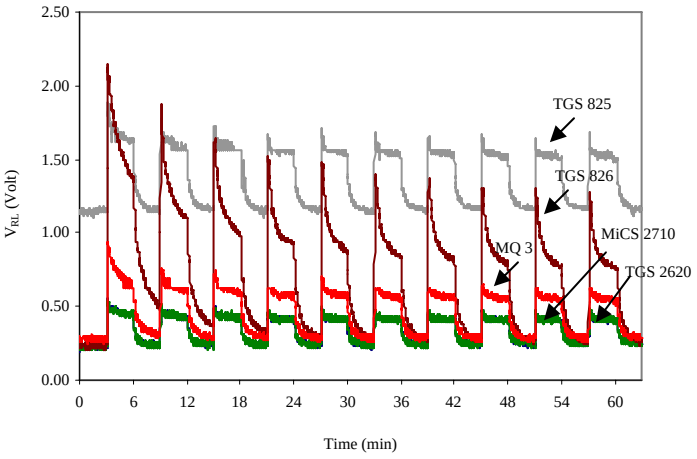

Figure 3. Typical dynamic fresh orange juice sensing response.

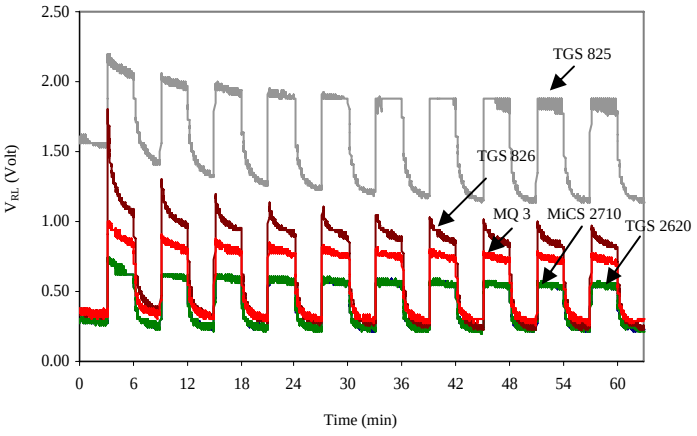

Figure 4. Typical dynamic ripe orange juice sensing response.

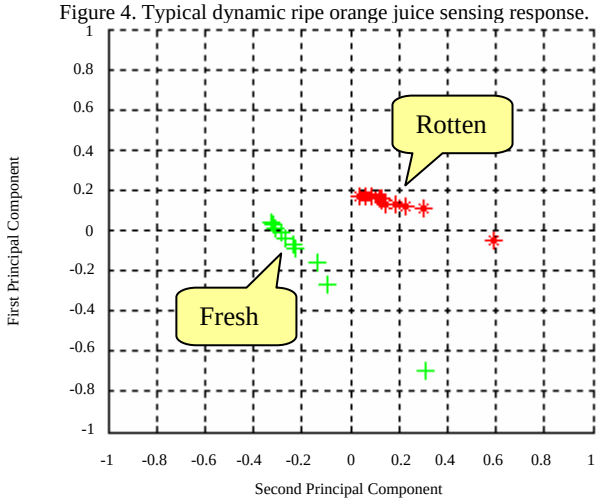

Figure 5. A plot of PCA result data.

VII. Conclusion

In conclusion, we have developed an electronic nose for effective fruit juice freshness recognition by deployment of commercial gas sensor array with compact electronic design for portable uses. The portable electronic nose system employs several small commercial gas sensors and low cost microcontroller system. The system processes sensor array inputs by time division multiplexing, calculates gas concentration, generates output to computer, and analyze gas concentration by applying Principal Components Analysis (PCA) technique used to investigate relationships between the individual points in the data set. In this case, the system is able to recognize between fresh orange juice and rotten orange juice. The tested system has shown satisfactory performance for typical ethanol vapor sensing. The successful application of the portable e-nose system will improve the quality of fruit products of Thailand and increase the use of new technology for farmer problem reduction.

Acknowledgment

We would like to thank Dr. Teerakiat Kerdcharoen for suggestion of Principal Components Analysis (PCA) technique.

References

[1] W. Pimpao, A. Tuantranont, M. Sangworasil, A. Wisitsoraat and T. Lomas, “Electronic Circuit System of Portable Gas Sensor Array”, The International Technical Conference on Circuits/Systems, Computers and Communications Vol.1 (2006) 133-136.

[2] W. Pimpao, T. Kerdcharoen, M. Sangworasil, A. Jomphoak and A. Tuantranont, “Design and Development of Gas Sensor Array System for Portable Electronic Nose”, International Conference On Applied Science (2006).

[3] Lindsay I Smith, “A tutorial on Principal Components Analysis”, February 26, 2002 1-26.

[4] Pascal STROBEL, Abderrazak LFAKIR, Maryam SIADAT, Martine LUMBRERAS, “A portative gas recognition system based on metal oxide gas sensor array”, IEEE (2004) 123-126..

[5] J. Watson, “Tin oxide gas sensor and its applications”, Sensor and Actuator 5 (1984) 29-42..

[6] Omar HELLI, Abderrazak LFAKIR, Maryam SIADAT and Martine LUMBRERAS, “Rapid evaluation of HzS/NOz concentration with a metal oxide gas sensor array”, IEEE (2003) 1320-1324..

[7] V. Coles, G. William, and B. Smith, “Selective studies on tin oxide based semiconductor gas sensors” Sensor and Actuator B3 (1991) 7-14.

[8] T. Oyabu, “Characteristics of SnO2 thin film gas sensor” J. Appl. Phys. 53 (1981) 2785-2787.

[9] H. Madhusudhana and N. Chanodrkar, “Response study of electron-beam evaporated thin-film tin oxide gas sensors” Sensor and Actuator B9 (1992) 1-8.

[10] H. Chueh. and J. Hatfield. “A real-time data acquisition system for a hand-held electronic nose (H2EN)” Sensor and Actuator B 83 (2002) 262-269.

[11] D.C. Dyer. J.W. Gardner, “High-precision intelligent interface for hybrid electronic nose” Sens. Actuators A 62 (1997) 724-728.

[12] J.W. Gradner, P.N. Barlett, “A brief history of electronic noses” Sens. Actuators B 18/19 211-220.

[13] E.L. Hines, E. Llobet, J.W. Gardner, “Electronic noses: a review of signal processing techniques” IEE Proc. Circuits Devices Syst. 149 (6) (1999) 297-310.

A wireless heart rate monitor for fitness exercise researches using 2.4 GHz RF transceivers

W. Siwaprapakorn[(1)] and B. Charoen[(2)]
[(1)] Graduate School, Faculty of Engineering, Khon Kaen University, Thailand
[(2)] Department of Electrical Engineering, Faculty of Engineering, Khon Kaen University, Thailand
E-mail: ee_kku@hotmail.com

***Abstract*- This paper presents the design and implementation of a heart rate monitoring system. This microcontroller-based system is developed for researches on fitness exercises, such as a a study of the relation between heart rates, energy expenditures, and intensity levels of aerobic exercises. The proposed system can be used for a long distance and support multi users where as most commercial heart rate monitor products support only short distance (using magnetic resonant from coil to communicate between transmitters and receivers) and are designed for individual or personal uses. The developed system, based on RF 2.4 GHz GFSK transceiver modules, can support multi channels up to 125 users. A simple threshold level detection algorithm is used to measure R-R interval of inputs from an ECG simulator. Results of heart rates computed from this algorithm correspond well with the known heart rates from ECG simulator. Single channel tests demonstrate that data can be transmitted and received successfully. Indoor and outdoor effective distances tests verify that the system can be used acceptably well up to a distance of 10 meters indoor and 100 meters outdoor. Multi channel tests yields proper functions and performances as expected.**

***Keywords*- Microcontroller, Electrocardiograph, Wireless system, Heart rate monitor**

I. INTRODUCTION

In sport sciences, it is well known that suitable exercise is a crucial factor to become healthy. One popular indicator for good health and appropriate intensity exercise is heart rate. A heart rate monitor (HRM) is a device used to 1) measure exercise stresses or intensity levels 2) monitor patients with obesity during their weight loss programs 3) monitor patients during their cardiac rehabilitation. Commercial HRMs [1] are widely available at various prices depend on specified features. Most commercial HRMs support only short distance monitoring since their main communication technology between transmitters and receivers is based on magnetic resonant from coil. Although HRMs can be developed in various ways [2]-[6], in general, they are designed for individual or personal uses.

Our main objective for this work is to design and implement a HRM system for fitness exercise researches. For this application, a HRM needs some additional features such as long operating distance and it must support multi users. For example, in aerobic exercises, there are many HRM users at the same time within a close distance. In such case, each device interferes other near by devices. With these specific requirements, commercial products are not suitable for our purposes. We propose to use RF 2.4GHz GFSK transceiver modules which support multi devices up to 125 channels, operates at much lower power consumption when compare with other 2.4 GHz devices such as Bluetooth or WLAN, and can be used for our long range requirement (up to 100 meters). Table I gives a general comparison of wireless technologies.

TABLE I
COMPARISON OF WIRELESS CONNECTION TECHNOLOGIES

Type	Coil	RF module	Bluetooth	Wireless LAN
Range	1 m	100 m	10 m	100 m
Speed	N/A	250kbps - 1Mbps	1-2 Mbps	11-54 Mbps
Power Consumption	Low	Low	Medium	High
Frequency	5 kHz	2.4 GHz	2.4 GHz	2.4 GHz
Cost	Low	Low	Medium	High

Figure 1 illustrates the overall concept of the HRM system developed for fitness exercise researches. Each pair of TX and RX must be set at different frequencies and addresses. Heart rate data on each receiver is transferred to a PC for further analyses, in either online (real-time) and offline modes.

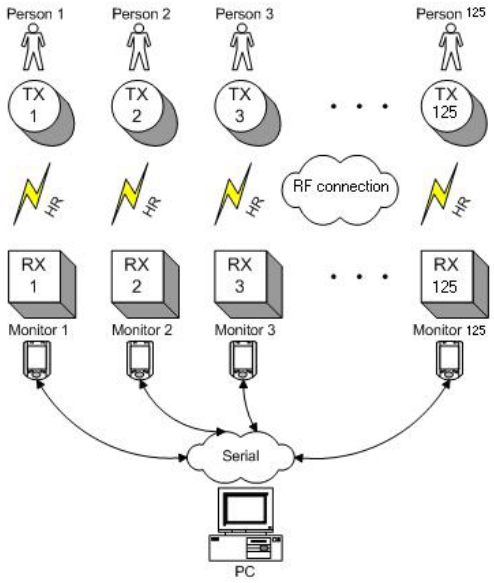

Figure 1. Heart rate monitor system for fitness exercise researches

II. MATERIALS AND METHODS

A detail of one channel HRM, composes of transmitter (TX) and receiver (RX), is shown in Figure2.

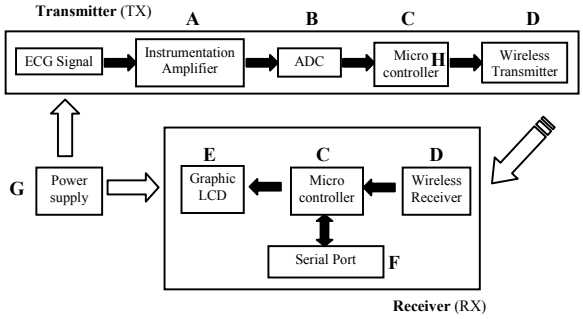

Figure 2. Block diagram of the single channel system

A. *Electrocardiograph (ECG) Instrumentation amplifier*

The ECG level is quite low in the range of a few mV. It has to be amplified to match with the input level of an analog to digital converter (ADC) for better resolution. A high precision and low offset instrumentation amplifier MAX4194 from Maxim Integrated Products, Inc [7] has been selected. This IC operates with a single 3 volts power supply.

The ECG amplifier gain can be set by selecting the value of one resistor (R_G). For our application R_G is initially set to 100 ohms to give a voltage gain of 500.

B. *Analog to digital converter*

The amplified ECG signal is digitized by the microcontroller internal 10 bits ADC. The ADC has maximum sampling rate of 15ksps, 1.5LSB absolute accuracy, 1LSB and 0.5LSB integral and differential nonlinearity respectively.

In this work the sampling rate is set at 500sps at 10 bits resolution which is 5 times of the ECG signal bandwidth (typically around 100 Hz).

C. *Microcontroller*

In this system, a microcontroller, is used in two separate parts of the system; Transmitter (TX) and Receiver (RX).

For the transmitter, the microcontroller processes ECG signals and detect heart rates using simple threshold level algorithm. After R-R intervals are detected, it is then used to calculate for instantaneous heart rates. Then the heart rate data is sent to the RF part for wireless transmission.

For the receiver, the microcontroller receives data from the RF part. Then data is sent to be displayed through a graphic LCD. Further analysis of the heart rate data on a PC can be done by interfacing these data through a serial port.

Microcontroller used in this system is ATMEL ATMEGA16 [8]. This chip includes flash memory 16 kB, internal RAM 1 kB, and a 10 bit ADC. In our application the microcontroller runs at 8 MHz clock and operates at 3 V supply. All program codes are in C programming language.

D. *RF transmission*

Laipac TRW-2.4G [9] wireless RF modules are used for sending and receiving data between transmitters and receivers. The operating frequency is 2.4 - 2.524 GHz ISM band, GFSK, and the data rate can be configured at either 250kbps or 1Mbps. This module supports frequency hopping and multi channel up to 125 channels. An interface to a microcontroller is obtained via a 3-wires serial bus. The RF output power can be adjusted from -20dBm to 0dBm (5dBm/step).

In this application, data rate is set at 250kbps and the output power is set to maximum (0dBm).

E. *Graphic LCD Display*

A Nokia 3310 Graphic LCD spare part [10] which is low cost and commonly available locally is selected to display heart rates and show menu of the heart rate monitor. This display has resolution of 84x48 pixels and can be interfaced through SPI bus. It can be configured to show characters in text mode as 14 columns x 6 rows.

F. *Serial Interface*

A PC interface to a microcontroller is required for acquiring either real time (online) or offline data for further analysis. In this work, the microcontroller interfaces to a PC via a serial port at 38400 bps, in 8 bits data format, no parity bit, and using 1 bit stop bit. At the PC, a LABVIEW program is used to display real time ECG signals.

G. *Power Supply*

This system operates with only a single 3 volts power supply from 2 AA batteries. The average current consumption of the system is approximately 20 mA.

H. *Heart Rate Calculation*

Figure 3 depicts the calculation of instantaneous heart rate from the R-R interval measurement (time between peak to next peak of ECG signals).

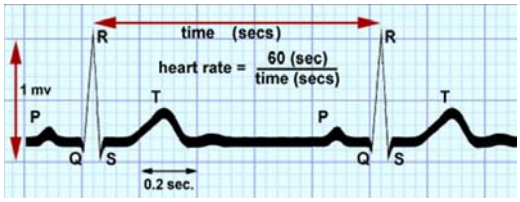

Figure 3. Heart rate calculations from R-R interval

III. EXPERIMENTS AND RESULTS

Experiment to verify system operations was divided into 3 parts; transmitter, wireless connection, and receiver parts.

1. *Transmitter(TX) part*

The amplified ECG signal measured by a 200 Msps DL1520 Yokogawa oscilloscope, as shown in Figure 4, shows that the gain of 500 is adequate for signals from an ECG simulator used initially in this experiment.

From Figure 4, the R-R interval = 496ms, using equation in Figure 3, gives heart rate = 60/0.496 = 120 beats/second.

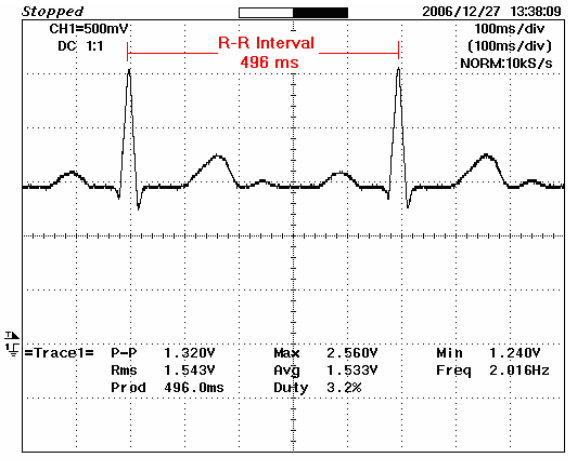

Figure 4. ECG signal at the instrumentation amplifier output

To verify that the ADC part is working properly, the digitized signal is sent through a serial port to be displayed on a PC. Figure 5 shows the digitized data, plotted by LABVIEW, from the microcontroller.

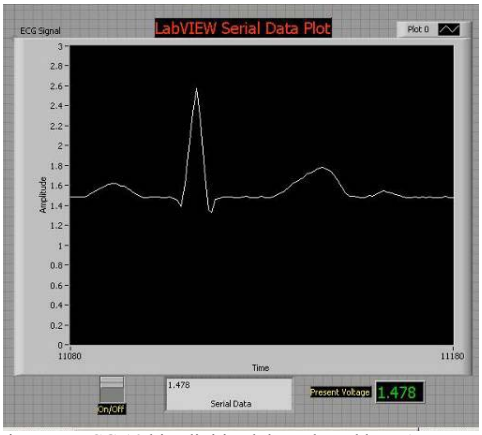

Figure 5. ECG 10 bits digitized data plotted by LABVIEW

The digitized ECG signal is then fed to the microcontroller which is running R-R interval detection program. The algorithm used to detect R-R interval is a simple threshold level detection method. More sophisticated and more robust algorithms can be used with the trade off of computational times. But for this initial test we will employ a simple algorithm to verify the concept of the proposed system. Figure 6 shows some heart rates which correspond well with those calculated from ECG simulator displayed in Figure 4.

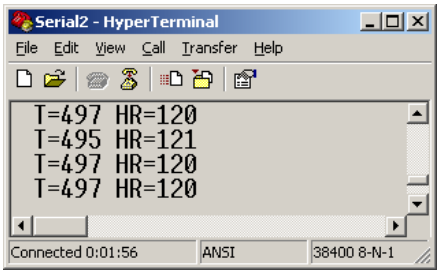

Figure 6. Heart rate calculates from microcontroller.

2. *Wireless connection part*

2.1 Operating Ranges Test

2.1.1 Indoor range, the RF wireless connection was tested for operating range with maximum RF output power, 0 dBm. By monitoring and comparing 350 Bytes data at serial ports of the transmitter and receiver. Byte-to-byte comparison is performed while the distance is varied until data differences occur. An indoor operating range of 10 meter can be achieved without data differences. Figure7 shows that the 350 bytes of sampling data at the transmitter and receiver are exactly the same at a 10 meters distance.

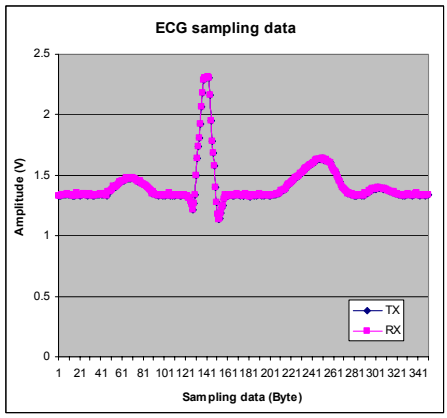

Figure 7. ECG sampling data from transmitter and receiver

2.1.2 Outdoor range, experiments were repeated for outdoor at the same RF output level. Test results show that maximum effective range is approximately 100 meters. This is considerably lower than the given specifications of the RF modules (200 meters for 250 kbps data rate). This may be caused by the test conditions and surrounding environment is not optimum. However, this operating range should be enough for our applications which are mostly outdoor activities.

2.2 Multi Channel Tests

Multi channel experiments, with 2 transmitters and receivers, are performed to verify their functionalities. This test can be divided into 6 cases as given in Table II.

TABLE II
MULTI CHANNEL TESTS FOR RF WIRELESS CONNECTION

Conditions	Configurations	Results
Same frequency Same address	TX1 ↓ RX1& RX2	Both RX get same data
	TX1&TX2 ↓ RX1	RX1 get some cross data from TX2
Same frequency Different addresses	TX1 ↓ RX1& RX2	Only RX1 (same address with TX1) get data
	TX1&TX2 ↓ RX1	RX1 get some data from TX1 due to interferences from TX2
Different frequencies Same address	TX1 TX2 ↓ ↓ RX1 RX2	Both perform well No interference & cross channel
Different frequencies Different addresses	TX1 TX2 ↓ ↓ RX1 RX2	Both perform well No interference & cross channel

From test results in table II, when multiple devices are used with different frequencies, the system works well and there is no interference between near by devices. But for the case which using the same frequency, such as single RX and multiple TXs, the RX gets interfered data or loses some data. And for a single TX and multiple RXs case, all RXs can get all correct data without interfering other devices. Address setting is used to set identity of each pair of TX and RX.

3. Receiver(RX) part

The overall system is tested by feeding ECG signals from an ECG simulator to a transmitter and monitoring data at the receiver. Figure 8 (a) shows a receiver board that displays heart rate on a Nokia 3310 graphic LCD. The displayed heart rate, in Figure 8 (b), is the same as calculated previously at the transmitter part in Figure 6. This result shows that the overall system works well as expected.

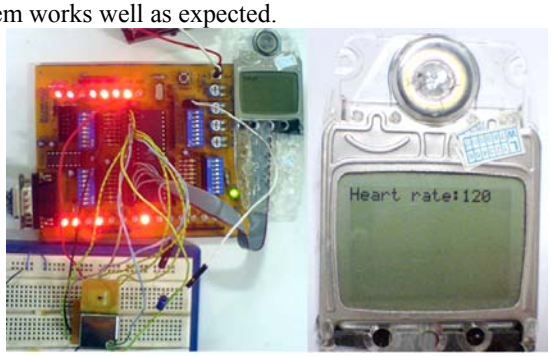

(a) (b)

Figure8. a) A receiver board b) A Nokia 3310 graphic LCD display showing the received heart rate.

IV. Discussion

For the ECG instrumentation amplifier part, the actual measured gain is 495 which a little bit lower than the calculated value due to the tolerance of the resistor R_G. This is not critical since we can change the gain to any desired values by changing the resistance of R_G.

For low power consumption operation, we design to use a microcontroller to operate at a low voltage supply (3V) and reduce clock speed to run at 8 MHz clock. System performances can be improved by trading off of the power consumption constrains.

According to the RF 2.4GHz GFSK transceiver modules datasheet, this module has features for switching frequency channel which support multi devices. However, from our experiments, it is found that adjacent channel frequencies may interference each other. For optimal and error free connection, the system should be set so that there is a frequency space (1-2 MHz) between adjacent channels. This will reduce the total number of channels that can be used at the same time. However, this problem can be fixed by employing frequency hopping to share bandwidth between channels.

Since this system is powered by 2 AA batteries, voltage drop may occur if used for a certain period of time. This affects the level of reference voltage at the ADC and may result in sampling data error. A boost converter circuit with battery voltage monitor should be incorporated for better regulation of the supply voltage.

Further development of this system is to measure actual human ECG signals via electrode chest strap and to investigate more accurate and robust algorithms for R peak detection and R-R interval calculation.

The system is intended to be eventually used in the study of the relation between heart rates, energy expenditures, and intensity levels of aerobic exercises. This is a collaboration research between the Department of Electrical Engineering, Faculty of Engineering, the Department of Pharmacology, Faculty of Medicine, and the Department of Physical Education, Faculty of Education, Khon Kaen University.

V. Conclusion

In this paper, a microcontroller-based system for heart rate monitor is presented. This multi users HRM system is aimed for fitness exercise researches such as the study of relation between heart rate and intensity levels of aerobic exercises. For our application which requires long distance operation, 2.4 GHz RF wireless transceiver modules is chosen for communication between transmitters and receivers. These modules can support multi users up to 125 users which is enough for our purposes.

Test results with an ECG simulator show that both multi users and single user configurations are working as required. From the system effective distance tests, the proposed system works well within the 10 meters indoor range and 100 meters outdoor range.

Acknowledgment

This work is partly supported by the graduate school of Khon Kaen university. Some sample devices are provided from Maxim Integrated Products, Inc.

References

[1] http://www.polarusa.com/comparison/fitness.html
[2] N. J. Holter, "New methods for heart studies: Continuous electrocardiography of active subjects over long periods is now practical", Science, no.134, pp.1214-1220, 1961.
[3] G. Qin and Z. Mu, "Heart rate monitor and method of estimating fitness", Proceedings of the Annual International Conference of the IEEE, Volume 3, 4-7 Nov. 1988, Page(s): 1429 - 1430.
[4] M. S. Alam, A. Chatterjea, and P. Ferriter, "Efficient microcontroller based portable heart monitoring system", IEEE 39th Midwest symposium, Volume 3, 18-21 Aug. 1996, Page(s):1264 - 1267.
[5] C. K. Lew and M. Moghavvemi, "Remote heart rate monitoring system based on electrocardiography", SCOReD 2002. Student Conference, 16-17 July 2002, Page(s):45 – 48.
[6] C. K. P. Ching, M. Z. M. Jenu, and M. N. Husain, "Fitness monitor system", TENCON 2003. Conference on Convergent Technologies for Asia-Pacific Region, Volume 4, 15-17 Oct. 2003, Page(s):1399 – 1403.
[7] http://www.maxim-ic.com/quick_view2.cfm/qv_pk/2006
[8] http://www.atmel.com/dyn/products/product_card.asp?part_id=2010
[9] http://www.wenshing.com.tw/data/rf-module/TRW-24G.pdf
[10] http://www.nxp.com/pip/PCD8544_1.html

An Algorithm of 3D Objects Connection for Dental Bridge Design

Teeraporn Kusalanukhun, Chanjira Sinthanayothin, Wichit Tharanon
Advanced Dental Technology Center (ADTEC),
National Science and Technology Development Agency (NSTDA)
111 Thailand Science Park, Pahon-Yothin Rd, Klong 1, Klong Luang, Pathumthani, 12120, Thailand
E-mail: teeraku@hotmail.com, cephsmile@gmail.com

***Abstract*- Dental restoration is the designed materials used to replace the missing teeth to restore function and morphology. One of the most common types is a bridge, which consists of one or more pontic or artificial teeth anchored by crowns at each end. To fill the gap between the pontic and the crowns, the open space must be bridged to avoid teeth shifting. This bridge is specifically designed for each patient and takes long time to create. Therefore, this paper presents the method for computer aided design using Borland C++ Builder® and OpenGL to connect this open space by 3D object modeling from 3D scanned dental data for design the crowns and bridges. Our technique starts from opening files of the scanned teeth in STL format and selecting the desired surfaces of both end teeth by defining the landmarks and fit them with cubic spline algorithm. Next, the landmarks are rearranged for point matching by comparison of the direction of cross product of the topmost point and the next point on both surfaces. Then the cylinder-like model is created for bridging the space. The bridge can be adjusted size and shape by scaling sections associated with the cubic spline algorithm. The 2D cross section can also be seen using the transformation from 3D frame to 2D contour. The result has shown that our method can be used to create the bridge and leads to the application on adding offset functions, which can be applied for the design of crowns and bridges to fit on individual. This can reduce the production time and also ease to transfer to computer aided production equipment.**

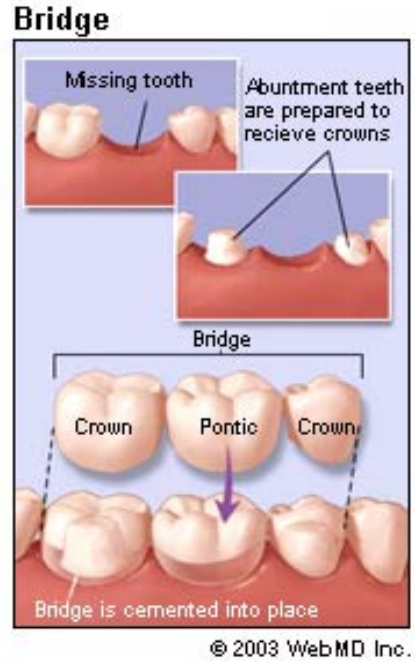

Figure 1 The characteristic of the dental bridge [2]

I. INTRODUCTION

When teeth are missing, the space must be filled to restore the beauty and to avoid several oral complications. The remaining teeth may drift out of position, which causes the change of patient's bite. This change may affect the ability to eat, speak and may produce pain in the jaw joint leading to gum disease or tooth decay [1]. Normally, the methods for tooth restoration are removable denture, bridge and implant. In this paper, the dental bridge is issued due to its reasonable stability, cost, and esthetic. Bridges are nonremovable appliances that are used to replace one or more missing teeth. A typical dental bridge is made up of a pontic (a false tooth) attached to two crowns that cover the surrounding abutment teeth as depicted in Fig. 1. Therefore, the bridge needs the appropriate design to fit on individual. Conventionally, the crowns and bridgework requires the skill and experience of dental technician. It also needs many processes and takes long time to complete. The novel techniques with computer aided design and fabrication have been developed for various dental applications. However, the commercial systems for design crowns and bridgework such as CEREC [3], DentalDesigner™ [4], etc., still have high cost and show no revealed source code. For this reason, the software tool for design the replacement teeth for the bridge application is initially developed in order to help the reduction of the software import to Thailand. In this paper, the focus is on the algorithm used for creating the connector that bridges the gap between each replacement teeth.

II. METHODS

A. Dealing with 3D Model

First of all, 3D tooth model must be imported to the program. Patient's cast model is scanned by the CT scanner and reconstructed into 3D computer model in STL file format which contains surface geometry information of a three

dimensional object. Our software has been written using Borland C++ Builder® and OpenGL to manage this STL model. It also has the user interface for viewing the 3D model with rotation, zoom and translation functions as shown in Fig.2.

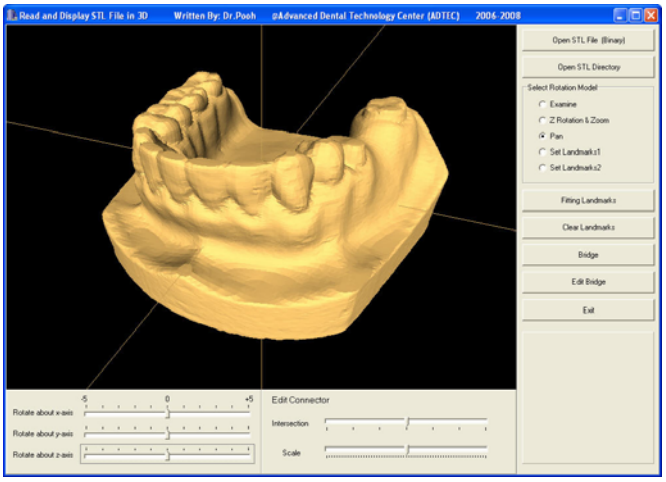

Figure 2 The viewing window of the program

B. Creating Connector

For the bridge part, the suitable standard tooth model is selected to place at the missing tooth, called a pontic. However, there is the gap between the crown and the pontic needed to be connected. Therefore, the algorithm for 3D object connection is performed for bridging them together. First, the desired surfaces for creating the connector of both sides are selected by defining the landmarks with any number of points and the program will fit curve to the circular shape with cubic spline interpolation based on the technique in *Numerical Recipes in C* [5]. One dimensional cubic spline fitting can be explained as in Eq. (1) – Eq.(6). But in our work, some modification has been applied on the interpolation of one dimension to three dimensions. With this method, a series of unique cubic polynomials is fitted between each of the data points with the condition that the curve obtained be continuous and appears smooth. This spline consists of weights attached to a flat surface at the points to be connected. A flexible line is then bent across each of these weights, resulting in a smooth curve. The first step of this approach is applying the three dimensional cubic spline where the one dimensional cubic spline line can be expressed as *G(x)* in Eq. (1) [6, 7].

$$G(x)=\begin{cases} g_1(x) & \text{if} \quad x_1 \le x < x_2 \\ g_2(x) & \text{if} \quad x_2 \le x < x_3 \\ \vdots & \\ g_{n-1}(x) & \text{if} \quad x_{n-1} \le x < x_n \end{cases} \tag{1}$$

where g_i is a 3rd degree polynomial defined by

$$g_i(x)=a_i(x-x_i)^3+b_i(x-x_i)^2+c_i(x-x_i)+d_i \tag{2}$$

for $i = 1, 2, \ldots, n\text{-}1$.

Since the piecewise function $G(x)$ will interpolate all of the data points, we can conclude that

$$G(x_i)=y_i \tag{3}$$

for $i = 1, 2, \ldots, n\text{-}1$. Since $x_i \in [x_i, x_{i+1}]$, $y_i = g_i(x_i)$

The coefficients a_i, b_i, c_i, and d_i in (2) are determined from the first and second derivatives of the n-1 equations of $g_i(x)$. The routine must ensure that $g_i(x), g_i'(x)$ and $g_i''(x)$ are equal at the interior node points for adjacent segments. Substituting a variable S_i for the $g_i''(x_i)$ and y_i for $s_i(x_i)$ will reduce the number of equations and simplify the tasks.

Given the spacing between successive data points is

$$h_i = x_i - x_{i-1} \tag{4}$$

Finally, the variables a_i, b_i, c_i and d_i in (2), or termed the weights of each n-1 equations, will be

$$\begin{aligned} a_i &= \frac{S_{i+1}-S_i}{6h} \\ b_i &= \frac{S_i}{2} \\ c_i &= \frac{y_{i+1}-y_i}{h} - \left(\frac{S_{i+1}+2S_i}{6}\right)h \\ d_i &= y_i \end{aligned} \tag{5}$$

When substituting these weights in (2), its 1st and 2nd derivatives, and including the condition of natural spline where 2nd derivative is equal to zero at the endpoints ($S_1 = Sn = 0$), the system can be determined in matrix equation as follows

$$\begin{bmatrix} 4 & 1 & 0 & \cdots & 0 & 0 & 0 \\ 1 & 4 & 1 & \cdots & 0 & 0 & 0 \\ 0 & 1 & 4 & \cdots & 0 & 0 & 0 \\ \vdots & \vdots & \vdots & \ddots & \vdots & \vdots & \vdots \\ 0 & 0 & 0 & \cdots & 4 & 1 & 0 \\ 0 & 0 & 0 & \cdots & 1 & 4 & 1 \\ 0 & 0 & 0 & \cdots & 0 & 1 & 4 \end{bmatrix} \begin{bmatrix} S_2 \\ S_3 \\ S_4 \\ \vdots \\ S_{n-3} \\ S_{n-2} \\ S_{n-1} \end{bmatrix} = \frac{6}{h^2} \begin{bmatrix} y_1 - 2y_2 + y_3 \\ y_2 - 2y_3 + y_4 \\ y_3 - 2y_4 + y_5 \\ \vdots \\ y_{n-4} - 2y_{n-3} + y_{n-2} \\ y_{n-3} - 2y_{n-2} + y_{n-1} \\ y_{n-2} - 2y_{n-1} + y_n \end{bmatrix} \tag{6}$$

Therefore, Eq. (6) is used to find the interpolation values in all dimensions. In this paper, data points can be any number with 10 control points on each segment such that the surface from defined landmarks can be drawn smoothly.

Next, the landmarks on both surfaces are rearranged for point matching by finding the highest point and comparison of the direction of cross product of the topmost point and the next point as illustrated in Fig.3, where $\vec{\mathbf{V}}_1$ is a cross product of $\overrightarrow{\mathbf{O_1A_1}}$ and $\overrightarrow{\mathbf{O_1A_2}}$ and $\vec{\mathbf{V}}_2$ is a cross product of $\overrightarrow{\mathbf{O_2B_1}}$ and $\overrightarrow{\mathbf{O_2B_2}}$. If the result of the dot product between $\vec{\mathbf{V}}_1$ and $\vec{\mathbf{V}}_2$ is

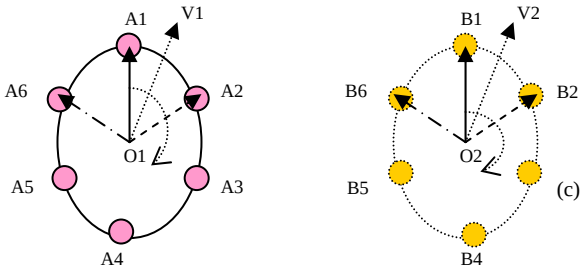

Figure 3 The landmark models from 2 surfaces.
Left, A1-A6 show the landmarks of surface1.
Right, B1-B6 show the landmarks of surface2.

more than zero, the landmarks of two surfaces are arranged in the same direction, otherwise they are reverse. Then the cylinder-like model is created for bridging the space with these arranged points as shown in Fig. 4. To illustrate this model in OpenGL, three points from both surfaces are matched to draw triangular primitive connectedly to form the 3D cylinder. The 3D viewing also involves the lighting that applies on each triangle. An amount of light that object receives at its vertices is determined from the orientation of the normal vector. The normal vector is calculated from the normalized cross products of two vectors on that surface. Due to the flat surface, all three vertices defining a surface share the same normal vector. Therefore, the normal vector needs to be specified only once for each set of three vertices [8].

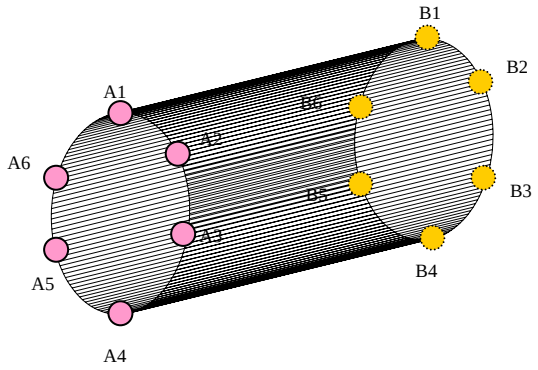

Figure 4 Creating the connector from arranged landmarks.

Moreover, the connector can be adjusted to the most suitable size and shape. The program is able to segment the connector into 1-10 sections by scaling the size of the cylinder according to the user interface. Each section can be scaled its cross section and shown in 2D by the transformation from 3D frame to 2D contour as shown in Fig.5. At first, the 3D positions in world coordinate (F_W) must be transformed to object coordinate (F_O) so that the cross section can be shown perpendicularly on the screen coordinate frame (F_S).

The 3D to 2D projection can be calculated from the generalized equations as the following [9]:

$$S_x = O_x * XSCALE / O_z + X_{Center}, \quad (7)$$
$$S_y = -O_y * YSCALE / O_z + Y_{Center}, \quad (8)$$

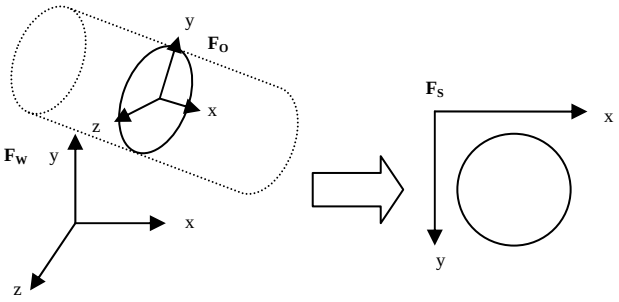

Figure 5 The transformation from world coordinate (F_W) to object coordinate (F_O) and to screen coordinate (F_S).

where S_x and S_y are positions in screen coordinate,
O_x, O_y, and O_z are positions in object coordinates,
XSCALE and *YSCALE* are Field Of View in x and y direction.
X_{Center} and Y_{Center} are half the screen width and half the screen height which are used to correct the alignment because the upper left of the screen is (0, 0). The selected segment is also adjusted at the 2D cross section and affects the size of that segment by inverse transformation.

In addition, the modification in shape in one section also changes curve of the cylinder so that cubic spline interpolation is used again to find three more control points between each segment for smooth the freeform connector.

III. Results

The experiment results with our tooth library have shown that the program can be used to view the 3D tooth model from STL files according to the user interface viewing.

For the 3D tooth connecting section (Fig. 6), user can define the landmarks with any number of point in circular direction (Fig. 6a), and obtain the closed surface, which has to be done

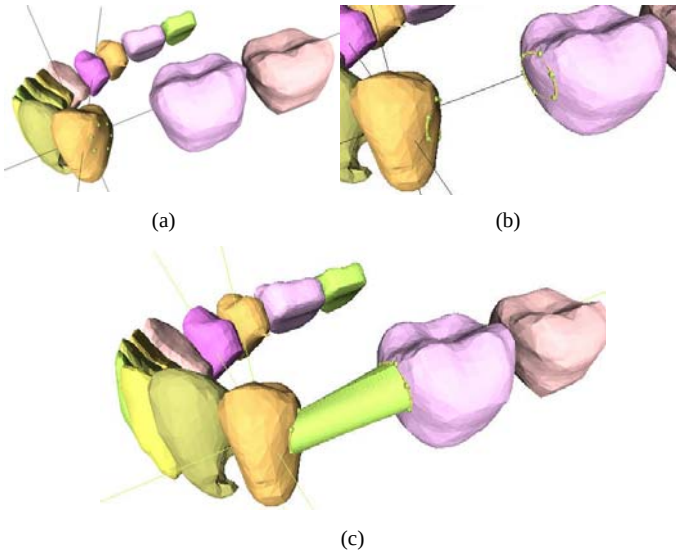

Figure 6 Steps for creating the connector.
(a) Define landmarks, (b) Fit curve on landmarks, and (c) Connect 2 surfaces

on both objects (Fig. 6b). Then 3D connector between 2 objects is generated from these surfaces (Fig. 6c). Moreover, to adjust size and shape of the connector to the most appropriate one, user is allowed to segment the connector and increase or decrease size of that cross section. Without the cubic spline algorithm, each segment was combined directly, which made the adjusted bridge bent sharply as shown in Fig. 7. Therefore, this method was not applied for the design. Alternatively, our program has the cubic spine interpolation step, which can adjust the outer surface of the connector smoothly as can be seen in Fig. 8. The example of the program for connecting two teeth with 10 smoothly adjustable segments is shown in Fig. 9 where the main window illustrates the 3D connector in mesh view and the small window presents the contour of selected section in 2D.

IV. Discussion and Conclusion

The results of the program have expressed that the discussed algorithm can be the basic for the development of the software for the dental bridge design. However, the program still needs further improvements on the 3D measurement and more user friendly on the adjustment functions. Moreover, the dental bridge also consists of the crown parts, which involve the 3D segmentation and offset on the prepared abutments. The integration of these 2 parts has been developing to present the most accurate size, shape, and anatomical features for computer aided design which will be an alternative choice replacing the conventional manual process afterwards.

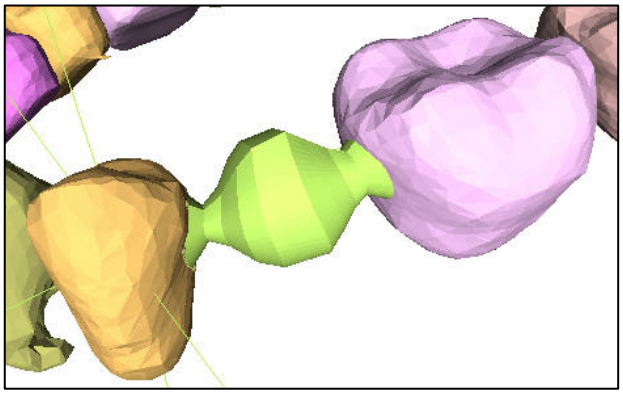

Figure 7 The adjustable connector without cubic spline algorithm

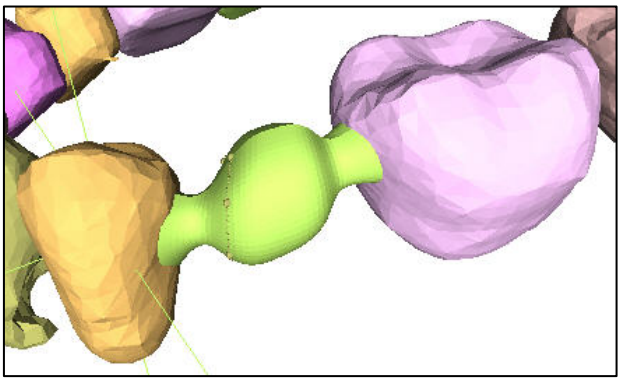

Figure 8 The adjustable connector with cubic spline algorithm

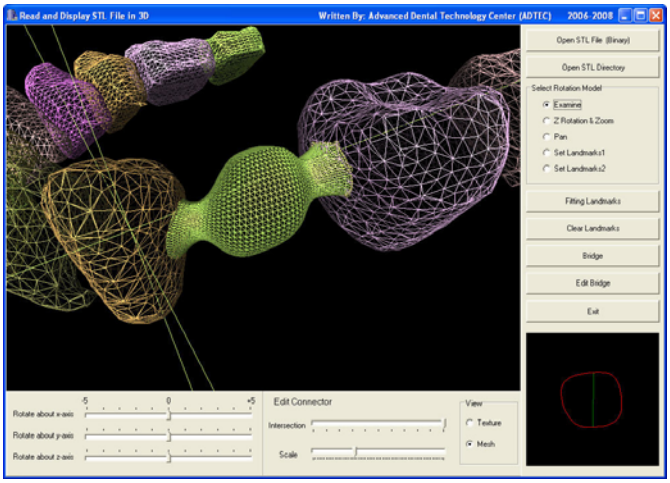

Figure 9 The smoothly adjustable connector between 2 teeth in mesh view and its 2D cross section

References

[1] "Dental bridges" [online], Retrieved January 3, 2007, available from http://www.smilechicago.com/html/bridges.html

[2] Charlotte E. Grayson, MD, "Dental health: Bridges" [online] Retrieved January 3, 2007, available from http://www.webmd.com/content/article/66/79611.htm

[3] Alex Touchstone, Randy J. Phillips, "Simplifying CAD/CAM dentistry," Reprinted from Dental Products Report, November 2005, available from http://www.cereconline.com/

[4] "3Shape DentalDesigner™" [online] Retrieved October 20, 2006, available from http://www.3shape.com/dentistry/dental_designer/dental_designer.htm

[5] William H. Press et al., "Cubic spline interpolation," chap. 3 in *Numerical Recipes in C: The Art of Scientific Computing*, 2nd ed, Cambridge University Press, 1992, available from http://www.nrbook.com/a/bookcpdf.php

[6] Sky McKinley and Megan Levine, "Cubic spline interpolation", *Student Projects in Linear Algebra*, College of the Redwood, [online] Retrieved November 20, 2006, available from http://online.redwoods.cc.ca.us/instruct/darnold/laproj/Fall98/SkyMeg/Proj.pdf

[7] Charles O'Neill, "Cubic spline interpolation" [online] Retrieved November 20, 2006, available from http://www.caselab.okstate.edu/ocharle/projects/cubicspline.pdf

[8] Shreiner D, Woo M, Neider J,and Davis T, *OpenGL Programming Guide: The Official Guide to Learning OpenGL*, Version 1.1, Addisson Wesley Longman, Inc, 1997

[9] Justine Deltener, "3D projection" [online] Retrieved November 16, 2006, available from http://www.inversereality.org/tutorials/graphics%20programming/ 3dprojection.html

Adaptive Thresholding for Iris Recognition

Peeranat Thoonsaengngam and Somying Thainimit
Kasetsart Signal and Image Processing Laboratory (KSIP Lab),
Department of Electrical Engineering, Kasetsart University,
50 Phaholyothin Rd. Jatujak, Bangkok, 10900, Thailand

***Abstract*-This paper presents an intensity-based iris recognition system. The system exploits intensity distributions of iris textures. The textures are enhanced and extracted using local histogram equalization and quotient thresholding. This thresholding technique partitions an iris image into regions of foregrounds and backgrounds such that a ratio between these two regions is the same for all iris images in a database. The extracted iris features are encoded in a way to accommodate a fast matching using a table lookup technique. Computational cost of our proposed 1:1 matching is 9 millisecond. The accuracy of the proposed system evaluated using CASIAv.1.0 iris database is 0.001413%EER.**

I. INTRODUCTION

The term 'biometrics' refers to the science and technology of authentication using physiological or behavioral characteristics of human such as fingerprints, signatures, faces, and irises. Among the biometrics, an iris pattern is a highly accurate and reliable characteristic. Flom and Safir [1] reported that the iris patterns are unique to individual and stable over time and across environments (e.g. occupations, humidity ect.). The uniqueness of iris patterns is the product of dense collections of iris structures and textures such as pigment frills, furrows, freckles, and crypts. These textures can be perceived easily. In addition, an iris is a protected organ located behind the cornea, but in front of the lens. This makes personal authentication possibilities life long.

The most successful commercial iris recognition system is a ramification of an algorithm proposed by John Duagman [2]. He uses 2D Gabor filters to extract phase information of an iris. Matching score of two iris codes is evaluated using hamming distance. After his work, several works are introduced. Wildes [3] analyzes iris features using 2-level Laplacian pyramid. Correlation of the obtained images is used to evaluate their similarity. Ma [4] analyzes and extracts iris features using circular symmetry filters. Sun [5] uses zero-crossings of wavelet transform to extract iris features. He represents the features using five geometric moments. Wen Yang [6] suggests using a group of 2D Gabor filters to detect a set of points, named key points. These points represent local iris texture. K. Miyazawa [7] analyzed an iris using 2D DFT. Only the obtained phase components are used to evaluate the match between two irises.

In this paper, we propose an intensity-based iris recognition system. The system aims to extract visible iris textures, which generally have low intensity level. These iris textures are extracted using local histogram equalization and a quotient thresholding [8]. In quotient thresholding, the threshold values for each image in the database are adapted to illumination of the image. Differences between our work and work in [8] are:

- We proposed to use intensity position of the extracted iris features instead of using its shape information. In [8], the extracted features are fitted with various sizes of circles. Diameter of the fitted circle describes the iris features.
- A new and fast matching technique is introduced in this paper. The proposed iris code is encoded to accommodate matching method, also to compensate effects of elastic distortion.
- The proposed method works on an unwrapped iris image, instead of an iris ring. This is to ease matching implementation.

The rest of this paper is organized as follows: section 2 describes our proposed iris recognition. Section 3 illustrates our experimental results and discussions. The last section, section 4 is our conclusion.

II. THE PROPOSED IRIS RECOGNITION

Our iris recognition approach is composed of five main steps: localization, normalization, feature extraction, feature encoding and matching. Their details are described in the following sections.

A. Iris Localization

Iris localization is to locate inner and outer boundaries of an iris. The inner boundary of an iris is a boundary separating the iris from the pupil, whereas the outer boundary is a boundary separating the iris from the sclera zone. Both boundaries can be located by exploiting intensity differences among organs (pupil, iris, and sclera) and a prior knowledge of circular-like shape of pupil and iris.

Since intensity level of a pupil is typically low and falls separately from intensity range of other eye components, pupil is detected using thresholding operation. Then, edge detection and edge thinning operations are applied over the thresholded regions. These operations yields edges belong not only to edges of the pupil but also of the other components such as eyelashes and reflected lights as shown in Fig. 1(a) and 1(c), respectively. To obtain only edges belong to the pupil, irrelevant edges are removed by examining its circular and diameter property. Fig. 1(b) and 1(d) shows corresponding results of Fig. 1(a) and 1(c), respectively. The obtained edges are fitted using circular model. The fitting results in two

parameters: r-inner and center, which denoted radius of an iris inner boundary and its center position, respectively. The obtained center position is used as reference point for the rest processes of our recognition system.

The iris outer boundary is detected by exploiting intensity difference between iris and sclera. Contrast enhancement algorithm [9] is applied to the image in order to improve contrast nearby the boundary of iris and sclera. The outer boundary is located by searching for abrupt change of average intensity of pixels along arc defined in Fig.2. The search is started nearby the inner boundary and moving outward. The outer boundary is located where the first abrupt change of the obtained average intensity occurs.

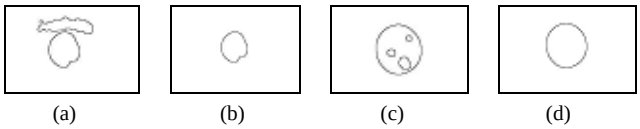

(a) (b) (c) (d)

Figure 1. Example results of pupil detection.

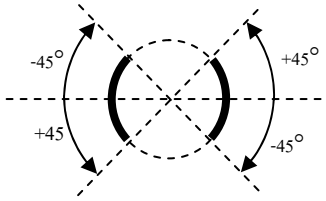

Figure 2. Arcs used in iris outer boundary detection.

B. *Iris Normalization*

Generally, acquired images of one iris have different iris sizes depending on an amount of incoming light. To compensate this variation, the localized iris is normalized into a fixed size rectangle using (1).

$$r_{input} = \{(i/N)\times(R_{outer} - R_{inner})\} + R_{inner},$$
$$\theta_{input} = (2\pi \times j)/M \qquad (1),$$

where, $(r_{input}, \theta_{input})$ is a polar coordinate of a point (x,y) on an input image as shown in Fig.3(a). R_{inner} is an iris inner boundary. R_{outer} is an iris outer boundary. A point (i,j) is a corresponding point of $(r_{input}, \theta_{input})$ on the rectangle that has a size of $N \times M$. Fig. 3(b) depicts an example result of the conversion.

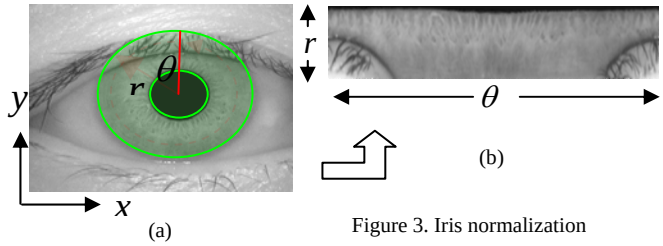

(a) (b)

Figure 3. Iris normalization

C. *Iris Feature Extraction*

In this paper, iris features are extracted using quotient thresholding (QT) technique. The QT technique is an adaptive thresholding proposed in [8]. The technique aims to extract dark pigmented iris textures such as crypts, freckles and moles. As these textures are visible and generally have low intensity values, thresholding technique can be used to extract these textures. However, thresholding operation is sensitive to image illumination. In order to obtain similar but distinguishable iris features, algorithm in [8] was proposed to compensate non-uniform illumination inhibited within an iris image using local histogram equalization (LHE) and proposed to compensate non-uniform illumination occurred across iris images in a database using quotient thresholding (QT).

The LHE is used not only for compensating non-uniform illumination, but also for enhancing informative iris features. The QT is an adaptive thresholding technique aiming to compensate uneven illumination among iris images. The compensation is done by varying the threshold values resulting in image partitioning, based on its histogram. The threshold value is varied until a ratio between the obtained foregrounds and backgrounds reach a pre-specified value. This value is fixed for all images in a database. By fixing this ratio instead of fixing a threshold value, similar iris patterns could be extracted from images of an iris captured under different lighting conditions.

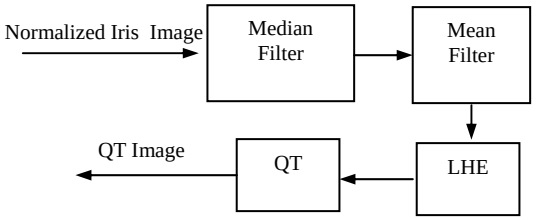

Figure 4. The proposed feature extraction algorithm.

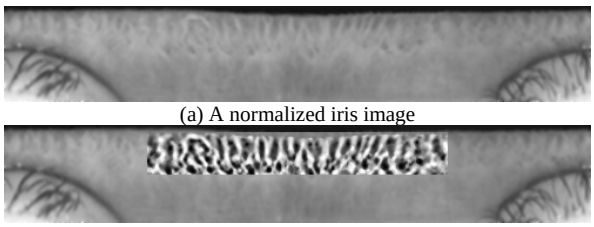

(a) A normalized iris image

(b) The corresponding enhanced iris image

(c) The obtained QT image

(d) Four divided parts for QT encoding

Figure 5. Image results from algorithm's progressive

In [8], the described process is applied over a segmented iris ring directly. This paper, we propose to apply the LHE and QT over a normalized iris image instead. This is to facilitate iris feature encoding and matching procedures. In addition noise

reduction using median and mean filters are applied prior the LHE. Fig. 4 shows our proposed feature extraction algorithm. Fig. 5(c) shows a result obtained from applied the proposed feature extraction on a normalized image shown in Fig. 5(a).

As our proposed is an intensity-based method, noises caused from eyelids and eyelashes can significantly degrade our system performance. To reduce this degradation, the proposed algorithm is performed only on area nearby pupil zone as indicated in Fig 5(b). Since eyelashes have very low intensity, they are usually segmented as one part of iris features. To reduce noisy pixels in our iris feature code, we invert the thresholded image before encoding the features. Surrounding pixels of dark iris textures are concerned in our proposed feature encoding and matching algorithm instead.

D. Feature Encoding

Instead of describing the obtained QT feature using its shape properties as in [8], we proposed to describe the QT features using its intensity position. Positions of the obtained foreground pixels, which represent iris features, are used to find the match between two irises. Its matching score is proportional to a number of matched foregrounds.

The encoding process is started from dividing the obtain QT image into 4 sections, indicated in Fig. 5(d). Each section has a size of 64 × 35 pixels. The background pixel is encoded as "0" and the foreground pixel is encoded as "1". For each section, one row of QT image generates a 64-bit QT code. Therefore, one iris image generates a template of 1120 bytes of QT code.

E. Feature Matching

This step is to find similarity of two QT codes. Its similarity is measured by counting a number of matches between foregrounds extracted from two irises. As we encode the foregrounds as "1", counting a number of matched foregrounds is equivalent to counting a total number of "1" resulted from performing AND operation between two QT codes.

Fast implementation of finding a total number of matched foregrounds is accomplished through a table lookup technique. A lookup table, called a matching score array, is created prior. Each cell of the array contains a normalized matching score, which is associated to a number of matched "1" between two binary QT codes. These two codes are row and column index of the cell.

To have a small size array, each row of the QT code, which is 64 bits, is separated into 4 parts. Each part is a 16-bit long. Thus, a matching score array of size 16x16 is used instead of an array of size 64x64.

Rotation and translation invariance can be achieved by shifting each part of the QT code in range of ±17 pixels horizontally and ±10 pixels vertically, independently. The maximum matching score of the shifted QT code represents its matching score. System matching score is a summation of the four best matching scores obtained from the four parts. The proposed method requires 102,900 times to perform AND operations. Therefore, $102{,}900 \times 4 = 411{,}600$ lookups are carried out.

III. EXPERIMENTAL RESULTS

We validated our proposed system using two databases: CASIA v.1.0 [10] and KSIP DB01R iris database [11]. The system performance is measured in term of Equal-Error-Rate (EER), which is equilibrium error of Fault Accept Rate (FAR) and Fault Reject Rate (FRR).

CASIA iris database is a public iris database. The database contains 756 iris images captured from 108 individual eyes, 7 images for each individual. This database requires $7c2 \times 108 = 2{,}268$ comparisons for generating the distribution of the intra-class matching distance and requires $108c2 \times 7^2 = 283{,}112$ comparisons for generating the distribution of the inter-class matching distance.

KSIP DB01R database contains 1920 iris images captured from 120 Thais volunteers. Eight images of their left and right eyes are captured. For this database, $8c2 \times 240 = 6{,}720$ comparisons are required for the distribution of the intra-class matching distance generation and $240c2 \times 8^2 = 1{,}835{,}520$ comparisons are required for inter-class matching distance generation.

TABLE 1
SYSTEM PERFORMANCE OF THE PROPOSED METHOD

QT ratio	CASIA v.1.0	KSIP DB01R
0.05	0.234734	0.818184
0.10	0.003532	0.605192
0.15	0.003355	0.524651
0.20	0.001413	0.484872
0.25	0.007771	0.515969
0.30	0.066726	0.586786
0.35	0.081708	0.657789
0.40	0.094629	0.740491

Our first experiment is finding QT ratio, which yields the best system performance. Table I indicates the obtained EER for each QT ratio. Empirically, the best system performance is obtained when QT ratio equals to 0.20. It yields 0.001413% EER using CASIA database and 0.484872% EER using KSIP database. The distribution of intra-class and inter-class matching distance obtained using the QT method with 0.2 QT ratio is shown in Fig. 6.

It is clearly seen that the proposed QT method is well perform with the CASIA iris database, but not with the KSIP iris database. This is due to inaccurate iris localization and occlusion problems. Irises in KSIP database is more difficult to locate, as pupils in CASIA database are manually filled with black circles and several pupils in KSIP database have their shape closed to an ellipsoid, not a circle. Fitting ellipsoid with circle often includes dark pupil regions within the segmented iris. In addition, KSIP irises are often occluded by eyelashes.

A reason for us to validate our system using CASIA database is that most existing iris recognition system evaluated

their systems using this database. Table II indicates our proposed system performance comparing to existing methods

Computational cost of our proposed system is shown in Table III. Our system is carried out in C++ on PC Pentium IV 2.4 GHz with 512 MB RAM. Matching time of our proposed method is reduced by half when comparing to one in [8], which reported 17 millisecond. for 1:1 matching. Even though, the 1:1 matching time is reduced significantly. The proposed system still needs 9 seconds for 1000 irises comparisons. This timing should be reduced further for large database usage.

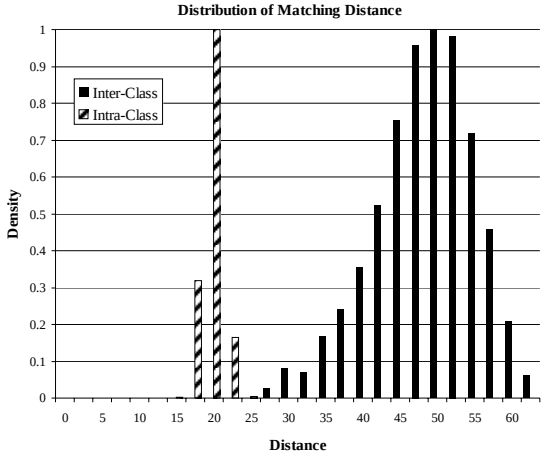

(a)

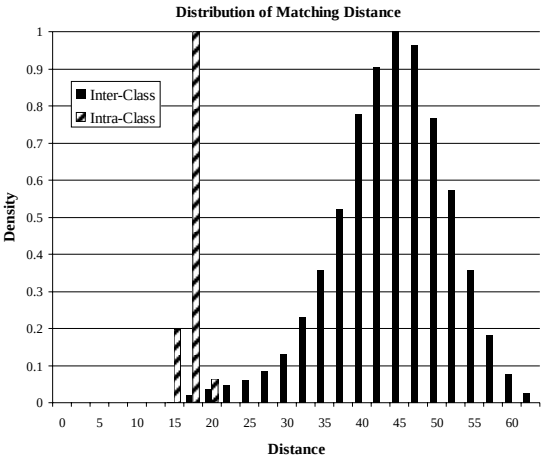

(b)

Figure 6. The distribution of inter- and intra- class matching distance of the proposed method using (a) CASIA v.1.0 database (b) KSIP DB01R database.

TABLE II
SYSTEM PERFORMANCE COMPARISONS (USING CASIA V.1.0)

Methods	EER (%)
Kazuyuki Miyazawa et al. [7]	0.0032
Peng Yao et al. [12]	0.2800
Chia-Te Chou et al. [13]	0.0229
Lu Chenhong [14]	0.1480
Thoonsangngam [8]	9.0810
Proposed method	0.0014

TABLE III
COMPUTATIONAL COST OF THE PROPOSED SYSTEM

Process	Computational Time (msec.)
Localization	234
Normalization	31
Enhancement	212
QT	16
1:1 Matching	9

IV. CONCLUSION

A new intensity-based iris recognition system is proposed in this paper. Intensity variations of iris textures are enhanced using local histogram equalization and are extracted using an adaptive quotient thresholding. Quotient thresholding partitions an iris image into regions of foreground and background such that a ratio between foregrounds and backgrounds is the same for all iris images in a database. Spatial corresponding between the obtained foreground pixels of the two irises is counted and used to measure its similarity. Effects of elastic distortions of an iris are reduced by partially match the extracted iris features. A system speed is reduced using a table lookup technique for searching for a matching score of two iris codes. Computational time of our proposed 1:1 matching algorithm is 9 msec. The proposed system accuracy is 0.001413%EER using CASIAv.1.0 and 0.484872%EER using KSIP DB01R.

REFERENCES

[1] L. Flom and A. Safir, “Iris recognition system,” U.S. Patent, 1987, 4,641,349.

[2] J. Daugman, “High confidence recognition of persons by rapid video analysis of iris texture”,European Convention on Security and Detection, no.408, pp.244-251, 1995.

[3] R.P. Wildes, J. Asmuth, G. Green, S. Hsu, R. Kolczynski, J. Matey and S. McBride, “A machine-vision system for iris recognition,” Mach. Vis. Applic., vol. 9, pp. 1-8, 1996.

[4] L.Ma, T.Tan, Y.Wang, and D.Zhang, “Personal identification based on iris texture analysis”, IEEE Transactions on Pattern Analysis and Machine Intelligence, vol. 25, no.12, pp. 1519-1533, 2003.

[5] Zhenan Sun, Yunhong Wand, Tieniu Tan, and Jiali Cui, “Cascading statistical and structural classifiers for iris recognition,” In Proceedings of ICIP, pp.1261-1264, 2004.

[6] L. Ma, T. Tan, D. Zhang, Y. Wang, "Local intensity variation analysis for iris recognition", Pattern Recognition, vol.37, no.6, pp. 1287-1298, 2004.

[7] K.Miyazawa, K.Ito, T.Aoki, K.Kobayashi, and H.Nakajima, “A phase-based iris recognition algorithm,” Proceedings of ICB, pp. 356-365, 2006

[8] P. Thoonsaengngam, K. Horapong, S. Thainimit, and V. Areekul, “Efficient iris recognition using adaptive quotient thresholding,” Proceedings of ICB, pp. 472-478, 2006.

[9] L.Hong, Y.wan and A.K.Jain, “Fingerprint image enhancement; algorithm and performance evaluation,” IEEE Transactions on PAMI, vol.20, no.8, pp.777-789, August 1998.

[10] http://nlpr-web.ia.ac.cn/english/irds/irisdatabase.htm

[11] http://ksip.ee.ku.ac.th/

[12] P. Yao, J. Li, X. Ye, Z. Zhuang, and B. Li “Iris recognition algorithm using modified Log-Gabor filters,” International Conference on Pattern Recognition, ICPR. vol. 4., pp. 461-464, 2006.

[13] Chia-Te Chou, Sheng-Wen Shih, Wen-Shiung Chen, and Victor W. Cheng, “Iris recognition with multi-scale edge type matching,” International Conference on Pattern Recognition, ICPR. vol.4. pp. 545-548, 2006.

[14] L. Chenhong, and L. Zhaoyang, “Efficient iris recognition by computing discriminable textons,” International Conference on Neural Networks and Brain, ICNN&B. vol. 2, pp. 1164 – 1167, 2005.

On-Line Signature Verification based on Time-Frequency Characteristics of Barycenter trajectory

P.Thumwarin[1], N.Suthithummathat[1] and T.Matsuura[2]
[1]Faculty of Engineering and Research Center for Communications and Information Technology
King Mongkut's Institute of Technology Ladkrabang, Bangkok 10520, Thailand, Email:ktpitak@kmitl.ac.th
[2]Faculty of Information Technology and Electronics, Tokai University
1117 Kitakaname, Hiratsuka, Kanagawa, 259-1292, Japan, Email:matsuura@dt.u-tokai.ac.jp

***Abstract*-We propose an on-line signature verification method based on time-frequency characteristics of barycenter trajectory. The barycenter is determined from the center point of signature and two adjacent pen-point positions with respect to time in handwriting process. The time-frequency characteristics of the barycenter trajectory are extracted by expanding the time sequences of velocity and trajectory of the barycenter into wavelet series. Then the corresponding wavelet coefficients are used as the input and output of the FIR(finite impulse response) system characterizing the handwriting motion in handwriting process. The impulse response of the FIR system is used as the individual feature for the particular signature. Finally, signature can be verified by using the K-L expansion of the obtained impulse response. Signature verification experiments are performed on database consisting of 600 signatures. As the results, the average of Type I(false rejection) and Type II(false acceptance) error rates were 2.66% and 1.33%, respectively.**

I. INTRODUCTION

In many countries, signature is the customary way to verify an individual in daily operations such as withdrawing cash from back account and making contract. Visual examination is popular method for signature verification. However, it usually takes long time for operation and there are occasions for the examiners to make some mistakes by the visual examination. In order to verify the signature effectively, an automatic system for signature verification is required. Signature verification is largely classified into two classes. One is off-line method based on only static visual information , the other is on-line method based on dynamics of handwriting process and has a major advantage that it very difficult to forge or copy the dynamics, which are not visible.

Many methods for on-line signature verification or writer recognition have been reported[1]-[8]. In those methods, dynamic features of handwriting have been used such as x, y coordinates of pen-point movement, pen-point velocity and its acceleration. In the work[4][5], the time-frequency characteristics of handwriting process were extracted by using pen-point position in handwriting process. It is considered that using pen-point position directly is not effective to extract the feature of handwriting. We use the barycenter determined from the center point of signature and two adjacent pen-point positions for the feature extraction. In the work[6][7][8], the handwriting feature was extracted by using Fourier approximation of handwriting process. We consider that such a method in [6][7][8] is not enough to extract the feature of handwriting. In this paper, the features of handwriting are extracted by expanding the time sequence of the trajectory and velocity of the barycenter of pen-point movement into wavelet series to extract the time-frequency characteristics of handwriting process. Furthermore, it is considered that the handwriting motion is an individual feature for signature verification. In this paper, the difference between the handwriting motions can be represented by that between FIR systems. Then the FIR system characterizing the handwriting motion is realized by considering the wavelet coefficients of the velocity and trajectory of the barycenter as the input and output of the FIR system, respectively. In order to represent the difference between the handwriting motions, the impulse response of the FIR system is used. Because it can be seen that the FIR system can be completely characterized by its impulse response[9]. In this case, the obtained impulse response is used as an individual feature of a particular signature. Finally, the K-L expansion of the impulse is used to verify signature.

II. PREPROCESSING

It is assumed here that signature is written on a graphical tablet to verify signature. The horizontal and vertical components of pen-point movement at a time, $t = \tau(\equiv t_n)$, in handwriting process are denoted here as $x(t_n)$ and $y(t_n)$, respectively, where τ is a constant sampling rate. In this section, in order to reduce fluctuation of handwriting, three kinds of normalization with respect to the size, location and duration time in handwriting process of signature are performed as follows:

First, in order to make a standard size of signature, the horizontal and vertical components, $x(t_n)$ and $y(t_n)$ are normalized as

$$\hat{p} = \frac{p(t_n) - p_{\min}}{p_{\max} - p_{\min}}, \quad (p = x, y), \tag{1}$$

where $p_{\min} = \min_{0 \le n \le N-1} p(t_n)$, $p_{\max} = \max_{0 \le n \le N-1} p(t_n)$ and N is a total number of sampled points of pen-point position. In the following $p(t_n), (p = x, y)$ are used to represent the normalized components of pen-point position.

Secondly, the location of signature is normalized as

$$c_p = \frac{1}{N}\sum_{n=0}^{N-1} p(t_n), (p = x, y), \quad (2)$$

$$\hat{p}(t_n) = p(t_n) - c_p, (n = 0,1,2,..., N-1), \quad (3)$$

where c_p is the center point of signature.

Thirdly, in order to reduce a fluctuation of pen-point movement in handwriting process, a trajectory of the barycenter determined from the center point of signature and two adjacent pen-point positions with respect to time in handwriting process, is used. The coordinates $r_x(t_n), r_y(t_n)$ of the barycenter are calculated as

$$r_x(t_n) = \frac{\hat{x}(t_n) + \hat{x}(t_{(n+1)})}{3}, r_y(t_n) = \frac{\hat{y}(t_n) + \hat{y}(t_{(n+1)})}{3}. \quad (4)$$

Furthermore, in order to reduce another fluctuation such as duration time in a part of handwriting process, a segmentation of handwriting process is performed. The pen-up signal is used as the segmentation point for separating a signature trace into a set of components strokes. Then in order to represent the handwriting process for each stroke, we define the followings

$$z_i(t_n) = r_x^{(i)}(t_n) + j r_y^{(i)}(t_n), \quad (5)$$

$$v_i(t_n) = z_i(t_{(n+1)}) - z_i(t_n), j = \sqrt{-1}, \ (i = 1,2,..., L), \quad (6)$$

where $z_i(t_n)$ represents barycenter trajectory and $v_i(t_n)$ corresponds to an average of the velocity between the two adjacent barycenter, L is the total number of stroke in a handwriting process after segmentation. In order to normalize the duration time in the part of handwriting process a piecewise-linear function(PLF) of $z_i(t_n)$ and $v_i(t_n)$ are determined by connecting their components with a straight line. The PLF can be described as

$$q(t) = \sum_{n=0}^{N} q(t_n)\phi_n(t), \ (q = z_i, v_i), \ t \in T_i, \quad (7)$$

where

$$\phi_n(t) = \begin{cases} \dfrac{t - t_{(n-1)}}{t_n - t_{(n-1)}}, t \in [t_{(n-1)}, t_n] \\ \dfrac{t_{(n+1)} - t}{t_{(n+1)} - t_n}, t \in [t_n, t_{(n+1)}] \\ 0, t \notin [t_{(n-1)}, t_{(n+1)}] \end{cases}$$

and T_i is the duration time in the i-th part of handwriting process. Using (7), the duration time in the i-th part of handwriting process is normalized as T_i^N . The T_i^N is determined by using training data for a particular signature.

III. FEATURE EXTRACION

In this section, in order to extract the time-frequency characteristics of the handwriting process, the $z_i(t_n)$ and $v_i(t_n)$ obtained in the preceding section are expanded into wavelet series as

$$q(t) = \sum_{l=0}^{M}\sum_{k=0}^{2^M-1} a_{l,k}^{(q)}\psi_{l,k}(t), \quad (q = z_i, v_i), \quad (8)$$

where $\psi_{l,k}(t)$ is orthonormal wavelet:

$$\psi_{l,k}(t) = 2^{l/2}\psi(2^l t - k), \quad l, k \in Z, \quad (9)$$

$$< \psi_{l,k}, \psi_{m,n} > \equiv \int_{-\infty}^{\infty} \psi_{l,k}(t)\psi_{m,n}(t)dt = \delta_{l,m}\delta_{k,n}, \quad (10)$$

where Haar function is used as mother wavelet $\psi_{l,k}(t)$, $\delta_{l,p}$ is Kronecker' delta and $a_{l,k}^{(q)}, (q = z_i, v_i)$ is the wavelet coefficients obtained through the inner product $a_{l,k}^{q} =< q, \psi_{l,k} >$ as shown in Fig. 1.

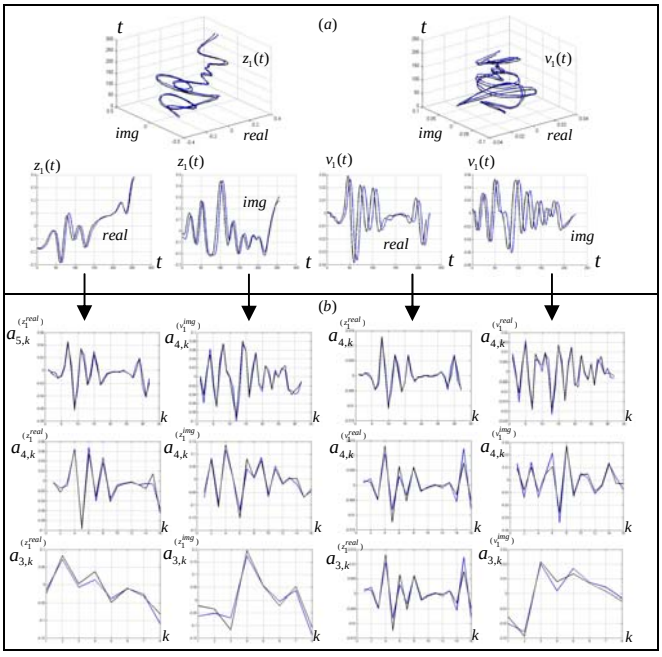

Figure 1. Z_i, V_i and their wavelet coefficients

For the simplicity of explanation, we define the following functions.

$$a_{M,k}^{(q)} = a_{M,k}^{(q^{(real)})} + j a_{M,k}^{(q^{(img)})}, (q = z_i, v_i), \quad (11)$$

$$\boldsymbol{a}_{\boldsymbol{M}}^{(\boldsymbol{q})} = [a_{M,1}^{(q)}, a_{M,2}^{(q)}, ..., a_{M,2^{M-1}}^{(q)}]', \quad (12)$$

$$\boldsymbol{f}_i = [\boldsymbol{a}_1^{(v_i)}', \ \boldsymbol{a}_2^{(v_i)}', ..., \boldsymbol{a}_M^{(v_i)}']' = [f_i(1), f_i(2), ..., f(\underline{N})]', \quad (13)$$

$$\boldsymbol{g}_i = [\boldsymbol{a}_1^{(z_i)}', \ \boldsymbol{a}_2^{(z_i)}', ..., \boldsymbol{a}_M^{(z_i)}']' = [g_i(1), g_i(2), ..., g(\underline{N})]', \quad (14)$$

where $a_{M,k}^{(q)}$ is wavelet coefficient, $\underline{N}$ is a total number of element in $\boldsymbol{f}_i$ and $\boldsymbol{g}_i$, $[.]'$ means the transposition. We consider a handwriting system characterizing the handwriting motion in the handwriting process. The handwriting system consists of subsystem describing the dynamic features in the corresponding part of handwriting process. The subsystem is realized by considering the wavelet coefficients $f_i(k)$ and $g_i(k)$ as the input and output of the i-th subsystem,

respectively. Fig. 2 shows the FIR system characterizing the handwriting system.

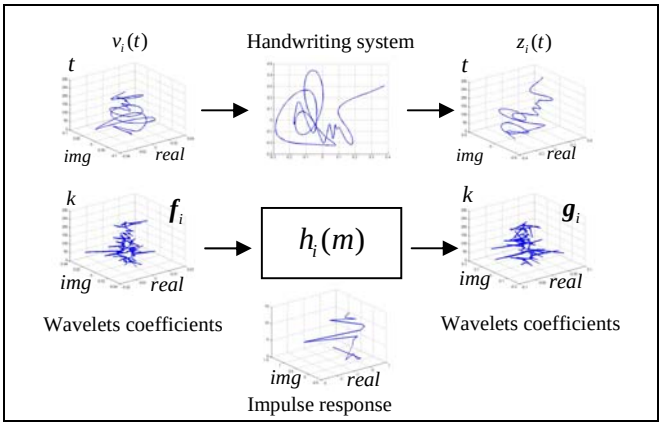

Figure 2. FIR system characterizing the handwriting system.

It is assumed that the subsystem can be described by

$$\hat{g}_i(k) = \sum_{m=0}^{M_i} h_i(m)\, f_i(k-m), (k = 0,1,...,K_i - 1), \quad (15)$$

where $\boldsymbol{h}_i' = [h_i(0), h_i(1), .., h_i(M_i)]$ is an impulse response of the subsystem, M_i is the order of the subsystem and $\hat{g}_i(k;\boldsymbol{h}_i)$ is an approximation of $g_i(k)$. $\boldsymbol{h}_i'$ means the transposition of $\boldsymbol{h}_i$. The impulse response $\boldsymbol{h}_i$ can be obtained by minimizing the least-square error at M_i as

$$E_i = \sum_{k=0}^{K_i-1} \left| g_i(k) - \hat{g}_i(k;\boldsymbol{h}_i) \right|^2 \to \min. \quad (16)$$

The details to determine the impulse response are reported in the work[7]. In order to characterize the handwriting motion in a whole handwriting process, the impulse responses of subsystems are combined as

$$\boldsymbol{h}^{\#} = [\boldsymbol{h}_1', \boldsymbol{h}_2', \boldsymbol{h}_3', ..., \boldsymbol{h}_L']', \quad (17)$$

where $\boldsymbol{h}^{\#}$ is a feature parameter vector used as the feature of handwriting. Fig. 3 shows the impulse response of the FIR system obtained from genuine signature and forgery. It can be seen from Fig. 3 that the impulse responses of the FIR system obtained from genuine signatures are quite similar and different from that obtained from the forgeries. Therefore it is considered that the obtained impulse response can be used as the individual feature of the particular signature.

IV. Signature Verification

In this section, the K-L expansion of the feature parameter vector obtained in the preceding section is used to verify signature. The signature verification procedures are given below.

1) Calculate the following covariance matrix R:

$$R = \frac{1}{P}\sum_{i=1}^{P} (\tilde{\boldsymbol{h}}_i^{\#} \tilde{\boldsymbol{h}}_i^{\#\prime}), \quad (\tilde{\boldsymbol{h}}_i^{\#} = \boldsymbol{h}_i^{\#} - \bar{\boldsymbol{h}}^{\#}), \quad (18)$$

$$\bar{\boldsymbol{h}}^{\#} = \frac{1}{P}\sum_{i=1}^{P} \boldsymbol{h}_i^{\#}, \quad (19)$$

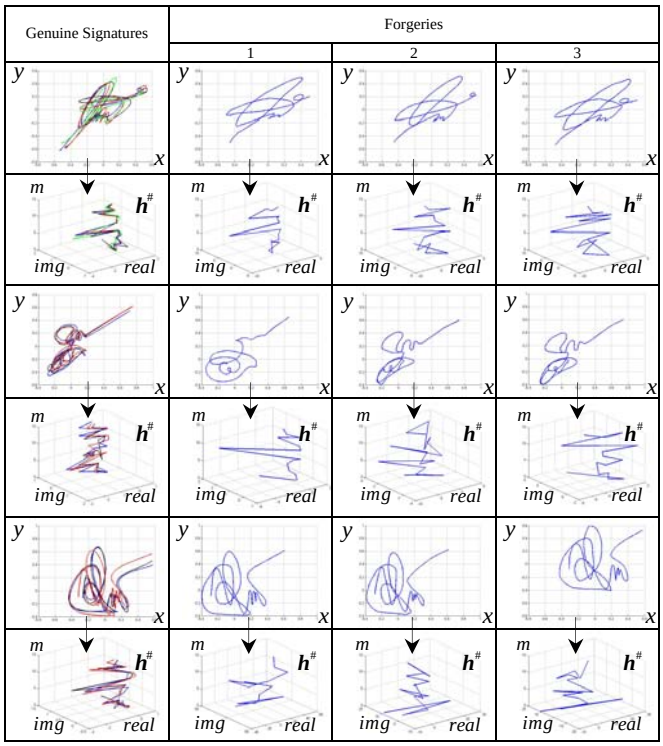

Figure 3. Impulse response obtained from genuine signatures and forgeries.

where $\boldsymbol{h}_i^{\#}$ is the feature parameter vector obtained from training data for the particular signature, P is a total number of training data.

2) Calculate the eigenvalues λ_k and the corresponding eigenvectors $\boldsymbol{u}_k$ of the covariance matrix R:

$$R\boldsymbol{u}_k = \lambda_k \boldsymbol{u}_k. \quad (20)$$

3) Form the transformation matrix U from the N^* eigenvectors corresponding to the largest eigenvalues of R as follows

$$U = [\boldsymbol{u}_1, \boldsymbol{u}_2, ..., \boldsymbol{u}_{N^*}] \quad (21)$$

where

$$\lambda_1 > \lambda_2 > ... > \lambda_{N^*}.$$

4) Compute the K-L coefficients $\boldsymbol{c}$

$$\boldsymbol{c} = U'\,\tilde{\boldsymbol{h}}^{\dagger} \equiv [c_1, c_2, ..., c_{N^*}], \quad \tilde{\boldsymbol{h}}^{\dagger} = \boldsymbol{h}^{\dagger} - \bar{\boldsymbol{h}}^{\#}, \quad (22)$$

where $\boldsymbol{h}^{\dagger}$ is the feature parameter vector obtained from the signature to be verified and $\bar{\boldsymbol{h}}^{\#}$ is obtained from (19).

5) The signature is verified as

$$\begin{array}{ll} \text{True} & \text{if } \|\boldsymbol{c}\| < \eta, \\ \text{False} & \text{otherwise,} \end{array} \quad (23)$$

where $\|\,.\,\|$ is Euclidean norm and η is a predetermined threshold value determined using training data set for a particular signature

V. EXPERIMENTS

Signature verification experiments were performed on database consisting of 300 genuine signatures and 300 forgeries collected from 10 particular writers for one year. In the experiments, the training data set of the feature parameter vectors was determined using 4 signatures selected randomly from the database for a particular signature. Fig. 5 shows the examples of Euclidean distance obtained from (23) using the signatures in our database. In the experiments, we use the threshold value at the point where the two types of error rates are nearly equal for a particular signature. Comparison of the experimental results for the proposed method and the method in the work[8] were shown in Table I. It can be seen in Table I that the proposed method is able to verify signature with better error rates in comparison with the work[8]. Fig. 4 shows the comparison of the impulse responses obtained from the proposed method and method in the work[8]. It can be seen from Fig. 4 that the impulse response obtained from the method in this paper is more suitable for signature verification than that obtained by using method in the work[8].

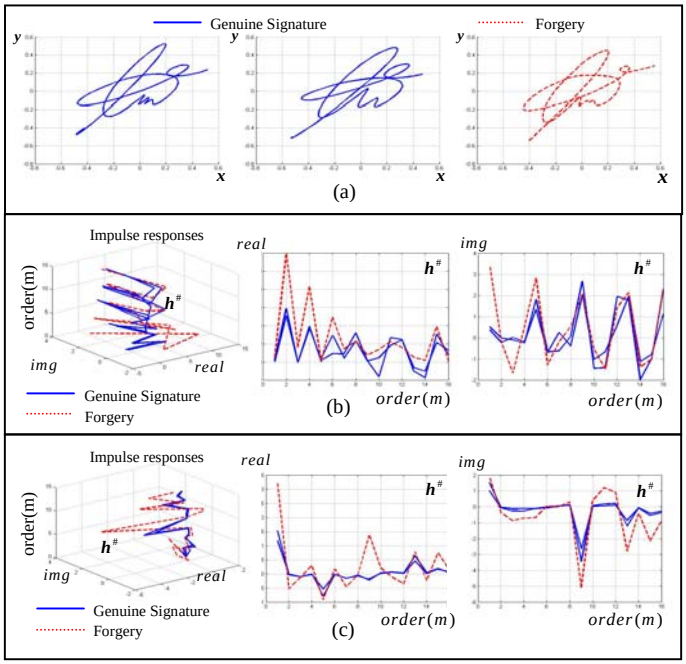

Figure 4 . (a) Genuine signatures and forgery, (b) impulse response (method in the work[8]) , (c) impulse response (the proposed method).

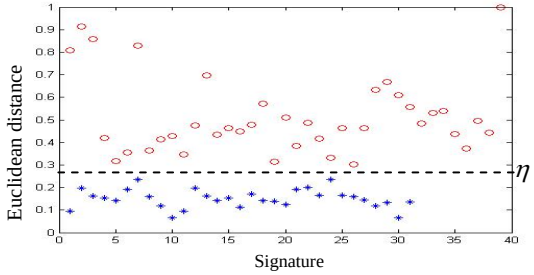

Figure5. Euclidean distances

TABLE I ERROR RATES

Persons	Number of data		Error rates (%) (proposed method)		Error rates (%) (method in work[8])	
	Genuin signatures	Forgeries	Type I	Type II	Type I	Type II
A	30	30	0	0	3.33	2.43
B	30	30	3.33	0	0	0
C	30	30	0	0	0	0
D	30	30	0	0	4.7	2.63
E	30	30	0	3.33	3.33	3.33
F	30	30	6.66	0	10	10
G	30	30	0	0	0	0
H	30	30	0	0	13.33	6.66
I	30	30	10	10	10	10
J	30	30	6.66	0	0	0
Average			2.665	1.33	4.469	3.505

VI. CONCLUSIONS

We proposed an on-line signature verification method based on time-frequency characteristics of barycenter trajectory of pen tip in signing process. In the proposed method. Haar wavelet was used to describe the above time-frequency characteristics. In order to extract the individual signing feature for a particular person, the wavelet coefficients of the velocity and the barycenter trajectory in signing process were used as the input and output of a FIR system characterizing the signing process. Then the impulse responses of the FIR system were defined as the individual signing feature. Signature verifications were performed by evaluating the difference between the impulse responses for genuine signature and forgery. It was found from our experimental results that the impulse responses can characterize the individual signing feature clearly and available for signature verification.

References

[1] R. Plamondon and Sargur N. Srihari, "On-Line and Off-Line Handwriting Recognition: A Comprehensive Survey," IEEE Trans. Pattern Anal. Mach. Intell., vol.22 no.1, pp. 63-84, 2000.

[2] M.Yoshimura, Y.Kato S.Matsuda and I.Yoshimura, "On-line signature verification incorporating the direction of pen movement," IEICE Trans., vol.E74, no.7, pp.2083-2092, 1991.

[3] Y.Komiya, T.Ohishi and T.Matsumoto, "A pen input on-line signature verifier integrating position, pressure and inclination trajectories," IEICE Trans. Inf. & Syst., vol.E84-D,no.7, pp.833-838, 2001.

[4] T.Matsuura and P.Thumwarin and S.Yamamoto : "Writer Recognition Based on Time-Frequency Characteristics of Handwriting Motion," ISPACS'99 Proceedings, pp.97-100, 1999.

[5] T.Matsuura, P.Thumwarin, "On-Line Writer Recognition for Thai Cursive Signature," NORSIG2000, pp. 49-51, 2000.

[6] P. Thumwarin and T. Matsuura, "On-line writer recognition for Thai numeral," IEICE Trans., vol.E86-A, no.10, pp.2535-2541, 2003.

[7] P. Thumwarin, "On-line writer recognition for Thai based on impulse response of FIR system characterizing handwriting motion," Doctoral Thesis, Tokai University JAPAN, 2004.

[8] P. Thumwarin and T. Matsuura, "On-Line Writer Recognition for Thai based on Velocity of Barycenter of Pen-Point movement," ICIP04, pp. II 889-892, 2004.

[9] A. V. Oppenheim, R. W. Schafer and J. R. Buck, Digital Signal Processing, Prentice-Hall, 1999, pp.23-43.

Signature Identification Using Linear Predictive Code Coefficients and Neural Network

T. Wijitpornchai, J. Koseeyaporn, and P. Wardkein
Department of Telecommunication Engineering, Faculty of Engineering,
King Mongkut's Institute of Technology Ladkrabang, Bangkok, 10520 THAILAND
pramote@telecom.kmitl.ac.th

***Abstract*- This paper presents a signature identification using linear prediction code (LPC) coefficients and Neural Network. The 2-D signature signal obtained from the tablet digitizer is separated into two 1-D signals. Each signal represents the information in horizontal and vertical direction versus time, (X,T) and (Y,T) respectively. These signals are modeled by the linear prediction system where the LPC coefficients represent the extracted features. The obtained feature vectors are fed as the input to the neural network for training and verification. The test results show that the average accuracy achieves 98.33% when using only either the (X,T) or the (Y,T) signals and 87.67% accuracy when using both of them to verify owner signature. In addition, for fraudulent situation, the proposed system provides 45% and 84% of accurate verification when inspecting either the (X,T) or the (Y,T) signals and both of signals, respectively.**

I. INTRODUCTION

Nowadays, there are many methods to identify person. Especially, the method of biometric which makes use of biology characteristic of each person such as, fingerprint, eye's pattern and ECG (Electro Cardiogram) to identify the uniqueness of human. However, a conventional way such as personal signature is still be the most popular one. For example, in banking system, the signature is employed to identify the owner of banking account. Another example is in an e-passport system; even though the biometric information such as fingerprint is an addition requirement but the conventional signature is remain used.

As stated above, personal signature which is handwriting of each person thus still be important. It is a simple, and a low cost technique which provides a high accuracy of identification. Conventionally, the decision of signature verification is done by a human (e.g. a bank teller); however, this task would be more convenient if it can be accomplished by an automated system.

In literature, the signature personal verification systems are classified into two methods, the first one is an off-line (statistical) technique and the second one is an on-line (dynamic) technique [1-11]. For the off-line technique, a 2-D image X-Y plane or horizontal and vertical data of signatures is collected and compared with image of owner signature that is previously collected. But this technique is easily fraudulent because the dynamic feature of the signature is not taken to be accounted. Therefore, the on-line technique is an alternative method. The data (X, Y, T) of a signature are collected where (X, Y) is a co-ordinate of each data point and T represents time at that point, respectively. For dynamic system (on-line), both similarity and stroke of the obtained signature are simultaneously used for personal verification. As a result, it is very difficult for one who attempts to fraud the signature without stoke information. Hence, most employed personal identification systems are based on dynamic handwritten technique.

In general, the dynamic method colleted signature signals with a tablet digitizer. The obtained signals are preprocessed (such as magnitude normalization, time normalization and DC canceling) by microprocessor and then discriminated their features for example velocity, and/or accelerate of signature signal [1],[3], or pressure, variation, vibration and consistency [2]. These features are then fed to be input of a decision process such as Hidden Markov Model, NNW (Neural Network) [12].

In this paper, the dynamic signature verification system is proposed where the handwritten feature extraction is based on linear predictive coding (LPC). The 2-D signature signal collected by a tablet is arranged into two of 1-D signals which are a (X, T) signal and a (Y, T) signal. The two groups of the LPC coefficients respectively obtained from a (X, T) signal and a (Y, T) signal are fed to be the input of a perceptron learning rule neural network for training and/or making a decision of signature verification.

The organization of this paper is given as follows. In section 2, the proposed handwritten identification system and preprocessing detail are described. The results are presented in section 3 where the conclusion and future work are summarized in section 4.

II. THE SIGNATURE IDENTIFICATION SYSTEM

In this work, the signature verification system is presented which is shown in Fig.1. As can be seen, the system is composed of three important procedures; the first one is the preprocessing such as time and magnitude normalization and DC filtering. For the second one, it is the feature extraction process. The LPC coefficients of each signal are determined in the last procedure. Finally, features of the signature signal in the form of LPC coefficients are kept for reference and/or verified.

A. Pre-processing

The 2-D signature signal obtained from the tablet (as an example shown in Fig. 2) is divided into two 1-D signals. These signals which are the (X,T) and the (Y,T) signals

representing information of the signature signal in horizontal and vertical direction, respectively.

Both 1-D signals are DC rejected by subtracting its mean value. In addition, they are normalized to have magnitude scale between -1 and 1 and time scale between 0 and 1000. The preprocessed version of the horizontal signal (X,T) and the vertical signal (Y,T) are illustrated in Fig. 3 (a) and (b), respectively.

B. LPC coefficients

Linear prediction is well-known to be a method for signal source modelling. It is not only dominant in speech signal processing but also wide-spread applied in other areas. The detail of linear prediction will be briefly reviewed as follows.

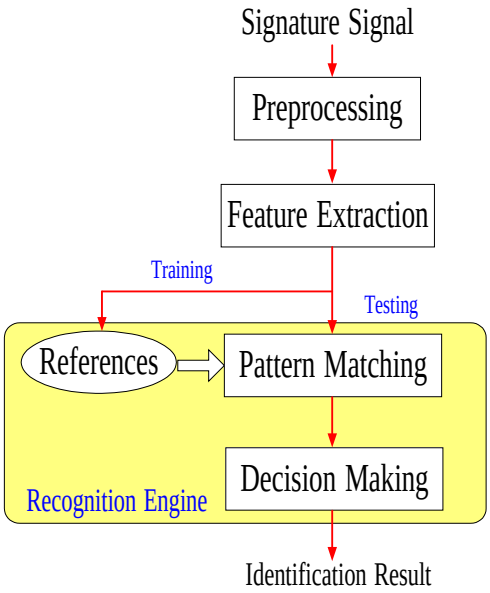

Figure 1. The procedures of the proposed signature verification system.

Figure 2. Example of test signature.

The objective of linear prediction is to form a model of a linear time-invariant digital system through the observation of input and output sequences. In other words, it attempts to estimate a set of coefficients which best describe the behaviour of an LTI system.

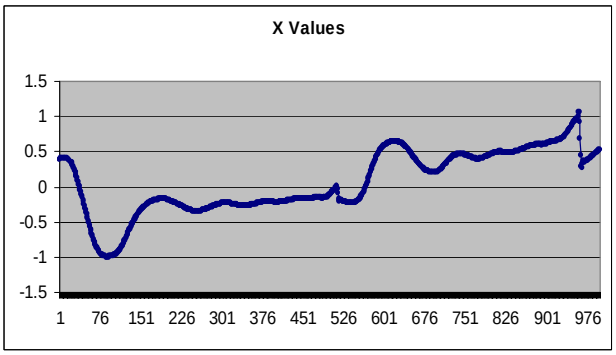

(a)

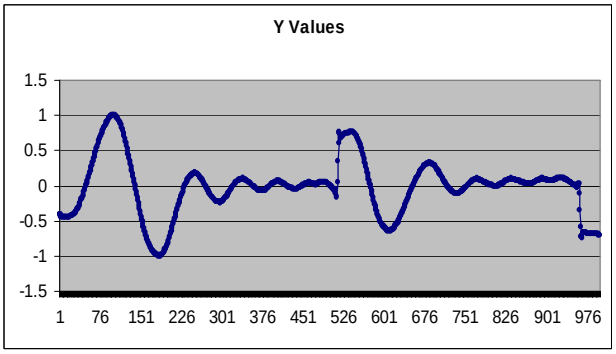

(b)

Figure 3. The preprocessed version of the signature signal
(a) The horizontal signal
(b) The vertical signal

Particularly, linear prediction determines a set of coefficients which provide *a prediction* for a forthcoming output sample $y'[n]$ given knowledge of previous input ($x[n]$) and/or output ($y[n]$) samples. This prediction can be expressed as the following difference equation

$$y'[n]=\sum_{k=0}^{p} a_k x[n-k]-\sum_{k=1}^{q} b_k y[n-k] \quad (1)$$

where a_k and b_k are *predictor coefficients*. It is noted that this estimator provides an inherent sensible way to model its properties even though the order of the system has not known in advance. In general, the most common form of linear prediction used in signal processing is one which the b_k coefficients are zero, so that the output estimate is made entirely on the basis of previous output samples, namely

$$y'[n]=-\sum_{k=1}^{q} b_k y[n-k] \quad (2)$$

which is called an *all-pole* model.

By using the relationship shown in (2), q is equal to order of coefficients, the resulted LPC coefficients of the pre-processed horizontal signature signal (X,T) and the pre-processed vertical signature signal are illustrated in Fig. 4(a) and (b), respectively.

C. *Artificial Neural Network*

An artificial neural network (ANN) is a mathematical structure which is designed for mimic information processing. The structure may have one neuron or multilayer perceptrons. For a one-neuron structure, the network is composed of a set of connected neuron. The neuron receives information through a number of input nodes and then internally processes it to produce a response. An example of a single layer perceptron network with four input nodes is demonstrated in Fig. 5. The process of neural network is typically divided into two stages. The first stage is a linear combination of inputs which is

$$w_{i1}x_1 + w_{i2}x_2 + w_{i3}x_3 + \mathrm{L} + w_{im}x_m$$

which w_{im} and x_i are weight and input vector, respectively. The obtained a linear combination of inputs is then used as the argument of a nonlinear activation function, $Y = f(V)$ which each output node is given by

$$y_i = g\left(\sum_{j=1}^{N} w_{ij}x_j - \mu_i\right) \qquad (3)$$

where

w_{ij} : Connection weight of branch *(i,j)*

x_j : Input data from node *j* in the input layer

μ_i : Threshold value of node *i* in the output layer

g : Activation function

N : Number of input nodes.

III. Simulation Results

In this section, the proposed procedures given in Fig. 1 are examined where one-hundred signature signals obtained from 20 persons (5 signatures from each person) are employed. As can be seen in Table I, by inspecting either the horizontal signature signal (X,T) or the vertical signature signal (Y,T), the results show that the proposed verification system can correctly identify signature 100% of accuracy for q = 10 and 20 and 95% for q = 30. For the case of using both signals ((X,T) and (Y,T) signals) in the inspecting process, the tested results provide 95% for q = 10, 90% for q = 20 and 78% for q = 30.

In addition, two situations of fraudulent signature which are the case that stroke, timing and sequence of the tested signature are unknown and known, respectively, are examined. The fraudulent signatures of these cases are forged by other 5 persons (5 signatures/person/case). The tested results of these situations where q = 10, 20 and 30 are given in Table II – IV, respectively. For the first case, the test results show 64% of accurate verification for q = 10, 20 and 30 when inspecting only the horizontal (X,T) or vertical (Y,T) signals and 88% of accuracy when inspecting both directions of signal for q = 10, 20 and 30. In the second case when stroke, timing and sequence of the signature are known, the test results show that the accurate verification decreases to 24% for q = 10, 26% for q = 20 and 28% for q = 30 when inspecting only the horizontal (X,T) or vertical (Y,T) signals. In addition, when inspecting both horizontal (X,T) or vertical (Y,T), the accuracy decreases to 80% for q =10, 20 and 30.

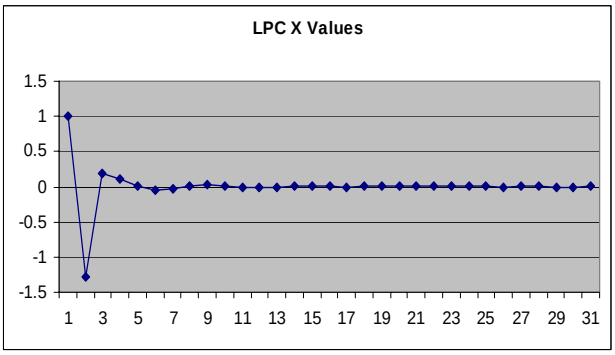

(a)

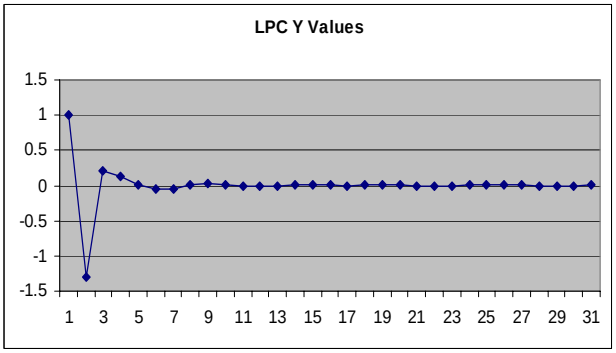

(b)

Figure 4. The resulted LPC coefficients of
(a) the preprocessed horizontal signal
(b) the preprocessed vertical signal.

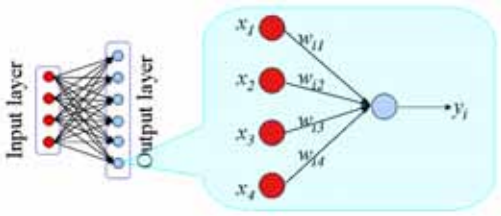

Figure 5. Single Layer Perceptron Network for N = 4.

TABLE I
TEST RESULTS FOR OWNER SIGNATURE (q = 10, 20 and 30)

q	Percentage of accurate verification	
	Inspecting in the (X,T) or the (Y,T) signals	Inspecting both the (X,T) and the (Y,T) signals
10	100	95
20	100	90
30	95	78

TABLE II

TEST RESULTS FOR FRADULENT SIGNATURE (q = 10)

Fraudulent signatures	Percentage of accurate verification	
	Inspecting in the (X,T) or the (Y,T) signals	Inspecting both the (X,T) and the(Y,T) signals
Unknown stroke, timing and sequence	64	88
Known stroke, timing and sequence	24	80

TABLE III

TEST RESULTS FOR FRADULENT SIGNATURE (q = 20)

Fraudulent signatures	Percentage of accurate verification	
	Inspecting in the (X,T) or the (Y,T) signals	Inspecting both the (X,T) and the(Y,T) signals
Unknown stroke, timing and sequence	64	88
Known stroke, timing and sequence	28	80

TABLE IV

TEST RESULTS FOR FRADULENT SIGNATURE (q = 30)

Fraudulent signatures	Percentage of accurate verification	
	Inspecting in the (X,T) or the (Y,T) signals	Inspecting both the (X,T) and the(Y,T) signals
Unknown stroke, timing and sequence	64	88
Known stroke, timing and sequence	32	80

IV. SUMMARY

In this paper, the signature verification system based on LPC coefficients is proposed. The information of the signature signal in horizontal direction and vertical direction (both are respected to time), respectively, (X,T) and (Y,T) are feature extracted by using LPC technique. The obtained LPC coefficients are fed to be the input of the ANN for verification. For owner signature verification, the test results show 98.33% of accuracy in average when either the (X,T) or the (Y,T) signals are inspected. But it provides averagely 87.67% of accurate verification when both of the (X,T) and the (Y,T) signals are inspected. For the fraudulent situation, the percentage of accuracy decreases to averagely 45% when either the (X,T) or the (Y,T) signals are inspected and to averagely 84% when both of the (X,T) and the (Y,T) signals are verified. For the future research, the number of LPC coefficients that is suitable for this system is further studied. Additionally, more signature signals are verified to prove accuracy of the proposed system in practical.

REFERENCES

[1] D. Penagos, N. Prabhakaran and V. Wunnava, "An Efficient Scheme for Dynamic Signature Verification," *Proc. IEEE Conf. Science and Technology*, pp. 451- 457, 1996.

[2] M. Palaniswami, N.Prabhakaran, S.Thacore and W. Subbarao, **"**Signature Identification Using Neural Networks," *Proc. IEEE Conf. EC3-Energy, Computer, Communication and Control Systems***,** vol. 2, pp. 149-152,1991.

[3] Y. Sato and K. Kogure, "On-Line Signature Verification Based on Shape, Motion and Writing Pressure," *Proc. Sixth Int'l Conf. Pattern Recognition*, pp. 823-826,1982.

[4] C.C. Tappert, C.Y. Suen, and T. Wakahara, "The State of the Art in On-Line Handwriting Recognition," *IEEE Trans. Pattern Analysis and Machine Intelligence*, vol. 12, pp. 787-808, 1990.

[5] P. Viviani and G. McCollum, "The Relation between Linear Extent and Velocity in Drawings Movements," *Neuroscience*, vol. 10, no.1, pp. 211-218, 1983.

[6] B. Wirtz, "Storke-Based Time Warping for Signature Verification," *Proc. Int'l Conf. Document Analysis and Recognition*, pp.179-182, 1995.

[7] R. Plamondon and G. Lorette, "Automatic Signature Verification and Writer Identification , the State of the Art," *Patter Recognition*, vol.22, no. 2, pp. 107-131, 1989.

[8] K. Huang and H. Yan, "On-line Signature Verification Based on Dynamic Segmentation and Global and Local Matching," *Optical Eng.*, vol. 34, no. 12, pp. 3480-3487, 1995.

[9] I. Nakanishi, "On-line Signature Verification Method Utilization Feature Extraction base on DWT" *Circuits and Systems, 2003. ISCAS '03. Proceedings of the 2003 International Symposium on***,** vol.4, no. 4, pp. 73-76, 2003.

[10] R. Plamondon, "The handwriting signature as a biometric identifier: Psychophysical model and system design", *European Conf. convention on security and detection*, no.488, 1995.

[11] R. Plamondon, "On-line and Off-line handwriting recognition a comprehensive survey", *IEEE Trans. pattern analysis and machine intelligence*, vol.22, no.1, pp. 63-84, Jan. 2000.

[12] T. Maneechote, "Signature verification using neural network", *King Mongkut's Institute of Technology Ladkrabang*, unpublished, 2004.

Generalized N-Tuple Machine on Signature Verification

Phongsan Nunsuk and Yuttana Kitjaidure
Faculty of Engineering King Mongkut's Institute of Technology Ladkrabang.
Ladkrabang, Bangkok 10520 Thailand.
Email: win_ff@hotmail.com and kkyuttan@kmitl.ac.th

***Abstract*- The problem of signature verification is a pattern recognition task used to discriminate two classes, genuine and forgery signature. In this paper, we propose on-line signature verification using n-tuple learning machine developed on entropy method. The n-tuple networks have predominantly been used as fast pattern classification and generalization ability, make the signature verification system particularly powerful that when verifying skilled forgeries. To increase the generalization ability of the network, we optimized the network synapses by the entropy estimation of all data that are trained to the n-tuple. Some network inputs will be connected to positions of the data that give the high entropy. In this work, we trained all parameters as binary patterns to the network. The results show the total error rate(TER) at 3%.**

I. INTRODUCTION

Personal identity verification has a great variety of applications including access to computer terminals, buildings, credit card verification. Algorithms for personal identity verification can be roughly classified into four categories[1] depending on physical/behavior and biometric/object as shown in figure 1.

Visual examination is the most popular approach for signature verification, yet there are many occasions for the examiners to make mistakes or lower their thresholds of acceptance. For instance, a previously written signature signed on the back of a credit card in a commercial transaction is more or less a challenge to the clerks. As a result, large financial losses may occur. It is clear that signature verification through visual examination can only judge the authentication roughly. Without expertise, human eyes can hardly analyze the detailed writing features. So there is a need for the machine to do this job instead.

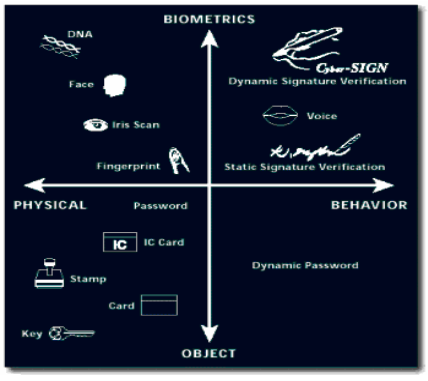

Figure 1. Personal identity verification.

Signature verification can be performed through the machine on-line or off-line. These two approaches and several other practical aspects related to the more general theme of handwriting recognition are discussed at length in the survey from Plamondon[2]. On-line signature verification methods can be further divided into two groups[2], direct methods (using the raw function of time) and indirect methods (using parameters). In the first case, the signature is stored as a discrete function to be compared to the standard from the same writer, that is previously computed during an enrolment stage. Such methods simplify data acquisition but the comparison process can become a hard task. On the other hand, the indirect methods require a lot of effort in preparing data to be processed, but the comparison process is quite simple and efficient. We used the later one with on-line signature verification.

In the rest of the paper, we describe the data acquisition in section 2, the pre-processing in section 3. The connection optimization is explained in section 4. The model of n-tuple used in this work is described in section 5. Experiments and results are shown in section 6. Finally, section 7 provides the conclusion.

II. DATA ACQUISITION

To acquire data in the dynamic verification system, we used a digital tablet, capturing dynamic information of signatures such as x-y position, pressure of pen and altitude of each sampling period as shown in figure 2. In this system, we use a WACOM Intuos size 12x12 inches.

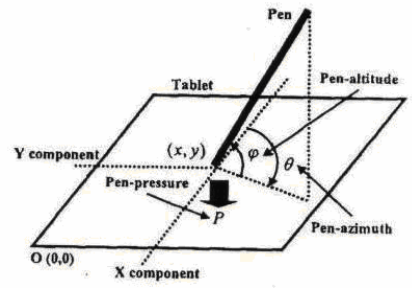

Figure 2. Parameters of the on-line signature.

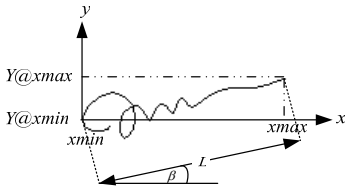

Figure 3. The angle between 0 to 45 degree

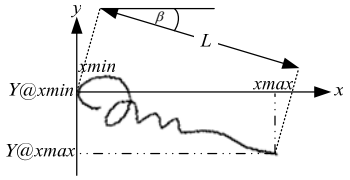

Figure 4. The angle between -45 to 0 degree

III. PREPROCESSING

Generally the preprocessing of signature verification includes the normalization of rotation, scaling, sampling points and binary image conversion, as follows.

A. *Rotation*

Set the angle of each signature to the most extensive.

Case I : the angle between 0 to 45 degree as shown in figure 3 ($Y@x\max - Y@x\min$ is positive).

$$L = X\max\cos\beta + Y@x\max\sin\beta \quad (1)$$

where β beginning with 0 increasing until 45 degree cause; L being maximum value. The signature is then rotated by (2) and (3).

$$X^*(t) = x(t)\cos\beta + y(t)\sin\beta \quad (2)$$

$$Y^*(t) = y(t)\cos\beta - x(t)\sin\beta \quad (3)$$

where $X^*(t)$ and $Y^*(t)$ are the positions of the signature data after rotation and β is the stable angle of signature obtained from (1).

Case II : the angle between -45 to 0 degree as shown in figure 4 ($Y@x\max - Y@x\min$ is negative).

$$L = X\max\cos\beta - Y@x\max\sin\beta \quad (4)$$

where β gives the maximum value of L. Then, the signature is rotated by (5) and (6).

$$X^*(t) = x(t)\cos\beta - y(t)\sin\beta \quad (5)$$

$$Y^*(t) = y(t)\cos\beta + x(t)\sin\beta \quad (6)$$

B. *Scaling*

Set the sizes of each signature to 10 cm on x-axis and 5 cm on y-axis.

$$x^*(t) = \frac{x(t) - x\min}{x\max - x\min} \times sizex \quad (7)$$

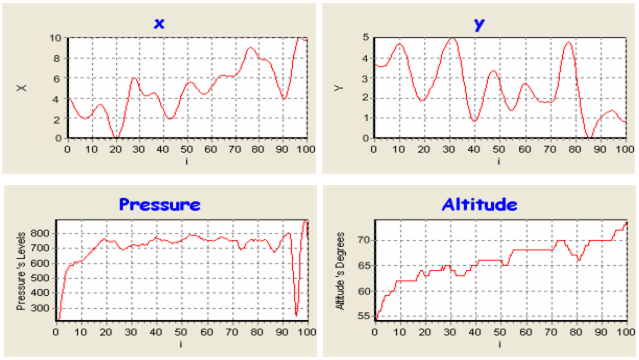

Figure 5. Images of all data after rotation and scaling

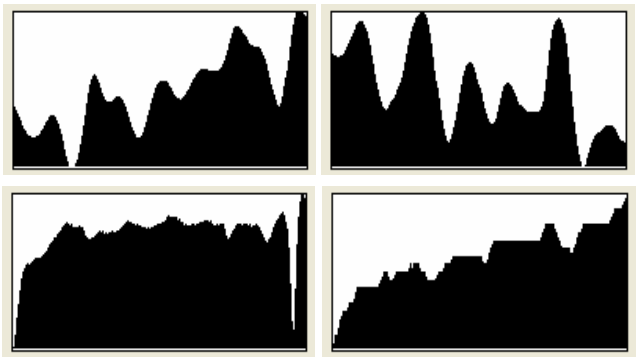

Figure 6. Binary images of all data

$$y^*(t) = \frac{y(t) - y\min}{y\max - y\min} \times sizey \quad (8)$$

where *sizex* and *sizey* are the sizes of signature on x-axis and y-axis respectively.

C. *Sample points*

Resampling 100 points from the individual x position, y position, pressure and altitude respectively.

D. *Binary image conversion*

Convert all feature graphs to binary image files namely bitmap of 200 x 100 pixels as shown in figure 6.

IV. CONNECTION OPTIMIZATION

The merit of n-tuple machine is the use of smaller number of connection by partially connected to the input field, which cause to increase the generalization ability.

Recently, the methods of network feature optimization in signature verification by used genetic algorithm(GA) has been proposed by[3]. The genetic algorithm is based on natural selection, the process drives biological evolution through inheritance, mutation, selection and recombination.In this work, we used entropy method to optimize the best horizontal input connected to the network.

Entropy Theory

The concept of Shannon's entropy[4][5] is the central role of information theory sometimes referred as measure of

uncertainty. The entropy of a random variable is defined in terms of its probability distribution[4] and can be shown to be a good measure of randomness or uncertainty.

The uncertainty is associated with the required amount of data so it can also be thought of as an information measure or quantifier. The value that quantifies uncertainty originally related to random variables which take different probabilities among a set of states. Shannon's entropy has become a very useful way of evaluating structure and pattern in the data.

To optimize the number of horizontal connections, the entropy is used by computing the probability distribution of data for each column of the input field from

$$P_{ij} = \frac{E_{ij}}{E_i} \tag{9}$$

where P_{ij} is the probability distribution at the sample point *i* pattern *j*. E_{ij} is the data at the sample point *i* pattern *j*. E_i is all data at the sample point *i*. The entropy (*H*) is defined in (10) and shown in figure 7.

$$H = -\sum_{j=1}^{n} P_{ij} \ln P_{ij} \tag{10}$$

where *n* is the number of patterns.

The columns of the input field that give the highest entropy will be connected to the network.

V. VERIFICATION PROCESS

Conventional n-tuple systems[6][7] have the desirable features of super-fast single-pass training, super-fast recognition and conceptual simplicity. In n-tuple machines, the basic model of a neuron is a standard Random Access Memory(RAM).

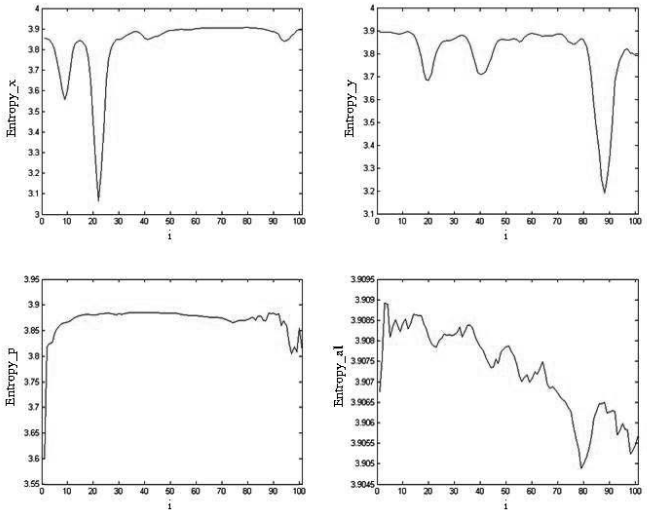

Figure 7. The entropy of all training data

The inputs to the neuron are binary values, which are used to form an address to the RAMs, while the output of the neuron is the data value stored at this address. By this configuration, the n-tuple network will have ability to generalization. The n-tuple is composed of a single layer feed forward as shown in figure 8.

In the training phase, all RAM locations are initially cleared or in undefined-state(u-state) as shown in figure 9. Training the n-tuple network is a single-pass process in which each discriminator is trained individually on a set of patterns as content addressable memory[8]. During the training all the sets of discriminator, which are addressed by the training parameters of the pattern, are set to 1. The process is repeated until all patterns of the training data are trained.

Testing the n-tuple network is performed by presenting an unknown pattern to network inputs. The Hamming distance(HM) proposed by Allinson and Kolcz[9] is used to measure the difference between the unknown binary bit strings and the stored memory. The address that gives the nearest in HM will fire the output.

Thresholding

The outputs of all nodes firing are collected. If the number of output nodes is greater than the preset value, the unknown image is approved, otherwise rejected. The threshold is the value under surface of standard normal score graph as shown in figure 10, we used 95% (-2 < z < 2)[10]. The threshold values are computed as

$$TH = \overline{X} + (Z \times SD) \tag{11}$$

where *TH* is the threshold value, $\overline{X}$ and *SD* are mean and standard derivation of the genuine signature scores.

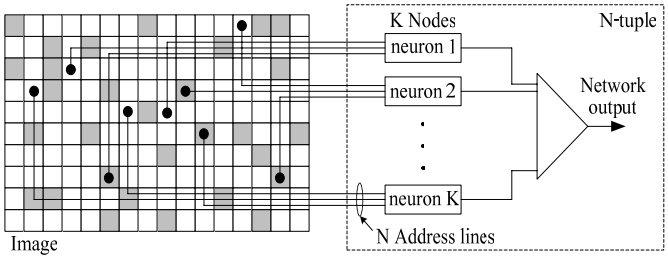

Figure 8. Structure of the n-tuple

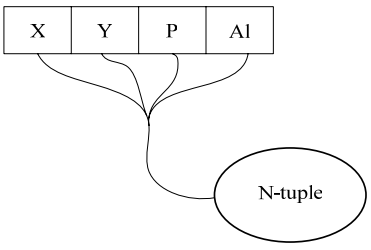

Address	Data
0000000000	u-state
0000000001	u-state
0000000010	u-state
0000000011	u-state
0000000100	u-state
0000000101	u-state
0000000110	u-state
0000000111	u-state
0000001000	u-state
⋮	⋮
1111111110	u-state
1111111111	u-state

Figure 9 Training phase of the n-tuple

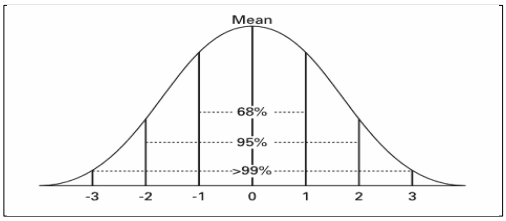

Figure 10. Standard score graph

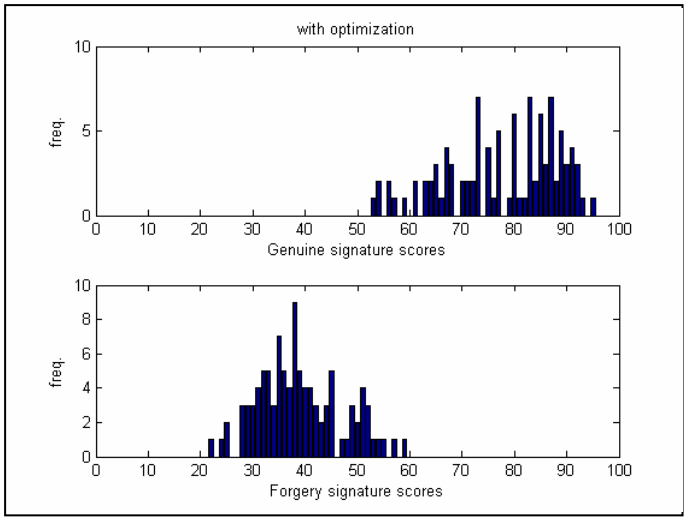

Figure 11. Scores of all testing data with optimization

VI. Experiments and Results

In the experimental, the database consists of totally 300 signatures, with 200 genuine signatures and 100 forgeries from five forgers. We use 100 genuine signatures to train the n-tuple and 100 genuine signatures and 100 forgeries for testing.

The n-tuple contains 100 tuples with 10 fan-ins each. Each tuple has 1 score, there for, the network has maximum 100 scores

In this paper, the higher entropy positions are connected to some synapses and a few number of synapses for lower entropy connections. From the experiment, the scores of all testing data with and without optimization are shown in figure 11 and 12 respectively, which the scores without optimization have large overlapped area than the optimization. As a result, the genuine signatures score have $\overline{X}$ = 77.6, SD = 10.7 and TH = 56. The system give the total error rate(TER) 3 %, false acceptance rate(FAR) 3 % and false rejection rate(FRR) 3 %.

VII. Conclusions

On-line signature verification using n-tuple has been proposed in this paper. The n-tuple networks have predominantly an ability of fast pattern classification and generalization. To increase the generalization, we optimized the network synapses by using the entropy technique, some of the network inputs will be connected to the positions of the data that give the highest entropy. The experiment has shown to support the assumption. To improve the network performance, we try to reduce the overlapped area between the genuine and forgery signature scores.

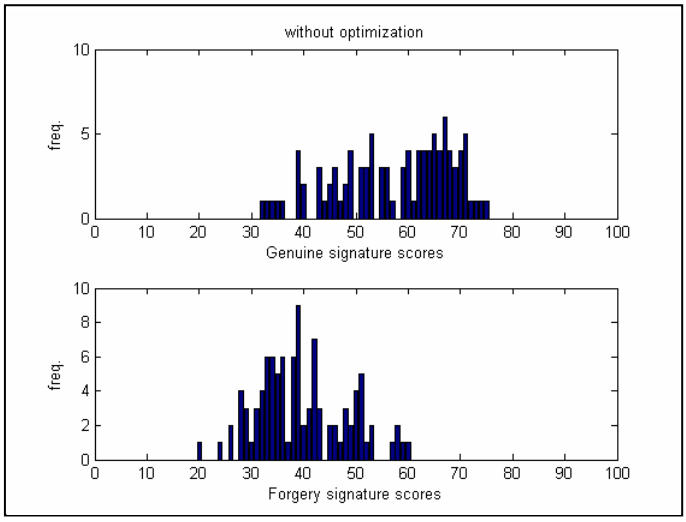

Figure 12. Scores of all testing data without optimization

References

[1] T.Ohishi, Y.Komiya and T.Matsumoto, “On-line Signature Verification using Pen-Position, Pen-Pressure and Pen-Inclination Trajectories”, Vol. 4, 3-7 Sept. 2000, pp.547-550.

[2] R. Plamondon, “On-line and Off-line Handwriting Recognition : A Comprehensive Survey”, *IEEE Transactions on Pattern Analysis and Machine Intelligence*, Vol. 22, No. 1, Jan. 2000, pp.63-84.

[3] W. Sardha Wijesoma, M. Mingming, E. Sung, “Selecting Optimal Personalized Features for On-line Signature Verification Using GA”, *IEEE* Systems, Man, and Cybernetics, Vol. 4, 8-11 Oct. 2000, pp. 2740-2745.

[4] A. Jesson, “Informed Assessments, An Introduction to Information, Entropy and Statistics”, Ellis Horwood, 1995.

[5] C.E. Shannon, “A mathematical theory of communication”, *Bell Syst. Tech. J.*, Vol. 27, pp.379-423, July, October 1948, 623-656.

[6] I. Aleksander and T. Stonham, “Guide to Pattern Recognition using Random-Access Memories”, IEE Proceddings on Computers and Digital Techniques, Vol.2, 1979, pp. 29-40.

[7] J.M. Bishop and R.J. Mitchell, “Auto-associative memory using n-tuple techniques”, Intelligent System Engineering, Winter, 1994, pp.222-229.

[8] P.Mazumder, J.H. Patel and W.K. Fuchs. “Methodologies for Testing Embeded Content Addressable Memories”, IEEE Transactions on Computer-Aided Design, Vol. 7, No. 1, Jan. 1988.

[9] N. Allinson and A. Kolcz, “Application of The CMAC Input Encoding Scheme in The N-Tuple Approximation Network”, IEE Proceedings on Computers and Digital Techniques, Vol. 141, 1994, pp. 177-183.

[10] T. Maneechot and Y. Kitjaidure, “Signature Verification Using N-tuple Learning Machine’, IEEE Engineering in Medicine and Biology Society, 2005, pp.2794-2797.

Detection Segment Retinal Blood Vessel of Anatomical Structures in Retinal Image

Chaichana Thanapong[1], Sookpotharom Supot[1,2], Turmchokkasam Sirichai[2],
Pintavirooj Chuchart[1] and Sangworasil Manas[1]
[1]Faculty of Engineering, and Computer Research and Service Center,
King Mongkut's Institute of Technology Landkrabang Bangkok 10520, Thailand.
[2]School of Engineering, Bangkok University, Pathumtani 12120, Thailand.
Email: s9061403@kmitl.ac.th

***Abstract*-We describe an automated method detection and extraction of blood vessels in retinal images. The proposed algorithm is composed of three steps: gaussian filtering, entropy thresholding and label filtering. First, the gaussian filter technique is to enhance visualization of the blood vessels in retinal image. Secondly, the entropy thresholding is to keep the spatial structure of vascular tree segments and remove a kind of lesion (i.e., hard exudates). Finally, label filter technique is used to remove misclassified pixels. The algorithm has been tested on ten hard exudates in ocular fundus images, and experimental results are compared with clinically generated vessel segmentation and are evaluated in terms of sensitivity and specificity. This method performs well in analyzing anatomical structures in retinal image.**

I. INTRODUCTION

The automatic detection of blood vessels in the retinal images can help physicians for the purposes of diagnosing ocular diseases, patient screening, clinical study, and etc. Information about blood vessels in retinal images can be used to detect the severe retinal diseases such as diabetic retinopathy from an abnormal retinal image. A typical fundus image of patient along with normal components such as arteries, veins, fovea and the optic disc is shown in Fig. 1. The example of lesion (i.e., hard exudates) can be observed on the retinal image.

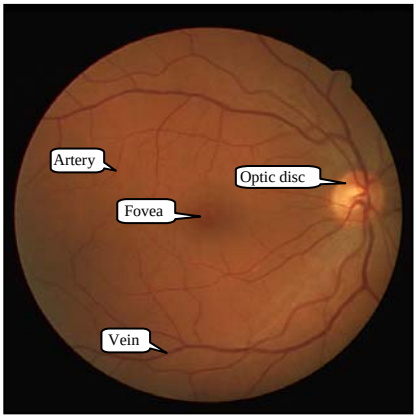

Figure 1. Magnetization as a function of applied field.
Note how the caption is centered in the column.

There are many previous works on extracting blood vessels in retinal images. In edge detection-based method [1], An efficient piecewise threshold probing technique was proposed in [3] where the matched-filter-response (MFR) image is used for mapping the vascular tree. A set of criteria is tested to determine the threshold of the probe region, and ultimately to decide if the area being probed is a blood vessel. Therefore, the different threshold techniques can be applied throughout the image for mapping blood vessels.

In this paper, we propose a new algorithm to remove hard exudates and extract blood vessels in ocular fundus images. The segmentation results are compared with clinically generated vessel segmentations and assessed in terms of their sensitivity and specificity of vessel identification.

II. THE PROPOSED ALGORITHM

The proposed algorithm is composed of three steps. Since blood vessels usually have lower reflectance compared with the background, we separate a green component of retinal image as shown in Fig. 2, we apply green component of retinal image with the gaussian filter to enhance blood vessels with the generation of a GMF image. Secondly, an entropy thresholding scheme can be used to distinguish between vessel segments and the background and remove hard exudates in the GMF image. A label filtering technique is used to remove misclassified pixels.

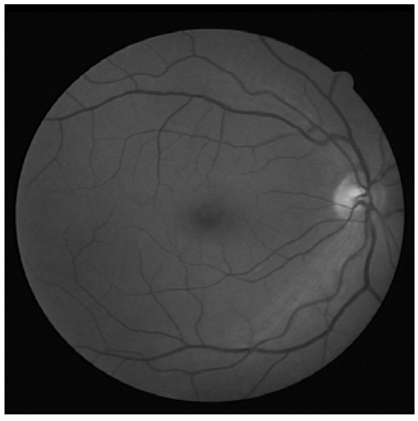

Figure 2. Green component of retinal image

A. Gaussian Filter

The section of a blood vessel is intensity profile which can be approximated by the Gaussian curve [6]. A single intensity

profile of the vessel is cross section, a significant improvement can be achieved by matching a number of cross sections of identical profile simultaneously. Thus, a kernel can be used which mathematical expression is as follows

$$f(x,y) = \frac{1}{\sqrt{2\pi}\sigma}\exp\left(-x^2/\sigma^2\right) \quad \text{for } |y| \le L/2, \qquad (1)$$

where L is the length of the segment for which fixed orientation has been assumed. The direction of the blood vessel here is assumed to be aligned along the y-axis. Because a vessel may be oriented at any angle, the kernel needs to be rotated for all possible angles. A set of twelve 15x16 pixel kernels is applied to convolve with the retinal image, and at each pixel only the maximum of their responses is retained, its GMF image is shown in Fig. 3, where we can see blood vessels are significantly enhanced.

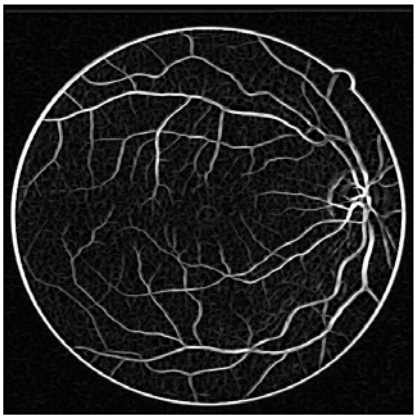

Figure 3. Gaussian filtering result with $\sigma = 1$

B. Entropy Thresholding

Secondly, the GMF image is processed by a proper thresholding scheme in order to extract the vessel segments from the background. An efficient entropy thresholding algorithm. We implement a entropy thresholding technique, described in [2] which can well preserve the spatial structures in the binarized/thresholded image. The co-occurrence matrix of the image F is an P x Q dimensional matrix $T = [t_{ij}]_{PxQ}$ that gives an idea about the transition of intensities between adjacent pixels, indicating spatial structural information of an image. Depending upon the ways in which the gray level i follows gray level j, different definitions of co-occurrence matrix are possible. Here, we made the co-occurrence matrix asymmetric by considering the horizontally right and vertically lower transitions. Thus, t_{ij} is defined as follows:

$$t_{ij} = \sum_{l=1}^{P}\sum_{k=1}^{Q}\delta \qquad (2)$$

where

$$\delta = 1 \quad if \begin{cases} f(l,k) = i & and \quad f(l,k+1) = j \\ f(l,k) = i & or \\ & and \quad f(l+1,k) = j \end{cases}$$

$$\delta = 0 \quad otherwise$$

The probability of co-occurrence p_{ij} of gray levels i and j can therefore be written as

$$p_{ij} = \frac{t_{ij}}{\sum_i \sum_j t_{ij}} \qquad (3)$$

If s, $0 \le s \ge L-1$, is a threshold. Then a can patition the co-occurrence matrix into 4 quadrants, namely A, B, C and D show in Fig. 4.

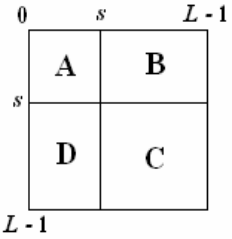

Figure 4. Partition of co-occurrence matrix

Let us define the following quantities:

$$P_A = \sum_{i=0}^{s}\sum_{j=0}^{s} p_{ij}$$
$$P_C = \sum_{i=s+1}^{L-1}\sum_{j=s+1}^{L-1} p_{ij} \qquad (4)$$

Normalizing the probabilities within each individual quadrant, we get the following cell probabilities for different quadrants:

$$P_{ij}^C = \frac{p_{ij}}{P_C} = \frac{t_{ij}}{\sum_{i=s+1}^{L-1}\sum_{j=s+1}^{L-1}} \qquad (5)$$
$$\text{for } s+1 \le i \le L-1, s+1 \le j \le L-1$$

Similarly,

$$P_{ij}^A = \frac{p_{ij}}{P_A} = \frac{t_{ij}}{\sum_{i=0}^{s}\sum_{j=0}^{s} t_{ij}} \qquad (6)$$
$$\text{for } 0 \le i \le s, 0 \le j \le s$$

The second-order entropy of the background can be defined as follows:

$$H_C^{(2)}(s) = -0.5 \sum_{i=s+1}^{L-1} \sum_{j=s+1}^{L-1} P_{ij}^C \log 2\, P_{ij}^C \quad (7)$$

Similarly, the second-order entropy of the object can be written as

$$H_A^{(2)}(s) = -0.5 \sum_{i=0}^{s} \sum_{j=0}^{s} P_{ij}^A \log 2\, P_{ij}^A \quad (8)$$

Hence, the total second-order can be written as

$$H_T^{(2)}(s) = H_A^{(2)}(s) + H_C^{(2)}(s) \quad (9)$$

The gray level corresponding to the maximum of $H_T^{(2)}(s)$ gives the optimal threshold for object and background classification. For the entropy thresholding result is shown in Fig. 5 where we can see blood vessels are clearly segmented from the background.

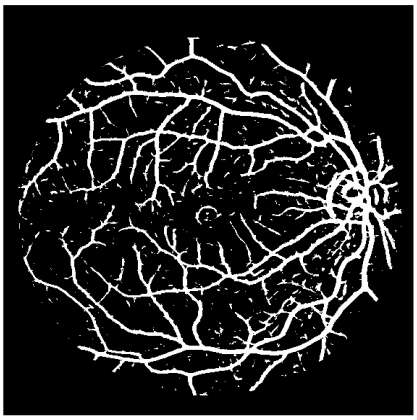

Figure 5. Entropy thresholding result

C. *Label filtering*

Label filtering is used to remove some misclassified pixels in image as shown in Fig. 5, we want to clean image and complete vascular tree structure. Label filtering is used to remove isolated pixels by using the concept of connected pixels labeling. The Label filtering tries to isolate the individual objects by using the eight-connected neighborhood and label propagation [5].The result after label filtering shows in Fig. 6.

III. Experiment and Results

On Pentium 4, CPU 2.6 GHz, using Matlab version 7.3, the computational time of the whole algorithm takes approximately a few minutes for each retinal image. We use the twenty sets are images of normalities. The retinal images and blood vessel ground truth data are obtained from the Image Sciences Institute [10]. In order to compare our of algorithm results with the state-of-the-art results obtained from [10] and hand-labeled groundtruth segmentations as shown in Fig. 7.

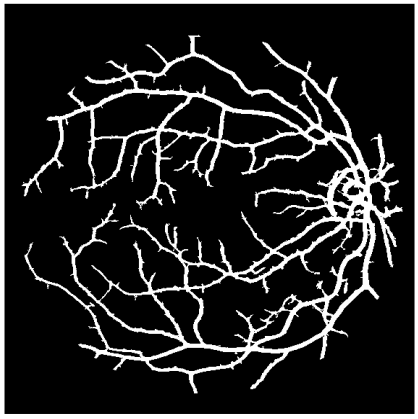

Figure 6. Label filtering result

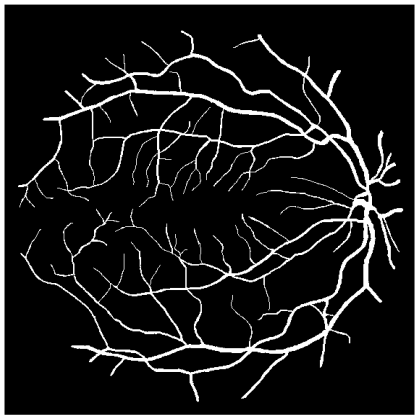

Figure 7. Hand-labeled ground truth segmentations of [10]

The performance of the blood vessel segmentation algorithm is conventionally measured using sensitivity and specificity. The definitions of the two indices are follows:

$$Sensitivity = \frac{Total\ number\ of\ \ positive\ correctly\ identified}{Total\ number\ of\ \ positives} x100 \quad (10)$$

$$Specificity = \frac{Total\ number\ of\ \ negatives\ correctly\ identified}{Total\ number\ of\ \ negatives} x100 \quad (11)$$

The resulting extracted blood vessel in terms of sensitivity and specificity using a stand set of hand-labeled segmentation data. The performance achieved is very promising, showing sensitivity and specificity of 78.16% and 95.75% respectively, and show the average sensitivity and specificity of the twenty test images obtained using other algorithms, the some result from other is shown in Fig. 8.

IV. CONCLUSIONS

In this paper, we have introduced an efficient algorithm for fully automated blood vessel detection in retinal image using the entropy thresholding scheme. It can be helpful in monitoring of the angiogenesis process stimulated more than otsu thresholding scheme [9]. The result of algorithm is compare otsu thresholding is shown in Fig. 9, and in this Fig. 9(e) can see thick blood vessel and thin blood vessel better than Fig. 9(d). In the future we can use algorithm help the doctor to analyse diabetic retinopathy.

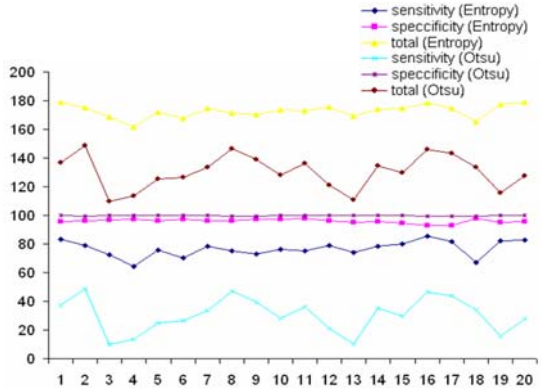

Figure 8. Compare result of Entropy thresholding and Otsu thresholding

REFERENCES

[1] Carsten Steger, "An unbiased detector of durvilinear structures," I*EEE Transactions on Pattern Analysis and Machine Intelligence.*, vol. 20, no. 2, February 1998.

[2] N.R. Pal and S.K. Pal, "Entropic thresholding," *Signal Processing.*, vol. 16, pp. 97-108, 1989.

[3] A. Hoover, V. Kouznetsova, and M. Goldbaum, "Locating blood vessels in retinal images by piecewise threshold probing of a matched filter response," *IEEE Trans. Medical imaging.*, vol. 19, no. 3, March 2000.

[4] N. Otsu, "A threshold selection method from gray-scale histograms," *IEEE Trans. Syst. Man. Cybern.*, vol. 9, no. 1, pp. 62-66, 1978.

[5] R.C. Gonzalez, R.E. Woods and S.L. Eddins, *Digital Image Processing Using Matlab*. Pearson Prentice Hall, 2004.

[6] S. Chaudhuri, S. Chatterjee, N. Katz, M. Nelson and M. Goldbaum, "Detection of blood vessels in retinal images using two-dimenal matched filters," *IEEE Trans. Med. Imageing*., vol. 8, on. 3, pp. 263-269, 1989.

[7] J.J. Staal, M.D. Abramoff, M. Niemeijer, M.A. Viergever and B. van Ginneken, "Ridge based vessel segmentation in color images of the retina," *IEEE Transactions on Medical Imaging.*, vol. 23, pp. 501-509, 2004.

[8] Sookpotharom Supot, Pintavirooj Chuchart and Sangworasil Manas, "Retinal blood vessel segmentation based on image thresholding by discrete curve evolution and fuzzy clustering," *Journal of Signal Processing.*, vol. 10, no. 6, pp.433-440, November 2006.

[9] R. Pajak, "Use of two-dimensional matched filters for estimating a length of blood vessels newly created in angiogenesis process," *Opto-Electronics Review.*, vol. 11, no. 3, pp.237-241, 2003.

[10] http://www.isi.uu.nl/Research/Databases/DRIVE/

(a) An image of diabetic retinopathy with hard exudates at early state.

(b) Gaussian filtering result with $\sigma = 0.5$

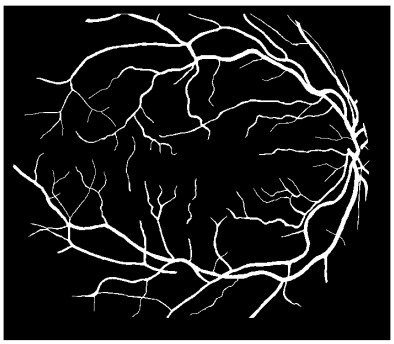

(c) Hand-labeled ground truth

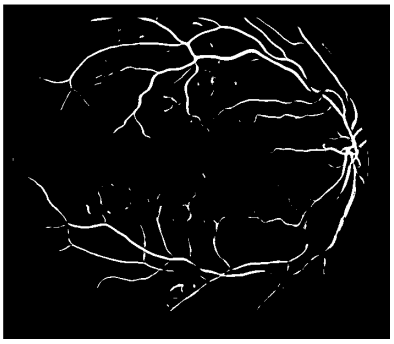

(d) Result from otsu thresholding [9]

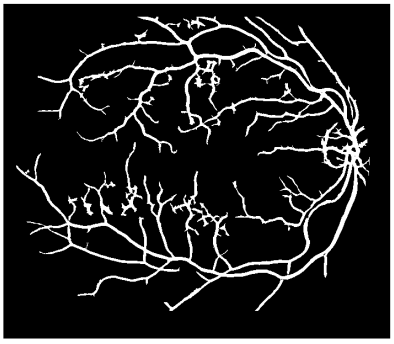

(e) Result from our algorithm

Figure 9. Result for an image with a lesion

Identification of Carcinoma *in Situ* from Segmented Squamous Cervical Cells

C. Aupayagoson, W. Chiracharit and K. Chamnongthai
Department of Electronic and Telecommunication Engineering
King Mongkut's University of Technology Thonburi
126 Pracha-uthit Road, Bangmod, Tung-kru, Bangkok 10140, Thailand

***Abstract* — This paper presents an identification approach for an early-state cervical cancer called carcinoma *in situ* (CIS). Size of nucleus and cytoplasm of a squamous cell in the Pap (Papanicolaou's) smear image is related to the cancer in CIS state. Segmentation techniques for the single squamous cell and the combined squamous cells are proposed. A proportion of the segmented nucleus area and the segmented cytoplasm area is computed and used as an indicator of the normal cells and the abnormal cells. To evaluate a performance of the proposed approach, 20 Pap smear images with 30 cells, 10 abnormal cells and 20 normal cells, have been tested. Experimental study with real ground-truth-known images demonstrated the feasibility and promising of the proposed techniques in discriminating between normal cell and abnormal CIS cell. The results reveal 80% accuracy approximately.**

I. INTRODUCTION

Cervical cancer is the second most common cancer in women worldwide, exceeded only by breast cancer [1]. The mortality related to cervical cancer can be reduced if this disease is detected at its carcinoma *in situ* (CIS) state, known as squamous intraepithelial lesion (SIL) [2].

Currently, the primary screening tool for detection of cervical cancer and its precursor is the Pap (Papanicolaou's) smear test [3]. In the Pap test, a large number of cervical cells obtained by scraping the cervical epithelium are smeared onto a slide which is then fixed and stained for cytologic examination. Each smear is then examined under a microscope for the presence of neoplastic cells [4]. Figure 1 shows an example of the Pap smear test [5]. The Pap smear is unable to achieve a concurrently high sensitivity and high specificity [6]. The accuracy of the Pap smear is limited by both sampling and reading errors [7]. Approximately 60% of false-negative smears are attributed to insufficient sampling, while the remaining 40% are due to reading errors. Because of the monotony and fatigue associated with reading Pap smears (50,000–300,000 cells per slide), the American Society of Cytology has proposed that a cyto-technologist should be limited to evaluating no more than 12,000 smears annually [8]. As a result, accurate Pap-smear screening is labor intensive and requires highly trained professionals.

However, Pap smear test is popular at this time even though the accuracy is limited. Because, it can be a final decision of pre-cancer and carcinoma *in situ*, while another method can not make these decisions.

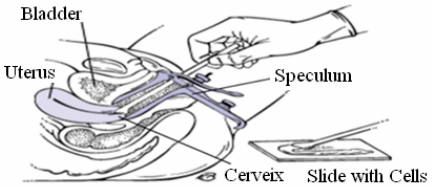

Figure 1. Pap smear test [5].

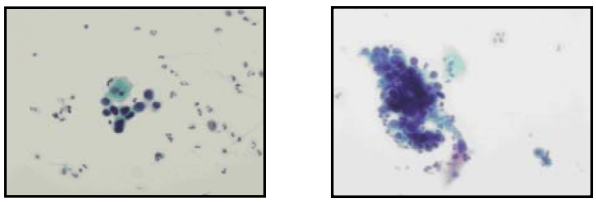

(a) (b)

Figure 2. Examples of Pap smear images: (a) single cells (b) combined cells.

Carcinoma *in situ* is the cervical cancer in the first stage, which is an abnormal deep-basal cell. This cell is a class of squamous cell. Therefore, if a final decision can be made accurately at the moment stage, the physician can be protect patient in due time. The incidence of cervical cancer mortality will be dramatically reduced. Figure 2 shows examples of Pap smear images with squamous cells.

From histological knowledge, the cytologist can make a final decision of carcinoma *in situ* by comparing between nucleus and cytoplasm in the cell.

There were some research works trying to find the comparison. For instance, Bak *et al.* [9] proposed an efficient segmentation method that exploits local information for automated cell segmentation. This method is proved to be resistant to the heavy noise and is not restricted to a particular noise environment represented by specific noise distribution form. Luck *et al.* [10] proposed the model and segmentation algorithm for reflectance confocal images of *in vivo* cervical tissue. Lassouaoui and Hamani [11] proposed genetic algorithms and multifractal segmentation of cervical cell image. Alan *et al.* [12] proposed segmenting cervical epithelial nuclei from confocal images by using Gaussian Markov random

fields. There is trying in several research papers in this field to develop the process. This paper applies shape-based approach by using a region size of cytoplasm campared to nucleus (C/N). Adaptive thresholding and segmentation of squamous cell is proposed. Carcinoma *in situ* cell is then identified.

In rest of this paper is arranged as follows. Section II discusses on the data collection and basis concept. The proposed method is in Section III. The experimental results are presented in Section IV. The paper ends in Section V with a summary.

II. Data Collection and Basic Concept

Class of squamous cell consists of deep basal cell, parabasal cell, intermediate cell and superficial cell, as shown in Figure 3. We have to know the structure of each cell in each class of squamous cell, because carcinoma *in situ* is the cervical cancer that happens in this class of deep basal cell. Table I shows comparison of size, color of cytoplasm, size of nucleus and ratio of cytoplasm and nucleus (C/N) of each normal squamous cell.

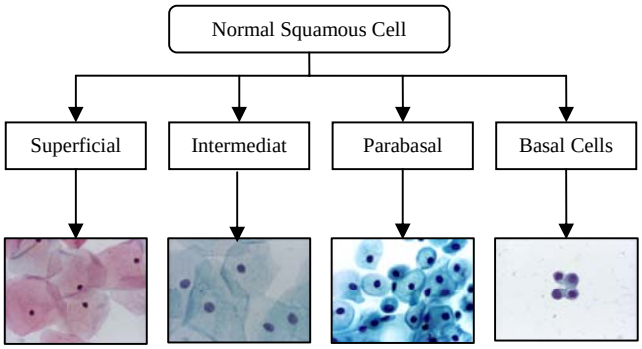

Fig.3. Types and structures of squamous cell.

Table I
Comparison of Size and Color of Normal Squamous Cell

	Deep basal	Parabasal	Intermediate	Superficial
Size of Cell	8-10µm	15-25µm	30-60µm	40-60µm
Color of Cytoplasm	dark blue	blue	pink or blue	orange
Size of Nucleus	7-9µm	8-13µm	10-12µm	5-7µm
Cytoplasm / Nucleus (C/N)	10/8	10/5	10/2	10/1

Table I shows a standard size, color of cytoplasm, size of nucleus and cytoplasm/nucleus (C/N) which is the data pointing to normal squamous cell and abnormal squamous cell. That is to say that if deep basal cell has a size of cytoplasm compared to nucleus less than 10/8 (C/N), it is carcinoma *in situ.*

This paper proposed an approach based on this basic concept. There are two problems of identifying squamous cells to be considered. Case I is for the cells with unclear border. Case II is for the overlapped cells.

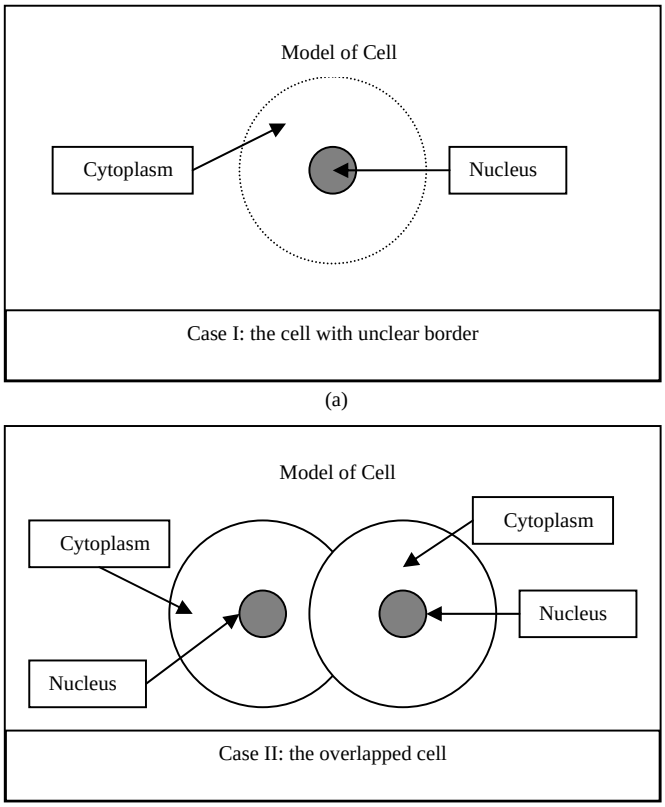

Figure 4. The problem conditions.

In the Figure 4 (a), the problem of this case is that the border of the cell cannot be detected clearly. Therefore the cell's area enclosed by this border is not clear. In Case II, shown in Figure 4 (b), the cells are overlapped.

III. Proposed Method

This paper proposes an identification approach for carcinoma *in situ* cervical cells according to the basic concept. The proposed approach can be described step by step as follows.

Step of software flow diagram in Figure 5 is:

Step 1: Input cell image,
Step 2: Grey level image is adjusted to reduce the background,
Step 3: Adaptive thresholded image for clear border cell,
Step 4: Binary image for cutting the remaining background,
Step 5: Image segmentation for detecting contour and area of the cell, and
Step 6: Classifying cell based on searching area by using basic set operation.

Each set may represent one object, as shown in Figure 6. Each pixel (x,y) has its status: belong to a set or not belong to a set. In the Case II, the logical operation is shown in Figure 7.

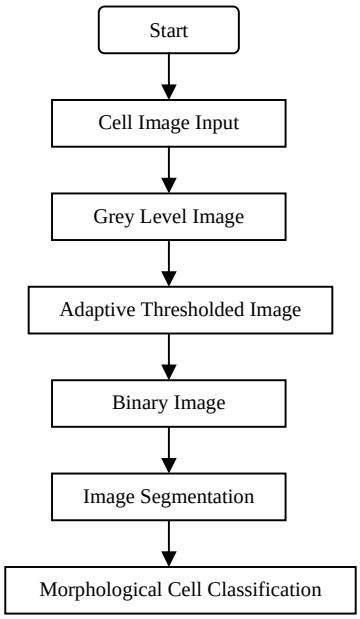

Figure 5. Software flow diagram.

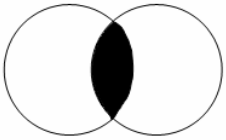

Figure 6. Case II for the intersection of A and B

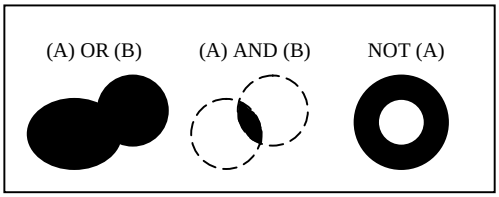

Figure 7. The morphological separation of the intersection of A and B.

IV. Experimental Results

A. Case I Results

In this case, the proposed approach is based on the basic concept that is to resolve the unclear border of the cell. The results are shown in Figure 8.

B. Case II Results

In this case, the results of the proposed approach based on the basis concept to separate the overlapped cells are shown in Figure 9.

The classification results of carcinoma *in situ* cells and normal cells are in the Table III, which C/N Range is a ratio of cytoplasm and nucleus (C/N). In the table, it shows a percentage of tested normal cells and tested abnormal CIS-cells. Fig. 10 shows the classification rate of normal cells and CIS cells from Table III. Twenty real Pap smear image with clinical ground-truth-known is used in the experiments. There are 30 cells: 20 normal cells and 10 carcinoma *in situ* cells. The C/N values are computed and ranged to find the relationship of the carcinoma *in situ* incidence. Figure 10 shows that the CIS cells with smaller C/N can be separated from the normal cells significantly.

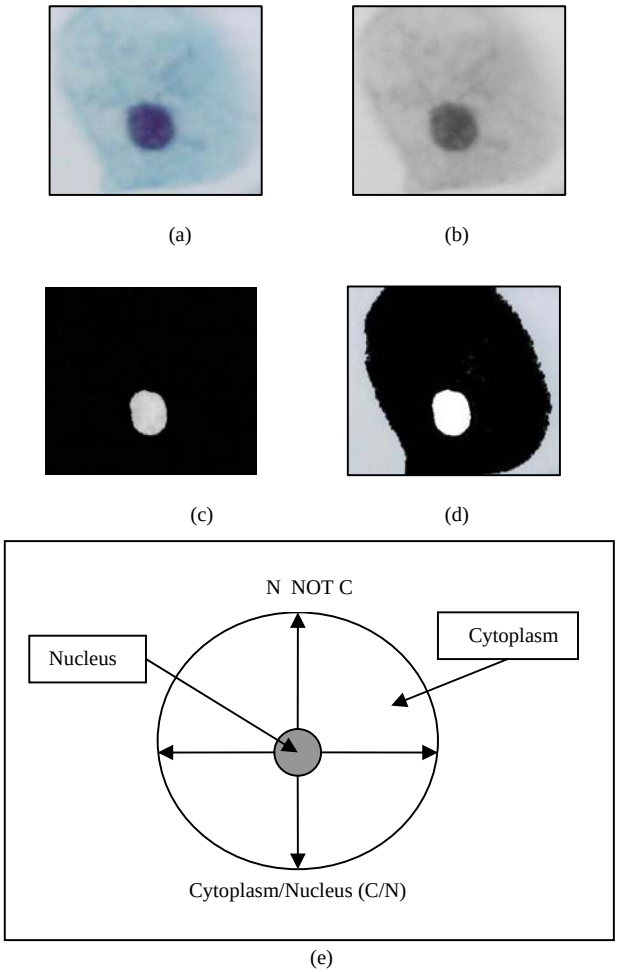

Figure 8. (a) Original image (b) gray level image (c) binary image of nucleus (d) binary image of cytoplasm and (e) nucleus subtracted from cytoplasm for searching nucleus area compared to cytoplasm area.

V. Conclusions

This paper proposes an identification approach for carcinoma *in situ* of Pap smear cervical-cell images. The segmentation of cytoplasm and nucleus of squamous cells is proposed. The results demonstrated that the proposed basis concept and approach reveal promising results from the experiments with the real samples cells.

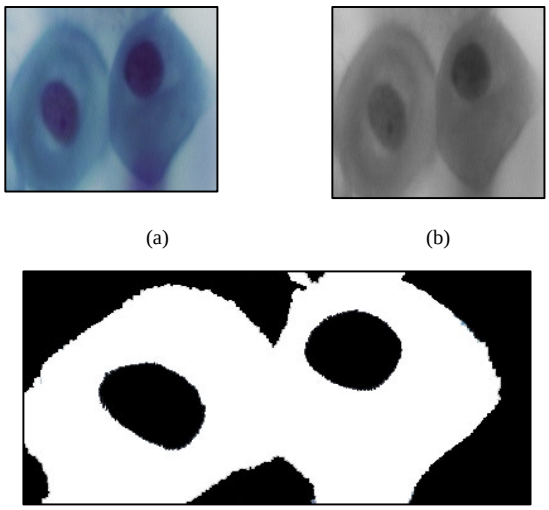

Figure 9. (a) Original image (b) gray level image (c) binary image of nucleus and cytoplasm and (d) concept for searching cytoplasm of cell B overlapped by cell A.

Table III
Classification Results

C/N Range	Normal Cells	CIS Cells
0 – 1.0	-	13.33%
1.0 – 2.0	-	10%
2.0 – 3.0	13.33%	3.33%
3.0 – 4.0	3.33%	-
4.0 – 5.0	20%	-
5.0 – 6.0	3.33%	-
6.0 – 7.0	-	-
7.0 – 8.0	3.33%	-
8.0 – 9.0	-	-
9.0 – 10.0	3.33%	-
10.0 – 11.0	3.33%	-
11.0 – 12.0	6.66%	-
12.0 – 13.0	6.66%	-
13.0 – 14.0	-	-
14.0 – 15.0	6.66%	-
15.0 – 16.0	-	-
16.0 – 17.0	3.33%	-
17.0 – 18.0	-	-
18.0 – 19.0	-	-
19.0 – 20.0	-	-

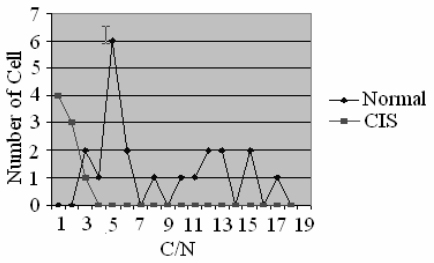

Figure 10. The classification results of normal and CIS cell.

ACKNOWLEDGMENT

The authors would like to acknowledge the suggestions of Pojana Maythangkul, M.D. and Somsak Laiweitwithaya, M.D. from Siriraj Hospital, Bangkok, Thailand.

REFERENCES

[1] American Cancer Society, Cancer Facts and Figures, 1995.
[2] T.C. Wright, R.J. Kurman, and A. Ferenczy, "Cervical Intraepithelial Neoplasia," *in Pathology of the Female Genital Tract*, A. Blaustein, Ed. New York: Spring-Verlag, 1994.
[3] R.J. Kurman, D.E. Henson, A.L. Herbst, K.L. Noller, and M.H.Schiffman, "Interim Guidelines of Management of Abnormal Cervical Cytology," *J. Amer. Med. Assoc.*, vol. 271, pp. 1866–1869, 1994.
[4] World Health Organization, *Cytological Screening in the Control of Cervical Cancer: Technical Guidelines*, Geneva, 1988.
[5] Family Doctor webpage, *Pap Smears*, http://familydoctor.org/138.xml.
[6] M.T. Fahey, L. Irwig, and P. Macaskill, "Meta-analysis of Pap Test Accuracy," *Amer. J. Epidemiol.*, vol. 141, no. 7, pp. 680–689, 1995.
[7] E.J. Wilkinson, "Pap Smears and Screening for Cervical Neoplasia," *Clin. Obstet., Gynecol.*, vol. 33, pp. 817–825, 1990.
[8] L.G. Koss, "The Papanicolaou Test for Cervical Cancer Detection: A Triumph and a Tragedy," *J. Amer. Med. Assoc.*, pp. 737–743, 1996.
[9] E.S. Bak, K. Najarian, J.P. Brockway "Efficient Segmentation Framework of Cell Image in Noise Environments," *IEEE EMBS*,CA, USA September 1-5, pp. 1802-1805, 2004.
[10] B.L. Luck, K.D. Carlson, A.C. Bovik and R.R. Richards-Kortum "An Image Model and Segmentation Algorithm for Reflectance Confocal Images of *in Vivo* Cervical Tissue", vol. 14, no. 9, pp.1265-2005, 2005.
[11] N. Lassouaoui, L. Hamami ," Genetic Algorithms and Multifractal Segmentation of Cervical Cell Images ", 2003.
[12] B.L. Alan, C. Bovik and R.R. Richards-Kortum, "Segmenting Cervical Epithelial Nuclei from Confocal Images Using Gaussian Markov Random Fields", pp.1069-1072, 2003.

Effect of D.C. Field-Induced Breakdown on GMR Heads at Slider-Bar Level

A. Siritaratiwat [1,2] N. Suwannata[2] and C. Sukprong [2]
[1]Industrial/University Cooperative Research Center in HDD Component, Khon Kaen University, 40002, Thailand.
[2]Department of Electrical Engineering, Khon Kaen University, 40002, Thailand.

***Abstract*- This paper shows the fluctuation of some stability parameters. The real data from QST tester shows no significance but the data analysis shows an interested sign. The standard error mean represents the possibility of error at higher applied field. The GMR boundary difference indicates the gap between lower 95% and upper 95% and its fluctuation represents the slider-bar quality. It is found that once the external field is applied, these two analyzed data step up and stay stable. That means some soft ESD may occur and possibly recover after the field is removed.**

I. INTRODUCTION

The recording head with GMR/TMR sensor has been recognized as the most sensitive device for the electrostatic discharge (ESD) effect. In the beginning of magnetoresistive film application for recording heads, the AMR sensor was used and the degree of ESD damage was in orders of 10 V [1-2]. However, the damage of recording head was less important due to its low sensitivity than that in recent years.

It has been currently alert that ESD effect is one of the most crucial effects to recording head when GMR sensor has been firstly manufactured. Many forms of damage such as the breakdown of read element and the bubble of insulator element have been presented [3-4]. They were all called as hard damage which is measurable in terms of resistance and amplitude changes. The visible abnormal increase of resistance and decrease of amplitude can be recognized as a head is totally damaged.

Many experiments have shown that it is due to worker activities and so, the human body model (HBM) has been used to model and simulate this phenomenon [5-6]. Since the dimension of head is scaled down, the ESD damage is becoming more severe.

In manufacturing, many protective possibilities are exercised and hard ESD damage of recording head is currently controllable. Nevertheless, in some process of manufacturing, it is found that some metallic or conductive devices are utilized. This possibly causes an electron move.

Corresponding Author: Apirat Siritaratiwat, Tel/Fax: +66-4334-7442
E-mail: apirat@kku.ac.th

Although an explicit damage cannot be detected by resistive and amplitude measurements, the contour of these two parameter curves are observable or some strange changes are shown. The resistance may be slightly decreased and suddenly increased as the U-shape. Finally it is stable as normal.

When using SEM or TEM to characterize the head, no damage could be observed. However, the soft ESD damage will be exhibited after using for a while. The charged device model (CDM) according to ESDA standard has been simulated to verify this effect.

In our previous demonstrations, a particular process, called "deshunting process", is clearly presented a use of conductive device. It is shown that the direct charge device model (DCDM) can cause a soft ESD effect due to the head conductor contacts [7-8]. This process that was once believed to reduce the ESD effect has been consciously considered in most recording-head production companies.

For more than a decade of ESD studies in recording heads, the Head Gimble Assembly (HGA) has been mainly subjected. This is because that there are many possible processes can be attacked by ESD. A small number of ESD study in Head Stack Assembly (HSA) and Hard-Disk Drive Assembly (HDA) has been published [9-10].

This firstly reports an ESD effect in slider bar level. The aim of this study is to ensure that the ESD effect will not be involved in the slider bar level, prior to transfer to the HGA level. Although standard means and deviations are set for measurements, their standard deviations have never been deeply considered.

II. EXPERIMENTAL SETUP

A couple of parallel charge plates are placed in variable distances and applied by voltage sources. An electric field produced by these two conductive plates is stable and continuous throughout the gap. A sample of slider bar is then inserted into a gap and placed on anti-static sticker as shown in Fig. 1. The voltage sources applied for these plates are DC in order to study the effect of applied field. The Quasi-Static Tester (QST) is used to measure static parameters such as resistance, amplitude, asymmetry and slope of the transfer curve. A number of samples are subjected in order to make sure that it is repeatable.

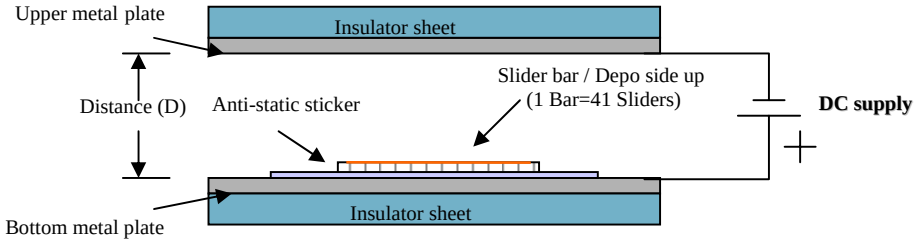

Figure 1 A couple of parallel conductive plates to apply a stable and continuous electric field.

III. RESULTS AND DISCUSSION

A voltage source of 3 steps; 10, 20 and 30 V is applied to fixed 10 cm gap conductive plates within 2 minutes. After applying a voltage of each step, a number of 35 samples are measured for static parameters by using the QST.

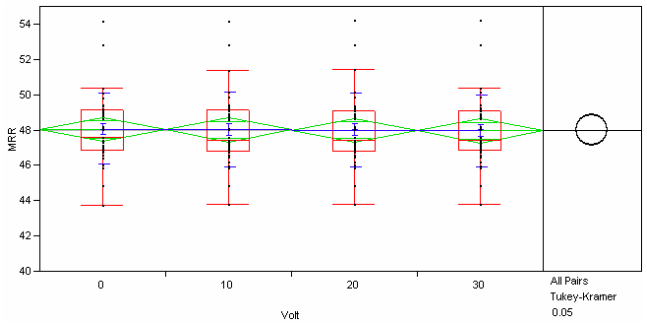

Figure 2 MRR measurements for E = 100-300 V/m.

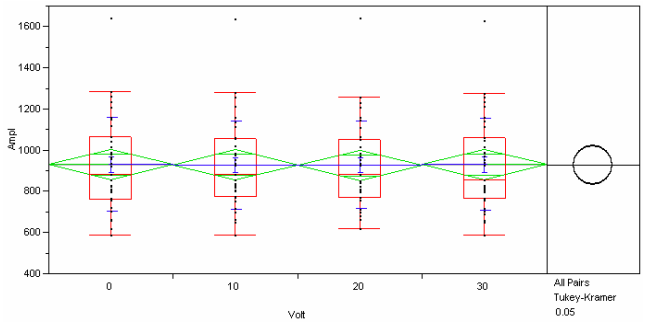

Figure 3 AMP measurements for E = 100-300 V/m.

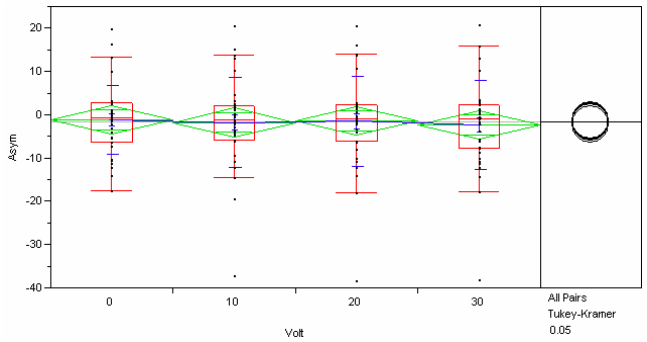

Figure 4 ASYM measurements for E = 100-300 V/m.

The results shown in Fig 2-5 are resistance (MRR), amplitude (AMP), asymmetry (ASYM) and slope (SLOPE). The Tables 1-4 show the means and standard deviations of each experiment.

TABLE 1
MEAN AND STANDARD DEVIATION OF MRR MEASUREMENT

Vap.	Mean	Std. Dev.	Std. Err. Mean	Lower 95%	Upper 95%
0	48.0600	2.00768	0.33936	47.370	48.750
10	48.0366	2.07583	0.35088	47.324	48.750
20	48.0166	2.06080	0.34834	47.309	48.724
30	47.9797	2.01871	0.34122	47.286	48.673

TABLE II
MEAN AND STANDARD DEVIATION OF AMP MEASUREMENT

Vap.	Mean	Std. Dev.	Std. Err. Mean	Lower 95%	Upper 95%
0	932.656	227.023	38.374	854.67	1010.6
10	930.294	213.790	36.137	856.85	1003.7
20	927.941	210.191	35.529	855.74	1000.1
30	931.996	223.443	37.769	855.24	1008.8

TABLE III
MEAN AND STANDARD DEVIATION OF ASYM MEASUREMENT

Vap.	Mean	Std. Dev.	Std. Err. Mean	Lower 95%	Upper 95%
0	-1.0765	8.0198	1.3556	-3.831	1.6784
10	-1.6637	10.3748	1.7537	-5.228	1.9002
20	-1.3810	10.4356	1.7639	-4.966	2.2037
30	-2.2293	10.2613	1.7345	-5.754	1.2955

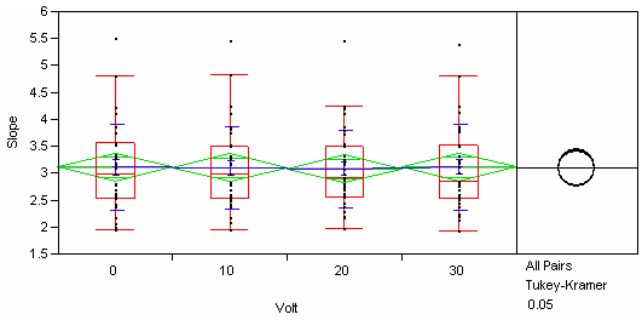

Figure 5 SLOPE measurements for E = 100-300 V/m.

It is expectedly found from Fig 2-5 and Table 1-4 that when an external electric field in an order of 100-300 V/m is applied to a covered slider-bar GMR head these stability parameters are not significantly changed. This is made under the consideration of mean and standard deviation measurements. The standard error mean is statistically calculated where the lower and upper 95% values are correlated with the mean.

The mean of MR is about 48 ohm and a slight fluctuation in a range of 47.9797-48.0600 ohm can be observed. The mean of AMP is about 930 µV with minimum and maximum of 927.941 and 932.656 µV.

The ASYM is varied in a negative range between -1.0765 and -2.293 %. It represents the asymmetry of transfer curve at varied magnetic field and is calculation by [11]

$$\text{ASYM} = \left[\frac{V^+ - V^-}{|V^+| + |V^-|} \right] \text{x}100\% \qquad (1)$$

The SLOPE parameter is calculated in ratio of changes between AMP and applied magnetic field. In this experiment, it changes from 3.09143 to 3.12160 µV /Oe.

It is seen from these results that, in particular, the direct measurement of electrical changes, MR and AMP, shows no obvious evidence because of covered head and very-high electric field protection. An indirect measurement in term of magnetic change is however in possibility and so, the other two parameters are studied.

It is seen in the ASYM measurement as shown in Table 3 that standard-deviations and standard-error means jump immediately after an electric field is applied and the GMR-BD (GMR Boundary Difference), calculated in equation (2), is stepped up as shown in Fig. 6. They seem to be stable under an applied field.

$$\text{GMR-BD} = (\text{Upper } 95\%) - (\text{Lower } 95\%) \quad (2)$$

In addition, the SLOPE measurement fluctuates after 20 V applied field. This is quite explicitly agreed with the ASYM measurement.

TABLE IV
MEAN AND STANDARD DEVIATION OF SLOPE MEASUREMENT

Vap.	Mean	Std. Dev.	Std. Err. Mean	Lower 95%	Upper 95%
0	3.12037	0.809469	0.13683	2.8423	3.3984
10	3.11389	0.764252	0.12918	2.8514	3.3764
20	3.09143	0.725575	0.12264	2.8422	3.3407
30	3.12160	0.792157	0.13390	2.8495	3.3937

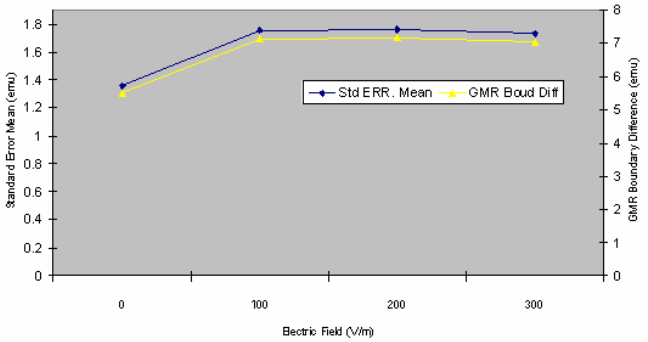

Figure 6 Relationships of applied field, standard-error mean and GMR boundary difference of ASYM measurement.

IV. Conclusion

It is seen from this experiment that 4 testing static parameters can be considered in detail because the raw data give no initiative sign. The measurements of MRR and AMP show no obvious changes but those of ASYM and SLOPE indicate some noticeable data. After evaluation of these last 2 measurements, it is found that the Standard Error Mean and GMR Boundary Difference seem to increase after an external electric field is applied. However, they tend to be stable for higher applied field. It is predictable that this change will be recovered after taking out an electric source. This is possibly due to the soft ESD effect and it will be predictably change again if a field is supplied. However, if the electric field gains higher, some change may be at risk.

Acknowledgements

The authors would like to thanks Western Digital (Bangpa-In) Co., Ltd. for facility provided.

References

[1] T. Hong and J. J. K. Lee, “Electrostatic discharge damage of MR heads”; *IEEE Tran Magn*, vol. 31, pp. 2624-2626, November 1995.
[2] J. Himle, “Off-track testing to evaluate ESD damage to MR heads”, *IEEE Tran Magn*, vol. 32, pp. 3455-3457, September 1996.
[3] A. Wallash and Y. K. Kim, “Magnetic changes in GMR heads caused by electrostatic discharge”, *IEEE Tran Magn*, vol. 34, pp. 1519-1521, July 1998.
[4] T. Ohtsu, H. Yoshida and N. Hatanaka, “Field emission noise caused by capacitance coupling ESD in AMR/GMR heads”, *J Electrostat*, vol. 56, pp. 303-309, October 2002.
[5] A. Wallash, “Electrostatic modeling and ESD damage of magnetoresistive sensors”, *IEEE Tran Magn*, vol. 32, pp. 49-53, January 1996.

[6] A. Siritaratiwat, N. Suwanata, J. Pinnoi and C. Pupaichitkul, "Voltage raised in Al_2O_3 gap of GMR head in the deshunting process", Proceedings of EOS/ESD Symposium, Portland, Oregon, USA, pp. 299-304, 9-13 September 2001.
[7] A. Siritaratiwat, N. Juthong and C. Puprichitkul, "Effect of deshunting sequences of magnetic head using charged device model", *J Magn Magn Mater*, vol. 272-276, pp. 2307-2309, 2004.
[8] A. Siritaratiwat, W. Surakampoltorn and M. Matsumoto, "Investigation of ESD prevention for GMR heads", *IEICE Tran Elec*, vol E88-C, pp. 1343-1347, June 2005.
[9] W. Boone J. Himle, T Porter and B. Perry, "A study of head stack assembly sensitivity to ESD", Proceedings of EOS/ESD Symposium, Orlando, USA, pp. 373-379, 1999.
[10] A Wallash, "ESD SPICE model and measurements for a hard disk drive", *Microelectron Reliab*, vol. 45, pp. 305-311, 2005.
[11] J. Zhu and M. Loera, "Amplitude and asymmetry correlation study between quasi-static and dynamic electrical testing of MR sensors", *IEEE Tran Magn*, vol. 34, pp. 1519-1521, July 1998.

A Study of RFID-Electromagnetic Field Effect on Recording Heads in Writing Process.

A. Pratoomthip[1,2], C. Sa-ngiamsak[2] and A. Siritaratiwat[2]
[1]Graduate school, Khon Kaen University, 40002 Thailand
[2]Department of Electrical Engineering, Khon Kaen University, 40002 Thailand

***Abstract*- This work is to study the effect of Radio Frequency Identification (RFID) system on MR recording heads, particular in writing process. The variations of current and antenna radius are compared with the angle between a 125 kHz RFID position and HGA. It is found from this result that a current flowing in loop antenna is rather effective than the other. This causes an additional current of 0.4% flowing in HGA compared with an ordinary 50 mA writing current. Although this will not apparently damage a head, it may interfere a writing process especially in a smaller head of the becoming technology.**

I. INTRODUCTION

Radio Frequency Identification (RFID) system is the convenient technology to identify specific data of objects. RFID technology is used in many applications such as livestock, commerce, security and industrial tasks. Generally, RFID system has two important parts which are Reader and Transponder (or Tag). The principle work of RFID is that a reader transmits energy with data in form of an electro magnetic field to a tag for data expression as show in Fig.1. The energy is changed to electric energy and then distributed to the tag circuit. The data with frequency carrier modulation is then reverse to reader for demodulate and reading data.

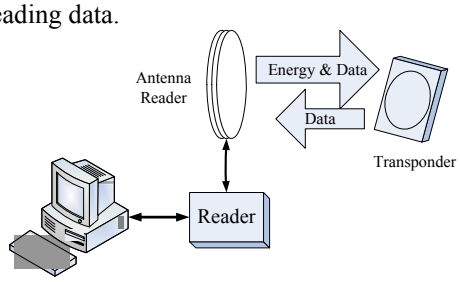

Figure 1. RFID system.

In hard disk drive industry, RFID technology has been applied for accuracy, rapidity and production time saving. However, the production process of hard disk drive components needs to be safely awared a temporary because of its high risks to be damage. Especially magnetoresistive heads (MR Heads) can be destroyed by a very low level of electrostatic discharge, electromagnetic interference etc. Therefore, the utilization of RFID may cause damage in the production components.

This work studies the effect of angle position, distance of RFID installation, current flow in loop antenna and antenna radius of RFID reader that may cause some change in writing process of MR heads. This advantage result show that how to choose an appropriate RFID equipment in the hard disk industry.

II. THEORY

A. Radiated Fields from RFID

To calculate the fields radiated by loop antenna of RFID, the potential function of loop antenna is expressed in (1) and explained in Fig. 2 [1].

$$\vec{A}(x,y,z)=\frac{\mu_o N}{4\pi}\int_c \vec{I}_e(x',y',z')\frac{e^{-jkR}}{R}dl'=\vec{A}_r+\vec{A}_\theta+\vec{A}_\phi \quad (1)$$

where $\vec{A}$ is a potential function of loop antenna,
(x,y,z) is a position of observation point,
μ_o is permeability of free space,
N is a number of turn of loop antenna,
$\vec{I}_e$ is a electric current in loop antenna,
(x',y',z') is an arbitrary position an loop antenna,
R is a distance from (x',y',z') to (x,y,z),
dl' is a tiny arc of loop antenna,
k is wave number,
$\vec{A}_r,\vec{A}_\theta,\vec{A}_\phi$ are potential functions in r-, θ- and ϕ- direction components, respectively.

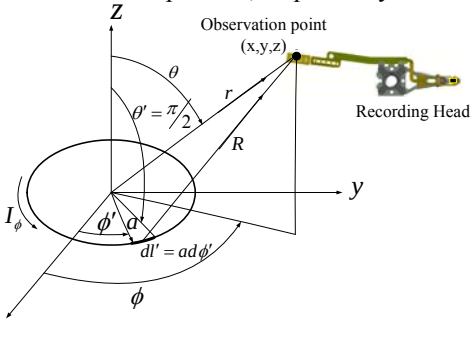

Figure 2. Position of loop antenna reader to observation point.

An electric current, $\vec{I}_e$, is normally composed of 3 component as show in (2)

$$\vec{I}_e=\bar{a}_r I_\phi \sin\theta\sin(\phi-\phi')+\bar{a}_\theta I_\phi\cos\theta\sin(\phi-\phi') \quad (2)$$

where ϕ is an angle between x-axis and observation point on the x-y plane,
ϕ' is an angle between x-axis and arbitrary position on loop antenna.

Since the loop antenna is initially assumed to be on the xy-plan, an electric current, $\vec{I}_e$, is therefore considered in the ϕ - component only as derived in (3).

$$\vec{I}_e = \vec{I}_\phi = I_o \tag{3}$$

where I_o is a current applied into a loop antenna.

The distance, R, can be calculated by (4)

$$R = \sqrt{r^2 + a^2 - 2ar\ \sin\theta\cos\left(\phi - \phi'\right)} \tag{4}$$

where r is a distance between the center of loop antenna and observation point,

a is a loop-antenna radius,

θ is a vertical angle between z-axis and r.

Due to the field is radiated in a free space, a wave number, k , is then computed by (5)

$$k = \omega\sqrt{\frac{\mu_o\varepsilon_o}{2}\left[\sqrt{1+\left[\frac{\sigma}{\omega\varepsilon_o}\right]^2}+1\right]} \approx \omega\sqrt{\mu_o\varepsilon_o} \tag{5}$$

where ω is an angular frequency,

ε_o is a permittivity of free space.

According to the assumption that a loop antenna is placed on the xy-plan the potential function, in (1), is then only composed of ϕ component as show in (6.1) and (6.2)

$$\vec{A}_\theta = \vec{A}_r = 0 \tag{6.1}$$

$$\vec{A}_\phi = \frac{a^2\mu_o NI_o\sin\theta}{4}\left(\frac{jk}{r}+\frac{1}{r^2}\right)e^{-jkr} \tag{6.2}$$

The radiated magnetic field of loop antenna, $\vec{H}$, can be calculated based on Maxwell's equation, in (7),

$$\vec{H} = \frac{1}{\mu}\nabla\times\vec{A} = \vec{H}_r + \vec{H}_\theta + \vec{H}_\phi \tag{7}$$

Since the potential function, $\vec{A}$,has only the ϕ-component, magnetic field in (7) is therefore composed of ϕ - components only as derived in (8.1), (8.2) and (8.3)

$$\vec{H}_r = j\frac{ka^2NI_0\cos\theta}{2r^2}\vec{a}_r\left[1+\frac{1}{jkr}\right]e^{-jkr} \tag{8.1}$$

$$\vec{H}_\theta = -\frac{(ka)^2\ NI_0\sin\theta}{4r}\vec{a}_\theta\left[1+\frac{1}{jkr}-\frac{1}{(kr)^2}\right]e^{-jkr} \tag{8.2}$$

$$\vec{H}_\phi = 0 \tag{8.3}$$

The radiated electric field, $\vec{E}$, can be calculated based on a Maxwell's equation as defined in (9)

$$\nabla\times\vec{H} = \vec{J} + j\omega\varepsilon\vec{E} \tag{9}$$

This electric field is radiated in free space and so, the term of $\vec{J}$ can be neglected due to the conductively of free space, σ , is approximately zero.

It is previously assumed that $\vec{H}$ components are only in r- and θ- directions. Thus, from (9), an electric field, $\vec{E}$, is that only in ϕ - direction as derived in (10.1) and (10.2)

$$\vec{E}_r = \vec{E}_\theta = 0 \tag{10.1}$$

$$\vec{E}_\phi = \eta\frac{(ka)^2\ NI_0\sin\theta}{4r}\vec{a}_\phi\left[1+\frac{1}{jkr}\right]e^{-jkr} \tag{10.2}$$

where η is an intrinsic impedance of free space or about $\approx 120\pi$.

The voltage drop, V_w, across a pair of HGA writing traces, as shown in Fig. 3, can be calculated by (11)

$$V_w = -\int_{r_1}^{r_2}\vec{E}\cdot d\vec{l} \tag{11}$$

From (11) can be easily written in (12)

$$V_w = -\left|\vec{E}\right|\cdot s \tag{12}$$

where s is a gap of HGA writing traces.

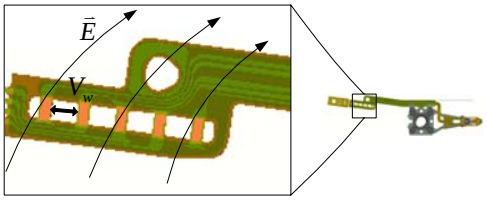

Figure 3. HGA traces.

B. Equivalent circuit of recording head in writing process.

An image of HGA is shown in Fig. 4 and its equivalent circuit of writing component is expressed in Fig. 5.

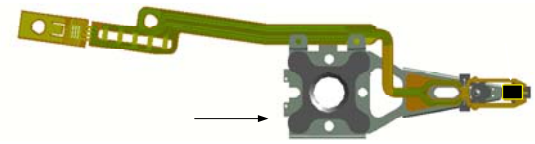

Figure 4. HGA sample.

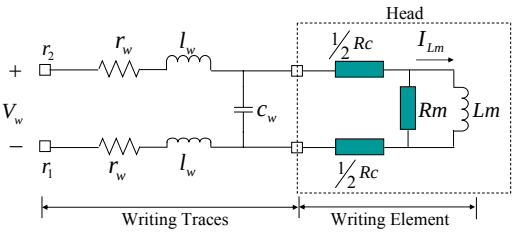

Figure 5. Equivalent circuit of HGA writing component.

In Fig. 5, the required parameters of 2 parts; writing traces and writing element, are that

r_w is resistance of writing trace,

l_w is an inductance of writing trace,

c_w is a capacitance of writing trace space,

R_c is the DC resistance of the coil,

R_m is resistance magnetic losses on the yoke,

L_m is impedance of the head inductance.

The formulas of r_w, l_w and c_w can be found from [2] and expressed in (13) - (15) where the values of R_c, R_m and L_m are defined by their specifications,

$$r_w = \frac{l}{\sigma_w . A_w} \tag{13}$$

$$l_w = \frac{Z_c}{v} \tag{14}$$

$$c_w = \frac{1}{v . Z_c} \tag{15}$$

where l is the length of writing traces,

σ_w is the conductivity of writing traces,

A_w is the cross-section area of writing traces,

Z_c is characteristic impedance of writing traces,

v is velocity of propagation in writing traces.

The characteristic impedance of writing traces, Z_c, can be defined in (16).

$$Z_c = \frac{30\pi}{\sqrt{\varepsilon_r'}} \frac{1}{\left[\frac{W_e}{s} + 0.441\right]} \tag{16}$$

where ε_r' is an effective relative permittivity of polyimide, expressed in Fig. 6,

$\frac{W_e}{s}$ is an effective width of the center conductor.

An effective width of the center conductor, $\frac{W_e}{s}$, can be defined in (17).

$$\frac{W_e}{s} = \begin{cases} \frac{w}{s} & ; \ \frac{w}{s} \geq 0.35 \\ \frac{w}{s} - \left(0.35 - \frac{w}{s}\right)^2 & ; \ \frac{w}{s} \leq 0.35 \end{cases} \tag{17}$$

where w is a wide writing traces,

s is a writing traces space.

The velocity of propagation in writing traces, v, can be defined in (18).

$$v = \frac{1}{\sqrt{\mu_0 \varepsilon_0 \varepsilon_r'}} \tag{18}$$

Therefore, a current, I_{Lm}, flowing in a pair of writing element calculated as a voltage, V_w, divided by a total impedance, as derived in (19)

$$I_{Lm} = \frac{R_m X_{cw} V_w}{(R_m + X_{Lm})\left(R_c + \frac{R_m X_{Lm}}{R_m + X_{Lm}} + X_{cw}\right)\left(\frac{\left(R_c + \frac{R_m X_{Lm}}{R_m + X_{Lm}}\right) X_{cw}}{R_c + \frac{R_m X_{Lm}}{R_m + X_{Lm}} + X_{cw}} + 2r_w + 2X_{lw}\right)} \tag{19}$$

where X_{cw} is capacitive reactance of c_w,

X_{lw} is inductive reactance of l_w,

X_{Lm} is inductive reactance of L_m.

C. *Writing traces information.*

A sample of structure of HGA writing traces and its dimension are shown in Fig. 6 and Table I, respectively [3].

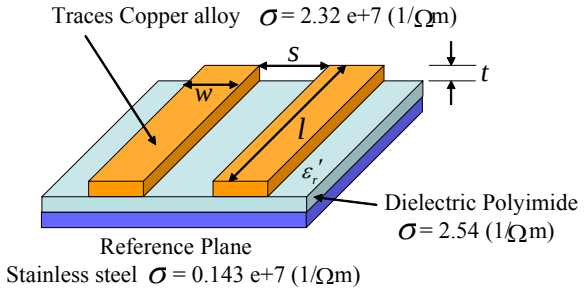

Figure 6. Structure of HGA writing traces.

Table I.
Dimension of HGA writing traces [4]

Dimension	Size
writing traces wide : w	35 µm.
writing traces space : s	50 µm.
writing traces thickness : t	18 µm.
writing traces length : l	50 mm.

III. RESULT ANALYSIS.

A. *Dependent of V_w - I_{Lm} on r and θ.*

The voltage drop, V_w, across a pair of HGA writing traces in (12), calculated as radiated electric field in (10.2), $\vec{E}$, dependent of r and θ. Such, V_w can find in (20) and shown in Fig. 7. The current, I_{Lm}, flowing in a pair of writing element calculated as a voltage, V_w. Such can find I_{Lm} in (21) and shown in Fig. 8. By parameter constant are N = 40 turns and I_o = 100 mA and s = 50 µm

$$V_w = -\left|\eta \frac{(ka)^2 NI_0 \sin\theta}{4r} \bar{a}_\phi \left[1 + \frac{1}{jkr}\right] e^{-jkr}\right| \cdot d \tag{20}$$

$$I_{Lm} = \frac{R_m X_{cw}\left(-\left|\eta \frac{(ka)^2 NI_0 \sin\theta}{4r} \bar{a}_\phi \left[1 + \frac{1}{jkr}\right] e^{-jkr}\right| \cdot d\right)}{(R_m + X_{Lm})\left(R_c + \frac{R_m X_{Lm}}{R_m + X_{Lm}} + X_{cw}\right)\left(\frac{\left(R_c + \frac{R_m X_{Lm}}{R_m + X_{Lm}}\right) X_{cw}}{R_c + \frac{R_m X_{Lm}}{R_m + X_{Lm}} + X_{cw}} + 2r_w + 2X_{lw}\right)} \tag{21}$$

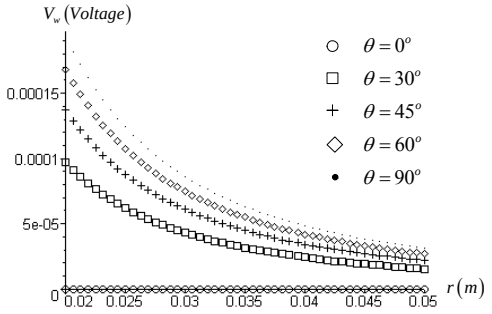

Figure 7. Voltage drop across a pair of HGA writing traces dependent of

r and θ.

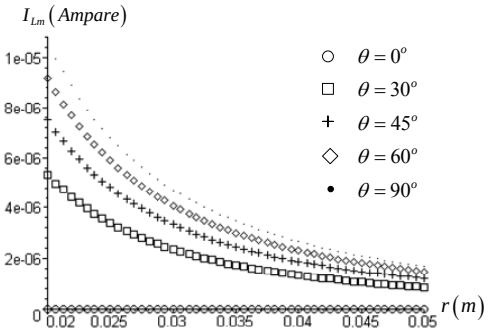

Figure 8. current flowing in a pair of writing element dependent of r and θ.

Therefore, from Fig. 7 and Fig. 8, its mean that the voltage, V_w, and the current, I_{Lm}, non linearly decrease when the distance, r, it long. A maximum voltage, V_w, and the current, I_{Lm}, are capture when the HGA is in the same xy-plane as an antenna loop. However a minimum voltage, V_w, and the current, I_{Lm}, are capture when the HGA perpendicular to an antenna loop.

B. Comparision of I_o - a affect on V_w and I_{Lm}.

The voltage drop, V_w, and the current, I_{Lm}, dependent of I_o and a. Such, can find in (20), (21) and shown in Fig. 9. and Fig. 10. By choose parameters r = 0.02 m. and θ=90° from Fig.7 are affects maximum V_w.

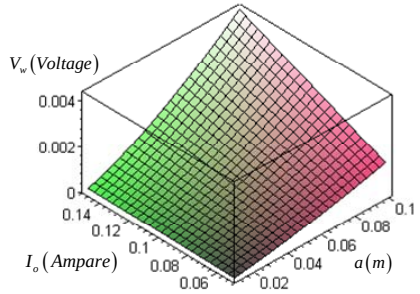

Figure 9. Voltage drop across a pair of HGA writing traces dependent of I_o and a.

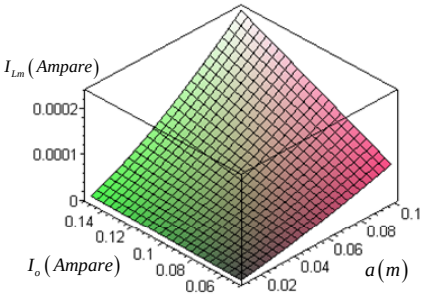

Figure 10. current flowing in a pair of writing element dependent of I_o and a.

Therefore, from Fig. 9 and Fig. 10, its mean that V_w and I_{Lm} increase when the radius of loop antenna, a, and current applied into a loop antenna, I_o, are increase. However V_w and I_{Lm} sensitive increasing dependent of a more than I_o. A maximum V_w and I_{Lm} when $I_o \approx$ 0.15 mA and $a \approx$ 0.1 m.

C. Percentage ratio of I_{Lm} and I_w.

Percentage ratio of I_{Lm} and I_w can find in (22) and shown in Fig. 11.

$$\frac{I_w}{I_{Lm}} \times 100\% \qquad (22)$$

where I_w is standard writing current flow in writing traces $\approx$ 50 mA.

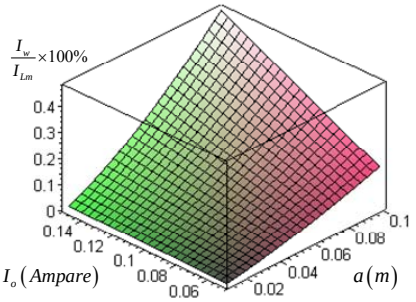

Figure 11. Percentage ratio of I_{Lm} and I_w dependent of I_o and a.

Therefore, from Fig. 11 it mean that I_{Lm} increase when the radius of loop antenna, a, and current applied into a loop antenna, I_o. However I_{Lm} sensitive increasing dependent of a more than I_o. A maximum V_w when $I_o \approx$ 0.15 mA and $a \approx$ 0.1 m.

IV. CONCLUSION.

The effect of electric field which derives from the RFID equipment in the recording head writing process was analyzed, it can identify the parameter which effects to the current flowing through the recording head are the angle θ, distance r, radius a and current flow in loop antenna I_o.

The radius a is the most effect parameter. A maximum ratio of I_{Lm} and I_w about 0.4% ,when a decrease approach zero and current flow in loop antenna I_o increase approach 150 mA.

RFID was designed to be used in the longer distance as in [5]. It indicated that the parameter of the RFID equipment should extend the size. Consequently, the electric field will be stronger which is the topic that will cause the error of the recording head test.

REFERENCES.

[1] C.A.Balanis, "Antenna Theory Analysis and Design", 2nd ed., J.Wiley, Arizona State, America, 1997

[2] C.R.Paul, "Introduction to Electromagnetic Compatibility", 2nd ed, J.Wiley, 2006

[3] K. B. Klaassen, J. C. L. van Peppen, and X. Xing, "Write-to-read coupling", *IEEE Trans Magn.*, vol. 38, pp. 61–67, Jan. 2002.

[4] N.Ruangsri, "Coil Design for Optimum Read Range of Magnetically-Coupled RFID System", EECON 29, 9-10 Nov, 2006.

The Effect of Head Protrusion on Recording Field for Perpendicular Recording System

D. Tongsomporn[1], A. Siritaratiwat[2*], N. Afzulpurkar[3], B. Bargmann[4]
[1] Microelectronics Field of Study, Asian Institute of Technology, Thailand
[2] KKU-Seagate Cooperation Research Laboratory, Department of Electrical Engineering, Khon Kaen University, Thailand
[3] School of Engineering and Technology, Asian Institute of Technology, Thailand
[4] Seagate Technology (Thailand) Co., Ltd., Nakorn Ratchasima, Thailand

***Abstract*-We developed a three-dimensional finite element model to analyze the effect of the heating from the integrated heater on the effective write field. We consider the effect of the heating into two phenomena; the protrusion of the main pole, and the shrinking of B-H curve of the pole material due to the rising temperature. The combination of these phenomena gives a stronger effective field of 8.3%. We also examine the effect using spin stand tester by measuring the magnetic write width. The experiment results show that the head protrusion also widens the written track. This may present adjacent track interference in the perpendicular recording system.**

I. INTRODUCTION

The increase in the areal density of hard disk drives requires the head to fly closer the medium into the order of 10 nanometers [1]. Thus, the variation of flying height for a few nanometers has an influential effect to the recording performance. The flying height variation may depend on many parameters, for example, the air-bearing surface (ABS) and the physical dimensions of slider head. Another cause to reduce the flying height is the head protrusion induced by ambient temperature and write current. Write-induced head protrusion (W-IHP) is caused by power dissipation generated in the head during writing that comprises Joule heating at the coil as well as eddy currents and hysteresis losses in the yoke [2]. However, in high density recording the integrated heater is introduced for the purpose to optimize the flying height of each individual head, so called an adaptive fly height. This heater introduces another protrusion term "heater-induced head protrusion (H-IHP)". Normally, H-IHP can produce a larger stroke than W-IHP. Therefore, the impact of H-IHP to the recording performance should be studied.

This paper investigates the dependence of the effective write field on the head protrusion and the rising temperature at the main pole using a simulation model. Then, we interpret the change of effective field properties into the variation of recording performance. Finally, we also experimentally study on the impact of head protrusion to electrical performance of the recording system using the spin stand tester.

II. MODELS AND SIMULATIONS

A. Simulation Model

We use the commercial ANSYS software to perform three-dimensional (3-D) finite-element modeling. Our model consists of a single main pole, a return pole, and a medium with soft under layer (SUL) as shown in Fig.1 (a). In this model, the main pole with a tapered-neck pole and a very small throat height is proposed as shown in Fig. 1 (b). To reduce the skew-angle sensitivity, the ABS of this main pole is designed to be trapezoidal shape with a wall angle of 15°. The recording system parameters are shown in Tab. I. It is the fact that the magnetic field magnitude depends on the potential difference between the main pole and the SUL. In this model, a positive magnetic scalar potential is applied to the top surface of the main pole and a zero potential is applied to the bottom surface of the SUL. To keep the same amount of magnetic flux flowing out to the return pole, a proportional negative potential is applied at the top surface of the return pole. The perpendicular and longitudinal components of the magnetic field are measured at the center of the recording layer.

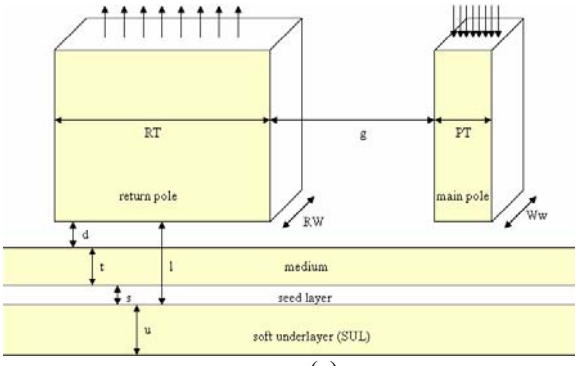

(a)

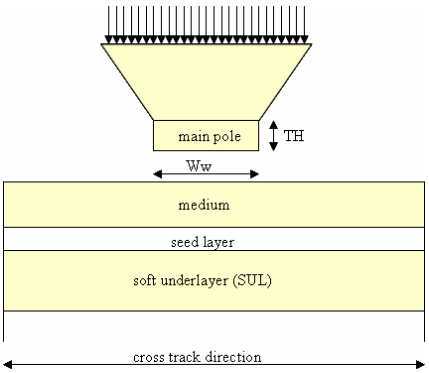

(b)

Figure 1 (a) A simulation model for perpendicular recording system and (b) A tapered-neck main pole with a small throat height.

* Corresponding author: apirat@kku.ac.th

TABLE I
SYSTEM PARAMETERS

Main-Pole Width	100 nm
Main-Pole Thickness	150 nm
Throat Height	50 nm
Wall Angle of Tapered Neck	45°
Wall Angle of Trapezoid-shaped ABS	15°
Bs of Main-Pole	2.4 KG
μr of Main-Pole	500
Return-Pole Width	20 μm
Return-Pole Thickness	2 μm
Bs of Return-Pole	16 KG
μr of Return-Pole	500
Head to media spacing, HMS	15 nm
Head to SUL spacing, HKS	35 nm
Media Thickness	15 nm
μr of Media	2
Interlayer Thickness	5 nm
SUL Thickness	200 nm
Bs of SUL	16 KG
μr of SUL	500

B. Write Field Comparison

It is well known that not only the field magnitude but also the angle between the write field and the easy axis of the medium grain effects to the writability of perpendicular recording heads. This effect can be evaluated using the Stoner-Wohlfarth model. This model gives the following relation [3]:

$$\frac{H_S}{H_K} = (\sin^{2/3}\theta + \cos^{2/3}\theta)^{-3/2} \qquad (1)$$

where H_S is the switching field, H_K is the anisotropy field of the medium, θ is an angle between the write field and the media easy axis.

The switching field H_S may be considered as an effective field H_{EFF} . This field can be obtained from

$$H_{EFF} = \sqrt{H^2_{PERP} + H^2_{LONG}} \times (\sin^{2/3}\theta + \cos^{2/3}\theta)^{3/2} \qquad (2)$$

where H_{PERP} is the field perpendicular to the medium plane, H_{LONG} is the longitudinal field which is the vector combination of the down-track and cross-track fields.

Fig.2 shows the write field components in the case that the magnetic scalar potential of 0.06 A is applied to the top surface of the main pole. The result exhibits the following magnitudes of the write field components and the field angle: $H_{DOWN-TRACK}$ = 1604 Oe, $H_{CROSS-TRACK}$ = 163 Oe, H_{PERP} = 8533 Oe, H_{EFF} = 10793 Oe, field angle = 17.15 degrees. H_{EFF} exhibits a peak value at the region above the trailing edge of the main pole. The maximum of the field angle is shifted from the trailing edge in the down-track direction. In this case the cross-track component is close to zero and it can be negligible. However, the cross-track component becomes significant if we plot the field in cross-track direction.

Fig.3 shows the dependence of the effective write field on the heating from the integrated heater. We may consider the effect of the heating into two phenomena; the protrusion of the main pole perpendicular to the medium plane, and the shrinking of B-H curve of the main-pole material due to the rising temperature [4]. Therefore, there are four difference sets of the input for this calculation as in Tab. II. In Case I, the condition is that the heater power is turned off. H_{EFF} exhibits a magnitude of 10793 Oe, therefore, it is equal to the effective field in Fig. 2. If only the rising temperature is considered (Case II), the magnitude of H_{EFF} is 10318 Oe or it is lower than that of the Case I by 3.92 %. If only the head protrusion is taken into account (Case III), the fly height reduction of 5 nm drives H_{EFF} to shows a magnitude of 12219 Oe or increased by 13.2% comparing to Case I. If both phenomena are combined in the simulation (Case IV), H_{EFF} exhibits a magnitude of 11693 Oe or increased by 8.3%.

Fig.4 shows the effective field measured above the trailing edge in all cases as a function of the cross-track position. It indicates an identical trend comparing to the effective field in the down-track position.

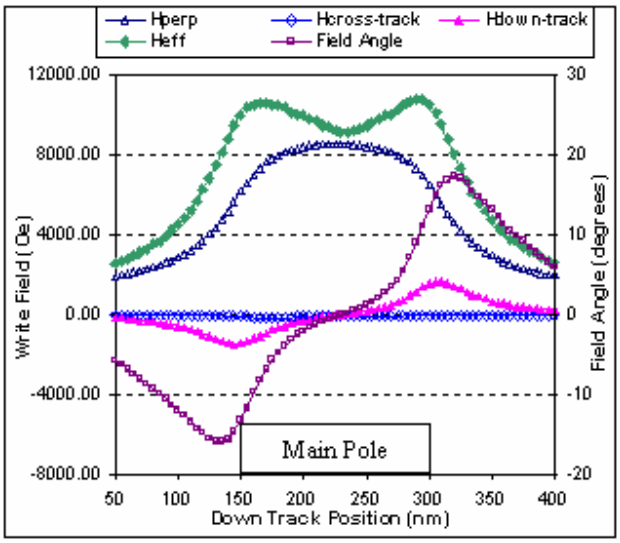

Figure 2. The write field components and the field angle in down-track position.

TABLE II
CALCULATION CONDITIONS

Case	Calculation Condition	HMS	B-H Curve
I	No protrusion and temperature	15 nm	As in Tab. I
II	Only temperature	15 nm	5% decrease of Tab.I
III	Only head protrusion	10 nm	As in Tab. I
IV	Both protrusion and temperature	10 nm	5% decrease of Tab.I

Fig.5 shows the magnitude of the effective field of all four cases above as a function of the applied magnetic scalar potentials. It shows that the difference of the effective field magnitude due to the effect of head protrusion and rising temperature becomes larger at higher magnetic scalar potential.

The rising temperature causes to decrease the effective field while the head protrusion leads to increase the field. However, the effect of the head protrusion is a dominant factor resulting that the effective field is increased by 8.3%. Normally, the stronger effective field gives a better writability. However, the wider pulse of the effective field in cross-track direction may lead to enlarge the written track and it may have a potential to interfere an adjacent track.

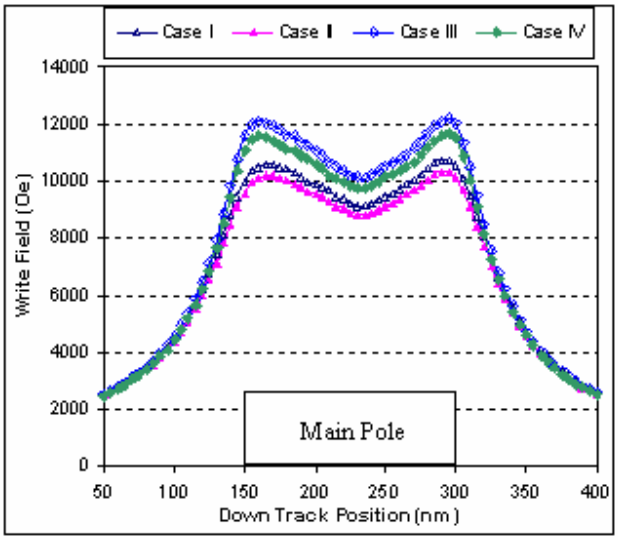

Figure 3. The dependence of the effective write field in down-track position on the heating from the integrated heater.

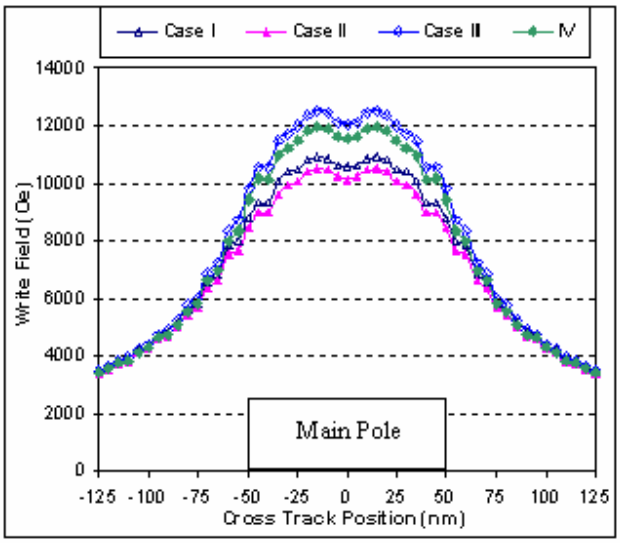

Figure 4. The dependence of the effective write field in cross-track position on the heating from the integrated heater.

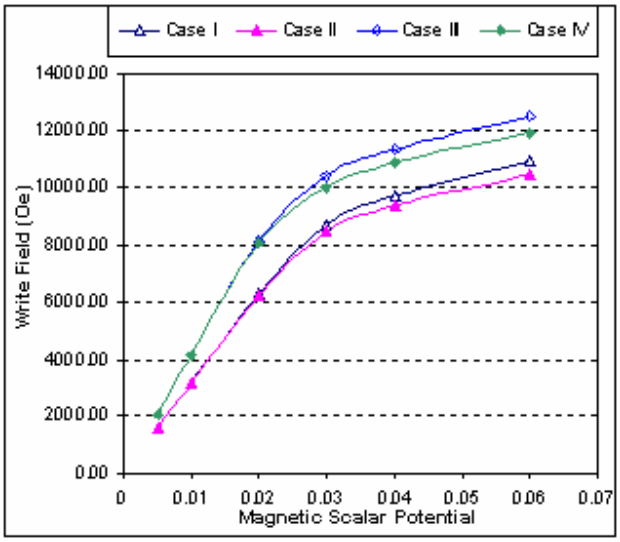

Figure 5. The magnitude of the effective field versus magnetic scalar potential from four cases of the heating effect.

TABLE III
TEST SETUP PARAMETERS

Linear Velocity (m/sec)	15.842
Written Wavelength (μm)	0.396
Write Frequency (MHz)	40
Write Current Amplitude 0-Pk (mA)	60
Skew Angle (degree)	-11

III. EXPERIMENT

In this experimental setup, a Seagate in-house built spin-stand tester was used. The heads used for this experiment are perpendicular magnetic recording (PMR) heads. The writer head is a trailing shielded single pole head (SSPH) and the reader head is a tunneling magneto-resistive (TMR) head. To investigate the dependence of the recording field on the head protrusion due to the heater power, we measure the dependence of the magnetic write width (MWW) on the flying height by increasing the heater power of 5 mW for each step. The heater power was applied in both write and read cycles. To prevent a head scratch to the media, we firstly measured the clearance between the head and media of all the heads and found out the contact power. It is well known that the head protrusion depends on both the heating from the heater and that from the write current. So, the MWW is measured at three different values of the write current; 50, 60, and 70 mA. The test setup parameters are shown in Tab. III.

The MWW is a very important parameter in characterizing magnetic recording heads. To measure the MWW using spin stand, microtrack profile has been widely used and it is considered to be a standard method. Using the microtrack profile method, the MWW value is defined from the width of a full-track profile at 50% of maximum amplitude [5].

In time-domain, the full-track profile $F(x)$ can be mathematically represented by the convolution between the reader response function and the magnetization of the data track as follows [5]:

$$F(x) = \int R(y)\, M(x - y)\, dy = \int R(y)\, [\theta(x - y) - \theta(x - y - MWW)]\, dy \quad (3)$$

where $R(x)$ is the reader response function, $M(x)$ is the magnetization of the data track in cross-track direction. Generally, $M(x)$ is assumed to have a rectangular shape.

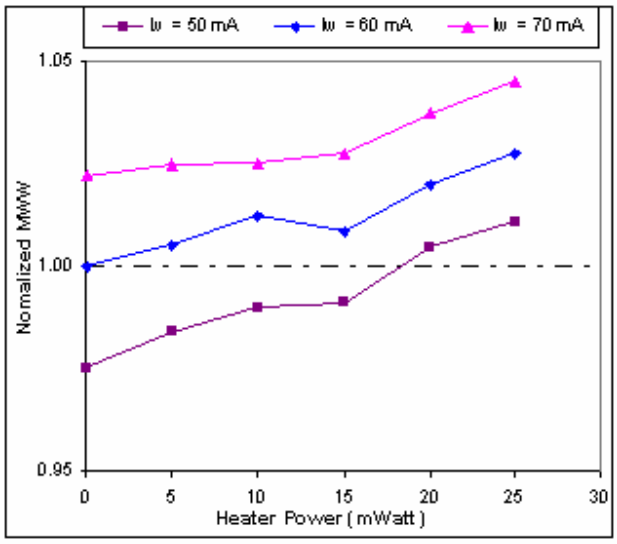

Figure 6. Normalized MWW at different heater powers and write currents.

Fig. 6 shows the plot of normalized MWW as a function of the heater power (normalized to the MWW value at no heater power and write current, I_w, is 60 mA). It exhibits that the higher heater power the larger MWW is. At I_w = 60 mA, the MWW is increased by 2.8% at the heater power of 25 mW. This experimental result agrees with the simulation result that the written track becomes wider due to the head protrusion and it may have a potential to interfere an adjacent track. It also exhibits similar trends when the write current is 50 mA and 70mA. The larger MWW at a higher write current can be classified into two phenomena; the increase of magnetic field due to higher magnetomotive force (mmf) or magnetic scalar potential across the effective gap, and the reduction of flying height due to W-IHP. It is the fact that the higher write current the larger W-IHP is.

IV. CONCLUSION

A 3-D finite element model has been developed to analyze the effective write field which is affected by H-IHP. The results show that the rising temperature which causes to lower *Bs* and μr of the main pole material (5%) decreases the effective field magnitude (3.92% lower than the case of no heating). In contrast, the head protrusion in the direction perpendicular to media plane (5 nm) increases the effective field (13.2% higher than the case of no head protrusion). The combination of these phenomena gives a stronger effective field of 8.3%.

The experiment results show that the head protrusion also widens the written track (through a measure of MWW) for 2.8% at the heater power of 25 mW. This may be explained by the simulation result in which the wider pulse of the effective field in cross-track direction due to head protrusion may lead to enlarge the written track. This larger written track may present adjacent track interference.

ACKNOWLEDGMENT

The authors would like to thank K. Vongsarath at Seagate Thailand for valuable suggestions on the technical issues of perpendicular recording heads and the support on the experiment.

REFERENCES

[1] Y. Li "Write-induced pole-tip-protrusion and its effect on head-disk interface clearance," *IEEE Trans. on Magnetics,* vol. 40, no. 4, pp. 3145-3147, July 2004.

[2] K. Aoki et al. "Thermal pole-tip protrusion analysis of magnetic heads for hard disk drives," *IEEE Trans. on Magnetics,* vol. 41, no. 10, pp. 3043-3045, October 2005.

[3] A. Shukh "Writability of perpendicular recording heads," *IEEE Trans. on Magnetics,* vol. 40, no. 4, pp. 2585-2587, July 2004.

[4] G. Bordin et al. "Temperature dependence of magnetic properties and phase transitions in a soft magnetic Co-based nanostructured alloy," *J.Phys. D: Appl. Phys.*, vol. 32, pp. 1795-1800, 1999.

[5] Z. H. Lin et al. "Full-track profile derivative method for track width measurements of magnetic recoding head," *IEEE Trans. on Magnetics,* vol. 41, no. 10, pp. 3067-3069, October 2005.

Design of High-Rate Modified Array Codes for Magnetic Recording System

W. Singhaudom, S. Noppanakeepong, P. Suphithi,
Faculty of Engineering, and Research Center for Communications and Information Technology (ReCCIT)
and I/U CRC in Data Storage Technology and Applications
King Mongkut's Institute of Technology Ladkrabang, Ladkrabang, Bankok 10520, THAILAND
Email: s5061230@kmitl.ac.th, knsuthic@kmitl.ac.th, ksupornc@kmitl.ac.th

***Abstract*- In applying iterative decoding methods to magnetic recording systems, the high-rate code must be considered. This paper presents design of high-rate Modified Array Codes, a type of Low Density Parity Check (LDPC) Codes, that have been known to possess many advantages required in magnetic recording system such as low error floor, capability of detecting and correcting burst error.**

***Index Terms*- Modified Array Codes, Low-density parity-check codes, high-rate codes, Magnetic recording.**

I. INTRODUCTION

Iterative decoding techniques of error correcting codes in magnetic recording system have been of great interest to replace the conventional error correcting codes. Turbo codes and Low Density Parity Check Codes (LDPC) utilize iterative decoding method which shows performance results close to the Shannon limit [1], [2]. However, many researches found that LDPC codes have better outperform Turbo codes for large block size such as [9].

In magnetic recording systems, higher-rate codes must be considered. One reason is that the internal clock rates of read channels inversely scale with code rate. A low code rate, therefore, means a large disadvantage in practice in hardware design. Furthermore, due to thermal instabilities in the media at high area densities, it may not be possible to reliably record at the higher symbol densities required by low code rates [4].

Recently, a type of LDPC codes coined "Modified Array Codes" is proposed [7] for use in communication system for medium code rate. The code is shown to have performance similar to regular/irregular LDPC codes, but possess attractive properties such as simple encoding, low error floor and capability of detecting and correcting burst error.

In this paper, we present a design of Modified Array Codes for high-rate applications such as magnetic recoding system. We show two sets of codes for block sizes common in magnetic recording systems. The effect of permutation matrix size is studied and together with iterative processing, coding gain is achieved.

II. LOW-DENSITY PARITY CHECK (LDPC) CODES

An LDPC code is a binary linear block code defined by a spare parity check matrix. It can be represented by the Bipartite Graph [5]. Suppose that a parity-check matrix $\mathbf{H}$ has n columns and m rows, and the codeword consists of n bits, which satisfy m checks, the number of message bits will be $k = (n-m)$, and the rate of code is $R_c = k/n$. The number 1's in the parity check matrix in rows and columns represents an edge between the $i-th$ bit node c_i and the $j-th$ check node f_j.

An example of the parity check matrix $\mathbf{H}$ of a LDPC code of dimension (m, n) = (3, 7) is shown in Eq. (1).

$$\mathbf{H} = \begin{bmatrix} 1 & 0 & 0 & 0 & 1 & 1 & 1 \\ 0 & 1 & 0 & 1 & 1 & 0 & 1 \\ 0 & 0 & 1 & 1 & 0 & 1 & 1 \end{bmatrix}_{m \times n} \quad (1)$$

The Bipartite or Tanner graph representing the LDPC code can be constructed as shown in Fig. 1.

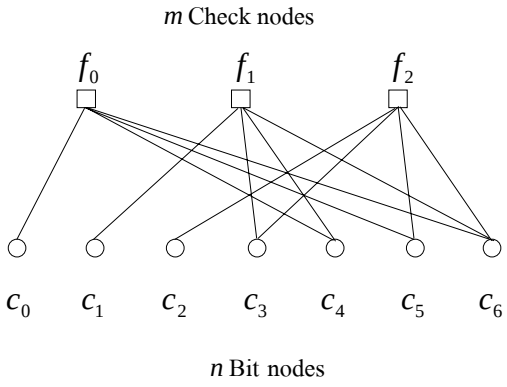

Figure 1. Bipartite or Tanner graph for LDPC code

A disadvantage of general LDPC code is that significant amount of memory is needed to store the parity-check matrix $\mathbf{H}$ due to long input message bits. An Array Code is a structured LDPC code which solves the memory problem since their parity-check matrix consists of the circulant permutation matrices and the identity matrices. In fact, the required memory for storing them can be reduced by a factor $1/p$, when p x p circulant permutation matrices are employed. Moreover, Array codes have capability to detecting and correcting burst error [6].

A. Modified Array Codes

To achieve efficient encoding and minimum distance properties, Eleftheriou [7] proposed a new Array Codes which is known as "Modified Array Codes". A parity-check matrix $\mathbf{H}$ of a modified array codes can be described in terms of the parameter (p, j, k) and has the form

$$\mathbf{H}(p,j,k) \triangleq \begin{bmatrix} \mathbf{I} & \mathbf{I} & \mathbf{I} & \cdots & \mathbf{I} & \cdots & \mathbf{I} \\ \mathbf{0} & \mathbf{I} & \mathbf{P} & \cdots & \mathbf{P}^{(j-2)} & \cdots & \mathbf{P}^{(k-2)} \\ \mathbf{0} & \mathbf{0} & \mathbf{I} & \cdots & \mathbf{P}^{2(j-3)} & \cdots & \mathbf{P}^{2(k-3)} \\ \vdots & \vdots & \vdots & \cdots & \vdots & \cdots & \vdots \\ \mathbf{0} & \mathbf{0} & \cdots & \mathbf{0} & \mathbf{I} & \cdots & \mathbf{P}^{(j-1)(k-j)} \end{bmatrix},$$

where p is prime and $j \le k \le p$, $\mathbf{0}$ is the p x p null matrix and $\mathbf{I}$ is the p x p identity matrix . The matrix $\mathbf{P}$ is a p x p circulant permutation matrix which shifts the identity matrix $\mathbf{I}$ to the right once given in Eq. (2). The permutation matrix can be used to shift the multiplied matrix to the right by i times for any integer i, $0 \le i < p$.

$$\mathbf{P} = \begin{bmatrix} 0 & 1 & 0 & & 0 \\ 0 & 0 & 1 & \cdots & 0 \\ \vdots & \vdots & \vdots & & \vdots \\ 0 & 0 & 0 & \cdots & 1 \\ 1 & 0 & 0 & & 0 \end{bmatrix} \qquad (2)$$

In [7], it is shown that for a modified array code, the minimum distance $d_{\min} = 6$ for $j = 3$ and $d_{\min} \ge 8$ for j = 4. Efficient encoding is achieved from $\mathbf{H}$ without the need to compute the generator matrix of the code. As the upper triangular form of $\mathbf{H}$, there are no cycles of length 4 in the corresponding Tanner graph.

The Modified Array Codes defined by $\mathbf{H}$ has codeword length $N = k \cdot p$, number of parity bit $M = j \cdot p$ and message block length $K = p \cdot (k - j)$ and finally, code rate is $R = 1 - j/k$.

B. Cycles of Modified Array Codes

To understand the cycle properties of Modified Array Codes, we will consider the following a more general from of a parity check matrix $\mathbf{H}$, i.e.,

$$\mathbf{H} = \begin{bmatrix} \mathbf{P}^{a_0 \cdot 0} & \mathbf{P}^{a_0 \cdot 1} & \mathbf{P}^{a_0 \cdot 2} & \cdots & \mathbf{P}^{a_0 \cdot p-1} \\ \mathbf{0} & \mathbf{P}^{a_1 \cdot 1} & \mathbf{P}^{a_1 \cdot 2} & \cdots & \mathbf{P}^{a_1 \cdot p-1} \\ \mathbf{0} & \mathbf{0} & \mathbf{P}^{a_2 \cdot 2} & \cdots & \mathbf{P}^{a_2 \cdot p-1} \\ \vdots & \vdots & \vdots & \cdots & \cdots \\ \mathbf{0} & \mathbf{0} & \cdots & \cdots & \mathbf{P}^{a_{j-1} \cdot p-1} \end{bmatrix} \qquad (3)$$

A cycle of length 2k exits in the Tanner graph of Modified Array Codes with the parity check matrix $\mathbf{H}$ and block row labels $a_0, a_1, \ldots, a_{j-1}$ if and only if there exists a close path $(i_1, j_1), (i_1, j_2), (i_2, j_2), (i_2, j_3), \ldots, (i_k, j_k), (i_k, j_1)$.

The possible cycles in $\mathbf{H}$ is 2k times, and then the length of the cycles in the permutation is described as shown below.

$$\mathbf{P}^{a_{i_1} \cdot j_1} \left(\mathbf{P}^{a_{i_1} \cdot j_2}\right)^{-1} \mathbf{P}^{a_{i_2} \cdot j_2} \left(\mathbf{P}^{a_{i2} \cdot j_3}\right)^{-1} \cdots \mathbf{P}^{a_{ik} \cdot j_k} \left(\mathbf{P}^{a_{ik} \cdot j_1}\right)^{-1}$$

From the result of short cycles properties in [8], the cycles of length 4 depends on the following permutation,

$$\mathbf{P}^{a_{i_1} \cdot j_1} \left(\mathbf{P}^{a_{i_1} \cdot j_2}\right)^{-1} \mathbf{P}^{a_{i_2} \cdot j_2} \left(\mathbf{P}^{a_{i2} \cdot j_1}\right)^{-1} = \mathbf{P}^{(a_{i_1} - a_{i_2})(j_1 - j_2)}$$

which is exact when it is equal to 1. This occurs when $(a_{i_1} - a_{i_2})(j_1 - j_2) \equiv 0$, which is clearly impossible since $i_1 \ne i_2$ and $j_1 \ne j_2$. Hence, there are no cycles of length 4 for Modified Array Codes.

III. THE SUM-PRODUCT ALGORITHM (SPA)

The sum-product algorithm (SPA) is a soft iterative decoding algorithm most commonly used to decode LDPC codes [2-3]. Given that y_i is the i^{th} received channel value corresponding to the i^{th} transmitted codeword c_i . Input of LDPC decoder is in the form of log likelihood ratios (LLRs) $L(c_i) = \log(P(c_i = 0 \mid y_i) / P(c_i = 1 \mid y_i))$.

From Fig 2, the basic operation in the decoding algorithm is shown. In the Tanner graph, the check nodes and bit nodes interchange soft information. Let the variable q_{ij} be the message (information) sent from the i^{th} bit node to j^{th} check node along a connecting edge, and r_{ji} is the message (information) sent from j^{th} check node to the i^{th} bit node along a connection edge. The information q_{ij} is computed based on the values sent from check nodes connecting to the i^{th} bit node excluding the j^{th} bit node.

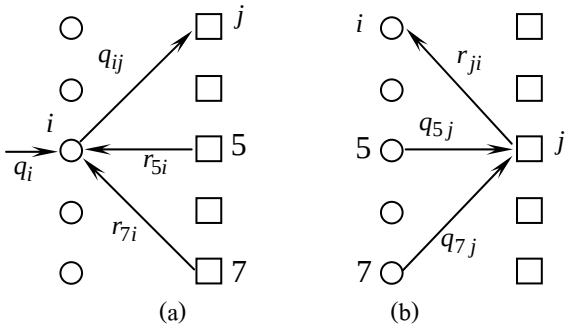

Figure 2. (a) A message is passed from i^{th} bit node to j^{th} check node and (b) A message is passed from the j^{th} check node to the i^{th} bit node.

The Operation of Log-Domain SPA Decoder

The operation of log-domain SPA decoder consists 5 steps, i.e.,

Step 1: Initialization. The LLR value of q_{ij} is set to be equal to the LLR value of the received channel values computed from

$$L(q_{ij}) = L(c_i) = 2y_i / \sigma^2, \qquad (4)$$

where σ^2 is variance of Gaussian noise.

Step 2: Update equation for the message from check nodes to bit nodes given by

$$L(r_{ij}) = \prod_{i' \in V_j \setminus i} \alpha_{i'j} \cdot \phi\left(\sum_{i' \in V_j \setminus i} \phi(\beta_{i'j}) \right), \quad (5)$$

where $\alpha_{ij} = \operatorname{sgn}\{L(q_{ij})\}$, $\beta_{ij} = |L(q_{ij})|$ and define $\phi(x) = \log\{(e^x + 1)/(e^x - 1)\}$ with the base of e. In addition, $V_{j\setminus i}$ represents all the bit nodes except the i^{th} bit node.

Step 3: Update equation for the message from bit node to check node is given by

$$L(q_{ij}) = L(c_i) + \sum_{j' \in C_i \setminus j} L(r_{j'i}) \quad (6)$$

Step 4: For i = 0, 1… n-1, the extrinsic output of decoder is given by

$$L(Q_i) = L(c_i) + \sum_{j \in C_i} L(r_{ji}) \quad (7)$$

Step 5: For i = 0, 1… n-1, the estimated channel input can be computed from

$$\hat{c}_i = \begin{cases} 1, \text{ if } L(Q_i) < 0 \\ 0 \text{ else} \end{cases} \quad (8)$$

If $\hat{\mathbf{c}}\mathbf{H}^t = \mathbf{0}$ or the number of iterations equals the maximum limit, stop, or else, go to Step 2.

IV. Simulation Results and Discussions

The current magnetic recording systems require high code rate such as 8/9 (0.88) and higher and the block size is around 1000 and 4000 bits. In this section, we present the design and performance of modified array codes at high-rate codes with block sizes which are common in magnetic recording systems.

A. Performance results with block size 1100~1300

The Modified Array Codes can be designed by fixing the code rate R and codeword length $N = k \cdot p$ to be around 1,100 – 1,300 bits, and then select p and k respectively. Due to the constraint of high code rates, the parameter j has to be low, given k. The relationship between j and k can be found in Table I. The targeted code rates are in the range of 0.88 – 0.9. Some examples of the designed codes are shown in Table 1.

Table 1: Code parameters with block size 1,100-1,300

j	3	3	3
k	31	29	25
p	37	43	53
$R_c = (1 - j/k)$	0.903	0.897	0.88
Message $p \cdot (k - j)$	1,036	1,118	1,166
Parity bit $j \cdot p$	111	129	159
Block size $k \cdot p$	1,147	1,247	1,325

For high-code rates, it can be observed that the parameter j is small compared with the parameter k. To select the best codes among designed codes, we simulate the performance and compare the results in AWGN channel, but the code rates and code lengths are tailored for magnetic recording systems.. The code performance in terms of the bit error rate (BER) compared with SNR is plotted. In the simulations, we refer to the input signal-to-noise ratio as electronics SNR in AWGN channel and defined it as

$$\left(\frac{E_b}{N_o}\right)_{dB} = \log_{10}\left(\frac{1}{R}\frac{E_c}{N_o}\right),$$

where E_c is the average energy of coded bits, E_b is the average energy of message bits and N_o is noise PSD. Each BER point is computed by using as many data packets as needed to collect at least 1000 error bits. The performance of the targeted block sizes are shown in Fig. 3. Note that the number of iterations in the decoding process is 30. Three modified array codes with code rates of ~0.9 are simulated in this paper. Three different values of p are considered, including 37, 43 and 53. The modified array codes with p = 37 has the worst performance than the other two, in particular, at BER = 10^{-5}, the codes with p = 43 and 53 need the SNR of 4.8 and 4.6 dB, which are less than for the code with p = *37*. The size of permutation matrix **P** evidently affects the code performance. It can be seen that performance is improved when the permutation matrix size increases. As the performance of the decoder is determined by the minimum distance of the code, the codes with larger **P** produces higher minimum distance.

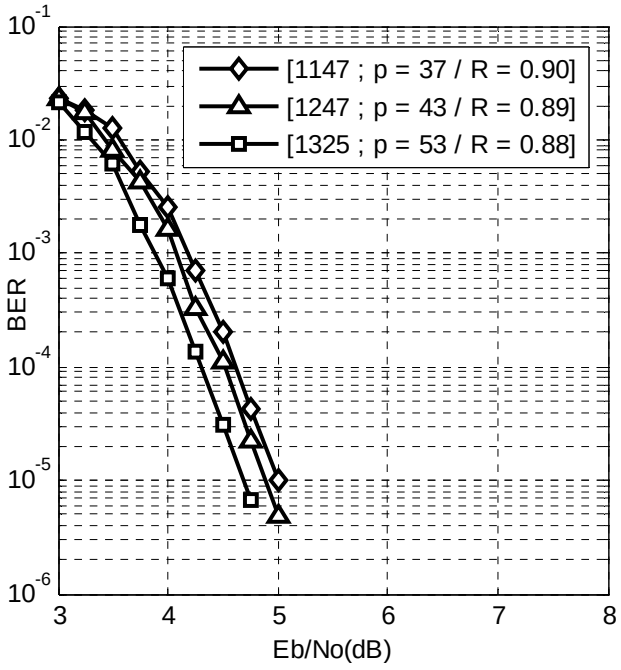

Figure 3. Performance results with block size 1100~1300 with various sizes of permutation matrix (after 30 iterations)

B. Performance results with block size 4000~4100

For this part, we fix the codeword length to be 4,000–4,100 bits, and then adjust the parameter *j*, *k*, and *p*, respectively. The code rate is targeted at 0.89 - 0.92, then the designed codes are shown in Table 2.

Table 2 : Code parameters with block size 4,000-4,100

j	5	5	5
k	61	53	47
p	67	79	89
$R_c = (1 - j/k)$	0.92	0.91	0.89
Message $p \cdot (k - j)$	3,752	3,792	3,738
Parity bit $j \cdot p$	335	395	445
Block size $k \cdot p$	4,087	4,187	4,183

Similar to the result in Fig. 3, the permutation matrix size affects the code performance. Three different values for p are considered, including 67, 79 and 89. The modified array code with p = 67 has the worst performance compared with the other two, in particular, at BER $=10^{-5}$, the code with p = 79 and 89 need 4.5 and 4.25 dB less than that of p = 67 code.

It can be seen that performance is improved when the permutation matrix size increases as well.

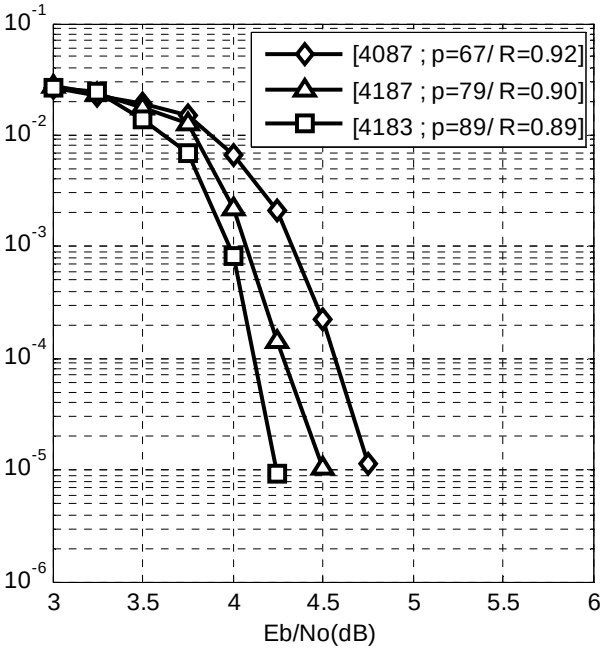

Figure 4. Performance results with block size 4000~4100 with various sizes of permutation matrix (after 30 iterations)

V. CONCLUSIONS

The design of high-rate Modified Array Codes at high code rate with block sizes suitable for magnetic recording system is illustrated. For high-rate codes, the simulation shows that the size of permutation matrix affects the code performance with larger *p* leads to higher minimum distance. This is valid for the both cases of considered block sizes. Modified Array Codes LDPC have been shown to possess suitable properties for magnetic recording system such as low-complexity encoding process, low error floor and capability of detecting and correcting burst. It is, therefore, possible to use the Modified Array Codes together with iterative decoding method, as the error correcting code in the magnetic recording channel. For future works, we plan to evaluate the performance of Modified Array Codes together with turbo equalization in realistic magnetic recording channel model.

REFERENCES

[1] C. Berrou, A. Glanvieux, and P. Thitimajshima, "Near Shannon limit error-correcting coding and decoding: Turbo-codes," in Proc. *IEEE Intl. Conf.*, pp. 1064-1070, May 1993.

[2] D.J.C. Mackey and R. Neal "Near Shannon limit performance of low density parity check codes," *Electronics Letters*, vol.33, pp. 457-458, Mar 1997.

[3] R. Gallager, "Low-density parity-check codes," *IRE Trans. Information Theory*, pp. 21-28, Jan 1962.

[4] Oenning, T.R.; Jaekyun Moon "Low density parity check coding for magnetic recording channels with media noise" *IEEE International Conference*, June 2001, pp.2189 -93.

[5] R. M. Tanner, "A recursive approach to low complexity codes," *IEEE Trans. Information Theory*, pp.533-547, Sept. 1981.

[6] M. Blaum, R. Roth, "New Array Codes for Multiple Phased Burst Correction," *IEEE Trans. Inform. Theory*, vol.39, No.1, Jan 1993, pp 66-77.

[7] E. Eleftheriou and S. Olcer, "Low-density parity check codes for digital subscriber lines," *Proc. 2002 Int. Conf. on Comm.*, pp.1752-1757., April – May, 2002.

[8] J. L. Fan, "Array codes as low-density parity-check codes," in *Proc.* 2nd *Int. Symp. Turbo Codes*, Best, France, Sep 2000, pp 543-546.

[9] Richardson T.J., Shokrollahi MA, Urbanke R.L. "Design of capacity-approaching irregular low-density parity-check codes," *Information Theory IEEE Trans.volume 47*, pp.619-637, Feb 2001.

Subblock Encoder Design of Modified Array-Based Low-Density Parity-Check Codes

P. Leekul, S. Chivapreecha, [+]K. Sripimanwat, and P. Supnithi
Faculty of Engineering and Research Center for Communications and Information Technology
I/U CRC in Data Storage Technology and Applications
King Mongkut's Institute of Technology Ladkrabang, Bangkok 10520
[+]National Electronics and Computer Technology (NECTEC), Thailand Science Park, Klongluang, Patumthani 12120
E-mail: s8060944@kmitl.ac.th, sorawat@telecom.kmitl.ac.th, ksripima@ieee.org, ksupornc@kmilt.ac.th

***Abstract* - Modified array code is considered a Quasi-cyclic LDPC codes with simple encoding structure. The parity-check matrix is based on identity matrix and permutation matrix. In this paper, we present a new encoding method with encoder circuit designs presented. The encoding is done on one subblock at a time compared to the direct XOR network and does not need matrix inversion. Both Serial and Semi-Parallel circuit structures are constructed for high-rate applications. The circuit complexity in terms of number of logic elements are compared against direct XOR networks for high-rate codes suitable for magnetic recording systems. The direct XOR networks show exponential complexity, while the proposed encoding methods are much simpler and show linear complexity.**

***Keywords*: Quasi-cyclic LDPC codes, FPGA, Modified array codes.**

I. INTRODUCTION

Low-density parity-check or LDPC code is a linear block code defined by a sparse parity-check matrix **H**. The sparseness results in large minimum distance, hence, a large number of correctable errors can be achieved. The codes when combined with iterative processing leads to a performance approaching the Shannon's limit in an additive white Gaussian noise channel. Low Density Parity Check (LDPC) codes was originally discovered in 1960 by Gallager [1] and in 1962, but the high-complexity hindered its usefulness. It was not until in 1996 when in [2], the author rediscovers LDPC and presents the decoding method using Belief Propagation. In [3], S. Y. Chung et. al. showed that LDPC code reaches a Shannon limit within 0.0045 dB. LDPC code comes into two types: regular LDPC code and irregular LDPC code. The encoding problem is typically complex and has been studied by many researchers [4-6]. A type of LDPC codes called quasi-cyclic LPDC (QC-LDPC) code has been studied recently due to the quasi-cyclic structure that allows simpler encoding scheme. In [4], the encoding is based on dividing the parity-check matrix **H** into submatrices to accommodate high-rate application. The encoding is still complex as matrix inversion is required. In [5] specific construction of QC-LDPC codes is based on Permutation matrix **P** to achieve a girth size of 12. The structure allows simpler encoding. In [6], encoding based on generator matrix **G** rather than **H** is presented instead. It is still based on breaking the matrix **H** into submatrices and then translates into the generator matrix **G**. In this paper, we present a block-type encoding of QC-LDPC codes for high-rate application. The simplicity is due to systematic encoding nature and encoding is done on a subblock basis. There is no matrix inversion required and for high-rate application, the numbers of encoding equations are small. In Section II, we review LDPC codes and QC-LDPC codes and some properties. In Section III, encoding equations are derived and encoder circuits are presented. The analysis results and discussions are shown in Section IV and the conclusions are in Section V.

II. LOW-DENSITY PARITY-CHECK (LDPC) CODES

A. *Array-based LDPC code*

An array-based LDPC code or Array code is a type of non-systematic LDPC codes with quasi-cycle property. The parity-check matrix **H** has a structure that allows efficient encoding process. The encoding is done with **H** rather than generator matrix **G** [6]. The quasi-cyclic property dictates that shifted message bits correspond to shifted parity-check bits.

The parity-check matrix **H** has the dimension (n-k) x n, where k is the message length and n is the code length. The matrix **H** can be built from the permutation matrix P with dimension size L x L given by

$$P_{LxL} = \begin{bmatrix} 0 & 1 & 0 & & 0 \\ 0 & 0 & 1 & \dots & 0 \\ : & : & : & & : \\ 0 & 0 & 0 & \dots & 1 \\ 1 & 0 & 0 & & 0 \end{bmatrix} \quad (1)$$

The matrix **P** is a shifted identity matrix **I** one time. The matrix **H** can be built from

$$\mathbf{H} = \begin{bmatrix} I & I & I & \dots & I \\ I & P & P^2 & \dots & P^{k-1} \\ I & P^2 & P^4 & \dots & P^{2(k-1)} \\ : & : & : & : & : \\ I & P^{j-1} & P^{2(j-1)} & \dots & P^{(j-1)(k-1)} \end{bmatrix} \quad (2)$$

Basically, the matrix P expands rowwise by j times and columnwise by k times, respectively.

B. Modified array-based LDPC code

A modified array-based LDPC code or a Modified Array code [7] is an array code with modification so that the codeword is systematic. The parity-check matrix **H** for modified array codes can be described by three parameters (q, j, k), where q is prime and integer number j and k. The matrix **H** has dimension jL x kL, i.e.,

$$\mathbf{H}(q,j,k)=\begin{bmatrix} I & I & I & \cdots & I & \cdots & I \\ 0 & I & P & \cdots & P^{(j-2)} & \cdots & P^{(k-2)} \\ 0 & 0 & I & \cdots & P^{2(j-3)} & \cdots & P^{2(k-3)} \\ & & & & \ddots & & \\ 0 & \cdots & 0 & I & P^{(j-2)} & \cdots & P^{(j-2)(k-j-1)} \\ 0 & 0 & \cdots & 0 & I & \cdots & P^{(j-1)(k-j)} \end{bmatrix} \quad (3)$$

(j | k-j)

The encoding complexity of the modified array code is linear [5]. An expansion of **H** matrix using **P** has a constraint that the rowwise expansion factor must be less than the column wise expansion factor, which is also less than the size of permutation matrix, i.e., $q \geq k \geq j$. The code rate can be computed from

$$R=\frac{k-j}{k}=1-\frac{j}{k} \quad (4)$$

Modified array code possesses a quasi-cyclic property and has a linear encoding complexity.

III. ENCODER CIRCUIT OF LDPC CODES

There are various ways to encode LDPC codes, but in this section, we review direct encoding method of LDPC code. The encoding complexity is linear. Encoding is transforming a message into a codeword. For systematic code, this means adding parity bits. A simple way is to exploit the relationship between coderword and the parity-check matrix **H**. Given a codeword **c** with dimension of 1xn and the corresponding matrix parity check **H** with dimension of (n-k)xn and **0** is a zero matrix with dimension of (n-k)xn. The encoding circuit uses to modulo-2 addition or XOR operation. Consider the relationship

$$\mathbf{cH}^T = \mathbf{0} \quad (5)$$

Transpose both sides of Eq. (5) to obtain

$$\mathbf{Hc}^T = \mathbf{0}^T \quad (6)$$

Let a systematic codeword **c** be in the form of

$$\mathbf{c}=\left[\, p_1\, p_2 \ldots p_{n-k} \;\middle|\; m_1 m_2 \ldots m_k \,\right]=[\mathbf{p}\quad \mathbf{m}] \quad (7)$$

where the parity bits are positioned at the front part and the message bits are at the back part. In this way, the encoding can be done efficiently. The transpose of codeword **c** in Eq. (6) can be written as

$$\mathbf{c}^T=\begin{bmatrix}\mathbf{p}\\ \mathbf{m}\end{bmatrix} \quad (8)$$

Substituting Eq.(8) into Eq.(6), the parity-check equation can be derived. For example, given that a parity-check matrix **H** of a (3, 6) code is

$$\mathbf{H}=\begin{bmatrix}1&0&0&1&0&1\\0&1&0&1&1&0\\0&0&1&0&1&1\end{bmatrix} \quad (9)$$

Rewrite Eq.(8) as

$$\mathbf{Hc}^T=\mathbf{0}^T \quad = \quad \begin{bmatrix}1&0&0&1&0&1\\0&1&0&1&1&0\\0&0&1&0&1&1\end{bmatrix}\begin{bmatrix}p_1\\p_2\\p_3\\m_1\\m_2\\m_3\end{bmatrix}=\begin{bmatrix}0\\0\\0\\0\\0\\0\end{bmatrix} \quad (10)$$

Then the parity-check equation can be listed as

$$\begin{aligned} p_1 + m_1 + m_3 &= 0 \\ p_2 + m_2 + m_1 &= 0 \\ p_3 + m_3 + m_2 &= 0 \end{aligned}, \quad (11)$$

where '+' is a modulo-2 addition or an XOR operation. The parity bits can then be found from

$$\begin{aligned} p_1 &= m_1 + m_3 \\ p_2 &= m_2 + m_1 \\ p_3 &= m_3 + m_2 \end{aligned} \quad (12)$$

A simple circuit diagram can thus be shown in Fig. 1.

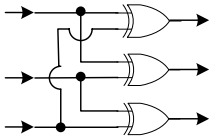

Fig. 1. Direct encoder of a (3, 6) code

Direct method is viable for the code with small k, but in practical applications, the message length can be up to 1024, for example. Given a code rate of ½, the codeword length is n = 2048. The number of parity-check equations is then 1024. The number of XOR operation can be very high and not suitable for encoder circuit design. In the next part, we propose a block-type encoder design.

A. *Subblock-Type Encoder Design of Modified Array Codes*

The encoder complexity can be reduced by encoding each subblock at a time. The matrix H consists of j subblocks rowwise and k subblocks columnwise. Consider a systematic codeword of length $N = kL$ with parity-check part at the front and the message part at the back, i.e.,

$$\mathbf{c} = \begin{bmatrix} \mathbf{p}_1 & \mathbf{p}_2 & \mathbf{p}_3 & \mathbf{p}_4 & \cdots & \mathbf{p}_j & \mathbf{m}_1 & \mathbf{m}_2 & \cdots & \mathbf{m}_{k-j-1} & \mathbf{m}_{k-j} \end{bmatrix} \quad (13)$$

Consider the equation

$$\mathbf{H}\mathbf{c}^T = \begin{bmatrix} I & I & I & \cdots & I & \cdots & I \\ 0 & I & P & \cdots & P^{(j-2)} & \cdots & P^{(k-2)} \\ 0 & 0 & I & \cdots & P^{2(j-3)} & \cdots & P^{2(k-3)} \\ & & & & \ddots & & \\ 0 & \cdots & 0 & I & P^{(j-2)} & \cdots & P^{(j-2)(k-j-1)} \\ 0 & 0 & \cdots & 0 & I & \cdots & P^{(j-1)(k-j)} \end{bmatrix} \begin{bmatrix} \mathbf{p}_1 \\ \mathbf{p}_2 \\ \vdots \\ \mathbf{p}_j \\ \mathbf{m}_1 \\ \mathbf{m}_2 \\ \vdots \\ \mathbf{m}_{k-j} \end{bmatrix} = \mathbf{0}^T, \quad (14)$$

where $\mathbf{p}_i$, $i = 1,2,\ldots, j$ is a subblock of parity bits of size LxL. Thus, each subsection of parity-check bits can be computed from two parts: the higher-indexed parity-check subsection and all the message subsections. The above equations can be written as a set of equations

$$\begin{aligned} \mathbf{p}_j &= \mathbf{m}_1 P^{(j-1)} + \mathbf{m}_2 P^{(j-1)2} + \mathbf{m}_3 P^{(j-1)3} + \cdots + \mathbf{m}_{k-j} P^{(j-1)(k-j)} \\ \mathbf{p}_{j-1} &= \mathbf{p}_j P^{(j-2)} + \mathbf{m}_1 P^{(j-2)2} + \mathbf{m}_2 P^{(j-2)3} + \cdots + \mathbf{m}_{k-j} P^{(j-2)(k-j+1)} \\ \mathbf{p}_{j-2} &= \mathbf{p}_{j-1} P^{(j-3)} + \mathbf{p}_j P^{(j-3)2} + \mathbf{m}_1 P^{(j-3)3} + \cdots + \mathbf{m}_{k-j} P^{(j-3)(k-j+2)} \\ &\vdots \quad\quad \vdots \quad\quad \vdots \quad\quad \vdots \\ \mathbf{p}_l &= \mathbf{p}_{l+1} P^{(l-1)} + \mathbf{p}_{l+2} P^{(l-1)2} + \cdots + \mathbf{p}_j P^{(l-1)(j-l)} \cdots + \mathbf{m}_{k-j} P^{(l-1)(k-l)} \\ &\vdots \quad\quad \vdots \quad\quad \vdots \quad\quad \vdots \\ \mathbf{p}_1 &= \mathbf{p}_2 + \mathbf{p}_3 + \cdots + \mathbf{p}_j + \mathbf{m}_1 + \mathbf{m}_2 \cdots + \mathbf{m}_{k-j} \end{aligned} \quad (15)$$

or in a simplified equation as

$$\begin{aligned} \mathbf{p}_j &= \sum_{i=1}^{k-j} \mathbf{m}_i P^{(j-1)i} \\ \mathbf{p}_l &= \sum_{i=1}^{j-l} \mathbf{p}_{l+i} P^{(l-1)i} + \sum_{i=1}^{k-j} \mathbf{m}_i P^{(l-1)(j-l+i)}; 1 \le l \le j-1 \end{aligned} \quad (16)$$

There is a total of j parity subblock equations. We start from the computation of $\mathbf{p}_j$ all the way to $\mathbf{p}_1$. Notice that subblock-type encoding does not require any real multiplication due to the fact that the result of a vector multiplying with permutation matrix is nothing but cyclic-shift the vector to the right by the power of the matrix **P.**

B. *Implementation of Subblock Encoder Circuit Using Serial Structure*

The parity subblocks in Eq. (14) can be implemented in Serial or Semi-Parallel structure. Here, we discuss the serial circuit type. According to Eq.(14), the amount of shifts in each equation is determined by the power of **P** matrix and it needs to be stored in ROM. The encoder circuit consists of shift and modulo-2 addition operations as shown in Fig. 2. We first compute the parity subblock $\mathbf{p}_j$. The message subblock $\mathbf{m}_1$ is first read into the top registers, then shifted by the amount of (j-1) times to the right. It is then placed at the bottom register. Next, the subblock $\mathbf{m}_2$ is read in and shifted by (j-1) times to the right. The output is moved to the bottom and XOR with previous stored subblock. The entire process is repeated until $\mathbf{p}_j$ is fully computed. Each subblock of $\mathbf{p}_l$ is computed similarly except that the previously computed parity subblocks will be used together with message subblocks.

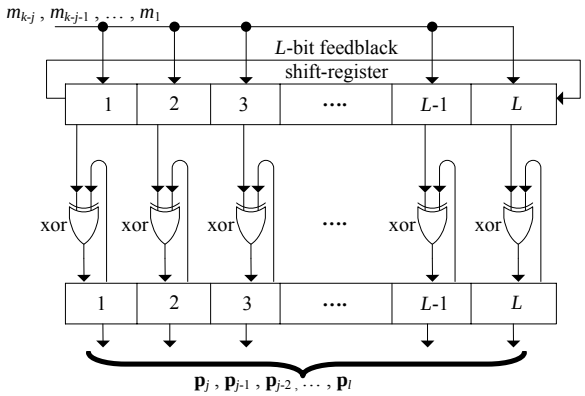

Fig. 2. Serial Encoder Circuit of Modified Array Codes

C. *Implementation of Subblock Encoder Circuit Using Semi-Parallel Structure*

To speed up the encoding process, and considering the encoding process in Eq. (15) and Eq. (16), the message subblocks are used in all equations, thus they can be shifted in advance and in Semi-Parallel, ready for the computation of higher-indexed parity subblocks as shown in Fig. 3.

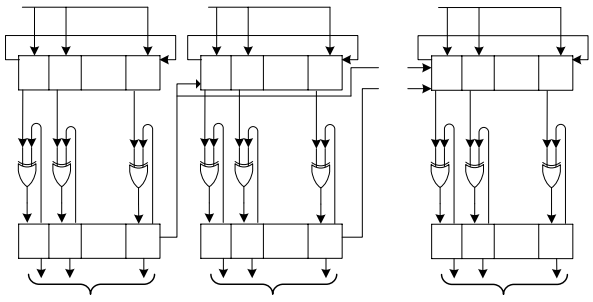

Fig. 3. Semi-Parallel Encoder Circuit of Modified Array Codes

IV. ANALYSIS RESULTS AND DISCUSSIONS

The circuit synthesis of serial and Semi-Parallel structure is performed on Quartus II with the utilized resources computed. The comparison of both designs against the direct XOR networks is illustrated in Table I.. The circuit analysis begins

with small message block size c = 361 bits and permutation matrix *P* of dimension 19x19. For this code, the complexity between Semi-Parallel circuit and direct XOR networks is similar, but for the block with large matrix *P* of dimension 43x43 and c = 1849 bits, XOR networks requires about 3 times logic elements than Semi-Parallel networks. Direct encoder circuits based on XOR Network requires much higher number of logic elements compared with subblock encoder for large message blocks. Larger message block size with larger permutation matrix size causes XOR networks to far exceed the complexity of subblock methods. In addition, direct XOR networks lack clock signal to synchronize the encoding process. For subblock encoding, serial circuits require less logic elements than the Semi-Parallel counterpart. The speed of Semi-Parallel circuit is of course faster. It is observed that Semi-Parallel encoding is 3 times faster than serial encoding circuits.

TABLE I. The Number of Required Logic Elements

Type		Quasi - Cyclic – LDPC Encoding		
Permutation Matrix	Block Size	Serial	Semi-Parallel	XOR Network
P = 19	c = 361	124	213	228
P = 29	c = 841	180	480	813
P = 37	c = 1369	236	849	1,801
P = 41	c = 1681	257	930	2,249
P = 43	c = 1849	269	1,049	3,314
P = 47	c = 2209	286	1,342	3,925
P = 59	c = 3481	359	1,978	13,001

The code rates of modified array codes analyzed here and listed in Table I ranges from 0.88 to 0.9. The high rate is suitable for many applications such as wireless/satellite communication under good conditions and high-density magnetic recording systems, for instance. The results from Table I is then plotted in Fig. 5. Notice the trend of required amount of logic elements. The direct XOR networks exhibit exponential increase as the block size goes up, while the serial subblock encoder shows linear complexity.

V. CONCLUSIONS

In this paper, we present a subblock encoder of modified array code, which is considered a type of quasi-cyclic LDPC codes suitable for high-rate applications such as magnetic recording systems and many other communication systems. The encoder equations are derived for each subblock at a time and then serial and Semi-Parallel circuit structures are presented. The circuit complexity in terms of number of logic

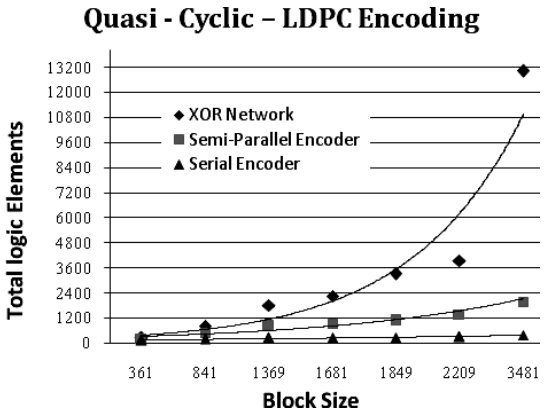

Fig. 5. The required number logic elements of direct XOR networks, Serial subblock encoder and Semi-Parallel subblock encoder

elements are compared for direct XOR networks, serial structure and Semi-Parallel structure. The direct XOR network exhibits exponential increase in complexity for large block size with lack of clock signal. The serial encoder has the lowest complexity for each message block size, but possess slower speed than the Semi-Parallel counterpart

REFERENCES

[1] R. G. Gallager, "Low density parity check codes," IRE Trans. Inform. Theory, vol. IT-8, pp. 21–28, Jan 1962.

[2] D. J. C. MacKay and R. M. Neal, "Good codes based on very sparse matrices," in Cryptography and Coding 5th IMA Conf., C. Boyd, Ed., Lecture Notes in Computer Science, no. 1025. Berlin, Germany: Springer, 1995, pp. 100–111.

[3] Chung, S.-Y., Forney, G. D., Jr., Richardson, T. J., and Urbanke, R. L., "On the design of low-density parity-check codes within 0.0045 dB of the shannon limit," *Electron. Lett.*, vol. 5, pp. 58–60, Feb. 2001.

[4] Z. Wang , Z. Cui, "A Memory Partially Parallel Decoder Architecture for QC-LDPC Codes" *IEEE 2005*

[5] M. P. C. Fossorier, "Quasi-Cyclic Low-Density Parity-Check Codes From Circulant Permutation Matrices" *IEEE Trans. Information Theory, vol. 50, no. 8, Aug. 2004*

[6] Zongwang Li, et.al., "Efficient Encoding of Quasi–Cyclic Low-Density Parity-Check Codes"*IEEE Trans. on Information Theory, Vol. 54, no. 1, Jan. 2006*

[7] S. Myung, K.Yang, J. Kim, "quasi - cyclic ldpc codes for fast encoding," *IEEE Trans. on Information Theory, vol. 51, no.8, Aug. 2000.*

Timing Recovery in Magnetic Recording Systems

Piya Kovintavewat
Faculty of Science and Technology, Nakhon Pathom Rajabhat University
85 Moo 3, Malaiman Rd., Muang District, Nakhon Pathom 73000, Thailand

***Abstract*— Timing recovery is a crucial component in a magnetic recording channel detector. Conventional timing recovery techniques are sufficient only when operating at high signal-to-noise ratio (SNR). However, iterative error-correction codes allow reliable operation at very low SNR, where conventional techniques fail. In this paper, we summarize the timing recovery schemes based on a per-survivor processing technique that are capable of working at low SNR. Results indicate that they perform better than conventional schemes.**

I. Introduction

Timing recovery is the process of synchronizing the sampler with the received signal. Sampling at wrong times can have a devastating impact on overall system performance. Therefore, the quality of synchronization is very important in a magnetic recording channel detector.

Conventional timing recovery techniques are based on a decision-directed phase-locked loop (PLL) [1], which consists of a timing error detector (TED), a loop filter, and a voltage-controlled oscillator (VCO). They are adequate only when the operating signal-to-noise ratio (SNR) is sufficiently high. Nonetheless, recent advances in error-control coding have made it possible to communicate reliably at very low SNR, where conventional techniques fail. Many timing recovery schemes that are capable of working at low SNR have been proposed in the literature [2], [3]. In this paper, we summarize all timing recovery schemes that are based on *per-survivor processing* (PSP) [4], a technique of jointly estimating a data sequence and unknown parameters, and also investigate their performances when operating in magnetic recording systems.

This paper is organized as follows. Section II briefly describes a system model. Section III explains how conventional timing recovery works and shows its performance. Per-survivor timing recovery and per-survivor iterative timing recovery are summarized in Sections IV and V, respectively. Finally, Section VI concludes the paper.

II. System Description

We consider the perfectly equalized PR-IV channel model shown in Fig. 1, where the read-back signal can be written as

$$p(t) = \sum_k a_k h(t - kT - \tau_k) + n(t), \tag{1}$$

where $a_k \in \{\pm 1\}$ is an input data sequence with bit period T, $h(t) = q(t) - q(t-2T)$ is a PR-IV pulse, $q(t) = \sin(\pi t/T)/(\pi t/T)$ is an ideal zero-excess-bandwidth Nyquist pulse, and $n(t)$ is additive white Gaussian noise (AWGN) with two-sided power spectral density $N_0/2$. The timing offset, τ_k, is modeled as a random walk model [5] according to $\tau_{k+1} = \tau_k + w_k$, where w_k is an independent and identically distributed (*i.i.d.*) zero-mean Gaussian random variable with variance σ_w^2, and σ_w determines the severity of the timing jitter. The random walk model is chosen because of its simplicity to represent a variety of channels by changing only one parameter.

At the front-end receiver, the read-back signal $p(t)$ is filtered by a low-pass filter (LPF), whose impulse response is $q(t)/T$, to eliminate the out-of-band noise, and is sampled at time $kT + \hat{\tau}_k$, creating

$$y_k = y(kT + \hat{\tau}_k) = \sum_i a_i h(kT + \hat{\tau}_k - iT - \tau_i) + n_k, \tag{2}$$

where $\hat{\tau}_k$ is the receiver's estimate of τ_k, and n_k is *i.i.d.* zero-mean Gaussian random variable with variance $\sigma_n^2 = N_0/(2T)$.

III. Conventional Timing Recovery

Conventional timing recovery is based on a PLL. A decision-directed TED [1] is used to compute the receiver's estimate of the timing error $\epsilon_k = \tau_k - \hat{\tau}_k$, which is the misalignment between the phase of the received signal and that of the sampling clock. In this paper, we consider the well-known Mueller and Müller (M&M) TED algorithm [6], where the estimated timing error is given by

$$\hat{\epsilon}_k = \frac{3T}{16}\{y_k \hat{r}_{k-1} - y_{k-1}\hat{r}_k\}, \tag{3}$$

where $\hat{r}_k$ is the k-th estimate of the noiseless *channel output* $r_k \in \{0, \pm 2\}$. The constant $3T/16$ ensures that there is no bias at high SNR so that $E[\hat{\epsilon}|\epsilon] = \epsilon$, for small ϵ. For simplicity, we assume perfect acquisition by setting $\tau_0 = 0$. Because our model has no frequency offset component, the sampling phase offset can then be updated by a first-order PLL according to

$$\hat{\tau}_{k+1} = \hat{\tau}_k + \xi\hat{\epsilon}_k, \tag{4}$$

where ξ is a PLL gain parameter [1]. Eventually, the Viterbi detector [7] performs maximum-likelihood (ML) equalization to determine the most likely input data sequence.

As depicted in Fig. 1, a conventional receiver performs timing recovery and ML equalization separately. Therefore, the overall performance of this system (also referred to as an *uncoded* system) is mainly determined by how good conventional timing recovery is. It has been shown in [2] that conventional timing recovery does not perform well in uncoded systems when the timing error is large. Thus, the need for efficient timing recovery schemes becomes increasingly crucial. Such timing recovery schemes can be developed using per-survivor processing (PSP) techniques [4].

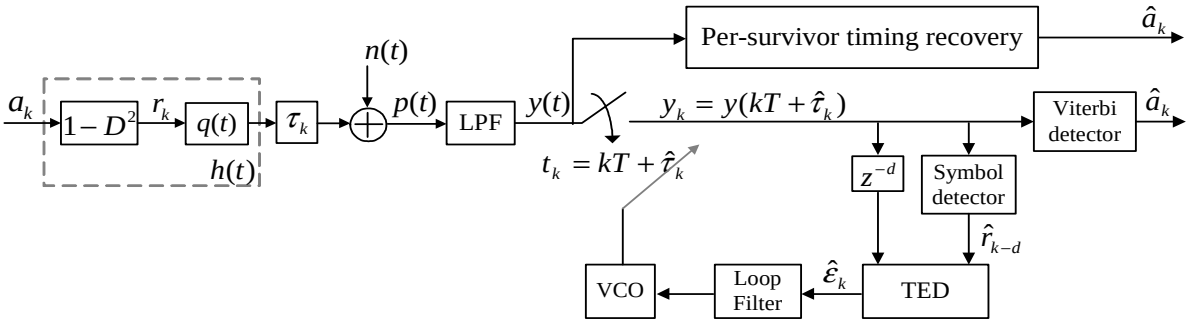

Fig. 1. The perfectly equalized PR-IV channel model with timing recovery.

IV. Per-Survivor Timing Recovery

To improve the performance of the conventional timing recovery, a reliable decision with zero decision delay can be extracted by utilizing the already-given information inside the trellis structure [7]. Specifically, each state transition in the trellis uniquely specifies a corresponding symbol. Hence, at least one state transition in each trellis stage will correspond to a correct decision. Utilizing that decision for the timing update operation will improve the performance of timing recovery.

A. Algorithm Description

With PSP, a new timing recovery scheme called *per-survivor timing recovery* was developed in [8], which jointly performs timing recovery and ML equalization, as also shown in Fig. 1. This scheme works in a similar fashion as the Viterbi algorithm does, except with an additional timing update operation. The key idea is to sample the received analog signal using different sampling phase offsets associated with each state transition. Additionally, each survivor path has its own PLL to update the sampling phase offset. In pseudocode, per-survivor timing recovery can be summarized as follows, where L is the length of an input sequence, and Q is the total number of trellis states in one stage. For details, a reader can refer to [8].

```
Initialize the sampling phase offset and
the path metric
for k = 1 : L (each time instant)
    for q = 1 : Q (each trellis state)
      sample the waveform y(t) using a PLL
      and the sampling phase offset, τ̂_k,
      associated with the starting state
      to get samples {y_k}
      compute the branch metrics
      compute the path metric
      update the survivor path
      update the next sampling phase
      offset, τ̂_{k+1}, using the information
      obtained from the survivor path that
      leads to state q
    end
end
decode a data sequence from the survivor
path that has the minimum path metric
```

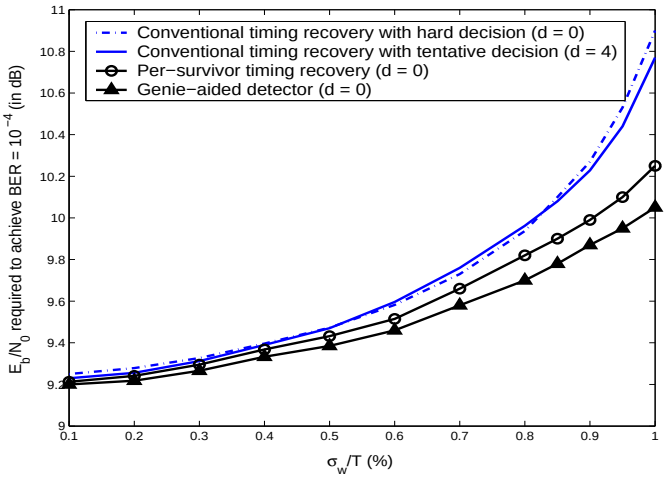

Fig. 2. Performance comparison of different timing recovery schemes [8].

B. Performance Results

Fig. 2 compares the performance of different timing recovery schemes by plotting the E_b/N_0 (in dB) requirement for bit-error rate (BER) 10^{-4} as a function of σ_w/T's, where a parameter d in the parenthesis denotes the total delay in the timing loop. The curve labeled "genie-aided detector" represents conventional timing recovery whose PLL has access to all correct decisions, thus serving as a lower bound for a timing recovery scheme that is based on a PLL. The tentative decision is obtained from the Viterbi detector with a (short) decision delay of $d = 4$. This is done by choosing the *best* survivor path at each time instant, and then the *tentative decision*, $\hat{r}_{k-d}$, is found by moving d steps backward along that survivor path.

Clearly, per-survivor timing recovery performs better than conventional timing recovery, especially when σ_w/T is large. This can be intuitively explained as follows. At each time instant, at least one state transition in each trellis stage will correspond to the correct decision. Using that decision to perform the timing update operation will help improve timing recovery performance. In other words, the PLL is *fully trained* if the correct path is chosen. By following this idea for an entire received signal, the overall performance is improved.

V. Per-Survivor Iterative Timing Recovery

Iterative error-control codes (ECCs) allow reliable operation at low SNR because of their large coding gains [9]. This means that timing recovery must also function at low SNR. A conventional receiver performs timing recovery and error-correction decoding separately. Specifically, conventional timing recovery ignores the presence of ECCs. Thus, it fails to work properly at low SNR.

Theoretically, joint ML estimation of timing offsets and message bits, which will jointly perform timing recovery, equalization, and decoding, is a preferred method of synchronization [10] but its complexity is huge. A solution based on the expectation-maximization (EM) algorithm [11] is also complex. Fortunately, a solution to this problem with complexity comparable to the conventional receiver has been proposed in [12], which will be referred to as *the NBM scheme*. It is realized by embedding the timing recovery step inside the turbo equalizer so as to perform timing recovery, equalization, and decoding jointly. Nonetheless, this scheme requires a large number of turbo iterations to provide a good performance even with a cycle slip [1] detection and correction algorithm as used in [12], especially when timing error is large.

To improve the performance of the NBM scheme, an iterative timing recovery scheme called *per-survivor iterative timing recovery* has been proposed in [13]. It is realized by first applying the per-survivor concept to the Bahl, Cocke, Jelinek, and Raviv (BCJR) algorithm [14], resulting in PSP-BCJR. Then, per-survivor iterative timing recovery iteratively exchanges soft information between PSP-BCJR and a soft-in soft-out (SISO) decoder.

Consider the *coded* PR-IV channel model shown in Fig. 3. The message bits $\{x_k\}$ are encoded by a serial concatenation of an error-correction encoder, an s-random interleaver [9] (i.e., the π block), and a $1/(1 \oplus D^2)$ precoder. The read-back signal $p(t)$ expressed as given in (1) is filtered by an LPF and is sampled at time $kT + \hat{\tau}_k$, creating y_k according to (2).

We also assume perfect acquisition. Because our model has no frequency offset component, the sampling phase offset can then be updated by a first-order PLL according to

$$\hat{\tau}_{k+1} = \hat{\tau}_k + \xi \frac{3T}{16}\{y_k \tilde{r}_{k-1} - y_{k-1}\tilde{r}_k\}, \tag{5}$$

where $\tilde{r}_k$ is the k-th *soft estimate* of the *channel output* $r_k \in \{0, \pm 2\}$ given by [12]

$$\tilde{r}_k = E[r_k|y_k] = \frac{2\sinh(2y_k/\sigma_n^2)}{\cosh(2y_k/\sigma_n^2) + e^{2/\sigma_n^2}}. \tag{6}$$

In the conventional receiver, conventional timing recovery is followed by a turbo equalizer [15] (see Fig. 3), which iteratively exchanges soft information between the SISO equalizer for the precoded PR-IV channel and the SISO decoder.

A. Algorithm Description

PSP-BCJR [13] is developed by embedding the timing recovery process inside the BCJR equalizer so as to perform timing recovery and ML equalization jointly. It works in a similar manner as per-survivor timing recovery does. Nevertheless, we update the timing estimate at each state based on the incoming branch that contributes the most to the state information. In pseudocode, PSP-BCJR can be summarized as follows.

```
FORWARD RECURSION:
Initialize the forward sampling phase
offset and the forward state information
for k = 1 : L (each time instant)
    for q = 1 : Q (each trellis state)
      sample the waveform y(t) using a PLL
      and the forward sampling phase
      offset, τ̂_k, associated with the
      starting state to get samples {y_k}
      compute the BCJR branch metrics
      compute the forward state
      information
      update the next forward sampling
      phase offset, τ̂_{k+1}, based on the most
      likely incoming branch that leads to
      state q
    end
end

BACKWARD RECURSION:
Initialize the backward sampling phase
offset and the backward state information
for k = L : 1 (each time instant)
    for p = 1 : Q (each trellis state)
      sample the waveform y(t) using a PLL
      and the backward sampling phase
      offset, τ̂^b_{k+1}, associated with the
      starting state to get samples {y^b_k}
      compute the BCJR branch metrics
      compute the backward state
      information
      update the next backward sampling
      phase offset, τ̂^b_k, based on the most
      likely incoming branch that leads to
      state p
    end
    compute a posteriori log-likelihood
    ratio (LLR) of the input bit, λ_k,
    using the forward and the backward
    state information
end
```

B. Performance Results

The per-survivor iterative timing recovery scheme is easily obtained by discarding the front-end PLL in Fig. 3 and replacing the BCJR equalizer with PSP-BCJR.

Consider a rate-8/9 system in which a block of 3636 message bits is encoded by a rate-1/2 recursive systematic convolutional encoder with a generator polynomial $[1, \frac{1 \oplus D \oplus D^3 \oplus D^4}{1 \oplus D \oplus D^4}]$, and then punctured to a block length of 4095 bits by retaining only every the eighth parity bit. The punctured sequence passes through an s-random interleaver with $s = 16$ to obtain an interleaved sequence of b_k. Both the SISO equalizer and the SISO decoder are implemented based on BCJR. We use the PLL gain parameter designed based on minimizing the RMS

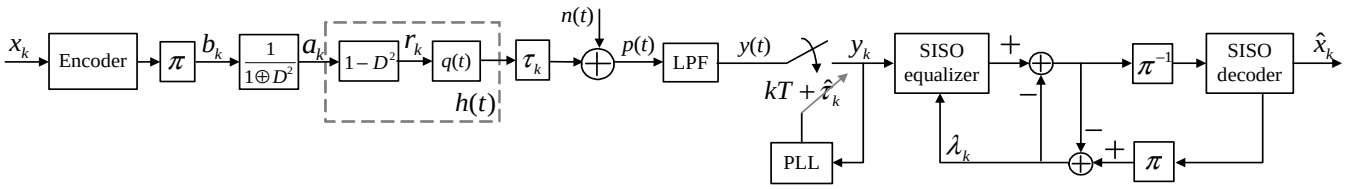

Fig. 3. A coded PR-IV channel model.

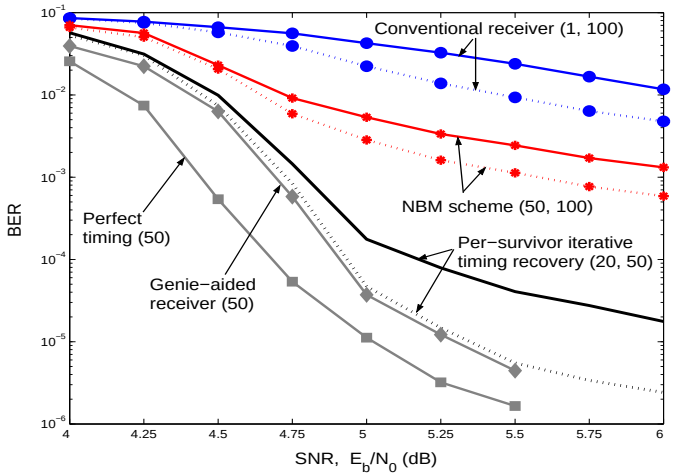

Fig. 4. Performance comparison with $\sigma_w/T = 1\%$ [13].

timing error, $\sigma_\epsilon = \sqrt{E[(\tau_k - \hat{\tau}_k)^2]}$, at $E_b/N_0 = 5$ dB. Each BER point was computed using as many data packets as possible until at least 100 sectors in error were collected at the 100-th iteration.

Fig. 4 compares the BER performance of different schemes for the system with a severe random walk parameter $\sigma_w/T = 1\%$, which implies a high probability of occurrence of a cycle slip. Note that the number inside the parenthesis in Fig. 4 indicates the total number of iterations used to generate each curve. The curve labeled "Perfect timing" represents the conventional receiver that uses $\hat{\tau}_k = \tau_k$ to sample $y(t)$. Clearly, per-survivor iterative timing recovery outperforms both the conventional receiver and the NBM scheme. This is because per-survivor iterative timing recovery can correct a cycle slip much more efficiently than the NBM scheme [13]. In addition, it performs similar to the genie-aided receiver and loses approximately a 0.35 dB relative to the system with perfect timing at BER = 10^{-5}.

VI. Conclusion

We summarized the timing recovery schemes that are based on per-survivor processing. It is clear that per-survivor timing recovery can perform better than conventional timing recovery, especially when the SNR is low and the timing error is large. By exploiting the presence of error-correction codes, per-survivor iterative timing recovery can perform even better than per-survivor timing recovery, but at the expense of increased complexity and the requirement of batch processing.

Simulation results has illustrated that per-survivor iterative timing recovery performs better than other iterative timing recovery schemes, especially when the timing error is severe. This is because it can correct a cycle slip much more efficiently than other schemes. Additionally, Kovintavewat *et al* [16] have proposed a reduced-complexity version of per-survivor iterative timing recovery, which has been shown to perform better than (full-complexity) per-survivor iterative timing recovery at low to moderate complexity regime.

References

[1] J. W. M. Bergmans, *Digital baseband transmission and recording*. Boston, Massachusetts: Kluwer Academic Publishers, 1996.

[2] P. Kovintavewat, *Timing recovery based on per-survivor processing*. PhD thesis, Georgia Institute of Technology, Georgia, USA., Oct 2004.

[3] J. R. Barry, A. Kavčić, S. W. McLaughlin, A. R. Nayak, and W. Zeng, "Iterative timing recovery," *IEEE Signal Processing Magazine*, vol. 21, pp. 89–102, Jan 2004.

[4] R. Raheli, A. Polydoros, and C.-K. Tzou, "Per-survivor processing: a general approach to MLSE in uncertain environments," *IEEE Trans. Commun.*, vol. 43, pp. 354–364, Feb/Mar/Apr 1995.

[5] A. N. Andrea, U. Mengali, and G. M. Vitetta, "Approximate ML decoding of coded PSK with no explicit carrier phase reference," *IEEE Trans. Commun.*, vol. 42, pp. 1033–1039, Feb/Mar/Apr 1994.

[6] K. H. Mueller and M. Müller, "Timing recovery in digital synchronous data receivers," *IEEE Trans. Commun.*, vol. COM-24, pp. 516–531, May 1976.

[7] G. D. Forney, "Maximum-likelihood sequence estimation of digital sequences in the presence of intersymbol interference," *IEEE Trans. Inform. Theory*, vol. IT-18, pp. 363–378, May 1972.

[8] P. Kovintavewat, J. R. Barry, M. F. Erden, and E. Kurtas, "Per-survivor timing recovery for uncoded partial response channels," in *Proc. of ICC'04*, vol. 27, no. 1, pp. 2715–2719, Paris, Jun 2004.

[9] C. Heegard and S. B. Wicker, *Turbo Coding*. Boston, Massachusetts: Kluwer Academic Publishers, 1999.

[10] H. Meyr, M. Moeneclaey, and S. A. Fechtel, *Digital Communication Receivers: Synchronization, Channel Estimation, and Signal Processing*. New York: John Wiley & Sons, Inc., 1997.

[11] C. N. Georghiades and D. L. Snyder, "The expectation-maximization algorithm for symbol unsynchronized sequence detection," *IEEE Trans. Commun.*, vol. 39, pp. 54–61, Jan 1991.

[12] A. R. Nayak, J. R. Barry, and S. W. McLaughlin, "Joint timing recovery and turbo equalization for coded partial response channels," *IEEE Trans. Magnetics*, vol. 38, pp. 2295–2297, Sept 2003.

[13] P. Kovintavewat, J. R. Barry, M. F. Erden, and E. Kurtas, "Per-survivor iterative timing recovery for coded partial response channels," in *Proc. of Globecom'04*, vol. 4, pp. 2604–2608, Texas, November 29 – Dec 2004.

[14] L. R. Bahl, J. Cocke, F. Jelinek, and J. Raviv, "Optimal decoding of linear codes for minimizing symbol error rate," *IEEE Trans. Inform. Theory*, vol. IT-20, pp. 248–287, Mar 1974.

[15] D. Raphaeli and Y. Zarai, "Combine turbo equalization and turbo decoding," in *Proc. of Globecom'97*, vol. 2, pp. 639–643, Nov 1997.

[16] P. Kovintavewat, J. R. Barry, M. F. Erden, and E. Kurtas, "Reduced-complexity per-survivor iterative timing recovery for coded partial response channels," *IEEE International Conference on Acoustics, Speech, and Signal Processing* (ICASSP 2005), Philadelphia, USA, vol. 3, pp. iii/841 iii/844, Mar 2005.

ECG Classification Using Fisher's Discriminant and Fuzzy c-mean

Sayan Rakbanjong and Yuttana Kitjaidure
King Mongkut's Institute of Technology Ladkrabang
3 Moo. 2 Chalongkrung Rd., Ladkrabang
Bangkok, 10520 Thailand
E-mail: rakbanjong@hotmail.com and kkyuttan@kmitl.ac.th

***Abstract*- In this paper, we propose a new algorithm for ECG classification that is less sensitive to the morphological variation of ECG. In the feature extraction process, the multiresolution wavelet transform and autoregressive modelling (AR) are applied together to obtain the feature vectors of ECG data. For the classifier, we have applied the fisher's discriminant and fuzzy c-mean working as hierarchical clustering with a top-down strategy. The results of experiments have confirmed good efficiency of the proposed algorithm. The investigations show that the method may find useful in practical applications for the classification of different type heartbeats.**

I. INTRODUCTION

The electrocardiogram (ECG) is a graphic record of the direction and magnitude of the electrical activity that is generated by depolarization and repolarization of the atria and ventricles. One cardiac cycle in an ECG signal consists of the P-QRS-T waves. The analysis of the ECG has been widely used for diagnosing many cardiac diseases. The most difficult problem faced by today's automatic ECG analysis is the large variation in the morphologies of ECG waveforms, not only of different patients or patient groups but also within the same patient. The ECG waveforms may differ for the same patient to such extend that they are unlike to each other and at the same time alike for different types of beats. This is the main reason that the beat classifier, performing well on the training data behaves badly, when presented with different patients ECG waveforms.

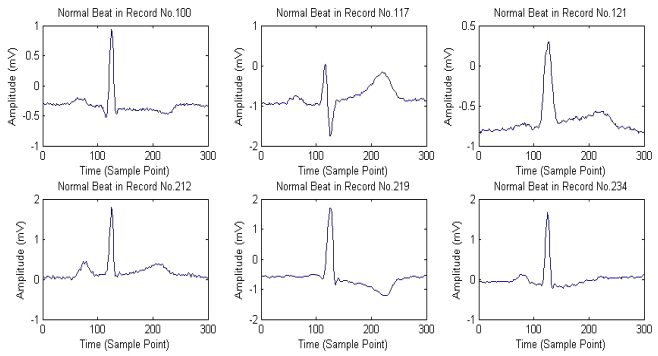

Figure 1. Normal ECG beat type in record No. 100, 117, 121, 212, 219, and 234.

Several algorithms have been developed in the literature for the detection and classification of ECG beats [1], [2], [3], [4] which various algorithms used ECG beat in the same class from only one person or record for training and testing those systems, in fact it may be unable to use in real situation due to above-mentioned reason. In this paper, we propose a new algorithm for ECG classification that is not complex model but gave a good efficiency. Fig. 1 represents the difference of ECG beat in the same class.

In the remainder of this paper, an overview of preprocessing algorithm for ECG data is firstly presented. Then, the feature extraction through the wavelet transform and autoregressive modelling (AR) is described in the next section. After that, in the classification, the Fisher's discriminant and fuzzy c-mean are presented. The training and testing process for each class of ECG are given next. Finally, the work is concluded and the suggestion for the future.

II. ECG DATA AND PREPROCESS

In this paper, ECG signal from Modified Limb Lead II (MLII) are chosen for processing due to they mostly found in the database. The recordings are digitized at 360 samples per second per channel. Each record has its respective annotation file that indicates the class of the heartbeat. We select different abnormal QRS complexes from several records. It is noticed that, there are six types of QRS complexes appeared frequently in the database. Therefore, we mainly deal with these six types heartbeats which include normal beat (NORMAL), left bundle branch block beat (LBBB), right bundle branch block beat (RBBB), paced beat (PACE), premature ventricular contraction (PVC) and atrial premature contraction (APC).

In the preprocessing phase, the continuous ECG signals must be separated into many segments which contain only one heartbeat. The extracted data of ECG complexes are centered around R peak, we have selected the segment of 250ms before the R peak point and 400ms after that with the R peak point is the 90th point. The R peak is detected using the Pan and Tompkins algorithm [5]. Thus, each segment must contain one ECG heartbeat. Fig. 2 shows typical waveforms of the six types of ECG segments described above.

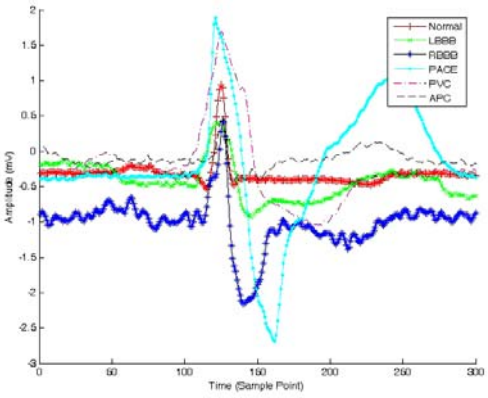

Figure 2. Typical waveforms of the six types of ECG segment.

III. FEATURE EXTRACTION

The recognition of heart rhythms requires generation of feature vectors which represents the original ECG segment. A good recognition system should depend on the features representing the ECG signals in such a way that the differences among the ECG waveforms are suppressed for the waveforms of the same type, while the differences should be emphasized for the waveforms of belonging to different types of heartbeats. We perform recognition process of heart rhythms on the single heartbeat of the ECG, proposing the description or representation by wavelet transform and AR model.

A. Wavelet Transform

From the wavelet multiresolution analysis properties [4], [6], and for any function $f(k) \in L^2(R)$, $f(k)$ can be expressed by the approximation and detail wavelet coefficients

$$f(x) = \sum_n a_{J,n}\phi_{J,n}(k) + \sum_{j=j_0}^{J}\sum_n d_{j,n}\psi_{j,n}(k) \qquad J > j_0, \qquad (1)$$

where $a_{J,n}$ are the approximation coefficients at scale level J, $\phi_{J,n}(k)$ is the scaling function, $d_{j,n}$ are the detail coefficients at scale level j, $\psi_{j,n}(k)$ is the wavelet function, and j_0 is the finest decomposed scale level. For simplicity, the wavelet coefficients will be written without the suffix n (e.g., $a_{j,n}$ and $d_{j,n}$ will be denoted as a_j and d_j, respectively). More detailed explanations of the wavelet transform theory and its applications are found in [6], [7], [8], and [9].

The selection of appropriate wavelet and the number of decomposition level are very important in analysis of signals using the WT. The number of decomposition levels is chosen based on the dominant frequency components of the signal. The level is chosen such that those parts of the signal that correlate well with the frequencies required for classification of the signal are retained in the wavelet coefficients. Usually, tests are performed with different types of wavelets and the one which gives maximum efficiency is selected for the particular application. Therefore, the wavelet used in this work is Daubechies wavelet of order 8, the chosen number of decomposition levels is 4. Thus, the ECG signals are decomposed into the details d_1 -d_4 and one approximation a_4.

Feature selection is also very important component, For each heartbeat, the detail wavelet coefficient d_1 are usually noise signals that must be eliminated and d_2, d_3, d_4 represent high frequency parts of the ECG signal. Since the approximation wavelet coefficients a_4 represent the main feature of each heartbeat, then we choose a_4 to be the feature of each heartbeat. For one heartbeat, the original signal contains 300 points, and a_4 contains 32 points. Fig. 3 shows the wavelet feature extraction of some normal heartbeats in record No. 100.

B. Autoregressive Modelling

In an AR process of order p, the signal $x[n]$ at time instant nth may be represented as a linear combination of p previous values of the same signal. Specifically, the process is modeled as

$$x[n] = \sum_{i=1}^{p} a[i]x[n-i] + e[n] \qquad (2)$$

where $a[i]$ is the ith coefficient of the AR model, $e[n]$ is a white noise with mean zero, and p is the AR order. Various methods are currently used to estimate the coefficients of the autoregressive process. The criterion used to evaluate the model order selection in this work is ARfit method [10]. Eventually, we select 4-order AR model to represent each heartbeat of ECG signals.

C. Generation of The Feature Vectors

The feature vector is composed of wavelet coefficients and AR coefficients. For each ECG heartbeat, the original signal is a vector of 300 dimensions $\{y_1, y_2, ..., y_{300}\}$. The wavelet coefficient for this is a vector of 32 dimensions $\{w_1, w_2, ..., w_{32}\}$, together with the AR coefficient vector of 4 dimensions

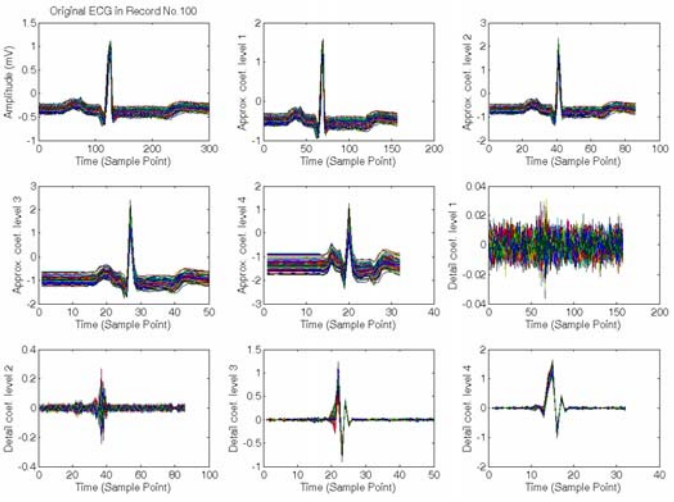

Figure 3. Wavelet transformation of normal heartbeats in record No.100.

$\{a_1, a_2, a_3, a_4\}$. Then wavelet coefficients and AR coefficients can be concatenated together to form the feature vector $\{w_1, w_2, ..., w_{32}, a_1, a_2, a_3, a_4\}$ for classification.

IV. ECG CLASSIFICATION

A. Fisher's Discriminant

Fisher's Linear Discriminant (FLD) [11], [12] is a widely used method for feature extraction and dimensionality reduction in pattern recognition. Fisher's idea is based on seeking projection direction $\boldsymbol{W}$ that separates the class means well (when projected onto the direction $\boldsymbol{W}$) while achieving a small variance around these means. Mathematically, FLD selects the projection $\boldsymbol{W}$ in such a way that the ratio of the between-class scatter matrix and the within-class scatter matrix is maximized.

For a *c*-class problem, the between-class scatter matrix is defined as

$$\mathbf{S}_B = \sum_{i=1}^{c} N_i (\boldsymbol{\mu}_i - \boldsymbol{\mu})(\boldsymbol{\mu}_i - \boldsymbol{\mu})^T \tag{3}$$

and the within-class scatter matrix as

$$\mathbf{S}_W = \sum_{i=1}^{c} \sum_{\mathbf{x}_k \in X_i} (\mathbf{x}_k - \boldsymbol{\mu}_i)(\mathbf{x}_k - \boldsymbol{\mu}_i)^T \tag{4}$$

where $\boldsymbol{\mu}_i$ is the mean samples of class $\boldsymbol{X}_i$, $\boldsymbol{\mu}$ is the mean sample of all classes, and N_i is the number of samples in class $\boldsymbol{X}_i$. If $\mathbf{S}_W$ is nonsingular, the optimal projection $\boldsymbol{W}_{opt}$ is chosen as a matrix with its orthonormal columns that maximizes the ratio of the determinant of between-class scatter matrix to the determinant of within-class scatter matrix obtained from the projected samples, i.e.,

$$\begin{aligned} \boldsymbol{W}_{opt} &= \arg\max_{\boldsymbol{W}} \frac{\left|\boldsymbol{W}^T \mathbf{S}_B \boldsymbol{W}\right|}{\left|\boldsymbol{W}^T \mathbf{S}_W \boldsymbol{W}\right|} \\ &= \left[\mathbf{w}_1 \quad \mathbf{w}_2 \quad ... \quad \mathbf{w}_m\right] \end{aligned} \tag{5}$$

where $\left\{\mathbf{w}_i \,|\, i = 1, 2, ..., m\right\}$ is the set of generalized eigenvectors of $\mathbf{S}_B$ and $\mathbf{S}_W$ corresponding to the *m* largest generalized eigenvalues $\left\{\lambda_i \,|\, i = 1, 2, ..., m\right\}$, where

$$\mathbf{S}_B \mathbf{w}_i = \lambda_i \mathbf{S}_W \mathbf{w}_i , \qquad i = 1, 2, ..., m \tag{6}$$

B. Fuzzy c-mean

Fuzzy c-means (FCM) [2], [13] is a data clustering technique wherein each data point belongs to a cluster to some degree specified by a membership grade.

Assume that the vectors representing the data under classification are denoted by $\mathbf{x}_k$ for $k = 1, 2, ..., p$ where $\mathbf{x}_k = \left[x_{k1}, x_{k2}, ..., x_{kN}\right]^T \in R^N$. Let these vectors be partitioned into *c* clusters, each represented by the center vector $\mathbf{c}_i = \left[c_{i1}, c_{i2}, ..., c_{iN}\right]^T$. Denote $\mathbf{U} \in R^{c \times p}$, the partition matrix of the elements u_{ij} represents the membership degrees of the data vector $\mathbf{x}_j (j = 1, 2, ..., p)$ in the *i*th cluster $(i = 1, 2, ..., c)$. The fuzzy clustering algorithms will search for the partition matrix and cluster centers such that the objective function *E* is minimized

$$E = \sum_{i=1}^{c} \sum_{j=1}^{p} u_{ij}^m d^2(\mathbf{x}_j, \mathbf{c}_i) \tag{7}$$

subject to

$$\sum_{i=1}^{c} u_{ij} = 1 \tag{8}$$

for $(j = 1, 2, ..., p)$. The parameter *m* controls the fuzziness of the clusters (typically *m*=2). The function $d(\mathbf{x}_j, \mathbf{c}_i)$ measures the distance between the data vector $\mathbf{x}_j$ and the center $\mathbf{c}_i$ of the *i*th cluster.

$$d^2(\mathbf{x}_j, \mathbf{c}_i) = (\mathbf{x}_j - \mathbf{c}_i)^T (\mathbf{x}_j - \mathbf{c}_i) \tag{9}$$

At the given data vectors $\mathbf{x}_j$, choose the number of clusters *c*, the weighting coefficient *m*, and the termination tolerance ε . Initialize the partition matrix $\mathbf{U}$ randomly in such a way that conditions $\sum_{i=1}^{c} u_{ij} = 1$ for all vectors $\mathbf{x}_j$ are satisfied. Then iterate through the following steps.

1) Determine the cluster prototypes $\mathbf{c}_i (i = 1, 2, ..., c)$

$$\mathbf{c}_i = \frac{\sum_{j=1}^{p} u_{ij}^m \mathbf{x}_j}{\sum_{j=1}^{p} u_{ij}^m} \tag{10}$$

2) Compute the distances $d_{ij}^2 (i = 1, 2, ...,c$ and $j = 1, 2, ...,p)$ between the input vector $\mathbf{x}_j$ and the cluster centers $\mathbf{c}_i$ using (9).

3) Update the partition matrix u_{ij} entries $(i = 1, 2, ...,c$ and $j = 1, 2, ...,p)$

$$u_{ij} = \frac{1}{\sum_{k=1}^{c} \left(\frac{d_{ij}}{d_{kj}}\right)^{2/(m-1)}} \tag{11}$$

If $d_{ij} = 0$ for some $i = I$, take $u_{Ij} = 1$ and $u_{ij} = 0$ for $i \neq I$, iterate until $\left\|\mathbf{U}^l - \mathbf{U}^{l-1}\right\| \leq \varepsilon$ for two succeeding iterations.

V. EXPERIMENT AND RESULTS

In the experiment, twenty-two difference patients taken from MIT-BIH arrhythmia database [14] have been considered, patients numbered 100, 107, 109, 111, 116, 117, 118, 119, 124, 200, 201, 207, 208, 212, 213, 217, 219, 221,

228, 231, 232, and 234. The ECG beats being classified are separated into two groups: one used in the learning and the other used in the testing mode, each feature vector of ECG beats is a vector of 36 dimensions from the feature extraction process described above.

A. Training Process

In the training process, the ECG feature vectors prepared for the training are processed by the Fisher's discriminant technique in order to seek new basis vectors $\{\mathbf{w}_i \,|\, i = 1, 2, ..., m\}$. After that each of the feature vectors is projected onto the new bases corresponding to *m* largest generalized eigenvalues $\{\lambda_i \,|\, i = 1, 2, ..., m\}$. The number of the *m* new bases is obtained from the number of vectors that give the best discriminated class when using FCM. From the experiment, six types of ECG according to Normal, RBBB, APC, LBBB, PVC, and PACE type are trained. However, by the FCM, only four clusters give the best separation in the first place. Therefore the process should be multistep clustering based on top-down strategy called hierarchical clustering.

In the first step, the FCM roughly separates all ECG data into four destined clusters such that Normal, RBBB, and APC are in the same class and LBBB, PVC, and PACE belong to the individual class respectively. In this step, the ECG feature vectors are projected onto 3 new bases by the Fisher's discrimination.

In the next step, Normal, RBBB, and APC beat types are further separated by projecting onto 2 new basis vectors via the Fisher's discrimination. In this second, the FCM will separate these three classes into four sub-clusters. Where the RBBB type composes of two clusters due to the distribution in this class.

B. Testing Process

In the testing process, the tested feature vectors are projected onto the 3 same bases as done in the training mode based on Fisher's discrimination technique. Then, the distances between the unknown feature vectors (in 3 dimensions) and the centers of each cluster (4 clusters) are calculated to classify them into the rough class. If they are in the mixed class (Normal, RBBB, and APC), they must be further classified by Fisher's discrimination and FCM again, otherwise the vectors belong to the single class.

TABLE I
EXPERIMENTAL RESULTS

ECG Beat Type	Training			Testing		
	Number	Correctly beat	Accuracy (%)	Number	Correctly beat	Accuracy (%)
Normal	1000	981	98.1	1000	978	97.8
LBBB	1000	981	98.1	1000	993	99.3
RBBB	1000	985	98.5	1000	942	94.2
APC	1000	951	95.1	500	489	97.8
PVC	1000	969	96.9	1000	942	94.2
PACE	1000	965	96.5	1000	956	95.6
Total	**6000**	**5832**	**97.20**	**5500**	**5300**	**96.36**

It is interesting to compare the obtained figures with the results presented in the literature by using different methods of beat classification. The comparison of proposed method with the different methods in [2] indicates high efficiency of the proposed approach.

VI. CONCLUSIONS

The new technique of ECG classification utilizing the multiresolution wavelet transform, autoregressive modelling, Fisher's discrimination, and fuzzy c-mean has been proposed in this paper. The feature sets have been carefully chosen to provide enough information and good accuracy. The wavelet transform is used to extract the ECG waveform features. Simultaneously, autoregressive modelling (AR) is also applied to obtain the temporal structures. The Fisher's discrimination and fuzzy c-mean are used to reduce the dimensions of feature vector and to classify the ECG beats respectively. The proposed algorithm is less sensitive to the morphological variation of ECG. The results of experiments have confirmed good efficiency of the proposed approach and also give good accuracy.

REFERENCES

[1] Qibin Zhao and Liqing Zhang, "ECG Feature Extraction and Classification Using Wavelet Transform and Support Vector Machine", Volume 2, 13-15 Oct. 2005 Page(s):1089 – 1092

[2] Stanislaw Osowski and Tran Hoai Lihn, "ECG Beat Recognition Using Fuzzy Hybrid Neural Network", IEEE Trans on BME, vol. 48, No. 11, pp 1265-1271, November 2001

[3] Nitikorn Silsirivanich and Panuthat Boonpramuk, "ECG Recognition Based on Hidden Markov Model for Heart Trouble Diagnostic" ECTI-CON 2006, pp 243-246

[4] Mahmoodabadi, S.Z.; Ahmadian, A.; Abolhasani, M.D.; Eslami, M.; Bidgoli, J.H., "ECG Feature Extraction Based on Multiresolution Wavelet Transform", IEEE-EMBS 2005, 01-04 Sept. 2005 Page(s):3902 – 3905

[5] J.Pan and W.J.Tompkins, "A real-time QRS detection algorithm"IEEE Trans.Biomed.Eng., Vol.BME-32, PP.230-236,1985

[6] C. Chui, "An Introduction to Wavelets", vol. 1 of Wavelet Analysis and Its Applications, ed. Academic Press, 1992.

[7] S. Mallat, "A Wavelet Tour of Signal Processing", second ed. Academic Press, 1999.

[8] Y. Tang, L. Yang, J. Liu, and H. Ma, "Wavelet Theory and Its Application to Pattern Recognition", vol. 36 of Machine Perception and Artificial Intelligence, eds. World Scientific, 2000.

[9] C. Sidney Burrus, Ramesh A. Gopinath and Haitao Guo, "Introduction to Wavelets and Wavelet Transforms", International Edition. Prentice Hall, 1998

[10] A. Neumaier and T. Schneider, 2001: "Estimation of parameters and eigenmodes of multivariate autoregressive models". ACM Trans. Math. Softw., 27, 27C57.

[11] S.Y. Kung, M.W. Mak, S.H. Lin, "Biometric Authentication A Machine Learning Approach", Prentice Hall, 2005

[12] Peter N. Belhumeur, Joao P. Hespanha, and David J. Kriegman, "Eigenface vs. Fisherface: Recognition Using Class Specific Linear Projection", IEEE Trans on Pattern Analysis and machine Intelligence, Vol. 19, No. 7, July 1997

[13] Vicenc Torra, "Fuzzy *c*-mean for fuzzy hierarchical clustering", IEEE International Conference on Fuzzy Systems 2005

[14] Goldberger AL, Zong W, Glass L, Hausdorff JM, Ivanov PCh, Mark RG, Mietus JE, Moody GB, Peng CK, Stanley HE. "PhysioBank, PhysioToolkit, and PhysioNet (http://www.physionet.org/)": Components of a New Research Resource for Complex Physiologic Signals. Circulation 101(23):e215-e220

ECG Data Compression by Wavelet-based Average Beat Subtraction (WABS)

S. Pathoumvanh[1], S. Airphaiboon[1], M. Sangworasil[1], K. Hamamoto[2]
Dept. of Electronic, Faculty of Engineering and Research Center for Communications and Information Technology (ReCCIT), King Mongkut's Institute of Technology Ladkrabang Bangkok 10520, Thailand[1]
Tokai University, Information Media Technology Dept. 1117 Kitakaname, Hiratsuka, Kanagawa 259-1292, Japan[2]

***Abstract* - This paper proposed a hybrid method for an ECG data compression method is based discrete wavelet transform (DWT). In order to increase the compression ratio, the preprocessing process is implemented by period detection and normalization of ECG wavelet coefficients. Then Run-Length Coding (RLE) is applied to each residual sequence obtained after average beat subtraction and threshold the differencing of residual data afterward. The difference between the actual period and the mean beat period for each beat are initially transmitted together with the standard mean beat to the decoder. At the decoder, original period of each beat are first recovered before re-ordered the wavelet coefficients and inverse wavelet transform is retrieved the reconstructed ECG signal. This experiment show the compression performance of the proposed method refer to the MIT/BIH arrhythmia database and the regular record 117 and the QRS complex record 203 have been employed to this experiment. The obtained of compression ratio is more than 20 with the percent root-mean-square difference (PRD) less than 1.5%.**

I. INTRODUCTION

Electrocardiogram (ECG) data provide cardiologists with essential information to diagnose heart disease in a patient. In an ambulatory monitoring system, the volume of ECG data is necessary large, as along period of time is required in order to gather enough information about the patient. As an example, with the sampling rate of 360 Hz, 11 bits/sample data resolution, a 24 hour record requires about 43 Mbytes per channel. Therefore, an effective data compression scheme for ECG signals is required in many practical applications including: ECG data storage, ambulatory monitoring system, ECG data transmission over telephone line or digital telephone network. Since it is often necessary to store or transmit ECG, efficient compression techniques are important to reduce transmission time or required storage capacity.

Previous ECG data compression techniques have been reported in the literature and include direct time-domain techniques [1], transform-domain techniques [2]–[4], average beat subtraction [8], and different modeling methods [5]-[7]. The main goal of the methods presented here is to achieve sufficiently high compression ratios (CR) without affecting the diagnostic characteristics of the ECG signals. In fact, the Simulation result from MATLAB presented here are based on different compression methodologies using the discrete wavelet transform (DWT) concept, with an enhanced coding scheme based on the combination of DWT, average beat subtraction, Threshold and Run-Length Coding. However, the main emphasis in this paper will study the compression characteristics of both regular ECG and complex QRS record.

II. COMPRESSION ALGORITHM

In this paper we propose an ECG compression method based on average beat subtraction of DWT coefficients and Run-Length coding. The block diagram of this method is shown in Fig. 1 and 2. This method initiates originally from the work of Hamilton and Tompkins, [8] "Compression of ambulatory ECG by average beat subtraction and residual differencing," and Ramakrishnan and Saha [9], "ECG data coding by wavelet based linear prediction". This proposed technique is also follows similar steps as in [8], [9], but it is more simple, provides higher CR and achieved with nearly constant ECG reconstruction error.

Fig.1 Show block diagram of compression process. When a beat is detected an average beat is aligned with that beat and subtracted by from the signal. The detected beat is then used to update the average beat estimate. After beat subtraction the residual signal is differenced. The differenced signal is Run-Length Coding and store along with the record of the beat location.

Fig.2 Show a block diagram of the operations required for decompression. The residual signal is decoded and first summed to undo the first differencing. The average beat is added to the residual signal as indicated by the stored beat locations. As beat reconstructed they are used the average beat estimate. As long as the average beat is initially equal to the average beat used in compression.

A. Discrete Wavelet transforms.

In this research method the first order of Discrete wavelet transform (DWT) express by (1), (2) and (3) is respectively determination of a scaling coefficient and Wavelet coefficient at a scale of *j-1* where $c_j(m)$ is a set of an input signal. The set of a scaling coefficient is denoted by $c_{j-1}(k)$ and the wavelet coefficient is denoting by $d_{j-1}(k)$. h_0 and h_1 are the filter coefficient.

$$c_{j-1}(k) = \sum h_0(m-2k)c_j(m) \tag{1}$$

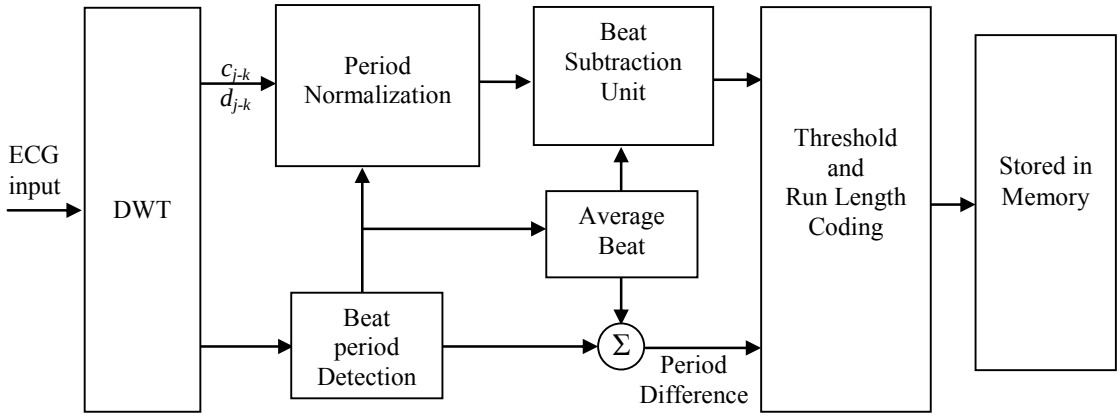

Fig.1 Block diagram of Compression process

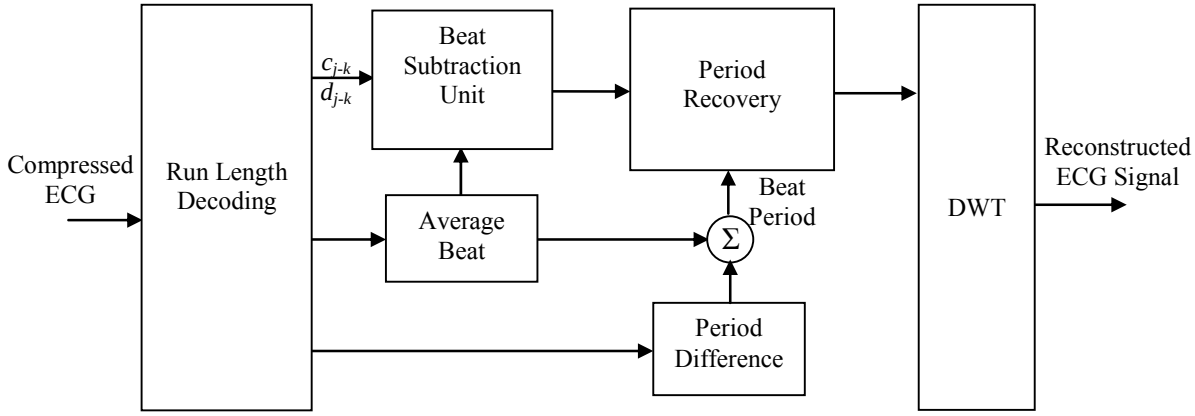

Fig.2 Block diagram of Decompression process

$$d_{j-1}(k) = \sum h_1(m-2k)c_j(m) \tag{2}$$

$$\begin{bmatrix} c_{j-1}(k) \\ d_{j-1}(k) \end{bmatrix} = \begin{bmatrix} h_0(n) \\ h_1(n) \end{bmatrix} \left[c_j(m) \right] \tag{3}$$

B. Period detection and Period Normalization

For period detection we define a cycle as the signal from one wave to the next. We used the technique reported in [8]. In this algorithm, the ECG is Band-pass filtered, differentiated, and squared. The squared signal is over a 150ms window. A period detection occurs when a peak is detected in the process signal which exceeds a variable detection threshold based on the previous detections and noise peaks.

For delineating cycles, we normalize the period of each isolated beat by up-sampled techniques and added the appropriate constant sampled to each individual beat. This converts the beats of differing periods into beats of a constant period, thus eliminating the effect of heart rate variability. The fixed length of the cycles is selected based on the maximum possible period of interval cardiac cycle.

C. Beat subtraction.

The ECG signal is generally composed of the number of beats repeated at fairly regular intervals. Since many of the beats are markedly similar. Intuitively this method should compress the signal by subtracting an average beat with individual period normalized beat signal. And the average beat or standard beat is estimated from mean value of 7 initial cycles of the ECG data. This value is initially sent to the decoder. During encoding, the difference between the actual period of a cycle and the average beat period is also transmitted.

D. Residual Threshold and Run-Length coding.

In this state, both residual of Approximation and Detail coefficients obtained from the subtraction process are needed to threshold before Run-Length coding. Due to this experiment PRD is limited to low values in order to guarantee preservation of clinically important features of the ECG waveform.

This experiment is proposed techniques based on selection threshold index (Δ) of the residual DWT coefficients of different beats between average beat and individual normalized ECG beat. It has been observed that Only ±50% of the maximum amplitude of residual DWT coefficients in the

region of Δ (which is a minor difference) can be set equal to zero, and the residual coefficient outside the region of Δ (which is a major difference) is still remain (see Fig. 3), because these coefficients are necessary for a negligible error in the reconstruction procedure of any significant structural information of the ECG beat. Then Run-Length Coding procedure is performed across the residual of Approximation and Detail coefficient. As a result, only the sequences of data and zero value elements of the DWT coefficients is transmitted or stored. In the decoder section, the inverse DWT (IDWT) is performed on the regained DWT coefficients and after following a period recovery procedure, The ECG signal is reconstructed.

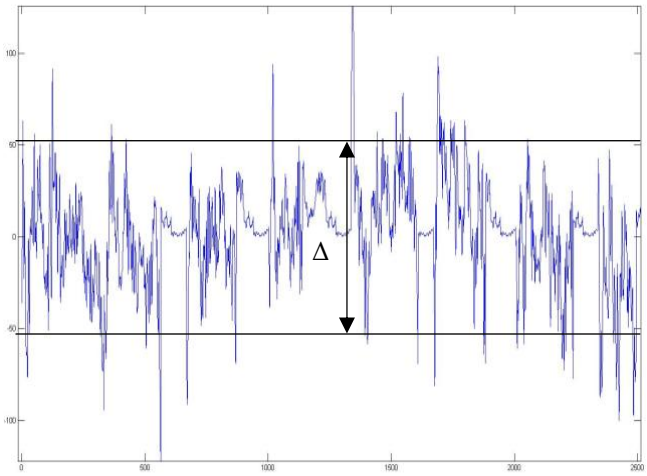

Fig.3 Threshold index selection of residual DWT coefficient of beat difference.

III. EXPERIMENTAL RESULT AND ANALYSIS

Most of the reported techniques are analysis the system based compression performance, and then compression ratio (CR) is defined as the ratio between the number of bits in the original signal and the number of bits used in reconstructed signal (4).

$$CR = \frac{x(i)}{x'(i)} \tag{4}$$

Let *x(i)*, and *x'(i)*, represent the values of the samples of the original and reconstructed signal, respectively. The perfect of reconstruction factor is frequently measured by the percent root-mean-square difference (PRD). And then, PRD factor is defined as (5).

$$PRD = \sqrt{\frac{\sum_{i=0}^{N-1}\left(x(i)-x'(i)\right)^2}{\sum_{i=0}^{N-1}x^2(i)}} \times 100 \tag{5}$$

TABLE I
Comparison of CR and PRD between the differences ECG MIT-BIH records

THRESHOLD INDEX (Δ)		40%	60%	80%	100%
MIT 203	CR	2.97	9.1	22.83	34.25
	PRD	4.3819	4.8908	5.1727	5.2285
MIT 117	CR	4	17.1	25.7	50.1
	PRD	1.447	1.378	1.3712	1.3431

The algorithmic approaches in this paper were implemented on a MATLAB-7.1. The methods were tested on abnormal ECG data from the MIT-BIH arrhythmia database files: (mit117, mit203 with sampling frequency 360 Hz).

The results in table I. shown the comparative performance results of CR and PRD values of the two ECG records to the Threshold index, which is based on the section of threshold index (Δ). In case of the original signal is uniform (as mit117) the possibility dropped the amplitude in the region of Δ equal to zero is allowed up to 100%, and without increase of any reconstruction error, and the factor of compression Ratio is increased. However, the QRS complex format (mit203) the possibility dropped is allowed only up to 50%, as the result format of reconstructed ECG is still remaining the original one, with increasing of a small reconstruction error, and the factor of Compression Ratio is increased up to 8:1.

According to the result listed in table 2, shown the overall analysis of the compression performance refer to equation (4) (this analysis of CR factor is not included size of bits transmitted the average beat of the original and Period difference, which is initially send to the Decoder ended). This proposed method is gained the improvement on the coding performance in term of CR and PRD over some resent methods including Wavelet-based pattern matching scheme [1], WHOSC [7], SPIHT [4], and so on.

TABLE II
The Maximum performance (CR and PRD) of the proposed method is compared with some recent algorithms.

Method	Proposed Method	Pattern Matching	WHOSC	SPIHT
Signal	MIT_BIH 117	MIT_BIH 117	MIT_BIH 117	MIT_BIH 117
CR	50.1	21.7	15.8	8
PRD%	1.34	1.76	1.74	1.18

As the results of the experiment of two ECG signals (mit117 and mit203) are shown in Fig.5 and Fig.6 respectively. Considering the figure 5, a first 6000 sample Database of record mit117 is used as the input of this system. And these results depicted that at a maximum CR of 50:1 is achieved with a low PRD at 1.34%. But for the record mit203 the maximum compression can be reach only 34:1 with the PRD of 5.22%, although this does not correlate to the lowest PRD value of the other arrhythmia types. However, the performance of the proposed algorithm is provides higher CR and smaller PRD for only the regular format ECG signal (Eg: 117, 102, 103 …), except for the case of QRS complex (203).

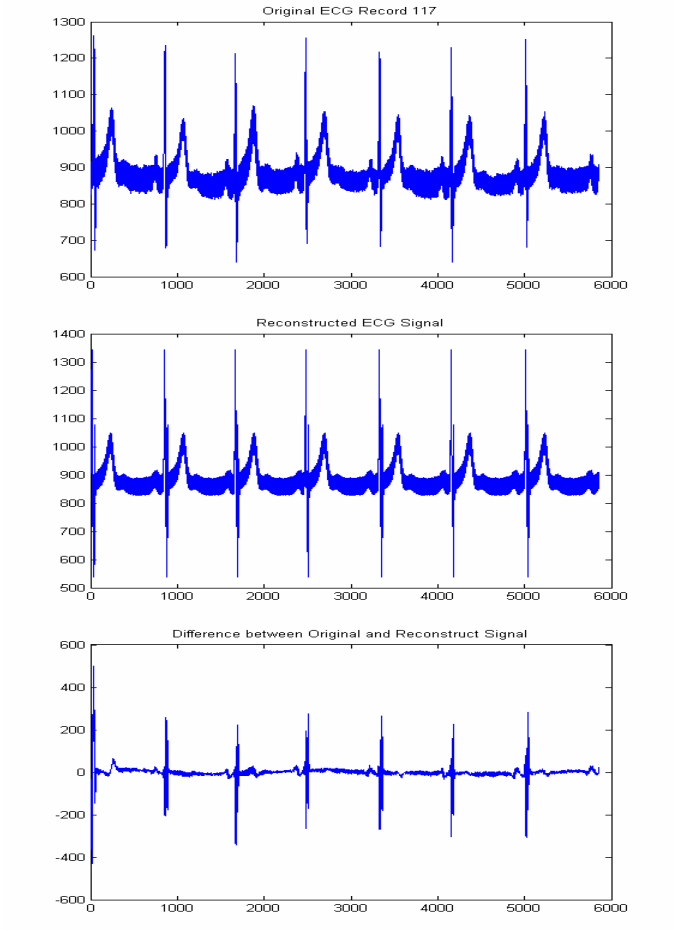

Fig.5 The result of proposed method on mit117 (a) Original signal, (b) Reconstructed signal, (c) Reconstruction error.

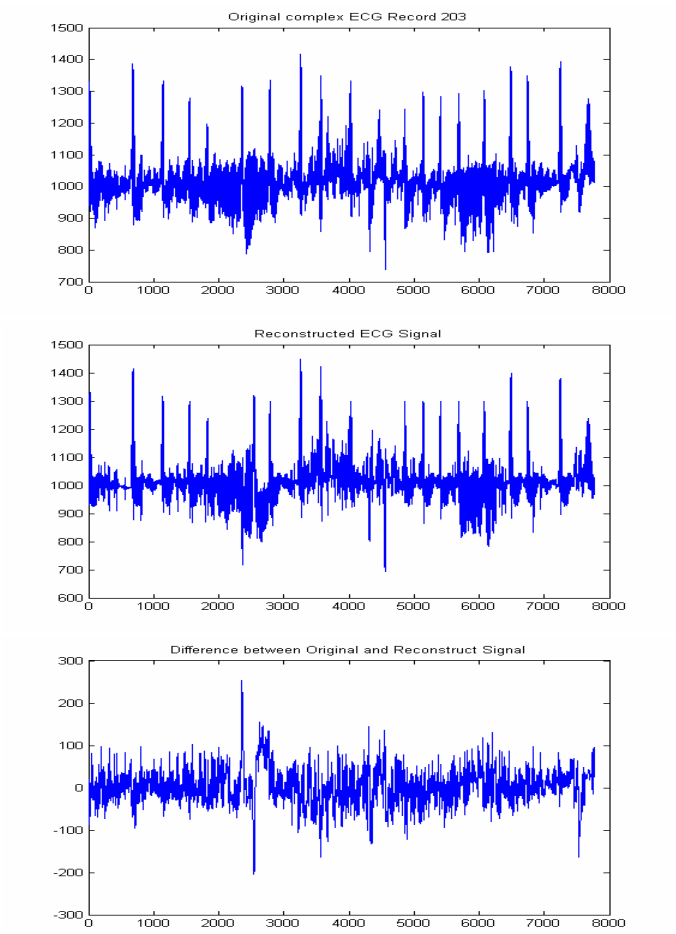

Fig.6 The result of proposed method on mit203 (a) Original signal, (b) Reconstructed signal, (c) Reconstruction error.

IV. CONCLUSIONS

The hybrid method of ECG compression by Wavelet based Average Beat subtraction has been proposed. This method consists of the QRS detection, period normalization, threshold technique of reduces the number of residual wavelet coefficients, and Run-Length Coding. The experiment results show that the average beat subtraction should produce relatively constant improvement in compression regardless of distortion level. However, our experiment indicate that a decrease of compression but increase the distortion level. It is because of the compression ratio (CR) depend upon the selected the Threshold index, and PRD is depend upon the number of beat selected to generate the mean beat at the average beat process and condition of the original ECG format.

REFERENCES

[1] Yanyan Hao, PinaMarziliano, "An Efficient Wavelet based Pattern Matching Scheme for ECG data compression, Biomedical Circuits and Systems, 2004 IEEE International Workshop, 2004.

[2] B. R. S. Reddy and I. S. N. Murthy, "ECG data compression using Fourier descriptors," IEEE Trans. Biomed. Eng., vol. BME-33, pp. 428–434, 1986.

[3] T. Blanchett, G. C. Kember, and G. A. Fenton, "KLT-based quality controlled compression of single lead ECG," IEEE Trans. Biomed. Eng., vol. 45, pp. 942–945, July 1998.

[4] Zhitao Lu, Dong Youn Kim, William A. Pearlman, " Wavelet Compression of ECG by the Set Partitioning in Hierarchical Tree (SPIHT) algorithm". IEEE Trans. Biomed. Eng., no. 12, Jan, 2000.

[5] B. Madhukar and I. S. N. Murthy, "ECG data compression by modeling," Comput. Biomed. Res., vol. 26, pp. 310–317, 1993.

[6] J. L. Cardenas-Barrera and J. V. Lorenzo-Ginori, "Mean-shape vector quantizer for ECG signal compression," IEEE Trans. Biomed. Eng., vol. 46, pp. 62–70, Jan. 1999.

[7] Robert S. H. Istepanian, Leontios J. Hadjileontiadis, "ECG Data Compression Using Wavelets and Higher Order Statistics Methods". IEEE TRANSACTIONS ON INFORMATION TECHNOLOGY IN BIOMEDICINE, VOL. 5, NO. 2, JUNE 2001

[8] P. S. Hamilton and W. J. Tompkins, "Compression of ambulatory ECG by average beat subtraction and residual differencing," IEEE Trans. Biomed. Eng., vol. 38, pp. 253–259, 1991.

[9] A. G. Ramakrishnam and S. Saha, "ECG coding by wavelet-based linear prediction," IEEE Trans. Biomed. Eng., vol. 44, no. 12, pp. 1253–1261, Dec. 1997.

[10] S. Claydokjan, K. Chitsakul, M. Sangworasil, S. Kondo. Realtime Electrocardiogram Compression Technique Using Wavelet Transform on MCS-51. 16th Biennial International EURASIP Conference Bio-Signal 2002 Proceeding. Czech Republic. Pp. 177-179.

Classification of Muscular Contraction Using EMG Topological Mapping

D. Sueaseenak[*‡], T. Chanwimalueang[*], K. Wong-ek[†], N. Laoopugsin[‡] and C. Pintavirooj[*]

[*]Research Center for Communication and Information Technology (ReCCIT), and
Department of Electronics, Faculty of Engineering,
King Mongkut's Institute of Technology Ladkrabang, Bangkok 10520 Thailand
[†]Department of Medical Technology, Faculty of Applied Health Science,
Thammasat University, Pratumthanee, Thailand
[‡]Faculty of Medicine, Srinakharinwirot University, Nakorn Nayok, Thailand
kpchucha@kmitl.ac.th

***Abstract*-We develop a multi-channel electromyogram acquisition system using PSOC microcontroller to record multi-channel EMG signals. An array of 4 x 4 surface electrodes is used to record the EMG signal. B-spline interpolation technique has been utilized to map the EMG signal on the muscle surface. The topological mapping of the EMG is then analyzed to classify the pattern of muscle contraction. The purposed system was successfully demonstrated to record EMG data and its surface mapping. The muscular contraction classification of mapping using Principle component analysis demonstrates promising results.**

Keywords— PSOC, EMG, PCA

I. INTRODUCTION

Electromyography (EMG) is the study of muscle electrical signals. EMG is sometimes referred to as myoelectric activity. Many muscular abnormalities such as muscular dystrophy, inflammation of muscle, peripheral nerve damages could results in an abnormal electromyogram [1-4]. EMG can be recorded by two types of electrodes; invasive electrode the so-called wire or needle electrodes and non-invasive electrode the so-called surface electrode. Wire or needle electrodes records individual muscle fiber action potentials which is an ideal choice to evaluate the muscle activity [7]. However, fine wire intramuscular electrodes require a needle for insertion into the muscle and may cause a significant pain. The choice of surface electrode is then preferable. However, when EMG is acquired from surface electrodes mounted directly on the skin, the signal is a composite of all the muscle fiber action potentials occurring in the muscles underlying the skin. Estimating this force in general is a hard problem due to difficulties in activating a single muscle in isolation, isolating the signal generated by a muscle from that of its neighbors, and other associated problems [5-6]. The clinical application of EMG can be classified into two mains categories. (i) Standard EMG [6] is recorded from discrete sites on a muscle and thus provides only a limited picture of the actual muscular electrical activity in the vicinity of the recording electrode. EMG,(ii) EMG, recorded by an array electrode array facilitates the clinical interpretation of electrical activities through the mapping of these signals on the muscle surface [7]. In this paper, a PSOC-based multi-channel surface electrode array data acquisition system is developed to acquire EMG data. The EMG signals are then mapped using B-spline interpolation technique. The EMG topological Mapping is then used for classification of muscular contraction. There exists a number of 2D-pattern classification [7-10], in this research, we applied the technique called principal component analysis which is very efficient and widely used for classification. [11]

The paper is organized as follows: Section II is devoted to the specification and design concept multi-channel electromyogram system. Section III described feature extraction and topological mapping process. Section IV briefly introduced Principle component analysis. The classification results is shown in section V. Conclusions and Discussion is provided in section VI.

II. DESIGN AND CONSTRUCTION OF MULTI-CHANNEL EMG

EMG measurement is accomplished by the instrument called electromyography. The system, in general, consists of instrument amplifier, notch filter, offset adjustment, isolator, main amplification, and the CRT display. The instrument amplifier is a front-end, high CMRR differential amplifier which functions to pick-up a low amplitude signal submersed in the high-frequency noise. The notch filter gets rid of the 50Hz noise while keeping the EMG signal intact. The offset adjustment maintains the baseline level especially during the subject's motion. The function of isolator is to separate the front-end section from the rear-end section to protect the possible electrical shock to the patient. The main amplification conditions the EMG prior to be display with CRT. The complexity of the electronic circuit becomes realized with the necessity to monitor the multi-channel of EMG. Such complicate designs, however, are made possible by the creation of entirely reconfiguration and programmable components the so-called Programmable System On Chip Microcontroller(PSOC Microcontroller).

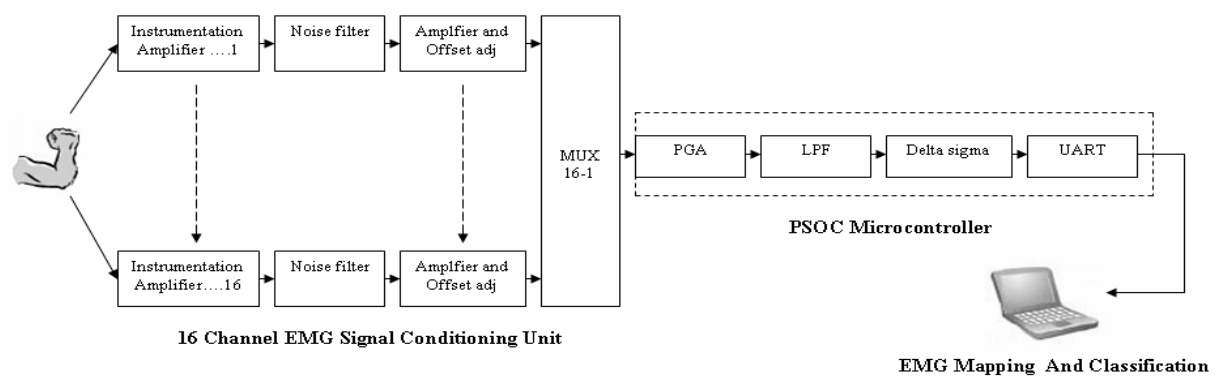

Figure 1. 16 channel electromyogram acquisition system

The designed EMG system is capable of monitoring 16 channels of EMG simultaneously. Each channel consists of 2 main parts; (i) EMG signal conditioning unit and PSOC microcontroller. Figure 1 shows diagram of multi-channel EMG acquisition system.

The EMG signal conditioning units consists of 3 sub-units

(i) Instrumentation Amplifier. This subunit uses the INA 2128 BUR-BROWN Integrated Circuit. The IC can achieve a CMRR up to 120 dB and gain up to 1000.

(ii) Noise filter. The function of the filter is to get rid of the 10-20 Hz noise which is classified as a motion artifact.

(iii) Amplifier and Offset Adjustment. The objective of this sub-unit is to Amplifier EMG signal and maintains the appropriate offset voltage prior to interface with the PSOC.

The PSOC microcontroller consists of 4 subunits

(i) PGA (Programmable Gain Amplification) This subunit acts as the buffer and the main amplification of EMG.

(ii) Low pass filter. The function of the filter is to remove of the high frequency noise. The cut-off frequency is at 500 Hz.

(iii) DELTA-SIGMA. This subunit functions as a 8-bit Analog to digital converter.

(iv) UART. This subunit functions to perform RS-232 interfacing unit with PC.

The captured EMG signal by the PC is displayed on the PC monitor. The display unit is written in C++ Builder. The function of PC is to display the Raw EMG signal (figure 3).

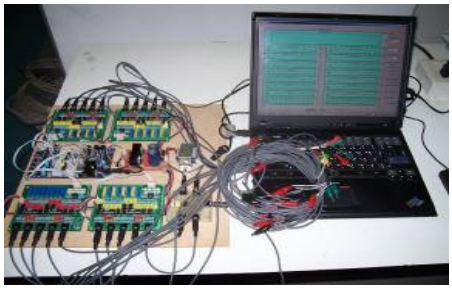

Figure 2. Multi-channel electromyogram acquisition system

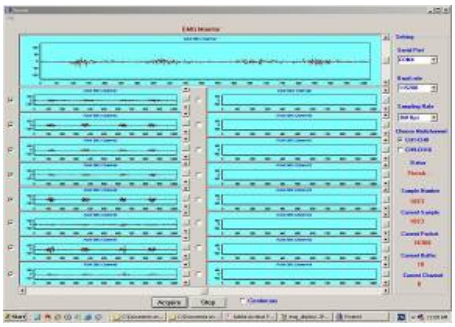

Figure 3. Raw EMG signal on laptop computer

III. EMG FEATURE EXTRACTION AND MAPPING

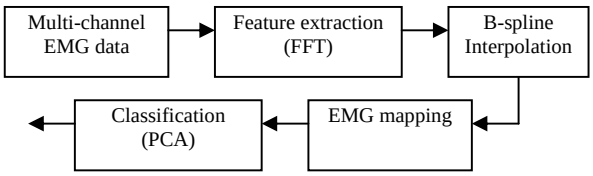

Figure 4. Feature extraction and mapping

Figure 4 show the feature extraction and mapping process. Each of the 16 EMG channels will be converted to frequency domain by taking the Fourier transform. The energy content of the EMG signal is then evaluated by computing area under the magnitude squared of the Fourier transform. The energy content on the 4x4 grid corresponding to the 4x4 electrode shown in figure 5 is then interpolated to derive the 49x49 topological maps which are later applied to PCA for muscular contraction classification. Figure 6 shows the topographical mapping of various muscular contractions.

Figure 5. 16 Channel electrode placements

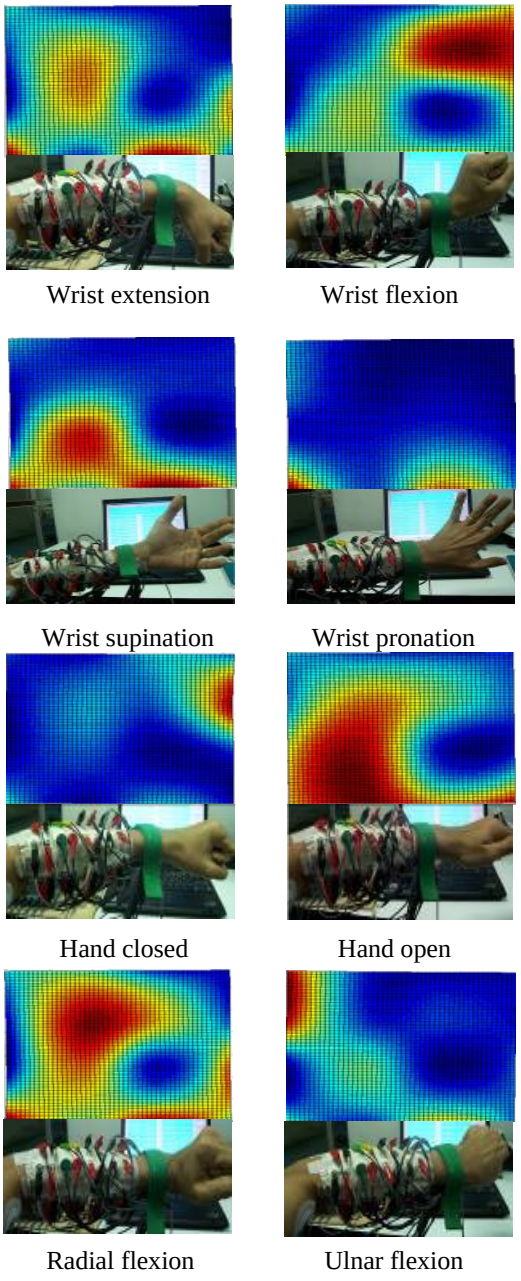

Figure 6. Topographical mapping of the EMG

IV. CLASSIFICATION USING PRINCIPAL COMPONENT ANALYSIS (PCA)

Principal Component Analysis (PCA) is a statistical technique which used to describe a large dimensional space with a relative small set of vectors. It is a popular technique for finding patterns in data of high dimension, and is used commonly in both face recognition and image compression. Application of PCA to face recognition is known as Eigen face. The Eigen face technique is a powerful yet simple solution to the face recognition dilemma. It uses much more information by classifying faces based on general facial patterns. Here we focus on the application of PCA for muscular-contraction classification

The procedure for using PCA is divided into 2 steps. (i) Training step and (ii) Classification step.

The Training step is as follow:

(i) Convert each cropped topological mapping matrix into a vector T_i of length N (N=imagewidth*imageheight). For the M data set, we let the training set represented by, $\{T_1, T_2, T_3, ..., T_M\}$ where M is the vector of N^2

(ii) Compute the mean vector Ψ and the set of deviation from the mean vector $\Phi = [\Phi_i, \Phi_2, ...\Phi_M]$ which is defined as

$$\Psi = \frac{1}{M}\sum_{i=1}^{M} T_i \quad (1)$$

$$\Phi_i = T_i - \Psi \quad (2)$$

(iii) Compute the covariance matrix C which is defined as

$$C = \frac{1}{M}\Phi\Phi^T \quad (3)$$

(iv) Compute the Eigen value and Eigen vector of C represented as

$$C\nu_i = \mu_i\nu_i \quad (4)$$

where μ_i is the corresponding Eigen value of Eigen vector ν_i

(v) Project each training set on the Eigen -space using the operation

$$\omega_K = (C\nu_k)^T(T_i - \psi) \quad (5)$$

$$1 \le k \le M', \quad 1 \le i \le M$$

where ν_k is ranked according to their significance. Therefore, for each topological mapping matrix we would have a set of M' weight

$$\Omega_k = [\omega_i, \omega_2, ..., \omega_{M'}] \quad (6)$$

which describe the contribution of Eigen space to the topological mapping matrix.

The Classification step is as follow:

(i) Project vector form of the tested topological mapping matrix T_p to the Eigen space using equation (4) to derive Ω_p. The tested topological mapping matrix is classified to class k which minimized

$$\varepsilon_k^2 = \left\|\Omega_p - \Omega_k\right\|^2 \quad (7)$$

with $1 \le k \le M$

V. EXPERIMENTAL AND RESULTS

The 5 patterns of topographical mapping of six muscular contraction of forearm (30 maps) are used in the training process of PCA. The topographical mapping of the five unknown contraction is then used as the tested set. Figure 7 shows the training sets , the derived Eigen-space and the result of classification.

TABLE I
The results of classification

Muscular contraction	% Accuracy
1.Wrist extension	80 %
2.Wrist flexion	100 %
3.Wrist pronation	80 %
4.Hand closed	100 %
5.Radial flexion	100 %
6.Ulnar flexion	100 %

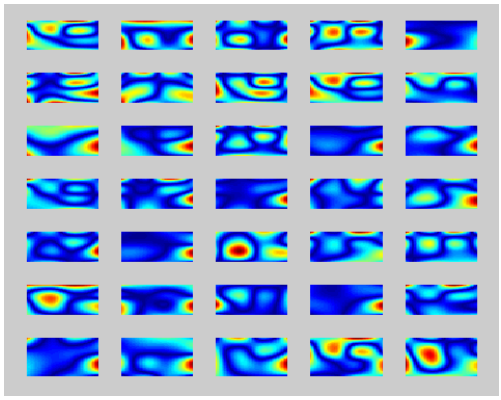

(a)

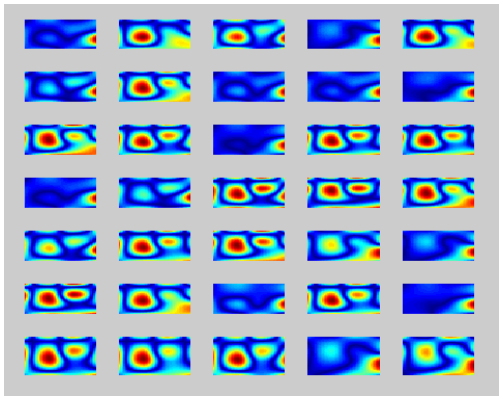

(b)

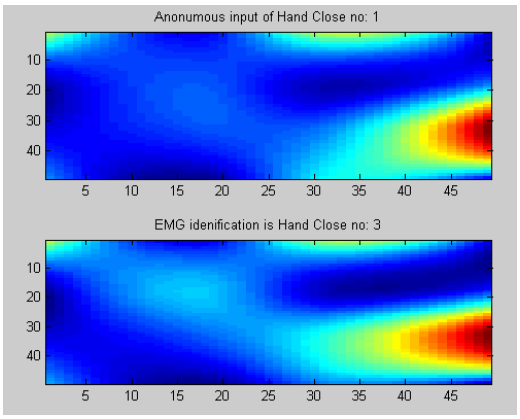

(c)

Figure 7 (a) Training Topological-Mapping Input of PCA; (b) Eigen space; (c) Result of classification

VI. CONCLUSION AND DISCUSSION

A multi-channel electromyogram acquisition system using PSOC is designed and constructed to perform a topological map of EMG signal on the muscle surface. The mapping for various pattern of muscular contraction are then recorded and later analyzed with principal component analysis (PCA) to classify the pattern of muscular contraction pattern. The classification result is very promising.

ACKNOWLEDGMENT

The authors wish to thank DEMAMEDICAL CO., LTD for supporting the ECG/EMG surface electrode and lead wire for measuring EMG signal in this research.

REFERENCES

[1] G. A. Bekey, C Chang, J Perry, M.M. Hoffer,"Pattern recognition of multiple EMG signals applied to the description of human gait," Proceedings of IEEE, vol. 65, pp. 674-689, 1977.

[2] S. Boisset, F Goubel, "Integrated electromygraphy activity and muscle work," J Applied Physiol, vol 35, pp. 695-702, 1972.

[3] C.J. DeLuca, "Use of the surface EMG signal for performance evaluation of back muscle," Muscle & Nerve, vol. 16, pp. 210-216, 1993.

[4] R. Plonsey, "The active fiber in a volume conductor," IEEE Trans Biomed Eng, vol. 21, pp. 371-381, 1974.

[5] K.S. Turker, T.S Miles, "Cross talk from other muscles can contaminate electromyographic signals in reflex studies of the human leg," Neuroscience Letters, vol. 111, pp. 164-169, 1990.

[6] J.W. Morrenhof, H.J. Abbink, "Cross-correlation and cross talk in surface electromyography," Electromyography, vol. 25, pp. 73-79, 1985.

[7] Basmajian JV, de Luca CJ. Muscles Alive – The Functions Revealed by Electromyography. The Williams & Wilkins Company; Baltimore, 1985.

[8] J. Cartinhour, " A Bayes classifier when the class distributions come from a common multivariate normal distribution " ,IEEE Transactions on Reliability, vol. 41, Issue 2, pp. 124 – 126, 1992.

[9] N.B. Karayiannis, M.M. Randolph-Gips, " Soft learning vector quantization and clustering algorithms based on non-Euclidean norms: single-norm algorithms " ,IEEE Transactions on Neural Networks, vol. 16, Issue 2, pp. 423 - 435, 2005.

[10] E. Alpaydin, M.I. Jordan, "Local linear perceptrons for classification ",IEEE Transactions on Neural Networks, vol. 7, Issue 3, pp. 788 - 794, 1996.

[11] Zhujie, Y.L. Yu, " Face recognition with Eigen faces " ,Proceedings of the IEEE International Conference on Industrial Technology, pp. 434 - 438, 1994.

An Automatic Classification of Microcalcification Clusters Using Shape and Distribution Features

W. Chiracharit
Department of Electronic and Telecommunication Engineering
King Mongkut's University of Technology Thonburi
126 Pracha-uthit Road, Bangmod, Tung-kru, Bangkok 10140, Thailand

***Abstract*-This paper presents an automatic approach to classify benign or malignant microcalcification cluster which is an important sign of early-stage breast cancer, appearing on digitized x-ray mammograms. The approach consists of two main processes: detection of microcalcification cluster and classification of clustered-microcalcification features. In the first process, clustered microcalcifications are located in time-frequency wavelet space. Shape of the detected microcalcification is then morphologically reconstructed. In the second process, the features based on shape of a single microcalcification and distribution of the cluster are extracted. Binary tree decision, artificial neural network and support vector machine are used as a classifier to evaluate the performance. The experimental results show 86% sensitivity and 85% specificity.**

I. INTRODUCTION

Breast cancer is the mortal disease of most women worldwide. In Thailand, the statistical incidence of the disease is the runner-up [1]. Unfortunately, because its causes are not certainly known, screening of the disease in an early stage by x-ray mammography is currently the best option. Examples of mammograms are shown in Fig. 1. There are many abnormalities visible on mammograms, e.g. circumscribed masses or speculated lesions. An important sign of early-stage breast cancer usually appearing on mammogram is clusters of a tiny calcium deposit called microcalcification.

However, a restriction of low-contrast x-ray imaging and human fatigue causes a high risk of film interpretation error. This makes a large number of unnecessary biopsy or miss-detected existent cancer each year. Accordingly, a computer-aided diagnosis (CAD) using digital image processing and pattern recognition techniques can provide a second reading for assisting radiologists to increase their diagnostic accuracy and patients' survival rate [2]. CAD helps in detecting hidden small microcalcifications and making another diagnostic result.

In detection of microcalcification cluster, the x-ray passing through the breast tissue is scattered and makes incomplete image. Microcalcifications appear on low-contrast breast-tissue background image. The challenge is described as more difficult than finding a polar bear in a blizzard. In reading mammogram to find microcalcifications, the presence of microcalcifications in the image is not certainly known. Its presentation sometimes looks similar to the background or noise. There is much information about the microcalcifications for the radiologists, but the image shows just something that may be the microcalcifications.

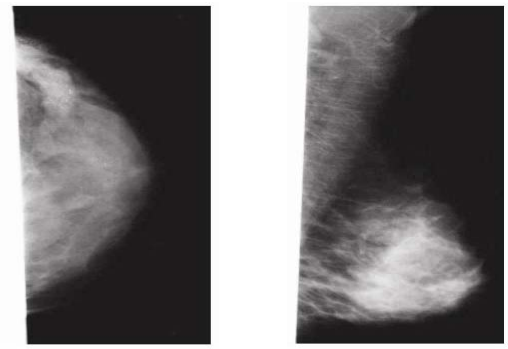

(a) (b)

Figure 1 Examples of mammograms: (a) cranio-caudad view (b) medio-lateral oblique view

In the previous works on detection of microcalcification, Dengler *et al.* [3] proposed the segmentation by using the difference between original and low-pass images and morphology. Smith *et al.* [4] subtracted a smoothed image obtained by the morphology techniques from an original. The smoothing techniques are erosion, median filter, median filter with hollow mask, *k*-nearest neighbor filter and Gaussian filter. Morrison and Linett [5] directly detected the microcalcification by modeling microcalcification signal by a Gaussian function, and finding points that get the least error. Wang and Karayiannis [6] utilized wavelet decomposition to cut low frequency components that related to image's background, inverse wavelet transform and thresholding to select only high frequency signals.

In classification of microcalcifications, it is a difficult task to distinguish microcalcification types between malignancy and benignancy, because of its imprecise pattern depended on property of x-ray attenuation of each patient's breast tissues and image acquisition. In previous works, based on clinical knowledge, the types are judged by their size, shape, and distribution of clustered microcalcifications. Shen *et al.* [7] developed a set of shape factor to measure a roughness of a segmented individual calcification. Kramer and Aghdasi [8] used statistical texture features computed from both original suspicious region and its wavelet-transformed subbands. The whole information of the clusters and their background image was analyzed. Sehad *et al.* [9] added a clinical parameter of

patient's age on morphological features. Verma and Zakos [10] determined a significance of single and combination of the features randomly selected. All of these tried to extract suitable input features to feed to classifier such as Bayesian classification, k-nearest neighbors, or neural network. Another system structure was proposed by De Vito *et al.* [11]. The architectural approach is a multiple expert system that combined recognition results of each feature type and finally decided.

In this paper, an automatic classification of detected microcalcification clusters is presented. The paper proceeds as follows. The analysis of mammographic microcalcification is in the Section II. Section III is microcalcification detection and Section IV is microcalcification classification. The experimental results are in Section V. The conclusions and discussion are in Section VI.

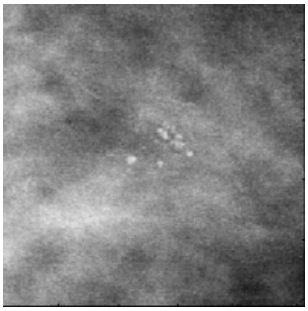

Figure 2 An example of microcalcification cluster

II. Mammographic Microcalcification Analysis

Microcalcification cluster looks like many bright small vary-shape spots [12]. Fig. 2 shows an example of mammographic microcalcification cluster. Normally, the mammogram consisting of the images of breast tissues, blood vessels, fat, microcalcifications, noises, chest muscle, air, other artifacts, etc. The intensity of breast tissue background increases or decreases slowly, while the intensity of small peak of microcalcification changes rapidly. They can be divided into three big groups: background, microcalcification and noise. The image signals of low-contrast background vary inconstantly, but totally are at high values. The image signals of microcalcifications are in minor group hidden in the image, and small noises are scattering throughout the entire image. In fact, the signals of the mammogram consist of many frequencies and intensities at any locations. Therefore, the microcalcification detection and classification without the flexibility of these changes may not succeed. The proposed approach is shown in Fig. 3. The details of each process are described in the next sections.

III. Microcalcification Detection

Firstly, the mammogram images are considered. Most image signals in the mammogram are an air, chest muscles or other artifacts that are not part of the breast. Therefore, to detect the microcalcifications without wasting time for processing these unrelated signals, the original mammogram image is divided into square regions of interest. Only the subblocks containing the breast images which may include the microcalcifications are considered. The other parts of the mammogram images are abandoned.

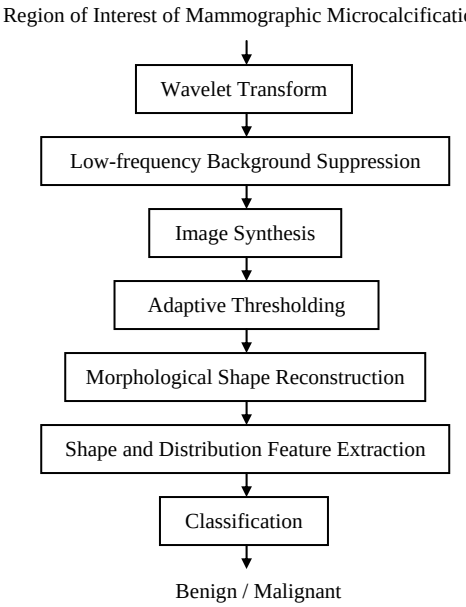

Figure 3 The automatic classification of microcalcification cluster

A. *Wavelet Transforms*

Since the microcalcification is related to high frequency component in frequency domain, and background behaves as low frequency signal. The spectrum of the signal or signal analysis in frequency domain is considered to be effective for the microcalcification detection.

Wavelet transform [13], [14] is an analysis for decomposing or mapping the signals into coarse and fine components in time-frequency domain. It can represent all of the non-stationary image signals, which is appropriate for the mammographic analysis. However, in typical wavelet transform, only low frequency component will be decomposed into higher levels up to a size of the image (e.g. eight levels available for 256×256 pixel-size). The high frequency components of microcalcification signals are not performed.

B. *Background Suppression*

The level of wavelet decomposition and the type of mother wavelet are the conditions of the transformation that must be found. Higher levels mean that finer approximation are analyzed with longer processing time, while the types of the mother wavelet refer to the quality of the output signals. This means that the low frequency component are considered to be background.

The digitization of mammograms is performed with 300 dot-per-inch resolution and 8-bit gray scale. Therefore it is possible

that the smallest point of microcalcification being about 85 microns can be detected. The average size of a single microcalcification is around 300 microns. Because of wavelet a half-down-sampling for every decomposition level, therefore there are three possible levels in order to detect the smallest microcalcification. Daubechies 4 mother wavelet with the similar shape as microcalcification is selected. The coefficient of low frequency component in the selected highest level is replaced by zero, in which case the highest level is two. Then, the signal without the low-frequency component after the inverse wavelet packet transform has no background signals.

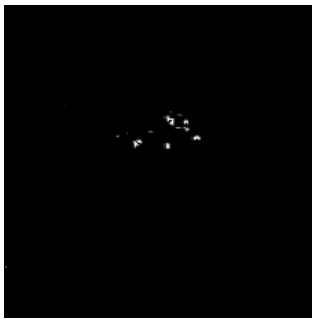

(a)

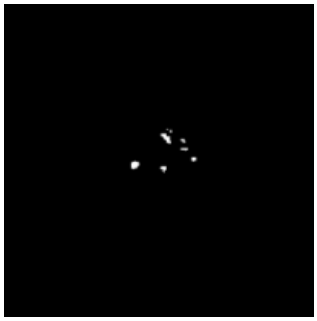

(b)

Figure 4 Examples of detected microcalcifications:
(a) thresholded synthesized-microcalcifications
(b) shape-reconstructed microcalcificatrions

C. Microcalcification Synthesis and Shape Reconstruction

After eliminating the background, the high frequency components representing only the microcalcifications are considered to be detected. All subband images are inverse-wavelet transformed. However, some noises and parts of background still remain in the reconstructed signal after the inverse wavelet packet transform, even though their amplitudes are very tiny compared with those of the microcalcifications. At the moment, some processes such as binarization for separating microcalcifications from the others are needed. The appropriate thresholding value has to be determined by using the image's histogram from which the microcalcifications are high-intensity minor part and other signals are low-intensity major part. The weighted threshold is balanced and selected. Then, the unwanted parts are cut. For example, the location of clustered microcalcifications in Fig. 2 is clearly detected, as shown in Fig. 4 (a).

The binarized microcalcifications may be detected with incomplete shape. The morphological closing is performed. The same location of microcalcifications in the original image is used to limit the boundary of morphological shape. The results are shown in Fig. 4 (b).

IV. MICROCALCIFICATION CLASSIFICATION

Classification of microcalcification clusters with features corresponding to a complex phenomenon of benign and malignant types is a hard problem. It requires suitable extracted features that can explain their exact clinical characteristic. The malignant type is typically different from the benign in shape, contour, size, number, or distribution in the cluster. Twelve features are chosen based on the characteristics of clustered microcalcifications in Table I [15].

TABLE I
CHARACTERISTICS OF MICROCALCIFICATIONS [14]

	Benign Type	Malignant Type
Shape	homogeneous rounded	dot-like or elongated form
Outline	Sharply	fragment with irregular
Size	generally larger	tiny
Number	solitary or numerous	very numerous
Distribution	Diffusely	clustered
Density	very fine and dense	differ granular

D. Shape and Distribution Feature Extraction

There are eight shape features. They are mean and standard deviation of Fourier descriptor, compactness chosen to describe the shape of the microcalcifications, mean and standard deviation of size of a single microcalcification, and mean and standard deviation of densities of microcalcification intensity.

There are four features representing the distribution of microcalcification cluster. Arrangement features are the distribution in the cluster that is represented by the area of the cluster, density, and mean and standard deviation of the distances between the micocalcification pairs.

E. Classifiers

Three classifiers are selected for two-class classification. The results are compared to find the best decision on the extracted features. The first classification is a simple binary tree decision. Each feature is decided into two classes. The decision tree is constructed for all possible paths and branches.

An artificial neural network learning with the back-propagation algorithm [16] is the second classifier for the more complex feature set. The feed-forward network is constructed with three layers.

The last classifier is support vector machine (SVM) [17], [18] which is a learning algorithm that is to find the largest separation margin between two classes. This is suitable for the high-variance feature set. Typically, only a few training samples will be the support vectors. In the experiments, there are three kernel functions based on the transformation or the

mapping of the input features into higher-dimensional feature space: linear kernel, polynomial kernel, and Gaussian radial basis function (RBF) kernel. The maximum soft margin is optimized from the dual form of SVM.

V. Experimental Results

Thirty mammogram films are from ten woman patients aged 35-62 years old. All mammograms are ground-truth known. The mammograms include both medio-lateral oblique (MLO) views and cranio-caudad (CC) views for both left and right breast images. Thirty-six regions of interest is cropped by the size of 256×256 pixels. There are 18 benign microcalcification clusters and 18 malignant microcalcification clusters.

TABLE II
Classification Results

	TPF	TNF	Classification Rate	A_z
Binary Tree	82%	76%	79%	0.74
Neural Network	84%	84%	84%	0.83
Linear SVM	84%	82%	83%	0.85
Polynomial SVM	86%	85%	86%	0.87
Gaussian-RBF SVM	85%	84%	85%	0.86

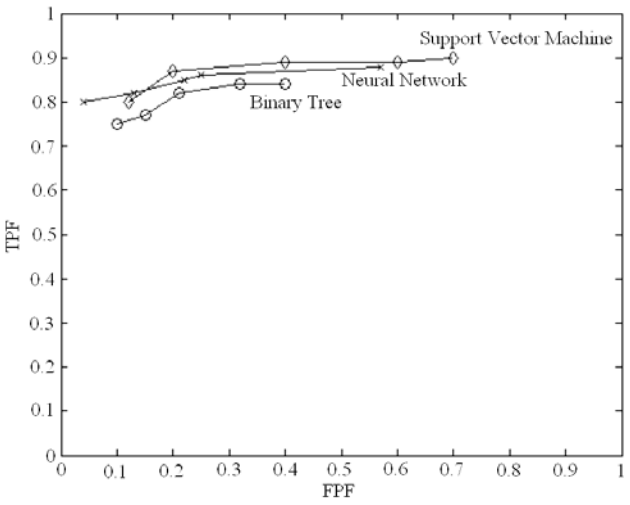

Figure 5 Comparison of ROC curves

The results of malignant or cancer case are true-positive and false-positive, and for benign or non-cancer case are true-negative and false-negative. They are used to compute sensitivity or true-positive fraction (TPF), and specificity or true-negative fraction or one minus false-positive fraction (1-FPF) [19]. The receive operating characteristic (ROC) curves are plotted to compare the results tested with different classifiers.

The experimental results are shown in Table II. The highest results is 86% sensitivity and 85% specificity by using polynomial support vector machine, shown in Fig. 5. The classification rate for all benign and malignant clusters is 86% area under ROC curve (A_z) is approximately 0.87. Although the results for any classifiers are not different, except binary tree, the results show significant results in both sensitivity and specificity.

VI. Conclusions and Discussions

This paper presents an automatic approach for classification of benign or malignant microcalcification cluster which is an important sign of early stage breast cancer appearing in mammogram. Clustered microcalcifications are detected and shape-reconstructed. Shape and distribution features are then extracted and classified. In the future, the CAD for full-field mammogram should be considered for the automatic diagnosis. All parts of mammogram should be analyzed.

References

[1] National Cancer Institute of Thailand, *Cancer Statistics webpage*, http://www.nci.go.th/statisti.htm.

[2] S.K. Moore, "Better Breast Cancer Detection", *IEEE Spectrum*, Vol. 38, No. 5, pp. 50-54, May 2001.

[3] J. Dengler, S. Behrens and J.F. Desaga, "Segmentation of Microcalcifications in Mammograms", *IEEE Trans. Med. Imag*., Vol. 12, No. 4, pp. 634-642, 1993.

[4] C.M. Smith, S.R. Nelson and S.M. Tuovila, "Morphological and Related Image Processing Techniques for the Detection of Microcalcifications in Mammographic Images", *IEEE Symp. Image Analysis & Interpretation*, Tucson, Arizona, USA, pp. 29-34, April 1998.

[5] S. Morrison and L.M. Linnett, "A Model Based Approach to Object Detection in Digital Mammography", *Proceedings of International Conference on Image Processing*, Vol. 2, pp. 182-186, October 1999.

[6] T.C. Wang and N.B. Karayiannis, "Detection of Microcalcifications in Digital Mammograms Using Wavelets", *IEEE Trans. Med. Imag*., Vol. 17, No. 4, pp. 498-509, 1998.

[7] L. Shen, R.M. Rangayyan and J.E.L. Desautels, "Application of Shape Analysis to Mammographic Calcifications", *IEEE Trans. Med. Imag*., Vol. 13, No. 2, pp. 263-274, 1994.

[8] D. Kramer and F. Aghdasi, "Texture Analysis Techniques for the Classification of Microcalcifications in Digitised Mammograms", *IEEE Conference in Africa*, Vol. 1, pp. 395-400, 1999.

[9] S. Sehad, S. Desarnaud and A. Strauss, "Artificial Neural Classification of Clustered Microcalcifications on Digitized Mammograms", *IEEE International Conference on Computational Cybernetics and Simulation*, Vol. 5, pp. 4217-4222, 1997.

[10] B. Verma and J. Zakos, "A Computer-aided Diagnosis System for Digital Mammograms Based on Fuzzy-neural and Feature Extraction Techniques", *IEEE Trans. Inform. Technol. Biomed.*, Vol. 5, No. 1, pp. 46-54, 2001.

[11] S. De Vito, F. Tortorella and M. Vento, "Automatic Classification of Clustered Microcalcifications by a Multiple Expert System", *IEEE International Conference in Image Analysis and Processing*, pp. 464-469, 1999.

[12] L. Tabar and P. B. Dean, *Teaching Atlas of Mammography*, Stuttgart, Thieme-Stratton, 1983.

[13] A. Graps, "An Introduction to Wavelets", *IEEE Computational Science and Engineering*, Vol. 2, No. 2, pp. 50-61, 1995.

[14] W.B. Richardson, "Applying Wavelets to Mammograms", *IEEE Engineering in Medicine and Biology Magazine*, Vol. 14, No. 5, pp. 551-560, 1995.

[15] S. Liu, *The Analysis of Digital Mammograms, Spiculated Tumor Detection and Normal Mammogram Characterization*, Ph.D. Thesis, Purdue University, 1999, p. 5.

[16] M. T. Hagan, H. B. Demuth, and M. Beale, *Neural Network Design*, MA, PWS Publishing Company, 1996.

[17] N. Cristianini and J. Shawe-Taylor, *An Introduction to Support Vector Machines and Other Kernel-based Learning Methods*, Cambridge University Press, 2000.

[18] B. Schölkopf, C.J.C. Burges and A.J. Smola, *Advanced in Kernel Methods: Support Vector Learning*, The MIT Press, 1999.

[19] T.G. Tape, University of Nebraska Medical Center, *Interpreting Diagnostic Tests webpage*, http://gim.unmc.edu/dxtests/reviewof.htm.

3D Shape-Recovery System Based on Photographic Tomography with Flexible Camera Orientation

P. Greesuradej,S. Gimjumpa, M. Sangworasil, C. Pintavirooj
Department of Electronics, Faculty of Engineering,
and Research Center for Communications and Technology (ReCCIT)
King Mongkut's Institute of Technology Ladkrabang Bangkok 10520, Thailand
kpchucha@kmitl.ac.th, ksmanas@kmitl.ac.th

***Abstract*- A 3D shape-recovery system based on photographic tomography is purposed in this paper. The system consists of a 12 digital camera mounted on the acrylic cases in flexible orientation. The photographs taken by these camera are served as projection data in the conebeam tomography. The 3D shape-recovery process can be divided into 2 steps; (i) calibration step and (ii) tomographic step. In the first step, all cameras capture a reference box performing the camera orientation to derive extrinsic camera calibration matrix. In the second step, the output volumetric data of the conebeam tomography is re-oriented using the extrinsic calibration matrix before undergoing a 3D backprojection step of tomography. The system is tested to recovery a varieties of object and the results are successfully.**

I. INTRODUCTION

3D shape recovering and modeling is the first step of the measurement chain in a number of applications including robot navigation, machine inspection, 3D object recognition, distance measurement, level control, profilometry, displacement measurement, and so on. Many techniques have been purposed for 3D shape recovering including stereo disparity [1-2], laser range finder [3-5], structured light [6-14], etc.

In this research, the concept of photographic tomography is applied for the 3d shape recovering system where the camera orientation can be varied arbitrarily and hence does not require the sophisticated circular scanning system for the camera around the object. The process is divided into 2 steps: (i) the camera calibration to determine the intrinsic and extrinsic parameters of the camera and (ii) modified tomographic process to reconstruct the pseudo cross-section of the object.

This work is organized as the following: - Section II discusses theory involved in tomography. Camera modelling is briefly introduced in section III. Shape extraction process are provided in section IV. Section V explained experiments and results. Discussions and conclusions are given in section VI.

Keywords: Image Reconstruction, 3D Rendering,Photographic Tomography, Cone-Beam Tomography

II. PHOTOGRAPHIC TOMOGRAPHY

The photographic tomography could be inferred as the one of a shape extraction system capable of reconstructing the volumetric data of an object from the sequence of photographs taken around the object.

The well-known algorithm for photographic cone-beam tomography is called Feldkamp cone-beam tomography [15]. The Feldkamp algorithm based on a 3D filtered backprojeciton. The generalized cone beam image reconstruction is expressed as follows:

$$f(x,y,z)=\frac{1}{2}\int_0^{2\pi}\frac{D_{SO}{}^2}{(D_{SO}-s)^2}R_\beta\left(\frac{D_{SO}t}{D_{SO}-s},\frac{D_{SO}z}{D_{SO}-s}\right)d\beta \qquad (1)$$

where $f(x, y, z)$ is the volumetric data, $R_\beta'(p, \zeta)$ is the two-dimensional silhouetted projection, β is the rotational angle, D_{SO} is the cone distance, and (t, s) are the coordinates which are rotated from (x, y). The 2D image taken from the camera normally is served as the projection data for Cone-beam photographic tomography

III. CAMERA MODELING

An photograph taken by a camera undergoes a linear transformation from the 3D projective space ρ^3 to the 2D projective space ρ^2 which can be described by the equation:

$$\begin{bmatrix}u\\v\\w\end{bmatrix}=K[I_3\,|\,O_3]\begin{bmatrix}R & -T\\ O_3^T & 1\end{bmatrix}\begin{bmatrix}x\\y\\z\\1\end{bmatrix} \qquad (2)$$

A scene point $[x\ y\ z\ 1]^T$ is expressed in a world Euclidean co-ordinate system and $[u\ v\ w]^T$ is the image of a scene point in pixel unit.

Matrix K in equation is eq (3) the intrinsic camera calibration matrix

$$K = \begin{bmatrix} fa & 0 & u_0 & 0 \\ 0 & fb & v_0 & 0 \\ 0 & 0 & 1 & 0 \end{bmatrix} \quad (3)$$

where f is the focal length of the projection, a and b is the conversion factor from physical unit to pixel unit and (u_0, v_0) is the principal point of the projection.

Matrix R and T contributes to the extrinsic camera calibration matrix. Rotation matrix R expresses three elementary rotation of camera Euclidean co-ordinate axes with respect to the world Euclidean Coordinate system- rotation along x, y and z are termed pan, tilt and roll respectively. Translation vector t gives three elements of the translation of the origin of the world co-ordinate system with respect to camera co-ordinate system.

To obtain M, observe each known point X=$[x\ y\ z\ 1]^T$ and its corresponding 2D image point $[u\ v\ w]^T$ yield an equation

$$\begin{bmatrix} x & y & z & 1 & 0 & 0 & 0 & 0 & -ux & -uy & -uz & -u \\ 0 & 0 & 0 & 0 & x & y & z & 1 & -vx & -vy & -vz & -v \\ & & & & & \vdots & & & & & & \end{bmatrix} \begin{bmatrix} m_{11} \\ m_{12} \\ \vdots \\ m_{34} \end{bmatrix} = 0 \quad (4)$$

or **AM=0**

If n such points are available, A will be of size 2n x 12. To solve for M, perform Singular Value Decomposition (SVD) of A to derive A=UDV^T. The last column of v is the solution for M. To separate extrinsic parameter, observe that M can be written as $M = [A|b]$ then $T = -A^{-1}b$. To determine R, we decompose A into a product of two matrices K and R using QR decomposition

IV. SHAPE EXTRACTION PROCESS

The entire process for the shape extraction from a series of photographs is shown as a diagram in Figure 1. This process starts with capturing a number of images of standard object (where the 3D coordinate with respect to the world coordinate is known) with camera in arbitrary orientation. The standard object is a cube with three axes of world coordinate passing through the lower corner of the cube. The 3D coordinates with respect to the world coordinate and their correspond image coordinates with reference to image coordinate system (which passes through the center of image) are used to compute the projection matrix M (Intrinsic and extrinsic camera calibration matrix) for each camera orientation as described in the previous section. The standard object is then replaced with object to be modelled. The series of image of the object are then captured with the same series of camera. The captured images are then turned into binary format where the background is equal to zero and the foreground is equal to one. As a result, this kind of shape extraction algorithm can extract the shape of any object regardless of the type of surface either the Lambertian or non-Lambertian surface. The binary images or the silhouetted projections are passed into the modified reconstruction algorithm in which the 3D reconstructed volume for each projection is reoriented such that the z-axis of world coordinate system is aligned with the camera co-ordinate system using the extracted rotation and translation matrix before implementing the general cone-beam tomography.

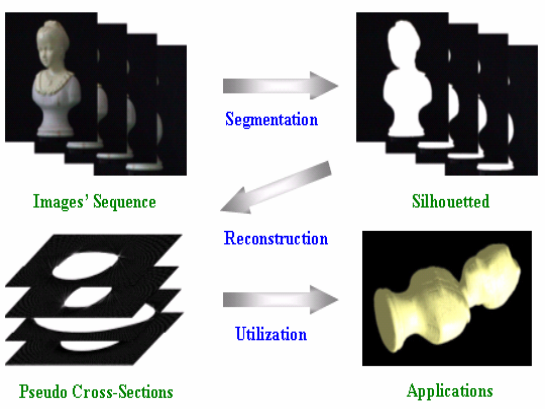

Figure 1. The process diagram of the photographic tomography

V. EXPERIMENT AND RESULTS

The 3D shaped recovery system shown in Figure 2 (a) is mainly composed of 12 USB cameras, and acrylic case. The cameras are installed on the case wall to capture photograph of object placed on the case floor. The taken photographs are forwarded to the Pentium 4 personnel computer via USB hub. Figure 2 (b) shows a reference box used in the camera calibration process. All cameras are requited to capture a reference box performing the camera orientation to derive extrinsic camera calibration matrix. Figure 3 (a) shows the photographs of object taken from 12 cameras. The shape-recovery results are shown in figure 3 (b) after performing surface rendering.

VI. CONCLUSION AND DISCUSSION

The 3D shape extraction using photographic tomography is studied extensively. The main idea of the method is that the tomographic imaging is used to reconstruct the stack of pseudo cross-sectional images from a series of photographs taken around the object. The shape of the stack can closely resemble the shape of original object. Compared with other 3D shape extraction techniques, the equipment used to collect the data for this technique is much lesser in complexity. It mainly consists of 12 digital cameras installed and taken the photograph around the object.

The proposed technique is tested successfully to generate the shape of a variety of objects. The shape with complex geometry such as hand requires more cameras to improve the shape recovery results. The application of real-time modelling is on progress.

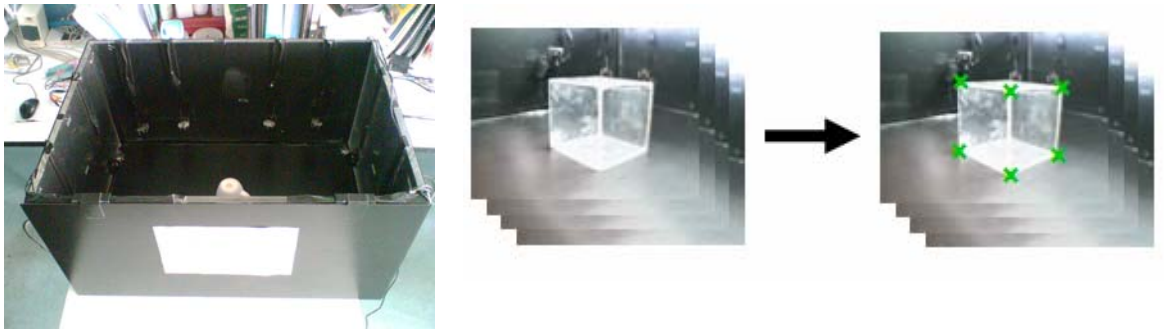

(a) (b)

Figure 2 (a) 3D Modelling system; (b) Camera Calibration

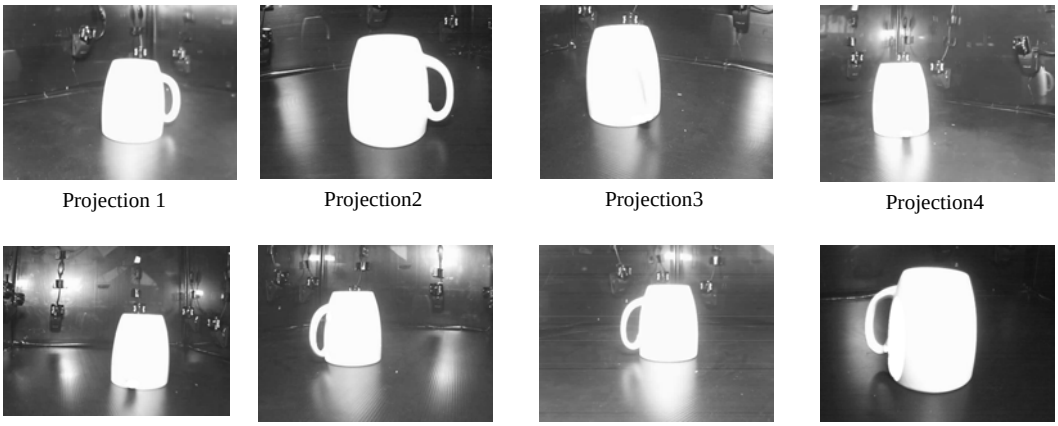

(a)

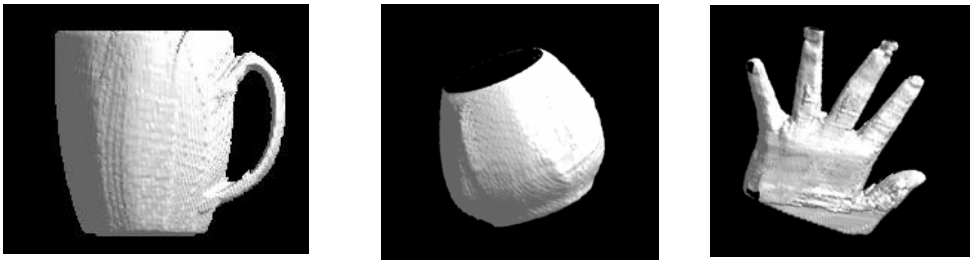

(b)

Figure 3 (a) Photograph Data of object taken from 12 cameras; (b) 3D model results

REFERENCES

[1] Barnard, S. T. and Fischler, M. A., " Computational Stereo", *ACM Computing Surveys,* vol. 14, no. 4, pp. 553-572, 1982.

[2] Dhond, U. R. and Aggarwal, J., " Structure from Stereo- A Review," *IEEE Trans. On Syst. Man. and Cybern*., vol. 19, no. 6, pp. 1489-1510, 1989.

[3] Bosch, T., Servagent, N., Chellali, R. and Lescure, M., "Three-Dimensional Object Construction Using a Self-mixing Type Scanning Laser Range Finder, *IEEE trans. Instrum. and Meas*., vol. 45, no. 5, pp. 1326-1329, 1998

[4] Beheim, G. and Frisch, K., " Range Finding using Frequency-modulated Laser Diode," *Appl. Opt.,* vol. 25, pp. 1439-1442, 1986.

[5] Okada, N., Kondo, E., Zha, H., Morooka, K. and Nagata, T., " 3-Dimensional Object Model Construction from Range Images Taken by a Range Finder on a Mobile Robot," *Proc. of the 1998 IEEE/RJS Int. Conf. Of Intell. Robot. and Sys*., pp. 1853-1858, 1998.

[6] Sato, Y., Hattori, K. and Otsuki, M., "Real-time Handy Rangefinder Cubicscope," *Proc. Int. Conf. ICARCV'94*, vol. 2, pp. 1148-1152, 1994.

[7] Sasoni, G., Carocci, M. and Rodella, R., " Calibration and Performance Evaluation of 3-D Imaging Sensor Based on the Projection of Structured Light," *IEEE Trans. on Instrum. Meas*., vol. 49, no. 3, pp. 628-636, 2000.

[8] Meadows., D. M. , Johnson, W. O. and Allen. J. B., "Generation of Surface Contours by Moiré Pattern," *Appl. Opt.,* vol. 9,pp. 942-947, 1970.

[9] Krattenthaker, W., Mayer, K. J. and Duwe, H. P., " 3D-Surface Measurement with Coded Light Approach", *Proc. Öesterr. Arbeitsgem. MusterKennung*, vol. 12, pp. 103-1114, 1993.

[10] Sansoni, G., Carocci, M. and Rodella, R., "3D Vision based on the Combination of Gray Code and Phase Shift Light Projection: Analysis and Compensation of the Systematic Errors," *Appl. Opt*., vol. 36, pp. 6565-6573, 1999.

[11] Hu. G. and Stockman, G., " 3-D Surface Solution using Structured Light and Constraint Propagation", *IEEE. Trans. Pattern Anal. Machine Intell.,* vol. 11, no.4, pp. 390-402, 1989.

[12] Alitschuler, M. D., " The Numerical Stereo Camera", *Proc. Soc. Photo-Opt. Eng. Conf. 2-D Math. Perception*, SPIE, WA, vol. 283. 1981.

[13] Sato, K. and Inokuchu, S., " Three Dimensional Surface Measurement by Space Coding ranfeimaging", *Journal of Robotic Systems,* vol.2 no. 1, pp. 27-39, 1985.

[14] Boyer, K. L. and Kak, A. C., " Color-coded Structured Light gor Rapid active ranging, *IEEE. Trans. Pattern Anal. Machine Intell.,* vol. 9, no.1, pp. 14-28, 1987.

[15] Keldkamp, L. A., Davis, L. and Kress, K., "Practical Cone-Beam Algorithm," J. Opt.Soc.Am. 1, pp 612-619.

Production Planning and Scheduling Approach in a Supply Chain

R. Masuchun
Faculty of Engineering
King Mongkut's Institute of Technology Ladkrabang
Bangkok 10520, Thailand

***Abstract*- This paper presents a linear integer programming model to plan and schedule production in a supply chain. In general, capacity constraints and operating sequences are ignored when generating MRP leading to many problems such as infeasible production plan on the shop floor. The approach proposed simultaneously plans and schedules for production at the same time capacity constraints and operating sequences are in consideration. The objective function of the proposed model is for scheduling purpose that is to minimize the makespan and tardiness of an order. Planning such capacity constraints and operating sequences as well as Bill of Material (BOM) is taken into consideration through several constraints. Numerical results verify that this model can be used to generate feasible and optimal schedule.**

I. INTRODUCTION

Problems always take place on shop floor since MRP and shop floor schedule are not synchronized. MRP does not consider capacity constraints and operating sequences; hence, production cannot be succeeded as planned [1-4]. Some jobs on schedule cannot be completed since the capacity is not enough. On the contrary, jobs requiring short operating time but not on the schedule cannot be alternatively put into operation as well because materials required have not arrived. Neither problem can be solved by solely conventional MRP or classic shop floor scheduling techniques. Advanced planning and scheduling is the solution to take capacity constraints and operating sequences into account when planning. This paper proposes an approach to simultaneously plan and schedule for production at the same time capacity constraints and operating sequences are in consideration. To consider both planning and scheduling, the scheduling part is handled through the objective function of maximizing efficiency of shop floor. The planning part including capacity consideration, operating sequences, and BOM procured or produced are taken into account by several constraints.

II. LITERATURE REVIEW

Research on advanced planning and scheduling has emphasized on heuristic approaches [2-3], [5-7]. Other research on mathematical modeling approach can also be found [8-10]. In [8], the relationship among items was ignored; in [9], only 2-level BOM was considered; and in [10], only makespan was considered in the objective function.

III. PROBLEM DESCRIPTION

When customer places an order, a due-date is set. Each order can comprise of more than one type of product. Each product requires certain subassemblies to be assembled into one unit of product. Each subassembly can be further congregated from certain components. Each component can be furthermore divided into certain items and so on. Subassemblies, components, and items can be either procured from outside or produced in-house. Either way requires some times to acquire. Fig. 1 displays four-level BOM of product A. Final product A comprises of one unit of subassembly x and four units of subassembly y. Two units of component i and five units of component j are assembled into one unit of subassembly x while one unit of subassembly y requires three units of component m and one unit of component n. Furthermore, one unit of component m comprises of one unit of item p and 2 units of item q.

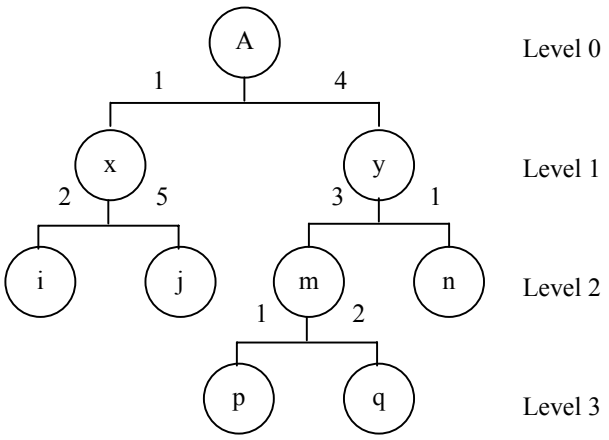

Figure 1. BOM of product A.

IV. MATHEMATICAL FORMULATION

Using the parameters and decision variables introduced in Table I, a linear integer programming model is constructed. The objective function is to maximize efficiency on the shop floor. In this paper, efficiency is defined in terms of both makespan and tardiness with constant multipliers of 5 and 2, respectively, as suggested in [11] so efficiency becomes a linear combination of makespan and tardiness. The objective function can be written as follows:

TABLE I
PARAMETERS AND DECISION VARIABLES

Parameters

O_{f,c,m_c} = Time required to obtain subassembly or component or item c belonging to final product f on the corresponding machine m_c

$n_{f,c}$ = Number of subassembly or component or item c required for one unit of final product f

$n_{f,f}$ = Number of final product f ordered

s_f = Arrival time of order consisting of final product f

DD_f = Due-date of final product f

M = A large positive constant

C(f) = Set of subassemblies or components or items required for final product or subassembly or component or item f

F = Set of final products

Decision Variables

t_{f,c,m_c} = Starting time of subassembly or component or item c belonging to final product f on the corresponding machine m_c

d_f = Completion time of order of final product f

y_i = 0 if $c_1 \in C(f_1)$ precedes $c_2 \in C(f_2)$ on the same machine $(m_{c_1} = m_{c_2})$; and 1 otherwise

ψ_f = 1 if $(d_f - DD_f) > 0$; and 0 otherwise

Objective function = Max (Efficiency)
= Min (Makespan and Tardiness)
= Min (5*Makespan + 2*Tardiness)

Makespan is the time taken to complete a set of final products and calculated as the time that the last final product in this group finished processing minus the time that the first item in this group starting processing. Tardiness is considered for each final product finished processing after its due-date and calculated as the difference between its finished time minus its due-date. A final product finishes processing before its due-date is not considered a tardy job and its tardiness is not included in the objective function. The objective function can be written as follow:

$$\text{Min } Z = \left[5 * \left\{ \underset{f}{\text{Max}}(d_f) - \underset{f}{\text{Min}}(S_f) \right\} + 2 * \left\{ \sum_f \psi_f (d_f - DD_f) \right\} \right].$$

Several constraints are needed to ensure an optimal and feasible schedule. The first and second constraints can be written as follow:

$$t_{f_1,c_1,m_{c_1}} + n_{f_1,f_1} * n_{f_1,c_1} * O_{f_1,c_1,m_{c_1}} \le t_{f_2,c_2,m_{c_2}} + y_i * M$$

or

$$t_{f_2,c_2,m_{c_2}} + n_{f_2,f_2} * n_{f_2,c_2} * O_{f_2,c_2,m_{c_2}} \le t_{f_1,c_1,m_{c_1}} + (1 - y_i) * M$$

$$\forall m_{c_1} = m_{c_2}, f_1 \in F, f_2 \in F,$$

$$c_1 \in C(f_1), c_2 \in C(f_2)$$

$$(f_1 = f_2) \rightarrow (c_1 \ne c_2)$$

Assuming that item c_1 belonging to final product f_1 and item c_2 belonging to final product f_2 demand processing on the same machine, only one of them can seize the machine and the other must wait until the machine is released. Ignoring the last terms in the first and second constraints, the first constraint ensures that item c_1 precedes item c_2 that is starting time of item c_1 plus the amount of total time required multiplied by total number needed must not exceed starting time of item c_2. On the contrary, the second constraint assures that item c_2 precedes item c_1 that is starting time of item c_2 plus the amount of total time required multiplied by total number needed must not exceed starting time of item c_1. For any given item c belonging to final product f, total number needed is calculated from number of item c required for one unit of final product f multiplied by number of final product f ordered. Since both constraints are conflicting and only one of them can be correct, they can be called either-or constraints. To be able to solve this model, a binary decision variable must be applied to each pair of either-or constraints. If this variable is 1, item c_2 precedes item c_1; otherwise item c_1 precedes item c_2.

The third constraint can be written as follow:

$$t_{f,c,m_c} + n_{f,f} * n_{f,c} * O_{f,c,m_c} \le t_{f,p,m_p}$$

$$\forall f, m_c, m_p, c \in C(p), p \in C(f)$$

For any given item c belonging to final product f and item p being the immediate parent of item c, the third constraint requires that item p cannot start processing until item c finishes its processing that is starting time of item c plus the amount of total time required multiplied by total number needed must not exceed starting time of item p. The last two constraints can be written as follow:

$$t_{f,f,m_f} + n_{f,f} * O_{f,f,m_f} \le d_f \qquad \forall f, m_f$$

$$t_{f,c,m_c} \geq s_f \qquad \forall f, m_c, c \in C(f)$$

The forth constraint defines the completion time of final product f. The fifth constraint makes sure that processing for any items assembled into final product f cannot be started until after order of final product f arrives.

The complete model can be rewritten as follow:

$$\text{Min } Z = \left[5 * \left\{ \underset{f}{\text{Max}}(d_f) - \underset{f}{\text{Min}}(S_f) \right\} + 2 * \left\{ \sum_f \psi_f (d_f - DD_f) \right\} \right]$$

subject to:

$$t_{f_1,c_1,m_{c_1}} + n_{f_1,f_1} * n_{f_1,c_1} * O_{f_1,c_1,m_{c_1}} \leq t_{f_2,c_2,m_{c_2}} + y_i * M$$

or

$$t_{f_2,c_2,m_{c_2}} + n_{f_2,f_2} * n_{f_2,c_2} * O_{f_2,c_2,m_{c_2}} \leq t_{f_1,c_1,m_{c_1}} + (1 - y_i) * M$$

$$\forall m_{c_1} = m_{c_2}, f_1 \in F, f_2 \in F,$$

$$c_1 \in C(f_1), c_2 \in C(f_2)$$

$$(f_1 = f_2) \rightarrow (c_1 \neq c_2)$$

$$t_{f,c,m_c} + n_{f,f} * n_{f,c} * O_{f,c,m_c} \leq t_{f,p,m_p}$$

$$\forall f, m_c, m_p, c \in C(p), p \in C(f)$$

$$t_{f,f,m_f} + n_{f,f} * O_{f,f,m_f} \leq d_f \qquad \forall f, m_f$$

$$t_{f,c,m_c} \geq s_f \qquad \forall f, m_c, c \in C(f)$$

$$t_{f,c,m_c} \geq 0 \qquad \forall f, m_c, c \in C(f)$$

$$y_i \in \{0,1\} \qquad \forall i.$$

V. Numerical Illustration

For an illustrative example, we consider two final products called product A and product B. Four-level BOM of product A and three-level of BOM of product B are shown in Figure 2. Each item requests a certain machine and requires certain amount of time for processing as shown in Table II. Values assigned to all other parameters required for solving this problem are shown in Table III. From table III, order 1 arrives at time 0 consisting of 150 units of product A with the due-date of 12000. At time 2, order 2 arrives demanding 100 units of product B with due-date of 11000.

The illustrative example was solved using the commercial software on a personnel computer. Starting time of each item is shown in Table IV and schedule on each machine is represented using Gantt chart as shown in Fig. 3.

TABLE II
Machine Requested and Time Required

Final Product	Item	Machine	Processing Time
A	r	M1	5
	s	M2	3
	p	M3	6
	q	M4	4
	x	M3	7
	y	M2	8
	A	M4	3
B	d	M1	5
	e	M2	4
	w	M4	9
	z	M3	6
	B	M1	4

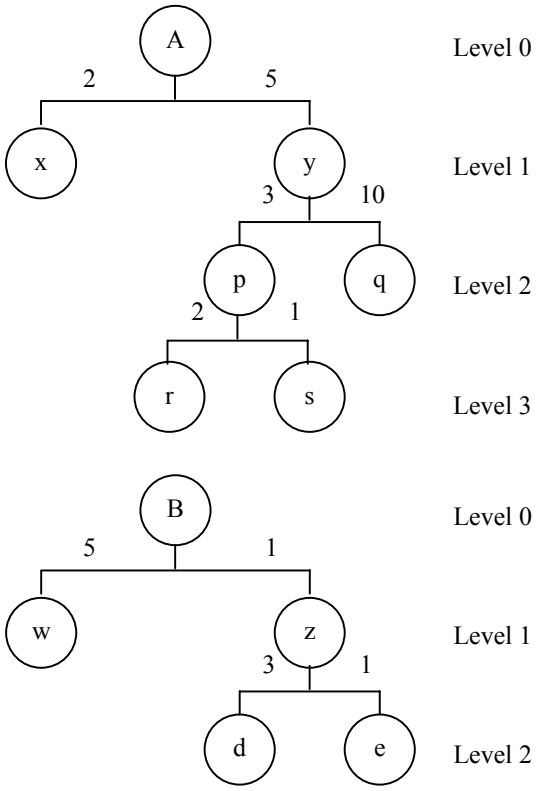

Figure 2. BOMs of product A and product B.

TABLE III
Values Assigned to all Other Parameters Required

Parameter	Value
M	100000
DD_A	12000
DD_B	11000
s_A	0
s_B	2
$n_{A,A}$	150
$n_{B,B}$	100

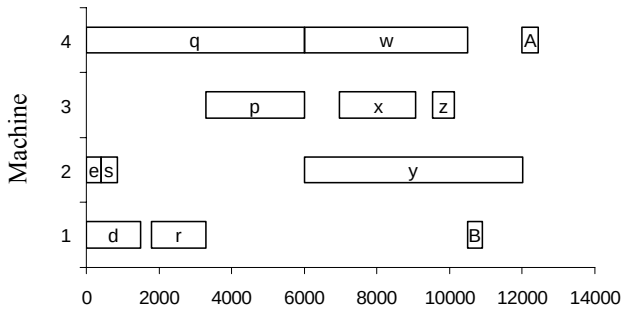

Figure 3. Schedule on each machine using Gantt chart.

TABLE IV
STARTING TIME OF EACH ITEM

Item	Value
R	1800
S	410
P	3300
Q	0
X	6960
Y	6000
A	12000
D	2
E	2
W	6000
Z	9540
B	10500

VI. CONCLUSION

In general, capacity constraints and operating sequences are ignored when generating MRP leading to many problems such as infeasible production plan on the shop floor. MRP and shop floor schedule should be synchronized. Planning and scheduling should be considered simultaneously. Solely conventional MRP or classic shop floor scheduling techniques cannot solve the problems. This paper presents a linear integer programming model to simultaneously plan and schedule for production at the same time capacity constraints and operating sequences are in consideration. The scheduling part is handled through the objective function of the proposed model that is to maximize efficiency of shop floor. The efficiency is defined in terms of makespan and tardiness. The planning part including capacity consideration, operating sequences, and BOM procured or produced are taken into account by several constraints. Numerical results verify that this model can be used to generate feasible and optimal schedule.

REFERENCES

[1] P.J. Billington, J.D. McClain, and L.J. Thomas, "Mathematical programming approaches to capacity-constrained MRP systems: Review, formulation and problem reduction," *Management Science*, vol. 29(10), pp. 1126-1141, 1983.

[2] C.C. Sum, and A.V. Hill, "A new framework for manufacturing planning and control systems," *Decision Sciences*, vol. 24(4), pp. 739-760, 1993.

[3] M. Taal, and J.C. Wortmann, "Integrating MRP and finite capacity planning," *Production Planning and Control*, vol. 8(3), pp. 245-254, 1997.

[4] S. VoB, and D.L. Woodruff, *Introduction to Computational Optimization Models for Production Planning in a Supply Chain*, Springer: Berlin, 2003.

[5] A.C. Bahl, and L.P. Ritzman, "An integrated model for master scheduling, lot sizing and capacity requirements planning," *Journal of the Operational Research Society*, vol. 35(5), pp. 389-399, 1984.

[6] B. Faaland, and T. Schmitt, "Scheduling tasks with due dats in a fabrication/assembly process," *Operations Research*, vol. 35(3), pp. 378-388, 1987.

[7] N.A.J. Hastings, P. Marshall, and R.J. Willis, "Schedule based MRP: An integrated approach to production scheduling and material requirements planning," *Journal of the Operational Research Society*, vol. 3(11), pp. 1021-1029, 1982.

[8] C. Dillenberger, L.F. Escudeero, A. Wollensak, and W. Zhang, "On practical resource allocation for production planning and scheduling with period overlapping setups," *European Journal of Operational Research*, vol. 75(2), pp. 275-286, 1994.

[9] R. Kolish, "Integration of assembly and fabrication for make-to-order production," *International Journal of Production Economics*, vol. 38(3), pp. 287-306, 2000.

[10] C. Moon, J.S. Kim, and M. Gen, "Advanced planning and scheduling based on precedence and resource constraints for e-plant chains," *International Journal of Production Research*, vol. 42(15), pp. 2941-2955, 2004.

[11] H. Ishibuchi, and T. Murata, "A multi-objective Genetic Local Search algorithm and its application to flowshop scheduling," *IEEE Transactions on Systems, Man, and Cybernetics-Part C: Applications and Reviews*, vol. 28(3), pp. 392-403, 1998.

Distributed Context Aware System for Travel Time Estimation Based on Cellular Probes in Metropolitan Environment

Panraphee Raphiphan, Arkady Zaslavsky
Caufield School of Information Technology,
Monash University
900 Dandenong Rd, Caulfield East, VIC 3145, Australia
{Panraphee.Raphiphan, Arkady.Zaslavsky}
@infotech.monash.edu.au

Wasan Pattara-Atikom, Passakon Prathombutr
National Electronics and Computer Technology Center
112 Thailand Science Park, Phahon Yothin Rd,
Pathumthani, 12120, Thailand
{wasan, prathom}@nectec.or.th

***Abstract*- Travel time estimation is an important component of Intelligent Transportation System (ITS). Many techniques for estimating travel time on various routes based on different types of sensors were proposed. In the past, stationary sensors were more popular, but they came with inflexibility, extra investment, and disruption to traffic flow during installation and maintenance. Global Positioning System (GPS) devices can also be used as mobile sensors but the signal penetration can be limited in the city environment. In this paper, we propose architecture of a context aware system for travel time estimation based on cellular probes in city environment. A cellular probe technique is our preference since necessary infrastructure is already in place without the weaknesses of stationary sensor techniques and GPS devices. The context analysis module in our system helps eliminate unrelated cellular probes from input data. Traffic data delivery methods are also discussed. Our system is very helpful for routes selection especially in the metropolitan area. The architecture of our system is open, flexible, extensible, and it can develop an evolutionary.**

I. INTRODUCTION

Travel time information is necessary for the journey planning and routes selection especially in the metropolitan area where people are interested in knowing time from an origin to the destination to plan a trip ahead. Travel time estimation is one important function in ITS.

Different approaches deployed various types of sensors for travel time estimation. A sensor is the hardware with assisted software that detects vehicles and converts the information into traffic flow data. Sensors that act as traffic data collectors can be stationary sensors and mobile sensors. We can categorize stationary sensors into intrusive detectors (installed in-roadway) and non-intrusive detectors (installed above roadway or sideline).

Intrusive detectors, such as inductive loop detectors (ILDs), have been used for several years to send traffic data to the traffic operators. However, this technology requires disruption to traffic flow during installation and maintenance, high failure rates in certain conditions, and inflexibility. Using non-intrusive detectors still lead to requirement of extra equipments installation just like the intrusive detectors. This is a time consuming task and needs extra investment. Deploying mobile sensors seems to be more flexible especially the cellular phone since the necessary infrastructures already exist and there is no disruption to traffic flow during installation and maintenance. In addition, mobile users are distributed all over the city, the number of mobile users is increasing day by day, and the problem of signal penetration is less than GPS in city environment.

To deploy cellular probe in travel time estimation, specifying valid cellular probes as samples is a primary challenge. There can be a lot of cellular phones that are un-related to the road traffic (e.g. mobile phone of pedestrians, in offices, in shopping mall, etc.) included in our input data set. Based on our literature review, some researches use cellular probes as traffic data originator, but very few of them offer the method of selecting valid samples in city environment and the majority of them do not apply the concept of context awareness to their systems.

"The context is any information that can be used to characterize the situation of an entity."[15] Almost any information available at the time of interaction can be classified as context. Context can include information such as identity, location, speed, acceleration, time of the day, date, season, temperature, people that are nearby, activities (e.g. walking, running), and schedules [19]. A system is context aware if it can extract, interpret and use context and adapt its functionality to the current context.

The public awareness of the actual traffic situation is very useful. It can assist the travelers in their route selection. Thus we design the context aware system for travel time estimation based on cellular information which can report the actual travel time through one of information representation methods.

Unlike other stationary sensor techniques, cellular phones are not designed to be the traffic data probes. Thus, additional works must be done to eliminate unrelated data based on context awareness concept. With our context analysis module, classifying related and unrelated cellular probes for further actual travel time calculation is possible.

This paper is divided into 4 parts. Part II reviews the existing travel time estimation techniques. Part III describes the

architecture and explanation of our system while the conclusion and future research can be found in part IV.

II. Travel Time Estimation Techniques

A sensor is a device with assisted software that detects vehicles and converts the information into traffic flow data. A sensor is an important component for the travel time or traffic condition estimation applications [17]. Different approaches applied various types of sensors as categorized in table1 [1, 2, 3, 4, 5, 7, 8, 9, 13]. Many travel time estimation algorithms were proposed based on each type of sensors or even data fusion algorithms for data from more than one type of sensors [18]. Some approaches apply various well known mathematic models in their algorithms.

TABLE 1
Examples of Sensor Technologies Used in Travel Time Estimation

Stationary Sensors	*Mobile Sensors*	*Mix Sensors*
Inductive Loop, Camera/ Video Image Processing, Microwave Radar, Passive and Active Infrared Devices, Ultrasonic, Passive Acoustic, Weight-in-Motion Detector, Magnetic Detector, Pneumatic Road Tubes, Piezoelectric Detector	Cellular Phone, GPS , Mobile devices equipped with video camera	Loop Detector + GPS Loop Detector + AVL

Most of stationary sensor techniques require installation of fixed infrastructure and dedicated instruments. For instance, video cameras incorporated with image processing algorithms to provide traffic flow information have a limitation if the weather condition is low visibility.

Mobile sensor techniques for traffic data collection have been studied lately. A probe vehicle and remote sensing method were primarily studied. Technologies in probe vehicle approaches include GPS, cellular phones, Automatic Vehicle Identification (AVI) and Automatic Vehicle Location (AVL). A remote sensing technology relies on satellite images to extract the traffic information. For more information of sensors technologies for ITS, readers can find in [16] and [17].

Satellite images associated with image processing can also provide the traffic data, but the same problem as using video camera or camera applied which is limitation on low visibility. In addition, cost of using satellite is quite high.

Cellular Phones as Probes

As the geo-location technology was developed, vehicle probes with cellular phones become attractive for many research groups. Cellular phone location tracking has been brought up to discuss as one part of the travel time estimation based on cellular information by many projects. The tracking data can come from either mobile phone equipped with GPS receiver, using Time Advance (TA), or triangulation method [2, 6]. However, the triangulation cannot tell the location of the phone within just a few meters [10]. Accuracy of a cellular geo-location technique remains as the challenge. Furthermore, tracking mobile phone position can lead to a privacy violation. This problem can be avoided by ignoring the data immediately after it is used and mobile phone numbers encryption so that it is not possible to know which phone made which trip [11]. In this section some examples of travel time estimation projects that rely on cellular probes are described.

In 2001, Ygnace and Drane [1] described the methodology and preliminary results from their study. The situation and environment were set up based on assumption that the location of cellular phones on the road are known by any of positioning techniques without proposing any methods to obtain positions.. The result from simulation tells that 5% of the total vehicle population per link is sufficient to allow precise estimation of travel time. This project is called INRETS which is the pilot of project named STRIP [2].

For STRIP project, the experiment was done on a stretch of 120 km of very crowded motorway. The distance between the mobile phone and the base station was obtained from the Time Advance (TA) when engaging in the phone call. The positions of mobile phones can then be calculated. All positions calculated to be out of threshold number centered on the motorway axis were discarded. Then a neuronal processing evaluates whether the mobile phone is located on the motorway or not, if yes, on which lane. The database of all time stamped locations of all mobile phones traveling on the motorway is used for travel time calculation [2]. Using TA to calculate positions must base on active cellular phones [6]. However, the possibility to have mobile phones in idle mode is higher.

Schneider and Mrakotsky [3] proposed a travel time estimation method by obtaining the coordinate of the cell transition of a mobile phone from GPS. This method is quite simple, but it needs vehicles carrying GPS receivers and mobile phones with special software installed. This can be a burden**.** The GPS coordinates gained at the moment of cell transition are registered via mobile phone and stored in the database. With the difference of the time stamp at cell transitions and the distance on the road between two cell transitions, the average speed was calculated.

It is noticeable that very few of cellular probe approaches offer methods to select valid samples in metropolitan areas. In addition, the majority of them do not apply context awareness concept to the systems.

III. Context Aware System for Travel Time Estimation Based on Cellular Probes in Metropolitan

Travel time information is an integral part of Intelligent Transportation System (ITS) especially for the journey planning and route selection. Sensors are necessary for making this task successful. Many stationary sensors have been used as traffic data collectors, but they come with inflexibility and requirement of extra equipments installation. Some of them come with disruption to traffic flow and some of them come with time consuming for installation. Mobile sensor can alleviate these obstacles, but some of them create other limitations as stated in part II. GPS has limitation in signal penetration in the city while cellular probe has fewer problems.

Satellite images can not perform well when the weather condition is not good such as when it is foggy or raining.

Calculating travel time information based on cellular probes has become an interest. Most projects have done experiment without offering solutions for selecting relevant cellular probes to the traffic. Nevertheless, selecting valid samples (here are appropriate cellular probes) is very important in order to get an accurate result. Our system thus provides the solution to this problem. Fig.1 presents overall architecture of our project.

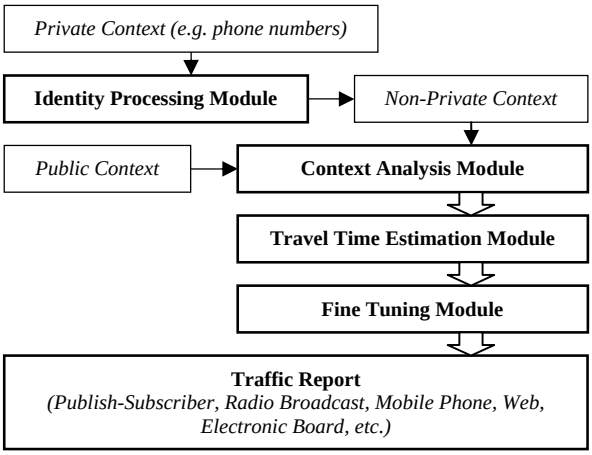

Figure 1. An architecture of a Distributed Context Aware System for Travel Time Estimation Based on Cellular Probes in Metropolitan Environment

The input of the system is context. Cellular phone locations, phone numbers, and base stations locations are examples of context attributes. Other context attributes are layout of the streets, building construction, events happening along the road, and type of cars as examples. For this project, some examples of context attributes are listed in Table 2. We aim to use minimum number of input context required, but provide the optimal, efficient, and accurate result.

To successfully deploy the system, the carrier's cooperation is important. The carrier who provides the cellular data can gain benefit from selling traffic data to mobile users. Anyhow, the carrier must strongly concern about each customer's privacy. Currently we cooperate with one of leading cellular phone operators in Thailand to provide us necessary data.

To track the cellular probes, the ID of each probe must be taken. The most convenient way is taking the phone number obtained from the mobile phone operator as the ID. However, the privacy consideration is important. This problem can be solved by converting a phone number into new unique number that can not tell what the original number is. Thus, to prevent our system from privacy violation, all "private context attributes" (e.g. phone numbers, names of mobile users, etc.) must get through the "identity processing module" which includes a one-way hashing function. Then they become non-private context attributes. For instance, an input phone number is hashed to another identity called "probe ID" that can represent each probe for a tracking purpose. With a one-way hashing function, after non-private context attributes are gotten and the input private context attributes are discarded, it is impossible to track back to get the original input. Locations of cellular phones in mobile networks can be obtained by using TA, triangulation, or detecting handover zone for instance [6].

TABLE 2
EXAMPLES OF CONTEXT ATTRIBUTES AND POSSIBLE USAGE

Context attributes	*Possible use of context attributes*
Location of mobile phones	- For cellular probe tracking - To help classifying related and un-related cellular probe to the traffic - For analyzing concentration and the location of groups of users
Phone number	- To generate the probe ID for tracking purpose - Can classify pre-paid and post-paid phone (for further analysis)
Location of base stations	- Can be used for map-matching - For analyzing and associate the mobile user within coverage area.
Layout of streets, buildings construction	- Can be used to compare with location of base station for our analysis. - Can be used to populate the geographic location and can provide navigation functionality.
Type of vehicles	- To help analyzing the density of cellular probe in particular location. (e.g. many passengers in buses, 1 driver in individual car)
Mobile users profile	- To help analyzing type of mobile users (e.g. bus driver, car driver, taxi driver) - To help personalizing the traffic report.
Time and Date	- To help analyzing the traffic congestion in particular location (e.g. high traffic in rush hour of the day, light traffic in the city during long weekend)
Weather condition	- To help analyzing the traffic congestion in particular location

Furthermore, the sample size of cellular probe is also one of important concerns. It was proved that 5% of the total vehicle population per link is sufficient to allow the precise estimation of travel time in the link. However, increasing number of sample size will result in more accuracy result [1].

Specifying valid cellular probes to be our samples while there are a lot of cellular phones that are un-related to the road traffic mixed in the input data set is a problem to be addressed. Thus, our system includes a context analysis module.

Context attributes are input of the "context analysis module" which consists of algorithm to analyze all context. Once context attributes go through the "context analysis module", we can tell either that cellular probe belongs to drivers of vehicles, pedestrians, or else. These can be told from situation of each probe extracted from input context attributes. Then we can choose valid samples to provide the accurate input for the next module, "travel time estimation module".

The travel time estimation module calculates the travel time based on travel time estimation algorithm. Travel time calculation can be as simple as taking the time-stamp difference of a tracked cellular probe between one reference location and another.

After obtaining the travel time information, the traffic report can be generated. There are many options to deliver traffic information to users. Traffic information can be broadcasted

through radio wave. Delivery through web application is another option such as in [3], but it might be inconvenient for drivers to access the web while they are already on the roads. Traffic information can also be presented on electronic boards mounted along the roads or at intersections, but data representation must be taking into account along with location selection to install electronic boards for the best perception. Colors maybe used to represent the traffic condition such as red, yellow, and green to specify the volume of traffic in each road. For example, [12] use color painted on a traffic map to represent traffic information based on pre-specified occupancy thresholds.

Moreover, the "publish/subscriber" technique may be chosen. Subscribed users may receive the traffic information through SMS on his/her mobile phone(s). This method is convenient for users, but well design of data representation is also needed. In addition, context awareness may be applied to help deliver appropriate information to each user based on his/her current location, his/her preference, his/her profile and user intent to support full pervasive computing environment.

Our travel time report will be very useful for journey planning or route selection which is quite important for drivers in the city. The obtained actual travel time information can also become useful parameter for other applications such as time of journey prediction.

IV. CONCLUSION

Travel time information is very important for the journey planning and route choice decision especially in the metropolitan area where people are interested in knowing the traffic condition along the route they are heading. This paper has proposed the architecture for estimating the actual travel time based on context and cellular probe. The cellular probes are chosen as our sensors because all necessary infrastructures are already in place thus there is no extra investment. Also there is no disruption to traffic flow during installation and maintenance. However, selecting valid samples (here are cellular probes) is a challenge. We apply concept of context awareness to the system to eliminate unrelated cellular probes from input data. Our system can develop an evolutionary. Building the prototype system is in progress and the prototype will be tested in Bangkok using cellular information provided from one of the major cellular phone service providers in Thailand. Employing our system to metropolitan area such as Bangkok, known as a city with serious traffic congestion problem, will help drivers make better decision to reach parts of the city. The actual travel time report can also help improving the traffic management and control. Thus the traffic congestion can be alleviated.

Our system can be extended to report other traffic information in addition to the travel time information. More modules can be added to make the system more functionality. Our system can also be expanded to include the traffic prediction based on any prediction algorithms in the future. Thus it is extensible, open and flexible.

ACKNOWLEDGMENT

Support from the National Electronics and Computer Technology Center (NECTEC) is thankfully acknowledged.

REFERENCES

[1] Jean-Lue Ygnace and Chris Drane, "Cellular Telecommunication and Transportation Convergence: a Case Study of a Research Conducted in California and in France on Cellular Position Techniques and Transportation Issues," *Intelligent Transportation Systems, Oakland*, pp.16-22, August 2001.

[2] J.-G. Remy, "Computing travel time estimates from GSM signaling messages: the STRIP project," *Proceeding of Intelligent Transportation Systems, Oakland*, 2001.

[3] W. Schneider and E. Mrakotsky, "Mobile Phones as a Basis for Traffic State Information," *Proceeding of Intelligent Transportation Systems*, 2005.

[4] Liang Zou, Jian-Min Xu, and Ling-Xiang Zhu, "Arterial speed studies with taxi equipped with global positioning receivers as probe vehicle," *Proceeding of Wireless Communications, Networking and Mobile Computing*, 2005.

[5] Yanying Li and M. McDonald, "Link travel time estimation using single GPS equipped probe vehicle," *IEEE 5th International Conference on Intelligent Transportation Systems*, September 2002.

[6] G. Rose**,** "Mobile Phones as Traffic Probes: Practices, Prospects and Issues," *Transport Reviews*, vol. 26, no. 3, pp.275-291, May 2006.

[7] B. Coifman, M. McCord, R.G. Mishalani, M. Iswalt and Y. Ji, "Roadway traffic monitoring from an unmanned aerial vehicle," *IEE Proc. Intell. Transp. Syst.* Vol.153, No. 1, March 2006.

[8] S. Lorkowski, P. Mieth, K.-U. Thiessenhusen, D. Chauhan, B. Passfeld, and R.-P. Schäfer, "Towards Area-Wide Traffic Monitoring-Applications Derived from Probe Vehicle Data," *Proc. of 8th International Conference on Applications of Advanced Technologies in Transportation Engineering, Beijing*, May 2004.

[9] K. Choi and Y. Chung, "A Data Fusion Algorithm for Estimating Link Travel Time," *Intelligent Transportation Systems*, Vol. 7, No. 3-4, pp.235-260, 2002.

[10] W.D.Jones, "Forecasting Traffic Flow," *IEEE Spectrum*, Vol. 38, Issue 1, pp. 90-91, 2001.

[11] J. White, J. Quick, and P. Philippou, **"**The use of mobile phone location data for traffic information**,"** *Road Transport Information and Control 2004*. pp. 321- 325, 2004**.**

[12] F.W. Cathey and D.J. Dailey, "Implementation of Traffic Management Using Transit Probes," *Proceedings of the 8th International IEEE Conference on Intelligent Transportation System*s, pp. 243- 247, 2005.

[13] D.J. Dailey and F.W. Cathey, "Virtual Speed Sensors Using Transit Vehicles as Traffic Probes," *Proc. of the IEEE 5th International Conference on Intelligent Transportation Systems*, pp.560-565, 2002.

[14] M. Satyanarayanan, "Pervasive computing: vision and challenges," *IEEE Personal Communications*, Vol. 8, Issue 4, pp.10-17, August 2001.

[15] A. K. Dey and G. D. Abowd, "*Toward a better understanding of context and context-awareness,*" GVU Technical Report GIT-gvu-99-22, College of Computing, Georgia Institute of Technology, 1999.

[16] Peter T. Martin, Yuqi Feng, and Xiaodong Wang, "Detector Technology Evaluation," http://www.mountain-plains.org/pubs/html/mpc-03-154/, visited on Jan. 15 2007.

[17] L. A. Klein, *Sensor Technologies and Data Requirements for ITS*, Boston: Artech House, 2001.

[18] A. Padovitz, A. Zaslavsky, S. W. Loke, "A Unifying Model for Representing and Reasoning About Context under Uncertainty," *11th International Conference on Information Processing and Management of Uncertainty in Knowledge-Based Systems (IPMU)*, France, July 2006.

[19] Mari Korkea-aho, "Context-Aware Applications Survey," http://users.tkk.fi/~mkorkeaa/doc/context-aware.html, visited on Jan. 16, 2007.

Ontology Development: An Integrated Engineering Approach

Paola Di Maio
School of Information Technology
Mae Fah Luang University, Chiang Rai Thailand
Paola{at}mfu.ac.th

Abstract - Ontology engineering (OE) is becoming increasingly critical to systems development, and more and more observers, researchers and scholars from all disciplines are learning to appreciate its practical importance and underlying relevance to knowledge based systems development. Yet the current understanding of ontology, especially regarding development and application of standard, methods and practices, according to recent research, does not meet the growing challenges arising from the complexity of increasingly dynamic environments. This paper, on the basis of recent research findings , analyzes ontology development activities as scheduled in the most commonly adopted ontology engineering methodologies (OEM), and identifies weaknesses in the application of certain 'standard' activities - such as requirements engineering, user centered engineering and knowledge engineering - which have become central to modern engineering practices overall. It concludes by suggesting that such activities can address at least in part some of the weaknesses in current OEM, and could be critical to the effective ontology development, therefore it advocates the integration of additional perspectives in the development of future OE methodologies.

I. INTRODUCTION

As we move from data and information centric architectures to knowledge based systems and economies, understanding and implementing ontology is becoming increasingly important for all stakeholders. An ontology is what delimits and formalizes the 'knowledge universe' underlying any information system. Gruber's early definition of an ontology [1] as "a formal specification of a conceptualization" is widely accepted, although novel and more specific interpretations of the word 'ontology' are being developed by the day to fit the variety of scopes and applications that ontology serves in different communities. Despite its importance and growing popularity, Ontology is still a domain largely dominated by theorists and academics.
Some of the weaknesses in existing instruments, demonstrated in recent research [2], need to be resolved in order for OEM to support participation of wider individuals and communities in building, maintaining and adopting conceptual and semantic frameworks.

Background
This paper takes into account the established trend towards 'agile' development practices [19] according to which planning and design activities in any system development are better undertaken iteratively and with ongoing input from users. It also takes into account the shift towards web based 'collaboration' and SOA architectures, and the need for shared, flexible and participatory development processes. It identifies key areas for improvement of existing OEM by suggesting the adoption of an integrated approach that incorporates approaches and best practices from other directly related and established engineering methods.

Problem Statement
Recent research [3], as well as empirical evidence gathered from direct observations of related work groups, shows that existing ontology engineering methodologies are not adequately supporting the growing challenges of ontology development in complex, dynamic environments. While novel methodologies are being proposed [4] that specifically attempt to support collaborative knowledge acquisition [5], no methodology to date addresses the knowledge lifecycle requirements satisfactorily and reliably. Additionally, among the other activities that have not been explicitly and systematically address by existing OEM are Knowledge Abstraction, and the overall application of principles of User Centered design. We discuss briefly their relevance to OE in further sections.

Scope Of Paper
In analyzing key research findings in this area, including studies that carry out detailed evaluation of established OE methodologies [7], we identify activities that, irrespective from the chosen method, are underspecified in ontology lifecycle - namely requirements analysis (as opposed to requirements specification), knowledge abstraction, as an intermediate step between knowledge elicitation and representation, and generally limited application of user centered principles of design

II. FROM SOFTWARE TO KNOWLEDGE ENGINEERING

'Fit for purpose' software and knowledge based programs are the result of highly challenging and articulate development projects, where, given the complexities, the risk of failure to meet expected outcomes is very high [6]. In recent years, Software Engineering methodologies have specialized and become quite sophisticated and sometimes increasingly structured in order to systematically reduce such risks. Methodologies, (IEEE, 1990) are generally composed of processes, activities and tasks.
The focus of Ontology Engineering methodologies is the structuring and representation of domain knowledge underlying system development. They are still being experimented and researched, and they are not yet

'standardized'. Currently a shift is taking place from data centric systems towards 'open' knowledge based and semantic systems, thanks to fast advancements in web technologies. It is therefore becoming paramount that an explicit integration of methodologies also takes place, to support adequately the development of systems that are increasingly hybrid in nature, and that increasingly rely on knowledge, unstructured content, and a semantic layer.

III. ONTOLOGY ENGINEERING METHODOLOGIES

Ontology Engineering methodologies are adopted to support the development conceptual, semantic and reasoning models underlying robust and usable knowledge systems. However research demonstrates that such methodologies are not yet sufficiently developed to fully support the growing challenges of distributed cognitive processes in dynamic social and knowledge environments. In particular weaknesses have been identified in various areas including Knowledge Acquisition, as well as in areas relating to the Organizational and Technical processes of the methods. [2]

Typical activities in OE

OEM have evolved dramatically over the past ten years, since the first workshop on Ontological Engineering was held at the 12th European Conference on Artificial Intelligence in 1996. Known methodologies analyzed by literature [7], [8], are summarized in Table 1. Ontology Engineering activities vary in scope and focus [7] depending on the methodology, but they can broadly be grouped in the following categories :

- *Development* (feasibility, specification, conceptualization, formalization, implementation)
- *Support* (knowledge acquisition, evaluation, integration, merging, aligning, documentation, configuration
- *Management* (scheduling, control, quality assurance)

Such activities above are generally carried out simultaneously, or in different order depending different focus and perspective, of each methodology which privileges and proposes a different sequence and emphasis on certain activities and tasks, as it can be seen from the example in figures 2, 4, 5, 6.

The comparative study of the most commonly adopted OE methodologies concludes that given the wide diversity of ontology development strategies, each offer advantages and shortfalls, and none covers satisfactorily the entire spectrum of processes involved in ontology building. Indicatively, Methontology is identified as the method that provides the most accurate descriptions of each activity, and On-To-Knowledge methodology describes more activities than the other approaches. [7]

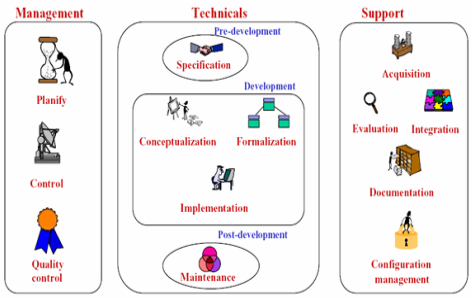

FIG 2 ACTIVITIES IN METHONTOLOGY METHOD

TABLE 1. ONTOLOGY ENGINEERING METHODOLOGIES

IDEF5
TOVE
Aspect theory
DODDLE (Domain Ontology rapiD DeveLopment Environment)
CLEPE/AFM
Cyc method
Uschold and King's
Gruninger and Fox's
KACTUS
METHONTOLOGY
SENSUS
ON-TO-KNOWLEDGE

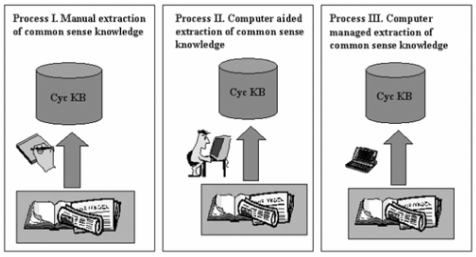

FIG 3 Processes in CYC Method

Among other shortcomings, OE methods overall, fail in varying degrees to adequately carry out essential activities such as requirements analysis, knowledge abstraction and fail to apply user centered design principles, and even when they do make a provision for such activities to be carried out, they are not necessarily undertaken at the right phase of the lifecycle, nor in sufficient detail. In Ontoknowledge for example [fig 4] and Methontology although there are explicit provision for 'requirements specification', there is not explicit provision for requirements analysis as a very distinct activities that should be carried out separately with distinct modalities (FIG 3) and end up with different deliverables, according to best practices [16], [17], [18]

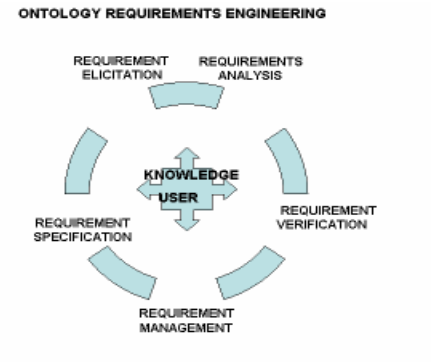

FIG 3

Similarly, 'knowledge conceptualization and representation' activities are bunched up in the same sub-process, while according to established knowledge engineering methodologies such as KADS, they are two very different activities that should be carried out separately in different phases of the knowledge lifecycle, resulting in different outputs [13]. The lack of in depth integration of different engineering perspective and approaches contributes to the weakness of the current OE methodologies, and contributes to limited accessibility and usability of knowledge and information currently being designed to be stored and exchanged on the web via commonly available browser based agents, thus inhibiting the full deployment of the vast application potential of the semantic web as intelligent agent.

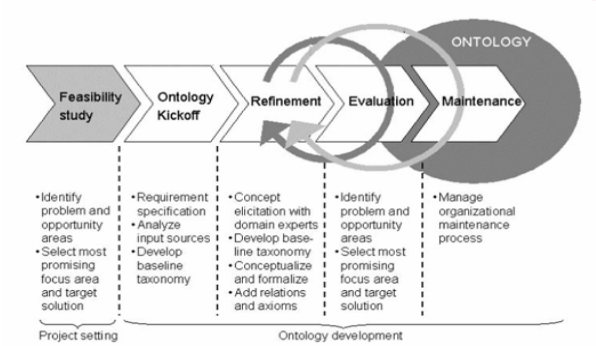

FIG 4 - Activities in Ontoknowledge Method

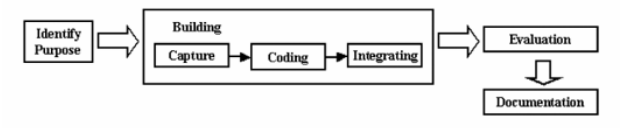

FIG 5 - Process in USHOLD KING Method

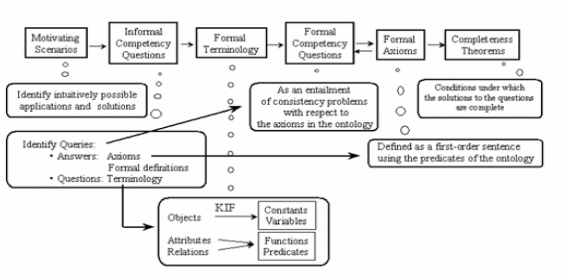

FIG 6 Processes in Gruninger and Fox Method

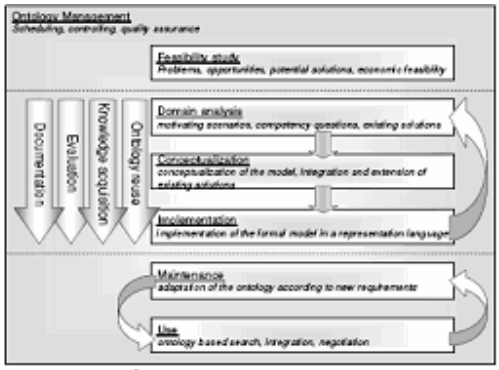

FIG 7 Ontology Engineering Activities
Source http://ontocom.ag-nbi.de/docs/odbase2006.pdf

Our comparative analysis of the processes, activities and techniques of recent studies [14], as well a empirical research and discussion in related workgroups, leads to the additional conclusion that:

1. Those methodologies which carry out requirement specification activities, do not have a sufficiently detailed, documented and structured 'requirements analysis' activity separately from the 'requirements specification' phase.
2. None of the methodology has a formal, iterative 'open consultation process' whereby all the stakeholders are requested to give feedback, and feedback is not scheduled as routine activity

None of the methodologies includes an intermediate process between knowledge acquisition (KA) activities and knowledge representation (KR), such as Knowledge Abstraction (Kab)

IV. RELATED ENGINEERING METHODS

After extensive review of related literature and studies, as well as direct observation and participation in related communities of practices [9], we conclude that at least three additional perspectives and approaches should be included in novel OE methodologies currently being developed:

Requirements Engineering (RE)
Requirements Engineering [10] is a key practice, although often underestimated and summarily carried out, especially

in ontology design. There are different kinds of requirements: operational, user, functional and non functional and each deserves to be developed systematically and independently from each other, and to be modeled into an Ontology Specification. RE consists of a set of detailed activities that should be undertaken in more structured form by OEM, namely requirements development (elicitation, analysis, specification, and verification/validation), and requirements management (fig 3). Getting the requirements wrong is likely to deliver unexpected limitations of the end result.

Knowledge Engineering (KE)

Knowledge engineering main contribution to modern development practices are methodologies that contain activities and techniques for the elicitation, analysis and structuring of knowledge. Although many such activities are common to other engineering practices, such as SE, KE is based on unique activities which are proper only to the 'Knowledge lifecycle', namely, knowledge acquisition, knowledge modeling, abstraction and representation. KADS [13], the best known structured methodology for knowledge engineering, formally includes systematic activities for knowledge analysis and design at different levels of abstraction. In recent discussions among peers in the ontology and related W3 workgroups [9], the lack of a properly defined and standardized Knowledge Abstraction [14] layer in semantic web technologies has emerged as a potential hindrance to the facilitation of knowledge dissemination and access on the web. A workgroup has been recently started with the purpose of analyzing the requirement for knowledge abstraction and making an explicit recommendation to the W3 consortium to develop and promote a Knowledge Abstraction standard as part of their knowledge exchange protocols.

User Centered Engineering (UE)

User centered design methods have become increasingly adopted in modern engineering and design, not only for software, but any type of product development as well [11] In this approach, 'User requirements' are central to the system lifecycle, and user involvement is 'wired' into the development process via the constant elicitation of needs, desires and considering all the feedback as input to the development cycle. Overall 'principles of good design' according to this approach [12] include simplifying the structure of tasks, increasing visibility of conceptual design and system logic, valuing user feedback and provisions to handle errors constructively. Ontology Engineering methodologies seem to lack a well defined UE perspective, although from informal exchanges with peers it appears that research in this directly is currently being undertaken.

V. CONCLUSION AND RECOMMENDATIONS

In order for Ontology Engineering methodologies to evolve to serve modern and future systems development, they will benefit from the integration of activities and tasks that have consolidated from years of practice in other related engineering disciplines, such as SE, KE and UE. In this paper we identify Requirements Analysis, Knowledge Abstraction and User Centered Design activities and principles as candidates for such inclusion. It is recommended that a more systematic evaluation is undertaken with a view to standardize their formal integration in OEM, and gain support from W3 consortium. Future research in this area should focus on impact and modalities of such systematic integration of the above men into one over arching, portable and lightweight ontology engineering framework.

VI. REFERENCES

[1] Gruber, T.R. (1995). Toward Principles for the Design of Ontologies Used for Knowledge Sharing, Int. Journal of Human-Computer Studies, Vol. 43, pp.907-928.

[2] Paslaru Bontas Simperl and Tempich. Ontology Engineering: A Reality Check. ontocom.ag-nbi.de/docs/odbase2006.pdf

[3] Holger Knublauch. Ontology-Driven Software Development Position Paper for the Workshop on Semantic Web Enabled Software Engineering,,Www.mel.nist.gov/msid/conferences/SWESE/repository/13on_agile_methods_and_oda.pdf

[4] 1st International Workshop on Semantic Technologies in Collaborative Applications STICA 06 - 15th IEEE International Workshops on Enabling Technologies: Infrastructures for Collaborative Enterprises (WETICE-2006) http://www.ag-nbi.de/conf/STICA06

[5] International Semantic Web Conference First International Workshop on Modular Ontologies http://www.cild.iastate.edu/events/womo.html

[6] Taxonomy Of Software Development Risk - http://www.stsc.hill.af.mil/resources/tech_docs/gsam3/chap6.pdf

[7] Gomez-Perez, Fernandez-Lopez, Corcho. Ontological Engineering: With Examples From the Areas of Knowledge Management, E-commerce and the Semantic Web Advanced Information and Knowledge Processing, 1610-3947 Springer Science & Business Media, 2004.

[8] Mizoguchi, Ikeda. Towards Ontology Engineering.The Institute of Scientific and Industrial Research, Osaka University, 567 Japan www.ei.sanken.osaka-u.ac.jp/pub/miz/miz-onteng.pdf

[9] Ontolog, ontolog.cim3.net

[10] Requirements Engineering A Good Practice Guide ww.comp.lancs.ac.uk/computing/resources/re-gpg/

[11] ttp://ieeexplore.ieee.org/iel5/8908/28166/01260240.pdf

[12] D. A. Norman's Principles for Transforming Difficult Tasks into Simple Ones .eecs.berkeley.edu

[13] KADS www.cs.vu.nl/~guus/papers/Schreiber92a.html

[14] Knowledge abstraction, Russell J. Abbott, Communications of the ACM archive Volume 30 , Issue 8 (August 1987)

[15] Pinto Martins, How Can Ontologies Be Built Springer-Verlag London 2004 Knowledge and Information Systems (2004) 6: 441–464

[16] "Requirements Analysis," Richard Thayer, SMC 10/97 Version 2, 1997

[17] "IEEE Guide for Software Requirements Specification," IEEE 830-1984

[18] "Software Requirements:Objects, Functions, and States", Prentice Hall, 1993

[19] Michael Hirsch, Moving from a Plan Driven Culture to Agile Development

[20] Conference on Software Engineering May 2005 http://www.cs.wustl.edu/icse05/ConferenceProgram/InvitedTalks/Hirsch.pdf

Note regarding illustrations: all images have been sourced and reproduced from the respective works cited above, except for table 1 and fig 3, which represent original content from this research.

A Satellite Collision Analysis During Orbit Deployment

Manop Aorpimai and Peerawat Artitthang
Department of Control and Instrumentation Engineering
Mahanakorn University of Technology, Bangkok, Thailand 10530

***Abstract*—This paper presents a relative motion analysis of satellites after separation from the same launch vehicle. It poses a more instructive geometry of the motion profile than conventional methods. Collision between spacecraft after a few orbital periods is theoretically possible, although they are separated at different time, and into different orbits. A novel criterion for collision-free orbit deployment is proposed, where the incremental velocities can be assigned for all satellites in a formation system with a safety margin guaranteed.**

I. INTRODUCTION

Recently, the risk of collision in space has been of high concern, especially for satellites orbiting in Low-Earth Orbit ($<1,000\,km$ altitude) where most space missions are being performed very actively. With a velocity of several kilometers per second, a millimeter-across debris can seriously harm an expensive satellite or even a space-walking man. A number of researchers have systematically studied the probability of the collision between satellites and space debris, both natural and man-made ones. Rigorous statistical mathematics are employed to predict the chance for collisions [1-3]. A similar approach has been applied for satellite and space tether collision prediction and avoidance [4].

There is another scenario that has a potential to cause a catastrophe in space, namely, the collision between spacecraft during their orbit deployment. The chance for collision is trivial when the number of satellites in the system is small, and little attention has been paid to this in the past. For future missions, however, a system comprised of multiple satellites coordinated in a close formation will become more common, as it is believed to help increase the system flexibility as well as reducing the total cost of the mission.

The deployment of these satellites from a single rocket (see, for example, figure 1) can potentially cause collision between spacecraft. Unfortunately, very few works have been reported on the analysis of the collision in this case, and none of them covers all possibilities for collision. The deployment strategy for multiple secondary payloads on the MLV-05 mission [5], for example, pays attention only on the along-track component of the incremental velocity vector (ΔV) at the deployment instance. It assumes that the radial and cross-track component will not affect the orbital period and hence the chance for collision. Ramanan [6] proposed a collision-free deployment strategy. His first assumption is that two satellites, S_1 and S_2, which are separated at the same time with different velocities will come back to exactly rendezvous again if the orbital period $P_1 = nP_2$ where $n = l$ and $l = 1,2,3,...$ and when $n = 1/k$ where $k = 1,2,3,...$ Therefore, his proposed strategy is simply to avoid such condition.

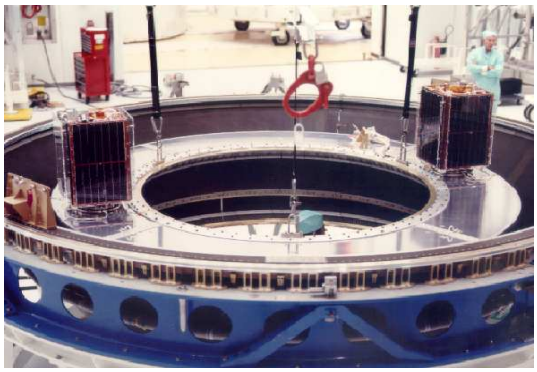

Figure 1. Multiple small satellites attached on the same launch vehicle

In this paper, it will be pointed out that, whatever the differential orbital period between satellites is, their relative motion which is closely related to both along-track and radial velocity components, can bring the satellites to a dangerously close approach. The closed-form solution proposed in this paper gives a more instructive description of the relative motion between satellites than the classic Clohessy-Wiltshire equations [7]. It then leads to a useful criterion for collision-free orbit deployment.

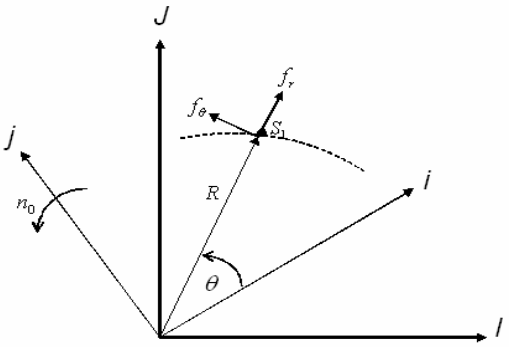

Figure 2. Coordinate System

II. ORBITAL DYNAMICS

Consider the motion of a satellite in the coordinate system shown in figure 2. (I, J) is an inertial frame with the origin at the centre of the Earth, and (i, j) is a rotating coordinate system which rotates with a constant angular rate n_0.

The equations of in-plane motion of the satellite viewed from the rotating coordinates can be derived as [8]

$$\ddot{R} - R\left(n_0 + \dot{\theta}\right)^2 + \frac{\mu}{R^2} = f_r \tag{1}$$

$$R\ddot{\theta} - 2\dot{R}\left(n_0 + \dot{\theta}\right)^2 = f_\theta \tag{2}$$

where R and θ are radius and phase of the satellite measured in the rotating frame, and f_r and f_θ are accelerations applied along the radial and along-track directions, respectively. μ is the gravitational parameter which is defined through $\mu \cong R_0^3 n_0^2$, where R_0 and n_0 are the orbital radius and frequency of a reference circular orbit, respectively. If we assume that the orbital radius of a satellite is in the vicinity of R_0, i.e. $r \ll R_0$, equations (1) and (2) can be linearised to first order approximation in r to give

$$\ddot{r} - 2R_0 n_0 \dot{\theta} - 3n_0^2 r = f_r \tag{3}$$

$$\ddot{\theta} + 2n_0 \dot{r} = f_\theta \tag{4}$$

If the applied accelerations are constant, both along the radial and along-track directions, equations (3) and (4) can be integrated to give

$$r = \left(\frac{f_r}{n_0^2} + \frac{2f_\theta t}{n_0}\right) + \Delta a_0 - R_0 e_0 \cos\left(n_0 t - \omega_0\right) \tag{5}$$

$$\begin{aligned}\theta = &-\left(\frac{f_r t}{R_0 n_0} + \frac{3}{2}\frac{f_\theta t^2}{R_0}\right) - \frac{3}{2}\frac{n_0}{R_0}\Delta a_0 t + 2e_0 \sin\left(n_0 t - \omega_0\right) \\ &+ \theta_0 - \left(\frac{2\dot{r}_0}{R_0 n_0} - \frac{4f_\theta}{R_0 n_0^2}\right)\end{aligned} \tag{6}$$

where

$$\Delta a_0 = \left(\frac{2R_0\dot{\theta}_0}{n_0} + 4r_0\right) \tag{7}$$

$$e_0 = \sqrt{\left(\frac{f_r}{R_0 n_0^2} + \frac{2\dot{\theta}_0}{n_0} + \frac{3r_0}{R_0}\right)^2 + \left(\frac{\dot{r}_0}{R_0 n_0} - \frac{2f_\theta}{R_0 n_0^2}\right)^2} \tag{8}$$

$$\omega_0 = \tan^{-1}\left(\frac{\dot{r}_0 n_0 - 2f_\theta}{3r_0 n_0^2 + 2\dot{\theta}_0 R_0 n_0 + f_r}\right) \tag{9}$$

The quantities in equations (7)-(9) represent the differential mean radius, eccentricity and argument of perigee at $t = 0$, respectively. Note that for the linerised dynamics, the motion caused by the acceleration component along the cross-track direction is de-coupled from the in-plane motion, and it expresses only simple harmonics oscillation [7].

III. COLLISION ANALYSIS

A spring mechanism is typically employed to separate each small satellite from the launch vehicle. The incremental velocity applied on the satellite can be assumed to be impulsive. The motion of the satellite, S_1, after the separation, relative to the launch vehicle that is orbiting in a circular orbit, can be found from equations (5)-(9) as

$$r = \Delta a_0 - R_0 e_0 \cos\left(n_0 t - \omega_0\right) \tag{10}$$

$$\theta = -\left(\frac{2\Delta V_{r1}}{R_0 n_0} + \frac{3}{2}\frac{n_0}{R_0}\Delta a_0 t - 2e_0 \sin\left(n_0 t - \omega_0\right)\right) \tag{11}$$

where

$$\Delta a_0 = \frac{2\Delta V_{\theta 1}}{n_0} \tag{12}$$

$$e_0 = \sqrt{\left(\frac{2\Delta V_{\theta 1}}{R_0 n_0}\right)^2 + \left(\frac{\Delta V_{r1}}{R_0 n_0}\right)^2} \tag{13}$$

$$\omega_0 = \tan^{-1}\left(\frac{\Delta V_{r1}}{2\Delta V_{\theta 1}}\right) \tag{14}$$

where ΔV_{r1} and $\Delta V_{\theta 1}$ are the incremental velocity components in the radial and along-track directions, respectively. Note that θ_0 and r_0 are zero, because the satellite is initially sitting on the launch vehicle.

The other satellites in the system may be deployed either at the same or different times after S_1. The relative motion between satellites can be described by differencing their relative motion with respect to the reference orbit. For example, if only the first two satellites, S_1 and S_2, are concerned, their relative motion will appear as an epicycle traveling with a constant along-track velocity. By applying equations (10)–(14), the centre of the epicycle $\left(r_{c0}, \theta_{c0}\right)$ is defined by the conditions at the epoch when S_2 is separated as

$$r_{c0} = \frac{2\delta V_\theta}{n_0} + 4r_{1t_2} \tag{15}$$

$$\theta_{c0} = \theta_{1t_2} - \frac{2\delta V_r}{R_0 n_0} \tag{16}$$

where δV_r and δV_θ are the differential applied velocities between the satellites. r_{1t_2}, θ_{1t_2} are the relative separation at t_2 when the second satellite is deployed. The radial amplitude of the epicycle is $R_0\delta e_0$ and the along-track amplitude is $2\delta e_0$, where δe_0 is the difference in eccentricity between the satellites orbits:

$$\delta e_0 = \sqrt{\left(\frac{2\delta V_\theta}{R_0 n_0} + \frac{3r_{1t_2}}{R_0}\right)^2 + \left(\frac{\delta V_r}{R_0 n_0}\right)^2} \tag{17}$$

The relative along-track drift rate is constant at

$$\delta\dot{\theta} = -\left(\frac{3\delta V_\theta}{R_0} + \frac{6n_0\delta r_{1t_2}}{R_0}\right) \tag{18}$$

This traveling epicycle can cause dangerously close approach, even though the two satellites have been deployed into orbits with an along-track separation and different orbital period. To visualise this, consider the relative motion between satellites in figure (3). In figure (3a), both satellites are separated at the same time, but a smaller along-track velocity has been applied on the second spacecraft. Obviously, it will appear to move forwards relative to the first satellite as its orbital period is shorter. Figure (3b) shows the motion when the second satellite is separated with the same differential velocity, but 10 seconds after the first satellite. We can see that the epicycle moves forward with the same rate in both cases. However, the difference in the eccentricity of the orbits, and the epoch of the separation cause the tail of the epicycle to start from the left-hand side. A collision occurs after 3 orbital periods, when the second satellite starts to move relatively rightward.

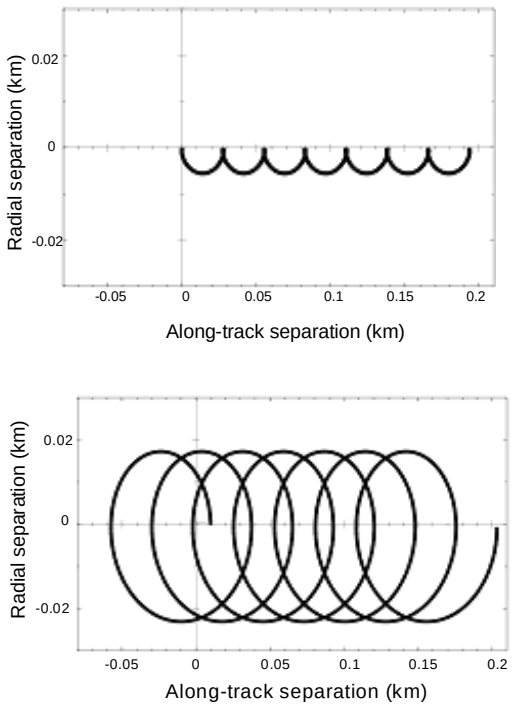

Figure 3. Relative motion between two satellites after orbit deployment

IV. COLLISION-FREE ORBIT DEPLOYMENT STRATEGY

So far, the cause of collision described above has never been paid attention, because its chance is trivial in practice, especially when the number of satellites in the system is small. However, the chance can potentially increase in the case of multiple satellite system, and when each satellite is equipped with some elongated parts.

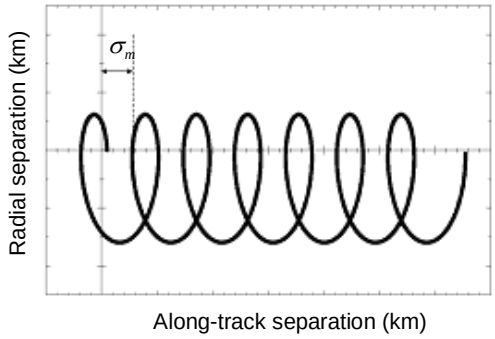

Figure 4. The safety margin for collision-free orbit deployment

In order to guaranteed that the spacecraft will not come back to collide, an adequate margin of closest approach after one orbital period (denoted by σ_m in figure (4)) can be assigned. From the shape and traveling velocity of the epicycle in equations (15)-(18), the criteria for the collision-free deployment can be set as

$$\left(\theta_{c0} - 2\delta e_0 + \frac{2\pi\delta\dot{\theta}}{n_0}\right) \le \sigma_m \tag{19}$$

It can be written in terms of differential incremental velocity as

$$-\left[\left(\theta_{1t_2} - \frac{12\pi r_{1t_2}}{R_0}\right) + \left(\frac{6\pi\delta V_\theta}{R_0 n_0} + \frac{2\delta V_r}{R_0 n_0}\right) + 2\sqrt{\left(\frac{2\delta V_\theta}{R_0 n_0} + \frac{3r_{1t_2}}{R_0}\right)^2 + \left(\frac{\delta V_r}{R_0 n_0}\right)^2}\right] \le \sigma_m \tag{20}$$

If the margin is zero the spacecraft will collide after one orbit. Note that this margin must have the same sign as the relative velocity, and if it is of the opposite sign to the relative velocity then there is a chance for collision as illustrated in figure (2b). When a safety margin is assigned, the differential velocity required for collision-free orbit deployment can be immediately worked out from equation (20).

If the satellites are separated simultaneously with only along-track velocities are applied, the differential incremental velocity will be proportional to the closest approach, and the criterion becomes

$$\delta V_\theta = \Delta V_{\theta 1} - \Delta V_{\theta 2} \le \frac{\sigma_m n_0}{6\pi + 4} \tag{21}$$

V. RESULTS

To validate the collision-free criteria proposed above, the deployment of two satellites to form a formation flying mission around a 700km altitude orbit is assumed. The closest approach between spacecraft is not allowed to be closer than 200 m. If the incremental along-track velocity assigned for the first satellite is $\Delta V_1 = 1.08 m/s$, the applied velocity for the second satellite can be calculated from equation (21) to give $\Delta V_{\theta 2} < 1.066 m/s$.

The errors in velocity magnitude and direction due to spring mis-alignment and the error of the launch vehicle heading can also be taken into account in the calculation. For example, it is possible that the velocity gain from the separation springs for both spacecraft can give an error up to 5% from their nominal values, and the combined error from the delta-V vector mis-alignment and the launcher's heading error can be up to 1 degree. The worst case scenario will occur when $\Delta V_{\theta 1}$ becomes smallest, i.e. $\Delta V_{\theta 1} = (\Delta V_1 - 0.05\Delta V_1)\cos(1^\circ)$, and $\Delta V_{\theta 2}$ becomes largest, i.e. $\Delta V_{\theta 2} = (\Delta V_2 + 0.05\Delta V_2)$, which will give the smallest σ_m. Note that there will be a radial velocity component applied on S_1 with an amount of $\Delta V_{r1} = (\Delta V_1 - 0.05\Delta V_1)\sin(1^\circ)$ in the worst case. From the given mission constraints, the incremental velocity required for S_2 can be calculated from equation (20), with $\theta_{1t_2} = r_{1t_2} = 0$ as both satellites are separated at the same time, and yields $\Delta V_2 < 0.977 m/s$.

By using this incremental delta-V, the relative motions between the spacecraft in nominal and worst cases are shown in figure (5a) and (5b), respectively. In figure (5a), S_2 moves away from S_1 with a larger excursion in the nominal situation, and the closest approach during the second orbit is about 2 km. In the worst case situation shown in figure (5b), however, the closest margin is guaranteed at 200 m as required.

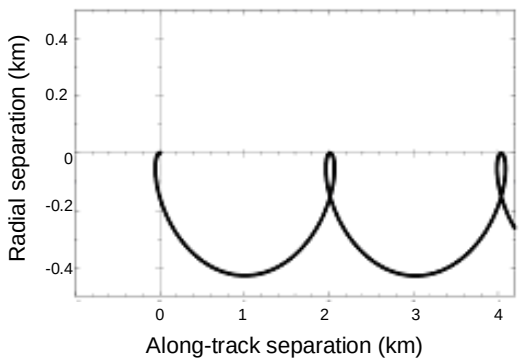

(a)

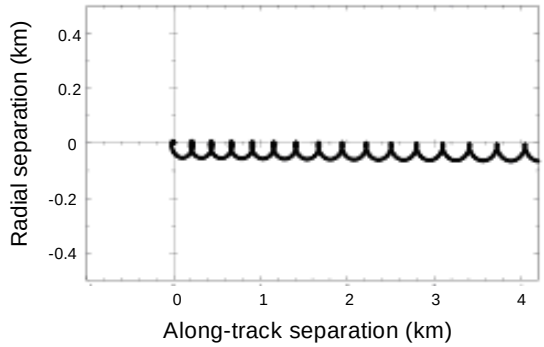

(b)

Figure 5. The motion after separation with a margin guaranteed

VI. CONCLUSIONS

The presented analysis of relative motion shows its simplicity and instructive geometry. Although a system of only two satellites is given in the example, the proposed criteria can be applied directly to the system that is comprised of multiple satellites. Any kind of orbit separation mechanism and structure can also adopt this criterion without any limitation. This gives a great benefit to new-generation launch vehicles when the design will be dedicated for multiple small satellites.

REFERENCES

[1] Khutorovsky, Z.N., Boikov, V., and Kamnesky, S.Y., "Direct Method for the Analysis of Collision Probability of Artificial Space Objects in LEO: Techniques, Results, and Applications," Proceedings of the First European Conference on Space Debris, ESA SD-01, ESA, Paris, 1993, pp.491-508.

[2] Chan, K.F., "Collision Probability Analysis For Earth Orbiting Satellites," Advanced in the Astronautical Sciences, Vol. 96, July, 1997, pp.1033-1048.

[3] Alfono, S., "Satellite Collision Probability nhancements," Journal of Guidance, Control, and Dynamics, Vol. 29, No. 3, May-June 2006.

[4] Petera, R.P., "Method for Calculating Collision Probability Between a Satellite and a Space Tether," Journal of Guidance, Control, and Dynamics, Vol. 25, No. 5, September-October 2002.

[5] Goodwin, J.S., and Wegner P., "Evolved expendable launch vehicle secondary payload adapter - Helping technology get to space," AIAA-2001-4701, AIAA Space 2001 - Conference and Exposition, Albuquerque, NM, Aug. 28-30, 2001.

[6] Ramanan, R.V., "Strategy for Deployment of Multiple Satellites for Collision-Free Relative Orbital Motion," Journal of Guidance, Control, and Dynamics, Vol. 23, No. 3, 2000, pp. 556-558.

[7] W.H. Clohessy and R.S. Wiltshire, "Terminal Guidance System For Satellite Rendezvous," Journal of Aerospace Sciences, Vol. 27, No. 9, Sept. 1960, pp. 653-658.

[8] Kaplan, M.H., "Modern Spacecraft Dynamics & Control," John Wiley & Sons, Inc., 1976.

Table of Contents

10:50 AM - 12:10 AM **Session TAM1-1** **Thursday,10 May 2007**

Microwave Technology 1

Chairperson : Denchai Worasawate, Kasetsart University

TAM1-1-1 **Design and Analysis of Fractal Microstrip Low Pass Filter using Radial-Line Stubs** **601**
10:50 AM
P.K.Singhal, Pramod Kumar, Neha Verma
Department of Electronics, CSE, IT Madhav Institute of Technology and Science, Gwalior, India

TAM1-1-2 **Performance Improvement of Broad-Beam Microstrip Reflectarray by Reduction of** **604**
11:10 AM **Elements Spacing**
Piyaporn Krachodnok, Rangsan Wongsan
School of Telecommunication Engineering,
Suranaree University of Technology, Nakhon Ratchasima, Thailand

TAM1-1-3 **Narrowband Ring Filter Design with Inductive Compensated Coupling Feed and** **608**
11:30 AM **Step-Impedance Resonator**
Ravee Phromloungsri, Ratthaya Suwanbunyaporn, Mitchai Chongcheawchamnan
Research Center for Electromagnetic Wave Applications(RCEWs),
Mahanakorn University of Technology, Bangkok, Thailand

TAM1-1-4 **A Dual-Band Bandpass Filter Using Stepped-Impedance and Load capacitive Hairpin** **612**
11:50 AM **Resonators for Mobile System**
Pongsathorn Chomtong, Sarawuth Chaimool, Prayoot Akkaraeakthalin
Department of Electrical Engineering, Faculty of Engineering,
King Mongkut's Institue of Technology North Bangkok, Bangkok, Thailand

10:50 AM - 12:10 AM **Session TAM1-5** **Thursday,10 May 2007**

Optical Communications

Chairperson : Athikom Roeksabutr, Mahanakorn University of Technology

TAM1-5-1 **Acousto-Optic Frequency Decoder and Its Applications** **616**
10:50 AM
Athikom Roeksabutr
Telecommunication Engineering Department,
Mahanakorn University of Technology, Bangkok, Thailand

TAM1-5-2 **Study on Backbone Network with WDM Via Optical Fiber** **619**
11:10 AM
Amornrat Mahaprom, Noppin Anantrasirichai
King Mongkut's Institute of Technology Ladkrabang, Bangkok, Thailand

TAM1-5-3 **Numerical Analysis of Pump Propagation Direction in Distributed Raman Amplifiers** **623**
11:30 AM
Nadir Hossain, A. W. Naji, V. Mishra, F.M. Abbou, M. A. Hasnayeen, A.A.R. Hairul, A.R. Faidz
Institute of Photonics Research & Applications, Multimedia University, Selangor, Malaysia

TAM1-5-4 **Performance Evaluation of 2-D Code Optical CDMA MAC Protocol over WDM** **627**
11:50 AM
Kidsanapong Puntsri
Department of Electronics and Telecommunication Engineering, Faculty of Industrial Education,
Rajamangala University of Technology Phranakhon, Bangkok, Thailand

10:50 AM - 12:10 AM **Session TAM1-7** **Thursday,10 May 2007**

Antenna Applications

Chairperson : Sompol Kosulvit, King Mongkut's Institute of Technology Ladkrabang

TAM1-7-1 **Resonances of a Chiral Filled Conducting Spherical Cavity** **631**
10:50 AM
Denchai Worasawate[1], Muhammad A. Shahzad[1], Monai Krairiksh[2]
[1]Kasatsart Advanced RF and EectromagNetics Laboratory,
Department of Electrical Engineering, Kasetsart University, Bangkok, Thailand
[2]Department of Telecommunication, Faculty of Engineering,
King Mongkut's Institute of Technology Ladkrabang, Bangkok, Thailand

TAM1-7-2 **Finite-Element Analysis of Aepatic Multiple Array Antenna for Microwave** **635**
11:10 AM **Coagulation Therapy**
Apichon Chintanasinton, Supan Tungjitkusolmun, Pattarapong Phasukkit
King Mongkut's Institute of Technology Ladkrabang, Bangkok, Thailand

TAM1-7-3 **Estimation of Heating Performances of a Coaxial-Slot Antenna for Treatment of Colon** **639**
11:30 AM **Carcinoma**
Apichon Chintanasinton, Supan Tungjitkusolmun, Pattarapong Phasukkit
King Mongkut's Institute of Technology Ladkrabang, Bangkok, Thailand

TAM1-7-4 **Reflector Shape Optimization for Wideband Uni-directional of CPW-fed Slot Antenna** **643**
11:50 AM
Sarawuth Chaimool[1], Prayoot Akkaraekthalin[1], Monai Krairiksh[2]
[1]Department of Electrical Engineering, Faculty of Engineering,
King Mongkut's Institute of Technology North Bangkok, Bangkok, Thailand
[2]Research Center for Communications and Information Technology (ReCCIT),
King Mongkut's Institute of Technology Ladkrabang, Bangkok, Thailand

10:50 AM - 12:10 AM **Session TAM1-10** **Thursday,10 May 2007**

DSP/Coding

Chairperson : Takao Onoye, Osaka University

TAM1-10-1 **Reconfigurable-based SoC Architecture for Media Processing** **647**
10:50 AM
Yukio Mitsuyama[1], Takao Onoye[1], Isao Shirakawa[2]
[1]Department of Information Systems Engineer, Osaka University, Osaka, Japan
[2]Department Policy and Management Informatics, University of Hyogo, Hyogo, Japan

TAM1-10-2 **Additional Steps of Convolutional Vector Symbol Decoding for General Data Sequence** **651**
11:10 AM
U. Tuntoolavest
Department of Electrical Engineering, Faculty of Engineering,
Kasetsart University, Bangkok, Thailand

TAM1-10-3 **MAP Decoding for Polynomial Ring Convolutional Trellis Codes for MPEG-4 Image** **655**
11:30 AM **Transmission System Over Rician Fading Channels**
Srijidtra Mahapakulchai
Department of Electrical Engineering, Kasetsart University, Bangkok, Thailand

TAM1-10-4	**Suitability of Cyclic-Prefix Modification for Signal Transmission in OFDM**	**659**
11:50 AM	Tawatchai Chontong, Noppadol Maneerat, Ruttikorn Varakulsiripunth *Research Center for Communications and Information Technology (ReCCIT),* *King Mongkut's Institute of Technology Ladkrabang, Bangkok, Thailand*	

1:00 PM - 2:40 PM	**Session TPM1-1** **Microwave Technology 2** Chairperson : Tuptim Angkaew, Chulalongkorn University	**Thursday,10 May 2007**
TPM1-1-1	**Feasibility Study of a Six-Port Reflectometer Design based on Inductively-Compensated**	**663**
1:00 PM	**Coupled Lines** Vitthaya Chamnanphrai[1], Ravee Phromloungsri[2], Mitchai Chongcheawchamnan[2] [1]*Telecommunication and Electronics Department, Faculty of Engineering,* *Rajamangala University of Technology Isan, Khon Kaen Campus, Thailand* [2]*Research Center for Electromagnetic Wave Applications (RCEWs),* *Mahanakorn University of Technology, Bangkok, Thailand*	
TPM1-1-2	**Impedance Analysis of a Shorted-End Curved Dipole on Reflector Plane using Method**	**667**
1:20 PM	**of Moments** Sompop Pimpol, Rangsan Wongsan *School of Telecommunication, Institute of Engineering,* *Suranaree University of Technology, Nakhon Ratchasima, Thailand*	
TPM1-1-3	**A Finite Element Method with Polygonal Elements for Analyzing a Band Gap**	**671**
1:40 PM	**Characteristic** Eny Sukani Rahayu, Tuptim Angkaew *Department of Electrical Engineering, Chulalongkorn University, Bangkok, Thailand*	
TPM1-1-4	**A Tri-Band Microstrip-to-Coplanar Stripline Transition**	**675**
2:00 PM	Kumron Meelarpkit[1], Mitchai Chongcheawchamnan[2], Chuwong Phongcharoenpanich[1] [1]*Research Center for Communications and InformationTechnology,* *King Mongkut's Institute of Technology, Ladkrabang, Bangkok, Thailand* [2]*Research Center for Electromagnetic Wave Applications (RCEWs),* *Mahanakorn University of Technology, Bangkok, Thailand*	
TPM1-1-5	**Simulations and Visualization of Electrostatic Field Strength Caused by Electrostatic**	**679**
2:20 PM	**Voltage Source in Homogeneous Material** Atthapol Wangsotorn[1], Pharkphum Direkpoke[2], Somchart Roongruangsorakarn[1], Kraisorn Chaisaowong[1,2,3] [1]*Department of Computer and Information Science,* *King Mongkut's Institute of Technology North Bangkok, Bangkok, Thailand* [2]*Department of Electrical Engineering, King Mongkut's Institute of Technology North Bangkok* [3]*Institute of Imaging & Computer Vision, RWTH Aachen University, Germany*	

1:00 PM - 3:00 PM **Session TPM1-3** **Thursday,10 May 2007**

Mobile Communication Technology

Chairperson : Zia Nadir, Sultan Qaboos University

TPM1-3-1 **Performance Study of CFP Contention Resolution Algorithm for Wireless** **683**
1:00 PM **Communication System**
Suvit Nakpeerayuth, Warakorn Srichavengsup, Lunchakorn Wuttisittikulkij
Department of Electrical Engineering, Faculty of Engineering,
Chulalongkorn University, Bangkok, Thailand

TPM1-3-2 **Computer-based 2D Simulations of SAR in Inhomogeneous Biological Domain Model** **687**
1:20 PM **Caused by Isotropic Antenna at 900 MHz and 1800 MHz**
Pharkphum Direkpoke[1], Atthapol Wangsotorn[2], and Kraisorn Chaisaowong[1,2,3]
[1]*Department of Electrical Engineering, Faculty of Engineering,*
King Mongkut's Institute of Technology North Bangkok, Bangkok, Thailand
[2]*Department of Computer and Information Science, Faculty of Applied Science,*
King Mongkut's Institute of Technology North Bangkok, Bangkok, Thailand
[3]*Institute of Imaging & Computer Vision, RWTH Aachen University, Germany*

TPM1-3-3 **Adaptive Channel Equalizer Design for Uplink WCDMA Rake Receiver** **691**
1:40 PM T. Phoopattanakul, W. Saenghiranwattana, K. Ruangsa-ad, C. Charoenlarpnopparut,
P. Boonyanant
Sirindhorn International Institute of Technology, Thammasat University, Thailand

TPM1-3-4 **Closed-Form Analysis of Equal Gain Combining for Wireless Communications** **695**
2:00 PM T.Phophongviwat[1], C.Chat-uthai[2]
[1]*Department of Electrical Power Engineering, Faculty of Engineering,*
Mahanakorn University of Technology, Bangkok, Thailand
[2]*Department of Electrical Engineering, Faculty of Engineering,*
King Mongkut's Institute of Technology Ladkrabang, Bangkok, Thailand

TPM1-3-5 **Artificial Immunity-Based Feature Extraction for Spam Detection** **698**
2:20 PM Burim Sirisanyalak, Ohm Sornil
Department of Computer Science,
National Institute of Development Administration, Bangkok, Thailand

TPM1-3-6 **Modification Of An Urban Area Okumura-Hata Propagation Model Suitable For** **702**
2:40 PM **Salalah-Oman**
Z. Nadir, N. Elfadhil, F. Touati, B. Suhail, M. Jamal, M. Abdulrahman,
Department of ECE, Sultan Qaboos University, Muscat, Sultanate of Oman

1:00 PM - 2:20 PM **Session TPM1-5** **Thursday,10 May 2007**

Communication Networks

Chairperson : Chalie Charoenlarpnopparut : Sirindhorn International Institute of Technology

TPM1-5-1 **A Design of Backpressure Scheme in Traffic Shaping over High speed network** **706**
1:00 PM Somchai Lekcharoen, Srisawad Yongyut
Faculty of Information Technology, Rangsit University, Bangkok, Thailand

TPM1-5-2	**Multicast Improvement Bandwidth Utilization in Inter-ring RPR Topology**	**710**
1:20 PM	Wuttichai Kwanmetakun, Pisai Setthawong, Surat Tanterdtid *Department of Telecommunications Science, Faculty of Science and Technology,* *Assumption University, Thailand*	
TPM1-5-3	**The Optimum route by QoS Based on Genetic Algorithms (QGAs)**	**714**
1:40 PM	Jittanun Kulsiri, Suvepon Sittichivapak, Kriengkai Vonglodjanaporn *Department of Telecommunication Engineering, Faculty of Engineering,* *King Mongkut's Institute of Technology Ladkrabang, Bangkok, Thailand*	
TPM1-5-4	**TCP-Friendliness Definition Revision & Implementation for Multi-Rate Multicast**	**718**
2:00 PM	**Congestion Control** Somnuk Puangpronpitag[1], Suchart Kummanee[2] [1]*Computer Science, Faculty of Informatics, Mahasarkham University, Thailand* [2]*Department of Computer Science, Faculty of Science,Khon Kaen University, Thailand*	

3:20 PM - 4:40 PM	**Session TPM2-1** **Antennas and Propagations** Chairperson : Danai Torrungrueng, Asian University	**Thursday,10 May 2007**
TPM2-1-1	**Design of Dual Wide-band Slot Antenna Fed by CPW**	**722**
3:20 PM	P. Pommas[1], N. Anantrasirichai[1], P. Rakluea[2], T. Wakabayashi[3] *Research Center for Communications and Information Technology (ReCCIT),* *King Mongkut's Institute of Technology Ladkrabang, Bangkok, Thailand* [2]*Department of Electronic and Telecommunication Engineering, Faculty of Engineering,* *Rajamangala University of Technology Thanyaburi, Pathumthanee, Thailand* [3]*School of Information Science and Technology, Tokai University, Kanagawa, Japan*	
TPM2-1-2	**A Compact U-Shaped Cross-Sectional Antenna on a U-Shaped Ground Plane for WLAN**	**726**
3:40 PM	Duang-arthit Srimoon[1], Chuwong Phongcharoenpanich[2], Monai Krairiksh[2] [1]*School of Computer Engineering, College of Engineering,* *Rangsit University, Pathumthani, Thailand* [2]*Faculty of Engineering & Research Center for Communications and Information Technology,* *King Mongkut's Institute of Technology Ladkrabang, Bangkok, Thailand*	
TPM2-1-3	**Fractal array antenna with NP generator model**	**730**
4:00 PM	Chatree Mahatthanajatuphat, Prayoot Akkaraekthalin *Department of Electrical Engineering, Faculty of Engineering,* *King Mongkut's Institute of Technology North Bangkok, Bangkok, Thailand*	
TPM2-1-4	**A New Compact WLAN 2.4 GHz CPW-fed Slot Antenna with Inverted-F Shaped**	**734**
4:20 PM	**Tuning Stub** Prapoch Jirasakulporn[1], Sarawuth Chaimool[2], Prayoot Akkaraekthalin[2] [1]*Pathumwan Institute of Technology, Bangkok, Thailand* [2]*Department of Electrical Engineering, Faculty of Engineering,* *King Mongkut's Institute of Technology North Bangkok, Bangkok, Thailand*	

3:20 PM - 4:40 PM | **Session TPM2-5** | **Thursday,10 May 2007**

Communication Systems 2

Chairperson : Usana Tuntoolavest, Kasetsart University

TPM2-5-1 **Throughput Analysis for Orthogonal Diversity of CSMA/CA Protocol by SFH/MC DS-CDMA** **737**
3:20 PM
Pichet Roumsamug[1], Pisakorn Sittiwatjana[2], Suvepon Sittichivapak[1]
[1]Department of Telecommunication Engineering, Faculty of Engineering,
King Mongkut's Institute of Technology Ladkrabang, Bangkok, Thailand
[2]Prince of Songkhla University, Phuket Campus, Phuket, Thailand

TPM2-5-2 **Users Capacity Increment of MLC-GSM Over Rayleigh Fading Channel** **741**
3:40 PM
Phichet Moungnoul, Wiphada Inkiew
Research Center for Communication and Information Technology,
King Mongkut's Institute of Technology Ladkrabang, Bangkok, Thailand

TPM2-5-3 **Proposal of PAPR Reduction Method for OFDM Signal without Side Information** **745**
4:00 PM
Pornpawit Boonsrimuang[1], Pisit Boonsrimuang[1], Kazuo Mori[2], Tawil Paungma[1], Hideo Kobayashi[2]
[1]Department of Telecommunication Engineering, Faculty of Engineering,
King Mongkut's Institute of Technology Ladkrabang, Bangkok, Thailand
[2]Division of Electrical and Electronic Engineering,
Graduate School of Engineering, Mie University, Japan

TPM2-5-4 **Interference Effect Comparison between IS-95B and CDMA2000 Cellular System over Nakagami Fading Channel** **749**
4:20 PM
Naphat Sutthaphol, Phichet Moungnoul
Research Center for Communication and Information Technology (ReCCIT),
King Mongkut's Institute of Technology Ladkrabang, Bangkok, Thailand

3:20 PM - 5:00 PM | **Session TPM2-10** | **Thursday,10 May 2007**

SS : Microwave and Antennas 1

Chairperson : Jun-ichi Takada, Tokyo Institute of Technology

TPM2-10-1 **Measurement Techniques of Transmissions from Ultra Wideband Devices** **753**
3:20 PM
Jun-ichi Takada
Graduate School of Science and Engineering, Tokyo Institute of Technology, Tokyo, Japan

TPM2-10-2 **Experimental Study and Analysis of Antenna Effects for UWB Radio Transmission** **757**
3:40 PM
Sanit Teawchim[1], Sathaporn Promwong[1], Jun-ichi Takada[2]
[1]Department of Information Engineering, Faculty of Engineering,
King Mongkut's Institute of Technology Ladkrabang, Bangkok, Thailand
[2]Graduate School of Science and Engineering, Tokyo Institute of Technology, Tokyo, Japan

TPM2-10-3 **Planar Source Characteristics Analysis for Wave Iterative Method Simulation** **761**
4:00 PM
Somsak Akatimagool, Sommart Kamkleing
Department of Teaching Training in Electrical Engineering, Faculty of Technical Education,
King Mongkut's Institute of Technology North Bangkok, Bangkok, Thailand

TPM2-10-4	**The Generalized Constant Circuit-Node Q Circles on the Extended T-Chart**	**765**
4:20 PM	P. Y. Chou, D. Torrungrueng *Department of Electrical and Electronic Engineering,* *Faculty of Engineering and Technology, Asian University, Chon Buri, Thailand*	
TPM2-10-5	**A Microstrip-Coplanar Waveguide Tight Coupler for a Single-Layer Substrate**	**769**
4:40 PM	Mitchai Chongcheawchamnan, Waikoon Sangworn, Ratthaya Suwanbunyaporn, Ravee Phromloungsri *Research Center for Electromagnetic Wave Applications (RCEWs),* *Telecommunication Engineering Department,* *Mahanakorn University of Technology, Bangkok, Thailand*	
8:30 AM - 10:10 AM	**Session FAM1-1** **Power Line Comm./ RFID** Chairperson : Chalie Charoenlarpnopparut, Sirindhorn International Institute of Technology	**Friday,11 May 2007**
FAM1-1-1	**Performance of Power Line Communication using Direct- Sequence Code Division**	**773**
8:30 AM	**Multiple Access with Turbo Coded** S. Chanakarn, C. Banjangkaprasert, N. Anantrasirichai *Research Center for Communications and Information Technology (ReCCIT),* *King Mongkut's Institute of Technology Ladkrabang, Bangkok, Thailand*	
FAM1-1-2	**TCP/IP Protocol over Power Line Communication System Contaminated with**	**777**
8:50 AM	**Impulsive noise** Oraya Rattanakanokkan, Suvepon Sittichivapak, Kriengkai Vonglodjanaporn *Department of Telecommunication Engineering, Faculty of Engineering,* *King Mongkut's Institute of Technology Ladkrabang, Bangkok, Thailand*	
FAM1-1-3	**Chaotic Direct Sequence Spread Spectrum for Power line Datacommunication**	**781**
9:10 AM	Narumon Thummakerd[1], Suvepon Sittichivapak[1], Kidsanapong Puntsri[2] [1]*Faculty of Telecommunication Engineering*, *King Mongkut's Institute of Technology Ladkrabang, Bangkok, Thailand* [2]*Department of Electronics and Telecommunication Engineering*, *Rajamangala University of Technology Phranakhon, Bangkok, Thailand*	
FAM1-1-4	**Evaluation Methods for Active RFID Equipments in Road Access Services**	**785**
9:30 AM	L. Kovavisaruch, T. Sanpechuda, J. Wisanmongkol, C. Mitrepant *National Electronics and Computer Technology Center (NECTEC), Pathumthani, Thailand*	
FAM1-1-5	**Data Recording with FAT16 in Removable Media of RFID Handheld Reader**	**789**
9:50 AM	Anukool Noymai, Urachada Ketprom, Chaichana Mitrpant *National Electronics and Computer Technology Center (NECTEC), Pathumthani, Thailand*	

8:30 AM - 10:10 AM **Session FAM1-5** **Friday,11 May 2007**

Mobile Communication Networks

Chairperson : Phongsak Keeratiwintakorn, King Mongkut's Institute of Technology North Bangkok

FAM1-5-1 **Performance Improvement of Paging Extensions for Mobile Internet Protocol based on** **793**
8:30 AM **Regional Registration and Multicasting**
Andrianus Yofy, Watit Benjapolakul
Department of Electrical Engineering, Chulalongkorn University, Bangkok, Thailand

FAM1-5-2 **Adaptive Protocol with Channel Variance Estimations for Cooperative Communications** **797**
8:50 AM
Chaiyod Pirak
Department of Teacher Training in Electrical Engineering,
King Mongkut's Institute of Technology North Bangkok, Bangkok, Thailand

FAM1-5-3 **Robust Ad Hoc Routing Protocol using Relative Mobility Information** **801**
9:10 AM
Suksun Mahakittikun, Peerapon Siripongwutikorn
Department of Computer Engineering,
King Mongkut's University of Technology Thonburi, Bangkok, Thailand

FAM1-5-4 **A QoS-Based Dynamic Source Routing for Multimedia Service in Mobile** **805**
9:30 AM **Ad Hoc Networks**
Wayan Mustiksa[1], Sakchai Thipchaksurat[1], Ruttikorn Varakulsiripunth[1], Hiroshi Ishii[2]
[1]Research Center for Communications and Information Technology (ReCCIT),
King Mongkut's Institute of Technology Ladkrabang, Bangkok, Thailand
[2]Department of Communication Engineering,
School of Information Technology and Electronics, Tokai University, Japan

FAM1-5-5 **Optimal Frequency Channel Assignment for WLANs Using Hybrid SIR and CSMA/CA** **809**
9:50 AM **Considerations**
Chutima Prommak, Boriboon Deeka
School of Telecommunications Engineering,
Suranaree University of Technology, Nakorn Ratchasima, Thailand

8:30 AM - 10:10 AM **Session FAM1-9** **Friday,11 May 2007**

Microwave Devices

Chairperson : Jaruek Jantree, Rajamangala University of Technology Suvarnabhumi

FAM1-9-1 **Compact Microstrip Two-layer Dual-Band Bandpass Filter Using Aperture-coupled** **813**
8:30 AM **SIR-Hairpin Resonator**
Sutatorn Promprathom[1], Jaruek Jantree[2], Sarawuth Chaimool[1], Prayoot Akkaraekthalin[1]
[1]Department of Electrical Engineering, Faculty of Engineering,
King Mongkut's Institute of Technology North Bangkok, Bangkok, Thailand,
[2]Department of Electrical Engineering, Faculty of Engineering and Architecture,
Rajamangala University of Technology Suvarnabhumi, Supanburi Campus, Thailand

FAM1-9-2	**Microwave Ablation Therapy for Lung Cancer using Open-Tip and Multi-Slot Coaxial**	**817**
8:50 AM	**Antenna**	
	D. Kiatkittisorn[1], M. Sangworasil[1,2], P. Phasukkit[1,2], S. Tungjitkusolmun[1,2]	
	[1]Faculty of Engineering,	
	King Mongkut's Institute of Technology Ladkrabang, Bangkok, Thailand	
	[2]Computer Research and Service Center,	
	King Mongkut's Institute of Technology Ladkrabang, Bangkok, Thailand	
FAM1-9-3	**Reducing Self Resonance Effect in High FrequencyInductors Using Capacitance**	**821**
9:10 AM	**Cancellation Technique**	
	K. Piboonwattanakit[1], V. Tarateeraseth[2], W. Khan-ngern[1]	
	[1]Research Center for Communications and Information Technology,	
	King Mongkut's Institute of Technology Ladkrabang, Bangkok, Thailand	
	[2]Srinakharinwirot University, Faculty of Engineering, Nakornnayok, Thailand	
FAM1-9-4	**A Minimized Bandpass Filter Using Two-Layers With Aperture-coupled for Microstrip**	**825**
9:30 AM	**Slow-Wave Open-Loop Resonator**	
	Apirada Namsang, Jaruek Jantree, Prayoot Akkaraekthalin	
	Department of Electrical Engineering, Faculty of Engineering,	
	King Mongkut's Institute of Technology North Bangkok, Bangkok, Thailand	
FAM1-9-5	**Bandwidth Enhancement of a CPW-Fed Rectangular Slot Antenna**	**829**
9:50 AM	P. Seangsae[1], N. Anantrasirichai[1], J. Nakasuwan [2], T. Wakabayashi[3]	
	[1]Research Center for Communications and Information Technology (ReCCIT),	
	King Mongkut's Institute of Technology Ladkrabang, Bangkok, Thailand	
	[2]Department of Electronic and Telecommunication Engineering, Faculty of Engineering,	
	Rajamangala University of Technology Thanyaburi, Pathumthanee, Thailand	
	[3]School of Information Science and Technology, Tokai University, Kanagawa, Japan	

8:30 AM - 10:10 AM	**Session FAM1-10**	**Friday,11 May 2007**
	SS : Microwave and Antennas 2	
	Chairperson : Rangsan Wongsan, Suranaree University of Technology	
FAM1-10-1	**Elliptical Patch Antenna Radiating Unidirectional Beam with Circular Polarization for**	**833**
8:30 AM	**Reader of RFID at UHF Band**	
	Rattapong Suwalak, Chuwong Phongcharoenpanich	
	Research Center for Communications and Information Technology (ReCCIT),	
	King Mongkut's Institute of Technology Ladkrabang, Bangkok, Thailand	
FAM1-10-2	**Parametric Study of a Vertically Polarized Concentric Circular Ring Antenna above**	**837**
8:50 AM	**the Reflector for High Gain Applications**	
	Souphanna Vongsack[1], Krittaya Chawanonphithak[1], Chuwong Phongcharoenpanich[1],	
	Sompol Kosulvit[1], Toshio Wakabayashi[2]	
	[1]Research Center for Communications and Information Technology,	
	King Mongkut's Institute of Technology Ladkrabang, Bangkok, Thailand	
	[2]School of Engineering, Tokai University, Kanagawa, Japan,	

FAM1-10-3	**Microwave-Based Durian Maturity Determination Using Microstrip Patch Antennas**	**841**
9:10 AM	Navapadol Kittiamornkul[1], Kamon Jiraseriamornkul[1], Kosin Chamnongthai[1,] Monai Krairiksh[2] [1]*Department of Electronic and Telecommunication Engineering,* *King Mongkut's University of Technology Thonburi, Bangkok, Thailand* [2]*Department of Telecommunication Engineering, Faculty of Engineering,* *King Mongkut's Institute of Technology Ladkrabang, Bangkok, Thailand*	
FAM1-10-4	**Interdigital Microstrip Resonator Sensor for Complex Permittivity Measurement**	**845**
9:30 AM	Somporn Seewattanapon[1], Tanee Somwong[2], Prayoot Akkaraekthalin[1] [1]*Department of Electrical Engineering, Faculty of Engineering,* *King Mongkut's Institute of Technology North Bangkok, Bangkok, Thailand* [2]*Department of Electrical Engineering, Faculty of Engineering and Architecture,* *Rajamangala University of Technology Suvarnabhumi, Nonthaburi, Thailand*	
FAM1-10-5	**A Miniaturized Dual-mode Bandpass Filter using Triangular Loop Resonator**	**849**
9:50 AM	Supachai Chotjit, Sarawuth Chaimool, Prayoot Akkaraeakthalin *Department of Electrical Engineering, Faculty of Engineering,* *King Mongkut's Institute of Technology North Bangkok, Bangkok, Thailand*	

10:30 AM - 12:10 AM	**Session FAM2-1**	**Friday,11 May 2007**
	Modulation and Channel Analysis	
	Chairperson : Keattisak Sripimanwat, National Electronics and Computer Technology Center	
FAM2-1-1	**Performance of MPSK Modulation in combined Flat Scintillation and**	**853**
10:30 AM	**Frequency-Selective Fading Channel for Satellite Mobile Communication System** N. Boonsongkusoljit, P.Supnithi *Research Center for Communications and Information Technology,Faculty of Engineering,* *King Mongkut's Institute of Technology Ladkrabang, Bangkok, Thailand*	
FAM2-1-2	**On the Interference Cancellation of OFDM System for Aeronautical Communication**	**857**
10:50 AM	Panit Lamun, Montree Kumngern, Phichet Moungnoul, Kobchai Dejhan *Faculty of Engineering and Research Center for Communication and Information Technology,* *King Mongkut's Institute of Technology Ladkrabang, Bangkok, Thailand*	
FAM2-1-3	**On the Performance of Adaptive MIMO-OFDM Systems over Severe Mobile Fading**	**860**
11:10 AM	**Channels** Hyundong Kim[1], Sangho Choe[2] [1]*The Catholic University of Korea, Bucheon-si, Korea* [2]*Beijing University of Posts and Telecommunications, Beijing, China*	
FAM2-1-4	**Proposal of Multi-level QAM-OFDM System with IDSI and IDAR Methods in Satellite**	**864**
11:30 AM	**Channel** Pisit Boonsrimuang[1], Kazuo Mori[2], Tawil Paungma[1], Hideo Kobayashi[2] [1]*Department of Telecommunication Engineering, Faculty of Engineering,* *King Mongkut's Institute of Technology Ladkrabang, Bangkok, Thailand* [2]*Division of Electrical and Electronic Engineering,* *Graduate School of Engineering, Mie University, Japan*	

FAM2-1-5	**QPSK Modulator Based On Phase Locked Loop**	**868**
11:50 AM	P. Wisartpong, J. Koseeyaporn, P.Wardkein *Department of Telecommunication Engineering, Faculty of Engineering,* *King Mongkut's Institute of Technology Ladkrabang, Bangkok, Thailand*	

10:30 AM - 12:10 AM	**Session FAM2-5** **UWB Channels** Chairperson : Sathaporn Promwong, King Mongkut's Institute of Technology Ladkrabang	**Friday,11 May 2007**
FAM2-5-1	**BER Performance of UWB Communications with Matched Filter and Correlation**	**872**
10:30 AM	**Receivers** Kultharee Teplee[1], Pichaya Supanakoon[1,2], Sathaporn Promwong[1,2], Jun-ichi Takada[3] [1]*Department of Information Engineering, Faculty of Engineering,* *King Mongkut's Institute of Technology Ladkrabung, Bangkok, Thailand* [2]*Research Center for Communications and Information Technology (ReCCIT),* *King Mongkut's Institute of Technology Ladkrabung, Bangkok, Thailand* [3]*Graduate School of Science and Engineering, Tokyo Institute of Technology, Tokyo, Japan*	
FAM2-5-2	**Modeling of Indoor UWB Channel by Using Finite Difference Time Domain Method**	**876**
10:50 AM	Phannipha Thaiwattanaporn[1], Pichaya Supanakoon[1,2], Sathaporn Promwong[1,2], Jun-ichi Takada[3] [1]*Department of Information Engineering, Faculty of Engineering,* *King Mongkut's Institute of Technology Ladkrabung, Bangkok, Thailand* [2]*Research Center for Communications and Information Technology (ReCCIT),* *King Mongkut's Institute of Technology Ladkrabung, Bangkok, Thailand* [3]*Graduate School of Science and Engineering, Tokyo Institute of Technology, Tokyo, Japan*	
FAM2-5-3	**Power Spectral Density Analysis of Ultra Wideband Signal Using Pulse Shape**	**880**
11:10 AM	**Modulation** Parinya Prommasuksakul[1], Pichaya Supanakoon[1,2], Sathaporn Promwong[1,2], Jun-ichi Takada[3] [1]*Department of Information Engineering, Faculty of Engineering,* *King Mongkut's Institute of Technology Ladkrabung, Bangkok, Thailand* [2]*Research Center for Communications and Information Technology (ReCCIT),* *King Mongkut's Institute of Technology Ladkrabung, Bangkok, Thailand* [3]*Graduate School of Science and Engineering, Tokyo Institute of Technology, Tokyo, Japan*	
FAM2-5-4	**Performance Investigation of UWB Rake Receiver in Realistic Indoor Channels**	**884**
11:30 AM	Worawoot Duangdeun, Monchai Chamchoy, Sathaporn Promwong *Faculty of Engineering, King Mongkut's Institute of Technology Ladkrabang, Bangkok, Thailand*	
FAM2-5-5	**Ultra Wideband Radio Propagation Channel with Corridor for Short Range Wireless**	**888**
11:50 AM	**Systems** Nisakorn Yingkajohn, Sathaporn Promwong, Pichaya Supanakoon *Department of Information Engineering, Faculty of Engineering,* *King Mongkut's Institute of Technology Ladkrabang, Bangkok, Thailand*	

1:00 PM - 3:00 PM **Session FPM1-1** **Friday,11 May 2007**

Communication Systems

Chairperson : Tanee Demeechai, Mahanakorn University of Technology

FPM1-1-1 **Modified Decision Feedback Adaptive Equalizer for Turbo Coded DS-CDMA Systems** **892**
1:00 PM
T. Udomsripaiboon[1], N. Sanpote[1], K. Sooksomsatarn[1], C. Benjangkaprasert[2]
[1]School of Information and Communication Technology ,
Narasuan University, Payao Campus, Payao,Thailand
[2]Research Center for Communications and Information Technology (ReCCIT),
King Mongkut's Institute of Technology Ladkrabang, Bangkok, Thailand

FPM1-1-2 **A Channel Estimation Method for Downlink STBC MC-CDMA System on Multi-Path** **896**
1:20 PM **Fading Channel**
Pattanapong Sookkaew, Montree Kumngern, Somyot Junnapiya, Kobchai Dejhan
Research Center for Communication and Information Technology,
King Mongkut's Institute of Technology Ladkrabang, Bangkok, Thailand

FPM1-1-3 **An Extend Bi-directional Arbitrated Decision Feedback Equalizer** **899**
1:40 PM
Samart Moodleah[1], Chawalit Benjangkaprasert[1], Keattisak Sripimanwat[2]
[1]Research Center for Communications and Information Technology (ReCCIT),
King Mongkut's Institute of Technology Ladkrabang, Bangkok, Thailand
[2]National Electronics and Computer Technology Center (NECTEC), Pathumthanee, Thailand

FPM1-1-4 **Narrowband Interference Suppression for UWB-TH System Based On Modified** **903**
2:00 PM **Template Waveform**
Eakaraj Pakdeechard, Monchai Chamchoy, Sathaporn Promwong
Faculty of Engineering, King Mongkut's Institute of Technology Ladkrabang, Bangkok, Thailand

FPM1-1-5 **A Survey on Non-Coherent QAM Receiver Structure in Noisy Channel** **907**
2:20 PM
Shahab Asoodeh, Alireza Rezazade
Department of Electrical and Computer Engineering, Shahid Behehsti University

FPM1-1-6 **Signal Transformation Using Harmonic Transform Based on OFDM** **911**
2:40 PM
Saiyan Saiyod, Sakchai Thipchaksurat, Ruttikorn Varakulsiripunth
Research Center for Communication and Information Technology (ReCCIT),
King Mongkut's Institute of Technology Ladkrabang, Bangkok, Thailand

1:00 PM - 3:00 PM **Session FPM1-5** **Friday,11 May 2007**

UWB Technology

Chairperson : Revee Phromloungsri, Mahanakorn University of Technology

FPM1-5-1 **Location Estimation Based on Modified TOA Measurements for UWB Network** **915**
1:00 PM
Tawatchai Jantaworn, Monchai Chamchoy, Sathaporn Promwong, Nikorn Sukutamtanti
Faculty of Engineering, King Mongkut's Institute of Technology Ladkrabang, Bangkok, Thailand

FPM1-5-2	**Accuracy Analysis of Focusing Resolution with TR EM Pulse Propagation for UWB**	**919**
1:20 PM	**Imaging Systems**	
	Tanaporn Payommai[1], Pichaya Supanakoon[1,2], Sathaporn Promwong[1,2], Nikorn Sukutamtanti[1], Jun-ichi Takada[3]	
	[1]Department of Information Engineering, Faculty of Engineering	
	[2]Research Center for Communications and Information Technology (ReCCIT), King Mongkut's Institute of Technology Ladkrabung, Bangkok, Thailand	
	[3]Graduate School of Science and Engineering, Tokyo Institute of Technology, Tokyo, Japan	
FPM1-5-3	**Performance Evaluation of Free Space Transmission Gain for Ultra Wideband Impulse**	**923**
1:40 PM	**Radio System**	
	Narongsak Manosittichai, Sathaporn Promwong	
	Department of Information Engineering, Faculty of Engineering, King Mongkut's Institute of Technology Ladkrabang, Bangkok, Thailand	
FPM1-5-4	**An Ultra-wideband CPW-Fed Elliptical Loop Slot Antenna**	**927**
2:00 PM	Rapeepan Keawon, Prayoot Akkaraekthalin, Vech Vivek	
	Department of Electrical Engineering, Faculty of Engineering, King Mongkut's Institute of Technology North Bangkok, Bangkok, Thailand	
FPM1-5-5	**Ultra Wideband Series-Fed Printed Dipole Antenna Arrays with a Log-periodic**	**931**
2:20 PM	**Structure**	
	Chittawan Choeysakul[1], Sarawuth Chaimool[2], Prayoot Akkaraekthalin[1,2]	
	[1]Communication Engineering, Thai-German Graduate School of Engineering, King Mongkut's Institute of Technology North Bangkok, Bangkok, Thailand	
	[2]Department of Electrical Engineering, Faculty of Engineering, King Mongkut's Institute of Technology North Bangkok, Bangkok, Thailand	
FPM1-5-6	**A Study of Interference Signal of Ultra Wideband to Wireless Local Areal Network**	**935**
2:40 PM	Pathamavadee Kositsakul, Sathaporn Promwong	
	Department of Information Engineering, Faculty of engineering, King Mongkut's Institute of Technology Ladkrabang, Bangkok, Thailand	

3:20 PM - 5:00 PM	**Session FPM2-1**	**Friday,11 May 2007**
	Antenna Technology	
	Chairperson : Chuwong Phongcharoenpanich, King Mongkut's Institute of Technology Ladkrabang	
FPM2-1-1	**Bandwidth Enhancement of a CPW-Fed Rectangular Slot Antenna**	**939**
3:20 PM	P. Seangsae[1], N. Anantrasirichai[1], J. Nakasuwan[2], T. Wakabayashi[3]	
	[1]Research Center for Communications and Information Technology (ReCCIT), King Mongkut's Institute of Technology Ladkrabung, Bangkok, Thailand	
	[2]Department of Electronic and Telecommunication Engineering, Faculty of Engineering, Rajamangala University of Technology Thanyaburi, Pathumthanee, Thailand	
	[3]School of Information Science and Technology, Tokai University, Kanagawa, Japan	

FPM2-1-2	**CPW-Fed Rectangular Slot Antenna with Tuning Stub for Dual Frequency**	**943**
3:40 PM	S. Kaewsupan[1], N. Anantrasirichai[1], P. Rakluea[2], T. Wakabayashi[3] *[1]Research Center for Communications and Information Technology (ReCCIT), King Mongkut's Institute of Technology Ladkrabung, Bangkok, Thailand* *[2]Department of Electronic and Telecommunication Engineering, Faculty of Engineering, Rajamangala University of Technology Thanyaburi, Pathumthanee, Thailand* *[3]School of Information Science and Technology, Tokai University, Kanagawa, Japan*	
FPM2-1-3	**Microstrip-Fed Acute Angle Wide-Slot Antenna**	**947**
4:00 PM	P. Wiriyacosol[1], C. Benjangkaprasert[1], N. Anatrasirichai[1], T. Wakabayashi[2] *[1]Research Center for Communications and Information Technology (ReCCIT), Department of Information Engineering, Faculty of Engineering, King Mongkut's Institute of Technology Ladkrabang, Bangkok, Thailand* *[2]School of Information Science and Technology, Tokai University, Kanagawa, Japan*	
FPM2-1-4	**Closed-form Expressions of Mutual Impedance between Perpendicular Thin Dipoles**	**951**
4:20 PM	T. Limpiti, M. Krairiksh *Research Center for Communications and Information Technology (ReCCIT), Department of Information Engineering, Faculty of Engineering, King Mongkut's Institute of Technology Ladkrabang, Bangkok, Thailand*	
FPM2-1-5	**Structural Analysis of Trapezoidal Dual Loop Antenna for Communication**	**955**
4:40 PM	**Performance Enhancement of LF-RFID** Supakit Kawdungta[1], Phairote Wounchoum[1], Chuwong Phongcharoenpanich[1], Danai Torrungrueng[2] *[1]Research Center for Communications and Information Technology, Department of Information Engineering, Faculty of Engineering, King Mongkut's Institute of Technology Ladkrabang, Bangkok, Thailand* *[2]Faculty of Engineering and Technology, Asian University, Chon Buri, Thailand*	
3:20 PM - 5:00 PM	**Session FPM2-5**	**Friday,11 May 2007**
	Communication Technology Chairperson : Keattisak Sripimanwat, National Electronics and Computer Technology Center	
FPM2-5-1	**An Implementation of a SCADA System based on Embedded TCP/IP Protocol Stack and**	**959**
3:20 PM	**Internet** Nguyen Ich Vinh, Watit Benjapolakul, Krisada Visavateeranon *Department of Electrical Engineering, Faculty of Engineering, Chulalongkorn University, Bangkok, Thailand*	
FPM2-5-2	**Channel Modeling and Simulated for Broadband Satellite**	**963**
3:40 PM	Ekavit Nukfron[1], Narong Hemmakorn[2], Suviporn Sitichepak[2] *[1]School of Graduate King Mongkut's Institute of Technology Ladkrabang , Bangkok, Thailand* *[2]Departments of Telecommunication Engineering, Faculty of Engineering, King Mongkut's Institute of Technology Ladkrabang, Bangkok, Thailand*	

FPM2-5-3	**Ionospheric Variability of foF2 at Low Latitude Station, Thailand**	**967**
4:00 PM	N. Wichaipanich, R. Attaviriyasuwon, N. Hemmakorn, P. Supnithi *Research Center for Communications and Information Technology (ReCCIT),* *Department of Information Engineering, Faculty of Engineering,* *King Mongkut's Institute of Technology Ladkrabang, Bangkok, Thailand*	
FPM2-5-4	**Improvement of Aggressive Fairness in RPR Based Dynamic Fair Rate Estimation**	**971**
4:20 PM	Thawatchai Rungsubsin, Siriwhaddhanah Pongpadpinit *Department of Telecommunications Science, Faculty of Science and Technology,* *Assumption University, Bangkok, Thailand*	
FPM2-5-5	**Investigation of Rain Attenuation on Vertical and Horizontal Polarizations of Thaicom**	**975**
4:40 PM	**Satellites** Pongputhai Udomareyasap, Donekeo Lakanchanh, Narong Hemmakorn, Nipha Leelaruji *Research Center for Communications and Information Technology (ReCCIT),* *Department of Information Engineering, Faculty of Engineering,* *King Mongkut's Institute of Technology Ladkrabang, Bangkok, Thailand*	

10:50 AM - 12:10 AM **Session TAM1-9** **Thursday,10 May 2007**

Image Technology

Chairperson : Akira Taguchi, Masashi Institute of Technology

TAM1-9-1	**Multiple Correspondences in Stereoscopy Using Frequency-Encoding Light Point**	**979**
10:50 AM	P. Tosranon [1,2], S. Bunluechokchai[2], C. Pintavirooj[1], M. Sangworasil[1] [1]*Research Center for Communications and Information Technology (ReCCIT),* *King Mongkut's Institute of Technology Ladkrabang, Thailand* [2]*Department of Industrial Physics and Medical Instrumentation,* *King Mongkut's Institute of Technology North Bangkok, Bangkok, Thailand*	
TAM1-9-2	**Automatic Alignment of White Blood Cell Using Principal Axis: The Improvement For**	**983**
11:10 AM	**Classification** P.Yampri[1], C.Pintavirooj[1], M. Sangworasil[1], P.Lertprasert[1], T.Rerksngaem[2] [1]*Research Center for Communication and Information Technology (ReCCIT)* *King Mongkut's Institute of Technology Ladkrabang, Bangkok, Thailand* [2]*Faculty of Allied Health, Thammasart University, Prathumthani, Thailand*	
TAM1-9-3	**Load Balancing Algorithm for Multipoint Video Conferencing Control Unit**	**987**
11:30 AM	Jirayu Charoenviriyaphap, Surin Kittitornkun *Department of Computer Engineering, Faculty of Engineering,* *King Mongkut's Institute of Technology Ladkrabang, Bangkok, Thailand*	
TAM1-9-4	**Continuous Thai Sign Language Recognition using HMM with Transition Models**	**991**
11:50 AM	Arunee Jaruwanawat, Nopporn Chotikakamthorn *Research Center for Communications and Information Technology,* *King Mongkut's Institute of Technology Ladkrabang, Bangkok, Thailand*	

1:00 PM - 3:00 PM **Session TPM1-7** **Thursday,10 May 2007**

Image Processing 1

Chairperson : Rachada Kangkachandra, Thammasat University

TPM1-7-1 **Shape-Based Object Segmentation by 2-Stage Level Set Method** **995**
1:00 PM Sarawut Tae-O-Sot[1], Supatana Auethavekiat[2], Somchai Jitapunkul[3]
[1]Department of Electrical Engineering, Naresuan University Phayao Campus, Phayao, Thailand
[2]National Electronics and Computer Technology Center, Patumthanee, Thailand
[3]Center of Excellence in Telecommunication Technology,
Department of Electrical Engineering, Chulalongkorn University, Bangkok, Thailand

TPM1-7-2 **Digital Image Compression using VPIC Algorithm in Wavelet Domain** **999**
1:20 PM K. Tongtar, N. Moongflangklang, F. Cheevasuvit
Department of Instrumentation Engineering, Faculty of Electrical Engineering,
King Mongkut's Institute of Technology Ladkrabang, Bangkok Thailand

TPM1-7-3 **Thai Banknote Verification and Recognition** **1003**
1:40 PM Narin Jeeranantasin, Pranchalee Rattanasakronchai
Department of Control System and Instrumentation Engineering,
King Mongkut's University of Technology Thonburi, Bangkok, Thailand

TPM1-7-4 **Locating and Reading Barcodes from Images Captured by Camera of Mobile Phone** **1007**
2:00 PM Sakda Suwanchatree, Pranchalee Rattanasakornchai
Control System and Instrumentation Engineering,
King Mongkut's University of Technology Thonburi, Bangkok, Thailand

TPM1-7-5 **Decision Combination of Multiple Classifier Systems for Multiresolution Face** **1011**
2:20 PM **Recognition**
P. Sermwuthisarn[1], W. Asdornwised[1], S. Jitapunkul[1], S. Marukatat[2]
[1]Department of Electrical Engineering, Chulalongkorn University, Bangkok, Thailand
[2]National Electronics and Computer Technology Center (NECTEC), Pathumthani, Thailand

TPM1-7-6 **On-Line Character Recognition for Khmer Numeral based on DP matching** **1015**
2:40 PM **of Barycenter Trajectory**
P. Thumwarin[1], S. Khem[1], K. Janchitrapongvej[1], T.Matsuura[2]
[1]Faculty of Engineering and Research Center for Communications and Information Technology ,
King Mongkut's Institute of Technology Ladkrabang, Bangkok, Thailand
[2]Faculty of Information Technology and Electronics, Tokai University, Kanagawa, Japan

3:20 PM - 5:00 PM **Session TPM2-3** **Thursday,10 May 2007**

Pattern Recognition and Others

Chairperson : Kosin Chamnongthai, King Mongkut's University of Technology Thonburi

TPM2-3-1 **The Use of Context-free Grammars in Isolated Word Recognition** **1019**
3:20 PM C. Chirathamjaree
Edith Cowan University, Australia

TPM2-3-2 **3:40 PM**	**Curvature Tree for Isolated Unconstrained Lao Handwritten Character Recognition** Khampheth Bounnady[1], Boontee Kruatrachue[1], Takenobu Matsuura[2] *[1]Computer Engineering Department, Faculty of Engineering,* *King Mongkut's Institute of Technology Ladkrabang, Bangkok, Thailand* *[2]Communications Engineering Department, Faculty of Information Technology and Electronics,* *Tokai University, Japan*	**1022**
TPM2-3-3 **4:00 PM**	**Combination of Self-Organizing Map and Fuzzy C-Means Algorithms for Project Performance Segmentation in Agricultural Technology Transfer and Service Centers** Sasithorn Mongkolsripattana, Anongnart Srivihok *Department of Computer Science, Faculty of Science, Kasetsart University, Bangkok, Thailand*	**1026**
TPM2-3-4 **4:20 PM**	**Automatic Floor-Mopping Robot** Wiruch Kongsin, Poj Tangamchit *Department of Control System and Instrument Engineering,* *King Mongkut's University of Technology Thonburi, Bangkok, Thailand*	**1030**
TPM2-3-5 **4:40 PM**	**Sansarn Offline: A Search Engine Tool for Managing, Archiving and Retrieving Offline Web Contents** Choochart Haruechaiyasak, Chatchawal Sangkeettrakarn *Human Language Technology (HLT) Laboratory,* *National Electronics and Computer Technology Center (NECTEC), Pathumthani, Thailand*	**1034**

3:20 PM - 5:00 PM **Session TPM2-7** **Thursday,10 May 2007**

Speech And Acoustic Technology

Chairperson : Rachada Kangkachandra, Thammasat University

TPM2-7-1 **3:20 PM**	**Combined Simulated Data Adaptation and Piecewise Linear Transformation for Robust speech recognition** Nattanun Thatphithakkul[1], Boontee Kruatrachue[1], Chai Wutiwiwatchai[2], Sanparith Marukatat[2,] Vataya Boonpiam[2] *[1]King Mongkut's Institute of Technology Ladkrabang, Bangkok , Thailand* *[2]National Electronics and Computer Technology Center, Pathumthani, Thailand*	**1038**
TPM2-7-2 **3:40 PM**	**Prosody-based Naturalness Improvement in Thai Unit-selection Speech Synthesis** A. Rugchatjaroen, A. Thangthai, S. Saychum, N. Thatphithakkul, C. Wutiwiwatchai *Human Language Technology Laboratory,* *National Electronics and Computer Technology Center (NECTEC), Pathumthani, Thailand*	**1042**
TPM2-7-3 **4:00 PM**	**Variable Momentum LMS Algorithm for Adaptive Howling Suppression in Audio Amplifier Systems** W. Loetwassana[1], R. Punchalard[2], J. Koseeyaporn[1], P. Wardkein[1] *[1]Department of Telecommunication Engineering, Faculty of Engineering,* *King Mongkut's Institute of Technology Ladkrabang, Bangkok, Thailand* *[2]Department of Telecommunication Engineering, Faculty of Engineering,* *Mahanakorn University of Technology, Bangkok, Thailand*	**1046**

TPM2-7-4	**The Improvement a New Method for a Front-End of Military Vehicles Sound**	**1050**
4:20 PM	**Recognition Using EHMM**	
	Yingyot Sa-nguanpuag[1], Panuthat Boonpramuk[2]	
	[1]Graduate school of Electrical engineering,	
	King Mongkut's University of Technology Thonburi, Bangkok, Thailand	
	[2] Instrumentation and Control System Engineering Department,	
	King Mongkut's University of Technology Thonburi, Bangkok, Thailand	
TPM2-7-5	**Precise Phone Boundary Detection using Selective Context-dependent Acoustic**	**1054**
4:40 PM	**Refinement**	
	Sirinoot Boonsuk, Proadpran Punyabukkana, Atiwong Suchato	
	Department of Computer Engineering,	
	Faculty of Engineering, Chulalongkorn University, Bangkok, Thailand	

8:30 AM - 9:50 AM	**Session FAM1-6**	**Friday,11 May 2007**
	Digital Signal Processing 1	
	Chairperson : Tanee Demeechai, Mahanakorn University of Technology	
FAM1-6-1	**Novel Precision Current-mode Full-wave Rectifier and Class B Push-Pull Current**	**1058**
8:30 AM	**Amplifier Using BiCMOS Current-controlled Current Conveyors**	
	Winai Jaikla[1], Montree Siripruchyanun[2]	
	[1]Electric and Electronic Program, Faculty of Industrial Technology,	
	Suan Sunandha Rajabhat University, Bangkok, Thailand	
	[2]Department of Teacher Training in Electrical Engineering, Faculty of Technical Education,	
	King Mongkut's Institute of Technology North Bangkok, Bangkok, Thailand	
FAM1-6-2	**Optical Diffraction-Based Object Dimensions Measurement in Reflection and**	**1062**
8:50 AM	**Transmission Modes**	
	Sarun Sumriddetchkajorn, Kosom Chaitavon	
	Photonics Technology Laboratory,	
	National Electronics and Computer Technology Center, Pathumthani, Thailand	
FAM1-6-3	**CCCDTAs-based Versatile Quadrature Oscillator and Universal Biquad Filter**	**1065**
9:10 AM	Winai Jaikla[1], Montree Siripruchyanun[2]	
	[1]Electric and Electronic Program, Faculty of Industrial Technology,	
	Suan Sunandha Rajabhat University, Bangkok, Thailand	
	[2]Department of Teacher Training in Electrical Engineering, Faculty of Technical Education,	
	King Mongkut's Institute of Technology North Bangkok, Bangkok, Thailand	
FAM1-6-4	**A Study of Optical Phase Retardation and Absorption Measurement by using a Fiber**	**1069**
9:30 AM	**Loop Mirror Architecture**	
	Kanitha Katanyukunanon[1], Sarun Sumriddetchkajorn[2], Toemsak Srikhirin[1]	
	[1]Department of Physics, Faculty of Science, Mahidol University, Bangkok, Thailand	
	[2]Photonics Technology Laboratory,	
	National Electronics and Computer Technology Center(NECTEC),	
	National Science and Technology Development Agency (NSTDA), Pathumthani, Thailand	

10:30 AM - 12:10 AM **Session FAM2-6** **Friday,11 May 2007**

Image Processing 2

Chairperson : Manas Sangworasil, King Mongkut's Institute of Technology Ladkrabang

FAM2-6-1 **Ultrasonic Reflection Tomography using Frequency Centroid-Shift Method** **1073**
10:30 AM
T. Onemanisone[1], C. Pintavi rooj[1], K. Wong-ek [2], S. Sangworasilp[1]
[1]Department of Electronics, Faculty of Engineering,
King Mongkut's Institute of Technology Ladkrabang, Bangkok, Thailand
[2]Department of Medical Technology, Faculty of Allied Health Science,
Thammasat University, Pathumthani, Thailand

FAM2-6-2 **Non-uniform Color Quantization for Content-based Image Retrieval** **1077**
10:50 AM
R. Sombutkaew, O. Chitsobhuk
Department of Computer Engineering, Faculty of Engineering,
King Mongkut's Institute of Technology Ladkrabang, Bangkok, Thailand

FAM2-6-3 **Image Coding Using Vector Quantization Based on Low-Frequency Component to** **1081**
11:10 AM **Determine Block Size**
Tanasak Phanprasit[1], Manas Sangworasil[1,2], Kosin Chamnongthai[3]
[1]Research Center for Communication and Information Technology (ReCCIT),
King Mongkut's Institute of Technology Ladkrabang, Bangkok, Thailand
[2]Computer Research and Service Center,
King Mongkut Institute of Technology Ladkrabang, Bangkok, Thailand
[3]Department of Electronic and Telecommunication Engineering,
King Mongkut's University of Technology Thonburi, Bangkok, Thailand

FAM2-6-4 **Image Coding Using Vector Quantization Based on System Error Compensate** **1085**
11:30 AM
Tanasak Phanprasit[1], Manas Sangworasil[1,2], Kosin Chamnonthai[3]
[1]Department of Electronics, Research Center for Communications and Information Technology,
King Mongkut Institute of Technology Ladkrabang, Bangkok, Thailand
[2]Computer Research and Service Center,
King Mongkut Institute of Technology Ladkrabang, Bangkok, Thailand
[3]Department of Electronic and Telecommunication Engineering,
King Mongkut's University of Technology Thonburi, Bangkok, Thailand

FAM2-6-5 **Direct Manipulation of 3D Curves with Pseudo- Physical Simulation Model** **1089**
11:50 AM
Pathawut Pichaichanlert, Nopporn Chotikakamthorn
Research Center for Communications and Information Technology,
King Mongkut's Institute of Technology Ladkrabang, Bangkok, Thailand

10:30 AM - 12:10 AM **Session FAM2-8** **Friday,11 May 2007**

Digital Signal Processing 3

Chairperson : K.R. Rao, The University of Texas at Arlington

FAM2-8-1 **Sequence Mirroring Properties of Orthogonal Transforms Having Even** **1094**
10:30 AM **and Odd Symmetric Vectors**
Do Nyeon Kim, K. R. Rao
Department of Electrical Engineering, University of Texas at Arlington, USA

FAM2-8-2	**Multi-Resolution Belief Propagation for StereoVision**	**1098**
10:50 AM	Preeyakorn Tipwai, Suthep Madarasmi *Department of Computer Engineering,* *King Mongkut's University of Technology Thonburi, Bangkok, Thailand*	
FAM2-8-3	**Estimating Radar Cross Section by Anisotropic Diffusion**	**1102**
11:10 AM	Sathit Intajag *King Mongkut's Institute of Technology Ladkrabang, Bangkok, Thailand*	
FAM2-8-4	**Fitting Model on BOD Response Curve**	**1106**
11:30 AM	Ekkawat Choona[1], Pakorn Kaewtrakulpong[1], Werasak Surareungchai[2], Pornpimol Sritongkam[2] *[1]Department of Instrumentation and Control System Engineering ,* *King Mongkut's University of Technology Thonburi, Bangkok, Thailand* *[2]Faculty of Engineering,Pilot Plant Development and Training Institute ,* *King Mongkut's University of Technology Thonburi, Bangkok, Thailand*	
FAM2-8-5	**Design of Adaptive Chrominance Delay Equalizer using Linear-Phase FIR Digital Filter**	**1110**
11:50 AM	V. Chutchavong, C. Benjangkaprasert, O. Sangaroon, K. Janchitrapongvej *Faculty of Engineering,* *King Mongkut's Institute of Technology Ladkrabang, Bangkok, Thailand*	

3:20 PM - 4:40 PM	**Session FPM2-6** **Image Processing 3** Chairperson : Vutipong Areekul, Kasetsart University	**Friday,11 May 2007**
FPM2-6-1	**Quantum Dot Molecule Chains and Their Polarization Photoluminescence**	**1114**
3:20 PM	N. Budsayaplakorn, S. Thainoi, S. Panyakeow *Department of Electrical Engineering, Faculty of Engineering,* *Chulalongkorn University, Bangkok, Thailand*	
FPM2-6-2	**3D Deformable Mesh Aided Dentistry**	**1117**
3:40 PM	C. Sinthanayothin, W. Bholsithi, W. Tharanon *Advanced Dental Technology Center (ADTEC),* *National Science and Technology Development Agency (NSTDA), PathumThani, Thailand*	
FPM2-6-3	**A Localization Method for Thailand License Plates**	**1121**
4:00 PM	Therdsak Chanfuangfoo[1], Pakorn Kaewtrakulpong[1], Supakorn Siddhichai[2] *[1]Department of Control System and Instrumentation Engineering ,* *King Mongkut's University of Technology Thonburi, Bangkok, Thailand,* *[2]National Electronics and Computer Technology Center (NECTEC), Pathumthani, Thailand*	
FPM2-6-4	**A Study of Normalized Cross Correlation Pattern Matching Algorithm in Thermal Imagery**	**1125**
4:20 PM	Sarun Sumriddetchkajorn, Armote Somboonkaew *National Electronics and Computer Technology Center, Pathumthani, Thailand*	

10:50 AM - 12:10 AM | **Session TAM1-2** | **Thursday,10 May 2007**

Processors

Chairperson : Prabhas Chongsatitwattana, Chulalongkorn University

TAM1-2-1 **Hardware Cryptography-Embedded Multimedia Mobile Processor** **1128**

10:50 AM

Masa-aki Fukase[1], Hiroki Takeda[1], Tomoaki Sato[2]

[1]*Faculty of Science and Technology, Hirosaki University, Japan*

[2]*Computer and Network Systems Center, Hirosaki University, Japan*

TAM1-2-2 **HDL Design and Verification of Digital Signal Processor for 2.4 GHz ZigBee Radio Receiver** **1132**

11:10 AM

T. Demeechai

Department of Telecommunication Engineering,

Mahanakorn University of Technology, Bangkok, Thailand

TAM1-2-3 **An Embedded Processor with Instruction Packing** **1135**

11:30 AM

C. Satayavibul, P. Chongstitvatana

Department of Computer Engineering,

Chulalongkorn University, Bangkok, Thailand

TAM1-2-4 **The AES Encryption Circuit on a Reconfigurable Hardware** **1139**

11:50 AM

J. Sripornprasert, P. Chongstitvatana

Department of Computer Engineering,

Chulalongkorn University, Bangkok, Thailand

1:00 PM - 2:40 PM | **Session TPM1-9** | **Thursday,10 May 2007**

Software Engineering and Applications

Chairperson : Prabhas Chongsatitwattana, Chulalongkorn University

TPM1-9-1 **Hardware Model Checking and Computational Temporal Logic(CTL)** **1143**

1:00 PM

Hamid Shojaei[1], Majid Nabi[2], Zainalabedin Navabi[2], Mohammad Reza Kakoee[1]

[1]*Islamic Azad University, Damavand Branch*

[2]*CAD Research Group, Faculty of Engineering, University of Tehran , Tehran, Iran*

TPM1-9-2 **Undeniable Fair Electronic Auction** **1147**

1:20 PM

Yongyuth Permpoontanalarp, Montri Apiromvorakarn

Department of Computer Engineering, Faculty of Engineering,

King Mongkut's University of Technology Thonburi, Bangkok, Thailand

TPM1-9-3 **A Cost Model for Bitmap Index Partition Techniques** **1151**

1:40 PM

Manlika Honghirun, Songrit Maneewongvatana

Department of Computer Engineering,

King Mongkut's University of Technology Thonburi, Bangkok, Thailaind

TPM1-9-4 **Towards Evolvable Safety Arguments** **1155**

2:00 PM

Paul Mason, Chadchai Mattayom

Shinawatra University, Bangkok, Thailand

TPM1-9-5	**Extending Cross-Tool Traceability to Source Code**	**1159**
2:20 PM	P. A. J. Mason *Shinawatra University, Bangkok, Thailand*	

1:00 PM - 3:00 PM	**Session TPM1-10** **Network Systems**	**Thursday,10 May 2007**
	Chairperson : Phongsak Keeratiwintakorn, King Mongkut's Institute of Technology North Bangkok	
TPM1-10-1	**Cellular Wireless Network Design with Genetic Algorithm**	**1163**
1:00 PM	Pakorn Leesutthipornchai[1], Naruemon Wattanapongsakorn[1], Chalermpol Charnsripinyo[2] [1]*Department of Computer Engineering,* *King Mongkut's University of Technology Thonburi, Bangkok, Thailand* [2]*National Electronics and Computer Technology Center, Pathumthani, Thailand*	
TPM1-10-2	**Performance Analysis of IEEE 802.11g Access Point under Heavy-Loaded Condition**	**1167**
1:20 PM	Roungsan Chaisricharoen, Thitiporn Pramoun *School of Information Technology, Mae Fah Luang University, Chiang Rai, Thailand*	
TPM1-10-3	**Time-Optimal Graph Algorithms for Finding Adjacent and Non-Adjacent**	**1171**
1:40 PM	**Nodes on a Completely Overlapping Network** Rasika Winit[1], Sanpawat Kantabutra[2], Saowaluk Rattanaudomsawat[3] [1]*Schools of Physics and Biological Earth and Environmental Science,* *Faculty of Science, the University of New South Wales, Sydney, Australia* [2]*The Theory of Computation Group, Computer Science Department,* *Chiang Mai University, Thailand* [3]*School of Information Technology, Mae Fah Luang University, Chiang Rai, Thailand*	
TPM1-10-4	**On the Effects of VLAN in WLAN-based Positioning System**	**1174**
2:00 PM	Chalermchai Khauphung[1], Phongsak Keeratiwintakorn[1], Kamol Kaemarungsi[2] [1]*Department of Electrical Engineering,* *King Mongkut's Institute of Technology North Bangkok, Bangkok, Thailand* [2]*National Electronics and Computer Technology Center (NECTEC), Pathumthanee, Thailand*	
TPM1-10-5	**On the Effect of Roadside Stations in Routing for Inter-Vehicle Communications**	**1178**
2:20 PM	Phitsanu Eamsomboon[1], Phongsak Keeratiwintakorn[1], Chaichana Mitrpant[2] [1]*Department of Electrical Engineering,* *King Mongkut's Institute of Technology North Bangkok, Bangkok, Thailand* [2]*National Electronics and Computer Technology Center (NECTEC), Pathumthanee, Thailand*	
TPM1-10-6	**The Improvement of TCP Performance in Heterogeneous Networks**	**1182**
2:40 PM	K. Kuprasert, P. Oothongsap *Department of Electrical Engineering, Faculty of Engineering,* *King Mongkut's Institute of Technology North Bangkok, Bangkok, Thailand*	

3:20 PM - 5:00 PM **Session TPM2-9** **Thursday,10 May 2007**

Simulation and Modelling

Chairperson : Nachol Chaiyaratana, King Mongkut's Institute of Technology North Bangkok

TPM2-9-1 **Early Warning of Internet Worms by ICMP Scan Data Visualization** **1186**
3:20 PM
Pitichai Pitimaneeyakul, Saroj K. Biswas
Department of Electrical and Computer Engineering, Temple University, Philadelphia

TPM2-9-2 **A Cost-Efficient Algorithm for Arbitrary CRCW PRAM Simulation** **1190**
3:40 PM
Martti Forsell
Platform Architectures Team,
VTT Technical Research Center of Finland, Oulu, Finland

TPM2-9-3 **Development of Low-cost Parachute Training Simulaion System** **1194**
4:00 PM
Sombat Hathairattananon, Thavida Maneewarn
Institute of Field Robotics (FIBO),
King Mongkut's University of Technology Thonburi, Bangkok, Thailand

TPM2-9-4 **Separation of Concerns in Modeling System Software for Automate Code Generation** **1198**
4:20 PM
Paniti Netinant
Computer Sceince Departmnet, Bangkok University, Bangkok, Thailand

TPM2-9-5 **Multidimensional Binary Clustering Tree for Surface Simplification of Point-Sampled** **1202**
4:40 PM **Surface**
Thanet Suphan, Chakrit Watcharopas
Department of Computer Science, Faculty of Science, Kasetsart University, Bangkok, Thailand

8:30 AM - 10:10 AM **Session FAM1-8** **Friday,11 May 2007**

Information Technology 1

Chairperson : Tong Srikhacha, The Telephone Organization of Thailand

FAM1-8-1 **Data Prediction by Support Vector Regression with a Decomposition Method** **1205**
8:30 AM
Phayung Meesad[1], Tong Srikhacha[2]
[1]*Department of Teacher Training in Electrical Engineering, Faculty of Technical Education*
[2]*Department of Information Technology, Faculty of Information Technology,*
King Mongkut's Institute of Technology North Bangkok, Bangkok, Thailand

FAM1-8-2 **Knowledge Management System with Root Cause Analysis for IT Service Desk in** **1209**
8:50 AM **Banking Business**
Padej Phomasakha Na Sakolnakorn[1], Phayung Meesad[2]
[1]*Faculty of Information Technology,*
King Mongkut's Institute of Technology North Bangkok, Bangkok, Thailand
[2]*Faculty of Technical Education,*
King Mongkut's Institute of Technology North Bangkok, Bangkok, Thailand

FAM1-8-3 **Web Metadata Design for Web Content Management** **1213**
9:10 AM
Natthaphon Sueb-Am, Mayuree Lertwatechakul
Department of Information Engineering, Faculty of Engineering,
King Mongkut's Institute of Technology Ladkrabang, Bangkok, Thailand

FAM1-8-4	**Towards Intelligent and Adaptive Digital Library Services: Associating Contents with**	**1217**
9:30 AM	**User Profile and Usage Pattern in Digital Libraries**	
	Yenruedee Chanwirawong, Md Maruf Hasan	
	School of Technology, Shinawatra University, Bangkok, Thailand	
FAM1-8-5	**Improve XML Web Services' Performance By Compressing XML Schema tag**	**1221**
9:50 AM	Tanakorn Wichaiwong, Chuleerat Jaruskulchai	
	Department Of Computer Science, Faculty of Science, Kasetsart University, Bangkok, Thailand	
10:30 AM - 11:50 AM	**Session FAM2-9**	**Friday,11 May 2007**
	Medical Engineering and Applications	
	Chairperson : Nachol Chaiyaratana, King Mongkut's Institute of Technology North Bangkok	
FAM2-9-1	**An Incremental Learning Algorithm Based-On Mahalanobis Distance for Breast**	**1225**
10:30 AM	**Cancer Diagnosis**	
	Sunantha Sodsee[1], Maytiyanin Komkhao[1], Phayung Meesad[2]	
	[1]*Department of Information Technology Faculty of Information Technology*	
	King Mongkut's Institute of Technology North Bangkok, Bangkok, Thailand	
	[2]*Department of Teacher Training in Electrical Engineering Faculty of Technical Education*	
	King Mongkut's Institute of Technology North Bangkok, Bangkok, Thailand	
FAM2-9-2	**Thalassaemia Classification by a Neural Network and a C4.5 Decision Tree**	**1229**
10:50 AM	P. Aksornpan[1], A. Assawamakin[2], N. Chaiyaratana[1], C. Limwongse[2]	
	[1]*Research and Development Centre for Intelligent Systems*,	
	Department of Electrical Engineering,	
	King Mongkut's Institute of Technology North Bangkok, Bangkok, Thailand	
	[2]*Division of Molecular Genetics, Department of Research and Development*,	
	Faculty of Medicine Siriraj Hospital, Mahidol University, Bangkok, Thailand	
FAM2-9-3	**A Numerical Model of Magnetic Fluid Flow in Blood Vessel with Nail-like Permanent**	**1233**
11:10 AM	**Magnet using Finite Element Method**	
	M. Lohakan[1,2], C. Seetao[2], S. Boonsang[1], C. Pintavirooj[1]	
	[1]*Research Center for Communication and Information Technology (ReCCIT),*	
	King Mongkut's Institute of Technology Ladkrabang, Bangkok, Thailand	
	[2]*Department of Teacher Training in Electrical Engineering Faculty of Technical Education ,*	
	King Mongkut's Institute of Technology North Bangkok, Bangkok, Thailand	
FAM2-9-4	**Reversal Transform for Prokaryotic Organisms**	**1237**
11:30 AM	Noppadon Khiripet, Jutarat Maneewattanapluk	
	National Electronics and Computer Technology Center, Pathumthani, Thailand	

1:00 PM - 3:00 PM	Session FPM1-8	Friday,11 May 2007

Information Technology 2

Chairperson : Tong Srikhacha, The Telephone Organization of Thailand

FPM1-8-1	**Computing the Diameter of a Point Set on a Completely Overlapping Network**	**1240**
1:00 PM	Saowaluk Rattanaudomsawat[1], Prapaporn Techa-angkoon[2] [1]*School of Information Technology,* *Mae Fah Luang University, Chiang Rai, Thailand* [2]*The Theory of Computation Group, Computer Science Department,* *Chiang Mai University, Chiang Mai, Thailand*	
FPM1-8-2	**Classification using Semi-Lazy Learned First Order Rules**	**1244**
1:20 PM	Sarawut Lueangampol, Sukree Sinthupinyo *Department of Computer Science, Faculty of Science and Technology,* *Thammasat University, Bangkok, Thailand*	
FPM1-8-3	**Object-Oriented Design for Thai Herbal Taxonomy**	**1248**
1:40 PM	Surangkana Rawungyot *School of Information and Communication Technology,* *Naresuan University, Phayao, Thailand*	
FPM1-8-4	**Computer Viruses Metadata**	**1252**
2:00 PM	Chittanond Pheunphiphop, Mayuree Lertwatechakul *Department of Information Engineering Faculty of Engineering,* *King Mongkut's Institute of Technology Ladkrabang , Bangkok, Thailand*	
FPM1-8-5	**Consensus of Decisiton Trees**	**1256**
2:20 PM	Suwimon Thaworncharoensukho, Sukree Sinthupinyo *Department of Computer Science, Faculty of Science and Technology,* *Thammasat University, Bangkok, Thailand*	
FPM1-8-6	**Combining learned rules in Ensembles of ILP**	**1260**
2:40 PM	Yutthasit Pukdeeboon, Sukree Sinthupinyo *Department of Computer Science, Faculty of Science and Technology,* *Thammasat University, Bangkok, Thailand*	

1:00 PM - 3:00 PM	Session FPM1-9	Friday,11 May 2007

Data Mining and Knowledge

Chairperson : Raymond Greenlaw, Armstrong University

FPM1-9-1	**Bottom-Up Hierarchical Clustering is CC-Complete**	**1264**
1:00 PM	Raymond Greenlaw[1], Sanpawat Kantabutra[2] [1]*Department of Computer Science,* *Armstrong Atlantic State University, Savannah, Georgia* [2]*The Theory of Computation Group, Computer Science Department,* *Chiang Mai University, Chiang Mai, Thailand*	

FPM1-9-2 **1:20 PM**	**LMC: Label-based Metadata Creation** Pitsanu Lousangfa, Naiyana Sahavechaphan, Jedsada Phengsuwan, Seksit Suwan *Large Scale Simulation Lab, National Electronics and Computer Technology Center(NECTEC), Pathumthani, Thailand*	**1268**
FPM1-9-3 **1:40 PM**	**RNET: Thailand IT Researcher Network Collection, Analysis and Visualization** K. Maleewong, C. Anutariya *School of Technology, Shinawatra University, Bangkok, Thailand*	**1272**
FPM1-9-4 **2:00 PM**	**Object-Oriented Data Structure for Text Association Rule Mining** Alisa Kongthon[1], Ralph Mueller[2], Alan L. Porter[3] [1]*National Electronics and Computer Technology Center, Pathumthani, Thailand* [2]*School of Industrial and Systems Engineering Georgia, Atlanta, USA* [3]*Search Technology university Blvd Norcross, USA*	**1276**
FPM1-9-5 **2:20 PM**	**Semantic Blog: An Approach to Knowledge Sharing and Knowledge Management** S. Wongwilai, C. Anutariya *School of Technology, Shinawatra University, Bangkok, Thailand*	**1280**
FPM1-9-6 **2:40 PM**	**In-Depth Analysis of the Quicksort's Efficiency based on the Threshold and Related Factors** Roungsan Chaisricharoen, Suwiphar Suwatthanaphiset *School of Information Technology, Mae Fah Luang University, Chiang Rai, Thailand*	**1284**

Design and Analysis of Fractal Microstrip Low Pass Filter using Radial-Line Stubs

P.K.Singhal, Pramod Kumar and Neha Verma
Department of Electronics, CSE and IT
Madhav Institute of Technology and Science
Gwalior 474 005, India
E-mail: pks_65@Yahoo.com

Abstract-The design of microstrip filter using radial line stub as reactive elements is investigated. Fractalization of this geometry has been proposed. The frequency response characteristics of specified microstrip radial-line stub filter is compared to the fractal microstrip radial-line stub.

1. Introduction

In microwave applications, it is often required to select or reject signals over specified frequency bands is often required. Filters accomplish this task. Depending on the application, low-pass, high-pass, band-pass or band-reject filtering may be provided [1], [2]. Filters employing open-circuited stubs are the simplest to design [3]. The stubs used are mostly straight and uniformly distributed. However, filters, which use a combination of both uniform and non-uniform characteristic impedance lines, can also be designed.

The non-uniform, characteristic impedance line considered here is a radial line. A low pass Butter- worth filter using radial line stubs is investigated. Fractals in this radial-line low-pass conventional filter have been done. The performance of the conventional and the fractalized geometries have been analyzed using the commercially available IE3D simulator [4]. The transmission line structures are assumed to be planar so that the filters may be realized in microstrip line.

2. Filter Design and Synthesis

A .Radial-line Elements

The standard geometry of a radial-line stub, as defined by Atwater [5], is shown in Fig. 1. The radial-line stub geometry is modified to an isosceles triangle, as shown in Fig. 2.

With the use of radial line stubs, the input impedance Z_{in} of the stubs is modified. For the low pass applications, the simplified expression for Z_{in} is [6]

$$Z_{in} = -jZ_0(l)\cot\left[\frac{\beta}{2}\left\{\frac{l_0^2}{l_0 - l} - (l_0 - l)\right\}\right] \quad (1)$$

$$= -jZ_{max}\cot\left[\frac{\beta l}{2}\left(1 + \frac{Z_{max}}{Z_{min}}\right)\right] \quad (2)$$

where,

$Z_{max} = Z_o(l)$ *and* $Z_{min} = Z_o(0)$

Thus equation (1) is the design equation for the radial-line stubs. It is to introduce the radial–line stub as a reactive element available for use in filter design. The proposed design technique is to use radial-line stubs in place of shunt capacitors and short sections of high impedance uniform transmission line for the series inductors. Using (1), the filter design equations for elements are

Inductors:

$$X_L = Z_o g_m = Z_L \sin(\theta_m) \quad (3)$$

Internal Capacitors (stubs):

$$B_c = \frac{g_m}{Z_o} = \frac{1}{Z_L}\tan(\theta_{m-1}/2) + \frac{1}{Z_{max}}\tan\left[\frac{\theta_m}{2}\left(1 + \frac{Z_{max}}{Z_{min}}\right)\right] + \frac{1}{Z_L}\tan(\theta_{m+1}/2) \quad (4)$$

End Capacitors (stubs):

$$B_C = \frac{1}{Z_L}\tan(\theta_{m\pm1}/2) + \frac{1}{Z_{max}}\tan\left[\frac{\theta_m}{2}\left(1 + \frac{Z_{max}}{Z_{min}}\right)\right] \quad (5)$$

where, Z_L is the characteristics impedance of the inductive line section, Z_O is the filter impedance level, and the electrical length θ is given by

$$\theta_m = \frac{2\pi\sqrt{\varepsilon_{eff}}}{c} lf \quad (6)$$

In equation (6), f is the match frequency i.e. $f = fc$ for inductors and $f \approx fc/2$ for capacitors and

$$\varepsilon_{eff} \equiv \frac{\varepsilon_{eff}\big|_{z=0} + \varepsilon_{eff}\big|_{z=l}}{2}$$

ε_{eff} is the effective relative permittivity. It is the average value of the wide and narrow ends of the stub.

To obtain the electrical length of the inductive line sections and the radial stubs, values for Z_L, Z_{max} and Z_{min} must be chosen.

B Low pass filter synthesis

The attenuation characteristics for a maximally-flat low pass (also called Butterworth) filter, can be mathematically expressed as [2]

$$L_{Ar}(\omega_1) = 10 \log_{10}\left[1 + \varepsilon\left(\omega/\omega_1\right)^{2n}\right] \text{dB} \quad (7)$$

The frequency ω_1 where the attenuation is L_{Ar} is defined as the pass band edge and

$$\varepsilon = |\text{antilog}_{10}(L_{Ar}/10)|-1 \quad (8)$$

Figure 1 shows LC Ladder Network Realization maximally flat low pass prototype filter [2], having resistor terminations at both the ends. The element values may be computed as [3]

$$g_o = 1 \quad (9)$$

$$g_k = 2\sin[(2k-1)\Pi/2n] \quad (10)$$

where $k = 1, 2, 3 \ldots n$

$$g_{n+1} = 1 \quad (12)$$

In this section simulation results for n = 5 equal ripple low pass filter will be presented, with passband ripple of 0.1dB.

A low pass microstrip filter using radial-Line stub, designed using the conventional technique [7, 8] for the following parameters,

Cut-off frequency, fc = 0.75 GHz, dielectric constant, εr = 4.7, substrate height, h = 1.6mm

Characteristics impedance, Z_0 = 50 Ω, Z_L= 100 Ω, Z_{max} = 50 Ω, Z_{min} = 20 Ω. Fig.5 shows the microstrip low pass filter using radial-line Stub.

3. Fractalised Low pass radial-line Filter

Fractalization has been done for this low pass radial-line filter, the rectangular shaped fractal of dimensions 4x3mm and 3x2 mm are etched out for the longer and shorter stubs respectively. The rectangular fractals and stubs are concentric. The length of rectangular fractals is oriented along the length of stubs.

4. Results and Discussion

Improvements in the frequency response of the filters have been obtained by fractalization. It is observed that the attenuation level of filter for the conventional geometry (Fig. 3) is 47 dB (Fig. 4) and for the fractalized geometry (Fig.5) is 50 dB (Fig. 6). The frequency response improves by 3 dB.

Acknowledgement

The authors thankfully acknowledge the financial support provided by M.P. Council for Science & Technology, Bhopal India.

References

[1] D.M.Pozar, "Microwave Engineering" (2/e), John Wiley and sons, 2000.

[2] G. L. Mathaei, L. Young and E.M.T. Jones, "Microwave Filter, Impedance Matching Networks and Coupling Structures", Artech House, Dedham, Mass, 1980.

[3] Jia-Shen G. Hong and M. J. Lancaster, "Microstrip Filters for RF/microwave Applications" (1/e), John Wiley and sons, 2001.

[4] IE3D Software Release – 8, Developed by M/S Zeland Software Inc.

[5] H. A. Atwater, "Microstrip Reactive Circuit Elements", *IEEE Trans*. Microwave Theory Tech., vol.MTT-31, pp.488-491, June 1983.

[6] R. E. Collin, "Foundation for Microwave Engineering", New York, McGraw-Hill, 1996

[7] F. Giannini, R.sorento, and J.Vrba, "Planar Circuit Analysis of Microstrip radial Stub," *IEEE Trans*. Microwave Theory Tech., vol.MTT-32, pp.1652-1655.

[8] D. W. Gardner, "A Closed –Form Model for Radial-Line Stub Elements in Microstrip circuits," University of Colorado M.S.E.E Thesis, Ann Arbor, MI: University Microfilms International, 1987.

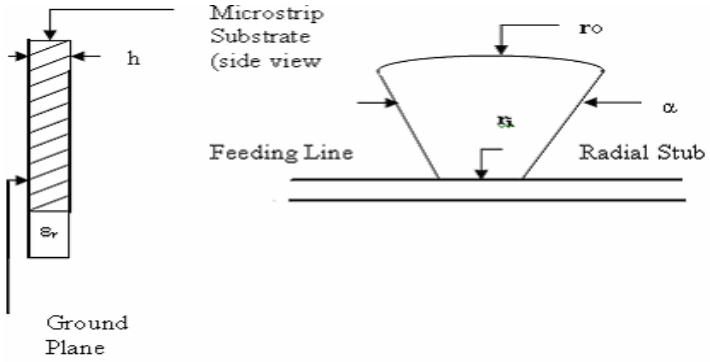

Figure 1. Radial Line Stub Geometry on Microstrip

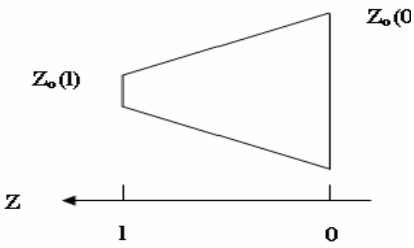

Figure 2. Modified Radial Line Stub Geometry

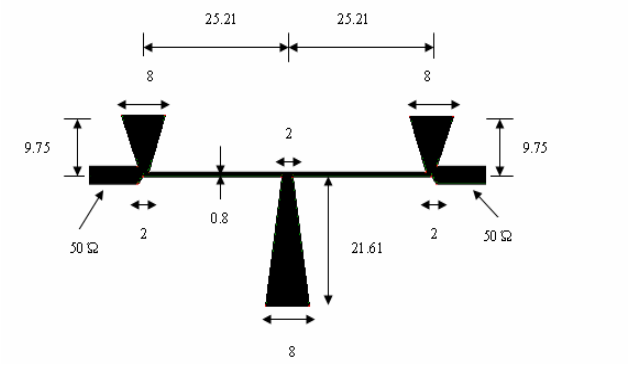

(All Dimensions are in mm)

Figure 3. Radial-Line microstrip Low Pass filter

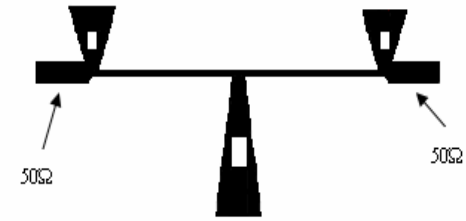

Figure 5. Radial-Line microstrip Fractal Low Pass filter

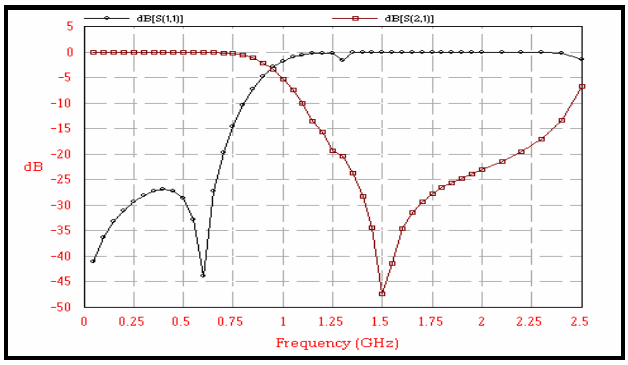

Figure 4. Response of Radial-Line Stub Microstrip Low Pass filter

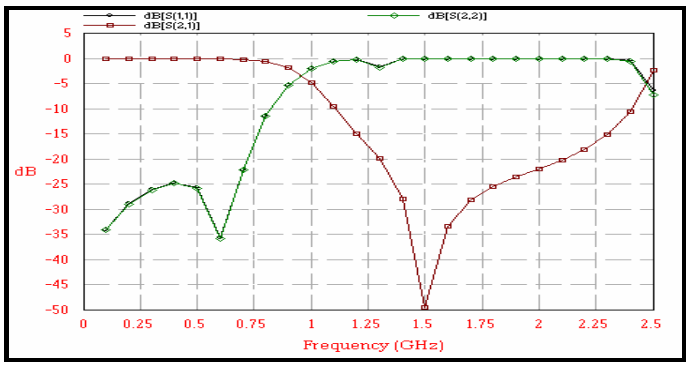

Figure 6. Response of Fractal Radial-Line Stub Microstrip Low Pass filter

Performance Improvement of Broad-Beam Microstrip Reflectarray by Reduction of Elements Spacing

Piyaporn Krachodnok and Rangsan Wongsan
School of Telecommunication Engineering, Suranaree University of Technology
Nakhon Ratchasima, 30000, Thailand
Email: priam@sut.ac.th

***Abstract*-This paper presents the effectiveness of reducing the center-to-center spacing of elements for broad beam microstrip reflectarray. For a given number of elements, it is shown that increased gain can be attainted for reduced center-to-center elements spacing with no significant change in array size.**

I. INTRODUCTION

A planar reflector or microstrip reflectarray is a printed low-profile antenna that consists of a grounded flat onto which a quasi-periodic array of resonant conducting element (patches or dipoles) is etched [1]-[4]. This operation is similar in concept to a parabolic reflector that naturally forms a planar phase front when a feed is placed at its focus. Each element phase can be adjusted to produce a required phase law over the antenna aperture.

In the wireless communication applications such as wireless local area network (WLAN) large-scale indoor base station [5], it is desirable the antenna which has wide beam to cover a broad area. The wide beam reflectarray for WLAN antenna is an alternative as shown in Fig. 1 [6]. A reflectarray configuration is attractive because it allows a single mechanical design to be used repeatedly for a wide variety of different coverage specifications. The only changes are required that the printed reflecting element dimensions can be changed for each design in order to generate the new shaped beam. Thus, many of the high recurring costs associated with shaped-reflector antennas can be eliminated with flat printed reflectarrays [7]. The flat geometry of a reflectarray also lends itself to easier placement and deployment on the WLAN large-scale indoor base station and also in terms of manufacture.

However, it is generally observed that when the antenna beam is enlarged, the antenna gain is reduced. In this paper, we have investigated the influence of the center-to-center spacing of reflectarray elements on the gain performance. To achieve such broad-beamwidth, phase of each array element in the reflectarray antenna is designed specifically to emulate the curvature of the backscatter function by using patches of different sizes. As the patch shape is not the aim of this work, it has been chosen to be simple to design regarding to the element position variation.

The first section, we will present the design approach as far as it concerns the center-to-center element spacing determination (Section II) and the reflection phase characteristic (Section III). In section IV, we apply this approach to calculate the radiation pattern of the proposed antenna. Finally, the conclusions are given in section V.

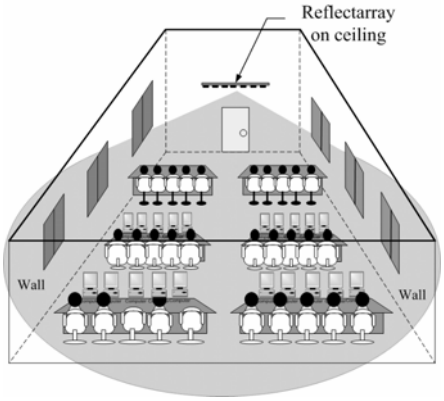

Figure 1. Reflectarray for WLAN large-scale indoor base station.

II. CENTER-TO-CENTER ELEMENT SPACING DETERMINATION

Fig. 2 shows the geometry of an infinite reflectarray element. As indicated, s is the center-to-center elements spacing in the x and y directions and L is the element size. To avoid the physical contacts among the adjacent elements, the grid spacing must be larger than the element size L,

$$\min\{s\} = L. \tag{1}$$

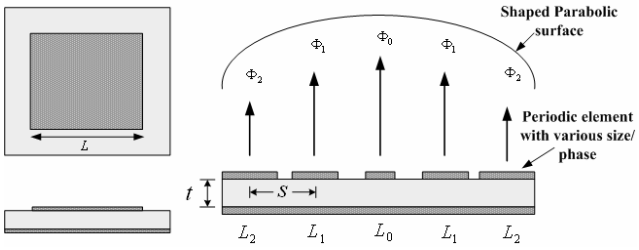

Figure 2. Geometry of an infinite reflectarray element.

The effective method for decreasing the grid spacing is to print the reflectarray elements on substrate, which reduces the size of reflectarray elements. In microstrip antenna, many

techniques have been reported to reduce the size of unit cell at a fixed operating frequency [8]. In general, reflectarray elements are half-wavelength structures at the 180° reflection phase and operated at a resonant frequency, which is given by

$$f_0 \cong \frac{c}{2L\sqrt{\varepsilon_r}}, \tag{2}$$

where c is the speed of light and ε_r is the relative permittivity of the grounded microwave substrate. From (2), it is found that the physical size of reflectarray elements will be decreased at a fixed operating frequency due to the use of the microwave substrate with a larger permittivity.

III. Reflection Phase Characteristic

A. Required Phase Delay

Fig. 3 illustrates the analysis model of a broad-beam microstrip reflectarray, which parameters used in this figure are described below:

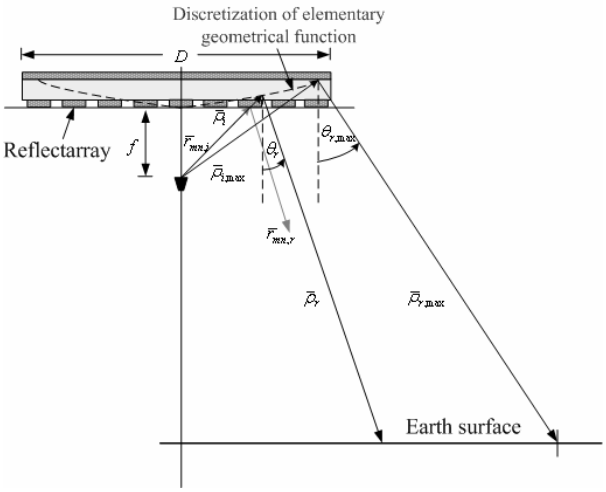

Figure 3. Analysis model of broad-beam microstrip reflectarray.

$\vec{r}_{mn,i}$ the vector from the feed to the *mn*-th reflectarray element, which can be obtained by using flat geometry;

$\vec{r}_{mn,r}$ the reflected vector from the reflectarray surface to far-field;

$\vec{\rho}_i$ the vector from the feed to the shaped reflector surface, which can be obtained by using curvature geometry;

$\vec{\rho}_r$ the reflected vector from the shaped reflector surface to far-field;

θ_i incidence angle;

θ_r reflection angle;

D diameter of the reflector;

f distance between the feed and the center of the reflectarray.

In general, the feed may be positioned at distance from the reflectarray. The path lengths from the feed to all reflectarray elements are all different, which lead to different phase delays. The required phase, which is induced on the array, has to compensate for phase delay $\Delta\Phi_{mn}$ between patch elements and surface of parabolic backscatter as expressed in (3).

$$\Delta\Phi_{mn} \text{ in degree} = \left[(1-N) k_0 \left(|\vec{\rho}_i| + \frac{z_b - f}{\sin\theta_r} - |\vec{r}_{mn,i}| \right) \right] \frac{180}{\pi}, \tag{3}$$

where (x_b, y_b, z_b) describes the coordinate of the parabolic backscatter function,

$$z_b = -\frac{x_b^2 + y_b^2}{4f} - f, \tag{4}$$

and N is integer. From (3) indicates that the compensating phase can be repeated every 360 degree and the portion that is an integer multiple of 360 degree can be deleted.

The required phase delays that related to the patch position are determined for shaping beam of reflectarray as shown in Fig. 4 with various center frequencies (f_0 = 10 GHz). These phases are duplicated the same radiating aperture as shape of parabolic backscatter. In the design, a standard X-band horn is functioned to be the primary feed and located at distance f = 25 cm. The cell elements are printed on a TACONIC substrate with thickness 0.762 mm and permittivity ε_r = 2.33 and 6.15. Because reduction of center-to-center element spacing changes the elements position, the phase delays are decreased.

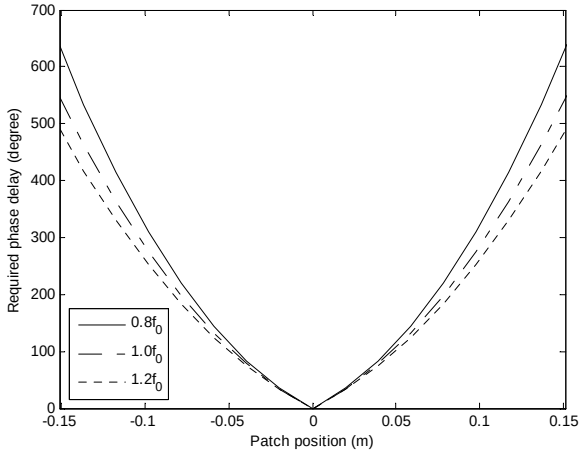

Figure 4. Calculated results of desired reflection phase properties.

B. Element Characterization

The most important and critical segment of the reflectarray design is its element characterization. To compensate for above phase delays, the elements must have corresponding phase advancements designed. Its phase change versus element change (patch size, etc.) must be calibrated correctly.

If the element design is not optimized, it will not scatter the signal from the feed effectively to form an efficient far-field beam. In this paper, the phase calibration technique is to use a full-wave method of moment and the infinite-array approach [6] to model the effect of the finite grounded dielectric substrate underlying the single radiator.

Fig. 5 shows simulated results of reflection phase of infinite array. The obtained results indicated that, if the element size L is excessively small, either the reflection phase cannot be made to cover the full required 0° to 360° phase range, or it changes excessively fast around the element resonance. This available phase shift rang is limited by the reflectarray antenna bandwidth (around 4%). In Fig. 5(c), the reductions of center-to-center spacing of reflectarray elements can reduce the slope of the phase response. For achieving reflectarray element with a reduced size at a fixed operating frequency, the use of a high-permittivity substrate is an effective method as shown in Fig. 5 (a)-(b).

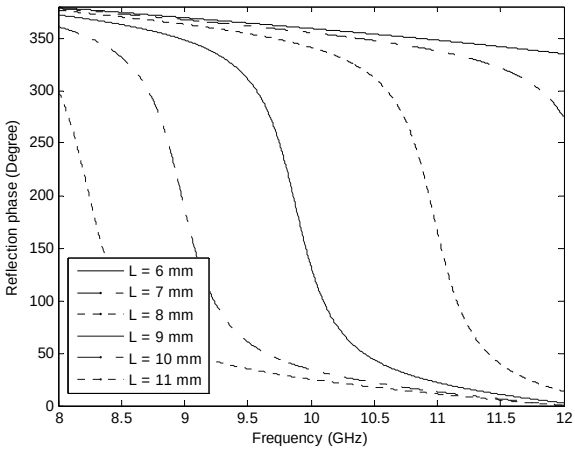

(a)

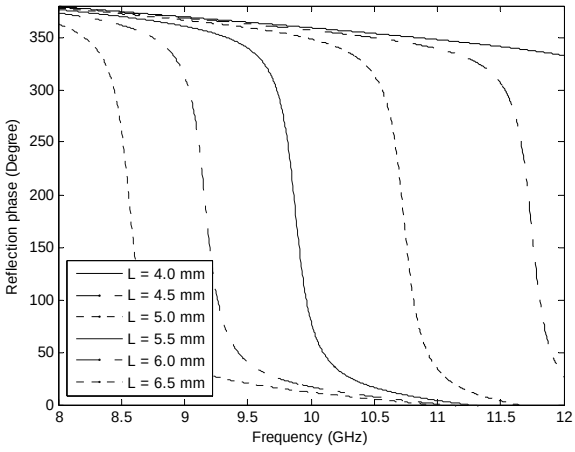

(b)

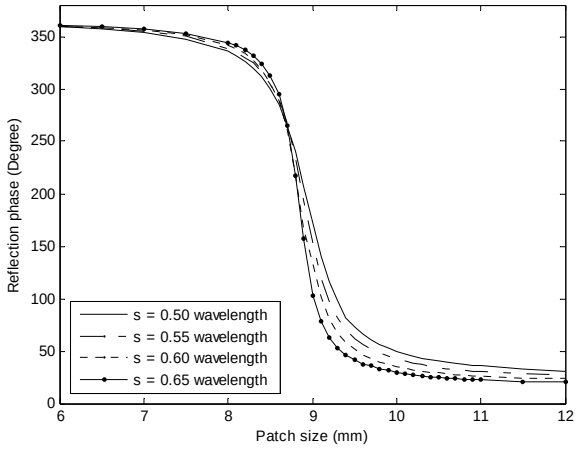

(c)

Figure 5. Simulated results of element characterization: (a) at ε_r = 2.33, s = 0.6 λ_0, (b) at ε_r = 6.15, s = 0.6 λ_0, (c) at ε_r = 2.33, f_0 = 10 GHz.

IV. Calculation of Radiation Pattern

With the compensating phases of all elements known, the far-field radiation patterns can be calculated by the conventional array theory [9], where the radiations of all elements are summed together as follow. Considering a planar array consisting of $M \times N$ elements that are nonuniformly illuminated by a low-gain feed, the reradiated field from the patches in an arbitrary direction, $\hat{u}$, will be of the form,

$$E(\hat{u}) = \sum_{m=1}^{M}\sum_{n=1}^{N} F(\vec{r}_{mn}\cdot\hat{a}_z)\cdot A(\vec{r}_i\cdot\hat{u}_r)\cdot A(\hat{u}\cdot\hat{u}_r) \cdot \exp\left[-jk_0\left(|\vec{r}_{mn}|+\vec{r}_i\cdot\hat{u}\right)-j\Delta\Phi_{mn}\right], \tag{5}$$

where F is the feed pattern function, A is the reflectarray element pattern function, $\vec{r}_i$ is the vector from the centre of reflectarray to *mn*-th element. $\hat{u}_r$ is the reflected field pointing direction, and $\Delta\Phi_{mn}$ is the required compensating phase of the *mn*-th element calculated by (3).

Table I
Characteristics of Reflectarray.

Grid spacing (wavelength)	HPBW (degree)	Maximum relative power (dBi)
0.3	68	32.91
0.4	72	28.80
0.5	72	24.33
0.6	72	21.18
0.7	72	18.67

The radiated field from (5) provides the radiation characteristics, which are shown in Table I and Fig. 6 for various center-to-center spacing of reflectarray elements. The

prescribed field requirements have been satisfied by an appropriate choice of the radiating patches selected from the complex design curves obtained in the analysis stage. The steepness of the pattern edges and the angular positions of these edges confirm that the antenna efficiently illuminates the target area to be covered (±65°). Because of phase change versus element change, each center-to-center elements spacing provides different characteristics such as -3 dB beamwidth (HPBW) and relative power. The maximum relative power is increased due to reduction of grid spacing. Thus, the HPBW is decreased and followed by the same order as the relative power.

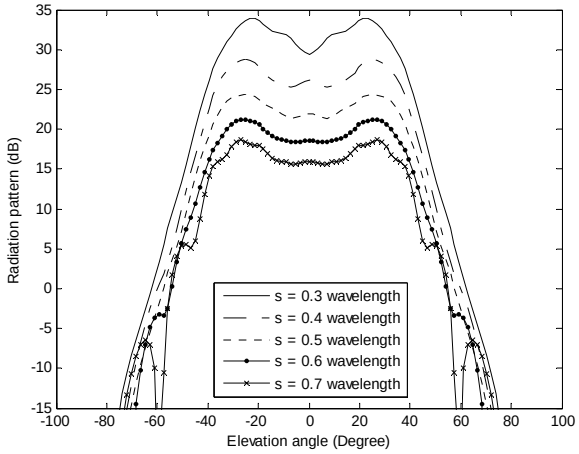

Figure 6: Radiation pattern of parabolic function.

V. CONCLUSIONS

A broad-beam microstrip reflectarray designed from square patch has been presented. The prescribed field requirements have been satisfied by an appropriate choice of the radiating patches array selected from the complex design curves obtained in the analysis stage. Simulation of this reflectarray demonstrates that reduction of center-to-center spacing of reflectarray elements can enhance bandwidth or reduce the slope of the reflection phase. In addition, the radiated power gain is improved with small significant change in HPBW.

ACKNOWLEDGMENT

This work was supported by the Research Department Institute of engineering, Suranaree University of Technology, Thailand.

REFERENCES

[1] R.E. Munson, H.A. Haddad, and J.W. Hanlen, "Microstrip reflectarray for satellite communications and RCS enhancement or reduction," U.S. patent 4 684 952, 1987.

[2] D.C. Chang and M.C. Huang, "Multiple-polarization microstrip reflectarray antenna with high efficiency and low cross-polarization," IEEE Trans. On Antenna and Propag., Vol.43, No.8, pp. 829-834, 1995.

[3] J.A. Encinar, "Design of two-layer printed reflectarrays using patches of variable size," IEEE Trans. On Antennas and Propag., Vol.49, pp.1403-1410, 2001.

[4] D. G. Kurup, M. Himdi, and A. Rydberg, "Design of an unequally spaced reflectarray," IEEE Antennas and Wireless Propag. Letters, Vol.2, pp.33-35, 2003.

[5] Peter F.M. Smulder, S. Khusial, and H.A.J. Herben, "A shaped reflector antenna for 60-GHz indoor wireless LAN access points," IEEE Trans. On Verhicular Technology, Vol. 50, No. 2, pp. 584-591, 2001.

[6] P. Krachodnok and R. Wongsan, "Design of microstrip reflectarray antenna using backscattering technique," ITC-CSCC 2006 Conference Proceedings, Thailand, Vol. 3, pp. 513-516, 2006.

[7] D.M. Pozar, S.D. Targonski, and R. Pokuls, "A shaped-beam microstrip patch reflectarray," IEEE Trans. On Antenna and Propag., Vol.47, Issue 7, pp. 1167-1173, 1999.

[8] Kin-Lu Wong, *Compact and Broadband Microstrip Antenna*.. John Wiley & Sons: New York, 2002, pp.22-86.

[9] J. Huang, "Analysis of a microstrip reflectarray antenna for microspacecraft applications," The Telecommunications and Data Acquisition Progress Report 42-120, pp. 153-173, 1995.

Narrowband Ring Filter Design with Inductive Compensated Coupling Feed and Step-Impedance Resonator

Ravee Phromloungsri, Ratthaya Suwanbunyaporn, and Mitchai Chongcheawchamnan

Research Center for Electromagnetic Wave Applications (RCEWs),
Mahanakorn University of Technology, Bangkok, Thailand, 10530

E-mail : ravee@mut.ac.th, and mitchai@ieee.org

***Abstract*—As a narrowband bandpass filter with wide stopband is needed for modern communication, a microstrip inductive-compensated coupling-fed ring bandpass filter with a SIR in loop resonator is proposed. Certain design approach for filter design procedure are derived based on ideal transmission line model. A designed narrowband bandpass filter operated at 2.4 GHz with a 5% bandwidth and wide stopband is presented. Simulated and experimental results of the design are performed to validate the technique proposed.**

***Index Terms* — Ring filter, narrowband, step-impedance resonator, inductive compensated, parallel-coupled lines**

I. INTRODUCTION

Microstrip ring resonators have found many applications in microwave communication circuits including oscillators [1], filters [2] ,tuned amplifiers [3], to name a few. For microwave bandpass filter design, ring resonator has been received much attention due to its simple design and narrow bandpass response [4]. However the multimode resonance inherent in ring resonator behavior partly contributes significant spurious magnitude in ring resonator based bandpass filter's response, which in turn degrades communication performance considerably.

Several techniques were proposed to alleviate the spurious response problem. Those proposed techniques have their own pros and cons. The first technique for spurious suppression, to the authors' knowledge, is applying a slow-wave coupler structure [5]. The technique though succeeds but lacks of a certain design rule. A simple technique such as cascading a low-pass filter [6] does not suit for practical applications as it increases passband loss, enlarges the filter bandwidth and, ultimately, reduces the signal-to-noise ratio.

Among the spurious suppression schemes, embedding a low-pass filter in a ring resonator [7] is in fact applicable. This is simply achieved by replacing a uniform-width transmission line in ring resonator loop with a step-impedance transmission line. This step-impedance ring resonator was proposed to apply with a step-width coupling-gap microstrip bandpass filter to provide narrow band response and large stop band [8]. Apart from its good performance, there is no certain design rule yet. Actually the concept of applying step-coupling feed to a microstrip ring filter design utilized in [8],[9] is originated from the works proposed for microstrip parallel-coupled filter [10] and hair-pin diplexer [11]. Non-uniform width coupling feed can effectively solve the spurious response in those circuits' passband by equalizing wave-mode velocities. We can therefore state that the spurious response in the filter is an outcome of unequal wave velocities in microstrip coupled lines. By this fact, techniques compensated wave-mode velocities are possible to apply for narrowband microstrip ring-resonator filter [12],[13].

So far, a simple yet effective technique to compensate wave velocities in parallel-coupled line is an inductive compensated coupled lines [14]. Consequently, in this paper, we first apply the technique combing with step-impedance ring loop to design a narrow band microstrip filter with wide stop band. Section 2 presents the background and the proposed technique's theories. Simulated and experiment results of the design 2.45 GHz microstrip filter of 5% bandwidth will be presented in Section 3. The paper is finally concluded in Section 4.

II. THEORY

A. Step Impedance Resonator (SIR)

Generally, step impedance resonators (SIR) which is a nonuniform transmission line resonator has been used in the filter design so as to reduce the circuits [15], to push the spurious passband to the higher frequency, and even to suppress the multiple spurious passbands [16]. The structures of SIR are shown in Fig. 1. Generally SIR structure is symmetrical and has two different characteristic admittances, Y_1 and Y_2, of corresponding electrical lengths θ_1 and θ_2. The admittance of the resonator from the open end, Y_i is given as [17]:-

$$Y_i = jY_2 \frac{2\left(K\tan\theta_1 + \tan\theta_2\right)\left(K - \tan\theta_1\tan\theta_2\right)}{K\left(1-\tan^2\theta_1\right)\left(1-\tan^2\theta_2\right) - 2\left(1+K^2\right)\tan\theta_1\tan\theta_2} \quad (1)$$

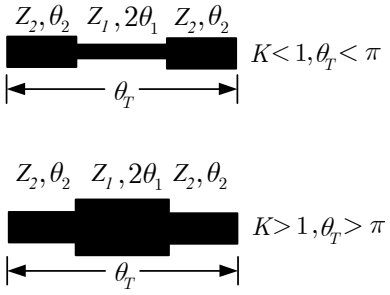

Fig. 1. Structure of the SIR [3].

where impedance ratio (K) is defined as Y_1/Y_2, and the total resonator electrical length $\theta_T = 2(\theta_1 + \theta_2)$. The anti-resonance condition can be obtained from the following condition:-

$$Y_i = 0 \tag{2}$$

Alternatively, the fundamental frequency can be express from the resonant condition as

$$K = \tan\theta_1 \tan\theta_2 \tag{3}$$

From (3), it is seen that the resonance condition not only depends on the lines length (θ_1 and θ_2) as in case of ordinary uniform impedance resonator (UIR), but also K. In addition, the previous work [17] indicated that zero transmission at other frequencies can be controlled by K. Here, we apply these properties of SIR to enhance the frequency response of bandpass filter based coupled feed ring resonator for obtaining sharp passband/stopband transition. The antiresonant condition shown in (2) will be applied at the desired zero frequencies which can be either located near passband or stopband. The solutions of K, θ_1, and θ_2 are fundamentally determined based on this fact.

B. Inductive Compensated Parallel-Coupled Lines

For microstrip parallel-coupled lines, the difference in phase velocities associated with the even- and odd-mode wave propagation contributes poor directivity in coupled lines, which in turn causes spurious response at filter stopband in bandpass filter. Obviously this is also unavoidable for microstrip ring filter with coupling feed. The technique used in this paper to eliminate the spurious response in the filter is to design coupling feed structure with high-directivity coupled lines. Normally microstrip parallel-coupled lines can not readily achieve directivity of better than 12 dB [18]. Nevertheless this can be simply surpassed with inductive compensated technique [14].

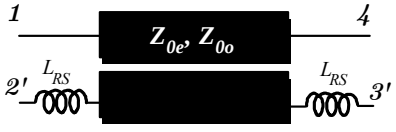

Fig. 2. Schematic of the inductive compensated parallel-coupled lines [19].

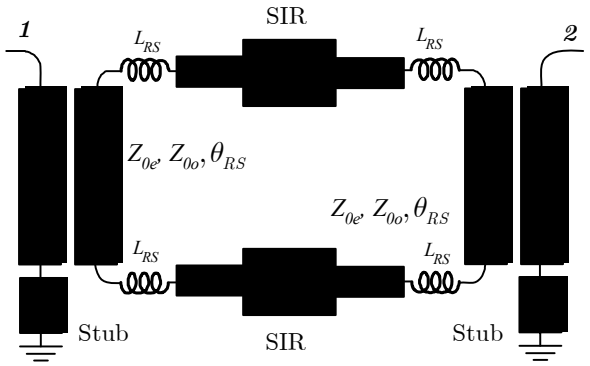

Fig. 3. Schematic of the proposed narrowband ring filter.

As shown in Fig. 2, the inductive compensated technique applied here is a modified one from their original structures [18]. Based on the four-port impedance parameters of the parallel-coupled lines model [19], the equation of the inductor (L_{RS}) for ring resonator designed at desired frequency (f_0) is presented [19]. This compensation inductors are related to the even- and odd-mode characteristic impedances ($Z_{0\mathrm{e}}$, $Z_{0\mathrm{o}}$) and effective even- and odd-mode permittivity ($\varepsilon_{\mathrm{effe}}$, $\varepsilon_{\mathrm{effo}}$).

After some mathematical manipulation, we obtain the optimum value of L_{RS} as shown:-

$$L_{RS} = \frac{1}{2\pi f_0}\mathrm{Im}\left\{\frac{\left(Z_o^2 + Z_{0o}^2\right)Z_C - 2Z_oZ_{0o}Z_{0e}\phi}{Z_oZ_C - Z_{0o}Z_{0e}\phi}\right\} \tag{4}$$

where $\phi = \cosh\theta_e - \cosh\theta_o$ and $Z_C = j\left(Z_{0o}\sin\theta_e - Z_{0e}\sin\theta_o\right)$ Equation (4) offers a closed-form expression to design the compensating inductances for achieving high directivity at f_0. The function of L_{RS} is to retard phase of the propagated signal.

It was clearly indicated that the zero-isolation frequency will be shifted to frequency which is lower than the original frequency [14]. This frequency can be simply shifted back to the desired frequency by modifying the electrical length of the compensated parallel-coupled line as shown:-

$$\theta_{RS} = \cot^{-1}\left\{\frac{4\pi f_0 L_{RS} - Z_{oo}\cot\theta_o}{2Z_{oe}}\right\} \tag{5}$$

In this paper, as mentioned above, an SIR and inductive compensated parallel-coupled lines are used in cooperated to form a new ring resonator bandpass filter. The proposed ring bandpass filter is shown in Fig. 3. Note that bandwidth tunable capability is succeeded with shorted stubs at coupling feeds. Sharp transition can be obtained by designing two zero frequencies (f_{Z1}, f_{Z2}) as shown in Fig. 4. Hence the proposed filter has many attractive characteristics which highly suits for wireless communication. These are sharp passband/stopband transition, wide stopband, tunable capability, and simple design and implementation.

The design procedure is very simple. The two zero frequencies are determined by solving the design equations of SIR where the compensated inductor and length of coupling feed are calculated from (5). Finally, if symmetry is passband response is needed, the short stub dimensions would be synthesized from the compensated inductor.

III. Design And Experimental Results

The technique validity is proven with a design of narrow bandpass filter operated at 2.45 GHz. The filter has a percentage bandwidth of 5. Sharp attenuation at both passband transitions are required. This is achieved with locating f_{Z1} and f_{Z2} at 1.9 and 2.6 GHz. The Taconic substrate, RF60-0600, was used to design the filter. The essential design parameters of the substrate are as follows:- $\varepsilon_r = 6.0$ $h = 1.52$ mm, and $\tan\delta = 0.002$. The effect of dispersive nature was neglected as the substrate used exhibits nearly nondispersive property in 9 GHz frequency region.

The design parameters obtained from (4)-(5) are summarized in Table I. All lumped inductors from ECKO (model 0603CS) were used in the design. To simulate the design circuit, the inductor model detail acquired from the manufacturer website was developed in the Advanced Design System™ software. Applying the obtained parameters calculated from the design equations, the circuit simulation results met all desired targets. Then the layout and EM simulation were performed with Momentum™. Special care was taken during the layout process, especially at all microstrip discontinuities. In our layout, the ground inductors were implemented with short stubs.

Fig. 5 a) and b) show the photograph of the PCB prototype and the layout, respectively. The circuit size excluding the input and output SMA connectors is around 2.2×1.8 cm^2. The measurement was performed with an HP8720C Vector Network Analyzer test system calibrated from 0.1 to 8 GHz with an SOLT calibration technique. HPVEE6.0™ software was used to collect the experimental data via GPIB card. Momentum™ and Matlab® were used for simulation, data post processing, and display.

The EM (dot line) and measured (thick line) results of the microstrip filter are shown in Fig. 6. A close view of the filter response at the passband is also plotted in the inset of Fig. 6. The measured results are in good agreement with the simulated results. The difference in filter response appeared is expected to caused by the in-house fabrication tolerance. From Fig. 6, the filter achieves bandwidth of 120 MHz at f_0 of 2.45 GHz. A 2.1 dB insertion loss is obtained at the center frequency. The f_{Z1} and f_{Z2} are occurred at 1.78 and 2.6 GHz, respectively. Large stopband response is obtained, which is less than -18 dB from 2.8 to 8 GHz. Harmonic responses at $2f_0$ and $3f_0$ are kept low, which are lower than –32 and -26 dB, respectively.

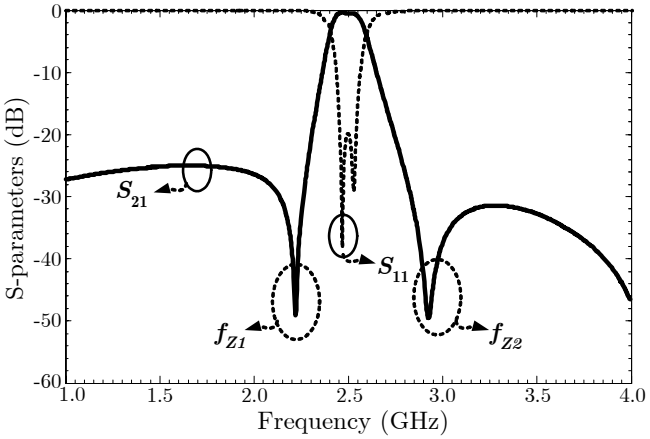

Fig. 4. Simulated frequency responses of the proposed narrowband ring filter based on coupling-fed and SIR.

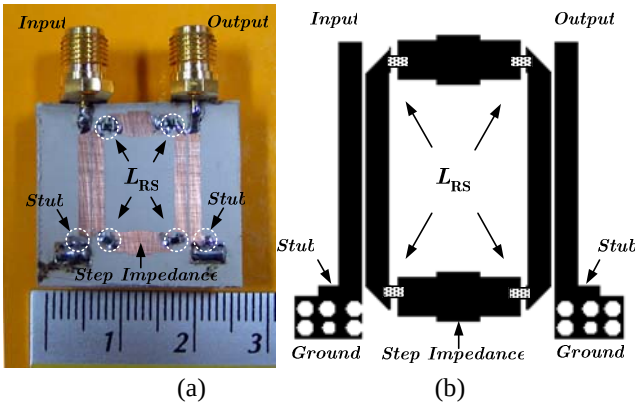

Fig. 5. (a) PCB photograph and (b) the circuit layout of the proposed ring bandpass filter.

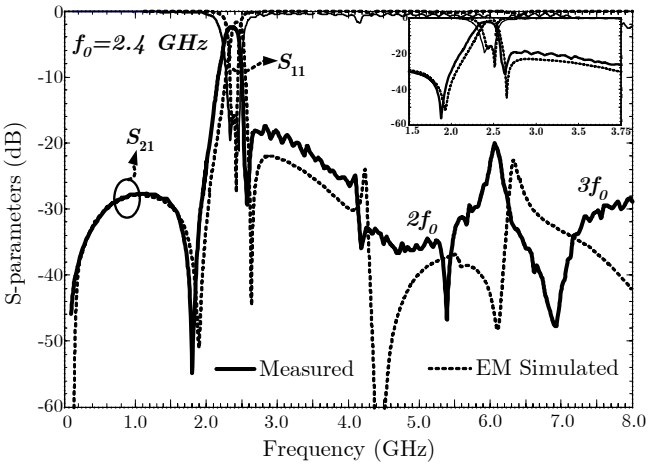

Fig. 6. Comparisons of EM simulated (------) and measured results (——) of the proposed ring bandpass filter.

IV. CONCLUSION

A novel narrowband coupling-fed ring filter based on inductive compensated technique and step-impedance resonator has been proposed. Sharp transition in filter response and hence narrow passband is achieved with introducing SIR in the loop resonator. A simple design approach for the filter has been presented and proven with the design microstrip filter at 2.4 GHz for 5% percentage bandwidth. It is believed that the technique is highly suitable for modern wireless communication systems.

V. ACKNOWLEDGMENT

This work is financially supported by the Thailand Research Fund (TRF) and the Commission on Higher Education (COE) under the grant number MRG4880184. The authors are grateful to TACONIC Inc. for supplying Taconic RF60-0600 microwave substrate for this research.

REFERENCES

[1] K. Chang, S. Martin, F. Wang, and J. I. Klein, "On the study of microstrip ring and varactor-tuned ring circuits", in 1987 *IEEE Trans. Microwave Theory Tech.*, vol. 35, no.12, pp. 1288-1295, 1987.

[2] P. Troughton, "Measurement techniques in microstrip", *Electron. Lett*., vol. 5, no. 2, pp. 25-26, 1969.

[3] H. Yabuki, M. Sakawa, M. Matsuo, and M. Makimoto, "Inductively compensated parallel-coupled microstrip lines and their applications", in 1996 *IEEE Trans. Microwave Theory Tech.*, vol. 44, no.5, pp. 723-728, 1996.

[4] K. Chang, *Microstrip Ring Circuits and Antennas*, Wiley New York, 1996.

[5] U. Karacaoglu, D. Sanchez-Hernandez, I. D. Robertson, and M. Guglielmi, "Harmonic suppression in microstrip dual-mode ring-resonator bandpass filter", in *IEEE Int. Microwave Symps*. Dig., pp. 1635-1638, 1996.

[6] J. Marti, and A. Grioa, "Harmonic suppressed microstrip multistage coupled ring bandpass filter", *Electron. Lett*., vol. 34, pp. 2140-2142, 1998.

[7] J.M. Carrol, and K. Chang, "Microstrip mode suppression ring resonator", *Electron. Lett*., Vol. 30, pp. 1861-1862, 1994.

[8] S. Srisathit, S. Patisang, and M. Chongcheawchamnan, "A microstrip stepped-width coupling gap and stepped-width ring resonator bandpass filter", *in* 2004 *ECTI Conf.*, vol. 1, pp.91-94, May 2004.

[9] P. H. Deng, M. I. Lai, S. K. Jeng, and C. H. Chen, "Design of matching circuits for microstrip triplexers based on stepped-impedance resonators ", *IEEE Trans. Microwave Theory Tech.*, vol. 54, no.12, pp. 4185-4192, Dec. 2006.

[10] S. Denis, C. Person, S. Toutain, B. Theron, and S. Vigeron, "Parallel coupled microstrip filter with phase difference compensation", *Electronics Lett*., vol. 31, No. 32, pp.1927-1928, Oct. 1995.

[11] S. Srisathit, S. Patisang, R. Phromloungsri, S. Bunnjaweht, S. Kosulvit, and M. Chongcheawchamnan, "High isolation and compact size microstrip hairpin diplexer," *IEEE Microwave and Wireless Components Letters***,** vol. 15, no. 2, pp. 101-103, February. 2004.

[12] J. Franresso, and C. E. Saavedra, "Narrowband bandpass filter exhibiting harmonic suppression", *Electronics Lett*., vol. 39, No. 9, pp.1189-1190, Aug. 2003.

[13] A. Griol, J. Marti, and L. Sempere, "Microstrip multistage coupled - lines", *Electron. Lett*., vol. 37, NO. 9, pp. 572-573, 2001.

[14] R. Phromloungsri, M. Chongcheawchamnan, and I. D. Robertson, "Inductively compensated parallel-coupled microstrip lines and their applications", *IEEE Trans. Microwave Theory Tech.*, vol. 54, no.9, pp. 3571-3582, Sept. 2006.

[15] J. S. Hong, and M. J. Langcaster, "Theory and experiment of novel microstrip slow-wave open-loop resonator filter", *IEEE Trans. Microwave Theory Tech.*, vol. 45, no.12, pp. 2358-2365, Dec. 2006.

[16] S. C. Lin, P. H. Deng, Y. S. Lin, C. H. Wang, and C. H. Chen, "Wide-stopband microstrip bandpass filters using dissimilar quarter-wavelength stepped-impedance resonators", *IEEE Trans. Microwave Theory Tech.*, vol. 54, no.3, pp. 1011-1018, Mar. 2006.

[17] M. Makimoto,and S. Yamashita, "Bandpass filters using parallel coupled stripline stepped impedance resonators", in 1980 *IEEE Trans. Microwave Theory Tech.*, vol. 28, no.12, pp. 1413-1418, Dec. 1980.

[18] T. Edward, *Foundation for Microstrip Circuit Design*, West Sussex, England: John Wiley & Son, pp. 173-228, 1992.

[19] V. K. Tripathi, "Asymmetric coupled transmission lines in an inhomogeneous medium", *IEEE Trans. Microwave Theory Tech.*, vol.23, no.9, pp 734-739, 1975.

Table I Parameters of the designed ring bandpass filter at 2.4 GHz

Sections #	Electrical parameters	Dimensions (mm)
SIR	Z1 = 40.0 Ω, $\theta_1 = 9.2^\circ$	$W_1 = 3.3$
		$L_1 = 3.0$
	Z2 =46.2 Ω, $\theta_1 = 15.7^\circ$	$W_2 = 2.6$
		$L_2 = 2.6$
Compensated Coupled Lines	Z_{0e} =78.44 Ω	W = 1.6
	Z_{0o} =33.38 Ω	S = 0.2
	$\varepsilon_{effe} = 4.869$	L = 15.6
	$\varepsilon_{effo} = 3.669$	$(\theta_{RS} = 0.45\pi)$
Stubs	$Z_s = 42.4$ Ω,	$W_s = 3.0$
	$\theta_s = 6.2^\circ$	L_s =1.0

A Dual-Band Bandpass filter Using Stepped-Impedance and Load capacitive Hairpin Resonators for Mobile Systems

Pongsathorn Chomtong, Sarawuth Chaimool, and Prayoot Akkaraeakthalin

Department of Electrical Engineering, Faculty of Engineering
King Mongkut's Institue of Technology North Bangkok,
1518 Pibulsongkram Rd., Bangsue, Bangkok 10800, Thailand
Phone:+662-9132500 Ext.8519 , Fax:+662-5857350 , E-mail:amakingkmitnb@hotmail.com, prayoot@kminb.ac.th

ABSTRACT

This paper presents a new dual-band bandpass Filter using stepped-impedance and capacitive load hairpin resonators for mobile systems. Based on resonant characteristics of a stepped-impedance resonator and load capacitive, the second resonant frequency can be tuned over a wide frequency range by adjusting its structure parameters. The stepped-impedance resonators and the resonators use capacitive load characteristic with a cross-coupled structure have been employed to build up a bandpass filter at center frequencies of 900 MHz and 1800 MHz. The experimental results of the fabricated filter agree very well with simulation expectations using IE3D package. The proposed filter has good performances and also small sizes.

Keywords: Stepped-impedance, cross-coupled filter, dual-band, bandpass filter, load capacitive.

1. INTRODUCTION

Nowaday there is increasing in the demand of using mobile. For mobile applications through the second-generation GSM and the third-generation WCDMA mobile communications, the RF transceivers should be able to receive and transmit for dual-band *i.e.* at 900 MHz and 1800 MHz. A GSM 900/1800 MHz dualband BPF was develop by using microstrip open-loop resonators.It is, of course, not suitable for constructing a dual - frequency filter of which the second frequency is not twice the first one.Thus, the resonators have to be modified. Intuitively, dual-band filters can be implemented by combination of two filter,which are design different passbands [1]-[2]. it can controll center freqyency by changing impedance therefor it development by parallel step-impedance for good mor than basic step-impedance and development hairpin resonators step-impedance for small struckture and good response. Open loop resonators use load capacitive for reduce size and tune first harmonics, therefore it has been developed to be a parallel a coupled line filter structure for good responses and smaller sizes [1]-[3]. These proposed filters employ coupled-line structures, therefore the sizes are considerably large and high selectivity characteristics can not be obtained. In this paper a crosscoupled structure with steppedimpedance resonators (SIR) and load capacitive has been used to design a dualband bandpass filter (BPF).

2.CROSS-COUPLED,STEPPED-IMPEDANCE AND LOAD CAPACITIVE RESONATORS

Design procedure for A dual-band bandpass filter using step-impedance and load capacitive hairpin resonators for mobile system it useing theory of load capacitive stepped-impedance and cross-couple .The theory load capacitive stepped-impedance and cross-couple structures have been discussed in the following.

2.1 Open-loop resonators use capacitive load

In this procedure useing theory of open-loop resonators use capacitive load.Fig. 1 shows the geometrical diagram of the miniaturize hairpin resonators and it equivalent circuit.These resonators are characterized by fundamental (odd-mode) and firstspurious (even-mode) resonances due to their coupleline section. As derived in the equations that describe the even-mode and odd-mode resonance are

$$\tan\frac{\theta_s}{2} = \frac{Z_{oo}}{Z_s}\cot\theta_{oo}$$

$$\cot\frac{\theta_s}{2} = -\frac{Z_{oe}}{Z_s}\cot\theta_{oe} \qquad (1)$$

Where θ_s is the electrical length of transmission line and Z_s is the characteristic impedance of the transmission line odd-mode and even-modecharacteristic impedance and corresponding coupling angle of the coupled-lines are Z_{oo},Z_{oe} and θ_{oo},θ_{oe} respectively.For this case the ratio of the couple-line characteristic impedance is

$$R = \frac{Z_{oo}}{Z_s} \quad (\text{at } f = f_0 \text{ odd-mode})$$

$$R = \frac{Z_{oe}}{Z_s} \quad (\text{at } f = f_1 \text{ even-mode}) \qquad (2)$$

Form Eq. (2) impedance ratio of greater than one causes the resonator to resonate at a frequency higher than initial fundamental frequency.Impedance ratio ofless than one makes the resonators to resonate at a frequency lower than initial fundamental frequency.These behaviors show that there is a special mechanism for resonance frequency tuning being offered by the internally couple-line hairpin

resonators.Acompact size of hairpin resonator can be designed if the initial frequency chosen for the half-wavelength resonator is higher than the desired operating frequency,with impedance ratio less than one .In structure of open-loop resonators use capacitive load electrical length θ_s are set to be λ/4.

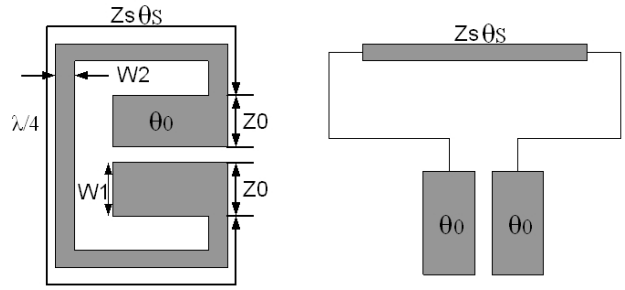

Fig. 1: *Schemetic of the miniaturize hairpin resonator and equivalent circuit of SIR.(a) Geometrical diagram of the miniaturized hairpin resonator.(b) An equivalent circuit of SIR with internal couple line.*

After using equations find the Open-loop resonators use capacitive load but the resonance frequency of first harmonic is not equal to the designing see in figure 2.

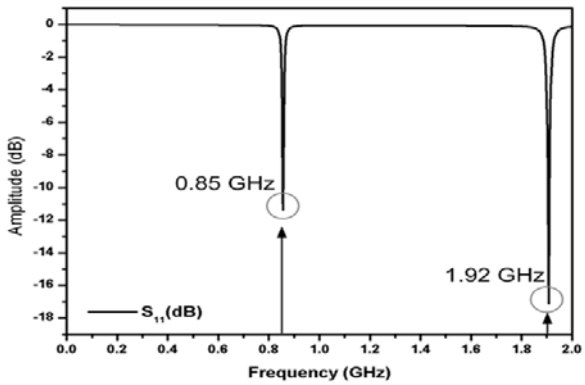

Fig. 2: *A simulated response of return loss.*

So ,we use a step-impedance technique to correct the first harmonic

2.2 A step-impedance line

Fig. 3 shows a basic stepped-impedance structure with a λ/4 length at lower frequency resonant, when electrical lengths θ_1 are set to be λ/4 respectively. Values of Z_1 and Z_2 represent the characteristic impedances of transmission lines that are implemented as a short circuited and open-circuit ends, respectively [1], [2]. A value *R* is the ratio between Z_1 and Z_2 .

$$R = \frac{Z_2}{Z_1} \tag{3}$$

The value of *R* can be *R*>1or *R*<1, however, it is found that we can control the first harmonic far away from the fundamental center frequency when *R* >1.

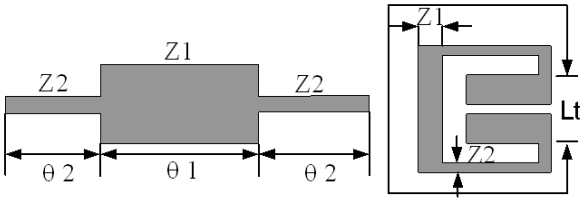

Fig. 3: *A structure of step-impedance line resonator*

The first harmonic can be found by the following equations

$$R = \tan^2 \theta_0$$
$$\theta_0 = \tan^{-1} \sqrt{R}$$
$$f_1 = \frac{\pi}{2 \tan^{-1} \sqrt{R}} f_0 \tag{4}$$

when f_1 is the first harmonic and f_0 is the fundamental frequency. A particular return loss response of the stepped-impedance structure can be obtained using IE3D program as shown in Fig.4.

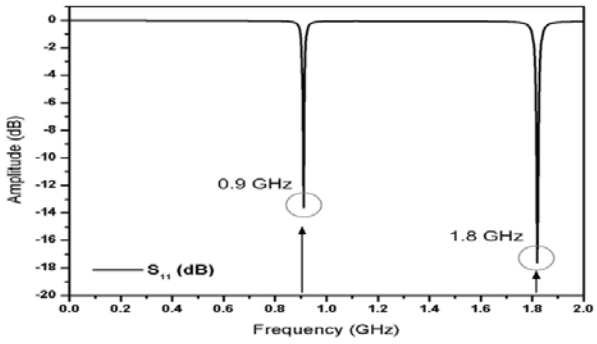

Fig. 4: *A simulated response of return loss stepimpedance.*

2.3 Hairpin-line resonators

The dual-band 900/1800 MHz line resonators are design to operate at the center frequency of 900 MHz.Due to the resonators are design at half wavelength at low frequency , so they generate the first harmonic at 1800 MHz.After that , the conventional line resonators are renovated to hairpin-line resonators as show in Fig.5 it has response of frequency at 900 MHz and 1800 MHz show in Fig.6

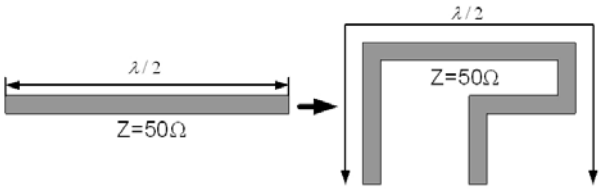

Fig. 5: *A structure of* hairpin-line resonators

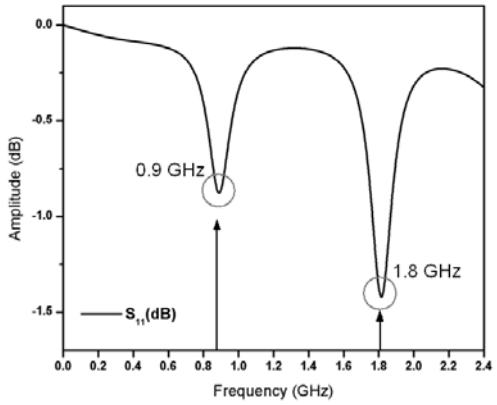

Fig. 6: *A simulated response of return loss* hairpin-line resonators.

2.4 A cross-couple structure

Theory of cross-coupled filter structures can be found in [4], [5]. This paper uses four stepped-impedance resonators in a cross-coupled structure to create a bandpass filter operated at centre frequencies of 900 MHz and its first harmonic of 1800 MHz as shown in Fig.7. The resonators must be properly placed so that four appropriate couplings can be obtained with a Chebyshev response. The equations of coupling coefficients K_{ij} can be found as following [6].

$$K_{12} = K_{34} = \frac{FBW}{\sqrt{g_1 g_2}}$$

$$K_{23} = \frac{FBWJ_2}{g1}$$

$$K_{14} = \frac{FBWJ_1}{g_1} \qquad (5)$$

$$Q_{ei} = Q_{eo} = \frac{g_0 g_1}{FBW} \qquad (6)$$

where FBW is the fractional bandwidth, g_0, g_1 and g_2 are the element values and J_1, J_2 are the admittance inverters in its equivalent circuit of the low-pass prototype. Q_{ei}, Q_{eo} are external quality factors of the resonators at the input and output.

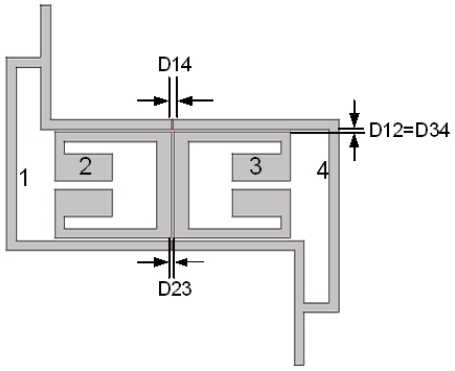

Fig. 7:*The proposed cross-coupled filter.*

3. IMPLEMENTATION AND RESULTS

The proposed filter has been designed on a substrate of GML-1000 with ε_r of 3.2, thickness of 0.762 mm and loss tangent of 0.004. The couplings between two resonators can be calculated by IE3D simulation program [7]. The stepped-impedances have been set to be Z_1 = 37.30 Ω and Z_2 = 50 Ω. Form equation (3)-(4), we find that the first harmonic is at frequency of 1800 MHz when the centre frequency is at 900 MHz. The line widths w of 37.30 Ω and 50 Ω are 2.87 mm and 1.83 mm, respectively. The values of θ_1 and θ_2 are calculated to be 37.3092 mm and 16.64 mm, respectively. The 50 Ω port has a width of 1.83 mm. and resonators use load capacitive has Zs 55 Ω Zoe 61.74 Ω Zoo 55 Ω are corresponding to the line widths w1 5.22 mm and w2 .083 mm. The 50 Ω port has a width of 1.83 mm. Form equations (1)-(2) we obtain a lowpass prototype of the proposed filter: g_0=1, g_1=0.7533, g_2=1.16552, j_1= -0.4513, j_2 =1.05789. The external quality factors are $Q_{ei} = Q_{eo}$ =21.5225. The coupling coefficients between the adjacent resonators can be found to be $K_{12} = K_{34}$ = 0.037353, K_{23} = 0.03176, K_{14} = 0.020974.

The next step of the filter design is to determine the couplings between adjacent resonators. It had been found that each of the three coupling structures has two dominant resonant frequencies, which are split off from the resonant condition as normally shown in Fig.4. The couplings between resonator i and j, K_{ij}, can be then calculated by

$$K_{ij} = \frac{f_b^{\,2} - f_a^{\,2}}{f_b^{\,2} + f_a^{\,2}}$$

where f_a and f_b are the lower and higer split resonant frequencies of a pair of couple resonators.

The distances of the final filter structure can be found to be D_{14}=0.3mm, D_{23}=0.4mm, and D_{12}=D_{34}=0.5 mm. Finally, we have simulated the values of return loss and insertion loss as results shown in Fig.8.

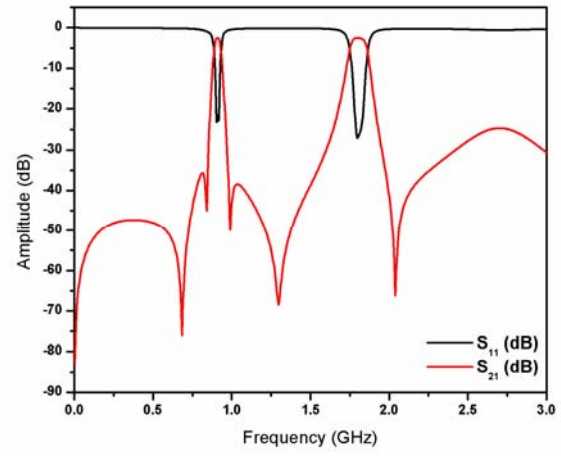

***Fig.8**: Simulated responses of S_{11} and S_{21}.*

From Fig.8, at the 900 MHz band we have S_{11}=-21 dB, S_{21}=-2.557 dB with a bandwidth of 60 MHz and at the 1800 MHz band we obtain S_{11}=-26 dB, S_{21}=-2.525 dB with a bandwidth of 180 MHz.

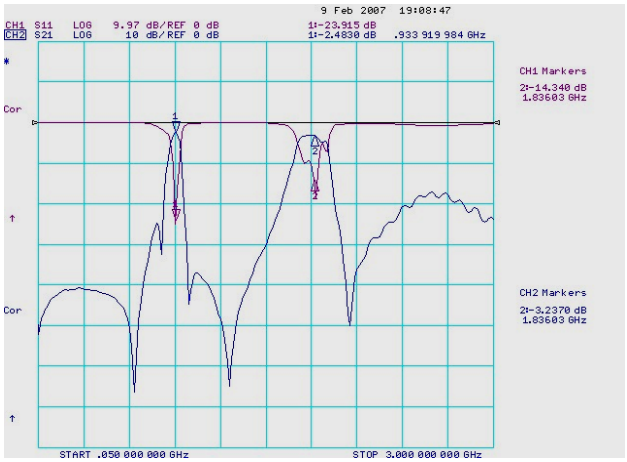

Fig.9: *Measured responses of S_{11} and S_{21}.*

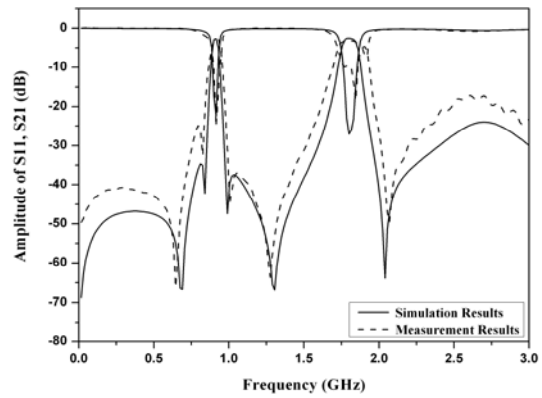

Fig.10: *Comparison between measured and simulated responses.*

Fig.9 shows measured responses at frequency of 900MHz with S_{11} = -23.91dB, S_{21}=-2.48dB and at frequency of 1800 MHz with S_{11}=-14.34 dB, S_{21}=-3.23dB.

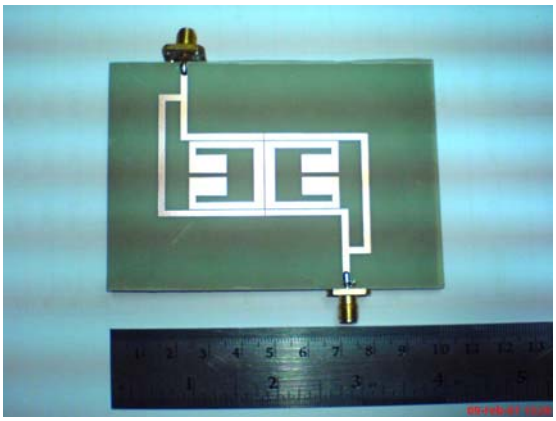

***Fig.11:** A photograph of the proposed BPF.*

Fig.10 comparisons between simulated and measured performance are shown.The photograph of the fabricated filter is shown in Fig.11.

4. CONCLUSIONS

A dual-band bandpass filter using cross-coupled stepped-impedance hairpin resonators for mobile systems has been proposed to operate at frequency bands of 900 and 1800 MHz. The results show good agreement between simulation and measurement. The proposed filter also demonstrates good performances, which it can be applied for other interesting frequency operation bands.

5. REFERENCES

[1] S.-F. Chang, Y.-H. Jeng, and J.-L. Chen, "*Dual-band step-impedance bandpass filter for multimode wireless LAN"* , Electron. Lett., Vol.40, no.1, Jan 2004.

[2] Anak Agung Alit Apriyana,and Zhang Yue Ping Nanyang Technological University, "*A Dual-band Wireless Transceiver*" ,IEEE 2003ElectronicsPacking Packaging Technology Conference

[3] J.-T. Kuo and T. Hsun, "*Design of Microstrip Bandpass Filter With a Dual-passband Response*" , *IEEE Trans. Microwave Theory and Tech.*,Vol.53, No.4, April 2005.

.[4] J-S Hong and M- J Lancaster, "*Cross –Coupled MicrostripHairpin Resonator Filter*",IEEE Transaction on microwave and techniques,Vol46,no.1,jan 1998

[5] J.S.Hong M J Lancaster, "*Back-to-Back Microstrip Open Loop Resonator Filters with Aperture.coupling"*. IEEE Trans Microwave Theory Tech,pp.1239-1242, 1999.

[6] HUN Num, "*A Design and Fabrication of Bandpass Filter 'using miniaturized Microstrip Square SIR*" IEEE.Catalogue pp 395-398, 2001.

[7] IE3D Users' Manual Release 8, Zeland Software, Inc Fremont, CA, 2001.

Acousto-Optic Frequency Decoder and Its Applications

Athikom Roeksabutr
Telecommunication Engineering Department
Mahanakorn University of Technology, Bangkok, 10530, THAILAND
E-mail : athikom@mut.ac.th

***Abstract*-The possibility of an acousto-optic frequency/tone decoder by means of a practical approach has been demonstrated by making use of a simple electronics feedback circuit to stabilize the sensitivity of fiber ring resonator. The applications of such a device have been proposed.**

I. INTRODUCTION

All-optical system is one of the key factors to maximize the speed of the optical systems in many applications such as optical communications and optical signal processing. One approach of such a system makes use of the replacing the electronics components with the optical components. The idea of imitation electronics devices in terms of optoelectronics or all-optical devices seems to be a simply way to research [1]-[3]. For instance, the microwave frequency optoelectronics tone decoder was firstly proposed in 1996 [4]. Consequently, the theory of this device was widely investigated [5],[6]. However, the practical demonstration of such a device has not yet been demonstrated due to the characteristic of high sensitivity of fiber ring resonator, which is the main part of the device. In this paper, we, for the first time to our knowledge, demonstrate the possibility of a practical device. The simple technique of employing a feedback electronics circuit to stabilize the output light intensity of fiber ring resonator is described. In addition, the concept idea to make use of this device in the applications as photonic switching, external modulator, and optical wavelength selection/multiplexer, is proposed.

II. SYSTEM DESIGN CONFIGURATION

As shown in figure 1, the configuration of an acousto-optic frequency decoder is a hybrid system consisting of optical and electrical parts. The optical part is composed of an ordinary fiber ring resonator with an acousto-optic (AO) phase modulator in its close loop. For very high frequency up to a few gigahertzes, the AO phase modulator can be an AO fiber transducer using zinc oxide (ZnO) circumferentially coated on an optical fiber surface [1]. The AO phase modulator is controlled by an electrical high frequency trigger signal. The electrical part is an electronics feedback system that supplies the DC voltage to a cylindrical PZT, which is wrapped by some part of the fiber in the loop. This technique is to set up the ring resonator at the phase resonance condition and also to compensate the ring resonator from the environment sensitivity. The key to lock up the desired electrical frequency arises from the structure of the phase modulator. By employing the theory of the acousto-optic resonator [2] as well as of the fiber ring resonator [4], the device performance at one particular desired frequency, defined from the thickness of ZnO layer, can be controlled by means of the output light intensity (I_o).

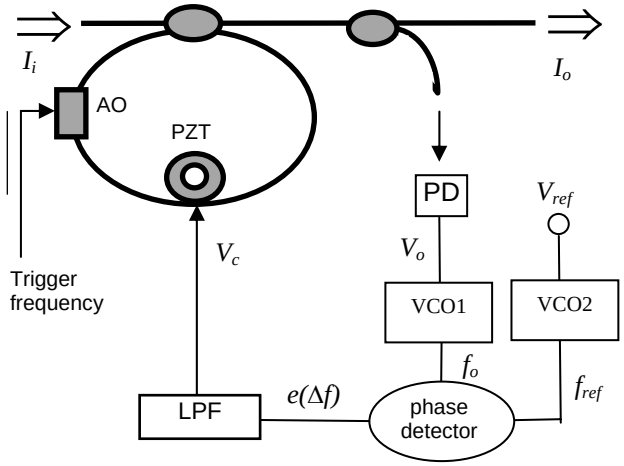

Figure 1. Schematic of an acousto-optic frequency decoder.

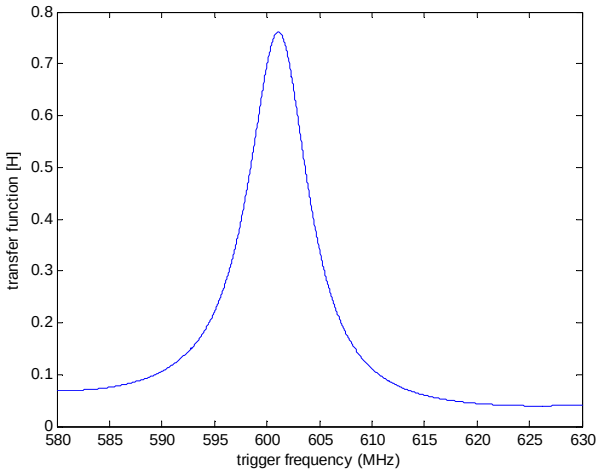

Figure 2. The output light intensity (I_o) as a function of frequency trigger.

Figure 2 shows an example of the output light intensity (I_o) when the electrical signal with different frequency is applied to

the AO phase modulator. As can be seen, although the input light (I_i) always remains at fix intensity, the output light will emerge only if an appropriate frequency is applied to the AO phase modulator.

In practice, the fiber ring resonator is very much sensitive to the environment [3]. Then, the electronics feedback system as shown in figure 1 is a need to stabilize the output light I_o. The stabilization circuit consists of two voltage control oscillators (VCO1 and VCO2), phase detector and active low pass filter (LPF). To photo detector (PD) defines the voltage (V_o) which is related to the reference voltage (V_{ref}) found from the characteristic point of fiber ring resonator so that the desired output light intensity is locked.

To verify the possibility of output light stabilization, the system as shown in figure 1 without an AO phase modulator is experimentally examined. The practical parameter values of VCO (VCO1 and VCO2) should be kept at low frequency to minimize the sensitivity. In the experiment, the minimum frequency of about 15 Hz is chosen. The maximum frequency is limited by the cut-off frequency of the active low pass filter (LPF) of about 140 Hz. The capture range of VCOs is varied between 20-40 Hz and the lock range is varied between 10-50 Hz. The phase detector employs an exclusive-OR gate. The characteristic between the DC voltage and frequency of VCO is illustrated in figure 3.

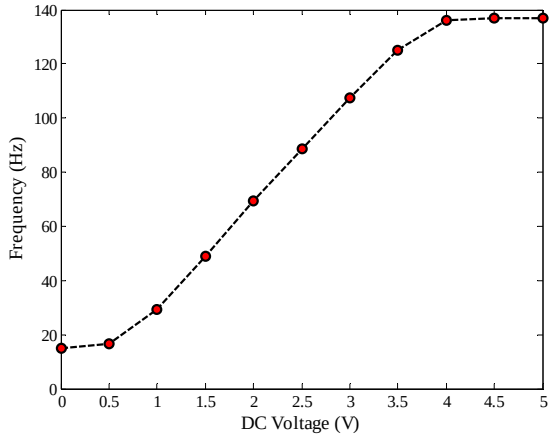

Figure 3. The characteristic between the DC voltage and frequency of VCO

The fiber ring resonator used in this experiment employs a single mode fiber and a 3-dB directional coupler. Some part of fiber in the loop was wound around a piezoelectric cylinder (PZT) that can expand radically to control the phase of the ring loop. A polarization controller (PC) is used to counter birefringence present in the resonator ring. Thus the polarization entering the coupler and the fiber ring will be in the same state. A He-Ne laser (λ = 633 nm) was used to excite the fiber ring resonator. The output light intensity of the ring resonator by means of electrical voltage (V_o) is sent through VCO1 and is compared to a reference signal from VCO2 (V_{ref} or V_r) corresponding to the desired operating point. If the frequency output from VCO1 (f_o) and the frequency output from VCO2 (f_{ref}) are different, an error signal $e(\Delta f)$ integrated by LPF will produce the DC voltage signal (V_c) to drive the piezoelectric cylinder (PZT). This mechanism makes compensation of the appropriate fiber length (phase shift) in the ring loop. Consequently, the output light intensity is stabilized even though the ring resonator is perturbed from the environment.

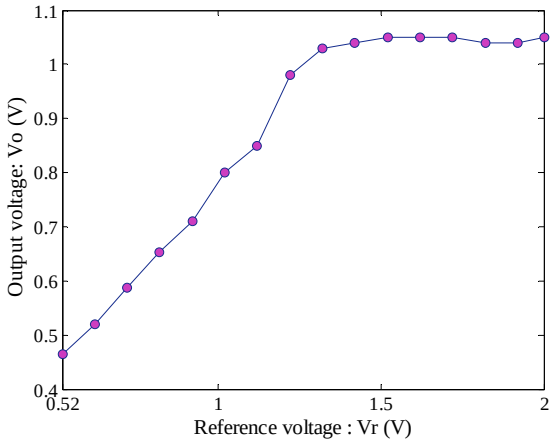

Figure 4. The relationship between the reference voltage and output voltage.

Figure 4 shows the output light intensity by means of output voltage (V_o) when the reference voltage (V_r) is varied. Once the operating point of the ring output is set at the lowest value, ie., V_r = 0.52 volt. As the reference voltage is increased, the output voltage is increased according to the characteristic of transfer function of the ring resonator itself until it reaches the maximum value at which the output voltage remains though the reference voltage keeps increasing. This experiment result verifies the possibility of system stabilization. In another word, the environment sensitivity is eliminated.

III. APPLICATIONS

A. Photonic Switching

The transfer function of an acousto-optic frequency/tone decoder, for example, shown in figure 1 is the characteristic of the photonics switching. The light signal from the input port (I_i) can be switched to the output port (I_o) only when an appropriate trigger signal (frequency in this case) is enabled. The speed of the switch depends on the characteristic of an AO transducer and the trigger frequency. If the ZnO-coated fiber [2] is performed, the speed in terms of gigahertz can be achieved.

B. External Modulator

From the transfer function of a fiber ring resonator as shown in figure 5, if the operating point is locked in the region of non-stable output, the small electrical frequency (depending on the AO phase modulator) applied to the acousto-optic frequency/tone decoder, shown in figure 1, will result in modulating the output light signal. The schematic of such a

device is very simple for an external light modulator in comparison with the electronic (internal) modulator when high frequency up to a few gigahertzes is considered. In addition, the response time of the modulation is quite fast [3].

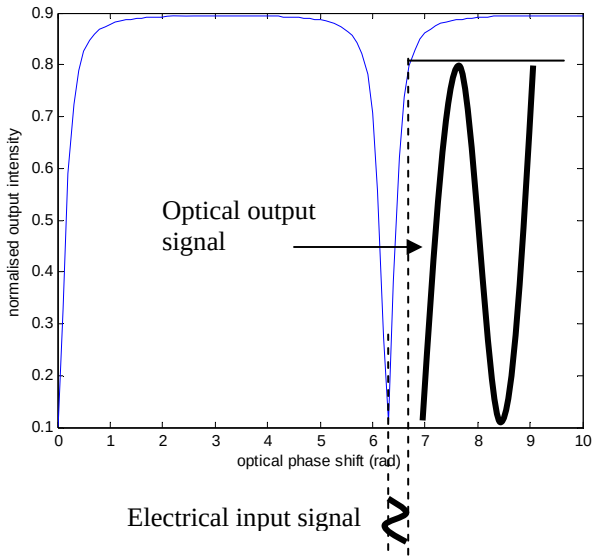

Figure 5. The concept idea of an external modulator.

C. Wavelength Selection/Multiplexer

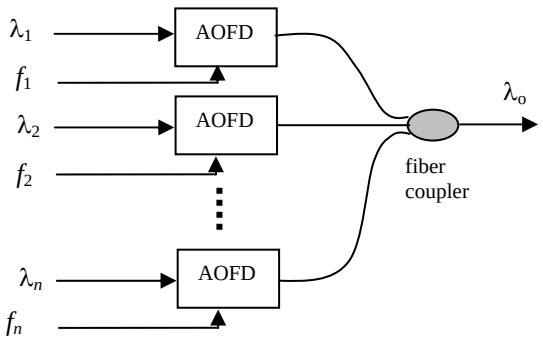

Figure 6. Structure of an optical wavelength selection.

The concept idea of an optical wavelength selection is expressed in figure 6. AOFD is an acousto-optic frequency/tone decoder which has the same structure as shown in figure 1. The input optical signal of each AOFD can be any wavelength, ie., λ_n with n an integer. Each AOFD needs trigger electrical signal at particular frequency to operate the AOFD (to control the output light). The output of all AOFDs is connected to an ordinary fiber coupler. It should be noted that the practical device needs an electronic feedback circuit with appropriate reference signal (V_r) to maintain the output of each AOFD at the desired operation. Once the output condition of each AOFD is set, the output signal corresponding to the input wavelength (λ_n) will emit when an electrical signal with appropriate frequency (f_n, n is integer) of each AOFD is enable. After passing through the fiber coupler the final optical signal is received. According to the characteristic of an AOFD, the output optical wavelength will depend on the trigger frequency (f_n). Consequently, the output wavelength can be selected. If more than one appropriate electrical signal is applied, more than one wavelength will be multiplexing at the output as the result.

IV. CONCLUSION

A simple electronic feedback system in the fiber ring resonator is experimentally demonstrated for the first time. This verify the possibility of using the fiber ring resonator in company with optical phase modulator in the fiber loop to sustain the desired output light by minimizing the sensitivity of the ring resonator due to the environmental effect. The principle concept for making use of such a device in terms of photonic switching, external modulator, and wavelength selection/multiplexer, have been explained.

ACKNOWLEDGMENT

The author would like to thanks Mr. Sommart Sang-ngern, a Ph.D. student at Mahanakorn University of Technology, for his great effort in making the successful experiment.

REFERENCES

[1] A. Roeksabutr and P. L. Chu, "Broadband Frequency Response of a ZnO Coated Fiber Phase Modulator," *IEEE Photon. Technol. Lett.*, vol. 9, no. 5, pp. 613-615, May 1997.

[2] A. Roeksabutr and P. L. Chu, "Design of High-Frequency ZnO-Coated Optical Fiber Acoustooptic Phase Modulators", *IEEE J. Lightwave Technol.* , vol. 16, no. 7, pp. 1203-1211, July 1998.

[3] A. Roeksabutr and W. Pornpanich, "Theory of Acousto-Optic Fiber Bragg Grating Coated with Zinc Oxide", *the 15th Annual Lasers and Electro Optics Society Meeting (LEOS2002)*, pp.821-822, Scotland, Nov 2002

[4] A. Roeksabutr, *Ph.D. Thesis*, ch. 8, University of New South Wales, 1996.

[5] A. Roeksabutr, "Microwave Frequency Optoelectronics Tone Decoder," *the 20th Electrical Engineering Conference (EECON-20)*, pp. 228-231, Bangkok, Nov 1997.

[6] A. Roeksabutr, :Electrode Effect of an Optical Fiber Acousto-Optic Resonator for Microwave Optoelectronics Frequency Decoder," *the 1998 IEEE Asia-Pacific Conference on Circuits and Systems (APCCAS1998)*, pp. 209-211, Nov 1998.

Study on Backbone Network with WDM Via Optical Fiber

Amornrat Mahaprom and Noppin Anantrasirichai
Research Center for Communications and Information Technology
And Department of Information Engineering, Faculty of Engineering
King Mongkut's Institute of Technology Ladkrabang, Bangkok 10520, Thailand
s5061105@kmitl.ac.th, kanoppin@kmitl.ac.th

***Abstract*- This paper studies the methodology of WDM Networks logical design, by using TOT (Telephone Organization of Thailand) backbone network for connecting between sub-networks. Bellman-Ford's algorithm is used for computing and simulation for optimal logical design of WDM network. There are three main parameters consider in this paper. Including minimum cost, shortest-path routing and re-computing of minimum cost to find out final shortest path. Furthermore, we have compared the result from logical computation with physical topology. Existing backbone optical network and traffic require of TOT are used as raw data for this study.**

I. INTRODUCTION

Design of WDM Backbone Network for connecting between Sub-networks is important. Not only considering about traffic of sub-networks all around Thailand but also the operating cost and losses in fiber optic also. Backbone network logical design is chosen for study how to make an optimal and efficiency routing in carrying increasing amounts of commercial traffic. Reliability and steady performances have become critical factors when designing and managing those networks. Large network today offer Service Level Agreements (SLAs) covering delay, port availability and losses across their network which must be maintained even if the network experiences congestion or failure. This provides strong incentives for designing conditions, i.e., fluctuating traffic patterns and intensities or topological changes caused by link and node failures [1].

In this paper, our focus is on logical design of TOT Backbone Network by considering three main parameters, Minimum Cost, Shortest-Path Routing and Re-computing of Minimum Cost in case of major category of failures,

II. ROUTING ALGORITHM

A. *Bellman Ford Algorithm*

Bellman-Ford Algorithm makes each node periodically broadcast its routing tables to all its neighbors. . This algorithm have to maintain the distance tables (which is a one-dimension array—"a vector"), which tell the distances and shortest path to sending packets to each node in the network. The information in the distance table is always updated by exchanging information with the neighboring nodes [2]. The number of data in the table equals to that of all nodes in networks (excluded itself). Each data contains the path for sending packets to each destination in the network and distance/ or time to transmit on that path (we call this as "cost"). The measurements in this algorithm are the number of hops, latency, the number of outgoing packets, etc.

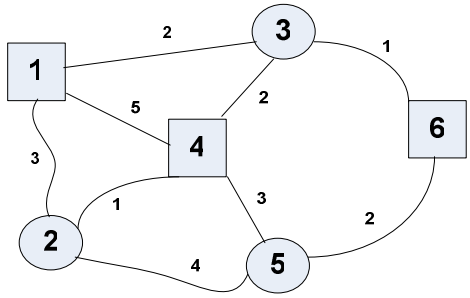

Figure 1. Sample Network with link cost

In Fig.1 if we would like to find the shortest-path between Node 2 to Node 6, from Node 2 that Node 1, 4 and 5 are neighbors and we can expect that the shortest link cost form Node 1, 4 and 5 to Node 6 are 3, 3 and 2 consequently. If we route through Node 1, the total cost is 3+3 which is equal to 6, on the other hand if we route through Node 4, the total cost is 1+3 which is equal to 4 and if we route through Node 5, the total cost is 4+2 which is equal to 6. Thus the shortest-path between Node 2 to Node 6 is routed through Node 4.

The starting assumption for distance-vector routing is each node knows the cost of the link of each of its directly connected neighbors. Next, every node sends a configured message to its directly connected neighbors containing its own distance table. Now, every node can learn and update its distance table with cost and next hops for all nodes network. Repeat exchanging until no more information between the neighbors.

Consider a node 2 to the destination node 6, the minimum cost can be found form

$$\begin{aligned} D_2 &= \min\{C_{21}+D_1, C_{24}+D_4, C_{25}+D_5\} \\ &= \min\{3+3, 1+3, 4+2\} \\ &= \min\{6,4,6\} \\ &= 4 \end{aligned} \quad (1)$$

Where C_{ij} is link cost between node i to node j, for example $C_{13}=C_{31}=2$ and $C_{ii}=0$. So the minimum cost from node 2 to node 6 is equal 4. Thus, we can calculate the other routing as follow: From node 1 to node 6

$$D_1 = \min\{C_{12} + D_2, C_{13} + D_3, C_{14} + D_4\} \quad (2)$$

While form node 4 to node 6

$$D_4 = \min\{C_{41} + D_1, C_{42} + D_2, C_{45} + D_5\} \quad (3)$$

For d, the distance to destination, we can consider Bellman-Ford Algorithm as follow:

1. Initial state

$$D_i = \infty \quad \text{Where } i \neq d \quad (4)$$

$$D_d = 0 \quad (5)$$

2. Update state (to find out the shortest-path to destination via neighbors) where $i \neq d$

$$D_i = \min\{C_{ij} + D_j\} \quad \text{For } j \neq i \quad (6)$$

This equation suggests that the form of neighbor-to-neighbor communication that will take place in the Distance-vector (DV) routing [3] - each node must know the cost of each of its neighbors' minimum-cost path to each destination. Hence, whenever a node computes a new minimum cost to some destination, it must inform its neighbors of this new minimum cost.

$$D_{ij} = 0 \quad (7)$$

$$D_{ij} = \min(C_{ik} + D_{kj}) \quad (8)$$

D_{ij} is the minimum cost from node i to destination node j. When update state node i will distribute vector $\{D_{i1}, D_{i2}, D_{i3}, ...\}$ to its neighbors.

B. Link Cost Calculation

In this paper, we calculate the link cost from 3 factors: the number of wavelength in each physical link N_λ, Total losses (L), and Distance (d) between nodes. The formula can be represented as

$$Link\ Cost = A + B + C \quad (9)$$

Where

$$A = (1/N_\lambda)^* w_1 \quad (10a)$$

$$B = L * w_2 \quad (10b)$$

$$C = d * w_3 \quad (10c)$$

Replace A, B, C in (9) with (10a)-(10c), Thus

$$Link\ Cost = ((1/N_\lambda)^* w1) + (d * w2) + (L * w3) \quad (11)$$

where
- N_λ is Number of wavelength
- d is distance (km)
- L is Losses
- w_1 is weight factor in term of number of wavelength
- w_2 is weight factor in term of distance
- w_3 is weight factor in term of losses

The total losses are from Fiber loss (0.2525 dB/km), Connection losses (0.5 dB/1 connection point) and Margin (4 dB/section). The weight setting are $w_1+w_2+w_3=1$ and $w_1=0.5$, $w_2=0.3$, $w_3=0.2$. The major factor of this study is on number of wavelength because it provides the minimum link cost and it is the main parameter in expansion/reduction of WDM capacity while the physical distance is not changed.

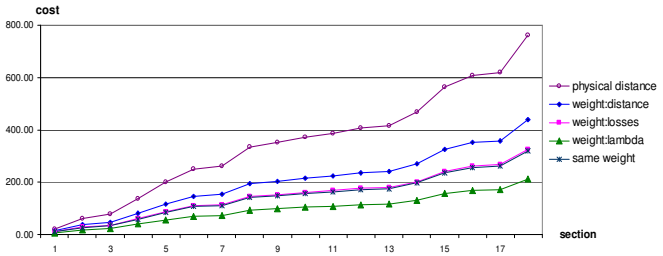

Figure 2. Link cost calculation in different weight setting

From (11) we will get backbone network with link cost as in Fig. 3

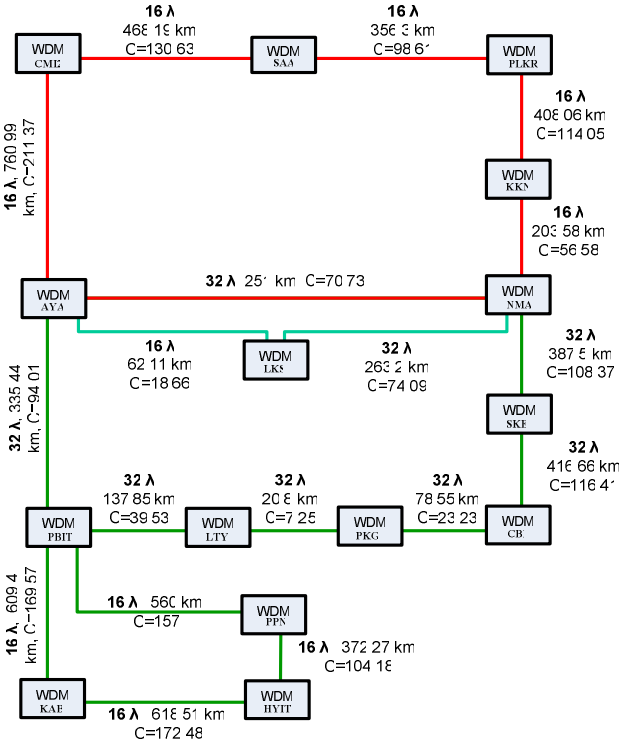

Figure 3. TOT Backbone Network with link cost

C. *Minimum Cost Calculation*

For all node i, the assign value are (n,D_i) where n is the shortest next hop and D_i is the minimum cost from node i to node j as (6). In case of none specific destination we have to assign n equal -1 for the first time calculation. The starting assumption for distance-vector routing is each node knows the cost of the link of each of its directly connected neighbors. Next, every node sends a configured message to its directly connected neighbors containing its own distance table. Now, every node can learn and update its distance table with cost and next hops for all nodes network. Repeat exchanging until no more information between the neighbors.

D. *Shortest Path Routing*

From *section C*, after exchanging cost until no more information between the neighbors, we will get shortest-path routing. In this paper we consider the condition from equation (7) and (8) and use Matlab to calculate Minimum Cost and Shortest-path.

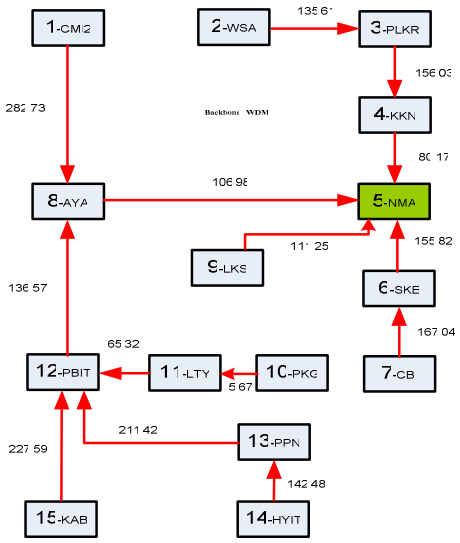

Figure 4. The shortest-path routing to destination Node 5

Fig. 3 show the example of calculate result to route a path connection between other nodes to destination node 5 with the shortest-path and minimum cost.

E. *Minimum Cost Re-computation*

It is beneficial to discuss the concept of critical links and our approach for finding them. Our goal is to compute a routing solution that protects the network performance against the failure of links that impact the network most on failure. In case of physical link failure, we have to re-routing path to the other route. We can follow up the process of *section D* by generate the link cost of failure to infinity and re-start calculate shortest-path and update its distance table with cost and next hops for all nodes network.

Fig. 4 shows the new shortest-path routing to destination Node 5 when the link failure occur between node 8 and node 5. The new path will be routed to avoid the broken link but the re-calculation is still being base on Bellman-Ford algorithm with the minimum link cost.

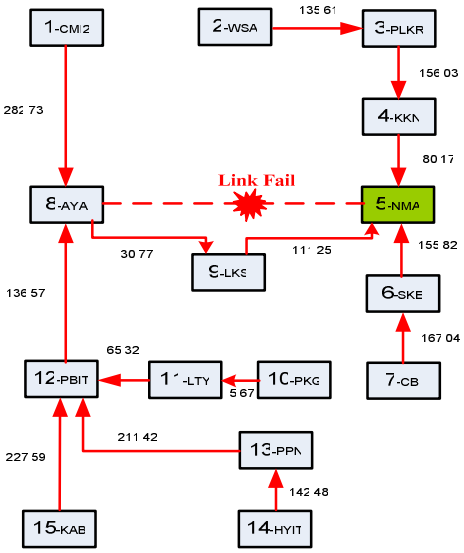

Figure 5. The new shortest-path routing to destination Node 5 with link failure

III. NUMERICAL RESULTS

In this section, we present the curves to compare the results of Physical distance and Logical Link Cost and between Logical and Physical Hop count. The parameters of node source to destination node, we have chosen node 5 and node 14 as destination nodes. Fig. 6 shows the comparison between Physical and Logical link cost of node i to node 5 and node 14 and Logical and Physical hop count. The same hop count on both techniques shows that the algorithm will provide the optimize path that match to the real network. Fig. 7 shows the Cost of distance and hop count in link failure between node 11 and node 12 that sorted by physical distance in each section. Fig. 8 shows the Cost of distance and hop count in link failure between node 5 and node 8 that sorted by physical distance in each section as shown.

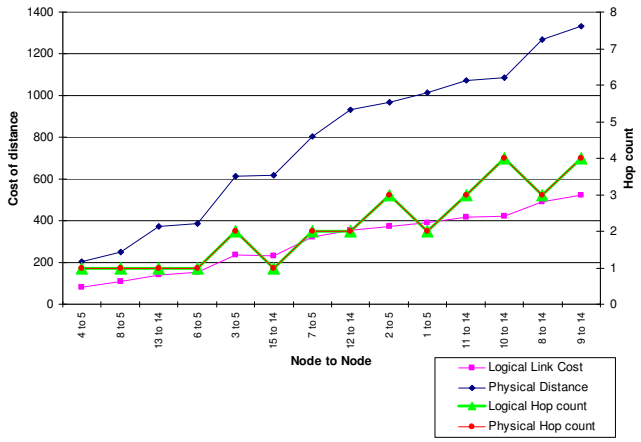

Figure 6. The comparison between Physical and Logical Cost Distance and Hop count

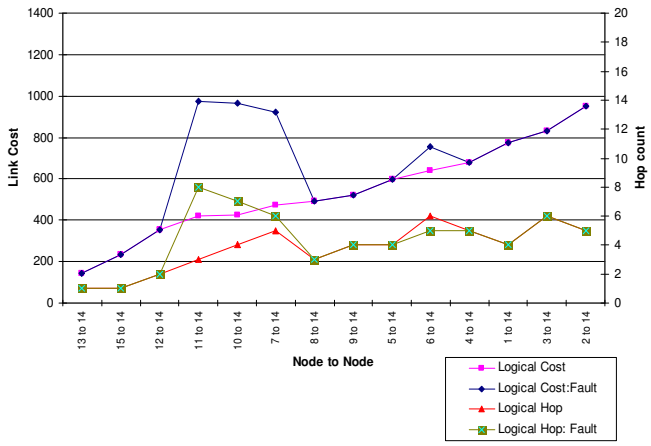

Figure 7. The new shortest-path routing to destination Node 5 with link failure

IV. CONCLUSIONS

Shortest-Path routing is introduced into design logical network for connecting between Sub-networks. Bellman-Ford's Algorithm is used for computing and simulation for optimal logical design of WDM network by considering in the link cost that can be calculated in term of number of wavelength in majority. Three main parameters consider in this paper including Minimum Cost, Shortest-Path Routing and Re-computing of Minimum Cost to find out final shortest path. Furthermore, the expansion or reduction of WDM network capacity can be changed by number of wavelength that updated link cost and new shortest-path.

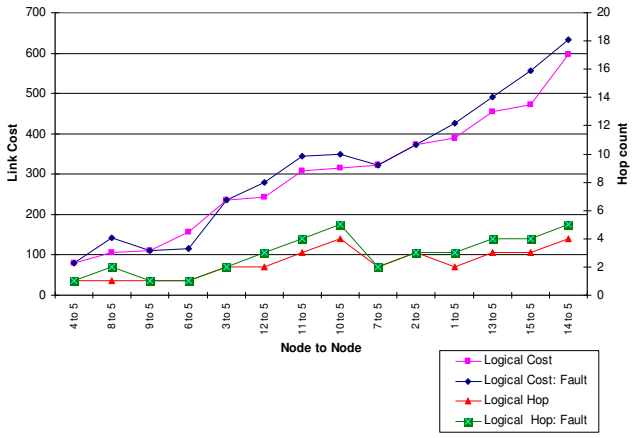

Figure 8. The new shortest-path routing to destination Node 5 with link failure

ACKNOWLEDGMENT

The authors would like to thank Assoc.Prof. Noppin Anantrasirichai for reading and helpful discussions.

REFERENCES

[1] Ashwin Sridharan, R. Guerin, and C. Diot. "Achieving Near-Optimal Traffic Engineering Solutions for Current OSPF/IS-IS Networks," Proceeding of *INFOCOM'2003*, April 2003.

[2] Andrew S. Tanenbaum, "Computer Networks," *Pearson Education*., pp.294-302.

[3] Martha E. Steenstrup, "Routing in Communications Networks" *Prentice Hall International, Inc.*, pp.136-145.

[4] Alberto Leon-Garcia and Indra Widjaja, "Communication Networks: Shortest-Path Routing" *McGrawhill*, pp.552-530.

Numerical Analysis of Pump Propagation Direction in Distributed Raman Amplifiers

Nadir Hossain*, A.W. Naji, V. Mishra, F.M. Abbou, M. A. Hasnayeen, A.A.R. Hairul, and A.R. Faidz
Institute of Photonics Research & Applications, Multimedia University,
63100 Cyberjaya, Selangor, Malaysia.
Email: nadir.hossain05@mmu.edu.my

***Abstract*-This paper presents a complete numerical analysis of co- and counter-propagating pump power in distributed Raman amplifier (DRA) for remotely pumped long haul optical fiber communication system (OFCS). The mathematical model to calculate the signal gain due to DRA is described. The intrinsic parameters of standard single mode fiber (SMF) are used to simulate the mathematical model DRA. Signal gain and signal propagation through the transmission fiber, with and without Raman gain using co- and counter-propagating pump power are investigated. The presented numerical analysis can be used as a design tool of long haul transmission link using DRA, especially to calculate the signal power budget of the long haul OFCS incorporated with a hybrid EDFA / DRA.**

***Keywords*-** Distributed Raman amplifier, Hybrid EDFA / DRA, Long haul OFCS.

I. INTRODUCTION

DRAs have emerged in recent years as a key technology for the modern optical fiber communication system [1]. The broad bandwidth of DRA makes it attractive for use in high capacity, long haul transmission system [2]. DRA expands the signal bandwidth through multi-pumping wavelength allocation [3] and offers improved noise characteristics [4]. Because of the high importance of DRA in modern long haul OFCS, a detailed analysis tools is essential in order to obtain the results of the system performance. Both analytical [5] and numerical [6] models of DRA have been reported. Co- [7] and counter-propagating [8] pumping schemes have been reported to maximize the power budget of remotely pumped long haul OFCS incorporated with hybrid EDFA / DRA. The position of inline Erbium doped fiber amplifiers (EDFAs) in the remotely pumped long haul OFCS are dependent on the pumping scheme of DRA. So, an analysis of power budget improvement due to DRA with respect to pump propagation direction is necessary to design a long haul OFCS incorporated with hybrid EDFA / DRA.

This paper focuses on the analysis of pump propagation direction in DRA using the numerical simulation of DRA mathematical model. This paper is organized as follows. Section II describes the pumping schemes of DRA followed by the DRA mathematical model in section III. Section IV presents the numerical simulation of the DRA mathematical model. Section V investigates the effects of pump propagation direction in DRA using the numerical simulation. This paper concludes with a summary in section VI.

II. DRA PUMPING SCHEMES

There are two pumping schemes to produce DRA in long haul OFCS incorporated with hybrid EDFA / DRA. They are co-propagating and counter-propagating pumping scheme as shown in Fig. 1. Referring to the Fig. 1(a), both the Raman pump and signal light propagates towards the same direction from the transmitter to the receiver. This is known as co-propagating pumping scheme. In case of counter-propagating pumping scheme, Raman pump light is provided from the receiver side and signal light propagates from the transmitter to the receiver as shown in Fig. 1(b).

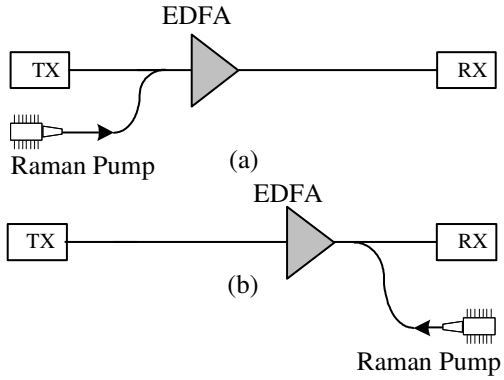

Figure 1. Two pumping schemes of DRA: co-propagating (Fig. 1(a)) and counter-propagating (Fig. 1(b)) pumping schemes.

III. MATHEMATICAL MODEL OF DRA

For the purpose of numerical modeling, pump power level is considered high enough to produce stimulated Raman scattering (SRS). During SRS the interaction between the co-propagating pump power (P_P^+) and signal power (P_S) as well as counter propagating pump power (P_P^-) and P_S are governed by the following set of coupled equations, derived from the Maxwell's equations [6, 9]:

$$\frac{dP_S}{dZ} = \frac{g_R}{A_{eff}} P_P^{\pm} P_S - \alpha_S P_S \tag{1}$$

$$\frac{dP_P^+}{dZ} = -\frac{\omega_P}{\omega_S} P_P^+ P_S - \alpha_P P_P^+ \quad (2)$$

$$\frac{dP_P^-}{dZ} = \frac{\omega_P}{\omega_S} P_P^- P_S + \alpha_P P_P^- \quad (3)$$

Where Z is the co-ordinate of the signal propagation direction, A_{eff} is the effective area of the fiber, g_R is the Raman gain coefficient as well as α_S and α_P account for fiber losses at the signal frequency (ω_S) and pump frequency (ω_P) respectively. The pump depletion must be included for a complete description of SRS but it can be neglected for the purpose of estimating the Raman threshold [6]. So, if we neglect the first term on the right hand side of equation (2) and (3), which is responsible for pump depletion, then equation (2) and (3) are readily solved to give:

$$P_P^+(Z) = P_{P_in}^+ e^{-\alpha_P L(Z)} \quad (4)$$

$$P_P^-(Z) = P_{P_in}^- e^{-\alpha_P L(Z)} \quad (5)$$

Where $P_{P_in}^+$ and $P_{P_in}^+$ is the co-propagating and counter propagating input pump power respectively as well as *L(Z)* is the distance between the pump source and *Z* co-ordinate of the transmission fiber. Now from equation (1) with the help of equation (4) and (5), we have,

$$\frac{dP_S}{dZ} = \frac{g_R}{A_{eff}} P_S P_{P_in}^{\pm} e^{(-\alpha_P Z)} - \alpha_S P_S \quad (6)$$

By solving equation (6) we have,

$$P_S(Z) = P_{S_in\ (Z)}\, e^{\frac{g_R P_{P_in}^{\pm}}{A_{eff}(-\alpha_P)}(e^{(-\alpha_P Z)}-1)-\alpha_S Z} \quad (7)$$

Where, $P_{S_in\ (Z)}$ is the input signal power at location *Z* of the transmission fiber. Now we can calculate the input signal power of the receiver from equation (7) as

$$P_S(L) = P_{S_in\ (0)} e^{\frac{g_R P_{P_in}^{\pm} L_{eff}}{A_{eff}} - \alpha_S L} \quad (8)$$

Where $L_{eff} = \frac{1}{\alpha_P}[1 - e^{-\alpha_P L}]$ (9)

Where, $P_{S_in\ (0)}$ is the signal power enters at the input of the transmission fiber, L is total transmission length, L_{eff} is the effective length of the transmission fiber within which signal is amplified due to the DRA. The total gain (G) due to the SRS in the transmission fiber is calculated from equation (8) as:

$$G = (P_{S_in(0)} e^{\frac{g_R P_{P_in}^{\pm} L_{eff}}{A_{eff}} - \alpha_S L} / P_{S_in(0)})$$

$$= e^{\frac{g_R P_{P_in}^{\pm} L_{eff}}{A_{eff}} - \alpha_S L} \quad (10)$$

Total signal attenuation in the transmission fiber is: $e^{-\alpha_S L}$
So, the net Raman gain is calculated as:

$$G_R = e^{\frac{g_R P_{P_in}^{\pm} L_{eff}}{A_{eff}} - \alpha_S L} * e^{-\alpha_S L}$$

$$= e^{\frac{g_R P_{P_in}^{\pm} L_{eff}}{A_{eff}}} \quad (11)$$

IV. NUMERICAL SIMULATION OF DRA MATHEMATICAL MODEL

Effective length of the DRA is calculated from the equation (9). Gain due to the DRA is calculated by iterative process using equation (4)-(5) and (11). Calculation of the Raman gain is started from the beginning of the effective length. Raman gain of the 1st meter of effective length is calculated according to the equation (11) by the input pump power at the beginning of effective length. The input pump power at the beginning of 2nd meter is then calculated from equation (4)-(5). Then the Raman gain of the 2nd meter of effective length is calculated according to the equation (11) by the input pump power at the beginning of 2nd meter. This process continues iteratively up to the end of the effective length. Total Raman gain is achieved by the cumulative gain through the whole effective length. The single mode fiber (SMF) parameters used to simulate the mathematical model is shown in Table 1. The typical values of A_{eff} , α_S and α_P are used for the purpose of numerical simulation as well as the value g_R is used according to the wavelength difference between pump and signal power.

TABLE I
INTRINSIC PARAMETERS OF SMF USED IN SIMULATION

L = 50 km.	$P^{-}_{P_in}$ = 200 mW.
$P_{S_in(0)}$ = 0.1 mW.	$P^{+}_{P_in}$ = 200 mW.
A_{eff} = 70 X 10^{-12} cm^2.	g_R = 3.9 X10^{-4} m/W.
λ_S = 1550 nm.	λ_P =1480 nm.
α_S = 0.20 dB/Km.	α_P = 0.24 dB/Km.

V. ANALYSIS OF PUMP PROPAGATION DIRECTION

In order to help the designers to calculate the power budget of a long haul OFCS incorporated with a DRA, a detailed analysis is carried out in this section using the numerical simulation of the DRA mathematical model. The comparison between co- and counter-pumped Raman gain at 1550 nm signal wavelength as a function of 1480 nm pump power using 50 km long transmission fiber for various signal power is shown in Fig. 2. From this Figure, 200 mW pump power shows a signal gain of 2.21 dB for 1 mW signal power, 4.49 dB for 0.1 mW signal power and 5.65 dB for 10 nW signal power using counter-propagating pump power as well as 0.44 dB for 1 mW signal power, 4.37 dB for 0.1 mW signal power and 5.43 dB for 10 nW signal power using co-propagating pump power. On the other hand, 2 watt pump power shows a signal gain of 9.95 dB for 1 mW signal power, 18.65 dB for 0.1 mW signal power and 50.53 dB for 10 nW signal power using counter-propagating pump power as well as 3.18 dB for 1 mW signal power, 16.33 dB for 0.1 mW signal power and 48.54 dB for 10 nW signal power using co-propagating pump power. According to the results in Fig. 2, counter-propagating pump power provides a higher gain than co-propagating pump power. This is because, signal power at the beginning of the effective length of co-propagating pumping scheme is higher than the signal power at the beginning of the effective length of counter-propagating pumping scheme and this higher signal power depletes the pump power at a higher rate. As a result, the signal gain is lower for the co-propagating pumping scheme.

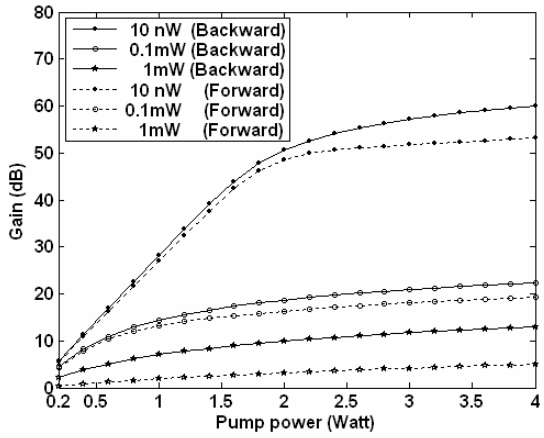

Figure 2. Comparison between Raman gain with respect to co- and counter-propagating pump power at 1550 nm signal wavelength as a function of 1480 nm pump power using 50 km long transmission fiber for various signal power.

The signal propagation characteristics at 1550 nm with (bold line) and without (dotted line) Raman effect as a function of position along a 50 km long transmission fiber using 200 mW pump power and co-propagating pumping scheme is shown in Fig. 3. The signal power at the input of the transmission fiber is 0.1 mW (-10 dBm). The input signal is amplified in the beginning 17.25 km effective length of the transmission fiber and after the effective length the signal power attenuates linearly due to the absorption of signal in the transmission fiber. Without Raman effect the signal power at the end of the transmission fiber is 0.010 mW (-20 dBm) but due to the Raman amplification signal power at the end of the transmission fiber is 0.018 mW (-17.26 dBm), which indicates a net Raman gain of 2.74 dB.

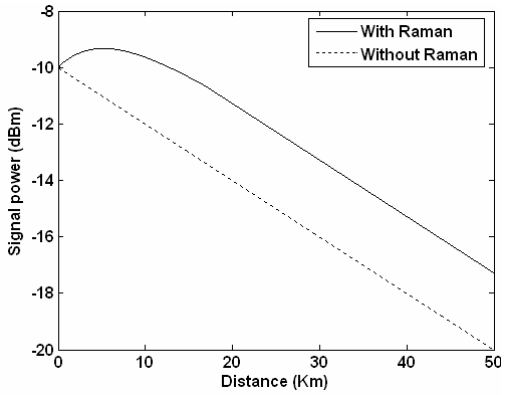

Figure 3. Signal power with and without Raman gain as a function of position along a 50 km long transmission fiber using co-propagating pump power.

Fig. 4 shows the signal propagation characteristics at 1550 nm with (bold line) and without (dotted line) Raman effect as a function of position along a 50 km long transmission fiber using 200 mW pump power and counter-propagating pumping scheme.

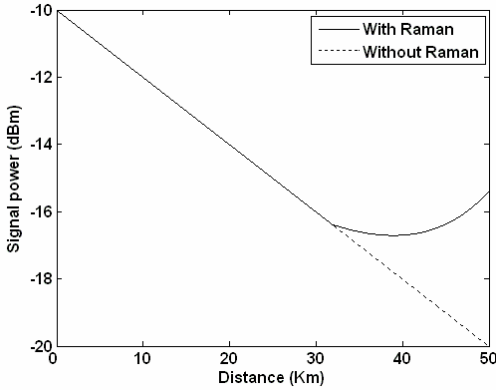

Figure 4. Signal power with and without Raman gain as a function of position along a 50 km long transmission fiber using counter-propagating pump power.

The input signal power at the input of the transmission fiber is 0.1 mW (-10 dBm). The input signal power attenuates in the beginning 32.75 km of the transmission fiber due to the absorption of signal in the fiber as well as the signal power amplifies due to the Raman effect in the last 17.25 km of the transmission length. Without Raman effect the signal power at

the end of the transmission fiber is 0.010 mW (-20 dBm) but due to the Raman amplification signal power at the end of the transmission fiber is 0.029 mW (-15.40 dBm), which indicates a net Raman gain of 4.60 dB. The analysis of co- and counter-propagating pumping scheme shows that the counter-propagating pumping scheme provides more amplification than the co-propagating pumping scheme for the same amount of pump power which justifies the findings in Fig. 2.

VI. CONCLUSION

DRA pumping schemes for long haul OFCS and the mathematical model of DRA to calculate the gain due to DRA are described. The approach to numerically solve the DRA mathematical model is investigated. The effects of pump propagation direction in DRA are analyzed using numerical simulation of the mathematical model. Signal amplification and signal propagation characteristics with and without Raman gain are investigated using co- and counter-propagating pumping scheme. These findings can be used to analyze the power budget improvement with respect to pump propagation direction, which is used to design a remotely pumped long haul OFCS incorporated with hybrid EDFA / DRA.

ACKNOWLEDGEMENT

The authors would like to thank all the members of Institute of Photonics Research & Applications (IPRA) at Multimedia University, Malaysia for their support.

REFERENCES

[1] N. Hossain, Mishra, V., Hairul, A. A. R., Abbou, F. M., Faidz, A. R., Al-Mansoori, H., Mahdi, M. A., and A. W. Naji, "Distributed Raman Amplifiers for Long-Haul OFCS", *MMU International Symposium on Information and Communications Technologies (M^2USIC'06),* PJ, Malaysia, pp. 188-192, November 2006.

[2] T. Tanka and T. Naito, "Raman amplifier based submarine transmission system", *Optical Fiber Technology*, Vol. 8, pp. 195-209, July 2002.

[3] S. V. Chernikov, S. A. E. Lewis, and J. R .Taylor, "Broadband Raman amplifiers in the spectral range of 1480-1620 nm", *Optical Fiber Communication Conference (OFC'99)*, San Diego, USA, pp. 117-119. February 1999.

[4] C. Fludger, A. Maroney and N. Jolley, "An analysis of the improvements in OSNR from distributed Raman amplifiers using modern transmission fibers", *Optical Fiber Communication Conference (OFC'2000)*, Baltimore, USA, pp. 100-102, March 2000.

[5] K. Mochizuki, "Optical fiber transmission systems using stimulated Raman scattering: Theory" *Journal of Lightwave Technology*, Vol. 3, No. 3, pp. 688-694, June 1985.

[6] E. A. Kunarajah, J. J. Lepley and A. S. Siddiqui, "An accurate numerical model for distributed Raman amplifiers", *European Conference on Optical Communication (ECOC'01),* Amsterdam, Netherlands, pp. 234-235, March 2001.

[7] J. P. Blondel, "Achievable Budget Improvement with Raman Amplification and Remotely Pumped Post amplification at Transmit Side of 622Mbit/s and 2.5Gbit/s Repeaterless System". *IEEE photonics technology letters,* vol. 7, no. 1, pp. 108-110, 1995.

[8] M. S. Chaudry, S. S. Sian, K. Guild, P. R. Morkel, and C. D. Stark, "Single-Span Transmission of 2.5 Gb/s Over 410 Km with Remote Amplification and Dispersion Compensation", *ECOC'94,* Florence, Italy, pp. 19-22, 1994.

[9] C. Headley, and G. P. Agrawal, *RAMAN AMPLIFICATION IN FIBER OPTICAL COMMUNICATION SYSTEMS,* 1st ed., New York: Academic Press, 2005, pp. 33-97.

Jd

Performance Evaluation of 2-D Code Optical CDMA MAC Protocol over WDM

Kidsanapong Puntsri
Department of Electronics and Telecommunication Engineering, Faculty of Industrial Education
Rajamangala University of Technology Phranakhon, Bangkok, Thailand
E-mail: k.puntsri@rmutp.ac.th

***Abstract*- We present the comparison of CDMA MAC protocol with and without beat noise by using 2-D optical CDMA MAC protocol over WDM networks. We use the asymmetric prime-hop sequence code. Moreover, we analyse the effect of the number of available wavelengths in terms of average number of attempted to transmissions per time slot (offered load), and beat noise is considered. The presented numerical results based on the throughput and delay time versus the offered load. We divide into two parts. The first one, we consider the effect of the number of available wavelengths. Another is the effect of with and without beat noise in the 2-D OCDMA over WDM systems.**

I. INTRODUCTION

In the middle of 80's, OCDMA (Optical code division multiple access) has been widely developed as high-optical communication network systems, where encoding and decoding are all performed in optical domain [1-2]. The advantageous function of the optical CDMA is the fact that it lets each user to access the network asynchronously and simultaneously without strict wavelength controls and timing synchronizations, but other systems needed such as in the case of wavelength division multiple access (WDMA) and time division multiple access (TDMA), respectively. In addition, optical CDMA local area networks allow shared access to a broadcast medium. However, the OCDMA has interference occur when the number of codeword are assigned increasing, call multiple access interference (MAI).

Especially, OCDMA will be operated on Ethernet passive optical networks (EPON) because of the EPON architecture is the key function in local area network (LAN). Moreover, it also can be upgradeable to Gigabit Ethernet and 10 Gigabit Ethernet, respectively, and in the future; when OCDMA are used on EPON, the capacity and bandwidth will increase [3-4].

In addition, many papers propose and focus on the physical layer of CDMA network [1-2, 6-7]; however, few papers have considered the MAC protocol with beat noise. Therefore, this article, we present the comparison of OCDMA MAC protocol with and without beat noise by using 2-D optical CDMA over WDM networks and asymmetric prime-hop sequence code is used. The family of asymmetric prime-hop sequence code has $p_s(p_h-1)$ of length p_s^2 and each code had Hamming weight p_s (prime number). At the source, tunable laser (or laser arrays) and tunable fiber delay-lines used to select the pulse wavelength and time position. Therefore, passive network of matched delay lines and corresponding optical filters required at the receiver.

This paper is organized as follows. In section II, the network model description is discussed, and the performance of 2-D asymmetric prime-hop sequence optical CDMA code over WDM networks is presented. In section III, the numerical results of the performance are reported with based on throughput and delay time. Finally, we give concluding in section IV.

II. PERFORMANCE ANALYSIS

A. Network Model

In figure 1, the network consists of a basic OCDMA, which the users are assigned with different optical code and share common transmission medium. The coding can be performed on to 1-dimension (1-D) either in time domain, or frequency domain, or performed on to 2-dimension (2-D) in both frequency and time domains simultaneously.

However, we focus on OCDMA over WDM PON networks. On each WDM grid $\lambda_n (n = 1,...,N)$, not a single channel, and M simultaneous users can be accommodated by individually assigning each user with a different code. Therefore, the total capacity of OCDMA over WDM PON becomes N times when compare with WDM PON. Moreover, we use 2-D coding, and the signals are transmitted over WDM channels [3-4]. The OCDMA over WDM PON is presented in figure 1.

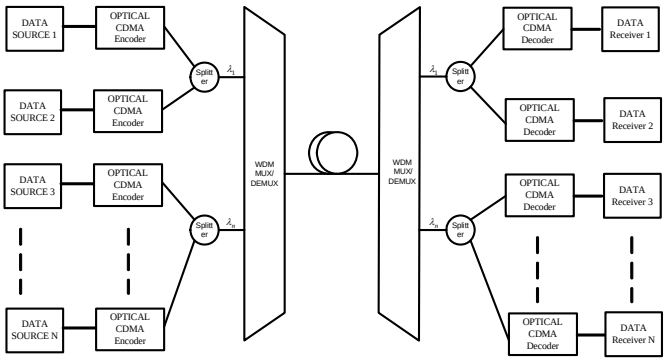

Figure 1. Optical CDMA network over WDM.

B. 2- D Optical CDMA Code

This article, we limit our analysis to OCDMA network that we use the asymmetric prime-hop sequence described by Tancevski et al. [5]. The advantages of 2-D codes in this family have low cross-correlations, nonexistent

autocorrelation side lobes and large cardinalities. Hence, the bits error rate of asymmetrical prime-hop sequence with beat noise is given by [5]

$$P_{error}(m)=\sum_{i=1}^{m-1}\binom{m-1}{i}2^{-(m-1)}\sum_{j=1}^{i}\binom{i}{j}\left(\frac{\langle\mu\lambda\rangle}{p_s^2}\right)^j\cdot \left(1-\frac{\langle\mu\lambda\rangle}{P_s^2}\right)^{i-j}\frac{1}{2}\left\{Q\left(\frac{p_sP_dD-jP_c}{\sqrt{2P_cP_c\binom{j}{2}\frac{1}{p_s}}}\right)+ Q\left(\frac{p_sP_d+jP_c+p_sP_dD}{\sqrt{2jP_dP_c+2P_cP_c\binom{j}{2}\frac{1}{p_s}}}\right)\right\} \quad (1)$$

Where $Q(x)$ is Q function, given by

$$Q(x)=\frac{1}{2\pi}\int_x^{\infty}\exp(-y^2/2)dy \quad (2)$$

and

$$\langle\mu\lambda\rangle=\frac{1}{\binom{p_h}{p_s}}\left[\binom{p_h-1}{p_s-1}\frac{(p_s-1)(p_s-2)+(p_h-2)}{p_h-2}+\binom{p_h-1}{p_s}\frac{p_s(p_s-1)}{p_h-2}\right] \quad (3)$$

is the average number of wavelengths common to any pairs of asymmetrical prime-hop sequences.
Hence,

p_s (prime code) is the number of pulses per wavelengths

p_h (prime code) is the number of available wavelengths

P_c is optical power of crosstalk pulse

P_d is optical power of bits data pulse

D is the threshold level

However, when consider the limiting case of negligible beat noise, i.e., all noise sources are neglected. This means that SNR is infinite [7]. Therefore, for positive signals of the term of Q function is zero in (1), and when the signals is negative Q function is 1 (in the case of when bit "0" is transmitted and j becomes greater than the threshold, we got $\theta = p_sP_dD$). We give the total probability of error when neglected beat noise, is [5]

$$P_{error}(m)=\frac{1}{2}\sum_{i=1}^{m-1}\binom{m-1}{i}2^{-(m-1)}\sum_{j=\theta}^{i}\binom{i}{j}\cdot \left(\frac{\langle\mu\lambda\rangle}{p_s^2}\right)^j\left(1-\frac{\langle\mu\lambda\rangle}{p_s^2}\right)^{i-j} \quad (4)$$

Additionally, the asymmetrical prime-hop sequences have a length in a time domain of p_s^2 chips and can be supported a maximum of $p_s(p_h-1)$ simultaneous users.

C. MAC protocol Analysis

We use the synchronous and random-access protocol for scheduling packets which is the length of a slot corresponds to L bits. A number of packets from many sources can be transmitted over the optical fiber in a single slot.

Moreover, some of the packets arrive at the receiver with bit errors because multiple-access interference (MAI) occurred by m simultaneous users increasing. We let $P_{error}(m)$ be the probability of a bit error when there are m simultaneous transmissions on the channel. The characteristics of $P_{error}(m)$ will depend upon the size, weight and family of the OCDMA code under consideration. Therefore, the probability of receiving a packet will occur without errors when m simultaneous transmissions on the channel are given by [7].

$$P_{correct}(m)=[1-P_{error}(m)]^L \quad (5)$$

and the condition of receiving a correct packet is

$$P_{correct}(m)=\begin{cases}[1-P_{error}(m)]^L, & 0\le m\le p_s(p_h-1)\\ 0, & p_s(p_h-1)\le m\le\infty\end{cases} \quad (6)$$

However, with suitable error-detection capability, at the receiver can detect and determine if one or more errors have occurred in the packets. For simplicity, the overhead required of error-detection is not considered. In a broadcast network, the sender can independently determine the success or failure of the transmission and queue the packet for retransmission after a random delay in the buffer.

From according above, we let M be a random variable that represents the number of simultaneous in a time slot. Therefore, the conditional distribution of the number of successfully received packets S is

$$P[S=s\mid M=m]=\binom{m}{s}P_{corect}^S(m)[1-P_{correct}(m)]^{m-s} \quad (7)$$

The steady-state throughput can be shown in equation (8).

$$\beta=E[S]=E[E[S\mid M]]=\sum_{m=1}^{\infty}mP_{correct}(m)f_m(m) \quad (8)$$

Where $f_m(m)$ is the steady-state probability distribution of composite arrivals, which include new and retransmission packets in queue. In this article, we assume that the composite arrival distribution is Poisson arrival with rate λ

$$f_M(m) = \frac{(\lambda T)^m}{m!} e^{-\lambda T} \tag{9}$$

Here, T is the temporal length of the packet.

Additionally, the choice of arrival distribution corresponds to an infinite user population. Giving $\gamma \equiv \lambda T$ to be the offered load (average number of attempted transmissions per time slot), so the throughput becomes

$$\beta = e^{-\gamma} \sum_{m=1}^{\infty} m P_{correct}(m) \frac{\gamma^m}{m!} \tag{10}$$

Then, the delay measured in the average number of retransmissions per packet, given by [6]

$$d = \frac{\gamma}{\beta - 1} \tag{11}$$

III. Numerical Results

In this section, we present the numerical results of OCDMA over WDM systems with and without beat noise. The asymmetric prime-hop code used with OCDMA chip-rates p_s^2, packets lengths set to $L = 1024$ bits and set $p_s = 13$. The results are shown two parts. The first one, we consider the effect of the number of available wavelengths (p_h), figure 2 and 3. Another is the effect of the comparison of OCDMA MAC protocol with and without beat noise when using the 2-D OCDMA over WDM systems, figure 4 and 5. However, it is based on throughput (β) and delay time (d) versus offered load (G).

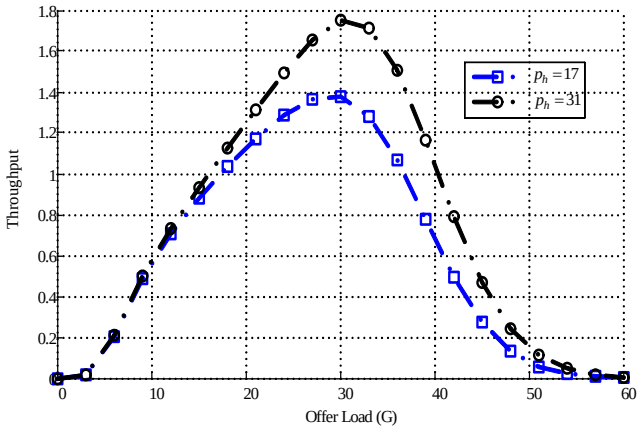

Figure 2. Throughput versus offered load with $p_h = 17$, 31

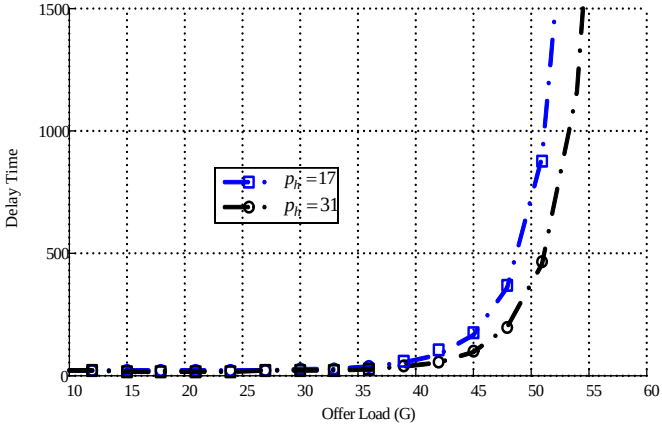

Figure 3. Delay time versus offered load with $p_h = 17$, 31

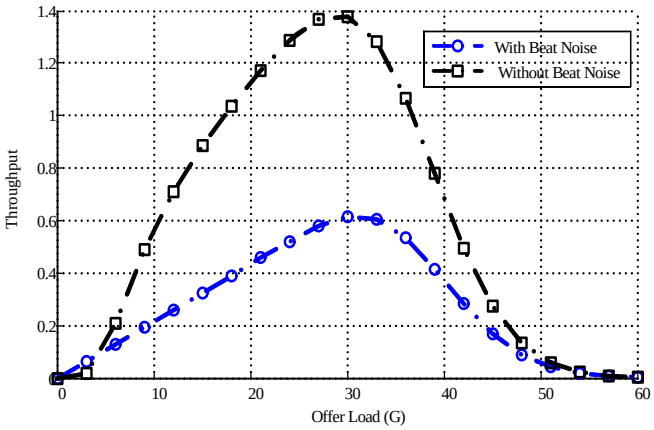

Figure 4. Throughput versus offered load with and without beat noise

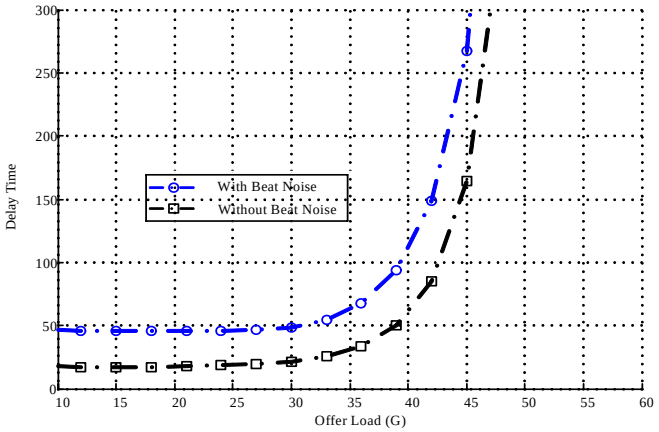

Figure 5. Delay time versus offered load with and without beat noise

Figure 2 compares the throughput versus offered load of OCDMA systems occurred without beat noise with $p_s = 13$, $p_h = 17$ and $p_h = 31$ (the available wavelengths), respectively.

We can see that the curves of throughput are parallel, but when a number of available wavelengths (p_h) increased, throughput increases.

Figure 3 plots the delay time as a function of the offered load for difference the number of available wavelengths (p_h) of OCDMA systems without beat noise. We set, again, the $p_s = 13$, $p_h = 17$ and $p_h = 31$, respectively. It is shown that the delay time start to increase at the offered load around 35-40 and then increases exponentially with the offered load. Additionally, the delay time decrease when the number of available wavelengths (p_h) increased.

Figure 4 shows the throughput with and without the beat noise versus offered load of OCDMA systems with $p_s = 13$ and the available wavelengths $p_h = 17$, respectively. It can be seen that the curves of throughput of without beat noise higher than the throughput with beat noise. Moreover, it clears that beat noise strongly affects the system performance and decreases the amount of simultaneous users.

Figure 5 plots the delay time as a function of the offered load for difference the number of available wavelengths (p_h) with and without beat noise. It is shown that the delay time start to increase at the offered load around 30-35 and then increases exponentially with the offered load. These means that beat noise has more effect in OCDMA system. Therefore, the beat noise is a very big problem and also is a big challenge how to reduce the beat noise effect in OCDMA systems.

IV. CONCLUSION

We propose performance evaluation of CDMA MAC protocol with and without beat noise by using 2-D optical CDMA over WDM networks. We use the asymmetric prime-hop sequence code. Moreover, we observe the effects of a number of available wavelengths in terms of average number of attempting to transmit per time slot (offered load), and also beat noise in system is considered. The presented numerical results based on the throughput and delay time versus the offered load. The results clear that the beat noise and prime code number has more effect in OCDMA system. Therefore, the beat noise is a very big problem and challenges to researcher who would like to reduce the beat noise effect in OCDMA systems.

ACKNOWLEDGMENT

This article was supported and received funding from Rajamangala University of Technology Phranakhon (RMUTP). Especially, the authors would like to special thanks to Mr.Sommart Sang-Ngern, a lecturer of the Department of Telecommunication Engineering, Mahanakorn University of Technology (MUT), Thailand for his review and discussions.

REFERENCES

[1] Kamath, P., Touch, J.D., Bannister, J.A., "*The need for media access control in optical CDMA networks*," *INFOCOM 2004*, Volume 4, pp. 2208 - 2219, 7-11 March 2004.

[2] Mohamed, M.A.A., Shalaby, H.M.H., El-Badawy, E.-S.A.-M., "*Performance Analysis of an Optical CDMA MAC Protocol With Variable-Size Sliding Window*," Journal of Lightwave Technology, vol. 24, Issue 10, pp.3590 - 3597, Oct. 2006.

[3] Galli, S., Menendez, R., Toliver, P., Banwell, T., Jackel, J., Young, J., Etemad, S., "*DWDM-compatible spectrally phase encoded optical CDMA*," *GLOBECOM '04. IEEE*, Vol.3, pp1888 – 1894, 29 Nov.-3 Dec. 2004.

[4] Kitayama, K, Xu Wang, Naoya Wada, "*OCDMA over WDM PON-solution path to gigabit-symmetric FTTH*," Journal of Lightwave Technology, vol. 24, Issue 4, pp. 1654 - 1662, April 2006.

[5] Tancevski, L.; Rusch, L.A, "*Impact of the beat noise on the performance of 2-D optical CDMA systems*," IEEE Communications Letters, vol 4, Issue 8, pp264 – 266, Aug. 2000.

[6] Srinivasan, M., Geetha, G., Meenakshi, M, "*Comparison of prime code, extended prime code and quadratic congruence code using a normalized throughput metric*," ICTON2004, vol. 2, pp.168 - 171, Sept. 2002.

[7] Stok, A., Sargent, E.H, "*System performance comparison of optical CDMA and WDMA in a broadcast local area network*," IEEE Communications Letters, vol. 6, Issue 9, pp.409 - 411, July 2004.

Resonances of a Chiral Filled Conducting Spherical Cavity

Denchai Worasawate[(1)], Muhammad A. Shahzad[(1)], and Monai Krairiksh[(2)]
(1) Kasetsart Advanced RF and ElectromagNetics Laboratory
Department of Electrical Engineering, Kasetsart University, Bangkok 10900, Thailand
fengdcw@ku.ac.th, http://karen.ee.ku.ac.th/
(2) Department of Telecommunication, Faculty of Engineering,
King Mongkut's Institute of Technology Ladkrabang, Bangkok 10520, Thailand
kkmonai@kmitl.ac.th

***Abstract*- The resonances of spherical resonator, with perfectly conducting wall and filled with a homogeneous isotropic chiral medium, is studied, using vector spherical wavefunctions. The aim of this work is to rewrite the equation in terms of vector spherical wavefunction and derive the characteristic equation for the problem when the relative chirality is one. Resonant frequencies of the first few modes for *n* = 1 and *n* = 2 are reported and discussed. These modes are hybrid modes. They are classed as either hybrid electric (HE) modes or hybrid magnetic (HM) modes.**

I. INTRODUCTION

Dielectric filled cavity resonators and dielectric resonators have been studied extensively because of their used in filters and antennas [1]–[4]. However, their used required a good knowledge of their resonant frequencies and *Q* factors. The resonances of a dielectric filled cavity resonator [5]–[6] and a dielectric sphere [7]–[9] have been presented in the past. The electromagnetic resonances and *Q* factor of a chiral sphere has been studied extensively in [10]. The resonances of spherical resonator, with perfectly conducting wall and filled with a homogeneous isotropic chiral medium, has been studied in [11]–[12]. The characteristic equations given in [11]–[12] does not work when the chirality approached the maximum limit given in [13] or the relative chirality defined in [10] approaches one and is invalid when it exactly equals to one. This paper is an extension of the work in [11]. In this paper, the characteristic equation of the problem in Fig. 1 is rewritten using the constitutive relation given in [10]. The detailed derivation of the characteristic equation is given for the case when the relative chirality is one. The characteristic equation is derived by forming solutions for the electromagnetic field inside the spherical resonator, which is completely filled with a chiral medium, in terms of the spherical vectorfunctions and enforcing the boundary condition on the tangential components of the electric filed on the surface of the sphere. The characteristic equation is solved by using the search function *fminsearch* provided by MATLAB [14].

II. THE SPHERICAL SOLUTIONS FOR A CHIRAL MEDIUM

The constitutive relations for a chiral medium are expressed as

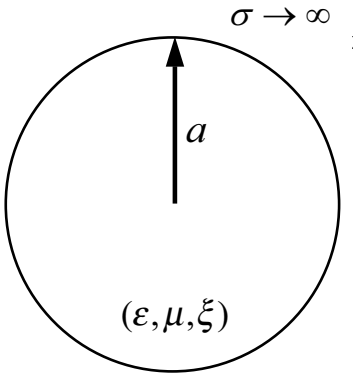

Figure 1. Geometry of the problem of resonances of a chiral filled conducting spherical cavity.

$$\mathbf{D} = \varepsilon \mathbf{E} - j\xi \mathbf{H} \tag{1}$$

$$\mathbf{B} = \mu \mathbf{H} + j\xi \mathbf{E}. \tag{2}$$

The electromagnetic field in a chiral medium can be decomposed in two parts, the right-handed wave ($\mathbf{E}_+$, $\mathbf{H}_+$) and the left-handed wave ($\mathbf{E}_-$, $\mathbf{H}_-$) [10]. The total electromagnetic field ($\mathbf{E}$, $\mathbf{H}$) can be written as

$$\mathbf{E} = \mathbf{E}_+ + \mathbf{E}_- \tag{3}$$

$$\mathbf{H} = \mathbf{H}_+ + \mathbf{H}_-. \tag{4}$$

Each of theses two wavefields ($\mathbf{E}_+$, $\mathbf{H}_+$) and ($\mathbf{E}_-$, $\mathbf{H}_-$) sees the chiral medium as an equivalent isotropic medium with respective medium parameters (μ_+, ε_+) and (μ_-, ε_-). The equivalent parameters ($\varepsilon_\pm$, $\mu_\pm$) and wave impedances $\eta_\pm$ are give as

$$\varepsilon_\pm = \varepsilon(1 \pm \xi_r) \tag{5}$$

$$\mu_\pm = \mu(1 \pm \xi_r) \tag{6}$$

$$\mu_\pm = \sqrt{\frac{\mu_\pm}{\varepsilon_\pm}} = \sqrt{\frac{\mu}{\varepsilon}} = \eta = \eta_0 \sqrt{\frac{\mu_r}{\varepsilon_r}} \tag{7}$$

where $\mu = \mu_o \mu_r$, $\varepsilon = \varepsilon_o \varepsilon_r$, and $\eta_o = \sqrt{\mu_o / \varepsilon_o}$ is the free-space wave impedance. The relative chirality ξ_r is defined by

$$\xi_r = \frac{\xi}{\sqrt{\mu\varepsilon}}. \tag{8}$$

For equivalent media, the wavenumber can be express in terms of free-space wavenumber as

$$k_\pm = \omega\sqrt{\mu_\pm \varepsilon_\pm} = k_o \sqrt{\mu_r \varepsilon_r}(1 \pm \xi_r) = k(1 \pm \xi_r). \tag{9}$$

These wavenumber are non-negative numbers when $-1 \le \xi_r \le 1$. In this paper, we assume that ξ_r is a positive number.

III. Fields Inside The Spherical Resonator

The resonant electromagnetic field inside a chiral filled conducting spherical cavity can be expressed as

$$\mathbf{E} = \sum_{m,n} \{ jc_{\{e,o\}mn}(\mathbf{N}^{(1)}_{\{e,o\}mn}(k_+ r) + \mathbf{M}^{(1)}_{\{e,o\}}(k_+ r)) + d_{\{e,o\}mn}(\mathbf{N}^{(1)}_{\{e,o\}mn}(k_- r) - \mathbf{M}^{(1)}_{\{e,o\}mn}(k_- r))\} \tag{10}$$

$$\mathbf{H} = -\frac{1}{\eta}\sum_{m,n} \{ c_{\{e,o\}mn}(\mathbf{N}^{(1)}_{\{e,o\}mn}(k_+ r) + \mathbf{M}^{(1)}_{\{e,o\}}(k_+ r)) + jd_{\{e,o\}mn}(\mathbf{N}^{(1)}_{\{e,o\}mn}(k_- r) - \mathbf{M}^{(1)}_{\{e,o\}mn}(k_- r))\} \tag{11}$$

where $\mathbf{M}^{(1)}_{\{e,o\}mn}(k_\pm r)$ and $\mathbf{N}^{(1)}_{\{e,o\}mn}(k_\pm r)$ are the vector spherical wavefunctions given in [10]. The subscript *o* indicates that the fields is odd with respect to ϕ and the subscript *e* indicates that the fields is even with respect to ϕ. $c_{\{e,o\}mn}$ and $d_{\{e,o\}mn}$ are the unknown expansion coefficients. The expansion coefficients can be obtained using the boundary condition at $r = a$. The tangential components of the electric field must vanish at $r = a$. Therefore

$$\mathbf{a}_r \times \mathbf{E} = 0 \tag{12}$$

where $\mathbf{a}_r$ is the unit radial vector. Using the expression for $\mathbf{M}^{(1)}_{\{e,o\}mn}(k_\pm r)$ and $\mathbf{N}^{(1)}_{\{e,o\}mn}(k_\pm r)$ given in [10] and the fact that these vector spherical wavefunctions are orthogonal, (12) can be expanded into two equations as

$$jc_{\{e,o\}mn} A - d_{\{e,o\}mn} B = 0 \tag{13}$$

$$jc_{\{e,o\}mn} C + d_{\{e,o\}mn} D = 0 \tag{14}$$

where

$$A = \frac{\hat{J}_n(k_+ a)}{k_+ a} \tag{15}$$

$$B = \frac{\hat{J}_n(k_- a)}{k_- a} \tag{16}$$

$$C = \frac{\hat{J}'_n(k_+ a)}{k_+ a} \tag{17}$$

$$D = \frac{\hat{J}'_n(k_- a)}{k_- a}. \tag{18}$$

Equations (13)–(14) for both odd and even modes are written in matrix form as

$$[Z][I] = [V] \tag{19}$$

where

$$[Z] = \begin{bmatrix} A & -B \\ C & D \end{bmatrix} \tag{20}$$

$$[I] = \begin{bmatrix} jc_{\{e,o\}mn} \\ d_{\{e,o\}mn} \end{bmatrix} \tag{21}$$

$$[V] = \begin{bmatrix} 0 \\ 0 \end{bmatrix}. \tag{22}$$

Solutions of (19) exist only when [Z] of (20) has zero determinant. This gives the characteristic equation for the chiral filled spherical resonator as

$$AD + BC = 0. \tag{23}$$

Let $ka = x$ be the roots of (23), where *x* is a positive real number and assume that $\xi_r \ne 1$. Substituting (15)–(18) into (23), we obtain

$$\hat{J}_n(x(1+\xi_r))\hat{J}'_n(x(1-\xi_r)) + \hat{J}_n(x(1-\xi_r))\hat{J}'_n(x(1+\xi_r)) = 0. \tag{24}$$

Equation (24) is the characteristic equation given in [11]. It is only valid for $\xi_r \ne 1$. When $\xi_r = 1$, $\hat{J}_n(x(1-\xi_r))$ and $\hat{J}'_n(x(1-\xi_r))$ are zero, nontrivial solutions for (24) do exist. The limiting values of $\hat{J}_n(z)$, and $\hat{J}'_n(z)$ as $|z| \to 0$ are used to derive the characteristic equation when $\xi_r \to 1$. These limiting values are [15, (10.1.4)]

$$\hat{J}_n(z) = \frac{z^{n+1}}{1 \cdot 3 \cdot 5 \ldots (2n+1)} \tag{25}$$

$$\hat{J}_n'(z) = \frac{z^n(n+1)}{1\cdot 3\cdot 5\ldots(2n+1)}. \quad (26)$$

When $\xi_r \to 1$, using (25) and (26), we obtain

$$\frac{\hat{J}_n(x(1-\xi_r))}{\hat{J}_n'(x(1-\xi_r))} = \frac{x(1-\xi_r)}{n+1}. \quad (27)$$

Dividing (24) with $\hat{J}_n'(x(1-\xi_r))$ and using the result from (27), (24) can be rewritten for $\xi_r \to 1$ as

$$\hat{J}_n(x(1+\xi_r)) + \frac{x(1-\xi_r)}{n+1}\hat{J}_n'(x(1+\xi_r)) = 0. \quad (28)$$

Since the characteristic equation is continuous at $\xi_r = 1$, the solutions when $\xi_r \to 1$ are the solutions when $\xi_r = 1$. Letting the relative chirality in (28) equal to one, we obtain the characteristic equation for $\xi_r = 1$ as

$$\hat{J}_n(2x) = 0. \quad (29)$$

After the roots x of the characteristic equation are obtained, the resonant frequency f_r can be computed by

$$f_r = \frac{x}{2\pi a\sqrt{\mu\varepsilon}} \quad (30)$$

IV. Numerical Results and Discussion

We solve for the roots of the characteristic equation numerically by using the function *fminsearch* provided by MATLAB [14]. The roots x of (24) and (29) are plotted in Figs. 1–4 for n = 1 and n = 2 as functions of the relative chirality. The solutions for the first few modes for $\xi_r = 0$ and $\xi_r = 1$ are shown in Table I. For the dielectric filled spherical cavity, TE and TM solutions are computed using (24) with $\xi_r = 0$. Each solution is in excellent agreement with that published in [16] and is used as an initial value for *fminsearch* for each mode. The electromagnetic field in a chiral sphere is always a hybrid mode (HEM mode). The HEM mode which reduces to the TM_{nr} mode when $\xi_r = 0$ is a hybrid magnetic mode called the HM_{nr} mode. The HEM mode which reduces to the TE_{nr} mode when $\xi_r = 0$ is a hybrid electric mode called the HE_{nr} mode. For each mode, x does not change much with respect to the relative chirality. We observe that x for $\xi_r = 1$ is a half of x for one of the TE modes. Equation (29) shows that the field inside the cavity is a TE mode with the wavenumber of 2k.

V. Conclusions

In this paper the resonances of a spherical cavity filled with a chiral medium are presented. This paper was previously presented by [6], but their characteristics equation becomes invalid when $\xi_r = 1$. Here we have reproduced the solution for the problem by using vector spherical function and explicitly discussed the problem when $\xi_r = 1$. This is interesting to see that the wave reduces to a TE mode with the wavenumber of 2k when $\xi_r = 1$.

Acknowledgment

Parts of this work were supported by the Thailand Research Fund (TRF) under the grant number RTA 4880002.

References

[1] S.A. Long, M.W. Mcallister, and L.C. Shen, "The resonant cylindrical dielectric cavity antenna," *IEEE Trans.Antennas Propagat*,. vol. AP-31,pp.406-412, May 1983.

[2] *Dielectric Resonators*, D. Kajfez and P. Guillon, Eds., Norwood, MA, Artech House, 1986.

[3] A.A. Kishk, M.R. Zunoubi, and D. Kajfez, "A numerical study of a dielectric disk antenna above grounded dielectric substrate," *IEEE Trans.Antennas Propagat.*, vol. 41, pp. 813–821, June 1993.

[4] A.A. Kishk, G. Zhou, and A.W. Glisson, "Analysis of dielectric resonator antennas with emphasis on hemispherical sphere," *IEEE Antennas Propagat. Mag.*, vol. 36, pp. 20–31, Apr.1994.

[5] L. Zhang, P. Wang, and C. Liang, "Resonant frequencies and Q-factors of a spherical cavity loaded by an eccentric dielectric sphere," *IEE Proc.-Microw, Antennas Propag.*, vol. 141, no. 5, pp. 342–350, Oct. 1994.

[6] P. Kandasamy and N. Okamoto, "Resonant modes of a concentric spherical cavity with conically stratified medium," *IEEE Trans. Microwave Theory Tech.*, vol. 49, pp. 111–118, Jan 2001.

[7] M. Gastine, L. Courtois, and J. L. Dormann, "Electromagnetic resonances of free dielectric spheres," *IEEE Trans. Microwave Theory Tech.*, vol. MTT-15, pp. 694–700, Dec. 1967.

[8] P. Affolter and B. Eliasson, "Electromagnetic resonances and Q-factors of lossy dielectric spheres," *IEEE Trans. Microwave Theory Tech.*, vol. MTT-21, pp. 573–578, Sept. 1973.

[9] M. S. Aly and T. T. Y. Wong, "Root nature of the transverse electric characteristic equation for a dissipative sphere," *IEEE Trans. Antennas Propagat.*, vol. 37, pp. 71–77, Jan. 1989.

[10] D. Worasawate, J.R. Mautz, and E. Arvas, "Electromagnetic resonances and *Q* factor of a chiral sphere," *IEEE Trans. Antennas Propagat.*, vol. 52, pp. 213–219, Jan.2004.

[11] A. Lakhtakia, V.K. Varadan, and V.V. Varadan, "Eigenmodes of a chiral sphere with a perfectly conducting coating" *J. Phys. D: Appl. Phys.*, vol. 22, pp. 825–828, 1989.

[12] H.T. Hui and E.K.N. Yung, "The quality factor of a spherical cavity filled with a chiral medium," *J. of Electromagn. Waves and Appl.*, vol. 15, No. 1 pp.41–52, 2001.

[13] I. V. Lindell, A. H. Sihvola, S. A. Tretyakov, and A. J. Viitanen, *Electromagnetic Waves in Chiral and Bi-Isotropic Media.* Boston: Artech House, 1994, p. 28.

[14] MathWorks, Inc. MATLAB Function Reference. [Online]. Available: http://www.mathworks.com/access/helpdesk/help/techdoc/ref/index.html. [Accessed Jan. 30, 2007].

[15] *Handbook of mathematical functions.*, M. Abramowitz and I. A. Stegun, eds., Washington, DC: National Bureau of Standards, 1964.

[16] *Time-Harmonic Electromagnetic Fields*, R.F. Harrington, New York: McGraw-Hill, 2001.

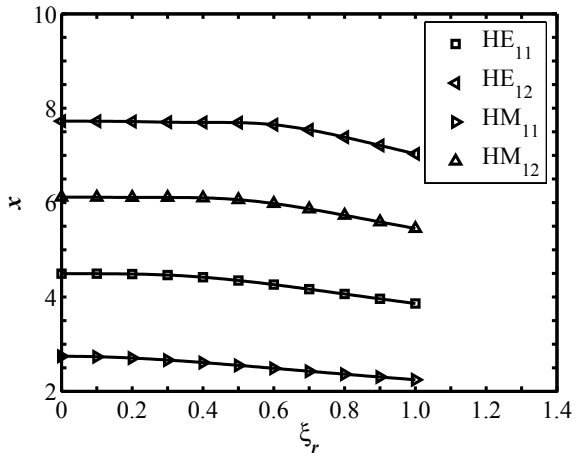

Figure 1. x for the 1st four modes for $n = 1$.

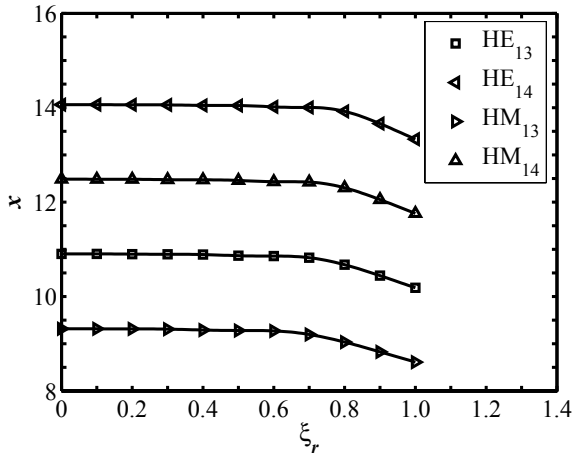

Figure 2. x for the high order modes for $n = 1$.

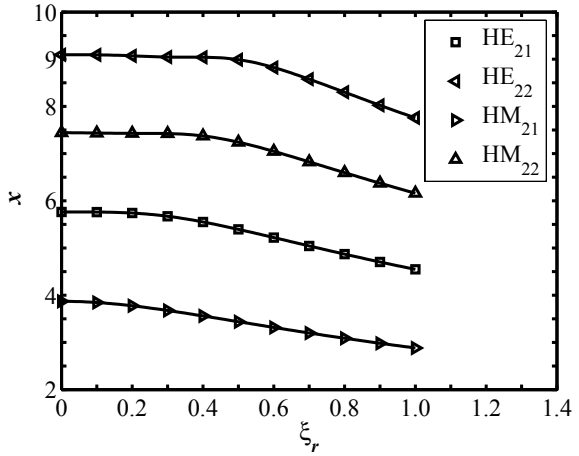

Figure 3. x for the 1st four modes for $n = 2$.

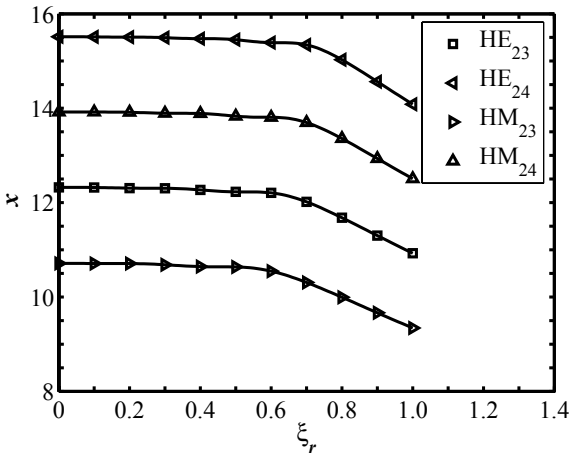

Figure 4. x for the high order modes for $n = 2$.

TABLE I

THE ROOTS OF THE CHARACTERISTIC EQUATION FOR $\xi_r = 0$ AND $\xi_r = 1$ FOR THE FIRST FEW MODES

MODE (HM_{nr} or HE_{nr})	x for $\xi_r = 0$	x for $\xi_r = 1$
HM_{11}	2.744	2.247
HE_{11}	4.493	3.863
HM_{12}	6.117	5.452
HE_{12}	7.725	7.033
HM_{13}	9.317	8.611
HE_{13}	10.904	10.186
HM_{11}	3.870	2.882
HE_{11}	5.763	4.548
HM_{12}	7.443	6.162
HE_{12}	9.095	7.758
HM_{13}	10.713	9.345
HE_{13}	12.323	10.927

Finite Element Analysis of Hepatic Multiple Array Antenna for Microwave Coagulation Therapy

Apinan Kathamma, Pattarapong Phasukkit, Supan Tungjitkusolmun
Faculty of Engineering
King Mongkut's Institute of Technology Ladkrabang, Thailand 10520
ktsupan@kmitl.ac.th

***Abstract* -This study presents a novel technique for increasing the extent of cancer tissue destruction zone by appropriate placements of microwave antennas at 2.45 GHz. We investigated the temperature distribution during microwave ablation of hepatic cancer treatment. We utilized coaxial multi-slot antenna and open-tip antenna designs in this study by placing in parallel with 10 mm spacing distance. Finite element analyses as well as *in vitro* experiments were performed to compare the resulting temperature distributions. From the results, the "microwave multi-antenna therapy" is able to destroy larger areas of unwanted tissue without having to increase the input power. The maximum lesion destruction zone from this technique was about twice as large as that of the resulting destruction zone created by a single microwave antenna, while the temperature distribution is also more uniformly distributed.**

I. INTRODUCTION

Microwave coagulation Therapy (MCT) is a treatment for hepatic cancer where cancer cells are destroyed by heat. Electromagnetic wave emitted from the distal end of a microwave antenna that is placed in the middle of the tumor will propagate through the surrounding tissue whereby "Joule heating" takes place. Temperature of cancer tissue that absorbs enough electromagnetic energy will then be elevated to 50 °C (a temperature level where cancer cells are destroyed or degraded) or higher. Different microwave antenna designs can result in different characteristics of energy and temperature distributions. Thus, a thorough investigation of various antenna designs is required to improve the efficacy of MCT.

Previous studies have proposed several antenna designs [2] such as different types of monopole antennas, and slot dipole antennas for destruction of unwanted heart tissue. However, further improvement in microwave antenna design is still much needed as the resulting tissue destruction zones from most previous designs were too small to completely destroyed large tumors. A tip-split antenna, formed by using two coaxial-fed slot antennas, was proposed for use at 2.45 GHz [3]. The resulting coagulation region from tip-split antenna was larger as current from both tips propagated into tissue. In addition, [5] utilized two coaxial slot antennas and placed them in a parallel array configuration with varying spacing distances between the two antennas, and input power levels. The experimental results from [5] showed that the maximum coagulation formed had a diameter of 3 cm.

Thus, we performed finite element analyses and *in vitro* experiments using multiple microwave antennas for destruction of hepatic cancer. In both simulation and *in vitro* experiments, we used open-tip and coaxial slot antennas and placed them in various configurations. In addition, we also varied the input power. Then, we determined and compared temperature distributions, as well as the specific absorption rate (SAR) distributions from simulation and *in vitro* experiments.

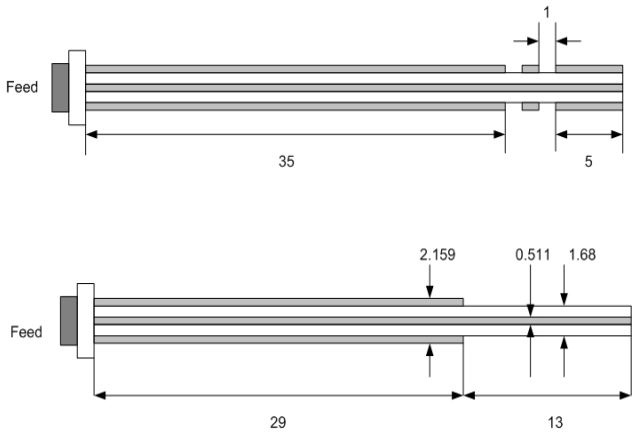

Fig. 1. Structures of a) Coaxial Multi-Slot b) Open-tips

TABLE I.
DIMENSIONS OF THE ANTENNAS

Diameter of the central conductor [mm]	0.511
Inner diameter of the outer conductor [mm]	1.68
Outer diameter of the outer conductor [mm]	2.159
Length from the tip to the slot [mm]	5.0
Width of the slot [mm]	1.0
Length of the antenna [mm]	42.0

TABLE II.
RELATIVE PERMITTIVITY AND CONDUCTIVITY OF MATERIALS INSIDE ANTENNAS

	Relative permittivity	Conductivity [S/m]
Inner dielectric of the antenna	2.03	-
Liver tissue	43.03	1.69

TABLE III.
THERMAL PROPERTIES OF THE MEDIA

	Liver
Thermal conductivity [W/m · K]	0.56
Specific heat [J/kg · K]	3600
Density [kg/m^3]	1060
Blood flow rate [m3/kg · s]	5x10^{-6}
Density of the blood [kg/m^3]	1060
Specific heat of blood [J/kg · K]	3960

TABLE IV.
VSWR OF COAXIAL MULTI-SLOT, OPEN-TIP ANTENNAS

Coaxial Multi-Slot(2 Slot)	VSWR 1.34:1
Open-tips	VSWR 1.35:1

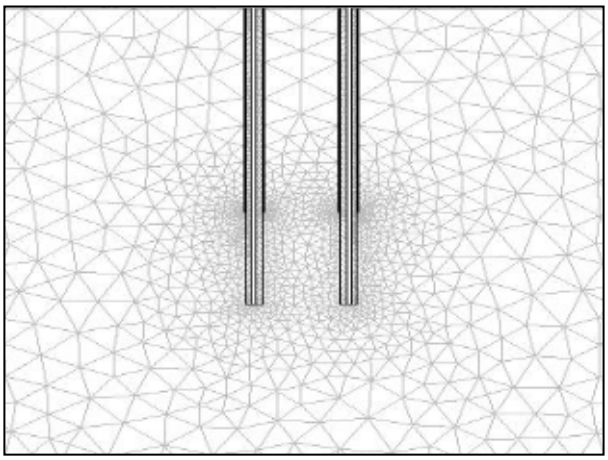

Fig. 2. Geometry of the antennas arrangement used in FEM.

In Fig. 2 shows geometry and mesh of the array antennas arrangement used in the FEM model. The distance of two antennas was 10 mm .In this study, we used results from finite element method compare with in-vitro experiment results.

II. METHODS

A. SAR (Specific Absorption Rate)

In order to evaluate the heating ability of the antenna, SAR distribution is widely used. The SAR shows the heat generated by the electric field in the tissue, and given by

$$SAR = \frac{\sigma}{\rho}\left|E^2\right| \qquad [W/kg] \qquad (1)$$

Where

σ = Conductivity of tissue [S/m]
ρ = Density of tissue [kg/m^3]
E = Electric field (rms) [V/m]

B. Bio-heat Equation

The bio-heat equation bellow was employed to analyze heat generation from electric energy. We solved the bio-heat equation to obtain the thermal distribution in hepatic cancer tissue.

$$\rho C\frac{\partial T}{\partial t}+\nabla\cdot(-k\nabla T)=\rho_b C_b \omega_b (T_b - T)+Q_{met}+Q_{ext} \qquad (2)$$

where

k = Thermal conductivity [W/m · k]
ρ_b = The blood density [kg/m^3]
C_b = Specific heat of blood [J/ (kg · K)]
ω_b = Blood perfusion [1/s]
Q_{met} = The energy generated by the metabolic process [W/m^3]
Q_{ext} = Spatial heat source [W/m^3]
ρ = Density [kg/m^3]
C = Specific heat [J/(kg · K)]

III. RESULTS

A. Simulation Results

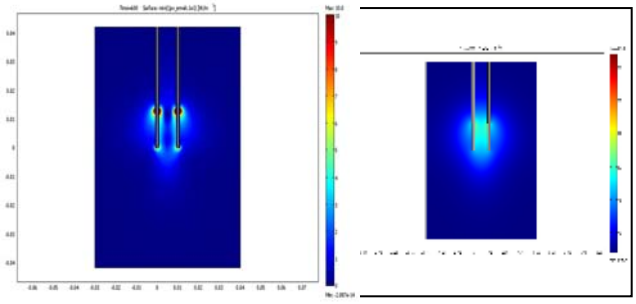

Fig. 3. SAR and temperature distribution of two open-tip antenna array spacing 10 mm

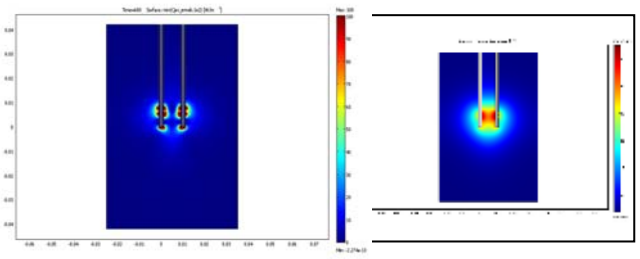

Fig. 4. SAR and temperature distribution of two coaxial-slot antenna array spacing 10 mm

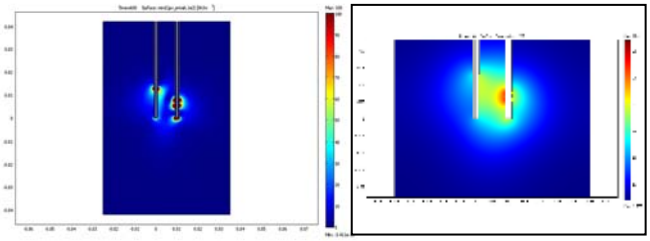

Fig.5. SAR and temperature distribution of open-tip and coaxial-slot antenna array spacing 10 mm

Fig. 3 shows SAR and temperature distributions in liver tissue of two open-tip antennas. From the results, electric field was highest at the tip of two open-tip antennas and the maximum temperature was 51.3 ^{o}C on the center of two antennas arrangement.

Fig. 4 shows SAR and temperature distributions in liver tissue of two coaxial- slot antennas. From the results, electric field was highest at the slot and tip of two coaxial-slot antennas. In this case the maximum temperature was 67 ^{o}C on the center of two antennas arrangement.

Fig. 5 shows SAR and temperature distributions in liver tissue of coaxial- slot and open-tip antennas. From the results, electric field was highest at the slot of coaxial-slot antennas and the tip of open-tip antennas. In this case the maximum temperature was 62 ^{o}C on the slot of coaxial- slot antennas.

B. Experiment Results

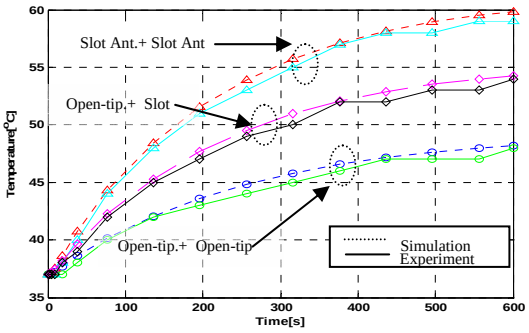

Fig. 6. The change of temperature at different time of three case experiments.

In Fig. 6 shows the change of temperature at different time and Fig.7 shows the lesion of hepatic tissue from *in vitro* experiments. We compare the results from finite element method with experiment results from Bird 54 Thermocouple thermometer. The finite element method results were similar with measured results.

Temperature exchanged of all antennas (Array Coaxial Slot Antenna). Maximum of temperature distributions in tissue and simulation equal 60 ^{o}C when insertion power at both antennas equal to 15 watts , and open-tip antenna have less than equal to 45 ^{o}C , ones equal power insertions to antenna.

(a)

(b)

(c)

Fig. 7. In-vitro experiment in liver tissue

a) Open-tip both b) Coaxial Slot both c) Open-tip with Coaxial Slot

IV. CONCLUSION

This paper performs the finite element method for analysis of microwave hepatic ablation (2.45 GHz). We present a new technique for increasing heat for destruction of cancer cells with various alignments of antennas. We aligned two antennas

in array style which has the spacing distance between two antennas equal to 10 mm. The heat occurred in *in vitro* tissue had temperature distribution similar to the result from finite element method. Using two slot antennas resulted in a destructed area of tissue that is larger than that of the open-tip antennas. In addition, lesions generated by multi array antennas were found to be significantly larger than those of single antennas.

REFERENCES

[1] A.S. Wright, F.T. Lee, Jr., and D.M. Mahvi, "Hepatic microwave ablation with multiple antennas result in synergistically lager zones of coagulation necrosis," *Ann Sure Oncol*, vol. 10, pp. 275-283, 2003.

[2] S. Labonte, A. Blais, S.R Legault, H.O Ali, L Roy, "Monopole antennas for microwave catheter ablation, " *IEEE Transactions on Microwave Theory and Tech.*, vol. 44, pp. 1832-1840, 1996.

[3] K. Saito, T.Taniguchi, H. Yoshimura, and K. Ito, "Estimate of SAR distribution of a tip-split array applicator for microwave coagulation therapy using the finite element method," *IEICE Trans Electron*, vol.E84-C, pp.948-954, 2001.

[4] K. Saito, Y. Hayashi, H. Yoshimura, K. Ito, "Heating characteristics of array applicator composed of two coaxial-slot antennas for microwave coagulation therapy," *IEEE Transactions on Microwave Theory and Tech.*, vol. 48, pp. 1800-1806, 2000.

[5] K. Saito, Y. Hayashi, H. Yoshimura, K. Ito, "Dielectric-loaded coaxial-slot antenna for interstitial microwave hyperthermia: longitudinal, control of heating patterns," *Int. J. Hyperthermia*, vol. 16, pp. 219-229, 2000.

[6] D. Haemmerich, S.T. Sraelin, S. Tungjitkusolmon, F.T. Lee, Jr., D.M. Mahvi, and J.G. Webster, "Hepatic bipolar radio-frequency ablation between separated multiprong electrodes, " *IEEE Trans Biomed Eng*, vol. 48, pp. 1145-1152, 2001.

Estimation of Heating Performances of a Coaxial-Slot Antenna for Treatment of Colon Carcinoma

Apichon Chintanasinton, Supan Tungjitkusolmun, Pattarapong Phasukkit
Faculty of Engineering
King Mongkut's Institute of Technology Ladkrabang, Thailand 10520
ktsupan@kmitl.ac.th

Abstract **Microwave hyperthermia is one of the modalities for cancer treatment. Microwave ablation is a method where current at frequency of 2.45 GHz is delivered to a small antenna probe in order to elevate surrounding tissue temperature. We have investigated various configurations of coaxial-slot antennas for microwave ablation. A coaxial-slot antenna aiming to generate intracavitary heat for colon carcinoma has been especially developed. This paper use finite element analyses of microwave ablation to predict heating distributions of different antenna designs. Configurations of slot antennas to bent 45° and 90° were considered In addition, we also performed *in vitro* experiments and the results show that coaxial-slot antenna can potentially be used for treatment of colon cancer.**

I. INTRODUCTION

In recent years, various types or medical applications of microwave have widely been investigated and reported. In 1996, Labonté et al [1] used microwave ablation as a treatment for supraventricular arrhythmias. Three monopole geometries were considered: open-tip, dielectric-tip, and metal tip. Subsequently in 2000, Saito [2] presented microwave ablation using coaxial-slot antenna for treatment of liver cancer. In 2003, Chiu [3] presented an expanded slot antenna called "(ETW) expanded tip wire antenna" by increasing the size of the slot for treatment of cardiac arrhythmias. In 2004 Bernardi et al. presented a new antenna called "Cap-Choke antenna" [4] by adding cap and choke at the tip of the antenna thus resulting in a specific heating region around of tip of the antenna which could be use for treatment of cardiac arrhythmias. In addition, Saito et al. [5] used two coaxial-slot antennas for treatment of interstitial cancer. In 2005, Christopher et al. [6] presented a new antenna called "triaxial antenna" and suggested that a larger destruction zone could be achieved in liver tumor. In 2006, Yang et al. [7] presented a floating sleeve antenna for the treatment of hepatic carcinoma, while Saito et al. [8] illustrated a treatment of bile duct carcinoma where the antenna was bent, so it could be inserted into mouth and passed through the esophagus to reach the bile duct.

Presently, more people are suffering from colon carcinoma than in the past, especially in the United States. Using microwave in the treatment of colon carcinoma is a new method for the treatment of colon carcinoma. Traditionally, the treatment of colon carcinoma has been performed using three main methods—the endoscope guided surgery, chemotherapy, and general surgery. In general surgery, patient will lose a lot of blood. In chemotherapy, patients may exhibit allergic reactions. In endoscope guided surgery, only a small incision is needed although this technique can generally cure colon cancer in the primary state.

In this paper, we present the treatment of colon carcinoma using flexible antenna that can be placed near the cancer tissue by inserting it through the anus. In section II, we discuss the method of the simulation and the structure of the antenna that is used in the experiment. In section III, presents the result of the simulation and *in vitro* experiment. The conclusion will be in section V.

II. METHODS

This section describes the physical configuration of the antennas used in this study, as well as principle equations related to analysis of specific absorption ratio and temperature distribution (bio-heat equation). Our microwave antennas operated at a frequency of 2. 45 GHz.

A. Structure of antenna

Figure 1 shows the structure of the coaxial slot antenna used in this study. The basic dimensions of the antennas are also listed in Table 1.

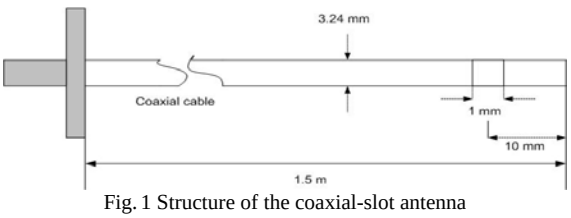

Fig. 1 Structure of the coaxial-slot antenna

B. SAR (Specific Absorption Ratio)

In order to evaluate the heating ability of the antenna, SAR distribution is widely used. The SAR shows the heat generated by the electric filed in the tissue, and given by

$$SAR = \frac{\sigma}{\rho}\left|E^2\right| \qquad [W/kg] \qquad (1)$$

where

σ : conductivity of tissue [S/m]

ρ : is the density of tissue $[kg/m^3]$

E : is the electric field (rms) [V/m]

C. Bioheat Equation:

The bioheat equation below was employed to analyze heat generation from electric energy [9]. We solve the bioheat equation to obtain the thermal distribution in hepatic cancer tissue

$$\rho C\frac{\partial T}{\partial t} + \nabla\cdot(-k\nabla T) = \rho_b C_b \omega_b (T_b - T) + Q_{met} + Q_{ext} \quad (2)$$

Where

k = Thermal conductivity [W/m*k]

ρ_b = Density of blood [kg/m^3]

C_b = Specific heat of blood [J/(kg*K)]

ω_b = Blood perfusion (Perfusion rate) [1/s]

Q_{met} = The energy generated by the metabolic processes [W/m^3]

Q_{ext} = Spatial heat source [W/m^3]

ρ = Density [kg/m^3]

C = Specific heat [J/(kg*K)]

Finite element modeling

In this study, we use a numerical method called finite element modeling (FEM) to simulate heating distribution of different antenna configurations. FEM helps us analyze complex partial differential equation [2] by dividing to domain of interest into many small regions where simpler algebraic equations can be formulated. The structure of a slot antenna is presented, and then we constructed the new type of the antenna. Later on we will construct the real antenna and validate it by experimenting with test tissue, and then we compared the result in the term of the change of temperature in test tissue. We utilized an FEM commercial software software, COMSOL (FEMLAB) *version 3.2b* (Comsol Inc., Burlington, MA).

Due to a tortuous characteristics of the colon, we used a bendable antenna in this study. A shape of a bendable antenna can be manipulated to follow the characteristics of the colon. Thus, we studied the angles (45° and 90°) of the bendable antenna and determined the temperature distribution inside colonic carcinoma tissue. We also performed *in vitro* experiments of microwave ablation using swine colon by inserting the antenna into a swine colon that was filled with air before microwave energy was delivered to the tissue.

Coaxial cable	mm
Inner conductor	0.5
Inner dielectric	1.92
Outer conductor	2.46

TABLE 1
DIMENSIONS OF THE ANTENNA

III. SIMULATION AND EXPERIMENT RESULTS

A. Simulation result

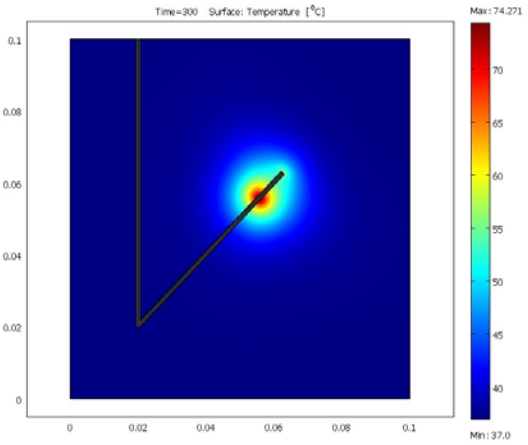

Fig. 2 Heating patterns around tip of the slot- antenna 45° (simulation result)

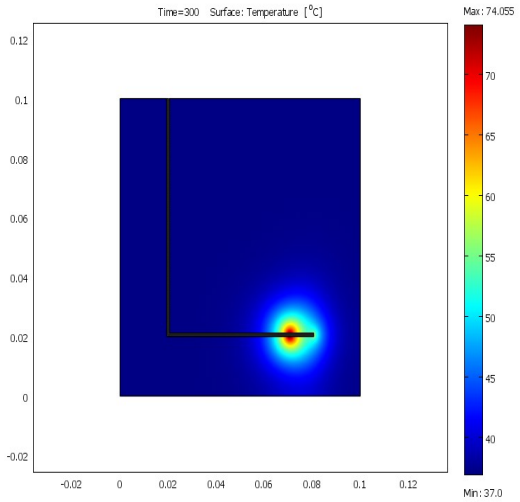

Fig. 3 Heating patterns around tip of the slot- antenna 90° (simulation result)

TABLE 2
PROPERTIES OF INNER DIELECTIC AND COLON

	Relative permittivity	Conductivity [S/m]	Density [kg/m^3]	Specific heat [J/kg.K]	Thermal conductivity [W/m.K]
Inner dielectric	2.03	0	70	1045	0.026
Colon	53.9	2.04	1043	3500	0.6

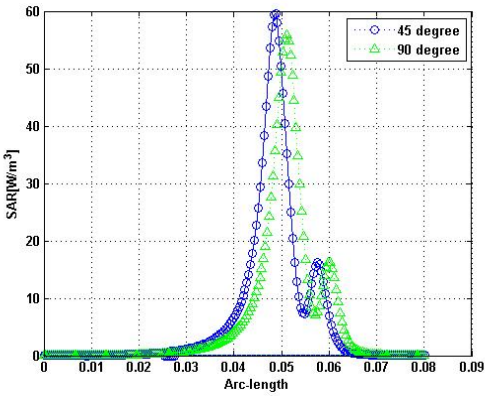

Fig. 4. Comparison SAR of open tip coaxial-slot antenna between 45^o and 90^o

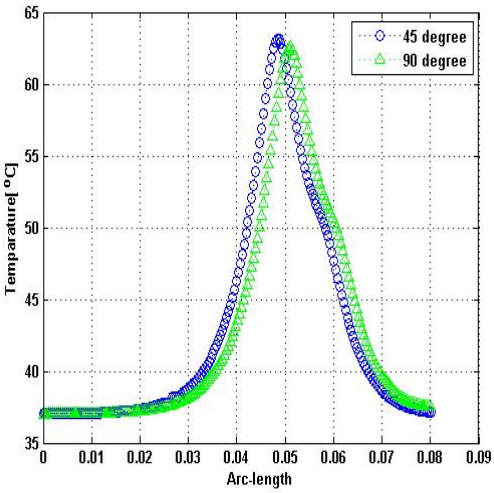

Fig. 5 Comparison of temperatures of open tip coaxial-slot antenna between 45 ^{o} and 90^o

In this section, we show the details of the simulation results. We applied 80 W of power to the antenna at a frequency of 2.45 GHz, and for a duration of 5 min, Fig 2 presents the temperature distribution calculated by FEM of the slot antenna with a bent angle of 45 ^{o}. Fig 3 is the temperature distribution of the slot antenna with a bent angle of 90 ^{o}. Fig 4 shows the comparison of SAR distributions in colon tissue by using the open-tip slot antenna with a 45 ^{o} and 90^o bent angle, measured at 2.5 mm away from the surface of the antenna. From this picture, we notice that SAR profiles have two peak values. The first value is SAR that occurs around the slot and the other peak occurs sat the tip of the antenna. When we compare the SAR at 45^o with 90^o, we found that the SAR at 45^o has slightly higher value than that of 90^o. Fig. 5 shows a comparison of temperature profile of slot antenna with a 45 ^{o} and 90^o bent angle measured at 2.5 mm away from the antenna. We found that the temperature at 45^o rises faster than that of 90^o. Thus, the simulation results illustrate that bendable antennas can potential destroy cancer tissue in colon. Next, we constructed a bendable antenna and performed *in vitro* experiment.

B.In vitro Experimental Results

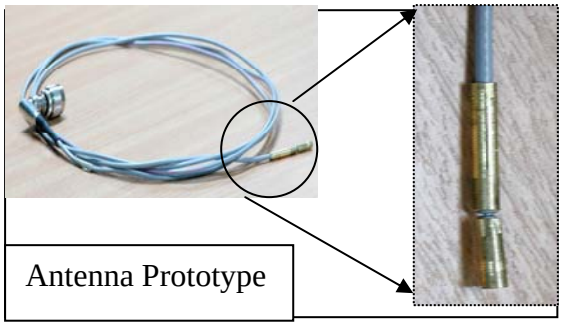

Fig. 6 antenna use in vitro experiment

(a) (b)

Fig. 7. Result of *in vitro* experiment in swine colon

Fig 6 is the prototype antenna that was used in the *in vitro* experiment. The antenna has copper covered at the tip that results in MW getting out around the slot. The fig. 7(a) is outer colon wall and Fig. 7(b) is inner colon wall of swine. The outer colon wall appeared to be destroyed in a greater extent compared to inner colon wall.

V. CONCLUSION

In this paper, we can conclude that a small antenna can be inserted into the colon. We simulated the angle of bendable slot antenna at 45^o and 90^o . The FEM simulation results show that bendable antennas can potential destroy cancer tissue in colon. We then performed in vitro experiments and discovered that a bendable slot antenna was able to destroy tissue along the colon wall. Thus, further studies are needed to improve the efficacy of the bendable slot antenna.

REFERENCE

[1] S. Labonte, A. Blais, S.R Legault, H.O Ali, L Roy, "Monopole antennas for microwave catheter ablation, " *IEEE Transactions on Microwave Theory and Tech.*, vol. 44, pp. 1832-1840, 1996.

[2] K. Saito, Y. Hayashi, H. Yoshimura, K. Ito, "Heating characteristics of array applicator composed of two coaxial-slot antennas for microwave coagulation therapy," *IEEE Transactions on Microwave Theory and Tech.*, vol. 48, pp. 1800-1806, 2000.

[3] H. M. Chiu, A. S. Mohan, R. Andrew, D. J. R. Gay, and D. L. Ross, " Analysis of novel expanded tip wire (ETM) antenna for microwave ablation of cardiac arrhythmias." *IEEE Trans Biomedical Engineering*, vol. 52, pp 890-899, July 2003.

[4] P. Bernardi, M. Cavagnaro, J. C. Lin, S. Pisa, and E. Piuzzi, " Distribution of SAR and temperature elevation lnduced in a phantom by a microwave cardiac ablation catheter." *IEEE Trans Microwave Theory Tech*., vol. 52, pp. 1978-1986, Aug 2004

[5] K. Saito, H.Yoshimura, K.Ito, Y.Aoyagi, and H. Horita, "Clinical trials of interstitial microwave hyperthermia by use

[6] L. Christopher, P. F. Laeseke, D. W. van der Weide, and Jr. F. Paul, "Microwave ablation with a triaxial antenna : result in ex vivo bovine liver." *IEEE Trans.Microwave Theory Tech.*,vol.53,pp.215-220,Jan2005.

[7] D. Yang, J. M. Bertram, C. Converse, A. P. O'Rourke J. G. Webster, S. C. Hagness, J. A. Will, and D. M. Mahvi,, " A floating sleeve antenna yields localized hepatic microwave Ablation." *IEEE Trans. Biomedical Engineering*., vol. 53, pp. 533-537, Mar 2006

[8] K. Saito, A. Hiroe, S. Kikuchi, M. Takahashi, and K. Ito "Estimation of Heating performances of a coaxial-slot antenna with endoscope for treatment of bile duct carcinoma." *IEEE Trans Microwave Theory Tech.*, vol. 54, pp. 3443-3449, Aug 2006

Reflector Shape Optimization for Wideband Uni-directional of CPW-fed Slot Antenna

Sarawuth Chaimool*[a], Prayoot Akkaraekthalin*[b], and Monai Krairiksh**
*Department of Electrical Engineering, Faculty of Engineering,
King Mongkut's Institute of Technology North Bangkok,
Pibulsongkram Rd., Bangsue, Bangkok 10800, Thailand,
E-mail: sarawuth@kmitnb.ac.th*[a]
**Faculty of Engineering and Research Center for Communications and Information Technology,
King Mongkut's Institute of Technology Ladkrabang, Bangkok 10520, Thailand

***Abstract*— The size and shape of the reflectors conductor of CPW-fed slot antennas using loading metallic strips and a widened tuning stub (CPW-FSLW) have been observed. By shaping the reflector, noticeable enhancements in both radiation pattern which provides uni-directional and bandwidth can be achieved while maintaining the easy fabrication and installation. Comparing each shapes for the same width reflector, the Λ-and inverted-Λ shape reflectors with a horizontal plate structure have noticeable enhancement both radiation pattern and impedance bandwidth.**

I. INTRODUCTION

In the past few years, printed circuit slot antennas have been extensively investigated. They have the advantages of being able to provide wide impedance bandwidth. Various feeding mechanisms have been proposed in the literature to improve the slot antenna's bandwidth. Many slot antennas fed by microstrip have been reported [1]. Another importance candidate which may complete favorably with microstrip for the many applications is coplanar waveguide (CPW). CPW transmission structures have several attractive features including low radiation, less dispersion, easy integration for MMIC and without the need for vias or holes through the substrate. One of the main issues with CPW-fed slot antennas is to provide an easy impedance matching to the CPW-line. CPW-fed antennas have been increasingly studied in recent years because of their large bandwidth operation. In order to obtain wideband CPW-fed slot antennas, several impedance tuning techniques have been reported in the literature based on a change of slot dimensions in bow-tie slots, a wide rectangular slot, coupling mechanism, dielectric resonator coupling, and other techniques. Their main drawback, however, is essentially a bi-directional radiator, with the back radiation being undesirable, which not only directs half of the power in potentially undesired directions but also increases the sensitivity of the antenna to its surrounding environment and prohibits the placement of such slot antennas on the platforms. Therefore, there are limit its use to a small number of applications.

The antenna should efficiently focus the RF/microwave signal towards the target and collect the back-scattered energy such as the base station antenna of mobile systems and point to point communications. A wideband antenna with uni-directional radiation pattern required for these applications. There are several techniques to reduce the level of back radiation from antennas using reflector[2]-[7]. However, they have a narrow bandwidth. Unfortunately, wideband printed circuit slot antennas with uni-directional radiation pattern have a small literature.

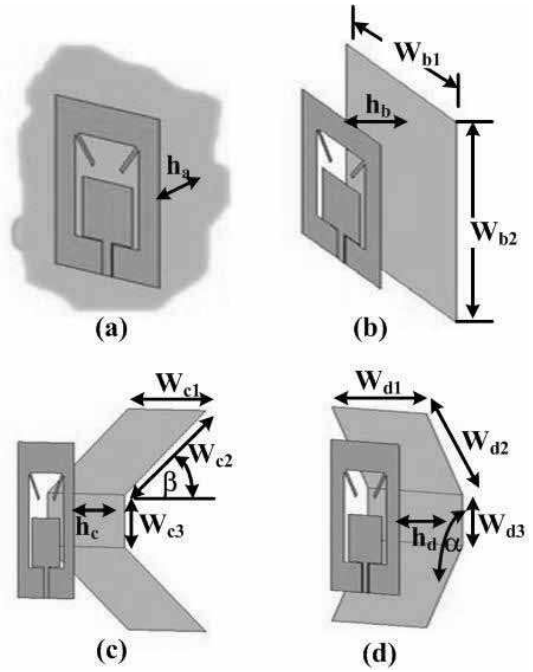

Fig. 1. CPW-fed slot antennas using loading metallic strips and a widened tuning stub above (a) infinite reflector, (b) finite reflector, (c) Λ-shape reflector with a horizontal plate, and (d) inverted-Λ-shape reflector with a horizontal plate.

This paper presents the enhancement of a uni-directional pattern and impedance bandwidth by optimizing the four types of reflector shape including infinite reflector, flat reflector, Λ-shape reflector with a horizontal plate and inverted-Λ-shape reflector with a horizontal plate. The goal in this study is the achievement on a uni-directional all frequencies in operating band and maintain impedance bandwidth equally an antenna without reflector. By shaping the reflector, noticeable

enhancements in both radiation pattern which provides uni-directional and bandwidth can be achieved while maintaining the easy fabrication and installation.

II. CPW-FSLW ABOVE VARIOUS TYPES OF REFLECTORS

In this study, the radiation element is an unbacked CPW-fed slot antennas using loading metallic strips and a widened tuning stub (CPW-FSLW) [8]. It is etched in the ground on the substrate FR-4 (ϵ_r=4.4) with a thickness 1.6 mm. This structure without a reflector radiates a bi-directional pattern and a low gain. Several types of reflector shape are considered in this paper including infinite reflector, finite reflector, Λ and inverted-Λ-shape reflectors with a horizontal plate. By changing the parameters of each reflector such as size of reflector, the distance between radiation element and reflector, and the angle between horizontal plate and the two sides slope reflector of Λ-and inverted-Λ shape reflectors with a horizontal plate are found to affect the impedance bandwidth, resonant frequency and radiation characteristics. These parameters are optimized to enhance the performance antenna. First, the CPW-FSLW located above an infinite reflector plane [Fig. 1(a)] is analyzed. As an example, we considered a CPW-FSLW above an infinite reflector plane with h_a.

An infinite sized reflector is not possible, and small reflector is necessary for base station and point-to-point antennas installation. Thereafter, the same CPW-FSLW antenna is analyzed above a flat finite reflector conductor.The reflector has dimensions of $W_{b1}\times$ W_{b2} and distance between the reflector and radiation element is h_b in Fig. 1(b).

The case for a simple bent conductor ground or corner ground was proposed in [4]. The Λ-shape reflector with the horizontal plate, which is a useful modification of the corner reflector. To reduce the overall dimensions of a large corner reflector the vertex can be cut off and replaced with a horizontal flat reflector ($W_{c1}\times W_{c3}$). The geometry of the proposed broadband CPW-FSLW with a Λ-shape reflector with the horizontal plate as shown in Fig. 1(c). The Λ-shape reflector, having a horizontal flat section dimensions of $W_{c1}\times W_{c3}$, is bent with a bent angle of β. The width of the bent section of the Λ reflector is W_{c2}. The distance between the antenna and the flat section is h_c.

For the last reflector, we modified the shape of the conductor reflector. Instead of a Λ-shape reflector, we took the conductor reflector to have the form of a inverted-Λ-shape reflector Fig. 1(d)]. The geometry of the inverted-Λ-shape reflector with the horizontal plate is shown in Fig. 1(d). The Λ-shape reflector, having a horizontal flat section dimensions of $W_{d1}\times W_{d3}$, is bent with a bent angle of α. The width of the bent section of the inverted-Λ reflector is W_{d2}. The distance between the antenna and the flat section is h_d.

III. CHARACTERISTICS OF ANTENNA BY REFLECTOR CONDUCTOR SHAPES

In order to obtain the uni-directional radiation, a plane reflector is placed parallel to the slot surface on the side of the dielectric substrate. The VSWRs and peak-gains of the

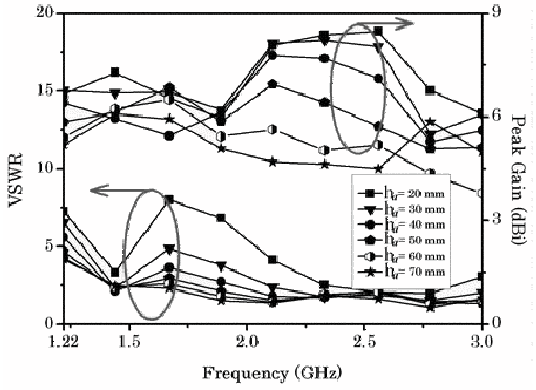

Fig. 2. Computedd VSWR and peak-gain of antenna above infinite reflector with different reflector distances (h_a).

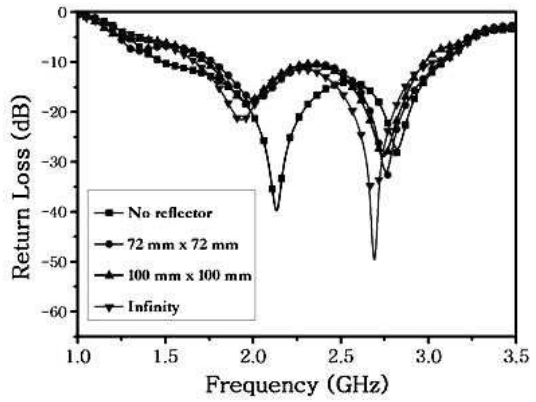

Fig. 3. Return loss of the CPW-FSLW antenna with different sizes of reflector plates where h_a and h_b are 70 mm.

CPW-FSLW antenna above infinite are calculated for different distances between the radiation element and an infinite reflector, as shown in Fig. 2. It can be seen that the matching of the antennas are affected by the distance between the reflector and radiator element. The matching of the antenna above infinite reflector gets worse when the distance between reflector and radiator element (h_a) is increased. Comparisons of the simulated gain obtained by six different distances h_a from 20 mm to 70 mm are also presented in Fig. 2. In these examples, the gain of the antenna increases as the reflector is positioned closer to the radiator element.

The return loss performance of the CPW-FSLW antenna for difference sizes of a finite reflector plate are simulated. IE3D is used to simulate the return loss of all antennas with finite reflector plates. Simulated return loss and directivity results of the CPW-FSLW antenna with different sizes of a reflector plate, including no-reflector, 72 mm$\times$72 mm, 100 mm$\times$100 mm, and infinite size reflector, are shown in Fig. 3. It can be seen that the resonant frequencies will shift lower when the reflector plate size increases. The 10-dB return loss bandwidth is about 1390 MHz for all antennas withwithout reflectors, which is 59% of the center frequency 2.355 GHz. The E-

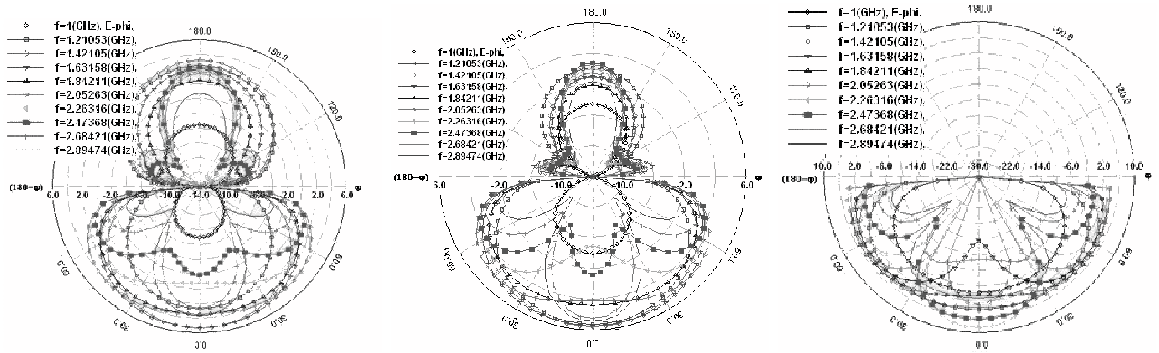

(a) (b) (c)

Fig. 4. Simulated radiation patterns in E-plane with different sizes reflector (a) 72 mm ×72 mm, (b) 100 mm × 100 mm, and (c) infinite size reflector.

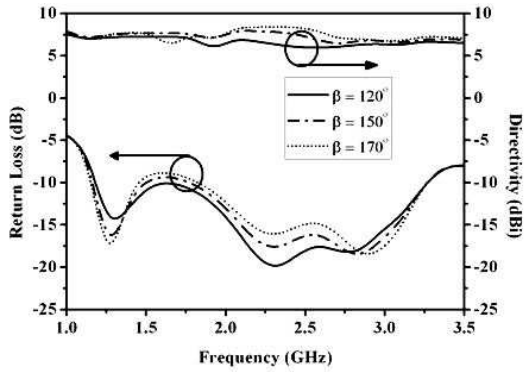

Fig. 5. Simulated return loss and directivity for the proposed antenna as a function β; h_c = 30 mm with W_{c1} = 72 mm, W_{c2} = 40 mm, and W_{c3} = 44 mm.

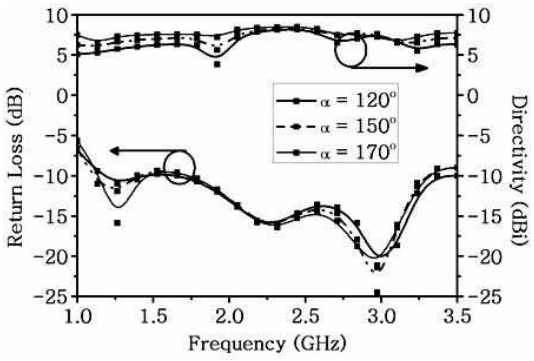

Fig. 6. Simulated return loss and directivity for the antenna as a function α; h_d = 30 mm with W_{d1} = 72 mm, W_{d2} = 40 mm, and W_{d3} = 44 mm.

plane patterns of the CPW-FSLW antenna with different sizes of a reflector plate have been calculated and given in Fig. 4. It can be seen that from Fig.4 that the backside lobe level decreases when the size of the reflector plate increases. The main lobe of both E- plane patterns of the two antennas change slightly when the size of the reflector plate increases from 100×100 mm^2 to infinity. It is obvious that there is no backward radiation in the case of an infinite reflector plate. Further studies are carried out to illustrate the effect of a finite reflector plate on the radiation performance of the CPW-FSLW antenna, as provided in Table I. It can be seen that the bandwidth and the peak gain change slightly when the size of the reflector plate increases from 72 mm ×72 mm size to 100 mm×100 mm. It is also noticed that the front-to-back ratio becomes higher when the size of the reflector increases, as we expected.

The cases for varying the angle β in the proposed design are also studied and the results of the simulated return loss are shown in Fig. 5. Here, the size of the flat reflector is fixed at 72 mm (W_{c1}) × 44 mm (W_{c3}) and the rectangular slope reflectors (W_{c2}×W_{c1}) are 40 mm×72 mm. Table II gives the corresponding simulated data. For obtaining maximum enhanced antenna gain, results indicate that β = 170^o is the optimal angle between the flat section and rectangular slop reflectors with h_c = 30 mm. On the other hand, it is seen that the decreases in β decreases the impedance bandwidth. This behavior is probably because the decrease in β corresponds to the lowering in the effective average substrate thickness in the proposed design, resulting in a smaller impedance bandwidth obtained.

Fig. 6 shows the simulated return loss for the CPW-FSLW above an inveted-Λ reflector with various of α. The flat reflector has dimensions of 44 mm × 72 mm (W_{d3} × W_{d1}) and the rectangular slope reflectors (W_{d2} × W_{d1}) are 40 mm × 72 mm. The distance h_d from the radiator element to the flat reflector is fixed to be 30 mm. The impedance bandwidth is significantly increased by increasing in the bent angle from 120^o to 170^o. The ferformance data of radiation pattern are listed in Table III. When the bent angles are 150^o and 170^o, the antenna's impedance bandwidth reaches about 38%. It can seen that the peak gain change slightly.

The radiation properties are computed for h_c and h_d = 30 mm with the same angle β and α = 170^o are shown in Fig. 7. It is interesting to observe that a uni-directional beam can be achieved all frequency in operating band.

TABLE I

ANTENNA PARAMETERS OF THE CPW-FSLW ANTENNA WITH DIFFERENT SIZES OF REFLECTOR PLATE WHERE h_b = 50 MM AND 70 MM.

Size of the reflector	Bandwidth (%, GHz)	Peak gain (dBi)	Front-to-back ratio (dB)
72 mm ×72 mm (h_b = 50 mm)	7.15%, 1.295-1.391 16.9%, 1.958-2.320 15.8%, 2.675-3.133	6.29	8.2
100 mm ×100 mm (h_b = 50 mm)	14.95%, 1.92-2.29 12.78%, 2.71-3.08	6.79	10.1
72 mm ×72 mm (h_b = 70 mm)	53%, 1.775-3.058	5.21	7.2
100 mm ×100 mm (h_b = 70 mm)	53%, 1.73-2.98	5.55	8.5
infinite size (h_a = 50 mm)	22.5%,1.85-2.32 12.2%, 2.70-3.05	7.49	∞
infinite size (h_a = 70 mm)	59%, 1.66-3.05	8.83	∞

TABLE II

CHARACTERISTICS OF THE ANTENNA ABOVE Λ REFLECTOR WITH h_c = 30 MM WITH W_{c1} = 72 MM, W_{c2} = 40 MM, AND W_{c3} = 44 MM.

β	120^o	150^o	170^o
10-dB Bandwidth (%, GHz)	[9.80, 1.26-1.39], [57.3, 1.79-3.23]	[12.0,1.23-1.40],[56.8, 1.80-3.23]	56.8, 1.23-1.40
Peak gain (dBi)	7.5	7.58	7.51
Front-to-back ratio (dB)	8.7	20	38

TABLE III

CHARACTERISTICS OF THE ANTENNA ABOVE INVERTED-Λ REFLECTOR WITH h_d = 30 MM WITH W_{d1} = 72 MM, W_{d2} = 40 MM, AND W_{d3} = 44 MM.

α	120^o	150^o	170^o
10-dB Bandwidth (%, GHz)	[5.13, 1.26-1.39], [63, 1.73-3.3]	[19.0, 1.14-1.38], [57.3, 1.79-3.23]	[11.1, 1.19-1.35], [59.3, 1.79-3.30]
Peak gain (dBi)	6.9	7.33	7.55
Front-to-back ratio (dB)	8.9	10	12.6

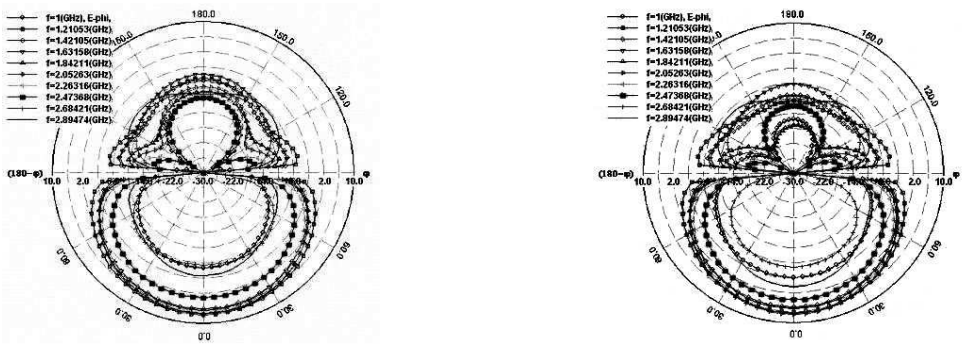

(a) (b)

Fig. 7. Simulated radiation patterns in E-plane with different sizes reflector when h_c = h_d = 30 mm (a) β = 170^o and (b) α = 170^o.

IV. CONCLUSION

This paper presented the investigations of a uni-directional CPW-fed slot antennas using loading metallic strips and a widened tuning stub of four different reflector shapes, namely infinite, finite, inverted-Λ and Λ-shape reflectors. By proper selection of reflector parameters, specially reflector distances, shaped, size, and angle of reflector, a wide impedance bandwidth and uni-directional can be achieved. Both Λ and inverted-Λ reflectors are the achievement on a uni-directional all frequencies in operating band and maintain good impedance bandwidth.

REFERENCES

[1] Y. Yoshimura, "A microstrip-line slot antenna," IEEE Trans. Microwave Theory Tech., pp. 760-762, Nov. 1972.

[2] B. Zheng and Z. Shen, "Effect of a finite ground plane on microstrip-fed cavity-backed slot antenna," IEEE Trans. Antennas Propag., vol. 53, no. 2, pp. 862-865, Feb. 2005.

[3] Y.-X. Guo, K.-M. Luk, and K.-F. Lee, "L-probe fed thick-substrate patch antenna mounted on a finite ground plane," IEEE Trans. Antennas Propag., vol. 51, no. 8, pp. 1955-1963, Aug. 2003.

[4] P. Li, K. L. Lau, and K. M. Luk, "A study of the wide-band L-probe fed planar patch antenna mounted on a cylindrical or conical surface," IEEE Trans. Antennas Propag., vol. 53, no. 10, pp. 3358-3391, Oct. 2005.

[5] R. Gardelli, G. L. Cono, and M. Albani, "A low-cost suspended patch antenna for WLAN access points and point-to-point links," IEEE Antennas and Wirel. Propagat. vol. 3, pp. 90-93, 2004.

[6] R. Chair, A. A. Kishk, K. F. Lee, C. E. Smith, and D. Kajfez, "Microstrip line and CPW fed ultra wideband slot antennas with U-shaped tuning stub and reflector," Progress In Electromagnetics Research, PIER 56, 163-182, 2006.

[7] A. R. Djordjevic, A. G. Zajic, and M. M. Ilic, "Enhancing the gain of helical antennas by shaping the ground conductor," IEEE Antennas and Wirel. Propagat. vol. 5, pp. 138-140, 2006.

[8] S. Chaimool, P. Akkaraekthalin, and V. Vivek, "Dual-dand CPW-fed slot antennas using loading metallic strips and a widened tuning stub," IEICE Trans Electronics, vol. E88-C, pp. 2258-2265; Dec. 2005.

Reconfigurable-based SoC Architecture for Media Processing

Yukio Mitsuyama Takao Onoye Isao Shirakawa†

Dept. Information Systems Eng.
Osaka University, Osaka Japan
{mituyama, onoye}@ist.osaka-u.ac.jp

†Dept. Policy and Management Informatics
University of Hyogo, Hyogo, Japan
sirakawa@ai.u-hyogo.ac.jp

Abstract— **An SoC architecure for media processing is prpoposed, which is based on coarse-grained reconfigurable logic cells. In order to attain high performance at low cost, a series of video decoding processes are executed by efficient cooperation between a host processor and reconfigurable logic cells. Four types of logic cells are introduced in the proposed architecture. Experimental results demonstrate that a multi-standard video decoder can be implemented in the proposed SoC with about 4 times as large hardware cost as a conventional MPEG-2 decoder.**

I. Introduction

For more than a decade, various coarse-grained reconfigurable architectures have been proposed[1] aiming at high performance, high flexibility, and low power consumption. Recently in addition to this, coarse-grained dynamically reconfigurable architectures[2], [3] have been proposed. These architectures support dynamic reconfiguration of each processing element (PE), and can utilize PE more efficiently, which leads to higher performance and flexibility. However, these conventional coarse-grained reconfigurable architectures usually suffer from large hardware cost. On the other hand, an embedded domain-specific reconfigurable architecture, which can provide higher throughput and lower power consumption than ordinary commercial FPGAs, is introduced in [4], [5]. However these reconfigurable architectures offer only limited type of computation, such as ME (Motion Estimation) or DCT (Discrete Cosine Transform), and there still remains considerable disadvantages in terms of area occupation against ASICs.

In this paper, considering trade-off among performance, flexibility, and hardware cost, an embedded domain-specific reconfigurable architecture is devised dedicatedly for media processing.

II. Design Approach

As shown in Fig. 1(a), modern SoC architecture is composed mainly of ASICs, processors, and shared memory. Specifically, an embedded processor performs the process at low computational cost but very complicated, while ASICs perform the process with high computational cost. Generally due to its high computational cost, video processing algorithms are implemented as ASICs to achieve high performance and low power consumption. As a result, several ASICs are employed to support the multi-standard video processing algorithms.

In order to develop an embedded domain-specific reconfigurable architecture (Fig. 1(b)), we address new area-efficient architecture, which is comparable in terms of performance and hardware cost to ASICs.

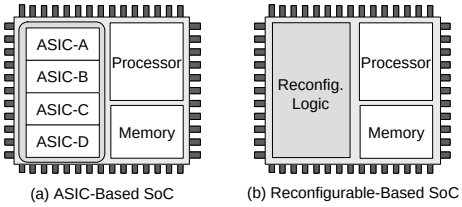

Fig. 1. Reconfigurable-based SoC.

In the course of constructing our domain-specific reconfigurable architecture, the necessary requirements are as follows.

A. Efficient cooperation with a host processor

As exemplified in Fig. 2, there exist data dependences in media processing, such as MPEG-2 decoding. Based on the data dependences and the results of software profiling of media processing, we employ a processor for header analysis, which includes the calculation of moving vector for MC (Motion Compensation). On the other hand, coarse-grained reconfigurable logic is used to execute VLD (Variable Length Decoding), IQ (Inverse Quantization), IDCT (Inverse Discrete Cosine Transform), and MC.

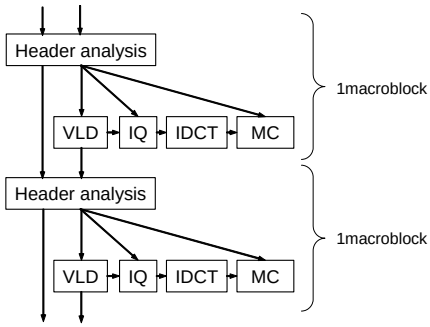

Fig. 2. Data dependency in media processing.

B. Reconfigurable architecture dedicated to media processing

In order to achieve high performance and area efficient implementation of media processing, the reconfigurable architecture must be suitable for performing the distinctive operations of media processing. In this paper, MPEG-2 MP@ML decoder, H.263 Baseline decoder, and MPEG-4 SP decoder are assumed as the target applications.

According to the software profiling results, the granularity, the function, and the ratio of various types of cells are determined. One of the reconfigurable cells is used as a look-up table, a register, and an access scheduler. Another cell is used as a memory, which can keep data during a dynamic reconfiguration. Others are used as computing unit. Basic structure of these heterogeneous cells as well as distinctive interconnect architecture is also introduced.

C. Dynamic reconfigurability

To achieve the decoding process of target applications, the proposed architecture performs VLD, IQ, IDCT, and MC operations in order for each macroblock. Thus dynamic reconfiguration is requested among these operations to raise area efficiency.

D. Reduction of configuration data

Dynamic reconfigurability requires an on-chip configuration memory, which stores multiple configurations. In order to change the configuration within a few cycles, conventional reconfigurable architectures have a configuration memory in each cell, while the size of configuration memory of conventional architectures is so large due to its excess flexibility. Then, the total area of configuration memory constitutes a large portion of reconfigurable logic in terms of area occupancy. Therefore, the reduction of the size of configuration data is indispensable for area-efficient reconfigurable logic.

In our reconfigurable architecture, the significant reduction of configuration data can be achieved, and enables to perform dynamic reconfiguration while the configuration memory is implemented as an external memory.

III. Reconfigurable Architecture

A. Overall Architecture

Overall architecture of our reconfigurable system is illustrated in Fig. 3, which consists mainly of a 32-bit RISC core as a host processor, a coarse-grained reconfigurable logic, a configuration memory, and a data buffer.

Configuration memory stores many of configuration data, and enables reconfigurable logic to change its context on runtime. Data buffer is a memory which can be accessed from both of processor and reconfigurable logic.

B. Reconfigurable Cell Architecture

As shown in Fig. 4, each of the cells consists of an interconnect part, which has the same structure for all kinds of cells, and a function part, having the different structure for each. The structure of interconnect part is made for suitable cooperation with adjacent cells.

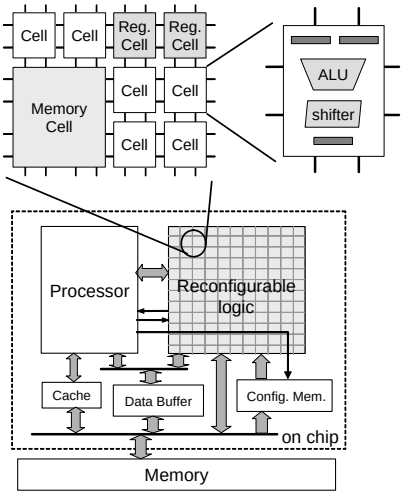

Fig. 3. Overall architecture.

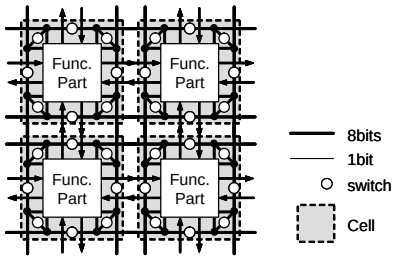

Fig. 4. Structure of reconfigurable array.

1) Interconnect: As illustrated in Fig. 5, the interconnect part is composed of eight 8-bit word lines "A0 $\sim$ A3, B0 $\sim$ B3" with eight switches, and eight 1-bit flag lines "fi0 $\sim$ fi3, fo0 $\sim$ fo3". Flag lines are used as carry-input, selector of multiplexer, write-enable of registers, and so on, where "fi0 $\sim$ fi3"are input from adjacent cells, and "fo0 $\sim$ fo3" are output to adjacent cells. Eight switches can change the connection of each two word lines, "A0 and B1", "A0 and B2", "A1 and B2", "A1 and B3", "A2 and B3", "A2 and B0", "A3 and B0", and "A3 and B1". Interconnection of word lines (i.e. status of switches) are defined by 8-bit configuration data.

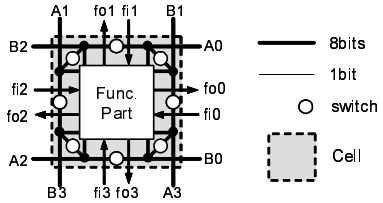

Fig. 5. Interconnect part.

2) Cell Variation: As illustrated in Fig. 6, reconfigurable logic adopts heterogeneous array architecture composed of four types of cells, i.e. basic cell, multiplication cell, register cell, and memory cell. Basic cell comprises 8-bit ALU and

basically supports ADD, SUB, AND, OR, and MUX operations. Multiplication cell executes 8-bit×8-bit multiplication. Register cell and memory cell provides 8-bit 16 words and 256 words storage, respectively. Memory cell occupies four times as large area as other types of cells.

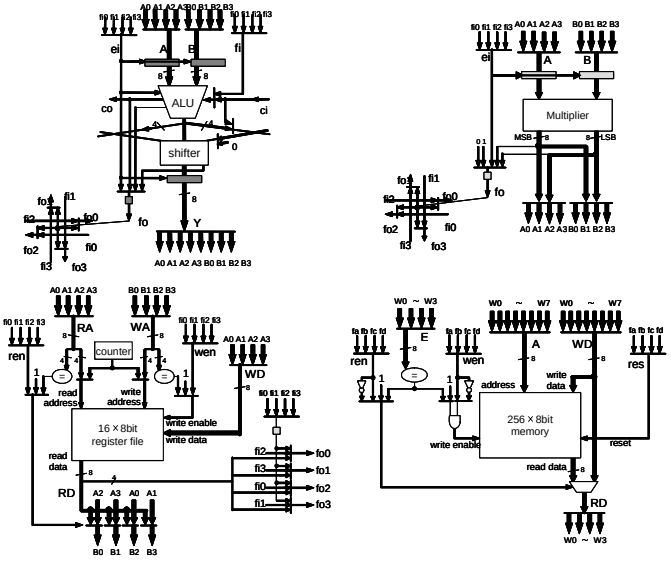

Fig. 6. Organization of function part of basic cell.

IV. Implementation Results

Evaluation of MPEG-2 decoder, H.263 decoder and MPEG-4 decoder implemented on the proposed reconfigurable system has been performed. In order to implement these decoding algorithms, as shown in Fig. 7, a heterogeneous yet based on basic pattern structure of four types of cells is proposed.

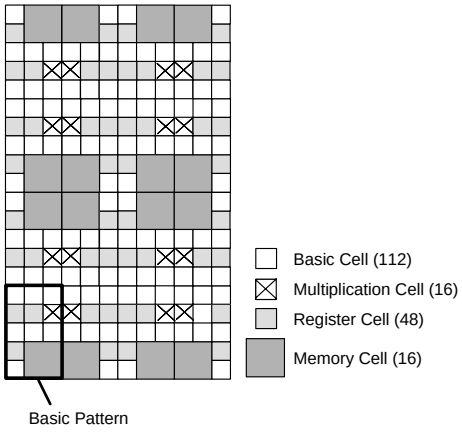

Fig. 7. Heterogeneous structure of 4 types of cells.

According to the software profiling results of MPEG-2 decoder, process partitioning between processor and reconfigurable logic is resolved as follows.

Processor: Header analysis, Calculation of moving vector, Control of reconfigurable logic.

Reconfigurable logic: VLD, IQ, IDCT, MC

The decode process is performed on macroblock basis. First, processor performs header analysis of a macroblock, then reconfigurable logic sequentially performs VLD, IQ, IDCT, and MC. Thus, the process, which is implemented on reconfigurable logic, is divided into some contexts, and performed with changing configuration of reconfigurable logic.

Particularly, MPEG-2 decoder and H.263 decoder are divided into three contexts of VLD/IQ, IDCT, and MC. On the other hand, MPEG-4 decoder is divided into four contexts of VLD, IQ, IDCT, and MC.

Since VLD operation does not fit to parallel processing, software implementation may achieve tolerable performance. However, the software implementation of VLD requires more high performance of host processor and lead to the increase of hardware cost. On the other hand, VLD, which is composed mainly of bit-level operations and look-up tables, can be implemented in hardware more efficiently than in software. Hence, in the proposed reconfigurable system, VLD operation is implemented in reconfigurable logic.

Table I shows the number of required cells for the context of each algorithms, and Table II shows the number of cycles for each context per one macroblock.

TABLE I
CELL UNILIZATION

		#cells			
		basic cell	mult. cell	reg. cell	mem. cell
	IDCT	52	12	9	8
MPEG-2	VLD/IQ	87	3	12	10
MPEG-2	MC	87	0	13	4
H.263	VLD/IQ	63	1	14	8
MPEG-4	VLD	83	0	13	9
MPEG-4	IQ	36	4	0	9
MPEG-4	MC	65	0	9	4

TABLE II
COMPUTATIONAL COST (1 MACROBLOCK)

		#cycles	
		Initialization	Operation
	IDCT	14	800
MPEG-2	VLD/IQ	32	140
MPEG-2	MC	57	515
H.263	VLD/IQ	32	25
MPEG-4	VLD	49	42
MPEG-4	IQ	29	394
MPEG-4	MC	44	496

Fig. 8 shows the process scheduling of typical macroblocks. In this performance estimation, processor and reconfigurable logic operate at the same clock frequency. The number of cycles for context switching of reconfigurable logic is 20 cycles, when the configuration data is transported over the configuration bus of 4×108-bit width. In our configuration mechanism, the configuration in each row of reconfigurable cell array can be performed in one cycle.

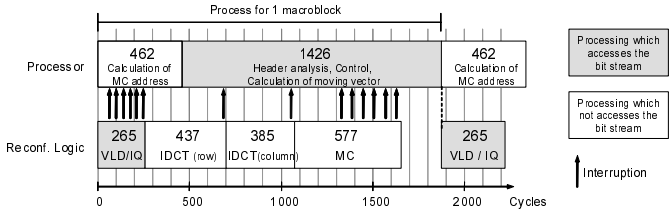

Fig. 8. Process scheduling on MPEG-2 decoder.

As shown in Fig. 8, while reconfigurable logic performs IDCT and MC for a macroblock, processor performes the header analysis for the next macroblock. Moreover, while reconfigurable logic performs VLD/IQ, processor operates the process, which does not need the bitstream.

As the results of process scheduling of MPEG-2 decoding, the numbers of cycles for operations of one macroblock are 1,888 and 1,664 on host processor and reconfigurable logic, respectively. On the other hand, for realtime processing of 720×480pixels 30fps MPEG-2 decoding, totally 40,500 macroblocks must be processed in one second, and thus a host processor must operate at the clock frequency of 77MHz or more. As for the reconfigurable logic, 68MHz of the clock frequency is requested. Critical path of the reconfigurable logic depends on the result of placement and routing. Implementation results by using Synopsys Design Compiler and HSPICE on a $0.18\mu m$ technology claim that the critical path of VLD/IQ, IDCT, and MC are 32.5ns, 8.8ns, and 11.0ns, respectively. When the reconfigurable logic operates at the maximum clock frequency, which are 30.8MHz, 114MHz, and 90.9MHz, realtime processing of MPEG-2 decoding can be attained. Considering the setting constraints of clock frequency on a real system, realtime processing of MPEG-2 decoding can be performed at the clock frequency of 30MHz for VLD/IQ and 90MHz for IDCT and MC.

However, these are almost the maximum clock frequency of VLD/IQ and MC. Thus, the proposed reocnfigurable architecture must preferably be implemented by more advanced technology.

In the same manner as MPEG-2 decoder, realtime processing of H.263 decoder and MPEG-4 decoder for 352×288pixels 30fps 384kbps bitstream can be implemented on the proposed reconfigurable system.

Table III summarizes implementation results, which demonstrate that multi-standard decoder can be implemented in the reconfigurable system with about 4 times as large hardware cost as a conventional MPEG-2 decoder.

TABLE III

IMPLEMENTATION RESULTS

Technology	$0.18\mu m$
Area of Reconfigurable logic	$4.94mm^2$
Delay on configurable cell	3.32μs
Size of configuration data	7,424bits/context
Configuration memory	8KB
Data buffer	6KB

V. CONCLUSIONS

The domain-specific area-efficient reconfigurable architecture, which has sufficient performance and flexibility for realtime processing of multi-standard decoder, has been proposed. In our reconfigurable architecture, the significant reduction of configuration data can be achieved, and enables to perform dynamic reconfiguration while the configuration memory is implemented as an external memory. Implementation results show that multi-standard decoder can be implemented in the reconfigurable system with about 4 times as large hardware cost as conventional MPEG-2 decoder.

ACKNOWLEDGEMENTS

The authors are grateful to Messrs. Rintaro Imai and Kazuma Takahashi for their assists throughout this research. Gratitude also goes to the members of the system architecture group, platform development center, Matsushita Electric Industrial Co., Ltd, for their helpful comments.

REFERENCES

[1] R. Hartenstein, " Coarse grain reconfigurable architectures," in *Proc. Asia and South Pacific Design Automation Conference (ASP-DAC2001)*, pp. 564-569, Feb. 2001.

[2] M. Motomura, " A dynamically reconfigurable processor architecture," in *Proc. Microprocessor Forum*, Oct. 2002.

[3] T. SUGAWARA, K. IDE, and T. SATO, "Dynamically Reconfigurable Processor Implemented with IPFlex's DAPDNA Technology," *IEICE Trans. on Information and Systems*, Vol.E87-D, No.8, pp.1997-2003, Aug. 2004.

[4] S. Khawam, S. Baloch, A. Pai, I. Ahmed, N. Aydin, T. Arslan, and F. Westall, "Efficient Implementations of Mobile Video Computations on Domain-Specific Reconfigurable Arrays," in *Proc. Design Automation and Test in Europe (DATE2004)*, Volume 2, pp. 1230-1235, Feb. 2004.

[5] S. Khawam, T. Arslan, and F. Westall, " Synthesizable reconfigurable array targeting distributed arithmetic for system-on-chip applications," in *Proc. Reconfigurable Architectures Workshop (RAW2004)*, pp. 150-157, April 2004.

[6] S. Kirkpatrick, C. D. Gelatt, Jr., and M. P. Vecchi, "Optimization by Simulated Annealing," *Science*, pp. 671-680, May 1983.

[7] V. Betz and J. Rose, "Directional Bias and Non-Uniformity in FPGA Global Routing Architectures," in *Proc. International Conference on Computer Aided Design (ICCAD96)*, pp. 652-659, Nov. 1996.

[8] V. Betz and J. Rose, "VPR: A New Packing, Placement and Routing Tool for FPGA Research," in *Proc. International Workshop on Field-Programmable Logic and Applications (FPL97)* pp. 213-222, Sept. 1997.

[9] C. Ebeling, L. McMurchie, S. A. Hauck, and S. Burns, "Placement and Routing Tools for the Triptych FPGA," *IEEE Trans. on VLSI*, pp. 473-482, Dec. 1995.

Additional Steps of Convolutional Vector Symbol Decoding for General Data Sequence

U. Tuntoolavest
Department of Electrical Engineering, Faculty of Engineering,
Kasetsart University, 50 Phahonyothin rd., Chatuchak, Bangkok, 10900 Thailand
Phone:+66-2-942-8555 ext1565, Fax:+ 66-2 -942-8555 ext1550 Email: fengunt@ku.ac.th

***Abstract*- Vector Symbol Decoding (VSD) is a verification-based decoding technique for linear codes with large nonbinary symbols. The decoding steps for VSD for Convolutional codes or conv. VSD are somewhat different from the basic VSD for block codes. The detailed decoding steps for conv. VSD was shown in previous work, but they were for the performance investigations purpose and simulations only since the codewords were assumed to be all-zero codewords. In the implementation viewpoints, additional steps are needed to allow for any data sequence and codeword. This work explains these additional steps, which is mainly the step for updating the memory of the decoder.**

I. INTRODUCTION

Vector Symbol Decoding is a general decoding technique for large nonbinary symbols. It can be applied for both block and convolutional codes. VSD principle was first proposed by Metzner and Kapturowski [1] in 1990 and rediscovered by **C.** Haslach and A.J. Han Vinck [2] in 1999. Seo [3] presented the idea of VSD for convolutional code (conv. VSD) in 1991. The use of alternative choices for block code was shown by Metzner in 2003 [4]. Conv. VSD with alternative choices was first proposed by Tuntoolavest and Metzner [5] in 2002.

Previous works [6,7,8] on conv. VSD were mostly in theory. Its performance was done analytically or by simulations. More recent works by Tuntoolavest and Intharasakul [9,10] also focused on the implementation of Vector Symbol Decoder for convolutional codes. The detailed decoding steps of convolutional VSD were explained in [11]. The most recent application of VSD was for packet network [12], which showed the modified concept of VSD to handle errors, deletions and mis-ordering of packets. Although those steps in [11] were enough to simulate the performance, there are more necessary steps in the algorithm when the decoder is to be implemented. Especially, the performance investigation assumed all-zero code words without lost of generality. In the implementation, the data can be anything and the decoding algorithm must also provide for any data sequence other than all-zero sequence. The main concept is that the syndrome must be updated and the effect of decoded symbols needs to be cleared out.

II. BACKGROUND

Conv. VSD is a decoding technique for nonbinary convolutional code with a large symbol size. The typical size is 32-bit/symbols. It uses a verification-based technique that can confirm correct symbols quite easily. Conv. VSD is more attractive than Block VSD in that it can usually confirm correct symbols when it has received only a few symbols without having to wait for the whole received sequence. This reduces the complexity of the decoder and the delay time.

VSD usually assumes availability of two alternative received values for each symbol because the second choice can help improve the performance and simplify the decoding process. This paper will consider a conv VSD with two choices since the result from [8] suggested that the implementation should allow two choices. Example of received sequence with two choices is shown in Fig. 1.

To understand conv. VSD, a (3,2,2) convolutional code with

$$G(D)=\begin{bmatrix}1+D+D^2 & D^2 & 1\\ D & 1+D^2 & 1+D+D^2\end{bmatrix} \qquad (1)$$

is used as an example. Note that this is the code used in the implementation in [9,10].

The alternative choices may come from diversity such as space diversity with multiple received antennas. The first choice of each symbol may come from the antenna with highest SNR and the second choice of each symbol may come from the antenna with the next highest SNR that has different symbol value from the first choice. That is the first and second choices for each symbol are assumed to be different.

To check whether there is any error, the syndrome is computed. Since the symbols are nonbinary, each symbol is viewed as an r-bit vector. The syndrome computation is done by

$$\mathbf{S} = \mathbf{H}\cdot\mathbf{Y} = \mathbf{H}\cdot(\mathbf{V}+\mathbf{E}) = \mathbf{H}\cdot\mathbf{E} \qquad (2)$$

Where **S** is the syndrome matrix, **H** is the parity check matrix and **Y** is the received symbol matrix, **V** is the codeword matrix and **E** is the error matrix.

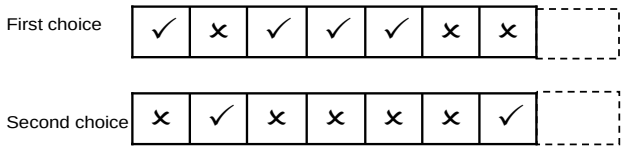

Figure 1. example of a received sequence with two alternative choices for each symbol where

✓ represents correct received symbol

✗ represents wrong received symbol

Supported by Kasetsart University Research and Development Institute

If the syndrome matrix **S** is a zero matrix, the decoder decides that no error occurs and it can transmitted the corresponding symbols out immediately. If **S** is not a zero matrix, the decoder will first try to correct the error using one syndrome vector from the first row of the syndrome matrix. For the (3,2,2) code, a syndrome vector involves 3 received symbols. If it can not correct, then it will increase the number of syndrome vector one by one.

Each additional syndrome vector involves three more received symbols. The decoder will also try to use second choice to correct the error symbol because when the second choice is correct, VSD can often substitute the wrong first choice with the correct second choice. If there are still some errors left, the decoder will then decode by using the concept called "null combinations" explained in [11]. Basically, null combination is a verification method that helps the decoder confirms all the correct codewords and discovers an error-locating vector, which reveals the positions of error symbols. Then the value of error symbols can be computed by matrix conversion.

The parity check matrix H for this (3,2,2) code was given in [5] as

$$H = \begin{bmatrix} 1&1&1&0&0&0&0&0&0&0&0&0&0&0&0 \\ 0&1&1&1&1&1&0&0&0&0&0&0&0&0&0 \\ 0&1&0&0&1&1&1&1&1&0&0&0&0&0&0 \\ 1&0&0&0&1&0&0&1&1&\cdots&\cdots&\cdots&\cdots&\cdots&\cdots \\ 1&1&1&1&0&0&0&1&0&\cdots&\cdots&\cdots&1&1&1 \\ 0&0&0&1&1&1&1&0&0&\cdots&\cdots&\cdots&0&1&1 \\ 0&0&0&0&0&0&1&1&1&\cdots&\cdots&\cdots&0&1&0 \\ \vdots&\vdots&\vdots&\vdots&\vdots&\vdots&\vdots&\vdots&\vdots&\cdots&\cdots&\cdots&1&0&0 \\ 0&0&0&0&0&0&0&0&0&0&0&0&1&1&1 \end{bmatrix} \quad (3)$$

Example: Suppose the transmitted symbols are ***A, B, C, D, E, F,…,Z*** where each alphabet represents an r-bit vector. Let the received sequence be as shown in fig. 2 where there is an error called $\mathbf{e_3}$ in the third symbol of the first choice and no error anywhere else. There is also a correct second choice for the third symbol.

Example of decoding steps:

1. The decoder begins by computing the first syndrome vector $\mathbf{s_1}$ according to (2) where the parity matrix for one syndrome comes from the first row and the first three columns of (3).

$$\mathbf{s_1} = \mathbf{H\,Y} = \mathbf{h_1\,Y} = [\,1\,1\,1\,]\,[\,\boldsymbol{A}\ \boldsymbol{B}\ (\boldsymbol{C} \oplus \boldsymbol{e_3})\,]^T$$
$$= \boldsymbol{A} \oplus \boldsymbol{B} \oplus \boldsymbol{C} \oplus \boldsymbol{e_3} \quad (4)$$

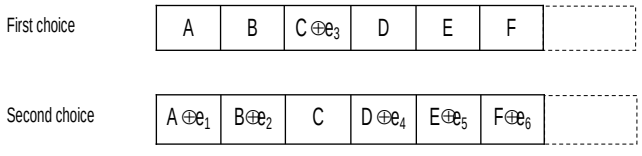

Figure 2 The first and second choice of the received sequence where e_i represent the error for the i^{th} received symbol and ⊕ represents r-bit exclusive-OR operation.

Where ⊕ is an r-bit XOR operation.

The basic decoding concepts indicate that the syndrome value must be zero if the received sequence is a codeword. Therefore,

$$\mathbf{H{\cdot}V} = \mathbf{h_1\,V} = [\,1\,1\,1\,]\,[\,\boldsymbol{A}\ \boldsymbol{B}\ \boldsymbol{C}]^T$$
$$= \boldsymbol{A} \oplus \boldsymbol{B} \oplus \boldsymbol{C} = \mathbf{0} \quad (5)$$

From (4) and (5),

$$\mathbf{s_1} = \mathbf{e_3} \quad (6)$$

Equation (6) shows that the first syndrome vector has the same value as the error. The decoder knows that error occurs since the syndrome is nonzero.

2. Then the decoder computes the differences for each symbol between its first and second choice as indicated in [11]. The differences are shown in fig. 3.

3. Next, the decoder compares the syndrome value to the differences shown in Fig. 3 and finds that the syndrome value is the same as the difference of the third symbol. This means that the third symbol is wrong and the error value has been revealed as the syndrome value. Knowing both the position of the error symbol and the error value, the decoder can easily correct this. It can be seen that the correction with one syndrome succeeds for the case of no more than one error symbol with a correct second choice.

The first three steps follow the steps explained in [11].

4. In the original decoding steps for the performance analysis, the decoder will then transmit the three correct symbols out as the start of the codeword. Then, the decoder will start again at the fourth received symbol and treat the fourth symbol (D) as the first received symbol and repeat step 1-3. If there is no error, the new first syndrome $\mathbf{s_1'}$ will be

$$\mathbf{s_1'} = [\,1\,1\,1\,]\,[\,\boldsymbol{D}\ \boldsymbol{E}\ \boldsymbol{F}]^T$$
$$= \boldsymbol{D} \oplus \boldsymbol{E} \oplus \boldsymbol{F} = \mathbf{0} \quad (7)$$

If the syndrome is zero as shown in (7), the decoder can transmit these three symbols out and start treating the seventh symbol as the first received symbol again.

If there are errors that can not be corrected with one syndrome, the decoder will increase the number of syndrome one by one. Each time, the decoder increase one syndrome, it has to take three more received symbols into the calculation for the case of (3,2,2) code. Note that for a (n,k,m) code, each syndrome involves n received symbols. If the decoder can correct with two syndromes, it will transmit six symbols out and restart and so on.

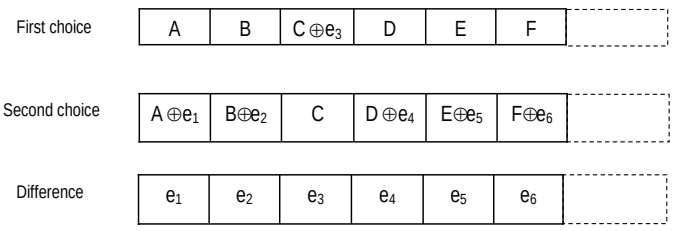

Figure 3 The differences between the first and the second choice for this example

It is important to emphasize that VSD has two main decoding parts. The first is called "correct with second choice" , which can be viewed as a screening part that helps reduce the number of error symbols. In this first part, the decoder can pick some correct second choices to replace the wrong first choices. The "correct with second choice" that uses one syndrome was explained in Step 1 to 3. The "correct with second choice" can also use many syndromes, where the error value and the error symbol index are found when the difference between the first and the second choice for that symbol is in the row space of the syndrome matrix.

The second part is called "correct with null combination" is the main part and more complicated. Briefly, this part can correct errors by using verification method to confirm the correct symbols and to find error locating vector that can locate the positions of the error symbols. The error values can then be discovered from the concept of

$$\mathbf{E} = \mathbf{H}^{-1} \cdot \mathbf{S} \qquad (8)$$

The details of "correct with second choice" and "decode with null combination" was explained in [4,11].

III. The Proposed Additional Decoding Step

A. Concept

This paper will focus on the Step 4 of section II. For the all-zero codeword (all transmitted symbols are zero-value), this original step worked. Since all-zero codeword can be assumed without lost of generality in the performance analysis, this was done for simplicity in previous works. However, for other applications, the data sequence can be anything and the codewords may not be all-zero codewords. In this more general case, additional step is needed to clear the memory out of the decoder because convolutional code is a code with memory. For step 4, when the decoder has output the first three symbols out, the decoder can not immediately treat the fourth symbol (***D*** in this example) as the first received symbol. To understand how to clear the memory, consider the following example.

Suppose again that the transmitted symbols are ***A, B, C, D, E, F,…,Z***. Computation of the second syndrome involves the symbols ***D***, ***E*** and ***F*** and the vector $\mathbf{h}_2$, which is the vector from the second row and the first six columns of the parity check matrix **H**.

$$\mathbf{h}_2 = [0\ 1\ 1 \quad 1\ 1\ 1] \qquad (9)$$

Therefore, the syndrome value will be

$$\mathbf{s}_2 = \mathbf{H}\,\mathbf{Y} = \mathbf{h}_2\,\mathbf{Y} = [0\ 1\ 1\ 1\ 1\ 1]\,[\boldsymbol{A\ B\ C\ D\ E\ F}]^{\mathrm{T}}$$
$$= \boldsymbol{B \oplus C \oplus D \oplus E \oplus F} = \mathbf{0} \qquad (10)$$

Comparing (7) and (10), it is obvious that the difference between the original step 4 and the new proposed step 4 is that for general date sequence where symbols ***B*** and ***C*** may be nonzero, they cannot be omitted.

When the calculation in (10) is performed by the decoder, the decoder has already known the values of symbols ***B*** and ***C*** since it has transmitted the first three symbols ***A***, ***B*** and ***C*** out. Therefore, (10) can be computed with no problem. Suppose there is no error in ***D***, ***E***, ***F*** or there is a wrong first choice with correct second choice, which can be corrected by one syndrome. The decoder can then transmit these three additional symbols out and go on to the next three received symbols. The vector $\mathbf{h}_3$ from the parity check matrix will then be

$$\mathbf{h}_3 = [0\ 1\ 0 \quad 0\ 1\ 1 \quad 1\ 1\ 1] \qquad (11)$$

Suppose there is an error in symbol ***G*** and symbol ***H***, the syndrome value will be

$$\mathbf{S}_3 = \mathbf{H}\,\mathbf{Y} = \mathbf{h}_3\,\mathbf{Y}$$
$$= [0\ 1\ 0\ 0\ 1\ 1\ 1\ 1\ 1]\,[\boldsymbol{A\ B\ C\ D\ E\ F\ (G \oplus e_7)\ (H \oplus e_8)\ I}]^{\mathrm{T}}$$
$$= \boldsymbol{B \oplus E \oplus F \oplus (G \oplus e_7) \oplus (H \oplus e_8) \oplus I}$$
$$= \boldsymbol{e_7 \oplus e_8} \qquad (12)$$

In this case, the decoder can not correct with one syndrome because the syndrome will not be a match for any difference. The decoder will then need to increase the number of syndrome to two.

$$\mathbf{S}_4 = \mathbf{H}\,\mathbf{Y} = \mathbf{h}_4\,\mathbf{Y}$$
$$= [1\ 0\ 0\ 0\ 1\ 0\ 0\ 1\ 1\ 1\ 1\ 1] \cdot [\boldsymbol{A\ B\ C\ D\ E\ F\ (G \oplus e_7)\ (H \oplus e_8)\ I\ J\ K\ L}]^{\mathrm{T}}$$
$$= \boldsymbol{A \oplus E \oplus (H \oplus e_8) \oplus I \oplus J \oplus K \oplus L}$$
$$= \boldsymbol{e_8} \qquad (13)$$

With two syndromes, the decoder finds that symbol ***H*** is wrong since the difference between the first and the second choice of symbol ***H*** has the same value as $\mathbf{s}_4$. Obviously, after the decoder corrects symbol ***H***, it can then correct symbol ***G***.

The main point is still that the decoder must update the memory with symbols ***A, B***, ***E*** and ***F***, which are known to the decoder, otherwise the results will be wrong. For more syndromes, the results are summarized in section IV.

B. Memory size

The memory size that the decoder has to keep for the updating purpose can be seen from the parity check matrix of the code. For this (3,2,2) code with the parity check matrix **H** in (3), the syndrome computations always involve no further than 12 previous symbols as seen by the fifth row of **H**. In other words,

$$\mathbf{h}_5 = [1\ 1\ 1 \quad 1\ 0\ 0 \quad 0\ 1\ 0 \quad 0\ 1\ 1 \quad 1\ 1\ 1] \qquad (14)$$

All following $\mathbf{h}_i$, i = 6,7,... are exactly the same as $\mathbf{h}_5$ and these $\mathbf{h}_i$, i = 5,6,7,...can be considered as being in the steady state, where $\mathbf{h}_i$, i = 1,2,3,4 may be considered as being in the transient state.

For a general (*n*,*k*,*m*) code, the syndrome computations will involve no more than $n \cdot k \cdot m$ previous symbols.

IV. Results

The updated memory can be summarized as shown in table 1 for the (3,2,2) code in consideration. It can be seen form table 1 that the syndrome calculation is in the steady state from $\mathbf{s}_5$ and the decoder will need no further than 12 previous symbols. Therefore, the memory of more than 12 decoded symbols can be cleared and the decoder can treat the 12th previous symbol as the start of the new received sequence. For example, computation of $\mathbf{s}_6$ can treat the 4th symbol as the new 1st symbol. With this clearing of memory, the decoder can

Table 1 Proposed syndrome calculation for the selected (3,2,2) code

parity vector	Proposed Syndrome Computation
$\mathbf{h}_1$ = [111]	$\mathbf{s}_1$ = XOR of received symbol 1,2,3
$\mathbf{h}_2$ = [011 111]	$\mathbf{s}_2$ = XOR of received symbol 2,3,4,5,6
$\mathbf{h}_3$ = [010 011 111]	$\mathbf{s}_3$ = XOR of received symbol 2,5,6,7,8,9
$\mathbf{h}_4$ = [100 010 011 111]	$\mathbf{s}_4$ = XOR of received symbol 1,5,8,9,10,11,12
$\mathbf{h}_5$ = [111 100 010 011 111]	$\mathbf{s}_5$ = XOR of received symbol 1,2,3,4,8,11,12,13,14,15
$\mathbf{h}_6$ = [000 111 100 010 011 111]	$\mathbf{s}_6$ = XOR of received symbol 4,5,6,7,11,14,15,16,17,18
$\mathbf{h}_7$ = [000 000 111 100 010 011 111]	$\mathbf{s}_7$ = XOR of received symbol 7,8,9,10,14,17,18,19,20,21

always use the calculation of $\mathbf{s}_5$ in the steady state without the need of $\mathbf{s}_6$, $\mathbf{s}_7$ and so on.

V. DISCUSSIONS

This paper shows that for general data sequence, it is necessary to clear the memory of the convolutional vector symbol decoder to obtain the correct results. This is because convolutional code has memory. The updating of memory was explained in concepts with some examples. The results showed the proposed syndrome calculation. This is more complicated than the original syndrome calculations used in the performance evaluation in previous work, which was explained in section II.

It should be emphasized that although the decoder must keep previous decoded symbol values for the calculation of later syndromes, those decoded symbols can still be transmitted out immediately after they are decoded. This means that the attractive feature of conv. VSD over block VSD still exits. This attractive feature is the fact that block VSD can decode the received sequence only when the whole block has been received as is the nature of block codes, while conv. VSD can decode and transmit out when only a few symbols have been received.

VI. CONCLUSIONS

The result is important and will be used for the implementation of conv. VSD decoder, which is under development on Field Programmable Gate Array (FPGA) board at this time. This works strengthen the point that it is a very big step to go from simulations to implementation as even algorithm may need to be modified and all assumptions must be reconsidered.

ACKNOWLEDMENT

The author would like to thank Mr. Auttaphud Seubnaung, a graduate student for alerting the author of the problem.

REFERENCES

[1] J.J. Metzner and E.J. Kapturowski, "A General Decoding Technique Applicable to Replicated File Disagreement Location and Concatenated Code Decoding," *IEEE Trans. Inf. Theory*, vol.36, pp.911-917, July 1990.

[2] C. Haslach and A.J. Han Vinck, "A Decoding Algorithm with Restrictions for Array Codes," *IEEE Trans. Inform. Theory*,vol.45, no. 7, pp.2339-2344, Nov. 1999.

[3] Y.S. Seo, A New Decoding Technique for Convolutional Codes, Ph.D. Thesis, Pennsylvania State U., May 1991.

[4] J.J. Metzner, "Vector Symbol Decoding with List Inner Symbol Decisions," *IEEE Trans. Comm.*, vol.51, Issue3, pp.371–380, Mar 2003.

[5] U. Tuntoolavest and J.J. Metzner, "Vector Symbol Decoding with List Symbol Decisions and Outer Convolutional Codes for Reliable Communications," *Integrated Computer-Aided Engineering Journal*, vol. 9, no. 2, 2002, p. 101-116, IOS Press, ISBN 1069-2509.

[6] U. Tuntoolavest, "Performance Comparison between a Maximum and a Non-maximum Distance Outer Code Decoding," *The 3rd International Symposium on Communications and Information Technologies Proceeding (ISCIT 2003)*, Sept 3-5,2003, Songkhla, Thailand.

[7] U. Tuntooolavest, "A Simple Method to Improve the Performance of Convolutional Vector Symbol Decoding with small symbol size." *IEEE TENCON 2004*, November, 21-24, 2004, Chiang Mai, Thailand.

[8] U. Tuntooolavest and A. Seubnaung, "Perforamnce investigation of Convolutional Vector Symbol Decoding Convolutional Vector Symbol Decoding with Larger than Two Choices and with Incomplete Second Choices," *Proceedings of Kasetsart Annul Conf.*, Jan 30 - Feb 2, 2007, Bangkok, Thailand.

[9] R. Intharasakul and U. Tuntoolavest, "State Diagram Design for Implementing Phase I of a Vector Symbol Decoder on an FPGA Board." *Proceedings of International Symposium on Communications and Information Technologies 2006 (ISCIT 2006)*, Oct 18-20, 2006, Bangkok, Thailand.

[10] U. Tuntoolavest and R. Intharasakul, "Nonbinary Convolutional Encoder for Vector Symbol Decoding on FPGA board," *Proceedings of Inernational Conference on Communications Technology 2006 (ICCT 2006)*, Nov 27-30,2006, Guilin, China.

[11] U. Tuntoolavest and J.J. Metzner, "Vector Symbol Decoding with List Inner Symbol Decisions and Outer Convolutional Codes for Wireless Communications," *2nd IEEE Electro/Information Technology Conference Proceeding (EIT2001)*, June 6-9,2001, Oakland University, USA.

[12] J.J. Metzner, "Simplification of Packet-symbol Decoding with Errors, Deletions, Mis-ordering of Packets, and No Sequence Numbers," unpublished. (submitted to *IEEE Trans. Inf. Theory*.)

MAP Decoding for Polynomial Ring Convolutional Trellis Codes for MPEG-4 Image Transmission System over Rician Fading Channels

Srijidtra Mahapakulchai
Department of Electrical Engineering, Kasetsart University, Thailand, E-mail:fengsjm@ku.ac.th

Abstract— **The crucial part of MAP decoding process is the computation of branch metrics. We derive the computation of new branch metrics, customized for Rician fading channels. These metrics are assigned in Viterbi decoder to perform MAP sequence detection. We also analyze the performance of our proposed MAP decoding with polynomial (non-systematic) ring trellis codes. These codes are based on the combination of polynomial ring convolutional codes and CPFSK modulation. The simulation results show the improvement in PSNR about $0.2 - 0.25$ dB on average.**

Keywords— **MAP decoding, Ring convolutional codes, Trellis-coded modulation, Joint source-channel coding, Rician fading channels.**

I. System Overview

The overall system block diagram is illustrated in Fig. 1.The MPEG-4 [1] source encoder produces the 4-ary symbol stream of the lowest frequency subband (LFS) and higher frequency subband (HFS) packet. Detail about the MPEG-4 EZW algorithm and the HFS packet structure can be found in [2]. This stream is passed though the

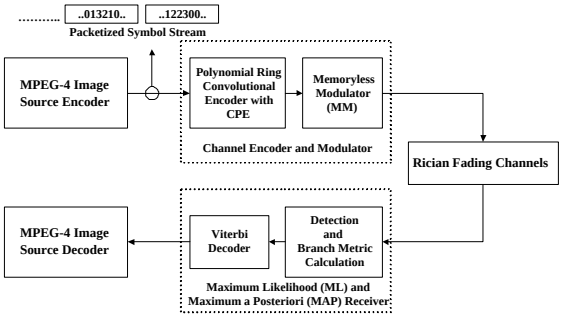

Fig. 1. System block diagram of the MPEG-4 still image transmission system using CPFSK and ring convolutional codes.

channel encoder and modulator system, which are a rate $\frac{1}{2}$ polynomial convolutional encoder (CE) over ring Z_4 and CPFSK with $h = \frac{1}{4}$, respectively. The CPFSK system is decomposed into a continuous phase encoder (CPE) and a memoryless modulator (MM)[3]. The overall encoder is the combination of the CE and the CPE. The MM maps a code symbol into the in-phase and quadrature phase components of a baseband CPFSK signal. These two components of a signal are then corrupted by noise and distortion from Rician fading channel [4]. At the receiver, we employ both the maximum likelihood (ML) and the maximum *a posteriori* (MAP) receiver consisting of a demodulation process, a branch metric calculator, and a Viterbi decoder[5]. The MAP receiver is applied only when a 4-ary zerotree symbol sequence in each HFS packet is transmitted. The decoded 4-ary stream is fed into MPEG-4 source decoder resulting in a reconstructed image.

II. Ring Convolutional Trellis-coded CPFSK and MAP Decoding Derivation

When an external convolutional encoder (CE) is used in conjunction with the CPFSK system (CPE+MM), the state of the overall encoder (CE+CPE) is of concern. Furthermore, a rate 1/2 CE is used in conjunction with a rate 1/2 CPE, and to be able to algebraically combine them into a single encoder, we need to first convert the CPE into an equivalent encoder of rate 2/4 [7]. To illustrate this, we first discuss the conversion in detail, and then we show how to combine the rate 1/2 CE with an equivalent encoder 2/4, resulting in the overall encoder of rate 1/4. From the block diagram shown in Fig. 2, we obtain four

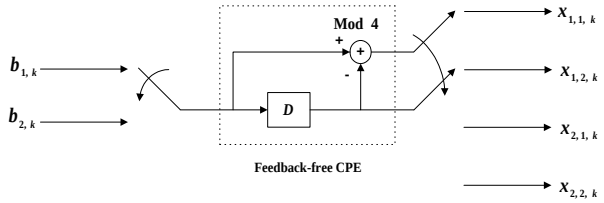

Fig. 2. The block diagram of an equivalent encoder of rate 2/4

equations corresponding to the four outputs $x_{1,1,k}$, $x_{1,2,k}$, $x_{2,1,k}$ and $x_{2,2,k}$ as: $x_{1,1,k} = b_{1,k} - b_{2,k-1}$, $x_{1,2,k} = b_{2,k-1}$, $x_{2,1,k} = b_{2,k} - b_{1,k}$, $x_{2,2,k} = b_{1,k}$. Note that the input $b_{2,k-1}$ is the initial value of the state which is stored in the delay D. That is why we have the first two equations. Moreover, the modulo sum of the first two equations results in the value of $b_{1,k}$ ($b_{1,k} = x_{1,1,k} + x_{1,2,k}$ *mod* 4) and for the modulo sum of the last two equations, we obtain the value of $b_{2,k} = x_{2,1,k} + x_{2,2,k}$ *mod* 4. Fig. 3 shows all possible phase transitions produced from the two input symbols $b_{1,k}$ and $b_{2,k}$. We observe that the value of $b_{2,k}$ is associated with the value of the phase state at time kT. In this section, the notation of the phase state $b_{2,k}$ is used in the same manner as that of the phase state $x_{2,k}$ explained [6]. The difference here is that $b_{2,k}$ is updated every two signal intervals, while $x_{2,k}$ is updated every signal interval. Therefore, we are now interested in finding $b_{2,k}$ for which the conditional probability $P(z_k|b_{2,k+1}, b_{2,k})$ is maximum. Note that z_k is the observed signal within two signal intervals. By assuming AWGN channel, the branch metric computation for MAP decoding within two signal intervals becomes

$$\lambda(s_{m,k}) = -\sum_{i=1}^{2N} z_{k,i} s_{m,k,i} - \frac{N_0}{2} \ln P(b_{2,k+1}|b_{2,k}). \quad (1)$$

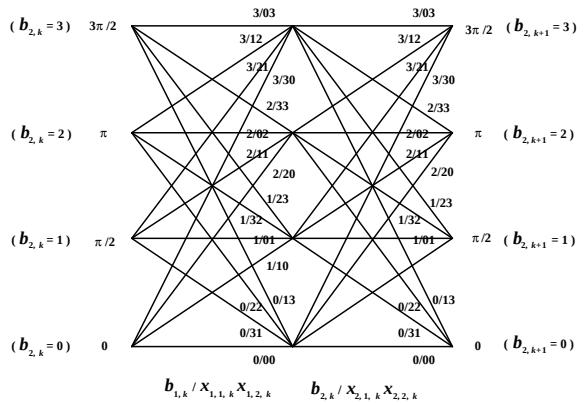

Fig. 3. The phase trellis diagram of the block diagram shown in Fig. 2.

In this case, the maximum number of possible path in the trellis that are required to compute the branch metric is 64. Moreover, the $s_{m,k}$ is the transmitted signal over two signal intervals. From the block diagram of CPE in Fig. 2, the four input-output relationships can be rewritten in another form as $X_{1,1}(D) = b_1(D) - Db_2(D)$, $X_{1,2}(D) = Db_2(D)$, $X_{2,1}(D) = b_2(D) - b_1(D)$, $X_{2,2}(D) = b_1(D)$. This is similar to taking the z-transform of the previous four equations, but we use the parameter D instead of z ; also, D is not a complex variable but a delay variable. Thus, we obtain the transfer function [7] as follows.

$$X = B \begin{bmatrix} 1 & 0 & 3 & 1 \\ 3D & D & 1 & 0 \end{bmatrix}, \qquad (2)$$

where X and B are row vectors corresponding to outputs $[X_{1,1}(D)\ X_{1,2}(D)\ X_{2,1}(D)\ X_{2,2}(D)]$ and inputs $[B_1(D)\ B_2(D)]$, respectively. Observe that the number 3 comes from -1 modulo 4.

For example, if the input row vector $B = [2D+1\ \ 1]$, we obtain the output row vectors $X = [D+1\ \ D\ \ 2D\ \ 2D+1]$. The block diagram of the overall encoder X is shown in Fig. 4. Notice that the realization of the overall encoder shows the relationship between input symbol u_k and four output symbols $x_{1,1,k}$, $x_{1,2,k}$, $x_{2,1,k}$ and $x_{2,2,k}$ without explicitly showing the value of the parameters $b_{1,k}$ and $b_{2,k}$. However, we can compute these parameters from the relationship from the block diagram shown in Fig. 2 described earlier. It is worth mentioning that the parameters $b_{1,k}$ and $b_{2,k}$ enable us to determine the transition of the phase state shown in Fig. 3. Fig. 5 shows the trellis diagram of the

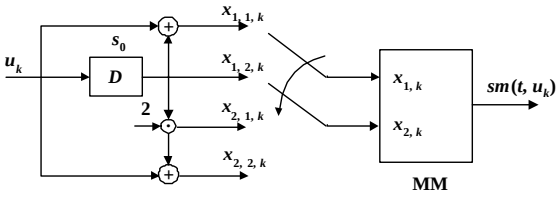

Fig. 4. The block diagram of overall encoder

block diagram in Fig. 4 as well as its corresponding phase trellis diagram. In this example, the total state numbers is

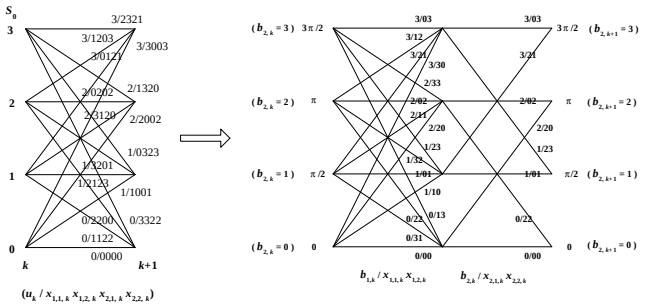

Fig. 5. The trellis diagram and the phase trellis diagram of the block diagram shown in Fig. 4.

four and the total path numbers in the trellis are 16. Emphasize that each path in the trellis diagram corresponds to the phase transition of two signal intervals and the value of S_0 is identical to the value of b_2. Therefore, the branch metric in Eq. (1) can be rewritten as

$$\lambda(s_{m,k}) = -\sum_{i=1}^{2N} z_{k,i} s_{m,k,i} - \frac{N_0}{2} \ln P(S_{0,k+1}|S_{0,k}). \qquad (3)$$

Next we would like to find the relationship between the state variable S_0 and input symbol u. By observing the structure of the overall encoder shown in Fig. 4, we found out that $S_{0,k+1} = u_k$. This fact is also evident by observing (in Fig. 5) that all branches entering the state $S_{0,k+1}$ corresponds to the input $u_k = S_{0,k+1}$. Thus, the branch metric in Eq. (3) now becomes $\lambda(s_{m,k}) = -\sum_{i=1}^{2N} z_{k,i} s_{m,k,i} - \frac{N_0}{2} \ln P(u_k|u_{k-1})$.

When the total state number of the overall encoder is greater than four, we may use $P(u_k|u_{k-1})$ more than one time. To see how one can combine $P(u_k|u_{k-1})$ into the branch metrics, let us first observe the structure of the overall encoder $G_{all}(D)$, whose block diagram is shown in Fig. 6. The block G'' contains only adders and multipliers connected according to the transfer function of $G_{all}(D)$; G'' does not contain any delay elements. The external multipliers, $a_1, \cdots, a_{m-1}$, are necessary whenever a reduction of the total number of states is possible. From Fig. 6, one sees

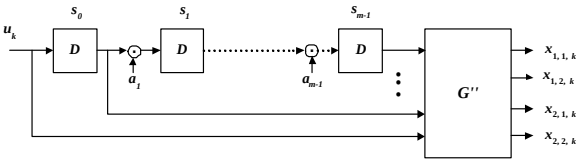

Fig. 6. The block diagram of the overall encoder, G_{all}.

that the first delay S_0 always contains the value of the previous input u_{k-1}. It implies that when we know the value of S_0, we then know what the previous input is. It also implies that at each state, all incoming branches are associated with the same input. This knowledge allows us to incorporate the source transition probabilities $P(u_k|u_{k-1})$ into each branch metric. Moreover, for a trellis having a total number of states more than four, one will have to use $P(u_k|u_{k-1})$ more than once. The method for automatically incorporating $P(u_k|u_{k-1})$ into all branch metrics must be

implemented. Note that the method is also necessary for performing a code search [10].

The technique used here is that for a given state number SN, the value of S_0 is automatically computed as follows

$$S_0 = SN \ mod \ 4, \tag{4}$$

where *mod* indicates a modulo operation. For instance, when the state number is five, the value of S_0 becomes 5 $mod\ 4 = 1$. It is worth mentioning that from the realization of the overall encoder shown in Fig. 6, the state number SN can be computed by

$$SN = S_0 + S_1 D_1 + S_2 D_2^2 + \cdots + S_{m-1} D_{m-1}^{m-1}, \tag{5}$$

where

$$D_i = \begin{cases} 2, & i = k, k+1, \ldots, m-1, \\ 4, & i < k, \end{cases}$$

and k = the minimum index i such that $a_i = 2$. Note that in the case when none of the external multipliers a_i is equal to two, $D_i = 4$, for all i. To verify the validity of Eq. 4, we simply substitute Eq. 5 into Eq. 4 and then show that it can be reduced to S_0. Observe that the terms $S_2 D_2^2, S_3 D_3^3, \ldots, S_{m-1} D_{m-1}^{m-1}$ contain a factor of 4 since D_i is either 2 or 4. As a result, the modulo 4 of these terms are identically zero. For the term $S_1 D_1$, we separate into two cases:

- *Case I when* $D_1 = 4$*:* the term $S_1 D_1$ contains a factor of 4 and so it is reduced to zero after a modulo 4 operation;
- *Case II when* $D_1 = 2$*:* the definition of D_i implies that $a_1 = 2$. In this case, S_1 can only be either 0 or 2 since from the realization of the overall encoder S_1 must contains a factor of a_1. Thus, the term $S_1 D_1$ also contains a factor of 4 and it is reduced to zero after a modulo 4 operation.

After knowing the value of $S_{0,k}$, we then use it as the value of u_{k-1}. Thus, at state number SN, the branch metric that corresponds to the current input u_k is incorporated with the source transition probability $P(u_k|u_{k-1}) = P(S_{0,k+1}|S_{0,k})$.

III. Rician Fading Channel Modelling

Let the transmitted baseband signal is $s_l(t)$. The received equivalent lowpass signal can be written as

$$r_l(t) = (1 + \beta e^{-j\phi}) s_l(t) + n_{wl}(t), 0 \le t \le T, \tag{6}$$

where n_{wl} is the complex-valued white Gaussian noise random process with two-sided spectral density $N_0/2$. Since the channel is sufficiently slow, the phase shift ϕ can be estimated from the received signal. Without loss of generality, we assume ϕ to be zero. The parameter β is defined as

$$\beta = \sqrt{(f_i(t)/\sqrt{2S})^2 + (f_q(t)/\sqrt{2S})^2}, \tag{7}$$

where $f_i(t)$ and $f_q(t)$ are the in-phase and quadrature phase components of the scattered multipath signal, which are Gaussian random variables with zero mean and variance equal to σ^2. S is the signal power, $S = Es/T$, where T is a symbol interval. Let γ_b be $(1+\beta)^2 E_s/N_0$. The probability density function of γ_b can be found in [4] as

$$p(\gamma_b) = \frac{1+\gamma}{\bar{\gamma_b}} e^{-\gamma-(1+\gamma)\gamma_b/\bar{\gamma_b}} I_0\left(2\sqrt{\frac{\gamma(1+\gamma)\gamma_b}{\bar{\gamma_b}}}\right), \tag{8}$$

where

$$\bar{\gamma_b} = \frac{1+\gamma}{\gamma} E_s/N_0, \tag{9}$$

and $\gamma = S/\sigma^2$ is the ratio of the direct path power to the scattered path power. If the direct path is blocked by any structures, the fading channel is called a Rayleigh channel. The channel can be simulated by letting the signal power S be small compared to the scattered path power σ^2.

IV. MAP Decoding Derivation for Rician Fading Channels

To construct the MAP decoder for the CPFSK system, we observe the data samples $z_{k,i}$. During time interval $kT \le t \le (k+1)T$, the observed samples can be written as $z_{k,i} = (1+\beta)s_{m,k,i} + n_{k,i}$ where $i = 1, 2, \cdot, N$. For a slowly fading channel, β is a constant during each signal interval. Al Semari *et al.* [8] assume that the fading values can de determined, *i.e.* they estimate channel state information (CSI). Therefore, this information can be incorporated into the decoding metric. We first follow this assumption. However, we shall show later that by using only the mean value of β, no estimation is necessary, and some improvement is still obtained. Assuming CSI, the conditional probability becomes

$$P(z_k|s_{m,k}) = \frac{1}{(\sqrt{\pi N_0})^N} e^{-\left[\sum_{i=1}^{N} \frac{(z_{k,i} - \alpha s_{m,k,i})^2}{N_0}\right]}, \tag{10}$$

where $\alpha = (1+\beta)$. The designed MAP decoding is based on a kind of probabilistic decoder known as Viterbi decoder [5]. This decoder is said to be "optimal" because it is the solution to the problem of maximum *a posteriori* probability (MAP) estimation of the state sequence of a finite-state discrete-time Markov process. This estimation problem is equivalent to finding the state sequence for $P(\mathbf{z}|\mathbf{x})P(\mathbf{x})$ is maximum, where $\mathbf{z}$ and $\mathbf{x}$ are the observed and state sequences respectively. By considering the first order Markov process and memoryless noise properties, we aim to search for the state sequence $\mathbf{x}$ which satisfies arg $\max_{\mathbf{x}} P(\mathbf{z}|\mathbf{x})P(\mathbf{x})$. And it is equal to

$$\arg \max_{\mathbf{x}} \prod_{k=0}^{K-1} P(z_k|x_k, x_{k-1}) P(x_k|x_{k-1}). \tag{11}$$

Since the natural log function, ln(.) is a monotonic function, we can apply this function to Eq.(11) without changing its solution. Also, we define the negative value of the component inside the summation as the branch metric, $\lambda(x_k, x_{k-1}) = -\ln P(z_k|x_k, x_{k-1}) - \ln P(x_k|x_{k-1})$. we obtain the branch metric $\lambda(s_{m,k})$ as $\lambda(s_{m,k}) = -\sum_{i=1}^{N} z_{k,i} s_{m,k,i} - \frac{N_0}{2\alpha} \ln P(x_{2,k+1}|x_{2,k})$. Since $P(x_{2,k+1}|x_{2,k}) = P(u_k|u_{k-1}) = P(u_{k+1}|u_k)$, where $\mathbf{u}$ is the input sequence. The new branch metric becomes $-\sum_{i=1}^{N} z_{k,i} s_{m,k,i} - \frac{N_0}{2\alpha} \ln P(u_k|u_{k-1})$. When an external encoder (CE) is included in the system, we have to consider the conditional probability $P(z_k|S_{0,k+1}, S_{0,k})$ instead of $P(z_k|x_{2,k+1}, x_{2,k})$ as explained in Section . The difference here is that the effect of the fading amplitude is included in the computation of the conditional probability

$P(z_k|S_{0,k+1}, S_{0,k})$ via the relationship in Eq. (10). Therefore the branch metric becomes

$$\lambda(s_{m,k}) = -\alpha_1 \sum_{i=1}^{N} z_{k,i} s_{m,k,i} - \alpha_2 \sum_{i=N+1}^{2N} z_{k,i} s_{m,k,i} - \frac{N_0}{2} \ln P(S_{0,k+1}|S_{0,k}), \quad (12)$$

where α_1 and α_2 are the constant fading amplitude during the first and second signal interval, respectively.

V. Simulation Results

The "Lena" image is used as our information source. This grayscale image has a size of 512×512 pixels. This image is compressed by using the subband coding technique and then the higher frequency subband (HFS)is packetized. For a noiseless channel, the peak signal to noise ratio (PSNR) of the reconstructed image and its compression ratio is 31.83 dB and 31:1, respectively.

TABLE I
The average PSNR of the reconstructed "Lena" image using ML and MAP decoding for Rician channel with $\gamma = -43$ dB

$\overline{\gamma_b}$ with $\gamma = -43$ dB	PSNR(dB) with ML decoding	PSNR(dB) with MAP decoding (Improvement in dB)
1.25	10.478	10.509 (0.031)
2.50	14.921	15.049 (0.128)
3.75	20.788	21.006 (0.218)
5.00	25.720	25.890 (0.170)
6.25	28.880	28.926 (0.046)
7.50	30.373	30.408 (0.035)

Table I, II and III summarize the average PSNRs for three Rician fading channels with $\gamma = -43, -33$ and -23 dB, respectively. Since γ is the ratio of the direct path power to the scattered path power, therefore $\gamma = -\infty$ dB is used for Rayleigh fading channel. For Table I, the maximum improvement is about 0.22 dB and it occurs at the average PSNR about 21 dB with $\overline{\gamma_b} = 3.75$ dB. The corresponding average symbol error rate (SER) is about 0.002. As γ increases, Table II shows the maximum improvement of about 0.26 dB at $\overline{\gamma_b} = 3.75$ dB. As expected, we also have slight improvement of the average PSNR about 22 dB.

Finally, from Table III, the maximum improvement is about 0.2 dB and it is located again at $\overline{\gamma_b} = 3.75$ dB. At this point, we have the average PSNR of about 25 dB which is higher than the results in the previous cases. The SER is of 0.00075.

VI. Conclusion and Future Work

In this work, we derive the branch metric for MAP decoding. This derivation is based on the use over Rician fading channel. The performances comparison of our proposed MAP and ML decoding are summarized. The improvement on average PSNRs is approximately 0.2-0.26 dB at SER of about 0.001.

TABLE II
The average PSNR of the reconstructed "Lena" image using ML and MAP decoding for Rician channel with $\gamma = -33$ dB

$\overline{\gamma_b}$ with $\gamma = -33$ dB	PSNR(dB) with ML decoding	PSNR(dB) with MAP decoding (Improvement in dB)
1.25	11.137	11.172 (0.035)
2.50	15.719	15.852 (0.133)
3.75	21.953	22.217 (0.264)
5.00	26.647	26.775 (0.128)
6.25	29.331	29.409 (0.078)
7.50	30.627	30.645 (0.018)

TABLE III
The average PSNR of the reconstructed "Lena" image using ML and MAP decoding for Rician channel with $\gamma = -23$ dB

$\overline{\gamma_b}$ with $\gamma = -23$ dB	PSNR(dB) with ML decoding	PSNR(dB) with MAP decoding (Improvement in dB)
1.25	13.613	13.690 (0.077)
2.50	19.469	19.676 (0.207)
3.75	25.129	25.333 (0.204)
5.00	28.783	28.816 (0.033)
6.25	30.474	30.475 (0.001)
7.50	31.138	31.138 (0.000)

VII. Acknowledgment

The author thanks Mr. Pakin Thanakulporn and Ms. Wanpen Janpanichsub for patiently running the simulation program. Moreover, the author appreciates all the comments from the reviewers. Finally, this work is financially supported by the faculty of engineering, Kasetsart university.

References

[1] ISO/IEC JTC1/SC29/WG11, "MPEG-4 video verification model version 11.0," *N2172*, Mar. 1998.
[2] R. E. Van Dyck, "MPEG-4 image transmission using MAP source controlled channel decoding," *IEEE J. Select. Areas Commun.*, vol. 18, pp. 1087-1098, June 2000.
[3] B. E. Rimoldi, "A decomposition approach to CPM, " *IEEE Trans. Info. Theory*, vol. 34, no. 2, pp. 260-270, Mar. 1988.
[4] H. M. Kwon, "Performance of continuous-phase frequency shift keying under fading," *IEEE Global Comm. Conf. (GLOBECOM'94)* vol. 3, pp. 1358-1362, November 1994.
[5] G. D. Forney, Jr, "The Viterbi algorithm," *Proc. of the IEEE*, vol. 61, pp. 268-278, Mar. 1973.
[6] S. Mahapakulchai and R. E. Van Dyck, "Source-controlled channel decoding of MPEG-4 imagery using CPFSK and ring convolutional codes," *Proc. IEEE Electro-Information Technology Conf.*, Chicago, IL, Jun. 2000.
[7] R. H. Yang, and D. P. Taylor, "Trellis-coded continuous-phase frequency-shift keying with ring convolutional codes, " *IEEE Trans. Information Theory*, vol. 40, pp. 1057-1067, Jul. 1994.
[8] S. A. Al-Semari, F. Alajaji, and T. Fuja, "Sequence MAP decoding of trellis codes for Gaussian and Rayleigh Channels," *IEEE Trans. on Vehicular Tech.*, vol. 48, pp. 1130-1140, July 1999.
[9] S. Mahapakulchai and R. E. Van Dyck, "Design of ring convolutional trellis codes for MAP decoding of MPEG-4 imagery," *Proc. IEEE Inter. Conf. Comm. (ICC 2001)*, June 2001.
[10] S. Mahapakulchai and R. E. Van Dyck, "Design of ring convolutional trellis codes for MAP decoding of MPEG-4 images," *IEEE Trans. Comm.*, vol. 52, No. 7, pp. 1033-1037, July 2004.

Suitability of Cyclic-Prefix Modification for Signal Transmission in OFDM

Tawatchai CHONTONG, Noppadol MANEERAT and Ruttikorn VARAKULSIRIPUNTH

Faculty of Engineering and Research Center for Communications and Information Technology (ReCCIT)
King Mongkut's Institute of Technology Ladkrabang,
Chalongkrung Road, Ladkrabang, Bangkok, Thailand 10520
Email:Tawatchai.c@gmail.com, kmnoppad@kmitl.ac.th, kvruttik@kmitl.ac.th

***Abstract*-The Conventional Orthogonal Frequency Division Multiplexing (OFDM) [1] transmission system uses a fixed-length Cyclic Prefix (CP) to reduce the Intersymbol Interferences (ISI) [2] and Intercarrier Interference (ICI) [3, 4] caused by channel delay under wireless environment. When the CP is less than the time delay of multipath fading channel, the efficiency of symbol decreased. When the CP equals to the time delay of multipath fading channel, the efficiency of symbol increases. In this paper, we introduce the OFDM system and then the efficiency of symbol decrement is solved using the important CP patterns in the interactive process of OFDM signals. We propose the Suitability of Cyclic Prefix (SCP) algorithm which the CP is adaptively which adjusted to the time delay in symbol duration in OFDM signal. The time delay of multipath fading channel is calculated from symbol duration method. Then the CP will be adjusted to SCP. The simulation result of SCP shown that the OFDM system can have transmit data rate higher than conventional CP.**

Keywords: **Orthogonal Frequency Division Multiplexing (OFDM), Cyclic Prefix (CP), Intercarrier Interference (ICI), Intersymbol Interferences (ISI), multipath fading channel**.

I. INTRODUCTION

As the demand for data communications rapidly increases with explosive growth of the Internet access and interactive multimedia services, broadband wireless access techniques are emerging as an attractive and economical alternative to wire-line access technologies. However, there exists fundamental challenge in high data rate transmission over a radio propagation channels. In the last few years, Orthogonal Frequency Division Multiplexing (OFDM) [1] has become very attractive for high data rate transmission over wired and wireless channels. OFDM transmits broadband signals by dividing the signals into a large number of narrowband channels to achieve resistance to such a long delay spread. In addition, a Cyclic Prefix longer than the maximum time delay is inserted between adjacent OFDM symbols, and a scheme called Cyclic Prefix is incorporated into the CP in order to completely eliminate both the intersymbol interference (ISI) [2] and the concurrently occurring intercarrier interference (ICI) [3, 4]. In the OFDM system, the CP is a well-known technique for maintaining the orthogonality between subcarriers against the multipath fading channel [3, 4] distortion in the present of multipath propagation paths whose excess delays are shorter than the CP. The intersymbol interference (ISI) occurs within the CP, and the CP is removed before decomposing an OFDM symbol into the subcarriers using a Fourier transform. However, the bit error performance is degraded in the presence of multipaths whose excess delays are longer than the CP. Because the ISI remained after the CP is removed, and the orthogonality between subcarriers is lost. The intercarrier interference (ICI) [3] also occurs. Therefore, the CP has to be long enough for an expected delay spread of the multipath fading channel, where as a shorter CP is more desirable because a long CP causes a decrease in transmission efficiency.

In this paper, we propose the suitability CP equalization OFDM transmission method. Under multipath fading channel environment, when the length of CP is longer than time delay or CP is less than the time delay, we will adjust the CP equal to the time delay. So the suitable CP length can be used to enhance bandwidth efficiency.

The rest of paper is organized as follow. In Section II, We introduce the OFDM system and propose the suitability of Cyclic-Prefix Modification. In Section III, We explain the SCP method which applied for efficiency increase of OFDM transmission. In Section IV, The result of simulation that the SCP applied to OFDM transmission is shown and compared to the conventional CP. Finally, conclusions are given in Section V.

II. OFDM SYSTEM AND THE SUITABILITY OF CYCLIC-PREFIX MODIFICATION

Figure 1 illustrates for the conventional OFDM transmission scheme. In the transmitter, a high-speed serial data stream is digitally quadrature modulated, converted to parallel low-speed modulated data streams, and fed to several traffic subcarrier channels. The modulated signals are frequency-division-multiplexed by an inverse fast Fourier transformation (IFFT) circuit which actually generates the OFDM symbol. A cyclic prefix is inserted in front of each OFDM symbol to eliminate both the intersymbol interference (ISI) and the intercarrier interference (ICI). The resulting OFDM is then converted to serial, converted into an analog by a digital-to-analog

(D/A), up-converted (U/C) to radio frequency band and transmitted in air.

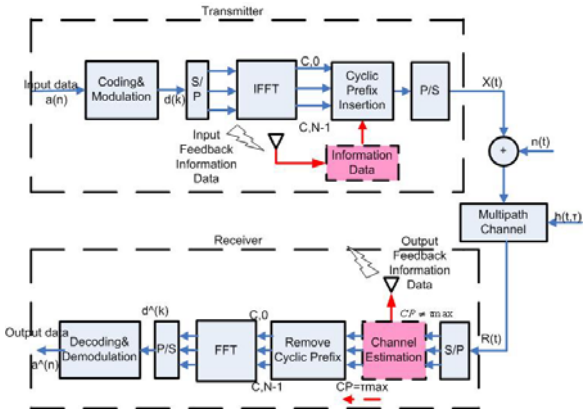

Figure1. The conventional OFDM system with proposed algorithm

After the received signal is down-converted (D/C) to lower frequency. The converted signals are sampled by an analog-to-digital (A/D) converter, converted to parallel and removed cyclic prefix. The sampled data are fed into an FFT circuit and demultiplexed as subcarrier-channel data. Finally, the data in these subcarrier-channel are demodulated by digital quadrature demodulator.

This paper proposed the SCP algorithm for OFDM system as the information data and channel estimation blocks. They are.applied into the transmitter and the receiver in Figure1. The OFDM transmission that the time delay is equal to and less than GI are shown in Figure 2a and Figure 2b respectively. The conventional method used the fix length CP. The SCP algorithm will adjust a suitable CP follow to the time delay.

The OFDM system start at the receiver to calculate the time delay from the time symbol duration. If the time delay is equal to the CP, the process in OFDM received is continued. If the time delay is not equal to the CP, the system will adjust the CP to suitable CP which calculated from the autocorrelation cyclic prefix method in channel estimation [5] block. The Cyclic Prefix method for the time symbol duration estimation will be explained in section III. Normally the guard interval is fixed to 16 points or 800 *n*s that is enough to cover the delay waves. We divide 800 *n*s to 16 parts (1part=50*n*s) for SCP points as shown Figure 3. The receiver sends SCP point data to the transmitter for a new SCP.

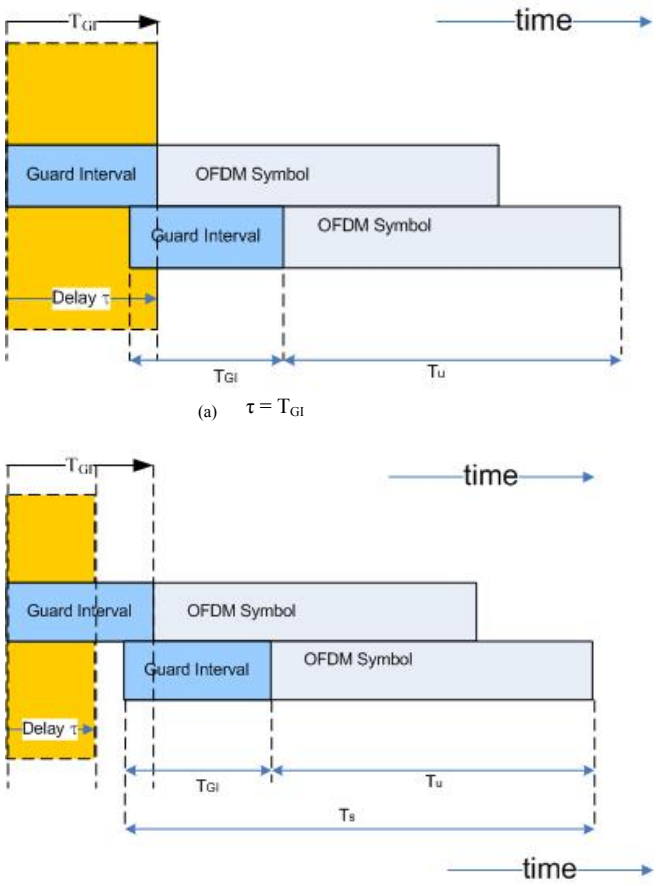

Figure2. Method with variable effective symbol duration

III. SUITABILITY OF CYCLIC-PREFIX METHOD

OFDM transmitted symbols can be expressed as a sum of single carrier modulated signals:

$$x_e(t) = \sqrt{\frac{2P}{N_c}} \sum_{k=0}^{Nc-1} \sum_{n=0}^{Nc-1} d_i(k) e^{2i\pi f_n (t-kT_s)} \cdot g(t-kT_s) \qquad (1)$$

Where f_n is the effective symbol length:

$$f_n = f_0 + n\Delta f$$

where $d_i(k)$ is the symbol sequence nth subcarrier of the ith OFDM symbol which is assumed to be centered, Nc is the number of sub-carriers, Δf is the frequency offset between carriers, f_0 is the frequency of the carrier, g(t) is the transmission pulse function and P is the average transmitting power. In Figure2, Ts = Tu +T_{GI} is the symbol duration, where Tu is the useful duration and T_{GI} is the guard interval duration. We assume to receive the complex signal:

$$r(t) = x(t)h(t) + n(t) \qquad (2)$$

where x(t) is the baseband signal of an OFDM modulation:

$$r(t) = \sqrt{\frac{2P}{N_c}} \sum_{k=0}^{Nc-1} \sum_{n=0}^{Nc-1} d_i(k) e^{2i\pi(\delta f_0 + n\Delta f)(t-t_0-kT_s)} \cdot g(t-kT_s) + n(t) \quad (3)$$

where t_0 is the time offset, δf_0 is the frequency offset and n(t) is AWGN (additive white Gaussian noise). Then we estimate the useful duration and the guard interval duration.

We compute the cyclic moment corresponding to the correlation between the signal and its conjugate version. Then the cyclic autocorrelation can be expressed by:

$$R_x(t,\tau) = E\{x(t)\cdot x^*(t-\tau)\} \quad (4)$$

and then (1) can be expressed by (5):

$$R_x(t,\tau) = \left(\frac{2P}{N_c}\right) \cdot \sum_{k,l=0}^{Nc-1} \sum_{m,n=0}^{N_c-1} E\{d_i(k)\cdot d_i^*(k)\} \cdot g(t-t_0-kT_s)\cdot g^*(t-t_0-lT_s)\cdot e^{2i\pi[(f_n+\delta f_0)(t-t_0-kT_s)]}\cdot e^{2i\pi[(f_n+\delta f_0)(t-t_0-lT_s)]} \quad (5)$$

Under the assumption that the emitted symbols are centered, we can deduce that:

$$R_x(t,\tau) = A\cdot \sum_{k=0}^{Nc-1} \sum_{n=0}^{N_c-1} g(t-t_0-kT_s)\cdot g^*(t-t_0-\tau-kT_s)\cdot e^{2i\pi[(f_n+\delta f_0)\tau]} \quad (6)$$

where $A = (2P\sigma_c^2)/Nc$ is a positive constant and σ_c^2 is the variance of emitted symbols: $\sigma_c^2 = E\{d_i(k)\cdot d_i^*(k)\}$

Besides, the summation terms can be separated, and the expression becomes:

$$R_x(t,\tau) = A\cdot \frac{\sin(\pi N_P \Delta f\tau)}{\sin(\pi\Delta f\tau)} \cdot e^{2i\pi\left[\left(f_0+\delta f_0+\frac{N_P-1}{2}\Delta f\right)\tau\right]} \sum_k g(t-t_0-kT_s) g^*(t-t_0-\tau-kT_s)\cdot \quad (7)$$

It is straightforward to see that $R_x(t,\tau)$ is time periodic with period equal to T_s:

$$R_x(t+T_s,\tau) = R_x(t,\tau)$$

The Fourier transform of R_x is discrete and is composed of peaks for the frequencies $\alpha_n = n/T_s$. For all the other frequencies, the value of transform is zero.

We compute the expression of the peaks in the Fourier transform. For $\alpha_n = n/T_s$, we have:

$$R_x^{a_n}(\tau) = \frac{1}{T_s}\int_0^{T_s} R_x(t,\tau)\cdot e^{-2i\pi a_n t}\cdot dt \quad (8)$$

Developing the expression and assume $t' = t - t_0 - kT_s$, we obtain:

$$R_x^{a_n}(\tau) = \frac{A}{T_s}\cdot e^{-2i\pi\left[\left(f_0+\delta f_0+\frac{N_P-1}{2}\Delta f\right)\tau + a_n t_0\right]} \cdot \int_{-\infty}^{+\infty} g(t')\cdot g^*(t'-\tau)\cdot e^{-2a_n t'}\cdot dt' \quad (9)$$

The term of cyclic correlation depends on the cyclic term of the pulse shape g (t). When we get the delay time from (9),we will change the SCP point follow to flowchart as shown in Figure3.

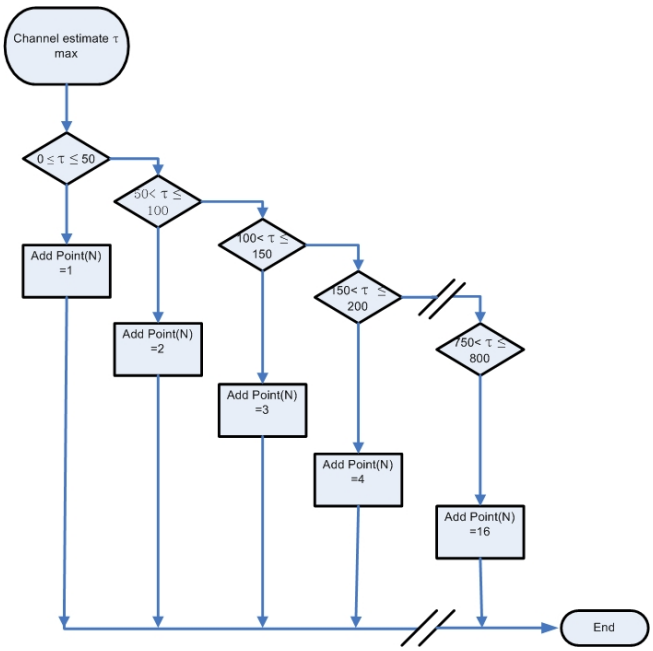

Figure3. Flowchart of Time Delay to SCP points

IV. Simulation Results

The parameters are shown in Table I. The modulation is BPSK. The data stream is converted to paralled bit stream by IFFT circuit with Number of FFT points (N) equal to 64. Each bit stream is modulated by 48 different subcarriers then combined with the extra 4 pilot signals. Totally 52 subcarriers are used. The symbol is applied with the SCP point follow to the time delay of multipath fading channel. The symbol is converted into serial bit and transmitted to the receiver.

TABLE I
Simulation Parameters

Parameters	Value
Channel Spacing	20 MHz
Number of FFT point (N)	64
Number Of Sub-carrier (M)	52
Sub-carrier Spacing (Δf)	312.5 kHz
Norminal Bandwidth ($M\Delta f$)	16.56 MHz
Symbol Duration (N)	36 (3.2μs)
Guard Interval (N)	SCP
Modulation	BPSK

From the simulation result, in the figure 4 the comparison data rate of BPSK modulation between the conventional CP and the SCP. The time delay of multipath fading channels are show between 0 - 0.8 μs. Then the SCP will be adjusted follow time delay. At the time delay equal to zero, the SCP can transmit data 11.25 Mb/s. It is better than the conventional CP still transmit data 9 Mb/s. The simulation result of SCP shows that the OFDM system can transmit data rate higher than conventional CP.

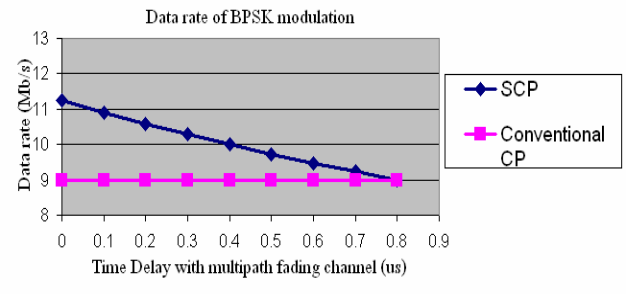

Figure4.Comparison of Data rate for Conventional CP and SCP

V.CONCLUSIONS

We propose the Suitability of Cyclic-Prefix (SCP) algorithm for OFDM transmission The OFDM system at the receiver to calculate the time delay from the symbol duration and system choose CP to suitable CP follow the time delay of multipath fading channel. Then receiver sends SCP point data to the transmitter for a new SCP. Simulation result the OFDM system with applied SCP can transmit data rate higher than conventional CP to 2.25Mb/s. This method can eliminate the time delay of multipath fading channel. The OFDM system with applied SCP can save time for data transmission and the system can be used beneficially.

REFERENCES

[1] R.W. Chang and R.A. Gibby, "A theoretical studyOf performance of an scheme", IEEE Trans. Commun., vol. COM-16, no.4, pp.529-540, Aug. 1968.

[2] J. A. C. Bingham, "Multicarrier modulation for data Transmission :An idea whose time has come," IEEE Commun. Mag., vol. 28, no. 5, pp. 5–14, May 1990.

[3] W.G. Jeon, K.H. Chang, and Y.S. Cho , "An equalization technique for orthogonal frequency-division miltiplexing systems in time-variant multipath channels," IEEE Tran. Commun., vol.47, no.1, pp.27-32, Jan 1999.

[4] D. Li and K. Yamashita, "An equalization technique for high-speed-mobile OFDM systems in Rayleigh multipath channels," IEICE Tran. Commun., vol.E87-B, no.1, pp.158-160, Jan 2004

[5] A.Walter, K.Eric and Q.Andre, "
OFDM parameters Estimation a time approach," IEEE 2000

Feasibility Study of a Six-Port Reflectometer Design based on Inductively-Compensated Coupled Lines

Vitthaya Chamnanphrai[1], Ravee Phromloungsri[2], and Mitchai Chongcheawchamnan[2]

[1]Telecommunication and Electronics Department, Faculty of Engineering,
Rajamangala University of Technology Isan, Khon Kaen Campus, Thailand, 40000
[2]Research Center for Electromagnetic Wave Applications (RCEWs),
Mahanakorn University of Technology, Bangkok, Thailand, 10530

E-mail : ravee@mut.ac.th, and mitchai@ieee.org

***Abstract* —The aims of this paper are to study the impact of directivity to the performance of an Engen's six-port reflectometer (SPR) and propose a simple technique based on inductive compensated coupled lines for an SPR design. Comparison of the performances of the SPR with compensated and uncompensated coupler designs is made at 2.4 GHz frequency. Based on the calculation data, the SPR with an inductive compensated coupler achieves small measurement error which is less than 5%.**

***Index terms* — Measurement error, directivity, six-port, impedance reflectrometer, microstrip coupled line.**

I. INTRODUCTION

The idea of using a six-port structure to determine the phase of a microwave signal was first presented in 1964 by Cohn and Weinhouse [1]. In fact, a six-port network can be considered simply as a system of one input, one output, and four power detector ports. With a deterministic signal applying at the input port, the unknown impedance at the output port can be determined from the DC powers measured at the detector ports [2]. The unknown impedance is obtained by solving a set of four characteristic equations, which is related to network parameters from these DC powers. In practice, a calibration procedure would be applied to determine the network parameters as they are sensitive to aging, atmosphere, and nonideality of the devices. After calibration is done, the power measurement will be performed. The three power ratio equations will be situated from the DC power reading and subsequently resort to derive both real and imaginary values of the unknown impedance. Therefore the direct application of a six-port structure, for example a network analyzer or an impedance reflectometer, is for complex impedance measurement. There are also some indirect applications such as a modern digital receiver, a permittivity measurement system, to name a few [2]-[4].

For complex impedance measurement application, several six-port design junctions were proposed [5]-[6]. It is well known that, apart from calibration errors, the measurement accuracy of a six-port reflectrometer (SPR) is governed by the error magnitude of the DC power measurement. Numerous effects; i.e. thermal noise, zero drift, network configuration; can easily harm the measurement accuracy [7]. The scope of this paper will focus on the network configuration solely.

It was already stated, without proofing, that the six-port configuration provides the accurate results when the phase difference of the "q-points" are 120^{o} at the operating frequency. In fact the q-points are the center of the circles obtained from the three power ratio equations already mentioned. There are various network configurations but only the structures proposed by C. Engen [8] are practicable for complex measurement application as its simplicity. The basic building blocks composed in the *preferred* structures are quadrature coupler, hybrid coupler, power divider, and directional coupler. Among these, a directional coupler is atleast included in the Engen's networks.

In fact directivity in directional coupler does impact to measurement accuracy. Such issue was also claimed by Engen without proofing. Thus, in this paper the relation between measurement error of the SPR proposed by Engen and the directivity of the applied directional coupler is exhaustively studied. The accuracy and the "q-points" distribution characteristic will be investigated for different unknown impedances and coupler directivities in Section 2. The benefit of the paper is to provide design criteria for directional coupler in Engen's SPR. Section 3 presents the feasibility of applying inductively compensated coupler in the SPR. Numerical results of the SPR operated at 900 MHz are presented for the measurement error obtained from the proposed technique. The paper is finally concluded in Section 4.

II. IMPACT OF DIRECTIVITY TO MEASUREMENT ERROR AND Q-POINTS DISTRIBUTION

A. Engen's six-port reflectometer

A six-port reflectometer (SPR) with nearly ideal "q-points" distribution shown in Fig. 1 includes only four quadrature hybrid couplers (Q) and one directional coupler (C). The ports P_3-P_6 are the power detector ports where P_1 and P_2 are the

input and output ports, respectively. The unknown load is connected at port 2 while port 1 connects to a sinusoidal source of testing frequency f_0 Quadrature hybrids in Fig. 1 can be simply implemented by either branch-line coupler or parallel-coupled lines. For the directional coupler, parallel-coupled lines highly suit for implementing in term of practical viewpoint.

As stated, a complex impedance can be determined by solving three power ratio equation set related to the "q-point" positions [9] as shown:-

$$\frac{P_i}{P_3} = K_i \left|\Gamma'_L - q_i\right|^2, \mathrm{i} = 4,5,6 \qquad (1)$$

where P_i is the power reading from the detector at port i, Γ'_L is the estimated reflection coefficient of an unknown load, K_i and q_i are constants related to the network parameters in Fig. 1 which are obtained from the calibration procedure.

The Γ'_L can be determined by solving the equation set in (1). The measurement accuracy which can be described with a percentage error (e) then can be defined as:-

$$\varepsilon = \left|\frac{\Gamma_L - \Gamma'_L}{\Gamma_L}\right| \times 100 \qquad (2)$$

where Γ_L is the exact reflection coefficient of the load.

Q-points distribution characteristic of the SPR is related to the coupler directivity. This is quite obvious since each q-point in the SPR in Fig. 1 is related to the S-parameter of the circuit as shown [10]

$$q_i = \frac{S_{i2} - (S_{i1}S_{22})/S_{21}}{S_{i1}/S_{21}} \qquad (3)$$

Eq (3) will be applied to plot the "q-points" distribution characteristic in a complex plane. If all the devices used in Fig. 2 are ideal and a 6-dB ideal directional coupler is used, from (2), the magnitudes of all "q-points" are equal and their phase differences are 90°, 135° and 135°.

B. Impacts of finite directivity on measurement errors and q-points distribution

Here we assume that all components used in Fig. 2 except the directional coupler is ideal. An ideal quadrature hybrid coupler shown in Fig. 2 a) can be mathematically modeled as shown

$$[S]_Q = \frac{-1}{\sqrt{2}}\begin{bmatrix} 0 & j & 1 & 0 \\ j & 0 & 0 & 1 \\ 1 & 0 & 0 & j \\ 0 & 1 & j & 0 \end{bmatrix} \qquad (4)$$

A directional coupler shown in Fig. 2 b) can be mathematically modeled as shown:-

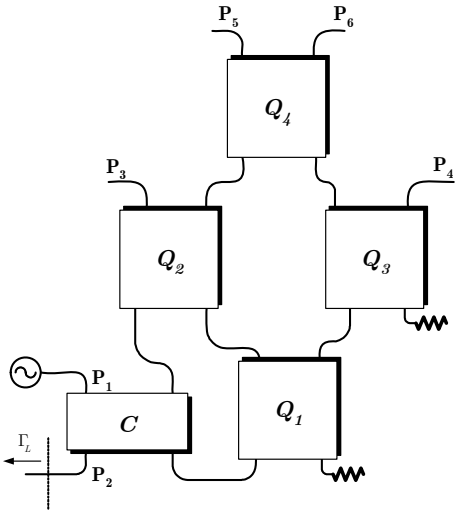

Fig. 1. Schematic diagram of the studied six-port junction [8].

$$[S]_C = \begin{bmatrix} a & C & I & -j\sqrt{1-C^2} \\ C & a & -j\sqrt{1-C^2} & I \\ I & -j\sqrt{1-C^2} & a & C \\ -j\sqrt{1-C^2} & I & C & a \end{bmatrix} \qquad (5)$$

where a are all ports return loss, C is the coupling factor and I is the Isolation coefficient.

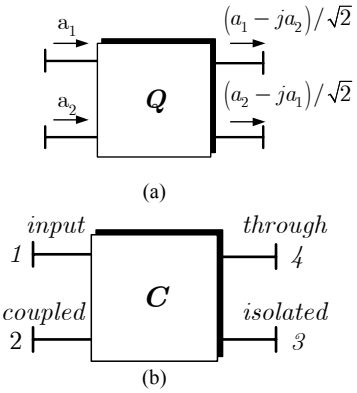

Fig. 2: a) Quadrature hybrid (Q) and b) directional couplers (C) [9].

$$D(dB) = C(dB) - I(dB) \qquad (6)$$

Applying the model from (3)-(5) in Fig. 1. The S-parameter of the SPR with finite directivity is obtained. The error magnitude and "q-points" distribution of the SPR designed based on a finite directivity coupler are calculated from (2) and (3), respectively.

Fig. 3 shows a percentage error of the SPR for different coupler's directivities, from 10 to 60 dB. The results were calculated for four different resistive terminations, i.e. R_L =5, 25, 50, and 100 Ω. The error obtained from the SPR estimation is increased when the coupler directivity decreases.

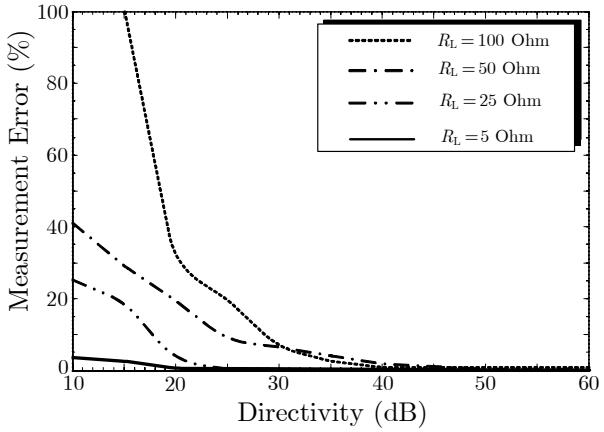

Fig. 3: Percentage measurement error of the SPR for different directivities.

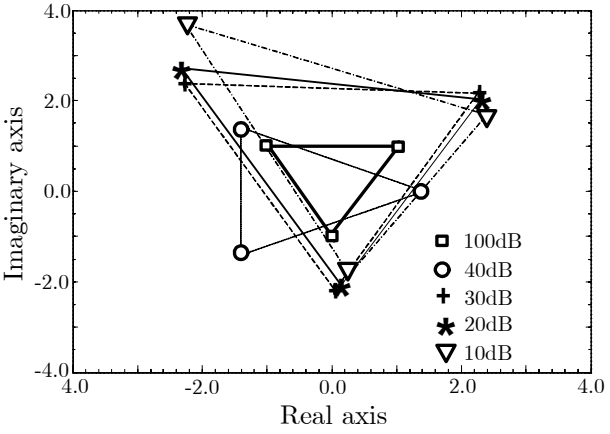

Fig. 4. Q-points distribution with different directivities.

It is shown that a directional coupler which greater than 40-dB directivity is needed to achieve less than 2% error.

The "q-points" distributions of the SPR for different directivities are shown in Fig. 4. The investigation was performed for five different cases, 10-, 20-, 30-, 40-, and 100-dB directivity. The "q-points" distribution of the 100-dB case, which can be considered as a perfect "q-points" distribution", is located at the positions for infinite directivity case. The "q-points" distribution starts to deviate from the perfect distribution when the directivity reduces.

III. Applying Inductively Compensated Coupled Lines to Six-port Reflectometer

A. Quadruply-Inductive Compensated Coupled Lines

Various compensated directional coupler capable to apply for SPR design exist but inductive compensated coupler [11] is chosen as its simple design and implementation. The singly and doubly-inductive compensated parallel-coupled lines, which were recently proposed [12] are not suitable for the SPR which requires symmetrical directional coupler. Rather a quadrupled inductive-compensated coupler shown in Fig. 5 is proposed for SPR design. Four equal inductors denoted by L_Q

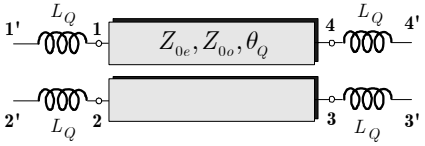

Fig. 5. Quadruply-inductive compensated parallel-coupled lines.

are connected in series at all coupled lines' ports. The uncompensated coupled lines ports are denoted by port 1-4 where the ports of the inductive-compensated coupled lines are labeled as port 1'- 4'. The isolation coefficient (S_{31}), in term of coupler electrical parameters (Z_0, Z_{0e}, Z_{0o}, ε_{effe}, ε_{effo}), is evaluated by terminating port 2', 3', and 4' with the characteristic impedances of the lines Z_0, while port 1' is terminated with voltage source with the output impedance Z_0. The maximum directivity at the operating frequency is occurred when the signal transmission of port 1 and 3 is null, i.e. $S_{31}(f) = 0$. By applying this condition, L_Q can be enumerated form [11]:-

$$L_Q = \frac{1}{2\pi f_0}\mathrm{Im}\left\{\frac{Z_0^2\left(\cosh\theta_e - \cosh\theta_o - Z_0 Z_A\right) - Z_B}{Z_A}\right\} \tag{7}$$

where $Z_A = Z_{0e}\sinh\theta_o - Z_{0o}\sinh\theta_e$ and

$$Z_B = \sqrt{Z_0^2\left(Z_{0e}^2 + Z_{0o}^2\right)\sinh\theta_e\sinh\theta_o - 2Z_0^2\left(\cosh\theta_e\cosh\theta_o - 1\right)}$$

Equation (7) offers a closed-form expression to design the compensating inductances for achieving high directivity at the center frequency f_0. However, the compensating inductances retard phase of the propagated signal, the zero-isolation frequency is shifted to frequency which is lower than the original frequency. Similar to the other lumped compensation techniques, the center frequency can be simply shifted back to original frequency by modifying the electrical length of the compensated parallel-coupled line as shown:-

$$\theta_Q = \cot^{-1}\left(\frac{4\pi f_0 L_Q - Z_{0o}\cot\theta_o}{2Z_{0e}}\right) \tag{8}$$

Then, the design equations for quadruply-inductive compensated microstrip coupled lines i.e. L_s and θ_f were calculated from (7) and (8) respectively.

B. Inductive Compensated Coupled Lines based SPR

A 6-dB nductive-compensated microstrip parallel-coupled lines operating at f_o of 2.4 GHz on RF60-0600 microwave substrate with electrical parameters (Z_{0e} = 86.74 Ω, Z_{0o} = 28.82 Ω, ε_{effe} = 4.502 and ε_{effo} = 3.303) were designed and simulated. The compensation inductors (L_Q) and the shorten electrical lengths (θ_Q) were calculated from (3) and (4), which are 0.7 nH and 0.47π, respectively.

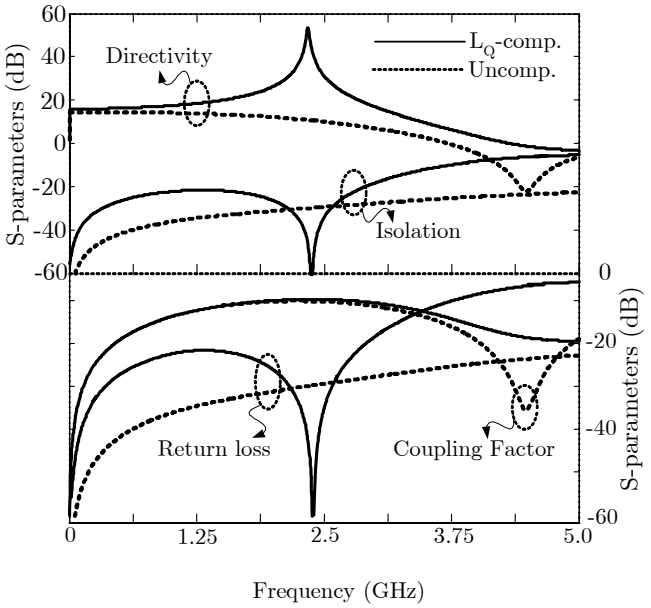

Fig. 6. Simulated results of compensated coupler

The coupled lines circuit based simulation results are shown in Fig. 6. It is shown that at f_0, the design provides directivity of more than 46 dB. To prove the validity of the proposed technique, a 6-dB uncompensated coupler was designed. The simulated result of the obtained directivity of the uncompensated coupler at 2.4 GHz is 16 dB. The designs were applied for coupled lines in the SPR shown in Fig. 1. Simulating the measuring of complex load Z_L = 25 +j30 Ω with uncompensated (13.8 dB) and quadruply compensated (46.2 dB) cases directivity. The q-points values and distribution of these cases were shown in table I, II and Fig. 7. These results are corresponded with ideal cases simulation.

Table I Simulated Q-values of 2.4 GHz SPR

D	Q_3		Q_5		Q_6	
(dB)	Re{}	Im{}	Re{}	Im{}	Re{}	Im{}
13.8	0.260	-1.82	2.390	1.680	-2.250	3.690
46.2	0.007	-0.97	1.013	0.998	-1.013	1.027

Table II Simulated measure impedances and errors of 2.4 GHz SPR

D (dB)	Real (Ω)	Imaginary(Ω)	% error
13.8 dB	20.81	49.63	37.81
46.2 dB	26.12	31.53	4.84

IV. CONCLUSION

A studied of the relation between microstrip coupled lines' directivity and measurement error of six-port reflectometer is presented. The error obtained from the SPR estimation is increased when the coupler directivities were decreased. From the investigation, it is shown that a directional coupler which greater than 40-dB directivity is needed to achieve less than

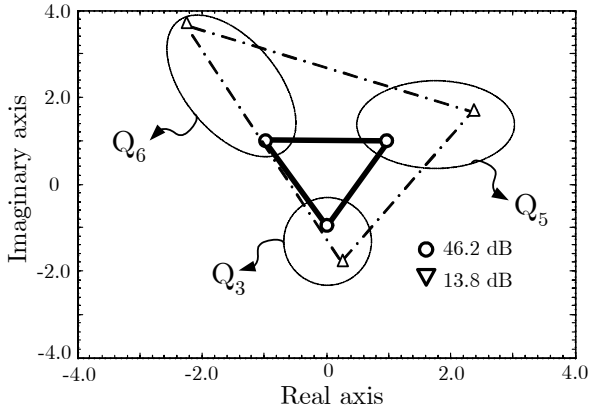

Fig. 7. Q-points distribution with 13.8 dB, and 46.2 dB directivities of 2.4 GHz microstrip SPR.

2% error for real loads and less than 5% for complex load. Design procedures for the compensation inductors have been provided to enhance coupled lines directivity. More important, the closed- form expressions for determining the compensation inductor values and coupled-line parameters are given to facilitate the design task considerably.

REFERENCES

[1] S. B. Cohn, and N. P. Weinhouse, "An automatic microwave phase measurement system", in 1964 *Microwave J.,* vol 7, no.2, pp. 49-56, Feb. 1964.

[2] S. Ovidiu, E. Moldovan, K. We, and R. G. Bosisio, "A new direct millimeter-wave six-port receiver ", in 2001 *IEEE Trans. Microwave Theory Tech.*, vol. 49, no.12, pp. 2517-2522, Dec. 2001.

[3] X. Z. Xiong, and V. F. Fusco, "Wideband 0.9 GHz 5.0 GHz six-port and its application as digital modulation receiver", in 2003 *IEE Proc.-Microw. Antennas Propag.,* vol 150, no. 4, pp. 301-307, Aug. 2003.

[4] N. G. Cutmore, D. A. Abernethy, and T. G. Evans, "Microwave technique for the on-line determination of moisture in coal", *J. Microwave Power and Electromag. Energy*, vol. 24, pp. 79-90, 1989.

[5] C.A. Hoer and K.C. Roe,"Using an arbitrary six-port junction to measure complex voltage ratios", *IEEE Trans. Microwave Theory Tech.*, vol. 23, pp. 978-984, Dec. 1975.

[6] S. P. Yeo, "Analysis of symmetrical six-port junction when configured as a six-port reflectometer", in 1992 *IEEE Trans. Microwave Theory Tech.*, vol. 41, no.2, pp. 193-197, April 1992.

[7] F. M. Ghannouchi, and R. G. Bosissio, "A comparative worst-case error analysis of some proposed six-port designs", in 1988 *IEEE Trans. Microwave Theory Tech.*, vol. 37, no.4, pp. 552-556, Dec. 1988.

[8] G. F. Engen, "Six-port measurement circuit", United States Patents, Aug. 1, 1978.

[9] G. F. Engen, and C. A. Hoer, "Application of 6-port junction to power-measurement ploblems", in 1972 *IEEE Trans. Microwave Theory Tech.*, vol. IM-21, pp. 470-474, Nov. 1972.

[10] P. I. Somlo, and J. D. Hunter, "Microwave impedance measurement", Peter Peregrinus, London, Chapt. 7, 1985.

[11] R. Phromloungsri, V. Chamnanphrai, and M. Chongcheawchamnan, "Quadruply-Inductive Compensated Parallel-Coupled Lines", in 2006 *Asia Pacific Microwave Con.*, Dec. 2006, pp. 2840-2843.

[12] R. Phromloungsri, and M. Chongcheawchamnan, "A high directivity design using an inductive compensation technique", in 2006 *Asia Pacific Microwave Con.*, Yogohama, Dec. 2006, pp. 1243-1246.

Impedance Analysis of a Shorted-End Curved Dipole on Reflector Plane using Method of Moments

Sompop Pimpol and Rangsan Wongsan
School of Telecommunication, Institute of Engineering,
Suranaree University of Technology, Nakhon Ratchasima, Thailand
E-mail: rangsan@sut.ac.th

***Abstract*-This paper presents the impedance analysis of a shorted-end curved dipole antenna on a square reflector plane. The current distribution of the curved dipole antenna can be solved numerically using the Method of Moment (MoM). A system of linear equations is generated to form matrix model and the inversion of this matrix can realize the current distributions, which are used to determine the impedance characteristics of this antenna. These simulation results have been validated with measurements on a fabricated prototype. The proposed antenna with simple structure is very suitable for UHF TV broadcasting station.**

I. INTRODUCTION

Broadcasting system has been extensively and continuously used for distributing information over wide range of the service area. The antenna applied for the broadcasting station of the ultra high frequency television (UHF TV) requires either unidirectional or omnidirectional beam with sufficient gain, high power handling, and bandwidth of each channel is 6 MHz [1]. Moreover, the antenna should possess physically strong structure, easy fabrication and cost effectiveness.

Most manufacturers offer configurations that can be used to broadcast a wide variety of azimuth and elevation patterns at either low or high power with their simple feeding system, low windload, and ability to be side- or top-mounted. Conventionally, the popular antenna utilized for this purpose is the UHF antenna panel system [2], which is one type of broadcasting antennas that contains horizontally polarized wire/patch dipoles as an array arrangement. To achieve omnidirectional pattern, however, the panel system must be placed around the tower at least four panels because the beamwidth of each panel is not much wide. In addition, the structure of conventional panel system is probably complex and required the fully feed system.

From these aforementioned literatures of the conventional UHF TV broadcasting antennas, it is obvious that the antenna which possesses simple structure and simple feeding system is desirable. An antenna made of curved-wire dipole, which the both ends are shorted on the metallic reflector plane, is an attractive one since the structure and feed system is very simple. Moreover, the beamwidth of curved-wire dipole is larger than straight dipole.

Most of substantial works related to the shaped or curved dipole structures. Krishnan *et al.* [3] presented a V-shaped wire-loop with a butterfly-like structure. The elliptically polarized radiation of S-shaped dipole antenna was presented by Elkamchouchi and Nasr [4]. Besides these, Dubost [5] presented the radiation impedance and bandwidth of a short-circuited dipole parallel to a perfect reflector plane. As far as we know, there is no information about the curved dipole that the both ends are shorted on a metallic reflector plane, which is necessary for the structure that requires the simple fabrication, simple feeder, and high power handling. Since impedance is the important characteristic that determines the efficiency of the antenna. Therefore, this paper focuses on the impedance of a shorted-ends curved dipole. Theoretical background of this antenna will be determined by using Method of Moments (MoM). The Pocklington's integral equations for total filed are first formulated and are subsequently solved by using Method of Moments to determine the unknown current densities. Finally, the input impedance of the antenna at the center feed will be determined and validated by measurement.

II. THEORY

The structure of a shorted-end curved dipole antenna is composed of a curved-wire dipole, which their both ends are short-circuited on a metallic reflector plane as shown in Fig.1. The curved-wire dipole of the length L, the wire radius b, and the curved radius a is aligned along ϕ-direction at which the feed center of this curved dipole is located at $\phi = \pi/2$. The dimension of a square reflector plane of the width W is one wavelength as shown in Fig.2.

The current distribution of the shorted-end curved dipole antenna can be obtained by using the Pocklington's integral equation and solved numerically using the method of moments. The point-matching technique is then used to satisfy the integral equation at discrete points on the axis of curved dipole rather than attempting to satisfy this equation everywhere on its surface [6]-[7]. Thus, a system of linear algebraic equations is generated to form the matrix model and the inversion of this matrix can realize the current distribution on the curved dipole, which is used to determine the input impedance of this proposed antenna.

In this work, the Pocklington's integral equation for the total field calculation, which are generated by an electric current source radiating in an unbounded free space [8], which can be written in the form of

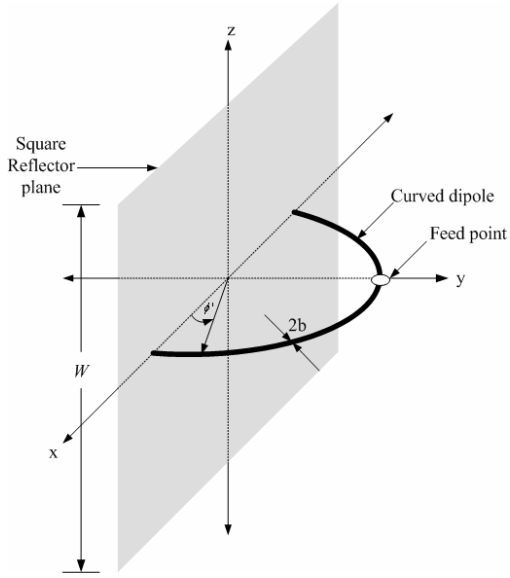

Figure 1. Geometry of the shorted-end curved dipole on a reflector plane.

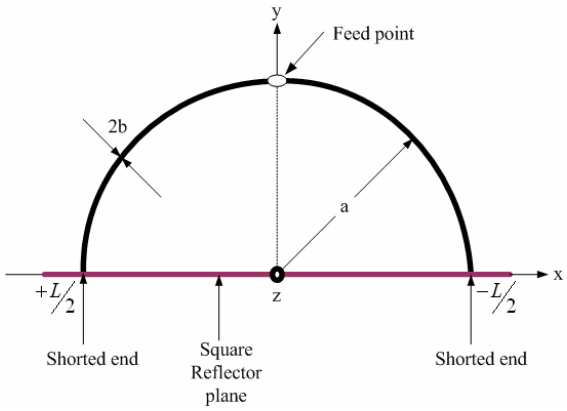

Figure 2. Analysis model of the shorted-end curved dipole on a reflector plane.

$$\int_{-L/2}^{+L/2} I_n\left(\phi'\right)\left(\frac{\partial^2}{\partial_\phi^2}+k^2\right)\frac{e^{-jkR}}{R}d\phi' \;=\; j4\pi\omega\varepsilon_0 E_\phi\,, \tag{1}$$

where E_ϕ is the radiated field due to the current $I_n\left(\phi'\right)$. Resulting from a source field E_ϕ, that could be caused by voltage applied at the antenna feed point or incident plane wave $E_{\phi'}^i$. Here ϕ' and ϕ are the source location variable and the observation location variable, respectively, and R is the distance from any one point on the source to the observation point. For small diameter wires, the current on element can be approximated by a finite series of odd-order even modes [7]. Thus, the current on the element can be written as a Fourier series expansion of the form:

$$I_n\left(\phi'\right)=\sum_{m=1}^{M} I_{nm}\,g_n\left(\phi'\right)\,, \tag{2}$$

where $g_n\left(\phi'\right)$ is entire domain basis functions [8], which is given by

$$g_n\left(\phi'\right)=\cos\left[\frac{\left(2m-1\right)\pi\phi_n'}{L_n}\right],\;\; 0\le\phi_n'\le\pi, \tag{3}$$

where L_n is the corresponding length of the n element.

After some rigorous derivations and using entire domain functions with Pocklington's integral equation, the integral equation for each element of the proposed antenna can be written as [8]

$$E_\phi^t=\frac{1}{j4\pi\omega\varepsilon_0}\sum_{m=1}^{M} I_{nm}\left\{\left(-1\right)^{m+1}\frac{\left(2m-1\right)\pi}{L_n}G_2\left(\rho,\rho',\phi,\phi'/z,\frac{L_n}{2}\right)\right.$$
$$\left.+\left[k^2-\frac{\left(2m-1\right)^2\pi^2}{L_n^2}\right]\times\int_0^{L_n/2} G_2\left(\rho,\rho',\phi,\phi'/z,\phi_n'\right)\cos\left[\frac{\left(2m-1\right)\pi\phi_n'}{L_n}\right]d\phi_n'\right\}, \tag{4}$$

where I_{nm} represents the unknown current coefficient of mode m on element n. Because of the proposed antenna comprises two elements such as driven and reflector elements. Therefore, n = 2 is the total number of elements. Green's functions is given as

$$G_2\left(\rho,\rho',\phi,\phi'/z,\phi_n'\right)=\frac{e^{-jkR_-}}{R_-}+\frac{e^{-jkR_+}}{R_+}\,, \tag{5}$$

where $R_\pm$ represents the distance from each wire radius to the center of any other wire which can be shown by

$$R_\pm=\sqrt{\left(a-a'\right)^2+\left(z-z'\right)^2+b^2+\left(\phi\pm\phi'\right)^2}\,. \tag{6}$$

From (4), in according with referred to as point-matching method, in matrix form can be expressed as

$$\left[V_m\right]=\left[Z_{nm}\right]\left[I_{nm}\right]\,, \tag{7}$$

where

$$Z_{mn}\;=\;\left\{\left(-1\right)^{m+1}\frac{\left(2m-1\right)\pi}{L_n}G_2\left(\rho,\rho',\phi,\phi'/z,\frac{L_n}{2}\right)+\left[k^2-\frac{\left(2m-1\right)^2\pi^2}{L_n^2}\right]\right.$$
$$\left.\times\int_0^{L_n/2} G_2\left(\rho,\rho',\phi,\phi'/z,\phi_n'\right)\cos\left[\frac{\left(2m-1\right)\pi\phi_n'}{L_n}\right]d\phi_n'\right\} \tag{8}$$

and

$$V_m\;=\;4\pi\varepsilon_0\,. \tag{9}$$

Finally, the unknown coefficients I_{nm} can be solved from the matrix model in (7) by using a number of matrix inversion techniques.

III. NUMERICAL RESULTS

For illustration, the shorted-end curved dipole antenna was designed to operate at the center frequency of 470 MHz. From the preliminary study it was found that, at this operating frequency, the radius of curvature *a* and the wire radius *b* should be 10.15 cm and 0.005 λ, respectively, so that the good matching condition and the proper gain of this antenna could be obtained. Computations for this proposed antenna have been made using the formulas of previous section. For the current itself, convergence was about 5.5 percent change in going from 30 to 50 segments. In our case, 40 segments for a half-wave length of antenna will give accurate results as shown in Fig.3. It is found that the appropriate length of this curved dipole should be half-wavelength due to the current magnitude at the both ends is zero.

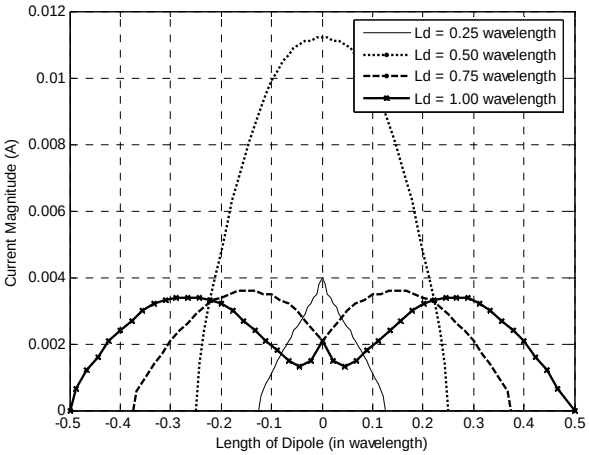

Figure3. Current distribution of curved dipole.

The length of curved dipole is the important parameter to characterize the impedance characteristics. The curved dipole length is varied from 0.25λ to 0.75λ while other parameters are fixed. The numerical results of the input resistance and reactance of a shorted-end curved dipole as a function of the frequency are illustrated in Figs. 4 and 5, respectively. From Fig. 4, it is obvious that the larger the length, the larger the resistance and the reactance. For the resonant frequency observed from the zero reactance, it can be seen that the resonant frequency will be higher when the dipole length is shortened. The resonant frequency of 470 MHz is realized when cavity length is around 0.5λ.

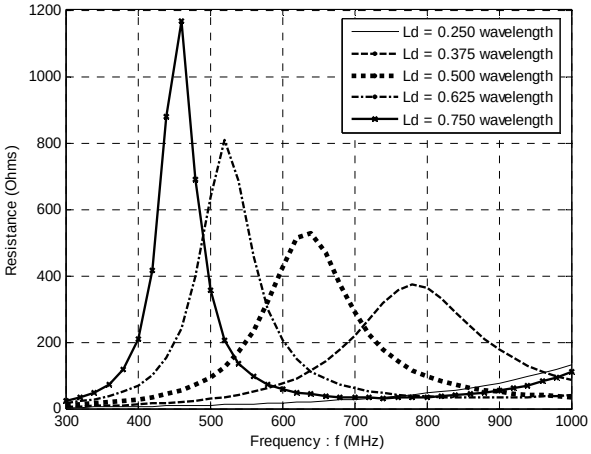

Figure 4. Input impedance characteristic of curved dipole.

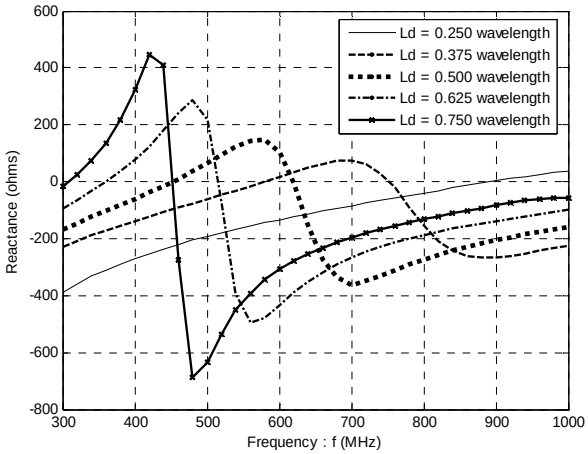

Figure 5. Input impedance characteristic of curved dipole.

IV. EXPERIMENTAL RESULTS

To verify the theoretical calculation, the curved dipole, which the both ends are short-circuited on the reflector plane is fabricated and the input impedance is measured by using an HP8720C Network Analyzer. The prototype of the fabricated antenna is shown in Fig. 6. To achieve impedance matching, the $\lambda/4$ coaxial balun (1:1) is mounted at the center gap of curved dipole to balance inherently unbalanced system. The measured results are superimposed as dashed line in Figs. 7 and 8. It should be pointed out that the good agreement between theory and experiment can be observed that the input impedance is around 50 Ω at the operating frequency of 470 MHz.

Figure 6. Photograph of the prototype of the shorted-end curved dipole.

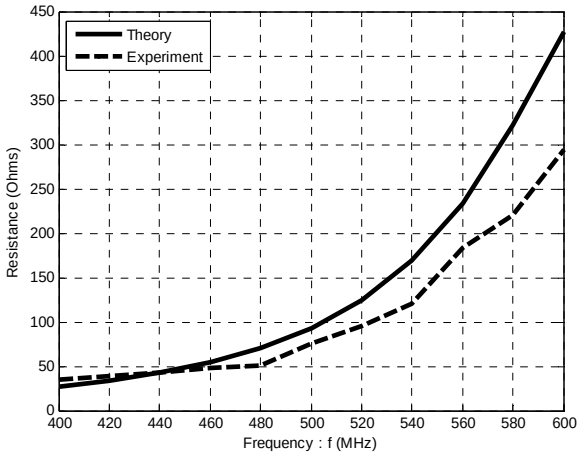

Figure 7. Input resistance of shorted-end curved dipole.

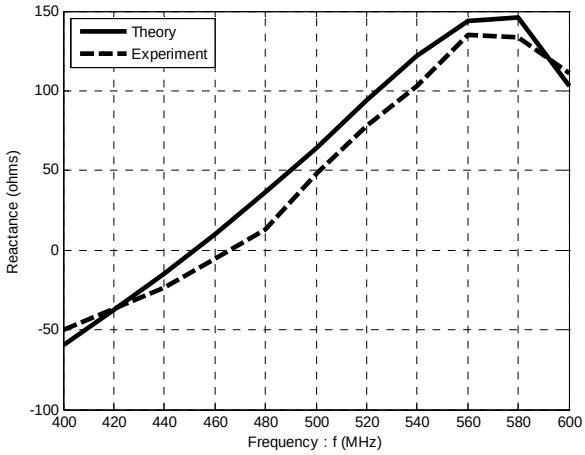

Figure 8. Input reactance of shorted-end curved dipole.

V. CONCLUSION

Input impedance is an important characteristic that affects the antenna efficiency. It must be well investigated so that the matched antenna can be designed. This paper focuses on the input impedance characteristics of a so-called shorted-end curved dipole on a reflector plane. This antenna is developed to be an UHF TV broadcasting antenna due to its simple structure and simple feeding system. In order to investigate input impedance of this antenna, the straightforward procedure is applied. Starting from formulations of integral equations of the structure based on the Pocklington's integral equation. The entire domain basis function is used in the Method of Moments to solve the electric current density on the curved dipole. The input impedance can be found from this current subsequently. From the numerical results, the frequency response of input impedance can be investigated, which is very useful to find the optimum matching condition by simply adjusting the length of curved dipole.

REFERENCES

[1] International Telecommunication Union, TRANSMITTING ANTENNA CHARACTERISTICS AT VHF AND UHF, Recommendation ITU-RBS.1195, 1995.

[2] D.Casciola, G.L. Mieers, and R.A. Surette, "UHF Antenna Choices," *IEEE Trans. On Broadcasting*, vol. 45, pp. 93-104, March 1999.

[3] S. Krishnan, L.-W. Li, and M.-S. Leong, "A V-Shaped Structure for Improving the Directional Properties of the Loop Antenna," *IEEE Trans. Antennas Propag*., vol.53. pp. 2114-2117, June 2005.

[4] H. Elkamchouchi and M. Abu Nasr, "THE S-SHAPED DIPOLE ANTENNA," *Proc. IEEE Microw. And Millimeter Wave Technology, 2004, ICMMT 4th International Conference*, pp. 19-22, August 2004.

[5] G. Dubost, "Flat Radiating Dipoles and Applications to Arrays," RESEARCH STUDIES PRESS A DIVISION OF JOHN WILEY & SONS LTD. pp. 28-36, 1981.

[6] R.F. Harrington, "Matrix methods for field problems," *Proc. IEEE*, vol. 55, pp. 136-149, February 1967.

[7] G.A. Thiele, "Calculation of the current distribution on a thin linear antenna," *IEEE Trans. Antennas and Propagation (Communications)*, vol. AP-14, pp.648-649, September 1966.

[8] C.A. Balanis, "Antenna Theory-Analysis and Design", USA, John Willey & Sons, Inc., 1982

A Finite Element Method with Polygonal Elements for Analyzing a Band Gap Characteristic of Square Lattice Photonic Crystals

Eny Sukani Rahayu and Tuptim Angkaew
Electrical Engineering Department, Chulalongkorn University
Bangkok, Thailand

***Abstract*–Finite element method (FEM) with polygonal elements employing the Wachspress shape functions to analyze the band gap characteristic of two-dimensional photonic crystals (2D PCs) is presented in this paper. The performance of the method compared with which of the linear triangular FEM is provided by showing the error calculation in order to observe the accuracy. The flexibility of meshing using polygonal elements with Wachspress shape function as the interpolation function is also presented. The results compared with those from linear triangular FEM show better accuracy than the linear triangular FEM with less number of unknowns.**

***Index Terms*–Polygonal elements, FEM, Wachspress shape function, 2D PCs and a band gap characteristic.**

I. INTRODUCTION

Photonic crystals (PCs) are periodic dielectric structures which can exhibit a photonic band gap (PBG) characteristic, where optical wave with frequency ranged in the band gap cannot propagate through the structures. In other words, the optical wave with that certain range of frequency is reflected by PCs [1]. This main property of PCs where these materials can control the propagation of optical waves is unique and gives great motivations in modifying and designing them to be high performance devices such as photonic integrated circuit (PIC) to support the next generation PICs in nanotechnology world [2,3,9]. Large contributions of two-dimensional (2D) PCs yield some devices such as lasers, couplers and most of optical devices used in optical networks [2,9]. One of the examples of 2D PCs is a square lattice PCs shown in Fig.1.

PC-based devices works at an operational frequency referred back to the band gap characteristic of such PC for a special purpose and in order to reduce the loss in the devices. Since the band gap is the most important property of PCs, the analysis of the band gap characteristic using improved numerical tools is advantageous as a starting point.

The band gap characteristic of such PCs depends on the geometry of the PC structures such as types of lattices, a filling ratio, and specifications of used materials. The geometry of the structures varies depending on the improved design of PCs and on the imperfect fabrication process. Therefore, the improvement in numerical tools to calculate the band gap characteristic is quite necessary to be investigated.

Several methods have been proposed and some of them are still used so far such as the famous plane wave expansion method (PWE) [4], finite difference time domain method (FDTD) [5], compact finite difference frequency domain method (FDFD) [7] and finite element method (FEM) [3,6,8]. The most flexible method in the application for any arbitrary shape and geometry structure of the calculation domain is the FEM so this method has been more suitable for analyzing even the real condition of PCs where there is a possibility of a non-ideal geometry of the structure or a deformation on the construction of PCs due to an imperfect fabrication process. The PWE will not be able to model such structures efficiently because the PWE can only model the ideal periodic dielectric structures while the two other methods, FDFD and FDTD are less flexible and less effective in modeling an arbitrary and curved-shape calculation domain than the FEM due to the grid based discretization [5,7].

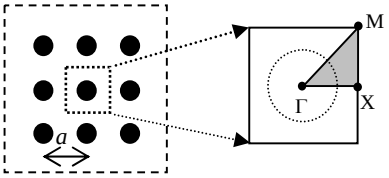

Figure 1. A square lattice PC shown with the first (zoomed area) and the irreducible (shaded area) Brillouin zone.

The FEM in previous works are formulated by incorporating Bloch theorem in the governing equations of TE and TM modes, which results in complicate FEM formulation. Recently, the 4th order finite difference formulation formulated directly from governing equations and employing periodic boundary conditions has been reported [7]. This finite difference formulation is straightforward and gives good computed results in numerical examples, but its method is not effective for the case of curved structure modeling. In this paper, the FEM for analyzing 2-dimensional PCs directly formulated from governing equations with PBCs are proposed to provide a straightforward FEM formulation for analysis band gap characteristic of 2D PCs using the polygonal FEM.

The FEM, which is known not a memory consuming numerical tool due to the sparse matrices, is such a tool used to find the approximate solutions of a boundary value problem

[3,8,12-14] which is imposed to the analyzed system. The system of 2D PCs is common to be discretizised over its domain of calculation using triangular elements as efficient shapes in modeling and simple interpolation function based on the barycentric coordinate [11,15,17]. Recently there is an improvement in meshing using generalized irregular polygonal elements called a polygonal FEM [12,16,18,19]. This work will implement polygonal FEM to calculate the band gap characteristic as a modified FEM. It is expected to be more efficient, effective and to provide a higher accuracy than the previous method in analysis of any arbitrary design of 2D PCs using the Wachspress shape function in the form of a rational basis function based on an area calculation [12,15,16]. Fig.2 shows the application of polygonal element meshes compared with the triangulation over the domain.

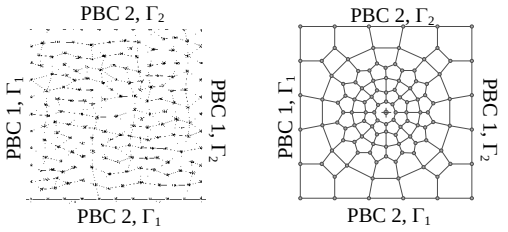

Figure 2. Samples of meshes on the same domain with triangular (left side) and polygonal (right side) elements shown with the imposed PBCs.

This paper is organized as follows. In section II, the polygonal finite element methods for analyzing the band gap characteristic is explained together with the Wachspress shape function used as the interpolation function for generalized polygonal elements. Section III shows the numerical results by comparing the approximation errors of band gap characteristic calculations between which from the linear triangular FEM and the polygonal FEM. Finally, section IV provides the conclusion of the work.

II. POLYGONAL FINITE ELEMENT METHOD

A. Governing Equations for TE and TM waves in 2D PCs

To calculate the band gap characteristic, the four Maxwell's equations are employed as basic equations. The medium of PCs is assumed to be lossless, isotropic and non-magnetic. The 2D PCs is a periodic dielectric structure, which is uniform along z-axis of coordinates system. The wave equations deriving from Maxwell's equations can be divided into 2 independent eigensystem equations, named as TE and TM modes. In TM modes, the electric field is polarized in *z*-direction while in TE mode, the magnetic field is polarized in *z*-direction. The general governing equation for both polarizations is expressed in (1) as follows

$$-\nabla \cdot p(x,y)\nabla u(x,y) = \frac{\omega^2}{c^2} q(x,y)u(x,y) \tag{1}$$

For TM mode, an unknown solution $u(x,y) = E_z(x,y)$ and constants $p(x,y)$ and $q(x,y)$ are equal to μ_r^{-1} and ε_r, respectively while for TE mode, $u(x,y) = H_z(x,y)$, $p(x,y) = \varepsilon_r^{-1}$ and $q(x,y) = \mu_r$. Here, ε_r is a relative permittivity of the medium while a relative permeability of the medium μ_r =1 for non-magnetic material, ω denotes the angular frequency of optical wave, and c is the speed of light in vacuum. The eigenvalue of the eigensystem equation in (1) is a resonant frequency of the PCs for a defined wave vector. Equation (1) is used in FEM formulation along with PBCs.

These boundary conditions employs the Bloch's function in order to model the periodic structure where the wave vectors are included. The wave vectors used as the input values are taken from the edges of the irreducible Brillouin zone of the unit cell of square lattice PCs determined by Weigner-Seitz cell algorithm [10] where the periodicity occurs. The approximate solution of FEM formulation is calculated for each sampled wave vector until the band gap characteristic is obtained for all the possible wave vectors.

The unit cell used as the calculation domain is the first Brillouin zone of square lattice PCs with a dielectric rod surrounded by an air medium due to the simple geometry. Fig.1 illustrates the square lattice PCs with the unit cell and the irreducible Brillouin zone with the suitable PBCs are shown in (2) for PBC 1 and (3) for PBC 2 as illustrated in Fig.2 based on [7]

$$u(x+a,y)|_{\Gamma_2} = e^{-jk_x a} u(x,y)|_{\Gamma_1} \tag{2}$$

$$u(x,y+a)|_{\Gamma_2} = e^{-jk_y a} u(x,y)|_{\Gamma_1} \tag{3}$$

where here u is an unknown solution on the boundary of the domain at edges Γ_1 or Γ_2 as shown in Fig.2. Symbol a denotes a length of periodicity of the square lattice points as shown in Fig.1 while k_x and k_y are particular wave vectors in x and y direction, respectively defined from the irreducible Brillouin zone as shown in Fig.1.

The unit cell domain is discretizised by finite elements. The linear unstructured triangulation in Fig.2 covers the curved domain sufficiently. However, the polygonal meshes are shown to have varied element shapes where the different n-gon elements can be conformed together by choosing a suitable interpolation function due to the linearity on the boundary so that the greater flexibility in meshing can be accomplished.

B. Wachspress shape functions

The main difference between triangular FEM and the polygonal FEM is the interpolation function. The Wachspress shape function is chosen as which for generalized convex polygon element which have properties explained in [12,15,17] where the construction is based on barycentric coordinate concept as well as the one for triangular elements.

The general shape function N_i^e in FEM is built to approximate the unknown field u within an element e using an expansion in (4).

$$\bar{u}^e = \sum_{i=1}^{n} N_i^e u_i^e \tag{4}$$

The Wachspress shape function used in (4) is formulated by (5)

$$N_i^e = \frac{\omega_i^e}{\sum_{j=1}^{n} \omega_j^e}; \text{ for } i = 1,2,...n \tag{5}$$

where ω_j is a non-normalized barycentric coordinate called a weight function for node *j* [18] yielding a polynomial as given in (6)

$$\omega_j = \frac{A(u_{j-1}, u_j, u_{j+1})}{A(u_{j-1}, u_j, p)A(u_j, u_{j+1}, p)} \text{ ; for } j = 1,2,..., n \quad (6)$$

so that when (6) is substituted into (5), the shape function becomes a ratio of polynomial A refers to a triangle area formed by three points as mentioned in the index with *P*(*x*,*y*) inside the element. Fig.3 shows an example of a polygonal element in a rectangular shape (*n*=5) with point *P*.

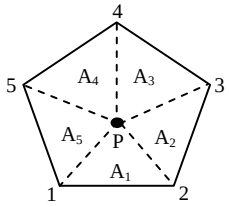

Figure 3. A pentagonal element as an example of polygonal elements.

An example calculation of a triangle area created by node *j*-1, *j* and *P*, $A(j-1, j, p)$ for $j = 2$, is formulated in (7) where it will give a positive number when the vertices are counterclockwise numbered.

$$A^e(1,2,p) = \frac{1}{2}\begin{vmatrix} x_1 & y_1 & 1 \\ x_2 & y_2 & 1 \\ x & y & 1 \end{vmatrix} \quad (7)$$

C. FEM Formulations

FEM formulation is built based on Galerkin method for both TM and TE modes based on the general formulation in (1). For TM mode case, the solution of the electric field E_z is approximated in the form of linear expansion of shape functions and unknown field parameter *u* as in (4). When the approximate field $\bar{u}$ is substituted in (1) for each kind of modes, a residual error *R*(*x*,*y*) will be obtained as in (8).

$$R = \frac{\partial^2 \bar{u}}{\partial x^2} + \frac{\partial^2 \bar{u}}{\partial y^2} + \left(\frac{\omega}{c}\right)^2 \varepsilon_r \bar{u} \quad (8)$$

According to the Galerkin's method, the integrals formed by integrating the product of residual error *R* and each shape function employed as a weighting function *w* are forced to zero as shown in (9) in order to minimize the error. By doing integration by part, a system of equations is obtained as given in (10)

$$\int_\Omega w_i R dxdy = 0; \text{ for } i = 1,2,...,n \quad (9)$$

$$\int w_i \frac{\partial \bar{u}}{\partial n} d\Gamma - \iint \left(\frac{\partial \bar{u}}{\partial x}\frac{\partial w}{\partial x} + \frac{\partial \bar{u}}{\partial y}\frac{\partial w}{\partial y} \right) dxdy + \iint w \left(\frac{\omega}{c}\right)^2 \varepsilon_r \bar{u} dxdy = 0; \text{ for } i = 1,2,..., n \quad (10)$$

Substituting (4) into (10) for unknown inside the element beyond the line integration and enforcing the PBCs in (2) and (3) for unknown on the element boundary will lead the formulation into eigensystem equation (12). The numerical integration is taken only inside the elements since nodes on element boundary will be imposed by the PBCs and the surface integration in (10) will be called as *f*(*x*,*y*). Numerical integration on polygonal element *e* is approached by means of partitioning it into *m* number of triangle e_Δ (sub-triangulation) and then using standard quadrature rules on triangles [18] where the element is the original physical element yielding an integration formulation as shown in (11)

$$\iint_e f(x,y)dxdy = \sum_{e_\Delta=1}^{m} \iint_{e,e_\Delta} f(x,y)dxdy = \sum_{e_\Delta=1}^{m} \int_0^1 \int_0^{1-\xi} f(\xi,\eta)\left|J_1^{e_\Delta}\right| d\xi d\eta \quad (11)$$

Finally, an eigensystem equation in matrix form as written in (12) can be obtained.

$$[A]\{u\} = \left(\frac{\omega}{c}\right)^2 [B]\{\phi\} \quad (12)$$

By solving (12) for a given wave vector *k*, the eigensolver computes a set of eigenvalues. These eigenvalues are plotted as a function of *k* yielding the band gap characteristic.

III. NUMERICAL RESULTS

The results from triangular FEM and polygonal FEM are validated by using results from plane wave expansion methods (PWE) as a semi analytical method by running MPB software with 128x128 resolutions. Fig.4 presents the results of band gap characteristic obtained by polygonal FEM for a square lattice PC of dielectric rods with ε_r=8.9 surrounded by an air medium for 5 numbers of bands using 4 gauss points.

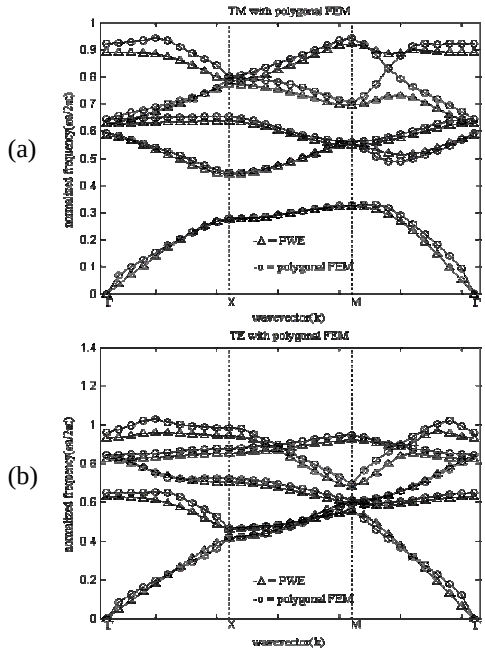

Figure 4. Band gap characteristic of a square lattice PC with ε_r=8.9 in a rod surrounded by an air medium for (a) TM and (b) TE mode.

The polygonal mesh is built by 116 number of nodes, 77 number of elements and 338 elements in sub-triangulation

while the triangular mesh is created from 186 number of nodes and 330 number of elements shown in Fig.2. The input wave vectors are sampled points from edges of the irreducible Brillouin zone (wave vector zone) by 10 cells for each edge plotted on horizontal axes. Certain parts of the bands look convergent with the comparative results especially for the lower bands and the error is around 3.713 %. It is convincible that this method can give greater accuracy with the proper design of the mesh.

Recent convergence test for 5 numbers of bands yields a graph shown in Fig. 5. The convergence rate test shows that the polygonal FEM with a polygonal mesh of all n>3 elements will give a quick step to converge than the linear triangular FEM until around 1000 numbers of unknowns.

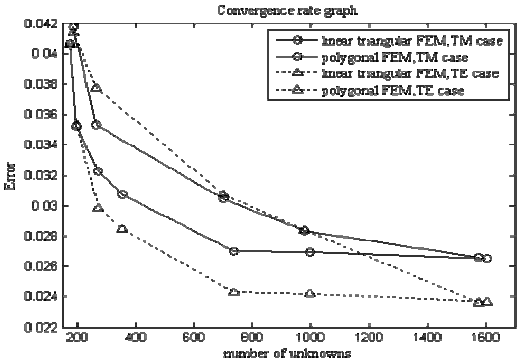

Figure 5. A comparative convergence rate graph between linear triangular FEM and polygonal FEM for both TE and TM mode cases.

Increasing unknowns until around 1600 numbers will bring the results into almost the same number of errors for both polygonal FEM and linear triangular FEM for each kind of modes with the same type of mesh where more refined elements are created in the rod rather than in the air medium. The more proper design of mesh is predicted to give better results.

Fig.6 shows a modification of polygonal mesh in Fig.2 which is combined with the linear triangular elements inside the rod called a mixed type mesh (right side of Fig.6) which indicates to give a better result i.e. 3.63 % where the number of triangle elements at least equal to the number of sub-triangulation created in polygonal mesh. It is shown that for un-fluctuating behavior of the system such as inside the rod where the field becomes more dominant rather than in the air medium, the use of linear triangular elements is enough while for the fluctuating one needs to use higher order elements such polygonal elements.

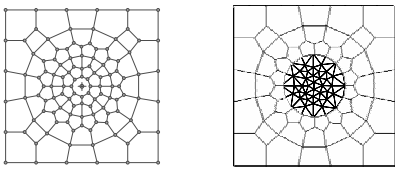

Figure 6. Comparison of a polygonal (left) and a mixed type mesh (right).

IV. CONCLUSION

Dealing with polygonal FEM, some parameters must be considered first in order to reduce the error or to increase the accuracy such as the numbers of used gauss points, external input values on boundary conditions, numbers of sub-triangulation elements depending on the problem. In this case, the polygonal FEM proves to give a higher accuracy than the linear triangular FEM where the lower error level is obtained by occupying less number of nodes (unknowns) and less number of elements.

REFERENCES

[1] S.G. Johnson and J.D. Joannopoulos, "Introduction to photonic crystals: Bloch's theorem, band diagram, and Gap (but no defects)", 2003,http://ab-initio.mit.edu/photons/tutorial/photonic-intro.pdf (accessed January, 2006).

[2] A.Yamilov, et.al., "Photonic band structure of ZnO photonic crystal slab laser", *Journal of Applied Physics* , vol. 98, 103102, 2005.

[3] B.P. Hiett, et.al., "Application of finite element methods to photonic crystal modeling", *IEE Proc.-Sci. Meas. Technol*., vol. 149, no. 5, 2002.

[4] J.D. Shumpert, "Modeling of periodic dielectric structures (Electromagnetic crystals)", A dissertation submitted in partial fulfillment of the requirements for the degree of Doctor of Phylosophy (Electrical Engineering), The University of Michigan, 2001.

[5] X. L. Yang, et.al., "Theoretical bandgap modeling of two-dimensional triangular photonic crystals formed by interference technique of three noncoplanar beams", *Optics Express 1053*, vol. 11, no. 9, 2003.

[6] B.P. Hiett, et.al., "Photonic band gaps in 12-fold symmetric quasycrystals", *Journal of Material Science: Materials in Electronics*, no. 14, page 413-416, 2003.

[7] Chin-ping Yu and Hung-chun Chang, "Compact finite-difference frequency-domain method for the analysis of two-dimensional photonic crystals", *Optic Express 1397*, Vol. 12, No. 7, 2004.

[8] W. Axmann and P. Kuchment, "An efficient finite element method for computing spectra of photonic and acoustic band gap materials I. Scalar case", *Journal of Computational Physics*, No. 150, page 468-481, 1999.

[9] Cuesta-Soto, et.al., "All-optical switching structure based on a photonic crystal directional coupler", *Optics Express 161*, Vol. 12, No. 1, 12 January 2004.

[10] C. Kittel, *Introduction to Solid State Physics, 7th edition*, John Wiley&Sons, Inc., 1996.

[11] Kenji K. and Tsutomo K., *Introduction to optical waveguide analysis, solving Maxwell's equations and the Schrodinger's equations*, John Wiley & Sons, Inc., 2001.

[12] N. Sukumar and A. Tabarei, "Conforming polygonal finite elements", International Journal for Numerical Methods in Engineering, No. 61, page 2045-2066, 2004.

[13] Giuseppe Pelosi, et.al., *Quick finite elements for electromagnetic waves*, Artech House, Inc., Boston, London, 1998.

[14] Jianming Jin, *The finite element method in electromagnetics*, John Wiley & Sons, Inc., 1993.

[15] M. Meyer, et.al., "Generalized barycentric coordinates on irregular polygons", *Journal of Graphic Tools*, Vol. 7, No. 1, page 13-22, 2002.

[16] N. Sukumar and E.A. Malsch, "Recent advances in the construction of polygonal finite element interpolants", *Arhcives of Computational Methods in Engineering*, Vol. 13, No. 1, page 129-163, 2006.

[17] J. Warren, et.al., "Barycentric coordinates for convex sets", *Advances in Computational and Applied Mathematics*, 2005.

[18] N. Sukumar and A. Tabarrei, "Numerical formulation and application of polygonal finite elements", *7th International ESAFORM Conference on Material Forming*, Trondheim, Norway, 2004.

[19] Timo Euler, et.al., "Polygonal Finite Elements", *IEEE Transactions on Magnetics*, Vol. 42, No. 4, April 2006

A Tri-Band Microstrip-to-Coplanar Stripline Transition

Kumron Meelarpkit [1], Mitchai Chongcheawchamnan[2], Chuwong Phongcharoenpanich[1]

Faculty of Engineering and Research Center for Communications and Information Technology,
King Mongkut's Institute of Technology, Ladkrabang, Bankokok, 10520, Thailand
[2]Research Center for Electromagnetic Wave Applications (RCEWs),
Mahanakorn University of Technology, Bangkok, 10530, Thailand

E-mail : mitchai@ieee.org, kpchuwon@kmitl.ac.th

***Abstract* —This paper first presents a tri-band microstrip (MS)-to-coplanar stripline (CPS) transition. Rather using a wideband transition for tri-band circuit integration, a triple band transition is proposed as the noise power of each band can be limited. The proposed transition is simple to implement thus suits for various applications. A MS-to-CPS transition design for operating at three simultaneous bands on a low-cost substrate has been performed. Simulated and experimental results are in good agreement. The proposed transition exhibits excellence insertion loss performance at three bands, which are 0.36, 0.78, and 0.82 dB, respectively.**

Index terms: Microstrip, coplanar stripline, transition, transmission line.

I. INTRODUCTION

Coplanar stripline (CPS) has a balanced structure [1] which ideally supports signal propagation with low common mode noise. Also, as being a uniplanar transmission line, low discontinuity parasitic and ease of mounting lumped component in CPS circuit are its main advantages. Therefore it has gained much attention for high-speed and wireless integrated circuit designs nowadays. In addition, balanced structure in CPS simplifies the issue of integration with some balanced subsystems, such as dipole antenna [2], baseband CMOS IC [3], singly or doubly balanced mixer [4], etc. There are several circuit and system designs based on CPS transmission line which show impressive performances, for example a wideband mixer [5], a high-Q resonator and low insertion loss filter [6], a wideband transition [7], a rectenna system [8], etc.

In developing and design process of CPS transmission circuit, a transition is usually to interface a CPS transmission line to another transmission line circuit [7],[9]. In addition, measurement the CPS circuit does need a transition to interface with measurement systems. Among the CPS transitions, microstrip (MS)-to-CPS transition is widely used as the microstrip transmission line is one of the most commonly found circuits [10]-[11]. In the past, there are a few MS-to-CPS transition proposed [7],[9],[12]-[13]. Most of the transitions are designed for wideband application to serve not only for circuit design but also for measurement system interfacing. However the wideband performance is sometimes not suitable for some certain applications. For example, applying a wideband transition to integrate with multi-band system may need extra filter for band separation to limit noise power in each band. It is quite obvious that a multi-band transition serves better for the circuit/system integration than a wideband transition.

The paper is organized as follows: Section II presents the design configuration of the MS-to–CPS transition. The circuit consists of coupled MS lines and dual-section open stub. The three cross-section view of the electric field distributions of microstrip line, coupled microstrip line, and CPS will be described. The MS-to-CPS transition operated for three simultaneous bands will be designed. Simulation and measurement of a tri-band MS-to-CPS transition will be presented in Section III. Comparison of measured and simulated transition performances will be also discussed and followed with the conclusion in Section IV.

II. A TRI-BAND MICROSTRIP-TO-COPLANAR STRIPLINE TRANSITION

Fig.1 shows a configuration of the proposed tri-band MS-to-CPS. The structure is composed of a dual-section microstrip line coupled with a dual-section open circuit transmission line. From Fig. 1, the dual-section transmission line has line width of W_1 and W_2 associating with length of l_1 and l_2, respectively. The dual-section open circuit transmission line has line width of W_3 and W_4 associating with length of l_3 and l_4, respectively. The input of the transition is a 50 Ω feed line of width W_F and length L_F. Note that a function of a 50 Ω feed line is only for signal launching, not regarding to transition function. The output of MS-to-CPS transition is a CPS of width W and gap G. Triple band operation in transition is succeeded with multi-band matching operation in dual-section MS line and open circuit MS line. The cross-section views of electric field (E-field) distribution for different reference planes are shown in Fig. 2. Fig. 2 (a) shows the MS line (plane A-A'). The E-field distribution from strip plane passes substrate to ground plane. Fig. 2 (b) shows E-field

distribution in coupled MS line section (plane B-B'). The E-field distributes from MS coupled to MS and passes substrate toward ground plane. For E-field in CPS line (C-C') shown in Fig. 2(c), since the configuration in the area has no ground plane but have two strips over the substrate, then the E-field distributes across only these two strips.

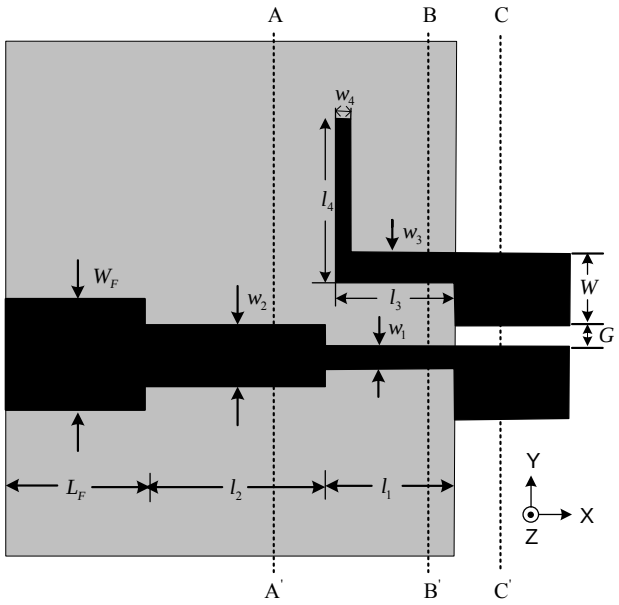

Figure 1. Configuration of the MS-to-CPS transition.

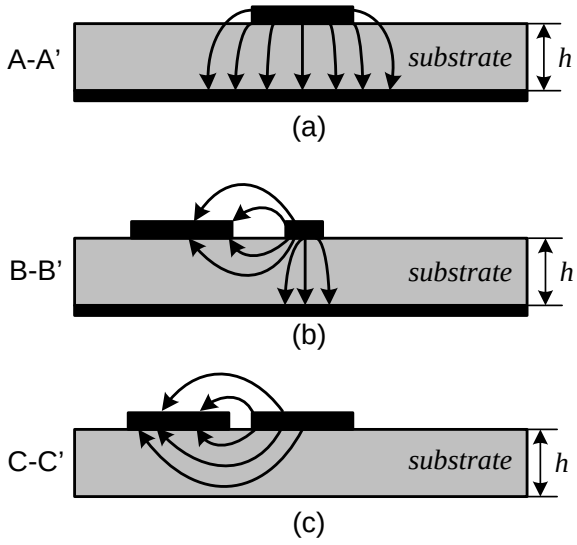

Figure 2. Cross-section view of the electric distributions: (a) microstrip line, (b) coupled microstrip line, and (c) CPS.

III. Results and Discussion

The proposed tri-band MS-CPS transition is designed for operating at 1800/1900 GSM band, WiMAX, and Wireless LAN. The bandwidth of each band was designed for supporting information bandwidth for each band application. In this paper, a low cost FR4 substrate is used to prove the concept. The parameters of substrate are as follows:- dielectric constant (ε_r) of 4.55 at 10MHz, thickness (h) of 1.6 mm, loss tangent of 0.02, and the conductor thickness (t) of 18 um. In the design stage, we assume that substrate is nondispersive media; that is its dielectric constant is independent with frequency.

In the initial design stage, the lengths of all transmission line sections were chosen at quarter-wavelength at the geometric mean frequency of upper- and lower-band center frequencies, i.e. 3.3 GHz. The width of each transmission line was initially selected at 115 ohm, which is equal to the differential impedance of the CPS line. With these initial design parameters, the circuit was simulated on Advanced Design System™ (ADS) platform and optimizer process was performed to reach the triple band operated. In our simulation setup, the number of cells per wavelength used in is equal to 25 at 7 GHz. This is the number compromising between speed and accuracy. The final design parameters associating with the circuit shown Fig.1 are listed in Table I. The lengths of 50 ohm line feeds at input and output ports are equal to quarter wavelength at 3.3 GHz. It should be noted that the digit number in millimeter dimension is one due to some limitations in our in-house fabrication process.

The MS-to-CPS transition with dimensions listed in Table I connected in back-to-back style was fabricated. Two SMA connectors from RADIAL were used for launching signal. Measurement was performed with an HP8710A network analyzer. The LRRM calibration method with a 3.5 mm calibration standard kit was done from 1 to 7 GHz. The measured data was collected via a GPIB port. The line feeds and connectors were de-embedded on ADS™ software.

TABLE I
Dimension of the Transition

Dimension	Unit(*mm*)
W	3
W1	1.8
W2	3
W3	1.4
W4	0.9
WF	3
L1	8.8
L2	11.2
L3	8.1
L4	11.3
LF	20
G	0.9

(a) top view

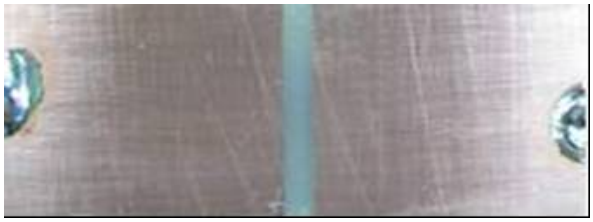

(b) bottom view

Figure 3. PCB photograph of the triple-band microstrip-to-coplanar stripline

The print circuit board (PCB) photograph of the experimental MS-CPS connected in back-back style fabricated on FR4 is shown in Fig. 3 (a) and (b). The circuit size is around 8.5×3 cm^2. Fig. 4 (a) and (b) show the measured and simulated results of the return loss of the transitions connected in back-to-back style. The designed transition operates at three simultaneous frequencies of 1.8, 3.5 and 6.5 GHz. The measured result at the third band somewhat differs from the electromagnetic (EM) simulated result. Apart from the result in the third band, the measured return loss performances of the transition are agreed very well with the EM simulated results. The distinct difference occurs at high frequency region is expected to produced mainly from dispersive in FR4 substrate.

It is well known that ε_r of the FR4 substrate decreases with an increase in frequency. The impact of ε_r decreasing in FR4 substrate to the return loss behavior at, especially, high frequency region is taken into account. Fig. 5 shows the return loss responses of the transition from 5 to 7 GHz for three different ε_r values. It is shown that the matching frequency is shifted to higher frequency when ε_r is smaller. The simulated results obtained in Fig. 5 supports that a frequency shift of matching at high-frequency band is possible came from a dispersive nature in FR4 substrate [14]. Another possible cause is the tolerance from our in-house fabrication process.

The comparison of EM simulated and measured insertion losses of the proposed transition are shown in Fig 6. Note that the effect of line feed and connector were excluded. The measured loss performance agrees with the simulated one very well. From measured results, the insertion losses at three desired bands are around 0.36, 0.78, and 0.82 dB.

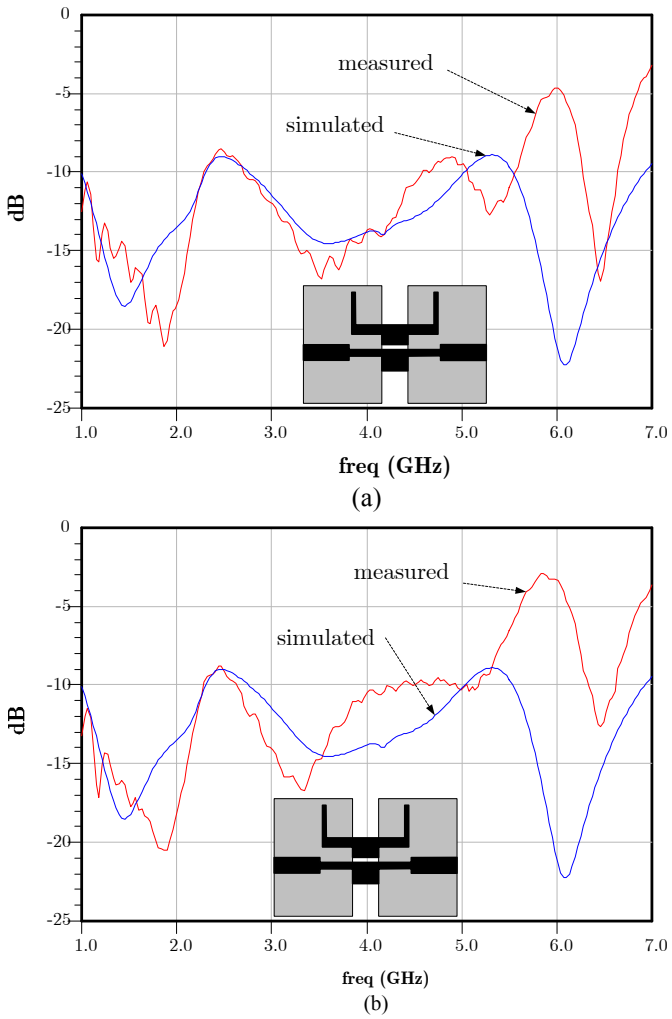

Figure 4. Simulated and measured results of the transition connected in back-to-back style (a) S11 and (b) S22

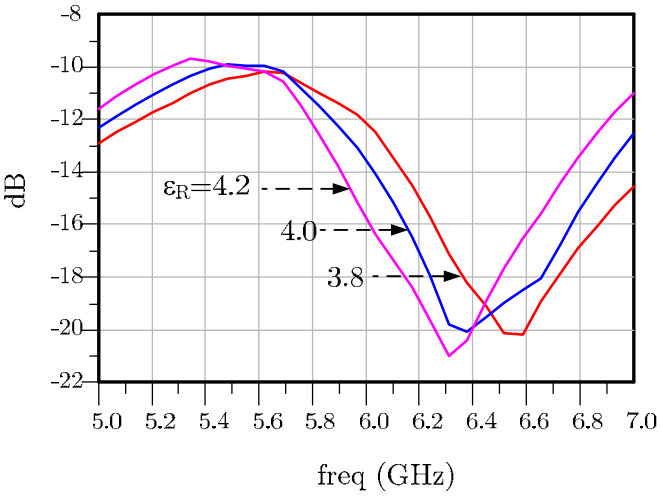

Figure 5. Impact of ε_r to return response of the transition

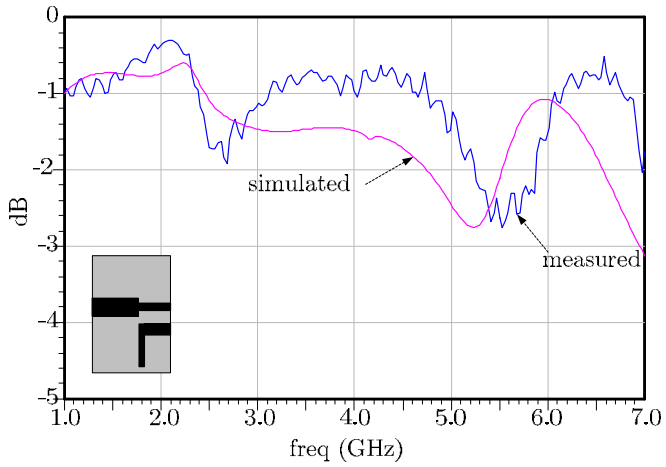

Figure 6. Comparison of measured and simulated insertion losses

IV. Conclusion

A simple triple-band microstrip-to-coplanar stripline for modern communication application has been presented. The circuit rather simple as it composes of a dual-section transmission line and a dual-section open stub. The proposed triple band transition was demonstrated with the design operated for GSM, WiMAX, and Wireless LAN applications. The experimental results confirm the technique proposed. The frequency shifting at high-frequency band is expected to come from dispersive nature of the substrate used combination with the limitation in fabrication process. In fact this can be simply corrected without any difficulty.

Acknowledgment

The authors would like to thank for Mr. Rattaya Suwanbunyaporn and Mr. Thatchawat Sukjiranon, the undergraduated students from Research Center of Electromagnetic-Wave Applications at Mahanakorn University of Technology, for print circuit board fabrication.

References

[1] G. Ghione., "CAD-Oriented analytical model for the losses of general asymmetric coplanar lines in hybrid and monolithic MICs," *IEEE Trans. Microwave Theory Tech*., vol. 41, no.7, pp. 1499 – 1510, Sep. 1993.

[2] R. Johnson, *Antenna Engineering Handbook,* McGraw-Hill Professional; 3rd edition, December 1, 1992)

[3] G. Chien, F. H. Weishi, Y. A. Tse, "A 2.4 GHz CMOS transceiver and baseband processor chipset for 802.11b wireless LAN application", *Solid-state Circuit Conference (ISSC),* 2003.

[4] S. A. Maas, *Microwave Mixer*, Artech House, 1999.

[5] N. Garg, L. B. Lok, I. D. Robertson, M. Chongcheawchamnan, and A. Worapishet, "1 to 20 GHz CMOS distributed mixer using asymmetric coplanar strip transmission lines", *Radio Frequency Integrated Circuit (RFIC) Symposium,* 2006.

[6] Y.H. Suh and K. Chang, "Coplanar stripline resonators modeling and applications to filter," *IEEE Trans. Microwave Theory Tech*., vol. 45, no.5, pp. 1289–1296, May. 2006.

[7] W. H. Tu and K. Chang., "Wide-band microstrip-to-coplanar stripline/slotline transition", *IEEE Trans. Microwave Theory Tech*., vol. 54, no.3, pp. 1084 – 1089, March 2006.

[8] Y.H. Suh and K. Chang, "A high-efficiency dual-frequency rectenna for 2.45-and 5.8-GHz wireless power transmission," *IEEE Trans. Microwave Theory Tech*., vol. 50, no.7,pp. 1784–1789, July 2002,

[9] T. Chiu and Y.S. Shen., "A broadband transition between microstrip and coplanar stripline," *IEEE Microwave and Wireless Components Lett.,* vol.13, pp. 66 – 68, Feb.2003.

[10] D. M. Pozar, *Microwave Engineering*, 2nd ed. New York: Wiley, 1998.

[11] K. C. Gupta, I. Bhal, and P. Bhartia, *Microstrip Lines and Slotline*, 2nd ed. Norwood, MA: Artech House, 1996.

[12] J. S. McLean and T. Itoh, "Analysis of a new configuration of coplanar stripline," *IEEE Trans. Microwave Theory Tech*., vol. 40, no.4, pp. 772–774 , May. 1992.

[13] R. N. Simons, N.I. Dib and L.P.B. Katehi, "Coplanar stripline to microstrip transition," *Electron. Lett*., vol. 40, no.4, pp. 772 – 774, April 1992.

[14] B. Brim, "EM simulator gets boost with 64-b code", *Microwave&RF*, 2002, p 122-124.

Simulations and Visualization of Electrostatic Field Strength Caused by Electrostatic Voltage Source in Homogeneous Material

Atthapol Wangsotorn[1)], Pharkphum Direkpoke[2)], Somchart Roongruangsorakarn[1)], and Kraisorn Chaisaowong[1),2),3)]
[1)] Department of Computer and Information Science, Faculty of Applied Science, King Mongkut's Institute of Technology North Bangkok
[2)] Department of Electrical Engineering, Faculty of Engineering, King Mongkut's Institute of Technology North Bangkok
[3)] Institute of Imaging & Computer Vision, RWTH Aachen University, Germany
atthaphol_w@hotmail.com, pharkphum_kmitnb@yahoo.co.th, scrkmitnb@yahoo.com, and kraisorn_kmitnb@yahoo.com

***Abstract*-During the usage of a mobile phone, human head is the most exposed organ to electromagnetic wave, which is propagated from the radio frequency device. Due to electromagnetic induction, electrical current occur in a proper conductive medium, such as our biological organ. Hence, we have to investigate their effect on the human health. In this work, we have used the computerized modeling and simulation technique to study the strength of electrostatic field caused by an electrostatic source in a homogeneous material volume. First, we have constructed a voxel-based homogenous model of human head consisting of electric elements, i.e. the resistances. Then, we have implemented the simulation of voltage distribution caused by virtual voltage source. Under the application of the numerical technique in combination with electromagnetic theory, we have then simulated and visualized the distribution of electrostatic field strength over the volume. The results conformed to the expected theoretical behavior, so that we can use our results for further step.**

I. INTRODUCTION

To-date, the telecommunication inventions enhance our life style, but they can also cause harmful effects to human health [1][2][3]. Mobile phone as such a device propagates electromagnetic wave into its surrounding, in which human head as the next human organ during its usage is included. Studies of effect of electromagnetic waves on human body can be done by a direct or an indirect way. Real experiments on animals for example are the direct method. But these in vivo experiments on animals raise the question of ethic and also need the high technology process [4]. An example of the indirect method is the experiment with a realistic phantom model, which is for example filled with liquid that are equivalent to physical and electrical properties of human. Even though, this method does not involve with the question of ethic, but it raises the question of cost. Moreover, it is a complicated and inflexible method. Another example of indirect method is the modeling of human head based on the computer database system. This model was constructed to contain the physiological, anatomical, and physical characteristics of human organs [5][6][7].

In order to calculate the effect of electromagnetic propagation on human head, such as increment of temperature in tissue or specific absorption rate of energy, we need to know the distribution of the electric field strength over the involved domain [8]. First, we have constructed a voxel-based homogenous model of human head. After that, we have evaluated our model by simulating the distribution of voltage over the volume model, and comparing with the real measurement on our real resistor lattice [9][10][11]. In this work, we were going further. We have used the results of the calculated voltage distribution to simulate the electric field intensity distribution over our three-dimensional model of human head. The results were also visualized.

II. MATERIALS AND METHODS

A. *The Finite difference to construct a three-dimensional model of human head*

Finite difference method is the method for finding of approximation answer on a homogeneous material problem. This method separates the volume domain space into equidistant sub-domain, i.e. a cubic (Fig.1a). A sub-domain is also known as a voxel, hence the finite difference is also called as a voxel-based model.

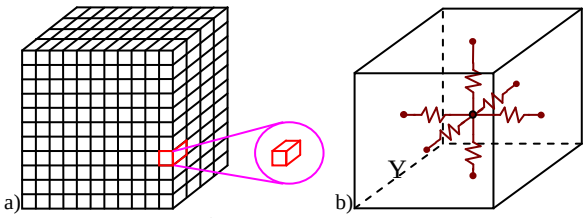

Figure 1. a) The separation of the volume domain into the small cubic, the so-called volume element (voxel). b) The structure of each voxel comprises of a reference node at the middle. Resistances modeling electrical properties spread out to the center of each rectangular side.

In order to model the electric properties of the sub-domain, each cubic has to be approached with an appropriate electrical element. Since the electrical current can be conducted in biological materials, the suitable electrical element of each voxel is resistance. Since, a cube has 6 joint sides, each voxel was assumed to contain 6 resistors, initiating at the center in the direction to each connection sides. The center point of each voxel is the referential node to the voltage of each single node (Fig.1b). Hence, several connected voxels result in a resistance lattice modeling human head (Fig. 2).

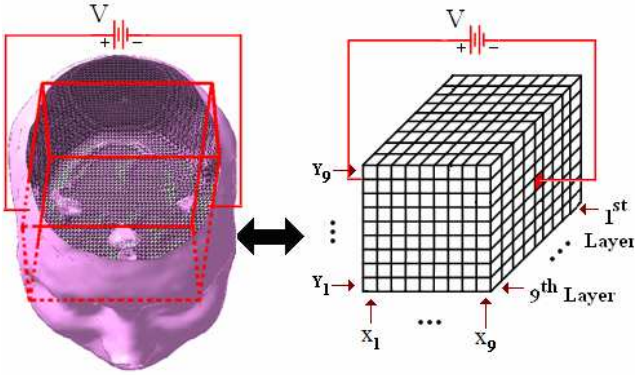

Figure 2. Human head was approached to a homogenous material of cubic form, and then modeled with the finite difference method, divided into 9x9x9 voxels. The injected voltage and grounding was then simulated at the showed position. (Note that each layer represents z coordinate) The voltage distribution was then simulated by the numerical calculation. (Fig from [12][13])

B. Electrical behavior of finite difference in 3D domain

Referring to the resistance structure within any voxel inside the volume model, any voxel *k* has six neighboring nodes i.e. *(k,1), (k,2), (k,3), (k,4), (k,5)* and *(k,6)* (Fig. 3). With the notation $V_{k,k}$ as the voltage value at the reference node k, $I_{k,i}$ the current flowing through between the reference node *k* and *i*, and the resistance value *R*, we finally formulized the sum of currents flowing through the node *k* in the three-dimensional circuit:

$$\sum_{i=1}^{6} I_{k,i} = \frac{3V_{k,k}}{R} - \sum_{i=1}^{6} \frac{V_{k,i}}{2R}, \qquad (1)$$

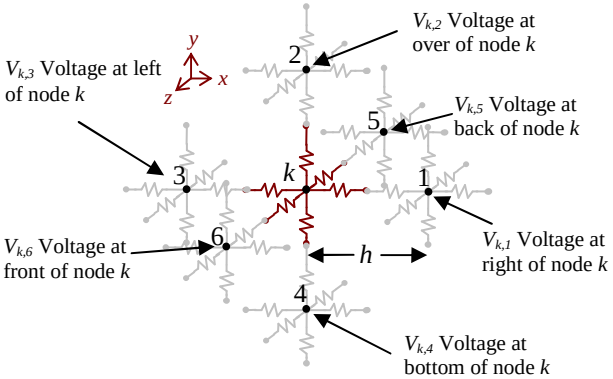

Figure 3. A voxel with its reference node *k* has normally 6 neighboring voxels. The distance between each node was denoted with *h*.

With the equation (1), the Kirchhoff's current law, and the fact that the sum of the inward and outward flowing currents at each node must be zero, we have concluded the linear equation:

$$0 = \frac{3V_{k,k}}{R} - \sum_{i=1}^{6} \frac{V_{k,i}}{2R}, \qquad (2)$$

with $k = 1, 2, 3, \ldots, (n_x \times n_y \times n_z)$,

where n_x, n_y, and n_z represents the number of element in *x*, *y*, and *z* axis.

To solve the linear equations system of three-dimensional domain, the equation can be written as matrix:

$$[I] = [A] \cdot [V], \qquad (3)$$

with [*I*]: the current vector of size $((n_x \times n_y \times n_z)+1)$,

[*A*]: the resistance matrix of size $((n_x \times n_y \times n_z)+1)^2$,

and [*V*]: the potential vector of size $((n_x \times n_y \times n_z)+1)$.

C. Numerical calculation of electrical field

In order to investigate electric field intensity, the gradient value of potential distribution was applied:

$$\vec{E} = -\vec{\nabla} V = -\left(\frac{\partial V}{\partial x}\hat{x} + \frac{\partial V}{\partial y}\hat{y} + \frac{\partial V}{\partial z}\hat{z}\right), \qquad (4)$$

with $\vec{E}$ represents the electric intensity field, and $\hat{x}, \hat{y}, \hat{z}$ unit vectors of *x*-, y- and z-axis.

For the numerical calculation of the gradient at any voxel, surrounded by neighboring voxels, we had to approximate the partial differentiation interval. For this purpose, we used the distance 2*h* between two neighboring reference nodes as the partial interval, so that the gradient value represents the center point of neighboring nodes:

$$\vec{\nabla} V_{k,k} \approx \frac{V_{k,1} - V_{k,3}}{2h}\hat{x} + \frac{V_{k,4} - V_{k,2}}{2h}\hat{y} + \frac{V_{k,5} - V_{k,6}}{2h}\hat{z}, \qquad (5)$$

with $V_{k,1}, V_{k,2}, V_{k,3}, V_{k,4}, V_{k,5}, V_{k,6}$ represents the voltages of neighboring nodes around node *k*.

Note that the estimation error of order $h^2, O(h^2)$ remains,

$$\vec{\nabla} V = \vec{\nabla} V_{k,k} + O(h^2), \qquad (6)$$

but we did not take it into account in this work.

For the boundary voxel, we applied the equation with the first forward divided difference, i.e. the distance between two adjacent nodes *h* as the partial interval, so that:

$$\frac{\partial V}{\partial x}\hat{x} = \frac{V_{k,1} - V_{k,k}}{h}\hat{x} \text{ or } \frac{\partial V}{\partial x}\hat{x} = \frac{V_{k,k} - V_{k,3}}{h}\hat{x}, \text{ for x-,}$$

$$\frac{\partial V}{\partial x}\hat{y} = \frac{V_{k,4} - V_{k,k}}{h}\hat{y} \text{ or } \frac{\partial V}{\partial x}\hat{x} = \frac{V_{k,k} - V_{k,2}}{h}\hat{x}, \text{ y-} \qquad (7)$$

$$\frac{\partial V}{\partial x}\hat{z} = \frac{V_{k,5} - V_{k,k}}{h}\hat{z} \text{ or } \frac{\partial V}{\partial x}\hat{z} = \frac{V_{k,k} - V_{k,6}}{h}\hat{z}, \text{ and z-axis.}$$

D. Numerical solving of linear equations system

Numerical solving of linear equations system can be done by several methods, e.g. the LU-decomposition method or the Gauss-Seidel method [14]. In this paper, we applied Gauss-Seidel method.

Since our matrix [*A*] has size of $((9x9x9)+1)^2$ or 532900 units, and if we focused on the characteristic of matrix [*A*], we found that a lot of positions has zero value (Fig. 4a). Only seven diagonals of the matrix show none zero value (Fig. 4b). Hence, in order to reduce the number of memory usage, we decided to collect the matrix elements lying on the principal diagonal as a single column matrix. As the next step, we have also defined other six single column matrixes to collect the other diagonal elements neighboring to the principal diagonal. Furthermore, we have defined another single column matrix to collect the information of voltage source position, which can be found in the first row of the matrix [*A*]. Finally, we have got a smaller matrix of size $[8((n_x \times n_y \times n_z)+1)]$ containing only

the diagonal elements of the matrix [*A*] and the voltage source position element (Fig. 4c). But since the information of the voltage position is a single value, we did not need to store other zero value for this special column, we have then got the new size of matrix [*A*] *NewS*:

$$NewS = 7((n_x \times n_y \times n_z)+1)+1, \quad (8)$$

so that, whereas the old size of matrix [*A*] = $((9x9x9)+1)^2$ = 532900 units. From equation (8), we have got the new size of matrix [*A*] = 7(730) + 1 = 5111 units.

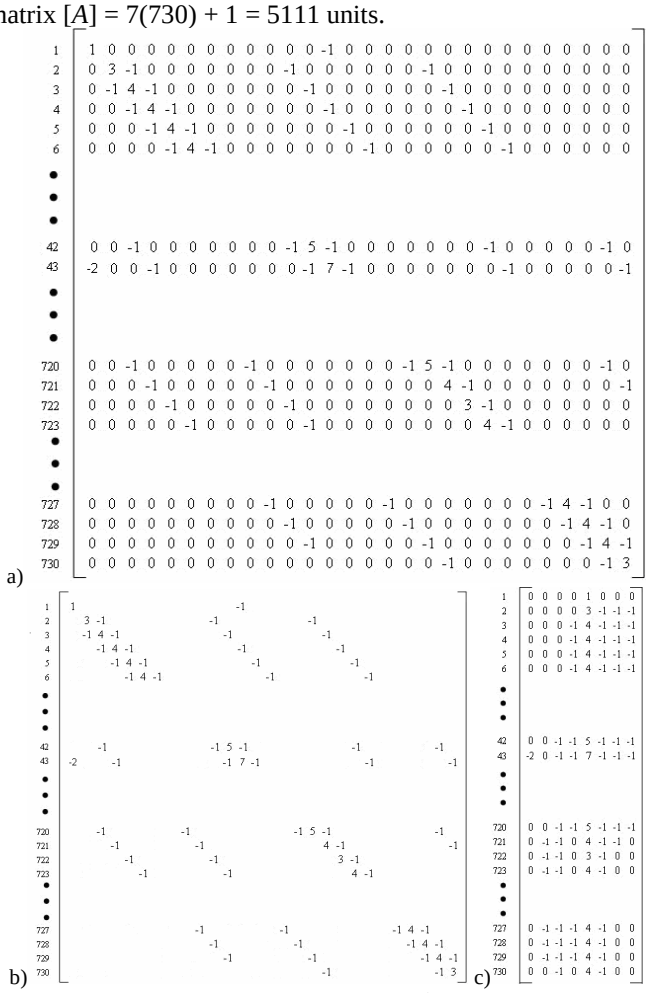

Figure 4. a) Since our volume model has the size of 9x9x9 units, the matrix [*A*] has the size of ((9x9x9)+1)2 = 532900 units, but containing about of zeros. b) Removing of zero elements show the value of matrix on seven diagonals. c) Collecting of specific values of diagonal elements together with the voltage source position value results into a new smaller matrix.

By collecting specific values of diagonal elements together with the voltage source position value into a new small matrix, the application of this *a priori* knowledge results in the total reduction of memory requirement over 99%.

III. RESULTS

A. *Simulation and visualization of potential distribution*

Assume that our model of human head is a cubic homogeneous volume domain. Then we separated it into connected small cubic sub-domains, by defining n_x = 9, n_y = 9, n_z = 9, whereas each voxel has six resistors and each resistor has a value of 5 *k*Ω. Each voxel has the dimension of 1 centimeter width. We then fed the electrostatic voltage source at point (1, 5, 5) and ground was connected at point (9, 5, 5) (Fig. 2). We then used the equations (1)-(2) to find the potential distribution over the whole volume model. The simulation results was satisfied both theoretical expectation and experimental verification (Fig. 5).

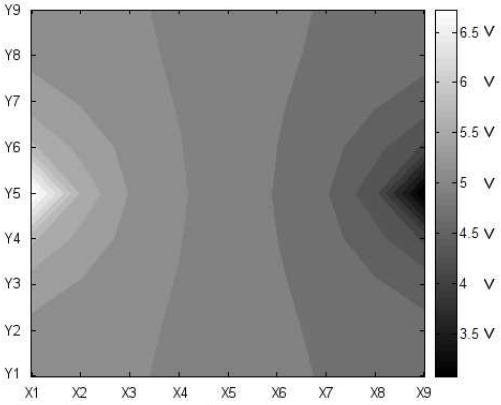

Figure 5. The equipotential line of potential distribution on 5th layer of z-axis. Color codes are shown in volt [V].

B. *Electrostatic field strength*

Finally, we have used the equations (3)-(7) under the application of the numerical method to find out the strength of electrostatic field caused by electrostatic voltage source on homogeneous material media, the depicted results are shown as table 1. We also have visualized the results, which were shown in figure 6 and 7.

Table 1. The values of the simulation of electrostatic field strength on the 5th layer (*xy* plane), which is the same layer of the voltage source, are shown a)b)c) by its vectorial components in *x*, *y*, and *z* direction, and d) its absolute value.

a) E_x on the 5th layer.

	x1	x2	x3	x4	x5	x6	x7	x8	x9
y9	3.0	3.9	5.4	6.1	6.3	6.1	5.5	4.1	3.1
y8	4.5	5.5	6.7	7.0	7.1	7.1	6.8	5.6	4.6
y7	10.1	10.3	10.0	9.1	8.7	9.1	10.1	10.5	10.2
y6	31.5	25.9	16.8	12.0	10.7	12.1	16.9	26.0	31.7
y5	129	83.1	27.5	14.6	12.0	14.7	27.6	83.4	129
y4	31.5	25.9	16.8	12.0	10.8	12.1	16.9	26.0	31.7
y3	10.1	10.4	10.1	9.1	8.8	9.2	10.2	10.5	10.3
y2	4.6	5.5	6.8	7.1	7.2	7.2	6.9	5.6	4.7
y1	3.0	4.0	5.5	6.2	6.4	6.2	5.6	4.1	3.1

b) E_y on the 5th layer.

	x1	x2	x3	x4	x5	x6	x7	x8	x9
y9	-5.0	-3.5	-2.0	-0.8	0.0	0.8	2.0	3.5	5.1
y8	-9.4	-5.9	-3.0	-1.2	0.0	1.2	3.0	5.9	9.5
y7	-25.4	-11.9	-5.0	-1.8	0.0	1.8	5.0	11.9	25.4
y6	-78.3	-19.1	-5.5	-1.6	0.0	1.7	5.5	19.1	78.5
y5	0.0	0.0	0.0	0.0	0.0	0.0	0.0	0.0	0.0
y4	78.2	19.0	5.5	1.6	0.0	-1.6	-5.5	-19.1	-78.4
y3	25.3	11.8	4.9	1.8	0.0	-1.8	-4.9	-11.8	-25.4
y2	9.3	5.8	3.0	1.2	0.0	-1.2	-3.0	-5.8	-9.4
y1	5.0	3.4	1.9	0.8	0.0	-0.8	-1.9	-3.4	-5.0

c) E_z on the 5th layer. Since on the voltage source was placed at this level, the differential value of voltage approaches to zero.

	x1	x2	x3	x4	x5	x6	x7	x8	x9
y9	0	0	0	0	0	0	0	0	0
y8	0	0	0	0	0	0	0	0	0
y7	0	0	0	0	0	0	0	0	0
y6	0	0	0	0	0	0	0	0	0
y5	0	0	0	0	0	0	0	0	0
y4	0	0	0	0	0	0	0	0	0
y3	0	0	0	0	0	0	0	0	0
y2	0	0	0	0	0	0	0	0	0
y1	0	0	0	0	0	0	0	0	0

d) Absolute value electrostatic field strength on the 5th layer.

	x1	x2	x3	x4	x5	x6	x7	x8	x9
y9	5.9	5.3	5.7	6.1	6.3	6.2	5.8	5.4	5.9
y8	10.4	8.0	7.3	7.1	7.1	7.2	7.5	8.1	10.5
y7	27.3	15.7	11.2	9.2	8.7	9.3	11.3	15.9	27.4
y6	84.4	32.1	17.6	12.1	10.7	12.2	17.8	32.3	84.7
y5	129	83.1	27.5	14.6	12.0	14.7	27.6	83.4	129
y4	84.3	32.1	17.6	12.2	10.8	12.2	17.8	32.3	84.6
y3	27.2	15.7	11.2	9.3	8.8	9.4	11.3	15.8	27.4
y2	10.4	8.0	7.4	7.2	7.2	7.3	7.5	8.1	10.5
y1	5.8	5.3	5.8	6.2	6.4	6.3	5.9	5.4	5.9

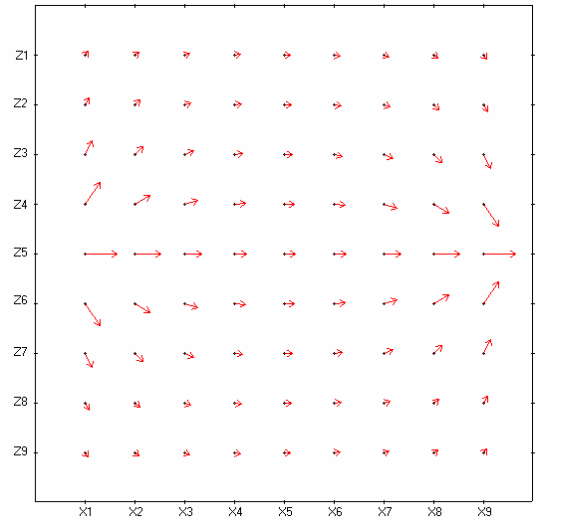

Figure 6. The arrows on the *zx* plane show both direction and size of electric field strength on the layer where $y = 4$.

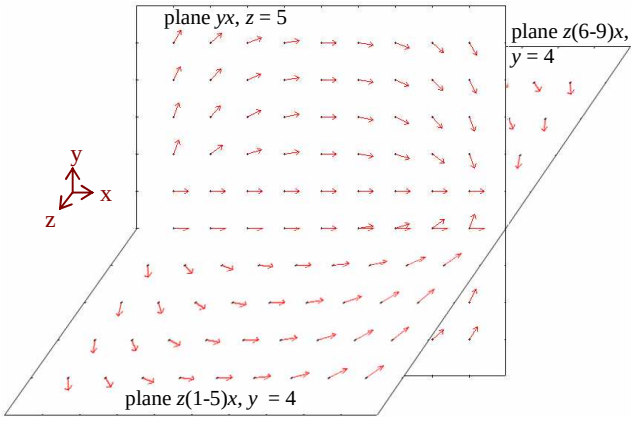

Figure 7. Cross view of two planes shows the direction of the simulated electric field distribution in the three dimensional domain. Cross line was at the level, where y = 4 and z = 5.

IV. Discussion

Even the fundamental theorem of this numerical implementation on a computerized voxel-based model was verified by the measurement of the voltage distribution on a real resistor lattice in an early study, further study will have to be launched in order to verify the current outcome. In order to study its effect on a closer-to-reality model of human domain, we shall use the voxel of size at least 1x1x1 mm^3. Furthermore, the integration of specific properties of human specimen e.g. density and conductivity will lead to the calculation of e.g. the specific absorption rate, so that the effect on human health can be quantified.

V. Conclusion

In this paper, we have simulated the electromagnetic propagation behavior of the electrostatic potential on a voxel-based biological domain model. By the mean of the computerized numerical method, we then calculated and visualized both the value and the direction of the electric field intensity distribution caused by electrostatic voltage source. The results fulfilled our expectation, hence can be used forwards further refinement and application.

Acknowledgment

This research was partly supported by a "Supporting Fund for General Researchers" 2005 of the Science and Technology Research Center, King Mongkut's Institute of Technology North Bangkok.

References

[1] Holmberg B., "Magnetic fields and cancer: animal and cellular evidence", Environ. Health Perspect., 103(S2):63-67, 1995.

[2] Körpinar M.A., Kalkan M.T., Morgul A., Birman H., Hacibekiroglu M., "The effect of electromagnetic field with a frequency of 144 MHz on the blood parameters and behavior of rats", in Proc. *2nd International Conference Biomedical Engineering Days*, pp82-84, Istanbul, 1998.

[3] Radzievsky, A.; Gordiienko, O.; Cowan, A.; Alekseev, S.I.; Ziskin, M.C.; "Millimeter-Wave-Induced Hypoalgesia in Mice: Dependence on Type of Experimental Pain", *IEEE Transaction on plasma science*, 32(4):1634-1643, 2004.

[4] Balzano, Q.; Chou, C.; Cicchetti, R.; Faraone, A.; Tay, R.Y.-S.; "An efficient RF exposure system with precise whole-body average SAR determination for in vivo animal studies at 900 MHz", *IEEE transactions on microwave theory and techniques*, 48(11):2040-2049, 2000.

[5] Kanda, M.Y.; Douglas, M.G.; Mendivil, E.D.; Ballen, M.; Gessner, A.V.; Chung-Kwang Chou, "Faster determination of mass-averaged SAR from 2-D area scans", *IEEE transactions on microwave theory and techniques*, 52(8):2013-2020, 2004.

[6] Ch. Sermpongpan and K. Chaisaowong. "Computer-based 3-Dimentionsal Modeling of Human Head: II. Assembly of physical parameters of anatomic specimen." In Proc. *The 28th Electrical Engineering Conference Thailand*, Phuket, pp1309-1312, 2005.

[7] R. Sutthaweekul, and K. Chaisaowong, "Computer-based 3-Dimentionsal Modeling of Human Head: I. Assembly of anatomic specimen." In Proc. *The 28th Electrical Engineering Conference Thailand*, Phuket, pp1305-1308, 2005.

[8] W. Wongrodjananan, and K. Chaisaowong. "Computer-Based Three-Dimensional Modeling of Human Head: Specific Absorption Rate of Energy in Human Tissue as the Quantitative Description of Electromagnetic Waves' Exposure." In Proc. *The 29th Electrical Engineering Conference Thailand*, Pattaya, pp577-580, 2006.

[9] K. Chaisaowong, and S. Roongruangsorakarn. "Computer-based 3-Dimensional Modeling of Electrical Potential Distribution: Surfacial Distribution in Homogenous Material.", in Proc. *The 2006 International Conference Electrical Engineering/Electronics, Computer, Telecommunications and Information Technology Association of Thailand*, Ubon Ratchathani, pp219-222, 2006.

[10] A. Wangsotorn, P. Direkpoke, S. Roongruangsorakarn, and K. Chaisaowong, "Simulations and Visualization of Voltage Distribution Caused by Electrostatic Voltage Source in Homogenous Material." In Proc. *The 3rd Joint Conference on Computer Science and Software Engineering*, Bangkok, pp1-7, 2006.

[11] P. Direkpoke, and K. Chaisaowong. "Two-Dimensional Simulations of Voltage Distribution Caused by Electrostatic Voltage Source in Homogenous Material: Theoretical and Experimental Validation." In Proc. *The 29th Electrical Engineering Conference Thailand*, Pattaya, pp589-592, 2006.

[12] K. Küper, "Scheringatlas Sectional Scan Anatomy v3.0", 1997.

[13] Glenn G. Chappell, "Advanced Computer Graphics: Marching cubes program", http://www.cs.uaf.edu/~cs481, 2004.

[14] Jeffreys, H. and Jeffreys, B. S, "Methods of Mathematical Physics, 3rd ed.", Cambridge, England: Cambridge University Press, pp305-306, 1988.

Performance study of CFP contention resolution algorithm for wireless communication system

Suvit Nakpeerayuth, Warakorn Srichavengsup and Lunchakorn Wuttisittikulkij
Electrical Engineering Department, Faculty of Engineering
Chulalongkorn University, Patumwan, Bangkok, Thailand
Tel: +66-2-218-6915, Fax: +66-2-218-6912
E-mail: wlunchak@chula.ac.th

***Abstract*- This paper presents a mathematical analysis of the system performance of three slot-based contention resolution algorithms for channel reservation namely *1/M, 1/n* and 1/(*M*-(*N*-*n*)) in terms of average number of successful users. The numerical results reveal that the system performance of the system depends on the number of users and the number of request slots per frame. Finally when comparing between all schemes it is found that the 1/*n* scheme is effective at systems with the number of slots greater than the number of users. However, when the number of users is large with respect to the number of slots per frame, the 1/(*M*-(*N*-*n*)) scheme offers relatively superior performance.**

I. INTRODUCTION

Medium access control (MAC) protocol is an essential part of a wireless access network which consists of a central base station and several wireless terminal users who communicate between them over a common wireless channel. Since in such a network users are usually geographically distributed over the service area and do not synchronize their transmission with each other, contention for uplink channel access becomes inevitable causing serious collision and usually resulting in low system throughput. Several MAC protocols have been developed to overcome this problem, for example ALOHA [1] and carrier-sense multiple access (CSMA) [2]. CSMA protocol and its variants such as CSMA/CD [3] and CSMA/CA [4] are widely used in most wired and wireless Local Area Networks.

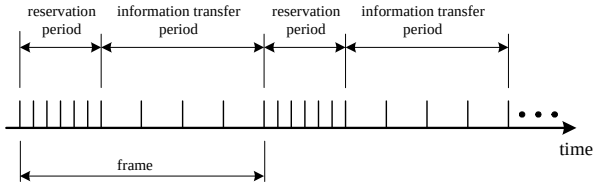

Figure 1. Frame structure.

In this paper we consider a specific class of MAC protocols as proposed in [5,6] which organizes the channel bandwidth into a frame structure that is composed of two alternate periods, namely reservation period and information transfer period, see an example of such a frame structure in Fig. 1. The reservation period consists of a fixed number of request slots, which are used by all users to reserve for channel bandwidth on a contention basis. A user who succeeds in the reservation process will be assigned the data slots by the base station in the information period for his information transmission. This class of MAC protocols has some interesting useful features, such as providing efficient bandwidth utilization, handling well with fluctuations in traffic demands, allowing Quality of Service guarantee, and offering fair channel access. One of the main problems in this protocol is how to resolve contention in reservation period in the most effective fashion. Reference [5] has addressed this problem comprehensively. Twelve contention resolution algorithms were introduced, mathematically analyzed and compared with existing classical protocols. Among these algorithms, the protocols called *Cascade Fixed Probability* (*CFP*) is considered one of the most appropriate for practical applications in high speed environment. However, the performance of the *CFP* has shown to be the least effective among all other schemes presented in reference [5], primarily due to its rigid contention resolution mechanism *i.e.* using a fixed value of access probability for all request slots. As a result, in this paper we attempt to improve the performance of the *CFP* by introducing a more flexible use of access probabilities; that is to use different values of probabilities for different slots as opposed to a single fixed value of access probability for all slots. It should be noted however that such a modification does not cause any fundamental changes to the *CFP*. In addition, the system performance can be improved as shown later in Section III. To achieve the desired performance improvement, one must be able to determine an appropriate set of probabilities. In this paper, we propose three different schemes namely 1/*M*, 1/*n* and 1/(*M*-(*N*-*n*)).

The paper is organized as follows. In the following section, we shall describe the details of *CFP* scheme. A complete system performance analysis of 1/*M*, 1/*n* and 1/(*M*-(*N*-*n*)) techniques is also mathematically derived in details. The numerical results and discussion are presented in Section III. Conclusions are given in Section IV.

II. REVIEW OF CFP SCHEME

In this section, we shall describe the detail of *CFP* scheme and its throughput performance derivation. The detailed description of the *CFP* algorithm and its throughput performance derivation can be found in [5] and [6]. However, the description of the *CFP* will be concisely presented again here to help understand the performance analysis.

In the *Cascade Fixed Prob* (*CFP*) scheme, each user will

attempt to make reservation on each request slot in sequence from the first slot to the last. In each slot, the user will decide whether it will access the present slot with certain probability of p and the value of this probability is the same for all users and fixed throughout all request slots.

Let $S_{CFP}[m,n]$ be the average number of successful users for the system with *m* users and *n* the number of request slots and $b[m,i,p]$ be the binomial probability that *i* out of *m* users access a particular request slot with permission probability *p*, which is expressed as:

$$b[m,i,p]=\binom{m}{i}p^i(1-p)^{m-i}\text{, where }\binom{m}{i}=\frac{m!}{i!(m-i)!}$$

In each request slot, only a single user can succeed in reservation, which will occur only when no other users access the slot. A more detailed analysis of $S_{CFP}[m,n]$ is formulated in a recursive form as follows:

$$\begin{aligned}S_{CFP}[m,n] &= b[m,0,p]S[m,n-1]\\ &+b[m,1,p](1+S[m-1,n-1])\\ &+\sum_{i=2}^{m}b[m,i,p]S[m-i,n-1]\\ &=b[m,1,p]+\sum_{i=0}^{m}b[m,i,p]S[m-i,n-1]\end{aligned}\quad(1)$$

where $m\ge 0, n\ge 0.$

The boundary conditions of (1) are $S_{CFP}[a,0]=S_{CFP}[0,b]=0$ where $a=0,1,2,.....,m-1,m$ and $b=0,1,2,.....,n-1,n$.

We can then find an appropriate permission probability $p_{CFP}[m,n]$ of each frame by differentiating (1) with respect to *p*, setting it to 0, *i.e.* $\frac{\partial}{\partial p}S_{CFP}[m,n]=0$ and determining *p* that gives the maximum average number of successful users $S_{CFP}[m,n]$.

III. Performance Analysis of Proposed Schemes

A. Description of 1/*M* scheme

In the *CFP* scheme, it is known that the system performance measured in terms of success probability depends on the value of *p* being used. Previous studies also show that an appropriate value of *p* exists and can be formulated as a function of the number of active users at the start of each frame (*M*) and the number of slots in each frame (*N*) as summarized in Section II. However, the computation time in determining the optimal $p_{CFP}[M,N]$ for each system configuration can be excessive, especially when the number of users and the number of slots are large. Therefore, it is felt useful to find a simple rule of thumb in determining appropriate value of *p* without having to perform excessive search for the optimum. For this reason, we propose a simple scheme in obtaining the effective value of *p* for the *CFP*. With this new scheme *p* is set to 1/*M* and hence this scheme is referred to as 1/*M*.

Let $S_{1/M}[m,n]$ be the average number of successful users for the system with *m* remaining users and *n* remaining request slots. $S_{1/M}[m,n]$ is computed as a recursive formula.

$$\begin{aligned}S_{1/M}[m,n] &= b[m,0,1/M]S_{1/M}[m,n-1]\\ &+b[m,1,1/M](1+S_{1/M}[m-1,n-1])\\ &+\sum_{i=2}^{m}b[m,i,1/M]S_{1/M}[m-i,n-1]\\ &=b[m,1,1/M]+\sum_{i=0}^{m}b[m,i,1/M]S_{1/M}[m-i,n-1]\end{aligned}\quad(2)$$

where $m\ge 0, n\ge 0.$

The boundary conditions of (2) are $S_{1/M}[a,0]=S_{1/M}[0,b]=0$ where $a=0,1,2,.....,m-1,m$ and $b=0,1,2,.....,n-1,n$.

B. Description of 1/*n* scheme

For the 1/*M* scheme, it is essentially the *CFP* scheme with *p* set to 1/*M*. Both CFP and its variant 1/*M* schemes apply a fixed value of access probability for all request slots. Study in [5] has shown that the early slots of *CFP* scheme usually support greater reservation demands than later slots, as the number of active users is generally higher at early slots than later slots. Therefore, using the same value of probability for early and later slots may not be effective in this situation. In the early slots, the value of probability should be small in order to avoid collisions. On the contrary, the users should attempt access the later slots at greater probability to reduce the number of idle slots and thus improving the overall system performance.

For these reasons, we propose the use of permission probability equal to 1/*n* (*n* = the number of remaining request slots in the system). In this scheme, the value of probability in the later slots is greater than the value of probability in the early slots. On average, it is expected that all request slots can be uniformly loaded and thus better utilized. The model for throughput analysis of this scheme is similar to that of the *CFP* scheme, though details may differ.

Let $S_{1/n}[m,n]$ be the average number of successful users for the system with *m* remaining users and *n* remaining request slots. In each request slot, only a single user can succeed in reservation, which will occur only when no other users access the slot. A more detailed analysis of $S_{1/n}[m,n]$ is formulated in a recursive form as follows:

$$\begin{aligned}S_{1/n}[m,n] &= b[m,0,1/n]S_{1/n}[m,n-1]\\ &+b[m,1,1/n](1+S_{1/n}[m-1,n-1])\\ &+\sum_{i=2}^{m}b[m,i,1/n]S_{1/n}[m-i,n-1]\\ &=b[m,1,1/n]+\sum_{i=0}^{m}b[m,i,p]S_{1/n}[m-i,n-1]\end{aligned}\quad(3)$$

where $m\ge 0, n\ge 0.$

The boundary conditions of (3) are $S_{1/n}[a,0]=S_{1/n}[0,b]=0$ where $a=0,1,2,.....,m-1,m$ and $b=0,1,2,.....,n-1,n$.

C. Description of $1/(M-(N-n))$ scheme

The problem of 1/*n* scheme is that it does not take the number of users into account. Accordingly, its performance can be significantly deteriorated when the number of users is relatively much higher than the number of slots available. This

is because all users will definitely place a reservation in one of the slots, collision will most likely be hard to avoid. To eliminate this problem, it is essential to find some means to limit the user attempts in accordance with the number of users and available slots. In this study, we propose a scheme which uses the permission probability for each slot equal to $1/(M-(N-n))$.

Let $S_{1/(M-(N-n))}[m,n]$ be the average number of successful users for the system with m remaining users and n remaining request slots. The average number of successful users of the $1/(M-(N-n))$ scheme can be expressed as follows:

$$\begin{aligned} S_{1/(M-(N-n))}[m,n] &= b[m,0,1/(M-(N-n))]S_{1/(M-(N-n))}[m,n-1] \\ &+b[m,1,1/(M-(N-n))](1+S_{1/(M-(N-n))}[m-1,n-1]) \\ &+\sum_{i=2}^{m} b[m,i,1/(M-(N-n))]S_{1/(M-(N-n))}[m-i,n-1] \qquad (4) \\ &= b[m,1,1/(M-(N-n))]+\sum_{i=0}^{m} b[m,i,1/(M-(N-n))]S_{1/(M-(N-n))}[m-i,n-1] \end{aligned}$$

where $m \geq 0, n \geq 0$.

The boundary conditions of (4) are $S_{1/(M-(N-n))}[a,0] = S_{1/(M-(N-n))}[0,b] = 0$ where $a = 0,1,2,....,m-1,m$ and $b = 0,1,2,....,n-1,n$.

IV. Numerical Results and Discussions

In this section, a numerical study is provided comparing the performance of the *CFP*, 1/*M*, 1/*n* and 1/(*M*-(*N*-*n*)) schemes. All results shown here are obtained from the mathematical formulations described in the previous sections. Computer simulations are also conducted to verify the accuracy of mathematical analysis.

Figures 2 and 3 illustrate the performance comparison of the *CFP*, 1/*M*, 1/*n* and 1/(*M*-(*N*-*n*)) schemes when the number of request slots equal to 8 and 32 respectively. The numerical result of *CFP* scheme is obtained by using appropriate permission probability $p_{CFP}[m,n]$. As we can see, the number of successful users of each scheme clearly increases with the number of slots in the area where the number of users is less than the number of slots available. However, when the number of users becomes greater than the number of slots, the *CFP*, 1/*M* and 1/(*M*-(*N*-*n*)) schemes still perform well whereas the number of successful users of the 1/*n* declines continuously. This is because 1/*n* scheme does not take the number of users into account. Therefore, its performance will clearly be degraded when the number of users is relatively much higher than the number of slots available whereas the *CFP*, 1/*M* and 1/(*M*-(*N*-*n*)) scheme can lower the risk of collision by reducing the permission probability and thus able to maintain efficient system performance. Note that the results of 1/(*M*-(*N*-*n*)) in the case of the number users more than the number of slots are not given here. This is because the probability of 1/(*M*-(*N*-*n*)) scheme will be negative in this situation.

Moreover, it is very interesting to see that the average number of successful users of 1/*M* is marginal less than the average number of successful users of *CFP* scheme. For this reason, if there are too many users and slots in the system the use of permission probability equal to 1/*M* helps reduce time to compute the appropriate permission probability $p_{CFP}[m,n]$ in the *CFP* scheme while maintains the throughput performance as high as the *CFP* scheme.

When comparing all the proposed schemes, it can be noticed that that 1/*n* scheme provide better performance than other schemes at systems with light to medium loads. In case of heavy load condition, the 1/(*M*-(*N*-*n*)) scheme offers relatively superior performance.

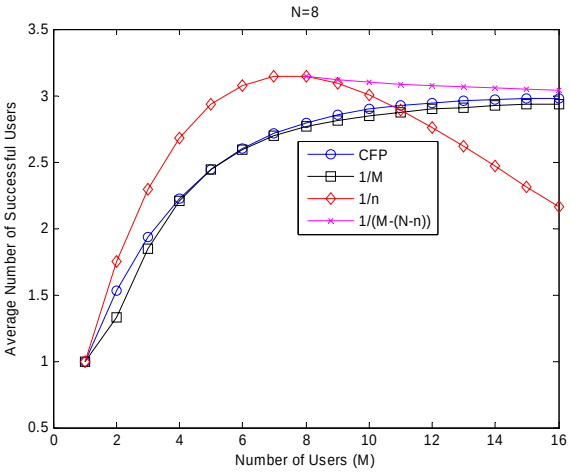

Figure 2. The average number of successful users vs the number of users (*M*) with the number of request slots (*N*) fixed at 8 for *CFP*, 1/*M* and 1/*n* and 1/(*M*-(*N*-*n*)) schemes.

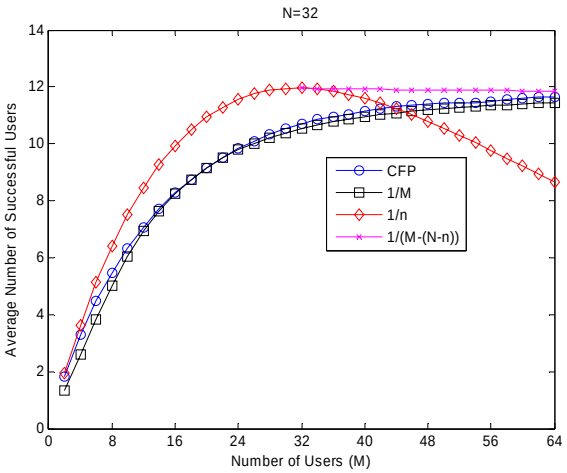

Figure 3. The average number of successful users vs the number of users (*M*) with the number of request slots (*N*) fixed at 32 for *CFP*, 1/*M* and 1/*n* and 1/(*M*-(*N*-*n*)) schemes.

ACKNOWLEDGMENT

This work was supported by the Cooperation Project between Department of Electrical Engineering, Chulalongkorn University, Thailand and Private Sector for Research and Development are acknowledged.

V. CONCLUSION

In this paper, we have introduced three new channel reservation schemes for media access protocols in high bit-rate wireless systems. The mathematical analysis derived in this paper enables us to numerically evaluate the performance of all proposed schemes. It is found that the performance of *CFP* scheme can be improved by assigning different access probabilities to different request slots. At low to medium loads, i.e. the number of slots is larger than the number of users, the $1/n$ scheme can provide substantial gain in comparison to that of original CFP scheme where the access probability is fixed and of the same value for all slots. At heavy load conditions, i.e. the number of slots is smaller than the number of users, the $1/(M-(N-n))$ scheme offers superior performance to the *CFP* counterpart. Based on this study, we find that the appropriate set of probabilities for each slot can be expressed as $1/[\max(M,N)-(N-n)]$, which is a combined formulation of the 1/n and $1/(M-(N-n))$ schemes. In addition to this, we have suggested the $1/M$ scheme which is a simple but effective scheme in determining appropriate probability for the *CFP* with the same access probability for all slots.

REFERENCES

[1] H.Peyravi, "Medium access control protocols performance in satellite communications", *IEEE Communication Magazine*, vol.373, pp. 62-71.

[2] A.S. Tanenbaum, *Computer Networks*, 3rd Edition, Prentice-Hall International, Inc., 1996.

[3] D. Bertsekas and R. Gallager, *Data Network*, 2nd Edition, Prentice Hall.

[4] Karol, M.J., "Distributed-Queueing Request Update Multiple Access (DQRUMA) for Wireless Packet (ATM) Networks", *IEEE Proc. of ICC*, Seattle, vol. 2, pp. 1224-1231, 1995.

[5] N. Sivamok, L. Wuttisittikulkij, and A. Charoenpanitkit, "New Channel Reservation Techniques for Media Access Control Protocol in High Bit-Rate Wireless Communication Systems", *IEEE Proc. of Globecom*, vol. 6, pp. 3558-3562, 2001.

[6] W. Srichavengsup, N. Sivamok, A. Suriya and L. Wuttisittikulkij, "A Design and Performance Evaluation of a Class of Channel Reservation Techniques for Medium Access Control Protocols in High Bit-Rate Wireless Communications", *IEICE Trans. Fund.*, vol. E88-A, July. 2005.

Computer-based 2D Simulations of SAR in Inhomogeneous Biological Domain Model Caused by Isotropic Antenna at 900 MHz and 1800 MHz

Pharkphum Direkpoke[1)], Atthapol Wangsotorn[2)], and Kraisorn Chaisaowong[1),2),3)]
[1)] Department of Electrical Engineering, Faculty of Engineering, King Mongkut's Institute of Technology North Bangkok
[2)] Department of Computer and Information Science, Faculty of Applied Science, King Mongkut's Institute of Technology North Bangkok
[3)] Institute of Imaging & Computer Vision, RWTH Aachen University, Germany
pharkphum_kmitnb@yahoo.co.th, atthapol_w@hotmail.com, and kraisorn_kmitnb@yahoo.com

***Abstract*-The modern wireless communication comforts human life, but mobile phones, for example, propagate the electromagnetic waves into environment, in which our head is also included. Therefore, we have to investigate their effect on the human health. For this purpose, a technique based on the application of computed simulation in combination with anatomic and physical model of human head was used. In this paper, we have simulated the two-dimensional distribution of SAR caused by isotropic antenna in inhomogeneous media, which consists of two layers of different specimens. We constructed a model containing an outer layer and an inner area which represents skull and brain respectively. Since the calculation of SAR depends on the electric field distribution, we assumed that the magnetic flux density would not depend on the varying of time. Our work focused on two frequencies, 900 MHz and 1800 MHz. The simulation was applied on a layered voxel-based cubic model. Electric field was fed by an isotropic antenna model which has the initial value of 20V/m. We found out that the maximal SAR in brain model was 0.1235 W/kg for 900 MHz and 0.1561 W/kg for 1800 MHz. Absorption effect of a low frequency radiation spreads over larger area than of that higher frequency.**

I. INTRODUCTION

To-date, the communication inventions enhance our life style, among them the wireless radio-frequency equipments are ubiquitous. Mobile phone as such a device propagates electromagnetic wave into its surrounding, in which human head as the next human organ during its usage is included. Although mobile phones provide convenient life, certain effects on human health remain unknown. Thus, we require methods to investigate their direct and indirect impact on the human health. Studies of effect of electromagnetic waves on human health can be done on several ways e.g. *in vivo* experiment on an animal [1][2], real measurement on a phantom model [3], or using computer-based numerical method with an application of a computer-based model [4]. Since the *in vivo* experiments on animals raise the question of ethic, real measurements on phantom models raise also a question of cost; numerical simulation with computer-based model remains an alternative method, which we have chosen to study the effect of electromagnetic wave on the human head. The so-called computer-based model of human head uses digital database comprising of the anatomic, physiologic, and physical characteristics of the human specimens. Application of various numerical methods can solve the problems of effect of electromagnetic wave on human health, since computerized numerical method provides a reasonable and flexible solution.

In order to quantify the effect of electromagnetic waves on human tissue, measurable quantity such as SAR (specific absorption rate) and temperature raise are to be investigated. Since the quantification measurement of temperature raise is extremely difficult to perform due to the very small temperature increments, which were reported to be less than 0.01°C [5], we have focused on the determination of SAR, which varies with the electric field intensity.

In this paper, we have studied electromagnetic theory of time varying field to simulate the electric field intensity on a planar domain of human head model. Then, we used the electric field intensity to calculate the specific absorption rate.

II. MATERIALS AND METHODS

A. The Finite Difference

Finite difference method is the method for finding of approximation answer on a homogeneous material problem. This method separates the domain of field space into equidistant sub-domain, i.e. a cubic (fig.1). A sub-domain is also known as a volume element (voxel), hence the finite difference is also called as a voxel-based model [6][7].

B. Construction of a Three-Dimensional Model

Application of a spherical structure, which comprises of different specimens on different layers, provides a simple layered head model (fig. 2a) [8]. The combination between the finite difference with the spherical layered model results in the multi-layers voxel-based model. In this paper, we have studied a two layers model consisting of an outer layer and an inner layer, which represents skull and brain respectively (fig. 2b).

C. Construction of a Two-Dimensional Model

Before we will apply the 3-dimensional model for our simulation, we have constructed a planar model to study the planar distribution of SAR. In the consideration of a cross section of figure 1 and 2b, we have got the square field domain. The outer boundary voxels represent skull. The voxels inside, we assumed them as brain (fig. 3).

D. Specific Absorption Rate (SAR)

The distribution of SAR in human head model was applied in this work to study effect of electromagnetic wave propagation through the human head. The application of this technique allows us to calculate the rate of energy absorption remaining in exposed human head specimen. This quantitative description has the unit of absorbed power per mass as W/kg or mW/g.

We can calculate the SAR for each specimen using the equation below [9]:

$$SAR = \frac{\sigma |E|^2}{2\rho}, \quad (1)$$

where E : Electric field intensity [V/m],
σ : Conductivity [S/m], and
ρ : Mass density of tissue [kg/m^3].

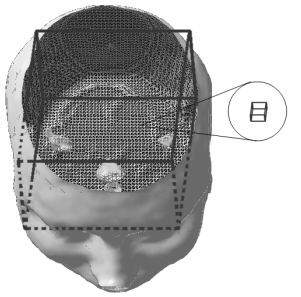

Figure 1 Separation of the volume space, which was used as the model of human head, into the small cubes, the so–called voxel (fig. from [7]).

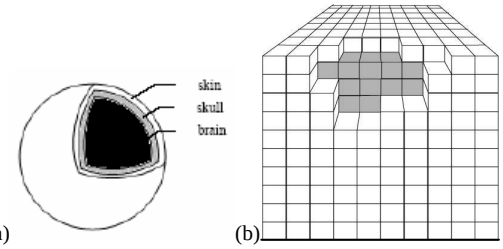

(a) (b)

Figure 2 (a) An example of a layered spherical head model with three layers consisting of skin, skull and brain. (b) The applied voxel-based model of human head consists of two layers. The white voxel-layer represents skull, and the gray brain.

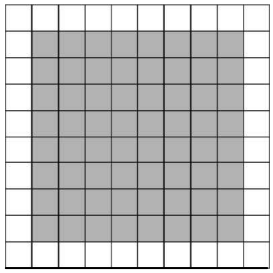

Figure 3 The planar field domain represents a voxel-based model of human head consisting of the boundary skull voxels (white) and the brain voxels (gray) therein.

E. Electric Field Intensity on a Plane

In order to calculate the SAR distribution on planar model, we have to know electric field intensity exposing to the planar domain [9]. In order to calculate SAR, we need to excerpt the electric field information out of the whole electromagnetic field. This allowed us to neglect the magnetic field, and hence also to assume that the magnetic field is not the time-varying field. We know that electric field caused by isotropic antenna as a point source propagating in any direction on plane. In general, the propagation of electric field can be expressed as [10]:

$$E = E_0 e^{-j\vec{k}\bullet\vec{r}} e^{j\omega t}, \quad (2)$$

where E : the distribution of electric field intensity,
E_0 : electric field intensity at ($\vec{r}$ = 0, t = 0),
$\vec{k}$: the propagation constant vector,
$\vec{r}$: the position vector,
t : time, and
ω : the radian frequency.

In our two-dimensional model of fig. 3, we can express $\vec{k}$ in terms of its x and y components:

$$\vec{k} \equiv k_x \hat{x} + k_y \hat{y} \quad , \quad (3)$$

where k_x and k_y represents k in x and y direction,
$\hat{x}$ and $\hat{y}$ are the unit vectors in x and y direction.

The position vector $\vec{r}$ can be similarly expressed as:

$$\vec{r} \equiv x\hat{x} + y\hat{y}, \quad (4)$$

so that $$E = E_0 e^{-jk(x+y)} e^{j\omega t}, \quad (5)$$

with $k_x = k_y = k$ in case of homogeneous media, and

x and y variable represents the distance from E_0 to E on x-axis and y-axis respectively.

The imaginary propagation constant can be expressed as explicit complex value [10]:

$$jk = \alpha + j\beta \quad \text{with } \alpha, \beta \in \Re, \quad (6)$$

where α : the attenuation coefficient, and
β : the phase constant.

Now we have got:

$$E = E_0 e^{-\alpha(x+y)} e^{-j\beta(x+y)} e^{j\omega t} \quad (7)$$

$$E = E_0 e^{-\alpha(x+y)} e^{j(\omega t + \beta(x+y))} \quad (8)$$

According to equation (1), SAR depends on the absolute value of E, so that:

$$|E| = E_0 e^{-\alpha(x+y)}. \quad (9)$$

The attenuation constant coefficient can be approximated in the dependency of frequency f [11]:

$$\alpha \approx \frac{\sigma(f)}{2}\sqrt{\frac{\mu(f)}{\varepsilon(f)}}, \quad (10)$$

where $\mu(f)$ is permeability of media, and
$\varepsilon(f)$ is permittivity of media.

F. Physical Parameters

One more important argument of a closer-to-reality human head model is the integrated physical parameter of human specimen. For all tissues, the relative magnetic permeability (μ_r) was set to 1 H/m [12]. The relative electric permittivity and the conductivity whose value depends on frequency are shown in table 1 [13]. In this work we have simulated two frequencies i.e. 900 MHz and 1800 MHz. In addition, the mass density of each tissue for calculating the SAR [13] is shown in table 2.

TABLE 1 VALUE OF THE RELATIVE PERMITTIVITY AND THE CONDUCTIVITY OF TISSUES MEASURED AT 900 MHZ AND 1800 MHZ (DATA FROM [13]).

Tissues	$\varepsilon_r(f)[F/m]$		$\sigma(f)[S/m]$	
	900MHz	1800MHz	900MHz	1800MHz
Skull	15.33	16.50	0.23	0.43
Brain	46.24	41.73	0.91	1.53

TABLE 2 THE MASS DENSITY OF EACH TISSUE (DATA FROM [13]).

Tissue	$\rho\left[kg/m^3\right]$
Skull	1772
Brain	1024

G. Discrete Technique of Electric Field Intensity in Each Element

In order to simulate the distribution of electric field intensity on the voxel-based planar domain of our head model, a technique was investigated to calculate under this condition. After separation of the exponential components of the equation (9) by the axial arguments, its calculation can be carried out on two steps:

$$|E| = E_0 e^{-\alpha x} e^{-\alpha y} \tag{11}$$

In order to calculate electric field intensity $E_{i,j}$ caused by any initial E_0 (fig. 4), we can first calculate $E_{i-1,j}$ which is also caused by E_0, on one hand. On the other hand, $E_{i,j}$ can be in analogue calculated also by using $E_{i,j-1}$. For a homogeneous media, both calculation sequences resulted in the same value of $E_{i,j}$.

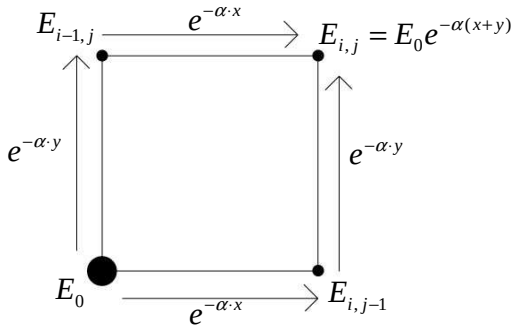

Figure 4 A point source (E_0) placed at the edge of a voxel. Arrows show the direction of calculation from point to point. $E_{i,j}$ is the electric field intensity caused by E_0 on the opposite position.

In case of inhomogeneous media however, electrical field has to cross continuous boundary, hence we used – as initial simplification – the approximated average value of both sequences to determine the value of the opposite position [12]:

$$E_{i,k} \approx \frac{E_{i,k|i-1,k} + E_{i,k|i,k-1}}{2} \tag{12}$$

where the index *i*, *k* represent x-axis position and y-axis position respectively,

$E_{ik|i-1,k}$ is the electric field intensity at position (*i*,*k*) caused by electric field intensity at position (*i-1*,*k*), and

$E_{ik|i,k-1}$ is the electric field intensity at position (*i*,*k*) caused by electric field intensity at position (*i*,*k-1*).

III. RESULTS

A. Electric Field Intensity Distribution

We have modeled an isotropic antenna, which propagates electric field intensity of 20V/m, and was placed at the center of the upper boundary of the planar model of 30x30 voxels by size (fig. 5). Each voxel is 5 mm width. The simulated results for the physical characteristics of specimen at 900 MHz and 1800 MHz were visualized and shown in figure 6, which shows that low frequency radiation has spread over larger area than higher frequency. Distribution of electric strength seems not to be different in term of both different frequency and different specimens.

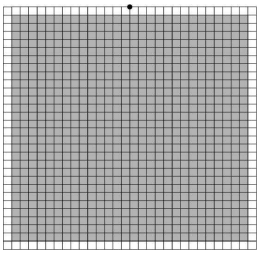

Figure 5 The two layers model consisting of skull and brain size of 30x30 voxels. The black point on the upper bound represents the position of the isotropic antenna.

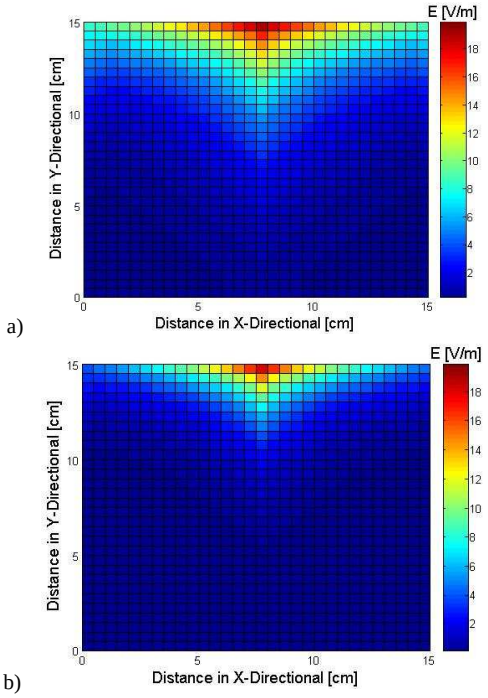

Figure 6 Visualization of electric field intensity distribution caused by a) 900 MHz and b) 1800 MHz isotropic antenna.

B. SAR Distribution

Finally, we calculated SAR distribution by using the equation (1). The visualization of SAR distribution caused by 900 MHz and 1800 MHz isotropic antenna was shown in figure 7. The maximum values of SAR in brain model are 0.1235 W/kg and 0.1561 W/kg in case of 900 MHz and 1800 MHz respectively. Moreover, both results show that there are very small values of SAR in skull layer; hence less amount of

energy was absorbed per mass unit in skull than in brain. Also here, we can see that lower frequency wave caused the larger area of absorption than the higher frequency field.

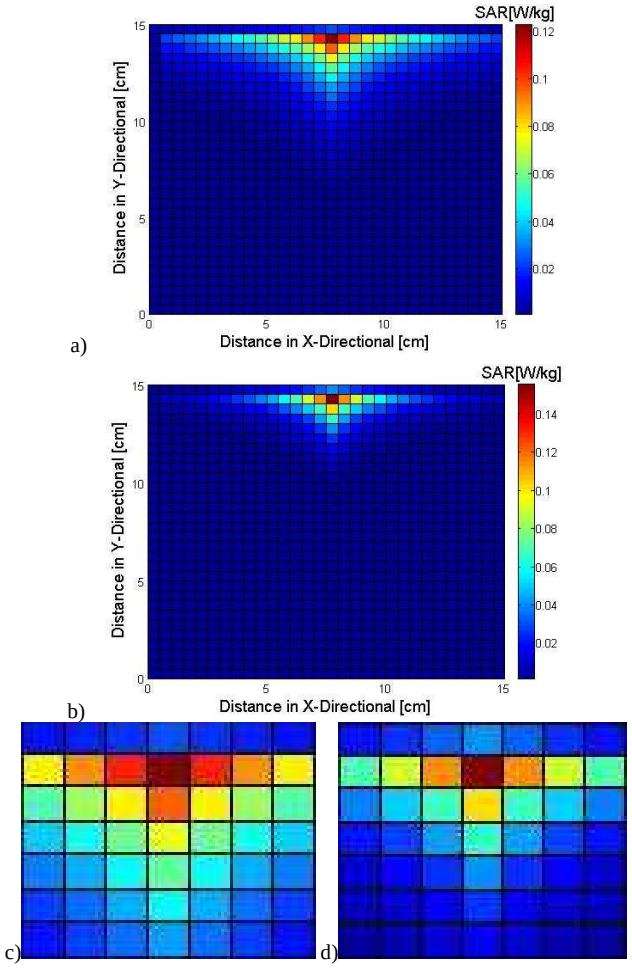

Figure 7 The visualization of SAR distribution caused by a) 900 and b) 1800 MHz isotropic antenna. c) and d) Magnifications of 7a) and 7b) respectively depicts the contrast of energy absorbed both in different specimens and different frequency causality.

IV. Summary

This work applied the finite difference method to construct the layered planar model of human head, consisting of skull and brain layers. Simulated electromagnetic wave propagation from isotropic antenna caused by higher frequency leads to a smaller absorption area, while lower frequency spreads over a larger absorption area. However, the largest value of SAR appears in the brain layer, which was exposed to higher frequency, thus in turn, SAR declines rather quickly than by lower frequency wave.

In consideration to the real biological domain, we concluded from our simulation results on the simplified model that first, the higher the frequency propagates from a device, the more involving specimen will absorb the energy. And second, that the quantity of the absorbed energy depends also on the specific mass density of each specimen, hence skull will absorbed less energy than brain.

V. Conclusions and Discussions

Our work was able to contrast the resulted SAR caused by two difference frequencies; but it is just a result of a simple model with the simple antenna. We still need to validate our results. The further step is the study of SAR distribution caused by the more complex antenna and the time varying field for approaching the realistic situation.

Acknowledgements

This paper was partly supported by a "Supporting Fund for General Researchers" 2005 of the Science and Technology Research Center, King Mongkut's Institute of Technology North Bangkok.

References

[1] Holmberg B., "Magnetic field and cancer: animal and cellular evidence", *Environ. Health Perspect*., 103(S2):63-7,1995.

[2] Körpinar M.A., Kalkan M.T., Morgul A., Birman H., Hacibekiroglu M., "The effect of electromagnetic field with a frequency of 144 MHz on the blood parameters and behavior of rats", *in Proc. Int. Conf. Biomedical Engineering Days*, pp 82-4, Istanbul, 1998

[3] Okano Y., Ito K., Ida I., Takahashi M., "The SAR Evaluation method by a combination of thermographic experiments and biological tissue-equivalent phantoms", *IEEE Trans on Microwave Theory and Techniques*, vol 48, issue 11, pp 2094-2103, 2000

[4] K. Chaisaowong, and S. Roongruangsorakarn. "Computer-based 3-Dimensional Modeling of Electrical Potential Distribution: Surfacial Distribution in Homogenous Material.", in Proc. *The 2006 International Conference Electrical Engineering/ Electronics, Computer, Telecommunications and Information Technology Association of Thailand*, pages 219-222, Ubon Ratchathani, 2006.

[5] W. Wongrodjananan and K. Chaisaowong. "Computer-Based Three-Dimensional Modeling of Human Head: Specific Absorption Rate of Energy in Human Tissue as the Quantitative Description of Electromagnetic Waves' Exposure." in Proc. *The 29th Electrical Engineering Conference Thailand*, page 577-580, Pattaya, 2006.

[6] P. Direkpoke and K.Chaisaowong. "Two-Dimensional Simulations of Voltage Distribution Caused by Electrostatic Voltage Source in Homogeneous Material: Theoretical and Experimental Validation", in proc. *The 29th Electrical Engineering Conference Thailand*, page 589-592, Pattaya, 2006.

[7] A. Wangsotorn, P. Direkpoke, S. Roongruangsorakarn, and K. Chaisaowong, "Simulations and Visualization of Voltage Distribution Caused by Electrostatic Voltage Source in Homogenous Material", in Proc. *The 3rd Joint Conference on Computer Science and Software Engineering*,pp1-7, Bangkok,2006.

[8] R. Sutthaweekul, and K. Chaisaowong, "Computer-based 3-Dimentionsal Modeling of Human Head: I. Assembly of anatomic specimen." in Proc. *The 28th Electrical Engineering Conference Thailand*, page 1305-8, Phuket, 2005.

[9] N. Homsup, "Use of the FDTD-ADI method for calculating SAR in human head models," In Proc. *The Fourth International Conference on Computation in Electromagnetics* (CEM2002), page 144-145, Bournemouth (UK), 2002.

[10] William H. Hayt, Jr., John A. Buck, "Engineering Electromagnetic", McGraw-Hill, Inc.: New York, 2001.

[11] Stuart M. Wentworth, "Fundamentals of Electromagnetics with Eng. Application", John Wiley & Sons, Inc.: Massachusetts, 2005.

[12] G. Scarella, O. Clatz, S. Lanteri, G. Beaume, S. Oudot, J. P. Pons, S. Piperno and J. Wiart, "Realistic Numerical Modelling of Human Head Tissue Exposure to Electromagnetic Waves from Cellular Phones*", C. R. Physique*, vol 7, pp 501-508, 2006

[13] Ch. Sermpongpan and K. Chaisaowong. "Computer-based 3-Dimentionsal Modeling of Human Head: II. Assembly of physical parameters of anatomic specimen." in Proc. The 28th *Electrical Engineering Conference Thailand*, page 1309-12, Phuket, 2005.

Adaptive Channel Equalizer Design for Uplink WCDMA Rake Receiver

T. Phoopattanakul, W. Saenghiranwattana, K. Ruangsa-ad, C.Charoenlarpnopparut and P.Boonyanant
Sirindhorn International Institute of Technology, Thammasat University, Thailand
E-mail : chalie@siit.tu.ac.th

***Abstract*—The heart of the Wideband Code Division Multiple Access (WCDMA) Rake receiver lies in the design of the the channel estimator and equalizer. The application of Least Mean Square (LMS) and other adaptive filtering algorithms to WCDMA uplink receiver was proposed in 2002. In this paper, we propose the equalizer design based on the optimization of adaptive filtering techniques namely Normalize Least Mean Square (NLMS), Block Least Mean Square (BLMS) and Recursive Least Square (RLS). The BER performance of the Rake receiver is minimized with respect to various adjustable filter parameters. Our extensive simulation results show that the best performance is obtained when NLMS is used with well-tuned filter parameters. The optimal parameter selection process employed in this paper is based on the theoretical estimate along with the simulation search procedures.**

I. Introduction

One of the most promising approaches to 3G is the WCDMA air interface, referred as UMTS Terrestrial Radio Access (UTRA). A transmitted signal was simulated according to the physical layer specification of the IMT-2000 WCDMA system [8]-[9] i.e. the chip rate of the system is 3.84 Mcps, the frame length is 10 ms and each frame is divided into 15 slots (2560 chip/slot) and spreading factors range from 256 to 4 in the uplink. Then, the data is transmitted in a frame-by-frame basis through a time varying channel which is corrupted by the multipath fading environment. The signal is also further corrupted by additive white Gaussian noise (AWGN) at the front end of the receiver. In this paper, the focus of the study involves the design of the WCDMA Rake receiver with the emphasis on the uplink direction and the power consumption and processing cost are not of much concerned. The design, therefore, will be optimized to yield the highest processing performance measured in terms of BER.

This paper is organized as follows. First, the short overview of WCDMA communications is introduced. The theory behind the system is explained in section II. Then, the parameters in each type of filters are optimally selected according to their limitations and objections explained in section III. Lastly, in section IV, the performance of the filters are tested and discussed.

II. WCDMA uplink system

A. WCDMA Transmitter

At the transmitter, the signal will be sent as data sequence through DPDCH channel, whereas control information such as the transmit power control and pilot channel are sent through DPCCH channel. Each channel signal passes through different component, depending on its unique spreading factor and power ratio between DPDCH and DPCCH. For DPDCH, the data can be sent using different bit rates (depending on the application). Each case operates on different value of complex orthogonal spreading codes and bit-per-frame ratios. Furthermore, in DPCCH, four groups of bits are introduced, namely pilot channel, TFCI, FBI, and TPC, each of which has its own function. For pilot channel, it is used for defining the desired signal for channel estimation at the receiver. The control sequence is spread by complex spreading factor regardless of the data bit rates, then attenuated by the power ratio (β). DPCCH usually have lower power than DPDCH due to the fact that DPDCH contains more important data than DPCCH.

After spreading, the signals are complexly added. The combined signals are then scrambled using orthogonal codes which would prevent the interference from other users that uses the same frequency. The output of the transmitter, before being modulated, is a spread spectrum signal $s(t)$ described by following equation,

$$s(t) = [d_d(t)w_d(t) + j\beta d_c(t)w_c(t)] \cdot c(t).$$

Fig. 1 shows the overall system of transmitter.

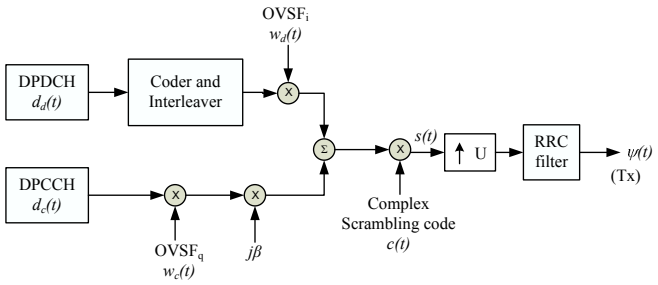

Fig. 1. WCDMA Transmitter

Throughout this paper, the simulation parameters are set according to Table I. We test the signal for 10 frames so altogether the signal contains 384,000 samples at four different bit rates varying from 12.2 kpbs to 384 kbps. The pilot channel is set according to 3GPP specification [10].

The input is usually up-sampled by the factor of 4, 8 or 16. In the experiment, we used the upsample factor of 4, thus, the chip rate after the upsampling becomes 15.36 Mcps. The pulse shape filter is put at the transmitter and the receiver for reducing the inter-symbol interference effect and the spectral bandwidth of baseband signals. Thus, we put the pulse shaping as a square root raised cosine type with the roll-off factor of 0.22 according

TABLE I

Transmitter parameter assignment

	I Channel				Q Channel
Bit Rate (kbps)	12.2	64	144	384	same as I channel
Bit per frame (bpf)	600	2400	4800	9600	150
Spreading Factor	64	16	8	4	256
N data (bit/slot)	10				0
N pilot (bit/slot)	0				6
Power Ratio P_Q/P_I (dB)	-5.46	-9.54	-11.48	-11.48	-

to the 3GPP specification. The amount of delay in the Rake receiver is adjusted by the path searcher (tracker).

B. Channel Model

The radio signal propagation through the air ("wireless channel") is influenced by many factors. Among them are reflections, diffraction, scattering and attenuation of the signal energy, caused by propagation loss and by natural obstacles such as buildings, mountains, etc. The well-known mathematical reference model due to Clarke [1] and its simplified simulation model due to Jakes [2] which have been widely used for Rayleigh fading channels. Multipath propagation is when signal from one transmitter takes different paths to get to the receiver. The receiver sees this as "echoes" with different arrival time and amplitude. With the usage of Rake receiver, these multipath signals are re-aligned and combined, by Maximum Ratio Combiner (MRC), to get a better signal-to-noise ratio (SNR) signal.

Assuming the maximum number of paths (or taps) to be L, the received signal at time t is

$$r(t) = s(t) \otimes h_b(t,\tau) + n(t),$$

where $n(t)$ is an additive white Gaussian noise (AWGN), $\otimes$ denotes the convolution operation, and $h_b(t,\tau)$ is the time-varying channel impulse response of a multipath channel and can be expressed as:

$$h_b(t,\tau) = \sum_{l=0}^{L-1} a_i(t,\tau)\exp[j(2\pi f_c \tau_i(t) + \phi_i(t,\tau))]\delta(\tau - \tau_i(t))$$

where $a_i(t,\tau)$ and $\tau_i(t)$ are the real amplitude and excess delay, *excess delay* is the relative delay of the l^{th}multipath component as compared to the first arriving component, the phase term $2\pi f_c \tau_i(t) + \phi_i(t,\tau)$ represents the phase shift due to free space propagation of the l^{th} multipath component, plus any additional phase shifts which are encounter in the channel,f_c is the carrier frequency and $\delta(\cdot)$ is the unit impulse response function.

In the simulation, we set the parameters, such as τ_i and a_i of channel impulse response $h_b(t,\tau)$ according to the 3GPP specification [10] shown in Table II. The adding phase shift $\phi_i(t,\tau)$ is randomly generated from $[-\pi,\pi]$, the carrier frequency for WCDMA is set at 2100MHz for the WCDMA [10].

For WCDMA uplink communications, the modulator is of QPSK type. However, we assumed that the modulator and demodulator are ideal and are ignored for simplicity. We followed the 6 cases of multipath Rayleigh fading channel according to the 3GPP specification 25.101 [3] as shown in Table II, for simulating the multipath Rayleigh fading channel.

TABLE II

3GPP specification 25.101

Case No.	Speed (km/hr)	Relative delay (ns)	Relative power (dB)
1	3	0 976	0 -10
2	3	0 976 20000	9 0 0
3	120	0 260 521 781	0 -3 -6 -9
4	3	0 976	0 0
5	50	0 976	0 0
6	250	0 260 521 781	0 -3 -6 -9

C. Base station Rake receiver

Upsampler block is compensated by downsampler block at the receiver side. The input to the receiver with chip rate of 15.36 Mcps is downsampled by factor of 4 (same as the upsampling factor) therefore, the chip rate after downsampling becomes 3.84 Mcps.

Rake receiver utilizes multiple correlators to separately detect strongest multipath components. Ideally, the Rake receiver should have L fingers, illustrated by Fig. 2 with $L = 3$. However, it is more practical to have M fingers ($M \leq L$) due to the complexity and hardware constraint.

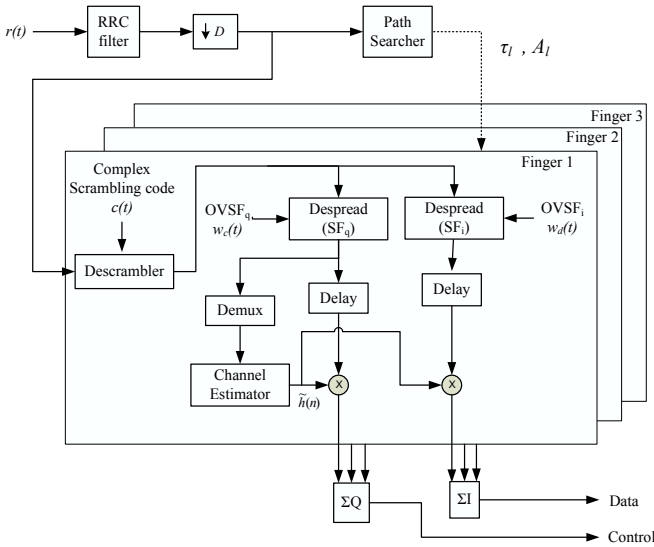

Fig. 2. Block diagram of Rake receiver

At the RAKE receiver, the first process is descrambling process and can be done by multiplying the input signal

with complex conjugate of the scrambling code. After descrambled at the receiver, the received l^{th}-path signal can be expressed as

$$\begin{aligned} r_l(t) &= [s(t)h_l(t) + n(t) + i(t)]c^*(t) \\ &= s(t)h_l(t)c^*(t) + n(t)c^*(t) + i(t)c^*(t) \\ &= [d_d(t)w_d(t) + j\beta d_c(t)w_c(t)]h_l(t) + n(t)c^*(t) + i(t)c^*(t) \end{aligned}$$

III. Channel equalizer by adaptive filter

Since the natural distortion and interference is usually predictable, it is necessary for the corrective system to identify and continuously adapt to the, often, time-varying condition. Such a system is called an adaptive equalizer [5]. In this paper, we compared three linear adaptive equalizers: NLMS, RLS and BLMS.

A. NLMS Algorithm

The normalized-LMS is similar to the standard LMS filter [5], but with the weight controller applying a weight adjustment. The NLMS algorithm sets an upper limit on scale factor (μ), resulting in more stable convergence and steady state coefficient values. The normalized μ is adjusted with the data as follow: (to avoid problem when $\|x(n)\|^2 \approx 0$, so, adding with an offset parameter (β))

$$\mu(n) = \frac{\alpha}{\|x(n)\|^2 + \beta}$$

where α is the scalar step size ($0 < \alpha < 2$), β is the offset parameter ($\beta > 0$) and $\|\cdot\|$ is the Euclidean norm.

The filter update algorithm is

$$w(n+1) = w(n) + \mu(n)e(n)x(n)$$

Fig. 3 and Fig. 4 demonstrates how the BER of NLMS

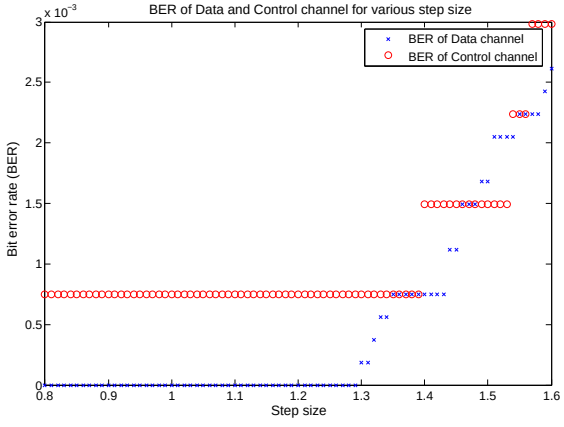

Fig. 3. BER performance at different step sizes values

algorithm behaves for various step size and offset value respectively. After many simulations, we found that an optimal step size mostly falls in the range of 0 to 1.29 (SNR = 0 dB). Later, we chose the step size $\alpha = 1$ for fast convergence speed and smaller BER. Clearly from Fig. 4, the larger offset (with step size α =1) results in the lower BER, since the offset ($\beta > 0$) is added to avoid the problem of $\|x(n)\|^2 \approx 0$. Here, we chose the optimal offset value = 50.

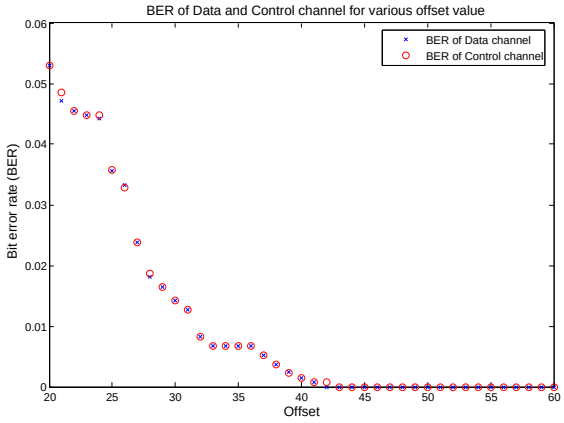

Fig. 4. BER performance at different step offset values

B. RLS Algorithm

The concept of Least Square method is based on the matrix inversion lemma. An important feature of this algorithm is that its rate of convergence is typically an order of magnitude faster than that of the simple LMS filter, due to the fact that RLS filter whitens the input data by using the inverse correlation matrix of the data. This improvement in performance, however, is achieved at the expense of computational complexity of the RLS filter [5].

There are at least three parameters the designer should carefully set. First is the forgetting factor, chosen in the interval $0 < \lambda < 1$. Since the signal is time-varying, the forgetting factor is usually optimal at the value between 0.95 and 1. Next, the filter length can be any designer's choice. From our experiment, using severely time-varying system, the more the filter length is, the higher the BER. Therefore, filter length of 1 is used. Lastly, the initial inverse autocorrelation matrix can be set by setting the value of regularization parameter. The optimal regularization parameter is tested and found to be just the identical matrix I alone.

We start by first obtaining the optimal forgetting factor. The relationship between forgetting factor (x axis) and BER (y axis) is shown in Fig 5. Note that Fig 5 is of bit rate=12.2 kbps and SNR=12dB. By testing the relationship between forgetting factor and BER at different bit rates and different SNR, we found that the optimal forgetting factor that makes the smallest BER is $\lambda = 1$.

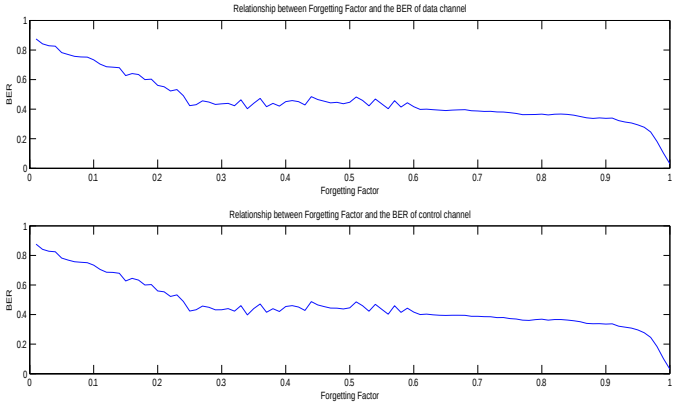

Fig. 5. Relationship between forgetting factor and BER

C. BLMS Algorithm

In Block LMS, the incoming data sequence $x(n)$ is sectioned into $L-sample$ blocks by means of serial-to-parallel converter, and the blocks of input data so produced are applied to an FIR filter of length M, one block at the time. The tap weights of the filter are updated after the collection of each block of data samples, so that adaptation of the filter proceeds on a block-by-block basis rather than on a sample-to-sample basis as in the conventional LMS algorithm. Block LMS algorithm is developed from the LMS algorithm, therefore it has several properties that are similar to those of the conventional LMS algorithm. However, one fundamental difference between them is the estimates of the gradient vector used in their respective implementations. Block LMS algorithm uses a more accurate estimate of the gradient vector, compared to the estimate of that of conventional LMS, because of the time-averaging, with the estimation accuracy increasing as the block size L is increased. Another disadvantage of BLMS is its slow adaptation behavior.

IV. Simulation and result

With the well-tuned of the parameters of adaptive filters, the simulation results measured in terms of BER using different adaptive algorithms at different bit rate and noise condition are reported.

For the NLMS algorithm; we found that the optimal step size of 1, offset = 50, leakage = 1 and filter tap of 32. The RLS algorithm; we found the best performance of BER when optimal forgetting factor of 1 and filter tap of 1. Note that the BER obtained by RLS algorithm has the lowest value of 0.000746 which is equivalent to 4 bits. These error bits occur during the initialization of the weight function $w(n)$ due to zero initial value for $w(n)$. Finally, the BLMS algorithm; we found the best performance of BER by setting step size = 0.01, leakage = 1, filter tap = 1, and block size = 2. The BER obtained by using BLMS algorithm has the lowest value of 0.001493 which is equivalent to 4 bits. These error bits occur during the initialization of the weight function $w(n)$ due to zero initial value for $w(n)$.we simulate the channel equalization using these 3 adaptive algorithms and the results are compared in Table III for data channel (I) and control channel (Q). Note that since moderate number of bits (over 10 frames) are simulated, the BER performance of the NLMS algorithm of zero might not be accurately represented, and only the trend can be used for conclusion.

V. Conclusion

In the WCDMA uplink transmission, the data and control signals are spread and scrambled before being modulates and propagates in the multipath environment. These multipath signals were received by the Rake receiver at the base stations. Here, we proposed to improve the performance of the Rake receiver by using channel estimator with various linear adaptive algorithms. The BER performance of several linear adaptive algorithms at various levels of SNR are compared. The optimal step size for NLMS is found to be $\alpha = 1$ and used throughout all later simulations. We discover that NLMS linear adaptive filter algorithm is the best algorithm in the specified environment as it has rapid convergence rate and the lowest miss-

TABLE III

BER of (a) Data channel and (b) control channel using three different adaptive algorithms

I-channel		Bit rates (kbps)	12.2 (kbps)	64 (kbps)	144 (kbps)	384 (kbps)
SNR (dB)	-3	NLMS	0.0000	0.0000	0.0000	0.0000
		RLS	0.0007	0.0054	0.0317	0.0597
		BLMS	0.0015	0.0078	0.0397	0.0524
	3	NLMS	0.0000	0.0000	0.0000	0.0000
		RLS	0.0007	0.0007	0.0007	0.0015
		BLMS	0.0015	0.0015	0.0019	0.0035
	12	NLMS	0.0000	0.0000	0.0000	0.0000
		RLS	0.0007	0.0007	0.0007	0.0007
		BLMS	0.0015	0.0015	0.0015	0.0015

(a)

Q-channel		Bit rates (kbps)	12.2 (kbps)	64 (kbps)	144 (kbps)	384 (kbps)
SNR (dB)	-3	NLMS	0.0000	0.0060	0.0575	0.0560
		RLS	0.0007	0.0037	0.0231	0.0328
		BLMS	0.0015	0.0052	0.0224	0.0224
	3	NLMS	0.0000	0.0000	0.0007	0.0000
		RLS	0.0007	0.0007	0.0007	0.0007
		BLMS	0.0015	0.0015	0.0022	0.0052
	12	NLMS	0.0000	0.0000	0.0000	0.0000
		RLS	0.0007	0.0007	0.0007	0.0007
		BLMS	0.0015	0.0015	0.0015	0.0015

(b)

adjustment among the three algorithms. It also has the best BER to be used at the adaptive channel estimator to achieve suitable result to cope with the distortion, delay, and Doppler affect of received signal.

VI. Acknowledgement

This research work is financially supported by The National Electronics and Computer Technology Center (NECTEC), National Science and Technology Development Agency (NSTDA), Thailand. The authors thanks reviewers for their constructive comments.

References

[1] R. H. Clarke, "A statistical theory of mobile-radio reception," Bell Syst.Tech. J., pp. 957-1000, Jul.-Aug. 1968.
[2] W. C. Jakes, Microwave Mobile Communications. Piscataway, NJ: IEEE Press, 1994.
[3] 3GPP TS25.101 v5.5.0(2002-12): Technical Speci.cation Group Radio Access Network; UE Radio Transmission and Reception (FDD)., Release 5.
[4] S.Makino, YKaneda, and N.Koisumi, "Exponentially Weighted Stepsize NLMS Adaptive Filter Based on the Statistics of a Room Impulse Response", IEEE Trans. Commun., vol. 1, no.1, pp.101-108, Jan.1993
[5] S. Haykin, Adaptive filter theory, Information and System Sciences Series, Prentice Hall, 4th ed., 2002.
[6] B. Sklar, "Rayleigh fading channels in mobile digital communication systems. Part I: Characterization," IEEE Commun. Mag., pp. 90-100,July 1997.
[7] T. S. Rappaport , Wireless Communications, Prentice Hall, New Jersey, first edition, 1996.
[8] Tero Ojanpera and Ramjee Prasad, "An Overview of Air Interface Multiple Access for IMT-2000/UMTS," IEEE Communications Magazine, vol. 36, pp. 88-95, September 1998.
[9] Erik Dahlman, Bjorn Gudmundson, Matts Nilsson, and Johan Skold, " UMTS/IMT-2000 Based on Wideband CDMA," IEEE Communications Magazine, vol. 36, pp. 70-80, September 1998.
[10] "UE Radio Transmission and Reception (FDD)", 3GPP, 3GTS 25.101 ver. 3.3.1, (06-2000).

Closed-Form Analysis of Equal Gain Combining for Wireless Communications Over Rayleigh Fading Channels

Narongrit Mekloi
Department of Electronic and Telecommunication Engineering, Faculty of Engineering
Rajamangala University of Technology Krungthep, Bangkok, 10120, Thailand

Abstract

Probability of outage is an important statistical measure in the design of cellular mobile radio systems which operate in a fading environment with multiple interferers. We derived the exact outage probability of dual branch equal gain combining (EGC) in wireless systems in presence of co-channel interference. The more general case with unequal power co-channel interferers is formulated and solved differently in this paper ending up with closed form solutions for Rayleigh fading channel models.

Keywords: Co-channel interference (CCI), Equal gain combining, Outage probability, Rayleigh fading

1. Introduction

Diversity technique is a well known method for mitigating the effects of multipath fading in wireless communication systems. Various techniques are used to combine the signals from multiple diversity branches. The most main of them are selection combining (SC), equal gain combining (EGC), maximal ratio combining (MRC) and hybrid diversity or called Generalized Selection Combining (GSC). The MRC need the knowledge of amplitude and phase of the signals to maximize the signal power. Therefore, the implementation needs some mechanism to measure these properties such as phase lock loop etc. For this reason, the EGC, which characterized as MRC with equal gain is employed in stead [1]. Equal gain combining is of a practical interest because it provides performance close to optimal maximal ratio combining but with greater simplicity [2].

Besides the probability of bit error, the outage probability is important measure of performance of mobile system operating in the presence of interferers over fading channels [3]. A system planner cans use outage probability calculations to assess the effects of various system configurations on the quality of service provided by the system. The outage probability is defined as the probability of failing to simultaneously achieve a signal-to-interference ratio (SIR) and a signal-to-noise ratio (SNR) sufficient to give satisfactory reception is an appropriate measure to evaluate the performance of a mobile radio systems. The outage probabilities based on either SNR or SIR have been reported [4]-[9].

Although previous studies on outage probability deal with a variety of channel models, the closed form of outage performance has not derived in literatures. Performance evaluation of EGC diversity systems is notoriously difficult only more so given that the closed form probability density function (pdf) of the EGC output is only available for dual diversity combining in Rayleigh fading. In this paper, we deal with the dual branch diversity EGC special case relevant to small-size/mobile communication units. Previous related work, performance evaluating of a broad class of modulation schemes employing EGC receivers in a variety of fading environment was analyzed in [10], where only the signal to noise ratio (SNR) was considered. However, an interference-limited fading environment as in cellular communication systems where the level of the co-channel interference is sufficiently high as compared to the thermal noise. The analysis in [11] was derived the SIR of EGC in co-channel interference, were only the ratio of mean signal power to mean interference power was considered in the case of equal interferer powers. In many operational environments, however, the interferer powers may be different.

In the following, we present a closed form of outage probability analysis of dual diversity using EGC in Rayleigh fading with CCI. Section 2, shows the system model for interference power calculation. The performance analysis is then derived in the Section 3. In Section 4, present numerical outage calculations for varying numbers of interferers for unequal power and the conclusion is provided in Section 5.

2. Signal and Receiver Model

Consider a communication systems in which the receiver with a dual diversity receiver operates in the presence of L independent co-channel interferers. Throughout this paper, it is assumed that the system performance is interference limited and that the effect of thermal noise is negligible. The 2 × 1 complex baseband received signal for dual-antenna diversity reception is given by

$$r(t) = s_0(t)\mathbf{A}_0 + \sum_{i=1}^{L} s_i(t)\mathbf{A}_i \qquad (1)$$

where L is the number of interfering signals, $s_i(t)$ (i=0,1,2,3,…,L) are the transmitting signals and $\mathbf{A}_i$ (i=0,1,2,3,…,L) are the M-dimensional direction of arrivals of desired signal (i=0) and ith interfering signals, respectively. We thus have the instantaneous SIR at the output of equal gain combiner, assuming interference power calculation over diversity branches is

$$\gamma = \Lambda_i \frac{\left|\sum_{j=1}^{M} \alpha_{s,j}\right|^2}{\sum_{j=1}^{L} \left|\beta_{i,j}\right|^2} \quad (3)$$

where $\Lambda_i \equiv P_s / P_i$, for $i = 1, 2, ..., L.$ is the power ratio of desired signal to the *i*th interfering signal, and $\alpha_{s,j}$ and $\beta_{i,j}$ are fading amplitudes of desired and interference signals and are zero-mean Gaussian distributed, respectively. The fading amplitudes $\alpha_{s,j}$ and $\beta_{i,j}$ are Rayleigh distributed as

$$f_\alpha(\alpha) = 2\alpha e^{-\alpha^2}, \qquad \alpha \geq 0. \quad (4)$$

3. Outage Probability

The outage probability is the probability of failing to achieve adequate reception of a wanted signal, is a useful statistical parameter for assessing the quality of radio reception in mobile communication systems. In EGC, the desired signals at the outputs of the antennas are co-phased, equally weighted and then summed to give the resultant desired signal. The exact outage probability can be derived for *M* = 2. The cdf of sum of two i.i.d. Rayleigh RVs is known [12], and the conditional outage probability for *M* = 2 is

$$\Pr(X < \sqrt{\gamma\omega}) = 1 - e^{-\gamma\omega} - \sqrt{\frac{\pi}{2}\gamma\omega} \times e^{-(1/2)\gamma\omega}\left[1 - erfc\left(\sqrt{\gamma\omega/2}\right)\right] \quad (5)$$

Letting $X = \sum_{j=1}^{M} \alpha_{s,j}$ and $\omega = \sum_{i=1}^{L} \left|\sum_{j=1}^{M} \beta_{i,j}\right|^2 / \Lambda_i$ when the interferers have unequal mean powers the pdf of α is given by [13, eq. (14.5-26)]

$$p_\alpha(\alpha) = \sum_{k=1}^{L} \frac{\Lambda_k}{M} \pi_k e^{-(\Lambda_k / M)\alpha}, \qquad u \geq 0 \quad (6)$$

where

$$\pi_k = \prod_{\substack{i=1 \\ i \neq k}}^{L} \frac{\Lambda_i}{\Lambda_i - \Lambda_k} \quad (7)$$

Averaging (5) with respect to (6) for $p_\alpha(\omega)$ gives the outage probability. In case of unequal interferer powers, using [14, eq.3.478, 6.286], is shown in the equation (8) at the bottom of the next page. The mathematical function ${}_2F_1(a,b,c;z)$ in (8) is the hypergeometric function [14].

4. Numerical Examples

In this section, we present some numerical results by plotting the outage probability SIR γ when the channel undergoes Rayleigh fading. To study outage for unequal interferer power distributions, define

$$\Lambda_{avg}(\text{dB}) = 10\log_{10}\frac{P_s}{\frac{1}{L}\sum_{i=1}^{L} P_i}$$

we define vector $q = [q_1, q_2, ..., q_L]$ of normalized interference power, where $\sum_{i=1}^{L} q_i = 1$. Power ratio

$$\Lambda_i(\text{dB}) = \frac{P_s}{P_i}(\text{dB}) = \Lambda_{avg}(\text{dB}) - 10\log(Lq_i).$$

Figure.1 plots the outage probability for the number of antennas (*M*) = 2 with number of interferences as a parameter for the case of non-identical interferer powers. Example for the interference power vector for L=6 is [0.05, 0.1, 0.15, 0.22, 0.23, 0.25]. As expect the system performance increases significantly as the number of interferences decreases. In Figure.2, we compare a Monte Carlo simulation of the outage probability using (3) with the analytical outage probability using the interference power calculation method for the case of unequal interferer powers. As shown, the analysis and simulation results agree closely.

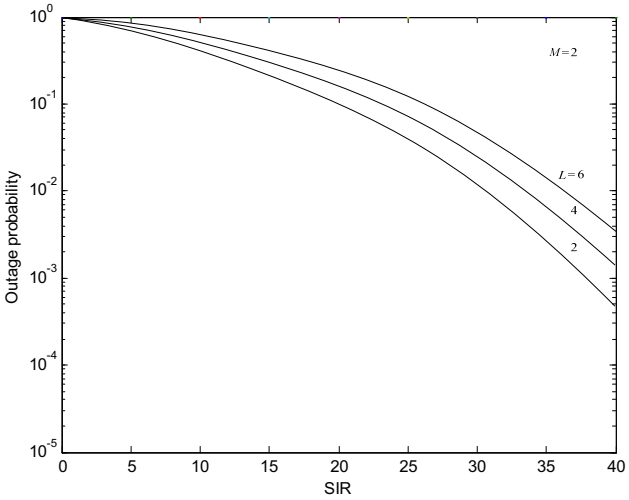

Fig. 1 Outage probability for non-identical ($\Lambda_{avg} = 10$ dB) interference power with *M* = 2 and *L* = 2, 4, and 6 interferences.

5. Conclusions

In regard to the EGC receiver performance analysis in Rayleigh fading channel, the framework in this paper has been presented in closed-from expressions for

outage probability for dual diversity systems. We have studied the effect of co-channel interference on the performance of digital cellular mobile radio systems. The new analysis method assumes that the interferers add in amplitude and phase, were the interfering signal components are across antenna array elements. The analysis assumed an arbitrary number of co-channel interferers with different average powers.

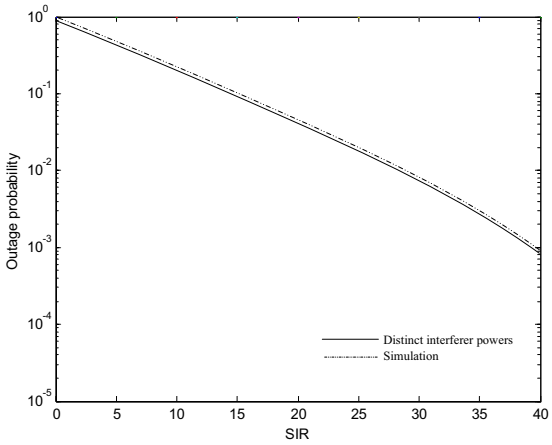

Fig. 2 Analytical outage probability for non-identical power calculation and Monte Carlo simulated outage probability for unequal interference power distributions with $L = 2$ interferers and $M = 2$ antennas. The interference power vector for $L = 2$ is [0.1, 0.9].

References

[1] D.G. Brennan, "Linear Diversity Combining Techniques", IEEE Proc., vol. 91, no. 2, Feb. 2003.

[2] G.K. Karagiannidis, D.A. Zogas and S.A. Kotsopoulos, "Statistical Properties of the EGC Output SNR Over Correlated Nakagami-*m* Fading Channels", IEEE Trans. Wireless Commun., vol. 3, no. 5, Sep. 2004.

[3] K.W. Sowerby and A.G. Williamson, "Outage Probability Calculations for Multiple Co-channel Interference in Cellular Mobile Radio Systems", IEE Proc., vol. 135, Pt.F, no. 3, June 1988.

[4] Y.D. Yao and A.U.H. Sheikh "Outage Probability Analysis for Microcell Mobile Radio Systems with Co-channel Interferers in Rician/Rayleigh Fading Environment", Electronics Letters, vol. 26, no. 13, 21 June 1990.

[5] T.T. Tjhung, C.C. Chai and X. Dong, "Outage Probability for Lognormal-Shadowed Rician Channels", IEEE Trans. Veh. Technol., vol. 46, no. 2, May 1997.

[6] J. Reig and N. Cardona, "Aproximation of Outage Probability on Nakagami Fading Channels with Multiple Interferers", Electronics Letters, vol. 36, no. 19, Sep. 2000.

[7] J.P. Pena-Martin and J.M. Romero-Jerez, "Outage Probability with MRC in Presence of Multiple Interferers Under Rayleigh Fading Channels", Electronics Letter, vol. 40, no. 14, July 2004.

[8] Y. Chen and C. Tellambura, "Performance Analysis of L-Branch Equal Gain Combiners in Equally Correlated Rayleigh Fading Channels" IEEE Trans. Commun., vol. 8, no. 3, March 2004.

[9] K. Sivannesan and N.C. Beaulieu, "Exact BER Analysis of Bandlimited BPSK with EGC and SC Diversity in Co-channel Interference and Nakagami Fading", IEEE Commun. Letters, vol. 8, no. 10, Oct. 2004.

[10] A. Annamalai, C. Tellambura and V.K. Bhargava, "Equal Gain Diversity Receiver Performance in Wireless Channels", IEEE Trans. Commun., vol. 48, no. 10, Oct. 2000.

[11] A. Shah and A.M. Haimovich, "Performance Analysis of Maximal Ratio Combining and Comparison with Optimum Combining for Mobile Radio Communications with Co-channel Interference", IEEE Trans. Veh. Technol., vol. 49, July 2000.

[12] S.W. Halpern, "The Effect of having Unequal Branch Gains in Practical Pre-detection Diversity Systems for Mobile Radio", IEEE Trans. Veh. Technol., vol3 VT-26, Feb. 1977.

[13] J. Proakis, *Digital Communications*, 4th. Ed., New York: McGraw-Hill, 2001.

[14] I. Gradshteyn and I. Ryzhik, *Tables of Integrals, Series and Products*, 5th ed. San Diego, CA: Academic, 1994**.**

[15] L. C. Andrews, *Special Functions for Engineers and Applied Mathematicians.* New York: Macmillian, 1985.

$$P_o(\gamma) = \sum_{i=1}^{L} \frac{\Lambda_k}{2} \pi_k \left[\frac{2\gamma}{\Lambda_k(\Lambda_k + \gamma)} - \pi\sqrt{\gamma}(\Lambda_k + \gamma)^{-3/2} + \frac{1}{3\sqrt{\pi}} {}_2F_1\left(\frac{3}{2}, 2, \frac{5}{2}; -\frac{\Lambda_k + \gamma}{\gamma}\right) \right] \quad (8)$$

Artificial Immunity-Based Feature Extraction for Spam Detection

Burim Sirisanyalak and Ohm Sornil
Department of Computer Science,
National Institute of Development Administration,
Bangkok, Thailand
burim@as.nida.ac.th,osornil@as.nida.ac.th

***Abstract*-Spam is considered a significant security problem for computer users everywhere. Spammers exploit a variety of tricks to conceal parts of messages that can be used to identify spam. This paper presents an email feature extraction technique based on artificial immune systems. The method extracts a relatively small set of features that can be used as inputs for a classification model. A Backpropagation neural network is employed as the spam detection model. The performance evaluation against a standard spam collection and reference systems shows that the proposed approach performs well compared to other systems with large sets of features, rules, or external evidences. The detection rate of the best system in this study is 92.4%, with 1% and 13.8% of false positive and false negative rates, respectively.**

I. INTRODUCTION

Spam, unsolicited, undesired, bulk email (or junk email), has been a significant security issue for computer users and a massive waste of time, disk spaces, and network bandwidths. As spam filters evolve better in abilities to identify and discard spam, spammers develop new tricks to circumvent the filters.

The most common method is to hide the parts of a message that make it spam, such as splitting words, dynamically generating messages by JavaScript, using images of words, encoding characters, ASCII art, etc. These methods are effective especially with HTML which provides a rich set of tools for creating messages. They can send rich messages with fonts, colors, and links which include images that are not attached but loaded when the email is displayed. Some spammers try to exclude words that are normally used in spam messages, fill the message with the nonsense tokens, and getting users to identify messages that contain spam words as non-spam (ham), for instance, word salad, white-out, invisible-ink, camouflage, HTML abuse, the daily news, random words, etc.

Effective spam filters must use multiple techniques to correctly filter messages. The best spam filter for any email account is the person who owns the account. Even as smart as most humans are, spammers try to trick them into reading spam messages that make it pass the filter or into not reporting the spam to the proper authorities, for example, fake legitimacy and sender unknown. Comprehensive discussions on the spammer tricks can be found in many sources such as [14].

This paper presents a method based on artificial immune systems to extract a set of features from email messages that can be used as input for a spam detection system. An artificial immune system (AIS) is a computational model inspired by mammalian immune systems. The main purpose of the immune system is to recognize all cells (or molecules) within the body and categorize those cells as self or nonself by learning through evolution. The harmful nonself elements of particular interest are the pathogens, such as viruses, bacteria, multi-cellular parasites and fungi. Artificial immune systems have been developed for a wide range of applications from data mining to information security [5,6]. In many cases, the applications have produced results comparable to, or better than, other standard techniques.

The rest of this paper is organized as follows. In Section 2, general and AIS-based spam filtering techniques are discussed. Section 3 presents our feature extraction and spam detection approach. In Section 4, the proposed method is evaluated against a standard content-based spam collection and reference systems. Section 5 provides concluding remarks on the research.

II. RELATED WORK

A role of the immune system is to protect our body from infectious agents such as viruses, bacteria, fungi and other parasites. On the surface of these agents are antigens that allow the identification of invading agents (pathogens) by the immune cells and molecules, thus provoking an immune response [9,10]. Recognition in the immune system is performed by lymphocytes. Each lymphocyte expresses receptor molecules of one particular shape on its surface (called antibody). An elaborate genetic mechanism involving combinatorial associations of a number of gene segments underlies the construction of these receptors. The overall immune response involves of three evolutionary methods: gene library evolution generating effective antibody, negative selection eliminating inappropriate antibodies and clonal selection cloning well-performing antibodies [10]. A more complete and accurate description of the immune system can be found in many biology texts.

There are a larger number of techniques for analyzing emails and determining whether they are indeed spam. Due to the fact that the response rate for spam is very low, spammers are forced to send out millions of copies of the same e-mails.

Content analysis techniques analyze the content of inbound emails and focuses on the commercial aspect of spam by detecting suspicious characteristics of legitimate and illegitimate offerings or information requests that spammers try

to hide from spam filters and email users at least until they open the emails. Nowadays, spammers change one or more characters of offensive words in their spam in order to foil content based filters. However, those changes are performed in such a way that human can understand meanings of the words without much difficulties [14], for instance, versions of the word 'Viagra', 'Vi@grA', 'V-iagra!', etc. cannot be detected by conventional spam filters. A number of content analysis techniques have been proposed. Keyword analysis, lexical analysis, bayesian analysis, and heuristic approaches. More filtering techniques and more a comprehensive description of spam filtering techniques can be found in many sources [2,4,14].

Regarding spam detection approaches based on artificial immune systems, Oda and White [12] describe a technique with a collection of detectors are created and combined randomly into new detectors. Digital lymphocytes have a receptor that can bind to more than one email message, through regular expressions. Emails are assigned final scored based on matched lymphocytes and results from other spam detection systems.

III. The Proposed Spam Detection Technique

The proposed spam detection method is a two-step approach. First, a set of message features are extracted from a training set of known spam and non-spam messages. The features are then used as input for a classification model to make a decision on the type (i.e., spam or non-spam) of unknown email messages.

A. *Artificial Immunity-Based Spam Feature Extraction*

1. Antibody generation: an initial set of antibodies is generated from a training set of email messages. The process consists of three parts. A MIME Parser parses values of MIME fields in each email. A HTML Parser selects and eliminates HTML tags. A list of stopwords is used to remove predefined unimportant words. The body and the subject parts of a message are parsed, and terms are identified based on delimited whitespace and stopmarks (".", "?", ";", ":", and "-"). The remaining terms become the initial set of base strings (antibodies).

2. The gene library: The gene library consists of two components: a library of base strings and a library of character matching patterns. A base string is a term found in spam messages whose age is greater than zero with all of its characters converted to small caps. Each base string in the library has an age associated with it. A character matching pattern has the form of: character =~ [$symbol_1$, $symbol_2$, …, $symbol_m$] (expressed here using the Perl's regular expression syntax), for instance a =~ [a, à, á, á, @]. A lymphocyte is represented as a regular expression formed by replacing each character in a base string with the right side of its corresponding character matching pattern, e.g., a base string "viagra" becomes a lymphocyte "vi[a, à, á, á, @]gr[a, à, á, á, @]". These lymphocytes are used to match terms from email messages. Both base strings and character matching rules are dynamically updated (evolving) with every message processed.

3. Learning Features: In feature extraction process (outlined in Fig. 1), lymphocytes matched with terms in spam messages have the age of their corresponding base strings increased by the spam-rate (*s-rate*) while those matched with terms in legitimate (non-spam) messages have the corresponding age decreased by nonspam-rate (*n-rate*). The increment represents the usefulness of the lymphocyte in identifying spam messages. In addition, each base string has its age decreased by the aging rate (*a-rate*) for every message processed. Once the age reaches zero, the base string is removed from the library (i.e., the lymphocyte dies off). Matching of antibodies and strings from emails is performed by edit distance [7] which represents the minimum number of insertions, deletions, and substitutions required to transform one string into the other.

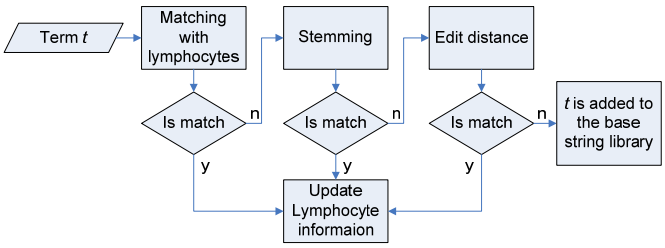

Figure 1. Feature extraction process.

B. *Spam Detection Model*

A Backpropagation neural network (Fig. 2), [13] is used as a spam detection model. It is a structure of small processing units, called neurons, connected in a systematic way. The neural networks used are Backpropagation feed forward neural networks, also known as multilayer perceptrons (MLP). The neurons are arranged in layers. Typically, there is one layer for input neurons (the input layer), one or more hidden layers for non-linear mapping, and one layer for output neurons (the output layer). Each layer is fully interconnected to the following layer.

The connections between neurons have weights associated with them, which determine the strength of influence one neuron has on the other. Information flows from the input layer through the hidden layer(s) to the output layer to generate predictions. By adjusting the connection weights during training to match predictions to target values for specific records, the network "learns" to generate better and better predictions. The computation of a backpropagation neural network consists of two passes: forward pass and backpropagation pass. The description here following.

Forward Pass: Input neurons have their activations set to the values of the encoded input fields. The activation of each neuron in a hidden or output layer is calculated as $a_i = \sigma(\sum_j w_{ij} o_j)$ where a_j is the activation of neuron *i*, *j* is the set of neurons in the preceding layer, w_{ij} is the weight of the connection between neuron *i* and neuron *j*, o_j is the output of

neuron *j*, and $\sigma(x)$ is the logistic transfer function:

$$\sigma(x) = \frac{1}{1+e^{-x}} \quad (1)$$

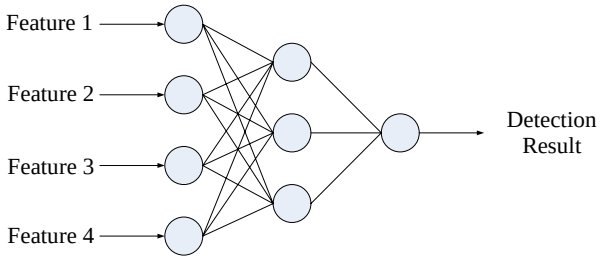

Figure 2. A Backpropagation neural network.

Backpropagation Pass: For each record, information flows through the network to generate a prediction, as described above. The prediction is compared to the target value found in the training data for the current record, and that difference is propagated back through the network to update the weights. To be more precise, the change value Δw for updating the weights is calculated as:

$$\Delta w_{ij}(n+1) = \eta \delta_{pj} o_{pi} + \alpha \Delta w_{ij}(n)$$

where η is the learning rate parameter, δ_{pj} is the propagated error (described below), o_{pi} is the output of neuron *i* for record *p*, α is the momentum parameter, and $\Delta w_{ij}(n)$ is the change value for w_{ij} at the previous cycle.

The value of α is fixed during training, but the value of η varies across cycles of training. η starts at the user-specified initial eta, decreases logarithmically to the value of low eta, reverts to the high eta value, and then decreases again to low eta. The value of η is calculated as:

$$\eta(t) = \eta(t-1) \cdot \exp\left(\log\left(\frac{\eta_{low}}{\eta_{high}} \right) \Big/ d \right) \quad (2)$$

where d is the user-specified number of eta decay cycles. If $\eta(t-1) < \eta_{low}$, then $\eta(t)$ is set to $\eta_{high} \cdot \eta$ continues to cycle thusly until training is complete.

The backpropagated error value δ_{pj} is calculated based on where the connection lies in the network. For connections to output neurons it is calculated as $\delta_{pj} = (t_{pj} - o_{pj}) o_{pj} (1 - o_{pj})$ where t_{pj} is the target value of output j for record p. For the weights that do not connect to the output neurons, δ_{pj} calculations take account of upstream error propagation, as $\delta_{pj} = o_{pj}(1 - o_{pj}) \sum_k \delta_{pk} w_{kj}$ where k is the set of neurons to which neuron *j*'s output is connected, w_{kj} is the weight between the current neuron and neuron *k*, and δ_{pk} is the propagated error for that weight for the current input record.

IV. Performance Evaluation

In this section, a series of experiments is carried out to evaluate our feature extraction technique. The data set used in this study is the SpamAssassin public corpus [15] which is widely used in evaluating spam detection systems. Two main types of settings are of interest: using the pruning phase and not using the pruning phase, (displayed in shaded areas). The pruning phase, *s-rate* and *n-rate* are set for a smooth adjustment of lymphocytes until reaching the number of lymphocytes needed. The remaining lymphocytes become the features used in spam detection systems. Details of all configurations are listed in Table I. If the pruning phase is not performed, living lymphocytes retained from the first phase are ordered by age, and the top required numbers of lymphocytes are selected as the features.

During training, 1,500 spam and 1,500 non-spam messages are used; and in order to measure the performance, 500 spam and 500 non-spam messages are used. Clementine [3], data mining software, is used to create every detection model; 30% of training data is set aside to prevent overfitting during detector model training.

Every configuration is executed 3 times with different initial weightings, each time we measure performance figures (detection rates and miss detection rates), and the average performance across the 3 iterations are calculated and reported.

TABLE I
Feature Extraction Configurations used in the Study

			Training			Pruning		
Configurations	*# Features*	*Initial Age*	*s-rate*	*n-rate*	*d-rate*	*s-rate*	*n-rate*	*d-rate*
Configuration 1	100	60	3	2	1	2	1	1
Configuration 2	150	60	3	2	1	2	1	1
Configuration 3	200	60	3	2	1	2	1	1
Configuration 4	100	60	3	2	1	-	-	-
Configuration 5	150	60	3	2	1	-	-	-
Configuration 6	200	60	3	2	1	-	-	-
Configuration 7	100	60	5	2	1	2	1	1
Configuration 8	150	60	5	2	1	2	1	1
Configuration 9	200	60	5	2	1	2	1	1
Configuration 10	100	60	5	2	1	-	-	-
Configuration 11	150	60	5	2	1	-	-	-
Configuration 12	200	60	5	2	1	-	-	-

TABLE II
Performance of Different Parameter Configurations

	Classification Rate (%)			Misclassification Rate (%)		
Configurations	Spam	Ham	Overall	Spam	Ham	Overall
Configuration 1	79.60	97.60	88.60	20.40	2.40	11.40
Configuration 2	82.00	95.80	88.90	18.00	4.20	11.10
Configuration 3	77.40	96.80	87.10	22.60	3.20	12.90
Configuration 4	79.20	95.40	84.30	20.80	4.60	15.70
Configuration 5	82.60	97.60	86.10	17.40	2.40	13.90
Configuration 6	79.00	96.60	87.80	21.00	3.40	12.20
Configuration 7	80.80	98.20	89.50	19.20	1.80	10.50
Configuration 8	82.60	98.20	90.40	17.40	1.80	9.60
Configuration 9	86.20	99.00	92.40	13.80	1.00	7.60
Configuration 10	80.20	96.20	88.20	19.80	3.80	11.80
Configuration 11	82.40	97.40	89.90	17.60	2.60	10.10
Configuration 12	81.00	97.80	89.40	19.00	2.20	10.60

First, different parameter configurations listed in Table I are studied. The results, in Table II, show that in general pruning gives better performance than not pruning, and the best parameter configuration is Configuration 9 which uses *s-rate* = 5, *n-rate* = 2, the number of lymphocytes = 200, and the pruning phase is applied.

Next, Configuration 9 is studied against three configurations of SpamAssassin. The results are shown in Table III. Note that, an important parameter of SpamAssassin (SA) is threshold with the default value of 5.0, represented as SA (threshold 5.0) in the table, as well as three other threshold values. With the SpamAssassin data, Oda and White [12] report the overall detection rate of 90%, with 84% and 98% spam and non-spam identification rates, respectively. Their work generates 1,000 lymphocytes and takes into account results from other spam detectors in making the decision. We also list their work in Table III and Fig. 3, for reference.

The results show that the proposed method performs well in relation to SpamAssassin, which as discussed in [12] uses over 700 complex heuristic tests to achieve similar results. In addition, Spam Assassin takes about 10 seconds in this environment to determine whether an email is spam, compared to less than a second far our system. Compared to [12], our system gives better performance on the same collection using five times less number of antibodies and not employing results from external detectors.

TABLE III
PERFORMANCE OF SPAMASSASSIN AND THE PROPOSED METHOD

	Classification Rate (%)			Misclassification Rate (%)		
	Spam	Ham	Overall	FN	FP	Overall
SA (Threshold 2.5)	86.80	99.80	92.80	13.20	0.20	7.20
SA (Threshold 4.0)	86.80	99.80	92.80	13.20	0.20	7.20
SA (Threshold 5.0)	58.60	100.00	79.30	41.40	0.00	20.70
SA (Threshold 7.5)	49.40	100.00	74.70	50.60	0.00	25.30
Configuration 9	86.20	99.00	92.40	13.80	1.00	7.60
Oda and White [12]	84.00	98.00	90.00	16.00	2.00	10.00

FN = False Negative FP = False Positive

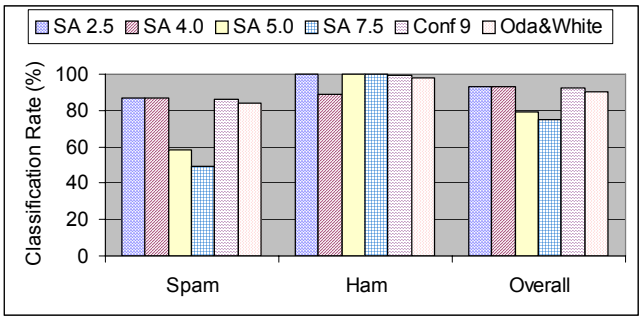

Figure 3. Performance of SpamAssassin and the proposed method.

V. CONCLUSION

This paper presents a feature extraction technique, based on artificial immune systems. Once a set of features is extracted, they are used as inputs to spam detection models. Features are represented as lymphocytes in AIS which are modeled by regular expressions of terms, constructed from base string and character matching rules, from the content of spam messages. The generation, updating, and elimination of lymphocytes are based solely on the content of spam and non-spam messages used in training. Different parameter settings of the method are studied with Backpropagation neural network which is used as spam detection model. The best feature extraction configuration is created by using *s-rate* = 5, *n-rate* = 2, the number of lymphocytes is 200, with the pruning phase applied. Its overall detection rate is 92.4% with the spam and the non-spam classification rates of 86.2% and 99.0%, respectively, which is comparable to more complex systems reported in literatures.

Due to the fact that the proposed method is not dependent upon languages, it is an attractive approach for multilingual spam detection. Since it is adaptive in nature; with a matching adaptive classification model, spam detection systems created can then be adaptive. This capability can be employed to support personalization by providing a base set of lymphocytes and allowing individual users to update their own lymphocytes based on their judgments and experiences with email messages.

REFERENCES

[1] S. Ahmed and F. Mithun, "Word Stemming to Enhance Spam Filtering," *Conference on Email and Anti-Spam (CEAS)*, California, July 2004.

[2] Barracuda Networks, "An Overview of Spam Blocking Techniques," Dec 2004. Available: http://whitepapers.zdnet.co.uk

[3] Clementine, "Clementine 8.0 Algorithms Guide," Integral Solutions Limited. 2003.

[4] Commtouch and Sybari, "Choosing the Best Technology to Fight Spam White Paper," April 2004. Available: http://www.commtouch.com

[5] D. Dasgupta and N. Attoh-Okine, "Immunity-Based System: A Survey," *IEEE International Conference in System, Man, and Cybernetics*, Orlando, October 1997.

[6] D. Dasgupta, "Immunity-Based Intrusion Detection Systems: A General Framework," *22nd National Information Systems Security Conference (NISSC)*, Virginia, October 1999.

[7] Dynamic Programming Algorithm (DPA) for Edit-Distance, "Dynamic Programming Algorithm (DPA) for Edit-Distance," June 2005. Avaiable: http://www.csse.monash.edu.au

[8] S. Forrest, B. Javornik, Robert. E. Smith and Alan S. Perelson, "Using Genetic Algorithm to Explore Pattern Recognition in the Immune System," *Evolutionary Computation*, Vol. 1, No. 3, pp. 191-211, 1993.

[9] S. Forrest, S. Hofmeyr, and A. Sommayaji, "Computer Immunology," *Association for Computing Machinery (ACM)*, Vol. 40, No. 10, pp. 88-96, 1997.

[10] J. W. Kim, "Integrating Artificial Immune Algorithms for Intrusion Detection," *Dissertation*, the University of London, July 2002.

[11] D. T. Larose, Discovering Knowledge In Data, John Wiley & Sons, Inc. 2005.

[12] T. Oda and T. White, "Developing an immunity to spam," *Genetic and Evolutionary Computation Conference (GECCO 2003)*, Chicago, July 2003.

[13] J. C. Principe, T. Simulations, and W. C. Lefebvre, Neural and Adaptive Systems, John Wiley & Sons. Inc. 2000.

[14] Process Software - a Platinum Equity Company, "Common Spammer Trick White Paper," September 2005. Available: http:// www.process.com

[15] SpamAssasin, "SpamAssasin public corpus," June 2005. Available: http://spamassassin.apache.org

Modification Of An Urban Area Okumura-Hata Propagation Model Suitable For Salalah-Oman

Z. Nadir, N. Elfadhil, F. Touati, B. Suhail, M. Jamal, M. Abdulrahman,
Dept of ECE, Sultan Qaboos University
Muscat, Sultanate of Oman
{nadir@squ.edu.om}

Abstract

The path loss, which represents signal attenuation as a positive quantity measured in dB, is defined as the difference (in dB) between the effective transmitted power and the received power, and may or may not include the effect of the antenna gains.

Imprecise propagation models lead to networks with high co-channel interference and a waste of power. In this paper, we aim to adapt a propagation model for Salalah (OMAN) as we examine the applicability of Okumura-Hata model in Oman in GSM frequency band. The study was carried out for urban area, since measurements provided from OmanMobile were about the urban areas. The study helped to design better GSM network for the city area. We will modify the propagation model used in Salalah city. We will accomplish this by investigating the variation in pathloss between the measured and predicted values, according to the Okumura-Hata propagation model for a cell in Salalah city. Then, we intend to modify the Okumura-Hata model according to the results obtained in our investigation. We will then verify our modified model by applying it for other cells and conclude the results. For the purpose the mean square error (MSE) was calculated between measured path loss values and those predicated on basis of Okumura-Hata model for an open area. The MSE is up to 6dB, which is an acceptable value for the signal prediction. Therefore, the model gave a significant difference in an open area that allowed necessary changes to be introduced in the model. That error was minimized by subtracting the calculated MSE (15.31dB) from the original equation of open area for Okumura-Hata model. Modified equation was also verified for another cell in an open area in Oman and gave acceptable results.

Keywords: propagation models. Okumura Hata Model, Pathloss,

I. INTRODUCTION

Mobile communications is currently at its fastest growth period in history; due to enabling technologies, which permit wide, spread deployment. Historically, growth in the mobile communications field has now become slow, and has been linked to technological advancements [1,2]. The need for high quality and high capacity networks, estimating coverage accurately has become extremely important. Therefore, for more accurate design coverage of modern cellular networks, signal strength measurements must be taken into consideration in order to provide an efficient and reliable coverage area. This article addresses the comparisons between the theoretical and the empirical propagation models. It was achieved that, the most extensively used propagation data for mobile communications is Okumura's measurements and this is recognized by the International Telecommunication Union (ITU) [3].

The cellular concept was a major breakthrough in solving the problem of spectral congestion and user's capacity. It offered high capacity with a limited spectrum allocation without any major technological change. The cellular concept is a system level idea in which a single, high power transmitter (large cell) is replaced with many low power transmitters (small cells). The area serviced by a transmitter is called a cell. Each small powered transmitter, also called a base station provides coverage to only a small portion of the service area. The power loss involved in transmission between the base station (BTS) and the mobile station (MS) is known as the path loss and depends particularly on the antenna height, carrier frequency and distance. At higher frequencies the range for a given path loss is reduced, so more cells are required to cover a given area. Base stations close to one another are assigned different groups of channels. So that, all the available channels (in frequency, time and space) are assigned to a relatively small number of neighboring base stations. Neighboring base stations are assigned different groups of channels so that the interference between base stations or interaction between the cells is minimized. As the demand for service increases, the number of base stations may be increased, thereby providing additional capacity with no increase in radio spectrum. The key idea of modern cellular systems is that it is possible to serve the unlimited number of subscribers, distributed over an unlimited area, using only a limited number of channels, by efficient channel reuse. [2]

II. THEORETICAL PROPAGATION MODELS

The propagation models are divided into two basic types; namely: Free space propagation and Plane earth propagation model.

A. Free Space Propagation Model

In free space, the wave is not reflected or absorbed. Ideal propagation implies equal radiation in all directions from the radiating source and propagation to an infinite distance with no degradation. Spreading the power over greater areas causes the attenuation. Equation (1) illustrates how the power flux is calculated.

$$P_d = P_t / 4\pi d^2 \ (W/m^2) \quad (1)$$

Where P_t is known as transmitted power and P_d is the power at a distance d from antenna. If the radiating element is generating a fixed power and this power is spread over an ever-expanding sphere, the energy will be spread more thinly as the sphere expands.

By having identified the power flux density at any point of a given distance from the radiator, if a receiver antenna is placed at this point, the power received by the antenna can be calculated. The formulas for calculating the effective antenna aperture and received power are shown in equations (2) and (3) below. The amount of power 'captured' by the antenna at the required distance d, depends upon the 'effective aperture' of the antenna and the power flux density at the receiving element. Actual power received by the antenna depends on; Aperture of receiving antenna A_o, wavelength of received signal λ, and power flux density at receiving antenna P_d.

Effective area A_e of an isotropic antenna is:

$$A_e = \lambda^2 / 4\pi \quad (2)$$

While power received is:

$$P_r = P_d \times A_e = P_t \times \lambda^2 / (4\pi d)^2 \quad (3)$$

$$P_r \ (dB) = P_t - 20 \log_{10}(4\pi) - 20 \log_{10} (d) + 20 \log_{10} (\lambda)$$

While equation (4) illustrates the path loss (L_p):

$$L_p = \text{Power transmitted } (P_t) - \text{Power received } (P_r) \quad (4)$$

When substituting equation (3) in equation (4), it yields equation (5):

$$L_p(dB) = 20 \log_{10} (4\pi) + 20 \log_{10} (d) - 20 \log_{10} (\lambda) \quad (5)$$

Then substituting (λ (in km) = 0.3 / f (in MHz)) and rationalizing the equation produces the generic free space path loss formula, which is stated in equation (6):

$$L_p(dB) = 32.5 + 20 \log_{10} (d) + 20 \log_{10} (f) \quad (6)$$

B. Plane Earth Propagation Model

The free space propagation model does not consider the effects of propagation over ground. When a radio wave propagates over ground, some of the power will be reflected due to the presence of ground and then received by the receiver. Determining the effect of the reflected power, the free space propagation model is modified and referred to as the 'Plain-Earth' propagation model. This model better represents the true characteristics of radio wave propagation over ground. The plane earth model computes the received signal to be the sum of a direct signal and that reflected from a flat, smooth earth. The relevant input parameters include the antenna heights, the length of the path, the operating frequency and the reflection coefficient of the earth. This coefficient will vary according to the terrain type (e.g. water, desert, wet ground etc). Path Loss Equation for the plane Earth Model is illustrated in equation (7).

$$L_{pe} = 40 \log_{10} (d) - 20 \log_{10} (h_1) - 20 \log_{10} (h_2) \quad (7)$$

Where d represents the path length in meters and h_1 and h_2 are the antenna heights at the base station and the mobile, respectively. The plane earth model in not appropriate for mobile GSM systems as it does not consider the reflections from buildings, multiple propagation or diffraction effects. Furthermore, if the mobile height changes (as it will in practice) then the predicted path loss will also be changed.

III. EMPIRICAL PROPAGATION MODELS

Empirical propagation models will be discussed in this section; among them are Okumura and Hata models.

A. Cellular Propagation Models

The two basic propagation models (free space loss and plane earth loss) would require detailed knowledge of the location, dimension and constitutive parameters of every tree, building, and terrain feature in the area to be covered. This is far too complex to be practical and would yield an unnecessary amount of detail. One appropriate way of accounting for these complex effects is via an empirical model. There are various empirical prediction models among them are, Okumura – Hata model, Cost 231 – Hata model, Cost 231 Walfisch – Ikegami model, Sakagami-Kuboi model. These models depend on location, frequency range and clutter type such as urban, sub-urban and countryside.

B. Okumura's Measurements

Okumura carried out extensive drive test measurements with range of clutter type, frequency, transmitter height, and transmitter power. It states that, the signal strength decreases at much greater rate with distance than that predicted by free space loss, as shown in Fig. 1. [3-5].

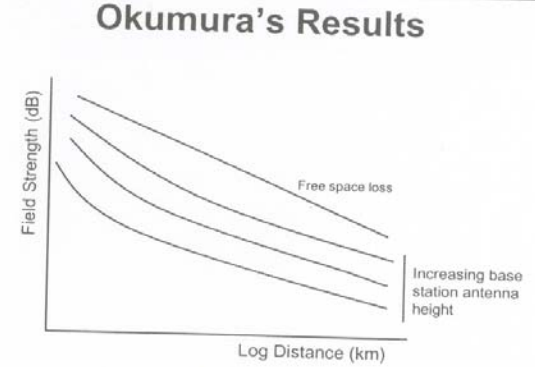

Figure 1: Okumura's Results [3]

C. *Hata's Propagation Model*

Hata model was based on Okumura's field test results and predicted various equations for path loss with different types of clutter. The limitations on Hata Model due to range of test results from carrier frequency *150Mhz to 1500Mhz*, the distance from the base station ranges from 1Km to 20Km, the height of base station antenna (h_b) ranges from 30m to 200m and the height of mobile antenna (h_m) ranges from 1m to 10m. Hata created a number of representative path loss mathematical models for each of the urban, suburban and open country environments, as illustrated in equations (8-10), respectively.

Path Loss for urban clutter:

$$L_p\,(\text{urban}) = 69.55 + 26.16\log(f) - 13.82\log(h_b) - a(h_m) + (44.9 - 6.55\log(h_b))\log(d) \quad (8)$$

$$a(h_m) = (1.1\log(f) - 0.7)h_m - (1.56\log(f) - 0.8) \quad (9)$$

Path loss for suburban clutter:

$$L_p\,(\text{suburban}) = L_p\,(\text{urban}) - 2\{\log(f/28)\}^2 - 5.4 \quad (10)$$

Path loss for the open country is :

$$L_p\,(\text{open country}) = L_p\,(\text{urban}) - 4.78\{\log(f)\}^2 + 18.33\log(f) - 40.94 \quad (11)$$

Hata model is not suitable for micro-cell planning where antenna is below roof height and its maximum carrier frequency is 1500MHz. It is not valid for 1800 MHz and 1900 MHz systems **.**

IV. Results and Discussions

TEMS tools were used to generate measurements of signal strength level for downlink and uplink at coverage areas for a cell in the road of Salalah, OMAN. However, the road of Salalah can be considered as an open area and therefore equations (8), (9) and (11) of Okumura-Hata model were used. After determining the path loss of the practical measurements for each distance, the study was carried on in order to make a comparison between the practical and theoretical values and the result is shown in Fig-2.

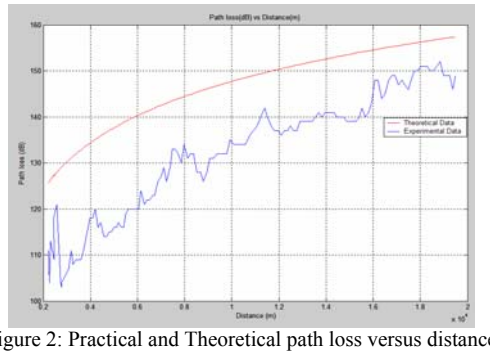

Figure 2: Practical and Theoretical path loss versus distance

From the above plot, the results clearly show that the measured path loss is less than the predicted path loss by a difference varying from 4 to 20 dB. However, there are several reasons which may cause that significant differences. First of all, in Japan there are few areas virtually satisfying the open area conditions; and if any, they are narrow. Because of that reason Okumura selected the value for urban area as standard for open area [5]. Moreover, the geographical situation of Japan is different from that in Oman. In Japan, rain which is the most effective factor that increases the path loss appears most of the time during the year, whereas in Oman most of the time the weather is clear. Therefore the radio signal propagation mechanism is different. Then, mean square error (*MSE*) was calculated between measured path loss value and those predicted by Hata model using the following equation [6]:

$$MSE = \sqrt{\left(\sum (P_m - P_r)^2 / (N-1)\right)} \quad (12)$$

Where;
P_m: Measured path loss (dB)
P_r: Predicted path loss (dB)
N: Number of Measured Data Points

The *MSE* was found 15.3148dB but the acceptable range is up to [6]. Therefore, the *MSE* is subtracted from the Hata equation for open area and the modified equation will be as following:

$$Lp_{\text{Modified}}\,(\text{open area}) = Lp\,(\text{urban}) - 4.78\{\log(f)\}^2 + 18.33\log(f) - 56.26 \quad (13)$$

The modified result of Hata equation in open area is shown in Figure 3 using modified equation and the *MSE* in this case is 5.6193dB, which is acceptable [6].

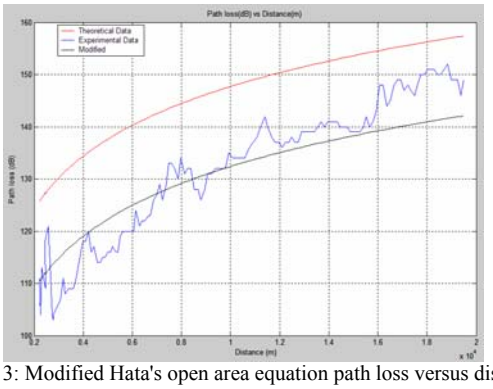

Figure 3: Modified Hata's open area equation path loss versus distance

In order to verify that the modified Hata's open area equation (13) is applicable for other open areas in Oman, another data generated from TEMS tool for another cell in the road of Salalah has been used. Therefore, based on that practical data, the propagation path loss and the distance have been determined and the result is shown in Figure 4.

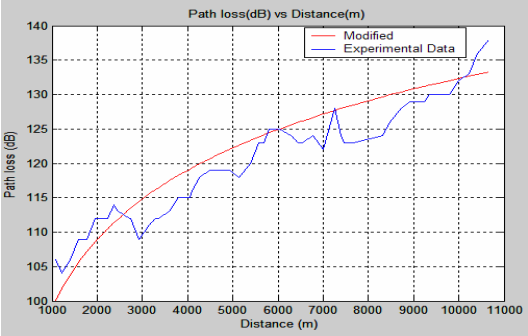

Figure 4: Modified Hata's open area equation path loss versus distance for another cell

By calculating the *MSE* for the second cell, it was found to be (3.2058dB) which is acceptable [6]. Therefore, the modified Hata's open area equation (13) was verified in order to be applicable in other open areas in Oman.

CONCLUSION

Generally, this work was focused for predicting the mean signal strength in different areas and with the signal variability as the mobile moves. However, most propagation models aim to predict the median path loss. But, existing predictions models differ in their applicability over different terrain and environmental conditions. Although there are many predictions methods based on deterministic processes through the availability of improved databases, but the Okumura-Hata model is still mostly used **[7].** That is because of the ITU-R recommendation for its simplicity and its proven reliability.

The effects of terrain situation predicted at 900MHz were analyzed. Results of radio signals propagation measurements for an open area in Oman were compared to those predicted based on Okumura-Hata model. However, the Okumura-Hata propagation model might not be fully adapted in Oman because there is no rain attenuation impact in Oman environment due to lack of rain. Therefore, further improvement of Okumura-Hata model in the open area has been suggested. This improvement was achieved by using mean square error (*MSE*) between measured and predicted path loss values in order to provide sufficient *MSE* for radio prediction The modified equation (13) was verified for a cell in another open area and the *MSE* was found to be 3.21dB which is accepted value for signal predication [6].

The measured data that provided by OmanMobile just covered the open area. Therefore, measurements for other areas (urban and suburban) should be obtained in order to compare all results (urban, suburban and open areas) with the predicted data based on Okumura-Hata model for Oman. Also, if more detailed environmental information is included in the model, better prediction results might be achieved.

ACKNOWLEDGMENT

The authors would like to express their sincere thanks to Mr Juma Al-Naabi, Head, Section of Quality Management – Network Division in OmanMobile Telecommunications Company LLC, without his help, valuable information and support this work could not be accomplished.

REFERENCE:

[1] D. Nobel, "The history of land to mobile radio communications," IEEE Transactions on Vehicular Technology, pp. 1406-1416, May 1962.

[2] V. H. MacDonald, "The cellular concept," *The Bell Systems Technical Journal*, vol. 58, no. 1, pp. 15-43, January 1979.

[3] A. Medeisis and A. Kajackas, "On the Use of the Universal Okumura-Hata Propagation Predication Model in Rural Areas", Vehicular Technology Conference Proceedings, VTC Tokyo, Vol.3, pp. 1815-1818, May 2000.

[4] Simon R.Saunders M. Hata, "Empirical Formula for Propagation Loss in Land Mobile Radio Services", *IEEE Transactions on Vehicular Technology,* vol VT 29 August 1980.

[5] Robert D.Wilson and Robert A. Scholtz, "Comparison of CDMA and Modulation Schemes for UWB Radio in a Multipath Environment", Proceedings of IEEE Global Telecommunications Conference, Vol. 2, Dec 2003.

[6] Jianhui Wu and Dongfeng Yuan, "Propagation Measurements and Modeling in Jinan City", IEEE International Symposium on Personal, Indoor and Mobile Radio Communications, Boston, MA, USA, Vol. 3, pp. 1157-1159, 8-11 September 1998.

[7] Y. Okumura et al., Field Strength and Its Variability in VHF and UHF Land-Mobile Radio Service, Review of the Electrical Communications Laboratory, Vol. 16, no. 9-10, September-October 1968.

The Design of a Backpressure Scheme in Traffic Shaping over High Speed Networks

Somchai Lekcharoen, and Srisawad Yongyut

Faculty of Information Technology
Rangsit University, Thailand
somchai@rangsit.rsu.ac.th and srisawad@gmail.com

***Abstract*-Congestion in VDSL network occurs when congestion builds up in the outgoing network and bandwidth is finite. Shaping mechanisms attempt smooth our this traffic. We used a 'leaky bucket' to achieve traffic shaping. But leaky buckets still have a lot of non-conforming frames. The solution to this problem lies in a backpressure algorithm under which no frames are non-conforming inside a VDSL network frame when congestion has built up. Congested nodes send backpressure feedback to neighboring nodes to inform them of unavailable buffering capacity, and this stops them from forwarding another frames until sufficient buffer becomes available. The potential advantages in backpressure networks are that they do not allow frame dropping. In this paper, we have proposed a backpressure algorithm that aims at detecting violations in parameter negotiation. Evaluation and comparison of backpressure with policing mechanisms, namely Leaky Bucket (LB), has shown that VDSL frames and backpressure help to improve throughputs and non-conforming frames. Backpressure meets its quality-of-service (QoS) requirements when source traffic is at low peak rate.**

KEY WORDS
VDSL network, Traffic shaping mechanism, Backpressure and Congestion Control.

I. INTRODUCTION

The ease and deployment speed of VDSL networks make these systems an option for improving efficiency in personal area networking (e.g., cell phone, laptop, ear phone). VDSL network performance is an important element of QoS and relates to the technical part of the Quality of Service parameters. It covers planning, development, operations and maintenance of the network. This focuses on user observable effects between the service access points. Network performance is focused on technical aspects.

A drawback of VDSL networks as compared wired networks is that they are generally less efficient and unpredictable. VDSL has limited bandwidth, high packet overheads, and is more prone to environmental factors such as obstructions, interference, weather and etc. Other issues related to VDSL network, Quality of Service (QoS) have been the relatively limited bandwidth and higher frame-error rates with high frame overheads. This could potentially limit the use of VDSL networks for delivering traffic for real-time applications such as Voice over IP (VoIP) telephony and multimedia applications. End-users have not expected only the mobility to provide QoS support.

In most VDSL networks, if a network device received more frames than it can forward, the device buffers experience backlog. However, when the buffer has filled up, the device begins to drop frames. This may lead to congestion collapse. This occurs when multiple frame streams are used some of the network resources before being dropped. Subsequent retransmissions use more network resources, resulting in degraded throughput.

An alternative approach is to perform hop by hop flow control, or backpressure at every link. Hop by hop flow control combines two mechanisms. The first is a strict portioning of the available buffer space among active flows, with selective backpressure on a per flow basis. The second is fair queuing to all shared resources by flows within a single network device. The result is twofold: frames are never dropped due to congestion within the network, and the available bandwidth is fairly divided up among all competing active flows. If there is no contention for priorities, each flow has access to the entire bandwidth on each link. However, but when there is such contention, each flow can access a fair share of the bandwidth.

In this paper, we are applying backpressure algorithmic concepts to network queue and evaluating the performance using VDSL network models. There are many previous studies involving policing mechanism [1][2][3], however backpressure algorithm in congestion control over VDSL network is not mentioned. Therefore, we proposed the performance comparison between backpressure and traditional policing mechanisms.

This paper is organized as follows. Section 2 is an overview of the most significant traffic policing mechanisms outlined in the literature. In Section 3 the backpressure algorithm is proposed. In Section 4 we defined the simulation model. Section 5 contains a performance evaluation of the proposed solution and comparison to backpressure, traditional policing mechanisms are presented. In Section 6, presents conclusion and recommendation for future research.

II. DESCRIPTION AND MODELING OF TRAFFIC SHAPING

Traffic shaping allows us to control the smooth rate of traffic sent or received on an interface during the entire active

phase. It must operate in real time. The mechanisms proposed are described in the following sections.

A. Requirement for shaping mechanism

aping mechanism system wants to smooth traffic connections by compromising the performance of other connections, and significantly improves the quality of service(QoS).

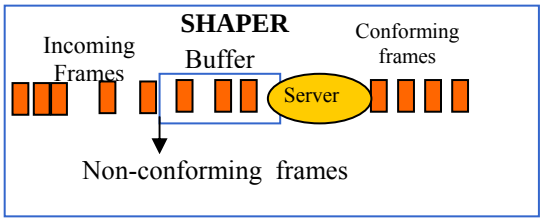

Fig. 1, Traffic shaping mechanism

Traffic shaping mechanism system allows us to ensure that there is a smooth rate of traffic data sent during the active phase and can be operated in real time. The mechanisms proposed is described in following sections.

A.1 Traffic source models

In our simulation, a single source can generate Burst/Silence traffic stream. Burst-periods and Silence-periods are strictly alternating[3].

B. Traffic shaping mechanism system

The Leaky Bucket Mechanism

The VDSL network must provide a large bandwidth and maintain the quality of service (QoS) guarantees. The Leaky Bucket (LB) mechanism (see figure 2) ensures that the source traffic does not exceed the negotiated rate. The bucket-size can be represented as a buffer with capacity N. If the buffer is filled up with frames until it is overflowing, then the frames are dropped. The server operates at a specific data rate, R. The LB is a commonly used for traffic control in high-speed networks

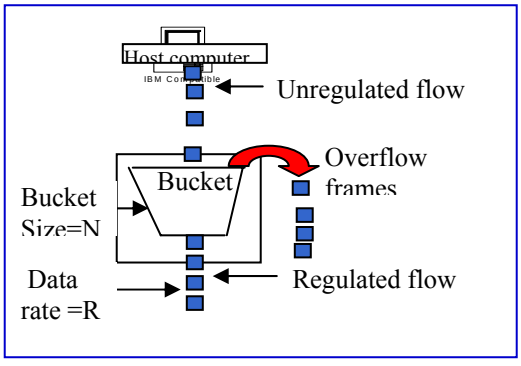

Fig. 2, Leaky bucket mechanism

III. BACKPRESSURE ALGORITHM

Traffic shaping mechanism systems can monitor traffic parameters as defined earlier, such as with peak rates (see Fig. 1). When an arriving frame is detected as being in excess of the receiving system capacity, the network monitor can mark the frame as non-conforming frames. The traffic sh

With backpressure algorithm works like a XON /XOFF techniques to prevent buffer overflows and transient congestion in network. Congestion control is invoked by triggering XON/XOFF flow control messages. The XOFF flow control message is sent upstream when buffer exceeds the upper threshold. When a server receives an XOFF signal, it temporarily stops sending frames until it received an XON signal from the same server, or until the time XOFF message expires. The XON signal is triggered when the buffer at the congested server has descended below the lower threshold.

When frames arrive to a buffer of server, the backpressure algorithm is activated. If the queue is not full and less than the threshold, then the server sends message to source hob that can send a double transmission rate to the receiver hob, and then the frame is transmitted without delay. If the buffer exceeds the upper threshold, the destination hop sends the message to source hop that can reduce it to a half transmission rate [5].

The backpressure algorithm is described as follows .

ALGORITHM

Goal: The goal is the flow control at every link. If the buffer exceeds the upper threshold, then the destination hop sends the message to source hop which can reduce it to a half transmission rate.

```
START_CHCK:
IF Simulation Time Reached THEN GOTO FINISH
ELSE
    { IF Q_DESTN  <  Q_THRESHOLD

     THEN  MARK  AS  HUNGRY FLOW

     ELSE   MARK  AS  RETARDING FLOW

 HUNGRY :  DOUBLE INPUT RATE

              GOTO START_CHECK

 RETARDING : REDUCE INPUT RATE INTO HALF

              GOTO START_CHECK
 }
```

Fig. 3, Backpressure algorithm.

IV. SIMULATION MODEL

The simulation model shown in figure 3 consists of a link processor which transmits frames into the link, and a finite buffer to hold frames. Frame arrival process is random and the inter-arrival time between frames follow a particular distribution function. Furthermore, the arriving frame is given to the link processor, which immediately starts transmitting

the frame; While the buffer is not empty, the link processor retrieves one frame at a time from the buffer in a first-in-first-out (FIFO) order, and transmits it onto the link. The link processor is never idle when there has been a frame waiting in the buffer.

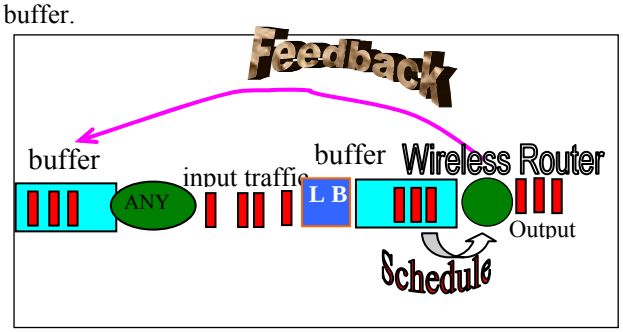

Fig.4, Simulation model

A. Input traffic

This research is mainly confined the discussion of data. Data sources are generally busty in nature whereas voice and video sources can be continuous or busty, it depends on the compression and coding techniques used.

B. Characteristics of queuing network model

There are three components with certain characteristics that must be examined before the simulation models are developed.

B.1 Arrival characteristics

The pattern of arrivals input traffic mostly is characterized as a *Poisson arrival processes*. The probability of the inter-arrival time between event t is defined by the *inter-arrival time probability density function (pdf)*. The following formula gives the resulting probability density function (pdf), where the inter-arrival time t is larger than some value x when the average arrival rate is λ events per second:

$$fx(t) = \begin{cases} e^{-\lambda t}, & for \quad t \geq 0 \\ 0, & for \quad t < 0 \end{cases}$$

$$p(t \leq x) = Fx(x) = \int_0^x e^{-\lambda x} dx = 1 - \lambda e^{-\lambda x}$$

$$p(t > x) = 1 - Fx(x) = \lambda e^{-\lambda x}$$

In this paper, we adopt the ON/OFF busty model [5], [6].

B.2 Service facility characteristics

In this paper, service times are randomly distributed by the *exponential probability distribution*. This is a mathematically convenient assumption if arrival rates are Poisson distributed. In order to examine the traffic congestion of output in VDSL downstream link (15Mbps) [7], the service time in the simulation model is specified by the speed of output link, given that a service time is 216 μs per frame where the frame size is 405 bytes [8].

V. RESULTS AND ANALYSIS

The comparison between backpressure (BP) and existing policing mechanism (LB, JW and TJW) is shown in figure 5-7.

A. The comparison between backpressure scheme and traditional policing mechanism.

This section shows simulation results from backpressure algorithms and traditional policing mechanism, and BP and LB performance are compared. The input frames (frame rate varies from 5 Mbps to 55 Mbps) with burst/silence ratio of 300:500 performed simulation results as shown in Figure 5. It clearly shows that the throughput of LB scheme is far better than the BP scheme. Throughput is one of factor of QoS to help guarantee a higher reliability of network performance. In conclusion, If source traffic is lower than the server performance (15 Mbps) then the throughput of BP is equal to LB.

In figure 6, the simulation results work in the sense that BP will produce non-conforming frames compared to traditional policing mechanism schemes. In other words, we can help conserve the conforming frames by reducing the number of non-conforming frames. A regular network may cause a poor QoS by higher non-conforming or dropped frames. The quality of telecommunication traffics non-conforming frame impact services and the efficient management of maintenance resources.

In figure 7, the simulation result determines greater utilization of backpressure algorithm comparing to traditional policing mechanisms with burst/silence ratio of 300:500. It is not problem when network congestion because the utilization is less than 80%.

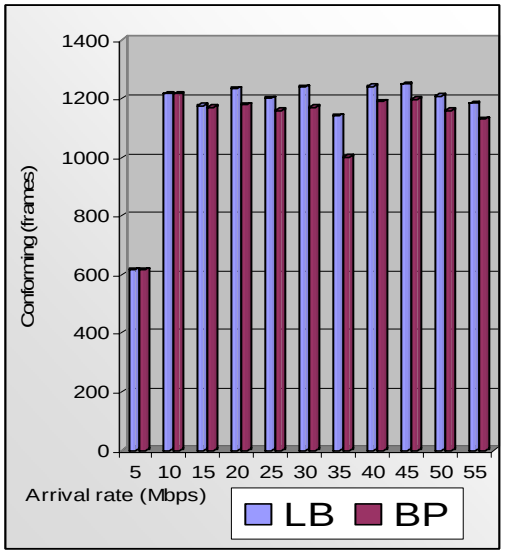

Fig. 5, illustrates comparison between conforming frame in BP and LB at burst : silence = 300:500

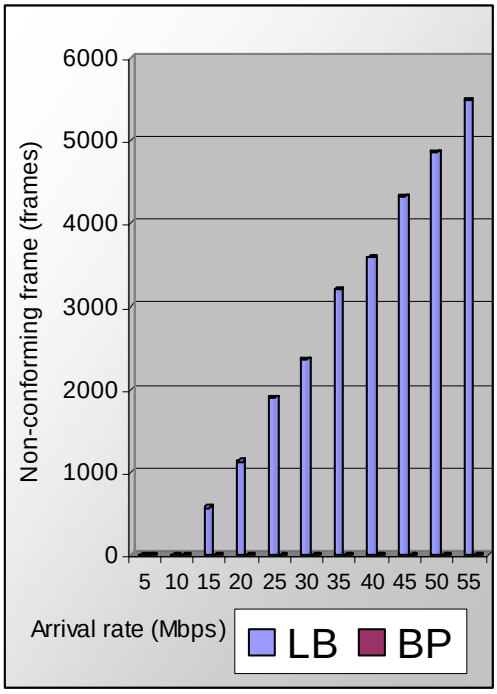

Fig. 6, illustrates comparison between non-conforming frame in BP and LB at burst : silence = 300:500

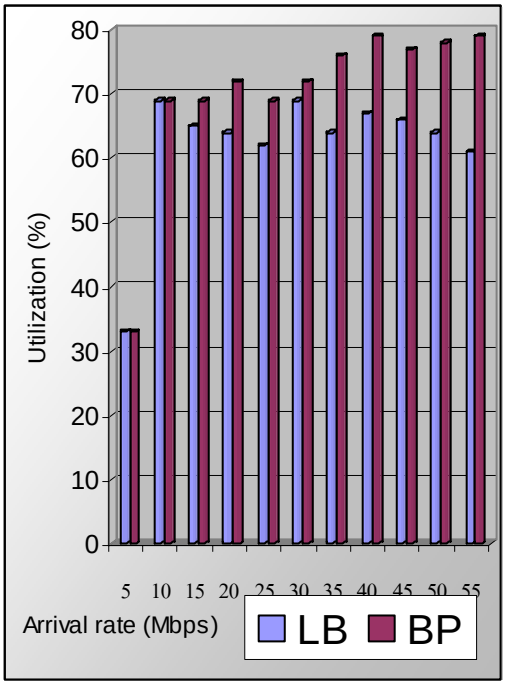

Fig. 7, illustrates the utilization comparison between BP, and LB at burst : silence = 300:500.

VI. Conclusions And Recommendations For Future Research

In this paper, we carried out a comprehensive study to investigate the performance of a backpressure scheme (BP) with a selected Leaky Bucket (LB) traffic shaping mechanism with fixed types of traffic. The study was accomplished through a simulation after developing an analytical queuing model.

We found that the BP within a non conforming frame outperforming LB. In our experience, if source traffics is lower than 20 Mbps because the data rate of server is 15 Mbps, the backpressure is the best in terms of throughput and non-conforming frames. BP is not problem about network congestion because the utilization is less than 80%.

BP meets its quality-of-service (QoS) requirements for VDSL network that have been relatively bandwidth and less delay time so it is suitable for telecommunication traffics.

In our future work, we will focus on the investigation of fuzzy control queuing systems in traffic shaping mechanisms.

References

[1] S. Lekcharoen, et. al., "QoS Sensitive Fuzzy Backoff Schemes in Policing Mechanisms," *IEE Mobility Conference*, 2005.

[2] P. Koutsakis and M. Paterakis. "Call-Admission-Control and traffic-policing mechanisms for the transmission of videoconference traffic From MPEG-4 and H.263 video coders in VDSL ATM networks," *IEEE transactions on vehicular technology*, Vol. 53, No. 5, 2004, pp. 1525-1530.

[3] S. Lekcharoen, et. al., "Performance Evaluation of VDSL Network with Fuzzy Control Policing Mechanisms," *Proceeding of International Conference on Telecommunications and Computer Networks (TCN'04*), 2004, pp. 56-60.

[4] S. Al-Wakeel Sami, R. Nasser-Eddine and A. Al-Wehaibi, "Evaluation of Fairness Strategies for ATM Congestion Control Policing Mechanisms," *Proceedings of the IASTED International Conference*,1999, pp. 200-204.

[5] M. Karol, S. J. Golestani and D. Lee, "Prevention of deadlocks and livelocks in lossless, backpressured packet networks," *IEEE INFOCOM 2000 - The Conference on Computer Communications* , No. 1, 2000, pp. 1333 – 1342.

[6] P. Pakdeepinit, et. al, "Performance Comparison of ATM Policy Mechanisms with Telecommunications Traffic," *Proceeding of The 6th World Multiconference on Systematics, Cybernetics and Informatics*, 2002, pp. 373-378.

[7]http://www.dlink.pl/docs/datenblatt /DEV3001 _datasheet_en.pdf.

[8] http:// www.etsi.org.

Multicast Improvement Bandwidth Utilization in Inter-ring RPR Topology

Wuttichai Kwanmetakun Pisai Setthawong Surat Tanterdtid
wuttihchaikwn@au.edu pisai@ieee.org surat.t@egat.co.th
Department of Telecommunications Science, Faculty of Science and Technology
Assumption University, Thailand 10240

***Abstract*-The IEEE 802.17 Standard, or Resilient Packet Ring (RPR) [1] was standardized in September 2004. Research on inter-ring traffic in RPR is a new development for expanding of the RPR ring by using bridge for interconnection. The standard multicast traffic is treated like broadcast traffic because it is source striped so the bandwidth is wasted from the last destination to the source. This paper presents the algorithm to control the multicast in inter-ring traffic to increase the bandwidth utilization. Our algorithm handles the multicast group to collect the members and distribute the multicast packets to the members. To control the striped multicast packets on the last destination in the local or remote ring by time-to-live (TTL) from enhanced topology discovery [3]. The OMNet++ [3] is used as simulator to test the proposed method and the results are compared with the Standard RPR. The results show that the bandwidth utilization of inter-ring RPR network is improved with the proposed solution, the degree of improvement depending on the location of the multicast members.**

I. INTRODUCTION

Resilient Packet Rings (RPR) [1] is a dual ring topology in which traffic is rotated in opposite directions on each ring; the inner ring is clockwise and the outer ring is counter-clockwise. RPR supports fiber optic and multi-packet platform such as the Synchronous Optical Network (SONET) [4] and the Ethernet frames [5]. Topology discovery (TD) is an important mechanism in RPR in order to exchange the information within the ring and complete topology's table of each node in the RPR network. Topology discovery is triggered periodically or by changes in the RPR network topology. Spatial reuse is used in RPR which allows the available bandwidth of the ring to transmit unicast traffic at the same time. Spatial reuse is made possible by the use of destination striped so it is used only for unicast traffic.

Inter-ring RPR is created by using bridge to expand the standard RPR as show in Fig 1. For inter-ring RPR, the functionalities of bridge provide to support the RPR network, such as Spanning Tree Algorithm (STA) [6].

On the other hand, multicast packets are striped at the source like broadcast traffic. This is known as source striping. Previous research [8] on multicasting was developed by using destination striped to remove the packet before it reaches the source. The time-to-live (TTL) value of multicast packet, which was from the topology discovery's information, will stripe the packet at the last member of the multicast group.

The standard of RPR and the existing literatures do not provided any ideas to support efficient multicast in the inter-ring RPR network. A novel idea is needed to reduce the duplicated traffic, such as unicast traffics that transmit for receivers. Broadcasting in the inter-ring RPR network affects the bandwidth utilization because if the broadcast packet is flooded through the bridges to other rings, the bandwidth utilization is dropped by the unwanted traffic.

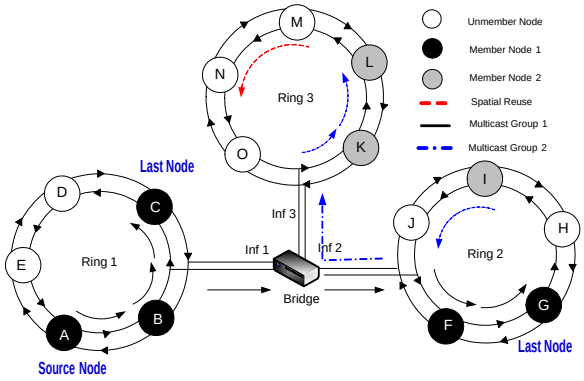

Fig 1. Node A sends the multicast packet to the members in the 3 inter-ring RPR which were connected by a single bridge.

The proposed algorithm denied the flooding from the multicast packet of the standard bridge to the rings which was no multicast member. The multicast traffic in the remote is striped at the last destination nodes of the multicast group.

The structure of this paper is organized as follows; the explanation of the multicast in the inter-ring RPR network is in the section 2. In section 3, the proposed algorithm and enhancement is illustrated using diagram. The remainder of this paper, the result and analyze of simulation, and conclusion are in section 4 and 5 respectively.

II. MULTICAST IN THE INTER-RING RPR TOPOLOGY

To implement the efficient multicast for the inter-ring RPR topology requires many developments to improve the standard of RPR and bridging. Enhanced bridging [3] is the new improvement for updating the performance of RPR to map the local address and the remote address, so the packet is forwarded directly to the remote destination. By Spatial Reuse Control Sublayer (SRCS) [7], the remote address is mapped to the local's table (bridge address) and compared to the global and local source address. The SRCS table is used to decide the next bridge in order to reach the destination bridge by using the bridge's table forward directly the destination address.

Enhanced Topology Discovery (ETD) and Enhanced Spanning Tree Algorithm (ESTA) [2] improve RPR to work more effectively. Topology Discovery is modified by adding

the bridge's indicator in the *TypeLengthValue* field for nodes to forward to other RPR rings directly. ESTA makes enhancements to the stage that information is interchanged between the bridges. By checking the best configuration for information interchange, if the ESPA message is not the last updated, the bridge will append its information and send to other bridges. When both tables are completed, STA and TD, the sender can forward the packet to destination across the bridge.

According to the IEEE 802.17 Standard [1], multicast packets use the MAC address to identify the multicast group within the destination address field. To transmit the packet in RPR, there are 2 types: 1) unidirectional multicast: the packet is transmitted on the chosen ringlet and the packet is striped at the source, and 2) bi-directional multicast: the packet is transmitted on both ringlets and the cleave point is end point for preventing the packet overlap. The RPR Media Access Control (MAC) Client sets the TTL value to control the cleave point.

For local RPR multicast [8], the best choice to use is identified from the location of the adjacent member node. If the closest node to the sender is too far, unidirectional multicast is chosen. If the gap between the adjacent members are very large, the sender can decide the node in the middle gap is the cleave point and bidirectional multicast is used.

Multicast in the Inter-ring RPR is not as simple. To apply the algorithm of the local RPR for the Inter-rings is more complicated. The nature of Multicast in Inter-ring is to increase efficiency by decreasing the unwanted traffic due to flooding from the bridges.

III. PROPOSED SOLUTION

The proposed solution focuses on increasing the bandwidth utilization for Multicasting via Inter-ring RPR. The standard multicast packet was striped at the source, so the algorithm set the priority of the striped packet depends on the TTL of last member in each ring. The TTL is limited to the last member of multicast, such that the bandwidth between the last member and the source node allows for spatial reuse.

The multicast of inter-ring RPR is more complicated because it has the bridge that uses the ETD and ESPA to improve the standard RPR to reduce the bridge's flooding. We modify the topology discovery in the *TypeLenghtValu*e (1byte) field in order to collect the multicast member's address, which is called the Registrar Massages (RM). The packet identification is set for the multicasting identification. So anytime, the source is sending the multicast packet, it has to flood the RM to collect the members. The bridge acts like the source to remote of each rings so if a ring has no members, the bridge does not forward to its interfaces on that ring.

A. Multicast Registration

Initially, the sender floods the RM to all nodes in the network. The bridge receives the packet and floods to every interface except the incoming interface. The number of the RM is set to the identities of the multicast group automatically. The interested nodes receive the packet and will respond to the sender by replying with a unicast packet.

For the nodes in the remote ring, the interested nodes reply to the bridge first. The bridge will create the bridge's forward table from the messages information by mapping the multicast and the adjacent bridge, after that it will forward to the sender.

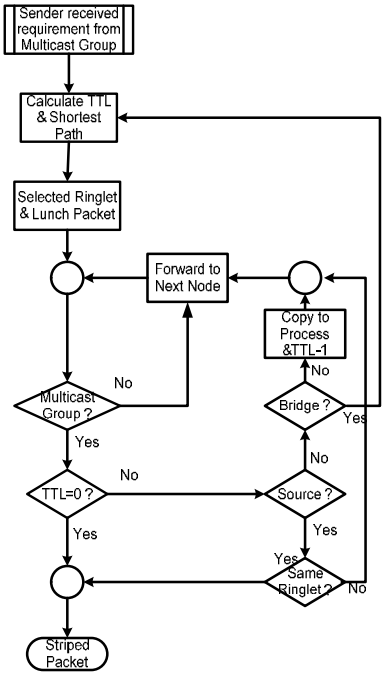

Fig 2. Flow chart of the multicast distribution is represented the proposed algorithm.

B. Multicast Distribution

The algorithm for multicast distribution is shown in Fig 2.When the multicast member's list is completed, the sender calculates the TTL to reach the last member node on the designated ringlet. The TTL of the multicast packet is decreased by each member node by 1 and the packet is copied to be processed at the MAC client layer. Other non-member nodes forward the multicast packet to the next node without decreasing the TTL. The last multicast member will decrease the TTL to zero and the packet is striped.

For Inter-ring RPR, when the bridge receives the multicast packet, it will check the destination from the bridge's forward table. The bridge will forward the multicast packet to the interface that the destination is on. After forwarding the packet to the other RRP rings, the bridge will re-calculate the TTL of the packet, by the bridge acting like the virtual source in the remote site so the same steps as the local ring can be repeated within each ring. If there are no multicast members in the remote site, the bridge will forward the packet to the next node in the local ring. The traffic in other RPR ring is not disturbed from the unwanted packet. This allows those parts of ring to create the spatial reuse traffic concurrently.

The algorithm is implemented to the nodes and the bridges to recognize the multicast group. In the case of the small network or single RPR ring, the enhanced multicast uses more

time in the registration period when it is compared with the standard multicast. On the other hand, the large network or inter-ring RPR, the enhanced multicast is very more valuable in the case of the video conference or the group distribution application because the unwanted traffic is avoided. We use the unused field of the frame format to implement so it does not require upgrading for any hardware or software.

IV. Simulation and Analysis of Proposed Solution

We conducted the OMNet++ simulator by configuring the parameters as shown in Table I.

TABLE I
CONFIGURATION PARAMETERS FOR OMNET++ SIMULATION

Parameter	Value
Link Capacities	2.4 Gbps(OC-48)
Packet Size	1,512 bytes data
Fairness Mode	Aggressive
Transit Buffer Size	6,144 bytes(4packets)
Link Delay	0.1ms

Initially, all nodes attach their information to the topology discovery message and flood to all nodes for completed topology's table and bridge's table. The topology discovery's table, includes collecting the multicasting member, is then created. In the simulation, we show the bandwidth utilization of multicast in inter-ring RPR, based on the following scenarios. Scenario 1 is measured time (ms) versus the link utilization of ring. By node A is a source node, after completed the multicast address's list, it calculated the TTL from the topology discovery's table for striped at the last destination.

For scenario 1, we measure the result of link utilization of each ring and compare with the standard multicasting. We can define the link utilization equation as:

$$Link\ Utilization = (TTL/Hop\ Count) * 100 \quad (1)$$

where *TTL* is the time-to-live of multicast, *Hop Count* is the number of passed node.

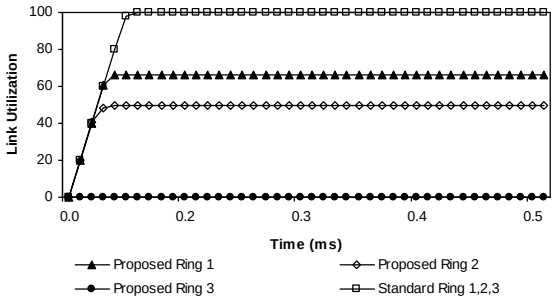

Fig 3. Graph of the link utilization in each rings for proposed multicast compare standard multicast.

The result of the simulation depends on the member's location as shown in Fig 3. The link utilization of the standard multicast in the ring 1, 2 and 3 is 100 percent from the source striped. When we applied our proposed algorithm, which was striped at destination, the graph of ring 1 will drop to approximate 66 percents from 3 members. The link utilization of the ring 2 is 50 percents from the 2 members in 5 nodes. The last ring 3 is 0 percents because no member is in the ring. When the link utilization was decreased, the bandwidth of each rings are more available to create other individual traffic so our proposed multicast use less bandwidth than standard multicast.

Next, we relocate the members in the ring 1and 2 by moving node C to D and G to I, in order to measure the link utilization and compare with the result in the previous scenario. The result of the link utilization in ring 1 and 2 increased by approximately 83.33 percent from the same number of members as in the previous scenario, as shown in Fig 4.

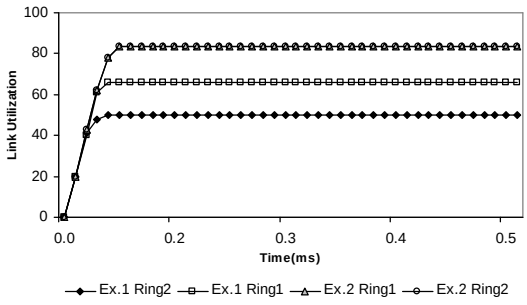

Fig 4. Graph of the link utilization, after relocation.

After we changed the node position, it affect to the link utilization which was increased, so the location of members is a major factor for the bandwidth usage.

For scenario 2, we use the topology shown Fig 1. We set the multicast group 1 as 200 Mbps, another multicast group as 400 Mbps and spatial reuse node M to N as maximum of bandwidth for testing the throughput of multicast traffic node M.

The result of the throughput at node M before applying the proposed multicast is 200 Mbps for multicast group 1's traffic, 400 Mbps for multicast group 2's traffic and the traffic of spatial reuse is 1.8 Gbps. The results of the proposed solution are shown in Fig 5. The throughput of spatial reuse is 2.4 Gbps that it is the maximum bandwidth of link capacity.

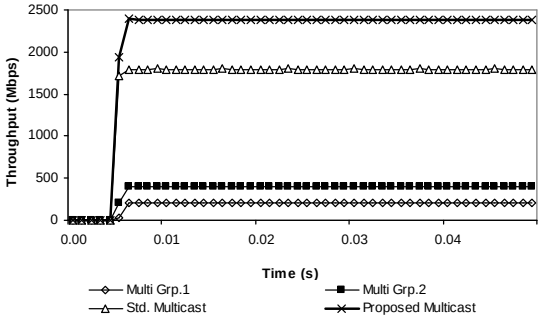

Fig 5. Graph of the throughput at node N compare the standard multicast and proposed multicast.

For scenario 3 in Fig 6, we applied the multicast traffic to the 3 inter-ring RPR with dual bridges. In this scenario, the traffic of ring 2 had to use for the route reach to the members in ring 3 so the traffic should limit less as possible and does not disturb the traffic in the ring 2.

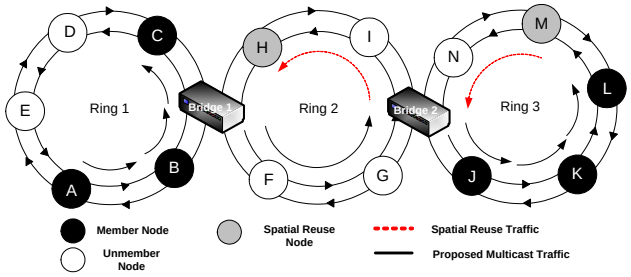

Fig 6. Node A sends the multicast packet to the members in the 3 RPR rings that were connected by dual bridges.

First, we start to transmit the multicast packet by using the standard multicast, after 0.05s, node M would transmit the spatial reuse traffic to node H. We measured the transmit rate at node H. For the results, the transmit rate of the standard multicast used full of bandwidth available but after 0.05s, the transmit rate dropped 50 percent from fairness mechanism for sharing the traffic with the spatial reuse as show at Fig 7.

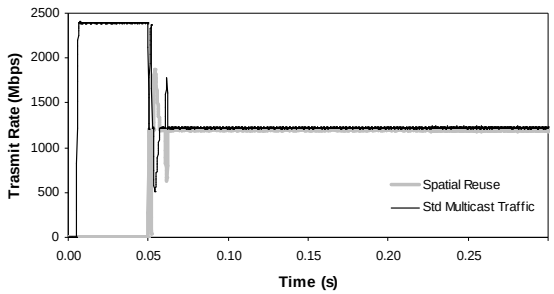

Fig 7. Graph of the transmit rate of standard multicast after the spatial reuse transmitted by measuring at node H.

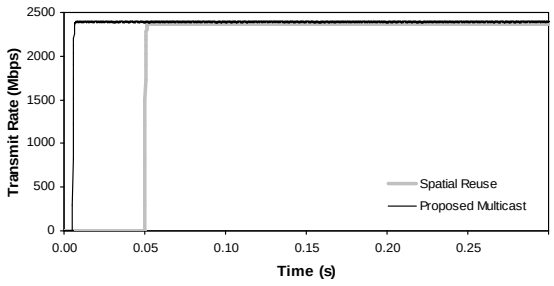

Fig 8. Graph of transmit rate of the proposed multicast after the spatial reuse transmitted by measuring at node H.

We also applied the proposed multicast instead the standard multicast and observe the transmit rate of the spatial reuse from nodes M to H. The transmit rate of spatial reuse doesn't drop during the multicast traffic as shown in Fig 8. When we compare the results of the 2 simulations, the proposed multicast avoid the multicast traffic to share the bandwidth of the spatial reuse so the transmit rate of spatial was full of bandwidth.

V. Conclusion

The simulation's results of the proposed multicast compared with the standard multicast show the increased bandwidth utilization in the inter-ring RPR from the lower link utilization and the throughput of the spatial reuse was full of link capacities during the multicasting. The proposed multicast algorithm uses less bandwidth than the standard multicast in the local and remote ring because the multicast traffic is limited at the last destination of each ring. The location of the member nodes impact the bandwidth usage of our multicast because we use only unidirectional multicast; nevertheless, it still better than the standard multicast. The cost upgrades of current RPR hardware and software is not required for implement the multicast in inter-ring RPR.

References

[1] IEEE 802.17 Working Group, "Resilient Packet Ring Access Method and Physical Layer Specifications," June 2004.

[2] P. Setthawong ,and S. Tanterdtid , "Efficient Traffic Management for Bridged Resilient Packet Ring Using Topology Discovery and Spanning Tree Algorithm", *The IASTED Network and Communication System NCS' 05*,April 2005 .

[3] A.Vargas,"The OMNet++ Discrete Event Simulation System", Proceedings of the European Simulation Multiconference ESM'01, Czech Republic, 2001.

[4] ANSI T1.105.01-2000, "Synnchoronous Optical Network (SONET) Automatic Protection".

[5] IEEE Standard 802.5-1989, " IEEE standard for token ring".

[6] IEEE 802.1D, Standards for Local and Metropolitan Area Networks: Media Access Control (MAC) Bridges, 1998.

[7] A. Kvalbein, S. Gjessing, and F. Davik, "Performance Evaluation of an Enhanced Bridging Algorithm in RPR Networks", *Proceedings 3rd International Conference on Networking ICN'04*,VOLUME II, 2004, 760–767.

[8] M. Maier, M. Scheutzow, M. Herzog, and M. Reisslein, "Multicasting in IEEE 802.17 Resilient Packet Ring", *IEEE CEC 2005*, July 2005.

The Optimum route by QoS Based on Genetic Algorithms (QGAs)

Jittanun Kulsiri, Suvepon Sittichivapak and Kriengkai Vonglodjanaporn
Department of Telecommunication Engineering, Faculty of Engineering,
King Mongkut's Institute of Technology Ladkrabang (KMITL),
Bangkok 10520, Thailand Tel +66-2737-2500 Ext.5028
Email: jittanuk@ais.co.th, jai_tel@hotmail.com

***Abstract*- We present another scheme, QoS based on Genetic Algorithms (QGAs), for finding the optimum route for wireless mesh networks. Our scheme was evaluated, based upon a critical factor as wireless channel quality, to decide whether each packet is successfully received and to define quality of service for improving the link quality and quantity in determining path. Simulation results show that our scheme outperforms with the original. Moreover, the time period of transmission by QGAs is less than the original when the packet size is higher or the population size is enlarging.**

Keywords: **Quality of Service, Genetic Algorithms, Optimum Routing, Wireless Mesh Network**

I. INTRODUCTION

Wireless mesh network (WMN) has grown considerably in popularity based on its several advantages in both metropolitan and rural applications, as showed in Fig. 1. This kind of network seeks to build a resilient and high performance infrastructure to provide users permeable Internet access. In a mesh network, each client accesses a local high speed access point (HAP), and multiple stationary HAPs communicate with one another over the wireless channel and form a multihop, wireless backbone for data delivery. This backbone ultimately forwards user traffic to a few gateway APs (GAPs) that additionally connect to the Internet via a wired connection or perhaps a WiMax link. Wireless devices have maximum utility since they can be used "anywhere at anytime".

The goal of WMNs is to process and forward packet data to other nodes and/or gateway. Therefore, a routing service is essential to WMNs applications. Much of recent work on wireless routing has been focusing on understanding the characteristics of the path performance metrics for finding the shortest path such as Dynamic Source Routing (DSR) [1], and Ad Hoc On-Demand Distance Vector Routing (AODV) [2]. Less attention has been paid to finding high-quality path in the face of lossy wireless links [3].

Nowadays, path optimum problem can be solved by many Artificial Intelligent (AI) techniques such as GAs, Tabu Search (TS), Evaluation Programming (EP), and etc [4]. As a result, a study on these AI techniques with speech recognition [5] is very interesting. GAs is chosen in this paper because (1) GAs can find nearly the optimum solution even for a large scale problem, and (2) GAs is simple to implement and understand.

In this paper, we present another scheme of the radio wireless mesh network, which is QoS metrics like desired

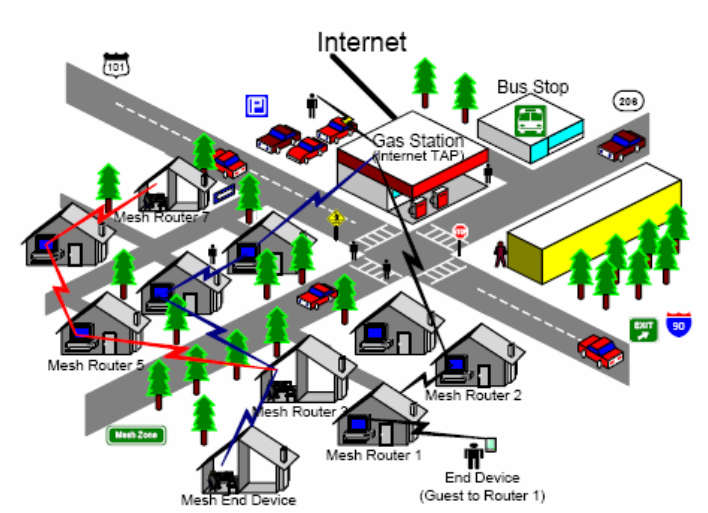

Fig.1: WMNs for metropolitan area networks

signal to noise ratio (S/N), packet loss, utilization and reliability of link in the path selection process to reduce a processing time and increase more accuracy before using GAs process to find an optimum route.

This paper is divided into 5 parts. The introduction is described in section I. The background and the system model are presented in section II and III respectively; whereas, the simulation results are presented in the section IV. Finally, our conclusion is given at the end of this paper.

II. Background

This section describes the wireless network architectures being focused on this paper, and provides a discussion of the Wireless link quality, Quality of Service, and Genetic Algorithms for wireless routing.

A. Wireless Mesh Network

Wireless mesh network is a mesh networking implemented over a Wireless LAN. This type of the Internet infrastructure is decentralized (with no central service provider), relatively inexpensive, and very reliable and resilient. Each node needs only transmission to the adjacent node. Nodes act as repeaters to transmit data from one node to another, allowing the extension of communications over distances, especially over rough or difficult terrain. Mesh networks are also extremely reliable as each node is connected to several other nodes. If one

node drops out of the network, due to hardware failure or any other reasons, its neighbors simply find another route. Extra capacity can be installed by simply adding more nodes. Mesh networks may involve either fixed or mobile devices. The solutions are as diverse as communications in difficult environments such as emergency situations, tunnels and oil rigs to battlefield surveillance and high speed mobile video applications on board public transport or real time racing car telemetry.

B. Wireless Link Quality

The signal strength received form transmitter is important for wireless systems. The loss in signal strength affected from several factor such as noise interference, fading, attenuation, and etc. Many wireless channel models have been proposed to predict the average received signal power. In this paper, we use the free space propagation model to predict received signal strength for the near sight and plane earth propagation model for the far sight. The received signal power (*Pr*) can be characterized as follow.

$$P_r = \begin{cases} \dfrac{P_t \times G_t \times G_r \times \lambda^2}{(4\times\pi)^2 \times d^2 \times L} & , \quad d \le \dfrac{4\times\pi\times H_r \times H_t}{\lambda} \\ P_t \times G_t \times G_r \times \left(\dfrac{H_r \times H_t}{d^2}\right)^2 & , \quad d > \dfrac{4\times\pi\times H_r \times H_t}{\lambda} \end{cases} \qquad (1)$$

From the equation, *Pt* is the transmitted power, *Gt* and *Gr* are the antenna gains at the transmitter and receiver, respectively, *d* is the distance between transmitter and receiver in meter, *Ht* and *Hr* are the heights of the transmitter and receiver, respectively, *L* is the system loss factor not related to propagation (In this paper, *L*=1), and λ is the wavelength in the meter.

The bit error rate (BER) of wireless link is resolute by link quality, modulation and code scheme. The link quality can be represented by signal to noise ratio (S/N) of packet at the receiver. Thus, BER of wireless channel is determined by SNR and modulation scheme or transmission rate. The modulations perform the general relationship between *BER* and *SNR* by the following equation

$$BER \; \alpha \; erfc(\sqrt{C \times SNR}) \quad , \quad SNR = 10 \times \log\left(\frac{P_r}{N}\right) \qquad (2)$$

where *BER* is bit error rate, *erfc (x)* is complementary function, *C* is constant, *Pr* is received signal power which derived from equation 1, and *N* is noise power.

The re-transmission is the factor for network performance with mention in IEEE802.11. When a transmitter send data packets to receiver and does not receive acknowledgments, the transmitter must perform re-transmission packet again. The classifications of the re-transmission have 2 modes, Hop-by-Hop Re-transmission (HHR) and End-to-End Re-transmission (EER). In this paper, we consider the HHR scheme because it is suitable for the characteristic of wireless mesh network such as having low number of packet re-transmission than the EER scheme, and implies a shortest time.

C. Quality of Service

Quality of Service (QoS) refers to the capability of a network to provide better service to selected network traffic over various technologies, including Frame Relay, Asynchronous Transfer Mode (ATM), Ethernet and 802.1 networks, SONET, and IP-routed networks that may use any or all of these underlying technologies [6]. The primary goal of QoS is to provide priority including dedicated bandwidth, controlled jitter and latency (required by some real-time and interactive traffic), and improved loss characteristics. The notion of QoS has been proposed to capture the qualitatively or quantitatively defined performance contract between the service provider and the user applications [7]. The basic function of QoS routing is to find a network path which satisfies the given constraints. In addition, our QoS routing algorithms consider the optimization of resource utilization and link reliability.

D. Genetic Algorithms

Genetic Algorithms (GAs) are adaptive heuristic random search algorithms premised on the evolutionary ideas of natural selection and genetics. The search is usually done with a group or population of binary strings, which are encoded forms of the decision variables. Each string is analogous to a chromosome and each binary bit is analogous to a gene on that chromosome. There are three operators used in the simple GA, selection, crossover, and mutation. Each having the following specific roles:

- Selection: exponentially spreads, over generations, above average fitted chromosomes by allowing them more offspring in next generations.
- Crossover: exploits genetic materials of the current population by breeding most interesting strings.
- Mutation: introduces diversity in population by flipping randomly chosen genes.

Using these operations, more fit members of the population are created over time and the population evolves to optimal or near optimal solutions.

III. System Model

In this paper, we simulate the connecting channel between source node and destination node of mesh topology over wireless communication system. The purpose is to achieve the most appropriate route for sending and receiving packet data. The proposed approach and process are as follows.

1. Individual routes of hop from QoS are determined to be utilized as candidate links prior to the process of GAs. In order to select a route for data transmission, the most important thing to be considered is the quality of the chosen route as it is able to be indicated by the following factors.

- BER: In case a route exhibits a large number of bit errors, it is considered poor quality. Additionally, more time is consumed for re-transmission.
- S/N: Signal strength received is compared to Noise power. A route exhibits low S/N value indicates the occurrence of noise interference of received data, resulted in eccentric signal.

Consequently, more time and energy are needed for re-transmission to obtain accurate data.

- Utilization: This factor considers the number of users of each route. A route with high volume of users is affected with the delay of data due mainly to the limitation of resource allocated to high utilization. Therefore, the route ought to be avoided.
- Link Reliability: This factor is considered to be significant for the selection of appropriate route owing to the fact that there are high tendencies of a route to confront with link down. As a consequence, although other factors prove effective, the opportunity of a successful transmission of data via the link is relatively low.

2. After obtaining the determined Link candidates in accordance with the defined criteria, the links, later, are evaluated to find the best route for transmission of data from source node to destination node by GAs, using Fitness Function under the condition of "minimum delay route" as shown in equation 3 as follow

$$Min\,T(L) = \sum_{i=1}^{M+N} \sum_{j=1}^{M+N} C_{ij} X_{ijk} + T_{re-tran} \qquad (3)$$

where *T(L)* is the period of time for a success of send-receive packet data from source node to destination node.

Cij is the period of time for a success of send-receive packet data between i node to j node.

$$X_{ijk} = \begin{cases} 1 & ,if\ link\ i,\ j\ is\ concluded\ in\ tour\ k \\ 0 & ,otherwise \end{cases}$$

N is number of locations to be visited

M is number of tours

$T_{re\text{-}tran}$ = time period for re-transmission

Fig. 2 shows the flow chart of the proposed QGAs algorithm. The characteristics of the algorithm are summarized as follows:

1) Set model parameter for QoS and error probability obtained from connecting channel as the initial distance, utilization and link reliability, respectively.
2) Create an initial population by randomly generating a set of feasible solution according to our scheme.
3) Determine the fitness function of each number in the population.
4) Apply GA operators to generate new population as mutation, crossover and reproduction, respectively.
5) Compare the results of all generation and choose the best ones.

IV. Simulation Results

We consider a mesh network topology with 50 nodes randomly placed over a 1000 x 1000 m^2, each node randomly positioned with communication range less than 120 meters. We perform experiments transmission packet as 1,000 packets with the sizes of data packets varying from 1,000, 2,000, 3,000 and 4,000 bits/packet. The physical radio characteristic of the transmission bit rate is 54 Mbps referred to IEEE802.11.

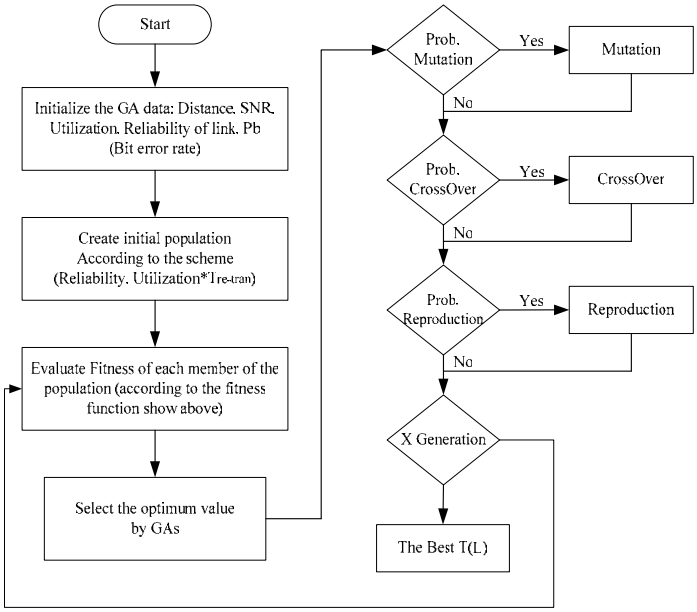

Fig. 2: Flow chart of the proposed QGAs Algorithm

In our simulated situation, we implement the link quality which uses the packet error probability to resolve whether or not each packet is received successfully based on the BER and packet length inferred by SNR at the receiver. Moreover, we consider about the QoS (Utilization and link reliability) for the path selection before using GAs process as well. The initial values of all factors are shown in Table 1.

For the GA parameters, the population size is 50, the value of parameter that optimizes the algorithm's performance as number of generation is 50, the probability of mutation and crossover are 0.5 and 0.75, respectively. The length of connections is 10 nodes.

The performance metrics that we have considered are the minimum delay routes from both of path finding time and transmission time.

Figure 3 illustrates the delay time (Fitness function) with the varied data packet sizes as 1,000, 2,000, 3,000 and 4,000 bits, respectively from both of our scheme and the original. It also shows a verifiable performance for our scenarios, especially for the 80% performance route; the link quality is affected the network connectivity. This implies that QGAs uses more number of hops to avoid the path consist of links having high

Table 1
Initial parameter in random scenario

Utilization (transaction/path)	1-54
Link Reliability (%)	0-100
SNR	0-20
Distance (m)	20-120
Simulation time (min)	2

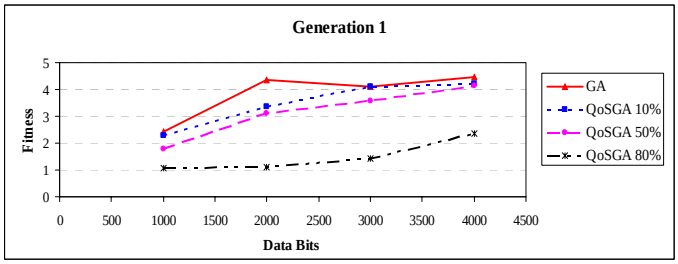

Fig.3: Comparison between original And QGAs at different packet sizes

Table 2
Simulation results in random scenario

Protocol / Metrics	GAs Original	QGAs at 10% performance link	QGAs at 50% performance link	QGAs at 80% performance link
Time period of finding route (sec)	1	1	1	1
Time period for complete transmission (sec)	1.854933	1.64921433	1.79043037	1.15131126

bit error rate and try to find the path having the least number of utilization or low possibility of link failure.

Figure 4 a) and b) reveal some of the chrematistic behaviors of both GAs and QGAs. As expected, the GAs and QGAs converge faster at lesser generation when the population is large. In fact, when the population size is 100, the GAs and QGAs reach a fitness level of 1st generation. For the population size of 50, the same GA also reaches a fitness level of 1st generation.

Figure 4 a) and b) show the results of our comparison when the population sizes are enlarged. The capability of QGAs in finding the optimum path for receiving – sending the data packet is better than the original algorithm.

Table 2 confirms that QGAs outperforms for finding the optimum route in wireless mesh network although the time of finding the QGAs route and the original are equal. This is due to the fact that QGAs need some time to search for the best quality route with Link reliability, utilization and chances of errors during transmission in order to reduce time period for re-transmission. From the reason, time period for complete transmission of QGAs is a lot less than that of the original.

V. Conclusions

In this paper, a new QoS base-on GA scheme is presented to find the optimum route between source and destination node with the consideration of the link quality and quantity.

The simulation results illustrate that QGAs can find the best route with the accurate data transmission compared to the original, although send-receive and network sizes are enlarged. This is because QGAs have a better path finding process based on concerned factors affecting communication. Thus, the time

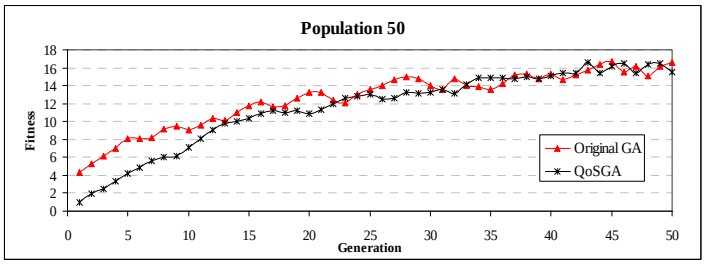

a)

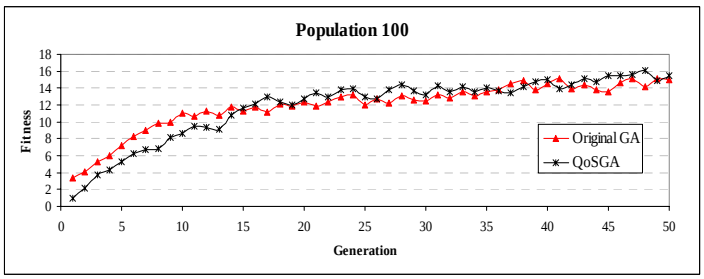

b)

Fig.4: Comparison of between original And QGAs at different population sizes

period for sending-receiving data is less with high quality of transmission.

References

[1]. D. B. Johnson, D. A. Maltz, and Y-C Hu., "The Dynamic Source Routing Protocol for Mobile Ad Hoc Networks (DSR)",IETF Mobile Ad Hoc Networks Working Group, Internet Draft, work in progress, 24 February 2003

[2]. C. E. Perkins, E. M. Royer and S.R. Das, "Ad Hoc Ondemand Distance Vector (AODV) routing," IETF internet Draft, work in progress, Nov 2002

[3]. D.De Couto, D. Aguayo, J. Bicket, and R.Morris, "A high-throughput path metric for multi-hop wireless routing", Proceedings of ACM MobiCom Conference, September 2003

[4]. B. Maxwell and S. Anderson. 1999. *Training Hidden Markov Models using Population-Based Learning*. In Genetic and Evolutionary Computation Conference, GECCO-99, 994

[5]. Wu Ying, Li Bin. "Jobshop Scheduling Using Genetic Algorithms" the 3rd International Conference on Signal Processing. ICS '96. Beijing

[6]. G.Apostolopoulos, R.Guérin, S. Kamat, A.Orda, S. Tripathi, "Intradomain QoS Routing in IP Networks: A Feasibility and Cost/Benefit Analysis", in IEEE Network Magazine, September/October 1999.

[7]. MONET research group," QoS Routing", University of Illinois at Urbana-Champaign http://cairo.cs.uiuc.edu/qosrouting/index.html

[8] A. Kershenbaum, Telecommunications Network Design Algorithm, New York, McGraw - Hill, Inc., 1993

[9] T. S. Rappaport, Wireless Communications Principles and Practice, Prentice-Hall, Inc., 2002

[10] M. Pioro and D. Medhi, Routing, Flow, and Capacity Design in Communication and computer Networks, Morgan Kaufmann Publishers, San Francisco, 2004

TCP-friendliness Definition Revision & Implementation for Multi-Rate Multicast Congestion Control

Somnuk Puangpronpitag
E-mail: somnuk.p@msu.ac.th
Computer Science, Faculty of Informatics,
Mahasarkham University

Suchart Kummanee[1]
E-mail: suchart.k@msu.ac.th
Computer Science Department, Science,
Khon Kaen University

***Abstract*- In this paper, we revise the definition of TCP-friendliness for multicast and introduce a new design of Multi-rate Multicast Congestion Control (MR-MCC) by applying a logarithmic receiver dependent policy to the Explicit Rate Adjustment (ERA) protocol. In our design, the receiver explicitly adjusts its reception rate according to the network conditions using Packet-pair Probe. Yet, the TCP-friendliness implementation has been revised in order to give a motivation for multicast deployment. A new multicast TCP-friendly bandwidth allocation scheme is used at any individual router to be multicast-favorable without causing TCP starvation. We have also implemented our MR-MCC design into a network simulator (ns2) and demonstrate via simulations a good performance.**

I. INTRODUCTION

Due to the tremendous growth of the multipart communication applications, such as software distribution, audio/video broadcasting and video conferences, multicast transmission has become significant since it is more bandwidth efficient for one-to-many communication than multiple unicast. However, the congestion control mechanism of multicast has not yet been standardized till now. Multi-Rate Multicast Congestion Control (MR-MCC) has been accepted as a key solution of multicast congestion control for the Internet [7]. Several MR-MCC proposals (such as [10], [4], and [6]) have been made including ours, Explicit Rate Adjustment (ERA) [12, 13].

TCP-friendliness is a main fairness goal for these previous MR-MCC proposals because it is a suggestion from IETF ([9], [1]) for new congestion control protocols running in the best-effort Internet. The purpose of TCP-friendliness is to protect Transmission Control Protocol (TCP) traffic (the majority of Internet traffic) from any new aggressive traffic.

TCP-friendliness definition in [8] demands that a non-TCP flow should receive similar bandwidth shares. In order to be TCP-friendly, previous MR-MCC proposals have been designed to allocate less than or equal bandwidth for a multicast flow in comparison to a TCP flow. However, we argue that the definition of TCP-friendliness for multicast congestion control protocol should be revised. An MR-MCC may serve several receivers, while a TCP flow serves only one. Hence, the MR-MCC flow should deserve more bandwidth than a single TCP (unicast) flow. Giving more bandwidth share would be an incentive to deploy multicast instead of multiple unicast, thus saving network bandwidth. Without this incentive, the overhead of multicast (such as Internet Group Management Protocol (IGMP), complex security issues and difficulties in congestion control) would not be attractive. Most receivers would then prefer to use multiple unicast, and not move to multicast.

Hence, in this paper, we propose to revise the definiton of multicast TCP-friendliness and modify ERA (our previous MR-MCC) by applying a logarithmic receiver dependent bandwidth allocation scheme [5] together with an estimation of an explicit target rate using a *Packet-pair Probe* (PP). The new design provides a multicast congestion control mechanism with responsiveness and a motivation for multicast deployment while not causing TCP bandwidth starvation. Hence, we contribute an innovative MR-MCC framework with a more incentive TCP-friendliness definition. In addition, we have built our design into a network simulator (ns2) and undertaken performance evaluation. The results show a favourable performance.

The remainder of this paper is organized as follows. We begin in Section II by discussion of background and related work. In Section III, we describe the rationale of our new design. The framework and algorithms of new ERA are proposed in Section IV. Section V shows the performance evaluation using network simulation technique. In Section VI, we conclude and discuss the future work.

II. BACKGROUND AND RELATED WORK

A. *Multi-Rate Multicast Congestion Control (MR-MCC)*

MR-MCC is based on the ability of a source to generate the same data at different rates over multiple multicast streams (using Layer Coding Transport (LCT) [7]). The multiple multicast groups are organized into logical layers. Each layer is each multicast group. The burden of congestion control is at the receiver's side. The source has only a passive role, so this approach is called receiver-driven. A receiver tunes its reception rate by subscribing to and unsubscribing from layers according to its network condition. Different receivers may subscribe at different levels of their own subscription rates, especially when they are in different network conditions

Receiver-driven Layered Multicast (RLM) [10] is the first proposal of MR-MCC. Packet-pair Layered Multicast (PLM) [4], Wave and Equation Based Rate control (WEBRC) [6] and ERA [12] are some previous proposals of MR-MCC.

[1] A postgraduate student at Khon Kaen University, Thailand

B. *TCP-friendliness*

More than 90% of today's Internet traffic is TCP-based. To protect the majority population from aggressive traffic, the Internet community [1] suggests that new congestion control mechanisms for traffic likely to compete with best-effort TCP traffic should be TCP-friendly. TCP-friendliness (also known as TCP compatibility) is actually the inter-protocol fairness towards TCP. The TCP-friendliness definition [8] demands that a TCP flow and a non-TCP flow should receive similar steady-state bandwidth shares, if they traverse the same path and thus face similar round trip delays and packet loss rates. Previous MR-MCC protocols have been designed to provide TCP-friendliness in such a strict manner by allowing the multicast flow to use less than or equal bandwidth share to TCP.

C. *Fairness Paradigm Between Multicast and Unicast*

As mentioned previously, a multicast flow may serve more than one receiver, while a unicast flow only serves one. If we want to give a motivation to use multicast instead of multiple unicast, the fairness definition between multicast and unicast must given the multicast flow a favor. There have been a few initial studies focusing on defining a better fairness paradigm between multicast and unicast. For example, Wang et al. have defined *Bounded Fairness* or *Essential Fairness* (against the current paradigm, Absolute Fairness), as the situation in which bandwidth allocated for multicast may not be the same as bandwidth allocated for unicast. The multicast flow in this sense of fairness may be allocated more bandwidth than TCP at a certain boundary. Furthermore, Legout et al. [5] proposed that the bandwidth allocation for multicast should consider the number of downstream receivers. They demonstrated three possible schemes of bandwidth allocation, namely Receiver Independence (RI), Linearly Receiver Dependence (LinRD) and Logarithmically Receiver Dependence (LogRD). They have also shown that LogRD is the best among three.

III. RATIONALES OF THE NEW DESIGN

Two main goals of MR-MCC design are responsiveness and TCP-friendliness. ERA was one of the successful MR-MCC design, proposed by Puangpronpitag et al. in [12, 13]. It is equipped with the "explicit receiving rate adaptation" using Packet-bunch Probe and TCP-friendly algorithm to provide responsiveness and TCP-friendliness. Like other previous MR-MCC designs, ERA uses a TCP-friendliness as a fairness paradigm. So, ERA will not use the bandwidth more than TCP even in the situation that an ERA flow may serve many more receivers than a TCP flow.

Hence, we revise the definition of TCP-friendliness for multicast and interpret it in a more relaxing way by allocating more bandwidth to the multicast flow correspondent to the number of its downstream receivers. We still believe in the key idea of TCP-friendliness to protect TCP from bandwidth starvation due to aggressive traffic. So, we apply LogRD bandwidth allocation policy at every router instead of the strict TCP-friendly rate. LogRD policy has been proven to provide more bandwidth allocated to multicast without starving TCP [5]. While this implementation should be more attractive for multicast deployment, it is still TCP-friendly in a way of not aggressive towards TCP.

To provide responsiveness, we still keep the "explicit receiving rate adaptation" using Packet-bunch Probe at the receiver operation. Moreover, LCT at source operation is also kept.

IV. FRAMEWORK AND ALGORITHMS

Multicast Support at network layer: Our design assumes IP multicast at the network layer. We also assume that there is a mechanism (such as, [3], [2]) to indicate the number of downstream receivers of the multicast flow at every router.

Network-assisted congestion control: Our design proposes LogRD bandwidth allocation policy to be implemented at each router.

Layered coding and receiver-driven: Our design uses a receiver-driven layered multicast approach to provide scalability for a very large heterogeneous group of receivers.

Explicit rate adjustment: We believe that finding a simple mechanism for explicit rate adjustment would simplify the congestion control problem. According to our algorithms, the receiver adjusts its reception rate to the target rate, which is explicitly calculated as the estimated available bandwidth. The details was described in [12]).

Receiver Coordination: The coordination of the receivers under the same bottleneck link is necessary to obtain intra-session fairness. In addition, this co-ordination is significant to utilize bandwidth efficiently and handle congestion properly. ERA provides the coordination by relying on *Session Announcement Message (SAM)* and *Rate Adaptation Interval (RAI)* as follows. The source sends a *SAM* at predefined times to provide information about the transmission session. *RAI* is a part of the information provided in *SAM*. The receiver can join a transmission session only after it has received a *SAM* and will adapt its reception rate every *RAI*.

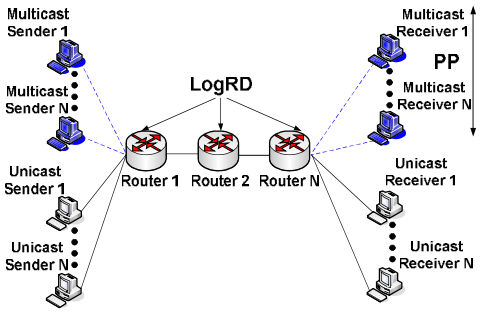

Figure 1 Modification of ERA design

Figure 1 shows the new of ERA design consisting of LogRD mechanism at the routers and Packet-bunch Probe (PP) at the receivers. The main part of ERA algorithms provided in [12]) are still same except the followings:

(1) We apply LogRD as the bandwidth allocation mechanism at each router as shown in Figure 2.

(2) The TCP-friendly rate in the old ERA's design is not used as a boundary of reception rate anymore. Yet, the LogRD bandwidth allocation (in (1)) will protect TCP from starvation while provide more bandwidth to multicast according to the number of its downstream receivers. The reception rate adaptation mechanism has been revised as follows:

LogRD algorithm at the router

Procedure LogRD (C, k, m, type) {

If type = 'UNICAST' **Then**

Return $\sum_{i=1}^{k} \frac{1}{k+(1+\ln m)} C$

Else If type = 'MULTICAST' **Then**

Return $\sum_{i=1}^{m} \frac{(1+\ln m)}{k+(1+\ln m)} C$

End If

}

when C = the available bandwidth,
k = the number of unicast flow
m= the number of multicast flow

Figure 2 LogRD algorithm

For every arrival of packet-pair, the receiver estimates the available bandwidth (R'_{pp}) using the technique mentioned in [12]. If the subscribed rate is higher than R'_{pp}, the receiver will immediately adapt its reception rate down to avoid overloading the network.

For every *Rate Adaptation Interval (RAI)*, the receiver calculates an estimated bandwidth R_{pp} as the minimum R'_{pp} during the last *RAI*. There may be a pathological case, when packet pairs are lost during severe congestion. Then, we may not have enough R'_{pp} to make a good estimation of available bandwidth (R_{pp}). In this case, we set R_{pp} to –1 to indicate severe congestion.

The receiver calculates its current subscribed rate (R_i) with respect to the number of subscribed layers (i) maintained at the receiver, and a data rate of each layer obtained from the session description.

1. The receiver then set the target reception rate (R_{TARGET}) as R_{pp}. If R_{pp}=-1, the receiver unsubscribes one layer to solve the severe congestion.
2. The receiver subscribes to or unsubscribes from layers according to the R_{TARGET} as follows:

```
If (Ri > RTARGET) Then
  Repeat Until (Ri ≤ RTARGET)
    If i > 0 Then
      Unsubscribe from a layer
      i = i -1
    Else
      EXIT the session
    End If
  Loop

Else If (Ri < RTARGET)
  Do While (Ri+1 < RTARGET)
    Subscribe to a layer
    i = i +1
  Loop
Else If (Ri = RTARGET)
  Maintain the current subscription level
End If
```

V. PERFORMANCE EVALUATION

A. Simulation Tools

We have integrated our algorithms into the ns2 network simulator [11] and conducted a performance evaluation to test our protocol extensively. Each simulation is run 20 times using a different Random Number Generator parameter. Results are averaged and quoted with respect to confidence intervals of 95%.Due to space limitation, some key simulation experiments are only sampled and summarized.

B. Simulation Scenarios & Parameters

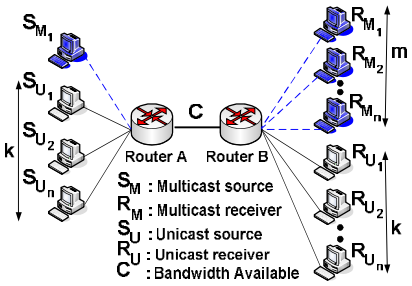

Figure 3 Simulation topologies

As shown in Figure 3, the topology used in our experiments is the dumbbell topology, having 1 multicast sender and k unicast (TCP) senders at one end and m multicast receivers and k unicast receivers at the other end as well as the bottleneck link at the middle. We randomly start the TCP source after 10 seconds and then start multicast source after 30 seconds to observe the responsiveness of the congestion control mechanism. We are interested in bandwidth allocation between TCP and multicast after increasing the number of multicast downstream receivers.

C. Experiment I : one downstream receiver

In this experiment, we use a multicast flow with one downstream receiver competing with a TCP flow. Figure 4 show the TCP-friendliness of our new ERA. So, LogRD at router can replace the function of TCP-friendly rate of the old design very well in case of one downstream receiver.

D. Experiment II: many downstream receivers

In this experiment, we use a multicast flow with several downstream receivers competing with a TCP flow. Figure 4 shows the results in case of 2 downstream receivers of multicast. From the figure, the multicast flow gains more bandwidth than the TCP flow. However, it does not starve the TCP connection. We have also run further experiments by increasing the number of multicast downstream receivers to 10 and 100 and still find that the new ERA mechanism does not starve the TCP connection. Moreover, the new ERA gains more bandwidth than TCP since it serves more receivers. This would inspire people to deploy multicast instead of multiple unicast that consumes more bandwidth.

In order to understand more about LogRD bandwidth allocation, we assume 400 Kbps of bandwidth and a multicast flow competing with a TCP flow. By increasing the number of

multicast downstream receivers, we calculate the bandwidth allocation between the multicast and TCP according to the algorithm described in Section IV. The results are shown in Table 1. From the results, it is clear that the logarithmic receiver dependent policy can give incentive to multicast deployment and does not starve the TCP connection even at 10,000 downstream receivers.

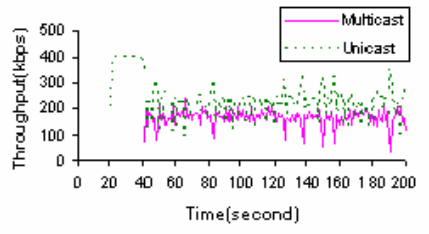

Figure 4 Experimental result I

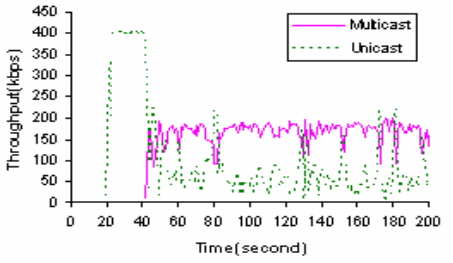

Figure 5 Experimental result II

Table 1 LogRD bandwidth allocation according to the number of multicast downstream receivers

# receivers	Multicast		TCP	
	Kbps	%	Kbps	%
1	200.00	50.00%	200.00	50.00%
2	251.47	62.87%	148.53	37.13%
3	270.91	67.73%	129.09	32.27%
4	281.88	70.47%	118.12	29.53%
5	289.18	72.29%	110.82	27.71%
6	294.51	73.63%	105.49	26.37%
7	298.63	74.66%	101.37	25.34%
8	301.95	75.49%	98.05	24.51%
9	304.70	76.17%	95.30	23.83%
10	307.03	76.76%	92.97	23.24%
100	339.44	84.86%	60.56	15.14%
1000	355.10	88.77%	44.90	11.23%
10000	364.32	91.08%	35.68	8.92%

One may argue that the TCP flow gains less bandwidth allocation. Yet, the reason is quite clear that the multicast flow must gain more bandwidth due to serving more receivers. If there is no incentive to use multicast as we proposed. The multiple unicast would be used instead. The network loads are then increased. Furthermore, in that case, the situation of the TCP flow will be even worse. For example, at 10 multicast receivers, from Table 1, we gain 307.03 Kbps for 1 multicast flow and 92.97 Kbps for 1 TCP flow. If the multicast flow is replaced with multiple unicast flows, there will be 11 unicast flows sharing 400 Kbps bandwidth. The TCP flow would gain only 36.36 Kbps instead (if the 11 unicast flows allocate bandwidth fairly). So, it would be far better to give some more bandwidth to the multicast flow when it serves more receivers.

VI. Conclusions and Future Work

Due to the strict definition of multicast TCP-friendliness, there has been no incentive to use MR-MCC. So, we have revised the definition of TCP-friendliness for MR-MCC that it should gain more bandwidth than TCP corresponding to its number of downstream receivers. Yet, MR-MCC should not starve TCP. To follow this new MR-MCC TCP-friendliness definition, our previous MR-MCC protocol (ERA) has been redesigned by changing the rate adaptation algorithm and applying a logarithmic receiver dependent policy at each router. After implementing and simulating by ns-2, the initial experimental results demonstrate that TCP is not starved due to our new protocol. Yet, our new protocol can be more attractive to be deployed as gaining more bandwidth. In the future, we plan to further experiment on our protocol to evaluate the performance extensively.

References

[1] B. Braden and et al., "Recommendations on Queue Management and Congestion Avoidance in the Internet", IETF, RFC 2309, April 1998.

[2] F. Filali, H. Asaeda, and W. Dabbous, "Counting the Number of Members in Multicast Communication", In Proceedings of Networked Group Communication, Massachusetts, USA, October 2002.

[3] H. W. Holbrook and D. R. Cheriton, "IP multicast channels: EXPRESS support for large-scale single-source applications", In Proceedings of ACM SIGCOMM, pp. 65-78, Harvard, USA, September 1999.

[4] A. Legout and E. W. Biersack, "PLM: Fast Convergence for Cumulative Layered Multicast Transmission", In Proceedings of ACM SIGMETRICS, pp. 13-22, California, USA, June 2000.

[5] A. Legout, J. Nonnenmacher, and E. W. Biersack, "Bandwidth-allocation Policies for Unicast and Multicast Flows", *IEEE/ACM Transactions on Networking*, vol. 9, No. 4, pp. 464-478, August 2001.

[6] M. Luby, V. K. Goyal, and S. Skaria, "Wave and Equation-based Rate Control: A Massively Scalable Receiver Driven Congestion Control Protocol", *Computer Communications*, October 2002.

[7] M. Luby and et al., "Layered Coding Transport (LCT) Building Block", IETF, RFC 3451, December 2002.

[8] J. Mahdavi and S. Floyd, "TCP-friendly Unicast Rate-based Flow Control", Technical note to the end2end-interest mailing list, 1997.

[9] A. Mankin, and et al, "IETF Criteria for Evaluating Reliable Multicast Transport and Application Protocols", IETF, RFC 2357, June 1998.

[10] S. McCanne, V. Jacobson, and M. Vetterli, "Receiver-driven Layered Multicast", In Proceedings of ACM SIGCOMM, August 1996.

[11] ns2, "Network Simulator -- ns 2", http://www.isi.edu/nsnam/ns.

[12] S. Puangpronpitag, R. Boyle, and S. Sanguangpong, "Explicit Rate Adjustment (ERA): Responsiveness, Network Utilization Efficiency and Fairness for Layered Multicast", *Journal of Systemics, Cybernetics and Informatics*, vol. 3, No. 4, February 2006.

Design of Dual Wide-band Slot Antenna Fed by CPW

P. Pommas [1], N. Anantrasirichai[1], P. Rakluea[2], T. Wakabayashi[3]
[1]ReCCIT, Faculty of Engineering, King Mongkut's Institute of Technology Ladkrabang
Bangkok, 10520, Thailand, E-mail: kanoppin@kmitl.ac.th
[2]Dept. of Electronic and Telecommunication Engineering, Faculty of Engineering
Rajamangala University of Technology Thanyaburi (RMUTT) Klong 6
Thanyaburi, Pathumthanee, Thailand
E-mail: paitoon_r@rmut.ac.th
[3]School of Information Science and Technology, Tokai University, Hirasuka, Kanagawa, 259-1292, Japan
E-mail: wakaba@et.u-tokai.ac.jp

***Abstract*- In this paper, the simple structure of slot antenna fed by coplanar waveguide (CPW) is considered for dual frequency. For increasing the antenna bandwidth, the conductor stub is proposed by overstep the central conductor (signal strip) into slot antenna. By sufficient choosing shape and size of conductor stub, can be achieved the wide bandwidth 23.8% (2.22-2.82 GHz) and 86.04% (3.88-9.74 GHz), which can use in WLAN applications coverage standard of IEEE 802.11b/g (2.4-2.4835 GHz), IEEE 802.11j (4.90-5.091), IEEE 802.11a (5.15-5.35 GHz), IEEE 802.16d (5.7-5.9 GHz). The simulation results of this slot antenna are analyzed by using MoM from IE3D Software [1].**

I. INTRODUCTION

Coplanar waveguide (CPW) transmission line has increased significantly in recent years. The antennas fed by CPW have several useful properties. The properties include wider bandwidth, better impedance matching, and lower radiation losses. Also slot antennas have wider impedance bandwidth as compared to microstrip patch antennas [2]. The advantages of CPW fed slot antenna is wideband antenna which many research introduced the several shape of slot antenna for use in Wireless Local Area Network (WLAN) communications systems [3]. However, conventional the CPW fed slot antennas is not large enough bandwidth to cover the demand of Wireless LAN communications systems.

In this paper presents a CPW fed slot antenna for dual frequency of WLAN application at low frequency band 2.4 GHz and high frequency band over 4 GHz. We will begins considering the simplest and most basic configuration of CPW-fed slot antenna. Finally, we will try to maximize bandwidth by using conductor stub to keep the return loss to minimum. The simulation results of bandwidth at low frequency 2.4 GHz is 23.8% and at high frequency over 4 GHz is 86.04%

II. ANTENNA DESIGN

In this paper, IE3D software package of Zeland [2] is used to design and simulation. This antenna is designed on dielectric constant ε_r = 2.2 and a thickness h = 1.575 mm at design frequency 2.4 GHz.

In this case, the parameters of slot antenna structure are as following:

Width of antenna, W_a = 72 mm
Length of antenna, L_a = 47 mm
Width of CPW feed line, S_f = 0.3 mm
Width of signal strip, W_f = 3.0 mm
Length of CPW feed line, L_f = 25 mm

In the design of CPW-fed slot antenna, we will begins to consider the simplest basic configuration and developing for wide band by using conductor tuning stub for maximize bandwidth.

A. Design Antenna on Simple Configuration

Figure 1 (a) shown the simple structure of CPW fed slot antenna at design frequency 2.4 GHz. For match impedance with 50 ohms transmission line, the CPW feed line has a signal strip W_f = 3.0 mm, a gap width S_f = 0.3 mm, and length of CPW feed line L_f = 25 mm ($\approx \lambda_g/4$). The length of slot antenna (L_a) depends on guide wavelength λ_g, which is approximately the half of the guided wavelength ($\approx \lambda_g/2$) at frequency 2.4 GHz. The length of slot antenna is given by

$$\lambda_g = \frac{\lambda_0}{\sqrt{\varepsilon_{eff}}} \tag{1}$$

$$\varepsilon_{eff} \approx \frac{\varepsilon_r + 1}{2} \tag{2}$$

$$Z = \frac{30\pi}{\sqrt{\varepsilon_{eff}}} \cdot \frac{K'(k_1)}{K(k_1)} \tag{3}$$

$$k_1 = \frac{w_f}{w_f + 2s_f} \tag{4}$$

$$k' = \sqrt{1-k^2} \tag{5}$$

$$\frac{K(k)}{K'(k)} = \frac{\pi}{\ln\left[2\frac{1+\sqrt{k'}}{1-\sqrt{k'}}\right]} \quad \text{for } 0 \le k \le \frac{1}{\sqrt{2}} \qquad (6)$$

$$\frac{K(k)}{K'(k)} = \frac{\ln\left[2\frac{1+\sqrt{k}}{1-\sqrt{k}}\right]}{\pi} \quad \text{for } \frac{1}{\sqrt{2}} \le k \le 1 \qquad (7)$$

where λ_0 is the free space wavelength at 2.4 GHz.

λ_g is the guided wavelength at 2.4 GHz.

ε_{eff} is an effective dielectric constant.

Z is the impedance.

.

In this case, the λ_0, λ_g, and L_a are 125mm, 98.82 mm and 47 mm, respectively.

B. Design Antenna with Stub Tuning

The stub tuning is proposed for maximize wide bandwidth, as shown in Figure 1(b) and 1(c). The procedure to increasing bandwidth of some frequency-band is:

1. Expanding the central conductor (strip signal) by overstepping into both side of slot antenna, Figure 1(b).
2. Next from case I, to overstepping the small conductor as shown in Figure 1 (c).

The parameters of conductor stub in Figure 1(b) are W_b and L_b which are adjusted for good matching. While Figure 1(c) adding three parameters of conductor stub, W_c, L_c, and L_d. Reasonable to maximize bandwidth, the value of W_b and L_b in case of minimum return loss is chosen. Finally, the W_c, L_c, and L_d is adjusted for wideband at high frequency.

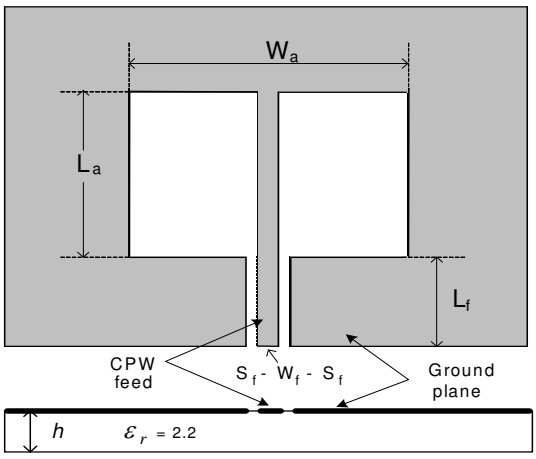

(a)

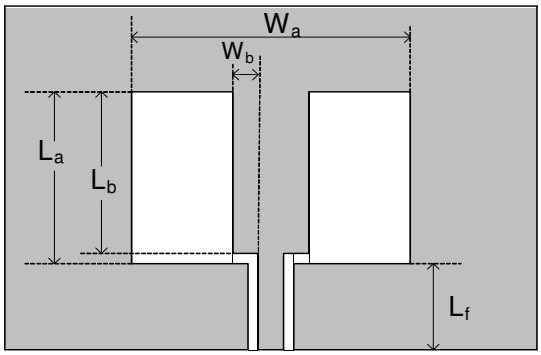

(b)

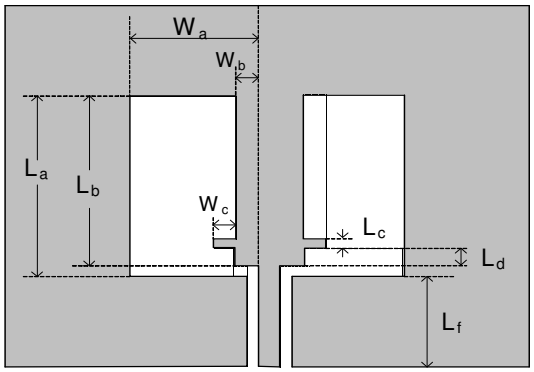

(c)

Figure 1. Configuration of the CPW fed slot antenna. (a) basic structure (b) with tuning L_b and W_b (c) with tuning L_c, W_c and L_d.

III. RESULTS

Figure 2 shown the simulation result of return loss (S_{11}) in varying value of W_a to 47, 72 and 80 mm by fixing L_a to 47 mm which the structure of antenna as shown in Figure 1(a).

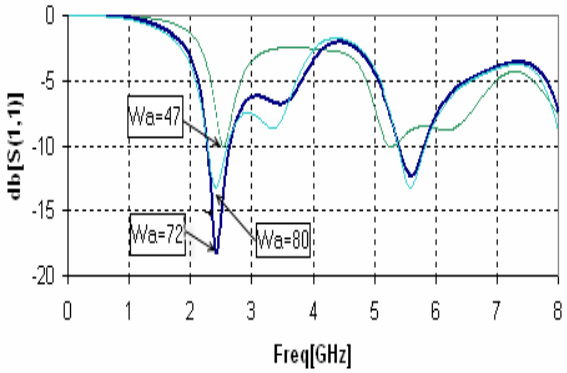

Figure 2. Simulation results of return loss by adjust W_a.

The best value of W_a for good matching is 72 mm. Thus, we will fix the value of L_a and W_a to 47 mm and 72 mm, respectively. In this case, the simulation results are shown in Table I.

TABLE I

Simulation results of Figure 1 (a) by fixed L_a = 47 mm.

W_a (mm)		47	72	80
Lower Frequency	Resonance Freq (GHz)	2.54	2.42	2.42
	Return Loss (dB)	-10.07	-18.33	-13.18
	BW (%)	0.79	13.38	12.34
Higher Frequency	Resonance Freq (GHz)	5.28	5.60	5.58
	Return Loss (dB)	-10.08	-12.31	-13.17
	BW (%)	1.51	6.77	7.48

From Figure 1(b), the central conductor is overstepped into slot antenna. The analytical affect of adjusting W_b and L_b will be considered, first analysis by fixed W_b to 8.5 mm and adjust L_b, and next choose L_b from first analysis base on return loss (S_{11}) and fixed it then adjust W_b. The simulation of return loss and bandwidth are shown in Figure 3-4 and Table 2-3, respectively.

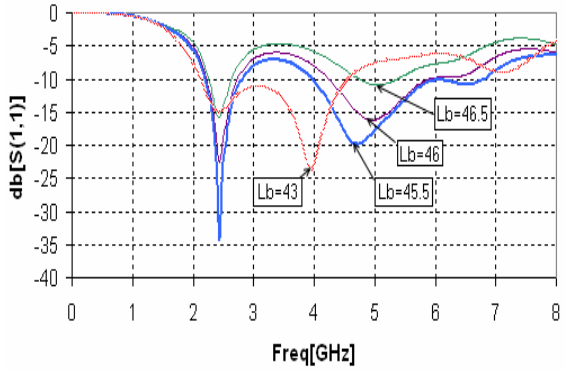

Figure 3. Simulation results of return loss by adjust L_b.

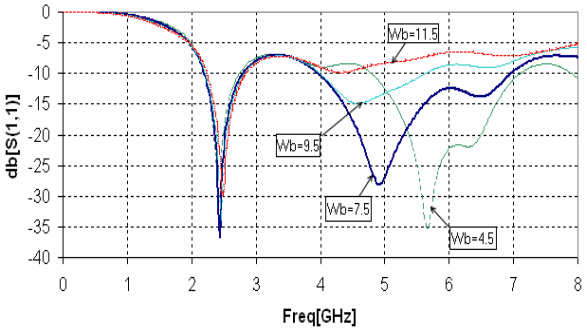

Figure 4. Simulation results of return loss by adjust W_b.

TABLE II

Simulation results of Figure 1(b), L_a=47 mm , W_a=72 mm, W_b= 8.5 mm.

L_b (mm)		43	45.5	46	46.5
Lower Frequency	Resonance Freq (GHz)	2.42	2.44	2.44	2.42
	Return Loss (dB)	-15.03	-34.35	-22.52	-15.76
	BW (%)	72.67	23.10	19.35	13.87
Higher Frequency	Resonance Freq (GHz)	3.94	4.7	4.94	5.04
	Return Loss (dB)	-23.72	-19.91	-16.18	-10.89
	BW (%)	-	52.31	32.74	12.22

TABLE III

Simulation results of Figure 1 (b): L_a=47 mm , W_a=72 mm, L_b = 45.5 mm.

W_b (mm)		4.5	7.5	9.5	11.5
Lower Frequency	Resonance Freq (GHz)	2.42	2.44	2.46	2.48
	Return Loss (dB)	-32.36	-36.79	-33.82	-30
	BW (%)	21.86	23.29	23.10	22.92
Higher Frequency	Resonance Freq (GHz)	5.66	4.92	4.6	-
	Return Loss (dB)	-35.28	-28.29	-14.93	-
	BW (%)	38.65	54.21	33.67	-

Figure 3 shown the low resonance frequency is slightly changed and high resonance frequency shift up when value of L_b is increased. Comparing between S_{11} for each value of L_b, we will choose L_b = 45.5 mm and use this value to find out W_b for better matching and wideband.

Figure 4 shown low resonance frequency is changed same as Figure 3, while high resonance frequency shift down when value of W_b is increased. In this case, the good matching can be achieved when L_b = 45.5 mm and W_b = 7.5 mm which are used to analyze for maximized bandwidth in next step.

Finally, we overstep the small conductor into slot antenna by adjust three parameters: L_c, W_c, and L_d, as shown in Figure 1(c). By sufficient choosing value of L_c = 1 mm, W_c = 5 mm and L_d= 6 mm, the simulation result of S_{11} is shown in Figure 5. In this case, we achieved the wide bandwidth at high frequency from 3.88 – 9.74 GHz (5.86 GHz or 86.04% of the center frequency 6.81 GHz) and at lower frequency from 2.22 - 2.82 GHz (0.6 GHz or 23.8%).

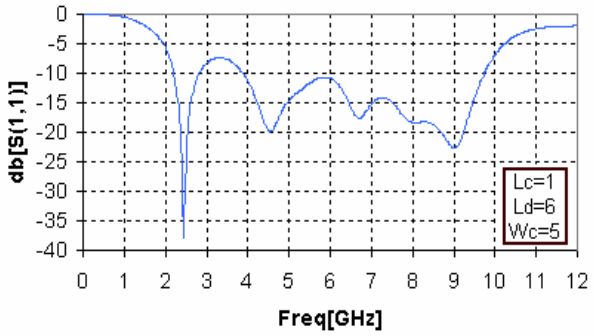

Figure 5. Simulation results of return loss by adjust L_c, W_c and L_d.

TABLE IV

Simulation results of Figure 5.

L_a = 47 mm, W_a = 72 mm, L_b = 45.5 mm, W_b = 7.5 mm, L_c = 1 mm, W_c = 5 mm, and L_d = 6 mm					
Lower Frequency			Higher Frequency		
S_{11} (dB)	Bandwidth (GHz)	Gain (dB)	S11 (dB)	Bandwidth (GHz)	Gain (dB)
-37.96	0.6	3.59	-22.69	5.86	4.43

Table IV shown the characteristic of return loss, gain and bandwidth of this slot antenna.

The radiation pattern gain xy-plane and xz-plane are shown in Figure 6-9. The antenna is obtained on center band of low frequency at 2.52 GHz and of high frequency at 6.8 GHz.

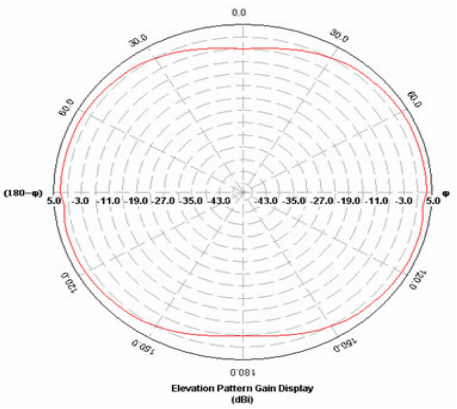

Figure 6. XZ plane at f = 2.52 GHz.

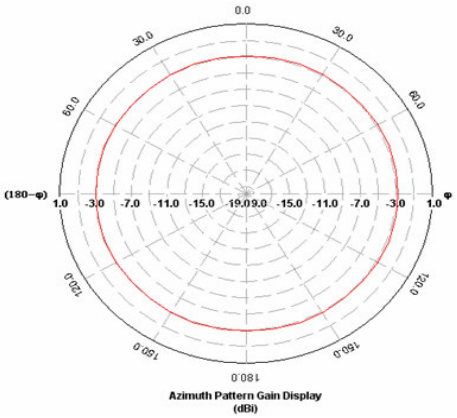

Figure 7. XY plane at f = 2.52 GHz.

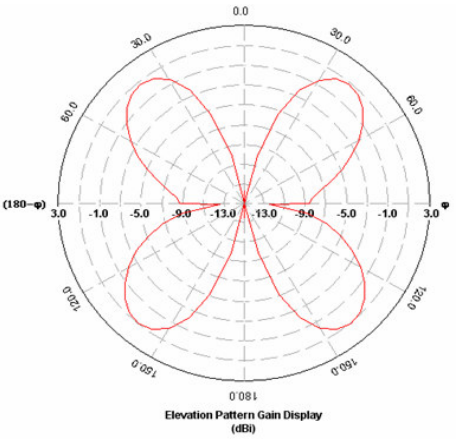

Figure 8. XZ plane at f = 6.8 GHz.

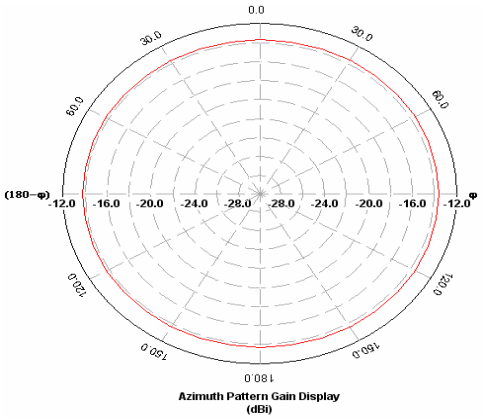

Figure 9. XY plane at f = 6.8 GHz.

IV. CONCLUSION

The slot antenna fed by CPW is designed for dual frequency 2.4 and 5 GHz bands. The stub tuning technique is proposed for wide-band which has two step tuning. By sufficient choosing size of conductor stub, can be achieved the wide bandwidth of 23.8% (2.22-2.82 GHz) and 86.04% (3.88-9.74 GHz), which can use in WLAN applications and communication system. The frequency bandwidth of the proposed slot antenna for dual frequency is large enough to coverage standard of WLAN communications systems.

REFERENCES

[1] IE3D User's Manual Release 9,Zeland software, Inc.,U.S.A., 2002.

[2] A.U. Bhobe, C.L. Holloway, M. Piket-May, "CPW fed wide-band hybrid slot antenna," *IEEE Transactions on Antennas and Propagation Society International Symposium*, Vol. 2, pp. 636-639, 2000.

[3] M. Nedil, T.A. Denidni, L. Talbi "Design of a Broadband Slot Antenna Fed by CPW for Wireless Application at 5.8 GHz," *Vehicular Technology Conference, 2004. VTC 2004-Spring*. 2004 IEEE 59th. Vol. 1, pp.18-21, May 2004.

[4] Horng-Dean Chen "Slot Antenna Coupled by Microstrip Line for Dual Frequency," *IEEE Transactions on Antennas and Propagation*, Vol. 51, No. 8, pp.1982-1986, August 2003.

[5] Tae-Hyun Kim and Dong-Chul Park, "Compact Dual-Band Antenna with Double L-Slits for WLAN Operations," *IEEE Antennas and Wireless Propagation Letters*, Vol.4, 2005, page 249-252.

[6] H.D. Chen, J.S. Chen, and Y.T. Cheng, " Modified inverted-L monopole antenna for 2.4/5 GHz dual-band operations," *Electron. Letter*, Vol.39, pp. 1567-1568, 2003.

[7] M.C. Mukandatimana, T.A. Denidni, L. Talbi "Design of a new dual-band CPW-fed slot antenna for ISM applications," *Vehicular Technology Conference, 2004. VTC 2004-Spring*. 2004 IEEE 59th. Vol. 1, pp.6-9, May 2004.

A Compact U-Shaped Cross-Sectional Antenna on a U-Shaped Ground Plane for WLAN

Duang-arthit Srimoon[1], *Chuwong Phongcharoenpanich*[2], *and Monai Krairiksh*[2]

[1] School of Computer Engineering, College of Engineering, Rangsit University, Muang, Pathumthani 12000, Thailand.
E-mail: ksduanga@yahoo.com

[2] Faculty of Engineering & Research Center for Communications and Information Technology, King Mongkut's Institute of Technology Ladkrabang, Bangkok 10520, Thailand.
E-mail: kkmonai@kmitl.ac.th

***Abstract*-This paper presents the compact and wideband U-shaped cross-sectional antenna on a U-shaped ground plane for WLAN system. The antenna prototype is fabricated for testing after the geometry is analyzed by using the FDTD method. The antenna element is contributed from a piece of rectangular thin metal-sheet which is folded to form a U-shaped, then, the bottom is etched to form a cross-strip at the center by two wide-slots, respectively. It is cross-placed on the U-shaped ground plane which is folded as its element. The antenna has overall dimension of 110 x 84 x 33 mm^3 with an impedance bandwidth (2:1 VSWR) of 40%, an average gain of 8.5 dBi., front-to-back ratio and cross-polarization level in both E-and H-plane greater than 20 dB across the bandwidth, and half power beam-width in both E- and H-plane of 80º at 2.45 GHz. The proposed antenna is suitable for implementing as an access point of the WLAN under the IEEE802.11 b, g standard.**

I. INTRODUCTION

Wireless communication systems are continuously developed in both transmitting and receiving the image, voice, and data. Especially for the wireless internet, it is growing very fast as we can see from the extending of the internet service providers (ISPs). Presently, wireless networks are used in everywhere with the name of WLAN (Wireless Local Area Network), since it is convenient to install without wiring a line for connecting [1]. The problem of drilling floor/wall is also negligible. However, the system must be under the IEEE 802.11b, g standard which operated in the ISM band or the frequency range of 2.4 - 2.484 GHz. Thus, antennas for this operating are the important equipment.

Compact antennas are required because the users need to suppress access points for the installation with the causes of the great point of view, light weigh, and easily to install. In order to decrease the antenna size, it can be treated to the ground plane. For this, it directly effects to the antenna performance especially for gain and front-to-back ratio. However, the technique for treating the ground plane with enhancing the antenna performance has been proposed in [2] but it is not the decreasing of the antenna size. The useful technique for decreasing the antenna size has been proposed in [3].

This paper describes the decreasing of the antenna size for using in WLAN operation that has not been proposed before as the geometry like this. The antenna develops from the U-shaped cross-sectional antenna on a U-shaped ground plane. The advantage is not only for it is a compact structure, it also provides a wide bandwidth in addition. The wideband antenna is more flexible than the narrowband antenna because when they are fabricated, it is not seriously to tune the operating frequency makes it easily to produce in the industrial part. For this reason, the material is also easily to find in the local market and not necessary to use an expensive substrate makes the antenna is low cost as well. The antenna was designed to have a mid-band at 2.45 GHz or closed to the central operating frequency of the WLAN. The analysis of the antenna was conducted by using the Finite-difference Time-domain (FDTD) method.

II. ANTENNA DESCRIPTIONS

For the antenna structure, it is the U-shaped cross-sectional antenna on a U-shaped ground plane as shown in Figure 1 [3]. The antenna element is contributed from a piece of rectangular brass sheet that has the thickness of 0.4 mm and is folded to form a U-shaped. The dimension have the length of a = 50 mm, the width of b = 52 mm, and the height of d = 30 mm. Then, the bottom is etched to form a cross-strip at the center by two wide-slots. The cross-strip have the width of w_1 = 10 mm, free-end-strip width of w_2 = 10 mm and the length of s = 14 mm, and the connected-strips width of t = 4 mm. The free-end-strip of the cross-strip is far from its front side connected-strip of l = 26 mm. The antenna element is cross-placed with the 1 mm thickness aluminium ground plane which is folded to form a U-shaped as its element with the size of 110 x 84 x 33 mm (G_x x G_y x G_z) for the length, the width, and the height,

respectively. They are separated by space with the thickness of h = 3 mm or the layer which has the dielectric constant close to unity. The antenna is fed by a probe pass-through a transmission line in the sequence at the center of the dimension a on the front side. The transmission line have the width of w_1 = 10 mm and the length of f = 14 mm while the probe is through-holed by the 50Ω SMA connector with the length of 2 mm. All dimensions are indicated as show in TABLE I.

Prototype of the U-shaped cross-sectional antenna on a U-shaped ground plane is fabricated with the dimensions and the materials as indicated above for comparison and to confirm the accuracy of the simulation. The antenna element is supported by foam beneath for the air layer.

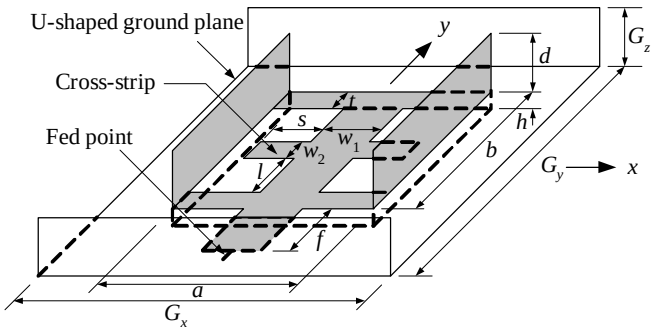

Figure 1. Structure of the U-shaped cross-sectional antenna on a U-shaped ground plane.

TABLE I
DIMENSIONS OF THE PROPOSED ANTENNA

Parameters	Dimensions (mm)
a	50
b	52
d	30
h	3
w_1	10
w_2	10
s	14
l	26
t	4
f	14
G_x	110
G_y	84
G_z	33
thickness (brass sheet)	0.4
thickness (ground-plane)	1

The analysis is carried out by the Finite-Difference Time-Domain method. This method is applied because it is simple to understand, capability, and flexibility. The detail of the FDTD theory can be found in [4] – [6]. For the simulation, a simple fed gap model is used, in which a voltage is introduced in one cell of the coaxial over a conducted plane. The return loss is obtained from the input impedance which is the ratio of the Fourier transform of the input voltage and the input current. The chosen PML is 8 grids. The virtual surfaces for the calculating of the radiation pattern are 10 grids from the outer boundary in all directions and 20 grids for the edges of the antenna components. The time step is 0.441 ps while the Gaussian half-width is 15 ps and the time delay is set to be 3 times of the Gaussian half-width. With the FDTD method, both the fed probe and the conducted material are assumed to be very thin.

The dimensions of the antenna were optimized by the simulation of the FDTD method as presented in [3]. Therefore, a and b are chosen under the assumption that they are about half of wavelength (λ_0). The width of w_1 and w_2 is defined to be nearly the 50Ω microstrip-line and the 100Ω for t which corresponded to the substrate layer height of h of the mid-band frequency (2.45 GHz). From the study, we found that the dimension of d is approximately $0.25\lambda_0$ and the width of the ground plane in the x-direction (G_x) is less sensitive to the input impedance thus it is fixed at 110 mm or $0.9\lambda_0$ in size for the good front-to-back ratio of ~20 dB and gain of ~8.5 dBi. G_z is assigned to equal with the appropriate height of d as described in [3]. Amount of s and l are used to tune the impedance matching and decreasing the cross-polarization level. To simplify the analysis, s is fixed at 14 mm while l, f, and G_y are varied for decreasing the antenna size.

III. SIMULATED AND MEASURED RESULTS

The first parameter to vary is G_y which is used for indicating the antenna size. When G_y is varied, all parameters are fixed as TABLE I except f that is also directly varied with G_y in the ratio of $\Delta G_y/2$ where ΔG_y is the differenced changing of G_y.

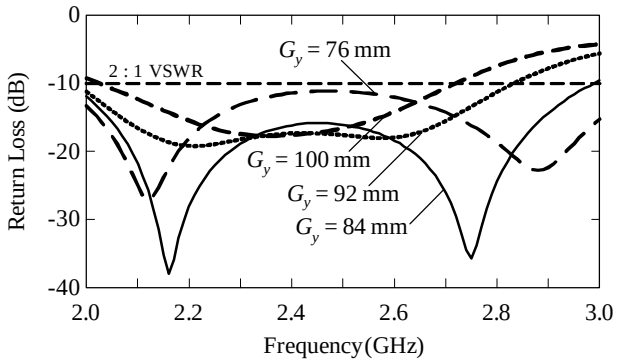

Figure 2. Simulated return losses of difference G_y.

Figure 2 shows the simulation results of the return loss of difference G_y. It is found that, G_y is mainly sensitive to the low and high frequency of the bandwidth (VSWR < 2 : 1) and slightly sensitive at the operating frequency of 2.45 GHz when G_y is decreased from 100 mm to 92 mm and to 84 mm. The impedance bandwidth is extended while the impedance matching is not change at 2.45 GHz but is greater at the low

and high frequency of the bandwidth. The resonant frequencies are clear to observe where the low resonant frequency is from the U-shaped cross-sectional antenna element and the high resonant frequency is from the U-shaped ground plane. When G_y is decreased to 76 mm, the impedance bandwidth is continuously extended but the impedance matching is become decrease. Notice that for the proposed antenna geometry with the operating frequency of 2.45 GHz, the proper size is about 110 x 84 x 33 mm^3.

The other parameter to be varied is *l*. As the varying of G_y, all dimensions are fixed as shown in TABLE I and *l* is changed between the length of 18 mm, 22 mm, and 26 mm. The simulation results of the return loss are shown in Figure 3. When *l* is increased from 18 mm to 22 mm and to 26 mm, the impedance bandwidth tends to narrow while the impedance bandwidth is better. Notice that the length of *l* can be used to tune the impedance matching. However, since the geometry of the antenna, *l* is bounded with the connected-strips.

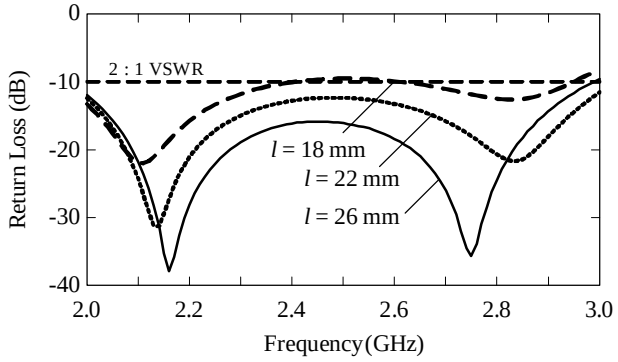

Figure 3. Simulated return losses of difference *l*.

After analysis, the appropriate parameters are chosen as in TABLE I. The simulated result of the return loss is agrees with the measured result as shown in Figure 4. The return loss of the fabricated antenna was measured using an HP 8510C Network Analyzer (50 MHz - 40 GHz) in anechoic chamber. Both simulated and measured return losses of the U-shaped cross-sectional antenna on a U-shaped ground plane provide the bandwidths of about 40% (VSWR < 2 : 1) at 2.45 GHz between the frequency range of 2.0 GHz to 3.0 GHz. Anyhow, the range of measured bandwidth is slightly narrower than the simulated one. The discrepancy is mainly due to the thickness of the constructed material of the antenna which is assumed to be very thin in the FDTD simulation but not in the practice.

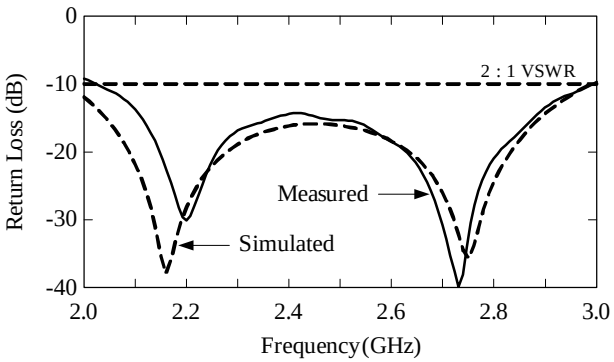

Figure 4. Measured return losses of the U-shaped cross-sectional antenna on a U-shaped ground plane.

The simulated far-field radiation patterns are computed by FDTD method while the measured radiation patterns are experimented in the anechoic chamber by using an HP8530A antenna measurement system at the operating frequency of 2.45 GHz

Figure 5(a) shows the simulated E-plane co- and cross-polarization patterns compared with the measured ones while Figure 5(b) are the results of H-plane. It is found that the front-to-back ratio is about 20 dB. The half power beam-width (HPBW) on the E-plane pattern is ~82° which is slightly difference from the H-plane pattern, which has the HPBW of ~80°. Moreover, the H-plane co-polarization pattern is more symmetry than the E-plane because of the antenna geometry and the position of the fed point. For HPBW, we can adjust by varying the dimensions of *a*, *b*, G_x, or G_y.

For the radiation patterns in Figure 5(a), the simulated E-plane cross-polarization is not show because it is very low when compared with the co-polarization.

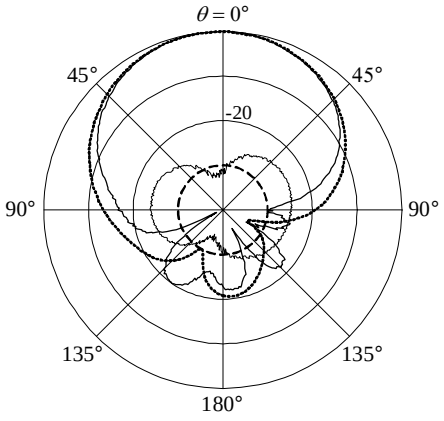

(a)

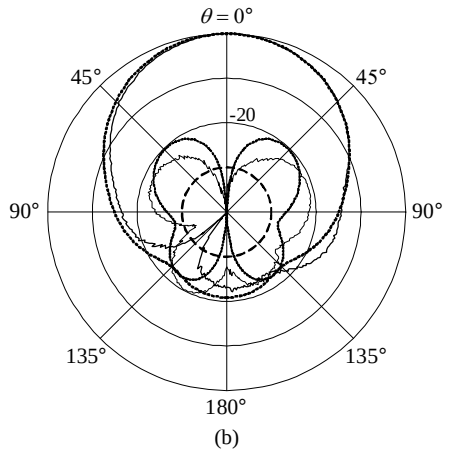

Figure 5. Measured co-polarization radiation patterns of the U-shaped cross-sectional antenna on a U-shaped ground plane at the frequency of 2.45 GHz (a) E-plane (b) H-plane

Figure 6 shows the measured antenna gains of the U-shaped cross-sectional antenna on a U-shaped ground plane across the bandwidth. Gain is high in the range of bandwidth and it is rapidly decrease out of the frequency range. The average gain is about 8.5 dBi.

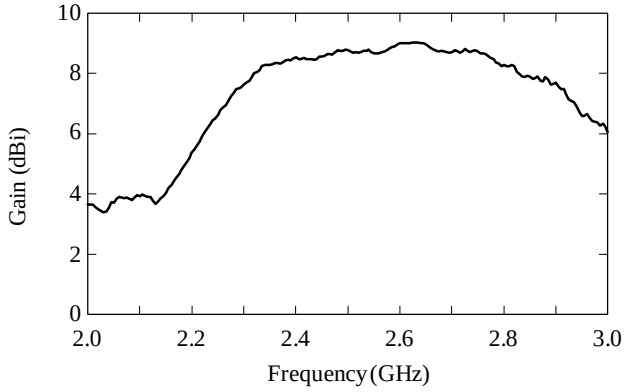

Figure 6. Antenna gain of the U-shaped cross-sectional antenna on a U-shaped ground plane between the frequency range of 2.0 - 3.0 GHz

IV. CONCLUSION

This paper presents the applying of the U-shaped cross-sectional antenna on a U-shaped ground plane with the WLAN. From the measurement, we found that the antenna has the HPBW in both E- and H-plane of ~80° and front-to-back ratio of >20 dB at the frequency of 2.45 GHz. The average gain is ~8.5 dBi. The measured return loss has a bandwidth of ~40% (2.0 GHz – 3.0 GHz). Advantages of this antenna are compact and wideband lead to benefit in constructing. The antenna is very suitable for implementing as a access point in the WLAN communication system.

V. REFERENCES

[1] R. Jordan and C. T. Abdallah, "Communications and networking: an overview," *IEEE Trans. Antennas Propagat. Mag.*, vol. 44, no. 1, pp. 185 - 193, Feb. 2002.

[2] S. Noghanian and L. Shafai, "Control of microstrip antenna radiation characteristics by ground plane size and shape," *Proc. Inst. Elect. Eng. Microwave Antennas Propagation*, vol. 145, no.3, pp.207-212, June 1998.

[3] D. Srimoon, C. Phongcharoenpanich, and M. Krairiksh, "A Probe-Fed U-Shaped Cross-Sectional Antenna with Tuning Stubs on a U-Shaped Ground Plane," *IEICE Trans. Commun.*, vol. E89-B, no. 5, May 2006.

[4] K. S. Yee, "Numerical solution of initial boundary value problems involving Maxwell's equations in isotropic media," *IEEE Trans. Antennas Propagat.*, vol. 14, no. 8, pp. 302-307, May 1996.

[5] A. Taflove, *Advance in Computational Electrodynamics: The Finite-Difference Time-Domain Method*, Norwood, MA, Artech House, 1998.

[6] J.P. Berenger, "Perfectly matched layer for the absorption of electromagnetic waves," *J. Computat. Phys.*, vol. 114, pp. 185-200, Oct. 1994.

[7] C. A. Balanis, *Antenna Theory Analysis and Design*, 2nd ed., New York: IEEE Press, 1997.

Fractal array antenna with NP generator model

Chatree Mahatthanajatuphat, Prayoot Akkaraekthalin
Department of Electrical Engineering, Faculty of Engineering, King Mongkut's Institute of Technology North Bangkok
1518 Pibulsongkram Rd., Bangsue, Bangkok 10800 Thailand
Email: cmp@kmitnb.ac.th, prayoot@kmitnb.ac.th

***Abstract*-This paper presents an array antenna using the technique of fractal geometry. The antenna is designed to operate at the frequency 2.45 GHz, which is used in the application of wireless LAN. A single fractal antenna is created by iterating an Narrow Pulse (NP) generator model at each side of normal square patch antenna. The advantage of fractal technique is that can reduce the antenna size compared with normal square patch antenna. The array elements are equally space between edges of each element, which equally space is 0.05 λ_g. It found that the size of antenna can be reduced and the side lobe of the radiation pattern can also reduce compared with the array of normal square patch antenna. However, the radiation patterns of the proposed antenna are still identically to the normal square patch antenna array. The properties of the antenna such as return losses, radiation patterns and gain have been carried out via numerical simulation and measurement.**

I. INTRODUCTION

Nowadays, wireless communication systems are becoming increasingly popular. There have been ever growing demands for antenna designs that possess the following highly desirable attributes: compact size, low profile, multi-band, and etc. There are varieties of approaches that have been developed over the year, which can be utilized to achieve one or more of these design objectives. Recently, the possibility of developing antenna design objective has been improved properties due to use of fractal concept. The term of the fractal geometries was originally coined by Mandelbrot [1] to describe a family of complex shapes that have self-similarity or self-affinity in their geometrical structure.

In the literature review, we have found the advantages of the fractal geometries, which support the attributes of compact size, and multi-band frequency operations. Recently, the antenna design, which has the characteristic of compact size by using the fractal technique, is known as Koch monopole antenna [2]. This fractal antenna is created by iterating the initial triangle pulse through a monopole antenna. Next, a miniaturization of loop antenna using fractal was known as Minkowski square loop antenna [3]. The fractal antenna was created by using the initial square pulse (SP) to iterative at each side of loop. The extended version of miniaturization square loop antenna was found in [4], which created by using the generator for 3/2 curve fractal to increase the electrical lengths in the fit small area.

Also, the fractal geometries still have the attribution of multi-band. The Sierpinski gasket monopole antenna in [5] was introduced by Puente. This popular antenna used the self-similarity properties of the fractal shape to translate into its electromagnetic behavior. The classic Sierpinski gasket can be generated by the Pascal triangle that was introduced in [6]. However, other antennas, which have the characteristic of multi-band created by fractal geometries, are following: Slot spiral antenna [7], multiple ring monopole antennas [8], coplanar waveguide (CPW) fed circular fractal slot antenna [9] etc.

In this paper, we used the attribute of compact size in fractal properties to design the fractal array antenna. The proposed antenna is created by using the technique of parallel feeding with fractal antenna. The antenna was designed by using the initial NP generator model [10]. The characteristics of fractal array antenna will be investigated by simulation using the full wave method of moments (MoM) software package from IE3D at the operating frequency of 2.45 GHz. Especially, the radiation pattern of the proposed antenna will be investigated to observe the magnitude of side lobe.

The organization of this paper is as follows. In section 2 and 3, a brief explanation on the antenna design will be given. Simulation and measured properties of the antenna will be discussed in section 4. Results are discussed in section 5.

II. COUPLING ANALYSIS

The NP generator model, as shown in Figure 1, is introduced to explain the iteration of the proposed antenna. The iteration depth W is smaller than a/3 [3]. In the proposed paper, the iteration depth W of the NP generator model is approximately 0.222a. The details of designed fractal antenna with NP generator model are described in [10].

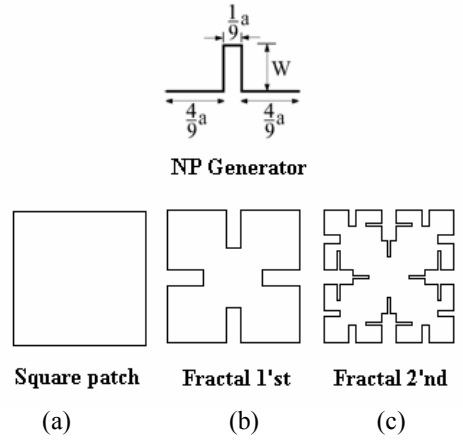

Figure 1. The NP generator model for (a) square patch, (b) first iteration, and (c) second iteration of fractal antenna.

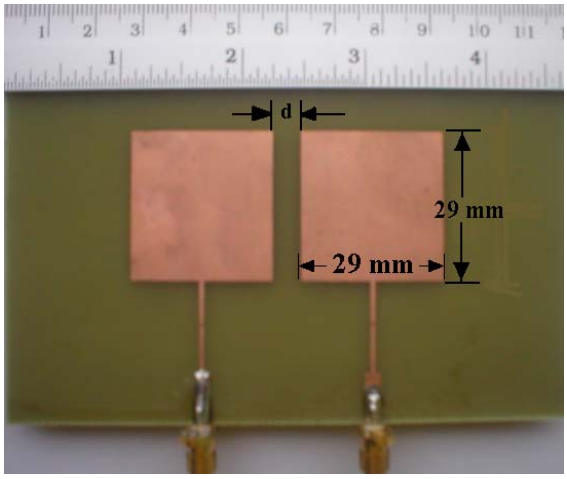

(a)

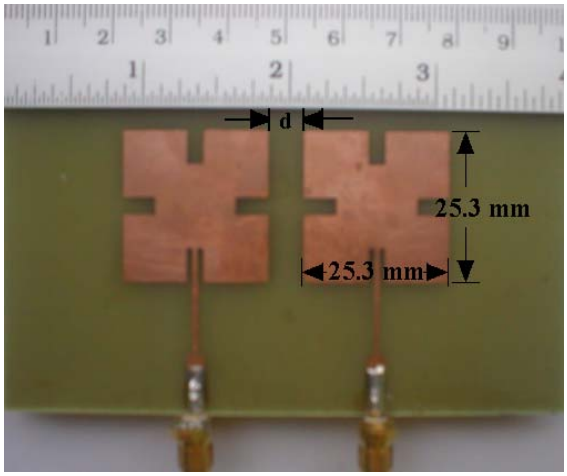

(b)

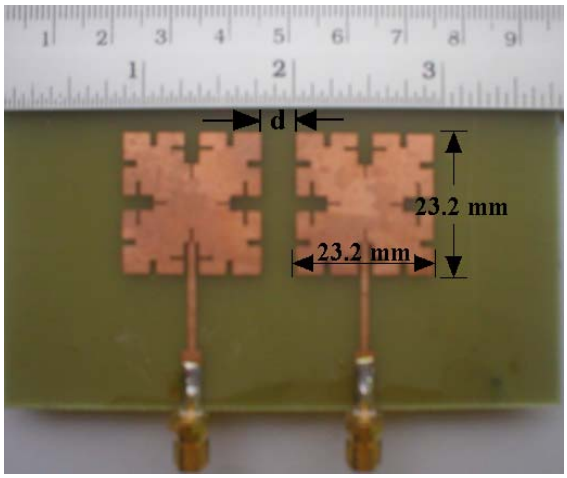

(c)

Figure 2. Experimental coupling coefficient of the antennas: (a) square patch, (b) the first iteration of fractal antenna, and (c) the second iteration of fractal antenna.

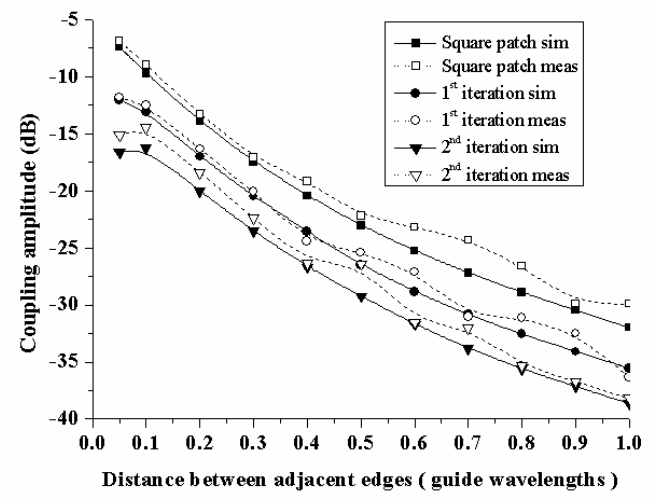

Figure 3. Coupling coefficients of all antennas.

Earlier designing the fractal array antenna, we have to investigate the coupling coefficient of the square patch antenna, 1st iteration of fractal antenna, and 2nd iteration of fractal antenna. Also, the substrate of 1.6 mm thick with dielectric constant of 4.1 was used in the experiment of coupling coefficient. The test of coupling coefficient S_{21} of the two square patch antennas, 1st iteration of fractal antennas, and 2nd iteration of fractal antennas were done with distance (d) between adjacent edges of the antennas, as shown in Figure 2. The distances (d) are following: 0.05λg, 0.1 λg, 0.2 λg, 0.3 λg, 0.4λg, until to λg.

Figure 3 shows that the simulation agrees well with the measurement. It can be clearly observed that the coupling coefficient will be reduced with the increment of the distance between adjacent edges of the antennas. The results indicate that the coupling of the fractal antennas with NP generator model is smaller than that of square patch antenna at the same distance.

III. ARRAY ANTENNA COFIGURATION

The fractal element mentioned previous section is used to create a 2x1 array antenna. The matching circuit and the array element are both on the same layer, as depicted in Figure 4. The material of the substrate is FR4 with dielectric constant 4.1, and the thickness of the substrate is 1.6 mm. The T-junction was used to design the power divider as to provide equal amplitude and in-phase feeding for each radiator. The radiator dimensions of the square patch array antenna, the 1st iteration, and the 2nd iteration of fractal array antenna, as shown in Figure 4, are 61x29 mm^2, 53.6x25.3 mm^2, and 49.4x23.2 mm^2, respectively. Also, the distance between adjacent edges of radiator is set to be 3 mm, which is 0.05λg. Therefore, the radiator dimensions of the 2nd iteration of 2x1 fractal array antenna with NP generator model is 35.21% smaller compared to the 2x1 array antenna of square patch.

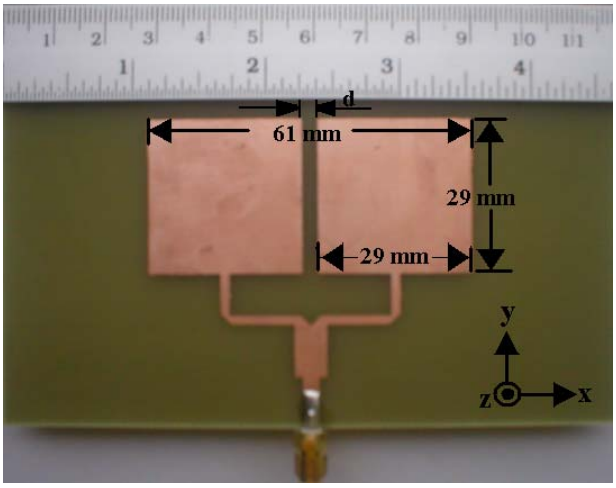

(a)

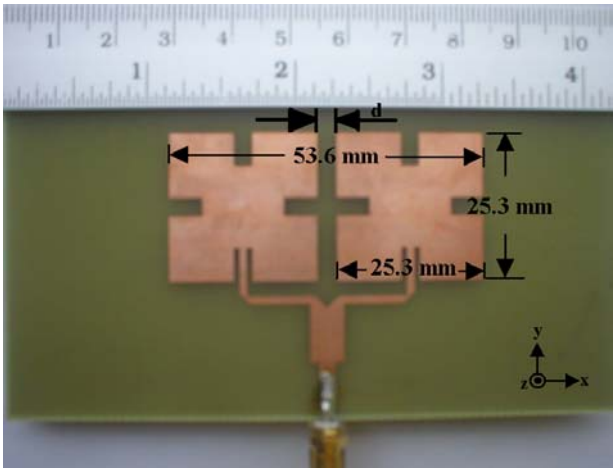

(b)

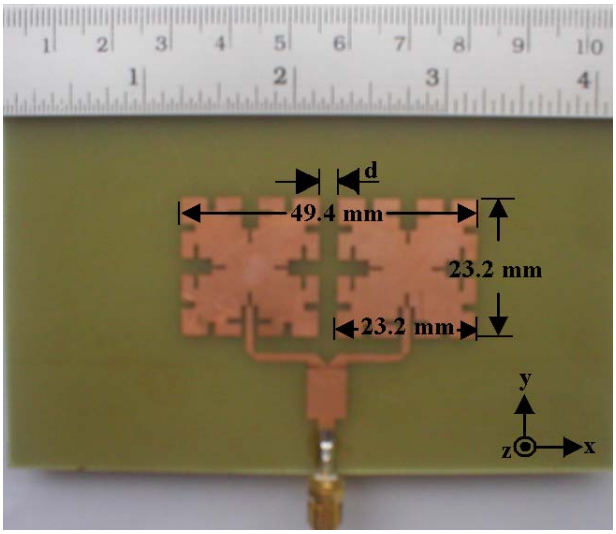

(c)

Figure 4. Geometry of the array antenna 2x1: (a) square patch, (b) the first iteration, and (c) the second iteration.

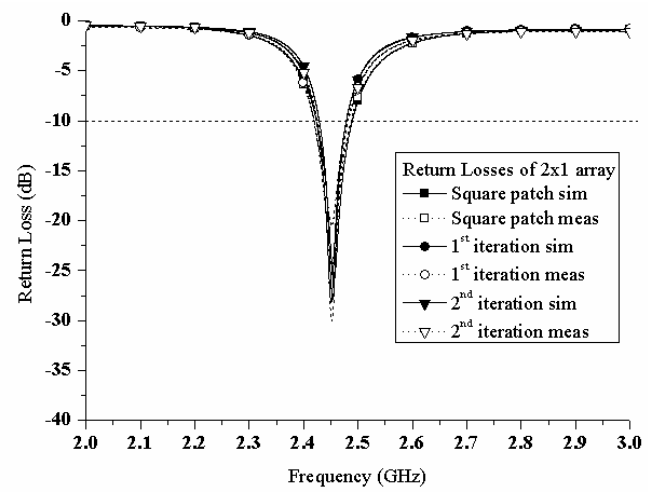

Figure 5. Simulated and Measured return losses for 2x1 array antenna.

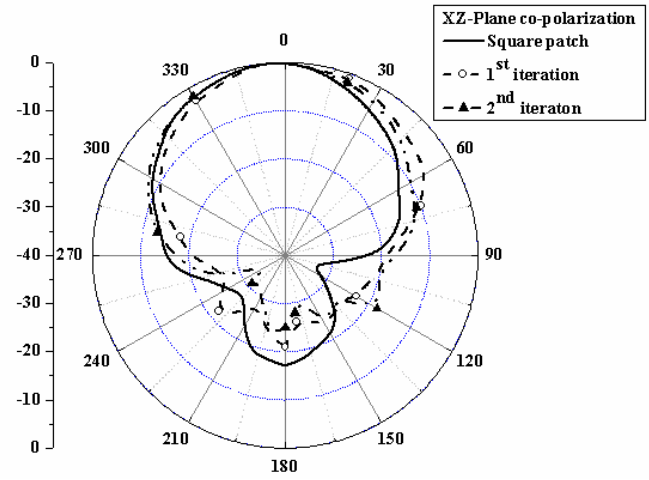

(a)

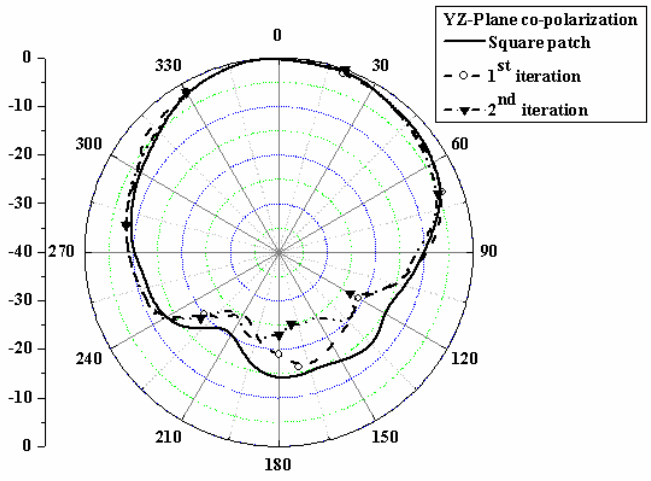

(b)

Figure 6. Measured radiation pattern of 2x1 array antenna at 2.45 GHz. (a) xz-plane and (b) yz-plane.

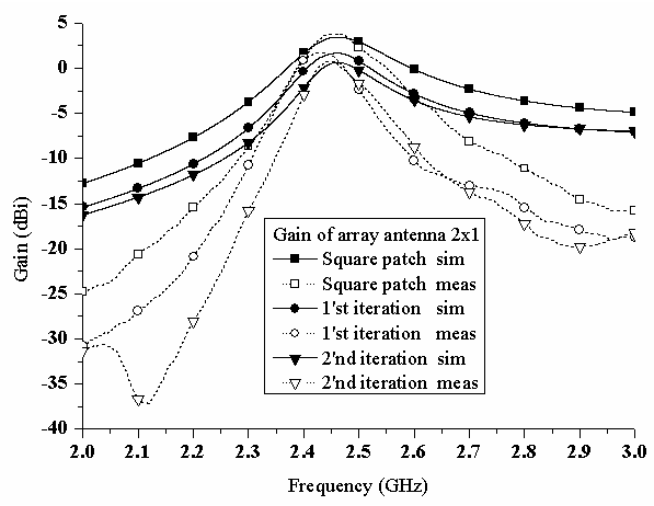

Figure 7. Simulated and Measured gain of 2x1 array antenna at 2.45 GHz.

IV. Results of Simulation and Experiment

The simulated and measured return loss of 2x1 array antennas are depicted in Figure 5. As the results show that the operating frequency of 2x1 array antennas are occurred at 2.45 GHz. Also, the simulation return losses agree well with the measured return losses. Figure 6 shows the measured radiation pattern of the 2x1 array antennas. The black lobe in the X-Z plane and Y-Z plane of 2x1 fractal array antenna with 2nd iteration NP generator model is smaller than that of the 2x1 array antenna with square patch about 5 dB. The maximum gains of radiation patterns in X-Z plane and Y-Z plane are approximately occurred at 0 degree at the resonance frequency of 2.45 GHz. Observing the results, the 3-dB beam width of the 2x1 fractal array antennas is approximately 60 degree for the measured radiation patterns. In Figure 7 depicts that the peak gains of simulation and measurement, which they occur at the operating frequency of 2.45 GHz. The peak gains of simulation are similar to that of measurement. In the simulation and measurement, the peaks gain of 2x1 array antenna with square patch, 1st iteration and 2nd iteration of fractal antenna are approximately 3 dB, 2 dB, and 1 dB, respectively.

V. Conclusion

In this paper, the experimental of the 2x1 fractal array antennas with the NP generator model have been investigated. The dimensions of the proposed antenna are approximately 35.21 % smaller than the 2x1 array antenna using square patch. The back lobe of 2x1 array antennas with square patch can be reduced approximately 5 dB, as using 2nd iteration of NP generator model. The radiation pattern of fractal array antennas are still similar to the direction radiation pattern, which have peaks gain about 2 dB, and 1 dB, respectively, for the 1st iteration and 2nd iteration of NP generator model. The 3-dB beam width of 2x1 fractal array antennas are approximately 60 degree larger than that of 2x1 array antenna with square patch.

References

[1] B.B. Mandelbrot, the Fractal Geometry of Nature, New York, W.H. Freeman, 1983.

[2] Puente, Romeu, Pous, Pamis and Hijazo, "Small but long Koch fractal monopole", IEEE Electronics Letters, vol. 34, pp. 9-10, January 1998.

[3] J. P. Gianvittorio and Y. Rahmat-Samii, "Fractal Antennas: A Novel Antenna Miniturization Technique, and Applications," IEEE Antennas Propagation Magazine, vol. 44, pp. 20-36, February 2002.

[4] H. M. Elkamchouchi and M. N. A. El-Salam, "Square loop antenna miniaturization using fractal geometry," Antenna and Propagation Society International Symposium, IEEE, vol. 4, pp. 254-257, June 2003.

[5] C. Puente, J. Romeu, R. Pous, X. Garcia, and F. Benitez, "On the Behavior of the Sierpinski Multiband Fractal Antenna," IEEE Transactions on Antennas and Propagation, vol. 46, pp. 517-524, April 1998.

[6] J. Romeu and J. Soler, "Generalized Sierpinski Fractal Multiband Antenna," IEEE Transactions on Antennas and Propagation, vol. 49, pp. 1237-1239, August 2001.

[7] Dejan S. Filipovic and John L. Volakis, "Novel slot spiral antenna designs for dual-band/multiband operation," IEEE Trans. Antennas Propagat., vol.51, pp.430-440, March 2003.

[8] C. T. P. Song, Peter S. Hall and H. Ghafouri-Shiraz, "Multiband Multiple Ring Monopole Antennas," IEEE Trans. Antennas Propagat., vol.51, pp.722-729, Apr 2003.

[9] Ji-Chyun Liu, Der-Chyuan Lou, Chin-Yen Liu, Ching-Yang Wu and Tai-Wei Soong, "Precise determinations of the CPW-FED circular fractal slot antenna," Microwave Opt. Technol. Lett., vol.48, pp.1586-1592, Aug 2006.

[10] Chatree Mahatthanajatuphat and Prayoot Akkaraekthalin, "An NP generator model for Minkowski fractal antenna," Proceeding of the 3rd ECTI, vol.2, pp.749-752, May 2006.

A New Compact WLAN 2.4 GHz CPW-fed Slot Antenna with Inverted-F Shaped Tuning Stub

Prapoch Jirasakulporn*, Sarawuth Chaimool**, and Prayoot Akkaraekthalin**
*Pathumwan Institute of Technology
Rama I Rd., Wangmai, Phatumwan, Bangkok, 10330, Thailand
**Department of Electrical Engineering, Faculty of Engineering,
King Mongkut's Institute of Technology North Bangkok,
Pibulsongkram Rd., Bangsue, Bangkok 10800, Thailand.

***Abstract*— In this paper, a new compact planar inverted-F antenna (PIFA) applicable to WLAN 802.11 b/g and bluetooth applications is proposed. The proposed antenna is a CPW-fed slot antenna with inverted-F shaped tuning stub on a FR-4 substrate, which is compact, cost-effectively and precisely to manufacture, with an omni-directional pattern and a sufficient bandwidth for all of above mentioned WLAN and bluetooth standards. The experimental results of the constructed prototype are presented, and are also compared with commercial software tool.**

I. INTRODUCTION

The use of the 2.4 GHz industrial, scientific, and medial (ISM) band is be coming an important means of wireless communications including WLAN 802.11 b/g and buletooth applications. These demands have stirred significant renewed interest in antenna design particularly at the ISM bands. Therefore, the development of appropriate antenna designs is imperative. Many antenna structures for ISM bands have been presented. [1]-[2]. An antenna printed on a substrate has some advantages compared to other antennas, like the planar inverted-F antenna (PIFA). It is usually cheaper and more precisely to manufacture.

In recent years, the demand for compact handheld communication devices has grown significantly. Devices having internal antennas have appeared to fill this need. Antenna size is a major factor that limits device miniaturization. In the past few years, new designs based on PIFA antennas have been used for handheld wireless devices because these antennas have low-profile geometry and can be embedded into the devices. Several antennas for mobile and WLAN communications devices are based on PIFA [3]-[6]. These kinds of inverted-F antennas printed on a dielectric substrate are shorted to the ground plane on the other side of the dielectric substrate. In this case, such inverted-F strip antennas can not be easily integrates in the printed circuit board of the system.

In this paper, a slot antenna with inverted-F shaped tuning stub printed on a FR-4 dielectric substrate and fed by a coplanar waveguide line is proposed. By using the inverted-F shaped tuning stub in a single layer, the proposed antenna no via hole is required in short circuiting the inverted-F strip to the ground plane. Furthermore, the opened and shorted sections of inverted-F tuning stub are fed toward center by feed line, which decreases the required area for the proposed design. Details of the design considerations of the proposed antenna and experimental results of the constructed prototype are presented.

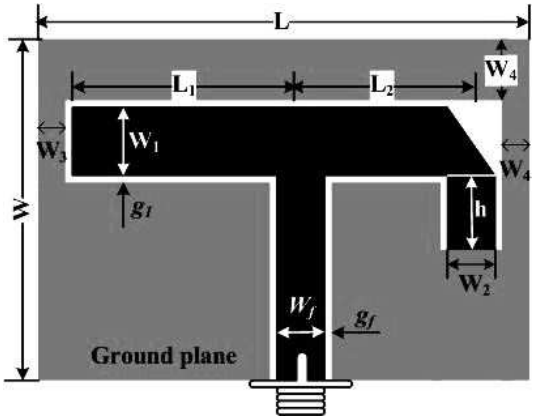

Fig. 1. Geometry of the proposed CPW-fed slot antenna with inverted-F shaped tuning stub.

II. ANTENNA DESIGN AND DISCUSSION

The configurations of the new compact CPW-fed slot antenna with inverted-F shaped tuning stub are depicted in Fig. 1. In this study, an inexpensive FR-4 substrate of thickness 1.6 mm and relative permittivity 4.4 was used for the dielectric substrate. The inverted-F tuning stub has a width of W_1, a length of L_1 for open section, and consists of a vertical shorting strip width and length of W_2 and h, respectively. A 50-Ω CPW feed line, having a signal strip of width W_f and a gap of distance g_f, is used to excite the slot. The spacing between the inverted-F tuning stub and edge of the ground plane is g_1. The miter of shorting strip is used to avoid right angle microstrip bend, which results in a poor current flow on tuning stub. The antenna has overall dimensions (W×L) of 28.3 mm× 30.1 mm.

In the study, the antenna of the proposed design for application in the WLAN 2.4 GHz band was studied. The design center frequency was chosen at 2.45 GHz, the center frequency of the WLAN 2.4 GHz band (2400-2483.5 MHz) or about 84

TABLE I

RESONANT FREQUENCY, INPUT IMPEDANCE, AND BANDWIDTH CHARACTERISTICS AS A FUNCTION OF THE GEOMETRICAL PARAMETERS

Parameters	$W_1\uparrow$	$W_2\uparrow$	$W_3\uparrow$	$W_4\uparrow$	$L_1\uparrow$	h↑
Resonant Frequency	↓	↓	↑	↑	↓	↓
Input impedance	↑	↑	↓	↓	↑	-
Bandwidth	-	↑	-	↓	↑	-

MHz. With the desired center operating frequency known, the total length L_1+ L_2+h of the inverted-F tuning stub can be first determined to be approximately one-quarter wavelength of the center operating frequency. For this reason, the total length of the inverted-F tuning stub was adjusted to be 21.04 mm. Also note that, in this design, the length of the shorting strip was selected to be 3.29 mm only (about 0.027λ) to achieve a lower height for the proposed antenna. Then, by the tuning the length L_1 of the open section of the inverted-F tuning stub and adjusting the width W_1, good impedance matching over wide frequency range can be achieved for the proposed design.

To achieve the best matching and enhance bandwidth performance, the length, width, and height of the inverted-F tuning stub and ground plane parameters are optimized. The trend of resonant frequency, input impedance, and bandwidth characteristics of each frequency is analyzed as a function of geometry parameters, as given in Table I. By observing from Table I the influence of various parameters on antenna performances, it can be seen that all parameters affect the resonant frequency of the antenna. As W_1, W_2, L_1, and h increased, the resonant frequency decreased, and vice versa. This was expected, since the height, h, and the length L_1, affect the total length of the PIFA. On the other hand, as W_4 increased, the resonant frequency so increased. Three parameters of the antenna including W_2, W_4, and L_1 affect the bandwidth of the proposed antenna. The size of the ground plane (W, L, W_2, W_3, and W_4) to a great extent also affects the resonant frequency, impedance matching, and radiation patterns. In addition, the calculated dimensions were also obtained by IE3D simulation software. The proposed antenna can be further enhances by adjusting those parameters.

The optimized design parameters for the proposed antenna are W_f = 2.73 mm, W = 28.3 mm, L = 30.1 mm, W_1 = 5.6 mm, W_2 = 3 mm, W_3 = 2.1 mm, W_4 = 1.5 mm, L_1 = 18.18 mm, L_2 = 2.86 mm, h = 3.29 mm, g_f = 0.3 mm, and g_1 = 0.6 mm.

III. SIMULATION AND EXPERIMENTAL RESULTS

In the study, a prototype of the optimal design for application in WLAN/bluetooth band was constructed as shown in Fig. 2. The characteristics impedance of the antenna were measured by an HP8510C network analyzer. Fig. 3 presents the comparison of the measured and simulated return loss S_{11} against frequency. From the obtained results, it is clearly seen that the bandwidth for WLAN 2.4 GHz band is obtained. We can see a very good agreement of the simulation and measurement results. The measured 10-dB bandwidth is about 100 MHz from 2400 to 2500 MHz.

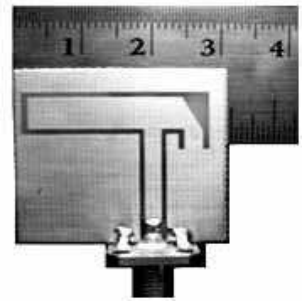

Fig. 2. Photograph of the fabricated prototype antenna.

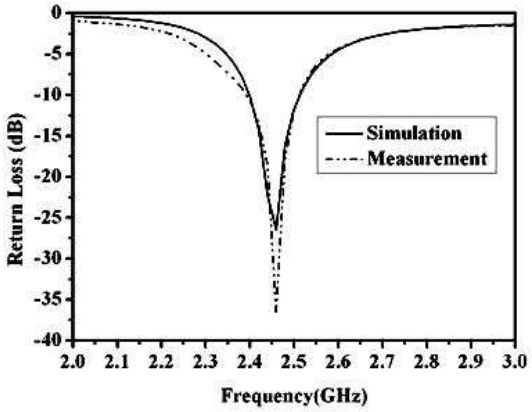

Fig. 3. Measured and simulated return losses for the proposed antenna with W_f = 2.73 mm, W = 28.3 mm, L = 30.1 mm, W_1 = 5.6 mm, W_2 = 3 mm, W_3 = 2.1 mm, W_4 = 1.5 mm, L_1 = 18.18 mm, L_2 = 2.86 mm, h = 3.29 mm, g_f = 0.3 mm, and g_1 = 0.6 mm.

The radiation characteristics of the proposed antenna have also been studied. Fig. 4 and 5 plot the simulated radiation patterns at 2.45 GHz. It is noted that the pattern in the azimuthal plane is omni-directional, which makes the proposed antenna have large radiation coverage in practical applications. The simulation results show that it is possible to build the proposed antenna, which does not only a compact size but furthermore fulfills the demand on bandwidth, impedance and radiation pattern. Other radiation pattern parameters of the proposed antenna as simulated are presented in Table II. The measured antenna gain for oprating frequencies within the WLAN band is also presented in Fig. 8. The proposed antenna shows a peak antenna gain of 2.55 dBi at 2.45 GHz.

TABLE II

THE RADIATION PARAMETERS OF THE NEW COMPACT CPW-FED SLOT ANTENNA WITH INVERTED-F SHAPED TUNING STUB

Radiation Parameters	2.4 GHz	2.45 GHz	2.4835 GHz
Directivity (dBi)	3.45	3.44	3.44
Gain (dBi)	2.49	3.03	2.92
Efficiency (%)	80.2	90.8	88.7

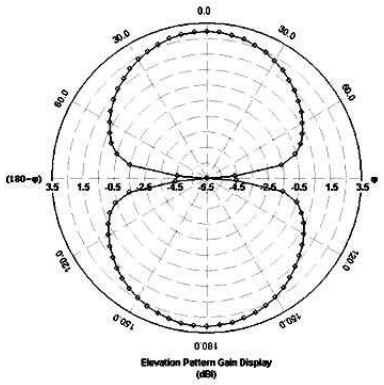

Fig. 4. Simulated radiation pattern of the proposed antenna at 2.45 GHz in elevation plane.

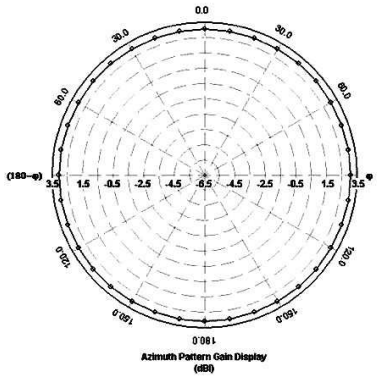

Fig. 5. Simualted radiation pattern of the proposed antenna at 2.45 GHz in azimuth plane.

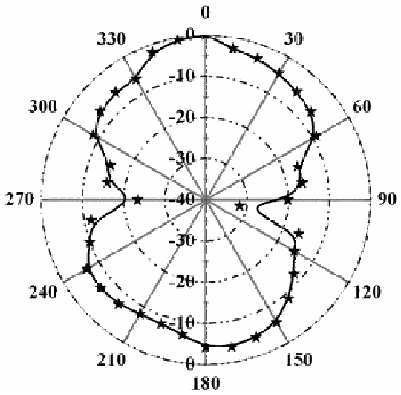

Fig. 6. Measured radiation pattern of the proposed antenna at 2.45 GHz in elevation plane.

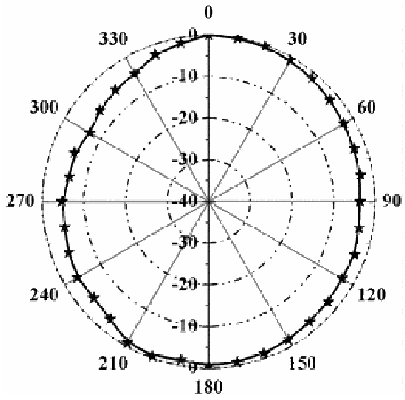

Fig. 7. Measured radiation pattern of the proposed antenna at 2.45 GHz in azimuth plane.

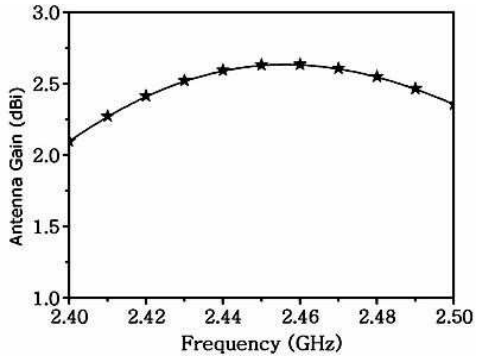

Fig. 8. Measured antenna gain for operating frequencies within the WLAN band.

IV. Conclusion

In this paper, a new compact CPW-fed slot antenna with inverted-F shaped tuning stub that covers the WLAN 802.11 b/g and bluetooth applications is proposed. And a prototype suitable for WLAN/bluetooth applications has also been constructed and studied. The constructed prototype meets the bandwidth requirement of the WLAN/bluetooth 2.4 GHz band, and good radiation characteristics have also been observed. In addition, the proposed antenna is compact, efficient, easy and cost-effective to manufacture.

References

[1] K.- L. Wong, *Planar antennas for wireless communication*, Hoboken, New jersey, John wiley& Sons, Inc., 2003.

[2] Z. N. Chen and M. Y. W. Chia, *Broadband planar antennas design and applications*, Southern Gate, Chichester, John wiley& Sons, Ltd., 2006.

[3] T. Taga and K. Tsunekawa, "Performance analysis of a built-in planar inverted-F antenna for 800 MHz hand portable radio units", IEEE J Select Areas Commun SAC-51(1987), 921-929

[4] M.J. Ammann and L.E. Doyle, "A loaded inverted-F antenna for mobile handset", Microwave Opt Technol Lett 28 (2001), 226-228.

[5] M. Ali and G.J. Hayes, "Analysis of integrated inverted-F antennas for bluetooth applications", 2000 IEEE-APS Conf Antennas Propagat for Wireless Commun, Waltham, MA, pp. 21-24.

[6] Y.L. Kuo, T.W. Chiou, and K.L. Wong, "A novel dual-band printed inverted-F antenna", Microwave Opt Technol Lett 31(2001).

Throughput Analysis for Orthogonal Diversity of CSMA/CA Protocol by SFH/MC DS-CDMA

Pichet Roumsamug[1] Pisakorn Sittiwatjana[2] Suvepon Sittichivapak[1]
1.Department of Telecommunication Engineering, Faculty of Engineering
King Mongkut's Institute of Technology Ladkrabang
2.Prince of Songkhla University, Phuket Campus, E-mail:masaki22hiroki@hotmail.com

***Abstract*-This paper presents the throughput for wireless local area network (WLAN) used orthogonal diversity antenna, vertical and horizontal polarization, and improved signal by multiuser detection of slow frequency hopping/multicarrier direct sequence-code division multiple access (SFH/MC DS-CDMA) technique over Nakagami fading channel. The numerical results presence in the number of path, number of carrier, Nakagami-m fading factor and number of user. The throughput of WLAN with Nakagami fading is analyzed. The throughput improvement of the SFH/MC DS-CDMA system. We have considered two type of antenna, including vertical polarization, horizontal polarization, and have analyzed their throughput versus offer load. We also found the vertical polarization is better than the horizontal polarization for throughput in all of the results.**

I. INTRODUCTION

More and More stations connect to wireless local area network (WLAN) and demand for various wireless services, which support data, voice, and video, has rapidly increased. The costs for installation and relocation for cable LAN's cable have increased. However, wireless LAN's offer many advantages in installation, maintenance, and relocation from the view point of cost and efficiency.

One of important research issues in wireless LAN is the design and analysis of MAC protocols or signal or antenna for high speed data bit rate. MAC protocols or orthogonal diversity for wireless communication have been widely studied[1-2]. There are also many for MAC protocols in fading channel. In this paper, we present analytical approach for the channel throughput by slow frequency hopping multicarrier direct-sequence code division multiple access (SFH/MC DS-CDMA) for two types of antenna: vertical polarization, horizontal polarization. We analyze and compare the throughput with each other.

II. CSMA/CA PROTOCOL

In the CSMA/CA protocol, a packet generated at a user terminal is transmitted to the access point after the carrier sensing becomes "idle." The CSMA/CA timing as shown in figure 1.

Here, when the expectation time length of a "busy" period as defined as $\overline{B}$ and the expectation time length of an "idle" period is defined as $\overline{I}$, and the expectation time length in which no collision occurs and packets are successfully transmitted is defined as $\overline{U}$, the throughput S is give by

$$S_{CSMA/CA} = \frac{\overline{U}}{\overline{B}+\overline{I}} \tag{1}$$

We obtain the sum of the expectation of useful transmission time as [3]

$$\overline{U} = \frac{M\left[1-(1-g)\right](1-g)^{M-1}}{1-(1-g)^{M}} + \left(\frac{1}{(1-g)^{(TP/a)M}}-1\right).\sum_{n=1}^{M}\left\{\left[np(1-p)^{n-1}+\left(np(1-p)^{n-1}(1-g)^{M-n}+(1-p)^{n}(M-n)g(1-g)^{M-n-1}\right).\frac{(1-p)^{n}(1-g)^{M-n}}{1-(1-p)^{n}(1-g)^{M-n}}\right]\cdot\binom{M}{n}\left[1-(1-g)^{(TP/a)}\right]^{n}(1-g)^{(TP/a)(M-n)}\right\} \tag{2}$$

and the expected value of the busy and the idle period as [3].

$$\overline{B}+\overline{I} = f\left[1-(1-g)^{M}\right]+1+a+\frac{a}{1-(1-g)^{(TP/a)M}}\left\{\left[1-(1-g)^{(TP/a)M}\right](1+a+f)+\left[a.\left(\sum_{k=1}^{\infty}\left\{(1-p)^{k}-(1-g)^{(TP/a)}\left[(1-p)^{k}-(1-g)^{k}\right]\right\}^{M}-(1-g)^{(TP/a)M}\right).\sum_{k=1}^{\infty}(1-g)^{kM}\right)\right]\right\}+\frac{a}{\left[1-(1-g)^{M}\right]} \tag{3}$$

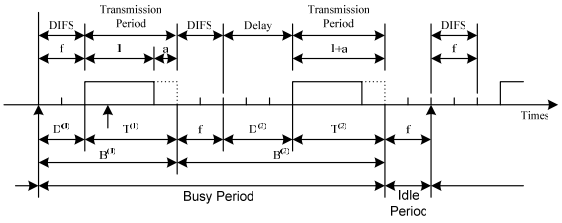

Figure1. Basic CSMA/CA Protocol

III. SYSTEM DESCRIPTION

A. *Transmitter Model*

The original bit stream having a bit duration of T_b is first serial-to-parallel (S-P) converted, as seen in the schematic, yielding U_k parallel stream. The assignment of bits to the activated subcarrier is controlled by the constant-weight code. Depending on the specific aims of the system design, we can

assign every $U_k - th$ bit to the same subcarrier and in this parallel system the bit-duration is hence extended to $T = U_k T_b$. This assists in mitigating the inter-symbol-interference (ISI) in a high-bit rate transmission scheme. Alternatively, the proposed parallel system can be used to maintain $T = T_b$ in each subchannel, hence assisting in high-rate or variable-rate transmission upon employing a different number of subcarriers, as well as highlight duration our further discourse. Theoretically, Q number of different information rate can be generated by changing the weight of code. The direct-sequence (DS) spread, transmitted signal of orthogonal diversity for the k[th] user can be formulated as

$$s_v(t) = \sum_{i=0}^{\infty}\sum_{k=1}^{K}\sum_{uk=1}^{Uk}\sqrt{\frac{2Eb_{uk}}{T}}b_{uk}^{(k)}(t)\cdot e^{j2\pi f_{v,uk}^{(k)}t}s_{uk}^{(k)}\left(t-iT_c\right) \quad (4)$$

$$s_h(t) = \sum_{i=0}^{\infty}\sum_{k=1}^{K}\sum_{uk=1}^{Uk}\sqrt{\frac{2Eb_{uk}}{T}}b_{uk}^{(k)}(t)\cdot e^{j2\pi f_{h,uk}^{(k)}t}s_{uk}^{(k)}\left(t-iT_c\right) \quad (5)$$

The DS spreading waveform the subcarrier frequency set and the phase angles introduced in the carrier modulation process. Let T_c the chip duration of the DS spreading waveform and $N = T_b/T_c$ of the symbol duration. We assume the FH interval is T_h and the number of data bit $N = T_b/T$, transmitted per hop is a positive integer, which is strictly larger than 1, implying slow FH

B. Nakagami Channel Model

We consider a frequency-selective multipath channel [4], whose complex low-pass impulse response for subcarrier u_k of user k is given by

$$h_{uk}^{(k)}(\tau) = \sum_{l=0}^{L-1}\alpha_{uk,l}^{(k)}e^{-j\phi_{uk,l}^{(k)}}\delta(t-lT_c) \quad (6)$$

Where l_pT_c is the relative delay of the $l_p - th$ path of user k with respect to the main path, the $\left\{\phi_{u_k,l_p}^{(k)p}\right\}$ are independent identically distributed (iid) random variables uniformly distributed in the interval $(0,2\pi)$, whilst the L_p tap weights $\left\{\alpha_{u_k,l_p}^{(k)}\right\}$ are independent Nakagami-m random variables of orthogonal diversity with a pdf of

$$P_{\alpha_l}(\alpha_l) = \frac{2m_l^{m_l}\alpha_l^{2m_l-1}}{\Omega_l^m\Gamma(m_l)}\exp\left(-\frac{m_l\alpha_l^2}{\Omega_l}\right) \quad (7)$$

Where $\Gamma(\cdot)$ represents the gamma function, and m is the Nakagami-m fading parameter. The parameter $\Omega_{u_k,l_p}^{(k)}$ is the second moment of $\alpha_{u_k,l_p}^{(k)}$

C. Receiver Model

In the traditional orthogonal diversity system, vertical and horizontal are used as an independent transmission channel. It means that the data streams transmitted in both antennas are uncorrelated

Let the user be the user-of-interest and consider the conventional matched filter base correlating receiver with maximum ratio combining (MRC). Upon exploiting the knowledge of the FH patterns, detection can be implement by demodulating only the U_k active subcarreir , or alternatively, all Q subcarrier can be always demodulated, while only U_k MRC output are according ti the FH patterns used for detection. The kth user employs BPSK modulation to transmit equal probability data bit $b_k(i)\in\{\pm 1\}$, at a common bit rate $1/T$. The number of matched filter in fig. are matched to the reference user's CDMA code used for spreading in the subband associated with the Q number of subcarrier, and assume to have achieved time synchronization. If we assume perfect estimates of channel tap weight and phase are variable, in order to synchronize the L number of path signals used correlating receiver for vertical polarization and horizontal can be expressed as

$$r_v(t) = \sum_{i=0}^{\infty}\sum_{k=1}^{K}\sum_{uk=1}^{Uk}\sum_{l=1}^{L}\sqrt{\frac{2E_{b_{uk}}}{T}}b_{uk,l}^{(k)}\alpha_{uk,l}^{(k)}e^{j2\pi f_{uk,l}^{(k)}(t)}.s_{uk,l}^{(k)}\left(t-iT-\tau_{uk,l}^{(k)}\right)+n(t) \quad (8)$$

$$r_h(t) = \sum_{i=0}^{\infty}\sum_{k=1}^{K}\sum_{uk=1}^{Uk}\sum_{l=1}^{L}\sqrt{\frac{2E_{b_{uk}}}{T}}b_{uk,l}^{(k)}\alpha_{uk,l}^{(k)}e^{j2\pi f_{uk,l}^{(k)}(t)}.s_{uk,l}^{(k)}\left(t-iT-\tau_{uk,l}^{(k)}\right)+n(t) \quad (9)$$

where $\alpha_{u_k,l_p}^{(k)}$ are independent Nakagami-m random variables of orthogonal diversity, horizontal and vertical, for horizontal polarization can be express as[5]

$$\alpha_h = \frac{\sin\gamma-\left(\kappa-j60\lambda\sigma-\cos^2\gamma\right)^{1/2}}{\sin\gamma+\left(\kappa-j60\lambda\sigma-\cos^2\gamma\right)^{1/2}} \quad (10)$$

and for vertical polarization[5]

$$\alpha_v = \frac{(\kappa-60\lambda\sigma)\sin\gamma-\left(\kappa-j60\lambda\sigma-\cos^2\gamma\right)^{1/2}}{(\kappa-60\lambda\sigma)\sin\gamma+\left(\kappa-j60\lambda\sigma-\cos^2\gamma\right)^{1/2}} \quad (11)$$

where $\kappa=\varepsilon/\varepsilon_0$ is the relative permittivity of the earth. σ is conductivity of the earth (good earth)[8].

IV. THROUGHPUT ANALYSIS

In this section, we consider multi-user detection of slow frequency hopping multicarrier direct sequence code division multiple access (multi-user detection of SFH/MC DS-CDMA) technique for vertical and horizontal polarization over Nakagami fading channel. The frequency hopping pattern are controlled by a set of constant-weight code $C(Q,U_k)$. A set of U_k number of active FH subcarrier frequencies from the Q outputs of the frequency synthesizer.

The average bit error probability for multi-user detection of SFH/MC DS-CDMA can be expresses as[4].

$$\overline{P_e} = \sum_{x=0}^{X-1} \binom{X-1}{x_h} . P_h^{x_h} \left(1-P_h\right)^{X-1-x_h} . P_b\left(x_h\right) \qquad (12)$$

where $0 \le x_h \le X-1$ and P_h is the probability of a hit from an interfering signal, which can be expressed as.

$$P_h\left(x\right) = \frac{U_k}{Q} \qquad (13)$$

where U_k represents the weight of constant - weight code employed. The multi-user detection of SFH/MC DS-CDMA designed supporting data, voice, and video service. We assume furthermore that each user transmits independently. Then average probability of a hit can be expressed as

$$P_h = \frac{1}{QM} \sum_{i=0}^{M} U_i \qquad (14)$$

Q-function can be represented as

$$Q\left(x\right) = \frac{1}{\pi} \int_0^{\frac{\pi}{2}} \exp\left(-\frac{x^2}{2\sin^2\theta}\right) d\theta \qquad (15)$$

the latter Q-function representation has the advantage of having finite integration limits that are independent of the argument x. Hence (15) allows us to obtain a convenient analytical BER expression for the scenario, where the multipath channel output are not identically distributed. In this paper, $\overline{\gamma}$ represents the average received signal-to-noise ratio (SNR) given by:

$$\overline{\gamma} = \left[\frac{q\left(L_p,\eta\right)}{2N_p}\left(\frac{L_p-1}{L_p}\right) + \frac{K_h, q\left(L_p,\eta\right)}{3N_p} + \left(\frac{2\Omega_0 E_b}{N_o}\right)^{-1}\right]^{-1} \qquad (16)$$

each received signal magnitude are same. The received signal magnitude $\gamma_l = \Omega_{q,l}^2 / \Omega_0$ represents by probability density function (pdf) over Nakagami fading channels for number of path L[th] are

$$P_{\gamma_{u_k}}\left(\gamma\right) = \frac{m^m \gamma_l^{m-1}}{\overline{\gamma}_l^m \Gamma\left(m\right)} \exp\left(-\frac{m}{\overline{\gamma}_l}\gamma_l\right) \qquad (17)$$

the average bit error probability over Nakagami fading channel for number of path L[th] can be expressed as.

$$P_b = \frac{1}{\pi} \int_0^{\frac{\pi}{2}} \prod_{l=1}^{L} \left(\frac{\sin^2\theta}{\sin^2\theta+1}\right)^{mL} d\theta \qquad (18)$$

according to the analysis of Alouini and Goldsmith [5] can be expressed in a closed -form as

$$P_b\left(x_h\right) = \sqrt{\frac{\gamma}{1+\gamma}} \frac{\Gamma\left(mL+\frac{1}{2}\right)}{\Gamma\left(mL+1\right)} \bullet {}_2F_1\left(1, mL+\frac{1}{2}; mL+1; \left(1+\gamma\right)^{-1}\right) \qquad (19)$$

where ${}_2F_1\left(a,b;c;z\right)$ is the hypergeometric function defined as[4].

$${}_2F_1\left(a,b;c;z\right) = \sum \frac{a_k b_k z^k}{c_k k!} \qquad (20)$$

Finally, the throughput of CSMA/CA protocol by multiuser detection of SFH/MC DS-CDMA technique for orthogonal diversity over Nakagami fading channel, we can be calculate throughput by (1) and (12) defined as

$$S = S_{CSMA/CA}\left(1-\overline{P_e}\right)^L \qquad (21)$$

for (21) L is the number of bit per packet to transmission.

V. NUMERICAL RESULT

The numerical results are shown and the throughputs of two types of polarization diversity (vertical polarization and horizontal polarization in the good earth's condition) are compared in this section. Figure2. plots the throughput versus offer load of the orthogonal diversity of the proposed SFH/MC DS-CDMA system with respect to the number of path $l_p = 1, 2, 3, 4, 5$. Note that as the number path increase, the throughput does increase a lot but the throughput does decrease when the offer load is high. Figure3. shown the throughput versus offer load are compared for two types of polarization diversity. We note that throughput increase when number of carrier increase $Q = 1, 2, 4, 8, 16$ in low-offered traffic while the throughput decreases in high-offered traffic. Figure4. Note that curves in presented, the throughput over Nakagami fading channel increase if offered load is low traffic, while the throughput in Nakagami fading channel model decrease when traffic increase. Figure5. Note that curves in presented, the throughput versus offer load with number of user, the throughput decrease in high user and high offered load. Finally, we note that the vertical polarization is more appropriate than the horizontal diversity in CSMA/CA by multiuser detection of SFH/MC DS-CDMA for wireless LAN system.

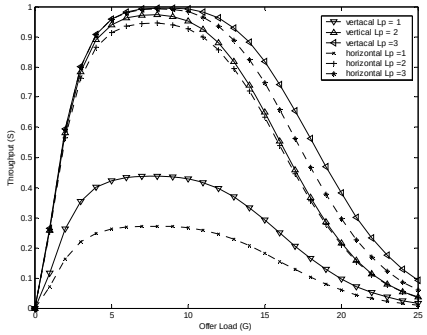

Figure 2. Throughput versus offer load for varying of the number of path (L_p=1,2,3 m=1 Q=1 User=32 SNR=15 dB)

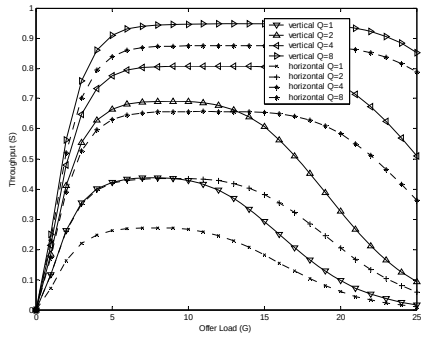

Figure 3. Throughput versus offer load for varying of the number of carrier (L_p=1 m=1 Q=1,2,4,8 User=32 SNR=15 dB)

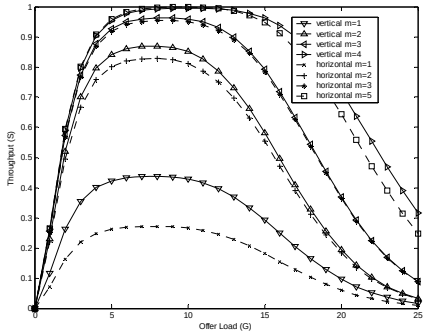

Figure 4. Throughput versus offer load for varying of the Nakagami-m fading factor (L_p=1 m=1,2,3,4 Q=1 User=32 SNR=15 dB)

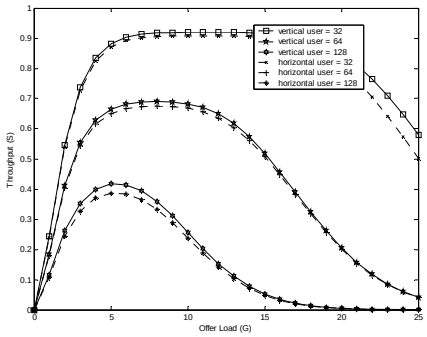

Figure 5. Throughput versus offer load for varying of the number of User (L_p=1 m=1 Q=4 User=32,64,128 SNR=15 dB)

VI. CONCLUSION

This paper presents the throughput for wireless local area network (WLAN) for orthogonal diversity antenna (vertical and horizontal polarization) by multiuser detection of SFH/MC DS-CDMA technique over Nakagami fading channel. The numerical results presence in the number of path, number of carrier, Nakagami-m fading factor and number of user. The throughput of WLAN with Nakagami fading is analyzed. The throughput improvement of the SFH/MC DS-CDMA system. We have considered two type of antenna, including vertical polarization, horizontal polarization, and have analyzed their throughput versus offer load. We also found the vertical polarization is better than the horizontal polarization for throughput in all of the results.

The main contributions of this are twofold: 1.the improvement of an analytical for the throughput of MAC protocol using multi-user detection SFH/MC DS-CDMA system for wireless LAN over Nakagami fading channel. 2.the throughput channel comparison for two types of antenna, vertical and horizontal polarization.

REFERENCE

[1] Al-Semari S.A. Guizani M, "Channel throughput of slotted ALOHA in a Nakagami fading environment," IEEE International Conference on, Volume 2, 8-12 June 1997 Page(s):605 - 609 vol.2.

[2] Jingshown Wu, Meng-Che Wu, "Dual-Polarization Frequency Reuse with Frequency Band Shifting Allocation" IEEE Transaction on Vehicular Technology, vol.49, No.6, November 2000

[3] Jae Hyun Kim, Jong Kyu Lee, "Performance Analysis of MAC Protocols for Wireless LAN in Rayleigh and Shadow Fading Channels." *Proceeding of IEEE Global Telecommunications Conference 1999*, vol. 5 pp2860-2864.

[4] Lie-Liang, Yang and Lajos Hanzo, "Blind Soft-Detection Assisted Frequency-Hopping Multicarrier DS-CDMA Systems" *Proceeding of IEEE Global Telecommunications Conference 1999*, volume. 1B pp 842-846.

[5] M.K. Simon and M.Alouini, "A unified approach to the probability of error for noncoherent and differentially coherent modulations over generalized fading channels," *IEEE Transaction Communications*, vol.45, pp.1625-1638, Dec 1998

[6] J.G.Proakis, " Digital Communication," 3rd Ed, New York, McGraw-Hill, 1995

[7] K. Bullington, "Radio propagation at frequencies above 30 megacycles," Proceedings of the IRE, pp. 1122-1136, October 1947

Users Capacity Increment of MLC-GSM Over Rayleigh Fading Channel

Phichet Moungnoul and Wiphada Inkiew
Faculty of Engineering and Research Center for Communication and Information Technology
King Mongkut's Institute of Technology Ladkrabang, Chalongkrung Road, Bangkok, 10520 THAILAND
E-mail: phichet@telecom.kmitl.at.th

***Abstract*-This paper proposes the Multi linear chirp frequency hopping (MLC/FH) technique for GSM system to increase the user capacity. Simulation used Rayleigh fading channel model for performance compare between GH-GSM and MLC/FH-GSM. From result shows that highest user capacity can increase up to 48 times to compare with conventional GSM system and also up to 6 times to compare with FH-GSM system.**

I. INTRODUCTION

The Global System for Mobile Communication (GSM) is very popular in the world. The number of GSM users increased very quickly, so providers have to increase number of base station more that system to increase the investment. Frequency Hopping (FH) [1] used to increase the GSM users capacity. This method can increase number of users more than GSM 8 times. The frequency allocations are defined to be used in different function as shown in Figure 1. In each frequency band, FDMA technique was employed to divide the whole bandwidth into sub-carrier frequency bandwidth of 200 kHz and each carrier frequency will be divided by using TDMA technique into 8 timeslots, and Ts_0 timeslot is used for signaling [2]. GSM system set time duration of each channel is 577 μs and hop to other frequency before through next frame. FH-GSM consisted of 2 types is Cyclic hopping and Pseudo random hopping as shown in Figure 2[3].

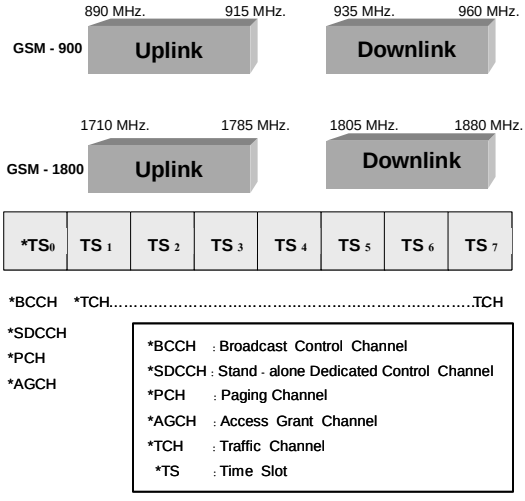

Figure 1.Frequency allocation and channel configuration of GSM

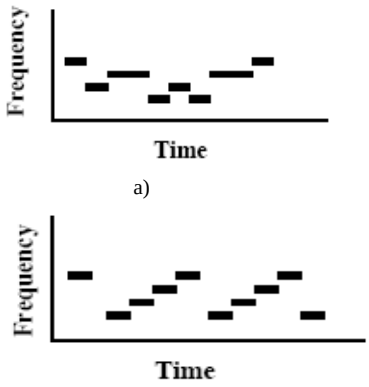

Figure 2.Hopping pattern of FH–GSM
a) Cyclic hopping b) Pseudo random hopping.

Pseudo-random hopping used random frequency hop, it have problem of frequency collision between hop. In causes from 2 users hop at the same time by accident and also in at that time it has synthesized at the same frequency thus it cannot detect user. The result is probably of data error that is affect to this system because the causes are happen always. Cyclic hopping can be solved for frequency collision but not good for the security. From [4] proposed technique prevents a collision problem. This paper used Pseudo-random hopping scheme for GSM because this scheme is good security and solved the collision problem by MLC technique. MLC/FH technique not only prevents a collision problem, it can be increase number of user per time slot and performance.

II. PRINCIPLE AND THEORY

A. FH – GSM System

In FH–GSM transmitted data in pattern of TDMA frame [1]. GSM base station will transmit frequency of each time duration channel (577 μs) and a frequency will hop to next channel after that. Uplink and downlink used the same frequency.

FH-GSM hopped 64 sequences. The type of hopped is Mobile Allocation Index Offset (MAIO) and Hopping Sequence Number (HSN).

MAIO have many data in sequence of frequency and also it can initial of hopped frequency. HSN has 64 sequences that function informed index of sequence. Actually frequency will

be changed as random when HSN not equal zero (0). If HSN equal zero (0), the system will be hopped in cyclic mode.

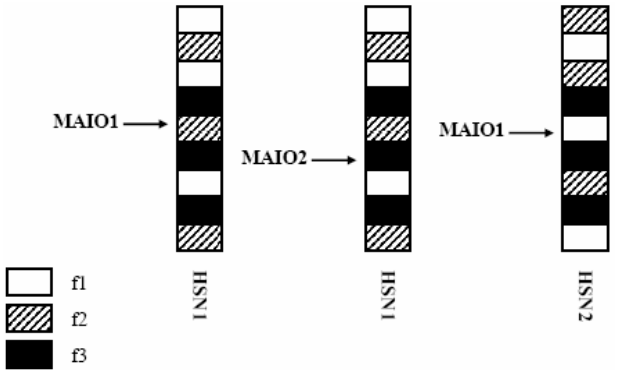

Figure 3.Hopping patterned with 3 MAIO frequencies for each HSN.

Advantage of hopped pattern in Figure 3 is set condition with different MAIO. It haven't problem about collision from hopping such as the frequency hopped of HSN is difference and MAIO is the same value. In case of HSN is same value both frequency and time channel. It will occur the interference at $1/n$ of burst signal, where n is the different value of hopped frequency sequence. It can decrease the performance of system as follow Figure 4.

Disadvantage of system is reduce one of channel because used one channel for BCCH (Broadcast Control Channel) which the base station use this channel for BSIC (Base Station Identification Code) and frequency decoding. Thus the system can be served the lower amount of users.

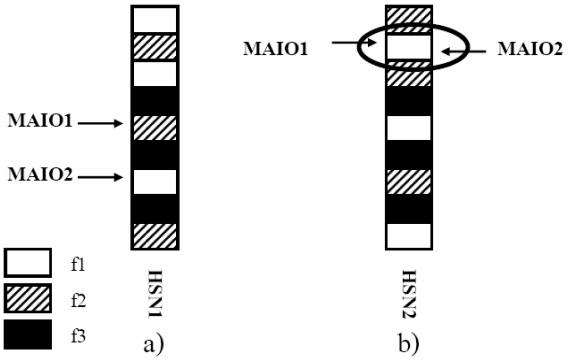

Figure 4.Hopping patterned with 3 MAIO frequencies in case the same of HSN a) No collision problem b) Collision problem.

III. PROPOSED SYSTEM

Transmitter and receiver block diagram of propose system as shown in Figure 5and Figure 6 respectively.

Figure 5 shows information of each user is passed to MLC modulator with parallel channel and multiplied with hopper. After that the data will sum in order to send Tx. Signal in the same antenna. MLC modulate signal as follow [4].

$$s_{mc}(t) = s_f(t) + s_b(t) \tag{4}$$

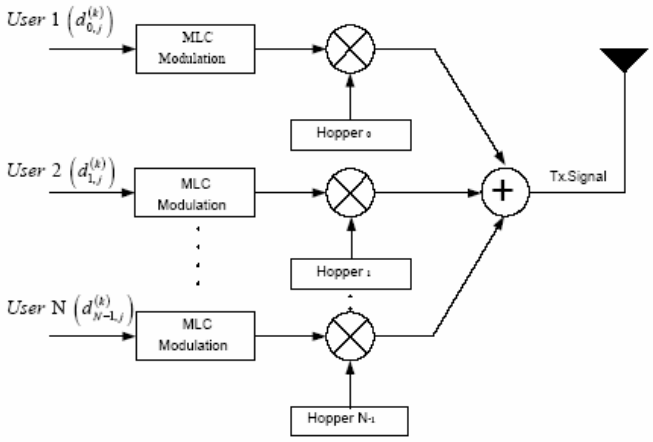

Figure 5.Block diagram of MLC/FH–GSM transmitter .

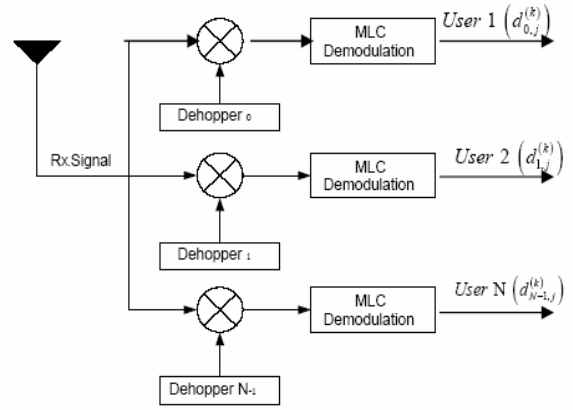

Figure 6.The block diagram at receiver side of MC – FH – GSM system.

And adjust center frequency value of f_{ch} as follow.

$$f_{ch} = f_{ch1} + (l_m - 1)W_d, \quad l_m = 1, 2, ..., L \tag{5}$$

$$L = 2^k \tag{6}$$

Where l_m is the hop level of user m
L is the number of all hop level
f_{ch} is center frequency of hop band
f_{ch1} is the center frequency of first(1^{st}) hop

From (5) can be write MLC/ FH –GSM signal for every user as follow [4,5,6].

$$\sum_i \sum_{l=0}^{N-1} \sum_{n=-\infty}^{\infty} \sum_{m=1}^{M} d_{l,i}^{(m)} s_{mf}(t)\, p_{T_h}(t - nT_h) \tag{7}$$

$$s_{mf}(t) = s_{mff}(t) + s_{mfb}(t) \tag{8}$$

$$s_{mff}(t) = A\cos\Big[2\pi\big(f_{ch1} + (l_m - 1 - b(t)/2)W_d\big)t + b(t)\mu_{fm}\pi t^2\Big], 0 \le t \le mT_c \tag{9}$$

$$\mu_{fm} = \frac{(M+1-m)\Delta f}{mT_c} \tag{10}$$

$$s_{mfb}(t) = A\cos\Big[2\pi\big(f_{ch1} + (l_m - 1 + b(t)/2)W_d - b(t)m\Delta f\big)(t - mT_c) + b(t)\mu_{bm}\pi(t - mT_c)^2\Big], \quad mT_c \le t \le T_h \tag{11}$$

$$\mu_{bm} = \frac{m\Delta f}{(M+1-m)T_c} \tag{12}$$

$$T_c = \frac{T_h}{(M+1)} \tag{13}$$

$$\Delta f = \frac{W_d}{(M+1)} \tag{14}$$

$$b(t) = \begin{cases} 1 & \text{Up Chirp} \\ -1 & \text{Down Chirp} \end{cases}, 0 \le t \le T_h \tag{15}$$

Where μ_{fm} is front chirp slope of user m^{th}

μ_{bm} is back chirp slope of user m^{th}

m is user sequence

T_h is hop bit duration

T_c is total time

$p(t)$ is unit amplitude pulse of duration T_c period

$d_{l,i}^{(m)}$ is the binary sequence of user m^{th}

l is the sequence of bit

i is the amount of bit

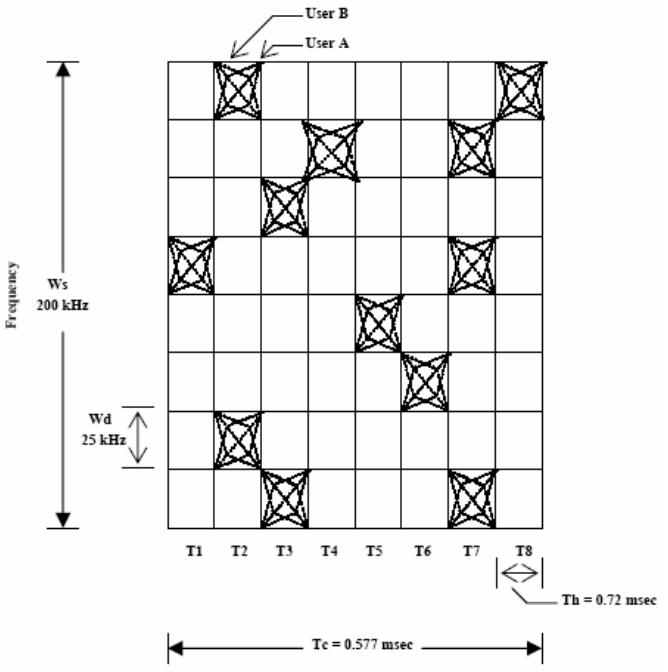

Figure 7 Solution for frequency code collision problem of users A and B in MLC/FH-GSM system

Receiver used dehopper for alternatives hopper process and MLC demodulator which correlator circuit used compared receive signal with reference signal. Figure 7 shows MLC/FH-GSM transmit signal in time–frequency domain of two users which has the same frequency as same as figure 4. It can see that occurred frequency collision of user A and user B will be different frequency characteristic. MLC demodulator can be separated the collision signal of each user and does not occur the error signal in users A and B. Figure 7.shows dispreading signal convert to data modulate band. This signal will compare and analyze of each bit in MLC demodulator. It can be decrease the error probability in MC-FH-GSM system.

IV. Experiment And The Results [7,8,9]

Simulate model of MC/FH-GSM detail of frequency and time bit duration as figure 8. Simulation result of performance and number of user compared between FH-GSM and MLC/FH-GSM as shown in figure 8, 9, 10 and 11.

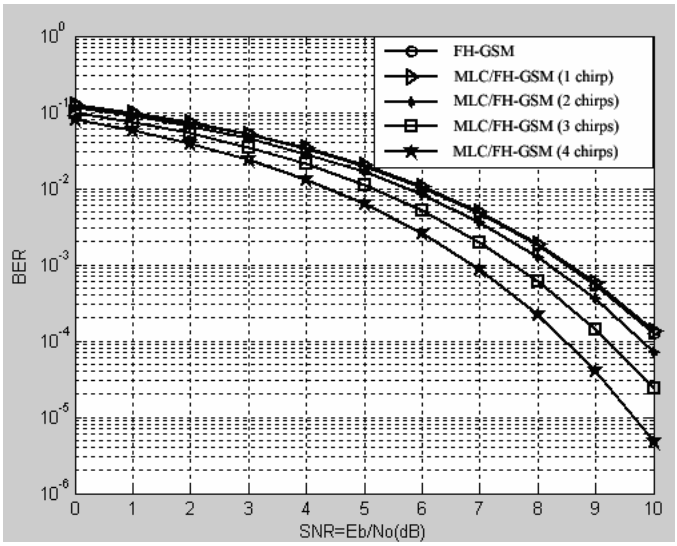

Figure 8.Performance comparative between MLC/FH-GSM and FH-GSM.

Figure 8 Show the experimental result from setting the number of user at 48. By vary SNR parameter that the BER value of FH-GSM system has the highest values when compare with MLC/FH-GSM system because of the FH-GSM system was defined frequency channel less than MLC/FH-GSM system.

Figure 9 shows performance as increase the number of user. When number of user increased continuously, FH-GSM system cannot support this amount of user because this system limited by number of hop. This result shows chirp modulation will make the system can serve the increase number of users. Because of chirp modulation will decrease the causes of data collision. Figure 10 can be estimated maximum of chirp rate which use in system not more than 12 chirps.

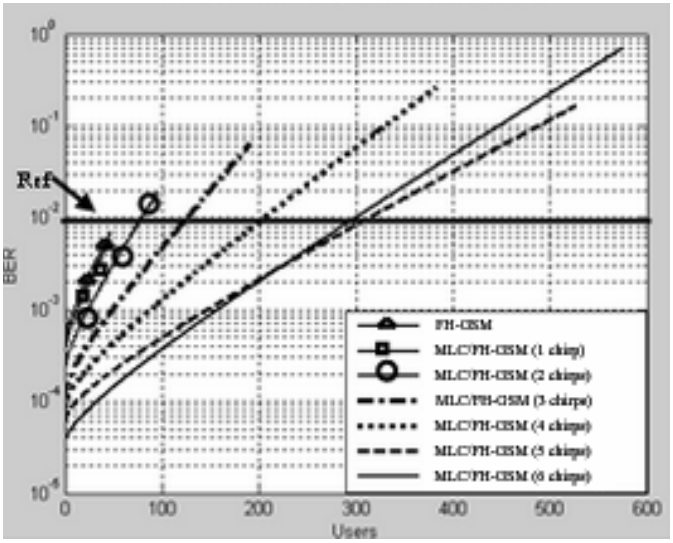

Figure 9.BER and Number of user compare between FH-GSM and MLC/FH-GSM system (Ideal channel).

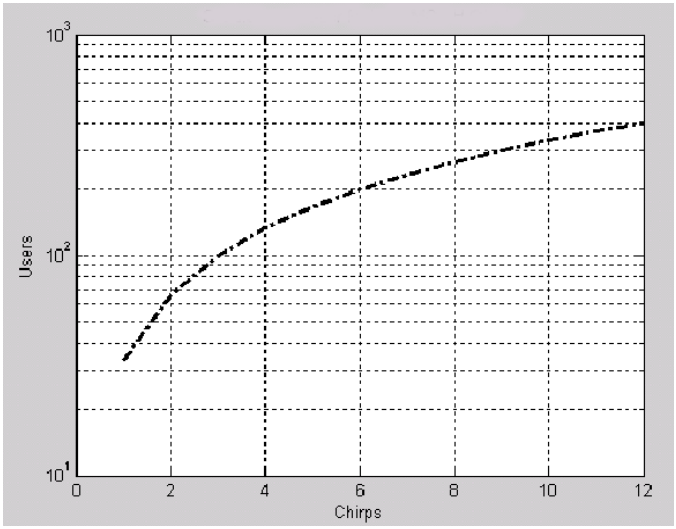

Figure 10.Comparative between number of GSM user and number of chirp.

Figure 10 shows comparative between maximum number of users and chirp rate. The initial period the trend of graph slope is increased. When the chirp rate is increased the slope will reduce continuously because number of user nearly upper bound.

Figure 11 shows performance of FH-GSM and MLC/FH-GSM over Rayleigh fading channel model. Performance of FH-GSM and MLC/FH-GSM system have lower value than experiment result in figure 9, because will have more signal distortion in system.

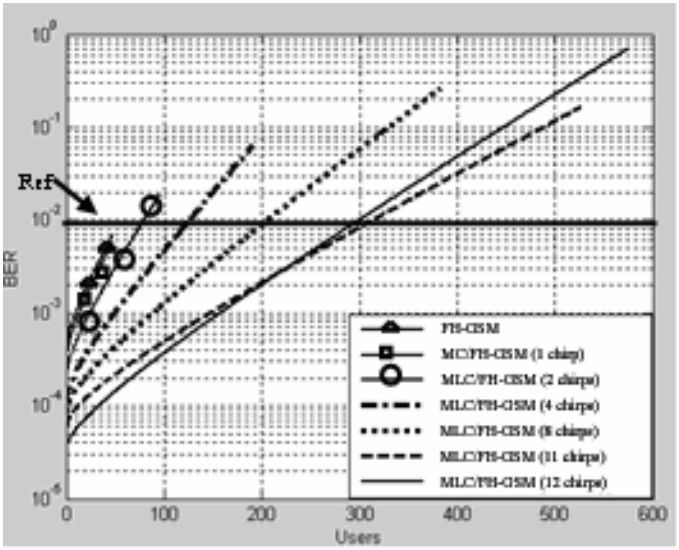

Figure 11.BER and number of user comparative between FH-GSM and MLC/FH-GSM system over Rayleigh Fading Channel model.

V. CONCLUSION

This paper proposes MLC/FH-GSM technique to solve collision problem and increase the performance greater than Pseudo random hopping FH-GSM system. Also this technique can serve the increasing of users. From result the chirp rate not more than 12 chirps. For voice service as BER 10^{-2}, the MLC/FH-GSM user capacity up to 6 times to compare with FH-GSM system.

REFERENCES

[1] C. Carneheim and M.Ljungberg, "FH-GSM Frequency Hopping GSM," in *Proc. of IEEE 44th VTC Sweden*, pp. 1155-1159, 1994.

[2] J. M. Hernando and F. P. Fontan, *Introduction to Mobile Communications Engineer*., Artech House, London, pp.375-424 1999.

[3] T. T. Nielsan and J. Wigard, *Performance Enhancements in a Frequency Hopping GSM Network.* Kluwer Academic Publishers, London, 2000.

[4] P. Moungnoul, S. Disapirom, S. Junpong, T. Paungma, "Collision Problem Solving in FH-CDMA by Multi Linear Chirp Technique," *ECTI-CON2005*, pp. 996-999, May 2005.

[5] C. Caini. And G. Riva, "A New Vector Quantization Technology for Performance Evaluation in Frequency Hopping Mobile Radio System," *Proc. of IEEE Communication Letters*, vol. 4 , No.8, pp. 252–254, August 2000.

[6] S. E. El-Khamy, S.E. Shahban, E. A. Thabet, "Frequency-Hopped Multi-User Chirp Modulation (FH/M-M) for Multipath Fading Channels," *IEEE Symp. Antennas and Prop*., Vol. 1, pp. 996-999, July 1999.

[7] J. G. Proakis, *Digital Communication*. McGraw-Hill, New York, 2001.

[8] H. Harada, R. Prasad, *Simulation and Software Ratio for Mobile Communications.*, Arteh House, London, 2002.

[9] J. G. Proakis, M. Salehi, G. Bauch, *Contemporary Communication Systems*. Brooks/Cole, 2004.

Proposal of PAPR Reduction Method for OFDM Signal without Side Information

Pornpawit Boonsrimuang†, Pisit Boonsrimuang†, Kazuo Mori*, Tawil Paungma† and Hideo Kobayashi*

† Department of Telecommunication Engineering, Faculty of Engineering,
King Mongkut's Institute of Technology Ladkrabang, Thailand
* Division of Electrical and Electronic Engineering, Graduate School of Engineering, Mie University, Japan
E-mail: pornpawit@bcommart.com , pisit@telecom.kmitl.ac.th , koba@elec.mie-u.ac.jp

Abstract— **The major drawback of orthogonal frequency division multiplexing (OFDM) is large Peak-to-Average Power Ratio (PAPR) of its time domain signal. To overcome the PAPR problem on OFDM signal, various PAPR reduction methods have been proposed up to today. The most of PAPR reduction methods such as PTS and SLM methods require the side information which causes the degradation of transmission efficiency and complexity of transmitter and receiver. In this paper, we propose a novel PAPR reduction method which can improve the PAPR performance without side information. The feature of proposed method is to use the common weighting factor over a frame including preamble and data symbols in which the common weighting factor is multiplied to the frequency domain signal over a frame so as to reduce the PAPR performance. The data symbols in one frame can be demodulated at the receiver by using the estimated common weighting factor. The common weighting factor can be estimated together with the channel frequency response by using the preamble symbol located at the start of every frame. This paper presents various computer simulation results to verify the effectiveness of proposed method in the multi-path fading channel.**

I. INTRODUCTION

Recently the OFDM technique has been received a lot of attentions especially in the field of wireless communications because of its efficient usage of frequency bandwidth and robustness to the multi-path fading. From these advantages, the OFDM has already been adopted as the standard transmission techniques in the wireless LAN systems and the terrestrial digital broadcasting system [1-2]. The OFDM technique is also considering as one of the candidate transmission techniques for the next generation of wireless communications systems. One of the limitations of using OFDM technique is the larger peak to averaged power ratio (PAPR) of its time domain signal as compared with the conventional single carrier transmission techniques [3]. The larger PAPR signal would cause the severe degradation of bit error rate (BER) performance due to the inter-modulation noise occurring in the non-linear amplifier.

From the above background, the PAPR reduction method is recognized as one of the essential research topics for the OFDM method employed in the wireless communications sytems. Up to today, various kinds of PAPR reduction methods were proposed including the selected mapping method (SLM) [4] and partial transmit sequence method (PTS) [5-6]. Although both methods can achieve the better PAPR performance by controlling the phase of data sub-carriers, these two methods are required to inform the phase information controlled for the data sub-carriers to the receiver as the side information (SI). Since the side information is required to inform the receiver symbol by symbol by using the data or control channels with the higher signal quality for the correct demodulation of data information at the receiver, the transmission efficiency would be degraded relatively and the system complexity would be increased. The size of side information depends on the number of clusters and discrete phases employed in the SLM or PTS methods. To improve the PAPR performance, the larger number of clusters and discrete phases are required which lead the proportional increasing of side information size.

To overcome the problem for the conventional PAPR reduction methods with using the side information, we propose a novel PAPR reduction method which is required no side information. The feature of proposed method is that the PAPR performance can be improved by multiplication of common weighting factor over one frame including preamble and data symbols. The original data can be recovered by multiplying the inverse of common weighting factor employed at the transmitter. In the proposed method, the inverse of weighting factor can be estimated by using the preamble symbols which are usually used in the conventional OFDM system to establish the synchronization of received signal and to estimate the channel frequency response of fading channel.

In the following of this paper, Section II presents the system model to be used in the following evaluations. Section III presents the proposed PAPR reduction method. Section IV presents the various computer simulation results to verify the effectiveness of the proposed method, and we draw some conclusions in Section V.

II. SYSTEM MODEL

In the OFDM system, the modulated signal in the frequency domain is converted to the time domain signal by using *IFFT*. The time domain signal for *l-th* symbol at *k-th* sample is given by the following equation.

$$y_{(l,k)} = \frac{1}{\sqrt{N}} \sum_{n=0}^{N-1} X_{(l,n)} e^{j\frac{2\pi kn}{N}} \quad (1)$$

where N is the number of *IFFT* points and $X_{(l,n)}$ is the modulated data for *l-th* symbol at *n-th* sub-carrier. Here the PAPR performance for the sampled time domain signal can be given by,

$$PAPR(dB) = 10\log_{10}\left(\frac{\max_{k=0\sim N-1}\left[\left|y_{(l,k)}\right|^2\right]}{E\left[\left|y_{(l,k)}\right|^2\right]}\right) \quad (2)$$

where $E[\ ]$ represents the average power of signal. The time domain OFDM signal given in (1) is input to the non-linear amplifier after adding the guard interval (GI). The output of non-linear amplifier can be expressed by the following equation.

$$s_{(l,k)} = F[\left|y_{(l,k)}\right|]e^{j\{\arg(y_{(l,k)})\}} \quad (3)$$

where, $F[\ ]$ represent the AM/AM conversion characteristics of non-linear amplifier. The non-linear amplifier assumed in this paper is the Solid State Power Amplifier (SSPA) of which input and output relationship is modeled by the following equation.

$$F[\rho] = \frac{\rho}{[1+(\rho/A)^{2r}]^{1/2r}} \quad (4)$$

where, ρ is the amplitude of input signal, A is the saturated output level, and r is the parameter to decide the non-linear level. The phase conversion of the non-linear amplifier is assumed to be linear in the following evaluation. Figure 1 shows the AM/AM conversion characteristics of SSPA when changing the parameter of r in (4).

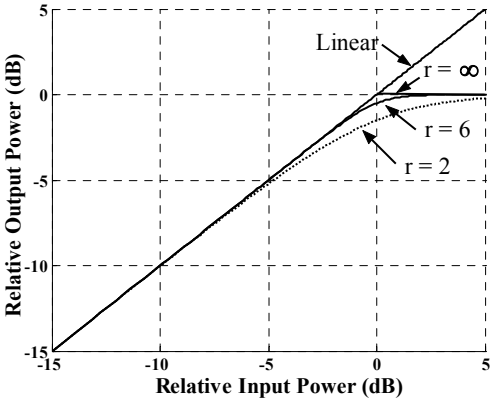

Figure. 1. Input-output relationship of SSPA.

III. PROPOSAL OF PAPR REDUCTION METHOD

A. Transmitter

Figure 2 shows the burst frame format to be used in the proposed OFDM system. In Fig. 2, two preamble symbols are inserted before the transmission of data symbols, which are used in the synchronization of received signal and the estimation of channel frequency response including the common weighting factor multiplied over a frame at the transmitter so as to reduce the PAPR performance. Fig.3 (a) shows the structure of proposed transmitter. By reoffering this figure, the following presents the detail of proposed method.

In the proposed method, the transmission time domain signal for *l-th* symbol of *k-th* sample at *i-th* iteration is given by the following equation.

$$\begin{aligned}\bar{y}_{(l,k)}^{(i)} &= \frac{1}{\sqrt{N}}\sum_{n=0}^{N-1}\left(X_{(l,n)}^{(i-1)}\cdot e^{j\theta_n^{(i)}}\right)e^{j\frac{2\pi kn}{N}} \\ &= \frac{1}{\sqrt{N}}\sum_{n=0}^{N-1}X_{(l,n)}^{(i)}\cdot e^{j\frac{2\pi kn}{N}}\end{aligned} \quad (5)$$

where $e^{j\theta_n^{(i)}}$ is the common weighting factor for *n-th* sub-carrier at *i-th* iteration, which is decided so as to reduce the PAPR performance. Here it should be noted that the common weighting factor at *n-th* sub-carrier has the same value over one frame. In the proposed method at the next *(i+1)-th* iteration, the new weighting factor for each symbol will be independently decided so as to obtain the better PAPR performance than the previous iteration. After the determination of weighting factor for all symbols including the preamble symbols, the new common weighting factor over one frame will be decided by taking the ensemble average of weighting factor obtained for all symbols.

As for the method to decide the weighting factor for each symbol, this paper employs the basic concept of time-frequency domain swapping algorithm [7]. In this algorithm, the error signal is calculated by the following equation in which the sampled time domain signal is detected as the error signal only when its amplitude level is greater than a certain reference level of *S*.

$$e_{(l,k)}^{(i)} = \begin{cases}\bar{y}_{(l,k)}^{(i)} & if\ \left|\bar{y}_{(l,k)}^{(i)}\right| \geq S \\ 0 & if\ \left|\bar{y}_{(l,k)}^{(i)}\right| < S\end{cases} \quad (6)$$

where the reference level *S* is decided on the basis of the average power of time domain signal. Here, the error signal is the composite signal in the time domain which includes all the larger amplitude level than the reference level of *S*. To determine the weighting factor for each sub-carrier, the time domain error signal given by (6) is converted to the frequency domain signal by *FFT*, which is given by the following equation.

$$E_{(l,n)}^{(i)} = \frac{1}{\sqrt{N}}\sum_{k=0}^{N-1}e_{(l,k)}^{(i)}\cdot e^{-j\frac{2\pi kn}{N}} \quad (7)$$

The weighting factor for *l*-th symbol at *n*-th sub-carrier can be obtained by subtracting the phase of error signal given in (7) from the phase of original signal. Then, the frequency domain signal to be used at the next iteration $(i+1)$ is given by the following equation.

$$X_{(l,n)}^{(i+1)} = \left|X_{(l,n)}^{(i)}\right|e^{j\arg\left\{X_{(l,n)}^{(i)}-E_{(l,n)}^{(i)}\right\}} \quad (8)$$

The weighting factor of *n*-th sub-carrier for *l-th* symbol can be given by,

$$\theta_{(l,n)}^{(i+1)} = \arg\left\{X_{(l,n)}^{(i+1)}\right\} - \arg\left\{X_{(l,n)}^{(i)}\right\} \quad (9)$$

After finishing the above procedures over all symbols, the common weighting factor for *n-th* sub-carrier at the *(i+1)-th* iteration can be obtained by taking the ensemble average for the weighting factors obtained for all symbols, which is given by,

$$\theta_n^{(i+1)} = \arg\left\{\sum_{l=1}^{L}e^{j\theta_{(l,n)}^{(i+1)}}\right\} \quad (10)$$

where L is the frame length including preamble and data symbols. By using (10), the transmission time domain signal at the *(i+1)-th* iteration can be given by,

$$\begin{aligned}\overline{y}_{(l,k)}^{(i+1)} &= \frac{1}{\sqrt{N}}\sum_{n=0}^{N-1}\left\{X_{(l,n)}^{(i)}\cdot e^{j\theta_n^{(i+1)}}\right\}\cdot e^{j\frac{2\pi kn}{N}} \\ &= \frac{1}{\sqrt{N}}\sum_{n=0}^{N-1}X_{(l,n)}^{(i+1)}\cdot e^{j\frac{2\pi kn}{N}}\end{aligned} \tag{11}$$

In the proposed method, the procedures from (5) to (11) are repeated up to reach either the predetermined target PAPR performance or predetermined number of iterations.

B. Receiver

Figure 3 (b) shows the structure of receiver for the proposed method. The received signal $r_{(l,k)}$ for *l-th* symbol at *k-th* sample after down converter (D/C) and Analog to Digital converter (A/D) as shown in Fig.3 (b) can be given by the following equation.

$$r_{(l,k)} = \overline{y}_{(l,k)}^{(P)} \otimes h_{(l,k)} + n_{(l,k)} \tag{12}$$

where $s_{(l,k)}$, $h_{(l,k)}$ and $n_{(l,k)}$ show the transmitted OFDM signal, impulse response of multi-path fading channel and Additive White Gaussian Noise (AWGN) for *l-th* symbol at *k-th* sample, respectively. In (12), P is the number of iterations which provides the best PAPR performance at the transmitter. The received signal as given in (12) is converted to the frequency domain signal by using *FFT* which is expressed by the following equation.

$$R_{(l,n)} = X_{(l,n)}^{(P)}\cdot H_{(l,n)} + N_{(l,n)} \tag{13}$$

where, $R_{(l,n)}$, $X_{(l,n)}^{(P)}$, $H_{(l,n)}$ and $N_{(l,n)}$ show the received signal, transmitted signal, channel frequency response and noise component in the frequency domain, respectively.

When assuming the operation environments such as the radio LAN system, the time variance of channel frequency response can be assumed as sufficiently slow because of very lower terminal moving speed. From this fact, the channel frequency response over one frame can be considered as static. Accordingly, the channel frequency response estimated by using two known preamble symbols inserted at the start of every frame can be used in the equalization of data symbols over one frame. The channel frequency response which is improved the estimation accuracy by taking the ensemble average over two preamble symbols, can be obtained by the following equation.

$$\begin{aligned}\hat{H}_n &= \frac{1}{2}\sum_{l=1}^{2}\left\{X_{(l,n)}^{P}\cdot H_n + N_{(l,n)}\right\}/X_{(l,n)} \\ &= H_n\cdot e^{j\psi_n} + N_{(l,n)}/X_{(l,n)}\end{aligned} \tag{14}$$

where $\hat{H}_n$ is the estimated channel frequency response affected by the common weighting factor and noise component. Here, $e^{j\psi_n}$ can be given by following equation.

$$\psi_n = \sum_{i=1}^{P}\theta_n^{(i)} \tag{15}$$

From (14), it can be observed that the common weighting factor can be estimated in the frequency domain by using preamble symbols. By using (14), the original data signal can be demodulated by employing the same manner as the conventional frequency domain equalization method in which the common weighting factor multiplied at the transmitter and the multi-path fading multiplied in the channel can be removed from the received signal.

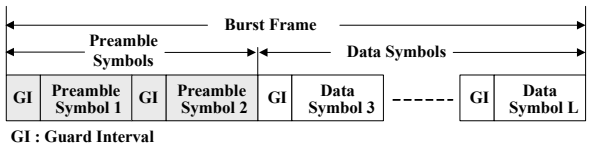

Figure. 2. Structure of burst frame format.

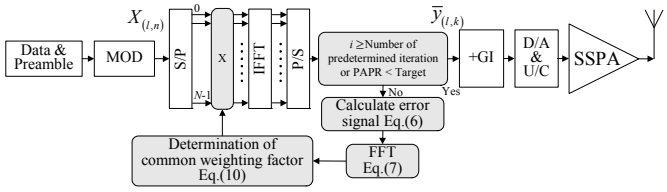

(a) Structure of proposed OFDM transmitter.

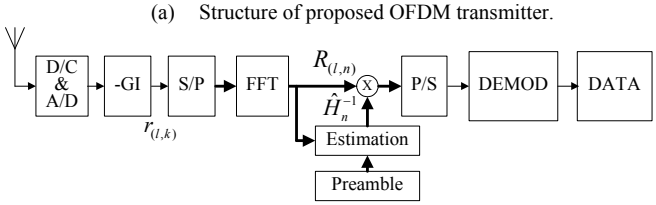

(b) Structure of proposed OFDM receiver.

Figure. 3. System model of proposed method.

IV. Performance Evaluation

This section presents the various computer simulation results to verify the performance of proposed method. The modulation method is assumed by 64QAM with coherent detection method. The multi-path fading is modeled by 16 delay paths having the exponential power delay profile with -1 dB decay constant. In the following simulations, the synchronizations both for the symbol timing and frequency offset are assumed to be established ideally by using two preamble symbols. The simulation parameters to be used in the following evaluations are shown in Table 1. In the simulations, the number of *FFT* points (N=256) is taken by 4 times larger than the number of sub-carriers (M=64) to evaluate the PAPR performance with higher accuracy.

TABLE I
SIMULATION PARAMETERS

Modulation	64QAM
Demodulation	Coherent
Allocated bandwidth	5MHz
Number of *FFT* points	256
Number of sub-carriers	64
Symbol duration	12.8us
Guard interval	1.28us
Non-linear amplifier	SSPA
Non-linear parameter of SSPA	r=2
Number of data symbols in one frame	12
Number of preamble symbols in one frame	2
Multi-path fading model	
Power delay profile	Exponential
Number of delay paths	16
Decay constant	-1 dB

Figure 4 shows the averaged PAPR performance both for the conventional OFDM and proposed methods when changing the number of iterations. The frame length is 12 symbols including 2 preamble symbols. From the figure, it can be seen that the proposed method can achieve the best PAPR performance when the number of iterations is larger than 8. The proposed method shows the better averaged PAPR performance than the conventional OFDM by 1.4 dB. From the results, the number of iterations is assumed by 8 in the following evaluations.

Figure 5 shows the PAPR performance for the conventional OFDM and proposed methods when the frame length is 12 symbols. The PAPR performance is evaluated by using the Complementally Cumulative Distribution Function (CCDF). From the figure, it can be observed that the proposed method can achieve the better PAPR performance than conventional OFDM about 1.9 dB at 10^{-1}. Here it should be noted that the degradation of BER performance of OFDM signal in the non-linear channel would be dominated by the PAPR performance at the CCDF larger than 10^{-1}.

Figure 6 shows the BER performances for the proposed and conventional OFDM methods in the multi-path fading channel when the input back-off (IBO) of non-linear amplifier is taken by -6 dB and -8 dB. From the figure, it can be observed that the proposed method can achieve much better BER performance than conventional OFDM method in the channel including the non-linear amplifier and multi-path fading.

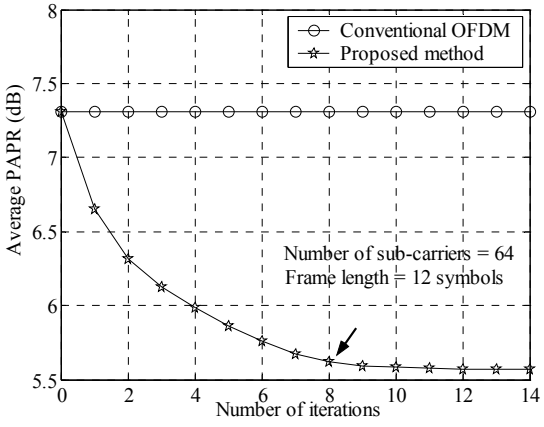

Figure. 4. Averaged PAPR performance versus number of iterations.

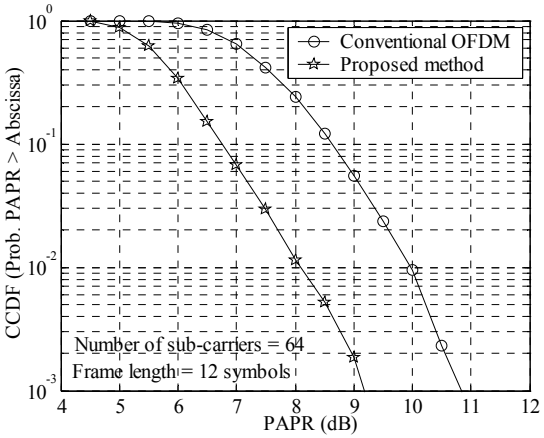

Figure. 5. PAPR performance for proposed method.

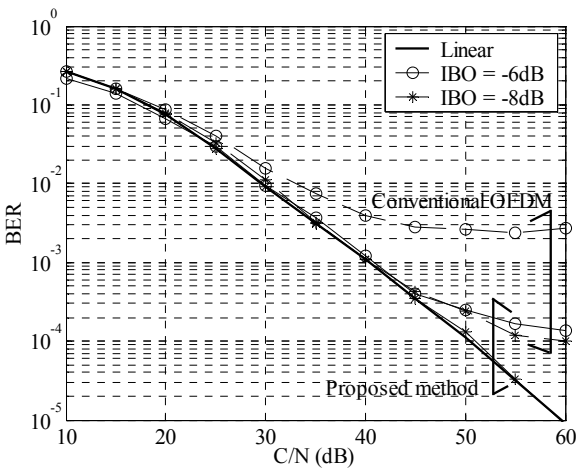

Figure. 6. BER performance of proposed method.

V. CONCLUSIONS

This paper proposed the PAPR reduction method for the OFDM signal without degradation of transmission efficiency. The feature of proposed method is to use the common weighting factor over one frame including the preamble symbols so as to improve the PAPR performance. In the proposed method, the time-frequency domain swapping algorithm is employed in the determination of common weighting factor. The common weighting factor can be removed from the received data symbols by using the frequency domain equalization. In the proposed method, the common weighting factor can be estimated together with the channel frequency response by using preamble symbols. Form this fact, the proposed method can achieve the better PAPR performance without loss of transmission efficiency. From the various computer simulation results, we confirmed that the proposed method can achieve the better PAPR performance and better BER performance than the conventional OFDM in the channel including non-linear amplifier and multi-path fading.

REFERENCES

[1] IEEE Std. 802.11a, High-speed Physical Layer in the 5GHz Band, 1999.

[2] IEEE 802.16 WG, *"SC-FDE PHY Layer System Proposal for Sub 11GHz BWA",* March 2001.

[3] D Dardari, V. Tralli and A Vaccari, *"A Theoretical Characterization of Nonlinear Distortion Effects in OFDM Systems,"* IEEE Trans. on Comm., vol. 48, no. 10, pp.1775-1764, Oct 2000.

[4] R. W. Bauml. R. F. H. Fischer and J.B. Huber, *"Reducing the peak-to-average power ratio of multicarrier modulation by selected mapping,"* IEEE Electro. Letter, vol. 32. no.22 pp.2056-2057, Oct. 1996.

[5] S. H. Muller and J. B. Huber, *"OFDM with reduce peak-to-average power ratio by optimum combination of partial transmit sequences,"* Electron. Letter, vol. 33, no. 5, pp. 368–369, Feb. 1997.

[6] L.J. Cimini, Jr. and N.R. Sollenberger, *"Peak-to-Average Power Ratio Reduction of an OFDM Signal Using Partial Transmit Sequences,"* IEEE Trans. on Comm., Letter, vol. 4, no. 3, pp86-88, March 2000.

[7] P. Boonsrimuang, K. Naito, K. Mori, T. Paungma and H. Kobayashi, *"PAPR Reduction of OFDM Signal by Use of DSI Method with Time-Frequency Domain Swapping Algorithm,"* IEICE Tran. on Comm., vol.E90-B, No.4, pp.1001-1006, Apr. 2007.

Interference Effect Comparison between IS-95B and CDMA2000 Cellular System over Nakagami Fading Channel

Naphat Sutthaphol and Phichet Moungnoul
Faculty of Engineering and Research Center for Communication and Information Technology
King Mongkut's Institute of Technology Ladkrabang, Chalongkrung Road, Bangkok, 10520 THAILAND
E-mail: ta_nee47@hotmail.com , phichet @telecom.kmitl.ac.th

***Abstract*- This paper proposes BER comparison between cdmaOne (IS-95B) and CDMA2000 for voice and WWW service over Nakagami fading channel model. The change of transmission data rate which direct effect to the quality of service (QoS). The performance in case perfect power control and imperfect power control is considered. Result shows the performance can be improve with maximum ratio combining (MRC) technique at the RAKE receiver. This technique can be increased performance by increase number of antenna and finger.**

I. INTRODUCTION

Mobile service is very popular in the world, developed of digital cellular from 2G to 3G for support voice and multimedia service. IMT-2000 was provide Mbps data rate for demand application such as broadband internet access, with most countries supporting one of two competing standard asCDMA2000 and Wideband-CDMA. CDMA2000 standard builds on cdmaOne to provide an evolution path to 3G [1]. The cdmaOne consist of 2 versions as IS-95A and IS-95B (2.5G) for higher data rate. Some techniques of CDMA2000 that consisted of cdmaOne have the ability of all data transmission at the same time.

In wireless communication system, the environment effect, such as reflection, diffraction and distortion from buildings or other obstacles, resulted to be the fading of transmitted signal. This fading effect can be described according to Nakagami Fading Model.

This paper considers the bit error rate between cdma2000 with IS-95B 3 channels and cdma2000 with 1 channel by studying the data rate changing which directly affects to the quality of service.

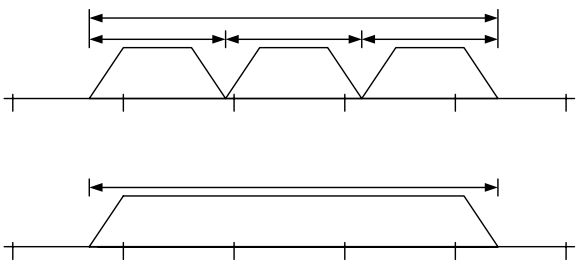

Figure 1. Frequency allocation Band of IS-95B and cdma2000 standard.

II. SYSTEM MODEL AND ANALYSIS OF SIGNAL TO INTERFERENCE SIGNAL RATIO

CDMA cellular system cell layout model consists of 19 cells for investigated interference [2] as shown in figure 2 and base station installed at the center of each cell.

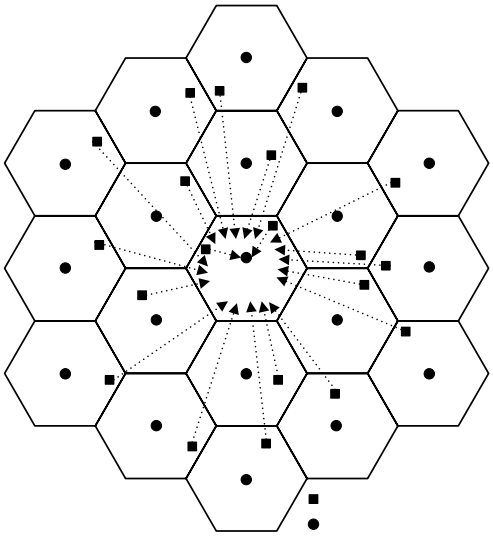

Figure 2. Model of 19 cells layout.

A. Transmitter Model

Figure 2 shows signal propagation path from the mobile subscribers to the base station and this paper assigned radius of cell is defined as 1 unit. There are k users which used the system in each cell at the same time. IS-95B and CDMA2000 transmitter uses BPSK modulation, as follow:

$$s_k(t) = \sqrt{2P}\, b_k(t)\, c_k(t) \cos(\omega_c t + \phi_k) \tag{1}$$

Where $s_k(t)$ is the transmitted of user k, P is the power of each user, ω_c is angular velocity of carrier, ϕ_k is the phase angle of user k carrier as uniform distribution at $[0, 2\pi]$

$$b_k(t) = \sum_{j=-\infty}^{\infty} b_{jk}\, p_{T_b}(t - jT_b) \quad ; b_{jk} \in \{-1, +1\} \tag{2}$$

$$c_k(t) = \sum_{j=-\infty}^{\infty} c_{jk}\, p_{T_C}(t - jT_c) \quad ; c_{JK} \in \{-1, +1\} \tag{3}$$

$b_k(t)$ is data sequence of user k which is binary pulse amplitude $(-1,+1)$ with same probability, $c_k(t)$ is code sequence of user k which is binary pulse amplitude $(-1,+1)$ with same probability, $P_{T_b}(t)$ and $P_{T_c}(t)$ is square waves with 1 unit height and pulse width equal to T_b (for bit sequence) and T_c (for chip sequence). G_p is the processing gain is equal to T_b / T_c.

B. Channel Propagation Model

By using frequency selective Nakagami-*m* fading channel [3], the model has the complex low pass equivalent impulse response for parallel signal u of user k^{th} as follow.

$$h_k^{(u)}(t) = \sum_{l=1}^{L_p} \beta_{kl}^{(u)} \exp(j\phi_{kl}^{(u)})\,\delta(t-\tau_{kl}^{(u)}) \tag{4}$$

The attenuation $\beta_{kl}^{(u)}$ in (4) has the probability density function (PDF), as follow.

$$p(\beta_{kl}^{(u)}) = M(\beta_{kl}^{(u)}, m_{kl}^{(u)}, \Omega_{kl}^{(u)})$$

$$M(R,m,\Omega) = \frac{2m^m R^{2m-1}}{\Gamma(m)\Omega^m} e^{-(m/\Omega)R^2} \tag{5}$$

Where $\Gamma(.)$ is Gamma function, m_{kl} is the Nakagami– m fading parameter of user k^{th} at signal path l and L is total number of signal paths.

C. Receiver Model

Transmit signal from each user will pass though the fading channel model. The channel consists of the amplitude attenuation (α) and delay time (from $d(t)$ to $d(t-\tau)$). The receive signal from any user, both internal and external cell stations are determined as (6).

$$r^{(q)}(t) = \sqrt{2P}\sum_{k=1}^{K}\sum_{l-0}^{L_k-1}\left\{\begin{array}{l}\alpha_{l\,k}^{(q)} c_k(t-\tau_{lk}^{(q)}) \\ b_k(t-\tau_{lk}^{(q)})\cos(\omega_c t+\varphi_{l\,k}^{(q)})\end{array}\right\} \tag{6}$$

$$+\sqrt{2P}\sum_{m=1}^{M}\sum_{l=0}^{L_k-1}\sum_{i=1}^{K}\left\{\begin{array}{l}\alpha_{l\,i}^{(q)}\left(\frac{d_{m,i}}{d_{0,i}}\right)^{\beta} c_i(t-\tau_{l\,i}^{(q)}) \\ b_i(t-\tau_{l\,i}^{(q)})\cos(\omega_c t+\varphi_{l\,i}^{(q)})\end{array}\right\} + n(t)$$

$r^{(q)}(t)$ is the received signal, P is power signal of each user from mobile subscriber to base station, $a_{lk}^{(q)}$ is amplitude attenuation of user k with branch l, τ_{lk} is delay time of user k with branch l, $\varphi_{lk}^{(q)} = \phi_k + \theta_{lk} - \omega_c \tau_{lk}^{(q)}$ is carrier phase with uniform distribution $[0, 2\pi)$, β is propagation path loss exponent (this paper is 4), $d_{0,i}$ distance from user i to home cell, $d_{m,i}$ $d_{0,i}$ distance from user i in cell m to home cell.

The receiver uses number of antenna as ξ branches, as shown in figure 3. Each branch uses the rake receiver [4] with MRC technique over J finger, as shown in figure 4 [5] and output signal as (7). From (7), the first term is the desire signal,

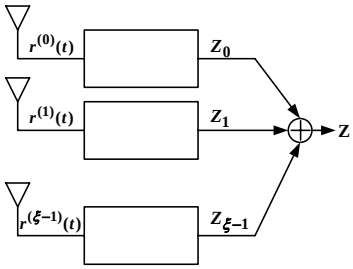

Figure 3. Receiver model at each antenna branch

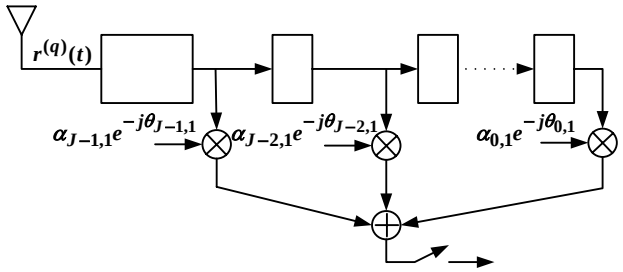

Figure 4. RAKE receive

second term is the self interference signal, third term is the interference signal from other users in cell, forth term is the interference signal from other users from the adjacent cell and the last term is AWGN(additive white Gaussian noise).

$$Z = \sum_{q=0}^{\xi-1} Z_q = \frac{\sqrt{2P}}{2}\sum_{q=0}^{\xi-1}\sum_{j=0}^{J-1} T b_0^1 \left[\alpha_{j1}^{(q)}\right]^2$$

$$+\frac{\sqrt{2P}}{2}\sum_{q=0}^{\xi-1}\sum_{j=0}^{J-1}\alpha_{j1}^{(q)}\sum_{\substack{l=0\\ l\neq j}}^{L_1-1}\left\{\begin{array}{l}\alpha_{l1}^{(q)}\cos(\varphi_{j\,l,1}^{(q)}) \\ \left[b_{-1}^1 R_{l1}(\tau_{jl}^{1,(q)}) + b_0^1 \hat{R}_{l1}(\tau_{jl}^{1,(q)})\right]\end{array}\right\} \tag{7}$$

$$+\frac{\sqrt{2P}}{2}\sum_{q=0}^{\xi-1}\sum_{k=2}^{K}\sum_{j=0}^{J-1}\left\{\begin{array}{l}\alpha_{j1}^{(q)} \\ \sum_{l=0}^{L_K-1}\left\{\begin{array}{l}\alpha_{l\,K}^{(q)}\cos(\varphi_{j\,l,1}^{(q)})\lambda \\ \left[b_{-1}^k R_{lk}(\tau_{jl}^{k,(q)}) + b_0^k \hat{R}_{lk}(\tau_{jl}^{k,(q)})\right]\end{array}\right.\end{array}\right\}$$

$$+\frac{\sqrt{2P}}{2}\sum_{q=0}^{\xi-1}\sum_{m=1}^{M}\sum_{i=1}^{K}\sum_{j=0}^{J-1}\left\{\begin{array}{l}\lambda\alpha_{j1}^{(q)} \\ \sum_{l=0}^{L_k-1}\left\{\begin{array}{l}\alpha_{li}^{(q)}\left(\frac{d_{m,i}}{d_{1,i}}\right)^{\beta}\cos(\varphi_{j\,l,1}^{(q)}) \\ \left[b_{-1}^i R_{li}(\tau_{jl}^{i,(q)}) + b_0^i \hat{R}_{li}(\tau_{jl}^{i,(q)})\right]\end{array}\right.\end{array}\right\}$$

$$+\int_{jTc}^{T+jTc} n(t)\alpha_{j1}^{(q)} c_1(t-jTc)\cos(\omega_c t+\varphi_{l1}^{(q)})dt$$

Analysis of signal to interference ratio (SIR) in this paper is consisted of 2 cases as perfect and imperfect power control.

D. Perfect power control SIR

Complete power control (V=0) is controlled power signal between mobile subscriber and base station, example of power

control by position of users is near or far from base station, SIR is calculated by

$$SIR = \frac{P_{Signal}}{\sigma^2_{Total}} \tag{8}$$

$$\sigma^2_{Total} = \sum_{q=0}^{\xi-1}\sum_{j=0}^{J-1}\left\{(E(I^2_{SI,j})+E(I^2_{MAI,j})+E(I^2_{OCI,j})+E(I^2_{NI,j})\right\} \tag{9}$$

$$= \sum_{q=0}^{\xi-1}\sum_{j=0}^{J-1}\left(\alpha^{(q)}_{j1}\right)^2\left\{\begin{array}{l}\dfrac{\left(\sqrt{2P}\right)^2T^2}{4}\dfrac{\sum_{l=0,l\neq j}^{L_1-1}\left(E(\alpha^{(q)}_{l1})^2\right)}{2Gp} \\ +\dfrac{\left(\sqrt{2P}\right)^2T^2}{4}\dfrac{\sum_{k=2}^{K}\lambda\sum_{l=0}^{L_k-1}\left(E(\alpha^{(q)}_{lk})^2\right)}{3Gp} \\ +\dfrac{\left(\sqrt{2P}\right)^2T^2}{4}\dfrac{1}{9}\dfrac{\sum_{m=1i=1}^{M}\sum^{K}\lambda\sum_{l=0}^{L_k-1}\left(E(\alpha^{(q)}_{li})^2\right)}{3Gp} \\ +\dfrac{N_oT}{4}\end{array}\right\}$$

For perfect power control, average power of each user is equal to $\left(\sqrt{2P}\right) = A$. First term in (7), can get the desire signal. Then take (9) in (8) to get (10) as

$$SIR_{per} = \frac{\sum_{q=0}^{\xi-1}\sum_{j=0}^{J-1}\left(\alpha^{(q)}_{j1}\right)^2}{\Omega_0\left\{\begin{array}{l}\sum_{l=0}^{L-1}e^{-l\delta}\dfrac{1}{2Gp}+\dfrac{(K-1)\lambda}{3Gp}\sum_{l=0}^{L-1}e^{-l\delta} \\ +\dfrac{K\lambda}{3Gp}\dfrac{M}{9}\sum_{l=0}^{L-1}e^{-l\delta}+\dfrac{No}{2Eb\Omega_0}\end{array}\right\}} \tag{10}$$

E. Imperfect power control SIR

From (10), if signal level from each user is not equals to A level and changed to A_k level. The probability density function [5] as follow:

$$p(A_k) = \frac{1}{2V}, \qquad A-V \le A_k \le A+V \tag{11}$$

Where V is maximum signal level of A_k. So the SIR value in (10) is:

$$SIR_{imper} = \frac{\sum_{q=0}^{\xi-1}\sum_{j=0}^{J-1}\left(\alpha^{(q)}_{j1}\right)^2}{\Omega_0\left\{\begin{array}{l}\sum_{l=0}^{L-1}e^{-l\delta}\left(1+\dfrac{V^2}{3A^2}\right)\dfrac{1}{2Gp} \\ +\sum_{l=0}^{L-1}e^{-l\delta}\dfrac{(K-1)\lambda}{3Gp}\left(1+\dfrac{V^2}{3A^2}\right) \\ +\sum_{l=0}^{L-1}e^{-l\delta}\dfrac{K\lambda}{3Gp}\dfrac{M}{9}\left(1+\dfrac{V^2}{3A^2}\right)+\dfrac{N_0}{2E_b\Omega_0}\end{array}\right\}} \tag{12}$$

$$Y = \frac{1}{\Omega_0}\sum_{j=0}^{J-1}\left(\alpha^{(q)}_{j1}\right)^2 \tag{13}$$

$$H = \frac{\xi}{\left\{\begin{array}{l}\sum_{l=0}^{L}e^{-l\delta}\left(1+\dfrac{V^2}{3A^2}\right)\dfrac{1}{2Gp}+\sum_{l=0}^{L}e^{-l\delta}\dfrac{(K-1)\lambda}{3Gp}\left(1+\dfrac{V^2}{3A^2}\right) \\ +\sum_{l=0}^{L}e^{-l\delta}\dfrac{K\lambda}{3Gp}\dfrac{M}{9}\left(1+\dfrac{V^2}{3A^2}\right)+\dfrac{N_0}{2E_b\Omega_0}\end{array}\right\}} \tag{14}$$

III. Analysis of Average Bit Error Rate

The cellular CDMA system performance analysis in this paper can be used the probability of error [3].

$$P_e(\sqrt{HY}) = \frac{1}{2}erfc(\sqrt{HY}) \tag{15}$$

$$erfc(x) = \frac{2}{\sqrt{\pi}}\int_x^{\infty}e^{-t^2}dt \tag{16}$$

Y_j is the attenuation from multipath signal which is Nakagami distribution power 2 and normalized as:

$$Y_j = \frac{\alpha_j^2}{\Omega_0} \tag{17}$$

The PDF of Y_j is,

$$P_{y_j}(Y_j) = \frac{Y_j^{(m-1)}}{\Gamma(m)}\left(\frac{m}{\lambda_j}\right)^m e^{(-m/\lambda_j)Y_j}, \quad Y_j \ge 0 \tag{18}$$

Assumed Y_j is not depend on statistic value, so

$$P_{y1,y2,.....,y_j}(Y_1,Y_2,.....Y_j) = \prod_{j=1}^{J}p_{y_j}(Y_j) \tag{19}$$

From (19), considering each channel in case of cdma2000 with N=3, bandwidth = 1.25 MHz and code rate = 1.2288 Mcps (3 x IS-95B) as:

$$P_{e(total)} = P_{e(f1)} + P_{e(f2)} + P_{e(f3)} \tag{20}$$

$P_{e(total)}$ is the statically independent event

$$\begin{aligned}P_{e(3\times IS-95B)} &= (P_{e(f1)} + P_{e(f2)} + P_{e(f3)}) \\ &-(P_{e(f1)}\bullet P_{e(f2)})-\left(P_{e(f1)}\bullet P_{e(f3)}\right) \\ &-(P_{e(f2)}\bullet P_{e(f3)}) \\ &+(P_{e(f1)}\bullet P_{e(f2)}\bullet P_{e(f3)})\end{aligned} \tag{21}$$

Incase of cdma2000 with one channel, 5 MHz bandwidth and code rate 3.6864 Mcps:

$$P_{e(cdma2000)} = \frac{1}{\pi}\int_0^{\frac{\pi}{2}}\prod_{j=1}^{J}\left(\frac{m\sin^2\theta}{He^{-\sigma(L-1)}+m\sin^2\theta}\right)^m d\theta \tag{22}$$

IV. Simulation and Result

Simulation for average BER is considered (21) and (22) with the system performance impact from the parameters changing with voice (8kbps) and WWW service (16kbps) These parameters is E_b/N_0, the number of user (K), signal attenuation rate (δ), the transmitted power control (V), the number of user in adjacent cell (M), voice activity factor (λ), number of signal path (L), Number of finger (J) and number of antenna (ξ), as shown in table 1.

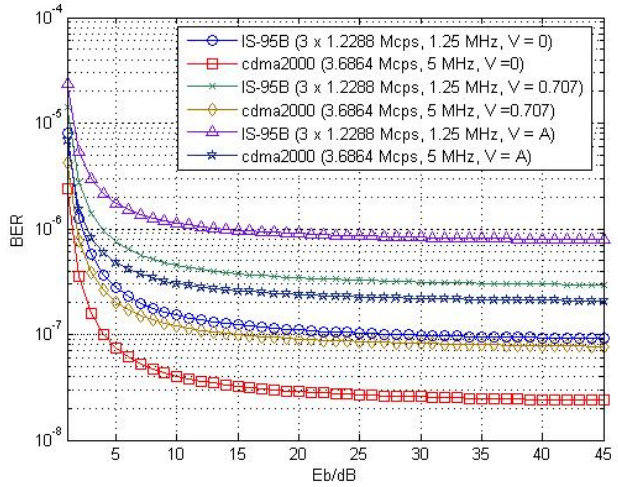

Figure 6. BER comparison between 3 x IS-95B and CDMA2000 for J=10, M=18, data rate 8 kbps (voice) and number of antenna 1 and 2 (perfect and imperfect power control)

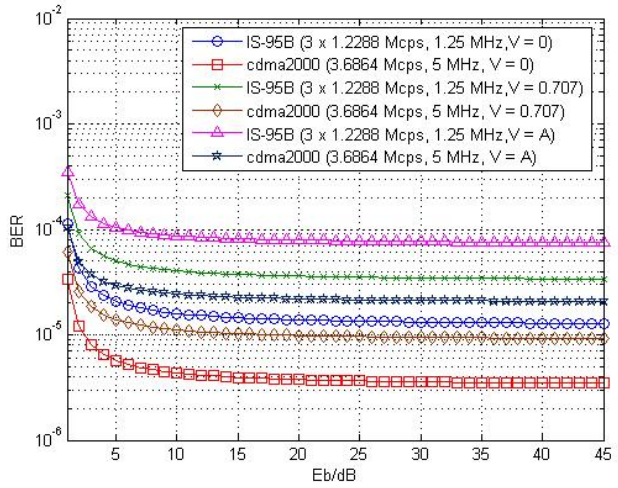

Figure 7. BER comparison between 3 x IS-95B and CDMA2000 for J=10, M=18, data rate 16 kbps and number of antenna 1 and 2 (perfect and imperfect power control)

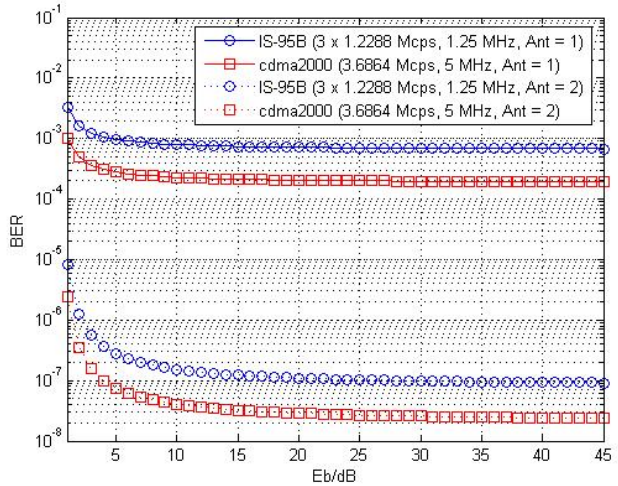

Figure 7. BER comparison between 3 x IS-95B and CDMA2000 for J=10, M=18, data rate 16 kbps and number of antenna 1 and 2 (perfect power control)

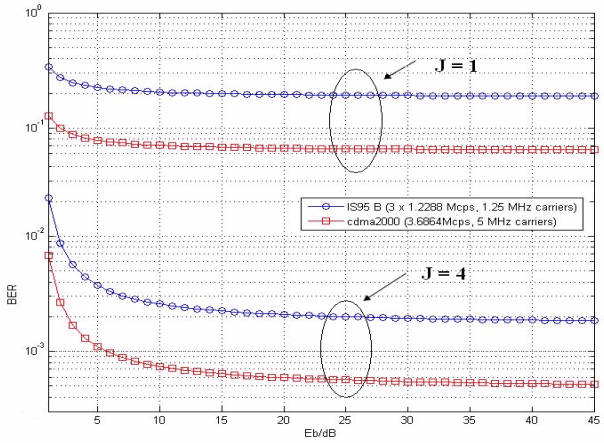

Figure 8. BER comparison between 3 x IS-95B and CDMA2000 for J=1 and 4

TABLE II
SIMULATION PARAMETER

Paremeter	IS-95B (f1)	IS-95B (f2)	IS-95B (f3)	CDMA 2000
Number of signal path	10	10	10	10
Data input	8,16kpbs	8,16kpbs	8,16kpbs	8,16kpbs
Voice activity	3/8	3/8	3/8	3/8
Maximum weighting	1	1	1	1

Result of simulation shows in figure 5, 6, 7 and 8. Figure 5 and 6 shows performance of perfect power control is better than imperfect power control. Performance of CDMA 2000 is better than 3xIS-95B in the same band with and data rate will increased, the performance will be decreased.

Figure 7 and 8 shows performance can be improve by increase number of antenna and number of finger.

V. CONCLUSION

The analysis of average BER on both systems shows the difference by using 5 MHz frequency bandwidth. Performance increases when compared to IS-95B, which uses 3 channels. Because of the interference between adjacent channel in IS-95B, in practice the system must be loose some bandwidth to reduce the adjacent interference.

Anyway the system investment can be reduced by improving the IS-95B performance close to CDMA2000 since it is the existing system. The performance can be compensation with the increasing of the number of finger and the number of antenna which leads to the adjacent interference reduction.

REFERENCES

[1] A. Goldsmith, *Wireless Communication.* Cambridge University Press, 2005.

[2] P. Moungnoul, V. Sinprayakun and T. Paungma, "BER Analysis of Cellular CDMA Reverse Link over Rayleigh Multipath Fading Channel," *Proc. of 2005 ECTI International Conference*, pp.418-421, May 12-13, 2005.

[3] M.K. Simon and M.S. Alouini, *Digital Communication over Fading Channels*. New York: John wiley & sons, Inc., 2000.

[4] T. Eng and L.B. Milstein, "Coherent DS-CDMA performance in Nakagami multipath Fading," *IEEE Trans. on Com*., Vol.43, No.2-4, pp. 1134-1143, February/March/April 1995.

[5] B.R. Tomiuk, N.C. Beaulieu and A.A. Abu-Dayya "General forms for maximal ratio diversity with weighting errors," *IEEE Trans. on Com.,* Vol.47, No.4, pp. 448-1492, April 1999.

Measurement Techniques of Transmissions from Ultra Wideband Devices

Jun-ichi Takada
Graduate School of Science and Engineering
Tokyo Institute of Technology
Meguro-ku, Tokyo 152–8550, JAPAN
Email: takada@ide.titech.ac.jp

***Abstract*—This paper reports the measurement techniques of transmissions from ultra wideband (UWB) devices summarized in ITU-R task group (TG) 1/8 to study the compatibility between ultra-wideband (UWB) devices and radiocommunication services. The author has published a paper with the similar title in September 2005 [1] based on the discussion of TG 1/8 until October 2004. As TG 1/8 has concluded the discussion and compiled the recommendation in October 2005, this paper provides the updated information on the background idea behind the measurement methods, as ITU-R recommendation does not contain any citations to the references, nor any "educational" description of the theoretical background.**

I. Introduction

To avoid the harmful interference of the ultra wideband (UWB) transmissions to the existing radio services, the transmission limit of the UWB devices shall be restricted. It is essential to define the transmission level of the UWB devices by the measurements. However, it is not so straightforward to measure the transmission characteristics of the UWB devices.

In the International Telecommunication Union Radiocommunication sector (ITU-R), task group (TG) 1/8 had been established in July 2002 to study the compatibility between ultra-wideband devices and radiocommunication services. TG 1/8 had been divided into four working groups (WGs), i.e. characteristics in WG 1, compatibility in WG 2, spectrum management framework in WG 3, and measurements in WG 4. The standard measurement techniques of emissions from UWB devices had been discussed in TG 1/8 WG 4.

The activity of TG 1/8 had been completed in October 2005 with four draft new recommendations (DNRs) and one draft new report submitted to study group (SG) 1 for spectrum management. After the approval of SG 1, member administrations (countries) have also approved these DNRs to be new recommendations (NRs) by letter ballot. Finally they are issued as NRs in May 2006 [2], [3], [4], [5].

This paper provides the update information to the previous paper [1] to describe the measurement techniques presented in the measurement recommendation [2]. Since ITU-R recommendation does not contain any citations to the references, nor any "educational" description of the theoretical background. Therefore, the paper provides the background idea behind the measurement methods, which is not available on the recommendation. To avoid the overlap, the changes from the previous paper [1] are more emphasized.

II. Philosophies of Measurements

Considering that the aim of the ITU-R recommendation is to provide the sufficient technical information to the administrations, it is not always necessary to provide the precise measurement method with tremendous cost and time. The regulatory or the compliance measurement procedure shall be simple enough to complete within a feasible period by using the off-the-shelf instruments. The measured value shall be reasonably meaningful from the view points of compatibility and/or coexistence with other radio systems, but it is not necessary that the measured value is completely identical to the real physical quantity.

III. Power Spectral Density

The UWB transmission is quantitatively evaluated by the power spectral density (PSD), of the power contained within a specified segment of spectrum, instead of the total power in the full frequency band. This is a reasonable criterion from the viewpoint of the impact of UWB transmission to other radiocommunication systems.

Three PSD values are used for different purposes; peak PSD, average PSD, and quasi-peak PSD.

Peak PSD mainly influences the RF front end of the receiver, e.g. the saturation of the low noise amplifier. Therefore, it is not necessary to evaluate the total peak power in the whole bandwidth, but the peak power within the sufficiently wide bandwidth that corresponds to the RF filter of the victim receiver. In the recommendation, the bandwidth of 50 MHz is used.

Average PSD is a measure of the interference to the victim system. To roughly estimate the effect of the interference, the interference signal power can be treated as the increase of the noise level.

Quasi-peak PSD is applicable in the frequency below 1000 MHz, which is a kind of weighted peak. This value is fully compatible with the unwanted emission [6].

Equivalent isotropic radiated power (EIRP) is used to evaluate the emission level. It is the product of the power supplied to the antenna and the antenna gain in a given direction relative to an isotropic antenna. EIRP is a direct measure of the emission, but it is a function of both direction and frequency, and it is rather difficult to find the maximum value.

IV. Spectral Emission Mask

The UWB transmission is spread over a very large frequency range and overlaps several frequency bands allocated to radio services. Therefore, it is a reasonable approach that the transmission level shall be restricted by the spectral transmission mask [4], just like the unwanted emission limit of unintentional emitters for electromagnetic compatibility (EMC). Although the emission limit itself is not the matter of the measurement, Appendix describes the conflicts of emission masks for communication and non-communication devices. Note that the mask value has the impact on the specification and the configuration of the instruments.

V. Frequency Domain vs Time Domain Measurement Approaches

Section 1.1 of recommendation [2] describes about two alternative approaches for the measurements.

One approach is the time domain measurement of the signal. The time domain data are transformed into the frequency domain data via the digital signal processing (DSP), such as the discrete Fourier transform (DFT). The second approach is a direct measurement of the UWB spectral characteristics in the frequency domain. There are equipment limitations that must be considered with respect to either of these measurement approaches.

The state-of-art single-end oscilloscope can measure a single-event waveform up to 20 GHz, while the quantization bits of A/D converter is limited to 8 bits. It is suitable for the peak PSD measurements with wider resolution bandwidth (RBW) that can not be achieved by the spectrum analyzer. Contrary, the relatively narrow dynamic range prevents the measurements of the low level emission outside the UWB bandwidth.

The IF-swept spectrum analyzers are typically designed to measure conventional narrow-band signals. The IF bandwidth of the spectrum analyzer is significantly smaller than the bandwidth of the UWB waveform, and is even smaller than the 50 MHz reference bandwidth for the peak power measurement. It is necessary to convert the narrow band measurement results into the estimate of the power within wider RBW. In addition, conventional spectrum analyzer is not so sensitive as to detect UWB signals at the very low emission limits applicable in specific frequency bands.

As is mentioned in Section 1.10 of the recommendation [2], the noise level of the spectrum analyzer is about -47 dBm/MHz at 1 GHz. Therefore, it is necessary to use a low noise amplifier (LNA) together with the appropriate RF preselection filter for the low level transmission measurement.

VI. Measurement Conditions

Section 1.4 of the recommendation [2] describes the measurement environments. A semi-anechoic chamber is suggested below 1000 MHz, while an anechoic chamber is recommended for above 1000 MHz.

As to the rotation of the equipment under test, the angular resolution of the measurement is not quantitatively specified but simply suggested as to "take sufficient measurements both in azimuth and elevation to ensure the maximum value has been recorded."

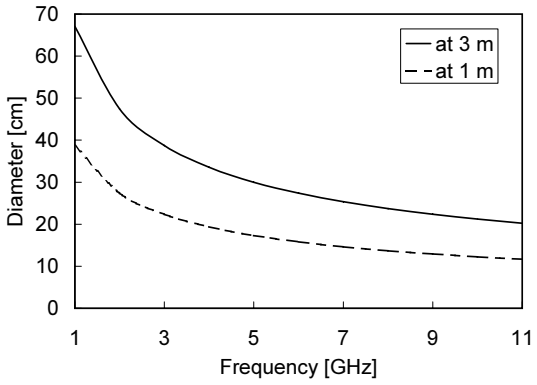

Fig. 1. Maximum UWB device size to satisfy far field condition.

Section 1.7 of the recommendation [2] describes the measurement distance. The distance of 3 m is normally recommended. It can be decreased to 1 m or less in case the signal is too weak, with taking care of the far field condition.

Figure 1 shows the maximun size (diameter) of the UWB device that satisfies the far field condition at 3 m and 1 m, which is derived by

$$r = \frac{2D^2}{\lambda}, \tag{1}$$

where r is the measurement distance, λ is the wavelength and D is the diameter of the sphere to enclose the device under test. For the high frequency, far field condition is more difficult to achieve in reality.

VII. Frequency Domain Measurements

Chapter 2 of the recommendation [2] describes the frequency domain measurements of PSD. First of all, the UWB bandwidth should be determined. Then, average and peak PSD measurements follow.

In the state-of-art IF-swept spectrum analyser, IF output is sampled at the constant frequency, e.g. 20 MHz. Within one frequency bin, the measurement is conducted during the period equal to the sweep time divided by the number of frequency bins in a sweep, to obtain the series of samples within a single frequency bin. The r.m.s. and peak detectors in the spectrum analyzer are digitally implemented to output the root-mean-square and the peak of the samples within the frequency bin for one sweep. The display function of max-hold trace mode is to trace the maximum values of all the frequency bins with respect to the multiple sweeps.

A. Determination of -10 dB bandwidth

Section 2.1 of the recommendation [2] describes the determination of -10 dB bandwidth. First, f_M is defined as the frequency with the maximum peak PSD. The spectrum analyser should be set up with 1 MHz resolution bandwidth

(RBW) and 1 MHz or greater video bandwidth (VBW), as well as with the max-hold trace mode. The lowest frequency below f_M and the highest frequency above f_M with the peak PSD 10 dB below the peak PSD at f_M are defined as f_L and f_H respectively. The UWB transmission is bounded by f_L and f_H, and the -10 dB bandwidth B_{-10} is defined as $f_H - f_L$.

B. Average PSD

Section 2.4 of the recommendation [2] describes the average PSD measurement.

Average PSD is measured by r.m.s. detector with the RBW of 1 MHz and the measurement period per frequency bin of 1 ms. In general, the maximum value of the average PSD tends to be smaller for impulsive signals with a low duty cycle when the measurement period becomes larger. Therefore, the measurement period is upper-bounded. Alternative measurements using zero span and power integration are also presented in the recommendation.

Moreover, the use of LNA and the radiometric measurement for the low level emissions are provided in sections 2.5 and 2.6, respectively.

C. Peak PSD

Section 2.7 of the recommendation [2] describes the peak PSD measurement.

The peak PSD of a UWB transmissions is defined as the peak power in a Gaussian filter with a bandwidth of 50 MHz. However, only the resolution bandwidths of 3 MHz or less can closely approximate the ideal Gaussian filter characteristics on the spectrum analysers. Therefore, the following scaling equation is used.

$$\mathrm{Limit}_{\mathrm{RBW}} = \mathrm{Limit}_{\mathrm{BW}} + 20\log_{10}\frac{\mathrm{RBW}}{\mathrm{BW}} \tag{2}$$

The measurement is made using a peak detector and max hold.

In fact, this equation is applicable for an impulsive signal, and it gives a conservative scaling of the peak PSD limit in general. When the signal appears to be noise-like, the complementary cumulative distribution function (CCDF) mode is used to test whether $10\log$ law can be applicable. If the CCDF falls within ± 2 dB error from the CCDF of a Rayleigh distribution in the range from 1 % to 99 %, the following scaling is applicable.

$$\mathrm{Limit}_{\mathrm{RBW}} = \mathrm{Limit}_{\mathrm{BW}} + 10\log_{10}\frac{\mathrm{RBW}}{\mathrm{BW}} \tag{3}$$

D. Conducted Measurements

Section 2.9 of the recommendation [2] describes the conducted measurements.

In case of the conducted measurement, the EIRP value is obtained by

$$\mathrm{e.i.r.p.}(f) = P(f) + G(f) \tag{4}$$

where $\mathrm{e.i.r.p.}(f)$ is the EIRP in dBm at the frequency f, $P(f)$ is the power in dBm measured at frequency f and at the antenna terminal, and $G(f)$ is the antenna gain in dBi measured at the frequency f in a given direction.

It is noted that the conducted measurement became only the measurement method approved in Japan. The major reason is described in Appendix.

VIII. Time Domain Measurements

Chapter 3 of the recommendation [2] describes the time domain measurements of PSD.

As is shown in Ref. [1], it is insufficient to use the oscilloscopes for the purpose to measure low emission levels due to the insufficient dynamic range. The time domain measurements by using oscilloscopes are only adequate to measure the highest emission limit. In particular, the peak PSD measurement with 50 MHz Gaussian filter is only possible in the time domain measurement.

Section 3.3 of the recommendation [2] presents the post processing of the time domain data. The complex antenna factor (CAF) of the measuring antenna is needed to reconstruct the electric field waveform from the antenna terminal voltage. In the frequency domain, the CAF $F_c(f)$, the complex electric field $E(f)$ and the terminal voltage with the matched impedance $V_0(f)$ are related as

$$F_c(f) = \frac{E(f)}{V_0(f)}. \tag{5}$$

By using discrete Fourier transform and its inverse, the filtered electric field strength can be reconstructed from the measured terminal voltage. The detail is presented in Ref. [7].

Section 3.4 of the recommendation [2] presents an alternative apparatus for peak power measurement. It combines a spectrum analyser with an oscilloscope. The spectrum analyser is used as the frequency down-converter together with the IF filter. The spectrum analyser IF output is an input to the oscilloscope. The IF output of the spectrum analyser is wide but its center frequency is much lower than the original RF signal. Therefore, the requirement for the sampling frequency of the oscilloscope is much relaxed. The Gaussian filtering is performed with digital signal processing without any phase distortion that would result from an analogue RBW filter.

IX. Conclusion

This paper has described the measurement techniques of the UWB emission, based on the ITU-R recommendation on the UWB measurement [2] to provide the updated background idea behind the measurement methods, in addition to the preceding paper [1].

Acknowledgement

This paper describes the personal opinion of the author himself, and does not represent the opinion of any party including NICT, ITU-R, or Ministry of Internal Affairs and Communications Japan. However, the author thanks all the members in NICT UWB Institute, NICT UWB Consortium, and ITU-R TG 1/8 WG 4, for their helpful discussions, suggestions, debate and encouragement.

REFERENCES

[1] J. Takada, S. Ishigami, J. Nakada, E. Nakagawa, M. Uchino and T. Yasui, "Measurement Techniques of Emissions from Ultra Wideband Devices," IEICE Trans. Fundamentals, vol. E88-A, no. 9, pp. 2252–2263, Sept. 2005.

[2] "Measurement techniques of ultra-wideband transmissions," Rec. ITU-R, SM. 1754, 2006.

[3] "Characteristics of ultra-wideband technology," Rec. ITU-R, SM. 1755, 2006.

[4] "Framework for the introduction of devices using ultra-wideband technology," Rec. ITU-R, SM. 1756, 2006.

[5] "Impact of devices using ultra-wideband technology on systems operating within radiocommunication services," Rec. ITU-R, SM. 1757, 2006.

[6] "Specification for radio disturbance and immunity measuring apparatus and methods — Part 1-1: Radio disturbance and immunity measuring apparatus — Measuirng apparatus," CISPR 16-1-1, second eds., 2006.

[7] S. Ishigami, and Y. Yamanaka, "Reconstruction of electric-field waveform radiated from UWB device by using the complex antenna factor," Proc. International Symposium on Electromagnetic Compatibility (EMC SENDAI '04), pp. 41-44, Jun. 2004.

[8] "Radio Frequency Devices," Part 15, Federal Communications Commission Rules, 2003.

[9] "Information Technology Equipment – Radio Disturbance Characteristics – Limits and Methods of Measurement," CISPR 22, Consol. Ed. 5.2, 2006.

[10] "Ordinance for Regulating Radio Equipment," Ministry of Internal Affairs and Communications, August 2006 (in Japanese).

APPENDIX: CONFLICT OF INTENTIONAL AND UNINTENTIONAL EMISSION MASKS

When UWB devices are permitted in United States, the average spectral mask level in the main UWB band 3.1–10.6 GHz has been chosen as −41.3 dBm/MHz [8]. It is noted that this emission level includes everything, i.e. UWB transmission and other emission. In the author's personal opinion, it was a challenge toward the existing conflict between two international regulations.

Any intentional emission of the radio is regulated by ITU-R, while unintentional emission of the radio is regulated by CISPR (Comité International Spécial des Perturbations Radioélectriques; International Special Committee on Radio Interference). Specifically, the ITU-R recommendation of the impact of UWB devices on the existing radiocommunication systems [5] and the CISPR standard on the radio disturbance characteristics of the information technology equipments [9] are to be compared. In CISPR [9], the upper limit of the unintentional average emission level in 3–6 GHz is 54 dBμV/m at 3 m for the reference bandwidth of 1 MHz, which is equal to −41.3 dBm/MHz e.i.r.p. although the recommended measurement method is slightly different from ITU-R [2]. However, much lower values are recommended for the transmission of UWB signal in the ITU-R recommendation [5]. Although ITU-R and CISPR have some contacts to each other, these two bodies decide the upper limits almost independently. As ITU-R should consider all the individual existing radiocommunication services, more conservative mask levels should be applied to the intentional emission.

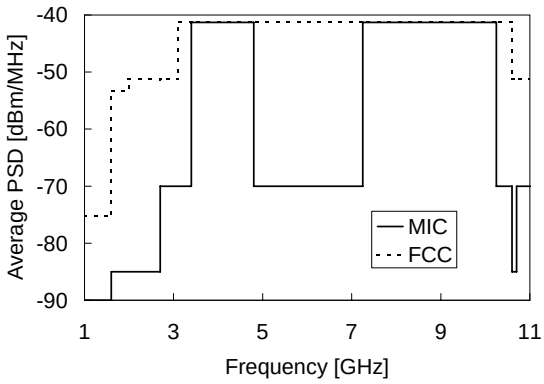

Fig. 2. Emission masks of average PSD of FCC indoor and MIC.

Considering the attitude of FCC that the regulation about the spectrum is basically the domestic matter as far as there is no interference outside US, it seems to the author rather natural that FCC chose more aggressive value, since the communication and non-communication signals can not be distinct with respect to the interference.

In Japan, however, the existing users of the radiocommunication services were not satisfied with the UWB devices to transmit up to the non-intentional emission limit. Ministry of Internal Affairs and Communications (MIC) finally approved the UWB systems in the Ordinance for Regulating Radio Equipment in August 2006 [10]. The spectral mask for the average PSD is presented in Fig. 2 in comparison with FCC indoor mask. For the compliance with the existing Japanese radio regulation, the UWB device should not be measured separately but should be integrated into the equipment such as PC. In case, PC itself may emit the power up to the limit of unintentional emission, and it is very difficult for the whole equipment to satisfy the UWB regulation. Therefore, the conducted measurement is needed to measure only the intentional transmission from the UWB device. In addition, it is not so easy to find the direction and frequency of the maximum transmission in the radiated measurement, since the antenna radiation pattern changes according to the frequency, and the measurement need tremendous time. They are the major reasons why the conducted measurement is only considered in Japan.

Experimental Study and Analysis of Antenna Effects for UWB Radio Transmission

Sanit Teawchim[1] , Sathaporn Promwong[1] and Jun-ichi Takada[2]
[1]Department of Information Engineering, Faculty of Engineering,
King Mongkut's Institute of Technology Ladkrabang,
Chalongkrung Rd., Ladkrabang, Bangkok 10520, Thailand.
Email: {s9061060,kpsathap}@kmitl.ac.th
[2]Graduate School of Science and Engineering, Tokyo Institute of Technology,
2-12-1-S6-4, O-okayama, Meguro-ku, 152-8550, Tokyo, Japan.
E-mail: takada@ide.titech.ac.jp

***Abstract*— This paper present the transmission gain of UWB system based on the extended Friis' transmission formula. The template waveform is considered at the receiver side to maximize the SNR for evaluation. An experimental evaluation of the antenna transfer function needs the three types of broadband antennas. The technique gives very accurate results and is very useful for design and evaluation of UWB impulse radio transmission systems, especially for the evaluation of waveform distortion effects.**

Keywords: **UWB, link budget, transmission gain, Friis' transmission formula**

I. INTRODUCTION

The propagation channel is in line of sight (LOS), Friis' transmission formula cannot be directly applied to the UWB radio as the bandwidth of the pulse is extremely wide. Furthermore, simple comparison between waveforms of transmitter and receiver is not significant because of the distortion of the waveform caused by the frequency response of the antenna.

In this paper, we discuss the free space link budget and transmission gain evaluation scheme for UWB impulse radio systems. This scheme is based on the Friis' transmission formula, adapted for UWB, in the sense that we would like to derive the equivalent antenna gain for UWB impulse radio systems. The transmission waveform and the receiver template waveform are keys for the extension of the Friis' transmission formula to UWB transmission signal.

II. THOERY

In this study, we focus on the link budget evaluation for UWB impulse radio system in free space.

A. Extension of Friis' Transmission Formula for UWB transmission System

The Friis' transmission formula [1] has been widely used, and can be applied to the calculation of these LOS channels.

$$G_{\text{Friis}}(f) = \frac{P_{\text{r}}(f)}{P_{\text{t}}(f)} = G_{\text{f}}(f)G_{\text{r}}(f)G_{\text{t}}(f), \tag{1}$$

where G_{r} and G_{t} are Rx and Tx antenna gain,

$$G_{\text{f}}(f) = \left(\frac{\lambda}{4\pi d}\right)^2 \tag{2}$$

is the free space propagation gain (less than unity in practice), $\lambda = \dfrac{c}{f}$ is the wavelength, c is the velocity of the light, f is the operating frequency, and d is the separation between transmitter and receiver antennas.

It is noted, however, that Eq. (1) is satisfied only at some certain frequency, and is not directly applicable to UWB systems. The Friis' transmission formula shall be extended to take into account the transmission signal waveform and its distortion as well [2].

Input signal $v_{\text{i}}(t)$ at the transmitter port is expressed as the convolution of an impulse input and the pulse shaping filter $h_{\text{i}}(t)$ as

$$v_{\text{i}}(t) = E_{\text{i}}\delta(t) * h_{\text{i}}(t), \tag{3}$$

where

$$\int_{-\infty}^{\infty} h_{\text{i}}^2(t)\mathrm{d}t = \int_{-\infty}^{\infty} |H_{\text{i}}(f)|^2 \,\mathrm{d}f = 1. \tag{4}$$

Friis' formula is extended taking into account the transmission waveform as

$$H_{\text{e-Friis}}(f) = \frac{V_{\text{r}}(f)}{E_{\text{i}}} = H_{\text{f}}H_{\text{i}}\mathbf{H}_{\text{r}} \cdot \mathbf{H}_{\text{t}}, \tag{5}$$

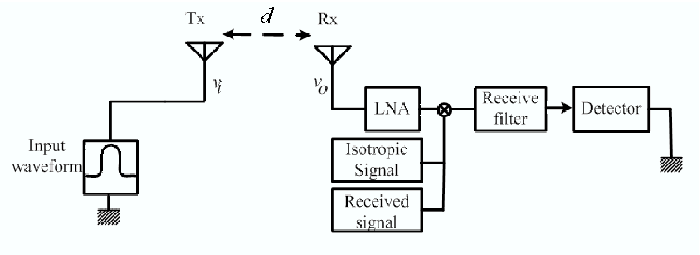

Fig. 1. Block diagram of transmission system for the extension of Friis' transmission formula to treat UWB signal.

where

$$\begin{aligned}\mathbf{H}_a &= \mathbf{H}_a(\theta_a,\ \varphi_a,\ f) \\ &= \hat{\boldsymbol{\theta}}_a H_{a\theta}(\theta_a,\ \varphi_a,\ f) + \hat{\boldsymbol{\varphi}}_a H_{a\varphi}(\theta_a,\ \varphi_a,\ f) \quad (6) \\ a &= \text{r } \textit{or } \text{t},\end{aligned}$$

is a complex transfer function vector of the antenna relative to the isotropic antenna,

$$H_{\mathrm{f}} = \frac{\lambda}{4\pi d}\exp(-\mathrm{j}kd), \quad (7)$$

is the free space transfer function where

$$k = \frac{2\pi}{\lambda}, \quad (8)$$

is the propagation constant.

B. Correlation Receiver

Let us consider a correlation receiver shown in Fig. 1. The output SNR is dependent on the choice of the template waveform. The correlator output $v_{\mathrm{o}}(\tau)$ is therefore expressed as

$$v_{\mathrm{o}}(\tau) = \int_{-\infty}^{\infty} v_{\mathrm{r}}(t) h_{\mathrm{w}}(t-\tau)\mathrm{d}t, \quad (9)$$

where $v_{\mathrm{r}}(t)$ is the receiver input waveform which is inverse Fourier transform, and $h_{\mathrm{w}}(t)$ is the template waveform. τ corresponds to the timing of the template waveform, and the optimum timing τ_{o} is chosen as

$$\tau_{\mathrm{o}} = \arg\max_{\tau} v_{\mathrm{o}}(\tau). \quad (10)$$

Hereafter $h_{\mathrm{w}}(t)$ is normalized as

$$\int_{-\infty}^{\infty} |h_{\mathrm{w}}(t)|^2 \mathrm{d}t = 2B, \quad (11)$$

where B is the signal bandwidth, so that the output noise power is constant as $N_0 B$, where $\frac{N_{\mathrm{o}}}{2}$ is power spectral density of AWGN.

Under the constraint of Eq. (11), $h_{\mathrm{wm}}(t)$ maximizes $v_{\mathrm{o}}(\tau_{\mathrm{o}})$ when $h_{\mathrm{wm}}(t)$ is a time-reversed and scaled version of $v_{\mathrm{r}}(t)$, i.e.

$$h_{\mathrm{wm}}(t) = \frac{\sqrt{2B}\, v_{\mathrm{r}}(\tau_{\mathrm{o}} - t)}{\sqrt{\int_{-\infty}^{\infty} |v_{\mathrm{r}}(t)|^2 \mathrm{d}t}}, \quad (12)$$

where τ_{o} is usually chosen so that $h_{\mathrm{wm}}(t) = 0$ for $t < 0$ to satisfy the causality. $h_{\mathrm{wm}}(t)$ is called the optimum template waveform hereafter. It is noted that the link budget evaluation is identical to that in Ref. [5] when $h_{\mathrm{wm}}(t)$ is used as the receiver template.

C. Isotropic Correlation Receiver

It is obvious from Eq. (12) that the optimum template waveform is not the simple time-reversed version of the transmitter waveform, but the channel characteristics including the antennas and the free space propagation. Therefore, it is not always feasible to adapt the template waveform to the angular-dependent antenna characteristics, since the waveform shall be generated at the clock rate of tens of gigahertz. Therefore, we consider a canonical template waveform $h_{\mathrm{wc}}(t)$. In this paper we have chosen $h_{\mathrm{wc}}(t)$ that is optimum for the isotropic and the constant gain antennas, i.e.

$$h_{\mathrm{wc}}(t) = \frac{\sqrt{2B}\, v_{\text{r-iso}}(\tau_{\mathrm{o}} - t)}{\sqrt{\int_{-\infty}^{\infty} |v_{\text{r-iso}}(t)|^2 \mathrm{d}t}}, \quad (13)$$

where

$$v_{\text{r-iso}}(t) = \int_{-\infty}^{\infty} H_{\mathrm{f}}(f) V_{\mathrm{t}}(f) \exp(\mathrm{j}2\pi f t)\mathrm{d}f \quad (14)$$

is the receiver input voltage for isotropic antenna including. The difference between the optimum and the isotropic templates indicates quantitatively the distortion of the waveform.

III. UWB Antenna Transfer Function Measurements

A. UWB waveform Transmission

The effect of the waveform distortion is more obvious when the bandwidth is wider. We considered the impulse

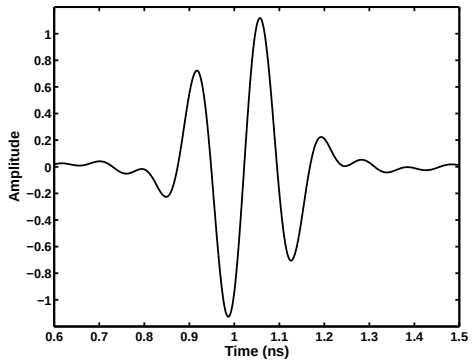

Fig. 2. The transmission waveform of UWB signal.

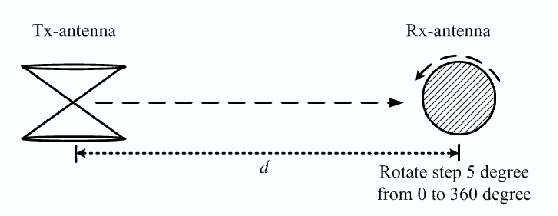

Fig. 3. Top view antenna setting.

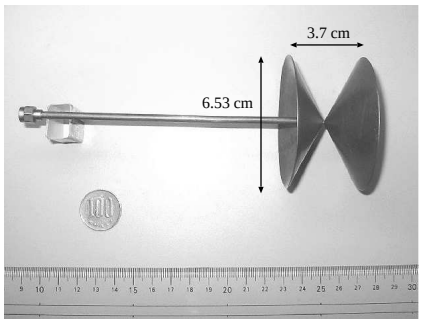

Fig. 4. Biconical antenna structure.

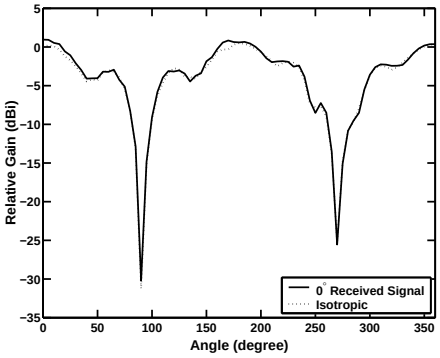

Fig. 5. Normalized UWB transmission gain for biconical–biconical link.

radio signal that fully covers the FCC band [4], i.e., $3.1 \sim 10.6$ GHz. The center frequency and the bandwidth were therefore set to be $f_0 = 6.85$ GHz and $f_\mathrm{b} = 7.5$ GHz, respectively. The transmit waveform assumed in the simulation was a single ASK pulse with the carrier frequency f_0. To satisfy the bandwidth requirement of f_b, the pulse length was set to be $\frac{2}{f_\mathrm{b}}$. Then the signal was band-limited by a Nyquist roll-off filter with roll-off factor $\alpha = 0$ (rectangular window) and passband $\left(f_0 - \frac{f_\mathrm{b}}{2},\ f_0 + \frac{f_\mathrm{b}}{2}\right)$. Figure 2 shows the transmit pulse waveform. The transmission process of the pulse waveform is simulated based on the measured transfer function of the antenna.

B. Experimental Setup and Measurement Model

The VNA was operated in the response measurement mode, where Port-1 was the transmitter port (Tx) and Port-2 was the receiver port (Rx), respectively. Biconical antennas with the maximum diameter of 65.3 mm and the length of 37 mm are used both as the standard antennas and as AUT. The measurement was done in the anechoic chamber. Both Tx and Rx antennas were fixed at the height of 1.75 m and separated at a distance of 4 m.

Figure 3 shows the orientations of the S_{21}, transfer function measurement for Tx and Rx antennas. The Tx antenna is fixed at pointing angle 0° and the Rx antenna is rotated from pointing angle 0° to 360° with each step at 5°.

IV. Experiment Results

In this section, standard broadband antennas and deployable antennas are used in the measurement for the link budget evaluation.

USA suggested the use of a biconical antenna, and log-periodic antenna for the frequency ranges of $30 - 200$ MHz, $200 - 960$ MHz, and $0.96 - 18$ GHz, respectively, for the compliance test of UWB transmitters [6]. We chose these two kinds of antennas, operating in the same frequency range.

1) Biconical Antenna: First, the same biconical antennas were used at both Tx and Rx sides. Figure 5 shows the normalized UWB transmission gain as a function of antenna pointing angle in E-plane. Well-known 8-shaped patterns were obtained. Two template waveforms were used for comparison, and the difference was rather small. The phase center of the biconical antenna is the feed point and it has theoretically the frequency independent gain at the broadside direction, and that is why the waveform distortion effect is small compared with the isotropic template.

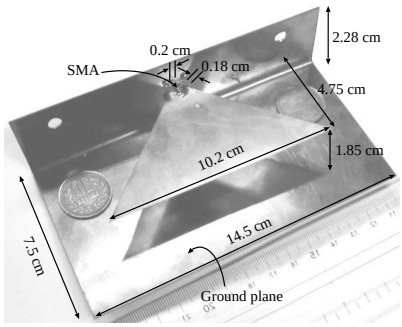

Fig. 6. Trapezoidal antenna with L-shaped ground plane.

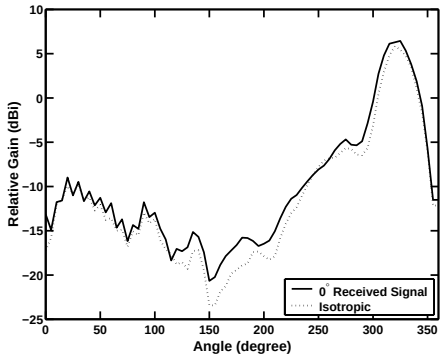

Fig. 7. Normalized UWB transmission gain for biconical–trapezoidal link.

2) Trapezoidal Antenna: A trapezoidal antenna with the L-shaped ground plane has been introduced by Duzdar and Kompa [7] and was later modified by Eskelinen [3]. We have chosen this antenna just for the ease of the fabrication The structure and dimensions of the antenna is shown in Fig. 6. The element shape itself is similar to that of a bow-tie antenna, but the L-shaped ground plane is parallel to the trapezoidal element to achieve the unidirectional characteristics.

Figure 7 shows the normalized UWB transmission gain pattern for biconical–trapezoidal link in E-plane. Note that 0° and 270° are the top and the broadside of the antenna, respectively. The peak is found at 320°. Therefore, the peak is elevated from the broadside of the antenna toward the top. The gain is relatively high, and the difference between two templates is small. As Refs.[1] consider the waveform transmission applications, the waveform distortion seems to be small.

V. Conclusion

This presented the evaluation scheme for UWB transmission gain, which includes the transmit waveform, the antennas, free space propagation, and the receiver correlator template. By using the definition, we have evaluated two types of broadband antennas. The performance can be evaluated only by the UWB transmission gain.

References

[1] H.T. Friis, "A note on a simple transmission formula," Proc. IRE, vol. 34, no. 5, pp. 254–256, May 1946.

[2] J. Takada, S. Promwong and W. Hachitani, "Extension of Friis' Transmission Formula for Ultra-Wideband Systems," IEICE Tech. Rep., WBS2003-8/MW2003-20, May 2003.

[3] P. Eskelinen, "Improvements of an inverted trapezoidal pulse antenna," IEEE Antennas Propagat. Mag., vol. 43, no. 3, pp. 82–86, June 2001.

[4] Federal Communications Commission, "Revision of Part 15 of the Commission's Rules Regarding Ultra-Wideband Transmission Systems," First Report and Order, FCC 02–48, Apr. 2002.

[5] S. Promwong, and J. Takada, "Free space link budget estimation scheme for ultra wideband impulse radio with imperfect antennas," IEICE Electronics Express, vol. 1, no. 7, pp. 188–192, July 2004.

[6] United States of America, "Working document towards the development of measurement procedures for assessing regulatory compliance of ultra-wideband emitters," ITU-R Document, 1-8/157-E, June 2004.

[7] A. Duzdar and G. Kompa, "A novel trapezoidal antenna fed by a ground image plane and backed by a reflector," Proc. European Microwave Conference (EuMC) 2000, vol. 2, pp. 1–4, Paris, France, Sept. 2000.

Planar Source Characteristics Analysis for Wave Iterative Method Simulation

Somsak Akatimagool and Sommart Kamkleing

Department of Teaching Training in Electrical Engineering, Faculty of Technical Education
King Mongkut's Institute of Technology North Bangkok, 1518 Pibulsongkram Road,
Bangsue, Bangkok, 10800, Tel. 0-2913-2500 ext. 3322 E-mail: ssa@kmitnb.ac.th

Abstract - This paper describes a wave iterative method (WIM) which has been specifically analyzed a planar source. Unlike traditional full wave analysis simulators which compute and display the overall wave in space and time domain, this method visualizes the scattering waves of time domain in the conductor, dielectric, and source meshes. The source mesh of wave iterative method, a square shape, is a planar excitation source. Based on an iterative formulation, the novel quasi-network characteristics of planar source is found and analyzed. The wave iterative method needs to modify by using quasi-network for the accuracy and efficiency simulation.

Keywords : Wave iterative method, Quasi-network, Planar source

I. INTRODUCTION

In the microwave circuit analysis and design, certain electromagnetic analysis method presents the simulated circuit parameters. The transmission line matrix method (TLM) is usually defined in the time domain [1]. This TLM method visualizes the scattering and spreading of the individual voltage impulses in a TLM mesh. The finite difference time domain (FDTD) is a kind of efficient methods of computational electromagnetics [2]. Recently, the iterative methods are used more extensively in solving electromagnetic problems. These methods are due to the augmentation of the computational capacities and to the simplicity of the formulation [4-5]. Already successfully tested in some simple, the wave concept iterative procedure (WCIP) has shown the great potential of development in solving electromagnetic problems [6-7].

An efficient wave iterative method (WIM) has been developed from the wave concept iterative procedure which has been specifically designed as an educational simulation tool. The formulation of the iterative method is based on the incident and reflected wave concept which propagate the alternating between the spectrum domain (modes) and the time domain (pixels). In the electromagnetic scattering on the pixel area, the boundary conditions are presented in several sub-domains: the metal, the dielectric, and the planar source. This paper presents a study and analysis of the effect of planar source involved in the quasi-network model which is added to the iterative process.

II. THEORY

The wave iterative method (WIM) is a numerical method used for the study of electromagnetic problems. The principle of this method is the concept of scattering wave propagation. The propagation of the incident wave ($\vec{A}$) and the reflected wave ($\vec{B}$) in the planar circuit can be shown in the fig.1.

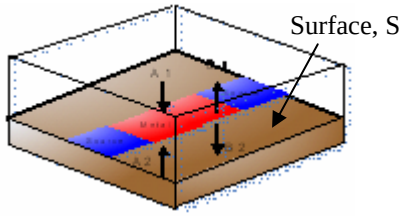

Fig. 1 Scattering wave of planar circuit

Considering the surface S to be a transverse section, the waves $\vec{A}$ and $\vec{B}$ are defined by (1)-(2):

$$\vec{A} = \frac{1}{2\sqrt{Z_0}}(\vec{E} + Z_0\vec{H}) \qquad (1)$$

$$\vec{B} = \frac{1}{2\sqrt{Z_0}}(\vec{E} - Z_0\vec{H}) \qquad (2)$$

when $\vec{E}$ and $\vec{H}$ are the tangent electric and magnetic field and Z_0 is the intrinsic impedance.

A.Quasi-Network of planar source

The planar source is the electromagnetic source which presents in the square pixel, shown in the fig.2.

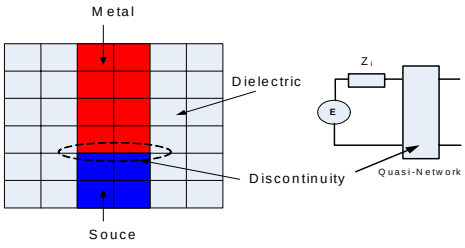

Fig. 2 Quasi-network of planar source

Appropriate equivalent circuits of the sub-domain of planar source represent the electric tangential field ($\vec{E}$) and source internal impedance (Z_i). The discontinuity between the planar source and the microstrip line presents a quasi-network which consists of a capacitor, inductor, and transformer, as shown in the fig. 3.

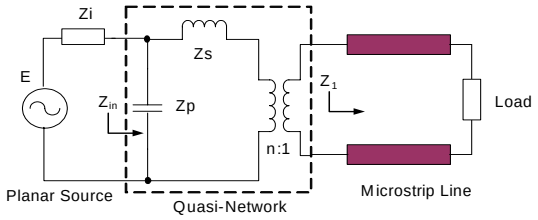

Fig. 3 Equivalent circuit of planar circuit

The ABCD parameter of a quasi-network is described by (3):

$$\begin{bmatrix} V_1 \\ I_1 \end{bmatrix} = \begin{bmatrix} n & \frac{Z_S}{n} \\ \frac{n}{Z_p} & \frac{Z_S+Z_p}{nZ_p} \end{bmatrix} \begin{bmatrix} V_2 \\ -I_2 \end{bmatrix} \quad (3)$$

and the Z parameter can be expressed as (4):

$$\begin{bmatrix} V_1 \\ V_2 \end{bmatrix} = \begin{bmatrix} Z_p & \frac{Z_p}{n} \\ \frac{Z_p}{n} & \frac{Z_s+Z_p}{n^2} \end{bmatrix} \begin{bmatrix} I_1 \\ I_2 \end{bmatrix} \quad (4)$$

From fig.3, the input impedance of planar circuit is written as (5):

$$Z_{in} = \frac{V_1}{I_1} = Z_p - \frac{Z_p^2}{n^2 Z_1 + Z_S + Z_p} \quad (5)$$

when Z_p is the parallel impedance of capacitor; Z_S is the series impedance of inductor; n is the ratio of transformer parameter; and Z_1 is the input impedance of microstrip line (without quasi-network) which is described by (6)-(7):

$$Z_{1(sc)} = jZ_0 \tan(\beta L) \quad \text{for Short Circuit} \quad (6)$$

$$Z_{1(oc)} = -jZ_0 \cot(\beta L) \quad \text{for Open Circuit} \quad (7)$$

The equivalent circuit of two ports network of the planar circuit can shows in the fig. 4.

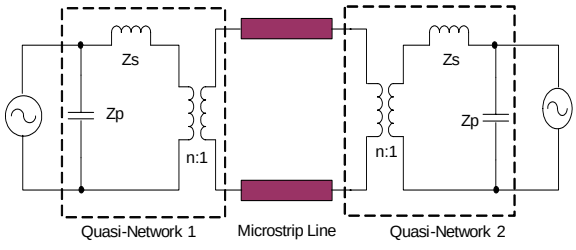

Fig. 4 Equivalent circuit of two port network

In the port 2, the ABCD parameter of a quasi-network is described by (8): Z_p

$$\begin{bmatrix} V_1 \\ I_1 \end{bmatrix} = \begin{bmatrix} \frac{1}{n}+\frac{Z_S}{nZ_p} & \frac{Z_S}{n} \\ \frac{n}{Z_p} & n \end{bmatrix} \begin{bmatrix} V_2 \\ -I_2 \end{bmatrix} \quad (8)$$

Fig.4 shows a structure composed of cascade ABCD networks of planar circuit; quasi-network 1, microstrip line and quasi-network 2. From equation (3) and (8), we represent the relation of ABCD parameter of the microstrip line as:

$$[ABCD_{Line}] = [ABCD_1]^{-1} \times [ABCD_{total}] \times [ABCD_2]^{-1} \quad (9)$$

B. Wave Iterative Method (WIM)

The wave iterative method is mainly a result of the building an iterative scheme that avoids the inversion of the integral operator to solve the boundary conditions problem owing to its waves based formulation [6]. On the printed surfaces, the boundary conditions are expressed in terms of waves rather than in terms of tangential fields. The whole printed surface is discredited by pixel-like functions. The scheme of the successive iterations is then given by

$$B = \hat{S}A + B_0 \quad in\ the\ pixel\ domain \quad (10)$$
$$A = \hat{\Gamma}B \quad in\ the\ mode\ domain$$

The toggling between the pixel and the mode representation of the waves A and B is ensured by a Fast Fourier Transform (FFT).

The diffraction operator ($\hat{S}$) of boundaries defines a built in the sub-domains; metal (M), dielectric (D) and source (S) area. The $\hat{S}$ operator can be written as (11):

$$\hat{S} = \begin{bmatrix} -M + \frac{(1-n^2)D}{1+n^2} + \frac{(-1+n_1-n_2)S}{1+n_1+n_2} & M + \frac{(2n)D}{1+n^2} + \frac{(2m)S}{1+n_1+n_2} \\ M + \frac{(2n)D}{1+n^2} + \frac{(2m)D}{1+n_1+n_2} & -M + \frac{(n^2-1)D}{1+n^2} + \frac{(-1-n_1+n_2)S}{1+n_1+n_2} \end{bmatrix} \quad (11)$$

when $n = \sqrt{\frac{Z_{01}}{Z_{02}}}$, $m = \frac{Z_0}{\sqrt{Z_{01}Z_{02}}}$, $n_1 = \sqrt{\frac{Z_0}{Z_{01}}}$, $n_2 = \sqrt{\frac{Z_0}{Z_{02}}}$ and 1, 2 are an order of layer.

Then, the iterative procedure rests on the balance conditions between the diffracted waves by the printed surfaces and the reflected waves by the circuit environment: substrate and enclosure. The advantage of wave iterative method is preserved by using a reflection operator ($\hat{\Gamma}$) defined in the spectral domain (TE and TM mode) from the admittance operator (Y_{mn}) as:

$$\hat{\Gamma} = \sum_{mn} |f_{mn}\rangle \Gamma_{mn}^{TE/TM} \langle f_{mn}| \quad (12)$$

where $Y_{mn}^{TE/TM}$ are the eigen values of the admittance operator, and

$$\Gamma_{mn}^{TE/TM} = \frac{Y_0 - Y_{mn}^{TE/TM}}{Y_0 - Y_{mn}^{TE/TM}} \quad (13)$$

when $Y_{mn}^{TE} = \frac{\gamma_{m,n}}{j\omega\mu}$, $Y_{mn}^{TM} = \frac{j\omega\varepsilon}{\gamma_{m,n}}$

The relation of the parameters Z and Y has the expression in the terms of the electric and magnetic filed as:

$$[Z]=[Y]^{-1}=\begin{bmatrix} \sum_{x,y}\left(\frac{E_{x,y(1)}}{H_{x,y(1)}}\right) & \sum_{x,y}\left(\frac{E_{x,y(1)}}{H_{x,y(2)}}\right) \\ \sum_{x,y}\left(\frac{E_{x,y(2)}}{H_{x,y(1)}}\right) & \sum_{x,y}\left(\frac{E_{x,y(2)}}{H_{x,y(2)}}\right) \end{bmatrix}_{Source} \quad (14)$$

The S parameter is defined as:

$$[S]=[Z-I][Z+I]^{-1} \quad (15)$$

III. QUASI-NETWORK PARAMETERS ANALYSIS

Fig.5 shows a microstrip structure. We can thus build an equivalent circuit for the discontinuity between the planar source and microstrip line (see in fig.3).

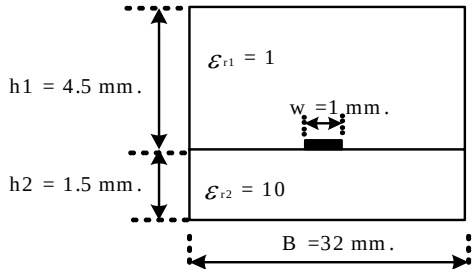

Fig. 5 Equivalent circuit of microstrip line

The analysis of the quasi-network by using WIM is done in 5 steps.

Step 1. Calculation of the input impedance (Z_{in}) of the planar circuit which is $\lambda/2$ of the length. From (5), when $Z_1=\infty$, thus we get:

$$Z_{in(\lambda/2)}=Z_p \quad (16)$$

Step 2. Calculation of the input impedance (Z_{in}) of the planar circuit which is $\lambda/4$ of the length. From (5), when $Z_1=0$, thus we get:

$$Z_{in(\lambda/4)}=\frac{Z_s Z_p}{Z_s+Z_p} \quad (17)$$

Step 3. Calculation of the input impedance (Z_{in}) of the planar circuit which is $3\lambda/8$ of the length. From (5), when $Z_1=-jZ_0\cot(\beta L)$, thus we get:

$$Z_{in}=Z_p-\frac{Z_p^2}{n^2 Z_1+Z_s+Z_p} \quad (18)$$

Step 4. From step (1) to (3), we calculated Z_p, Z_s and n of the quasi-network. The element values of the network at several frequencies can be found in table 1.

Table 1. Quasi-network parameters

f (GHz)	ε_{eff}	Z_c	Z_p	Z_s	n
6.950	7.276	57.98	-j157	+j32.93	0.939
4.730	6.981	64.41	-j215	+j24.65	0.958
3.615	6.721	59.71	-j218	+j18.74	1.013
1.850	6.417	59.47	-j493	+ j1.05	1.105
1.485	6.362	59.52	-j565	+ j8.44	1.031

Step 5. In the last step, we calculated the C_p, L_s for different frequency.

Table 2. Capacitor and inductor of quasi-network

f (GHz)	C (pF)	L(nH)	n	λ (mm)
6.950	0.15196	0.75406	0.939	16
4.730	0.15597	0.82930	0.958	24
3.615	0.15645	0.82498	1.013	32
1.850	0.17393	0.90324	1.105	64
1.485	0.18969	0.90477	1.031	80

For each frequency, the quasi-network elements of planar source are represented for the wave iterative method (WIM) simulation.

IV. NUMERICAL RESULTS

In this section, we present some examples of correction by using quasi-network of planar source for efficiency WIM simulation.

A. Input impedance of microstrip circuit

The input impedance of the open circuit-microstrip line is now studied in fig. 6. The circuit consists of the open-end line connected to a planar source.

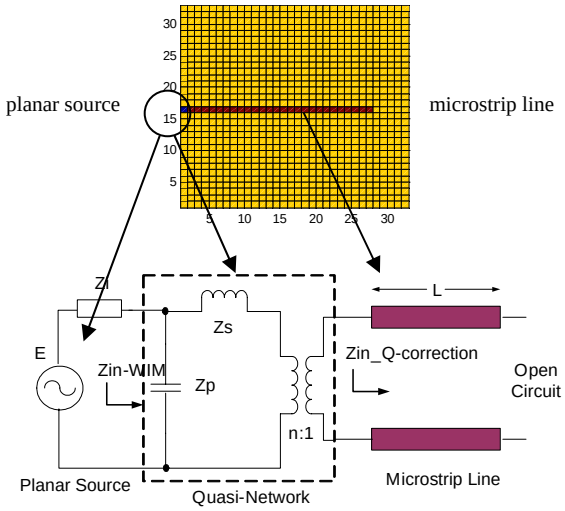

Fig. 6 Open circuit-microstrip line

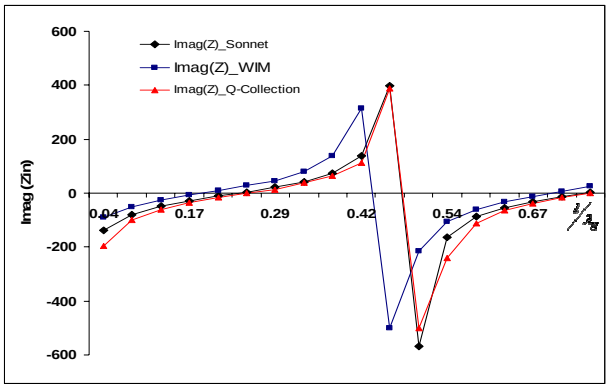

Fig. 7 Comparison of the input impedance obtained by WIM, WIM_(Q-correction) and SONNET Lite

In fig. 7, the input impedance of open circuit-microstrip line is plotted against normalized wavelength of line (l/λ_g). The trace of input impedance of the WIM shows the shift in resonance frequency. After to correct by using the quasi-network (Q-correction), the simulated results by the WIM (Q-correction) are compared with SONNET Lite, they are in very good agreement.

B. Microstrip circuit

The proposed approach is checked by considering the circuit given in fig. 8. The structure of the microstrip is shown in fig. 5, where $h_1 = 4.5$, $h_2 = 1.5$, w=1 mm, L=30 mm, $\varepsilon_{r1} = 1$ and $\varepsilon_{r2} = 10$.

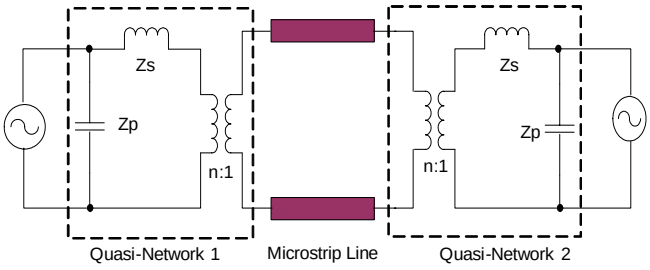

Fig. 8 Two ports network of microstrip line

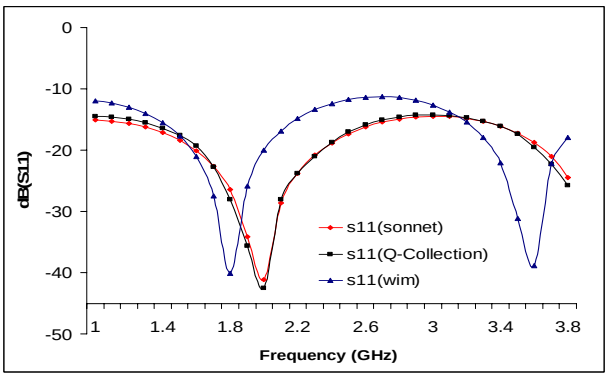

(a) dB (S11)

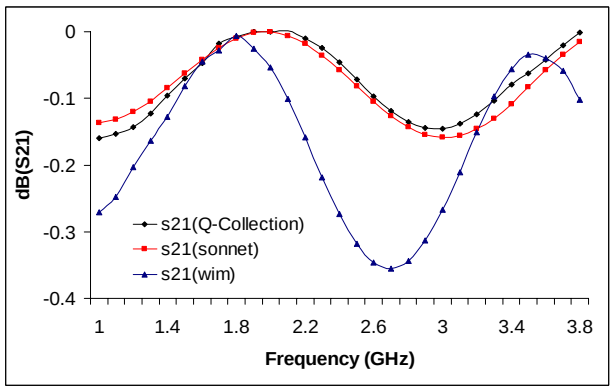

(b) dB (S21)

Fig. 9 Comparison of the S-parameter obtained by WIM, WIM_(Q-Collection) and SONNET Lite

Frequency variation of the dB(S11) and dB(S21) of the microstrip line is plotted in fig. 9. Better agreement between WIM (Q-correction) and SONNET Lite results can be obtained.

V. CONCLUSION

The efficiency and accuracy of WIM simulation has been presented to solving electromagnetic problems. In this case, the quasi-network of planar source has been characterized. The WIM is properly conceived to apply in microstrip line. The obtained results are very similar to the results of SONNET Lite simulation.

REFERRENCE

[1] P.Russer, B.Bader, “The alternating Transmission Line Matrix (ATLM) Scheme”, IEEE MTT-S Intern. Microwave Sym. Digest., Orlando FL, USA, May 1995.

[2] W.H.Yu and R.Mittra, “A New Sub-girding Method for the Finite Difference Time Domain (FDTD) Algorithm”, Microwave Opt. Tech. Letter, Vol. 21, pp. 330-333, June 1999.

[3] Yan Zhang, Ben-Qing Gao et al., “Analysis and Application of New Quasi-Network Characteristics of Nonuniform Mesh in FDTD Simulation”, IEEE Trans. on Microwave Theory and Techniques, Vol. 50, N° 11, pp. 2519-2526, November, 2002.

[4] F.Bouzidi, H.Aubert, D.Bajon, H.Baudrand. "Equivalent Network Representation of Boundary Conditions Involving Generalized Trial Quantities: Application to Lossy Transmission Lines with Finite Metallization Thickness". IEEE Trans. on Microwave Theory and Techniques, Vol. 45, N° 6, pp. 869–876, June 1997.

[5] D.Bajon, H.Baudrand; “Application of Wave Concept Iterative Procedure (WCIP) to Planar Circuits”, Microtec’2000, Hannovre, pp.864-868, Septembre 2000.

[6]. S.Akatimagool, D.Baujon, H.Baudrand, “Analysis of Multi-layer Integrated Inductor with Wave Concept Iterative Procedure”, IEEE MTT-S Intern. Microwave Sym. Digest., Arizona, USA, May 2001.

[7]. N.Raveu, T.P.Vuong, et al., “Wave Concept Iterative Procedure applied to cylinders”, IEE proc. Microwave and Antennas Propag.. Vol. 151, N° 5, October 2004.

The Generalized Constant Circuit-Node *Q* Circles on the Extended T-Chart

P. Y. Chou and D. Torrungrueng
Department of Electrical and Electronic Engineering, Faculty of Engineering and Technology,
Asian University, Chon Buri, 20150, Thailand
Phone: 038-754-450, Fax: 038-754-460, Email: chouman_b@hotmail.com, dtg@asianust.ac.th

***Abstract*-The extended T-chart has been developed for solving problems associated with conjugately characteristic-impedance transmission lines (CCITLs) with *active* characteristic impedances. In this study, the constant circuit-node *Q* circles, denoted by Q_n, are constructed on the extended T-chart to assist in designing lossless matching networks for these CCITLs. The circles can be easily generated, and the procedures of obtaining these circles are discussed in detail.**

Keywords: CCITLs, active characteristic impedances, constant circuit-node *Q*, standard T-chart, extended T-chart.

I. INTRODUCTION

The T-chart has been developed for solving problems associated with conjugately characteristic-impedance transmission lines (CCITLs) with *passive* characteristic impedance ($\mathrm{Re}\{Z_0^{\pm}\} \geq 0$), where $Z_0^{\pm}$ are characteristic impedances of CCITLs [1]-[4]. A recent study has shown that CCITLs implemented by periodically loaded lossless lines can exhibit *active* characteristic impedances ($\mathrm{Re}\{Z_0^{\pm}\} < 0$) [5]. Interestingly, the associated magnitude of the voltage reflection coefficient for this case can be greater than or equal to unity for *passive* load terminations. In addition, the standard T-chart has recently been extended, called the extended T-chart, for CCITLs with active characteristic impedances [6].

Fig. 1 represents a lossless CCITL, terminated in a *passive* load impedance Z_L, possessing the propagation constants β^+ and β^-, with conjugate characteristic impedances Z_0^+ and Z_0^-, for propagation in the *forward* and *reverse* directions, respectively. For impedance matching problems shown in Fig. 2, a lossless network matches an arbitrary load impedance Z_L to a CCITL with active characteristic impedances. Previously, the generalized constant circuit-node *Q* circles on the standard T-chart were developed in [7]. In this paper, the generalized *Q* circles are extended to

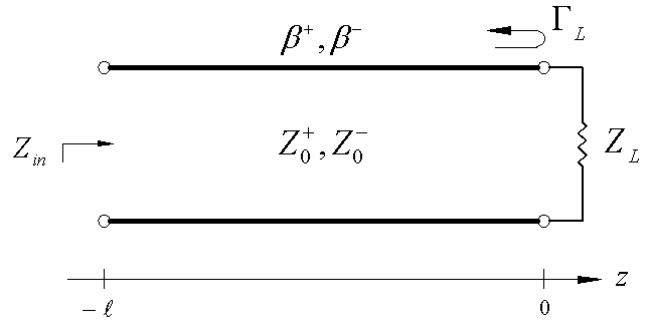

Figure 1. A lossless CCITL terminated in a passive load impedance Z_L.

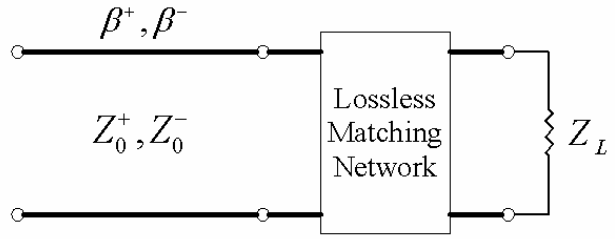

Figure 2. A lossless network matching an arbitrary load impedance Z_L to a CCITL with active characteristic impedances.

be plotted on the extended T-chart for problems associated with Fig. 2. At each node in the lossless matching network, the value of the circuit-node *Q*, denoted by Q_n, is determined by using the equivalent input impedance at the node. By definition, Q_n is the ratio of the magnitude of its reactance to its resistance at the node [8]. Therefore, several equivalent series input impedances can have the same Q_n. In this paper, equations of constant-Q_n contours will be shown and plotted on the extended T-chart for some phase angles ϕ of $Z_0^{\pm}$.

This paper is organized as follows. Section II presents the theory of CCITLs with active characteristic impedances in brief. The construction of the generalized constant-Q_n circles is illustrated in Section III. Section IV shows some numerical results. Finally, conclusions are provided in Section V.

II. THEORY OF CCITLS

This section provides the necessary background of CCITLs for constructing the constant-Q_n circles in the next section. CCITLs are lossless, and generally possess *different* characteristic impedances, Z_0^+ and Z_0^-, for propagation in the *forward* and *reverse* directions. It can be shown that the characteristic impedances $Z_0^{\pm}$ must be complex conjugate of one another [1], which can be expressed as

$$Z_0^+ = \left(Z_0^-\right)^*, \tag{1}$$

where the superscript * denotes the complex-conjugate symbol. For convenience, let us define $Z_0^{\pm}$ as

$$Z_0^{\pm} = |Z_0| e^{\mp j\phi}, \tag{2}$$

where $|Z_0|$ and ϕ are the absolute value and the argument of Z_0^-, respectively.

For *active* characteristic impedances, it is required that

$$\mathrm{Re}\left\{Z_0^{\pm}\right\} < 0. \tag{3}$$

Using (2) and (3), it is found that the argument ϕ must lie in the following range:

$$90^\circ < \phi \le 180^\circ \ \cup \ -180^\circ < \phi < -90^\circ. \tag{4}$$

The reflection coefficient at the load Γ_L for CCITLs is given by [1]

$$\Gamma_L = \frac{z_L z_0^- - 1}{z_L z_0^+ + 1}, \tag{5}$$

where z_L is the normalized load impedance and $z_0^{\pm}$ is the normalized characteristic impedances, where the normalized impedance z of an arbitrary impedance Z is defined as

$$z = \frac{Z}{|Z_0|}. \tag{6}$$

Using (2) and (6), $z_0^{\pm}$ is found to be

$$z_0^{\pm} = e^{\mp j\phi}. \tag{7}$$

It should be pointed out that when the argument ϕ lies within the range specified in (4), the magnitude of the reflection coefficient of the load $|\Gamma_L|$ is always greater than or equal to unity for a passive load termination. In the next section, the construction of the generalized constant-Q_n circles on the extended T-chart is illustrated.

III. Construction of the Generalized Constant-Q_n Circles on the Extended T-Chart

The generalized constant-Q_n circles on the extended T-chart are constructed by using the same concept as constructing the generalized constant-Q_n circles on the standard T-chart [7]. To derive equations for the generalized constant-Q_n circles, it is better to express the normalized impedance z in terms of its corresponding reflection coefficient Γ. Using (5), z can be expressed as

$$z = \frac{1+\Gamma}{z_0^- - z_0^+ \Gamma}. \tag{8}$$

For convenience in manipulation, let $\Gamma = \Gamma_r + j\Gamma_i$ and $z = r + jx$. Substituting Γ and z into (8) and using (7) yield the following equation:

$$r + jx = \frac{1+\Gamma_r + j\Gamma_i}{e^{j\phi} - e^{-j\phi}\left(\Gamma_r + j\Gamma_i\right)}. \tag{9}$$

In [8], Q_n is defined as

$$Q_n \equiv \frac{|x|}{r}. \tag{10}$$

Depending on the signs of x, (10) can be rearranged as follows:

$$\left[\Gamma_r - \frac{\sin\phi}{Q_n\cos\phi - \sin\phi}\right]^2 + \left[\Gamma_i + \frac{\cos\phi}{Q_n\cos\phi - \sin\phi}\right]^2 = \frac{\left(Q_n^2+1\right)\cos^2\phi}{\left(Q_n\cos\phi - \sin\phi\right)^2} \tag{11}$$

$$\left[\Gamma_r + \frac{\sin\phi}{Q_n\cos\phi + \sin\phi}\right]^2 + \left[\Gamma_i - \frac{\cos\phi}{Q_n\cos\phi + \sin\phi}\right]^2 = \frac{\left(Q_n^2+1\right)\cos^2\phi}{\left(Q_n\cos\phi + \sin\phi\right)^2}, \tag{12}$$

for $x > 0$ and $x < 0$, respectively. Thus, (11) and (12) are the equations of the generalized constant-Q_n circles in the case of CCITLs with active characteristic impedances. It should be pointed out that (11) and (12) are identical to those in the passive case [7]. Note that these two circle equations depend on the argument ϕ defined in (4) in a complicated fashion.

In the next section, numerical results of the generalized constant-Q_n circles on the extended T-chart will be illustrated.

IV. Numerical Results

Fig. 3 shows the plot of $Q_n = 5$ circles generated on the extended T-chart when $\phi = 180^\circ$. Note that the horizontal line across the extended T-chart represents the contour $x = 0$, the region below it corresponds to $x > 0$ and the region above it corresponds to $x < 0$. From Fig. 3, the constant-Q_n circles for $x > 0$ and $x < 0$ are symmetric about the contour $x = 0$. In addition, it is observed that these constant-Q_n circles intersect both open-circuited (OC) and the short-circuited (SC) locations.

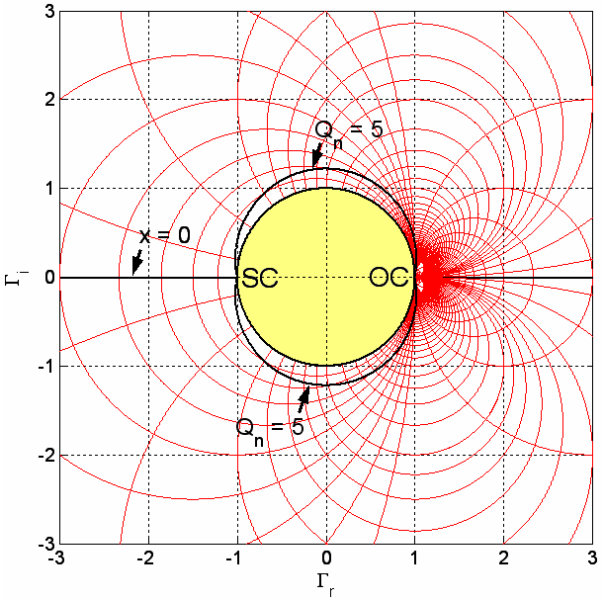

Figure 3. Plot of $Q_n = 5$ circles on the extended T-chart when $\phi = 180^\circ$.

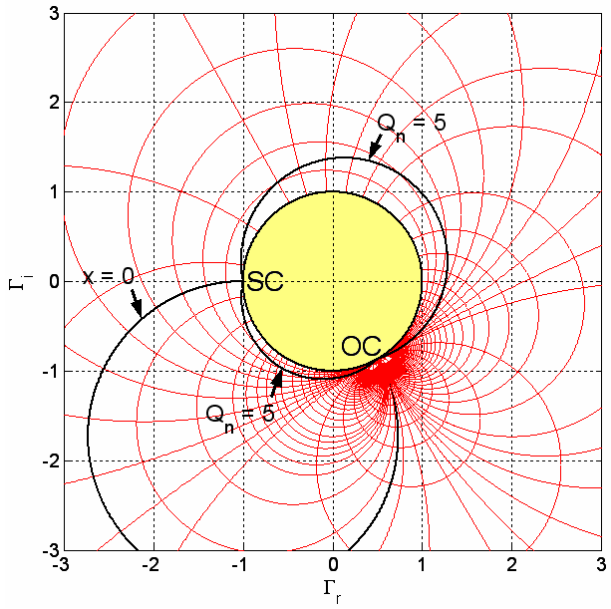

Figure 4. Plot of $Q_n = 5$ circles on the extended T-chart when $\phi = 150^\circ$.

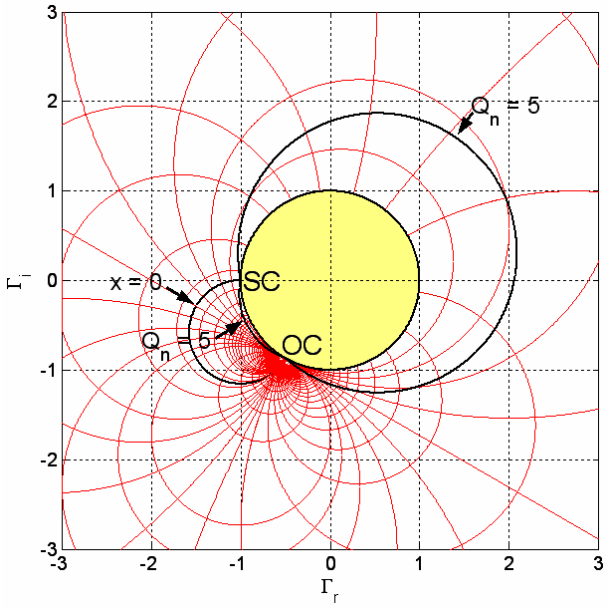

Figure 6. Plot of $Q_n = 5$ circles on the extended T-chart when $\phi = 120^\circ$.

As illustrated in Section III, the constant-Q_n circles depend on the argument ϕ. To illustrate this dependence graphically, let us consider several cases in the valid range of ϕ defined in (4). Fig. 4 shows the plot of $Q_n = 5$ circles on the extended T-chart when $\phi = 150^\circ$. Note that, outside the unit circle on the extended T-chart, the region outside the circle $x = 0$ corresponds to $x < 0$, and that inside the circle $x = 0$ corresponds to $x > 0$. The $Q_n = 5$ circle for $x < 0$ is larger than that for $x > 0$. In this case, the constant-Q_n circles are no longer symmetric about the contour $x = 0$.

Next, consider the case when $\phi = -150^\circ$. When the argument ϕ becomes negative, the center of the circle $x = 0$ is at the upper part of the extended T-chart. Fig. 5 illustrates the plot of $Q_n = 5$ circles on the extended T-chart when $\phi = -150^\circ$. Note that, outside the unit circle on the extended T-chart, the region outside the circle $x = 0$ corresponds to $x > 0$, and that inside the circle $x = 0$ corresponds to $x < 0$. Note that Figs. 4 and 5 look like the mirror image (about the horizontal axis) of each other.

Fig. 6 shows the plot of $Q_n = 5$ circles on the extended T-chart for $\phi = 120^\circ$. Note that the region $x > 0$ (inside the circle $x = 0$) becomes smaller as ϕ decreases from $\phi = 150^\circ$ (in Fig. 4) to $\phi = 120^\circ$. Fig. 7 illustrates the plot of $Q_n = 5$ circles on the extended T-chart when $\phi = -120^\circ$. Note that the region $x < 0$ becomes smaller as ϕ increases from $\phi = -150^\circ$ (in Fig. 5) to $\phi = -120^\circ$. Figs. 6 and 7 follow the same characteristics as in Figs. 4 and 5, respectively.

When $\phi \neq 180^\circ$, the contour $x = 0$ is not a horizontal line, and the constant-Q_n circles for $x > 0$ and $x < 0$ are not a symmetrical image of each other, as shown in Figs. 4 to 7. However, there are still some common properties that can be observed. For example, it can be seen that all constant-Q_n circles are intersected at the SC and OC points on the chart.

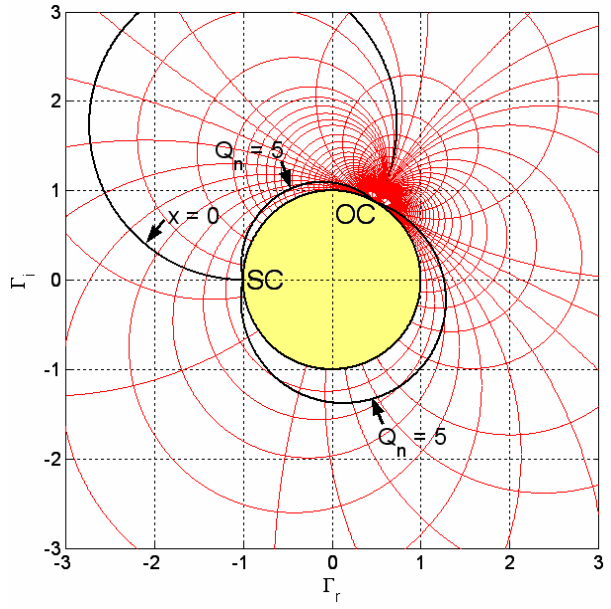

Figure 5. Plot of $Q_n = 5$ circles on the extended T-chart when $\phi = -150^\circ$.

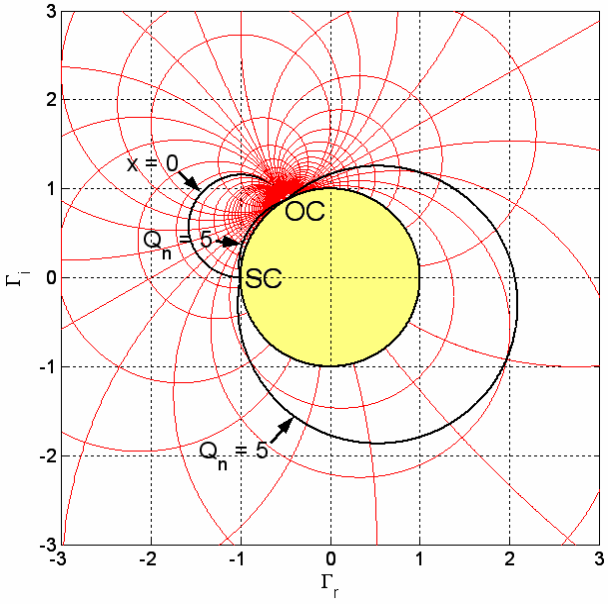

Figure 7. Plot of $Q_n = 5$ circles on the extended T-chart when $\phi = -120^\circ$.

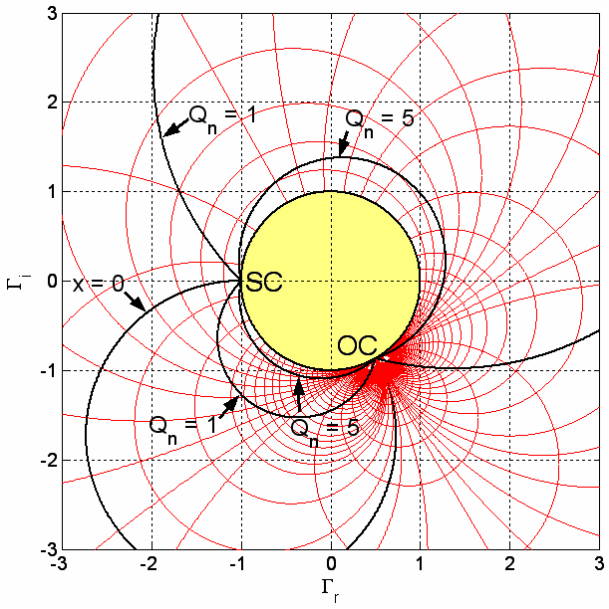

Figure 8. Plot of constant-Q_n circles on the extended T-chart for $Q_n = 1$ and $Q_n = 5$ when $\phi = 150^\circ$.

Constant-Q_n contours can be obtained by simply superimposing each constant-Q_n circle in the Γ plane as shown in Fig. 8 when $\phi = 150^\circ$. From the figure, it is observed that as Q_n increases, the closer the circles are from the unit circle for both $x > 0$ and $x < 0$, except at the short-circuited and open-circuited points on the extended T-chart. Therefore it is possible to obtain a very large constant-Q_n circle when Q_n is very small.

V. Conclusions

In this study, we extend the generalized constant-Q_n circles on the standard T-chart to be plotted on the extended T-chart. It is found that associated circle equations for both cases are the same. The only difference is the valid range of ϕ for plotting. In this case, we concentrate on the region that is outside the unit circle in the Γ plane. It is found that all constant-Q_n circles are intersected at the short-circuited and open-circuited points on the extended T-chart. In addition, the circles for $x > 0$ and $x < 0$ are generally not a symmetrical image of each other, except when $\phi = 180^\circ$. The generalized constant-Q_n circles on the extended T-chart can be employed as a tool in the design of lossless matching network when dealing with CCITLs with active characteristic impedances with a specified Q_n.

References

[1] D. Torrungrueng and C. Thimaporn, "A Generalized ZY Smith Chart for Solving Nonreciprocal Uniform Transmission-Line Problems," *Microwave and Optical Technology Letters*,vol. 40, no. 1, pp. 57-61, 2004.

[2] D. Torrungrueng, C. Thimaporn, and N. Chamnandechakun, "An Application of the T-Chart for Solving Problems Associated with Terminated Finite Lossless Periodic Structures," *Microwave and Optical Technology Letters*, vol. 47, no. 6, pp. 594-597, December 20, 2005.

[3] D. Torrungrueng and C. Thimaporn, "Application of the T-chart for Solving Exponentially Tapered Lossless Nonuniform Transmission-Line Problems," *Microwave and Optical Technology Letters*, vol. 45, no. 5, pp. 402-406, June 5, 2005.

[4] D. Torrungrueng and C. Thimaporn, "Applications of the ZY T-Chart for Nonreciprocal Stub Tuners," *Microwave and Optical Technology, Letters*, vol. 45, no. 3, pp. 259-262, May 5, 2005.

[5] S. Lamultree and D. Torrungrueng, "On the Characteristics of Conjugately Characteristic-Impedance Transmission Lines with Active Characteristic Impedance," 2006 Asia-Pacific Microwave Conference Proceedings, vol. 1, Yokohama, Japan, pp. 225-228, December 12-15, 2006.

[6] D. Torrungrueng , P.Y. Chou and M. Krairish, "An Extended ZY T-Chart for Conjugately Characteristic-Impedance Transmission Lines with Active Characteristic Impedances," submitted to Microwave and Optical Technology Letters.

[7] D. Torrungrueng and P.Y. Chou, "The Generalized Constant Circuit-Node *Q* Circles," Proceedings of the 2006 ECTI International Conference, Ubon Rachathani, Thailand, pp. 757-760, May 10-13, 2006.

[8] G. Gonzalez, *Microwave Transistor Amplifiers Analysis and Design*, 2nd Ed., Prentice Hall, NJ, 1997.

A Microstrip-Coplanar Waveguide Tight Coupler for a Single-Layer Substrate

Mitchai Chongcheawchamnan[1], Waikoon Sangworn[1,2], Ratthaya Suwanbunyaporn[1], and Ravee Phromloungsri[1]

[1]Research Center for Electromagnetic Wave Applications (RCEWs),
Telecommunication Engineering Department,
Mahanakorn University of Technology, Bangkok, Thailand, 10530

E-mail : mitchai@ieee.org

Abstract — **In this paper, a tight coupler designed for a single layer substrate is proposed. The technique extends the previous proposed concept which combines the microstrip line and coplanar waveguide structure to apply with multi-coupled lines, leading to a more tight-coupling design for standard PCB manufacturing process. Validation on the proposed technique is demonstrated with experiment on a 3-dB coupler fabricating with the in-house process in laboratory. From the measured results, tight coupling, being extremely difficult to achieve on a single-layer standard process, is achieved simply.**

Index Terms — **Microstrip (MS), coplanar waveguide (CPW), Lange coupler, , tight coupler, quadrature.**

1. INTRODUCTION

It is well known that a coupler is commonly used in various microwave circuits and systems. Though there are yet numerous structures proposed for coupler realization, only coupled-lines structure is always preferable for industrial application [1],[2]. This is because not only its wide band operation and simple profile, but also ease of integratibility. Design coupled lines [3] with various transmission line technologies, for example microstrip, coplanar waveguide, stripline, etc., can be done. However microstrip and coplanar waveguide technologies are mostly chosen as the process is more likely compatible with the mostly used fabrication processes nowadays, i.e. CMOS, MWMIC, and MMIC [2].

In view of coupling coefficient, coupler can be classified into two categories which are loose and tight coupling [4]. It has been well known that a tight coupling design is frequently used in microwave design. The most applied tight coupler is a quadrature 3-dB coupler [5],[6] as it is a basic building block to implement a balanced mixer [7], balanced amplifier [8], etc. More tight coupling design is also desirable for a coupled-line phase shifter [9]. Nevertheless a tight coupling design issue is always problematic.

Originally, parallel-coupled lines, the simplest coupled-lines structure, were proposed but since their failure to achieve tight coupling, then tandem coupled [10], multi-coupled [11]-[16] and multi-layer coupled lines [17]-[21] were invented. A tandem coupled line structure, composed of two loose coupled lines, can achieve very tight coupling design but only for narrow band operation. Additionally, the tandem structure needs air–bridges and consumes around twice of the circuit size required for parallel-coupled lines. Multi-coupled lines structure such as Lange coupler [15] or three-coupled lines [16] is very promising as the design provides a large bandwidth and small size. Besides, at least two substrate layers are demanded as it does need air bridges. Multi-layer couplers can provide a compact design. Still the approach does not suit for a single substrate layer.

Clearly neither of the abovementioned approaches is appropriate for the simplest standard fabrication process, hence a standard PCB process. Previous tight coupler implementation can not therefore avoid extra fabrication cost. Recently, there is an approach proposed [22] using a structure employing the microstrip (MS) and coplanar waveguide (CPW) transmission lines which is a pure single-layer circuit. The structure is succeeded with three-finger CPW coupled line structure. The bottom metal beneath the CPW coupled lines is etched and air-bridges needed are replaced with via holes. However the technique was demonstrated with a 3-dB quadrature coupler on thin substrate layer as the coupling performance partly relies on ground capacitances. Henceforth this paper presents an extended work of such mix-mode coupled lines to achieve tight coupling design with arbitrary substrate thickness. Section 2 illustrates the topology proposed. Section 3 reports the design details and results from simulation and experiment. Section 4 summarizes the work in this paper and future work.

2. PROPOSED TOPOLOGY

In fact, it is well known that multi-coupled line structure can provide a tight coupling design. Therefore here we apply the five-finger CPW coupled lines to attain a tight coupling. The structure of the proposed circuit is shown in Fig. 1. From the top view shown in Fig. 1 a), the layout of the circuit in the top view is similar to a standard Lange coupler except the introducing of conductor lines of width W_1 and length L_1. Via holes are applied to short these lines with the lower conductor plane shown in Fig. 1 b). Clearly that these lines of width W_1 operate as ground for the upper plane. The five-finger coupled lines have width of W and length of L. These coupled lines places at distance of D from the upper ground planes. The feed lines of W_2 are designed for attaining 50-Ω characteristic impedance.

Table 1
Summarized proposed coupler dimension

W	= 0.8 mm	L_1	= 16.2 mm
W_1	= 1.9 mm	L_2	= 29 mm
W_2	= 3 mm	S	= 0.2 mm
W_3	= 17.8 mm	D	= 5.5 mm
L	= 17 mm	h	= 1.6 mm

The bottom view of the circuit layout is shown in Fig 1 b). The conductor plane lies beneath the five-coupled lines are etched away. This makes the connecting between five-coupled lines simple with via holes. The dimensions of the open ground at the bottom plane are W_3, L_3, and L. The cross section view of the proposed circuit is shown in Fig. 1c).

3. Design And Experimental Results

In this paper, a 3-dB quadrature coupler on a low-cost FR4 substrate (thickness of 1.6 mm, dielectric constant of 4.4, loss tangent of 0.02) was designed to validate the proposed topology. A design procedure of this work begins with the same approach proposed in [22]. As the analysis approach is based on a quasi-static TEM model [4], the given formulae presented are not sufficiently accurate. Therefore the design procedure done in this paper indeed heavily relies on the electromagnetic (EM) calculation. Here the Momentum™ (EM software simulation) in Advanced Design System 2005 (ADS) software suite was used through out the whole design stage. EM optimization process was performed at the final stage with the constraints of 0.2 mm conductor width and space dimensions according to the limitation in our in-house fabrication process.

The dimensions of the design parameters obtained are summarized in Table I. The photographs of top and bottom views of the 3-dB coupler with SMA connector are shown in Fig. 2 a) and b), respectively. All via holes in the circuit were implemented with 0.8-mm diameter conductor wire. The size of the fabricated circuit excluding the SMA connectors is 2.3 $\times$1.78 cm^2. Circuit measurement was performed with HP8720C 2-port vector network analyzer. The SOLT calibration technique was done from 1 to 4 GHz. Two 3.5-mm standard loads were used to terminate at other two ports while measuring was performed. Six measurement data sets were collected via GPIB port and subsequently formed to four-port data by the developed program written in MATLAB™. Finally the 4-port data in S4P format was then plot in graphs with the ADS software.

Simulated (dotted line) and measured (line) performances of the experimental circuit are shown in Fig. 3 to Fig. 5. Fig. 3 shows the directed (S31) and coupling (S21) performances. Excellent agreement between simulated and measured S31 and

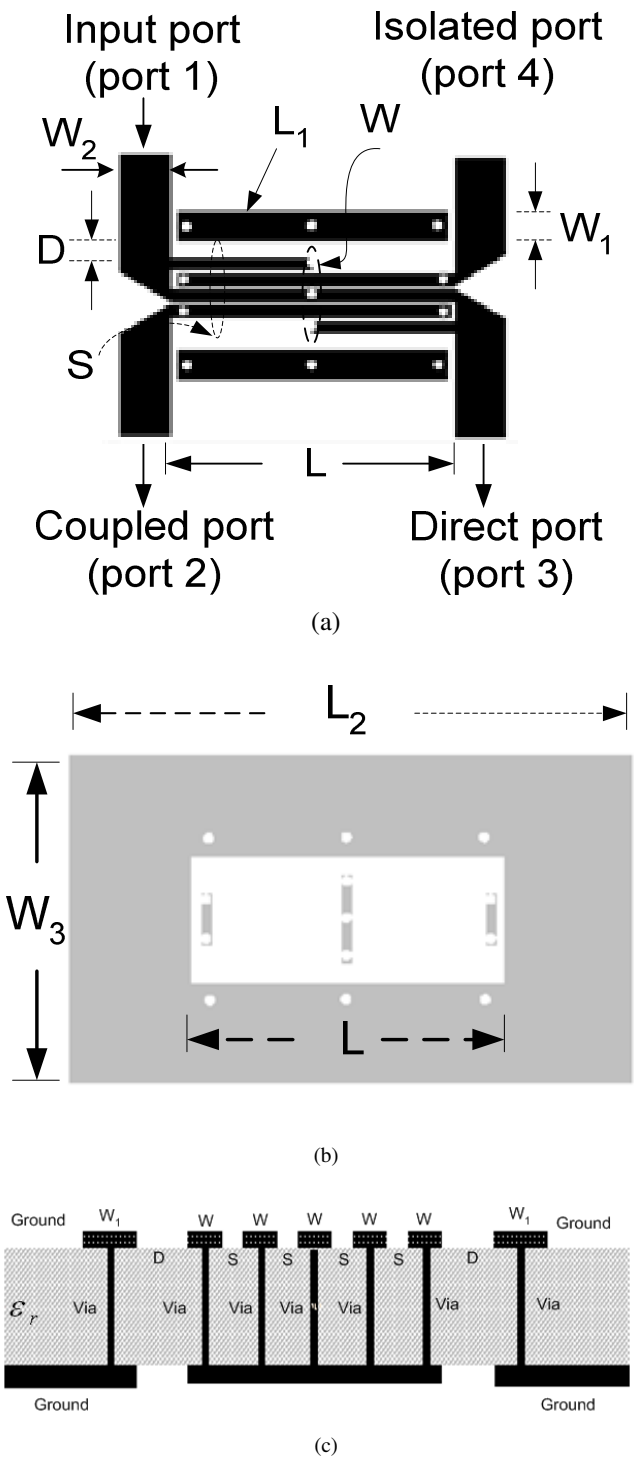

Fig. 1. Layout of the proposed circuit, (a) Top view. (b) Bottom view. (c) Cross-section view

S21 are obtained. The coupler achieves -3.60 dB and -3.61 dB for measured S21 and S31, respectively, which are 0.5 dB less than the theoretical performance of a 3-dB coupler. The authors believe that this 0.5 dB loss is mainly resulted from the loss tangent behavior in FR4.

Fig. 4 shows the performances of isolation (S41) and return losses (S11). Good return and isolation performances are obtained from 1 to 3.4 GHz. At 2.45 GHz, the design achieves

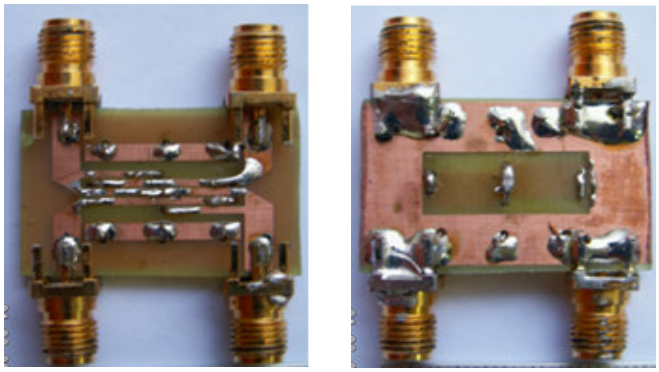

(a) (b)

Fig. 2. PCB Photographs of the experimental circuit, (a) Top (b) Bottom view.

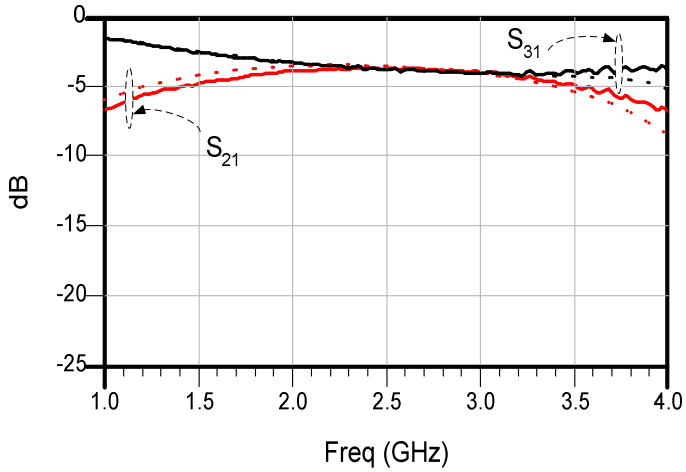

Fig. 3. Simulation and measured results of the coupled and direct ports : EM simulated (- - -), measured results (——) of the experimental circuit.

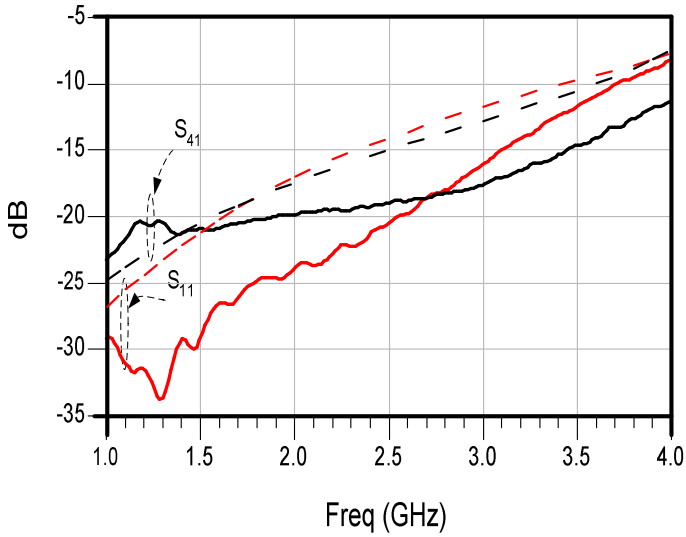

Fig. 4. Simulation and measured results of the return and isolation losses: EM simulated (- - -), measured results (——) of the experimental circuit.

S41 and S11 of -19 and -22 dB respectively. At high frequency, S41 and S11 are clearly degraded as the loss mechanism and dielectric constant are frequency dependent.

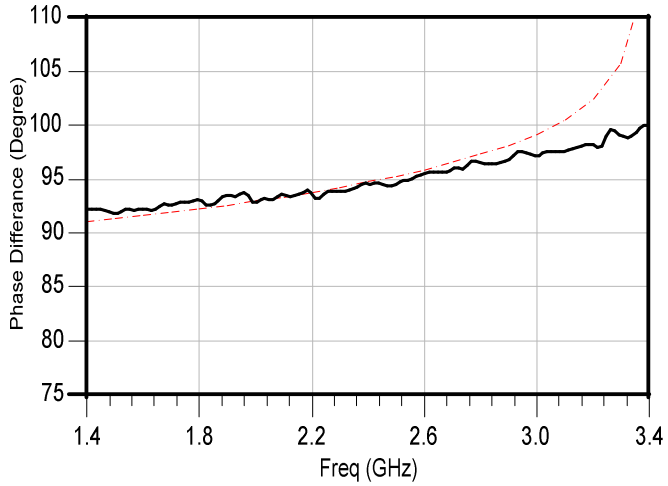

Fig. 5. Measured and simulated results of relative phase difference: EM simulated (- - -), measured results (——) of the experimental circuit.

The phase difference between the direct and coupled ports from 1.4 to 3.4 GHz is shown in Fig. 5. Nearly 90 degree, the theoretical phase difference, is obtained. A difference between measured and simulated results at high frequency region is expected to come from the dispersive nature of the FR4 which was not taken into account in our simulation.

4. CONCLUSION

A tight coupler based on five-finger coupled lines has been proposed and its experimental results demonstrate excellence performance. The circuit can achieve tight coupling on a purely single substrate layer, making it more suitable for low cost fabrication process such as a standard PCB prototyping. As shown from the experimental circuit prototyping with the in-house fabrication process, good yield performance is also gained from the proposed topology. Closed form design equations are under investigated and will be presented for facilitate the design task.

REFERENCES

[1] Kai Chang, *Enclycopedia of RF and Microwave Engineering*, Wiley-Interscience , 2005.

[2] D. M. Pozar, *Microwave Engineering*, 2nd ed. New York: Wiley, 1998.

[3] R. Mongia, I. . Bahl, and P. Bhartia, *RF and Microwave Coupled-Line Circuits*, Artech House, 1999.

[4] E. G. Cristal, "Coupled-transmission-line directional couplers with coupled lines of unequal characteristic impedances," *IEEE Trans. Microw. Theory Tech.*, vol. MTT-4, no. 7, pp. 337–346, Jul. 1966

[5] D. P. Andrews and C. S. Aitchison, "Wide-band lumped element quadrature 3-dB couplers in microstrip," *IEEE Trans. Microw. Theory Tech.*, vol. 48, no. 12, pp. 2424–2431, Dec. 2000.

[6] C. V. B. Maciel, D. F. M. Argollo, and H. Abdalla, "Broadside suspended stripline 3 dB couplers," in *SBMO Int. Microw. Conf.*, São Paulo, Brazil, Aug. 1993, vol. 1, pp. 117–122.

[7] S. A. Maas, *Microwave Mixers*, Artech House, 1988.

[8] G. H. Martin, et al**,** *Balanced amplifier device*, US Patent, 4571554

[9] B. M. Schiffman, B.M., "A New Class of Broad-Band Microwave 90-Degree Phase Shifters"**,** *IEEE Trans. Microw. Theory Tech.*, vol. MTT-6, no. 2, pp. 232–237, Jul. 1958.

[10] T.-Y Chang, C-L Liao, C. H. Chen, "Coplanar-waveguide tandem couplers with backside conductor**",** *IEEE Microwave and Wireless Components Letters,*, vol. 13, no. 6, pp. 214–216, June. 2003.

[11] J. Lange, "Interdigitated stripline quadrature hybrid," *IEEE Trans. Microw.Theory Tech.*, vol. MTT-17, no. 12, pp. 1150–1151, Dec. 1969.

[12] V. Tulaja, B. Schiek, and J. Kohler, "An interdigitated 3-dB coupler with three strips," *IEEE Trans. Microw. Theory Tech.*, vol. MTT-26, no. 9, pp. . 643–645, Sep. 1978.

[13] A. Presser, "Interdigitated microstrip coupler design," *IEEE Trans. Microw. Theory Tech.*, vol. 26, no.10, Oct 1978.

[14] D. Kajfez, Z. Paunovic, and S. Pavlin, "Simplified design of Lange coupler," *IEEE Trans. Microw. Theory Tech.*, vol. MTT-26, no. 10, pp. 806–808, Oct. 1978.

[15] R. Waugh and D. LaCombe, "Unfolding the Lange coupler," *IEEE Trans. Microw. Theory Tech.*, vol. MTT-20, no. 11, pp. 777–779, Nov. 1972.

[16] S. M. Perlow and A. Presser, "The interdigitated three-strip coupler," *IEEE Trans. Microw. Theory Tech.*, vol. MTT-32, no. 10, pp. 1418–1422, Oct. 1984.

[17] L. Krishnamurthy, V. V. Tuyen, R. Sloan, K. Williams, and A. A. Rezazadeh, "Broadband CPW multilayer directional couplers on GaAs for MMIC applications," in *High-Freq. Postgraduate Student Colloq.*, Sep. 2004, pp. 183–188.

[18] M. Nedil, T. A. Denidni, and L. Talbi, "CPW multilayer slot-coupled directional coupler," *Electron. Lett.*, vol. 41, pp. 706–707, Jun. 2005.

[19] S. Al-Taei, P. Lane, and G. Passiopoulos, "Design of high directivity directional couplers in multilayer ceramic technologies," in *IEEE MTT-S Int. Microw. Symp. Dig.*, May 2001, pp. 51–54.

[20] Q. H. Wang, T. Gokdemir, D. Budimir, U. Karacaoglu, A. A. Rezazadeh, and I. D. Robertson, "Fabrication and microwave characterization of multilayer circuits for MMIC applications," *Proc. Inst. Elect. Eng.—Microw., Antennas, Propag.*, vol. 143, pp. 225–232,Jun.1996.

[21] D. Willems and I. Bahl, "An MMIC-compatible tightly coupled line structure using embedded microstrip," *IEEE Trans. Microw. Theory Tech.*, vol. 41, no. 12, pp. 2303–2310, Dec. 1993.

[22] Jui-Chieh Chiu, Chih-Ming Lin, "A 3-dB quadrature coupler suitable for PCB circuit design," *IEEE Trans. Microw. Theory Tech.*, vol. 54, no.9, Sep 2006

Performance of Power Line Communication using Direct- Sequence Code Division Multiple Access with Turbo Coded

S. Chanakarn, C. Banjangkaprasert, N. Anantrasirichai
ReCCIT, Department of Information Engineering, Faculty of Engineering,
King Mongkut's Institute of Technology Ladkrabang,
Chalongkrung Rd., Ladkrabang District, Bangkok 10520, Thailand
E-mail: chai_mea@hotmail.com, kbchawal@kmitl.ac.th, kanoppin@kmitl.ac.th,

Abstract *- This paper presents the performance of the power line communication (PLC) using direct-sequence code division multiple access (DS-CDMA) technique with turbo code. In the decoding algorithm of the turbo code is using the attractive log-maximum a posteriori algorithm (Log-MAP) decoder. It is demonstrated that the performance of the system can be improved. The simulation results are verified the bit error rate (BER) performance of the power line communication systems.*

I. INTRODUCTION

Due to its omnipresence, the electric power distribution grid offers a tremendous potential for extended fast and reliable communication services. Currently, the exploitation has just started and still is far from complete. Various fields of applications can be envisioned, starting, for example, with simple inexpensive services embodied into household appliances, where data rates of some kilobits per second are sufficient. A next level might be Internet access over the wall socket, where speed is in the lower megabit range up to high-speed networking that includes fast Internet access, voice over IP, and home entertainment.

There are limits in transfer power line systems[1-4] which are in part due to some difficulties found when sending the data system. Some examples of these difficulties include impedance value (change all the time), interference signal in the power line system, attenuation which has a high value. Power line channel system[4] will insert interference signal from the source, including high voltage systems which occur from circuit breaker's working, transient occurs from thunderbolts and tools. Medium voltage systems occur from ON-OFF capacitors and switching, low voltage system occurs from working of electrical equipment when it connects to the system. These effects are used to transfer the data signal.

Direct sequence code division multiple access (DS-CDMA)[5-6] is a candidate access technique for a third generation mobile system[6]. In DS-CDMA system, signal transmission over time-varying multipath mobile radio channel produces intersymbol interference (ISI), multiple access interference (MAI), and other time-varying effect from the channel.

A turbo code, which were discovered by C. Berrou *et al.* in 1993 provide significant improvement in the quality of data transmission over a noisy channel [7]. The iterative log-maximum a posteriori algorithm (Log-MAP) is an important kind of turbo decoding algorithms [8-9].

In this paper, the performance of the power line communication using direct-sequence code division multiple access (DS-CDMA) technique with turbo coded is presented in order to increase potential and decrease bit error rate, which occurs from interference of the signal in power line systems.

II. A MULTIPATH MODEL FOR POWER LINE CHANNELS

A simple approach to rough estimation of the transfer function of power line channels was presented by Hensen [1]. A straight line can interpolate the attenuation increasing with higher frequencies, so a simple equation can be found to calculate the amplitude of the channel transfer function. As this approach does not consider multipath propagation and the resulting notches of the channel transfer function, more detailed models had to be developed. Multipath propagation approaches, which are suitable for describing the transmission behavior of power line channels, have been proposed by Philip's [2] and Zimmermann [3]. Philip's' echo model describes the channel impulse response as a superposition of N direct pulses representing the superposition of signals from N different paths. Each of these impulses is multiplied by a complex factor ρ_i and delayed by time τ_i. The factors ρ_i represent the product of reflection and transmission factors along each echo path. This leads to the complex channel transfer function

$$H(f) = \sum_{i=1}^{N} \rho_i e^{-j2\pi f \tau_i} \quad (1)$$

This model allows realistic reproduction of notches of the channel transfer function and is therefore well suited to describe indoor channels where the low-pass characteristic of the channel is not relevant. For the description of channels that show such low-pass behavior like typical European access networks, Zimmermann has proposed an adapted echo model that contains an additional attenuation factor [3]. This model represents the superposition of signals from N different paths,

each of which is individually characterized by a weighting factor g_i and length d_i. Furthermore, frequency-dependent attenuation is modeled by the parameters a_0, a_1, and k. Eventually, the following equation can be formed

$$H(f) = \sum_{i=1}^{N} g_i e^{-(a_0 + a_1 f^k) d_i} e^{-j2\pi f \frac{d_i}{v_p}} \quad (2)$$

The Eq.(2) describes a universal and practically useful form of the complex transfer function for power line channels. While the first exponential function describes attenuation, the second one, including the propagation speed v_p, represents the echo scenario. The parameters for the multipath model can be obtained from measurements of the complex channel transfer function. The attenuation parameters a_0 (offset of attenuation), a_1 (increase of attenuation), and k (exponent of attenuation) can be obtained from the magnitude of the frequency response. To determine the path parameters d_i and g_i, the impulse response is necessary. The impulse response gives information about the time delay of each path, which is proportional to d_i. The weighting factors g_i can be obtained from the amplitude of each impulse.

III. DIRECT SEQUENCE CODE DIVISION MULTIPLE ACCESS

DS-CDMA is the method that allows the data signal to directly modulate with digital signal. The data signal can be achieved in both an analog and a digital signals. The data signal will multiply the code signal directly and then bring the signal to modulate with the carrier signal. This paper will consider the data transfer through power line channels by the DS-CDMA system, which has the following model.

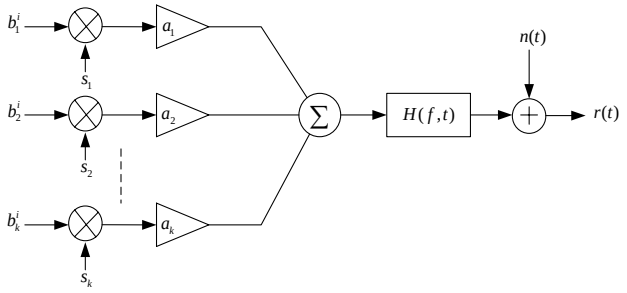

Fig. 1 Transmitter Model

In consideration of the data transfer model in the DS-CDMA system through power line channel, which has noise in additive white Gaussian noise (AWGN), and assign users in the system for k people, b_k^i is a data bit at i of user k (which has T_s time period of signal), a_k is size of acceptable signal from receiver k, s_k is spread code of user k, which has chip equal to L_c, allows the following formula to be formed :

$$s_k(i) = \sum_{i=0}^{L_c - 1} s_i(i) x(t - iT_c) \quad (3)$$

A formula showing the collective signal from the receiver can be written as follows:

$$r(t) = \sum_{i=0}^{\infty} \sum_{k=1}^{K} a_k^i b_k^1 s(t - iT_s) * h(t) + n(t) \quad (4)$$

Receivers in DS-CDMA system's duty is separate to each user, where the users' receiver including despread code of each user and integration circuit can be shown in the Fig. 2 :

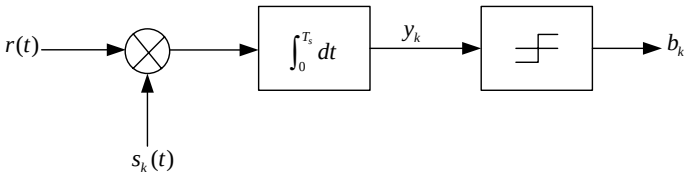

Fig. 2 Receiver Model

We observed that each user's receiver using only the own spread data in separate wanted signal then bring the signal past to bit decision circuit in order to get the designed data. If y_k is outcome signal from user k's receiver at iT_S, we can write following formula:

$$y_k = \int_0^{T_S} r(t) s_k(t) dt \quad (5)$$

The decision output of the detector can be defined as

$$b_k = \mathrm{sgn}(y_k) \quad (6)$$

IV. TURBO CODES [8]

A. Turbo Encoder

Turbo coding, illustrated in Fig. 3, uses a parallel forward error control (FEC) encoding scheme. With this scheme, the information is systematically encoded by two separate encodes. Often, the two encodes are identical, and to ensure that they do not product the same output, the information bits are reordered through the use of a pseudorandom interleaver before the second encoding stage. This pseudorandom interleaver is often referenced to as the turbo interleaver to distinguish it from channel interleavers. The information bits and the parity bits generated by the two encoders are then transmitted over the channel. In a typical turbo encoding scheme, the parity bits are punctured in a repeating pattern to increase the code rate, but this is not a requirement and puncturing refers to the omission of certain parity check bits in the code so as to increase the data rate.

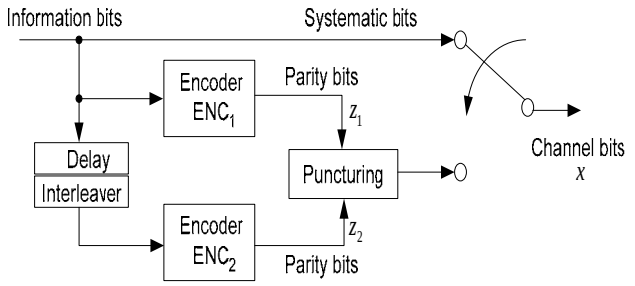

Fig. 3 Rate ½ turbo encoder.

B. Turbo Decoder

In this paper, we using the attractive Log-Map decoding algorithm, therefore we will briefly describe the Log-Map decoding turbo codes in this section. The general structure of the iterative turbo decoder is shown in Fig.4 [10]. Two component decoders (dec1 and dec2) are linked by interleavers (I). In this figure, u_k is the systematically encoded channel output bit, Y_{1k}, Y_{2k} are the parity bits transmitted from the associated component encoder respectively, Λ_{12}, Λ_{21} are the extrinsic information from the other component decoder, and $\hat{u}_k$ is the output of the hard decision (HD) of the last component decoder after the iteration is finished.

According to output *Y*, the MAP algorithm count the probability

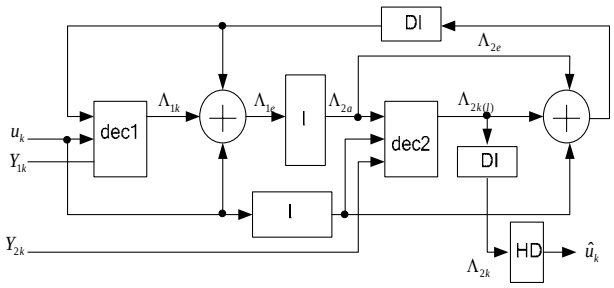

Fig 4. Turbo decoder schematic.

of every u_k = +1 and u_k = -1. That is the $L(u_k \mid Y)$,

$$L(u_k \mid Y) = In\frac{P(u_k = +1 \mid Y)}{P(u_k = -1 \mid Y)}$$

$$= In\frac{\sum(s',s) \Rightarrow u_k = +1 \alpha_{k-1}(s')\gamma_k(s',s)\beta_k(s)}{\sum(s',s) \Rightarrow u_k = +1 \alpha_{k-1}(s')\gamma_k(s',s)\beta_k(s)} \quad (7)$$

$$L(u_k \mid Y) = \left\{ \ln \sum_{(s',s)\Rightarrow u_k=+1} e^{A_{k-1}(s')+\Gamma_k(s',s)+\beta_k(s)} - \ln \sum_{(s',s)\Rightarrow u_k=-1} e^{A_{k-1}(s')+\Gamma_k(s',s)+\beta_k(s)} \right\} \quad (8)$$

Then if we use the approximation:

$$\ln \sum_i e^{x_i} \approx \max(x_i) \quad (9)$$

$$L(u_k \mid Y) = \left\{ \max_{(s',s)\Rightarrow u_k=+1} [A_{k-1}(s') + \Gamma_k(s',s) + B_k(s)] - \max_{(s',s)\Rightarrow u_k=-1} [A_{k-1}(s') + \Gamma_k(s',s) + B_k(s)] \right\} \quad (10)$$

This is the Max-Log-Map algorithm. However the performance is slightly degraded compared to the MAP algorithm due to the approximation of Eq. (9). When used for the iterative decoding of turbo codes, it is found that the degradation results a drop in performance of about 0.35 dB. However, the approximation can he made exact by using the Jacobian equation:

$$\log\{\exp(x_1) + \exp(x_2) + ... + \exp(x_n)\} = \max_{i\in(1,2,...,n)}(x_i) + \log\left\{\sum_i^n \exp(x_i - \max(x_i))\right\} \quad (11)$$

when $\Delta = \exp(x_1) + \exp(x_2) + ... + \exp(x_n) = \exp(x_\Delta)$ $f_{(x)}(x = |x_\Delta - x_n|)$ can be thought of as a correction term.

Therefore the Log-Map algorithm is given by

$$\log\{\exp(x_1) + \exp(x_2) + ... + \exp(x_n)\} \approx \max_{i\in(1,2,...,n)}(x_i) + f_{(x)}(x = |x_\Delta - x_n|) \quad (12)$$

V. NUMERICAL RESULTS

The BER performance of the proposed DS-CDMA with turbo coded for the PLC channel receiver is presented in this section. Besides the measurement data in Fig. 5, simulation results are derived from the following parameters [9], length of transmission information is equals to 1 kbits, the length of the individual path of the PLC channel is 200 m, frequency response of PLC channel is 20 MHz, an attenuation parameter $a_0 = 9.4\times10^{-3}$ and $a_1 = 7.8\times10^{-10}$, exponent of the attenuation factor $k = 0.7$ and weighting factor for path $g_i = 0.64$. And the parameters for the turbo code system : code generator metric = [1 1 1;1 0 1] with constraint length = 3, channel code rate $R = \frac{1}{2}$ and using Log-Map decoding algorithm, number of iteration for turbo decoder = 1, and DS-CDMA have chip rate = 128 bits.

Fig. 5 shows the BER performance comparison of the system with transfer data range = 1000 bits. From Fig. 5, it is evident that the performance of the system using DS-CDMA with turbo code technique provides a less BER than using only DS - CDMA.

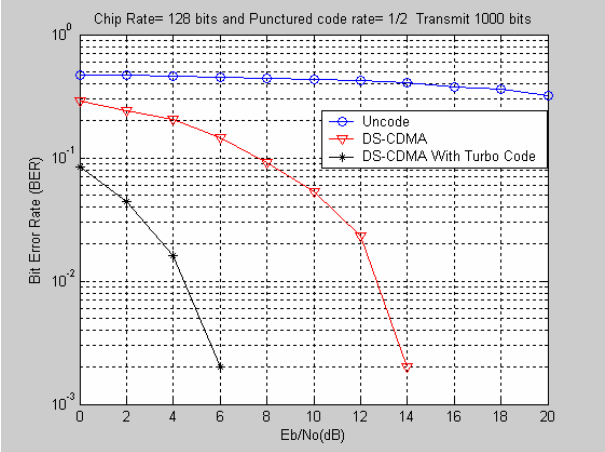

Fig. 5 BER comparison (Data = 1000 bits)

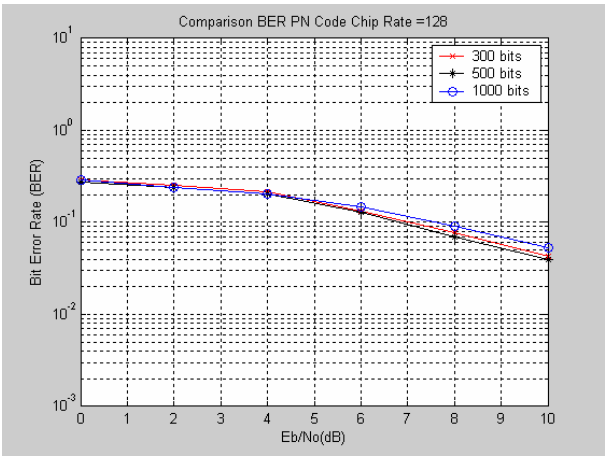

(a) DS-CDMA

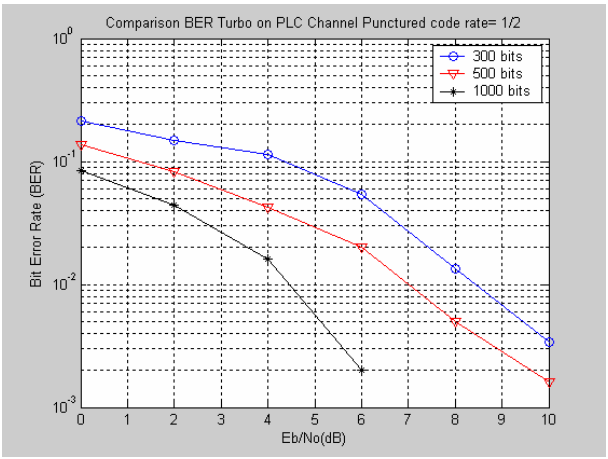

(b) DS-CDMA with turbo code

Fig. 6 BER comparison

Fig. 6 shows the BER performance comparison of the system in verities transfer data rate. Fig. 6(a) shows the BER performance of the system by using DS-CDMA technique with data range = 300, 500, and 1000 bits, respectively. Fig. 6(b) shows the BER performance of the system by using DS-CDMA with turbo codes technique with data range = 300, 500, and 1000 bits, respectively. From the Fig 6(a), it is seen that the performance of the system is slightly same. And from the Fig. 6 (b), it is demonstrated that the performance of the system by using DS-CDMA with turbo code can be increased, if the transfer data is increased.

VI. CONCLUSION

This paper presents the performance of the power line communication using DS-CDMA with turbo code through the Additive White Gaussian Noise (AWGN) channel. From the simulation results, it can be concluded that the efficiency of the power line communication systems can greatly improved by using DS-CDMA with turbo code method.

REFERENCES

[1] C. Hensen and W. Schulz, " Time Dependence of the Channel Characteristics of Low Voltage Power – Lines and its Effects on Hardware Implementation," AEÜ Int'l. J. Electronics and Communications, Vol.54, No.1, Feb. 2000, pp. 23–32.

[2] H. Philipps, "Modelling of Powerline Communication Channels," Proc. 3rd Int'l. Symp. Powe - Line Commun. and its Applications, Lancaster, UK, 1999, pp. 14–21.

[3] M. Zimmermann and K. Dostert, "A Multipath Model for the Power line Channel," IEEE Trans. Communications, Vol. 50, No. 4, April. 2002, pp. 553–59.

[4] M. Zimmermann and K. Dostert, " Analysis and Modeling of Impulsive Noise in Broad – Band Power Line Communications," IEEE Trans. Electromagnetic Compatibility, Vol. 44, No. 1, Feb. 2002, pp. 249–58.

[5] M.B. Pursley, "Direct-Sequence Spread-Spectrum Communications for Multipath Channels," IEEE, Microwave Theory and Techniques, Vol. 50, Issue 3, March 2002, pp. 653 – 661.

[6] G. Mandyam and J. Lai, "Third-Generation CDMA System for Enhanced Data Servides," Academic Press, 2002.

[7] C. Berrou, A. Glavieux, and P. Thitimasjshima, "Near Shannon Limit Error - Correcting Codings and Decoding : Turbo Code," In proc. IEEE ICOC, 1993, pp.1064-1070.

[8] S. Jiang, X. F. Su, D. L. Xiao and H. Sun, " Simplification on Log - MAP Algorithm and its Application in Raylaeigh Channel," In proc. IEEE PACRIM, 2000,pp. 231-233.

[9] S. Haykin and M. Moher, "Modern Wireless Communications," Prentice-Hall,2005.

[10] L. X. Zhong; M. Z. Gang; Y. Y. Zheng; C. Y. Min, "A simplification of the Log-MAP algorithm for turbo decoding " In Proc. IEEE Asia - Pacific Conference on Circuit and System, Vol. 2, 6-9 Dec. 2004, pp.1057 - 1060 .

TCP/IP Protocol over Power Line Communication System Contaminated with Impulsive noise

Oraya Rattanakanokkan, Suvepon Sittichivapak and Kriengkai Vonglodjanaporn
Department of Telecommunication Engineering, Faculty of Engineering, King Mongkut's Institute of Technology Ladkrabang (KMITL), Bangkok, Thailand 10520 Tel +66-2737-2500 Ext.5028
Email: oraya_rat@hotmail.com

***Abstract*- In this paper, we present the throughput, probability of bits error and average retransmission on various signals to noise ratio when comparing of M-ary parameter and bits rate of Power Line Communication (PLC) system base on the physical layer. Our study indicates that the system using TCP/IP and M-ary FSK modulation scheme for solving packet loss and packet corrupt correction that is affected by impulsive noise channels can provided the high efficiency and throughput enhancement.**

I. INTRODUCTION

Nowadays, one of wireline communication technology that are attractive for the provision of narrow-band communications that is Power line Communication (PLC). It uses existing electric lines to transmit data communication for home users or small business. Power lines in-house are low voltage lines on the basic of European standard, in particular the European CENELEC standard EN 50065 [1]. The advantage of using PLC is that it can reduce or eliminate the cost of wiring new networks. However, the noises in PLC are present in many types. The typical noises over power line are background noise, thermal noise, narrowband noise, impulsive noise etc. This paper, our main interest is impulsive noise and ignores other noises. An impulsive noise have caused by variety of sources, such as switching noise, adverse channel environments in a communication system, clicks from computer keyboards, and so on.

The main contribute of this paper is proposed to use TCP/IP and M-ary FSK modulation for studying the performance of PLC that is affected by impulsive noise. Simulation results are given to support the scheme in terms of the probability of bits error, average packets retransmission and throughout compared with signal to noise ration (SNR) when M=2 and 4. In order to, our can be analyze the optimum performance of system and reliability.

The remainder of this paper is organized as follows. Section II reviews the architecture and standard of the PLC, Impulsive noise model, M-ary FSK modulation scheme and protocol stack respectively, section III describes the simulation, section IV presents the simulation results, and section V describe the conclusions

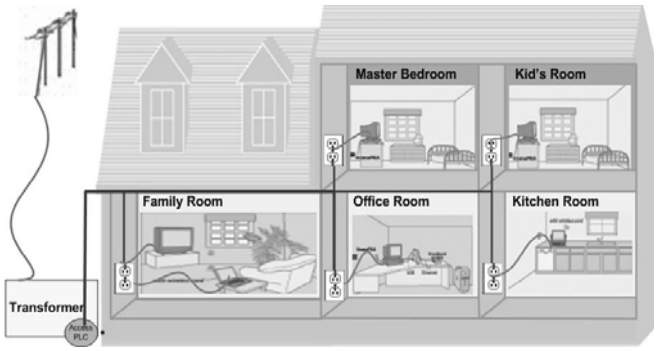

Figure 1: Typical Architecture of PLC

II. POWER LINES

A. Power Line Architectures and Standard

In power line system where the transmission medium is the electrical power network based on the European CENELEC standard EN 50065 include parameters as show in Table I. This standard rules the use of frequency range from 3 to 148.5 kHz on Low voltage while the range from 95 to 148.5 kHz is for the use, mainly, within buildings and operating home users. The architecture of PLC system is shown in Fig. 1. With the systems provided, the user can be send-receive data via power lines that are already installed. The data will be transferred data with TCP stack protocol. With the chosen modulation scheme of M-ary FSK, this M-ary parameter is the number of frequencies used in the modulated signal. Using M-ary FSK, a binary 1 for a high frequency and binary 0 for low frequency [2-4].

TABLE I
PARAMETER AND STANDARD PLC

Parameter	PLC
Standard	EN 50065 (specific standard)
AC frequency	50 or 60 Hz.
Low Voltage level	220 - 400 V.
Frequency range for in-house	95 - 148.5 KHz.
Transmission Rate	1 - 10 Mbps
Usable distance	about 500 meter
Work law	use send - receive data by electric lines in house

B. Impulsive Noise Model

Impulsive noise is non-stationary, binary state sequence of impulse with random amplitudes and random instances of occurrence. An impulsive noise sequence can be modeled as an amplitude-modulation binary state sequence, and express as [5-6]

$$n_I(m) = n(m)b(m) \tag{1}$$

Where *b(m)* is binary-value random sequence of ones and zeros, that signals the presence or absence of noise pulse, and *n(m)* is random noise process. the autocorrelation and power spectrum are express as binary state function depend on the "on/off" state of impulsive noise at time m. A real impulsive-type noise sequence, $n_I(m)$, as the output of channel filter excited by an amplitude modulation random binary sequence as

$$n_I(m) = \sum_{k=0}^{P-1} h_k n(m-k) b(m-k) \tag{2}$$

Where h_k is impulse response of a filter that models the duration and the shape of each impulse.

An alternative for an impulsive noise sequence is binary model, in which the state S_0 corresponds to the "off" condition when impulsive noise is absent; in this state, the model emits zero-valued samples. The state S_1 corresponds to the "on" condition; in this state the model emits short-duration pulses of random amplitudes and durations. The probability of a transition from state S_i to state S_j is denoted by a_{ij}. In its simplest form, as shown in Fig.2, the model is memoryless, and the probability of a transition to state S_i is independent of the current state of the model. In this case, the probability that at time t+1

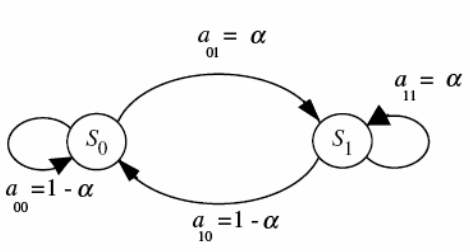

Figure 2. A binary-state model of an impulsive noise generator.

the signal is in the state S_0 is independent of the state at time t, and is given by

$$P(s(t+1)=S_0 \mid s(t)=S_0) = P(s(t+1)=S_0 \mid s(t)=S_1) = 1-\alpha \tag{3}$$

where s_t denotes the state at time t. Likewise, the probability that at time t+1 the model is in state S_1 is given by

$$P(s(t+1)=S_1 \mid s(t)=S_0) = P(s(t+1)=S_1 \mid s(t)=S_1) = \alpha \tag{4}$$

In general, the power line is share by all of users connected that impulsive noise may be present different on time of day depend electronic device are plug-in.

C. M-ary FSK

The M-ary communication scenarios that the M-ary is form multi-level of symbol. These symbols are indexed m by the integers 0 through M-1. In here, we consider the M-ary Frequency Shift Keying (M-ary FSK) where the source wishes to send one of M symbols. The M signal waveforms, u_0, u_1,… u_{M-1} or u_m, that are available to the transmitter. The u_m controls a switch that selects the modulated frequency from a bank of M oscillators. The modulation is continuous phase at the edges of symbols. Mathematically can write as

$$u_m(t) = \sqrt{\frac{2E_s}{T_b}} \cos\left(2\pi f_c t + 2\pi m \Delta f t\right) \tag{5}$$

where $E_s=kE_b$ is the energy per symbol, $T=kT_b$ is the symbol interval, f_c is carrier frequency, and Δf is the frequency separation between successive frequencies that is, $\Delta f = f_m - f_{m-1}$ for all $m = 0,1,2,\ldots,M-1,\ 0 \le t \le T$, when M is an integer power of 2and $f_m = f_c + m\Delta f$.

D. Protocol Stack

TCP/IP is a communication protocol stack designed to provide a reliable data stream between two hosts. It is a popular means of communicating data over a network. A reliable transport typically uses a connection-oriented to establish connection [7]. The data can be transmitted from transmitter to receiver on time digital duplex (TDD) channel. In a TDD that shares carriers between the uplink and downlink, the resource being switched in time so users are allocated one or more time slots for uplink and downlink transmission. The main advantage to TDD operation is that it allows asymmetric flow which is more suited data transmission. Therefore, the PLC system presented in this paper operated base on TDD scheduling algorithm, which is basically operated with the by-exchanges of round-robin policy, many be wasted by exchanges of POLL or NULL packets even when there no data waiting for transmission in queues. The transmitter will transmit and receive from receivers that are allocated address and are active at that time. If there is nothing to send, the transmitter may either omit that receivers or transmit a NULL packet.

III. SIMULATION

The TCP/IP over PLC system of this simulation as show in Fig. 3 that consist of three parts: 1) Transmitter 2) Noise and Receiver, respectively.

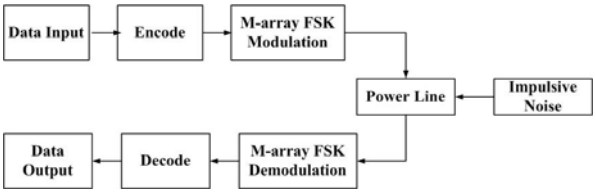

Figure 3. Block diagram of system.

Method of the transmitter is describes as follows. The input data are encoded by binary code and then modulated using M-ary FSK modulation, M-ary parameter vaule are set to 2 and. 4 over TDD channel with TCP/IP protocol. Outputs from the transmitter are sent to the receiver via power line. The received signal includes the effect of impulsive noise channels, with zero mean and 1-sided power spectral density. In the receiver, the received signals are demodulated and sent to decoder module. This received data stems are compared against with the input data stems from the transmitter. The differences from the comparison are used for calculating the BER. The program simulated of this paper, as show in Fig.4

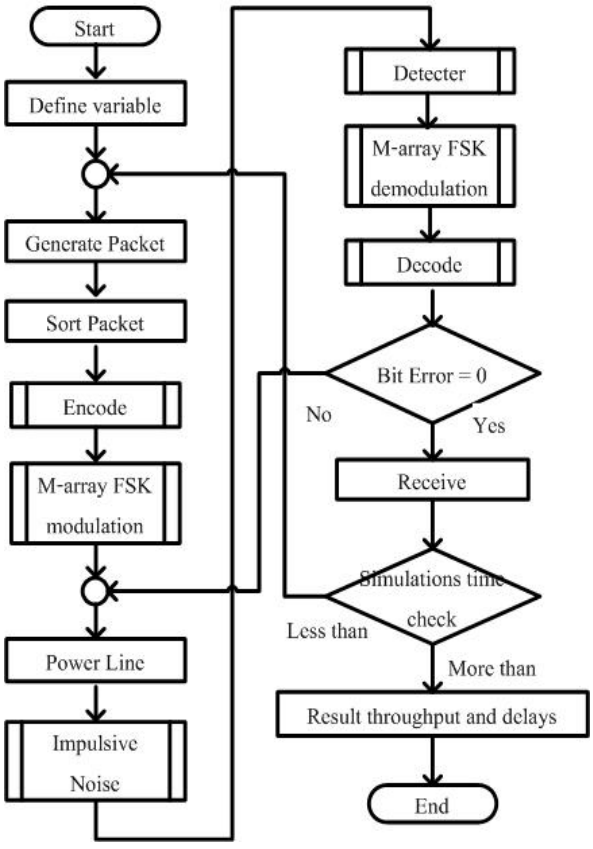

Figure 4. Flow chart of TCP/IP over PLC system contaminated with Impulsive noise

This paper uses TCP/IP protocol for flow control. Packet loss and packet corruption are main problems in PLC system. We solve these problems using TCP/IP. An acknowledgment (ACK) is generated only after the receiver receives the data correctly. TCP transmitter is guaranteed that the data have reached the receiver correctly when it receives an ACK. Also, Negative Acknowledgement (NAK) is generated when the packet loss or packet corruption. In the case that binary code cannot correct the packet corruption, the NAK packet is send out to the transmitter for requesting packet retransmission. Then, the transmitter will keep retransmitting the packet until it corrects.

IV. SIMULATION RESULTS

In this section, we present simulation results that show performance improvement of PLC system when using TCP/IP and M-ary FSK modulation scheme. In the simulation, we compared M-ary parameters of FSK modulation that are two and four. The bit rates used for M=2 are 10 kbps, 20 kbps, 30 kbps and 20 kbps, 40 kbps, 60 kbps for M=4. For the noise on power line, we considerate impulsive noise and ignore other noise. Therefore, we indicate the occurrence of impulsive noise with various SNR from 0 to 12 and amplitude of impulsive noise.

Fig. 5 shows the probability of bits error. The data contaminated with impulsive noise of PLC for the case of M=2 and M=4 when various bit rate. The result shows that the probability of bits error decreased when SNR increases (decreased noise). And in the case of M=4 the probability of bits error is lower than in the case of M=2 at same the symbol rate, that the symbol rate of M=4, if we rewrite in bit rate form it has double value of M=2. In the same trend, Fig. 6 shows the average packets retransmission decreases as SNR increases. However, the both figures have show in the relation between the data transmission and the average packets retransmission when the data has a few bit errors rate, the number of average packets retransmission is also low.

Fig. 7 shows the throughput is succeeding packets complete in transmission. They illustrate the throughput of data using TCP/IP over PLC system that has effect of impulsive noise. The curves present the different throughput that has performed by TCP/IP and M-ary. The results of increasing M-ary value, which can be increase throughput due to one symbol, have number of bits increasable. At M=4 that has throughput higher than M=2 and the throughput will be limit to maximum bit rate of each M-ary value, which depends the effect from impulsive noise as show in SNR. According to the throughput curve where SNR is equal to five (Selected SNR value can be seen all vary M-ary) the throughput of M=4, bit rate=20 kbps approaches the maximum bit rate more rapidly than M=2, bit rate 10 kbps that represent the same symbol rate and the both M=2 and M=4 at the symbol rate increases to 20 symbols/s, 30 symbols/s and show the same result as previous above.

Therefore, the relation of all simulate figures when considered the throughput of M=4 and bit rate =20 kbps these are given the optimum performance of system because this M-

ary value can be transfer many data and low probability of bits rate. Both values are conceded for simulation result that shows perform of TCP/IP protocol and M-ary FSK method. In this perform increasing the noise immunity of data transmissions and perform can be improve performance of PLC system.

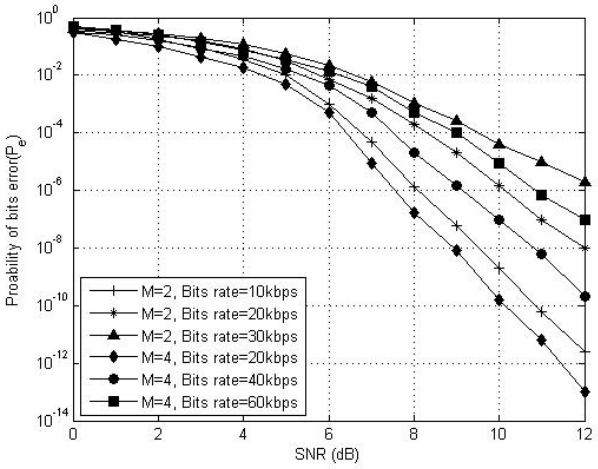

Figure 5. Probability of bits error versus SNR when M=2 and 4

V. CONCLUSION

In this paper, we presented a simulation of procedure to evaluate the throughput of PLC system with corrupted by impulsive noise that we considered data transmission on TDD channel used TCP/IP protocol and M-ary FSK method. An advantage of TCP/IP designed to provide a reliable data stream between two hosts and M-ary FSK increased the noise immunity of modulation format that data receive have correction and reliability. Therefore, the simulation results also indicate that the TCP/IP and M-ary FSK method can provide a useful tool for performance improvement.

REFERENCES

[1] K. Dostert, *Powerline Communications,* Prentice-Hall, Inc., New Jersey, 2001, pp. 73-76

[2] N. Pavlidouetal., "Power Line Communications: State of the Art and Future Trends", *IEEE Communication Magazine,* Abril 2003.

[3] J. G. Proakis, M. Salehi and G. Bauch, *Contemporary Contemporary Communication Systems, 2nd ed* Prentice-Hall, Inc., New Jersey, 2001, pp. 311-315

[4] F. J. Canete et al., "Modeling and evaluation of the Indoor Power Line Transmission Medium", *IEEE communication Magazine,* Abril 2003.

[5] S. V. Vaseghi, B.P.Millner, "Speech Recognition in Impulsive Noise", *IEEE Proc., ICASSP-95*, vol.1, pp. 437-440

[6] S. V. Vaseghi, *Advanced Digital Signal Processing and Noise Reduction, 2nd ed,* John Wiley & Sons Ltd., New York, 2000, pp. 355-376

[7] A. Chockalingam, "Performance of TCP/IP Protocol Stack on Correlated Fading DS-CDMA Wireless Link", *IEEE Transactions on Vehicular Technology, vol.49,* January 2000.

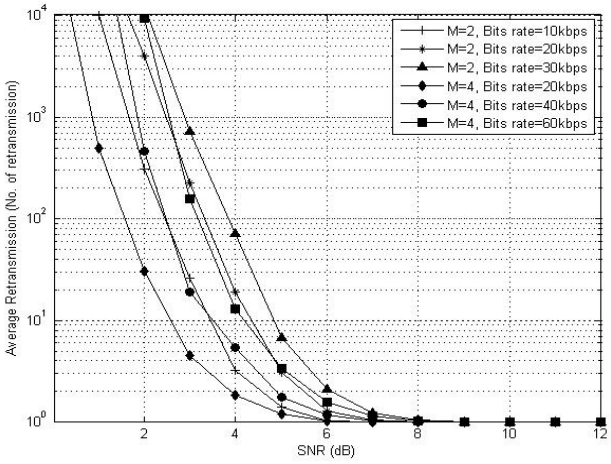

Figure 6. Average Retransmission versus SNR when M=2 and 4

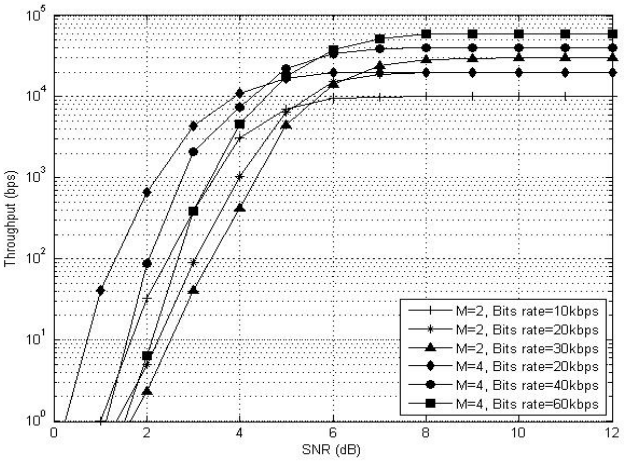

Figure 7. Throughput versus SNR when M=2 and 4

Chaotic Direct Sequence Spread Spectrum for Power line Datacommunication

[1]Narumon Thummakerd, [1]Suvepon Sittichivapak, [2]Kidsanapong Puntsri
[1]Faculty of Telecommunication Engineering,
King Mongkut's Institute of Technology Ladkrabang Bangkok 10520, Thailand
[2]Department of Electronics and Telecommunication Engineering, Faculty of Industrial Education
Rajamangala University of Technology Phranakhon, Bangkok 10300, Thailand

***Abstract*- Recently, communication in power line system is very interesting in data communication because of convenient and inexpensive solution. In this paper, we propose the modulation data with binary Chaos Shift Keying (CSK) scheme. Additionally, we combined the data with Direct Sequence Spread Spectrum (DSSS) technique for data communication in power line system, and impulsive noise is considered.**

I. INTRODUCTION

Chaotic signals are nonperiodic waveforms, generated by deterministic systems, which are characterized by a continuous "noise-like" broad power spectrum. In the time domain, chaotic signals appear random signals what are indistinguishable [1]. Chaotic systems are characterized by "sensitive dependence on initial conditions" [2]; an arbitrarily small perturbation eventually causes a large change in the state of the system. Equivalently, chaotic signals decorrelate rapidly with themselves. The autocorrelation function of a chaotic signal has a large peak at zero and decays rapidly. Thus, chaotic signals share many of the properties of stochastic processes; they also possess a deterministic structure that makes it possible to generate noise-like chaotic signals in a theoretically reproducible manner. In particular, a continuous-time chaotic system can be used to generate a wideband noise-like signal with robust and reproducible statistical properties.

Due to its wide-band nature, a signal comprising chaotic basis functions is potentially more resistant to multipath propagation than one constructed of sinusoids. Thus, chaotic digital modulation, where the digital information signal to be transmitted and mapped to chaotic waveforms, is potentially useful in propagation environments where multipath effects dominate. [3]

In this paper, we investigate the chaotic signals over direct sequence spread spectrum (DSSS) for power line data communication with impulsive noise. The article composes of the following sections. Section II, we mainly use the theory of binary Chaos Shift Keying (CSK) and DSSS communication system to explain and study the power line and impulsive noise model in power line system. By the way, the simulation model is proposed in section III, while section IV presents the result of the simulation itself. Finally, the conclusions are given in section V.

II. THEORY

A. Chaotic signal and Binary Chaos Shift Keying(CSK)

In a binary Chaos Shift Keying (CSK), each symbol is represented a weighted sum of chaotic basis functions, $g_j(t)$. The binary CSK transmitter is shown in Fig.1. The sample function $s_i(t)$ composes with $g_1(t)$ or $g_2(t)$, depending on whether symbol "1" or "0" is transmitted. From Fig. 1, the required chaotic basis functions could be generated by different chaotic circuits or produced by a single chaotic generator, whose output is multiplied by two different constants.

In both cases, the transmitted binary information is mapped to the bit energies of chaotic sample functions. In the chaotic digital communications systems, as in the conventional communications schemes, the transmitted symbols could be recovered using either coherent or noncoherent demodulation techniques.

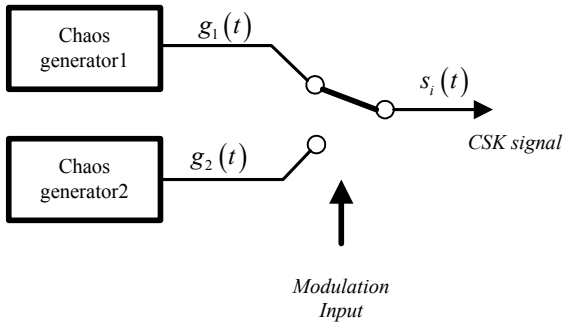

Fig. 1 Chaotic Sift keying modulation.

B. Coherent Demodulation of CSK

Coherent demodulation is accomplished by reproducing copies of the basis functions in the receiver, typically by means of a synchronization scheme [3]. When the synchronization is exploited, the synchronization scheme must be able to recover the basis function ($s_i(t)$) from the corrupted received signal.

If a single sinusoidal basis function is used, a narrow-band phase-locked loop (PLL) will be used to recover it. Noise corrupting the transmitted signal is suppressed because the low-pass property of the PLL. When an inherently wideband chaotic basis function is used, the synchronized circuit must

also be wideband in nature. Typically, both of the amplitude and phase of the chaotic basis function must be recovered from the received signal. Because of the wideband property of the chaotic basis function, narrow-band linear filtering cannot be used to suppress the additive channel noise. Fig.2 exhibits a coherent (synchronization-based) receiver using the binary CSK modulation with two basic functions, $g_1(t)$ and $g_2(t)$. The synchronization circuits, which is working at the receiver base, will try to reproduce the basic functions again but including the as-received noisy sample function, $r_i(t) = s_i(t) + n(t)$.

An acquisition time, Ts, is allowed the synchronization circuits to lock the incoming signal. The recovered basis functions $\hat{g}_1(t)$ and $\hat{g}_2(t)$ are then correlated with $r_i(t)$ for the remainder of the bit duration, T. A decision is made on the assumption of the relative closeness of $r_i(t)$ when $\hat{g}_1(t)$, and $\hat{g}_2(t)$ is multiplied by the observation variables, z_{i1} and z_{i2} respectively.

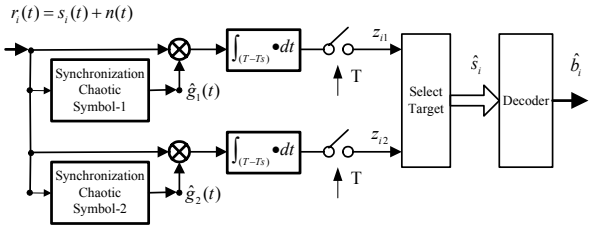

Fig. 2 Coherent Demodulation of CSK

C. *Direct Sequence Spread Spectrum system*

The main objective of spread spectrum (SS) sequence is protecting the communication signals from any interfere and illegally exploit by unintended users. In some contexts, it is important that the unintended user could not determine whether a communication signal is active or not. [2]

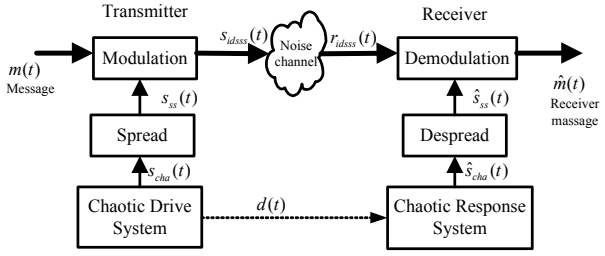

Fig. 3 Chaotic Spread Spectrum System.

This requirement of the communication signal must provide a low probability of detection (LPD) and commonly referred to LPD signals. In some case, a low probability of detection (LPD) also named a low probability of intercept (LPI) which is provide some different in the working processes. LPI signals may be detectable but extracting features from them is very difficult. Frequently, both of LPD and LPI capabilities are desired in application [2].

To achieve these objective, a SS system usually operates with communication bandwidth, B, which is much wider than the massage bandwidth. Since a bit interval of T seconds results in a message bandwidth of approximately $1/T$ Hz, the communication bandwidth consists of approximately BT non-overlapping signal intervals. The different SS module strategies could utilize this wide communication bandwidth to create uncertain released signal in a different way.

In Direct Sequence (DS), a broadband modulation waveform is used to spread the signal energy over the entire communication bandwidth at each real time of application. An unintended user, who uses an intercept bandwidth of $1/T$ Hz, will only receive a fraction of the signal power. On the other hand, if the intercept bandwidth is equal to the communication bandwidth, B, the received noise will increase with a factor BT. Vice versa, the SNR of the intercepted signal is significantly reduced.

According to the DS, the required signal spreading is achieved by modulating of the message signal with a noise-like waveform that has nearly uniform power spectrum over the communication bandwidth. The modulation waveform should display considerately complicate and unpredictable when it is viewed by an unintended user even it is being completely deterministic and easily recreated at the various communication receivers, in facts. So, the chaotic signals are the good candidates to work as the modulation waveform for SS communication systems because of their broadband and noise-like characteristics. Furthermore, the synchronized chaotic systems can be used at the communication receivers to coherently de-spread the received signal.

Many variations of SS communication systems which created on synchronized chaotic systems are possible to apply in a real application. For example, Fig. 3 illustrate one possible approach. The primary signal processing components of the transmitter consist of a chaotic drive system, followed by a whitening filter and a DS modulator. The receiver consists of a synchronizing chaotic response with the subsystem followed with identical whitening filter and a demodulator. The RF section of this system has been omitted. We assume that the transmitter and communication receiver are linked through a common drive signal, $d(t)$. The transmitter and communication receiver form a chaotic drive system and a stable response subsystem, respectively. Then, the output signal of the response subsystem, $\hat{s}_{cha}(t)$, will synchronize to the signal, $s_{cha}(t)$, present at the transmitter. The purpose of the whitening filter is to product a nearly uniform power spreading from the chaotic signal, $s_{cha}(t)$. The whitened signal, $s_{ss}(t)$, will be a nearly ideal spreading signal because of its broad and uniform Fourier spectrum. If the message signal, $m(t)$, is multiplied by $s_{ss}(t)$ at the modulator, the transmitted signal, $s_{idsss} = m(t) + s_{ss}(t)$, will also have a broad Fourier spectrum. By property scaling $s_{ss}(t)$, the average power in s_{idsss} will nearly the same as the average power in $m(t)$. Since s_{idsss} occupies a bandwidth which is larger than the bandwidth of $m(t)$ by a factor of approximately BT, they

must be decrease with the power spectral density of s_{idsss}. By making the communication bandwidth very large, the transmitted signal, in principle, can be hidden in the background noise which would make it very difficult to detect.

The communication receivers can easily recover the transmitted message since the dispreading signal, $\hat{s}_{ss}(t)$, will identify the spreading signal, $s_{ss}(t)$. Once the transmitter and receiver have synchronized, the demodulator performs the reverse of the modulation operation then $m(t)$ can be recovered. The required SNR of the recovered message is as same as the requirement from the conventional system which is having the same error rate with the same baseband modulation scheme.

D. Power Line system

Cable of power line system is not designed for transmitted data in telecommunication. It provided high impedance and more noise. The noise is impulsive noise. Fig. 3 shows the Bernoulli-Gaussian Model in impulsive noise process. The random time of the presence of the impulses is modeled by a binary Bernoulli-Gaussian, $b(m)$; and the amplitude of the impulses is modeled by Gaussian process, $n(m)$.

Probability of Bernoulli process [4], $b(m)$, is as the following equation:

$$P_B\left(b(m)\right)=\begin{cases}\alpha & for \quad b(m)=1\\ 1-\alpha & for \quad b(m)=1\end{cases} \tag{1}$$

Means of Bernoulli process is:

$$\mu_b=\mathrm{E}\left[\left(b(m)\right)\right]=\alpha \tag{2}$$

and a variance is:

$$\sigma_b^2=\mathrm{E}\left[\left(b(m)-\mu_b\right)^2\right]=\alpha\left(1-\alpha\right) \tag{3}$$

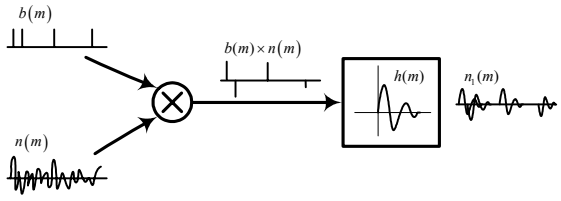

Fig. 3 The impulsive noise model.

E. Power-line Network Channel Model

Channel transfer function of a matched transmission powerline follows. In the case of unmatched junctions, part of a propagating signal reflects back to the transmitter at branch junctions due to impedance mismatch and the remainder travels through [5]. The propagation along a wire follows, so one can easily express the multipath network channel model as:

$$H(f)=\sum_{i=1}^{N} g_i e^{-\alpha(f)d_i} e^{-j\beta(f)d_i} \tag{4}$$

where N is the number of significant arrived paths at the receiver, di is the length of ith path and gi is the weighting factor of the ith path. This formulation is basically similar to what has been mentioned in [6], however, with a model for propagation constant that is appropriate for overhead MV power-lines, rather than underground cables in Europe.

III. SIMULATION MODEL

From the flow chart in Fig. 4, the main block composes of the carrier, full signal, modulation, spreading sequence, noise, de-spreading sequence, filter, and demodulation.

At first, Carrier block is chaotic signal that generated by Lorenz generator. Afterward, the full massage block will add the signal from any input massage. Then the modulation block is used in modulating the CSK with full message signals. From the modulation block, the spreading sequence block spreads module signal with the Bernoulli sequence method. The noise block is generated by Bernoulli-Gaussian Model in power line system, which generates impulsive noise and added that synchronized signal into the power line data communication. In additions, the DSSS signal is generated by dispreading sequence block and the demodulation block is also uses to retrieve the binary information that already been sent.

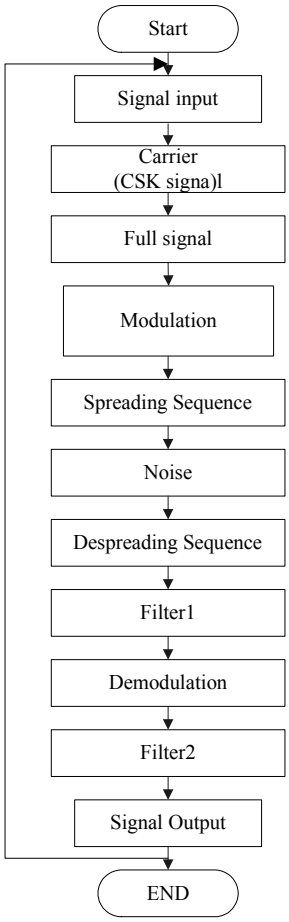

Fig. 4 Flow-chart of simulation.

IV. SIMULATION RESULTS

The simulation results is shown in Fig. 5, 6, and 7. The input signal '01100010' shows in Fig. 5(a). Fig. 5(b) presents the chaotic shift keying signal for modulation. Fig. 5(c) shows the plotted signals after passed out from the module and the spread spectrum processes. Fig. 5(d) illustrates signal receiver that pass dispreading sequence and filter1 processes. The Impulsive noise in the power line system and chaotic generator is shown in the Fig. 6 and 7, respectively.

V. CONCLUTION

A method of generating a chaotic sequence in direct sequence spread spectrum system takes advantage of their noise-like features. From the simulation results, it is clearly observed that the power line communication system has impulsive noise. However, from the simulation method, it is able to receive the correct massages just as same as the massage before encoding one.

For the future plan, we will focus on the bit error rate of CSK and DSSS method including the performance of the system when any part of modulation has changed.

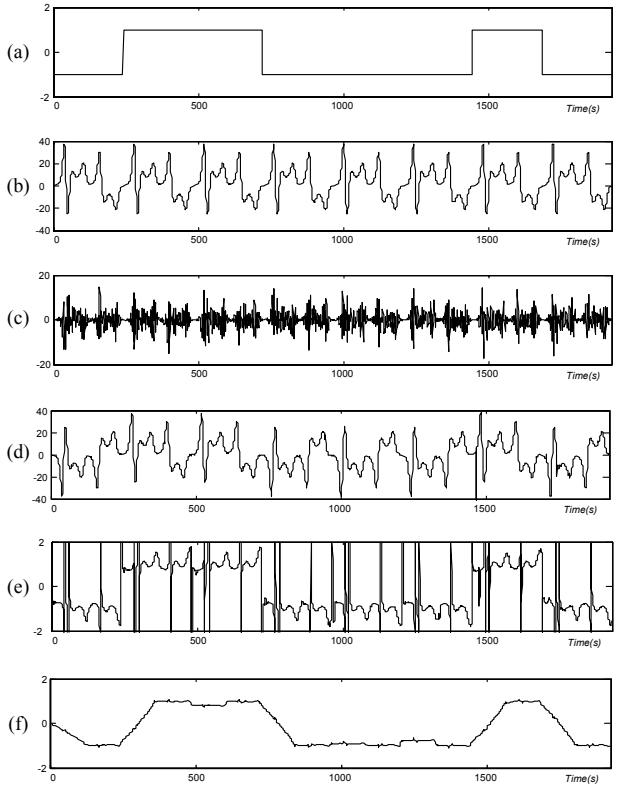

Fig. 5 Signal waveform: (a) Input signal '01100010', (b) CSK modulation signal, (c) Transmitter signal, 5 (d) Despreading signal, 5(e) Demodulatonion signal and 5(f) Output signal

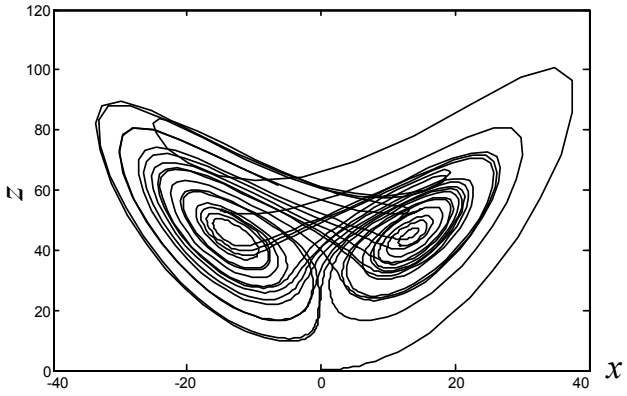

Fig. 6 Chaotic generator is generated by Lorenz generator.[5]

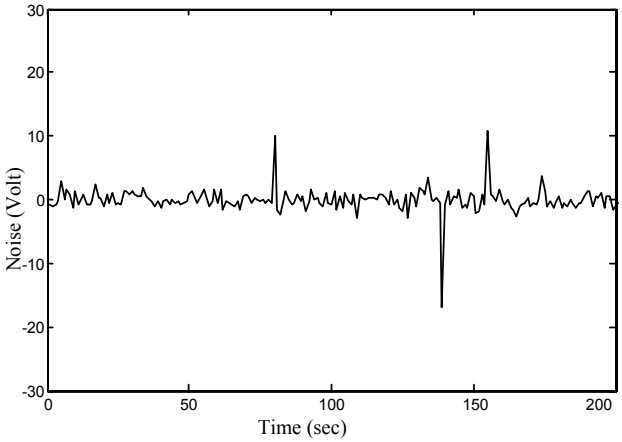

Fig. 7 Impulsive noise signals.

REFERENCES

[1] Sathyanaraya S. Rao and Sephen P. Howare, *Corrleation Performance of chaotic Signals in Spread Spectrum System,* Proc. 1996 IEEE Digital Signal Processing Workshop, Loen, Norway, September 1-4,1996, pp 506-509.

[2] Kevin M. Cuomo, Alan V.Oppenheim, and Steven H.Isabelle, *Spread Spectrum Modulation and Signal Masking Using Synchronized Chaotic Systems.* Research Laboratory of Electronics Massachusetts institute of Technology Cambridge, Massachusetts, Febuary,1992, pp.19-22.

[3] Jerry L.Hudgins, Theodore F.Bogart Jr., Kartikeya Mayaram, Michael Peter Kennedy, Geza Kolumban, *Nonlinear Circuit*,CRC Press LLC, 2000, pp.24-29.

[4] Saeed V. Veseghi. *Advanced Digital Signal Processing and Noise Reduction,* 2nd edition. New York,2000, pp.360-361.

[5] Cheng, David K., "Fundamentals of Engineering Electromagnetic," New York, Addison-Wesley, 1992.

[6] Zimmerman M., Dostert, K., "A multipath model for the power-line channel," IEEE Transactions on Communications, Vol. 50, No. 4, pp. 553-559, April 2002.

Evaluation Methods for Active RFID Equipments in Road Access Services

L. Kovavisaruch, *Member IEEE*, T. Sanpechuda, J. Wisanmongkol, and C. Mitrepant
National Electronics and Computer Technology Center (NECTEC), 112 Thailand Science Park,
Phahon Yothin Road, Klong Luang, Pathumthani 12120, THAILAND

***Abstract*—Position and orientation of the RFID reader and tags play an important role to the system performance in the actual installation. However, most RFID manufacturers rarely provide information on how to install the reader and tags for a specific application. In this paper, we investigate two methods to determine the best installation position of the RFID reader for road access services. An Anechoic Chamber Test and simulation provide the basic information for reader installation in the ideal environment. The field test determines the best installation position in the actual environment. The information obtained by the first method can be utilized to reduce the number of experiments in the second method.**

I. INTRODUCTION

Recently, RFID has been actively researched as a result of an announcement from Wal-Mart and US Department of Defense (DoD) who required their vendors to utilize RFID for their inventory-stock inspection by the year of 2005 [1]. RFID applications are not limited to tracking traceability logistic access control, but also widely used in transportation. In the world where security and time become a critical issue in road access control, many important places enforce vehicle to stop and verify its identity before accessing the facilities. System such as Automatic Vehicle Identification (AVI), which applied RFID technology, can be employed for security control and also help reducing the queuing time.

RFID system is a system that detects and identifies each tag based on data communication between readers and tags. The tags can be either active or passive tag. A choice between active tag and passive one is always an issue in most applications; each has significant advancetage and disadvantage. The active tag provides longer reading-range and greater penetration. The disadvantage of active tags is that the battery needs to be replaced every 2-3 years. Although the passive tags provide shorter range and poorer penetration than the active tags, the battery is not required for the passive tags. Besides the readers and tags, the system also includes a server for storing the information to validate the access code from the tags [2].

There are several RFID products available in the market. However, the information provided by most vendors of each product is insufficient for installation the reader and tags in the actual environment. In particular, the microwave wavelength products, of which performance effectiveness can be adversely affected by the environment factors such as humidity and metal. In addition, positions and orientation of the reader and tags also crucially affect the readability results.

This paper explains two methods to determine a position and orientation of the reader and tags for the best reception rate. The first method requires an access to either the anechoic chamber or electromagnetic simulation software to obtain the radiation pattern, while the second method is based on the actual installation. The first method provides the position for the ideal installation and it might not be the best position in the actual installation. The second method can determine the best position in the actual installation but it is time consuming process to obtained accurate results. The main advantage of the second method is that it does not require the knowledge of radiation patterns. However, the radiation patterns can be also utilized to reduce the number of experiments in the second method.

The paper is organized as follows: In Section II, brief specifications of the equipments under test are given. The outlines of the experiments are also discussed in Section II. The radiation patterns from the anechoic chamber and electromagnetic simulation are given in Section III. The detail on the experiments to determine the best position and orientation of the reader in the actual installation is given in Section IV. Summary is given in Section V.

II. EQUIPMENTS AND EXPERIMENTS

A. Equipments

In the experiment, a 2.4 GHz active RFID development kit (F2M07-KIT) made by Free2move Company is used as shown in Figure 1. The kit consists of RFID reader, tags, and configuration software. The developer can use the configuration software to encode tag information, set the communication protocol between reader and tags, and configure reader baud rate and output power. Detail specifications of the reader and tags are given in [3].

Figure 1 Reader and tags

The communication protocol between reader and tags is set to be Reader Talks First (RTF) so that the reader continuously transmits the signal and the radiation pattern can be measured in the anechoic chamber. In all experiments, the reader is set to transmit at the maximum power of 0 dBw or 1 watt to obtain the highest performance of both reader and tags.

The reader and tag utilize meander line antenna as shown

in Figure 2. The meander line antenna often used in the application that required a limited space, such as reader or tags. Nevertheless, its radiation pattern resembles monopole antenna. Unfortunately, the radiation patterns of the meander line antenna cannot be expressed in closed forms. In order to obtain the radiation pattern, either the full wave electromagnetic simulation or measurement in the anechoic chamber is required. It can be seen from Figure 2a that the reader is designed to utilize the diversity technique to obtain the best signal form both antennas. Since both reader and tag use the same type of antenna, we measure and simulate only the radiate pattern from the reader.

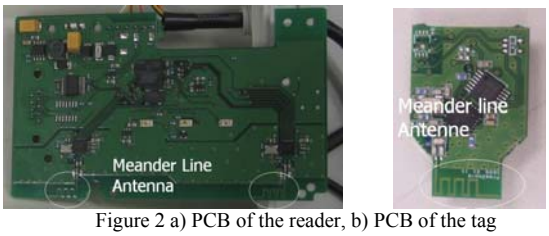

Figure 2 a) PCB of the reader, b) PCB of the tag

B. *Experiment*

An objective of the experiment is to determine the best location and orientation of the reader and tags placement on the car windshield. In this experiment, we first measured the radiation pattern of the reader to obtain the direction of the maximum transmitted power. Figure 3 illustrates the flowchart for the first experiment.

Then, the best location and orientation of the reader in the actual installation are determined by the readability of the tag. The reader is attached to either next to booth station or pole and faced the front to the road. The readability test is performed by increasing the reader tilt angle with respect to the wall toward the vehicle. If the readability is increased with respect to the previous tilt angle, then we continue to increase the tilt angle until the readability of the tags decrease. The tilt angle before decreasing in readability of the tags is the optimum reader orientation. The procedure for this experiment is summarized in Figure 4. Seven tags are attached to the windshield to determine the best tags location for all tilt angles.

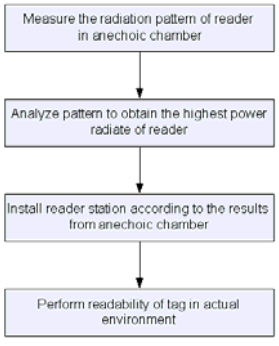

Figure 3. Flow chart for the first experiment

III. IDEAL TEST

In this section, the radiation patterns are obtained so that the best position and orientation of the reader can be determined. The radiation pattern can be obtained by either testing in the anechoic chamber or full wave electromagnetic simulation. The results from both methods are presented in this section.

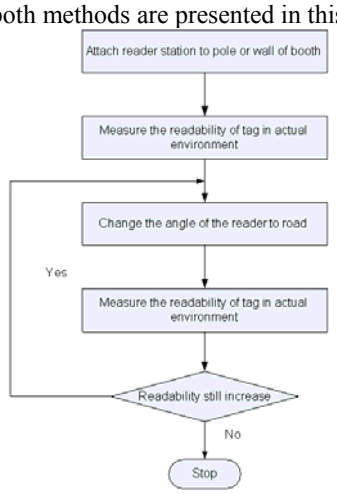

Figure 4. Flow chart for the second experiment

A. *Radiation Pattern Measurement in The Anechoic Chamber*

It would be beneficial to know the 3-D radiation pattern of the antenna. However, it is very difficult and unnecessary to measure the complete representation of antenna radiation properties [4]. Therefore, in this paper, we measured only radiation pattern of E-field of reader in E-plane and H-plane in the anechoic chamber, which considered as a controlled environment. The anechoic chamber is provided by Electrical and Electronic Product Testing Center (PTEC). Both field components (E_θ and E_ϕ) have been measured. Figure 5 shows test setup in the anechoic chamber for the radiation pattern measurement. For the H-plane, we face the reader directly to the horn antenna and then rotate it by 360° with respect to the stationary horn antenna. For the E-plane, the reader lied directly to the horn antenna and then is rotated 360° with respect to the horn antenna.

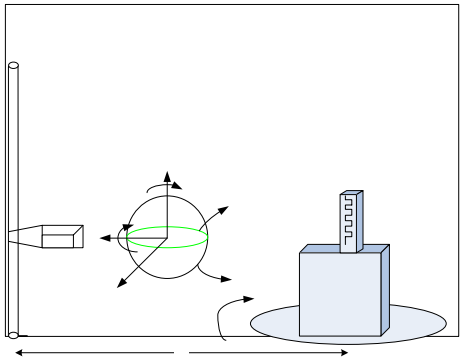
Figure 5. Testing in anechoic chamber for reader radiation pattern

The dot line in Figure 6 shows the normalized polar plot of E-field radiation pattern in H-plane. From the Figure 6, we observe that the reader radiation pattern resembles to the azimuth radiation pattern of monopole [7]. The reader almost equally radiates electromagnetic field for all angles. However, the reader radiates the lowest power at about 110° to the receiver. The power and signal cables in the back of the PCB, as shown in Figure 2, might cause the power drop at this angle.

The solid line in Figure 6 illustrates the normalized polar plot of E-field in E-plane. From Figure 6 suggests that the radiation pattern resembles the elevation radiation pattern of monopole antenna, that is it radiate most power in one side of the antenna. It can be also seen that the reader radiates most of the total power when it is rotated about 160° with respect to the horn antenna. In other words, it radiates most power from the top right corner of the reader. The directivity of this antenna can be obtained from this equation

$$D = \frac{P(\theta,\phi)_{\max}}{P(\theta,\phi)_{ave}}$$

where $P(\theta,\phi)_{\max}$ is the maximum power pattern and $P(\theta,\phi)_{\text{ave}}$ is the average radiation power pattern. From the measured radiation pattern, the directivity is 3.67 dB

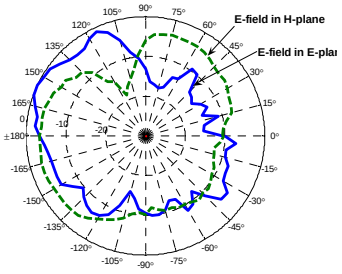

Figure 6. Radiation pattern of total E field in H plane and E Plane from testing in anechoic chamber

B. *Simulation Results*

While testing in anechoic chamber is the best way to obtain the realistic radiation patterns, it is expensive and time consuming process. If full wave electromagnetic simulation software is available, the radiation pattern can be obtained by the simulation. By using in house FDTD software, we can obtain the radiated pattern of the reader antenna. Figure 7 displays radiation pattern of E-field in E-plane and H-plane, respectively.

From the simulation, the radiation patterns form both azimuth and elevator resemble to those from the theoretical model of a dipole antenna [7]. The result is different from the measured radiation pattern since the simulation does not include the effect from other electronic components and other metal parts in the reader. However, the direction of maximum radiating power is similar to the measured radiation pattern.

IV. FIELD TEST

We propose a technique to determine the best position for the reader in the actual installation with knowledge of radiation patterns. The radiation patterns help to determine the initial set up of the reader and it will reduce the number of experiments in the actual installation. However, this method is also valid when the radiation pattern is not available but it will require more number of experiments.

A. *Experimental Setting*

A field experiment has been performed on an actual road in front of National Electronics and Computer Technology Center (NECTEC) building. The experiment consists of two main cases: 1) readability of tags when the reader placement at its highest and lowest radiated power, and 2) readability of tags when attached the reader to side of wall or pole.

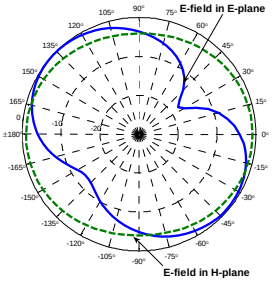

Figure 7. Radiation pattern of Total E field in H plane and E plane from simulation

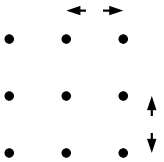

Figure 8. Grid of reader station at one measurement

In each measurement, the reader locates half wavelength space on the grid as shown in figure 8, which was 6.25 cm in this case. This type of measurement commonly uses to characterize both the small-scale and the large-scale statistics of the channel [6]. We repeated each measurement 180 times. The placement of the first test is based on the radiation patterns from in Section III. We installed the reader with the best direction (to place the top right corner of the reader faced down to the windshield of the vehicle as shown in Figure 9a). The reader station is 3 m high. We have measured the reading-range for 10 and 15 m. Then, we compare the results from the worst direction of reader to the tags. We also attach 7 tags on the windshield of vehicle to observe the best tags position on the windshield as shown in Figure 10.

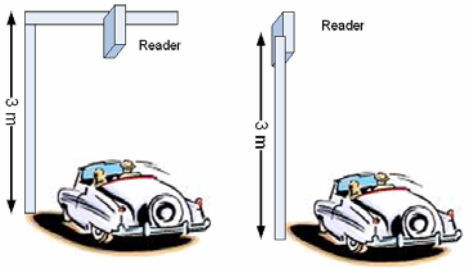

Figure 9 a) Field test the first case, b) Field test the second case

In the second test, we have attached the reader next to the pole at the height of 3 m from the floor, as shown in Figure 9b, and facing the front of the reader to the road. Then, we compare the results of the readability of tag when the reader is rotated with 30° increasing step with respect to the pole. In every measurement, the vehicle is located 10 m away from the reader station. At the same time, we also observe the best tags location on windshield of the vehicle by attaching seven tags on the windshield.

B. *Results*

The results from the first test are shown in Table 1. At 10 m, while the average readability of the best direction was

97.06%, the average readability of worst direction was 53.34%. As the distance between reader and tags is increased to 15 m, the readability of the worst direction deteriorates to 1.43 % while there was still 80% chance of reading the tag in the best direction.

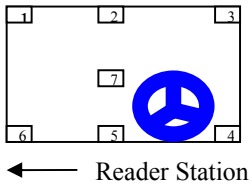

Figure 10 Tags positions on the windshield.

When the reader position is set to radiate maximum power to the tags according to the radiation pattern at the distance of 10 m, the readability is insensitive to the tag position. All tags can be read more than 90%. When the distance between the reader station and vehicle is increased to 15 m, the readability of tag is affected by tag position. Tag 1 gives the best performance while tag 5 gives the worst performance. In the worst radiating direction, only tag 1,3,6,7 can be read more than 50% and most tags cannot be read when the distance is 15 m.

TABLE 1 READABILITY OF EACH TAG IN FIRST CASE

Tag	Readability in best direction (%)		Readability in worse direction (%)	
	10 m	15 m	10 m	15 m
1	100	98.89	80	3.89
2	93.89	92.78	49	0
3	98.89	81.11	80	0
4	100	88.89	38.89	1.11
5	97.22	16.11	13.8	0
6	98.33	95	56.67	0
7	91.11	90	55	5
Ave	97.06	80.40	53.33	1.43

The results from the second test are shown in Table 2. The results suggest that the readability of tag has increased as we rotate the reader towards the car. The average readability reaches the peak at the angle of 120°, and then starts to decline at the angle 150°. These results are consistent with the radiation pattern in E-plane in Section III.

In terms of the tag position on the windshield of the vehicle, tag 4 outperformed the rest. Tag 1 and 6 were the second best. On the other hand, tag 5 provided the worst performance.

V. SUMMARY

Most specifications of RFID products provide the reading range for the ideal case, which is not suitable for the actual application. Besides, there is no information about the reader or tag radiation pattern that will help installation to obtain the most effective performance from the equipment. By testing in the anechoic chamber, we can obtain radiation patterns. However, this kind of test is often too expensive. Full wave simulation of the antenna is an alternative method for obtaining the radiation patterns. When the radiation patterns are known, the best orientation of the reader can be determined. We also perform readability tests when the reader is installed in the typical environment without any knowledge of radiation patterns. The results suggest that by increasing the tilt angle of the reader in respect to the pole towards the vehicle, the average readability is increased and the best orientation can be obtained. The best angle for readers in the field test is also consistent with the radiation pattern in H-plane from the anechoic chamber. The radiation patterns from simulation can also be utilized to estimate the best angle. Although, the radiation patterns from the simulation are not exactly the same as the radiation pattern from the anechoic chamber test, this information can be used to reduce number of experiments in the field test.

In terms of tags position, results show that the closest tags to the reader station do not always provide the best performance. This may cause by the surrounding environment or even the type of the vehicle. However, from the test, the nearest tags do provide the second best performance. This brings to another intrigue issue to find the relationship between the position of tag on windshield and the type of vehicle which will be further investigated.

The usability of active RFID equipments on the road access service is highly possible with some limitations on the tag and reader placement for the best performance. The readability of tags will perform differently in diverse environments and at the different vehicle speeds. Hence, it is always recommended to test practically in actual conditions before making the final decision.

TABLE 2 READABILITY OF EACH TAG IN SECOND CASE

Tag / °	1 (%)	2 (%)	3 (%)	4 (%)	5 (%)	6 (%)	7 (%)	Ave (%)
0	29	17	43	87	4	26	1	27
30	100	97	99	100	53	97	41	75
60	100	99	100	100	12	100	98	78
90	96	91	92	79	7	97	95	72
120	100	77	50	96	98	99	97	79
150	90	89	24	94	48	99	41	63
Ave.	86	78	68	93	37	86	62	

ACKNOWLEDGMENT

Authors would like to thank Dr. Kraison Anchaleeworapan, and Mr. Anake Meemoosor from PTEC for their support on equipment testing in Anechoic Chamber and also a great support on experimentation from Dr. Urachada Ketprom, and Mr. Anukool Noymai.

REFERENCES

[1] M. A. Jones, D. C. Wyld, J.W. Totten, "The adoption of RFID technology in the retail supply Chain" *Coastal Business Journal* Vo. 4 No. 1, Spring 2005 p 29-42

[2] K. Finkenzeller, RFID Handbook: Fundamentals and Applications in Contactless Smart Cards and Identification. New York: Wiley,2003

[3] Free2Move:F2M07 [Online] Available: http://www.free2move.se/pdf/RFID_broschyr.pdf

[4] Electrical and Electronic Products Testing Center (PTEC). [Online] Available: http://ptec.nectec.or.th/

[5] W L. Stutzman, G. A. Thiele, "Antenna theory and design ", 2nd Ed, John Wiley, c1998.

[6] C.C. Chong Y. Kim S.S. Lee , "UWB indoor propagation channel measurements and data analysis in various types of high-rise apartments", *Vehicular Technology Conference*, Vol. 1, pp. 150- 154, Fall. 2004

[7] J. D. Kraus and R. J. Marhefka, "Antennas:for all applications", 3rd edition, McGraw Hill, 2003.

Data Recording with FAT16 in Removable Media of RFID Handheld Reader

Anukool Noymai, Urachada Ketprom and Chaichana Mitrpant
National Electronics and Computer Technology Center (NECTEC)
112 Thailand Science Park, Phahon Yothin Road, Klong Luang, Pathumthani 12120, THAILAND

***Abstract*--Different types of media such as hard disk, flash drive and memory card require different memory formats. File Allocation Table (FAT) file system is ideal for use with devices that are optimized for quick media removal. FAT16 is a common file system for Windows family of operating systems in hard disk and also in removable media. When transferring data from hard disk to other types of media, the memory format of hard disk must be preserved. Even though the typical memory card size of RFID handheld reader is small (512MB or less), it must preserve the file system format of the hard disk and thus reduces the storage capacity. Different memory space will be allocated when not only identification number, but also with additional information is recorded for the RFID offline handling purpose. Based on the understanding of how data are recorded with FAT16, RFID users can benefit the most from the limited memory capacity in removable media. This paper aims to inform RFID users with options on recording data into the removable media with the adjustment regarding the number of identified items and any related information to the items.**

***Index Terms*—handheld RFID, removable media, FAT**

I. INTRODUCTION

Recently, Radio Frequency Identification (RFID) has been the topic of interest within both academic and industry domains [1]. RFID system consists of three major components: reader, transponder (tag) and data server. The communication between tag and reader uses a defined radio frequency protocol transmitted through signals as shown in Figure 1. Applications of RFID range from systems such as animal identification, access control, to supply-chain management. Employing RFID technology is considered a good approach in automated identification of products, with the prospect that tags could eventually replace barcode used ubiquitously at present. Comparing to barcode, RFID provides better reading range, requires no line-of-sight, and allows multiple products to be read simultaneously. RFID reader has two types: stationary and handheld. A stationary reader is fixed at a read location while handheld can move to anywhere. Handheld RFID reader records data into its internal memory or removable media. A cable is a mean to transfer recorded data in the internal memory to personal computer (PC), but a cable is not necessary when transferring data from a removable media to PC.

In order to transfer data from the removable media into the hard disk of a PC, the memory format FAT must also be transferred along with the data. In addition to the format, data will be arranged in the removable media according to the standard of FAT file system. Currently there are three FAT file system types: FAT12, FAT16, and FAT32. The FAT file system is ideal for removable media that is used in consumer electronic devices, such as digital cameras, media players, Flash drives and so on. FAT12 is, of course, the only file system that can be used on floppy disks. Windows supports FAT16 and FAT32 for hard disk volumes and removable media [2]. For the simplification of the process, the researchers begin with the implementation of the FAT16 on the removable media instead of FAT32. The concept of optimization records is always the goal of application developer; Sandisk released an application note on optimization of CF Host Operation for improve the read performance [3]. This paper applies this similar concept to optimize memory space for each RFID data types and its related information.

Anatomy of FAT16 file system

File Allocation Table (FAT) 16 structure information consists of 6 parts: (1) *Master Boot Record (MBR)* (2) *Volume ID* or *Boot Sector* (3) *Reserved Sector* (4) *FAT1*, *FAT2* (5) *Files and Directories* and (6) *Data Region* [3]. Each part is used for locating data in the file system.

Master Boot Record (MBR)

A *Master Boot Record* (MBR) is the first sector in memory (first 512 bytes). It contains a Boot Code area and partition information area accommodating up to four partitions as displayed in Figure 2. The first 446 out of 512 bytes in the MBR are assigned to the Boot Code area**.** This code is primarily used only for booting a computer from a hard disk. In case of removable media, all data in the Boot Code area is set to 0x00 because a boot code is not required. Taking up 16 bytes each, Partition 1 to Partition 4 contain data indicating the Starting Sector (SS) locations and the numbers of sectors in corresponding partitions. SS can also be referred to as the location of *Volume ID.* A memory card usually contains one partition whose information is stored in Partition 1, and Partition 2 -4 contain no data or 0x00. Next to these four partitions is the *footer* with 2-byte memory consisting of 0x55 and 0xAA. All data in the MBR area is very important because if this area is damaged, all data in the memory card will be unreadable.

Volume ID or Boot Sector

Volume ID consists of one sector with many details such as Bytes per Sector, Sector per Cluster, Number of Reserved Sector, Number of FAT, Maximum Root Directory Entries,

and Sectors per FAT. Volume ID is often the starting sector in the FAT layout system shown in Figure 3.

Reserved Sector

This area is reserved for operating systems other than windows such as DOS and OS/2 for the purpose of compatibility. In removable media, the number of sectors reserved will be indicated by the field in the Boot sector.

FAT1, FAT2

FAT1 and FAT2 hold information about cluster locations and how to connect data from these clusters together. To locate

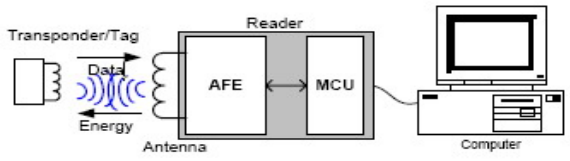

Figure 1. RFID system

FAT1, we must add the number of reserved sector in Volume ID to Starting Sector (SS) as shown in the Eq.2.

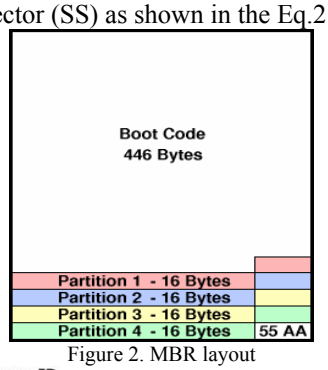

Figure 2. MBR layout

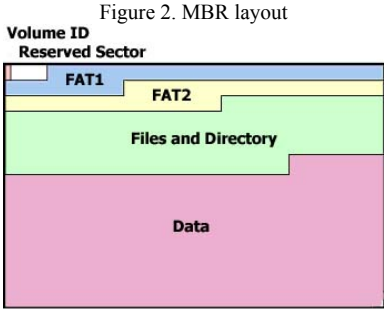

Figure 3. FAT16 File system layout

0	1	2	3	4	5	6	7	8	9	A	B	C	D	E	F
meida type		ps.		cluster 2		cluster 3		cluster 4		cluster 5		cluster 6		cluster 7	
cluster 7		cluster 8		cluster 9		cluster 10		cluster 11		cluster 12		cluster 13		cluster 14	
cluster..		cluster..		cluster..		cluster..		cluster..		cluster..		cluster..		cluster.n	

ps. = partition state

Figure 4. File Allocation Table (FAT)

0	1	2	3	4	5	6	7	8	9	A	B	C	D	E	F
file/folder name								file extension			fa	nt	create time		
create date		lad		lat		lmd		lmt		fc		fs			

fa = file attributes
nt = reserved for NT
lad = last access date
lat = last access time
lmd = last modified date
lmt = last modified time
fc = first cluster
fs = file size

Figure 5. Files and Directories Structure, Short Filename Format

0	1	2	3	4	5	6	7	8	9	A	B	C	D	E	F
41	4E	49	4D	41	4C	20	20	54	58	54	20	00	00	7A	00
00	00	00	00	00	00	00	00	00	00	02	00	00	00	00	00

A N I M A L T X T . . z

Figure 6. Data structure with a file name

0	1	2	3	4	5	6	7	8	9	A	B	C	D	E	F
41	4E	49	4D	41	4C	20	20	20	20	20	20	00	00	7A	00
00	00	00	00	00	00	00	00	00	00	04	00	00	00	00	00

A N I M A L . . z .

Figure 7. Data structure with a folder name

Then, the location of FAT2 can be calculated by adding the value of Sector per FAT (SPF) to FAT1. Both data format and memory in FAT1 are the same as in FAT2.

Data inside FAT will be grouped into clusters. A cluster contains data in hexadecimal format. Cluster #0 and #1 are pre-determined by the type of media and partition state displayed in Figure 4. Next, Cluster #2 indicates the location of the next cluster that contains the data but if Cluster # 2 contains FFFF, this indicates the end of data in that cluster.

$$\text{Volume ID Starting location} = SS \quad (1)$$

$$\text{FAT1 Starting location} = SS + Res \quad (2)$$

$$\text{FAT2 Starting location} = SS + Res + SPF \quad (3)$$

$$\text{Files and Directory Starting Location} = SS + Res + (2*SPF) \quad (4)$$

$$\text{Data Region Starting location} = SS + Res + (2*SPF) + \ldots + ((MRDE*32)/BPS) \quad (5)$$

SS = Starting Sector, Res = Reserved, SPF = Sector per FAT,
MRDE = Maximum Root Directory Entries, BPS = Bytes per Sector

Here is an example of setting SS equal five. This number "five" behaves as a pointer to indicate the Volume ID sector. This sector #5 contains all information of Volume ID such as Bytes per Sector, Sector per Cluster, Number of Reserved Sector, Root entries, and Sectors per FAT. This information will further be used to calculate the starting sector of FAT1 and FAT2 as in Eqs.2-3. The number of sectors used up for FAT memory space is limited by Sector per FAT in the field of Volume ID. Next, it is possible to identify the starting location of Files and Directory and Data Region by Eqs.4-5 using information retrieved from the data in Volume ID as well.

Files and Directories

Information in FAT indicates the location of Files and Directory. When the first sector location of a file or a directory is known, the next step is to use data in the cluster fields of FAT to link data between sectors. An entry in File and Directories area contains 32 bytes. The first 8 bytes of memory in the sector are translated to the name of file in ASCII. Another 3 of 8 bytes is the extension file name. The next 5 bytes and 16 bytes are information of time stamp for modification of time and date as shown in Figure 5. The name of the recorded file is set to follow the short filename format of 8 characters only for simplification. The file extension ".txt" or "0x54 0x58 0x54" in the record is an example shown in Figure 6. For data recording in the directory (folder), the data in the extension field of 3 bytes will contain 0x20 0x20 and 0x20 indicating that it is not a file but a folder instead as shown in Figure 7.

Data Region

This area contains data records inside the sectors. The capacity of sector will be indicated in the *Volume ID* as Bytes per

Ssector. The starting location of data region can also be calculated using Eq. 5. The location of the data region must follow the files and directories area as in Figure 3.

II. RFID DATA RECORDS IN FAT16 FILE SYSTEM

In an RFID handheld reader, two main alternatives to record data in a removable medium are such that recording all information of an item into a file, or recording only the unique numbers of items into a file and leave other information to database server.

1. One ID in one file (OID)

This alternative is the simplest format for recording. Each file contains only one ID and that file has enough memory space for recording information associated with that ID. The only disadvantage is that it creates many storage files and requires extra time to locate each ID. One possible use of OID is to update the status of an animal such as feeding time and amount in the farm management application. Farm labor can update information through RFID handheld reader by typing information from the handheld keyboard and saving it to the memory card. It is necessary to reserve an equal capacity of each file to guarantee enough memory space. Typically, not all recorded files require the same memory resulting in inefficient memory utilization. Searching for an ID must follow the procedure for locating data from Eqs.1- 5 in the previous section. This procedure will be repeated in each file. This alternative is suitable for acquiring detailed information of an item in addition to an ID. To store this information in limited memory, a memory card can only save small numbers of items. Human involvement is necessary in the process of updating the information for often status changes of an item on the site.

2. Many IDs in one file (MID)

This alternative is for collecting only ID information so it is possible to include more IDs in the memory card than the OID alternative. There is only one file recorded in MID. Searching an ID is also a faster process because MID requires a locating procedure once for only one file in the card. Memory capacity of the card is used sufficiently. Only ID number is recorded and thus there is not enough information to decipher these ID numbers unless connecting to the data server. Limited information is suitable when only checking IDs is required. This is a typical recording format in the present. Majority of RFID handler associates RFID usage to replace a barcode system because of its unique number and non-line-of-sight advantage. Only ID is important for tracking the status of such application and RFID handheld reader will be less expensive when the function of keying update information is not required. This is useful for application that needs no human involvement for updating information. MID alternative is suitable for storing as many IDs as possible in a limited memory of a removable media for the application with the first priority on the amounts of ID detection.

IV. CASE STUDIES OF DATA RECORD

RFID in livestock application identifies an animal with a unique number. For the purpose of comparison in this paper, we set the unique identification number to be 15 digits following the draft of animal ID in Thailand [4]. In this paper, we make an assumption to record 15 digits of Animal IDs separated into 3 digits of country, 2 digits of animal species, and the other 10 digits are the running number of the animal. In addition to 15-digit ID, an RFID handheld reader may also retrieve updated information by farm labor and records that information into the removable media. To record unique IDs of animal into a file called “animal.txt” previously shown as an example in Figure 6, the ASCII data will be recorded with the details of country code, animal code and running number of the animal as shown in Figure 8. A simple way to understand the data recording scheme is to discuss two recording alternatives with the following examples.

1. One ID in one file (OID)

To record each animal ID into a file, extra information for farm management will be added to the previously stored information into the continuous sectors shown in Figure 9. As an example, the first ID is saved into the file “animal01.txt” while the second ID is saved into the file “animal02.txt”. The detailed of FAT system for this structure is displayed in Figure 10. Although equal memory capacity is reserved for all files but information saved in the file can be different so number of sectors used to record data will also be different.

Details in the “animal01.txt” file are country code, animal code and running number of animal and extra information of day month year to record this ID as shown in Figure 11. The left part of the figure indicates the ASCII data in the recorded sectors. To explain this ASCII data, the right part of the figure is shown only for comparison purpose for animal ID of 764091111111111 and date of record on 07/01/29 or January 29, 2007. Details in the “animal02.txt” file are country code, animal code and running number of animal and extra information of quantity of food as shown in Figure 12.

2. Many ID in one file (MID)

Figure 13 specifies three ID sample records in both ASCII data and also the 15 digit information for explanation. The ASCII data is the exact record in the FAT16 system. MID recording scheme can record many IDs into only one file which simplifies ID locating procedure from locating volume ID, Reserved, FAT1 FAT2, File and Directories and Data Region in Figure 10 only for one file. In the case of many files in OID, this procedure must be repeated for every file.

Combination of OID and MID might be used for utilizing the memory capacity in the memory card. Given the memory card with capacity of 1 gigabyte, and unique identification number of an animal is 15 bytes, it is possible to make decision on number of files and memory of bytes per file utilizing the memory capacity in the card. We assume that a file takes the space of a whole cluster, which contains multiple sectors of size 512 Bytes. For newer versions of Windows from Windows2000, the possible numbers of sectors in a cluster must be in the set $\{2^n: 0 \le n \le 7\}$. Furthermore, the maximum number of clusters for FAT16 is $2^{16} = 65{,}536$. Based on this information, we would like to identify appropriate the number of sectors per cluster so that a fifteen-byte identification

number with the following data can be stored efficiently in a 1 Gigabyte memory card: date (6 bytes), quantity of feed in kg. (2 bytes), and premises ID (13 bytes). Therefore, an entry of record would occupy 15 + 6 +2 + 13 = 36 bytes. We first investigate all possible numbers of sector by creating the data table. From Table 1, one can see that the number of sector per cluster must be in the set $\{2^n: 5 \le n \le 7\}$; otherwise, the number of cluster would exceed the number specified (2^{16} = 65,536). Maximum number of entries in a file will be the number of cluster divided by the entry size. The number of entries per file from this process is not always the integer number, in case of the decimal number, it must be rounded down. The decimal fraction reflects the memory that cannot store a complete record and is considered wasted. The exact number of used memory is the rounded number multiplied by the size of one entry record. It is possible to see the wasted memory in a cluster by comparing the available memory BPC in Table1 with the used BPC shown in Table 2. To utilize the capacity for the most entries of ID records of 15 bytes with least memory waste, the number of sector per cluster must be set to $\{2^n: n = 7\}$ for the number of files or total clusters of 16384, while this cluster utilization for an entry of 36 bytes creates the same result in number of entries. One can decide on the most number of clusters instead for the purpose of file categorization.

V. CONCLUSION

In this paper, we specified two options of data recording: One ID One file (OID) and Many IDs One File (MID). OID is an option for handling offline information very often. Additional information such as date and premises are commonly reserved for updating the status in the central database system. This option is suitable only for limited numbers of data entries to be identified because memory space must be reserved in advance. While MID is an option for only IDs requirement from multiple entries and this option simplifies the ID search within one file in contrast to the OID option that must search many files before finding an ID. This characteristic of each option implies the OID is appropriate for an application with low speed and small data such as animal identification, but MID will be more appropriate for an application with high speed and high data such as item identification in the warehouse. Utilizing memory in the memory card requires decision from RFID user. User can obtain the most benefit from removable media when user can identify the characteristics of the data required for each application.

ACKNOWLEDGMENT

Author would like to thank Mr. Poonperm Makapun for his support on FAT16 information study.

REFERENCES

[1] K. Finkenzeller, RFID Handbook: Fundamentals and Applications in Contactless Smart Cards and Identification. New York: Wiley,2003

[2] Microsoft [Online] Available: http://download.microsoft.com/download/5/b/5/5b5bec17-ea71-4653-9539-204a672f11cf/LocFileSys.doc

[3] Sandisk, Optimization of CF Host Operation, Application Note Version 1.1 Document No. 80-36-00233 , February 2005

[4] J. Dobiash , "FAT16 Structure Information" [Online] Available: http://home.teleport.com/~brainy/fat16.htm

[5] NECTEC, *Draft of Thailand National Animal ID,* August 2006

Figure 8. Details in the "animal.txt" file

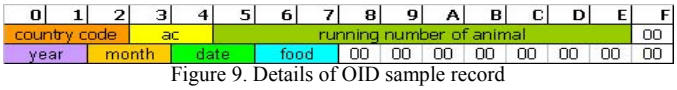

Figure 9. Details of OID sample record

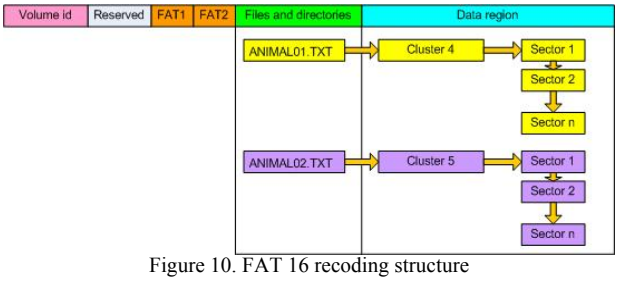

Figure 10. FAT 16 recoding structure

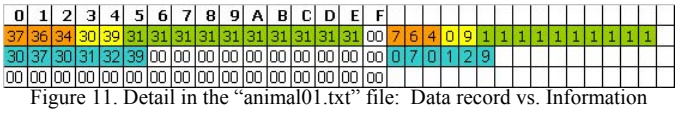

Figure 11. Detail in the "animal01.txt" file: Data record vs. Information

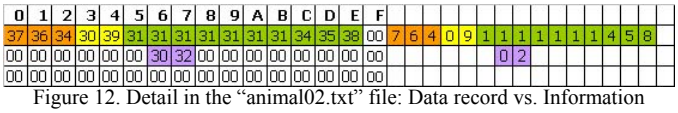

Figure 12. Detail in the "animal02.txt" file: Data record vs. Information

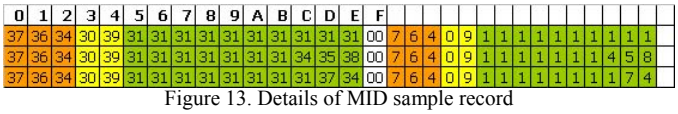

Figure 13. Details of MID sample record

Table 1. Combinations of different set up for FAT 16 system

BPS	SPC	BPC =BPS*SPC	Total clusters 1GB/BPC	EPC = BPC/15	EPC = BPC/36
512	1	512	2097152	34.13	14.22
512	2	1024	1048576	68.27	28.44
512	4	2048	524288	136.53	56.89
512	8	4096	262144	273.07	113.78
512	16	8192	131072	546.13	227.56
512	32	16384	65536	1,092.27	455.11
512	64	32768	32768	2,184.53	910.22
512	128	65536	16384	4,369.07	1820.44

Table 2. Comparison of used memory for different data records

	Data 15 bytes per entry (ID only)			Data 36 bytes per entry (ID + date+ quantity+premises)		
Total clusters	Floor (EPC)	Total Entries	Used BPC	Floor (EPC)	Total entries	Used BPC
65536	1,092	71,565,312	16,380	455	29,818,880	16,380
32768	2,184	71,565,312	32,760	910	29,818,880	32,760
16384	4,369	71,581,696	65,535	1820	29,818,880	65,520

BPS = byte per sector, SPC = sector per cluster, BPC = byte per cluster, EPC = entry per cluster, Total clusters = number of clusters in 1 gigabytes, Total entries = number of entries in 1 gigabytes

Performance Improvement of Paging Extensions for Mobile Internet Protocol based on Regional Registration and Multicasting

Andrianus Yofy and Watit Benjapolakul
Department of Electrical Engineering, Chulalongkorn University, Bangkok 10330, Thailand
Email: yofyptmn@yahoo.com, watit.b@eng.chula.ac.th

***Abstract*-Paging extensions for Mobile Internet Protocol (P-MIP) only reduces the number of registrations in Mobile Internet Protocol (Mobile IP). P-MIP still uses similar registration procedure of Mobile IP which has high number of lost packets and long handoff latency if the distance between the Mobile Node and Home Agent is large. In this paper, we propose to combine P-MIP, Mobile IP Regional Registration, and multicasting to improve the performance of P-MIP. Simulation results show that the proposed method can reduce the signaling cost, the number of lost packets, and handoff latency of original P-MIP significantly.**

I. INTRODUCTION

Mobile Internet Protocol (Mobile IP) [1] is a proposal from Internet Engineering Task Force to support internet in mobile and wireless devices. Mobile IP assigns two IP addresses to Mobile Node (MN): Home Address which is assigned by the Home Agent (HA) in the home network and Care-of Address (CoA) which is assigned by a Foreign Agent (FA) in the foreign network. CoA is updated every time the MN changes its network. The MN detects whether it has changed its network by checking the Agent Advertisement message that is sent periodically by every FA. Whenever it moves to a new network, the MN registers to the HA through the present FA. When there is a node called Correspondent Node (CN) wants to send data to the MN, it must first send data to the HA. The HA then forwards the data to the MN through the latest FA.

As the basic protocol for mobile internet, Mobile IP still suffers a lot of problems, e.g. security, handoff latency, encapsulation overhead, triangle routing, and signaling load [1]. Paging Extensions for Mobile IP (P-MIP) [2] is one of the proposals that improve the performance of Mobile IP. P-MIP differentiates the state of the MN, which can be active or idle. An active MN is a MN which has just sent or received data. P-MIP uses paging to handle the location management of an idle MN. The wireless system uses paging procedure to search an idle MN when there is a message for that MN. Here, an idle MN does not need to register its precise location to the system whenever it moves. Paging decreases the signaling overhead related to registration and location system database updates. Paging also reduces the power consumption of the MN since the idle MN does not need to register with the system whenever it roams. However, P-MIP only concentrates to reduce the number of registrations and still uses the same registration method as Mobile IP, in which the registration may have long handoff latency and high number of lost packets if the distance between the MN and the HA is large.

In this paper, we propose to enhance the performance of P-MIP in terms of the number of lost packets and handoff latency. We use regional registration so that the MN does not need to register to the HA if it moves to the new network. We employ Protocol Independent Multicast-Sparse Mode multicast protocol [3] to send the data packets from Gateway Foreign Agent (GFA) to the FAs in the vicinity of the MN to make the MN able to accept the packets as soon as possible after handoff.

Several works have been done related to our work. Ref. [4] improved the performance of P-MIP by combining it with Mobile IP Regional Registration [5]. Ref. [6] combined P-MIP and Mobile IP Post Registration to reduce the number of lost packets and handoff latency of P-MIP. Ref. [7] has proposed Multicast for Mobility Protocol (MMP) which utilizes Core Based Trees multicast protocol in local domain to provide efficient location management and routing for the MN.

This paper is structured as follows. Section II discusses about the overview of P-MIP, Mobile IP Regional Registration, P-MIP Regional Registration, and P-MIP Post Registration methods. Section III explains our proposed method which is applied during MN's active time. Section IV presents the performance evaluation. Finally, section V concludes this paper and gives explanations of our future work.

II. OVERVIEW OF PAGING EXTENSIONS FOR MOBILE IP, MOBILE IP REGIONAL REGISTRATION, PAGING MOBILE IP REGIONAL REGISTRATION, AND PAGING MOBILE IP WITH POST REGISTRATION METHODS

A. Paging Extensions for Mobile IP (P-MIP)

Two or more networks construct a paging area in P-MIP. P-MIP extends the Agent Advertisement message in Mobile IP to contain a "P" bit to support paging. An active MN has to register to HA whenever it moves to a new network. In contrast, an idle MN does not need to register in the same situation and only registers when it changes its paging area or if there is data destined for that MN. If a CN wants to send packets to the MN, it will send them to the HA. The HA then delivers the packets to the registered FA. The registered FA first finds whether it has any information in the record for the MN. If a record exists, then that FA checks the operational state of the MN. If the MN is active, the FA forwards the packets to the MN. If the MN is

idle, the registered FA sends Paging Request messages to all other FAs that reside in the same paging area, as well as broadcasts the Paging Request on its own network. When the idle MN which has moved to another network receives that message, it registers with the HA through the current FA. After receiving Registration Reply message, the MN sends Paging Reply message to the registered FA through the present FA to inform its new location. After the registered FA receives Paging Reply message, that FA forwards any buffered packets toward the MN through the present FA. The incoming packets from the HA are then forwarded to the MN via present FA.

B. Mobile IP Regional Registration

In Mobile IP, the MN registers to the HA every time the MN changes its network. This causes high signaling load and long signaling delay during registration if the distance between MN and HA is large. Mobile IP Regional Registration [5] solves this problem by introducing a new entity called Gateway Foreign Agent (GFA). GFA is a local administrator for some FAs. When moving from one network to another within the same GFA, the MN does not need to register to the HA. Instead, the MN performs regional registration with the GFA by using a pair of registration messages. Regional Registration Request and Regional Registration Reply messages are used locally within a domain by the MN, the FAs, and GFA for regional registration. Mobile IP Regional Registration can reduce the signaling load and delay significantly. This also means that Mobile IP Regional Registration has lower number of lost packets and handoff latency than Mobile IP.

C. Paging Mobile IP Regional Registration

Ref. [4] proposed to combine P-MIP and Mobile IP Regional Registration. In this scheme, when there are packets for the MN, the HA sends the packets to the GFA. The GFA then checks the operational state of the MN. If it is active, the GFA encapsulates the packets and forwards them to present FA. The FA then delivers the packets to the MN. If the MN is idle, the GFA buffers incoming packets and sends Paging Request messages to all FAs that reside in the same paging area under that GFA. When the MN receives the Paging Request message, it registers to the GFA through the current FA. After receiving the Regional Registration Reply message, the MN sends a Paging Reply message to the GFA. Finally, the GFA sends the buffered and incoming packets to the MN.

D. Paging Mobile IP Post Registration

Ref. [6] improved the performance of P-MIP by using the idea of Mobile IP Post-Registration. Registration delay method is proposed in two phases, i.e. when the MN is active and when there are incoming data packets for the MN. Post-Registration scheme is used during active state to reduce the movement detection time. In P-MIP, the movement is detected when the MN receives Agent Advertisement message in Network Layer (Layer 3) periodically every one second. Using the Post-Registration method, the MN can detect that it has moved to another FA area fast since the MN uses Link Layer beacons which are sent every 100 ms to detect the movement.

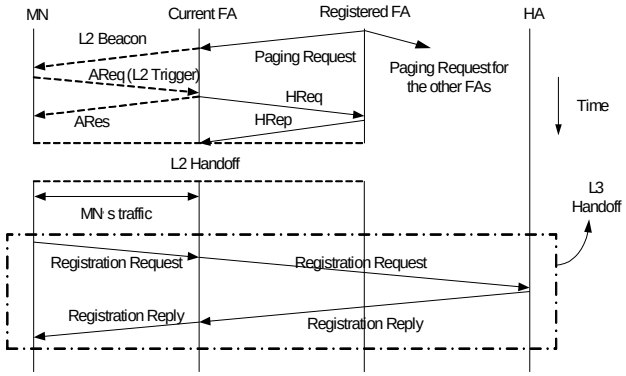

Figure 1. Signaling time diagram while the Mobile Node is entering the active state in [6].

When there are packets destined to the MN, the MN defers the registration process and keeps using the registered FA's CoA while the MN is on the current FA's subnet through the Bi-directional Edge Tunnel (BET). The BET is established between the registered FA and the current FA. Then, the MN can receive these packets fast before the MN registers to the HA. Fig. 1 shows the signaling time diagram of this work while the MN is entering the active state.

III. PROPOSED METHOD

P-MIP reduces the signaling load and power consumption in Mobile IP but still has high number of lost packets and long handoff latency. In this paper, we propose to combine P-MIP, Mobile IP Regional Registration, and multicasting to improve the performance of P-MIP. We use regional registration so that the active MN does not need to report to HA every time it moves to the new network. We employ Protocol Independent Multicast-Sparse Mode [3] to send packets from GFA to FAs in the vicinity of the MN to make the MN able to accept the packets fast after the handoff process. Hierarchical topology of Mobile IP Regional Registration is used in our work. Some FAs are grouped into two or more paging areas under the administration of one GFA. Non-overlapping paging area scheme is employed. The MN, the GFA and the FAs are assumed to support security, authentication, paging and multicasting. The hierarchical topology of the proposed method is shown in Fig. 2.

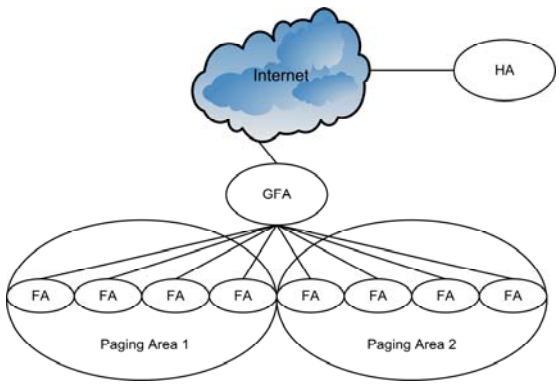

Figure 2. Hierarchical topology of the proposed method.

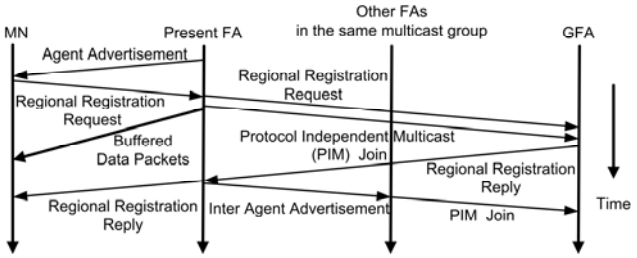

Figure 3. The signaling time diagram of regional registration of an active MN in the proposed method.

The MN is assigned with one multicast address within the GFA domain. Every FA broadcasts multicast addresses in the Agent Advertisement. The GFA uses the multicast address to multicast downlink data packets to FAs in the vicinity of an active MN. Multicasting is only applied locally within the GFA domain. If an active MN detects that it has moved to a new network, it conducts registration to the GFA. The MN uses Agent Advertisement for movement detection as in Ref. [2]. During registration, the multicast group and tree of the MN are constructed. After receiving Regional Registration Request message from the MN, the FA sends Protocol Independent Multicast (PIM) Join message to the GFA to form the multicast tree. The multicast group members are the FAs surrounding the present FA. The present FA constructs the multicast group by sending Inter-Agent Advertisement message to neighbor FAs every time the present FA receives Regional Registration Reply message from the GFA. The Inter-Agent Advertisement message contains the multicast address that neighbor FAs have to join. Neighbor FAs then join the multicast group by sending PIM Join message to the GFA. Fig. 3 shows the registration process of an active MN in the proposed method.

When there are data packets from the HA to the MN, the HA will first send the packets to the GFA. The GFA then checks the state of the MN. If the MN is in active state, the GFA multicasts the packets to the MN's multicast group. If the MN is in idle state, the GFA buffers the incoming packets and sends Paging Request messages to all FAs that reside in the last reported paging area visited by the MN. Every FA then broadcasts Paging Request message in its own area. When the idle MN receives the Paging Request message and finds that it is still located in the last registered FA, the MN sends Paging Reply message to the GFA and sets its state to be active. Otherwise, the MN conducts regional registration to GFA as explained in the previous paragraph. When the FA receives Regional Registration Reply message from the GFA, it sets the state of the MN to be active and relays the message to the MN. After receiving Regional Registration Reply message, the MN sends Paging Reply message to the GFA. The GFA then multicasts and forwards the buffered and incoming packets to the MN's multicast group. Present FA forwards the packets, while other FAs in the same multicast group buffer the packets and forward the packets as soon as the MN moves to their network. Fig. 4 shows the signaling time diagram when the HA sends packets to an idle MN in the proposed method.

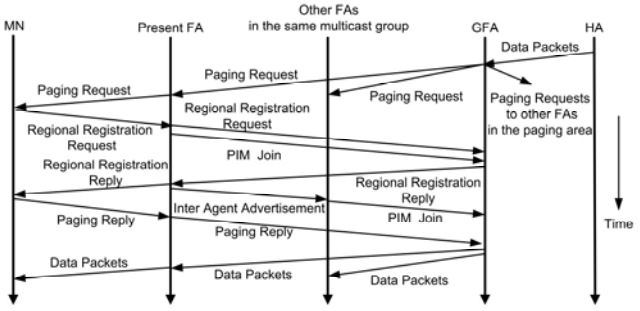

Figure 4. The signaling time diagram when the HA sends packets to an idle MN through the GFA in the proposed method.

IV. Performance Evaluation

We simulate Mobile IP, Paging Mobile IP, P-MIP Post Registration, P-MIP Regional Registration, and the proposed method using Borland Delphi 7.0. We adapt the network model in Ref. [6] in our simulation. HA sends Constant Bit Rate 500-bytes packets with 10 ms period as the traffic source. Wireless LAN 802.11 with 100 ms period of beacon is chosen to be the Link Layer. The FA broadcasts Agent Advertisement message every one second. There are two paging areas where both paging areas contain a number of cells. Each cell is associated with one FA in an overlapping cell scenario with 122 m diameter and 1 m overlapping area. We assumed that all links have 5 Mbps transmission rate and every link has 3 ms transmission delay. The active MN percentage is 5 % [2]. Protocol Independent Multicast-Sparse Mode [3] is used as multicasting protocol. We apply one GFA, one straight moving MN, and one HA in the simulation. We vary the speed of the MN and the number of hops between the GFA and the HA to evaluate the signaling cost, handoff latency, and the number of lost packets. Fig. 5 shows the simulation model.

In Fig. 6, we show the impact of MN's speed on signaling cost. There are 50 cells in one paging area. The number of hops between GFA and HA is set to be 40. The duration of the simulation is 342.259 s. There are three time periods. Every period lasts for 112 s. There are 95 % of idle time and 5 % of active time for the MN in one period.

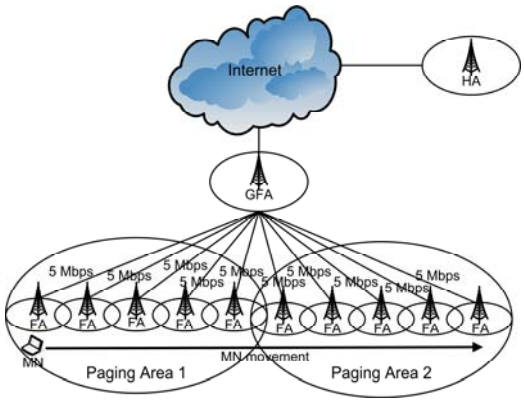

Figure 5. Simulation model with overlapping cell scenario.

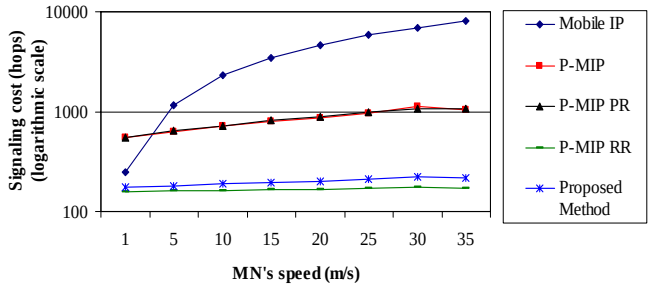

Figure 6. Signaling cost as the function of MN's speed.

Signaling cost of every method increases as the MN's speed increases. It is because of more cell boundary crossings and more registrations at higher MN's speed. The signaling cost of the proposed method is much lower than that of Mobile IP, P-MIP, and P-MIP Post Registration (P-MIP PR) since the MN only registers to the GFA and not to the far away HA. However, the signaling cost of our method is a little bit higher than that of P-MIP Regional Registration (P-MIP RR) because of increased signaling cost of the multicasting messages.

With the same model parameters, we investigate the handoff latency and the number of lost packets as shown in Fig. 7 and Fig 8. In overall, the handoff latency and the number of lost packets depend on the movement detection used by each method. P-MIP PR has the best performance since it uses Link Layer for movement detection, whereas the other methods use Network Layer (i.e. use Agent Advertisement that is broadcast every 1 second). However, the proposed method has lower handoff latency and the number of lost packets than Mobile IP, P-MIP, and P-MIP RR. It is because the MN can reduce the signaling delay by conducting regional registration to the GFA. Moreover, the MN can receive the packets fast since the present FA forwards the buffered packets to the MN after it receives Regional Registration Request message from the MN.

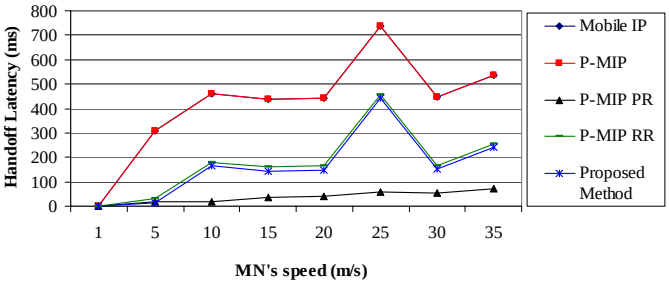

Figure 7. Handoff latency as the function of MN's speed.

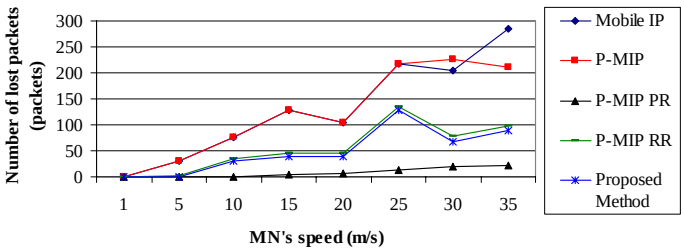

Figure 8. The number of lost packets as the function of MN's speed.

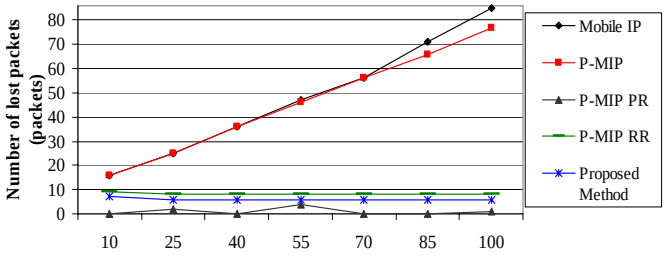

Figure 9. The number of lost packets as the function of the number of hops between GFA and HA.

We vary the number of hops between GFA and HA to see the impact on the number of lost packets. The parameters are 15 cells in a paging area, 15 m/s of the MN's speed, and one period of data with 233.934 s of simulation time. As we can see from Fig. 9, the number of lost packets in the proposed method and P-MIP RR are not influenced by the number of hops. It is not similar to Mobile IP and P-MIP where the registration messages to the HA have to experience longer delay if the number of hops between GFA and HA is increased. P-MIP PR is also not influenced by the number of hops since it can defer the registration in Network Layer and use Link Layer registration so that it can accept data packets faster than the other methods.

V. Conclusion And Future Work

In this paper, we propose to combine P-MIP, regional registration, and multicasting to improve the performance of P-MIP. The simulation results show that the proposed method can reduce the signaling cost, handoff latency, and the number of lost packets of P-MIP. In the future, we will study how to apply Link Layer as the movement detection mechanism in the proposed method to make further improvement to the present results.

Acknowledgment

The authors wish to thank AUN/SEED-Net's Collaborative Research Support Project (JFY 2006) for supporting this research work.

References

[1] C. E. Perkins, "Mobile Networking Through Mobile IP," *IEEE Internet Computing*, vol. 2, January-February 1998, pp. 58-69.

[2] X. Zhang, J. G. Castellanos, and A. T. Campbell, "P-MIP: Paging Extensions for Mobile IP," *ACM Mobile Networks and Applications (MONET)*, vol. 7, April 2002, pp. 127-141.

[3] B. Fenner, M. Handley, H. Holbrook, and I. Kouvelas, "Protocol Independent Multicast - Sparse Mode (PIM-SM)," *Internet Draft*, draft-ietf-pim-sm-v2-new-12.txt, March 2006.

[4] T. Poungkong and W. Benjapolakul, "A Comparative Analysis on Signaling Cost of Mobile IP Regional Registration with Paging Support," *IEEE Communication Society*, WCNC 2005, vol. 3, March 2005, pp. 1415-1420.

[5] E. Fogelstrom, A. Jonsson, and C.E. Perkins, "Mobile IP Regional Registration," *Internet Draft*, draft-ietf-ip4-reg-tunnel-02.txt, July 2006.

[6] K. Chiratana and W. Benjapolakul," Improvement of Paging Extensions in Mobile Internet Protocol based on Post Registration," *IEICE Trans. Inf. & Syst.*, vol. E89-D, no.12, December 2006, pp. 2848-2855.

[7] C. L. Tan and S. Pink," Mobicast: A Multicast Scheme for Wireless Networks," *Mobile Networks and Application*, no. 5, 2000, pp. 259-271.

Adaptive Protocol with Channel Variance Estimations for Cooperative Communications

Chaiyod Pirak
Department of Teacher Training in Electrical Engineering
King Mongkut's Institute of Technology North Bangkok, Bangkok, Thailand 10800
Email: chaiyod.p@gmail.com

***Abstract*— A cooperative communication system is one of prominent communication systems for the future wireless communications because it could provide a diversity gain achieved by the cooperation among users in the wireless network. In this paper, we propose a time-reversal technique for channel variance estimations, including a least square (LS), a modified LS, a minimum mean-square error (MMSE), and a modified MMSE estimations, for the proposed minimum symbol-error-rate (SER)-based adaptive protocol in the cooperative communication systems. Simulation results show that the proposed adaptive protocol with the modified LS estimation is the best scheme because it provides a closed SER to the ideal scheme with the lowest complexity.**

I. Introduction

Multiple-input multiple-output (MIMO) communication systems have been recognized as the communication scheme for the future wireless communications due to their diversity gain that results in a lower error probability. Recently, a generalized MIMO system called cooperative communication [1] has been proposed for realizing such diversity gain of the conventional MIMO system. By the cooperation of the active users equipped with a single antenna in the wireless networks, the generalized MIMO system can be established in a distributed fashion. In addition, the coverage range of such communication is also expanded, which results in less power consumption for a particular user who communicates with far-away destinations, and in turn prolongs a battery life.

Recently, various protocols have been proposed for the cooperation system [1], in which each user acts as a relay to assist other users transmit their information. A relay can either amplify the received signal and forward it, or decode the received signal first and then forward it. In addition, outage probability performance has been analyzed for such cooperation systems. The direct benefit of cooperatively working with more users is the diversity gain that comes at the price of the reduced transmission rate since the cooperation partners need to sacrifice their time slots for transmitting the source information. In [2], we proposed an adaptive protocol based on minimizing a tight approximate symbol error rate (SER). The proposed protocol can achieve the maximum achievable diversity gain in the system without sacrificing any transmission rate or total transmit power. In addition, this protocol is able to determine the best cooperation strategies in accordance with the changing environment. One of the most essential parameters needed for the source node to compute such approximate SER, used in the adaptation process, is a short-term channel variance. Previously, it was assumed known to the source node. In this paper, it is estimated through a pilot signal transmission. There has been studied that a pair of outgoing and incoming fading channels between a transmitter and a receiver is approximately reciprocal for slowly-varying channels [3]. Hence, we further exploit the reciprocity of slowly-varying fading channels to better estimate that of short-term channel variance using a time-reversal technique. The main contributions of this paper are as follows,

- We propose the time-reversal technique for channel variance estimations including a least square (LS) estimation, a modified LS estimation, a minimum mean-square error (MMSE) estimation, and a modified MMSE estimation.
- We numerically investigate the performance of the adaptive protocol with various kinds of channel variance estimations. We can show that the adaptive protocol with the modified LS estimation is the best scheme because its performance is close to the ideal scheme and its complexity is the lowest.

This paper is organized as follows. In Section II, we describe system models. In Section III, we describe a signal transmission in a transmission period. In Section IV, we propose a signal transmission in an acquisition period. The simulation results are shown in Section V, and we conclude this paper in Section VI.

II. Signal Transmission and System Models

For the sake of exposition, we consider cooperative communications in the wireless network with two phases, three users (i.e. one user acts as a source node and the other users act as relay nodes), and one destination. We consider the half-duplex communication system, i.e. a transceiver transmits or receives the signal in separate time slots, with two periods: an acquisition period and a transmission period. During the transmission period, the source and relay nodes cooperatively communicate with the destination. There are two transmission phases in this period. In Phase I, user 1 transmits a modulated signal to its destination, while user 2 and user 3 also receive this transmitted signal due to a broadcast nature of wireless channels. In Phase II, user 2 and user 3, or either of them relay the received signal to user 1's destination in an amplify-and-forward fashion. Likewise, in the next communication periods, user 2 and user 3 act as the source node, respectively, and the other users act as the relay nodes. In both phases, all users transmit signals through orthogonal channels by using a time-division multiple access (TDMA) scheme [1], [2], [4]. Due to the symmetry of the three users, we will analyze only user 1's performance by considering user 1 as the source node, user 2 as relay 1, and user 3 as relay 2. In this study, we employ an M-PSK modulation scheme. In order to maintain a fixed transmission rate, e.g. rate=1, an adaptive modulation scheme is considered. Specifically, for a

noncooperation strategy where no relay nodes are employed, BPSK modulation is used. For a 1-relay cooperation strategy where either relay 1 or relay 2 is employed, QPSK modulation is used. Finally, for a 2-relay cooperation strategy where both relay 1 and relay 2 are employed, 8-PSK modulation is used. In general, for an arbitrary transmission rate, the constellation of the adaptive modulation can be adjusted accordingly.

During the acquisition period, the source node determines the best cooperation partners by using a pilot-assisted technique in conjunction with a time-reversal technique described in Section IV. Then, the source node notifies the destination as well as the corresponding relay nodes about its cooperation strategy via some control channels. Here since we focus on a fixed transmission rate of 1, and there are 3 users in the cooperation system, the number of data packets in each transmission period with certain cooperation strategy must be in an order multiple of $6i,\ i \in \mathbb{I}$, so that all cooperation strategies' communications will be terminated at the end of the transmission period simultaneously. In addition, the total transmit power P per data packet is fixed for all cooperation strategies.

III. Signal Transmission in Transmission Period

In this section, we describe a signal transmission in the transmission period, including channel and signal models, a SER analysis, and the proposed asymptotic minimum SER-based adaptive protocol. In Phase I, the source node broadcasts its transmit signal to the destination and the relay nodes. The received signal z_{1B} at the destination, z_{12} at relay 1, and z_{13} at relay 2 can be expressed as follows,

$$z_{1B} = \sqrt{P_1} h_{1B} u + n_{1B}, \tag{1}$$

$$z_{12} = \sqrt{P_1} h_{12} u + n_{12}, \tag{2}$$

$$z_{13} = \sqrt{P_1} h_{13} u + n_{13}, \tag{3}$$

where P_1 is the transmit power of the source node; u is the transmitted symbol; $h_{1B}, h_{12},$ and h_{13} are the channel coefficients from the source to the destination, relay 1, and relay 2, respectively; and $n_{1B}, n_{12},$ and n_{13} are the additive noises modelled as zero-mean, complex Gaussian random variables with variance N_0. In Phase II, the relay nodes amplify the received signals and forward them to the destination with the transmit power $\tilde{P}_2$ and $\tilde{P}_3$ for relay 1 and relay 2, respectively. The received signal at the destination can be written as

$$y_{2B} = \frac{\sqrt{\tilde{P}_2}}{\sqrt{P_1|h_{12}|^2+N_0}} h_{2B} z_{12} + n_{2B}, \tag{4}$$

$$y_{3B} = \frac{\sqrt{\tilde{P}_3}}{\sqrt{P_1|h_{13}|^2+N_0}} h_{3B} z_{13} + n_{3B}, \tag{5}$$

$$\tilde{P}_2 = \begin{cases} 0; \text{ If relay 1 is not selected} \\ P_2; \text{ Otherwise.} \end{cases},$$

$$\tilde{P}_3 = \begin{cases} 0; \text{ If relay 2 is not selected} \\ P_3; \text{ Otherwise.} \end{cases},$$

where h_{2B} and h_{3B} are the channel coefficients from relay 1 and relay 2 to the destination, respectively; and n_{2B} and n_{3B} are also additive Gaussian noises with zero-mean and variance N_0. In addition, the channel coefficients $h_{1B}, h_{2B}, h_{3B}, h_{12}$, and h_{13} are modelled as slowly-varying Rayleigh fading channels with variances $\delta^2_{1B}, \delta^2_{2B}, \delta^2_{3B}, \delta^2_{12}$ and δ^2_{13}, respectively. These channel coefficients are assumed to be known to the destination node so that the maximum-ratio combining (MRC) [5] can be performed.

A. Symbol Error Rate Analysis

In this section, we derive an approximate SER for cooperation systems with the M-PSK modulation. The output of the MRC detector at the destination can be expressed as follows [5],

$$y = a_1 z_{1B} + a_2 y_{2B} + a_3 y_{3B}, \tag{6}$$

$$a_1 = \sqrt{P_1} h^*_{1B} / N_0,$$

$$a_2 = \begin{cases} 0; \text{ If relay 1 is not selected} \\ \dfrac{\sqrt{\frac{P_1 \tilde{P}_2}{P_1|h_{12}|^2+N_0}} h^*_{12} h^*_{2B}}{\left(\frac{\tilde{P}_2|h_{2B}|^2}{P_1|h_{12}|^2+N_0}+1\right) N_0}; \text{ Otherwise.} \end{cases},$$

$$a_3 = \begin{cases} 0; \text{ If relay 2 is not selected} \\ \dfrac{\sqrt{\frac{P_1 \tilde{P}_3}{P_1|h_{13}|^2+N_0}} h^*_{13} h^*_{3B}}{\left(\frac{\tilde{P}_3|h_{3B}|^2}{P_1|h_{13}|^2+N_0}+1\right) N_0}; \text{ Otherwise.} \end{cases}$$

Assuming that the transmitted symbol u has a unit average energy, then the approximate SNR of the MRC output can be written as follows [4], [5],

$$\gamma \approx \gamma_1 + \gamma_2 + \gamma_3, \tag{7}$$

where $\gamma_1 = P_1|h_{1B}|^2/N_0,\ \gamma_2 = \frac{P_1 \tilde{P}_2 |h_{12}|^2 |h_{2B}|^2}{N_0\left(P_1|h_{12}|^2+\tilde{P}_2|h_{2B}|^2\right)},\ \gamma_3 = \frac{P_1 \tilde{P}_3 |h_{13}|^2 |h_{3B}|^2}{N_0\left(P_1|h_{13}|^2+\tilde{P}_3|h_{3B}|^2\right)}$. Computing the conditional SER and averaging it over the Rayleigh fading channels [6], and using a tight upper bound on SER derived in [2], we can derive the approximate SER of such system as follows. First, for the noncooperation strategy, we can show that the approximate SER with the BPSK modulation can be written as,

$$P_{BPSK} \approx \frac{N_0}{4P\delta^2_{1B}}. \tag{8}$$

Second, for the 1-relay cooperation strategy where relay 1 is selected, we can show that the approximate SER with the QPSK modulation can be written as,

$$P^{relay\ 1}_{QPSK} \approx 4CN_0^2 \cdot \frac{P_1\delta^2_{12} + P_2\delta^2_{2B}}{P_1^2 P_2 \delta^2_{1B}\delta^2_{2B}\delta^2_{12}}, \tag{9}$$

where $C = \left[\frac{9}{32} + \frac{1}{4\pi}\right]$ and $P = P_1 + P_2$. Likewise, for the 1-relay cooperation strategy where the relay 2 is selected, we can show that the approximate SER with the QPSK modulation can be written as follows,

$$P^{relay\ 2}_{QPSK} \approx 4CN_0^2 \cdot \frac{P_1\delta^2_{13} + P_3\delta^2_{3B}}{P_1^2 P_3 \delta^2_{1B}\delta^2_{3B}\delta^2_{13}}, \tag{10}$$

where $P = P_1 + P_3$. Finally, for the 2-relay cooperation strategy, we can show that the approximate SER with the 8-PSK modulation can be written as,

$$P_{8PSK} \approx \frac{DN_0^3}{E} \cdot \frac{\left(P_1\delta^2_{12} + P_2\delta^2_{2B}\right)\left(P_1\delta^2_{13} + P_3\delta^2_{3B}\right)}{P_1^3 P_2 P_3 \delta^2_{1B}\delta^2_{2B}\delta^2_{3B}\delta^2_{12}\delta^2_{13}}, \tag{11}$$

where $D = \left[\frac{-13}{128} + \frac{23}{12\sqrt{2}}\right],\ E = \frac{1}{2}\left[1 - \frac{1}{\sqrt{2}}\right]$, and $P = P_1 + P_2 + P_3$.

B. The Asymptotic Minimum SER-based Adaptive Protocol

Now the most desirable protocol is the protocol that is able to achieve the asymptotic minimum error probability in an averaging sense under high-enough SNR regimes, expressed as

$$\arg \min_{\text{number \& index of cooperation partners}} Pr(error)$$
$$\text{s.t. fixed rate and total transmit power constraints.} \tag{12}$$

The procedures of the proposed adaptive protocol can be described as follows,

1) The source node acquires a short-term channel variances [5], i.e. $\delta^2_{1B}, \delta^2_{2B}, \delta^2_{3B}, \delta^2_{12}$, and δ^2_{13}, within the acquisition period described in the following section. This channel variances will be used as if they were the exact short-term channel variances during the upcoming transmission period given that the channel is slowly varying.
2) The source node calculates the approximate SER derived in Section III-A for such cooperation strategies, and then compares them all. The best cooperation strategy that results in the asymptotic minimum SER will be chosen for the upcoming transmission period.
3) The source node notifies the chosen cooperation partners and the destination about the cooperation strategy decision via some control channels.

IV. Signal Transmission in Acquisition Period

In this section, we propose the time-reversal approach for the instantaneous channel variance estimations. In this paper, we assume that each pair of inter-user channels is reciprocal, i.e. $h_{21} \approx h_{12}, h_{31} \approx h_{13}, h_{B1} \approx h_{1B}, h_{B2} \approx h_{2B}$, and $h_{B3} \approx h_{3B}$. This assumption is adequately consistent because the channels are slowly varying, resulting from slowly changing in each node's location [3]. In the acquisition period, all short-term channel variances, i.e. $\delta^2_{1B}, \delta^2_{2B}, \delta^2_{3B}, \delta^2_{12}$, and δ^2_{13}, are being estimated to be used in an adaptation process of the proposed adaptive protocol in Section III-B. We employ a time average approach for estimating such short-term channel variances, expressed as

$$\bar{\delta}^2_{ij} = \frac{1}{M}\sum_{k=1}^{M} |h^k_{ij}|^2, \ \exists i \in \{1,2,3\} \text{ and } \exists i \in \{2,3,B\}, \quad (13)$$

where M stands for a number of pilot blocks sent in this period and $|h^k_{ij}|^2$ denotes the k^{th}-block instantaneous channel variance of the sender node i and the receiver node j.

There are two transmission phases in this period. In Phase I, the instantaneous channel variances $|h_{12}|^2$ and $|h_{13}|^2$ are to be estimated at the source node. In Phase II, the instantaneous channel variances $|h_{1B}|^2, |h_{2B}|^2$ and $|h_{3B}|^2$ are to be estimated at the destination node. Then, they will be sent to the source node via the control channels. In Phase I-State I, the source node broadcasts the pilot signal, i.e. $u = 1$, to the destination and the relay nodes. The received signal z^I_{1B} at the destination, z^I_{12} at relay 1, and z^I_{13} at relay 2 can be expressed as follows,

$$z^I_{1B} = \sqrt{P_1} h_{1B} + n_{1B}, \quad (14)$$
$$z^I_{12} = \sqrt{P_1} h_{12} + n_{12}, \quad (15)$$
$$z^I_{13} = \sqrt{P_1} h_{13} + n_{13}, \quad (16)$$

In Phase I- State II and III, the relay nodes performs a time-reversal complex-conjugate mirror [3] by complex-conjugating the received signal. Then, this complex-conjugated received signal is amplified and forwarded to the destination by the relay 1 and relay 2, respectively. Due to the broadcast nature of wireless channels, this relayed signal also propagates back to the source node. The received signal at the source node can be written as

$$y^I_{21} = \frac{\sqrt{P_2}}{\sqrt{P_1|h_{12}|^2+N_0}} h_{21} z^{I*}_{12} + n_{21}, \quad (17)$$
$$y^I_{31} = \frac{\sqrt{P_3}}{\sqrt{P_1|h_{13}|^2+N_0}} h_{31} z^{I*}_{13} + n_{31}. \quad (18)$$

Substituting z^I_{12} and z^I_{13} in (15) and (16) into (17) and (18), respectively, to arrive at

$$y^I_{21} = \frac{\sqrt{P_1P_2}}{\sqrt{P_1|h_{12}|^2+N_0}} h_{21} h^*_{12} + \frac{\sqrt{P_2}}{\sqrt{P_1|h_{12}|^2+N_0}} n^*_{12} + n_{21}, \quad (19)$$
$$y^I_{31} = \frac{\sqrt{P_1P_3}}{\sqrt{P_1|h_{13}|^2+N_0}} h_{31} h^*_{13} + \frac{\sqrt{P_3}}{\sqrt{P_1|h_{13}|^2+N_0}} n^*_{13} + n_{31}. \quad (20)$$

By the assumption that the channels are reciprocal, i.e. $h_{21} \approx h_{12}$ and $h_{31} \approx h_{13}$, we have

$$y^I_{21} = \xi_{21}|h_{12}|^2 + \frac{\xi_{21}}{\sqrt{P_1}} n^*_{12} + n_{21}, \quad (21)$$
$$y^I_{31} = \xi_{31}|h_{13}|^2 + \frac{\xi_{31}}{\sqrt{P_1}} n^*_{13} + n_{31}, \quad (22)$$

where $\xi_{21} = \frac{\sqrt{P_1P_2}}{\sqrt{P_1|h_{12}|^2+N_0}}$ and $\xi_{31} = \frac{\sqrt{P_1P_3}}{\sqrt{P_1|h_{13}|^2+N_0}}$.

Similarly, in Phase II-State I, the destination node broadcasts the pilot signal to the source and the relay nodes with the power P. The received signal z^{II}_{B1} at the source, z^{II}_{B2} at relay 1, and z^{II}_{B3} at relay 2 can be expressed as follows,

$$z^{II}_{B1} = \sqrt{P} h_{B1} + n_{B1}, \quad (23)$$
$$z^{II}_{B2} = \sqrt{P} h_{B2} + n_{B2}, \quad (24)$$
$$z^{II}_{B3} = \sqrt{P} h_{B3} + n_{B3}, \quad (25)$$

In Phase II-State II-IV, the source and relay nodes perform a time-reversal complex-conjugate mirror to the received signal, and amplify and forward the resulting signal back to the destination, respectively. By the assumption that the channels are reciprocal, i.e. $h_{B1} \approx h_{1B}, h_{B2} \approx h_{2B}$ and $h_{B3} \approx h_{3B}$, we have

$$y^{II}_{1B} = \xi_{1B}|h_{1B}|^2 + \frac{\xi_{1B}}{\sqrt{P}} n^*_{1B} + n_{B1}, \quad (26)$$
$$y^{II}_{2B} = \xi_{2B}|h_{2B}|^2 + \frac{\xi_{2B}}{\sqrt{P}} n^*_{2B} + n_{B2}, \quad (27)$$
$$y^{II}_{3B} = \xi_{3B}|h_{3B}|^2 + \frac{\xi_{3B}}{\sqrt{P}} n^*_{3B} + n_{B3}, \quad (28)$$

where y^{II}_{1B}, y^{II}_{2B} and y^{II}_{3B} are the received signals transmitted from the source, relay 1, and relay 2 to the destination, respectively; and $\xi_{1B} = \frac{P}{\sqrt{P|h_{1B}|^2+N_0}}, \xi_{2B} = \frac{P}{\sqrt{P|h_{2B}|^2+N_0}}$ and $\xi_{3B} = \frac{P}{\sqrt{P|h_{3B}|^2+N_0}}$. Here, $n_{21}, n_{31}, n_{B1}, n_{B2}$ and n_{B3} are modelled as zero-mean, complex Gaussian random variables with variance N_0. Now we estimate the instantaneous channel variances $|h_{12}|^2, |h_{13}|^2, |h_{1B}|^2, |h_{2B}|^2$ and $|h_{3B}|^2$ from (21)-(22) and (26)-(28), respectively. For the sake of simplicity, we just only show the derivation of estimating $|h_{12}|^2$. The remaining ones can be estimated in the same way.

A. Least Square Estimation

The objective function for the LS estimation can be written as

$$\widehat{|h_{12}|^2}_{LS} = \arg\min_{|h_{12}|^2} \|y^I_{21} - \xi_{21}|h_{12}|^2\|^2. \quad (29)$$

After some algebraic manipulation, it can be shown that

$$\widehat{|h_{12}|^2}_{LS} = y^I_{21}/\xi_{21}. \quad (30)$$

From the fact that $|h_{12}|^2$ is a positive-value variable, we further propose the modified LS channel variance estimation by taking an absolute operator to (30), to arrive at

$$\widehat{|h_{12}|^2}_{MLS} = \left|y^I_{21}/\xi_{21}\right|. \quad (31)$$

B. Minimum Mean-Square Error Estimation

We employ a linear finite impulse response (FIR) filter, w_{12}, to estimate the channel variance as follows,

$$|h_{12}|^2 = w_{12} y^I_{21}. \quad (32)$$

The objective function for computing w_{12} is based on minimizing a mean-square error expressed as

$$w_{12} = \arg\min_{w} \mathrm{E}[\|\,|h_{12}|^2 - w y_{21}^I\|^2]. \quad (33)$$

After some algebraic manipulation and from the identity that $\mathrm{E}[\|\,|h_{12}|^2\|^2] = 2\delta_{12}^4$, we have

$$\widehat{|h_{12}|^2}_{MMSE} = \frac{y_{21}^I}{\xi_{21} + \beta}, \quad (34)$$

where $\beta = \frac{N_0(1+\xi_{21}^2/P_1)}{2\xi_{21}\delta_{12}^4}$. In a similar reason to Section IV-A, we further propose a modified MMSE channel variance estimation as follows,

$$\widehat{|h_{12}|^2}_{MMMSE} = \left| \frac{y_{21}^I}{\xi_{21} + \beta} \right|. \quad (35)$$

V. Simulation Results

In this section, based on simulations, performance evaluation of the proposed adaptive protocol employing the time-reversal channel variance estimations is carried out. Adaptive modulation with BPSK, QPSK, and 8-PSK constellations are employed. The total transmit power is fixed to be P=1 W, and the bandwidth efficiency is 1 bit/s/Hz. In addition, one acquisition period consists of 2 pilot blocks, i.e. $M = 2$, and one transmission period consists of 6 data packets so that all cooperation strategies' communications will be terminated at the end of the transmission period simultaneously. The channel variances are $\delta_{1B}^2 = 1, \delta_{2B}^2 = 1, \delta_{3B}^2 = 1, \delta_{12}^2 = 10$, and $\delta_{13}^2 = 5$. For a fair comparison, we illustrate the average SER curves as function of P/N_0.

In Fig.1, we show the average SER versus SNR(dB) for different cooperation strategies in quasi-static Rayleigh fading channels, i.e. the channels are constant over a pair of consecutive acquisition and transmission periods and change in a period-by-period basis, with a normalized Doppler shift $f_d T_s$ of 0.005 with f_d being the Doppler shift and T_s being the symbol duration. It turns out that the adaptive protocol with the modified LS and MMSE estimations yields the closed error probability to the ideal scheme, in which all channel variances are assumed to be known to the source node. This result suggests that the adaptive protocol with the modified LS estimation is the best scheme because its performance is close to the ideal scheme and its complexity is the lowest (see (31)). It is worth noticing that the proposed adaptive protocol achieves the maximum diversity of 3, and yields a remarkably lower SER.

In Fig.2, we show the MSE for the proposed time-reversal channel variance estimations in the source-destination link. It is worth noticing that the modified MMSE estimation yields the lowest MSE at the price of high computational complexity. In addition, because of the knowledge about the noise and channel variances, the MMSE estimations yield the lower MSEs than the LS estimations in low SNR regimes.

VI. Conclusion

In this paper, we have proposed the time-reversal technique for channel variance estimations, including the LS, modified LS, MMSE, and modified MMSE estimations, for the adaptive protocol in the cooperative communication systems. We have also proposed the signal transmission strategy for such systems. Simulation results indicated that the adaptive protocol with the modified LS and MMSE estimations yielded a remarkably lower SER that is close to the ideal scheme, in which a SNR difference of 0.5 dB at SER of 10^{-5} was observed. On the other hand, such

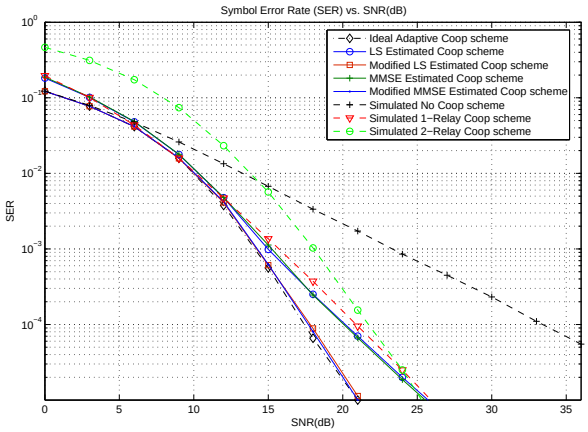

Fig. 1: The curves of the average SER for different cooperative protocols in quasi-static Rayleigh fading channels.

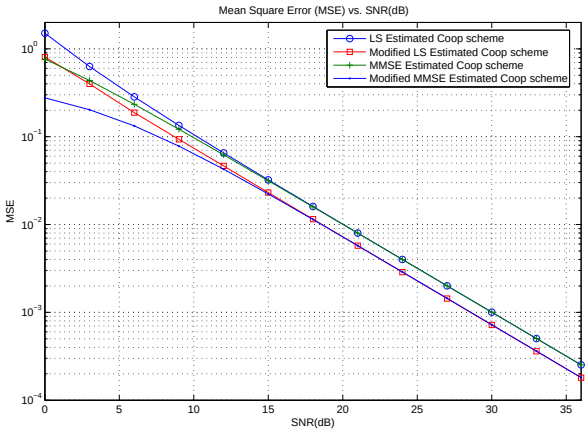

Fig. 2: The curves of the MSE for the proposed time-reversal channel variance estimations in the source-destination link.

protocol with the LS and MMSE estimations yielded the worst performance, in which a SNR difference of 5 dB in comparison with that of ideal scheme at SER of 10^{-5} was observed. For a complexity comparison, the modified LS estimation had a lower complexity than the modified MMSE estimation. As a result, the adaptive protocol with the modified LS estimation provided the best performance among all other schemes for the cooperative communication systems.

References

[1] J.N. Laneman, D.N.C. Tse, and G. W. Wornell, "Cooperative diversity in wireless networks: efficient protocols and outage behavior," *IEEE Trans. Infor. Theory*, Vol. 50, pp. 3062-3080, Dec. 2004.

[2] C. Pirak, Z. J. Wang, and K.J.R. Liu, "An adaptive protocol for cooperative communications achieving asymptotic minimum symbol-error-rate," *Proceedings of IEEE ICASSP 2006*, Vol. IV, pp. 53-56, May 2006.

[3] P. Kyritsi, G. Papanicolaou, P. Eggers, and A. Oprea, "MISO time reversal and delay-spread compression for FWA channels at 5 GHz," *IEEE Ant. and Wireless Prop. Letters*, Vol. 3, pp. 96-99, 2004.

[4] M.O. Hasna and M.-S. Alouini, "End-to-end performance of transmission systems with relays over Rayleigh-fading channels," *IEEE Trans. Wireless Commu.*, Vol. 2, pp. 1126-1131, Nov. 2003.

[5] D.G. Brennan, "Linear diversity combining techniques," *Proceedings of the IEEE*, Vol. 91, No. 2, pp. 331-356, Feb. 2003.

[6] M.K. Simon and M.-S. Alouini, "A unified approach to the performance analysis of digital communication over generalized fading channels," *Proceedings of the IEEE*, Vol. 86, No. 9, pp. 1860-1877, Sept. 1998.

Robust Ad Hoc Routing Protocol using Relative Mobility Information

Suksun Mahakittikun and Peerapon Siripongwutikorn
Department of Computer Engineering, King's Mongkut University of Technology Thonburi
emails: i.suksun@gmail.com peerapon@cpe.kmutt.ac.th

***Abstract*— Ad hoc On-Demand Distance Vector (AODV), a widely deployed routing protocol in ad hoc networks, performs well in networks of high user density and low mobility. However, its performance drops for sparse networks with highly mobile users due to frequent broken links. This paper presents Mobility-Aware AODV (MA-AODV) routing protocol, which improves upon AODV by incorporating speed and direction of node movement in selecting neighbors. In particular, nodes with low relative mobility tend to form links with each other to increase the path lifetime. Compared to standard AODV, our simulation results show that MA-AODV only introduces minor overheads but reduces the amount of routing overheads caused by broken routes and route rediscovery. Furthermore, approximately 10% improvement in the packet delivery ratio is observed in MA-AODV under node mobility.**

I. INTRODUCTION

Mobile wireless networks have increasingly become more popular. Even in the absence of wired infrastructures such as access points, mobile devices or nodes can communicate by forming a Mobile Ad Hoc Network (MANET). In a MANET, packets sent by one node are forwarded by other nodes over the wireless medium until reaching the destination. Nodes in a MANET executes Ad hoc routing protocol in a distributed manner to determine the next-hop to forward packets.

One of the most well-known ad hoc routing protocols is Ad hoc On-Demand Distance Vector (AODV), which has been standardized by IETF [1]. A source node discovers a route to a given destination by broadcasting a Route REQuest (RREQ) packet with an originator's ID and a unique sequence number. Each immediate node along that path records the packet ID and the sequence number of the RREQ packet, creates a new routing entry whose destination field is the originator node with the next hop ID as the upstream neighboring node from which it receives the RREQ packet, as well as other related fields, and then rebroadcast. Upon receiving the RREQ packet, the destination responds with the Route REPly (RREP) packet back to the source by using the route recorded by the intermediate nodes in the forward path. If some intermediate node happens to have the entry for that destination, it returns an RREP packet itself. The immediate nodes along the reverse path is thus able to add the next node to forward the packet to this destination in their routing table. The route is said to be active if there are packets destined for this destination. A timer is used to purge inactive routing entry from the tables. Also, a node that detects a broken route will report to its upstream nodes back to the source so that the routing tables can be updated and the source initiates a new route discovery. To prevent routing loops, each routing entry utilizes per-node sequence numbers to ensure that the routes are loop-free. A node increments its sequence number whenever there is a change in its local connectivity information or requesting a new RREQ.

Broken routes, mostly caused by relative mobility, seriously decreases the end-to-end packet delivery ratio and increases the packet delay because of considerable amount of time and routing overheads to detect the broken routes and rediscover the new route to the destination. For example, in a multiple access link layer protocol such as IEEE 802.11b, a broken link leads to the absence of acknowledgment packets even if the node has successfully attempted the transmission. The retry attempts will be made for another 15 times before giving up, leading to significant amount of delay. Many techniques have been proposed to maintain good network performance under mobility. The problem is that AODV only maintains a single path for a given destination. Therefore, when the path is broken, data packets are simply dropped by nodes along the broken path.

In [2], [3], on-demand multi-path routing are proposed, whereby each neighboring node in a primary route also maintain its own backup route. When the node on a primary route detects a link failure, it transmits a route update message to its neighbors. The neighbor receiving this message then activates the backup route. [2] also introduces the term of goodness of preferential path probability to classify the goodness value. Recent work in [4] proposed the scheme that comes closest to ours work. The link breakage is reduced by enhancing the route discovery process of AODV using the concept of mobility aware agent. A mobile agent used at each node periodically broadcasts mobility information to its neighbors to collect node status and the selection of best neighbors for a given destination is done at each intermediate node. In this way, the agent attempts to establish a path between two nodes with minimum number of intermediate nodes. However, it does not clearly state the neighbor selection mechanism and how to elect the goodness value. In neighbor detection algorithm, [5] suggested using the Signal to Noise Ratio (SNR) value that is measured whenever a packet that contains an AODV message is received. A neighbor is classified good neighbor if the quality of the wireless physical channel is good enough to carry traffic. Note that this metric is representative of the distance, and may not correctly reflect how long two nodes

will remain neighbors.

In this paper, we propose the Mobility-Aware AODV (MA-AODV) routing protocol, which enhances AODV by selecting neighbors to forward packets based on relative mobility. Specifically, a node will select neighbors that would remain in its transmission range longest to extend the path lifetime. As shown in Fig. 1, nodes n and m on the right would remain neighbors longer than that in the left as they move in the same direction. A longer path lifetime not only reduces time and overheads spent on the new route discovery but also increases the packet delivery ratio as less packets are dropped due to broken links.

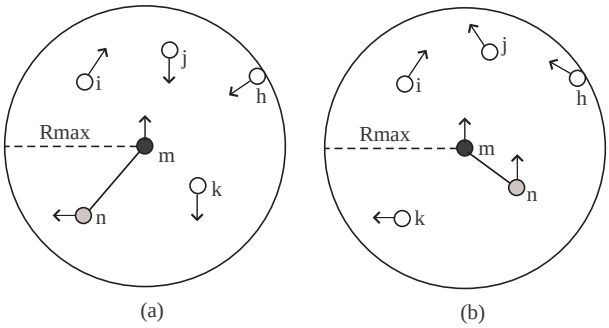

Fig. 1. Illustration of moving direction for each mobile node and its neighboring node: (a) Shorter session time. (b) Longer session time.

The rest of the paper is organized as follows. Section II describes the concept of relative mobility and how it is used to enhance the neighbor selection process in MA-AODV. In section III, we evaluate the performance of MA-AODV by means of simulation and compare its performance with standard AODV. Section IV concludes the paper.

II. Mobility-Aware AODV (MA-AODV)

In our work, we assume that the nodes use the same transmission range R and have a Global Positioning System (GPS) receiver to acquire its own coordinate, and this information is embedded into transmitted frames in the MAC level. Each node also uses the network interface that works in a promiscuous mode, which listens or eavesdrops every packets in its reception range, to mobility information of other nearby nodes. Fig. 2 illustrates walking routes of two mobile nodes moving independently and coordinate information is embedded to beacon packets broadcast periodically every one second by node M. The square and asterisk points indicate the sending and receiving of the beacons respectively by node M and N, while the dashed lines indicate the time period that M and N move out of one another coverage area.

Each node m maintains the position of all its neighbors n within its proximity for the last two updates. This information can easily be added to AODV routing update or HELLO messages that are already exchanged periodically. The relative velocity and other related parameters such as direction and the remaining session time can be established by using this

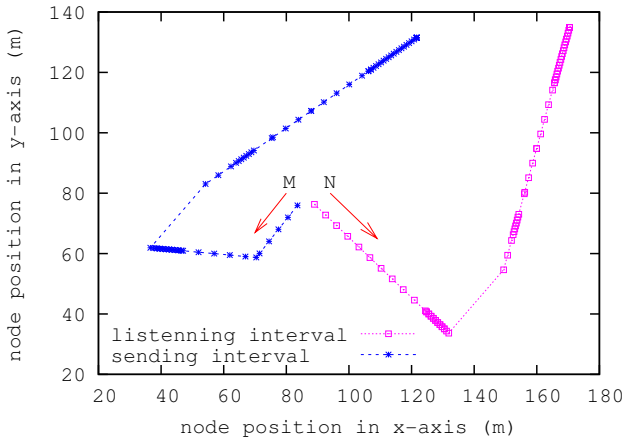

Fig. 2. Walking route of two nodes with periodic HELLO beacons.

information. Let

$$\underline{\boldsymbol{p}}_m(t) = [x_m(t)\ y_m(t)]^T \tag{1}$$

be the coordinate vector of node m at time t in the Euclidean space. Define $d_{m,n}(t)$ as the distance between node m and n at time t, which is given by

$$d_{m,n}(t) = \|\underline{\boldsymbol{p}}_m(t) - \underline{\boldsymbol{p}}_n(t)\| \tag{2}$$

where the operator $\|\cdot\|$ is an L_2 norm[1]. For every time interval τ, node m estimates the instantaneous velocity $v_{m,n}(t)$ that each of its neighbors n *moves outward* from the center of a circle where m is located along a *virtual* straight line toward the circumference.

$$v_{m,n}(t) = \frac{d_{m,n}(t) - d_{m,n}(t-\tau)}{\tau} \tag{3}$$

As shown in Fig. 3, the virtual straight line (the dashed line straightline) means that it is not the actual movement path. Rather, it is invented to model the distance that n moves out of the transmission coverage of m. The negative value of $v_{m,n}(t)$ indicates the inward movement while the positive value indicates the outward movement. Suppose the current

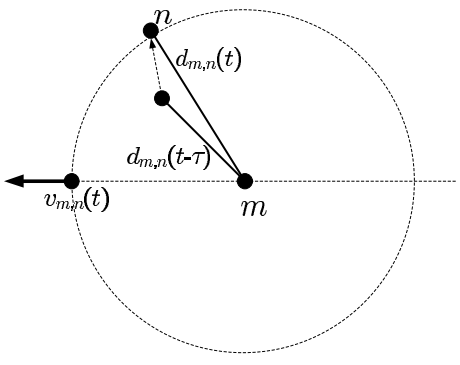

Fig. 3. Instantaneous velocity $v_{m,n}(t)$ of n moving out of m's transmission coverage.

[1]For a vector $\boldsymbol{a} = [a_1 a_2 \ldots a_n]$, $\|\boldsymbol{a}\| = \sqrt{\sum_{i=1}^{n} a_i^2}$

distance of n from m is $d_{m,n}(t)$. If n is moving away from m, it will take another $R - d_{m,n}(t)$ before n moves out of the transmission coverage of m. If n is moving closer from m, it will take another $d_{m,n}(t) + \frac{R}{2}$ before n moves out of the transmission coverage of m. Therefore, we can estimate the remaining session lifetime of n with respect to m at time t as

$$S_{m,n}(t) = \begin{cases} \frac{R - d_{m,n}(t)}{|v_{m,n}(t)|} & v_{m,n}(t) > 0 \\ \frac{R + d_{m,n}(t)}{|v_{m,n}(t)|} & v_{m,n}(t) < 0 \end{cases} \quad (4)$$

MA-AODV enhances the neighbor selection in the route discovery and route reply processes of standard AODV with the estimated session lifetime as described below. In standard AODV, the originator node initiates a RREQ. An intermediate node only responds the first RREQ, and then rebroadcasts. The RREQ finally reaches the destination or some intermediate node that has a route to the destination. In this phase every nodes can recognize and create a fresh routing entry containing next hop address used to reach the originator of RREQ. Also, a RREP is sent back to the originator to create another routing entry used to reach the destination of RREQ. Since the RREQ can traverse different paths to the destination, each intermediate node may receive multiple RREPs back from the destination. RREPs generated by the RREQ packet with the same sequence number are said be duplicates.

The process of updating the routing entry when receiving RREP gives the preference to various metrics in the following order: (i) sequence number, (ii) hop counts, (iii) expiration timer, and (iv) the estimated remaining session lifetime $S_{m,n}(t)$. A highest sequence number is given the highest priority as it represents the route reply for the newest RREQ. For RREPs with the same sequence number, they are duplicates and the one with lowest hop counts is selected. For duplicate RREPs with the same hop count, the one with highest expiration timer is selected as it represents the most recent route. The one with low expiration timer may imply that it is a cached route. For duplicate RREPs with the same hop count and expiration timer, it means they may be returned from the same intermediate node (or destination node) but traverse different reverse paths. This scenario is actually not uncommon. As shown in Fig. 4, node a receives multiple RREPs from different neighbors b and c, which in turn receive the RREPs from the same intermediate node when tracing back. In this case, both routes may have the same number of hop counts as well as the expiration timer. Therefore, the one with highest $S_{m,n}(t)$ is selected to ensure that the path will have a higher probability to remain longest.

III. Simulation Results

The simulation is implemented with OMNET++, a discrete-event simulation language based on C++[2]. The performance metrics are the packet delivery ratio and the routing overheads. The packet delivery ratio is the total number of received packets divided by the total number of packets sent, computed from all the nodes. The routing overhead is the number of packets generated by the routing protocol. The network consists of 50 nodes initially randomly placed in an area of 700 x 700 m^2. The MAC layer is IEEE 802.11b CSMA/CA with RTS/CTS and the common transmission range $R = 100$ m. The nodes move according to the random waypoint mobility model [6] with velocity selected from the range $(0, v_{\max})$. Five source nodes are selected to generate a constant bit rate traffic to a randomly selected destination at 10 packets/second (1460 bytes per packet) for 100 packets before terminating the session, and then selecting a new destination until the simulation terminates. Therefore, there are at most five concurrent sessions in the network to avoid the bandwidth saturation due to broadcast traffic. We implement the neighboring node detection module in the MAC layer using crossing layer concept introduced in [7]. Each data point is averaged from 15 runs, where each simulation run lasts 150 seconds.

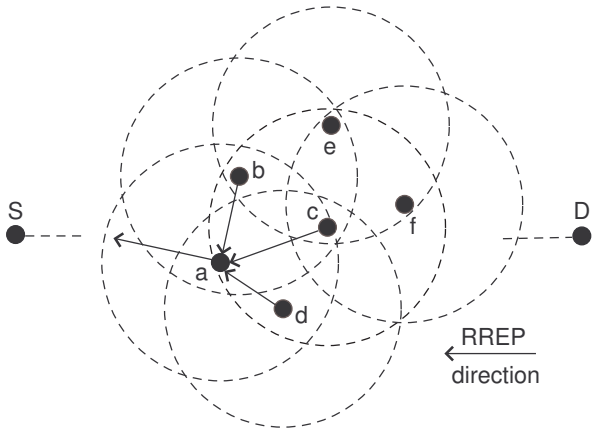

Fig. 4. Duplication of route reply from neighboring node known for the destination address.

Fig. 5 shows the packet delivery ratio as a function of the maximum speed $v_{\max}$. Both protocols have gradually decreasing delivery ratio as expected. However, MA-AODV performs slightly better in low mobility and the amount of improvement over standard AODV is approximately 10% as the mobility increases (from $v_{\max} > 6$ m/s). For instance, at $v_{\max}$ = 12 m/s, AODV delivers about 40% of total packets, while MA-AODV delivers about 53% due to its mobility awareness.

The amount of routing overhead packets shown in Fig. 6 indicates that MA-AODV generates less routing overheads because it maintain a longer path lifetime, and hence less overheads are generated due to the route update and rediscovery. The only additional overhead generated by MA-AODV is local update of node positions. While AODV does not have this update, it generates more routing overhead in RREQ flooding to discover a new route as a result of broken paths, which is more clearly observed when the velocity increases.

When increasing the network load by adding more sessions to the network, the packet delivery ratio drops for both AODV

[2]www.omnetpp.org

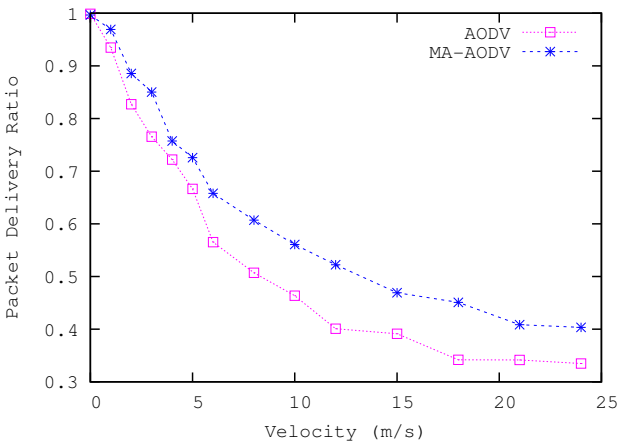

Fig. 5. Comparison of packet delivery ratio in AODV and MA-AODV as a function of the maximum velocity.

and MA-AODV as shown in Fig. 7.

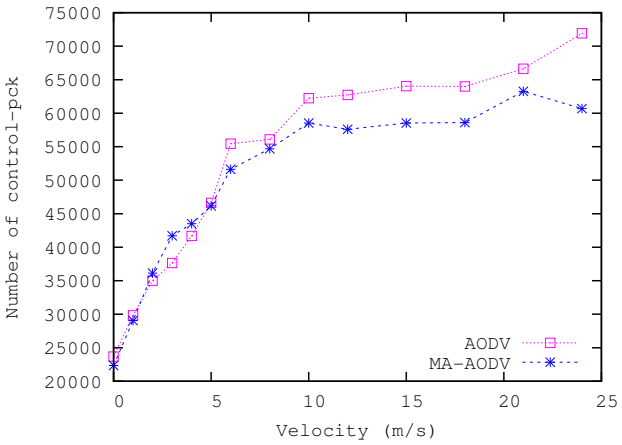

Fig. 6. Number of control packet vs. velocity.

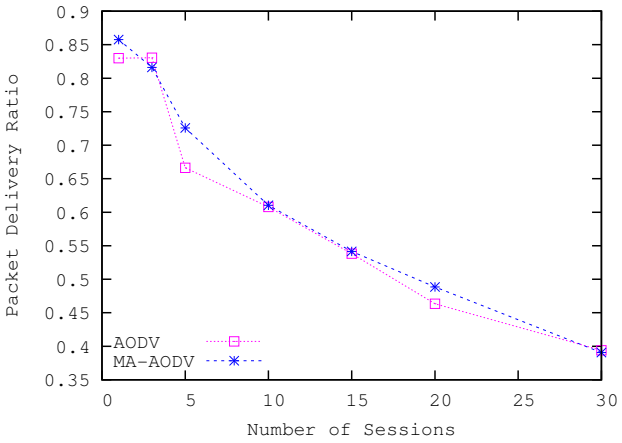

Fig. 7. Packet Delivery Ratio vs. Number of sessions ($v_{\max}$ = 5 m/s)

IV. Conclusion

In ad hoc networks, node mobility caused broken routes and leads to the route update and route rediscovery processes that waste time and network resources. Therefore, it is desirable to use the path that remains as long as possible. This paper proposes a MA-AODV ad hoc routing protocol, which enhances the neighbor selection process in standard AODV by using the estimated session lifetime. Each node estimates how long its neighbors will remain in its coverage area, or the remaining session lifetime, based on the history of coordinates broadcast by the neighbors. Compared to standard AODV, our simulation results show that MA-AODV reduced the amount of routing overheads caused by broken routes and route rediscovery. Therefore, packets are delivered with less end-to-end delay and more network resources are left to deliver packets. It has been shown that MA-AODV improves the packet delivery ratio approximately 10% over AODV.

References

[1] C. Perkins, E. Belding-Royer, and S. Das, "Ad hoc on-demand distance vector (aodv) routing," RFC3561, IETF MANET Working Group, Tech. Rep., July 2003.

[2] F. Jing, R. Bhuvaneswaran, Y. Katayama, and N. Takahashi, "On-demand multipath routing protocol with preferential path selection probabilities for manet," in *IEEE AINA*, vol. 2, Apr. 2006.

[3] S.Motegi and H. Horiuchi, "Aodv-based multipath routing protocol for mobile ad hoc networks," *IEICE TRANSACTIONS on Communications*, no. 9, pp. 2477–2483, 2004.

[4] M. Idrees, M. Yousaf, S. Jaffry, M. Pasha, and S. A. Hussain, "Enhancement in aodv routing using mobility aware agents," in *Proc. IEEE Symposium of Emerging Technologies*, Sept. 2005, pp. 98–102.

[5] S. Krco and M. Dupcinov, "Improved neighbor detection algorithm for aodv routing protocol," *IEEE communications letters*, vol. 7, no. 12, pp. 584–586, 2003.

[6] T. Camp, J. Boleng, and V. Davies, "A survey of mobility models for ad hoc network research," *Wireless Communication & Mobile Computing (WCMC)*, vol. 2, no. 5, pp. 483–502, 2002.

[7] J. S. Z. Ren and W. Guo, "A cross-layer aodv routing protocol," in *Proc. IEEE ICMA*, July. 2005, pp. 2150–2155.

A QoS-Based Dynamic Source Routing for Multimedia Service in Mobile Ad Hoc Networks

Wayan MUSTIKA*, Sakchai THIPCHAKSURAT*, Ruttikorn VARAKULSIRIPUNTH*, Hiroshi ISHII**
*Faculty of Engineering and Research Center for Communications and Information Technology (ReCCIT)
King Mongkut's Institute of Technology Ladkrabang (KMITL), Bangkok, Thailand 10520
**Department of Communication Engineering, School of Information Technology and Electronics, Tokai University, Japan
Email: mus_thicks@yahoo.com, {ktsakcha, kvruttik}@kmitl.ac.th, ishii@dt.u-tokai.ac.jp

***Abstract* - The growth of real-time multimedia applications in mobile ad hoc networks (MANETs) will be increasingly popular in the near future. To support such kind of applications, Quality of Service (QoS) features are desired. However, the mobile nature, limited resources, and dynamic topology of MANETs make it complicates to provide QoS guarantee in such network. In this paper, we propose a routing scheme for multimedia service based on multiple QoS constraint called QoS-Based Dynamic Source Routing (QDSR). It applies the source routing mechanism defined by the Dynamic Source Routing (DSR) to reduce routing overheads and improve throughput. QDSR gathers information about end-to-end delay, available bandwidth and signal strength during route discovery and uses the information in route decision process. We evaluate the performance of our proposed scheme by means of simulation. The result shows that QDSR provides the higher throughput and lower packet loss rate than those of DSR.**

***Keywords*: QoS routing, mobile ad hoc networks, Dynamic Source Routing.**

I. INTRODUCTION

A Mobile Ad Hoc Network (MANET) consists of wireless mobile nodes with no predetermined topology or central control. The nodes intercommunicate through single-hop or multi-hop paths in a peer-to-peer fashion and operate both as hosts as well as routers. Such network can be used in the situation where either there is no any wireless communication infrastructure present or such infrastructure cannot be used such as in battlefields, emergency search-and-rescue operations, and disaster environments [1]. Collaborative computing and communication in smaller areas (educational buildings, conferences, etc.) also can be set up using MANETs.

Since MANET is characterized by its fast changing topology, extensive research efforts have been devoted to the design of routing protocols for MANETs [1, 4, 5]. However, the most existing work is based on non-QoS requirement for example the source node attempts to transmit data to the destination node without any delay or bandwidth guarantee. As the real-time applications such as multimedia stream, live voice and video conference grow rapidly and sensitive with delay and bandwidth, QoS features become more important. However, the mobile nature, limited resource, and dynamic topology of MANETs make it complicates to provide QoS guarantee in such network.

There are many researches on QoS support in MANETs include QoS models [6], Layered QoS [2], QoS Medium Access Control (MAC) [7], and QoS routing [3, 8] which only consider with a single QoS constraint and sometimes it is not suitable to the highly unpredictable ad hoc environment. In order to guarantee the real-time and multimedia applications with QoS requirement, we propose a QoS-Based Dynamic Source Routing (QDSR) protocol. The protocol finds the route that meets the multiple QoS constraints and has a better chance for surviving over a period of time from node movement. The multiple QoS constraints considered here are delay, bandwidth and signal strength. The rest of the paper is organized as follows. In Section II, we introduce all related works. The proposed scheme QDSR is presented in Section III. Section IV presents our simulation and results. Finally, conclusion and future work are given in Section V.

II. RELATED WORK

A. MANETs Routing Protocols

Routing protocols in ad hoc networks can be classified into three groups [1]: *Proactive* (*Table Driven*), *Reactive* (*On-Demand*) and *Hybrid* as shown in Fig. 1.

A.1 Proactive (Table Driven) routing protocols

Proactive routing protocols come as a natural extension of protocols for the wired network. In these routing protocols, each node has a number of tables to maintain routing information to every other node in the network and these tables are updated periodically. Examples of proactive routing protocols are DSDV, WRP, CGSR [1] and so on. Since using periodic update, these protocols allow some significantly overheads and consume bandwidth in the network.

A.2 Reactive (On-Demand) routing protocols

Unlike proactive routing protocols, reactive routing protocols neither maintain nor periodically update their route tables. Several reactive routing protocols have been proposed such as DSR, AODV, TORA [1, 5] and so on. These routing protocols were designed to overcome the overheads occurred in proactive protocols.

DSR is one of the more commonly accepted routing protocols [5]. In DSR, when a node wishes to send data packets and does not have any routing information, it initiates a route discovery by flooding all of its neighbors with route request (RREQ) packets. Each neighbor broadcasts this

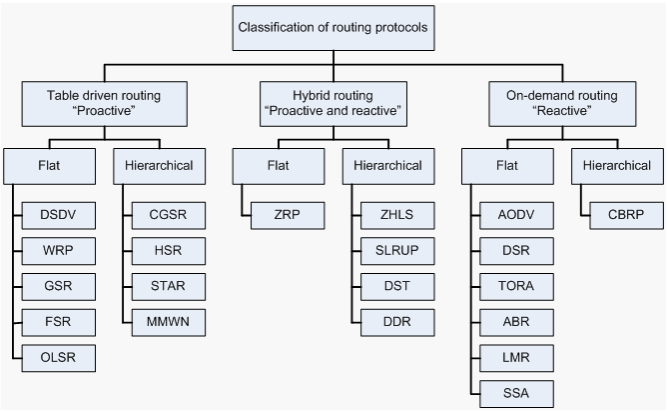

Figure 1. Classification of routing protocols

RREQ, adding its own address in the header of packet. When the RREQ is received by the destination or by a node that have a route to destination, a route reply (RREP) is generated and sent back to the sender along with the addresses accumulated in the RREQ header. Route maintenance is invoked when the source node detects the broken link and then it can choose any other route to the destination node or invokes the route discovery again to find the new route to destination.

A.3 Hybrid routing protocols

Hybrid routing protocols combine proactive and reactive routing protocols. These protocols are designed to increase scalability when the wireless networks become larger. All nodes in the network are separated into groups. Each group is called a cluster. All clusters form a hierarchical infrastructure. In these routing protocols, the proactive maintains routes in a cluster and reactive maintains routes between clusters. Several hybrid routing protocols have been proposed such as ZRP, ZHLS, DDR [1] and so on.

B. QoS Routing

QoS routing is the critical issue in MANETs due to mobility, mobile nature, and resource limitation. Some technical challenges are described in terms of designing optimal routes, providing reliable transmission, robustness, efficiency in resource utilization, adaptability, and unlimited mobility.

Normally, QoS routing protocols can be classified into two main groups. The first group concerns with some traditional protocols extended with QoS features. Their goal is to eliminate among the selected routes that do not meet the given criteria. The second group takes into account QoS aspect within the routing algorithm. Two types of constraints exist such as application specific [8, 10] (e.g. bandwidth or delay) and network specific features (e.g. congestion, energy constraint and link stability) [9, 11]. We can conclude that most of QoS routing protocols merely focus only on one application's QoS requirement based on a single QoS constraint which is not usually suitable to the highly unpredictable and dynamic ad hoc environment.

III. QoS-Based Dynamic Source Routing Protocol

In MANETs, the data service can be classified into two groups. The first group is the non real-time data service which bandwidth is not so sensitive and allows the delay during transmission. Examples of this service are file transfer, web documents and other traditional datagram applications. The second group is the real-time data service which bandwidth and delay are very sensitive such as on-demand multimedia stream, video and audio conference, etc. This kind of traffic needs QoS guarantee on the route. The proposed scheme constitutes an extension of DSR routing protocol, in which QoS features are embedded in the selection and maintenance of the routes.

A. QDSR procedures

QDSR relies on three procedures: route discovery, route reservation and route maintenance.

1. Route discovery

QDSR adds a QoS header to an ordinary route request (RREQ) packet and has the following fields: <*packet_type*, *source_addr*, *dest_addr*, *seq_num#*, *route_list, link_info* (*delay*, *bandwidth*, *signal*), *slot_array_list*, *traffic_type*, *bw_slot_req*, *qos_function*, *TTL*, *data*>. The following QoS metrics are used in our proposed scheme to provide the network layer with QoS requirement that are used during route discovery:

- **Delay**: The end-to-end delay from a source to a destination that the application can tolerate.
- **Bandwidth**: The lowest bandwidth that the application can tolerate on the route.
- **Signal Strength**: More stable route through dynamic network topology that has probability of surviving longer.

In this paper, we consider the combination of delay, bandwidth, and signal strength as the QoS function for selecting the appropriate route from source to destination.

a) Source node algorithm

When a source node wishes to send the real-time data packets, it first checks its resource availability such as free slots for bandwidth. If there is no resource available, the route discovery is canceled and the upper layer is informed. If the source node has sufficient resource, it will check the route in the route cache whether there is a route to the destination that satisfies the traffic requirement. If no valid route is stored in the route cache, the source node will place the information in RREQ header, initializes the QoS function and broadcasts the RREQ packet to its neighbors.

b) Intermediate node algorithm

This algorithm is executed by intermediate nodes on receiving a RREQ packet. From Fig. 2, we can explain the process of intermediate nodes as the following steps:

1. If the pair <*dest_addr*, *seq_num#*> for the RREQ is seen recently, check whether Time to Live (TTL) is zero or not, if TTL counts down to zero, we drop the RREQ and do not

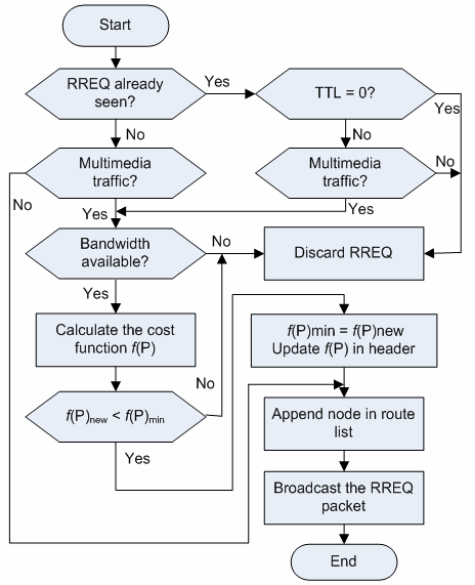

Figure 2. Intermediate node algorithm

process it further. TTL can limit the length of delivery path and control the flooding traffic.

2. Check whether the route request is searching for the path of multimedia traffic or common data traffic. If the traffic is multimedia traffic, the intermediate node calculates the available bandwidth from the source to this node using path bandwidth calculation and records the state of the data slots to the *slot_array_list*. If the result does not satisfy the QoS requirement, we drop the RREQ.
3. Compute the QoS function including the link delay, available bandwidth and received signal strength. The QoS function of path P is given by a heuristic formula (1):

$$f(P) = 1/\left((d - D(P))^{\alpha} + BW(P)^{\beta} + \left(S(P)/Rt\right)^{\gamma}\right) \qquad (1)$$

where $D(P)$ is the delay at given path, d is the maximum delay that application can tolerate, $BW(P)$ is the available path bandwidth, $S(P)$ is the minimum signal strength along the path, and Rt is the received signal threshold. α, β and γ are fixed parameters used to show relative importance about delay, bandwidth and signal strength in QoS routing.

4. Decrement TTL by one and append the address of this node to the *route_list* to track the route which the packet has traversed.
5. Selectively re-broadcast RREQ packet based on the QoS function. In order to reduce the broadcast storm and routing overhead, an intermediate node can re-broadcast a second RREQ packet only if it has lower QoS function than the first RREQ packet, otherwise the RREQ will be discarded.

c) Destination node algorithm

When the first RREQ packet with QoS enabled reaches the destination, the node starts the timer interval and during that time the node examines the QoS function of every arrived RREQ packet. When the timer interval expired, the destination node selects the RREQ packet that has the lowest QoS function and sends the route reply (RREP) packet carrying this route to the source node. When another RREQ packet with the same sequence number arrives after the threshold time interval, it will not be considered and do not process it further. Fig. 3 shows the process of destination node when receive RREQ packets.

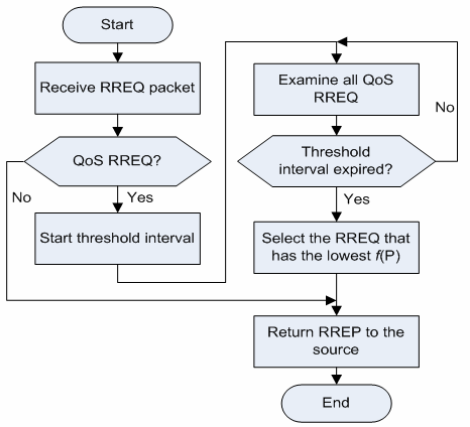

Figure 3. Destination node and route decision algorithm

2. Resource reservation procedure

On receiving the RREQ packet, the destination node reserves resource using a TDMA-based bandwidth reservation model. As a RREQ packet travels from the source to the destination, it automatically sets up the reverse path from the destination back to the source. From the RREQ packet, we can obtain the state of data slots and according to the information recorded within the RREQ packet. The destination can set up a QoS route and reserves resources (slots) hop-by-hop backward to the source. If the reservation operation fails or the resource are not available, a route error (RRER) packet is sent.

3. Route maintenance

If the destination node does not receive the data packet in reserved time slot, it considers that the link is broken and uses its dedicated control time slot to broadcast a route error (RERR) packet with finite TTL. Any node in the QoS route will forward the RERR packet to the source. On receiving the RERR packet, the source can re-establish a new RREQ with QoS enabled.

IV. Simulation and Result

Network Simulator (NS-2) is used to analyze the performance of QDSR. The performance of our proposed scheme is then compared to DSR. Only the route discovery procedure has been implemented and the maintenance procedure is the one implemented in DSR.

A. *Simulation model and parameters*

The simulations were run using an ad hoc network model composed of 8 nodes that moved randomly at uniform speed over a rectangular area 800 x 800m flat space. The simulation parameters and constant values for $f(P)$ in Eq.(1) are shown in Table I and II, respectively.

TABLE I. SIMULATION MODEL

Parameter	Value
Simulation area	800 x 800m
Number of nodes	8 nodes
Max speed	0 - 10 m/s
Node movement	Random
Transmission range	250 m
Source / Packet size	CBR / 512 bytes
Sending rate	20 packets/sec

TABLE II. CONSTANT VALUES

Constant	Value
α	0.3
β	0.3
γ	0.4
Max delay (d)	1 sec
Rt	3.65×10^{-10}

B. *Simulation results*

The result of simulation is shown in Fig. 4. We notice that QDSR improves the average throughput in comparison to DSR. When the mobility is increased, the performance of DSR will be significantly degraded. Adding more QoS criteria in the selection of intermediate nodes along the path leads to a more reliable data transmission which improves the throughput.

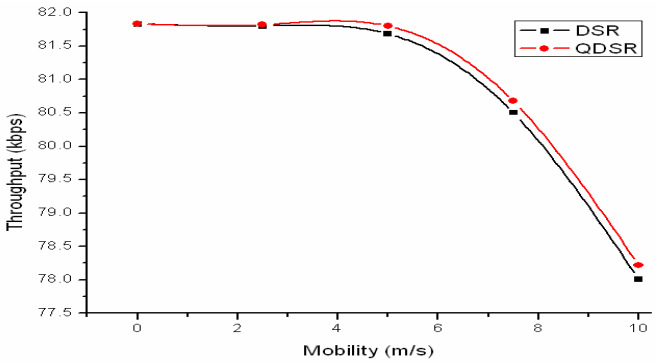

Figure 4. Average throughput versus mobility

In Fig. 5, we show the packet loss rate versus mobility. It also shows that the packet loss rate is proportional to the node's mobility. When the network becomes congested or the route is broken frequently due the mobility, many packets will be discarded or lost. The lower packet loss rate implies the more stable route. Since our proposed scheme involves the multiple QoS constraints and selects the most feasible and stable route, the probability of broken route can be decreased and that leads the lower packet loss rate than those on DSR.

V. CONCLUSION AND FUTURE WORK

We propose a new approach for QoS-aware routing to support multimedia applications in mobile ad hoc networks.

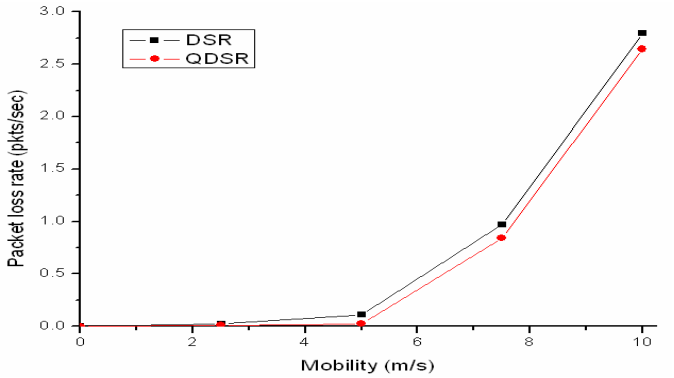

Figure 5. Packet loss rate versus mobility

Our proposed scheme, QDSR, considers with multiple QoS constraints such as delay, bandwidth, and signal strength to find the most feasible route from the source node to the destination node. It also selects the most stable links which leads to longer-lived routes and reduces route maintenance. We can conclude that our proposed scheme provides the improvement in terms of throughput and lower packets lost for real-time traffic and multimedia services in small networks.

Our future works will consequently consist in adding more functionalities such as improving the maintenance procedure and analyzing the effect of QoS function parameters on the performance of our proposed scheme.

REFERENCES

[1] Mehran Abolhasan, Tadeusz Wysocki, and Eryk Dutkiewicz,"A Review of Routing Protocols for Mobile Ad Hoc Networks," *Ad Hoc Networks*, Volume 2, Issue 1, Pages 1 – 22, January 2004.

[2] P. Mohapatra, J. Li, and C. Gui, "QoS in Mobile Ad Hoc Networks," IEEE Wireless Communications, pp. 44 - 52, June 2003.

[3] B. Zhang and H.T. Mouftah, "QoS Routing for Wireless Ad Hoc Networks: Problems, Algorithms, and Protocols," *IEEE Communications Magazine*, Volume 43, Issue 10, Page(s):110 – 117, Oct. 2005.

[4] C.E. Perkins and P. Bhagwat, "Highly Dynamic Destination-Sequenced Distance-Vector routing (DSDV) for Mobile Computers," *Proceedings of SIGCOMM '94*, pp. 234 - 244, August 1994.

[5] D.B. Johnson, D.A. Maltz, and Y-C. Hu, "The Dynamic Source Routing for Mobile Ad-hoc Networks," *IETF Internet draft*, 19 July 2004.

[6] G.S. Ahn, A.T. Campbell, A. Veres, L.H. Sun, "Supporting Service Differentation for Real-Time and Best-Effort Traffic in Stateless Wireless Ad Hoc Networks (SWAN)", *IEEE Transactions on Mobile Computing*, Vol.1, No.3, pp.192-207, 2002.

[7] IEEE 802.11e/D6.0, "Draft Amendment to Standard for Information Technology – Telecommunications and Information Exchange between Systems – LAN/MAN Specific Requirements – Part 11: Wireless Medium Access Control (MAC) and Physical Layer (PHY) Specifications: Medium Access Control (MAC) Quality of Service (QoS) Enhancements," Nov. 2003.

[8] C.R. Lin and J.-S. Liu, "QoS Routing in Ad Hoc Wireless Networks", *IEEE Journal on Selected Areas in Communications,* Vol. 17, No. 8, pp. 1426-1438, August 1999.

[9] J. Li, D. Cordes and J. Zhang, "Power-Aware Routing Protocols in Ad Hoc Wireless Networks," *IEEE Wireless Communications*, December 2005.

[10] R. Sivakumar, P. Sinha, V. Bharghavan, "CEDAR : A Core Extraction Distributed Ad Hoc Routing Algorithm ", IEEE JSAC, vol.17,no. 8, pp 1454-65, Aug. 1999.

[11] R. Dube, C. D. Rais, K-Y Wang, and S. K. Tripathi, "Signal Stability-Based Adaptive Routing (SSA) for Ad Hoc Mobile Networks," *IEEE Personal Communications*, Volume 4, Issue 1, pp. 36 - 45, Feb. 1997.

Optimal Frequency Channel Assignment for WLANs Using Hybrid SIR and CSMA/CA Considerations

Chutima Prommak, Boriboon Deeka
School of Telecommunications Engineering, Suranaree University of Technology
Nakorn Ratchasima, Thailand 30000
cprommak@sut.ac.th, M4740452@sut.ac.th

***Abstract*-This paper presents a novel frequency channel assignment algorithm for Wireless Local Area Networks (WLANs). The proposed algorithm accounts the physical signal quality (considering SIR level in the service area) and the system throughput (considering the medium access control protocol, CSMA/CA). A multi-objective integer linear programming problem is defined. The proposed objective function separates the physical signal quality and the system throughput contributions in order to differently change the weights of the two characteristics of WLANs. Numerical results are presented and the jointed impact of signal quality and the system throughput are evaluated.**

I. INTRODUCTION

Frequency channel assignment is one of complicated tasks in the Wireless Local Area Networks (WLANs) design due to not only the limited unlicensed frequency spectrum in which the networks can operate but also the unique Medium Access Control (MAC) functionalities specified by the Institute for Electrical and Electronic Engineers (IEEE) 802.11 working group [1].

The IEEE 802.11b and 802.11g operate at the 2.4 GHz band while the IEEE 802.11a operates at the 5 GHz band. In North America, 83.5 MHz bandwidth is available in the 2.4 – 2.4835 GHz band while 300 MHz bandwidth is allocated in the 5.15 – 5.35 MHz (lower-band) and 5.725 – 5.825 MHz (upper-band). The 802.11 standard divides the 2.4 GHz band into eleven channels with center frequencies located 5 MHz apart as shown in Figure 1. Each channel has a frequency bandwidth of 22 MHz. Among these eleven channels are three channels whose bandwidths do not overlap each other. Those channels are 1, 6 and 11, as there is a frequency space of 3 MHz between channels 1 and 6 as well as between channels 6 and 11. These three channels are called the non-overlapping channels, and they can be assigned to adjacent APs without interfering with each other. The remaining channels overlap with one of the three non-overlapping channels and are called the overlapping channels.

Since a limited number of channels exist in the available frequency spectrum for an 802.11 WLAN, a multi-cell network deployment requires that some channels are reused. Reuse of frequency channels in neighboring cells can cause interferences in the service area. Thus, frequency channels of APs must be carefully assigned in the multi-cell WLANs.

The issues on quality of signal in the target service areas and the concerns about system throughput are two important metrics to be accounted in the frequency channel assignment process. However, in the majority of the published papers, the attention is focused on either one of the two aspects. Traditionally, the frequency channel assignment used in the cellular network design is based on the use of channel-separation matrix [2, 3] and the graph coloring approaches [4]. Recent study in [5] shows that the frequency channel assignment for WLANs using the signal quality based approach outperform those using the traditional channel-separation based approach and yield WLAN systems with higher signal quality in the service area. However [5] does not consider throughput of the WLAN system. Recent work [6] considers the medium access control (MAC) protocol in the frequency channel assignment procedures but only focuses on maximizing system throughput and does not consider coverage of signal in the service area.

In this paper we propose a hybrid technique that allows to optimize both criteria (signal quality and system throughput). We present a multi-objective integer programming model for the frequency channel assignment problem (FCAP) for WLANs. The proposed model takes into account the interference level and the WLANs' MAC protocol to reflect the target criteria.

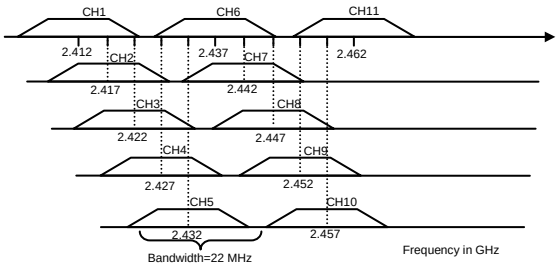

Figure 1 Frequency spectrum allocation for IEEE 802.11b and 802.11g

The rest of the paper is organized as follows. The next section describes the problem definition of the FCAP for WLANs and gives the mathematical formulation of the FCAP model. Section III gives numerical results and discussion. Section IV provides conclusions.

II. Problem Definition and Formulation

In WLANs context, the Frequency Channel Assignment Problem (FCAP) involves assigning frequency channels from a set of available channels to the access points (APs) in WLANs. In this paper we jointly determine the locations to install APs while considering fixed level of AP transmitting power (which is a given value). The proposed FCAP model takes into account two important aspects of the WLAN operation, including the signal quality in the service area and the system throughput.

A. System Throughput Considerations

In WLANs, user terminals rely on a common (broadcast) transmission medium. Only one terminal can occupy the medium at a time. If multiple terminals simultaneously transmit, a collision may occur and the signal could be corrupted. The IEEE 802.11 standard specifies a Medium Access Control (MAC) protocol, called Carrier Send Multiple Access/ Collision Avoidance (CSMA/CA), to coordinate transmission of the user terminals. This coordination is achieved by means of control information. This information is carried explicitly by control messages traveling in the medium (i.e. ACK messages) and can be provided implicitly by the medium itself through the use of a carrier-sensing mechanism before each transmission to check if the channel is either active or idle.

Control messages and message retransmission due to collisions consumes medium bandwidth. They are overhead required by a MAC protocol that coordinates transmissions of user terminals. According to the throughput analysis of the CSMA/CA protocol, the AP throughput varies depending on the number of users connecting with the AP [7]. As the number of wireless users in the AP coverage area increases, the AP throughput decreases. An efficient frequency channel assignment technique accounting for the CSMA/CA protocol can help improve the AP throughput, resulting in higher system throughput.

Thus, the important objective function for the FCAP with the system throughput consideration is to maximize the system throughput which is a summation of throughput of all APs used in the network. This objective can be written as follows:

$$f_1\text{: } max \sum_{\forall j \in A} t_j \qquad (2)$$

We adopt a throughput estimation technique developed in [6] to compute AP throughput (t_j). Please refer to [6] for detail equation and parameters to compute t_j.

B. Signal Quality Considerations

In the proposed FCAP model, we consider signal quality in the network because the service availability of the network depends on availability of the radio signal and the level of interferences in the area. In particular, we adopt the signal-quality based approach presented in [5] which considers the signal to interference ratio (SIR) that is assessed at all STPs in the target service area. Thus, the important objective function for FCAP with the signal quality consideration is to maximize the signal coverage availability by maximizing the number of STPs whose SIR are greater than the specified threshold. This objective can be written as follows:

$$f_2\text{: } max \sum_{\forall g \in G} x_g \qquad (1)$$

C. Math Model

On the basis of the signal quality and the system throughput considerations, the problem of assigning the best frequency channels to APs in WLANs, accounting the interference level and the CSMA/CA functionalities, can be mathematically formulated as the hybrid model written below.

$$f_3\text{: } max \quad w_1 \sum_{\forall j \in A} t_j + w_2 \sum_{\forall g \in G} x_g \qquad (3)$$

The objective function f_3 is a popular approach used to deal with multi-objective optimization problems [8], transforming the problem f_1 and f_2 into a single objective function that maximizes a combination of the two problems by using factors w_1 and w_2 to weight the importance of each problem.

TABLE I
NOTATION USED

Notation	Definition
A	Set of access points (APs) in the network. $\|A\|$ is the total number of APs used in the network.
G	Set of Signal Test Points (STPs). It represents locations in the service area where the signal to interference ratio (SIR) level are assessed. $\|G\|$ is the total number of STPs in the service area.
s_g	SIR assessed at STP g, $g \in G$
s_t	SIR threshold
x_g	Binary variable equals 1 if $s_g > s_t$; 0 otherwise
t_j	Throughput of AP j, $j \in A$
f_j	Frequency channel of AP j, $j \in A$
w_1	Weight ascribed to the system throughput consideration
w_2	Weight ascribed to the signal quality consideration

III. Numerical Results and Discussion

To evaluate the performance of the proposed hybrid FCAP model (f_3), we conducted numerical experiments using the same test scenario as that used in [6] where the building floor is divided into grid granularity of 5 m., a uniform distribution of user terminals was considered and the 16 AP candidate locations were given. The Two-Ray-Ground model was used to predict the signal strength. We considered three non-overlapping frequency channels (1, 6, and 11) for the frequency assignment and used the SIR threshold of 10 dB. We used $w_1 = w_2 = 0.5$.

We compared frequency channel assignment solutions obtained by the three FCAP models, f_1 (the throughput based model), f_2 (the signal quality based model) and f_3 (the hybrid model), where the solutions were found by using the patching algorithm [6]. The resulting WLAN systems using the frequency channels obtained by each model were compared in term of the coverage area and the system throughput.

Figure 2 and 3 compare the system throughput and the coverage area of the WLAN system using frequency channels obtained by the model f_1, f_2 and f_3. We can see that the hybrid model, f_3, yields the WLAN system with high system throughput and good signal coverage. Figure 2 shows that f_1 results in the highest system throughput while f_2 results in the lowest system throughput. We can see that f_3 results in very high system throughput, much better than that of f_2 and only slightly less than that of f_1. Figure 3 shows that f_1 results in the lowest coverage area while f_2 and f_3 result in the highest coverage area.

We conducted another set of numerical experiments to study effects of number of users in the service area on the performance of the FCAP model. We considered three scenarios of the use density; low, medium and high. We used a uniform distribution of 0 to 2 users per grid in the low user density scenario, 2 to 4 users per grid in the medium user density scenario, and 4-6 users per grid in the high user density scenario.

From figure 4 and 5, we can observe that in all case of user density f_3 results in higher system throughput compared to that of f_2 and results in better signal coverage compared to that of f_1. Although f_1 yields WLAN system with higher system throughput but it results in much less signal coverage compared to that of f_3. For example, in case of high user density, coverage area of the WLAN system using f_1 is 50.8% less than that using f_3.

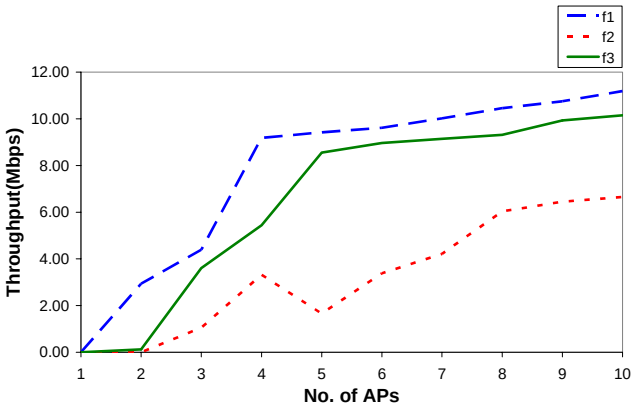

Figure 2. System throughput comparison as the number of APs increases

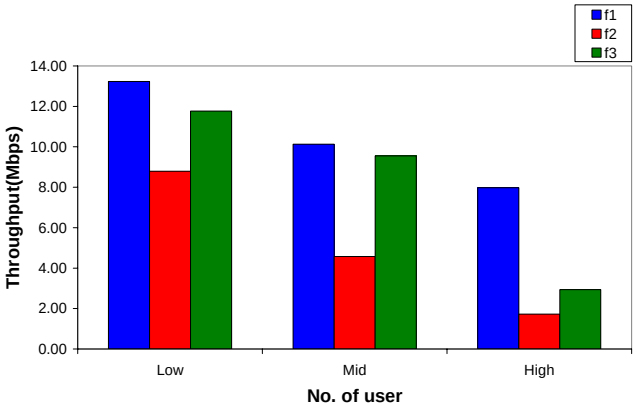

Figure 4. System throughput comparison as the number of users increases

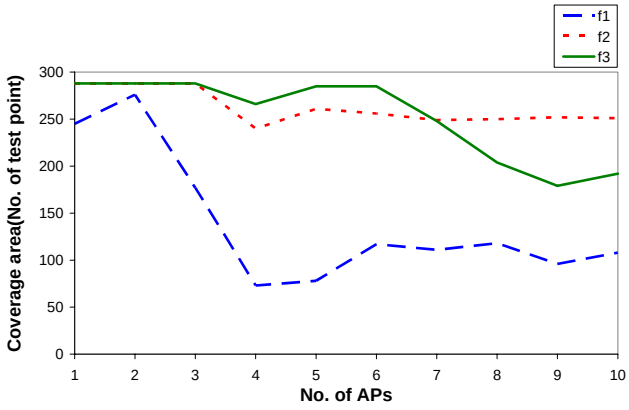

Figure 3. Coverage area comparison as the number of APs increases

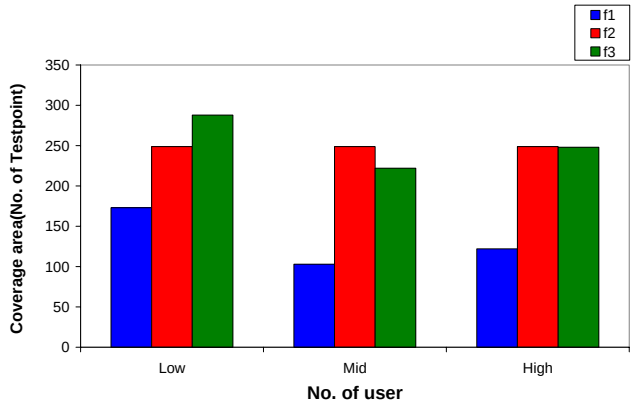

Figure 5. Coverage area comparison as the number of users increases

IV. Conclusion

A novel hybrid model that accounts the system throughput and the signal quality in the service area has been formulated as a multi-objective linear programming. The numerical results show that the hybrid model can enhance the WLAN system performance in term of system throughput and coverage area while the signal quality based model results in low system throughput and the throughput based model results in poor signal coverage.

Acknowledgment

This work has been supported in part by the SUT (Suranaree University of Technology) research fun through the grant "Quality-of-Service Network Planning for Large Scale Wireless LANs".

References

[1] "IEEE standard for information technology- telecommunications and information exchange between systems- local and metropolitan area networks- specific requirements Part II: wireless LAN medium access control (MAC) and physical layer (PHY) specifications," *IEEE Std 802.11g*, 2003, pp. i-67.

[2] K. N. Sivarajan et al., "Channel assignment in cellular radio," *IEEE Trans Veh. Technol*, p. 846-850, May 1989.

[3] S. U. Thiel, S. Hurley, and D. H. Smith, "Frequency assignment algorithms," Dept. of Computer science, University of Wales Cardiff, UK, Ref. RCCM 070, April 1997.

[4] C.-W. Sung and W.-S. Wong, "A graph theoretic approach to the channel assignment problem in cellular systems," in *Proc. 45th IEEE Veh. Technol Soc. Conf.*, July 1995

[5] C. Prommak and B. Deeka, "On the Analysis of the Optimal Frequency Planning for Wireless Local Area Networks", *The Fourth PSU Engineering Conf. (PEC-4)*, pp. 77-81, December 2005.

[6] X. Ling and K. Lawrence Yeung "Joint Access Point Placement and Channel Assignment for 802.11 Wireless LANs," *IEEE Wireless Communications and Networking Conf.*, pp. 1583-1588, 2005.

[7] F. Cali, M. Conti, and E. Gregori, "Dynamic tuning of the IEEE 802.11 protocol to achieve a theoretical throughput limit," *IEEE/ACM Trans. On networking*, vol. 8, pp.785-799, 2000.

[8] Y. Colletter and P. Siany, *Multi-objective Optimization: Principles and Case Studies (Decision Engineering)*. Springer-Verlag, 2003.

Compact Microstrip Two-layer Dual-Band Bandpass Filter Using Aperture-coupled SIR-Hairpin Resonator

Sutatorn Promprathom[1], Jaruek Jantree[2], Sarawuth Chaimool [1] and Prayoot Akkaraekthalin [1]

[1]Department of Electrical Engineering, Faculty of Engineering, King Mongkut's Institute of Technology North Bangkok, 1518 Pibulsongkram Rd. Bangsue, Bangkok 10800,Thailand
[2]Department of Electrical Engineering, Faculty of Engineering and Architecture, Rajamangala University of Technology Suvarnabhumi, Thailand.

***Abstract*- A compact two-layer dual-band bandpass filter using aperture-coupled microstrip stepped-impedance hairpin resonator is proposed and designed to operate at 2.4 and 5GHz band. The proposed dual-band filter is composed of four stepped-impedance hairpin resonator located on two stacked microstrip layers. To validate the design and analysis, a prototype of the dual-band bandpass filter was fabricated and measured. It is shown that the measured and simulated performances are in good agreement. The prototype of the dual-band bandpass filter achieved insertion losses of 2.29 and 2.978 dB, return losses of 20 and 15 dB at 2.4 and 5GHz band, respectively. As result, a significant reduction of approximately 50 % is achieved.**

I. INTRODUCTION

Microwave planar bandpass filters are mostly employed in wide applications of wireless communication systems in the present day [1]. Recently, in exploring advanced dual-band wireless systems, filters with dual-band operation for microstrip devices have become quite popular. Therefore, dual-band filters have been widely studied in several papers. This type of dual-band filter was initially reported in [2]-[8] by the combination of two individual filters with two specific single passbands. Extra impedance-matching networks must be used to design the input and output structure of the filter. Unfortunately, this solution suffers from high insertion loss and large overall size in its resultant filter block. Using the basic topology of a stopband filter in [3] and [4], uniform transmission line is interrupted with multiple shunt stubs of unequal lengths so as to enforce the emergence of dual passbands relying on multiple transmission zeros. Parallel-coupled microstrip dual-band filter without any external feeds is originally presented in [5] to realize the controllable dual-passband bandwidth at the two specified frequencies. On the other hand, an increasing interest has been recently moving to utilize the stepped-impedance resonator (SIR) for constructing the dual-band resonators by properly selecting the relevant impedance or strip width ratio [6]-[8].

As a consequence, this approach may cause some problematic issues, such as large size and extra loss in design. To resolve this problem, two–layer or multilayer filter designs become suitable approaches for a filter-size reduction. For instance, these two-layer filter structures have been presented in [9] and [10]. In approaches, open-loop resonators have been employed. In the same perspective, another two-layer design with one aperture for the mixed coupling has been investigated in [11]. From previous approaches, it can be noted that only open-loop resonators with one type of coupling have been considered.

This paper presents a four-pole chebyshev function dual-band bandpass with aperture-coupled microstrip resonators. By using two-layer technique, the dual-band filter has a compact size, which is much smaller than single layer. In addition, the cross-coupling between nonadjacent resonators creates transmission zeros that improve the selectivity.

In section II, theories and guidelines for calculating the geometric parameters of SIRs have been presented. The design procedures for the filter are given in section III. The simulation results are compared with the measured data. Finally, brief conclusions are draws in section IV.

II. CHARACTERISTICS OF STEPPED-IMPEDANCE RESONATOR

The basic structure of a half-wavelength microstrip stepped-impedance resonator (SIR) is shown in Figure 1. It consists of two lines of different characteristic impedance Z_1 and Z_2 and of electrical lengths θ_1 and θ_2 , respectively. To simplify the theory analysis, the basic structure of a half-wavelength SIR, show in Figure 1. Ignoring the effect of the step discontinuity, the fundamental resonance condition of a SIR can be derived by examining the input admittance Y_{in} of the composite transmission line from the open plane, and it can be written as [12].

$$Y_{in} = jY_2 \frac{Y_2 \tan\theta_1 \tan\theta_2 - Y_1}{Y_2 \tan\theta_1 + Y_1 \tan\theta_2} \tag{1}$$

The resonance condition given by $Y_{in} = 0$ can be described as follows:

$$\tan\theta_1 \tan\theta_2 = R \tag{2}$$

where the impedance ratio R is defined by

$$R = \frac{Z_2}{Z_1} = \frac{Y_1}{Y_2} \tag{3}$$

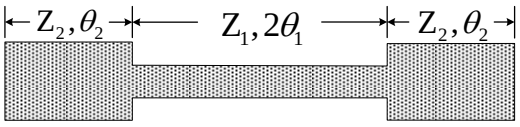

Figure 1. Basic structure of the stepped-impedance resonator (SIR)

The relationship between the total electric length θ_T and the resonator and electric length θ_1 is given by

$$\theta_T = 2(\theta_1 + \theta_2) \quad (4)$$

$$\theta_T = 2\left(\theta_1 + \tan^{-1}\left(\frac{R}{\tan\theta_1}\right)\right), \quad R \neq 1 \quad (5)$$

$$\theta_T = \pi, \quad R=1 \quad (6)$$

From Eq. (4), it can be shown that the resonator length reaches a minimum value for 0< R < 1 and a maximum value when R>1, which means that we should choose a very small value of R in order to obtain the smallest filter size. It may be shown that the first spurious resonance frequency is given by [12]

$$\frac{f_{s1}}{f_0} = \frac{\pi}{2\tan^{-1}\sqrt{R}} \quad (7)$$

From Eq. (7), it is clear that the spurious response can be controlled by the characteristic impedance ratio R. In this design, we set f_0 and f_{s1} to be 2.442and 5.250 GHz, respectively.

III. Filter Design and Measured Results

A. Coupling Coefficients

In order to design filters with required specifications, such as bandwidth, it is necessary to evaluate the coupling coefficients *k* between two adjacent resonators. In this way, the dependence of the electric coupling and magnetic coupling can be expressed as a function of the distance. However, the mixed coupling coefficient depends on the dimensions and the location of the apertures. It has been known that the coupling coefficient of two coupled resonators can be extracted from resonant-mode splitting [9].

Figure 2 shows the simulated resonant frequency responses of coupled resonator structures. Two split resonant-mode frequencies are easily identified by the two resonant peaks. To simulate the frequency responses of these basic coupling coefficients, full-wave simulator (IE3D) was used. The coupling coefficient can be graphically estimated from these two resonant frequencies, and they are extracted using the following relation

$$k_{ij} = \pm\frac{f_b^{\,2} - f_a^{\,2}}{f_b^{\,2} + f_a^{\,2}} \quad (8)$$

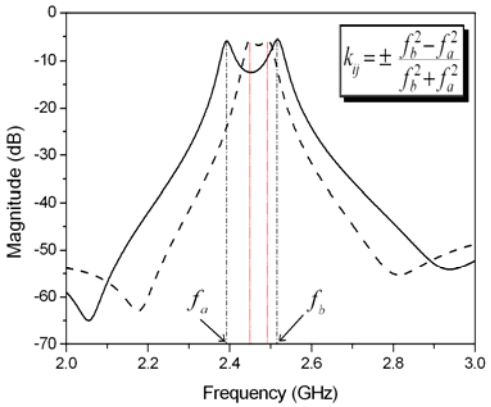

Figure 2. Resonant responses of coupled resonator structures.

where f_a and f_b are the lower and higher split resonant frequencies of a pair of couple resonators.

Figure 3 shows the three possible coupling coefficient curves as a function of distance d for the electric and magnetic couplings or aperture dimensions dx, dy for mixed coupling, respectively. From these results, it can be seen that the mixed coupling increases as aperture sizes are increased.

B. U-Shaped Defected Ground Structure (DGS)

A compact duable equilateral U-Shaped DGS unit is proposed in [13]. The dimension structure of U-Shaped DGS shown in Figure 4 with proper design, the stopband performances of the structure consists of two slot defected areas. Therefore, the dimension must be optimized to get the proper high performance stopband response.

C. Measured results

Based on the proposed design, dual-band bandpass filter prototype using two layer substrates was fabricated. The filter prototype was built with GML 1000 substrates with a relative dielectric constant of 3.2 a loss tangent of 0.004 and thickness of 0.762 mm by using a standard printed circuit board (PCB) process. Figure 5 shows cross-sectional view of two-layer dual-band bandpass filter. The optimized filter layout parameters have been obtained in the following d_{14}= 0.544mm, d_{12}= 0.477mm, d_{23}= 0.85mm, d_x= 4.52mm and d_y= 3.2695mm, W_a = 0.7mm, W_b = 0.3mm, L_a = 3.76mm and L_b = 3.0mm, respectively.

Figure 6 shows a prototype, where only the two resonators on the top layer are visible. To examine the filter performances, experimental measurements were carried out using an Agilent 8719ES network analyzer. Figure 7 shows the simulated and experimental results of S_{11} and S_{21}. It can be observed that the simulated and measured results display a good agreement. The measured return losses in both 2.4GHz and 5GHz bands are higher than 18 dB while the measured insertion losses are 2.29 dB and 2.978 dB, respectively.

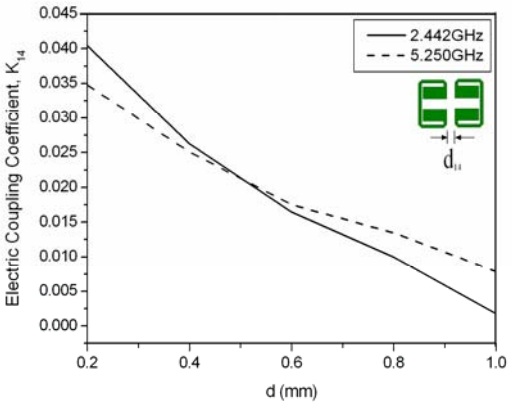

(a)

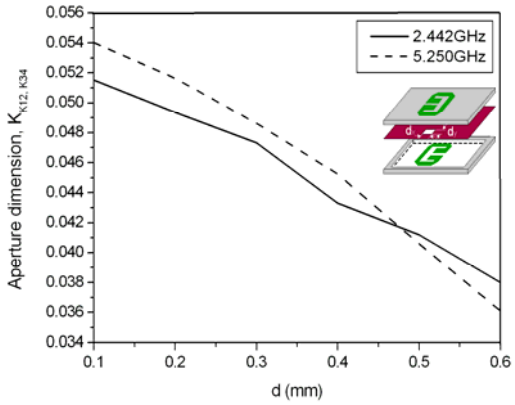

(b)

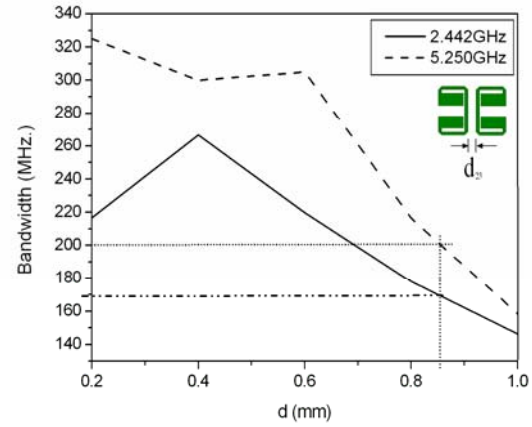

(c)

Figure 3. Typical coupling coefficients of the different coupling structure (a) Electric coupling, (b) Magnetic coupling and (c) Mixed coupling.

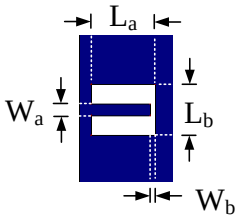

Figure 4. Dimensions structure of U-Shaped DGS.

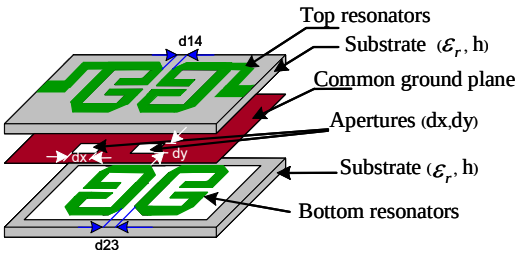

Figure 5. Cross-sectional view of the proposed filter.

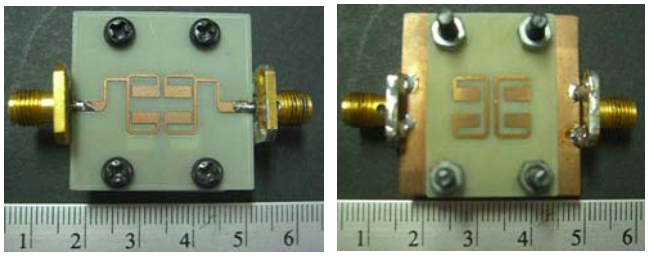

(a) (b)

Figure 6. Photograph of the fabricated circuit prototype. (a) Top-layer and (b) Bottom-layer

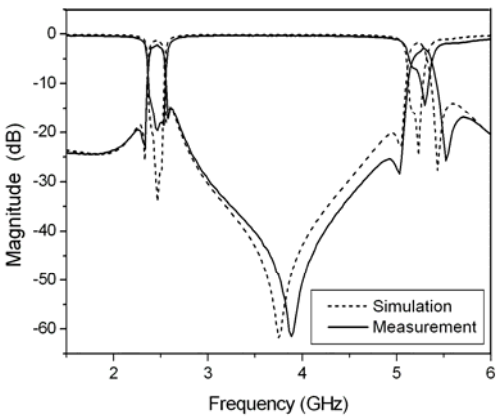

Figure 7. Comparisons of simulated and measured responses.

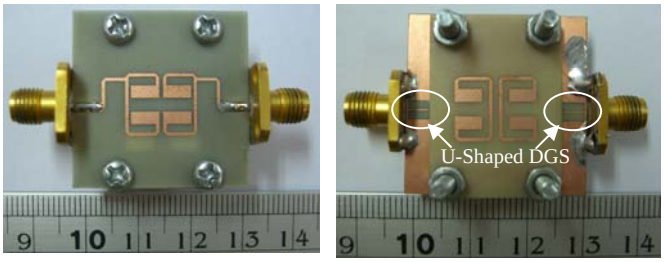

(a) (b)

Figure 8. Photograph of the fabricated circuit prototype with U-Shaped DGS. (a) Top-layer and (b) Bottom-layer

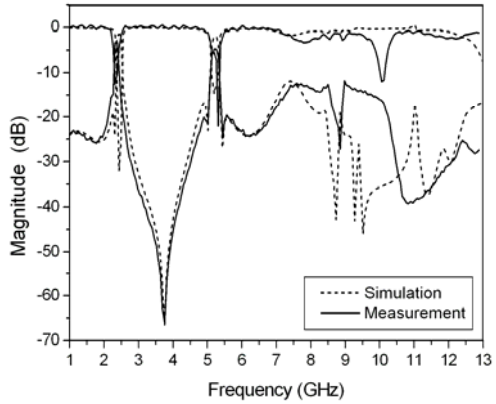

Figure 9. Comparisons of simulated and measured responses with U-Shaped.

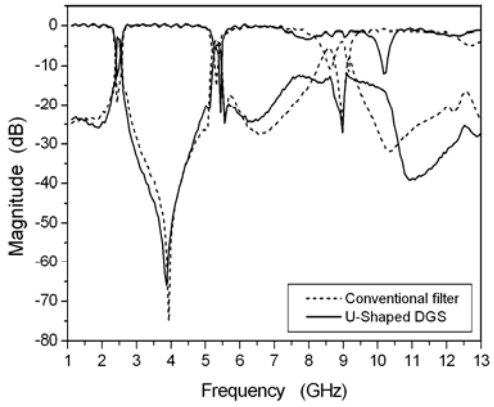

Figure 10. Comparisons of measured responses.

Figure 8 shows photograph of the U-Shaped DGS. Figure 9 shows the comparisons of simulated and measured responses of the proposed filter with U-Shaped DGS. Designed defected ground structure shows that the stopband performances of the proposed filter have drastically improved, that the measured harmonic suppression of better than -10 dB up to about 13GHz is shown in Figure 10.

IV. CONCLUTION

In this paper, a new compact dual-band bandpass filter using aperture-coupled microstrip SIR-hairpin resonator on a two-layer structure has been proposed and investigated. In the proposed design, the couplings between the filter resonators have been achieved through apertures etched in the common ground placed between the two layers. Base on this architecture, we can easily achieve a significant size reduction of 50% compared with conventional single-layer filters. Furthermore, the aperture coupled technique used in the design is efficient, simple and easy to be implemented. In addition, a good agreement has been achieved between experimental and simulated results. With these features, the proposed dual-band bandpass filter is suitable for compact microwave systems.

ACKNOWLEDGMENT

This research has been partially supported by the Graduate College, King Mongkut's Institute of Technology North Bangkok, Thailand.

REFERENCES

[1] I. C. Hunter, L. Billonet, B. Jarry, and P. Guillon, "Microwave filters-applications and technology," IEEE Trans. Microw. Theory Tech., vol.50, no.3, pp. 794-805, Mar. 2002.

[2] H. Miyake, S. Kitazawa, T. Ishizaki, T. Yamada, and Y. Nagatom, "A miniaturized monolithic dual band filter using ceramic lamination technique for dual mode portable telephones," IEEE MTT-S Int. Dig., vol.2, pp. 789-792, Jun. 1997.

[3] C. Quendo, E. Rius, and C. Person, "An original topology of dual-band filter with transmission zeros," IEEE MTT-S Int. Dig., vol.2, pp. 1093-1096, Jun. 1996.

[4] V. Palazzari, S. Pinel, J. Laskar, L. Roselli, and M. M. Tentzeris, "Design of an asymmetrical dual-band WLAN filter in liquid crystal polymer(LCP) system-on- package technology," IEEE Trans. Microw. Wireless compon. Lett., vol.15, no.3, pp. 165-167, Mar. 2005.

[5] S. Sun, and L. Zhu, "Coupling dispersion of parallel-coupled microstrip lines for dual-band filters with controllable fractional pass bandwidths," IEEE MTT-S Int. Dig., Jun. 2005.

[6] S. F. Chang. Y.H. Jeng, and S. C. Chang, "New dual-band bandpass filters with step-impedance resonators comb and hairpin structures," in Proc. Asia Pacific Microwave Conf., 2003, pp.739-769.

[7] S. F. Chang, Y. H. Jeng, and J. L. Chen, "Dual-band step-impedance bandpass filters for multimode wireless LANs," Electron. Lett., vol.40,no. 1, pp.38-39,2004.

[8] H. M. Lee, C. R. Chen, C. C. Tsai, and C. M. Tsai, "Dual-band coupling and feed structure for microstrip filter design," IEEE MTT-S Int.Dig.,pp.1971-1974, Jun. 2004

[9] J. S. Hong, and M. J. Lancaster, "Aperture-coupled microstrip open-loop resonators and their applications to the design of novel microstrip bandpass filter," IEEE Trans. Microw. Theory Tech., vol.47, no.9, pp. 1848-1855, Sep. 1999.

[10] J. T. Kuo, C. F. Jou, and C. C. Chen, "Design of microstrip band-pass filters with aperture coupled miniaturized hairpin resonators," in Proc. Asia Pacific Microwave Conf., 2001, pp.421-424.

[11] A. Djaiz, and T. A. Denidni, "A reduced-size two-layer bandpass filter," Microw. Opt. Tech. Lett, vol.44, no.6, pp. 512-515, Feb. 2005.

[12] M. Makimoto, and S. Yamashita, "Bandpass filters using parallel coupled stripline stepped impedance resonators," EEE Trans. Microw. Theory Tech., vol.MTT-28, no.12, pp. 1413-1417, Dec. 1980.

[13] Sio-Weng Ting, Kam-Weng Tam and R.P.Martins,"Miniaturized Microstrip Lowpass Filter With Wide Stopband Using Double Equilateral U-Shaped Defected Ground Structure," IEEE Trans. Microw. Wireless compon. Lett., vol.16, no.5, pp. 240-242, May. 2006.

Microwave Ablation Therapy for Lung Cancer using Open-Tip and Multi-Slot Coaxial Antenna

D Kiatkittisorn[1], M Sangworasil[1,2], P Phasukkit[1,2], and S Tungjitkusolmun[1,2]

Faculty of Engineering[1], Computer Research and Service Center[2]

King Mongkut's Institute of Technology Ladkrabang, Bangkok, Thailand 10520

ktsupan@kmitl.ac.th

***Abstract* -This paper presents the treatment of pulmonary carcinoma using microwave coagulation therapy with open-tip and multi-slot coaxial antennas. Because lung is a common site for cancer and usually has substantial functional reserve, MW ablation of lung cancers is an attractive option for minimally invasive treatment. We performed finite element analysis simulation of microwave ablation and analyzed heating characteristics of open-tip and multi-slot coaxial antennas. We also performed *in vitro* experiments and analyzed heating characteristics in swine-lung tissue during application of microwave energy through open-tip and coaxial-slot antennas. The validity of the analysis was confirmed by comparison of the results from the simulation and *in vitro* experiments.**

Keyword: MCT, lung Cancer, open-tip, multi-slot

I. INTRODUCTION

Microwave coagulation therapy (MCT) has been used extensively for the treatment of hepatocellular carcinoma [1], [2]. Microwave ablation technique is minimally invasive, thus it requires shorter recovery period compared to surgical resection. In the treatment, a thin microwave antenna is inserted into the tumor, and the microwave energy provided by the antenna heats up the tumor to produce the coagulated region covering cancer cells. The input power of the antenna is usually less than 50 W. The goal of microwave ablation is to elevate the temperature of unwanted tissue to above 50 °C where cancer cells are destroyed [3].

From our literature review, no previous studies have discussed the use of microwave ablation for treatment of lung cancer. However, previous studies using radio-frequency (RF) ablation for lung cancer have been reported [4]. Using microwave is potentially more effective than using RF due to air-filled anatomical structure of the lung. For RF ablation of lung carcinoma, the major problem is that the size of coagulated region is generally insufficient due to low RF energy deposited in lung tissue.

In this paper, we used finite element method (FEM) to determine electromagnetic fields and heating patterns of various antenna designs. Then we constructed the antennas with desirable characteristics and utilized them to perform *in vitro* experiments using swine lung tissue.

II. MATERIALS AND METHODS

(a) Open-tip and multi-slot coaxial antennas

Fig. 1 (a) and (b) show the configuration of the open-tip antenna (OTA) and multi-slot coaxial antenna (MSCA). Table 1 lists all related structural parameters of the antennas. Here, d_a is the diameter of the antenna; d_b is the thickness of the dielectric; d_c is the thickness of the conductor; d_g is the length from the tip to the center of the slot; and d_f is the width of the slot. We used a thin semi-rigid coaxial with a diameter of 3.6 mm. Table 2 provides values for the relative permittivities of the materials used in the antennas.

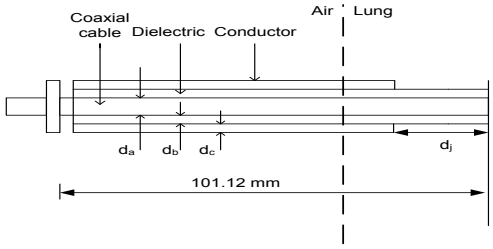

(a)

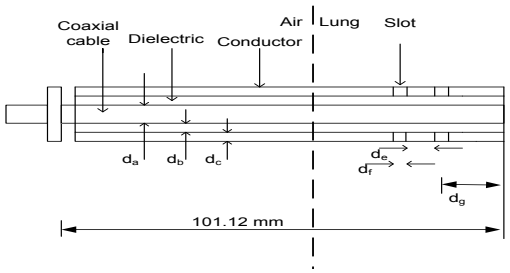

(b)

Figure 1. Structural configuration of (a) OTA and (b) MSCA

TABLE 1

THE DIMENSION AND RELATIVE PERMITTIVITIES OF THE COAXIAL ANTENNAS USED IN MW

Dimension of Antenna	
da (diameter of the coaxial antenna) [mm]	3.66
db(thickness of the dielectric), dc (thickness of the conductor), de (length between the slots), d_f (width of the slot) [mm]	1
dg(length from the tip to the center of the slot) [mm]	6.5
d_j(length of the tip) [mm]	18.82
Relative permittivity	
ϵ_{ri} (relative permittivity of the inner dielectric) [mm]	2.03
ϵ_{rc} (relative permittivity of the catheter) [mm]	2.36

TABLE 2

ELECTRICAL AND THERMAL PROPERTIES OF THE TISSUE [5]-[6]

Electrical and Thermal properties of the media	Lung
Thermal conductivity [W/m · K]	0.3158920
Relative permittivity	20.476801
Conductivity [S/m]	0.8041280
Blood flow rate [m3/kg · s]	6.67×10^{-6}
Density of the blood [kg/m^3]	1060
Specific heat of blood [J/kg · K]	3960

(b) Finite element studies of coupled thermal-electromagnetic analyses

Since our goal is to compare the characteristics of different antenna designs in terms of energy and heating distribution, we performed all analyses using the bio-heat and Maxwell's equations. Finite element analysis was utilized to obtain approximate numerical results of the complex coupled thermal-electromagnetic problems by dividing the domain of interest into many small areas with simple geometry. We describe the bio-heat equation and calculation of the specific absorption ratio (SAR) in this section.

Bio-heat equation

We can calculate the temperature distribution inside the biological tissue by solving the bio-heat transfer equation

$$\rho c \frac{\partial T}{\partial t} = \nabla \bullet (k \bullet \nabla T) + \rho_b \rho_b c_b \omega_b (T_b - T_b) + Q_{met} + Q_{ext} \qquad (1)$$

where T is the temperature (˚C), t is the time (s), ρ is the density (kg/m^3), c is the specific heat (J/ kg· K), k is the thermal conductivity (W/m·K), ρ_b is the density of the blood (kg/m^3), c_b is the specific heat of the blood (J/kg·K), w_b is the blood perfusion rate (m^3/kg·s), T_b is the temperature of the blood (˚C).

The first, second, and third terms on the right hand side of (1) denote thermal conduction, heat dissipation by the blood flow, and heat generation by the electric field (Q_{ext}), respectively. Q_{met} is the amount of heat generated by metabolic process and is comparatively much smaller than the previous terms. Thus Q_{met} is considered negligible in this study.

Calculation of SAR

We can calculate SAR using equation (2):

$$SAR = \frac{\sigma}{\rho}\left|E^2\right| \qquad [W/kg] \qquad (2)$$

where σ is the electrical conductivity [S/m]

ρ is density $[kg/m^3]$ and

E is the electric field intensity (rms) [V/m]

Software simulation

In this study we performed finite element analyses using COMSOL version 3.2b. We ran all simulations on a PC with Intel Pentium M, 1.5 GB of RAM, and 50 GB of Hard disk space. There were three types of MW antennas used—OTA, 1-slot MSCA, and 2-slot MSCA. For each case, we set the input power to 80 W, for a duration of 30 s.

In vitro Studies

We constructed the OTA, 1-slot MSCA, and 2-slot MSCA using the semi-rigid coaxial cables. We tested each antenna in *in vitro* experiments using swine lung tissue. The microwave power generator was built in house and was able to supply 0-100 W to the MW antenna. Swine lung tissue was placed in a saline bath and MW energy was delivered to each antenna. In addition, we measured SAR and temperature distribution along the shaft of each antenna using the Bird Site Analyzer (Electronic Corporation, Cleveland (Solon) Ohio, USA).

III. RESULTS

Fig. 2 illustrates SAR distributions along the axial surface of OTA, 1-slot MSCA, and 2-slot MSCA from finite element analyses. Table 3 lists VSWR for each antenna used. Table 3 lists Voltage Standing Wave Ratio (VSWR) measured with the Bird Site Analyzer in *in vitro* experiment. Graph 1 shows the distribution of SAR in lung tissue from the three antennas. Fig. 3 compares temperature distributions of the three antennas along their axes. Graph 2 shows corresponding temperature distributions and Fig. 4 displays temperature gradients within lung tissue for in vitro experiment.

TABLE 3

VSWR VALUES OF EACH ANTENNA MEASURED WITH BIRD SITE ANALYZER

Coaxial 1 Slot	VSWR: 1.33:1
Coaxial 2 Slot	VSWR: 1.45:1
Open-tip	VSWR: 1.29:1

Simulation Results

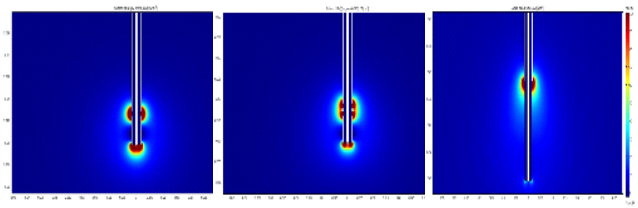

(a) (b) (c)

Fig. 2 the quantities of SAR distributions of the antennas in pulmonary tissue (a) 1-slot (b) 2-Slot c) Open-tip

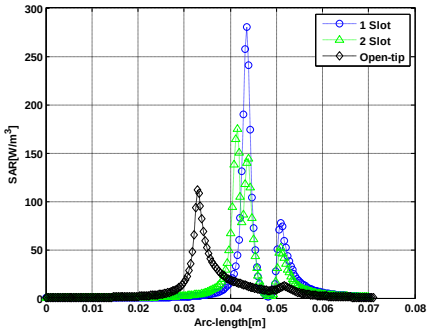

Graph 1. SAR distributions within lung tissue from the simulation of 1-slot, 2-slot, and open-tip antennas

Fig. 2 shows the simulation values of SAR in pulmonary tissue corresponding to the 1slot, 2 slot, and open-tip respectively. SAR values relates to the values of electric field by Eq. (2). Graph 1 shows that the 1 slot has the highest level of whole electrical field, and the 2 slot has the highest level of electric field around the slots. Finally the pen-tip has lower level of electric field than the 1 and 2 slots.

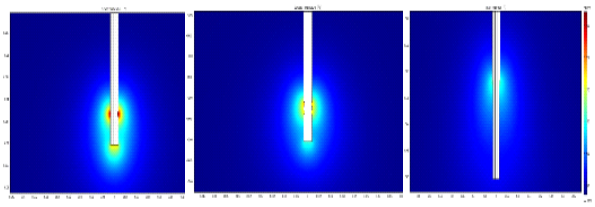

(a) (b) (c)

Fig. 3 the quantity of temperature distribution in pulmonary tissue. (a) 1-slot (b) 2-Slot (c) Open-tip

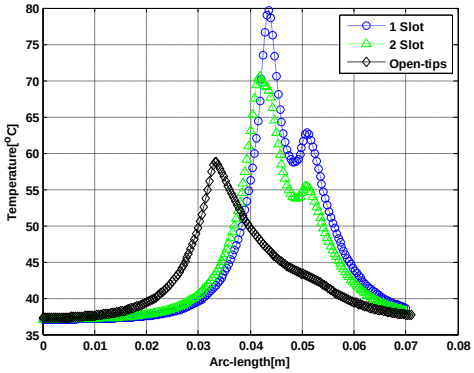

Graph 2. graph shows the comparison of temperature distributions from the simulation of 1-Slot, 2-Slot, Open-tip coaxial antennas in pulmonary tissue

Fig. 2 and graph 2 show the level of temperature distribution of the tree types of the antennas in pulmonary tissue. As shown in fig. 2 and graph 2, the 1 slot has the highest level of temperature. The 1 and 2 slots have the temperature distributions around the slots and the tips of the antennas. The open-tip has lower level of temperature than the 1 and 2 slots

Experiment Results

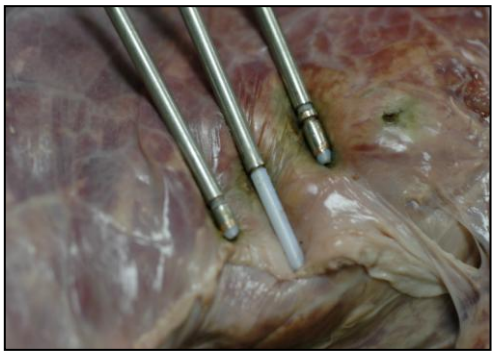

Figure 4. Lesions created in swine lung tissue using 1-slot MSCA, OTA, and 2-slot MSCA.

Fig. 4, in vitro experiment, shows that the analysis with the finite element method gave the simulation result similar to the in vitro experiment.

IV. Conclusions

This study presents 2 different antenna designs—OTA and MSCA—for use in lung cancer treatment. Due to high electrical resistivity in lung compared to other tissues, using microwave ablation can be potentially more effective than RF ablation. With OTA design, the location with optimal SAR occurs at regions adjacent to the outer conductor. For MSCA, optimal SAR is distributed close to the slots. From both FE analyses and in vitro experiments, 1-slot MSCA appeared to have a higher maximum temperature compared to that of OTA. When we increased the slot from 1 to 2, the maximum temperature in lung tissue decreased, however, the maximum temperature region was more widely distributed. The different results obtained from each antenna design can be applied to appropriate treatment criteria

References

[1] T. Seiki, M. Wakabayashi, T. Nakagawa, T. IToh, T. Shiro, K. Kunieda, M. Sato, S.Uchiyama, and K. Inoue, "Ultrasonically guided percutaneous microwave coagulation therapy for small carcinoma," *Cancer*, vol.74, no. 3, pp. 817-825, 1994.

[2] R. Murakami, S. Yoshimatsu, T. Matsukawa, M. Takahashi and K. Sagara, "Treatment of hepatocellular carcinoma: Value of percutaneous microwave coagulation," *Amer. J. Rentgenol*., vol. 164, pp. 1159-1164, 1995.

[3] J. P. McGahan, J. M. Brock, H. Tesluk, W. –Z. Gu, P. Schneider, and P. D. Browing, "Hepatic ablation with use of radiofrequency electrocautery in the animal model." J.Vasc. Inter. Radiol., vol.3, pp.291-297, 1992.

[4] Steven C. Rose, MD, Patricia A. Thistlethwaite, MD, PhD, Patrick E. Sewell, MD, and Ralph B. Vancd, MD, "Lung Cancer and Radiofrequency Ablation," J. Vasc. Inter. Radiol, vol. 17, pp. 927-951, 2006

[5] J. W. Valvano, J. R. Cochran, and K. R. Diller, "Thermal Conductivity and Diffusivity of Biomaterials Measured with Self-Heated Thermistors," International Journal of Thermophysics, vol. 6, No.3, 1985

[6] F. A. Duck, Physical Properties of Tissue. New York: Academic, 1990.

Reducing Self Resonance Effect in High Frequency Inductors Using Capacitance Cancellation Technique

K. Piboonwattanakit[1], V. Tarateeraseth[2], W. Khan-ngern[1]

[1]King Mongkut's Institute of Technology Ladkrabang (KMITL),
Research Center for Communications and Information Technology (ReCCIT),
Faculty of Engineering, Bangkok, Thailand, E-mail: kkveerac@kmitl.ac.th
[2]Srinakharinwirot University, Faculty of Engineering, Ongkharak, Thailand, E-mail: vuttipon@swu.ac.th

***Abstract*-This paper presents the simulation of the parasitic capacitance cancellation technique of inductor using mutual capacitance. Its mutual capacitance can be emulated using two small capacitors, connected with circuit. The simulation using PSpice program to simulate mutual capacitance concept is presented. The objective of this paper is to analyze the high frequency inductor performance using PSpice simulation. Finally, the simulation results show that the performance of inductor is improved.**

I. INTRODUCTION

The EMI filter is typically composed of inductors and capacitors, which is considered only the inductors in this paper. Theoretically, the impedance of inductor is increased while the frequency increased. Therefore, the inductor's operation frequency range is limited because of the parasitic capacitance, which makes an inductor changing to a capacitor at high frequency. The parasitic capacitance is usually lumped together as an equivalent parallel capacitance (EPC), and the winding loss and core loss of the inductors are usually lumped together as an equivalent parallel resistance (ESR), paralleled to the inductance L [1]. Fig. 1 shows a simple model for inductor.

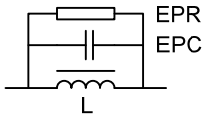

Figure 1. Equivalent circuit for a practical inductor.

The advantages of PSpice simulator, when comparing with practical experiment, can minimize the experiment time. Because there are too many equivalent and step in the practical experiment, if some mistakes take place, it must takes time to repair them. By simulation, it can be more convenient, rapid and high accuracy.

II. THE SIMULATION PROCEDURE USING PSPICE PROGRAM

The simulation of winding capacitance cancellation, by PSpice program, is simulated the measured results of network analyzer by its AC sweep mode with 150 kHz for initial frequency, 1000 Hz for step frequency, and 30 MHz for final frequency. The inputs of PSpice circuit are connected to AC source, 1 V, then, calculating the simulated results following Eqn. (1). The inputs and outputs of PSpice circuit are connected to resistor 50 ohm because the impedance of connectors of network analyzer is 50 ohm for matching impedance. The voltage probe is used to measure difference voltage across the resistor. Fig. 2 shows the circuit for measurement with four ports balances ENA RF [3], and Fig. 3 shows the simulated circuit using PSpice program.

$$\text{Inductor filtering performance} = 20\log\frac{V_{out}}{V_{in}}\ \text{dB} \qquad (1)$$

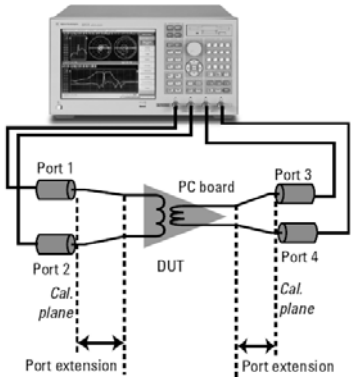

Figure 2. The method of network analyzer (Agilent E5070B/E5071B).

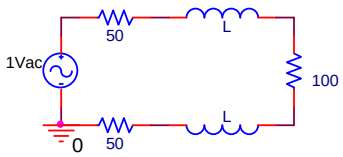

Figure 3. The simulation of PSpice program

The simulation of parasitic capacitance and resistance are emulated by capacitor and resistor of PSpice program, paralleled to the inductance L, as shown in Fig. 4. The parasitic capacitance and resistance are measured by impedance analyzer.

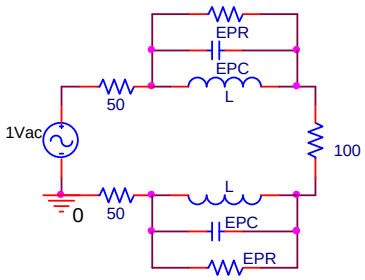

Figure 4. The parasitic capacitance is emulated by PSpice program.

III. Simulated Results

At frequencies higher than the self resonance frequencies of the inductors, the inductors perform like capacitors, and therefore, the filter with parasitic capacitance is worse more than the filter without parasitic capacitance as shown in Fig. 5.

Fig. 5 shows the simulation of parasitic capacitance, which effects to performance of the EMI filter. As shown in Fig. 5 (a), the inductors are connected with capacitances. As shown in Fig. 5(b), the inductors are connected without capacitances. The self-parasitic of two inductors, measured by impedance analyzer, are $L_1 = L_2 = 3.21$ mH, EPC_1=$EPC_2 = 30$ pF, and EPR_1=$EPR_2 = 15.7$ kΩ. The compared result is shown in Fig. 6, which is compared between simulated results of with and without parasitic capacitances as shown in Figs. 5 (a)-(b), respectively. The performance of inductor with parasitic capacitance has a resonance frequency around 500 kHz, which makes the inductor performance worse more than inductor without parasitic capacitance.

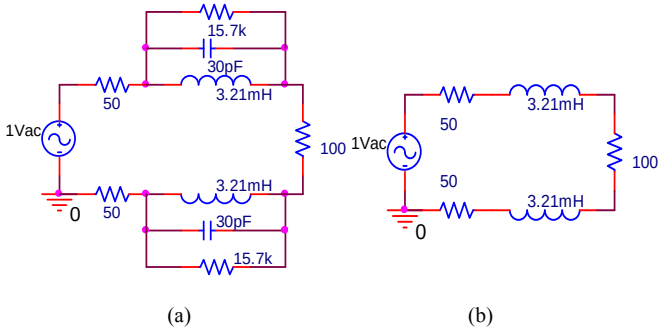

Figure 5. The simulation of inductor
(a) with parasitic capacitance (b) without parasitic capacitance.

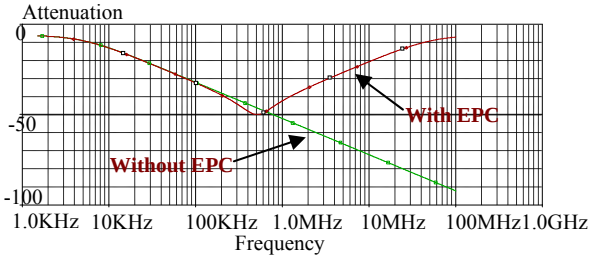

Figure 6. The simulation of inductor
(a) with parasitic capacitance
(b) without parasitic capacitance.

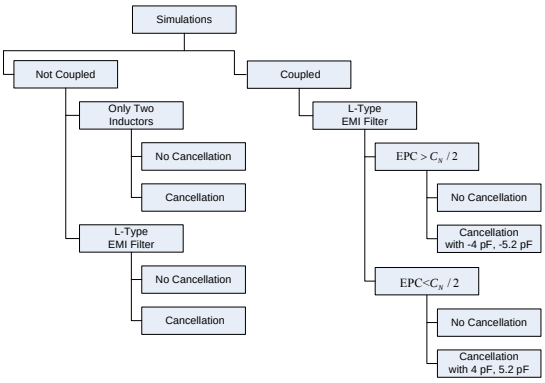

Figure 7. The simulation flowchart.

Fig. 7 shows the simulation flowchart to implement and verify the presented method.

A. *The inductors are not coupled*

In the first simulations, two inductors are not coupled, which are two inductors and L-Type EMI filter. The self-parasitic of two inductors is shown in Fig. 8 (a), L-Type EMI filter is shown in Fig. 8 (b) [1].

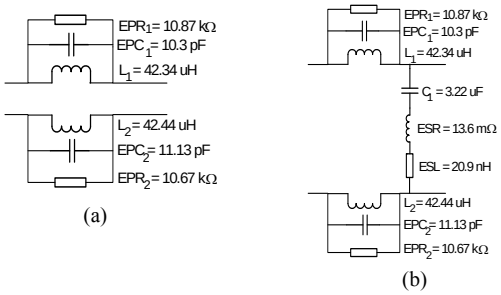

Figure 8. Self-parasitic capacitance of two inductor windings
(a) Two inductors (b) L-Type EMI filter.

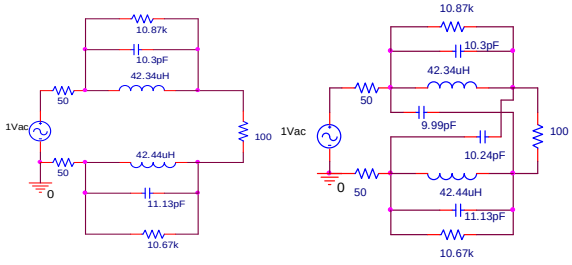

Figure 9. The simulation for canceled parasitic capacitance
(a) Two inductors without EPC cancellation
(b) Two inductors with EPC cancellation.

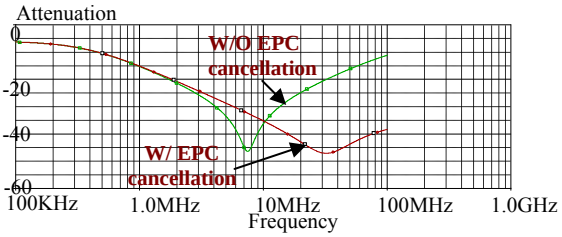

Figure 10. Improvement of inductor filtering performance at high frequencies due to the EPC cancellation for two inductors.

The two simulations for two inductors are inductor without parasitic capacitance cancellation and inductor with parasitic capacitance cancellation as shown in Figs. 9 (a)-(b), respectively. The capacitance of two cancellation capacitors is $N_1 = 9.99$ pF and $N_2 = 10.24$ pF, which are a little bit smaller than EPC_1 and EPC_2 [1].

In Fig. 10, the simulation results are compared between Figs. 9 (a)-(b). The two inductors have a resonance frequency about 7.5 MHz, which makes the inductor performance worse above 10 MHz. After EPC is canceled, the resonance moves to about 28 MHz. The result of this simulation is similarly with the experiment of [1].

The two simulations for L-Type EMI filter are inductor without parasitic capacitance cancellation and inductor with parasitic capacitance cancellation as shown in Figs. 11 (a)-(b), respectively. The one capacitor is used for L-Type EMI filter, simulated $C = 3.22$ μF, ESL=20.9 nH and ESR=13.6 mΩ [1].

In Fig 12, the result is compared between Figs. 11 (a)-(b). The L-Type EMI filter has a resonance frequency about 7 MHz. The filter's performance improves above 10 MHz. At the frequency about 670 KHz, it has a resonance frequency due to the series resonance (ESL) of C_1. The result of this simulation is still similarly with the experiment of [1].

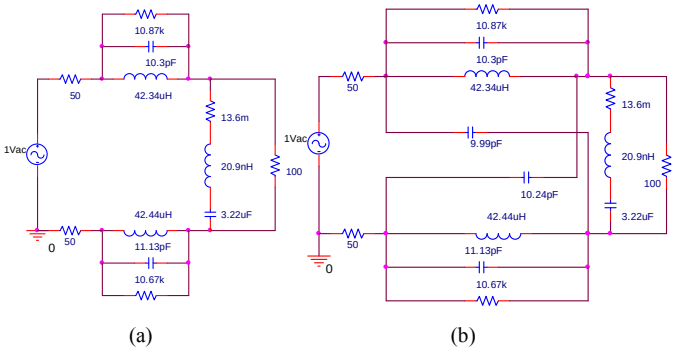

Figure 11. The simulation of L-Type EMI filter (a) L-Type EMI filter without EPC cancellation (b) L-Type EMI filter with EPC cancellation.

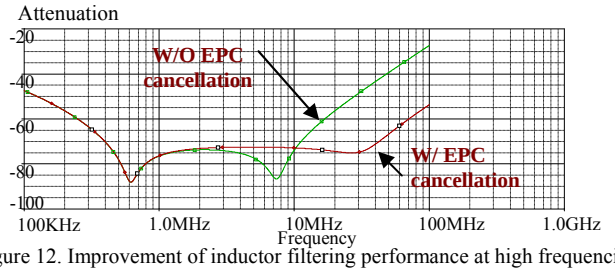

Figure 12. Improvement of inductor filtering performance at high frequencies due to the EPC cancellation for L-Type EMI filter.

B. *The inductors are coupled*

In the second simulation, the two inductors are coupled, which presents only L-Type EMI filter. The coupled inductor is located on one core. There are three kinds of parasitic capacitances in the inductor: turn-to-turn capacitance C_a, turn-to-core capacitance C_b, and winding-to-winding capacitance C_c as shown in Fig. 13. Their effects can be represented by EPC and C_N. EPC represents the effect of C_a and C_b. C_N represents the effect of C_c and C_b, i.e., the parasitic capacitance between two windings [1]. In the simulation each winding of the coupled inductor for L-Type EMI filter has an inductance of 20 μH. It is assumed that the inductance for one winding is L. Fig. 14 shows the self-parasitic capacitances of inductors are coupled. An L-Type EMI filter is built using one capacitor ($C = 477$ nF, ESL=18.5 nH and ESR=35.4 mΩ). The C_N is 14.8 pF [1].

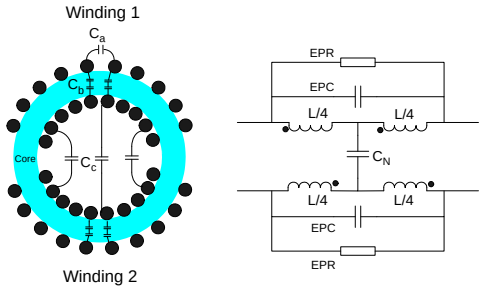

Figure 13. Parasitic capacitance between two coupled inductors winding (a) Inductor structure (b) Equivalent circuit.

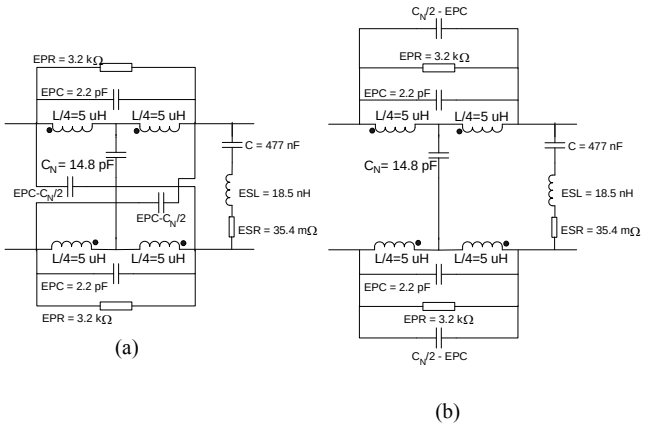

Figure 14. Self-parasitic capacitance of L-Type EMI filter (a) For $EPC > C_N/2$ (b) For $EPC < C_N/2$.

For $EPC > C_N/2$, the equivalent winding capacitance is positive, then two cancellation capacitors with a capacitance of -5.2 pF each need to parallel with two winding to cancel the winding capacitance 5.2 pF. The three simulations for L-type EMI filter are inductor without parasitic capacitance and inductor with −4 pF parasitic capacitance cancellation and inductor with −5.2 pF parasitic capacitance cancellation, as shown in Figs. 15 (a)-(c), respectively.

In Fig. 16, the simulation results are compared among Figs. 15 (a)-(c). The inductor of −5.2 pF EPC cancellation achieves the best performance above 5 MHz because the parasitic capacitance is almost canceled. For inductor with −4 pF, EPC cancellation is worse more than −5.2 pF EPC cancellation. For the inductor without EPC cancellation, the filter performance is worse above 5 MHz. This result is quite similarly with experiment [1].

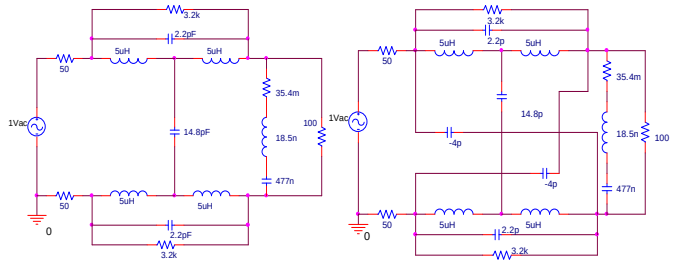

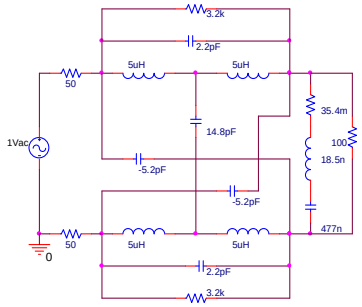

Figure 15. The simulation of L-Type EMI filter are coupled
(a) Inductor without EPC cancellation
(b) Inductor with −4 pF EPC cancellation
(c) Inductor with −5.2 pF EPC cancellation

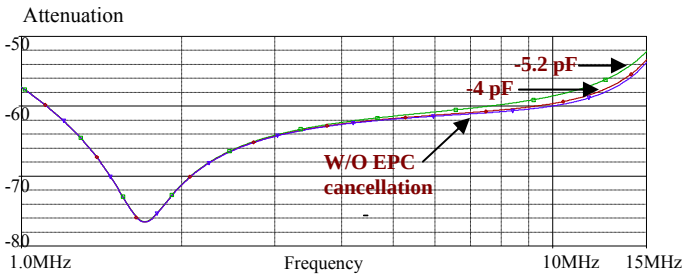

Figure 16. Improvement of inductor filtering performance at high frequencies for L-Type EMI filter.

For $EPC < C_N / 2$, the equivalent winding capacitance is negative, then, two cancellation capacitors with a capacitance of 5.2 pF each need to parallel with two winding to cancel the winding capacitance -5.2 pF. The three simulations for L-Type EMI filter are inductor without parasitic capacitance cancellation, inductor with 4 pF parasitic capacitance cancellation and inductor with 5.2 pF parasitic capacitance cancellation as shown in Figs. 17 (a)-(c), respectively.

In Fig. 18, the simulation results are compared among Figs. 17 (a)-(c). The inductor of 5.2 pF EPC cancellation achieves the best performance above 5 MHz because the parasitic capacitance is almost canceled. For inductor with 4 pF, it is worse more than 5.2 pF EPC cancellation. For the inductor without EPC cancellation, the filter performance is worse above 5 MHz. This result is in a good agreement with the experiment [1].

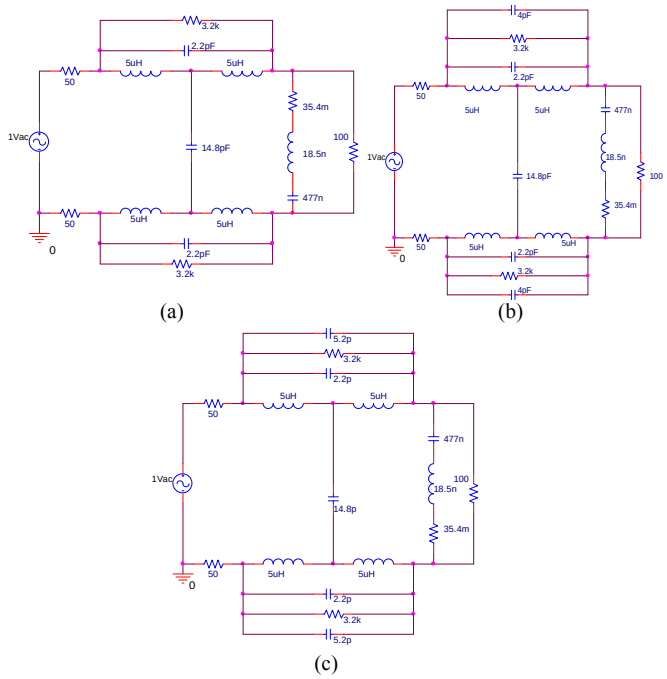

Figure 17. The simulation of L-Type EMI filter are coupled
(a) Inductor without EPC cancellation (b) Inductor with 4 pF EPC cancellation (c) Inductor with 5.2 pF EPC cancellation

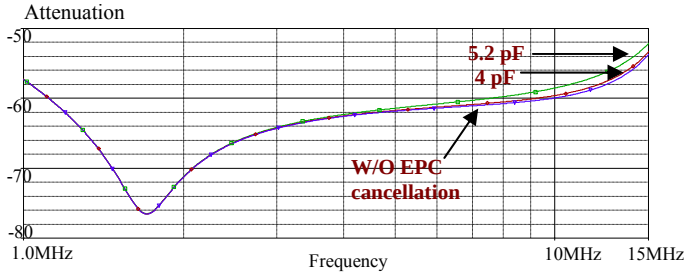

Figure 18. Improvement of inductor filtering performance at high frequencies for two inductors.

IV. Conclusion

The method and design of a mutual capacitance concept to cancel the effects of parasitic capacitance of inductors are discussed in this paper. This concept is verified by the simulation for ensuring Wang's proposed method [1]. With this concept, it can be applied for EMI filter design to efficiently improve its performance. Finally, it can be seen that the simulation are convenient, fastnesses, and high accuracy.

V. References

[1] S. Wang, F. C. Lee, and J. D. van Wyk, "Inductor Winding Capacitance Cancellation Using Mutual Capacitance Concept for Noise Reduction Application," *IEEE Trans. Power Electron.*, vol. 48, no. 2, pp. 311-318, May 2006.

[2] F. J. Monssen, *Orcad PSpice with circuit analysis*, Prentice Hall, Inc., New Jersey, 2001.

[3] *Agilent E5070B/E5071B ENA Series RF Network Analyzers User's Guide*: 5th ed., Agilent Technologies, 2004.

A Minimized Bandpass Filter Using Two-Layers With Aperture-coupled for Microstrip Slow-Wave Open-Loop Resonator

Apirada Namsang, Jaruek Jantree, and Prayoot Akkaraekthalin
Faculty of Engineering, King Mongkut's Institute of Technology North Bangkok
1518 Pibulsongkram Rd., Bangsue, Bangkok 10800, Thailand, email: japirada747@hotmail.com

***Abstract*- This research proposes a new microstrip slow-wave open-loop resonator bandpass filter using a multilayer, resulting in size reduction. This filter structure consists of two microstrip layers supporting four resonators by inserting two apertures in a common ground plane. Each resonator is laid difference 180° with others. This filter has been designed at the operating frequency about 2.8 GHz, and a bandwidth of 80 MHz. The full-wave simulator IE3D has been employed to design the slow-wave open-loop resonator. The filter is not only sized reduction, but also low passband insertion loss and high return loss.**

I. INTRODUCTION

RF and microwave bandpass filters are presently required in wide applications of communication systems [1-2], for designing of compact and high performance microwave devices. The microstrip filter is one of the most important components, especially needs to reduce in size and norrrow-band.

Nevertheless there are several disadvantages of the planar filter. One of those is the spurious resonant frequency occurs at $2f_0$, and $3f_0$ where f_0 is the center frequency of a bandpass filter. Not only for suppress the resonant frequency but the high performance filter also need a wider upper stopband for reducing the interference from out of band signal. There are many ways which are proposed such as using microstrips parallel coupled lines to extend the electrical length and compensate the difference of the phase velocities [3]. The wiggly-line stripline filter is also another way of suppression the spurious frequency [4]. Besides, many bandpass filters using stepped impedance resonators to shift away the first higher order resonant frequency have been also proposed [5]. Otherwise planer cross-coupled filters have been proposed, which mostly based on open-loop microstrip resonators [6]. These filters provide the frequency transmission zero and also compact structure. As these best performances a microstrip slow-wave open-loop resonator [7] is designed by using asymmetrical capacitive load which including compact in size and a wide upper stopband.

Another disadvantage is the whole size of the planar filter which mostly implemented on a single microstrip is too large. To overcome the size problem there have been rapidly interested in multilayer structure devices [8-9]. This technique

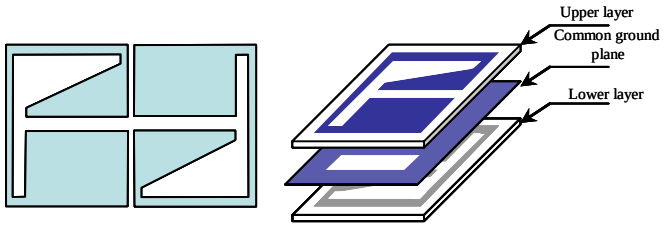

(a) (b)

Figure 1. (a)Conventional micristrip slow-wave open-loop resonator bandpass filter and (b) micrstrip multilayer slow-wave open-loop resonator bandpass filter.

is based on the electric coupling, magnetic coupling and aperture coupling using square stepped impedance open loop resonators.

In this research, we proposed a technique to reduce size of the slow-wave filter but still keep the fundamental properties and also control spurious responses by adjusting the widths and gaps of the aperture. Figure1 (a) and (b) show the conventional and proposed multilayer structures, respectively. The proposed multilayer resonator structure consists of two resonators for the same area on upper layer and another two resonators are laid in the bottom one which the ground plane is inserted between them, resulting in 50% size reduction.

II. A MULTILAYER FILTER STRUCTURE

Figure2 shows the enlarge view of a stack of four resonators of the proposed bandpass filter. These resonators are placed on the external side of the two dielectric substrates that are separate by a common ground plane. Each resonator will be located 180° in different of layout together. Figure 2(a) shows two resonators which are on the upper layer, figure 2(b) shows others are on the lower layer. That means the layout of the upper layer resonator on the left hand side is placed as same as the lower layer resonator on the right hand side. By the way the layout upper layer resonator on the right hand side is placed as same as the lower layer resonator on the left hand side.

The upper and lower layers produce the essential couplings which influence to the characteristic of this filter. Such the upper layer generates the electric couplings that will appear between the resonators. Similarly, in the lower layer the

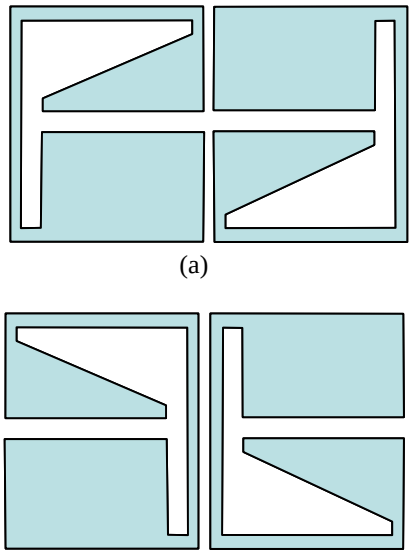

(a)

(b)

Figure 2. A view of the proposed multilayer bandpass filter (a) upper layer (b) lower layer

resonators are set in order to produce the magnetic couplings.

Besides that the aperture couplings between the two layers are certainly by inserting two identical apertures on the central common ground. The proposed multilayer bandpass filter uses slow-wave open-loop resonator bandpass filter located on the outer side of both dielectric substrates with a common ground plane in between and apertures on the common ground plane. These resonators are placed near each other with a specified space d.

III. Design And Results

A. *Coupling structures*

This proposed structure filter produces necessary couplings between adjacent resonators including electric coupling, magnetic coupling and aperture-coupling. Besides, filter designing always requires for good performances such as bandwidth so that it is essential to evaluate the coupling coefficient k between two adjacent resonators. The IE3D commercial electromagnetic simulation software, which is based on the method of moments and proven to be quite accurate in its prediction, has been used to simulate the frequency responses of the three basic coupling structures. In this method the factor of the electric and magnetic coupling depend on the distance between the two resonators on each layer. However, the mixed or aperture coupling will be depended on the dimension of aperture.

Due to the electric coupling behavior, in each structure can be sprit the two vital frequencies which are spirited off from the resonance situation. Then the coupling coefficient can be determined from them which extracted by following

$$k_{ij} = \pm \frac{f_2^{\,2} - f_1^{\,2}}{f_2^{\,2} + f_1^{\,2}} \qquad (1)$$

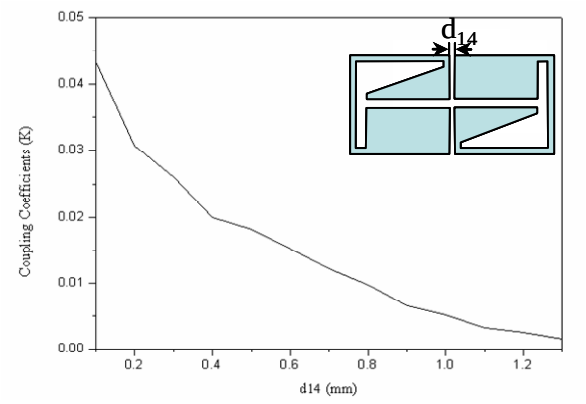

(a)

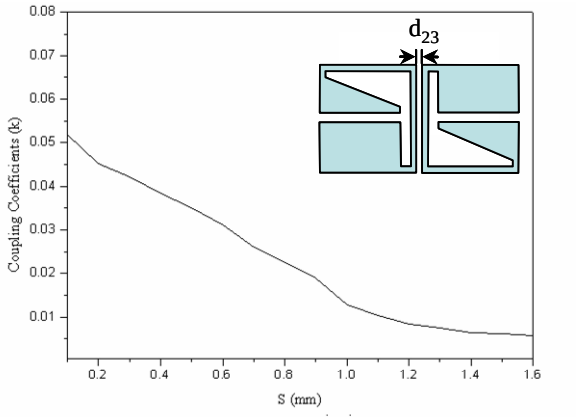

(b)

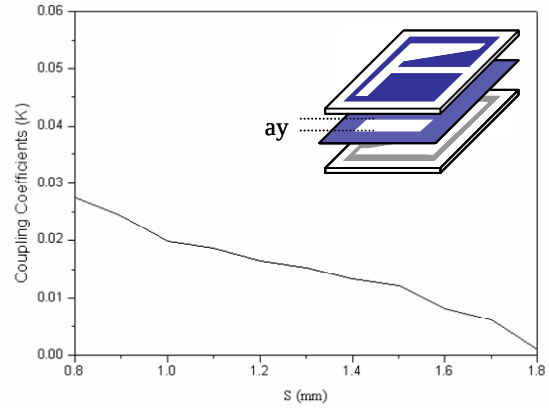

(c)

Figure 3.Variation of the coupling coefficient K versus the distance s between two coupled resonators, (a) electric coupling (b) magnetic coupling and (c) mixed coupling.

where f_1 and f_2 are the sprit resonance frequencies. The external quality factor may be characterized by

$$Q_e = \frac{f_0}{f_{3dB}} \qquad (2)$$

where f_0 and f_{3dB} are the resonant frequency and 3 dB bandwidth of the input or output resonator when it alone is externally excited.

In this proposed filter is fabricated on a standard microwave substrate of GML 1000 substrate with a relative dielectric permittivity, ε_r of 3.2 and dielectric thickness, h of 0.762 mm from Roger Corp. Figure 3(a), (b) and (c) show an electric coupling, magnetic couplings, and aperture couplings respectively. The distance d between the two resonators is influence the variation of the coupling coeffient K.

B. Spurious suppression

This proposed resonator filter is also evaluated by IE3D microwave software to determine the characteristics of an asymmetry parallel coupled line diction to define the excitation of two mode of electromagnetic performance which known as odd- and even-mode[7]. Normally, when we can find the odd- and even-mode response of any resonator, the first spurious suppression can be obtained. In figure 4 shows an asymmetrical parallel coupled-line, supporting the odd- and even-modes. So we can basically predict how far that resonator filter can press the harmonic.

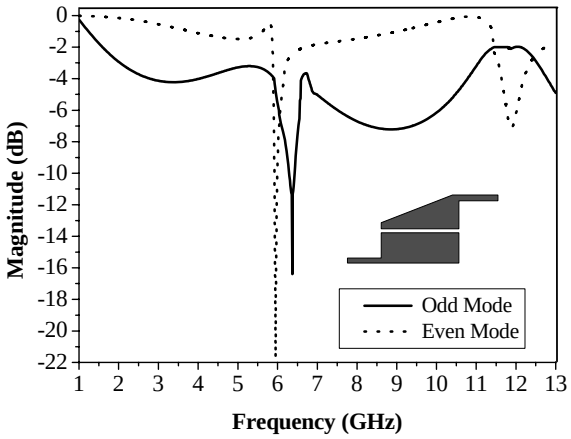

Figure 4. Frequency responses (S_{21}) of the asymmetrical triangle-rectangular coupler with odd- and even-mode excitations

C. Resonator Optimization

This proposed filter is a four resonator bandpass filter, which consists of the two slow-wave open-loop resonators on the top layer and others on the bottom layer which separate by the common ground plane. The filter has been then fabricated on a microwave substrate GML 1000 with a relative dielectric constant of 3.2 and a thickness of 0.762 mm. The value of gab g has been set to be 0.5 mm. In order to have a maximally flat passband bandwidth of 80 MHz (or the fractional bandwidth of FBW=28.6%) at f_0 = 2.8 GHz, the external quality factor Q_e as follows:

$$Q_e = \frac{g_1}{FBW} = 26.41017127 \qquad (3)$$

The coupling coefficients $K_{12} = K_{34}$ which are defined by the dimension of the apertures. By the ways the coupling coefficients K_{23} and K_{14} values are calculated by the space d_{23} and d_{14}. The values of the low pass prototype were synthesized with element values as $g_0 = 1$, $g_1 = 0.7553$, $g_2 = 1.2222$, $J_1 = 0.2576$, $J_2 = 0.9453$, so that the coupling coefficients can be calculated as follows

$$K_{12} = K_{34} = \frac{FBW}{\sqrt{g_0\, g_1}} = 0.02174 \qquad (4)$$

$$K_{23} = \frac{FBW \cdot J_2}{g_2} = 0.02204 \qquad (5)$$

$$K_{14} = \frac{FBW \cdot J_1}{g_1} = 0.003204 \qquad (6)$$

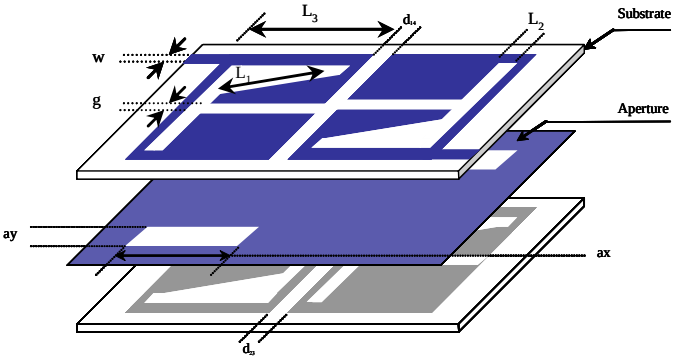

Figure 5. The multilayer open-loop resonator filter layout

Figure 5 illustrates the layouts of the multilayer open-loop resonator filter. Then the resonator layout parameters have been obtained in the following: L_1 = 8.09 mm, L_2 = 0.634 mm, L_3 = 8.889 mm, g = 0.501 mm, w = 0.381 mm and spacing d_{14} = 0.89 mm, d_{23} = 0.87 mm. The aperture dimension ay = 1.5 mm, ax = 5.94 mm.

Figure 6 shows a photograph of the fabricated filter using a proposed filter. Figure 7(a) shows the measurement and simulated response which is being analytical from the IE3D software. The measured center frequency is 2.75 GHz with insertion loss approximately -3 dB. The passband return loss is greater than 10 dB. Figure 7(b) illustrates a wide upper stopband. We can see the spurious frequencies are rejected more than 25 dB up to 10 GHz.

IV. CONCLUSION

We have presented a technique for reducing size of a bandpass filter by using the multilayer structure of cross coupled slow-wave open-loop resonator with apertures. This bandpass filter has been designed at the high frequency about 2.8 GHz. Otherwise this filter is not only compact 50% in size

but also having a wider upper stopband. This filter can suppress spurious response and move it far away longer than 10 GHz. The filter has been optimized using IE3D microwave software.

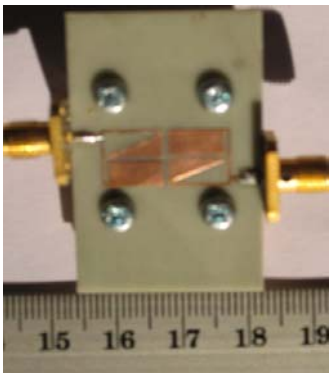

Figure 6. A photograph of the fabricated bandpass filter

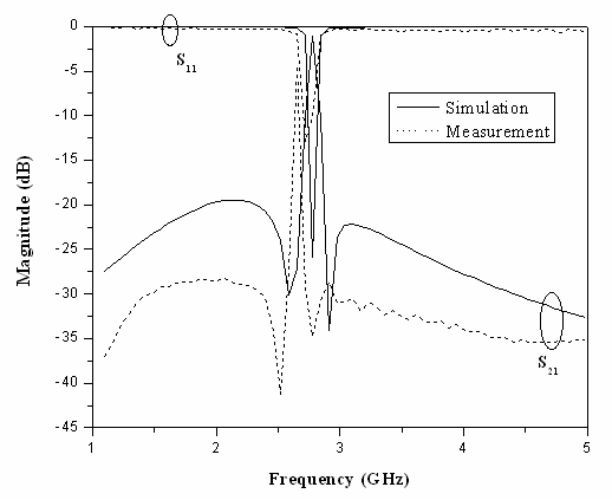

(a)

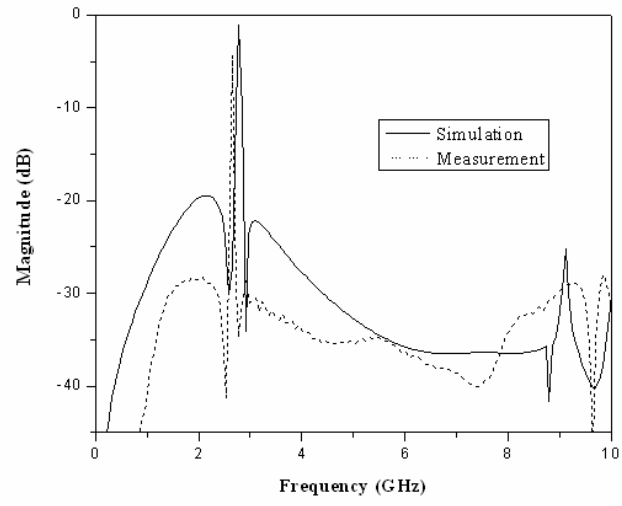

(b)

Figure 7. Comparison of measured and simulated responses of the proposed filter (a) passband response (b) wideband response

REFERENCES

[1] Ian C. Hunter, Laurent Billonet, Bernard Jarry, and Pierre Guillon, "Microwave filters - applications and technology," IEEE Trans. on Microwave Theory and Tech., Vol.50, pp.794-805, Mar 2002.

[2] J. S. Hong and M. J. Lancaster "Microstrip filter filter for RF/microwave applications,"John Wiley& Son Inc., 2001.

[3] J.-T. Kuo, S.-P. Chen, and M. Jiang, "Parallel-coupled microstrip filters with over-coupled end stages for suppression of spurious responses," IEEE Microw. Wireless Compon.Lett., Vol.13, no.10, pp.440-442, Oct. 2003

[4] T. Lopetegi, M. A. G. Laso, J. Hernandez, M.Bacicoa, D. Benito, M. J. Garde, M. Sorolla, and M. Guglielmi, "New microtrip "wiggly-line" filters with spurious passband suppression," IEEE Trans. on Microwave Theory and Tech., Vol.49, no.9, pp.1593-1598, Sep. 2003.

[5] M. Makimoto and S. Yamasashita, "Bandpass filters using parallel coupled stripline stepped impedance resonators," IEEE Trans. on Microwave Theory and Tech., Vol.MTT-28, pp.1413-1417, Dec 1980.

[6] J.S. Hong and M.J. Lancaster, "Couplings of microstrip square open-loop resonators for cross-coupled planar microwave filters," IEEE Trans. on Microwave Theory and Tech., Vol.44, pp.2099-2109, Dec. 1996.

[7] P. Akkaraekthalin, J. Jantree, "Microstrip slow-wave open-loop resonator filters with reduced size and improved stopband charactereisticd," IEICE Trans.Electron., Vol. E89-C, No. 12, Dec. 2006.

[8] A. Djaiz Tayeb and A. Denidni, "A design and fabrication of a new stacked bandpass filter using multilayer microstrip structure for wireless applications," IEEE Trans.Microwave Theory Tech, 2003.

[9] J. S. Hong and M. J. Lancaster, "Aperture coupled microstrip open-loop resonators and their applications to the design of novel microstrip bandpass filter," IEEE Trans. Microwave Theory Tech, vol. 47, pp.l8l8-1855, Sept. 1999.

Bandwidth Enhancement of a CPW-Fed Rectangular Slot Antenna

P. Seangsae [1], N. Anantrasirichai[1], J. Nakasuwan [2], T. Wakabayashi[3]
[1]ReCCIT, Faculty of Engineering, King Mongkut's Institute of Technology Ladkrabang
Ladkrabang, Bangkok, 10520, Thailand
E-mail: kanoppin@kmitl.ac.th
[2]Dept. of Electronic and Telecommunication Engineering, Faculty of Engineering
Rajamangala University of Technology Thanyaburi (RMUTT) Klong 6
Thanyaburi, Pathumthanee, Thailand
E-mail: jintana@rmut.ac.th
[3]School of Information Science and Technology, Tokai University, Hirasuka, Kanagawa, 259-1292, Japan
E-mail: wakaba@et.u-tokai.ac.jp

***Abstract*- This paper investigated wideband coplanar waveguide (CPW) fed rectangular slot antenna with rectangular planar patch and slot tuning. A rectangular slot antenna is excited by a 50 ohm CPW with slot tuning on rectangular planar patch for wireless applications. By adjusting size of rectangular planar patch and of slot tuning on rectangular planar patch, can easily achieve a wideband. The proposed antenna is designed to operate from 1.38 to 6.04 GHz which is suitable for applications in WLAN (Wireless Local Area Network) according to IEEE 802.11 a/b/g standards and covered the WiMAX (Worldwide Interoperability for Microwave Access, IEEE 802.16e). The characteristics of antenna are proposed and analyzed for bandwidth, return loss, input impedance and VSWR. The simulation results are analyzed by IE3D Zeland software.**

I. INTRODUCTION

Recently, there is growing research activity on multi-frequency and broadband and wideband antennas for various wireless communication applications such as WLAN (Wireless Local Area Network) or WiMAX (Worldwide Interoperability for Microwave Access. In particular, a great interest in coplanar waveguide (CPW) fed slot antenna has been presented in the paper because the CPW fed slot antennas have the advantage of wide bandwidth, simplest structure and easy integration with active devices [1]. The CPW fed slot antennas have been designed for wideband applications by rectangular and square slot and enhance bandwidth by optimizing a tuning stub [2, 3, 4].

In this paper, we propose a CPW fed slot antenna for wideband application in WLAN communication and WiMAX. Owing to the slot tuning on rectangular planar patch inset around the side edge of the rectangular slot antenna, a new resonant frequencies can be excited and enhance the operating bandwidth of the wideband by adjusting parameter of slot tuning on rectangular planar patch, which simulation covers the bandwidth of 1.38 to 6.04 GHz is enough for wireless communication. Detail of the proposed CPW fed slot antenna designs are described, and simulation results for obtained wideband performance are presented by using IE3D Zeland software.

II. ANTENNA STRUCTURE

Figure 1, shows the structure of the proposed CPW-fed rectangular slot antenna with slot tuning on rectangular planar patch at designed frequency 1.5 GHz. The slot antenna is on FR4 substrate of dielectric constant 4.5 (ε_r) and substrate of thickness 1.6 mm (h). The dimension of dielectric substrate is 53x61.5 mm^2. The proposed antenna consists of rectangular slot has a length Lx = 44.8 mm and Ly = 25.5 mm. A 50 ohms coplanar waveguide with gap width S = 0.5 mm and centre conductor width Wc = 5.4 mm and the end of CPW feed line connected to rectangular planar patch of dimensions width Wx = 27.8 mm and Wy = 15.5 mm. The both slot tuning etched at the middle of rectangular planar patch, the spacing between rectangular planar patch and edge of the ground plane is G = 1.6 mm. The slot tuning consist of four parameters which three parameters of slot tuning: Lh, Lw and Ls, affect the wideband operation other one is Lv fixed to 2 mm. The characteristic of the proposed antenna and details of designing are discussed in the following section.

The guide wavelength is given by

$$\lambda_g = \frac{c/f}{\sqrt{\varepsilon_{eff}}} \tag{1}$$

Where ε_{eff} is an effective dielectric constant which can be computed by using the following equation.

$$\varepsilon_{eff} \approx \frac{\varepsilon_r + 1}{2} \tag{2}$$

In this case, ε_{eff} = 2.75 and λ_g = 120.6 mm, and dimension of rectangular slot antenna in length and width (Ly and Lx) is about $0.58\lambda_g$ ($Lx = 0.37\lambda_g$ and $Ly = 0.21\lambda_g$).

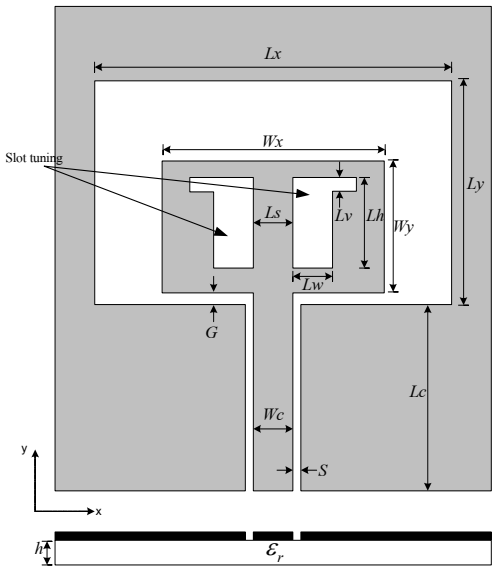

Figure 1. Structure of the proposed antenna.

III. SIMULATION RESULTS

The proposed antenna was designed and studied for bandwidth enhancement. The theoretical analysis was performed using the IE3D simulate software package of Zeland [5]. The CPW feed line is designed with the centre conductor width *Wc* = 5.4 mm, coplanar waveguide with gap width *S* = 0.5 mm, and length CPW feed line of *Lc* = 26 mm for match with 50 Ohms characteristic impedance. There are three designs for show the enhancement of this antenna, the first is CPW fed rectangular slot antenna, second is rectangular planar patch inside of the slot, and third is slot tuning inside of the planar patch. The proposed design can be further enhanced by rectangular conductor patch and with slot tuning on rectangular planar patch. The main proposed of this paper is to show the effect of adjusting three parameters: *Lh*, *Lw* and *Ls* of slot tuning. The result of S11 in three designs are shown in Figure 2, which fixing value of the parameters: *Lx, Ly, Wx, Wy, G, Wc, S*, *Lv* and *Lc* as a first step. The initial value of three parameters of slot tuning of *Lh* = 11 mm, *Lw* = 2 mm and *Ls* = 5.4 mm are proposed for begin adjusting. From Figure 2, the bandwidth of proposed antenna will be increased when using conductor stub tuning (rectangular planar patch) and slot tuning. For more bandwidth enhancement from Figure 2, the adjusting of three parameters will be considered in next step.

A. Effect of Adjusting Lh of Slot Tuning

In this case, we fixed *Lw* = 2 mm, *Ls* = 5.4 mm and vary the length *Lh* of slot tuning to 11 mm, 11.3 mm, 11.5 mm and 12 mm, respectively. The effect on the resonant frequencies and bandwidth are investigated as shown in Figure 3. Its shown that the bandwidth at return loss -10 dB about 4 GHz, the lowest resonance frequency of each value of *Lh* is same but highest resonance frequency is shift down when *Lh* is increased. From Figure 3, the best matching for wideband is at *Lh* = 12 mm, which return loss is 50 dB at ~4.2GHz.

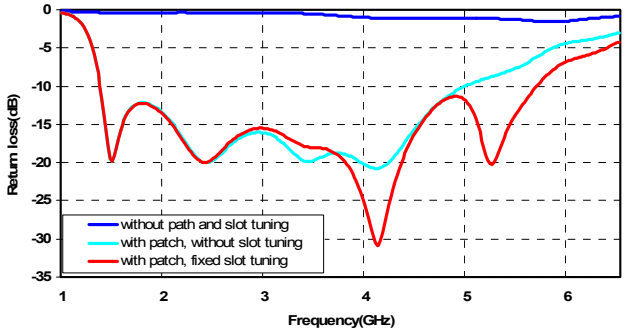

Figure 2. Comparison return loss of three designs.

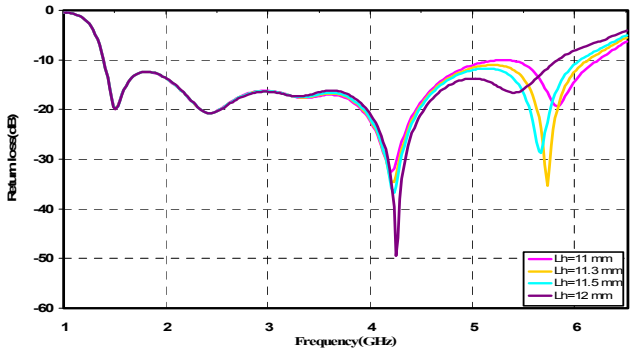

Figure 3. Simulation return loss for difference *Lh*.

B. Effect of Adjusting Lw of Slot Tuning

The effect of the width *Lw* of slot tuning on return loss is considered. Herein, the *Lw* is chosen to 3.7 mm, 4.2 mm, 4.7 mm and 5.7 mm, while *Lh* = 11.5 mm, *Ls* = 5.8 mm are fixed.

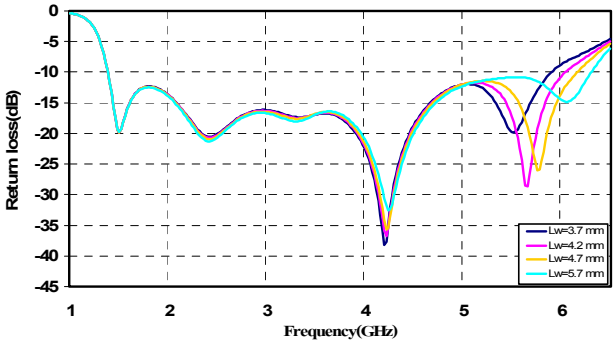

Figure 4. Simulation return loss for difference *Lw*.

The typical simulation results are shown in Figure 4, when we focus to the high resonance from 4 to 6 GHz, it can be found that the resonance frequency near 4 GHz is slightly

chanced but the resonance frequency near 6 GHz is shift up when value of *Lw* is increased and wider bandwidth.

C. Effect of Adjusting Ls of Slot Tuning

The effect of distance between both slot tuning (*Ls*) on the return loss is considered by vary values of *Ls*: 4.8 mm, 5.8 mm, 6.2 mm and 7 mm, respectively, while *Lh* = 11.5 mm and *Lw* = 4.2 mm, as shown in Figure 5. The resonance frequencies slightly changed and return loss is much change.

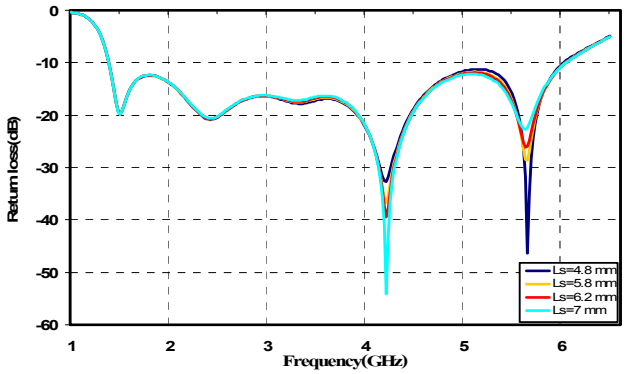

Figure 5. Simulated return loss for difference *Ls*.

D. Characteristic of Return Loss

We optimized and investigates the effect of adjusting three parameters of the antenna for enhance bandwidth covers IEEE 802.11a/b/g (2.4-2.4835GHz, 5.15-5.35GHz and 5.725-5.875GHz) WLAN applications and WiMAX (2-6 GHz). Finally, the dimension of slot tuning is *Lh* = 11.5 mm, *Lw* = 4.2 mm and *Ls* = 4.8 mm for sufficient choosing. Figure 6, shown the frequency band and maximum bandwidth coverage at 1.38 GHz to 6.04 GHz which all of parameters are shown in Table 1.

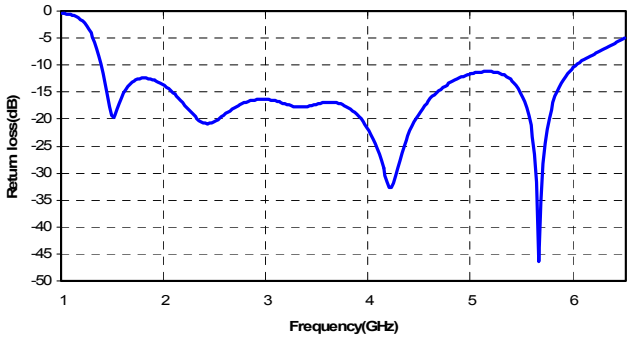

Figure 6. Simulated S_{11} of the proposed antenna.

E. Characteristic of Input Impedance

The input impedance Z_{in} is the complex number, which fined out by using the S_{11} parameter and characteristic impedance Z_o of transmission line. The characteristic of input impedance for this slot antenna is shown in Figure 7.

TABLE 1
Parameters of the proposed antenna designs.

	without patch and slot tuning (mm)	with patch, without slot tuning (mm)	with patch and slot tuning (mm)
Lx	44.8	44.8	44.8
Ly	25.5	25.5	25.5
Lc	26	26	26
Wc	5.4	5.4	5.4
S	0.5	0.5	0.5
Wx	-	27.8	27.8
Wy	-	15.5	15.5
G	-	1.6	1.6
Lv	-	-	2
Lh	-	-	11.5
Lw	-	-	4.2
Ls	-	-	4.8
	-	BW=1.38~5 GHz	BW=1.38~6.04 GHz

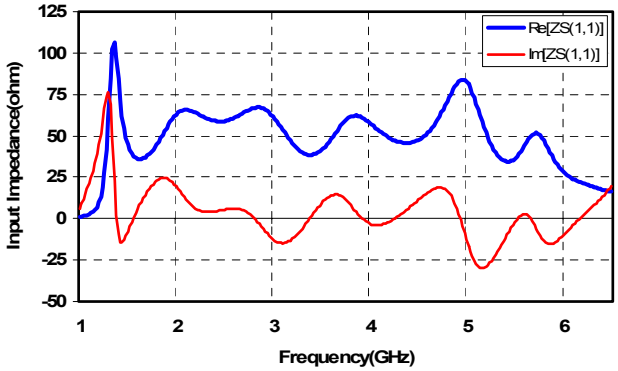

Figure 7. The simulation results of input impedance.

F. Characteristic of VSWR

Figure 8, shown voltage standing wave ratio (VSWR) of this slot antenna. In this case, the maximum VSWR for wideband is 1.035 at frequency 5.68 GHz.

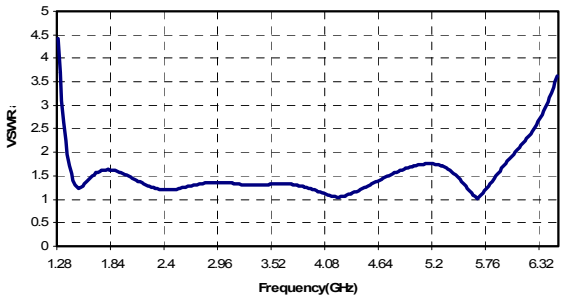

Figure 8. Simulation results of VSWR.

G. Radiation Patterns

The radiation patterns of this antenna for five frequencies: 2.4 GHz, 3.5GHz, 4.2 GHz, 4.8GHz, 5.2GHz and 5.7 GHz are shown in Figure 9.

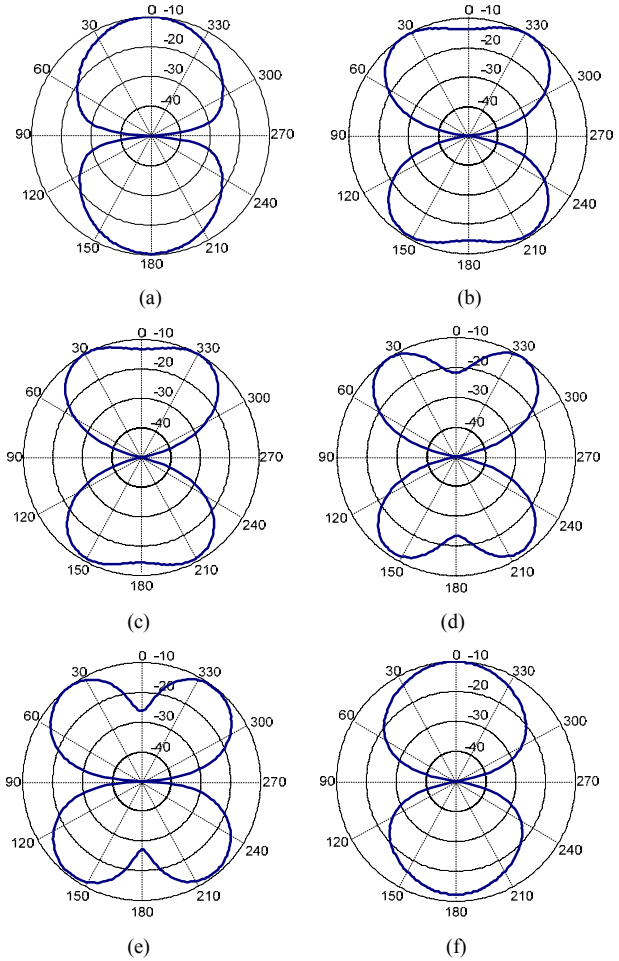

Figure 9. Simulated radiation patterns of E-plane, (a) 2.4 GHz, (b) 3.5 GHz, (c) 4.2GHz, (d) 4.8 GHz,(e) 5.2 GHz, (f) 5.7 GHz

IV. CONCLUSION

This paper presented the bandwidth enhancement of CPW fed slot antenna by rectangular conductor patch and slot tuning on rectangular planar patch. This slot antenna easy to fabrication and can achieved the wideband from frequency range 1.38 – 6.04 GHz coverage IEEE 802.11 a/b/g standard (2.4-2.4835 GHz, 5.15-5.35GHz and 5.725-5.875GHz) for WLAN and WiMAX (IEEE 802.16e, 2-6 GHz).

REFERENCES

[1] Ramaesh Garg, Prakash Bhartia, Inder Bahl and Apisak Ittipiboon, Microstrip Antenna Design Handbook, Artech House, Inc., 2001.

[2] Alpesh U.Bhobe, Christopher L. Holloway, Melinda Piket-May. "Wide-band Slot Antennas With CPW-Feed Line:Hybrid and Log-Periodic Designs," *IEEE Trans. Antennas Propagat*, Vol.52, No. 10, pp. 2545-2554, 2004.

[3] Chen, H. D., "Broadband CPW-fed square slot antennas with a widened tuning stub," *IEEE Trans. Antennas and Propagat*., Vol. 51, No. 8, pp. 1982-1985, August 2003.

[4] M. A. Saed. "Broadband CPW-Fed Planar Slot Antennas With Various Tuning Stubs," *Progress In Electromagnetics Research*, PIER 66, 199-212, 2006.

[5] IE3D User's Manual Release 9,Zeland software, Inc.,U.S.A.,2002.

Elliptical Patch Antenna Radiating Unidirectional Beam with Circular Polarization for Reader of RFID at UHF Band

Rattapong Suwalak and Chuwong Phongcharoenpanich

Faculty of Engineering and Research Center for Communications and Information Technology,
King Mongkut's Institute of Technology Ladkrabang, Bangkok 10520 Thailand, E-mail: kpchuwon@kmitl.ac.th

***Abstract*- This paper presents elliptical patch antenna that radiates unidirectional beam with circular polarization. This antenna is proposed for installing at the reader of the Radio Frequency Identification (RFID) at Ultra High Frequency (UHF) band. The center frequency is 923 MHz with the bandwidth from 920 MHz to 925 MHz. The antenna structure is simple because we use the single feed for circular polarization. The prototype antenna was fabricated to measure the characteristics. The pattern is unidirectional pattern with directivity around 8.93 dBi and axial ratio of 1.88 dB at the center frequency. The obtained bandwidth is 15 MHz.**

I. INTRODUCTION

At present, Radio Frequency Identification (RFID) system becomes very popular due to their usefulness in many applications such as identification, logistics and many others [1]. The antenna designs for both readers and tags are hot research topics. The operating frequency depends on different applications. The ultra-high frequency band is desired for long range applications. The antenna at reader plays a vital role in communication between the reader and the tags. The antennas that can communication with various tag orientations is desirable. Therefore, the antenna radiating the circular polarization is needed to cope with this problem [2]-[4]. In addition, for convenient installation the flat structure is required [5]-[10]. In literature, there are many researches involving with flat structure with circular polarization [2]-[10]. However, all of them focus on the design at microwave frequency that printed circuit board (PCB) is convenient to use for microstrip antenna fabrication with many configurations. To apply the similar concept to the UHF band, the authors proposes to use elliptical patch antenna with single feed to radiate circular polarization. The antenna is designed to achieve the unidirectional beam to direct at the tag direction. The structure is made of metallic plate with air substrate to avoid dielectric loss. The structure is flat with the feeding structure is easy. The antenna is expected to use for reader of RFID system.

II. ANTENNA STRUCTURE

The antenna structure is composed of three metallic plates as shown in Fig.1. The top plate is cut as the elliptical geometry with the major and minor axes of u_x and u_y, respectively. The middle plate is rectangular configuration with two opposite truncated corners whereas the remained two corners are not truncated. The length and the width of the rectangular one are v_x and v_y, respectively. The radius of the truncated corner is denoted by r. At the non-truncated corner, there are two square holes of the size s_h. The distance between the center of the hole and the corner is d. The bottom plate acts as the ground with the length and width of w_x and w_y, respectively. This structure is excited by the linear electric probe. The spacing between the bottom plate and the middle plate and the middle plate and the top plate are t_1 and t_2, respectively. The feeding location is x_p and y_p offset from the top and the right sides, respectively.

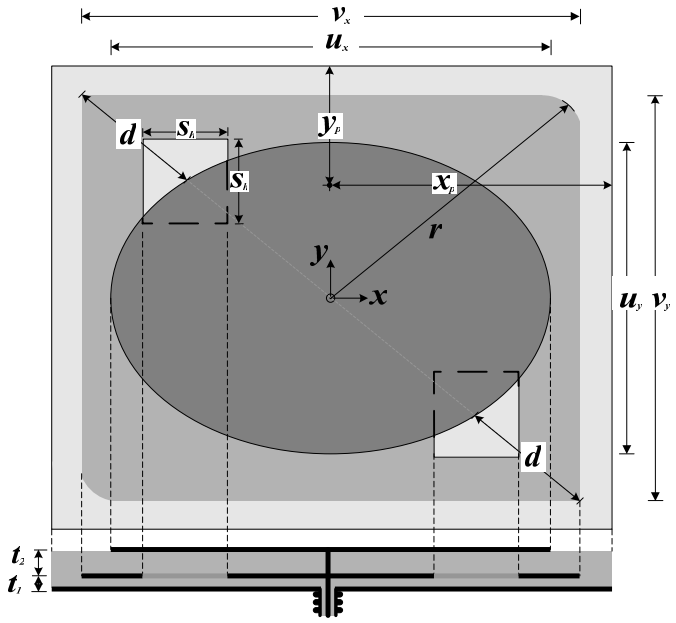

Figure 1. Antenna Structure

III. PARAMETRIC STUDY

In order to find the suitable parameters to obtain the unidirectional pattern with the circular polarization, the hole and the patch sizes must be varied. The other parameters have the size corresponded the operating frequency scaled from the references [2]. The initial antenna parameters are tabulated in Table 1.

Table1 Antenna Parameters

Parameters	Electrical Size	Physical Size at 923 MHz
u_x	0.44λ	14.21 cm
u_y	0.29λ	9.59 cm
v_x	0.58λ	18.80 cm
v_y	0.47λ	15.40 cm
r	0.25λ	8.20 cm
t_1	0.008λ	2.60 mm
t_2	0.034λ	11.10 mm
d	0.17λ	5.38 cm
x_p	0.34λ	10.90 cm
y_p	0.16λ	5.25 cm

The variation of axial ratios versus the hole size is shown in Fig.2. It is found that the suitable hole size with minimum axial ratio is 3.38 cm.

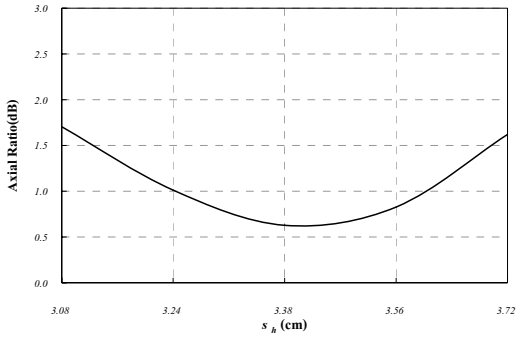

Figure 2. Axial ratio versus s_h

The axial ratio of the antenna in xz-plane for different hole sizes is illustrated in Fig.3. It is found that the axial ratio is lowest at angle of zero degree. However, when the angle is 90 degree offset, the axial ratio becomes very high. So, the circular polarization is significantly obtained at the angle of zero degree.

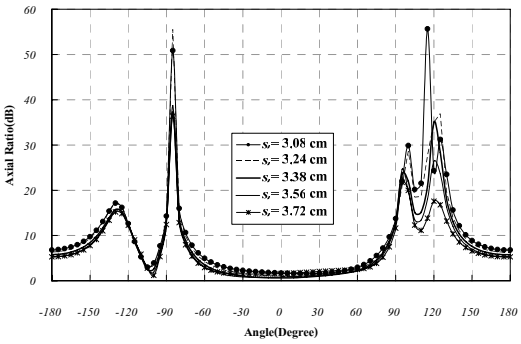

Figure 3. Axial ratio versus angle for different s_h

The magnitude of S_{11} as a function of frequency for various hole sizes is shown in Fig.4. It is obvious that the hole size affects the resonant frequency and level of $|S_{11}|$. To obtain the resonant frequency of 923 MHz with $|S_{11}|$ better than -10 dB, the hole size of 3.38 cm is selected.

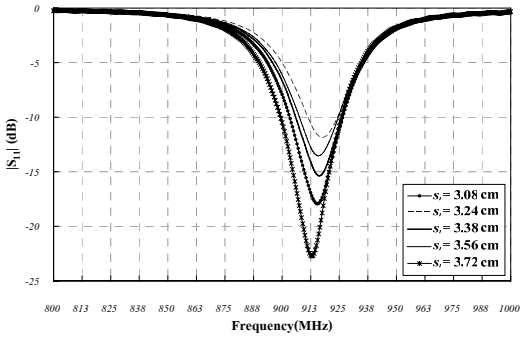

Figure 4. Magnitude of S_{11} versus frequency for different s_h

The axial ratio as a function of additional patch size is shown in Fig.5. The other parameters are the same as Table 1. It is evident that δ = 1.17 cm achieves the minimum axial ratio.

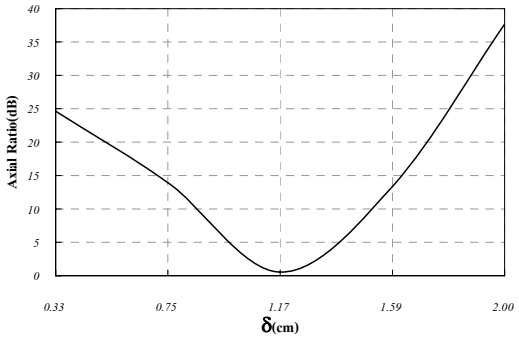

Figure 5. Axial ratio versus δ

The axial ratio in xz-plane for different additional patch sizes is shown in Fig.6. It is found that the minimum axial ratio is accomplished at angle of zero degree. When comparing among different δ, δ = 1.17 cm has the lowest axial ratio. This parameter is used for the guideline of the antenna design.

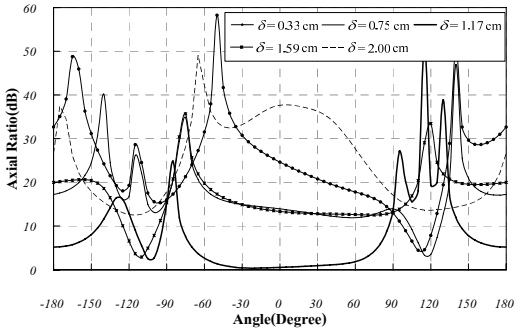

Figure 6. Axial ratio versus angle for different δ

In order to clarify the matching condition of the antenna for various δ, the magnitude of S_{11} for different δ is illustrated in Fig. 5.

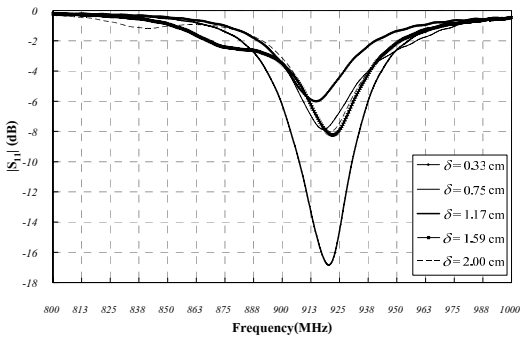

Figure 7. The magnitude of S_{11} versus frequency for different δ

The directivity of the antenna as a function of the frequency is shown in Fig.8. As expected, the directivity is increased when the frequency is higher because the dimension of the antenna per wavelength is larger. At the center frequency of 923 MHz, the directivity is 8.93 dBic.

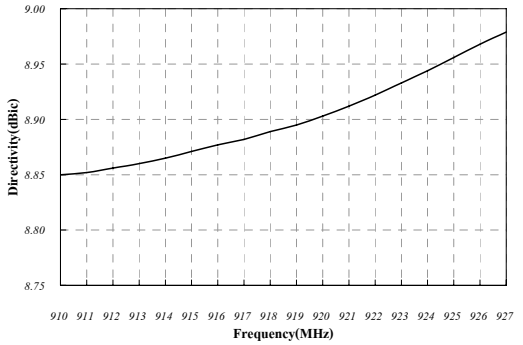

Figure 8. Directivity versus frequency

The axial ratio as a function of the frequency is shown in Fig.9. It is evident that the minimum axial ratio is occurred at 918 MHz. However, along the frequency range of 910-926 MHz, the acceptable axial ratio of less than 3 dB is accomplished. At the frequency of 923 MHz, the axial ratio is 1.88 dB.

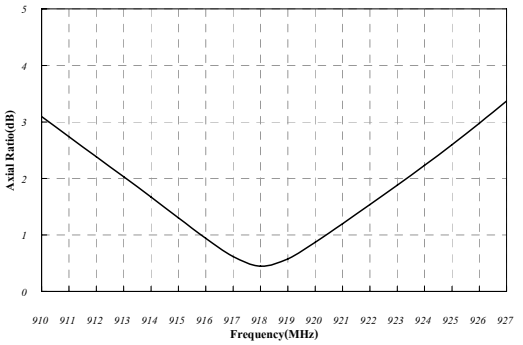

Figure 9. Axial ratio versus frequency

The axial ratio as a function of angle in xz- and yz-planes is shown in Fig.10(a) and Fig.10 (b), respectively. We have changed the frequency at 913, 917, 921 and 925 MHz. It can be seen that the axial ratio is slightly different for various frequencies. When comparing among the different angles, it is found that the angle of zero degree yields the minimum axial ratio.

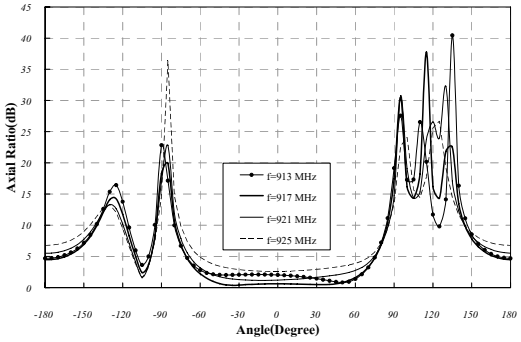

(a) xz - plane

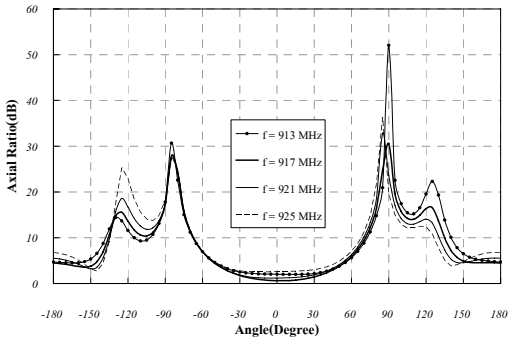

(b) yz - plane

Figure 10. Simulated axial ratio versus angle

IV. MEASURED RESULTS

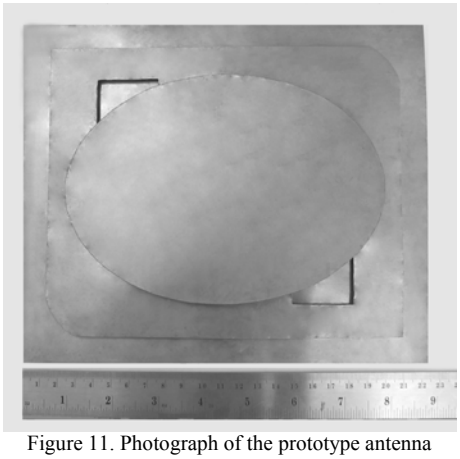

Figure 11. Photograph of the prototype antenna

In order to verify the principle, the prototype antenna was fabricated to operate at the frequency of 923 MHz as shown in Fig.11. The physical dimension is shown in Table 1. The measurement of radiation pattern is set up at the frequency of 923 MHz. The radiation pattern in xz- and yz- planes are plotted and compared with the simulated results as shown in Fig.12(a) and Fig.12(b), respectively. It is seen that the results are reasonable agreement. The unidirectional is obtained. The measured beamwidths in xz- and yz- planes are 100 and 70

degrees, respectively. The measured front-to-back ratio in both planes is 12.7 dB.

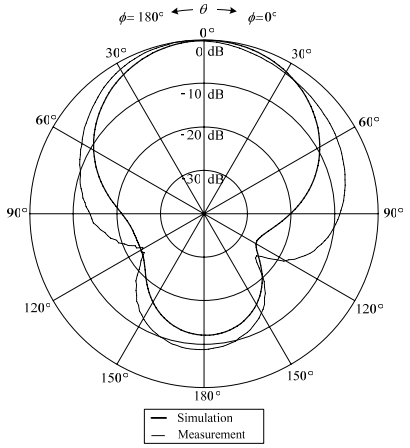

(a) xz - plane

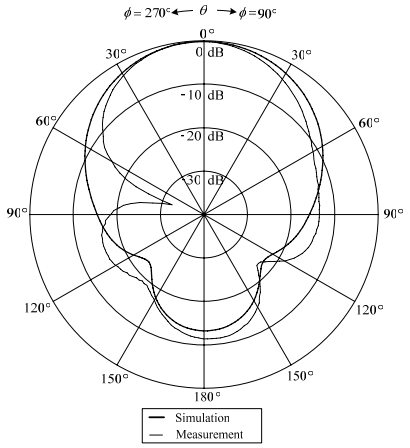

(b) yz – plane

Figure 12. Simulated and measured patterns

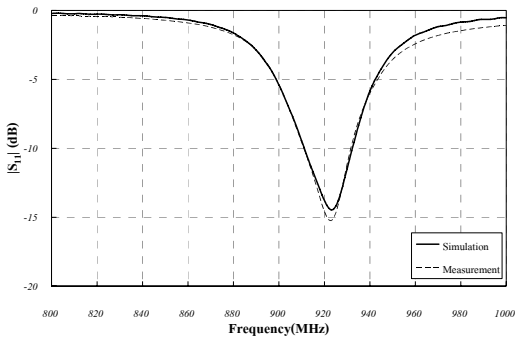

Figure 13. Simulated and measured magnitude of S_{11}

The magnitude of S_{11} as a function of frequency from simulation and measurement is disposed in Fig.13. It is found that the simulated and measured results agreed very well. The obtained impedance bandwidth of $|S_{11}|$ better than -10 dB is 2.2 % (912 - 932 MHz).

V. Discussions And Conclusions

The UHF-RFID antenna is proposed in this paper using the elliptical patch antenna to radiate the circular polarization. The antenna structure is simple because it need only single feeder and it is free from dielectric loss. The parametric study of the antenna is presented. It is obvious that the antenna radiates unidirectional beam with the beamwidth in xz- and yz- planes are 100 and 70 degrees, respectively. The axial ratio is 1.88 dB and the directivity is 8.93 dBic, respectively. From the results, it can confirm that this antenna can be used as the reader antenna of the UHF-RFID system.

References

[1] K. Finkenzeller, "RFID handbook: Fundamentals and applications in contactless smart cards and identification", John Wiley and Sons, Ltd., 2003.

[2] C. S. Lee and V. Nalbandian, "Planar circularly polarized microstrip antenna with a single feed," *IEEE Trans. Antennas Propagat*., vol. 47, pp. 1005–1007, 1999.

[3] C. S. Lee, V. Nalbandian, and F. Schwering, "Circularly polarized microstrip antenna with a single coaxial feed," *IEEE Trans. Antennas Propagat.*, vol. 44, pp. 1426–1427, 1996.

[4] C. S. Lee, V. Nalbandian, and F. Schwering, "planar, single-feed, circularly polalized microstrip antenna with enhanced bandwidth," *IEEE Trans. Antennas Propagat*., vol. 3, pp. 1368–1371, 1998.

[5] D. M. Pozar and S. M. Duffy, "A Dual-band Circularly Polarized Aperture-coupled Stacked Microstrip Antenna for Global Positioning Satellite (GPS)," *IEEE Trans. on Antennas and Propagation*, vol.45, no.11, pp. 1367-1374, 1997.

[6] S. Yuminaga and Y. Yamada, "A Triple-layer patch antenna capable of triple-frequency operation," *Digest of the 2003 Antennas and Propagation Society International Symposium,* vol. 4, pp. 138–141, 2003.

[7] Q. Jinghui; Q. Wenyi; and Y. Caitian; and Z. Lingling, "A triple-frequency circularly polarized microstrip antenna," *Proceeding of the 2005 Asia-Pacific Microwave Conference*, vol. 4, 3 pages, 2005.

[8] Richards, W.; Yuen Lo; and Harrison, D, "Planar circularly polarized microstrip antenna with a single feed," *IEEE Trans. Antennas Propagat.*, vol. 29, pp. 38-46, 1981.

[9] C.Y. Huang; J.Y. Wu; and K.L. Wong, "Cross-slot-coupled microstrip antenna and dielectric resonator antenna for circular polarization," *IEEE Trans. Antennas Propagat*., vol. 47, pp. 605–609, 1999.

[10] W.S. Chen; C.K.Wu; and K.L. Wong, "Square-ring microstrip antenna with a cross strip for compact circular polarization operation," *IEEE Trans. Antennas Propagat*., vol. 47, pp. 1566–1568, 1999.

Parametric Study of a Vertically Polarized Concentric Circular Ring Antenna above the Reflector for High Gain Applications

Souphanna Vongsack[1], Krittaya Chawanonphithak[1]Chuwong Phongcharoenpanich[1], Sompol Kosulvit[1], and Toshio Wakabayashi[2]
[1]Faculty of Engineering and Research Center for Communications and Information Technology, King Mongkut's Institute of Technology Ladkrabang, Bangkok 10520 Thailand, E-mail: kpchuwon@kmitl.ac.th
[2]School of Engineering, Tokai University, Hiratsuka, Kanagawa 259-12, Japan, E-mail: wakaba@dt.u-tokai.ac.jp

***Abstract*- This paper presents the parametric study of a vertically polarized concentric circular ring antenna above the reflector for high gain applications. The proposed antenna is designed to achieve unidirectional pattern with high gain for the point-to-point communication application in wireless Local Area Network (WLAN). The operating frequency of this antenna is 2.45 GHz. The CST software based on FIT (Finite Integral Technique) is used as the simulation tool for investigating the antenna characteristics. From the simulation, the antenna bandwidth, frequency range and gain are 28.30%, 2.00-2.66 GHz and 9.19 dBi, respectively. Moreover, the good radiation characteristics with vertical polarization and front-to-back ratio better than 20 dB are obtained in both E-plane and H-plane.**

I. INTRODUCTION

It is well-known that the antenna is a significant part of wireless system to make the communication successfully. The conventional antenna for the wireless Local Area Network communication system radiates the omnidirectional beam. However, for some specific application of the long range service area such as the point-to-point communication between the buildings, the unidirectional antenna is preferred. Generally, the unidirectional antenna with the high gain, low side lobe level and narrow beamwidth is desirable. Thus, many researches have continuously developed the unidirectional antennas as published in [1]. Usually, the unidirectional beam can be obtained by using microstrip fundamental mode [2], horn antenna [3], reflector antenna [4] and many others. Moreover, the unidirectional antenna can be achieved by using some specific antenna that is arranged to from the array configuration [5]-[6]. Most unidirectional antenna has complicated structure with the expensive material. However, the structure of a concentric circular ring antenna above the reflector is simple and cost-effective.

Historically, the probe excited circular ring is designed to radiate the bidirectional pattern [7]. The unidirectional beam is carried out by placing the antenna above the reflector or ground plane. To realize the unidirectional pattern, the reflector should be placed near one side of the ring aperture [8]. From the previous work we found that the side lobe level is not good and directivity is not so high. But, the proposed antenna has an impedance bandwidth (2:1 VSWR) of 28.30%. The centre frequency is 2.45 GHz, and the obtained frequency range is 2.00-2.66 GHz. From the simulation, the concentric circular ring antenna above the reflector has the unidirectional pattern with the gain of 9.19 dBi. The polarization is vertically linear polarization, the front-to-back ratio in both E-plane and H-plane is better than 20 dB. Moreover, the design of this antenna is simple, and the fabrication uses the low cost materials. Therefore, this antenna is interested for utilizing in the point-to-point wireless Local Area Network communication system.

The content of this paper are divided into five sessions. In section II, the antenna structure is described. Then, the parametric study and conclusion of antenna parameter are presented. The last session is conclusion.

II. ANTENNA STRUCTURE

The structure and design of the antenna is easy and straightforward. For the specified operating frequency, a choice of the ring radius is first chosen to achieve the condition that only the dominant mode can be propagated inside the cylindrical waveguide. The structure of a concentric circular ring antenna above the reflector for high gain application consists of a linear electric probe of the length *l* aligned along the *y* axis, and the distance from probe to reflector is *h*, and it is surrounded by an inner ring of the radius *a*. The radius of an outer ring is *b*; the lengths of inner and outer circular ring are *t* and *d*, respectively. The distance between inner and outer circular ring is supported by the post of the length *p*. The traveling wave along *z* axis is accomplished by using an electric probe fed in the radial direction as shown in Fig.1. It is noted that the probe is shielded by dielectric rod of the length *l*/2.

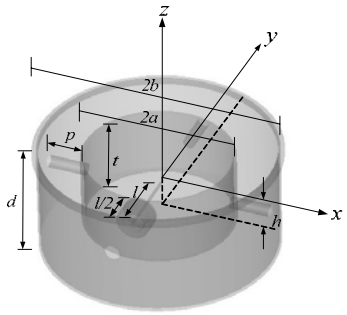

Fig.1 A concentric circular ring antenna above the reflector

The antenna was made from two material types, i.e. the outer circular ring and the reflector are made of aluminum and the inner circular ring is made of brass. The initial parameters for the parametric study are tabulated as shown in Table 1.

Table1 Antenna Parameters

Parameters	Electrical Size	Physical Size
a	0.59λ	72.71 mm
b	0.95λ	116.59 mm
l	0.26λ	33.00 mm
h	0.26λ	32.00 mm
t	0.29λ	35.53 mm
d	0.43λ	53.43 mm
p	0.17λ	21.94 mm
ε_r (dielectric constant)	10	10
Location of the Probe	$\rho = a$, $\phi = 90^o$, $z = 0$	

III. PARAMETRIC STUDY

A concentric circular ring antenna above the reflector is designed to operate at frequency of 2.45 GHz. The parametric study of six parameters is investigated in this section, i.e. the inner ring radius (a), outer ring radius(b), length of inner ring (t), length of outer ring (d), distance from probe to reflector (h), and probe length (l), respectively.

A. Effect of radius and length of inner ring

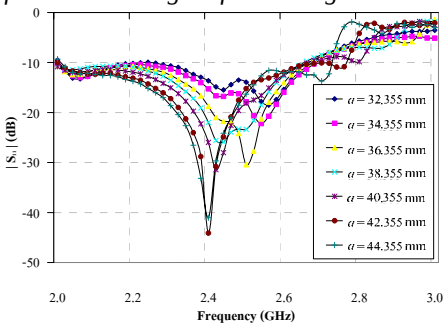

Fig.2 Frequency response of return loss as a function of inner ring radius

Figure 2 shows the frequency response of return loss as a function of inner ring radius. The different radii of inner ring are analyzed whereas all other parameters are fixed as following Table 1. The radius of inner ring affects to the front-to-back ratio as illustrated in Fig.3. From Fig.3, it is obvious that a of 42.355 mm is the suitable value of inner ring radius because it provides the optimum front-to-back ratio.

Moreover, the influence of the length of inner ring (t) is studied by fixing the radius of inner ring at 42.355 mm for simulation. The different lengths of inner ring are analyzed from 13.765 mm to 21.765 mm. Figure 4 and Figure 5 show the frequency response of return loss and front-to-back ratio as a function of inner ring length, respectively. From the results it is obvious that the inner ring length (t) of 17.765 mm is suitable for the antenna design because the best front-to-back ratio is obtained.

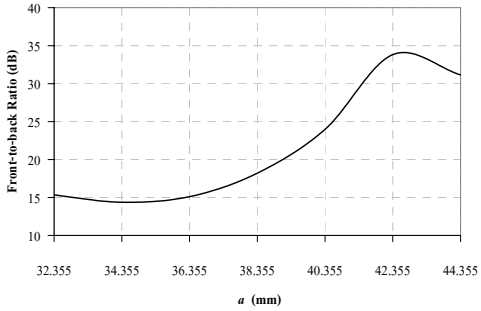

Fig.3 Front-to-back ratio as a function of inner ring radius

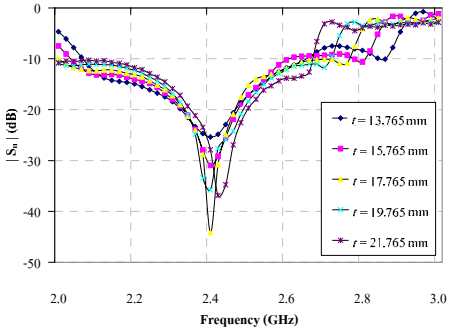

Fig.4 Frequency response of return loss as a function of inner ring length

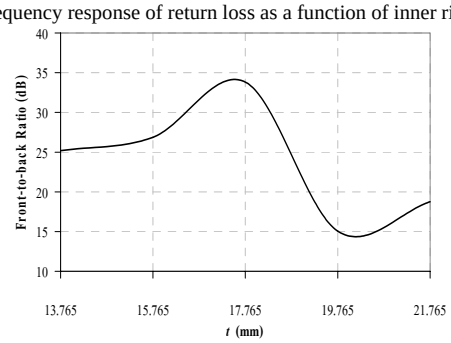

Fig.5 Front-to-back ratio as a function of inner ring length

B. Effect of radius and length of outer ring

The effects of different radii of outer ring are investigated from 54.295 mm to 62.295 mm while the radius and length of inner ring is fixed at 42.355 mm and 17.765 mm, respectively. Figure 6 and Figure 7 shows the frequency response of return loss as a function of outer ring radius and front-to-back ratio for various radii of outer ring. From the simulated results it is obvious that the outer ring radius (b) of 58.295 mm is suitable for the antenna design because the front-to-back ratio is the maximum at 58.295 mm as can be seen in Fig.7.

Furthermore, the simulation is performed to study the influence of the outer ring length by fixing a=42.355 mm, t=17.765 mm and b=58.295 mm while the outer ring lengths are varied from 45.43 mm to 57.43 mm. From Fig. 8, the outer ring length is not much affected to the return loss. Figure 9 shows the front-to-back ratio for various outer ring lengths. From the simulated results, it is obvious that the outer ring length (d) of 47.43 mm is the suitable for the antenna design.

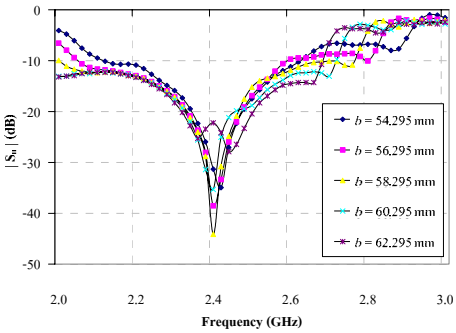

Fig.6 Frequency response of return loss as a function of outer ring radius

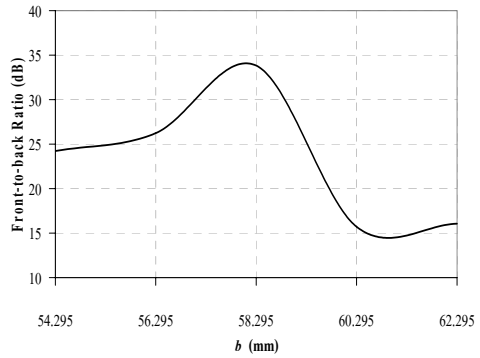

Fig.7 Front-to-back ratio as a function of outer ring radius

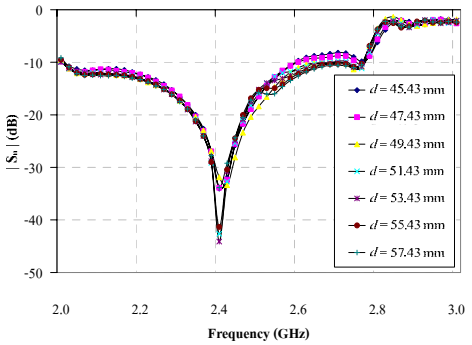

Fig.8 Frequency response of return loss as a function of the outer ring length

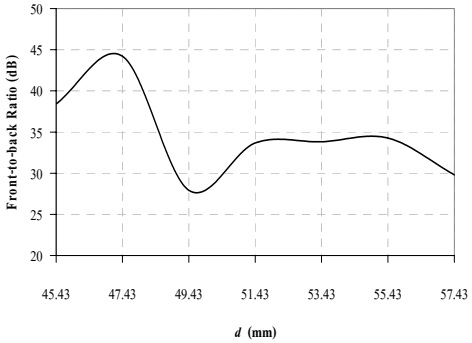

Fig.9 Front-to-back ratio as a function of outer ring length

C. Effect of distance from probe to reflector

In this section, the simulation is conducted to study the antenna characteristics of the distance from probe and reflector by using *a*=42.355 mm, *t*=17.765 mm, *b*=58.295 mm and *d*=47.43 mm. The distances from probe to reflector are investigated from 28 mm to 40 mm. The frequency response of return loss as a function of distance from probe to reflector is shown in Fig.10. The front-to-back ratio for various distances from probe to reflector is shown in Fig.11. From the simulated results, the distance from probe to reflector (*h*) of 32 mm is suitable for the antenna design.

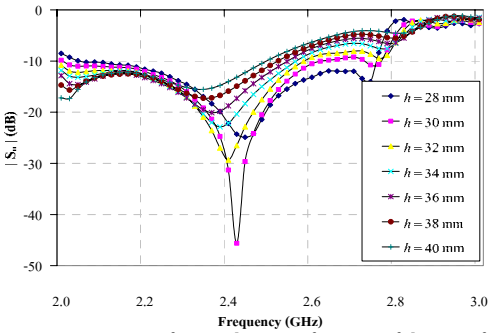

Fig .10 Frequency response of return loss as a function of distance from probe to reflector

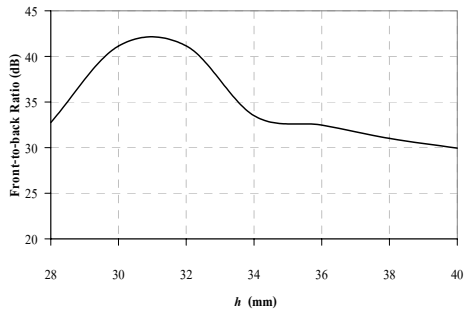

Fig.11 Front-to-back ratio as a function of distance from probe to reflector

D. Effect of probe length

The influence of the probe length (*l*) are also studied by fixing *a*=42.355 mm, *t*=17.765 mm, *b*=58.295 mm, *d*=47.43 mm, and *h*=32 mm. The probe lengths are investigated from 29 mm to 45 mm. From the simulation, it is found that the probe length (*l*) have much influence to return loss as illustrated in Fig.12. From the simulated results, the probe length of 33 mm is chosen for the antenna design because it provides the best resonance.

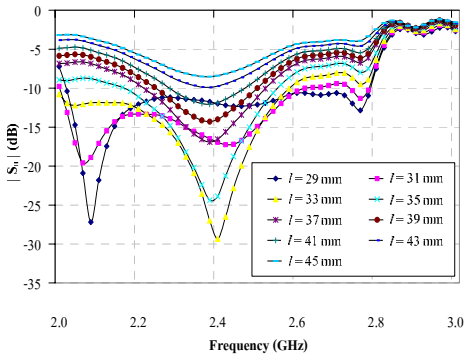

Fig.12 Frequency response of return loss as a function of probe length

IV. SIMULATION RESULTS

A. Radiation Characteristics

From the previous section, the appropriate parameters were selected as inner ring radius (*a*) of 42.355 mm, inner ring length (*t*) of 17.765 mm, outer ring radius (*b*) of 58.295 mm, outer ring length (*d*) of 47.43 mm, distance from probe and reflector (*h*) of 32 mm, and probe length (*l)* of 33 mm. The proposed antenna provides the unidirectional pattern with the vertically linear polarization. The half-power beamwidth (HPBW) in both in E-plane and H-plane are 64.1^{o} and 64.8^{o}, respectively. The front-to-back ratio (F/B) in both planes is greater than 20 dB. Figure 13 shows the simulated radiation pattern in H-plane that it consists of co-polarization and cross-polarization and in E-plane the result shows only co-polarization because cross-polarization is less than co-polarization more than 40 dB. The maximum gain of the proposed antenna is 9.19 dBi at the frequency 2.45 GHz as can be seen in Fig.14.

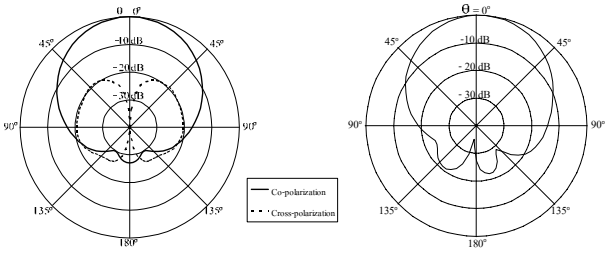

(a) H-plane (XZ-plane) (b) E-plane (YZ-plane)

Fig.13 The radiation pattern

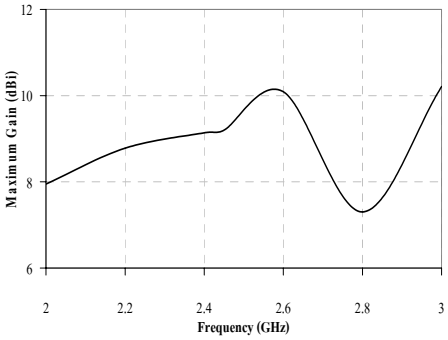

Fig.14 Frequency response of maximum gain

B. Impedance Characteristics

The impedance bandwidth (VSWR<2) of the proposed antenna is 28.30% and the resonant frequency is 2.45 GHz as shown in Fig. 15.

C. Polarization Characteristics

The simulated axial ratio of main lobe in H-plane is approximately 120 dB as shown in Fig.16. Therefore, this antenna radiates the dominantly vertically linear polarization.

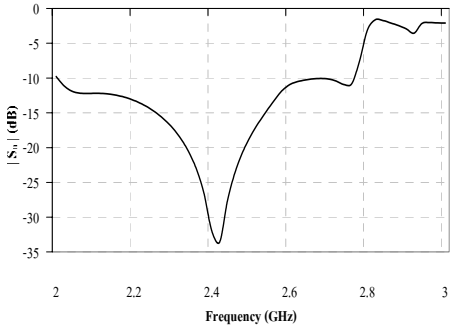

Fig.15 Frequency response of return loss

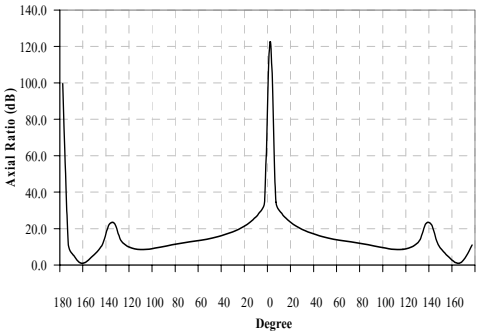

Fig.16 Axial ratio

V. DISCUSSIONS AND CONCLUSIONS

This paper describes a vertically polarized concentric circular ring antenna above the reflector with simple structure, low cost and high gain. The parametric study is also presented for finding the suitable parameters to meet the requirement of high gain. From the simulation results, it confirms that this antenna is suitable for applying in point-to-point communication of wireless Local Area Network (WLAN) system.

Acknowledgement

The author wish thanks AUN/Seed-Net Program for support the scholarship.

REFERENCES

[1] R. C. Johnson and H. Jasik, *Antenna Engineering Handbook*, McGraw Hill, New York, 1984.

[2] J. R. James and P. S. Hall, *Handbook of the Microstrip Antenna*, vol. 1-3, Peter Peregrinus, 1989.

[3] C. A. Balanis, "Horn antennas," chapter 8 in *Antenna HandbookTheory, Applications and Design* (Y. T. Lo and S. W. Lee, eds.), Van Nostrand Reinhold Co., New York, 1988.

[4] A. W. Love (eds.), *Reflector Antennas*, IEEE Press, New York, 1988.

[5] W. H. Kummer, "Basic array theory," *Proc. IEEE*, vol. 80, no. 1, pp. 127-140, Jan. 1992.

[6] R. Tang and R.W. Burns, "Array technology," *Proc. IEEE*, vol. 80, no.1, pp. 173-182, Jan. 1992.

[7] S. Kosulvit, C. Phongcharoenpanich, M. Krairiksh and T. Wakabayashi, "Design of a Bidirectional Antenna Using a Probe Excited Circular Ring," *Proceedings of the 1999 Thailand-Japan Joint Symposium on Microwaves*, Pattaya, pp. 55-59, Sept. 1999.

[8] C. Phongcharoenpanich, I. Rattanachote, P. Wounchoum, S. Kosulvit, and M. Krairiksh, "Design of a probe Excited Circular Ring above the Reflector for Bridging Outdoor Wireless LAN," *Digest of the Antenna and Propagation Society International Symposium.* Vol. 2, pp. 950-953. June 2003.

Microwave-Based Durian Maturity Determination Using Microstrip Patch Antennas

Navapadol Kittiamornkul, Kamon Jiraseriamornkul*, Kosin Chamnongthai* and Monai Krairiksh***
* Department of Electronic and Telecommunication Engineering, Faculty of Engineering,
King Mongkut's University of Technology Thonburi
** Department of Telecommunication Engineering, Faculty of Engineering,
King Mongkut's Institute of Technology Ladkrabang
Bangkok Thailand

***Abstract*-Since durian has specific properties such as big peel, non-uniform shape, rough skin, etc. The non-destructive maturity determination is difficult to perform. This paper proposes microwave free-space measurement by using two microstrip patch antennas as transmitter and receiver operating in 2.4 GHz of frequency to determine the scattering parameters after passing through durian which can be calculated in term of complex permittivity. This method can save the costs that the results can be calculated from the amplitude of wave, no need the network analyzer. The results show that the technique can provide fast durian maturity determination with 72.22% accuracy.**

I. INTRODUCTION

Thailand can make a lot of export values from the agricultures. Durian is the one of the commercial fruits with highest export value. In fruit quality control, it is very important to know the maturity of durian before exporting. There are many methods to determine their qualities, both in destructive and non-destructive. In non-destructive way, it is very difficult to determine because durian has massive of its thickness peel, non-uniformity shape and roughness prickle. In the quality determination of fruit, Ketsa and Dangkanit [1] presented the relation between the maturity of durian and the chemical compound in the prickle of durian which destructive technique. Javier et al. [2] and Yang [3] presented the vision system for fruit determination with color, size and shape. Lee et al. [4] and Slaughter [5] presented near infared to determine chemical structure inside tomato and peach. However, the infared technique is not appropriate for pericarp fruit. T. Anupun et al. [6] presented the durian maturity determination by knocking and then took its signal to analyze for determination of frequency response. But the result showed low accuracy because of non-linearization of knocking. W. Kongratanaprasert et al. [7] presented non-destructive maturity determination of durian by force vibration and ultrasonic. T. Rutpralom et al. [8] presented non-destructive durian maturity determination by using microwave free-space measurement.

In this paper, we present the non-destructive technique of durian maturity determination by using microwave moisture sensing. This method using 2.45 GHz of microwave beam to measure the scattering parameters between the transmitter and the receiver. Then we calculate them in term of complex permittivity which is used to classify the property of a durian. Then the result is compared with percentage dry weight of durian after drying.

This method can save the costs because the results are calculated from the amplitude of the wave, do not need the network analyzer. The basic concept, experimental result and conclusion are showed in next chapter.

II. BASIC CONCEPT

A. Basic Microwave Material Interaction

When microwaves are directed towards a material, part of the energy is reflected, part is transmitted through the surface, and part of it is absorbed. The proportions of energy, which fall into these categories, have been defined in term of the dielectric properties. The fundamental electrical property though which the interactions are described is the complex relative permittivity of the material, ε^*. It is mathematically expressed as

$$\varepsilon^* = \varepsilon' - j\varepsilon'' \qquad (1)$$

where ε' = dielectric constant, and
ε'' = dielectric loss factor

The absolute permittivity of a vacuum, ε_0, is determined by

$$C_0 \mu_0 \varepsilon_0 = 1 \qquad (2)$$

where C_0 = speed of light in free space
μ_0 = magnetic constant = 1.26×10^{-6} H/m
ε_0 = 8.854×10^{-12} F/m

B. Free Space Method

This method use beams of electromagnetic radiation that pass through the dielectric sample as shown in Figure 1. The wave travels from the radiating antenna to the receiving antenna through the two media of air and sample.

The total reflection and transmission coefficients are given by

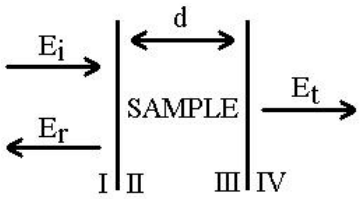

Fig1. Reflection/transmission measurement configuration

For lossy materials, the total reflection and transmission coefficients are given by

$$r = r_{12} = \frac{\sqrt{1} - \sqrt{\varepsilon_r}}{\sqrt{1} + \sqrt{\varepsilon_r}} \quad (3)$$

$$t = (1 - r_{12}^2)e^{-j\Theta} \quad (4)$$

where $\Theta = k_0 \sqrt{\varepsilon_r} d$, $k_0 = \frac{2\pi}{\lambda_0}$, (5)

Here, ε_r is the relative permittivity of the sample, and λ_0 is the wavelength in free space.

To find the permittivity by using any root-finding method, in (3) and (4) should be solved simultaneously. In order to simplify the solution of the equations, let $\sqrt{\varepsilon_r} = a - jb$. The expressions for reflection and transmission coefficients then become

$$r = r_{12} = \frac{1 - (a - jb)}{1 + (a - jb)} \quad , \quad t = \frac{4(a - jb)e^{-j\Theta}}{(1 + a - jb)^2} \quad (6)$$

and the amplitudes of reflection and transmission coefficients can written as

$$|r| = \frac{\sqrt{(1-a)^2 + b^2}}{\sqrt{(1+a)^2 + b^2}} \quad (7)$$

and

$$|t| = \frac{4\sqrt{a^2 + b^2}e^{-k_0 db}}{(1+a)^2 + b^2} \quad (8)$$

From (7) and (8), we get the final equation as

$$\sqrt{2a(1 - |r|^4) - (1 - |r|^2)^2} \cdot \exp\left\{-k_0 d \sqrt{\frac{2a(1 + |r|^2)}{(1 - |r|^2)} - (1 + a^2)}\right\} - |t| a = 0 \quad (9)$$

that depend on a .

The real and imaginary parts of the permittivity are then calculated by using the following simple equations

$$\varepsilon_r' = a^2 - b^2 \text{ and } \varepsilon_r'' = 2ab \quad (10)$$

The amplitudes of reflection and transmission coefficients together with the thickness of the sample uniquely determine the complex dielectric permittivity of cement-based specimens.

III. Experimental Setup

In the experiment, 2 microstrip patch antennas have been designed as shown in Fig.2, the dimension of the microstrip patch antenna is a = 90 mm, b = 90 mm, c = 5 mm.

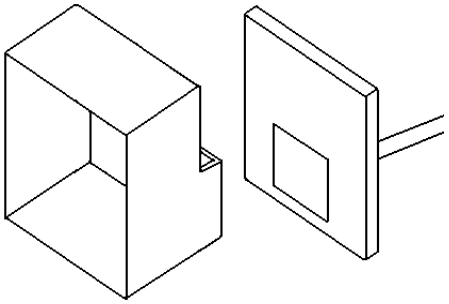

Fig 2. The designed microstrip patch antenna.

The measurement setup is shown in Fig.3 to determine the voltage that transmitted and reflected. Then change into transmission and reflection coefficient. Finally the data is calculated for permittivity by using Matlab software.

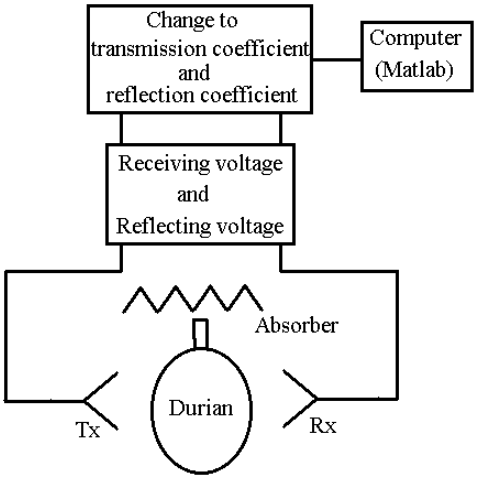

Fig 3. Measurement setup.

IV. Result

18 durians (Monthong) weight 4-4.5 kg. are sampled from Rayong market . The experiment for permittivity of durians determination is shown in Fig. 6, the transmitter and receiver antenna are placed in the same vertical level and close contact to durian surface to prevent non-direct signal path go to the

receiver antenna. The transmission and reflection coefficient is measured and calculated for real part of complex permittivity of durian.

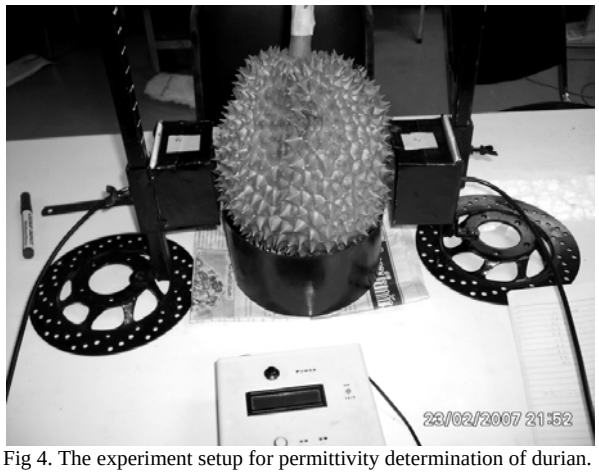

Fig 4. The experiment setup for permittivity determination of durian.

The voltage can change into the amplitude of the transmission and reflection coefficients by the following graphs.

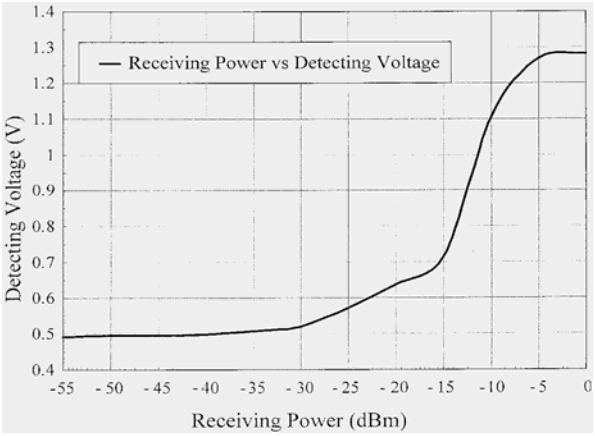

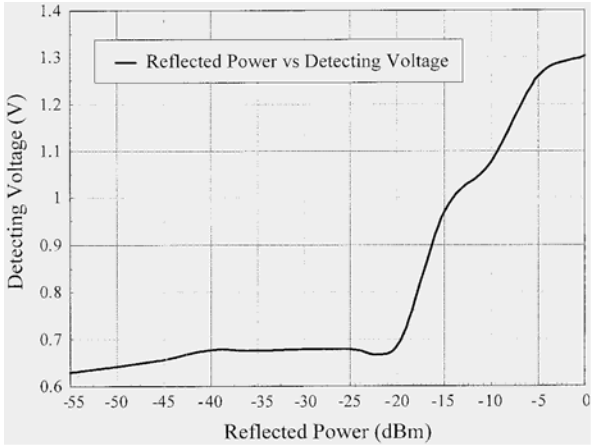

Fig 5. The amplitude transmission and reflection coefficients from measured voltages.

A. Dry-Weight Percentage Determination

The standard maturity classification of durian has been proposed by Peerapong [5] 50 g. of durian pulp is fumed 65 C° for 48 hours, Percentage dry-weight can be obtained from Equation (11).

$$\%Dry-weight = \frac{W_{after}}{W_{before}} 100\% \qquad (11)$$

Where W_{after} is weight after fuming
W_{before} is weight before fuming

From his result, he found that the % dry-weight threshold value is 30, the % dry-weight of immature durian is less than 30% and the % dry-weight of mature durian is more than 30% so in our experiment, we use this dry-weight percentage result as a standard maturity classification.

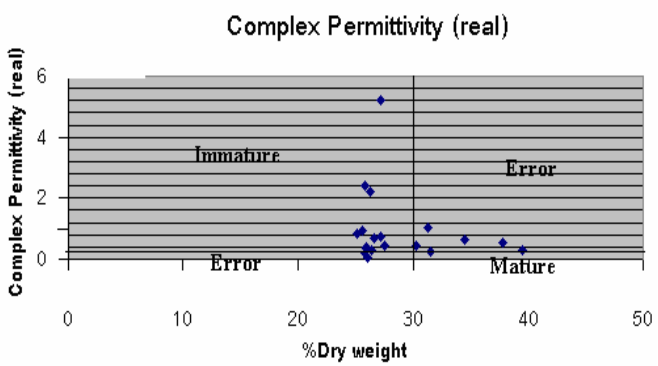

Fig 6. The result of 18 durian samples between real part of complex permittivity and %dry-weight.

From graph in Fig.6 above, it shows that the real part of complex permittivity is more than 0.4 and %dry-weight is less than 30% means durian is immature. Real part of complex permittivity is less than 0.4 and %dry-weight is more than 30% means durian is mature. In the left lower and right upper region of the graph are the error regions. The error occurs from non-uniform shape of durian causes incorrect sample length.

V. Conclusion

This paper presents nondestructive durian maturity determination by using microwave free space measurement. The complex permittivity of material such as agricultural products can be determined with fast and accurate. The results show that this technique gives 72.22**%** accuracy.

References

[1] Ketsa S. and Daungkanit T., 1999, "Firmness and Activities of Polygalacturonase, Pectinesterese, β-Galactosidase and Cellulase in Ripening Durian Havested at Difference Stages of Maturity", Scientia Horticulture, 1999, pp. 184-188.

[2] Javier, C., Filioberto, P., Jordi, M., Pedro, D. and Juan, C.B., 1996, Robust Low-Cost Vision System for Fruit Grading", IEEE International Conference on Electrotechnical, Vol. 3, pp. 1710-1713.

[3] Yang, Q., 1996, "Apple Stem and Calyx Identification with Machine Vision", Elsevier Science on Postharvest Biology and Technology, Vol. 3, pp. 229-236.

[4] Lee, K.J., Hruschka, W.R., Abbott, J.A., Noh, S.H. and Chen, Y.R., 1997, "Comparison of Statistical Methods for Calibrating Soluble Solid Measurement from NIR Interactance in Apples", Proceedings Korean Society Agriculture Machinery.97 Winter, Vol. 1, pp. 206-212.

[5] Slaughter D.C., BarrettD., Boersig M., 1996, "Nondestructive Determination of Soluble Solids in Tometoes using Near-Infrared Spectroscopy", J.food Sci. 61, 1996, pp. 695-697.

[6] Anupun T., Wichet S. and Anek S., 1997, "Investigation of Change in Resonant Frequency Related Index with Respect to Durian Quality", Research report to Thailand research fund, Division of Science and Technology Research for Manufacturing and Administration, October 1997.

[7] Kongrattanaprasert, S., Arunrungrusmi, S., Pungsiri, B., Chamnongthai, K. and Okuda, M., 2001, "Nondestructive Maturity Determination of Durian by Force Vibration and Ultrasonic", IEEE International Symposium on Circuits and Systems, Thailand, 6-9 May 2001, pp. 441-444.

[8] Rutpralom T., Chamnongthai K. and Kumhom P., 2006, "Nondestructive Durian Maturity Determination by Using Microwave Free Space Measurement", IEEE International Symposium on Circuits and Systems 2006**,** Thailand

[9] Sergey N. Kharkovsky, Mehmet F. Akay, Ugur C. Hasar, Student Member, and Cengiz D. Atis, "Microwave-based durian maturity determination using microstrip patch antennas" IEEE transactions on instrumentation and measurement, vol.51, No.6, December 2002

[10] Peerapong S., 1998, "Growth and Development of Durian Fruit Monthong and the Effect of Ethephon Preharvest Treatment", Department of Horticulture, Kasetsart university, 1998.

Interdigital Microstrip Resonator Sensor for Complex Permittivity Measurement

Somporn Seewattanapon[1], Tanee Somwong[2] and Prayoot Akkaraekthalin [1]

[1]Department of Electrical Engineering, Faculty of Engineering, King Mongkut's Institute of Technology North Bangkok, 1518 Pibulsongkram Rd. Bangsue, Bangkok 10800, Thailand
[2]Department of Electrical Engineering, Faculty of Engineering and Architecture, Rajamangala University of Technology Suvarnabhumi, 7/1 Nonthaburi 1 Rd., Maung, Nonthaburi, Thailand.

***Abstract*- The interdigital microstrip resonator sensor in two configurations for measurement of complex permittivity in compact areas of material under test is proposed. As a consequence, the characteristics of resonator including resonant frequency and bandwidth vary with dielectric constant and loss tangent of material. Limitations in the frequency response performance of the proposed sensors have been carefully studied. It has been found that the proposed sensors have great potentials for practical applications in view of low cost and monolithic integration capability with the driving circuit.**

I. INTRODUCTION

In numerous applications, a nondestructive monitorization of dielectric properties of materials is required. The electromagnetic radiation of the microwave region is widely used by microwave sensors. Microwave dielectric measurement methods generally fall into two categories: non-resonant and resonant methods. Non-resonant methods mainly include reflection and transmission/reflection techniques [1]–[3]. Resonant methods, mainly including resonator and resonant perturbation methods, have relatively higher accuracy than non-resonant ones [4]–[8]. In resonant methods, the sample under measurement is introduced to a resonator thus altering the electromagnetic boundaries of the resonator, and the electromagnetic properties of the sample are deduced from the change of the resonant properties of the resonator. Due to its high accuracy and its flexibility in sample preparation, the resonant method is widely used for low-loss samples, powders, small size samples and samples of irregular shapes. The sensors based on waveguide and coaxial lines are bulky and not convenient for integration with electronic circuits.

A planar transmission lines are used in order to develop a compact sensor to measure the permittivity [9]. Several investigators have used microstrip resonators for the determination of dielectric constant and dielectric loss of materials. The resonator structure is very simple, low cost, and easy to remove samples. The microwave sensors based on an interdigital microstrip resonator sensor for the complex permittivity materials have been developed. A software procedure has been also created that allows the direct identification of the complex permittivity as a function of the resonant frequency and the 3-dB bandwidth. The measurement system is shown in Fig.1, consisting of a sensor, a detector, a VCO and a processor unit.

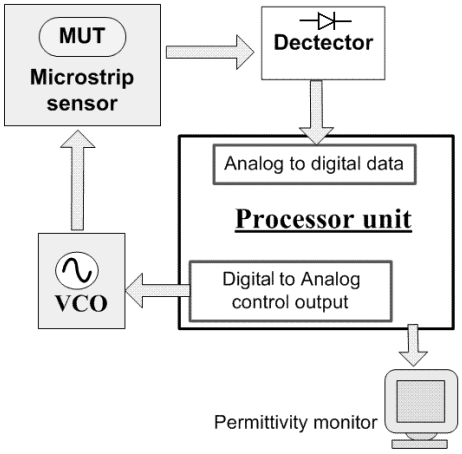

Fig. 1 Block diagram of the dielectric permittivity measurement system

Complex permittivity measurement can be performed by choosing the sensor that best fits to the user's specifications, thus adapting the measurement capability to the case of interest. Changes in permittivity manifest them selves as changes in resonant frequency of the microstrip sensor. A voltage controlled signal source and appropriate electronics are interfaced to the resonator under computer control. Different process can be used as sensor – a coaxial probe having a big size, can be used for large area samples and has a higher penetration depth, while the planar microstrip sensor is more suitable for small areas of the material under test (MUT).

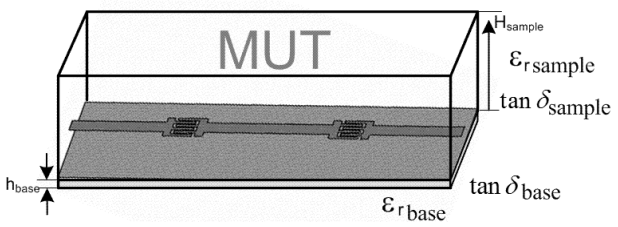

Fig. 2 3-D geometry of the proposed microstrip sensor

This paper proposes new microstrip resonant sensors to obtain high measurement performances with a wide range of dielectric constant including small size, low cost, and high sensitivity. The sensor allows monitoring the MUT properties by placing it above the strip (see an example of MUT location in Fig. 2) and performing continuous measurements at a fixed frequency of transmission characteristic. A 3-D geometry of the proposed microstrip sensor is shown in Fig. 2. The microstrip resonant sensor is on a dielectric layer, called the base substrate. It has known parameters including a thickness (h_{base}) and a complex relative permittivity (ε_{rbase}) and a loss tangent ($\tan\delta_{base}$). The MUT is a dielectric layer with unknown dielectric constant ($\varepsilon_{rsample}$) and loss tangent ($\tan\delta_{sample}$), called the sample layer. The thickness of this layer is also known. From [10], the results suggest that for the finite thickness greater than 10 mm as long as $\varepsilon_{rsample} \geq 2.1$, the MUT can be assumed as infinitely thick with good approximation. From Fig. 2, there are two layers, the base substrate and the sample layer with unknown relative permittivity and loss tangent; therefore it is posible to determine the relative permittivity and loss tangent of the material.

II. MICROSTRIP SENSOR TOPOLOGIES AND SIMULATION RESULTS

In this paper, two microstrip sensors with different operating of frequency ranges have been investigated and compared in terms of their dielectric constant ranges and performances. In Fig.3, the microstrip sensor structure is designed on interdigital microstrip resonator model which included Cg , Cp and a resonator. The model of a interdigital microstrip resonator was simulated using IE3D [11]. The MUT was also included in the simulation and the object parameters of the MUT including thickness, dielectric constant and loss tangent were varied for each simulation. The considered topologies are shown in Fig.4. Fig.4 (a) illustrates the layout of the microstrip sensor type A using interdigital microstrip resonator for a lower frequency bandwidth with a center frequency of 876 MHz for air-filled MUT or a dielectric constant of 1. In Fig.4 (b), the configuration type B contains the same structure with Fig.4 (a) but operates at a higher frequency band with a center frequency of 3.835 GHz. The resonators were constructed using interdigital microstrip resonators. The responses of microstrip sensors type A and type B for different values of permittivities of the MUT are shown in Fig.5 and 6, respectively.

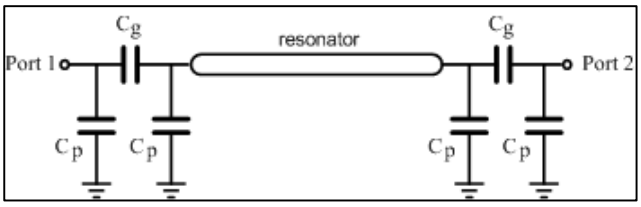

Fig. 3 The proposed microstrip sensor model [11]

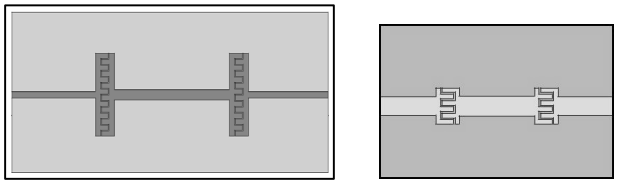

Fig.4 Interdigital microstrip resonators on FR4 substrate
(a) type A for low frequency band and size of 120*60mm
(b) type B for high frequency band and size of 37*24mm.

As a microstrip sensor typeA, a variation of the complex permittivity of the MUT causes a variation of the resonant frequency and 3-dB bandwidth which a dielectric constant are changing from 2.1 to 9. The result resonant frequency will be changing of 876-634 MHz. This can identify materials [12] by related approximate equation (1).

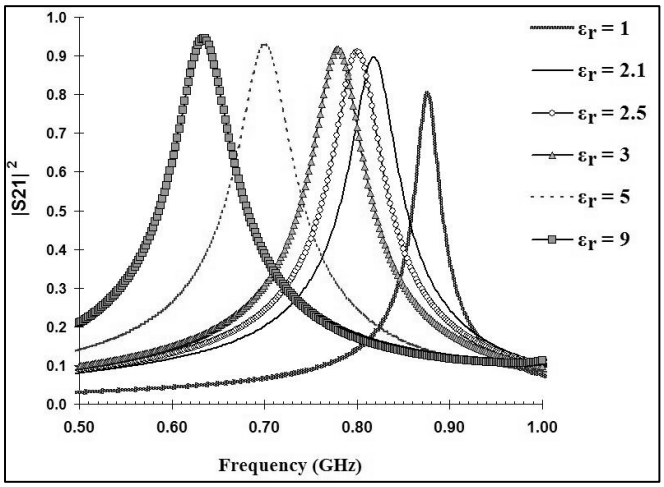

Fig. 5 Typical simulated response of the microstrip sensor type A for different values of permittivity of MUT.

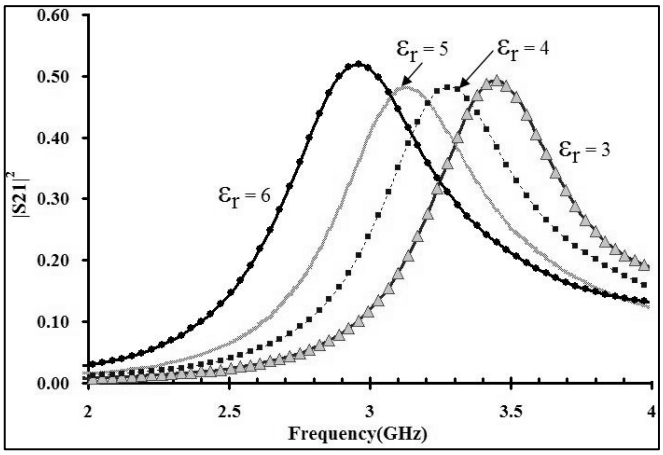

Fig. 6 Typical simulated response of the interdigital microstrip resonator structure type B for different values of the permittivity of MUT.

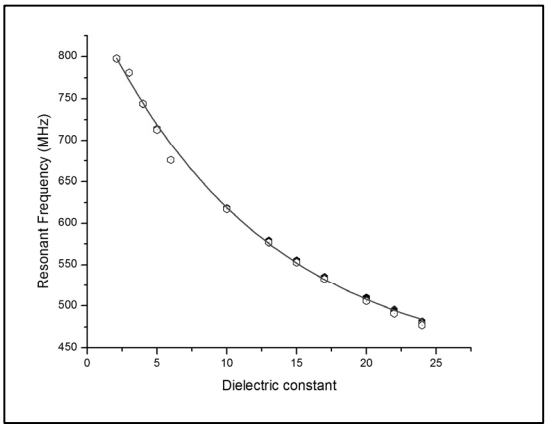

(a)

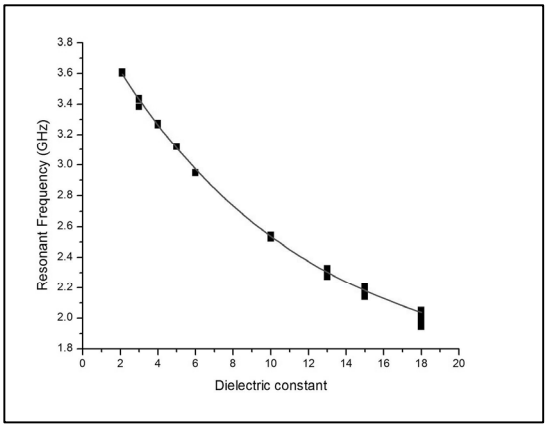

(b)

Fig. 7 Dependent of (a) the resonant frequency type A and (b) the resonant frequency type B on the dielectric constant of MUT

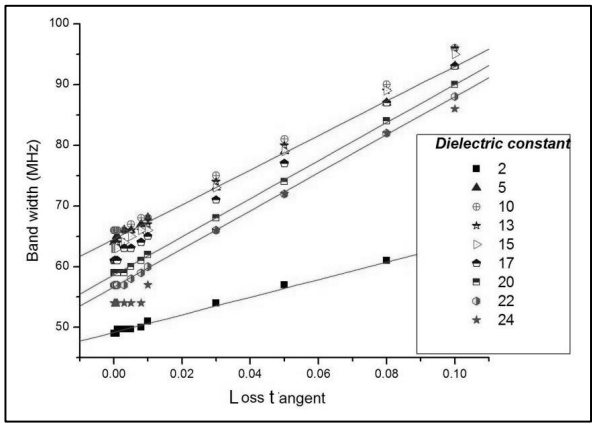

(a)

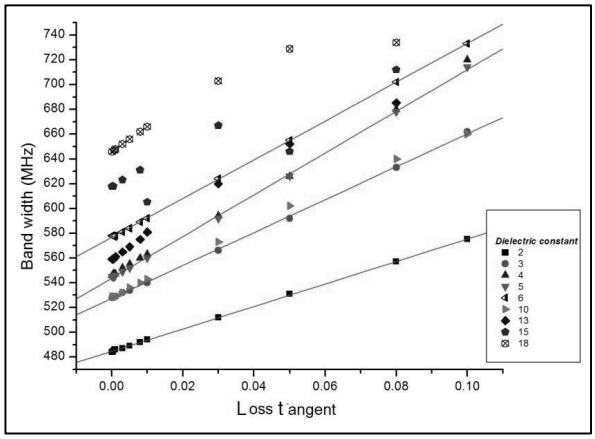

(b)

Fig. 8 Dependent of (a) the bandwidth type A and (b) the bandwidth type B on loss tangent of MUT

III. CHARACTERIZATION OF SENSORS

In this session, the characteristic responses of microstrip sensors are shown in Fig. 7 and Fig. 8. The complex permittivities in a wide range of sequence MUT are simulated by IE3D software which an effect output response has two parameters. These are resonant frequency response (Fig.7) and bandwidth response (Fig.8). In Fig.7, the output response of changed dielectric constant in X-axis is resonant frequency response in Y-axis. The resonant frequency point is related a loss tangent in many values which start from 0.0001 to 0.1. In resonant frequency response, the sensor type A is stable variability more than type B because a response after the dielectric constant of 12 in type B will be fluctuated. Therefore, the operative resonant frequency designed in this model should be careful at high frequency. The approximate equations (1) and (2) are used for dielectric constant calculation and equation (1) is used for sensor type A which is limited in range of dielectric constant not over of 24. In Fig.8, the output response of changed loss tangent in X-axis is

$$\varepsilon_r = 389.35e^{f_r/(-177.3)} - 1.99 \quad (1)$$

$$\varepsilon_r = 130.1e^{f_r/(-1.097)} - 2.729 \quad (2)$$

bandwidth response in Y-axis. The bandwidth response is determined for each value of dielectric constant. Subsequently, the bandwidth responses of sensors type A and type B are shown in Fig. 8. The trends of bandwidth response are linear responses but some responses are not. In Fig.8 (a), it can be seen that increasing of bandwidth response has a minimal change from loss tangent lower of 0.008. These minimal changes can not be classified into a loss tangent of MUT different response from Fig.8 (b). Fig.8 (b) is explicitly classified more than Fig.8 (a). Therefore, the high frequency sensor design can be identified MUT in loss tangent session , such as sensor type B which an approximate equations are becoming to be classified MUT and (3),(4),(5) equations are used to calculate loss tangent which their dielectric constants have been obtained in the following: 2.0,3.0,5.0. In other words, the effective bandwidth responses of microstrip -sensor type B at dielectric constant over of 13 are nonlinear. The approximate equations of sensor type A can be limitly used , which a loss tangent lower than 0.008 may result in error.

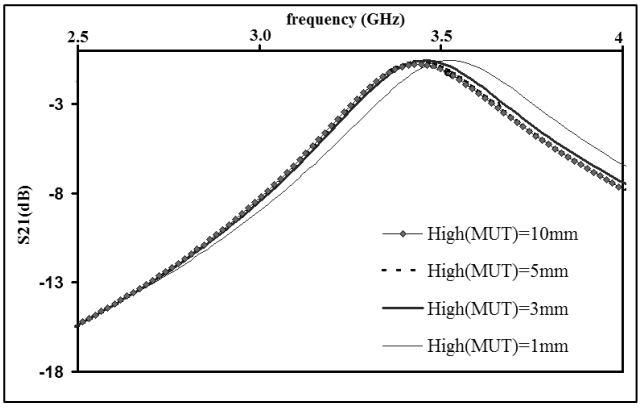

Fig. 10 Dependence of response on MUT thickness (h_{base})

$$\tan\delta = 0.001102BW - 0.53382 \quad ; \varepsilon_r = 2.0 \qquad (3)$$
$$\tan\delta = 0.000753BW - 0.39709 \quad ; \varepsilon_r = 3.0 \qquad (4)$$
$$\tan\delta = 0.000639BW - 0.36827 \quad ; \varepsilon_r = 5.0 \qquad (5)$$
$$\tan\delta = 0.001102BW - 0.53382 \quad ; \varepsilon_r = 2.0 \qquad (6)$$
$$\tan\delta = 0.003189BW - 0.18703 \quad ; \varepsilon_r = 22.0, 24.0 \qquad (7)$$

The MUT is represented by the dielectric layer. Its thickness (h_{base}) in Fig.2. Fig.10 shows the typical frequency response of the sensor for different thicknesses of the MUT. Since the effect of the finite thickness increases with decreasing h_{base}, the result of Fig.10 suggests that for height (MUT) greater than 5 mm, the MUT can be assumed as infinitely thick with good approximation.

V. CONCLUSION

For the purpose of determining of complex permittivities of dielectric materials, the resonator sensors have been proposed. Two resonator sensors based on interdigital microstrip resonators have been designed and analysed. The resonant frequency and bandwidth of the sensors have been simulated and investigated, resulting in formulation of permittivity equations for MUT with each sensor. These proposed sensors have very high performances with low cost and simplicity for manufacturing, therefore, they may be useful for permittivity characterization for a wide range of materials.

REFERENCES

[1] J. R. Mosig, J.-C. E. Besson, M. Gex-Fabry, and F. E. Gardiol, "Reflection of open-ended coaxial line and application to nondestructive measurement of materials," *IEEE Trans. Instrum. Meas.*, vol. IM-30, no.1, 1981, pp. 46-51.

[2] W. B. Weir, "Automatic measurement of complex dielectric constant and permeability at microwave frequencies," *Proc. IEEE*, vol. 62, pp.33–36, Jan. 1974.

[3] J. Baker-Jarvis, M. D. Janezic, J. H. Grovenor Jr., and R. G. Geyer, "Transmission/reflection and short-circuit line methods for measuring permittivity and permeability," NIST Tech. Note 1355 (revised), Dec.1993.

[4] W. E. Courtney, "Analysis and evaluation of a method of measuring the complex permittivity and permeability of microwave insulators," *IEEE Trans. Microwave Theory Tech.*, vol. MTT-18, pp. 476–485, Aug. 1970.

[5] Y. Kobayashi and M. Katoh, "Microwave measurement of dielectric properties of low-loss materials by the dielectric rod resonator method," *IEEE Trans. Microwave Theory Tech.*, vol. 33, pp. 586–592, July 1985.

[6] E. J. Vanzura, R. G. Geyer, and M. D. Janezic, "The NIST 60-millimeter diameter cylindrical cavity resonator: Performance evaluation for permittivity measurements," NIST Tech. Note 1354, Aug. 1993.

[7] V. R. K. Murthy and R. Raman, "A method for evaluation of microwave dielectric and magnetic parameters using rectangular cavity perturbation technique," *Solid State Commun.*, vol. 70, no. 8, pp. 847–850, 1989.

[8] A. W. Kraszewski and S. O. Nelson, "Observations on resonant cavity perturbation by dielectric objects," *IEEE Trans. Microwave Theory Tech.*, vol. 40, pp. 151–155, Jan. 1992.

[9] A.K. Verma,Nasimuddin and A.S. Omar " Microstrip resonator sensors for determination of complex permittivity of material in sheet, liquid and paste forms" *IEE* Proc.-Microw. Antennas Propag., Vol.152, No. 1, February 2005.

[10] C.K. Ong "Amendment of Cavity Perturbation Method for Permittivity Measurement of Extremely Low-Loss Dielectrics" *IEEE Trans. Instrum. Meas.*, vol.48, no.6 , pp.10311037,December 1999.

[11] S.Seewattanapon, P. Akkaraekthalin, and V.Vivek,"A CPW Capacitively Coupled Resonator Bandpass Filter and Its Lump Element Model" Int.Symp. On Communications and Information Tech, Pattaya, Thailand.Oct22-23,2002.

[12] E.Fratticcioli and R.Sorrentino, "A Simple and Low Cost Measurement System for the Complex Permittivity Characterization of Materials", *IEEE* IMTC2003 conf. Proceedings, Vail CO, pp.524-528., 20-22 May, 2003.

[13] E.Fratticcioli, R.Sorrentino, "A Planar Resonant Sensor for the Complex Permittivity Characterization of Materials". *IEEE* MTT-S Int. Microwave Symp.Dig., Seattle,WA,pp.647-650,June2-7,2002.

A Miniaturized Dual-mode Bandpass Filter using Triangular Loop Resonator

Supachai Chotjit, Sarawuth Chaimool, and Prayoot Akkaraeakthalin

Department of Electrical Engineering, Faculty of Engineering
King Mongkut's Institute of Technology North Bangkok,
1518 Pibulsongkram Rd., Bangsue, Bangkok 10800, Thailand
Phone: +662-9132500 Ext.8519, Fax: +662-5857350, Email:prayoot@kminb.ac.th

Abstract- In this paper, miniaturized dual-mode microstrips bandpass filter using the triangular loop structure is proposed by contain excellent performance. The proposed filter shows a 3.6% fractional bandwidth at the center frequency of 1.4 GHz with a return loss of better than 10 dB and an insertion loss of less than 2 dB. The size of the proposed structure is 50% less than conventional dual-mode microstrip triangular loop resonator filter at the same center frequency.

I. INTRODUCTION

Modern microwave communications systems such as satellite and mobile communications systems require compact size, high performance, and low-cost bandpass filters. Therefore, dual-mode microstrip filters have been widely used in wireless communications systems because of their advantages in applications requiring high-quality narrow-band microwave bandpass filters with features such as small size, low mass, and low loss.

Dual-mode microstrip resonators are attractive since a single dual-mode resonator can be utilized as a doubly tuned resonant circuit and, hence, the number of resonators required for a prescribed filter degree is reduced by half, resulting in a reduced-size filter structure [1]. Many authors [2]-[4] have proposed the dual-mode microstrip loop and patch resonators for miniaturization of the dual-mode microstrip filters. Recently, a dual-mode loop resonator using the properties of microstrip open-loop resonator has been proposed for miniaturization of the microstrip dual-mode filters [5].

A bandpass filter based on a dual-mode resonator can achieve Chebyshev, elliptic, or quasi-elliptic responses if the feed lines, notches, or stubs are properly arranged [6]-[10]. The strength and nature of the coupling between the degenerate modes of the dual-mode resonator are mainly determined by the perturbation's size and shape [6]. For instance, a bandpass filter based on a dual-mode microstrip square-patch resonator having a perturbation in the form of a corner cut can produce a Chebyshev characteristic [5], whereas one with a perturbation in the form of a small conductor patch attached to an outer corner of the same dual-mode resonator exhibits an elliptic characteristic. This is because the perturbation's shape on a patch resonator determines the nature of the coupling, whether it is inductive or capacitive. A perturbation in the form of a corner cut produces the inductive effect, while the capacitive effect is obtained by the perturbation in the form of a patch.

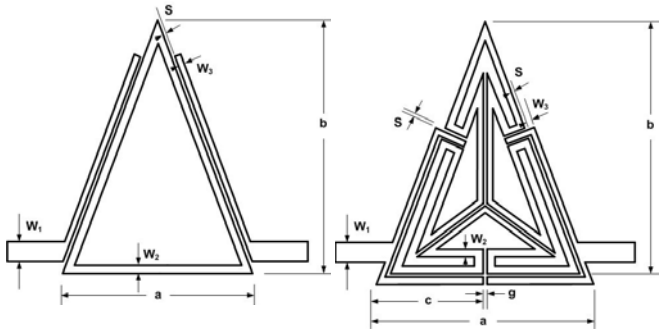

Fig. 1. *Configuration of the conventional dual-mode triangular loop structure (a) and the proposed miniaturized dual-mode triangular loop structure (b) the resonator dimensions are a = 20 mm, b = 27 mm, w_1 = 1.83 mm, w_2 = 1 mm, w_3 = 0.5 mm, c = 10.7 mm, s = 0.12 and g = 0.2 mm.*

A microstrip triangular loop resonator which reduces or eliminates some of the limitations of dual-mode bandpass filters based on microstrip loops. To allow easier coupling between the modes of two separate dual-mode resonators, we need the structure which is not symmetric with respect to two orthogonal planes. A simple structure which fulfills this requirement is a triangle although other solutions are possible. The triangular microstrip loop has several advantages, it has smaller size than a triangular patch as used in [1]. Differences in the resonant frequencies of the two modes can be easily adjusted be changing the height of the triangle. There is no need to couple the two modes of a given dual-mode resonator by inserting a perturbation. Filters with transmission zeros both at real frequency (attenuation poles) and at imaginary frequencies (group-delay flattening) can be designed with the same arrangement [11].

In this paper, we have proposed a miniaturized dual-mode microstrip filter using the degenerate mode of a modified triangular loop structure, which has a size reduction of more than 50% at the same center frequency compared with the conventional triangular loop structure [11].

II. DUAL – MODE RESONATOR

Single-mode microstrip resonator, such as broad side edge coupled filters, have been long established. However, single-mode filters have limited applications in microwave areas due to their low performance in terms of insertion loss and narrow bandwidth in pass-band regions. Hence, to improve the filter performance, the dual-mode microstrip resonating filters are more commonly adopted. The basic idea is to constructively couple two resonating modes, TM^{z100} and TM^{z010}, inside a resonator for a better performance. Planar dual-mode filters were first introduced in [12].

The triangle loop dual-mode resonator is simply a wavelength long microstrip line whose two ends are joined to form a triangle. Two of the sides of the triangle are always maintained equal, i.e., the triangle is isosceles. The structure is therefore, symmetric with respect to a plane going orthogonally through the middle of its bottom edge. Two degenerate modes can exist in such a structure, one with a magnetic wall (mode 1) and the other with an electric wall (mode 2) along the symmetry plane [11].

The proposed dual-mode resonator has been shown in Fig. 1(b). It consists of three identical arms, each of which may be viewed as a line with a triangular ring stub. The triangular ring stub increases the resonator perimeter significantly and hence decreases the resonance frequency. The proposed structure uses the space inside the loop efficiently when compared with the conventional triangular loop resonator shown in Fig. 1(a).

The resonance frequency of the both structures has been compared. Fig. 2 shows that the resonance frequency of the proposed resonator is much smaller than the conventional dual-mode triangular loop resonator for the same dimensions. The simulated results are given in Fig. 2. The resonant responses are obtained from both structures with the same size. It can be noticed that the proposed structure has a resonant frequency of 1.4 GHz, compared to 2.8 GHz of the conventional triangular loop structure. This means the proposed structure can be made smaller than the conventional structure when they resonate at the same frequency.

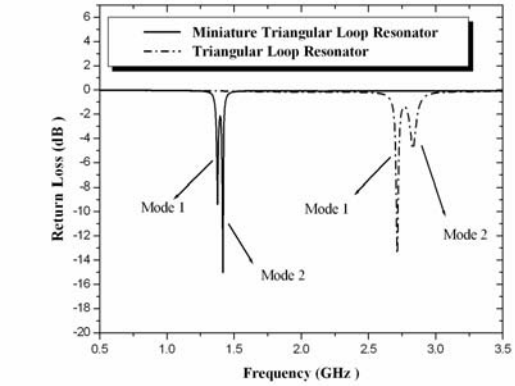

Fig. 2. Simulated return loss for the dual-mode triangular loop structure (broken line) and proposed miniaturized dual-mode triangular loop structure (full line).

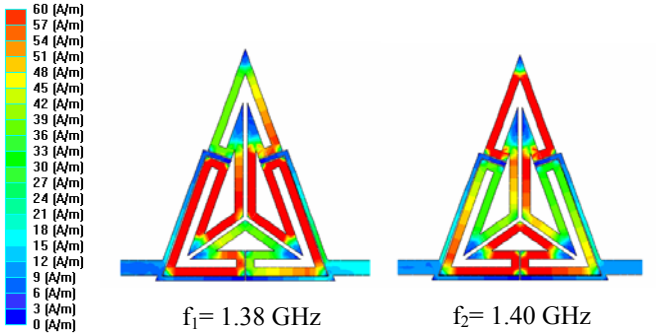

Fig. 3. Simulated current distribution for two resonance frequency of degenerated modes. (a) Mode 1 (magnetic wall along two side of the triangle). (b) Mode 2 (electric wall along two side of the triangle).

The simulated current distribution of the two modes can be easily computed from a full-wave simulation. In this study, the commercial software package, IE3D, is used for this purpose as well as for the analysis and the design of the resonator. By inspecting the current distribution patterns in Fig. 3, we can see that mode 1 is actually an even mode, while mode 2 is an odd mode. The current distribution of mode 1 is shown in Fig. 3(a). It can be seen that a high concentration is at the top tip and the center of the bottom edge of the triangle which called the electric wall. Fig. 3(b) shows the current distribution on the microstrip loop for mode 2. The field is mostly concentrated on the two lateral sides of the triangle which called the electric wall.

To observe the mode splitting, the dual-mode loop resonator has been simulated with different relative values of the length (a) and the height (b) of the base. The simulated split resonance frequencies of these degenerate modes of the triangular loop resonator as a function of are shown in Fig. 4. The split between the mode frequencies decreases as the height of the triangle increases from 15 mm up to 35 mm.

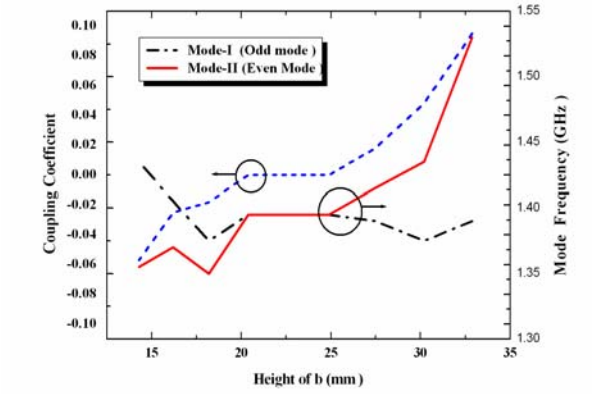

Fig. 4. Simulated coupling coefficient and two resonance frequencies of degenerate mode against the height of triangle.

This situation can also be seen from the coupling coefficient computed using the relationship between the split in the resonance frequency of two modes and the coupling, as described by [15]

$$k = \frac{f_{02}^2 - f_{01}^2}{f_{02}^2 + f_{01}^2} \tag{7}$$

where f_{01} and f_{02} are resonance frequency of mode 1 and mode 2, respectively. The coupling coefficient between the resonant frequency of mode 1 and mode 2 is also shown in Fig. 4.

Since we need to split mode of equilateral triangular loop resonator for design a bandpass filter, the mode splitting is achieved by changing height of the isosceles triangle, where $b < \sqrt{3}a/2$. We found that the resonant frequency of mode 1 was exited at lower than mode 2. The coupling coefficient becomes negative coupling coefficient (or electric coupling). Where $b > \sqrt{3}a/2$, it is found that the resonant frequency of mode 1 was exited at higher than mode 2, the coupling coefficient becomes positive coupling coefficient (or magnetic coupling). When $b = \sqrt{3}a/2$, the coupling coefficient becomes zero since the dual-mode resonator is a simple microstrip loop resonator.

III. Dual – Mode Filter

The equivalent circuits of the dual-mode triangular loop filter for even and odd modes. The impedance of the two networks at the feed point can be derived as follows [13] shown in Fig. 5.

$$Z_{even} = jZ_x\left(\frac{y_s \tan\theta_2 - 1}{y_s(1 - \tan\theta_1 \tan\theta_2) + \tan\theta_1 + \tan\theta_2} - \frac{1}{y_g}\right) \tag{1}$$

$$Z_{odd} = jZ_x\left(\frac{1}{(\cot\theta_1 + \cot\theta_2)} - \frac{1}{y_g}\right) \tag{2}$$

where Z_0 is the terminated impedance, Z_{even} and Z_{odd} are the input impedances of the half-circuits corresponding to the even and odd modes about the symmetric line, respectively. $\theta_1 = \beta l_1$, $l_1 = \sqrt{a^2 + b^2}$, $\theta_2 = \beta l_2$, $l_2 = a/2$, $y_g = 2\pi f c_g Z_x$, and $y_s = 2\pi f c_s Z_x$, C_g and C_s are the equivalent capacitances of the coupling gap and top tip of triangle, respectively. For design, the center frequency and Z_x are usually the prespecified parameters, where w_2, C_g, and C_s are the circuit variables to be lossless. The S -parameters of transmission and reflection for the triangle circuit are given by [14]

$$S_{11} = (\Gamma_{even} + \Gamma_{odd})/2 \tag{3}$$

$$S_{21} = (\Gamma_{even} - \Gamma_{odd})/2 \tag{4}$$

where

$$\Gamma_{even} = \frac{Z_{even} - Z_o}{Z_{even} + Z_o} \tag{5}$$

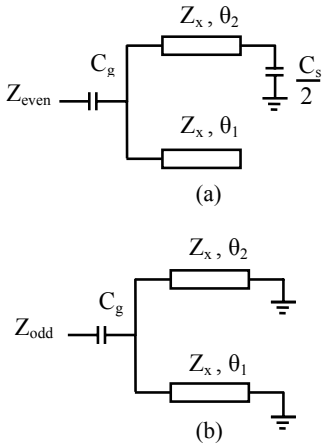

Fig. 5. *Equivalent circuits of the triangular loop dual-mode filter: (a) even mode; (b) odd mode.*

$$\Gamma_{odd} = \frac{Z_{odd} - Z_o}{Z_{odd} + Z_o} \tag{6}$$

Finally, the frequencies f_{z1}, f_{z2}, at which the transmission zeros are located, can be obtained by solving by setting insertion loss S_{21}=0.

The proposed dual–mode microstrip bandpass filter was fabricated on a GML-1000 substrate having a thickness of 0.762 mm and relative dielectric constant of 3.2. The filter dimensions are a = 20 mm, b = 27 mm, w_1 = 1.83 mm, w_2 = 1 mm, w_3 = 0.5 mm, c = 10.7 mm, s = 0.12 and g = 0.2 mm. Fig. 6 shows the photograph of the fabricated filter. The simulated bandwidth is about 3.6%, while the measured bandwidth is 5.7% at the center frequency of 1.4 GHz.

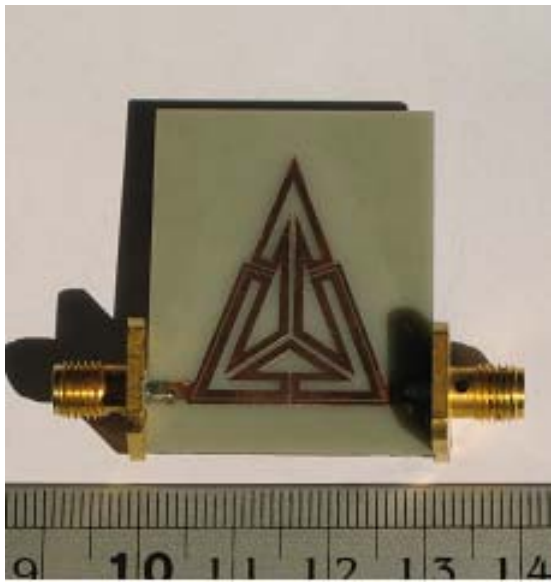

Fig. 6. *A fabricated of proposed dual-mode microstrip filter.*

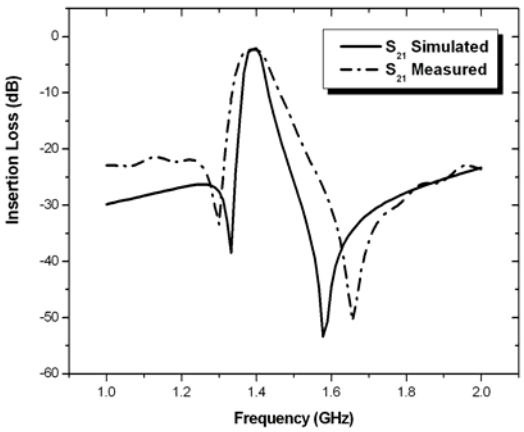

Fig. 7*. Simulated and measured responses (S_{21}) of the proposed filter.*

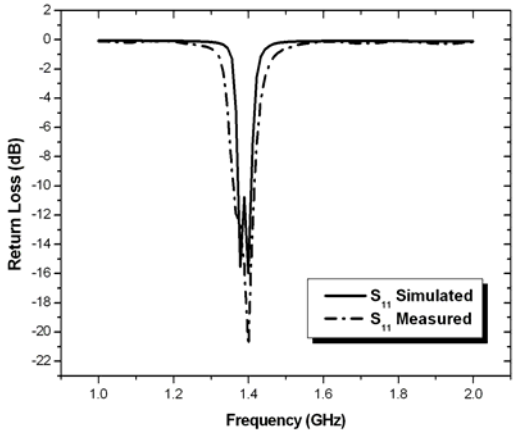

Fig. 8. *Simulated and measured responses (S_{11}) of the proposed filter.*

Fig. 7 shows the simulated and measured frequency responses, the measured insertion loss of filter is 2.3 dB, higher than the simulated value of 2 dB. The loss is due to circuit loss including conductor and dielectric losses. The return loss is better than 10 dB within passband as shown in Fig. 8. The simulated and measured results are in good agreement.

IV. CONCLUSION

A dual-mode band-pass filter with a 3.6% bandwidth at the center frequency of 1.4 GHz has been designed and fabricated to demonstrate the application of the proposed triangular loop resonator for designing the compact microstrip filters. Also, it has a size reduction of about 50% with respect to conventional triangular loop structure. The proposed filter responses have been measured resulting in good agreement with simulation expectations. The magnetic and electric coupling between degenerate mode of the dual-mode the proposed triangular loop resonator was identified depending on the height of triangle.

REFERENCES

[1] J.-S. Hong and S. Li, "Theory and experiment of dual-mode microstrip triangular patch resonators and filters," IEEE Trans. Microw. Theory Tech., vol.52, no. 4, pp. 1237-1243, Apr. 2004.

[2] J.S. Hong and M.J. Lancaster, "Bandpass characteristics of new dual-mode microstrip square loop resonators," Electron. Lett., vol. 31, no.11, pp.891-892, May 1995.

[3] J. S. Hong, "Microstrip bandpass filter using degenerate mode of a novel meander loop resonator," IEEE Microw, Guide Wave Lett., vol. 5, no.11, pp.371-372, Nov. 1995.

[4] L. Zhu, P. –M. Wecowski, and K. Wu, "New planar dual-mode filters using cross-slotted patch resonator for simultaneous size and low conduction," IEEE Trans. Microw. Theory Tech., vol. 47 no. 5, pp. 650-654, May 1999.

[5] A.Görür, "A novel dual-mode bandpass filter with wide stopband using the properties of microstrip open-loop resonator," IEEE Microw. Wireless Compon. Lett., vol. 12, no. 10, pp. 386-388, Oct. 2002.

[6] R. R. Mansour, "Design of superconductive multiplexers using single-mode and dual-mode filters," IEEE Trans. Microwave Theory Tech., vol. 42, pp. 1411-1418, July 1994.

[7] S. J. Fiedziuszko, J. A. Curtis, S. C. Holme, and R. S. Kwok, "Low loss multiplexers with planar dual mode HTS resonators," IEEE Trans.Microwave Theory Tech., vol. 44, pp. 1248-1257, July 1996.

[8] L. Zhu, P.-M. Wecowski, and K. Wu, "New planar dual-mode filter using cross-slotted patch resonator for simultaneous size and loss reduction," IEEE Trans. Microwave Theory Tech., vol. 47, pp. 650-654, May 1999.

[9] L.-W. Hsieh and K. Chang, "Dual-mode elliptic-function bandpass filter using one single patch resonator without coupling gaps," Electron. Lett., vol. 36, no. 24, pp. 2022-2023, Nov. 2000.

[10] M. Matsuo, H. Yabuki, and M. Makimoto, "Dual-mode stepped-impedance ring resonator for bandpass filter applications," IEEE Trans. Microwave Theory Tech., vol. 49, pp. 1235-1240, Jul. 2001.

[11] R.Wu and S. Amari, "New trinagular loop resonators for bandpass dual-mode filter applications," *IEEE MTT-S Dig.,June 2005*.

[12] I. Wolff and N. Knoppik, "Rectangular and circular microstrip disk capacitors and resonators," IEEE Trans. Microw. Theory Tech vol.22, no.10, pp.857-864, Oct. 1974.

[13] M.H. Weng, C.H. Hung and W.N. Chen, "Dual-mode bandpass filters using triangular ring resonators with coupling stubs," Microwave opt Lett., vol. 43, no. 6, pp. 512-515, Dec. 2004

[14] K.K.M. Cheng, "Design of dual-mode ring resonators with transmission zeros," Electron Lett., vol.33, no. 16, pp.1392-1393, July 1997.

[15] L.-H. Hsieh and K. Chang, "Dual-mode quasi-elliptic-function bandpass filters using ring resonators with enhanced-coupling tuning stubs," IEEE Trans. Microwave Theory Tech., vol. 50, pp. 1340-1345, May 2002.

Performance of MPSK Modulation in combined Flat Scintillation and Frequency-Selective fading channel for Satellite Mobile Communication System

N. Boonsongkusoljit and P.Supnithi
Faculty of Engineering and Research Center for Communications and Information Technology
King Mongkut's Institute of Technology Ladkrabang (KMITL), Bangkok, 10520, Thailand
Email: s8060910@kmitl.ac.th, ksupornc@kmitl.ac.th

***Abstract*- Satellite communication with land mobile terminals in VHF and UHF bands is affected by ionospheric scintillation and multipath fading that causes strong variation in received signal power. In this paper, the performance of MPSK modulation in combined flat scintillation and frequency selective multipath fading channel with various fading conditions is presented. It is shown that for frequency-selective channels, Viterbi detector reduces the error floor, thus providing reduction of average bit error rate.**

I. INTRODUCTION

Satellite mobile communication in UHF band and lower frequency bands has been recently planned [1]. Combined scintillation and multipath fading channels are common in mobile satellite communication and have become impediments to reliable transmission system.

Scintillation effects are caused by non-uniform electrical charge distribution in the ionosphere layer. The phenomenon is maximum near the geomagnetic equator and smallest in the mid-latitude regions [1]. It is statistically modeled as Rician or Rayleigh fading with finite signal decorrelation time and limited coherent bandwidth of the transmission channel [2]. If the modulated signal is transmitted through the ionosphere with electrical charge fluctuation, there would be an effect on signal amplitude, the signal level swings rapidly up and down from normal level. The frequency-selective multipath fading channel is characterized by rural area power delay profiles defined in COST207 models [3].

The fading can be "flat"or "frequency selective" depending upon delay spread in communication medium and symbol rate, when the delays are short compared to the symbol rate, the medium is flat fading channel. Conversely, when the delays are long compared to the symbol rate, the channel is considered frequency-selective fading channel.

Previously in [4], the performance of MPSK modulation in combined scintillation and flat multipath fading system is analyzed.

In this paper, we simulate the performance of combined channels for mobile satellite communication with MPSK, specifically, QPSK modulation scheme. The performance is shown in terms of bit error rate versus signal-to-noise ratio (SNR) and the plots are then illustrated.

The paper is organized as follows. In Section II, system model and basic definitions are reviewed. Section III describes the channel model. In Section IV, simulation results and discussions for scintillation channel, combined scintillation and frequency selective multipath fading channel. Finally, the conclusions are given in Section V.

II. SYSTEM MODEL AND BASIC DEFINITION

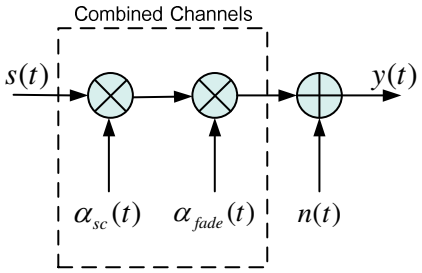

Fig. 1. Combined scintillation and multipath fading channel model

In combined scintillation-multipath channel given in Fig. 1, the received signal $y(t)$ is

$$y(t)=\sum_{n=-\infty}^{\infty}\alpha_{sc}(t)\cdot\alpha_{fade}(t)\cdot s(t-nT_s)+n(t) \qquad (1)$$

where $\alpha_{sc}(t)$ and $\alpha_{fade}(t)$ are scintillation and multipath fading coefficients, respectively, $s(t)$ is the modulated MPSK signal and $n(t)$ is an additive white Gaussian noise (AWGN) with zero mean and variance $\sigma^2 = N_0/2$ W/Hz.

In M-ary phase shift keying (MPSK) modulation is a common modulation scheme employed in satellite and wireless channel due to spectral efficiency. Each k-bit information sequence is mapped to a waveform of equal amplitude and M possible phases. The signal $s_i(t)$ can be expressed as

$$s_i(t)=\sqrt{\frac{2E}{T}}\cos\left(\omega_0 t-\frac{2\pi i}{M}\right);\quad \begin{matrix}0\le t\le T_s\\ i=1,...,M\end{matrix}, \qquad (2)$$

where E is the symbol energy over each the duration T_s and ω_0 is the radian frequency of the carrier. For an AWGN channel assuming coherent detection, the probability of bit error at high SNR can be expressed in terms of digital SNR $\left(E_b/N_0\right)$.

$$P_B \approx \frac{2Q\left(\sqrt{\frac{2E_b \cdot \log_2 M}{N_0}} \sin\frac{\pi}{M}\right)}{\log_2 M} \quad (3)$$

where $Q(x)$ is a Q-function, E_b is average bit energy and N_0 is the noise power spectral density.

III. CHANNEL MODEL

A. *Scintillation model*

Scintillation effects are caused by non-uniform electrical charge distributions in the ionosphere which depends on the ionosphere condition, location, season, solar activity and local time. Ionospheric scintillation is maximum near the geomagnetic equator and smallest in the mid-latitude regions. The received signal from scintillation effect causes amplitude signal fluctuations [1].

The intensity of scintillation is often measured by the scintillation index S4 which S4 can be found from standard deviation value to mean value of the received signal envelope.

In general, scintillation index has values $0 \le S4 \le 1$. When S4 = 0 is ideal non-fading channel, with $0 < S4 < 1$, it is Rician fading channel, and with S4 = 1, it is Rayleigh fading channel [6].

The scintillation coefficient $\alpha_{sc}(t)$ is statistically modeled as a non-zero mean, complex Gaussian random process [2].

$$\alpha_{sc}(t) = \sqrt{K_s} \cdot e^{j\phi} + n_{\text{scint}}(t), \quad (4)$$

where K_s is proportional to the signal power received via the line of sight path, ϕ is a random phase shift uniformly distributed over the interval $[-\pi, \pi]$ and $n_{\text{scint}}(t)$ is a complex Gaussian process that arises from scattered signal propagation over random paths due to atmospheric scintillation effects. The average signal power received over the scattered paths is proportional to $\sigma_{nsc}^2 = E\left|n_{sc\,\text{int}}(t)\right|^2$. Envelope signal power of scintillation coefficient $r_{sc} = \left|\alpha_{sc}(t)\right|$ has a Rician probability density given by:

$$P_{rsc}(r) = \frac{2r}{\sigma_{nsc}^2} \cdot e^{-\gamma} \cdot e^{-r^2/\sigma_{nsc}^2} \cdot I_0\left\{2r\sqrt{\gamma/\sigma_{nsc}^2}\right\} \quad (5)$$

where $\gamma \equiv K_s / \sigma_{nsc}^2$ is the ratio of received specular to scattered signal power and γ can be related to the scintillation index S_4 [6], then can be expressed as

$$S_4 = \sqrt{1 - \left\{\gamma/(\gamma+1)\right\}^2}. \quad (6)$$

The coefficient $\alpha_{sc}(t)$ can be generated in the time or frequency domain with the basic idea is to filter an independent complex Gaussian sequence to generate the scattered component $n_{\text{scint}}(t)$ and then combine the result with the specular component to produce $\alpha_{sc}(t)$. The magnitude-squared filter frequency response $\left|H_{sc}(f)\right|^2$ is matched to the power spectrum of $n_{\text{scint}}(t)$, *i.e.*,

$$\left|H_{sc}(f)\right|^2 = P_{sc}(f) = \int_{-\infty}^{\infty} d\tau \cdot R_{sc}(\tau) \cdot e^{-2\pi j f \tau} \quad (7)$$

The process is shown in Fig. 2, the filter frequency response is designed to have linear phase with $phase\left\{H_{sc}(f)\right\} = 2\pi\Delta f$, where Δ is typically set to half the duration of the filter impulse response.

$$h_{sc} = \int_{-\infty}^{\infty} df \cdot H_{sc}(f) \cdot e^{2\pi j f \tau} \quad (8)$$

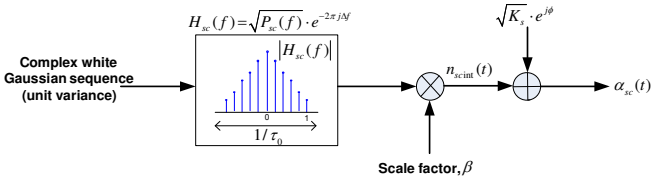

Fig. 2. Scintillation coefficient simulation model

For the discrete frequency response $\bar{H}_{sc}(k)$ of the discrete-time filter $\hat{h}_{sc}$ is computed from (8) as follows:

$$\bar{H}_{sc}(k) = \mathrm{e}^{-(\pi\tau_0 k F_s/N)^2/2} \cdot \mathrm{e}^{-(2\pi j(L/2)k/N)} \quad (9)$$

where $0 \le k \le N/2$ F_s is a sampling rate that is two to three times the maximum bandwidth of the square–root Gaussian filter and $N \ge L$ is the number of points computed. Finally, $\hat{h}_{sc}(k)$ is computed via inverse discrete Fourier transform.

$$\hat{h}_{sc}(k) = \frac{1}{N} \cdot w(k) \cdot \sum_{l=0}^{N-1} \hat{H}_{sc}(l) \cdot \exp\left(2\pi jkl/N\right) \quad (10)$$

where $0 \le k \le L-1$, $w(k)$ is a window function, L sampled in extent. Normally a Hamming window is used.

Given $\hat{h}_{sc}(k)$, the sampled scattered component $n_{sc\,\text{int}}(k/F_s)$ can generated via discrete convolution with a white, unit variance complex Gaussian input sequence $\xi(k)$ as follows:

$$n_{sc\,\text{int}}(k/F_s) = \beta \cdot \sum_{l=0}^{L-1} \hat{h}_{sc}(l) \cdot \xi(k-l), \quad (11)$$

where the scaling constant β is chosen to yield the desired output variance.

$$\beta = \sqrt{\sigma_{nsc}^2 / \sum_{l=0}^{L-1} \hat{h}_{sc}^2(l)} \quad (12)$$

As noted above, the value σ_{nsc}^2 is typically computed in terms of the desired Rician factor via $\sigma_{nsc}^2 = 1/(1+\gamma)$.

B. *Frequency-selective fading model*

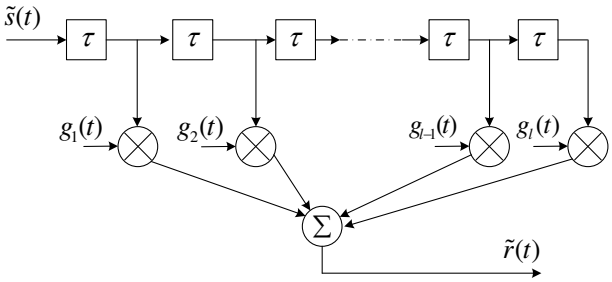

Fig. 3. Frequency-selective multipath fading channel model.

The complex envelope of the received signal $r(t)$ is

$$\tilde{r}(t)=\sum_{i=1}^{l} g_i(t)\cdot\tilde{s}(t-\tau_i) \tag{13}$$

where $\tilde{s}(t)$ is the complex envelop of the transmitted signal, l is the number of taps, $g_i(t)$ is the complex gains [3] and τ_i is path delays associated with the taps.

Multipath fading effects occur as the satellite signal is not only received via the direct path but also reflected from objects in the surrounding area. Each area contains different conditions which cause varying degrees of additions and subtractions of signal. In process of simulation, the frequency selective multipath fading channel is characterized by typical rural area (non-hilly) power delay profiles defined in COST207 models [3]. The COST207 models are useful for simulating GSM and other systems (up to 2 GHz band); the model describes the channel impulse response in terms of a set of Doppler characteristics at various specified time delays.

The power and delay profiles of the simple 6 path form for rural area are given in Table 1.

TABLE I
TYPICAL RURAL AREA POWER DELAY PROFILE DEFINED BY COST207 [2]

Delay (μs)	Fractional Power	Doppler Category
0.0	0.602	RICE
0.1	0.241	CLASS
0.2	0.096	CLASS
0.3	0.036	CLASS
0.4	0.018	CLASS
0.5	0.006	CLASS

In a tapped delay model, each channel has a Doppler spectrum $P_s(f,\tau_i)$, where i is the index of the tap. The following two types of Doppler spectra are defined in the COST 207 model, where $f_{\max}$ represents the maximum Doppler frequency of the channel.

- CLASS is the classical (Jakes) Doppler spectrum and is used for paths with delays not in excess of 500 ns $(\tau_i \le 0.5\mu s)$

$$P_s(f,\tau_i)=\frac{A}{\sqrt{1-\left(f/f_{\max}\right)^2}} \tag{14}$$

- RICE is the sum of a classical Doppler spectrum and one direct path. This spectrum is used for the shortest path of the model for propagation in rural areas.

$$P_s(f,\tau_i)=\frac{0.41}{2\pi f_{\max}\sqrt{1-\left(f/f_{\max}\right)^2}}+0.91\delta(f-0.7f_{\max}) \tag{15}$$

where $|f|\le f_{\max}$ and A is a normalization constant chosen so that $\int P_s(f,\tau_i)\,df=1$.

IV. SIMULATION RESULTS AND DISCUSSIONS

The performance of QPSK modulation in combined channels is simulated in this section. The channel is the product channel of flat scintillation and frequency selective multipath fading. The performance is in terms of bit error rate and the signal-to-noise (SNR) ratio is defined by E_b/N_0, where E_b is average bit energy and N_0 is the noise power spectral density in Watts/Hz.

In the simulation, QPSK modulation is selected with scintillation index S4 = 0 (no scintillation), 0.3, 0.6 and 0.9 respectively. The frequency selective multipath fading channel has 6 channel taps with delay profile [0, 0.1, 0.2, 0.3, 0.4, 0.5] μs and fractional power profile [0.602, 0.241, 0.096, 0.036, 0.018, 0.006]. Carrier frequency in the satellite mobile system is set to be 320 MHz and users' speed is 10 km/hours. The block size is 2048 bits with bit rate of 10 Mbps and noise in the system is AWGN.

In Fig. 4, we illustrate BER performance of QPSK modulation in flat scintillation channel as the scintillation index varies. It is evident that as the scintillation intensity level increases, the BER performance degrades. e.g., BER = $1\text{x}10^{-5}$, with S4 = 0.9, there is an SNR loss of 33 dB compared with the case of AWGN channel (S4 = 0).

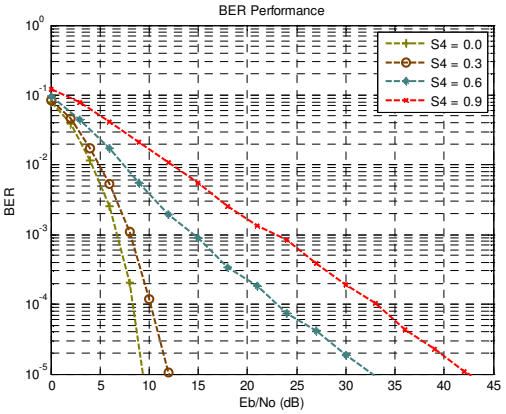

Fig. 4. BER performance of QPSK modulation in flat scintillation fading channel for S_4 = 0, 0.3, 0.6 and 0.9.

In Fig. 5, we illustrate the case of combined flat scintillation and frequency selective multipath fading channel with COST207 channel model. As scintillation index increases, the system performance in terms of bit error rate degrades. At low values of S4, the SNR loss is incrementally less than at high values of S4.

In addition, like any other fading channels, there exist irreducible error floors as the SNR increases, the error floors are caused by the delay spread. Compared with scintillation channels alone and channels in [4], the frequency-selective multipath fading causes more severe performance. Thus, to reduce the floors, the Viterbi detection is implemented to correct the intersymbol interference; the results are reduction of bit error rate and absence of error floors as shown in Fig. 6.

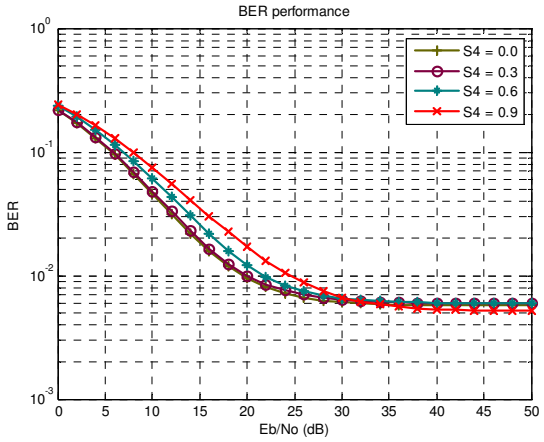

Fig. 5. BER performance of QPSK modulation in combined flat scintillation and frequency selective fading channel.

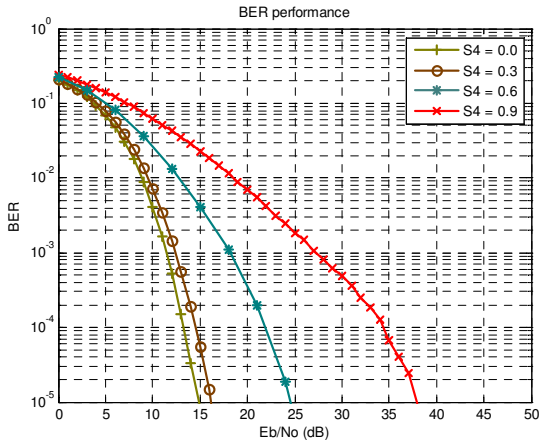

Fig. 6. BER performance of QPSK modulation in combined flat scintillation and frequency selective fading channel with Viterbi detector.

V. CONCLUSIONS

In this paper, we have simulated the performance of QPSK modulation in combined flat scintillation and frequency selective multipath fading channel. The system performance degrades as the scintillation intensity level increases and when combined with terrestrial frequency selective multipath fading, the bit error rate has additional loss and there are error floors occurring at high SNR. The error floors caused by the delay spread of the channel which can reduce the floors with the use of equalizers such as Viterbi detector.

ACKNOWLEDGMENT

I would like to acknowledge Prof. Nipa Leelaruji and Prof. Narong Hemakorn for providing suggestion and supportive facility at Satellite Communication Lab (SCL), ReCCIT, KMITL. In addition, I am grateful to student members of the lab for advice and proofreading assistance.

REFERENCES

[1] P.A. Kullstam and M.J. Keskinen, “Ionospheric Scintillation Effects on UHF Satellite Communications”, *MILCOM 2000* Proceedings, Vol.2, Oct.2000, pp.779-783.

[2] Zhong Ye and Edgar H. Satorius, “Channel Modeling and Simulation for Mobile User Objective System (MUOS)—Part I: Flat Scintillation and Fading”, *ICC 2003* - IEEE International Conference on Communications, vol. 26, no. 1, May 2003, pp. 3503-3510.

[3] Gordon L.Stuber, *Principles of Mobile Communication*, Second Edition, Kluwer Academic Publishers 2001.

[4] Boonsongkusoljit N. and Supnithi P. "Performance of MPSK Modulation in Satellite Mobile Communication Systems", *ECTI 2006*, May 2006, pp.457-460.

[5] Bernard Sklar, *Digital Communications Fundamental and Applications*, Prentice-Hall, 2nd Ed, 2001.

[6] Wongtrairat, W., Leelaruji , N., Hemmakorn, N. and Supnithi, P., "Performance of MPSK in Satellite Mobile Channels with Combined Ionospheric Scintillation and Flat Fading Channels”, *IRST 2006*, July 2006.

[7] Shaft P., "On the Relationship Between Scintillation Index and Rician Fading", *IEEE Trans. Comm*, May 1974, pp. 731-732.

[8] COST 207 Management Committee, "COST 207: Digital Land Mobile Radio Communications," *Final Report*, *Commission of the European Communities*, 1989.

On the Interference Cancellation of OFDM System for Aeronautical Communication

Panit Lamun, Montree Kumngern, Phichet Moungnoul, and Kobchai Dejhan
Faculty of Engineering and Research Center for Communication and Information Technology,
King Mongkut's Institute of Technology Ladkrabang, Bangkok 10520, Thailand
Tel: 66-2326-4238, 66-2326-4242, Fax: 66-2326-4554,
E-mail: panitlamun@hotmail.com, montree_kumngern@yahoo.com, {phichet, kobchai}@telecom.kmitl.ac.th

***Abstract*–This paper addresses an interference cancellation of orthogonal frequency division multiplexing (OFDM) system for aeronautical channel in the future. In this system, each sub-carrier contains all symbols transmitted in a given frame. Each symbol in the sub-carrier will be separated by orthogonal Hadamard sequences. The proposed method used with the multiple receiver antennas, called "minimum mean square error–diversity combiner (MMSE-DC)". The E_b/N_0 performance of the proposed system are improved. Simulation results shown the proposed system is better performance than MMSE-DC for 3dB at the BER of 10^{-4}.**

I. INTRODUCTION

Orthogonal frequency division multiplexing (OFDM) system is commonly used for high-data-rate applications in fading channels and has been chosen for several new standards such as digital audio broadcasting and wireless LAN [1], [2]. At the present, the number of fight is growth in regional and global air travel. Thus the channel bandwidth will be occupied. Since the OFDM system consists of a high-bit-rate and high spectral effiency [3], this element would be the most reasonable for solve to increase the demand of fight traffic and increase number of channel per system in the future. For the airport, the aeronautical channel scenarios consist of several conditions such as en-route scenarios, arrival and takeoff scenario, taxi scenarios, parking scenarios, aircraft flying over ground station. The interference of these communications will decrease the performance of OFDM system. In this paper, an interference cancellation of OFDM system for aeronautical channel is presented. The taxi and parking scenarios are considered.

II. SYSTEM MODEL

A. Transmitter system

The OFDM transmitter with interference cancellation for aeronautical communication is shown in Fig. 1. The input data stream rate R (bits/sec) though a serial-to-parallel converter which provides N parallel data streams, the data rate be R/N bits/sec. The output of parallel data that have the time interval is N time of original data. Let x_q is number parallel data q, spread by orthogonal Hadamard sequence [4] $w_q=[w_{q,0},w_{q,1},..,w_{q,N-1}]$, for q=0,1,…, N-1. After the spreading, the data rate is recovered to R bits/sec. x_q denotes QPSK modulated signal in complex form, i.e., $x_q=\alpha_q+j\beta_q$, the spread signal can be expressed as

$$X_{q,k} = x_q w_{q,k} = \alpha_q w_{q,k} + j\beta_q w_{q,k} \tag{1}$$

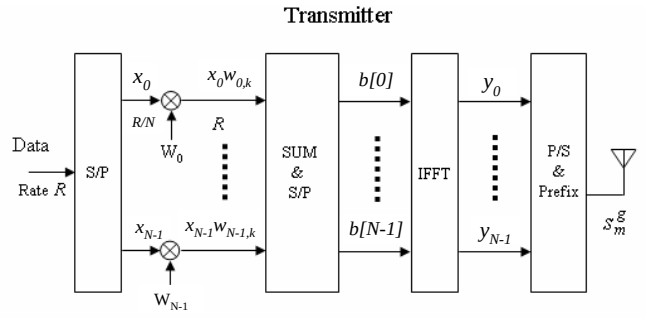

Fig. 1. Block diagram of OFDM transmitter system.

when k=0,1,…,N-1. The process is called orthogonal code division multiplexing (OCDM). After that, each spread signal is summed and a second serial to parallel converter, given as

$$b[k] = \sum_{q=0}^{N-1} x_q w_{q,k} \tag{2}$$

The signal b[k] is parallel signal. It applied to the input of inverse fast Fourier transform (IFFT) for convert frequency domain to time domain, express as

$$y_m = \sum_{k=0}^{N-1} b[k] e^{j2\pi\left(\frac{km}{N}\right)}; m = 0,1,\ldots,N-1 \tag{3}$$

Then, the output N parallel streams of IFFT can be added the guard time of each frame, called a cyclic prefix, to prevent the multipath fading channel. The cyclic prefix is actually a copy of the last portion of the data symbol appended to the front of the symbol during the guard interval. Then all symbols of each frame is $N_S=N+N_g$, for N_g is the number of guard-samples that added to the frame. The equation can be given by

$$s_m^g = \sum_{k=0}^{N-1} b[k] e^{j2\pi\left(\frac{km}{N}\right)}; m = -N_g,\ldots,N-1 \tag{4}$$

From the above detail, the N incoming data symbols consist of $[x_0,x_1,\ldots,x_{N-1}]$. This data symbols are applied to the input of OFDM transmitter and can express in matrix D_N follows as

$$D_{\tilde{N}} = \begin{bmatrix} x_0 & x_0 & \cdots & x_0 \\ x_1 & x_1 & \cdots & x_1 \\ \vdots & \vdots & \vdots & \vdots \\ x_{N-1} & x_{N-1} & \cdots & x_{N-1} \end{bmatrix} \begin{matrix} \leftarrow W_0 \\ \leftarrow W_1 \\ \vdots \\ \leftarrow W_{N-1} \end{matrix}$$
$$\begin{matrix} \uparrow & \uparrow & \cdots & \uparrow \\ f_0 & f_1 & \cdots & f_{N-1} \end{matrix}$$

It can be observed that the proposed method is every transmitter sub-carriers f_k contain all data symbols, x_0, x_1,…x_{N-1}, which each symbol is separated from each other by orthogonal Hadamard sequence. When compared with the ordinary OFDM, one sub-carrier spread to only one sub-carrier and w_q are not Hadamard sequence. Consider $W_q=[w_{q,k}]$, it will equal 1, when q=k and will equal 0 when q≠k, hence it can see that the ordinary OFDM system is a special case of proposed OFDM system, expressed in matrix D_N follows as

$$D_N = \begin{bmatrix} x_0 & 0 & \cdots & 0 \\ 0 & x_1 & \cdots & 0 \\ \vdots & \vdots & \vdots & \vdots \\ 0 & 0 & \cdots & x_{N-1} \end{bmatrix} \begin{matrix} \leftarrow W_0 \\ \leftarrow W_1 \\ \vdots \\ \leftarrow W_{N-1} \end{matrix}$$
$$\begin{matrix} \uparrow & \uparrow & \cdots & \uparrow \\ f_0 & f_1 & \cdots & f_{N-1} \end{matrix}$$

B. Receiver system

The interference cancellation MMSE-DC receiver in the OFDM system for aeronautical communication is shown in Fig. 2. The system consists of multiple receiver antennas. The received signal from each receiver antenna is separated to remove the guard time and converted from serial to parallel next. After that, this signal will be processed by fast Fourier transform (FFT), the resulting output is signal in frequency domain. Again, this output signal is converted from parallel to serial. The output can be expressed as (5)

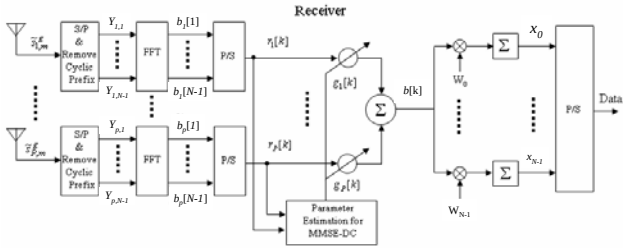

Fig. 2. Block diagram of MMSE-CD receiver in OFDM system.

$$r_p[k] = H_p^{(0)}[k]b_p^{(0)}[k] + \sum_{l=1}^{L} H_p^{(l)}[k]b_p^{(l)}[k] + N_p[k] \quad (5)$$

Eq. (5), let the receive antenna is p antennas, when p=1,2,…,P, $b_p^{(0)}[k]$, b is the required signal, $H_p^{(0)}[k]$ is the frequency response of channel of required signal of p-th receive antennas, $b_p^{(l)}[k]$ is l-th interference signals, $H_p^{(l)}[k]$ is the frequency response of channel consistence with the interference of p-th receive antennas, $N_p[k]$ is Gaussian noise of p-th receive antennas which is equal zero and noise power equal σ_n^2. On the next step, the signal of each receive antenna is summed, so called diversity combiner (DC) and weight with $g_p[k]$. The equation can be given as

$$b[k] = G^H[k]r[k] \quad (6)$$

where r[k] is the signal vector of receive antenna, G[k] is the weight of vector, $G^H[k]$ is the defining of conjugate and transpose of vector G[k]. By using MMSE algorithm detection is

$$MMSE = \min E\left\{ \left| G^H[k]r[k] - b^{(0)}[k] \right|^2 \right\} \quad (7)$$

Also, G[k] in (6) and (7) can be calculated by [3], and expressed as

$$G[k] = (R_r[k])^{-1} H^{(0)}[k] \quad (8)$$

where $H^{(0)}[k]$ is channel frequency response vector P×1, $R_r[k]$ is correlation matrix P×P of receive antenna which is transmitted with same sub-carrier, given by

$$R_r[k] = E\left(r[k]r^H[k]\right) = \sum_{l=0}^{L} H^{(l)H}[k]H^{(l)}[k] + \sigma_n^2 I_P \quad (9)$$

Also, I_P is the identical matrix P×P. The signal b[k] of (6) can be achieved by linear summing of each antenna and weight with MMSE algorithm, called MMSE-DE. After that, the output of b[k] must be despread by product with W_q. The output of each despread is summed, given by

$$x_q = \sum_{k=0}^{N-1} b[k]W_q \quad (9)$$

The x_q must be modulated by QPSK, and it parallel-to-serial converted to recovering the original data.

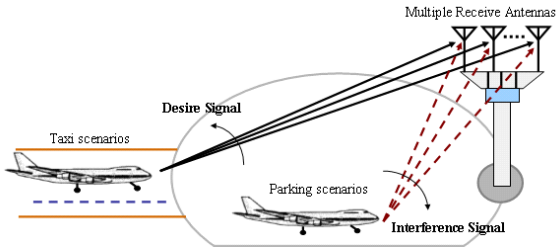

Fig. 3. The communication between aircrafts and an airport ground station.

C. Aeronautical Channel model

The aeronautical channel scenarios consist of several conditions such as en-route scenario, arrival and takeoff scenario, taxi scenario, parking scenario, aircraft flying over ground station [7]. In this paper, only taxi and parking channel scenarios will be considered. The taxi scenario is the applied when the aircraft is on the ground and traveling toward or from the terminal while parking scenario is applied when the aircraft is on the ground and traveling at very slow speed close to the terminal or is parked at the terminal. In Fig. 3, we let the taxi scenario is the channel of

desire signal. In this case, the speed of aircraft approximately about 15m/s. If we use the carrier about 5GHz, the maximum doppler frequency is 250Hz, the channel is Rician fading and the factor *k* is 6.9dB [7]. Again, we let the channel of the parking scenario as shown in Fig. 3 is interference signal. The speed of aircraft about 5.5m/s, at the same carrier, the maximum doppler frequency is 91.7Hz, the channel is Rayleight fading.

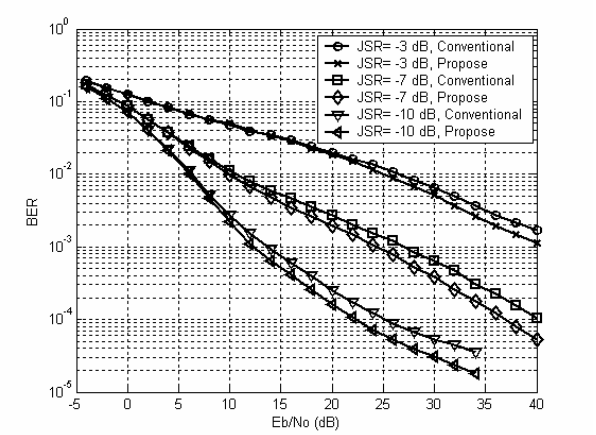

Fig. 4. BER performance of the original OFDM MMSE-DC compared with proposed OFDM system with respect to three receive antennas with JSR is:-3dB, -7dB, and -10dB.

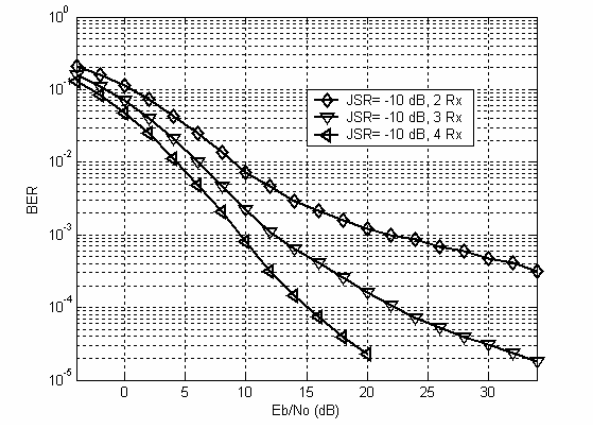

(a)

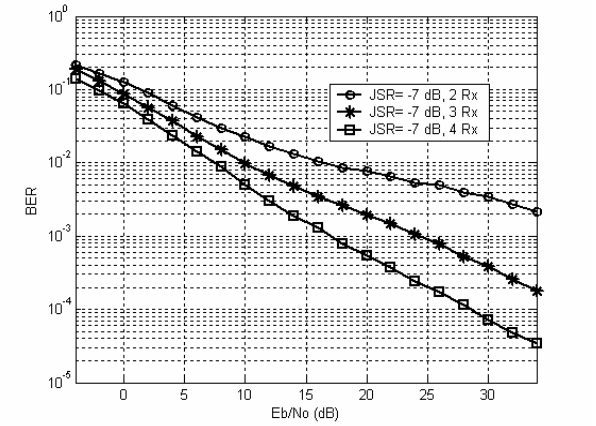

(b)

Fig. 5. BER performance of proposed OFDM system with respect to different receive antennas, (a) JSR=-10dB and (b)-7dB.

III. Simulation Results

The proposed systems in Figs. 1 and 2 are evaluated by using computer simulation. In the simulation, the system consists of N_C=N=64 carriers, each spread is 7.68kHz from each other, giving a total bandwidth is 492kHz and an OFDM symbol duration of T_{FFT}=130μs. A guard time of T_g=32.5μs and the carrier frequency is 5GHz [7]. Fig. 4 shows the Bit Error Rate (BER) performance of the original OFDM MMSE-DC compared with proposed OFDM system. In this simulation, it used three receive antennas with JSR is -3dB, -7dB, and -10dB, respectively, when JSR=10log(P_I/P_S), also P_I and P_S denotes the average power of interference and desire signal, respectively. In this figure, it can see that the proposed OFDM system give better performance compared with original OFDM MMSE-DC. Proposed OFDM is better than original OMDM MMSE-DC by 3dB at the BER of 10^{-4} for JSR=-7dB and -10dB. The BER performance of proposed OFDM system with respect to different receive antennas for JSR=-10dB and -7dB shown in Fig. 5(a) and (b), respectively. When we use the receive antenna R_x=2, 3, and 4, the BER performance in Fig. 5(a) for JSR=-10dB give better performance compared with Fig. 5(b) for JSR=-7dB. In this case, we can evaluate that the performance of aeronautical communication can be improved by increase the receive antenna at an airport ground station.

IV. Conclusions

We show that when the aircraft is on the ground and traveling on the runway, the communication between an aircraft and ground station will be disturbed from the interference signals. In this paper, an interference cancellation of aeronautical communication is presented. The performance of aeronautical communication can be increased by canceling the interference signals. The simulation results demonstrate that the performance of the system can be improved. When the power of interference signal increased, the JSR will be increased too, in this case the performance of the system can be increased by increasing the receive antenna combined with MMSE-DC algorithm. The performance of aeronautical communication can be increased by improving the ground station without changing the system of aircraft.

References

[1] ETSI ETS 300 401, "Radio broadcasting systems: digital audio broadcasting (DAB) to mobile, portable and fixed receiver," February 1995.

[2] R. V. Nee, G. Awater, M. Morikura, H. Takanashi, M. Webster, and K. W. Halford, "New high-rate wireless LAN standards," *IEEE Communications Magazine*, pp. 82-88, December 1999.

[3] T. Keller, L. Piazzo, P. Mandarini, and L. Hanzo, "Orthogonal frequency division multiplex synchronization techniques for frequency-selective fading channel," *IEEE Journal on Selected Areas in Communications*, vol. 19, pp. 999-1009, December 1999.

[4] D. Gerakoulis and E. Geraniotis, *CDMA: access and switching*, John Wiley & Sons, New York, 2001.

[5] D. Gerakoulis and P. Salmi, "An interference suppressing OFDM system for ultra wide bandwidth radio channels," *IEEE Conference on UWB Systems and Technologies*, pp.259 -264, 2002

[6] H. Zhang and Y. Li, "Clustered OFDM with adaptive antenna arrays for interference suppression," *Proceeding of IEEE International Conference on Communications*, 2003.

[7] E. Haas, "Aeronautical Channel Modeling," *IEEE Transactions on Vehicular Technology*, vol. 51, pp. 254-264, March 2002.

[8] P. Hoeher and E. Haas, "Aeronautical channel modeling at VHF-band," *Proceeding of IEEE Vehicular Technology Conference*, pp. 1961-1966, 1999.

On the Performance of Adaptive MIMO-OFDM Systems over Severe Mobile Fading Channels

Hyundong Kim and Sangho Choe
The Catholic University of Korea, Bucheon-si, Korea
Beijing University of Posts and Telecommunications, Beijing, China
Tel: +82-2-2164-4870, Fax: +82-2-2164-4777
E-mail: schoe@catholic.ac.kr

***Abstract*— Adaptive multiple input multiple output orthogonal frequency division multiplexing (MIMO-OFDM) system adaptively changes modulation scheme per subcarrier depending on channel state information (CSI) via feedback channel. CSI feedback channel delay including propagation delay, processing delay, frame delay degrades the data capacity of adaptive modulation system. This paper evaluates the two least square (LS) based multi-step autoregressive predictions, high rate prediction (HRP) and low rate prediction (LRP), over severe mobile fading channels and presents an adaptive MIMO-OFDM system with a linear predictor that is robust to the delay and the channel estimation error. Via computer simulation, we verify that LRP based MIMO-OFDM improves data capacity compared to HRP based MIMO-OFDM.**

I. INTRODUCTION

Adaptive OFDM improves data capacity for cellular systems by changing adaptively modulation order per each subcarrier according to the feedback CSI [1,2]. In practical communication systems, the CSI feedback channel has multiple symbol delays, such as processing delay and propagation delay, which result in the CSI mismatch to degrade system performance.

To compensate the multiple symbol delays via feedback channels, several minimum mean square error (MMSE) based autoregressive (AR) high rate prediction (HRP) schemes for adaptive OFDM systems have recently been proposed [3,9-10]. HRP is sensitive to CSI feedback delay d due to its fixed sample span, especially at the high channel estimation error conditions [5]. As a linear prediction filter, this paper chooses least square (LS) rather than MMSE [4], since MMSE is difficult to get the weight vector over time-varying mobile fading. This paper also investigates low rate prediction (LRP) whose sample span for prediction is extensible depending on the delay d. As a result, LRP that has a d times larger sample span than HRP is more robust to the multiple symbol delays [5].

To compensate the multiple symbol delays effectively in adaptive MIMO-OFDM, we employ the low rate prediction (LRP) scheme [5]. We evaluate the two prediction schemes, LRP and HRP, in terms of minimum sum of error squares (MSES) and mean square error (MSE) versus the delay d in MIMO-OFDM channels and verify that LRP based MIMO-OFDM is less sensitive than HRP based MIMO-OFDM over mobile fading channels with a large CSI delay and a small channel estimation signal to noise ratio (CESNR). Via computer simulation, we verify that LRP based MIMO-OFDM improves data capacity over HRP based MIMO-OFDM.

The organization of the rest of the paper is as follows. Section II explains the two fading channel prediction methods, HRP and LRP. Section III addresses the proposed adaptive SISO (single input single output) / MIMO-OFDM system with a multi-step predictor and Section IV demonstrates the simulation results for the proposed adaptive MIMO-OFDM. Finally we conclude this paper in Section V.

II. MULTI-STEP FADING CHANNEL PREDICTION

CSI feedback channel has multiple symbol delays such as processing delay and propagation delay. Hence this paper employs a multi-step channel prediction scheme to mitigate adaptive system performance degradation due to the CSI mismatch by the feedback delay. This paper compares and analyzes the two autoregressive (AR) multi-step prediction schemes, the conventionally well-known high rate prediction (HRP) and the recently proposed low rate prediction (LRP), in multipath fading channels. As an AR prediction filter, LS is used.

A. High Rate Sample Based Multi-step Prediction

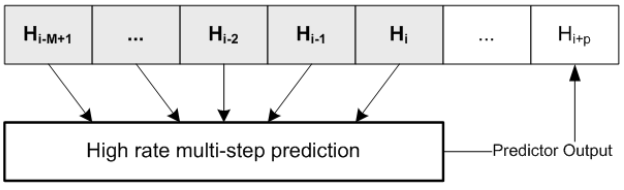

Fig. 1. High rate samples based multi-step prediction.

HRP, described in Fig 1, predicts the future p th channel samples $\hat{H}_{i+p}$ based on the previous contiguous M (=filter length) samples $\{H_i, H_{i-1}, ..., H_{i-(M-1)}\}$, whose sampling rate is the same as the OFDM symbol rate f_s, as follows:

$$\hat{H}_{i+p} = \sum_{j=1}^{M} w_j H_{i-(j-1)}, \quad (1)$$

where p is the prediction step size and w_j is the jth element of HRP weight vector $\mathbf{w}_h = [w_1 \ w_2 \ ... \ w_M]$. The weight vector $\mathbf{w}_h$ is derived by

$$\mathbf{w}_h = \mathbf{\Phi}_h^{-1} \mathbf{z}_h, \quad (2)$$

where $\mathbf{\Phi}_h = \mathbf{U}_h \mathbf{U}_h^H$ is the $M \times M$ autocorrelation matrix of HRP data matrix $\mathbf{U}_h$ [4] (the superscript H denotes the Hermitian transpose) given as

$$\mathbf{U}_h = \begin{bmatrix} H_M & H_{M+1} & \cdots & H_N \\ H_{M-1} & H_M & \cdots & H_{N-1} \\ \vdots & \vdots & \ddots & \vdots \\ H_1 & H_2 & \cdots & H_{N-M+1} \end{bmatrix}.$$

M and N denote the filter length and the number of samples for generating the weight vector, respectively. $\mathbf{z}_h = \mathbf{U}_h \mathbf{d}_h^H$ is the $M \times 1$ cross correlation vector of the data matrix $\mathbf{U}_h$ and the desired output vector $\mathbf{d}_h = [H_{M+1} \ H_{M+2} \ ... \ H_{N+1}]$ [4]. HRP has a fixed sample span M so it is sensitive to CSI feedback delay d [5], especially when the channel estimation error is high.

B. Low Rate Sample Based Multi-step Prediction

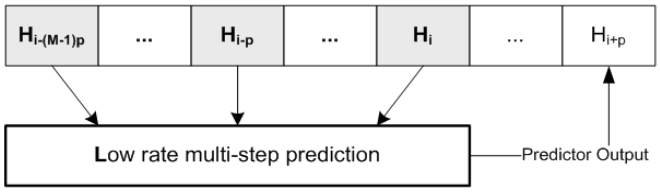

Fig. 2. Low rate samples based multi-step prediction.

LRP, described in Fig. 2, predicts the p th future samples $\tilde{H}_{i+p}$ based on the previous M channel samples whose index difference is p: $\{H_i, H_{i-p}, ..., H_{i-(M-1)p}\}$. That is, the sampling rate of LRP is f_s / p which is p times lower than HRP. H_{i+p} can be obtained by the following equation (3).

$$\tilde{H}_{i+p} = \sum_{j=1}^{M} \tilde{w}_j H_{i-(j-1)p}, \quad (3)$$

where p is the prediction step size and $\tilde{w}_j$ is the jth element of LRP weight vector $\mathbf{w}_l = [\tilde{w}_1 \ \tilde{w}_2 \ ... \ \tilde{w}_M]$ which is obtained from

$$\mathbf{w}_l = \mathbf{\Phi}_l^{-1} \mathbf{z}_l, \quad (4)$$

where $\mathbf{\Phi}_l = \mathbf{U}_l \mathbf{U}_l^H$ is the autocorrelation matrix of data matrix $\mathbf{U}_l$

$$\mathbf{U}_l = \begin{bmatrix} H_{(1+(M-1)p)} & H_{(1+Mp)} & \cdots & H_{(1+(N-1)p)} \\ H_{(1+(M-2)p} & H_{(1+(M-1)p)} & \cdots & H_{(1+(N-2)p)} \\ \vdots & \vdots & \ddots & \vdots \\ H_1 & H_{1+p} & \cdots & H_{(1+(N-M+1)p)} \end{bmatrix} \quad (5)$$

and $\mathbf{z}_l = \mathbf{U}_l \mathbf{d}_l^H$ is the cross correlation matrix of LRP data matrix $\mathbf{U}_l$ and desired output matrix $\mathbf{d}_l = [H_{(1+Mp)} \ H_{(1+(M+1)p)} \ ... \ H_{(1+Np)}]$. LRP that has an expandable sample span dM proportional to the delay d is more robust to CSI feedback delay d than HRP [5].

C. Performance comparison

This paper compares the two LS based prediction schemes, HRP and LRP, in terms of MSES (minimum sum of error squares) $E_{\min}$

$$\begin{aligned} E_{\min} &= E_d - E_{est} \\ &= \sum_{i=M}^{N} |d(i)|^2 - \sum_{i=M}^{N} |d(i \mid \mathbf{u}_i)|^2 \\ &= \sum_{i=M}^{N} |d(i)|^2 - \mathbf{z}^H \mathbf{\Phi}^{-1} \mathbf{z}, \end{aligned} \quad (6)$$

where $E_d = \sum_{i=M}^{N} |d(i)|^2$ is the energy of desired output samples $d(i)$ and $E_{est} = \sum_{i=M}^{N} |d(i \mid \mathbf{u}_i)|^2$ is the energy of estimated output samples $\hat{d}(i \mid \mathbf{u}_i)$ when the ith prediction filter input vector $\mathbf{u}_i = [u_i \ u_{i-1} \ ... \ u_{i-M+1}]$ is given. That is, $\mathbf{u}_i = [H_i \ H_{i-1} \ ... \ H_{i-M+1}]$ for the HRP method and $\mathbf{u}_i = [\tilde{H}_i \ \tilde{H}_{i-p} \ ... \ \tilde{H}_{i-(M-1)p}]$ for the LRP method.

HRP and LRP are compared in Fig. 3 in terms of MSES versus CSI feedback delay in a Vehicular A channel [7]. Assume the mobile speed is 60km/h. Fig. 3 shows that when the delay d is less than 5 there is no big MSES difference between LRP and HRP. But when the delay d is greater than 5, the MSES difference between LRP and HRP gets greater, That is, as the feedback delay increases,

MSES of HRP increases but MSES of LRP is within the range of 10^{-4} to 10^{-2}. Fig. 4 compares MSE of HRP, i.e., $E\left[\left|H_{i+p}-\hat{H}_{i+p}\right|^2\right]$, and MSE of LRP, i.e., $E\left[\left|H_{i+p}-\tilde{H}_{i+p}\right|^2\right]$, for the variation of the CSI feedback delay *d*. We employ Vehicular A channel for fading channel and assume the mobile speed is 60km/h. As the CSI feedback delay increases, the MSE curve for HRP has a steeper slope than that for LRP. From the results in Fig. 3 and Fig. 4, we can confirm that LRP is more robust to the delay *d* than HRP especially in mobile fading channels.

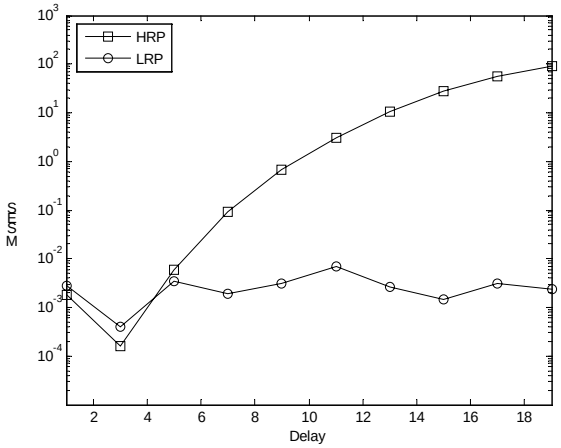

Fig. 3. MSES comparison of HRP and LRP in Vehicular A channel when the mobile speed is 60km/h.

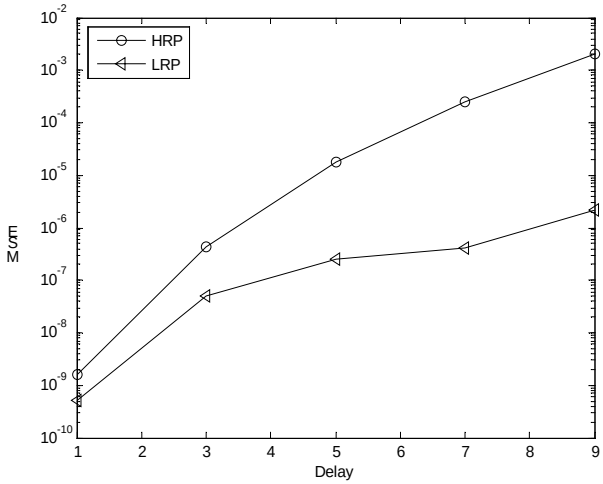

Fig. 4. MSE comparison of HRP and LRP in Vehicular A channel when the mobile speed is 60km/h.

III. ADAPTIVE MIMO-OFDM SYSTEM WITH A PREDICTION FILTER

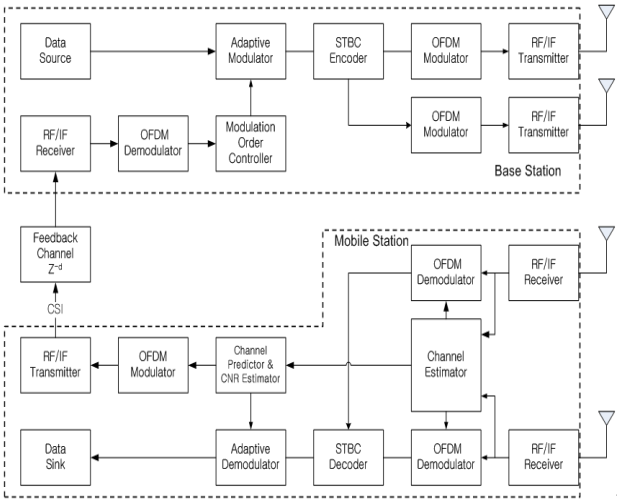

Fig. 5. Adaptive MIMO-OFDM system with a multi-step channel predictor.

A block diagram of adaptive MIMO-OFDM with a multi-step channel predictor is shown in Fig. 5. This paper employs a 2×2 space-time block code (STBC) for MIMO operation [6]. For adaptive operation, we add an adaptive modulator block and a channel predictor block to the fixed MIMO-OFDM system and establish a CSI feedback path with the feedback delay *d*. Mobile station (MS) receiver compensates the CSI damage due to the delay *d* using the multi-step channel predictor. MS feedbacks CSI to its serving base station (BS) and the BS assigns bit loading information per each modulation symbol depending on the CSI.

TABLE 1. SYSTEM PARAMETERS

Parameter	*Value*
bandwidth	20MHz
sampling frequency	25MHz
carrier frequency	5GHz
number of used subcarriers	1536
number of virtual unused subcarriers and DC subcarrier	512
number of total subcarriers	2048
number of transmit antennas	2
number of receive antennas	2
effective symbol period	81.92usec
cyclic prefix length	18.08usec

IV. SIMULATION RESULTS

In this section, we provide simulation results that demonstrate the performance of the proposed SISO / MIMO-OFDM system with a multi-step predictor. In computer simulation, we consider the Jakes model [8]

whose fading parameters are the same as Vehicular A channel model [7]. Assume the mobile velocity is 60km/h. Among the total 2048 subcarriers, the number of used (traffic or pilot) subcarriers is 1536. The adaptive MIMO-OFDM system parameters are shown in Table 2.

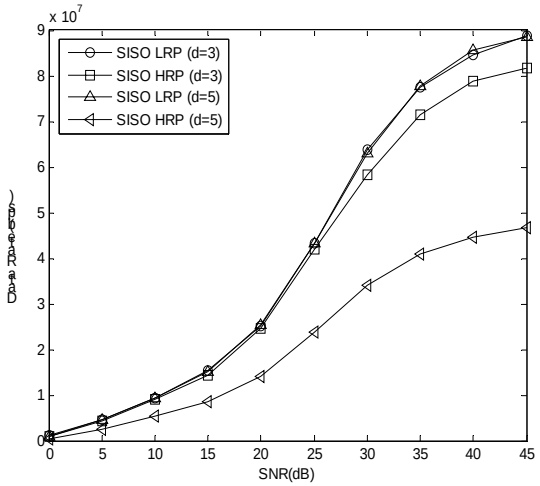

Fig. 6. Data rates of SISO LRP and HRP versus SNR and CSI feedback delay for CESNR 50dB.

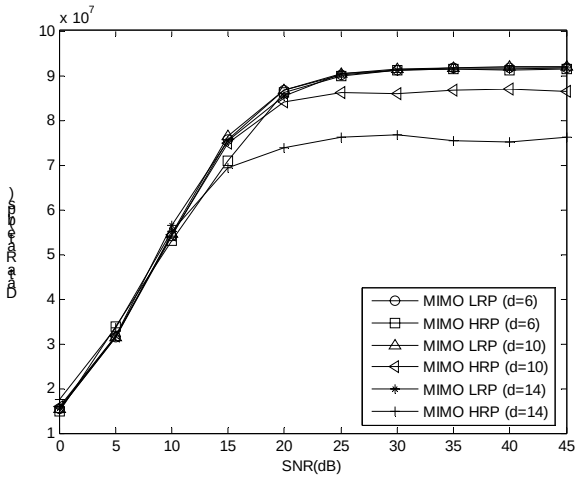

Fig. 7. Data rates of MIMO LRP and HRP versus SNR and CSI feedback delay for CESNR =50dB.

Fig. 6 compares the data rate of SISO LRP and SISO HRP versus signal-to-noise ratio (SNR) when CSI feedback delay varies. Assume CESNR (channel estimation signal to noise ratio) is equal to 50dB. In case of SISO HRP, the maximum allowable data rate (= data capacity) decreases from 82Mbps to 48Mbps when the delay *d* increases 3 to 5. But in case of SISO LRP, the increase of delay does not make a big change of data rate. For SISO LRP, the data capacity is 88Mbps. On the other hand, Fig. 7 compares the data rate of MIMO LRP and MIMO HRP versus signal-to-noise ratio (SNR) when CSI feedback delay varies. Assume also CESNR is set to 50dB. For the space-time diversity gain, MIMO-OFDM assumes constant channel for the two symbol period. For the delay *d*=6, MIMO HRP and MIMO LRP has a similar data capacity of 92Mbps. But as the delay increases while MIMO LRP has no big change of data rate MIMO HRP reduces the data rate a lot. For instance, for *d*=14, MIMO HRP has a reduced data capacity of 76 Mbps and MIMO LRP keeps the maximum data capacity of 92Mbps.

V. CONCLUSION

This paper has presented an adaptive MIMO-OFDM with an LS based linear prediction filter which compensates CSI feedback delay effectively over mobile fading channels. This paper has compared MSES and MSE between the two linear autoregressive prediction schemes, LRP and HRP, and has confirmed that LRP is more robust to the severe MIMO-OFDM channels. Via computer simulation in Vehicular A channels, we verify that LRP based MIMO-OFDM improves data capacity compared to conventionally proposed HRP based MIMO-OFDM.

ACKNOWLEDGEMENT

"This research was supported by the MIC, Korea, under the ITRC support program supervised by the IITA" (IITA-2006-(C1090-0602-0011))

REFERENCES

[1] W.T. Webb and R. Steele, "Variable rate QAM for mobile radio," IEEE Trans. Commun., vol. 43, pp. 2223-2230, Jul.1995.

[2] M. R. Souryal and R. L. Pickholtz, "Adaptive Modulation with Imperfect Channel Information in OFDM, " *Proc. IEEE Int. Conf. Commun*, Helsinki, pp. 1861-1865, June, 2001.

[3] A. Duel-Hallen, S. Hu, and H. Hallen, "Long Range Prediction of fading signals," *IEEE Signal Process. Mag.*, vol. 17, pp. 62-75, May 2000.

[4] S. Haykin, Adaptive Filter Theory, Prentice-Hall, 1991.

[5] S. Choe and M. Uysal, "Robust Autoregressive Predictive Power Control Method for Mobile CDMA Systems," *Electron. Lett.*, vol. 42, issue 15, pp. 866-868, July 2006.

[6] S. Alamouti, "A simple transmit diversity technique for wireless communications", *IEEE J. Select. Areas Commun.*, vol. 16, pp. 1451-1458, Oct. 1998.

[7] Recommendation ITU-R M.1225, Guidelines for Evaluation of Radio Transmission Technologies for IMT-2000, 1997.

[8] W. C. Jakes, Microwave Mobile Communications, New York: Wiley, 1974.

[9] S. Falahati, A. Svensson, T. Ekman, and M. Sternad, "Adaptive Modulation Systems for Predicted Wireless Channels," *IEEE Trans. Commun.*, vol. 52, pp. 307-316, Feb. 2004.

[10] M. Munster and L. Hanzo, "MMSE channel Prediction Assisted Symbol-by-Symbol Adaptive OFDM," *Proc. IEEE Int. Conf. Commun.*, New York, NY, pp. 416-420, April, 2001.

Proposal of Multi-level QAM-OFDM System with IDSI and IDAR Methods in Satellite Channel

Pisit Boonsrimuang†, Kazuo Mori*, Tawil Paungma† and Hideo Kobayashi*

† Department of Telecommunication Engineering, Faculty of Engineering,
King Mongkut's Institute of Technology Ladkrabang, Thailand
* Division of Electrical and Electronic Engineering, Graduate School of Engineering, Mie University, Japan
E-mail: pisit@telecom.kmitl.ac.th , koba@elec.mie-u.ac.jp

Abstract- **The future satellite communication systems are required to support the higher transmission data rate for providing the multimedia services by employing the efficient modulation method such as multi-level QAM. However, the employment of conventional single carrier transmission method with multi-level QAM would cause the fatal degradation of signal quality due to the non-linear amplifiers located at the earth station and satellite. To overcome this problem, we have proposed the multi-level QAM-OFDM technique with IDAR method designed for non-linear satellite channel. However, the proposed method could not mitigate the non-linear distortion sufficiently when modulation level becomes higher such as 64QAM. This paper proposes the combined scheme for PAPR reduction method employed at the transmitter and OFDM-IDAR method employed at the receiver so as to enable the usage of higher multi-level QAM method. The proposed method can achieve the higher transmission data rate with keeping the better bit error rate performance even in the non-linear satellite channel.**

I. INTRODUCTION

One of the disadvantages of using the OFDM is that its time domain signal has the larger PAPR (Peak to Average Power Ratio), which causes the degradation of BER (Bit Error Rate) performance in the non-linear amplifier [1]. From this reason, the OFDM has been considered as unsuitable transmission technique for the non-linear satellite channel, although it has a potential capability to improve the transmission data rate by employing the multi-level QAM with less complexity of transmitter and receiver.

To solve PAPR problem in the OFDM scheme, we proposed the OFDM-IDAR (Improved Decision Aided Reconstruction) method, which can mitigate the non-linear distortion at the receiver and achieve the higher transmission data rate with keeping the better BER performance even in the satellite channel [2]. However, the proposed OFDM-IDAR method has some limitation on the usage of higher level of modulation method such as 64QAM for achieving the higher transmission data rate. Because its higher level of modulation method causes a lot of decision error due to the non-linear amplifiers located at the transmit earth station and satellite, and the IDAR method could no more mitigate the non-linear distortion sufficiently. To reduce the non-linear distortion, it is required to improve the PAPR performance as much as possible for the OFDM signal at the transmission side. If the PAPR performance of OFDM signal can be improved somehow at the transmission side, the non-linear distortion can be reduced and accordingly the IDAR method could achieve the better BER performance at the receiver even when the higher level of modulation method is employed. In this paper, we propose the OFDM-IDAR method in conjunction with the PAPR reduction method, which allows the employment of higher level of modulation method in the non-linear satellite channel. As for the PAPR reduction method, we propose the improved DSI (Dummy Sub-carrier Insertion) method [3], which can achieve the better PAPR performance than the conventional DSI method [4].

In this paper, Section 2 firstly presents the satellite system model including the non-linear amplifiers at the earth station and satellite. Section 3 proposes the improved dummy sub-carrier insertion (IDSI) method as the PAPR reduction method at the transmit earth station and also propose the IDAR method as the mitigation method of non-linear distortion at the receive earth station. Section 4 presents the various computer simulation results to verify the effectiveness of proposed OFDM-IDAR with IDSI method in the non-linear satellite channel, and Section 5 draws some conclusions.

II. SATELLITE SYSTEM MODEL

Figure 1 shows the typical satellite system model assumed in the following evaluations. The non-linear amplifiers assumed at the transmit earth station and satellite are the Solid State Power Amplifier (SSPA) and Traveling Wave Tube Power Amplifier (TWTA), respectively. The input-output relationships of AM-AM and AM-PM characteristics both for SSPA and TWTA are assumed in the following evaluations [2]. The downlink signal from the satellite to the received earth station, which corresponds to the output signal of TWTA, is given by the following equation.

$$s_{dw}(t) = F_c\left[\left|s(t)\right|\right] \cdot e^{j\left\{\arg(s(t)) + \Phi_c(s(t))\right\}} \qquad (1)$$

where $s(t)$ is the modulated OFDM signal, and $F_c[\,]$ and $\Phi_c[\,]$ are the composite AM-AM and AM-PM conversions characteristics of SSPA and TWTA as shown in Fig.1.

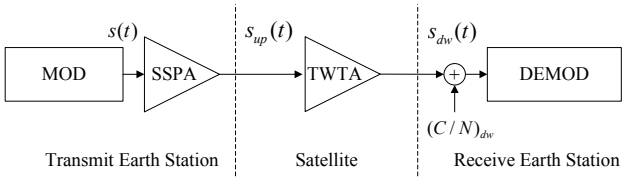

Figure 1. Satellite system model.

III. PROPOSAL OF OFDM-IDAR WITH IMPROVED DSI METHOD

A. Proposed DSI Method at Transmit Earth Station

This section proposes the improved DSI (IDSI) method, which can achieve better PAPR performance as compared with the conventional DSI method. Fig.2 shows the structure of proposed OFDM symbol represented in the frequency domain. The OFDM symbol consists of *M* data sub-carriers and *L* dummy sub-carriers that are placed at the both ends of data sub-carriers.

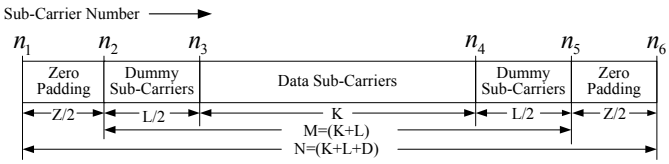

Figure 2. Structure of proposed OFDM symbol in frequency domain.

Figure 3 shows the block diagram of proposed IDSI method at the transmission side that employs the time-frequency domains swapping algorithm for the determined phase values for the dummy sub-carriers. In the proposed method, the target PAPR and the maximum number of iterations are firstly set. From Fig.3, the modulated data sub-carriers and dummy sub-carriers in the frequency domain are converted to the time domain signal by *IFFT*. The time domain signal at the *i-th* iteration is given by the following equation.

$$x_k^{(i)} = \frac{1}{\sqrt{N}} \sum_{n=0}^{N-1} X_n^{(i)} e^{j\frac{2\pi kn}{N}} \tag{2}$$

where N is the number of *IFFT* points and $X_n^{(i)}$ is the frequency domain data including the data, dummy and null sub-carriers at the *i-th* iteration, which is given by,

$$X_n^{(i)} = \begin{cases} A_n & n_3 \le n \le n_4 - 1 \\ D_n^{(i)} & n_2 \le n \le n_3 - 1 \text{ and } n_4 \le n \le n_5 - 1 \\ 0 & \text{others (zero padding)} \end{cases} \tag{3}$$

where A_n is the frequency data for information and $D_n^{(i)}$ is the frequency data for dummy sub-carriers at *i-th* iteration. At the initial iteration (*i=0*), the frequency data for all dummy sub-carriers are given by 0.

In the time-frequency domain swapping algorithm, the error signal is calculated by the following equation in which the sampled time domain signal is detected as the error signal only when its amplitude level is greater than a certain reference level of *S*.

$$e_k^{(i+1)} = \begin{cases} x_k^{(i)} & \text{if } \left|x_k^{(i)}\right| \ge S \\ 0 & \text{if } \left|x_k^{(i)}\right| < S \end{cases} \quad (0 \le k \le N-1) \tag{4}$$

where the reference level *S* is usually decided on the basis of the average power of input signal. The time domain error signal given by (4) is converted to the frequency domain signal by *FFT*, which is given by the following equation.

$$E_n^{(i+1)} = \frac{1}{\sqrt{N}} \sum_{k=0}^{N-1} e_k^{(i+1)} \cdot e^{-j\frac{2\pi nk}{N}} \quad (0 \le n \le N-1). \tag{5}$$

By using (5), the frequency domain signal both for the data and dummy sub-carriers to be used at the next iteration *(i+1)* is given by the following equation.

$$D_n^{(i+1)} = \alpha \cdot e^{j\left[\arg\left\{D_n^{(i)} - E_n^{(i+1)}\right\}\right]} = \alpha \cdot e^{j\theta_n^{(i)}}$$
$$n_2 \le n \le n_3 - 1 \text{ and } n_4 \le n \le n_5 - 1 \tag{6}$$

where α is the constant amplitude level which can be decided by the averaged amplitude level of data sub-carriers. Here, it should be noted that these determined phases are carried out only for the dummy sub-carriers and the data sub-carriers are kept as the same as the original data information. In the time-frequency swapping algorithm, (2) to (6) are repeated up to reach either the predetermined PAPR or the predetermined number of iterations.

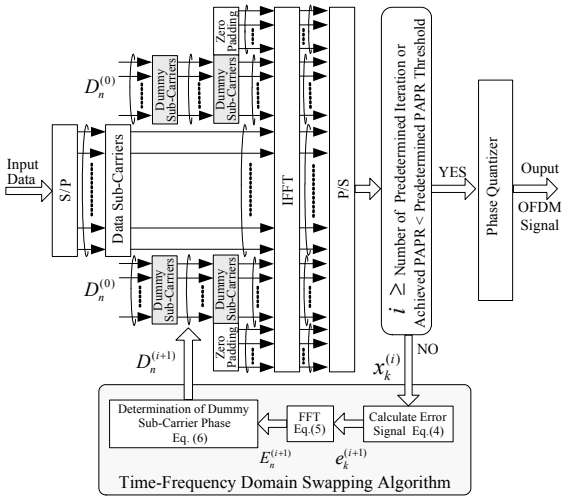

Figure 3. Structure of proposed IDSI method.

The phase value of $\theta_n^{(i)}$ for each dummy sub-carrier, which is obtained by the above time-frequency domain swapping algorithm, has the continuous (analogue) value because of using the time-frequency domains swapping algorithm. However, the IDAR method is required to use the decision data at the receiver for the reconstruction of inter-modulation noise. If the continuous phase is used for each dummy sub-carrier, the accuracy of decision phase at the receiver would be degraded relatively and the complexity of IDAR receiver would be increased. From these reasons, the continuous phase value is quantized to the discrete value at the "Phase Quantizer" as shown in Fig.3. The output of "Phase Quantizer" can be given by the following equation.

$$\tilde{\theta}_n^{(i)} = \min_{k=1\sim J} \left|\theta_n^{(i)} - \tilde{\theta}_k\right| \tag{7}$$

where $\tilde{\theta}_k$ is the predetermined discrete phase value and given by the following equation.

$$\tilde{\theta}_k = 2\pi \cdot \frac{(k-1)}{J} \quad k = 1 \sim J \tag{8}$$

where the discrete phase value is given by equal phase step from *0* to 2π and *J* is the number of discrete phase value. By using (7), the transmitted dummy sub-carrier is given by the following equation.

$$X_n^{(i)} = \alpha \cdot e^{j\tilde{\theta}_n^{(i)}} \ , n_2 \le n \le n_3 - 1 \ and \ n_4 \le n \le n_5 - 1 \qquad (9)$$

Here it should be noted that if J is taken by larger number, the PAPR performance could be improved. However, the complexity of IDAR method at the receiver side would be increased because the decision of dummy sub-carriers is required to perform by using the larger number of discrete phase. The selection of optimum value for J is evaluated in Section 4.

B. OFDM-IDAR Method for Satellite Channel

Figure 4 shows the structure of receiver for the proposed OFDM-IDAR with IDSI method. In Fig.4, the received downlink RF signal $s_{dw}(t)$ given in (1) is first down converted to the base band signal and digitized by A/D converter. The received time domain sampled signal after removing the guard interval (GI) is given by the following equation.

$$r_k = s_{dw,k} + w_k = y_k + i_k + w_k \qquad (10)$$

where, $s_{dw,k}$, w_k, y_k and i_k represent the output signal of TWTA, additive noise in the downlink, transmitted desired signal and inter-modulation noise on the *k-th* time domain sampled signal, respectively. Here, the inter-modulation noise is assumed to add the desired signal y_k linearly. It should be noted that the inter-modulation noise at the output of non-linear amplifier is unable to express separately as given in (10), because it is strongly related to the desired signal y_k. However, the inter-modulation noise is reconstructed separately in the IDAR method by using the decision data at the receiver. Although it is inappropriate to express the inter-modulation noise separately, (10) is given here just as the assumption so as to explain the following IDAR algorithm clearly. The received time domain sampled signal given by (10) is converted to the frequency domain signal by *FFT*, which is given by the following equation.

$$R_n = Y_n + I_n + W_n \qquad (11)$$

where, the capital letter represents the frequency domain signal, which corresponds to its small letter given by (10) in the time domain. The decision for data information and dummy sub-carriers can be made by the following equation.

$$\hat{S}_n = \min_X \left| R_n - X_n \right| \qquad (12)$$

where $\hat{S}_n$ is the decision data both for the data and dummy sub-carriers at the *n-th* sub-carrier. Here it should be noted that the decision for dummy sub-carrier is made by using (7).

The decision data in the frequency domain is converted to the time domain signal $\hat{s}_k$ by *IFFT*, which corresponds to the reconstructed transmitted time domain signal. In the IDAR method, the time domain signal $\hat{s}_k$ is used for the reconstruction of inter-modulation noise. This is based on the fact that the OFDM time domain signal converted from the decision data in the frequency domain, which includes even some decision errors, would be almost the same as the original time domain signal without error [2]. From this fact, the inter-modulation noise can be reconstructed by using the decision data in the time domain.

By using the time domain signal $\hat{s}_k$, the output time domain signal of SSPA and TWTA can be reconstructed by using the same manner as processed at the earth station and satellite. In the IDAR method, the operations of non-linear amplifiers both for the SSPA and TWTA are conducted on the digital sampled data by assuming the same AM-AM and AM-PM conversion characteristics as that operated in the radio frequency. The time domain signal at the output of SSPA and TWTA as shown in Fig.4 is given by the following equation.

$$\hat{s}_{dw,k} = F_C\left[\left|\hat{s}_k\right|\right] \cdot e^{j\left\{\arg(\hat{s}_k) + \Phi_C\left(\left|\hat{s}_k\right|\right)\right\}} \qquad (13)$$

where, $\hat{s}_k$ is the time domain signal converted from the frequency domain decision data given in (12), F_C and Φ_C are the AM-AM and AM-PM conversions characteristics which are the composite characteristics of SSPA and TWTA. Here, the composite characteristics of SSPA and TWTA can be estimated by using the low PAPR preamble symbols. By using (13), the inter-modulation noise incurred at the SSPA and TWTA can be estimated by the following equation.

$$\begin{aligned} \hat{d}_k &= \hat{s}_{dw,k} - \hat{s}_k \\ &\approx \hat{s}_k + \hat{i}_k - \hat{s}_k \approx \hat{i}_k \end{aligned} \qquad (14)$$

The inter-modulation noise given by (14) is then converted to the frequency domain signal $\hat{C}_n$ by *FFT*. By subtracting $\hat{C}_n$ from (11), the frequency domain signal coped with the inter-modulation noise can be obtained by the following equation.

$$\begin{aligned} \hat{R}'_n &= R_n - \hat{C}_n = Y_n + \left\{ I_n - \hat{I}_n \right\} + W_n \\ &\approx Y_n + W_n \end{aligned} \qquad (15)$$

The above procedures are repeated until the better performance can be achieved in the IDAR method.

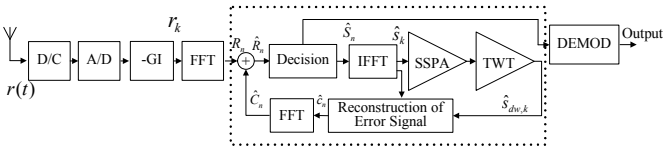

Figure 4. Structure of proposed receiver for OFDM-IDAR with IDSI method.

IV. PERFORMANCE EVALUATIONS

This section presents the various computer simulation results to demonstrate the performance of OFDM-IDAR with IDSI method in the non-linear satellite channel. In the following evaluation, the uplink C/N is assumed to be the noise free condition and only the downlink noise is added to the received signal. The input back-off (IBO) for the transmit earth station amplifier of SSPA is fixed by – 4 dB.

Figure 5 shows the BER performance for the proposed method when changing the number of discrete phase J for the "Phase Quantizer" as shown in Fig.3. In the figure, the BER performance for the case of continuous phase is also shown. In the simulations, IBO for satellite TWTA is taken by -6 dB and the downlink C/N is 26 dB. From the figure, it can be observed that the BER performance of proposed method is almost the same as the case of continuous phase when J is larger than 18. From these results, the following simulation for IDSI method is assumed to use 18 as the number of discrete phase.

Figure 6 shows the PAPR performances for the proposed IDSI and conventional OFDM methods. In the figure, the PAPR performance with the case of continuous phase is also shown. The PAPR performance is evaluated by using the Complementary Cumulative Distribution Function (CCDF). From the figure, it can be seen that the PAPR performance for the IDSI method can be improved as increasing the number of discrete phase, while the performance is almost the same as the case of continuous phase when the number of discrete phase is 18. From these results, J is assumed to use 18 in the following evaluations for the proposed method.

TABLE I SIMULATION PARAMETERS.

Allocated bandwidth	26MHz
Modulation method	64QAM
Detection method	Coherent
No. of *FFT* points (N)	512
No. of sub-carriers (M+L)	128
Symbol duration	4.92μs
Guard interval	0.5μs
No. of dummy sub-carriers (L)	24
Number of discrete phases (J)	18
Transmission data rate	115.1Mbit/s

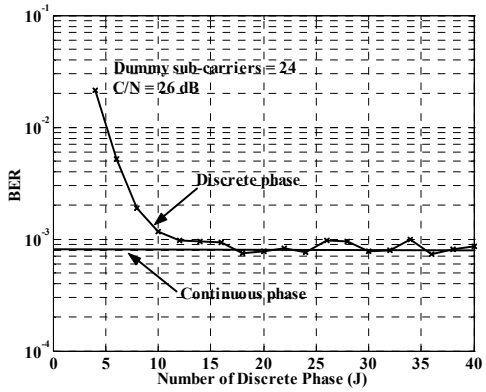

Figure 5. BER performance when changing the number of discrete phase.

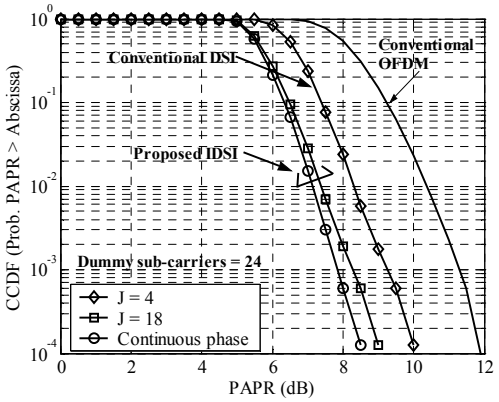

Figure 6. PAPR performance.

Figure 7 shows the BER performances for the conventional single carrier (SC), OFDM-IDAR and proposed OFDM-IDAR with IDSI methods when changing the downlink $(C/N)_{dw}$. In the simulation, the optimum IBO of satellite TWTA for these methods are taken by -15 dB, -6 dB and -6 dB, respectively based on the optimized IBO [2]. From the figure, it can be observed that the proposed method can achieve much better BER performance than that for the conventional SC and OFDM-IDAR methods of which BER performances have error floor at the higher C/N. From these results, it can be concluded that the proposed OFDM-IDAR with IDSI method could achieve the higher transmission data rate with keeping the better BER performance in the non-linear satellite channel.

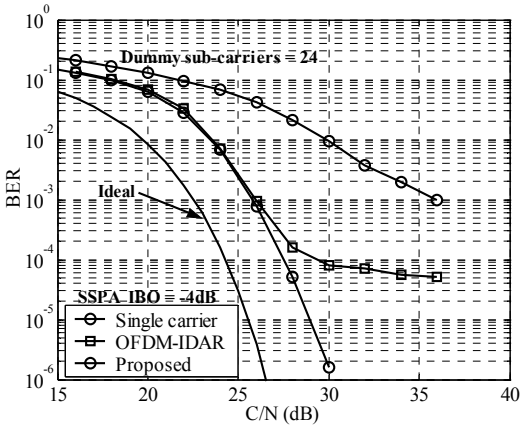

Figure 7. BER performance when changing C/N.

V. CONCLUSIONS

This paper proposed the OFDM-IDAR with IDSI method, which can reduce the PAPR performance at the transmitter by using the proposed IDSI method and can mitigate the non-linear distortion at the receiver by using the IDAR method, respectively. This paper presented various computer simulation results to verify the effectiveness of proposed method in the non-linear satellite channel. From the computer simulation results, we confirmed that the proposed method could achieve the higher transmission data rate with keeping the better BER performance in the non-linear satellite channel.

REFERENCES

[1] C.E. Dimakis, S.S. Kouris and S.A. Kosmopoulos, *"Performance Evaluation of 16-QAM Signaling Through Nonlinear Channel in an AWGN and Interference Environment: A Simulation Approach,"* IEE Proc., Vol137, no 5, pp315-322, Oct. 1990.

[2] P. Boonsrimuang, K. Mori, T. Paungma and H. Kobayashi, *"Employment of QAM-OFDM Technique in Satellite Channel,"* Technical Report of IEICE, SAT2004-98, pp21-23, July 2004.

[3] P. Boonsrimuang, K. Naito, K. Mori, T. Paungma and H. Kobayashi, *"PAPR Reduction of OFDM Signal by Use of DSI Method with Time-Frequency Domain Swapping Algorithm,"* IEICE Tran. on Comm., vol.E90-B, No.4, pp.1001-1006, Apr. 2007.

[4] Heung-Gyoon Ryu, Jae-Eun Lee and Jin-Soo Park, *"Dummy Sequence Insertion (DSI) for PAPR Reduction in the OFDM Communication System,"* IEEE Trans. on Consumer Electronics, Vol. 50, No. 1, Feb 2004.

[5] C. Rapp, *"Effects of HPA-Nonlinearity on a 4-DPSK/OFDM-Signal for a Digitial Sound Broadcasting System,"* in Proceedings of the Second European Conference on Satellite Communications, Liege, Belgium, pp. 179-184, Oct. 22-24, 1991.

[6] A. A. M. Saleh, *"Frequency independent and frequency dependent nonlinear model of TWT amplifiers,"* IEEE Trans. Commun., vol. COM-29, pp. 1715–1720, Nov. 1981.

QPSK Modulator Based On Phase Locked Loop

P. Wisartpong, J. Koseeyaporn, and P.Wardkein
Department of Telecommunication Engineering, Faculty of Engineering,
King Mongkut's Institute of Technology Ladkrabang, Bangkok, 10520 THAILAND
pramote@telecom.kmitl.ac.th

***Abstract*- In this paper, a new scheme for phase shifter implemented on phase locked loop (PLL) is proposed. It can be accomplished by placing a gain controller either between a loop filter and a VCO or between a summing circuit and an integrator of a conventional PLL. This gain controller is employed to control phase shifting where the phase shift is inversely proportional to its gain. The advantage of this technique is that the phase shift is not a function of the running frequency of a VCO. Hence, the identical phase shifters can be achieved. In addition, the proposed scheme is applied for a QPSK modulator to illustrate its practical application where the experimental results confirm well with the theoretical expectation.**

I. INTRODUCTION

PLL is well known to be one of negative feedback system applications. It is employed in many fields, such as in communication system for FM modulation, FM demodulation, frequency synthesizer, frequency doubler, frequency multiplier, and frequency divider. Also in control system, it is used for phase synchronize to deliver power to motor and in power electronic for phase synchronize to control on-off switched.

Recently, A.W. Houghton and P.V. Brennan [1] proposed phase shifter for application in antenna beam steering by PLL. This proposed technique is based on the summing between input feeding voltage and output phase error voltage. Although it is quite simple; however, the disadvantage of such method is that phase shift is dependent directly on the running frequency (ω_r) of VCO. In addition, this method can be applied for the case that error frequency is small. When the difference between frequency input (ω_i) and frequency running (ω_r), ($\omega_i - \omega_r$) are large, the accuracy of this method thus decreases.

In this paper, an alternative technique to shift phase of signal is proposed which is based on gain adjustment. The proposed system can be easily implemented by adding a gain controller to the conventional PLL. The obtained phase output is found to be proportional to gain of this gain controller. Also, the proposed phase shifter with PLL technique can provide an accurate result because phase difference is directly determined without any approximation. In addition, the phase shifting is not dependent on the frequency running (ω_r) of VCO. Hence, the phase shifters whose phase shifting characteristics are identical can be easily constructed.

Moreover, the phase shift of the proposed technique can be electronically controlled. It is accomplished by constructed the gain controller with devices such as OTA. For this case, gain of this controller is adjusted by the biasing current which results in phase shifting be electronically controlled.

To verify the validation of the proposed method, the experiment is established by using a commercial PLL IC4046. Furthermore, this proposed phase shifter is modified to be QPSK modulator where the experimental results confirm the theoretical expectation.

The organization of this article is given as follows. The brief review of PLL is discussed in section II. In section III, the phase shifter that is proposed by [1] is described and followed with the proposed technique. The application of the proposed PLL for a QPSK modulator is explained in section IV. The experimental results are demonstrated in section V. Finally, the conclusions are given in section VI.

II. PRINCIPLE OF PLL

In this section, a brief review of a conventional PLL as shown by the block diagram in Fig.1 is given. It is noted that the notations in Fig.1 are

$\phi_i(s)$: Laplace transform of phase input function ($\phi_i(t)$)

$\phi_o(s)$: Laplace transform of phase output function ($\phi_o(t)$)

$\varepsilon(s)$: Laplace transform of phase error ($\varepsilon(t)$)

$V_L(s)$: Laplace transform of loop filter output ($v_L(t)$)

$\omega_o(s)$: Laplace transform of frequency output of VCO ($\omega_o(t)$)

$F(s)$: Transfer function of loop filter

$I(s)$: Laplace transform of Integrator $I(t)$

$\omega_r(s)$: Laplace transform of frequency running of VCO in PLL.

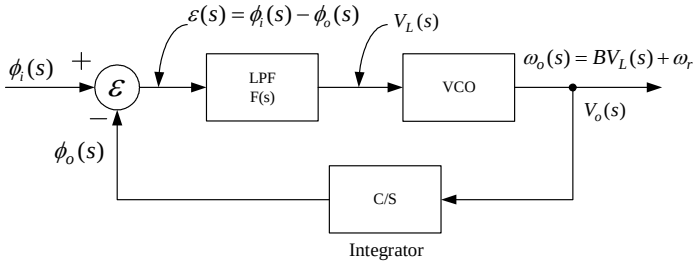

Figure 1. Block diagram of a conventional PLL.

From Fig. 1, the relationship of the system can be written as

$$\frac{BCF(s)}{S}\phi_o(s)+\phi_o(s)=BCF(s)\phi_i(s)+\omega_r(s) \quad (1)$$

where B is the sensitivity of VCO and C is gain of integrator. By substituting a transfer function of the loop filter as $F(s)=\frac{A}{1+GS}$, where A is gain of the loop filter, into (1), it then yields

$$\frac{ABC}{S(1+GS)}\phi_o(s)+\phi_o(s)=\frac{ABC}{S(1+GS)}\phi_i(s)+\omega_r(s). \quad (2)$$

For convenience, let $D = ABC$ and then (2) is rewritten to be

$$GS^2\phi_o(s)+S\phi_o(s)+D\phi_o(s)=D\phi_i(s)+GS^2\omega_r(s)+S\omega_r(s). \quad (3)$$

By taking inverse Laplace transform to both sides of (3), it thus becomes

$$G\frac{d^2\phi_o(t)}{dt^2}+\frac{d\phi_o(t)}{dt}+D\phi_o(t)=D\phi_i(t)+G\frac{d^2\omega_r(t)}{dt^2}+\frac{d\omega_r(t)}{dt}. \quad (4)$$

Since $\omega_r(t)$ is not a function of time, the first and second derivative of this term (shown in the right-side of (4)) is zero. Therefore,

$$G\frac{d^2\phi_o(t)}{dt^2}+\frac{d\phi_o(t)}{dt}+D\phi_o(t)=D\phi_i(t). \quad (5)$$

From (5), the solution for $\phi_o(t)$ can be determined by solving this differential equation. In general, $\phi_o(t)$ is composed of two parts which are homogeneous solution (natural response) and particular solution (force response). For this work, only steady state response is of interest, the natural response is therefore ignored. To determine the force response, let $\phi_i(t)$ be assumed as follows

$$\phi_i(t)=\omega_i t+\theta_i \quad (6)$$

where ω_i is an input frequency. Then $\phi_o(t)$ has the following form,

$$\phi_o(t)=at+b \quad (7)$$

where *a*, *b* are constant.
By replacing $\phi_o(t)$ shown in (7) into (5), hence

$$\phi_o(t)=\omega_i t+\theta_i+\frac{\omega_i}{D}. \quad (8)$$

Therefore,

$$\varepsilon(t)=\phi_i(t)-\phi_o(t)=-\frac{\omega_i}{D} \quad (9)$$

where $\varepsilon(t)$ is phase difference between input and output vary with $-\omega_i/D=-\omega_i/ABC$. As can be seen, the phase difference $\varepsilon(t)$ can be adjusted by A, B and C.

III. PHASE SHIFTER BASED PLL

Recently, A.W. Hougton et al. [1] proposed a phase shifter based on PLL where its application is for antenna beam forming. The block diagram of this work can be depicted as Fig. 2.

In similar to the analyses of the PLL shown in Fig. 1, the error phase voltage of [1] is

$$\varepsilon(t)=\frac{\omega_i-C\omega_r}{ABC}+\frac{v_i}{A}. \quad (10)$$

It is seen in (10) that error phase voltage is proportion to ω_i, ω_r and v_i. However, this scheme cannot provide an accurate phase shift since the ω_r term is difficult to be determined.

To improve this limitation, an alternative technique to shift phase is proposed as given in Fig. 3. As can be seen, the gain controller which can be placed at one of these positions which are either between the loop filter and the VCO or between the summing circuit and the integrator. By selecting gain of the gain controller be inversely proportional to v_i, the phase shift of the proposed scheme is found to be proportional to voltage input as given by

$$\varepsilon(t)=\frac{-v_i\omega_i}{ABC}. \quad (11)$$

It is noted that, this gain controller can be either voltage amplifier or divider circuits.

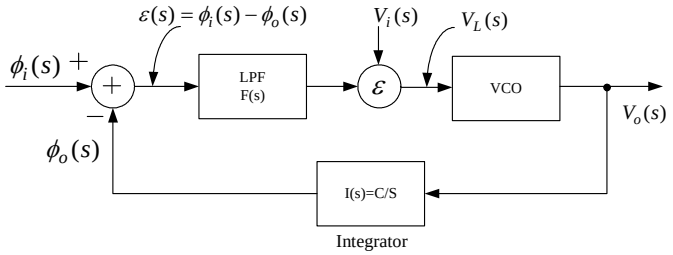

Figure 2. Block diagram of the phase shift scheme proposed by [1].

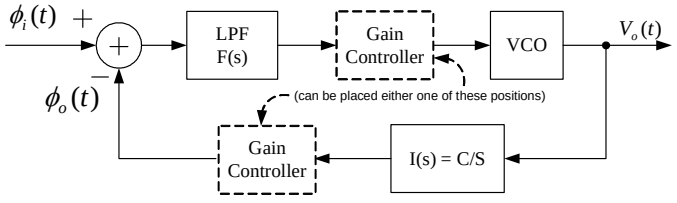

Figure 3. The proposed phase shift scheme.

IV. THE PROPOSED QPSK MODULATOR

Based on the proposed phase shift scheme described in previous section, the application for QPSK modulator is experimented. The proposed phase shifter based on PLL is employed to be the phase detector for $0°-180°$ of phase range. For the case of conventional QPSK signal, 4 phases required for modulating signals are selected to be $45°$, $135°$, $-45°$, and

$-135°$. The experimented circuit of the QPSK modulator is shown in Fig. 4. As shown in Fig. 4, the circuit depicted inside the dash line is the gain controller which can shift phase by adjusting its gain. In addition, the design of the modulation codes are given in Table I.

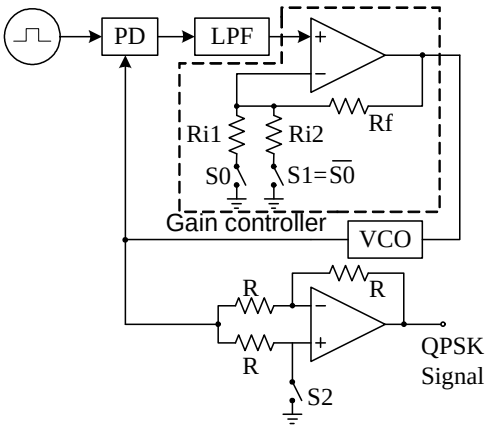

Figure 4. The proposed QPSK scheme.

TABLE I
MODULATION CODE DESIGN

θ	D1	D0	A	S0	S1($\overline{S0}$)	S2
45	0	0	A0	ON	OFF	OFF
135	0	1	A1	OFF	ON	OFF
-45	1	0	A0	ON	OFF	ON
-135	1	1	A1	OFF	ON	ON

As shown in Table I, the switch S0 is controlled by D0 (close when logic D0 = 1 and open when logic D0 = 0). Contrarily, the switch S1 is controlled by $\overline{D0}$, its operation is thus opposite to that of S0. For the switch S2, it is controlled by logic D1 where on and off operation (when logic D1 = 1 and 0, respectively) of this switch controls gain of the amplifier to be -1 or 1, respectively.

V. EXPERIMENTAL RESULTS

To confirm the proposed phase shifter by PLL as mentioned above, the experiment is setup by using a commercial PLL IC4046 as the circuit shown in Fig. 5. It is noted that R1= 50KΩ, R2=50KΩ, R3=1KΩ, Ri=1KΩ, C1=1nF, and C2=0.1μF are employed in this circuit. The results of phase shift for the 49KHz and 50KHz running frequency are illustrated in Fig. 6. It is obvious that the phase shifting characteristic of the proposed technique is independent on the running frequency. In addition, the phase shift is shown to be inversely proportional to gain of the gain controller.

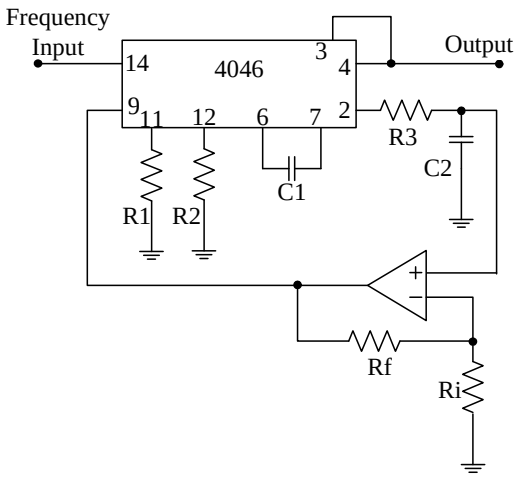

Figure 5. The experiment phase shifter using IC4046.

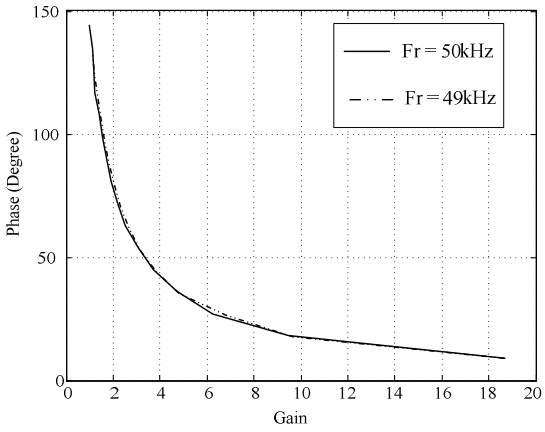

Figure 6. Phase shifting versus controller gain varying of the proposed scheme for running frequency is 49KHz and 50KHz.

For the experiment of the QPSK modulation, the proposed QPSK scheme shown in Fig. 4 is setup with IC XR-2206 for a VCO, X-OR for a phase detector and first order RC for a loop filter as shown in Fig. 7. The example of experimental result is shown in Fig. 8-10. The obtained QPSK signals therefore confirm the application of the proposed phase shift scheme in practical.

VI. CONCLUSIONS

A new scheme for phase shifting is proposed in this work. The concept of the proposed technique to control phase shifting is based on gain of a gain controller. The gain controller is chosen to have its gain be inversely proportional to the input voltage. In the conventional PLL circuit, this gain controller can be placed either between the loop filter and the VCO or between the integrator and the summing circuit. The phase output of the proposed scheme is found to be independent on the running frequency. The identical phase shifter circuits therefore can be achieved. For practical application, the proposed phase shifting scheme has been applied for the QPSK modulator where the experimental result confirms the contribution of the proposed technique.

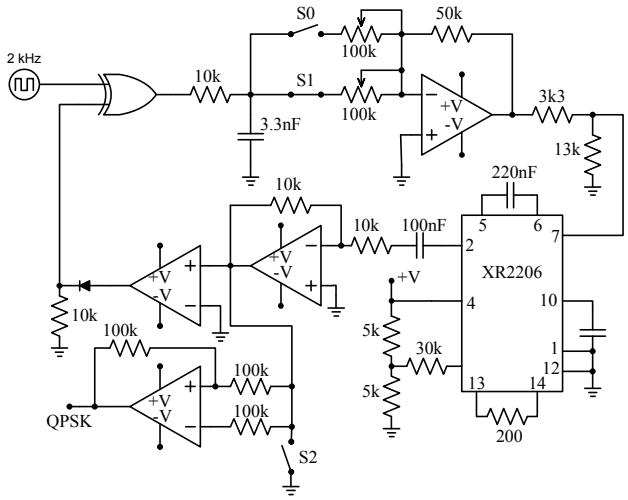

Figure 7. The experimental circuit for the proposed QPSK phase shifter.

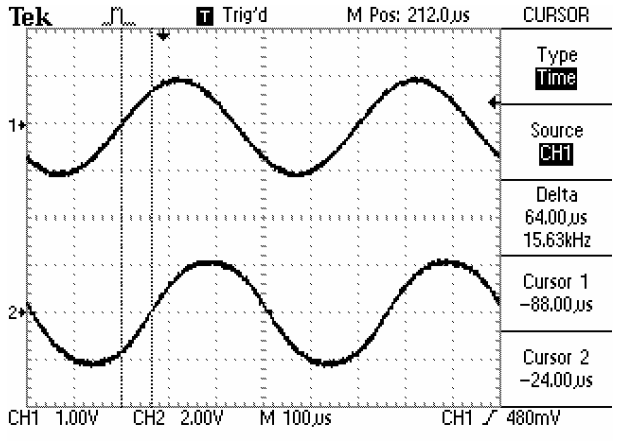

(a)

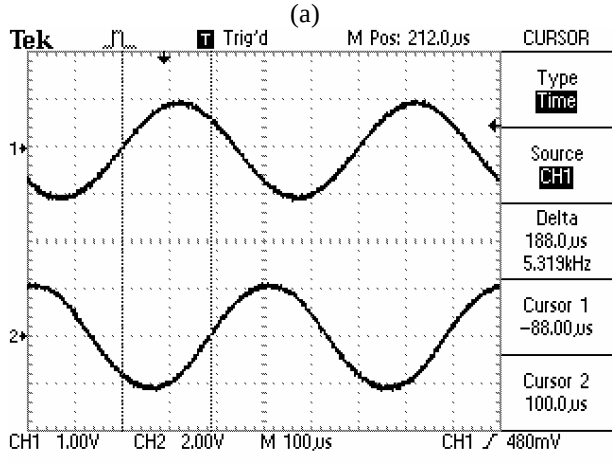

(b)

Figure 8. Result of the QPSK signals
where the upper trace is carrier signal and the lower trace is QPSK signal for phase shift (a) $45°$ and (b) $135°$, respectively.

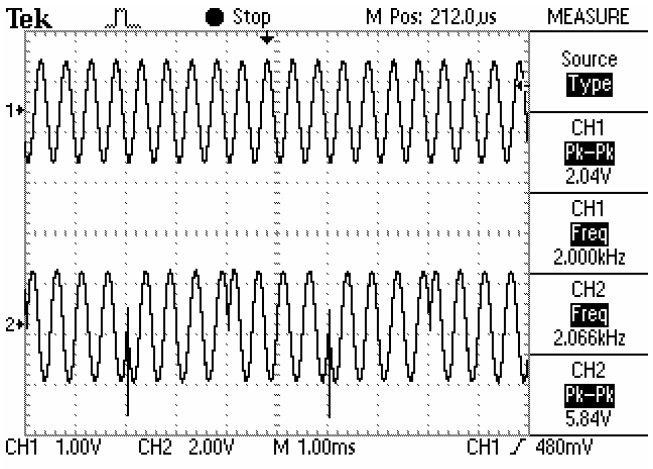

Figure 9. Demonstration of the signals of the proposed QPSK modulator where the upper trace is a carrier signal and the bottom trace is QPSK signal.

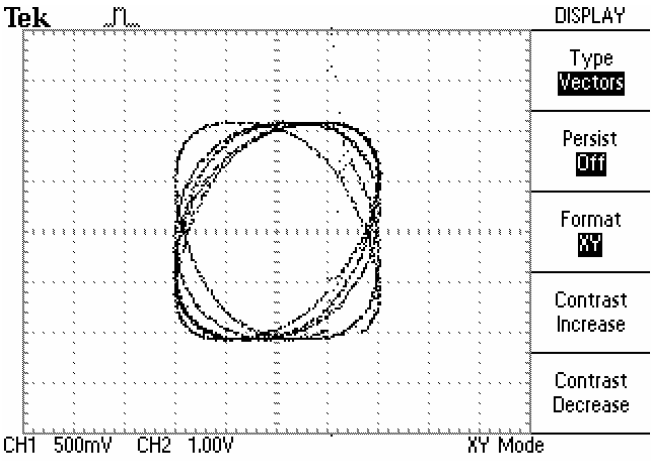

Figure 10. Illustration of the lissajous curve of the QPSK modulation signals.

ACKNOWLEDGMENT

The authors would like to thank Telecommunication Engineering Department MUT for encouragement.

REFERENCES

[1] A.W. Houghton, P. V. Brennan, "Phased array control using phase-locked-loop phase shifters," IEE Proceedings-H, vol. 139,No. 1, February 1992.
[2] H. Zarei, A. Ecker, P. Jinho , D.J. Allstot, "A full-range all-pass variable phase shifter for multiple antenna receivers," ISCAS 2005 , vol 3, pp. 2100-2103, May 2005.
[3] A. Ashrafi, R. Adhami, and P. Cox, "A simple wide-band frequency independent quadrature phase shifter," System theory,2002 proceeding of the thirty-forth southeastern symposium on System Theory , pp. 188 – 191, March 2002.
[4] R. Adler, "A study of locking phenomena in oscillators," Proc. IRE, vol.34, pp. 351-357, June 1946.
[5] WilliamF.Egan, "Phase-Lock Basics," Jhon wiley & Sons, Inc., 1988.

BER Performance of UWB Communications with Matched Filter and Correlation Receivers

Kultharee Teplee*, Pichaya Supanakoon*,†, Sathaporn Promwong*,† and Jun-ichi Takada‡
*Department of Information Engineering, Faculty of Engineering,
†Research Center for Communications and Information Technology (ReCCIT)
King Mongkut's Institute of Technology Ladkrabung, Bangkok 10520, THAILAND
E-mail: {s8061011,kspichay,kpsathap}@kmitl.ac.th
‡Graduate School of Science and Engineering, Tokyo Institute of Technology,
2-12-1-S6-4, O-okayama, Meguro-ku, 152-8550, Tokyo, Japan
E-mail: takada@ide.titech.ac.jp

***Abstract*— In this paper, the bit error rate (BER) performance of ultra wideband (UWB) communications with matched filter and correlation receivers are analyzed. The rectangular passband, modulated rectangular and modulated Gaussian waveforms, which is satisfied the UWB signal definition and Federal Communications Commission (FCC) indoor and outdoor limit spectral masks, are used as the transmitted UWB signal. The complex form of Friis' transmission formula is considered as the UWB free space channel. Therefore, the distortion effects caused from the channel are included. The BER performance of each waveform is shown and compared. The results are discussed in the conclusion.**

I. INTRODUCTION

An ultra wideband (UWB) radio technology has become an important topic for microwave communication because of its low cost and low power consumption potentials [1]-[3]. The UWB differs from the convectional narrow band radio frequency (RF) and spread spectrum (SS) technologies. The UWB uses an extremely wideband of RF spectrum to transmit the data with very short pulses and power spectral density (PSD) in the range of ultra wide frequency spectrum instead of using narrow carrier frequency in traditional RF technologies. The UWB is a unique and new usage of recently legalized frequency spectrum. The UWB technology is specified the frequencies ranging from 3.1 GHz to 10.6 GHz by Federal Communications Commission (FCC) [4]. The FCC defined the UWB signal as those, which have a fractional bandwidth equal or greater than 0.20, or occupied bandwidth equal or greater than 500 MHz.

The Friis' transmission formula [5] is widely used to calculate the free space path loss for narrow band communications. After that, the complex form of Friis' transmission formula is developed for UWB communications [6]-[8]. The matched filter and correlation receivers are used as the UWB receivers [9]-[12]. Although, the performances of UWB communications are analyzed [13], [14], there are no considerations about the FCC regulation of UWB signal and distortion of UWB signal caused by channel. After that, the rectangular waveform distorted by UWB free space channel is used to derive the theoretical BER performance [15]. However, there are no considerations about other causal waveforms.

In this paper, the BER performance of UWB communications with matched filter and correlation receivers are analyzed. The rectangular passband, modulated rectangular and modulated Gaussian waveforms, which is satisfied the UWB signal definition and FCC indoor and outdoor limit spectral masks [16], are used as the transmitted UWB signal. The complex form of Friis' transmission formula is considered as the UWB free space channel. The spectral density of received signal considering the distortion caused by free space channel is evaluated. At the receiver, the matched filter and correlation receivers with frequency transfer functions, which is satisfied the constant noise power condition between the input and output, are used. The BER performance of each waveform is shown and compared.

This paper is organized as follows. Sections 2 and 3, the UWB waveform models and analysis of BER performance are briefly discussed, respectively. Next the analysis results are illustrated in Sec. 4. Finally, the conclusions are discussed in Sec. 5.

II. UWB WAVEFORM MODELS

For UWB waveforms, the rectangular passband, modulated rectangular and modulated Gaussian waveforms are considered as the UWB transmitted waveform (v_{t}) in time domain and its spectral density (V_{t}) in frequency domain. These waveforms can satisfy the FCC definition of UWB signal and FCC spectral masks for indoor and outdoor limits. The parameters obtained from maximum bandwidth, amplitude and average power optimizations, which is proposed in [16], are used.

A. Rectangular Passband Waveform

The rectangular passband transmitted waveform in time domain and its spectral density function are given by

$$v_{\mathrm{t}}(t) = \frac{A}{f_{\mathrm{b}}}[f_{\mathrm{H}}\mathrm{sinc}(2f_{\mathrm{H}}t) - f_{\mathrm{L}}\mathrm{sinc}(2f_{\mathrm{L}}t)], \quad (1)$$

$$V_{\mathrm{t}}(f) = \begin{cases} \frac{A}{2f_{\mathrm{b}}} & ||f| - f_{\mathrm{c}}| \le \frac{f_{\mathrm{b}}}{2} \\ 0 & ||f| - f_{\mathrm{c}}| > \frac{f_{\mathrm{b}}}{2} \end{cases}, \quad (2)$$

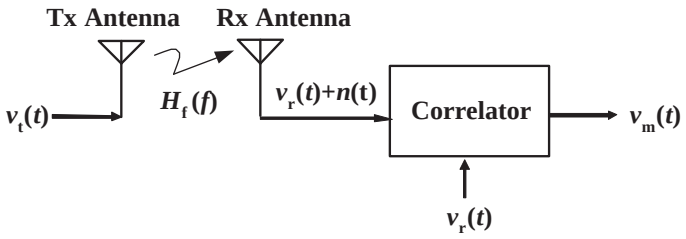

Fig. 1. Block diagram of matched filter receiver system.

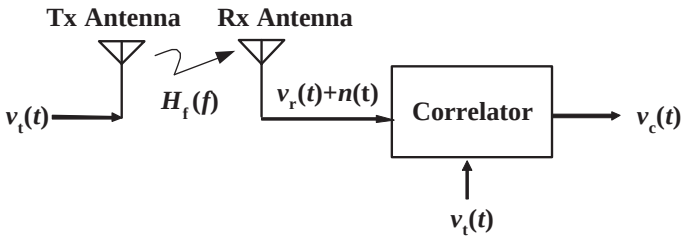

Fig. 2. Block diagram of correlation receiver system.

where A is the maximum amplitude, $f_{\rm b}$ is the occupied bandwidth, $f_{\rm c}$ is the center frequency, $f_{\rm L} = f_{\rm c} - f_{\rm b}/2$ and $f_{\rm H} = f_{\rm c} + f_{\rm b}/2$ are the minimum and maximum frequencies.

B. Modulated Rectangular Waveform

The modulated rectangular transmitted waveform in time domain and its spectral density function are given by

$$v_{\rm t}(t) = \begin{cases} A\sin(2\pi f_{\rm c}t) & |t| \le \frac{t_{\rm b}}{2} \\ 0 & |t| > \frac{t_{\rm b}}{2} \end{cases}, \quad (3)$$

$$V_{\rm t}(f) = \frac{At_{\rm b}}{j2} \begin{Bmatrix} \mathrm{sinc}[t_{\rm b}(f-f_{\rm c})] \\ -\mathrm{sinc}[t_{\rm b}(f+f_{\rm c})] \end{Bmatrix}, \quad (4)$$

where A is the maximum amplitude, $f_{\rm c}$ is the carrier frequency and $t_{\rm b}$ is the pulse width of waveform.

C. Modulated Gaussian Waveform

The modulated Gaussian transmitted waveform in time domain and its spectral density function are given by

$$v_{\rm t}(t) = Ae^{-(t/d)^2}\sin(2\pi f_{\rm c}t), \quad (5)$$

$$V_{\rm t}(f) = \frac{Ad\sqrt{\pi}}{j2} \begin{bmatrix} e^{-\pi^2 d^2 (f-f_{\rm c})^2} \\ -e^{-\pi^2 d^2 (f+f_{\rm c})^2} \end{bmatrix}, \quad (6)$$

where A is the maximum amplitude of envelope waveform, $f_{\rm c}$ is the carrier frequency and d is the $1/e$ characteristic decay time.

III. Analysis of BER Performance

In this section, the analysis of BER performance is theoretically discussed. The UWB waveform models discussed in Sec. 2 are used as the UWB transmitted waveforms. For UWB free space channel, the complex form of Friis' transmission formula is used [6]-[8]. The transmitting (Tx) and receiving (Rx) antennas are considered to have one constant gains. The frequency transfer function of free space channel $H_{\rm f}$ can be written as

$$H_{\rm f}(f,d) = \frac{c}{4\pi|f|d}e^{-j2\pi fd/c}, \quad (7)$$

where d is the transmitter-receiver (T-R) separation distance and c is the velocity of light. This equation is satisfied for both positive and negative frequencies as it satisfies the causality.

The spectral density of UWB received signal $V_{\rm r}$ is calculated by using multiplication between $H_{\rm f}$ and $V_{\rm t}$, which can be written as

$$V_{\rm r}(f,d) = H_{\rm f}(f,d)\cdot V_{\rm t}(f). \quad (8)$$

This spectral density of UWB received signal includes the distortion effect caused by UWB free space channel.

The matched filter and correlation receivers with frequency transfer functions satisfied constant noise power condition between input and output are considered. For matched filter receiver or optimum correlation receiver, the spectral density of template signal is the complex conjugate of $V_{\rm r}$. The block diagram of matched filter receiver system is shown in Fig. 1. For correlation or transmitted template signal receiver, the spectral density of template signal is the complex conjugate of $V_{\rm t}$. Figure 2 shows the block diagram of correlation receiver system. The receiver gains of both receivers are satisfied the constant noise power condition. Therefore, the frequency transfer functions of matched filter and correlation receivers, ($H_{\rm m}$ and $H_{\rm c}$), can be written as

$$H_{\rm m}(f,d) = \frac{\sqrt{2f_{\rm b}}}{\sqrt{\int_{-\infty}^{\infty}|V_{\rm r}(f,d)|^2df}}V_{\rm r}^*(f,d), \quad (9)$$

$$H_{\rm c}(f,d) = \frac{\sqrt{2f_{\rm b}}}{\sqrt{\int_{-\infty}^{\infty}|V_{\rm t}(f,d)|^2df}}V_{\rm t}^*(f,d), \quad (10)$$

where * is the complex conjugate operator.

The spectral densities of output signal from matched filter and correlation receivers, ($V_{\rm m}$ and $V_{\rm c}$), can be written as

$$V_{\rm m}(f,d) = H_{\rm m}(f,d)\cdot V_{\rm r}(f,d), \quad (11)$$

$$V_{\rm c}(f,d) = H_{\rm c}(f,d)\cdot V_{\rm r}(f,d). \quad (12)$$

The signal-to-noise ratio (SNR) gain of these receivers are defined as the ratio between average power of received signal at receiver input and that at receiver output. The SNR gains of matched filter and correlation receivers, $G_{\rm m}$ and $G_{\rm c}$ can be respectively written as

$$G_{\rm m} = \frac{\int_{-\infty}^{\infty}|V_{\rm m}(f,d)|^2df}{\int_{-\infty}^{\infty}|V_{\rm r}(f,d)|^2df}, \quad (13)$$

$$G_{\rm c} = \frac{\int_{-\infty}^{\infty}|V_{\rm c}(f,d)|^2df}{\int_{-\infty}^{\infty}|V_{\rm r}(f,d)|^2df}. \quad (14)$$

The efficiency of receiver is considered by using correlation coefficient between received and template signals. The correlation coefficients of matched filter and correlation receivers, $C_{\rm m}$

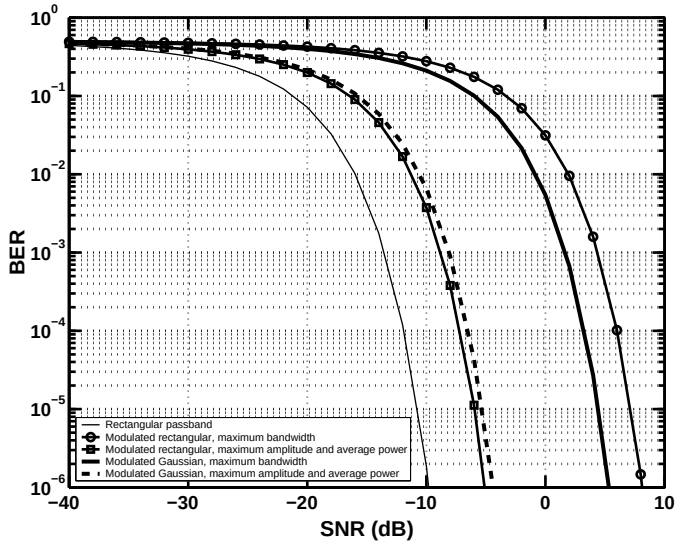

Fig. 3. BER performance of matched filter receiver for UWB waveforms satisfied FCC indoor limit spectral mask.

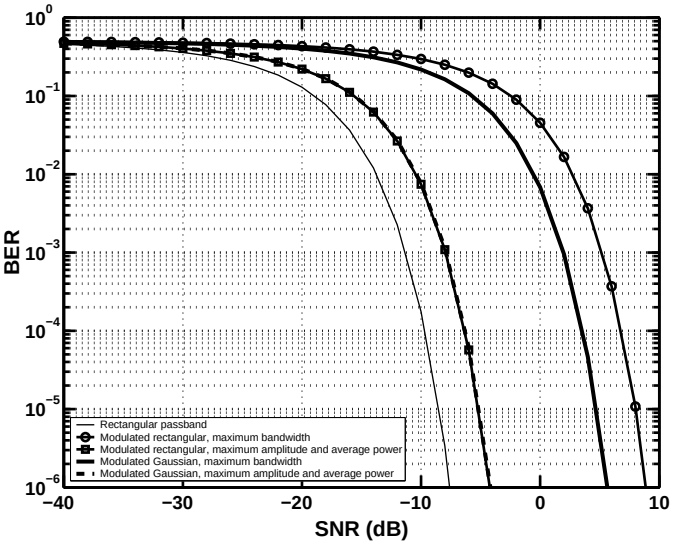

Fig. 4. BER performance of correlation receiver for UWB waveforms satisfied FCC indoor limit spectral mask.

and $C_{\rm c}$ can be respectively written as

$$C_{\rm m} = \frac{\max|\int_{-\infty}^{\infty} V_{\rm m}(f,d)e^{j2\pi ft}df|}{\sqrt{\int_{-\infty}^{\infty}|V_{\rm r}(f,d)|^2df\cdot\int_{-\infty}^{\infty}|H_{\rm m}(f,d)|^2df}}, \quad (15)$$

$$C_{\rm c} = \frac{\max|\int_{-\infty}^{\infty} V_{\rm c}(f,d)e^{j2\pi ft}df|}{\sqrt{\int_{-\infty}^{\infty}|V_{\rm r}(f,d)|^2df\cdot\int_{-\infty}^{\infty}|H_{\rm c}(f,d)|^2df}}, \quad (16)$$

The UWB modulation schemes can be classified in to the antipodal modulation scheme such as binary pulse amplitude modulation (BPAM) and orthogonal modulation scheme such as on-off keying (OOK) and pulse position modulation (PPM) with modulation index of $\delta = 1$ [17]. In this paper, only BER performance of antipodal modulation scheme is considered. For orthogonal modulation scheme, the BER performance can be evaluated in the same way as shown in [15], [18]. The BER performance of matched filter and correlation receivers, $B_{\rm m}$ and $B_{\rm c}$, in additive white Gaussian noise (AWGN) for antipodal modulation scheme can be respectively written as

$$B_{\rm m} = Q\left(\sqrt{\frac{2C_{\rm m}G_{\rm m}f_{\rm b}S}{B_{\rm r}N}}\right), \quad (17)$$

$$B_{\rm c} = Q\left(\sqrt{\frac{2C_{\rm c}G_{\rm c}f_{\rm b}S}{B_{\rm r}N}}\right), \quad (18)$$

where $B_{\rm r}$ is the bit rate, S/N is the SNR at input of receiver and

$$Q(x) = \frac{1}{\sqrt{2\pi}}\int_x^{\infty} e^{-t^2/2}dt, \quad x \geq 0.$$

The SNR is normalized by average power of rectangular passband waveform, which is the theoretical maximum average power of UWB signal, for considering FCC spectral masks. Moreover, the distortion effect caused from UWB channel, occupied bandwidth and bit rate are also included to analyze the BER performance.

IV. Analysis Results

In this section, the analysis results of BER performance are shown. The BER performance of transmitted waveforms, which are the rectangular passband, modulated rectangular and modulated Gaussian waveforms, are analyzed. The T-R separation distance is set to be 10 m, while the bit rate is set to be 110 Mbps. These parameters are based on the IEEE 802.15.3a [19]. The parameters of each waveform, which obtained from the maximum bandwidth, amplitude and average power optimizations satisfied FCC spectral masks for indoor and outdoor limits [15], are used.

Figures 3 and 4 show the BER performances of matched filter and correlation receivers for UWB waveforms satisfied FCC indoor limit spectral mask, respectively. The BER performances of rectangular passband waveforms are lowest for both matched filter and correlation receivers. The BER performances of maximum amplitude and average power optimizations are less than that of maximum bandwidth optimizations. That is because the maximum bandwidth optimizations are much less average power and slightly more bandwidth compared with maximum amplitude and average power optimizations [16]. For comparison between modulated rectangular and Gaussian waveforms, the BER performance of modulated rectangular and Gaussian waveforms with maximum amplitude and average power optimizations are almost the same and are better than the others.

The BER performances of matched filter and correlation receivers for UWB waveforms satisfied FCC outdoor limit spectral mask are shown in Figs. 5 and 6, respectively. The BER performances of rectangular passband waveforms are also lowest for both matched filter and correlation receivers. For

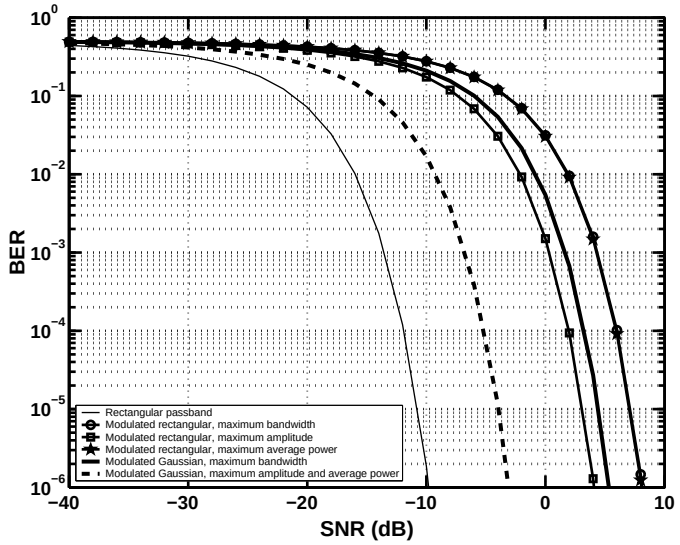

Fig. 5. BER performance of matched filter receiver for UWB waveforms satisfied FCC outdoor limit spectral mask.

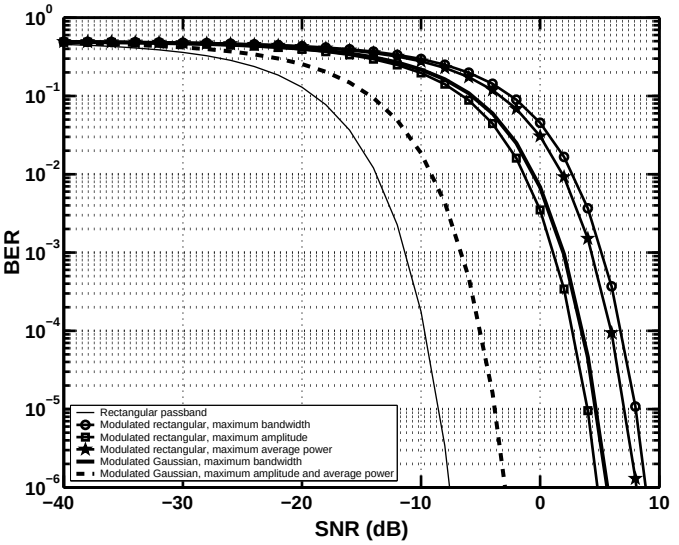

Fig. 6. BER performance of correlation receiver for UWB waveforms satisfied FCC outdoor limit spectral mask.

comparison between modulated rectangular and Gaussian waveforms, the BER performance of modulated Gaussian waveform with maximum amplitude and average power optimizations are clearly better than the others.

V. Conclusion

In this paper, the BER performance of UWB communications with matched filter and correlation receivers are analyzed. The rectangular passband, modulated rectangular and modulated Gaussian waveforms, which is satisfied the UWB signal definition and FCC indoor and outdoor limit spectral masks, are used as the transmitted UWB signal. From the results, the BER performance of rectangular passband waveform with matched filter receiver is the ideal theoretical bound, which is the minimum BER performance case. The modulated rectangular and Gaussian waveforms with maximum amplitude and average power optimizations are appropriate for FCC indoor limit spectral mask, while the modulated Gaussian waveform with maximum amplitude and average power optimizations is appropriate for FCC outdoor limit spectral mask.

References

[1] K. Siwiak, "Ultra-Wide Band Radio: Introducing a New Technology," *2001 Spring IEEE Vehicular Technology Conference (VTC)*, vol. 2, pp. 1088-1093, May 2001.

[2] K. Siwiak, "Ultra-Wide Band Radio: The emergence of an Important RF Technology," *2001 Spring IEEE Vehicular Technology Conference (VTC)*, vol. 2, pp. 1169-1172, May 2001.

[3] K. Siwiak, "Impact of ultra wide band transmissions on a generic receiver," *2001 Spring IEEE Vehicular Technology Conference (VTC)*, vol. 2, pp. 1181-1183, May 2001.

[4] Federal Communications Commission, "Revision of Part 15 of the Commission's Rules Regarding UWB Transmission Systems," First Report, FCC 02-48, Apr. 2002.

[5] H. T. Friis, "A Note on a Simple Transmission Formula," *Proc. IRE*, Vol 34, no 5, pp. 254-256, May 1946.

[6] J. Takada, S. Promwong and W. Hachitani, "Extension of Friis' Transmission Formula for UWB Systems," *Technical Report of IEICE*, WBS2003-8/MW2003-20, May 2003.

[7] S. Promwong, W. Hachitani and J. Takada, "Experimental Evaloation Scheme of UWB Antenna Performance," *Technical Meeting on Instrument and Measurement*, IEE Japan, IM-03-35, June 2003.

[8] S. Promwong, W. Hachitani, J. Takada, P. Supanakoon and P. Tangtisanon, "Experimental Study of Ultra-Wideband Transmission Based on Friis' Transmission Formula," *The Third International Symposium on Communications and Information Technology (ISCIT) 2003*, vol. 1, pp. 467-470, Sept. 2003.

[9] X. Xu and R. M. Narayanan, "Impact of Different Correlation Receiving Techniques on The Imaging Performance of UWB Random Noise Radar," *2003 IEEE International Geoscience and Remote Sensing Symposium (IGARSS)*, vol. 7, pp. 4525-4527, July 2003.

[10] S. Promwong, J. Takada, P. Supanakoon and P. Tangtisanon, "Path Loss and Matched Filter Gain for UWB System," *2004 International Symposium on Antenna and Propagation (ISAP)*, pp. 97-100, Aug. 2004.

[11] S. Promwong, J. Takada, P. Supanakoon and P. Tangtisanon, "Path Loss and Matched Filter Gain of Free Space and Ground Reflection Channels for UWB Radio Systems," *IEEE TENCON 2004 on Analog and Digital Techniques in Electrical Engineering*, pp. 125-128, Nov. 2004.

[12] J. Wu, Y. Zhao and H. Xiang, "Performance of Ultra-Wideband Correlation Receiver Using Rectangular Template Signal in AWGN Channel," *2005 International Conference on Wireless Communications, Networking and Mobile Computing*, vol. 1, pp. 348-351, Sept. 2005.

[13] Z. Bai, W. Zhang, S. Xu, W. Liu and K. Kwak, "On The Performance of Multiple Access DS-BPAM UWB System in Data and Impage Transmission," *IEEE International Symposium on Communications and Information Technology (ISCIT)*, vol. 2, pp. 851-854, Oct. 2005.

[14] J. Cha, K. Kwak, C. Lee, J. Jeong and I. Lee, "Chaotic-OOK UWB Modem Using New Unipolar ZCD Codes for Wireless Pan," *International Conference on Consumer Electronics (ICCE)*, pp. 197-198, Jan. 2006.

[15] P. Supanakoon, K. Teplee, S. Promwong, S. Keawmechai and J. Takada, "Theoretical SNR Gain and BER Performances of UWB Communications with Matched Filter and Correlation Receivers," *The International Technical Conference on Circuits/Systems, Computers and Communications (ITC-CSCC 2006)*, no. 3, pp. 269-272, July 2006.

[16] P. Supanakoon, K. Wansiang, S. Promwong and J. Takada, "Simple Waveform for UWB Communication," *The 2005 Electrical Engineering/Electronics, Computer, Telecommunication, and Information Technology International Conference (ECTI-CON 2005)*, pp. 626-629, May 2005.

[17] I. Oppermann, M. Hamalainen and J. Iinatti, *UWB Theory and Applications*, John Wiley & Sons, 2004.

[18] J. G. Proakis, *Digital Communications*, 4th edition, McGraw-Hill, 2001.

[19] J. Foester, "Channel Modeling Sub-committee Report Final," *IEEE P802.15-02/368r5-SG3a*, Nov. 2002.

Modeling of Indoor UWB Channel by Using Finite Difference Time Domain Method

Phannipha Thaiwattanaporn*, Pichaya Supanakoon*,†, Sathaporn Promwong*,† and Jun-ichi Takada‡
*Department of Information Engineering, Faculty of Engineering,
†Research Center for Communications and Information Technology (ReCCIT)
King Mongkut's Institute of Technology Ladkrabung, Bangkok 10520, THAILAND
E-mail: {s8061008,kspichay,kpsathap}@kmitl.ac.th
‡Graduate School of Science and Engineering, Tokyo Institute of Technology,
2-12-1-S6-4, O-okayama, Meguro-ku, 152-8550, Tokyo, Japan
E-mail: takada@ide.titech.ac.jp

***Abstract*— In this paper, a two-dimensional (2-D) transverse magnetic (TM) mode finite difference time domain (FDTD) method is used to simulate the indoor radio wave propagation and model the indoor ultra wideband (UWB) channel. The modulated Gaussian pulse, which is satisfied the UWB signal definition and Federal Communications Commission (FCC) indoor limit spectral mask, is used as the UWB excitation signal. The free space path loss obtained by using FDTD method is shown and verified by comparing with that obtained by using Friis' transmission formula. After that, the path loss in example indoor environment is evaluated. The line-of-sight (LOS) and obstructed (OBS) environments are considered. Furthermore, these obtained data are modeled the path loss by using regression model. The probability density function (PDF) and cumulative distribution function (CDF) of fading are evaluated. The results are discussed in the conclusion.**

I. INTRODUCTION

Recently, ultra wideband (UWB) radio technology has become an important topic for microwave communication because of its low cost and low power consumption potentials [1]. The UWB technology is different from other radio frequency (RF) technologies. Instead of using narrow carrier frequency, the UWB transmits pulses with power spectral density (PSD) in the range of ultra wide frequency spectrum. The Federal Communications Commission (FCC) [2] specified that UWB signal has a frequency spectrum ranging from 3.1 GHz to 10.6 GHz. The FCC defined the UWB signal as those which have a fractional bandwidth equal to or greater than 0.20, or occupied bandwidth equal to or greater than 500 MHz.

The power density of UWB signal is considered to be the noise for other communication systems because its power spectrum is below the FCC part 15 noise limit. The UWB receiver collects the power of received signal to rebuild the pulse. Therefore, the UWB radio technology can coexist with other RF technologies without interference.

The indoor radio communications have become more and more interesting in recent time, which several researchers report the wideband impulse response measurement [3]. Such data is useful to predict the maximum allowable data rates in order to the intersymbol interference and in the exploration of such techniques as diversity and equalization. The effective design, assessment and installation of radio communication in indoor environment require the accurate characterization of radio wave propagation. Therefore, it is also important to consider the propagation behavior in indoor environment.

A ray tracing technique has been demonstrated to be promising for indoor radio propagation [4]. A finite difference time domain (FDTD) method [5], [6] is the alternative method for modeling channel. Although the FDTD method requires more computer resources compared with the ray tracing technique, the simulation of indoor environment requires the computer resources less than that of outdoor environment. Furthermore, the FDTD method can be calculated the scattered fields more accurately compared with ray tracing technique for complex lossy structures with finite dimensions encountered in indoor environment. Therefore, the FDTD method is usually used to model the narrow band channel [7], [8]. For UWB communications, there are many researches that used the FDTD method to model the channel [9], [10]. However, there is no consideration about path loss model with FCC regulation of UWB signal.

In this paper, the two-dimensional (2-D) transverse magnetic (TM) mode FDTD method, which is satisfied the numerical stability condition [11] and with perfectly matched layer absorbing boundary condition (PML ABC) [12], is used to simulate the indoor radio wave propagation and model the indoor UWB channel. The modulated Gaussian pulse, which is satisfied the UWB signal definition and FCC indoor limit spectral mask [13], is used as the UWB excitation signal. The free space path loss obtained by using FDTD method is shown and verified by comparing with that obtained by using Friis' transmission formula [14]. which has the high accuracy for UWB channel [15]. After that, the path loss in example indoor environment is evaluated. The line-of-sight (LOS) and obstructed (OBS) environments are considered. Furthermore, these obtained data are modeled the path loss by using regression model. The probability density function (PDF) and cumulative distribution function (CDF) of fading are evaluated.

II. FDTD METHODS

The 2-D TM mode finite difference equations are directly derived from Maxwell's curl equations in time domain. To obtain discrete approximation of continuous partial differential equations, the centered difference approximation is used on both time and space first-order partial difference. The entire computation domain is the collection of all the unit cells. The dimensions of unit cell along x and y directions are Δx and Δy, respectively. The node with subscript indices i and j corresponds to the node number in x and y directions. The time step is indicated with the superscript index n. The time interval of each time step is Δt. After simple arrangement, the 2-D TM mode finite difference equations are described as [5],[6]

$$H_x|_{i,j}^{n+\frac{1}{2}} = H_x|_{i,j}^{n-1/2} + \left(\frac{\Delta t}{\mu_{i,j}}\right)\left(\frac{E_z|_{i,j-\frac{1}{2}}^{n} - E_z|_{i,j+\frac{1}{2}}^{n}}{\Delta y}\right), \quad (1)$$

$$H_y|_{i,j}^{n+\frac{1}{2}} = H_y|_{i,j}^{n-1/2} + \left(\frac{\Delta t}{\mu_{i,j}}\right)\left(\frac{E_z|_{i+\frac{1}{2},j}^{n} - E_z|_{i-\frac{1}{2},j}^{n}}{\Delta x}\right), \quad (2)$$

$$E_z|_{i,j}^{n+1} = C_{\mathrm{a}}|_{i,j} E_z|_{i,j}^{n-1} + C_{\mathrm{b}}|_{i,j}\left(\frac{H_y|_{i+\frac{1}{2},j}^{n+\frac{1}{2}} - H_y|_{i-\frac{1}{2},j}^{n+\frac{1}{2}}}{\Delta x} + \frac{H_x|_{i,j-\frac{1}{2}}^{n+\frac{1}{2}} - H_x|_{i,j+\frac{1}{2}}^{n+\frac{1}{2}}}{\Delta y}\right), \quad (3)$$

with the electric field updating coefficients at node (i, j) are given by

$$C_{\mathrm{a}}|_{i,j} = \left(1 - \frac{\sigma_{i,j}\Delta t}{2\varepsilon_{i,j}}\right) \Big/ \left(1 + \frac{\sigma_{i,j}\Delta t}{2\varepsilon_{i,j}}\right), \quad (4)$$

$$C_{\mathrm{b}}|_{i,j} = \left(\frac{\Delta t}{\varepsilon_{i,j}}\right) \Big/ \left(1 + \frac{\sigma_{i,j}\Delta t}{2\varepsilon_{i,j}}\right), \quad (5)$$

where H is the magnetic field, E is the electric field, μ is the magnetic permeability, ε is the electric permittivity and σ is the electric conductivity. The maximum time step is limited by stability restriction of finite difference equation [11].

The modulated Gaussian pulse, which is satisfied the UWB signal definition and FCC indoor limit spectral mask, is used as the UWB excitation signal V_{S}. The expression of this pulse is [7]

$$V_{\mathrm{S}}|^{n} = Ae^{-[(n-n_0)\Delta t/d]^2}\sin[2\pi f_{\mathrm{c}}(n-n_0)\Delta t], \quad (6)$$

where A is the maximum amplitude of envelope signal, f_{c} is the carrier frequency, d is the $1/e$ characteristic decay time and n_0 is the delayed time step.

The tangential field components on four mesh walls must be specified in such a way that outgoing waves are not reflected. The FDTD simulation in this paper uses the PML ABC [12].

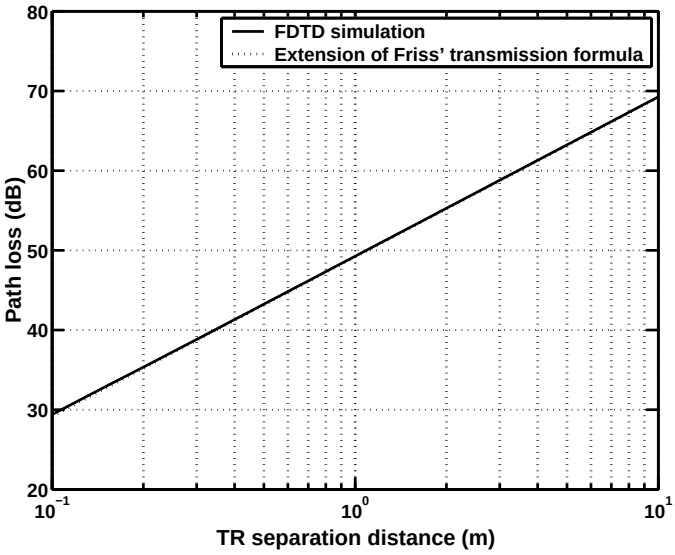

Fig. 1. Free space path loss obtained from FDTD simulation compared with that obtained from Friis' transmission formula.

TABLE I
ELECTROMAGNETIC PROPERTIES OF DIFFERENT MATERIALS.

Material	Electromagnetic property
Gypsum board	$\varepsilon_{\mathrm{r}} = 2.80$, $\sigma = 0.15$
Plywood door	$\varepsilon_{\mathrm{r}} = 2.88$, $\sigma = 0.21$
Brick wall	$\varepsilon_{\mathrm{r}} = 3.30$, $\sigma = 0.11$
Dry concrete wall	$\varepsilon_{\mathrm{r}} = 5.00$, $\sigma = 0.70$

III. UWB CHANNEL MODEL

In this section, the path loss obtained from FDTD method is modeled. First, the 2-D TM FDTD simulation is done in the free space environment. The cell sizes in x and y directions are $\Delta x = \Delta y = 0.005$ m. The PML ABC with 16 layers is used to reduce the reflection error at edges. The time interval of each time step is $\Delta t = 11.79$ ps, which is satisfied the numerical stability condition. For UWB excitation signal, the parameters of modulated Gaussian signal, which is satisfied the UWB signal definition and indoor limit spectral mask, are $f_{\mathrm{c}} = 7.34$ GHz, $d = 0.11$ ns and $A = 0.27$ V. These signal parameters are the maximum amplitude and average power optimizations with bit rate of 100 Mbps [13].

Figure 1 shows the free space path loss obtained from FDTD simulation compared with that obtained from Friis' transmission formula along transmitter-receiver (TR) separation distance 0.1 to 10 m. From the figure, the path loss obtained from FDTD simulation coincides very well with that obtained from Friis' transmission formula. There is root mean square (RMS) error only 0.13 dB. This verifies that FDTD simulation can be modeled the path loss of UWB channel.

Subsequently, the FDTD simulation is done in the room structure with excitation signal located at point S. The dimension of this room is shown in Fig. 2. The room consists of gypsum board, plywood door, metallic cabinet, brick and dry concrete walls. The metallic cabinet is assumed to be the perfect

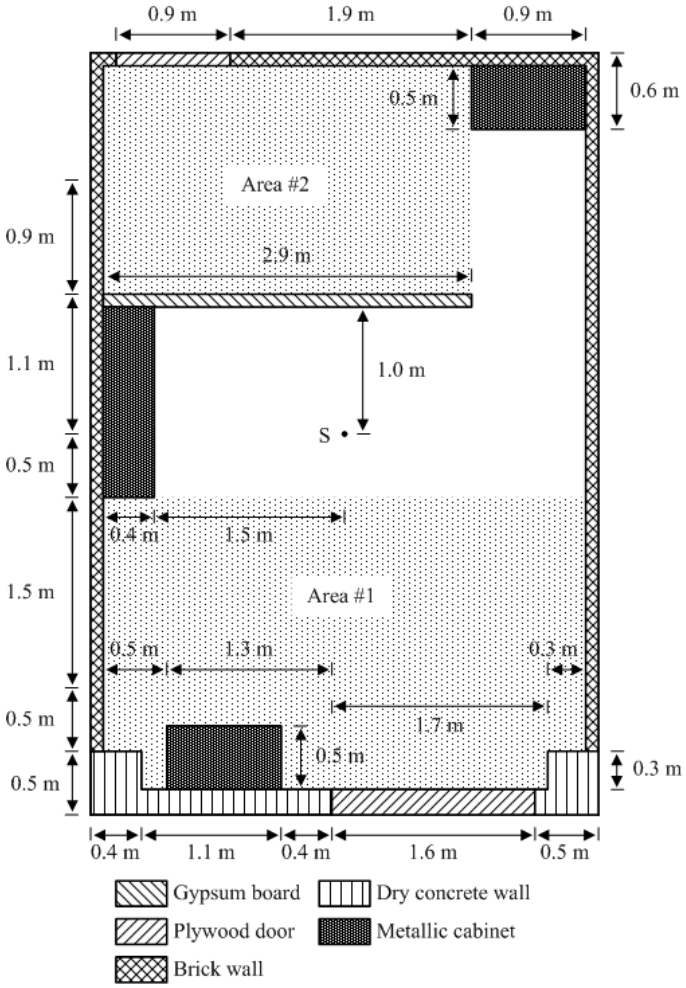

Fig. 2. Layout of room environment.

conductor. The electromagnetic properties of other materials are listed in Table 1 [4]. The two areas, Area #1 and Area #2, as shown in Fig. 2 are considered for LOS and OBS environments, respectively. The UWB path loss of both considered areas in dB at note (i, j) can be evaluated by using

$$PL|_{i,j} = 10 \log \left[\frac{\sum_n (V_{\mathrm{S}}|^n)^2}{\sum_n \left(V_{\mathrm{R}}|^n_{i,j}\right)^2} \right], \tag{7}$$

where V_{R} is the received signal.

The TR separation distance d at node (i, j) is computed by using

$$d = \sqrt{[(i - i_{\mathrm{S}})\Delta x]^2 + [(j - j_{\mathrm{S}})\Delta y]^2}, \tag{8}$$

where $(i_{\mathrm{S}}, j_{\mathrm{S}})$ is the node of UWB excitation signal.

For modeling path loss, the linear regression model based on log-distance path loss model [16] is used. The model can be realized by curve fitting on a scatter plot of obtained path loss and then derived the path loss exponent n from

$$PL(d) = \overline{PL}(1) + 10n \log(d) + X_\sigma, \tag{9}$$

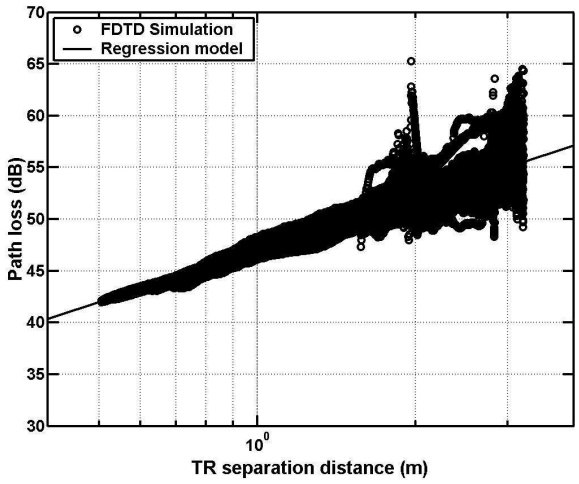

Fig. 3. Scatter plot of path loss obtained from FDTD simulation and regression model in Area #1.

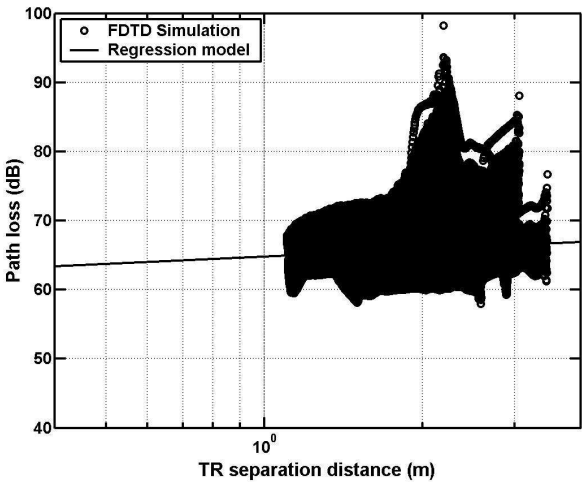

Fig. 4. Scatter plot of the path loss obtained from FDTD simulation and regression model in Area #2.

where $PL(d)$ is the path loss in dB at TR separation distance of d (m), $\overline{PL}(1)$ is the average large-scale path loss at TR separation distance is 1 m, X_σ is the fading parameter with standard deviation of σ in dB. When plotted on a log-distance graph, the path loss model is a straight line and n can be determined from the slope of $10n$ dB per decade. The value n and σ depend on the specific propagation environment. The main objective of this simulation is to determine $\overline{PL}(1)$, n and X_σ of UWB signal propagation in Area #1 and Area #2.

Figure 3 shows the scatter plot of path loss obtained from FDTD simulation and regression model in Area #1, which is the LOS environment. The 323,081 data are used to model the path loss. For this area, the model parameters are $\overline{PL}(1) = 47.00$ dB and $n = 1.68$. The scatter plot of path loss obtained from FDTD simulation and regression model in Area #2, which is the OBS environment, is shown in Fig. 4. The 207,861 data are

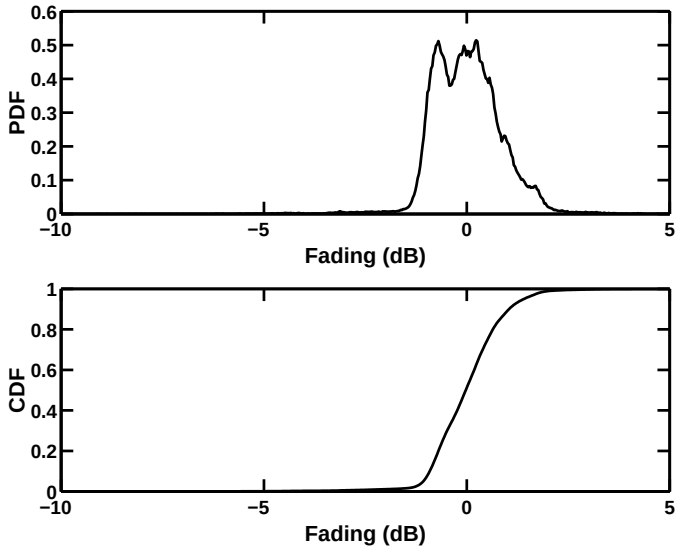

Fig. 5. PDF and CDF of fading in Area #1.

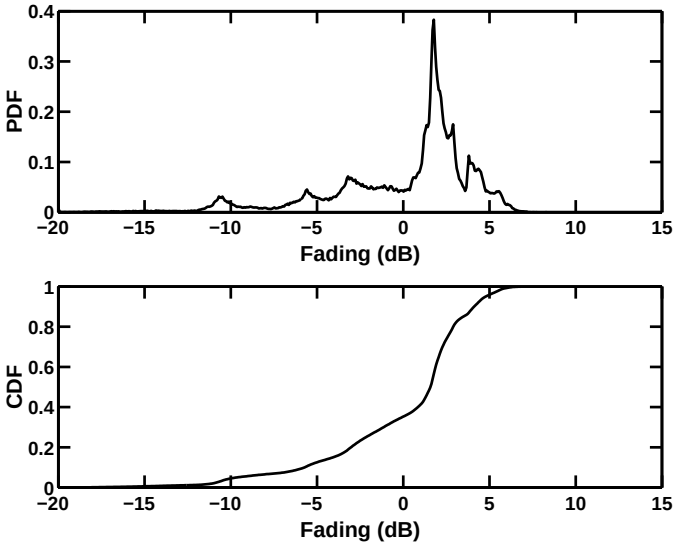

Fig. 6. PDF and CDF of fading in Area #2.

used to model the path loss. For this area, the model parameters are $\overline{PL}(1) = 64.79$ dB and $n = 0.35$.

For considering the fading parameter X_σ, the statistic model is used. The PDF and CDF of fading are evaluated. Figure 5 shows the PDF and CDF of fading in Area #1. The statistic parameters of this area are the standard deviation of $\sigma = 0.86$ dB and zero mean. The PDF and CDF of fading in Area #2 are shown in Fig. 6. The statistic parameters of this area are the standard deviation of $\sigma = 4.21$ dB and zero mean. We can see that the fading in Area #2, which is OBS environment, is more fluctuate than that in Area #1, which is LOS environment.

IV. Conclusion

In this paper, the 2-D TM mode FDTD method is used to simulate the indoor radio wave propagation and model the path loss of UWB channel. The free space path loss obtained by FDTD method is verified with that obtain by Friis' transmission formula. By using FDTD method, the numerous data can be obtained for modeling indoor UWB channel. It is flexible to model the different environment according to desire accuracy by setting cell size. This simulation can be applied to arbitrary bandwidths or types of UWB signals. In order to develop a reliable UWB product for WPAN applications, a good understand of UWB channel model of specific environment is essential for link budget. Therefore, FDTD method provides a high flexible and convenient tool for modeling UWB channel.

References

[1] K. Siwiak, "Ultra-Wide Band Radio: Introducing a New Technology," *2001 Spring IEEE Vehicular Technology Conference (VTC)*, vol. 2, pp. 1088-1093, May 2001.

[2] Federal Communications Commission, "Revision of Part 15 of the Commission's Rules Regarding UWB Transmission Systems," First Report, FCC 02-48, Apr. 2002.

[3] A. M. D. Turkmani, D. A. Demery and J. D. Parsons, "Measurement and Modelling of Wideband Mobile Radio Channels at 900 MHz," *IEEE Proceedings I on Communications, Speech and Vision*, vol. 138, no. 5, pp. 447-457, Oct. 1991.

[4] R. Yao, Z. Chen and Z. Guo, "An Efficient Multipath Channel Model for UWB Home Networking," *2004 IEEE Radio and Wireless Conference*, pp. 511-516, Sept. 2004.

[5] K. S. Yee, "Numerical Solution of Initial Boundary Value Problems Involving Maxwell's Equations in Isotropic Media," *IEEE Transactions on Antennas and Propagation*, vol. 14, pp. 302-307, 1966.

[6] A. Taflove, *Computational Electrodynamics: The Finite-Difference Time-Domain Method*, Norwood, MA: Artech House, 1995.

[7] P. Supanakoon, T. Subson, M. Chamchoy, P. Rawiwan, S. Promwong and P. Tangtisanon, "FDTD Simulation for Site-Specific Modeling of Indoor Radio Wave Propagation," *24th Electrical Engineering Conference (EECON-24)*, pp. 874-879, Nov. 2001.

[8] P. Supanakoon, P. Rawiwan, P. Tangtisanon and J. Takada, "Indoor Radio Wave Propagation Modeling Using Modified FDTD Method," *2001 International Symposium on Communications and Information Technology (ISCIT 2001)*, pp. 441-444, Nov 2001.

[9] H. Zhou, C. Yang and F. Wang, "Simulation of Indoor Ultra Wideband Propagation Channel Modeling," *2005 International Conference on Wireless Communications, Networking and Mobile Computing*, vol. 1, pp. 333-336, Sept. 2005.

[10] P. Supanakoon, P. Thaiwattanaporn, S. Keawmechai and S. Promwong, "Indoor Radio Wave Propagation of UWB Signal Using FDTD Method," *The International Technical Conference on Circuit/Systems, Computers and Communications (ITC-CSCC 2006)*, vol. 3, pp. 265-268, July. 2006.

[11] A. Taflove and M. E. Brodwin, "Numerical Solution of Steady-State Electromagnetic Scattering Problems Using The Time-Dependent Maxwell's Equation," *IEEE Transections on Microwave Theory and Techniques*, vol. 23, pp. 623-630, 1975.

[12] J. Berenger, "A Perfectly Matched Layer for The Absorption of Electromagnetic Wave," *Journal on Computational Physics*, vol. 14, pp. 185-200, 1994.

[13] P. Supanakoon, K. Wansiang, S. Promwong and J. Takada, "Simple Waveform for UWB Communication," *The 2005 Electrical Engineering/Electronics, Computer, Telecommunication, and Information Technology International Conference (ECTI-CON 2005)*, pp. 626-629, May 2005.

[14] J. Takada, S. Promwong and W. Hachitani, "Extension of Friis Transmission Formula for UWB Systems," *Technical Report of IEICE*, WBS2003-8/MW2003-20, May 2003.

[15] P. Supanakoon, P. Tangtisanon, S. Promwong and J. Takada, "Accurate Analysis of Extension of the Friis' Transmission Formula for UWB Channels," *The First Electrical Engineering/Electronics, Computer, Telecommunication and Information Technology Annual Conference (ECTI-CON 2004)*, pp. 291-294, May 2004.

[16] T. S. Rappaport, *Wireless Communication: Principles and Practice*, Prentice Hall PTR, 2nd Edition, 2002.

Power Spectral Density Analysis of Ultra Wideband Signal Using Pulse Shape Modulation

Parinya Prommasuksakul*, Pichaya Supanakoon*,†, Sathaporn Promwong*,† and Jun-ichi Takada‡
*Department of Information Engineering, Faculty of Engineering,
†Research Center for Communications and Information Technology (ReCCIT)
King Mongkut's Institute of Technology Ladkrabung, Bangkok 10520, THAILAND
E-mail: {s8061019,kspichay,kpsathap}@kmitl.ac.th
‡Graduate School of Science and Engineering, Tokyo Institute of Technology,
2-12-1-S6-4, O-okayama, Meguro-ku, 152-8550, Tokyo, Japan
E-mail: takada@ide.titech.ac.jp

***Abstract*— According to satisfy the Federal Communications Commission (FCC) indoor and outdoor limit spectral masks, a good understanding of power spectral density (PSD) of ultra wideband (UWB) signal and how it is influenced by modulation without and with time hoping (TH) is necessary. In this paper, the PSD of UWB signal using pulse shape modulation (PSM) without and with TH is analyzed. The orthogonal pair of modulated Gaussian waveforms, which satisfied the UWB signal definition and FCC indoor and outdoor limit spectral masks, are considered. The PSD of UWB signal is analyzed and shown. The results are discussed in the conclusion.**

I. Introduction

Almost all communication systems employ the sinusoidal signal as a transmitted waveform. Its information is mapped via the modulation. The result is that the power spectral density (PSD) of this signal is well concentrated in specific frequency band. It easily suppresses noise and interference by using bandpass filter. Unfortunately, the narrowband system is sensitive to fading. Furthermore, frequency spectrum is divided into many narrow frequency bands causing deficient spectrum for new communication system.

An ultra wideband (UWB) refers to a technology, which makes the use of a signal waveform occupied a very large bandwidth. The Federal Communications Commission (FCC) in US defines the UWB signal, which is any signal where the fractional bandwidth is equal to or greater than 0.20, or the occupied bandwidth is equal to or greater than 0.50 GHz. The fractional and occupied bandwidth are defined as [1]

$$\text{Fractional bandwidth} = \frac{2(f_{\mathrm{H}} - f_{\mathrm{L}})}{f_{\mathrm{H}} + f_{\mathrm{L}}}, \quad (1)$$

$$\text{Occupied bandwidth} = f_{\mathrm{H}} - f_{\mathrm{L}}, \quad (2)$$

where f_{L} and f_{H} are the lowest and highest frequencies at the -10 dB point, respectively.

The main concern about UWB communications is that they occupy a portion of spectrum where other narrowband communications already operate, so a regulation is necessary in order to avoid co-existence interference problems. Therefore, the FCC regulates the indoor and outdoor spectral masks to limit the maximum emission of unlicensed UWB signals for guaranteeing the protection to the already existent and planed radio services. The UWB communications specified FCC indoor and outdoor spectral masks are undetectable by other communication systems and having the PSD below past 15 noise limit. Furthermore, the UWB radio technology is an ideal candidate that can be utilized for commercial, short-range, low power, low cost, indoor and outdoor communication systems such as wireless personal area networks (WPANs) [2]-[5].

Numerous UWB waveforms have been proposed [6]. The waveform designs are reviewed, but no considered about the UWB signal definition and spectral masks specified by FCC. The signal processing and numerical techniques are used to design the UWB waveform [7]-[14]. Although the waveform has very high effective spectral in designed frequency range, these algorithms are complex. Therefore, the simple waveforms for UWB communications are proposed [15]. After that, the orthogonal pairs of simple UWB waveforms are developed for pulse shape modulation (PSM) scheme [16]. Although, these waveforms have the closed form expressions in both time and frequency domains, they are considered only the PSD of one UWB waveform. There is no consideration about the PSD of pulse train of UWB signal using modulation scheme.

In this paper, the PSD of UWB signal using modulation scheme is analyzed. The modulation scheme is focused on the PSM without and with time hoping (TH) [17]. The orthogonal pair of modulated Gaussian waveforms, which satisfied the UWB signal definition and FCC indoor and outdoor limit spectral masks [16], are considered. The PSD of UWB signal consists of the continuous and discrete components. The discrete component presents greater interference to narrowband communication system than the continuous component. The PSD of UWB signal using PSM without and with TH is analyzed and shown. The capability of PSM with TH that suppressed the discrete component is discussed in the conclusion.

This paper is organized as follows. Section 2, the PSD of UWB signal using PSM is briefly described. Next, the PSD analysis results are demonstrated in Sec. 3. Finally, the conclusions are drawn in Sec. 4.

II. PSD OF UWB SIGNAL USING PSM

In this section, we will first introduce the UWB waveform model. After that, we will investigate the PSD of UWB signal using PSM without and with TH.

1) UWB Waveform Model: The UWB waveforms that used for PSM scheme are the orthogonal pair of modulated Gaussian waveforms. The orthogonal pair of modulated Gaussian waveforms in time domain, f_1 and f_2, and their spectral density functions, F_1 and F_2, are given by [16]

$$f_0(t) = A_0 e^{-(t/d)^2} \sin(2\pi f_c t), \quad (3)$$

$$f_1(t) = A_1 e^{-(t/d)^2} \cos(2\pi f_c t), \quad (4)$$

$$F_0(f) = \frac{A_0 d\sqrt{\pi}}{j2} \begin{bmatrix} e^{-\pi^2 d^2 (f-f_c)^2} \\ -e^{-\pi^2 d^2 (f+f_c)^2} \end{bmatrix}, \quad (5)$$

$$F_1(f) = \frac{A_1 d\sqrt{\pi}}{2} \begin{bmatrix} e^{-\pi^2 d^2 (f-f_c)^2} \\ +e^{-\pi^2 d^2 (f+f_c)^2} \end{bmatrix}, \quad (6)$$

where f_c is the carrier frequency, d is the $1/e$ characteristic decay time, A_0 and A_1 are the maximum amplitudes of waveform envelopes f_0 and f_1, respectively.

2) PSD of UWB Signal Using PSM without TH: The PSM without TH uses the orthogonal pair of waveforms to represent the bits '0' and '1'. The UWB signal using PSM without TH can be presented as

$$s(t) = \sum_{n=-\infty}^{\infty} \left[(1-d_n) f_0(t - nT_s) + d_n f_1(t - nT_s) \right], \quad (7)$$

where d_n is the digital data in sequence of n, T_s is the time interval of bit data, f_0 and f_1 are the waveforms representing bits '0' and '1', respectively.

The probability distribution function (PDF) of d_n is

$$P\{d_n\} = \begin{cases} p & d_n = 1 \\ 1-p & d_n = 0 \end{cases}, \quad (8)$$

where p is the probability of d_n is the bit '1'.

For considering radiated PSD, the transmitter (Tx) antenna is assumed to be the isotropic antenna. The internal circuit and Tx antenna impedances are assumed to be the same real value R. That is the ideal with maximum radiated PSD. In this paper, the path loss and measurement system are not considered. Therefore, the radiated PSD of UWB signal using PSM without TH can be derived as

$$S_R(f) = \lim_{N\to\infty} \frac{1}{4RNT_s} \left| \sum_{n=-N/2}^{N/2} \begin{bmatrix} (1-d_n)F_0(f) \\ +d_n F_1(f) \end{bmatrix} e^{-j2n\pi f T_s} \right|^2. \quad (9)$$

3) PSD of UWB Signal Using PSM with TH: The PSM with TH is used to suppress the discrete component of PSD. The UWB signal using PSM with TH can be presented as

$$s(t) = \sum_{n=-\infty}^{\infty} \begin{Bmatrix} (1-d_n) f_0(t - nT_s - T_n) \\ +d_n f_1(t - nT_s - T_n) \end{Bmatrix}, \quad (10)$$

where T_n is the TH.

The PDF of T_n is the uniform distribution in the range of $-T_s/2$ to $T_s/2$, which can be written as

$$P\{T_n\} = \begin{cases} \frac{1}{T_s} & -\frac{T_s}{2} \le T_n \le \frac{T_s}{2} \\ 0 & \text{elsewhere} \end{cases}. \quad (11)$$

The radiated PSD of UWB signal using PSM with TH is considered in the same way of that without TH, which can be derived as

$$S_R(f) = \lim_{N\to\infty} \frac{1}{4RNT_s} \left| \sum_{n=-N/2}^{N/2} \begin{matrix} \{(1-d_n)F_0(f) \\ +d_n F_1(f)\} e^{-j2\pi f(nT_s+T_n)} \end{matrix} \right|^2. \quad (12)$$

III. PSD ANALYSIS RESULTS

The orthogonal pair of modulated Gaussian waveforms is used as the UWB signal for representing bits '0' and '1'. The waveform parameters, which obtained from the maximum amplitude and average power optimizations [16], are considered for both FCC indoor and outdoor limit spectral masks. The parameters R and N are set to be $50\ \Omega$ and $1,000$ bits, respectively. The bit rate is assumed to be 110 Mbps, therefore T_s is equal to 9.09 ns. For FCC indoor limit spectral mask, the waveform parameters are $A_0 = A_1 = 3.76$ V, $d = 0.11$ ns and $f_c = 7.34$ GHz. The time domain waveforms and their PSD compared with FCC indoor limit spectral mask are shown in Fig. 1. For FCC outdoor limit spectral mask, the waveform parameters are $A_0 = A_1 = 3.18$ V, $d = 0.13$ ns and $f_c = 6.85$ GHz. Figure 2 shows the time domain waveforms and their PSD compared with FCC outdoor limit spectral mask. The PSD of each waveform is the same with another for both cases.

For analyzing PSD of UWB signal using PSM without and with TH, two cases of p are considered for FCC indoor and outdoor limit spectral masks. For the first case, the parameter p is set to be 0.0 or 1.0, which all bits are '0' or '1'. Another case, the parameter p is set to be 0.5, which the bits '0' and '1' are equal.

Figures 3 and 4 show the PSD of UWB signal using PSM without TH compared with FCC indoor and outdoor limit spectral masks, respectively. The continuous and discrete component characteristics of PSD for FCC indoor and outdoor limit spectral masks are the same. The PSD of $p = 0.0$ or 1.0 is more than the FCC indoor and outdoor limit spectral masks up to 29.99 dB, while that of $p = 0.5$ is more than the FCC indoor and outdoor limit spectral masks up to 26.98 dB. That because the discrete component of $p = 0.5$ is less than that of $p = 0.0$

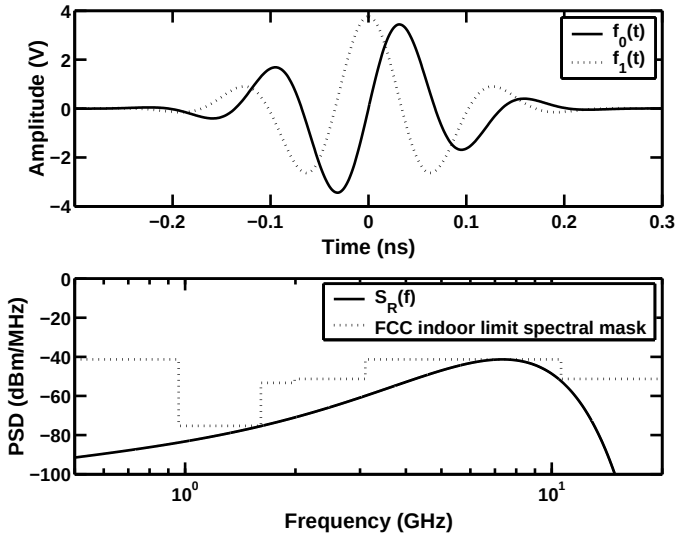

Fig. 1. Time domain waveforms and their PSD compared with FCC indoor limit spectral mask.

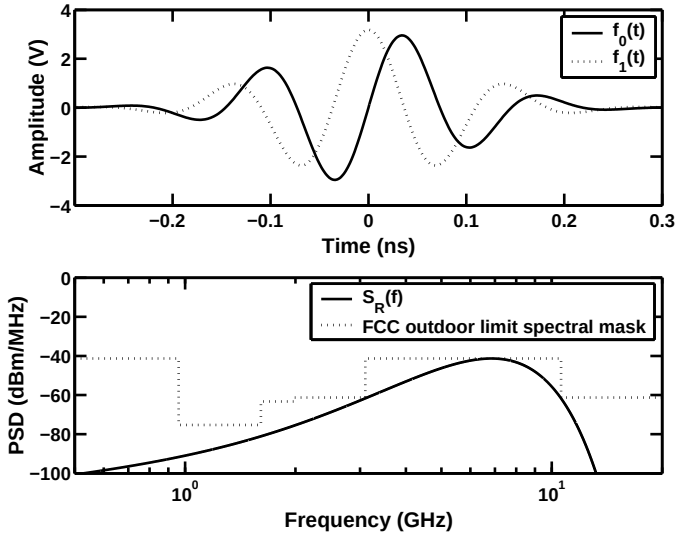

Fig. 2. Time domain waveforms and their PSD compared with FCC outdoor limit spectral mask.

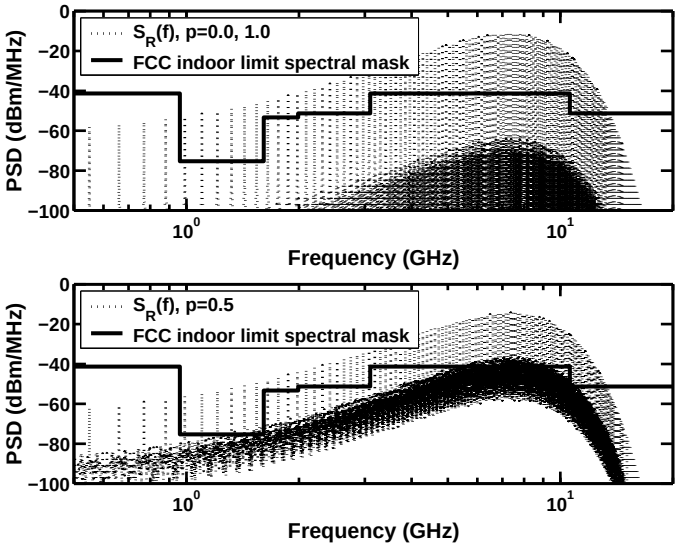

Fig. 3. PSD of UWB signal using PSM without TH compared with FCC indoor limit spectral mask.

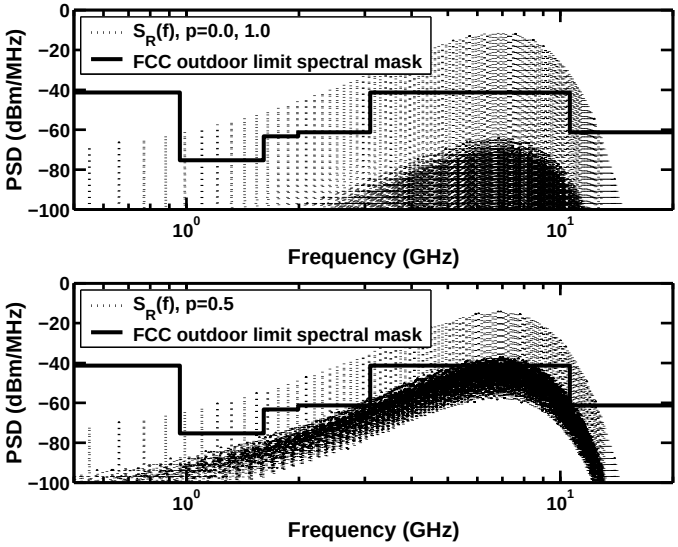

Fig. 4. PSD of UWB signal using PSM without TH compared with FCC outdoor limit spectral mask.

or 1.0. Therefore, the PSD of $p = 0.5$ is decreased from that of $p = 0.0$ or 1.0 about 3 dB. Although this orthogonal pair of modulated Gaussian waveforms is well designed to satisfy the FCC indoor and outdoor limit spectral masks, their PSD using PSM without TH exceeds the FCC indoor and outdoor limit spectral masks very much. Then, the technique that uses to suppress the discrete component of PSD is necessary.

In this paper, the PSD of UWB signal using PSM with TH is considered to suppress the discrete component. The PSD of UWB signal using PSM with TH compared with FCC indoor and outdoor limit spectral masks are shown in Figs. 5 and 6, respectively. The continuous and discrete component characteristics of PSD for FCC indoor and outdoor limit spectral masks are little difference. For FCC indoor limit spectral mask, the PSD of $p = 0.0$ or 1.0 is more than the FCC indoor limit spectral mask up to 8.07 dB, while that of $p = 0.5$ is more than the FCC indoor limit spectral mask up to 7.73 dB. For FCC outdoor limit spectral mask, the PSD of $p = 0.0$ or 1.0 is more than the FCC indoor limit spectral mask up to 8.37 dB, while that of $p = 0.5$ is more than the FCC indoor limit spectral mask up to 8.32 dB. The PSD of $p = 0.5$ is decreased from that of $p = 0.0$ or 1.0 about 0.34 and 0.05 dB for FCC indoor and outdoor limit spectral masks, respectively. The discrete component of UWB signal using PSM with TH is less than that of without TH about 22 dB for $p = 0.0$ or 1.0, and 19 dB for $p = 0.5$. Although the PSD of UWB signal using PSM with TH is extremely reduced compared with that of without

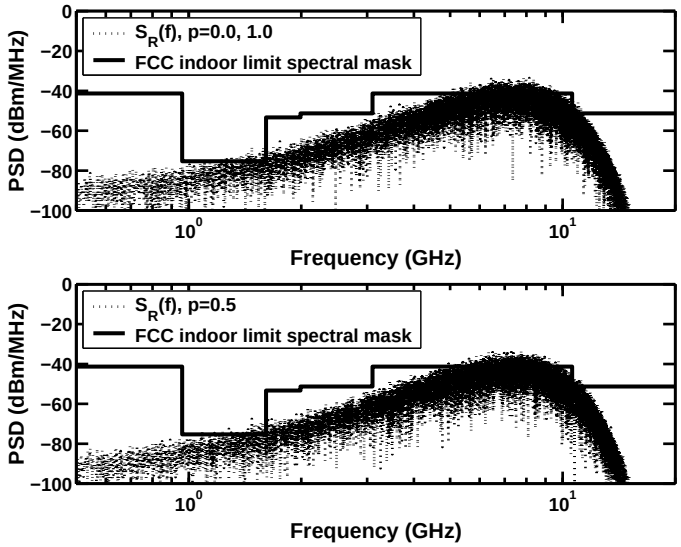

Fig. 5. PSD of UWB signal using PSM with TH compared with FCC indoor limit spectral mask.

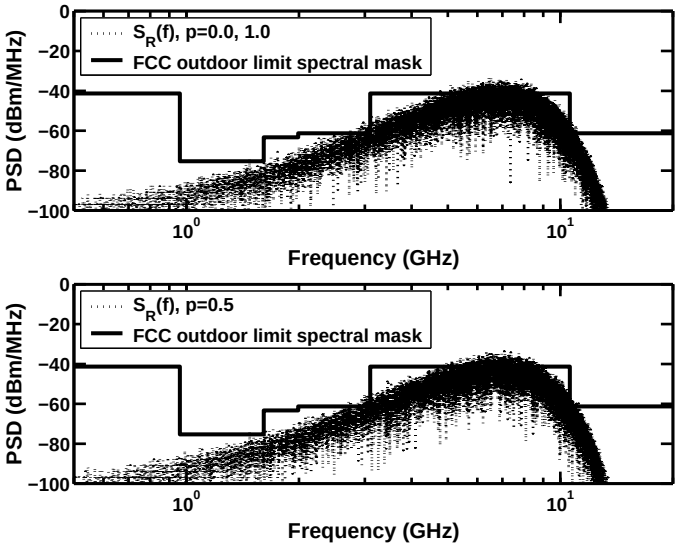

Fig. 6. PSD of UWB signal using PSM with TH compare with FCC outdoor limit spectral mask.

TH, their PSD still exceeds the FCC indoor and outdoor limit spectral masks. Therefore, the peak power of UWB signal must decreases to satisfy the FCC indoor and outdoor limit spectral masks.

IV. Conclusion

In this paper, the PSD of UWB signal using PSM without and with TH is analyzed. The orthogonal pair of modulated Gaussian waveforms, which satisfied the UWB signal definition and FCC indoor and outdoor limit spectral masks, are considered. From the results, we can see that the PSD characteristics of UWB signal for FCC indoor and outdoor limit spectral masks are almost the same. The PSM with TH can be suppressed the discrete component of the PSD about 20 dB. But this is not sufficient. The peak power of UWB signal must decreases about 9 dB to satisfy the FCC indoor and outdoor limit spectral masks.

References

[1] Federal Communications Commission, "Revision of Part 15 of the Commission's Rules Regarding UWB Transmission Systems," First Report, FCC 02-48, Apr. 2002.

[2] K. Siwiak, "Ultra-Wide Band Radio: Introducing a New Technology," *2001 Spring IEEE Vehicular Technology Conference (VTC)*, vol. 2, pp. 1088-1093, May 2001.

[3] K. Siwiak, "Ultra-Wide Band Radio: The emergence of an Important RF Technology," *2001 Spring IEEE Vehicular Technology Conference (VTC)*, vol. 2, pp. 1169-1172, May 2001.

[4] K. Siwiak, "Impact of Ultra Wide Band Transmissions on A Generic Receiver," *2001 Spring IEEE Vehicular Technology Conference (VTC)*, vol. 2, pp. 1181-1183, May 2001.

[5] J. Farserotu, A. Hutter, F. Platbrood, J. Gerrits and A. Pollini, "UWB Transmission and MIMO Antenna Systems for Nomadic User and Mobile PAN," *Wireless Personal Communications*, no. 22, pp. 197-317, 2002.

[6] B. Allen, S. A. Ghorashi and M. Ghavami, "A Review of Pulse Design for Impulse Radio," *2004 IEE Seminar on Ultra Wideband Communications Technologies and System Design*, pp. 93-97, Jul. 2004.

[7] M. Ghavami, L. Miscael, R. Khono, "Hermite Function Based Orthogonal Pulses for Ultra Wideband Commuincation," *WPMC*, 2001.

[8] C. A. Corral, S. Sibecas, S. Emami and G. Stratis, "Pulse Spectrum Optimization for Ultra-Wideband Communication," *Proc. 2002 IEEE Conference on Ultra Wideband Systems and Techniques*, pp. 31-35, May 2002.

[9] L. B. Michael, M. Ghavami and R. Kohno, "Multiple Pulse Generator for Ultra-Wideband Communication Using Hermite Polynomial Based Orthogonal Pulses," *Proc. 2002 IEEE Conference on Ultra Wideband Systems and Techniques*, pp. 47-51, May 2002.

[10] J. Han and C. Nguyen, "A New Ultra-Wideband, Ultra-Short monocycle pulse generator with reduce ringing," *IEEE Microwave Wireless Compon. Lett.*, vol. 12, pp. 206-208, June 2002.

[11] R. Dilmaghani, M. Ghavami, B. Allen, H. Aghvami, "Novel UWB Pulse Shaping Using Prolate Spheroidal Wavefunctions," *IEEE PIMRC*, 2003.

[12] S. Ciolino, M. Ghavami, H. Aghvami, "UWB Pulse Shape Modulation System Using Wavelet Packets," *International Workshop on Ultra Wideband Systems*, 2003.

[13] A. B. Parr, B. L. Cho and Z. Ding, "A New UWB Pulse Generator for FCC Spectral Masks," *2003 Spring IEEE Vehicular Technology Conference (VTC)*, pp. 1664-1666, 2003.

[14] A. B. Parr, B. L. Cho, K. Wallace and Z. Ding, "A Novel Ultra-Wideband Pulse Design Algorithm," *IEEE Communications Letters*, vol. 7, no. 5, pp. 219-221, May 2003.

[15] P. Supanakoon, K. Wansiang, S. Promwong and J. Takada "Simple Waveform for UWB Communication," *The 2005 Electrical Engineering/Electronics, Computer, Telecommunication, and Information Technology International Conference (ECTI-CON 2005)*, pp. 626-629, May 2005.

[16] P. Supanakoon, P. Prommasuksakul, S. Promwong, P. Sithiyopasukul and J. Takada, "Simple Orthogonal Waveforms Satisfied FCC Indoor and Outdoor Spectral Masks for UWB Communications," *The International Technical Conference on Circuits/Systems, Computers and Communications (ITC-CSCC 2006)*, no. 3, pp 261-264, July 2006.

[17] I. Oppermann, M. Hamalainen and J. Iinatti, *UWB Theory and Applications*, John Wiley & Sons, 2004.

Performance Investigation of UWB Rake Receiver in Realistic Indoor Channels

Worawoot Duangdeun, Monchai Chamchoy, and Sathaporn Promwong
Faculty of Engineering, King Mongkut's Institute of Technology Ladkrabang
Chalongkrung Rd., Ladkrabang, Bangkok 10520, Thailand
Email: worawoot_wislab@yahoo.co.th

***Abstract*— The performance investigation of wireless communication system based on the realistic indoor channels are necessary to design the receiver. In this paper, the performance of 2 ultra wideband (UWB) Rake receivers for realistic indoor channels are proposed. The UWB Rake receivers with minimum mean square error (MMSE) and least square (LS) channel estimators are compared. By using the channel impulse response between human body shadowing and Saleh-Valenzuela (S-V) realistic indoor channel model are combined. As the simulation results, the performance of Rake receiver with the MMSE channel estimator is better than with the LS channel estimator for all UWB indoor channels. Therefore, the MMSE channel estimator can be used for the UWB Rake receiver in the realistic indoor environment.**

I. INTRODUCTION

Ultra-wideband technology is an attractive candidate for short-range wireless communication. The definition of the Federal Communications Commission (FCC)was formulated the emission limits for UWB of effective isotropic radiated power (EIRP) below -41.3 dBm/MHz, low power consumption, low cost structure and the frequency range of 3.1$\sim$10.6 GHz [1]. The UWB communication system has high bandwidth and high data rate support. Therefore, the UWB is provided to wireless personal area network (WPAN) and applied to use in home environment or office area. For UWB system, the data are transmitted using nano-second baseband pulses and without the need for mixers. Since finding time resolution for accurate ranging or positioning is easier than narrowband, EIRP has very low power, intersymbol interference (ISI) simply occurred for high data rate. Consequently, Rake receiver is suitable for this system. The Rake receiver is used for CDMA technology and wideband technology. Because the structure of Rake receiver can separate multi-path for adjusting the received signal to increase SNR level and purge ISI on the received signal.

The channel estimator is very important for Rake receiver. Because it estimates the amplitude or gain of the received signal and the results of the gain combining of signal is followed by it and the number of signal are arrived. The important parameters for channel estimation are PDF of channel impulse response (CIR), noise variance and number of pilot signals per data range (for data aided). Therefore, the performances of UWB Rake receiver based on the different complexity of the estimation parameters are investigated.

The S-V channel model of UWB communication is proposed for the multi-path channel in indoor environment. This model is dived into 4 groups of environments, namely, CM1-CM4. CM1 describes a line-of-sight (LOS) scenario with distance between transmitter and receiver of less than 4 meters. CM2 describes the same range but for a non-LOS situation. CM3 represents a non-LOS scenario for distances between TX and RX of 4-10 meters. Finally, CM4 describes an environment with strong delay dispersion, resulting in a delay spread of 25 ns. For CM1-CM4, the models did not fix the environment location, because the models are adjusted for universal stochastic model of the wireless propagation channel and can be developed for analyzing the UWB communication system. On the other hand, the human body may obstruct the propagated signal between TX and RX. Therefore, the effects of human body shadowing are important issue for designing UWB receiver in realistic environment.

Several literatures have studied the performance of UWB Rake reception for indoor channel [2]-[4]. These investigations do not consider the human body shadowing effects. However, the performance of UWB communication in the realistic environment is still necessary for designing the receiver, especially when propagated signal is shadowed by the human body. Therefore, in this paper, the combining of channel impulse responses between the human body shadowing and the S-V multi-path indoor channel are investigated.

The rest of the paper is organized as follows: Section II presents the transmitter signal model, S-V channel models, measurement channel impulse response, and Rake receiver models. Section III summarizes the performance results of the realistic indoor channel and Section IV is conclusion.

II. SYSTEM MODEL

For the UWB system, transmitted signal has a very small pulse width and no carrier frequency. The indoor CIR of the human body shadowing are very important issue in the wireless personal area network (WPAN) communication. And the UWB Rake receiver with MMSE and LS channel estimators are presented.

A. Transmitter Signal Model

The characteristic of Gaussian doublet waveform is almost uniformly distributed on frequency spectrum of UWB technology. Specifically, the second derivative of the Gaussian pulse is chosen for non carrier modulation of the UWB signal and

then it is given by [5]-[7]

$$p(t) = \sqrt{E_p}\sqrt{\frac{8}{3\tau}}\left(1 - 4\pi\left(\frac{t - T_c}{\tau}\right)^2\right) e^{-2\pi\left(\frac{t-T_c}{\tau}\right)^2}, \quad (1)$$

where E_p is energy of signal, τ is time scaling factor by set to 0.2877 ns, T_c is time chip of next bit. In this time, the Bi-Phase Modulation (BPM) has been experimented and expressed as

$$s(t) = \sum_{i=-\infty}^{\infty} b_i p(t - iT_s), \quad (2)$$

where $p(t)$ is the Gaussian doublet waveform, $b_i \in \{-1, +1\}$ are bi-phase modulation symbols, i is bit number, T_s is bit duration.

B. Channel Model

Nowadays, there are several channel models which are used for analyzing wireless communication system. Each model is designed suitable for specific situation such as indoor and outdoor environment. However, there is no model which combines the effects of channel impulse responses with the human body effects. Thus, in the paper, the combination of the human body shadowing effects based on measurement channels in [8]-[9] and the realistic S-V channel model is considered.

The realistic channel for IEEE 802.15 study group 3a has been developed by Saleh-Valenzuela (S-V model) and proposed for the real indoor channel model, where the clusters and rays are multi-path components [10]. This multi-path channel can be expressed as

$$h(t) = \sum_{l=0}^{L}\sum_{k=0}^{K} \alpha_{k,l}\delta(t - T_l - \tau_{k,l}), \quad (3)$$

where the real value of multi-path gain is defined by $\alpha_{k,l}$ for cluster l and ray k. The lth cluster arrives at T_l and its kth ray arrives at $\tau_{k,l}$ which is relative to the first path in cluster l. However, the multi-path channels consist of four different models, namely, CM1, CM2, CM3 and CM4. The detail of the four different groups is provided in [11]. The CIR of the human body channel is derived as in the S-V model except the clusters of arrivals.

The combination of 2 CIRs between the S-V multi-path indoor channel models (in each CM groups indoor channel) and the human body shadowing are summarized for each CIRs or described by $h_{com} = h_{sv} + h_{human}$, where h_{sv} is the CIR of S-V model and h_{human} is the CIR of the human body shadowing. Fig. 1 shows are example of the CIR of S-V model for CM4, the CIR of the human body shadowing from measured channel [12] and the combining of 2 CIRs between the S-V model and the human body shadowing, respectively.

C. Rake Receiver Model

In ideal Rake receiver, the number of multi-paths per bit duration is combined as time and amplitude arrivals. Therefore, the SNR of Rake receiver is higher than conventional receiver. In this investigation, the Rake receiver based on MRC

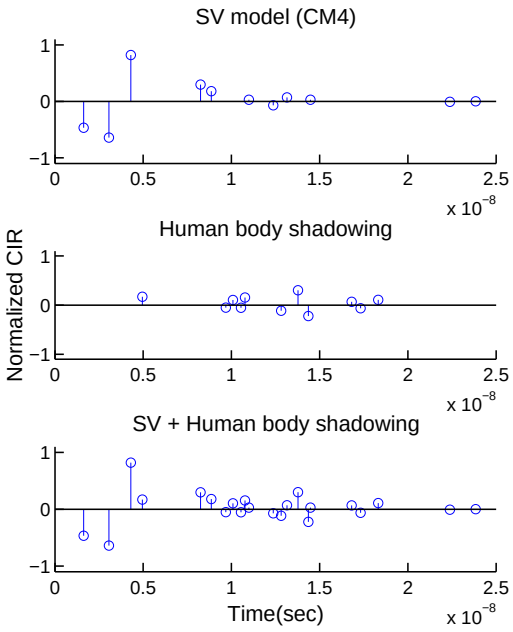

Fig. 1. The CIR of the S-V model for CM4, the human body shadowing from measured channel, and the combining of the S-V model and the human body shadowing, respectively.

combining is employed. The received signal for UWB BPM transmitter can be expressed as

$$r(t) = \sum_{i=-\infty}^{\infty} b_i \sum_{l=0}^{L-1} \alpha_l p(t - \tau_l - iT_s) + n_0(t), \quad (4)$$

where α_l is channel impulse response with multi-path component, τ_l is chip arrival times and n_0 is AWGN noise with two side spectra density of $N_0/2$.

In the case of no ISI and when the noise is AWGN, the optimal receiver is a filter matched to the received waveform. Typically, this is implemented in Rake receiver structure with M fingers, which can be represented as the filter with response given by

$$f(t) = \sum_{m=0}^{M-1} \beta_m p(-t - \theta_m), \quad (5)$$

where the Rake delays are θ_m. The sampled output of the Rake receiver is then

$$\begin{aligned} y_n &= [r(t) * f(t)]|_{t=nT} \\ &= \sum_{i=-\infty}^{\infty} b_i \sum_{l=0}^{L-1}\sum_{m=0}^{M-1} \alpha_l \beta_m R_p(nT - iT + \theta_m - \tau_l) \\ &\quad + \widetilde{n}_0(nT), \end{aligned} \quad (6)$$

where $R_p(t) \triangleq \int_{-\infty}^{\infty} p(\tau)p(\tau + t)d\tau$ is the time auto-correlation of the pulse shape and $\widetilde{n}_0(t) = \sum_{m=0}^{M-1} \beta_m \cdot \int_{-\infty}^{\infty} n_0(\tau)n_0(-t + \tau - \theta_m)d\tau$ is filtered noise.

It is well known that the optimal combiner for the AWGN multi-path channel is MRC, where $M = L$ fingers, $\beta_m = \alpha_m$ and $\theta_m = \tau_m$. For UWB-based high rate, it is anticipated

that spreading codes will be short, and therefore MRC is suboptimal even when the noise is AWGN. This motivates a smarter choice of combining weights β_m and finger delays θ_m to combine the signal energy while compensating for the effects of ISI and narrowband interference.

D. Channel Estimation Model

Nowadays, the training sequence is popular in wireless communication, easily applied to other communication and low complexity for estimating channel response. Therefore, the least square (LS) and minimum mean square error estimators (MMSE) are used in our investigation.

The LS estimation method is used to estimate channel impulse response of the received signal. For this method, it does not require an expression for the PDF $p(r,h)$ in order to estimate the unknown parameter h or the channel impulse response (CIR) but requires the training sequence. The LS estimation for this investigation can be expressed as [13]

$$\hat{\mathbf{h}}_{LS} = (\mathbf{S}^T\mathbf{S})^{-1}\mathbf{S}^T\mathbf{y}, \tag{7}$$

where $\mathbf{S}$ is the known observation matrix containing the transmitted data, $(\ )^T$ and $(\ )^{-1}$ denote the transpose and inverse matrices, respectively, and $\mathbf{y}$ is the received signal.

For the special case of time variant channel with AWGN, the linear MMSE estimator of the CIR can be used. Therefore, the MMSE estimator is used [14]. The result is

$$\hat{\mathbf{h}}_{MMSE} = R_c\mathbf{S}^T(\mathbf{S}R_c\mathbf{S}^T + \sigma_n^2 I)^{-1}\mathbf{y}, \tag{8}$$

where R_c is covariance matrix of $R_c = E\{\mathbf{h}\mathbf{h}^H\}$ [15], $\mathbf{S}$ is matrix of data signals, σ_n^2 is the variance of noise and I is identity matrix.

A natural optimal criterion is minimization of the mean square error and can be expressed as

$$MSE(\hat{\mathbf{h}}_{LS,MMSE}) = E[(\hat{\mathbf{h}}_{LS,MMSE} - \mathbf{h})^2], \tag{9}$$

where $\hat{\mathbf{h}}_{LS,MMSE}$ is the LS or MMSE channel estimation result and $\mathbf{h}$ is channel impulse response.

III. Performance Results

In this investigation, the LS and MMSE estimators are used to estimate the channel impulse responses of the received signal, according to CM1-4 models and the combining of the channel impulse response between the S-V model and the human body shadowing. The mean square errors of the channel estimator versus the signal to noise ratio are shown in Fig. 2. From the results, the MSE decreases as the SNR increases. Therefore, the performance of MMSE estimator is higher than LS estimator. For the example, the mean square error at 10^{-1} of the MMSE and the LS estimator differ by about 5 dB of SNR.

The performances of the 3 different UWB Rake receivers namely, the Rake receiver with perfect channel estimation, MMSE and LS channel estimators,and the correlation receiver with perfect synchronization are evaluated. The CIR combination of 4 S-V channel models and the human body shadowing

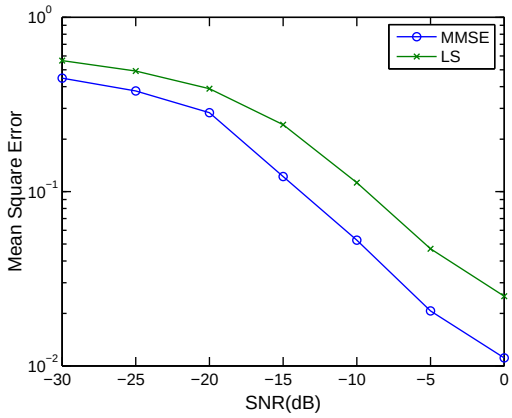

Fig. 2. Mean square errors versus SNR of the least square and minimum mean square error estimator.

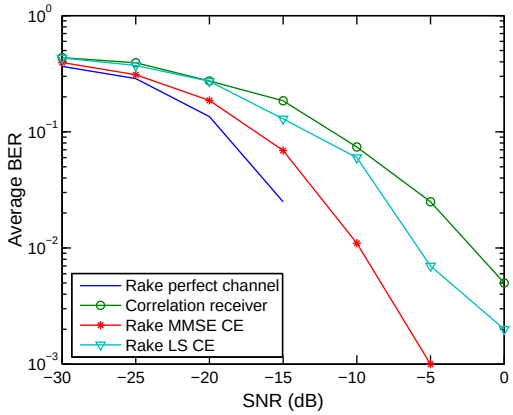

Fig. 3. Average BER performance of 4 UWB receivers in realistic indoor channel based on the combining of CM1 and human body shadowing effects.

are considered. Fig. 3- Fig. 6 show the performances of the UWB receivers for CM1-CM4 environments, respectively.

The performances of the UWB receivers based on the line-of-sight communication with the distance of 0-4 meters or the CM1 environment are shown in Fig. 3. It can be observed that the performance of Rake receiver with perfect channel estimator is best among overall and the correlation receiver with perfect synchronization is the worst for all receivers. Moreover, the performance of MMSE Rake receiver is better than LS Rake receiver by about 5 dB at BER of 10^{-2}.

Fig. 4-Fig. 6 show the performances of the UWB receivers for CM2-CM4 environments. As the results, the performances of the UWB receivers for all environments are similar with CM1 performance. Then, the performance of UWB Rake receiver with perfect channel estimator is best for all receivers, the receiver with MMSE channel estimator is better than LS channel estimator and correlation receiver, respectively. However, the UWB Rake receiver with the MMSE estimator can be used in the realistic indoor channel.

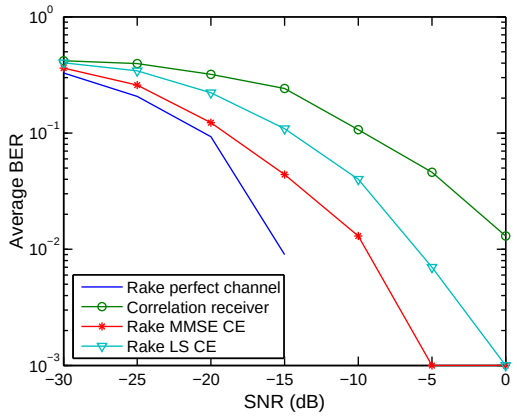

Fig. 4. Average BER performance of 4 UWB receivers in realistic indoor channel based on the combining of CM2 and human body shadowing effects.

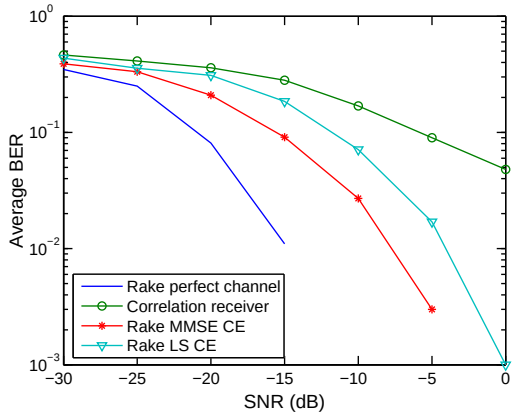

Fig. 5. Average BER performance of 4 UWB receivers in realistic indoor channel based on the combining of CM3 and human body shadowing effects.

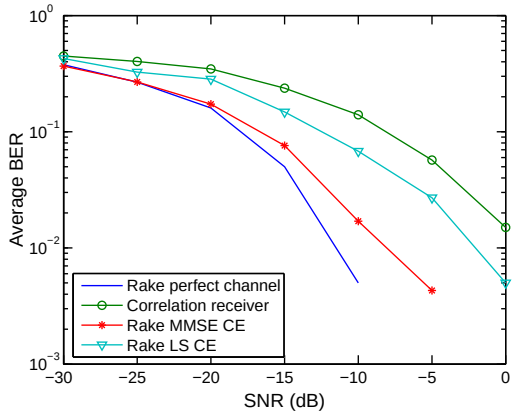

Fig. 6. Average BER performance of 4 UWB receivers in realistic indoor channel based on the combining of CM4 and human body shadowing effects.

IV. Conclusions

The performances of the UWB Rake receivers with LS and MMSE channel estimators in realistic environment are investigated. The performance of the Rake receiver with perfect channel estimation, LS and MMSE channel estimations and the correlation receiver with perfect synchronization are compared, based on the combining of the channel impulse response of the human body shadowing and the S-V channel model. As the simulation results, the mean square error (MSE) for all receivers decreases as SNR increases. The performances of the Rake receiver with perfect channel estimation are best for all receivers and environments. Moreover, the performances of the Rake receiver with MMSE channel estimator are better than with the LS channel estimator for all realistic indoor environments but it has much higher complexity than the LS estimator. Therefore, the MMSE channel estimator is one of the candidate for UWB Rake receiver in realistic indoor channel.

References

[1] Federal Communications Commission, First order and report: Revision of part 15 of the Commission's rules regarding UWB transmission systems, Apr. 22, 2002.

[2] D. Wang, D. Liu, and G. Yue, "Performance comparison of two kinds of UWB Rake receiver," *Proc. IEEE Circuits and Systems*, vol. 1, pp. 329-332, 2004.

[3] W. Q. Malik, D. J. Edwards, and C. J. Stevens, "Experimental evaluation of RAKE receiver performance in a line-of-sight ultra-wideband channel," *UWBST&IWUWBS*, pp. 217-220, 2004.

[4] A. Rajeswaran, V. S. Somayazulu, J. R. Foerster, "RAKE performance for a pulse based UWB system in a realistic UWB indoor channel," *IEEE Int.Conf. Communications*, vol. 4, pp. 2879-2883, 2003.

[5] M. Z. Win and R. A. Sholtz, "Impulse radio: how it works," *IEEE Commun. Lett.*, vol. 2, pp. 36-38, Feb. 1998.

[6] F. Ramirez-Mireles and R. A. Scholtz, "System performance analysis of impulse radio modulation," *RAWCON 98*, pp. 67-70, 1998.

[7] R. A. Scholtz and M. Z. Win, *Impulse Radio in Wireless Communication TDMA versus CDMA*, Kluwer Academic Publishers, Chapter 7, pp.245-267, 1997.

[8] A. Pradabphon, N. Kaewboonruean, M. Chamchoy, P. Supanakoon, and S. Promwong, "Experimental evaluation scheme of UWB radio propagation channel with human body," *Proc. ISCIT 2005*, pp. 638-641, 2005.

[9] A. Pradabphon, W. Doungdeun, M. Chamchoy, P. Supanakoon, and S. Promwong, "Investigation of Ultra-Wideband Pulse Distortion Due to the Body Shadowing," *Proc. ICICS 2005*, pp. 831-835, 2005.

[10] A. Saleh and R. Valenzuela, "A statistical model for indoor multi-path propagation," *IEEE Journal on Select. Areas Commun.*, vol. 5, pp. 128-137, Feb. 1987.

[11] J. Foerster et al., "Channel model sub-committee report final," *IEEE P802.15 Working Group for Wireless Personal Area Networks, P802.15-02/490rl-SG3a*, Feb. 2003.

[12] W. duangdeun M. Chamchoy, and S. Promwong, "Performance Investigation of UWB Rake Receiver with the Human Body Shadowing Effect," *The 21st International Technical Conference on Circuits/Systems, Computers and Communications*,,pp. II-261-II-264, 2006.

[13] Steven M. Kay, *Fundamentals of Statistical Signal Processing: Estimation Theory*, Prentice-Hall, 1993.

[14] T. Kailath, "Adaptive matched filters", In: R. Bellman (ed.), *Mathematical Optimization Techniaues*, University of California Press, pp. 109-140, 1963

[15] S. Haykin, *Adaptive Filter Theory*, 3^{rd} *Edition*, Prentice-Hall, 1996.

Ultra Wideband Radio Propagation Channel with Corridor for Short Range Wireless Systems

Nisakorn Yingkajohn[1], Sathaporn Promwong[1], and Pichaya Supanakoon[1]
[1]Department of Information Engineering, Faculty of Engineering,
King Mongkut's Institute of Technology Ladkrabang,
Chalongkrung Rd., Ladkrabang, Bangkok 10520, Thailand.
Email: {s6064609,kpsathap,kspichay}@kmitl.ac.th

***Abstract*— Ultra wideband (UWB) is currently wide interesting technology of wireless communication technology in building and home entertainment so the line-of-sight (LOS) and non-line-of-sight (NLOS) environments have effect on attenuation and other. In this paper, the LOS/NLOS propagation channel for UWB radio communications are evaluated. A vector network analyzer (VNA) is used to measure the frequency transfer functions of the radio channels over the frequency ranged from 3.1 10.6 GHz. The biconical antennas are used as transmitter (Tx) and receiver (Rx) antennas. The measurement is performed in the corridor with LOS and NLOS (wall obstruction) environments along the distance from 1-7 m. The matched filter is used at the receiver to maximize signal-to-noise ratio (SNR) of the received signal. The results are discussed in the conclusion.**

Keywords: **UWB line-of-sight, non-line-of-sight, path loss**

I. INTRODUCTION

Ultra Wideband (UWB) technology, a revolutionary approach to radio communications, allows systems to operate across a range of frequency bands defined by FCC [1] with negligible interference to existing systems in that band. This is because UWB uses very low power spectral density (PSD), while maintaining a high data rate. The UWB techniques can also provide reliable location information, high resolution imaging and work efficiently in a cluttered environment. The UWB technology is an ideal candidate that can be utilized for commercial, short-range, low power and low cost indoor communication systems such as wireless personal area networks (WPANs) [2], [3]. Moreover, this channel model was mainly aimed for short range applications (i.e. $<$ 10 m).

Indoor environment is one of the operating environments defined in [4] based on the applications envisioned for IEEE 802.15.4a standard as identified in [5]. Several channel measurements based on the indoor environments have been reported in the literature [6]-[9], but most of these measurements were conducted on the IEEE 802.15.4a standard, which was conducted in a flat. Furthermore, these measurements were aimed to investigate propagation channel for long range applications. This implies that more channel measurements are required in order to gain more profound knowledge of the UWB channel behaviors in this environment.

This paper report an extensive UWB measurement campaigns conducted in the types of corridor. The aim of this paper is to present the measurement of line-of-sight (LOS) and non-line-of-sight (NLOS, wall obstruction) environments along the distance from 2 to 7 m. The UWB path loss is evaluated and shown. The path loss characteristics are discuses. The frequency transfer functions of the radio channels are measured by using a vector network analyzer (VNA) over the frequency ranged from 3.1 GHz $\sim$ 10.6 GHz. The biconical antennas are used as transmitter (Tx) and receiver (Rx) antennas. The measurement data in term of the distance and frequency dependency of transmission gain are analyzed. Based on this, more measurement results can be provided for the standardization activities in IEEE 802.15.3a channel modeling.

II. ULTRA WIDEBAND ANALYSIS

A. UWB transmission theory

The Friis' transmission formula [10] has been widely used to evaluate the link budget for the narrowband LOS channels.

The UWB transmission signal waveform, its distortion due to the channel, and the receiver. Friis' transmission formula is extended for calculating the UWB free space link budget. For free space model, channel transfer function $H_{\rm c}$ are expressed as

$$H_{\rm c,f}(f,d) = H_{\rm f}(f,d)\vec{H}_{\rm r}(f,\frac{\pi}{2},\pi)\cdot\vec{H}_{\rm t}(f,\frac{\pi}{2},0), \quad (1)$$

where $H_{\rm f}$ is the free space transfer function which is expressed as

$$H_{\rm f}(f,d) = \frac{c}{4\pi f d}e^{-j2\pi f d/c}. \quad (2)$$

The complex transfer function vector of the antenna $\vec{H}_a$ relative to the isotropic antenna towards the $(\theta,\ \varphi)$ direction

$$\vec{H}_a(f,\theta,\varphi) \quad = \quad \hat{\theta}H_{a\theta}(f,\theta,\varphi) + \hat{\varphi}H_{a\varphi}(f,\theta,\varphi), \quad (3)$$

where a = r *or* t, θ and φ are the azimuthal and polar angles of spherical coordinates. Unit vectors $\hat{\theta}$, $\hat{\varphi}$ express the polarization and are defined with respect to the local spherical coordinates of the antennas.

The receiver input voltage $v_{\rm r}(t)$ of free space model is given as

$$v_{\rm r}(t,d) = \int_{-\infty}^{\infty} H_{\rm c,f}(f,d)V_{\rm t}(f)e^{j2\pi f t}{\rm d}f, \quad (4)$$

where $V_{\mathrm{t}}(f)$ is the spectral density of the transmitted signal that is calculated by using Fourier transform of its time domain waveform as

$$V_{\mathrm{t}}(f) = \int_{-\infty}^{\infty} v_{\mathrm{t}}(t) e^{-j2\pi ft} \mathrm{d}t. \quad (5)$$

At the receiver, the matched filter $H_{\mathrm{MF}}(f)$ is using for improvement signal-to-nosie ratio (SNR) of the received signal waveform that can be written as below

$$H_{\mathrm{MF}}(f) = \frac{\sqrt{2f_{\mathrm{b}}} H^{*}_{\mathrm{Friis}}(f)}{\sqrt{\int_{-\infty}^{\infty} |H_{\mathrm{Friis}}(f)|^2 df}}, \quad (6)$$

which satisfies the following constant noise output power condition

$$\int_{-\infty}^{\infty} |H_{\mathrm{MF}}(f)|^2 df = 1. \quad (7)$$

In this case, the output waveform when $E_i = 1$, and the spectrum of the receiver output are $h_{\mathrm{e-Friis}}(t)$ and $H_{\mathrm{e-Friis}}(f)$, respectively. The waveform of the output from the match filter $v_{\mathrm{MF}}(t)$ and the spectrum of the output from the matched filter $V_{\mathrm{MF}}(f)$ are

$$\begin{aligned} v_{\mathrm{MF}}(t) &= h_{\mathrm{e-Friis}}(t) * h_{\mathrm{MF}}(t) \\ &= \frac{h_{\mathrm{e-Friis}}(t) * h_{\mathrm{MF}}(-t)}{\sqrt{\int_{-\infty}^{\infty} h^2_{\mathrm{e-Friis}}(t) dt}}, \end{aligned} \quad (8)$$

$$\begin{aligned} V_{\mathrm{MF}}(f) &= H_{\mathrm{e-Friis}}(f) H_{MF}(f) \\ &= \frac{|H_{\mathrm{e-Friis}}(f)|^2}{\sqrt{\int_{-\infty}^{\infty} |H_{\mathrm{e-Friis}}(f)|^2 df}}, \end{aligned} \quad (9)$$

take its maximum as

$$\max_t v_{\mathrm{MF_t}} = \frac{\int_{-\infty}^{\infty} V_{\mathrm{MF}}(f) df}{\sqrt{\int_{-\infty}^{\infty} |H_{\mathrm{e-Friis}}(f)|^2 df}}, \quad (10)$$

Eq.(10)is the UWB extension of Friis' transmission formula. It includes three elements, namely the frequency characteristics of free space propagation, and the spectrum of the transmit signal. It is clear from Eq.(10)that the transmission gain of the UWB cannot be defines as the product of gains of antenna and a free space channel as a Friis' formula[10]. Instead, the total transmission gain including the effect of the waveform can be obtained as Eq.(10).

B. Path loss

The path loss PL [11] can be defined as the ratio between the maximum amplitude of the transmitted signal waveforms and output waveform of the matched filter

$$PL(dB) = 20 \log \frac{max|v_{\mathrm{t}}(t)|}{max|v_{\mathrm{MF}}(t)|}. \quad (11)$$

TABLE I
PARAMETERS OF EXPERIMENT

Parameter	Value
Frequency range	3 GHz - 11 GHz
Number of frequency point	801
Dynamic power range	80
Tx antenna height	1.5 m
Rx antenna height	1.5 m
Distance between Tx and Rx	1-7 m
Distance increment step by	0.5m

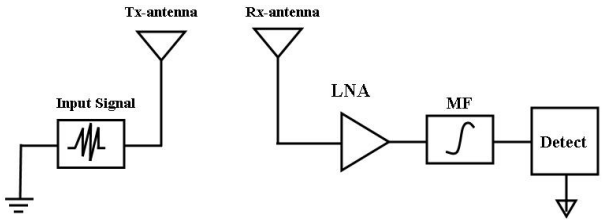

Fig. 1. Block diagram of System Analysis for UWB.

III. EXPERIMENTAL SYSTEM

A. Experiment setup

The UWB radio channel transfer function is measured. The measurement system consists of the VNA model HP-8510C, the S-parameter test set (HP-8514B), the frequency synthesized sweeper (HP-83620A), the biconial antenna pair and the personal computer. The VNA is operated in the response measurement mode, where PORT1 is the Tx port and PORT2 is the Rx port. The biconical antennas with the maximum diameter of 65.3 mm and the length of 37 mm are used as the Tx and Rx antennas. Table 1 lists the main parameters of the experiments.

The measurement is done on 12 floor Engineering Building at King Mongkut's Institute of Technology Ladkrabang (KMITL). Two models are considered for the LOS and NLOS environments, respectively. The first model for LOS environment and second model for NLOS environment are shown in Fig 2.

B. Transmitted signal waveform

The effect of the waveform distortion is more obvious when the bandwidth is wider. We considered the impulse radio signal with center frequency is at the center of lower band of preliminary UWB transmission mask for impact analysis of Japan. That is $f_{\mathrm{c}} = 4.1$ GHz. Three cases of the spectral bandwidths are considered. The bandwidths are set to be $B = 0.5$, 0.95 and 1.4 GHz, which are the minimum UWB bandwidth defined by FCC, middle and maximum UWB bandwidths of the lower band. The UWB transmitted signal in the simulation was the passband rectangular pulse. Figure 3 shows the transmitted pulse waveforms with 0.5, 0.95 and 1.4 GHz bandwidths. The expression of this pulse in time domain

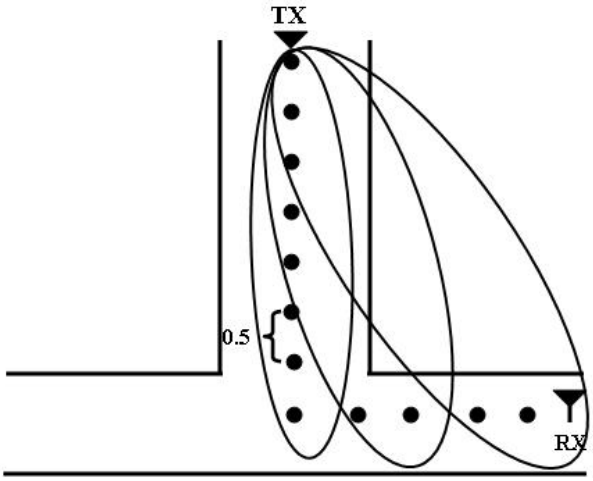

Fig. 2. The measurement model with corridor.

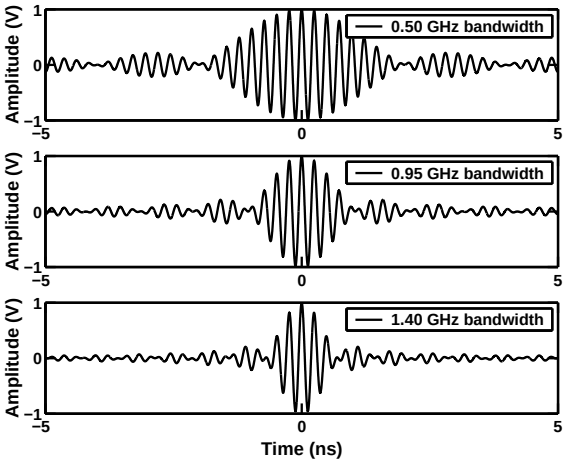

Fig. 3. UWB transmitted signal waveform.

$v_{\rm t}(t)$ and its spectral density function $V_{\rm t}(f)$ were

$$v_{\rm t}(t) = \frac{\sqrt{2}}{\sqrt{B}}\left[\ f_{\rm H}{\rm sinc}(2f_{\rm H}t) - f_{\rm L}{\rm sinc}(2f_{\rm L}t)\ \right], \quad (12)$$

$$V_t(f) = \begin{cases} \frac{1}{\sqrt{2B}} & ||f| - f_c| \le \frac{B}{2} \\ 0 & ||f| - f_c| > \frac{B}{2} \end{cases}, \quad (13)$$

where ${\rm sinc}(x) = \sin(\pi x)/(\pi x)$, $f_{\rm L} = f_{\rm c} - B/2$ and $f_{\rm H} = f_{\rm c} + B/2$ are the lower and upper frequencies.

IV. Results and Discussion

The transmission losses of UWB signals with optimum and isotropic matched filters in corridor LOS and NLOS environments are evaluated. The three cases of signal bandwidths, that are 0.50, 0.95 and 1.40 GHz, are considered. Fig. 4 shows the transmission losses of 0.50 GHz signal bandwidth with optimum and isotropic matched filters in corridor LOS and NLOS environments along the distance from 2 to 7 m. The transmission loss of optimum matched filter is less than that of isotropic matched filter about 1.8 and 6.79 dB for the LOS and NLOS, respectively. The obstruction loss is about 12.47 dB.

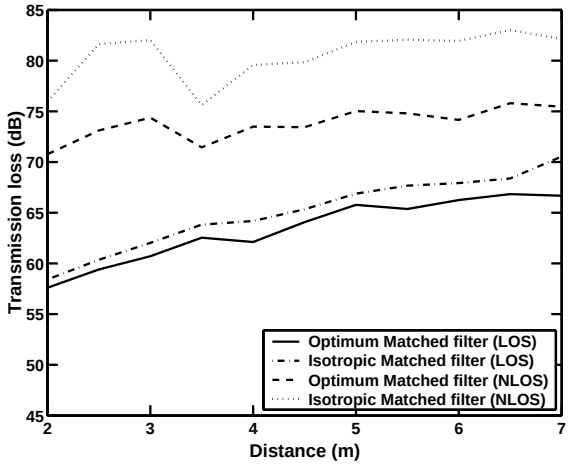

Fig. 4. Transmission losses of 0.5 GHz bandwidth along the distance from 2 to 7 m.

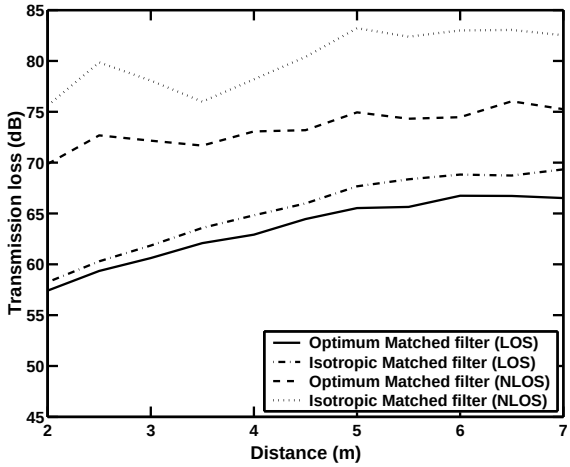

Fig. 5. Transmission losses of 0.95 GHz bandwidth along the distance from 2 to 7 m.

The transmission losses of 0.95 GHz signal bandwidth with optimum and isotropic matched filters in corridor LOS and NLOS environments along the distance from 2 to 7 m are shown in Fig. 5. The transmission loss of optimum matched filter is less than that of isotropic matched filter about 1.65 and 6.70 dB for the LOS and NLOS, respectively. The obstruction loss is about 12.94 dB.

Fig. 6 shows the transmission losses of 1.40 GHz signal bandwidth with optimum and isotropic matched filters in corridor LOS and NLOS environments along the distance from 2 to 7 m. The transmission loss of optimum matched filter is less than that of isotropic matched filter about 1.71 and 6.70 dB for the LOS and NLOS, respectively. The obstruction loss is about 12.42 dB.

V. Conclusion

In this paper, UWB radio propagation channel with corridor for short range wireless systems. From the results, the

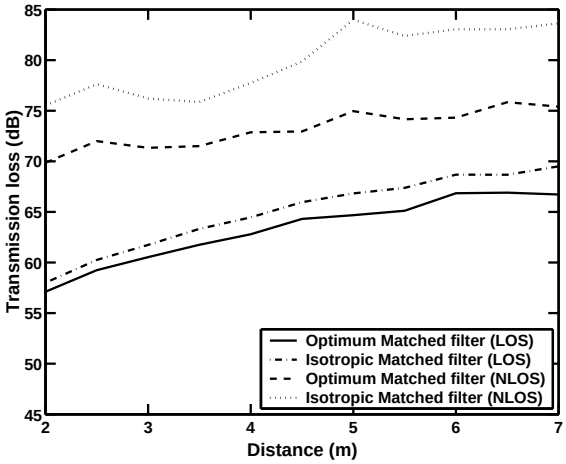

Fig. 6. Transmission losses of 1.4 GHz bandwidth along the distance from 2 to 7 m.

transmission loss of the optimum matched filter is better than that of the isotropic matched filter for all cases of the signal bandwidths. The obstruction loss of each signal bandwidth is almost the same. Based on this, the measurement results can be used for the standardization activities in IEEE 802.15.3a channel modeling.

REFERENCES

[1] Federal communications commission Revision of part 15 of the commissions rules regarding ultra-wideband transmission systems, First Report and Order, ET Docket $98-153$, FCC $02-48$, April 2002. On line available at [http://www.fcc.gov].

[2] M. Ghavami, L.B.Michael,R.Kohno, "*Ultra wideband signals and systems in communcation engineering*," John Wiley-Sons,Ltd, 2004.

[3] T. B. Welch, R. L. Musselman, B. A. Emessiene, P. D. Gift, D. K. Choudhury, D. N. Cassadine, and S. M. Yano, "The effects of the human body on UWB signal propagation in an indoor environment," IEEE J. Select. Areas Commun., vol. 20, no. 9, pp. $1778-1782$, Dec. 2002.

[4] A. F. Molisch, B. Kannan, C. C. Chong, S. Emami, A. Fort, J. Karedal, J. Kunisch, H. Schantz, U. Schuster and K. Siwiak, IEEE 802.15.4a Channel Model Final Report, IEEE 802.15-04-0662-00-004a, San Antonio, TX, USA, Nov. 2004.

[5] Application Requirement Analysis. IEEE P802.15-03/0489r4.

[6] S. S. Ghassemzadeh, R. Jana, C. Rice, W. Turin and V. Tarokh, Measurement and modeling of an ultra-wide bandwidth indoor channel, IEEE Trans. Commun., vol. 52, no. 10, pp. 1786-1796, Oct. 2004.

[7] J. Foerster and Q. Li, UWB Channel Modelng Contribution from Intel, IEEE P802.15-02/445r1-SG3a, Jun. 2002.

[8] J. Keignart, J. B. Pierrot, N. Daniele, A. Alvarez, M. Lobeira, J. L. Garcia, G. Valera and R. P. Torres, Radio Channel Sounding Results and Model, Deliverable D31, IST-2001-32710-U.C.A.N., Nov. 2002.

[9] M. Pendergrass and W. C. Beeler, Empirically based statistical UWB channel model, IEEE P802.15-02/240SG3a, Jul. 2002.

[10] J. Takada, S. Promwong and W. Hachitani, Extension of Friis Transmission Formula for Ultra-Wideband Systems, IEICE Tech. Rep., WBS2003-8/MW2003-20, May 2003.

[11] United States of America, Path Loss Calculations for Ultra Wideband Signals in Indoor Environments, ITU-R Document 3K/30-E, pp. 1-14, Nov. 2003.

Modified Decision Feedback Adaptive Equalizer for Turbo Coded DS-CDMA Systems Using SOVA Decoding

T. Udomsripaiboon*, N. Sanpote*, K. Sooksomsatarn* and C. Benjangkaprasert**
*School of Information and Communication Technology, Narasuan University Payao Campus, Payao, 56000 Thailand.
** Research Center for Communications and Information Technology (ReCCIT), and
Faculty of Engineering, King Mongkut's Institute of Technology Ladkrabang, Bangkok 10520, Thailand.
Email: noah8622@hotmail.com, kbchawal@kmitl.ac.th

***Abstract*- This paper presents a modified decision feedback adaptive equalizer for turbo coded direct-sequence code division multiple access (DS-CDMA) system using soft output viterbi algorithm (SOVA) decoding. The modified decision feedback equalizer (MDFE) structure is based on the decision feedback equalizer (DFE) structure. And the adaptation process of the equalizers is using the most commonly least mean square (LMS) adaptive algorithm. The simulation results are shown that the bit error rate (BER) performance of the MDFE with the SOVA decoding outperforms other equalizers structure such as the finite impulse response (FIR) equalizer and the conventional decision feedback equalizer (DFE).**

I. INTRODUCTION

Direct sequence code division multiple access (DS-CDMA) is a candidate access technique for a third generation mobile system [1]. In DS-CDMA systems, signal transmission over time-varying multipath mobile radio channel produces intersymbol interference (ISI), multiple access interference (MAI), and other time-varying effect from the channel. In this case, a DS-CDMA receiver with channel equalization is generally required to mitigate the effect of ISI and MAI signals. There are many kinds of the equalizers structure such as the finite impulse response (FIR) equalizer, the conventional decision feedback equalizer (DFE) [2,11] and the modified decision feedback equalizer (MDFE) [3]. The last one equalizer structure that was proposed by author can improve the performance of the system, which is considered in this paper.

Turbo coding [4] has been adopted as a channel coding scheme for several third generation mobile system in particular third generation partnership project (3GPP) for high data rates. It provides significant improvements in the quality of data transmission over a noisy channel. Iterative log-maximum a posteriori algorithm (Log-MAP) and soft output viterbi algorithm (SOVA) decoding are an important kind of turbo decoding algorithms [5-7]. However, SOVA is less complex [7]: the algorithm shares some operations [8]. Therefore, SOVA solutions have to be considered in this paper.

In this paper presents a modified decision feedback adaptive equalizer for turbo coded direct-sequence code division multiple access (DS-CDMA) system using soft output viterbi algorithm (SOVA) decoding.

The paper is organized as follows. Section II, the system model for the DS-CDMA system is presented. In section III presents the turbo codes system herein including turbo encoder and the prime candidates SOVA decoding turbo codes. Section IV, the conventional decision feedback equalizer and the modified decision feedback equalizer are presented. In section V presents the least mean square adaptive algorithm for update the coefficient of the equalizers. Computer simulations for several situations to demonstrate the performance of the system and conclusions are given in section VI and VII, respectively.

II. SYSTEM MODEL

We consider the real signal model of an Additive White Gaussian Noise (AWGN) *K*-user synchronous DS-CDMA channel that the baseband received signal [3] is defined as:

$$r(n) = \sum_{i=0}^{\infty} \sum_{k=0}^{K-1} d_i^k c_k (n - i\tau) * h_k(n) + n(n) \qquad (1)$$

where modulation scheme is linear. d_i^k is the *k*th symbol of duration T_s, transmitted by user *i*. and T_c is the chip duration ($T_c = T_s / L_c$) and $c_k \in \{-1,1\}$.

The minimum value of τ is: $\tau = T_s + (W\text{-}1)\ T_c$.. $n(n)$ is a complex additive white gaussian noise with zeros mean and a variance of σ^2.

The spread signal is transmitted over the frequency and time selective channels, where $h_k(n)$ is given as follows [2]:

$$h_k(n) = \sum_{i=0}^{W-1} a_i^k \delta(n - iT_c) \qquad (2)$$

whose impulse response is given by:

$$a(n) = \left\{ \begin{array}{ll} 0.5\left\{1 + \cos(\frac{2\pi}{A}(n-2))\right\}, & n = 1,2,3 \\ 0 & ,otherwise \end{array} \right\} \qquad (3)$$

where the factor *A* is introduced to allow scaling to customize the simulated ISI.

III. TURBO CODES [9]

Parallel concatenation of at least two component codes with interleaver in between them forms a parallel-concatenated interleaved code, also known as a turbo code. A turbo code encoder with two component codes is shown in the Figure 1. Special types of convolutional codes, called recursive systematic convolutional codes (RSC), are used as the building blocks of a turbo code encoder.

The encoder ENC_1 and ENC_2 of the two component RSCs encode the same input information bits $x(n)$ but in a different order, because of the interleaver before the ENC_2. Appropriate puncturing of parity bits ($d2_n, d3_n$) from two encoders can produce a turbo code of desired rate ($d2,3_n$). In this study, two memory-2 recursive systematic convolutional codes (generate matrix 7_8, 5_8) are used as component codes and the puncturing matrix is used to get overall turbo code of rate ½ following the design in [6]. A fixed pseudorandom interleaver is used. It has been selected among randomly generated interleavers based in frequency of low-weight output codeword for weight-2 input sequences following methodology in [10].

The Figure 2 shows the structure of a turbo decoder. The two decoders (log-maximum a posteriori algorithm (Log-MAP) or soft output viterbi algorithm (SOVA) decoding) Decoder 1 (DEC_1) and Decoder 2 (DEC_2), corresponding to the constituent encoders ENC_1 and ENC_2, are serially connected through the same interleaver that is used in the encoder.

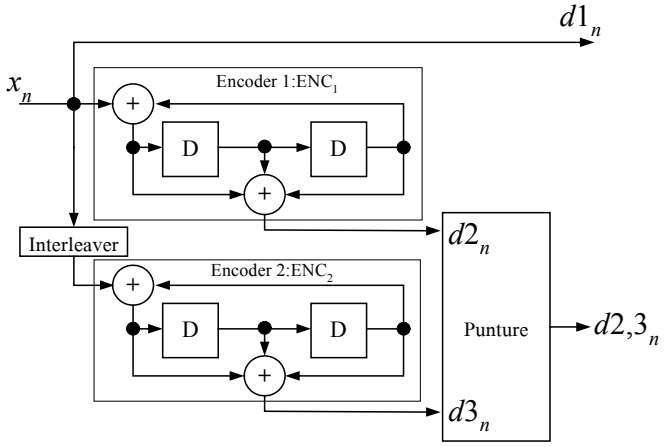

Figure 1. Turbo Encoder

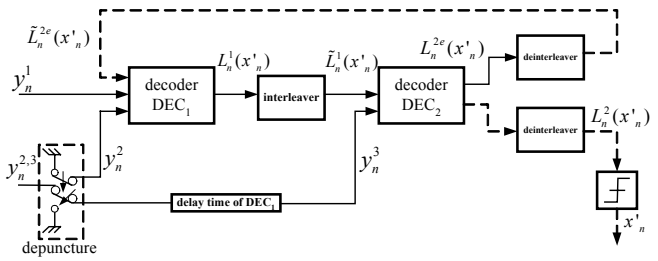

Figure 2. Turbo Decoder

The iterative turbo decoding is implemented using SOVA and Log–MAP algorithms in the soft input soft output (SISO) decoders described in [9,10]. Appropriate soft output $y_n^1, y_n^{2,3}$ from the depuncture y_n^2, y_n^3 are used as inputs of both the decoders. The values of a priori probability distribution for information bits $\tilde{L}_n^{2e}(x'_n), \tilde{L}_n^1(x'_n)$ are initialized for the first iteration by assuming information bits to be equally probable. However, after the first decoding step $\tilde{L}_n^{2e}(x'_n)$ will be available from the soft outputs of information bits $L_n^1(x'_n), L_n^{2e}(x'_n)$ computed in the previous decoding stage. The SISO decoder of [10] can be used to compute extrinsic information corresponding to both information bits $L_n^1(x'_n), L_n^{2e}(x'_n)$ and coded bits $L_n^2(x'_n)$ in general. However, for iterative decoding of a turbo code only $L_n^{2e}(x'_n)$ are required, and it is passed to next decoder after each decoding step to improve the correction capacity of decoding. Detection is made after the final iteration by adding the a posteriori probability values of the information bits $L_n^2(x'_n)$ from the output of the last decoding stage to the values of a priori distributions $\tilde{L}_n^1(x'_n)$.

In this paper SOVA solutions have to be considered. We will briefly describe the attractive SOVA decoding turbo codes in next section.

The Viterbi Algorithm (VA) [12] was originally proposed for decoding of convolution codes. Here we will present SOVA algorithm which development by VA. The SOVA estimates the soft output information for each transmitted binary symbol in the log-likelihood function $L(x'_n)_{SOVA}$, as follows:

$$L(x'_n)_{SOVA} = \log\frac{P_r(s_n = 1 \mid y_1^\tau)}{P_r(s_n = 0 \mid y_1^\tau)} \approx \log\frac{e^{-\mu_{\tau,\min}}}{e^{-\mu_{t,s}}} \approx \mu_{t,s} - \mu_{\tau,\min} \quad (4)$$

where P_r is a *posteriori* probability , s_n is the spread signal of the transmitted symbol, $\mu_{\tau,\min}$ is the minimum path metric as the maximum likelihood (ML) , $\mu_{n,s}$ is the minimum path metric of the paths with complementary symbol to the ML symbol at time *n*. If the ML symbol at time *n* is 1, then its complementary symbol is 0. Therefore, we can write [5]:

$$P_r(s_n = 1 \mid y_1^\tau) \approx e^{-\mu_{\tau,\min}} \quad (5)$$

$$P_r(s_n = 0 \mid y_1^\tau) \approx e^{-\mu_{n,s}} \quad (6)$$

IV. THE EQUALIZER STRUCTURES

A. Decision feedback equalizer (DFE) structure

The DFE, first introduced by Austin[11], shows significant performance gain by adding decision feedback filter to linear equalizer (LE). It consists of feed-forward filter and decision feedback filter. The DFE that has feed-forward filter of *M*-1 taps and feedback filter of *N*-1 taps. We assume that the input

vector, R_n^k, and filter coefficient vector, $W_{w,v}$ with time index n is given by:

$$R_n^k = [r^k(n) r^k(n-1) \ldots r^k(n-(M-1)) \; y_{H1}^k(n-1) \ldots y_{H1}^k(n-(N-1))]^T \quad (7)$$

$$W_{w,v} = [w_0 \; w_1 \ldots w_{M-1} \quad v_1 \ldots v_{N-1}]^T \quad (8)$$

where $r^k(n)$ is the input signal and $y_{H1}^k(n)$ is the decision value of the equalizer output.

Then, the output before decision of the DFE can be expressed as:

$$y_{d1}^k(n) = \sum_{i=0}^{M-1} w_i r^k(n-i) + \sum_{i=0}^{N-1} v_i y_{H1}^k(n-(i+1)) \quad (9)$$

$$= W_{w,v}^H R_n^k \quad (10)$$

where H stand for Hermitian transpose, $y_{d1}^k(n)$ is the output before decision of the DFE can be expressed as:

$$y_{d1}^k(n) = y_{ff1}^k(n) + y_{fb1}^k(n) \quad (11)$$

The error between the desired signal $d^k(n)$ and the filter output $y_{ff1}^k(n)$ is defined as:

$$e_{ff1}(n), e_{fb1}(n) = d^k(n) - y_{ff1}^k(n) \quad (12)$$

B. The modified DFE equalizer (MDFE) Structure [3]

This section, the modified decision feedback equalizer (MDFE) structure is presented. The equalized output signal of the MDFE adaptive equalizer is the sum of the outputs of the feed-forward part and feedback part of the equalizer. Decisions made on the equalized signal are only feedback to a feedback part of the equalizer. By this structure, it is suitable for turbo code decoding of the DS-CDMA systems. Therefore, the output $y_{ff2}^k(n)$ of the feed-forward part is given by:

$$y_{ff2}^k(n) = \sum_{i=0}^{M-1} w_i r^k(n-i) \quad (13)$$

The output $y_{fb2}^k(n)$ of the feedback part is given by:

$$y_{fb2}^k(n) = \sum_{i=1}^{N-1} v_i y_{df2}^k(n-(i+1)) \quad (14)$$

where $y_{df2}^k(n)$ is the decision output of $y_{ff2}^k(n)$ can be expressed as:

$$y_{df2}^k(n) = sign\left[y_{ff2}^k(n) \right] \quad (15)$$

Then, the output $y_o^k(n)$ of the MDFE can be expressed as:

$$y_o^k(n) = y_{ff2}^k(n) + y_{fb2}^k(n) \quad (16)$$

The error between the desired signal $d^k(n)$ and the filter output $y_{ff2}^k(n)$ of MDFE is given as:

$$e_{ff2}(n), e_{fb2}(n) = d^k(n) - y_{ff2}^k(n) \quad (17)$$

V. The Adaptive Algorithm for The Equalizers

The general problem is to estimate the desired discrete time signal $d^k(n)$ using past values $d^k(n\text{-}1)$, $d^k(n\text{-}2)$, …, and samples from a reference signal $\{r^k(n)\}$, from Eq.(8), the weights of feedback part of the equalizer using the least mean square (LMS) algorithm [2] are updated according to:

$$w(n+1) = w(n) + \mu_{ff} e_{ff}(n) r^k(n) \quad (18)$$

where μ_{ff} is a fixed step-size parameter of feed-forward filter part.

The weights of feedback filter part are updated as:

$$v(n+1) = v(n) + \mu_{fb} e_{fb}(n) y_{df}^k(n) \quad (19)$$

where μ_{fb} is a fixed step-size parameter of feedback filter part.

VI. Numerical Results

The BER performance of the modified decision feedback equalizer (MDFE) structure with SOVA decoding for turbo code DS-CDMA system receiver is presented in this section. The simulation results are obtained from the communication system over both ISI and MAI channels. The main system parameters are defined as follows: length of transmission information 15 kbits (15 x 1024), support 4 users, filter length of feed-forward part M = 11, feedback part N = 10, power of each user = 8 dB, and with 10 independents computer runs.

For turbo code parameters are defined as follows : channel code rate R = 1/2, and the number of iteration for turbo decoder = 1, code generator metric:

$$G = \left[1, \quad \frac{1 + D^2}{1 + D + D^2} \right] \tag{20}$$

with constraint length = 3.

Figure 3 shows the convergence processes of feed-forward and feedback part with adaptive algorithm for the equalizers with the Eb/No = 15 dB. Figure 4 shows the average BER performance of the perfect power control versus Eb/No for various values of the MDFE with SOVA decoding receiver. From this figure, it is seen that the MDFE provides a lowest BER performance for every Eb/No values.

Finally, Figure 5 shows the BER performance of the equalizer as a function of the number of decoder iterations. From Figure 5, it is evident that the BER performance of the equalizer is directly proportional to the number of decoder iterations.

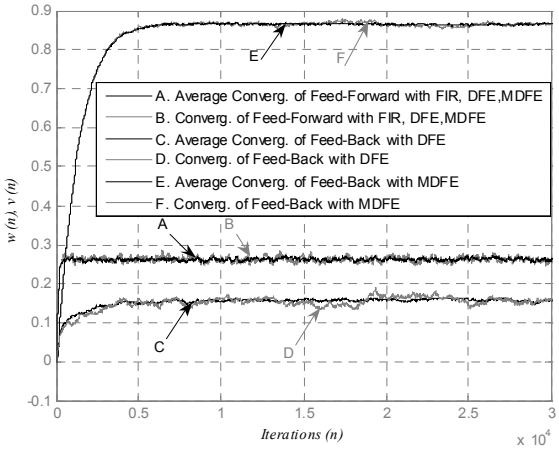

Figure 3. The convergence processes of feed-forward coefficients and feedback coefficients of the equalizers with Eb/No = 15 dB.

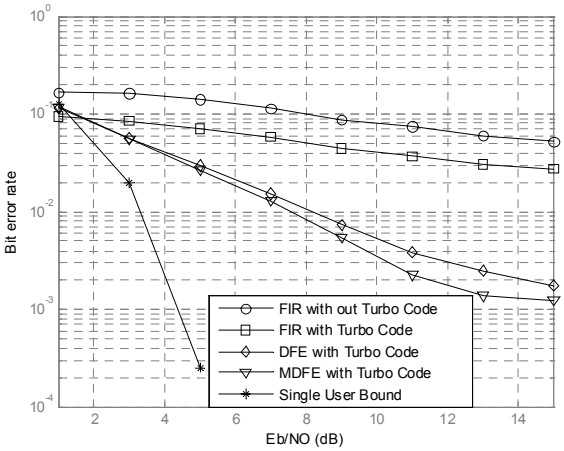

Figure 4. The BER performance of the equalizers using SOVA decoding.

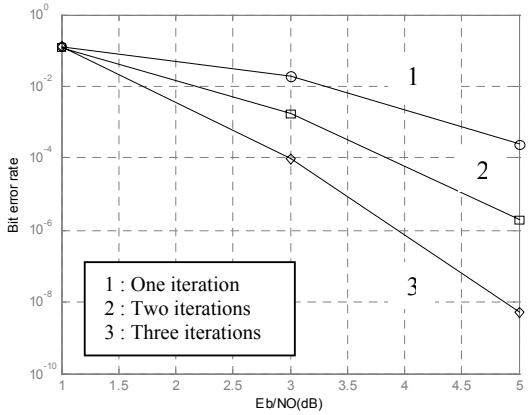

Figure 5. The BER performance of Single User Bound (SUB) as a function of Eb/No and multiple iterations.

VII. CONCLUSION

In this paper presents a powerful adaptive equalizer that using the LMS algorithm to control the adaptation process of the modified decision feedback equalizer (MDFE) and followed by the attractive SOVA algorithm for the turbo decoding process of the communication system. Our simulation results shown that the BER performances of the MDFE for the DS-CDMA communication systems are greatly outperformed then other equalizers. Finally, the performance of the equalizer is achieved as a function of the number of decoder iterations.

REFERENCES

[1] G. Mandyam and J. Lai, "Third-Generation CDMA systems for enhanced data services", Academic Press, 2002.

[2] S. Haykin, "Adaptive filter theory", Prentice-Hall, 2002.

[3] T. Udomsripaiboon, C. Mingkwan, C. Benjangkaprasert, O. Sangaroon, K. Janchitrapong-vej, "Soft output decision feedback equalizer using variable step-size algorithm for turbo codes DS/CDMA systems," In Proc. IEEE ISPACS, pp.505-508, Dec. 2005.

[4] C. Berrou, A. Glavieux, and P. Thitimasjshima, "Near shannon limit error-correcting codings and decoding: turbo code", In Proc. IEEE ICOC, pp. 1064-1070, May 1993.

[5] D. Divsala and F. Pollara, "On the design of turbo codes", The Telecommunication and Data Acquisition Progress Report, Jet Propulsion Laboratory, pp.99-121, 1995.

[6] S. Benedetto, D. Divsala, G. Montorsi and F. Pollara, "Soft-output decoding algorithms in iterative decoding of turbo codes", The Telecommunication and Data Acquisition Progress Report, Jet Propulsion Laboratory, pp.63-87, 1996.

[7] P. Robertson, E. Villebrum, P. Hoher, "A comparason of optimal and sub-optimal MAP decoding algorithms operating in the log domain," In Proc. IEEE ICC, pp. 1009-1013, June 1995.

[8] C. Chaikalis, M. S. Khaligh, N. Panayotopoulos, "Reconfiguration between soft output viterbi and log maximum a posteriori decoding algorithms," In Proc. IEE 3G2000, pp. 316-320, March 2000.

[9] A. Giulietti, B. Bougard and L. V. Perre, "Turbo codes desirable and designable", Kluwer Academic Publisher, 2004.

[10] P. Jung and M. Nashan, "Performance evaluation of turbo codes for short frame transmission systems", Electronics Letters, Vol. 30, No. 2, pp. 111-113, Jan. 1994.

[11] M. Austin, "Decision-feedback equalization for digital communication over dispersive channels", M. I. T. RES. Lab. Election., Tech. Rep. 461, 1967.

[12] S. Haykin and M. Moher, "Modern wireless communications", Prentice-Hall, 2005.

A Channel Estimation Method for Downlink STBC MC-CDMA System on Multi-Path Fading Channel

Pattanapong Sookkaew, Montree Kumngern, Somyot Junnapiya, and Kobchai Dejhan
Faculty of Engineering and Research Center for Communication and Information Technology,
King Mongkut's Institute of Technology Ladkrabang, Bangkok 10520, Thailand
Tel: 66-2326-4238, 66-2326-4242, Fax: 66-2326-4554,
E-mail: montree_kumngern@yahoo.com, {somyot, kobchai}@telecom.kmitl.ac.th

***Abstract*–This paper describes a channel estimation method for space–time block code multi–carrier code division multiple access (STBC MC–CDMA) system as operating on multi-path fading channel with minimum mean square error (MMSE) detection scheme. In the proposed method, the design of orthogonal preamble symbols in time domain for separate impulse response of each channel is presented and threshold method in which an optimal threshold value can be selected to eliminate the noise signal in channel estimation. The simulation results are shown that the proposed technique can improve the performance of the system.**

I. INTRODUCTION

MC-CDMA system is expected that it has received a great deal for future fourth-generation wireless systems (4G) [1]. MC-CDMA inherits from orthogonal frequency division multiplexing (OFDM) characteristics such as high spectral efficiency and robustness against multi-part propagation, while from CDMA the benefit of a multiple access flexibility. In the past, a diversity technique as transmitter [2], [3] combined with STBC MC-CDMA [4] have been reported. It is a multi-input single-output (MISO) and a multi-input multi-output (MIMO) communication. Therefore, the effect of fading channel can be reduced. However, good performance of multiple antennas STBC MC-CDMA also depends on an accuracy of channel estimation of receiver part.

In this paper, a channel estimation technique for STBC MC-CDMA system is presented. The proposed technique based on least square (LS) channel estimation which can separate the channel impulse response of each transmit antenna by designing the preamble symbol with orthogonal in time domain and combined with threshold method. This proposed technique can reduce noise in the channel estimation.

II. MODEL OF SYSTEM

A. Transmitter and Receiver

Fig. 1(a) shows the block diagram of downlink STBC MIMO MC-CDMA system. The system uses N_C sub-carriers, N_t=2 be the number of transmit antennas and N_r=2 be the number of receive antennas. As Fig. 1(a), a stream of modulated signal of the u-th users is serial-to-parallel converted, where every V symbols are grouped into a vector. Each group vector is spread by the same Hadamart's sequence. After spreading, the spread vector of the v-th subdata, when v=1,2,…,V, are summed with symbol of other user. After that, a data with serial stream is converted to a parallel stream. A STBC will be applied to the MC-CDMA using Alamoutti's sequence [3]. To convert the frequency domain into the time domain, inverse fast Fourier transform (IFFT) is used. The outputs of IFFT are enters a parallel to serial converter and transmit to the receiver over the wireless channel.

At receiver, alternative transmit process will be used to detect the original data. In this paper, MMSE [3] single user detect scheme is investigated.

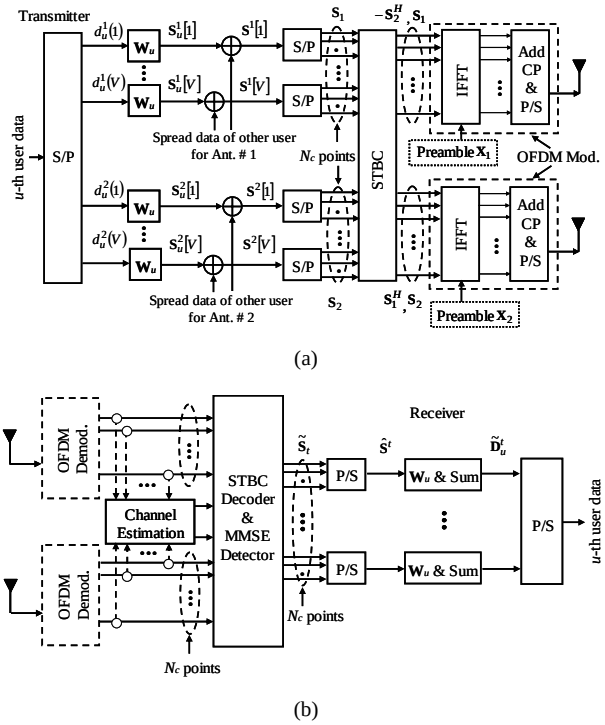

Fig. 1. Block diagram of MIMO MC-CDMA: (a) transmitter model, (b) receiver model.

B. Preamble Symbol Design and Channel Estimation

As the transmitter, a preamble for the 2 antennas is considered in this investigation. The preamble symbol is designed to be orthogonal in the time domain. It uses for separating the result of channel impulse response. The preamble for 2 transmit antennas can be formulated in the frequency domain by [2]

$$X_t(k) = X_1(k)e^{-j2\pi(t-1)N_t N_g k/N_c} \quad (1)$$

where $x_1(k)$ is the preamble symbol of the first transmit antenna as k-th subcarrier and N_g is the sample number of guard time interval. By using IFFT criterion, (1) can be expressed in the time domain by

$$x_t(n) = x_1\{(n-(t-1)N_t N_g)\}_{N_c} \quad (2)$$

when n=0,1,…,N_C-1. In (2), the preamble symbol of the t-th transmit antennas is the preamble symbol of the first transmit antenna with delay by (t-1)$N_t N_g$. Note that each multipath fading path of t-th transmit antennas to r-th receiver antennas are uncorelate and assumed that the two period of symbols are constant. After transmitted, the preamble symbol of each frame from each transmit antenna through the multipath fading channel. The received signal can be expressed by

$$x_r(n) = \sum_{t=1}^{N_t} x_t(n) \otimes h_{tr}(n) + n_r(n) \quad (3)$$

Assume the every receive antennas are received the signal at the same time. By using FFT criterion, it can be written as

$$X_r(k) = \sum_{t=1}^{N_t} X_t(k) H_{tr}(k) + N_r(k) \quad (4)$$

when $H_{tr}(k)$ is the channel frequency response as k-th subcarrier of t-th transmit antenna to r-th receive antenna. $N_r(k)=FFT\{n_r(n)\}$ is noise signal. The sum of channel frequency response from every transmit antennas can be approximated by Least square algorithm, as

$$\hat{H}_r(k) = X_r(k)/X_t(k) \quad (5)$$

To simplify for separating the channel impulse response of each transmit antenna, (5) is converted into the time domain, expressed as

$$\hat{h}_r(n) = \sum_{t=1}^{N_t} h_{tr}(n-(t-1)N_t N_g) + \tilde{n}_r(n) \quad (6)$$

If the time period of result from the channel impulse response is less than the guard time interval, the signal from t-th transmit antenna have channel impulse response to the r-th receive antenna. The receiver can be made orthogonal in time domain, as follows

$$\hat{h}_{tr}(n) = \hat{h}_r(n+(t-1)N_t N_g) \quad (7)$$

In the case of the results from channel impulse response decreased as exponential formula, the receive power signal is a few in the time domain. Accordingly, it can be neglected some of the sample of impulse response these low power signals, because these sample are sum between signal and the strong noise power. Whereas the low E_b/N_o can be achieved by using threshold level, which is relate E_b/N_o at receiver as shown in (8). The channel impulse response from each transmit antenna in (7) measured the level of signal by selecting only the channel impulse response sample have more power than or equal to the level of threshold, expressed as

$$Threshold = \beta \times Eb/No \quad (8)$$

$$\tilde{h}_{tr}(n) = \begin{cases} \hat{h}_{tr}(n), & if \left|\hat{h}_{tr}(n)\right|^2 \geq Threshold \\ 0, & Other \end{cases} \quad (9)$$

Eq. (9) will be converted to channel frequency response with FFT formula. This process is used for MMSE detection as follow [3].

III. Simulation Results

To evaluate the system performance, computer simulations to verify the performance of the MIMO MC-CDMA system of Fig. 1 were conducted following an extended specification of an IEEE 802.11a as listed in Table. The indoor propagation channel model in [5] is used for this simulation.

TABLE
Simulation Condition.

System parameters	Configuration
Occupied bandwidth	20MHz
FFT size (N_c)	64
Guard Interval (T_g)	0.8μs
Total symbol duration ($T_s=T_{FFT}+T_g$)	4μs
Subcarrier spacing ($1/T_{FFT}$)	312.5kHz
Length of Spreading code (M)	32
Modulation	QPSK
Center frequency (f_c)	5GHz
Transmission Rate	32Mbit/s
Multi-path channel Model	
Delay profile	Exponential
Number of paths	4
RMS Delay spread	50ns
Maximum Doppler frequency	33.4Hz

Fig. 2 shows the optimal threshold values depend on E_b/N_o of the system. The threshold level to give minimum MSE (β=0.003) of all E_b/N_o values (8dB, 12dB, and 16dB). Fig. 3 shows the comparison between MSE and Eb/N_o of system. The comparative of channel estimation with β=0.003 and conventional method, from the results the proposed channel estimation to increase the better performance. If E_b/N_o are large the performance of two method, it will be same. Accordingly, in case of the E_b/N_o will be increased, some of channel impulse response sample has low power will be cancelled and effect to the performance of the system. Fig. 4 shows the BER performance of channel estimation in 1 user. By the proposed method gives better performance than conventional method. As BER=10^{-4}, the use power of proposed method more than the perfect channel

estimation of SISO MC-CDMA, MISO MC-CDMA and MIMO MC-CDMA are 0.8dB, 1.3dB and 1.9dB, respectively. Fig. 5 shows the performance of three systems alternate with number of user. The results compared between the proposed channel estimation and perfect channel estimation shown the E_b/N_o=16dB.

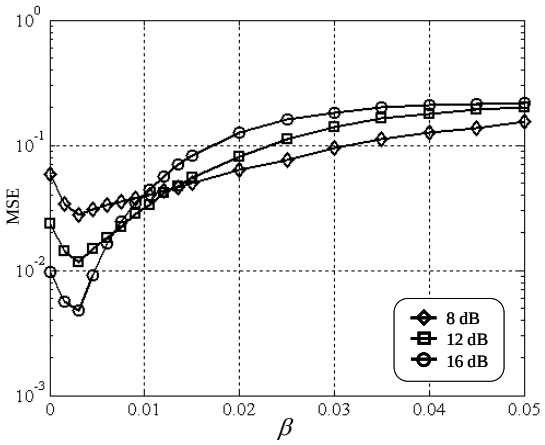

Fig. 2. The best of β level with Eb/No=8, 12 and 16 dB.

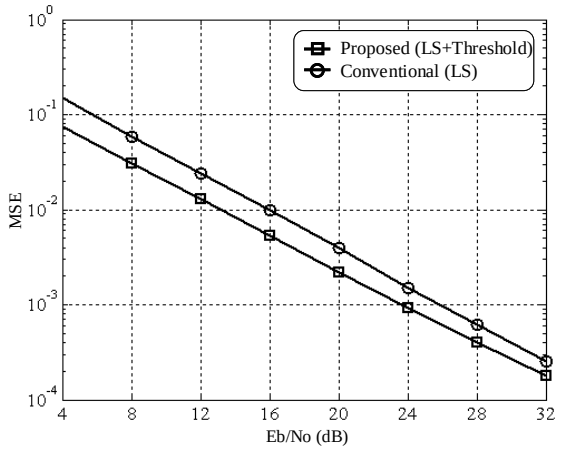

Fig. 3. Comparison of MSE between proposed channel estimation and conventional channel estimation.

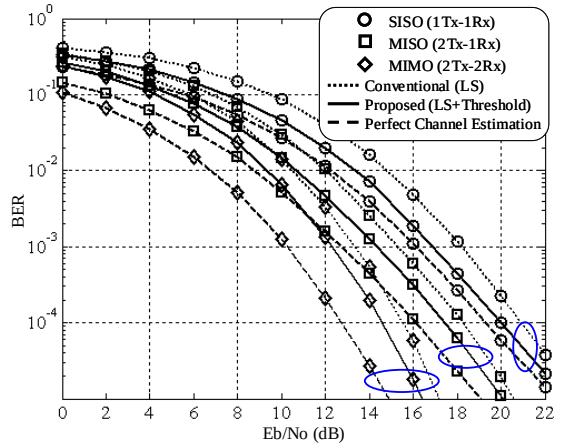

Fig. 4. Channel estimation performance for different systems in case of 1 user.

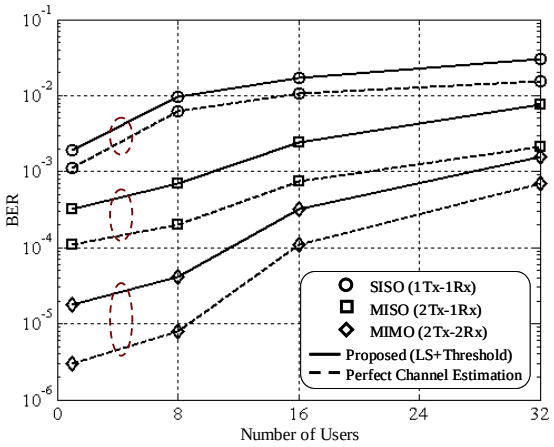

Fig. 5. Comparison of BER between number of users for SISO MC-CDMA, MISO-CDMA, and MIMO-CDMA systems.

IV. Conclusions

In this paper, we introduced a STBC MC-CDMA multipath fading channel estimation employing MMSE detector. The proposed method designs the preamble symbol with orthogonal in the time domain to simple for separate the channel impulse response of each transmit antenna and using the threshold technique to cannel noise in the channel estimation. The simulation results can be demonstrated that the proposed technique provides good performance.

References

[1] F. Fazel and S. Kaiser, "Multi-carrier and spread spectrum systems," Chichester, Wiley & Son, 2003.

[2] Y.-H. You, W.-G. Jeon, J.-H. Paik, M.-J. Kim, D.-S. Kim, and H.-K. Song, "Performance evaluation of OFDM-CDMA with multiple antennas for broadband wireless access networks," *IEEE Transactions on Vehicular Technology*, vol. 54, pp. 385-398, January 2005.

[3] X. Cai and A. N. Akansu, "Multicarrier CDMA systems with transmit diversity," *Proceeding of IEEE Vehicular Technology Conference*, vol. 6, pp. 2817-2821, 24-28 September 2000.

[4] S. M. Alamouti, "A simple transmit diversity technique for wireless communications," *IEEE Journal on Selected Areas in Communications*, vol. 16, pp. 1451-1458, October 1998.

[5] A. Doufexi, S. Armour, M. Butler, A. Nix, D. Bull, and J. McGeehan, "A comparison of the HIPERLAN/2 and IEEE 802.11a wireless LAN standards," *IEEE Communications Magazine*, vol. 40, pp. 172-180, May 2002.

An Extend Bi-directional Arbitrated Decision Feedback Equalizer

Samart Moodleah[1], Chawalit Benjangkaprasert[1], Keattisak Sripimanwat[2]

[1]Research Center for Communications and Information Technology (ReCCIT), and
Department of Information Engineering, Faculty of Engineering,
King Mongkut's Institute of Technology Ladkrabang
Bangkok 10520, Thailand,
Email: s7061159@kmitl.ac.th, kbchawal@kmitl.ac.th

[2]National Electronics and Computer Technology Center (NECTEC), Thailand

***Abstract*- An Extend bi-directional arbitrated equalizer (E-BAD) algorithm is presented whose performance is improved from the conventional bi-directional arbitrated equalizer (BAD) algorithm while complexity is linear in the channel length. Modified method uses the benefit of low correlation errors among forward, reverse and extend soft-decision feedback equalizer (SD-DFE). The low correlation errors among three equalizers gain the whole algorithm performance to outperform to the conventional BAD.**

I. INTRODUCTION

The nonlinear classical decision feedback equalizer (DFE) technique is introduced by M.Austin [1] whose complexity and performance lie between that of linear equalization and equalization based on maximum likelihood (ML) or maximum *a posteriori* (MAP). The better performance of ML and MAP techniques has high complexity whose grow as A^L where A is the alphabet size and L is the channel length. Meanwhile, the error propagation is the big deal of DFE even with the perfect decision feedback. Many works proposed the way to mitigate error propagation by using dual decision feedback whose threshold is set for difference feedback. Threshold technique, however, may not be the best error propagation mitigating strategy. In fact, nonlinear equalizer (DFE) may outperform a linear equalizer by several decibels [2]. Recently work, a new bi-directional arbitrated equalizer (BAD) was proposed [3] and shown that the performance is better than classical DFE.

The BAD algorithm work by running the parallel forward and reverse equalizer DFE separately. The low correlations among errors over the entire block data in forward and reverse equalizers are adopted. The best match received data is decided. Each equalizer is separately designed for forward and reverse channel and the channel is assumed to be known to the receiver.

This work is supported by the National Electronics and Computer Technology Center (NECTEC) Thailand under the QT5001 project.

The BAD use the benefits of low correlation error between forward and reverse equalizer. In this paper, the extend equalizer is added in the BAD algorithm to gain the low correlation error by adding the third soft-decision feedback equalizer. We propose an E-BAD that the performance outperforms to the conventional BAD by adding soft-decision feedback equalizer.

The rest of this paper is organized as follows. In Section II, we start with the definition and the operation of the BAD algorithm. We then proceed with a detail for explanation in the modify of BAD algorithm. In Section III, we give the simulation result then the E-BAD result is compared with that of several other equalization methods.

II. THE PREVIOUS STRUCTURE AND THE PROPOSED STRUCTURE

A. BAD algorithm

The BAD [3] uses bi-directional DFE equalizer to recover channel inputs in forward and reverse direction as depicted in Fig. 1. Define the input sequence of uncoded as binary phase shift keyed (BPSK) data as a , $a_k \in \{\pm 1\}, k = 0,..., N-1$ over the channel impulse response $h_k, k = -L2,..., L1$. The receive data sequence $r_k, k = 0,..., N-1$ can be expressed as

$$r_k = \sum_{i=-L_2}^{L_1} a_{k-i} h_k + w_k \qquad (1)$$

where w_k is an Additive White Gaussian Noise (AWGN) with variance σ^2 . The channel h_k and noise variance σ^2 are assumed known to the receiver. The channel is assumed to be time-invariant for the duration of the packet data sequence.

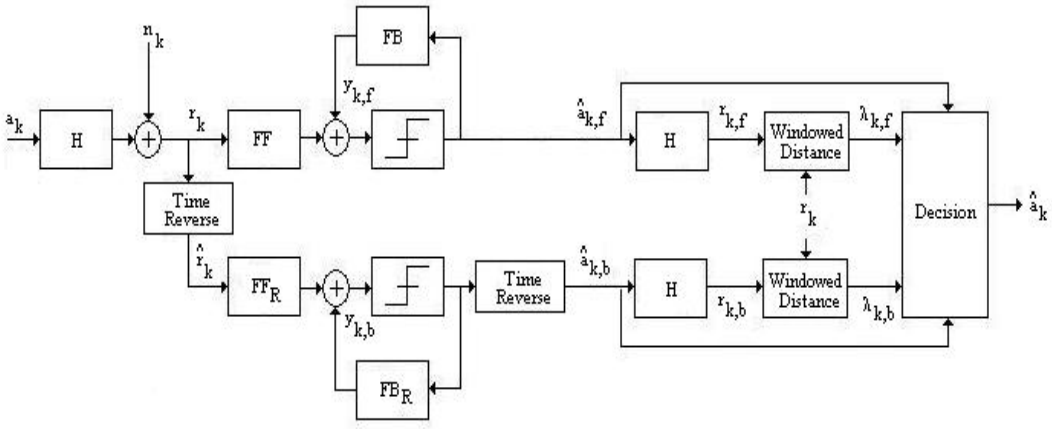

Fig. 1 Schematic of Bi-directional Arbitrated Decision Feedback Equalizer

The BAD equalizer consists of two DFE instructors which are separately designed for forward and reverse direction. The time-reversal operator for a length of N sequence of r_k can be expressed as

$$\hat{r}_k = r_{N-k} + 1, \qquad k = 0,\ldots,N-1 \qquad (2)$$

The upper DFE consists two filters: a feedforward filter tap coefficient $F = \{f_k\}, \{k = 0,..,M_f\}$ of length $M_f + 1$, and a causal feedback filter $B = \{b_k\}, \{k = 0,..,M_b\}$ of length M_b.

The equalizer tap coefficients are computed by using Recursive Least-Squares (RLS) algorithm. Hence, the equalized signal can be described as

$$y_{k,f} = \sum_{j=0}^{Mf} f_i r_{k-i} + \sum_{i=1}^{Mb} b_i \hat{a}_{k-i,f} \qquad (3)$$

At time k, $\hat{a}_{k,f}$ is made by slicing $y_{k,f}$ of both DFE directions which are separately designed by regarding to asymmetric channel. The lengths M_f and M_b depend largely on the channel are minimum, mixed, or maximum phase and on the length L_1 and L_2 [4].

Consider the ISI cancellation, the upper DFE is designed for normal channel and the lower DFE is independently designed for the time-reversal channel h_k. We can say that the precursor ISI is canceled by the upper DFE. While the lower DFE cancels the postcursor ISI.

The BAD algorithm has three stages: (1) bi-directional processing with forward and reverse DFEs, (2) data reconstruction and error calculation, and (3) data symbol arbitration. The output of two DFE are $\hat{a}_{k,f}$ and $\hat{a}_{k,b}$ from forward DFE and reverse DFE respectively, at the first stage.

In the second stage, the estimated data $\hat{a}_{k,f}$ and $\hat{a}_{k,b}$ are reconstructed pass through the channel to form noise-free signal. This tries to estimate of the received data r_k : reconstructed data can be expressed as

$$\hat{r}_{k,f} = \sum_{i=-L_2}^{L_1} h_i \hat{a}_{k-i,f} \qquad (4)$$

$$\hat{r}_{k,b} = \sum_{i=-L_2}^{L_1} h_i \hat{a}_{k-i,b} \qquad (5)$$

The final stage in BAD is the arbitration stage. The purpose of arbitration state is to arbitrate the symbol decision between $\hat{a}_{k,f}$ and $\hat{a}_{k,b}$ based on the minimum error in windowed size $W_1 + W_2 + 1$. The computation parameter is given by

$$\lambda_{k,f} = \sum_{j=-W1}^{W2} r_{k+j} - \hat{r}_{k+j,f}^{\,2} \qquad (6)$$

$$\lambda_{k,b} = \sum_{j=-W1}^{W2} r_{k+j} - \hat{r}_{k+j,b}^{\,2} \qquad (7)$$

The decision $\hat{a}_k$ can be formulated under criteria as

$$\hat{a}_k = \begin{cases} \hat{a}_{k,f}, & \lambda_{k,f} \le \lambda_{k,b} \\ \hat{a}_{k,b}, & \lambda_{k,f} > \lambda_{k,b} \end{cases} \qquad (8)$$

B. *Extend Bi-direction Arbitrated DFE (E-BAD) Algorithm*

In this section, the E-BAD algorithm is described. In the second state of BAD algorithm, data is re-constructed and an accumulation error is computed for forward and reverse equalizer. In the Extend BAD, we re-construct and calculate error again from difference source. The additional source is Soft Decision Feedback symbol and the BAD symbol is another input to the second state. Following the same method, the low correlation error is used again for make the best match with original received data. The soft-decision feedback equalizer is illustrated in Fig. 2. A soft decision feedback calculation can be expressed as follows [5]:

$$z_k = \tanh(\frac{y_k}{\alpha}) \tag{9}$$

$$\alpha = 10^{\frac{SNR}{10}} \left| HH^T \right\| FF^T \left| \right. \tag{10}$$

where T is the transpose operator.

The Extend BAD is depicted in Fig. 3. Using Eqs. (4), (5), (6), (7) and (8) to find the possibly correct data as the first times second BAD state.

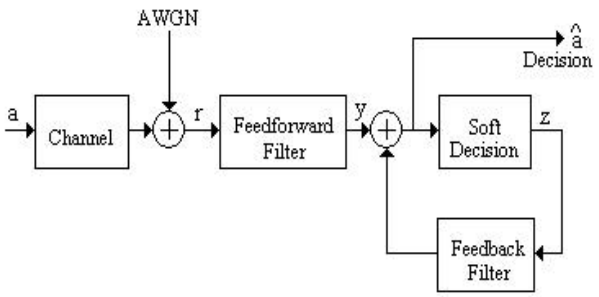

Fig. 2 Soft Decision Feedback Equalizer (SD-DFE)

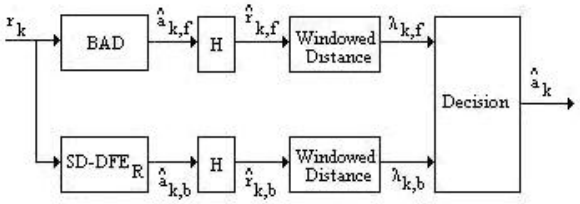

Fig.3 An Extend Bi-directional Arbitrated DFE (E-BAD)

III. Simulation Results Analysis

We first illustrate the performance of DFE structure among conventional DFE, SD-DFE, and Ideal DFE to show the degradation due to error propagation in DFE structure. We then show the performance of an Extend BAD algorithm that used SD-DFE structure in an extension block and compared to conventional BAD in Fig. 4. The simulation model is based on an uncoded MEEPR4 magnetic recording channel with binary input that are $H(D) = 5 + 4D - 3D^2 - 4D^3 - 2D^4$. The equalizer tap coefficients are chosen to be 31 and 9 for feed forward and feedback equalization, respectively. Windowed Distance size W is selected to 15 for simplicity. Each BER point was calculated using several 4,096 data blocks as need to collected 1,000 error bits.

A conventional BAD lag behind E-BAD whose 12 dB perform BER at 1.25e-5 and 0.79e-5, respectively. The Ideal BAD structure performance is better than E-BAD and BAD that of 0.6 dB and 0.8 dB at BER 2e-5.

Less error propagation of Ideal DFE structure in the Ideal BAD perform better performance than the other BAD algorithm. Even we reduce burst error of BAD structure by adding an Extend SD-DFE. The key to improve performance of BAD algorithm is to reduce error propagation in the structure as shown in the Ideal BAD.

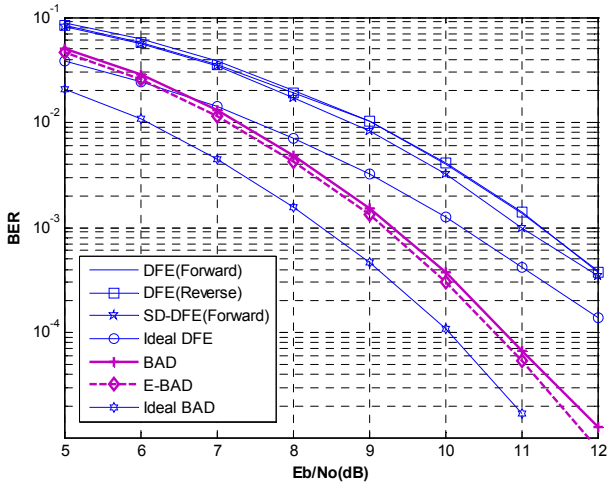

Fig. 4 E-BAD performance compared to other equalization method

IV. Conclusions

In this paper, an Extend Bi-directional Arbitrated Decision Feedback Equalizer had been presented. The traditional BAD algorithm is improved by adding another equalization symbol from an extend SD-DFE. Among equalization symbol posses the low correlation errors whose the benefit is used in arbitration state. E-BAD performance is better than conventional BAD over MEEPR4 channel with data uncoded system. The performance is improved due to burst error is

mitigated using among three equalization data. In fact, the BAD performance can by further improved by reducing error propagation in BAD structure. E-BAD is the modification level of BAD algorithm and perform better performance which can be used to several environment provided that the channel are known to the receiver.

REFERENCES

[1] M. Austin, "Decision feedback equalization for digital communication over dispersive channel", *MIT Research Laboratory of Electronics Technical Report 437*, Aug 1967.

[2] S. Pornchai, R. Lopes, and S. W. McLaughlin, "Reduced Complexity Turbo Equalization for High-Density Magnetic Recording Systems," *IEEE Trans. Magn*, vol. 39, no.5 Sep 2003.

[3] J.K Nelson, A.C. Singer, U. Madhow, and C.S. McGahey, "BAD: Bidirectional Arbitrated Decision-Feedback Equalization", *IEEE Trans. Comm.*, vol. 53, no. 2, Feb 2005.

[4] J. Proakis, *Digital Communications*, 3rd ed. New York: McGraw-Hill, 1995.

[5] J. Balakrishnan, "Mitigation of error propagation in decision feedback equalization", Master thesis, Cornell University, Aug 1999.

Narrowband Interference Suppression for UWB-TH System Based On Modified Template Waveform

Eakaraj Pakdeechard, Monchai Chamchoy, and Sathaporn Promwong
Faculty of Engineering
King Mongkut's Institute of Technology Ladkrabang
Chalongkrung Rd., Ladkrabang, Bangkok 10520, Thailand
Email: s7061172@kmitl.ac.th

***Abstract*— The narrowband interference can affect the performance of the UWB time hopping (TH) system. Therefore, interference suppression technique is important for UWB communication to operate over spectrum with established narrowband system. In this paper, the interference suppression technique based on modified template waveform for correlation receiver is employed, where the modulation techniques and path loss model are considered. Our study demonstrates that the BER performance of the modified template waveform is better than the original one. Therefore, the modified template waveform based correlation receiver is simple and low complexity technique which can improve the system performance significantly.**

I. INTRODUCTION

Ultra wideband (UWB) radio technology has a great interest in wireless networking. UWB offers many advantages which can be described as the potential for low cost, low power transmission, high data rates and immunity to multipath. Instead of using a narrow carrier frequency, UWB transmits pulses of power spectral density (PSD) in the range of the ultra wide frequency spectrum. The Federal Communications Commission (FCC) defines UWB as any signal that occupies more than 500 MHz in the frequency range of 3.1-10.6 GHz with the maximum emission power of -41.3 dBm/MHz [1]. Because of the transmission at low power, the UWB signal is considered to be noise for other communication systems. Therefore, UWB radio technology can coexist with other RF technologies without interference. Unfortunately, at close proximity, UWB radio can induce interference and degrade the throughput of the other system.

Numerous literatures study on UWB interference to other existence narrowband system [2]-[8]. On the other hand, there are few research study on the influence of narrowband interference (NBI) to UWB communication system. Especially, the IEEE 802.11a wireless LAN system operates at 5 GHz bands which overlaps the UWB spectrum [9]. This system uses orthogonal frequency division multiplexing (OFDM) based transmission. In [10], the coexistence of UWB system and wireless LANs is investigated for LOS and NLOS propagation scenarios. The results show that wireless LAN interference can greatly impact the performance of the UWB receiver. Similarly, the interference from a nearby NBI will affect UWB performance also provides in [11]. While the analytical approach of the IEEE 802.11a interference on UWB systems is given in [12]. Therefore, the interference suppression technique is required for UWB communication.

In this paper, we propose the modified template waveform based correlation receiver for interference suppression. The proposed waveform is the filtered Gaussian doublet pulse by using notch-filter to reject the narrowband interference (IEEE802.11a WLAN). Our simulation illustrates that the modified template waveform based correlation receiver allows significant performance improvement in the presence of the narrowband interference.

The organization of the paper is as follows. In Section II, the models of UWB time-hopping transmission and IEEE 802.11a interference are provided. The performance simulation and results will be given in Section III and the conclusion is given in Section IV.

II. SYSTEM MODELS

A. The UWB Transmitter Model

A common method for implementing the UWB signal is widely referred to as Impulse Radio (IR) [13]. Therefore, Gaussian doublet pulse shape is considered as a transmitted waveform and is given by

$$p(t) = A(1 - \frac{2t^2}{\xi^2}) \exp\left[-(t/\xi)^2\right], \quad (1)$$

where A is the maximum amplitude, ξ is the $1/e$ characteristic delay time. This waveform is the second derivative of the Gaussian pulse.

Modulation method for UWB time-hopping in the transmission are considered. The most common method of time-based techniques modulation is pulse position modulation (PPM) which may be expressed as

$$s_{\mathrm{PPM}}(t) = \sum_{n=-\infty}^{+\infty} p(t - nT_f - T_{c_n} - T_{p_n} - \tau_k), \quad (2)$$

where T_f represents the time duration of the frame, $p(t)$ is the Gaussian doublet pulse, T_f denotes the pulse repetition time, T_{c_n} is the time shift related to the PN code sequence, T_{p_n} represents the time shift from the pulse position modulation scheme and τ_k is the time delay.

Another common method of modulation is to invert the pulse. This is known as bi-phase modulation (BPM) and is

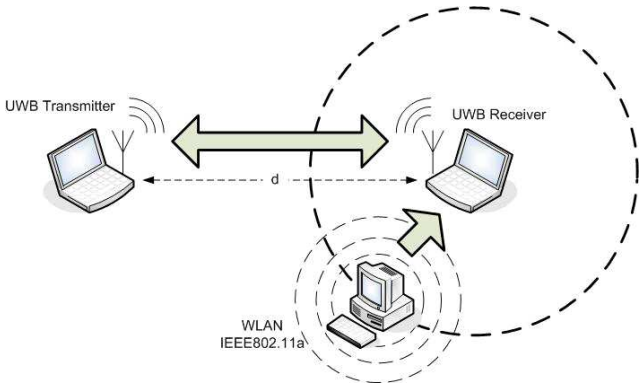

Fig. 1. Model of UWB transmission in the presence of the IEEE 802.11a interference.

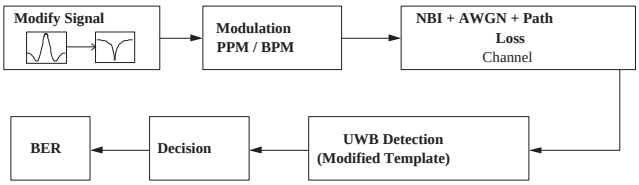

Fig. 2. The block diagram of the NBI suppression technique based on modified template waveform.

given by

$$s_{\mathrm{BPM}}(t) = \alpha_k \sum_{n=-\infty}^{+\infty} p(t - nT_f - T_{c_n} - \tau_k), \qquad (3)$$

where α_k represents the modulation symbol sequence for BPM ($[-1, 1]$).

B. IEEE 802.11a NBI and Path Loss Model

The NBI transmitted signal can be represented as [9]

$$s_{\mathrm{NBI}}(t) = w_T(t) \cdot \Re\left\{ \sum_{k=-N_{ST}/2}^{k=N_{ST}/2-1} c_k e^{j2\pi k \Delta F (t-T_G)} e^{j2\pi f_c t} \right\}, \qquad (4)$$

where N_{ST} is the total number of subcarrier, c_k is the set of coefficients transmitted, T_G is the guard time and ΔF represents the subcarrier frequency spacing, $w_T(t)$ is a time-windowing function that defines the boundaries of the subframe which assume a rectangular $w_T(t)$ with unit amplitude.

In order to calculate the SINR of the UWB system in the presence of the IEEE 802.11a interference, the empirical path loss model is employed. Therefore, the SINR at the UWB receiver is given by

$$SINR_{\mathrm{UWB}} = P_R(d) - 10\log(NBI_{802.11a} + N_{\mathrm{UWB}}), \qquad (5)$$

where $NBI_{802.11a}$ and N_{UWB} are interference and noise power at the UWB receiver, respectively. The propagation path loss model may be expressed as

$$PL(d) = PL(d_0) + 10n\log_{10}\left(\frac{d}{d_0}\right);\ d \geq d_0, \qquad (6)$$

where n is the path loss exponent which indicates the rate of the path loss increases with distance and d represents the T-R separation distance. Fig. 1 illustrates the UWB time-hopping system in the presence of IEEE 802.11a interference.

C. The Modified Template Waveform

Due to the UWB transmitted signal occupies an ultrawide bandwidth which cover the IEEE802.11a wireless LAN system operation. From [14], the IEEE802.11a wireless LAN can affect the performance of the UWB time-hopping system. Therefore, the interference suppression technique is required. We propose the modified template waveform technique which is simple and low complexity structure. This suppression technique involves the filtered UWB transmitted signal $p(t)$ by using the notch filter for reject bandwidth of the IEEE802.11a wireless LAN. Moreover, we consider the modified template waveform use to transmit and detect signal in the UWB system as shown in Fig. 2. The modified transmitted waveform is given by

$$u(t) = \sum_{w=-W}^{+W} \alpha_w p(t - wT_c). \qquad (7)$$

Therefore, the modified template waveform is given by

$$M(t) = u(t) - u(t - \delta), \qquad (8)$$

where T_c is one sample per bin period, the coefficients of the filter are $\{\alpha_w\}$ for $w = [-W, ..., W]$ and the number of taps on each side of the notch filter is W.

Fig. 3 shows the template waveform for the UWB correlation receiver. A left side pulse in the figure is the original template waveform, while the modified template waveform is shown in the right figure.

D. The UWB Receiver Model

A transmitted signal passes through the wireless channel including the transmitter and receiver antennas. Therefore,

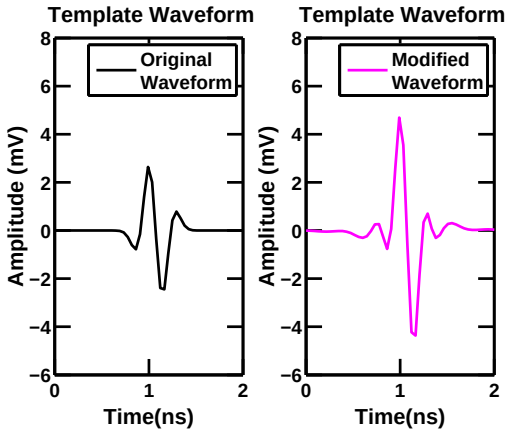

Fig. 3. The template signal waveform based correlation receiver. The left figure is the original template waveform and the right figure is the modified template waveform.

the total received signal for UWB PPM transmitter can be expressed as

$$r_{\mathrm{PPM}}(t) = \sum_{n=-\infty}^{+\infty} p(t - nT_f - T_{c_n} - T_{p_n} - \tau_k) + s_{\mathrm{NBI}}(t) + n(t), \quad (9)$$

and for UWB BPM transmitter,

$$r_{\mathrm{BPM}}(t) = \alpha_k \sum_{n=-\infty}^{+\infty} p(t - nT_f - T_{c_n} - \tau_k) + s_{\mathrm{NBI}}(t) + n(t), \quad (10)$$

where $s_{NBI}(t)$ represents the IEEE 802.11a interference and $n(t)$ is the additive white Gaussian noise.

The receiver considers the received signal $r(t)$ and decide based on an observation of the received signal for the decided bit, it uses correlation receiver signal with the template signal. Therefore, the received signal with the PPM transmission may be expressed as

$$r_{\mathrm{PPM,k}} = \sum_{n=-\infty}^{+\infty} \int_{\tau_k+nT_f}^{\tau_k+(j+1)T_f} r_{\mathrm{PPM}}(t) \cdot v(t - nT_f - T_{c_n} - T_{p_n} - \tau_k)dt, \quad (11)$$

and for the BPM transmission

$$r_{\mathrm{BPM,k}} = \sum_{n=-\infty}^{+\infty} \int_{\tau_k+nT_f}^{\tau_k+(j+1)T_f} r_{\mathrm{BPM}}(t) \cdot v(t - nT_f - T_{c_n} - \tau_k)dt, \quad (12)$$

where $v(t) = p(t) - p(t - \delta)$ represents the template signal. Therefore, in the case of the modified template waveform based correlation receiver, $v(t)$ is replaced by $M(t)$.

III. Performance Simulation and Results

The effects of NBI on the UWB time-hopping system, the IEEE 802.11a wireless LAN physical layer [15] with the operating frequency bands of 5.15-5.25 GHz, 5.25-5.35 GHz, and 5.725-5.825 GHz were generated by the computer simulation. The empirical path loss exponent in equation (6), n equals to 1.73 [16]. Consequently, the UWB transmitted power (EIRP) was set to be -41.3 dBm/MHz based on the FCC requirements [1]. The Gaussian doublet pulse width of 0.28 ns was assumed for the transmitting waveform. The pulse repetition time $T_f = 5$ ns, therefore, the transmission rate equals to 200 Mbps. Antennas are assumed to be omni-directional radiation pattern. Suppose that the transmitter and the receiver are perfectly synchronized. Therefore, the correlation receiver can be obtained for detecting the PPM and BPM symbols. The UWB and the NBI simulation parameters are listed in Table I.

Referring to the model of the UWB time-hopping in the presence of the IEEE 802.11a interference as shown in Fig. 1. The influence of the NBI increases as the T-R separation distance increases. Therefore, three observation points at 1, 5 and 10 meter are investigated to verify the performance of the modified template waveform for the UWB time-hopping system. However, the BER performance of the UWB system depends on the T-R separation distance between UWB transmitter and receiver. Moreover, it also depends on the separation between UWB receiver and wireless LAN interferer. The separation distance between the UWB receiver and the NBI depends on the SINR. Hence, the continuous transmission of the interferer was assumed for entire simulation time for the considered UWB system.

TABLE I
UWB AND NBI SIMULATION PARAMETERS.

Quantity	Values
UWB data rate	200 Mbps
UWB transmitter power	-41.3 dBm/MHz
UWB bandwidth	7.5 GHz
UWB center frequency	6.85 GHz
T-R separation	1, 5, and 10 m
Pulse width	0.28 ns
Pulse repetition time	5 ns
PPM time shift	0.188 ns
NBI frequency bands	5.15-5.25 GHz
	5.25-5.35 GHz
	5.725-5.825 GHz
NBI data rate	54 Mbps
Path loss exponent	1.73

Fig. 4 shows the UWB performance of the original template waveform and the modified template waveform on the influence of the IEEE 802.11a wireless LAN interferer. The BER performance of the UWB-PPM without modified template (PPM), the UWB-BPM without modified template (BPM), the UWB-PPM modified template waveform (mPPM) and the UWB-BPM modified template waveform (mBPM) are illustrated by the cycle solid line, the square solid line, the cycle dot line and the square dot line, respectively, for the transmission rate of 200 Mbps at the three different observation points.

Fig. 4(a)-(c) show the comparison of BER performances for the observation points at 1, 5, and 10 meter, respectively. As predicted, it can be seen that the UWB correlation receiver with the modified template waveform (mBPM, mPPM) always outperform the UWB-PPM and UWB-BPM that without the modified template (BPM, PPM).

From these results, it is found that the modified template waveform performs better than the original template waveform. Therefore, this NBI suppression technique can improve the performance of UWB system. In addition, it is clearly observed that the involvement of the T-R separation distance with the average BER performance are direct variation.

IV. Conclusion

In this paper, the narrowband interference suppression technique for UWB-TH system based on modified template waveform is investigated. The system performance was characterized in term of the bit error rate. Simulation results show that the modified template waveform outperforms the original

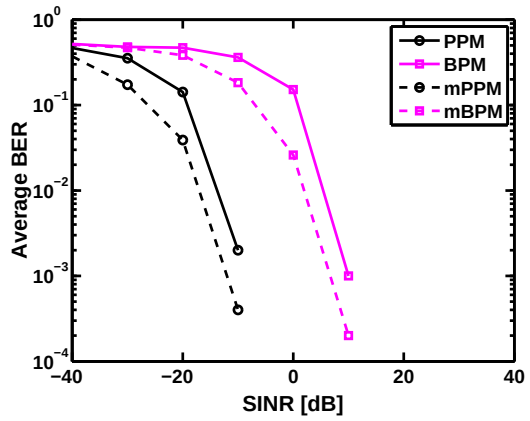

(a) 1 m.

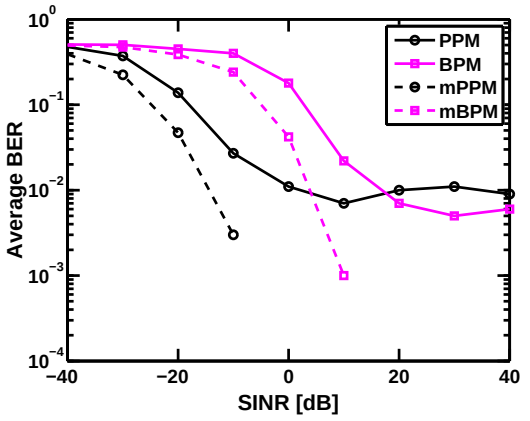

(b) 5 m.

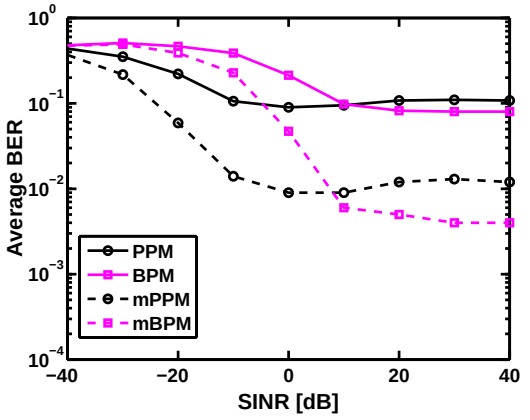

(c) 10 m.

Fig. 4. Average BER vs SINR for UWB correlation receiver with the original and modified templates waveform. The T-R separation distance was set to be 1, 5, and 10 meter, respectively.

one. In addition, it is found that the BER performances of the PPM are better than the BPM in the presence of the NBI for the entire range of the SINR. Moreover, the NBI can significantly affect to the UWB correlation receiver depended on the probability of signal overlap and the T-R separation distance of the IEEE 802.11a interferer to the UWB receiver.

REFERENCES

[1] Federal Communications Commission, First order and report: Revision of part 15 of the Commission's rules regarding UWB transmission systems, Apr. 22, 2002.

[2] R. Giuliano and F. Mazzenga, "On the coexistence of power-controlled ultrawide-band systems with UMTS, GPS, DCS1800, and fixed wireless systems," *IEEE Trans. Vehicular Technology*, vol. 54, no. 1, pp. 62-81, Jan. 2005.

[3] R. D. Wilson, R. D. Weaver, M.-H. Chung, R. A. Scholtz, "Ultra wideband interference effects on an amateur radio receiver," *Proc. Ultra Wideband Systems and Technologies*, pp. 315-319, 2002.

[4] D. Landi and C. Fischer, "The effects of UWB interference on GSM systems," *Proc. International Zurich Seminar on Communications*, pp. 86-89, 2002.

[5] G. Yue, L. Ge, and S. Li, "Analysis of ultra wideband signal interference to DSSS receiver," *Proc. IEEE Workshop on Signal Processing Advances in Wireless Communications*, pp. 229-233, 2003.

[6] S.-S. Choi and W.-J. Oh, "Analysis the interference of pulse position modulated UWB into IEEE 802.11 a WLAN," *Proc. UWBST & IWUWBS*, pp. 328-331, 2004.

[7] G. Yue, L. Ge, and S. Li, "Ultra wideband impulse radio signal interference to code division multiple access system," *Proc. Personal, Indoor and Mobile Radio Communications*, vol. 3, pp. 2437-2441, 2003.

[8] M. Hamalainen, J. Saloranta, J.-P. Makela, I. Oppermann, and T. Patana, "Ultra wideband signal impact on IEEE802.11b and Bluetooth performances," *Proc. Personal, Indoor and Mobile Radio Communications*, vol. 1, pp. 280-284, 2003.

[9] R. van Nee and R. Prasad, *OFDM for Wireless Multimedia Communications*, Artech House, 2000.

[10] J. Bellorado, S. S. Ghassemzadeh, L. J. Greenstein, T. Sveinsson, and V. Tarokh, "Coexistence of ultra-wideband systems with IEEE-802.11 a wireless LANs," *Proc. Global Telecommunications Conference*, vol. 1, pp. 410-414, 2003.

[11] X. Chu and R. D. Murch, "The effect of NBI on UWB time-hopping systems," *IEEE Trans. Wireless Communications*, vol. 3, no. 5, pp. 1431-1436, Sept. 2004.

[12] B. Firoozbakhsh, T. G. Pratt, and N. Jayant, "Analysis of IEEE802.11a interference on UWB system," *Proc. Ultra Wideband Systems and Technologies Conference*, pp. 473-477, 2003.

[13] M. Z. Win and R. Scholtz, "Impulse radio: How it works", *IEEE Communication Letters*, vol. 2, no. 1, Jan. 1998.

[14] E. Pakdeechard, M. Chamchoy and S. Promwong, "A study on Performance of UWB System in the Presence of IEEE 802.11a Interference," *ISCIT 2005 Beijing Conference*, pp. 936-939, 2005.

[15] IEEE Standard 802.11a: Part 11: Wireless LAN Medium Access Control (MAC) and Physical Layer (PHY) Specifications High Speed Physical Layer in the 5 GHz Band, 1999.

[16] M. Chamchoy, S. Promwong, P. Tangtisanon, and J. Takada, "Characterization of In-Home UWB Channnel with Different Antenna Directivity," *Proc. IEEE Regian 10 Conference*, vol. C, pp. 129-132, 2004.

A Survey on Non-Coherent QAM receiver structure in Noisy Channel

Shahab Asoodeh, Alireza Rezazade
Dept. of electrical and Computer Engineering
Shahid Behehsti University
Asoodehshahab@gmail.com

Abstract- **In wireless receiver, carrier's phase derivation and mismatching of I/Q are so considerable. Recently Independent Component Analysis (ICA) has been proposed that does not need to phase estimation. But the noise of channel leads to break down of performance. In this paper, the structure of QAM receiver based on Noisy ICA is proposed with assumption of presence of channel noise. Simulations result high Signal to Interference Rejection Ratio (SIRR) especially in low Signal to Noise Ratio (SNR).**

I. INTRODUCTION

For demodulation of QAM signal, receiver needs synchronized sinusoidal with received signal. Synchronization of local oscillator can be accomplished by Phase Locked Loop (PLL) and nonlinear analog method [1] that need more number of signal's period otherwise the performance will be broken down. Also mismatching of used signals' amplitudes of demodulation in QAM receiver can lead to go down the performance [10]. In order to solve these problems Independent Component Analysis (ICA) has been applied when frequency of local oscillator and received signal are the same [3]. On the other hand, the error of ICA method will be increased when the noise of channel are assumed [7-9]. In order to reduce the effect of noise, methods have been introduced such as time signal filtering and Primary Component Analysis (PCA) [5]. Since these methods can not totally omit that, Noisy ICA (NICA) have been considered [4,5]. In this paper, the performance of NICA-based QAM receiver with the presence of noise has been studied.

II. QAM RECEIVER MODEL

The general form of received QAM signal in the time interval $kT < t < (k+1)T$ has been shown in (1).

$$r(t) = A_{mc}(k) g_T(t) \cos(w_c t) + A_{ms}(k) g_T(t) \sin(w_c t) + n(t) \quad (1)$$

Where $\{A_{mc}(k)\}$ and $\{A_{ms}(k)\}$ are the sets of used amplitudes for n-bit sequence mapping, $g_T(t)$ and w_c are the frequency response of shaping filter and angle frequency of carrier signal, respectively and finally $n(t)$ is symbol of AWGN in channel.

Received signal is summation of two PAM signals having 90° phase difference plus additive noise to both signals. Demodulator divides QAM received signal to $y(k) = [y_1(k) \quad y_2(k)]^T$ at which $y_1(k)$ and $y_2(k)$ are the estimated value of $A_{mc}(k)$ and $A_{ms}(k)$ in the time interval $kT < t < (k+1)T$. A QAM demodulator has been shown in Fig.1 [1].

For ideal *I/Q* separation in receiver, phase and frequency of local oscillator and carrier signal must be the same. Local oscillator signals in Fig.1 are considered as (2) and (3).

$$v_1 = A\cos(w_c t + \alpha) \quad (2)$$

$$v_2 = B\cos(w_s t + \beta) \quad (3)$$

Where α and β show the phase differences between received signals and local oscillator signals. Suppose that noise in (1) can be represented as (4).

$$n(t) = n_{wc}(k)\cos(w_c t) + n_{rem}(t) \quad (4)$$

Where $n_{wc}(k)$ and $n_{rem}(t)$ are the noise elements in w_c frequency and other frequencies in time interval $kT < t < (k+1)T$ .in this case $s_i(t)$ in Fig.1 can be obtained as (5).

$$\begin{aligned} s_i(t) &= \frac{1}{2} A g_T(t) A_{mc}(k)[\cos(2w_c t + \alpha) + \cos(\alpha)] \\ &+ \frac{1}{2} A g_T(t) A_{ms}(k)[\sin(2w_c t + \alpha) - \sin(\alpha)] \\ &+ \frac{1}{2} A g_T(t) n_{wc}(k)[\cos(2w_c t + \alpha) + \cos(\alpha)] \\ &+ n_{rem}(k) A g_T(t)\cos(w_c t + \alpha) \end{aligned} \quad (5)$$

Subsequently, the output of LPF can be shown as (6).

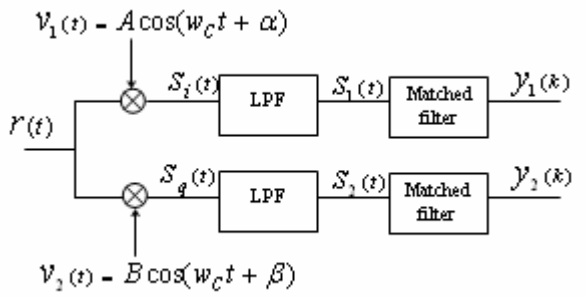

Fig. 1. Block diagram of a QAM demodulator

$$s_1(t) = \frac{1}{2}Ag_T(t)A_{mc}(k)\cos(\alpha) - \frac{1}{2}Ag_T(t)A_{ms}(k)\sin(\alpha) + \frac{1}{2}Ag_T(t)n_{wc}(k)\cos(\alpha) \quad (6)$$

And finally the sampled output of matched filter is written as (7).

$$y_1(k) = \frac{1}{2}AA_{mc}(k)E_g\cos(\alpha) - \frac{1}{2}AA_{ms}(k)E_g\sin(\alpha) + n_1(k) \quad (7)$$

Where $E_g = \int_0^T g_T^2(t)dt$ is the energy of shaping filter's frequency response and $n_1(k)$ is defined as $n_l(k) = \frac{1}{2}An_{wc}(k)E_g\cos(\alpha)$. After doing same steps for *Q*-branch and combination of both results, the output can be finally presented as follow.

$$y(k) = Ma(k) + n(k) \quad (8)$$

Where $a(k)$, $y(k)$, $n(k)$ and M are the transmitted symbols vector, match filter's output signals vector, noise vector in k[th] signaling time interval and linear transmission matrix or mixer matrix, respectively which are formulated as follow.

$$a(k) = [A_{mc}(k) \quad A_{ms}(k)]^T \quad (9)$$

$$y(k) = [y_1(k) \quad y_2(k)]^T \quad (10)$$

$$n(k) = [n_1(k) \quad n_2(k)]^T \quad (11)$$

$$M = \begin{pmatrix} A\cos(\alpha) & -A\sin(\alpha) \\ B\sin(\beta) & B\cos(\beta) \end{pmatrix} \quad (12)$$

In the above formulation for ease of calculation we suppose $E_g = 2$. These formulations show that channel noise appears in linear manner in QAM receiver and does not have any affect on mixer matrix and due to this characteristic, ICA can be used in the presence of noise [4].

III. NOISY ICA IN QAM RECEIVER

The general ICA-based structure for QAM signaling has been described in [3]. In this paper, we use the NICA (Noisy ICA) method [4] for *I/Q* separation in QAM receiver. According to (8) it can be readily shown that outputs $y_1(k)$ and $y_2(k)$ appear linearly in terms of symbol vectors and noise in the QAM receiver.

The main target of NICA process for QAM signaling is to determine the matrix W in (13) in order that $A_{mc}(k)$ and $A_{ms}(k)$ can be estimated with use of $y_1(k)$ and $y_2(k)$.

$$\hat{a}(k) = Wy(k) \quad (13)$$

Where $\hat{a}(k)$ and W are the estimated vector of $a(k)$ and estimated of reverse matrix of *A*, respectively. On the other hand, the amplitude of separated signals can not be determined in the ICA algorithm because the value of $a(k)$ and M are not definite [5,6]. This problem can be solved with the assumption of unit variance for separated signals [5]. In other words we determine the elements of matrix W in order that variances of estimated signals become unit. For QAM signaling, variances of transmitted symbols are determined in *I* and *Q* braches. This is because the QAM signals can be considered as two PAM signals modulated with orthogonal phases. If the amplitude of these signals be symmetric, variance of PAM signals will be as follow. [1]

$$\sigma_{PAM}^2 = \frac{M^2 - 1}{3} \quad (14)$$

Where M is the number of signals' amplitudes. Hence, the amplitudes of detected signals must be multiplied by $\sqrt{(M^2-1)/3}$ gained from (14). Also in order to decrease the volume of computations, it can be estimated just one row of matrix *W* or coefficient vector and another coefficient vector can be gained with augmenting 90° to first vector's phase.

To determine the NICA algorithm for QAM receiver, it has been assumed in [4] that the covariance matrix of noise is definite. Moreover, $n(k)$ in output of match filter will be white [1] and therefore its covariance matrix can be obtained from multiplication of unit matrix by noise variance which can be estimated by primitive transmitted data.

NICA algorithm includes two steps pre-process and main process. In the former, initially the average of received signals is forced to become zero and received signals are made quasi-white as follow [4].

$$\hat{y}(k) = (C - \Sigma)^{-\frac{1}{2}}y(k) \quad (15)$$

Where $C = E(yy^T)$ and $\Sigma = E(nn^T)$ are the covariance matrix of input signal and noise, respectively. According to (8), (15) can be rewritten as follow.

$$\hat{y}(k) = \boldsymbol{B}a(k) + n(k) \quad (16)$$

$$\boldsymbol{B} = (C - \Sigma)^{-\frac{1}{2}}M \quad (17)$$

In the main process, an initial *2*1*dimension vector *w* (one of the columns of matrix W^T) are placed in (18) [4] and this procedure will be done iteratively in order to reach the constant value for *w*.

$$w_{new} \leftarrow E(\hat{y}(w^T \hat{y})^3) - 3(I + \hat{\Sigma})wE((w^T \hat{y})^2) \quad (18)$$

Where

$$\hat{\Sigma} = (C - \Sigma)^{-\frac{1}{2}} \Sigma (C - \Sigma)^{-\frac{1}{2}} \quad (19)$$

As it was said, the next row of matrix *W* can be gained from addition 90° to phase of first row. Hence the transmitted symbols are estimated using (13). The NICA algorithm can be presented as Fig.2.

IV. SIMULATION AND RESULTS

In this section the performance of 16-QAM receiver based on NICA is simulated according to presented method in [3]. In this method for measurement of systems performance, Signal to Interference Rejection Ratio *(SIRR)* has been introduced which is defined as follow.

$$SIRR = \frac{1}{2}\left[\left|20\log(\frac{h_{11}}{h_{12}})\right| + \left|20\log(\frac{h_{21}}{h_{22}})\right|\right] \quad (20)$$

Where h_{ij}s are the elements of matrix $\boldsymbol{H}$ defined as follow.

$$\boldsymbol{H} = \boldsymbol{WB} \quad (21)$$

In ideal state, $\boldsymbol{B}$ will be the reverse of $\boldsymbol{W}$ and therefore $\boldsymbol{H}$ will become unit matrix, in this case *SIRR* will be indefinite. In this section, results are presented based on 1000 independent experiments and calculation of average *SIRR*. In any iteration α is the value with uniform distribution in $\left[0 \quad 2\pi\right]$ and $\beta = \alpha + \varphi$. The values of *A* and *B* are assumed 1 and $A(1-\Delta)$. Indeed, φ represent the phase difference between received signal and receiver local oscillator signals and Δ is the symbol of amplitude mismatch of *I* and *Q* branches. Results show that use of proposed NICA instead of SICA [3], *SIRR* will be increased and therefore the error due to noise will be decreased. The values of average *SIRR* are shown in the table 1 for both NICA and SICA [3]. From the results derived in *SNR=2dB* it is clear that the values of average *SIRR* for the different values of φ and Δ are constant approximately, this point shows that NICA algorithm is so robust rather phase and amplitude variety as well as SICA. In other words, receiver has the same performance for different values of phase difference between received signal and local oscillator signals. The values of *SIRR* for different *SNR* and 2000 symbols are depicted in fig.3. In simulations Δ and φ are supposed to be 0.1 and 10, respectively. From fig.3 it is evident that for a constant *SNR* the average value of *SIRR* for NICA is higher than SICA, so with use of NICA in the QAM receiver, estimated signals are much similar to transmitted signals. The average values of SIRR in terms of the number of symbols are illustrated in Fig.4. It is readily seen that the average values of *SIRR* is increased with the increase of number symbols and proposed NICA algorithm has the higher values of *SIRR* for most number of symbols. Consequently, the errors derived from the channel noise will be decreased with use of proposed NICA algorithm in non-coherent QAM receiver.

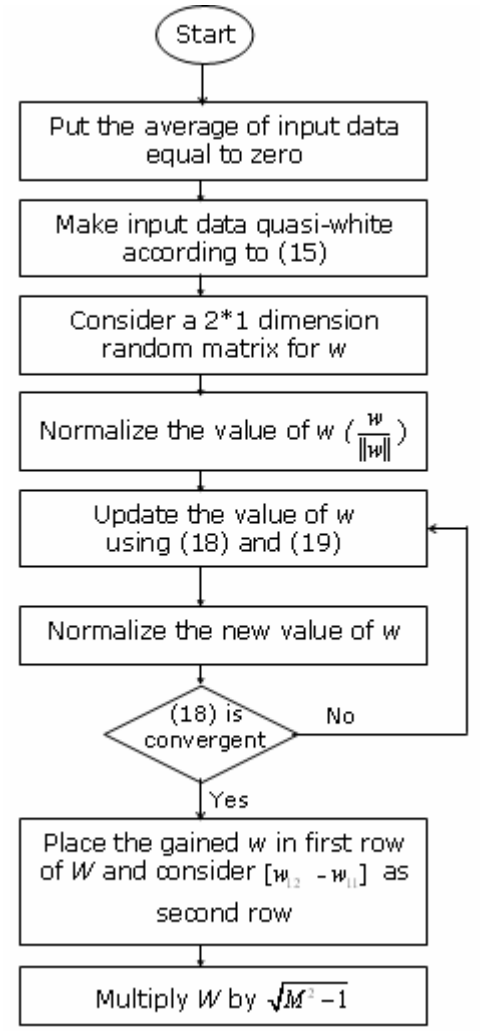

Fig. 2. Proposed NICA algorithm form QAM receiver

TABLE I
The average values of *SIRR* in SICA and NICA for different values of Δ and φ

Δ \ ϕ	0°		1°		10°		20°	
	SICA	NICA	SICA	NICA	SICA	NICA	SICA	NICA
0%	42.51	42.71	42.83	43.06	42.43	43.36	41.86	43.01
1	42.63	42.87	42.60	42.88	42.77	42.96	41.81	43.42
2	43.09	42.97	43.14	43.37	42.38	42.83	41.36	42.67
3	43.10	42.91	43.27	43.09	42.53	43.17	41.70	42.98
4	42.92	42.86	42.98	43.12	42.62	42.97	41.34	43.00
5	43.15	43.32	43.08	43.26	42.63	43.18	41.78	42.93
10	43.26	43.23	42.71	42.90	42.74	43.01	41.89	43.30
15	42.84	42.89	43.02	43.28	42.75	43.17	41.29	42.70
20	42.84	42.83	42.88	42.94	42.79	43.33	41.37	42.68

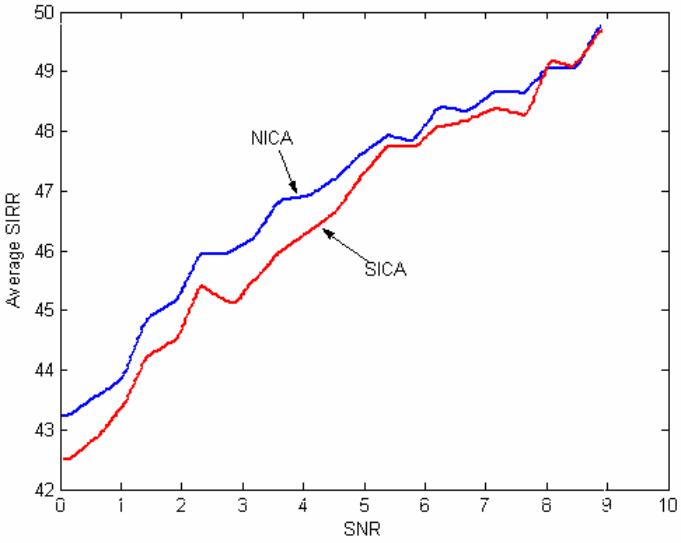

Fig.3. The average value of *SIRR* in terms of *SNR* for 2000 symbols

V. CONCLUSION

In this paper, we showed that in case of presence of channel noise in QAM receiver, the output of demodulator is the linear combination of transmitted symbols and noise. An ICA based non-coherent receiver was introduced which leads to higher values of *SIRR* especially for low *SNR* and hence is so robust against channel noise.

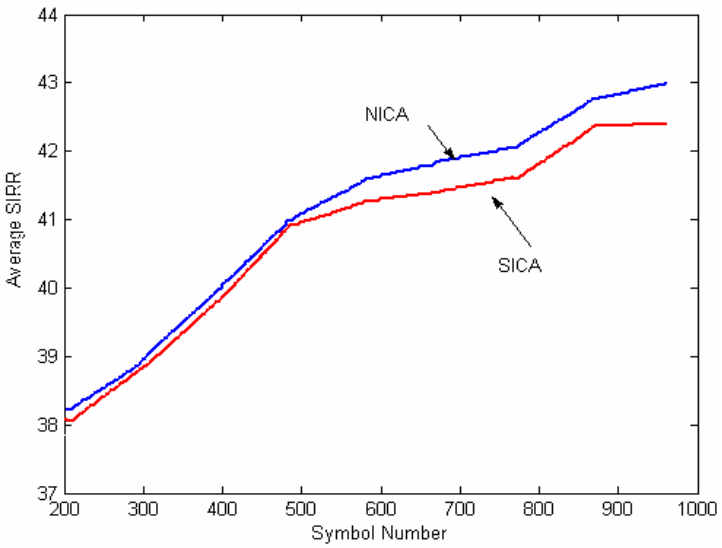

Fig.4. The average value of *SIRR* in terms of number of symbols in SNR=2dB

REFRENCE

[1] J. G. Proakis and M. Salehi, "*Communication System Engineering*", second Edition, Prentice Hall, 2002.

[2] A. Hyvarinen, "Fast and Robust Fixed-Point Algorithms for Independent Component Analysis", *IEEE Trans. on Neural Network*, vol. 10, no. 3, May 1999.

[3] I. Kostanic, W. Mikhael, "ICA Based Non-Coherent QAM Receiver Architecture", IEEE Int. Conf. on Neural Network and Signal processing, pp.1350-1353, Nanijing, China, 2003.

[4] A. Hyvarinen, "Fast ICA for Noisy Data using Gaussian Moments", Proc. Of IEEE Int. Sym. on Circuits and Systems, pp.57-61, vol.5, Jun 1999.

[5] A. Hyvarinen, J. Karhumen and E. Oja, "*Independent Component Analysis*", John Wiley, 2001.

[6] F. M. Ham and I. Kostanic, "*Principles of Neural Networks for Science and Engineering*", McGraw Hill, 2001.

[7] P. Comon, "Independent Component Analysis-a New Concept?", Signal Processing, vol. 36, no.3, pp. 287-314, 1994.

[8] A. Hyvarinen, "A Family of Fixed-Point Algorithms for Independent Component Analysis", IEEE Int. Conf. on Acoustic, Speech and Signal processing, pp. 3917-3920, Germany, 1997.

[9] A. Hyvarinen and E. Oja, "*A Fast Fixed-Point Algorithm for Independent Component Analysis, Neural Computation*", vol. 9, no. 7, pp. 1483, 1492, 1997.

[10] M. Valkama, M. Renfors and V. Koivunen, "Advanced Methods for I/Q Imbalance Compensation in Communication Receivers", *IEEE Tran. On Signal Processing*, vol. 49, no. 10, pp. 1335-1344, Oct.2001.

Signal Transformation Using Harmonic Transform Based on OFDM

Saiyan SAIYOD, Sakchai THIPCHAKSURAT, and Ruttikorn VARAKULSIRIPUNTH
Faculty of Engineering and Research Center for Communication and Information Technology (ReCCIT)
King Mongkut's Institute of Technology Ladkrabang (KMITL), Bangkok, Thailand
Email: {s8060055, ktsakcha, kvruttik}@kmitl.ac.th

***Abstract*- In this paper, we propose a new transformation for orthogonal frequency division multiplexing (OFDM) systems with Harmonic transform. The main idea of our research is to improve performance of estimating a small frequency offset in a signal with a large carrier frequency. The most appealing feature of OFDM is the simplicity of the receiver design due to the efficiency of frequency offset. OFDM can cope with the effects of frequency-selective multipath channels. OFDM is more sensitive to carrier frequency offset than the one of single-carrier systems. To solve those problems, the Harmonic transform can be applied. In this paper, we evaluate the performance of our proposed system in the terms of the accuracy of estimation and computational complexity. Finally, we show the improvement of our purposed system comparing with the conventional fast-Fourier transform (FFT).**

***Keywords*-OFDM, Fourier transform, Harmonic transform**

I. INTRODUCTION

Use of wireless access to the Internet has exploded in recent years with appearance of mobile Internet access services such as wireless LAN (WLAN) systems. In the near future people will demand much higher data rate in wide coverage to transfer large data files or enjoy high quality video streaming anytime anywhere.

OFDM is well known for its sensitivity to the time and frequency offset [1], [2]. There have been several papers on the subject of synchronization for OFDM in recent year. Moose gives the maximum likelihood estimator for the carrier frequency offset which is calculated in the frequency domain after taking the FFT [3], [4], [5], [6].

In the problem of frequency offset estimation, there have been proposed in [7], [8], [9] for warped discrete Fourier transform (WDFT). It is efficient to resolve closely spaced sinusoids. Harmonic transform (HT) [10] is a new method of spectrum analysis. This paper, we use this method to transform the signal.

The rest of the paper is organized as follows. We consider the OFDM system model and problem definition in section II, while section III illustrates main idea of Harmonic transform. We develop the Harmonic transform based on OFDM in section IV. In selection V, we discuss on results for computation complexity of proposed receivers, with Fourier transform and Harmonic transform. Finally, in section VI, some conclusions are drawn.

II. OFDM SYTEM MODEL AND PROBLEM DEFINITION

A. OFDM System Model.

Firstly, we introduce some basic of OFDM : Orthogonal Frequency Division Multiplexing). The "orthogonal" part of the OFDM name indicates that there is a precise mathematical relationship between the frequencies of the carriers in the system. Fig. 1 shows the spectrum of an OFDM. The conventional OFDM signal is generated at baseband by taking the inverse fast Fourier transform (IFFT) of quadrature amplitude modulated (QAM) or phase-shift keyed (PSK). In the fig. 2, an OFDM symbol has a useful period T and proceeding each symbol is a cyclic prefix of length T_g, which is longer than the channel impulse response so that there will be no intersymbol interference (ISI) [11]. The frequencies of the complex exponentials are $f_k = k/T$,and the useful part for $2N+1$ subcarriers is given by

$$u(t) = \sum_{k=-N}^{N} c_k e^{j 2\pi f_k t} \quad , 0 \le t \le T \qquad (1)$$

A carrier frequency offset of Δf causes a phase rotation of $2\pi t\Delta f$. The carrier frequency offset is not correct a rotation of the constellation and a spread of the constellation points similar to additive white Gaussian noise (AWGN) [2].

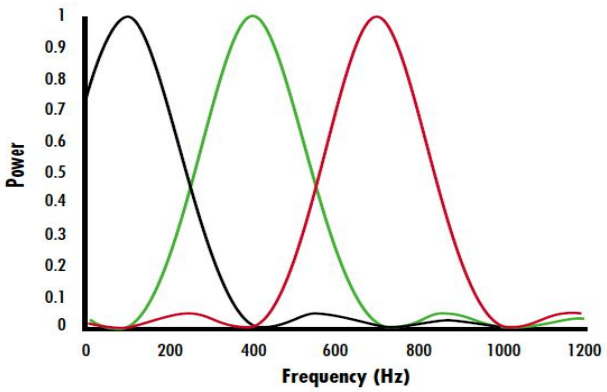

Figure 1. Spectrum frequency domain of OFDM.

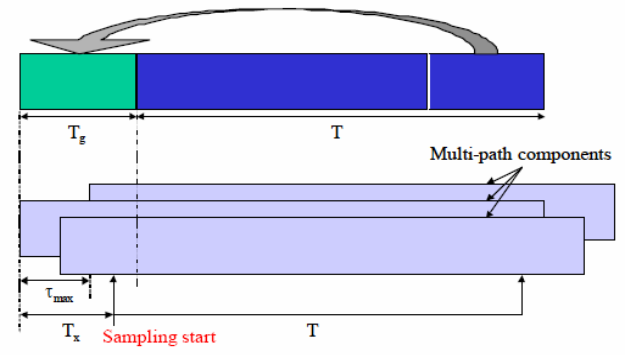

Figure 2. Multipath fading of OFDM

Figure 3 illustrates a general system overview of OFDM. At the transmitter, the signal is defined in the frequency domain. It is a sampled digital signal, and it is defined such that the discrete Fourier spectrum exists only at discrete frequencies. Each OFDM carrier corresponds to one element of discrete Fourier spectrum. The amplitudes and phases of the carriers depend on the data that is transmitted. The data transmissions are synchronized at the carriers, and can be processed together, symbol by symbol.

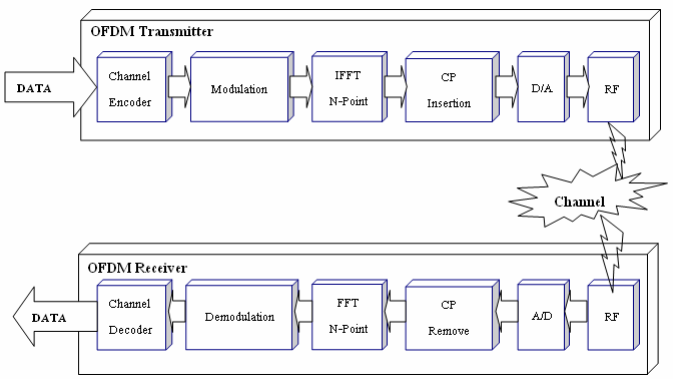

Figure 3. General system overview of OFDM.

B. Problem definition.

The main problem with reception of radio signals is fading caused by multipath propagation. Also, there are intersymbol interference (ISI), shadowing, interference. This makes link vary. As a result of the multipath propagation, there are many reflected signals, which arrive at the receiver at different time. Delayed signals are the result of reflections from terrain features such as trees, hills or mountains, or objects such as people, vehicles or buildings as shown in Fig. 2. These echoes cause ISI. The time delay of each OFDM symbol is the time-shifting property in signals, which indicates that a shift of a function in time corresponds to multiplication of the harmonic function by a complex function of harmonic number k [12]. Therefore, we use Harmonic transform to analysis the signals in OFDM symbol caused by multipath propagation.

III. HARMONIC TRANSFORM

Harmonic is a new method of spectrum analysis, which is proposed to provide an impulse-train spectrum for signals that are comprised of time-varying harmonics.

The Fourier transform (FT) represents signal $f(t)$ in term of sinusoids of various frequencies, that is defined as

$$F(\omega) = \int_{-\infty}^{+\infty} f(t) e^{-j\omega t} dt \qquad (2)$$

The original signal is recovered by the inverse Fourier transform (IFT)

$$f(t) = \frac{1}{2\pi} \int_{-\infty}^{+\infty} F(\omega) e^{-j\omega t} d\omega \qquad (3)$$

For signals consisting of fixed frequency components, the FT effectively reveals their frequency contents and is generally able to represent the signals with an acceptable resolution within a narrow band of spectra. However, this capability deteriorates quickly when the frequency components are time-varying as shown in Fig. 4

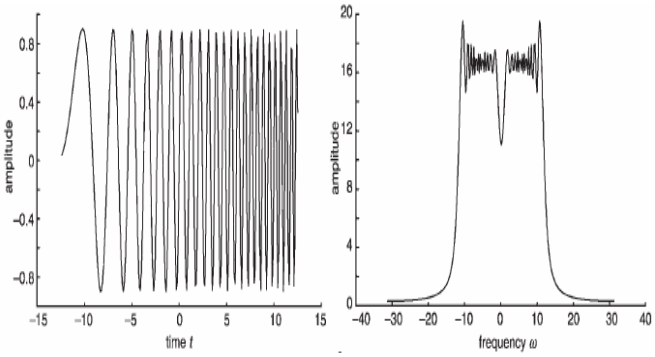

Figure 4. Fourier transforms of signals
Left: Waveforms Right: Corresponding spectra

One solution to avoid the deterioration is the warped Fourier transform, in which the signal is warped in time before calculation of the spectrum. Harmonic transform has a built-in warping function.

The time-varying harmonic signal generally contains harmonics whose nominal instantaneous frequencies are expressed by

$$c_k(t) = (k+1)c_0(t), \quad k = 1, 2, 3, \ldots \qquad (4)$$

where $c_0(t)$ is the frequency of the fundamental and $c_k(t)$ is the frequency of the kth harmonic component.

Now let us consider a time-varying harmonic signal in the time-frequency plane. For simplicity, only the nominal instantaneous frequency of the fundamental and the first two harmonics are given in Fig. 5(b). The Fourier transform of the signal, as shown in Fig. 5(c), can be treated as the linear

integration of the signal along the time axis in the time-frequency plane, which fails to distinguish the harmonic components. A better solution is to integrate the signal along the nominal instantaneous frequency of every component, rather than along the time axis, to obtain an impulse-train spectrum, as shown in Fig. 5(a). This is the basic concept of the harmonic transform (HT).

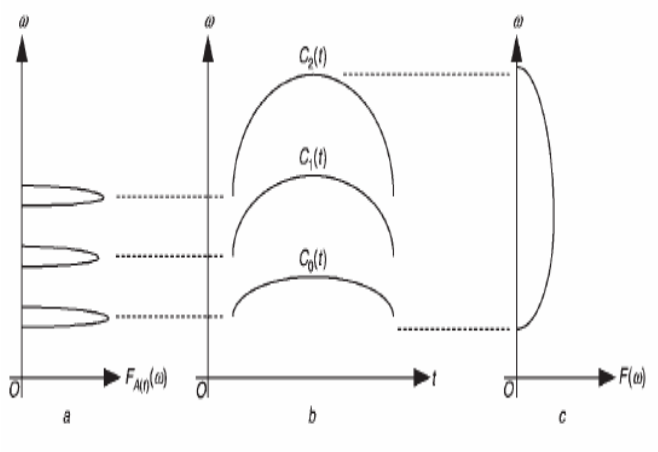

Figure 5. Concept of harmonic transform
a: Harmonic transform
b: Time-frequency representation
c: Fourier transform

The Harmonic transform of $f(t)$ is defined by

$$F_{\varphi_{u(t)}}(\omega) = \int_{-\infty}^{+\infty} f(t)\varphi_u'(t)e^{-j\omega\varphi_u t}\,dt \qquad (5)$$

where $\phi_u(t)$ is the unit phase function, which is the phase function of the fundamental divided by its nominal instantaneous frequency and $\phi'_u(t)$ is the first-order derivative of $\phi_u(t)$. The requirement for $\phi_u(t)$ is that it should be differentiable and invertible on $(-\infty, +\infty)$. HT of the signal will be scaled if the nominal instantaneous frequency of any harmonic is used. The inverse harmonic transform (IHT) is

$$F(t) = \frac{1}{2\pi}\int_{-\infty}^{+\infty} F_{\varphi u(t)}(\omega)e^{-j\omega\varphi_u(t)}\,d\omega \qquad (6)$$

It is noted that the Harmonic transform becomes the Fourier transform when $\phi_u(t) = t$. Fig. 6 shows FT and HT of speech. Clear peaks representing the fundamental and harmonics are seen in the HT, while the same observation cannot be made from the FT.

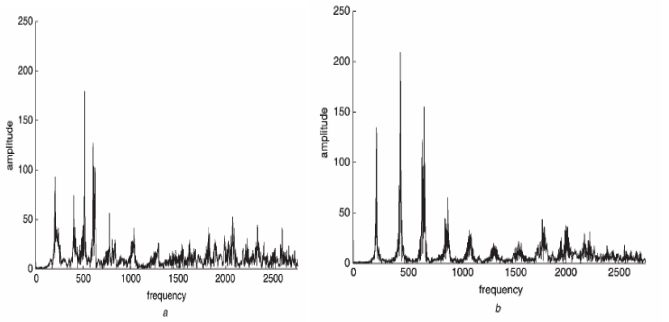

Figure 6. Transform of speech.

IV. HARMONIC TRANSFORM BASED ON OFDM

A basic diagram of an OFDM system under proposed scheme is shown in Fig.7. We consider the transformation of an OFDM system. We substitute IHT and HT into IFFT and FFT, respectively.

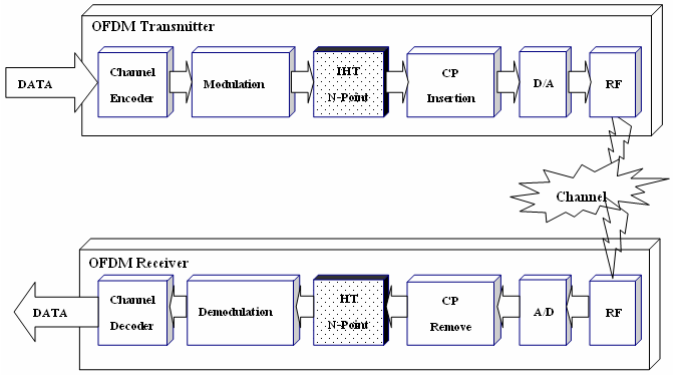

Figure 7. OFDM system based on HT.

In figure 8, we present the block diagram of channel estimation based on Harmonic transform using same pilot sequences [13] that to measure the number of multipath (NoM). While signal to interference plus noise power ratio (SINR) is used to calculate interference plus noise level (I+N level). The most important issue is that the receiver should know the number of multipath and interference plus noise level for each subcarrier to setup parameter of Harmonic transform.

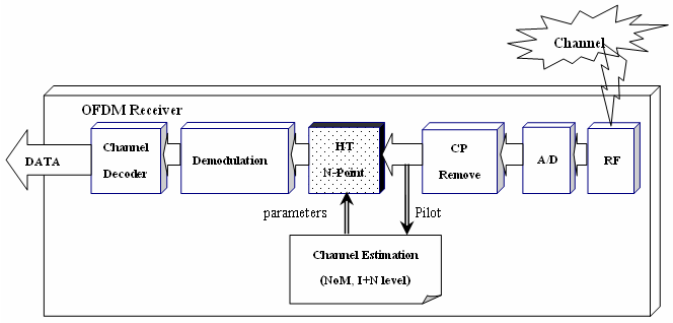

Figure 8. Block diagram of channel estimation based on HT .

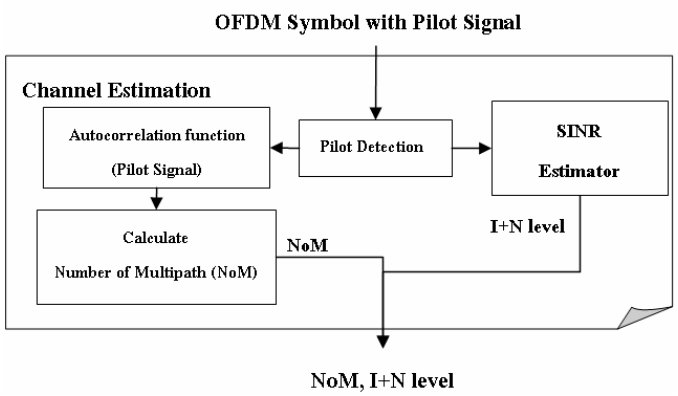

Figure 9. Procedure of channel estimation for HT.

The I+N level for each subcarrier is estimated by calculating vector error of the received symbols from the reference symbols. SINR estimator takes the average values of vector error over adjacent sub carriers.

In order to estimate channel multipath delay desired locations and interfering channels, same pilot symbols are received OFDM symbol signals from the transmitters. The Pilot detection will prepare pilot signals for next function.

First part of the algorithm is estimating number of multipath. In this method, Autocorrelation function will be used. We can calculate number of multipath by peak of pilot signals counting. The NoM will be used in Harmonic transform as a number of harmonic.

Second part of the algorithm is SINR Estimator, which estimate SINR for calculate I+N level of each subcarrier. The I+N level will be used in Harmonic transform for setup parameter of each subcarrier.

V. DISCUSSIONS

We now compare the performance of the HT with FT based on OFDM systems. The use of Fourier transform in conventional OFDM is not flexible and very sensitive to carrier frequency offset, which is much more affected by carrier frequency errors. A small frequency offset at the receiver compromises the orthogonally between the sub channels, causes a degradation in a system performance. The channel estimation after taking FFT has been researched and more complexity cause of no more information from FFT.

In the case of HT based on OFDM is the best way to achieve flexibility. It can adapt on condition of environments, when signals are very strong echoes. In bad environments, the HT will be adapted and have more efficiency. But it has more computational complexity. In other hand, good environments, the computational complexity of our proposed system similar as the conventional OFDM. Therefore, the conventional transmitter can use for our proposed scheme. It does not design any more for transmitter. However, we can reduce design and computational complexity of channel estimation after taking FFT in the conventional OFDM.

Harmonic transform based on OFDM especially in the multipath propagation, interference and fading environment is a promising technique for digital communications including mobile multimedia.

VI. CONCLUSIONS

We propose a new signal transformation using Harmonic transform based on OFDM. The main idea of our research is to improve performance of frequency offset estimation. Therefore, the receiver can reduce computational complexity after take FFT. Our proposed system is flexibility and computes on condition of environments. However, transmitter can process with the conventional OFDM. The computational complexities of transformation in receiver depend on environments. But it still has an accuracy frequency offset.

REFERENCES

[1] Bruce McNair, Leonard J.,and Nelson S.,"A Robust Timing and Frequency Offset Estimation Scheme for Orthogonal Frequency Division Multiplexing (OFDM) Systems",*Vehicular Technology Conference, 1999 IEEE 49th*, Vol.1, 16-20 May 1999, pp. 690 – 694.

[2] Timothy M. Schmidl and Donald C. Cox, "Robust Frequency and Timing Synchronization for OFDM", *IEEE Transaction on communications*, Vol.45, No. 12, December 1997. p.1613-1621

[3] Van De Beek, Sandell M. and Borjesson P.O., "ML estimation of time and frequency offset in OFDM systems", *IEEE Trans. Signal Process.*, 1997, Vol.45, No.7, pp. 1800-1805.

[4] Jing Lei and Tung-Sang Ng, "Pilot-Tone-Based Maximum Likelihood Estimator for Carrier Frequency Offset in OFDM Systems", *IEEE International Conference*, 2003, p.2046-2050.

[5] Lee J., Lou H. and Toumpakars D., "Maximum likelihood estimation of time and frequency offset for OFDM systems", *Electronics Letters 28th*, October 2004, Vol.40 No.22. p.

[6] Lee J., Lou H. and Toumpakaris, "Approximate Maximum Likelihood Estimation of Integer Carrier Frequency Offset in OFDM Systems", *Communications IEEE International Conference on Volume 4*, 2005, pp. 2543-2547

[7] Makur A. and Mitra K., "Warped Discrete-Fourier Transform: Theory and Application", *IEEE Transaction on Circuits and System*, Vol 48, No.9 , September 2001, p. 1086-1093.

[8] Franz S., Mitra K., Schmidt J.C. and Doblinger G., „"Warped Discrete Fourier Transform: A New Concept in Digital Singal Processing", *(ICASSP '02).IEEE International Conference*, Vol 2, 2002, p.1205–1208.

[9] Venkataramanan R. and Prabhu K.M.M. "Estimation of Frequency Offset using Warped DFT", *Signal Processing,* Vol. 86, Feb. 2006, p. 250-256.

[10] Zhang F., Bi G. and Chen Y.Q.,"Harmonic Transform", *IEE Proc.-Vis Image Signal process*., Vol.151, No. 4, August 2004, p. 257-263.

[11] Batariere M. Baum K. and Krauss T.P., "Cyclic Prefix Length Analysis for 4G OFDM System", *Vehicular Technology Conference, 2004. VTC2004-Fall. 2004 IEEE 60th* , 2004, pp.543-547.

[12] Roberts M.J. , *Signals and Systems : analysis using transform methods and MATLAB*. Mc graw Hill, Singapore, 2004.

[13] Simeone O., Bar-Ness Y., "Pilot-Based Channel Estimation for OFDM Systems by Tracking the Delay Subspace", *IEEE Transactions on Wireless Communications*, Vol.3, No.1 January 2004. p.315-325.

Location Estimation Based on Modified TOA Measurements for UWB Network

Tawatchai Jantaworn, Monchai Chamchoy, Sathaporn Promwong and Nikorn Sukutamtanti
Faculty of Engineering
King Mongkut's Institute of Technology Ladkrabang
Chalongkrung Rd., Ladkrabang, Bangkok 10520, Thailand
Email: s8061052@kmitl.ac.th

***Abstract*— The location estimation technique for UWB wireless network is very importance issue in mobility management. In this paper, the estimation accuracy based on TOA measurement for direct-calculation method is improved by using CLEAN algorithm. The performance criterias such as TOA and distance estimation errors are compared. As the simulation results, the CLEAN algorithm can increase the estimation accuracy, especially for low SNR region, more than conventional TOA measurement.**

I. INTRODUCTION

Ultra-wideband (UWB) technology has been seen as one promising solution for future short-range indoor radio communication systems. The technology offers many advantages over conventional narrowband and wide-band systems (CNWS) such as high bit rate services, low power consumption, very large capacity and accuracy positioning capabilities [1]. Because of the advantages of this technology, therefore, it was considered as the suitable wireless transmission media for IEEE WPAN working groups [2]. The Federal Communication Commission (FCC) [3] specifies that UWB has a frequency spectrum ranging from 3.1 to 10.6 GHz. The FCC defined the UWB signal as those which have a fractional bandwidth is greater than 0.20 or occupied bandwidth is equal to or greater than 500 MHz.

The radio signal is used as the key for several location estimated techniques. Time of arrival (TOA) measurement, angle of arrival (AOA) and signal strength can be used for the location estimation. The most popular method for estimating location is directly solve a set of simultaneous equations based on the time difference of arrival (TDOA). For accurate solution, this method must be obtained for x-y plane locating with 3 sensors and 2 TDOA measurements, and x-y-z plane locating with four sensors [4]. In the case of undecided system, to avoid the convergence problems, the double maximum likelihood [5] and the spherical interpolation techniques have been proposed [6]. However, the DFP quasi-Newton algorithm [7] was employed in the UWB precision assets location system [8]. The CLEAN algorithm initial used to improve radio-astronomical maps of the sky [9]. Also, it has been used in more narrow-band communication channel characterization problems [10]. Based on the advantage of the CLEAN algorithm, it can eliminate unwanted signal, such as interference and noise. In the communication system, the signal to noise ratio is reduced by several factors such as the multipath component, the long T-R separation between transmitter and receiver, and so on. These impairments lead to the higher location estimation error. Therefore, several methods are introduced to improve the estimated accuracy. Although the CLEAN algorithm is proposed for radio-astronomical maps, for the position estimation, the CLEAN algorithm can be used to eliminate unwanted signal from TOA measurements. Due to the TOA estimation error of each array sensor is not possible to completely remove the unwanted signal. Therefore, the CLEAN algorithm is involved for reducing noise in TOA measurements.

In this paper, the modified TOA measurement by using the CLEAN algorithm for position estimation based on the direct-calculation method is investigated. The channel measurements are examined in the indoor environment for the frequency ranging from 3.0 GHz to 11 GHz. The rest of paper is organized as follows. Section II presents the measurement method, measurement equipment and model under investigated. Section III briefly examines the direct-calculation method, Signal to noise ratio and summary step of the CLEAN algorithm. Section IV describes the simulation results of the modified TOA measurement by using the CLEAN algorithm, probability of TOA and distance errors and finally, the conclusion.

II. TOA MEASUREMENT METHOD

The UWB channel characterizations can be achieved by performing measurements in time domain or in frequency domain. The real-time channel measurement can only be obtained in time domain. Unfortunately, receiver noise, jitter, and synchronization are mainly degrade factors for the TOA measurement. On the other hand, when the vector network analyzer (VNA) is used, the TOAs can be obtained by performing the inverse discrete Fourier transform (IDFT) of the measured channel frequency responses.

A. Measurement Equipment

The vector network analyzer (VNA) is used as the frequency domain channel sounder. Then, the transmit and receive antennas are connected to the VNA with the double-shielded low-loss cables. The experiments were made while the transmit antenna was located in a fixed position, and the receive antenna was moved within the precisely measurement grids of 8×8

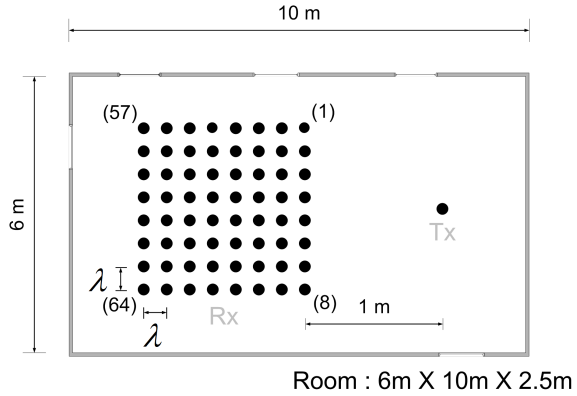

Fig. 1. Measurement model.

TABLE I
EXPERIMENT PARAMETERS.

Parameter setting	Value
Frequency Range	3.0∼11.0 GHz
Frequency Resolution	1601 points
Tx Antenna Height	1 m
Rx Antenna Height	1 m
Polarization	Vertical
T-R Separation	1∼1.3065 m

positions. The linear inter-distance of the synthesized array antenna is set to λ at the center frequency of 6.85 GHz. The 30 dB ultra-wideband and low-noise amplifier is used to compensate the loss in the cables. The biconical antennas are used to measure the UWB channel for presenting the channel characterizations with omni-directional propagation. The dynamic range for the VNA (HP 8510C) is exceeded 80 dB. Table I lists the main parameters of the experiments.

B. Measurement Location

In this experiment, the real indoor environment is investigated. Fig. 1 shows the measurement plane of the 8×8 grids of the receive antenna. The distance of the first array sensor plane and the transmitter site about 1 m. The measurement room, 10 m long, 6 m wide, and 2.5 m high, is used. The walls of the room are made of autoclaved aerated concrete internationally known as AAC, which is lighter weight than the conventional one. The ceiling and floor are made of chipboard and wood, respectively.

III. SIMULATION MODELS

In this paper, the modified UWB channel measurements in indoor environment are used to estimate the TOA and distance by using the CLEAN algorithm based on direct-calculation method. Therefore, the performance criterias such as TOA and position estimations for direct-calculation method are analyzed.

A. Direct Calculation Method

The direct-calculation method is algorithm for basic position estimation method. This method do not require knowledge of variance or distribution of the TOA estimation error and the direct-calculation method also do not require an accurate initial position estimation as described and derived in [11],

$$\sqrt{(x-x_i)^2+(y-y_i)^2} = c(t_i - t_0), \tag{1}$$

where c is the speed of light, t_i is the TOA at sensor i, t_0 is the transmit time, x, y and x_i, y_i are the coordinates of the tag and the sensor, respectively.

B. CLEAN Algorithm

Generally, CLEAN algorithm is introduced for evaluating the receiver signal of the more narrow-band communication channel. On the other hand, it also provides the advantage of array response from the actual signal for UWB communication. In this algorithm, the actual signal is called dirty signal. The steps in the CLEAN algorithm are as follows [13]:

1. Generate the dirty spectrum to the input data over a window spectrum in time.
2. Search the spectrum output window over time for the peak response.
3. Determine and store the amplitude and time of peak response.
4. Estimate the signal corresponding to the peak response and store waveform.
5. Generate the spectrum response to this estimated waveform.
6. Update the spectrum response by subtracting a gain factor of the response to the estimated signal from the previous spectrum response.

$$\mathbf{C}_n(t) = \mathbf{C}_{n-1}(t) - \gamma \widehat{\mathbf{C}}_{k,n-1}(t), \tag{2}$$

where k is an index of the largest response in $\mathbf{C}_{n-1}(t)$, $\mathbf{C}_n(t)$ is the beamformer response at the nth interation, and $\widehat{\mathbf{C}}_{k,n-1}(t)$ is the estimated response to the kth impulse at time $n-1$.

7. Add the current signal amplitude, scaled by gain factor, to the appropriate place in a list of signal location.
8. If a stopping criterion (a threshold on the signal level or residual energy) is not met, go to step 2.
9. Generate a list of the signals found, including amplitude and the time of arrival.
10. Form the CLEAN map by convolving the list of signals with delta functions.

C. SNR Calculation

The signal to noise ratio (SNR) compares the level of a desired signal (such as peak response) to the level of background noise for measuring the clarity of the signal in a transmission channel. The SNR of each array is defined as magnitude of signal between the first arrival of the channel impulse response and the average noise floor. Therefore, the SNR is given by

$$\mathbf{SNR}_{(k)}[dB] = 20\log_{10}[\frac{A(i)_k}{A_{ave}(n)_k}], \tag{3}$$

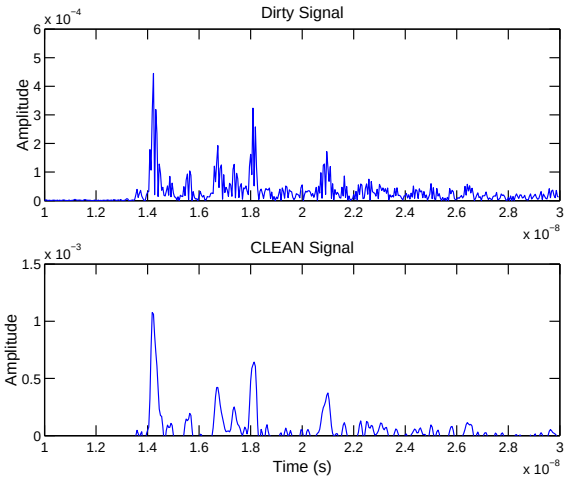

Fig. 2. The channel responses of the conventional and modified TOA measuremnts.

where $A(i)$ is the magnitude of the first arrival at the kth array, $A_{ave}(n)$ is the average noise floor at the kth array

IV. Numerical Results

The results of the channel impulse responses for the conventional and modified TOA measurements by using CLEAN algorithm are shown in Fig. 2. Consequently, the results of the SNR improvement are listed in Table. II. From Fig. 2, the impulse responses of the modified TOA measurement with the CLEAN algorithm are smoother than conventional measurement. Therefore, the TOA can simply to find more than without the CLEAN algorithm. From Table. II, shows the SNR of all arrays. The SNR of the improved TOA measurement arrays by using CLEAN algorithm are higher than the conventional one, for example the SNR at the 30th array is 33.37 dB and 38.36 dB, respectively.

For location estimation based on direct-calculation method, the distance estimated errors with and without CLEAN algorithm are shown in Fig.3. From the results, the distance error trends to increase as the distance between the transmitter and the receiver increase, both for with and without the CLEAN algorithm. For example, the distance error at the 12th array is 3.227 meter and 3.2407 meter and at the 61th array is 3.3225 meter and 3.3361 meter, respectively. The TOA and the distance errors with the CLEAN algorithm are lower than the conventional measurement.

Fig. 4 shows the distance error versus SNR (dB) for the location estimation. The SNR of the position estimation with the CLEAN algorithm is higher than without the CLEAN algorithm for all arrays. Moreover, the distance error for the location estimation with the CLEAN algorithm at the low SNR is lower than without the CLEAN algorithm. Because at the long distance, the CLEAN algorithm can improve the SNR by eliminating the unwanted signal.

TABLE II
SNR comparison of conventional and modified TOA measurements in dB

Array No.	Dirty	CLEAN	Array No.	Dirty	CLEAN
1	33.08	37.34	33	33.44	38.06
2	33.00	38.05	34	33.22	37.77
3	32.71	37.50	35	31.08	37.89
4	31.28	38.82	36	33.83	37.47
5	32.86	37.10	37	32.39	37.41
6	32.84	37.76	38	32.93	37.91
7	31.44	37.00	39	33.13	37.61
8	31.34	37.35	40	32.13	37.18
9	32.32	38.75	41	33.06	38.57
10	33.32	38.08	42	32.42	37.63
11	33.19	38.90	43	32.33	37.31
12	32.94	37.36	44	31.87	37.40
13	33.91	38.21	45	30.78	38.93
14	32.95	37.99	46	33.62	36.93
15	31.02	37.00	47	33.29	37.82
16	33.32	38.89	48	31.11	37.16
17	30.50	38.04	49	32.77	38.46
18	32.89	38.97	50	32.71	37.50
19	30.52	37.46	51	32.11	37.20
20	30.15	37.95	52	31.60	37.80
21	31.50	37.69	53	31.61	37.46
22	31.60	36.99	54	31.61	37.31
23	31.77	38.11	55	31.91	37.05
24	32.67	38.46	56	32.01	38.44
25	33.33	38.46	57	31.26	38.51
26	31.93	38.06	58	31.39	36.71
27	32.98	37.85	59	32.22	37.28
28	32.98	37.98	60	31.01	37.54
29	32.61	37.00	61	31.86	37.46
30	33.37	38.36	62	32.23	37.54
31	32.57	38.02	63	31.37	38.71
32	31.96	38.18	64	31.61	38.74

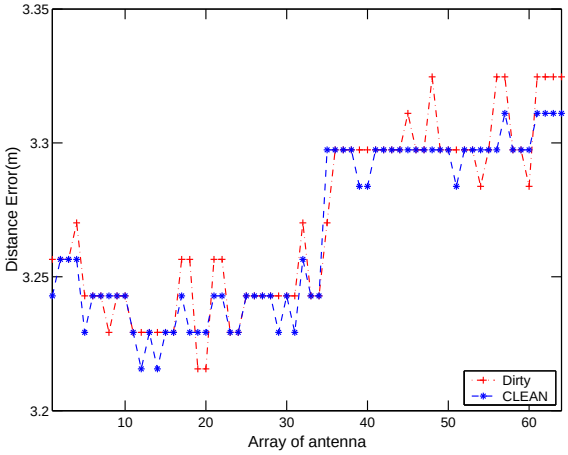

Fig. 3. The distance error for conventional and modified TOA measurements.

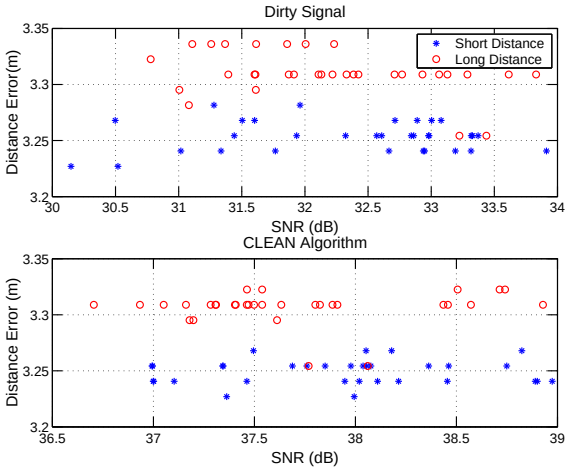

Fig. 4. The distance error versus the SNR (dB) for short and long T-R separation distances

V. CONCLUSIONS

In this paper, the modified TOA measurement for location estimation based on the direct-calculation method in ultra-wideband network is proposed. The CLEAN algorithm is introduced as the effective approach to eliminate the unwanted signal. The numerical results show that the TOA and distance errors trend to be linear. Therefore, the CLEAN algorithm is used to improve the estimated accuracy of the TOA estimation based on direct-calculation method. In addition, the CLEAN algorithm also provides the SNR improvement for location estimation in low SNR region.

REFERENCES

[1] R. A. Scholtz, R. Weaver, E. Homier, J. Lee, P. Hilmes, A. Taha, and R. Wilson, "UWB radio deployment challenges," *Proc. IEEE Personal, Indoor, and Mobile Radio Communications (PIMRC'00)*, vol. 1, pp. 620-625, 2000.

[2] http://ieee802.org/15 IEEE 802.15 Working group for WPAN

[3] Federal Communications Commission, "Revision of Part 15 of the Commission's Rules Regarding UWB Transmission Systems," *First Report and Order, FCC 02-48*, Apr. 2002.

[4] B. T. Fang,"Simple solution for hyperbolic and related position fixes," *IEEE Trans. Aerosp. Elecctron. Syst.*, vol. 26 pp. 748-753, Sept. 1990.

[5] Y. T. Chan and K. C. Ho, "A simple and efficient estimator for hyperbolic location," *IEEE Trans. Signal Processing*, vol. 42, pp. 1905-1915, Aug. 1994.

[6] H. C. Schau and A. Z. Robinson, "Passive source location employing intersecting spherical surfaces from time-of-arrival differences," *IEEE Trans Acoust. Speech, Signal Processing*, vol. 35, pp. 1661-1669, Dec. 1987.

[7] R. Fletcher and M. J. D. Powell, "A rapidly convergent desent method for minimization," *Computer Journal*, vol. 6, pp. 163-168, 1963.

[8] R. J. Fontana, E. Richley, and J. Barney, "Commercialization of an ultra wideband precistion asset location system," *in Proc. IEEE Conf. UWB systems and Technologies, 2003.*

[9] J. A. Hogbom, "Aperture synthesis with a nonregular distribution of interferometer baselines," *Astronomy Astrophys. Suppl.*, vol. 15, p. 417, 1974.

[10] R. G. Vaughan and N. L. Scott, "Super-resolution of pulsed multipath channels for delay spread characterization, *IEEE Trans. Commun.*, vol. 47, pp. 343347, Mar. 1999.

[11] K. Yu and L. Oppermann, "Performance of UWB Position Estimation Based on Time-of-Arrival Measurement," *in Proc. IEEE Conf. UWB Systems and Technologies 2004*, pp. 400-404, May 2004.

[12] J. Foerster, "Channel Modeling Sub-committee Report (Final)", *IEEE 802.15 Wireless Personal Area Networks*, Nov. 18, 2002.

[13] R. Jean-Marc Cramer, Moe Z. Win and Robert A. Scholtz, "Evaluation of the Multipath characteristics of the Impulse Radio Channel," *IEEE*, vol. 2, pp. 864-868, 8-11 sept.1998.

Accuracy Analysis of Focusing Resolution with TR EM Pulse Propagation for UWB Imaging Systems

Tanaporn Payommai*, Pichaya Supanakoon*,†, Sathaporn Promwong*,†, Nikorn Sukutamtanti* and Jun-ichi Takada‡
*Department of Information Engineering, Faculty of Engineering,
†Research Center for Communications and Information Technology (ReCCIT)
King Mongkut's Institute of Technology Ladkrabung, Bangkok 10520, Thailand
E-mail: {s8061065,kspichay,kpsathap,ksnikorn}@kmitl.ac.th
‡Graduate School of Science and Engineering, Tokyo Institute of Technology,
2-12-1-S6-4, O-okayama, Meguro-ku, 152-8550, Tokyo, Japan
E-mail: takada@ide.titech.ac.jp

***Abstract*— The focusing resolution is very important performance for ultra wideband (UWB) imaging system. In this paper, the accuracy of focusing resolution with time-reversal (TR) electromagnetic (EM) pulse propagation is analyzed. The TR EM pulse propagation is done via the numerical simulation of finite difference time domain (FDTD) method. The modulated Gaussian pulse is used as the UWB EM pulse. The directional error of focusing resolution at specific locations is shown. The results are discussed in the conclusion.**

I. Introduction

Recently, ultra wideband (UWB) radio technology based on the transmission of short duration pulses has gained much interest because of its low cost and low power consumption potentials [1]-[3]. Federal Communications Commission (FCC) [4] defined the UWB signal as those, which have a fractional bandwidth equal or greater than 0.20, or occupied bandwidth equal or greater than 500 MHz. The fractional and occupied bandwidth are defined as

$$\text{Fractional bandwidth} = \frac{2(f_{\mathrm{H}} - f_{\mathrm{L}})}{f_{\mathrm{H}} + f_{\mathrm{L}}}, \quad (1)$$

$$\text{Occupied bandwidth} = f_{\mathrm{H}} - f_{\mathrm{L}}, \quad (2)$$

where f_{L} and f_{H} are the lowest and highest frequencies at the -10 dB point, respectively.

The FCC established different technical standards and operating restrictions for three types of UWB devices based on their potential to cause interference. These three types of UWB devices are 1) imaging systems, 2) vehicular radar systems and 3) communications and measurement systems. The applications of UWB imaging systems include ground penetrating radar (GPR), wall, through-wall, surveillance and medical imaging systems. Furthermore, the UWB imaging systems are designated as three classes, which are low-frequency, mid-frequency and high-frequency imaging systems. The FCC spectral masks of these UWB imaging systems are shown in Fig. 1. In this paper, we focus on only high-frequency imaging system.

The focusing resolution is important performance of imaging system. There are many focusing techniques for imaging systems, such as depth-focused echo imaging [5], aperture focusing technique [6], [7] and auto-focusing algorithm [8]. The time reversal (TR) algorithm is widely used for UWB imaging system because its simplicity and high focusing resolution [9]. This TR algorithm can be directly performed by using the FDTD method [10], [11]. The use of FDTD method for TR is purposed in [12]. Although, the focusing resolution of TM ER pulse propagation is proposed [13], there is no considered about its accuracy.

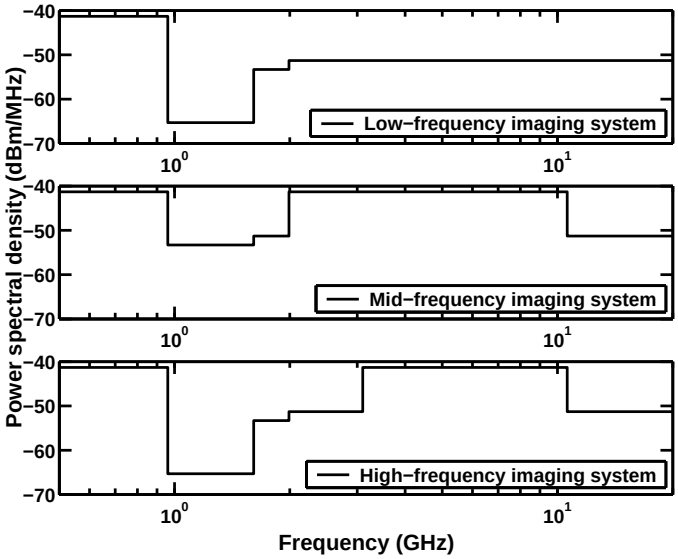

Fig. 1. FCC Spectral masks of UWB imaging systems [4]

In this paper, the accuracy of focusing resolution with TR electromagnetic (EM) pulse propagation is analyzed. The TR EM pulse propagation is done via the numerical simulation of two-dimensional (2-D) transverse magnetic (TM) mode finite difference time domain (FDTD) method. The modulated Gaussian pulse is used as the UWB EM pulse. The directional error of focusing resolution at specific locations is shown. The results are discussed in the conclusion.

The rest of this paper is organized as follows. Section 2, the FDTD method used in this paper is described. Next, the results of accuracy analysis are demonstrated in Sec. 3. Finally, the conclusions are discussed in Sec. 4.

II. FDTD METHOD

A. Conventional FDTD Algorithm

The 2-D TM mode finite difference equations are directly derived from Maxwell's curl equations in time domain. Maxwell's curl equation can be written as [14]

$$\mu\frac{\partial\vec{H}}{\partial t} = -\nabla\times\vec{E}, \tag{3}$$

$$\varepsilon\frac{\partial\vec{E}}{\partial t} = \nabla\times\vec{H}, \tag{4}$$

where H is the magnetic field, E is the electric field, μ is the magnetic permeability and ε is the electric permittivity.

To obtain discrete approximation of the continuous partial differential equations, the centered difference approximation is used on both the time and space first-order partial differences. The entire computation domain is the collection of all the unit cells. The dimensions of the unit cell along x and y directions are Δx and Δy, respectively. The node with subscript indices i and j corresponds to node number in x and y directions. The time step is indicated with the superscript index n. The time interval of each time step is Δt. After simple arrangement, the 2-D TM mode of finite difference equations are described as [10], [11]

$$H_x|_{i,j}^{n+\frac{1}{2}} = H_x|_{i,j}^{n-1/2} + \left(\frac{\Delta t}{\mu_{i,j}}\right)\left(\frac{E_z|_{i,j-\frac{1}{2}}^{n} - E_z|_{i,j+\frac{1}{2}}^{n}}{\Delta y}\right), \tag{5}$$

$$H_y|_{i,j}^{n+\frac{1}{2}} = H_y|_{i,j}^{n-1/2} + \left(\frac{\Delta t}{\mu_{i,j}}\right)\left(\frac{E_z|_{i+\frac{1}{2},j}^{n} - E_z|_{i-\frac{1}{2},j}^{n}}{\Delta x}\right), \tag{6}$$

$$E_z|_{i,j}^{n+1} = C_{\mathrm{a}}|_{i,j}E_z|_{i,j}^{n} + C_{\mathrm{b}}|_{i,j}\left(\frac{H_y|_{i+\frac{1}{2},j}^{n+\frac{1}{2}} - H_y|_{i-\frac{1}{2},j}^{n+\frac{1}{2}}}{\Delta x} + \frac{H_x|_{i,j-\frac{1}{2}}^{n+\frac{1}{2}} - H_x|_{i,j+\frac{1}{2}}^{n+\frac{1}{2}}}{\Delta y}\right), \tag{7}$$

with the electric field updating coefficients at node (i,j) are given by

$$C_{\mathrm{a}}|_{i,j} = \left(1-\frac{\sigma_{i,j}\Delta t}{2\varepsilon_{i,j}}\right)\Big/\left(1+\frac{\sigma_{i,j}\Delta t}{2\varepsilon_{i,j}}\right), \tag{8}$$

$$C_{\mathrm{b}}|_{i,j} = \left(\frac{\Delta t}{\varepsilon_{i,j}}\right)\Big/\left(1+\frac{\sigma_{i,j}\Delta t}{2\varepsilon_{i,j}}\right), \tag{9}$$

where the parameter σ is the electric conductivity.

B. TR FDTD Algorithm

To reversing the time direction, the time sequence of conventional FDTD algorithm is reversed. The EM waves, E^n and $H^{n-1/2}$, are computed form $H^{n+1/2}$ and E^n, respectively. Therefore, the 2-D TM mode of time reversal FDTD can be written as [12]

$$E_z|_{i,j}^{n} = C_{\mathrm{a}}|_{i,j}E_z|_{i,j}^{n+1} - C_{\mathrm{b}}|_{i,j}\left(\frac{H_y|_{i+\frac{1}{2},j}^{n+\frac{1}{2}} - H_y|_{i-\frac{1}{2},j}^{n+\frac{1}{2}}}{\Delta x} + \frac{H_x|_{i,j-\frac{1}{2}}^{n+\frac{1}{2}} - H_x|_{i,j+\frac{1}{2}}^{n+\frac{1}{2}}}{\Delta y}\right), \tag{10}$$

$$H_y|_{i,j}^{n-\frac{1}{2}} = H_y|_{i,j}^{n+1/2} - \left(\frac{\Delta t}{\mu_{i,j}}\right)\left(\frac{E_z|_{i+\frac{1}{2},j}^{n} - E_z|_{i-\frac{1}{2},j}^{n}}{\Delta x}\right), \tag{11}$$

$$H_x|_{i,j}^{n-\frac{1}{2}} = H_x|_{i,j}^{n+1/2} - \left(\frac{\Delta t}{\mu_{i,j}}\right)\left(\frac{E_z|_{i,j-\frac{1}{2}}^{n} - E_z|_{i,j+\frac{1}{2}}^{n}}{\Delta y}\right), \tag{12}$$

C. Numerical Stability Condition

The maximum time step is limited by the stability restriction of the finite difference equation. The numerical stability condition of 2-D FDTD is specified as [15]

$$\Delta t \le \frac{1}{c\sqrt{\frac{1}{\Delta x^2}+\frac{1}{\Delta y^2}}}, \tag{13}$$

where c is the velocity of light in free space.

In this paper, the magic time step condition is used to obtain the minimum numerical error. The magic time step condition is defined as

$$\Delta t = \frac{1}{c\sqrt{\frac{1}{\Delta x^2}+\frac{1}{\Delta y^2}}}. \tag{14}$$

D. Excitation of UWB EM Wave

The modulated Gaussian pulse is used as the UWB EM wave excitation V_{S}. The expression of this pulse is

$$V_{\mathrm{S}}|^n = Ae^{-[(n-n_0)\Delta t/d]^2}\sin[2\pi f_{\mathrm{c}}(n-n_0)\Delta t], \tag{15}$$

where A is the maximum amplitude of the envelope signal, f_{c} is the carrier frequency, d is the $1/e$ characteristic decay time and n_0 is the delayed time step.

E. PML ABC Treatment

The tangential field components on the four mesh walls must be specified in such a way that outgoing waves are not reflected. The FDTD simulation in this paper uses the perfectly matched layer adsorbing boundary condition (PML ABC) [16]. The PML ABC can effectively absorb propagation wave by using nonphysical lossy media adjacent to the outer-grid boundaries backed by perfectly conducting walls. The field components are

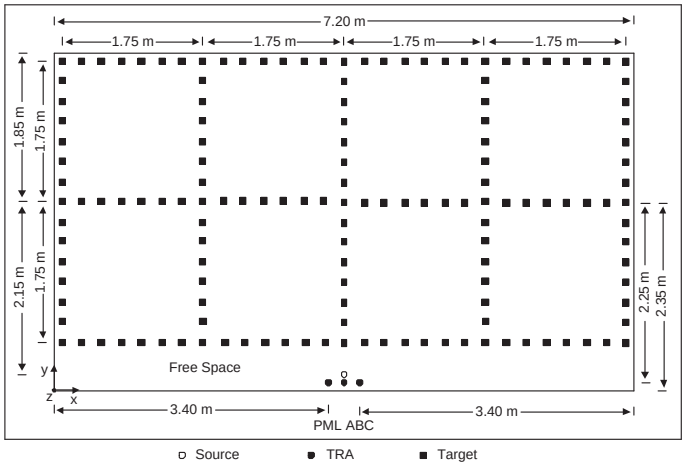

Fig. 2. Dimensions of simulation model and locations of target

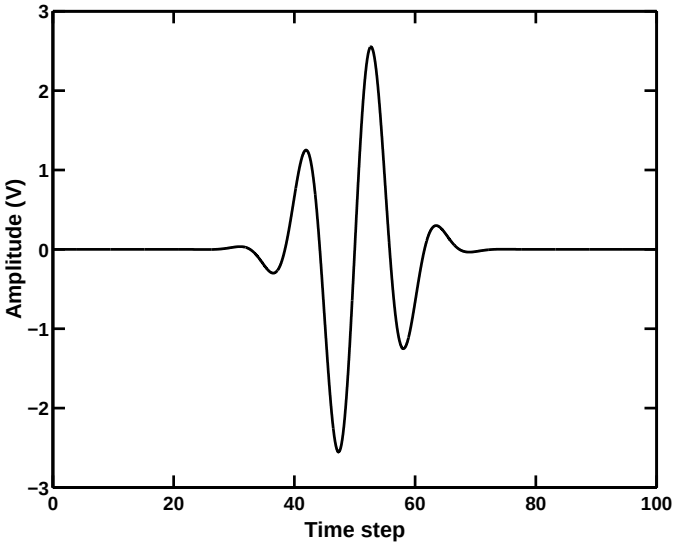

Fig. 3. Time domain waveform of UWB EM wave excitation.

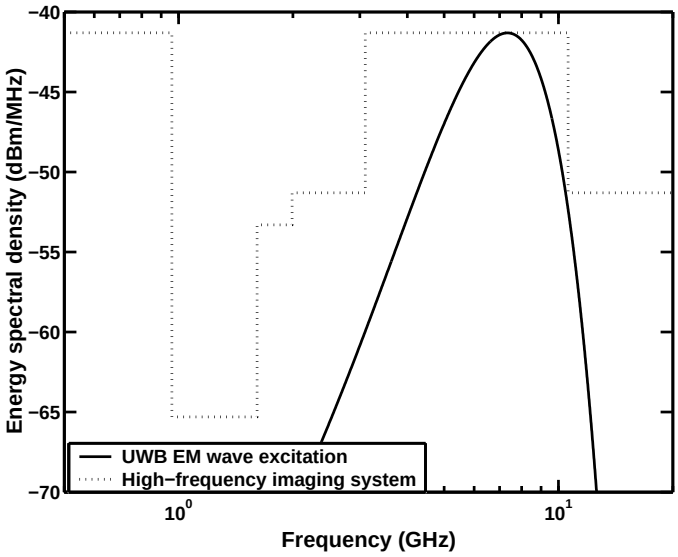

Fig. 4. Energy spectral density of UWB EM wave excitation compared with FCC spectral mask of high-frequency imaging system.

split into two subcomponents. The electric and magnetic losses, $\sigma_{\rm e}$ and $\sigma_{\rm h}$, inside the PML medium are specified by satisfying the PML impedance-matching condition

$$\frac{\sigma_{\rm e}}{\varepsilon} = \frac{\sigma_{\rm h}}{\mu}. \tag{16}$$

After the specification of electric and magnetic losses, EM waves inside the PML medium is rapidly attenuated. The explicit exponentially difference field-updating equations [11] are used to replace the conventional FDTD algorithm.

The electric loss inside the PML legion is assumed to increase with depth from zero at $\rho = 0$ to a maximum value of $\sigma_{\max}$ at $\rho = \delta$ by the quadratic ramping

$$\sigma_{\rm e}(\rho) = \sigma_{\max}\left(\frac{\rho}{\delta}\right)^2, \tag{17}$$

where $\sigma_{\max}$ is chosen to bound the PML reflection coefficient. The PML reflection coefficient at normal incident has the following expression,

$$R(0) = e^{-2\sigma_{\max}\delta/(3\varepsilon c)}. \tag{18}$$

III. Accuracy Analysis Results

The simulation model is done in free space medium with three transceivers as the TR array (TRA) and one source point. The accuracy of focusing resolution is analyzed along both horizontal and vertical axes. The dimensions of simulation model and locations of targets are shown in Fig. 2. All targets are perfect conductors and the increment of each target location along the horizontal and vertical axes is 0.25 m.

Subsequently, the 2-D TM mode of FDTD simulation is used to model this structure. The cell sizes in x and y directions are $\Delta x = \Delta y = 0.005$ m. The PML ABC with 16 layers is used to reduce the reflection error at the edges of the simulation boundaries. The dimension of total lattice is $872 \times 1,472$ cells. The time interval of each time step is $\Delta t = 11.79$ ps which is satisfied the numerical stability condition. The total time steps of this simulation is $n = 2,500$. For the UWB EM wave excitation, the parameters of modulated Gaussian pulse are $f_{\rm c} = 7.34$ GHz, $d = 0.11$ ns, $A = 2.79$ V, and $n_0 = 50$. The time domain waveform of UWB EM wave excitation and its energy spectral density are shown in Figs. 3 and 4, respectively. This waveform is well satisfied the FCC spectral mask of high-frequency imaging system.

First, the UWB EM wave source is excited by using the 2-D TM mode of conventional FDTD algorithm. The UWB EM wave propagates to each target and reflects back to the TRA. Then, each element of TRA is recorded the reflected UWB EM waves, and the directed UWB EM wave from source is eliminated. Next, the reflected UWB EM wave of each target is separated and performed the TR algorithm. The TR EM wave of each TRA element is transmitted by using the 2-D TM mode of TR FDTD algorithm. The TR EM waves focus back to each

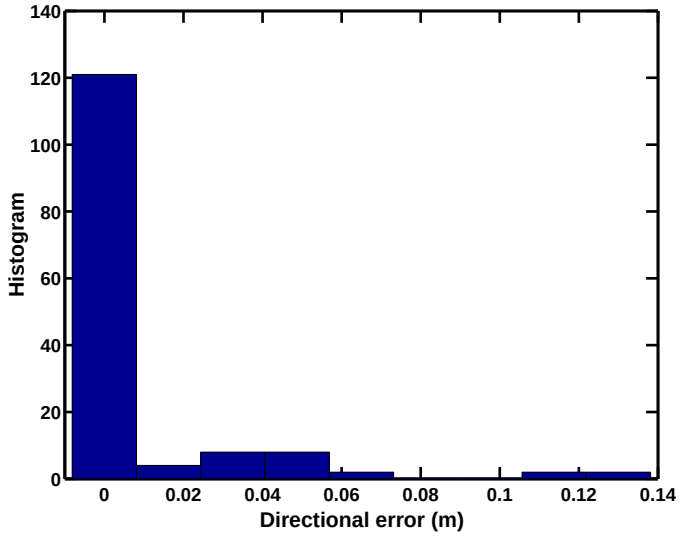

Fig. 5. Histogram of directional error.

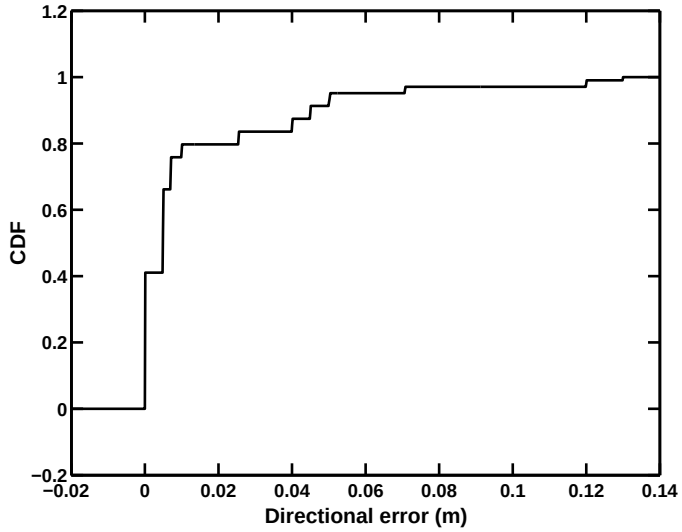

Fig. 6. CDF of directional error.

target. The accuracy of focusing resolution is considered in the terms of directional error.

The directional error e indicates the resolution accuracy of TR EM waves that focus back to the target and it can be written as

$$e = \sqrt{e_{\mathrm{x}}^2 + e_{\mathrm{y}}^2}, \tag{19}$$

where e_{x} and e_{y} are the directional error of TR EM waves that focus back to the target along the x and y directions, respectively.

The histogram and cumulative distribution function (CDF) of directional error are shown in Figs. 5 and 6 respectively. There are 26 error targets from all 147 targets, which is about 17.69 %. All directional errors are less than 0.13 m. The mean and standard deviation of directional error are only 0.01 m and 0.02 m, respectively.

IV. Conclusion

In this paper, the accuracy of focusing resolution with TR EM pulse propagation is analyzed. The TR EM pulse propagation is done via the numerical simulation of FDTD method. The directional error of all target is evaluated. The histogram and CDF of directional error are shown. From the result, there are error targets about 17.69 %. The average and standard deviation of directional error are 0.01 m and 0.02 m, respectively. In future work, the improvement of directional error by increasing the elements of TRA is investigated.

References

[1] K. Siwiak, "Ultra-Wide Band Radio: Introducing a New Technology," *2001 Spring IEEE Vehicular Technology Conference (VTC)*, vol. 2, pp. 1088-1093, May 2001.

[2] K. Siwiak, "Ultra-Wide Band Radio: The emergence of an Important RF Technology," *2001 Spring IEEE Vehicular Technology Conference (VTC)*, vol. 2, pp. 1169-1172, May 2001.

[3] K. Siwiak, "Impact of ultra wide band transmissions on a generic receiver," *2001 Spring IEEE Vehicular Technology Conference (VTC)*, vol. 2, pp. 1181-1183, May 2001.

[4] Federal Communications Commission, "Revision of Part 15 of the Commission's Rules Regarding UWB Transmission Systems," First Report, FCC 02-48, Apr. 2002.

[5] M. Soumekh, "Depth-Focused Interior Echo Imaging," *IEEE Transactions on Image Processing*, vol 8, no. 11, pp. 1608-1618, Nov. 1999.

[6] L. J. Busse, "Three-Dimensional Imaging Using a Frequency Domain Synthetic Aperture Focsing Technique," *IEEE Transactions on Ultrasonics, Ferroelectrics and Frequency Control*, vol 39, no. 2, pp. 174-179, March 1992.

[7] M. Li, W. Guan and P. Li, "Improved Synthetic Aperture Focusing Technique with Applications in High-Frequency Ultrasond Imaging," *IEEE Transactions on Ultrasonics, Ferroelectrics and Frequency Control*, vol 51, no. 1, pp. 63-70, Jan. 2004.

[8] S. D. Silverstein, "A Robust Auto-Focusing Algorithm for Medical Ultrasound: Consistent Phase References from Scaled Cross-Correlation Functions," *IEEE Signal Processing Letters*, vol 8, no. 6, pp. 177-179, June. 2001.

[9] M. E. Yavuz and F. L. Teixeira, "A Numerical Study of Time-Reversed UWB Electromagnetic Wave in Continuous Random Media," *IEEE Antennas and Wireless Propagation Letters*, vol 4, pp. 43-46, 2005.

[10] K. S. Yee, "Numerical Solution of Initial Boundary Value Problems Involving Maxwell's Equations in Isotropic Media," *IEEE Transactions on Antennas and Propagation*, vol. 14, pp. 302-307, 1966.

[11] A. Taflove, *Computational Electrodynamics: The Finite-Difference Time-Domain Method*, Norwood, MA: Artech House, 1995.

[12] R. Sorrentino, L. Roselli and P. Mezzanotte, "Time Reversal in Finite Difference Time Domain Method," *IEEE Microwave and Guided Wave Letters*, vol 3, no. 11, pp. 402-404, Nov. 1993.

[13] P. Supanakoon, T. Payommai, S. Promwong, P. Sithiyopasukul and J. Takada, "Study on Focusing Resolution of Time-Reversed Ultra Wideband Electromagnetic Waves by Using Finite Difference Time Domain Method," *The International Technical Conference on Circuits/Systems, Computers and Communications (ITC-CSCC 2006)*, no. 1, pp 289-292, 10-13 July 2006.

[14] C. A. Balanis, *Advanced Engineering Electromagnetics*. John Wiley, 1989.

[15] A. Taflove and M. E. Brodwin, "Numerical Solution of Steady-State Electromagnetic Scattering Problems Using The Time-Dependent Maxwell's Equation," *IEEE Transections on Microwave Theory and Techniques*, vol. 23, pp. 623-630, 1975.

[16] J. Berenger, "A Perfectly Matched Layer for The Absorption of Electromagnetic Wave," *Journal on Comptattional Physics*, vol. 14, pp. 185-200, 1994.

Performance Evaluation of Free Space Transmission Gain for Ultra Wideband Impulse Radio System

Narongsak Manosittichai* and Sathaporn Promwong*
*Department of Information Engineering, Faculty of Engineering,
King Mongkut's Institute of Technology Ladkrabang,
Chalongkrung Rd., Ladkrabang, Bangkok 10520, Thailand.
Email: {s9061058,kpsathap}@kmitl.ac.th

***Abstract*— An ultra wideband impulse radio (UWB-IR) is applied for short-range system such as wireless local area network (WLAN) and wireless personal area network (WPAN) on office and home networking. The characteristics of indoor propagation channel are very complicated and difficult to predict. Therefore, the performances of transmission signal shall be considered. In this paper, we discuss the performance of UWB-IR transmission signal. The template signal receiver is considered at receiver side to maximize the signal-to-noise ratio (SNR) for evaluation. The experiment results are used to evaluate the transmission signal waveform based on Friis' transmission formula. This technique gives very accurate results and is useful to design and evaluate the UWB-IR systems, especially for the performance evaluations of waveform distortion.**

I. Introduction

Today the wireless personal area networks (WPANs) are required to have high data rate, low power consumption and low cost. The ultra wideband impulse radio (UWB-IR) technology is an ideal candidate focusing on WPAN.

Federal Communications Commission (FCC) is currently working on setting emission limits that would allow UWB-IR communication systems to be deployed on an unlicensed band following the part 15 rules for radiated emissions of intentional radiators [1].The frequency range of UWB-IR signal for wireless communications is from 3.1 GHz to 10.6 GHz. The UWB-IR transmitter sends pulses with ultra high bandwidth and the UWB-IR receiver collects the power of received signal for rebuilding the pulses. Since the power spectral density (PSD) level of UWB-IR signal may be below the noise level of other systems, UWB-IR technology can exist with other RF technology without interference.

The antennas of UWB-IR communication systems are significantly pulse-shaping filters. Any distortion of the signal in the frequency domain causes the distortion of the transmitting pulse shape. Consequently, this will increase the complexity of the detection mechanism at the receiver [2]. Moreover, low cost, geometrically small and still efficient structures are required for typical wireless applications. Therefore, the antenna design for UWB-IR signal radiation is the one of main challenges [3].

Even if the channel is in line-of-sight (LOS), Friis' transmission formula cannot be directly applied to the UWB-IR system as the bandwidth of the pulse is extremely wide. Furthermore, simple comparison between the waveforms of transmitter and receiver is not significant because of the distortion of the waveform caused by the frequency response of the antenna.

In this paper, we discuss the free space transmission waveform evaluation scheme for UWB-IR systems. This scheme is based on the Friis' transmission formula, adapted for UWB-IR. The transmitted waveform and the receiver template waveform are keys for the extension of Friis' transmission formula to UWB system. An experiment is carried out using two types of broadband antennas for UWB operation in an indoor environment.

II. Ultra Wideband Thoery

In this study, we focus on the performance evaluation for UWB-IR system in free space.

A. Extension of Friis' Transmission Formula for UWB transmission System

UWB-IR transmission systems have attracted a great deal of attention because of its potential applications on short-range, high-speed, and low-power wireless communications. In order to minimize the interference with existing systems, UWB is expected to be mainly used in indoor wideband environments.

In narrowband systems, the link budget of the free space propagation loss is usually estimated by using Friis' transmission formula [4]. However, it is not directly applicable to the UWB impulse radio transmission system, as the formula is expressed as a function of the frequency. Moreover, the waveform may be distorted due to the frequency characteristics of the antenna. [5] treats the special cases of the constant gain and the constant aperture, but no general discussion had been made although it suggested the use of the time-domain antenna effective length.

The Friis' transmission formula has been widely used, and can be applied to the calculation of these LOS channels.

$$G_{\text{Friis}}(f) = \frac{P_{\text{r}}(f)}{P_{\text{t}}(f)} = G_{\text{f}}(f) G_{\text{r}}(f) G_{\text{t}}(f), \tag{1}$$

where G_{r} and G_{t} are Rx and Tx antenna gain,

$$G_{\text{f}}(f) = \left(\frac{\lambda}{4\pi d}\right)^2 \tag{2}$$

is the free space propagation gain (less than unity in practice), $\lambda = \frac{c}{f}$ is the wavelength, c is the velocity of the light, f

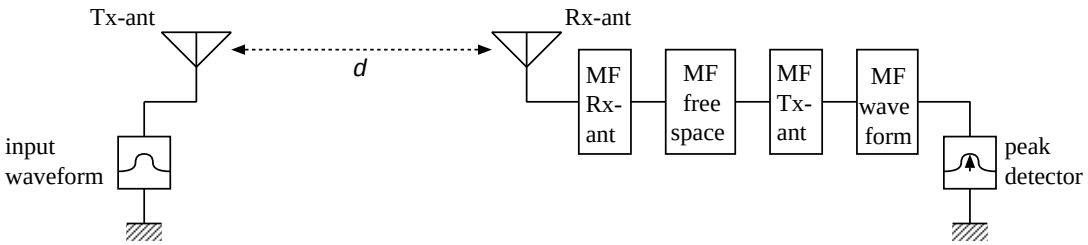

Fig. 1. Block diagram of transmission system for UWB-IR signal.

is the operating frequency, and d is the separation between transmitter and receiver antennas.

It is noted, however, that Eq. (1) is satisfied only at some certain frequency, and is not directly applicable to UWB systems. The Friis' transmission formula shall be extended to take into account the transmission signal waveform and its distortion as well [6], [7].

Input signal $v_{\rm i}(t)$ at the transmitter port is expressed as the convolution of an impulse input and the pulse shaping filter $h_{\rm i}(t)$ as

$$v_{\rm i}(t) = E_{\rm i}\delta(t) * h_{\rm i}(t), \tag{3}$$

where

$$\int_{-\infty}^{\infty} h_{\rm i}^2(t){\rm d}t = \int_{-\infty}^{\infty} |H_{\rm i}(f)|^2\,{\rm d}f = 1. \tag{4}$$

Friis' formula is extended taking into account the transmission waveform as

$$H_{\text{e-Friis}}(f) = \frac{V_{\rm r}(f)}{E_{\rm i}} = H_{\rm f}H_{\rm i}\mathbf{H}_{\rm r}\cdot\mathbf{H}_{\rm t}, \tag{5}$$

where

$$\begin{aligned}\mathbf{H}_a &= \mathbf{H}_a(\theta_a,\ \varphi_a,\ f)\\ &= \hat{\boldsymbol{\theta}}_a H_{a\theta}(\theta_a,\ \varphi_a,\ f) + \hat{\boldsymbol{\varphi}}_a H_{a\varphi}(\theta_a,\ \varphi_a,\ f), \quad (6)\\ a &= \text{r } \textit{or } \text{t},\end{aligned}$$

is a complex transfer function vector of the antenna relative to the isotropic antenna,

$$H_{\rm f} = \frac{\lambda}{4\pi d}\exp(-{\rm j}kd), \tag{7}$$

is the free space transfer function where

$$k = \frac{2\pi}{\lambda}, \tag{8}$$

is the propagation constant. Unit vectors $\hat{\boldsymbol{\theta}}_{\rm a}$, $\hat{\boldsymbol{\varphi}}_{\rm a}$ express the polarization and are defined with respect to the local polar coordinates of each of the antennas. The following relations can be easily derived.

$$\hat{\boldsymbol{\theta}}_{\rm r} = \hat{\boldsymbol{\theta}}_{\rm t}, \tag{9}$$

$$\hat{\boldsymbol{\varphi}}_{\rm r} = -\hat{\boldsymbol{\varphi}}_{\rm t}. \tag{10}$$

At the receiver, the matched filter $H_{\rm MF}(f)$ is introduced to maximize the signal-to-noise ratio (SNR) of the receiver output, as shown in Figure 1.

$$H_{\rm MF}(f) = \frac{H^*_{\text{e-Friis}}(f)}{\sqrt{\displaystyle\int_{-\infty}^{\infty} |H_{\text{e-Friis}}(f)|^2\,{\rm d}f}}, \tag{11}$$

which satisfies the following constant noise output power condition

$$\int_{-\infty}^{\infty} |H_{\rm MF}(f)|^2\,{\rm d}f = 1. \tag{12}$$

In this case, the output waveform when $E_{\rm i} = 1$, and the spectrum of the receiver output are $h_{\text{e-Friis}}(t)$ and $H_{\text{e-Friis}}(f)$, respectively. The waveform of the output from the matched filter $v_{\rm MF}(t)$ and the spectrum of the output from the matched filter $V_{\rm MF}(f)$ are

$$\begin{aligned}v_{\rm MF}(t) &= h_{\text{e-Friis}}(t) * h_{\rm MF}(t)\\ &= \frac{h_{\text{e-Friis}}(t) * h_{\text{e-Friis}}(-t)}{\sqrt{\displaystyle\int_{-\infty}^{\infty} h^2_{\text{e-Friis}}(t){\rm d}t}}, \quad (13)\end{aligned}$$

$$\begin{aligned}V_{\rm MF}(f) &= H_{\text{e-Friis}}(f)H_{\rm MF}(f)\\ &= \frac{|H_{\text{e-Friis}}(f)|^2}{\sqrt{\displaystyle\int_{-\infty}^{\infty} |H_{\text{e-Friis}}(f)|^2\,{\rm d}f}}, \quad (14)\end{aligned}$$

taking its maximum as

$$\begin{aligned}\max_t v_{\rm MF}(t) &= \int_{-\infty}^{\infty} V_{\rm MF}(f){\rm d}f\\ &= \sqrt{\int_{-\infty}^{\infty} |H_{\text{e-Friis}}(f)|^2\,{\rm d}f}. \quad (15)\end{aligned}$$

Equation (15) is the UWB extension of Friis' transmission formula. It includes three elements, namely the frequency characteristics of the antennas, the frequency characteristics of free space propagation, and the spectrum of the transmit signal. It is clear from Eq. (15) that the transmission gain of the UWB signal can not be defined as the product of gains of antennas and a free space channel as Friis' formula (1). Instead, the total transmission gain including the effect of the waveform can be obtained as Eq. (15). For the normalization, the reference isotropic antenna with $H_{\rm Iso}(f) = 1$ is considered. The UWB transmission gain can be defined as

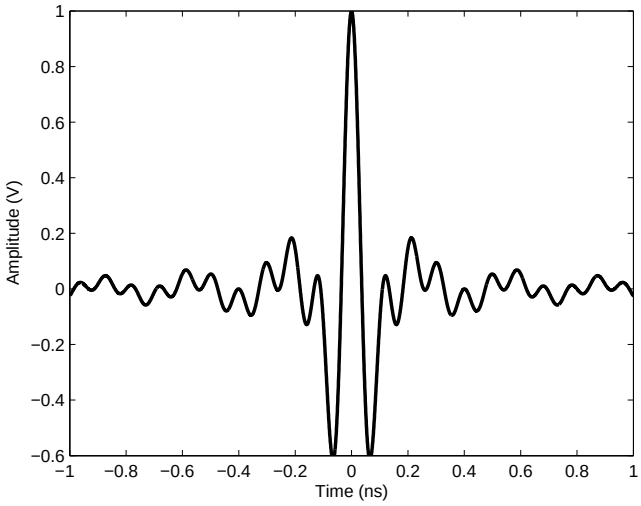

Fig. 2. The transmission waveform of UWB-IR signal.

$$G_{\mathrm{UWB}} = \max_{t} v_{\mathrm{MF}}(t) / \max_{t} v_{\mathrm{MF,Iso}}(t). \qquad (16)$$

III. Measurement Systems

A. UWB Signal Model

The rectangular density spectral waveform covering the FCC band [8], i.e., that is 3.1 GHz $\backsim$ 10.6 GHz is used to test the distortion of the received UWB waveform.The UWB transmission signal is set in the full UWB spectrum bandwidth. The minimum and maximum frequencies are $f_{\min}$ = 3.1 GHz and $f_{\max}$ = 10.6 GHz, respectively. The spectral bandwidth is f_{b} = 7.5 GHz and equation is

$$v_{\mathrm{t}}(t) = \frac{1}{\mathrm{f_b}}[f_{\max}\mathrm{sinc}(2f_{\max}t) - f_{\min}\mathrm{sinc}(2f_{\min}t)] \qquad (17)$$

where $f_{\min}$ = 3.1 GHz, $f_{\max}$ = 10.6 GHz, f_{b} = $f_{\max} - f_{\min}$ and $\mathrm{sinc(x)} = \sin(\pi x)/(\pi x)$. This signal waveform in time domain is shown in Fig. 2.

B. Experimental Setup and Measurement Model

The vector network analyzer (VNA) was operated in the response measurement mode, where Port-1 was the transmitter port (Tx) and Port-2 was the receiver port (Rx), respectively. The Tx antenna is a Biconical antennas with the maximum diameter of 65.3 mm and the length of 37 mm used as the standard antennas [9]. The Rx antenna is a commerial, small-size , low profile antenna developed by Skycross Lnc.,(USA) [10] used as the AUT. The measurement was done in the meeting room at Department of Information Engineering (KMITL). Tx and Rx antenna are fixed on labtop computer at the height of 1.40 m from ground. Rx antenna is separated at a distance of 1.43 m.

It is noted that the calibration is done at the connectors of the cables to be connected to the antennas. Therefore, all the impairments of the antenna characteristics are included in the measured results. The setup is sketched in Fig. 3.

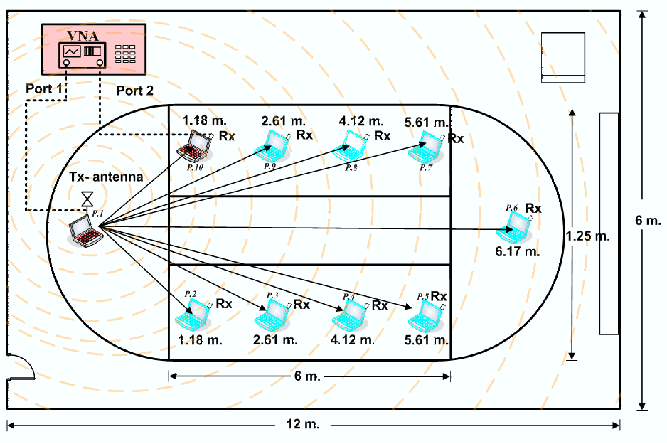

Fig. 3. The measurement model setup.

TABLE I
Experimental Setup Parameters.

Parameter	Value
Frequency range	3 GHz to 11 GHz
Number of frequency points	801
Dynamic power range	80 dB
Tx antenna height	1.40 m
Rx antenna height	1.40 m
Distance between Tx and Rx	1.18 to 6.17 m

C. Parameters of Experiment and Calibration Techniques

The important parameters for the experiments are listed in Table I.

IV. Results and Discussion

From the results of experiment by using the VNA. The data measured shows that BER of signal will be considered in two part are effect from opening and closing laptop computer.

Fig.4. shows BER performance of correlation receiver for UWB-IR with laptop computer (open). The transmitted rate has increasing BER when SNR has risen in every points of observation. Moreover, in the 2^{nd} position (P.2) has the minimum BER because of the distance that is too close (1 m). However, in the 6^{th} position (P.6) has the maximum BER because the received antenna is too far (6.17 m).

Fig.5. shows BER performance of correlation receiver for UWB-IR with laptop computer (closed). From analytical result, transmitted rate has decreasing BER when SNR has risen in every points of observation. Moreover, in the 2^{nd} position (P.2) has the minimum BER and the 6^{th} position (P.6) has the maximum BER, respectively. In the same way of laptop computer (open) case.

V. Conclusion

In this paper, we discuss the performance evaluation of free space transmission gain with laptop computer for UWB-IR, which comparison between opening and closing laptop

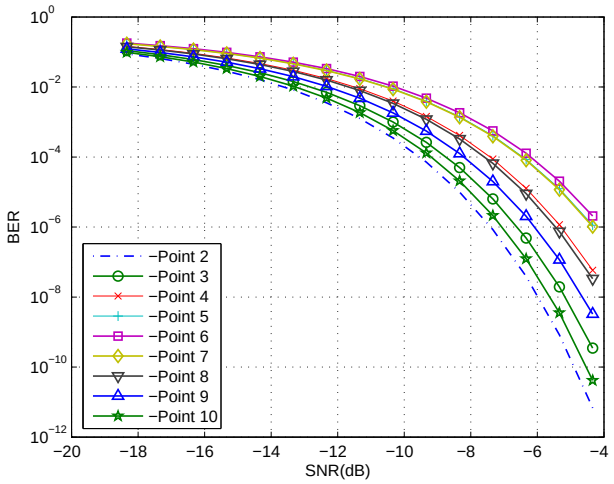

Fig. 4. BER performance of correlation receiver for UWB impulse radio with laptop computer : open.

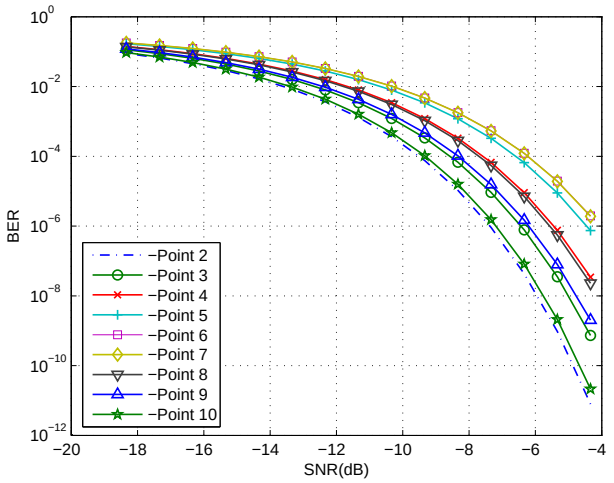

Fig. 5. BER performance of correlation receiver for UWB impulse radio with laptop computer : closed.

computer. Every points of investigation express a BER of an opening part is more increasing than close one. Obviously, BER varies to distance between transmitted and received antenna and setting position of antenna.

REFERENCES

[1] K. Siwiak, "Impact of ultra wide band transmissions on a generic receiver," Proc. 2001 Spring IEEE Veh. Tech. Conf. (VTC), Rhodes, Greece, vol. 2, pp. 1181–1183, May 2001.

[2] H.F. Harmuth and S. Ding-Rong, "Antennas for Nonsinusiodal Wave — Part I: Radiators," IEEE Trans. Elec. Mag. Compat., vol. EMC-25, no. 1, pp. 13–24, Feb. 1983.

[3] H.F. Harmuth and S. Ding-Rong, "Antennas for Nonsinusiodal Wave — Part II: Sensors," IEEE Trans. on Elec. Mag. Compat., vol. EMC-25, no. 1, no. 2, pp. 107–115, May 1983.

[4] H.T. Friis, "A note on a simple transmission formula," Proc. IRE, vol. 34, no. 5, pp. 254–256, May 1946.

[5] United States of America, "Path loss calculations for ultra-wideband signals in indoor environments," ITU-R Document 3K/30-E, pp. 1–14, Nov. 2003.

[6] J. Takada, S. Promwong and W. Hachitani, "Extension of Friis' Transmission Formula for Ultra-Wideband Systems," IEICE Tech. Rep., WBS2003-8/MW2003-20, May 2003.

[7] A.H. Mohammadian, A. Rajkotia, and S.S. Soliman, "Characterization of UWB Transmit-Receive Antenna System," Proc. IEEE Conf. Ultra Wideband Syst. Tech. (UWBST) 2003, Nov. 2003.

[8] Federal Communications Commission, "Revision of Part 15 of the Commission's Rules Regarding Ultra-Wideband Transmission Systems," First Report and Order, FCC 02–48, Apr. 2002.

[9] S. Promwong, and J. Takada, "Free space link budget estimation scheme for ultra wideband impulse radio with imperfect antennas," IEICE Electronics Express, vol. 1, no. 7, pp. 188–192, July 2004.

[10] Skycross Inc., "3.1 – 10 GHz UWB Antenna for Commercial UWB Applications," `http://www.skycross.com/`

An Ultra-wideband CPW-Fed Elliptical Loop Slot Antenna

Rapeepan Keawon, Prayoot Akkaraekthalin,and Vech Vivek
Department of Electrical Engineering, Faculty of Engineering,
King Mongkut's Institute of Technology North Bangkok,
1518, Pibulsongkram Rd., Bangsue, Bangkok 10800, Thailand
Tel.: +662-9132500-24 Ext. 8515, Fax.: +662-5857350, E-mail: prayoot@kmitnb.ac.th

Abstract- **In this paper, we present a new Coplanar Waveguide-fed elliptical loop slot antenna for ultra-wideband applications. This antenna consists of a 50 Ω coplanar waveguide feeding line. Proper parametric results of an optimal structure with a bandwidth of 146.26 % are thus achieved. Experimental investigations are also presented and the obtained results confirm high antenna performances.**

I. INTRODUCTION

Ultra-wideband technology has experienced a blooming growth in the past few years and has become the most promising candidate for future short rang high-speed indoor data communications. In 2002, the U.S. Federal Communication commission officially allocated the spectrum from 3.1-10.6 GHz for unlicensed UWB communication application, which meets the 802.15.3 protocal requirements. The interest of the Coplanar Waveguide (CPW)-fed slot antennas has been increasingly studied in recent years. CPW-fed antennas also have many attractive features including low radiation loss, less dispersion, easy integration for monolithic microwave integrated circuits (MMIC) and simple configuration with a single metallic layer, since no backside processing (via holes) is required for integration of devices, thus the designs of these antennas have recently become more and more attractive. One of the main issues with CPW-fed slot antennas is to provide an easy impedance matching to the CPW line. In order to obtain broadband CPW-fed slot antennas, several impedance tuning techniques have been reported in literatures based on a change of slot dimensions in bow-tie slot [1]-[3], a square slot fed by a CPW [4]-[5] and CPW-fed equilateral hexagonal slot [6]. However, up to now the CPW-fed slot antenas designed by using these techniques have impedance bandwidths generally less than 60-110 %. In this paper, an alternative method for proposed radiator is an Ultra-wideband CPW-fed elliptical loop slot antenna that requires an additional stub for input impedance matching and offers more wide bandwidth. The antenna consists of a circular CPW stub surrounded by a slot elliptical loop. For designing, a widened tuning stub is used, and the parameters of the location and size of the tuning stub can control the coupling between the CPW-fed line and the radiating loop slot leading to large bandwidth of 146.26 %. In this study several designs are experimentally investigated, and the characteristics of input impedance radiation pattern are analyzed and discussed.

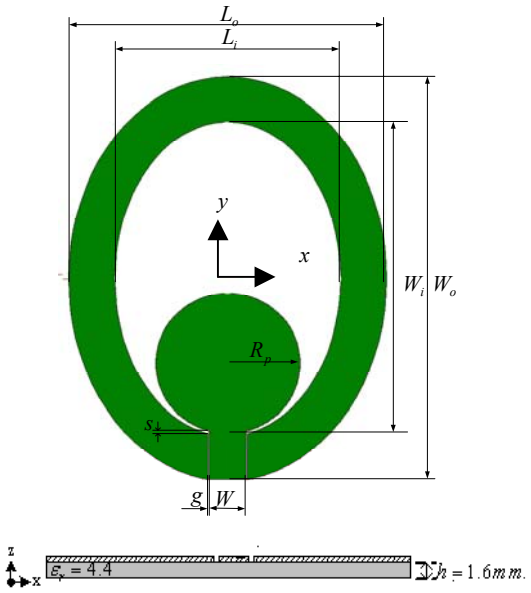

Figure 1. Geometry of the proposed CPW-fed elliptical loop slot antenna.

II. ANTENNA DESCRIPTION

The geometry of the propose CPW-fed elliptical loop slot antenna is shown in Fig. 1. The proposed antenna is farbricated on an inexpensive FR-4 substrate with thickness (h) of 1.6 mm and relatively permittivity (ε_r) of 4.4. The printed elliptical loop radiating slot has a side width of W_o, W_i and a length of L_o, L_i. A 50Ω CPW has a signal strip of width W and a gap of the spacing g between the signal strip and the coplanar ground plane. The widened tuning stub with circular tuning stub in the elliptical loop slot has a side radius of R_p. The spacing between the tuning stub and edge of the ground plane is S. The antenna geometric parameters are designed and optimized using IE3D resulting in W_o = 72 mm, W_i = 56 mm, L_o = 55 mm, L_i = 39 mm, W = 6.37 mm and g = 0.5 mm. Thus, six parameters of adjusting include W_o, W_i, L_o, L_i, R_p and S. The overall antenna size is thus 72 × 55 mm^2, therefore, the details of the design, simulation and measurement will be described in following sections.

III. PARAMETER STUDY AND IMPLEMENTATION

A. *Elliptical loop slot*

First, a CPW–fed line is designed with the strip width W = 6.37 mm and gap with g of 0.5 mm, corresponding to the characteristic impedance of 50 Ω. Simulation has been carried out by using IE3D. The proposed design can be futher enchanced by adjusting parameters of elliptical loop slot width (W_o, W_i) and (L_o, L_i) Fig. 2 shows the simulated return losses for different elliptical slots (W_o = 72,79,89,93 and 100 mm).

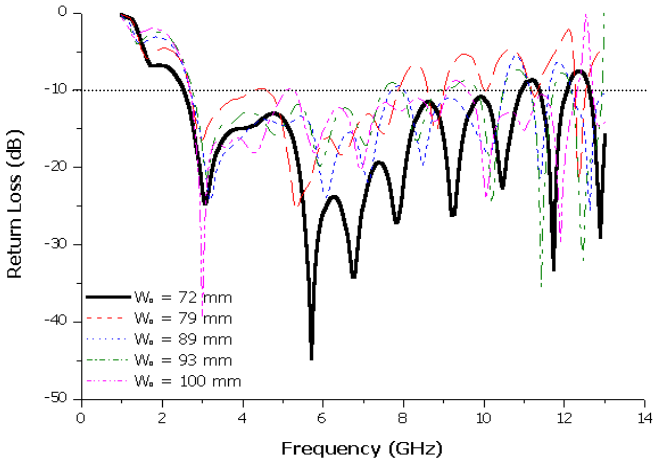

Figure 2. Simulated return losses for the different width (W_o) elliptical slot with W_i = 56 mm, L_o = 55 mm, L_i = 39mm, W = 6.37 mm, R_p = 12.5 mm and S = 0.5 mm.

The results, when W_o is chosen in a rang of about 72 to 100 mm, obtain much enhanced impedance bandwidth (also see Table 1). It can be observed that the return losses for the case of W_o =72 to 100 mm, all frequencies between and in the much higher resonant modes have a return loss larger than 10 dB. The maximum impedance bandwidth is obtained to be as large as 10.67 GHz or about 140.21 % of the center frequency, which is at 7.61 GHz. Fig. 3 shows the simulated return losses for different elliptical slots (W_i = 56,57,58,59 and 60 mm).

Table 1 : Performance of the proposed CPW-fed elliptical loop with various tuning W_o

	W_o (mm)	f_c (MHz)	BW (%,GHz)
Antenna1	72	7.61	140.21,10.67
Antenna2	79	3.41/6.25	41.28,1.41/51.68,3.23
Antenna3	89	5.17	95.74,4.95
Antenna4	93	3.58/6.46	52.23,1.87/36.06,2.33
Antenna5	100	3.88/7.15	59.27,2.30/53.00,3.79

It can be seen that the maximum impedance bandwidth (also see Table 2) is as large as 10.67 GHz or about 67.2 % of the center frequency, which is at about 7.61GHz. The optimized antenna dimension of W_o = 72 mm and W_i = 56 mm.

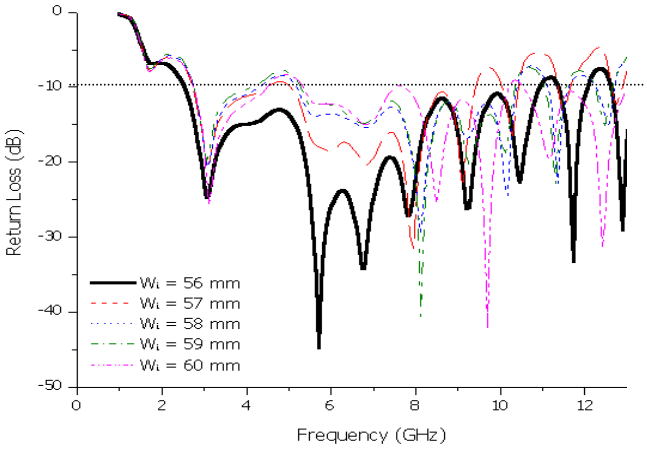

Figure 3. Simulated return losses for the different width (W_i) elliptical slot with W_o = 72 mm, L_o = 55 mm, L_i = 39 mm, W = 6.37 mm, R_p = 12.5 mm and S = 0.5 mm.

Fig. 4 Shows the simulated return losses for different elliptical slots (L_o = 55,62,69,76 and 83 mm). The results, when L_o is chosen in the rang of about 55 to 83 mm, obtain much enchanced impedance bandwidth (also see Table 3). Fig. 5 shows the simulated return losses for different elliptical slots (L_i = 39,40,41,42 and 43 mm). It can be seen that the maximum bandwidth (also see Table 4) is as large as 10.67 GHz.

Table 2 : Performance of the proposed CPW-fed elliptical loop with various tuning W_i

	W_i (mm)	f_c (MHz)	BW (%,GHz)
Antenna1	56	7.61	140.21,10.67
Antenna2	57	3.59/7.20	46.79,1.68/60.27,4.34
Antenna3	58	3.51/7.74	42.16,1.48/67.57,5.23
Antenna4	59	3.35/7.79	34.62,1.16/65.46,5.10
Antenna5	60	5.37	41.34,2.16

Table 3 : Performance of the proposed CPW-fed elliptical loop with various tuning L_o

	L_o (mm)	f_c (MHz)	BW (%,GHz)
Antenna1	55	7.61	140.21,10.67
Antenna2	62	3.60/7.21	48.33,1.74/59.91,4.32
Antenna3	69	3.42/7.19	63.45,2.17/63.69,4.58
Antenna4	76	3.44/7.00	52.03,1.79/52.14,3.65
Antenna5	83	3.29	45.28,1.49

B. Circular tuning stub

The simulated return losses for various tuning stub radius shown in Fig. 6. In this case, the optimal tuning stub is obtained by varying R_p. Many prototypes (antennas 1 to 5) have been simulated and their designed parameters and performances are listed in Table 5 for comparision.

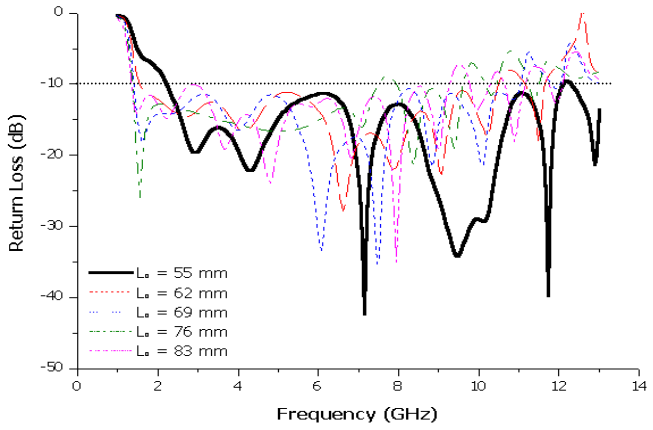

Figure 4. Simulated return losses for the different width (L_o) elliptical slot with W_o = 72 mm, W_i = 56 mm, L_i = 39 mm, W = 6.37mm, R_p =12.5 mm and S= 0.5 mm.

Table 4: Performance of the proposed CPW-fed elliptical loop with various tuning L_i

	L_i (mm)	f_c (MHz)	BW (%,GHz)
Antenna1	39	7.64	140.21,10.67
Antenna2	40	3.64/4.28	48.90,1.74/99.06,4.24
Antenna3	41	3.42/7.19	49.58,1.80/69.49,5.40
Antenna4	42	3.44/7.00	48.75,1.76/60.85,4.43
Antenna5	43	3.29	112.87,6.84

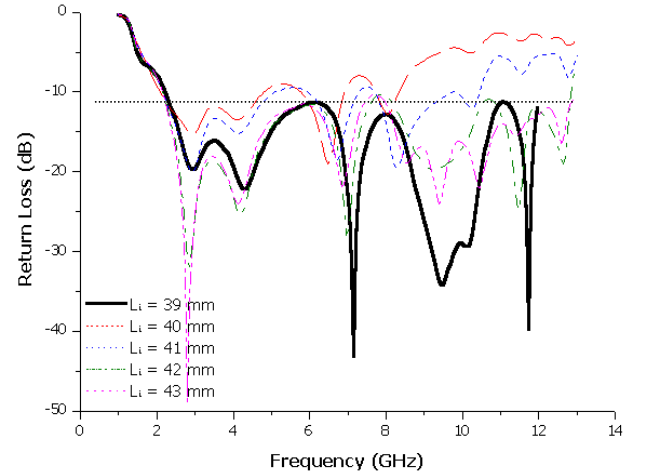

Figure 5. Simulated return losses for the different width (L_i) elliptical slot with W_o = 72 mm, W_i = 56 mm, L_o = 55 mm, W = 6.37 mm, R_p = 12.5 mm and S = 0.5 mm.

The width of W_o is fixed to be 72 mm, W_i = 56 mm and S = 0.5 mm. and the length of L_o is fixed to be 55 mm, L_i = 39 mm and S = 0.5 mm for antenna 1 to 6 in Table 5, which R_p is varied to be 10.5,11.5,12.5,13.5 and 14.5 mm. It is noted that an impedance bandwidth larger than 111 % can be obtained when R_p is chosen in a rang from 11.5 to 13.5 mm. The results also show that the radius of R_p has a significant effect on the impedance bandwidth of a CPW. When a radius of stub is selected, this new resonant mode (higher frequency) can be shifted. Finally, The proposed antenna has been constructed as shown in Fig. 7, and then tested using a calibrated vector network analyzer. Measured result of S_{11} compared with simulation is shown in Fig. 8. We can see a very good agreement of the measurement and simulation results.

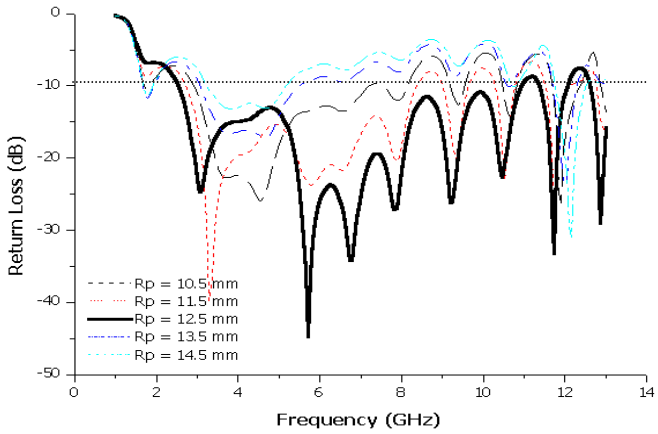

Figure 6. Simulated return losses for the different width (R_p) elliptical slot with W_o = 72 mm, W_i = 56 mm, L_o = 55 mm, W = 6.37 mm, L_i = 39 mm and S = 0.5mm.

Far-field radiation patterns of the proposed antenna with the largest operating bandwidth using the designed parameters of W_o = 72 mm, W_i = 56 mm, L_o = 55mm, L_i = 55 mm W = 6.37 mm, R_p = 12.5 mm and S = 0.5 mm have been then measured.

Table 5: Performance of the proposed CPW-fed elliptical loop with various tuning R_p

	R_p (mm)	f_c (MHz)	BW (%,GHz)
Antenna1	10.5	6.29	111.44,7.01
Antenna2	11.5	6.69	118.53,7.93
Antenna3	12.5	7.61	140.21,10.67
Antenna4	13.5	6.04	114.40,6.91
Antenna5	14.5	7.21	86.82,6.26

Fig. 9 shows the plots of pattern measured in x-z and y-z planes at frequencies of 3.4 GHz, 6.8 GHz, and 8.9 GHz. From the results,

it demonstrates that all the operating frequencies have the similar radiation pattern. It is also noted that all design exhibit an omnidirectional profile in lower frequencies for the x-z plane and bidirectional for the y-z plane. As the frequency increases, Antenna 3 radiates either with strong side lobes (3.4 GHz) and multiple lobes (6.8 GHz).

Figure 7. The constructed antenna.

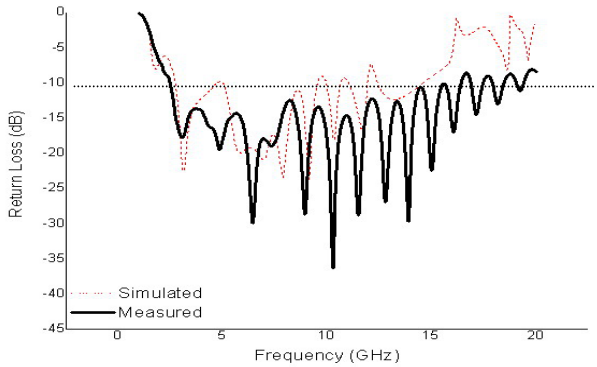

Figure 8. Measured and Simulated return losses for W_o = 72 mm, W_i = 56 mm, L_o = 55mm, L_i = 39 mm W = 6.37 mm, S and g= 0.5 mm.

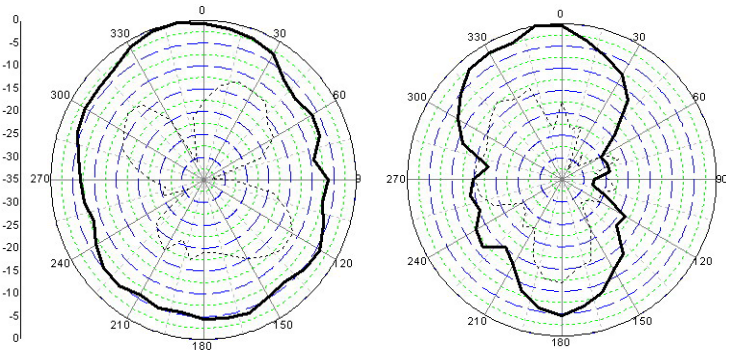

(a)

IV. CONCLUSION

This paper presents study and design of an ultra-wideband CPW-fed elliptical loop slot antenna. It is seen that the antenna has a bandwidth of 2.56 – 16.57 GHz or about 146.26 % at return loss higher 10 dB. The constructed elliptical loop slot antenna has been compared with CPW square slot antenna. It is found the proposed antenna has a wider bandwidth than CPW-fed square slot antenna.

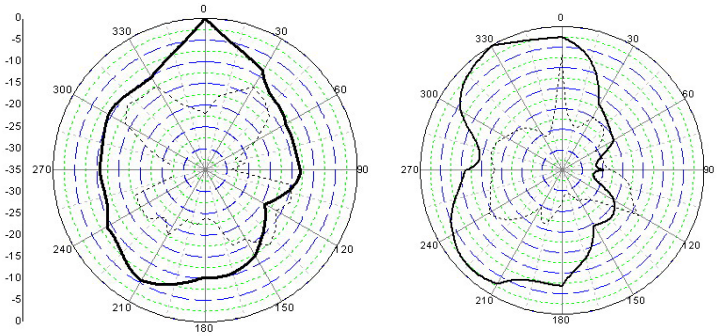

(b)

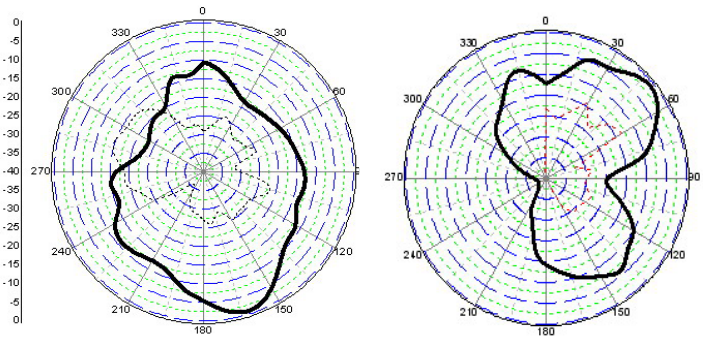

(c)

Figure 9. x-z and y-z plane for antenna (a) 3.4 GHz (b) 6.8 GHz (c) 8.9 GHz.

REFERENCES

[1] P.L.Chin, A.Z. Elsherbeni, and C.E. Smith, "Characteristics of Copla-nar Bow-Tie Patch Antennas," *Antennas and Propagation Society International symposium,* vol. 1, pp.398-401, 2002.

[2] P.L.Chin, A.Z. Elsherbeni, and C.E. Smith, "A Coplanar Waveguide Bow-Tie Aperture Antennas," *Antennas and Propagation Society International symposium,* vol. 1, pp.565-567,2002.

[3] E.A. Soliman, S. Brehels, P. Delmotte, G.A.E.Vonden bosch, and E. Begne, "Bow-Tie Slot Antenna Fed by CPW," *Electron. Lett.,* vol.35, pp..514-514,1999.

[4] Horng-Dean Chen, "Broadband CPW-Fed Square Slot Antennas Wiith a Widened Tuning Stub," *IEEE Trans. Antennas. Propagat.,* vol. 51,No.8,pp.1982-1986, August 2003.

[5] R. Chair, A. A. Kishk, and K. F. Lee, "Ultrawide-band Coplanar waveguide-Fed Rectangular Slot Antenna," *IEEE Antennas.Wireless Propag.Lett.,* vol. 3, pp.227-229, August 2004.

[6] K. Sarikha, V. Vivek, and P. Akkrakethalin. "A Broadband CPW-fed Equilateral Hexagonal Slot Antenna," *29th EECON.* Vol. 3, 2005.

Ultra Wideband Series-Fed Printed Dipole Antenna Arrays with a Log-periodic Structure

Chittawan Choeysakul*, Sarawuth Chaimool**, and Prayoot Akkaraekthalin*,**

*Communication Engineering, Thai-German Graduate School of Engineering
**Department of Electrical Engineering, Faculty of Engineering
King Mongkut's Institute of Technology North Bangkok 1518 Piboonsongkram Rd.
Bangsur, Bangkok 10800, Thailand, Phone: 662-9132500-24 EXT.8402, Fax :+662-5857350
Email: chittawan_thai@yahoo.com, prayoot@kmitnb.ac.th

***Abstract*- In this paper, a novel microstrip antenna using log-periodic and series-fed techniques is proposed to increase operation frequency. This is modification of quasi-Yagi with log-periodic as driver and series-fed to get wider bandwidth and same pattern as end-fire pattern. The prototype antenna measurement shows more than 100 % bandwidth ($S_{11} \leq$ -10dB) and gain of 2-8 dBi. The enhanced performances have been confirmed by both simulation using IE3D and measurement.**

Keywords: Ultra wideband antenna, Log –Periodic arrays, Quasi-Yagi antenna

I. INTRODUCTION

The popularity of using wireless communication makes huge demand for high quality of every part of elements. The most important part of wireless communication systems is an antenna. Antenna is needed in a number of communication systems such as radar, civilian, and military systems. At present, antenna is modified to improve efficiency in various ways upon specialists of each system including microstrip antenna. Microstrip antennas have been extensively studied due to their low profile, low-cost, light-weight, and ease of fabrication. However, microstrip antennas also have some limitations such as narrow bandwidth [1], lower gain, and poor end-fire radiator except tapered slot antennas.

This paper proposes a new antenna using a combination of a quasi-Yagi antenna and a series-fed dipole array antenna in order to increase bandwidth. Normally, a quasi-Yagi microstrip antenna [2],[3] is modified from a classical Yagi-uda dipole. However, the microstrip has certainly uniplanar, therefore the second director or more added will perform as conducting reflectors which lift main lobe. Resolving this problem, series-fed dipole array technique [4] is used to combine them together. The result after combination could be a new antenna, which provides advantages of those characteristics. In addition to this work, it is also used log-periodic technique with driver element to increase operation bandwidth [5]. The proposed antenna could be able to increase up the efficiency ultra wideband operation.

The most interesting approach for this is a modified antenna using many techniques to obtain advantages of each technique. The proposed antenna is fabricated on FR-4 substrate and is demonstrated to achieve an ultra-wideband bandwidth (more than 100% for 10 dB return-loss), which is keeping end-fire pattern. The results will be confirmed by both of IE3D simulation and measurement.

II. DESIGN AND FABRICATION

The beginning ideas and theories of quasi-Yagi antenna have been developed by W. R. Deal, N. Kaneda [2]. In this paper, the quasi-Yagi had been modified to be a new structure. A design of ultra-wideband series-fed printed dipole antenna arrays with a log-periodic structure is conducted and simulated by IE3D (Zeland).

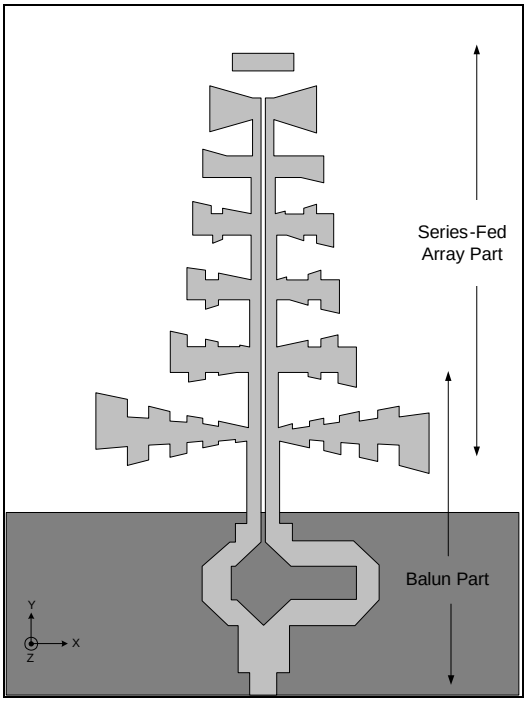

Figure 1. Schematic diagram of the Ultra Wideband Series-Fed Printed Dipole Antenna Arrays with a Log-periodic Structure on front and back side are depicted as shaded and black.

The UWB series-fed printed dipole antenna arrays with a log-periodic structure are fabricated on FR4 substrate, containing metallization on both sides. The top metallization consists of series-fed, which has pair of driver and 6 arrays and

a director fed by a broadband microstrip to coplanar strip transition. The microstrip arms are a balun used for introducing a half-wavelength delay (as center frequency). The bottom metallization is a truncated ground plane used as a reflector.

At last, the optimal new antenna is obtained in **Fig.1**. The new antenna consists of 3 main parts; the first one is microstrip-to-coplanar strips (CPS) balun part [7]. Secondly, it is series-fed dipole arrays part [4], and the last one is called a log-periodic part.

A. Design of balun

This research proposes an ultra-wideband microstrip antenna (3-12 GHz) based on quasi-Yagi antenna [7]. However, limitation of quasi-Yagi antenna requires high dielectric. Because of, the driver and director are placed on same place, then it would work for only broadband. However, balun is very interesting for end-fire antenna designing. Because of, it is major structure to increase band, reducing size, easy to fabricated and very sensitive. In addition to the ground plane, it will reduce the backside of the surface wave travelling which has the same direction as radiation.

The balun is designed for center frequency at 6 GHz. The others interesting structure are L_{dri} and S_{ref} because those values are designed for starting operation frequency point, therefore length of main driver (L_{dri}) and separation from truncated ground S_{ref} will cover starting frequency of 4GHz instead 6GHz (f_0) of quasi-Yagi concept. However, a balun is still designed at 6GHz (f_0) following to quasi-Yagi concept. The schematic diagram of balun part is shown as **Fig.2**.

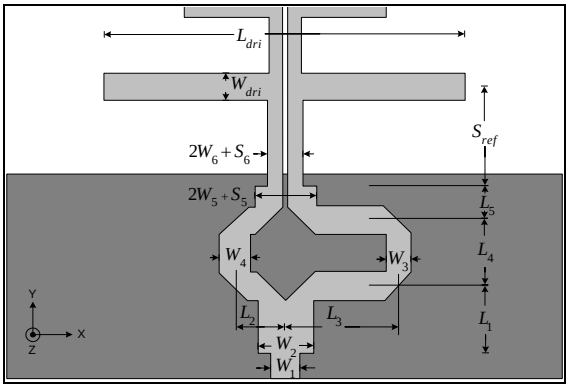

Figure 2. Schematic diagram of Balun part.

From **Fig. 2** The optimized dimensions of Balun part is *(unit:mm)* L_{dri}=38.6, L_1=7.208, L_2=5.424, L_3=12.124, L_4=7.332, L_5=3.5424, S_{ref} =11.2, S_5, S_6 =0.6, W_{dri}=3.016, W_1=3.016, W_2=5.832,W_3 =2.616, W_4=3.216, W_5=3.016 *and* W_6=1.608.

B. Design of a series-fed part

Next, we use a series-fed technique [7], which the operation bandwidth is restricted by lengths of the longest and the shortest dipole elements. Therefore, dipoles are placed on the front side of substrate by using a directing connection CPS between dipoles for resolving "conducting reflector problem". First structure is to replace the position of normally director. This is changing to general quasi-Yagi, the modified antenna is not called quasi-Yagi anymore.

The end of the series-fed is a parasitic director. Its dimension is designed for the end of operation frequency (11 GHz) instead 6GHz (f_0) following to quasi-Yagi concept. Because of The parasitic director element on the top plane simultaneously directs the antenna propagation toward the end-fire direction, and acts as an impedance matching element. **Fig.3** shows structure of the series-fed antenna.

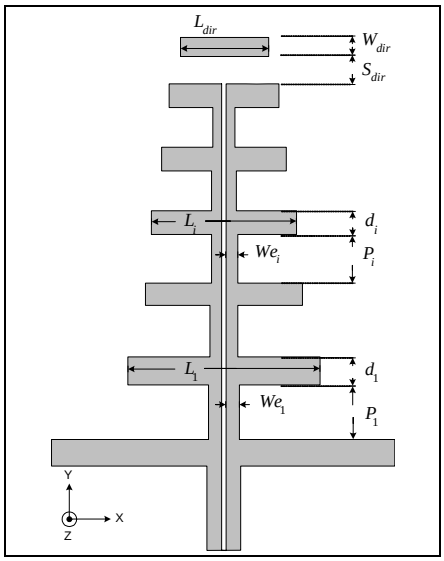

Figure 3. Schematic diagram of the element parts.

From **Fig.3** the dimensions after adjustment are (unit:mm) P_1=6.88, P_2=5.66, P_3=5.4, P_4=4.75, P_5=4.39, d_1 =3.0, d_2=2.71, d_3=2.52, d_4=2.51, d_5=2.71, L_1=21.4, L_2=17.8, L_3=16.2, L_4=14.2, L_5=12.2, L_{dir}=7.2, We_1=1.50, We_2=1.3, We_3=1.2, We_4=1.0, We_5=0.95, W_{dir}=2.216 and S_{dir}=3.284

C. Design of a Log-periodic part

Lately, we use a Log-periodic technique. The proposed log-periodic on quasi-Yagi antenna adopts new driver elements in order to achieve maximum bandwidth. This structure is replaced to the main driver and every series-fed dipole element. Every element is modified by same theory but difference scale. Designing of schematic diagrams of every log-periodic part are as follows:

If f_1 and f_2 are one period apart, they will be related to geometric ratio (τ) by [8]

$$\Delta=\ln(f_2)-\ln(f_1)=\ln\left(\frac{1}{\tau}\right) \quad (1)$$

Typical designs of Log-periodic dipole arrays have apex half angles (α)as [8]

$$10^\circ \le \alpha \le 45^\circ \text{ and } 0.95 \ge \tau \ge 0.7 \quad (2)$$

Maximum value of frequency span (Δ) is related with minimum value of τ, as 0.7. From **Fig.4** the dimensions of

log-periodic are defined by the inverse of the geometric ratio τ are [8]

$$\frac{1}{\tau} = \frac{l_{n+1}}{l_n} = \frac{R_{n+1}}{R_n} \quad (3)$$

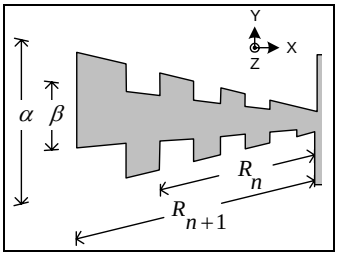

Figure 4.. Schematic diagram of the Log-periodic part.

Designing of log-periodic part has been described in [8] and hence it is not repeated here. From **Fig. 4** the dimensions after adjustment are τ = 0.7, the value of β is estimated as value of W_{dri} as 3.016 mm, and the other important value is α. Since the value of it is much, it is possible that the value interfere with truncated ground plane. Therefore 30° (9.834 mm) was used after adjustment.

III. MEASUREMENT AND RESULTS

Fig.5 shows the prototype of ultra-wideband series-fed printed dipole antenna arrays with a log-periodic structure. This prototype is fabricated on FR4 substrate with ε_r=4.4 and substrate thickness is 1.6 mm.

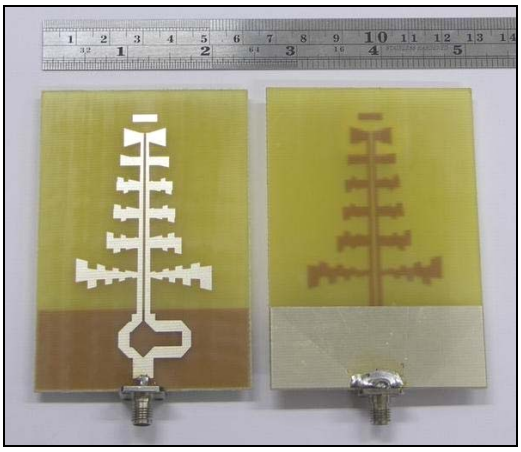

(a) *(b)*

Figure 5. The antenna prototype (a) front-side and (b) back-side.

The HP8910C network analyzer was used for this measurement. **Fig.6** plots both simulation and measurement results for input return loss. The simulated and measured bandwidths (return loss ≤ 10 dB) that have consistent term are 118% and 121%, respectively that cover the Ultra wideband. Additionally, the gain of the antenna have been measured and its can be observed that the peak gains increase to more than 6 dBi at 7GHz and 11 GHz.

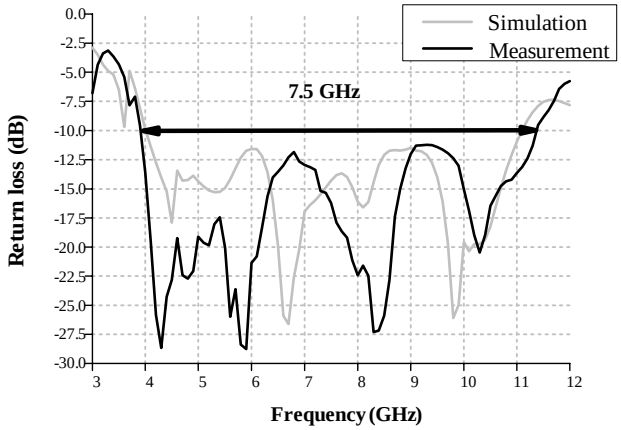

Figure 6. Measured and simulated return losses of the proposed antenna.

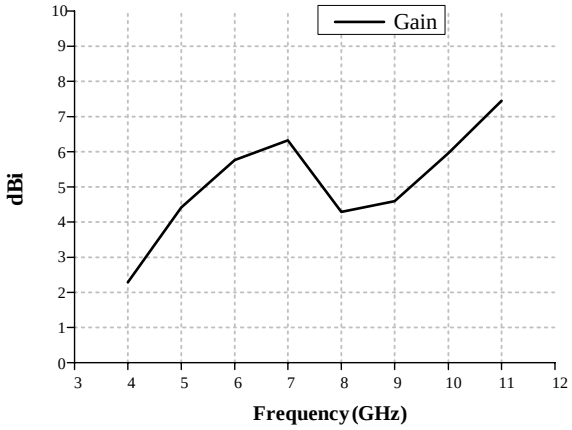

Figure 7.. Measured gain versus frequency.

IV. CONCLUSION

The ultra wideband series-fed printed dipole antenna arrays with log-periodic structure has been proposed and demonstrated. The antenna is based on a modified of the proposed techniques, which achieve ultra-wideband operation. A 100% bandwidth is obtained and it is also keeping end-fire pattern radiation. The antenna is compact and easy to fabricate, and it achieves extremely wide bandwidth and good end-fire radiation characteristics.

REFERENCES

[1] R. Garg, P. Bhartia, I. Bahl, and A. Ittipiboon, *Microstrip Antenna Design Handbook*, Artech House, Norwood, MA, 2001.

[2] W. R. Deal, N. Kaneda, J. Sor, Y. Qian, and T.Itoh, "A new quasi-Yagi antenna for planar active antenna arrays ," *IEEE Trans. Antennas Propag.*, vol. 48, no. 6, pp. 910-918, June. 2000.

[3] L. C. Kretly and A. S. Ribeiro, "A novel tilted dipole quasi-Yagi antenna designed for 3G and blue-tooth applications," *IEEE Trans. Microwave Theory Tech.*, pp. 303-306, 2003.

[4] Shau-Gang Mao and Siou-Li Chen, "*Broadband Series-Fed Printed Dipole Arrays in Uniplanar Configulation*" URSI EMTS, pp.960-962, 2004.

[5] L. C. Kretly and C. E. Capovilla, "Patches driver on the quasi-Yagi antenna: analyses of bandwidth and radiation pattern," *IEEE Trans. Microwave Theory Tech.*, pp. 313-316, 2003.

[6] CH Choeysakul, CH Sarawuth, A Prayoot "A new quasi-Yagi antenna with a log-periodic dipole array director." ECTI Conf., pp. 753-756. June 2006:

[7] N. Kaneda et al., "*A Broadband Microstrip-to-Waveguide Transition Using Quasi-Yagi Antenna*" IEEE Trans. Microwave Theory Tech., Vol.47 ,No. 12, Dec.1999, pp 2562-2567.

[8] C. A. Balanis, *Antenna Theory*, 3rd Edition, John Wiley and Sons, New Jersy, 2005.

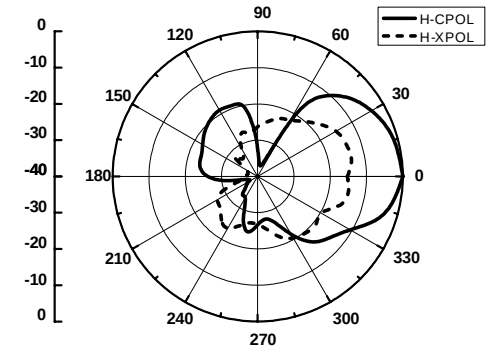

(a) 5 GHz

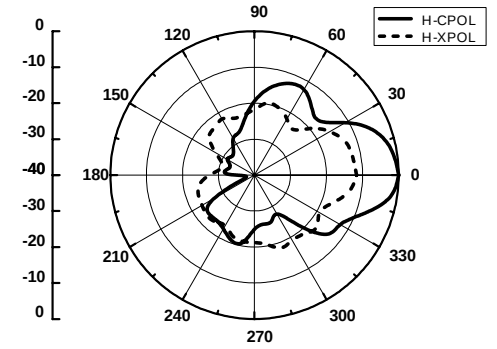

(b) 7 GHz

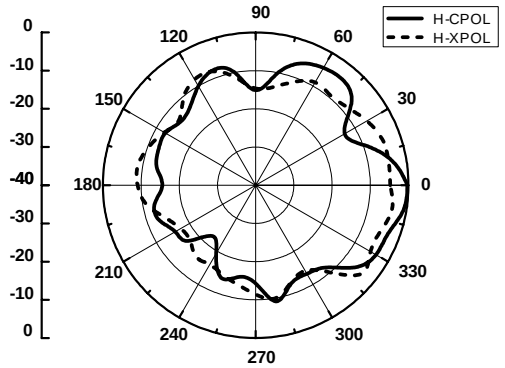

(c) 9 GHz

Figure 8. Measured the H plane co- and cross-polarized radiation pattern of the proposed antenna (a) 5GHz, (b) 7GHz, and (c) 9GHz.

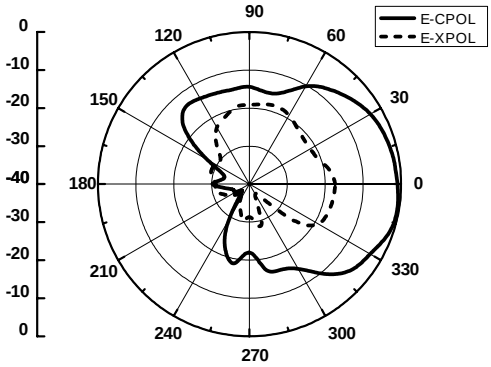

(a) 5 GHz

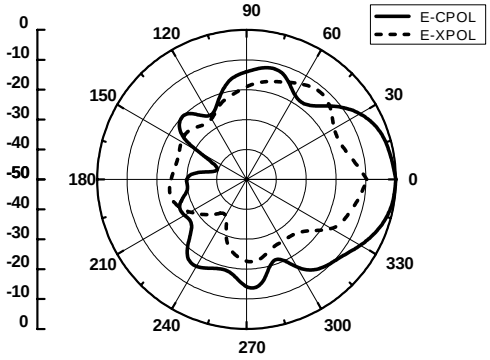

(b) 7 GHz

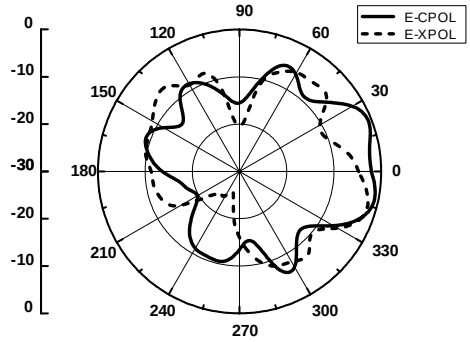

(c) 9 GHz

Figure 9. Measured the E plane co- and cross-polarized radiation pattern of the proposed antenna (a) 5GHz, (b) 7GHz, and (c) 9GHz.

A Study of Interference Signal of Ultra Wideband to Wireless Local Areal Network

Pathamavadee Kositsakul, Sathaporn Promwong
Department of Information Engineering, Faculty of engineering,
King Mongkut's Institute of Technology Ladkrabang, Thailand
E-mail:oui_iey@hotmail.com

***Abstract*— This paper studies about the presence of ultra wideband (UWB) system to performance of IEEE 802.11a (WLAN). From our study, it indicates that UWB interference can cause a significant increase in the bit error rate (BER) of IEEE 802.11a. Then, we purpose a model to evaluate bit error rate by using Binary Phase Shift Keying modulation (BPSK). The model has purpose to investigate that the distance can increase the bit error rate of IEEE 802.11a when it operates simultaneously with UWB.**

I. INTRODUCTION

Recently, Ultra Wideband (UWB) [1] technology has attracted a lot of interest in the research community. UWB offers the potential for high data rates, low-power transmissions, low cost, robustness to multipath fading, and excellent geolocation capabilities. Given these superior capabilities, it is expected that UWB will quickly become a critical and integral part of the future home and office environments. As specified by the FCC [2], UWB can operate in the frequency range of 3.1 GHz ~10.6 GHz with an indoor emission limit of -41 dBm/MHz. IEEE 802.11a [3] wireless systems also operate in the 5 GHz U-NII bands, which overlaps the allowed UWB band, and will most likely co-exist with UWB technology that shown in Fig. 1. Therefore, UWB radio technology can induce interference and degrade the throughput of IEEE 802.11a system. This system studies the coexistence of UWB system and IEEE 802.11a in both Line of sight (LOS) and Non Line of sight NLOS propagation scenarios. The results show that UWB interference can greatly impact the performence of the IEEE 802.11a receiver that present in Fig. 2.

In this paper, we analyze about effect of UWB interference occurring while it works with IEEE 802.11a system [4]. We use a BPSK modulation and keep watching BER to SNR in every bit rates operating. In order to measure any impact or interference of UWB transmission to IEEE 802.11a system. In section II, the model of IEEE 802.11a transmission and UWB interference are provided. The Experiment setup and result will be given in Section III and IV respectively and a brief conclusion is given in Section V.

II. THEORY

A. The IEEE 802.11a Transmitter Model

The IEEE 802.11a signal used to transmit can be represented as [5]

$$s_{BPSK}(t) = m(t)\sqrt{\frac{2E_b}{T_b}}\cos(2\pi_{f_c}t + \theta_c) \quad (1)$$

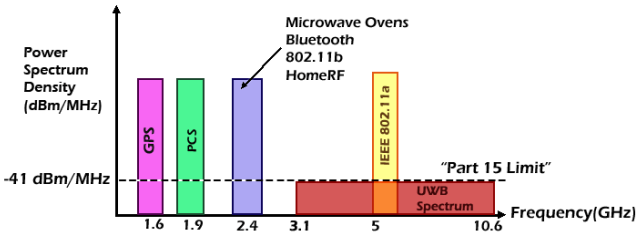

Fig. 1. Range of IEEE.802.11a frequency overlapping with UWB frequency.

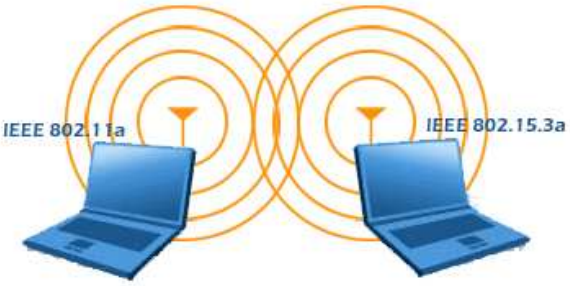

Fig. 2. Interference between IEEE.802.11a and UWB transmission.

where $\cos(2\pi_{\mathrm{f_c}}\mathrm{t})$ is applied as the carrier, and the data signal $\mathrm{m(t)}$ is applied as the modulating waveform.

B. The transmitted signal waveform of UWB and Path Loss Model

In this paper, we use BPSK modulation [6] method for UWB transmission incorporating Orthogonal Frequency Division Multiplexing (OFDM) [7]. BPSK modulation is a common method to invert the pulse. This is Eq. (2) and (3).

$$v_t(t) = \frac{1}{\mathrm{f_b}}[\mathrm{f_H}sinc(2\mathrm{f_H}t) - \mathrm{f_L}sinc(2\mathrm{f_L}t)] \quad (2)$$

$$V_t(f) = \begin{cases} \frac{1}{2f_b} & ||f| - f_c| \le \frac{f_b}{2} \\ 0 & ||f| - f_c| \ge \frac{f_b}{2} \end{cases} \quad (3)$$

where t represents the time duration, f is a frequency, $\mathrm{f_c}$ is a center frequency, $\mathrm{f_b}$ is a bandwidth frequency, $\mathrm{f_L} = \mathrm{f_c} - \frac{\mathrm{f_b}}{2}$ is minimized frequency, $\mathrm{f_L} = \mathrm{f_c} + \frac{\mathrm{f_b}}{2}$ is maximum frequency, and $\arcsin \mathrm{x} = \frac{\sin(\pi_{\mathrm{x}})}{\pi_{\mathrm{x}}}$ is waveform that has maximum magnitude equal to 1 at $\mathrm{t} = 1$. Fig.. 3 and 4 illustrate block diagram

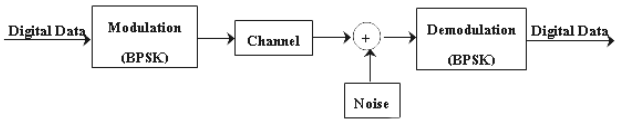

Fig. 3. Diagram of only IEEE 802.11a transmission.

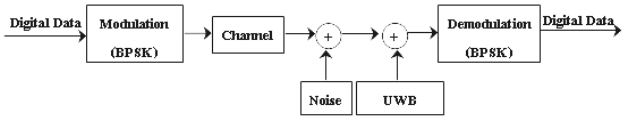

Fig. 4. Diagram of IEEE 802.11a transmission with presence of UWB transmission

about IEEE 802.11a transmission and with a presence of UWB transmission. The propagation path loss model may be expressed as

$$PL(d)[\mathrm{dB}] = 20\log\left[\frac{\max|\mathrm{v_t(t)}|}{\max|(\mathrm{v_r(t)}|}\right] \quad (4)$$

C. The IEEE 802.11a Receiver Model

A transmitted signal pass through the wireless channel including the transmitter and receiver antennas. Therefore, the total received signal from BPSK transmitter can be expressed as

$$r_{BPSK}(t) = m(t)\sqrt{\frac{2E_b}{T_b}}\cos^2(2\pi_{f_c}t + \theta_c) + V_t(f) + n_(t) \quad (5)$$

where $\mathrm{V_t(f)}$ represents UWB interference [8] and $\mathrm{n(t)}$ is additive white Gaussian noise.

D. The UWB Receiver Model

A received waveform of UWB transmission that works with IEEE 802.11a is $\mathrm{v(t)}$ that can be present as Eq. 6.

$$v(t) = \frac{h(t) * h(-t)}{\sqrt{\int_{-\infty}^{\infty} h^2(t)dt}} \quad (6)$$

For the spectrum of output from UWB transmission is $\mathrm{V(f)}$ present in Eq. 7.

$$V(f) = \frac{|H(f)|^2}{\sqrt{\int_{-\infty}^{\infty} |H(f)|^2 df}} \quad (7)$$

TABLE I
EXPERIMENTAL SETUP PARAMETERS

Parameter	Value
Frequency range	3 GHz ∼ 11 GHz
Number of frequency points	801
Tx antenna height	2.2 m
Rx antenna height	1.8-2.05 m
Antenna type	Biconical

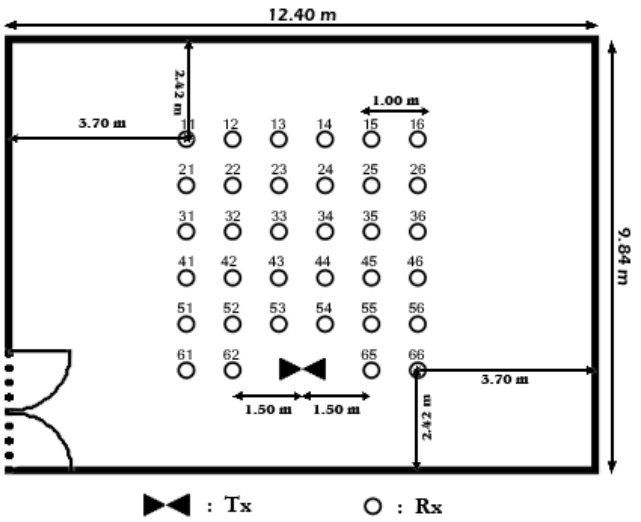

Fig. 5. Model 1 arranged antennas in horizontal view.

III. EXPERIMENTAL SETUP

In our analysis of interference of UWB working together with IEEE 802.11a, we propose a model to notice the characteristics of UWB interference which affects to IEEE 802.11a system [9]. Simulating a UWB signal at a frequency range of 3 GHz ∼ 11 GHz and IEEE 802.11a signal at 5.2 GHz that is performed in an anechoic chamber. The Vector Network Analyzer (VNA) generates transmitted signal and translates received signal. We use a biconical antenna to send and receive the signal. For all of detail about parameter is present in table 1. About transmitted bit rate, we define at 6 and 9 Mbps and pick 4 points from 64 points to compare BER to SNR in different angle. Our model aims to investigate the characteristics of horizontal UWB interference to IEEE 802.11a system by setting the antennas as Fig. 5 without changing in height of antennas.

IV. RESULT AND DISCUSSION

From the result, when we transmit only the IEEE 802.11a signal or UWB signal, the result shows that in a higher bit rate has more BER value than lower bit rate. About the SNR value, it has arisen when the bit rate are incresed. However, in every bit rates, raising SNR makes the BER decrease. Fig. 6 and 7 depict BER to SNR in only IEEE 802.11a transmission and UWB transmission respectively. From that graph, we can learn we should send the signal in lower rate because it provides better SNR than in higher rate. Moreover, when UWB and IEEE 802.11a signal perform in the same time, the BER will be risen more than only IEEE 802.11a transmission. Similarly, when SNR have arisen, they cause BER deplete. Fig. 8 and 9 illustrate the comparison between IEEE 802.11a transmission and IEEE 802.11a transmission with presence of UWB transmission at 6 Mbps and 9 Mbps respectively.

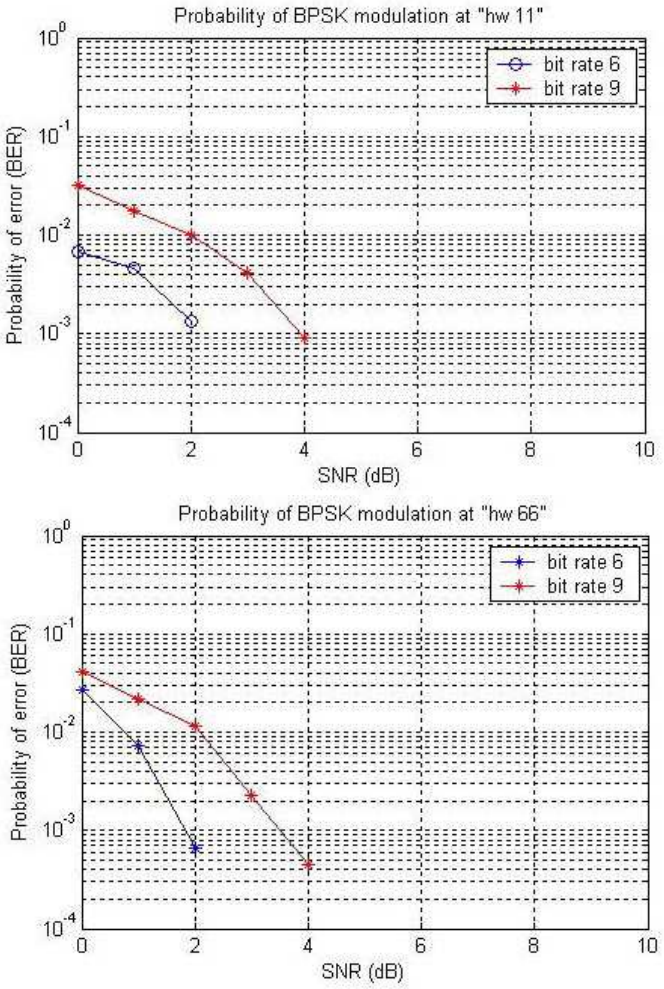

Fig. 6. BER to SNR in only IEEE 802.11a transmission.

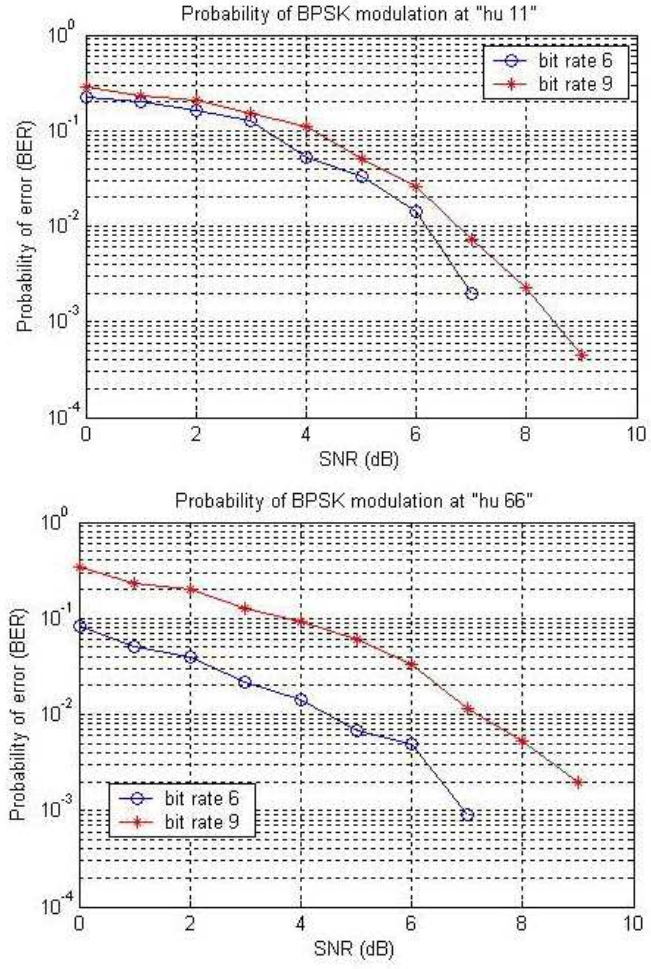

Fig. 7. BER to SNR in only UWB transmission.

V. Conclusions

In this paper, it purposes effect of UWB signal to IEEE 802.11a performance. We use a model to investigate its effect. From IEEE 802.11a transmission, UWB transmission, and IEEE 802.11a transmission with the coexistence of UWB, the result arriving from the model shows that when we send in higher bit rates, they always result in increasing BER. Especially, IEEE 802.11a transmission with the coexistence of UWB has higher BER more than IEEE 802.11a or UWB transmission themselves. Then we can conclude that UWB transmission makes interference to IEEE 802.11a transmission in every single bit rates and especially, in higher bit rate, it can notice obviously.

References

[1] M.Z. Win and R.Scholtz, "Impluse radio: How it works", IEEE Communication Letters, vol2, no.1, Jan. 1998.

[2] Federal Communications Commission,"Revision of Part 15 of the Commission's Rules Regarding UWB Transmission Systems, " First Report, FCC 02-48, Apr. 2002.

[3] Institute of Electrical and Electronics Engineers, High-speed Physical Layer in the 5 GHz Band, IEEE Std 802.11a-1999, Sept 1999.

[4] B. Firoozbakhsh and T. Pratt, "Ultra Wideband Communications; Coexistence with IEEE 802.11a," Georgia Institute of Technology, Atlanta, GA, GTBI Advisory Board Report, Jun. 2003.

[5] D. Landi and C. Fischer, "The effects of UWB interference on GSM systems," Proc. International Zuurich Seminar on Communications,pp. 86-89, 2002.

[6] W.C. Chung and D.S.Ha,"On the perfoermance of bi-phase modulated UWB signals in a multipath channel," Proc. IEEE Vehicular Techonology Conference, vol. 3, pp. 1654-1658, 2003.

[7] R. Van Nee and R. Prasad, OFDM for Wireless Multimedia Communications, Artech House, 2000

[8] K. Siwiak, "Impact of ultra wide band transmissions on a generic receiver," Proc. 2001 Spring IEEE Veh. Tech. Conf. (VTC), Rhodes, Greece, vol. 2. pp. 1181-1183, May 2001.

[9] B. Firoozbakhsh, T. Pratt and N. Jayant, "Analysis of IEEE 802.11a Interference on UWB Systems," in Proc. IEEE Conf. on Ultra Wideband Systems and Technology (UWBST2003), Nov. 2003.

[10] G.Yue, L. Ge, and S. Li, "Analysis of ultra wideband signal interference to DSSS receiver," Proc. IEEE Workshop on Signal Processing Advances in Wireless Communications, pp. 229-233,2003.

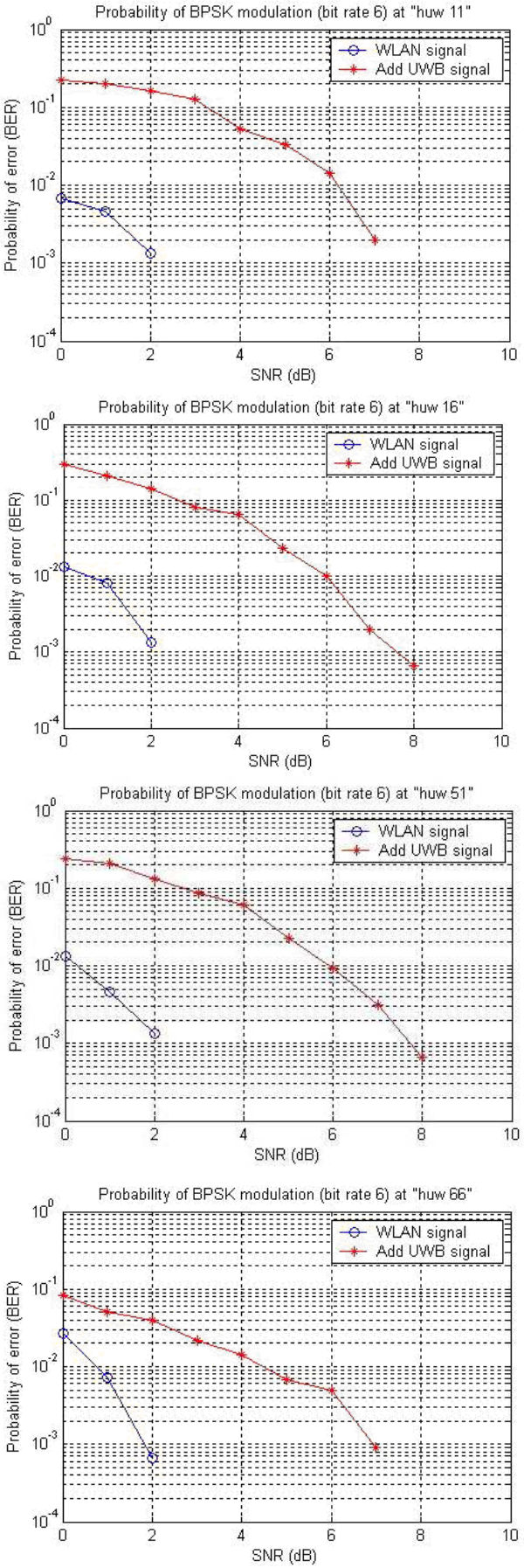

Fig. 8. BER to SNR in IEEE 802.11a in presence of UWB transmission at 6 Mbps.

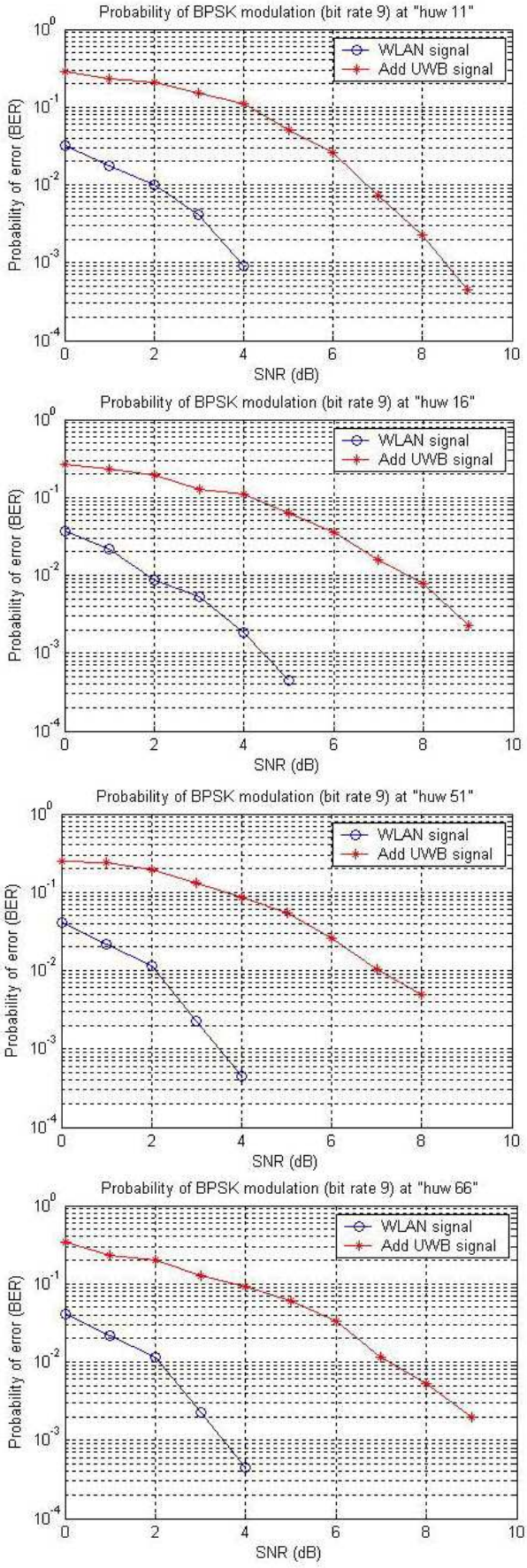

Fig. 9. BER to SNR in IEEE 802.11a in presence of UWB transmission at 9 Mbps .

Bandwidth Enhancement of a CPW-Fed Rectangular Slot Antenna

P. Seangsae [1], N. Anantrasirichai[1], J. Nakasuwan [2], T. Wakabayashi[3]
[1]ReCCIT, Faculty of Engineering, King Mongkut's Institute of Technology Ladkrabang
Ladkrabang, Bangkok, 10520, Thailand
E-mail: kanoppin@kmitl.ac.th
[2]Dept. of Electronic and Telecommunication Engineering, Faculty of Engineering
Rajamangala University of Technology Thanyaburi (RMUTT) Klong 6
Thanyaburi, Pathumthanee, Thailand
E-mail: jintanan@rmut.ac.th
[3]School of Information Science and Technology, Tokai University, Hirasuka, Kanagawa, 259-1292, Japan
E-mail: wakaba@et.u-tokai.ac.jp

***Abstract*- This paper investigated wideband coplanar waveguide (CPW) fed rectangular slot antenna with rectangular planar patch and slot tuning. A rectangular slot antenna is excited by a 50 ohm CPW with slot tuning on rectangular planar patch for wireless applications. By adjusting size of rectangular planar patch and of slot tuning on rectangular planar patch, can easily achieve a wideband. The proposed antenna is designed to operate from 1.38 to 6.04 GHz which is suitable for applications in WLAN (Wireless Local Area Network) according to IEEE 802.11 a/b/g standards and covered the WiMAX (Worldwide Interoperability for Microwave Access, IEEE 802.16e). The characteristics of antenna are proposed and analyzed for bandwidth, return loss, input impedance and VSWR. The simulation results are analyzed by IE3D Zeland software.**

I. INTRODUCTION

Recently, there is growing research activity on multi-frequency and broadband and wideband antennas for various wireless communication applications such as WLAN (Wireless Local Area Network) or WiMAX (Worldwide Interoperability for Microwave Access. In particular, a great interest in coplanar waveguide (CPW) fed slot antenna has been presented in the paper because the CPW fed slot antennas have the advantage of wide bandwidth, simplest structure and easy integration with active devices [1]. The CPW fed slot antennas have been designed for wideband applications by rectangular and square slot and enhance bandwidth by optimizing a tuning stub [2, 3, 4].

In this paper, we propose a CPW fed slot antenna for wideband application in WLAN communication and WiMAX. Owing to the slot tuning on rectangular planar patch inset around the side edge of the rectangular slot antenna, a new resonant frequencies can be excited and enhance the operating bandwidth of the wideband by adjusting parameter of slot tuning on rectangular planar patch, which simulation covers the bandwidth of 1.38 to 6.04 GHz is enough for wireless communication. Detail of the proposed CPW fed slot antenna designs are described, and simulation results for obtained wideband performance are presented by using IE3D Zeland software.

II. ANTENNA STRUCTURE

Figure 1, shows the structure of the proposed CPW-fed rectangular slot antenna with slot tuning on rectangular planar patch at designed frequency 1.5 GHz. The slot antenna is on FR4 substrate of dielectric constant 4.5 (ε_r) and substrate of thickness 1.6 mm (h). The dimension of dielectric substrate is 53x61.5 mm^2. The proposed antenna consists of rectangular slot has a length Lx = 44.8 mm and Ly = 25.5 mm. A 50 ohms coplanar waveguide with gap width S = 0.5 mm and centre conductor width Wc = 5.4 mm and the end of CPW feed line connected to rectangular planar patch of dimensions width Wx = 27.8 mm and Wy = 15.5 mm. The both slot tuning etched at the middle of rectangular planar patch, the spacing between rectangular planar patch and edge of the ground plane is G = 1.6 mm. The slot tuning consist of four parameters which three parameters of slot tuning: Lh, Lw and Ls, affect to wideband operation, the other one is Lv fixed to 2 mm. The characteristics of the proposed antenna and details of designing are discussed in the following section.

The guide wavelength is given by

$$\lambda_g = \frac{c/f}{\sqrt{\varepsilon_{eff}}} \tag{1}$$

Where ε_{eff} is an effective dielectric constant which can be computed by using the following equation.

$$\varepsilon_{eff} \approx \frac{\varepsilon_r + 1}{2} \tag{2}$$

In this case, ε_{eff} = 2.75 and λ_g = 120.6 mm, and dimension of rectangular slot antenna in length and width (Ly and Lx) is about $0.58\lambda_g$ ($Lx = 0.37\lambda_g$ and $Ly = 0.21\lambda_g$).

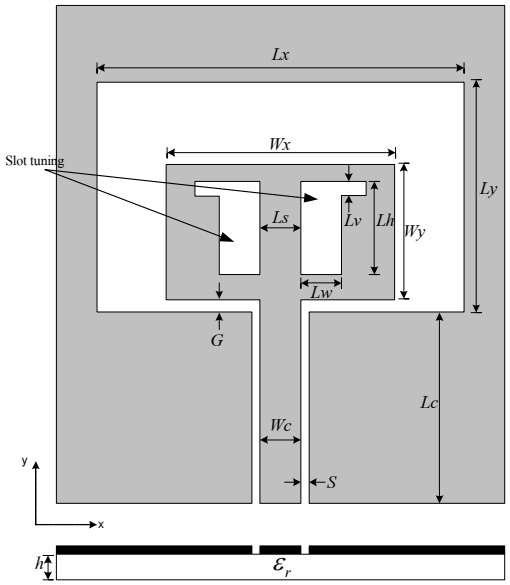

Figure 1. Structure of the proposed antenna.

III. SIMULATION RESULTS

The proposed antenna was designed and studied for bandwidth enhancement. The theoretical analysis was performed using the IE3D simulate software package of Zeland [5]. The CPW feed line is designed with the centre conductor width *Wc* = 5.4 mm, coplanar waveguide with gap width *S* = 0.5 mm, and length CPW feed line of *Lc* = 26 mm for match with 50 ohms characteristic impedance. There are three designs for show the enhancement of this antenna, the first is CPW fed rectangular slot antenna, second is rectangular planar patch inside of the slot, and third is slot tuning inside of the planar patch. The proposed design can be further enhanced by rectangular conductor patch and with slot tuning on rectangular planar patch. The main proposed of this paper is to show the effect of adjusting three parameters: *Lh*, *Lw* and *Ls* of slot tuning. The result of S11 in three designs is shown in Figure 2, which fixing value of the parameters: *Lx, Ly, Wx, Wy, G, Wc, S*, *Lv* and *Lc* as a first step. The initial value of three parameters of slot tuning of *Lh* = 11 mm, *Lw* = 2 mm and *Ls* = 5.4 mm are proposed for begin adjusting. From Figure 2, the bandwidth of proposed antenna will be increased when using conductor stub tuning (rectangular planar patch) and slot tuning. For more bandwidth enhancement from Figure 2, the adjusting of three parameters will be considered in next step.

A. Effect of Adjusting Lh of Slot Tuning

In this case, we fixed *Lw* = 2 mm, *Ls* = 5.4 mm and vary the length *Lh* of slot tuning to 11 mm, 11.3 mm, 11.5 mm and 12 mm, respectively. The effect on the resonant frequencies and bandwidth are investigated as shown in Figure 3. Its shown that the bandwidth at return loss -10 dB about 4 GHz, the lowest resonance frequency of each value of *Lh* is same but highest resonance frequency is shift down when *Lh* is increased. From Figure 3, the best matching for wideband is at *Lh* = 12 mm, which return loss is -50 dB at frequency 4.2GHz.

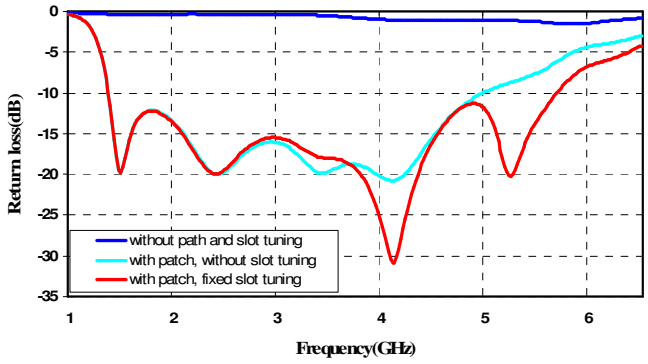

Figure 2. Comparison of return loss of three designs.

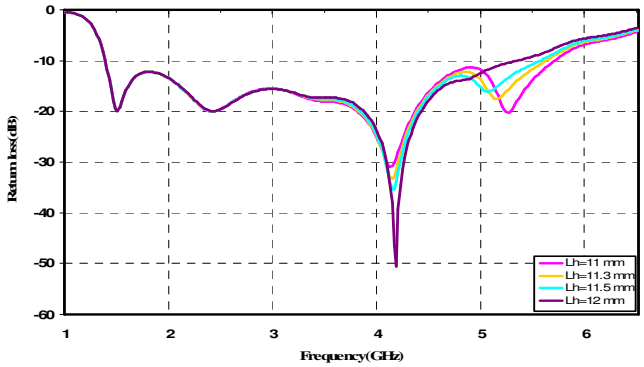

Figure 3. Simulation return loss for difference *Lh*.

B. Effect of Adjusting Lw of Slot Tuning

The effect of the width *Lw* of slot tuning on return loss is considered. Herein, the *Lw* is chosen to 3.7 mm, 4.2 mm, 4.7 mm and 5.7 mm, while *Lh* = 11.5 mm, *Ls* = 5.8 mm are fixed.

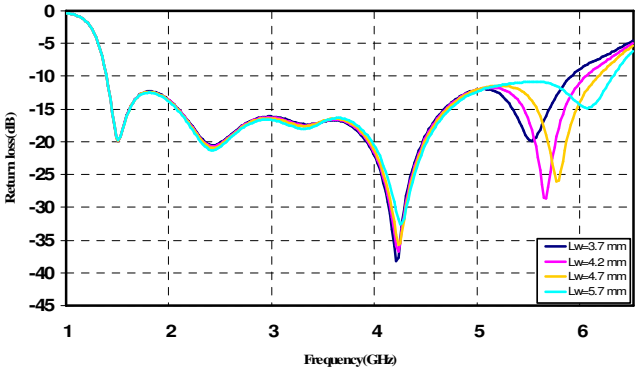

Figure 4. Simulation return loss for difference *Lw*.

The typical simulation results are shown in Figure 4, when we focus to the high resonance from 4 to 6 GHz, it can be found that the resonance frequency near 4 GHz is slightly

chanced but the resonance frequency near 6 GHz is shift up when value of *Lw* is increased and wider bandwidth.

C. Effect of Adjusting Ls of Slot Tuning

The effect of distance between both slot tuning (*Ls*) on the return loss is considered by vary values of *Ls*: 4.8 mm, 5.8 mm, 6.2 mm and 7 mm, respectively, while *Lh* = 11.5 mm and *Lw* = 4.2 mm, as shown in Figure 5. The resonance frequencies slightly changed and return loss is much changing.

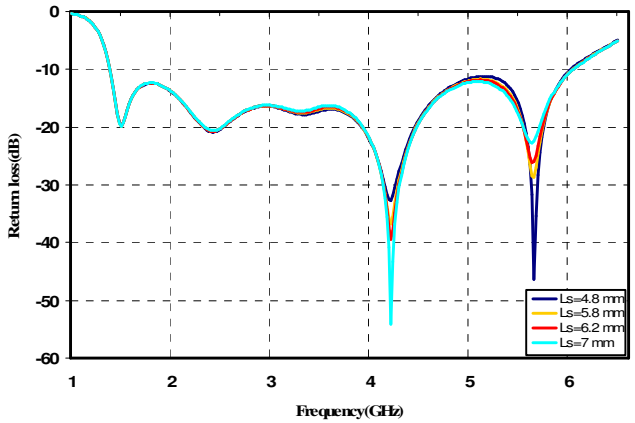

Figure 5. Simulated return loss for difference *Ls*.

D. Characteristic of Return Loss

We optimized and investigated the effect of adjusting three parameters of the antenna for enhance bandwidth covers IEEE 802.11a/b/g (2.4-2.4835GHz, 5.15-5.35GHz and 5.725-5.875GHz) WLAN applications and WiMAX (2-6 GHz). Finally, the dimension of slot tuning is *Lh* = 11.5 mm, *Lw* = 4.2 mm and *Ls* = 4.8 mm for sufficient choosing. Figure 6, shown the frequency band and maximum bandwidth coverage at 1.38 GHz to 6.04 GHz which all of parameters are shown in Table 1.

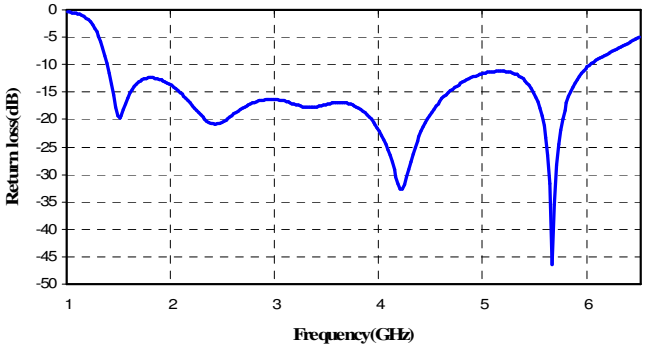

Figure 6. Simulated S_{11} of the proposed antenna.

E. Characteristic of Input Impedance

The input impedance Z_{in} is the complex number, which fined out by using the S_{11} parameter and characteristic impedance Z_o of transmission line. The characteristic of input impedance for this slot antenna is shown in Figure 7.

TABLE 1
Parameters of the proposed antenna designs.

	without patch and slot tuning (mm)	with patch, without slot tuning (mm)	with patch and slot tuning (mm)
Lx	44.8	44.8	44.8
Ly	25.5	25.5	25.5
Lc	26	26	26
Wc	5.4	5.4	5.4
S	0.5	0.5	0.5
Wx	-	27.8	27.8
Wy	-	15.5	15.5
G	-	1.6	1.6
Lv	-	-	2
Lh	-	-	11.5
Lw	-	-	4.2
Ls	-	-	4.8
	-	BW=1.38~5 GHz	BW=1.38~6.04 GHz

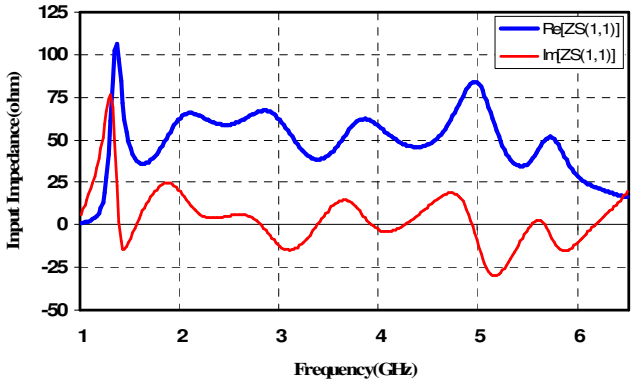

Figure 7. The simulation results of input impedance.

F. Characteristic of VSWR

Figure 8, shown voltage standing wave ratio (VSWR) of this slot antenna. In this case, the maximum VSWR for wideband is 1.035 at frequency 5.68 GHz.

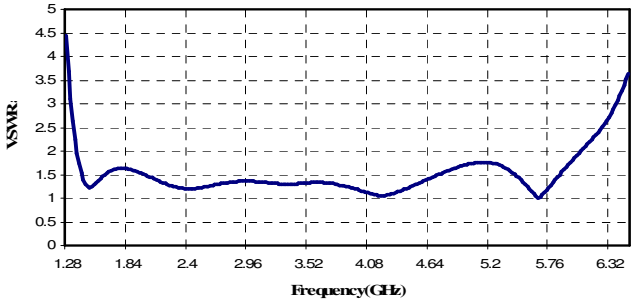

Figure 8. Simulation results of VSWR.

G. Radiation Patterns

The radiation patterns of this antenna for five frequencies: 2.4 GHz, 3.5GHz, 4.2 GHz, 4.8GHz, 5.2GHz and 5.7 GHz are shown in Figure 9.

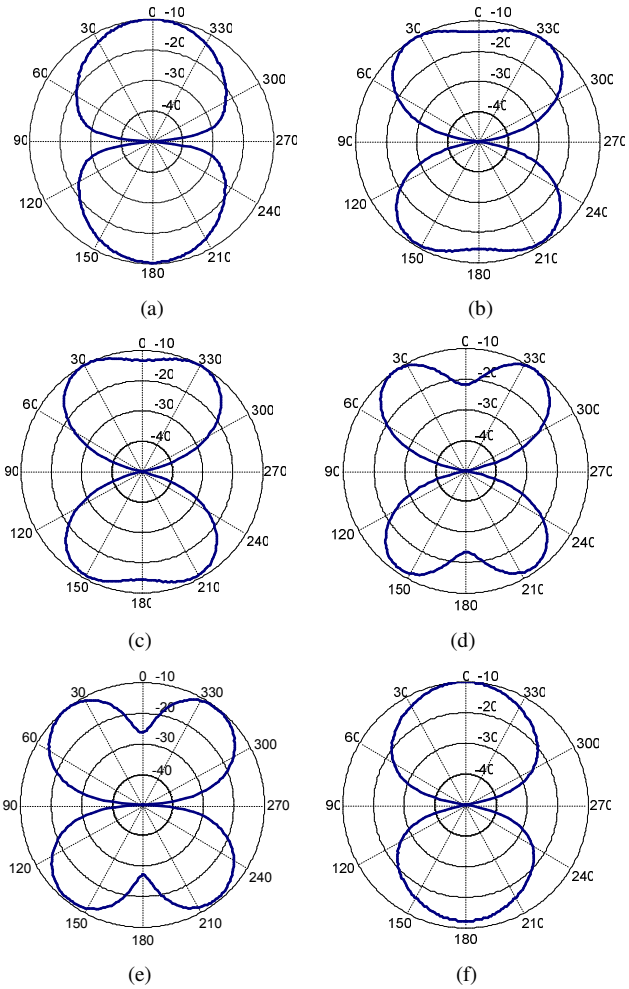

Figure 9. Simulated radiation patterns of E-plane, (a) 2.4 GHz, (b) 3.5 GHz, (c) 4.2GHz, (d) 4.8 GHz,(e) 5.2 GHz, (f) 5.7 GHz

IV. CONCLUSION

This paper presented the bandwidth enhancement of CPW fed slot antenna by rectangular conductor patch and slot tuning on rectangular planar patch. This slot antenna easy to fabrication and can achieved the wideband from frequency range 1.38 – 6.04 GHz coverage standard of IEEE 802.11 a/b/g (2.4-2.4835 GHz, 5.15-5.35GHz and 5.725-5.875GHz) for WLAN and WiMAX (IEEE 802.16e, 2-6 GHz).

REFERENCES

[1] Ramaesh Garg, Prakash Bhartia, Inder Bahl and Apisak Ittipiboon, Microstrip Antenna Design Handbook, Artech House, Inc., 2001.

[2] Alpesh U.Bhobe, Christopher L. Holloway, Melinda Piket-May. "Wide-band Slot Antennas With CPW-Feed Line:Hybrid and Log-Periodic Designs," *IEEE Trans. Antennas Propagat*, Vol.52, No. 10, pp. 2545-2554, 2004.

[3] Chen, H. D., "Broadband CPW-fed square slot antennas with a widened tuning stub," *IEEE Trans. Antennas and Propagat*., Vol. 51, No. 8, pp. 1982-1985, August 2003.

[4] M. A. Saed. "Broadband CPW-Fed Planar Slot Antennas With Various Tuning Stubs," *Progress In Electromagnetics Research*, PIER 66, 199-212, 2006.

[5] IE3D User's Manual Release 9, Zeland software, Inc.,U.S.A.,2002.

CPW-Fed Rectangular Slot Antenna with Tuning Stub for Dual Frequency

S. Kaewsupan[1], N. Anantrasirichai[1], P. Rakluea[2], T. Wakabayashi[3]

[1]ReCCIT, Faculty of Engineering, King Mongkut's Institute of Technology Ladkrabang
Ladkrabang, Bangkok, 10520, Thailand
E-mail: s8061003@kmitl.ac.th, kanoppin@kmitl.ac.th

[2]Dept. of Electronic and Telecommunication Engineering, Faculty of Engineering
Rajamangala University of Technology Thanyaburi (RMUTT) Klong 6
Thanyaburi, Pathumthanee, Thailand
E-mail: jintanan@rmut.ac.th
E-mail: s8061003@kmitl.ac.th, kanoppin@kmitl.ac.th

[3]School of Information Science and Technology, Tokai University, Hirasuka, Kanagawa, 259-1292, Japan
E-mail: wakaba@et.u-tokai.ac.jp

***Abstract*—A rectangular slot excited by coplanar waveguide (CPW) with tuning stub is introduced to obtain a dual frequency operation. Prototype of the proposed antenna designed for WLAN operations in the 2.4 and 5.2 GHz bands. The antenna and CPW feed line are printed on the same side of a single conducting layer, thus simplifying the fabrication process. The characteristics of antenna are proposed and analyzed for instance input impedance, return loss, bandwidth, VSWR, and far field radiation patterns. The obtained impedance bandwidth for two operating bands can reach about 55.2% for the 2.4 GHz band and 12.97% for the 5.2 GHz band. Finite Difference Time Domain method (FDTD) is introduced to analyze this antenna. A verification of simulation procedure is confirmed by IE3D software which is based on the Method of Moments (MOM).**

I. INTRODUCTION

Recently, great advances have been made in wireless local area network (WLAN) communications, and in order to satisfy the IEEE 802.11 WLAN standards in the 2.4 GHz band (2.4 -2.484 GHz) and 5.2-GHz band (5.15-5.35 GHz), many wireless communication devices are now designed to be capable of dual-band operation in the 2.4 and 5.2-GHz bands. For this reason, dual-band antennas for WLAN operation are in demand accordingly.

Dual-frequency microstrip antennas are generally classified into two types: multiresonator antennas, such as multilayer patch antennas, and reactive loading antennas using etching slots on the patch and/or short circuit vias. Thus, the research for new microstrip configurations with wider bandwidth or dual band has been dominant feature of the research literature, and much effort continues to be expended [1]

The coplanar waveguide (CPW) fed antennas have been widely used for wireless communications owing to their many attractive features such as wide bandwidth, simplest structure of a single metallic layer, no soldering points, easy integration with MMICs, and broad bandwidth, etc [2]. Etching the slot and the feed line on the same side of the substrate eliminates the alignment problem needed for etching on both sides of the substrate. The coplanar waveguide (CPW) is such a transmission line that can achieve this. In addition, the CPW has lower loss than the microstrip line. For the available designs, the patch antenna fed by CPW reported in [1] is capable of dual band but two metallic layer are require for this antenna, the CPW-fed square slot antenna reported in [3] is capable of broad but single-band operation only, and some related designs applied for single metallic WLAN operations have been reported in [4-8] realize dual band operations. However, the lower mode has a narrow impedance bandwidth. In this paper, a novel and simple wideband dual-frequency, easy harmonic adjusting design of the rectangular slot fed by coplanar waveguide (CPW) with tuning stub is presented. The antenna and feed line structure are placed on the same single conductor side of the substrate, thus simplifying the fabrication process, it can be shown that this antenna is suitable for WLAN application, details of the antenna design are described and simulated results are presented and discussed.

II. FDTD METHOD

This software is a full wave electromagnetic simulation code for conventional three dimension (3D) passive structures, which are base on the FDTD algorithm that can predict and analysis of the electromagnetic responses of complex problems. The analytical space consists of $70\times249\times100$ cells with the cell dimension $\Delta x = 0.1575$ mm., $\Delta y = \Delta z = 0.25$ mm. The time step satisfies the following courant condition.

$$\Delta t \le \frac{1}{v_{\max}\sqrt{(1/\Delta x)^2 + (1/\Delta y)^2 + (1/\Delta z)^2}} \quad (1)$$

For source excitation of the antenna is input voltage $V(t)$ base on Gaussian pulse and express as

$$V(t) = e^{-\left(\frac{t-t_0}{T}\right)^2} \quad (2)$$

Where t_0 the center of the pulse, T is is the pulses width at its $1/e$ characteristic delay point.

III. ANTENNA DESIGN

The geometry of the proposed CPW-fed rectangular slot antenna with tuning stub for wideband and dual-frequency operations is shown in Figure 1. For the design studied here, the antenna is etched on the same side of RT/Duroid 5880 substrate with the dielectric constant of 2.2 (ε_r)and the substrate thickness of 1.575 mm (h), while the other side without any metallization. A CPW transmission line, which consists of a center conductor strip width of w_f and a gap distance of s between the conductor strip and the coplanar ground plane, is used for feeding the antenna. Two equal finite ground planes, each with dimensions of length L_{cpw} is situated symmetrically on each side of the CPW feed line. The basis of the antenna structure is a rectangular slot, which has the dimensions of length L and width W. To achieve the desired dual-frequency operations and for easy upper frequency control range, the feed line is connected with the tuning stub, which comprises both the horizontal and vertical sections with dimensions.

The guide wavelength is given by

$$\lambda_g = \frac{c/f}{\sqrt{\varepsilon_{eff}}} \tag{3}$$

Where ε_{eff} is an effective dielectric constant which can be computed by using the following equation.

$$\varepsilon_{eff} \approx \frac{\varepsilon_r + 1}{2} \tag{4}$$

To investigate the performance of the proposed antenna configurations in terms of achieving the wideband dual frequency operations, the Finite Difference Time Domain method (FDTD) was used for required analysis and obtaining the proper geometry parameters in Figure 1.

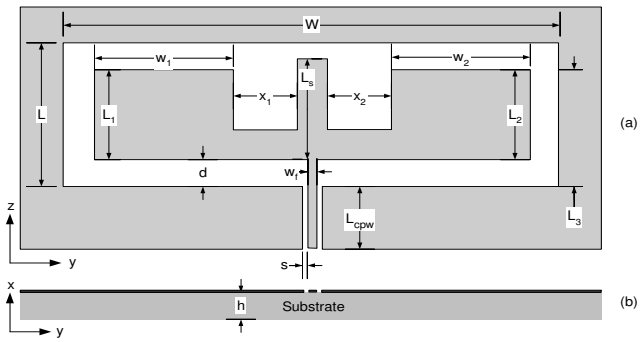

Figure 1. CPW-fed rectangular slot antenna with tuning stub (a) top view (b) cross section

Finally, the antenna dimension is obtained to be

L	= 14 mm.	L_1	= 9 mm.
W	= 48.25 mm.	L_2	= 9 mm.
L_{cpw}	= 7.5 mm.	L_3	= 12.5 mm.
w_f	= 0.75 mm.	x_1	= 5.5 mm.
s	= 0.25 mm.	x_2	= 5.5 mm.
d	= 2.5 mm.	w_1	= 15 mm.
L_s	= 10 mm.	w_2	= 15 mm.

IV. RESULTS AND DISCUSSION

The antennas are analyzed by using Finite-Difference Time-Domain (FDTD) Method and comparing with IE3D software which is based on the Method of Moments (MOM).

The resonant mode at 2.4 GHz band is achieved by W and L parameter adjusting. The upper resonant mode occurs by L_s L_1, L_2, x_1, and x_2 adjusting. In this paper, we will show to adjust the W, L_1, L_2, and Ls parameters by fixing the value of other parameters.

A. *Affect of adjusting the W parameter.*

In this case, the W is adjusted to be 46.25 mm, 48.25 mm, and 50.25 mm, respectively. The simulation result of return loss (S_{11}) are shown in Figure 2. Thus, the lower resonant can shift to any frequency.

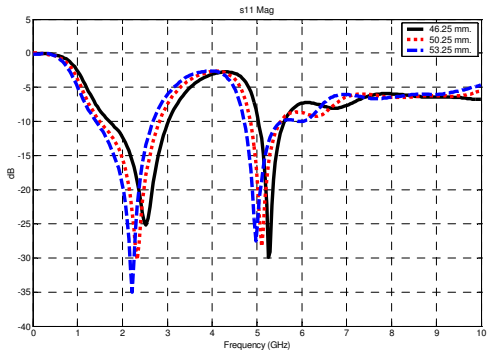

Figure 2. The return loss in the case of W adjusting

B. *Affect of adjusting the L_1 and L_2 parameter.*

The length of L_1 and L_2 are adjusted to 7, 8 and 9 mm, the resulting show that the spacing between the lower and upper resonant frequency can optimize by this condition (see Figure 3).

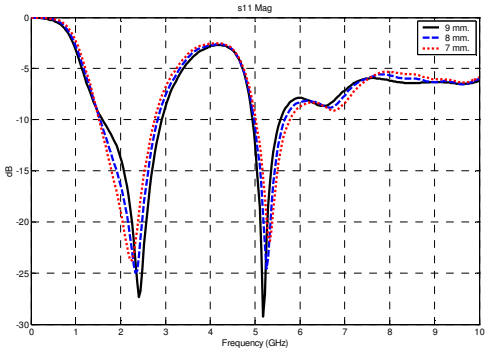

Figure 3. The return loss in the case of L_1 and L_2 adjusting

C. *Affect of adjusting the L_s parameter.*

To follow this condition, the upper resonant can select to the frequency requirement that shown in figure 4.

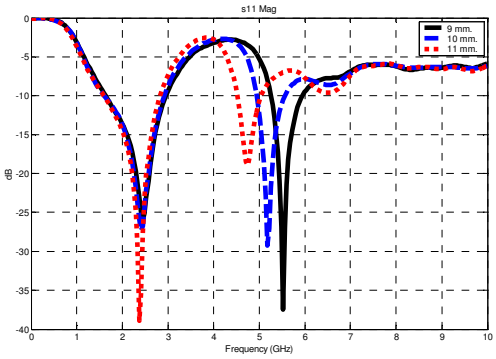

Figure 4. The return loss in the case of L_s adjusting

D. The characteristics of proposed antenna.

Figure 5 shows the simulated return loss against frequency for the proposed CPW-fed rectangular slot antenna with W-shaped tuning stub which simulated by FDTD method and MoM.

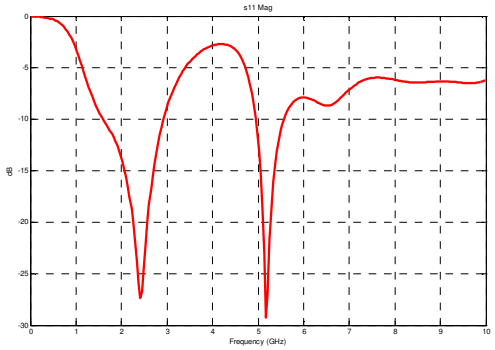

(a) FDTD

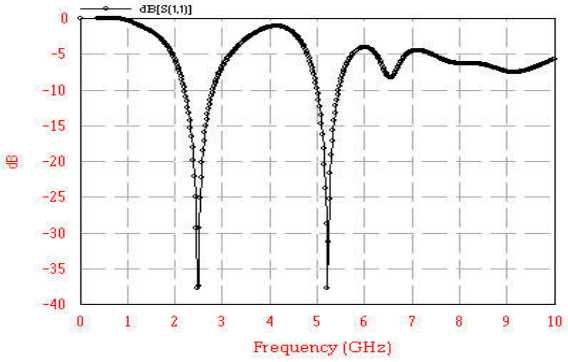

(b) MOM

Figure 5. Simulated return loss of proposed CPW-fed rectangular slot antenna with tuning stub.

The simulation in lower band achieves a -10 dB impedance bandwidth of 55.2% ranging from 1.59 GHz to 2.92 GHz with respect to the centre frequency at 2.41 GHz, and the simulated bandwidth for the upper mode ranging from 4.9 GHz to 5.57 GHz or about 12.97% referred to the centre frequency at 5.17 GHz. Obviously, the antenna can operate over the bands which cover the required bandwidths of the IEEE 802.11 WLAN standards in the bands at 2.4 GHz (2.4–2.4835 GHz), 5.2 GHz (5.15–5.35 GHz) [8]. Figure 6-7 show the simulated of VSWR and input impedance.

Typical radiation characteristics of the frequencies across the lower and higher bands for the proposed dual-band antenna are also examined. The radiation patterns for E_θ are nearly omnidirectional at both operating frequencied. The radiation patterns have symmetric characteristic because the antenna structure is symmetrical. Figures 8-9 show the radiation patterns in the azimuth cut (x–y plane) for the antenna at the lower band of 2.41 GHz, and at the higher band of 5.17 GHz.

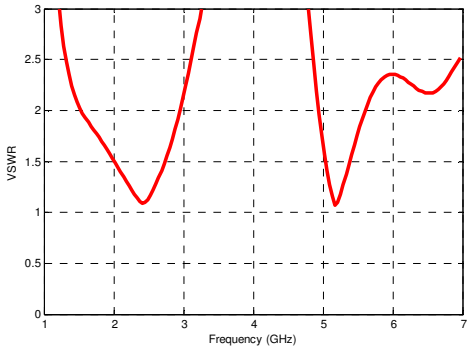

Figure 6. Simulated VSWR of proposed CPW-fed rectangular slot antenna with tuning stub.

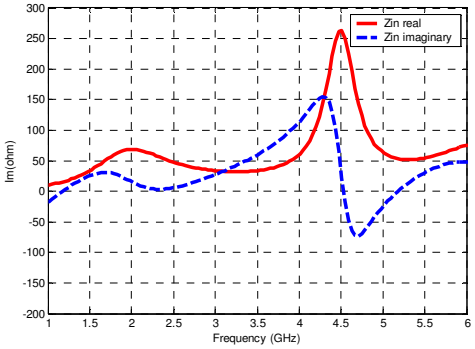

Figure 7. Simulated input impedance of proposed CPW-fed rectangular slot antenna with tuning stub.

V. CONCLUSION

Broadband dual-frequency operations of a simple CPW-fed rectangular slot antenna with tuning stub suitable for WLAN operations in the 2.4 and 5.2 GHz bands have been studied. By the connecting of a tuning stub to the CPW feed line, the proposed antenna can provide dual-band and wide impedance bandwidths of 55.2% ranging from 1.59 GHz to 2.92 GHz with respect to the centre frequency at 2.41 GHz, and the simulated bandwidth for the higher mode ranging from 4.9 GHz to 5.57 GHz or about 12.97% referred to the centre frequency at 5.17 GHz. Also, good antenna performances of operating frequencies across the two bands can be obtained.

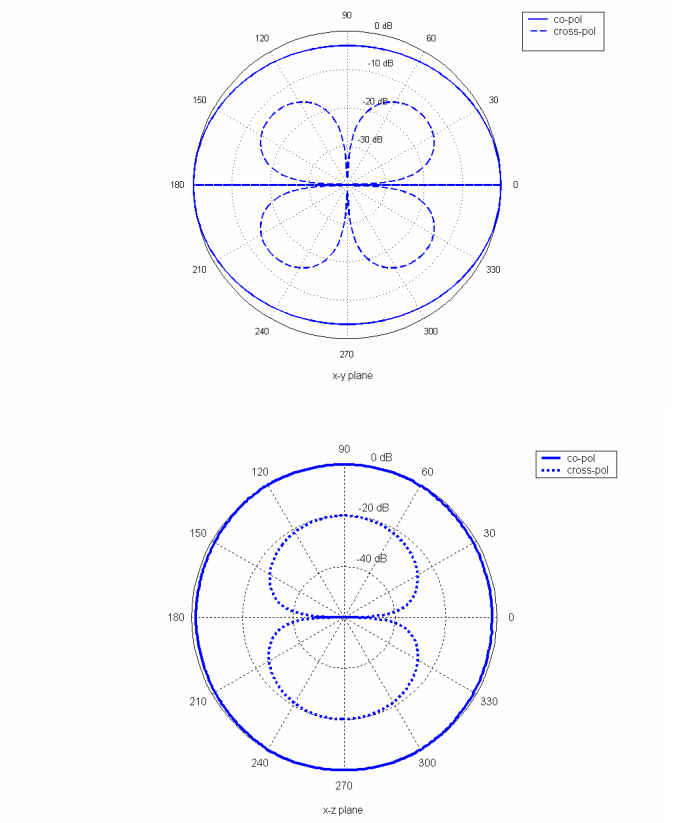

Figure 8. Simulated radiation patterns at 2.41 GHz for the proposed antenna in Figure 1.

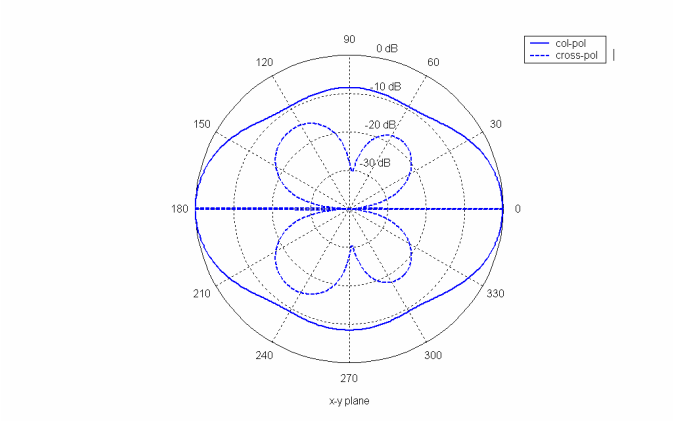

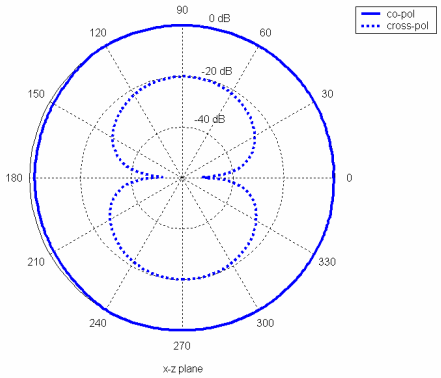

Figure 9. Simulated radiation patterns at 5.17 GHz for the proposed antenna in Figure 1.

ACKNOWLEDGEMENT

The authors would like to thank Rajamanggala University of Technology Thanyaburi Pathumtanee, Thailand, for support the IE3D User Manual Release 10, Zeland Software.

REFERENCES

[1] A. Belguessoum, G.Y. Delisle, "A Novel Dual frequency operation of CPW Coupled Patch Antenna," Antennas and Propagation Society International Symposium, 2005 IEEE, pp. 446-449, July 2005.

[2] W.-C. Liu, "Broadband dual-frequency meandered CPW-fed monopole antenna", Electron. Lett., Vol. 40 No. 21, pp. 1319-1320, October 2004.

[3] Shih-Yuan Chen, Powen Hsu, "A CPW-Fed Horn-Shaped Slot Array Antenna For 5 GHz WLAN Access Point," European Conference on Wireless Technology 2004, Amsterdam, pp. 281-284.

[4] Yu-De Lin, Member, IEEE, and Pei-Ling Chi, "Tapered Bent Folded Monopole for Dual-Band Wireless Local Area Network (WLAN) Systems," Antennas and Wireless Propagation Letters, Vol. 4, pp. 355-357, 2005.

[5] W.C. Liu and W.R. Chen, "CPW-fed compact meandered patch antenna for dual-band operation," Electron. Lett., Vol. 40 No. 18, pp. 1094-1095, Sept. 2004.

[6] W.C. Liu, "Wideband dual-frequency double inverted-L CPW-fed monopole antenna for WLAN application," IEE Proc.-Microw. Antennas Propag., Vol. 152, No. 6, pp. 505-510, December 2005.

[7] Gaoming Chill, Binhong Li and Dongsheng Qi, "A Dual-frequency Antenna Fed By CPW," Antennas and Propagation Society International Symposium, 2005 IEEE, pp. 459-462 vol. 1B, July 2005.

[8] T.H. Kim and D.C. Park, "CPW-fed compact monopole antenna for dual-band WLAN applications," Electron. Lett., Vol. 41 No. 6, pp. 291-293, March 2005.

[9] Yongxi Qian and Tatsuo Itoh, FDTD Analysis and Design of Microwave Circuits and Antennas Software and Application, Realize Inc., 1999.

[10] Allen Taflove, Computational Electrodynamics The Finite-Difference Time-Domain Method, Artech House, Inc., 1995.

[11] *IE3D User Manual Release*. 10, Zeland Software, June 2003.

Microstrip-Fed Acute Angle Wide-Slot Antenna

P. Wiriyacosol[1], C. Benjangkaprasert[1], N. Anatrasirichai[1] and T. Wakabayashi[2]
[1]Research Center for Communication and Information Technology (ReCCIT) and Faculty of Engineering
King Mongkut's Institute of Technology Ladkrabang, Chalongkrung Road, Ladkrabang, Bangkok, 10520 Thailand
[2] School of Information Science and Engineering, Tokai University, Hirasuka, Kanagawa, 259-1292 Japan

***Abstract*—Investigation was carried out on the novel microstrip-fed acute angle wide-slot antennas. These antennas were designed for 2–3 GHz covering Wi-Fi (IEEE 802.11b/g at 2.4–2.4835 GHz) and WiMax (IEEE 802.16 at 2.3 GHz and 2.5 GHz) applications. The antennas achieved the omni-directional radiation pattern and high average gain. Details of the antenna design and simulation results are presented and discussed.**

I. INTRODUCTION

Wide-slot antennas have been studied since 1993. Kahrizi M., Sarkar T. K., and Maricevic Z. A. [1] presented the calculation involved the wide open slot by the Method of Moments. Further investigations by [2] and [3] revealed that wider slot width created wider bandwidth, which was preferable. Microstrip antennas with wide basic rectangular slot then appeared to be an interesting alternative in antenna design.

A wide-slot antenna with acute angle shapes at 45° were first developed by [4] as another novel design alternative. The width of the bandwidth characteristic was maintained while the area of the antenna structure was reduced. The antenna structure was kept simple. The microstrip feed was also kept simple for the ease of manufacturing. In this paper, acute angle shape antennas at 60° were brought into consideration for further understanding.

IEEE 802.16 standard was established by IEEE standards board in 1999. In 2005, IEEE 802.16e standard was developed to serve mobile applications. Presently more applications were found in the frequency range of 2.3 GHz and 2.5 GHz which was the overlapped range to IEEE 802.11b/g standard which operated at 2.4–2.4835 GHz. In this study wide-slot antennas with acute angle shapes were developed to yield the bandwidth covering 2.3, 2.4–2.4835 and 2.5 GHz to satisfy these standards. The Method of Moments (MoM) was adopted to analyze the proposed antennas by simulation through IE3D software from Zeland, Inc, as referred in [5].

II. METHODOLOGY

A. Principle

The slot is edged on the ground plane, while the microstrip feed line is on the other side of the substrate. The middle layer is the substrate with permittivity ε_r F/m and thickness h mm.

As suggested in [6], the wavelength of the fundamental frequency (λ_o) is found from (1).

$$\lambda_o = \frac{c}{f} \tag{1}$$

When light velocity $c = 2.998 \times 10^8$ m/s, and f is the operating frequency used by the antenna in receiving and sending signals.

Effective dielectric constant (ε_{eff}) is known from (2)

$$\varepsilon_{eff} = \frac{\varepsilon_r + 1}{2} + \frac{\varepsilon_r - 1}{2}\left[1 + 12\frac{h}{W_m}\right]^{-\frac{1}{2}} \tag{2}$$

Guided wavelength (λ_g) is determined by (3).

$$\lambda_g = \frac{\lambda_o}{\sqrt{\varepsilon_{reff}}} \tag{3}$$

There are two steps in designing a microstrip antenna, ie. the slot design and the microstrip feeding design.

Slot design

The geometry of an acute angle wide-slot antenna is shown in Fig. 1. The related structural parameters were illustrated in Fig. 2. The slot is responsible for creating resonance. In principle, the length of the slot (L) should be one half of the guided wavelength (λ_g). The antenna designed according to this approach is then a half-wavelength antenna, i.e.

$$L = 0.5\lambda_g \tag{4}$$

At this stage of investigation, the width of wide-slot (W) was kept larger than 0.1 of L so that $W > 0.1L$ or $W > 0.05\lambda_g$.

The acute angle wide-slot has a width $W = W_v = W_h = 9.00$ m and the total length $L = L_v + L_h = 61$ mm ($\approx 0.7\ \lambda_g$). Other parameters were found from tuning for the optimum matching point with 50-Ω transmission line.

Microstrip feed line design

Reference [7] presented equations for width of the feed line (W_m) by (5).

$$\frac{W_m}{h} = \frac{2}{\pi}\{B' - 1 - ln(2B' - 1) + \frac{\varepsilon_r - 1}{2\varepsilon_r}\left[\ln(B' - 1) + 0.39 - \frac{0.61}{\varepsilon_r}\right]\} \tag{5}$$

For $\frac{W_m}{h} \geq 2$, $B' = \frac{120\pi^2}{2Z_o\varepsilon_r^{\frac{1}{2}}}$ and Z_o was a characteristic impedance.

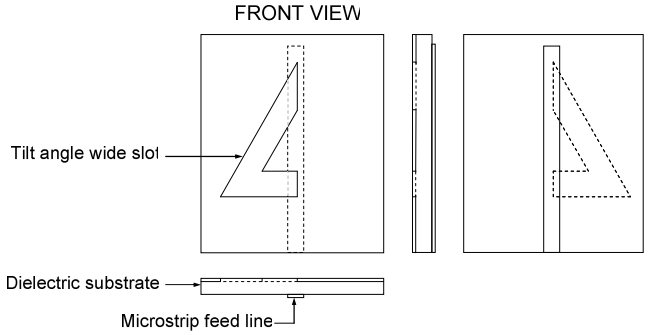

Figure 1. Configuration of the microstrip-fed acute angle wide-slot antenna

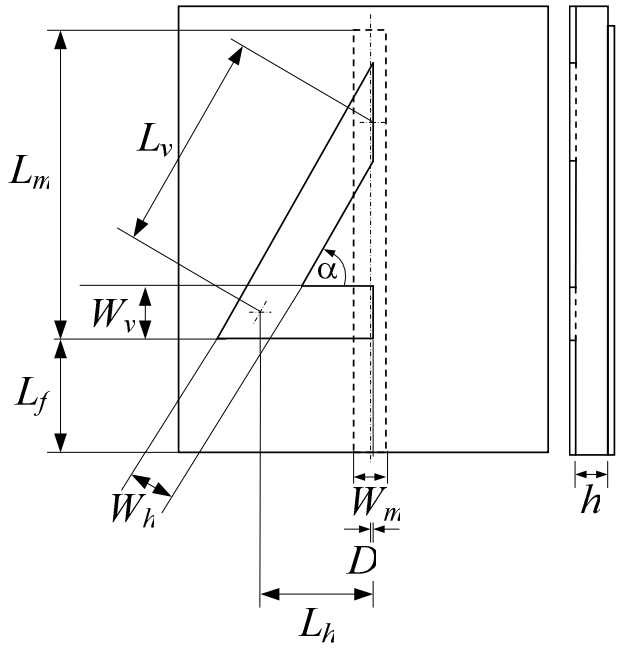

Figure 2. Structural parameters of the microstrip-fed acute angle wide-slot antenna

W_m was determined by numerical method. The theoretical guided wavelength of the lowest order resonant frequency at 2.44 GHz was 91.41 mm. The width of a microstrip feed line was 4.853 mm. The length of a microstrip feed line L_m, and the width of a slot W_s were obtained by arbitrarily adjusting for the optimum matching condition.

The calculated dimensions were then truncated as listed in TABLE I. These dimensions were used in designing a single frequency linear slot antenna. The characteristic of this antenna satisfied to the design objective.

B. Materials

A commercial substrate RT/duroid 5880 was used with the dielectric constant (ε_r) of 2.2 and the substrate thickness (h) of 1.575 mm with the copper coating thickness 0.035 mm.

III. Results

A. Tuning the design parameters

Simulation revealed that for the $0.5\lambda_g$ open slot width the frequency for best matching occurred at a value slightly higher than the designed value. To keep the best matching at the designed frequency, the slot length was allowed to be slightly higher than the original designed value, and position of the feed line was slightly adjusted.

The effects of structural parameters were then studied in the search for the optimum matching. The offset position of the feed line was found to affect input impedance of the antenna as suggested earlier by [8]. Some details of the techniques used in tuning D for the second matching frequency in WLAN range was described in [9–11]. These studies used the technique of varying the offset distance D of an antenna to adjust the characteristic $|S_{11}|$ for two very close frequencies until the wide bandwidth was obtained for that antenna.

The effect of the offset distance D on the characteristic $|S_{11}|$ on the microstrip-fed acute angle wide-slot antenna is shown in Fig. 3 suitable value of offset distance D created wider bandwidth for an antenna. In this case the suitable value for D was between –0.5 mm and 1.0 mm.

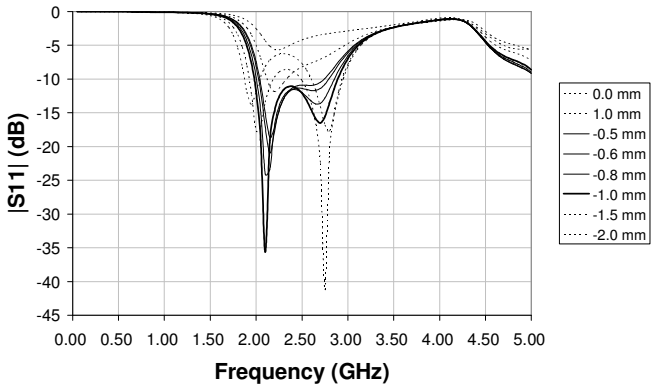

Figure 3. Effect of D on the characteristic $|S_{11}|$ on the microstrip-fed 60° angle wide-slot antenna

After matching was found on the selected frequency, L_m was slightly adjusted for the best matching. The effect of Lm is illustrated in Fig. 4. L_m was also found to affect bandwidth and the suitable value for L_m was between 55 mm to 59 mm. $|S_{11}|$ was reduced between frequencies 2 to 3 GHz until it became a wide bandwidth. As L_m increased $|S_{11}|$ also increased until it lost the wide bandwidth characteristic. It was found that L_m was not a very sensitive parameter and possible error in L_m due to manufacturing should have very little effect on antenna characteristic.

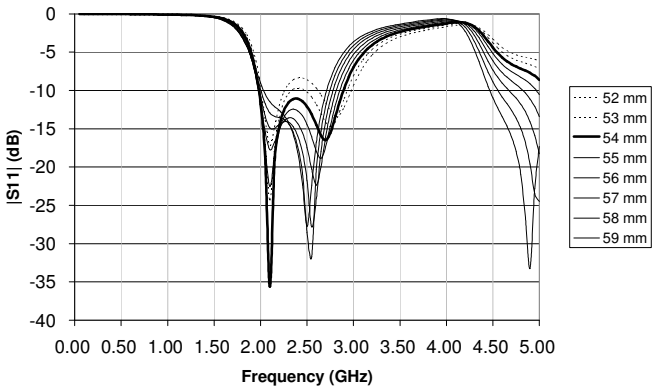

Figure 4. Effect of L_m on the characteristic $|S_{11}|$ on the microstrip-fed 60° angle wide-slot antenna after final matching

B. *Result Antenna Characteristic*

After optimum matching the final dimensions of the microstrip feed line and the antenna were found as shown in TABLE I. The characteristic $|S_{11}|$ of the result 60° angle antenna at was compared with 60° angle antenna which was done by [4] is shown in Fig. 5.

Simulations were run on the design antennas to study their performance characteristics. Fig. 6, 7 and 8 showed far-field radiation patterns at 2.3 GHz, 2.4 GHz and 2.5 GHz respectively which indicated that the far-field radiation patterns were omni-directional. The antennas were linearly polarized in those frequency ranges. The maximum gain in the usual ranges of applications was shown in Fig. 9. The gain was higher than 2 dBi and was considered satisfactory.

TABLE I
THE OPTIMUM DIMENSIONS FOR ACUTE ANGLE WIDE-SLOT ANTENNAS

α (degree)	L_h (mm)	L_v (mm)	L_m (mm)	W_m (mm)	D (mm)	–10 dB BW (%)	f_c (GHz)
45	28.50	40.50	58.77	4.80	–0.88	10.57	2.46
60	20.37	40.75	54.20	4.80	–0.90	18.11	2.43

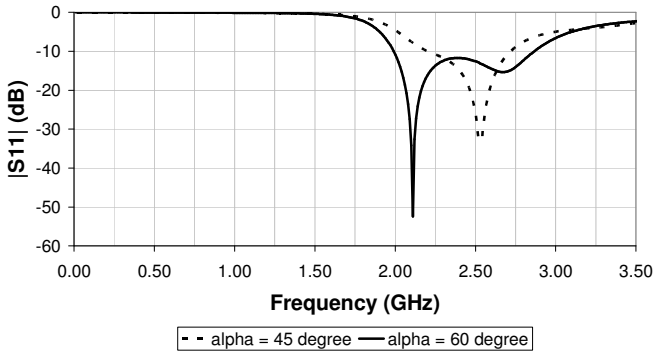

Figure 5. Characteristic $|S_{11}|$ of the 60° angle wide-slot antenna

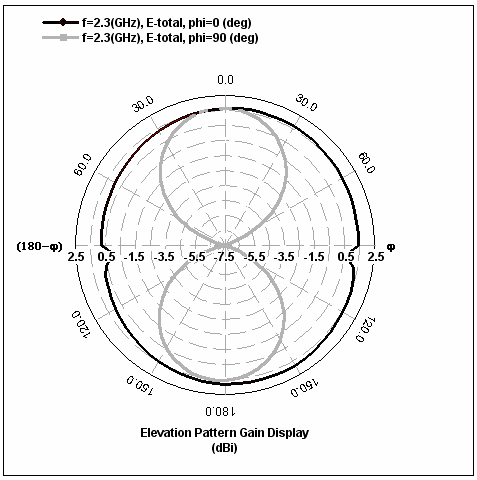

Figure 6. Far-field radiation patterns at 2.3 GHz of the microstrip-fed 60° angle wide-slot antenna

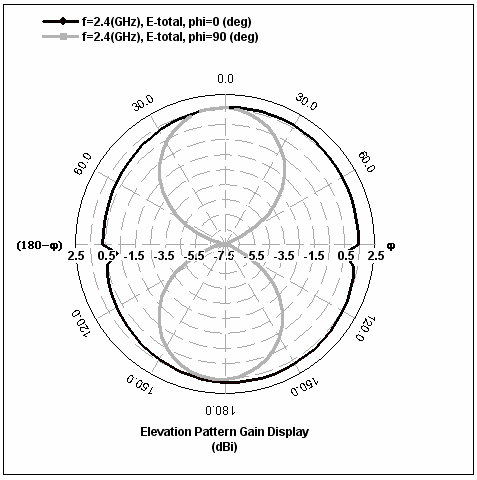

Figure 7. Far-field radiation patterns at 2.4 GHz of the microstrip-fed 60° angle wide-slot antenna

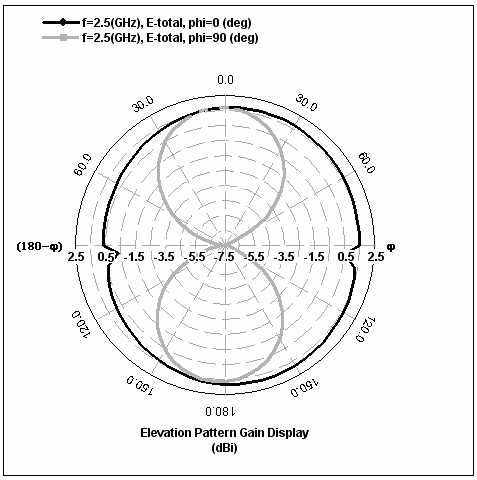

Figure 8. Far-field radiation patterns at 2.5 GHz of the microstrip-fed 60° angle wide-slot antenna

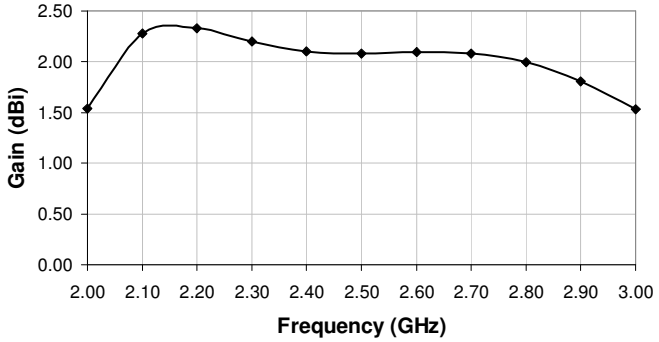

Figure 9. Maximum gain in the utilized frequency range of the microstrip-fed 60°angle wide-slot antenna

IV. CONCLUSION

The 45° and 60° acute angle wide-slot antennas satisfied IEEE 802.16, IEEE 802.16e and IEEE 802.11b/g standard requirements. These antennas are being further developed to satisfy the 3.5 GHz and 5.2 GHz applications, and also to satisfy the dual frequency applications.

These acute angle wide-slot antennas appeared suitable for wide bandwidth applications. The variation of the angle α between 45° and 60° had little effect on the wide bandwidth characteristic. Possible deviation in the angle α due to manufacturing would have little if any effect on the antenna performance. The acute angle wide-slot antenna structure is therefore considered to be a good alternative in antenna design.

ACKNOWLEDGMENT

The authors would like to express their appreciation to Faculty of Engineering, Rajamangala University of Technology Thanyaburi for their kind permission for the use of the licensed IE3D simulation program in this study.

REFERENCES

[1] M. Kahrizi, T. K. Sarkar, and Z. A. Maricevic, "Analysis of a widw radiator," *IEEE Trans. Microwave Theory Tech.*, vol. 41,A247, no.1, pp. 29–37, Jan. 1993.

[2] Jia-Yi Sze and Kin-Lu Wong, "Bandwidth Enhance of a Microstrip-Line-Fed Printed Wide-Slot Antenna," *IEEE Tran. Antennas and Propagation*, vol. 49, no. 7, July 2001.

[3] Jen-Yea Jan and Jia-Wei Su, "Bandwidth Enhancement of a Printed Wide-Slot Antenna With a Rotate Slot," *IEEE Trans. Antennas and Propagation*, vol. 53, no.6, June 2005.

[4] C. Jamjank, "Study on characteristics of angular microstrip slot antenna," *Master Thesis*, Department of Information Engineering King Mongkut's Institute of Technology Ladkrabang, 2006.

[5] *IE3D User's Manual Release 9*, Zeland Software, Inc., U.S.A., 2002

[6] C. A. Balanis, *Antenna Theory Analysis and Design*, John Wiley & Sons, Inc., 1997.

[7] E. O. Hammerstadt, Equations for microstrip circuit design, Proceedings of the fifth European Microwave Conference, Microwave Exhibitions & Publishers, pp. 268–272, 1975.

[8] Y. Yoshimura, "A Microstripline Slot Antenna," *IEEE Trans. Microwave Theory Tech.*, vol. 20, pp. 760–762, November 1972.

[9] P. Rakluea T. Wakabayashi P. Wiriyacosol and N. Anantrasirichai, "Right AngleFShaped Slot Antenna for IEEE 802.11b/g/j Applications," *Proceedings of Progress in Electromagnetic Research Symposium (PIERS 2006)*, Japan, Aug. 2006.

[10] P. Wiriyacosol, N. Anantrasirichai, C. Benjangkaprasert and T. Wakabayashi, "Creating Dual-Frequency on Simple-Structured Slot Antennas for IEEE 802.11 a/b/g/h/j Applications," *Proceedings of IEEE TENCON 2006*, Hong Kong, Nov. 2006.

[11] P. Wiriyacosol , N. Anantrasirichai , C. Benjangkaprasert and T. Wakabayashi, "Dual-Frequency Microstrip-Fed Basic-Structured Slot Antennas for Wireless LAN Applications," *Proceedings of International Symposium on Antennas and Propagation (ISAP 2006),* Singapore, Nov. 2006.

Closed-form Expressions of Mutual Impedance between Perpendicular Thin Dipoles

T. Limpiti and M. Krairiksh
Faculty of Engineering and Research Center for Communications and Information Technology
King Mongkut's Institute of Technology Ladkrabang, Bangkok, Thailand
Phone/Fax : +66-2-737-3000 Ext. 3327, E-mail : s8060939@kmitl.ac.th, kkmonai@kmitl.ac.th

***Abstract*-Analytic expressions are derived and presented for the mutual impedance between two thin perpendicular center-fed dipoles of arbitrary size. The current distribution on the antennas is assumed to be sinusoidal. The expressions are in terms of summation of sine-integrals and cosine-integrals. Mutual impedance curves are presented. The accuracy of the formulas is favorably compared with results from digital computation and electromagnetic simulator. An application of interest is in a dielectric property determination.**

I. INTRODUCTION

Most radiating antenna systems are often suffered from the effect of one antenna upon another in addition to determing the interfered pattern due to guy wires acting as parasitic elements or antennas adjacent to the fed antenna. To find the input impedance or finding induced currents on other wires, it is necessary to determine the unknown quantity which links the various elements called the mutual impedance. Mutual impedance analysis has been published for a long time. King has presented the mutual impedance between unequal length dipoles in echelon which the advantage of this work is ease for using because the expressions are performed in closed-form [1]. Digital computation of the mutual impedance between two arbitrary lengths antennas with unlimited geometrical configuration has been extended [2]. However, the expressions are not in closed-form. Over the past ten years the mutual impedance has been investigated such as the mutual impedances between nonplanar-skew sinusoidal dipoles which have been well documented by Richmond and Geary [3], or sinusoidal electric and magnetic dipoles [4].

Many useful applications of mutual coupling are published such as the dielectric property measurement of subsurface using linear dipoles [5]. One of the most interesting methods is the measurement of amplitudes of transmission and reflection coefficients [6]-[7]. The advantage of this method is that this is no need to measure phase but it is quite complicate to measure amplitudes of both transmission and reflection coefficients.

Although sufficient data of the parallel-in-echelon configuration has been presented in the past for solving the conventional problems, a knowledge of the mutual impedance between perpendicular thin dipoles is accordingly required. Consequently, the purpose of this paper is to present the new closed-form expressions for easily computing the exact mutual impedance between two thin center-fed perpendicular dipoles of arbitrary size. The calculation is assumed for the case of sinusoidal current distribution in each antenna, induced EMF method is used and restricted to two antennas of equal size. The formulations of the mutual impedance are expressed in terms of sine-integrals and cosine-integrals in section II. Analysis by using formulation of mutual coupling for dielectric determination are presented in section III. It shows the possibility to determine dielectric property by measuring mutual coupling of parallel and perpendicular dipoles. This paper is concluded in section IV.

II. MUTUAL IMPEDANCE OF PERPENDICULAR DIPOLES

A. *Near-zone Field of a Thin Dipole*

Consider two center-fed dipoles of length L when the primary antenna is placed along the z axis of a cartesian coordinate system. Its feed point, which is assumed to have infinitesimal spacing, is located at the origin. The secondary antenna with the same configuration, is separated by a distance d and h along y and z axis, respectively, as shown in Fig. 1. As pointed out in [8]-[9], the near-zone field of a thin dipole in free space is

$$E_y = j\frac{\eta I_m}{4\pi y}\left(\frac{(z-H)e^{-jkR_1}}{R_1}+\frac{(z+H)e^{-jkR_2}}{R_2}-\frac{2z\cos(kH)e^{-jkr}}{r}\right). \quad (1)$$

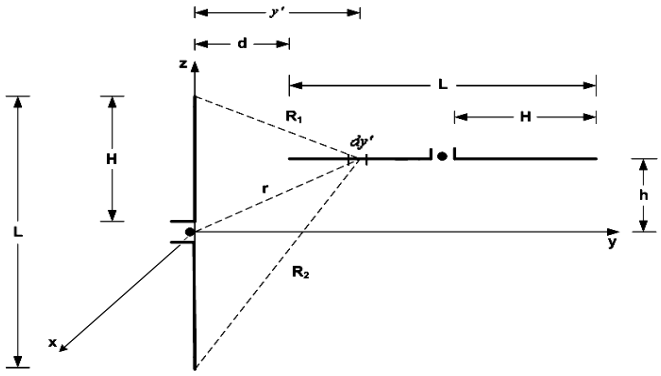

Figure 1. Geometry of two perpendicular dipole antennas.

The antenna current distribution $I_2(y')$ is assumed to be sinusoidal and given by

$$I_2(y') = \begin{cases} I_m \sin[k(y'-d)] & ; \quad d<y'<H+d \\ I_m \sin[k(2H+d-y')] & ; H+d<y'<2H+d \end{cases} \tag{2}$$

where I_m and η denote the maximum current and the intrinsic impedance, respectively.

B. Derivation of Mutual Impedance

With the induced emf method, the mutual impedance between the two antennas in Fig. 1. is defined by

$$Z_{21} = -\frac{V_{21}}{I_1(0)} \tag{3}$$

where V_{21} denotes the open-circuit voltage at the terminals of the secondary antenna, due to the feed-point current $I_1(0)$ in the primary antenna. The open-circuit voltage at the terminal of the secondary antenna which results from the voltage induced along the length of the antenna may be found by the application of reciprocity theorem.

$$V_{21} = -\frac{1}{I_2(0)} \int E_{y21} I_2(y')\, dy' \tag{4}$$

where $I_2(0)$ and E_{y21} are the feed-point current of the secondary antenna and the parallel component of electric field at the secondary antenna due to the primary antenna respectively.

Substituting (1), (2) and (4) into (3), one obtains a standard expression for mutual impedance [8]

$$Z_{21} = -\frac{1}{I_1(0) I_2(0)} \int E_{y21} I_2(y') dy'. \tag{5}$$

Integration of E_{y21} and $I_2(y')$ with respect to y' in (5) can be carried out directly, resulting in

$$Z_{21} = -j \frac{\eta I_{1m} I_{2m}}{4\pi I_1(0) I_2(0)} \left[\left\{ \int_d^{H+d} \sin\left[k(y'-d)\right] + \int_{H+d}^{2H+d} \sin\left[k(2H+d-y')\right] \right\} \times \left(\frac{(z-H)e^{-jkR_1}}{yR_1} + \frac{(z+H)e^{-jkR_2}}{yR_2} - \frac{2z\cos(kH)e^{-jkr}}{yr} \right) dy' \right]. \tag{6}$$

The geometry of Fig. 1 reveals that

$$R_1 = \sqrt{(H-h)^2 + y'^2} \tag{7}$$

$$R_2 = \sqrt{(H+h)^2 + y'^2} \tag{8}$$

$$r = \sqrt{h^2 + y'^2}. \tag{9}$$

The mutual resistance and the mutual reactance are obtained from real and imaginary parts of the complex expression (6). Although Eq. (6) can be evaluated by digital computation method, derived-form computation is more convenient.

Inserting (7)-(9) into (6), and following the integrations to yield the most general expressions for the mutual impedance between two infinite thin perpendicular center-fed antennas, the mutual resistance and reactance of the perpendicular dipoles are shown in (10) and (11), respectively.

$$\begin{aligned} R_{21} = \frac{15}{d\sin^2(kH)} \Big[& (h-H)\Big\{\cos(kd)\big(Ci(u_1)-Ci(u_0)+Ci(v_1)-Ci(v_0)\big)+\cos(k(2H+d))\big(Ci(m_1)+Ci(m_4)-Ci(u_0)-Ci(v_0)\big) \\ & +\sin(kd)\big(Si(u_1)-Si(u_0)+Si(v_1)-Si(v_0)\big)+\sin(k(2H+d))\big(Si(m_1)-Si(m_4)-Si(u_0)-Si(v_0)\big)\Big\} \\ & +(h+H)\Big\{\cos(kd)\big(Ci(u_2)-Ci(u_3)+Ci(v_2)-Ci(v_3)\big)+\cos(k(2H+d))\big(Ci(m_2)+Ci(m_5)-Ci(u_3)-Ci(v_3)\big) \\ & +\sin(kd)\big(Si(u_2)-Si(u_3)+Si(v_2)-Si(v_3)\big)+\sin(k(2H+d))\big(Si(m_2)+Si(m_5)-Si(u_3)-Si(v_3)\big)\Big\} \\ & +2h\cos(kH)\Big\{\cos(kd)\big(Ci(u_5)-Ci(u_4)+Ci(v_5)-Ci(v_4)\big)+\cos(k(2H+d))\big(Ci(u_5)+Ci(v_5)-Ci(m_3)-Ci(m_6)\big) \\ & +\sin(kd)\big(Si(u_5)-Si(u_4)+Si(v_5)-Si(v_4)\big)+\sin(k(2H+d))\big(Si(u_5)+Si(v_5)-Si(m_3)-Si(m_6)\big)\Big\}\Big] \end{aligned} \tag{10}$$

$$X_{21} = \frac{15}{d\sin^2(kH)}\Big[(h-H)\Big\{\sin(kd)\Big(Ci(u_0)-Ci(u_1)+Ci(v_1)-Ci(v_0)\Big)+\sin\big(k(2H+d)\big)\Big(Ci(u_0)-Ci(v_0)+Ci(m_1)-Ci(m_4)\Big)$$
$$+\cos(kd)\Big(Si(u_1)-Si(u_0)+Si(v_0)-Si(v_1)\Big)+\cos\big(k(2H+d)\big)\Big(Si(v_0)-Si(u_0)-Si(m_1)+Si(m_4)\Big)\Big\}$$
$$+(h+H)\Big\{\sin(kd)\Big(Ci(u_3)-Ci(u_2)+Ci(v_2)-Ci(v_3)\Big)+\sin\big(k(2H+d)\big)\Big(Ci(u_3)-Ci(v_3)+Ci(m_2)-Ci(m_5)\Big)$$
$$+\cos(kd)\Big(Si(u_2)-Si(u_3)-Si(v_2)+Si(v_3)\Big)+\cos\big(k(2H+d)\big)\Big(Si(v_3)-Si(u_3)-Si(m_2)+Si(m_5)\Big)\Big\}$$
$$+2h\cos(kH)\Big\{\sin(kd)\Big(Ci(u_4)-Ci(u_5)-Ci(v_4)+Ci(v_5)\Big)+\sin\big(k(2H+d)\big)\Big(Ci(v_5)-Ci(u_5)-Ci(m_3)+Ci(m_6)\Big)$$
$$+\cos(kd)\Big(Si(u_5)-Si(u_4)+Si(v_4)-Si(v_5)\Big)+\cos\big(k(2H+d)\big)\Big(Si(u_5)-Si(v_5)+Si(m_3)-Si(m_6)\Big)\Big\}\Big] \quad (11)$$

where

$$u_0 = k\left[(H+d)-\sqrt{(H-h)^2+(H+d)^2}\right]$$
$$u_1 = k\left[d-\sqrt{(H-h)^2+d^2}\right]$$
$$u_2 = k\left[d-\sqrt{(H+h)^2+d^2}\right]$$
$$u_3 = k\left[(H+d)-\sqrt{(H+h)^2+(H+d)^2}\right]$$
$$u_4 = k\left[d-\sqrt{h^2+d^2}\right]$$
$$u_5 = k\left[(H+d)-\sqrt{h^2+(H+d)^2}\right]$$
$$v_0 = k\left[\sqrt{(H-h)^2+(H+d)^2}+(H+d)\right]$$
$$v_1 = k\left[\sqrt{(H-h)^2+d^2}+d\right]$$
$$v_2 = k\left[\sqrt{(H+h)^2+d^2}+d\right]$$
$$v_3 = k\left[\sqrt{(H+h)^2+(H+d)^2}+(H+d)\right]$$
$$v_4 = k\left[\sqrt{h^2+d^2}+d\right]$$
$$v_5 = k\left[\sqrt{h^2+(H+d)^2}+(H+d)\right]$$
$$m_1 = k\left[\sqrt{(H-h)^2+(2H+d)^2}+(2H+d)\right]$$
$$m_2 = k\left[\sqrt{(H+h)^2+(2H+d)^2}+(2H+d)\right]$$
$$m_3 = k\left[\sqrt{h^2+(2H+d)^2}+(2H+d)\right]$$
$$m_4 = k\left[(2H+d)-\sqrt{(H-h)^2+(2H+d)^2}\right]$$
$$m_5 = k\left[(2H+d)-\sqrt{(H+h)^2+(2H+d)^2}\right]$$

III. Simulation Results

In order to determine the accuracy of the formulas (10) and (11), two thin perpendicular center-fed dipole antennas in Fig. 1 have been analyzed. The mutual impedance are calculated using the formulation (10) and (11), and compared to the results obtained from digital computation [2], and electromagnetic simulator [10]. The comparisons of mutual impedance are shown in mutual impedance curves which spacing between two antennas are extended to two wavelength.

A. Comparison with Digital Computation and Electromagnetic Simulator

As can be easily seen from the curves in Fig. 2, the mutual impedance obtained from the closed-form formulas of this paper are in agreement with those obtained from digital computation [2], and electromagnetic simulator [10]. However, there are deviations of both real and imaginary parts within the range of spacing between antennas d/λ is equal to 0.2-0.6. If the value obtained from the electromagnetic simulator is set as a reference value, resistance values of the closed-form formulations are more accurate than those from digital computation. On the other hand, reactance value of the digital computation is more accurate than those from the closed-form formulations.

B. Mutual Impedance for Different Heights

Height variation shows the trend of mutual impedance which both antennas are half-wavelength and height of the secondary antenna are varied within half of the primary antenna length range. Fig. 3 and 4 present mutual resistance and mutual reactance curves in terms of the parameter d/λ, respectively. It can be noticed from Fig. 3 that the mutual resistance becomes higher as the height increases at the spacing between antennas equals 0.2-0.4 d/λ. However, it decreases to zero as the spacing between antennas increases. Fig. 4 shows that the mutual reactance becomes higher as the height increases at the spacing between antennas equals 0.2 d/λ while it decreases as the spacing between antennas increases.

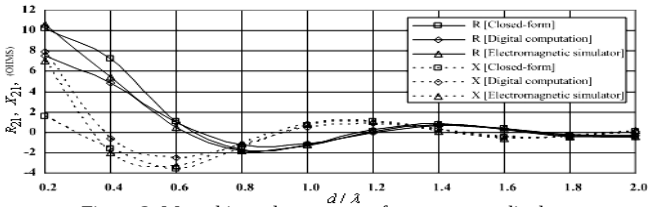

Figure 2. Mutual impedance curves for two perpendicular half-wavelength antennas.

C. *Mutual Coupling in Different Dielectrics*

A new concept for dielectric determination using linear dipoles to measure magnitude of mutual coupling are presented. The presented method uses the concept of switching the antennas configuration which between perpendicular and parallel-in-echelon. The mutual coupling curves with various dielectrics and spacing between antennas, at 2.45 GHz, extended from 0.2-0.8 d / λ are presented in Fig. 5. It can be noticed that there are cross points between S_{21} of perpendicular and parallel-in-echelon configurations with the same spacing. Thus, the cross points can notify the unknown dielectric constant of the object. The result in Fig. 5 is based on the halfwave dipoles in free space and the cross points of mutual coupling of parallel and perpendicular dipoles are in the range of $10 \le \varepsilon_r \le 40$. In order to utilize this method in higher ε_r range, the dipoles must be halfwave long in higher dielectric constant. Fig. 6 shows the results when the dipoles are halfwave in ε_r = 81. It is clear that the dielectric constant in the range of $90 \le \varepsilon_r \le 100$ can be determined.

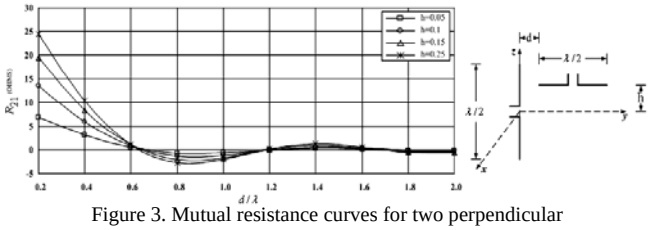

Figure 3. Mutual resistance curves for two perpendicular half-wavelength antennas with various height.

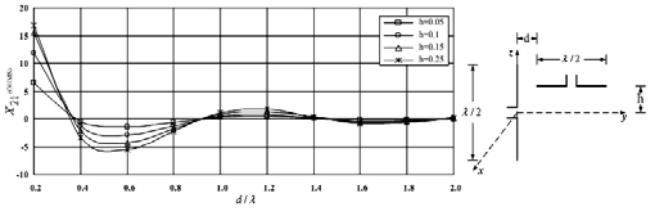

Figure 4. Mutual reactance curves for two perpendicular half-wavelength antennas with various height.

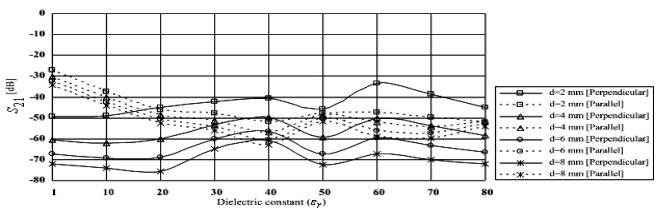

Figure 5. Mutual coupling curves for two perpendicular and parallel half-wavelength antennas with various dielectrics.

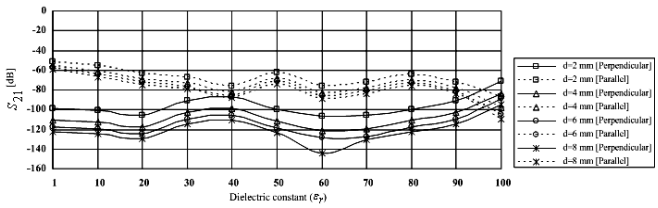

Figure 6. Mutual coupling curves for two perpendicular and parallel half-wavelength of ε_r =81 antennas with various dielectrics.

IV. CONCLUSION

Analytic expressions are derived and presented for the mutual impedance between two thin perpendicular center-fed dipoles of arbitrary size. Both antennas are assumed to have sinusoidal current distribution. The mutual impedances are calculated and presented. In addition, as shown with the mutual impedance curves in Fig. 2, calculated values of mutual impedance using the presented expressions compared with values from digital computation and electromagnetic simulator. The accuracy of the formulas is favorably compared and the integrations in the expressions contain no special functions, furthermore, they are in suitable forms for implementation. This paper has shown an application of these expressions in determination of lossless dielectric property. The future work will be focused on determination of lossy dielectrics.

ACKNOWLEDGMENT

This work was supported by the Thailand Research Fund under contract No. RTA 4880002.

REFERENCES

[1] H. E. King, "Mutual impedance of unequal length antenna in echelon," *IRE Trans. Antennas Propagat.*, vol. 5, No.3, pp.306-313, 1957.

[2] H. C. Baker and A. H. Lagrone, "Digital computation of the mutual impedance between thin dipoles," *IRE Trans. Antennas Propagat.*, vol. AP-10, No.2, pp.172-178, 1962.

[3] J. H. Richmond and N. H. Geary, "Mutual impedance of nonplanar-skew sinusoidal dipoles," *IEEE Trans. Antennas Propagat.*, vol. 23, No.5, pp.412-414, 1975.

[4] K. Liu, C. A. Balanis and G. C. Barber, "Exact mutual impedance between sinusoidal electric and magnetic dipoles," *IEEE Trans. Antennas Propagat.*, vol. 39, No. 5, pp.684-686, 1991.

[5] A. Shostak, V. Zagoskin, L. Ligthart and V. IIjushenko, "Analysis of a linear dipole antenna system for measurement the complex dielectric permittivity," *Microwave, Radar and Wireless Communication, MIKON-2002, 14th Int. Conf.*, pp.294-298, 2002.

[6] Z. Ma, and S. Okamura, "Permittivity determination using amplitudes of transmission and reflection coefficients at microwave frequency," *IEEE Trans. Microwave Theory Tech.*, vol. 47, No. 5, May 1999.

[7] S. N. Kharkovsky, F. Akay, U. C. Hasar, and C. D. Atis, "Measurement and monitoring of microwave reflection and transmission properties of cement-based specimens," *IEEE Trans. Instrum. Meas.*, vol. 51, No. 6, pp.1210-1218, December 2002.

[8] K. F. Lee, *Principles of Antenna Theory*, John Wiley & Sons, 1984.

[9] C.A. Balanis, *Antenna: Theory Analysis and Design*; 2nd Edition, John Wiley & Sons, 1997.

[10] CST Microwave Studio 2006.

Structural Analysis of Trapezoidal Dual Loop Antenna for Communication Performance Enhancement of LF-RFID

Supakit Kawdungta[1], Phairote Wounchoum[1], Chuwong Phongcharoenpanich[1], and Danai Torrungrueng[2]

[1]Faculty of Engineering and Research Center for Communications and Information Technology,
King Mongkut's Institute of Technology Ladkrabang, Bangkok 10520, Thailand, E-mail: kpchuwon@kmitl.ac.th
[2]Faculty of Engineering and Technology, Asian University, Chon Buri 20150, Thailand, E-mail: dtg@asianust.ac.th

***Abstract*-This paper presents the structural analysis to enhance the communication performance of a trapezoidal dual loop antenna with walk-through gate installation for Low-Frequency Radio Frequency Identification (LF-RFID) system. Its structure will be optimized by means of Genetic Algorithm (GA) in conjunction with the Numerical Electromagnetic Code (NEC) simulation to maximize the percentage of volume for communication achievement. Subsequently, the prototype antenna was fabricated and measured the percentage of volume to confirm the communication performance. The obtained percentages of volume in *x*, *y* and *z* axes are 100%, 93.08% and 91.12%, respectively.**

***Keywords*: RFID, Trapezoidal dual loop antenna, Genetic Algorithm, Numerical Electromagnetic Code, Percentage of Volume**

I. INTRODUCTION

At present, Radio Frequency Identification (RFID) system becomes popular due to their usefulness in many applications. The animal identification in the farm is one of the most promising applications of RFID system at low frequency (LF). This system can assist increase the facilitation and efficiency. The LF band of 125 kHz and 134.2 kHz is used for human and animal safety. The principle of magnetic coupling is applied to communicate between readers and tags. The antenna is a key device to enhance the communication performance of this system. Conventionally, the rectangular- and circular-loop antennas are used as the reader antenna. It is found that those antennas cannot communicate with some tag orientations due to their generating null fields. Recently, the trapezoidal dual loop antenna has been proposed to improve the communication performance in various tag orientations [1]. In addition, the two trapezoidal dual loop antennas must be installed in parallel to make a walk-through gate for animal passing. Therefore, the individual antenna parameters and combined parameters of two antennas affect the communication performance. This paper presents the structural analysis to optimize the system performance. The Genetic Algorithms (GA) is used as an optimization tool, where the optimizing characteristics were simulated by Numerical Electromagnetic Code (NEC) [2]. The communication performance is expressed in terms of percentage of volume for communication achievement. The optimized results are used for the antenna design in the LF-RFID system. The prototype antenna will be fabricated with walk-through gate installation to measure the percentage of volume. Measured results confirm the usefulness of the antenna for further animal identification applications.

II. A TRAPEZOIDAL DUAL LOOP ANTENNA FOR LF-RFID

The proposed antenna consists of two adjacent trapezoidal dual loop antennas made of the conducting wire as shown in Fig. 1(a). The width, total height and angle of the slant line are denoted by a, b and ψ, respectively. The spacing between two trapezoidal dual loops along the slant line is represented by δ.

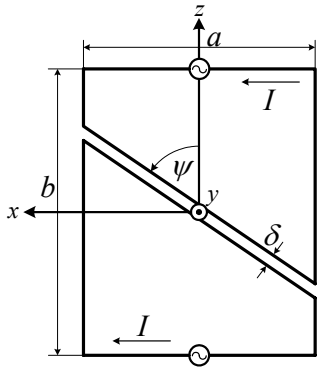

(a) Trapezoidal loop antenna.

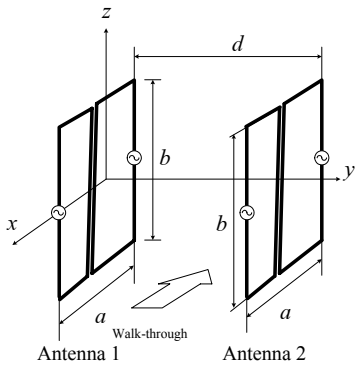

(b) Walk-through gate arrangement.

Figure 1. Antenna configuration and arrangement.

In the animal identification, two trapezoidal dual loop antennas are installed in walk-through gate arrangement as

illustrated in Fig. 1(b). The distance between two trapezoidal dual loop antennas is equal to *d*.

III. METHOD OF ANALYSIS

The structural analysis of the antenna will be optimized by GA. It is well known that GA is robust search techniques based on the principle of evolution. GA maintains a population of encoded solution, and guides the population towards the optimum solution. This process is facilitated through an evaluation procedure, or fitness function, that determines the fitness or worth of each member of the population. Probabilistic genetic operators are employed to recombine highly fit individuals and search the solution space for better and better solutions. Fig. 2 shows a flow chart of the GA used in this paper.

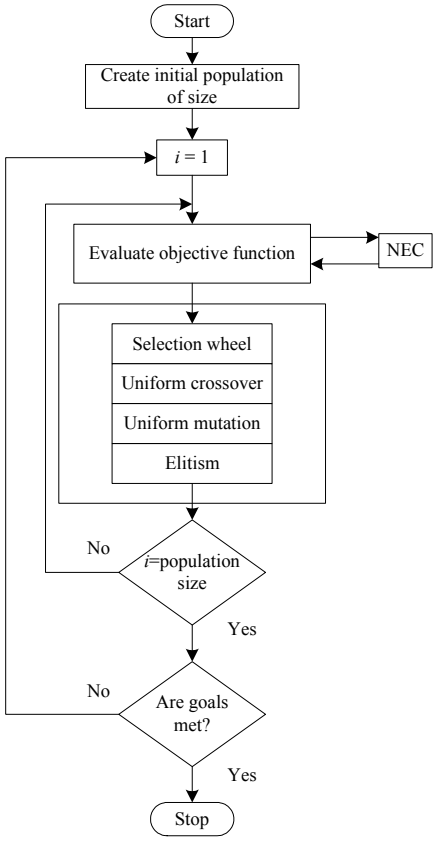

Figure 2. Flow chart of GA used in this paper.

In this paper, GA implements selection wheel for selecting variable in mating pool and uses uniform crossover and mutation operator. The elitism operator forces the best member of each population to progress to the next generation. With a population size of 50, crossover probability is 0.8 and mutation probability is 0.05. The operator parameters are chosen by using the rule of thumb [3].

GA begins a search with a large population of randomly generated individuals that are solutions to a problem. This randomness produces a diverse population of possible solutions representing a broad cross section of the entire solution space. For the problem at hand, each individual in the population represents an antenna design. This random altering of a small percentage of the population helps maintaining the global nature of the search. New population are produced and evaluated for many generations until the population converges to the same solution, or some other stopping criteria are met.

The goal of the design process is to develop the antenna meets or exceeds the desired performance. The desired antenna performance in this paper is the uniformly maximum magnetic field intensity and the percentage of volume.

The percentage of volume for communication achievement is probability of all points in the space that have magnetic field strength stronger than the activation field intensity (H_t) of a tag.

This paper considers the percentage of volume in three principal axes (*x*-axis, *y*-axis and *z*-axis). So the fitness function (F) in this case is the percentage of volume in three axes.

$$F = [P_{vx},\ P_{vy},\ P_{vz}], \tag{1}$$

where P_{vx}, P_{vy} and P_{vz} are the percentages of volume in *x*, *y* and *z* axes, respectively.

The evaluation of percentage of volume starts from considering percentage of line (P_l). It is determined by considering a tag goes through gate along a straight line from the entrance to the exit. If some points in the line (parallel to the *x*-axis) has $H(x,y,z) \geq H_t$, then the percentage of that line is 100%. However, if every point along the line has $H(x,y,z) < H_t$, the percentage of line is 0%. Note that $H(x,y,z)$ is the magnetic field intensity simulated by NEC at any point parallel to the *x*-*z* plane. (H_t is assumed to be 175 mA/m for the ISO card). The evaluation of the percentage of surface is subsequently calculated by (2).

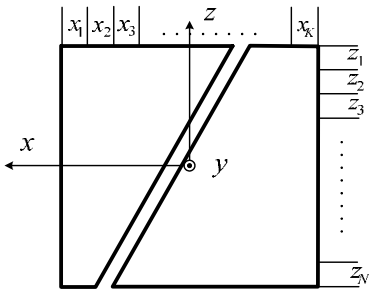

Figure 3. Consideration of the percentage of line parallel to the *x*-*z* plane.

$$P_s(y_m) = \frac{\sum_{n=1}^{N} P_l(z_n)}{N}\ , \tag{2}$$

where N is the total number of lines along the *z* axis, $P_s(y_m)$ is the percentage of surface in the *x*-*z* plane, $P_l(z_n)$ is the percentage of line along the *x* axis. Note that $P_s(y_m) \leq 100\%$. The subdivided area is shown in Fig.3.

The percentage of surface is consequently used to evaluate the percentage of volume (P_v) by equation (3).

$$P_v = \frac{\sum_{m=1}^{M} P_S(y_m)}{M} \quad , \tag{3}$$

where M is the total number of surface parallel to the x-z plane between two gate as shown in Fig.4. Note that $P_v \leq 100\%$.

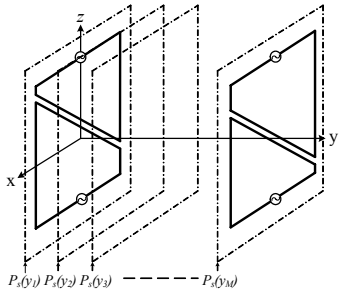

Figure 4. Consideration of the percentage of volume.

In addition, the considered volume must cover all regions between two antennas. Therefore, this paper uses the following dimension to obtain the percentage of volume: x-axis from -0.3m to 0.3 m, y-axis from 0 to 1 m and z-axis from -0.45m to 0.45 m.

IV. Structural Analysis

Fig.5 shows trapezoidal dual loop antennas set up in walk-through gate arrangement. The total width (b), the length (a) and the distance between antennas (d) are equal to 60 cm, 90 cm and 1m, respectively. These parameters are chosen due to the physical dimension for the actual animal identification in the farm.

In the previous work [1], the antenna parameters are varied but it cannot cover the entire space of applications. Hence, this paper separates the walk-through gate antenna into six models by considering the ψ angle to cover 0° to 360°. In each of the six models, there are two cases of study. The first case is that Antennas 1 and 2 are fed in-phase, and the other is that the Antennas 1 and 2 are fed 180° out-of-phase. All of them are optimized by using GA.

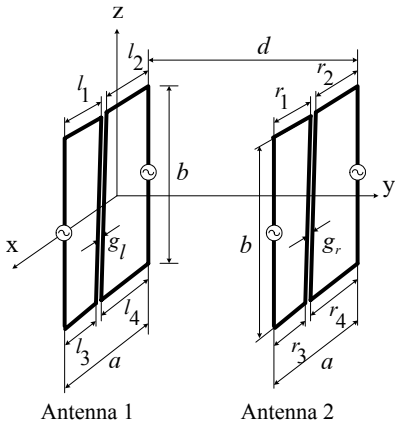

(a) Type I.

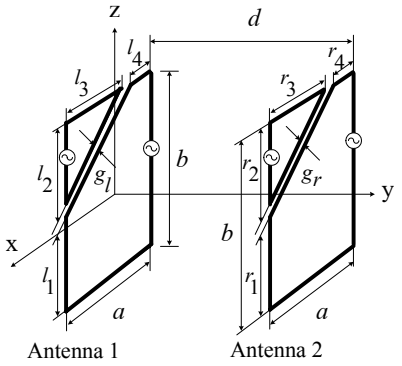

(b) Type II.

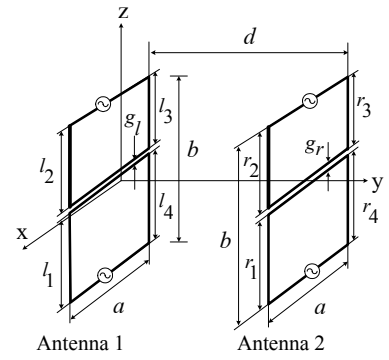

(c) Type III.

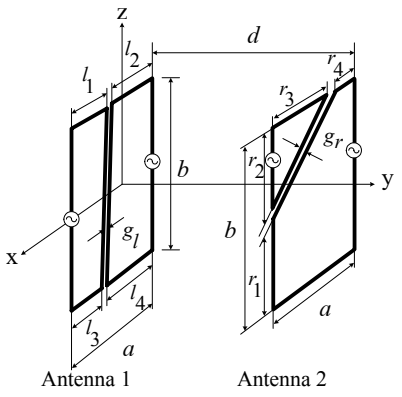

(d) Type IV.

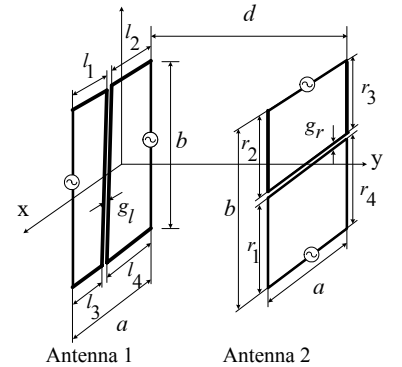

(e) Type V.

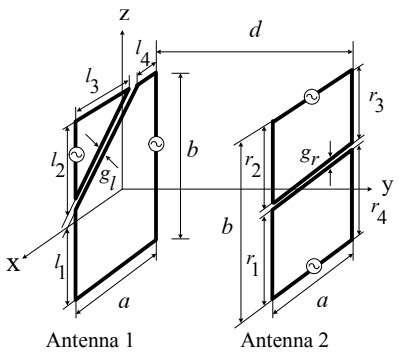

(f) Type VI.

Figure 5. Trapezoidal dual loop antennas with walk-through gate arrangement of 6 types.

When the intricate manipulation by genetic algorithms is completed, it is found that the optimum model is shown in Fig.6 with the out-of-phase excitation. It has the percentage of volume as P_{vx} = 93.82%, P_{vy} = 91.32% and P_{vz} = 70.78%, respectively.

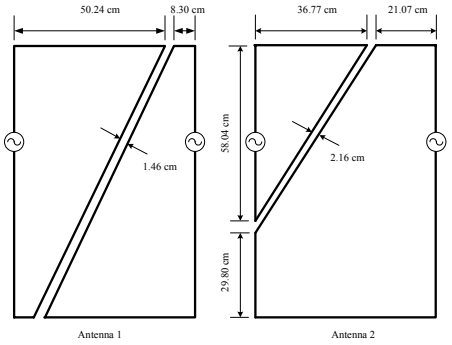

Figure 6. The actual dimension of the optimum trapezoidal dual loop antennas for the walk-through gate arrangement.

TABLE I

ANTENNA DESIGN PARAMETERS

Parameters of Antenna 1	Unit (cm)	Parameters of Antenna 2	Unit (cm)
l_1	50.24	r_1	29.80
l_2	8.30	r_2	58.04
l_3	8.30	r_3	36.77
l_4	50.24	r_4	21.07
g_l	1.46	g_r	2.16

V. MEASURED RESULTS

The measurement set up is carried out in the case that the trapezoidal dual loop antennas with the some dimension as in the optimum model are installed as the walk-through gate configuration shown in Fig.7. The prototype trapezoidal dual loop antenna is constructed by using the wire No. 24 AWG with 17 turns. The left-hand side is Antenna 1 and the right-hand side is Antenna 2. The tag under test is the ISO card.

Figure 7. Fabricated trapezoidal dual loop antennas for the walk-through gate arrangement.

The measured percentages of surface versus the distance along the *y* axis is shown in Fig.8. It is found that the measured percentages of volume are P_{vx} = 100%, P_{vy} = 93.08% and P_{vz} = 91.12%, respectively. The results are significantly better than the previous work [1].The discrepancy between the simulation and measurement is found because the area of tag in the measurement that is larger than the detected point in the simulation. Moreover, the coupling of the magnetic field in other axes around the tag is also making contributes to this discrepancy.

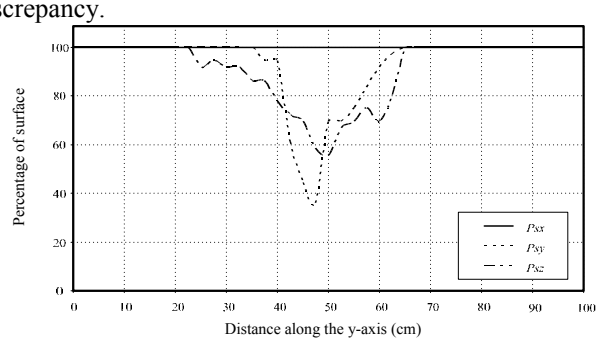

Figure 8. Measured percentage of surface versus the distance along the *y* axis.

VI. CONCLUSIONS

The genetic algorithms in conjunction with NEC are employed to optimize the trapezoidal dual loop antennas with walk-through gate arrangement. Results show the enhancement of communication performance over the previous work. This configuration was also fabricated and tested. The measurement data for percentages of volume are as follows: P_{vx} = 100%, P_{vy} = 93.08% and P_{vz} = 91.12%, respectively. This antenna can be efficiently used in RFID system at low frequency.

REFERENCES

[1] C.Mansap, P.Wounchoum, C.Phongcharoenpanich and D.Torrungrueng, "Trapezoidal dual loop antenna for Radio Frequency Identification (RFID) system at Low Frequency," *Proceedings of the 2006 Asia-Pacific Microwave Conference*, Yokohama, vol.3, pp.1478-1481, Dec.2006.

[2] G. J. Burke and A. J. Poggio. Numerical Electromag-netics Code (NEC) Method of Moment, Part I-III.Lawrence Livermore Nat. Lab., Livermore, CA, 1981.

[3] J.J. Grefenstette, "Optimization of control parameter for genetic algorithms", *IEEE Trans. on System, Man and Cybernetics*, Vol 16, No.1, July 1986, pp.122-128.

[4] S. D.Roger, "Design and realization of GA-optimized wire monopole and matching network with 20:1 bandwidth", *IEEE Trans. on Antennas and Propagation,* Vol.51, No 3, March 2003, pp.493-502.

An Implementation of a SCADA System based on Embedded TCP/IP Protocol Stack and Internet

Nguyen Ich Vinh Watit Benjapolakul Krisada Visavateeranon
Dept. of Electrical Engineering, Faculty of Engineering
Chulalongkorn University, Bangkok, Thailand
Email: vinhni82@hotmail.com, watit.b@eng.chula.ac.th

***Abstract* -- A new way of implementing SCADA systems is proposed by means of embedded TCP/IP boards and Internet. This kind of embedded boards and ADSL technology are used to integrate Internet as the communication network in the system. The public nature of Internet makes the idea obviously be a low-cost solution providing a high operation flexibility on SCADA systems. The experimental results show that the solution can work in a real-time manner and it is possible to deploy this idea in newly building or upgrading general SCADA systems.**

***Keywords:* Internet, Web-based SCADA, TCP/IP.**

I. INTRODUCTION

Supervisory Control and Data Acquisition (SCADA) systems are now becoming more and more popular in industrial processes and the demands in functionality and high performance have been increasing rapidly. Furthermore, the fast development of microprocessor manufacturing and Internet technology makes it more efficient and cost-saving to design such systems with the embedded network protocol modules.

The Internet has now been dedicating a new and highly-efficient medium for sharing information all over the world. The development of web technologies allows information to be displayed numerically and graphically on any conventional Internet browser. Via Internet browsers (or web-browsers), end users can access, monitor the real-time data and even control the field devices and equipments.

In [1] Andrew, et al. presented a remote data acquisition system for experimenting using power system's hardwares. The application software, based on the server/client module, has the task of performing the data communication over the Internet. Data Socket Server module created by National Instruments, which eliminates the difficulties of Transmission Control Protocol (TCP) programming, was used. The system is protected by password-authentication, approved Internet Protocol (IP) addresses and a physical protection scheme for the power hardwares. The research gave users the ability to monitor the data, which had been logged and saved in the server's database, in the forms of trends and tables via web-browsers. However, the real-time criterion was not mentioned in this work. Again in power system's application, Zhang Donglai, et al. [2] proposed an internet-based SCADA system. A TCP module, which is manufactured by Ubicom, namely IP2012, was used to collect necessary data and transmit those data to the Internet. This module also supports the User Datagram Protocol (UDP). However, UDP is not as reliable as TCP, and it is not preferably used in Internet-based telemetry systems. PPPoE (Point to Point Protocol over Ethernet) was employed to connect the data in the IP2012 directly to the Internet. This led to complexity in term of programming. Nevertheless, this research did not mention about the data transfer speed actually achieved and the system's security issue, though these concerns are very important.

In order to give a solution to improve the communication ability, Wei-Fu Chang, Yu-Chi Wu and Chui-Wen Chiu [3] built a model of a web-based remote load supervision and control. Programmable Logic Controllers (PLCs) were used to collect data from and give control to field devices. The server/client model was used again with two given options: first, the PLC is connected to an RS-232/TCP-IP converter for the data to be sent to the Internet, and remote users can both access the data directly via the IP address of the converter and the server's database; second, there is no converter, but the PLCs are connected to server PC and the data is stored in the server's database. The implemented system followed the second option. A Visual Basic (VB) program was developed in the client PC allowing the client users to connect to the database in the server PC. The data were both displayed on the VB screen and the web-browsers. The control commands to the loads were also issued via these two kinds of interface softwares. In a more general sense, M. Mahmud, et al. [4] used both Ethernet and Internet to build a SCADA system. Under the server/client framework, the system consists of several RTUs (Remote Terminal Units) and one SCU (SCADA Central Unit). The SCU was connected in the same Ethernet/LAN network with the RTUs. A data acquisition card was installed at each RTU to collect the data, and then these data were sent to the database at the SCU to be stored for further use. A VB program was developed in both computers at RTU side and SCU side for data monitoring and remote control. Users anywhere can also access the SCU database using web-browsers. Here, the security issue was not strictly considered in this research. The dial-up technology was used to connect the SCU to the Internet, causing a lot of problems with the speed of transferring data, since the dial-up network is quite slow. A more theoretical analysis about the advantages of utilizing Internet in SCADA applications and a comparison between Internet and other communication options was given in [5], by Robert H. McClanahan. Medida, et al. [6] presented a SCADA system based on the Internet for energy management system (EMS), using Java to make the SCADA database accessible and available to the remote Human Machine Interfaces (HMI) through web-browsers. No vendor dependent hardware, software and application are required at the remote location for SCADA but an Internet connection to gain access to the system from any corner of the world. In [7], Duo Li, et al. proposed a conceptual design for SCADA system with regards to all available Internet technologies. An implementation example was also given with Java and a web-based server application, Internet browser was used as the interface between system and users. Discussions about the security matter and some of Internet-related problems such as congestions, time constraint are given in [8-9].

In this paper, a solution to implement an Internet-based SCADA system is proposed with the presence of an embedded TCP/IP Protocol stack. The solution provides the following features:

- Automatically collect the latest data.
- Real-time data is displayed on web-browser interfaces, users can issue command controls from any internet-connected place.
- Security issue is carefully considered with: two layers of firewalls from router to server and client computers; user authentication and IP approval. This helps reduce the threat of the public nature of the Internet.
- New sites/devices can be added/deleted/tracked.
- Overall data transfer speed and time can also be tracked.

The paper is organized as follows. Section 2 depicts the general idea to build the solution. Section 3 describes the deployment scheme including hardware and software design, and initial experimental results. Discussions and conclusions are given in section 4.

II. System Architecture

The solution is built based on the client-server model with Internet being the communication network (See Fig. 1). Network programming techniques are used to develop the system's software.

- Server Tier

The server is built as a Web-based application composed of four functional modules: Real-time Data Acquisition, Active Data Objects and Remote Data Service, Device Control and Security Management.

These modules bring the ability to collect data from data acquisition part, display data on HMI softwares in real time, give control commands on devices and ensure the security of the entire system.

- Client Tier

There can be more than one client computers in the system, as long as authenticated. Client users can monitor data in real-time and issue supervisory control commands.

There are two communication methods:

1. Via Web-browsers

Authorized users can access and use the provided functions of the system through the web-based application built in server computer.

2. Via the IP addresses of the TCP/IP Protocol Stack

With IP-supported Protocol Stack, client users can interact directly with system's data and devices by a VB program.

- TCP/IP Protocol Stack

This is a special hardware embedded with a Dynamic Link Library (DLL) module. Supporting TCP/IP protocol, this module interfaces with the field device, collects data and sends these data to the Internet. It also has the tasks of receiving the control commands from the users and placing them on the field devices.

- Field Devices

These are the equipments in the real world from which the Protocol Stack collects data. They also perform the actions following the control commands from system's users.

III. Deployment Prototype

See Fig. 2. Internet is used as the communication network between server and client users; the SCADA center lies within the Ethernet LAN network with field devices.

A. Hardware Components

1. Server PC with Windows XP Service Pack (SP) 2, 3.0 GHz for CPU Speed and 1 GB for RAM Memory.
2. Client PCs with Windows XP Service Pack (SP) 2, 2.0 GHz for CPU Speed and 1 GB for RAM Memory.
3. Modem/Router.

Containing a built-in modem, the router has the task of connecting the system with one ISP (Internet Service Provider), making the system available on the Internet.

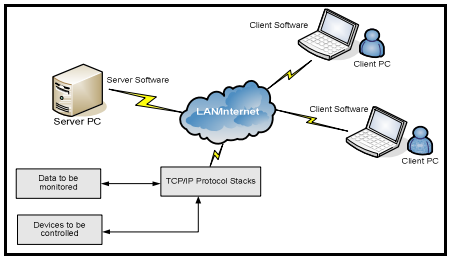

Fig. 1. General System Architecture

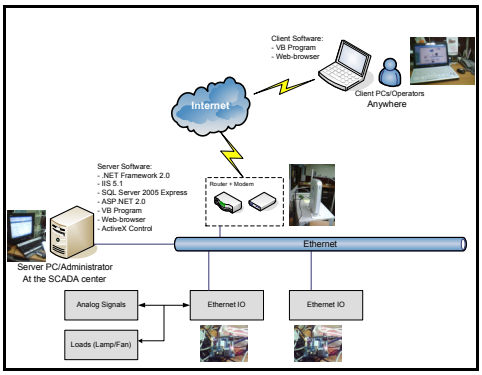

Fig. 2. Deployment Prototype Architecture

4. Ethernet IO boards.

See Fig. 3. The boards, developed by Design-Gateway with a LAN connector, are connected into the Ethernet network together with the server computer. They collect data from the field devices and transmit these data to the server. Additionally, with a network processor, the boards can support the TCP/IP protocol.

5. Field Devices

A voltage signal, which is simulated as the real-time data, will be fed to the Ethernet IO boards. Digital data or text file can also be used.

A fan and a lamp, connected to the Ethernet IO boards, are used to simulate the supervisory control function. They may receive the ON/OFF or Speed Increase/Decrease commands from the users.

B. System Software

- Data Management

The Web-based application in the server is built using the latest technologies from Microsoft, including Internet Information Service (IIS) 5.1, .NET Framework 2.0, SQL Server 2005 (MySQL is also supported), ASP.NET 2.0.

- Real-time Data Acquisition (RTDA): See Fig. 4.
- Real-time Data Viewer (RTDV): See Fig. 5.

This is an ActiveX control embedded into the Active Server Pages at server computer. It gives the ability to display the real-time data on web-browsers. Data can also be displayed on the HMI software written in VB at both server and client sides.

- Supervisory Control (See Fig. 6.)

Being integrated in the web-based application software on the server computer, this module allows placing control commands on devices. The communication is done within the Ethernet network established among the server and all the boards. Therefore, the communication is faster and more reliable.

Since more than one device can be installed in the system, the following functions can be added: devices add/remove and devices tracking by using the IP address of the Ethernet IO board to which the

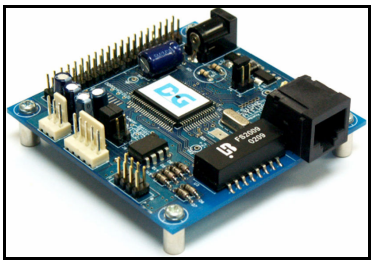

Fig. 3. Ethernet IO Board.

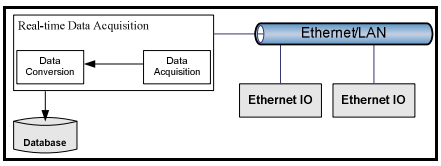

Fig. 4. RTDA Module.

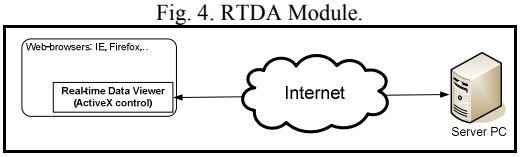

Fig. 5. RTDV Module.

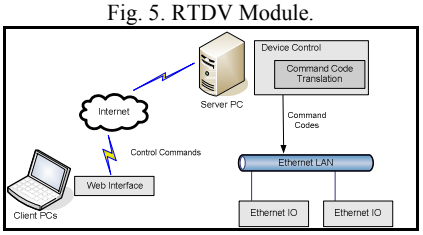

Fig. 6. Supervisory Control Module.

device is connected. A number of possible causes are given if any IP address is found missing.

Users can also use both the VB program and the web-browser to perform this function. At the client side, the communication is done over Internet.

- Security Management

There are four tools to be used: user authentication, permission distribution, IPs approval and router configuration. Two types of system operators are defined which are administrator and users. The administrator can create or delete accounts (users), pass or withdraw the right of other users. These jobs are done on web-interface, giving the administrator the ability to manage the system from any place as long as connected to the Internet. Normal users only have the right to perform actions which have been defined or distributed by the administrator. The IP approval tool is activated only when necessary, since it may reduce the flexibility of the system. A user with legal username and password may still not be able to access the system if the computer being in use does not have the IP address which is in the approval list. We can also use the router configuration page to perform the IP approval feature.

Firewalls in the router and in each computer using the system should also be turned on to prevent unwanted outsiders.

- System Performance Consideration

- The use of the IP-supported Ethernet IO boards makes it possible for the system administrator to add/remove/track the field devices. This lead to a flexible operation.
- Users can be anywhere; only an internet connection is required. This provides an easy and unlimited-range operation.
- Every necessary change to the system is done within the SCADA center, on the server PC.

Regarding the real-time issue, we have two communication stages, one is from the Ethernet IO board to the server and another is from the server to the client computer. Since the communication among the server and IO boards is in Ethernet network, the experimental results showed that we can achieve the real-time satisfactory and the data transfer speed can be up to 200 kbps. However, the communication over Internet between server and client computer may not be real-time and it depends on the Internet's traffic intensity. Nevertheless, the use of Asymmetrical Digital Subscriber Line (ADSL) technology gives a quicker access speed and we still can perform system's functions in a real-time fashion most of the time. A display of the estimated values of the data transfer speed from the IO boards to the client computer and the variance time between the server and client side are given. This brings a visual view about the performance of the system.

C. Implementation Results

Throughout the paper, we can see there are two ways to build the system software by using a VB program and using web-based software tools. Fig. 7 is a simple VB program used to connect to the IO boards directly over Internet and to do some testing experiments. Login step is illustrated in Fig. 8. After successful login, user can enter the overall web-based interface with the entire system, see Fig. 10. From here, user can perform the full system's features as mentioned.

The real-time data display functions are depicted in Fig. 11. Here, approximated numbers describing the data transfer speed and time between server and client side are also given. Fig. 9 describes the possible actions users can place on attached devices. Experimental system allows users to turn on/off a lamp, turn on/off as well as change the speed of a motor/fan.

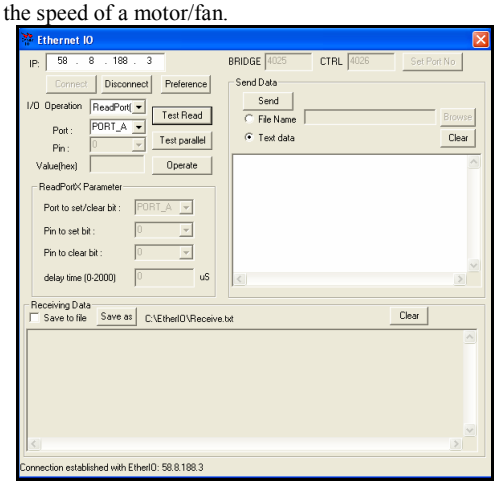

Fig. 7. Operation on Ethernet IO board over Internet using VB.

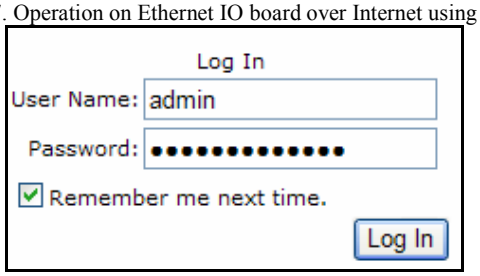

Fig. 8. Login Screen.

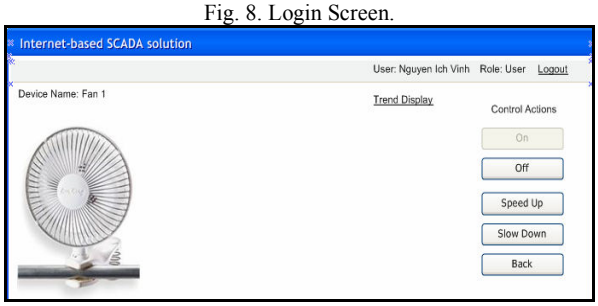

Fig. 9. Control Actions

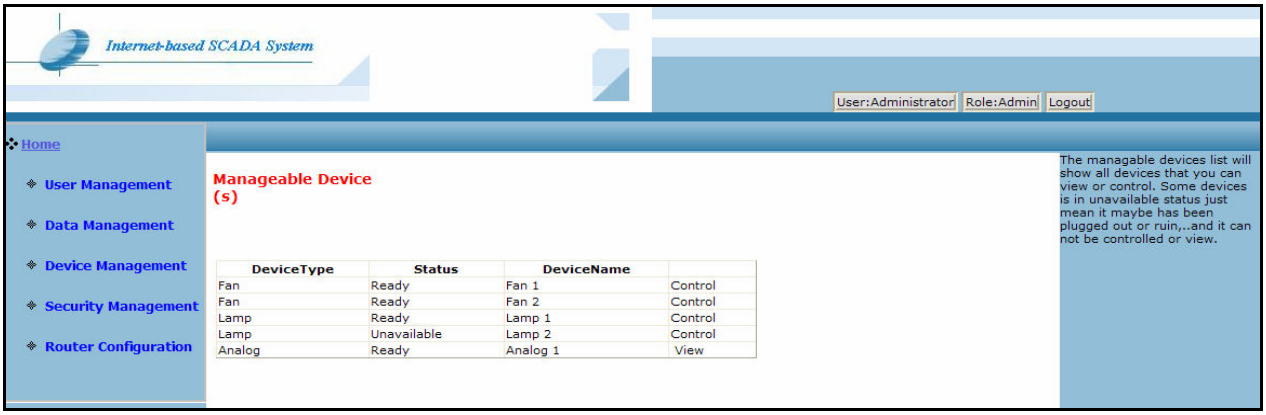

Fig. 10. Overall Web-based Interface

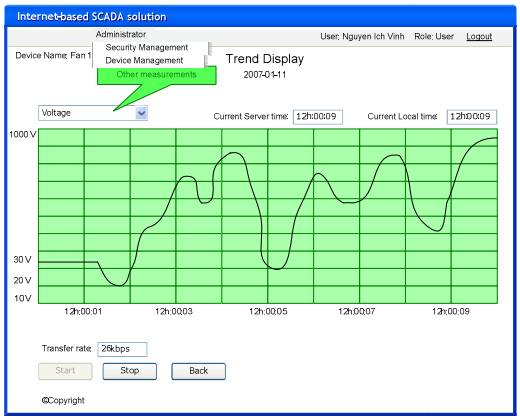

Fig.11. Real-time Data Display

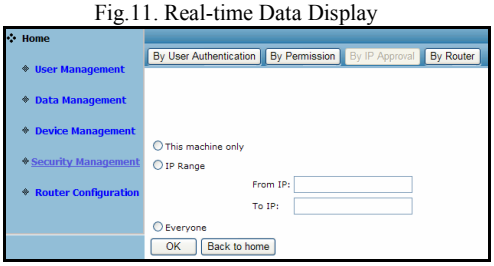

Fig. 12. Security Management by IP Approval.

See Fig. 12 for security management by IP approval. Other tools can be accessed by clicking the next tabs.

The web-based interface is friendly and easy-to-use. Information about how to perform each system's feature is also provided on the right column accordingly. Users can use this information for more appropriate actions.

IV. Conclusions

It is now becoming more and more visible and desirable for the ability to monitor data and even to place control commands on devices in a real-time manner with Internet used as the communication network. In this paper, an implementation of SCADA systems with real-time data monitoring, device control and security features has been presented. The proposed system was built on a web-based solution with IIS, ActiveX control and ASP programming; a VB program was also used as a testing tool and as optional HMI software. First experimental results showed that we can achieve the system's features as stated. Users, as long as stay connected to Internet, can monitor system's data in a real-time fashion and perform control actions on system's devices. The security issue has also been considered carefully. The presented solution is low-cost and easy to implement, while it still provides a high flexibility feature by using the IP-supported hardware components. With the development of hardware devices and Internet-based software technologies, this solution promises to give a more and more stable and reliable method in upgrading or newly building SCADA systems for various industries. The solution proposed in this research is most suitable for such applications as Fuel Unloading/storage and Feed, Water Supply Monitoring, Irrigation, Flood Warning, Oil and Gas Tracking.

Further study on this research can be based on other web technologies such as Java or Ajax to provide a more interactive operating environment in the system. A web camera server can also be added at the device or process places to provide a visual image of the devices' reactions for better system's performance evaluation.

Acknowledgement

Financial support from the AUN/SEED-Net JICA project for this presented research is greatly acknowledged.

A great thank is sent to Mr. Dao Quang Minh, who is an IT expert, for his significant advices on IT-related matters in the research.

References

[1] A. Golder, K. Miu, C. Nwankpa, S. Carullo, "Remote Hardware Power System Loading Studies over the World Wide Web". Power Symposium. 2005. Proceedings of the 37th Annual North American. p. 9-15.

[2] Z. Donglai, F. Hong, W. Chao, Z. Ying, "Low Cost and High Performance Power System Telemetry Data Transmission System based on Embedded Ethernet and ADSL". IEEE Transmission and Distribution Conf. and Ex. 2005. p. 1-5.

[3] W. Chang, Y. Wu, C. Chiu, "Development of a Web-based Remote Load Supervision and Control System". Electrical Power and Energy Systems 28. 2006. 401-407, 2006 Elsevier Ltd.

[4] M. Mahmud, M. R. Karim, M. M. Islam, K. M. Rahman, "Supervisory Control and Data Acquisition (SCADA) through Internet". Second Int/ Conf on Electrical and Computer Engineering ICECE 2002, Dhaka, Bangladesh.

[5] R. McClanahan. "The Benefits of Networked SCADA Systems Utilizing IP-Enabled Networks". IEEE Rural Electric Power Conf. 2002. p. C5-7.

[6] S. Medida, Sreekumar N, K. V Prasad, "SCADA-EMS on the Internet". Energy Management and Power Delivery Conf. 1998. vol. 2. p. 656-60.

[7] D. Li, Y. Serizawa, M. Kiuchi, "Concept Design for a Web-based Supervisory Control and Data Acquisition (SCADA) System". IEEE Transmission and Distribution Conf. and Ex. 2002. vol. 1. p. 32-36.

[8] J. Pollet, "Developing a Solid SCADA Security Strategy". Sicon/02_Sensors for Industry Conf. USA. 19-21 Nov. 2002.

[9] C. Labovitz, A. Ahuja, A. Bose, F Jahanian, "Delayed Internet Routing Convergence". IEEE/ACM Transactions on Networking. 2001. Vol. 9. No. 3.

Channel Modeling and Simulated for Broadband Satellite

Ekavit Nukfron* Narong Hemmakorn** Suviporn Sitichepak**

*School of Graduate King Mongkut's Institute of Technology Ladkrabang Bangkok Thailand
Email:E_nukfron@hotmail.com
**Departments of Telecommunication Engineering, Faculty of Engineering
King Mongkut's Institute of Technology Ladkrabang Bangkok Thailand

Abstract

This paper presented the effects of attenuation from rain rate together with rain drop size distribution analysis on the model of transmitter broadband satellite in Ka-band frequency. We illustrated a new model by simulating transmission broadband signal and studied the rain attenuation which has effects to high frequency. The results of the model were represented by the relation between error probability and S/N. Moreover, the numbers of re-transmission cycles for completing the amount of data were also presented. The attenuation would be illustrated in log normal distribution forms and in PDF terms. The simulation would be run by taking error probability (Pe) of noise at 0.4, 0.04, 0.004 and 0.004.

Keywords : Ka-band, broadband satellite

I. INTRODUCTION

The rapid growth of telecommunication services, both in satellite and terrestrial links using higher frequency bands above 10 GHz has highlighted the need for estimating the effects of hydrometer such as rain, clouds, fog and gangues. The demand of ultra wide bandwidth for high speed, high quality, and multimedia transmission was driving the use of the higher radio frequency spectrum. However, attenuation and fading due to rain have long been recognized as a major limitation to reliable communication systems operating at higher frequencies. The presence of hydrometer in radio wave propagation, particularly rain, can produce major impairments to microwave propagation. Raindrops can be absorbed and scattering radio wave energy in signal attenuation, which can degrade the reliability and performance of the communication links. Rain attenuation can be obtained through measurement or predicted from knowledge of rain rate and drop size distribution. The modeling of the rain drop size distribution in temperature and tropical region is different. It is because tropical region has experiences heavy rain rate compared to temperature region.

Rain-induced attenuation on satellite earth communication links at frequency above 10 GHz is the predominant signal impairments. However, for the design of law margin systems, especially those at high frequency and low elevation angles, scintillation effects must be accounted for to complete a link budgets accurately. With an increased demand for direct-to-user satellite services, Ka-band has become a preferred alternative for many new systems as it offers a large bandwidth needed to support the anticipated need for capacity. While offering a solution to the problem of spectrum congression, Ka-band suffers from fading due to rain. Fade depths of dBs are commonly caused by rain. However, the ITU-R has mentioned that the attenuation in Ka-band is more than in C/Ku-Band and sensitive to location.

Chi and Chen[1] studied effect of rain fading of Ka-band for Taiwan and analyzed new model for LMDS. The results compared signal between measured and simulated in BER and S/N. Filip and Vilar[2] studied effect to channel capacity of satellite link which have effect amplitude scintillation and rain attenuation for optimal utilization. Paraboni, Masini and Eila[3] have found new model for analysis attenuation in high frequency. After that Germont and Filip[4] have brought Paraboni, Masini and Eila's model to analysis and to predict fade detection and also Germont and Filip[4] prove fading terms BER and S/N. Otherwise, M.Aloini, A.Borgsmiller and G.Steffes[5] presented many factors effect to Ka-band and create another model for high performance in the system. This paper presented the analysis of rain attenuation from rain rate and drop size distribution. The research was similar to A.Maitra[6] and Sekine,Chen and Musha[7] but considered in different frequency.

This paper presented new model for analysis broadband satellite at frequency Ka-band (30/20) GHz and the effect of the model was in the high value attenuation. The noise had log normal distribution forms The rain attenuation in Ka-band are described in section 2. In section 3, new model consider in new analysis. Analytical model was illustrated the relation between error probabilities versus S/N in binary bits and re-transmission for completing the data in section 4 and finally conclusion in section 5

II. RAIN ATTENUATION IN Ka-BAND

The capacity of white noise (AWGN) is given by Shannon's Expression method [8] by

$$C = BLog_2\left(1+\frac{S}{N}\right) \quad \text{(b/s)} \qquad (1)$$

B is the channel bandwidth in hertz and S/N is signal-to-noise power ratio for the channel in order to make the

analysis independence for the actual bandwidth of the channel can be written as

$$\frac{C}{B} = Log_2\left(1+\frac{S}{N}\right) \quad \text{(b/s)/Hz} \tag{2}$$

Where C/B represents the channel capacity due to propagation fading, the term S/N in (2) is random with un arbitrary but defines distribution depending on the type and characteristics of the fading process considered, the channel capacity is also random. The random variable of the channel capacity imposes performance degradation on the system that utilizes the channel. Therefore, one many wish to determine the probability density function (PDF) and cumulative (CDF) of the channel knowing those of S/N on equivalently, those of the fading process. The standard transformation of random variable, the PDF of C/B can be written in term of S/N. The rain attenuation reflected the signal to noise ratio level detailed in [2], [3] and [9]

$$\left(\frac{S}{N}\right) = \left[\frac{S}{N}\right]_0 - A \quad \text{(dBw)} \tag{3}$$

$\left[\frac{S}{N}\right]_0$ is signal to noise ratio level (dB) in clear condition

A is Attenuation from rain in satellite link

The CDF of the channel capacity is given by

$$F_{\frac{C}{B}}(Y) = F_{\frac{C}{A}}(X) = \Pr ob\left\{\frac{C}{B}\langle Y\right\} = \Pr ob\left\{\frac{S}{N}\langle f^{-1}(y)\right\} \tag{4}$$

$$= \Pr ob\left\{A\rangle\left(\frac{S}{N}\right)_O - f^{-1}(y)\right\} \tag{5}$$

$$= F_{\frac{C}{A}}\left[\left(\frac{S}{N}\right)_O - f^{-1}(y)\right] \tag{6}$$

if $y = \frac{C}{B}$

$$f^{-1}(y) = 10Log(2^y - 1) \tag{7}$$

so that

$$F_{\frac{C}{X}}(X) = P\{A\rangle X\} = \int_X^\alpha P_A(a)da \tag{8}$$

$$\text{X} = \left(\frac{S}{N}\right)_O - 10Log(2^y - 1) \tag{9}$$

A is approximately log normal distribution random variable. Therefore, the overall long-term distribution PDF of rain attenuation along the link has the term [10]

$$P_A = \begin{cases} \frac{1}{a\delta\sqrt{2\pi}}.\exp\left\{-\frac{(\ln a-\mu)^2}{2\delta^2}\right\} & a\rangle 0 \\ 0 & a\langle 0 \end{cases} \tag{10}$$

Where the term mean and standard variation will be discussed in later. We can expressed as

$$F_{\frac{C}{B}}(Y) = F_{\frac{C}{A}}(X) = \int_x^\alpha P_A da = Q\left(\frac{\ln x-\mu}{\delta}\right) \tag{11}$$

So that

$$Q = \int_\varphi^\alpha \left(1/\sqrt{2\pi}\right)e^{\frac{-t^2}{2}}.dt$$

For the log normal distribution, we have

$$P = F(\ln A) = \int \frac{1}{\delta\sqrt{2\pi}}.\exp\left[-\frac{(x-\mu)^2}{2\delta^2}\right].dx = Q\left(\frac{\ln A-\mu}{\delta}\right) \tag{12}$$

and

$$\frac{\ln A-\mu}{\delta} = Q^{-1}(P) = \alpha\ln A+\beta \tag{13}$$

$$\mu = \frac{-\beta}{\delta} \tag{14}$$

$$\delta = \frac{1}{\delta} \tag{15}$$

Equation (14) and (15) are mean and standard deviation respectively. They can be find by linear regression, where the slop δ and intercept β. From equation (12) we can get A (attenuation due to rain). This paper considered rain attenuation from rain drop size distribution and the specific attenuation A in dB/km due to rain is calculated by integrating over all of the drop size as

$$A = 4.343\int Q(D,\lambda,m)N(D)dD \tag{16}$$

Q is the attenuation cross section which is a function of the drop diameter D, the wavelength of the radio wave λ and the complex refractive index of the water drop m, which is a function of the function and temperature, and N(D) is the drop size distribution. The attenuation cross section Q is found by applying the classical scattering theory of Mie's for a plane wave impinging upon a spherical absorbing particle. By N(D) for Gamma distribution can be written

$$N(D) = N_T A^{n+1}D^n \exp\left[-\text{AD}/\Gamma(n+1)\right] \ (m^{-3}.mm^{-1}) \tag{17}$$

N(D) for Log normal distribution can be written

$$N(D) = \frac{N_T}{\sigma D\sqrt{2\pi}}.\exp\left[-\frac{1}{2}\left(\frac{\ln(D)-\mu^2}{\sigma}\right)\right] \ (m^{-3}.mm^{-1}) \tag{18}$$

Consider in Log normal distribution terms and froms (12)

$$P = F(\ln A) = \int_{\ln A}^\alpha \frac{1}{\delta\sqrt{2\pi}}.\exp\left[\frac{-\left(x-\mu^2\right)}{2\delta^2}\right].dx = Q\left(\frac{\ln A-\mu}{\delta}\right)$$

And (16), (18) -- [6], [7], [11]

$$A = 4.343\int Q(D,\lambda,m).N(D)dD$$

The cross section Q is expended as

$$Q(D,\lambda,m) = \frac{\lambda^2}{2\pi}.\sum_{n=1}^{\alpha}(2n+1)\,\mathrm{Re}[a_n + b_n]$$

$$A = (4.343)\left(\frac{\lambda^2}{2\pi}\right).\sum_{n=1}^{\alpha}(2n+1)\,\mathrm{Re}[a_n + b_n].\frac{N_T}{\sigma D\sqrt{2\pi}}.\exp\left[-\frac{1}{2}\left(\frac{\ln D - \mu^2}{\delta}\right)\right] \quad (19)$$

Where a_n and b_n are the Mie scattering coefficients and analysis in Bessel function [13], [14], which are complex function of m, D and λ. In equation(19), *A* is rain attenuation analysis in rain drop size distribution having log normal distribution term. We can be find N(D) for log normal distribution[7] and written as.

$$N(D) = \frac{N_T}{D(2\pi)^{\frac{1}{2}}\ln\sigma}.e^{-\left[\ln\left(\frac{D}{D_M}\right)/2\ln\sigma\right]^2}$$

Case 1 (Showers) $5\langle R\langle 50mm/hr$

$$N_T = 40R^{0.64}$$

$$D_M = 1.14 + 0.18\ln R$$

$$\sigma = e^{0.29-0.001R}$$

Case 2 (Showers) $5\langle R\langle 50mm/hr$

$$N_T = 46R^{0.55}$$

$$D_M = 0.222 + 0.397\ln R$$

$$\sigma = e^{0.5--.0035R}$$

Case 3 (Thunderstorms) $50\langle R\langle 200mm/hr$

$$N_T = 8.8^R$$

$$D_M = 1.76 + (7.33*10^{-4}).\ln R$$

$$\sigma = 1.37$$

III. MODELING CONSIDERATIONS

We designed the model for considering and simulating the generation of the random variables r_o and r_1 which constitute the input to the detector. The research has begun by generating a binary sequence of 0 and 1 that occur with equal probability and being mutually statistically independent. To accomplish this task, the random number generator was used to generate a uniform random number in range (0,1). If the generated number is in the range (0,0.5), the binary is 0. Otherwise, it is a 1. Additive noise components n_0 and n_1 are taken in equation (12) and (19), we analysis in rain rate is 50mm/hr and diameter of rain is 10mm. From [15]

$$\gamma_r = kR^{\alpha} \quad (20)$$

and

$$A = a_n R^{b_n} \quad (21)$$

From CCIR recommendation at 20GHz

$$a_n = K_H = 0.0751 \text{ (Horizontal Polarization)}$$
$$a_n = K_V = 0.0691 \text{ (Vertical Polarization)}$$

and

$$b_n = \alpha_H = 1.099 \text{ (Horizontal Polarization)}$$
$$b_n = \alpha_V = 1.065 \text{ (Vertical Polarization)}$$

Take value in (19), attenuation (*A*) was found from rain with rain rate at 50mm/hr and diameter of rain at 10 mm

Case 1 (Showers) $5\langle R\langle 50mm/hr$

A=-3.7369 dB/km

Case 2 (Showers) $5\langle R\langle 50mm/hr$

A=-3.186 dB/km

Case 3 (Thunderstorms) $50\langle R\langle 200mm/hr$

A=-3.4852 dB/km

The mean and standard deviation in PDF can be found from

$$\ddot{A} = \alpha R^{\beta}$$

and

$$\frac{\ln A - \mu}{\delta} = \delta\ln A + \beta$$

that

$$\mu = \frac{\beta}{\alpha} \qquad \delta = \frac{1}{\delta}$$

Horizontal Polarization has

$$\mu = \frac{\beta}{\delta} = \frac{1.099}{0.0751} = 14.633821$$

$$\delta = \frac{1}{\delta} = \frac{1}{0.0751} = 13.31557927$$

Vertical Polarization has

$$\mu = \frac{\beta}{\delta} = \frac{1.065}{0.069} = 15.4347826$$

$$\delta = \frac{1}{\delta} = \frac{1}{0.069} = 14.4927536$$

From $P = F(\ln A) = Q\left(\frac{\ln A - \mu}{\delta}\right)$, the PDF terms is in log normal distribution

IV. RESULT FROM SIMULATED

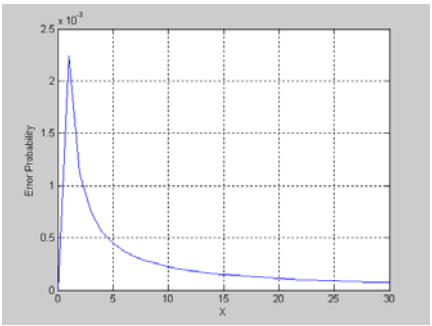

Figure 1 Simulation PDF rain attenuation

Figure 1 was the noise signal which was log normal distribution format. It was considered by using rain rate at 50 mm/hr and rain diameter at 10 mm. The noise was dope into the channel model ($P = F(\ln A) = Q\left(\frac{\ln A - \mu}{\delta}\right)$) by using different error probability (Pe).

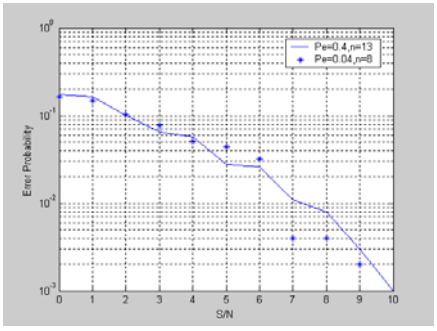

Figure 2 Illustrate Probability and S/N
Pe (0.4and 0.04)

The result from taking noise with error probability (Pe) at 0.4 and 0.04 was illustrated in figure 2. The system with Pe(0.4) needed to re-transmit data totally 13 times comparing to 8 times from Pe(0.04). In addition, the output error probability around the lower zone of S/N (0.1-4 dB) was not much different between Pe(0.4) and Pe(0.04). When the S/N got higher (more than 5 dB), the output error probability from Pe(0.4) was tentatively lower than Pe(0.04)

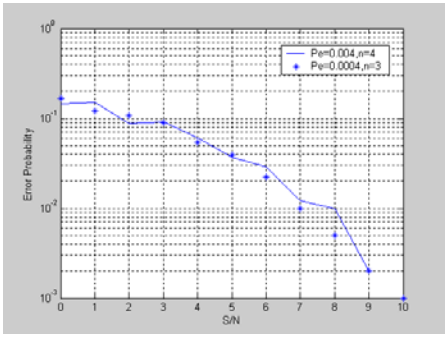

Figure 3 Illustrate Probability and S/N
Pe (0.04and 0.004)

Figure 3 was illustrated the result from taking noise with error probability (Pe) at 0.004 and 0.0004. The system with Pe(0.004) and Pe(0.0004) required data re-transmission wholly 4 and 3 times respectively. For the relation between error probability and S/N of the system by taking Pe(0.004) and Pe(0.0004), there was likely similar.

CONCLUSION

In this paper, the Ka-band transmission system was newly modeled by analyzing error probability from considering the noise from rain drop size and the high-value attenuation from rain. The results were shown in relation between error probability and S/N (in binary bits). Determinately, the higher the error probability was taken to the system, the more the re-transmissions were required by system. In conclusion, the rain rate and rain drop size destroyed the quality of Ka-band transmission channel.

ACKNOWLEDMENT

This research was financially supported by University of the Thai Chamber of Commerce (UTCC) Bangkok, THAILAND.

REFERENCE

[1] Chih-Yuan Chu and K.S.Chen. “Effects of Rain Fading on the Efficiency of the Ka-band LMDS System in the Taiwan Area” IEEE Transactions on vehicular Technology, Vol.54,No.1,January, 2005
[2] Miodrag Filip and Enric Vilar “Optimum Utilization of the Channel Capacity of a Satellite Link in the Presence of Amplitude Scintillation and Rain Attenuation”
IEEE Transactions on Communications,Vol.38 .No11 November,1990
[3].Paraboni,G.Masini amd A.Elia “The effect of precipitation on microwave LMDS networks-performance analysis using a physics raincell model” IEEE Journal on Selected Areas in Communications ,Vol .20,No3,March 2002
[4] Boris Gremont, Miodrag Filip,Paul Gallois and Stephen Bate “Comparative Analysis and Performance of Two Predictive Fade Detection Schemes for Ka-Band Fade Countermeasures” IEEE Journal on Selected Areas in Communications ,Vol .17,No2,February 1999
[5] Mohamed-Slim Alouini,Scott A.Borgsmiller and Paul G.Steffes “Channel Characterization and Modeling for Ka-Band Very Small Aperture Terminals” Proceedings of The IEEE,Vol.85.,No 6,June 1997
[6] A.Maitra “Three-Parameter Rain Drop Size Distribution Modeling at Tropical Location” Electronics Letters 11th May 2000, Vol36,No10
[7] Matsuo Sekine,Chii-Dong Chen and Toshimitsu Musha “ Rain Attenuation from Log-Normal and Weibull Rain Drop Size Distributions”
IEEE Transactions on Antenna and Propagation,Vol AP-35,No3,March 1987
[8] V.K.Bhargava,D.Haccoun,R.Matayas and P.P.Nuspl, Digital Communications by Satellite :Modulation, Multiple Access and Coding. New York: Wiley,1981
[9]. G.Hendrantoros,R.J.C. Bultitude and D.D.Falconer “Use of cell-site diversity in millimeter-wave fixed cellular systems to combat the effects of rain attenuation” IEEE Journal on Selected Areas in Communications ,Vol .20,No3,March 2002
[10]. K.Karimi and H.Helmken. “A study of satellite channel utilization in the presence of rain attenuation in Florida” Proceedings IEEE South-eastcon’94 Creative Technology Transfer –A global Affair,1994,pp196-200
[11] M.A.Awang and J.Din “ Comparison of the Rain Drop Size Distribution Model in Tropical Zone” 2004 RF and Microwave Conference, October 2004
[12] Dusan Cermak,Onderj Fiser and Vladiimir Schejbal “Electromagnetic Scattering by rain drops” Cost 280
[13] Craig F.Borhren,Absorption and Scattering of Light by Small Particles, John Wiley & Sons ,Inc 1983
[14]D.Barnet
www. lboro.ac.uk/departments/el/research/optics/matmie/mfiles.html
[15] ITU-R Recommendation 838 P-series “Specific Attenuation Model for Rain for Use in Prediction Methods”

Ekavit Nukfron was born in Thailand in 1976. He received the Bachelor’s degree on telecommunications engineering from Mahanakorn University (MUT) in 1997 and received M.Eng. (Telecommunications) from King Mongkut’s Institute of Technology Ladkrabang (KMITL) in 2000. Now he is a Ph.D candidate in Telecommunication (KMITL) with the main research area in wave propagation and broadband satellite. He is also a lecturer in the faculty of science, University of the Thai chamber of Commerce (UTCC).

Ionospheric Variability of foF2 at low latitude station, Thailand

N. Wichaipanich, R. Attaviriyasuwon, N. Hemmakorn, and P. Supnithi
Faculty of Engineering and Research Center for Communications and Information Technology
King Mongkut's Institute of Technology Ladkrabang, Bangkok, Thailand
E-mail: s8060913@kmitl.ac.th, s6064123@kmitl.ac.th, khnarong@kmitl.ac.th, ksupornc@kmitl.ac.th

***Abstract* - In this paper, we study the variability of critical frequency (foF2) in F2-layer of the ionosphere. The foF2 data are obtained from the ionosonde at Chumphon campus of King Mongkut's Institute of Technology Ladkrabang (latitude 10.72°N and longitude 99.37°E), Thailand. The measurement data in 2004 and 2006 are analyzed diurnally and seasonally and compared with solar activity. The data established are proposed as equatorial input values used in the model development of the International Reference Ionosphere (IRI).**

Keywords: Equatorial Ionosphere, Ionospheric Variability, Ionogram, Critical Frequency

I. INTRODUCTION

The ionosphere is the ionized region in the earth's atmosphere extending from about 50-2000 km above the earth surface, containing the oxygen which ionizes resulting into free electrons and ions. The ionization level differs depending on the time and height of ionosphere. The F2 region of the ionosphere is the most effective layer for long distance high frequency (HF) radio communication as it is above other layers where the signals reflect. The F2 layer is the high altitude layer that has the most irregularity of electron density, which also severely affects to satellite signal using VHF and UHF bands. Accurate characteristics of the F2 layer are important to atmosphere understanding and design of HF, VHF and UHF communication systems. The knowledge of the critical frequency of (foF2) layer is essential in the range of usable HF frequencies and implication in atmospheric study. The critical frequency is usually given in terms of average value. This parameter is taken into consideration of the effect of time of the day, seasons, solar cycle and the coordinate location of the station on the surface of the earth. Even though the HF radio system is well studied and the F2 layer characteristics have been measured and compiled in many catalogs, continuous data collection is essential responding to continually changing atmospheric conditions and emerging digital HF radio systems.

Many results on ionospheric variability have been published in the literature. In [1], the ionospheric variability using hourly values data of different characteristics from nine ionospheric stations in the Northern hemisphere for one year of high solar activity is presented. In [2], the variability of foF2 at low and mid-latitude, obtained from 14 locations, is analyzed using the reduced standard deviation (r.s.d) technique. The monthly foF2 data are shown to depend on hours, seasons and solar cycle phase. Hourly foF2 data during 1967-89 are examined to quantify F-region ionospheric variability in [3]. In addition, variabilities from day-to-day and hour-to-hour of the ionospheric characteristics are done in. Ezquer et al. [4] presented the variability of the critical frequency and propagation factor M(30000)F2 observed at Tucuman in Argentina. The data are analyzed for different seasonal conditions and two levels of solar activity: low and high [5]. The deviation of hourly values of foF2 from the monthly median values is used to study the variability of foF2 for the period of high and low solar activity in [6]. Zhang et al. presented the ionospheric characteristic parameters to obtain from ionograms record by the DPS-4 digisonde at Hainan, China and analyzed the diurnal and seasonal behavior of the ionosphere variability [7]. Bilitza et al. presented the monthly variability of foF2; data from two equatorial stations in the African longitude sector are used to analyze variation diurnal, seasonal and solar activity effects [8]. A quantitative study on ionosphere variability is necessary for developing such a model for the International Reference Ionosphere. Recently, the observation of ionospheric variability in Thailand is conducted to analyze the ionospheric height changes [9] and the spread F phenomenon of the ionosphere [10]. Despite many studies of foF2 in many parts of the world and a few studies of ionospheric conditions in Thailand [9-10], the observation of the ionospheric variability of foF2 in Thailand is scarce.

In this paper, we study on the ionopheric variability of foF2 using data from bottomside ionograms recorded by the ionosonde at Chumphon campus of King Mongkut's Institute of Technology Ladkrabang (KMITL), Thailand, located near the magnetic equator. The measurement data in 2004 and 2006 are analyzed based on the diurnal, seasonal period and solar activity**.** The ionosonde technique is described in Section II and then the ionogram is explained in Section III. The experiment setup and measurement method is described in Section IV followed by Results and Discussions in Section V. Finally, in Section VI, the conclusions are made.

II. IONOSONDE TECHNIQUE

One of the traditional techniques used to monitor ionosphere is the ionosonde (or ionopheric sounder). This technique is still widely used today. The ionosonde is special radar that sweeps the shortwave band frequencies; it transmits

pulsed radio wave into the ionosphere and receives an echo in return [11]. The delay time is computed by multiplying the speed of light with the value of one-half the echo (propagation time up to the point of reflection) as the apparent altitude of reflection (h'(F)), then h'(F) will be higher than the actual altitude of reflection h(F); this value depends on the sounding frequency and the electron density distribution up to the point of reflection.

III. IONOGRAM

Ionogram is a photographic display of echo strength as a function of transmitted frequency produced by a sweep-frequency ionosonde [11]. In the frequency of sweep of the ionosonde, as the frequency of the pulsed radio wave is increased step-by-step, the echo returns from sequentially higher altitudes, where electron density is higher. By using observation technique, the echo is returned at an altitude below where maximum electron density. The maximum frequency with echo corresponding to the maximum electron density is referred as a critical frequency. Any pulse signals with frequency exceeding critical frequency will penetrate the ionosphere. Ionogram is used to infer the structure of the ionospheric layers and, hence, to predict radio transmission concentration.

The delay time of the echo pulse is illustrated as apparent height (h') versus frequency (f) with the ionogram shown in Fig. 1. The figure shows the apparent height in the F layer (h'F) and the critical frequencies in the F2 layer for ordinary waves (foF2) and extraordinary waves (fxF2) , by extra-ordinary frequency waves higher than ordinary waves. We also read the ionogram trace directly to obtain minimum value for apparent height of the F2 layer, the critical frequencies. Minimum apparent heights for the daytime F1 layer and E regions. Since electron densities are low in the D region and ionosonde cannot be used for detecting echoes.

The ionogram measurement is divided into topside and bottomside ionograms [11]. In this paper, we use bottomside ionogram. A major difference between topside and bottomside sounding is that the sounding pulse transmits from a point, where an electron density level already exists in the topside sounding, whereas for bottomside sounding, the pulse is transmitted from ground level, where the electron density is zero. In Fig. 2, the idealized topside and bottomside ionograms are shown. The ionograms vary greatly in appearance depending on several factors such as geographic locations, sunspot numbers, seasons, local time and degrees of noise.

IV. EXPERIMENTAL SETUP

The parameters used to study variability of critical frequency (foF2) of ionosphere are shown in Table 1. The data were collected from the ionosonde station located at Latitude 10.72°N, Longitude 99.37°E and magnetic latitude 3.22° at the Chumphon campus of King Mongkut's Institute of Technology Ladkrabang (KMITL), Thailand. The ionosonde station is near the magnetic equator. The ionosonde continuously transmits radio waves from 2 to 30 MHz for each round with transmission starts from 2 MHz and increases the frequency with an increment of 100 KHz s^{-1} up to 30 MHz The echoes from the ionosphere provide the bottom plasma density profile every 5 minutes. The sampled data interval is 15 minutes.

The analysis is done on hourly and yearly bases. The data analyzed in 2004 and 2006 are compared with moderate and low solar activities, respectively. Seasonal effects were investigated by using data (combining the hourly values of foF2 for all days of the months) from three months for each season: March Equinox (February, March, April), June Solstice (May, June, July), September Equinox (August, September, October) and December Solstice (November, December, January). We select years with comparable solar activities. Table 2 lists the years selected from the Chumphon station and average annual sunspot numbers.

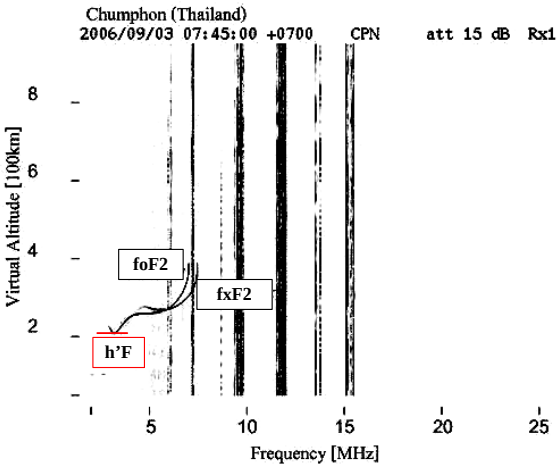

Fig. 1. Ionogram recorded at Chumphon.

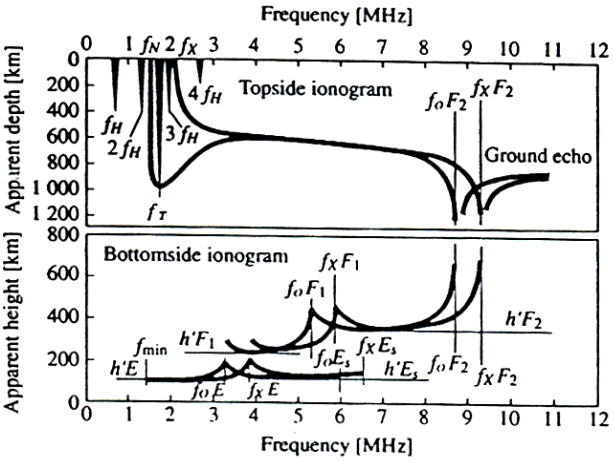

Fig. 2. Topside and bottomside ionograms.

Following the example of [3], [8] and others, we use the monthly mean of foF2 (μ) and standard deviation (σ) to evaluate the monthly variability as seen in the ionosonde data. Therefore, the relative standard deviation **VR** is given by:

$$VR\left[\%\right] = \left(\sigma/\mu\right) * 100 \qquad (1)$$

TABLE I
OBSERVATION PARAMETER OF IONOSONDE AT CHUMPHON

System	Frequency Modurated-Continuous Wave (FM-CW) With pseudo-random Tx/Rx switching
Peak Tx Power	20 W
Average Tx Power	10 W
Frequency Range	2-30 MHz
Sweep Rate	100 kHz s^{-1}
Sweep Repetition Period	5 min
Antenna	height 27 m, Folded dipole

TABLE II
DATA-YEARS USED IN THIS STUDY AND THEIR AVERAGE SUNSPOT NUMBER

Solar activity	Low	Moderate
Chumphon	2006 (Rz = 15.2)	2004 (Rz = 40.44)

The hourly values are representative of the monthly-hourly averages for the day of month. These monthly averages are used to compute the seasonal averages. On other hand, it is a good measure for describing the average deviation from monthly averages, but it is more difficult to interpret in terms of probability. The probability of the foF2 values falling between $\pm\sigma$ centered around μ is obtained for each hour in each seasons of the years under investigation.

V. MEASUREMENT RESULTS

Figure 3-4 show the diurnal variation patterns of the relative standard deviation (VR) of foF2 observed at Chumphon, Thailand, respectively. Each plot shows the variation of local time for four seasons. Generally, the average diurnal of VR follows the same trend at all solar activity levels. Variability is lowest during daytime (6-15%), and increases during nighttime (15-60%) and reaches highest values during sunrise (30-60%) with a second peak during sunset (15-30%). The variability percentage is evident during nighttime, resulting from the lower monthly mean μ , The lower values of μ during nighttime causes recombination of electron density, This reverse relation is also found during daytime, the variability percentage changes during daytime is due to higher values of μ and causes ionization of electron density.. Therefore, the peaks at sunrise and sunset are the results of the onset and turnoff of solar ionization.

Considering the variation for each seasons of all solar activities of Chumphon data, we find the June solstice values in the afternoon section is higher than data for other seasons, resulting in the lowest foF2 data in the afternoon. Seasonal effects in the Chumphon data are most likely a result of seasonal changes in the buildup of the equator anomaly crests.

The diurnal variation pattern of the relative standard deviation averaged over the whole year for low and moderate solar activity is shown in Fig. 5. The average diurnal of VR follows the same trend at all solar activity levels. The variability percentage for the year 2004 is lower than the year 2006, because in 2004 has solar activity values higher than year 2006, while the foF2 data in 2004 are higher than that in 2006. Therefore, the variability percentage in 2004 lower than year 2006.

Figure 6 show comparisons diurnal foF2 data of in 2004 and 2006 with moderate and low solar cycle, respectively. Generally, the average diurnal of foF2 follows the same trend at all solar activity levels, the foF2 values increase during sunrise, decrease during sunset, and increase during sunrise again. The foF2 values in 2006 are less than those in 2004, because of solar activity is higher in 2004. The results of the percentage variability of foF2 decrease during daytime and increase during nighttime, which is the most irregularity of electron density in the ionosphere as a result of the most irregularity of percentage variability in nighttime.

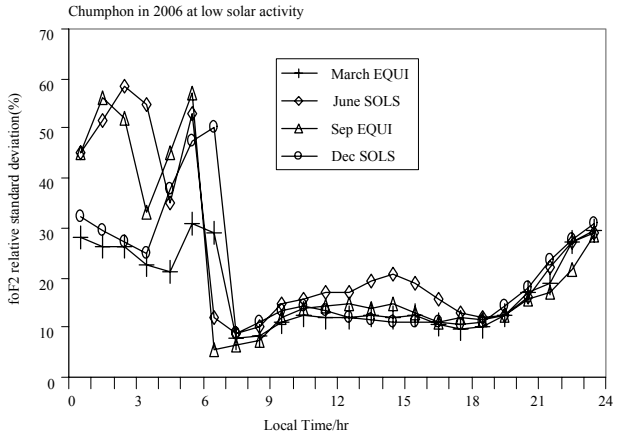

Fig. 3. Diurnal variation of the relative standard deviation for all season and low solar activity for Chumphon (2006).

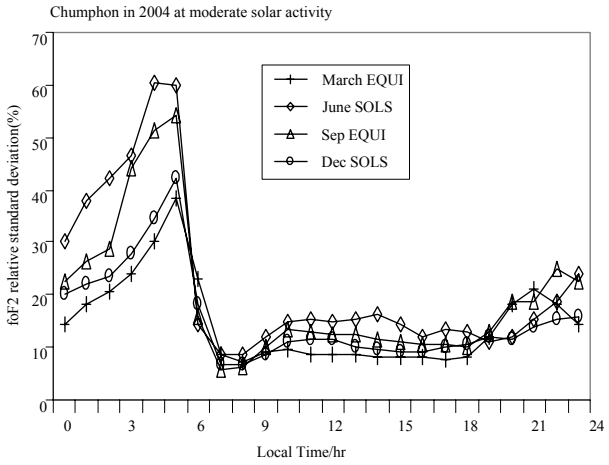

Fig. 4. Diurnal variation of the relative standard deviation for all season and moderate solar activity for Chumphon (2004).

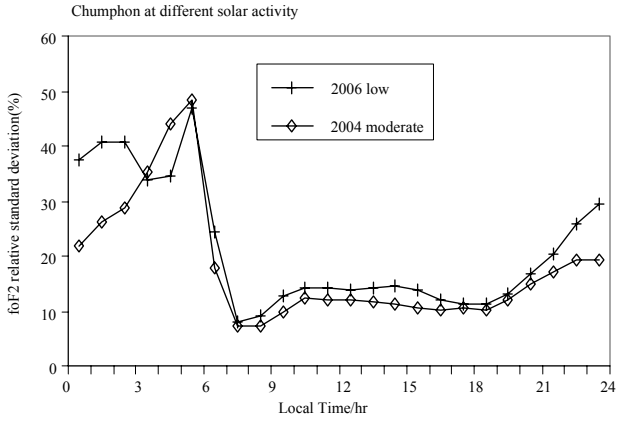

Fig. 5. Diurnal variation of the relative standard deviation Averaged over the whole year for low and moderate solar activity for Chumphon.

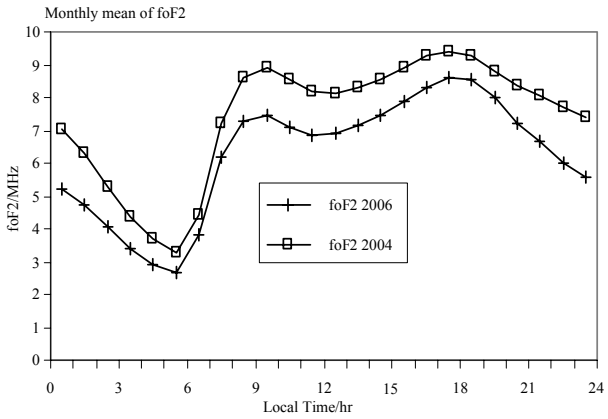

Fig. 6. Comparison diurnal variation of variability of foF2 observed at Chumphon, Thailand.

VI. CONCLUSIONS

The hourly interval foF2 data obtained from bottomside ionograms are recorded by the ionosonde at the low latitude station Chumphon, Thailand in 2004 and 2006, respectively. The data analyzed and compared with relation to monthly variability with local time, season and solar activity.

The variability of VR is lower during daytime hours than during nighttime, the maximum variability occurs at pre-sunrise hours for all solar activities. The percentage of variability is typically 6-15% during daytime, 15-60% during nighttime, 30-60% at sunrise and 15-30% at sunset. From the results, we find the maximum of solstice in the afternoon section in June in Chumphon data for all solar activities. Relative variability generally decreases with increasing solar activity most noticeable during nighttime. The changes of relative variability can be explained in terms of absolute foF2 values (higher foF2 values result in lower percentage variability). From the experimental results in this paper, we found the variability of VR nearly the results of Bilitza et al. [8]. However, the results in this paper higher than the results of Bilitza et al. [8] during nighttime, because the different of intensity of sunspot activity in each year and geographic location. The monthly relative variability values obtained by this study can be used in development of a variability model for the International Reference Ionosphere.

ACKNOWLEDGMENT

The authors are grateful to the National Institute of Information and Communications Technology (NICT), Japan for the necessary equipment and for the Research Center for Communication and Information Technology (ReCCIT) for the use of facility in this research.

REFERENCES

[1] S.M. Radicella, M.-L. Zhang, L. Romanelli, and A. Figliola, "A critical analysis of monthly medians and variability of ionospheric parameter," *Adv. Space Res,* vol. 15 (2), pp. 45-50, 1995.

[2] T.L. Gulyaeva, S. Aggaewal, K.K. Mahajan, and S. Shastri, "Variability of foF2 at low and middle latitudes," *Ads. Space Res.* Vol. 22 (6), pp. 847-850, 1998.

[3] J.M. Forbes, S.E. Palo, and X. Zhang, "Variability of the ionosphere," *J.Atmos. Solar-Torres. Phys.* Vol. 62 (8), pp. 685-693, 2000.

[4] S.S. Kouris, and D.N. Fotiadis, " Ionospheric variability: a comparative statistical study," *Adv. Space Res.* Vol. 29 (6), pp. 977-985, 2002.

[5] R.G. Ezquer, M. Mosert, and R.J. Corbella, "Variability of critical frequency and M(3000)F2 at Tucuman and San Juan," *ICTP Conference*, pp. 85-94, 2002.

[6] J.O. Adeniyi, A.A. Willoughby, and S.M. radicella, " Variability in Equatorial foF2," *ICTP Conference*, pp. 79-84, 2002.

[7] M.-L. Zhang, J.K. Shi, X. Wang, and S.M. Radicella, " Ionospheric variability at low latitude station: Hainan, China," *Adv. Space Res.* vol. 34, pp. 1860-1868, 2004.

[8] D. Bilitza, O.K. Obrou, J.O. Adeniyi, and O. Oladipo, " Variability of foF2 in the equatorial ionosphere" *Adv. Space Res.* vol. 34, pp. 1901-1906, 2004.

[9] R. Attaviriyasuwon, T. Boonchuk, N. Leelaruji, N. Hemmakorn, "Observation of ionospheric height changes at Chumphon near the magnetic equator" *ICICS Conference*, pp. 1169-1172, 2005.

[10] V. Yamvinij, N. Hemmakorn, N. leelaruji, P. supnithi, " The spread F phenomenon of the ionosphere in Thailand" *IASTED International Conference*, pp.467-469, 2006.

[11] T. Ondoh, and K. Marubashi, *Science of Space Environment.* Ohmsha, Ltd., 2000.

[12] N. Wakai, H. Ohyama, and T. Koizumi, "Example of typical ionogram," Manual of Ionogram Scaling Third Version, 1987.

[13] H. Rishbeth, and M. Mendillo, "Patterns of F2-layer variability," *J.Atmos. Solar-Torres. Phys.* Vol. 63, pp. 1661-1680, 2001.

[14] J.O. Adeniyi, O.A. Oladipo, and S.M. Radicella, "Variability of foF2 and comparison with IRI Model For an equatorial station," *The Abdus Salam International Centre for Theoretical Physics*, 2005.

[15] S. Saito, and T. Maruyama, "Ionospheric height variations observed by ionosondes along magnetic meridian and plasma bubble onsets," *Ann. Geophys*., 24, pp. 2991-2996, 2006.

Improvement of Aggressive Fairness in RPR Based Dynamic Fair Rate Estimation

Thawatchai Rungsubsin g4719574@au.edu
Siriwhaddhanah Pongpadpinit winyu@scitech.au.edu
Department of Telecommunications Science, Faculty of Science and Technology
Assumption University, Thailand 10240

***Abstract*-The IEEE 802.17 Resilient Packet Ring (RPR) is the latest standard for ring based packet in the Metropolitan Area Network (MAN). Some scenarios of RPR in the aggressive mode suffer from severe and permanent oscillation which make system unstable and cause low bandwidth utilization. In this paper, we propose a novel dynamic fair rate estimation method. The proposed method produces higher bandwidth utilization, achieves system stability and supports fairness weight which does not obtain in the original aggressive mode. The proposed method is compared with conventional algorithms [1] & [7] and higher bandwidth utilization with minimum oscillation is obtained.**

I. INTRODUCTION

The RPR [1] is a Media Access Control protocol (MAC) of the ring topology in the MAN. It combines the advantages of the Synchronous Optical Network (SONET) [2] and the Ethernet [3] by providing protection in case of links failure and maximizing the bandwidth utilization. The RPR uses the buffer insertion method [4] and consists of dual unidirectional rings which use to transmit the data traffic and control message between two adjacent nodes. It provides automatic topology discovery, fast protection mechanism, multiple classes of services, dynamic bandwidth allocation, spatial reuse through destination-stripping and fairness [5]. The RPR MAC layer is designed to control the transmission of frames on the ring [5]. Frames are allowed to add to the ring only if the transit queue is empty and there is no frame to transit. The transiting frame arrives to a node and is temporary stored in the transit queue when the node adds the local frames. To avoid frame losses in the ring, node stops to add frame when the transit queue occupancy for Fairness Eligible (FE) traffic exceeds the configured threshold (High threshold). The architecture of RPR node can be designed into single transit queue (1TB) [8] and dual transit queue (2TB) as illustrated in Fig. 1.

RPR congestion control operates to avoid buffer over flow in the case of demand for the bandwidth is greater than the total available bandwidth. The congestion domain is defined within the region specified by two boundary nodes. The node which attaches upstream of the most congested link is called head node of the congestion domain. The opposite end of the region is called tail node. The head node estimates fair rate to limit the amount of FE traffic which is distributed to upstream node in the congestion domain as fairness control message (FCM). The tail node tasks to stop the distribution of FCMs by dropping those FCMs.

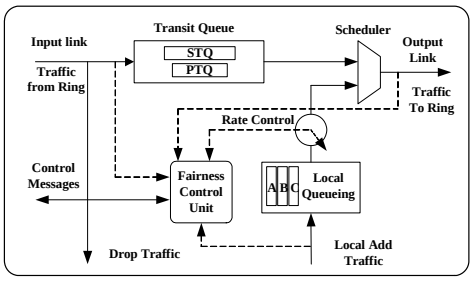

Figure 1. RPR node architecture.

Aggressive mode fairness operates unfair sharing of the bandwidth and unstable for the parking lot scenario where head node transmits the modest traffic [7]. The main reason of these deficient is the application of own local add traffic as the fair rate estimate which it is less than actually fair rate. The proposed algorithm uses dynamic rate control by observing the STQ occupancy to determine the fair rate estimation.

The structure of this paper is organized as follows: the explanation of aggressive mode is in Section 2. Section 3 is the proposed algorithm. The results of the simulation and conclusion are in Section 4 and 5 respectively.

II. AGGRESSIVE FAIRNESS MODE IN FAIR RATE

Aggressive mode is developed from the Spatial Reuse Protocol (SRP) [6]. It is defined as a congested station when the occupied buffer is either greater than the configured threshold which is known as the *stqLowThreshold* or the sum of the local add traffic (*addRate*) and the transit traffic (*fwRate*) is greater than the total available bandwidth. Head node estimates the fair rate by using its own *addRate* and distributes this rate across congestion domain every time interval (*agingInterval*). The original aggressive algorithm [1] is shown in the Table I.

TABLE I
THE ORIGINAL AGGRESSIVE FAIRNESS MODE

Current State		Row	Next State	
State	**Condition**		**Action**	**State**
INIT		1	*L = R*	UNCG
UNCG	*AgingInterval Expired && (STQ > STQLowThreshold)*	2	*L = LpAddRate*	CGST
	AgingInterval Expired	3	*L = R*	UNCG
CGST	*AgingInterval Expired && (STQ <= STQLowThreshold)*	4	*L = R*	UNCG
	AgingInterval Expired	5	*L = LpAddRate*	CGST

Where *L* is the estimated Fair Rate, *R* is the unreserved rate (Normally equal to link capacity (*C*) – reserved rate for A0 traffic [5]), *LpAddRate* is local add traffic of a head node, UNCG is uncongested state and CGST is congested state.

III. DYNAMIC FAIR RATE ESTIMATION

To solve the problem of modest traffic transmission in head node, a new fair rate estimation that does not depend on the local add traffic is proposed. The proposed algorithm is separated into two parts: (1) maximum and minimum rate estimation values and (2) STQ occupancy control.

The maximum rate of the algorithm which is the upper bound of fair rate is defined as:

$$Max_Rate = (R - LpaddRate) * W_i / \sum_{n-1} W_n \quad (1)$$

where R is the unreserved rate, *LpAddRate* is the local add traffic of the congestion domain, W_i is the weight station of node i and W_n is the total weight in the congestion domain n. (1) shows that the traffic of the head node is excluded in the maximum rate calculation. The minimum rate which is the lower bound of fair rate is the same as the Zhou fair rate estimation [7] which is defined as.

$$Min_Rate = R * W_i / \sum_n W_n \quad (2)$$

Our algorithm observes STQ occupancy to control the fair rate estimation. When STQ occupancy is greater than the *stqMedThreshold* (Normally equal to (*stqHighThreshold* + *stqLowThreshold)/2*) and the occupancy rate is increasing, the algorithm will reduce the fair rate by gradually decreased to the *Min_Rate* using:

$$L = L_c - (L_c - Min_Rate) / \alpha \quad (3)$$

where L is the estimated fair rate, L_c is the current fair rate and α is the coefficient factor (default value is 64). Otherwise if the STQ occupancy is lower than the *stqMedThreshold* and occupancy rate is decreasing, the fair rate will be gradually increased up to the *Max_Rate* as:

$$L = L_c + (Max_Rate - L_c) / \alpha \quad (4)$$

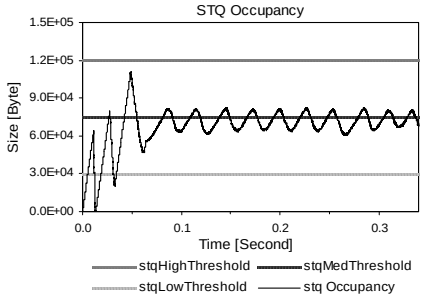

Figure 2. STQ Occupancy Control *stqhighThreshold* is configured as 120000 byte, *stqLowThreshold* is configured as 31812 byte.

(3) and (4) show that we control the STQ occupancy oscillated around *stqMedThreshold*. The first reasons is to avoid the unwanted effects of the local station stops to transmit local traffic when STQ occupancy greater than *stqHighThreshold*. The second is the switching state between CGST to UNCG when STQ occupancy lower than *stqLowThreshold*. The STQ occupancy control is illustrated in Fig. 2.

If the STQ occupancy falls below the *stqLowThreshold* and the scenario remains unchanged, the lower bound will be increased in order to avoid unwanted state changed (CGST switch to UNCG) which causes the *Min_Rate* drops below the actually fair rate. The *Min_Rate* can be calculated using:

$$Min_Rate = max\ (Min_Rate, L) \quad (5)$$

Otherwise the upper bound will be decreased to avoid buffer overflow in the STQ when the active transmitting node in the congestion domain is increased. The *Max_Rate* can be obtained from:

$$Max_Rate = min\ (Max_Rate, lpAddRate) \quad (6)$$

TABLE II
THE IMPROVEMENT OF FAIRNESS ALGORITHM

Row	Next State	
	Action	State
1	$L = R$	UNCG
2	*If ($\sum W_n$ changed) {* *Max_Rate = (R – LpaddRate) * W_i / $\sum_{n-1} W_n$* *Min_Rate = R * W_i / $\sum_n W_n$ }* *L = Min_Rate*	CGST
3	$L = R$	UNCG
4	$L = R$ *Min_Rate = max (MinRate, L)*	UNCG
5	*If ($\sum W_n$ increase)* *Max_Rate = min (Max_Rate,LpAddRate)* *If (STQ rate increase) && (STQ > stqMedThreshold)* *L = L_c – (L_c – Min_Rate) / α* *Else if (STQ rate decrease) && (STQ > stqMedThreshold)* *L = L_c + (Max_Rate – L_c) / α*	CGST

The congestion domain status and fairness control message are determined as the standard of aggressive fairness. The main difference between the proposed algorithm and the aggressive mode is the fair rate estimation method. The state diagram of the proposed algorithm is shown in the Table II.

IV. EXPERIMENTAL METHODOLOGY

The simulations are based on java simulator and the experimental results are compared with the standard aggressive mode [1] and Zhou algorithm [7].

TABLE III
CONFIGURATION PARAMETER FOR FAIRNESS MODES

Parameter Name	Value
Link Capacity	1000 Mb/s
Packet size	500 [B] (fixed)
stqLowThreshold	31812
stqHighThreshold	120000
ageCoef, lpCoef	4,64

The configured parameters of the simulator are as shown in the Table III. We simulate the performance with different scenarios where the traffic generations are FE traffic.

A. Convergence for all nodes transmits greedy traffic.

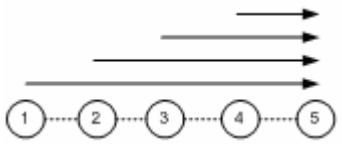

Figure 3. The parking lot scenario with the link capacity of 1Gb/s.

Consider the scenario in Fig. 3 where all traffics transmit the greedy traffic at the time 0.01s with link delay of 1ms. Fairness algorithm defines the head node and tail node of the congestion domain to be Node 4 and Node 1 consequently. The experimental results are shown in Fig. 4 and Fig. 5.

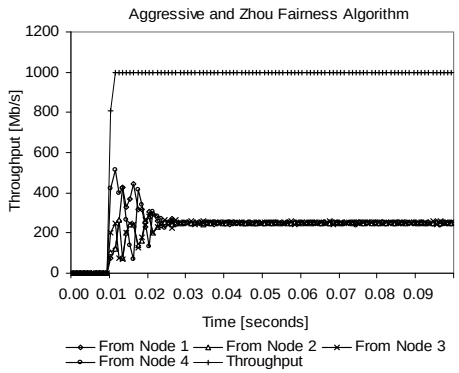

Figure 4. The results of aggressive fairness mode when all nodes transmit greedy traffic.

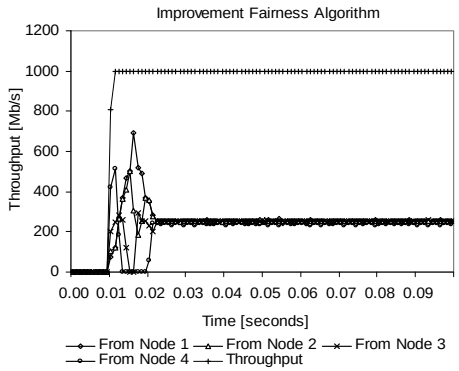

Figure 5. The results of the proposed algorithm when all nodes transmit greedy traffic.

All tested algorithms perform to achieve fair sharing of the total available bandwidth. Fig. 4 shows that the results of the aggressive mode and the Zhou algorithm are identical. The system reaches stable state at time 0.026s while the proposed algorithm reaches the stable state at time 0.022s as show in Fig. 4 and 5 respectively. This is proved that the proposed algorithm reaches stable state faster than the aggressive and Zhou algorithm.

B. Convergence for head node transmits modest traffic.

To simulate the deficient of aggressive mode, the same scenario as in the previous section is used when node 4 transmits the traffic of 50Mb/s. The experimental results are as shown in Fig. 6 -8.

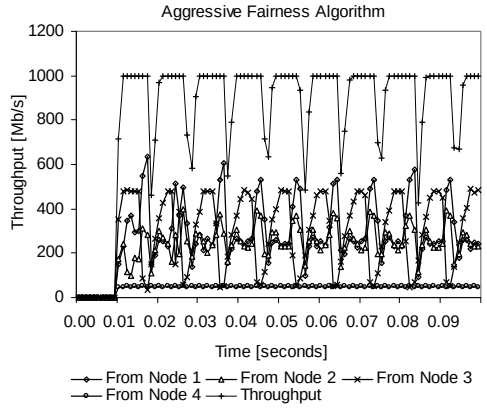

Figure 6. The result of aggressive fairness mode when head node transmits modest traffic.

We consider the results of aggressive mode are as show in Fig. 6. The each traffic oscillates and the system unable to reaches the stable state and become low link utilization.

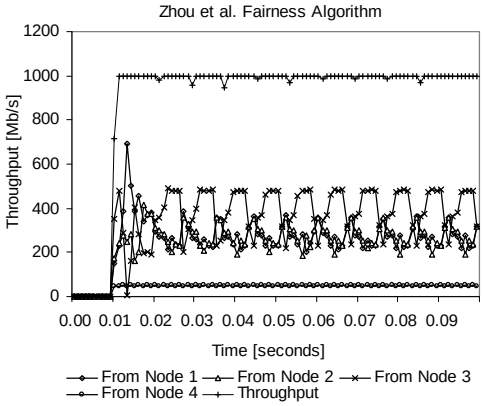

Figure 7. The result of Zhou algorithm when head node transmits modest traffic.

The results from Zhou algorithm, as shown in Fig. 7, improve deficient of the aggressive mode which only alleviated the range of traffic oscillation of each node and overall throughput loss. The system also unable to reaches the stable state.

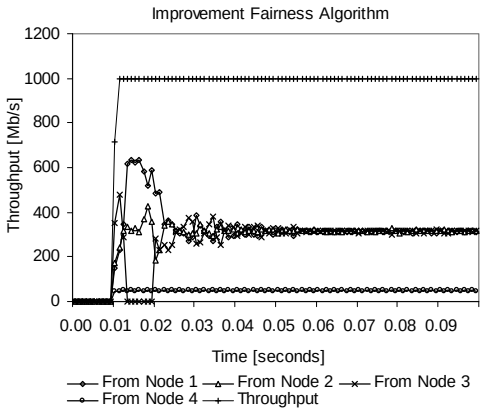

Figure 8. The result of our improvement fairness algorithm when head node transmits modest traffic.

Fig. 8 shows that our algorithm achieves bandwidth fair sharing and maximizes bandwidth utilization. The system reaches stable state at time 0.046s. These are proved that the proposed algorithm solves the deficient of head node transmits with modest traffic which is mentioned in the previous section.

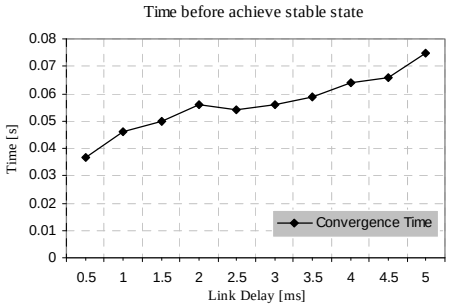

Figure 9. The comparison between difference link delays.

The graph of link delay versus stable state is shown in Fig. 9 where the scenario in Section B is re-applied with various link delays.

C. Convergence for weighted fairness.

In this section, we show that the proposed algorithm supports weighted fairness. The scenario in Fig. 2 is reconsider, the weight of the transmitting node 1, 2 and 3 were set as 2, 3 and 4 respectively.

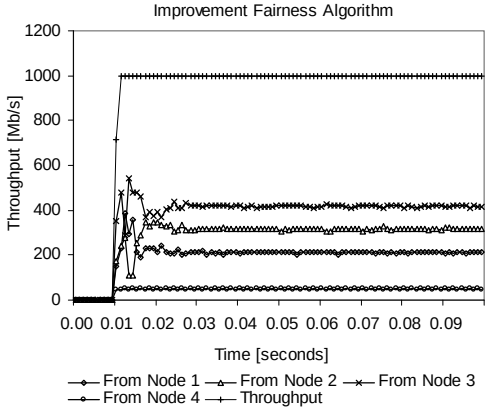

Figure 10. The result of our improvement algorithm with weighted fairness.

Fig. 10 shows the throughput of individual node, demonstrating that all nodes are able to obtain the fair sharing of bandwidth proportional to their weights. In order to test system stability, dynamic scenario is used in the next sub-section.

D. Convergence for dynamic scenarios.

In this section, the congestion domain is increased to 9 nodes as illustrated in Fig. 11 in order to test the proposed algorithm with the dynamic scenario. Fairness algorithm determined the head node and tail node of the congestion domain as Node 8 and Node 1 respectively.

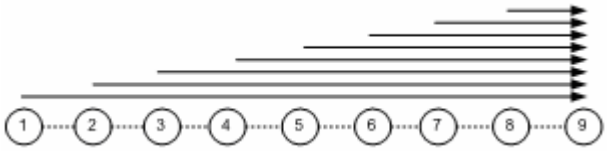

Figure 11. The parking lot scenario with the link capacity of 1Gb/s and link delay of 1ms.

The dynamic scenario shows that all active nodes transmit traffic to the destination node (node 9). To simulate the convergence when head node transmits modest traffic (node 8) of 50Mb/s and the rest nodes transmit greedy traffic with the link delay of 1ms. All nodes start to transmit traffic at the time 0.01s except the node 4 and 5 start to transmit traffic at the time 0.3s. Finally when the time 0.6s, the node 2 and 3 stop to transmit traffic.

Consider the results of dynamic scenario as shown in Fig. 12 at the time 0.01s where node 1, 2, 3, 6, 7 and 8 start to transmit traffic, the system became stable state at the time 0.03s until 0.3s. At the time 0.3s the traffics from node 4 and 5 start to transmit, the proposed algorithm detects this changed and perform to achieve stable state at the time 0.33s and when the time 0.6s node 4 and 5 stop to transmit the traffic. The system became to stable state again when the time 0.64s. The result shown that, our algorithm achieves fair sharing for bandwidth with dynamic scenario.

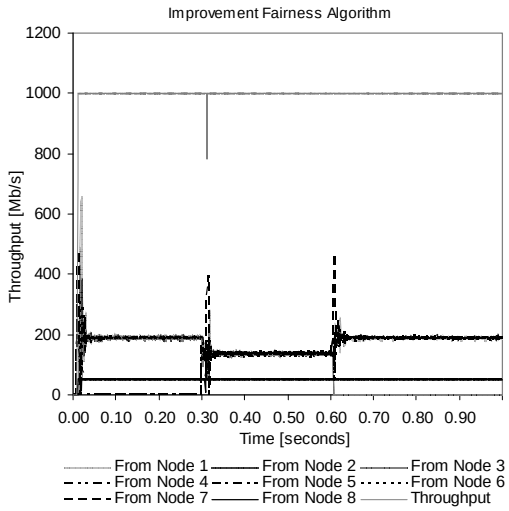

Figure 12. The result of dynamic scenario.

V. CONCLUSION

In this paper, we show that in some scenarios the aggressive mode performs low link utilization and unfair for sharing of bandwidth. The result from the section 4B, the average throughput of the aggressive algorithm approximate to 911.69 Mb/s and the average throughput of Zhou algorithm approximate to 982.33 Mb/s but each traffic unable to achieve the stable state. We propose the improvement algorithm which uses dynamic fair rate estimation. The average throughput of proposed algorithm able to reach to the maximum link capacity (approximate 1000 Mb/s) and each traffic achieve the stable state. The simulation's results verify that our algorithm achieve fair sharing for bandwidth, gain the maximum throughput, faster convergence time and support the fairness weights.

REFERENCES

[1] IEEE 802.17 Working Group, "Resilient Packet Ring Access Method and Physical Layer Specifications," June 2004.

[2] ANSI T1.105.01-2000: Synchronous Optical Network (SONET) Automatic Protection.

[3] IEEE Standard 802.5–1989, "IEEE standard for token ring".

[4] E. Hafner, Z. Nendal, and M. Tschanz, "A digital loop communication system," IEEE Transactions on Communications, vol. 22, no. 6, pp. 877–881, June 1974.

[5] F. Davik, M. Yilmaz, S. Gjessing, and N. Uzun, "IEEE 802.17 Resilient Packet Ring Background and Overview," Simula Research Laboratory, Tech. Rep. 2003-11, December 2003. [Online]. Available: http://www.simula.no

[6] D. Tsiang and G. Suwala, "The Cisco SRP MAC layer protocol," August 2000, IETF, RFC 2892.

[7] X. Zhou, G. Shi, H. Fang, and L. Zeng, "Fairness algorithm analysis in Resilient Packet Ring," in Proceedings of the 2003 International Conference on Communication Technology (ICCT 2003), vol. 1, April 9-11 2003, pp. 622–624.

[8] F. Yuan and C. Huang, "Performance Analysis for Resilient Packet Rings with Single Transit Buffer", IEEE ICT 2002, June 2002.

Investigation of Rain Attenuation on Vertical and Horizontal Polarizations of Thaicom Satellites

Pongputhai Udomareyasap, Donekeo Lakanchanh, Narong Hemmakorn and Nipha Leelaruji
Faculty of Engineering and Research Center for Communications and Information Technology
King Mongkut's Institute of Technology Ladkrabang (KMITL), Bangkok, 10520, Thailand,
Email:s9060928@kmitl.ac.th, s8060949@kmitl.ac.th, khnarong@kmitl.ac.th, klnipa@kmitl.ac.th

Abstract **This paper present the effect of rain attenuation on Ku band satellite propagation path with difference polarizations.The vertical and horizontal polalized signal received from Thaicom 2 and Thaicom 3 satellites by one dish antenna with two LNBs. The observation of rainfall rate and rain attenuation at KMITL Bangkok Thailand are investigated.The reduction of satellite signal passing through the same rain rate on difference polizations has some difference . Finally the rainfall rate and rain attenuation are estimated and compared to ITU-R rain attenuation prediction model.**

Keywords Ku band rain attenuation, vertical and horizontal polarizations, yearly cumulative time of rainfall rate, ITU-R model.

I. INTRODUCTION

Rainfall attenuation has been recognized as the main source of atmospheric attenuation in satellite links. Raindrops absorb and scatter radio wave energy, resulting in signal attenuation. It causes both attenuation and depolarization.The result is reduction in separation between vertical and horizontal polarizations in an orthogonal polarized signal. B.Fong et.al. had reported the effect of rain attenuation on orthogonally polarized LMDS (local multipoint distribution service) system in tropical region. The attenuation from both polarized is 2 dB difference. [1]

This paper is to study the difference in attenuation due to polarizations from two Thaicom satellites with difference polized signals. Both Thaicom satellites are located at the same position as the detail listed in table 1. The signals are received by one antenna and convert to IF frequencies. The polarizations are separated by two LNBs and received by two receivers. The experiment had been carried out in one year from January to December 2006 and denoted that from 14 June 2006 Thaicom 5 had been replaced to Thaicom 3 at the same position. Furthermore the authors proposed the cumulative time of rainfall rate in year 2005 and 2006 compare to ITU-R model.

II. EXPERIMENT METHOD

Fig.1. is illustrated the configuration of the propagation experiment system at KMITL. The pulse numbers of rain gauge are counted to data logger and recorded by the computer parallel with the satellite signals.

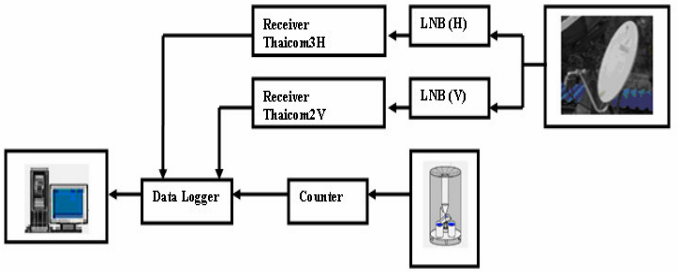

Fig.1. The experiment block diagram of rain attenuation on two polarizations of Ku band system .

The data of the received signal and the rainfall amounts are sampled at every 1-second and the dynamic range of attenuation of the instrument is approximately 15 dB below the clear sky level. The resolution of the tipping-bucket type rain gauge is 0.5 mm/tip. Since June 2006 the data from Thaicom3 are changed to Thaicom 5 with the same parameters.The receiving parameters are listed in table1.

TABLE I
PARAMETER OF RECEIVING SYSTEM

Parameters	Thaicom2	Thaicom3 (Thaicom 5)
Polarization	Vertical	Horizontal
Down link frequency	12.567 GHz	12.594GHz
IF frequency	1.467 GHz	1.280 GHz
Antenna diameter	0.5 meter	0.5 meter
Position satellite	78.5° E	78.5° E
Elevation angle	59.83°	59.83°
Azimuth angle	239.652°	239.652°
Sample data interval	1-second	1-second
Rain guage type	Tipping bucket	
Longitude (KMITL)	100.7° E	
Latitude (KMITL)	13.7° N	

Calibration of receiving system

The recording system has been calibrated by signal generator with the normal level of Thaicom2 and Thaicom3 before collecting data.The received signal from Thaicom 2 equal to -63.752 dBm while Thaicom 3 is -60 dBm. These are the reference values. The strength of signal are measured at AGC output of receivers. For calibration of satellite level, the signal generator is replaced to satellite signal. The calibration level is step in dB value. When the rainfall rate and satellite level has been converted to correct unit we can calculate the rain attenuation or losses of signal during rain by equation:

$$L_r = P_{ref} - P \qquad (1)$$

Where L_r : Rain attenuation level (dB)
P : Measuring signal level (dBm)
P_{ref} : Reference level (dBm)

III. EXPERIMENT RESULTS

A. Rainfall Rate and Rain Attenuation Measurement Results

The results of rain attenuation on 4 June 2006 are presented in Fig. 2 and Fig. 3. From the configurations, the rainfall rate 90 mm/hr caused to signal attenuate 12 dB via horizontal polarized signal and 9 dB from vertical polarized signal .This is the result of one event. The attenuation depends on rain intensity and period of measurement.

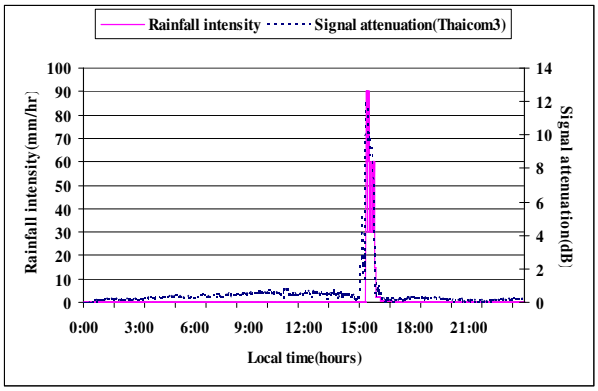

Fig. 2. Example of intense rainfall event and signal attenuation in horizontal polarization on June 4,2006.

The reliability of satellite link is described by the yearly cumulative time of rain attenuation. The result at 0.01% cumulative time of rainfall rate cause rain attenuation about 9 dB and 11 dB from Thaicom2 and Thaicom3 respectively as shown in Fig. 4. and Fig. 5.The attenuation difference between both satellites is 2 dB which is the difference in polarizations.

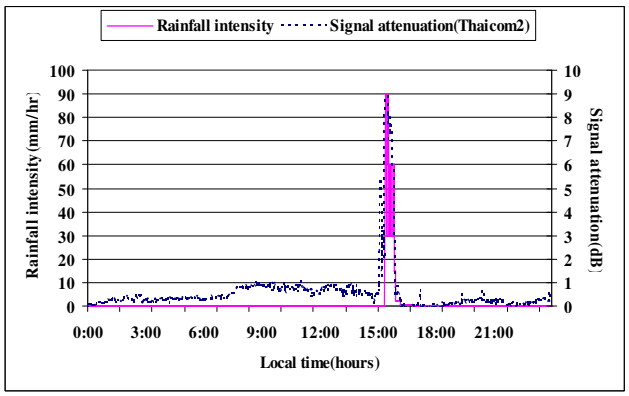

Fig. 3. Example of intense rainfall event and signal attenuation in vertical polarization on June 4,2006.

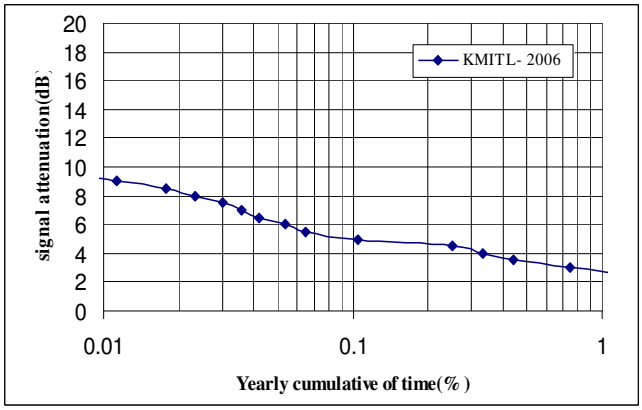

Fig. 4. Cumulative time distribution of rain attenuation in Thaicom2 (vertical polarization) .

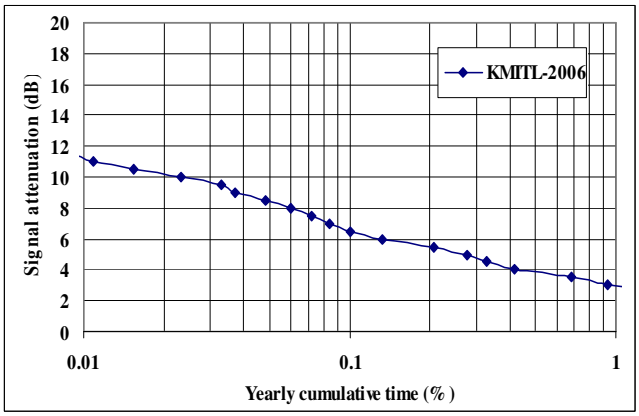

Fig. 5. Cumulative time distribution of the rain attenuation in Thaicom3 (horizontal polarization).

B. Measurement and Predicted Rainfall Rate by ITU-R.model.

The yearly reliability of satellite signal should be 99.99% in each year. Fig.6. indicated one year cumulative distribution of rainfall rate. It is indicated the short percentage time of rainfall rate exceed 0.01%, the rainfall rate is 94 mm/hr.

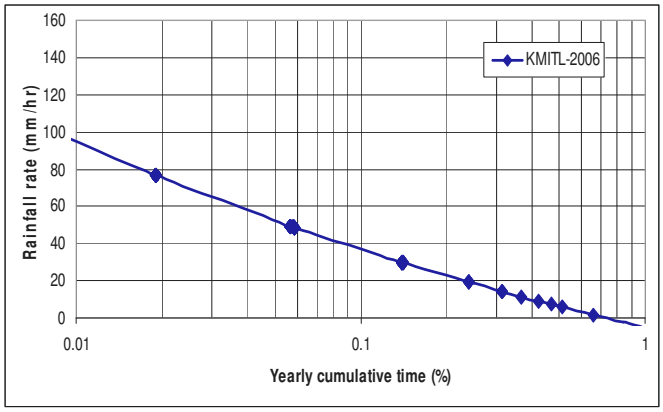

Fig. 6. Yearly cumulative time of rainfall rate on year 2006.

The rain attenuation in Fig.7. are indicated one year cumulative distribution time of rain attenuation from both polarizations included the result of ITU-R prediction model. The rainfall rate is more effective to satellite signal. In Fig. 7. we found that the yearly cumulative time of rainfall rate at 0.01% the rain attention is about 9 dB from vertical polarization and 11.5 dB from horizontal polarized signal. The signal attenuation from horizontal polarization of Thaicom3 is higher than the vertical polarization of Thaicom2 about 2.5 dB. The comparison of rain attenuation between ITU-R model and measured value are indicated that the measuring results from horizontal polarization are closed to ITU-R zone N.

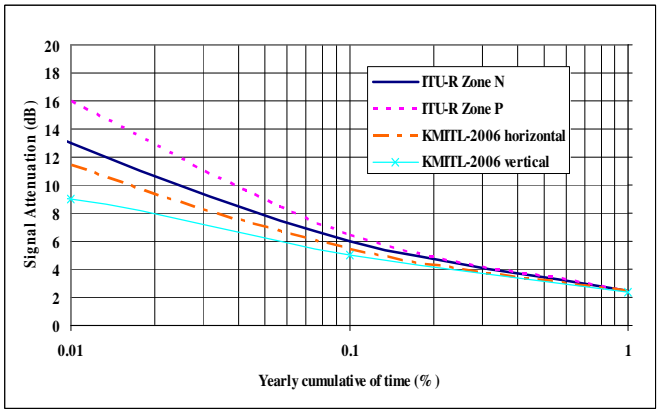

Fig.7. Comparison between ITU-R zone P, zone N and rain attenuation at KMITL.

Moreover, we also proposed the comparison of rainfall rate in year 2005 and 2006 with ITU-R model which presented in Fig. 8. The rainfall rates are measured in every 1 minute. We found that at 0.01% of cumulative time distribution of rainfall rate in year 2005 is about 155 mm/hr and 165 mm/hr in year 2006 which close to ITU-R zone N. The ITU-R rain zone model is shown in Fig. 9. Thailand is located between zone P and N.

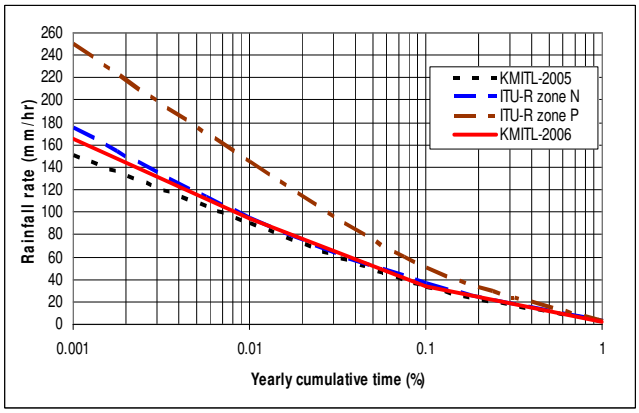

Fig. 8. One year comparison between rainfall rate in year 2005 and 2006 at KMITL and ITU-R zone P, zone N model.

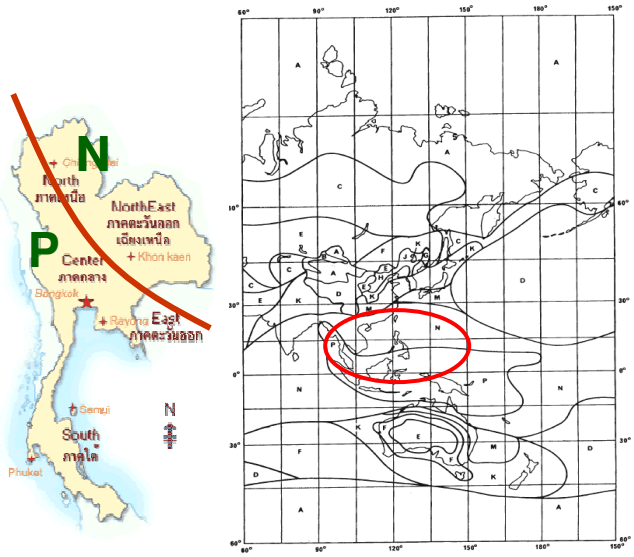

Fig. 9. ITU-R P.837-1 rain zone

IV. CONCLUSION

This paper present the effect of rain attenuation on vertical and horizontal polarized signal of Ku band satellites.The studies are received strength of signal from Thaicom2 and Thaicom3 include Thaicom5 by one antenna and two LNBs in difference polizations.The satellite signals pass through the same propagation path because both satellites have same elevation angle.The effect of rain probably small difference in practical.The monthly and yearly cumulative time distribution of rainfall rate and rain attenuation at KMITL, Bangkok are closed to ITU-R zone N model. From the results, the rain attenuation on both sattellites of Ku band are about 11.5 dB and 9 dB at 0.01% of exceed time. The result of satellite attenuation from horizontal polarized signal is higher than the vertical polarized signal which is same as the investigation result of B. Fong et al.[1].

ACKNOWLEDGEMENT

The authors are grateful thanks to AUN/SEED – Net and King Mongkut's Institute of Technology Ladkrabang for technical support.

REFERENCES

[1] B. Fong, P.B. Rapajic, G.Y. Hong and A.C.M. Fong, "The Effect of Rain Attenuation on Orthogonally Polarized LMDS System in Tropical Rain Regions", IEEE Antennas and wireless Propagation Letters, Vol.2, 2003, pp. 66-67

[2] T.Boonchuk, "*The rain Attenuation Characteristic at 12.7 GHz on Earth-Space Path in Bangkok* ", Faculty of Engineering and Research Center for Communication and Information Technology (ReCCIT), 2003.

[3] Koji Yasakawa**,** Matsuichi Yamada, "*The 11.9 GHz rainattenuation and site diversity effect on the earth-space paths of low elevation angles*",Radio Science Volume 20 Number 6 ,1985.

[4] Recommendation ITU-R P.839-3, "*Rain height model for prediction methods*", ITU-R P.839-3, 2001.

[5] Recommendation ITU-R P.838-2, "*Specific attenuation model for rain for use in prediction methods*", ITU-R P.838-2, 2003.

[6] Recommendation ITU-R P.618-7, "*Propagation data and prediction methods required for the design of Earth-space Telecommunication system*", ITU-R P.618-7, 2001.

[7] Recommendation ITU-R P.837-4, "*Characteristics of precipitation for propagation modeling*", ITU-R P.837-4, 2001.

[8] Crane.R.K (1980); "Prediction of Attenuation by rain", IEEE Trans. Commun., COM-28.

[9] J. Surayana et al, " *Study of prediction models compared with the measuement results of rainfall rate and Ku band rain attenuation at Indonesian tropical cities*", ICICS 2005 Bangkok, Thailand.

[10] Dennis Roddy, "*Rain Attenuation P.92-97*", Satellite Communication, New York: McGraw-Hill, 1996

Multiple Correspondences in Stereoscopy Using Frequency-Encoding Light Point

P. Tosranon [1,2], S. Bunluechokchai[2], C. Pintavirooj[1], M. Sangworasil[1]
[1]Department of Electronics, Faculty of Engineering, and
Research Center for Communications and Information Technology (ReCCIT)
King Mongkut's Institute of Technology Ladkrabang, Thailand
[2]Department of Industrial Physics and Medical Instrumentation
King Mongkut's Institute of Technology North Bangkok
Bangkok 10520, Thailand
Email: Kpchucha@kmitl.ac.th

***Abstract*- Stereoscopy is the method to recover depth from the scene. This method suffers from the correspondent problem especially when there are multiple points to extract 3D information from the scene. This paper concentrates on the solution to correspondent problem. Our idea is to project the binary-coding light point on the object while capturing the image sequences. The image sequences are later analyzed to detect the binary code of various projected points. The correspondence of points on the right and left image are established when the binary code is similar. Our technique has been tested to extract the shape of the face model. The result is very promising.**

I. INTRODUCTION

Shape extraction is the first step of many 3D applications, including a 3D modeling, object recognition, robot navigation, machine inspection, geometry measurement, and so on. To satisfy these applications, it requires an appropriate shape extraction method. Nowadays, several shape extraction systems are proposed, and each one is suitable in the limited range of applications. Some of those, including stereoscopy, laser range finder, structured-light projection, and shape from shading, will be reviewed here concisely.

The first 3D perception method, which was explored for a long time, is stereoscopy [1]. Its concept is simulated from the human visual system by using two images from two different angles to perceive the depth of the scene. Practically, an orientation of each camera as well as a correspondent problem is elaborate, and the decision for the points of landmark must be done manually. Laser range finder technique [2] straightforwardly measures the distances from the viewer to points on surfaces in the scene by using the time-of-flight of a laser beam. Giving a high precision of a depth map, the "Laser Plane Range Finder" [3] is claimed about 0.5 mm in depth's resolution. Commonly, the machine is fragile and costly. Structured-light projection technique [4] projects some light patterns, for instance – plane or grid, onto a surface of the object, captures the scene, and then computes the shape from the distorted light. This has a main advantage in that the discontinuity and monotony of the surface are abruptly replaced by the readily-computed artificial light pattern. This method, similar to the stereoscopy, suffers from the correspondent problem. Shape from shading [5] – the shape information could be inferred from only a monocular image if the illuminating position and the surface property were known. However, the result sensitively depends on the surface's reflectance property. For some kinds of images, never does the shape from shading provide a correct solution [6].

In the tomographic process [9] , by directly replacing the projections of an object with the silhouetted photographs from sufficient viewpoints, one can acquire the pseudo cross-sections of an object, which means that only the outlines are correct, regardless to the internal regions [7, 8]. Therefore, the photographic tomography could be inferred as the one of shape extraction systems capable of reconstructing the volumetric data of an object from the sequence of photographs taken around the object. This technique, however, suffers from concave occlusion. In this paper, we revisit the stereoscopy method with an objective to facilitate the corresponding process. Our idea is to project the binary-coding light point on the object while capturing the image sequences. The corresponding point on the right and left images blinks at the binary coding. The captured video image is then analyzed, decoded the binary code among various points to establish correspondence.

This work is organized as the following: - Section 2 discusses stereoscopy. Binary-encoding process is provided in section 3. The experiments and results is discussed in section 4. Discussion and conclusions are given in section 5.

II. STEREOSCOPY

The 3D coordinate of the object can be recovered from the scene using stereoscopy techniques. In the technique, the two identical and perfectly aligned cameras, namely left and right cameras, take the image of the same object. The 3d coordinate of the world points, as shown in figure 1, can be derived as follows:

$$Z = f - \frac{fB}{x_2 - x_1} \quad (1)$$

$$X = \frac{x_1}{f}(f - Z) \quad (2)$$

$$Y = \frac{y_1}{f}(f - Z) \quad (3)$$

Where

(X, Y, Z) is the 3d coordinate of the world point W,

(x_1, y_1) is the image of world point in the left camera,

(x_2, y_2) is the image of world point in the right camera,

B is the distance between the two cameras.

f is the focal distance of the camera.

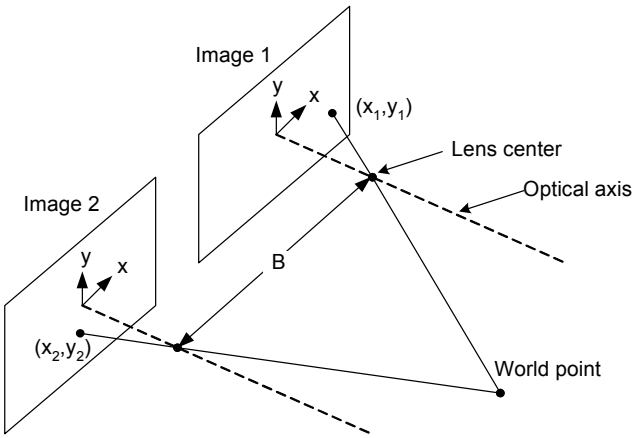

Figure 1. Stereoscopy system

III. FREQUENCY-ENCODING PROCESS

One of the major drawbacks of shape recovery using stereoscopy is the problem of point correspondence. To overcome the problem, the point projected on the object will be binary encoded. Firstly this method project a mask pattern of an all illuminated dots to the object. The left and right

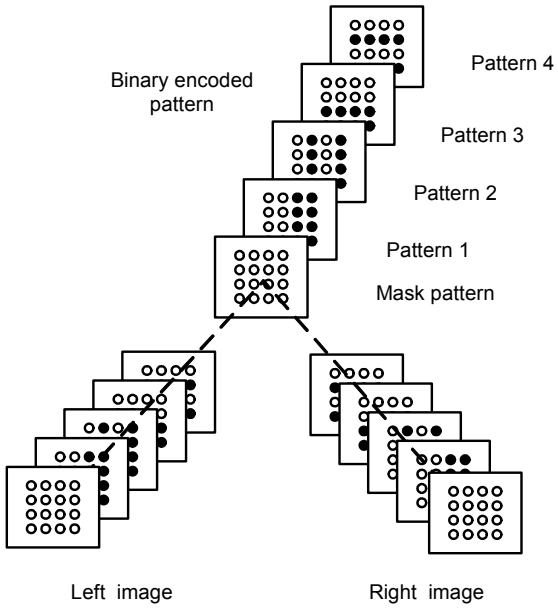

Figure 2. Frequency-Encoding Process

cameras image all the dots and keeps their positions. In the following steps, a series of patterns consisting of patterns one to four is projected and then a series of left and right images is stored. After all the patterns were projected, all dot positions of image series were analyzed for blinking dots to assign a bit one or zero. Figure 2 shows the configuration of 4x4 points and the binary-encoded light pattern. In each case, four bits is required for the encoding process. The light will be projected one frame per one bit and hence 4 frames are required. Bit "0" means that the black dot is projected, while bit "1" means that a white dot is projected. In case of the first point, for example, the black dot will be projected for all the 4 frames. For the second point, the first three frames will project the black dot and the fourth frame will project the white dot contributed for "0001".

IV. EXPERIMENTS AND RESULTS

Figure 3 shows the experimental set up. The 4 mm focal length two identical and perfect-aligned cameras are installed on the rail. The distance between cameras is 10 cm. The object is located at 50 cm from the camera plane. The 32x32 dot will be projected on the object with the NEC VT47 projector. The number of dots is hence 1024 dots. The number of bit required is 10 bits and hence 10 frames are required. The size of the light point projected on the model is 2 mm. The distance between point centers of the successive point both horizontally and vertically is 7.5 mm. The image capture card is Matrox

Meteor-II installed on a Pentium IV 2.8 GHz. The acquisition time of the 10-Bit pattern is about 30 seconds. The computational time for the 3D coordinate is 2-3 seconds. The total time is about 35 seconds. Figure 4 shows 10 bit binary-encoded light pattern used in the experiment which has ten patterns. The first pattern represents the first digit of each binary encoded light point while the last pattern represents for the last digit. Figure 5(a) shows the left image of all projected points and figure 5(b) displays the right image of all projected points. The dot correspondence obtained from figure 5(a) and 5(b) was used to reconstruct three dimensional object as shown in figure 5(c).

Figure 3. Experiment Setup

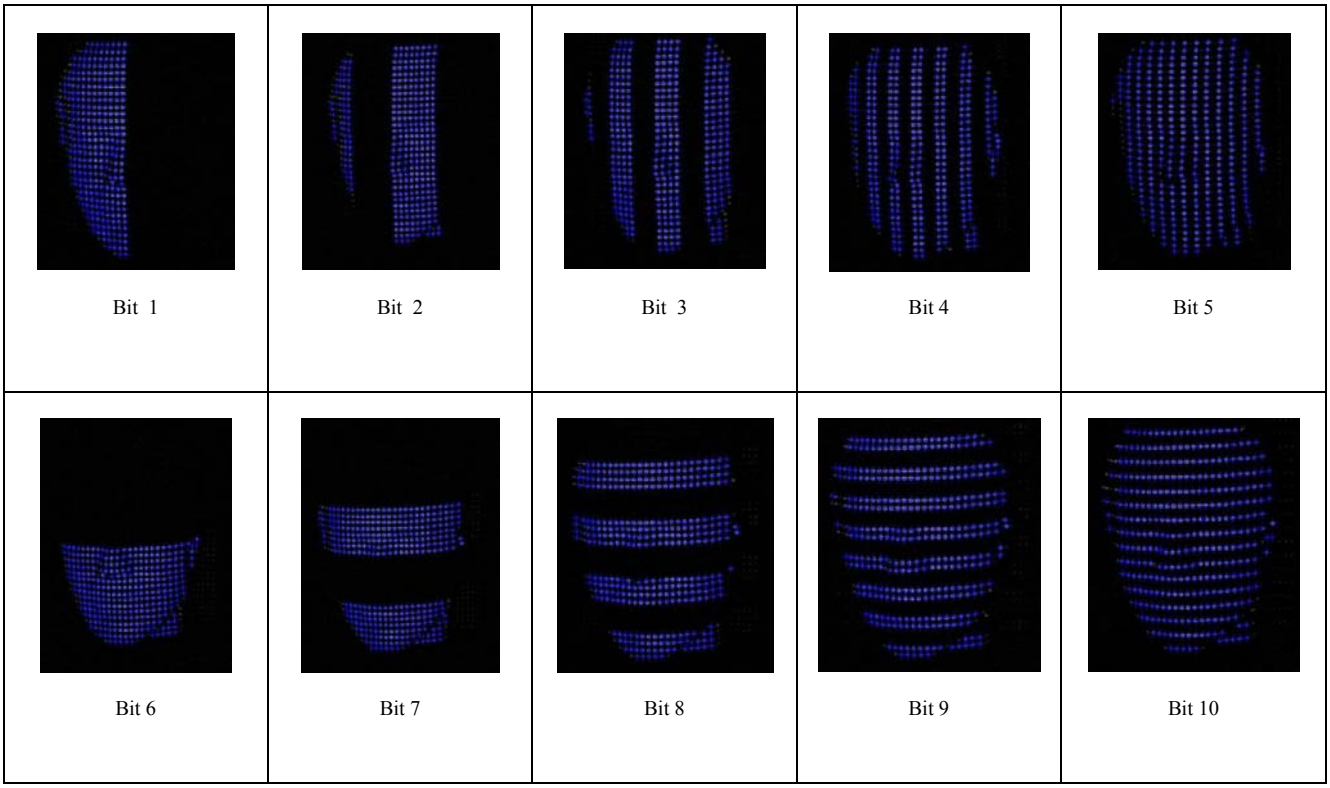

Figure 4. Bit binary-encoded light pattern

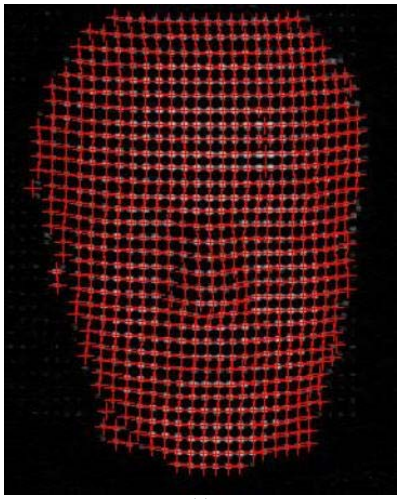

(a)

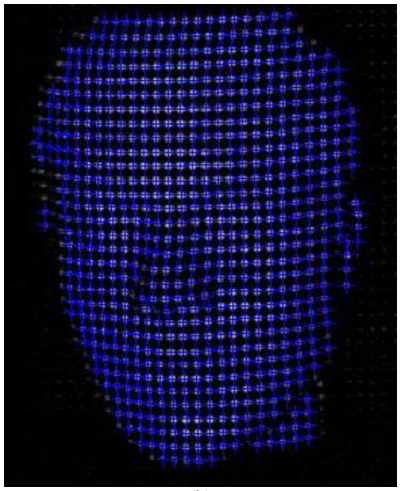

(b)

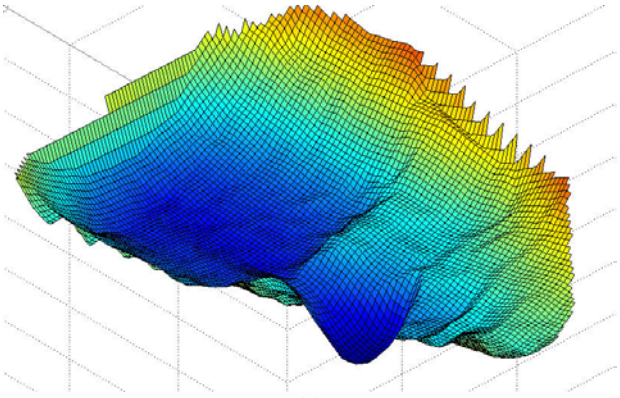

(c)

Figure 5 (a) Left Image (all projected points) ; (b) Right Image(all projected points; (c) Shape Extraction Result

V. CONCLUSIONS AND SUGGESTIONS

The purposed technique to correspondence establishment of shape extraction using stereoscopy technique has been discussed in this paper. The technique exploits the binary-coding light pattern by projecting multiple points which blinks at distinct binary code on the object while recording the image sequence. The captured video image is then analyzed, decoded the binary word among various points and established correspondence. The modified stereoscopy can be hence applied for real-time application.

REFERENCES

[1] Dhond U. R., Aggarwal J. "Structure from Stereo - A Review." IEEE Trans. on Syst. Man. and Cybern. vol. 19, no. 6, 1989. pp. 1489-1510.

[2] Bosch T. et. al. "Three-Dimensional Object Construction Using a Self-mixing Type Scanning Laser Range Finder." IEEE Trans. Instrum. and Meas. vol. 45, no. 5, 1998. pp. 1326-1329.

[3] Center for Machine Perception (CMP). "Laser Plane Range Finder." [Online]. Available: http://cmp.felk.cvut.cz/.

[4] Meadows D. M. et. al. "Generation of Surface Contours by Moiré Pattern." Appl. Opt. vol. 9, 1970. pp. 942-947.

[5] Zhang R. et. al. "Shape from Shading: A Survey." IEEE Trans. Pattern Anal. Machine Intell. vol. 21, no. 8, Aug 1999. pp. 690-706.

[6] B.K.P. Horn et. al. "Impossible Shaded Images." IEEE Trans. Pattern Analysis and Machine Intelligence. vol. 15, no. 2, Feb 1993. pp. 166-170.

[7] Gering, D.T., Wells, W.M., III. "Object modeling using tomography and photography". Multi-View Modeling and Analysis of Visual Scenes, 1999. (MVIEW '99) Proceedings. IEEE Workshop on. pp. 11-18.

[8] Johnson A.J. et. al. "Three-Dimensional Surface Reconstruction of Optical Lambertian Objects Using Cone-Beam Tomography." Proc. Int. Conf. on Image Processing. vol. 2, 1999. pp. 663 -667.

[9] C. Pintavirooj, W. Withayachumnankul, S. Tungjitkusolmun, and K. Chitsakul, "3D Shape Recovery Based Radon Transform," Proc. ISCIT2001, Thailand, November 2001. pp. 377-380.

[10] Anil K. Jain and U.C. Davis. Fundamental of Digital Image Processing. Prentice-Hall International, Inc. 1989.

[11] Kak A.C., Slaney M. Principles of Computerized Tomographic Imaging. New York : IEEE Press. 1988.

[12] W.E. Lorensen, and H.E. Cline, "Marching Cubes: A High Resolution 3D Surface Construction Algorithm," Computer Graphics (Proc. SIGGRAPH), Vol. 21, No. 3, July 1987. pp. 163-169.

[13] Gouraud, H., "Continuous Shading of the Curved Surface," IEEE Trans. Computers, vol. 20, no. 6, 1971. pp.623-629.

[14] Phong, B.T., "Illumination for Computer Generated Pictures," Communications of the ACM, vol. 18, no. 6, 1975. pp. 311-317.

[15] C. Pintavirooj and M. Sangworasil, "3D Modeling Based on Radon Transform with Application in Volume Measurement," Journal of WSCG, vol. 10, 2002. pp. POS33.

Automatic Alignment of White Blood Cell Using Principal Axis: The Improvement For Classification

P.Yampri[†], C.Pintavirooj[†], M. Sangworasil[†], P.Lertprasert[†], T.Rerksngaem[‡]
[†]Research Center for Communication and Information Technology (ReCCIT), and
Department of Electronics, Faculty of Engineering,
King Mongkut's Institute of Technology Ladkrabang, Bangkok 10520 Thailand
[‡]Faculty of Allied Health, Thammasart University, Prathumthani, 12121

***Abstract*-Numbers of white blood cells in different classes help doctors to diagnose patients. A technique for automating the differential count of white blood cell is presented. The proposed system takes an input, color image of stained peripheral blood smears. The process involves segmentation, feature extraction and classification. The segmentation procedure, a novel simple algorithm, is proposed for localization of white blood cells and the different cell components are separated with automatic thresholding. Features extracted from the segmented nucleus are motivated by the concept of the well-known Eigen face. The derived Eigen value and Eigen vector contributes to the important feature in the classification process. To further improve the performance, the concepts of principal axis are adopted to automatically align the white blood cell prior to the classification process. The results of the classification are very promising.**

I. INTRODUCTION

White Blood cell composition reveals important diagnostic information about the patients as well as patient follow-up. One of the important counts required by hematologist is differential blood count in which an expert counts 100 white blood cells on the smear at hand and computes the percentage of occurrence of each type of cell counted. The result gives important information about patient's health status and plays an important role in diagnosis. Counting each classes of the white blood cell manually is a tedious, time consuming and qualitative process. An automated differential white blood cell counter is attempting to perform the counting process automatically by analyzing smear images of white blood cell. The process of counting blood cells on smear image requires three steps (1) segmentation, (2) feature extraction and (3) classification.

Automatic white blood cell analysis requires good segmentation algorithm to locate white blood cell. Many conventional image segmentation methods are based on thresholding selection, edge detection or region growing. Among all, thresholding techniques is the simplest method yet produces the acceptable results. They usually combined with mathematical morphology operation to improve the accuracy of segmentation [1-3]. Edge detection performs poorly on cell images because not all cell boundaries are sharp and hence it is difficult to get all the edge information and locate the cell accurately [4]. Region growing methods group neighbouring pixels of similar characteristics to form a segmented region. The method provides reasonably accurate segmentation result of simple scenes with few object and little texture. Region growing methods is hence rarely used for segmenting white blood cell.

Feature extraction is the important process for automated white blood cell classification. The accuracy rate of the subsequent classification relies on the number of extracted feature as well as the characteristic of the feature. Features of white blood cell can be classified into 3 groups: (1) Morphological feature, (2) color feature and (3) texture feature. Morphological feature includes shape and size of nucleus, shape and size of white blood cell, number of nucleus lobe, cell circularity, and nucleus rectangularity [6]. Color feature results from the unique and distinguish characteristic of individual white blood cell to the blood smear. The color information of nucleus is then served as an important feature. Texture features results from the specific granule and chromatin in the nucleus. Texture feature includes mean, standard deviation, skewness, kirtosis, entropy of luminance. A number of classifiers have been purposed for white blood cell classification including Bayes classifiers [7], learning vector quantization (LVQ) [8] and multilayer perceptrons [9]. Performance results vary significantly in the literature depending data set and the extracted features ranging from 61% to 78% with the neuron network achieves the highest accuracy.

In this paper, we introduce the classification of white blood cell based on using principal component analysis to a representative dataset of images of white blood cell. The system functions by projecting white blood cell images onto a feature space that spans the significant variations among known white blood cell images. These significant features are termed "*Eigen cells*" because they are the principal components of the set of training white blood cell image.

The concepts have been widely used for face recognition which is known as *"Eigen faces"* [10]. The performance of the principal component analysis, however, requires that the cell images must be in the same orientation. To rectify the problem, the concepts of principal axis are used to automatically align the white blood cell before the classification process.

II. SEGMENTATION

Images of blood smear are imported to the computer via a color CCD camera. Each color blood-smear image is disintegrated into tristimulus components, i.e. red, green and blue image. We elect to use the green component due to the high contrast between the nucleus and cytoplasm provided as shown in figure. The nucleus is first segregated using automatic thresholding [11]. The noise remained in the segmented image is removed using basic morphological process which is erosion and dilation. The centroid of the nucleus is then determined to locate the nucleus position. The white blood cell is then cropped at the centroid location and later used in the subsequent process.

III. EIGEN CELL

Principal Component Analysis (PCA) is a statistical technique which used to describe a large dimensional space with a relative small set of vectors. It is a popular technique for finding patterns in data of high dimension, and is used commonly in both face recognition and image compression [12]. Application of PCA to face recognition is known as Eigen face. The Eigen face technique is a powerful yet simple solution to the face recognition dilemma. It uses much more information by classifying faces based on general facial patterns. Here we focus on the application of PCA for white blood cell classification –the so-called Eigen cell

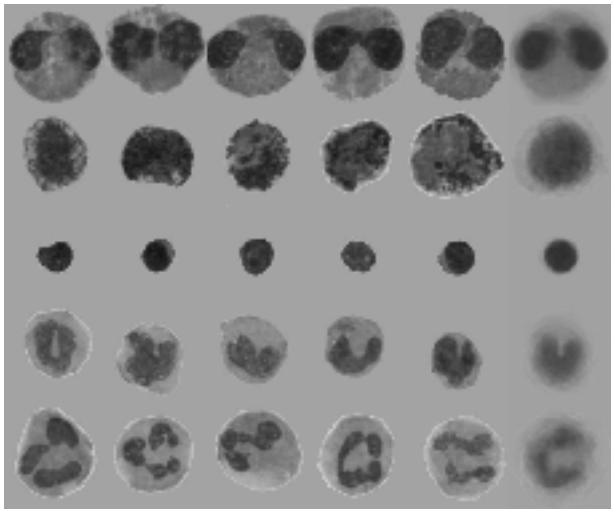

Figure 1 Sample of white blood cell (column 1:5) and averaged Cell (column 6). Row 1: Eosinophil; Row 2: Basophil; Row 3: Lymphocyte; Row 4: Monocyte; Row 5: Neutrophil

The procedure for using Eigen cell is divided into 2 steps. (i) Training step and (ii) Classification step.

The Training step is as follow:

(i) Convert each cropped white-blood-cell image into a vector T_i of length N (N=imagewidth*imageheight). For the M data set, we let the training set represented by, $\{T_1, T_2, T_3, ..., T_M\}$ where T_i is the vector of N^2

(ii) Compute the mean vector Ψ and the set of deviation from the mean vector $\Phi = [\Phi_i, \Phi_2, ...\Phi_M]$ which is defined as

$$\Psi = \frac{1}{M}\sum_{I=1}^{M} T_i \quad (1)$$

$$\Phi_i = T_i - \Psi \quad (2)$$

Figure 1 show the mean vector for each white blood cell (after converted to matrix)

(iii) Compute the covariance matrix C which is defined as

$$C = \frac{1}{M}\Phi\Phi^T \quad (3)$$

(iv) Compute the Eigen value and Eigen vector of C represented as

$$Cv_i = \mu_i v_i \quad (4)$$

Where μ_i is the corresponding Eigen value of Eigen Vector v_i

(v) Project each training set on the Eigen cell-space using the operation

$$\omega_K = (Cv_k)^T (T_i - \psi) \quad (5)$$

$$1 \le k \le M', \ 1 \le i \le M$$

Where v_k is ranked according to their significance. Therefore, for each cell image we would have a set of M' weight

$$\Omega_k = [\omega_i, \omega_2, ..., \omega_{M'}] \quad (6)$$

Which describe the contribution of Eigen Cell to the cell image.

The training process and classification process is summarized in figure 2 and 3 respectively

The classification step is as follow:

(i) Project vector form of the tested cell image T_p to the Eigen cell space using equation (4) to derive Ω_p. The tested cell image is classified to class k which minimized

$$\varepsilon_k^2 = \left\| \Omega_p - \Omega_k \right\|^2 \qquad (7)$$

With $1 \le k \le M$

IV. AUTOMATIC ALIGNMENT USING PRINCIPAL AXIS

The principal axis of arbitrary 2D binary shape of size J x K is the axis that passes through the center of gravity of the shape, namely centroid. Hence the principle axis trends to balance the mass on either side of the axis. In this research, the concepts of principal axis are adopted to align the white blood cell. The axis of white blood cell has a distinct direction. To compute the principal axis, the white blood cell is converted to binary such that on their nucleus remained. Then the covariance matrix of second-order central moment is evaluated on the binary image, .i.e.

$$\mathrm{U} = \begin{bmatrix} \mathrm{U}_{(2,0)} & \mathrm{U}_{(1,1)} \\ \mathrm{U}_{(1,1)} & \mathrm{U}_{(0,2)} \end{bmatrix} \qquad (8)$$

Where Row Moment of Inertia, U(2,0) is defined as

$$U(2,0) = \frac{1}{K^2} \sum_{j=1}^{J} \sum_{k=1}^{K} (x_k - \bar{x}_k)^2 F(j,k)$$

Column Moment of Inertia as

$$U(0,2) = \frac{1}{J^2} \sum_{j=1}^{J} \sum_{k=1}^{K} (y_j - \bar{y}_j)^2 F(j,k)$$

And Row-Column Cross moment of Inertia as

$$U(1,1) = \frac{1}{JK} \sum_{j=1}^{J} \sum_{k=1}^{K} (x_k - \bar{x}_k)(y_j - \bar{y}_j) F(j,k)$$

And where the centroid $(\bar{\mathrm{x}}_\mathrm{k}, \bar{\mathrm{y}}_\mathrm{j})$ is defined as

$$\bar{x}_k = \frac{M(1,0)}{M(0,0)}$$

$$\bar{y}_j = \frac{M(0,1)}{M(0,0)}$$

Where

$$M(m,n) = \frac{1}{J^n K^m} \sum_{j=1}^{J} \sum_{k=1}^{K} (x_k)^m (y_j)^n F(j,k)$$

The principal direction of the white blood cell is then the Eigen value of the covariance matrix *U*. Figure 2 shows the results of the automatic alignment of the white blood cell.

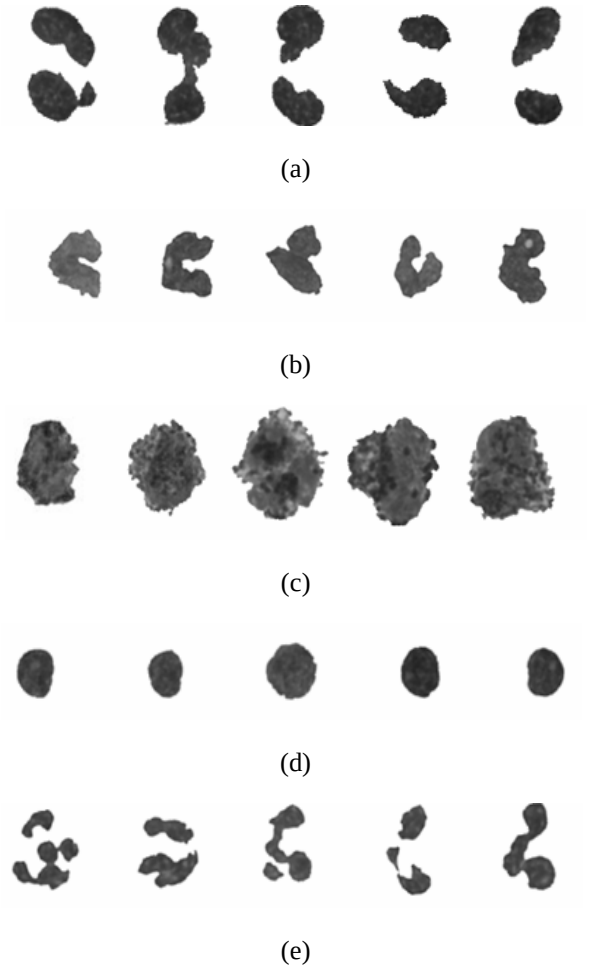

(a) (b) (c) (d) (e)

Figure 2 Aligned White Blood Cell (Only Nucleus Shown); (a) Eosinophil (b) monocyte (c) Basophil (d) Lymphocyte (e) Neutrophil

V. EXPERIMENTAL RESULTS AND DISCUSSION

A library set of 50 patterns of white blood cell is used in the training process. 100 samples of blood smear image which are not in the trained group are used for classification. Before classification, the white-blood cell image requires the pre-processing step to segment only the cell nucleus image and align the individual images as described in section IV. To further improve the performance, the white blood cell is divided based on the number of nucleus lobes into 2 groups which are (i) one lobes and (ii) more -than- one lobes. Each group is then trained and classified separately. For comparison purpose, the classification result is shown in table 1 without the alignment and table 2 with alignment process. The averaged accuracy of 93.64 % can be achieved

with the alignment process while that without the alignment process is only 78.18 %.

Table I
Classification results without alignment

Cell name	Classi-fied No	Misclassified No / As	% Accuracy
Eosinophil	25	16/ Neutrophil	36
Basophil	10	3 / Monocyte	70
Lymphocyte	25	0	100
Monocyte	25	4 / Lymphocyte	84
Neutrophil	25	1 / Eosinophil	96

Table II
Classification results with alignment

Cell name	Classi-fied No	Misclassified No / As	% Accuracy
Eosinophil	25	0	100
Basophil	10	3 / Monocyte	70
Lymphocyte	25	0	100
Monocyte	25	3 / Lymphocyte	88
Neutrophil	25	1 / Eosinophil	96

VI. DISCUSSION AND CONCLUSION

The automatic alignment of white blood cell prior to the application of the principal component analysis has been applied to improve the classification of white blood cell. The alignment is based on using the principal axis. The results of the classification shows significantly improved

REFERENCE

[1] C. Di Rubeto, A. Dempster, S. Khan, B. Jarra, "Segmentation of Blood Image using Morphological Operators", Proceeding 15th International Conference on Pattern Recognition, vol. 3, pp. 397-400, 2000

[2] M. B. Jeacocke, B. C. Lovell, " A multi-resolution Algorithm for Cytological Image Segmentation" , Proceeding of the 1994 Second Australian ands New Zealand Conference on Intelligent Information Systems, pp. 322-326, 1994.

[3] D. Anoraganingrum, "Cell Segmentation with Median Filter and Mathematical Morphology Operation", Proceeding International Conference on Image Analysis and Processing, pp. 1043 -1046, 1999.

[4] I. Cseke, "A Fast Segmentation Scheme for White Blood Cell Images", Proceedings. 11th IAPR International Conference Pattern Recognition, Conference C: Image, Speech and Signal Analysis, vol III, pp. 530-533, 1992.

[5] J. Theerapattanakul, J. Plodpai, S. Mooyen, C. Pintavirooj, " Classification of White Blood Cell Using Adaptive Active Contour " ,ICCAS 2004 , Bangkok Thailand

[6] P.L. Rosin, "Measuring shape: ellipticity, rectangularity, and triangularity", Proceedings. 15th International Conference on Pattern Recognition, vol. 1, pp. 952 – 955, 2000.

[7] J. Cartinhour, " A Bayes classifier when the class distributions come from a common multivariate normal distribution " ,IEEE Transactions on Reliability, vol. 41, Issue 2, pp. 124 – 126, 1992.

[8] N.B. Karayiannis, M.M. Randolph-Gips, " Soft learning vector quantization and clustering algorithms based on non-Euclidean norms: single-norm algorithms " ,IEEE Transactions on Neural Networks, vol. 16, Issue 2, pp. 423 - 435, 2005.

[9] E. Alpaydin, M.I. Jordan, " Local linear perceptrons for classification " ,IEEE Transactions on Neural Networks, vol. 7, Issue 3, pp. 788 - 794, 1996.

[10] Zhujie, Y.L. Yu, " Face recognition with Eigen faces " ,Proceedings of the IEEE International Conference on Industrial Technology, pp. 434 - 438, 1994.

[11] C. Di Ruberto, A. Dempster, S. Khan, B. Jarra, " Automatic thresholding of infected blood images using granulometry and regional extrema " , Proceedings. 15th International Conference on Pattern Recognition, vol. 3, pp. 441 - 444, 2000.

[12] P.L. Venetianter, T. Roska, " Image compression by cellular neural networks " , Proceedings. 15th International Conference on Pattern Recognition, vol. 45, Issue 3, pp. 205 - 215, 1998.

LOAD BALANCING ALGORITHM FOR MULTIPOINT VIDEO CONFERENCING CONTROL UNIT

Jirayu Charoenviriyaphap and Surin Kittitornkun
Dept. of Computer Engineering, Faculty of Engineering,
King Mongkut's Institute of Technology Ladkrabang,
Bangkok, 10520 Thailand
c_jirayu@msn.com, kksurin@kmitl.ac.th

***Abstract*-Today videoconferencing is more popular because the Internet is more widespread and faster than it was in the past few years. Multipoint videoconferencing requires a multipoint control unit (MCU) to mix video/audio and manage the floor. MCU load increases as much as user's growth worldwide. Therefore, distributed MCUs can balance the load from all users. However, we need to equally balance the MCUs by introducing a load-balancer. The contribution of this paper is the balancing algorithm taking into account of %CPU used, %memory used and %bandwidth used.**

I. INTRODUCTION

Videoconferencing is very popular because people do not need to spend the time for conference just 1-2 hours but take more time in traveling. And now internet is faster and cheaper than past e.g. ADSL, leased line and broadband. And internet price is cheaper. Videoconferencing is one choice to saving time and money. Multipoint videoconferencing requires a multipoint control unit (MCU) to manage the floor and connection, encode and decode video from users, mix audio and send to users. Encoding and decoding video and mixing audio consume a lot of resources. When we talk about resource computer, we almost think about CPU, memory and harddisk but for MCU another resource that is important is network resource. Except encoding and decoding video and mixing audio, MCU has a task to manage connection both signaling and data packet.

MCU load increases as much as user's growth. For supporting large users Centralized MCU is changed to distributed MCU and optimized MCU. When we distributed MCUs there are problems about balance of MCU load. Therefore we need to manage MCUs to work equally and accordingly. The main contribution of this paper is the balancing algorithm taking into account of %CPU used, %memory used and %bandwidth used.

This paper is organized as follows. Section II explains H.323 and general load balancing algorithms. We describe our own algorithm and show the experimental results in Section III and IV, respectively. Section V concludes this paper and suggests some future works.

II. H.323 AND LOAD BALANCING ALGORITHM

A. H.323 Multipoint Conference

H.323 protocol is developed by ITU-T (International Telecommunications Union- Telecommunications section) for real-time multimedia communication over IP.

Today H.323 conference system is one of the most famous conference systems. H.323 basically supports one-to-one remote conference, and H.323 also supports multipoint conference using MCU (Multipoint Control Unit).

MCU communicates with all hosts. MCU collects audio and video streams from all hosts, mixes them, and distributes the mixed stream to all hosts. In other words, MCU holds one-to-one conference with all hosts. Therefore, when the number of hosts increases, CPU and network load on MCU become heavier and conference system may become overloaded. To avoid this bottle neck about load on MCU, conference system should adopt the method of distributing the load on MCU. The existing method of load sharing is using multiple MCUs as Fig.1. It distributes the hosts of which MCU has to take care to two or more MCUs to reduce the load on each MCU. This method reduces the load on each host, but it has some problems. When the number of hosts increase, the number of MCUs which is required for load sharing also increases. And the number and location of hosts change dynamically in the conference. But, the number and location of MCUs should be static. Therefore if the number of hosts becomes enormous, MCUs may become overload after all. And if hosts crowd around somewhere, the MCU near the hosts should deal with them, and becomes overload after all.

B. MPEG4MCU [1]

MPEG4MCU [1] can be partitioned into 2 sections as follows

a) Audio Section

Each Connection object corresponds to each client. The client always sends encoded audio stream to the MPEG4MCU. The decoded audio is used by the DetectVoice function for detecting the speaking client.

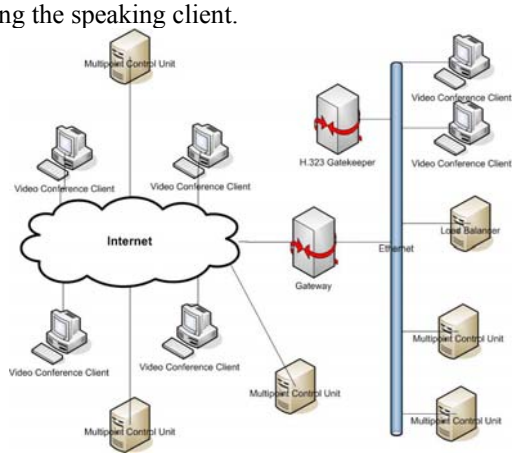

Figure 1 Distributed MCUs [6] Video Conference

b) Video Section

When the video stream from the client come to, the MPEG4MCU will decode and then detect whether this terminal is in the position for video displaying or not. If it is, it copies the video data to the center video buffer in the appropriate position. Finally, it reads the video data from the center video buffer, encode, and then send back to the terminal.

Note that, at any time, the MPEG4MCU will display only 4 users in the video position. So the video data of users outside the video position are still decoded and then leave these resulted in the waste of the network incoming traffic and the CPU Load of the MPEG4MCU.

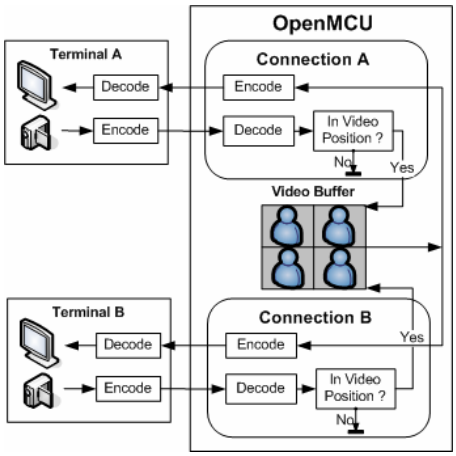

Figure 2 Block Diagram of MPEG4MCU in the video section with 2 terminals

C. Load balancing algorithms

In load-balancing schemes, the two most important policies are information policy and location policy. Information policy will collect load information of each host for location policy decision. When a new task location policy has will consider sending this task to proper host by load information from information policy.

GLOBAL: Every *P* seconds, *load information center* (LIC), receives load updates from all the other hosts and assembles them into *load vector,* which is then broadcast to all the other hosts. When the task arrives to host A, A will look at load vector to find the lowest load host and send the task to. [3]

RANDOM: This algorithm uses only local load information. When a job is found to be eligible for load balancing, it is sent to a randomly selected host. [3]

CENTRAL: In Global algorithm, placement decisions are made by each host using the load vector. In the [3] CENTRAL algorithm, the LIC acts as a central scheduler for all the hosts, in addition to receiving load information from the other hosts periodically. When a host decides that a job is eligible for load balancing, it sends a request to the LIC, together with the current value of its load. The LIC selects a host with the shortest queue length and informs the originating host to send the job there. It is assumed that the loads of all the hosts are known to the placement decision maker(s), with some delay. [3]

THRHLD: A number of randomly selected hosts, up to a limit *Lp* (probing limit), are polled when an eligible job arrives, and the job is transferred to the first host whose load is below load threshold *TI.* If no such host is found, the job is processed locally. [3]

LOWEST: This is similar to THRHLD except that, instead of using a threshold for the placement, a fixed number of hosts *L,,* are polled and the most lightly loaded host is selected. The probing stops if an empty host is found. [3]

Credit-based: The credit-based load-balancing model focuses on these two policies. We assign a numerical value, called credit, to every host. The credit indicates load of the host. The lower its credit has chance to take new task. The credit of each host changes in accordance with the behavior of the system and interaction [2]

III. OUR LOAD BALANCING ALGORITHM

There are two important policies, information policy and location policy in dynamic load balancing algorithm.

A) Information policy:

Load information from each host is very small size when compare with data packets in video conference. So we make decision to collect load from all MCUs to Load Balancer (LB) periodically.

The task of MCU is encoding and decoding video, mixing video and audio and managing floor and transfer data. Therefore load of MCUs is combining of computation load and communication load

$$C_{MCU} = C_{CP} + C_{NW} \quad (1)$$

C_{MCU} = MCU Credit

C_{CP} = Computation Credit

C_{NW} = Communication Credit

A.1) Computation credit is combining of central processing unit (CPU) and memory available because MCU task is encoding and decoding video, mixing video and audio that consume CPU resource and memory.

$$C_{CP} = f_{CP}(W_{cpu}A_{cpu}, W_{mem}A_{mem}) \quad (2)$$

A_{cpu} =Available Central Processor Unit (CPU) (%)

A_{mem} = Available Memory (%)

W_{cpu} = Weight number for CPU load

W_{mem} = Weight number for Memory used

f_{CP} = Computation Weight Function

MCU has variations of CPU powers, memory capacities and network performance. We use MCU_j to represent one of the MCUs in a heterogeneous network of MCUs [4]. We also use

variable P to represent the total number of MCUs in the system. The CPU weight of a workstation refers to its computing capability relative to the fastest workstation in a distributed system. The value of the CPU weight is less than or equal to 1. Since the CPU weight is a relative ratio, it can also be represented by the CPU speed of each node measured by millions of instructions per second (MIPS). If $V_{cpu}(j)$ is the speed of MCU_j in MIPS, j = 1, …, the CPU weight can be expressed as follows:

$$W_{cpu}(j) = \frac{V_{cpu}(j)}{Max_{i=1}^{P} V_{cpu}(i)} \quad (3)$$

Similarly, the memory weight is calculated by comparing the memory sizes among the MCUs:

$$W_{mem}(j) = \frac{Mem_j}{Max_{i=1}^{P} Mem_i} \quad (4)$$

Where Mem_j is the amount of user available memory space in MegaBytes on MCU_j for j = 1, …, P.

A.2) Communication credit is network bandwidth available and delay between host and client. Because each MCU is not on the same network bandwidth and speed between host and client will be different.

$$C_{NW} = W_{bw} A_{bw} + T \quad (5)$$

A_{bw} = Bandwidth usage (%)

T = Percentage of delay time between MCU and client (%)

W_{bw} = Weight number for bandwidth used

$$W_{bw}(j) = \frac{BW_j}{Max_{i=1}^{P} BW_i} \quad (6)$$

H.323 video conference acceptable delay is between 150 – 300 ms [8] so if MCU has delay from MCU and Client > 300 ms we will not choose it and we use 300 ms to convert delay time from ms to percent as below:

$$T = \begin{cases} (300 - delaytime^*) \times 0.33 & delaytime \le 300ms \\ -\infty & delaytime > 300ms \end{cases} \quad (7)$$

* Size of test packet = 64 kilobyte (Maximum size of ping command)

B) Location Policy:

When LB gets load information from each host, LB will convert received load to credit and collect in LB. Conversion method needs to weight the receiving load from each host.

Whenever a new conference room is created, LB will compute the collected credit of each MCU and select any MCU with the highest credit at that moment to serve that new room.

IV. EXPERIMENT AND RESULTS

Our experiment is consist of, Load balancer, MCU and Call generator as show in Fig 3.

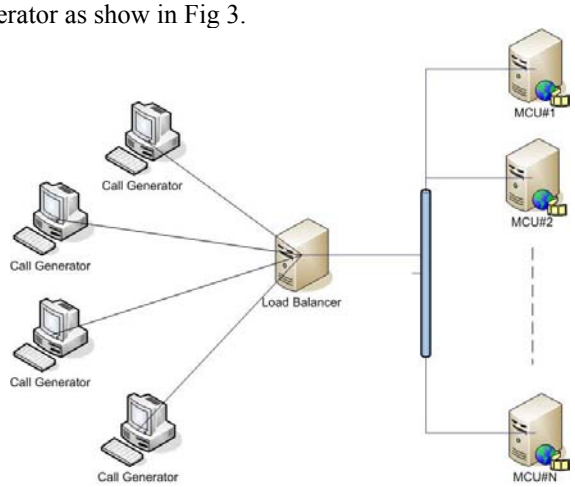

Figure 3 Environment in our experiment using our load balancing algorithm in Eq. (2)

A)Load Balancer(LB)

Load balancer (LB) is an opensoure application from www.codeproject.com that we enhance to collect memory and bandwidth used by the applications to calculate computation and communication credits. LB is developed using Microsoft Visual C++. NET 2003 with winpcap library version 3.01.

B)MCU

We install MPEG4MCU from [1] with no Gatekeeper on several machines as follows:

1) MCU1 = Pentium D CPU 3.0GHz, Memory = 512 MB
2) MCU2 = Pentium 4 CPU 2.8 GHz, Memory = 512 MB
3) MCU3 = Pentium M CPU 1.4 GHz, Memory = 768 MB
4) MCU4 = Celeron 2.6 GHz, Memory = 384 MB

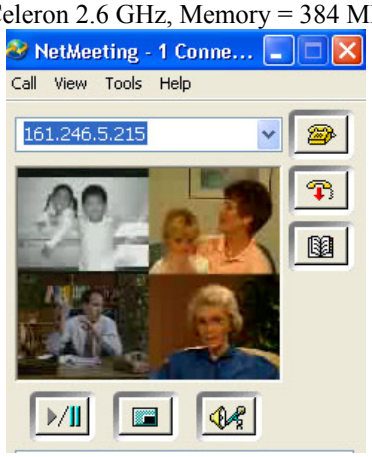

Figure 4. Netmeeting with OpenMCU [7]

C)Call generator

We use call generator from [1] that can send and receive audio and video with following parameters:

Video codec = MPEG-4
Frame rate = 10 Frames/sec
Audio codec = G.711-uLaw-64k (PCM)
Audio Sampling rate = 8 kHz
Users per room = 4 users per room

D) Results

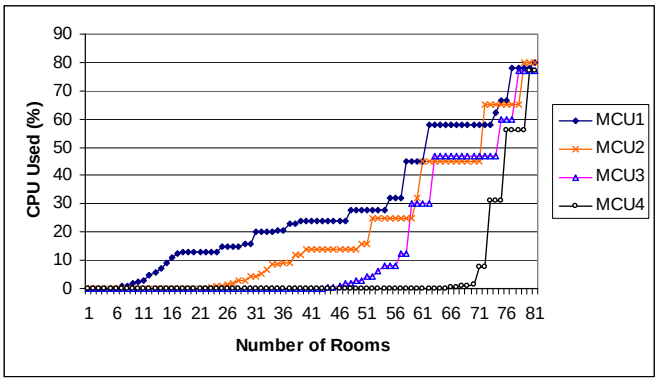

Figure 5. %CPU Used on each MCU

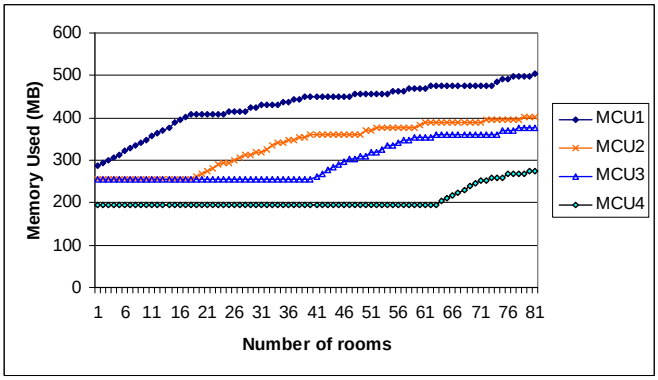

Figure 6. Memory Used in MegaBytes on each MCU

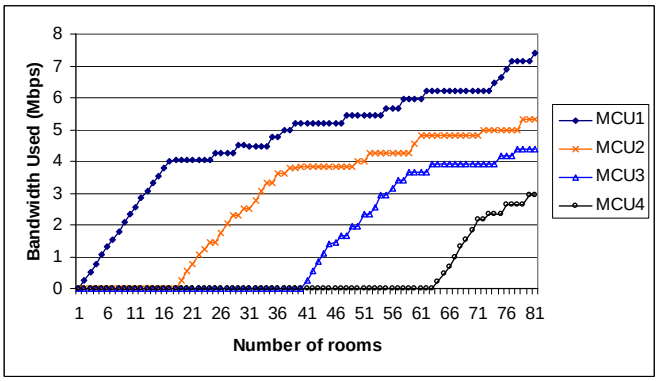

Figure 7. Bandwidth Used in Mbps on each MCU

From the experiment, the proper weighting function between CPU and memory is:

$$f_{CP}(W_{cpu}A_{cpu}, W_{mem}A_{mem}) = W_{cpu}A_{cpu}^2 + W_{mem}A_{mem} \quad (8)$$

we use weighting function (f_{CP}) according to Eq.(8). It can be noticed in Fig. 5, 6, and 7 when we start adding conference rooms until 23 rooms into the system, the LB chooses only MCU1 because MCU1 has the fastest CPU. Then, the LB chooses MCU2 together because of low % CPU used. At 46 rooms in the system, the LB just chooses MCU3 because MCU1 and MCU 2 are quite loaded. Eventually, when Room 70 is added, it is redirected to MCU4 which has the slowest CPU but the least %CPU used.

After we use LB with weighting function, CPU, memory and bandwidth used of all MCUs gradually increase together and no MCU has critical CPU, memory and bandwidth used at anytime.

VI. CONCLUSION

This paper presents a load balancing algorithm for videoconference multipoint control unit (MCU) to manage distributed MCUs in video conference system. We take into account the computation load(%CPU load and %memory used) on the MCUs and communication load between each MCU and its H.323 clients. The decision is based on credit that is a sum of weighted available loads. The load balancer picks the MCU with the highest credit to serve the newly arriving videoconference room.

For future work, we will do more experiments by setting up MCUs running on a variety of CPUs with different memory sizes over an emulated IP network using NISTNET [9] as shown in Fig. 15. Hence, we will measure CPU load, memory used, and bandwidth used in order to compute the proper weighting function for different MCU specification and different network environments. Finally, we will compare our algorithm with others.

REFERENCES

[1] C. Traiperm and S. Kittitornkun, "High Performance Video Conference Multipoint Control Unit with MPEG-4 Codec", ECTI-Con 2005, May 12-13, 2005

[2] Ka-Po Chow and Yu-Kwong Kwok, "On Load Balancing for Distributed Multiagent," *IEEE Transactions on Computing Parallel and Distributed Systems*, 2002, pp. 787-801

[3] Songnian Zhou, " A Trace-Driven Simulation Study of Dynamic Load balancing," *IEEE Transactions* on *Software Engineering,* Volume 14, Issue 9, Sept. 1988

[4] Li Xiao, Xiadong Zhang and Yanxia Qu, "Effective load sharing on heterogeneous networks of workstations," *14th International Proceeding Parallel and Distributed Processing Symposium, 2000. IPDPS 2000.*

[5] T. Kawasaki and K. Okamura, "Evaluation on Scalability of Conference System using Request-Routing," *18th International Conference on Advanced Information Networking and Applications (AINA'04)*, 2004

[6] R. Ventakesha Prasad, H. N. Shankar and H. S. Jamadagni, S. Vijay, "Server Allocation Algorithm for VOIP Conferencing," *Distributed Frameworks for Multimedia Applications*, 2005.

[7] OpenH323 Project, http://www.openh323.org

[8] Prasad Calyam, Mukundan Sridharan, Weiping Mandrawa1 and Paul Schopis, "Performance measurement and analysis of H.323 traffic," *PAM 2004 : passive and active network measurement,* Antibes les Pin, Frances, 19-20 April 2004

[9] Mark Carson and Darrin Santay, NIST Net: a Linux-based network emulation tool, Computer Communication Review (ACM SIGCOMM), 33(3):111-126, 2003.

Continuous Thai Sign Language Recognition using HMM with Transition Models

Arunee Jaruwanawat and Nopporn Chotikakamthorn
Faculty of Information Technology, and
Research Center for Communications and Information Technology
King Mongkut's Institute of Technology Ladkrabang, Bangkok Thailand
(E-mail: s5066025@kmitl.ac.th)

***Abstract*-This paper addresses the problem of continuous Thai sign language recognition. Sign language is typically composed of hand shapes and gestures formed by the movement of hands, arms and perhaps body also. One of the problems in performing continuous sign recognition is the existence of hand and arm movement in transition between two signs. This spontaneous transition movement conveys no meaning. However, not taking it into account results in poor recognition performance. This papers proposes the inclusion of algorithmic-based HMM transition movement models within a HMM-based sign language recognition system. A transition movement is represented by a single-state HMM model, of which its model parameters are obtained algorithmically based on the HMM parameters of the two signs involved in the transition. This avoids the need to collect extensive training data for modeling all possible transition movements in a conventional manner. In addition, to realize continuous sign language recognition, in this paper a pruning strategy for reducing the complexity of a Viterbi search is also described. Based on the experiment result, inclusion of such model within a HMM-based recognizer was found to offer improved recognition performance.**

***Keywords*- Sign Language, Hidden Markov Model, Transition Movement**

I. INTRODUCTION

People with hearing and speech impairments communicate within their communities through the use of a sign language. Use of this specialized language, however, is limited to those who have acquired knowledge of the language. This largely prevents deaf people from communicating with those outside their communities. Also, while currently there exists a speech recognition system, allowing a computer user to input textual data through voice, there is not yet an equivalent product for deaf people. A sign language recognition system has been seen as an enabling technology to allow for natural human-computer interaction, as well as to assist in communications between those who understand the sign language as those who do not.

Previous works in continuous sign language recognition, with the emphasis on problems related to transition movement, include those of [1-6]. In [1], equipped with an electronic glove device and a 6-DOF tracking sensor, a method was proposed to segment continuous sentences such that transition movement can be removed before the segmented data being processed by a HMM-based recognizer. This 'hard' pre-segmentation strategy is, however, suboptimal as compared to a 'soft' segmentation inherent in a general HMM-based pattern recognition method, where segmentation and recognition are jointly performed to achieve optimal result. In [2, 4], transition movements are first extracted. This extracted data is then used to perform data clustering using a Dynamic Time Warping (DTW) method. The so-obtained clusters are used to form HMM models for transition movements. The problem with this method based on conventional HMM model construction is its need for extensive training data to sufficiently cover possible transition movement patterns.

In [3], a large vocabulary sign language recognition is considered. Due to a large sign database, extensive Viterbi search is required. The solution suggested in [3] is based on a two-stage classification strategy. A sign gesture input is first classified into one of the clusters of similar signs. Then, a Viterbi search is performed on a small subset of HMM models corresponding to signs belonging to that cluster. Although efficient computation is obtained, this two-stage classification method is suboptimal for the search is performed over a subset of a set of all feasible solutions. It also results in poorer recognition rate as compared with a direct search over all feasible HMM models [1].

Most research works in sign language recognition deal with languages used by people of large population such as American and Chinese sign languages. However, it is known that a sign language, like its spoken language counterpart, is different from one region to another. For Thai sign language, early works include those of [5-6]. In [5, 6], a Thai sign language recognition system based on a statistical-based estimator was described. The method performs a pre-segmentation of input data from an electronic glove into static and dynamic gestures. Recognition is performed from the classified data using a Bayesian estimator. The method can perform recognition of signs with certain regularity in the movement patterns. However, it cannot deal with signs of irregular patterns, as well as transition movements. A solution to automated Thai sign language recognition based on HMM models was suggested in [5]. Use of HMM models allows signs of arbitrary movement patterns to be handled in a unified manner. However, the method in [5] was applied on a single-sentence basis. In [6] a method was developed to classify periodic gestures as found in Thai sign language and those with non-periodic nature, of which transitional gestures form a large part of them. However, the method in [6] can not differentiate between some non-periodic and yet meaningful gestures from those due to transition movements. No known work has been done on recognition of continuous Thai sign language containing both periodic and non-periodic gestures.

In this paper, a problem of continuous Thai sign language recognition is considered. In particular, the problem due to the existence of a transition movement is addressed. It is known that, by neglecting such spontaneous movement in modeling the recognition system, recognition performance is degraded [3]. The method described in this paper is based on a HMM model. Unlike those in [2, 4], this paper proposes an algorithmic-based method for construction of a transition model. This avoids the need for

collection and processing of extensive training data for transition movements. Also, it can be used to handle transition movement between any two arbitrary signs. To address complexity in performing Viterbi search on continuous signs, a pruning strategy based on the detection of static signs is also described.

This paper first introduces a general framework of a Thai sign language recognition system in Section 2. Then, a detailed discussion on modeling a transition movement is described in Section 3. A Viterbi search strategy is also given. Experimental result is provided in Section 4, with concluding remarks given in Section 5.

II. THAI SIGN LANGUAGE RECOGNITION SYSTEM

Like other sign languages, Thai sign language is composed of hand shapes and gestures formed by the movement of hands, arms and body. Sometimes, facial expression also plays a crucial role in sign interpretation. Here, only part of the gestures formed by hand shapes and movement of hands and arms are considered. In this study (see Figure 1), a sign gesture is roughly classified into static (posture) and dynamic gestures. Dynamic gestures are further classified into sign movements and transition movements.

- Static gesture (posture) is a sign of which there is no hand or arm movement. Only the hand posture that defines the meaning of the sign.
- Dynamic gesture contains a hand/arm movement. It is further divided into
  - dynamic signs, which are meaningful hand movement, and
  - transition movements, which occur during the transition from one sign to another and convey not meaning.

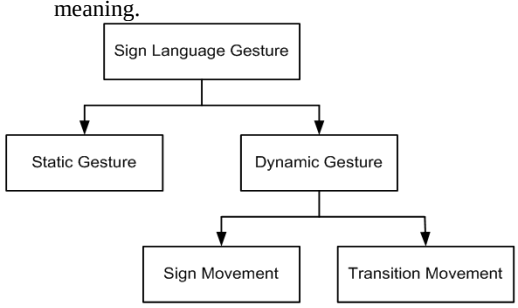

Figure 1. Classification of Thai sign gestures

An overall view of the Thai sign language recognition system, which contains the work described here as its part, is illustrated in Figure 2.

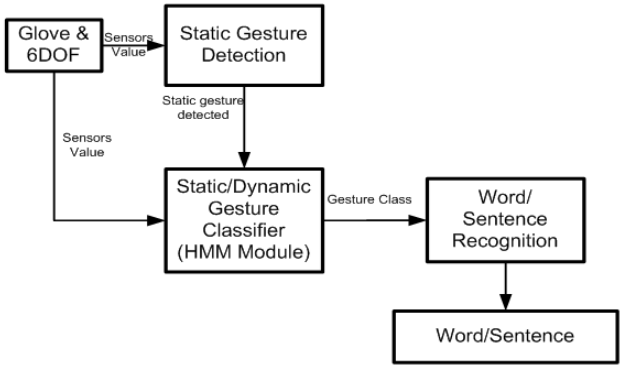

Figure 2. Block diagram of the continuous Thai sign language recognition system.

From the figure, the system is composed of four main parts. The first one is responsible for acquisition of hand shapes and movements. Here, an electronic glove with a 6-DOF electro-magnetic sensor is used as an acquisition device. The second part is the HMM-based gesture recognizer. The third part is the static gesture detector. The result of the detection is used to assist the HMM recognizer in selecting feasible Viterbi paths (pruning). And the last part is the word/sentence recognizer. This part uses the result from the gesture recognizer, along with a sign language model, to produce the final recognized word/sentence. In this paper, the focus is mainly on the second and, to a lesser extent, the third parts of the system.

III. CONTINUOUS THAI SIGN LANGUAGE RECOGNITION WITH ALGORITHMIC-BASED TRANSITION MODELS

A. Modeling the transition movement

Here, an HMM model is adopted for the recognition of both static and dynamic signs. As pointed out by previous work [2, 4], transition movement should be incorporated in the model to improve recognition rate. Instead of directly training the model using data of transition movements, in this paper we propose that a transition movement is modeled using a single state HMM of which its model parameters are obtained algorithmically at run-time. Thus, given two signs (the last states of the word models A and B respectively) connected by a particular transition movement, the series of interconnected HMM models is described by Figure 3.

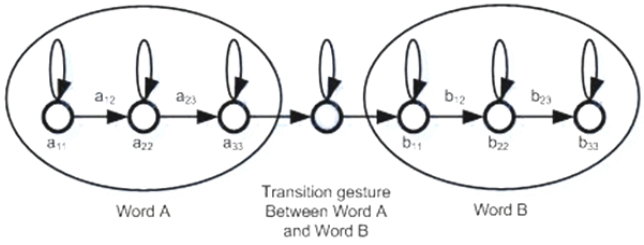

Figure 3. Series of HMM states, connected by a transition state, to model continuous signing.

In our study, a single-state HMM transition model is constructed at run-time based on HMM parameters corresponding to the last state of Word A and the first state of Word B. To explain the algorithm, some notations for HMM models are first introduced. Let (π, A, μ_i, U_i) be an HMM model parameters corresponding to the first word (Word A in Figure 3). Here, π is the initial probability of being in the first state. **A** is a matrix of state transition probabilities. In addition, μ_i is the means vector of the i^{th} state outcome and U_i is the corresponding covariance matrix. Similarly, (π', A', μ_i', U_i') are HMM parameters corresponding to the second word (Word B in Figure 3). In addition, we define $(\overline{\pi}, \overline{A}, \overline{\mu}, \overline{U})$ as model parameters corresponding to the single-state transition model. These parameters are obtained below.

First, because each transition model is designed for a particular pair of sign words, its initial probability can be set to $1 - a_{33}$, where a_{33} is the probability that the system, once reaching the last state in

Word A, remains on the same state. Next, because the model contains a single state, $\overline{A}$ is scalar. It is set to 1 - π'. The model parameters related to the outcome probability is obtained according to the following equations.

$$\bar{\mu} = \frac{\mu_3 + \mu'_1}{2} \quad (1)$$

$$\overline{U}_{11} = \frac{U_{3,11} + U'_{1,11}}{2} \quad (2)$$

$$\overline{U}_{12} = \overline{U}_{21}^{T} = 0 \quad (3)$$

$$\overline{U}_{22} = \begin{bmatrix} \sigma_1^2 & & & \\ & \sigma_2^2 & & \\ & & \ddots & \\ & & & \sigma_N^2 \end{bmatrix} \quad (4)$$

From Eq. (2), $\overline{U}_{11}$ is the $M \times M$ top-left submatrix of $\overline{U}$, where M is the number of data points obtained from an electronic glove. Similarly, $U_{3,11}$ and $U'_{1,11}$ are the $M \times M$ top-left submatrice of U_3 and U'_1 respectively. In Eqs (3, 4), $\overline{U}_{12}$, $\overline{U}_{21}$, and $\overline{U}_{22}$ are the remaining submatrice of $\overline{U}$ (see Figure 4, for an illustration). The size N of $\overline{U}_{22}$ is equal to the number of data points obtained from a 6-DOF electromagnetic location sensor (N = 6). The variance parameters in Eq. (4) are obtained from the following equation.

$$\sigma_i^2 = \{|\mu_{3,M+i} - \mu'_{1,M+i}| / \alpha\}^2 \quad (5)$$

Here, $\mu_{3,M+i}$ is the mean value at the third state in the first word model, corresponding to the ith data point from the location sensor. In addition, $\mu'_{1,M+i}$ should be interpreted similarly. From the same equation, α is a scaling factor, arbitrarily chosen as 6.

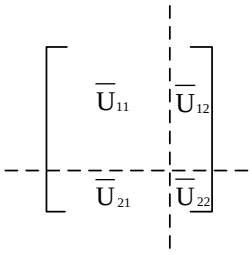

Figure 4. Decomposition of $\overline{U}$ into four submatrice

B. Viterbi search strategy

Generally, pattern recognition by HMM model involves a search for a best path (i.e., a sequence of HMM states) using a Viterbi algorithm. However, for continuous sign language recognition, with medium to large vocabulary support, the search complexity and space is increased significantly. To maintain the search complexity and memory space requirement to a practically realizable level, certain search strategy must be applied to a standard Viterbi algorithm. Here, by observing that many words in Thai sign language are composed at least partly of static signs, those static moments are detected and utilized (along with some heuristic rules) as part of the pruning strategy in an attempt to keep the number of active paths to an acceptable figure. The search strategy used here is summarized in Figure 5.

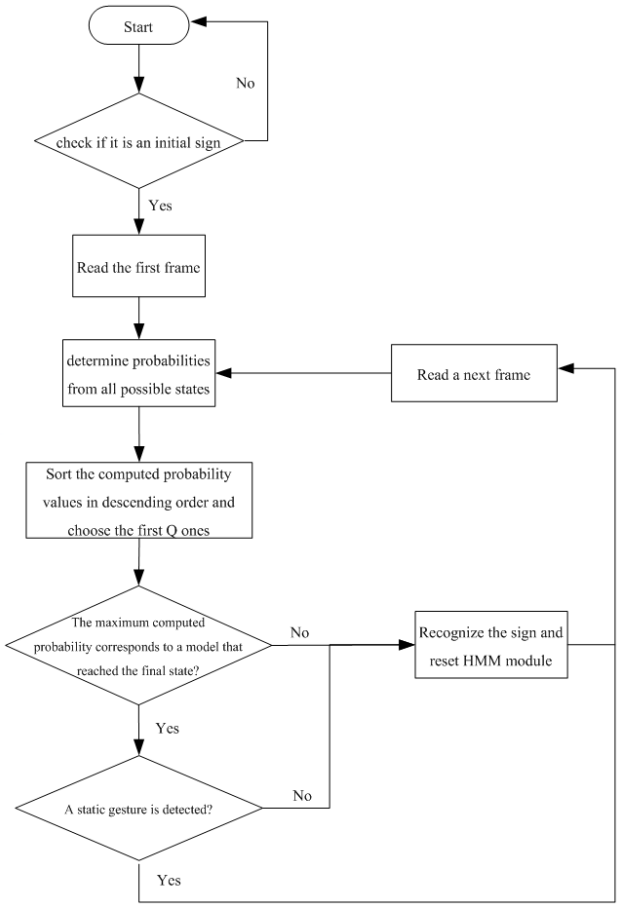

Figure 5. A flow chart describing a pruning strategy, to be used with a standard Viterbi algorithm

From Figure 5, the parameter Q is the maximum number of feasible Viterbi paths that can be kept at any time instance. Therefore, from time to time, rules must be enforced to select Q best paths from all candidates. Here, in addition to a simple accumulated probability sorting, it is proposed that a detection of static sign is used to significantly reduce infeasible paths. Detail of a static sign detector is not given here. It is, however, similar to that used in [6].

IV. EXPERIMENTAL RESULT

The experiment was carried out based on 13 sentences of everyday use. Each sentence is composed of 2-3 words on average and was selected from [7]. For each sentence, 20 data sets were collected using a right-hand electronic glove and a 6-DOF location sensor. A signer performed each sentence by starting in the pre-defined initialized position. In summary, 40 data sets were collected for each sign word. Of these, 30 sets were used for training and the remaining data sets were used for testing.

Two HMM-based sign language recognition techniques were applied to the same data sets. The first one employed the proposed transition models as part of the HMM models. The second one did not model the transition movement. For the latter model, each HMM sign model was simply connected to the next one. The results are shown in Tables 1 and 2. From the tables, it is seen that the proposed method offers noticeable performance improvement. It is noted, however, that this is achieved without additional work on training the transition movement.

Table 1. Recognition performance using the method with algorithmic-based transition models

Sentence	Word sequence	Accuracy (%)
1. I was born in Denmark.	Born-Denmark	100
2. I met him in Denmark.	Meet-Him-Denmark	80
3. Please, sit down.	Please-Sit	100
4. Your mom is fine.	Mother-Fine	95
5. Today is Monday.	Today-Monday	95
6. I take a rest on Friday.	Friday-Rest	80
7. I have ten relatives.	Relative-Ten	85
8. I have ten goats.	Goat-Ten	85
9. I study English on Monday.	Monday-Study-English	90
10. I'll go swimming in the day after tomorrow.	Swim-The day after tomorrow	100
11. Orange has a sour taste.	Orange-Sour	90
12. Elephant is big.	Elephant-Big	80
13. Frog eat fly.	Frog-Eat-Fly	90

Table 2. Recognition performance using the method without modeling transition movement.

Sentence	Word sequence	Accuracy (%)
1. I was born in Denmark.	Born-Denmark	75
2. I met him in Denmark.	Meet-Him-Denmark	70
3. Please, sit down.	Please-Sit	85
4. Your mom is fine.	Mother-Fine	80
5. Today is Monday.	Today-Monday	85
6. I take a rest on Friday.	Friday-Rest	70
7. I have ten relatives.	Relative-Ten	70
8. I have ten goats.	Goat-Ten	75
9. I study English on Monday.	Monday-Study-English	75
10. I'll go swimming in the day after tomorrow.	Swim-The day after tomorrow	80
11. Orange has a sour taste.	Orange-Sour	75
12. Elephant is big.	Elephant-Big	70
13. Frog eat fly.	Frog-Eat-Fly	75

V. CONCLUSION

In this paper, the problem of modeling transition movements for Thai sign language recognition has been addressed. The transition models, based on algorithmic construction at run-time, have been described. It has been verified through the experiment that the use of the proposed transition model offers improved performance over the standard HMM-based method without transition movement modeling. The improvement is attained without the need for additional training work for modeling these spontaneous movements.

REFERENCES

[1] F. Gaolin and G. Wen, *"A SRN/HMM system for signer-independent continuous sign language recognition"*, Automatic Face and Gesture Recognition, 2002. Proceedings. Fifth IEEE International Conference on, 20-21 May 2002 Page(s): 297 -302

[2] G. Wen, F. Gaolin, Z. Debin and C. Yiqiang, *"Transition Movement Models for Large Vocabulary Continuous Sign Language Recognition"*, Automatic Face and Gesture Recognition, 2004. Proceedings. Sixth IEEE International Conference on, 17-19 May 2004 Page(s):553 - 558

[3] Y. Guilin, Y. Hongxun, L. Xin and J. Feng, *"Real Time Large Vocabulary Continuous Sign Language Recognition Based on OP/Viterbi Algorithm"*, Pattern Recognition, 2006. ICPR 2006. 18th International Conference on, Volume 3, 20-24 Aug. 2006 Page(s):312 - 315

[4] G. Fang, W. Gao and D. Zhao, *"Large-Vocabulary Continuous Sign Language Recognition Based on Transition-Movement Models"*, Systems, Man and Cybernetics, Part A, IEEE Transactions on Volume 37, Issue 1, Jan. 2007 Page(s):1 – 9

[5] C. Siam and V. Wuttichai, *"Isolated Thai Sign Language Recognition System using Hidden Markov Models"*, Proceedings of the 25th National Electrical Engineering Conference (EECON-25), Hadyai, Thailand, November 21-22, 2002.

[6] Worawit Werapan, *"Gesture Segmentation and Recognition Techniques for Automated Thai Sign Language Translation"*. Master of Science in Information Technology School of Graduate Studies, King Mongkut's Institute of Technology Ladkrabang, 2005.

[7] The National Association of the Deaf in Thailand, *The Thai Sign Language Dictionary: Revised and Expanded Edition*, Thai Watana Panich, 1990.

Shape-Based Object Segmentation by 2-Stage Level Set Method

Sarawut Tae-O-Sot[1], Supatana Auethavekiat[2] and Somchai Jitapunkul[3]
[1]Electrical Engineering Department,
Naresuan University Phayao Campus, Phayao, 56000, Thailand
[2] National Electronics and Computer Technology Center, Patumthanee 12120, Thailand
[3]Center of Excellence in Telecommunication Technology,
Department of Electrical Engineering,
Chulalongkorn University, Bangkok, 10330, Thailand

***Abstract*- In this paper, we propose the shape-based object segmentation method. Our method is divided into two stages. In the first stage, we estimate the coefficients of the eigenshape of the object and the pose parameters to match the eigenshape to the actual object shape. In the second stage, we fine tune the result of the first stage. Level set method is used in the second stage. We test our method on both synthetic and cardiac MRI. From the experiment, our method gave the boundary that was near the actual boundary in every test.**

I. INTRODUCTION

Extracting organs from medical images is a tedious and time consuming task. So, automatic segmentation is preferable. The desired accuracy of medical image segmentation is high; however, segmentation algorithms, which work well on general image, do not give the satisfy results because medical images have poor contrast, high noise and missing boundary information.

Active contour methods, introduced by Kass *et al*. [1], are widely accepted as the efficient segmentation algorithm. Edge contour is extracted according to image force, defined by gradient of the image, and internal force, defined by the curve characteristic. This method fails to extract edges at the sharp corner. Melladi *et al*. [2] introduced level set for image segmentation. Edge is extracted as the pixels with the zero signed distance value. Both active contour and level set method use intensity gradient to define image force. Estimation of this gradient is very sensitive to noise. Chan and Vese [3] defined image force as the function of the region homogeneity. Their method works well on segmenting regions with no distinct edge.

Image information alone is not sufficient for extracting organs in medical images, because the intensity variation among organs is not always distinct. In addition to image information, object shape must also be considered. Chen *et al*. [4] used mean shape of the training set as prior knowledge. The contour must minimize the sum of distance from the extracted object to the mean shape and image energy. Leventon *et al*. [5] derived shape parameters by PCA on a set of signed distance of training images. Segmentation is under the influence of image force and shape parameters estimated by MAP. The shape parameters are estimated every iteration of level set computation. Tsai *et al*. [6] also represented the model by parameters derived from PCA. Tsai method estimated the coefficients of the eigenvector and used the estimated coefficient to construct the segmentation results.

Because we cannot find all eigenvectors from the limited number of training data, error from the image reconstructed by PCA is unavoidable. However, segmenting curve from Tsai is still useful. To improve the segmentation result, fine tuning process, which can move the contour to the actual boundary, is considered. However, from our review, there is no work specific on this issue. Nonetheless, it can improve the results with very few noticeable differences on complexity.

In this paper, we propose the two-stage level set segmentation method. In the first stage, we adopted the algorithm by Tsai *et al*. to estimate and extract the object shape. In the second stage we fine tune the result by moving the edge inside the area near the estimated shape (from the first stage). In this stage, we applied the segmentation technique of Chan and Vese.

The rest of this paper is organized as follows. Section II explains how we extract the shape information and reconstructed the object shape for the given image (first stage). The fine tuning (second stage) is described in Section III. Section IV shows experimental results and discussion. We then conclude this paper in Section V.

II. SHAPE INFORMATION EXTRACTION AND SHAPE RECONSTRUCTION

A. Training Image Alignment

Object shapes are built from the set of objects extracted by experts. The shapes are represented by binary format with pixel value "one" inside the object and otherwise "zero". All training shapes are aligned to the same pose and scale. Following the algorithm of Tsai *et al*. we align binary images by estimating the pose parameter giving the minimum cost. The cost function is defined as follow:

$$E_{align} = \sum_{i=1}^{n} \sum_{\substack{j=1 \\ j \neq i}}^{n} \left\{ \frac{\iint_{\Omega} \left(\tilde{I}^{i} - \tilde{I}^{j} \right)^2 dA}{\iint_{\Omega} \left(\tilde{I}^{i} + \tilde{I}^{j} \right)^2 dA} \right\}, \quad (1)$$

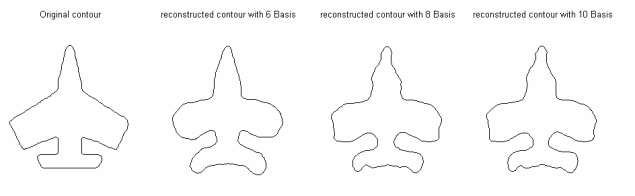

(a) (b) (c) (d)

Figure 1. The error of shape reconstruction. (a) Original Shape. (b) – (d) Reconstructed Shape using 6, 8 and 10 bases.

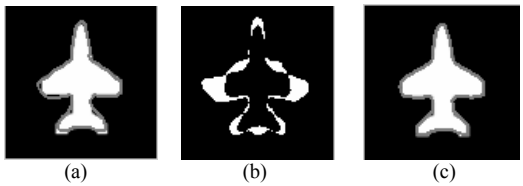

(a) (b) (c)

Figure 2. (a) boundary from the first stage. (b) Active region of (a) with b=1 and k=2. (c) Segmenting curve after fine tuning.

where $\tilde{I}^i(\tilde{x},\tilde{y}) = I^i(T[\mathbf{p}][x\ y\ 1]^T)$, the i th binary image, and Ω denotes the image domain. The pose parameter, $\mathbf{p}$, consist of x-, y-translation, scale and rotation. The optimal pose parameters are found by gradient descent method.

B. Shape Representation

Signed distance function is used to represent the object shape. Pixels inside and outside the object have the negative and positive signed distance value, respectively. The magnitude of the signed distance function represents the distance of the pixel to the nearest edge. The boundary is embedded in the pixels with the zero signed distance value. The shape variation is captured via mean-offset functions $\{\tilde{\boldsymbol{\Psi}}_1, \tilde{\boldsymbol{\Psi}}_2, ..., \tilde{\boldsymbol{\Psi}}_n\}$, which are the value of n signed distance function subtracted by their mean level set function $\overline{\boldsymbol{\Phi}}$ at that position. The mean level set function is defined by,

$$\overline{\boldsymbol{\Phi}} = \frac{1}{n}\sum_{i=1}^{n} \boldsymbol{\Psi}_i, \tag{2}$$

where $\boldsymbol{\Psi}_i$ is the signed distance function of image i. Each mean offset function is stored in lexicographical order forming $N = N_1N_2$ elements vector. The n principal bases from n training curves are found by eigenvalue decomposition of $(1/n)\mathbf{S}\mathbf{S}^T$, where $\mathbf{S}$ is the $N\times n$ matrix defined by $\mathbf{S} = [\tilde{\boldsymbol{\Psi}}_1\ \tilde{\boldsymbol{\Psi}}_2\ ...\ \tilde{\boldsymbol{\Psi}}_n]$. Eigenvalue decomposition is defined by following equation:

$$\frac{1}{n}\mathbf{S}\mathbf{S}^T = \mathbf{U}\Sigma\mathbf{U}^T. \tag{3}$$

The n orthogonal bases are stored in each column of $\mathbf{U}$. We re-order the column of $\mathbf{U}$ from N_1N_2-D vector into $N_1\times N_2$ matrix, called eigenshape ($\boldsymbol{\Phi}$). The magnitude of eigenvalue shows the degree of variation among the training shapes in the direction of the corresponding eigenshape. Small eigenvalue indicates small variation from the mean value. Small variation can be ignored, so, at this eigenshape direction, the mean level set is sufficient to represent the entire set of training shapes. Thus, the shape can be represented as follow:

$$\boldsymbol{\Phi}[\mathbf{w}] = \overline{\boldsymbol{\Phi}} + \sum_{i=1}^{k} w_i \boldsymbol{\Phi}_i, \tag{4}$$

where $k \le n$ and w_i is the result of projecting image to $\boldsymbol{\Phi}_i$. By varying $\mathbf{w}$, the shape is changed. The pose of the object can be changed by adding the pose parameter into equation (4) as shown in equation (5).

$$\boldsymbol{\Phi}[\mathbf{w},\mathbf{p}](x,y) = \overline{\boldsymbol{\Phi}}(\mathbf{p}) + \sum_{i=1}^{k} w_i \boldsymbol{\Phi}_i(\mathbf{p}) \tag{5}$$

C. Segmentation Process

The segmentation follows the algorithm of Chan and Vese [3], which segments an image into two regions with homogenous intensity. This segmentation is the problem of minimizing the following function:

$$\begin{aligned} E(C) = {} & \lambda_i \int_{inside(C)} \left| I(x,y) - \hat{I}_i \right|^2 dxdy \\ & + \lambda_o \int_{outside(C)} \left| I(x,y) - \hat{I}_o \right|^2 dxdy \end{aligned} \tag{6}$$

which is equivalence to the energy function of $\mathbf{w}$ and $\mathbf{p}$ parameter defined in equation (7).

$$\begin{aligned} E(\mathbf{w},\mathbf{p}) = {} & \lambda_i \int_{\Omega} \left| I - \hat{I}_i \right|^2 H(-\boldsymbol{\Phi}(\mathbf{w},\mathbf{p}))dA \\ & + \lambda_o \int_{\Omega} \left| I - \hat{I}_o \right|^2 H(\boldsymbol{\Phi}(\mathbf{w},\mathbf{p}))dA. \end{aligned} \tag{7}$$

where

$$H(x) = \begin{cases} 1 & \text{if } x < 0 \\ 0 & \text{if } x \ge 0. \end{cases}$$

The optimal $\mathbf{w}$ and $\mathbf{p}$ are found by gradient descent method. The boundary of an object is extracted from the zero level of $\boldsymbol{\Phi}(\mathbf{w},\mathbf{p})$.

III. Fine Tuning Process

Because we use fewer bases than the available basis, the extracted boundary does not exactly match the boundary of an object as shown in Figure 1. In this Figure the error exists; although, we use all eigenshapes. Nevertheless, we found that the extracted boundary is near the actual boundary. By fine tuning the extracted boundary, it is possible to move the boundary to the actual boundary. We applied the segmentation algorithm of Chan and Vese in our fine tuning stage; however, we restrict the area that the boundary can moves. We call this area "active region" and define the area by the following function:

$$A_{Active} = \left| H(\boldsymbol{\Phi}_k[\mathbf{w}_k + b\boldsymbol{\sigma}_k, \mathbf{p}]) - H(\boldsymbol{\Phi}_k[\mathbf{w}_k - b\boldsymbol{\sigma}_k, \mathbf{p}]) \right|, \tag{8}$$

where b controls region size and $\boldsymbol{\sigma}$ is the standard derivation of the eigenshapes. A_{Active} is one in the active region and zero, otherwise. For a small b, the active region is narrow. The active region would be narrow on the region that the curve has low variation, and vice versa. To build the active region, we use only the eigenshape with large variation (large eigenvalue). Figure 2(b) shows the active region of fighter jet image boundary from first stage, as shown in figure 2(a), with b=1 and k=2.

Now, the signed distance values are changed by the following equation,

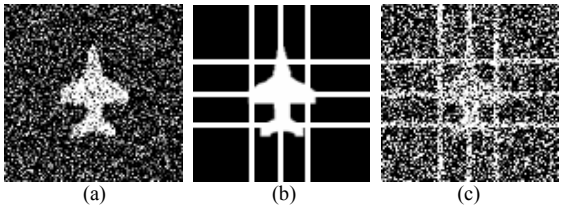

(a) (b) (c)

Figure 3 Examples of synthetic image which have been tested. (a) Fighter jet image with noise. (b) Fighter jet image with occlusion. (c) Fighter fet image with noise and occlusion.

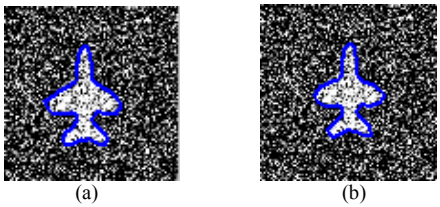

(a) (b)

Figure 4. (a) Segmenting curve of the first stage. (b) Segmenting curve after fine tuning.

$$\frac{\partial \Phi}{\partial t} = \delta(\Phi) A_{Active} \left[\mu K + \lambda_i (I - \hat{I}_i)^2 - \lambda_o (I - \hat{I}_o)^2 \right], \quad (9)$$

where K and is a curvature of the level set function.

IV. Experiment

A. Quality Assessment

In this paper, we used two techniques, area similarity [7] and distribution of distance from reference boundary, to measure and compare the quality of our segmentation method to Tsai's method. In order to have the absolutely correct segmentation result, we used the synthetic image to assess the segmentation method.

1) Area Similarity: In this method, we compare the area of the segmented object with the reference object. Let A and A_R be the binary images of segmenting curve and the reference object templates which pixel with value "one" lies inside the object and pixel with value "zero" lies outside the object. Area similarity can be calculate by

$$S_{area} = \frac{2n(A_R \wedge A)}{n(A_R) + n(A)} \quad (10)$$

where $\wedge$ is "and" operator and $n(\cdot)$ is the number of the pixel inside the object.

2) Distribution of Distance from Reference Boundary: This technique shows the number of pixels on the curve which are far from reference curve for each distance range. Let distance from any point (x,y) to curve C be

$$D(x,y) = \begin{cases} -\min\limits_{(i,j)\in C} \sqrt{(x-i)^2 + (y-j)^2}, (x,y) \text{ is inside } C \\ \min\limits_{(i,j)\in C} \sqrt{(x-i)^2 + (y-j)^2}, (x,y) \text{ is outside } C. \end{cases} \quad (11)$$

The distribution of distance from pixels on the extracted boundary to the reference boundary indicates the accuracy of the segmentation. If the distribution concentrates near zero, the accuracy of segmentation is high.

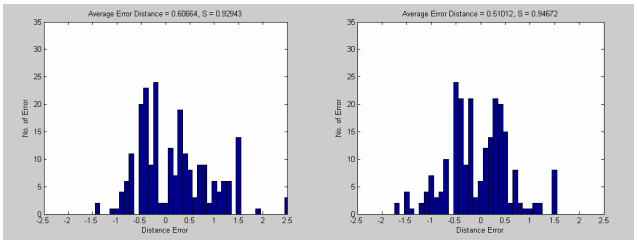

(a) (b)

Figure 5. (a) Distribution of distance from reference curve of Figure 3(a). (b) Distribution of distance from reference curve of Figure 3(b).

B. Result and Discussion

We test our proposed method with synthetic and medical image. The performance of our method is compared with Tsai's method by the proposed assessment.

1) *Synthetic image:* We used fighter jet images, which are the jet shape binary image, in this experiment. The eigenshapes were calculated from 12 training shapes. In the algorithm of Tsai *et al*., we approximated the coefficients of k eigenshapes, then we used this result as the result of the first stage in our algorithm. In this experiment, we corrupted the jet image by adding noise and occlusion which can be shown in Figure 3. The example of Tested image with noise adding is shown in Figure 3(a). Figure 3(b) shows the image with occlusion and Figure 3(c) shows the image corrupted by both noise and occlusion. In this experiment, we vary the parameter b, the size of active region, and the number of basis k. the experimental result show that our proposed method outperforms in all three cases. Increasing k does not always improve the performance of the first state but, surely, reduce the computational time because more parameters have to calculate. The segmentation performance seems always increase when we increase b and it would saturate at some point. However, in binary image with occlusion, the segmentation performance would drop when b still increase. This means that too much b would decrease the prior information. The curve from the first stage is just the good initial for the second stage but, finally, the curve would act like traditional Chan-Vese algorithm when too much b is used. Figure 4 shows the segmentation result of our proposed method comparing with Tsai's Method when we set b=1 and k=2. Figure 4(a) and 4(b) show the result of Tsai *et al*. method and our method respectively. Comparing Figure 4(a) with 4(b), we found that our extracted boundary fit more into the object than the boundary from Tsai's method. Figure 5(a) and 5(b) are the graphs showing the distribution of distance from reference boundary from the result of Tsai's method and our method, respectively. The result of our algorithm had the range of the distribution distance from -1.75 to 1.5 which is less than the range from Tsai's method (-1.5 to 2). In addition, the number of the pixels with the distance larger than +1 is less in our results. The average error distance and the area similarity of the results from the method of Tsai and our method are shown in Table 1. It is very clear that our method gave the result with smaller average error distance and higher area similarity.

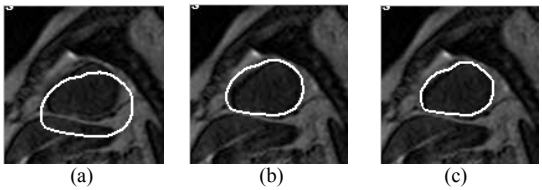

(a) (b) (c)

Figure 6. Segmentation result of cardiac MRI. (a) Initial curve. (b) Segmentation result of Tsai's method. (c) Segmenting curve after fine tuning.

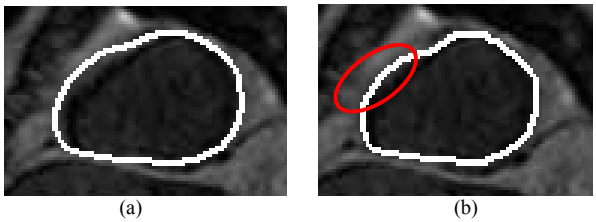

(a) (b)

Figure 7. (a) Enlarged image of Figure 5(a). (b) Enlarged image of Figure 5(b).

2) *Medical Image:* In this experiment, the eigenshapes of heart were calculated from 16 training shape, extracted manually. We test the proposed segmentation method with the cardiac MRIs which are from the same source of our test images. The results of Tsai's and our method are shown in Figure 6(b) and 6(c) respectively. The initial curve is shown in Figure 6(a). These test images have low contrast, so they are hard to evaluate visually. We enlarged and increased the contrast of Figure 6(b) and 6(c) and showed them in figure 7(a) and 7(b) respectively. We found our method gave the boundary that was closer to the true boundary than Tsai's method.

V. CONCLUSION

In this paper, we propose the 2-stage level set segmentation method. In the first stage, we adopt the method of Tsai to extract the object shape. In the second stage, we fine tune our extracted shape by the method of Chan and Vese. We restrict the area that the boundary can move. After comparing our method to the method of Tsai with synthetic and medical images, we found the improvement over Tsai's method in all cases.

TABLE I

SOME COMPARISON BETWEEN TSAI'S AND OUR PROPOSED METHOD

Test Image	average error distance		Area Similarity	
	Tsai's Method	Our method	Tsai's Method	Our method
Jet	0.769	0.391	0.9323	0.9798
Jet+30dB -noise	0.773	0.603	0.9302	0.9434
Jet +Occlusion + 30 dB -noise	1.758	1.572	0.8873	0.8911

ACKNOWLEDGMENT

This work was supported by the cooperative research fund of Digital Signal Processing Research Laboratory, Chulalongkorn University, Thailand.

REFERENCES

[1] M. Kass, A. Witkin, and D. Terzopoulos, "Snakes: Active Contour Models," *International Journal of Computer Vision*, vol. 1, No. 4, pp. 321-331, 1988.

[2] R. Malladi, J. A. Sethian, B. C. Vemuri, "Shape modeling with front propagation: a level set approach," *IEEE Transactions on Pattern Analysis and Machine Intelligence*, vol. 17, No. 2, pp.158 – 175, , February 1995.

[3] T. F. Chan, L. A. Vese, "Active contours without edges," *IEEE Transactions on Image Processing*, vol. 10, No. 2, pp.266 – 277, February 2001.

[4] Y. Chen, S. Thiruvenkadam, H. D. Tagare, F. Huang, D. Willson, E. A. Geiser, "On the incorporation of shape priors into geometric active contours," *IEEE Workshop on Variational and Level Set Methods in Computer Vision*, pp. 145-152, July 2001.

[5] M. E. Leventon, W. E. Grimson, O. Faugeras, "Statistical shape influence in geodesic active contours," *5th IEEE EMBS International Summer School on Biomedical Imaging*, June 2002.

[6] A. Tsai, A. Yezzi, W. Wells, C. Tempany, D. Tucker, A. Fan, W. E. Grimson, A. Willsky, "A shape-based approach to the segmentation of medical imagery using level sets," *IEEE Transactions on Medical Imaging*, vol. 12, No. 2, pp.137 – 154, , February 2003.

[7] C. Pluempitiwiriyawej, J.M.F Moura, Yi-Jen Lin Wu, Chien Ho, "STACS: new active contour scheme for cardiac MR image segmentation," *IEEE Transactions on Medical Imaging*, vol. 24, No. 5, pp.593 – 603, , May 2005.

Digital Image Compression using VPIC algorithm in Wavelet Domain

K.Tongtar, N. Moongflangklang and F.Cheevasuvit
Department of Instrumentation Engineering, Faculty of Engineering,
King Mongkut's Institute of Technology Ladkrabang Bangkok, Thailand 10520.
s5061229@kmitl.ac.th, nanfa_blue@yahoo.com, kcfusak@kmitl.ac.th

***Abstract*-This paper proposes an efficient method to improve the quality of digital image compression using Visual Pattern Image Coding (VPIC) in wavelet domain. Wavelet based compression gives higher quality of the reconstructed image with high PSNR and less amount of minimum mean square error compared to VPIC. However, its compression ratio is reasonably low. Therefore, the proposed method combines the advantages obtained from both wavelet transform and VPIC to achieve high compression ratio while preserve the quality of the reconstructed image. The proposed algorithm can be separated in to three main processes. First, wavelet transform is used to decompose the low and high frequency coefficients. Then, the LL coefficients are reserved, while one of the high frequency sub-bands (HL, LH, and HH) is selected based on its Standard Deviation (SD). The sub-band having the highest information distribution usually contains proper edge information, which could be used to improve VPIC algorithm. Finally, the LL and the selected sub-bands are decomposed to obtain the result image. The experimental results show that the proposed compression algorithm can achieve high compression ratio while still maintain good image fidelity and minimum mean square error.**

I. INTRODUCTION

Several algorithms are proposed for digital image compression such as Block Truncation (BTC), Vector Quantization (VQ) and Visual Pattern Image Coding (VPIC). BTC[1], [2] was first proposed in 1979 by Delp and Mitchell, to compress monochrome images. BTC is an efficient method for block correlated signals. It quantizes block data into two values by preserving the first moment and the second moment. The advantages of BTC are its simple computation, easy implementation and fine edge preservation. The main drawback of BTC is its high bit rate. VQ[3] was proposed in 1980 by Linde, Buzo and Gray also called "LBG" algorithm . It separates an image into blocks (4x4 pixels), which we can determine intensity vector of pixels. Drawback of this method is its high complexity coding and low quality of edge image.

BTC and VQ are similar in that the image to be coded is first partitioned into a large number of smaller sub-images or blocks. Each block is then coded either by extracting certain intrinsically high-information quantities which are transmitted in reduced form(as in BTC), or by marking a comparison between the block and a set of preordained vectors or "typical" sub-image, the index of the "closest" vector being transmitted instead of the original block(as in VQ).

VPIC[4] was proposed in 1990 by Chen and Bovik. High compression ratio with low computational complexity is the main advantage for VPIC. However, the algorithm produces higher minimum mean square error and lower PSNR compared to other techniques.

This paper is organized as follows. Section II describes the overview of proposed method. Section III presents applying of VPIC. Section IV is experimental results and the final is the conclusions.

II. OVERVIEW OF PROPOSED METHOD

In this paper, we presents the compression method applying VPIC encoding with selection of wavelet sub-bands containing 4 separated the frequency bands (LL, LH, HL and HH). Only the LL sub-band is inversed with no modification. One of the other sub-bands is selected based on maximum SD value. This sub-band is used as input to VPIC. Then, the LL sub-band and the result of VPIC are used as input to inverse wavelet transform in order to compressed information as shown in figure 1.

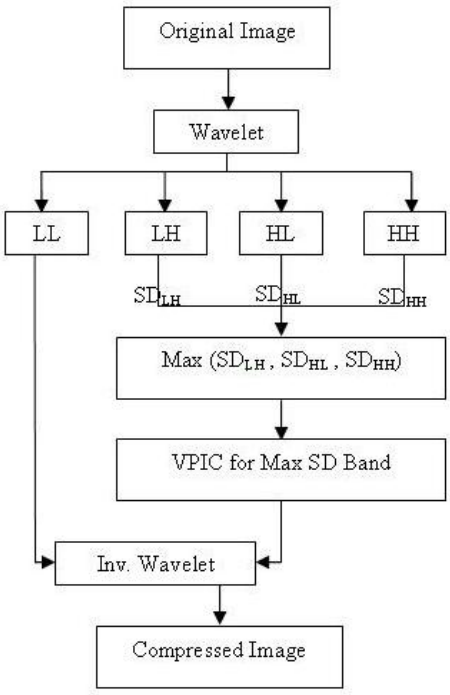

Fig.1 Show the overview of proposed method.

III. Implementation of The Proposed Algorithm

In this section, we apply VPIC to encode image information into binary blocks, and then each binary block is classified as the uniform or edge block based on its gradient magnitude in final stage.

A. Image Coding

In order to reduce the computation time, in the first stage, algorithm is initiated by separating image into sub-blocks (4x4 pixels). Then, the mean intensity of the pixel in each sub-block is calculated as shown in (1). This mean value is used to translate the intensity sub-block into binary sub-block. If the intensity value in the pixel is equal or greater than the mean intensity value, we assign the value of "1" to that pixel, otherwise assign "0".

$$Mean = \left(\sum_{i=1}^{4} \sum_{j=1}^{4} I(i,j) \right) / 16 \tag{1}$$

where $I(i,j)$ is sub-block of image.

Next stage, determine the value of $\Delta_x b_{i,j}$ and $\Delta_y b_{i,j}$ of each sub-block illustrated in (2) and (3) respectively to calculate the value of gradient magnitude and orientation $\angle \Delta b_{i,}$, which can be calculated using (4) and (5) respectively. The gradient value is used to separate between uniform sub-block and edge sub-block while the $\angle \Delta b_{i,j}$ is used to determine the direction of edge in each sub-block.

$$\begin{aligned} \Delta xb_{i,j} = {} & AVE\{ I_{n,m} : 4i+2 \le n \le 4i+3, 4j \le m \le 4j+3 \} \\ & -AVE\{ I_{n,m} : 4i \le n \le 4i+1, 4j \le m \le 4j+3 \} \end{aligned} \tag{2}$$

$$\begin{aligned} \Delta yb_{i,j} = {} & AVE\{ I_{n,m} : 4i \le n \le 4i+3, 4j+2 \le m \le 4j+3 \} \\ & -AVE\{ I_{n,m} : 4i \le n \le 4i+3, 4j \le m \le 4j+1 \} \end{aligned} \tag{3}$$

where $I_{n,m}$ is intensity of pixels in sub-block.

$$|\nabla b|_{i,j} = \sqrt{(\Delta xb_{i,j})^2 + (\Delta yb_{i,j})^2} \tag{4}$$

$$\angle \Delta b_{i,j} = \tan^{-1} \left(\frac{\Delta yb_{i,j}}{\Delta xb_{i,j}} \right) \tag{5}$$

Ultimately, we compare the gradient magnitude value $|\nabla b|_{i,j}$ with the threshold $|\nabla I|$ [1] to classify the class of sub-block. If the $|\nabla b|_{i,j} \le |\nabla I|$, that sub-block is defined as uniform block, and can go to image coding stage. Otherwise, it is defined as edge block. The edge block is compared to 28 pattern blocks to find the most similarity for the next encoding process. Figure 2 shows the 14 examples of the pattern blocks.

B. Coding Analysis

In coding stage, the binary coding is constructed based on the class of each sub-block from the previous stage. The coding information composes of 6-bit mean intensity, 6-bit gradient magnitude value, 5-bit number of pattern block and 1-bit sub-block type. Moreover, two additional bits called sub-band ID are used to identify the sub-band, whose the SD value is maximum. Figure 3 presents the data format obtained after VPIC coding. Table I shows the number of bits for each field of the information coding.

C. Decoding Analysis

At the decoder, the class of sub-block is determined from the received compressed bitstream. If the sub-block is a uniform block, a 4x4 pixel block is created and the mean intensity of each pixel is estimated. In contrast, if the sub-block is an edge block, the pattern block that matches with the information of that sub-block is applied. The mean intensity and gradient magnitude value are used to calculate low and high intensity value. The low intensity value is represented by "0" pixel, high intensity value is represented by "1" as shown in (6).

$$xH+yL=16*Mean \tag{6}$$

where x is "1" in the pattern block number
y is "0" in the pattern block number

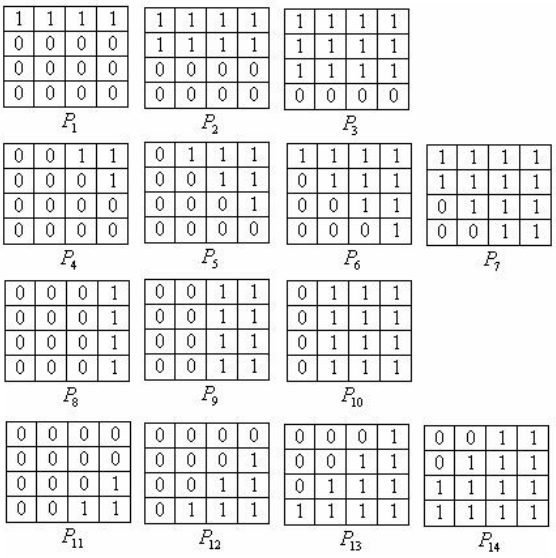

Fig.2 Show 14 examples pattern blocks (a) 90° patterns; (b) 45° patterns; (c) 0° patterns; (d) -45° patterns.

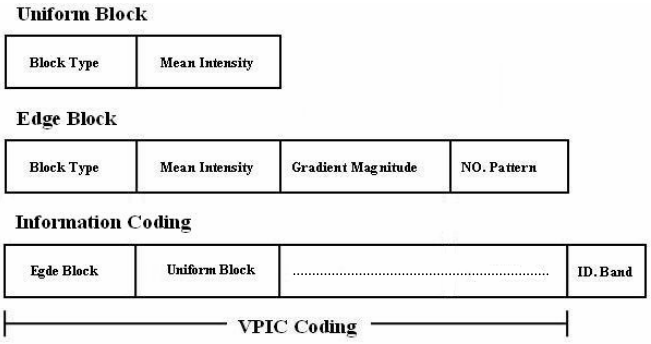

Fig.3 Coding pattern of proposed method.

TABLE I
DETAIL OF INFORMATION CODING.

	Uniform Block	Edge Block
Block type	1	1
Mean intensity	6	6
Gradient	0	6
Pattern number	0	5
Total	7	18

For example, we would like to find the low and high intensity value of pattern block P1 as shown in figure 2.

Given

$$4H+12L=16*Mean \quad (6.1)$$

From (5)

$$|\nabla b|_{i,j} = \sqrt{(\Delta xb_{i,j})^2 + (\Delta yb_{i,j})^2}$$

Where $(\Delta xb_{i,j}) = \frac{4H-4L}{8}$ and $(\Delta yb_{i,j}) = 0$

$$|\nabla b|_{i,j} = \sqrt{\left(\frac{4H-4L}{8}\right)^2}$$

$$8|\nabla b_{i,j}| = 4H-4L \quad (6.2)$$

Given (6.1)-(6.2)

$$16L = 16*Mean - 8|\nabla b|_{i,j}$$

$$L = \frac{16*Mean - 8|\nabla b|_{i,j}}{16} \quad (7)$$

Substitute L in (6.2)

$$H = \frac{16*Mean - 12L}{4} \quad (8)$$

Equation (7) and (8) can be used to calculate the low and high intensity value of P1 pattern block.

IV. EXPERIMENTAL

This section presents the experimental results of the proposed compression techniques. The experiments are conducted using the grayscale images of "Lena", "Girl", "Baboon", "Camera man" and "Woman with 512x512 pixels size. The original images are decomposed using wavelet transform. Daubechies 9 wavelet is used in this paper. The wavelet coefficients of 4 sub-bands (LL, LH, HL, and HH) are coded at 8 bits/component. Figure 3 displays wavelet coefficients for all four sub-bands of Lena image.

As previously mentioned, the LL sub-band is preserved without any modification. The VPIC coding is performed on the chosen high frequency sub-bands, which its SD value is maximum. At the decoder side, both information of the LL and the selected high frequency sub-bands are used to decode and reconstruct the result image.

For example, the SD values of all the high frequency sub-band of Lena image is presented in Table II. The sub-band having the highest SD value is the HL band. Table III shows the MSE of the reconstructed image using different combinations of LL and one of the high frequency sub-band. The minimum MSE also occurs in the case of the combination of the LL and HL sub-band information.

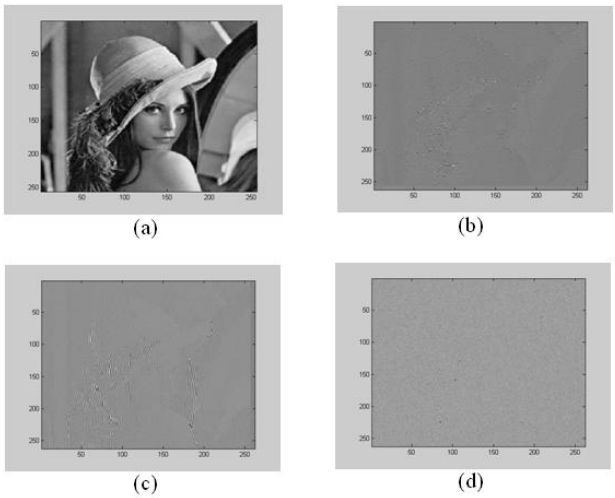

Fig.3 Result of wavelet transform of Lena
(a) LL band; (b) LH band; (c) HL band; (d) HH band.

TABLE II
STANDARD DEVIATION VALUE OF 3 SUB-BANDS OF LENA IMAGE.

Band	Standard Deviation
LH	1.7861
HL	4.7285
HH	0.2979

TABLE III
MSE OF WAVELET TRANSFORM OF LL BAND WITH OTHER BAND.

Wavelet	MSE
LL+LH	5.8584
LL+HL	1.0933
LL+HH	6.9073

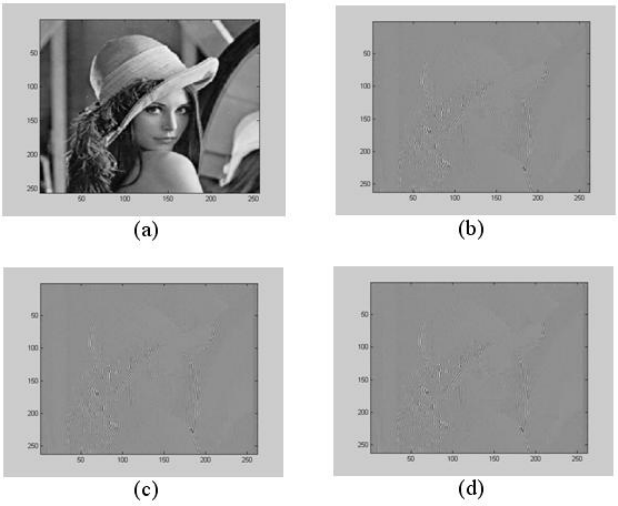

Fig. 4 (a) LL Band; (b) HL Band;
(c) gradient value =10; (d) gradient value = 30.

Figure 4 shows wavelet coefficients of the LL sub-band (a), the HL sub-band (b) of the original Lena image and those of the HL sub-band of the reconstructed image using gradient threshold = 10 (c) and 30 (d). Table IV show the results of the HL sub-band after VPIC coding with different gradient thresholds. The higher the value of the threshold, the lower the chance to find the edge blocks. As the number of the edge blocks decrease, the compression ratio will be higher.

Table V compares the MSE values of different tested images obtained from VPIC and the proposed technique (Wavelet and VPIC) algorithm with various gradient thresholds.

TABLE IV
THE INFORMATION OF LENA IMAGE IN HL BAND WITH PROPOSED METHOD.

	Gradient (threshold) = 10	**Gradient (threshold) = 30**
Edge block	55	26
Uniform block	4041	4070
compression ratios	17.9066	18.1039

TABLE V
THE MSE VALUE OF VPIC AND THE PROPOSED METHOD

Image Name	**VPIC**		**Wavelet & VPIC**	
	Gradient (threshold)		**Gradient (threshold)**	
	10	**30**	**10**	**30**
Lena	34.62	45.8	4.8	5
Cameraman	62.4613	74.7471	10.5215	10.6232
Woman	9.8507	13.2069	1.4746	1.5046
Girl	57.3144	71.5343	6.2108	6.2108
Baboon	287.5341	327.7233	53.2742	53.4756

TABLE VI
THE RELATION OF INFORMATION SIZES AND QUALITY FACTORS

Feature	**Wavelet**	**VPIC**		**Wave & VPIC**	
		Gradient (threshold)		**Gradient (threshold)**	
	LL+HL	**10**	**30**	**10**	**30**
Information size	130KB	21.1KB	16.3KB	68.7KB	68.6KB
MSE	1.0933	34.62	45.8	4.8	5
PSNR	47.7436	32.74	31.5	41.34	41.14

Table VI shows the results of information sizes and quality factors (MSE and PSNR) for three compression techniques (Wavelet, VPIC, and the proposed combination of Wavelet and VPIC). From the table V, the proposed technique offers lower size of the information while producing slightly higher MSE value compared to wavelet based technique. However, the proposed technique produces lower MSE value even though the information size is larger than that of VPIC technique.

V. CONCLUSION

This paper presents an image compression algorithm using a combination of VPIC and wavelet based coding techniques to improve compression quality factors of MSE and PSNR. The value of minimum mean square error and good image fidelity are improved by conserving the coefficients of the low frequency component (LL band) of wavelet transform which represents the smooth of image data. The coefficient of the other three sub-bands provides additional information, which is less important and can be neglected with less amount of perceptually effect. However, if some of the information from high frequency sub-bands is included in the encoded bitstream accompany with the information from LL sub-band, the quality of the reconstructed image could be improved. This paper proposed a method to choose the appropriate high frequency sub-band base on standard deviation. Then, the selected sub-band is encoded using VPIC technique. Consequently, the proposed compression algorithm can achieve high compression ratio while still maintains good image fidelity and minimum mean square error.

REFERENCES

[1] E. J. Delp and O. R. Mitchell, "Image compression using block truncation coding," IEEE Trans.Commun., vol. COM-27, pp. 1335-1341, Sept. 1979.

[2] O. R. Mitchell and E. J. Delp, "Multilevel Graphics representation using block truncation coding," Proc. IEEE, vol.68, July 1980

[3] A. Gersho, R.M. Gray, "Vector Quantization and Signal Compression", Kluwer Academic Publishers 1992.

[4] D.Chen and A. C. Bovik, "Visual pattern image coding," IEEE Trans. Commun.,vol. COM-38,no. 12, pp. 2137-2146, Dec. 1990

Thai Banknote Verification and Recognition

Narin Jeeranantasin and Pranchalee Rattanasakronchai
Department of Control System and Instrumentation Engineering
King Mongkut's University of Technology Thonburi
126 Prachauthit Rd. Bangmod , Tungkru , Bangkok , Thailand 10140
E-mail : Narin_je@hotmail.com , Pranchalee.rat@kmutt.ac.th

***Abstract* - This paper introduces the approach to check Thai banknotes by employ 2 following steps; 1. Check the invisible fibers of banknote to identify that it is legal banknote or counterfeit banknote. 2. Perform banknote recognition by using rule base for classify the types of banknote. This classification is based on the recognition of number " 1 ", " 2 " and " 5 " which appear on each banknote. In the experiment, 30 samples of 5 types of Thai banknotes (20 baht, 50 baht, 100 baht and 1,000 baht) were used to test the efficiency of this approach. While 5 samples of each type were used in the training system.**

Keywords : Thai Banknote , Invisible Fibers , Rule Base

I. INTRODUCTION

Nowadays, there are the widespread of counterfeit banknotes and the technique to produce counterfeit bank-notes is more complicated. However, the techniques for manufacturing and printing the banknote were also improved to prevent the imitation [1]. for example, adding invisible fibers on the banknote, using various fine color, using watermark, adding metal color fibers, using rare material on banknote. Therefore, these distinctive information on the banknote are useful for identify the counterfeit banknote.

There are many approaches to perform banknote recognition [2]. In this research, the invisible fibers investigation technique is introduced to identify the counterfeit banknote. Subsequently, the banknote recognition is performed by rule base approach, which analyzes the numeric numbers which appear on the banknote. There are many researches on recognition applications by using rule base technique; For example, The alphabet and symbol recognition by using Rule Base technique in [3], The number recognition from hand-writing by using the Rule Base technique in [4], and The name place recognition on Chinese language by using the Rule Base technique in [5]. All of the mentioned researches indicate the good efficiency of rule base technique.

This research describes the method to investigate the banknotes by focusing on the invisible fibers, which can be seen only under the ultraviolet (UV) light. There are 3 kinds of invisible fibers; red, green and blue invisible fibers. These fibers are able to be detected by taking the image of banknote under the UV light and using the property of color model: HSV (Hue,Saturation,Value) to detect the invisible fibers on the image. Later on, the image will be passed through the recognition step.

II. SYSTEMS

The hardware structure of this system, which appeared on figure 1, is composed of (1) ultraviolet light bulb to perceive the invisible fibers on the banknote, (2) The tested banknote (3) digital camera to take the data image of tested banknote, and (4) computer to perform image processing.

The structure of software system is displayed on figure 2, (1) the image of tested banknote is imported to the software system, (2) Identify the banknote. If it is legal banknote then performs the banknote recognition on step (3). However, if the banknote is counterfeit, the system will deny and indicate the result on output (4).

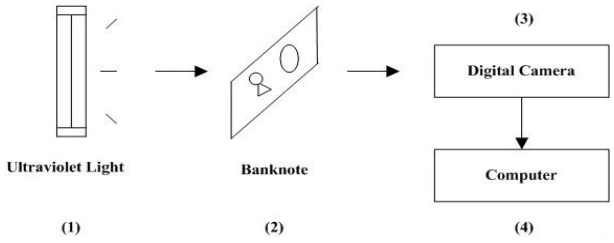

Figure 1. Hardware System

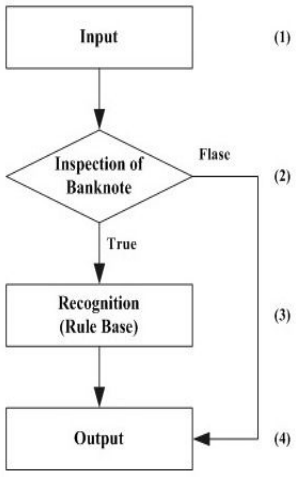

Figure 2. Software System

III. CONCEPTS

1.The invisible fiber is made from very high technological manufacturing process. It has a distinctive property; cannot be seen by human eye under the normal lighting. Hence, this is an essential point to prove the banknote.

2.Every banknote is composed of 3 types of invisible fibers which are different on features and positions

3.This research employs IF…THEN rules to perform number recognition for classify the type of banknote.

IV. ALGORITHMS

A. Characteristic of the invisible fibers

The invisible fibers, which added into the front side and back side of the banknote, are used to prevent the imitation. The size of each fiber is not similar and they are randomly distributed on the banknote also. It is difficult to imitate.

The invisible fibers are able to be detected when the banknote is illuminated by ultraviolet light. The figure 3 shows the image of banknote under the normal lighting. While the figure 4 displays the image of legal banknote under the illumination from ultraviolet bulb. The various colors of invisible fibers are appeared on the image. Whereas the figure 5 is the image of counterfeit banknote under the ultraviolet light. No invisible fibers can be detected from this image.

Because the important feature of invisible fibers are their distinctive colors. Hence, in this research, the HSV color model (Hue, Saturation, Value) is employed to detect the invisible fibers on the banknote and determine that the tested banknote is legal or counterfeit.

Figure 3. Image of banknote under the normal light

Figure 4. Image of legal banknote under the ultraviolet light

Figure 5. Image of counterfeit banknote under the ultraviolet light

Table 1
Result of inspection the banknote from Invisible Fiber.

Type of banknote	20 Baht (legal)	50 Baht (legal)	100 Baht (legal)	500 Baht (legal)	1000 Baht (legal)	Counterfeit banknote
Amount	30 items	30 items	30 items	30 items	30 items	50 items
Legal banknote	30	30	30	30	30	0
Counterfeit banknote	0	0	0	0	0	50

From the table 1, the result of inspection the banknote by detecting the invisible fiber is proved that it can separate between the legal banknote and counterfeit banknote.

B. Rule base technique

"Rule base" is one method in the expert system, which described in artificial intelligent science, and can apply to perform pattern recognition. This rule base technique employs the "If … Then" rules [6] as following.

$$R_n = IF \ldots\ldots THEN \ldots\ldots \quad (1)$$

Whereas the R_n is one of the rules, "IF" is the condition and description of that rule, and "Then" is a part of conclusion or action to be executed.

The rule bases, which are the same pattern in equation 1, will be created to describe the property of each type of Thai banknote, and used to perform banknote recognition.

V. BANKNOTE RECONITION

The banknote recognition step will prove the Arabic numbers on the front-side of Thai banknotes, which can be classified into 5 types: 20 baht, 50 baht, 100 baht, 500 baht, and 1000 baht. Figure 6 (a) shows the images of Arabic numbers from each kind of actual Thai banknotes, while the images in figures 6 (b) are the first character of each kind of Thai banknotes. The image of numbers will be passed to the thinning algorithm. The results are displayed on figure 6 (c).

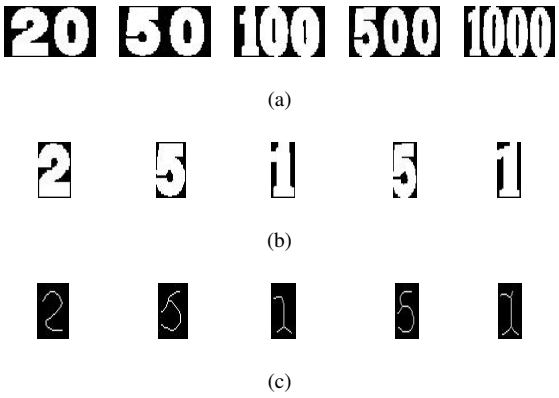

Figure 6. (a) Images of numbers from each kind of Thai banknote, (b) First number of each banknote, (c) Results after perform thinning algorithm with images from figure 6 (b).

The first step of banknote recognition is finding the histogram of the image of numbers, which appears on the tested banknotes, as shown on figure 6 (a). Hence, the software will know the coordination of first number. Subsequently, the image of the first number will be reduced by thinning method. The result is similar to images in figures 6 (c).

Finally, the thinning image of the first number will be separated into 9 regions in figures 7. The software will count the number of white pixels in each region, and compare to the standard value of each number [" 1 ", " 2 " and " 5 "] by equation (2) to find the error.

$$E = | P_n - \bar{\mu}_n | \quad (2)$$

- E is the error value.
- P_n is number of white pixels in region n.
  n is region of image (n = 1, 2, 3,…, 9)
- $\bar{\mu}_n$ is the standard value of white pixel in each region. These standard values are obtained from the learning step with 5 samples, and finding the average of these 5 samples. Hence, after finished the learning, we will obtain 3 set of $\bar{\mu}_n$ [" 1 ", " 2 " and " 5 "].

The error value, which calculated from standard value $\bar{\mu}_n$ of " 1 ", will be kept as parameter $\sum E_1$, calculated from standard value $\bar{\mu}_n$ of " 2 ", will be kept as parameter $\sum E_2$, and calculated from standard value $\bar{\mu}_n$ of " 5 ", will be kept as parameter $\sum E_5$. Subsequently, these errors will be used in rule base equations from (3)-(5), R_1, R_2 *and* R_3 are the recognition rules of each numeric character 1, 2 and 5.

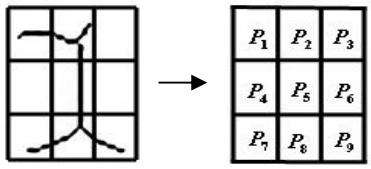

Figure 7. Separate thinning figure into 9 regions

$$R_1 : IF\ Min((\sum E_1),(\sum E_2),(\sum E_5)) = \sum E_1\ THEN\ Output = 1 \quad (3)$$

$$R_2 : IF\ Min((\sum E_1),(\sum E_2),(\sum E_5)) = \sum E_2\ THEN\ Output = 2 \quad (4)$$

$$R_3 : IF\ Min((\sum E_1),(\sum E_2),(\sum E_5)) = \sum E_2\ THEN\ Output = 5 \quad (5)$$

- By consideration on equation (3), if the minimum value among these three errors is $\sum E_1$, hence, the tested thinning image is " 1 ".
- By consideration on equation (4), if the minimum value among these three errors is $\sum E_2$, hence, the tested thinning image is " 2 ".
- By consideration on equation (5), if the minimum value among these three errors is $\sum E_5$, hence, the tested thinning image is " 5 ".

After knowing the first number of tested banknote, we will find the number of digits by using histogram, and, hence multiply the first number to the number of digit. We will obtain the actual number, which appears on the tested banknote. The proposed method is shown in figure 8.

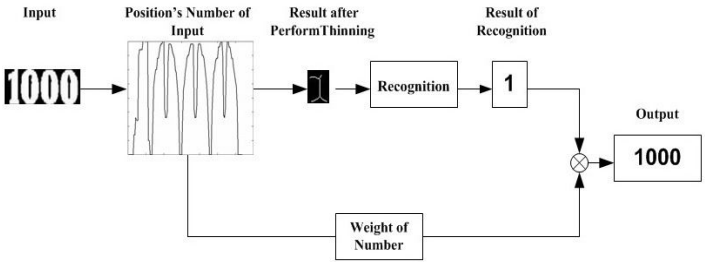

Figure 8. The Structure of System

VI. RESULT OF THE EXPERIMENT

In this testing, we used 5 types of legal Thai banknotes and counterfeit Thai banknotes as well. Figure 9 shows the images of those 5 types. The invisible fibers of each Thai banknote, which have different in features and positions, is a key feature to determine that the tested banknote is legal or counterfeit.

After the tested banknote is proved, the number, which appear on the banknote and has a certain size and coordinate, will be performed the recognition process.

The result of this testing is shown on table 2. The system indicates the 100% accuracy for separating the counterfeit banknotes from legal banknotes, and 100% accuracy to classify the types of banknotes. Except the 1,000 baht banknotes, this system gives only 96.67% accuracy to recognize this type. Because there is a complicated graphic beneath the number " 1,000 " on the banknote, as shown in figure 9 (f).

Table 2
Result of the Experiment

Type of banknote	20 Baht (legal)	50 Baht (legal)	100 Baht (legal)	500 Baht (legal)	1000 Baht (legal)	Counterfeit banknote
Amount	30 items	30 items	30 items	30 items	30 items	50 items
No. of banknotes which can be recognized correctly	30	30	30	30	29	Rejected
% Accuracy on the recognition process	100	100	100	100	96.67	n/a

The 50 samples of counterfeit banknote are use for testing the inspection, 10 samples of each type. The result of the test is it can reject all of counterfeit one.

(a)

(b)

(c)

(d)

(e)

(f)

Figure 9. Image of each type of Thai Banknotes (a) 20 baht banknotes. (b) 50 baht banknotes. (c) 100 baht banknotes. (d) 500 baht banknotes. (e). 1000 baht banknotes (f) 1000 baht banknote which has a complicated graphic beneath the number " 1,000 " on the banknote.

VII. CONCLUSION

This research proposes the method for proving the banknotes by checking the invisible fibers and performs banknotes recognition by using rule base method, which is one technique in pattern recognition application.

From the testing with 30 items of each kinds of Thai banknotes, this proposed system can give the 100% accuracy for separating counterfeit banknote from legal banknote, and 100% accuracy for recognize each types of banknote. However, the system gave the accuracy only 96.67% for recognize 1000 baht bank notes.

REFERENCES

[1] Bank of Thailand, " Knowledge about Bank-Note", Insurance Quality Publication of Financial Institution. Bangkok , August 2005. pp. 13

[2] A.Leelasantitham, S. Pattaramalai and K. Chamnongthai "Inspection of Water Mark on Currency Note by Using Correlation Mapping and Neural Network ", IEEE , pp.403-406, 1998

[3] M.Ahmed, and R.Ward, "A Rotation Invariant Rule-Based Thinning Algorithm for Character Recognition", IEEE Trans. Pattern Analysis and Machine Intelligence, Vol. 24, pp. 1482-1490, 2002.

[4] D.Gorgevik, D.Cakmakov , and V. Radevski, "Handwritten Digit Recognition Using Statistical and Rule-Based Decision Fusion", IEEE ,pp. 131-135, 2002

[5] J.H.Zheng, H.Y.Tan,K.Y.Liu, and Y.Zhao," Automatic Recognition of Chinese place names: A Statistical and Rule-based Combined Approach ", IEEE ,Vol 4, pp.2204-2209, 2001

[6] G.F.Luger, W.A.Stubblefield, "Artificial Intelligence:Structures and Strategies for Complex Problem Solving", Adison Wesley Logman, 1995, ISBN 0805311963

Locating and Reading Barcodes from Images Captured by Camera of Mobile Phone

Sakda Suwanchatree and Pranchalee Rattanasakornchai
Control System and Instrumentation Engineering
King Mongkut's University of Technology Thonburi
126 Pracha-utid Road, Bangmod, Thungkru, Bangkok, Thailand
Tel. 0-2470-9096 E-mail: sakda_suwanchatree@gmail.com, Pranchalee.rat@kmutt.ac.th

***Abstract*-The system of locating and reading 1-D barcodes which captured by mobile-phone's camera is studied. In this paper we still developed program and tested it on the personal computer. At first, the location of barcode in a captured image is found by using Morphological method. Finally, the code will be decoded by reading the numeric characters under barcode image. For this step, the Rule base method was employed to recognize the numeric character, 0-9, which leaning with 20 samples each character. For the experiment, various barcode of commercial products is used to test the efficiency of this work.**

Keywords: Barcode, Morphological, Rule Base

I. INTRODUCTION

In these days, almost all commercial products have barcode labels which can be read by optical scanner called barcode reader. The identity of products will be encoded to numeric and stored in the widths and spacings of printed parallel lines. The advantage of the barcodes is the safe and rapid availability of the information about product from production to shop. The standard of barcode that used in Thailand is EAN-13 (European Article Numbering).

In the recent years, a mobile phone's performance has increased rapidly and its camera also. Some of those have more than over mega-pixel range image sensor cameras. In this propose, we use a mobile phone to find and read barcode label. The consumers can read the information of goods (i.e. type, size, price, etc.) from barcode by using a camera in mobile phone.

For method for finding and reading barcode image with mobile phone can be found in [1] and [2].

In this paper, we proposed an image recognition algorithm for 1-D barcode for EAN-13 standard. At first, the barcode in image that captured by camera of mobile phone is found by Morphological method. And then the numeric under the barcode will be read by Rule base method.

This paper is organized into 5 sections. In Section II is a brief conclusion of EAN-13 barcode. Section III is proposed method for locating and reading barcode. Experimental results is given in Section IV. And conclusion can be found in Section V.

II. THE EAN-13 BARCODE

For 1-D barcode, there are many standards that used in the world. In Thailand, the barcode system follow standard of EAN that developed by European Article Numbering. The EAN-13 barcode consists of 13-numeric characters. The first-three-numeric characters are the country code which is885 for Thailand's country code. Then the next 4 characters, 4^{th}-7^{th}, are the manufacturer code. For 8^{th} to 12^{th} numeric characters are product code. And the last one is the checksum digit. Figure 1 shows an example of the EAN-13 standard barcode. More information of EAN-13 Barcode can be found in [3].

Figure 1. Example of EAN-13 barcode

III. PROPOSED APPROACH

The block diagram of proposed method, as show in Figure 2, which consists of two steps: the first step is the location of barcode. When location of barcode is found, the next step is reading numeric characters under barcode. In this paper, the input images are captured by camera of mobile phone which having resolution 1 Mega pixels as shown in Figure 3.

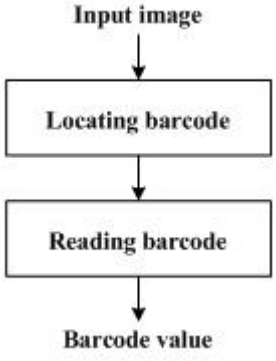

Figure 2. Block diagram of the proposed method

Figure 3. Input image captured with a camera of mobile phone

A. Locating of barcode

In locating of barcode, we use Morphological method to find the location of barcode, as illustrate in Figure 4, which explain in the following steps:

- At first, an input image as showed in Figure 3 was converted into grayscale image. Then edge of grayscale image is found by edge detection which uses the following mask.

$$\begin{bmatrix} -1 & -1 \\ 1 & 1 \end{bmatrix}$$

- After that, average value of image edge will be calculated in a horizontal line by using mask as showed below.

$$\begin{bmatrix} \frac{1}{13} & \frac{1}{13} & \frac{1}{13} & \frac{1}{13} & \frac{1}{13} & \frac{1}{13} & \frac{1}{13} & \frac{1}{13} & \frac{1}{13} & \frac{1}{13} & \frac{1}{13} & \frac{1}{13} & \frac{1}{13} \end{bmatrix}$$

- Input image is converted into binary image. Next, pixel group is classified to be an object by labeling technique. Then small size of objects will be compared with β (in this paper β = 10,000 pixels which is to obtain from experimental). The objects which have pixel numbers less than β will be removed from binary image.

- In this step, the hole inside object will be filled by using dilation in a morphological method. And the edge which connects to object will be removed, as illustrated in Figure 5.

- The last step for locating the barcode is finding top position, bottom position, left position and right position of object then the barcode region is extracted, as illustrated in Figure 6.

B. Reading barcode

After the barcode to be found, the numeric code under barcode will be read by the following steps as shown in Figure 7.

- Barcode region image is converted to binary image by Otsu thresholding technique [4]. This binary image is reduced noise which to remove object smaller then five pixels. And edge connected object is removed.

- Each bar of barcode is detected by labeling technique. After that, the first and last bars, which are standard bar of barcode, are scanned to find the width of barcode region. Then the width of standard bar will be calculated by division the width of barcode region with 95, because, in EAN-13 standard, there are 95 units per a barcode.

- The first pixel-group from labeling is determined to be the first digit of numeric code. The first digit which detected from barcode image is illustrated in Figure 9(a).

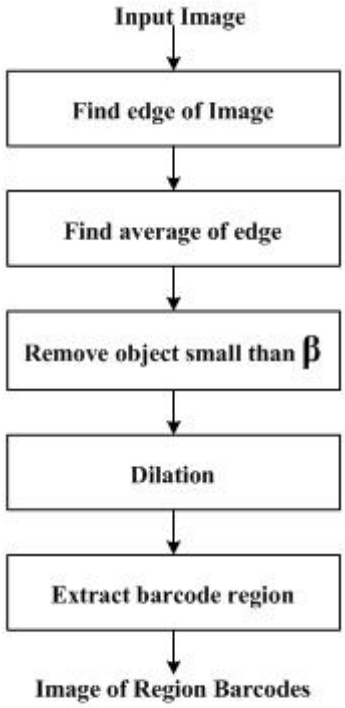

Figure 4. Block diagram of locating barcode

Figure 5. The barcode region is found by proposed locating method

Figure 6. The segmented barcode region image from input image

- 2nd – 7th digit of numeric code will be detected by referring from left-side and middle standard bar. A position of 2nd digit is left-hand side of left-side standard bar by plus double of standard-bar's width. And a position of 7th digit is middle position of middle-standard bar by minus double of standard-bar's width. For 8th – 13th digit of numeric code will be referred from middle and right-side standard bar. A position of 8th digit is middle position of middle standard bar by plus double of standard-bar's width. And a position of 13th is right-hand side of right-side standard bar by minus double of standard-bar's width. The left-side standard bar, middle standard bar and right-side standard bar positions are shown in Figure 8. The detection's results of 2nd – 7th and 8th – 13th are shown in Figure 9(b) and 9(c), respectively.

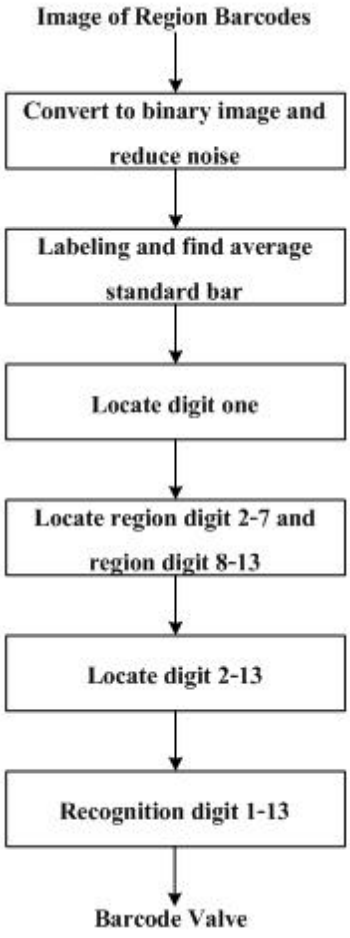

Figure 7. Block diagram of reading barcode

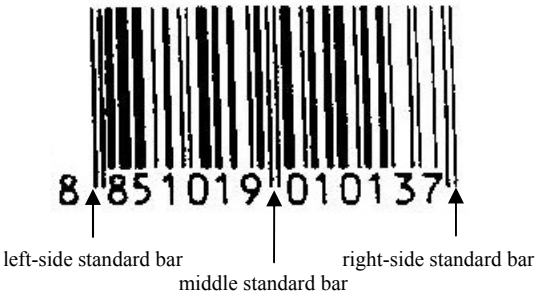

Figure 8. Left-side standard bar, middle standard bar and right-side standard bar position

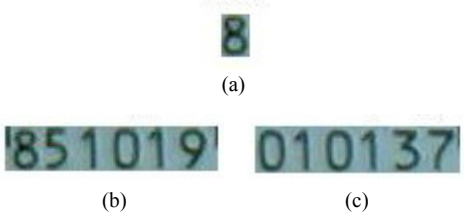

Figure 9. (a) First digit (b) second - seventh digit region (c) eighth - thirteenth digit region

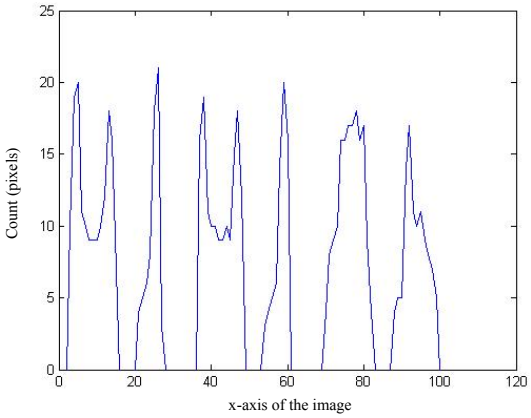

Figure 10. Histogram of 8^{th} - 13^{th} digit region image

- When 2^{nd} - 7^{th} digit region image and 8^{th} - 13^{th} digit region image were obtained, both images are completed numeric characters by dilation operation. Therefore the noise of images is reduced. Subsequently, the histograms of these images are found for cutting each numeric character at the points that have zero count. These points mean the separation of each numeric character. Histogram of 8^{th} - 13^{th} digit region image is shown in Figure 10.
- Next each digit of 1^{st} – 13^{th} numeric code is found values by Rule base method which is Artificial Intelligence system used for recognition. This rule base technique employs the "If … Then" rules as shown following in equation (1). For this step, the

images of each numeric character will be reduced by thinning method. The thinning image of each character will be separated into 9 parts. Subsequently, the software will count the number of white pixels in each region, and compare to the standard value of each numeric character, 0-9, by equation (2) to find the error (E).

$$R_n = IF \ ..... \ THEN \ ..... \quad (1)$$

Where the R_n is one of the rules, "IF" is the condition and description of that rule, and "Then" is a part of conclusion or action to be executed.

$$E = | P_n - \bar{\mu}_n \ | \quad (2)$$

Given that, p_n is number of white pixels in the n[th] part, n is part of image (n=1, 2,…, 9). $\bar{\mu}_n$ is the standard value of each part which obtained in the learning step from 20 samples per a character of 0-9 numeric characters. Finally, these errors will be used in rule base equations as shown in equation (3) - (13).

$$R_0 : IF \ Min(\sum E_0, \sum E_1 \ldots \sum E_9) = \sum E_0 \ THEN \ Output = 0 \quad (3)$$

$$R_1 : IF \ Min(\sum E_0, \sum E_1 \ldots \sum E_9) = \sum E_1 \ THEN \ Output = 1 \quad (4)$$

$$R_2 : IF \ Min(\sum E_0, \sum E_1 \ldots \sum E_9) = \sum E_2 \ THEN \ Output = 2 \quad (5)$$

$$R_3 : IF \ Min(\sum E_0, \sum E_1 \ldots \sum E_9) = \sum E_3 \ THEN \ Output = 3 \quad (6)$$

$$R_4 : IF \ Min(\sum E_0, \sum E_1 \ldots \sum E_9) = \sum E_4 \ THEN \ Output = 4 \quad (7)$$

$$R_5 : IF \ Min(\sum E_0, \sum E_1 \ldots \sum E_9) = \sum E_5 \ THEN \ Output = 5 \quad (8)$$

$$R_6 : IF \ Min(\sum E_0, \sum E_1 \ldots \sum E_9) = \sum E_6 \ THEN \ Output = 6 \quad (9)$$

$$R_7 : IF \ Min(\sum E_0, \sum E_1 \ldots \sum E_9) = \sum E_7 \ THEN \ Output = 7 \quad (10)$$

$$R_8 : IF \ Min(\sum E_0, \sum E_1 \ldots \sum E_9) = \sum E_8 \ THEN \ Output = 8 \quad (11)$$

$$R_9 : IF \ Min(\sum E_0, \sum E_1 \ldots \sum E_9) = \sum E_9 \ THEN \ Output = 9 \quad (12)$$

From (3) - (12), $R_0, R_1, R_2 \ldots, R_9$ are the recognition rules of each numeric character, 0, 1, 2…, 9. And the values of $\sum E_0, \sum E_1, \sum E_2 \ldots, \sum E_9$ are summations of errors (E) of 0-9 character image, respectively. R_0 – R_9 will be chosen from the minimum value of $\sum E_0, \sum E_1, \sum E_2 \ldots, \sum E_9$. If the minimum value equals $\sum E_1$, hence, this tested image is the "i" numeric character.

IV. EXPERIMENTAL RESULTS

In the experiment, we used 20 barcode-sample images for testing our proposed algorithm which experimental results are show in Table1. A sample images are captured by 1 mega-pixel-mobile-phone's camera. From 20 samples of barcode images, 100% of samples can be located and detected to be barcodes and 80% of samples can be read their all numeric code under them correctly.

TABLE 1
EXPERIMENTAL RESULTS

Number of barcode (patterns)	Number of correct location (patterns)	Efficiency location (%)	Number of correct reading (patterns)	Efficiency of reading (%)
20	20	100	16	80

The reason that makes the barcode locating fail is region of barcode smaller than β. And the false of reading numeric of barcode is a size of numeric is too small to read and surface of label has reflected then it is difficult to read.

For this paper, our algorithm to locate and read 1-D barcode is in the studying step then we still developed program and tested it on the personal computer. In future work, we will implement on mobile-phone system.

V. CONCLUSION

In this paper, we propose method of locating and reading barcodes form images captured by camera of mobile phone. In locating barcodes use Morphological method to locate barcode and reading barcode use Rule Base method to recognize number under barcode to read barcode value. The experimental results with 20-pattern barcodes have 100% efficiency for the locating of the barcode and 80% efficiency for the reading of numeric character.

REFERENCES

[1] E. Ohbuchi, H. Hanaizumi and A.-H. Lim, "Barcode readers using the camera device in mobile phones," International Conference on Cyberworlds, Tokyo, Japan, pp. 260-265, Nov. 2004.

[2] Kongqiao Wang, Yanming Zou, and Hao Wang, "Bar Code Reading from Images Captured by Camera Phone", IEEE International Conference on Mobile Technology, Applications and Systems, 2005.

[3] http://www.export911.com/e911/coding/ean13.htm

[4] N. Otsu, "A threshold selection method from gray-level histograms," IEEE Transactions on Systems, Man and Cybernetics, vol. 9, no. 1 pp.62-66, 1979.

[5] D.Gorgevik, D.Cakmakov, and V. Radevski, "Handwritten Digit Recognition Using Statistical and Rule-Based Decision Fusion", IEEE, pp. 131-135, 2002.

Decision Combination of Multiple Classifier Systems for Multiresolution Face Recognition

P. Sermwuthisarn[1], W. Asdornwised[1], S. Jitapunkul[1], and S. Marukatat[2]
[1]Department of Electrical Engineering, Chulalongkorn University, Bangkok, Thailand
[2]National Electronics and Computer Technology Center (NECTEC), Pathumthani, Thailand

Abstract- **In this paper, we propose an amelioration of the Principal Component Analysis (PCA) for face recognition using an ensemble method to multiresolution analysis. Indeed, the input data are first decomposed into several frequency subbands by Discrete Wavelet Transform (DWT) for representation. We consider several fusions of frequency subbands. Then, for each fusion, PCA is used in feature extraction and classification is done independently. The final decision is obtained from the majority vote of decision from each fusion. The experimental results show that our proposed method outperforms both PCA and Two-Dimensional Principal Component Analysis (2DPCA) in term of recognition accuracy rate.**

I. INTRODUCTION

Face recognition is one of the most interested pattern recognition problems which are growing in many applications. Among face recognition algorithms, appearance-based approach [1] is the most popular. This approach relies on the pixel intensity-derived features. It can be further classified in 3 categories, which are holistic matching method, featured-based matching method and hybrid method [1]. Holistic matching method is used in this work. Holistic matching method uses the whole face region as the raw input to a recognition system, therefore it is also known as appearance-based method. In this approach, Principal Component Analysis (PCA) is widely used as feature extraction technique. PCA selects components at the source resolution that are optimal for minimizing mean square error in reconstructing the original input [2]. For classification, where discriminability among classes puts an additional constraint on representations, PCA is no longer optimal.

Features utilizing multiresolution have been demonstrated to preserve discriminability better than a single scale representation. Multiresolution is widely used techniques for signal representation. Wavelet decomposition is the most widely used multiresolution technique in image processing. The components are chosen to provide good representations of the input signal at several resolutions. The full set of components provides an exact reconstruction of the original signal. In Ref. [3], PCA and wavelet transform were using to reduce computation complexity. PCA was applied to extract meaningful features from one mid-range frequency subband. Moreover, Linear Discriminant Analysis (LDA) has also been used with multiresolution to reinforce discriminant power [4]. LDA was incorporated into low frequency subimage of three-level pyramid structured wavelet decomposition. While there are 2 main motivations for representation an image in several resolutions. First, a given feature may be best observed at some scale, but the appropriate scale may not be known. Second, several features may be of interest, but no single resolution is satisfactory for all features. For example, in Ref. [5], a hybrid (local/global) model of the localized kernel feature and multiresolution feature for face representation and recognition has been presented. This approach exploited the intrinsic discriminating power of the face kernels. They were not only capable of exhibit performance comparable with other hybrid kernel methods, but also computationally efficient. In Ref. [6], the author investigated the performance of a technique for face recognition. This approach based on the computation of 25 local autocorrelation coefficients. It operated at a speed of one face per second and gave the good performance. In Ref. [7], the authors investigated the use of eigenface-like features computed on different portion of input image. They performed PCA to provide an adaptive basis for multiresolution and multiresolution provided localization to PCA. The feature extraction point of view was analyzed that projection to high dimensional spaces also enhances the chance of obtaining better feature. In Ref. [8], the authors considered an ensemble classifier working on frequency subbands similar to this work. Indeed, they first compared each individual subband. They considered the fusion of best performing subbands. It was shown that the fusion improve recognition accuracy compare to using a single subband. The studied papers of multiresolution have been demonstrated that information integrating from multiple sources is essential for reliably performing. Therefore, we also consider multiple classifier system, in which each classifier focuses on some particular resolutions, in order to improve the recognition accuracy.

The multiple classifier systems have been used in several pattern recognition works. They are powerful solutions to difficult pattern recognition problems involving large class sets and noisy input. Because, they allow simultaneous use of arbitrary feature descriptors and classification procedures. Decisions by the classifiers can be represented as rankings of classes so that they are comparable across different types of classifiers and different instances of a problem [9]. There are heterogeneous classifier ensembles and homogeneous classifier ensembles. The heterogeneous ensemble method integrates various pattern recognition algorithms as experts in a committee machine. In Ref. [10], the authors used the sum rule and RBF-based integration strategies to combine three face classifiers based on PCA, ICA, and LDA representations. This

approach could improve the performance of face identification system. However, each classifier is appropriate in different kind of database. Therefore, the dynamics face recognition committee was proposed in Ref. [11]. The authors formulated gating network to determine suitable weights for the experts. This face recognition system could combine the strong points of each representation and performed the better performance.

The homogeneous ensemble method relies on the same type of classifier in the system. It has been used in non-face and face recognition frameworks. In Ref. [12], the authors used multiresolution wavelet analysis and an ensemble of classifier for the early diagnosis of Alzheimer's disease. They performed on event related potential EEG signal which were used with the ensemble of classifiers based Learn++ algorithm. Parallel Consensus Neural Network (PCNN) in Ref. [13] is another homogeneous ensemble method that uses neural networks to satellite data classification. Indeed, each network is trained on different input full wavelet tree representations. Then, the decision is taken by class-specific weighted averages in the framework of consensus theory. However, the small size of face database makes it not suitable for applying this neural network based approach. In face recognition framework, multiresolution was applied to multiple classifier systems in the several previous works [5-8]. The experimental results of the previous works demonstrated that there was hidden information in many resolutions. They used the homogenous expert to classify and gave various decisions. Multiple classifier systems were the simple way to combine decisions and gave the better result.

In this paper, we consider face recognition from intensity images in multiresolution analysis and the homogeneous ensemble classifier. In this work, the input image is first decomposed into several frequency subbands. Four groups of frequency subbands are chosen due to their information coverage. For each group different kinds of fusion are considered. PCA is used in each group to reduce computational load while retaining meaningful features. We can further consider these 4 groups as independent classifiers in parallel classifiers system [14]. Thus new decision can be drawn from the majority vote of these 4 classifiers. Experimental results show that our proposed method outperform the classical approach of "PCA" and its recent extension of "2DPCA" [15] on the well known ORL face database.

II. BACKGROUND

A. *Multiresolution Analysis*

Multiresolution methods provide powerful signal analysis tools, which are widely used in feature extraction, image compression and denoising applications. Wavelet decomposition is the most widely used technique in image processing. Images have typically locally varying statistics that result from different combinations of abrupt features like edges, of textured regions and of relatively low-contrast homogeneous regions. While such variability and spatial nonstationarity defied any single statistical characterization, the multiresolution components are more easily handled. Wavelet transform can be performed for every scale and translation, resulting in continuous wavelet transform (CWT), or only at multiples of scale and translation intervals, resulting in discrete wavelet transform (DWT). Since, CWT provides redundant information and requires a lot of computation, generally DWT is preferred.

B. *Ensemble Method*

Ensemble method is one of the major developments in machine learning in the past decade. It finds a highly accurate classifier by combining many moderately accurate component classifiers. Bagging, Boosting, and Random Subspace methods are the most successful techniques for constructing ensemble classifier [16, 17].

There have been many previous studies on how to create the ensemble of models. The methods for constructing the ensemble of models can be categorized into five groups [16] : 1) Bayesian voting, which creates an ensemble of model by sampling them from an estimated posterior model distribution; 2) Manipulating the training examples, which creates multiple subset of training examples and trains a classifier for each subset; 3) Manipulating input features, which creates a number of subsets of the input features and a classifier is built for each subset of input features; 4) Manipulating the output targets or error-correct output code (ECOC) [18], which converts a multiple class problem into a set of binary class problems; 5) Injecting randomness, that generates ensembles of classifiers by injecting randomness into the learning algorithm.

Among the five categories, our work is closely related to the third method, which creates multiple classifiers by manipulating input features. This method only works when the input features are highly redundant. And it is optimal for multiresolution input.

C. *PCA and Eigenface for Face Recognition*

PCA was also knows as the Karhunen Loeve (KL) expansion in communication theory or Hotelling transform in image processing. It is a well-known approach for feature extraction. It is a method of identifying patterns of data, and expressing the data in a way to highlight their similarities and differences. The basic idea of PCA is to discard all redundancy existing in the original set of features thus allows representing the same object in a more compact way. Therefore the dimension of the image can be greatly reduced. In face recognition, the eigenface method is more generally called "PCA", which is used to find a low dimensional representation of face image data.

D. *Fusion*

There are 3 architectures of fusing frequency subbands [8], which are "data fusion", "feature fusion", and "decision fusion". We fuse raw pixel values of the frequency subbands in data fusion as shown in Fig. 1. The block diagram of feature fusion is shown in Fig. 2. We fuse feature vectors that exacted from the frequency subbands. For decision fusion, we fuse in classification decisions of the frequency subbands as showed in Fig. 3.

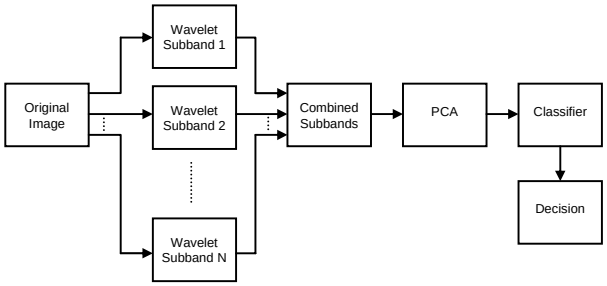

Figure 1. Block diagram of the data fusion scheme

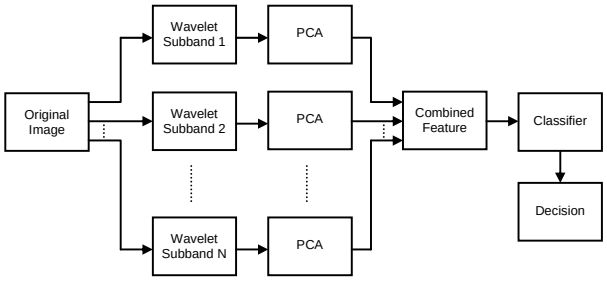

Figure 2. Block diagram of the feature fusion scheme

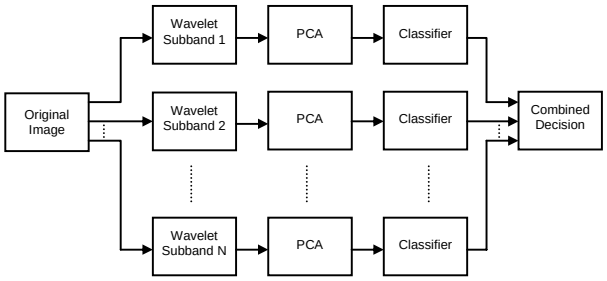

Figure 3. Block diagram of the decision fusion scheme

III. Proposed Method

There are many fusion techniques in [8] as shown in previous section. The authors proposed only trend to select group of frequency subbands for fusing. In this paper, we propose new architecture for fusing frequency subbands. We use the conception of multiple classifier systems to decide the results of each fusion again.

The schematic of the wavelet decomposition, which used in this paper is shown in Fig. 4. There is approximation (A), horizontal detail (H), vertical detail (V), and diagonal detail (D) coefficients respectively. A 128 x 128 pixels original face image is decomposed in the first level, and four 64 x 64 pixels resolution frequency subband images A1, H1, V1 and D1 are obtained. In the second level, we decompose only A1, yielding four 32 x 32 frequency subband images A2, H2, V2 and D2. And in the third level, we decompose A2 component to produce four 16 x 16 frequency subband images. In summary, we obtain 12 different subband images from the original face image and input them into the multiple classification scheme in Fig. 1-3. The octave decomposition is used in our proposed. We found that classification performance of individual H, V, and D were very low [3].

We define the group of frequency subbands in each level from octave DWT. The several frequency subbands are decomposed as Fig. 4. It consists of information from the different stage networks. Each stage has alike original input data with different time frequency resolutions. We divide the group of frequency subbands to 4 levels.

0 level : The 128 x 128 pixels of original image.
1 level : A1H1V1D1
2 level : H1V1D1A2H2V2D2
3 level : H1V1D1H2V2D2A3H3V3D3

Our proposed scheme in Fig. 5 is the fusion of fusion architecture. First, the original image is decomposed to be 3 level octave tree DWT. The frequency subbands are concatenated to 1-3 level groups of subbands. Then, we use similarly fusion scheme for fusing every level of frequency subbands. The fusion blocks in Figure 5 are three types of fusion, which are Fig. 1, Fig. 2, and Fig. 3. Finally, we combine all decision of fusion blocks together with decision fusion (majority vote). It gives the final decision. We choose Daubechies 4 wavelet for the experiments because it gave the optimum results [3, 4].

IV. Experimental Results

We tested on ORL face database in Appendix B [19]. The database has 400 pictures, which made up from 10 pictures of 40 people. The images are 112 x 92 pixels, 8 bit gray scale images. The pictures show variation in background lighting, scale, orientation and facial expression. The tolerance in scale is about 20% and tolerance for tilting is about. All of face images are scaled to 128 x 128 pixels resolution. We use first 5 images for training and last 5 images for testing. In recognition stage, we conserve 90% of energy for reducing computation.

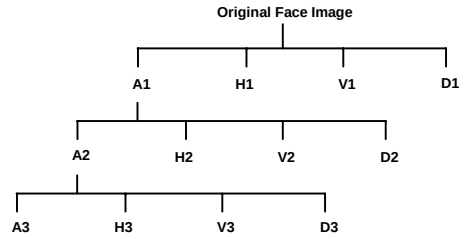

Figure 4. Wavelet decomposition tree in the study

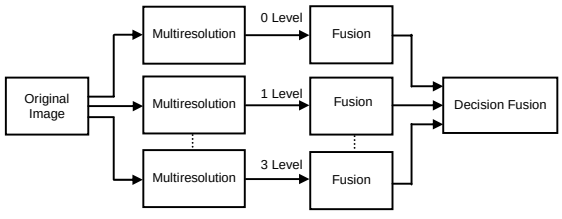

Figure 5. Block diagram of the proposed fusion scheme

The nearest neighbor classifier is chosen for classification. We evaluated comparatively three different distances namely the $L1$, the $L2$ norm, and the normalized correlation coefficient (CC). The top 3 results of PCA on single wavelet transform subband are shown in Table 1. Our proposed method's recognition accuracy rates are shown in Table 2. For example, in 1-3 level (Data Fusion), the 1 level, 2 level, and 3 level are selected to be multiresolution input and data fusion is chosen in fusion block in Fig. 5. The subbands in each level are fused by data fusion separately. After that, three level display 3 individual decision result. The decision fusion is used to combine 3 decisions and give final decision. Almost fusing several subbands levels give better accuracy recognition rate than original and single subband. It shows that manipulating the input features of ensemble method and multiple classifier systems are appropriate to our proposed method. The 0-3 level fusing subbands which first fused by decision fusion gives the best result.

Our best architecture can improve recognition accuracy rate to the ORL database. We compared our proposed method's best result to the classic PCA approach's result and the new approach of PCA which is called "2DPCA" [15] result. The size of images tested for PCA and 2DPCA is 112 x 92 pixels. The result in Table 3 indicate that our proposed give the best result which better than PCA 15.5% and better than 2DPCA 2.5%.

V. CONCLUSIONS

In this paper, a framework of ensemble frequency subbands are proposed for face recognition to be one approach to select group of fusing frequency subbands. One of the advantages of adding redundant features is good for classification problem as long as the redundant information supplied to ensemble classifiers is not harmfully correlated. But it has to spend more computation time and more complexity than 2 compared methods. If there are high speed enough CPU and large enough memory machine in the future, our proposed method will be one option.

TABLE I
TOP 3 RESULTS OF PCA ON SINGLE WAVELET TRANSFORM SUBBAND AND D3

Wavelet Subband	L1	L2	CC
A1	85.5	78	84.5
A2	86.5	80.5	83.5
A3	86.5	78.5	87
D3	53.5	59.5	69

TABLE II
OUR PROPOSED METHOD'S RESULTS

Level Fusion	L1	L2	CC
0 level (original)	85.5	78.5	85
1-3 level (Data Fusion)	75	82	93
1-3 level (Feature Fusion)	81	83	88.5
1-3 level (Decision Fusion)	79	82	92.5
0-3 level (Data Fusion)	84	78.5	91.5
0-3 level (Feature Fusion)	84	81	89.5
0-3 level (Decision Fusion)	84.5	84	**94**

TABLE III
THE TOP RECOGNITION ACCURACY COMPARISONS OF PCA AND 2DPCA

Method	PCA	2DPCA	Proposed (Best)
Accuracy (%)	78.5	91.5	**94**

ACKNOWLEDGMENT

Thanks to Thailand Graduate Institute of Science and Technology (TGIST) and Cooperation Project between Department of Electrical Engineering and Private Sector for Research and Development, Chulalongkorn University, Thailand.

REFERENCES

[1] W. Zhao, R. Chellappa, A. Rosenfeld, and J. Phillips, "Face Recognition A Literature Survey," *ACM Computing Surveys*, vol. 12, pp. 399-458, 2003.

[2] M. A. Turk and A. P. Pentland, "Eigenfaces for Recognition," *Journal of Conitive Neuroscience*, vol. 3, no. 1, pp. 71-86, March 1991.

[3] G. C. Feng, P. C. Yuen, and D. Q. Dai, "Human Face Recognition Using PCA on Wavelet Subband," *SPIE Journal of Electronic Imaging*, vol. 9, no. 2, pp. 226- 233, 2000.

[4] J. T. Chien and C. C. Wu, "Discriminant Waveletfaces and Nearest Feature Classifiers for Face Recognition," *IEEE Trans. Pattern Analysis and Machine Intelligence*, vol. 24, no. 12, December 2002.

[5] M. Pavlou and N. M. Allinson, "Unsupervised Multiresolution Face – Kernel Recognition Models," *Invited Talk Proc. Irish Machine Vision & Image Processing Conference 2005*, Belfast, Northern Ireland, August 2005.

[6] F. Goudail, E. Lange, T. Iwamoto, K. Kyuma, and N. Otsu, "Face Recognition System Using Local Autocorrelations and Multiscale Integration," *IEEE Trans. Pattern Analysis and Machine Intelligence*, vol. 18, no. 10, October 1996.

[7] V. T. Brennan, "Principal Component Analysis with Multiresolution," PhD thesis, University of Florida, May 2001.

[8] H. K. Ekenel and B. Sankur, "Multiresolution Face Recognition," *Image and Vision Computing*, vol. 3, no. 5, pp. 469-477, 2005.

[9] T. K. Ho, J. J. Hull, and S. N. Srihari, "Decision Combination in Multiple Classifier Systems," *IEEE Trans. Pattern Analysis and Machine Intelligence*, vol. 16, no. 1, January 1994.

[10] A. K. Jain, X. Lu, and Y. Wang, "Combining Classifiers for Face Recognition," *in Proc. ICME 2003*, pp. 13-16, Baltimore, MD, July 2003.

[11] T. Ho-Man, "Face Recognition Committee Machine: Methodology, Experiments and A System Application," Master thesis, Chinese University of Hong Kong, July 2003.

[12] G. Jacques, J. L. Frymiare, J. Kounios, C. Clark, and R. Polikar, "Multiresolution Wavelet Analysis and Ensemble of Classifiers for Early Diagnosis of Alzheimer's Disease," *Proc. of 30th IEEE Int. Conf. on Acoustics, Speech and Signal Processing 2005*, vol. 5, pp. 389-392, Philadelphia, PA, March 2005.

[13] J. A. Benediktsson, J. R. Sveinsson, O. K. Ersoy, and P. H. Swain, "Parallel Consensual Neural Networks," *IEEE Trans. Neural Networks*, vol. 8, no. 1, pp. 54-64, 1997.

[14] N. M. Wanas, "Multiple Classifier System," Focus Group, PAMI Lab, December 2003.

[15] P. Sanguansat, W. Asdornwised, S. Jitapunkul, and S. Marukatat, "Two-Dimensional Linear Discriminant Analysis of Principle Component Vectors for Face Recognition," *IEICE-Trans. on Inf. and Sys.*, vol. E89-D, no. 7, pp. 2164-2170, 2006.

[16] T. G. Dietterich, "Learning Research: Four Current Direction," *AI Magazine*, pp. 97-136, winter 1997.

[17] R. Polikar, "Ensemble Based Systems in Decision Making," *IEEE Circuit and Systems Magazine*, pp. 21-45, 2006.

[18] T. G. Dietterich and G. Bakiri, "Solving Multiclass Learning Problems via Error-Correcting Output Codes," *Journal of Artificial Intelligence Research*, vol. 2, pp. 263-286, 1995.

[19] http://www.cl.cam.ac.uk/research/dtg/attarchive/facedatabase.html

On-Line Character Recognition for Khmer Numeral based on DP matching of Barycenter Trajectory

P. Thumwarin[1] S. Khem[1] K. Janchitrapongvej[1] and T.Matsuura[2]
[1] Faculty of Engineering and Research Center for Communications and Information Technology
King Mongkut's Institute of Technology Ladkrabang, Bangkok 10520, Thailand, Email:ktpitak@kmitl.ac.th
[2]Faculty of Information Technology and Electronics, Tokai University
1117 Kitakaname, Hiratsuka, Kanagawa, 259-1292, Japan, Email:matsuura@dt.u-tokai.ac.jp

***Abstract*-We propose an on-line character recognition method for Khmer numeral based on DP matching of barycenter trajectory. First, the barycenter is determined from the center point of script and two adjacent pen-point positions with respect to time in handwriting process. Then the barycenter trajectory and its direction changes are used to describe the features of handwritten characters. Finally, the numeral is recognized by calculating the dissimilarity between the features of handwritten character using Dynamic Programming(DP) matching. Character recognition experiments are performed on database consisting of 5000 Khmer numerals. As the result, the average of recognition rate was 95.9%.**

I. INTRODUCTION

Many methods for on-line character recognition have been reported[1][2][3]. In those methods, the pen-point position is used to recognize the character. It is considered that using pen-point position directly is not effective to extract the feature of the handwritten character. In this paper, the barycenter determined from the center point of script and two adjacent pen-point positions is used instead of pen-point position to extract the feature of the handwritten character. We considered that the feature of the handwritten character can be described by two features, the barycenter trajectory and its direction change. Finally, the incorporation of the barycenter trajectory and its direction changes into DP matching is used to recognize the character.

II. PREPROCESSING

It is considered that there are fluctuations depending on many factors such as age, habit, psychological and mental state, physical or practical conditions in handwriting process of writer. For instance, size, location, shape, and duration time in handwriting process of the same alphabet are never precisely the same even they were written by the same writer.

Fig.1 shows Khmer numeral 'one' written by different writers. From Fig.1, we can see that the characters are written in different sizes, locations and styles. In order to recognize the character effectively, such fluctuations of handwriting should be reduced.

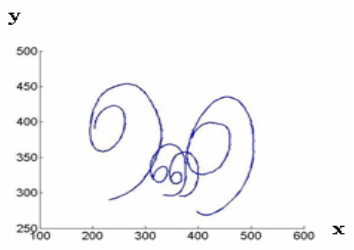

Figure 1: Khmer numeral 'one' written by different people.

It is assumed here that Khmer numerals are written on a graphical tablet to recognize the character. The horizontal and vertical components of pen-point position at a time, $t = n\tau(\equiv t_n)$, in handwriting process are denoted here as $x(t_n)$ and $y(t_n)$, respectively, where τ is a constant sampling rate.

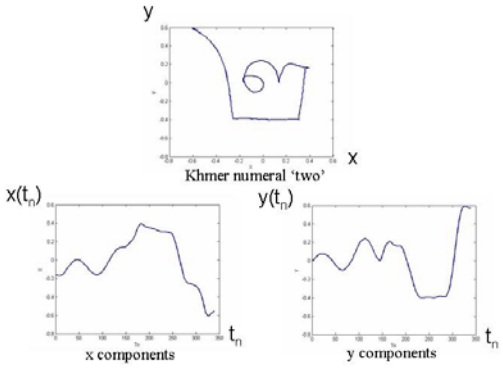

Figure 2: Khmer numeral 'two', its x components and y components (top to down , left to right).

Fig.2 shows Khmer numeral 'two' and its x, y components with respect to time in handwriting process. In order to reduce the fluctuation of handwriting, two kinds of normalization with respect to the size and location in handwriting process are performed as follows:

1) Normalization of size

The size of the script is standardized after removing the duplicated points of pen-point position. In order to make a standard size of script, the horizontal and vertical components, $x(t_n)$ and $y(t_n)$ are normalized as

$$\hat{p}(t_n) = \frac{p(t_n) - p_{\min}}{p_{\max} - p_{\min}}, \; p = (x, y), \quad (1)$$

where $p_{\min} = \min_{0 \le n \le N-1} p(t_n)$, $p_{\max} = \max_{0 \le n \le N-1} p(t_n)$, (2)

and N is a total number of sampled points of pen-point position.

2) Normalization of location

The location of the script is normalized as follows:

$$c_p = \frac{1}{N} \sum_{n=0}^{N-1} \hat{p}(t_n), \; p = (x, y), \quad (3)$$

$$\tilde{p}(t_n) = \hat{p}(t_n) - c_p, \; n = 0,1,2...N-1, \quad (4)$$

where c_p is the center point of script.

Fig.3 shows Khmer numeral 'two' before and after normalization. It can be seen from Fig.3 that the fluctuation of handwriting character can be reduced by using the normalization.

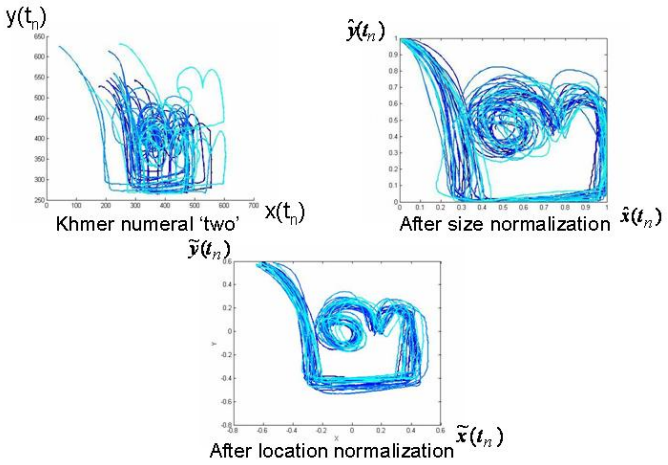

Figure 3: Khmer numeral 'two', after size normalizaton, and location normalization (left to rigth; top to down).

In order to reduce a fluctuation of pen-point movement in handwriting process, a trajectory of the barycenter determined from the center point of script and two adjacent pen-point positions with respect to time in handwriting process is used. The coordinates $(r_x(t_n), r_y(t_n))$ of the barycenter shown in the Fig.4 are calculated by the following equations:

$$r_x(t_n) = \frac{\tilde{x}(t_n) + \tilde{x}(t_{n+1}) + 0}{3},$$

$$r_y(t_n) = \frac{\tilde{y}(t_n) + \tilde{y}(t_{n+1}) + 0}{3}, \quad (5)$$

$$(n = 1,2,3..N-1),$$

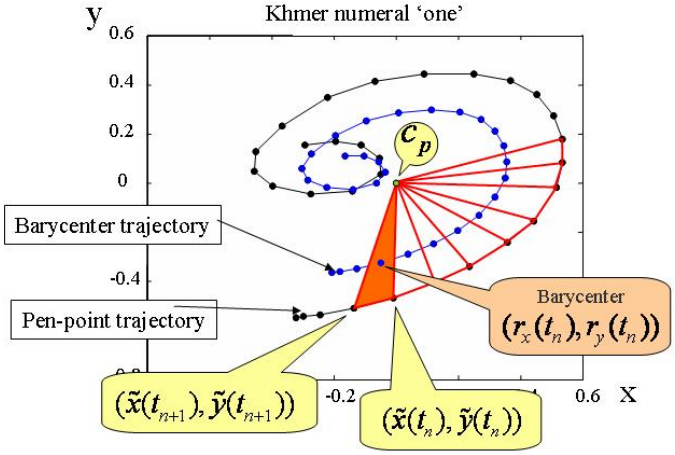

Figure 4: Khmer numeral 'one'.

III. FEATURE EXTRACTION

In this paper, we consider that the handwriting feature of Khmer numeral can be represented by two features, barycenter trajectory and its direction changes. The two features can be described as follows:

$$z(t_n) = r_x(t_n) + j r_y(t_n), \quad (6)$$

$$\theta(t_n) = \arctan\left(\frac{r_y(t_{n+1}) - r_y(t_n)}{r_x(t_{n+1}) - r_x(t_n)}\right), \quad (7)$$

where $z(t_n)$ is the complex function representing barycenter trajectory, and $\theta(t_n)$ represents the direction changes of the barycenter at the time t_n.

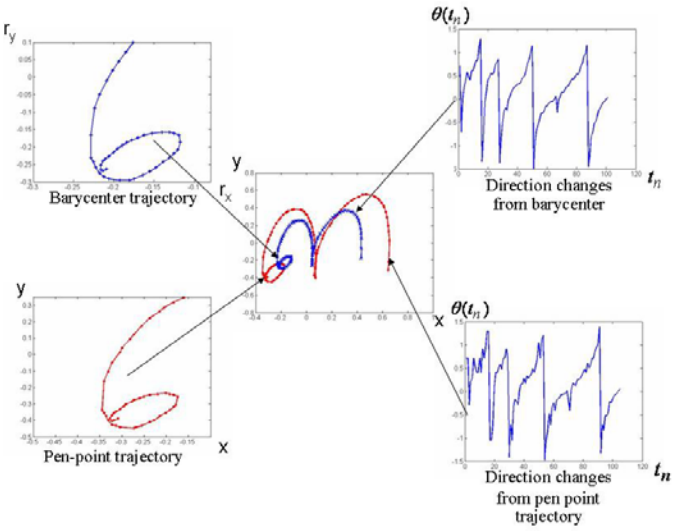

Figure 5: $z(t_n)$ and $\theta(t_n)$ obtained from the pen-point position and barycenter.

Fig.5 shows the comparison of $z(t_n)$ and $\theta(t_n)$ obtained from pen-point position and the barycenter. It can be seen from fig.5 that $z(t_n)$ and $\theta(t_n)$ obtained from the barycenter

are less sensitive than those obtained from the pen-point position.

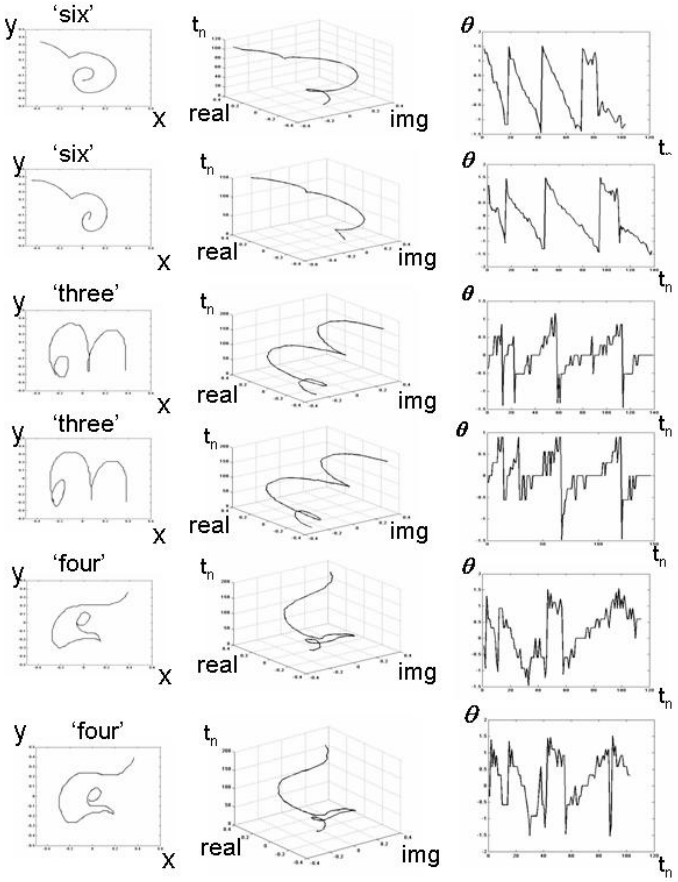

Figure 6: Khmer numerals, their complex features, and their direction changes from left to rigth.

Fig.6 shows $z(t_n)$ and $\theta(t_n)$ obtained from the same and different Khmer numerals. It can be seen from Fig.6 that $z(t_n)$ and $\theta(t_n)$ obtained from same numeral class are similar and different from those obtained from different numeral class. Therefore, we consider that the $z(t_n)$ and $\theta(t_n)$ can be used as the features of handwriting characters for Khmer numeral recognition.

IV. CHARACTER RECOGNITION

It is well known that the duration time in handwriting process obtained from the same character are never precisely the same. It is considered as the fluctuation in time-axis of handwriting character. To recognize the character effectively, Dynamic Programming(DP) matching method[4] is used to calculate the dissimilarity between the features of the reference handwriting character and a character to be recognized. With DP matching technique, the fluctuation of the duration time in handwriting process can be reduced. The DP matching can be performed as follows:

1) The feature parameter vectors of handwriting process are given by

$$\mathbf{z}^r = \left[z^r(1), z^r(2), z^r(3)..., z^r(I)\right]', \quad (8)$$

$$\mathbf{z}^t = \left[z^t(1), z^t(2), z^t(3)..., z^t(L)\right]', \quad (9)$$

$$\boldsymbol{\theta}^r = \left[\theta^r(1), \theta^r(2), \theta^r(3)..., \theta^r(I)\right]', \quad (10)$$

$$\boldsymbol{\theta}^t = \left[\theta^t(1), \theta^t(2), \theta^t(3)..., \theta^t(L)\right]', \quad (11)$$

where $z^r(t_n)$, $z^t(t_n)$, $\theta^r(t_n)$ and $\theta^t(t_n)$ are the barycenter trajectory and its direction changes obtained from preceding section, $\mathbf{z}^r$ and $\boldsymbol{\theta}^r$ are the feature parameter vectors for reference character, $\mathbf{z}^t$ and $\boldsymbol{\theta}^t$ are the feature parameter vectors for character to be recognized, and I and L are the number of elements in the feature parameter vectors for the reference character and the character to be recognized, respectively.

2) In order to obtain a good matching between the feature parameter vectors, a warping function $w(k)$ is defined as sequence

$$\mathbf{w} = w(1), w(2), w(3), ..., w(K), \quad (12)$$

where $w(k) = (i_k, l_k)$, $(1 \le i_k \le I; 1 \le l_k \le L)$, with the initial condition as $w(1) = (1,1)$, and the terminal condition as $w(K) = (I, L)$. K is the number of warping points obtained from DP matching

3) The dissimilarity between the feature parameter vectors is calculated by

$$S = \frac{1}{I+L} \min_{w} \left(\sum_{k=1}^{K} d(w(k)) g_k \right), \quad (13)$$

where

$$d(w(k)) = \left| z^r(i_k) - z^t(l_k) \right| + p \left| \theta^r(i_k) - \theta^t(l_k) \right|,$$
$$g_k = (i_k - i_{k-1}) + (l_k - l_{k-1}), \quad (14)$$

The minimum cost of matching two features are calculated by

$$h(w(k)) = \min \begin{Bmatrix} h(i_k - 1, l_k - 1) + 2d(i_k, l_k) \\ h(i_k - 1, l_k) + d(i_k, l_k) \\ h(i_k, l_k - 1) + d(i_k, l_k) \end{Bmatrix}, \quad (15)$$

Equation (13) can be rewritten as

$$S = \frac{1}{I+L} h(w(K)), \quad (16)$$

where $h(w(1)) = 2d(w(1))$, p is the weight for θ.

Fig.7 shows the warping function of matching two vectors, $\mathbf{z}^r$ and $\mathbf{z}^t$. It can be seen that timing differences between two patterns are eliminated by the warping function.

It is assumed that the reference patterns of known classes for Khmer numerals 'zero', 'one', 'two', 'three', …, 'nine' are defined by $\{C_0, C_1, C_2, ..., C_9\}$, respectively.

Then an unknown character x is assigned to a class $C_i \in \{C_0, C_1, C_2, ..., C_9\}$

$$\text{if } S_{\min}(C_i, x) = \min_l \{S(C_l, x)\},\ l = 0,1,2,...,9, \qquad (17)$$

where $S_{\min}(C_i, x)$ is the dissimilarity between the feature parameter vectors obtained from an unknown pattern x and that obtained from the reference pattern of known class C_i.

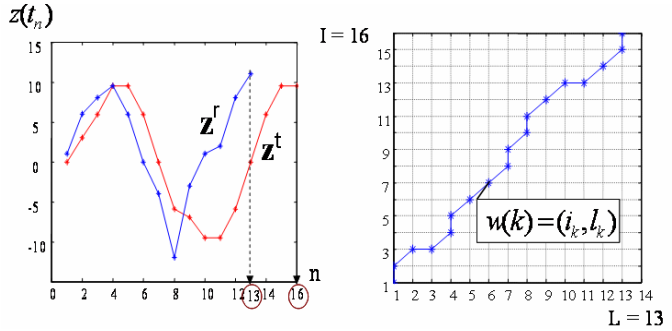

Figure 7: Reference vector $\mathbf{z}^r$, test vector $\mathbf{z}^t$ (left), and the warping function (right).

V. EXPERIMENTS

Character recognition experiments were performed on a database consisting of 5000 Khmer numerals written by 20 people. In the experiments, 100 scripts for each Khmer numeral(0,1,…,9) are selected randomly from the database and used as the test data, and the training data for each Khmer numeral consisting of 5 scripts selected randomly from the database. The examples of some Khmer numerals in our database are shown in Fig.8.

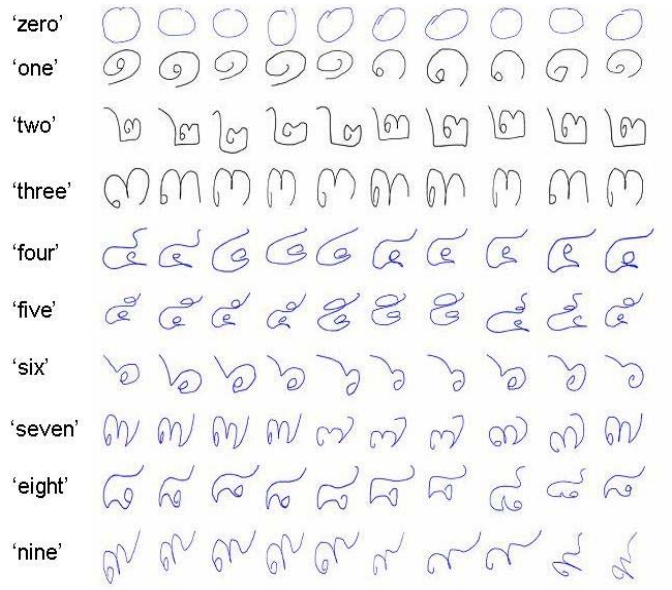

Figure 8: Some Khmer numerals in database.

The experimental results are shown in Table I. Table I shows the comparison of the experimental results of the proposed method using pen-point position and the barycenter. It can be seen from Table I that the recognition rate obtained from the barycenter is better than that obtained from pen-point position. The average of recognition rates was 95.9%, and it can be seen from Table I that the recognition rates obtained from numeral 'nine' and 'seven' are less than those obtained from other numerals because the handwriting style for numeral 'nine' and 'seven' obtained from some writers are similar. Fig.9 shows Khmer numeral 'nine' and 'seven' which were not correctly recognized.

Table I: Recognition rates of Khmer numerals.

Khmer numeral	Recognition rates (%)	
	Using pen-point	Using barycenter
'Zero'	96	96
'One'	63	94
'Two'	85	92
'Three'	98	99
'Four'	98	99
'Five'	74	92
'Six'	100	100
'Seven'	95	99
'Eight'	83	96
'Nine'	85	92
Average	87.7	95.9

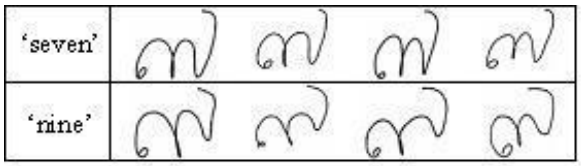

Figure 9: Numeral 'seven' (first row) , and numeral 'nine' (second row).

VI. CONCLUSION

We proposed an on-line character recognition method based on DP-matching of barycenter trajectory. The barycenter, determined from the center point of the script and two adjacent of pen-point positions, was used to reduce the sensitivity of pen-point movement in handwriting process. The character was recognized by the incorporation of the barycenter trajectory and its direction changes in DP matching. The experimental results show that the proposed method is useful for on-line character recognition for Khmer numeral.

REFERENCES

[1] R. Plamondon and Sargur N. Srihari, "On-Line and Off-Line Handwriting Recognition: A Comprehensive Survey," IEEE Trans. Pattern Anal. Mach. Intell., vol.22 no.1, pp. 63-84, July 2000.

[2] T.Matsuura and P.Thumwarin, "On-Line Thai Numeral Recognition" IEEE Asia Pacific Conference on Circuits and Systems, pp. 445-448, December 2000.

[3] Yuichi Nakatani, Daisuke Sasaki, Youji Liguni, Member, IEEE, and Hajime Maeda, Member, IEEE, "Online Recognition of Handwritten Hiragana Character Based Upon a Complex Autoregressive Model", IEEE Trans. Parttern Ana. Mach. Intell. , vol. 21 no. 1, pp. 73-76, January 1999.

[4] HIROAKI SAKOE, and SEIBI CHIBA, "Dynamic Programming Alogorithm Optimization for Spoken Word Recognition ", IEEE Trans. Acoustics. Speech. Signal Processing., vol. ASSP-26 no.1, pp. 43-49, Febraury 1978.

The Use of Context-free Grammars in Isolated Word Recognition

C. Chirathamjaree
Edith Cowan University
2 Bradford Street
Mt. Lawley, WA 6050 AUSTRALIA

***Abstract*-A method using non-recursive context-free grammars is presented for the recognition of isolated words. Some form of 'training' is required to combat problems of variations in speech. In the training mode, one grammar for each word in the vocabulary is constructed directly from a set of sample strings of 'features' represented by symbols. In the recognition mode, an incoming string is analyzed to determine which grammar, if any, could have generated it. The word corresponding to such grammar is then said to have been recognized.**

I. INTRODUCTION

An isolated word recognition (IWR) system is one which can recognize human utterances. Short pauses are required before and after utterances to be recognized. Following the common practice in the filed of pattern recognition [1], an IWR system can be considered to consist of a feature extractor (FE) or a pre-processor of some sort followed by a recognizer or classifier (Figure 1). The FE transcribes the input speech signal into strings of symbols representing various parameters extracted from the signal. A decision is made by the recognizer on this simplified representation as to which word in the vocabulary, if any, has been spoken.

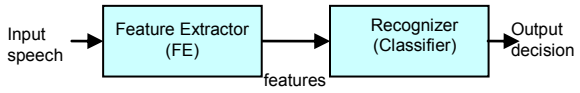

Figure 1. An isolated word recognition system.

The classical decision-theoretic methods [1,2] from the filed of pattern recognition have commonly been used to produce recognizers for processing strings of symbols generated by the FE. Another promising approach, which stemmed from the fields of mathematical linguistics and computer science, is to make use of the techniques of formal language theory [3]. The essence of this method is the use of formal grammars to model a FE and to classify a pattern by determining which of a number of formal grammars [4] or sets of rules could have generated it. This paper presents the application of linguistic methods to the modeling of a FE and the recognition of isolated words from a limited vocabulary.

II. THE FORMAL GRAMMARS IN ISOLATED WORD RECOGNITION

In general, a person does not always speak the same word in the same way. This may be due to the emotional and physical states of the speaker, the ambient noise level of the surrounding and free variation from trial to trail. Hence, some form of 'training' is usually required in order to combat problems of variations in speech. This is done by having the user speaking each word in the vocabulary a number of times until the representative rules for the construction of each word are formed.

In IWR systems, words are spoken in isolation with short gaps between utterances. This leads to the following assumptions:-

(a) Only a finite number of symbols are generated by the FE and only one symbol can be represented at a particular time.

(b) Each word uttered results in a sequence of symbols of some finite length.

The problem of designing a recognizer in an IWR system can be broadly divided into two areas: the construction of models based on formal grammars, known as grammar inference [5,6,7], to represent characteristics of the symbol-generating source and the search for suitable decoding methods for efficiently analyzing the strings from the source using rules or grammars of the models previously created.

In outline, the basis of the linguistic method is simply explained (Figure 2). In the training (learning) mode, a user repeats each word in the vocabulary a number of times. Each time the same word is spoken, a similar but not necessarily the same string of symbols is produced by the FE. Grammar-based models, one for each word in the vocabulary, are then automatically constructed and stored in the system memory for future use. In addition to producing all the strings in the sample set, each model is also capable of predicting other similar strings. Model building is considered to be the encoding of strings. In the recognition mode, an incoming string is processed using suitable decoding algorithms to determine which model, if any, corresponds or nearly so to the word spoken. If the most compatible model is found, the corresponding word is then indicated as to have been recognized. Otherwise, the recognition fails and the word is rejected.

In IWR systems, unlike many applications of grammar inference where the class of grammars to be inferred is precisely defined, it is not clear what types of grammars best represent the FE. In principle, regular or finite-state grammars (FSG's) would be adequate since each training set can consist only of a finite number of finite-length strings. The FSG approach is simple, offers well-established characteristics and its sequential nature is similar to that of the string symbols. In addition, many efficient computational techniques are known for the FSG methods. This paper presents a method using non-recursive context-

free grammars (CFG's) for the recognition of isolated words. The CFG approach is selected because it enables useful complexity to be generated without requiring inordinate computing power. In addition, a CFG may have fewer nodes and/or links than a finite-state grammar using the same data. Another motivation behind the use of the non-recursive CFG approach is to determine whether there is any advantage from the use of a more powerful grammar in isolated word recognition.

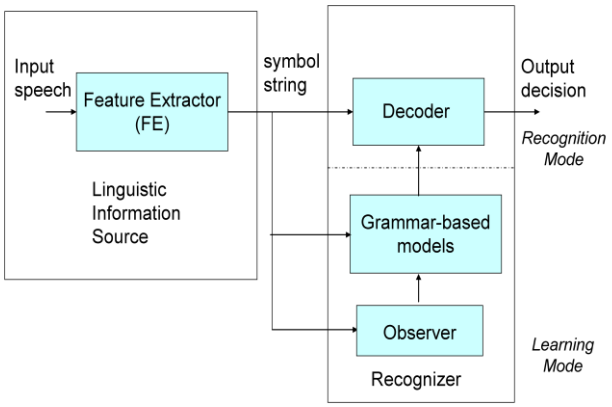

Figure 2. A grammar-based IWR system.

Some notation and terminology are now introduced. Precise and complete definition of context-free grammars (CFG's) are available elsewhere [3,4,8].

A CFG consists of:

1. A finite set of *non-terminals* $A_1, A_2, \ldots, A_r$;
2. A finite set of *terminals* $b_1, b_2, \ldots, b_s$;
3. A set of *rewriting rules* (or just *rules*) of the form $A \rightarrow \beta$; where A is a non-terminal and β is a non-empty string of terminals or non-terminals, or both;
4. A *start symbol*, which is one of the non-terminals.

Any CFG can be transformed into an equivalent Chomsky normal form [4] in which the rules are of the following forms only:

Bielement rules: $A \rightarrow BC$
Terminating rules: $A \rightarrow a$

where A, B and C are non-terminals and a is a terminal.

III. Computation of the Minimization Matrix

Before the inference method can be given, it is necessary to describe the minimization matrix, M, which forms the basis of the inference process of the CFG's.

For a given CFG in Chomsky normal form and for a string, S, the minimization matrix, M, (M-matrix) is a 3-dimensional, n x n x r matrix where n is the length of S and r is the number of non-terminals in the grammar. Let a_j represent the j^{th} symbol of S. Element m_{ijk} of M denotes the minimum number of symbol alterations (insertions, deletions or substitutions) required if the length-i substring of S, whose first symbol is a_j, is to be generated by the grammar from A_k, the k^{th} non-terminal.

M-matrix can be computed iteratively by the following procedure.

Part 1: Terminating rules

m_{1jk} = 0, if and only if $A_k \rightarrow a_j$ is a rule of the CFG

m_{1jk} = 1, otherwise.

For i=2,3,…,n:

$$m_{ijk} = \max\left[(i-1), \sum_{u=j}^{j+i-1} m_{1uk}\right].$$

Part 2:Bielement rules

$$m_{1jk} = \min_{p,q \in P_k} \left\{\min\left[m_{1jp} + H(q), m_{1jq} + H(p)\right]\right\}$$

where P_k is the set of ordered pairs (p,q) such that $A_k \rightarrow A_pA_q$

For i=2,3,…,n:

$$m_{ijk} = \min_{p,q \in Pk} \left\{\min\left[x, \min_{1 \le u < i} (m_{ujp} + m_{i-u,j+u,q})\right]\right\}$$

where $x = \left[m_{ijp} + H(q), m_{ijq} + H(p)\right]$

IV. Inference Procedure

In the learning mode, a learning algorithm is employed to automatically construct one grammar for each word in the specified vocabulary. The inference process produces rewriting rules directly from the observed sample strings in response to the words spoken. Rule or production probabilities are also estimated during the learning process.

Inference algorithms of the CFG's are based on the criterion of maximizing the similarity between various strings of the same word. The basis of the inference process is now explained. The first grammar, called the *skeleton grammar* G_1, is constructed from the first string in the sample set such that G_1 can generate only that string. Other strings are then individually processed in the search for incompatibility between each string and the current grammar. If the nth observed string, S_n can be derived from the $(n-1)^{th}$ inferred grammar G_{n-1}, then $G_n = G_{n-1}$ and no augmentation of G_{n-1} is required. Otherwise, G_{n-1} is augmented such that G_n is produced which can generate the present string. For the CFG approach, the matching process between an incoming string and a CFG involves the computation of the *M-matrix* whose elements reveal the shortcomings of the grammar in relation to its ability to generate the string.

V. Recognition Scheme

In the recognition mode, each unknown string presented to the recognizer is classified or decoded using the rules obtained in the learning mode. The recognition process consists of three main levels of operation in terms of the complexity involved. The recognition always starts at the lowest level (level 1). A higher level is applied only if the previous one fails to classify a string according to some criteria.

Level 1: In this simplest level of the recognition process, an incoming string is tested by means of a parsing algorithm to determine which grammar, if any, could have generated it. If the string is accepted by one grammar only, the corresponding word is indicated at the output. For unsuccessful matching, the method of level 2 is applied to decode the string. When two or more grammars can generate the string, it is necessary to employ a stochastic algorithm to find one 'best word' that is most likely to have produced the string. If two or more such words are possible, the string is rejected.

Level 2: In this level, a technique is utilized to determine the 'closest match' for the string i.e. the grammar that could nearly have generated the string. It is basically a dynamic programming method of optimizing the similarity between two functions.

Level 3: This is the highest and most complicated level of the recognition process where the operations in the two lower levels have to be performed in order to reach level 3. It is applied when there exist two or more closest-matched words corresponding to the string. Another stochastic algorithm is employed to select the most likely closest-matched word. The string is rejected if two or more such words are found.

The foregoing recognition scheme is not too restrictive in the sense of immediate rejection of an erroneous string but rather trying to find a grammar that could most likely have generated the string. This can be very useful in many applications involving noisy strings.

VI. Results and discussion

The experimental IWR system has been constructed based on the use of the CFG's outlined in this paper to model the FE. The vocabulary consists of ten digits 'ZERO' to 'NINE' uttered by a single speaker. The speech signal of the spoken digits is of telephone-grade quality. This is obtained from a normal telephone set via a circuit representing two local lines. Ten of CFG's for the recognition of the spoken digits 'ZERO' to 'NINE' were generated from a total of 100 strings, of average length 3.6 symbols. The testing set consists of 500 strings in total with 50 strings for each of the ten digits spoken. The average length of testing strings is 3.4 symbols per string.

The non-recursive CFG approach yields the average recognition rate of 72.8% using the training and testing set as described above. In another experiment using FSG's approach, the recognition rate using the same training and test set as above gives an average recognition rate of 73.4%. From the results obtained, it seems that the use of FSG's and CFG's to model a FE offers comparable recognition performances with less than 1% variation between them. This, in a way, is to be expected since the learning algorithms for the inference of both types of grammars are based on a similar criterion of maximizing the similarities between strings in the sample set.

It appears that there is no advantage gained for the use of non-recursive CFG's over that of FSG's, as far as recognition performance and computational requirement are concerned. This may be because only an isolated word, and not a sentence, needs to be recognized and this does not require the information of the syntax of the words concerned. There are, however, other situations where there may be an advantage for using a CFG approach. One example is the recognition of connected speech.

The previous sections have described an incremental method for the construction of non-recursive CFG's. This is appropriate for applications such as the recognition of isolated words, where finite-length strings only are involved. The method presented is guaranteed to yield non-recursive CFG's that are capable of producing all the given strings, irrespective of the order in which they are presented. Any other strings generated by the grammar will resemble those in the training set. The method also produces compact grammars having a near-minimal number of rules and non-terminals.

The representation of strings by a set of rules of formal grammars instead of direct storage of strings make possible the 'generalization' of strings in the training set. This reduces the size of the training set needed compared with the approach of using template matching techniques in order to cover the same number of strings. Extension of the method to the construction of stochastic CFG's, by counting the frequency of use of rules, is straightforward. Future work on the recognition of words in connected speech is planned.

VII. Conclusion

Techniques of formal language theory or the syntactic methods provide a useful approach to the solution of classification and description in an isolated word recognition system where only a finite number of features (represented by symbols) are generated for each utterance. The method presented for the generation of grammars from sample strings enables grammars of useful complexity to be generated without requiring inordinate computing power. Comparison with an approach using DTW (Dynamic Time Warping) is planned for futture work.

References

[1] P. O. Duda, P. E. Hart, and D. G. Stork, *Pattern Classification*, John Wiley, New York, 2001.

[2] K. S. Fu, *Syntactic Pattern Recognition and Applications*, Prentice-Hall, Englewoods Cliffs, 1982.

[3] N. Chomsky, *Aspects of the Theory of Syntax*, MIT Press, Cambridge, Massachusetts, 1964.

[4] J. E. Hopcroft, R. Motwani, and J. D. Ullman, *Introduction to Automata Theory, Languages, and Computation*, 2nd Ed., Addison-Wesley, Reading, Massachusetts, 2000.

[5] K. Clarkson, and T. G. Dietterich, *Grammatical Inference, The Handbook of Artificial Intelligence*, pp. 494-511, William Kaufmann, Inc, 1982.

[6] T. G. Evans, "Grammatical inference techniques in pattern analysis", *Software engineering*, Volume (2), pp. 183-202, Academic Press, 1971.

[7] L. Miclet, *Grammatical Inference, Syntactic and Structural Pattern Recognition: Theory and Applications*, World Scientific, 1990.

[8] A. V. Aho, and J. D. Ullman, *The Theory of Parsing, Translation, and Compiling, Vol. I: Parsing*, Prentice-Hall, Englewood Cliffs, New Jersey, 1972.

Curvature Tree for Isolated Unconstrained Lao Handwritten Character Recognition

Khampheth Bounnady*, Boontee Kruatrachue*, Takenobu Matsuura **
*Computer Engineering Department, Faculty of Engineering,
King Mongkut's Institute of Technology Ladkrabang, Bangkok Thailand 10520.
**Communications Engineering Department, Faculty of Information Technology and Electronics,
Tokai University 259-1292, Japan. E-mail: s6060215@kmitl.ac.th, kkboonte@kmitl.ac.th, matsuura@dt.u-tokai.ac.jp

***Abstract*- Lao handwritten characters can naturally be represented as a sequence of curve in clockwise and counter clockwise directions. This paper proposed the use of this curve sequence as a main feature in Lao handwritten character recognition system. Since, there can be variation and noise in a handwritten that usually generates small curve segment. Also, some curve segments when written in fast speed can be decreased to small curve segment. Hence, it is hard to distinguish between real curve and noisy curve. To overcome this problem, small curve segment is treated as both real curve and noise curve. The noise curve segment is omitted from the sequence while the real curve is remained. Each uncertain curve segment causes two possible representations. So, instead of single curve sequence, a tree of curve segment is form and use as a main feature in recognition. The proposed method can recognize different handwritten Lao character very well in comparing to the conventional method such as elastic matching.**

Keywords- *feature tree, curvature feature, distinguish feature, handwritten Lao character, Lao recognition.*

I. INTRODUCTION

Many methods for online character recognition have been proposed [1]. However a few methods for Lao character recognition have been proposed [6,7]. In this paper, a new method for unconstrained Lao handwritten recognition is proposed. Fig 1. shows the example of Lao characters and Fig. 2 shows the unconstrained Lao handwritten, where characters are written out of proportion and varied in amount of rotation (slant) and writing style. Most zone features [1] are less effective due to the out of proportion since some characters will have big, small or omitted head.

The proposed method will be compared with elastic matching which provides a very good recognition rate and has been widely used since the early [2] and recently handwritten recognition research [3,4]. The elastic matching can be used to performed matching the unknown writing with the prototype character and the unknown writing is recognized as the character with the closest match.

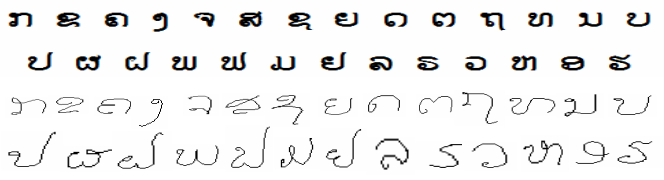

Fig 1. Example of Lao isolated handwritten and printed characters

Fig 2. Variation of Lao handwritten.

The elastic matching by finds the optimal alignment distance among all the n points of both matched characters by summing distance of all the matched points. The disadvantage of elastic matching is the overall shape matching of character which has also been observed by other researcher [3]. This is a problem in Lao handwritten as shows in Fig. 3, where the overall shape matches to the wrong character and miss the small curvature in the top. The elastic matching misses dominant point due to equally treatment of all the point in the matching.

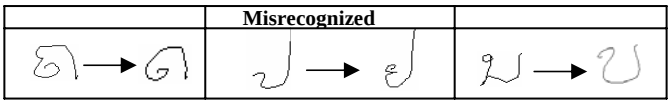

Fig 3. Misrecognized characters by elastic matching method.

Handwritten Lao character is usually continuous drawing of curves (mostly single stroke). It is naturally to represent handwritten Lao as a sequence of curve segment with clockwise and counter clockwise direction as the main feature. Even though this feature quite coincides with the way writers learn to write Fig. 4, it may consist of noisy curves. Usually, the noise curve segment can be distinguished from the real curve by the high amount of curvature of the real signal. But when the written speed is fast, the curvature is reducing close to the noisy curve as shown in Fig. 4. These noisy curves are hard to distinguish with normal noise reduction technique such as Fourier expansion or Fourier descriptor due to the similarity in frequency and amplitude.

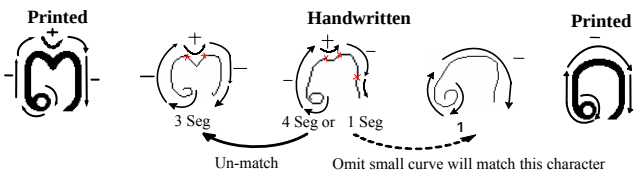

Fig 4. Uncertain segment with small curvature.

In order to successfully use the curvature sequence in the recognition, one may have to identify real curvature from the noisy one. As shown in Fig. 4, the character ๆ consist of three curvatures in sequence. If all small curvature is treated as noise and omitted. It will match to another character ๅ that has one clockwise curvature. On the other hand, if treated all curvature as real curve the character will have 4 curvatures and can't match to the correct character with three curvature segments. So in the proposed method, we classify curve feature into three groups, noise, real and uncertain segments. The noise group consists of the noise curves that can be identified and are ignored. The uncertain group consists of noise and real signal that can't be distinguished. The real group has high curvature enough to be certain as a real signal. A binary tree of curve sequence is formed, the branch in the tree represents uncertain curve segment. So the feature of a handwritten character is not just a single sequence of curve but a tree of curve segments. The noisy curves are discarded and the real curves still remain in the tree. In other word, we discard the certain noise out but keep all possibility of the uncertain and real curve segment and form them in the tree. For detail of tree generation will be descript later in section three.

Since all possible segments still remain in the tree, we postpone the determination of the uncertain segment until we compare with another character. So in order to find a similarity (or dissimilarity) with another character, it is liked comparing two trees for all possible representation of curve sequence of both characters. Since this method needs to compare between two characters in order to select the closet representation of the two characters, this technique is suitable for similarity based pattern recognition.

The tree representation guarantees to have one correct sequence of curve, but also contains a lot of other noisy sequences. Hence, more additional curve features are added in order to make noisy curve dissimilar enough to make the correct sequence pair the most similar. In order to show the effectiveness of this approach, the comparison of the recognition results obtained from the proposed method using the curvature tree and the elastic matching are given.

II. CURVATURE SEQUENCE EXTRACTION OF LAO HANDWRITTEN

Lao handwritten is input as a sequence of X,Y coordinates samples from input device with the rate of 100 samples per second. In order to extract curvature sequence, the following steps are performed: 1) Translate the X,Y coordinate sequence into the direction sequence and the length sequence. 2) Translate the direction sequence into the angle sequence by subtracting the current direction from the next direction in the sequence. 3) Find segmentation points and then curvature sequence is defined by adding the angle between consecutive segmentation points.

The direction of pen trajectory is represented as real number call directional code [5]. Examples of the directional code calculation are shown in Fig. 5. The 45-degree means one unit (360-degree is 8 units). The directional code can be calculated

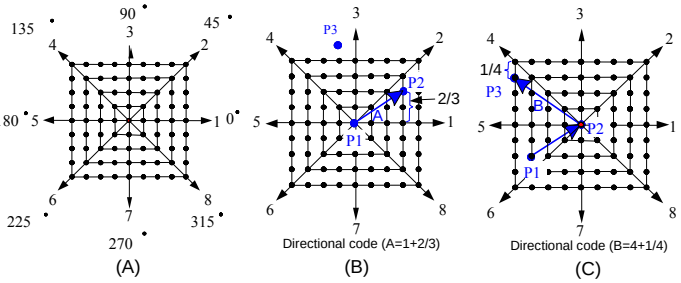

Fig 5.The directional code calculation,(A) The directional code,(B)Directional code calculation of vector A, (C) Directional code calculation of vector B.

as a real number. As shown in Fig. 5, the directional code of vectors A and B are given as 1 + 2/3 and 4+1/4, respectively.

The angle between two consecutive segments of pen trajectory is defined as the difference between the corresponding directional codes, the current directional code minus the previous one. With the above angle, the directions of pen trajectory, counter clockwise and clockwise can be represented as positive and negative angles, respectively. The angle of a curve segment represented as the sum of the angles of the consecutive segments and the length of curve segment is represented as the sum of the length of the segments in the curve segment. It can be seen that the angle for curve segment is rotation invariant and shape invariant. As shown in Fig.6, the directional code for the rotation of any counter clockwise 90 degree turn is 2.0 and the directional code for whole circle 270 turn is 6 independent of exact shape. In the following the whole character is represented as the sequences of curve segments with clockwise and counter clockwise directions.

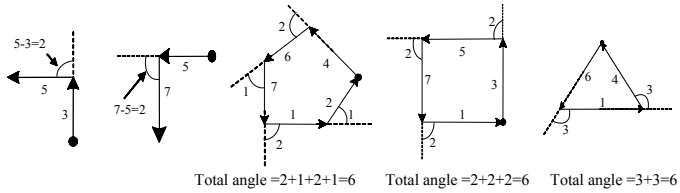

Fig 6. Rotation invariant and shape invariant.

Consecutive segments with the same direction of clockwise or counter clockwise are treated as one angle. A point separating pen trajectory into two curve segments with clockwise and counter clockwise directions is defined here as a segmentation point. In other words, a segmentation point is the point changing the direction of pen trajectory from the clockwise to the counter clockwise and vice versa. Some researchers [5] have used the dominant point or point where the pen trajectory turns the direction quickly. We consider the segmentation points in the pen trajectory of Lao handwritten by improving the above dominance point in the literature [5]. In order to represent Lao handwritten with segmentation points effectively, the noise such as small variation or fluctuation in the pen trajectory should be removed. In this paper the noise cancellation is made as show in Fig. 7(A) and 7(B). When the direction of pen trajectory is not in alignment but in zigzags (clockwise and counter clockwise curve segments with small equal angle), the zigzags is considered as a straight line. In other words, the pen trajectory with the zigzags segments is

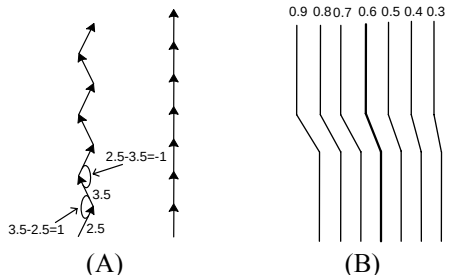

Fig 7. (A) Quantized noise cancellation, (B) The threshold 0.6 curvature

considered as a straight line if sum of the angles of curve segments between the consecutive segmentation points is equal to zero. As show in Fig. 7(B), a pen trajectory has a noise such as small and quick change of curvature. In this case pen trajectory is considered as a straight line or zigzag line according to the amount of the angle of the curve segments between two segmentation points. That point is not considered as the segmentation point if the angle is less than a selected threshold angle. In the example in Fig. 7(B), pen trajectory is considered as straight line if amount of the angle of the curve segments is less than threshold value (0.6), otherwise a zigzag line. It can be seem that the direction of pen trajectory is determined using the angle of curve segment in the trajectory. However some Lao characters such as ถ and ฦ have same clockwise direction of pen trajectory. In this case we can not recognize two characters as different using the angle. Thus we introduce the change of the x, y coordinates and the length of the curve segment of pen trajectory as other features of handwritten Lao character.

III. CURVATURE TREE REPRESENTATION

This section explains construction of curvature tree for all possible uncertain segments. The sequence consisting of clockwise and counter clockwise curve segments is used to construct curvature tree using the following steps:

1) Classify each curve segment as one of the following segments, noise, uncertain and real using length and angle of the segment. Then discard the noise segment by merging noise segment with the previous segment and subsequent segment.

2) Re-classify each merged segment as one of the following segments, uncertain and real. If any adjacent uncertain segments has the same amount of angles but different signs (-clockwise,+ counter clockwise), then both uncertain segments are treated as a noises with zero angle and merge both adjacent segments as mentioned above.

Construct binary tree of curve segments consisting of the real and uncertain segments.

The noise of segment can be reduced using the combinations of the angle of the curve segment and the length of the segment. The real curve segment should have high curvature and significant size. Some noise segments may have high curvature with short length or small curvature with long length, but not both. Hence, the noise segment can be classified here using angle-length feature, the angle multiplied by the length (the ratio of the length over the summation of the entire segments length). If the angle-length feature is less than a threshold value (0.017) then the segment is considered as a noise segment. If it is between 0.017 and 0.4, then it is considered as an uncertain segment and furthermore if it is greater than 0.4, then it is considered as a real segment. These threshold values 0.017 and 0.4 got from our handwriting database. Since our database is from 18 writers and we have rotation invariant feature, this threshold should be suitable for other writer. The segment contaminated with noise is removed from the pen trajectory and then the angle and the length of segment are added to both adjacent segments (previous and subsequent segments). After noise removal, the angle and the length of the merged segment change due to the addition. The noise classification of the merged segments is repeated until this classification results in only uncertain and real segments without noise. Up to now the curve sequence has been represented by a sequence of clockwise and counter clockwise curve segments with some uncertain segment. In the next step a binary tree of all possible representation is formed, where each uncertain segment can be treated as a noise or real segment and forms the binary branch of the tree. When uncertain segment is treated as a noise segment, the adjacent segments (three segments) are merged together, as shown in Fig. 8. The figure also shows the tree representation of character ถ. Each node of tree consists of sum angle and sum length. As mentioned in the introduction, the purpose of feature tree is to keep all the possible representations of a character. At this moment, we still don't know which the real curve sequence is because of some uncertainty. But, the real representation can be identified by comparing with the other characters.

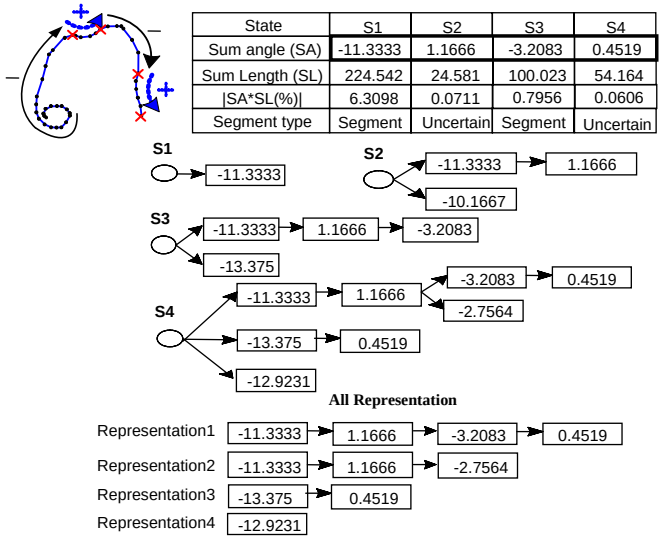

Fig 8. Curvature tree representation and merge of uncertain segment treated as a noise.

IV. RECOGNITION USING PROTOTYPE MATCHING

It is assumed that the character to be recognized has some segments, and the prototypes are prepared in each segment. For the convenience of explanation, it is assumed the character to

be recognized has p segments and the number of character classes with p segments, is s_p. Then the character X is represented as

$$X \equiv X_{p=} (\xi_{1,}\ldots,\xi s_p)^T \quad (1)$$

X_p is corresponding to the branch of the alternate curvature tree for the character X then the character X is recognized as follows (Fig. 9)

(Step.1) calculate the distance between prototype P_k and X as

$$d\left(X_p, P_k\right) = \left\| X_p - P_k \right\| \quad (2)$$

where $d\left(X_p, P_k\right)$ is the Euclidean distance between X_p and prototype P_k of the *k*th character class with p segments.

(Step.2) calculate the minimum distance as

$$\underline{d}_{s_p}(r) = \min_{1 \le k \le s_p} d\left(X_p, P_k\right) \quad (3)$$

(Step.3) character x is recognize as $X \in C_r$ (The *r*th character class)

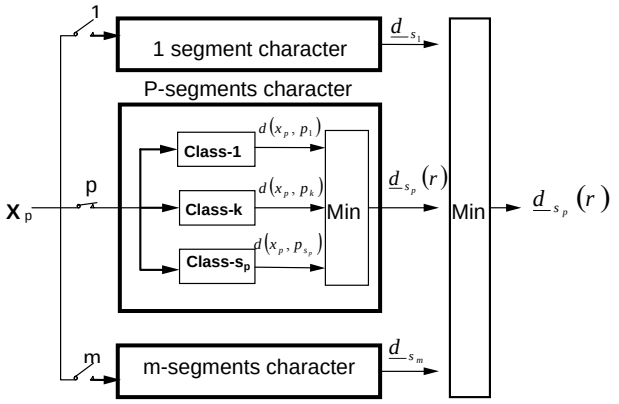

Fig 9. Lao handwritten recognition system

V. EXPERIMENTAL RESULTS

The proposed curvature tree and the elastic matching method are compared. In experiment we used PC with 1.4 GHz Pentium 4 and using our database consisting of 24321 handwritten Lao characters belonging to 27 classes. The prototypes of characters consisting of 3729 handwritten Lao characters. The recognition rates of each method are shown in Table I

TABLE I
COMPARISONS OF RECOGNITION METHODS

Method	Recognition Rate (%)	Average Time (s)
curvature tree	96.78	0.0204
Elastic Matching	94.05	1.2356

Some of characters misclassified by our method and elastic matching method in the experiment are shown in Fig. 10.and Fig.11, respectively. It can be seem from Fig.10 that it is rather difficult for out method to recognize some of characters having small loop or curve, but it easy to recognize curve segment with clockwise or counter clockwise direction in pen trajectory. While it can be also seem from Fig.11 that the elastic matching method can not recognize a curve segment with clockwise or counter clockwise direction in pen trajectory but it is easy to recognize a character with similar shape except for the direction, clockwise or counter clockwise of pen trajectory.

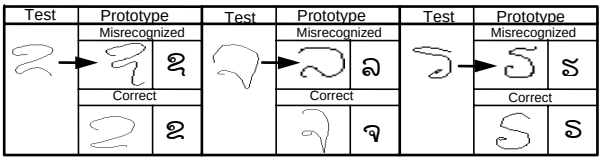

Fig 10. Example of misrecognized in our method.

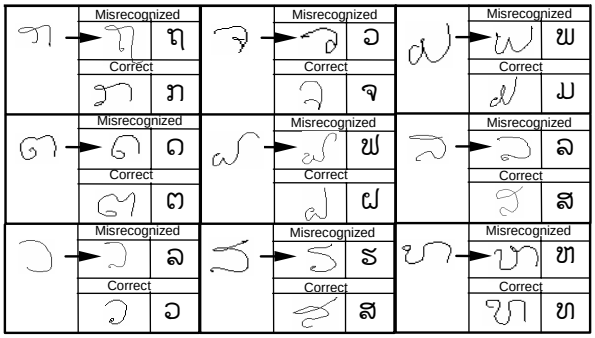

Fig 11. Example of misrecognized in elastic matching.

VI. CONCLUSIONS

This paper proposed an unconstrained isolated Lao handwritten recognition method by using curvature tree. In the proposed method, as unique features of Lao handwritten, different characters with similar shapes having small or large curve segments with clockwise and counter clockwise directions, were take into account. The proposed method can recognize correctly Lao handwritten with above features though the elastic matching method having been used widely can not do this. It was found from our experiments using our data base that the recognition rate of our method was higher than that of elastic matching method and average time requited to the recognition of our method is faster than elastic matching method.

REFERENCES

[1] Rejean Plamondon, Sargur N. Srihari, "On-Line and Off-Line Handwriting Recognition A Comprehensive Survey", IEEE Trans, vol.22, no.1, pp.63-83, January 2000.

[2] D.J Burr, "Designing a Handwriting reader ", IEEE Trans. PAMI vol. PAMI-5, no 5, pp. 555-559, 1983.

[3] Seiishi Uchida, Hiroaki Sakoe, "Eigen deformation for elstic matching base handwritten character recognition", Pattern Recognition, Vol. 36, Issue 9, pp 2031-2040. September 2003.

[4] Claus Bahimann and Hans Burkardt, "The Writer independent Online Handwriting Recognition System frog on hand and cluster Generative Statistical Dynamic Time Warping", IEEE Trans, vol.26, no.3, pp.299-310, March 2004.

[5] H. Yuen, "A chain coding approach for real-time recognition of on-line handwritten characters", ICASSP'96, Atlanta, USA, 1996.

[6] Khampheth Bounnady, Boontee Kruatrachue, Somkiat Wangsiripitak "On-line Lao Handwritten Recognition with Proportional Invariant Feature", WEC'05, April 27-29, 2005, Istanbul, Turkey, pp41-44.

[7] Khingtong Intawongkam and Kosin Chamnongthai, "A method of Hand Writing Lao Alphabet Recognition by Using Back-Propagation Neural Networks", 21th Electrical Engineering Conference (EECON), 1998.

Combination of Self-Organizing Map and Fuzzy C-Means algorithms for project performance segmentation in Agricultural Technology Transfer and Service Centers

Sasithorn Mongkolsripattana, Anongnart Srivihok
Department of Computer Science, Faculty of Science,
Kasetsart University, Bangkok, Thailand
Email: {g4764238, anongnart.s}@ku.ac.th

***Abstract*- Currently, there are more than six thousands Agricultural Technology Transfer and Service Centers (ATSC) which conduct training to target groups in Thailand. Project performance measurements are significant for management and strategic planning for ATSC. Therefore, the assessments of their performances are not simple since all data are enormous and stored in huge database. This study aims to introduce a new tactic in segmenting ATSC performances. Clustering and ranking data set are two key steps in this approach. Firstly, apply two data mining techniques: SOM (Self-Organizing Maps) and Fuzzy C-Means algorithms to cluster ATSC data related to their project performances. SOM algorithm is used to calculate the appropriate number of clusters. Three measurement indices: SD validity index, DB and PBM index are used for SOM. Later, the same ATSC data set is clustered by Fuzzy C-Means algorithm. Secondly, data are ranked on their project performance scores. There are four levels of project performance: high, above average, average and low. Results revealed that ATSC can be clustered in six groups. The majority of ATSC project performances are in average and low levels, whereas some are in above average and no center is in high level.**

I. INTRODUCTION

Data mining is an integral part of knowledge discovery [1], which is the process of discovering useful knowledge in large database. Many industries [2] including finances, public health, education, and engineering have applied this method in their business. Clustering [1] is one of the most useful tasks in data mining. The main objective of the clustering algorithm is to find groups of closely related objects.

A. Previous Work

In case of using two-stage method to cluster data is certainly not new. Kuo et at. [3] proposed a two-stage method which is a combination of the SOM and K-Means algorithms for Market Segmentation. And then results were compared with the conventional two-stage method by Wilk‘s Lambda for measuring. The results indicate that the proposed method is better than the conventional two-stage method. Weng and Liu [4] used a combination between SOM and K-Means algorithms for one to one market recommendation system. The results show that the optimal number for clustering was 9 groups which have the best CV (Coefficient of Variance) values. Chaimeun and Srivihok [5] proposed the principles of data mining to cluster Thai handicraft customers by using a hybrid algorithm including SOM and K-Means algorithm. Mongkolsripattana and Srivihok [6] purposed the approach in clustering Technology Transfer Center performances by using two steps: clustering and ranking data set. First two data mining techniques (SOM and K-Means algorithms) used to cluster data according to their project performances. Second, project management efficiency scores (p score) were calculated for ranking TTC according to their management performances. The disadvantages of this research is that data set used in experimenting is small.

The above literatures have applied two-stage methods including SOM and K-Means algorithms. The majority used SOM algorithm to find the optimal number of clusters because K-Means algorithm requires an input which is a predefined number of clusters, k. Fuzzy C-Means algorithm is an extension of K-Means algorithm (it also requires an input which is a predefined number of clusters). It allows an object to partially belong to multiple clusters because of it has a membership function. Fuzzy C-Means algorithm is frequently used in many fields including pattern recognition, image processing and data mining. Albayrak and Amasyali [7] used unsupervised clustering method to developed medical diagnostic system by using Fuzzy C-Means algorithm. This algorithm was used for classification Thyroid patients and then compared performances with K-Means algorithm. Results reveal that Fuzzy C-Means algorithm give better results than K-Means algorithm in correct classified samples. Mingoti and Lima [8] presented the comparisons of clustering performance among SOM, Fuzzy C-Means, K-Means algorithms and Agglomerative Hierarchical. The results show that Fuzzy C-Means algorithm has the best performances in all cases and is stable in the presence of outliers and overlapping. And other methods are affected by the amount of overlapping and outliers. From this research Fuzzy C-Means algorithm has better performance, we will propose two-stage methods which combine SOM and Fuzzy C-Means algorithms for clustering ATSC data.

B. *Agricultural Technology Transfer and Service Center (ATSC)*

The policy for ATSC was established in Thailand in 1999. In these days, there are more than six thousands centers in each subdistrict (tumborn) of Thailand. ATSC provide services and training in agriculture to inhabitants in the neighborhood areas. Examples of a variety of trainings include training on rice cultivation, mango plantation and others. On monthly basis, ATSC have to report their progresses for planning and work practices on the provided web site.

II. CLUSTERING METHOD

Clustering is a division of data into clusters of similar objects. Each cluster consists of objects that are similar between themselves and dissimilar to objects of other clusters.

A. *Self-Organizing Maps (SOM)*

SOM [9] is one of the popular and powerful neural network algorithm which is unsupervised learning. Clustering using the SOM technique consists of six steps described below [10].

1) Initialize the weight vectors (*w*)
2) Calculate Distance: Calculate equation (1)

$$D(j) = \sum_{i=1}^{n} \left(w_{i,j} - x_i \right)^2 \quad (1)$$

Given *i* is input data, *j* is number of clusters as final result, *D*(j) is the distance between instance data and center of cluster, *x* is attribute of data.

3) Compare *D(j)* from each cluster
4) From step 3 we calculate cluster that least value by (2)

$$w_{i,j}(new) = w_{i,j}(old) + \alpha \left(x_i - w_{i,j}(old) \right) \quad (2)$$

When *w(new)* is a new weight, *w(old)* is an old weight

5) Decrease α
6) Go to step 2 and recomputed until *D(j)* has not change.

B. *Fuzzy C-Means (FCM) algorithm*

FCM is a clustering technique which allows one piece of data which belongs to two or more clusters with different membership function between 0 and 1. This method developed by Dunn [11] and improved by Bezdek [12]. The steps of the Fuzzy C-Means algorithm are given below [7].

1) Choose *c* initial centroids, *c* is the number of cluster.
2) The membership matrix (*U*) is randomly initialized

$$U_{ij} = 1 \Big/ \left(\sum_{k=1}^{c} \left(\frac{d_{ij}}{d_{kj}} \right)^{\frac{2}{(m-1)}} \right) \quad (3)$$

Where d_{ij} is the Euclidian distance between i_{th}, centroid (c_i) and j_{th} data point, *m* is a weighting exponent, and u_{ij} is between 0 and 1.

3) Calculate centroids (c_i)

$$C_i = \left(\sum_{i=1}^{n} U_{ij}^{\ m} x_i \right) \Big/ \left(\sum_{j=1}^{n} U_{ij}^{\ m} \right) \quad (4)$$

4) Compute dissimilarity between centroids and data points. Stop if its improvement over previous iteration is below a threshold

$$J(U, c_1, c_2, \ldots c_c) = \sum_{i=1}^{c} J_i = \sum_{i=1}^{c} \sum_{j=1}^{n} U_{ij}^{\ m} \left\| c_i - x_j \right\|^2 \quad (5)$$

5) Compute a new *U* using Equation 3. Go to Step 3.

III. EVALUATION OF CLUSTERING

Three indices are used for evaluating the efficiency of data clustering. The first index was proposed by Halkidi et al. [13], they reported that SD validity index proposed an optimal number of clusters. The second method, Davies-Bouldin (DB) index [14] is well-known for cluster validity. And the last index is PBM-Index, the new validity index proposed by Pakhiraa [15]. In this paper, three indices used to evaluate the optimal number of clusters.

IV. RESEARCH METHODOLOGY

A. *Research Design*

The framework for this study includes three steps; it is depicted in figure 1.

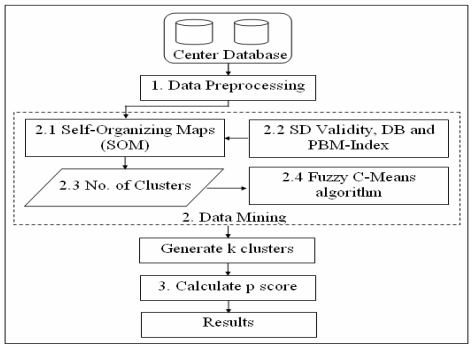

Figure 1. System Framework for the study

1) *Data Preprocessing*: We selected transaction data from ATSC including Center Profile and Activity Profile from tables in database were retrieved from Sending Activity Table, Committee Meeting Table and Sending Report Tables. In order to get the complete data set, incomplete data, noise and duplicate observations were discarded.

2) *Data Mining*: In this phase, two data mining techniques: SOM and Fuzzy C-Means algorithms used to cluster ATSC data.

Step 1: SOM is used to group data into 2-10 groups and then SD validity index, DB and PBM-Index were applied to find the optimal number of clusters which is the output of this phase. The lower index value reveals the better power of clustering for SD validity and DB index. On the order hand, the bigger value of PBM-Index is the better performance of cluster.

Step 2: Fuzzy C-Means algorithm is used for clustering ATSC data. The number of cluster or k value is derived from step 1. In this step ATSC data are segmented based on their work performances.

3) *Calculate p score*: After clustering have finished, p score in each group is calculated according to six attributes of project management which include (1) number of trainings (*Activity*), (2) number of participants in each training (*Target*), (3) the different between actual and planning technology transferred projects (*PE*), (4) the different between actual and expected participants (*TE*), (5) number of committee meetings (*Meeting*) and (6) number of submitted report (*Report*). The

real value of each attribute is adjusted in level ranged from 1 to 5. The p score of group is calculated from the sum of the average value of each attribute in that group, it was defined as

p score = sum score of (Activity + Target + PE + TE + Meeting + Report) (6)

From Table III, Cluster 1 includes the mean score of *Activity*, *Target*, *PE*, *TE*, *Meeting* and *Report* equal to 2.14, 2.06, 3.02, 3.02, 2.00 and 3.00 respectively. Thus, p score is 15.24 (2.14+2.06+3.02+3.02+2.00+3.00 = 15.24).

To rank ATSC, their performances are divided in 4 levels and the total p score is 30 points.

1) High: p score is ranged from 24 to 30 points.
2) Above average: p score is ranged from 18 to 23 points.
3) Average: p score is ranged from 15 to 17 points.
4) Low: p score is less than 15 points.

V. Experiment and Results

A. Experiment data

In this study, 68,281 transactions (in year 2005) obtained from working data of ATSC in Thailand. Center Profile and Activity Profile are the components of data set. Center Profile consists of general data of ATSC, such as Sub district ID, District ID, Province ID, Zone and other. Activity Profile is work practices of ATSC in each month. Clustering attributes in Activity Profile including

1) Technology Transfer Activity (*Activity*) is the numbers of technology transferred activity are organized in one ATSC. They are divided in 5 groups.

G1: No activity G2: 1 activity G3: 2 activities
G4: 3 activities G5: More than 3 activities

2) Agriculturist Target (*Target*) is the number of participants attending at each training. It is divided in 5 groups.

G1: No person G2: 1-50 persons G3:51-100 persons
G4:101-150 persons G5: More than 151 persons

3) Project-Expected (*PE*) is the different between actual technology transferred projects and planning. They are divided in 5 groups.

G1: Less than -1 G2: -1 G3: 0
G4: 1 G5: More than 1

4) Target-Expected (*TE*) is the different between actual and expected participants attending in each training. They are divided in 5 groups.

G1: Less than -50 G2: -50 to -1 G3: 0
G4: 1 to 50 G5: More than 50

5) Committee meeting (*Meeting*) is the meeting provided at ATSC in one month. They are divided in 5 groups.

G1: No meeting G2: 1 times G3: 2 times
G4: 3 times G5: More than 3 times

6) Report submission (*Report*) is the total number of reports sends to the head quarters by the web site. It is divided in 5 groups.

G1: No report G2: 1-5 reports G3: 6-10 reports
G4:11-15 reports G5: 16-20 reports

B. Results

Table I. depicts the results of clustering ranging from 2 to 10 clustered by using SOM algorithm. At the number of cluster equals 6 has the minimal value of SD validity and DB index. In part of the PBM-Index has the maximum value in clusters numbers equal 9. Thus, we choose cluster numbers equal 6 for the next step because two indices that give the same results.

TABLE I
CLUSTERING BY SOM ALGORITHM USING DIFFERENT INDEX FOR MEASUREMEN

No. of clusters	Validity Index		
	SD	DB	PBM
2	1.893	1.384	1.651
3	1.683	0.844	20.637
4	1.808	0.689	2.373
5	1.791	0.678	0.067
6	**1.677**	**0.622**	0.670
7	2.220	0.706	0.213
8	2.144	0.646	0.927
9	2.646	0.662	**33.633**
10	2.641	0.661	0.004

This phase, Fuzzy C-Means algorithm is applied for ATSC data segmentation in 6 clusters. Results are depicted in Table II. Characteristics of each cluster are as follows:

Cluster 1: It is the smallest cluster (10.77%). Technology transfer and Committee meeting in this cluster are about 1 activity and 1 time respectively. The number of participants in training is about 1-50 persons. Report submission is between 6-10 reports per month. P score is 15.24 which is average level. In order to improve the performances, ATSC in this cluster should increase numbers of activities, participants and meetings.

Cluster 2: It is the second largest cluster (19.05%) and has the smallest p score, 12.21 which is the low level. This group has neither Technology transfer and nor participants in training. Committee meeting is 1 time per month. To improve their performances, they should increase numbers of technology transfers, participants and meetings in each month.

Cluster 3: This cluster contains 10,407 transactions (15.24%), Technology transfer in this cluster is about 1-2 activities. The number of participants in training is about 1-150 persons. Committee meeting is 1 time per month. Report submission is between 1-5 reports per month. P score is 13.87 which is low level. In order to improve the performances, ATSC in this cluster should increase numbers of all attributes.

Cluster 4: It is the largest cluster (22.64%). Technology transfer is about 1 activity. The number of participants in each training is 1-50 persons. Committee meeting is 1 time per month. Report submission is 11-15 reports. P score is 16.28 which is average level. In order to improve the performances, ATSC should increase the numbers of training, participants and meetings in each month.

Cluster 5: This group has the maximum p score, 19.26 which is in above average level. Technology transfer activity is about 1-3 activities or more. The participants in training is more than 51 persons. Committee meeting is 1 time per month. Report submission is 11-15 reports. In order to improve their

performances, ATSC should increase committee meeting. It has 11,022 transactions (16.14%).

Cluster 6: It is the third largest cluster (16.22%). This group has Technology transfers and participants in training for this month about 1-2 activities and 1-100 persons respectively. Committee meeting is 1 time per month. This group has the maximum number of report submission, 16-20 reports. P score is 16.87 which is average level. To improve their performances, they should increase all attributes except number of report submission.

TABLE II
CLUSTERING ATSC BY FUZZY C-MEANS (USING 6 CLUSTERS)

Factors		Clusters					
		1	2	3	4	5	6
		7306	13008	10407	15462	11022	11076
Activity	No	0	12971	1942	0	0	2138
	1	6333	37	6168	13238	1594	6351
	2	935	0	2247	2224	5289	2532
	3	37	0	35	0	2086	55
	>3	1	0	15	0	2053	0
Target	No	10	13008	1972	62	0	2163
	1-50	6822	0	6643	14402	127	7175
	51-100	474	0	1551	998	4593	1738
	101-150	0	0	239	0	2638	0
	>150	0	0	2	0	3664	0
PE	<-1	26	1496	107	44	90	320
	-1	138	2548	270	303	170	571
	0	6814	8964	9574	14443	9954	9855
	1	299	0	348	613	75	303
	>1	29	0	108	59	733	27
TE	<-50	23	1417	98	42	87	318
	-1 to -50	139	2623	270	258	155	548
	0	6832	8968	9585	14501	9973	9878
	1-50	270	0	325	581	145	279
	>50	42	0	129	80	662	53
Meeting	No	587	1983	1003	1129	1135	868
	1	6327	10129	8644	13135	8871	9388
	2	290	746	613	972	766	706
	3	40	49	72	59	115	53
	>3	62	101	75	167	135	61
Report	No	0	0	2017	0	3	0
	1-5	0	4030	8390	0	1507	0
	6-10	7306	3440	0	0	2107	0
	11-15	0	5538	0	15462	5371	0
	16-20	0	0	0	0	2034	11076

TABLE III
CALCULATION P SCORE FOR EACH CLUSTER

Attributes	Clusters					
	1	2	3	4	**5**	6
Activity	2.14	1.00	2.04	2.14	**3.42**	2.05
Target	2.06	1.00	2.01	2.06	**3.89**	1.96
PE	3.02	2.57	3.01	3.02	**3.11**	2.92
TE	3.02	2.58	3.01	3.03	**3.10**	2.93
Meeting	2.00	1.94	2.00	2.03	**2.02**	2.01
Report	3.00	3.12	1.81	4.00	**3.72**	5.00
p score	15.24	12.21	13.87	16.28	**19.26**	16.87

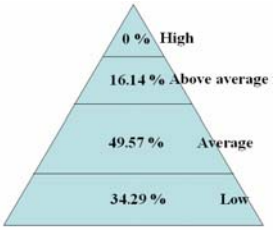

Figure 2. Ranking ATSC according to their practice work scores (p score).

VI. CONCLUSION

This study introduces a new method in segmenting ATSC performances. Clustering and ranking data set are two key steps in this method. Using SOM algorithm and three measurement indices, SD validity, DB and PBM, results show that data set should be segmented in six clusters. Then ATSC data set is clustered by using Fuzzy C-Means algorithm. The characteristics of majority ATSC include the number of technology transfers are about 1-2 activities and 1-50 participants per month. The different between number of proposed and actual projects is zero. In the same way, the different between number of proposed and actual participants is zero. Majority committee meeting is one time per month. Lastly, the number of report submission is about 1-20 reports.

This study suggests the project measurement by using performance scores (p score) to segment ATSC management. The majority of the centers are in average and low levels, whereas some are in above average and no center is in high level. When applying data clustering and p score ranking, the administrator can evaluate ATSC operations by comparing with other centers in the same or different clusters. This method will provide advantages for the manager to increase the productivity and services in their Centers by accentuating on the attributes which have low p score.

REFERENCES

[1] U. Fayyad, G. Piatetsky and P. Smyth, "Knowledge discovery and data mining : towards a unifying framework," *AAAI Press*, 1996, pp. 156.

[2] P.N. Tan, M. Steinbach, and V. Kumar, Introduction to data mining. Pearson Education, Inc., USA, 2006.

[3] R.J. Kuo, L.M. Ho and C.M. Hu, "Integration of self-organizing feature map and k-means algorithm for market segmentation," *International Journal of Computers and Operations Research*, vol. 29, Taiwan, 2002, pp. 1475-1493.

[4] S.S. Weng, and M.Liu, "Feature-based recommendations for one-to-one marketing," *Expert systems with Applications*, vol. 26, 2004, pp.493-508.

[5] O. Chaimeun, and A. Srivihok, "Clustering of Thai handcraft customers using combined som and k-means algorithm," A Scientific and Technical Publish Company. *OACTA Press*, 2005.

[6] S. Mongkolsripattana, and A. Srivihok, "Clustering of technology transfer centers by using som algorithm and project performances," *The 3rd Asia-Pacific International Conference on Knowledge management*, Hong Kong, China, 2006.

[7] S. Albayrak, and F.Amasyali, "Fuzzy c-means clustering on medical diagnostic systems," *Turkish Symposium on Artificial Intelligence and Neural Networks*, TAINN, 2003.

[8] S. Mingoti, and J. Lima, "Comparing som neural network with fuzzy c-means, k-means and traditional hierarchical clustering algorithms," *European Journal of Operational Research*, 2006, pp. 1742-1759.

[9] T. Kohonen, Self-Organizing Maps. Springer Inc., Berlin, 1995.

[10] A.K. Jain, and R.C. Dubes, Algorithms for Clustering Data. Prentice Hall Inc, New York. pp.368, 1998.

[11] J.C. Dunn, "A fuzzy relative of the ISODATA process and its use in detecting compact well-separate clusters," *Journal of Cybernetics*, vol. 3, 1976, pp. 32–57.

[12] J.C. Bezdek, Pattern Recognition with Fuzzy Objective Function Algorithms. New York: Plenum, 1981.

[13] M. Halkidi, M. Vazirgiannis, and Y. Batistakis, "Quality scheme assessment in the clustering process," *Proceedings of the 4th PKDD Conference*, pp. 265-276, Lyon, September 2000.

[14] F. Kovacs, C. Legany and A. Babos, "Cluster validity measurement techniques," *6th International Symposium of Hungarian Researchers on Computational Intelligence*, Budapest, Hungary, 2005.

Automatic Floor-Mopping Robot

Wiruch Kongsin, Poj Tangamchit
Department of Control Systems and Instrumentation Engineering,
King Mongkut's University of Technology Thonburi, Bangkok, Thailand 10140
Tel (66-2)470-9006, Email wiruch_kongsin@yahoo.com, ipojchit@kmutt.ac.th

***Abstract*- We designed and implemented a robot capable of mopping smooth floor. The robot mechanism consists of two main parts: the motor driving part and the cloth cleaning part. The driving part has two rear wheels combining with a mop-head wheel in the front with cloth for mopping rolled around it. The cloth cleaning part has a brush mechanism within the cleaning chamber to remove dirt from the cloth rolled into it. We designed the navigation algorithm using the behavior-based structure to cover a working area as much as possible without wetting the floor too much. The effectiveness of the algorithm was tested on simulation and a real robot.**

I. INTRODUCTION

Thai households usually have no floor-carpet due to hot and humid weather. Therefore, the most common method to clean a floor is to mop with a damp cloth. Therefore, instead of vacuum cleaning, we designed a floor mopping robot to clean a smooth floor. The robot imitates the mopping action on the floor by using a cloth to clean the floor combining with a cloth cleaning mechanism. We proposed a navigation algorithm that is suitable for mopping in that the robot should be efficient but not wetting the floor too much. With this bottom line, the robot has to cover as large area as possible while minimizing repeatedly mops the same area.

II. RELATED WORK

Yong-Joo and Yoshio Watanabe[1] implemented a vacuum robot cleaning in households. Their design was based on the idea that good cleaning robots must have small size and light weighting order to use a small amount of energy for cleaning large areas and save time. It defined navigation algorithms for moving to be three patterns as 1.random, 2.zigzagging, 3.rectangular as shown in Figure 1.

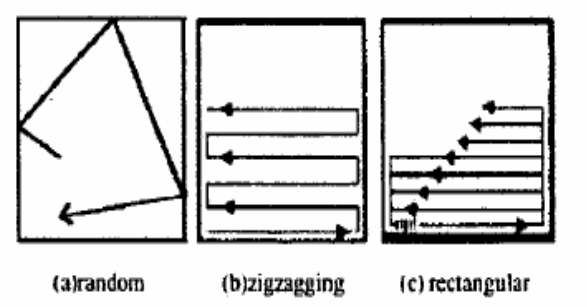

Figure 1. The navigation way

We utilized the idea of navigation algorithm from this research and used as a tested with our robot

Joon, Yoon and Jin [2] proposed a navigation algorithm for a floor-cleaning robot by using a triangular cell map. The experiments were made to compare it with the rectangular cell map to the cell map at to be triangular patterns. It can move in twenty directions around itself. While the rectangular pattern will move in eight directions. The navigation method used for both patterns are.

First: To follow side walls continuously until it moves around the room and gathers information by using templates with seven patterns.

Second: To search the uncleaned areas by visiting the closet unexplored area.

III. ROBOT HARDWARE

A. Cleaning system for the robot

The main function of the cleaning part is to wash cloth that is used for cleaning floor. Figure 2. shows the structure of the cleaning mechanism. It includes a tank for containing clean water. Inside the cleaning mechanism, there are rollers to rotate the cloth used mopping the floor and to take a cloth to a tank for cleaning a cloth. Which the system of rollers will have one roller at cleaning a cloth.

When: "1" is the knob of cloth.

"2" is the cleaning roller.

"3" is the rollers for feeding the cloth.

"4" is the outlet for draining.

"5" is the inlet for filling water.

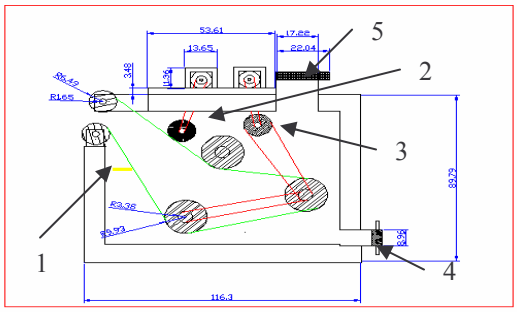

Figure 2. The cleaning mechanism

The operation of the cleaning system is as follows. Motors which are attached to the front rollers will rotate a cleaning cloth and rub it with the floor. After that, the cloth will be fed into the rollers inside a tank for cleaning.

In that moment, the rollers will pull the other part of the cloth out to clean again. The inner of the cleaning tank is filled with clean water and bristled brushes. The brushes is continuously rolled in order to whisk dirt out of the cloth while the clean water inside a tank will help dispel dirt out of the cloth. (This is similar to operation in a washing machine.) In the next step, when a cloth is readily clean, it will continually move out following the rotation of the rollers, while there is a squeezing knob that removes excessive water from the cloth and makes it ready to be used again.

B. The structure of the robot

The robot will move into many areas depending on the navigation program using the occupancy grip method.

The driving mechanism includes two wheels and two motors controlled by a microcontroller. We utilized PID controllers to control motors on the wheels. It controls both wheels that make same speed of the both wheels. Which controller will receive values from encoders on the both wheels of the robot and it send into the both wheels. It has one roller to rotate cloth into the cleaning mechanism. It also has two rollers to adjust cloth tightness. Which it want a face cloth to touch the floor for to increase the efficiency of mopping.

The sensor system includes infared distance measuring sensors and front bumping sensors. When the sensors detect obstacles, it will invoke a program to avoid the obstacles. The safe avoiding distance was calculated depended on the distance measuring from the infared sensors and the front bumper sensors.

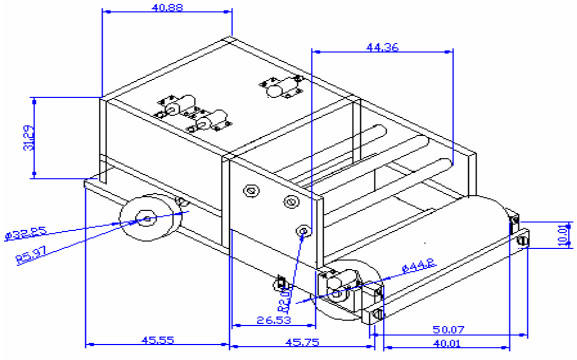

Figure 3. The complete structure of the robot

Figure 3, 4 shows the drawing and the construction of the real robot. It includes with the moving system and the cleaning system.

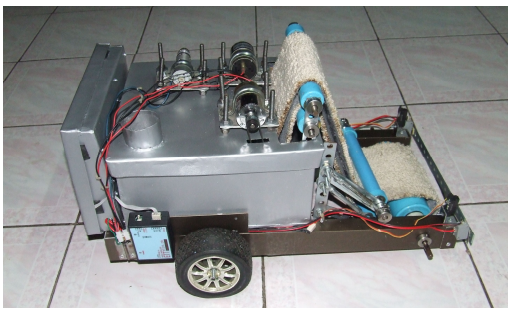

Figure 4. The floor-mopping robot

IV. NAVIGATION ALGORITHM

Behavior-based [4] approach is utilized to control the robot in a working area. We designed the control behaviors as follows .

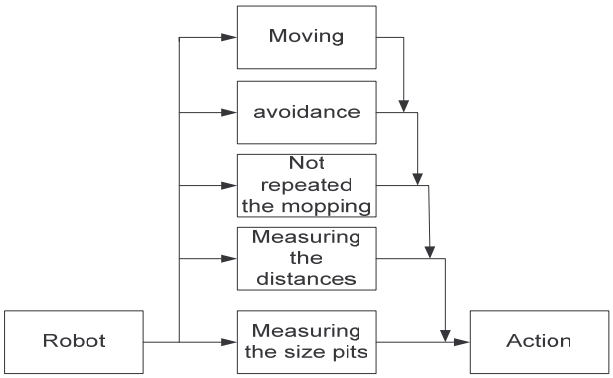

Figure 5. Behavior-base for the mopping robot

- *Moving* is the behavior for the moving of the robot from one place to another. By moving around, the robot build map according to the data from its sensors. It records the position of detect obstacles and the places that already visited and use that information to decide the place to go next. When there are many uncleaned areas to visit, it random the place to go based on four directions: left, right, up, down.
- *Avoidance* is the behavior to avoid obstacles such as wall, bed, and etc. It uses sensors to detect obstacles and keeps data into the map model.
- *Not repeated the mopping* is the behavior to avoid going to the same places that already been visited.
- *Measuring the size pits* is the behavior to search for free spaces in the map model (free space is still not keep into map model). The robot will try to go to the largest space that has not been visited.

  We calculate the largest free space from the current map by using the Component Labeling [3] that is four components. We will label the value at to be zero to put in Array. Therefore, we compare the space size and prepare a sequence by large space to equal 1 at spaces small than

first to equal 2 and decreasing a sequence. It use for to calculate to find the moving way.

- *Measuring the distances* is the behavior to measure for to find the closet free space that has not been visited by referring to the map model. The robot will try to go to the closet space that has least repeated visit. The way is to distribute out to four directions (four zones include Left, Right, Up, Down) as Figure 6. by to keep in such the value of distances by keeping values in map model continuously until to meet zero and ten values and to calculate best distance into its zone. Which will take best distance in four zones to calculate the best distance into this four zone . Formula used to find the distances as equation (1) is.

$$Distance_N^Z = \sum_{begin}^{End} value\ in\ Map\ Model \qquad (1)$$

When: N is the number of the line for to distribute into four directions.

Z is the number of the line in each zones.

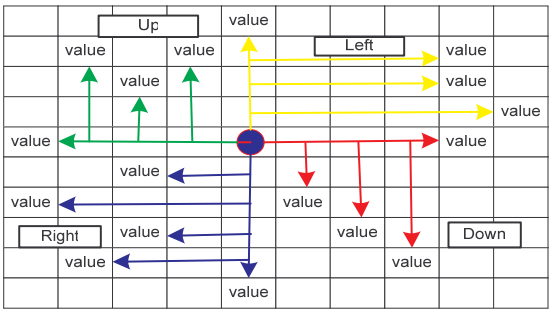

Figure 6. To show the way for finding distance in map model

To calculate for to find the best distance

To find the best distance for moving into the not cleaning area at the case is the center among the ready mopping area to find as equation (2) is.

$$Scores_n = best\ distances_n + best\ spaces_n \qquad (2)$$

When: n is the number of zone in four zones

When we obtain the ready value of four zones and to find best distances for to control the robot to move the target.

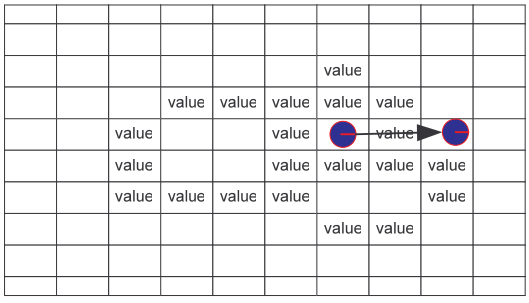

Figure 7. The case of robot searches a exit.

V. Simulation Results

In Beginning the robot will move randomly inside the map. The beginning value of the map will be all zero.

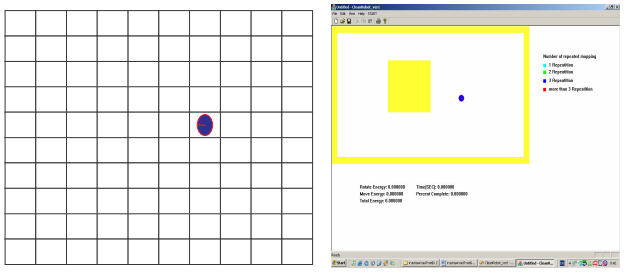

Figure 8. Show to begin simulation and map model

In simulation, we measured the efficiency of the robot which includes the rotation energy as the indication of energy in the rotation of the robot, moving energy as the indication of energy in the moving of the robot, total energy is to sum between rotate energy and moving energy. All energy is "Unit" for energy.

The indication of time in cleaning as time has that unit is second, The indication of cover area at cleaning as percent complete has that unit is percent (%).

Besides, we still have the indication of repeating number to divide four color that include sky-blue as one repeating , green as two repeating, blue as more than two repeating.

This experiment will made at 120 sec. By we divide two experiment that have obstructs and not obstructs. Such experiment include zigzagging, random, random (map) by moving so that.

1. Zigzagging will move from left to right and button to below .
2. Random will move not sure directions to depend on to rand for to select directions
3. Random has map model that will move to like normal random but it will add map model for using the navigation and not repeating.

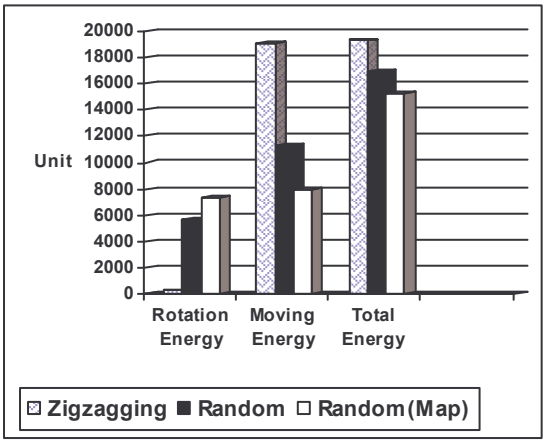

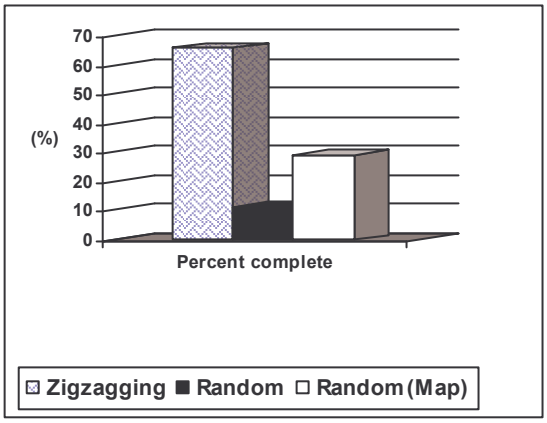

Figure 9. The energy and complete percent having no obstacles

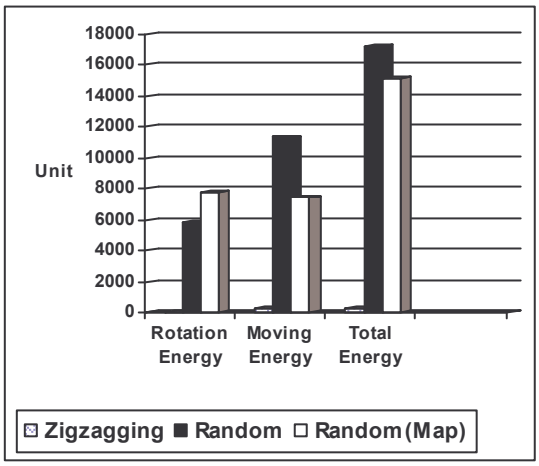

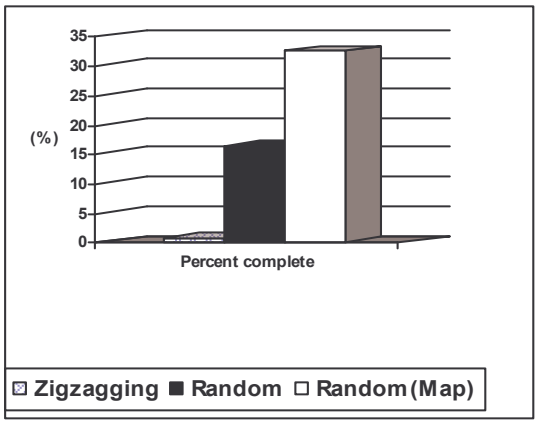

Fig ure10. The energy and complete percent having obstacles

VI. Real Results

In experimentation, we define the area to test the Automatic Floor-Mopping Robot. By we define as the square room and we can define inside room to have the number, position and size obstructs to want. From experimentation, we appear that in case having a lot of obstructs will use the many energies, many mopping numbers and in case having little obstructs will use the little energies, many mopping numbers. Again factory is to put the position obstructs and the size obstructs. It still has other factory to effect with energies of the robot such as sundry error to happen the robot. The mopping experimentation appears that sufficiency in cleaning. It will goodly clean the floor. It depend the dirty that adhere the floor. It adheres many or little on floor. It have many or little for the number of dirty.

VII. Conclusion

We implemented a floor-mopping robot. Its effectiveness was measured using three navigation algorithms: zigzagging, random ,random (map). We discovered that when there were not much obstacles the energy of zigzagging use the most energy but the completeness of the area is best. The total energy of the random (map) algorithm uses little energy, while the percent completeness of random (map) was less than zigzagging but it is more than random.

In the area is much obstacles the total energy of random (map) use the energy less than the random and the completeness of the area is best. The total energy of the zigzagging algorithm uses very little energy and completion because the robot detained much obstacles.

We conclude from three pattern that zigzagging appropriate with the area having no obstacles and the random (map) appropriate with the area having obstacles

In real experimentation, we appear that clean the room satisfactorily. It can avoid obstacles fairly.

References

[1] Yong-Joo oh and Yoshio Watanabe, “Development of Small Robot for Home Floor Cleaning”, Kanagawa University, Yokohama, Japan 2002

[2] Joon Seop Oh, Jin Bae Park, Yoon Ho Choi, “Complete Coverage Navigation of Clean Robot based on Triangular Cell Map”, Dept of Electrical & Computer Eng., Yonsei University and School of Electronic & Mechanical Eng., Kyonggi University, Pusan, KOREA 2001

[3] Dr. Bai-ling Zhang,, School of Computer Science & Mathematics, Victoria University of Technology

[4] D. Langer, et al, “A Behavior-base system for off-road navigation ” IEEE Transactions on Robotic and Automation, Vol.10, no.6, pp. 776-783, 1994

Sansarn Offline: A Search Engine Tool for Managing, Archiving and Retrieving Offline Web Contents

Choochart Haruechaiyasak Chatchawal Sangkeettrakarn

Human Language Technology (HLT) Laboratory
National Electronics and Computer Technology Center (NECTEC)
Thailand Science Park, Klong Luang, Pathumthani 12120, Thailand
Email: [choochart.haruechaiyasak, chatchawal.sangkeettrakarn]@nectec.or.th

Abstract

Today the World Wide Web has become widely accepted as the world's largest information resource. These information are generally available for users who have accessible Internet connection. However, the problem known as digital divide still exists among people who live in rural areas, especially of developing countries. To alleviate this problem, we have developed a search engine tool called Sansarn Offline with the purpose of managing, archiving and retrieving contents obtained from the Internet. Sansarn Offline is designed to accommodate two main tasks: content administration and content retrieval. For the first task, content administrator will use the tool to collect, manage and index Web pages obtained from the Internet. These contents are then organized into some predefined categories and recorded into some removable media such as CD-ROMs and DVDs. The second task involves user entering query through the interface and the tool looking up from the index and returning search results to the user. Since the contents and their indexes are stored on the removable media, the retrieval process can be done without the Internet connection. Another advantage is that the tool could yield search results which are more focused than those from regular search engines because the Web contents are selected and filtered by the administrator to match the real information need of the users.

1 Introduction

Due to the enormous growth of the Web contents available online, the Internet is now considered as the world's largest information and knowledge resource. Internet usage and applications are extremely varied and could range from e-mailing to online shopping. One of yet another important applications is to use the Internet as a public library to search for information and knowledge. Some of the interesting projects include, for example, Wikipedia [8] and Google Book Search's Library Project [6]. Wikipedia is a free well-known online encyclopedia. The outstanding feature of Wikipedia is the use of collaborative concept in which each user is allowed to edit and share the definitions and contents of the posted articles. Currently there are over *1,600,000* articles available in English and many in other languages. Google's Library Project has collaborated with many universities in order to scan and export contents of many books into digitized format. Users are then able to search and retrieve the book contents which match their interests. Besides these examples, there are many other Web sites which provide great information and knowledge and are publicly available.

These information and knowledge are however only accessible by users who could connnect to the Internet. Today, the problem known as *digital divide* still exists among people who live in rural or remote areas, especially of developing countries. The digital divide problem can be generally described as the lack of computer equipments, network infrastructure, and knowledge in IT. Therefore, one of our main goals is to bridge this gap for the users who have difficulties in accessing the Internet and the Web. To accomplish this goal, we have developed a search engine tool called *Sansarn Offline* which could be used to manage, archive and retrieve contents obtained from the Internet.

The process of using Sansarn Offline consists of two main tasks: content administration and content retrieval. For the first task, content administrator will use the tool to collect Web pages from the Internet. The tool currently supports many different document

formats such as *html*, *pdf* and *txt*. We will extend the tool in the next version to support the collection of images and other types of multimedia contents. Once a Web page is retrieved, each word token appearing on the page will be extracted and indexed using the widely adopted *inverted file* technique [4]. All contents with the index are then organized into some predefined categories and recorded into some removable media such as CD-ROMs and DVDs. The second task involves user entering search query through the interface. The tool then looks up from the index and returning search results to the user. Since the contents and their indexes are stored on the removable media, the retrieval process can be done without the Internet connection. Therefore, this tool could alleviate the problem of inaccessible Web contents. Another advantage is that the tool could yield search results which are more focused than the ones obtained by using regular search engines. This is because the content administrator would select, filter and collect only high quality Web contents which match the users' information need.

Our second goal is to provide and distribute the tool to interested users without any licensing fee. Therefore, our project will be based on the open-source software concept. With the thorough survey of the open-source Information Retrieval (IR) libraries and tools, we found *Lucene* to be a suitable choice for implementing our IR platform. *Lucene* is one of the most widely used IR library currently maintained under the Apache project [7]. Lucene provides the core indexing and searching functions which are very efficient and scalable [1]. The key success to the high scalability is the intelligent algorithm in managing the inverted index files between the memory and the secondary storage. The users may set the number of index segments and their sizes according to the system specification in order to optimize the indexing and searching performance. Lucene library, however, only comes with the support of English language. To extend the library to support other languages, developers must add language-specific analysis package into the library. Integrating and extending Lucene library is very simple and easy, since its creator has designed the framework via the object-oriented programming concept of Java [2]. This object-oriented feature is another reason that makes Lucene a very attractive choice for implementing our platform.

To make Sansarn Offline support both English and Thai texts, we have developed a Thai-language analysis package, *ThaiAnalyzer*, which could be integrated seamlessly within the Lucene framework. In addition ThaiAnalyzer, our tool includes two other functions which support the content administrator and general users. We have designed our the interface to be user-friendly so that users with little or no programming skill could use the tool with ease.

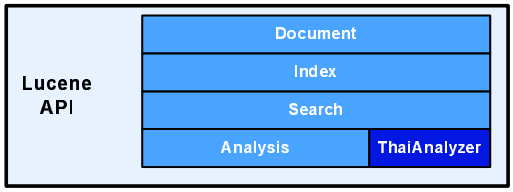

Figure 1. Lucene layer with ThaiAnalyzer package.

To demonstrate the usage, we will use Sansarn Offline tool to collect and index some useful Web pages and then distribute them among high schools in rural areas of Thailand where Internet connection is slow or not available. Students can search for useful information on CD-ROMs as if they are connected to the Internet. Our first prototype includes contents related to subjects taught among high school classes in Thailand.

The remainder of this paper is organized as follows. In next section, we give some details on Lucene library and the implementation of ThaiAnalyzer package. Section 3 gives the discussion on the system design and architecture of Sansarn Offline. Section 4 gives the conclusion.

2 Lucene Library with ThaiAnalyzer Package

Lucene was designed and implemented based on the object-oriented programming framework of Java. Figure 1 illustrates the *Lucene* API which is organized into the following four packages.

- *Document*: In Lucene, a text is organized as a document which represents a collection of fields. Before a text document could be indexed, it must be created by constructing a new instance of *Document* class. The seach results are also returned in the form of *Documents*.

- *Index*: Index contains many different classes responsible for indexing process. *IndexWriter* is the main class whose task is to create a new index and add documents into an existing index.

- *Search*: Search contains classes related to search operations. *IndexSearcher* is the main class whose task is to search within the given index directory for matching documents.

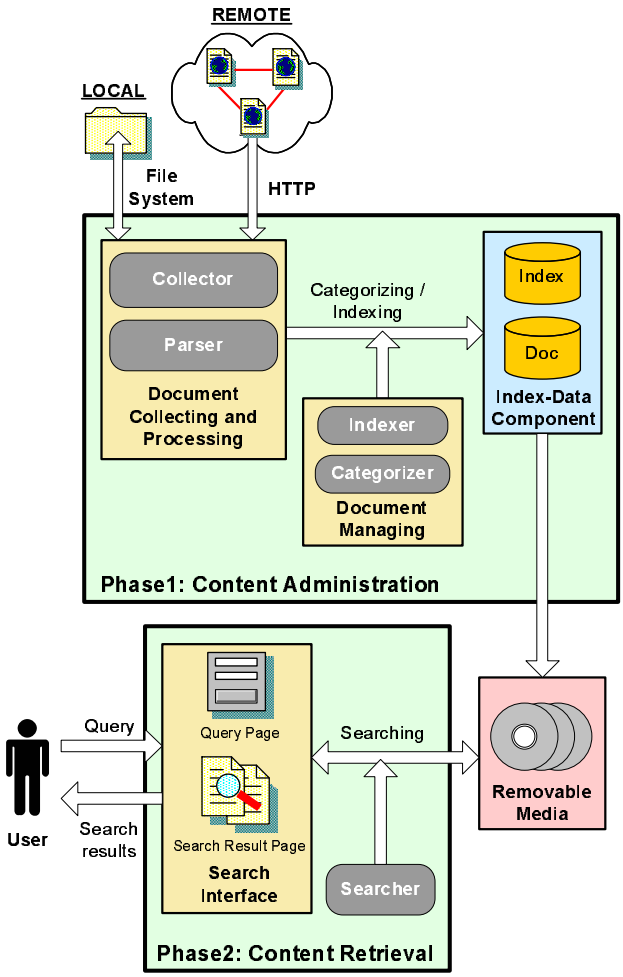

Figure 2. Sansarn Offline: System functionalities.

- *Analysis*: Analysis contains classes for performing the text processing. Different *Analyzer* classes are provided for various specific tasks such as stopword removal and stemming which are suitable only for English language. To make the analysis applicable to Thai language, we developed *Thai-Analyzer* package whose basic task is to tokenize Thai texts into a set of words [3].

3 Sansarn Offline: System Architectural Design

Figure 2 illustrates the overall architecture of *Sansarn Offline*. The system consists of two functions: *content administration* and *content retrieval*. For the first function, there are four important modules which support the content administration function.

- *Collector*: To provide flexibility, the *Collector* module contains various classes for collecting documents from either remote servers or local file system. For remote documents, i.e., Web pages, the collector functions exactly as a Web crawler.
- *Parser*: This module contains classes for removing HTML tags or pre-specified XML tags.
- *Indexer*: This module contains classes which perform indexing functions. Indexer package contain higher-level classes which make use of the *Index* package from Lucene library.
- *Categorizer*: This module contains classes which perform automatic categorization of collected contents into predefined subjects or categories. This module will be implemented and added into the tool in the next version.

The outputs from the first phase are data contents with the index which are then recorded into some removable media such as CD-ROMs or DVDs. The second *content retrieval* function consists of two modules which support the retrieval of contents for the users.

- *Searcher*: This module contains classes which perform searching functions. *Searcher* contain higher-level classes which make use of the *Search* package from Lucene library.
- *Search Interface*: This module provides a GUI-based interface which connects to the searcher module in order to pass the query from the users and to return the search results back to the users.

Sansarn Offline is implemented in Java by using Eclipse tool [5]. Using Java offers several advantages including platform-independent and open-source development. Our first application of Sansarn Offline is to collect useful and related Web pages from the Internet which are related to the class materials taught in high schools. The contents and the tool could enhance the teaching and learning outside classes. The CD-ROMs containing the contents, indexes and tool will be distributed to many high schools in Thailand. This project is a part of a main project whose goal is to use IT to develop schools in rural areas of Thailand.

We have collected the contents related to many subjects such as astronomy, physics, biology and chemistry. These contents were obtained from many educational Web sites. Figure 3 shows parts of table of contents which we have collected. Users are allowed to browse according to the organized subjects and click on

Figure 3. Example: Table of contents.

the links to read the full Web page. Besides browsing, another retrieval mode is the keyword search. Users can enter query of one or more keywords to search for Web pages. The returned search results show the snippets with the highlighted terms similar to typical search engines. User can click on the link to view the full page content. Since the retrieval process is done on the controlled Web pages which are stored on the CD-ROM, the results are more focused than using general search engines. Another advantage is that the response time depends only on the I/O activity of the computer which is generally more reliable than the network. Our tool also allows the users to set some configuration such as the color used to highlight the terms in the results and number of results shown per page.

4 Conclusions

We proposed a search engine tool called *Sansarn Offline* with the purpose of managing, archiving and retrieving contents obtained from the Internet. Sansarn Offline is a free open-source software which has been developed by using *Lucene* IR (Information Retrieval) library. However, Lucene doesn't support retrieval of Thai texts. Therefore, we have developed a Thai-language analysis package called *ThaiAnalyzer* whose task is to segment Thai written texts into word tokens. Sansarn Offline consists of two main functions which directly support two user groups: content administration and content retrieval. The first function is used by content administrator whose task is to collect, manage and index Web pages obtained from the Internet. The second function is carried out by general users who need the information. Sansarn Offline allows searching for information stored on the removable media, therefore the retrieval process could be done offline or without connection to the Internet. As part of our project, we have planned to distribute the contents and the program to some high schools in rural area where Internet connection is not available. Future works of this project include the automatic categorization of contents and other intelligent search features such as search result clustering which could organize and represent search results into meaningful concepts. For example, search results returned from the query "gravity" could be organized into clusters such as "definition", "experiments", "history" and "Isaac Newton".

References

[1] D. Cutting and J. Pedersen, "Optimization for dynamic inverted index maintenance," *Proc. of the 13th int. ACM SIGIR conf.*, pp. 405–411, 1989.

[2] D. Cutting, J. Pedersen, and P. Halvorsen, "An object-oriented architecture for text retrieval," *Proc. of Intelligent Text and Image Handling (RIAO 91)*, pp. 285–298, 1991.

[3] C. Haruechaiyasak et al., "Sansarn Look!: A Platform for Developing Thai-Language Information Retrieval Systems," *Proc. of the 21st International Technical Conference on Circuits/Systems, Computers and Communications (ITC-CSCC 2006)*, pp. 85–88, 2006.

[4] G. Salton, *Automatic Text Processing*, Addison Wesley, 1989.

[5] Eclipse - An Open Development Platform, *http://www.eclipse.org*

[6] Google's Book Search: Library Project An enhanced card catalog of the world's books, *http://books.google.com/googleprint/library.html*

[7] Overview - Apache Lucene, *http://lucene.apache.org/java/docs/index.html*

[8] Wikipedia: The Free Encyclopedia, *http://wikipedia.org*

Combined simulated data adaptation and piecewise linear transformation for robust speech recognition

Nattanun Thatphithakkul[1], Boontee Kruatrachue[1], Chai Wutiwiwatchai[2], Sanparith Marukatat[2] and Vataya Boonpiam[2]
[1]King Mongkut's Institute of Technology Ladkrabang,
Bangkok 10520, Thailand
[2]National Electronics and Computer Technology Center,
Pathumthani, 12120, Thailand

***Abstract*- This paper proposes a combination of simulated data adaptation and piecewise linear transformation (PLT) for robust continuous speech recognition. The original PLT selects an appropriate acoustic model using tree-structured HMMs and the acoustic model is adapted by the input speech in an unsupervised scheme. This adaptation can improve the acoustic model if the input speech is long enough and is correctly transcribed in the adaptation process. Indeed, an incorrect transcription can drastically degrade the acoustic model. Our proposed method increases the size of adaptation data by adding noise portions from the input speech to a set of pre-recorded clean speech, of which correct transcriptions are known. We investigate various configurations of the proposed method. Evaluations are performed with additive noisy continuous speech. The experimental results show that the proposed system reaches higher recognition rates than MLLR and PLT.**

I. INTRODUCTION

It is commonly known that a speech recognition system trained by speech in a clean or nearly clean environment cannot achieve good performance when working in noisy environment. Research on robust speech recognition is then necessary. Gales [1] has classified the techniques of robust speech recognition into 4 approaches: 1) robust feature approach, 2) clean speech estimation approach, 3) robust model approach, and 4) combination of three previous approaches. This paper focuses on the model-based approach, which has achieved good recognition results [1]. The model-based approach aims to create or to adapt the acoustic model in specific environments. Several techniques of model adaptation have been proposed such as maximum likelihood linear regression (MLLR) [2], maximum a posteriori (MAP) [3], parallel model combination (PMC) [4], and piecewise linear transformation (PLT) [5].

In this work, we are interested in the adaptation technique of piecewise linear transformation with model selection based tree-structured cluster (MSTC) [5, 6], proposed by Zhang, Sugimura and Furui [5]. This technique is based on unsupervised acoustic model adaptation using the incoming speech. It was proven to be efficient in both the recognition accuracy and computational cost. However, a problem of the PLT is that the acoustic model may not be well adapted if the incoming speech is very short. Moreover, in the unsupervised adaptation, a wrong transcription strongly degrades the adapted model. These 2 problems can be solved by a recently proposed technique called simulated-data adaptation [7]. Indeed, the simulated-data adaptation process aims to increase the data used in adaptation by adding the background noise extracted from the current input signal to existing clean speech. Since correct transcriptions of the clean speech are known, using the simulated-data is supervised adaptation.

This paper presents a new adaptation scheme which applies simulated-data adaptation to piecewise linear transformation (called S-PLT hereafter). S-PLT combines the strength of both techniques; PLT allows selecting a good initial acoustic model while simulated-data adaptation enlarges the size of the adaptation data. S-PLT uses the MLLR adaptation technique. The proposed method is compared with other model adaptation techniques.

The proposed system was evaluated in 3 groups of environments. The first group contained a clean environment and 9 types of noisy environments that have been trained in the system. The second group contained isolated-words. The third group contained continuous-speech. Noisy speech of second and third group were prepared by adding noise signals from an exhibition in Thailand (NAC 2005) to the clean speech taken from NECTEC-ATR Thai speech corpus [8] at various SNR (0, 10, 15 dB).

We will review the PLT in the next section. Section 3 reviews the simulated-data adaptation. Section 4 describes our proposed models. Section 5 describes the data used in these works and experimental results are reported in Section 6. Section 7 concludes this paper with future works

II. PIECEWISE LINEAR TRANSFORMATION (PLT)

The PLT method is composed of 2 main steps namely MSTC [5, 6] model selection and MLLR adaptation [2]. In the training step, a wide variety of noise data were collected and classified into noise clusters using hierarchical clustering. The root node includes all noises and all SNR conditions and each leaf node consists of only one noise at one SNR condition. Intermediate nodes in this tree contain similar noises from different environments and from different SNR. A noise-added speech HMM is constructed for each node. Using this tree structure, an unknown noise environment which is similar to combination of known environments should be handled by

non-leaf HMM. The resulting tree-structured HMM allows representing both known and some unknown noises. In the recognition phase, the noise-cluster HMM which is best fitted to the input speech was selected and adapted by the input speech itself using the MLLR method.

III. SIMULATED DATA ADAPTATION

A. *Noise portion extraction*

Simulated-data adaptation begins with identifying silence parts which are supposed to be background noise of the current input signal. We assume that there are short periods of silence at the beginning and the end of the input signal. A phone-based HMM is used to segment the input signal into speech and silence portions. In this work, we use 64 HMMs of Thai phonemes including a special phoneme of silence "sil", form a speech recognizer. Fig. 1 illustrates this HMM structure. Noise portions are the signal regions labeled with silence "sil".

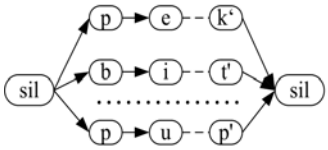

Figure 1 HMM architecture for noise extraction.

B. *Background- noise addition*

Given noise portions extracted from the input signal, several issues need to be considered in adding background noise to the pre-recorded clean speech. First we concatenate noise portions extracted from the input signal. There are two noise-only regions in the input signal, at the beginning and at the end of the signal as shown in Fig. 2. These noise portions are duplicated and concatenated so that the duration of noise signal is equal to the duration of clean-speech being added.

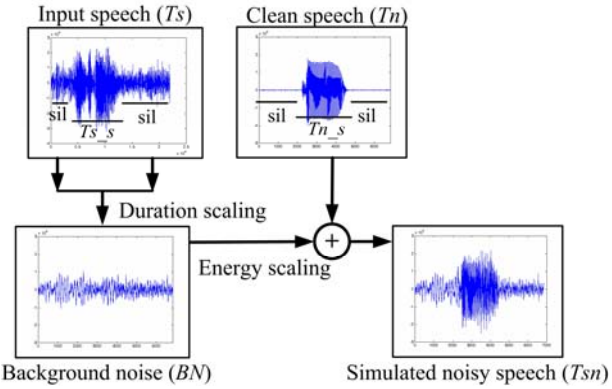

Figure 2 Background-noise addition.

Second, simulated speech for adaptation should have a similar SNR to the input speech. However, estimation of SNR is not trivial and remains unsolved. The simulated-data adaptation relies on a simple signal-energy scaling. Let "Train-S" be a set of pre-recorded clean speech, of which correct transcriptions are known. We denote by Tn and Ts the current input signal and a clean speech in the Train-S set. Tn_s and Ts_s is the speech portion of Tn and Ts and Tn_sil and Ts_sil is the silence portion of Tn and Ts. First, a scale_factor is calculated as follows:

$$EngS = sum(abs(Ts_s))/length(Ts_s) \quad (1)$$

$$EngC = sum(abs(Tn_s))/length(Tn_s) \quad (2)$$

$$scale_factor = EngC/EngS \quad (3)$$

where |T| denotes the energy of a signal T. EngS and EngC is respectively the energy averaged over all Ts_si and Tn_si extracted from Ts and Tn. Next, the background noise, BN, given by the noise-portion extraction step, is multiplied by the scale_factor and added to Tn, resulting in a simulated noisy-speech Tsn as shown in Equation (4). The signal Tsn is then included in the adaptation set.

$$Tsn = BN*scale_factor + Ts \quad (4)$$

C. *Adaptation-data preparation*

Adaptation data set is a key element in our robust speech recognition system. Two variations of the proposed method are considered. The first one uses only the pre-recorded clean speech with known transcription. This is called supervised adaptation. The second variation includes the input speech in the adaptation set with its label transcribed automatically. This second variation is called semi-supervised adaptation.

Beside these two variations, other important parameters including the selection of speakers and lexicon in the Train-S data are required to adjust. Basically, we selected speakers and words that can be correctly recognized by our clean speech model. Moreover, selected words should cover all phones presented in the system.

IV. COMBINED SIMULATED DATA ADAPTATION AND PLT

Combined simulated-data adaptation [7] and PLT [5], called S-PLT is shown in Fig. 3.

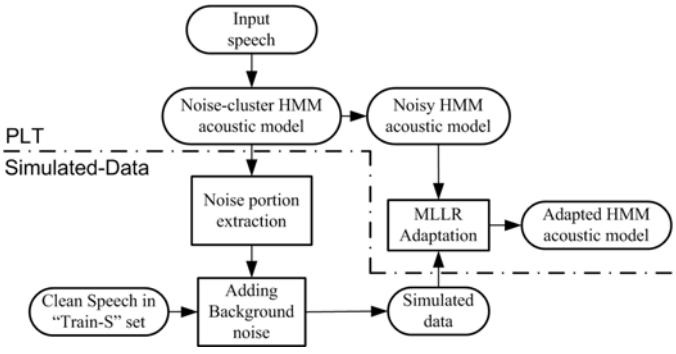

Figure 3 Combine simulated-data adaptation and PLT process (S-PLT) for HMM adaptation.

The basic idea is to adapt the model selected from the tree-structured cluster using the adaptation data prepared by the simulated-data process either in supervised or semi-supervised

mode. The adapted HMM is then used to recognize the incoming signal.

V. Experimental Setting

Our domain is continuous speech recognition using monophone-based HMMs representing 64 Thai phones. The aim of using context-independent phone model is the flexibility to add any word in the recognition lexicon. Each monophone HMM consists of 5 states and 16 Gaussian mixture per state. 12 MFCC, 1 log-energy, and their first and second derivatives are used as recognition features. The clean model is trained by phonetically-balanced utterances read by 32 speakers. The total number of training utterances is 32,000. In all experiments, clean-speech data are taken from the NECTEC-ATR corpus [8].

D. Noise data for training

Eight kinds of noise from JEIDA, including crowded street, machinery factory, railway station, large air-condition, trunk road, elevator, exhibition in a booth, and ordinary train, and one large-size car noise from NOISEX-92 are considered. All noises and the clean speech are preprocessed by resampling to 8 kHz. Noisy speech is prepared by adding the noise from JEIDA or NOISEX-92 to the clean speech of the NECTEC-ATR corpus at various SNRs (5, 10 and 15 dB).

E. Noise data for testing

Two test sets, "Test-1" and "Test-2", are used in evaluation. Test-1 contains 3,200 utterances from 640 words uttered by 5 male speakers. Test-2 contains 1,950 utterances from 390 sentences uttered by 5 male speakers.

An exhibition (NSTDA Annual Conference S&T in Thailand) recorded over four days in March 2005, are added to clean-speech utterances at three SNR levels: 0, 10 and 15 dB. This test set represents speech with different noise from the training set.

F. Simulated-data for adaptation (Train-S set)

In order to constitute the Train-S set for model adaptation, speakers and lexicon are selected from the NECTEC-ATR corpus. For speaker selection, we limited to male-speakers with clear speech and randomly selected speech signals of four speakers are used in the experiment, denoted as "MIX" speaker.

For word selection, the selected lexicon should cover all 64 phones presented in the system. According to these criteria, two sets of train-s are prepared. The first set (Train-S1) contains 22 words and the second set (Train-S2) contains 10 sentences, both are the minimum set of isolated-words and continuous speech that cover 64 phones used in the recognizer

VI. Experimental results

In this section we investigate various settings of S-PLT and compare them to other robust speech recognition techniques. Subsection A evaluates different settings of our system. Subsection B compares our proposed system to conventional methods.

A. Effects of type MLLR adaptation and type Train-S in simulated-data adaptation

In our experiments the acoustic model before adaptation can be either a clean-speech model or the model selected by the MSTC algorithm. For each model, we test adaptation in both supervised and semi-supervised modes. Semi-supervision means that the input speech is also included in the adaptation data. Table I defines four systems varying on the supervision made of adaptation and the initial acoustic model

Table I Definition of comparative systems

	Initial AM	
	Clean	MSTC
supervised	S-MLLR1	S-PLT1
Semi supervised	S-MLLR2	S-PLT2

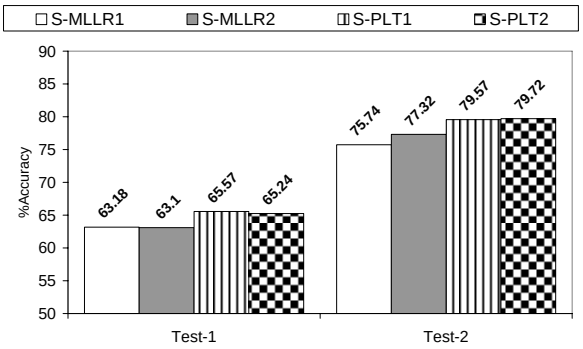

Figure 4 Recognition accuracies of S-MLLR and S-PLT evaluated by Test-1 and Test-2.

Fig. 4 shows the experimental results from various settings using the Train-S1 set in adaptation. According to these results, using the MSTC algorithm to initialize the acoustic model gives better accuracy than using the clean model. As expected, since the MSTC-selected model is closer to the real environment than the clean model and hence give the higher performance. For semi-supervised adaptation, results show that it rather suit for continuous speech (Test-2) than for isolated word (Test-1). This may be due to the fact that for the isolated word case, the signal is too short and no useful information can be automatically and reliably extracted. It is then better to rely only on assured transcription as in supervised adaptation. On the other hand, for continuous speech the signal is long enough to compensate the incertitude concerning the transcription thus make it useful for model adaptation.

Next, we investigate the use of continuous speech as adaptation data. For this propose, we ran the experiment on the Test-2 set with the Train-S2 adaptation data. Fig. 5 summarizes the results from this experiment. We can see that using the Train-S2 outperforms the use of Train-S1 in every case. This is due to the increasing in the size of the adaptation data. However, the computational time unavoidably increases as a drawback.

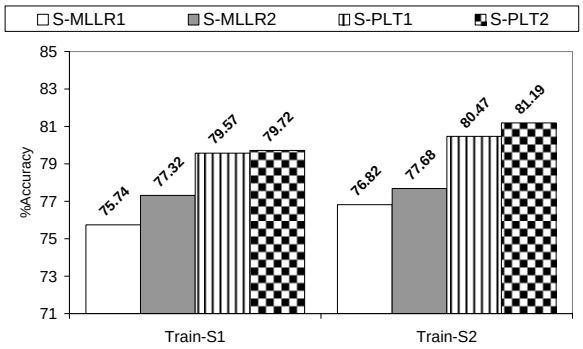

Figure 5 Recognition accuracies of S-MLLR and S-PLT with different Train-S evaluated by Test-1.

B. Comparison with conventional methods

In this subsection, several robust speech recognition techniques including ours are compared. The first one is a baseline system without any implementation for robust speech recognition. The second system, denoted as "MLLR", uses online acoustic-model adaptation based on the well-known MLLR approach. The third system, called "MSTC", uses model selection based on the tree-structured cluster model without any adaptation. The forth system called "PLT" uses the PLT method (see section III). The fifth and the sixth systems are S-MLLR2 and S-PLT2. The Train-S2 is used in adaptation.

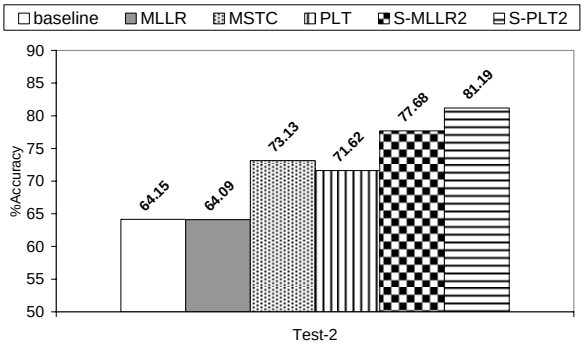

Figure 6 Comparison of baseline, MLLR, MSTC, PLT, S-MLLR2 and S-PLT2 systems evaluated by Test-2.

Fig. 6 shows comparative results. According to the results, it is obvious that our proposed methods, S-MLLR2 and S-PLT2, outperform other conventional methods. In the case of S-MLLR2 we gain approximately 14% improvement of recognition accuracies over the conventional MLLR model. S-PLT2 achieves approximately 10% improvement of recognition accuracies over the PLT-based method. Moreover, the PLT's accuracy is lower than that of the MSTC but both systems perform worse than the S-PLT2. We believe that the continuous speech signal is not long enough, so that purely unsupervised adaptation can always improve the initial acoustic model. This underlines the benefit of using clean speech with known transcription in simulated-data adaptation.

VII. CONCLUSIONS AND FUTURE WORK

This paper proposed combined simulated-data adaptation and PLT in acoustic-model adaptation. The approach solved limitations of the conventional unsupervised MLLR adaptation in the PLT method. The adaptation data were increased by adding a noise-signal extracted from the input signal to a pre-recorded set of clean speech. Since correct transcriptions of simulated-data are given, adaptation is more effective than using only the input speech with unknown transcription. Experiments showed that our technique achieved over 10% improvement of recognition accuracy comparing to the original PLT.

Future works include an evaluation of the proposed model by a larger set of speech from various real environments. Further improvement of noise extraction and noise addition in simulated-data adaptation will also be investigated.

REFERENCES

[1] M.J.F. Gales, "Model-based techniques for noise robust speech recognition," PhD thesis University of Cambridge, 1995.

[2] M.J.F. Gales and P.C. Woodland, "Mean and variance adaptation with in the MLLR framework," Comput. Speech Lang. vol.10, pp. 249–264, 1996.

[3] J.L Gauvain and C.H. Lee, "Maximuma posteriori estimation for multivariate Gaussian mixture observations of Markov chains," IEEE Trans. Speech Audio Process. vol. 2, pp. 291–298, 1994.

[4] M.J.F Gales and S. Young, "An improved approach to the hidden Markov model decomposition of speech and noise," Proc. of ICASSP, pp. 233–236, 1992.

[5] Z.P. Zhang, T. Sugimura and S. Furui, "Tree-structured clustering methods for piecewise linear transformation-based noise adaptation," IEICE Trans. Inf. and Syst. vol. 9, pp. 2168-2176, 2005.

[6] T. Kosaka, S. Matsunaga, and S. Sagayama, "Speaker-independent speech recognition based on tree-structured speaker clustering," Computer Speech Language, vol. 10, pp. 55–74, 1996.

[7] T. Nattanun, K. Boontee, W. Chai, M. Sanparith and B. Vataya, "A simulated-data adaptation technique for robust speech recognition," Proc. of INTERSPEECH, pp. 777–780, 2006.

[8] S. Kasuriya, V. Sornlertlamvanich, P. Cotsomrong, T. Jitsuhiro, G. Kikui and Y. Sagisaka, "NECTEC-ATR Thai speech corpus," Proc. of COCOSDA, pp. 105-111, 2003.

Prosody-based Naturalness Improvement in Thai Unit-selection Speech Synthesis

A. Rugchatjaroen, A. Thangthai, S. Saychum,
N. Thatphithakkul and C. Wutiwiwatchai
Human Language Technology Laboratory,
National Electronics and Computer Technology Center (NECTEC)
Patumthani, Thailand

***Abstract*-This paper presents naturalness improvement in Thai unit-selection text-to-speech synthesis (TTS) based on prosody modeling. Although several modeling approaches of prosodic parameters in Thai speech have been proposed, they have not been proven to provide a promising performance when practically assembling in a synthesizer. In this paper, two learning machines for phrase break and phoneme duration prediction are integrated in a Thai unit-selection TTS system. Evaluations focusing on the naturalness improvement are conducted both subjectively and automatically. The listening test gives 0.47 MOS improvement from the baseline system and the objective measures obviously show the better quality of the proposed system.**

I. INTRODUCTION

Text-to-speech synthesis (TTS) has been widely implemented in many kinds of applications. It is particularly important for people with disabilities. At present, there are some developed systems for Thai, which almost present in the way of unit-selection algorithm. There exist some TTS systems developed based on the demisyllable-unit concatenation algorithm with prosody modification. However, automatic controlling of prosodic parameters is still far from natural human sounds.

To improve the naturalness of synthetic speech in Thai, several components need to be considered, including word segmentation [9]-[11], sentence boundary detection [12], and grapheme-to-phoneme conversion [14]-[16]. Prosodic prediction often employs intelligent learning machines or statistical models trained by a large prosody-annotated speech corpus. Given the predicted parameters, modifying speech signals can be performed efficiently by Time Domain Pitch Synchronous OverLab-Add (TD-PSOLA) [4].

At present, Vaja [1], a Thai speech synthesizer developed by NECTEC in Thailand, is utilizing the unit-selection technique on a well-organized speech corpus named TSynC [6]. The current version, treated as baseline system in this paper, incorporated a simple rule-based phrase breaking model and had no prediction of phoneme duration. This paper presents the improvements by objective and subjective tests on a modified system, where in a machine-learning based phrase break detection and a linear-regression based duration model are incorporated. The next section will describe two Thai prosodic-parameter prediction algorithms, including phrase breaking and duration modeling. Section III presents experiments, and results. Conclusion and future works are given in Section IV.

II. PROSODY-MODIFIED THAI TTS SYSTEM

Recently, modeling of two prosodic parameters, phrasal pauses and phoneme durations for Thai, has been extensively researched [2, 3, 7, 8]. This section reviews proposed algorithms, which will be integrated in the baseline TTS system. Figure 1 shows an overall structure of our TTS system with the two additional modules for phrase breaking and phoneme duration prediction. An example of intermediated outputs is given beside.

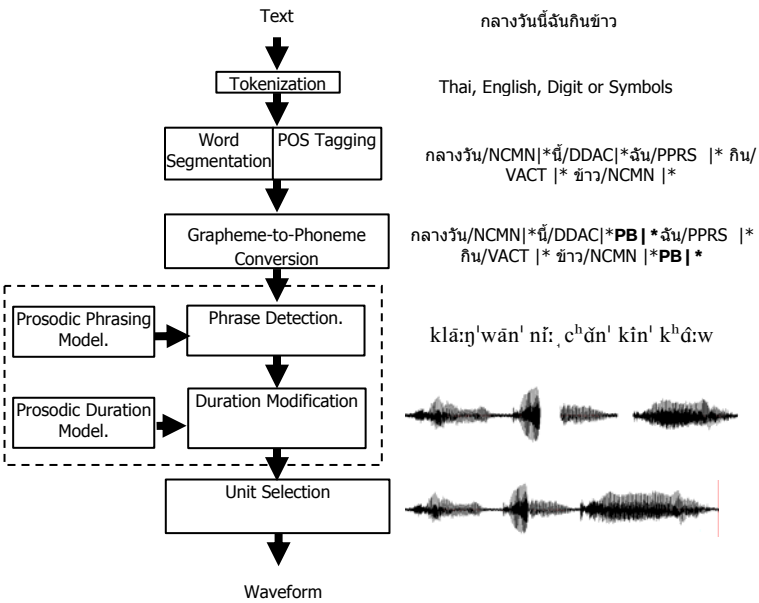

Figure 1. A structure of baseline Thai TTS system.

To predict prosodic parameters, a set of information (features) is extracted from an annotated speech corpus as shown in Table I. P and D denotes the task of phrase break and phoneme duration prediction.

TABLE I
FEATURES USED FOR PROSODY PREDICTION

Feature	Description	P	D
POS	Part-of-speech (POS) of four contextual words	✓	✓

Feature	Description	P	D
NSyl	The number of syllables between the previous phrase break and the current juncture	✓	
NWrd	The number of words between the previous phrase break and the current juncture	✓	
SylRatio	The ratio of *NSyl* and the total number of syllables in the previous phrase	✓	
WrdRatio	The ratio of *NWrd* and the total number of syllables in the previous phrase	✓	
Phone	Five phonemes including the current phoneme and four contextual phonemes		✓
PosWrd	Position in word (begin, mid, end)		✓
PosPhr	Position in phrase (begin, mid, end)		✓
Tone	Tone of the current syllable (five Thai tones)		✓

A. *Phrase break prediction*

In this section, we describe a practical approach for phrase detection. In literatures [7, 8], five candidates of the learning methods; for Thai POS sequence model, CART, RIPPER, SLIPPER and neural network, were used in prosodic phrase-break prediction. Experiments mostly showed that CART gave almost the highest performance. Since CART can be simply implemented and consumes a small processing time, this paper uses CART to predict phrase breaks.

Some features related to sentence boundaries proposed in [7, 8] are difficult to incorporate in the practical system due to unsolved problems of Thai sentence boundary detection. Not only an unreliable result, but also a high computational time is required by the current sentence breaking module. Therefore this paper ignores such features and proposes a new set of features independent of sentence boundaries as shown in Table I.

B. *Phoneme duration prediction*

Duration modeling for Thai speech synthesis is dominated by control factors (*Phone*, *PosWrd*, *PosPhr*, *Tone*), which depend on the structural design of Thai syllables, positional difference in phrase and syllable, and syllabic tones as shown in Table I.

Prediction is done by statistical linear regression based on the quantification theory as shown in the following equation.

$$\hat{y}_i = \bar{y} + \sum_f \sum_c x_{fc}\delta_{fc}(i) \quad i = 1,2,3,...,N \qquad (1)$$

where N represents the total number of data,

$\hat{y}_i$ represents the predicted phoneme duration of the i-th sample,

$\bar{y}$ represents the average duration of the phoneme,

x_{fc} represents the regression coefficient, and

$\delta_{fc}(i)$ represents the characteristic function [3] producing 0 or 1 corresponding to affected factors.

The predicted duration is exploited as the first criterion for speech unit selection in TTS. It serves later as a target value for waveform duration modification if the duration difference between the selected unit and the target value exceeds a threshold value. Duration modification is based on Time-Domain Pitch Synchronous OverLap-and-Add (TD-PSOLA) [4].

These trained models and wave-form modification technique are integrated into the baseline system resulting a new naturalness improved Vaja system.

III. EXPERIMENTS

Experiments are performed in two approaches, an objective and subjective test. Each test used different data sets and measurements as described in two following subsections. The last subsection shows experimental results.

A. *Experimental Data*

The TTS system uses a Thai speech corpus named TSynC [6], containing 2,644 paragraph, 15,716 phrase breaks, 5,200 utterances, 5,089 unique words and 30,096 tonal syllable patterns, varied on 89 Thai phonemes. Every paragraph was manually tagged with sentence-end markers, word and phrase breaks, and word POSs, by linguists. The data were divided into five subsets and performed cross-validation. Each of five cross-validation experiments utilized a training set of 2,115 paragraphs and 12,639 phrase breaks in average and a test set of the remaining data. Average results of those five sets are reported.

B. *Experimental Measurement*

Both objective (automatic) and subjective (listening) tests are performed to reflect the improvement of the system.

- *Objective evaluation of phrase breaking*

Missing or misplaced phrase breaks can distort the meaning of utterances, as well as the naturalness of synthetic speech. To measure the quality of phrase detection automatically, we compute

$$Precision = \frac{t_B}{t_B + f_B} \qquad (2)$$

$$Recall = \frac{t_B}{t_B + f_{\neg B}} \qquad (3)$$

$$F - measure = 2\frac{Precision\ Recall}{Precision + Recall} \qquad (4)$$

where t_B, f_B and $f_{\neg B}$ denote correct acceptance, false acceptance, and false rejection rates of phrase break prediction.

- *Objective evaluation of duration modeling*

Fluctuation of phoneme duration in a syllable conveys a different meaning of the whole word in an utterance. Differences between the predicted duration and the targeted duration observed from an actual human speech are shown as

an average duration error (in ms), which is calculated by the following equation.

$$\text{Average duration error} = \frac{\sum_{i=1}^{N} |D_{pi} - D_{ti}|}{N} \quad (5)$$

where D_{pi} is the predicted duration of the i-th phoneme,

D_{ti} is the targeted duration of the i-th phoneme,

N is the total number of phonemes in the test set.

- *Subjective evaluation*

A listening test using the MOS scale [5] is conducted. The values 1 to 5 in the MOS scale rank the quality of speech utterance from the worst to the best. Three test cases (S1, S2 and S3) were set up in an office room using 45 test utterances (3 cases * 15 sentences/case). The three cases are as follows.

- S1 contains 15 utterances of natural speech.
- S2 contains 15 utterances generated by the baseline TTS system.
- S3 contains 15 utterances generated by the prosody-modified TTS system.

The test is performed by prompting three versions of each of 15 sentences to a listener, starting by S1 followed by S2 and S3, which can be shuffled. The listener gives scores to each version based on the question "how natural is the utterance?" and steps to the next sentence.

The experiment is done by 20 subjects, who are NECTEC staffs aged between 22 – 38 years old (27.9 years in average). Seven of them are females and thirteen are males.

C. Experimental Result

According to the objective and subjective tests, results are presented as follows.

- *Objective Test*

This subsection shows results averaged from the five cross-validation data sets. Phrase detection in the several research works revealed that the accuracy was varied by the different features. In real situation, some features such as *POS*, *NSyl*, and *NWrd* are not precise since the previous modules; word segmentation, POS tagging, and grapheme-to-phoneme (G2P) conversion are not perfect.

TABLE II
RESULTS OF FOUR PHRASE BREAKING MODELS.

Model	Feature	Precision	Recall	F-measure
Baseline	*Rule based*	33.2	34.6	33.9
1	*POS*	77.8	65.9	71.4
2	*POS + NSyl*	74.1	70.2	72.1
3	*POS + NSyl + NWrd*	73.8	70.8	72.3
4	*POS + NSyl + NWrd + SylRatio + WrdRatio*	74.2	69.4	71.7

Table II compares four models of phrase breaking with different input features. All features are base on perfect word segmentation, POS tagging, and G2P conversion.

The results show that using *POS*, *NSyl* and *NWrd* achieves the best performance. Adding more features, e.g. in the 4th model, is noisy and hence lowers the overall accuracy.

Our word segmentation with POS tagging yields 66.6% accuracy, whereas our G2P module achieves 87.2% accuracy when the input text is perfectly segmented into words. We also compute F-measure of the phrase break prediction model when working with such imperfect word segmentation and G2P conversion. Results are illustrated in Figure 2. In the case of using actual word segmentation and G2P conversion (white pieces), which is the real situation, results show that using *POS* and *NSyl* gives the highest accuracy. Interestingly, no matter what perfect or imperfect G2P is used with the ideal word segmentation, only little changes of accuracy are obtained. The reason is that both still produce the similar number of syllables, which is one of a key feature in the phrase breaking module.

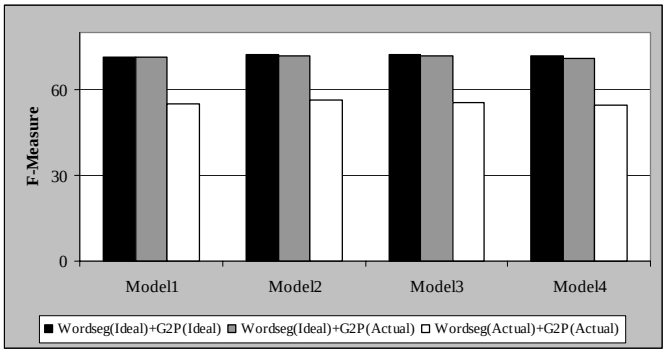

Figure 2. F-measure results of 4 models based on ideal and actual word segmentation and G2P modules.

The graph in Figure 2 obviously shows that the accuracy of phrase breaking can be significantly improved if a better word segmentation is obtained. Improving the word segmentation module can be done by a carefully treat of abbreviation, numbering, and special symbols in the input text.

In the same way, evaluations of duration modeling were also set up using five cross-validation training and test data sets. The average duration error achieves 21.4 ms and 22.9 ms given ideal and actual phrase breaks respectively. Comparing to the baseline TTS system where average duration errors are 24.9 and 25.5 ms for the ideal and actual phrase breaks, 3.5 and 2.6 ms error reductions are obtained. To express more detailed results, we count the number of phonemes, whose predicted durations lie in a $\pm t$ interval from their targeted durations. Figure 3 plots the relative counts with respect to the value of t.

We can observe that durations of over 80% of phoneme samples are well predicted, i.e. less than 20 ms average duration error. In Thai, the phoneme duration plays a critically important role on the vowel length. Short and long vowels in Thai carry different meanings and have been designed as separated units. Therefore, the system must be able to generate

at least the distinguishable durations of these two vowel groups. Hansakunbuntheung [3] showed that short and long vowels differ at approximately 50 ms in average. We then set a threshold to modify the phoneme duration by TD-PSOLA if the duration difference between the unit selected from TSynC and its targeted value exceeds 40 ms.

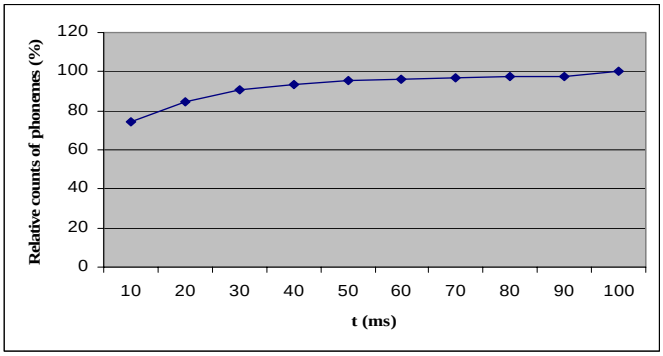

Figure 3. Relative counts of phonemes whose durations lie in $\pm t$ distance from their targeted values.

- *Subjective Test*

Table III reports MOS results of the listening test described in Section II.

TABLE III
MOS OF THREE TEST CASES

Case	Source	Naturalness score
S1	Natural speech	4.85
S2	Synthetic speech from the baseline system	2.14
S3	Synthetic speech from the prosody-modified system	2.56

The results show that a 0.42 improvement of MOS is obtained by the prosody-modified TTS system comparing to the baseline system. A major reason of the improvement comes from better phoneme durations predicted by the intelligent duration model. It is noted that some subjects gave a lower score to some prosody-modified utterances, which contain unnatural false-breaks. Such false-breaks happen more in the proposed phrase-break detector, where breaks are determined at every word juncture; while the baseline system considers only at white-spaces.

IV. CONCLUSION AND FUTURE WORKS

In this paper, phrase-break and phoneme-duration prediction modeling were optimized the practical use in a Thai unit-selection TTS system. In phrase-break improvement, a new set of features was proposed as an input to CART. To predict appropriate phoneme durations, a linear regression model was developed and TD-PSOLA was applied to modify speech signals. These proposed models were evaluated by an objective test and gave 73.8% precision, 70.8% recall and 72.2% F-measure. Moreover, duration prediction gave 3.5 and 2.6 ms reduction of average duration errors for ideal and actual phrase-break detection. A subjective test reported that the prosody-modified TTS system achieved 0.42 MOS improvement of naturalness over the baseline system.

Although the implemented system reaches an acceptable quality, there are several issues of naturalness, which can improve for example, G2P conversion of hardly literate words such as named entities, word segmentation, and other prosody information includes tonal information etc.

ACKNOWLEDGMENT

We would like to thank the members of HLT and IMG laboratory of NECTEC who spent their valuable time to join our subjective test.

REFERENCES

[1] P. Mittrapiyanurak, C. Hansakunbuntheung, V. Tesprasit and V. Sormlertlumvanich, "Issues in Thai Text-to-Speech Synthesis: The NECTEC Approach", *NECTEC Technical Journal Thailand*, vol. 2, No. 7, pp. 36-47, June 2000.

[2] C. Hansakunbuntheung, V. Tesprasit, R. Siricharoenchai, Y. Sagisaka, "Analysis and Modeling of Syllable Duration for Thai Speech Synthesis", *Proc. European Conference on Speech Communication and Technology*, Geneva-Switzerland, pp.93-96 (2003-9).

[3] V. Tesprasit, P. Charoenpornsawat and V. Sornlertlamvanich, "Analysis and Modeling of Syllable Duration for Thai Speech Synthesis", *Proc. European Conference on Speech Communication and Technology*, Geneva-Switzerland, pp.325-328 (2003-9).

[4] F. Charpentier and E. Moulines, "Pitch synchronous waveform processing techniques for text-to-speech synthesis using diphones", *European Conference on Speech Communication and Technology*, vol. I, pp. 013-019, 1989.

[5] M. Viswanathan, "Measuring speech quality for text-to-speech systems: development and assessment of a modified mean opinion score (MOS) scale", *Computer, Speech and Language19*, pp. 55-83, 2005.

[6] C. Hansakunbuntheung, V. Tesprasit and V. Sornlertlamvanich, "Thai Tagged Speech Corpus for Speech Synthesis", *The Oriental COCOSDA 2003*, pp. 97-104, 2003.

[7] V. Tesprasit, P. Charoenpornsawat and V. Sornlertlamvanich, "Learning Phrase Break Detection in Thai Text-to-Speech", *Interspeech 2003*, pp. 113-116, 2003.

[8] C. Hansakunbutheung, A. Thangthai, C. Wutiwiwatchai and R. Siricharoenchai. "Learning Methods and Features for Corpus-Based Phrase Break Prediction on Thai", *Interspeech 2005*, pp. 325-328, 2005.

[9] W. Aroonmanakun, N. Thubthong, P. Wattuya, B. Kasisopa, and S. Luksaneeyanawin, "Automatic Thai transcriptions of English words", *Southeast Asian Linguistics Society Conference 14 (SEALS 14)*, 2004.

[10] J. Inrut, P. Yuanghirun, S. Paludkong, S. Nitsuwat, and P. Limmaneepraserth, "Thai word segmentation using combination of forward and backward longest matching techniques", *International Symposium on Communications and Information Technology (ISCIT)*, pp. 37–40, 2001.

[11] T. Theeramunkong and S. Usanavasin, "Non-dictionary-based Thai word segmentation using decision trees", *The First International Conference on Human Language Technology Research (HLT)*, pp. 1–5, 2000.

[12] P. Mittrapiyanurak and V. Sornlertlamvanich, "The automatic Thai sentence extraction", *International Symposium on Natural Language Processing (SNLP)*, pp. 23–28, 2000.

[13] K. Sileverman, "The Structure and Processing of Fundamental Frequency Contours", *Ph.D. Thesis, University of Cambridge*,1987.

[14] S. Meknavin and B. Kijsirikul, "Thai grapheme-to-phoneme conversion, Burnham, D. (Ed.)", *Interdisciplinary Approaches to Language Processing: The International Conference on Human and Machine Processing of Language and Speech*, NECTEC, 1997.

[15] P. Tarsaku, V. Sornlertlamvanich, R. Thongprasirt, "Thai Grapheme-to-Phoneme using Probabilistic GLR Parser" In Proc. Eurospeech, volume 2, pp. 1057 – 1060, 2001.

[16] P. Charoenpornsawat and T. Schultz, "Example-Based Grapheme-to-Phoneme Conversion for Thai", *Interspeech 2006*, pp. 1268-1271, 2006.

Variable Momentum LMS Algorithm for Adaptive Howling Suppression in Audio Amplifier Systems

W. Loetwassana† R. Punchalard‡ J. Koseeyaporn† and P. Wardkein†
† Department of Telecommunication Engineering, Faculty of Engineering
King Mongkut's Institute of Technology Ladkrabang, Bangkok, THAILAND 10520
E-mail: s9060015@kmitl.ac.th
‡Department of Telecommunication Engineering, Faculty of Engineering
Mahanakorn University of Technology, Nongjok, Bangkok, THAILAND 10530

***Abstract*-It is well-known that acoustic feedback causes a howling phenomenon in an audio amplifier system. This problem not only annoys hearing but also can damage an amplifier system. The adaptive howling suppressor (AHS) in an audio amplifier system is thus proposed in this paper. The algorithm employed in adaptive process is achieved by using the variable momentum least mean square (VMLMS). With this algorithm, the performance improvement and higher convergence rate can be success. The proposed AHS, which is placed between a preamplifier section and a power amplifier section, acts as a notch filter whose frequency characteristic can reduce the howling spectrum. The simulation results show good improvement in the howling suppression of the proposed algorithm. Moreover, the proposed suppressor provides faster rate when has compared with the LMS and NLMS algorithms at the same environment condition.**

I. INTRODUCTION

An amplifier system often encounters with the problem such as whistling or howling which is caused by the acoustic feedback of a loudspeaker to a microphone. This problem does not only cause hearing annoyance but also can damage the amplifier system.

In literatures, many researchers attempt to mitigate the howling effect in amplifier systems with various techniques. The frequency shift method [1] is one of the proposed techniques but it has complicated in the modulation device. Later, the adaptive feedback cancellation (AFC) [2] which employs an adaptive finite impulse response (FIR) filter to identify the impulse response of the acoustic feedback is proposed. By using this technique, the unwanted feedback signal (howling) is estimated and subtracted from the microphone signal (speech signal). Unfortunately, this method requires large number of coefficients (>1000). Correspondingly, a simple least mean square algorithm (LMS) is not suitable employment because it leads to slow adaptation and can not completely eliminated the howling effect. For this reason, literature [2] used recursive least square (RLS) for adaptation algorithm but its disadvantage is high complexity. Nevertheless, the AFC method is usually employed to reject a howling phenomenon in a hearing aids system such as [5], [6]. This is because of short impulse response requirement in the AFC and the simplicity of the algorithm such as the LMS or normalized least mean square (NLMS) is still suitability for the work. The adaptive howling suppressor (AHS) methods [3], [4] are proposed. The AHS requires low number of coefficients (about 100) of the system and performs as notch filter characteristic in order to cancels a howling spectrum. This method can also reduce the howling effect in an audio amplifier system.

Because of, both LMS and NLMS algorithms are often used in the AHS system due to its simplicity. They are well-known that the convergence rate is directly proportional to the adaptation step size. When the step size is large, not only the convergence rate is increased but the excess mean square error (MSE) as well. To eliminate this drawback, the variable momentum least mean square (VMLMS) algorithm [8] is proposed. Therefore, it is applied for the AHS system which can provide both high convergence rate and low excess MSE is thus employed in the proposed system.

The paper is organized as follows. The howling in an audio amplifier system is described in section II. In section III, the adaptive howling suppressor is discussed. The simulation results are illustrated in section IV. Finally, conclusions are then given in section V.

II. THE HOWLING IN AN AUDIO AMPLIFIER SYSTEM

The acoustic feedback in an audio amplifier system is generally occurred when an audio signal produced by a loudspeaker travels back to a microphone either directly or being reflected from the walls, floor or ceiling (see Fig. 1(a)). This feedback system is modeled as shown in Fig. 1(b) where the $s(n)$ and $f(n)$ represent a speech signal and a feedback signal (howling), respectively, and n is discrete time index.

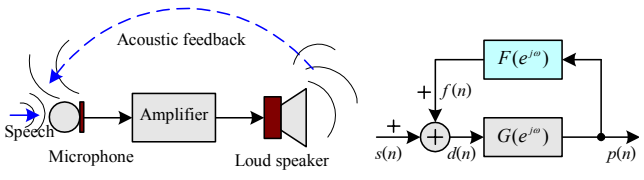

a). System b). Model

Figure 1. The acoustic feedback in an audio amplifier system

In this block diagram, $G(e^{j\omega})$ and $F(e^{j\omega})$ is the amplifier transfer function and the acoustic feedback transfer function respectively. The loudspeaker output signal $p(n)$ is fed back and passed through $F(e^{j\omega})$ to be the howling signal $f(n)$ to the microphone again. Then the composite signal $d(n) = s(n) + f(n)$ is amplified in $G(e^{j\omega})$ before being sent to the loudspeaker. The closed loop transfer function of the system model can be written as

$$T(e^{j\omega}) = \frac{G(e^{j\omega})}{1 - G(e^{j\omega})F(e^{j\omega})} \quad (1)$$

As can be seen, the system will become unstable if a frequency component of the feedback signal produces the $|G(e^{j\omega})F(e^{j\omega})| > 1$ and $\angle G(e^{j\omega})F(e^{j\omega}) = m2\pi$ (where m is an integer). For this condition, the oscillation phenomenon will occur. In case that the oscillation signal has the frequency in the audible range of human hearing, it is called a howling signal.

To eliminate this howling signal, the AHS that which performs as notch filter is proposed in this paper. With frequency reject characteristic of the notch filter, the howling signal is thus suppressed. The proposed system is discussed in the following section.

III. Adaptive Howling Suppressor

A. Principle of the AHS system

The proposed AHS system can be depicted in Fig. 2. The AHS inserted between a preamplifier section and a power amplifier section of the audio amplifier system. The structure of the AHS is illustrated in Fig. 3. This structure is based on an adaptive periodic noise canceller, and is modified from a well-known adaptive line enhancement (ALE) [7]. The signals $d(n)$ and $e(n)$ shown in Fig. 3 represent input and output of the system, respectively.

When the oscillation occurs, the input $d(n)$ is composed of a speech signal $s(n)$ and a periodic howling signal $f(n)$. Thus, from the point of view of an adaptive filter, the speech signal may be considered as broadband while the howling signal considered as narrowband where $s(n)$ is uncorrelated with $f(n)$ [3]. Both signals are passed through the delay unit (Δ sample) that causes delay about 1 ms (16 sample at 16 kHz sampling rate) which is sufficient to make $s(n - \Delta)$ and $s(n)$ uncorrelate each other but there is still a strong correlation of periodic component between $f(n - \Delta)$ and $f(n)$ [4]. The adaptive FIR filter attempts to adapt the system to minimize mean square error $e(n)$.

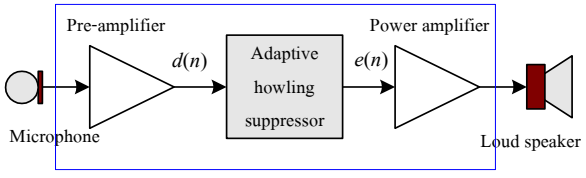

Figure 2. The adaptive howling suppressor implemented in audio amplifier

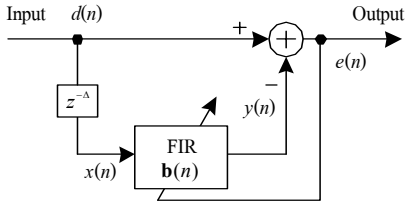

Figure 3. The structure of adaptive howling suppressor

After that, the adaptive FIR filter has reached to the optimum estimate of the periodic component. Thus, after subtraction we are left with mainly the speech component and it is a desirable signal.

B. Notch characteristic

From Fig. 3, let us consider the output equation of the AHS system as follows

$$e(n) = d(n) - \sum_{k=0}^{N-1} b_k(n)x(n-k) \quad (2)$$

or

$$e(n) = d(n) - \sum_{k=0}^{N-1} b_k(n)d(n-k-\Delta) \quad (3)$$

where $b_k(n)$ are coefficients of the N^{th} order FIR which are adjusted by the VMLMS algorithm. By assuming that adaptation of the FIR filter has converged, hence $b_k(n) \rightarrow b_k$. The AHS transfer function can then be obtained by

$$\frac{E(e^{j\omega})}{D(e^{j\omega})} = H(e^{j\omega}) = 1 - e^{-j\Delta\omega}\sum_{k=0}^{N-1} b_k e^{-jk\omega} \quad (4)$$

As shown in (4), it is seen that when the adaptive algorithm has converged thus, the transfer function of the AHS system is notch filter characteristic.

C. VMLMS algorithm

The VMLMS algorithm which is employed for the coefficient adaptation of the adaptive FIR filter is given by [8]

$$\mathbf{b}(n+1) = \mathbf{b}(n) + \mu e(n)\mathbf{x}(n) + \alpha(n)\big(\mathbf{b}(n) - \mathbf{b}(n-1)\big) \quad (5)$$

where

$$\mathbf{b}(n) = \big[b_0(n)\ b_1(n)\ b_2(n)\ \cdots\ b_{N-1}(n)\big]^{\mathrm{T}} \quad (6)$$

$$\mathbf{x}(n) = \big[x(n)\ x(n-1)\ \cdots\ x(n-N+1)\big]^{\mathrm{T}} \quad (7)$$

or

$$\mathbf{x}(n) = \big[d(n-\Delta)\ d(n-1-\Delta)\ \cdots\ d(n-N+1-\Delta)\big]^{\mathrm{T}} \quad (8)$$

It is noted that $\mathbf{b}(n)$ and $\mathbf{x}(n)$ are a coefficient vector and an input vector, respectively. In addition, $e(n)$ is a scalar of error signal (output of the AHS system), μ is a constant step size of

the algorithm that controls the convergence rate and the algorithm stability [7], [8] and $\alpha(n)$ is a scalar of momentum factor which bounded as $0 \le \alpha(n) < 1$ [8]. Also, $[\cdot]^T$ denotes the matrix transpose.

In equation (5), the last term is a momentum which the acceleration of convergence is controlled by the momentum factor. It is adjusted to large value in transient state in order to obtain high convergence rate and contrarily to be small value in steady state for low adaptation speed. Thus, if the step size of the algorithm can be accomplished a very small value and the low excess MSE is obtained. The adjustment of the momentum factor can be given by

$$\alpha(n) = \gamma\alpha(n-1) + \rho e(n)\mathbf{x}(n)^{\mathrm{T}}\left(\mathbf{b}(n-1) - \mathbf{b}(n-2)\right) \qquad (9)$$

which it can found in [8]. In the above equation, the algorithm is updated under a past difference of coefficient vector, a past momentum factor, a current input vector, a current error signal scalar, a constant γ and ρ, respectively where $0 < \gamma < 1$ and $\rho > 0$ [8]. The adaptation of momentum factor is bounded as the condition which is given by

$$\alpha(n) = \begin{cases} \alpha_{\min} & ;\ \text{if}\ \ \alpha(n) < \alpha_{\min} \\ \alpha_{\max} & ;\ \text{if}\ \ \alpha(n) > \alpha_{\max} \\ \alpha(n) & ;\ \text{otherwise} \end{cases} \qquad (10)$$

where $\alpha_{\min}$ and $\alpha_{\max}$ are lower and upper bounds of the momentum factor, respectively. The constant $\alpha_{\max}$ is normally selected near unity while the value of $\alpha_{\min}$ is chosen near or equal to zero. The initial value $\alpha(0)$ is usually taken to be $\alpha_{\max}$.

IV. Simulation Results

In this section the computer simulations are performed to examine the performance of the proposed AHS system. The adaptive 100th order FIR filter and the delay unit (Δ = 16 samples) are used where the sampling rate is at 16 kHz. For the environment set up, the amplifier system is set to oscillate at 1.6 kHz. The tested input signal of the AHS thus comprise of a speech signal and a 1.6 kHz howling signal. The speech signal is artificially generated with a speech-shaped noise using zero mean and unity variance white Gaussian noise signal through a 12th order auto regressive (AR) filter [6].

With the above set-up environment, the proposed algorithm is implemented with the parameters μ = 0.0001, γ = 0.999, ρ = 0.9, $\alpha_{\max}$ = 0.7 and $\alpha_{\min}$ = 0. The normalized power spectrum of an artificial speech with a howling signal (input of the AHS system) illustrated in Fig. 4. It is seen that the sine signal to broadband signal ratio (SBR) [7] is about 20 dB.

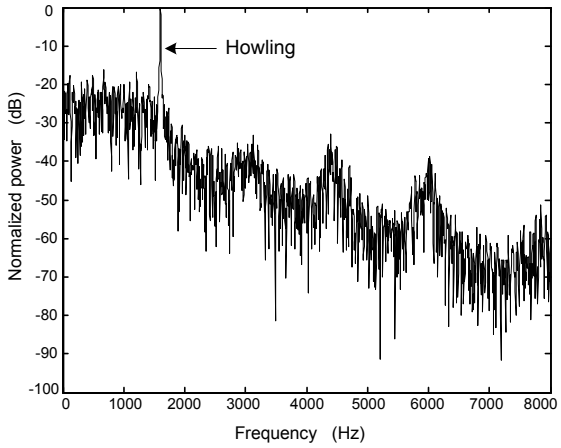

Figure 4. Power spectrum of AHS input with howling signal

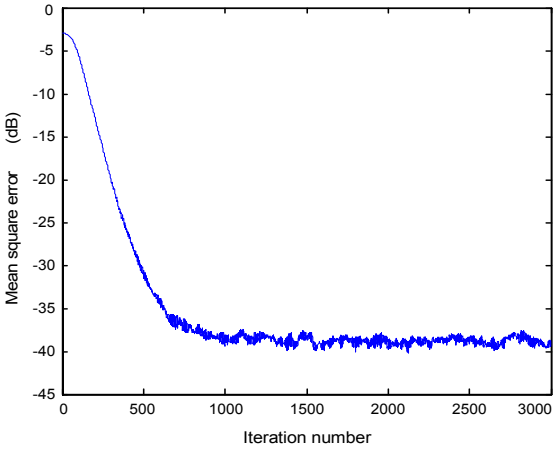

Figure 5. Convergence of AHS system using VMLMS algorithm

Fig. 5 shows the convergence behavior of the proposed algorithm where the MSE approaches the steady state about 500 iterations. As can be seen, the howling signal is almost completely suppressed after 500 iterations. When the algorithm approaches the steady state, the transfer function and output normalized power spectrum of the AHS system can be demonstrated in Fig 6 and Fig. 7, respectively. In Fig. 6, the magnitude response illustrates the notch filter characteristic of the AHS system where its depth is 1.6 kHz. Thus, the howling spectrum has been reduced as the result magnitude given in Fig. 7.

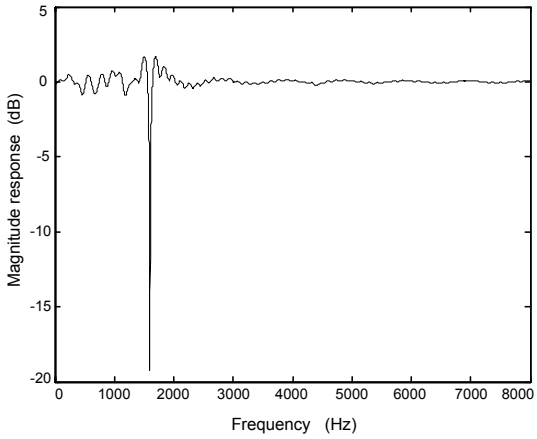

Figure 6. Transfer function of AHS system

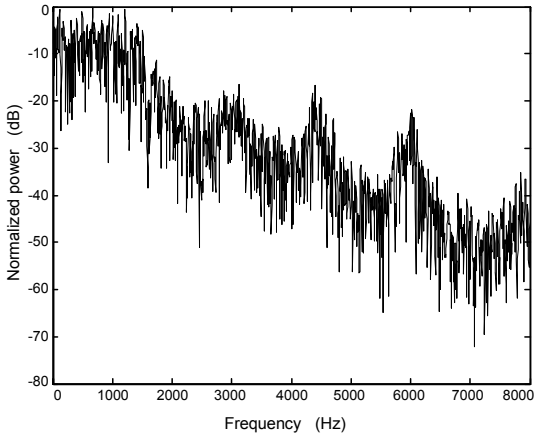

Figure 7. Power spectrum of the AHS output without howling signal

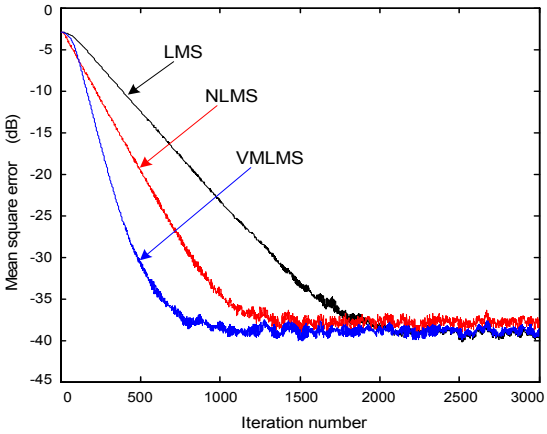

Figure 8. Comparison of convergence behavior

The convergence behavior of the proposed algorithm has been also compared with both LMS and NLMS algorithms where the parameter μ is set to be 0.0001 and 0.01, respectively. These algorithms are then performed in the same environment setup as previous discussion. As results shown in Fig. 8, the MSE convergence behavior of the proposed algorithm is superior to both LMS and NLMS algorithms.

V. CONCLUSIONS

An amplifier system often encounters with a howling problem due to an acoustic feedback of a loudspeaker to a microphone. The system will become unstable if a frequency component of the feedback produces larger than unity open loop gain and the loop phase is a multiple of 2π where the howling effect is occurred. The adaptive howling suppressor in an audio amplifier system using the VMLMS algorithm is thus proposed in this paper. The simulation results of the proposed algorithm show good result in howling suppression. Moreover, the comparison shows that the proposed algorithm provides faster convergence rate than the LMS and NLMS algorithms which are performed in the same environment.

REFERENCES

[1] M. R. Schroeder, "Improvement of acoustic-feedback stability by frequency shifting," *J. Acoust. Soc. Amer.*, vol. 36, no. 9, pp. 1718-1724 Sept. 1964.

[2] T. V. Waterschoot, G. Rombouts and M. Moonen, "On the Performance of Decorrelation by Prefiltering for Adaptive Feedback Cancellation in Public Address Systems," *IEEE Benelux Signal Processing Symposium*, pp. 167-170, 2004.

[3] J. B. Foley, "Adaptive Periodic Noise Cancellation for the Control of Acoustic Howling," *IEE Colloquium Adaptive filters*, pp. 7/1-7/4, 1989.

[4] G. Schmidt and T. Haulick, "Signal Processing for in-car Communication Systems," *Signal Processing*, pp. 1307-1326, Oct. 2005.

[5] J. A. Maxwell and P. M. Zurek, "Reducing Acoustic Feedback in Hearing Aids," *IEEE Trans. Speech and Audio Processing*, vol. 3, no. 4, pp. 304-313, July 1995.

[6] M. G. Siqueira and A. Alwan, "Steady-State Analysis of Continuous Adaptation in Acoustic Feedback Reduction Systems for Hearing-Aids," *IEEE Trans. Speech and Audio Processing*, vol. 8, no. 4, pp. 443-453, July 2000.

[7] J. R. Treichler, "Transient and Convergent Behavior of the Adaptive Line Enhancer," *IEEE Trans. Acoustics Speech and Signal Processing*, vol. 27, no. 1, pp. 53-62, Feb. 1979.

[8] W. Loetwassana, R. Punchalard, J. Koseeyaporn and P. Wardkein, "A Modification of Momentum LMS with Variable Momentum Factor," *IEEE Int. Symp. Communications and Information Technologies* (ISCIT-2006), pp. W2A-3 - W2A-6, 2006.

The Improvement a New Method for a Front-end of Military Vehicles Sound Recognition Using EHMM

Yingyot Sa-nguanpuag*, Panuthat Boonpramuk**

*Graduate school of Electrical engineering, KMUTT, email: s6403514@st.kmutt.ac.th
** Instrumentation and Control System Engineering Department, KMUTT, email: panuthat.boo@kmutt.ac.th

ABSTRACT

The propose of this investigated was to implement military vehicles sound recognition by using Ergodic Hidden Markov Model (EHMM) pattern recognition system. The system used real cepstral coefficient and normalization of cepstral coefficient as feature vectors and used wavelet transform as front-end process. Real cepstral coefficient gave a good result when using small database but the recognition rate decreased when using more type of vehicles. Cepstral coefficient normalization cannot improve the recognition rate, so this method was unsuitable for military vehicles sound recognition. Using wavelet transform and real cepstral coefficient gave the best recognition rate comparing with using only real cepstral coefficient as feature extraction. In conclusion, Wavelet transform could improve the recognition rate up to 97.77% (increased 14.44% when compared with the real ceptral coefficients).

Keywords: Military Vehicles Sound, Errgodic Hidden Markov Model, Real Cepstral Coefficient, Normalization of Cepstral Cofficient, Wavelet Transform.

1. INTRODUCTION

Generally, Speech recognition system is performed by the pattern template matching as shown in Fig. 1 [1]. In order to improve recognition rate (or robustness), Many works have been shown those techniques such as pre-processing algorithm, feature normalization, recognizer improving [2]. So, most of researchers are focus into two fields of automatic speech recognition (ASR) system; feature extraction and recognizer. Nowadays, HMM recognizer is accepted be good method for good recognition rate. It applies the statistical method to making template of speech references.

A great deal of efforts has been paid in developing new feature vector extraction techniques for automatic speech recognition (ASR) system. In the last two decade, several methods were proposed which used pattern features in HMM-based speech recognition. As a result, the Cepstral coefficient of speech waveform became a standard feature set for speech recognition system.

For the system which apply cepstral coefficient as feature vector, the cepstral mean normalization is the simply method to increase the recognition rate and robustness. The papers[3][4] have been shown the improving recognition rate by the two new feature normalization, i.e. Cepstral Max Normalization (CMN) and Cepstral Standard-Score Normalization (CZN), in addition to Cepstral Mean Normalization (CMN). The normalized feature vector is changed the mean values to the zero mean for distinguishing the difference of different feature to similar feature.

Though of military vehicles sound signal don't look like speech signal. Real cepstral coefficient and normalization of cepstral coefficient as feature vectors of military vehicles sound signal doesn't accepted be good method for HMM recognition. Therefore this paper proposed developing feature vectors together wavelet Transform and Cepstral Coefficient for HMM recognizer.

This research to try analysis military vehicles sound spectral make to feature vector, and it mean of "Real Cepstral". The coefficient reduced by FFT military vehicles sound signal, and after that the feature vector to import process EHMM recognition for produce reference military vehicles sound model, And it matching for test recognition rate.

In this paper presents the review of military vehicles in next section. The recognition is simulated by EHMM algorithm. In section III, the results are presented comparing the effect of real cepstral and normalization of cepstral as feature vectors and used wavelet transform as front-end process to the recognizers in clean sound. Finally, in section IV a conclusion of this research work is given.

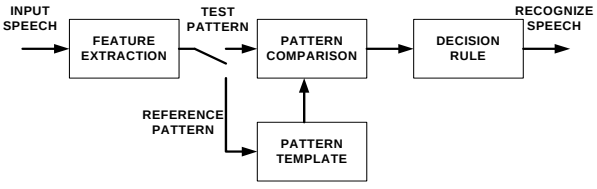

***Fig. 1** Pattern recognition approach.*

2. MILITARY VEHICLES

Military vehicles incorporate all forms of wheeled and tracked vehicles including the full range of body types found in commercial vehicles. However, there are also bodies and equipment that are unique to military operations. They include all types of trucks, tractors, truck tractors, personal carriers, tanks, self-propelled guns, motorized and mechanized special purpose

equipment, trailers, vans, and special purpose towed vehicles.

The principal distinction between these vehicles and their commercial counterparts is that military vehicles are specifically designed for military purposes. This includes combat operations and the transportation of cargo, personnel, or equipment; towing other vehicles or equipment; and operations, both cross country and over roads, in close support of combat vehicles and troops. They are designed and constructed to endure the rigors of the military environment ant to continue to operate at, or above, a prescribed minimum performance level in this environment. They have excellent cross-country performance capabilities over all types of terrain where tactical or combat operations can be conducted. This includes snow and ice, rocky terrain, swamps, and desert sands. In order to negotiate water barriers with a minimum of preparation, all sensitive equipment is either permanently waterproofed to prevent damage by immersion, or designed to function underwater [5].

3. EXPERIMENTAL DETAILS AND RESULTS

3.1 Performance evaluation

The performance of the algorithm proposed herein was investigated by implementation using the Borland c++ builder programming language and Matlab. For testing and evaluating the proposed algorithm, military vehicle sound cited from Armored car V150; Truck, Utility: ¼ Ton 4x4, M151 Series; Truck, Utility: Armament Carrier, Armored, 1 ¼ Ton, 4x4, M1025 (HMMWV); Cargo truck 2 ½ Ton KM 250; Truck, 10 Ton, 6x6, MB2028 and Carrier, Personnel, Full-Tracked, Armored, M113.

The simulation, 6 military vehicles sound are collected each with 5 samples for 5 seconds at the clean sound. The sounds have been recorded from the front and back of the vehicles was approximately one meter.

3.2 Wavelet Transform

Wavelet Transform represents the next logical step: a windowing technique with variable-sized regions. Wavelet analysis allows the use of long time intervals where we want more precise low-frequency information, and shorter regions where we want high-frequency information.

Dyadic analysis filter banks are constructed from the following basic unit. The unit can be cascaded to construct dyadic analysis filter banks with either a symmetric or asymmetric tree structure.

Each unit consists of a lowpass (LP) and highpass (HP), followed a decimation by a factor of 2. The filters are halfband filters with a cutoff frequency of Fs/4, a quarter of the input sampling frequency. Each filter passes the frequency band that the other filter stops.

The unit decomposes its input into adjacent high-frequency and low-frequency subbands. Compared to the input, each subband and has half the bandwidth (due to the half-band filters) and half the sample rate (due to the decimation by 2).

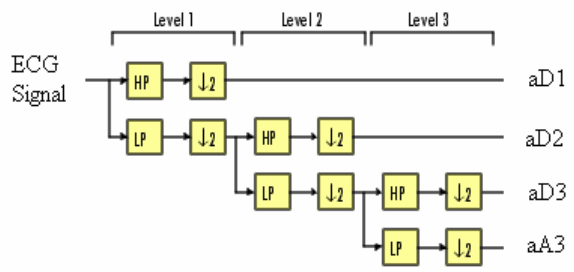

HP = highpass filter with fc=1/4 of fs.

LP = lowpass filter with fc=1/4 of fs.

aA3 = approximation coefficient.

aD1, aD2, aD3 = detail coefficient

Fig. 2 *Wavelet decomposes 3 layers.*

Synthesis filter banks are constructed from the following basic unit. The unit can be cascaded to construct dyadic synthesis filter banks with either a asymmetric or symmetric tree structure as illustrated in the figure3. The unit consists of a lowpass (LP) and highpass (HP).

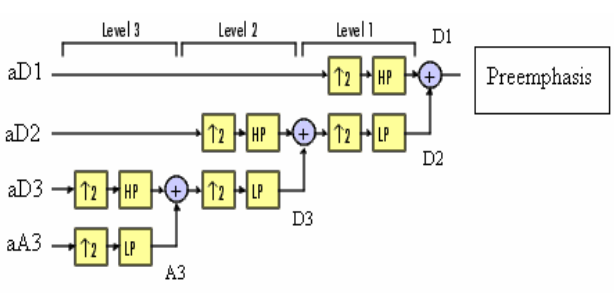

D1, D2, D3 = detail coefficient reconstruction.

A3 = approximation coefficient reconstruction.

Fig. 3 *Wavelet Synthesis 3 layers.*

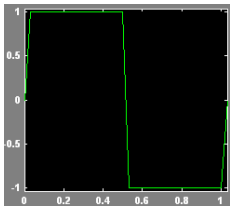

Fig. 4 *Haar Wavelet function used in this paper.*

3.3 Feature Normalizetation

The principles of the 3 techniques of feature vectors normalization which use in this paper are described.

3.3.1 Cepstral Mean Normalization (CMN)

The sequence of feature vector of a speech signal is given by

$$\mathbf{A} = \boldsymbol{a}(0)\boldsymbol{a}(1)\kappa\ \boldsymbol{a}(I-1) \quad (1)$$

where $\boldsymbol{a}(i) = (a_{i1}, a_{i2}, \text{L}\ , a_{ip}, \text{L}\ , a_{iP})^T$, I is the number of frames in each word. P is cepstrum dimension. The average value of whole coefficients in each dimension of feature vectors is obtained by

$$\mu_j = \frac{1}{I}\sum_{i=0}^{I-1} a_{ij}, (j = 1,2,...,P) \quad (2)$$

The normalization of Eq.1 by Eq.2 can be represented by

$$\tilde{\mathbf{A}} = \tilde{\boldsymbol{a}}(0)\tilde{\boldsymbol{a}}(1)\text{L}\ \tilde{\boldsymbol{a}}(i)\ \text{L}\ \tilde{\boldsymbol{a}}(I-1) \quad (3)$$

where $\tilde{\boldsymbol{a}}(i) = (\tilde{a}_{i1}, \tilde{a}_{i2}, \text{L}\ , \tilde{a}_{ip}, \text{L}\ , \tilde{a}_{iP})^T$ and $\tilde{a}_{ij} = a_{ij} - \mu_j$.

3.3.2 Cepstral Mean Max Normalization (CMMN)

The maximum value of whole coefficients in each dimension of feature vectors is obtained by

$$M_j = \max_i(\tilde{a}_{ij}) \quad (4)$$

The normalization of Eq.1 by Eq.4 can be represented by

$$\tilde{\mathbf{A}} = \tilde{\boldsymbol{a}}(0)\tilde{\boldsymbol{a}}(1)\text{L}\ \tilde{\boldsymbol{a}}(i)\ \text{L}\ \tilde{\boldsymbol{a}}(I-1) \quad (5)$$

where $\tilde{\boldsymbol{a}}(i) = (\tilde{a}_{i1}, \tilde{a}_{i2}, \text{L}\ , \tilde{a}_{ip}, \text{L}\ , \tilde{a}_{iP})^T$

and $\tilde{a}_{ij} = \dfrac{a_{ij} - \mu_j}{M_j}$.

3.3.3 Cepstral Standard-Score Normalization (CZN)

The standard-score value of coefficient in each dimension of feature vectors is obtained by

$$SD_j = \frac{1}{I}\sum_{i=0}^{I-1} (\tilde{a}_{ij})^2 \quad (6)$$

The normalization of Eq.1 by Eq.6 can be represented by

$$\tilde{\mathbf{A}} = \tilde{\boldsymbol{a}}(0)\tilde{\boldsymbol{a}}(1)\text{L}\ \tilde{\boldsymbol{a}}(i)\ \text{L}\ \tilde{\boldsymbol{a}}(I-1) \quad (7)$$

where $\tilde{\boldsymbol{a}}(i) = (\tilde{a}_{i1}, \tilde{a}_{i2}, \text{L}\ , \tilde{a}_{ip}, \text{L}\ , \tilde{a}_{iP})^T$

and $\tilde{a}_{ij} = \dfrac{a_{ij} - \mu_j}{SD_j}$.

3.4 Feature Extraction

The military vehicles sound feature extraction is a difficult take witch has attracted a great deal of interest. It is very important take because EHMM recognition processes depend on the quality of the features extracted.

The parameter values used in the simulations for 10kHz sampling frequency are as follows. The number of bits per sample of the military vehicles sound waveform was 16 bits. The coefficient (a) of pre-emphasis filter ($H(z) = 1 - az^{-1}$) is 0.97. The analysis window is Hamming window. The analysis frame length and frame overlap are 256 points and 128 points, respectively. The baseline feature vectors are 8 dimensions of FFT cepstral analysis. The Real Cepstral is the inverse Fourier transforms of the military vehicles sound spectrum in each sequence show in Fig. 5. The normalization of cepstral coefficient as feature vectors and used wavelet transform as front-end applied to the FFT cepstral feature vector show in Fig. 6-7.

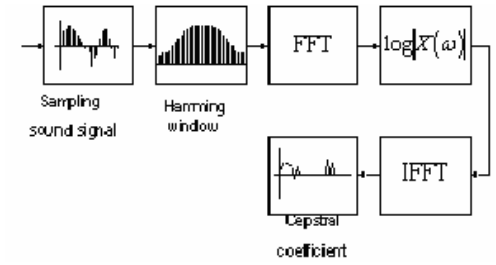

Fig. 5 *Real Cepstral Coefficient Feature Extraction.*

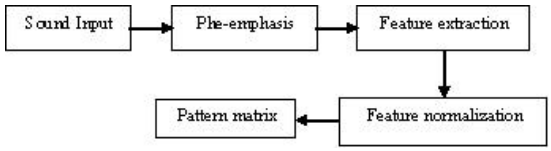

Fig. 6 *Cepstral Coefficient Normalization.*

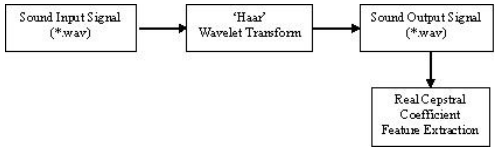

Fig. 7 *Wavelet Transform Process.*

3.4 Recognizers and Templates

For compared the overall of performance, The Errgodic Hidden Markov model (EHMM) recognition was investigated. It used to make statistical templates form as a model. The EHMM setting is given by 8 states of diagonal transition matrix and single Gaussian Mixture parameter. The likelihood between test and references pattern is obtained by Viterbi's algorithm.

3.5 Results

The result of this simulation, baseline feature vector, CMN, CMMN and CZN, shown in Table 1, respectively. The evaluated recognition rate of the baseline feature vectors, when tested with a large sample size the recognition rate were decreased. For CMN,CMMN and CZN, the recognition rate will be decreased when compared with the real ceptral coefficients.

TABLE 1: *Recognition rate on normalization of cepstrum as feature vectors feature vector simulation with EHMM engine.*

Normalized technique	The front of vehicle sample train data	The front of vehicle sample test data	The end of vehicle sample test data
Baseline	100	100	50
CMN	73.33	43.33	10.00
CMMN	56.66	33.33	10.00
CZN	53.33	33.33	13.33

Furthermore, using wavelet transform Coiflets, Haar family before extraction feature vectors processed, it can increase recognition rate. Because of wavelet transform consists of a lowpass (LP) and highpass (HP). After decomposed, Approximation (A) of military vehicles sound original signal is result of Lowpass filter, as well as and result of Highpass filter is detail (D). The process selected detail subband essential of filter banks from wavelet transform before extraction feature vectors processed. The result of this simulation shown in Table 2

TABLE 2: *Recognition rate on real cepstrum as feature vectors and used wavelet transform as front-end process simulation with EHMM engine.*

Signal Condition	The front of vehicle sample train data	The front of vehicle sample test data	The end of vehicle sample test data
Haar D1 + Cepstrum	93.33	96.66	73.33
Haar D2 + Cepstrum	73.33	63.33	60
Haar D3 + Cepstrum	50	33.33	13.33
Haar D1,2 + Cepstrum	100	100	90
Haar D1,3 + Cepstrum	100	100	90
Haar D2,3 + Cepstrum	90	76.66	50
Haar D1,2,3 + Cepstrum	100	100	93.33
Haar D1,2,3,4 + Cepstrum	100	100	66.66

Note:
Haar D… = Wavelet Transform decomposes used Haar function, and selected Detail of any Layer before extraction feature vectors.

4. DISCUSSION AND CONCLUSIONS

The purposes of the paper are to study the effects of the feature vector normalization techniques, such as CMN, CMMN, CZN and analysis filter banks of wavelet transform are separate feature frequency of signal out off original signal before extraction feature vector with Real Cepstral processed, that affect to the recognizer in the military vehicles recognition system and to increase the recognition rate compared with the Real Cepstral front-end. [6] The simulation results show that the recognition rate is increase by using function Haar3. Because of waveform function look like the military vehicles sound signal which sharp of Wavelet family are effectively of decompose and synthesis signal. The result at table 3 show the recognition rate average on real cepstrum and normalization of cepstrum as feature vectors and used wavelet transform as front-end process simulation with EHMM engine. The simulation results show that the recognition rate is increase by using Haar3 function wavelet transform accuracy was average is approximately 97.77%.

In the future work, we will implement the system in to aiming at a high degree of noise robustness, it is still obligatory to perform noise compensation in the recognition unit using either model adaptation techniques and/or implement the system in to DSP chip.

Table 3. *Recognition rate average on real cepstrum and normalization of cepstrum as feature vectors and used wavelet transform as front-end process simulation with EHMM engine.*

Signal Condition	Recognition rate (%)
Real cepstrum	83.33
CMN	42.22
CMMN	33.33
CZN	33.33
Real cepstrum as feature vectors and used wavelet transform as front-end process (Haar D1,2,3)	97.77

5. REFERENCES

[1] L.R. Rabiner, B.H. Juang, *Fundamentals of Speech Recognition*, PTR Prentice Hall, Inc., NJ, 1993.

[2] S. Jitapunkul, S. Luksaneeyanawin and et al., "Recent Advances of Thai Speech Recognition in Thailand," *IEEE Asia-Pacific Conference of Circuits and Systems (IEEE APCCAS 98)*, pp. 173-176, 1998.

[3] B. Panuthat, T. Funada, and H. Nomura, "Study on Improvement of Word Recognization by Using Normalization of Cepstrum Coefficients," *Proc. Spring Meet Acoust. Soc. Japan*, 3-Q-1, pp. 155-156, March, 2003.

[4] M. Ballang and B. Panuthat, "The Improvement of Thai-Speech Recognition Rate By Using Normalization of Cepstral Coefficients," *Proceeding of 27th Electrical Engineering Conference (EECON 27)*, pp. 181-184, 2004.

[5] Ordnance School, *Technical Manual 9-8000*, 2000

[6] Sa. 2LT.Yingyot and B. Panuthat, "Military Vehicles Sound Recognition Using EHMM," *Proceeding of 28th Electrical Engineering Conference (EECON 28)*, pp. 1045-1048, 2005.

[7] S. Nitikron and B. Panuthat, "ECG Recognition Based on Hidden Markov Model for Heart Trouble Diagnostic" *ECTI Annual Conference*

Precise Phone Boundary Detection using Selective Context-dependent Acoustic Refinement

Sirinoot Boonsuk Proadpran Punyabukkana and Atiwong Suchato
Spoken Language Systems Research Group, Department of Computer Engineering,
Faculty of Engineering, Chulalongkorn University, Bangkok, Thailand
Tel: +66-2-218-6959, Fax: +66-2-218-6955
E-mail: g48sbn@cp.eng.chula.ac.th ,{Proadpran.P, Atiwong.S}@chula.ac.th

***Abstract*- This paper proposes an automatic method for locating phone boundaries in speech utterances based on HMM-based forced alignment together with some context-dependent refinements. HMM-based forced alignment has been a preferred method for speech segmentation in many applications. However, the resulting boundaries are usually not consistent with real boundaries, defined based on abrupt changes in acoustic properties, which are often required in a number of applications such as landmark- and segment-based speech recognizers. In this work, the boundary refinement process fine-tunes boundary locations by utilizing acoustic features selected according to boundary types, categorized by their manners of articulation. Several acoustic measurements are combined with spectral features to form the set of acoustic features to be selected from. Performances of the refinements on different boundary types are investigated on a development set. Refinements working well are identified and these refinements are applied to an unseen test set. The maximum accuracy of 87.13% is achieved from speaker-independent speech segmentation experiments on 490 continuous speech utterances. This introduces a 14.7% error reduction when compared to the baseline HMM-based forced alignment.**

I. INTRODUCTION

Precise phone boundary labeling in speech waveform plays an important role in speech recognition and speech synthesis systems. Information on the timing of phone boundaries is usually needed in many applications. Relying on manual labeling, speech segment boundaries in a speech utterance could be located by having labelers listen to the computer playback of that utterance, visually observe its associated waveform and spectrogram, and mark down their timing. Although manual labeling by human is reliable and accurate, it is not at all feasible for large speech corpus since generating the associated labels for all boundaries is laborious and very time-consuming. Another disadvantage of manual labeling is possible inconsistency. Automatic segmentations, in which automatic methods are used for finding the location (or, more specifically, timing), of boundaries between all adjacent speech units when the sequence of speech units, or phonetic transcription, associated with the utterance of interest is a required prerequisite, are usually desirable.

Currently, techniques based on Hidden Markov models (HMMs) have been widely used in automatic speech recognition systems, as well as in performing forced alignments, where HMM-based recognizer is employed to find the most probable sound unit boundaries for speech utterances with known transcriptions, i.e. phonetic sequences without associated time labeling. Phone boundaries proposed by HMM forced alignment are not always, and are rarely, placed precisely at acoustic abruptness. Although it is not crucial for typical HMM-based speech recognizer, such precision is necessary for many other applications such as landmark- and segment-based speech recognizer, as well as other applications in need of acoustic-phonetic analysis. Some post refining methods were employed to improve the precision of sound unit boundaries from HMM forced alignment. Various refining techniques, such as HMM itself [1], Artificial Neural Networks (ANN) [2], Multi-Layer Perceptrons (MLP) [3, 4], Dynamic Time Warping (DTW) [5] and Gaussian Mixture Models (GMM) [6], have been proposed as post-processing techniques. Attempts to explicitly capture abrupt acoustic changes were also made. Andre-Obrecht [7] detected the sequential abrupt changes of some model parameters for speech segmentation. Dusan and Rabiner [8] relied on Spectral Transition Measures (STM) as their feature vectors.

The sound units in this work are phones, each of which possesses homogeneous acoustic characteristics, i.e. there are no significant changes during its interval. This paper proposes a method for locating phone boundaries. In such an approach, the system attempts to mimic manual labeling by incorporating information from spectrogram and temporal acoustic features in speech waveform. Several acoustic features [9] and temporal cues are combined in order to refine phone boundaries proposed by the forced alignment process.

II. BACKGROUND

A. Acoustic Characteristics of Phone Boundaries

Human's speech production is described as a two-staged process. Firstly, a source signal is produced either at the vocal folds or constrictions in the speaker's vocal tract. Then, the source signal is acoustically shaped according to the transfer function of the vocal tract at the moment the sound is produced. When vocal folds vibrate as a part of speech production, the corresponding sound is said to be 'voiced'. Otherwise, it is 'unvoiced'. Acoustic shaping of the source signal depends on the resonance properties of the vocal tract which change over the course of uttering phonemes due to the changing configuration of related articulators. Therefore, phonemes can be distinguished by their spectral shapes of the

resulting speech signals. There are marked changes in vocal tract configuration when the articulation translates from one phone to another. Consequently, abrupt discontinuities [10] manifest in the speech signal during phone transitions in both time and frequency domains. Examples of abrupt acoustic changes, marked by vertical solid lines, can be clearly observed in the spectrogram of the speech utterance /*n-aa-j^-s-a-ng-aa-s-a-p^-sp-ph-a-s-ii*/ shown in the upper panel of Figure 1.

B. HMM-Based Forced Alignment

HMM-based forced alignment is basically a speech recognition process that relies on HMM. However, with a known phonetic sequence, the decoding process in a typical recognition reduces from finding the best possible path in the network, whose topology is defined with an associated grammar, of HMM acoustic models to just finding the most likely state sequence, emitting the observed acoustic feature vectors, in a network that has only one path, constrained by the known phonetic sequence. Therefore, there are no substitution, insertion, and deletion errors. Still, the most likely state sequence might not always yield phone boundaries that precisely locate at abrupt acoustic changes as required in some applications. Figure 1 also illustrates an example of a set of phone boundaries resulted from an HMM forced alignment (lower panel) compared to ones precisely conform with abrupt acoustic changes (upper panel).

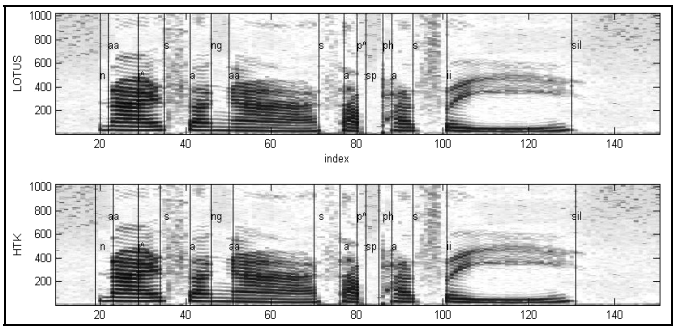

FIGURE 1. SPECTROGRAM OF A SPEECH UTTERANCE DESCRIBED IN THE CONTEXT WITH PHONE BOUNDARIES (UPPER PANEL) AND WITH AN HMM FORCED ALIGNMENT RESULT (LOWER PANEL)

III. PROPOSED METHOD

A. Overview

Figure 2 describes our overall boundary detection system. It is divided into two steps: 1) HMM forced alignment is used to propose rough phone boundaries. 2) The boundaries proposed in the first step are refined using context-dependent acoustic measurements. In this work, the aspect of contexts that concerns with which acoustic measurements will be used is a broad categorization of speech sounds based on their manners of articulation. Specifically, the boundary types of interest in this work include *stop-vowel*, *stop-sp*, *sp-stop*, *sp-nasal*, *vowel-sp*, *nasal-sp*, *vowel-nasal*, *vowel-stop*, *vowel-semivowel*, *nasal-vowel*, *fricative-vowel*, *affricate-vowel*, and *semivowel-sp*, where *sp* represents silence or a short pause. These boundaries make up to more than 90% of all boundaries and they are the only ones refined in this work. Speech frames in the vicinity of the initially proposed boundaries, including the frame where the boundaries are originally in, are considered candidates for locations of refined boundaries. Selected acoustic measurements are extracted from these speech frames and used as features for deciding where boundaries should be refined to.

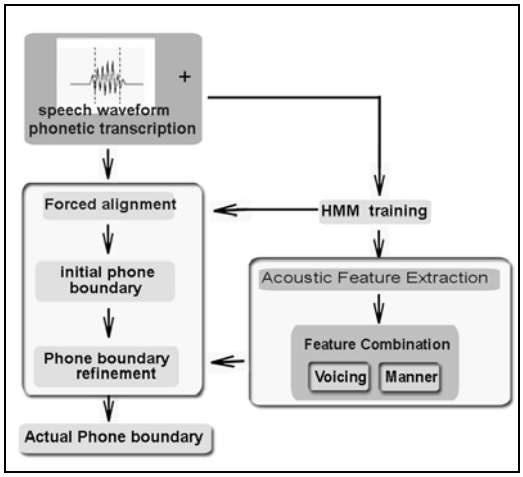

FIGURE 2. BLOCK DIAGRAM OF THE PROPOSED METHOD

B. Acoustic measurements

The set of acoustic measurements for the refining task is selected so that each of them reflects some aspects of acoustic difference. These measurements are:

1) Difference in the total signal energy in the speech frame of interest and the one in the preceding frame.
2) Correlation coefficient between the speech signal in the frame of interest and the speech signal in the preceding frame.
3) Difference in the Zero-Crossing Rate (ZCR) obtained from the speech signal in the frame of interest and the one from the preceding frame.
4) Energy ratios in different frequency bands between the speech signal in the frame of interest to the one in the preceding frame. Five frequency bands are used. Their ranges are: 1) below 400 Hz., 2) from the first formant frequency to the second formant frequency, 3) from the second formant frequency to the third formant frequency, 4) from the third formant frequency to 5,000 Hz., and 5) from 5,000 Hz. to 8,000 Hz.
5) Difference in the first formant frequency, as well as the second formant frequency, of the speech signal in the frame of interest and the ones from the preceding frame.

Only the last two measurements are applied to boundary types where there is no change in voicing property across the boundaries. Energy ratios in specific frequency bands are used with different boundary types according to a heuristic derived

from their acoustic-phonetic characteristics. For boundary types where the voicing property of the phones changes, the first three measurements are applied together with the last two since the first three since the first three measurements are closely related to voicing detection [11].

C. *Boundary Refining*

The location of each initial boundary proposed by HMM forced alignment is refined in order to obtain a location that is precisely at its corresponding acoustic discontinuity, if it is not there already. A refining region is defined around the frame, indexed n_o, containing each initial boundary. The region spans from the frame at n_o- γ to the frame at n_o- γ. The size of each refining region is an important factor to the resulting accuracy. An optimal size depends also upon the characteristic of results from the initial force alignment. A large refining region allows recovery of largely deviated boundaries, yet it may detect false alarms. A small refining region might not uncover real boundaries if the HMM force alignment propose heavily deviated boundaries.

Speech frames falling into the refining region are candidates for the real boundaries. The decision rules adopt in this work for selecting the best candidate in a refining region are based on the assumption that the most likely boundary, in a short-time speech interval, must demonstrate the maximum acoustic change. Therefore, candidates with the maximum difference (lowest correlation coefficient), demonstrated across all acoustic measurements, are picked as the resulting boundaries.

IV. Experiment Details

A. *Speech Corpus*

Large vOcabulary Thai continUous Speech recognition (LOTUS) corpus [12] is used. In this task, the phonetically distributed (PD) set containing 5,000 lexical items and manual transcriptions with phone boundaries information for every speech utterance is used to evaluate the performance of the proposed method. Developing and test sets contain the total of 28,828 and 22,145 boundaries, respectively. Utterances were recorded in a quiet environment at 16 kHz. sampling rate.

B. *Baseline System*

HMM forced-alignment is used as our baseline. A 39-dimensional feature vector (MFCCs together with their deltas and accelerations) is extracted every 10 ms. The observation frame size is 25 ms. A Hamming window is applied to each frame before the feature extraction. Five-state left-to-right HMMs are used as acoustic models for triphones representing 76 phonemes in Thai language. Gaussian mixtures with five components are used as probability density functions governing how each state in the HMMs emits its output.

C. *Evaluation*

To evaluate the performance of the proposed refining method, the detection accuracy percentage, which is the percentage of a ratio between the number of boundaries correctly located to the total number of boundaries tested, is measured. To determine whether a boundary is located correctly tolerance thresholds are set in terms of the numbers of frames allowed to be deviated from the frame marked in the associated manually prepared labels. The frame size used for extracting acoustic measurements for refining is either 7.5 ms. or 15 ms. for this work. The accuracies of the refined boundaries are compared with the ones obtained from the forced alignment alone.

Refinements are first performed on all of the thirteen boundaries types in the test set, and the result is compared with the performance obtained without the refinements in order to evaluate the performance of the method. The benefit obtained from the refinement of each boundary type is observed in terms of its contribution to the overall improvement on the development set. We then opt to apply the refinement on only the boundary types showing significant benefits as observed on the development set to the refinement on the test set. Note that since the test set is treated as if it was an unseen data set and the selective refinement is judged based on observations made on the development set, which is a different set than the test set, the accuracy obtained in this case should be an unbiased reflection of the performance of the proposed method even though the refinement is not applied to all boundaries.

V. Results and Discussions

Table I shows the boundary detection accuracy of the proposed method on the test set compared to the one obtained from the baseline system when refinement is performed on every boundary types. Note that the detection was test on 22,145 boundaries in the test set and the frame size used in this case is 15 ms. The performance is evaluated at a 1-frame tolerance level. The proposed method yields a 3.5% error reduction.

TABLE I.
BOUNDARY DETECTION PERFORMANCE WHEN UNSELECTIVE REFINEMENT IS APPLIED

Tolerance (frames)	%Accuracy (out of 22,145 boundaries)	
	frame size = 15 ms.	
	Baseline	Proposed
1	84.91	85.44

Figure 3 listed figures of merit of the proposed refinement on the thirteen boundary types. The figures of merit are evaluated based on the performance of the refinement of 28,828 boundaries in the development set. The larger the figure of merit, the more benefit its corresponding boundary type receives from the refining. Even though the overall boundary detection result improves over the baseline method, not all boundary types are fully benefited from the refinement. A few of them worsen the result.

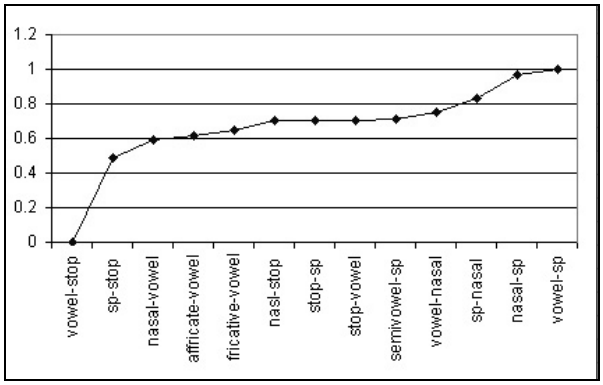

FIGURE 3. FIGURE OF MERIT OF THE REFINEMENT ON ALL BOUNDARY TYPES

Table II shows the boundary detection accuracies when the refinement is selectively applied to only the boundary types receiving significant benefits from the refinement performed on the development set. These boundary types include the top five of boundary types shown in Figure 3. The refining regions used in these cases are 2 frames.

TABLE II
BOUNDARY DETECTION PERFORMANCE WHEN SELECTIVE REFINEMENT IS APPLIED

Tolerance (frames)	%Accuracy (out of 22,145 boundaries)			
	frame size = 7.5 ms.		frame size = 15 ms.	
	Baseline	Proposed	Baseline	Proposed
1	54.54	60.53	84.91	87.13
2	78.26	80.51	94.98	95.11

From the table, we can see that when the frame size used is 7.5 ms., the proposed method yield the detection accuracy of 60.53% and 80.51% with 1-frame and 2-frame tolerance levels respectively. These introduce error reductions of 13.2% and 10.4% over the baseline method. When the frame size used is 15 ms., the proposed method yield the detection accuracy of 87.13% and 95.11% with 1-frame and 2-frame tolerance levels respectively. These introduce error reductions of 14.7% and 2.6% over the baseline method.

Typically, phone boundaries are considered as accurate when they are located within 10-20 ms. from their correct locations. Therefore, according to this criterion, the best boundary detection accuracy from our method is the accuracy obtained when the tolerance level is one 15-ms frame which is 87.13% with 14.7% error reduction over the baseline.

Results from another experiment suggest that the top five beneficiaries observed from the development set are located correctly with the overall accuracies of 93.36% when tested on the test set. These boundary types are located with 82.32% accuracy via the HMM forced alignment.

Table III shows another measure of the performance of the proposed method compared to the one of the baseline method. The table lists average deviation in frames when the frame sizes are 7.5 ms. and 15 ms. These average deviations are calculated by dividing the total number of frames for which all of the detected boundaries deviated from their corresponding true locations with the total number of boundaries. The less the average deviation, the better its corresponding method performs. From the table, the proposed method also shows a better performance than the baseline in this aspect.

TABLE III.
AVERAGE DEVIATION (FRAMES)

Detection Method	Frame size	
	7.5 ms.	15 ms.
Baseline	2.00	0.87
Proposed	1.86	0.78

VI. CONCLUSION AND FUTURE WORKS

This paper proposes a method for locating phone boundaries using context-dependent refinement on HMM forced alignment. The proposed algorithm achieves 87.13% detection accuracy when the refining is applied on some specific boundaries. Further investigation is needed on the adjustment of refining area, the frame size for the feature extraction procedure, as well as additional acoustic features.

REFERENCES

[1] A. Sethy and S. Narayanam, "Refined speech segmentation for concatenative speech synthesis," in Proc. ICSLP , Denver, USA, pp.145-148, September 2002.

[2] D.T. Toledano, "Neural network boundary refining for automatic speech segmentation," in Proc. ICASSP, Istanbul, Turkey, pp.3438-3441, June 2000.

[3] K.S. Lee, "MLP-Based Phone Boundary Refining for a TTS Database," IEEE Trans Audio, Speech and Language Processing, vol. 14, pp.981-989, May 2006.

[4] E.-Y. Park, S.H. Kim, and J.H. Chung, "Automatic speech synthesis unit generation with MLP based postprocessor against auto-segmented phoneme errors," in Proc. ICASSP, Phoenix, AZ, pp.2985-2990, March 1999.

[5] S. Paulo and L.C. Oliveira, "Improving the Accuracy of the Speech Synthesis Based Phonetic Alignment Using Multiple Acoustic Features," in Proc. PROPOR, Faro, Portugal, pp.31–39, June 2003.

[6] L.J. Wang, Y. Zhao, M. Chu, J.L. Zhou, and Z.G. Cao, "Refining Segmental Boundaries for TTS database Using Fine Contextual-Dependent Boundary Models," in Proc ICASSP, Quebec, Canada, pp.641-644, May 2004.

[7] R.A. Obrecht, "Automatic Segmentation of Continuous Speech Signals," in Proc. ICASSP, Tokyo, pp-2275-2278, 1986.

[8] S. Dusan and L. Rabiner, "On the Relation between Maximum Spectral Transition Positions and phone Boundaries," in Proc. Interspeech/ICSLP, Pittsburgh, PA, USA, September 2006.

[9] C.Y. Lin, J.S.R. Jang, and K.T. Chen, "Automatic Segmentation and Labeling for Mandarin Chinese Speech Corpus for Concatenation-based TTS," International Journal of Computational Linguistics and Chinese Language Processing, No. 2, Vol. 10, PP.145-166, June 2005.

[10] P. Leelaphattarakij, P. Punyabukkana, and A. Suchato, "Locating Phone Boundaries from Acoustic Discontinuities using a Two-staged Approach," in Proc. Interspeech/ICSLP, Pittsburgh, PA, USA, September 2006.

[11] D. Meen and T. Svendsen, "Improving Phone Label Alignment by Utilizing Voicing Information," in Proc. SPECOM, Patras, Greece, October 2005.

[12] R. Thongprasert, T. Charoenporn, W. Sinthupinyo, and V. Sornlertlamvanich, "Development of Very Large Corpora in Thailand," in Proc. 6th Natural Language Processing Pacific Rim Symposium Post-Conference Workshop, Tokyo, Japan, November, 2001.

Novel Precision Current-mode Full-wave Rectifier and Class B Push-Pull Current amplifier Using BiCMOS Current-controlled Current Conveyors

Winai Jaikla* and Montree Siripruchyanun**
*Electric and Electronic Program, Faculty of Industrial Technology,
Suan Sunandha Rajabhat University, Dusit, Bangkok, 10300, THAILAND Email: jnai2004@yahoo.com
**Department of Teacher Training in Electrical Engineering, Faculty of Technical Education,
King Mongkut's Institute of Technology North Bangkok, Bangkok, 10800, THAILAND Email: mts@kmitnb.ac.th

***Abstract*- This article introduces a novel version for implementing current-mode precision full-wave rectifier and class B push-pull current amplifier. The features of the proposed circuits are that: it can rectify and amplify current signal with controllable output magnitude via an input bias current: the output current save ideally free from temperature variation. In addition, direction of the output current signals can be arbitrarily controlled by current in the circuits to be either positive or negative without changing circuit topology, which differs from the previous literatures. Circuit descriptions merely consist of 3 BiCMOS CCCIIs. The performances of the proposed circuits are investigated through PSPICE. They show that the proposed circuits can function as a current-mode precision full-wave rectifier and push-pull current amplifier where input current range from -80μA to 80μA can be achieved at ±2.5V power supplies. The maximum power consumption is 1.43mW. In addition, the highest frequency is restricted at up to megahertz range.**

***Index Terms*- full wave rectifier, BiCMOS, current-mode, class B, current amplifier, push-pull**

I. INTRODUCTION

A precision rectifier is extensively used in signal processing circuits, for instance, in an AC to DC converter, in a signal polarity detector, in a peak signal detector, in an amplitude demodulation circuit, and in an automatic gain control system [1-2]. Basically, a voltage-mode precision rectifier employs an operational amplifier and a diode [3]. The output signal confronts a zero-crossing distortion due to characteristic of the diode [4]. This problem has been subsequently solved by proposing the novel circuit without a diode [5]. In addition, the precision rectifiers are modified to use other active elements to achieve wider frequency response, for example, current conveyor [6] and current feedback operational amplifier [7].

Since a low-voltage operating circuit becomes necessary as in portable and battery-powered equipment, the current-mode technique is ideally suited for this purpose more than the voltage-mode one. Presently, there is a growing interest in synthesizing the current-mode circuits because of more their potential advantages such as larger dynamic range, higher signal bandwidth, greater linearity, simpler circuitry and lower power consumption [8-9]. From our investigations, there are seen that the previous literatures have proposed the current-mode precision rectifiers [10-12]. Unfortunately, the output magnitude of those proposed circuits can not be adjusted. Consequently, they require a proper amplifier to achieve appropriate level of output signal. Furthermore, in case of opposite polarity of output signal is required, it must be unavoidably changed the circuit topology or added a current inverter. This makes the circuit more complicated. Some of them employ a number of passive elements, which is not suitable for realizing into an integrated circuit [13]. The operations of all mentioned circuits, moreover, are dependent on temperature.

On the other hand, the current amplifiers find wide applications, particularly in a system that requires a low power supply voltage, such as in communication system, instrumentation system, biomedical system, etc. [14]. Recently several current amplifiers have been proposed, however, their current gain cannot electrically and linearly be tuned [15]-[17]. Basically, class-A current amplifiers have linear characteristics. However, they require DC bias currents that restrict the allowable signal swing range and lead a high-power consumption. The DC power consumptions of class-A amplifiers do not depend on the signal amplitude but it is determined by the DC bias current and voltage of the power source. On the other hand, class-B amplifiers require no DC bias current, thus there is no power consumption when no signal is processed in the amplifiers. In addition, the DC power of the class-B amplifiers vary with the magnitude of the processing signal, thus quite good power efficiencies are expected.

The purpose of this paper is to introduce novel current-mode precision rectifier and class B push-pull current amplifier, whose output magnitude and polarity are electronically controllable without changing a circuit topology or adding any more circuit. They can be applied in an automatic control via a microprocessor. Each circuit construction consists of 3 CCCIIs. The PSPICE simulation results are also shown. They confirm that the proposed circuits provide a wide range of input current, temperature-insensitive, wide range of frequencies. In addition, controllability of the output magnitude and polarity can be achieved via an input bias current and control current, respectively.

II. CIRCUIT PRINCIPLE

A. BiCMOS Current Controlled Current Conveyor (BiCMOS CCCII)

CCCII is a versatile analog building block which is similar to the conventional Current Conveyor (CCII) except that the CCCII has a finite input resistance (R_X) at the X terminal. CCCII has the advantage of electronic adjustability over the CCII, because it allows the adjustment of intrinsic resistance R_X via the bias current I_B as shown in the following equation.

$$R_X = \frac{V_T}{2I_B}. \tag{1}$$

Where V_T is the thermal voltage. The matrix-relationship between the voltage and current variables among port X, Y and Z of an ideal CCCII can be described by the following matrix equation

$$\begin{bmatrix} i_y \\ v_x \\ i_z \end{bmatrix} = \begin{bmatrix} 0 & 0 & 0 \\ 1 & R_x & 0 \\ 0 & \pm 1 & 0 \end{bmatrix} \begin{bmatrix} v_y \\ i_x \\ v_z \end{bmatrix}. \tag{2}$$

Where the positive and negative signs of the current i_z denote the positive (CCCII+) and negative type (CCCII-), respectively. The symbol and the equivalent circuit of the CCCII+ are illustrated in Fig.1.

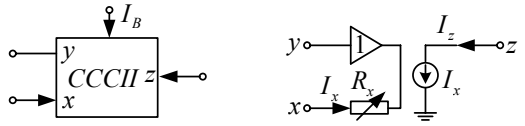

(a) (b)

Figure 1. CCCII (a) symbol (b) equivalent circuit

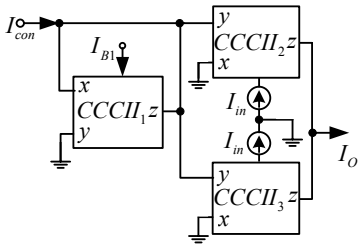

Figure 2. Proposed current-mode full-wave circuit

B. The proposed current-mode rectifier circuit

Fig. 2 displays the proposed current-mode rectifier circuit. Considering the circuit in Fig. 2 and using the CCCII properties described in section A, we will receive

$$i_{z2} = \begin{cases} \frac{I_{con}}{2I_{B1}} I_{in} & \text{if} \quad I_{in} > 0 \\ 0 & \text{if} \quad I_{in} < 0 \end{cases}, \tag{3}$$

$$i_{z3} = \begin{cases} 0 & \text{if} \quad I_{in} > 0 \\ \frac{I_{con}}{2I_{B1}} I_{in} & \text{if} \quad I_{in} < 0 \end{cases}, \tag{4}$$

and

$$I_o = i_{z2} + i_{z3} = \frac{I_{con}}{2I_{B1}} |I_{in}|. \tag{5}$$

It can be seen form Eq. (5) that the circuit in Fig. 2 can perform as a precision current-mode full-wave rectifier whose output magnitude can be controlled via controlled current I_{con} or I_{B1} and is theoretically temperature independent.

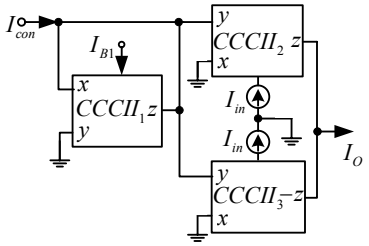

Figure 3. Proposed class B push-pull current amplifier circuit

C. The proposed class B push-pull current amplifier circuit

Fig. 3 shows the proposed class B push-pull current amplifier. Considering the circuit in Fig. 3 and using the CCCII properties described in section A, we will receive

$$i_{z2} = \begin{cases} \frac{I_{con}}{2I_{B1}} I_{in} & \text{if} \quad I_{in} > 0 \\ 0 & \text{if} \quad I_{in} < 0 \end{cases}, \tag{6}$$

$$i_{z3} = \begin{cases} 0 & \text{if} \quad I_{in} > 0 \\ -\frac{I_{con}}{2I_{B1}} I_{in} & \text{if} \quad I_{in} < 0 \end{cases}, \tag{7}$$

and

$$I_o = i_{z2} + i_{z3} = \frac{I_{con}}{2I_{B1}} I_{in}. \tag{8}$$

It can be seen from Eq. (8) that the circuit in Fig.3 can perform as class B push-pull current amplifier whose current gain can be controlled via control current I_{con} or I_{B1} and which is temperature independent.

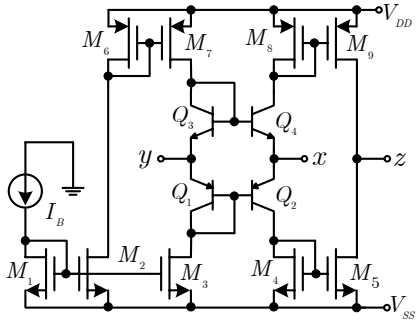

Figure 4. Internal construction of BiCMOS CCCII

III. SIMULATION RESULTS

To prove the performances of the proposed circuits, the PSPICE simulation program was used for the examinations. The PNP and NPN transistors employed in the proposed circuit were simulated by using the parameters of the PR200N and NR200N bipolar transistors of ALA400 transistor array from

AT&T [18]. The PMOS and NMOS transistors were simulated by using the parameters of a 0.35µm TSMC CMOS technology [19]. The aspect transistor ratios (W/L) of PMOS and NMOS are 55/2.4µm and 12/2.4µm, respectively. The circuit was biased with ±1.5V supply voltages. Fig. 4 displays the internal construction of the CCCII used in the proposed circuit. Fig.5 shows DC transfer characteristics of proposed rectifier, where $I_{B1}=50\mu A$ and $I_{con}=100\mu A$. It can be seen that the proposed circuit can provide a wide range of input currents and that the polarity of the output current can easily be changed by the change of polarity of the control current I_{con}. Fig. 6 shows the output current versus temperature variations at $27^{\circ}C$, $50^{\circ}C$ and $100^{\circ}C$. It is clearly observed that the output current is almost not dependent on the temperature variations due to internal temperature compensation in the CCCIIs used in the circuit, as explained earlier.

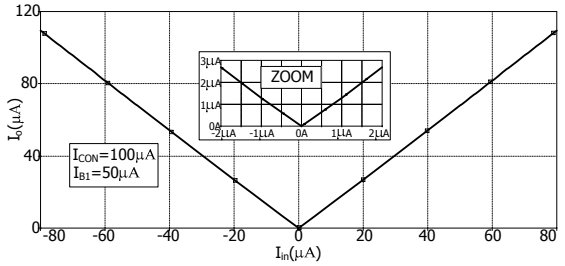

(a) *with* $I_{con} = 100\mu A$

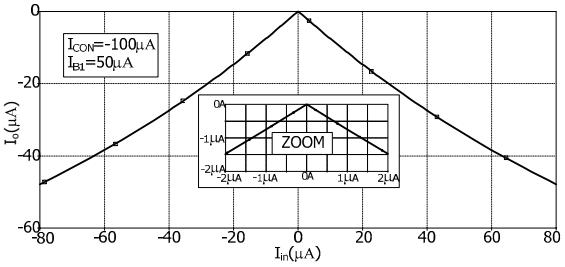

(b) with $I_{con} = -100\mu A$

Figure 5. DC transfer characteristics of proposed rectifier

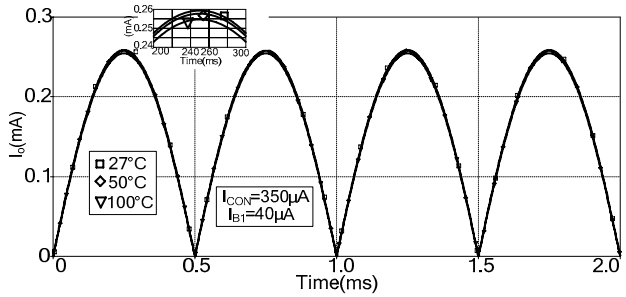

Figure 6. Output current with temperature variations

The output current responses with various input frequencies are also shown in Fig. 7. They confirm that the proposed circuit can rectify when frequency is up to megahertz range without disturbing magnitude of the output current. Fig. 8 displays the output currents as a function of the control current I_{con} while $I_{in}= 50\mu A$. These figures prove that the magnitude of the output current can easily be controlled electronically in accordance with the theoretical anticipations.

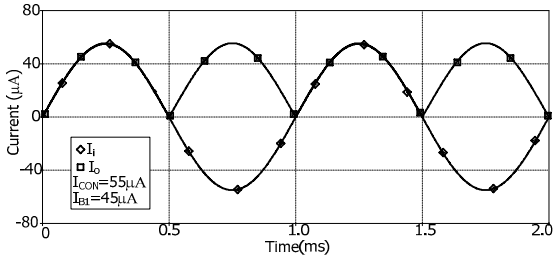

(a) 1kHz

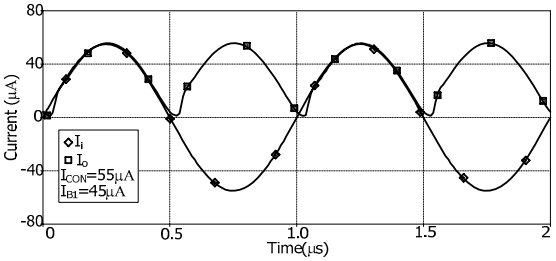

(b) 1MHz

Figure 7. The results of output current with various input frequencies

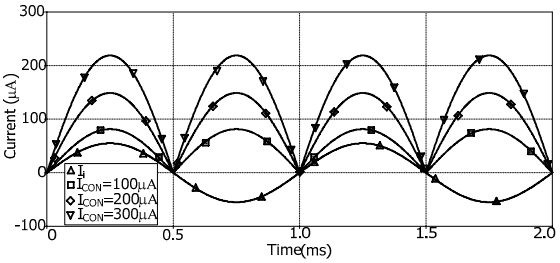

Figure 8: Output currents relative to input current

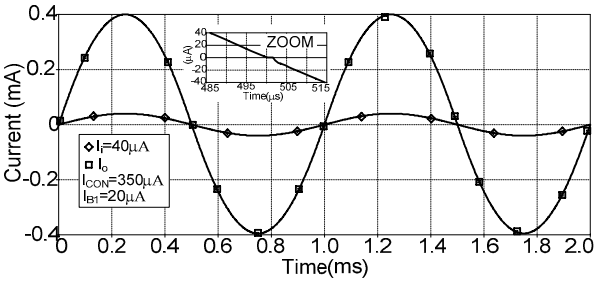

Figure 9. Output current due to input current of proposed current amplifier

The proposed controllable gain class B push-pull current amplifier in Fig. 3 was tested by setting $I_{in}=40\mu A$ and $f=1kHz$, the results obtained are shown in Fig. 9. Fig. 10 shows the current transfer characteristic of the proposed current amplifier circuit. Fig. 11 represents plots of the current gain $Ai = I_{out}/I_{in}$ versus the control current. Fig. 12 shows the output current relative to temperature variations at $27^{o}C$, $50^{o}C$ and $100^{o}C$. Fig. 13 insists that the proposed circuit can also amplify current signal when frequency is up to megahertz range. Slight cross over distortion at high frequency stems from the parasitic elements in the CCCIIs.

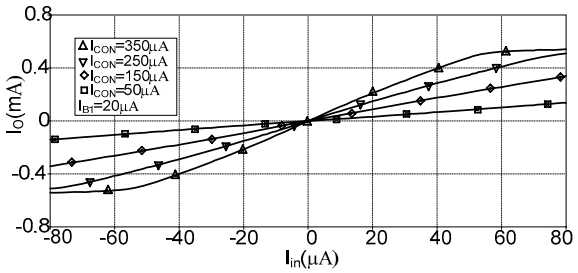

Figure 10. DC transfer characteristics of proposed current amplifier circuit

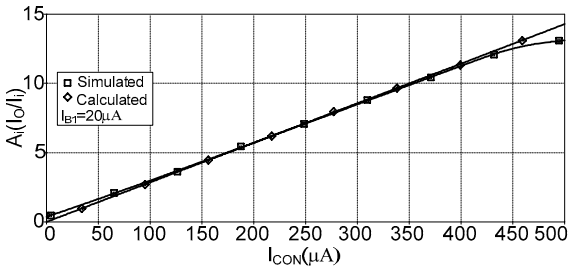

Figure 11. Current gain of proposed current amplifier circuit where I_{con} is varied

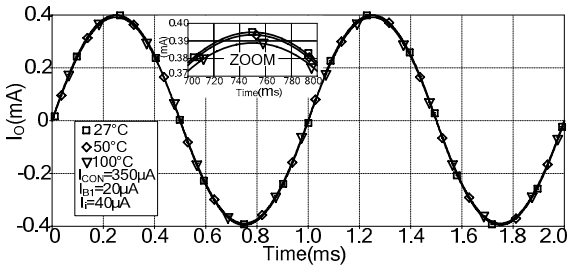

Figure 12. Output current with temperature variations

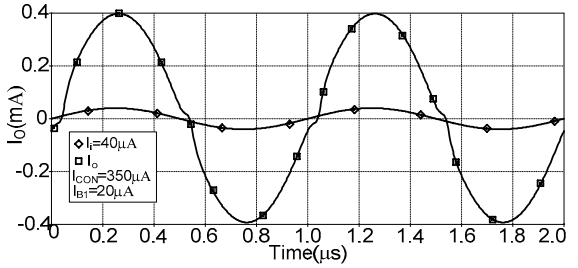

Figure 13. The results of output current with input frequency 1MHz

IV. CONCLUSIONS

The novel current-mode precision rectifier and push-pull current amplifier, based on BiCMOS CCCIIs, which can rectify and amplify an input current with electronic controllability of output magnitude, have been reported in this paper. In addition, direction of the output current signal can be arbitrarily controlled by current in the circuit to be either positive or negative without changing circuit topology, which differs from the previous literatures. Each circuit description merely consists of 3 CCCIIs. The performances of the proposed circuits have been also investigated through PSPICE. They show that the proposed circuits can function as a current-mode precision full-wave rectifier and class B push-pull current amplifier where input current range from *-80μA* to *80μA* can be achieved at *±2.5V* power supplies. The maximum power consumption is 1.43mW. Furthermore, the highest frequency is restricted at up to megahertz range. With claimed outstanding features, it is very appropriate to further develop the proposed circuits to be a part of a monolithic chip for working in a current-mode signal processing.

REFERENCES

[1] C. Toumazou, F. J. Lidgey and S. Chattong, "High frequency current conveyor precision full-wave rectifier," *Elec. Lett*., vol.30, pp.745-746, 1994.

[2] B. Boonchu and W. Surakampontom, "A CMOS Current-mode squarer/rectifier circuit," *IEEE Transactions on Circuits and Systems I*, Vol. 1, pp. 405-408, 2003.

[3] R. F. Coughlin and F. Drisoll, *Operational Amplifier and Linear Integrated Circuit*. Prentice Hall of India, New Dehli, 1998.

[4] J. G. Gift Stephan, "Novel precision full-wave rectifier," *Proceeding of 7th IEEE International Conference on circuit and system.*, Vol. 1, pp.206-209, 2000.

[5] S. Jun and D. M. Kim, "CMOS precision half-wave rectifier transconductance," *IEICE Trans. on Fundamentals*, Vol. E80-A, pp.2000-2005, 1997.

[6] A. Monpapasorn, K. Dejhan and F. Cheevasuvit, "A full-wave rectifier using a current conveyor and current mirror," *International Journal of Electronics*, Vol. 88, pp. 751-758, 2001.

[7] J. G. Stephan, "New precision rectifier with high accuracy and wide bandwidth," *Inter. Journal of Electronics*, vol. 92, pp. 601-617, 2005.

[8] C. Toumazou, F.J. Lidgey and D.G. Haigh, *Analogue IC design: the current-mode approach*, Peter Peregrinus, London, 1990.

[9] D. R. Bhaskar, V.K. Sharma and S.M.I. Rizvi, "New curren-mode universal biquad filter," *Microelectronics Journal*,Vol.30, pp. 837-839, 1999.

[10] K. Anuntahirunrat, W. Tangsrirat, V. Riewruja, W. Surakampontorn, "Sinusoidal frequency doubler and full-wave rectifier based on translinear current-controlled current conveyors," *International Journal of Electronics*, Vol. 91, pp. 227-239, 2004.

[11] S. Khucharoensin and V. Kasemsuwan, "High performance CMOS current-mode precision full-wave rectifier (PFWR)," *IEEE Transactions on Circuits and Systems I*, Vol. 1, pp. 41-44, 2003.

[12] V. Riewruja and R. Guntapong, "A low-voltage wide-band CMOS precision full-wave rectifier," *International Journal of Electronics*, Vol. 89, pp. 467-476, 2002.

[13] A. Anwar, M. Khan, A. el-ela and M.A. Al-turaigi, "Current-mode precision rectifier," *Inter. Journal of Electronics*, vol. 79, pp. 853-859, 1995.

[14] G. Palmisano, G. Palumbo, S. Pennisi, "*CMOS Current Amplifiers", Kluwer Academic Publsihers*, 1999.

[15] [16]S. Jun, D.M. Kim, "Fully differential current operational amplifier", *Elec. Lett.*, vol. 34, 1998, pp. 62-63.

[16] G. Palmisano, S. Pennisi, "Low-voltage continuous-time CMOS current amplifier with dynamic biasing", *Proc. ISCAS2001*, pp. I-312-I-315.

[17] R.H. Zele, S. Lee, D.J. Allstot, "An alternative push-pull amplifier circuit-dual to conventional circuits", *Proc. 37th Midwest Symposium Circuits and Systems*, pp. 1127-1130 , Aug 3-5, 2004.

[18] D. R. Frey "Log-domain filtering: an approach to current-mode filtering," *IEE Proc. Circuit Devices Syst.,* vol. 140, no. 406-416, 1993.

[19] E. Yuce, S. Tokat, A. Kızılkaya and O. Cicekoglu, "CCII-based PID controllers employing grounded passive components," *International Journal of Electronics. (AEU),* 2005.

Optical Diffraction-based Object Dimensions Measurement in Reflection and Transmission Modes

Sarun Sumriddetchkajorn and Kosom Chaitavon

Photonics Technology Laboratory
National Electronics and Computer Technology Center
112 Thailand Science Park, Phahonyothin Rd., Klong 1, Klong Luang, Pathumthani 12120, Thailand
Phone: +66-2564-6900 ext. 2102, Fax: +66-2564-6974, E-mail: sarun.sum@nectec.or.th

***Abstract* - This paper proposes to simultaneously analyze far-field diffraction patterns in both reflection and transmission modes in order to investigate the dimensions of a micron-size object. Our experimental demonstration shows a promising result obtained from both modes of operation. However, the quality of all edges of the object induces a variation in optical intensity, causing a small fluctuation in our measurement. This result also implies that if both modes of operation provide different results, a surface perpendicularity problem might occur on the object and our proposed non-invasive diffraction-based dimensions analyzer structure can be used to investigate this issue.**

I. INTRODUCTION

There are several optically noninvasive techniques for measuring shape and size of an object [1]. These include vibration insensitive approaches such as a time of flight method, an optical triangulation approach, a moiré technique, and a laser speckle pattern sectioning method, where a high resolution electronic controller is required and a minimum object size is limited to submillimeters. A smaller object size can also be accurately investigated by using an interferometric method but it needs a very good vibration control system. In addition, because these techniques typically operate in the reflection mode in which only one surface (e.g., front surface) of the object is analyzed, it is not appropriate to use in applications where the effect of front and back surfaces of the object (e.g., a harddisk slider) need to be taken into consideration. Hence, it would be highly desirable to have a measurement system that can determine the object dimensions in both reflection and transmission modes and it is also insensitive to the vibration.

One promising optical metrology approach is Fourier Optics [2] that can be used to analyze the object size and dimensions through its near-field or far-field diffraction pattern. Previously, it was used in a transmission mode for classifying biological cells [3], studying small cracks [4], and determining size and shape of the objects [5-6]. With this in mind, this paper proposes to simultaneously investigate the far-field diffraction patterns of the micron-size object in both reflection and transmission modes.

II. OUR PROPOSED ARCHITECTURE

Fig.1 shows our proposed non-contact diffraction-based dimensions analyzer architecture. In our scheme, an incident collimated optical beam having an operating wavelength of λ passes through an optical beam splitter (BS) where the amplitude of the optical beam is equally split into two optical beams. One optical beam is reflected by 90° to the right hand side and it is blocked by an absorber. Another optical beam travels through the BS and it partially falls on a micron-size object. In this way, part of the optical beam that hits the front surface of the object will be reflected back to the BS. It is then directed by the BS to a spherical lens (S1) where it is Fourier transformed onto a camera 1 (Cam1) located at a distant of F from the lens S1. Similarly, the remaining part of the incident optical beam will pass through all edges of the object and then a mirror (M) sends it to the Cam2 via another Fourier transform lens S2. Two recording diffraction patterns will be analyzed by an electronic control unit (ECU). By assuming that our tested object is a rectangle like a harddisk drive slider, a normalized optical intensity of the diffraction pattern in a reflection mode can be mathematically written as follows [2].

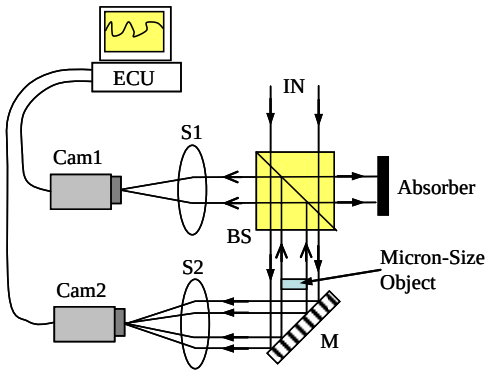

Fig.1 Our non-contact vibration-insensitive diffraction-based dimensions measurement architecture.

$$I(x,y) = K\left|\left[\frac{\sin\left(\frac{\pi d_x x}{\lambda F}\right)}{\frac{\pi d_x x}{\lambda F}}\right]\left[\frac{\sin\left(\frac{\pi d_y y}{\lambda F}\right)}{\frac{\pi d_y y}{\lambda F}}\right]\right|^2, \quad (1)$$

where K is a constant. d_x and d_y are the dimensions of the object in the x and y axes, respectively. Similarly, a normalized optical intensity of the diffraction pattern in a transmission mode can also be expressed as.

$$I(x,y) = K\left|\delta(x,y) - \left[\frac{\sin\left(\frac{\pi d_x x}{\lambda F}\right)}{\frac{\pi d_x x}{\lambda F}}\right]\left[\frac{\sin\left(\frac{\pi d_y y}{\lambda F}\right)}{\frac{\pi d_y y}{\lambda F}}\right]\right|^2. \quad (2)$$

From eqns(1) and (2), it is obvious that the object sizes along the x and y axes can be verified from the far-field diffraction pattern. The spacing between adjacent diffracted order beams also depends on λ and F.

III. Our Experimental Demonstration

We follow our proposed structure shown in Fig.1 by using a measured 638-nm wavelength laser diode with a fiber-connectorized collimator that provides a measured 3-mm 1/exp(2) output optical beam diameter with a < 0.3 mrad optical beam divergence. A camera available in our laboratory is used in our experiment having 640×480 active pixels with a pixel pitch of 8.4 μm and it is interfaced through our computer via a 10-bit frame grabber. A spherical lens has a focal length of 30 cm and our test object is a very fine and well fabricated harddisk drive slider. Its measured dimensions is 691μm × 835 μm by using a scanning electron microscope (SEM) as shown in Fig.2.

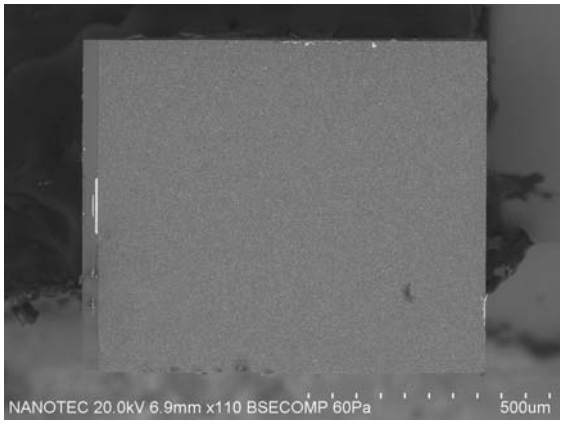

Fig. 2 SEM Image of our test object

Fig.3 shows snap shots of two far-field diffraction patterns obtained from the reflection and transmission modes. These two far-field diffraction patterns agree very well with our mathematical expressions in eqns(1) and (2). By determining the spacing between adjacent diffracted order beams and using eqn(1) or eqn(2), the length and the width of the object can be determined.

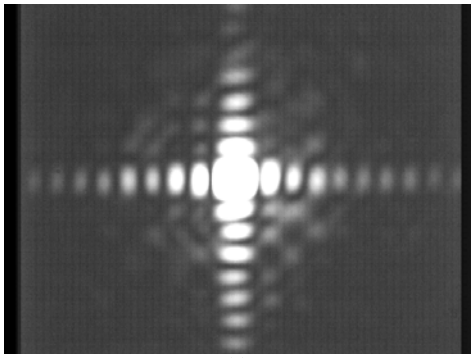

(a)

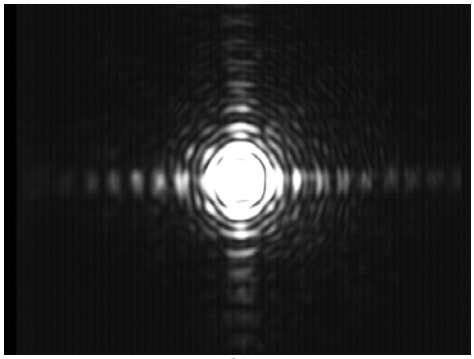

(b)

Fig.3 Far-field diffraction patterns from our rectangular object observed in (a) reflection and (b) transmission modes.

Table 1 Our Experimental Result

Modes of Operation	**Dimensions of Object from Diffracted Order Beams**			
	Left	**Right**	**Top**	**Bottom**
Reflection	690 μm	696 μm	800 μm	794 μm
Transmission	691 μm	696 μm	815 μm	800 μm

From Fig.3, as there are four wings on each diffraction pattern, the diffracted order beams on the left and right hand sides are used to determine the width of the object while the diffracted order beams on the top and bottom sides are used for calculating the length of the object. Another good thing about using this well-fabricated rectangular object as well as its Fourier transform for our analysis is the symmetry of the far-field diffraction pattern that provides an orientation invariant property. As a result, when the object is rotated, its far-field

diffraction pattern is also changed accordingly without affecting the spacing between adjacent diffracted order beams. Table 1 summarizes our calculated data, indicating that both modes of operation give similar results. This result also implies that if both modes of operation provide different results, a surface perpendicularity problem might occur on the object which more or less can affect the performance of the harddisk drive slider. Note that the surface perpendicularity of the object cannot be investigated directly from the SEM. In addition, if we compare our experimental result in Table 1 with our SEM result, there are errors of < 5 μm and < 40 μm along the width and the length of the object, respectively. These errors come from a variation in optical diffraction intensity that can affect the spacing between adjacent diffracted order beams. Hence, based on our experimental result, our proposed non-contact diffraction-based dimensions analyzer architecture is a low cost and vibration insensitive optical system that can be used to analyze the dimensions of a small object and has the possibility to examine the surface perpendicularity of the object.

IV. CONCLUSION

This paper proposes a far-field diffraction analyzer for simultaneously determining the object dimensions in both reflection and transmission modes of operation. Our experiment shows that both modes of operation give similar measuring results. In addition, if both modes of operation are employed, our far-field diffraction analyzer structure is a low cost and vibration insensitive optical system that has the possibility to indicate the surface perpendicularity problem of the object. However, a change in optical diffraction intensity has to be taken into consideration in order to reduce measuring errors. In the future, we plan to increase the number of test samples and statistically analyze our experimental result in order to clearly see the possibility of deploying it in the field.

ACKNOWLEDGEMENTS

This work is partially supported by Western Digital Corporation (Banpa-In), Thailand. Authors would also like to thank Chakkrit Supavasuthi, Krisda Siangchaew, Ittipon Cheowanish, Parot Burapachit, and Laddawan Supadee for their valuable discussions and preparing samples.

REFERENCES

[1] F. Chen, G. M. Brown, and M. Song, "Overview of three-dimensional shape measurement using optical methods," *Opt. Engg.*, Vol. 39, pp. 10-22, Jan. 2000.

[2] J. W. Goodman, *Introduction to Fourier Optics*, Mc-GrawHill, 1968.

[3] R. E. Kopp, J. Lisa, J. Mendelsohn, B. J. Pernick, H. Stone, and M. R. Wohlers, "Method for classifying biological cells," *US Patent*, 4213036, Jul. 15, 1980.

[4] X. Li, A. K. Soh, C. Huang, C. H. Yang, and H.- J. Shi, "Detection of small cracks and cavities using laser diffraction," *Opt. Engg.*, Vol. 41, pp. 1295-1308, Jun. 2002.

[5] G. Urcid and A. Padilla, "Far-field diffraction patterns of circular sectors and related apertures," *Appl. Opt.*, Vol. 44, pp. 7677-7969, Dec. 2005.

[6] A. Borovoi, E. Naats, U. Oppel, and I. Grishin, "Shape characterization of a large nonspherical particle by use of its Fraunhofer diffraction pattern," *Appl. Opt.*, Vol. 39, pp. 1989-1997, Apr. 2000.

CCCDTAs-based Versatile Quadrature Oscillator and Universal Biquad Filter

Winai Jaikla* and Montree Siripruchyanun**
*Electric and Electronic Program, Faculty of Industrial Technology,
Suan Sunandha Rajabhat University, Dusit, Bangkok, 10300, THAILAND Email: jnai2004@yahoo.com
**Department of Teacher Training in Electrical Engineering, Faculty of Technical Education,
King Mongkut's Institute of Technology North Bangkok, Bangkok, 10800, THAILAND Email: mts@kmitnb.ac.th

***Abstract*- In this article, a novel circuit, which can function both as quadrature oscillator and universal biquad filter (lowpass, highpass and bandpass functions) is introduced. The features of the circuit are that, working as quadrature oscillator, the oscillation condition and oscillation frequency can be adjusted independently with the input bias currents: functioning as universal biquad filter, the quality factor and natural frequency can be tuned orthogonally via the input bias currents: the circuit can work as either the quadrature oscillator or the universal biquad filter without changing circuit topology: it provides output signals both in current-mode and voltage-mode simultaneously. The circuit description is very simple, consisting of merely 2 Current Controlled Current Differencing Transconducatance Amplifiers (CCCDTAs), 1 voltage buffer and 2 grounded capacitors. Without any external resistors and using only grounded elements, this circuit is then suitable for IC architecture. The PSPICE simulation results are depicted. The given results agree well with the theoretical anticipation. The circuit was biased with ±1.5V supply voltages.**

***Index Terms*- Biquad filter, Current-mode, CCCDTA**

I. INTRODUCTION

An oscillator and a filter are 2 basic important building blocks which are frequently employed in electrical engineering works. A quadrature oscillator is widely used because the circuit provides two sinusoids with 90° phase difference, as for example in telecommunications for quadrature mixers and single-sideband [1]. In similar, nowadays, the applications and advantages in the realization of various active transfer functions, called as universal biquad filters, have received considerable attention. A universal filter may be used in phase locked loop FM stereo demodulators, and crossover networks used in three-way high fidelity loudspeakers [2]. However, a current-mode universal filter has being been more popular than voltage-mode one. This is due to operating in low-voltage environment as in portable and battery-powered equipment. Since a low-voltage operating circuit becomes necessary, the current–mode technique is ideally suited for this purpose more than the voltage-mode one. Presently, there is a growing interest in synthesizing the current-mode circuits because of more their potential advantages such as larger dynamic range, higher signal bandwidth, greater linearity, simpler circuitry and lower power consumption [3]. However, from our investigations, there are seen that the previous literatures have proposed the universal filters and the quadrature oscillators require too many components and component matching conditions [4]. Some universal filters require floating capacitors, which is not ideal for IC implementation [5]. In addition, each circuit can work only one function, either quadrature oscillator or universal filter. Recently, the versatile quadrature oscillator and biquad filter using current controlled current differencing buffered amplifier (CCCDBA) was proposed [6]. Unfortunately, it is rather complicated topology, due to consisting of 3 CCCDBAs and 2 grounded capacitors, which results in low frequency of operation and high power consumption.

The purpose of this paper is to introduce a current-mode universal biquad filter, based on CCCDTA as the active building block recently proposed in [7], providing three standard transfer functions (lowpass, highpass and bandpass). The natural frequency can be adjusted independently from the quality factor. Moreover, in case of no input current and appropriated condition, the proposed circuit can provide quadrature sinusoidal signals in both voltage-mode and current-mode simultaneously. The circuit construction consists of 2 CCCCTAs, 1 voltage buffer and 2 grounded capacitors. The PSPICE simulation results are also shown, which are in correspondence with the theoretical analysis.

II. CIRCUIT PRINCIPLE

A. The Current Controlled Current Differencing Transconductance Amplifier (CCCDTA)

Since the proposed circuit is based on CCCDTAs, a brief review of CCCDTA is given in this section. Basically, the CCCDTA is composed of translinear elements, mixed loops and complementary current mirrors. Generally, CCCDTA properties are similar to the conventional CDTA, except that input voltages of CCCDTA are not zero and the CCCDTA has finite input resistances R_p and R_n at the p and n input terminals, respectively. These parasitic resistances are equal and can be controlled by the bias current I_{B1} as shown in Eq. (1)

$$\begin{bmatrix} V_p \\ V_n \\ I_z \\ I_x \end{bmatrix} = \begin{bmatrix} R_p & 0 & 0 & 0 \\ 0 & R_n & 0 & 0 \\ 1 & -1 & 0 & 0 \\ 0 & 0 & 0 & \pm g_m \end{bmatrix} \begin{bmatrix} I_p \\ I_n \\ V_x \\ V_z \end{bmatrix}. \quad (1)$$

When $$R_p = R_n = \frac{V_T}{2I_{B1}} \quad (2)$$

and $$g_m = \frac{I_{B2}}{2V_T}. \quad (3)$$

Where g_m is the transconductance of the CCCDTA and V_T is the thermal voltage. The symbol and the equivalent circuit of the CCCDTA are illustrated in Figs. 1(a) and (b), respectively.

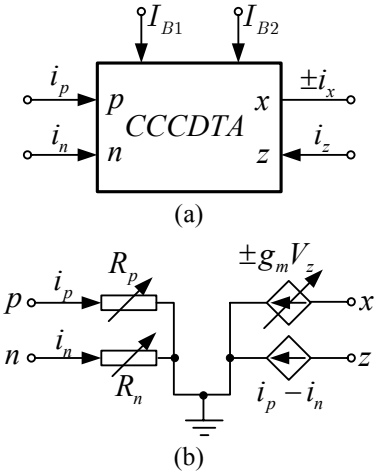

Figure 1. CCCDTA (a) Symbol (b) Equivalent circuit.

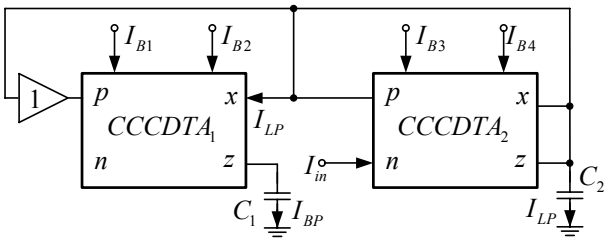

Figure 2. Proposed circuit working as universal filter

B. The operation of proposed circuit working as a universal biquad filter

Fig. 2 demonstrates the circuit scheme of the proposed circuit working as the universal filter. The depicted bias currents; I_{B1}, I_{B2}, I_{B3} and I_{B4} are respectively the input bias currents of CCCDTA1 and CCCDTA2. From the circuit and the CCCDTA properties in section A including routine analysis, the following current transfer functions are obtained

$$\frac{I_{HP}}{I_{in}} = \frac{s^2}{s^2 + \left(\frac{2}{R_{p2}} - g_{m2}\right)\frac{s}{C_2} + \frac{g_{m1}}{R_{p1}C_1C_2}}, \quad (4)$$

$$\frac{I_{LP}}{I_{in}} = \frac{g_{m1}/C_1C_2R_{P1}}{s^2 + \left(\frac{2}{R_{p2}} - g_{m2}\right)\frac{s}{C_2} + \frac{g_{m1}}{R_{p1}C_1C_2}}, \quad (5)$$

$$\frac{I_{BP}}{I_{in}} = \frac{s/C_2R_{P1}}{s^2 + \left(\frac{2}{R_{p2}} - g_{m2}\right)\frac{s}{C_2} + \frac{g_{m1}}{R_{p1}C_1C_2}}. \quad (6)$$

From Eqs. (4)-(6), the parameters ω_0 and Q_0 can be expressed as

$$\omega_0 = \sqrt{\frac{g_{m1}}{R_{P1}C_1C_2}}, \quad (7)$$

$$Q_0 = \omega_0 \frac{C_2}{(2/R_{P2}) - g_{m2}}. \quad (8)$$

For easy consideration, if $I_{B1}=I_{B2}=I_B$ and $C_1=C_2=C$, Eqs. (7) and (8) can be reduced to

$$\omega_0 = \frac{I_B}{V_TC}, \quad (9)$$

$$Q_0 = \frac{I_B}{4I_{B3} - (I_{B4}/2)}. \quad (10)$$

It is obviously found that, from Eqs. (9) and (10), the quality factor can be adjusted by I_{B3} or I_{B4} without affecting the pole frequency. Reversely, the pole frequency can be controlled via I_B. In addition, bandwidth (BW) of the system can be expressed by

$$BW = \frac{\omega_0}{Q_0} = \frac{4I_{B3} - (I_{B4}/2)}{V_TC}. \quad (11)$$

In the same view, the bandwidth can be linearly tuned by I_{B3}. Another advantage of the proposed circuit is that the high Q_0 circuit can be obtained by setting $I_{B4}/2$ close to $4I_{B3}$, which differs from conventional universal filters in such that the maximum Q_0 is limited by component values.

C. Circuit Sensitivities

The sensitivities of the proposed circuit are low and can be found as

$$S_{I_B}^{\omega_0} = 1;\ S_C^{\omega_0} = -1, \quad (12)$$

and

$$S_{I_B}^{Q_0} = 1;\ S_{I_{B3}}^{Q_0} = \frac{-4I_{B3}}{4I_{B3} - (I_{B4}/2)},\ S_{I_{B4}}^{Q_0} = \frac{I_{B4}}{8I_{B3} - I_{B4}}. \quad (13)$$

D. The operation of proposed circuit working as a quadrature oscillator

If no input current applied to the circuit as shown in Fig. 3, system characteristic equation can be expressed as

$$s^2 + \left(\frac{2}{R_{p2}} - g_{m2}\right)\frac{s}{C_2} + \frac{g_{m1}}{R_{p1}C_1C_2}. \quad (14)$$

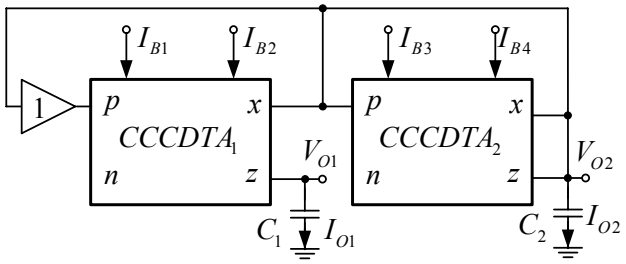

Figure 3. Proposed circuit working as quadrature oscillator

From Eq. (14), it can obviously be seen that the proposed circuit can be set to be an oscillator if

$$\frac{2}{R_{p2}} = g_{m2}. \quad (15)$$

Eq. (15) is called as condition of oscillation, this is achieved by $I_{B3}= I_{B4}/8$, then the oscillation frequency of this system can be obtained as

$$\omega_0 = \sqrt{\frac{g_{m1}}{R_{P1}C_1C_2}}. \quad (16)$$

If letting $I_{B1}=I_{B2}=I_B$ and $C_1=C_2=C$, Eq. (16) can be reduced to

$$\omega_0 = \frac{I_B}{V_T C}. \quad (17)$$

It can be seen that the oscillation frequency (ω_0) can be linearly controlled by bias current.

Furthermore, the quadrature sinusoidal signals can be simultaneously obtained at I_{O1} and I_{O2} or V_{O1} and V_{O2} as seen in Fig. (3), in current-mode and voltage-mode, respectively. The free terminals of I_{O1} and I_{O2} can be achieved by using multiple Z-terminal output CCCDTAs.

E. Non-ideal case

For non-ideal case, the I_z and I_x of CCCDTA can be respectively characterized by

$$I_z = \alpha_p I_p - \alpha_n I_n, \quad (18)$$

and

$$I_x = \beta V_z. \quad (19)$$

Where α_p, α_n and β are transferred error values deviated from one. In the case of non-ideal and brief consideration, the ω_0 and Q_0 are changed to

$$\omega_0 = \sqrt{\frac{\alpha_p\beta_1\beta_b g_{m1}}{R_{p1}C_1C_2}}, \quad (20)$$

$$Q_0 = \omega_0 \frac{C_2}{\left(1+\alpha_{p2}\right)/R_{P2} - \beta_2 g_{m2}}. \quad (21)$$

III. Simulation Results

To prove the performances of the proposed circuit, the PSPICE simulation program was used for the examination. The PNP and NPN transistors employed in the proposed circuit were simulated by respectively using the parameters of the PR200N and NR200N bipolar transistors of ALA400 transistor array from AT&T [6]. Fig. 4 depicts schematic description of the CCCDTA used in the simulations, the ideal voltage buffer was used in the simulations. The CCCDTAs were biased with ±1.5V power supplies, the capacitor values of C_1 and C_2 are 1nF. Firstly, the operation as the universal biquad filter is verified. The gain responses of the proposed universal filter are shown in Fig. 5. It shows that the proposed filter obtains LP, HP and BP responses at the same time. By varying I_{B4} to 100μA, 200μA and 3000μA, only the quality factor is changed as shown in Fig. 6. Therefore, it is confirmed that the quality factor can be adjusted by I_{B3} or I_{B4} which is linearly independent of the pole frequency, as mentioned.

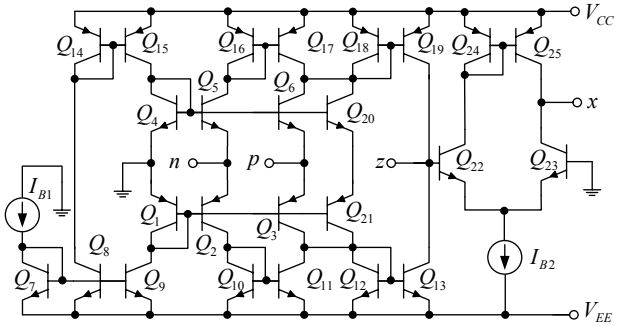

Figure 4. Internal construction of CCCDTA

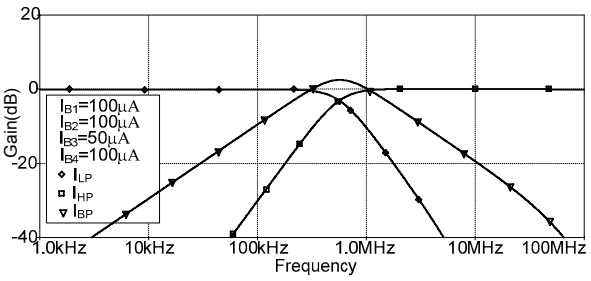

Figure 5. Gain response of the proposed circuit working as universal biquad filter

Fig. 7, 8 and 9 show the responses when operating as quadrature oscillator, where the total harmonic distortion (THD) is about 1.12% and the maximum operating frequency is approximately 1.58MHz.

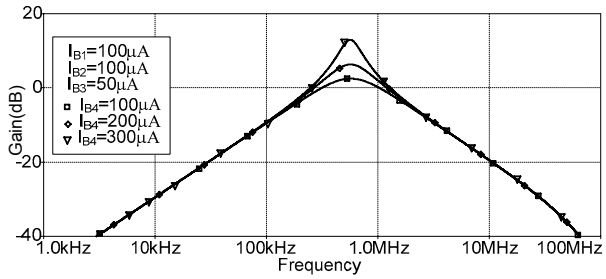

Figure 6. BP response when I_{B3} is varied

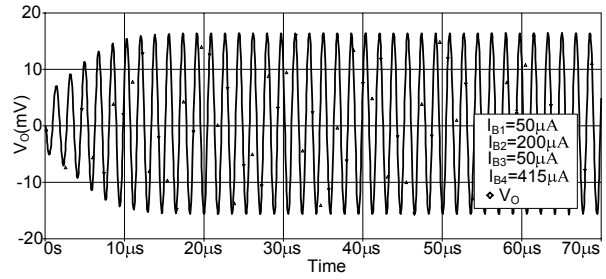

Figure 7. The simulation results of waveforms when working as quadrature oscillator

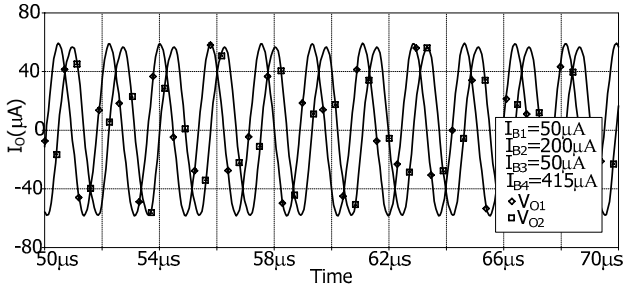

Figure 8. The simulation results of current waveforms of quadrature oscillator

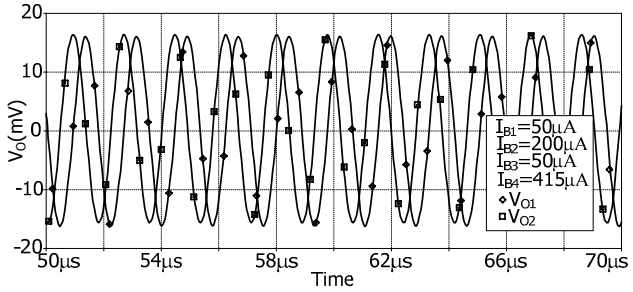

Figure 9. The simulation results of voltage waveforms of quadrature oscillator

IV. CONCLUSION

The novel circuit, which can function both as quadrature oscillator and current-mode universal biquad filter has been presented. The proposed circuit can work as either the quadrature oscillator or the universal biquad filter without changing a circuit topology. Working as current-mode universal biquad filter, the quality factor and pole frequency can be tuned orthogonally via the input bias currents. When no input current and suitable condition, the proposed circuit can function as a quadrature oscillator. Its oscillation condition and oscillation frequency can be adjusted independently with the input bias currents. It can provide quadrature sinusoidal signals in both voltage-mode and current-mode simultaneously. The PSPICE simulation results are well agreed with the theoretical anticipation with maximum power dissipation of 1.03mW at ±1.5V supply voltages. Since it consists of merely 2 CCCCTAs, 1 voltage buffer and 2 grounded capacitors, this circuit is then suitable for an IC architecture.

REFERENCES

[1] I. A. Khan and S. Khawaja, "An integrable gm-C quadrature oscillator," *Int. J. Electronics*, vol. 87, no. 1, pp.1353-1357, 2000.

[2] M. A. Ibrahim, S. Minaei and H.A. Kuntman, "A 22.5 MHz current-mode KHN-biquad using differential voltage current conveyor and grounded passive elements," *Int. J. Electron. Commun. (AEU)*, vol. 59, pp. 311-318, 2005.

[3] C. Toumazou, F.J. Lidgey and D.G. Haigh, *Analogue IC design: the current-mode approach*, Peter Peregrinus, London, 1990.

[4] C. Toumazou and F.J. Lidgey, "Universal active filter using current conveyors," *Electronics Letters*, vol. 22, pp.662-664, 1986.

[5] M. Sagbas, and K. Fidanboylu, "Electronically tunable current-mode second-order universal filter using minimum elements," *Electronics Letters*, vol. 40, no. 1, pp.2-4, 2004.

[6] W. Jaikla and M. Siripruchyanan, "A Versatile Quadrature Oscillator and Universal Biquad Filter Using CCCDBAs," *Proceedings of ECTI con 2006,* Ubon-ratchathani, Thailand, pp.501-504, May 2006.

[7] W. Jaikla and M. Siripruchyanun, "Current Controlled Current Differencing Transconductance Amplifier (CCCDTA): A New Building Block and Its Applications," *Proceedings of ECTI conference 2006,* Ubon-ratchathani, Thailand, pp. 348-351, May 2006.

[8] D. R. Frey, "Log-domain filtering: an approach to current-mode filtering," *IEE Proc. Circuit Devices Syst.*, Vol. 140, pp.406-416, 1993.

A Study of Optical Phase Retardation and Absorption Measurement by using a Fiber Loop Mirror Architecture

Kanitha Katanyukunanon[1], Sarun Sumriddetchkajorn[2], and Toemsak Srikhirin[1]

[1]Department of Physics, Faculty of Science, Mahidol University
272, Rama VI Rd., Phayathai, Ratchathewi, Bangkok 10400, Thailand

[2]Photonics Technology Laboratory
National Electronics and Computer Technology Center (NECTEC)
National Science and Technology Development Agency (NSTDA)
112 Thailand Science Park, Phahonyothin Rd., Klong 1, Klong Luang, Pathumthani 12120, Thailand

***Abstract* – This paper proposes and experimentally demonstrates a fiber-connectorized optical system that can be used to study both the optical transmittivity and phase retardation of the material. Our key idea comes from the inherent advantage of the fiber loop mirror (FLM) in which all optical components are easily connected to each other without the need of a precise free-space optical alignment. In addition, its two output optical powers can be controlled via adjusting the phase retardation inside the FLM. Our experimental proof of concept using three known waveplates shows promising results which agree very well with our theoretical analysis.**

I. INTRODUCTION

A variety of optical sensing structures has been proposed and demonstrated for measuring some optical properties of materials. For example, an optical absorption coefficient (α) can be determined by using a typical optical spectrometer [1] where the optical power emerging from the test material is compared to the incident optical beam power, also called the optical transmittivity. Apart from the α of the material, another interesting parameter of the material is its birefringence (Δn) which tells us how different states of polarized lights refract into the material and suffer different phase delay. It is sometimes mentioned as a phase retardation ($\Delta\phi$) as well. In this case, another instrument such as a polarimeter is needed. With this in mind, it is obvious that only one equipment can handle in measuring only one interesting parameter. In addition, these instruments are designed and implemented in a free-space architecture and therefore a precise free-space optical alignment is a very important issue. Hence, it would be desirable to have a fiber-based optical instrument in which more than one parameters (e.g., both optical transmittivity and $\Delta\phi$) can be investigated.

One of the promising fiber-based optical structures is the fiber loop mirror (FLM) [2]. Since its invention in 1988, it has been proposed and experimentally demonstrated for optical fiber current sensors [3], liquid-level sensors [4], microwave filters [5], and multiwavelength 2x2 add-drop switches [6]. Based on the operating principle of the FLM, this paper proposes and experimentally demonstrates how the FLM structure can be explored in investigating both the optical transmittivity and the $\Delta\phi$ of the material [7].

II. OUR PROPOSED ARCHITECTURE

Fig.1 shows our proposed FLM-based absorption and phase retardation measurement structure. In our proposed FLM-based structure, an optical beam is fed in at the IN port and it passes through a fiber-optic circulator where the optical beam is allowed to go from the left to the right hand sides. Once the optical beam comes out of the fiber-optic circulator, it then travels to a 2x2 fiber-optic coupler in which its amplitude is split into two equal amplitude optical beams. In this case, one optical beam travels clockwise passing through a polarization controller (PC) and two fiber-optic collimators. Another optical beam also travels anticlockwise passing two fiber-optic collimators and then the PC.

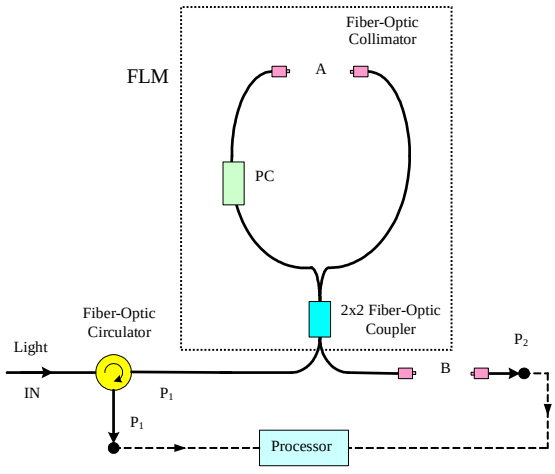

Fig. 1 Our proposed FLM-based optical absorption and phase retardation measurement architecture.

From the basic operation of the FLM, the relationship between output optical powers at the port1 and port2 can be written as follows [2].

$$\frac{P_1}{P_1+P_2} = 4K(1-K)|J|^2, \quad (1)$$

and

$$\frac{P_2}{P_1+P_2} = 1-4K(1-K)|J|^2, \quad (2)$$

where

$$J = e^{j\Delta\phi}\sin^2\theta + \cos^2\theta. \quad (3)$$

Here, θ is the orientation angle of the phase retardation plate and K is the coupling ratio of the 2x2 fiber-optic coupler. Δϕ is equal to 2πLΔn/λ and it is the phase retardation between the ordinary and extraordinary rays. Δn is the birefringence of the material (e.g., an optical fiber), L is the length of the optical fiber, and λ is the operating wavelength.

This basic FLM operation implies that if we have a test sample inside the FLM (i.e., at A), the Δϕ of the sample can inherently determined by just rotating the test sample on the plane normal to the propagation direction of the optical beam and then measuring the optical power ratio expressed in eqn(1) or eqn(2). Apart from the Δϕ of the test sample, the optical transmittivity of the test sample can also be investigated by just inserting the test sample at the position B outside the FLM and initially adjusting the FLM in such a way that we obtain the maximum P_2. These two operations indicate that both the optical transmittivity and the Δϕ of the test sample can be studied in our proposed FLM-based architecture.

III. Our Experimental Demonstration

To verify our proposed FLM-based absorption and phase retardation measurement concept, our experimental setup is shown in Fig.2. In this case, a tunable laser diode in the C-band telecomm region is connected to the fiber-optic circulator via a fiber-connectorized/angle polished contact (FC/APC) adapter. A 2x2 fiber-optic coupler having K of 50% splitting ratio is also employed. Two mechanically controlled PCs (e.g., PC1 and PC2) are inserted inside the FLM in order to easily and initially adjust the appropriate Δϕ of the FLM. In addition, a photodetector (PD) is used to measure both the output optical powers P_1 and P_2. In our experiment, we also use three known zero-order waveplates as our test samples and they are situated on a rotational stage having 2.5 deg per step. The first two known zero-order waveplates are the quarter waveplate (QWP1) (i.e., a 90-deg waveplate) and the half waveplate (HWP1) (i.e., a 180-deg waveplate) designed to operate at a 1550-nm wavelength [8]. The last one is the HWP designed to operate at a 632.8-nm (HWP2). For our optical absorption analysis, we initially adjust the two PCs inside the FLM such that we have a maximum optical output power at the port2.

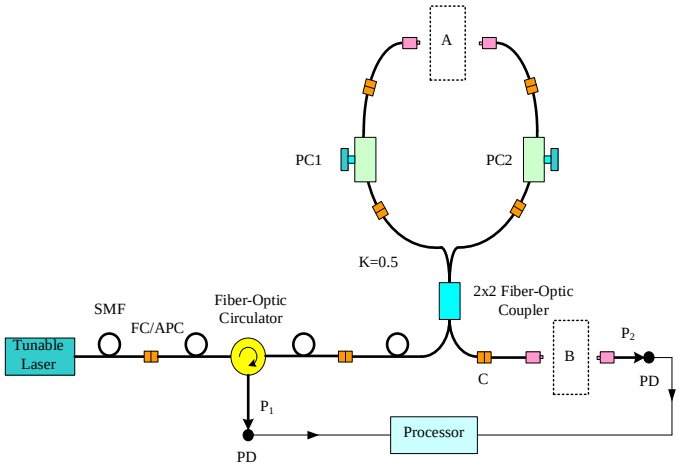

(a)

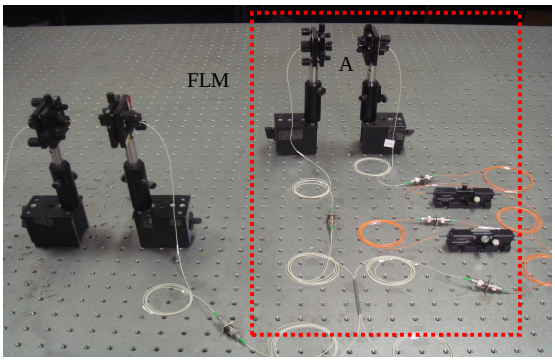

(b)

Fig. 2 (a) Schematic illustration of our experimental setup and (b) photograph of our experimental setup taken at the FLM section. SMF: Single mode optical fiber.

Before testing the sample, we have to make sure that there is less amount of the optical beam reflected back from the FLM to the port1. This can be analyzed by looking at the optical isolation of the system and it is defined as the ratio between the output optical power at the port2 and the output optical power at the port1. In this case, the measured optical isolation is 33.1±1.2 dB over a 20 nm wavelength band. In other words, the ratio of P2 and P1 in our proposed FLM-based absorption and phase retardation measurement architecture is about 2089 which is high enough for investigating the test samples. The optical less of our proposed FLM-based absorption and phase retardation measurement architecture is also an important system issue. A measured optical loss of 2.47 dB is determined and it is limited by eight FC/APC adapters (0.2 dB), a one-way trip through the fiber-optic circulator (0.5 dB), two PCs (0.13 dB), and free-space coupling efficiency at the locations A and B (1.64 dB). Another important system issue is the polarization dependent loss (PDL). In this case, by scrambling the state of polarization of the input light in front of the fiber-optic circulator, a measured PDL of 0.38 dB is obtained.

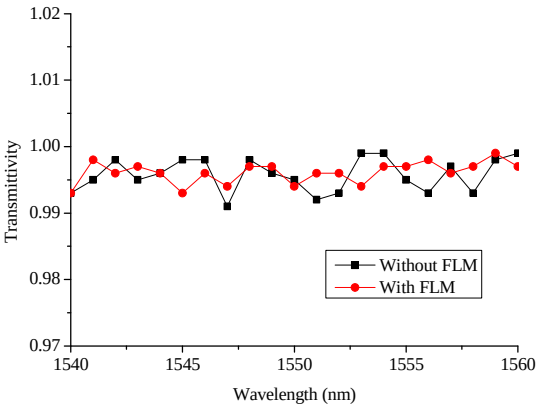

(a)

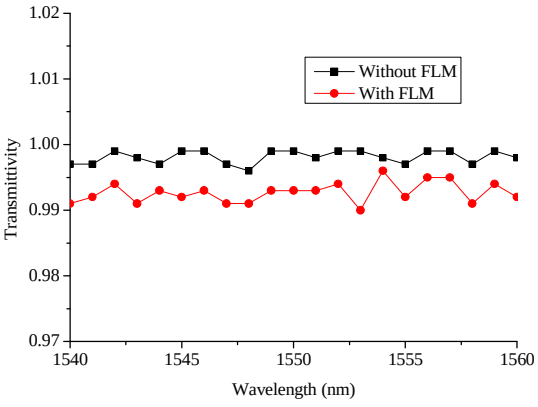

(b)

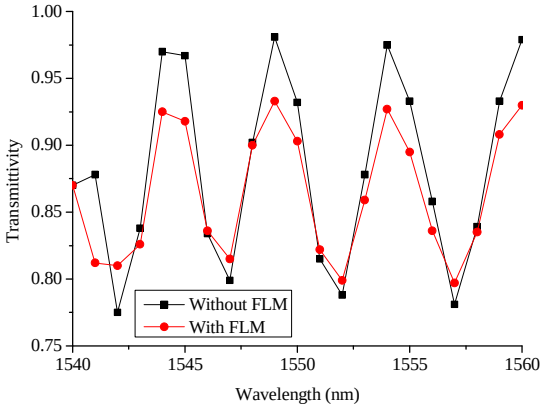

(c)

Fig. 3 Measured optical transmittivity versus operating wavelength for (a) QWP1, (b) HWP1, and (c) HWP2.

Later on, we place the test sample at the position B and our measured optical transmittivities are shown in Fig.3. We also compare our experimental results obtained from our proposed

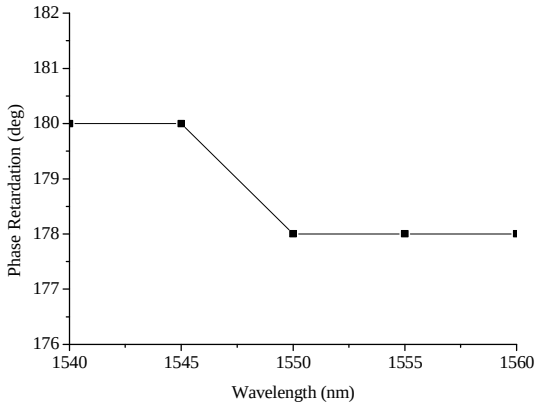

(a)

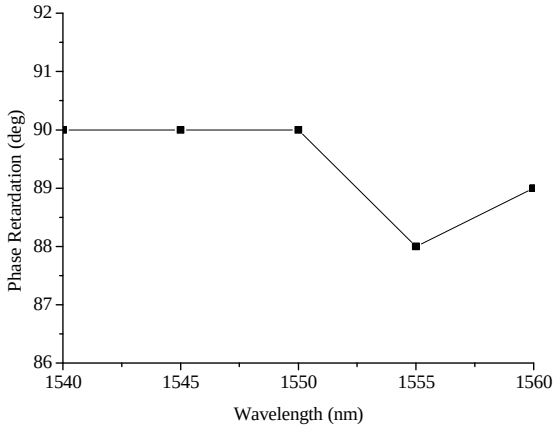

(b)

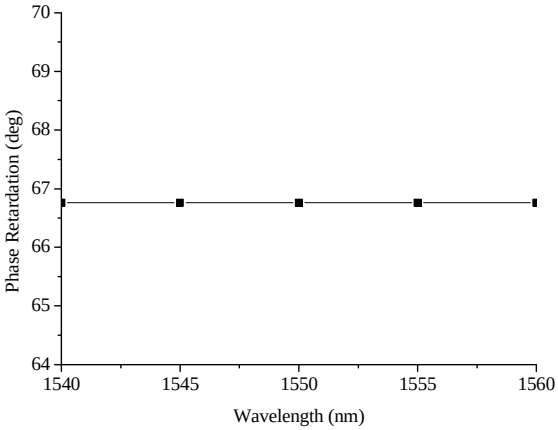

(c)

Fig. 4 Measured optical phase retardation versus operation wavelength for (a) QWP1, (b) HWP1, and (c) HWP2.

FLM-based absorption and phase retardation measurement architecture with a typical spectrometer architecture. This can be done by just connecting the tunable laser directly at the position C. It can be observed that our experimental results for the HWP1 and QWP1 obtained from both architectures have less than 0.84% difference in measured optical transmittivity. For the HWP2, a variation of the measured optical transmittivities versus operating wavelength is much higher compared to the previous two samples. This is because at the 1540-1560 nm operating wavelength, the HWP2 which is optimally designed to operate at the 632.8 nm with a low optical loss value induces the Fabry-Perot interference effect. The FLM also pays an important role in inducing the optical loss in the structure and therefore a higher 6.6% difference in measurement between the two architectures is obtained. In addition, there is a very small < 0.9% fluctuation in our measured optical transmittivity values, limited by a < 3% accuracy of our PD used in our experiment [9].

For our $\Delta\phi$ analysis of the test sample, we initially adjust the two PCs inside the FLM so that we have a maximum reflected optical power at the port1. Then we insert our test sample at the position A and rotate it from 0 to 45 deg. Fig. 4 shows our $\Delta\phi$ measurement which agrees quite well with our theoretical analysis. There is also a 2 deg difference between our experimental results and the expected values and it is limited by our rotational stage. Note that for the HWP2, its phase retardation is reduced to 0.191x360 = 68.7 deg at the 1550 nm wavelength [10]. By varying the operating wavelength, $\Delta\phi$ values with a small error of < 2 deg are achieved, pointing out that our waveplate samples are indeed zero-order waveplates.

IV. CONCLUSIONS

We have proposed and experimentally demonstrated an FLM-based optical absorption and phase retardation measurement structure. Our key idea comes from the use of the inherent FLM operation, allowing the flexibility to control the optical output powers via varying phase retardation inside the FLM. Without the test sample, our proposed FLM-based absorption and phase retardation measurement system offers a very high measured optical isolation of 33.1 dB, a 2.47 optical loss, and a PDL of 0.38 dB. Our experimental demonstration using three known zero-order waveplates shows promising results associated with the expected values. Our experiment also confirms that these three waveplates are designed as zero-order waveplates. For our optical transmittivity study, our experimental result from the FLM-based structure corresponds to the result obtained from a non FLM system. In the future, we plan to test the performance of our FLM-based absorption and phase retardation measurement structure with other samples.

ACKNOWLEDGMENT

This work is financially supported by the National Electronics and Computer Technology Center. Kanitha Katanyukunanon would also like to thank the Thailand Graduate Institute of Science and Technology for the financial support during her study.

REFERENCES

[1] B. Henderson, "Optical spectrometers," Chap. 20 in *Handbook of Optics*, Vol. II, M. Bass, E. W. Van Stryland, D. R. Williams, and W. L. Wolfe, Eds., McGraw-Hill, 1995.

[2] D. B. Mortimore, "Fiber loop reflectors," *J. of Lightwave Technol.*, Vol. 6, pp. 1217-1224, 1988.

[3] J. Blake, P. Tantaswadi, and R. T. De Carvalho, "In-line Sagnac interferometer current sensor," *IEEE Trans. on Power Del.*, Vol. 11, No. 1, pp. 116-121, 1996.

[4] D. Bo, Z. Qida, L. Feng,G. Tuan, Z. Lifang, L. Shuhong, and G. Hong, "Liquid-level sensor with a high-birefringence-fiber loop mirror," *Appl. Opt.*, Vol. 45, No. 30, pp. 7767-7771, 2006.

[5] E. H. W. Chan and R. A. Minasian, "Sagnac-loop-based equivalent negative tap photonic notch filter," *IEEE Photon. Technol. Lett.*, Vol. 17, No. 8, pp. 1740-1742, 2005.

[6] S. Sumriddetchkajorn and N. A. Riza, "Fiber-connectorized multiwavelength 2×2 switch structure using a fiber loop mirror," *Opt. Commun*., Vol. 175, pp. 89-95, 2000.

[7] S. Sumriddetchkajorn, "Absorption and phase retardation measurement in a fiber-loop mirror configuration," *Thailand Patent Application*, 2007.

[8] Product Catalog, Thorlabs, Inc., 435 Route 206, North Newton, New Jercy, USA, 07860.

[9] 818-IR Detector Specifications, Newport Corporation, 150 Long Beach Blvd., Stantford, Connecticut, USA, 2006/2007.

[10] L. Xanthe, Private Communication, CASIX, Inc., P. O. Box 1103, Fuzhoum Fujian 350014, China, Feb. 2007.

Ultrasonic Reflection Tomography Using Frequency-Centroid Shift Method

T. Onemanisone[1], C. Pintavi rooj[1], K. Wong-ek [2], S. Sangworasilp[1]
[1]Biomedical Signal and Image Processing Laboratory
Research Center for communication and Information Technology (ReCCIT)
Department of Electronics, Faculty of Engineering
King Mongkut's Institute of Technology Ladkrabang, Bangkok, Thailand.
[2] Department of Medical Technology, Faculty of Allied Health Science,
Thammasat University, Pratumthanee, Thailand
jackki_lucky@hotmail.com, kpchucha@kmitl.ac.th.

***Abstract*- The application of parametric spectral analysis for attenuation estimation on the reflected ultrasound signal of soft biological tissue. The attenuation coefficient used to estimate the projection data which used to reconstruct the image model. Tomogram of the soft tissue can be reconstructed by using its projections resolved from the ultrasonic broadband pulsed waves which pass through the tissue. While a data from ultrasonic transmission mode tomography cannot be used to image the character of soft tissue where shadowed by a bone, an ultrasonic reflection mode tomography is realized to be a solution for this. There are many ways to extract the projections, in most case the attenuation coefficient, of the tissue from the pulsed wave. Almost all of these methods were proved to implement with the transmission mode signal, but however, some adaptation may takes benefit from those method to implement with the reflection mode. We choose the spectral centre-frequency or centroid shift method to be analyzed because its advantage in a computational viewpoint. The simple filtered back-projection algorithm was implemented to reconstruct the tomographic images of the soft tissue suffered by bone. The results show the successful of this method over the transmission mode tomography.**

I. INTRODUCTION

The measurement of acoustic attenuation in biological tissue has received much interest in the field of ultrasound tissue characterization. Over the past decade, several clinical applications have shown a correlation between attenuation values and pathological states. For most biological tissues, the attenuation appears to be almost linearly dependent on frequency in the range of medical frequencies. Therefore, spectral analysis may lead to an estimation of attenuation. Generally, the attenuation estimation uses spectral methods. Many methods based on pulse echo techniques have been proposed for the estimation of the attenuation coefficient. They are based on either a time domain or a frequency domain processing of the reflected pulses. Then the ultrasonic computed tomography has an advantages over the X-ray computed tomography in some viewpoint; not only it is considered to be safer for a patient, but also we can record its waveform in the function of time and convert into function of frequency for spectrum analysis. However, the major problems of the ultrasound are expanded into two cases. Firstly, the diffraction and refraction of the ray while it get through the interfaces of the tissue where having difference reflective indexes make it travels not in the straight line, so we cannot use the line integral geometry as in the X-ray case. The approaches to this problem are somewhat more complicate, known as the Fourier diffraction theorem [6] and the filtered back-propagation algorithm [7]. But anyway, we still can use the straight line integration if we assume the soft biological tissue having a little change in the refractive index. But, the reflected pulse also contains the character of the tissue; brings us a possibility to utilize this waveform.

The conventional pulse-echo B-scan imaging [5] is one method that use the reflected pulse for reconstruct the tomogram, but the image only shows the interfaces of tissue, not the local properties of it. In the other hand, the ultrasonic transmission mode can image the local properties such as the refractive index or the attenuation coefficient of the tissue from the received pulse, many methods was reviewed in [3]. Recently, we used the reflected pulse to find the integrated attenuation coefficient using the linear least-square fitting method [1]. The simulated results show how the reflection mode superior over the transmission mode tomography where the tissue is shadowed by a bone.

II. REFLECTION-MODE ULTRASONIC TOMOGRAPHY

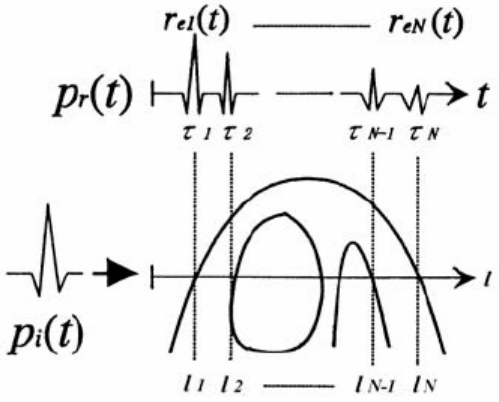

Figure 1. The waveform of incident and reflected pulse. Where the reflections occur at the tissue interfaces.

When the specimen is issued by the broadband ultrasonic pulse $p_i(t)$, the reflection of the pulse will occur every time it passes each interface where the refractive indexes are difference, subsequently return us the attenuated waveform pr(t) as illustrated in figure 1. Only the latest pulse in the waveform or $r_{en}(t)$ that we need, because it passes the entire tissue's length from l_1 to l_N and reflected at the N^{th} interface. The equations for the reflected waveform and concern parameters are written below. Keep in mind that we never know about the character of the reflectance and transmittance between each layer.

$$P_r(t) = \sum_{n=1}^{N} r_{en}(t) \tag{1}$$

$$r_{en}(t) = \sqrt{R_n}\left(\prod_{k=1}^{n-1} T_K\right) \times P_i(t-\tau_n) \times e^{-2\int_{l_1}^{l_N} \alpha(x,y,f_0)dl} \tag{2}$$

Where R_n and T_K are the reflectance and transmittance of the power at the n^{th} interface, τ_n is the delay time corresponding to the distance from the transducer to the n^{th} interface, and $\alpha(x, y, f)$ is the frequency-dependent attenuation coefficient of the tissue at coordinate (x, y). The latest reflected pulse must be converted to be in the frequency domain as shown in equation 3

$$R_{eN}(f) = \sqrt{R_N}\left(\prod_{K=1}^{N-1} T_K\right) \times P_i(f) \times e^{-2\int_{l_1}^{l_N} \alpha(x,y,f)dl} \times e^{-2j\int_{l_1}^{l_N} \beta(f)dl} \tag{3}$$

Where $\beta(f)$ is the phase shift of the reflected pulse $R_{eN}(f)$ and $P_i(f)$ is the incident pulse insonified along the object; T_K and R_N are transmittance and reflectance respectively which are never known for the case.

III. Evaluation of Attenuation Coefficient and Projection Data.

The latest ultrasound signal $r_{en}(t)$ reflected by a biological tissue is digitized with a sampling interval $\Delta t = 1/F_S$ in N samples (F_S is the sampling frequency, T is the signal duration). On this signal $r_{en}(t)$, a window of T_W seconds (N_W samples) is shifted with a constant step T_r (N_r samples). In each window centered at position τ_i, the spectrum is evaluated with a spectrum estimator and we estimate the center frequency or spectral centroid defined by

$$f_C(\tau_i) = \frac{m_1(\tau_i)}{m_0(\tau_i)} \tag{4}$$

Where

$$m_j(\tau_i) = \int_{-\infty}^{+\infty} f^i . R_{en}(\tau_i, f) df \tag{5}$$

Due to the random position of scatters in the medium, the output of the estimator fluctuates. The variance of the estimate is reduced by averaging the spectra of incident pulse independent (uncorrelated) the lasted pulse and/or echo signals.

With the classical assumption of a linear-with-frequency attenuation:

$$\alpha(x, y, f) = \beta(x, y).f \tag{6}$$

Where α is varied along to x and y axis with which attenuates by frequency f which equals to β then multiplied by frequency f; the system of this equation shows that they are the relation of linear-with-frequency attenuation which can be reviewed the detail in [2]. While the centroid-shift obtained as :

$$\beta = \frac{-8.68}{c\sigma^2(\tau)} \times \frac{df_C}{d\tau} \tag{7}$$

Where df_c is the spectral center-frequency which differ by the time $d\tau$ both of relation are expressed in *(MHz/s)*, then c is denoted for the speed of ultrasound in the tissue which is expressed in *(m/s)*; and finally, $\sigma^2(\tau)$ is Spectral variance of ultrasonic pulse in function of time, is expressed in *(MHz^2)*. Furthermore, the process of deriving the projection data shown as figure 2,

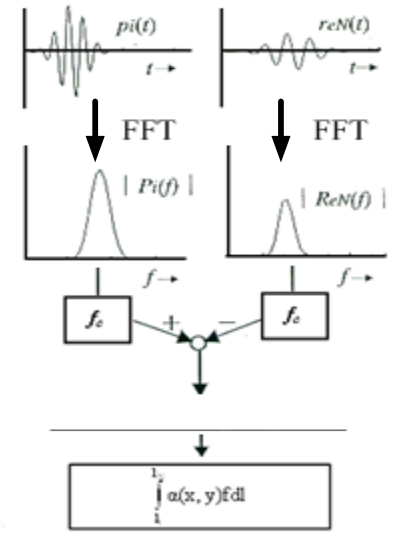

Figure 2. The process of derive the projection data

Figure 2 shows the process of deriving the projections where $p_i(t)$ and $r_{eN}(t)$ are the incident and the reflected pulse. Both Signals are converted into frequency domain by taking Fast Fourier Transform. The power spectrum is then computed. The spectrum centroid for each spectrum, equation (5), is derived. Then the centroid shift (df_c) between both spectrum can be computed Finally, the integration of attenuation coefficient β along the ultrasonic path is derived from equation (7) which is the a projection to be used in the reconstruction process.

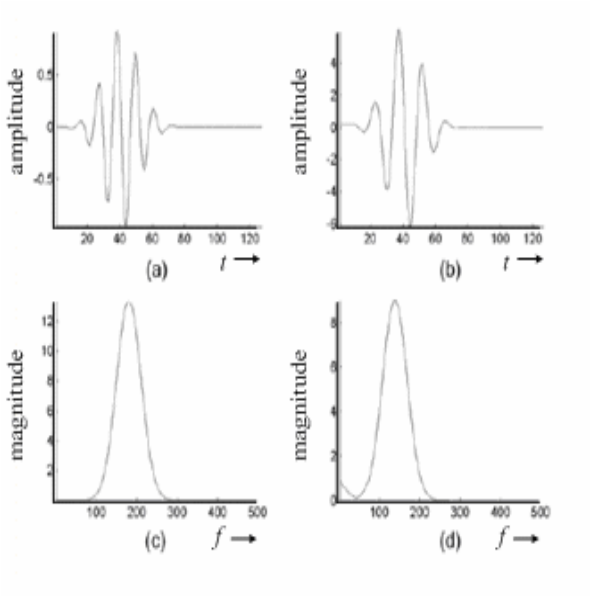

Figure 3. (a) and (b) are the incident pulse and reflected pulses. (c) and (d) are the power spectrum of incident pulse and reflected pulses respectively.

Figure 3 is the noise-free incident and reflected pulse respectively, which are converted into frequency domain then find the power spectrum of them, after that determine the spectral center-frequency f_c from those power spectrum and finally used the obtained values in attenuation estimation procedure.

IV. SIMULATION

A. Methods

This part starts from define parameters which are used inside Phantom or image model that used in this research; the detail of each size of the small phantom are filled as of the parameter. While the filled parameters are conformed to the characters of Human's abdomen, the detail of those parameter are shown as Table 1.

TABLE I
PARAMETERS IN CREATED PHANTOM

Center Coordinate(x,y)	Radius r	Gray Level	Alpha α
(00.00,00.00)	55.95	1.00	Bone
(00.00,-1.27)	53.39	0.50	Muscle
(15.29,00.00)	14.60	0.19	Tissue 1
(-15.29,00.00)	19.81	0.19	Tissue 2
(00.00,24.32)	15.95	0.09	Fat
(00.00,6.95)	3.20	0.15	Tissue 3
(00.00,-6.95)	3.20	0.15	Tissue 3
(-5.56,-42.05)	3.20	0.15	Tissue 3
(00.00,-42.05)	1.60	0.15	Tissues 4
(4.17,-42.05)	2.40	0.15	Tissue 4

Tomographic model created by using the parameters in Table 1, while it is summary of center coordinate of image *(x,y)*, radius in unit *(mm)*, gray level *(ρ)*is expressed begin from *0* to 1, respectively. In the simulation process, the model was issued by the *3.5 MHz* broadband ultrasonic pulse (figure3a), sampled at *40 MHz*, along the vertical axis, its latest reflected pulse were then calculated and resolved by the spectral center-frequency method to get the value of the integrated attenuation coefficient. Do this repeatedly on the horizontal axis from left to right; we got the array of attenuation coefficients, or called as the projection at the zero angle. Next, the model was rotated by the degrees of two to simulate and obtain the second projection. The process keeps going until we got 90 projections from the half-plane stepping rotation. Subsequently, the model was reconstructed from all of the projections using the simple filtered back-projection algorithm.

B. Results

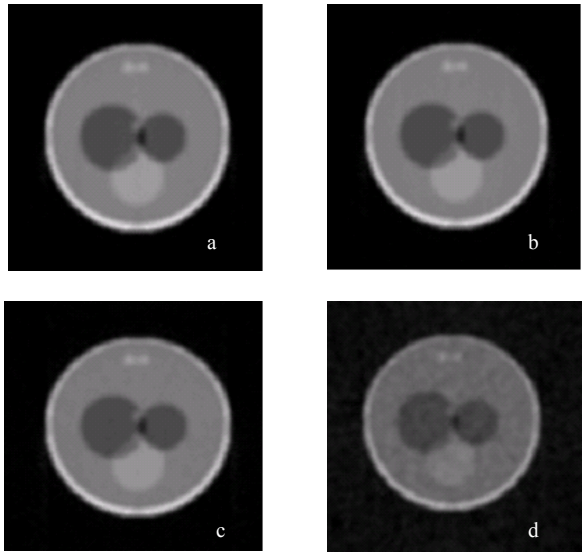

Figure 4. Reconstructed models:
(a) from noise-free object
(b) to (d) are 40dB, 30.45dB, 15dB signal to noise ratio objects.

The reconstructed results are shown in the figure 4 for different cases of image models. The profiles of the reconstruction are plotted against the original profiles in figure 5. To provide numerical evidence, we opt to use the Mean Square Error (MSE) for deriving the error between the reconstructed image and the original image. The formula of MSE is given by

$$MSE = \frac{\iint \left[o(x,y) - o'(x,y)\right]^2 dxdy}{\iint \left[o(x,y)\right]^2 dxdy} \times 100 \qquad (8)$$

The Error obtained the formula above are shown as table 2.

As we can see, the reconstructed result from the noisiest image (figure 4. a) still maintains its pattern, **this caused by the low-pass filters in filtered back-projection algorithm** that suppress most of the noise out with the trade of some blurring. The 17.73% of error in the noise-free image case mainly dues to the back-projection process.

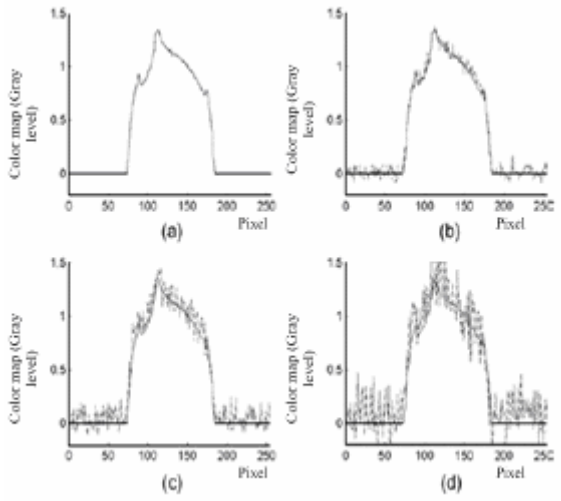

Figure 5. Profiles at 128th line of the reconstructed model, which against to those reconstructed models in figure 4, (real profiles are remarked as solid line, reconstructed profiles as blue dash line)

TABLE II
ERROR OF RECONSTRUCTED MODELS

Signal Per Noise (dB)	Mean Square Error (%)
Noise-Free	17.73
40	29.45
30.45	48.05
15	68.73

V. DISCUSSION AND CONCLUSION

The ultrasonic reflection mode tomography using the frequency centroid-shift method to resolve the integrated attenuation coefficient from the reflected waveform was purposed in this paper. The simulated demonstrated the promising results in the case of the wave path obstructed by the bone. Also the noise sensitivity of the reconstruction process is in the acceptable level. This method might be appropriately utilized in the medical diagnostic to gain the benefits of the ultrasound over the conventional X-ray tomography. Further work may be done in the following manners: Firstly, this method should be implemented in the real-world experiment for realizing more problems that never seen from the simulation. Secondly, we may reduce the noise level in the waveform by using the interpolation algorithm. And the last suggestion is – doing the tomograms of the organ followed by the volume rendering to view the tissue in 3-dimensional style is also possible.

REFERENCES

[1] K.Hamamoto, B.Andreas, T.Shiina, and M.Ito, "Basic Investigation on Reflection Mode Ultrasonic Attenuation Tomography", Jpn. J. Appl. Phys., Japan, vol. 34 (May 1995), pp. 2812-2816.

[2] T. Baldeweck, P. Laugier, A. Herment, and G. Berger, "Application of Autoregressive Spectral Analysis for Ultrasound Attenuation Estimation: Interest in Highly Attenuation Medium", *IEEE TRANSACTIONS ON ULTRASONICS, FERROELECTRICS, AND FREQUENCY CONSTROL*, VOL.42, NO.1, January 1995, pp. 99-110.

[3] A.C.Kak, and K.A.Dines, "Signal Processing of Broadband Pulsed Ultrasound: Measurement of Attenuation of Soft Biological Tissues", *IEEE Transactions on Biomedical Engineering, IEEE Press*, July 1978, pp. 321-344.

[4] A.C.Kak, and M.Slaney, "Princicles of Computerized Tomographic Imaging", *IEEE Press*, NY, 1988.

[5] M.Fatemi, and A.C.Kak, "Ultrasonic B-Scan Imaging: Theory of Image Formation and a Technique for Restoration", *Ultrason. Imaging*, vol. 2, 1980, pp. 1-47.

[6] M.Slaney, and A.C.Kak, "Diffraction Tomography", *Proc. S.P.I.E.*, vol. 413, Apr. 1983, pp. 2-19.

[7] A.J.Devaney, "A Filtered Backpropagation Algorithm for Diffraction Tomography", *Ultrason. Imaging*, vol 4, 1982, pp. 336-350.

Non-uniform Color Quantization for Content-based Image Retrieval

R. Sombutkaew and O. Chitsobhuk
Department of Computer Engineering, Faculty of Engineering,
King Mongkut's Institute of Technology Ladkrabang, Bangkok, Thailand.
ksrattik@kmitl.ac.th, kcoracha@kmitl.ac.th

***Abstract*- Color-based image retrieval usually uses color histogram as image feature. Regular color histogram is uniformly quantized. However, color variation is non-uniformly distributed. Consequently, uniform quantization may lead to inappropriate separation of colors. Similar colors can be treated as dissimilar because of the uniform quantization of each color axis. This causes inefficiency of the retrieval performance. Therefore, this paper proposes non-uniform color quantization used for color histogram generation. The proposed non-uniform color histogram incorporated with color correlogram is stored in the database as image indices. Retrieval results using the proposed color features have been compared with uniform color features to show the improvement of the proposed retrieval system..**

I. INTRODUCTION

With the growth of development in image technology and the increase in the number of pictorial archives, this creates a need for efficient and effective methods and techniques to store and retrieve images from large databases. Color is known as powerful information for image content analysis, recognition, and visualization. Among several color features, a color histogram is the most commonly used since it is efficient to compute and insensitive to image rotation and translation. Several color histograms have been proposed in the literature [1,2]. Most of color histogram generations are based on uniform quantization of color space. Uniformly quantized histogram is simple and easy to calculate. However, color deviation is non-uniformly distributed. Consequently, uniform quantization may lead to inappropriate separation of colors. Similar colors can be treated as dissimilar or vise versa. This causes inefficiency of the retrieval performance. Therefore, this paper presents non-uniform color quantization for color histogram generation. The proposed non-uniform color histogram incorporated with color correlogram is used as image indices and stored in the database. To retrieve similar images to the query, these color features of the query image are compared to those of the images in the database. The most similar images are retrieved and order according to their distances to the query.

II. COLOR QUANTIZATION

A. *Uniform color quantization*

Most of color features are uniformly quantized [1,2,3]. Even though uniform quantization is fast and simple, it may lead to inappropriate separation of colors. Bountha et. al. [1] uniformly quantizes R, G, and B into 4 groups as shown in fig. 1. Also, uniform quantized HSI color proposed in [2] separates Hue into 51 equal ranges for colors and 17 equal ranges for gray scale as shown in fig. 2. We can see from fig. 1 and fig. 2 that some similar colors are considered as dissimilar.

B. *The proposed non-uniform color quantization*

We have researched the visual properties of the HSI color space and its usefulness in content based image retrieval applications. The proposed non-uniform color quantization is based on HSI color model as shown in fig. 3 and 4. The HSI color space is divided into achromatic, low chromatic, and high chromatic sub-regions. Each sub-region is separated based on the value of saturation. In achromatic sub-region, the lightness component is clearly more important and is used to separate color into 4 groups (saturate: 0-0.2, 4 levels of intensity). In the low chromatic sub-region, the chromatic component can be perceived but the perceived color differs according to the hue and lightness. Therefore, hue and lightness are used to separate color into 54 groups (saturate: 0.21-0.6, 3 levels of intensity and 18 subgroups for each level). In the high chromatic sub-region, nearly the same color is perceived regardless of saturation. Therefore, hue is used for the high chromatic quantization, which separate color into 36 groups (saturate: 0.61-1.0, 2 levels of intensity and 18 subgroups for each level).

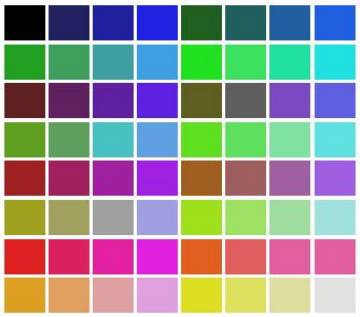

Figure 1. Representation of uniform RGB color quantization [1]

C. *The Propose Indexing Algorithm*

In the proposed indexing algorithm, each image in the database is quantized and segmented using JSEG algorithm [4]. Then, color histogram and correlogram are extracted from each region in the segmented image. These features are stored in the database and used as image indices to retrieve relevant

images from the database. Color histogram is generated based on the proposed non-uniform color quantization as described in section 2. Color correlogram [5] is a spatial extension of the histogram. Given any pixel of color in the image, color correlogram gives the probability that a pixel at distance away from the given pixel is of color can be calculated as followed.

$$\gamma^{(k)}_{C_iC_j}(I) \cong \Pr_{P_1 \in I_{c_i}, P_2 \in I_{c_j}} [p_1 \in I_{c_i}, p_2 \in I_{c_j}, |p_1 - p_2 = k|] \quad (1)$$

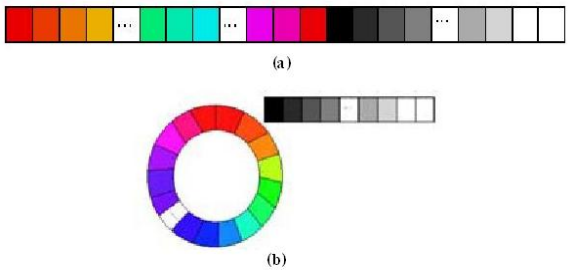

Figure 2. Representation of uniform HSI color quantization [2]

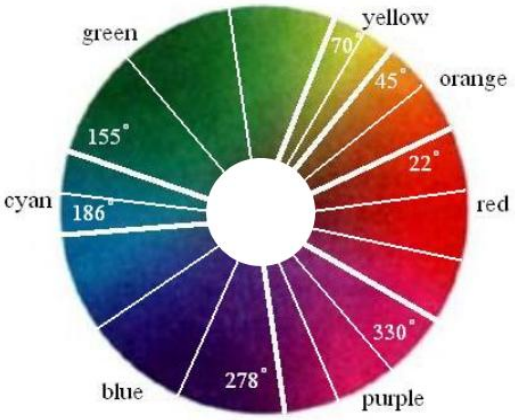

Figure 3. The proposed non-uniform hue quantization

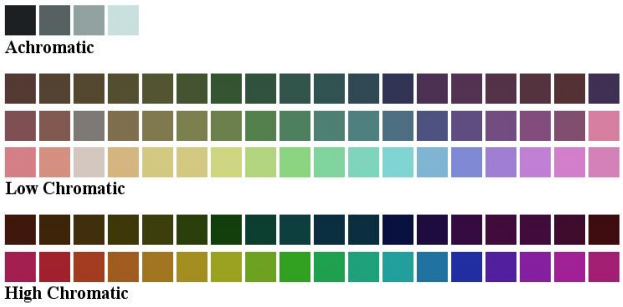

Figure 4. Representation of the proposed non-uniform HSI quantization

D. The Proposed Retrieval System

In the proposed system, users are allowed to impose their desired requirements on the query image using rectangular box. The Region of Interest (ROI) selection area is then segmented into N regions using JSEG algorithm as in the indexing process. Each region in the ROI is exacted color feature, color histogram and color correlogram as same as previous section. In matching process between selected ROI and indexing form database is performed using similarity comparision between the exacted features. The similarity measured by modified L1 distance [6] of color histogram and color correlogram as in equation 2 and 3, respectively.

$$|I - I'|_{h_1 d_1} \triangleq \sum_{i \in [m]} \frac{|h_{c_i}(I) - h_{c_i}(I')|}{1 + h_{c_i}(I) + h_{c_i}(I')} \quad (2)$$

$$|I - I'|_{\gamma_1 d_1} \triangleq \sum_{i \in [m]} \frac{|\gamma^{(k)}_{c_i,c_j}(I) - \gamma^{(k)}_{c_i,c_j}(I')|}{1 + \gamma^{(k)}_{c_i,c_j}(I) + \gamma^{(k)}_{c_i,c_j}(I')} \quad (3)$$

where I and I' are the query and the indexing image. $h_{c_j}(I)$ and $h_{c_i}(I')$ are the color histograms and $\gamma^{(k)}_{Ci,Cj}(I)$ and $\gamma^{(k)}_{Ci,Cj}(I')$ are color correlogram of I and I' images, respectively.

To retrieve relevant images, hierarchical query is performed instead of static query, which searches for N query regions to retrieve N query results and uses all the retrieved results to produce a single query result. Static query requires a large amount of search time due to a large number of regions containing in each indexing image. Even though hierarchical query requires less amount of search time, it is possible that a mistake from one level can propagate to next levels and cause retrieval errors at the end of query. Therefore, in this paper, two-level search is proposed, which not only can reduce the search time compared to the static search algorithm but also can reduce the effects of the mistakes propagating from one level to the next.

The hierarchical search [1] is a combination of the static search and the traditional hierarchical search. In the first-level query, the most important regions from user's query, usually the largest regions at the center of user's query, are matched with the regions in the indexing images using the static search technique. To select the important region for first-level search, we consider the window positioned at the center of selected ROIs. The region covering more than 20% at the window is chosen and used to search for the first-level. The indexing images, which contain all the most important regions and have matching errors less than predefined thresholds, are retrieved from the database. The refinement search is performed in the second-level query to look for the remaining regions in user's query from first-level retrieved images.

During matching task, the distance between the ROIs and feature of the indexing images in the database is calculated as shown in equation 4. Let the color histogram weight be 0.8 and the correlogram weight be 0.2.

$$\text{Distance } (I\text{-}I') = \begin{pmatrix} |I - I'|_{h_1 d_1} * weigth\,(\text{Histogram}) + \\ |I - I'|_{\gamma_1 d_1} * weigth\,(\text{Correlogram}) \end{pmatrix} \quad (4)$$

III. The Experimental Results

We have conducted the experiments using the proposed indexing approach. Color features of regional non-uniform color histogram and a its corresponding correlogram are used as image indices. These features are extracted from regions in the indexing images and the selected ROI of user's query. The database consists of 2,000 images from internet and Corel stock photo gallery, and video clips. The images in the database can be categorized into 7 categories; building creature, foodstuff, human, material, natural, and plant. These images are indexed based on the proposed indexing algorithm as described in section III. The indices of each image will later be used for retrieval process. We have performed the retrieval experiments using a query set consisting of 70 queries, each chosen to represent various situations such as different objects and colors, different views of the ROI, spatial translations and backgrounds. The retrieval performance of all the queries is shown in fig. 5 and fig. 7.

The retrieval performance [7] is evaluated using average precision at each recall level (x) as follow:

$$\overline{P}(r) = \sum_{i=1}^{N_q} \frac{P_i(r)}{N_q} \qquad (5)$$

where $\overline{P}(r)$ is the average the precision at the recall level r, N_q is the number of queries used, and $P_i(r)$ is the precision at recall r for the $i-th$ query.

An example of retrieval results using the proposed non-uniform color quantization compared to uniform color quantization are presented in fig. 5 and fig.8 while corresponding recalls and precisions for each technique are shown in fig. 6 and fig. 7, respectively. In addition, a comparison of the average retrieval performance of recall and precision is shown in fig. 9. From experimental results, the retrieval performance of using the proposed color features is better than those of using uniformly quantized color features.

IV. Conclusion

In this paper, non-uniform color quantization used for color histogram generation is developed based on visual properties of the HSI color space and its usefulness in content based image retrieval applications. The objective is to construct a suitable representation for color histogram, which helps to prevent colors that are perceptually similar from being treated as dissimilar. The non-uniform color histogram incorporated with color correlogram is used to search for similar images to the query from the database. Retrieval results using the proposed color features have been compared with uniform color features to show the improvement of the proposed retrieval system. From the results, it can be seen that the proposed non-uniform color quantization outperforms the uniform quantization in most cases of recall and precision.

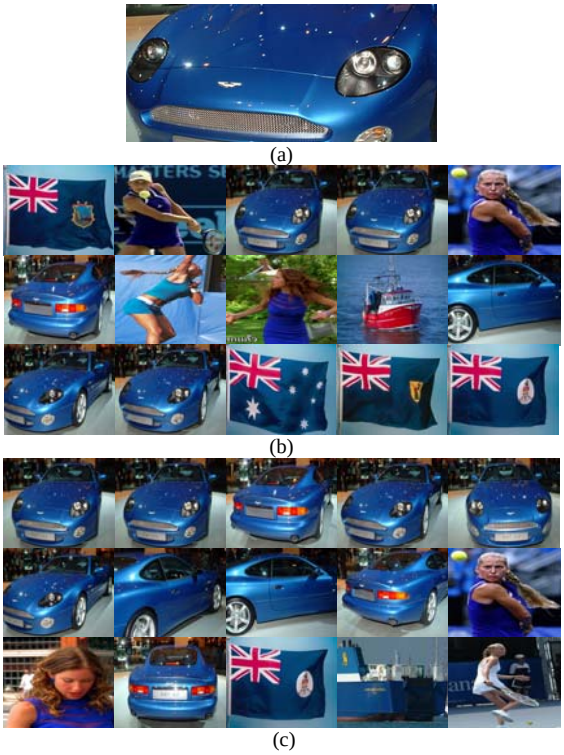
(a)

(b)

(c)

Figure 5. An example of retrieval results of query (a) using uniform (b) and the proposed non-uniform (c) HSI color quantization

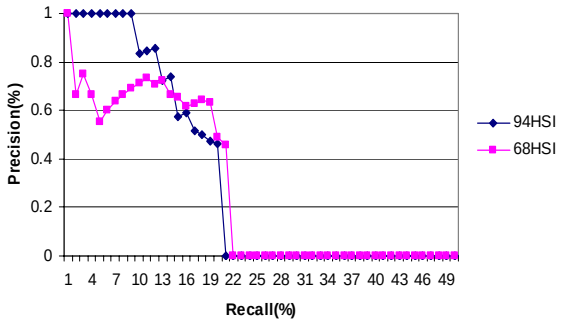

Figure 6. Retrieval performance corresponding to fig. 5.

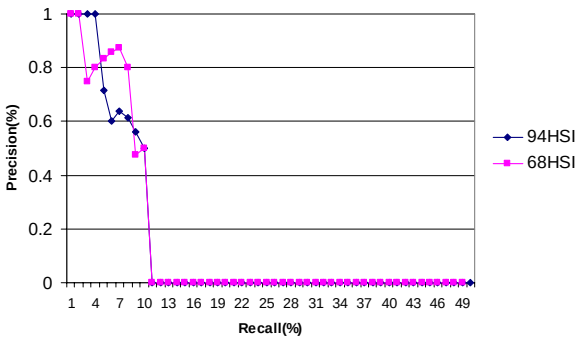

Figure 7. Retrieval performance corresponding to fig. 8.

Figure 8. An example of retrieval results of query (a) using uniform (b) and the proposed non-uniform (c) HSI color quantization

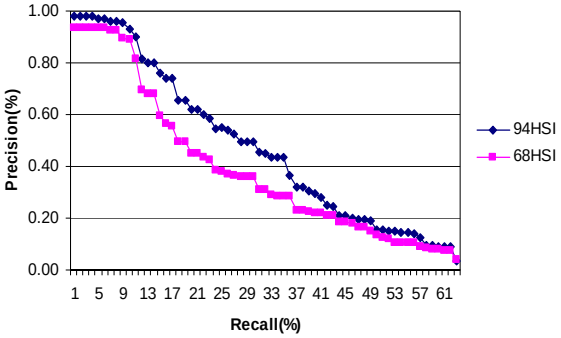

Figure 9. A comparison of the average retrieval performance of the proposed non-uniform quantization and the uniform quantization.

REFERENCES

[1] T. Bounthanh, O. Chitsobhuk and S. Mitatha, "Hierachical Region of Interest Query and Indexing for Content-Based Image Retrieval" Digital Signal Processing and its Applications, Russia, March 12-14 2003,pp.281-284.

[2] S. Soral, G Qian and S. Pramanik, "Segmentation and Histogram Generation Using the HSV Color Space for Image Retrieval", International Conference on Image Processing, USA, 2002, pp. II-589 - II-592.

[3] R. Sombutkaew and O Chitsobhuk, "Color Image Query Using Hierachical Search by Region of Interest with Color Indexing", International Conference on Control Automation and Systems, Thailand, 2004,pp 810-813

[4] Y. Deng, B.S. Manjunath and H. Shin, "Color Image Segmentation" Proc.of IEEE Computer Society Conference on Computer Vision and Pattern Recognition, Fort Colins, 1999, pp.446-451.

[5] J. Huang, S. R. Kumar, M. Mitra, W.J. Zhu and R. Zabih "Image Indexing Using Color Corellograms" 1997 IEEE Computer Society Conference on Computer Vision and Pattern Recognition, 1997, pp.762-768.

[6] G. Pass and R. Zabih, "Histogram Refinement for Content-Based Image Retrieval"IEEE Workshop on Applications of Computer Vision,1996, pp.96-102.

[7] R. Baeza-Yates and B. Riberiro-Neto, Modern Information Retrieval, Addison-Wesley Inc., United State, 1999.

Image Coding Using Vector Quantization Based on Low-Frequency Component to Determine Block Size

Tanasak PHANPRASIT[1] Member, Manas SANGWORASIL[1,2] Nonmember and
Kosin CHAMNONGTHAI[3] Regular Member

[1] Department of Electronics Faculty of Engineering and Research Center for Communications and Information Technology (ReCCIT) King Mongkut Institute of Technology Ladkrabang (KMITL) Chalongkrung Rd., Ladkrabang, Bangkok, Thailand 10520. Email: tanasak.p@bu.ac.th
[2] Computer Research and Service Center King Mongkut Institute of Technology Ladkrabang(KMITL) Chalongkrung Rd., Ladkrabang, Bangkok, Thailand10520,Email ksamanas@kmitl.ac.th
[3] Electronic and Telecommunication Engineering Department of King Mongkut's University of Technology Thonburi (KMUTT), Bangkok, Thailand 10140. Email kosin.cha@kmutt.ac.th

***Abstract*-Image coding requires a small bit rate for high-speed data transmission and a small space for data storage. Simultaneously, the peak signal to noise ratio (PSNR) has to be maintained. This paper proposes a method of image coding design using wavelet transform (WT). By applying the WT for defining groups of pixels with the same intensity in spatial domain, the groups of pixels are allocated in a low frequency range. Hence, locations of pixels are the key factor to determine the size of each block. In this method, image blocks with appropriate size in the image set are initiated, and then used wavelet transform to decompose each block into sub-band components. The low-frequency components (LL) of each block is selected as representative of the block, and their vertical (HL), horizontal (LH) and diagonal (HH) are used to define 3D vectors. The 3D vectors are then classified into 8 groups corresponding to quadrants of spatial coordinates. Magnitudes of vectors in each group are coded as representatives of each block. By applying the proposed method, performance has been improved which indicated by lower bit rate (75%) and better PSNR (4.23%) (Airplane from table 2) compared to the A Genetic Grey-Based Neural Network with Wavelet Transform for Search of Optimal codebook (WT+GGCLN) methods.**

I. INTRODUCTION

Data compression is the mapping of data set into a bit stream to decrease the number of bits required to represent the data set. The data storage space is saved, and memory access time is fastened in case of applying an efficient image coding. In order to enhance the efficiency of communication system for real-time image transmission, we need to decrease the bit rate, and simultaneously maintain PSNR for image quality. To satisfy the mentioned conditions, many developments and researches are undertaken, and results have been published. M. Antonini, M. Barlaud, P. Mathieu, and I. Daubechies in [1] propose wavelet transform as a tool to reduce memory sizes, and increase the quality of image by using multi-resolution codebook. They design codebook by using a well known splitting technique. The initial codebook is generated by splitting the centroid (center of gravity) of this training set. This splitting technique classifies data image into code vectors and determines mean squared error (MSE). In the splitting technique, median of group data is analyzed without the consideration of the interpixel information. Hence, the adjacent block with high frequency data is not considered in the process. Furthermore, the process with 1 bpp compensates PSNR by using two different sizes of blocks, 2x2 (N = 256) and 4x4 (N = 128), which results in higher PSNR. Chaur-Heh Hsieh group in [2] applies several fast search algorithms based on TIE with multiple control points and the Haar wavelet transform. TIE is constructed with multiple control vectors. A systematic way for determining the control vector is developed. A codebook with 256 code vectors is generated by the fast fuzzy C-mean algorithm with block size of 4x4. L. Chin-Yuan and C. Chin-Hsing in [3], apply wavelet transform to reduce bit rate using in data transmission and data storage. The image quality is improved by using multi resolution codebook designed by the genetic algorithm and the grey-base designed competitive learning network. Both of these techniques provide a better quality of image. However, designing the codebook with this technique considers only the center of each group which calculated from individual pixel in the same group. The codebook composes of two different block sizes (e.g., 2x2 with 512 code vectors and 4x4 with 64 code vectors). The results shown that the bit rate is 0.84 bpp.

In this paper, the authors aim to find VQ-based coding method as discussed in [4]-[9] with low bit rate and high PSNR. We propose a novel technique which utilizing frequency components to determine size of blocks. One of the main advantages of the proposed method is that the size of each block is adjustable to minimizing coding errors. Section 2 describes problem analysis in an image coding. Sections 3 to 4 an image coding system and codebook design. Finally, experimental results and a conclusion are in sections 5 and 6, respectively.

II. PROBLEM ANALYSIS IN IMAGE CODING

One issue of researches in image coding is to find coding methods with low bit rate and high PSNR. As conventional method, L. Chin -Yuan etc. [3] proposed A Genetic Grey-Based Neural Networks with Wavelet Transform for Search of Optimal codebook in order to enhance PSNR as quality. However, bit rate is still high, because of multi-resolution.

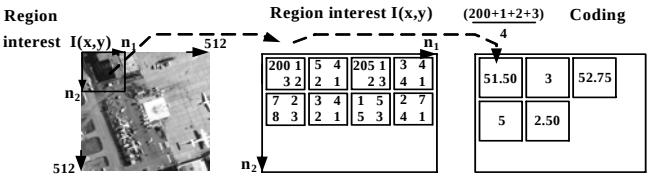

Figure 1. A simple of coding conventional method.

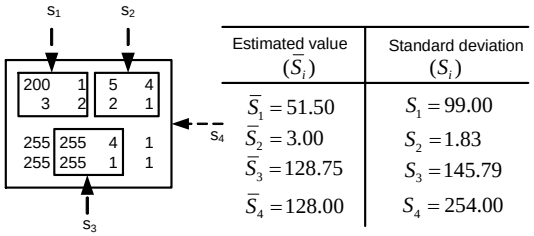

Figure 2. A case of image sample in block for coding.

As shown in figure 1, the conventional method employs average of intensity in the 2x2 blocks for coding. Normally, if we enlarge a block for coding, bit rate is decreased. On the other hand, since coded data is generated from intensity average in the block, PSNR becomes worse. In this paper, we raise "To decrease bit rate while maintaining PSNR" as theme, and declare it as problem statement.

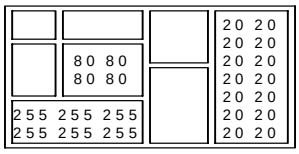

Figure 3. The similar intensity pixel.

In figure 2, small block will absorb distortions between intensity values and their averages. That means PSNR is decreased according to block size. However, block size should be enlarged to cover area consisting of similar intensity values in order to decrease bit rate maintaining PSNR as shown in figure 3. Therefore, we should determine block location and size depending on adjacent pixels that have similar intensity values. In frequency domain as shown in figure 4, spectrum representing block that contains similar-intensity pixels is located in low frequency range. On the other hand, a block with different-intensity pixels will be located in high frequency range.

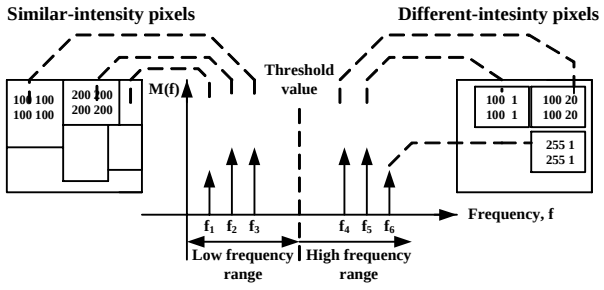

Figure 4. An analysis of the signal in frequency domain.

Obviously, we can use frequency components to determine block location and size in spatial domain. Separating the low frequency components and high frequency components can be done in many ways. One way is the decomposition of the image using a Discrete Wavelet Transform (DWT) [10]-[12], which is being used in a number of different applications.

III. AN IMAGE CODING SYSTEM

The system of image compression mentioned in this paper can be described as follows. Image data coding proposed in this paper consists of encoding stage and decoding stage.

3.1 Encoding System

Encoding process, due to the aim for high PSNR, (encoding processing step) consists of three important processes. First process, the 512x512 input-image (X_i) is divided into 256 of 32x32 square blocks (Bn) which is called input vector. Second process consists of two important steps: Interpixel codebook and Nearest Neighbor Rule. The Nearest Neighbor Rule is an error retrieved from the calculation of mean square error (MSE) between input vector and code vector in the following formula:

$$d(X_i, X_i'') = \frac{1}{K}\sum_{m}^{K}[X_i(m) - X_i''(m)]^2, \qquad (1)$$

where

$d(X_i, X_i'')$ is mean square error,

$X_i(m)$ is input vector,

$X''(m)$ is code vector, and

K is dimension of code vector

The third process is finding the index. The index is the result of the comparison between input vector and code vector with the least error. The index is then used to indicate position of code vector which is kept in the Interpixel codebook.

3.2 DECODING SYSTEM

Decoding process, in order to have the image reconstructed, the decoding process needs to have the reverse process of the encoding. Result is that the image data or reconstruction (X_o).

IV. CODEBOOK DESIGN

In the present, wavelet transform is a popular research topic applying for signal processing such as image and sound signals. It is an effective display technique for analyzing time and frequency [13]. Moreover, this technique is widely accepted. In the paper, wavelet transform is applied to determine a block location and size which depend on adjacent pixels that have similar intensity values as shown in figure 3. A group of vector code from a wavelet's theory is also implemented to experiment assumptions. And the mother function of wavelets, $\Psi(x)$, can be any function if it satisfies the following condition

$$\int_{-\infty}^{\infty} |\Psi(x)|^2 \, dx < \infty \tag{2}$$

Basically, a mother wavelet function is derived from its corresponding mother scaling function $\Phi(x)$ which satisfies the scaling equation

$$\Phi(x) = \sum_{i \in Z} c_i \Phi(2x - i) \tag{3}$$

For any integer j, the vector space V^j is define as

$$V^j = span\{\Phi_i^j(x), \forall i \in z\} \tag{4}$$

$$\Phi_i^j(x) = \Phi(2^j x - i), i, j \in z \tag{5}$$

If V^j satisfies the following four multi resolution analysis conditions

Condition 1: $f(x) \in V^j \Leftrightarrow f(2^{-j}x) \in V^0, \forall j \in z$
Condition 2: $\bigcap_{i \in z} V^i = \{0\}$
Condition 3: $\bigcup_{i \in z} V^i = L^2(R)$
Condition 4: $... \subset V^{-2} \subset V^{-1} \subset V^0 \subset V^1 \subset V^2 \subset ...$

That the mother wavelet is given by

$$\Psi(x) = \sum_{i \in z} (-1)^i c_{1-i} \Phi(2x - i) \tag{6}$$

One of the most important characteristics of the wavelet transform is multi resolution. The wavelet transform converts the pixel values of an image to its wavelet representation, without losing any information, in the spatial domain. In this paper, the Interpixel codebook is designed by applying the wavelet transform theory. The Interpixel codebook design consists of the following steps:

Step 1: The input image size 512x512 pixels are separated into 256 square sub-blocks. Each sub-block has 32x32 pixels and nominated as E_1 to E_{256}.

Step 2: Analyze the characteristics of each sub-block to define address of sub-block associated with frequency of input image.

- Each sub-block is decomposed into 5 levels. The five level wavelet transform is performed on image to generate the corresponding transformed coefficients.
- 3D vector ($\vec{B}_1, \vec{B}_2, \vec{B}_3, .., \vec{B}_{256}$) is constructed by using the coefficient values of LH_5, HL_5, and HH_5 sub-bands to determine of the unit vector i, j, k.
- Find magnitudes (B_1, B_2, B_3,…B_{256}) of 3D vectors which can be described are:

Step 3: Divide sub-blocks into eight groups (*Total_group*) according to 3D vector signs and *Small_group* less than 256 blocks, as shown in (7)-(8).

$$Total_group = \begin{Bmatrix} Big_group(m)(-\hat{i}, -\hat{j}, -\hat{k}); m = 1, \\ Big_group(m)(-\hat{i}, -\hat{j}, \hat{k}); m = 2, \\ .., Big_group(m)(\hat{i}, \hat{j}, \hat{k}); m = 8 \end{Bmatrix} \tag{7}$$

$$Big_group(m) = \begin{Bmatrix} Small_group(1), Small_group(2), \\ .., Small_group(n) \end{Bmatrix} \tag{8}$$

Step 4: Find amount code vector (block size in figure 3 corresponding to resolution of step value) by applying the following equation.

$$Bit(bit_for_calculator) = Log_2(small_grouproup) \tag{9}$$

- If *Bit* for calculator more than real bit, step = Max/2
- If *Bit* for calculator less than real bit, step = step/2

Step 5: Find Interpixel codebook from sub-blocks size 32x32 pixels, as shown in figure 5 (Address of sub-blocks is defined as address of E_1 to E_{256}).

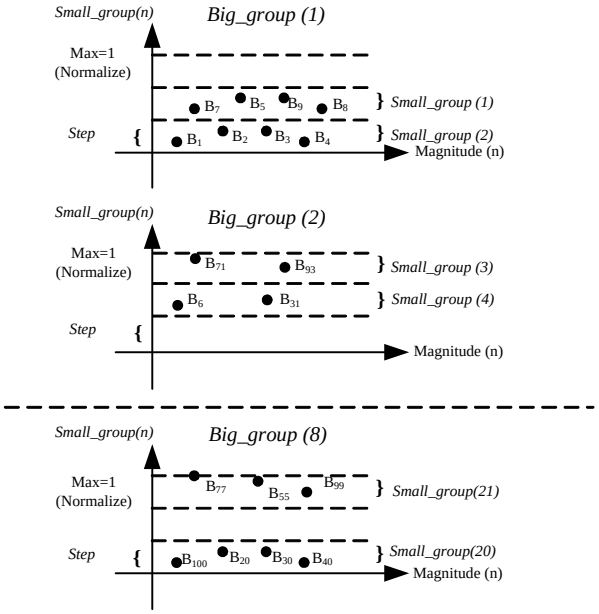

Figure 5. A grouping sample of magnitude value

where *small_ group* is on integer value (1, 2,..,256).

And find Interpixel codebook by applying the following equation.

$$C_{Small_group(n)}(1, j) = \frac{1}{m} \sum_{i=1}^{m} (X_{i,j}); j = 1, 2, .., 1024 \tag{10}$$

V. EXPERIMENTS AND RESULTS

For evaluating the performance of proposed image coding method, the image coding has been produced by specification

Pentium(R) 4 CPU 3.01 GHz, Block size 32x32, codebook size 210, and Image size 512x512.

Table 1 shown PSNR and MSE of the "Airplane", "Girl", "Lena" and "Pepper" image reconstructed from three bit rates of size 0.38, 0.44 and 0.50. Table 2 shown bit rate, compression ratio of the "Airplane", "Girl" and "Lena" image reconstructed from bit rate size 0.48 and the test of PM system using the three standard images, block size 4x4 are demonstrated in figure 6, and Set Partitioning in Hierarchical Trees (SPIHT) [14]-[15] is a wavelet-based image compression coder. It first converts the image into its wavelet transform and then transmits information about the wavelet coefficients. The decoder uses the received signal to reconstruct the wavelet and perform an inverse transform to recover the image.

TABLE I
PSNR and MSE of the images reconstructed from bit rates of various sizes designed by the LBG [4] and the proposed method (PM).

Algorithms	Images	0.38 bpp PSNR	0.38 bpp MSE	0.44 bpp PSNR	0.44 bpp MSE	0.50 bpp PSNR	0.50 bpp MSE
PM	Airplane	27.02	129.12	28.03	102.33	28.83	85.11
LBG		24.11	252.35	25.29	192.30	26.34	132.94
PM	Girl	28.80	85.70	29.96	65.61	30.33	60.26
LBG		27.68	109.62	28.51	91.60	29.69	77.09
PM	Lena	28.02	102.57	28.81	85.51	29.65	70.47
LBG		25.26	146.89	26.37	127.01	27.06	106.71
PM	Pepper	26.50	145.55	27.20	123.88	27.93	104.71
LBG		24.82	214.33	25.59	179.51	26.78	136.48

TABLE 2
Bit rate, Compression ratio, PSNR and MSE of the images reconstructed from SPIHT [14]-[15], LBG, WT+GGCLN [3] and the proposed method

Algorithms	Images	Bit rate (BR)	Compression Ration (CR)	PSNR	MSE
PM	Airplane	0.48	16.59	28.83	85.11
WT+GGCLN		0.84	16.89	27.66	111.43
LBG		0.50	16.00	24.11	222.31
SPIHT		0.50	N/A	37.44	11.72
PM	Lena	0.48	16.59	29.65	70.47
WT+GGCLN		0.84	16.89	29.52	72.61
LBG		0.50	16.00	25.26	146.89
SPIHT		0.50	N/A	37.25	12.25
PM	Girl	0.48	16.59	30.33	60.26
WT+GGCLN		0.84	16.89	31.90	41.98
LBG		0.50	16.00	27.68	109.62
SPIHT		0.50	N/A	38.50	9.18

VI CONCLUSIONS

This paper proposes a method for image coding design using vector quantization based on low-frequency component to determine block location and size in spatial domain. The experiments on the propose method have been performed with four standard images. The experimental results reveal proposed method is evaluated as 0.48bpp, and 28.83dB for bit rate and PSNR respectively, that is improved by 75% and 4.23% for bit rate and PSNR comparing with the conventional method (WT+GGCLN).

Figure 6. Experimental results: show in table 1

REFERENCES

[1] M. Antonini , M. Barlaud, P. Mathieu, and I. Daubechies, " Image Coding Using Wavelet Transform, " *IEEE Trans. Image Processing*, vol.1, no.2, pp.205-220, 1992.

[2] Chaur - Heh Hsieh and Yong - Jzu Liu, "Fast Search Algorithms for Vector Quantization of Images Using Multiple Triangle Inequalities and Wavelet Transform," *IEEE Trans. Image Processing*, vol.9, no.3, pp.321 - 328, 2000.

[3] L. Chin - Yuan, C. Chin - Hsing, "A Genetic Grey – Based Neural Networks with Wavelet Transform for Search of Optimal codebook," IEICE Trans. Fundamentals, vol. e86-a, no. 3, pp. 715-721, 2003.

[4] Y. Linde, A. Buzo, and R. M. Gray, "An algorithm for vector quantizer design," *IEEE Trans. Commun.*, vol.COM-28, no. 1, pp. 84-95, Jan. 1980.

[5] R. M. Gray, "Vector Quantization," *IEEE Trans. Acoust., Speech Signal Process.*, vol. 1, no. 2, pp. 4-29, 1984.

[6] A. Gersho and R. M. Gray, Vector Quantization and Signal Compression, Kluwer Academic, Norwell, Ma, 1992.

[7] E. A. Riskin, T. Lookabaugh, P. A. Chou, and R. M. Gray, "Variable rate vector quantization for medical image com-pression," *IEEE Trans. Med. Imaging*, vol. 9, no. 3, pp. 290-298, 1990.

[8] E.Yair, K. Zeger, and A. Gersho, "Competitive learning and soft competition for vector quantizer design," *IEEE Trans. Signal Process.*, vol.40, no.2, pp.294-309, 1992.

[9] K. Zeger, J. Vaisey, and A. Gersho, "Globally optimal vector quantizer design by stochastic relaxation," *IEEE Trans. Signal Process.*, vol.40, no.2, pp.310-322, 1992.

[10] R. C alderbank, I. Daubechiess, W. Sweldens, and B.- L. Yeo, "Wavelet transforms that map integers to integer," Journal of Appl. And Comp. Harmon. Analy., vol. 5, pp 332-369, 1998.

[11] A. Graps, "An introduction to wavelet," *IEEE Computation Science and Engineering*, vol.2, no. 2, pp. 50-61, 1995.

[12] R. Calderbank, I. Daubechies, W. Sweldens, and B.-L. Yeo, "Wavelet transforms that map integers to integers," Journal of Appl. And Comp. Harmon. Analy., vol. 5, pp 332-369, 1998.

[13] S.C. Tai, Data Compression, Unalis, 1998.

[14] Jarvi, A., Lehtien, J., Nevalainen, O.: Variable Quality Image Compression System Based on SPIHT, *Signal Processing: Image Compression*, 14(9), 1999, 683-696.

[15] Said, A., Pearlman, W.A.: A New, Fast, and Efficient Image Codec Based on Set Partitioning in Hierarchical Trees, *IEEE Transactions on* Circuits and System for Video Technology, 6(3), 1996, 243-250.

Image Coding Using Vector Quantization Based on System Error Compensate

Tanasak PHANPRASIT[1] Member, Manas SANGWORASIL[1,2] Nonmember and
Kosin CHAMNONGTHAI[3] Regular Member

[1] Department of Electronics Faculty of Engineering and Research Center for Communications and Information Technology (ReCCIT) King Mongkut Institute of Technology Ladkrabang (KMITL) Chalongkrung Rd., Ladkrabang, Bangkok, Thailand 10520. Email: tanasak.p@bu.ac.th
[2] Computer Research and Service Center King Mongkut Institute of Technology Ladkrabang(KMITL) Chalongkrung Rd., Ladkrabang, Bangkok, Thailand10520,Email ksamanas@kmitl.ac.th
[3] Electronic and Telecommunication Engineering Department of King Mongkut's University of Technology Thonburi (KMUTT), Bangkok, Thailand 10140. Email kosin.cha@kmutt.ac.th

***Abstract*-Vector Quantization (VQ) is Lossy image compression system (irreversible compression). The information loss then causes reconstruction containing loss information. Moreover, system error non-compensation will cause low peak signal to noise ratio (PSNR). Therefore, this paper proposes a method of system error compensation on VQ. At encoding system, system error compensation (e2) is calculated difference image between input image (X_i) and the reconstruction image (X_i'). It is decomposed by 2-dimentional 3-level Discrete Wavelet Transform (DWT). System error is known by looking at the sub-band LL3. At decoding system, system error is composed by 2-dimentional 3-level Inverse Wavelet Transform (IDWT). However, before the composition, LH3 HL3 and HH3 must be set to zero. The reconstructed image and system error compensate will be combined in order to construct an output image (X_o). By applying the proposed method, performance has been improved which indicated by better PSNR (11.63%) compared to the A Genetic Grey-Based Neural Network with Wavelet Transform for Search of Optimal Codebook (WT+GGCLN) methods.**

I. INTRODUCTION

Vector quantization, which has been widely applied in speech and image coding [1]-[2], provides an efficient technique for signal compression due to it excellent rate-distortion performance. Image storage and transmission pose an important problem to the development of intelligent communication systems due to memory and bandwidth requirements. In image data transmission, the 3rd generation communication (3G) [3], is currently installed in mobile phones is used, and expected to be popular for the near future [4]. We need to decrease the bit-rate, and simultaneously maintain PSNR for image quality. To overcome this problem, several PSNR and bit-rate improved algorithms [5]-[6] have been proposed. The algorithms can be roughly categorized as lossy and lossless approaches [7]. M. Antonini, M. Barlaud, P. Mathieu, and I. Daubechies in [8] propose wavelet transform as a tool to reduce memory sizes, and increase the quality of image by using multi-resolution codebook. They design codebook by using a well known splitting technique. The initial codebook is generated by splitting the centroid (center of gravity) of this training set. This splitting technique classifies data image into code vectors and determines mean squared error (MSE). In this system, and the process is analyzed system error compensation on VQ is not taken into consideration**.** Furthermore, the process with 1 bpp compensates PSNR by using two different sizes of blocks, 2x2 (N = 256) and 4x4 (N = 128), which results in higher PSNR. L. Chin-Yuan and C. Chin-Hsing in [9], apply wavelet transform to reduce bit-rate using in data transmission and data storage. The image quality is improved by using multi resolution codebook designed by the genetic algorithm and the grey-base designed competitive learning network. Both of these techniques provide a better quality of image. The codebook composes of two different block sizes (e.g., 2x2 with 512 code vectors and 4x4 with 64 code vectors). The results shown that the bit-rate is 0.84 bpp. However, this system, the process is analyzed and also same as [8].

The focus of this paper is a system error compensated approach utilizing wavelet transform and vector quantization techniques, hoping to achieve the best result in term of compression ratio with acceptable recovery quality. This new approach will be called error compressed vector quantization. The paper is organized in the following way. Section 2 describes problem analysis in an image coding. Sections 3 and 4 a coding system and image quality enhancement techniques mixed scheme technique. Finally, experimental results and a conclusion are in sections 5 and 6, respectively.

II. PROBLEM ANALYSIS IN AN IMAGE CODING

One of research issues in image coding is to find coding methods with low bit-rate and high PSNR. In [9] L. Chin-Yuan and C. Chin-Hsing propose A Genetic Grey-Based Neural Networks with Wavelet Transform for Search of Optimal codebook. In this paper, a new image compression technique combining the genetic algorithm (GA) and the grey-based competitive learning network (GGCLN) in the wavelet transform domain. This method can enhance PSNR as quality. However, bit-rate is still high because of multi-resolution.

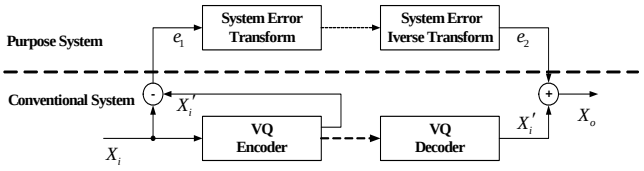

Figure 1. A simple of VQ coding system.

As shown in Fig. 1, the conventional system employs average of intensity in the 2x2 blocks for coding. Normally, if we enlarge a block for coding, bit-rate is decreased. On the other hand, since coded data is generated from intensity average in the block, in addition to, is system error non-compensation, PSNR becomes worse. In this paper, we raise "To decrease bit-rate while maintaining PSNR" as theme, and declare it as problem statement. The system error compensate can be calculated, is defined as

$$e_1 = X_i - X_i' \quad (1)$$

$$e_2 = \mathrm{T}^{-1}(e_1) \quad (2)$$

$$X_o = X_i' + e_2 \quad (3)$$

$$X_o = (X_i - e_1) + e_2 \quad (4)$$

$$X_o = X_i - e_1 + \mathrm{T}(e_1) \quad (5)$$

Where e_1 is system error, e_2 is system error compensate, T^{-1} is inverse transform, X_i is input image, X_i' is reconstructed image and X_o is output image. Therefore, if system error compensates approaches system error as close as possible the output image will approach input image, and the image has low bit-rate and high PSNR, is define as (5).

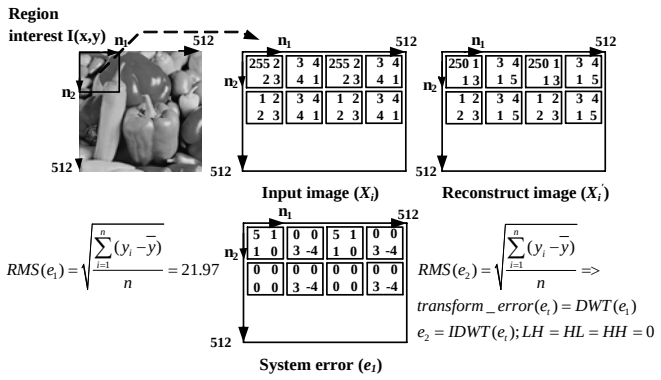

Figure 2. A case of image sample in block for coding.

In system error as shown in Fig. 2, the system error compensate is transform system error. Obviously, we can use transform system error components ($e_t = DWT(e_1), e_2 = IDWT(e_t); LH = HL = HH = 0$) to determine the system error compensate.

III. CODING SYSTEM

The system of image compression can be described as follows.

3.1 Encoding / Decoding System

In this paper image data coding consists of encoding stage and decoding stage that are demonstrated in Fig. 3. The aim of encoding process is to produce the image with high PSNR. Therefore, the development of encoding process is necessary. The process consists of two steps. The first step is the closed loop control. In this step, the image is reconstructed from the relationship between the codebook and the nearest neighbor rule. The codebook designed by Quadrant technique [10]. In the second step, to reduce the system error, the 3-level DWT is applied to transform to the system error in frequency domain then, only the low frequency component is transmitted to the decoding process.

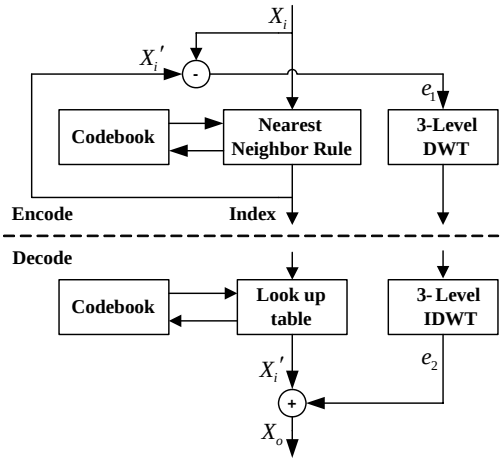

Figure 3. Diagram of implementation error added VQ.

The image is compressed in a lossy style. The system error and system error compensate can be calculated, is defined as (1) and (2). In order to cover all frequency, the Haar wavelet is applied as wavelet transform. The system error will be decomposed by 3-level wavelet transform. Only the sub-band LL will be transmitted and sub-bands LH, HL, and HH are discarded.

Decoding process, in order to have the image reconstructed, the decoding process needs to have the reverse process of the encoding. Furthermore, the system error will be inverse transformed in the three levels which will yield the system error compensate. Then the construction of output image is generated from the merging of reconstruction image and system error compensate.

IV. IMAGE QUALITY ENHANCEMENT TECHNIQUES

Image coding using vector quantization based on system error compensated in this paper can be accomplished by 3 different techniques:

- **Techniques 1** Closed Loop Control (CLC)
- **Techniques 2** System Error Compensation (SEC)
- **Techniques 3** Combination of CLC and SEC (CLC+SEC)

Details of each technique are mentioned in the following subsections.

4.1 Closed Loop Control

The closed system that demonstrated in Section 3.1 (encoding processing step) consists of three important processes. First process, the 512x512 input images is divided into 4,096 of 8x8 square blocks which is called input vector. Second process consists of two important steps: codebook and Nearest Neighbor Rule. The Nearest Neighbor Rule is an error retrieved from the calculation of mean square error (MSE) between input vector and code vector as follows

$$d(X_i, X_i'') = \frac{1}{K}\sum_{m}^{K}[X_i(m) - X_i''(m)]^2, \qquad (6)$$

where $d(X_i, X_i'')$ is mean square error,

$X_i(m)$ is input vector,

$X_i''(m)$ is code vector, and

K is dimension of vector.

(a) 26.70 dB, 0.13 bpp (b) Closing up

Figure 4. A sample of basic VQ on image.

The third process is to find the index and image data or reconstruction image. The index is the result of the comparison between input vector and code vector with the least error. The index is then used to indicate position of code vector which is kept in the codebook.

(a) Original image (b) System error

Figure 5. Quantization error of basic VQ on an image.

The result is the image data of the reconstruction as shown in Fig. 4. The figure shows the serious blocky effect of implement basic VQ. The blocky effect and loss of information is more pronounced when the error image in Fig. 5 is inspected as, it is associated with quantization error.

4.2 System Error Compensation

Compression in the VQ pattern basically causes information loss. The information loss then causes reconstruction containing loss information. Moreover, system error non-compensation will cause blocky effect to occur. Therefore, the VQ compression needs improvement to contain system error compensation. The system error compensation consists of two main processes. In the first process, system error is calculated from input image of size 512x512 pixels, and the reconstruction image. In the second part, system error is decomposed into 4 sub-bands (LL_1, LH_1, HL_1, HH_1). Then LL_1 will be decomposed further into 4 sub-bands (LL_2, LH_2, HL_2, HH_2). However, only sub-band LL_2 is used for further decomposition until the pixel of data exist in the block is reduced to 64x64 (LL_3, LH_3, HL_3, and HH_3). Result of the decomposition allows us to know system error by looking at the sub-band LL_3. The other three sub-bands (LH_3, HL_3, and HH_3) will be discarded.

4.3 Combination of CLC and SEC

Due to the blocky effect and loss information that occur during the image reconstruction, the combination of CLC and SEC is used to solve the problems. The combination of CLC and SEC consists of three parts. In part I, input of decoding processing step consists of index and system error. Part II consists of a look up table, codebook and inverse wavelet transform (IDWT). In this second part, system error, 64x64 pixels, in sub-band LL_3 LH_3 HL_3 HH_3 is composed to sub-bands LL_2 LH_2 HL_2 and HH_2. However, before the composition, LH_3 HL_3 and HH_3 must be set to zero. After that, LL_2 LH_2 HL_2 and HH_2 will be composed further into sub-band LL_1 LH_1 HL_1 and HH_1 respectively. Finally, the all four sub-bands will be composed by IDWT in order to construct system error compensate. In part III, the reconstructed image and system error compensate will be combined in order to construct an output image, the value of output image is defined as (3) to (5). The quality of the output image is demonstrated in Fig. 7.

(a) 27.57 dB, 0.13 bpp (b) Closing up

Figure 7. A sample of image system error compensate.

V. EXPERIMENTS AND RESULTS

For evaluating the performance of proposed image coding method, the image coding has been produced by specification Pentium(R) 4 CPU 3.01 GHz, Block size 32x32, Codebook size 210, and Image size 512x512.The value of *PSNR* is also calculated for evaluating the system performance.

5.1 VQ Based on CLC

The tests of CLC system using the four standard images are “Airplane”, “Girl”, “Lena”, “Pepper” and block size 4x4. The results reveal the PSNR and bit-rate as in Table 1. The result of PSNR comparison between low frequency image and high frequency image are shown in Table 1. They reveal the

advantage of CLC system in low frequency image, rather than in high frequency image.

5.2 VQ Based on CLC and SEC

The tests of CLC+SEC system using the four standard images, block size 4x4 and block size 32x32 show in Table 1. The results reveal the PSNR and bit-rate as shown in Table 1. According to Table 2, the CLC+SEC system are better than the CLC system.

TABLE I
The image reconstructed from proposed CLC + SEC system

Images	CLC+SEC		CLC	
	PSNR (dB)	Bit rate (bpp)	PSNR (dB)	Bit rate (bpp)
Airplane	26.07	0.13	25.53	0.13
Girl	29.31	0.13	27.90	0.13
Lena	27.96	0.13	27.66	0.13
Pepper	26.81	0.13	26.70	0.13

5.3 Varied bit-rates

Table II and III show the PSNR and MSE of the "Airplane" "Girl", "Lena" and "Pepper" image reconstructed from four bit-rate 0.38 bpp, 0.44 bpp, 0.48 bpp and 0.84 bpp blocks size 4x4 designed by the LBG and CLC systems. The LBG design algorithm is an iterative algorithm which alternatively solves two optimality criteria (Nearest Neighbor and Centroid Condition). The algorithm requires an initial codebook by the *splitting* method. According to Table II and III the average PSNR produced by CLC is 1.96 dB higher than that by the typical VQ (LBG). Further, the average PSNR produced by the proposed CLC+SEC system is 6.69 dB higher than that by VQ(LBG) conventional algorithm. The comparison between WT+GGCLN and CLC, CLC+SEC systems is shown in Table IV which shows the compression ratio (CR) of [512*512*8 / (512*512*7.71/(4*4))] = 16.59 for CLC, and [((512*512) + (64*64))*8 / (((512*512*7.71) /(4*4))+(8*64*64))] = 13.38 for CLC+SEC respectively. From the experimental simulation, the reconstructed images obtained from the CLC+SEC is significantly better than those from the CLC system.

TABLE II
PSNR and MSE of the images reconstructed from designed by the LBG and CLC system.

Algorithms	Images	0.38 bpp PSNR MSE	0.44 bpp PSNR MSE	0.48 bpp PSNR MSE
CLC	Airplane	27.02 129.30	28.03 102.33	28.83 85.13
LBG		24.11 252.39	25.29 192.30	26.34 132.94
CLC	Girl	28.80 85.63	29.96 65.55	30.33 60.27
LBG		27.68 109.62	28.51 91.60	29.69 77.09
CLC	Lena	28.02 102.61	28.81 85.56	29.65 70.56
LBG		25.26 146.89	26.37 127.01	27.06 106.71
CLC	Pepper	26.45 147.26	27.20 123.85	27.93 104.73
LBG		24.82 214.33	25.59 179.51	26.78 136.48

TABLE III
PSNR and MSE of the images reconstructed from designed by the WT+GGCLN and CLC+SEC system.

Algorithms	Image	0.84 bpp PSNR MSE
CLC+SEC	Airplane	33.41 29.65
WT+GGCLN		27.66 111.45
CLC+SEC	Girl	33.64 28.12
WT+GGCLN		31.90 41.98
CLC+SEC	Lena	33.25 30.76
WT+GGCLN		29.52 72.62
CLC+SEC	Pepper	32.28 38.46
WT+GGCLN		NA NA

TABLE IV
Compression ratio by the WT+GGCLN and CLC+SEC system

Compression ratio (Cr)		
CLS+SEC	CLC	WT+GGCLN
13.38	16.59	16.89

VI. CONCLUSIONS

This paper proposes a method for image coding design using vector quantization based on system error compensate. The experiments on the propose method have been performed with four standard images. The experimental results reveal proposed method is evaluated as 0.84 bpp, and 33.15 db for bit-rate and PSNR respectively, that is improved by 11.63 % for the average PSNR comparing with the conventional method.

REFERENCES

[1] A. Gersho and R. M. GRAY, Vector Quantization and Signal Compression. Norwell, MA: Kluwer, 1992.

[2] Y. Linde, A. Buzo, and R. M. Gray, "An algorithm for vector quantizer design," IEEE Trans. Commun., vol.COM-28, no. 1, pp. 84-95, Jan. 1980.

[3] P. Chaudhury, W. Mohr, and S. Onoe, "The 3GPP proposal for IMT-2000 , " IEEE Commun. Mag., vol.37, pp. 72 - 81, Dec. 1999.

[4] S. Ohmori ,Y. Yamao , and N. Nakajima, " The future Gen-erations of Mobile Communication Based on Broadband Access Technologies, " IEEE Communications Magazine, pp. 136-137, Dec 2000.

[5] C.D. Bei and R. M. Gray, "An improvement of the minimum distortion encoding algorithm for vector quantizaton," IEEE Transs. Commun., vol. COM-33, pp. 1132-1133, Oct. 1985.

[6] Chaur - Heh Hsieh and Yong - Jzu Liu, "Fast Search Algorithms for Vector Quantization of Images Using Multiple Triangle Inequalities and Wavelet Transform," IEEE Trans. Image Processing, vol.9, no.3, pp.321 - 328, 2000.

[7] C. -H. Hsieh and Y. -J. Liu, "Fast search algorithms for vector quantization of images using multiple triangle inequalities and wavelet transform," IEEE Trans. Image Processing, vol. 9, pp. 321-328, Mar. 2000

[8] M. Antonini , M. Barlaud, P. Mathieu, and I. Daubechies, " Image Coding Using Wavelet Transform, " IEEE Trans. Image Processing, vol.1, no.2, pp.205-220, 1992.

[9] L. Chin - Yuan, C. Chin - Hsing, "A Genetic Grey – Based Neural Networks with Wavelet Transform for Search of Optimal codebook," IEICE Trans. Fundamentals, vol. e86-a, no. 3, pp. 715-721, 2003.

[10] C. Tengcharoen, R. Varakulsiripunth, T. Phanprasit and M. Sanworasil, "Stereo Image Compression by Quadrant Vector Quantization", *IVCNZ'03 Proceedings*, pp.210-214, (2003).

Direct Manipulation of 3D Curves with Pseudo-Physical Simulation Model

Pathawut Pichaichanlert and Nopporn Chotikakamthorn
Faculty of Information Technology and
Research Center for Communications and Information Technology
King Mongkut`s Institute of Technology Ladkrabang, Bangkok, Thailand
Tel: +66-2-326-4331, Fax: +66-2-326-4332
E-mail: patha_wut@hotmail.com

Abstract - **The task of 3D-object modeling is made difficult due to at least two reasons. First, 3D modeling software generally has a high learning curve due to its complicated commands. Secondly, object manipulation is generally unnatural. A 3D direct manipulation with physically based simulation is one such solution. However, use of physically based simulation for this purpose is inappropriate due to its high computational complexity, and reduction in design flexibility. This paper presents a gesture-based 3D-manipulation technique where a 3D object responses to manipulation according to certain parameters. By adopting a pseudo-physical simulation approach, complexity requirement is lower than a physically based approach. In addition, a user still gains flexibility and efficiency in manipulation an object. The pseudo-physical simulation model is described for a Bezier curve object type. Extension to other object types is achieved by requiring that an object skeleton is modeled by a curve segment(s). The simulation model imposes two types of pseudo-physical constraints onto a curve, namely the length and bending angle constraints. A prototype of a 3D-curve-modeling tool has been developed. By adjusting a combination of model parameters, curves can reflect differences in the associated physical properties by being shaped differently to the same gesture-based manipulation.**

I. INTRODUCTION

Currently, 3D modeling has been widely used for various applications. Depending on an interaction technique adopted, as well as the underlying virtual object mathematical model, ease of use of a 3D modeling tool may vary. Direct manipulation based on a 2-D mouse is universally used in current 3D modeling tools as a principal interaction technique. However, in using a 2D-pointing device for 3D virtual object manipulation, a mouse-keyboard compound command is generally required. This can affect ease of learning and usage retention. In addition, 3D virtual objects are based on either a mathematical model of parametric curve, or a polygon model. With such models, virtual objects generally response to manipulation in a way that is quite different from real objects. Thus, time is required to develop a skill needed to efficiently model an object so that it has an intended shape.

A technique of 3D direct manipulation has been proposed for various virtual reality and simulation applications, to provide a more natural human computer interaction. This can result in reduced learning time. Currently, many VR devices have been developed for 3D direct manipulation techniques. An electronic glove is perhaps the most widely used VR device for such purpose because it allows gesture-based interaction to be performed. It is this type of VR device that is applied for our study.

In addition to an interaction technique used, a mathematical model of a virtual object also affects how natural the interaction experience is. To allow virtual objects to react more naturally to user manipulation action, physically based rules may be applied in performing shape manipulation [1-2]. In [1], a virtual spring model is used to make object manipulation more realistic. In [2], a different physically based model is applied so those virtual 3D objects behave more like a real object. In [3], direct manipulation using physically based sculpting with B-spline surface is developed to simplify object manipulation. However, such physically based simulations generally require high computation, and may be inappropriate for interaction applications. In addition, such physical rules impose a rigid constraint on how virtual objects are manipulated, and thus reducing design flexibility.

In this paper, use of a gesture-based 3D direct manipulation technique in combination with a pseudo-physical simulation model is proposed for 3D-curve modeling. Gesture-based interaction has been proposed for 3D-curve manipulation [4-5]. For example, in [4], a specialized input device called ShapeTape is used to obtain a shape of a tangible stripe object in controlling a computer-generated curve. Such approach is, however, inflexible for its degree of freedom is limited by the input device physical characteristics. Instead, an electronic glove is adopted in this paper to achieve more flexibility in performing object manipulation. The pseudo-physical simulation method is applied in defining the shape of a manipulated curve. The model used is composed of two pseudo-physical constraints imposed on a curve object With this simulation model, by varying the model parameters, 3D curves can behave differently to the same manipulation to

mimic different types of string material (such as robe or wire). The technique can also be extended to model 3D surface object shapes by using the skeleton technique [6].

The rest of the paper is organized as follows. In section 2, a 2D direct manipulation technique for Bezier curve modeling is described. In section 3, a 3D direct manipulation technique for Bezier curve is given. In section 4, detail of the pseudo-physical simulation method is provided. The modeling tools developed under the proposed method with results are explained in section 5. The paper ends with some concluding remarks.

II. 2D DIRECT MANIPULATION OF A BEZIER CURVE

A. Bezier curve

Bezier curve is defined by control points, which in turn define shape and characteristic of a curve. Four control points are used here for a Bezier curve. Such cubic Bezier curve will refer to simply as a Bezier curve. Points on the curve can be obtained according to the following equation.

$$\boldsymbol{R}(t) = (1-t)^3\boldsymbol{P}_0 + 3t(1-t)^2\boldsymbol{P}_1 + 3t^2(1-t)\boldsymbol{P}_2 + t^3\boldsymbol{P}_3 \quad (1)$$

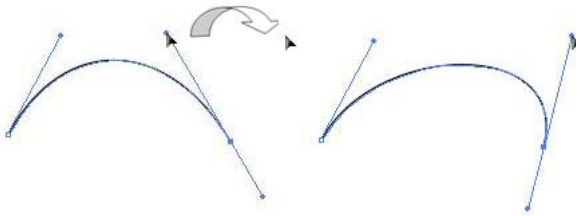

Figure 1. 2D direct manipulation of a Bezier curve as typically performed by a drawing tool

From the equation, $\boldsymbol{P}_0$, $\boldsymbol{P}_1$, $\boldsymbol{P}_2$, $\boldsymbol{P}_3$ are four control points (which are represented here as vectors from the origin).

B. Direct manipulation of a Bezier curve

Usually direct manipulation of a Bezier curve is performed at its control points. In 2D direct manipulation, a pointing device (e.g., a mouse) is used to manipulate the control points. Figure 1 illustrates how a Bezier curve is typically manipulated in a 2D graphic drawing tool.

C. Multiple-segment Bezier curve

Bezier curve can be used to represent many shapes. However, many of them cannot be well represented by a single curve segment. In that case, multiple segments of Bezier curve are used to represent complex shapes. If two or more segments are directly combined, however, it will result in discontinuity at the intersection.

Let s_1 and s_2 be the first and second consecutive segments, respectively. Bezier curve is continuous if the following condition is met.

$$\boldsymbol{P}_{3s1-1} - \boldsymbol{P}_{3s1} = -(\boldsymbol{P}_{3s2-2} - \boldsymbol{P}_{3s1}) \quad (2)$$

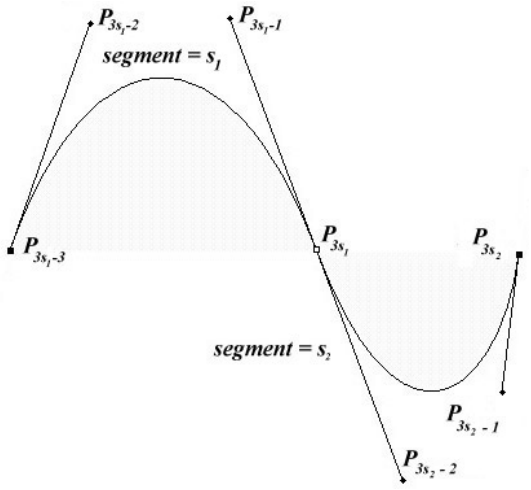

Figure 2. Preserving continuity at the intersection of two Bezier segments.

D. Bezier curve fragmentation

Fragmentation is an algorithm for splitting one segment into two segments, to realize a more complex curve. From definition of De Casteljau's algorithm [7], a polynomial $B(t)$ in Bernstein form of degree n can be expressed as

$$B(t) = \sum_{i=0}^{n} \beta_i^{(0)} b_{i,n}(t), \in [0,1] \quad (3)$$

where $b_{i,n}$ is a Bernstein basis polynomial. The polynomial at point t can be evaluated with the following recurrence relation.

$$\beta_i^{(0)} = \beta_i, i = 0,..,n \quad (4)$$

$$\beta_i^{(j)} = \beta_i^{j-1}(1-t) + \beta_{i+1}^{j-1}t, i = 0,..,n-j, j = 1,..,n \quad (5)$$

where

$$\boldsymbol{B}(t) = \beta_0^n \quad (6)$$

When choosing a point t_0 to evaluate a Bernstein polynomial, we can use the two diagonals of the triangle scheme to construct a division of the polynomial in (3) into

$$\boldsymbol{B}_1(t) = \sum_{i=0}^{n} \beta_0^i b_{i,n}\left(\frac{t}{t_0}\right), \in [0, t_0] \quad (7)$$

and

$$\boldsymbol{B}_2(t) = \sum_{i=0}^{n} \beta_{n-i}^i b_{i,n}\left(\frac{t-t_0}{1-t_0}\right), \in [t_0, 1] \quad (8)$$

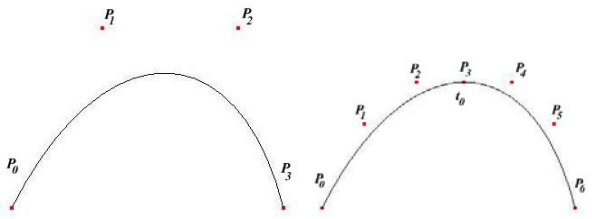

Figure 3. Bezier curve fragmentation at t_0

III. 3D DIRECT MANIPULATION OF A BEZIER CURVE

Here, 3D direct manipulation technique for curve shaping is performed through an electronic glove device using gesture-based human-computer interaction technique.

A. Gesture-based direct manipulation of a Bezier curve

A gesture-based direct manipulation technique was developed to model a Bezier curve. By using a (one or two-handed) electronic glove device, hand position and orientation are used to control the curve parameters. In particular, the hand position is used to control the position of $\boldsymbol{P_1}$ ($\boldsymbol{P_2}$), while its orientation (denoted by unit vectors $\boldsymbol{V_1}$ $\boldsymbol{V_2}$) is used to control the control point direction. See Figure 4 for illustration.

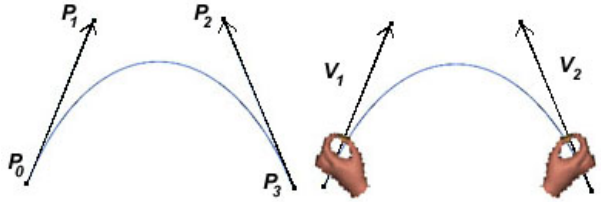

Figure 4. Manipulation of control parameters of a Bezier curve using hand position and orientation

This control can be expressed mathematically by the following equations.

$$\boldsymbol{P_1} - \boldsymbol{P_0} = \alpha \boldsymbol{V_1} \tag{9}$$

$$\boldsymbol{P_2} - \boldsymbol{P_3} = \beta \boldsymbol{V_2} \tag{10}$$

Only the direction part of the above equations is controlled by a hand orientation. The length parameters (α and β) are controlled by the two pseudo-physical constraints to be explained later.

By substituting (9)-(10) into (1), we arrive at

$$\begin{aligned}\boldsymbol{R}(t) = {} & (t-1)^2(2t-1)\boldsymbol{P_0} + 3t(1-t)^2\alpha\boldsymbol{V_1} \\ & + 3t^2(1-t)\beta\boldsymbol{V_2} + t^2(3-2t)\boldsymbol{P_3}\end{aligned} \tag{11}$$

where α and β are control parameters, whose values are obtained under the pseudo-physical constraints to be described shortly.

B. Collision detection

To perform 3D direct manipulation, collision between an electronic glove device and the object under manipulation must be detected. Here, a simple spherical shape with its center at a user palm is used as a collision proxy. In addition, line segments are used in rendering of a Bezier curve. Thus, collision point is calculated by using the method of line segment-sphere intersection [8].

From method of line segment-sphere intersection, $\boldsymbol{R}$ (t_1) and $\boldsymbol{R}$ (t_2) is start and end point of line segment that collides with sphere.

C. Curve control parameter mapping

As previously stated, a Bezier curve is manipulated by changing its control-point parameters. However, it is the hand orientation and position that are measured when gesture-based direct manipulation is applied. Therefore, there is a need to map the measured hand position and orientation to Bezier curve parameters. To do this, consider first Figure 4. From the figure and (9) - (10), the control points' positions and orientations are defined by $\boldsymbol{P_0}$, $\boldsymbol{P_3}$, $\boldsymbol{V_1}$, $\boldsymbol{V_2}$, α, and β. The left and right hand positions can be directly mapped to $\boldsymbol{P_0}$ and $\boldsymbol{P_3}$, respectively. In addition, hand orientations can be directly mapped to $\boldsymbol{V_1}$, and $\boldsymbol{V_2}$.

$$\begin{aligned} a_1 &= (1-t_1)^2(1+2t_1) & a_2 &= (1-t_2)^2(1+2t_2) \\ b_1 &= 3t_1(1-t_1)^2 & b_2 &= 3t_2(1-t_2)^2 \\ c_1 &= 3t_1^2(1-t_1) & c_2 &= 3t_2^2(1-t_2) \\ d_1 &= t_1^2(3-2t_1) & d_2 &= t_2^2(3-2t_2) \end{aligned} \tag{12}$$

$\boldsymbol{R}$ (t_1) and $\boldsymbol{R}$ (t_2) are points on Bezier curve that collide with user hand(s) using a collision detection method as described in Section III-*B*. From this, the vector $\boldsymbol{V}_1$ and $\boldsymbol{V_2}$ can be calculated from

$$\boldsymbol{V_1} = \frac{1}{\alpha}\frac{c_2\boldsymbol{R}(t_1) - c_1\boldsymbol{R}(t_2) + (a_2c_1 - a_1c_2)\boldsymbol{P_0} + (c_1d_2 - c_2d_1)\boldsymbol{P_3}}{b_1c_2 - b_2c_1} \tag{13}$$

$$\boldsymbol{V_2} = \frac{1}{\beta}\frac{b_2\boldsymbol{R}(t_1) - b_1\boldsymbol{R}(t_2) + (a_2b_1 - a_1b_2)\boldsymbol{P_0} + (b_1d_2 - b_2d_1)\boldsymbol{P_3}}{b_2c_1 - b_1c_2} \tag{14}$$

With the above equations, all curve parameters except α and β are mapped from user hand positions and orientations. These two parameters are obtained by imposing pseudo physical constraints as described next.

D. Pseudo physical constraints

As noted, α and β are two curve parameters left not matched to any hand parameters. Here, these remaining curve parameters are defined by two pseudo-physical constraints. The constraints are imposed on a curve object to mimic physical properties of different string-type objects (such as elastic rope and wire etc.). These constraints are described below.

1) Length constraint: this constraint imposes a limit on how a curve length can vary from its original value. For example, a wire has a strong length constraint so that it tends to being bended sharply in response to a shape manipulation, to retain its original length.

2) Bending angle constraint: this constraint imposes a limit on how much a bending angle is allowed for a curve. For example, an elastic rope has a strong bending constraint. Therefore, it tends to stretch in response to a shape manipulation, to avoid sharp bend.

E. Multiple-segment Manipulation Modes

In direct manipulation of multiple-segment Bezier curve, we can choose from different manipulation modes to affect the

object's shape differently. First, let $\boldsymbol{V}_{12}$ and $\boldsymbol{V}_{21}$ represents control vectors as described in Figure 5(a). If both sizes and directions of $\boldsymbol{V}_{12}$ and $\boldsymbol{V}_{21}$ are equal, the Bezier curve is continuous over multiple (two) segments. If the two have opposite direction with arbitrary sizes, the two segments form G^1 continuity. If the two have arbitrary size and direction, the two curves can be manipulated independently. In summary, manipulation modes of multiple-segment Bezier curve supported by the system are G^2 *connected*, G^1 *connected* and G^0 *connected* (Split) mode.

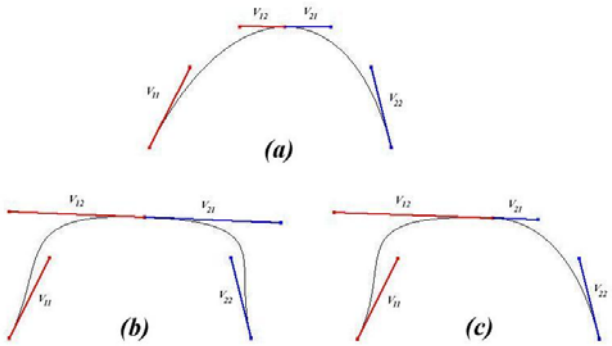

Figure 5. (a) Multiple-segment Bezier curve; (b) Bezier curve in G^2 *connected* mode; (c) Bezier curve in G^1 *connected* mode

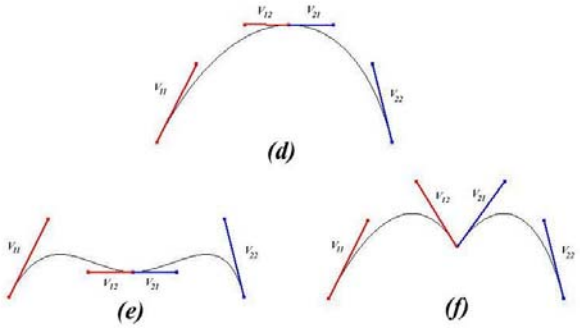

Figure 6. (d) Multiple-segment Bezier curve; (e) Bezier curve in G^2 *connected* mode; (f) Bezier curve in G^0 *connected* mode

IV. PSEUDO-PHYSICAL SIMULATION

A pseudo-physical simulation technique is applied here to provide a physical-like property to a 3D virtual object. The technique is much simpler than a common physically based method. The two types of constraints as explained in Section III-*D* are combined into the following cost function

$$C = w_1 \Delta L + w_2 (1 - \cos\theta_{\max}) \qquad (15)$$

where C is a cost value to minimize, w_1 and w_2 are user definable parameters. From the same equation, ΔL is a normalized length difference as defined by

$$\Delta L = \frac{L - L_0}{L_0} \qquad (16)$$

From (15) and (16), L is the current curvature length, and L_0 is the original length. In addition, $\theta_{\max}$ is the largest bending angle along the curve. From Figure 7 the angle is obtained by finding the angle $\theta(t)$ between the vectors $\boldsymbol{R}_t\boldsymbol{R}_{t-1}$ and $\boldsymbol{R}_{t+1}\boldsymbol{R}_t$. Then, $\cos\theta_{\max}$ is obtained from

$$\cos\theta_{max} = \max_{t=0\to 1} \cos\left(\frac{\mathbf{R}_t\mathbf{R}_{t-1} \bullet \mathbf{R}_{t+1}\mathbf{R}_t}{\left|\mathbf{R}_t\mathbf{R}_{t-1}\right|\left|\mathbf{R}_{t+1}\mathbf{R}_t\right|}\right) \qquad (17)$$

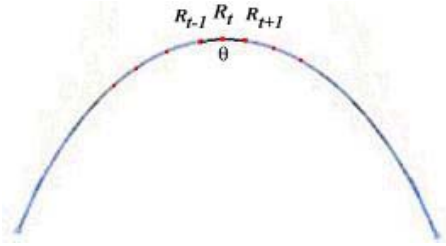

Figure 7. Calculation of a bending angle along a Bezier curves.

From (15) and (16), L is implicitly a function of α and β. Also, from (11) R_t is implicitly a function of α and β. Therefore, $\theta_{\max}$ and C are all the functions of α and β.

From (15) - (17), we can calculate C (α, β) from w_1, w_2, ΔL and M. and C must be minimized with respect to α and β. As a result, α and β are obtained from.

$$(\alpha_{\min}, \beta_{\min}) = \arg \min_{\alpha,\beta} C(\alpha, \beta) \qquad (18)$$

V. SOFTWARE PROTOTYPE AND RESULTS

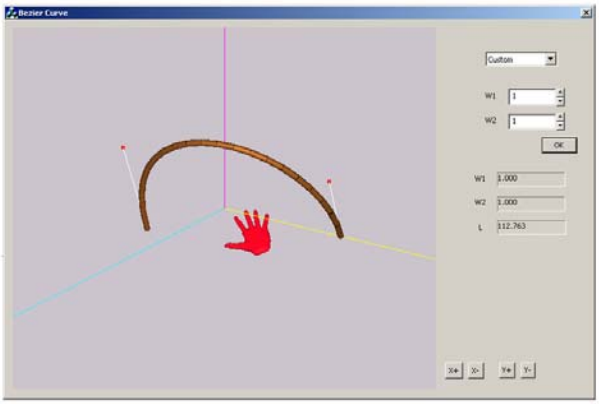

Figure 8. Software prototype

A software prototype was developed using Visual C++ and OpenGL library for graphic display. Experiments were performed with one-handed and two-handed electronic glove (CyberGlove®) configurations. Different values of w_1 and w_2 were tested. Figure 9 shows the result of the manipulation. Figure 10 compares the shapes obtained using different sets of w_1 and w_2.

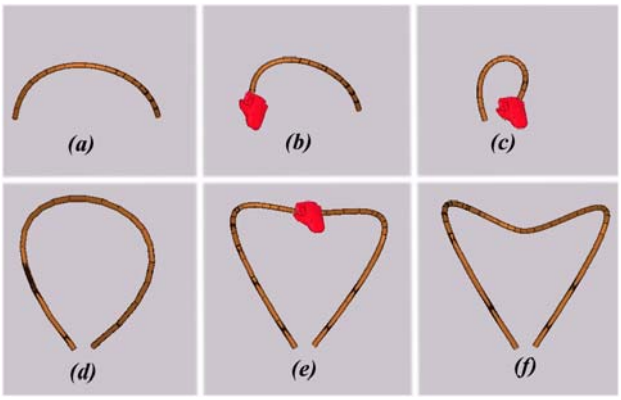

Figure 9. (a) normal Bezier curve; (b) and (c) curve end-points translation by hand gesture; (d) gesture-based manipulation with pseudo-physical constraints; (e) gesture-based manipulation with auto-fragmentation operated in the non-continuous mode; (f) the final shape

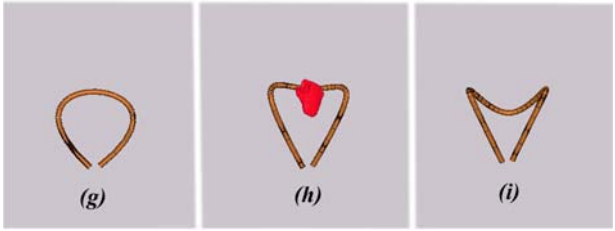

Figure 10. (g) Pseudo-physical constraints using different parameter; (h) manipulation with auto-fragmentation; (i) final shape

Figure 9a shows a normal Bezier curve before manipulation. The manipulated curve shown in Figure 9b and 9c was obtained by translating the curve end-point with gesture-based manipulation. Using gesture-based manipulation with pseudo-physical constraint with w_1 = 1.0 and w_2 = 1.0, the manipulation result is shown in Figure 9d. By using auto-fragmentation operated in the non-continuous mode, a more complex shape was obtained as shown in Figure 9e. Figure 10 shows the same curve undergone similar manipulation, but with different set of constraint parameters (w_1 = 0.3 and w_2 = 14.0).

VI. Conclusion

In this paper, a pseudo-physical simulation method for 3D direct manipulation of a 3D curve has been described. The method features the ease of use of a 3D direct manipulation metaphor, and a simulated real-object behavior of a virtual object. Unlike a physically based simulation approach, with its simple equation the proposed pseudo-physical method can reduce processing time and offers more flexibility in designing 3D curves. Software tool has been developed based on the proposed method and was applied to manipulate simple and complex curve shapes.

References

[1] Shi-Min Hu , Hui Zhang , Chiew-Lan Tai and Jia-Guang Sun , "Direct Manipulation of FFD: efficient explicit solutions and decomposible multiple point constraints" ,Springer-Verlag 2001

[2] Kevin T. Mcdonnell and Houng Qin , "Dynamic Sculpting and Animation of Free-form Subdivision Solids" IEEE2000

[3] Colette J. Mullenhoff , "Physically-Based B-Spline Surface Sculpting", Department of Computer Science,The University of Utah December 1998

[4] Tovi Grossman , Ravin Balakrishnan , Karan Singh , "An Interface for Creating and Manipulating Curves using a High Degree-of-Freedom Curve Input Device" CHI 2003

[5] Ignacio Llamas , Alexander Powell , Jarek Rossignac , Chris D. Shaw , "Bender: A Virtual Ribbon for Deforming 3D Shapes in Biomedical and Styling Applications" , ACM Symposium on Solid and Physical Modeling 2005.

[6] Steave Capell , Seth Green , Brian Curless , Tom Duchamp and Zoran Popovic 2002. "Interactive Skeleton-Driven Dynamic Deformations". ACM 2002

[7] Wolfgang Boehm, Andreas Muller, "Computer Aided Geometric Design" , pages 587-605 year of publication 1999 , ISSN:0167-8396

[8] Rhoad, R.; Milauskas, G.; and Whipple, R. "Geometry for Enjoyment and Challenge", rev. ed. Evanston, IL: McDougal, Littell & Company, 1984.

[9] Fuhua Cheng and Chi-Cheng Lin, "Clipping of Bezier Curves",ACM 1985.

Sequence Mirroring Properties of Orthogonal Transforms Having Even and Odd Symmetric Vectors

Do Nyeon Kim and K. R. Rao, *Fellow, IEEE*
E.E. Dept., 416 Yates Street
UTA, Box 19016
Arlington, TX 76019 USA

***Abstract*-This paper presents sequence mirroring properties for discrete orthogonal transforms consisting of the even and odd symmetric row vectors. As an application, mirroring an image (horizontally or vertically) and rotation by 90°, 180° and 270° in the spatial domain is implemented by changing the signs of the 2D orthogonal transform coefficients of the original image appropriately.**

I. INTRODUCTION

As the discrete transforms, in general, have been utilized in a number of image/video compression/coding schemes, it is helpful to implement the mirroring/resizing operations in the transform domain. This paper presents sequence mirroring properties for discrete orthogonal transforms consisting of the even and odd symmetric row vectors. These properties are valid for DCT [1], DST (also all their integer revisions – integer DCT (IntDCT) [5], IntDST [8], integer cosine transform (ICT) [2], IST [8] etc.), slant [9], and Hadamard transforms. Variants of ICT are developed for H.264 [3], WMV9 [4] and AVS China [6], and they also hold these inherent properties. Orthogonal transforms that are not symmetric include MDCT, Haar transform and Hartley transform. This property for the DCT has been presented by Shen and Sethi [7], but it is generalized for other transforms in this paper. We show specific applications using some of these transforms.

II. PROPOSED ALGORITHM

We can prove sequence mirroring properties for discrete orthogonal transforms consisting of even and odd symmetric row vectors as follows. Let $[S_4]$ be one of these orthogonal matrices of size (4×4) and be defined as

$$[S_4]=\begin{bmatrix} a & b & b & a \\ c & d & -d & -c \\ e & -f & -f & e \\ g & -h & h & -g \end{bmatrix} \begin{matrix} even \\ odd \\ even \\ odd \end{matrix} . \quad (1)$$

Since $[S_4]$ is orthogonal, it follows that $[S_4]^T[S_4]=[I]$, where the superscript T represents transpose, and I is the identity matrix. For later use, let column vectors of $[S_4]^T$ be

$$[S_4]^T=(\underline{s}_{R,0}, \underline{s}_{R,1}, \underline{s}_{R,2}, \underline{s}_{R,3}) \quad (2)$$

$$=(\underline{e}_R, \underline{o}_R, \underline{e}_R, \underline{o}_R) \quad (3)$$

where $\underline{e}_R$ and $\underline{o}_R$ represent even and odd symmetric column vectors of $[S_4]^T$. Also, let column vectors of $[S_4]$ be

$$[S_4]=(\underline{s}_{C,0}, \underline{s}_{C,1}, \underline{s}_{C,2}, \underline{s}_{C,3}) \quad (4)$$

where $\underline{s}_{C,n}$ for n = 0, …, 3 are column vectors of $[S_4]$.

Let an input sequence or column vector be $\underline{x}$. We can get the mirrored transform coefficients $\underline{X}_M$ if we set input sequence in reverse order and then transform it.

$$\underline{X}_M=[S_4][J_4]\underline{x} \quad (5)$$

where the permutation matrix

$$[J_4]=\begin{bmatrix} 0 & 0 & 0 & 1 \\ 0 & 0 & 1 & 0 \\ 0 & 1 & 0 & 0 \\ 1 & 0 & 0 & 0 \end{bmatrix} \quad (6)$$

is the opposite diagonal unit matrix. The matrix multiplication $[S_4][J_4]$ arranges the column vectors of $[S_4]$ in reverse order. Thus the signs of elements of odd symmetric row vectors of $[S_4]$ are changed whereas the signs of elements of even symmetric row vectors are not changed while absolute values of elements of $[S_4]$ are not changed, since $[S_4]$ is a matrix having either even or odd symmetric rows. Thus

$$\underline{s}_{C,0}=[K_4^I]\ \underline{s}_{C,3} \quad \text{and} \quad \underline{s}_{C,1}=[K_4^I]\ \underline{s}_{C,2} \quad (7)$$

where

$$[K_4^I]=diag(1, -1, 1, -1). \quad (8)$$

It is noted a diagonal element of $[K_4^I]$ is the positive number one if the corresponding column vector of $[S_4]$ is of even symmetry, and an element is the negative number one if the corresponding column vector is of odd symmetry. From (8), $[S_4][J_4]=(\underline{s}_{C,3}, \underline{s}_{C,2}, \underline{s}_{C,1}, \underline{s}_{C,0})$

$$= \left(\left[K_4^I\right] \underline{s}_{C,0}, \left[K_4^I\right] \underline{s}_{C,1}, \left[K_4^I\right] \underline{s}_{C,2}, \left[K_4^I\right] \underline{s}_{C,3} \right)$$
$$= \left[K_4^I\right] \left(\underline{s}_{C,0}, \underline{s}_{C,1}, \underline{s}_{C,2}, \underline{s}_{C,3} \right)$$
$$= \left[K_4^I\right] \left[S_4\right]. \quad (9)$$

Let the mirrored sequence of an input sequence $\underline{x}$ be $\underline{x}_M$. From (10), we can compute $\underline{X}_M$ transform coefficients of $\underline{x}_M$ as

$$\underline{X}_M = \left[S_4\right] \underline{x}_M = \left[S_4\right]\left[J_4\right] \underline{x}$$
$$= \left[K_4^I\right] \left[S_4\right] \underline{x} = \left[K_4^I\right] \underline{X} \quad (10)$$

or

$$\underline{x}_M = \left[S_4\right]^T \underline{X}_M = \left[S_4\right]^T \left[K_4^I\right] \underline{X}. \quad (11)$$

We can generalize transforms represented by (1) for size *N*.

$$\left[S_N\right]^T = \left(\underline{s}_{R,0}, \underline{s}_{R,1}, \ldots, \underline{s}_{R,N-2}, \underline{s}_{R,N-1} \right)$$
$$= \left(\underline{e}_R, \underline{o}_R, \ldots, \underline{e}_R, \underline{o}_R \right) \quad \text{for } N \text{ even}$$
$$= \left(\underline{e}_R, \underline{o}_R, \ldots, \underline{o}_R, \underline{e}_R \right) \quad \text{for } N \text{ odd.} \quad (12)$$

We refer to orthogonal transforms represented by (1) as type 1 orthogonal transform, and the type 1 includes DCT, DST and slant transform.

The Hadamard transform has a similar property. Let $\left[S^{WH}\right]$ be a matrix of size (8×8) representing the Hadamard transform. Then,

$$\left[S^{WH}\right]^T = \left(\underline{e}_R, \underline{o}_R, \underline{o}_R, \underline{e}_R, \underline{o}_R, \underline{e}_R, \underline{e}_R, \underline{o}_R \right). \quad (13)$$

To change an input vector into reverse order, the signs of elements of even symmetric row vectors of $\left[S^{WH}\right]$ are not changed however the signs of elements of odd symmetric row vectors are changed.

Similarly with (9), we can compute $\underline{X}_M^{WH}$ transform coefficients of the mirrored sequence of an input sequence $\underline{x}$ as

$$\underline{X}_M^{WH} = \left[S^{WH}\right]\left[J_8\right]\left[x\right] = \left[K_8^{II}\right] \underline{X}^{WH} \quad (14)$$

where $\left[J_8\right]$ is a permutation matrix and the opposite diagonal unit matrix of size (8×8), and

$$\left[K_8^{II}\right] = diag\left(1, -1, -1, 1, -1, 1, 1, -1\right). \quad (15)$$

We can get the signs of (15) in the same manner explained in (8). We refer to orthogonal transforms represented by (13) as type 2 orthogonal transform, and the type 2 includes the Hadamard transform.

Thus we can mirror a sequence in the transformed domain just by changing signs of transform coefficients. Applications of these very useful properties for compressed-domain image editing by using the DCT have been presented in [7]. Two-dimensional extension is presented in the next section.

III. Two-Dimensional Extension

Mirroring or rotation of an image is illustrated using an (8×8) block. Given

$$\left[x\right] = \begin{pmatrix} x_{00} & x_{01} & \cdots & x_{07} \\ x_{10} & x_{11} & \cdots & x_{17} \\ \vdots & \vdots & \ddots & \vdots \\ x_{70} & x_{71} & \cdots & x_{77} \end{pmatrix}, \quad (16)$$

horizontally mirrored sequence of $\left[x\right]$ is

$$\left[x_h\right] = \begin{pmatrix} x_{07} & x_{06} & \cdots & x_{00} \\ x_{17} & x_{16} & \cdots & x_{10} \\ \vdots & \vdots & \ddots & \vdots \\ x_{77} & x_{76} & \cdots & x_{70} \end{pmatrix}. \quad (17)$$

Similarly, we can get the vertically mirrored sequence of $\left[x\right]$, $\left[x_v\right]$. $\left[x\right]$ rotated by 90° is

$$\left[x_{90^o}\right] = \begin{pmatrix} x_{70} & x_{60} & \cdots & x_{00} \\ x_{71} & x_{61} & \cdots & x_{01} \\ \vdots & \vdots & \ddots & \vdots \\ x_{77} & x_{67} & \cdots & x_{07} \end{pmatrix}. \quad (18)$$

Let $\left[x\right]$ rotated by 180° be $\left[x_{180^o}\right]$, and $\left[x\right]$ rotated by 270° be $\left[x_{270^o}\right]$.

Image can be represented as nonoverlapping blocks of size $N \times N$ (for example $N = 8$). Each block can be represented as a matrix $\left[x\right] = \{x(n_1, n_2)\}_{n_1,n_2=0}^{7}$ shown in (16). Let $\left[S_8\right]$ be an orthogonal transform of size (8×8). Then we can compute the two-dimensional transform coefficients matrix $\left[X\right]$ of an input image block or matrix, $\left[x\right]$ as follows:

$$\left[X\right] = \left[S_8\right]\left[x\right]\left[S_8\right]^T. \quad (19)$$

Let the 2D-transform of horizontally mirrored sequence $\left[x_h\right]$ be $\left[X_H\right]$ and the 2D-transform of vertically mirrored sequence $\left[x_v\right]$ be $\left[X_V\right]$. Then we can compute $\left[X_H\right]$ and $\left[X_V\right]$ as follows:

$$\left[X_H\right] = \left[X\right]\left[K_8\right] \quad (20)$$

$$\left[X_V\right] = \left[K_8\right]\left[X\right] \quad (21)$$

where the matrix $\left[K_8\right]$ can be $\left[K_8^I\right]$ or $\left[K_8^{II}\right]$ depending on the associated orthogonal transform. Here $\left[K_8^I\right]$ is defined as

$$\left[K_8^I\right] = diag\left(1, -1, 1, -1, 1, -1, 1, -1\right) \quad (22)$$

and $\left[K_8^{II}\right]$ is defined in (15).

Thus we can select a group of consecutive 2D-transform blocks of an image and flip horizontally according to the following steps:

1. Apply the (8×8) 2D-transform to the nonoverlapping blocks of size (8×8) of the image.
2. Set the size of a rectangular block to be horizontally flipped. Horizontal and vertical sizes should be integer multiples of eight according to the transform size.
3. Compute transform-domain image flipping for each 2D-transform block by using (20).
4. Rotate horizontally transform blocks within the rectangular block. The most left transform block goes to the most right, and vice versa.

In general this is applicable to $(N \times N)$ 2D-transforms having even and odd symmetric vectors by choosing $[K_8^I]$ appropriately. We can also rotate an image block by 90° in the 2D-transform domain by using the proposed scheme. Let us denote the 2D-transform of the 90°, 180° and 270° rotated blocks in the spatial domain $[x_{90^o}]$, $[x_{180^o}]$ and $[x_{270^o}]$ as $[X_{90^o}]$, $[X_{180^o}]$ and $[X_{270^o}]$ respectively. Then we can compute 2D-transform of rotated blocks in the spatial domain using (9) as follows:

$$[X_{90^o}] = [S][x]^T[J_8][S]^T = [S][x]^T[S]^T[K_8^I] = [X]^T[K_8^I] = [X_V]^T. \quad (23)$$

Let the symbol $\otimes$ represent element-by-element multiplication.

$$[X_{180^o}] = [K_8][X][K_8] = [W] \otimes [X] \quad (24)$$

where the matrix $[W]$ can be $[W^I]$ or $[W^{II}]$ depending on the associated orthogonal transform. Here the matrices $[W^I]$ and $[W^{II}]$ are defined as

$$[W^I] = \begin{bmatrix} 1 & -1 & 1 & -1 & 1 & -1 & 1 & -1 \\ -1 & 1 & -1 & 1 & -1 & 1 & -1 & 1 \\ 1 & -1 & 1 & -1 & 1 & -1 & 1 & -1 \\ -1 & 1 & -1 & 1 & -1 & 1 & -1 & 1 \\ 1 & -1 & 1 & -1 & 1 & -1 & 1 & -1 \\ -1 & 1 & -1 & 1 & -1 & 1 & -1 & 1 \\ 1 & -1 & 1 & -1 & 1 & -1 & 1 & -1 \\ -1 & 1 & -1 & 1 & -1 & 1 & -1 & 1 \end{bmatrix} \quad (25)$$

$$[W^{II}] = \begin{bmatrix} 1 & -1 & -1 & 1 & -1 & 1 & 1 & -1 \\ -1 & 1 & 1 & -1 & 1 & -1 & -1 & 1 \\ -1 & 1 & 1 & -1 & 1 & -1 & -1 & 1 \\ 1 & -1 & -1 & 1 & -1 & 1 & 1 & -1 \\ -1 & 1 & 1 & -1 & 1 & -1 & -1 & 1 \\ 1 & -1 & -1 & 1 & -1 & 1 & 1 & -1 \\ 1 & -1 & -1 & 1 & -1 & 1 & 1 & -1 \\ -1 & 1 & 1 & -1 & 1 & -1 & -1 & 1 \end{bmatrix}. \quad (26)$$

Similarly, using (9)

$$[X_{270^o}] = [S][J_8][x]^T[S]^T = [K_8][S][x]^T[S]^T = [K_8^I][X]^T = [X_H]^T. \quad (27)$$

We can also show (24) and (27) by using $[x]^T \Leftrightarrow [X]^T$, where the symbol $\Leftrightarrow$ indicates forward and inverse 2D-DST pair.

IV. Applications

A. Integer DCT for H.264

We use the integer DCT designed for the Fidelity Range Extension (FRExt) [3] of the H.264/MPEG-4 Advanced Video Coding (AVC) standard. The integer DCT is defined as follows:

$$[S^{FRE}] = [SF^{FRE}]\,[H^{FRE}] \quad (28)$$

where

$$[SF^{FRE}] = diag\{1/(16\sqrt{2}), 1/(17\sqrt{2}), 1/(8\sqrt{5}), 1/(17\sqrt{2}), 1/(16\sqrt{2}), 1/(17\sqrt{2}), 1/(8\sqrt{5}), 1/(17\sqrt{2})\}$$

and $[H^{FRE}]$ is defined by Eq. (14) in [11].

B. DCT and DST

The type 2 DCT for N = 8 and the type 1 DST for N = 9 are defined in matrix form as follows:

$$[S^{C2}]_{mn} = \sqrt{2/N}[k_m k_n]\cos[m(n+\tfrac{1}{2})\pi/N] \quad (29)$$

$m, n = 0, 1, \ldots, N\text{-}1$

$$[S^{S1}]_{mn} = \sin(mn\pi/N) \qquad m, n = 1, 2, \ldots, N \quad (30)$$

where $k_p = 1/\sqrt{2}$ for $p = 0$ and $k_p = 1$ otherwise.

C. Slant Transform

The slant transform [9] is defined as follows:

$$[S^{SL}] = [SF^{SL}]\,[H^{SL}] \quad (31)$$

where

$$[SF^{SL}] = \sqrt{1/8}\; diag(1, \sqrt{7/3}, 3\sqrt{5}, 17\sqrt{105}, 1, 1, 3\sqrt{5}, 3\sqrt{5})$$

and

$$[H^{SL}] = \begin{bmatrix} 1 & 1 & 1 & 1 & 1 & 1 & 1 & 1 \\ 1 & \frac{5}{7} & \frac{3}{7} & \frac{1}{7} & -\frac{1}{7} & -\frac{3}{7} & -\frac{5}{7} & -1 \\ 1 & \frac{1}{3} & -\frac{1}{3} & -1 & -1 & -\frac{1}{3} & \frac{1}{3} & 1 \\ \frac{7}{17} & -\frac{1}{17} & -\frac{9}{17} & -1 & 1 & \frac{9}{17} & \frac{1}{17} & -\frac{7}{17} \\ 1 & -1 & -1 & 1 & 1 & -1 & -1 & 1 \\ 1 & -1 & -1 & 1 & -1 & 1 & 1 & -1 \\ \frac{1}{3} & -1 & 1 & -\frac{1}{3} & -\frac{1}{3} & 1 & -1 & \frac{1}{3} \\ \frac{1}{3} & -1 & 1 & -\frac{1}{3} & \frac{1}{3} & -1 & 1 & -\frac{1}{3} \end{bmatrix}.$$

D. Hadamard Transform

The Hadamard transform [8] is defined by Eq. (5.107) in [10].

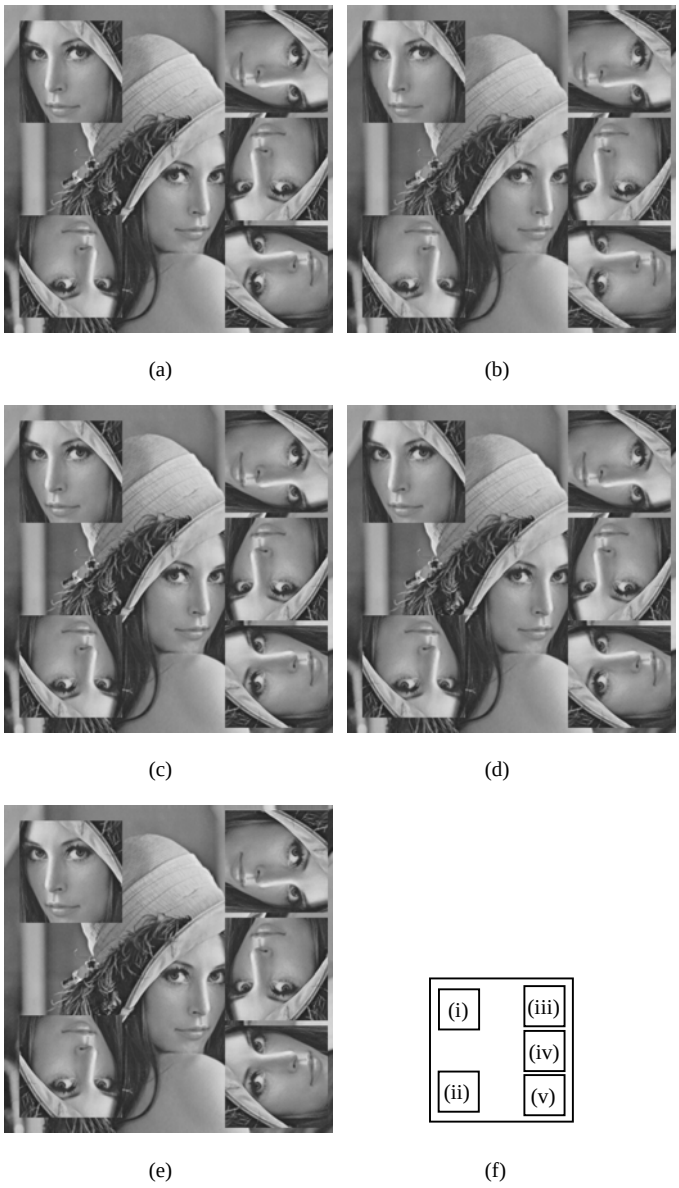

Figure 1. Mirroring or rotation of portion of Lena image in the spatial domain by manipulating the 2D-transform coefficients of the original block: (i) horizontal mirroring, (ii) vertical mirroring, (iii) rotation by 90°, (iv) rotation by 180°, and (v) rotation by 270° for (a) IntDCT of H.264, (b) Slant transform, (c) Hadamard transform (d) DST, and (e) DCT. Here the number of each block in images is shown in (f).

E. Simulations

Using Eqs. (16)-(26), the 2D-transform domain manipulation is utilized to obtain image mirroring and rotation by 90°, 180°, and 270° in spatial domain. Note that image mirroring and rotation by 90°, 180°, and 270° in spatial domain is accomplished by changing the signs of the 2D-transform coefficients of the original image appropriately. These operations are implemented on the Lena image (see Fig. 1).

ACKNOWLEDGMENT

Do Nyeon Kim acknowledges the support by the Korea Ministry of Information and Communication.

REFERENCES

[1] K. R. Rao and P. Yip, *The transform and data compression handbook*. CRC Press, 2001.

[2] W. K. Cham, "Development of integer cosine transforms by the principle of dyadic symmetry," *IEE Proc. I, Commu., Speech & Vision*, vol. 136, pp. 276-282, Aug. 1989.

[3] G. J. Sullivan, P. Topiwala and A. Luthra, "The H.264/AVC advanced video coding standard: overview and introduction to the fidelity range extensions", in *Proc. SPIE Conf. on Applications of Digital Image Processing XXVII*, pp. 53-74, Aug. 2004.

[4] S. Srinivasan et al., "Windows media video 9: overview and applications," Signal Processing: Image Communication, vol. 19, pp. 851-875, Oct. 2004.

[5] Y.-J. Chen and S. Oraintara, "Video compression using integer DCT," in *Proc. IEEE ICIP*, pp. 844-845, Sept. 2000.

[6] W. Gao *et al*., "AVS – The Chinese next-generation video coding standard", NAB, Las Vegas, Nevada, April 2004.

[7] B. Shen and I. K. Sethi, "Inner-block operations on compressed images," in *Proc. of the Third ACM International Conference on Multimedia*, pp. 489-498, San Francisco CA, 1995.

[8] V. Britanak, P. Yip and K. R. Rao, *Discrete cosine and sine transforms*. Orlando, FL: Academic Press (Elsevier), 2007.

[9] W. K. Pratt, W.-H. Chen and L. R. Welch, "Slant transform image coding," *IEEE Trans. Commun*., vol. 22, pp. 1075-1093, Aug. 1974.

[10] A. K. Jain, "Fundamentals of digital image processing," Englewood Cliffs, NJ: Prentice Hall, 1989.

[11] S.-K. Kwon, A. Tamhankar and K. R. Rao, "Overview of H.264/MPEG-4 part 10," J. Vis. Commun. Image R., vol. 17, pp. 186-216, April 2006.

Multi-Resolution Belief Propagation for Stereovision

Preeyakorn Tipwai and Suthep Madarasmi
Computer Engineering Department, King Mongkut's University of Technology Thonburi
126 Pracha-utid Rd., Bangmod, Toongkru, Bangkok 10140, THAILAND

***Abstract*-We propose a multi-resolution algorithm for stereo matching. The algorithm works with a grid matching and an inter-grid matching stereo model in terms of message passing in a Bayesian belief propagation (BBP) framework. The local smoothness and other constraints are expressed within each resolution scale grid and also between grids in a single paradigm. The matching within a single resolution grid contains data matching costs and smoothness costs. The inter-grid matching helps avoid the local minimum problem in finding the optimal solution by bringing features closer at the coarse level and yet providing a full-scale solution at the finest level. The results on real and synthetic images are presented, showing an increase in the accuracy of the disparity map.**

I. INTRODUCTION

The majority of machine vision algorithms work on 2-D cases. Stereo matching computes the third dimension by finding the matching features in each of the left and right images, and then measures the distances to objects containing these features by triangulation; that is, by intersecting the lines of sight from each camera to the object.

Considerable progress in stereo vision has been achieved by formulating the problem in terms of energy minimization. Lucas and Kanade [1] presented an iterative image registration technique with an application to stereo vision. They used the spatial intensity gradient of the images to find a good match using the Newton-Raphson's iterative method. The difficulty of this approach is in its requirement of considerable hand-guidance, so a method to automate the process is needed.

Marapane and Trivedi [2] proposed a multi-primitive hierarchical method for stereo matching. Each matching module uses a simple minimum distance based classifier to choose correspondences. Average contrast, average angle, and slope are used as attributes for comparing similarity of the linear features. Edge contrast and angle are also compared. However, an analysis found that the system is formulated as a nonsymmetrical matching process.

Boykov *et. al.* [3] proposed a method for computing dense visual correspondence based on general assumptions about scene geometry. For each pixel, the plausible disparity with the largest connected component is selected. A variable region of support is used to decrease false matches near the object boundaries. A suitable correlation measure method and sufficiently large window size are important, but a window may encompass more than a single smooth disparity region if the size is too large.

Tomasi and Manduchi [4] proposed a representation using intrinsic curves and transforming stereo matching into a nearest neighbor problem. The image positions are stored by their appearance instead of image intensities with the objective to store image points that look similar in the same place, so correspondences are trivially established. Occlusions are also easily found as points that lie isolated in some location. However, different image points can look the same, making memory locations crowded, and corresponding points in the images can look different, causing points that should be in the same memory location to vary.

Bayesian Belief Propagation (BBP) has recently become the choice algorithm for energy minimization in solving computer vision-related optimization problems. Good optimization algorithms for stereo vision based on BBP have been developed. Kolmogrorov [5][6], Wainwright *et. al* [7] and Meltzer *et. al* [8] applied the Tree Re-weighted Belief Propagation (TRBP) to the stereopsis problem. Sun *et. al* [9][10] proposed a variety of BBP for stereo matching with a line process for depth discontinuity and a binary process for occlusion handling. Belief Propagation methods produce highly accurate results in practice. However, several iterations are required to propagate data within a large neighborhood, and distant features are often not successful in propagating their constraints. Felzenszwalb and Huttenlocher [11] proposed a coarse-to-fine BBP approach with an added approximation to reduce the computational complexity inherent in the classical BBP algorithm. The top-down manner of the coarse-to-fine architecture helps the multi-stage process to escape a local minimum in the parameter space. This significantly speeds up the convergence process since the search space is narrowed for each subsequent finer level with a larger lattice. The problem in such approaches, though, occurs when the coarse level solution is incorrect, since the error will copied to the finer scale resulting in an incorrect solution at the finest level.

In this paper, we propose the use of a multi-resolution, coarse-and-fine, pyramid image architecture to belief propagation for stereo matching. It helps avoid the local minimum problem by bringing features closer at the coarse level and yet provides a complete solution at the finest level

II. BELIEF PROPAGATION

Figure 1 shows belief propagation as a Markov network. $I=\{I_p\}$ in solid circles are the *observed nodes* or data. $D=\{d_p\}$ in dashed circles are the *hidden nodes* or computed variables. In stereovision, I is data given by the stereo pair and D is the disparity image. The objective is to search for the values of the hidden variables D which provide the optimal solution, given the observed variables I. Therefore, using Bayes' Rule, the goal is to solve the following equation:

$$\arg\max_d P(D \mid I) = \frac{P(I|D)P(D)}{P(I)} \quad (1)$$

where *P(D|I)* is the conditional probability of *D* given *I*. *P(I|D)* is the conditional probability of *I* given *D* which is generally image formation model or the *data constraint*, and *P(D)* is the prior probability such as the *smoothness constraint*. *P(I)* is the evidence probability which may be assumed to be constant and can, therefore, be ignored.

Using negative log probabilities, the global optimization can be formulated in an energy minimization framework:

$$\arg\min_{d} E(D \mid I) = E(I \mid D) + E(D) \tag{2}$$

where *E*, in stead of *P*, is the cost or energy function.

Bayesian belief propagation (BBP) works by passing messages around within a predefined neighborhood. In Figure 1, m_p is called the local evidence, the message sent from an observed node I_p to the corresponding hidden node d_p. It is considered the data constraint revealing how much the value of the computed variable matches the data. Since I_p is known, m_p is a function of d_p, written as $U_p(d_p)$.

$$m_p = U_p(d_p) \tag{3}$$

m_{pq} is a message sent from a hidden node d_p to its neighbor d_q. The message carries the evidence from the observed node and messages from all other neighbors of the sender, combined with the smoothness between the sender and the receiver. First initialized using a uniform random distribution, it is then iteratively updated using the update rule in (4).

$$m_{pq}^{new} = \alpha \min_{d_p}\left\{ V_{pq}(d_p, d_q) + m_p + \sum_{k \in N(p) \setminus q} m_{kp} \right\} \tag{4}$$

where $V_{pq}(d_p,d_q)$ is the smoothness function between nodes d_p and d_q and $k \in N(p) \setminus q$ is all the other neighbors of the sender node d_p except the receiver neighbor d_q.

After passing messages for a number of iterations, the solution is computed by finding the maximum belief for each node *p*. However, as the messages are cost functions showing the error of the solution, the minimum disbelief must be used to represent the maximum belief. The disbelief of node *p* is obtained by the summation of all messages and evidence the node receives:

$$disbelief_p = m_p + \sum_{q \in N(p)} m_{pq} \tag{5}$$

The optimal solution is the one with the maximum belief.

$$d_p = \arg\max_{d_p}(disbelief_p) \tag{6}$$

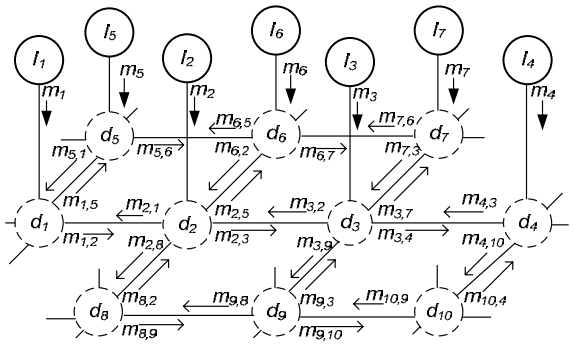

Figure 1. Belief Propagation Presented as a Markov Network.

III. Coarse-and-Fine Belief Propagation

The coarse-and-fine stereo matching includes grid matching and inter-grid matching. Let $I^0 = \{I_L^0, I_R^0\}$ be the original stereo images, where I_L is the left image and I_R is the right image. They are sub-sampled into N-1 coarser levels $I^n = \{I_L^n, I_R^n\}$, *n = 1,2,..N-1,* to make the image pyramid of *N* levels. Let $D^n = \{d_i^n\}$ be the scene property or disparity at level *n.* Within each grid the data constraint through differences in matched points and the smoothness constraint are both enforced to find the disparity labeling. In addition, another constraint called the *inter-grid* constraint requires the disparity at the contiguous coarse and fine levels to be consistent.

The data cost is expressed in terms of an energy function:

$$E(I \mid D) = \lambda_D \sum_{n=0,..,N-1} E^{DATA(n)} \tag{7}$$

where λ_D is the weight for the data constraint. $E^{DATA(n)}$ is the data constraint at grid level *n*, coarse or fine, defined by the summation of the energy at every pixel p given by:

$$E^{DATA(n)} = \sum_p \left(I_R^n(x_p, y_p) - I_L^n(x_p - d_p, y_p) \right)^2 \tag{8}$$

The prior includes grid smoothness and inter-grid consistency:

$$E(D) = \lambda_S \sum_{n=0,..,N-1} E^{S(n)} + \lambda_I \sum_{n=0,..,N-2} E^{I(n)} \tag{9}$$

where λ_S and λ_I are the smoothness and inter-grid weighing factors, respectively. At each grid level, the grid smoothness energy is defined by the smoothness prior:

$$E^{S(n)} = \sum_p \sum_{q \in N(p)} E_{pq}^S(d_p^n, d_q^n) \tag{10}$$

$E_{pq}^S(d_p^n, d_q^n)$ is the smoothness energy between nodes *p* and *q*, which are both at the same level *n*, computed from:

$$E_{pq}^S(d_p^n, d_q^n) = (d_p^n - d_q^n)^2 . \tag{11}$$

The inter-grid energy $E^{I(n)}$ measures the consistency between the disparities d_p at level *n* and d_q at it's adjacent coarser level *n+1*, between the coarse and fine levels. At each pixel *p* of fine level *n*, $E^{I(n)}$ is calculated by:

$$E^{I(n)} = \sum_p E_{pq}^I\left(d_p^{n+1}, d_q^n\right) \tag{12}$$

$$E_{pq}^I(x,y) = \begin{cases} 0, & |x \times S - y| < S - 1 \\ 1, & otherwise \end{cases} . \tag{13}$$

Message passing in the coarse-and-fine structure is illustrated in Figure. 2. The grid matching is in the messages m_{left}, m_{right}, m_{up}, m_{down}, which are sent to neighborhood pixels in the same grid level. The inter-grid matching is in the message m_{above} sent to corresponding pixel in the coarser level, and $m_{below1,2,3,4}$ sent to four corresponding pixels in the finer level.

A. Computing Local Evidence

The local evidence, or data constraint, at pixel *p* on level *n* can be computed via

$$m_p^n(d_p^n) = \left[I_R^n(x_p, y_p) - I_L^n(x_p - d_p^n, y_p) \right]^2 . \tag{14}$$

B. Computing Intra-grid Message

To send a message at the same grid level, the message is computed by

$$m_{pq}^{new}(d_p^n) \leftarrow \min_{dp} \lambda_S E_{pq}^S(d_p^n, d_q^n) + \lambda_D m_p(d_p^n) + \sum_{k \in N(p) \setminus q} m_{kp}(d_p^n) \quad (15)$$

, where $p=(x,y)$, m_{pq} is m_{left}, m_{right}, m_{up}, m_{down} *when* $q = (x+1,y)$, $(x-1,y)$, $(x,y+1)$, and $(x,y-1)$, respectively.

C. Computing Inter-grid Message

To send the inter-grid message, the message is calculated by:

$$m_{pq}^n(d_p^n) \leftarrow \min_{dp} \lambda_I E_{pq}^I(d_p^n, d_q^{n+1}) + \lambda_D m_p(d_p^n) + \sum_{k \in N(p) \setminus q} m_{kp}(d_p^n) \quad (16)$$

, where $p=(x,y)$ in level n, m_{pq} is m_{above}, when $q = (x/2,y/2)$ in level $n+1$, or

$$m_{pq}^n(d_p^n) \leftarrow \min_{dp} \lambda_I E_{qp}^I(d_q^{n-1}, d_p^n) + \lambda_D m_p(d_p^n) + \sum_{k \in N(p) \setminus q} m_{kp}(d_p^n) \quad (17)$$

, where $p=(x,y)$ on level n, m_{pq} is m_{below1}, m_{below2}, m_{below3}, m_{below4}, when $q=(2x,2y)$, $(2x+1,2y)$, $(2x,2y+1)$, $(2x+1,2y+1)$, respectively, in level $n-1$.

D. Belief Propagation Algorithm

The belief propagation algorithm is used to find a solution for the disparity image as described below:

1. For every level n, compute the data cost for every pixel by:

$$m_p^n(d_p^n) = \left[I_R^n(x_p, y_p) - I_L^n(x_p - d_p^n, y_p) \right]^2$$

2. All messages are initialized to 0.

$$m_{pq}^n(d_p^n) \leftarrow 0$$

3. For each iteration i = 1…T, update the following messages:

3.1 Intra-grid messages:

$$m_{pq}^n(d_p^n) \leftarrow \min_{dp} \lambda_S E_{pq}^S(d_p^n, d_q^n) + \lambda_D m_p(d_p^n) + \sum_{k \in N(p) \setminus q} m_{kp}(d_p^n)$$

3.2 Inter-grid message to the coarser grid level:

$$m_{pq}^n(d_p^n) \leftarrow \min_{d_p} \lambda_I g(d_p^n, d_q^{n+1}) + \lambda_D m_p(d_p^n) + \sum_{k \in N(p) \setminus q} m_{kp}(d_p^n)$$

3.3 Inter-grid message to the finer grid level:

$$m_{pq}^n(d_p^n) \leftarrow \min_{d_p} \lambda_S g(d_q^{n-1}, d_p^n) + \lambda_D m_p(d_p^n) + \sum_{k \in N(p) \setminus q} m_{kp}(d_p^n)$$

4. At level 0, compute disbeliefs for each pixel p:

$$disbelief_p^0(d_p^0) \leftarrow \lambda_D m_p(d_p^0) + \sum_{k \in N(p) \setminus q} m_{kp}(d_p^n)$$

5. Choose the value for disparity of each pixel p to the one with maximum belief or the minimum disbelief:

$$d_p^0 = \arg\min_{d_p} disbelief_p^0(d_p^0)$$

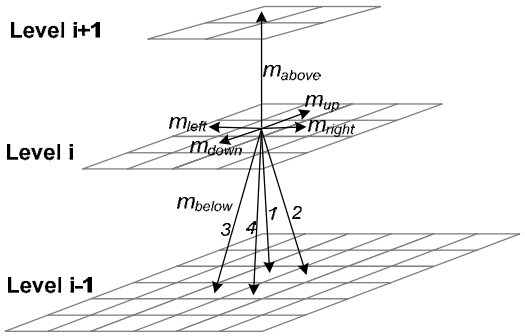

Figure 2. Message Passing in Coarse-and-Fine BBP.

IV. Experimental Results

We ran the coarse-and-fine Bayesian belief propagation algorithm on three types of stereo pairs which are those of random dot images, synthetic images, and real images.

Figure 3 shows the comparison of the stereo results from one level, coarse-to-fine, and our coarse-and-fine BBP. The results show that the coarse-and-fine algorithm can reduces some errors in the other algorithm.

The results for synthetic images are shown in Figure 4. The disparity images are shown in both coarse and fine levels, which appear to be so clean.

Figure 5 to 6 are the stereo results for real images. In figure 5 are the result for the tree images which looks very promising. Illustrated in Figure 6 are the intermediate results of the algorithm at different iterations, which show how the pixels propagate the right solution to the whole image. A result of Tsukuba stereo pair is shown in Figure 7. Compared to the ground truth image, our algorithm yields an accurate disparity image which has only some error in some non-texture areas.

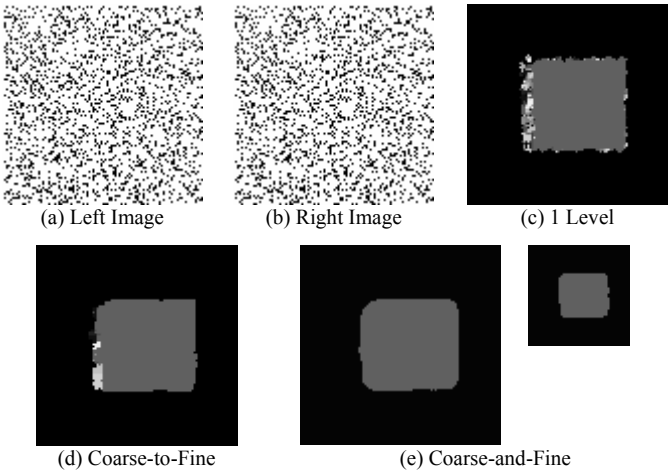

(a) Left Image (b) Right Image (c) 1 Level

(d) Coarse-to-Fine (e) Coarse-and-Fine

Figure 3. Stereo Result for the random dot square images

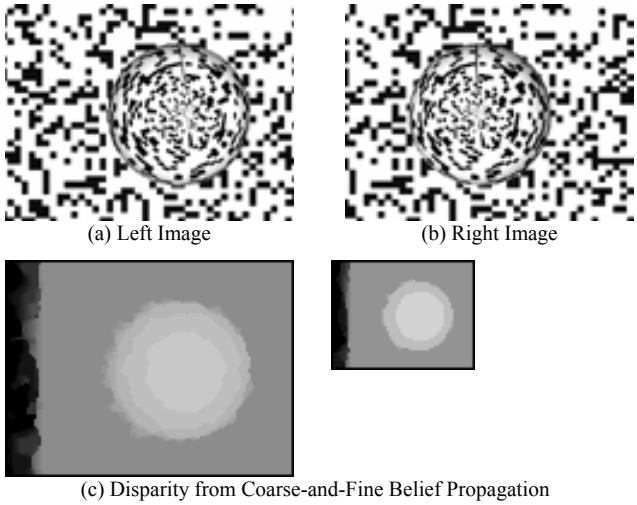

(a) Left Image (b) Right Image

(c) Disparity from Coarse-and-Fine Belief Propagation

Figure 4. Stereo Result for the Synthetic Sphere Image Pair

(a) Left Image

(b) Right Image

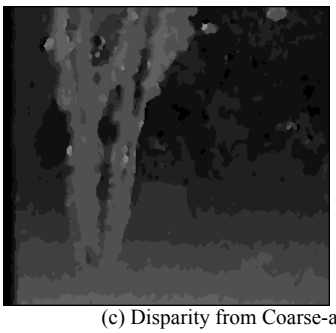

(c) Disparity from Coarse-and-Fine Belief Propagation

Figure 5. Stereo Result for the Real Trees Image Pairs

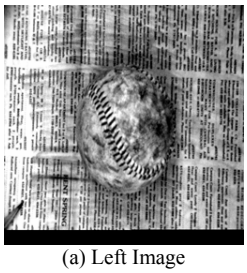

(a) Left Image

(b) Right Image

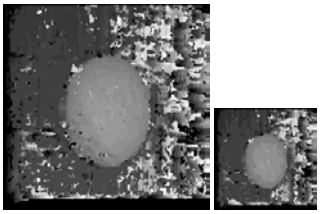

(c) iteration 1

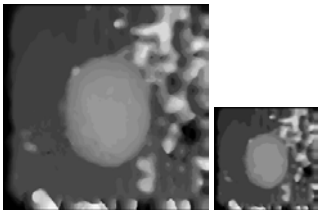

(d) iteration 2

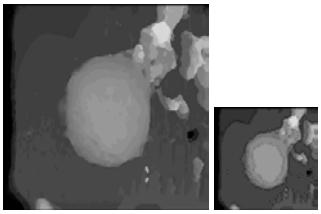

(e) Disparity at iteration 3

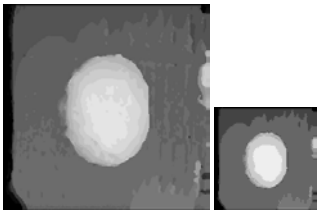

(f) Disparity at iteration 5

Figure 6. Stereo Results for the Real Baseball Image Pair at several levels

V. CONCLUSION

We have presented a coarse-and-fine belief propagation algorithm for stereo vision to help get the distant features of the coarse level closer in order to not get stuck at a local minimum solution in the fine level. We present results for synthetic, random-dot, and real images, showing an increase in the accuracy of the disparity map. Our main contribution is in the mechanism for belief propagation in a multi-resolution grid. The algorithm is a connectionist one, since it manages to find a solution by only communicating within a neighborhood. Thus, it lends itself to parallel implementations for improved speed. In general the algorithm converges by the 2nd to 3rd iteration. Thus, the number of iterations is indeed very low.

REFERENCES

[1] Lucas, B.D., Kanade, T., "An Iterative Image Registration Technique with an Application to Stereo Vision," Proceeding of Imageing Understanding Workshop, pp. 121-130, 1981.

[2] Marapane, S.B. and Trivedi, M.M., "Multi-Primitive Hierarchical (MPH) Stereo Analysis," IEEE Transactions on Pattern Analysis and Machine Intelligence,Vol. 16, 1994, No. 3, pp. 227-240.

[3] Boykov, Y., Veksler, O., Zabih, R., "Fast Approximate Energy Minimization via Graph Cuts," IEEE Transactions on Pattern Analysis and Machine Intelligence, Vol. 23, No. 11, 2001, pp. 1222-1239.

[4] Tomasi, C. and Manduchi, R., "Stereo matching as a nearest-neighbor problem," IEEE Transactions on Pattern Analysis and Machine Intelligence, Vol. 20, No. 3, 1998, pp. 333-340I.

[5] V. Komogorov. "Convergent tree-rewrighted message passing for energy minimization, " Technical Report 2005-38, 2005, Microsoft Research.

[6] V. Komogorov and M.J. Wainwright. "On the optimality of tree-rewrighted max-product mesage passing, " Uncertainty in Artificial Intelligence, 2005.

[7] M.J. Wainwright, T. Jaakkola, and A.S. Willsky. "Exact MAP estimates by (hyper)tree areement," Advance in Neural Processing Systems (NIPS), 2003, MIT Press.

[8] T. Meltzer, C. Yanover, and Y. Weiss, "Globally optimal solution for energy minimization in stereo vision using reweighted belief propagation," the Tenth IEEE International Conference on Computer Vision, 2005, pp. 428 – 435.

[9] J. Sun, H.-Y. Shum, and N.-N. Zheng, "Stereo matching using belief propagation," IEEE Transactions on Pattern Analysis and Machine Intelligence, Vol. 25, No. 7, 2003, pp. 1-14.

[10] J. Sun, Y. Li, S.-B. Kang, H.-Y. Shum, "Symmetric stereo matching for occlusion handling, " IEEE Conference of Computer Vision and Pattern Recognition, Volume 2, 20-25, June 2005, pp. 399 – 406.

[11] P. Felzenwalb and D. HuttenLocker, "Efficient belief propagation for early vision," IEEE Conference of Computer Vision and Pattern Recognition, 2004, pp. 261-268.

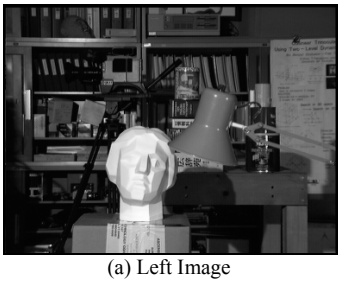

(a) Left Image

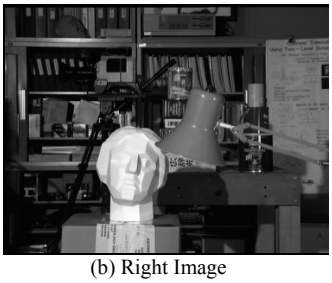

(b) Right Image

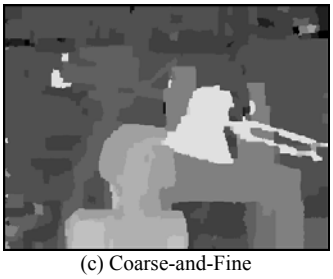

(c) Coarse-and-Fine

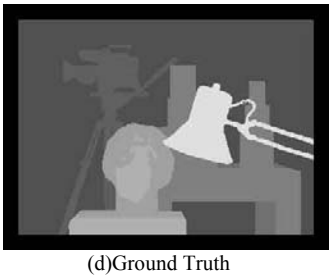

(d)Ground Truth

Figure 7. Stereo Result for the Tsukuba Image Pair

Estimating Radar Cross Section by Anisotropic Diffusion

Sathit Intajag

King Mongkut's Institute of Technology Ladkrabang, Department of Instrumentation Engineering,
Faculty of Engineering, Ladkrabang, Bangkok, THAILAND 10520

Abstract- **Speckle effects are commonly observed in synthetic aperture radar (SAR) images, which apply to many fields, such as agriculture and forestry. The human eye is capable of deriving meaningful information from SAR images; however, an automatic or semi-automatic processing algorithm has difficulty distinguishing the objects in the images because of noise effects present in those images. This paper presents an estimation method for SAR images, which employs an anisotropic diffusion algorithm. In the proposed scheme, a SAR image is transformed into a logarithmic domain where the diffusion process is used to grow homogeneous regions in the noise environment until the regions reach some criteria for homogeneity; consequently, the segmented image in the logarithm domain is converted to the intensity domain by an exponential function. To grow radar cross section (RCS) regions the adaptive diffusion method is introduced with a tensor technique in which tensor data are varied with the neighboring pixels. Our diffusion algorithm will stop itself by a standard deviation divided by mean, which provides according to the homogeneity criteria. Results are shown on both synthetic and satellite SAR images. The evaluation of the proposed method employs the theoretical gain of equivalent numbers of looks (*ENL*).**

I. INTRODUCTION

Many land applications of SAR images [1, 2], such as agriculture or forestry, use information from intensity data. The accuracy of these applications requires methods for identifying changes between images gathered at different times or with a single set of image at a single time, in which preprocessing to reduce speckle is an essential step. Due to the image noise by coherent effects, the overlapping of signatures of various land categories, and the strong effect of the local topography, even forest mapping turns out to be very difficult.

Typically, when it comes to filtering speckle noise to estimate radar cross section (RCS), a spatial domain and many spatial filters are provided as described by Oliver and Quegan [3]. However, the anisotropic diffusion method has been developed to achieve a good trade-off between noise removal and boundary region preservation. Generally, the anisotropic diffusion model is formulated to eliminate additive noise. Speckle noise is multiplicative in nature; however, the multiplicative noise may be transformed to the additive noise by a logarithmic function [4, 5]. Furthermore, the proposed method modifies the diffusion process [6] for filtering the speckle noise by using the standard deviation divided by mean criteria to stop the iteration process.

The proposed scheme is a region-based estimation algorithm. The region-based methods postulate that neighboring pixels within the same RCS or region have similar intensity values, of which the split-and-merge [9] technique is probably the most well known. The general procedure is to compare a pixel with its immediate surrounding neighbors. If a criterion of homogeneity in RCS is satisfied, the pixel can be classified into the same region as one or more of its neighbors. In order to achieve success in estimation RCS method choosing the criteria for homogeneity is of the utmost importance.

Using anisotropic diffusion to smooth out noisy (in our assumption as the same to obtain RCS) is usually embedded with another mechanism such as watershed transformation [7] and thresholding technique [10]. In this paper, the anisotropic diffusion is employed to estimate RCS of SAR images in the logarithm domain. The diffusivity value of the diffusion process uses a structure tensor in order to discriminate textures. When the image regions have the same textures, they are grown and bounded by a diffusion mechanism. This estimation method is the same as region growing but without marker set or seeds. On the other hand, our diffusion algorithm can stop the iteration process within a standard deviation divided by mean criteria, which is provided according to the homogeneity criterion.

Section 2 presents the handling of backgrounds by the proposed method that consists of speckle noise modelling, anisotropic diffusion, and diffusion tensor. Section 3 describes the method of enhancing the SAR images in a logarithm domain. The experimental results of the despeckled images are given in Section 4 and the final Section is our conclusion.

II. RELATED WORKS

A. Speckle modeling

Generally, speckle noise is modeled with intensity and amplitude formats. The proposed method works on intensity data, which is transformed to a logarithm domain. The intensity of a SAR image $F_L(x, y)$ at a pixel coordinate (x, y), where the SAR image is assumed as the average of L looks, can be expressed by

$$F_L(x,y) = I(x,y)R_L(x,y) \tag{1}$$

where R_L is the speckle noise with L looks and I represents the radar cross section of the imaged surface [3].

The multiplicative model of speckle noise suggests performing a logarithmic transformation on the equation (1), giving

$$\tilde{F}_L = \tilde{I} + \tilde{R}_L \tag{2}$$

where $\tilde{F}_L = \ln(F_L)$, $\tilde{I} = \ln(I)$, and $\tilde{R}_L = \ln(R_L)$. From the transformation, $\tilde{R}_L$ becomes stationary white noise, we get the additive noise model, $\tilde{F}_L$ [4, 5].

An equivalent number of looks or *ENL* [11] is often used to estimate the speckle noise level in a SAR image, which is formulated by the ratio of mean to variation in the homogenous image area as given by:

$$ENL = E(F)^2 / V(F), \quad (3)$$

where $E(F)$ and $V(F)$ denote the mean and variance that are estimated from the homogenous area, respectively. In our scheme, *ENL* is employed to measure the degree of speckle reduction, by the meaning of: the higher the *ENL* value, the stronger the speckle noise reduction.

B. Anisotropic Diffusion

Anisotropic diffusion is derived for nonlinear diffusion. It was first proposed and has attracted much deserving attention in the field of image processing by Perona and Malik [12]. In their work, nonlinear diffusion was used to reduce noise while enhancing the true location of edge images. This diffusion is introduced with a space- and time-variant diffusion coefficient, $c(x, y, t)$, as formulated by

$$\frac{\partial f(x,y,t)}{\partial t} = div\left[c(x,y,t)\cdot\nabla f(x,y)\right] \quad (4)$$

where $f(x,y,t)$ is an image pixel value at discrete time steps (t^{th} iterations, for $t = 0$ the representation is the original data: $f(x,y,0) = f(x,y)$). *div* is the divergence operator and $\nabla f(x,y)$ denotes the gradient of images.

To allow the diffusion process to run smoothly from intra-region in RCS to inter-region of the another RCS and thus preserve edges, the region boundaries need to be identified. Obviously, the boundaries are not available a priori, and the best way to estimate the boundary locations by using an edge detector. Perona and Malik [12] claimed that the simplest gradient of images at time t ($\nabla f(x,y,t)$) works excellently; consequently, the diffusion coefficient, $c(x, y, t)$, is given by:

$$c(x,y,t) = g\left(\left|\nabla f(x,y,t)\right|\right) \quad (5)$$

The diffusivity function $g\left(\left|\nabla f(x,y,t)\right|\right)$ is provided to enhance the edges of objects in an image by smoothing the original image while preserving brightness discontinuities. Perona and Malik [12] defines the function as

$$g\left(\nabla f(x,y,t)\right) = \left(1 + \frac{\left\|\nabla f(x,y,t)\right\|^2}{K^2}\right)^{-1} \quad (6)$$

where K denotes a parameter controlling the diffusion strength. The enhancing process is obtained by gradient magnitude $\left|\nabla f(x,y,t)\right|$: where if $\left|\nabla f(x,y,t)\right|$ is large, then the diffusion will be low to preserve the edges. If $\left|\nabla f(x,y,t)\right|$ is small, then the diffusion will tend to smooth the pixel $f(x,y)$.

Catté *et al*. [13] used a Gaussian function (G_σ) with a small variance for convolution with the gradient magnitude term by replacing $g\left(\left|\nabla f(x,y,t)\right|\right)$ with $g\left(\left|G_\sigma * \nabla f(x,y,t)\right|\right)$. The regulation of Catté *et al*. [13] provides edge sharpening and is more stable than the Perona and Malik method. Form the Perona and Malik method, Weickert and Benhamouda [8] studied in more detail about the discrete implementations, a regularization factor.

C. Diffusion tensor

This is a technique to develop a directed diffusion by using local geometric structures. It is adapted from coherence enhancing diffusion (CED) proposed by J. Weickert in 1999 [6]. He suggested many useful properties of nonlinear diffusion under some general assumptions, which concern with the input images and some conditions imposed on the diffusion tensor, D, which was used to replace the diffusion coefficient, $c(x, y, t)$. A formulation of CED equation is expressed by:

$$\frac{\partial f(x,y,t)}{\partial t} = div\left[D\cdot\nabla f(x,y)\right] \quad (7)$$

The diffusivity tensor is a function of image gradient, where D is defined in a matrix framework as follows.

$$D = \begin{bmatrix} d_{11} & d_{12} \\ d_{21} & d_{22} \end{bmatrix} \quad (8)$$

This matrix is constructed by the smoothing perpendicular [17] of the image gradient and an integration scale ρ by using the convolution of an image $f(x, y)$ with a Gaussian kernel G_σ to obtain a smoothed version of the image with standard deviation σ, $f_\sigma(x,y) = G_\sigma * f(x,y)$, where * represents the convolution operator. Accordingly, the diffusivity tensor can be attained by a componentwise convolution of terms $\nabla f_\sigma(x,y)\left(\nabla f_\sigma(x,y)\right)^T$, which are partial derivatives, and a Gaussian G_ρ that is given as:

$$S_\rho\left(\nabla f_\sigma(x,y)\right) = G_\rho * \left(\nabla f_\sigma(x,y)\left(\nabla f_\sigma(x,y)\right)^T\right) \quad (9)$$

where T denotes a transposition of matrix. The structure tensor, S_ρ, is symmetric and positive semi-definite.

$$S_\rho = \begin{bmatrix} s_{11} & s_{12} \\ s_{21} & s_{22} \end{bmatrix} \quad (10)$$

In the CED [6], an integration scale ρ takes positive values. The diffusion process along coherent structures is based on the construction of a diffusion tensor whose eigen-directions coincide with the eigenvectors of the structure tensor and provide the different eigenvalues; namely,

$$\begin{aligned} \lambda_1 &= \alpha, \\ \lambda_2 &= \alpha + (1-\alpha)e^{\left(\frac{-C}{(\mu_1-\mu_2)^{2m}}\right)}, \end{aligned} \quad (11)$$

where μ_1 and μ_2 are the eigenvalues of the structure tensor and C, m, and α are parameters controlling the shape of the exponential form.

The CED method based on the structure tensor provides a local description for boosting up the ridge and valley [14], which is effective of enhancing images such as a fingerprint or a blood vessel [15]. In our paper, this diffusion method is modified to remove the speckle noise by preserving the information detail.

III. Estimate RCS by Anisotropic Diffusion

To smooth out the speckle noise by anisotropic diffusion, the proposed method uses logarithmic transformation to convert the multiplicative noise to additive noise. In practice, we employ a natural logarithm by adding the image data with 1 for convenience in calculation. The SAR image in an additive model as seen in Eq. (2) is an optimal model to process with the anisotropic diffusion methods. After the noise is smoothed out by the diffusion process, the image data is converted to the intensity domain by an exponential function.

The anisotropic diffusion, which is used to estimate RCS, is modeled by Eq. (7) when the diffusivity tensor D is

modified to reduce speckle noise in the logarithm domain and to discriminate textures in each region. In modification, the diffusion coefficient is constructed along boundaries of the homogeneous areas by using a local gradient of the smoothed image $f_\sigma(x,y)$. Generally, the Gaussian smoothing used for the structure tensor dislocates the edges in feature space leading to inaccurate results [16]. However, a nonlinear structure tensor based on a nonlinear matrix-valued diffusion method can tackle these dislocations.

The diffusion tensor *D* is decomposed as

$$D = \begin{bmatrix} d_{11} & d_{12} \\ d_{21} & d_{22} \end{bmatrix} = V^T \begin{bmatrix} \lambda_1 & 0 \\ 0 & \lambda_2 \end{bmatrix} V \tag{12}$$

where the parameters: λ_1 and λ_2 are conductivity values and *V* denotes the rotation matrix [17]. These parameters are calculated by a first-order derivative in the neighborhood of a coordinate pixel (*x*,*y*). In the proposed scheme, λ_1 and λ_2 represent conductivity of the gradient, expressed as

$$\lambda_2 = e^{-\frac{\|\nabla f_\sigma\|^2}{K^2}}, \quad \|\nabla f_\sigma\| = \sqrt{\left(\nabla_x f_\sigma(x,y)\right)^2 + \left(\nabla_y f_\sigma(x,y)\right)^2} \tag{13}$$
$$\lambda_1 = 0.2\lambda_2$$

where $\nabla_x f_\sigma$ and $\nabla_y f_\sigma$ are the gradients with respect to *x* and *y* directions, respectively. The parameter *K*, which is used to define λ_2, represents the controlling of the diffusion strength as the same in Eq. (6). The matrix *V* represents a local coordinate system, which is defined as

$$V = \frac{1}{\|\nabla f_\sigma\|} \begin{bmatrix} \nabla_x f_\sigma & -\nabla_y f_\sigma \\ \nabla_y f_\sigma & \nabla_x f_\sigma \end{bmatrix}. \tag{14}$$

In the RCS estimation algorithm, the diffusion process is completed by a standard deviation to mean criteria. The mean of RCS, $\hat{\mu}$, and standard deviation, $\hat{\sigma}$, are estimated in a homogeneous region, where $C_0 = \hat{\sigma}_0/\hat{\mu}_0$ is calculated before taking the diffusion process and $C_t = \hat{\sigma}_t/\hat{\mu}_t$ is formulated between the running of the diffusion process at the t^{th} iteration. When the ratio C_0/C_t is more than the defined value *R*, the iteration processes stop.

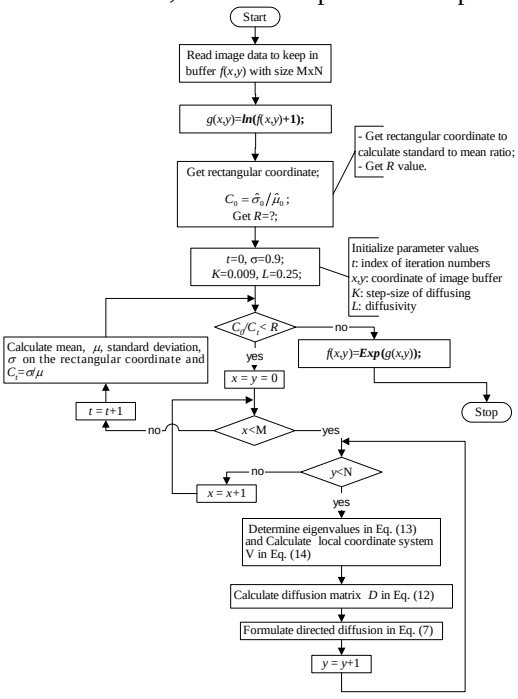

Fig. 1 RCS estimation algorithm

Fig. 1 illustrates our RCS estimation algorithm. The algorithm will get a SAR input and transfer the input data by taking logarithm. A user identifies a homogeneous region of the input data in rectangular coordinates and defines a homogeneity criterion *R*. The algorithm will calculate the standard to mean ratio, C_0, and go to the step of initialization of anisotropic diffusion parameters. Consequently, the diffusion process and measuring the homogeneity region will be started and operated until the ratio C_0/C_t is greater than the defined value *R*, and then the iteration processes are finished.

IV. Experiments and Results

Several illustrations and evaluations have been done on ERS-1/AMI and JERS-1/SAR satellite data [18]. These test data are selected from West-Thailand in Kanchanaburi province (coordinates 99°5′ E; 14°0′ N). The area consists of sparse forest, river, urban, and agricultural lands. Fig. 2(*a*) illustrates the ERS-1 image, which has a pixel spacing of 15 m and the image size, 256×256 pixels with 8 bits per pixel (taken on 22 November 1991). Fig. 3(*a*) shows the JERS-1 image with a pixel spacing of 12.5 m and the image size, 256×256 pixels with 16 bits per pixel (taken on 22 September 1992).

The experimentation results, which are depicted in Fig. 2(*b*~*d*) and 3(*b*~*d*), are processed by RCS estimation algorithm at a difference ratio of the homogeneous criteria, *R*. The homogeneous areas that are employed to estimate the standard deviation to mean values, are defined on the rectangular coordinates [(142, 84), (154, 100)] for Fig. 2 and [(27,170), (57, 193)] for Fig. 3. These results correspond with Table 2 and 3 that show the algorithm's parameters depending on the given value *R*.

Table 1 and 2 illustrate the numerical results of the RCS of each object from the ERS-1 and JERS-1, respectively. In the Tables, *R* is defined in the rough scale from 4 to 22. The *R* criterion provides the iteration processes with a halting mechanism, when the diffusion process propagates until the noise ratio is greater than the homogeneous criteria.

Table 1. The numerical results from ERS-1 image.

R	Iterations	Mean	Variance	*ENL*
-	-	39.39	33.90	45.77
4	195	21.85	2.61	182.97
6	292	21.80	1.10	433.45
8	389	21.83	0.69	692.03
12	625	21.84	0.30	1586.36
20	1409	22.00	0.10	5071.30
22	1639	22.03	0.06	7713.72

Table 2. The numerical results from JERS-1 image.

R	Iterations	Mean	Variance	*ENL*
-	-	62.37	72.04	53.99
4	416	33.52	6.28	178.90
6	575	32.59	2.79	380.67
8	725	32.38	1.46	716.65
12	1136	32.23	0.86	1210.25
20	1811	31.60	0.33	3000.51
22	1899	31.53	0.27	3746.68

The 3rd column of Table 1 and 2 provides the means of RCS, which represents water region in Fig. 2 and 3. In Fig. 2(*d*), the expected RCS of water region at *R*=22 equal to 22.03. For Fig. 3(*d*), the expected RCS of water region at *R*=22 equal to 31.35. As seen from the column of variance, the values decrease when *R* increase and that of the causes of the higher *ENL*.

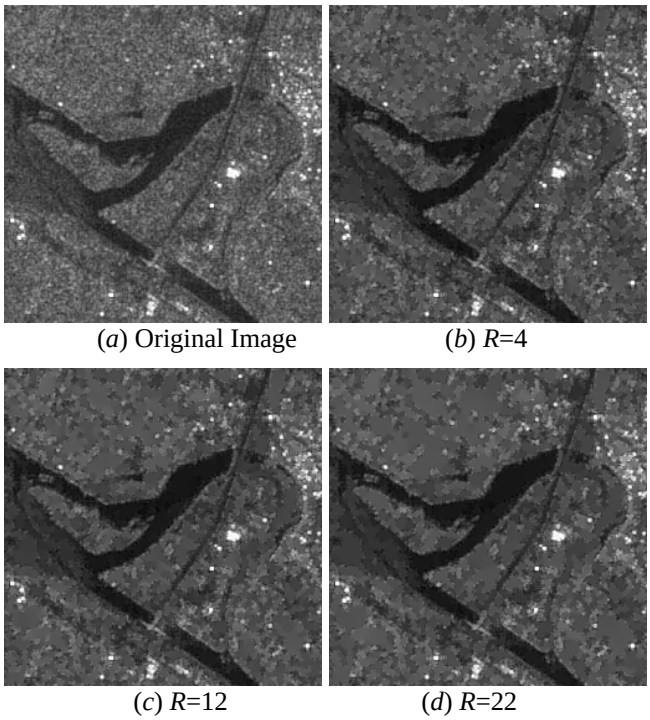

(*a*) Original Image (*b*) *R*=4

(*c*) *R*=12 (*d*) *R*=22

Fig. 2. Despeckled results of ERS-1 image for different ratio *R*.

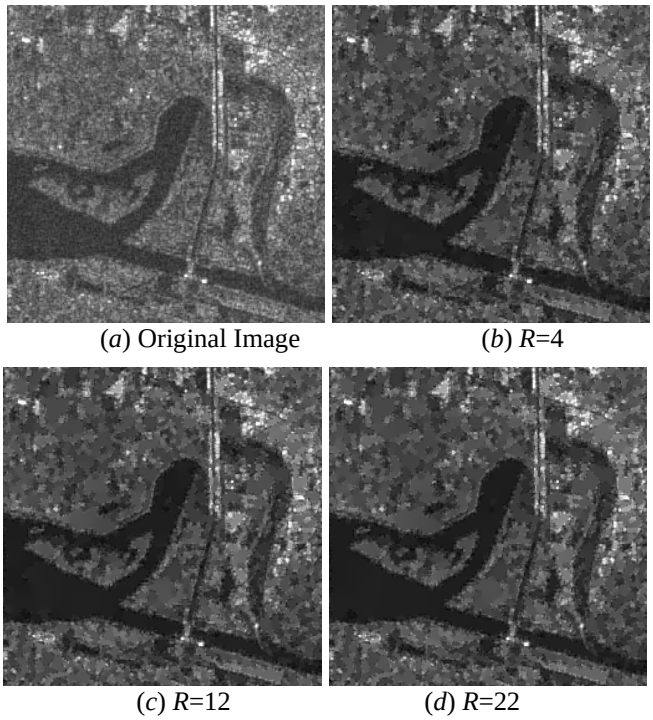

(*a*) Original Image (*b*) *R*=4

(*c*) *R*=12 (*d*) *R*=22

Fig. 3. Despeckled results of JERS-1 image for different ratio *R*.

V. Conclusions

The RCS estimation of SAR images is important in an estimation for classification of agriculture, forestry and different terrain types, which was the motivation our research. The algorithm modifies the diffusion process by the decomposition of the diffusion tensor to improve the criterions of contour pixels and to grow the regions of each RCS object in optimum boundary. The superior performance of the adaptive diffusion method is in maintaining the homogeneous region boundaries in each region and booting up the boundary magnitude as seen from the *ENL* values in Table 1 and 2. The proposed algorithm can use the knowledge of SAR images to adapt the parameters of anisotropic diffusion for estimating RCS, such as the numbers of iteration and the growing region process were given by the homogeneity criteria.

References

[1] M.C. Dobson, L.E. Pierce, and F.T. Ulaby, "Knowledge-based land-cover classification using ERS-1/JERS-1 SAR composites," *IEEE Trans. Geosci. Remote Sensing*, vol. 34, no. 1, pp. 83-99, Jan. 1996.

[2] I. Ben Ayed, A. Mitiche, and Z. Belhadj, "Multiregion level-set partitioning of synthetic aperture radar images," *IEEE Trans. on Pattern Anal. Machine Intell.*, vol.27, no. 5, pp. 793-800, May 2005.

[3] C. Oliver and S. Quegan, *Understanding Synthetic Aperture Radar Images*. Boston, MA: Artech House, 1998.

[4] A. K. Jain, *Fundamentals of Digital Image Processing*. USA: NJ, Prentice-Hall, 1989.

[5] Hua Xie, L. E. Pierce, and F. T. Ulaby, "Statistical properties of logarithmically transformed speckle," *IEEE Trans. Geosci. Remote Sensing*, vol. 40, no. 3, pp. 721-727, Mar. 2002.

[6] J. Weickert, "Coherence enhancing diffusion filtering," *Intl. Jour. of Computer Vision*, Vol. 31 (2/ 3), pp. 111-127, 1999.

[7] J. Weickert, "Fast segmentation methods based on partial differential equations and the watershed transformation," P. Levi, R.-J. Ahlers, F. May, M. Schanz (Eds.), *Mustererkennung*, Springer, Berlin, 93-100, 1998.

[8] J. Weickert and B. Benhamouda, "Why the Perona-Malik filter works," *Technical Report DIKU-97/22*, Dept. of Computer Science, University of Copenhagen, Denmark, 1997.

[9] X. Wu, "Adaptive split-and-merge segmentation based on piecewise least-square approximation," *IEEE Trans. on Pattern Anal. Machine Intell.*, vol. 15, no. 8, pp. 808-815, 1993.

[10] S. Manay and A. Yezzi, "Anti-geometric diffusion for adaptive thresholding and fast segmentation," *IEEE Trans. Image Processing*, vol. 12, no. 11, pp. 1310-1323, 2003.

[11] S. Solbo and T. Eltoft, "Homomorphic wavelet-based statistical despeckling of SAR images," *IEEE Trans. Geosci. Remote Sensing*, vol. 42, no. 4, pp. 711-721, April, 2004.

[12] P. Perona and J. Malik, "Scale-space and edge detection using anisotropic diffusion," *IEEE Trans. on Pattern Anal. Machine Intell.*, vol. 12, pp. 629-639, 1990.

[13] F. Catté, T. Coll, P. L. Lions and J. M. Morel, "Image selective smoothing and edge detection by nonlinear diffusion", *SIAM J. Numer. Annal.* vol. 29, no. 1, pp. 182-193, 1992.

[14] A. Lopez, F. Lumbreras, J. Serrat, and J. Villanueva, "Evaluation of methods for ridge and valley detection," *IEEE Trans. on Pattern Anal. Machine Intell.*, Vol. 21, No. 4, pp. 327-335, 1999.

[15] S. Intajag and V. Tipsuwanporn, "Blood vessel enhancement by directed diffusion," *International Conference on Control, Automation and Systems (ICCAS-2004)*, Bangkok, Thailand, pp. 101-106, Aug. 2004.

[16] S. Intajag and K. Paithoonwatanakij, "Automated edge detection by a fuzzy morphological gradient," *IEICE Trans. Fundamentals*, vol. E86-A, no.10, pp. 2678-2689, Oct., 2003.

[17] M. Nitzberg, D. Mumford and T. Shiota, *Filtering, Segmentation and Depth*. Germany, Springer-Verlag, 1993.

[18] SAR and optical sensor image, http://www.eorc.nasda.go.jp/EORC/Gallery/Southeast_Asais/Thailand/kanchana_01.html.

Fitting Model on BOD Response Curve from Biosensor

Ekkawat Choona[1,a], Pakorn Kaewtrakulpong[2,b], Werasak Surareungchai[3,c], Pornpimol Sritongkam[4,d]
Department of Instrumentation and Control System Engineering[1, 2], Faculty of Engineering,
Pilot Plant Development and Training Institute[3, 4]
King Mongkut's University of Technology Thonburi
126 Prachautid, Bangmod, Toongkru, Bangkok, 10140, Thailand.
Email: S8403506@st.kmutt.ac.th [a], pakorn.kae@kmutt.ac.th [b],
werasak .sur@kmutt.ac.th [c], pornpimol@pdti.kmutt.ac.th [d]

***Abstract*-This paper presents determination of BOD by fitting model of time response curve from biosensor. Unlike previous method, the proposed method is a rapid, simple, compact and inexpensive determination of BOD measurement. The method consists of two phases: data collection and model fitting. In the data collection phases, we acquired data of eight degrees of added glucose and glutamic acid (GGA) substrate which covered the degree of water pollution. In the fitting phases, Iterative Least Square (ILS) is applied to fit the data to a Second Order Plus Dead Time (SOPDT) model. We compared the results to those obtained from recorder chart analysis by human experts. The technique requires less time consumption than BOD_5 and BOD_7. The algorithm is to be integrated into our on-going BOD analysis Machine.**

I. INTRODUCTION

BOD - biochemical oxygen demand is a method to measure a request of oxygen in a sample of water. It can be used to infer quality of the water or degree of pollution [1]. The BOD values indicate the amount of biodegradable organic material and the oxygen used to oxidise inorganic material such as sulphides and ferrous iron. The BOD test finds its main application in measuring waste load of treatment plant and evaluates the BOD removal efficiency of such treatment systems.

The BOD has been determined conventionally by taking a sample of water, aerating it, placing it in a sealed bottle, incubating for a period of time at $20 \pm 1\,^{\circ}C$ in the dark. The oxygen consumption in the water is determined at the end of incubation. For the American standard, the incubation time is five days and the BOD value obtained from this method is named BOD_5 [1] Whereas for the Swedish standard, the incubation time is set to seven days and the result is called BOD_7[2]. However, it has limitation of being time consuming and is not suitable for on-line measurement process. It is necessary to develop an alternative which requires less time for BOD evaluation. This could be achieved by biosensor.

The fast determination of BOD by biosensor is performed on a sample of water [4] confused with glucose and glutamic acid (GGA) [3, 6-8]. These approaches can provide quantitative or semi-quantitative analytical information using an integrated device.

The biosensor response curve from BOD measurement can be modeled using kinetic or dynamic models. The advantage of this method is a rapid, simple, compact and inexpensive determination of BOD measurement. It also uses less substrate than BOD_5 and BOD_7 and enabled possibilities of implementation for on-line monitoring applications. However, the conversion of difference current from the response curve to a BOD value is still done by experts on a chart recorder.

Since method of calculating BOD value depends on expertise of the human operators, it is a slow and complicated measurement process. From these drawbacks of the current method, this paper focuses on estimation and prediction of biosensor response curve by an Iterative Least Square (ILS) method on the time response curve. Typical response curve can be shown in Figure 1. The curve bears similarity to a time response of a Second Order Plus Dead Time (SOPDT) system; therefore, it is used as the model in our work.

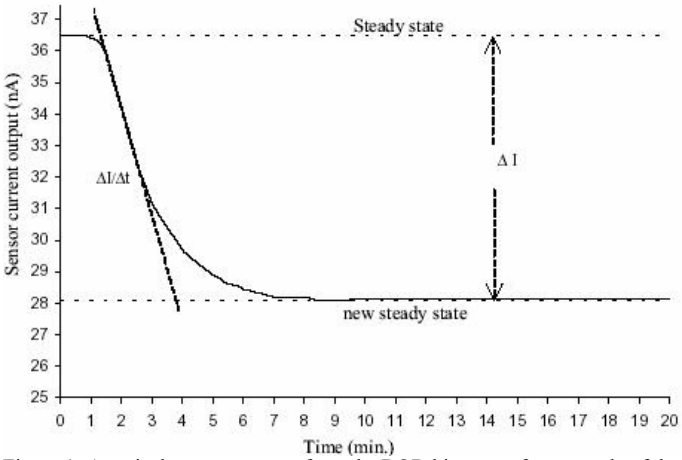

Figure 1. A typical response curve from the BOD biosensor for a sample of the synthetic wastewater. The initial current change ($\Delta I / \Delta t$) and current difference (ΔI) between two steady states were the sensor responses for sensor BOD measurements in the kinetic or dynamic models.

The paper is organized as follows. After general introduction presented in this section, our proposed method is described in Section II. In Section III, we present some experimental results. Finally, conclusion and future work are drawn in Section IV.

II. PROPOSED METHOD

The method consists of two phases: data collection and model fitting. In the data collection phase, we start by acquiring electrical current data from biosensor. In the fitting phases, we use iterative least square method to model a non-linear function. The time response of an SOPDT system is chosen as the model which includes four parameters.

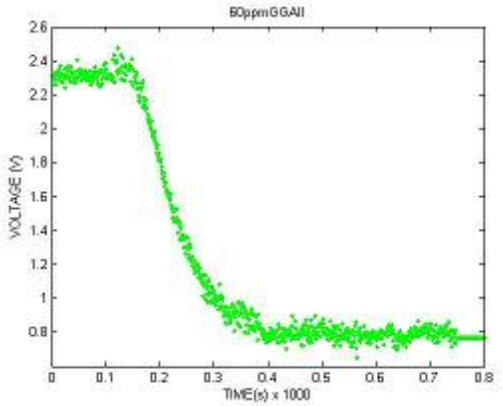

Figure 2. The change of electrical current using BOD sensor

A. Parameter Model Consideration

The change of signal is non-linear form. Before adding GGA, the signal is at a high and stable level. When GGA is added, the level of signal gradually decreases. Finally, the signal reaches another steady level. The decrease of signal level depends on the amount of added GGA. The response resembles the time response of an SOPDT which can be expressed as

$$y(t) = -k(1-(1+\frac{t-t_d}{\tau})e^{\frac{-(t-t_d)}{\tau}})u(t-t_d)+y_s \qquad (1)$$

this is function of SOPDT where k is the change in y(t) between the two steady states, τ is the system time constant, t_d is the delay time and y_s is the initial value of y(t). u(•) is the standard unit step function.

This model estimation is performed by an ILS estimator. The technique repeatedly applied a Least Square (LS) estimator to a liberalized form of non-linear function. Details are explained in the sequel.

B. Least Square Estimation

The method of least squares assumes that the best-fit curve of a given type is the curve that has the minimal sum of the deviations squared (*least square error*) from a given set of data. The LS is an optimization technique to find an approximate solution for system of linear equations which have no exact solution. It can be written as

$$\hat{\boldsymbol{\theta}} = (\mathbf{A}^T\mathbf{A})^{-1}\mathbf{A}^T\mathbf{b} \qquad (2)$$

where $\hat{\boldsymbol{\theta}}$ is the LS estimate of the equation $\mathbf{A}^{\mathrm{T}}\mathbf{y}=\mathbf{b}$. $(\mathbf{A}^T\mathbf{A})^{-1}\mathbf{A}^T$ is the pseudo inverse.

Since the response signal is non-linear, plain LS estimation can not be employed. So, we use Gauss-Newton algorithm to overcome the problem of plain LS estimation.

C. Iterative Least Squares

The LS finds its use in many applications and some researches try to overcome its limitation on linear function by applying several techniques to adjust the model for the LS [11-12]. The parameters of model are estimated iteratively until minimum error is reached [13-14]. Among these, Gauss-Newton algorithm can be used to solve this nonlinear least square problem.

A system of nonlinear equations can be written as

$$\mathbf{g_1}(\boldsymbol{\Phi}) \approx \mathbf{y}_1 . \qquad (3)$$

It can be approximated by Taylor series as

$$\frac{\partial \mathbf{g_1}}{\partial a}\Delta\boldsymbol{\Phi}_a + \frac{\partial \mathbf{g_1}}{\partial b}\Delta\boldsymbol{\Phi}_b + \cdots + \frac{\partial \mathbf{g_1}}{\partial n}\Delta\boldsymbol{\Phi}_n = \mathbf{y}_1 - \mathbf{g}_1\left(\boldsymbol{\Phi}^k\right). \qquad (4)$$

This form can be solved by LS estimator. Subsequent guesses $\boldsymbol{\Phi}^k$ for the parameter vector are produced by the recurrence relation

$$\boldsymbol{\Phi}^{k+1} = \boldsymbol{\Phi}^k - (\mathbf{J}_f(\boldsymbol{\Phi}^k)\mathbf{J}_f(\boldsymbol{\Phi}^k)^{\mathrm{T}})^{-1}\mathbf{J}_f(\boldsymbol{\Phi}^k)\mathbf{f}(\boldsymbol{\Phi}^k) \qquad (5)$$

where $\mathbf{f} = (\mathbf{f}_1 \ldots \mathbf{f}_n)$ and $\mathbf{J_f}(\boldsymbol{\Phi})$ are Jacobian of $\mathbf{f}$ at $\boldsymbol{\Phi}$. The matrix inverse is never computed explicitly in practice. we use

$$\boldsymbol{\Phi}^{k+1} = \boldsymbol{\Phi}^k + \boldsymbol{\Delta}^k \qquad (6)$$

and we compute update Δ^k by solving the linear system

$$\mathbf{J}_f(\boldsymbol{\Phi}^k)\mathbf{J}_f(\boldsymbol{\Phi}^k)^{\mathrm{T}}\boldsymbol{\Delta}^k = -\mathbf{J}_f(\boldsymbol{\Phi}^k)\mathbf{f}(\boldsymbol{\Phi}^k) \qquad (7)$$

where

$$\mathbf{J}_f(\boldsymbol{\Phi}^k) = \begin{bmatrix} \frac{\partial \mathbf{g_1}_{(x_1,y_1)}}{\partial \boldsymbol{\Phi}_1{}^k} & \frac{\partial \mathbf{g_1}_{(x_1,y_1)}}{\partial \boldsymbol{\Phi}_2{}^k} \cdots & \frac{\partial \mathbf{g_1}_{(x_1,y_1)}}{\partial \boldsymbol{\Phi}_n{}^k} \\ \vdots & \vdots & \vdots \\ \frac{\partial \mathbf{g_1}_{(x_n,y_n)}}{\partial \boldsymbol{\Phi}_1{}^k} & \frac{\partial \mathbf{g_1}_{(x_n,y_n)}}{\partial \boldsymbol{\Phi}_2{}^k} \cdots & \frac{\partial \mathbf{g_1}_{(x_n,y_n)}}{\partial \boldsymbol{\Phi}_n{}^k} \end{bmatrix} \qquad (8)$$

$$\boldsymbol{\Phi}^k = \begin{bmatrix} \Delta\boldsymbol{\Phi}_1 \\ \Delta\boldsymbol{\Phi}_2 \\ \vdots \\ \Delta\boldsymbol{\Phi}_n \end{bmatrix} \qquad \mathbf{f}(\boldsymbol{\Phi}^k) = \begin{bmatrix} \mathbf{y}_1 - \mathbf{g}_{1(x_1,y_1)}\left(\boldsymbol{\Phi}^k\right) \\ \vdots \\ \mathbf{y}_n - \mathbf{g}_{1(x_n,y_n)}\left(\boldsymbol{\Phi}^k\right) \end{bmatrix} \qquad (9)$$

$\mathbf{g}_{\mathbf{1}(x,y)}\left(\mathbf{\Phi}^k\right)$ is the model function around point (x, y) and $\mathbf{\Delta\Phi}_1 \ldots \mathbf{\Delta\Phi}_n$ is the parameter vector. The Gauss-Newton method is an iterative procedure and the parameter vector is initiated by an initial guess. Then the time response function of an SOPDT equation can be formed by

From equation (1), members of the Jacobian matrix can be found by

$$\begin{aligned}
\frac{\partial y}{\partial k} &= -(1-(1+\frac{t-td}{\tau})e^{\frac{-(t-td)}{\tau}})u(t-td) \\
\frac{\partial y}{\partial \tau} &= -k(\frac{t-td}{\tau^2})e^{\frac{-(t-td)}{\tau}}[1-(1+(\frac{t-td}{\tau}))]u(t-td) \\
\frac{\partial y}{\partial td} &= k\frac{(-e^{\frac{-(t-td)}{\tau}})}{\tau}[1-(1+\frac{t-td}{\tau})]u(t-td) \\
\frac{\partial y}{\partial y_s} &= 1
\end{aligned} \tag{10}$$

After substituting (10) into (8), it can be formed in linear equations as (2).

III. Experimental Result

The data collection to evaluate the performance of our proposed method was performed from sample water confused with added GGA of 5, 10, 20, 30, 40, 50, 60 and 70 parts per million. Eight degrees of GGA was added which covered the degrees of water pollution. Each degree of added GGA was evaluated three times. An example of the collected data is shown in Figure 3. Each data was modeled using ILS on the time response of an SOPDT. We compared the results to those obtained from recorder chart analysis by human experts.

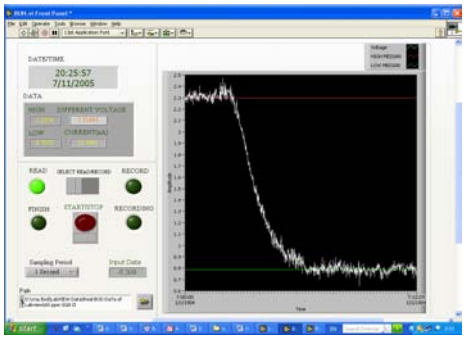

Figure 3. Data collection by LabVIEW program which used in data keeping. It spends time about fifteen minutes for data keeping and shows low, high, and different of voltage. The data is estimate by simple technique and convert to electrical current. It is automatic record.

Figure 4 shows performance of the estimation by our proposed method. The axis x and axis y of graph are time and voltage, respectively.

From experimental results, it can be seen that the estimate produced the best results. The error of estimation which compared with the results from expert is shown in Table I. The results were compared in nanoampere with an average of three measures for each GGA substrate. These results would be used to calculate the BOD value.

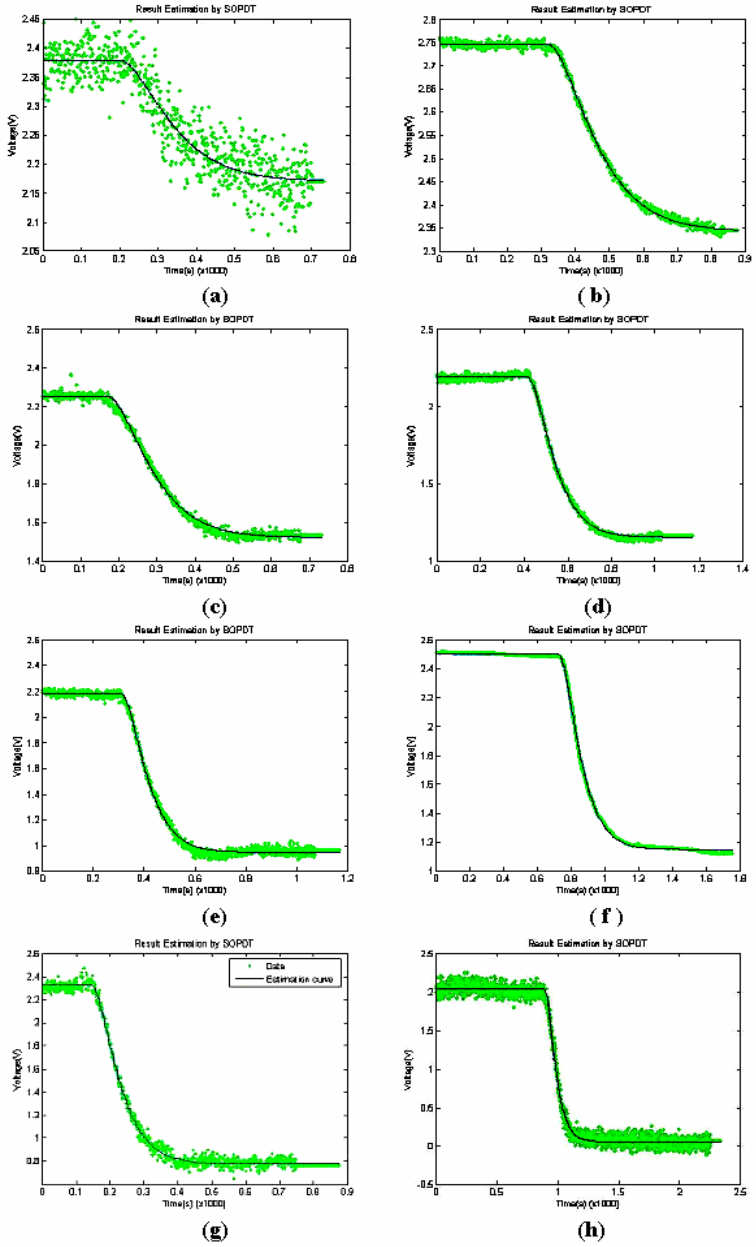

Figure 4. Results of estimation for each degree of added GGA by our proposed method which using MATLAB program. (a) 5 parts per million (b) 10 parts per million(c) 20 parts per million (d) 30 parts per million (e) 40 parts per million(f) 50 parts per million (g) 60 parts per million (h) 70 parts per million

IV. Conclusion and Future work

In this paper, we proposed a technique to estimate the timer domain response curve of current drawn from a BOD sensor. ILS estimation based on Gauss-Newton algorithm was applied. It requires less time consuming than that of BOD_5 and BOD_7. It also showed accurate results when compared with those from human expert. Moreover, our approach can be applied to model other nonlinear systems. The algorithm is to be integrated into our on-going BOD analysis Machine.

TABLE I
Error of estimation

	Recoreder	Estimation	Recoreder	Estimation	ERROR
GGA (ppm)	I (nA)	I (nA)	Average I (nA)	Average I (nA)	%
5	2.2500	2.2440	2.5833	2.5220	2.3742
	3.0000	2.7320			
	2.5000	2.5900			
10	4.0000	4.2960	3.7500	4.6357	23.6178
	3.7500	4.5260			
	3.5000	5.0850			
20	7.0000	7.1640	7.2500	7.5787	4.5333
	7.2500	7.8040			
	7.5000	7.7680			
30	11.0000	10.8840	10.4167	10.2770	1.3408
	10.2500	10.3530			
	10.0000	9.5940			
40	13.2500	12.8700	13.5000	13.4857	0.1062
	13.5000	13.2680			
	13.7500	14.3190			
50	15.0000	14.7480	14.6667	14.7143	0.3250
	14.0000	14.0380			
	15.0000	15.3570			
60	16.5000	15.9320	16.7500	16.1690	3.4687
	17.0000	16.4060			
70	20.2500	20.4130	19.9167	19.9877	0.3565
	19.5000	20.3260			
	20.0000	19.2240			

Acknowledgment

This work has been funded by the Pilot Plant Development and Training Institute (PDTI), King Mongkut's University of Technology Thonburi.

References

[1] APHA, "Standard methods for the examination of water and wastewater," *American Public Health Association Water Works Association*, 1992, pp.5.1-5.6.

[2] SIS-Standardiseringskommissionen i Sverige. Water analysis Determination of biochemical oxygen demand, BOD, of water—dilution method (Svensk Standard SS 02 81 43 E), 1st ed. Stockholm: The Swedish Standards Institution, 1979. p. 1–9.

[3] I. Karube, T. Matsunaga, A. Mitsuda, and S. Suzuki, " A microbial electrode BOD sensors," *Biotechnol Bioeng*, vol. 19(10), 1 977, pp. 1535–1547.

[4] J. Liu, L. Bjornsson, and B. Mattiasson B. "Immobilised activated sludge based biosensor for BOD measurement," *Biosens Bioelectron*, vol. 14(12), 2000, pp. 883–893.

[5] J. Liu, and B. Mattiasson, "Microbial BOD sensors for wastewater analysis," *water research*, vol. 36, 2002, pp.3786-3802.

[6] C. Preininger, W. Klimant, and O. Wolfbeis, "Optical fiber sensor for biological oxygen demand," *Anal Chem*, vol. 66(11), 1994, pp.1841–1846.

[7] K. Riedel, R. Renneberg, M. K.uhn, and F. Scheller, "A fast estimation of biochemical oxygen demand using microbial sensors," Appl Microbiol Biotechnol, vol 28, 1988, pp.316–318.

[8] K. Riedel K, P. LangeK, J. Stein,, M. Kuhn, Ott P, and F. Scheller, "A microbial sensor for BOD," Water Research, vol. 24, 1990, pp.883–887.

[9] C. Jeng-Ming and C. Bor-Sen, "System parameter estimation with input/output noisy data and missing measurements," *IEEE transaction on signal processing*, vol. 48, 2000, pp.1548-1558.

[10] K.W. Chenug, H.C. So, W. Ma, and Y.T. Chan, "Least squares algorithms for time-of-arrival-based mobile location," *IEEE transaction on signal processing*, vol.52, 2004, pp.1121-1128.

[11] B. Tawfik, and D. Durand, "Nonlinear parameter estimation by linear association: application to a five parameter passive neuron model," *IEEE transaction on biomedical engineering*, vol.41, 1994, pp.461-469.

[12] S. Lu, And K. Chon, "Nonlinear autoregressive and nonlinear autoregressive moving average model parameter estimation by minimizing hypersurface distance," *IEEE transaction on signal processing*, vol.51, 2003, pp.3020-3026.

[13] W. Xiong-liang, and W. Zheng-ming, "Super-resolution SAR Imaging via nonlinear regressive model parameter estimation method," Proceeding *of the computer graphics CGIV'05*, 2005, pp.1-6.

[14] J. Jih-Gau, L. Bo-Shian, and L. Chien-Kuo, "Parameter estimation of nonlinear system based on hybrid intelligent method," Proceeding *of the 2004 IEEE international conference on systems, man and cybernetics*, 2004, pp.3365-3370.

[15] M. Sanjeev Arulampalam, S. Maskell, N. Gordon, and T. Clapp, "A tutorial on particle filters for online nonlinear/non-Gaussian Bayesian tracking,", *IEEE transaction on signal processing* vol. 50, 2002, pp.174-188.

Design of Adaptive Chrominance Delay Equalizer using Linear-Phase FIR Digital Filter

V. Chutchavong, C. Benjangkaprasert, O. Sangaroon and K. Janchitrapongvej
Research Center for Communication and Information Technology (ReCCIT),
and Department of Information Engineering, Faculty of Engineering,
King Mongkut's Institute of Technology Ladkrabang,
Bangkok, THAILAND 10520

***Abstract*-This paper describes the design of adaptive video equalizer based on a linear-phase FIR filter with least mean square (LMS) algorithms. In color video waveform transmission, inequalities of delay between luminance and chrominance channel is a potential source of picture impairment. Delay inequalities cause horizontal registration errors and hue between the luminance-chrominance content of picture and will make picture look smeared. As the simulation results, the modulated 20T sine-square pulse test signal with color sub-carrier 4.43 MHz for PAL system is utilized. It can be seen that the proposed adaptive equalizer based on linear phase FIR filter can equalized the chrominance delay distortions without causes gain error and provides a wide range of time-delay control.**

I. INTRODUCTION

In recent years, adaptive filtering has been receiving a great deal of attentions in the area of communications, sonar, radar, mechanical design, and biomedical electronics. Adaptive filters are self-designing system, which can adjust them to difference environments, so the use of adaptive filter provides a significant performance over the use of a fix filter. Basic classes of adaptive filtering applications are recognized, namely adaptive equalizer. Therefore, in this paper design the adaptive equalizer using LMS adaptive algorithm, which has always been attractive to the researchers in adaptive signal processing because of its simplicity and its robustness to numerical errors [1].

Unlike the IIR digital filter design problem, whereas it is not possible to design an IIR transfer function with exact linear-phase. So, many researches are always possible to design FIR digital filters with exact linear-phase [2]. In color video system, the linear distortions divided into the gain distortion only, group-delay distortion only and both gain & group-delay distortions. Adaptive amplitude chrominance distortion is described in ref. [3]. In this paper, we examine specially occurrence the group-delay distortion only hence it's necessary linear-phase FIR filter. As the effects of group-delay error are the picture look less sharp, look smeared and causes to utilize the color hue.

In addition, the pulse and bar test signal which has been used to measure linear waveform distortion in TV system is a special 20T sine-squared pulse with a 4.43 MHz color sub-carrier for PAL system [6], [8]. As a result, the proposed adaptive equalizer can be equalized the group-delay distortion in good agreement.

II. LINEAR PHASE FIR FILTER BASED ON LMS ADAPTIVE ALGORITHM

A. Linear Phase FIR Digital Filter

In this section, we pointed out why it is important to have a transfer function with a linear-phase property. It turns out it is always possible to design an FIR transfer function with an exact linear-phase response, whereas it is not possible to design an IIR transfer function with exact linear-phase. We first consider the realization of FIR digital filters. Recall that a causal FIR filter of order N is characterized by a transfer function $H(z)$ [2].

$$H(z) = \sum_{k=0}^{M} h(k) z^{-k} \tag{1}$$

where $h(k)$ are samples of its impulse response, a polynomial in z^{-1} of degree M . In the time domain, the input-output relation of the above FIR filter is given by

$$y(n) = \sum_{k=0}^{M} h(k) x(n-k) \tag{2}$$

where $y(n)$ and $x(n)$ are the output and input sequences, respectively. A linear-phase FIR of order M is either characterized by a symmetric impulse response

$$h(n) = h(M-n) \tag{3}$$

or by an antisymmetric impulse response

$$h(n) = -h(M-n) \tag{4}$$

The symmetry (or antisymmetry) property of a linear-phase FIR filter can be exploited to reduce the total number of multipliers into almost half of that in the direct form implementations of the transfer function.

To see this, consider the following manipulations of the discrete convolution equation, assuming that M is an even integer corresponding to type I or type III system [4]:

$$y(n) = \sum_{k=0}^{M/2-1} h(k)x(n-k) + h(M/2)x(n-M/2) + \sum_{k=0}^{M/2-1} h(M-k)x(n-M+k) \quad (5)$$

For type I system, we use (3) to obtain

$$y(n) = \sum_{k=0}^{M/2-1} h(k)(x(n-k) + x(n-M+k)) + h(M/2)x(n-M/2) \quad (6)$$

Equation (6) implies structures with $M/2$ coefficient multipliers rather than the M coefficient multipliers of the general direct form. Fig. 1 shows the direct form structure for a linear-phase FIR system when M is an even implied by (6).

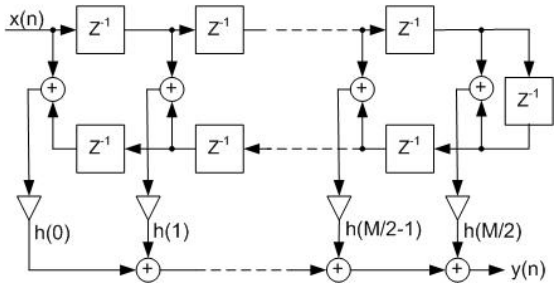

Figure 1 Direct form structure for a linear-phase FIR system when M is an even.

B. LMS Adaptive Algorithm

One of the most well known algorithms in adaptive signal processing is the Least Mean Square (LMS) adaptive algorithm proposed by Widrow and Hoff [1]. The most commonly used structure in the implementation of adaptive filter is the transversal structure given by

$$y(n) = \mathbf{w}^T(n)\mathbf{x}(n) \quad (7)$$

where,

$$\mathbf{w}(n) = [w_0(n) \quad w_1(n) \quad ..... \quad w_{N-1}(n)]^T \quad (8)$$

$$\mathbf{x}(n) = [x(n) \quad x(n-1) \quad ..... \quad x(n-N+1)]^T \quad (9)$$

where $\mathbf{w}(n)$ is tap-weight vector of FIR filter, $\mathbf{x}(n)$ is input vector, and the error signal $e(n)$ is written as

$$e(n) = d(n) - y(n) \quad (10)$$

where $d(n)$ is desire signal.

The conventional LMS algorithm is a stochastic implementation of the steepest-descent algorithm. It simply replaces the cost function $\xi = E[e^2(n)]$ by its instantaneous coarse estimate $\hat{\xi}(n) = e^2(n)$. Substituting $\hat{\xi}(n) = e^2(n)$ for ξ in the steep-descent recursion (10), and replacing the iteration index k by the time index n, we obtain

$$\mathbf{w}(n+1) = \mathbf{w}(n) - \mu\nabla e^2(n) \quad (11)$$

where ∇ is the gradient operator defined as the column vector

$$\nabla = \left[\frac{\partial}{\partial w_0} \quad \frac{\partial}{\partial w_1} \quad ..... \quad \frac{\partial}{\partial w} \right] \quad (12)$$

We note that the *i*th element of the gradient vector $\nabla e^2(n)$ is

$$\frac{\partial e^2(n)}{\partial w_i} = 2e(n)\frac{\partial e(n)}{\partial w_i} \quad (13)$$

Substituting (10) in the last factor on the right-hand side of (13) and noting that $d(n)$ is independent of w_i, we obtain

$$\frac{\partial e^2(n)}{\partial w_i} = -2e(n)\frac{\partial y(n)}{\partial w_i} \quad (14)$$

Substituting for $y(n)$, we get

$$\frac{\partial e^2(n)}{\partial w_i} = -2e(n)x(n-i) \quad (15)$$

Using (13) and (15), we obtain

$$\nabla e^2(n) = -2e(n)x(n) \quad (16)$$

Substituting, this result in (11). So that we have LMS algorithm as follows

$$\mathbf{w}(n+1) = \mathbf{w}(n) + 2\mu e(n)\mathbf{x}(n) \quad (17)$$

where μ is the step-size parameter.

III. Chrominance-to-Luminance Gain & Delay Distortions

In color video waveform transmission, linear distortions cause by gain distortion only, group-delay distortion only and both gain & group-delay distortions. The pulse and bar test signal, which has been used to measure linear waveform distortion in TV systems, by a special 20T sine-squared pulse. This pulse is formed by the linear addition of a 20T-pulse to the pulse modulated on the color sub-carrier can be expressed as follows [6].

$$x(n)=\begin{cases}\dfrac{1}{2}\sin^2\left(\dfrac{\pi t}{40T}\right)+\dfrac{A}{2}\sin^2\left(\dfrac{\pi(t-\tau}{40T}\right)\cos\omega_c t & ;|t|\le 20T\\ 0 & ;|t|>20T\end{cases} \tag{18}$$

where A is the gain of 20T sine-squared pulse, τ is delay time, T = 0.1 μs. For the Phase Alternating Line (PAL) system t is instantaneous time, $\omega_c = 2\pi f_c$ and the color sub-carrier $f_c = 4.43$ MHz.

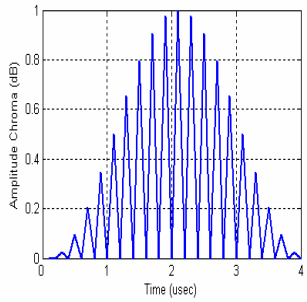

Figure 2 The Modulated 20T sine-square pulse test signal

Fig. 2 shows the undistorted modulated 20T sine-square pulse test signal, which we defined gain or $A=1$ and the delay time or $\tau = 0$. In this paper, we will defined $A=1$ but adjust τ value, because we examine specially occurrence the group-delay distortion shown in Fig. 3.

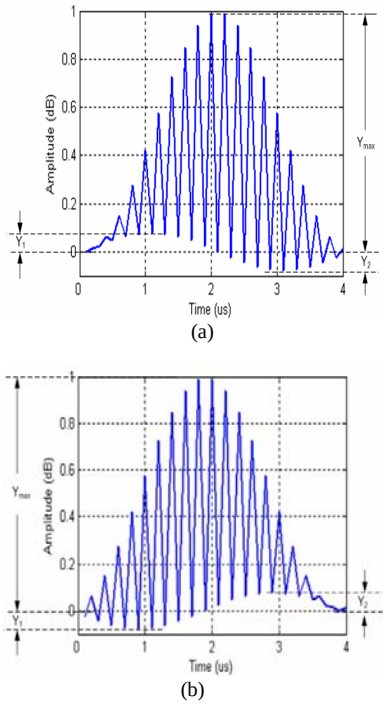

Figure 3 Group-delay distortion of the modulated 20T sine-square pulse.

From Fig. 3 (a) shows the modulated 20Tsine-square pulse is occurring a group-delay distortion only at $\tau = 200$ ns, that the peak pulse height $y_1 = 0.08$ and $y_2 = -0.08$ or $Y_1 = Y_2$ we obtain unity gain ($A = 0$ dB) given by

$$\tau = \frac{4T_0}{\pi}\sqrt{-y_1 y_2} \tag{21}$$

where y_1 and y_2 is the normalize of the single peak the following as

$$y_1 = \frac{Y_1}{Y_{\max}} \tag{22}$$

$$y_2 = \frac{Y_2}{Y_{\max}} \tag{23}$$

Fig. 3 (b) shows group-delay distortion only at $\tau = -200$ ns, that the peak pulse height $y_1 = -0.08$ and $y_2 = 0.08$. The baseline shape will indicate whether chrominance is lagging or leading luminance. The group-delay distortion will cause color hue and make the picture look smeared [7].

IV. Simulations And Results

A. *Design of Adaptive Equalizer*

Fig. 4 shows block diagram of an adaptive equalization of group-delay of chrominance distortion by using linear-phase FIR filter and LMS adaptive algorithm. Herein, $x(n)$ is input signal, which have been occurred the chrominance group-delay distortion by using the modulated 20T sine-square pulse test signal. $d(n)$ is the desire signal or no group-delay error. $y(n)$ is the output signal, which is modified the group-delay distortion, and $e(n)$ is the error signal [9].

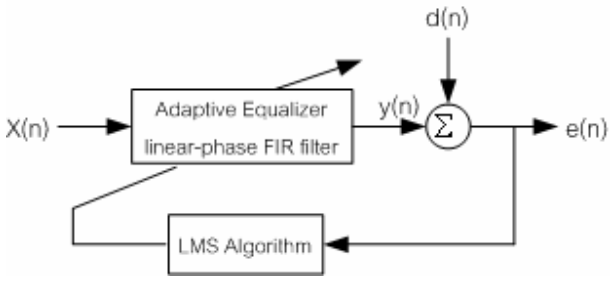

Figure 4 Block diagram of an adaptive equalization of chrominance signal

The linear-phase structure was discussed section, and the equation of adaptive equalizer linear-phase FIR based on LMS adaptive algorithm is given as

$$y(n) = \sum_{i=0}^{N/2-1} w_i(n)(x(n-i)+x(n-N+i)) + w(N/2)x(n-N/2) \tag{22}$$

B. Experimental Results

Herein, the proposed adaptive equalizer linear-phase FIR with LMS adaptive algorithm is used to correcting the distorted modulated 20T sine-square pulse test signal, which have been occurred the chrominance group-delay distortion only.

We first consider the chrominance delay inequalities between luminance-chrominance without gain error $(A=1)$ [9]. We determine the group-delay distortion only at 200 ns and -200 ns, which the baseline will be a symmetrical positive and negative peaks indicate the presence of group-delay distortion only shown in Fig. 5 (a) and (c) respectively. In this case, other parameters chose are $N=50$, and step-size $\mu=0.02$. Fig. 5 (b) and (d) show the output signal is equalized by using adaptive linear-phase FIR digital filter with LMS adaptive algorithm As the results, the proposed adaptive equalization can be equalized the chrominance delay distortion, which the baseline will be flat indicates no group-delay distortion..

Next, we used the input signal is the modulated 20T sine-square pulse has the both low-gain chrominance distortion at -2 dB ($A<1$) and group-delay distortion at +300 ns as shown in Fig. 6 (a), and the both high-gain chrominance distortion at 2 dB ($A>1$) and group-delay distortion at -300 ns as shown in Fig. 6 (c). The both of figure have the baseline are an asymmetrical positive and negative peaks indicate the presence of the both gain and group-delay distortion. Fig. 6 (b) and (d) show the low gain chrominance distortion only at -2 dB ($A_l=-2$ dB) and high gain chrominance distortion only at 2 dB ($A_h=2$ dB), respectively.

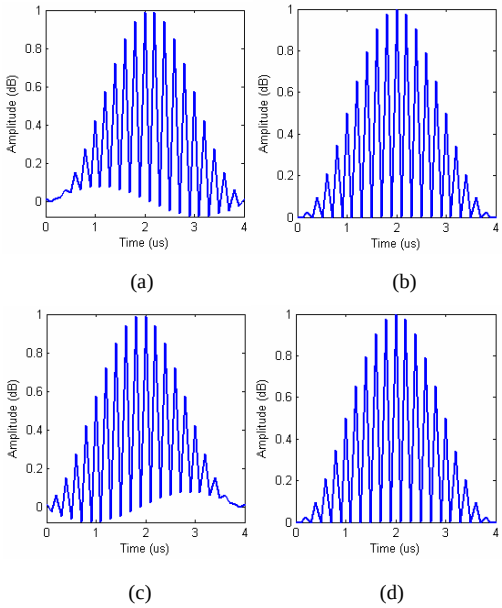

Figure 5 Group-delay distortion of chrominance signal equalized by using adaptive linear-phase FIR digital filter with LMS algorithm.

As the result, the proposed adaptive equalizer can be equalized the chrominance delay distortion only, which the baseline will be enhanced and compressed the amplitude chrominance indicates the presence of gain distortion only.

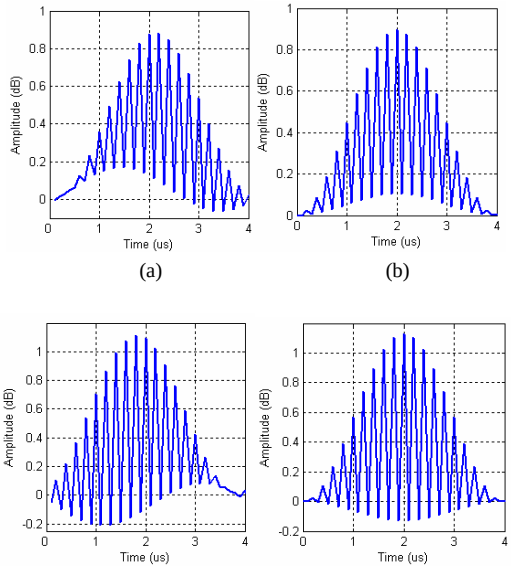

Figure 6 Gain and Group-delay distortion of chrominance signal equalized by using adaptive linear-phase FIR digital filter with LMS algorithm.

V. CONCLUSION

In this paper, an adaptive video equalizer is designed by using a linear-phase FIR structure with LMS adaptive algorithm. It is shown that the proposed adaptive equalizer can be equalized the chrominance group-delay distortion at color sub-carrier 4.43 MHz for PAL system. From the simulation results, the symmetry of linear-phase FIR filter with even order degree is adopted. Therefore, its can be exploited to reduce the total number of multipliers into almost half of that in the direct form. As the results, the modulated 20T sine-square pulse is used to examine the characteristics of the proposed adaptive equalizer. Simulation results show the performance achievable.

REFERENCES

[1] B. Farhang-Boroujeny, *Adaptive Filters Theory and Applications*, John Wiley, 1998

[2] Sanjit K. Mitra, *Digital Signal Processing*, 3rd ed., McGraw-Hill, 2006

[3] V. Chutchavong, C. Benjangkaprasert, and K. Janchitrapongvej, "Gradient-based Algorithm by using VSLMP Technique for the Amplitude Chrominance Distortion", *Proceeding Laos Journal on Applied Science*, vol. 1, pp. 610-617, Nov. 2006.

[4] Alan V. Oppenheim, Ronald W. Schafer, *Discrete-Time Signal Processing*, Prentice Hall, 1989.

[5] Peter Nagel, "Frequency-Domain Design Method for Linear-Phase and Minimum-Phase FIR Equalizers", *IEEE Trans. Circuits and Systems*, vol. 47, No. 11, pp. 1347-1351, Nov. 2000.

[6] K. Janchitrapongvej, and T. Ikeda, "Equalization of the relative Luminance-to-Chrominance Gain in Video Signal Transmission", *International Journal of IL ITS*, vol. 40, 1986.

[7] http://pdfserv.maxim-ic.com/en/an/AN3634.pdf

[8] P. Wolf, "Modification of the Pulse-and-Bar Test Signal with Special Reference to Application in Color Television", *Journal of the SMPTE*, pp. 15-19, 1996.

[9] V. Chutchavong, K. Janchitrapongvej, and C. Benjangkaprasert, "An Adaptive Equalization of Amplitude Chrominance Distortion by using the Variable Step-Size Technique", *Proceeding ICCAS 2004*, pp. 2065-2069, Aug. 2004.

Quantum Dot Molecule Chains and Their Polarization Photoluminescence

N. Budsayaplakorn, S. Thainoi and S. Panyakeow
Semiconductor Device Research Laboratory
Department of Electrical Engineering, Faculty of Engineering, Chulalongkorn University,
Bangkok 10330, Thailand

***Abstract*-Quantum dot molecules (QDMs) were grown on nanopropeller templates which were obtained by thin-capping-and-regrowth MBE process. Thin-capping-and-regrowth was done on as-grown quantum dots (QDs) at low temperature. All processes are self-assembled method which provides defect-free structures. The length of nanopropeller templates was extended by applying several cycles of thin-capping-and-regrowth as well as by using proper thin-capping thickness. Longer nanopropellers result in the possibility of growth of longer chains of QDMs if QDs are grown with suitable thickness in final cycle. Chains of QDMs stretch along [1 $\bar{1}$ 0] crystallographic direction. With their alignment in one specific direction, chains of QDMs demonstrate optical anisotropy. The polarization dependence of photoluminescence (PL) spectrum of QDM chains was measured. The QDMs grown with difference conditions were compared in term of degree of anisotropy. The optical anisotropy increases when length of aligned QDs is increased. However, it is reduced when the density of QDMs become high.**

I. INTRODUCTION

Quantum dots have been attracting interest for applications in optoelectronic devices and quantum computing as well as the fundamental physics of QDs. Their unique physical properties lead to high performance optoelectronic devices, for example, QDs lasers have low threshold current density, high temperature stability, high gain etc.[1] Because of their applicability of optoelectronic devices in fibre-optical communication, polarization dependence of QDs photoluminescence is required as one fundamental optical property. The polarization-uncontrolled laser has problems such as increasing of relative intensity noise which leads to a deterioration of bit error rate.[2] Polarized emission property of QDs was proposed to be arised from asymmetric shape, anisotropic composition and anisotropic strain of QDs.[3-5] Recently, coupling of aligned QDs was introduced that it also contributes to polarization anisotropy.[6]

QDs can be modified to form laterally close-packed QDs, which are so-called quantum dot molecules, by the GaAs-thin-capping and regrowth of InAs-QDs at low temperature on the as-grown QDs.[7] QDMs obtained by this technique have formation pattern of QDs stretching along [1 $\bar{1}$ 0] crystallographic direction. The advantage of this growth process, which is a self-assembled technique, is the possible growth of defect-free nanostructure. In our previous work, we proposed the modified MBE growth process for extending the length of QDMs.[8] The thin-capping-and-regrowth done for several cycles with proper thin-capping thickness was applied for this purpose. In this paper, we reported further experimental result i.e. the polarization-dependence PL intensity of long chain of QDMs. Polarization-dependence measurement system was set up by modifying the conventional PL measurement system. A half wave plate was placed in front of samples to adjust the polarized direction of incident laser and polarizer was placed between samples and a monochromator. The light emerging from polarizer is corresponding to Malus's law and was measured by a detector.

II. QUANTUM DOT MOLECULE CHAINS

After oxide desorption under As_4 overpressure of 8×10^{-6} Torr, 300 nm of GaAs buffer layer was grown on GaAs(100) substrates with growth rate of 0.6 ML/s at 580 °C. Afterward, the substrates were cooled down to 500 °C. This temperature which was used as a reference temperature was checked by RHEED-pattern transition from (2x4) to (2x2) reconstruction. 1.8 ML of InAs was deposited to form QDs using low growth rate of 0.01 ML/s. The growth interruption time of 30s was applied to obtain uniform QDs before the substrates were reduced to 470 °C. The QDs were thin-capped by GaAs and the growth interruption of 25 s was applied at retaining temperature of 470 °C. After that, InAs QDs were regrown with different depositions of InAs thickness. The thicker thin-capping thickness was deposited, the more InAs amount was required to form QDs. The thickness was estimated by observing RHEED transition into clear spotty pattern. As the results, the necessary thickness of InAs for the cases of the samples thin-capped with 6, 9, 12 and 15 ML of GaAs are 0.6, 0.75, 0.82 and 0.875 ML, respectively. After QDs-regrowth and annealing for 25 s, the QDs locating at the center of nanopropellers are nucleated above the QDs buried in GaAs thin-capping layer due to the seeding effect of strain as well as both of nanopropeller's blades stretch along [1 $\bar{1}$ 0] crystallographic direction due to strain anisotropy. Thin-capping-and-regrowth processes were done for several cycles in order to extend length of nanopropeller's blades.

The samples thin-capped with 9, 12 and 15 ML of GaAs and regrown QDs with InAs were used to compare the surface of samples by atomic force microscope (AFM). The nanopropeller length is statistically summarized in Fig.1 as

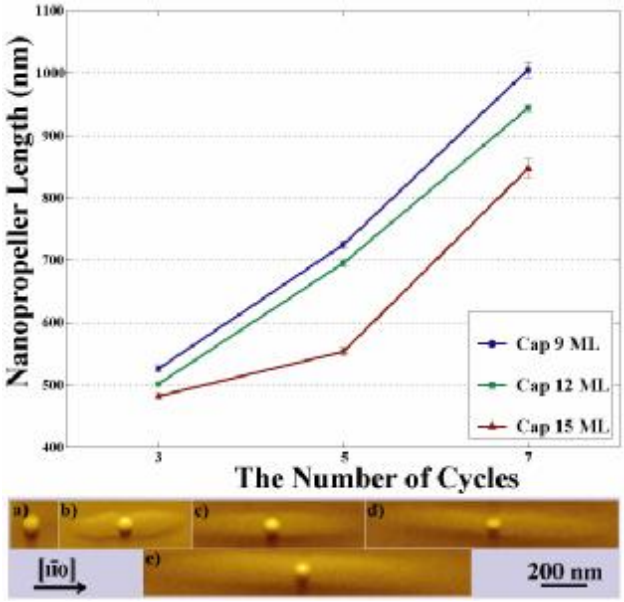

Figure 1. Nanopropeller length as a function of the number of cycles of thin-capping-and-regrowth for thin-capping thickness of 9 ML, 12ML and 15 ML. And AFM images of as-grown QDs and nanopropeller from 9ML-thin-capping for 1,3,5 and 7 cycles in a), b), c), d), and e)

well as the AFM images of as-grown QDs and nanopropeller QDs from 9ML-thin-capping for 1,3,5 and 7 cycles are shown in Fig.1 a), b), c), d) and e), respectively.

Corresponding to all thin-capping thicknesses, the nanopropeller length is increased when capping-and-regrowth process is more repeated. Considerably, the length of nanopropellers with thin-capping thickness of 9 ML is consistently longer than the length of nanopropeller with thin-capping thickness of 12 and 15 ML. However, the length fluctuation is lowest at thin-capping thickness of 12 ML and is highest at thin-capping thickness of 15 ML. For example, the standard deviations of length of nanopropellers with thin-capping of 9 ML, 12 ML and 15 ML for 7 cycles are 185.6, 123.6 and 196.36 nm, respectively.

The chains of QDMs were achieved by depositing further InAs in the last cycles. The additional QDs are likely to locate on the nanopropeller's blade templates. The chains of QDMs ordering along [1 $\bar{1}$ 0] direction can be attained by depositing with appropriate InAs amount. The QDMs from 1 cycle of 9ML-thin-capping-and-regrowth which originate from isolated nanopropellers contain 10 QDs per group in average. And the numbers of QDs per QDM form 5 cycles of thin-capping-and-regrowth and final-cycles regrowth thickness of 1.5 ML are 25 and 22 for thin-capping thickness of 9 ML (sample1 shown in Fig.2 a)) and 12 ML (sample2 shown in Fig.2 b)), respectively. The QDs densities of QDMs chains increase from densities of as-grown QDs (3.2×10^{9} cm^{-2}) and nanopropeller QDs (1.8×10^{9} cm^{-2}) to 2.7×10^{10} cm^{-2} and 2.24×10^{10} cm^{-2} for sample1 and sample2, repectively. When final-cycles regrowth thickness increase to 1.8 ML (sample3 shown in Fig.2 c)), the QDs density is raised up to 3.38×10^{10} cm^{-2}.

III. Polarization Dependence of QDM Chains

All samples used to perform PL measurement were capped with 10 nm of GaAs at 470 °C. And the substrate temperature was ramped up to 500 °C while the growth of GaAs was suspended. Further 90 nm of GaAs was grown when substrate temperature was stable.

All samples were excited by Ar^{+} laser at wavelength of 488 nm. The peaks of PL spectra of sample1, sample2 and sample3 are at 1.17 eV and full widths at half maximum are 50 meV at 77 K. In order to measure polarization dependence of the peaks, The polarized direction of laser were adjusted by retarding a halfwave plate and a polarizer was used to filter light emerging from the samples before the light entered into monochromator. The polarized direction of laser was adjusted to obtain the highest excitation of electron in QDMs by observing PL intensity at the peaks. After that, the polarizer was retarded to determine the highest intensity and set that

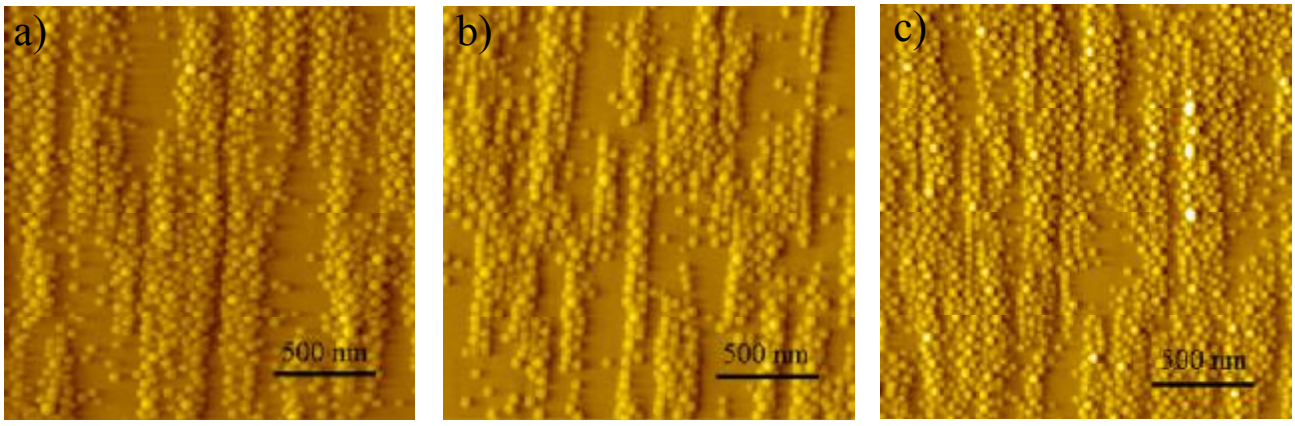

Figure 2. The AFM image of QDMs from 5 cycles of thin-capping-and-regrowth with 9 ML and 12 ML of thin-capping thickness and 1.5 ML of final-cycles regrowth thickness in a) and b), repectively and with 9 ML of thin-capping thickness and 1.8 ML of final-cycles regrowth thickness

direction to be angle of zero.

The polarization dependence of PL peaks from as-grown QDs was not observed in this experiment. QDMs in sample1, sample2 and sample3, however, demonstrated clear polarization dependence. The degree of linear polarization P defined by

$$P = \frac{I_{\max} - I_{\min}}{I_{\max} + I_{\min}}$$

where $I_{\max}$ and $I_{\min}$ are the maximum and minimum PL intensity. The degree of polarization at PL peaks of sample1, sample2 and sample3 are 35.15%, 29.72% and 21.35%. The PL spectrum of sample1 at each angle from 0° to 90° are shown in fig.3 as well as the peak intensity of PL spectrum was plotted on the upper right side as a function of polarization angle θ. The results of peak intensity of PL spectrum exhibit existence of two orthogonal components of PL peak intensity. The peak intensity of PL spectrum was thus fitted by

$$I = A\sin^2(\theta + \delta) + B\cos^2(\theta + \delta)$$

where A and B correspond to the peak intensities of PL spectrum in each of their component and δ correspond to the deviation angle due to zero-angle setting error. A and B imply for the PL intensity in polarization direction along [1 $\bar{1}$ 0] and [1 1 0] directions, respectively. The optical anisotropy of QDM chains is resulted from the difference in the square of the magnitude of the wave vectors between [1 $\bar{1}$ 0] and [1 1 0] directions. It is arised from the difference in amount of coupled QDs in each direction.

The measurement results of the peaks of PL spectrum can be comparatively explained. Sample1 have stronger polarization dependence than sample2. That is in an agreement with the AFM result that nanopropeller templates

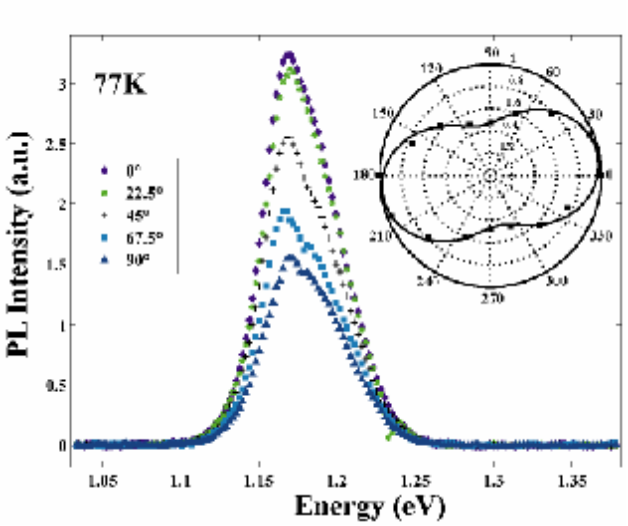

Figure 3 PL spectrum of QDMs from 9ML thin-capping and regrowth for 5 cycles (sample1) which polarized in angle of 0° to 90° and peak of PL spectrum as a function polarized angle

of sample1 are longer than that of sample2. It also implies that the number of coupled QDs aligning along [1 $\bar{1}$ 0] direction in sample1 is greater than that in sample2. In contrast, sample3 have weaker optical anisotropy, because sample3 have high density of QDs which lead to greater amount of coupling in [1 1 0] direction.

IV. Conclusion

Nanopropeller used for QDM template can be extended by applying many cycles of thin-capping-and-regrowth and proper selection of thin-capping thickness as the parameters of thin-capping-and-regrowth process. Polarization dependence of QDMs was observed in PL spectrum of QDMs. Alignment of coupled QDs along [1 $\bar{1}$ 0] rather than [1 1 0] is the origin of optical anisotropy. Longer nanopropeller template with proper overgrowth thickness gives longer ordering of ODs as well as stronger anisotropy. On the other hand, if the density of QDs which is resulted from the density of as-grown QDs and overgrowth thickness is too high, the anisotropy will be limited.

Acknowledgment

This research is financially supported by Asian Office of Aerospace Research and Development (AOARD), U.S. Air Force, Thailand Research Fund (TRF), Nanotechnology Center of Thailand (Nanotech), and Chulalongkorn University.

References

[1] Y. Arakawa and H. Sakaki, Appl. Phys. Lett., vol. 40, pp. 939-941, 1982

[2] D. V. Kuksenkov, H. Temkin, and S. Swirhun, Appl. Phys. Lett., vol. 67, pp. 2141-3, 1995.

[3] H. Saito, K.Nishi, S. Sogou, and Y. Sugimoto, Appl. Phys. Lett., vol. 71, pp. 590, 1997

[4] Y. Nabetani, T. Ishikawa, S. Noda, and A. Sasaki, J. Appl. Phys., vol. 76, pp. 347, 1994

[5] M. Henini, S. Sanguinetti, S. C. Fortina, E. Grilli, M. Guzzi, G. Panzarini, L. C. Andreani, M. D. Upward, P. Moriarty, P. H. Beton, and L. Eaves., Phys, Rev. B, vol. 57, pp. 6815, 1998

[6] N. T. C. Swe, C. Wissawinthanon, and S. Panyakeow, "Theoretical investigation on the optical polarization anisotropy of photoluminescence from InAs/GaAs linearly aligned quantum dots", EECON-29 Proceedings, 2006

[7] S. Suraprapapich, S. Thainoi, S. Kanjanachuchai, and S. Panyakeow, J. Vac. Sci. Technol. B vol. 23(3), pp. 1217, 2005

[8] S. Ruangdet, N. Budsayaplakorn, C. C. Thet, S. Thainoi, S. Kanjanachuchai, and S. Panyakeow, "Long chains of self-assembled InAs quantum dot molecules by modified MBE growth technique", MBE2006 14th International Conference Molecular Beam Epitaxy, 2006.

3D Deformable Mesh Aided Dentistry

C. Sinthanayothin, W. Bholsithi, W. Tharanon
Advanced Dental Technology Center (ADTEC), National Science and Technology Development Agency (NSTDA)
111 Thailand Science Park, Phahon Yothin Rd, Klong 1, Klong Luang, Pathumthani 12120, Thailand
cephsmile@gmail.com, cephsmile@hotmail.com

***Abstract*- The 3D shapes encountered in designing in dentistry and maxillofacial applications. It is difficult to design and edit some features of crowns, some part of skull and anatomical model for rapid prototyping.**

Therefore, this paper presents 3 dimensional deformable mesh using thin plate spline through the following 4 steps: The first step, the program was written to open, display and allow the user to interact with the 3D STL file by using Borland C++ Builder ™ and OpenGL library. Second step, the deformable region was manually defined by locate the surface control points. Then the surface control points were fitted and the patch surface were created automatically using cubic spline technique. Third step, the control points in the patch surface were manipulated in the direction as required. The last step, the control points manipulation can change the shape of the 3D object using the thin plate spline algorithm.

The results from the research have shown that the 3D deformable mesh by applying thin plate spline technique can do either restrict a deformation to a limited local region or also create a new shape by making very large area deformations as well. Therefore 3D deformable mesh is powerful alternative, which can make a small deformation in an exiting shape and modify the shape without affecting its original overall characteristics.

I. INTRODUCTION

In the past, dental crown design has been done by manual process along with expertise of dental crown designer to get dental crown with shape resemble to actual teeth. However, manual process cannot fulfill the growing demands of dental crown from increasing number of aging people. Therefore, the computer design for dental crown has become the new trend after there is a commercial CAD/CAM product for dental crown design such as CEREC™ 3D CAD/CAM system [1] for designing

However, it is quite difficult to design and manipulate dental crown shape due to natural complexity of 3D structure, which takes time to modify the shape of the dental template to have the shape that suit for each patient.

This paper presents a technique for 3D deformable mesh aided dentistry based on thin plate spline technique [2]. With this algorithm, the users are allowed to see the movement of 3D mesh, in the direction that they have been decided. Therefore, the users who needs to developed software for dental designer; CAD/CAM editing application; virtual animation or further study in 3D would find this technique more informative and useful. In recent years, some algorithms for deformable mesh model have been proposed [3][4]. Some approaches construct surfaces that interpolate from 2D data [5]. Others provide means for the direct drawing of surfaces like commercial CAD/CAM software. An alternative to these shape change techniques is the warping or deformation of existing shapes like the technique proposes in the research.

However, mostly 3D deformable mesh techniques are applied in the research or CAD/CAM technology areas. The techniques are also available in dentistry application but they are expensive commercial software such as 3shape dental designer™ [6], GeoMagic Dental ™ [7] and so on.

II. METHODS

A. 3D STL Viewer & User Interaction

First step, the graphics user interface of 3D deformable mesh has been designed using C++ Builder® and OpenGL library. The users are allowed to interact with the 3D object by rotating, zooming and panning as shown in Figure 1.

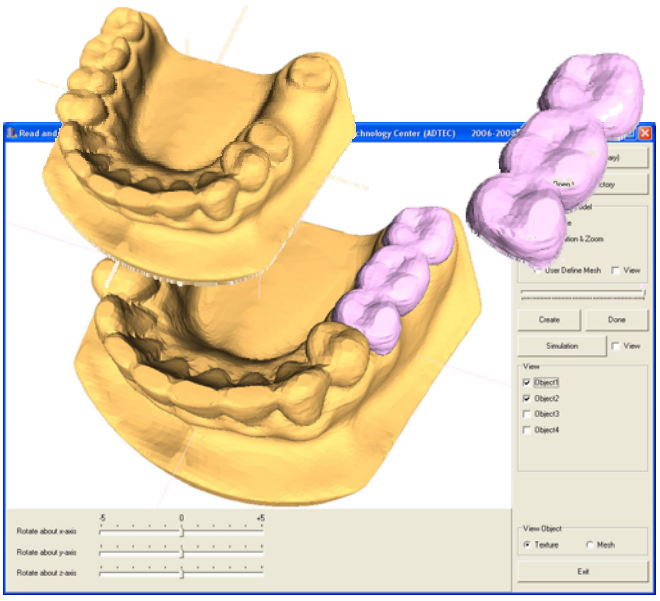

Figure1: The 3D visualization of dental cast and crown.

This software is also allowed to open the 3D object up to 100 objects with the different color set in the same time as well. The 3D STL data format has been used in this research.

B. Surface Control Points and Cubic Spline fitting

Next step is to define the area to perform dental crown shape manipulation by applying surface control points and then apply cubic spline interpolation to fit the landmarks with the mesh of

3D dental model. The landmark placement will be 4 x 4 landmark set to form a mesh of 3 x 3 on 3D object as shown in Figure 2.

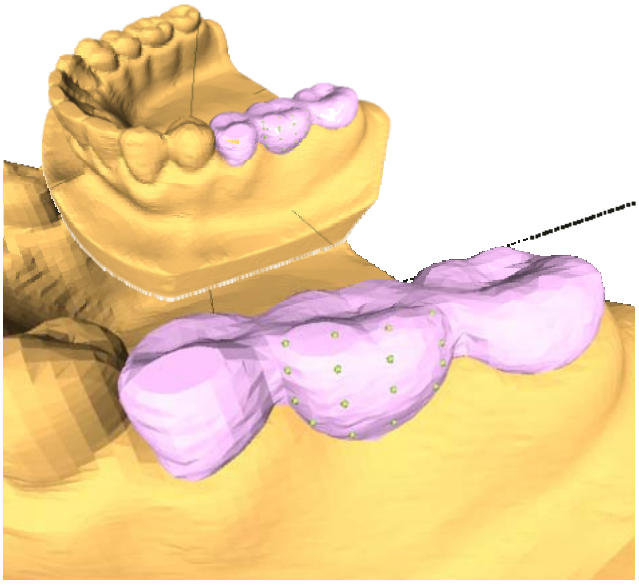

Figure2: Manual Location of Landmarks onto the 3D Object.

After landmark placement, the next step is to perform 3D cublic spline interpolation to form a mesh and create minor landmarks between major landmarks in very smooth way in both horizontal and vertical. For this experiment we have chosen the natural spline technique [8]. The results of cublic spline interpolation can be shown in Figure 3.

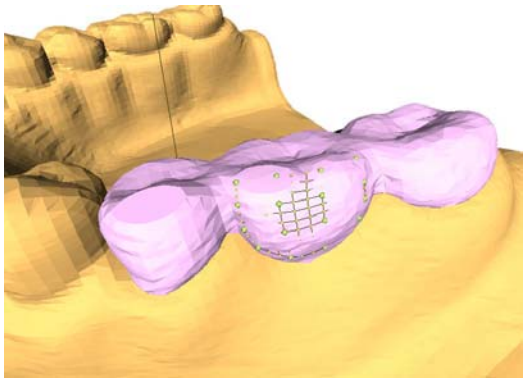

Figure 3: Automatic creating of the patch surface using cubic spline technique.

C. Adjusting the Surface Control points

The next step after performing 3D cubic spline interpolation is to manipulate the surface control point by moving the set of landmark to the direction that need the change of the 3D object shape as shown in Figure 4. This is the way to set the shape change landmarks for performing 3D thin plate spline

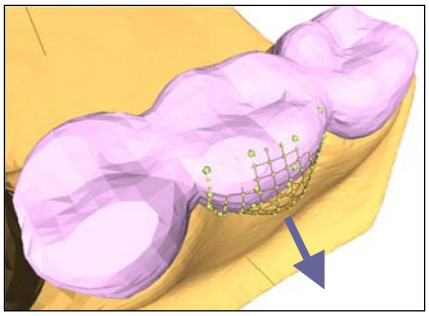

Figure 4: Adjusting of the patch surface in order to move to the required direction.

D. 3D Deformable Mesh using Thin Plate Spline

After manipulating surface control points by applying cubic spline interpolation and adjust the patch landmarks, the next step is to manipulate the mesh of the object by 3D thin plate spline to perform image manipulation by calculating the linear affine factor A and nonlinear weighting factor W from 2 set of landmarks from initial positions X which has been modified into matrix P and final positions V according to the following equations.

$$\begin{bmatrix} K & P \\ P^T & zeros(4,4) \end{bmatrix} \begin{bmatrix} W^T \\ A^T \end{bmatrix} = \begin{bmatrix} V \\ zeros(4,3) \end{bmatrix} \quad (1)$$

$$K = \begin{bmatrix} 0 & U(r_{1,2}) & \dots & U(r_{1,N-1}) & U(r_{1,N}) \\ U(r_{2,1}) & 0 & \dots & U(r_{2,N-1}) & U(r_{2,N}) \\ \dots & \dots & \dots & \dots & \dots \\ U(r_{N-1,1}) & U(r_{N-1,2}) & \dots & 0 & U(r_{N-1,N}) \\ U(r_{N,1}) & U(r_{N,2}) & \dots & U(r_{N,N-1}) & 0 \end{bmatrix} \quad (2)$$

$$U(r)_{r>0} = |r|, r = \sqrt{(P_{xi}-x)^2 + (P_{yi}-y)^2 + (P_{zi}-z)^2} \quad (3)$$

X is a matrix of initial position (the landmarks from step B) which can be expressed as

$$X = \begin{bmatrix} x_1 & y_1 & z_1 \\ \dots & \dots & \dots \\ x_N & y_N & z_N \end{bmatrix} \quad (4)$$

P is the modified matrix for X with the additional matrix one of N x 1

$$P = \begin{bmatrix} ones(N,1) & X \end{bmatrix} = \begin{bmatrix} 1 & x_1 & y_1 & z_1 \\ \dots & \dots & \dots & \dots \\ 1 & x_N & y_N & z_N \end{bmatrix} \quad (5)$$

V is a matrix of the final positions (the landmarks from step C) which can be expressed as

$$V = \begin{bmatrix} x_1' & y_1' & z_1' \\ \dots & \dots & \dots \\ x_N' & y_N' & z_N' \end{bmatrix} \quad (6)$$

The solution for both weighting factor W and affine factor A can be expressed as the following equation

$$\begin{bmatrix} W^T \\ A^T \end{bmatrix} = \begin{bmatrix} K & P \\ P^T & zeros(4,4) \end{bmatrix}^{-1} \begin{bmatrix} V \\ zeros(4,3) \end{bmatrix} \quad (7)$$

W is a matrix of the weighting factors for non-rigid (nonlinear) registration which can be expressed as

$$W = \begin{bmatrix} w_1 & \dots & w_N \end{bmatrix} = \begin{bmatrix} w_{x1} & \dots & w_{xN} \\ w_{y1} & \dots & x_{yN} \\ w_{z1} & \dots & w_{zN} \end{bmatrix} \quad (8)$$

A is a matrix of the affine factors for rigid and linear transformation (e.g. Rotation, Translation, and Scaling) which can be expressed as:

$$A = \begin{bmatrix} a_1 & a_x & a_y & a_z \end{bmatrix} = \begin{bmatrix} a_{11} & a_{1x} & a_{1y} & a_{1z} \\ a_{21} & a_{2x} & a_{2y} & a_{2z} \\ a_{31} & a_{3x} & a_{3y} & a_{3z} \end{bmatrix} \quad (9)$$

Use weighting and affine factors to define function of coordinate $f(x, y, z)$ everywhere in the plane as shown in (1), (2), and (3)

$$f(x, y, z) = a_1 + a_x x + a_y y + a_z z + \sum_{i=1}^{N} w_i U(P_i - r) \quad (10)$$

The result on 3D thin plate spline calculation can be shown in Figure 5. Figure 4 is showing the direction of mesh movement for patch surface manipulation.

The original crown with texture will be shown in Figure 5(A) while the original crown displayed in mesh can be seen in Figure 5(C). The final form of crown with texture after applying 3D thin plate spline following to the moving patch surface can be seen in Figure 5(B) while the final form of crown with mesh can be displayed in Figure 5(D).

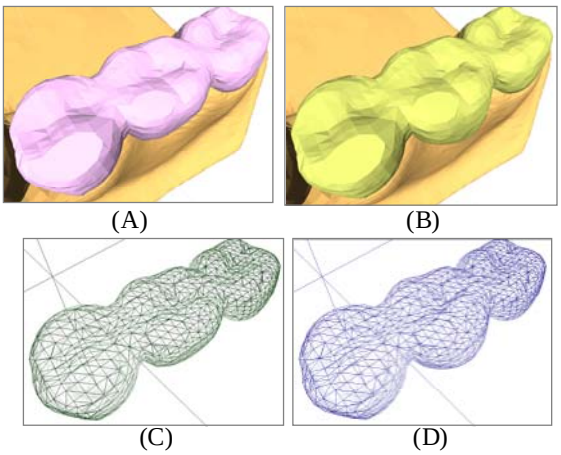

(A) (B)

(C) (D)

Figure 5: 3D Deformable Meshes Result on Crown Object.
(A) Original crown object.
(B) Crown after applied TPS follows to the patch surface.
(C) Original crown object display in mesh.
(D) Crown after applied TPS follows to the patch surface display in mesh.

III. RESULTS

After testing the algorithm for surface manipulation, the actual experiment on second lefty molar of the mandible can be shown in Figure 6 and Figure 7 step by step.

Figure 6 is showing the original dental crown (the second molar of the mandible) before the surface shape manipulation.

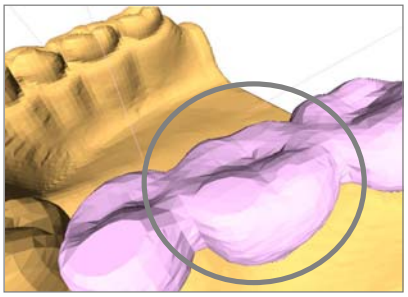

Figure 6: Original crown object to be under Manipulation

Figure 7 is showing the deforming of dental crown from the original crown shown in Figure 6. Figure 7(A) is showing the original crown with the mesh on the targeted area while the magnified mesh in Figure 7(B) is showing the original positions of the mesh. Figure 7(C) is showing the direction of the mesh after performing surface manipulation and Figure 7(D) is showing the final form of dental crown after surface manipulation and 3D thin plate spline.

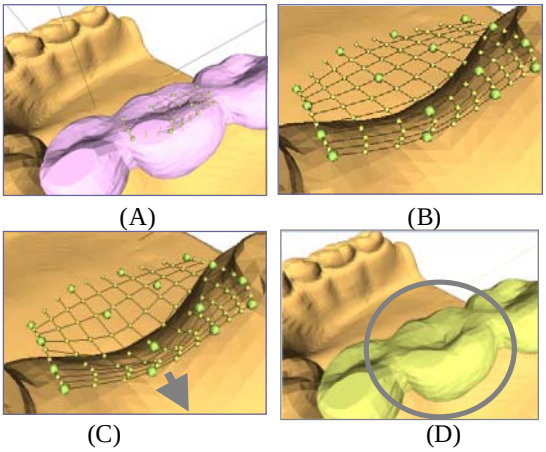

(A) (B)

(C) (D)

Figure 7: 3D deformable meshes steps on top of crown.
(A) Crown with the patch surface on the top.
(B) Display of patch surface.
(C) The middle of the patch surface sinks into bottom.
(D) Crown after applied TPS follows to the patch surface.

Figure 8 is showing example of manipulating left mandible. Figure 8(A) is showing the original mandible with texture along with mesh and direction of surface manipulation. Figure 8(B) is showing the results of manipulation on mandible in mesh. Figure 8(C) is showing the original mandible in mesh. Figure 8(D) is showing the results of manipulation on mandible in mesh. Figure 8(E) and 8(F) are showing the magnified section of original mandible within circle from Figure 8(C) and 8(D) respectively.

Figure 9 is showing the result of image manipulation on the left cheekbone. Figure 9(A) is showing original skull in texture with mesh that moves to the final point. Figure 9(B) is showing the final image in texture after surface manipulation. Figure 9(C) is showing the magnified version of the original part in mesh while Figure 9(D) is showing the magnified version of the manipulated part in mesh.

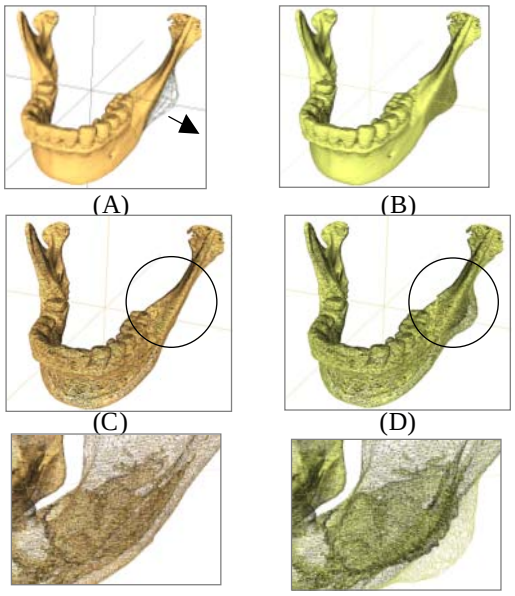

(A) (B) (C) (D) (E) (F)

Figure 8: 3D deformable meshes steps on mandible.

(A) Original mandible object with showing the direction of patch surface manipulation.
(B) Mandible after applied TPS follows to the patch surface.
(C) Original mandible display in mesh.
(D) Mandible after applied TPS display in mesh.
(E) Magnified area from Circle area in Figure 9 (C)
(F) Magnified area from Circle area in Figure 9 (D)

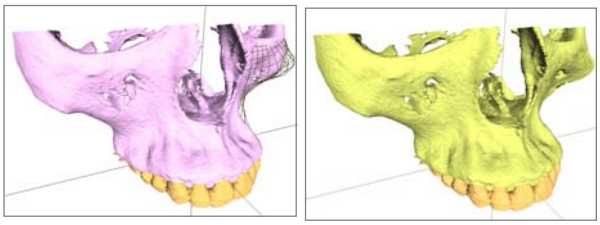

(A) (B)

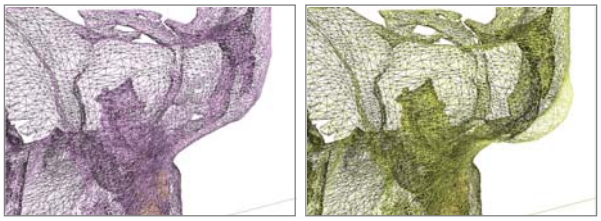

(C) (D)

Figure 9: 3D deformable meshes steps on maxilla

(A) Original maxilla with showing the direction of patch surface manipulation.
(B) Maxilla after applied TPS follows to the patch surface.
(C) Expand of the original maxilla display in mesh.
(D) Expand of the maxilla after applied TPS display in mesh.

IV. Discussions and Conclusions

The results after performing mesh deformation with cubic spline interpolation and thin plate spline have shown that it can deform dental crown, mandible and skull at the targeted area without distorting other areas.

Further improvements will be focused on faster image distortion algorithm [9] along with better segmentation of target area which require the generation of new vertices and form new triangles in between the old vertices.[10]

References

[1] Sirona Dental Systems GmbH, "CEREC Software", available online at http://www.cereconline.com/ecomaXL/index.php?site=Cerec_software

[2] F. L. Bookstein, "Principal Warps: Thin Plate Splines and the Decomposition of Deformations." IEEE Trans. on Patt. Anal. And Mach. Intel., Vol. 11, No.6, 567-585, June 1989, available on line at www-cse.ucsd.edu/classes/sp03/cse252/bookstein.pdf

[3] I. Llamas, A. Powell, J. Rossignac, C. Shaw. Bender: A Virtual Ribbon for Deforming 3D Shapes in Biomedical and Styling Applications. Proceedings of the 2005 ACM symposium on Solid and physical modeling. Pages: 89 – 99, available on line at www.gvu.gatech.edu/~jarek/papers/Bender.pdf

[4] W. Welch and A. Witkin, Free-Form Shape Design Using Triangulated Surfaces. International Conference on Computer Graphics and Interactive Techniques Proceedings of the 21st annual conference on Computer graphics and interactive techniques. Pages: 247 - 256, available on line at /www1.acm.org/pubs/articles/proceedings/graph/122718/p257-celniker/p257-celniker.pdf

[5] M.W. Lee and S. Ranganath, 3D deformable face Model for Pose Determination and Face Synthesis, available on line at ieeexplore.ieee.org/iel5/6462/17274/00797605.pdf

[6] 3Shape DentalDesigner™, available on line at www.3shape.com/dentistry/dental_designer/dental_designer.htm

[7] GeoMagic Dental™, available on line at www.geomagic.com/en/products/dental/

[8] Sky McKinley and Megan Levine, Cubic Spline Interpolation, Student project, Fall 1998, available online at online.redwoods.cc.ca.us/instruct/darnold/laproj/Fall98/SkyMeg/Proj.PDF

[9] J. Müller et. al., A Template-Deformation Method for Facial Reproduction, Proceedings of the 4th International Symposium on Image and Signal Processing and Analysis, 2005. Pages: 359-364, available online at ieeexplore.ieee.org/iel5/10202/32543/01521317.pdf

[10] M.M. Karimi, et. al. , A 3-D Deformable Surface Method for Automatic Hippocampus-Amygdala Complex Segmentation, Nuclear Science Symposium Conference Record, 2004 IEEE, October 16-22, 2004, Pages: 3725 – 3729, available online at ieeexplore.ieee.org/iel5/9892/31438/01466690.pdf

A Localization Method for Thailand License Plates

Therdsak Chanfuangfoo [1,a], Pakorn Kaewtrakulpong [1,b], Supakorn Siddhichai [2,c]
Department of Control System and Instrumentation Engineering [1]
Faculty of Engineering, King Mongkut's University of Technology Thonburi
126 Prachautid, Bangmod, Toongkru, Bangkok 10140, Thailand
National Electronics and Computer Technology Center (NECTEC) [2]
Thailand Science Park, Pathum Thani 12120, Thailand
Email: s8403503@st.kmutt.ac.th [a], pakorn.kae@kmutt.ac.th [b], supakorn.siddhichai@nectec.or.th [c]

***Abstract*-A license plate localization (LPL) is a key that bring a good final result for automatic license plate recognition system (ALPRS). Switching algorithm for Thailand license plate localization is presented. Eleven plate detection techniques were used to generate candidate plate regions based on gradient and color. All of Thailand license plates can be detected, including plates complex problem. Experimental results correspond to 99.07%, 0.93% and 1.48% for correct extraction rate, missed detection rate, and false alarm rate, respectively. However, some problems still occur due to similar texture of grilles, logos, headlights, and plate.**

I. INTRODUCTION

An automatic license plate recognition system (ALPRS) has many applications such as law enforcement, toll collection, and car parking systems. ALPRS involves three steps: license plate localization (LPL), text segmentation (TS), and text recognition (OCR). In this paper, the focus is on LPL as it is a key step which determines the accuracy of the final ALPRS results.

There are many types of Thailand license plate such as private car, pickup truck, rental car, diplomat car, etc (see Table I). These plates differ in size, color, and format. In this paper, an LPL approach which can detect all types of Thailand license plates is presented. For national security reason, military and royal plates are not included in this research work.

Existing LPL systems can only detect limited types of license plate. Difficulty arises when old plates, dirty plates, damaged plates, and complex scene such as vehicle with large or complex bumper, are encountered. Other problems include fast moving vehicles and changing outdoor environments. The proposed approach utilizes important characteristics of license plate to form switching algorithm for license plate localization.

Well known plate region extraction techniques include binarized image approach [1], edge and gradient detection [2][3], plate color [4][5], and text detection approach [6]. The binarized image approach requires a good threshold value and often fails if intensities of plate and bumper are alike. Edge and gradient technique generates many candidates in complex scene which leads to ambiguity in segmentation. Color-based approach often fails if colors of plate and bumper are similar or when lighting condition is unstable. Text detection also fails if the text is connected to screws or merged with borders.

TABLE I

STYLES OF THAILAND LICENSE PLATE UNDER CONSIDERATION

Plate Type	Character/ plate color	Size (WxH cm)	Category	Example
A1	Black/graphic	34x15	Private car (not more 7 persons) (graphic plate)	
A2	Black/white	34x15	Private car (not more 7 persons)	
A3	Green/white	34x15	Pickup truck	
A4	Blue/white	34x15	Private car more 7 persons	
A5	Red/white	34x15	Private Tuk tuk	
A6	White/light green	34x15	Corporate rental car	
A7	Black/yellow	34x15	Taxi	
A8	Green/yellow	34x15	3-wheel Tuk tuk	
A9	Blue/yellow	34x15	4-wheel Tuk tuk	
A10	Red/yellow	34x15	Large regional bus	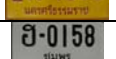
B1	Black/white	30x15	Private car (old generation)	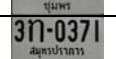
B2	Black/white	30x15	Private car (old generation)	
B3	Black/red	30x15	New car waiting to be registered	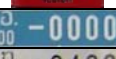
C1	White/Blue	38.7x11	International organization car	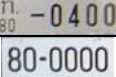
C2	Black/white	38.7x11	Diplomat car	
D1	Black/white	43x21	Truck	
D2	Black/yellow	43x21	Local bus	
E1	-	-	Modified plate (unlawful)	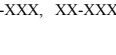

* There are four character formats for A1 to A10 : XX-X, XX-XX, XX-XXX, XX-XXXX

II. LICENSE PLATE LOCALIZATION SYSTEM

The LPL system consists of two parts, candidate plate detection and plate verification. Firstly, eleven plate detection techniques are used to determine candidate plates. The plate verification part is explained in Section IV. If a plate is not verified, the next of the eleven detection algorithms is used. The LPL system and its details are shown in Figure 1.

III. CANDIDATE PLATE DETECTION

An image sub-sampling is carried out prior to plate region detection. Plate candidate regions are then determined. There are eleven plate detection techniques using color and gradient

density. A switching algorithm selects which techniques to use in the detection, see Figure 1(b).

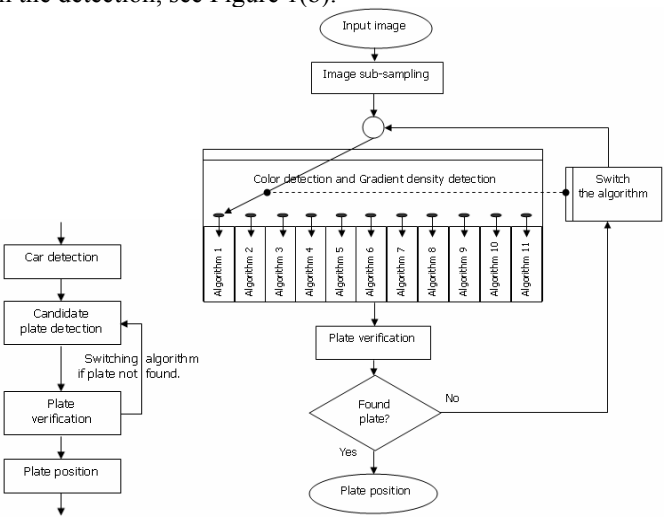

Figure 1. LPL system and its details
a) LPL system b) detail of LPL

A. *Image Sub-Sampling*

Comb-type problem is often found in captured images where cars move quickly. Sub-sampling the image, keeping only odd or even lines from both horizontal and vertical directions, can solve this problem. Moreover, sub-sampled images result in faster processing time with its smaller dimension, see Figure 2.

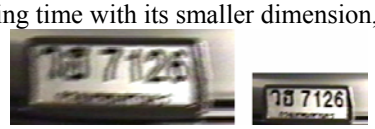

a) b)

Figure 2. Image sub-sampling
a) original image b) sub-sampled image

B. *Colors Detection*

There are five background colors on Thailand license plate: white, yellow, red, light green, and blue. HSV color model is a logical model for color detection. However, this model is unstable in white, gray, and black. This instability problem can be solved using chromatic thresholding [10], see Figure 3. Subsequently, HSV color model can be used to detect yellow, red, light green, and blue background. Detected background colors can then be encoded, see Table II. In chromatic thresholding, cylindrical area is defined in RGB cube covering gray scale part of the model. This cylindrical area can be used to detect white, gray, and black.

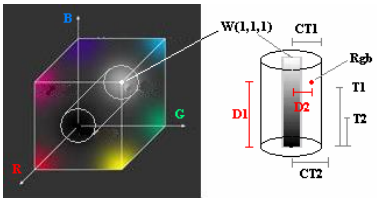

Figure 3. Rgb color model and cylindrical model

$$D_1 = \sqrt{\|\overline{RGB}\|^2 - \left(\frac{\overline{RGB}\cdot\overline{W}}{\|\overline{W}\|}\right)^2} \quad (1)$$

$$D_2 = \frac{\overline{RGB}\cdot\overline{W}}{\|\overline{W}\|} \quad (2)$$

From (1) and (2), D1 is the distance from origin on black (0,0,0) to $\overline{RGB}$ diagonal axis and D2 is the perpendicular distance from of $\overline{RGB}$ to diagonal axis. $\overline{RGB}\in(0,1)$, $\overline{W}=(1,1,1)$. Color code of these gray points (as shown in Table II.) can be determined as shown in (3) where $CT1=0.1250$, $CT2=0.2499$, $T1=0.8627$, $T2=0.5$.

$$colorcode = \begin{cases} 1 & if \quad D_1 > T_1 \quad and\ D_2 \le CT_1 \\ 2 & if \quad T_2 \le D_1 \le T_1 \quad and\ D_2 \le CT_1 \\ 3 & if \quad D_1 \le T_2 \quad and\ D_2 \le CT_2 \\ 0 & Otherwise \end{cases} \quad (3)$$

Subsequently, HSV values of yellow, red, light green, and blue can be determined by a standard conversation [7].

The colors are encoded using (4) where $H \in (0,360)$, $S,V,R,G,B \in (0,1)$, $YT1=21.6$, $YT2=64.8$, $YT3=0.4$, $RT1=21.6$, $RT2=327.6$, $RT=0.4$, $LGT1=140.4$, $LGT2=187.2$, $LGT3=0.35$, $BT1=187.2$, $BT2=252$, $BT3=0.35$.

$$colorcode = \begin{cases} 4 & if \quad YT_1 \le H \le YT_2 \quad and \quad S > YT_3 \quad and \quad colorcode \ne 1,2,3 \\ 5 & if \quad H \le RT_1 \text{ or } H > RT_2 \quad and \quad S > RT_3 \quad and \quad colorcode \ne 1,2,3 \\ 6 & if \quad LGT_1 < H < LGT_2 \quad and\ S > LGT3 \quad and \quad colorcode \ne 1,2,3 \\ 7 & if \quad GT_1 < H < BT_2 \quad and \quad S > BT_3 \quad and \quad colorcode \ne 1,2,3 \end{cases} \quad (4)$$

Finally, binary image of each color code is formed (see (5)).

$$\text{Binary Image}(Color) = \begin{cases} 1 & if \quad ColorCode = Color \\ 0 & Otherwise \end{cases} \quad (5)$$

C. *Gradient Density Detection*

Gradient density of the plate image can be calculated from the red channel in (6). Intensities in red channel show clearly the differences between plate characters and background of Thailand license plates.

$$\text{Gray Image}(x_i, y_j) = RGB[\text{Red}(x_i, y_j)] \quad (6)$$

Since gradient of texts in license plate will dominate in horizontal direction, a window of size $1 \times N_1$ is run over the image, where $N_1 = 4$, for gradient detection and noise reduction (see (7)).

$$\text{Gradient Image}(x_i, y_j) = \frac{\sum_{k=0}^{(N/2)-1} \text{GrayImage}(x_{i+k}, y_j) - \sum_{k=N/2}^{(N-1)} \text{GrayImage}(x_{i+k}, y_j)}{N/2} \quad (7)$$

Next, high gradient density regions are determined, see (8).

$$DensityGradientDetection(x_i, y_j) = \frac{\sum_{k=0}^{7} Gradient\ \text{Image}(x_{i+k}, y_j)}{7} \quad (8)$$

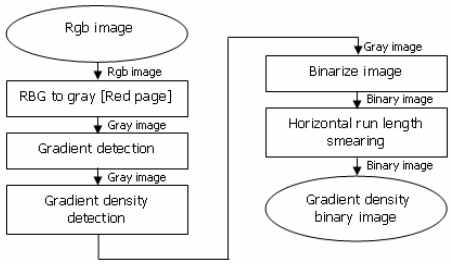

Figure 4. Block diagram of gradient density detection

The gradient density image is binarized. The color and gradient density selection uses threshold value equal to 50. And the gradient density selection uses threshold value equal to 30, see (9).

$$DensityGradientBinary\ \text{Image}(x_i, y_j) = \begin{cases} 1 & if \quad DensityGradientBinary\ \text{Image}(x_i, y_j) \ge Threshold \\ 0 & Otherwise \end{cases} \quad (9)$$

Finally, horizontal run length smearing [7] with gradient density binary image are used to fill gap of gradient with threshold value of 15, see Figure 4.

D. Switching Algorithm for Candidate Plate Detection

From eleven pre-processing algorithms for candidate plate detection using switching method in Table III, they can be categorized into three groups as follows.

1. Color and gradient density selection.
2. Color selection.
3. Gradient density selection.

Color and gradient density selection provides high accuracy result because color and gradient data are the main features of license plate. However, the accuracy depends on color integrity and gradient density. The color selection uses only color data to detect candidate plate region as some of the plates have little gradient. If the color of the plate is similar to that of the vehicle bumper, this method will fail since license plate region and bumper region will be joined together. In outdoor environment with changing light conditions, gradient density selection is more tolerant to changing light condition than color data. Segmentation problem will occur in a license plate with complex scene as many spurious gradients will be generated.

The algorithms order by efficiency and frequency of successful plate detection of Thailand license plate are shown in Table III.

TABLE II
BACKGROUND COLOR CODES

Code	Color
0	Unclassified
1	White
2	Gray
3	Black
4	Yellow
5	Red
6	Light green
7	Blue

TABLE III
ORDER OF SWITCHING ALGORITHM

Order	Algorithm
1	White color and gradient density selection (WGS)
2	Yellow color and gradient density selection (YGS)
3	Red color and gradient density selection (RGS)
4	Light green color and gradient density selection (LGGS)
5	Blue color and gradient density selection (BGS)
6	White color selection (WS)
7	Yellow color selection (YS)
8	Red color selection (RS)
9	Light green color selection (LGS)
10	Blue color selection (BS)
11	Gradient density selection (GDS)

The first to fifth algorithms are color and gradient density selection as shown in Figure 5. The binary image from the color detection will be processed horizontal run length smearing with threshold value of gap 15. After that, we uses AND operation between the binary image and gradient density binary image. The output of this is candidate plate. Finally, the candidate plate feeds to plate verification process.

The sixth to tenth algorithms are color selection algorithms. The process is similar to Figure 5 except the And operation as shown in Figure 6(a).

The eleventh algorithm is gradient density selection, see Figure 6(b). The method uses the gradient density binary image with processing in horizontal to vertical histogram [9] to confirm position of candidate plate. The horizontal to vertical histogram can reduce the noise of gradient.

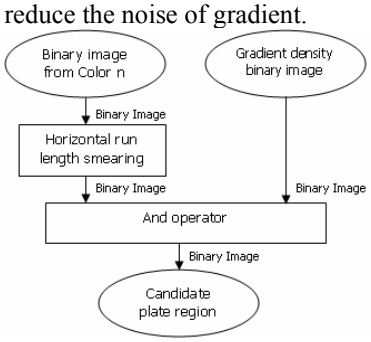

Figure 5. Block diagram of color and gradient density selection

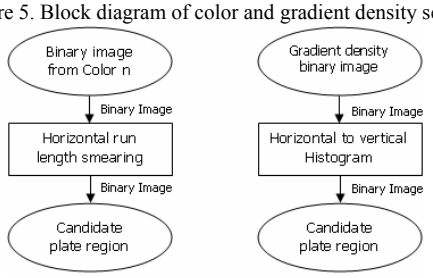

a) b)

Figure 6.Block diagram of color and gradient density selection
a) Color selection b) Gradient density selection

IV. PLATE VERIFICATION

In case of there are more than one candidate regions, the candidates will be verified. Component labeling is carried out to determine the position and properties of their regions. The plate verification technique can be divided into three steps.

1) The width and aspect ratio of height/width are checked to reduce candidate plate regions. The width varies in range 56-125 pixels and respect ratio of height/width varies in range 0.14-0.52.

2) Detect the average number of objects in horizontal line. A threshold is determined for each candidate region using iterative thresholding selection [7]. The iterative thersholding selection conditions are:

Threshold value is initialized to 127 in all algorithms, except algorithms that pass red, light green or blue steps in switching algorithm.

For red, the threshold is set at 20% of P-tile method [7].

For light green or blue, the threshold is set at 80% of P-tile method [7].

The image from light green and blue must be binary inverse because the color of character is white. Next, objects in binary image that are smaller than 10 pixels are removed. Then, number of objects along 3 horizontal lines is counted. The three lines are called L_1, L_2 and L_3. The position of L_1 object starts at $H/4$ and the total height of all lines are limited to $H/2$,see Figure 7(a). Each line is 1 pixel apart. Only objects with $1 \le a \le 8$ and $b \le 18$ will be counted. Then, average number of objects along the three lines must be between 6 to 14 objects. Otherwise, if it is between 3 and 6, then 3 to 8 objects within this region must be considered for being a character. Number of objects that maybe text will be counted when height of

object is between 20 to 24 pixels with aspect ratio of width/height between 0.14 to 0.96. And the center of height of object is between $H/6-((H/6)\times 4)$, see Figure 7(b).

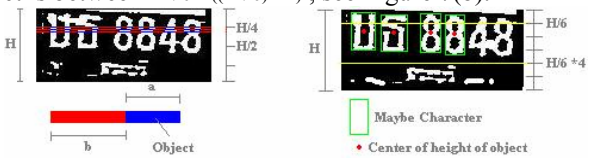

a) b)

Figure 7. Plate verify step 2.

a) Horizontal line scan image b) Maybe character image

3) The last step, width of plate is considered by region growing [8] which it must be between 50 to 125 pixels. The region growing uses the seed point from binary image. In this experiment, a windows of size 1x10 is used starting at $x=(w/2)-7$, $y=H/2$ and sliding the window to bottom until all pixels in window are background (pixel="0"). Then shift window 1x10 to bottom 1 pixel and put seed point in gray image to process region algorithm with eight neighbors. The region growing uses threshold of 70 and expands area of growth to Left-2, Right+4, Top-3 and bottom+7.

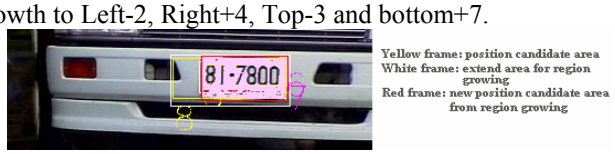

Figure 8. Result from region growing

V. Experimental Results

The proposed method was evaluated at three locations: the Bangkok express way and two semi-indoor parking lots with controlled light source. Manual vehicle detection was used in express way test and photo sensors were used in parking lot tests. For the second parking lot, all of the license plates were setup for testing on one car. The program was written in Visual C++ 6.0 in a Pentium 4 2.4GHz/1GB RAM with IDS falcon card capture (768x576 pixels).

Experimental results are shown in Table V. These results correspond to 99.07%, 0.93% and 1.48% for correct extraction rate, missed detection rate, and false alarm rate, respectively. Computation time varied between 0.39 to 1.266 seconds, depending on the number of detection techniques used. Frequency of detection algorithms used are shown in Table IV.

Grilles, logos, and headlights of vehicles have similar characteristics that of license plates. The thresholds in proposed method support for license plate detection with many sizes, colors and formats, so false alarms happened.

VI. Conclusion and Future Work

A switching algorithm for Thailand license plate localization is presented. Eleven plate detection techniques were used to generate candidate plate regions based on gradient and color. All of Thailand license plates can be detected, including some other complex plate localization problems. Experimental results show high accuracy. However, some problems still occur due to similar texture of grilles, logos, headlights, and plate.

Acknowledgment

This research is supported by Thailand Graduate Institute of Science and Technology (TGIST) fund under National Science and Technology Development Agency, Thailand.

TABLE IV
Frequency of Using Algorithm

	Place of testing		
	Express way	Parking1	Parking2
Algorithms 1-5	95	329	77
Algorithms 6-10	3	6	11
Algorithm 11	1	5	2

TABLE V
Experimental Results

Plate type	Place of testing					
	Express way		Parking 1		Parking 2	
	Correct extraction	False alarm	Correct extraction	False alarm	Correct extraction	False alarm
A1					1/1	
A2	30/30	1	291/294	6	21/21	1
A3	24/24		1/1		8/8	
A4	1/1		1/1		8/8	
A5					5/5	
A6					5/5	
A7	5/5		7/7		10/10	
A8					5/5	
A9					5/5	
A10					5/5	
B1	1/1				2/2	
B2	8/8		41/41		2/2	
B3	1/1		1/2		2/2	
C1					3/3	
C2					2/2	
D1	17/17				2/2	
D2	12/12				2/2	
E1			3/4			
Total	99/99	1	345/350	6	91/91	1
Rate	100%	1.01%	98.5%	1.72%	100%	1.09%
Processing time (sec.)	0.39-1.01		0.43-1.26		0.43-1.03	
Average	Correct extraction 99.07%, False alarm = 1.481%, Time processing =0.39-1.26 second.					

References

[1] S. Ozbay and E. Ercelebi, "Automatic vehicle identification by plate recognition", *Engineering, Computing and Technology Trans.* 2005.

[2] D. Gao and J. Zhou, "Car license plate detection from complex scene", *ICSP* 2000.

[3] P. Dubey, "Heuristic approach for license plate detection", *AVSS IEEE*, 2005.

[4] K.K. Kim, K.I, Kim, J.B. Kim and H.J. Kim, "Learning-base approach for license plate recognition", *SPSW IEEE*, 2000.

[5] E.R. Lee, P.K. Kim and H.J. Kim, "Automatic recognition of car license plate using color image processing", *ICIP IEEE*, 1994.

[6] C.M. Lee and A.Kankanhalli, "Automatic extraction of characters in complex scene image", *IJPRAI*, vol 9 , pp. 67-82, 1995.

[7] R. Jain, R. Kasturi, B.G. Schunck, *Machine Vision*. McRacw-Hill, 1995.

[8] L. Pitas, Digital Image Processing Algorithms and Application. John Wiley & Sons, 2000.

[9] X. Hong-ke, Y. Fu-hua, J. Jia-hua and S. Huan-sheng, "A new approach of the vehicle license plate location", *PDCAT IEEE*, 2005.

[10] T. Borerakarawin, P. Kaewtrakulpong and A. Prateepasen, "A Machine Vision Method For Maturity Grading Of Pineapples", *ACIAR03*, pp 178-182, 2003.

A Study of Normalized Cross Correlation Pattern Matching Algorithm in Thermal Imagery

Sarun Sumriddetchkajorn and Armote Somboonkaew

Photonics Technology Laboratory
National Electronics and Computer Technology Center
112 Thailand Science Park, Phahonyothin Rd., Klong 1, Klong Luang, Pathumthani 12120, Thailand
Phone: +66-2564-6900 ext. 2102, Fax: +66-2564-6974, E-mail: sarun.sum@nectec.or.th

***Abstract*-This paper studies the performance of deploying a normalized cross correlation pattern matching algorithm in independently tracking three desired regions on thermal imagery. In our experiment with five subjects under test, we observe that the orientation angles of the subject along three axes can be tracked with a wider angle in color-based than in gray-based thermal images. However, as there are three color planes in the color-based thermal image, the measured learning time is about twice of that in the gray scale-based thermal image. For the searching time, both color and gray scale-based thermal images show similar performance of ~ 8 ms per tracking zone using the Duo Core technology.**

I. INTRODUCTION

As the price of a thermal imaging camera is gradually going down, thermal images have been exploited in several applications in order to investigate some interesting parameters through the change of the object temperature. Especially, it has been deployed to distinguish in real time a person who might affect from severe acute respiratory syndrome at the airport check point [1] and to analyze the subject's deceptive level during crime investigation [2-3]. For these applications, an independent tracking approach of the desired areas on the subject's face is very important. Because there are some difficulties in locating and tracking desired regions of interest in the thermal image, complicated feature extraction and feature tracking techniques are required. These include the use of a threshold adjustment [4], a multicast multifeature fuzzy connectedness framework [5], and a rigorous data training-based support vector method [6]. Although these tracking techniques promise to provide good tracking results, the operating time is slow due to their complicated computing processes, which is not appropriate to use for independently searching several zones in real-time applications. Hence, it would be highly desirable to have a simple image matching technique and yet still provides an acceptable tracking performance.

II. OUR EXPERIMENTAL DEMONSTRATION

Keeping in mind that geometric features of the subject's face taken from a thermal imaging camera is difficult to observe, we choose to use a holistic or appearance-based approach to identify our desired zones. In this method, it generally operates directly on a pixel intensity array without the detection of facial features [7]. One of the appearance-based pattern matching algorithms is the normalized cross correlation (NCC) technique. In this case, a normalized amplitude of the NCC is used in order to distinguish the desired areas from their surrounding regions and it can be calculated as follows [8].

$$R(i,j)=\frac{\sum_{x=0}^{L-1}\sum_{y=0}^{K-1}\left[w(x,y)-\bar{w}\right]\left[f(x+i,y+j)-f(i,j)\right]}{\left\{\sum_{x=0}^{L-1}\sum_{y=0}^{K-1}\left[w(x,y)-\bar{w}\right]^2\right\}^{1/2}\left\{\sum_{x=0}^{L-1}\sum_{y=0}^{K-1}\left[f(x+i,y+j)-f(i,j)\right]^2\right\}^{1/2}}, \quad (1)$$

where $\bar{w}$ is an array intensity value of the pixels in the reference template w and it is computed only once. w(x,y) and f(x,y) are the subimage having KxL pixels and the image having MxN pixels ($M \geq K$, $N \geq L$), respectively. i and j vary from 0 to M-1 and from 0 to N-1, respectively.

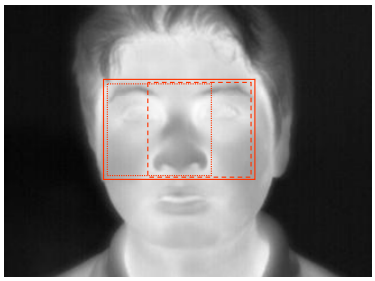

(a)

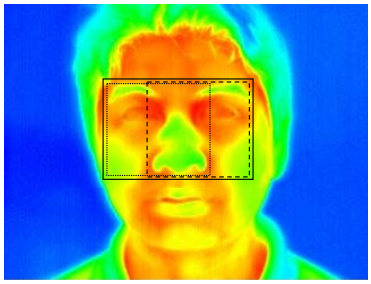

(b)

Fig.1 An example of our thermal image taken in (a) gray scale palette and (b) rainbow palette. Small dash line, large dash line, and solid line indicate our regions of interest 1, 2, and 3, respectively.

In our study, we have recorded thermal images at a measured speed of 20 frames/second (fps) (or 50 ms in one frame) by using a far-infrared (i.e., 7.5-13 μm wavelength band) camera having an uncooled focal plane array-based microbolometer with its thermal sensitivity of 0.080 mK, a 24°×18° field of view, and a 320×240 active pixels. We also divide our study into two cases. One is to perform the NCC on the gray scale-based thermal image while another case is to do the same on the color-based thermal image. In addition, there are three tracking zones as shown in Fig.1. One zone covers the right eye and the nose and the second zone encompasses the left eye and the nose. These two areas have approximately 81×76 pixels. The last zone includes two eyes and the nose and it has about 119×76 pixels. Five subjects (i.e., A, B, C, D, and E) as shown in Fig.2 are tested and our study is investigated under a notebook computer having an Intel DuoCore 1.83GHz with 512 MB RAM. In addition, an NCC threshold is set to 0.6 in a full scale range of 1.0.

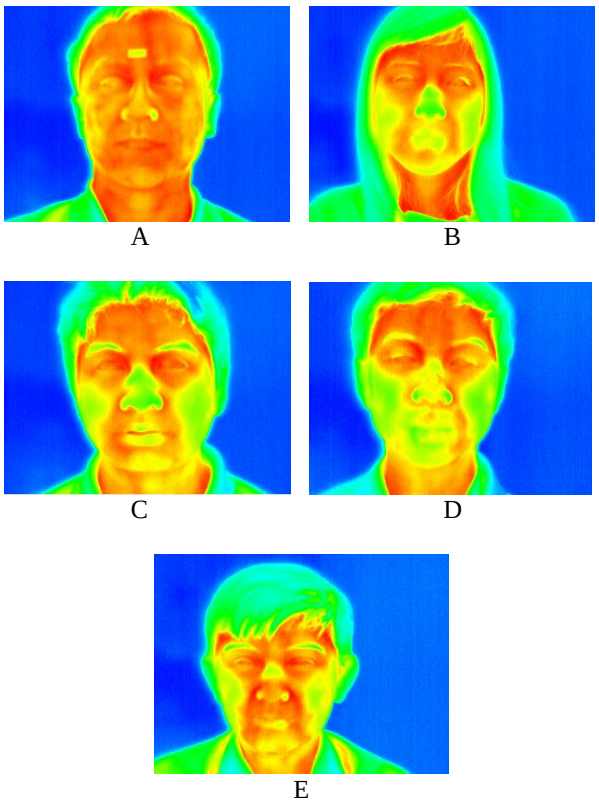

Fig.2 Color-based thermal images of our five subjects under study.

As our experiment aims to study only the performance of using the NCC to independently match and track three separate regions of interest, we manually locate these three desired regions in each subject. In addition, maximum rolling angle, maximum pitch angle, and maximum rotation angle for each subject are investigated as shown in Fig.3. We can see that

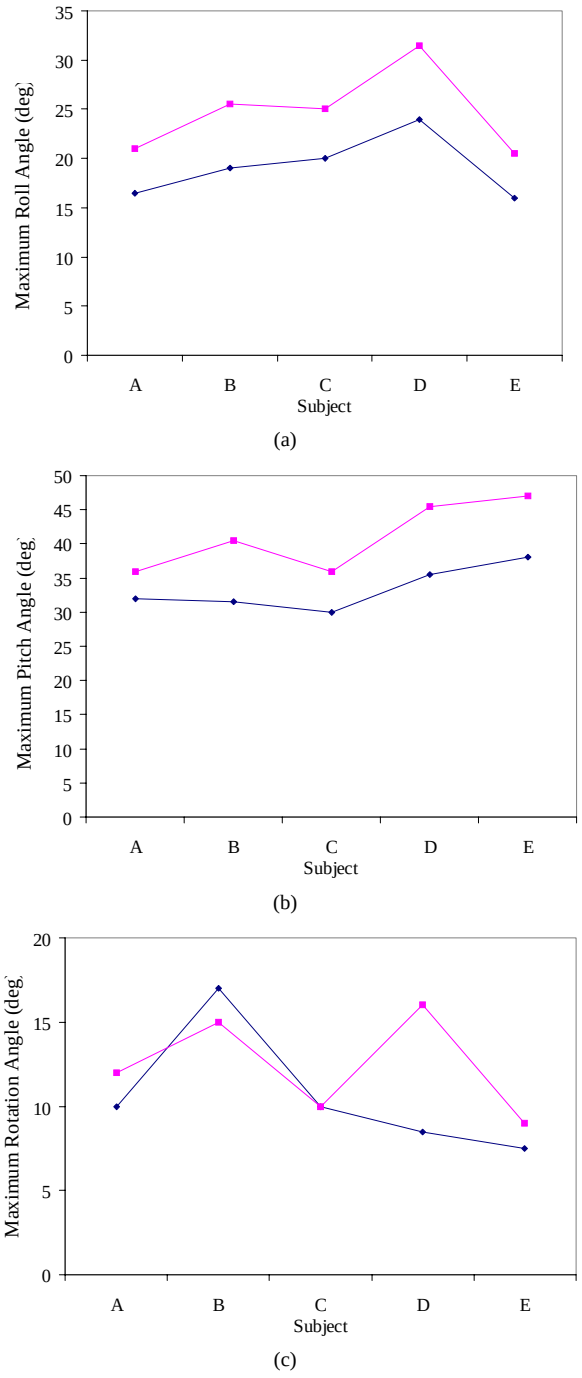

Fig.3 Maximum located orientations of the subject's regions of interest when the subject (a) rotates from left to right, (b) tilts from top to bottom, and (c) inclines from left to right.

when the subject rotates his/her face from left to right along the roll axis as shown in Fig.3(a) or tilts from top to bottom along the pitch axis (see Fig.3(b)), the NCC matching method shows a better 5-7 deg tracking angle in color-based thermal images. For the case of inclining subject's face from left to right as shown in Fig.3(c), the NCC matching method gives similar

performance for both gray scale-based and color-based thermal images. Apart from the maximum orientation of the subject, pattern learning and matching times are also important parameters. An average measured pattern learning time for color-based thermal images is 5,616 ms while it is only 2,796 ms for gray scale–based thermal images. The average measured searching time on three separate zones of 25 ms (or ~8 ms per zone) is achieved for both color palettes. This result implies that if we deploy this NCC for independently matching and tracking three different zones on the subject's face during recording data, a recording speed is expected to reduce from 20 fps to 13 fps. However, if we consider only one tracking zone, this algorithm will slightly alter the recording speed from 20 fps to 17 fps, thus very practical to use in real time applications.

III. CONCLUSION

This paper shows that a simple and widely used NCC pattern matching algorithm can be deployed to independently track the desired zones on the thermal image, especially, in the roll and pitch axes. It can also be applied for both gray scale- and color-based thermal images, and still offers similar searching speed via a DuoCore-based CPU. As the color-based thermal image has three different color planes, tracking orientation of the subject is more robust but with slower learning time. In a practical point of view, our experimental result for five subjects confirms that merely the NCC can be used during recording thermal imaging data without affecting too much on the recording speed. In the future, we will employ an appropriate thresholding algorithm to help us automatically and systematically define three desired regions of interest. We will also increase the number of subjects and will statistically analyze the result.

REFERENCES

[1] Y. K. Ng Eddie, W. Muljo, and B. S. Wong, "Study of facial skin and aural temperature," *IEEE Engg. in Med. And Biol.*, Vol. 25, pp. 68-74, May/June 2006.

[2] S. Sumriddetchkajorn and A. Somboonkaew, "A non invasive method for analyzing psychophysiological data," *Thailand Patent Application*, 0601002047, May 8, 2006.

[3] S. Sumriddetchkajorn, A. Somboonkaew, I. Promduang, N. Sumriddetchkajorn, and T. Sodsong, "Thermal analyzer for deceptive detection," *Tech. Rep*, Nat. Electronics and Computer Tech. Ctr., Thailand, 2006.

[4] I. Pavlidis and P. Symosek, "The imaging issue in an automatic face/disguise detection system," *Proc. IEEE Workshop on Computer Vision Beyond the Visible Spectrum: Methods and Applications*, pp. 15-24, South Carolina, USA, Jun. 2000.

[5] I. A. Kakadiaris, G. Passalis, T. Theoharis, G. Toderici, I. Konstantinidis, and N. Murtuza, "Multimodal face recognition: combination of geometry with physiological information," *Proc. Computer Vision and Pattern Recognition*, Vol. 2, pp. 1022-1029, June 2005.

[6] W. Xiaoyu, C. Jihong, W. Pingjiang, and H. Zhihong, "Infrared human face auto locating based on SVM and a smart thermal biometrics system," *Proc. Int. Conv. On Intelligent Systems Design and Applications*, 2006.

[7] S. G. Kong, J. Heo, B. R. Abidi, J. Paik, and M. A. Abidi, "Recent advances in visual and infrared face recognition – a review," *Comp. Vis. And Image. Under.*, Vol. 97, pp. 103-105, 2005.

[8] *NI Vision Concepts Manual*, National Instruments Corp., 11500 North Mopac Expressway, Austin, Texas, USA, Nov. 2005.

Hardware Cryptography-Embedded Multimedia Mobile Processor

Masa-aki Fukase [†], Hiroki Takeda [†], and Tomoaki Sato [‡]

[†] Faculty of Science and Technology, Hirosaki University, E-mail: {slfuka , gs06411}@eit.hirosaki-u.ac.jp
[‡] Computer and Network Systems Center, Hirosaki University, E-mail: tsato@cc.hirosaki-u.ac.jp

ABSTRACT

Since cutting-edge ubiquitous devices need power conscious high-speed operation, embedded software approaches so far taken do not always continue to play the key role in ubiquitous computing. Single chip processors are most promising solutions for overall demand of ubiquitous devices. We have so far developed a hardware cryptography-embedded multimedia mobile processor, HCgorilla and its software support system. In this article, we focus on the hardware of HCgorilla. Firstly, we show the structure of HCgorilla. The architecture, implementation, and verification are described in detail. Then, we evaluate the hardware in view of area, the number of devices, power consumption, and clock speed.

Keywords: Hardware cryptography, multimedia, moblie, ubiquitus, single chip processor.

1. INTRODUCTION

Internet owes its outstanding expansion in recent years to the development of handheld multimedia devices. The latest cellular phones are embedded with various functions like GPS, music, and the game, etc [1, 2]. The performable features of these devices have mainly relied on embedded software. However, such approach obviously contradicts power conscious design.

Cutting-edge ubiquitous devices need power conscious, high-speed, secure, and user friendly processing. ICT techniques corresponding to these demands are as follows. Java is one of the most promising solutions for user friendly multimedia processing. Power consciousness for mobility must be satisfied together with high speed for quick response. Not only so called security chip but also data protection is important to practically prevent privacy, prevention, intrusion, etc.

In order to fulfill demands for the Java execution of power conscious high speed and the cryptography of large quantity of multimedia data, it is expedient to develop a single VLSI processor system with built-in functions covering those schemes [3]. We have so far developed multimedia mobile processor named gorilla [4, 5], hardware cryptography-embedded processor named RAP (random addressing-accelerated processor) [6, 7], and a hardware cryptography-embedded multimedia mobile processor named HCgorilla [8-17].

In this article, we focus on the hardware of the latest version of HCgorilla. Firstly, we show the structure of HCgorilla. The architecture, implementation, and verification are described in detail. Then, we evaluate the hardware in view of area, the number of devices, power consumption, and clock speed.

This work has been financially supported in part by the president of Hirosaki University and the dean of the Faculty of Science and Technology of Hirosaki University.

2. PROCESSOR STRUCTURE

Our strategies for developing HCgorilla are as follows.

a. Making use of practically simple structure for a full-length RNG (random number generator). For this aim, LFSR (linear feedback shift register) is best suited. This requires trivial additional chip area and power dissipation. A tiny *n*-bit LFSR produces the huge *n*-th power of 2 random numbers.
b. Cooperating with Java compatible media processing. This makes it possible for HCgorilla to have efficient performance for media processing as well as cryptography.
c. Following H/S co-design in order for HCgorilla to have many PC-like sophisticated features as well as the role for ubiquitous computing.

Table 1 summarizes architectures related to HCgorilla. Firstly, one of our previous works for downsizing, power reduction, and speedup in ubiquitous computing was the development of a series of Java-embedded multimedia processor and a multimedia mobile processor core, gorilla. Another previous work was the development of RAP. Considering the unification of RAP and gorilla has advantageous potential for multimedia security, we have developed a hardware cryptography-embedded multimedia mobile processor architecture, HCgorilla.

In order to lighten the burden on hardware design, the ISA (instruction set architecture) of HCgorilla is made compact. The ISA of HCgorilla consists of 2 SIMD (single instruction stream multiple data stream) mode cipher instructions and 61 Java compatible media instructions.

The cipher instructions are the random addressing instructions *rsw* and *rlw*. Java instructions like *bipush, iadd, isub* are carefully selected from the 202 Java bytecodes for ever growing usage of Java in mobile fields [18]. Each instruction is composed of a 1-byte opcode and 0 to 2 1-byte operands. Since ISA succeeds various aspects of Java, opcodes are Java bytecodes. Operands are grammatically equal to opcodes but are actually dependent on them.

Table1: *Exploration of hardware cryptography-embedded multimedia mobile processors*

Name	Architecture								Microarchitecture				
	ISA		Core parallelism										
	No. of instructions	Format	No. of cores	ILP	Pipelining			Hardware crypto-graphy	Control	Chip	Process	Clock Speed (MHz)	Current status
					Regular		Waved						
					Degree	Number							
gorilla.1	16	JVM	2	2-degree	8	2 media pipes	2-wave EX	Not available	Wired logic	gorilla035	0.35μm	240	4.9-mm chip
gorilla.2					7					gorilla035v2		200	Synthesis
RAP	17	RISC	1	Not available	5	1 cipher pipe	Not available	SISD		Not available	FPGA	45	FPGA
HCgorilla.1	18	JVM	2	2-degree	8	2 cipher-embedded media pipes	Not available	SISD		HCgorilla035	0.35μm	150	4.9-mm chip
HCgorilla.2	63				7	3 (2 media pipes and a cipher pipe)	2-wave EX	SIMD		HCgorilla018	0.18μm	400	2.8-mm chip
										HCgorilla018 v2			Synthesis
										HCgorilla018 v3			5.9-mm chip

According to ISA, the latest version, HCgorilla018v3 has double core structure as shown in Fig. 1. Each core has two media pipes and a cipher pipe. These pipes are partly wave-pipelined. This results in the formation of heterogeneous pipelines. The register file plays the role of a pseudo-streaming buffer. The register file and data cache are quasi 2-port I/O. Although the register file and data cache are physically shared by the two cores considering hardware resource, they are logically divided. Each division is allocated to a corresponding core.

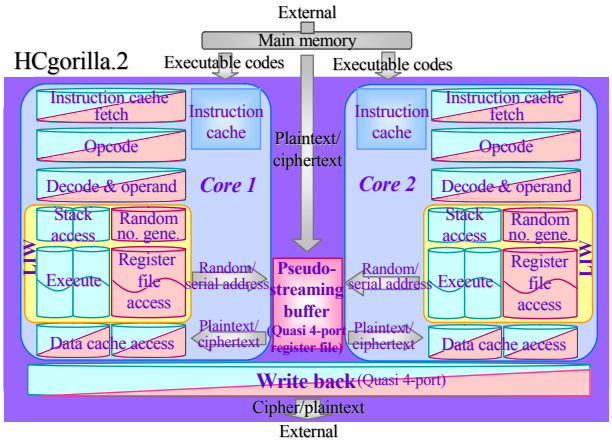

Fig. 1: *Organization of HCgorilla018v3*

The cipher pipes are built in RNGs. They are connected to data cache that writes the content of a specified register file location in data cache directly addressed by RNG output. The cipher pipe enables multimedia stream cipher due to an extremely long cycle of random numbers. It is easily produced by making RNG with LFSR.

The architectural aspects of HCgorilla are summarized as follows.

a. Direct connection of a built-in RNG and a data cache without additional chip area and power dissipation.
b. Interpreter type Java CPU to enhance sophisticated multimedia processing.
c. Multicore and LIW (long instruction word) to swiftly deal with large quantity of multimedia data. LIW is not so broad like VLIW (very long instruction word). Yet, LIW is effective to enhance multimedia communication.
d. Microprogramming techniques for respective cores that cover PicoJava in conjunction with LIW.
e. Wave-pipeline for execution units that brings about PC-like high speed and low power dissipation proper to mobile devices.

We have been developing HCgorilla018 by using 0.18-μm CMOS standard cell technology. Design environments we have used are basically Synopsys and Cadence tools. Fig. 2 shows the resultant logic synthesis of HCgorilla018v3.

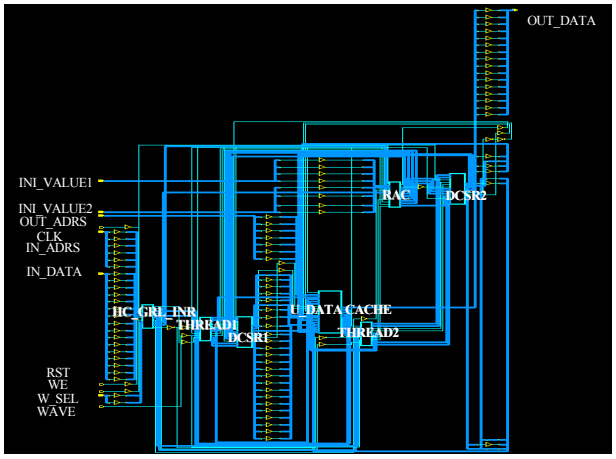

Fig. 2: Logic synthesis *of HCgorilla018v3*

Fig. 3 shows the verification of the hardware parallellism of HCgorilla that is under a dual mode bidirectional processing at 400MHz. The horizontal axis shows time in nanosecond. For the sake of well understanding the timing relation, the pipelined structure is added in the above. The test bench of this simulation describes dual mode processing that activates both cores and LIW. LIW covers two media streams. While core 1 simultaneously executes the SIMD mode encryption and the two arithmetic operations (*add* and *sub*), core 2 executes the SIMD mode decryption and other arithmetic operations (*or* and *and*). The encryption within core 1 works for 32 1-byte graduation elements stored in the register file. On the

other hand, the arithmetic operations by using Java instructions work for stacks. Thus, the encryption and the arithmetic operations are completely independent.

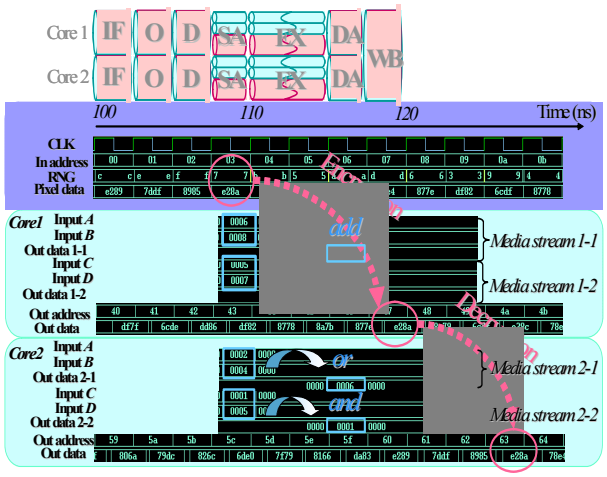

Fig. 3: *Simulation of the 400-MHz operation of HCgorilla018v3*

3. PROCESSOR EVALUATION

HCgorilla018v3 is evaluated in view of various aspects. Related chips are compared. The difference of process technology and chip area is taken into account of by scaling them. Fig. 4 shows the area of HCgorilla018v3 and related chips. Cache and register file occupies wide area in any case.

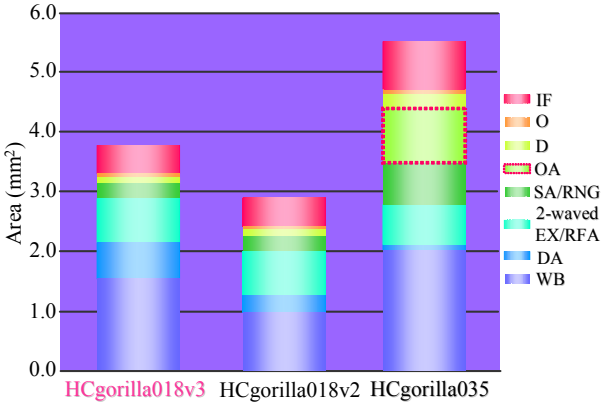

Fig. 4: *Area of HCgorila018v3 and related chips*

Fig. 5 shows the number of transistors of HCgorilla018v3 and related chips. The dotted line shows scaling by using chip core size ratio between HCgorilla018v3 and HCgorilla018v2. The usage of the chip core size in this scaling is because we are setting core utilization as large as possible in any case. From the estimation shown by the dotted line, HCgorilla018v3 is made compact.

Fig. 6 shows the power consumption of HCgorilla derivatives. The parameters *A*, *B*, and *C* represent test programs. In the case of SIMD mode encryption and decryption, each core executes the random addressing instructions *rsw* and *rlw*, respectively. In the case of Java and SIMD mode cipher, it runs a test program whose threads simultaneously execute Java instructions, *rsw* and *rlw*.

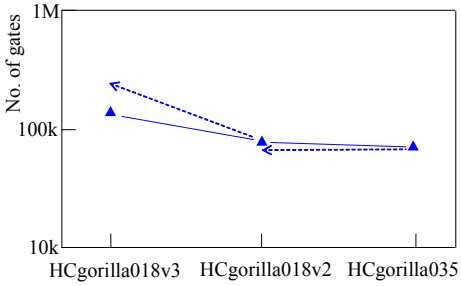

Fig. 5: *Number of gates of HCgorilla018v3 and related chips*

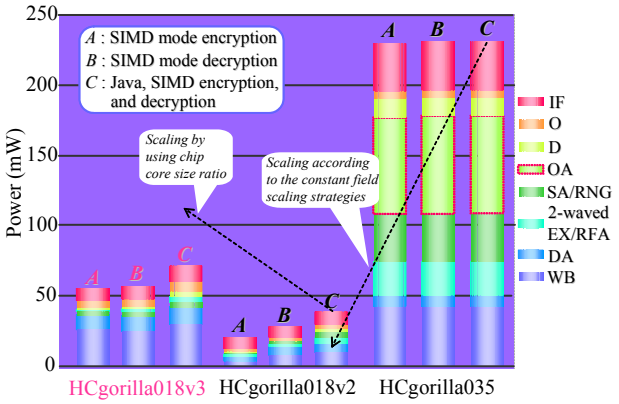

Fig. 6: *Power consumption of HCgorilla018v3 and related chips*

Dotted lines in fig. 6 show the effect of process technology and chip core size. Scaling between HCgorilla018v3 and HCgorilla018v2 has been done by using chip core area ratio. Then, scaling between HCgorilla018v2 and HCgorilla035 has been done according to core area ratio and constant field scaling strategies [19]. From the estimation shown by the dotted lines, HCgorilla018v3 has architectural improvement on the power reduction.

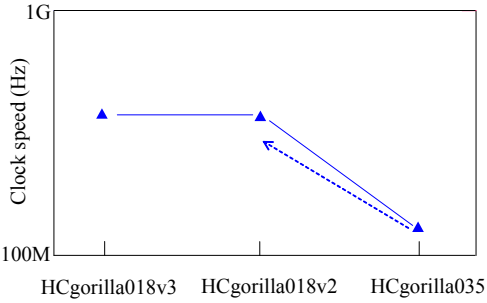

Fig. 7: *Clock speed of HCgorilla018v3 and related chips*

Fig. 7 shows the clock speed of HCgorilla018v3 and related chips. The dotted line between HCgorilla035 and HCgorilla018v2 is drawn by scaling according to the

constant field scaling strategies. This shows the architectural design effort of HCgorilla.2.

4. CONCLUDING REMARKS

In order to make power conscious, high-speed, secure, and user friendly ubiquitous devices, we have developed HCgorilla018v3. This is the latest version of the hardware cryptography-embedded multimedia mobile processor, HCgorilla. It has the parallelism of double core and six pipes. HCgorilla018v3 has been compactly designed in view of chip area and number of devices. HCgorilla018v3 has further improved multimedia mobility. It consumes less power and operates at higher clock. It also has both Java and cryptographic streaming capability.

The next step of this study will be as follows.

1. Further expanding the register file and data cache from the practical viewpoint of streaming SIMD.
2. Real chip implementation and its evaluation. The chip implementation requires effort to suppress the increase of power dissipation and the decrease of clock speed.
3. Combining HCgorilla and cutting-edge other single chip processors like security chips. They compliment each other.

ACKNOWLEDGMENT

This work is supported by VLSI Design and Education Center (VDEC), the University of Tokyo in collaboration with Synopsys, Inc. and Cadence Design Systems, Inc.

REFERENCES

[1] L. Garber, "Company Makes First Multipurpose Programmable Mobile Chip," Computer Magazine, Vol. 38, No. 10, p24, 2005.

[2] M. Takahashi, "The development of a multimedia SoC for cellular phone applications," The Journal of the IEICE, Vol. 84, No. 11, pp.790-795, 2001.

[3] A. Jerraya et al., "Multiprocessor Systems-on-Chips," Computer Magazine, Vol. 38, No. 7, pp. 36-40, 2005.

[4] M. Fukase et al., "Development of a Multimedia Mobile Processor," Proc. of ISCIT 2004, pp. 672-677, 2004.

[5] M. Fukase et al., "Hardware Cryptography-Embedded Multimedia Mobile Processor," Technical Report of IEICE, Vol. 104, No. 735, pp. 31-36, 2005.

[6] M. Fukase et al., "Power Conscious Endeavor in Processors to Speed Up Random Sampling", Proc. of SCI2003, Vol. V, pp. 111-116, 2003.

[7] M. Fukase et al., "Development of a Multimedia Stream Cipher Engine," Proc. of ISPACS 2006, pp. 562-565, 2006.

[8] M. Fukase et al., "Cryptographic System by a Random Addressing-Accelerated Multimedia Mobile Processor," Proc. of SCI2004, Vol. II, pp. 174-179, 2004.

[9] M. Fukase et al., "Exploiting a Hardware Security-Embedded Multimedia Mobile Processor System and its Application," Proc. of ITC-CSCC, pp. 7C3L-3-1-7C3L-3-4, 2004.

[10] M. Fukase et al., "Design of a Hardware Security-Embedded Multimedia Mobile Processor," Proc. of ISCIT 2004, pp. 362-367, 2004.

[11] Y. Sato et al., "Simultaneously Multithreaded Multimedia Mobile Processor Embedded with Hardware Cryptography," Social Information, Vol.14, No. 2, pp. 97-107, 2005.

[12] M. Fukase et al., "Low Energy Digital Electronics for Multimedia Ubiquitous Environments," Proc. of EIC'05, pp. 409-414, 2005.

[13] M. Fukase et al., "Hardware Cryptography-Embedded Multimedia Mobile Processor for Ubiquitous Computing," Proc. of 12th NASA Sympo. on VLSI, pp. 1.2.1-1.2.6, 2005.

[14] M. Fukase et al., "Hardware Cryptography for Ubiquitous Computing," Proc. of ISCIT2005, Vol. 1, pp. 462-465, 2005.

[15] M. Fukase et al., "Hardware Cryptography-Embedded Multimedia Mobile System," Proc. of WMSCI2006, Vol. III, pp. 225-230, 2006.

[16] M. Fukase et al., "Innovative Ubiquitous Cryptography and Sophisticated Implementation," Proc. of ISCIT2006, 2006.

[17] M. Fukase et al., "Hardware/Software Co-Design of a Secure Ubiquitous System," Springer Lecture Notes in Artificial Intelligence (In press).

[18] D. S. Kochnev et al., "Surviving Java for Mobiles," IEEE pervasive COMP., Vol. 2, No. 2, pp. 90-95, 2003.

[19] Sze, VLSI TECHNOLOGY, p. 495, McGraw-Hill, 1983.

HDL Design and Verification of Digital Signal Processor for 2.4 GHz ZigBee Radio Receiver

T. Demeechai
Mahanakorn University of Technology
Department of Telecommunication Engineering
51 Cheum-Sampan Road, Nongchok
Bangkok 10530, Thailand

***Abstract*-This paper describes design and verification of a digital signal processor of a receiver for the IEEE 802.15.4 PHY or ZigBee radio at the 2.4 GHz ISM band. This design achieves an improvement over a recent work, as the resulting circuit requires smaller silicon area and potentially lower power.**

I. INTRODUCTION

The IEEE 802.15.4 standard and ZigBee wireless technology are designed to satisfy the market's need for a low-cost, standard-based and flexible wireless network technology, which offers low power consumption, reliability, interoperability and security for control and monitoring applications with low to moderate data rates. The IEEE 802.15.4 standard specifies the physical (PHY) and medium access control (MAC) layers at the 868 MHz, 915 MHz and 2.4 GHz ISM bands [1], [2]. This paper presents a design and verification of a digital signal processor for a radio receiver conforming to the IEEE 802.15.4 PHY at the 2.4 GHz ISM band. This processor receives a digitized form of an IF signal obtained after quadrature downconversion and outputs the detected PHY payload. More information on the specification of this processor can be found at the author's URL [3]. The present work is indeed an improvement over a recent work [4], in which the author has participated.

In this paper, a brief introduction of the related standard is given first. The design principle and verification method are then explained. Results on the verification and estimated silicon area on an FPGA are also presented before the paper is concluded.

II. PROTOCOL DATA UNIT AND MODULATION SCHEME

According to the IEEE 802.15.4 PHY standard, the physical layer protocol data unit (PPDU) is a packet that consists of three concatenated components. The first component in the PPDU is the synchronization header (SHR) which allows a receiver to synchronize and lock onto the bit stream. The second component is the PHY header (PHR) which contains frame length information. The third component is the PHY payload which carries the data of the PHY packet. The SHR is composed of a preamble field that provides synchronization information to a receiver and a start-of-frame delimiter (SFD) field that indicates the end of the SHR. The preamble field is composed of 32 binary zeros. The SFD field is a fixed octet, i.e., a fixed eight-bit binary pattern. The PHR is an octet which contains a seven-bit frame length field that specifies the total number of octets contained in the PHY payload. The PHY payload has a variable length and carries the data of the PHY packet. For all packet types of length five octets or greater than seven octets, the PHY payload contains the MAC sublayer frame.

The IEEE 802.15.4 PHY at the 2.4 GHz band employs a spread-spectrum offset quadrature phase-shift keying (OQPSK) with half-sine pulse shaping as the modulation scheme. However, since signal obtained from OQPSK with half-sine pulse shaping can be deemed as a minimum-shift keying (MSK) signal, MSK with a suitable encoding can be employed instead of the OQPSK. In the modulation scheme, during each four-bit data symbol period, four information bits are used to select one of 16 nearly orthogonal pseudo-random (PN) sequences to be transmitted. The PN sequences for successive data symbols are concatenated, and the aggregate chip sequence is modulated onto the carrier at 2 Mchip/s using MSK. Since MSK is employed instead of the OQPSK, the 16 PN sequences mentioned above must be properly derived from Table 20 of [1]. Note also that each PN sequence derived will have 32 chips, where there are 31 chips uniquely identifying a four-bit symbol.

III. DESIGN PRINCIPLE

There are two major components in the processor: an FM demodulator and a symbol detector as shown in Figure 1.

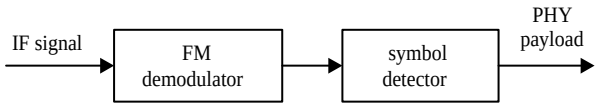

Figure 1. Block diagram of the processor.

The FM demodulator receives a digitized form of an IF signal obtained after quadrature downconversion and outputs a signal representing an estimate of the instantaneous frequency of the IF signal. The symbol detector receives the estimated instantaneous frequency signal and performs acquisition and tracking of symbol timing as well as detection of successive symbols for each PPDU.

For the FM demodulator, the IF frequency of 2 MHz is assumed. Due to quadrature downconversion, there are 2 IF signals, i.e., I-phase and Q-phase signals, as shown in Figure 2. Both of them are represented in digital form by a stream of five-bit two's complement numbers at 8 Msample/s, and accordingly the system clock frequency is 8 MHz. The two IF signals are processed independently by component FM demodulators, and the outputs are then combined simply by addition. A classical FM demodulator is adopted for each component FM demodulator.

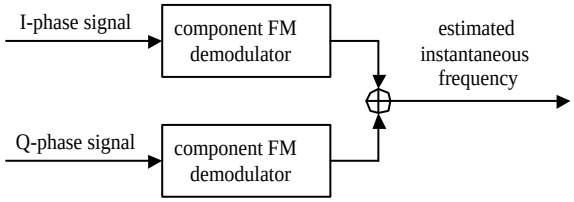

Figure 2. Block diagram of the FM demodulator.

The symbol detector has two modes of operations, i.e., the acquisition mode where the detector attempts to lock onto the received signal timing and the tracking mode where the acquired timing is fine-tuned while successive symbols are detected. Switching between the two modes behaves as shown in Figure 3.

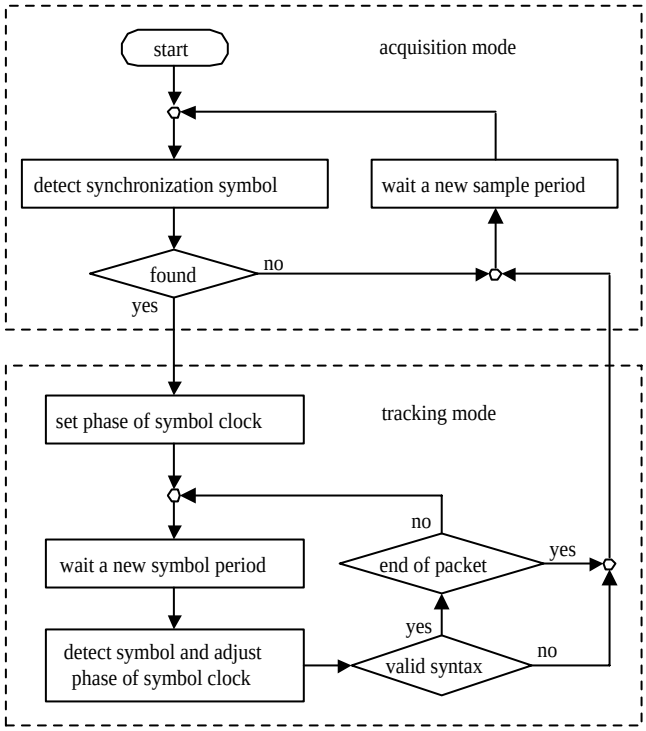

Figure 3. Symbol detector flow of operations.

The detector is in the acquisition mode when start, until a synchronization symbol is detected. Once a synchronization symbol is detected, the detector enters the tracking mode. When entering the tracking mode, the phase of a symbol-rate clock that represents the received signal timing at a resolution of one sample period is set. In the tracking mode, for every symbol period, a successive symbol is detected and the phase of the symbol-rate clock is adjusted. The operation mode will switch from the tracking mode to the acquisition mode, if the last symbol detected is the last symbol of the packet or the successive symbols detected violate the PPDU format. It may be noted that such a violation is possible only before the SFD is detected and it occurs when a detected symbol that follows a synchronization symbol is neither a synchronization symbol nor constituting the SFD.

Realization of the symbol detector is based on the structure shown in Figure 4.

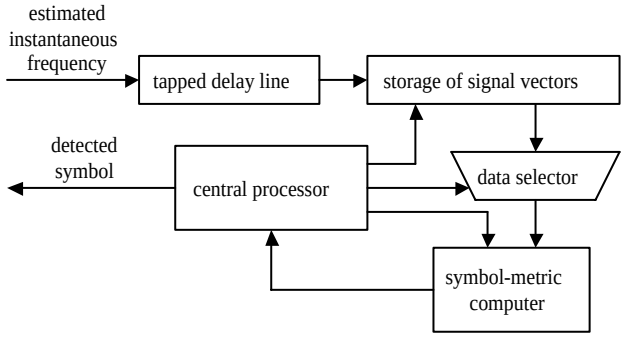

Figure 4. Symbol detector structure.

The tapped delay line is a parallel-output shift register that implements a sliding-window storage of the input. The operations of the symbol detector rely only on the likelihood metrics of 16 candidate symbols, computed from the received signal at properly determined time intervals. A single symbol-metric computer based on the matched-filter principle is employed for the computation of all the likelihood metrics.

In the acquisition mode, the storage of signal vectors and the data selector bypass the output of the tapped delay line to the symbol-metric computer, so that the tapped delay line and the symbol-metric computer act as a sliding correlator for the synchronization symbol. Once in the acquisition mode the output of the symbol-metric computer is significant that signifies presence of a synchronization symbol, the received signal timing is acquired, and the symbol detector enters the tracking mode with the phase of the symbol-rate clock set accordingly.

For every symbol period in the tracking mode, the storage of signal vectors keeps three signal vectors. Each of the three vectors is to be inputted through the data selector to the symbol-metric computer in the process of symbol detection and symbol-rate clock-phase adjustment. The first vector corresponds to the received signal over a symbol period that is

synchronized with that of the previously detected symbol. This vector is used in symbol detection, based on a selection of the best among 16 candidate symbols. It takes 16 system clock periods to accomplish the selection by the central processor. The second and third vectors correspond to the received signals over the symbol periods that are one-sample-early and one-sample-late compared to that of the first vector. Based on an early-late synchronization style, these vectors are used in the process of fine-tuning the acquired timing that adjusts the phase of the symbol-rate clock. It takes 4 system clock periods to accomplish the fine-tuning. Noting that a symbol period equals 128 system clock periods, we should see that the symbol detector activity is quite low in the tracking mode that processes the major part of the data packet.

It may be noted that, although this design is based on the same algorithm as the recent design [4], the symbol detector of this design uses a sequential-processing architecture instead of a parallel-processing one. Compared to the recent design, the use of sequential processing in this design results in a substantial reduction of registers and combinatorial circuits. The number of required slices on a Virtex-II FPGA for this design is found to be 464, that is quite small compared to the 4,039 slices required by the recent design. In addition, because the recent design uses a bank of 16×3 matched filters that are all-time active, the present design also results in a substantial reduction of circuit activity. Therefore, the present design achieves an improvement, as the resulting circuit requires smaller silicon area and potentially lower power.

IV. VERIFICATION

This design is completed as a set of VHDL source codes and has been verified at the HDL level as shown in Figure 5.

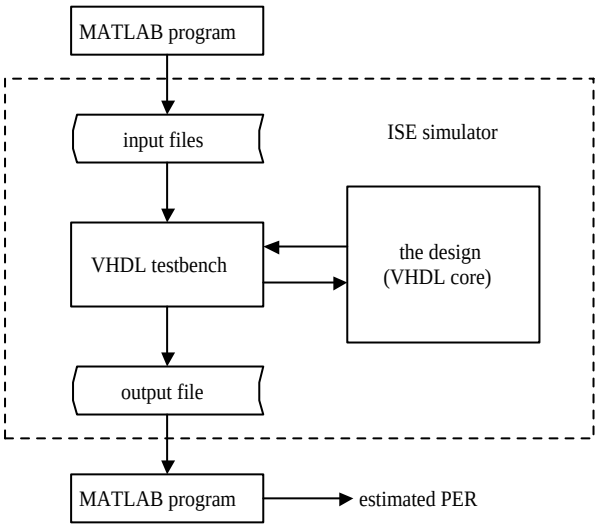

Figure 5. Design verification.

A MATLAB program was used to make input files that store an integer representation of the quantized I-phase and Q-phase IF signals, according the following criteria: (1) the frame length is 20 octets; (2) the two IF signals are corrupted by independent Gaussian noise processes; (3) the power spectral densities of noise and signal are the same; (4) the quantizer is of uniform-type with five-bit two's complement representation, and therefore the quantizer output is an integer that ranges from -16 to 15; (5) the quantizer input is automatic-gain-controlled such that its average power is $(q^{-1}(15))^2/2$, where $q^{-1}(\cdot)$ is the associated uniform dequantizing function. A VHDL test bench was simulated to get the input data from the input files for the core, get the detected data frames from the core output, and write the results to an output file from which the packet error rate (PER) can be estimated. Thanks to the Xilinx university program for the donation of the ISE platform that includes the ISE simulator. Table I shows the simulation results on the detection performance.

TABLE I
DETECTION PERFORMANCE

input SNR (dB)	no. of transmitted packet	no. of packet errors	PER (%)
2.1	2000	21	1.05
2.2	3000	28	0.94

It should be noted that, while Annex E.2.2 of [1] states that a typical low-cost detector implementation is expected to meet the 1% PER requirement as SNR values of 5-6 dB, this design meets the requirement at SNR of 2.2 dB for the above simulated environments.

V. CONCLUSIONS

In this paper, design and verification of a digital signal processor that receives an IF signal and outputs the detected PHY payload for a 2.4 GHz ZigBee radio receiver have been presented. This design employs a sequential-processing architecture, which results in an improvement over a recent work. Namely, the resulting circuit requires smaller silicon area and potentially lower power.

REFERENCES

[1] IEEE standard for information technology – telecommunications and information exchange between systems – local and metropolitan area network specific requirements – part 15.4: wireless medium access control (MAC) and physical layer (PHY) specifications for low-rate wireless personal area networks (LR-WPANS), May 2003.

[2] Khanh Tuan Le, "Designing a ZigBee-ready IEEE 802.15.4-compliant radio transceiver," available online since Nov 2004 at http://rfdesign.com/mag/radio_designing_zigbeeready_ieee/

[3] http://www.corescomm.com/products/ZB_IFP250/ZB_IFP250.html

[4] W. Jirakittidul, S. Chanyavilas, T. Demeechai, P. Sirisuk and A. Worapishet, "FPGA implementation of base-band signal processing for 2.45GHz ZigBee radio receiver," in Proceedings of ECTI-CON 2005, pp. 60-63.

An Embedded Processor with Instruction Packing

C. Satayavibul, P. Chongstitvatana
Department of Computer Engineering
Chulalongkorn University
Phayathai road, Bangkok 10330, Bangkok, THAILAND
g49cst@cp.eng.chula.ac.th , prabhas@chula.ac.th

Abstract - **This work proposes a design of, SX4, a resource efficient 32-bit processor. SX4 is designed for a limited resource embedded system. The performance of SX4 has been improved by the "instruction packing" method. The measurement on the performance improvement is evaluated. Instruction packing reduces the code size by 33.0% at the same time it improve the speed of the processor by 17.1%. The proposed design has been realized on a FPGA device. SX4 processor requires 10,020 equivalent gates. Its maximum frequency is 63 MHz. In term of cycle consumed, it compares very well to commercial 32-bit Xilinx's microprocessor, Micro Blaze.**

I. INTRODUCTION

Nowadays, the embedded devices are playing important role in daily life. Computer exists in many things, such as mobile phone and automatic vending machine. As a result, the research in this area has many objectives: to improve the performance, to minimize code size, to minimize power consumption or to reduce cost of production depend on their functional purposes.

According to its working environment, the embedded devices have to be built to fit its surrounding conditions. A modern mobile phone needs a high performance processor for its multimedia applications, while most of the other devices don't require such high performance.

This is the main motivation of the work, to develop a resource efficient processor with adequate performance. The main focus of this work is to apply instruction packing method to reduce the size of executable code and also to improve the performance of a processor. The performance improvement is possible due to the reduction in number of cycle in fetching instructions. Such method is done by putting more than one instruction into same memory address space, which reduces the code size. As the code segment and data segment of the proposed processor share the same memory bus, instruction packing eases the memory bottle neck problem by reducing instruction traffic between processor and memory. Moreover, the proposed method requires little amount of additional resource so that the enhanced processor is still very resource efficient. Pipelining is another option for improving the processor's performance but it requires large modification on processor's data path which can violate the resource efficient criteria.

II. PROCESSOR DESIGN

SX4 is a 32-bit processor with no pipelined execution. Its design is based on the design of stack-based processor, SMC [1]. Fig. 1 demonstrates system overview of the proposed processor. Additional perpherals are attached to the system via memory-mapped I/O. SX4's instruction set is also based on SMC's ISA. SMC's zero-address instructions, which operate with data on top of stack, are replaced by one-address instructions in SX4 so that there is no stack-based operation in SX4. The processor operates with memory as shown in Fig. 1. One part of memory is writable; another part is read only (ROM). The ROM stores the code segment.

A. Data path

This processor data path is improved from the previous stack-based processor, SMC. (see Fig. 2) The processor has 32-bit data width. It consists of five registers: PC (program counter), IR (instruction register), AC (Accumulator), FP (frame pointer) and BUFFER.

B. Instruction Set Architecture

SX4 uses three instruction formats: Short, Long1 and Long2.(see Fig. 3) The Short format instruction, which is 16-bit wide, consists of two parts: 8-bit opcode and 8-bit operand. The long instruction formats are 32-bit wide. Long1 format has 8-bit opcode and 24-bit operand. Long2 format has 4-bit opcode, 20-bit operand and another extra 8-bit operand.

SX4 instructions can be divided into four categories: arithmetic&logic, data manipulation, control and misc (see Table I). Unary instruction operates on AC. The binary instruction needs one more element, which depended on the addressing mode. It can be either an immediate value of the operand or a local variable stored in the activation record. LD and ST access global memory. GET and PUT access local variables. CALL creates a new activation record. RET restores the previous activation record and returns to the caller.

The processor's operation is similar to an accumulator machine. This design uses an activation record, instead of general purpose registers. Although the activation record is slower than register, but there is some benefit of using the activation record. Firstly, it reduces size of the processor. Moreover, the activation record eliminates register saving and restoring during a function call.

Normally, the SX4 processor takes one cycle for instruction fetch and one more cycle for executing the instruction. But for some complex instruction, execution needs two cycles to

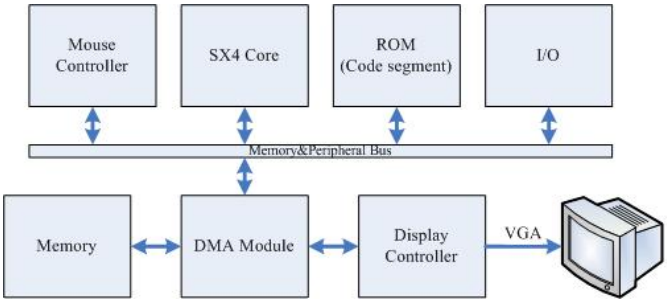

Figure 1. System overview of the proposed processor.

complete. As a result, overall performance of SX4 is around 2 to 3 cycles per instruction.

III. INSTRUCTION PACKING

As mentioned earlier, the embedded devices are designed to fit their working environment. In this paper, we introduce an instruction packing method, which causes little impact to the resource of a processor. The resource increased from including the instruction packing is less than 10% of the original design while it reduces code size and cycle consumed in program execution.

Instruction packing is done by putting two short instructions in the same memory address space (see Fig. 4). As two instructions are stored in one word, the processor will have two instructions after one instruction fetch. There is a case in which two short instructions can not be packed together. The instruction, which is the destination of CALL or JMP, cannot be placed in the most significant half word (31^{st} – 16^{th} bit). This is due to the proposed design's architecture does not suport half word directional in CALL and JMP instruction. Says, the program can not jump to the instruction placed in the most significant half word. As a result, such instructions can not be packed with the earlier instruction. Fig. 4 illustrates example of such case. The GET LED_addr instruction is the destination of the later IJX instruction, therefore it can not be packed with the earlier LIT 0 instruction. Hence, NOP instruction is packed with the LIT 0.

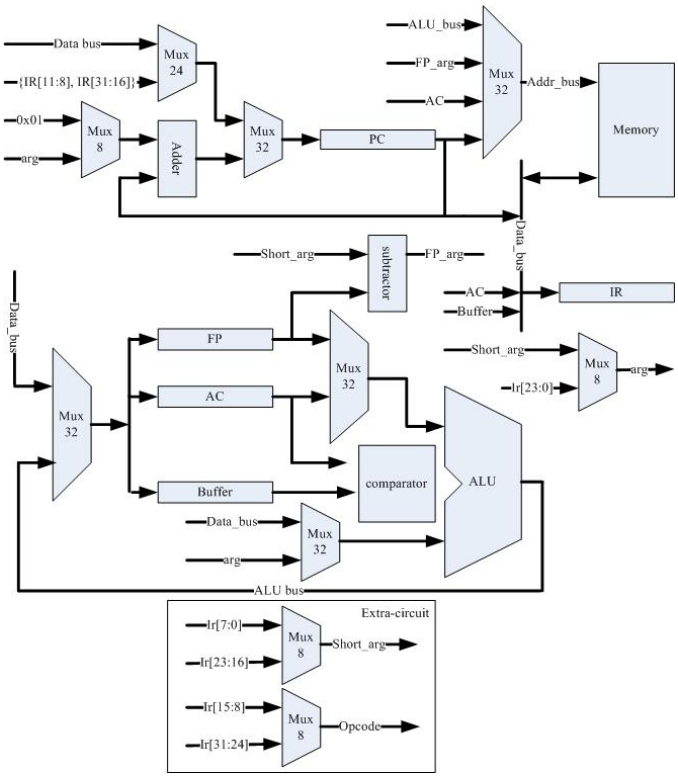

Figure 2. The data path of the proposed processor.

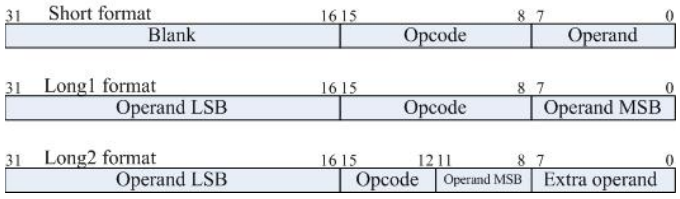

Figure 3. The proposed ISA format.

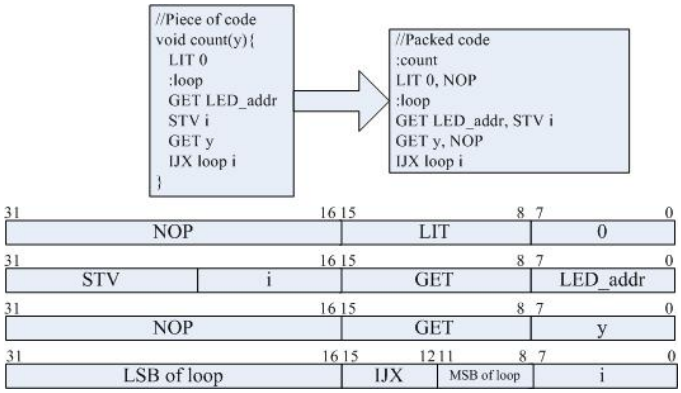

Figure 4. Example of instruction packing.

In the best case, instruction packing can reduce the program size by 50% and improve processor's throughput by 25%. This method also reduces program's code size. To include instruction packing on SX4, there is a small modification of the control unit. The data path needs two 8-bit MUX to select which half word is used. The extra circuit is shown in Fig. 2.

A complier plays a role in packing the code for the processor. Improvement in performance also depends on how well the code has been packed.

TABLE I
THE LIST OF THE PROPOSED PROCESSOR'S INSTRUCTIONS.

Instruction category	Instruction
Arithmetic&logic	ADD, SUB, MUL*, DIV*, BOR, BAND, BXOR, MOD*, ADDI, SUBI, MULI*, DIVI*, BORI, BANDI, BXORI, MODI*
Data manipulation	LD, ST, LDL, STL, LDX, STV, GET, PUT, INC, DEC
Control	JMP, JT, JF, JMPL, JTL, JFL, IJX, CALL, RET
Misc.	LIT, LITL, NOP

* indicates the instruction has not yet been implemented.

See the following function written in a machine code as follow:

```
add:
    get a  // 2 cycles consumed
    add b // 2 cycles consumed
    ret 3   // 3 cycles consumed
```

The code above can be optimized by packing GET and ADD instruction together as follow:

```
add:
    get a add b // 3 cycles consumed
    ret 3   // 3 cycles consumed
```

As a result, the packed code runs one cycle faster than the unpacked code, hence the performance improved by 14%.

IV. MEASUREMENT

In this section we test the processor with a suite of benchmarks. There are seven programs used in the measurement. There are seven test suites used in this paper: Bubble, Merge, Quick, Fibonacci, Hanoi, Sieve and AES.

Bubble: bubble sort 100 items of data. The initial data is ordered in descending order.

Merge: merge sort 100 items of data. The initial data is ordered in descending order.

Quick: quick sort the descending ordered data. The following number indicates number of data items.

Fibonacci: calculate the value of Fibonacci 10. The program is written in recursive function.

Hanoi: solves the 6 disks Hanoi problem.

Sieve: finds all prime numbers which less than 100.

AES: AES (Advance Encryption Standard) (128, 128) bit key block cipher [2].

To test the processor, we divide the measurement into three steps. Firstly, the instruction packed SX4 is compared to the original SX4 (see Table II, III). The test result shows that the SX4 executes packed code faster than unpacked code by 17.1% averaging over all benchmarks. Also packed program code size is 33.0% smaller than unpacked programs.

Secondly, code size comparison between packed SX4 program and other processors' (see Table IV, V). One of them is the stack-based processor [1]. The stack-based ISA is widely known to achieve a compact executable code [3].

TABLE II
THE COMPARISON BETWEEN
PACKED CODE SIZE AND UNPACKED CODE SIZE.

Test program	Unpacked code size (Byte)	Packed code size (Byte)	Size reduce
Bubble	96	64	33.3%
Merge	388	224	42.3%
Quick	200	168	16%
Fibonacci	100	68	32%
Hanoi	180	116	35.6%
Sieve	152	92	39.5%
AES	1,336	912	31.7%

The total equivalent gates needed in Micro Blaze system, the processor and 8kbytes of block ram is 315,528 gates. The Micro Blaze alone needs about 55,000 gates. The test program is written in C programming language and compiled by gnu C compiler. We use Xilinx On-Chip Peripheral Timer/Counter to measure the number of cycle consumed during execution. The numbers of cycle shown in Table V are the number of cycle that Micro Blaze takes to finish the test program and stop the timer. In term of cycle, the SX4 compares very well with Xilinx Micro Blaze. If running at the same frequency, the proposed processor will be about 15% slower than Micro Blaze, except for Fibonacci and Hanoi test suite. Because of the use of activation record, SX4's function call is very simple and fast. Therefore, SX4 defeats Micro Blaze on heavily recursive call programs. SX4 code size is about 60% of the Micro Blaze code size. In term of performance, Micro Blaze's maximum frequency is 91 MHz while the proposed design's is 63 MHz.

V. RELATED WORK

Processor proposed in paper [1] uses stack-based instruction approach to achieve the resource efficient criteria. Its operations take elements on the top of stack so it does not require general purpose registers. Performace is the major weakness of the stack-based processor. Many methods, include instruction packing [4] , are applied to improve the performance. But the stack-based operations, which require a lot of memory accesses, have limitted the processor's performance.

There are many approaches in instruction packing. One of them is the use of Instruction Register File (IRF) [5, 6]. IRF

TABLE III
THE PERFORMANCE COMPARISON BETWEEN
PACKED CODE AND UNPACKED CODE.

Test program	Unpacked code Cycle consumed	Packed code Cycle consumed	Speedup
Bubble	327,706	282,953	13.7%
Merge	34,712	27,888	19.7%
Quick			**14.8%**
20 items	5,388	4,575	15.1%
60 items	32,948	28,116	14.7%
100 items	82,908	70,856	14.5%
Fibonacci	3,875	3,112	19.7%
Hanoi	4,398	3,708	15.7%
Sieve	2,341	1,859	20.6%
AES	59,710	50,640	15.2 %

TABLE IV
THE COMPARISON BETWEEN
PACKED CODE SIZE AND THE STACK-BASED PROCESSOR CODE SIZE.

Test program	Stack-based code size (Byte)	Packed code size (Byte)	Comparison
Bubble	124	64	51.6%
Quick	187	168	89.8%
Fibonacci	50	68	136%
Hanoi	153	116	75.8%
Sieve	137	92	67.2%
AES	650	912	140.3%

keeps the frequently occurring pair of instructions in the program. This approach indicates multiple instructions by indexing the IRF.

Similar to instruction packing, code compression aimed for reducing the code size. The well-known code compression examples are ARM Thumb [7] and MIPS16 [8]. The special instruction set is designed to offer small code size. Number functions are unavailable in code compression mode. As a result, the performance of the processor drop while operating in code compression mode.

TABLE V
THE COMPARISON BETWEEN
THE PROPOSED PROCESSOR AND XILINX MICRO BLAZE.

Category	Xilinx Micro Blaze	Proposed processor	Comparison
Circuit size (Equivalent gate)	315,528* 55,000**	10,020	3.2% 18.2%
Code size (byte)			
Bubble	172	64	37.2%
Merge	396	224	56.6%
Quick	264	168	63.6%
Fibonacci	112	68	60.7%
Hanoi	168	116	69.0%
Sieve	132	92	69.7%
AES encryption	1,524	912	60.0%
Performance (cycle consumed)			
Bubble	248,354	282,953	114.0%
Merge	23,389	27,888	119.2%
Quick			
20 items	4,131	4,575	111.0%
60 items	24,439	28,116	115.1%
100 items	73,442***	70,856	96.5%
Fibonacci	4,810	3,112	64.7%
Hanoi	4,102	3,708	90.4%
Sieve	1,195	1,859	155.6%
AES	43,500	50,640	116.4%
Maximum frequency (MHz)	91	63	0.69

* 8kbyte of Block ram is included in the equivalent gate count.
** approximated equivalent gate count of Micro Blaze processor. Block ram is excluded.
*** indicates external memory is used to hold the Micro Blaze program's Stack/Heap section.

VI. CONCLUSION

The design presented here of a 32-bit processor with instruction packing achieves the main objective, to design a resource efficient adequate performance processor. We divide the conclusion into three points of view. First of all, in term of resource consumed, the proposed design has been realized on a Xilinx Spartan3 FPGA device. It consumes 10,020 equivalent gates. Secondly, in term of code size, the result is still satisfactory. SX4's code size is obviously smaller than the conventional 32-bit processor. The proposed processor code size also comparable to the stack-based processor [1], which is a 16-bit processor. Finally, the number of cycle of SX4 executing the benchmark suites are comparable to a commercial processor, Micro Blaze. However, the maximum frequency of the SX4 is significantly lower than Micro Blaze's. To be fair, these results are based on small set of benchmarks and should be taken as preliminary result. Our current work is expanding on this result to include larger and more diversed benchmark suite and better code generation quality.

VII. REFERENCES

[1] A. Burutarchanai, P. Nanthanavoot, C. Aporntewan, and P. Chongstitvatana, "A stack-based processor for resource efficient embedded systems," Proc. of IEEE TENCON 2004, Thailand, 21-24 November 2004.

[2] J. Daemen and V. Rijmen, "The Rijndael Block Cipher: AES proposal," 1999.

[3] P. Nanthanavoot and P. Chongstitvatana, "Code-Size Reduction for Embedded Systems using Bytecode Translation Unit," Conf. of Electrical/Electronics, Computer, Telecommunications, and Information Technology (ECTI), Thailand, 13-14 May 2004.

[4] P. Nanthanavoot, A. Burutarchanai and P. Chongstitvatana, "Instruction packing for a 32-bit resource efficient processor," National Science and Technology Development Agency (NSTDA) Annual Conference, Thailand, 27-30 March 2005 .

[5] S. Hines, G. Tyson and D. Whalley, "Reducing instruction fetch cost by packing instructions into register windows," Microarchitecture, 2005. MICRO-38. Proceedings. 38th Annual IEEE/ACM International Symposium on Microarchitecture MICRO 38**,** 12-16 Nov. 2005. Page(s):11 pp.

[6] S. Hines, J. Green, G. Tyson and D. Whalley, "Improving Program Efficiency by Packing Instructions into Registers," ACM SIGARCH Computer Architecture News , Proceedings of the 32nd Annual International Symposium on Computer Architecture ISCA '05, May 2005.

[7] Advanced RISC Machines Ltd., "An Introduction to Thumb," March 1995.

[8] K. D. Kissell, "MIPS16: High-density MIPS for the Embedded Market," In Proc. of Real Time Systems '97 (RTS97), 1997.

The AES Encryption Circuit on a Reconfigurable Hardware

J. Sripornprasert, P. Chongstitvatana
Department of Computer Engineering
Chulalongkorn University
Phayathai road, Bangkok 10330, Bangkok, THAILAND
g49jsr@cp.eng.chula.ac.th, prabhas@chula.ac.th

***Abstract*-This work presents an AES encryption circuit implemented by a special type of machine called "Hardware Multiplexing" (HWMX). Hardware Multiplexing is a kind of reconfigurable embedded processor. By using dynamic reconfiguration concept, HWMX operates AES Algorithm correctly with efficient resources. HWMX consists of two cores 1) Register Bank and 2) Reconfigurable Core. The first part stores temporal results for next round computation. The second part, an important core of HWMX, processes as a reconfigurable system. This approach allows HWMX to pursue AES encryption application by splitting AES circuit into four segments and execute one segment per round, putting the temporal result of each segment into Register Bank. By using time-multiplexing hardware the resource consumed is less than a conventional circuit.**

I. INTRODUCTION

Presently, the embedded system plays critical role of computation in everyday life. At the same time, application is becoming more complex. Therefore, circuit area must be enlarged to provide more complex functionality. As a result, the circuit size could not match for budgetary environment. Hardware Multiplexing (HWMX) is a good solution for embedded systems with limited resources.

HWMX does have contribution to economic resources and its flexibility makes it suitable for embedded systems. Moreover, AES encryption is an instance of problem that we are interested in. This work demonstrates how to apply the concept of Hardware Multiplexing to implement an AES encryption circuit efficiently.

II. RELATED WORKS

The paper [1] describes the fundamental concept of Hardware Multiplexing which it provided the simulation result. This work also provides the simulation result. The simulation compares between HWMX and a general processor which illustrates HWMX's advantages.

In [2], a reconfigurable AES core using FPGA is represented. Their work presents a reconfigurable component for saving resources, S-Box. The S-Box is an important part of ByteSub process. It uses large area because of ByteSub look-up table (Encryption/Decryption). To reduce ByteSub look-up table area, a reconfigurable S-Box would be used ByteSub value stored in S-Box counts on whether it is Encryption or Decryption. This concept saves 50% of overall resource area. However, the reconfiguration of entire data path (not only S-Box) which relies upon current function is the core concept of HWMX.

Another work [3], proposed a design of Reconfigurable AES Encryption/Decryption for mobile terminals. It made up of Reconfigurable Crypto-Unit (RCU) and Reconfiguration Control Logic (RCL). The RCU has the multiplier which supports encryption, decryption, error correction and error detection. The RCU obtain control signals from the RCL. The RCL is reconfigured by Control Unit. Consequently, the RCU and the RCL give overall system more flexibility.

When a computation task is larger than the available area, it is needed to be partitioned. The work [4] proposed methods to partition a design into reconfigurable blocks. This work states two partition methodologies, Level-Based partition and Clustering-Based partition. If Level-Based partition is applied to a task, the independent subtasks will be put into reconfigurable area. On the other hand, The Clustering-Based partition will put dependent subtasks into reconfigurable area. As a result, Level-Based partition spends a little time of execution delay but it has expensive communication time and vice versa for Clustering-Based partition.

III. OPENCORE AES IP-CORE

We compare our work with an Opencore AES engine. The work [6] meets Rijndael's specification and has publicly available information (Fig. 1).

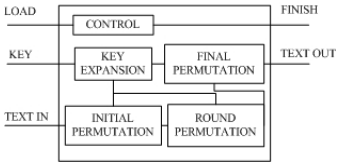

Figure 1. Opencore AES architecture which finishes its task by 12 cycles. It starts when completely load 128-bits key and 128-bits data into machine.

Opencore AES IP-Core has five modules integrated into a structure. There are four modules that are connected to each other. A group of modules does transformation and computes a RoundKey per each round. The Opencore Encryption cipher

consumes chip area about 40,000 equivalent gates. This synthesized result comes from FPGA Xilinx spartan3 xcv200.

IV. Overview of AES Encryption and Hardware Multiplexing

This section describes a basic background of AES Encryption. Moreover, some fundamental concept of how to apply HWMX to the AES core would be described.

A. AES Encryption Background

AES encryption [5] is an iterated block cipher with a variable block length and a variable key length. The block length can be independently specified to 128, 192 or 256 bits. The round transformation is composed of four different transformations. From Rijndael's proposal we obtain Table I.

TABLE I
FOR 1ST -TO 9TH OF AES ENCRYPTION USES LEFT SIDE TABLE, BUT FINAL ROUND USES RIGHT SIDE.

Round(State, RoundKey){
ByteSub(State);
ShiftRow(State);
MixColumn(State);
AddRoundKey(State);
}
	FinalRound(State,RoundKey){
	ByteSub(State);
	ShiftRow(State);
	AddRoundKey(State);
	}

* The intermediate cipher result is called *State.*

B. Hardware Multiplexing Architecture

HWMX contains two essential components, Register Bank (RB) and Reconfigurable Data Path (RDP), as show in Fig. 2.

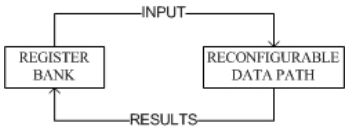

Figure 2. RB and RDP work together by sharing input, output and temporal result.

From Fig. 2, HWMX manages process cycles around RB and RDP. RB keeps three types of data, input, output and temporal results. These data comes from RDP's unit, which links with Control Unit. The Control Unit outputs fix sequence of control signal to RB and the Control Unit issues commands to the sequence ROM as a pointer to the desired sequence. (See Fig. 3)

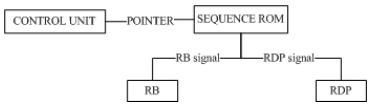

Figure 3. Control Unit send pointer to sequence ROM for RB signal and RDP signal.

The RDP realized the AES circuit by dividing it into four modules, Transposer, KeyExpansion, cipherSB and cipherMX. At any time, the RDP will be configured as one of these modules (Fig.4).

As you see in Fig. 4, there are two types of execution that is Initial Round and Others Round (1^{st}-10^{th} Round). Initial Round is a round which provides data ready to be executed in next round. In 1^{st}-10^{th} Round, all of processes will change. These rounds calculate the final result when they reach 10^{th} round. Execution sequence is discussed in detail again in EXECUTION section.

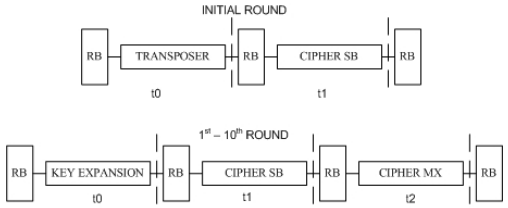

Figure 4. AES Encryption instance has two types of loop that has to be executed along the encryption.

V. Implementation

This section presents briefly the details of HWMX architecture and then shows the AES Encryption. HWMX has two main cores. There are Double Register Banks and Reconfigurable Data Path, called RDP.

Double Register Banks: Each bank contains sixteen 32-bit registers. These cores are designed to store any temporal results that come from RDP and then RDP will fetch these temporal results to compute next results.

Reconfigurable Data Path (RDP): RDP has a self-reconfigurable capability. It changes its circuit to maximize utilization and minimize resource usage. The idea to achieve this encryption by minimum resources consumption is to break an entire circuit into smaller fragments. If a fragment is too large that means circuit spends expensive resource but if a fragment is too small that means circuit wastes time. In this paper, AES Encryption circuit is divided into four modules, a Transposer, a CipherSB, a CipherMixColumn and a KeyExpansion. We assume method of reconfiguration by using Multiplexer. Reconfiguration happens when Multiplexer swaps itself to connect to other modules. By this assumption, the reconfiguration time is zero. Because there is no known practical and fast reconfiguration method at present, this assumption is amounted to a best case scenario.

VI. Experiment

We illustrate how an AES circuit based on HWMX work by comparing it to two conventional designs, one in based on a general purpose processor and the second one is an AES engine.

Traditional CPU: the CPU fetches instructions, and then decodes them. After that, The CPU executes instructions. All of these steps run on the same data path, no matter what operations are.

The AES engine: the special purpose AES engine has its circuit designed specific for the task. It has fast data-flow style execution which can be parallelized. It can be much faster than a general purpose processor trade in by the size of the circuit.

The AES based on HWMX: a HWMX circuit changes its data path (the reconfigurable unit) from time to time to share resource among different part of computation. It can trade off the speed with the size of the circuit. Table II shows the sequence of multiplexing the reconfigurable units. This is a sequence of data paths that it uses to find the result. (See Table II)

TABLE II
TABLE II SHOWS THE SEQUENCE HWMX OF EXECUTION. INITIAL ROUND PREPARES DATA INPUT READY TO PROCESS NEXT ROUND. 1st-10th ROUND DOES ENCRYPTION TO FIND OUTPUT.

Initial Round	1st-10th Round
Transposer cipherSB	KeyExpansion cipherSB cipherMX*

*cipherMX in final round would not do mix column operation.

First of all, RDP selects the Transposer module (Fig. 5) to be used. It fetches input data and input key from RB. After it finishes matrices transpose operation ,it stores the results into RB. The cipherSB module (Fig. 6) replaces the Transposer module. To prepare encryption, the cipherSB does addRoundKey. When it gets the end of addRoundKey process, RDP begins encryption. The AES encryption iterates the intermediate results for 10 rounds (see Table II). Each round has the same sequence. Firstly, the KeyExpansion module (Fig. 7) is the first module which RDP selects. The KeyExpansion module causes a new Round Key that other modules need to manipulate the Round Cipher. The KeyExpansion module finds a Round Key, and then it places them into RB. Thereafter, the cipherSB would replace the KeyExpansion module. Instead of doing addRoundKey process again, the cipherSB does ByteSub. The intermediate results from the cipherSB would be stored to RB. Finally, the cipherSB transforms itself to the cipherMX module (Fig. 8). At the beginning, the cipherMX module fetches data, and then executes shiftRow, mixColumn and addRoundKey. These set of operation which consist of the KeyExpansion, the cipherSB and the cipherMX module would be executed that sequence until they reach 10th round encryption. Furthermore, the final result is store into RB. Fig. 5-8 illustrate each component.

VII. CONCLUSION

The following paragraphs compare among HWMX, Traditional CPU and AES engine. Any advantages and disadvantages would be discussed.

Figure 5. Inside the Transposer module, matrix transpose module transforms input to ready-to-use form.

Traditional CPU: a general purpose processor has its performance disadvantage due to its generic data path. However, the processor can perform other general purpose task as well.

The AES engine: an AES engine is built to be specific encryption hardware. Certainly, this approach has highest performance. On the other hand, it consumes the largest area when compares to others and can not do anything but AES Encryption.

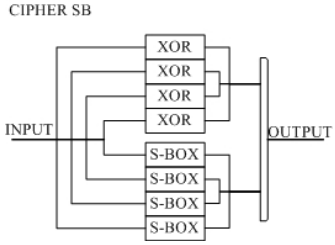

Figure 6. Inside cipherSB module, there are four S-Boxes and four XORs module to find ByteSub result.

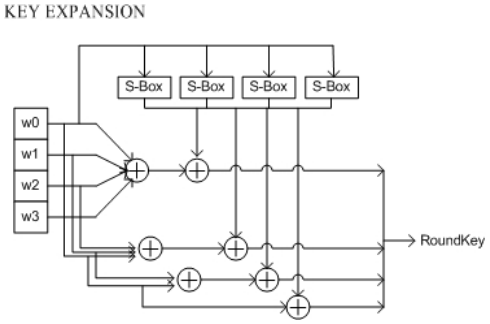

Figure 7. KeyExpansion module is the most complicated module, so this reason is why KeyExpansion is the largest part.

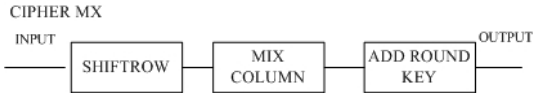

Figure 8. The cipherMX module consists of three sub-modules to do three operations, ShiftRow, MixColumn and AdddRoundKey.

The AES based on HWMX: HWMX does the AES encryption by RDP. RDP has the advantage of a flexible data path by reconfigurable ability. The ability of partition hardware into a smaller fragment helps to overcome the resource problem. Although the speed of HWMX is traded off with the resource, it can be designed to be "in-between" the performance of the general purpose processor and the special engine. This flexibility is shown in Table III.

This paper demonstrates a design of AES circuit based on HWMX concept. The comparison is made between the proposed design, AES engine, and a general purpose processor, Intel 8051 [8], which has a published performance figure. From Table III, HWMX spend around 10 thousand gates less than AES engine three times and two times for Intel 8051 [5]. The reason that HWMX is smaller than any other because its core, RDP. However, its speed is still slower than the specific AES Encryption engine. The Bottleneck

Communication is a major problem according to nature of Level-Based partition. Each module that RDP change operates on 128-bits bus but HWMX bus is Double 32-bits bus. Therefore, it wastes 2 cycles to load data into each module. Nevertheless, if HWMX has 128-bits bus instead, it will be much faster. Anyway, that is not the sole purpose of HWMX. HWMX idea is more general than a circuit that does only AES encryption.

TABLE III
RESOURCES AND CYCLES USAGE SUMMARY SHOW THAT HWMX TAKE AN ADVANTAGE ON EQUIVALENT GATES.

	Equivalent gates	128-bit Encryption Cycles	Freq (MHz).
HWMX	10830	202	75.644
AES engine	40621	12	137.299
Intel 8051	38203* 37902**	48780* 4878**	12.00* 18.906**

* original 8051 [5], ** Oregano 8051 [8]

VIII. FUTURE WORKS

In this paper, HWMX never do the physical dynamic self-reconfigurable circuit. The technology of hardware has not reaches the actual self-reconfigurable yet. Presently, we are working on a study of integrating two Xilinx spartan3 boards, one is master and other is slave. Master board consists of Double Register Banks and Microblaze. Slave board is reserved only for RDP. Master board handles storing temporal results and request to Microblaze for reconfiguration. Microblaze, then, put bitstream that store in it memory into slave board via JTAG.

REFERENCES

[1] K. Piromsopa, P Bavonparadon and P Chongstitvatana, "Hardware multiplexing: towards a resource efficient reconfigurable processor." *3rd International Symposium on Communications and Information Technologie*s, Songkhla, Thailand, 2003

[2] X. Jian, L.Yuan-Feng, D. Zi-Bin and S. Yi, "Design and Implementation of AES IP-Core Using FPGA," *ASIC, 2005. ASICON 2005. 6th International Conference On*, Shanghai, China, 2005, pp.765-768.

[3] T. Pionteck, T. Staake, T. Steifmeir, L.D. Kabulepa and M. Glesner, "Design of Reconfigurable AES Encryption/Decryption Engine for Mobile Terminals," *Circuits and Systems, 2004. ISCAS '04. Proceedings of the 2004 International Symposium on*, Vancouver, BC, Canada, 2004, II- pp.545-8.

[4] K.M.G. Purna and D. Bhatia, "Temporal and Scheduling Data Flow Graphs for Reconfigurable Computers," *Computers, IEEE Transactions on*, 1999, pp.579-590.

[5] National Institute of Standards and Technology (NIST), FIPS Publication 197, "Advanced Encryption Standard (AES)," November 2001.

[6] R. Usselmann, AES IP-Core, www.opencore.org, 2002.

[7] K. Compton and S. Hauck, "Reconfigurable Computing: A Survey of System and Software," ACM Computing Survey, NY, USA, 2002, 171-210.

[8] http://www.oregano.at/ip/ip01.htm.

Hardware Model Checking and Computational Temporal Logic(CTL)

Hamid Shojaei, *Majid Nabi, *Zainalabedin Navabi, Mohammad Reza Kakoee
Islamic Azad University, Damavand Branch
shojai@cad.ece.ut.ac.ir
*CAD Research Group, ECE Department, Faculty of Engineering
University of Tehran / Tehran, Iran
{mnabi, kakoee}@cad.ece.ut.ac.ir, navabi@ece.neu.edu

***Abstract*-We use symbolic model checking to verify a VHDL design. This paper mainly focuses on Computational Tree Logic (CTL) for model checking problem. We have explained these two terms "CTL" and "model checking" for providing a clear idea about these two. Most importantly we have explored the ways of uses of CTL formulae in the case of model checking. The importance of the model checking, the ways of specifying properties in CTL and some most commonly used CTL formulae in checking are also stated. Also the uses and importance of fairness constraints in CTL formula and the conversion of CTL operators have also been included in this paper. Lastly, we have given an example of the processes of model checking.**

I. INTRODUCTION

Hardware systems are generally specified as a set of interacting finite state machines (FSMs). Network protocols and CPU controllers are such systems that their base structures consist of finite state machines. Therefore, checking the correctness of these systems is a major issue in the digital system design and the verification.

Current techniques for testing FSMs are simulations and testing. But the problems with the simulation are: it can not run for ever; it will be many times slower than the simulated system; can be very expensive; and there is no guarantee that all the possible runs will be simulated. Testing also suffers from similar disadvantages. There are some additional disadvantages such as, not all (infinite) inputs can be presented; input patterns needs to be automatically generated; no guarantee that bad inputs will be presented; and especially messy for concurrent systems like multi-component systems. These two can reveal the presence of bugs but can never establish the absence of bugs. This is a fundamental limitation for safety-critical systems. For these reasons, the application of model checking is increasing day by day. Model checking uses transition systems (*Kripke Structure*) to model systems and *temporal logics* to specify properties. It makes the verification problem reduced to graph algorithmic problems that can be fully automated [1, 2, 3, 6] and relatively easy to use. It is very successful in verifying hardware communication protocols and other many *embedded systems.* It is increasingly popular in industry. Besides, there are some robust tools such as SPIN, SMV, COSPAN, VIS, SMART etc. that can be easily and effectively used as verification tools. But the problem is that as the number of interacting components increases the size of the transition system increases exponentially which creates a very serious problem namely the state explosion problem.

The use of modeling checking in place of simulation or testing is now common in most of the cases of hardware, software, concurrent systems, reactive systems design verification. This checking uses *temporal logic* (mainly CTL) to specify the properties to be verified. In our paper, we have explored a brief idea on how we can use Computational Tree Logic (CTL) for model verification purpose. We have explained about the model, the CTL formula, the necessity of *fairness* in CTL formula and lastly a full elaborative example of model checking.

II. SYMBOLIC MODEL CHECKING

Symbolic CTL model checking is a formal verification technique which has proven itself practical in the verification of hardware specifications and implementations. A design of N latches is considered as a state machine containing 2**N states, and the temporal logic CTL is used to reason about the design. Symbolic representation and manipulation of the design allows the state machine to be traversed without explicitly building it, thus making the technique feasible for N=100 and more. The foremost step to verify a system is to specify the properties that the system should have. For example, we may want to show that some concurrent processes never deadlock. These properties are represented by *temporal logic*.

Computational Tree Logic (CTL) is one of the versions of *temporal logic*. It is currently one of the popular frameworks used in verifying properties of concurrent systems [4]. In this paper; we take consideration of only this type of logic for model checking. Once we know which properties are important, the second step is to construct a *formal model* for that system. The model should capture those properties that must be considered for the establishment of correctness. Model checking includes the traversing the state transition graph (*Kripke Structure*) and verifying that if it satisfies the formula representing the property or not, more concisely, the system is a model of the property or not. Each CTL formula is either true or false in a given state of the *Kripke Structure*. Its truth is evaluated from the truth of its sub-formulae in a recursive fashion, until one reaches atomic propositions that are either true or false in a given state.

A formula is satisfied by a system if it is true for all the initial states of the system. Mathematically, say a *Kripke*

Structure K = (S, S0, R, AP, L) (system model) and a CTL formula Ψ (specification of the property) are given. We have to determine if $K \models \Psi$ holds (K is a model of Ψ) or not. $K \models \Psi$ holds iff $K, s0 \models \Psi$ for every $s0 \in S0$. If the property does not hold, the model checker will produce a counter example that is an execution path that can not satisfy that formula.

III. STANDARD CTL FORMULAE

Formulae in standard CTL are built from atomic propositions which correspond to variables in the model being verified, standard Boolean operators (e.g., AND, OR, XOR, NOT), and temporal operators. Each temporal operator consists of two parts: a path quantifier (*A* or *E*) and a temporal modality (*F*, *G*, *X*, *U*). There are two different path quantifiers: *A* indicates that the modality defines a property that should be true on all the possible paths and *E* indicates that the property needs only hold on some paths. The temporal modalities describe the ordering of events in time along a path and have the following meaning:

$F\phi$: (reads ϕ holds sometime in the future) is true on a path if there exists a state in the path where formula ϕ is true.

$G\phi$: (reads ϕ holds globally) is true on a path if ϕ is true at every state in the path.

$X\phi$: (reads ϕ holds in the next state) is true on a path if ϕ is true in the state reached immediately after the current state in the path.

$\phi \cup \psi$: (reads ϕ holds until ψ holds, called strong until) is true on a path if ψ is true in some state in the path, and ϕ holds in all preceding states.

The semantics of the CTL operators are stated below:

K, s |= EX (Ψ) there exists s' such that s → s' (R(s, s')) and K, s' |=Ψ. It means that s has a successor state s' at which Ψ holds.

K, s |= EU (Ψ1, Ψ2) iff there exists a path L = s0, s1, … from s and k >= 0 such that: K, L(k) |= Ψ2 and if 0 ≤ j < k, then K, L(j) |= Ψ1.

K, s |= AU(Ψ1, Ψ2) iff for every path L = s0, s1, … from s there exists k >= 0 such that: K, L(k) |= Ψ2 and if 0 ≤ j < k, then K, L(j) |= Ψ1.

AX (Ψ): It is not the case there exists a next state at which Ψ does not hold i.e. for every next state Ψ holds.

EF (Ψ): There exists a path L from s and k >= 0 such that: K, L(k)|=Ψ.

AG (Ψ): It is not the case there exists a path L from s and k>= 0 such that: K, L(k)|= Ψ i.e. for every path L from s and every k >= 0;K, L(k)|=Ψ

AF(Ψ) : For every path L from s, there exists k>= 0 such that: K, L(k)|= Ψ.

EG(Ψ): It is not the case that for every path L from s there is a k >= 0 such that K,L(k)|=Ψ. It means that there exists a path L from s such that, for every k>= 0: K, L(k) |= Ψ.

Some basic CTL operators among those stated above are shown graphically for easy understanding in Figure 1. In this figure, if it is assumed that in the filled states, the formula *f* holds then we can say that the formula EF*f*, AF*f*, EG*f* and AG*f* are satisfied in the initial states (a) in the figures 1.a, 1.b, 1.c and 1.d, respectively.

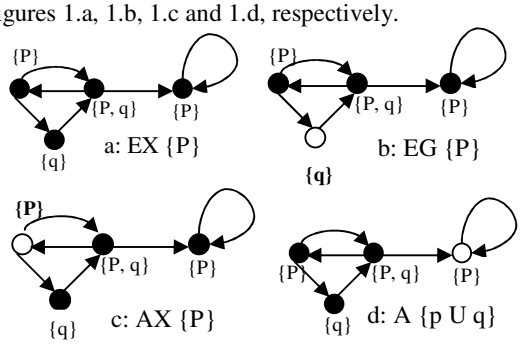

Figure 1: Basic CTL Operators

IV. CTL FORMULA CONVERSION

For a universal *CTL* formula, all states in a design that are reachable from the initial states should be checked. However for an existential *CTL* formula only one case from the initial states should be found that satisfies the formula. It is clear that algorithms of existential *CTL* formula can be implemented easier than universal *CTL* formula, so universal formulae are converted to existential formulae. Therefore all universal path quantifiers are replaced with the appropriate combination of existential quantifiers and *Boolean* negations. Also "*finally*" operators are converted to "*until*" operators. This returns a new formula that shares absolutely nothing with the original formula (not even the strings). The "*original Formula*" field of each new sub-formula is set to point to the formula passed as an argument. In addition, if and only if the original formula is of type *AG, AX, AU, AF, or EF*, the "*converted flag*" is set. These conversions are as below:

TABLE I
CONVERSION OF CTL FORMULAE

Formulae	Converted Formulae
AX f	*~ EX (~f)*
EF f	*E (True U f)*
AG f	*~ EF(~f)*
AF f	*~ EG (~f)*
A (f U g)	*~E[~g U (~f ∧ ~g)] ∧ ~EG ~g*

V. UNWINDING

We usually use the Computation Tree Logic (CTL) for specifying these kinds of formula for model checking. It is one of the versions of *temporal logic*. State Transition Graph (STG) is used to derive the computation trees. Now the question is that how we can build a tree from the STG? The graph structure is unwound into an infinite tree rooted at the initial state. Figure 2 shows an example of unwinding a graph (traffic-light controller; R, G and Y indicate RED, GREEN and YELLOW respectively) into a tree. All possible computations of the system being modeled are represented by the paths in the tree. Formulae in CTL refer to the computation tree derived from the model. CTL is classified as branching time logic because it has operators that describe the branching structure of this tree.

The formula *EG (RED)* is true as there is at least one path which in all its states; there is RED (the path *R, R, R*

…….). The formula E *(RED U GREEN)* is also true as there is at least a path (*R, R, G……*) where all the states hold *R* until we reach a state with *G*. But the formula *AF (GREEN)* is false as there is at least one path in which no state is with the atomic proposition *G*.

Figure 2: Unwinding of state transition graph.

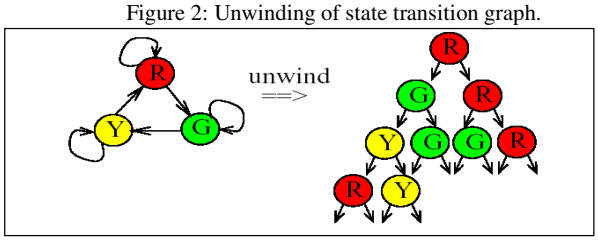

VI. Expressing Properties in CTL

CTL formulas are sometime problematical to interpret. For this, a designer may fail to understand what property has been actually verified. Here we want to add some common constructs of CTL formula used in hardware verification.

1. *AG (Request → AF Acknowledgement)*: For all reachable states (*AG*), if *Request* is asserted in the state, then always at some later point (*AF*), we must reach a state where *Acknowledgement* is asserted. *AG* is interpreted relative to the initial states of the system whereas *AF* is interpreted relative to the state where *Request* is asserted. A common mistake would be to write *Request → AF Acknowledgement* in place of *AG (Request → AF Acknowledgement)*. The meaning of the former is that if *Request* is asserted in the initial state, then it is always the case that eventually we reach a state where *Acknowledgement* is asserted, while the latter requires that the condition is true for any reachable state where *Request* holds. If *Request* is identically true, *AG (Request → AF Acknowledgement)* reduces to *AG AF Acknowledgement*.
2. *AG (AF DeviceEnabled)*: The proposition *DeviceEnabled* holds infinitely often on every computational path.
3. *~AG(busy)*: The device should not be always busy.
4. *AG (EF start)*: From any reachable state, there must exist a path starting at that state that reaches a state where *start* is asserted. In other words, it must always be possible to reach the restart state.
5. *EF (x ∧ EX (x∧ EX x)) → EF (y ∧ EX EX z)*: If it is possible for *x* to be asserted in three consecutive states, then it is also possible to reach a state where *y* is asserted and from there to reach in two more steps a state where *z* is asserted.
6. *EF (~Ready ∧ Started)*: It is possible to get to a state where *holds started*, but *ready* does not hold.
7. *AG (Send → A (Send U Receive))*: It is always the case that if *Send* occurs, then eventually Receive is true, and until that time, *Send* must continue to be true.
8. *AG (in → AX AX AX out)*: Whenever *in* goes high, *out* will go high within three clock cycles.
9. *AG(~storage_coke→ AX storage_coke)*: if the coke storage of a vending machine becomes empty, it gets recharged immediately.
10. *AG AF ((~storage_coke ∨ ~storage_coffee) ∧ (storage_coke ∧ storage_coffee))*: the recharge transaction of a vending machine (of coke and coffee) takes place infinitely often.

VII. Fairness Properties in CTL

In verifying concurrent systems, we are occasionally interested only in correctness along *fair* execution [5]. It is often necessary to introduce some notion of *fairness*. For example, if there are two processes trying to use a shared resource using an arbiter, we may wish to consider only those executions in which the arbiter does not ignore one of its request inputs from either of the processors forever. Alternatively, we may want to consider communication protocols that operate over reliable channels which have the property that no message is ever continuously transmitted but never received. A *fairness constraint* can be an arbitrary set of states, usually described by the formula of the logic. If *fairness constraints* are interpreted as a set of states, then a fair path must contain an element of each constraint infinitely often. If *fairness constraints* are interpreted as CTL formulas, then a path is *fair* if each constraint is true *infinitely often* along the path. The path quantifiers in the logic are then restricted to fair path [6]. An example of a *fairness* condition is *P* that restricts the system to only those paths where *P* is asserted infinitely often. Basically we use *fairness constraints* to rule out undesired executions. Let us discuss this with an example.

In Figure 3 (a), the two processes (*PR1* and *PR2*) want to use the shared resource using the arbiter. Figure 3 (b) shows the corresponding STG. For this example, the atomic propositions are, $AP = \{idle_1, waiting_1, using_1, idle_2, waiting_2, using_2\}$ where, $idle_i$, $waiting_i$ and $using_i$ mean that process *i* is idle, waiting for and using the resource respectively. Here, the state *0* is the initial state. The *AP*s that are "True" in a specific state are expressed by a labeling function *L*. So, from the Figure 3 (b), we can find that $L(0) = \{ idle_1, idle_2\}$; $L(1) = \{ waiting_1, idle_2,\}$; $L(2) = \{ using_1, idle_2 \}$; $L(3) = \{ idle_1, waiting_2\}$; $L(4) = \{ idle_1, using_2\}$; $L(5) = \{ waiting_1, waiting_2 \}$; $L(6) = \{ using_2, waiting_1\}$; *and* $L(7) = \{ using_1, waiting_2 \}$. From this, we can make some assertions about a computation of the above graph. These are a) If at some stage process 1 is waiting then at some later stage it is using the resource (the path (1, 2) or (3, 4) or (5, 6, 7)); b) at no stage both processes are using the resource (all the states); c) If a process is waiting then it does so until it starts to use the resource (as in a)) and d) There is a stage at which both processes are waiting (5).

A computation in which 3, 5 and 7 are visited infinitely often but 4 and 6 are visited only finitely often is really unfair. So, it may be the case that the computation in the sequence 3, 5, 7, 3, 5, 7 … goes on infinitely. In this case, process2 never gets the access to the shared resource and as a result the formula $AG (waiting_2 \rightarrow AF (using_2))$ is "False". But we, of course want to see this formula "True" for the correctness of the design. To avoid such unwilling thing, we can put the constraints that any fair path must visit the any of the states got applying by the rule ($\sim waiting_2$ V $using_2$). This rule gives us all the states except (3, 5 and 7). Note that, it is clear from the graph that from the states 3, 5 and 7, if we want to hit any others states that must be visited; we have only to options either 4 or 6. In these two states, the process 2 gets the resource to use. So, it satisfies $AG (waiting_2 \rightarrow AF (using_2))$. For any design, we may need to add more than one *fairness constraints.* Here, we see the same problem if a computation goes infinitely often over the

path 0, 3, 4, 0, 3, 4 …or 0, 1, 2, 0, 1, 2…or 1, 5, 6, 1, 5, 6… . Here, we have just tried to narrate the necessity of *fairness* with example.

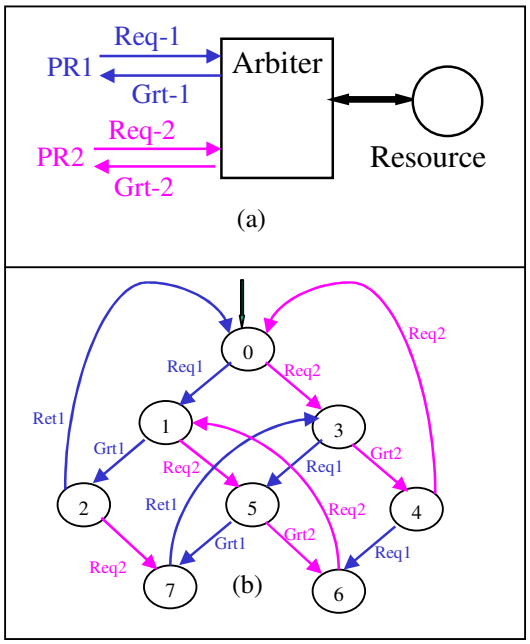

Figure 3 (a): Two processes use the shared resource using the arbiter; (b) the state transition graph

VIII. CASE STUDY

In this section we use the controller part of a simple processor, *SAYEH* and we verify this controller by standard *CTL*. The architecture of this processor is simple, but it has enough hardware for our work in formal verification and test and testability research. The processor has a 16-bit data bus and a 16-bit address bus. The processor has 8 and 16-bit instructions. Short instructions may contain shadow instructions, which effectively pack two such instructions into a 16-bit word.

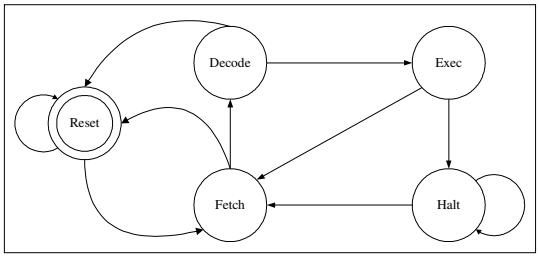

Figure 5: State machine of *SAYEH* Controller

The controller of *SAYEH* has five states*: reset, halt, fetch, decode,* and *exec*. External signals *ExternalReset* and *instruction* control transitions between states of this state machine. The state machine of *SAYEH* controller is shown in Fig. 5.

With *CTL*, all properties of this state machine are written. These properties are in three classes. With these three classes that are explained below, each state machine will be completely verified. The three classes are as follows:

The first class of properties should be checked for all states. This class is divided into three sets of properties: "There is no deadlock in any state". This property is expressed in ECTL as Equation 1.

$$AG((Pstate = S) \rightarrow EX(Pstate != S)) \quad \forall S \in \{reset, fetch, decode, exec\} \qquad (1)$$

"States are reachable from the initial state (reset)". This property is presented in ECTL as Equation 2.

$$AF(Pstate = S) \quad \forall S \in \{reset, fetch, decode, exec\} \qquad (2)$$

"Each state is reachable from any state". This property is shown in ECTL as Equation 3.

$$AG((Pstate = exec) \rightarrow EX(Pstate != reset)) \qquad (3)$$

The second class of properties is different from one state to another. In this class of properties *"immediate states after each states"* are checked. For example:

$$AG((Pstate = exec) \rightarrow EX(Pstate != reset)) \qquad (4)$$

The third class of properties is to check transitions between states with respect to the input signals and instructions. For example:

$$AG((Pstate = exec \ \& \ External\,\mathrm{Re}\,set = 1) \rightarrow AX(Pstate != reset)) \qquad (5)$$

IX. CONCLUSIONS

Formal verification replaces simulation in certain applications. For testing the correctness of a digital system that consists of FSMs verification is efficient and easy to use. This is an exact method and does not require test data. Model checking has many important advantages over the mechanical theorem provers or proof checkers for verification of the different hardware and protocols. In the cases like protocol design, network design and many others where it is more complex and expensive to check/test after the implementation, model checking can be brilliantly used in those cases to find the bug before the implementation. In model checking, CTL, an important family of *temporal logic* is effectively and increasing used to specify the properties of the model to be verified.

REFERENCES

1. E. M. Clarke, J. R. Burch, O. Grumberg, D. E. Long and K. L. McMillan, "Automatic verification of sequential circuit designs", Phil. Trans. R. Soc. Lond. A; pp. 105- 120. 1992.
2. E. M. Clarke, E. A. Emerson, and A. P. Sistla, "Automatic Verification of Finite-State Concurrent Systems Using Temporal Logic Specifications," in ACM Transitions on Programming Languages and Systems, 8(2), pp. 244–263, 1986.
3. Jerry R. Burch, M. Clarke, David E. Long, L. McMillan, David L. Dill, " Symbolic Model Checking for Sequential Circuit Verification", IEEE Transactions on Computer-Aided Design of Integrated Circuit and Systems; Vol. 13, No. 4, 1994.
4. Steve Easterbrook and Victor Petrovykh, "*Model-Checking over Multi-Valued Logics*", in *Proceedings of Formal Methods Europe (FME'01)*, March 2001
5. Michael Huth, "Logic in Computer Science: tool-based modeling and reasoning about systems", IEEE Session T1C; 2000.
6. E. M. Clarke, E. A. Emerson and A. P. Sistla, Automatic Verification of Finite-State Concurrent Systems Using Temporal Logic", ACM Transactions on Programming Languages and Systems, Vol. 8, No. 2, pp. 244-263, April 1986.
7. Edmund M. Clarke, Jr., Orna Grumberg and Doron A. Peled, "Book: "Model Checking", The MIT Press; Second printing 2000.

Undeniable Fair Electronic Auction

Yongyuth Permpoontanalarp and Montri Apiromvorakarn
Department of Computer Engineering, Faculty of Engineering
King Monkut's University of Technology Thonburi
126 Pracha-Utid Road, BangMod, Tung-Kru, Bangkok 10140, Thailand

***Abstract*- Fair e-auction is an e-auction which employs the fair exchange protocol. All existing approaches to fair e-auction achieve the fair exchange property between a single bidder and an auctioneer. But they do not offer the fair exchange between all bidders and an auctioneer. So, a malicious auctioneer can deny receiving bids from some legitimate bidders but do receive bids from conspired bidders. We propose a new fair e-auction protocol which provides the fair exchange for all bidders, called the undeniable fairness.**

I. INTRODUCTION

Many internet-based applications involve electronic exchange of information between senders and receivers, for example, e-mail, e-payment and e-auctions. E-auction involves the exchange of information between bidders and auctioneers. For example, after a bidder submits a bid to an auctioneer, the auctioneer will send back a bid receipt to the bidder. But, if one party behaves dishonestly, then the exchange becomes unfair to the other party. In particular, a malicious auctioneer may deny bids based on the bidders and amount, but receive bids from conspired bidders only. Thus, the conspired bidder can be the bid winner easily.

Fair e-auction is an e-auction which uses the fair exchange protocol. The fair exchange protocol (eg.[1,2,3,4,5,6,7]) allows both sender and receiver to exchange information such that either all of parties have the exchanged information or none of them do. There are three main approaches to fair exchange, depending on the use of a trusted third party (TTP). TTP is an additional infrastructure to mediate the exchange between a sender and a receiver. The first approach (eg. [1]) does not use TTP at all. The second approach (eg. [2,3]) uses online TTP to mediate the exchange. This approach is suitable for commercially practical use, but it has an additional cost on TTP. The third approach (eg. [4,5,6,7]) uses offline TTP, and is also called optimistic fair exchange. TTP is involved only when there is a dispute between sender and receiver.

All existing approaches to the fair exchange and fair e-auction achieve the fair exchange property between a single bidder (sender) and an auctioneer (receiver). But they do not offer the fair exchange between all bidders and an auctioneer. Thus, a malicious auctioneer can deny receiving bids from some bidders but do receive bids from conspired bidders. Note that the conspired bidders can intentionally reveal their identities to the auctioneer in some way when their bids are submitted. So, denied bidders will have much less chance to compete and are likely to be bid losers.

In this paper, we propose a new fair exchange protocol for e-auction which offers the undeniable fairness. The undeniable fairness means in addition to the usual fair exchange that an auctioneer cannot refuse to receive bids sent by any bidder. Moreover, we analyze the practicality of our new protocol for e-auction. Also, we consider open-bid e-auction only in this paper. A preliminary result of our work here is reported in [8].

II. RELATED WORKS

In the following, we discuss an online TTP approach. We use the following notations throughout the paper. Let *S, R*, *m* mean sender, receiver and message that *S* wants to exchange with *R*, respectively. $S \rightarrow R : M$ means that *S* sends *M* to *R*. $A_X(m)$ means public key encryption on message *m* by *X*'s public key, and $S_X(m)$ means *X*'s signature on message *m*. Also, *k(m)* stands for symmetric encryption of *m* by key *k*, and *h(m)* means hash of message *m*. $Mac_k(m)$ means message authentication code of message *m* by key *k*.

A. Abadi et. al.'s Approach [3]

Abadi et. al. presents an interesting fair exchange which uses online TTP in a minimal way. In particular, TTP does not store state information during the exchange. The following presents their simplified version.

1. $S \rightarrow R$: $k(m), A_{TTP}(k, S, R, h(k(m)))$
2. $R \rightarrow TTP$: $A_{TTP}(k, S, R, h(k(m))), h(k(m))$
3. $TTP \rightarrow R$: $h(k(m)), k$
4. $TTP \rightarrow S$: $S_{TTP}(A_{TTP}(k, S, R, h(k(m))))$

In step (2), *R* sends *h(k(m))* computed from *k(m)* in step (1). After step (2), TTP compares *h(k(m))* with *h(k(m))* in $A_{TTP}(k, S, R, h(k(m)))$ to verify that *R* gets the correct *k(m)* before issuing decryption key *k* in step (3). In step (4), TTP sends a receipt to *S* on behalf of *R*.

Again, malicious *R* can deny receiving message from legitimate *S* by not performing step 2. As a result, no exchange can be taken place.

III. UNDENIABLE FAIRNESS

Definition 1 Undeniable Fair e-auction
The undeniable fair e-auction means that

1. Either both a bidder and an auctioneer have exchanged information or none of them do, and
2. An auctioneer cannot deny receiving bids sent by any bidder by ignoring to participate into an agreed message-exchange protocol with the bidder. □

While (1) means the fair exchange between one bidder and one auctioneer, (2) deals with the fair exchange between all

bidders and one auctioneer. The undeniable fairness is also called the fairness for all bidders.

Our system provides the undeniable fairness in a loose sense in that if an auctioneer has denied receiving bids from some bidders, then soon the auctioneer will not be able to receive any further bids from any bidders. Thus, to always offer the bidding service to all bidders the auctioneer will have to receive all submitted bids. The strict undeniable fairness would require a sequential bid receiving because an undeniable fair auctioneer must read bid as soon as the bid arrives. In other words, the sequential bid receiving for all bids ensures the undeniable fairness. But our undeniable fair exchange system offers a more flexible bid reading in that an auctioneer can read bids in a non-sequential order.

Our system uses TTP to mediate the exchange between a bidder and an auctioneer. Before an auctioneer can read a bid message sent to her, the auctioneer has to obtain a key and an approval from TTP. TTP provides a reading queue of sent but unread bid messages for an auctioneer. To constrain bid receiving by auctioneer, TTP specifies a window of receivable bids in the reading queue. Only messages in the window can be read by the auctioneer and they can be read in any order. The window can be slid in forward direction across only messages that have been already read. If message at the leftmost of the window is not read, then the window cannot be slid. So, no additional messages can be read.

The size of windows is important since it indicates the trade-off between the flexibility for bid reading and the undeniable fairness. If the window is wide, then the auctioneer has a great flexibility to read any bid messages in the window. But the undeniable fairness is weak since the auctioneer can still read many other bids while denying reading some bid in the wide window. However, if the window is small, then the flexibility is decreased but the undeniable fairness is strong.

The size of the window should be adjustable dynamically as the bidding proceeds. If the system is highly fair for all bidders, then the window should be wide to allow for flexible reading. But if the system is not undeniably fair, then the window should be small to regain the fairness.

IV. UNDENIABLE FAIR E-AUCTION PROTOCOL

Our protocol is based on Abadi et. al.'s approach [3]. The protocol consists of two parts, namely basic protocol and dispute resolution protocol. Basic protocol describes steps used for exchanging messages between sender and receiver. However, dispute resolution protocol is used when there is a dispute occurring between bidder and auctioneer.

A. Basic Notations

1) $Q(R)$ = a unique running sequence number (called the bid number) generated by TTP for each bid that any bidder requests to send to auctioneer R
2) $Min_Q(R)$ = the smallest bid number of unread bid in R's reading queue (ie. the earliest unread bid in the queue)
3) $W(R)$ = receiver R's window
4) TS = the total number of sent bids by a bidder to an auctioneer
5) TR = the total number of received bids by an auctioneer
6) $Ratio_{fair}$ (a system parameter) = TR/TS where $TR \leq TS$
7) S_{all} = the set of all bidders' identities

B. Basic Assumptions

We assume that only TTP has a pair of private and public keys. All bidders and auctioneers have TTP's public key. Also, each bidder and each auctioneer have share keys with TTP, namely k_s and k_r, respectively. Moreover, TTP is trusted on all aspects, but both bidders and auctioneers are not trusted.

C. Basic Protocol

Before a bidder can send a bid to an auctioneer, the bidder must submit a request to TTP for a sending ticket. The ticket contains necessary information for the auctioneer to read the bid. Then, the bidder sends both ticket and encrypted bid to the auctioneer. To read the encrypted bid, the auctioneer requests the key from TTP. After TTP issues the key to the auctioneer, TTP sends out the receipt of the bid to the bidder.

TTP provides for each auctioneer R a reading queue of bids sent to R by any bidder. Bids in the reading queue are ordered according to their sending requests to TTP. When R requests to read a bid in the queue, TTP computes a range of receivable bids in the queue that are allowed to read by R.

Initially, $W(R)$=1

1) Bidder S sends an authenticated request for ticket to TTP.
$S \rightarrow TTP : S, R, h(k(m)), Mac_{ks}(S, R, h(k(m)))$
2) TTP issues a signed ticket to bidder.
$TTP \rightarrow S : S_{TTP}(Q(R), h(k(m)))$

$Q(R)$ is the bid number for m that S wants to send to R. The ticket consists of $Q(R)$ and $h(k(m))$.

3) The bidder sends the signed ticket, encrypted message and encrypted key to the auctioneer R.
$S \rightarrow R : S_{TTP}(Q(R), h(k(m))), k(m), A_{TTP}(k, S, R, h(k(m)))$

R can verify the validity of TTP's signature in the ticket, and verify that the ticket is for the encrypted bid $k(m)$.

4) The auctioneer requests from TTP the decryption key k to read bid m.
$R \rightarrow TTP : S_{TTP}(Q(R), h(k(m))), A_{TTP}(k, S, R, h(k(m))), h(k(m)), Mac_{kr}(h(k(m)))$

Then, TTP verifies its own signature in the ticket and verifies that the ticket corresponds with the encrypted key. Also, TTP verifies that the request is actually from R and that R received the correct $k(m)$.

5) TTP checks if R is currently allowed to read m.
If $Min_Q(R) \leq Q(R) \leq Min_Q(R)+W(R)$, then
$TTP \rightarrow R : h(k(m)), k_r(k)$
Else
$TTP \rightarrow R : S_{TTP}(\text{"Request is refused"})$
Go to step 4)

TTP allows R to read m if m is in R's window on bids in the reading queue.

6) TTP sends an evidential receipt of bid m by R to the bidder S.
$TTP \rightarrow S : S_{TTP}(A_{TTP}(k, S, R, h(k(m))))$

TTP certifies that TTP has released the decryption key for $A_{TTP}(k, S, R, h(k(m)))$. S can use this receipt with $k(m)$ to prove to a third party with the help of TTP that R has received m.

V. CALCULATION OF WINDOW SIZE

Definition 2 The system is fair for all bidders and auctioneer R if and only if $\frac{\sum_{S1 \in S_{all}} TR(S1, R)}{\sum_{S2 \in S_{all}} TS(S2, R)} \geq Ratio_{fair}$ where $TS(S,R)$ and $TR(S,R)$ mean the total number of sent and received bids, respectively, between S and R. □

Suppose that there are bidder S and auctioneer R such that $TR(S,R)_{period(S,R)}/TS(S,R)_{iperiod(S,R)} < Ratio_{fair}$. We call R as an unfair auctioneer and S as an unfairly treated bidder.

Indeed, $Ratio_{fair}$ defines an acceptable degree of the fairness for all bidders. If $Ratio_{fair}$ is large (ie. TR is closed to TS), then it results in a strict kind of bid receiving in that many submitted bids must be received by auctioneers soon after the bids are sent. However, with a large $Ratio_{fair}$, the system provides a stronger level of fairness due to the large TR. If more number of bid messages is received, then less number of bid messages can be denied.

The following algorithm generates a new window size $W(R)$ from an input window size $W'(R)$. The algorithm is involved in step (5) of the basic protocol.

Algorithm 1 Window Computation for auctioneer R
Input: $W'(R)$, $TR(S,R)$ and $TS(S,R)$ for all bidders S
Output: $W(R)$: positive integer
If the system is fair for all bidders and auctioneer R, then

$$W(R) = \lceil Ratio_{fair} \times TS_C(R) \rceil$$

where $TS_C(R)$ is the number of currently unread bids in R's reading queue
Else /* unfair for all senders */
If $UF\%(R) < T(UF\%)$ and $0 < W'(R)$ then

$$W(R) = \left\lceil W'(R) - (W'(R) \times \frac{UF\%(R)}{T(UF\%)}) \right\rceil$$

Else $W(R) = 1$
where $W'(R)$ is the last $W(R)$ when the system is fair at the last time but if the system has never been fair, then $W'(R)=1$, $S_{UF}(R)$ is the set of all unfairly treated bidders by auctioneer R, $T(UF\%)$ is the threshold of the highest acceptable degree of the unfairness in percentage and $UF\%(R)$ is the current degree of the unfairness by R in percentage which is defined by the following:

$$n = \frac{\sum_{j1 \in S_{UF}(R)} TR(j1, R)}{\sum_{j2 \in S_{UF}(R)} TS(j2, R)}, \quad UF\%(R) = 100 - (\frac{n}{Ratio_{fair}} \times 100\%)$$ □

Our method for window reduction is to reduce the window size according to the degree of the unfairness occurred. The higher the degree of the unfairness occurs, the more reduction the window size is. $UF\%(R)$ is compared with $T(UF\%)$ to reduce the window. A larger $Ratio_{fair}$ produces faster window reduction. As a result of the fast window reduction, the severity of the unfairness is low since the amount of bids that can be read by an unfair auctioneer during the unfairness is small.

VI. DISPUTE RESOLUTION PROTOCOL

Dispute resolution protocol is used when there is a dispute between bidder and auctioneer. For example, R may claim that she does not receive an encrypted bid in step (3) of the basic protocol for a bid message number $Q(R)$. As a result, R's window cannot be slid over $Q(R)$. In such case, R may engage in a dispute resolution protocol to provide a pre-committed receipt of bid message number $Q(R)$.

7) $R \rightarrow TTP : S_R(R, Q(R))$
8) $TTP \rightarrow R$: ok
9) $TTP \rightarrow S$: "Q(R) is pre-committed"

After (7), TTP will treat message number $Q(R)$ as if it has been read by R. And S can resolve the dispute by contacting TTP. In such case, TTP may act as a mediator for the actual message exchange. Note that here we show the use of auctioneer's private key, but other message authentication methods, for example MAC or passwords are allowed.

VII. ANALYSIS

We apply our protocol to a case study in e-auction. In our case study, bidders submit their bids on round basis. In each round, all losing bidders from the previous round submit their bids. After that, the auctioneer will read all those submitted bids and announce the round winner. Assume that there is only one round winner. There are two consecutive phases for the bidding where the second phase stands for a final period of bidding times (eg. last 30 minutes). The second phase requires stronger undeniable fairness than the first phase since the unfairness in the second has a direct effect on a bid winner.

In the first phase, there are 10 rounds. Let i be the number of bidders taking part in the second phase. Assume that there are $2i$ rounds in the second phase. Assume that there are 30 bidders in the first phase and 15 bidders in the second phase. In the first phase, $Ratio_{fair}$ is set to 50% and it is increased at the beginning of the second phase and becomes 100% at the middle of the second phase. The increment of $Ratio_{fair}$ prevents the auctioneer to behave unfairly to all bidders in the second phase. Also, $T(UF\%)$ is set to 50%.

First, we shall discuss the first phase. Figure 1 shows the change of $W(R)$ in the first round when all bids are submitted and the auctioneer starts to read (TS=30 and TR=1…30). Initially, the system is not fair, so $W(R)$ is 1. When TR=15, the system becomes fair (so $W(R)$ = 8) and then the auctioneer gets the flexibility for bid reading. After that, $W(R)$ is decreased toward 0 because $TS_C(R)$ is reducing. Figure 2 shows $W(R)$ in the second round. Initially, the system is fair and then the auctioneer gets the flexibility. Later, as $TS_C(R)$ is reducing, $W(R)$ is decreasing. All other rounds are similar to the second round.

Figure 3 shows the 1st round of the second phase. The size of $W(R)$ here is smaller than that in the first phase since only 15 bidders take part. $Ratio_{fair}$ is increasing towards 100%. At the 16th round of the 2nd phase, $Ratio_{fair}$ becomes 100%. So, from the 16th round onwards, $W(R)$ is mostly 1.

Now, we discuss the unfairness case. Suppose that in the first round of the first phase, bidders submit their bids more than expected. Thus, the system will be unfair and the window

should be reduced. Figure 4 shows the window reduction in the second round (*TR*=30) when *TS* is increasing towards 150 and *T(UF%)=50%. W(R)* is started to reduce from 15 at *TS*=61 and becomes 1 at *TS*=113. Thus, even though the number of submitted bids is more than the expected number (ie. 30) for a round, the auctioneer cannot process those excessive bids due to the reduction of *W(R)*. In other words, *W(R)* must not be more than 30. Otherwise, the auctioneer can read submitted bids on the next round while denying reading some bids on a current round.

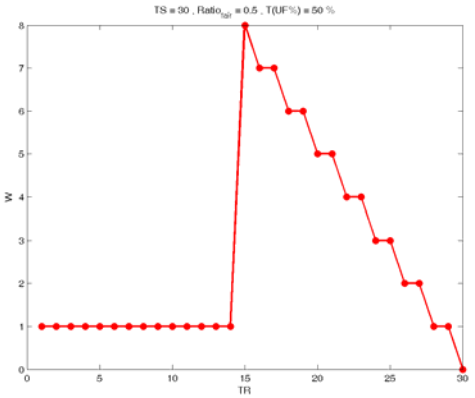

Figure 1. Window size in the 1st round of phase 1

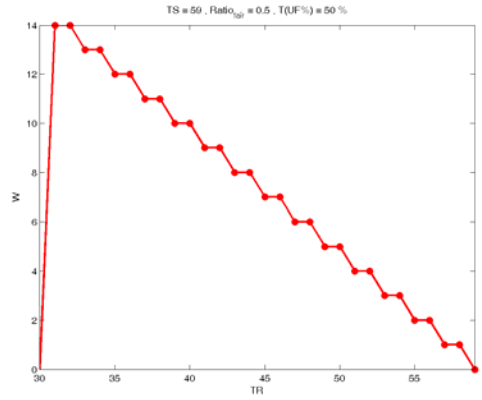

Figure 2. Window size in the 2nd round of phase 1

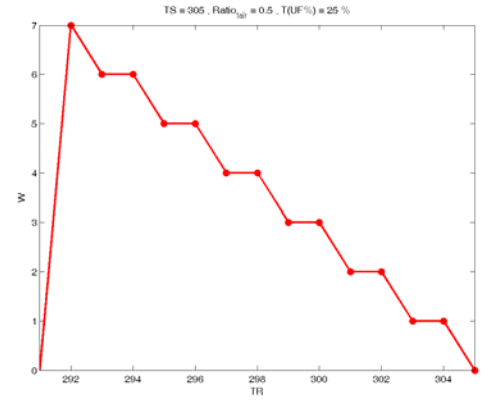

Figure 3. Window size in the 1st round of phase 2

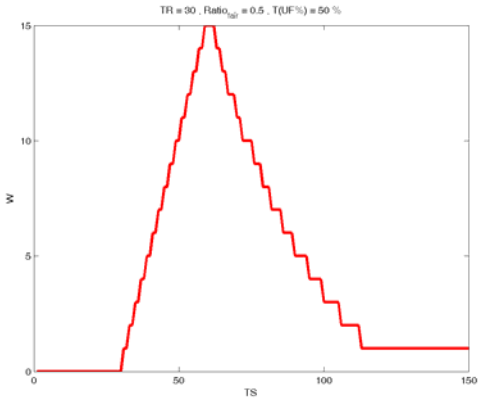

Figure 4. Window reduction during the unfairness

Our window reduction works fine if the amount of *TS* can be restricted. Without the restriction, when *TS* and *TR* are very large, *W(R)* can be much greater than the expected number of bids in a round. Due to space limit, our protocol presented here does not restrict *TS*. But our extended protocol to restrict *TS* is presented in [9] where it can also prevent the denial of service attack on the number of submitted bids in each round.

VIII. CONCLUSION

In this paper, we present a new fair e-auction which offers the undeniable fairness. The undeniable fairness is achieved by using $Ratio_{fair}$ and the window mechanism to constraint message receiving. Also, we have applied our protocol to a case study. The result looks promising. As a future work, we aim to apply our undeniable fair protocol to other applications.

ACKNOWLEDGMENT

We would like to thank anonymous reviewers for their comments. The first author would like to acknowledge support from the National Research Council of Thailand.

REFERENCES

[1] S. Even, O. Goldreich and A. Lempel, A randomized protocol for signing contracts, *Communications of the ACM*, 28(6), pp.637-647, 1985.

[2] R.H. Deng, L. Gong, A.A.Lazar and W. Wang, Practical protocols for certified electronic mail, *J. of Network and Systems Management*, 3(4), pp. 279-297, 1996.

[3] M. Abadi, N. Glew, B. Horne and B. Pinkas, Certified Email with a Light On-line Trusted Third Party: Design and Implementation, In Proc. of World Wide Web Conference, ACM, pp. 387-395, 2002.

[4] N. Asokan, V. Shoup and M. Waidner, Optimistic Fair Exchange of Digital Signatures, *IEEE Journal of Selected Areas in Communications*, 18(4), pp. 591-606, 2000.

[5] S. Micali, Simple and Fast Optimistic Protocols for Fair Electronic Exchange, In Proc. of ACM symposium of Principles of Distributed Computing, ACM, pp. 12-19, 2003.

[6] S.Gurgens, C. Rudolph and H.Vogt, On the security of fair non-repudiation protocols, *International Journal of Information Security*, 4(4), pp. 253-262, 2005.

[7] G. Wang, Generic Non-Repudiation Protocols Supporting Transparent Offline TTP, *Journal of Computer Security*, 14(5): 441-467, 2006.

[8] M. Apiromvorakarn and Y. Permpoontanalarp, Undeniable Fair Exchange, In Proceedings of the 6th WSEAS International Conference on Multimedia, Internet & Video Technologies, Lisbon, Portugal, 2006.

[9] M. Apiromvorakarn, Undeniable Fair Exchange, *M.Eng Thesis*, King Mongkut's University of Technology Thonburi, Thailand, 2006.

A Cost Model for Bitmap Index Partition Techniques

Manlika Honghirun, Songrit Maneewongvatana
Department of Computer Engineering
King Mongkut's University of Technology Thonburi

***Abstract*- Bitmap indexes are efficient for online analytical processing (OLAP) applications and decision support systems that involve complex queries. They use a single bit in each key value instead of a list of row identifiers to indicate the specific value of data. The vital benefit of bitmap index is that Boolean operations can be easily manipulated on the bitmap strings. However, many scientific applications usually operate on floating point numbers and simple bitmap index scheme would generate too many bitmaps. The issue of using bitmap indexes in high cardinality attributes can be solved by assigning a bitmap to cover an interval of attribute values. This method requires partitioning of the attribute domain. We present the cost model for predicting the performance of two bitmap indexes partition techniques. The first technique called equal density of bitmap index partition technique and the second is equal interval of bitmap index partition technique. We verify our analytical results by a detailed experimental study and imply the suitable bitmap index partition technique for certain data and query distributions.**

I. INTRODUCTION

An index is a feature in a database allowing rapid access to some associated data in a table. It can improve performance of queries but it may decrease the performance on updates. In traditional indexing techniques, most DBMSes use B-tree or its variants as an index structure [5]. However, B-tree is not suitable for some systems such as online analytical processing (OLAP) or decision support system (DSS) due to the nature of operations on database which consists of a lot of complex queries and very few updates.

Bitmap index is another type of index that is particularly useful in the above applications. It uses only single bit for each key value instead of a list of row identifiers. The associated bit is set if and only if the record's value fulfils the property in focus. Since, the values are now bit, Boolean operations can be easily manipulated on the bitmap string. Moreover, Building and maintaining bitmap indexes usually costs less time and space for attributes with limited number of values (low cardinality). One major problem of simple bitmap indexes is that it cannot handle high cardinality domains effectively. This problem can be solved by assigning a bitmap to cover an interval of attribute values [3]. Bitmap partition techniques would determine proper intervals that each bitmap covers.

In this paper, we focus on the equal density and equal interval partitioning techniques for bitmap indexes when the attributes have high cardinality. We propose a simple yet accurate cost model for predicting the performance of two bitmap indexes partition techniques.

II. RELATED WORKS

Several database vendors including Oracle, Red Brick Systems, and Sybase have the introduced bitmap indexing to support complex query applications and application that support multidimensional analysis [1, 3, 5, 6, 7].

A detailed discussion on designing bitmap indices based on different encoding schemes is presented in [6]. In particular, space and time complexities are evaluated for multi-component indexed and each of these encoding schemes is suitable for different types of queries. In [1], an encoded bitmap indexing for data warehouses is presented. The domain of the indexed attribute is encoded by the mapping. It solves the problems of sparsity, at the same time, improves the space utilization and shortens the maintenance and processing range searches. In scientific data communities, the common attributes are non-discrete [7]. Wu and Buchmann presented an algorithm for processing one-sided range queries called GenericRangeEval and studied analytically and experimentally the performance behavior of multi-dimensional queries. A related task of finding an optimal partition with respect to data and query distribution is proposed in [3]. Typically, Bitmap is used for low cardinality attributes since the overall space requirement depends on the cardinality attributes. For high cardinality attributes, partitioning technique of associating a range of continuous values to a single bitmap is generally applied to reduce the space requirement [4]. Existing partition techniques include equal interval and equal density partition. In [2], the authors presented the techniques on partitioning the attributed domain into intervals for a bitmap that minimize candidate check cost, which is the cost of verifying whether candidate records satisfy the condition in the query or not.

III. BITMAP INDEXES PARTITION TECHNIQUES

The goal of partitioning is to dividing the attribute domain into k disjoint intervals. Each interval corresponds to a bitmap.

Let $\{L_i, U_i\}$ denote an interval I_i of data set, where $1 \le i \le k$, L_i is the lower boundary and U_i is the upper boundary interval i. The length of interval in interval i equal to U_i - L_i

$$I_i = U_i - L_i \quad (1)$$

A. *Equal Interval Partition Technique (E.I.)*

This technique partitions attribute domain so that each interval has the same length. If the data set is random, the numbers of data records in all intervals are roughly the same. In the other hand, if the data are clustered, the numbers of data records in all intervals can be very different and depend on the data distribution.

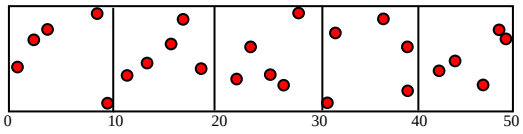

Figure 1. An example of equal interval partition technique
(Assume the data distribution is uniform)

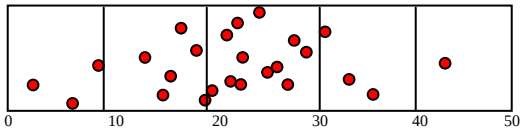

Figure 2. An example of equal interval partition technique
(Assume the data distribution is not uniform)

B. *Equal Density Partition Technique (E.D.)*

For non-uniform data distributions, equal interval partitioning is not suitable because the density of data records will be different (shown in Fig. 2). Some intervals may have a lot of data records while some have much fewer. If the high density interval is used during candidate check process, the cost would be rather high. This problem can be solved by the equal density partition technique which tries to partition each interval to the roughly same number of data records.

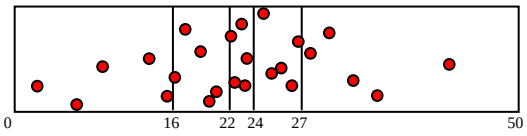

Figure 3. An example of equal density partition technique
(Assume the data distribution is not uniform)

IV. THE COST MODEL

A. *Candidate Check Cost*

To answer the query, the records that fall into specific intervals must be checked to make sure that they really satisfy the query condition. The candidate check cost (C_c) which dominates the query time [6] consists of the *candidate interval cost* and *candidate record cost*. The candidate interval cost is required to locate the desired intervals. The candidate record cost is proportional to the number of records falling into the interval.

Fig. 4 explains the candidate check cost (C_c) by means of an example. An attribute domain X with eight records is partitioned into five intervals. The first column lists the X value of each record. Assume the query X= 13, the answer would be in interval I_2 which has the range [10,20) and it has two candidate records 18 and 13 which the bit equal to 1. However, only the last record is a true match. All candidates must be checked during candidate record check.

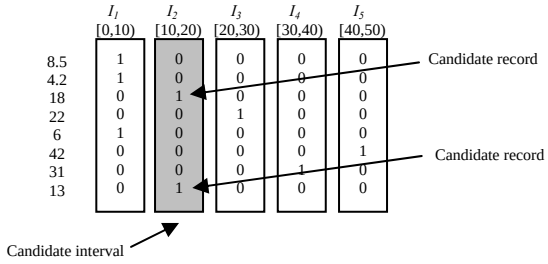

Figure 4. The candidate record cost and candidate interval cost of equal interval partition technique

In this paper, we verify our analytical results by a detailed experimental study and consider only normal and uniform distribution. The probability density functions are as the follow,

$$f(x) = \frac{1}{\sigma\sqrt{2\pi}} e^{-\frac{1}{2}\left(\frac{x-\mu}{\sigma}\right)^2} \quad \text{For} \quad -\infty < x < \infty \qquad (2)$$

$$f(x) = \begin{cases} \dfrac{1}{b-a} & \text{For } a < x < b, \\ 0 & \text{For } x < a \text{ or } x > b, \\ \dfrac{1}{2(b-a)} & \text{For } x = a \text{ or } x = b \end{cases} \qquad (3)$$

Equations in (2) and (3) are the probability density function of normal distribution and uniform distribution respectively.

The distribution function is denoted by

$$\int_{-\infty}^{\infty} f(x)dx = 1 \qquad (4)$$

The following is the probability of data records to appear in interval i:

$$p_i = \int_{L_i}^{U_i} f(x)dx \qquad (5)$$

Assume the number of data records equals to n. For equal density partition technique, the number of data records in each interval equals to n/k, the probability of data that fall in each interval equals to $1/k$.

For equal interval partition technique, each interval has the same length of interval. Therefore, we know the certain L_i and U_i and can calculate the number of data records that appear in each interval (r_i).

$$r_i = p_i * n \qquad (6)$$

The followings are the candidate record cost and the candidate interval cost

$$\text{Candidate record cost} = \sum(r_r p_r) \qquad (7)$$

$$\text{Candidate interval cost} = \sum(I_r p_r) \qquad (8)$$

Therefore, the candidate check cost is

$$\text{Candidate check cost } (C_c) = \sum(r_r p_r) + \sum(I_r p_r) \quad (9)$$

Where r_r = number of data records in range r of query
p_r = probability of data retrieval in range r of query
I_r = number of intervals scans in range r of query

B. Disk Access Cost

The candidate check cost can partially predict the performance of two bitmap index partition techniques. In typically situations, the data set is too large to fit in memory and it requires massive amount of storage. Therefore, the cost model needs to add the cost of storage or disk access cost. We can hypothetically divided data records and bitmap indexes into two classes: active and inactive. Active records and corresponding indexes are placed in buffer space in RAM. Inactive portions are stored in hard disk and need to be fetched if once required. Disk access cost would be added to our cost model when bitmap indexes of data retrieval are not in buffer and we need to access bitmap indexes in the disk storage. We define the disk access cost (C_d) of bitmap index partition technique as the follow,

$$\text{Disk access cost } (C_d) = \sum_{i=1}^{n} \left((1 - p_{q_i}) \times n_{q_i} \right) \quad (10)$$

Where p_{q_i} is the probability of queries fall in interval i of data record or the probability of bitmap indexes are in memory and n_{q_i} = Number of queries that fall in interval i of data record.

C. Cost Model for Predicting the Performance of Bitmap Indexes Partition Techniques

From above, we can define the overall cost model for predicting the performance of bitmap indexes partition techniques:

$$\text{Total Cost } (C_t) = P_d C_c + P_b C_d \quad (11)$$

Where P_d = The percentage of data records which could be contained in disk
P_b = The percentage of bitmap indexes which could be contained in disk
C_c = Candidate check cost
C_d = Disk access cost

V. PERFORMANCE OF BITMAP INDEX PARTITION TECHNIQUES

We perform detailed experiments, to predict and compare the performance of two bitmap index partition techniques. We consider only normal and uniform distributes for data and query distributions. The main assumptions are as follow,

1) *Data and Query Distribution are normal.*
2) *Data Distribution is normal and Query Distribution is Uniform.*

We ignore the case when the data distribution is uniform because the records that fall into specific intervals are roughly the same. Even queries fall into different intervals, the number of data records to be scanned is roughly the same.

The experiments are parameterized with the cover conditions between data set and queries. When data and query distributions are normal, it covers 6 possible conditions.

TABLE I
THE CONDITIONS FOR DATA AND QUERY DISTRIBUTION ARE NORMAL

Conditions					
No.	Means	S.D.	No.	Means	S.D.
1	$\mu_q = \mu_d$	$\sigma_q = \sigma_d$	4	$\mu_q < \mu_d$	$\sigma_q = \sigma_d$
2	$\mu_q = \mu_d$	$\sigma_q < \sigma_d$	5	$\mu_q < \mu_d$	$\sigma_q < \sigma_d$
3	$\mu_q = \mu_d$	$\sigma_q > \sigma_d$	6	$\mu_q < \mu_d$	$\sigma_q > \sigma_d$

From Table I μ_d and μ_q are the means of data set and queries respectively. σ_d and σ_q are the standard deviation of data set and queries respectively.

If data distribution is normal and query distribution is uniform, we consider only the means of data set and queries. It covers 3 conditions: condition 1 is $\mu_q = \mu_d$, condition 2 is $\mu_q < \mu_d$, condition 3 is $\mu_q > \mu_d$.

A. Compare the Candidate Check Cost

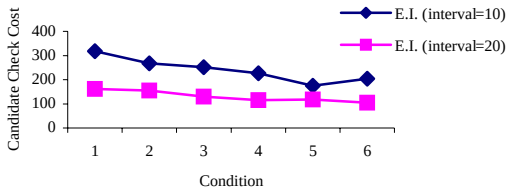

Figure 5. The candidate check cost of equal interval partition technique

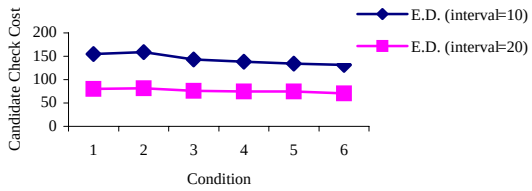

Figure 6. The candidate check cost of equal density partition technique

Fig. 5 and Fig. 6 show the comparison of the candidate check cost when the number of intervals equal to 10 and 20. The number of intervals of data record affects to the candidate check cost. Intuitively, larger number of intervals gives smaller candidate check cost. Similarly, when data distribution is normal and query distribution is uniform, the same behavior applies. Then, considering the candidate check cost between E.I. and E.D. At the same number of intervals E.D. give the less candidate check cost. However, this candidate cost is not the whole cost. It excludes the disk access cost which would be added to our total cost when the number of intervals increases. Therefore, we need to trade off between candidate check cost and disk access cost.

B. *Compare the Disk Access Cost*

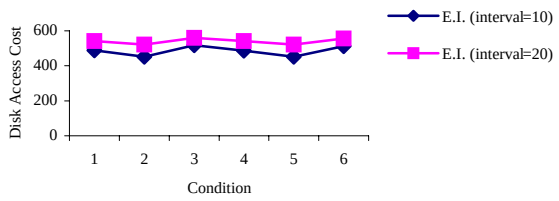

Figure 7. The disk access cost of equal interval partition technique

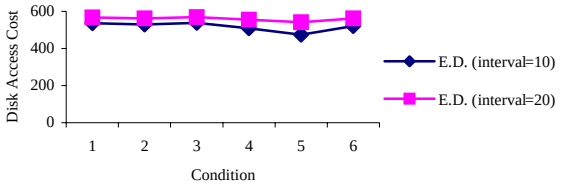

Figure 8. The disk access cost of equal density partition technique

Fig. 7 and Fig. 8 are the comparison of the disk access cost when the number of intervals equal to 10 and 20. The disk access costs increase when the number of intervals increases because the increasing of number of intervals requires massive amount of storage. If data distribution is normal and query distribution is uniform, the disk access costs are similarly to data and query distributions are normal. At the same number of intervals E.I. gives the less disk access cost. However, the feature of today's common memory technology is rapid developed and tends to be low-cost of high performance storage such as RAM. If high performance storage is cheap, increasing memory can decrease the disk access cost.

C. *Compare the Total Cost*

TABLE II
THE TOTAL COST OF EQUAL INTERVAL PARTITION TECHNIQUE

Condition	P_b =10%	P_b =20%	P_b =50%	P_b =80%
1	335.1076	383.9751	530.5778	677.1805
2	285.8723	331.1226	466.8735	602.6244
3	278.0062	329.7893	485.1388	640.4882
4	252.2186	300.958	447.1761	593.3943
5	202.2957	247.4028	382.724	518.0453
6	235.3191	286.5013	440.0478	593.5944

TABLE III
THE TOTAL COST OF EQUAL DENSITY PARTITION TECHNIQUE

Condition	P_b =10%	P_b =20%	P_b =50%	P_b =80%
1	193.0005	246.6622	407.6472	568.6323
2	195.9168	248.8335	407.5839	566.3342
3	182.5854	236.375	397.7437	559.1124
4	175.1335	225.9802	378.5205	531.0607
5	168.4384	215.8452	358.0658	500.2864
6	170.4524	222.5958	379.0262	535.4565

Tables II and III show the total cost of E.I. and E.D. with the different percentage of bitmap indexes which contained in disk (P_b) and the percentage of data record which contained in disk (P_d) equal to 90%. The total costs of E.D. less than the total costs of E.I. for all conditions and its increase when P_b increases. For data distribution is normal and query distribution is uniform, the total costs are similarly to data and query distributions are normal. Thus, the performance or the capacity of memory affects to the performance of two bitmap index partition techniques.

VI. CONCLUSION AND FUTURE WORK

We proposed a simple cost model for predicting the performance of two bitmap index partition techniques (equal density and equal interval partition technique). The candidate check cost and disk access cost are added in our cost model.

If data and query distributions are normal or data distribution is normal and query distribution is uniform, equal density partition technique is more efficient than equal interval partition technique. In a very high performance or capacity of storage (memory and disk) situation, the disk access cost literal affects to the performance of bitmap indexes partition techniques and may be equal to 0. Thus, our cost has only the candidate check cost and we can partition bitmap indexes in a highly number of intervals to reduce the candidate check cost. However, in general situation the partitioning bitmap index is important. We need to trade off between the candidate check cost and disk access cost. If the number of intervals increases, the candidate check cost will be decreased, but the disk access cost also increased, too.

For future work, we aim to improve the cost model for two bitmap index partition techniques by adding other dynamic factors in multi-database system environment such as CPU load, local CPU speed, etc. which affect the performance of retrieval data record. Then, our experiments will work with the real data set and queries.

REFERENCES

[1] Chan, C.-Y. and Ioannidis, Y., 1999, "An Efficient Bitmaps Encoding Scheme for Selection Querirs", *International Conference On Management of Data*, pp. 215-226.

[2] Chan, C.-Y. and Ioannidis, Y., 1999, "Bitmap Index Design and Evaluation", *International Conference On Management of Data*, pp. 355-366.

[3] Koudas, N., 2000, "Space Efficient Bitmap Indexing", *The Ninth International Conference on Information Knowledge Management CIKM*, McLean,VA USA, pp. 194–201.

[4] Maneewongvatana, S., 2003, "Bitmap Index Partition Techniques for Continuous and High Cardinality Discrete Attributes", *International Conference on Intelligent Technologies*, pp. 643-650.

[5] O'Neil, P. and Quass, D., 1997, "Improved Query Performance with Variant indexes", *International Conference On Management of Data*, pp. 38-49.

[6] Stockinger, K., 2001, "Design and Implementation of Bitmap Indices for Scientific Data", *International Database Engineering and Application Symposium*, pp. 47-57.

[7] Wu, M.-C. and Buchmann, A., 1998, "Encoding Bitmap Indices for Data Warehouses", *The 14th IEEE International Conference Data Engineering*, pp. 220-230.

Towards Evolvable Safety Arguments

Paul Mason & Chadchai Mattayom
Shinawatra University, Shinawatra Tower III, Viphavadi Road, Bangkok, Thailand

***Abstract*-Most safety critical systems must be certified before entering service. This normally involves submission to the industry regulator of a safety case (a reasoned argument and supporting evidence) that the system is acceptably safe to operate.**

The 'traditional' safety case is presented as a linear document. However, the level of detail often obscures the arguments presented so graphical notations have been developed to improve scrutability. Effective as these are, they lack means of representing evolution (i.e., changes) to an argument. This paper therefore extends one such notation to better manage safety case evolution.

I. INTRODUCTION

Safety critical systems must normally be certified before entering service. Typically, this involves submission to the appropriate regulatory body (e.g., the Civil Aviation Authority) of a safety case, a reasoned argument with supporting evidence that the system is acceptably safe to operate.

'Traditional' safety cases are presented as a linear document. They can run to several volumes (with hundreds of cross-references) so making sense of a body of arguments and evidence on this scale can be extremely difficult. Graphical notations have therefore been developed to improve their structure and scrutability. Examples include ASCAD (Adelard Safety Case Development) [1], and GSN (Goal Structuring Notation) [2].

While popular, such techniques lack means of representing changes to an argument. For example, an in-service 'safety incident' may invalidate the evidence on which an argument was originally based. Moreover, commercial forces dictate that the systems themselves must evolve. Put simply, the cost of incorporating multiple redundancies and in-built diagnostics that help critical systems meet stringent safety and reliability requirements mean developers strive to extend their 'shelf-life' through periodic revisions incorporating appropriate technological advances. Hence, just as the systems themselves change, so must their safety cases.

This paper introduces an approach (with tool support) which extends GSN (arguably the best known graphical safety argument notation) to better manage revisions to safety cases.

The rest of the paper is organized as follows. Section two provides an overview of Goal Structure Notation, as well as configuration management models with potential for managing their evolution. Section three introduces modifications to GSN based on these models to enable versioning of safety cases which is illustrated in Section four. Section five offers some conclusions.

II. FOUNDATIONS

This section introduces the foundations for our work, and sets out the contribution of the paper. Two aspects are considered, means of structuring safety cases, and means of managing their evolution.

A. Structuring Safety Cases Using GSN

The 'spine' of a goal structure has three core elements: i) *goals* (denoted as rectangles), constraints on the target system or its development process (note goals can be decomposed into sub-goals); ii) *strategies* (denoted as parallelograms) - courses of action for achieving a goal; and iii) *solutions* (denoted as circles) - pieces of analysis or evidence.

Additional elements can be added to provide *context*, e.g., operational conditions (denoted as rounded corner rectangles); and strategies often need some *justification* or are based on some *assumption* (denoted as ellipses) – see Figure 1.

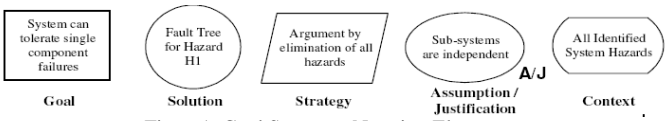

Figure1. Goal Structure Notation Elements

B. Managing Safety Case Evolution

This aspect of our work draws on software configuration management (SCM) theory, the discipline of managing the evolution of complex software systems. SCM helps developers perform coordinated changes to software by accurately recording the composition of versioned software products, thus enabling their evolution as revisions and variants, while maintaining consistency between interdependent components [3].

We can adapt this perspective to the safety case domain as performing coordinated changes to safety cases (reflecting changes to the systems they describe), by accurately recording the composition of versioned safety cases, thus enabling their evolution as *revisions* (intended to supersede their predecessor and the focus of this paper) and *variants* (intended to coexist), while maintaining consistency between interdependent components.

SCM theory distinguishes between *product* space and *version* space. These represent descriptions of a system (or in our case GSN elements of a safety argument) and the organisation of versions of these descriptions respectively.

Different revisions/variants of a safety case can be produced by combining different elements (either individual entities or larger fragments of a goal structure) and different versions of these elements into what is termed a *configuration*. The degree

of flexibility permitted in producing such combinations depends on the version model being used. Conradi & Westfechtel [4] distinguish three such models:

- ***Product First*** - the product structure is selected first, followed by the versions of each module (such that each configuration has the same structure);
- ***Version First*** - the product version is selected first which uniquely determines module versions (allowing different versions to be structured differently, though in the event of change, new versions are created for all 'parents' of the affected module - this is known as version proliferation); and
- ***Intertwined model*** - components and versions are selected in alternating order, preventing version proliferation (Figure 2).

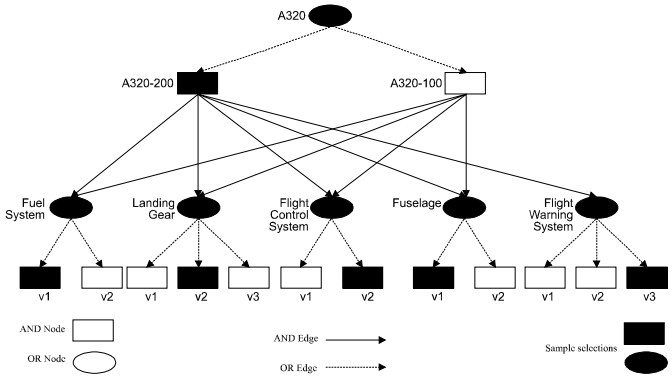

Figure 2. Intertwined Configuration Model

Note [5] address change management in the context of GSN. However, while presenting a systematic process for examining the impact of change (termed *challenges*) to the validity of a safety argument (termed the *damage phase*), they do not discuss means of structuring revisions (or variants) that may occur as a result (termed the *recovery phase*). The contribution of this paper is therefore to provide version management of safety arguments represented in GSN using an Intertwined model.

III. VERSIONING SAFETY CASES IN GSN

This section addresses structuring of versions using *AND/OR* graphs, together with use of GSN to express, analyse and manage change in safety cases.

A. AND/OR Graphs

Figure 2 showed how AND/OR graphs using an *Intertwined* model can capture the interplay between product and version space without the structural restriction and version proliferation problem of the *Product First* and *Version First* models respectively.

Recall AND/OR graphs contain two types of nodes and two types of edges. OR nodes (represented as ellipses) depict version clusters, while AND nodes (represented as rectangles) correspond to actual versions (in this case goals, strategies, solutions and other GSN elements); shading denotes selection. AND edges meanwhile show composition, whereas OR edges describe either a *revision* (successor relationship) or *variant* (coexistence relationship) between two goal structure fragments.

Finally, because Goal Structure Notation itself uses rectangles (denoting goals) ellipses (denoting assumptions/justifications), some 'syntactic sugar' is necessary when integrating the two conventions. GSN symbols are therefore depicted 'inside' AND nodes as illustrated for the core elements in Figure 3.

Figure 3. Intertwined GSN: Core Elements

B. Managing Change Using Intertwined GSN

Challenges to a safety case may come from various sources. For example, operational use may challenge *evidence* (e.g., hazard analysis) on which the original safety argument was based. Additional certification *requirements* must also be considered. For example, a safety case argued partly on the basis of having satisfied the evaluation criteria of an international standard such as IEC615803 [6] would be challenged if these criteria were changed in any way. Moreover, any changes in *context* need to be addressed, such as the emergence of new hazards.

Kelly & McDermid [5] use a cross (x) to indicate a challenge to a GSN element; we preserve this formalism. However, as the purpose of this work is to maintain different versions of a safety argument, semantics of the cross here are that the affected elements are pending investigation. Thus, when the argument is recovered – either by introducing new elements, or where no action is deemed necessary as the argument still holds – then the cross is removed. Note the rationale underlying both actions is captured using the UML Note symbol (a 'dog-eared' rectangle). Again, this enhances the audit-trail for engineers revisiting the safety case in future.

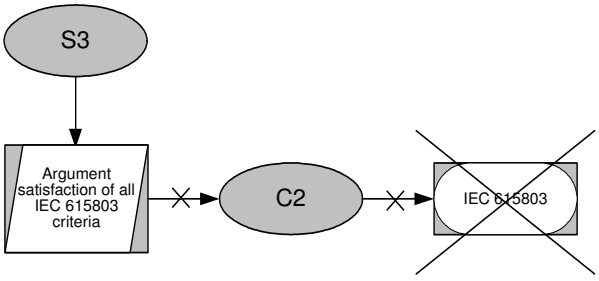

Figure 4. Requirements Challenge Example

Figure 4 illustrates a context challenge where safety is being argued on the basis that all criteria for systems developed according to the afore-mentioned IEC 615803 standard have been addressed. Hence, the set of criteria defined by this standard provide context to a strategy. If however the requirements change, the current argument may be invalidated.

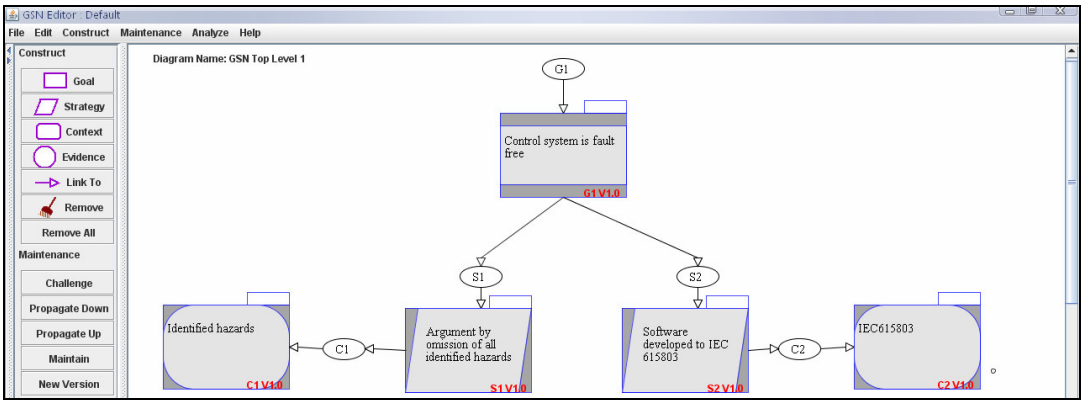

Figure 5. Top Level Goal Structure for Control System (developed using iGSN Tool)

Having identified an immediate challenge to a safety argument, engineers can use the goal structure to determine the extent of the 'damage', i.e. which other elements are affected. As a rule, [5] note that changing a core item (goal, strategy or solution) challenges items higher up (parents) and items lower down children) the goal structure, as well as context items (to the left and right). However, changes in context, justifications and assumptions challenge not only the core items that introduce them, but all child goals strategies and solutions.

After establishing the full extent of damage, engineers can determine what action is necessary to recover the safety argument. This is where an intertwined goal structure can be used to manage their evolution, providing full audit trail history. We demonstrate this in the following section.

IV. INTERTWINED GSN WORKED EXAMPLE

We now consider a simplified safety argument for a control system (C/S) where the top level goal is to show the system is fault free (Figure 5).

Strategies demonstrating that the top level goal has been met are to argue that all identified hazards have been addressed (in the context of all known hazards) and that the system has been developed to meet all IEC 615803 evaluation criteria (the standard itself providing context)[1].

The strategy of addressing all known hazards is realized by demonstrating that unintended opening of the press after Point of No Return, and unintended closing of the press can only occur due to component failure. These goals are satisfied by appeal to fault tree analysis and results of hazard directed testing.

The strategy of demonstrating IEC 615803 compliance is realized by demonstrating that the formal specification has been validated and that all software safety functions perform correctly. These goals are again satisfied by direct evidence (the VDM and architecture specification and dynamic analysis results respectively).

Given this initial safety case, we now consider a brace of challenges to its arguments and the process of recovering them, i.e. versioning of the safety case. The first challenge is to a solution to the goal that unintended closing of the press can only occur as a result of component failure, which may be invalidated by operational use. Recall challenges to core GSN elements propagate up the goal structure, here invalidating the top level claim (Figure 6).

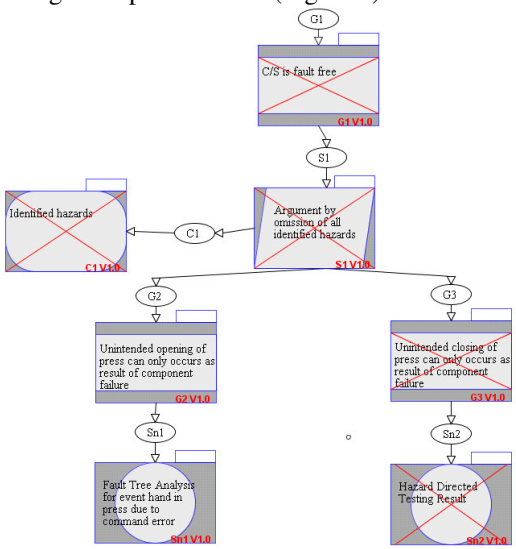

Figure 6. Hazards Challenge (Damaged Argument)

In this case, recovery of the damaged argument is relatively straightforward, requiring only that further hazard directed testing is undertaken and the results included as a solution (Figure 7).

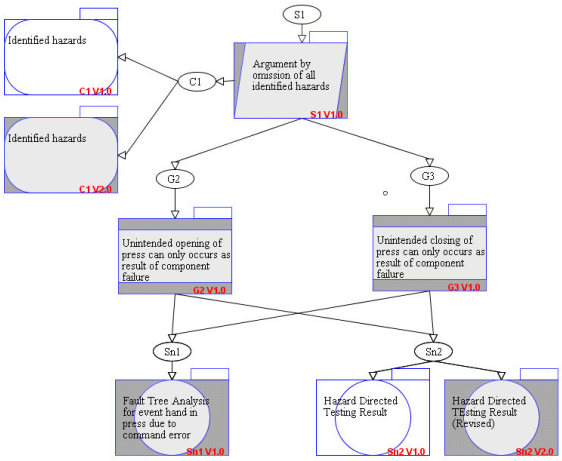

Figure 7. Hazards (Recovered Argument)

[1] Decomposition of the two strategies our safety argument is based on shows their damaged and recovered forms only (Figures 6-9).

In the second challenge we assume the context to our strategy of demonstrating IEC 615803 compliance is challenged by revisions to the standard itself. Recall that challenges to context propagate to all children of the core goal structure element to which the context is attached (see Figure 8).

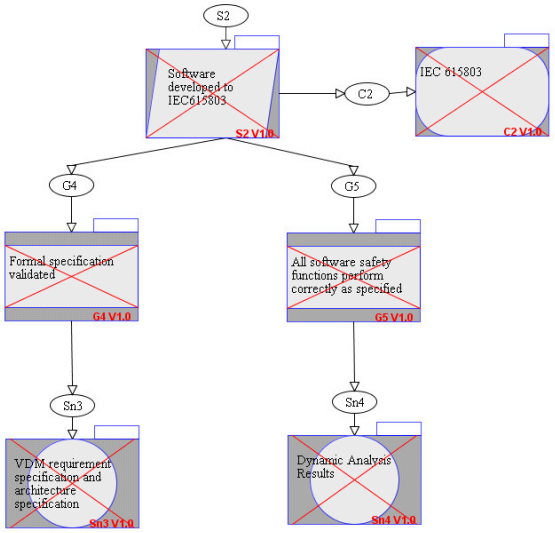

Figure 8. IEC 615803 Challenge (Damaged Argument)

Having assessed the challenge and identified the damage to the existing argument, engineers can begin steps towards its recovery. That may involve inserting new evaluation criteria (as additional goals), and evidence of their satisfaction (solutions), as well as revisions to existing criteria. See Figure 9.

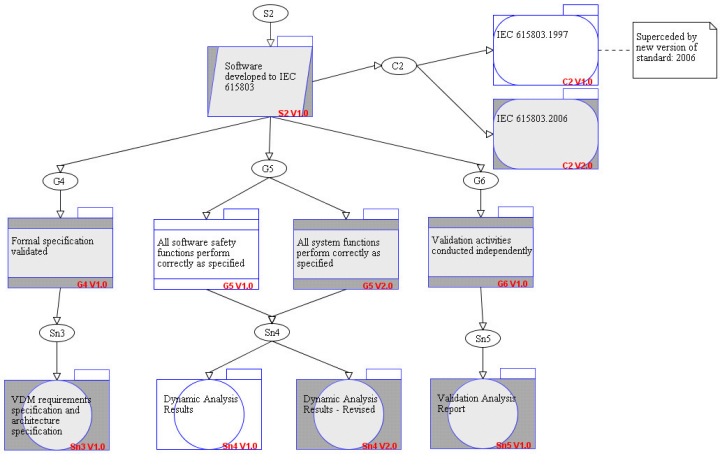

Figure 9. IEC 615803 (Recovered Argument)

Notice the UML Note convention on the original context element recording the reason IEC 615803 is no longer valid. In practice rationale would be attached to all obsolete goal structure items.

Of course arguments in this form don't show the constituent items making up each safety case version. This is accomplished by projecting the relevant nodes (N) and edges (E)[2] from the goal structure. For example, for the (partial) safety arguments in Figures 6 and 7, we can determine the following (partial) safety case revisions:

SC.$_{v1}$ = N1 + E1 where:
N1 = {G1.$_{v1}$, S1.$_{v1}$, C1.$_{v1}$, G2.$_{v1}$, G3.$_{v1}$, Sn1.$_{v1}$, Sn2.$_{v1}$} and
E1 = {<G1.$_{v1}$, S1.$_{v1}$>, <S1.$_{v1}$, C1.$_{v1}$>, <S1.$_{v1}$, G2.$_{v1}$>, <S1.$_{v1}$, G3.$_{v1}$>, <G2.$_{v1}$, Sn1.$_{v1}$>, <G3.$_{v1}$, Sn2.$_{v1}$>, <G2.$_{v1}$, Sn2.$_{v1}$>, <G3.$_{v1}$, Sn1.$_{v1}$>}

SC.$_{v2}$ = N2 + E2 where:
N2 = {G1.$_{v1}$, S1.$_{v1}$, C1.$_{v2}$, G2.$_{v1}$, G3.$_{v1}$, Sn1.$_{v1}$, Sn2.$_{v2}$} and
E2 = {<G1.$_{v1}$, S1.$_{v1}$>, <S1.$_{v1}$, C1.$_{v2}$>, <S1.$_{v1}$, G2.$_{v1}$>, <S1.$_{v1}$, G3.$_{v1}$>, <G2.$_{v1}$, Sn1.$_{v1}$>, <G3.$_{v1}$, Sn2.$_{v2}$>, <G2.$_{v1}$, Sn2.$_{v}2$>, <G3.$_{v1}$, Sn1.$_{v1}$>}

We could then find the symmetric difference (properties specific to SC.$_{V1}$ and SC.$_{V2}$) between the two arguments to determine how they have changed.

V. INTERTWINED GSN WORKED EXAMPLE

Traditional' means of presenting safety cases as a linear document are inadequate as the level of detail often obscures the arguments presented. Graphical techniques such as Goal Structure Notation have therefore been developed to improve their structure and scrutability. However, GSN currently lacks the ability to record versions of safety arguments. This is especially important as industries like aerospace and defence offset huge development costs through revisions and variants of their systems.

What safety practitioners require therefore is an effective and efficient means for configuration management of safety cases; the actual level of effectiveness and efficiency depends on the underlying configuration model. An Intertwined approach has been shown to combine both qualities and was therefore the model adopted here.

This combination of GSN and Intertwined configuration model was shown to have great potential for configuration management of safety cases, especially when supported by a CASE tool. Further testing on larger case studies is currently being undertaken to determine scalability.

REFERENCES

[1] P.Bishop, & R. Bloomfield, A Methodology for Safety Case Development, *Procs. Safety-Critical Systems Symposium*, Feb., 1998

[2] T. Kelly & R. Weaver, The Goal Structuring Notation - A Safety Argument Notation, *Procs. Dependable Systems and Networks Workshop on Assurance Cases*, July 2004

[3] W. Babich, *Software Configuration Management*, Addison-Wesley, 1986

[4] R.Conradi & B. Westfechtel, Version Models for Software Configuration Management, *ACM Computing Surveys*, Vol. 30., No. 2, 1998

[5] T. Kelly & J. McDermid, A Systematic Approach to Safety Case Maintenance, *Reliability Engineering and System Safety*, vol. 71, pp. 271-284, 2001\

[6] IEC, Standard IEC 61508: Functional Safety of Electrical/Electronic/Programmable Electronic Safety Related Systems, 1998

[2] An Edge is denoted by a pair <a, b>, where a is the source node and b the target node

Extending Cross-Tool Traceability to Source Code

P. A. J. Mason
Shinawatra University, Shinawatra Tower III, Viphavadi Road, Bangkok, Thailand

***Abstract*- Traceability is the term describing means to record and navigate relationships between system development artifacts. While simple in theory, in practice the range of separate CASE tools engineers use to express these artifacts, and a lack of well defined approaches to their integration, mean traceability is difficult to achieve across the complete lifecycle, especially to source code documents. This paper describes a framework known as MAST (Meta-modeling Approach to System Traceability) which offers one possible solution to that problem.**

I. INTRODUCTION

Traceability is the term software engineers use to describe mechanisms for recording and navigating relationships between development artifacts, including requirements, design and source code. While establishing and maintaining these relationships imposes a sizable administrative overhead, the many benefits include helping verify a system meets its requirements, tracking the effects of changes and determining the rationale underpinning a design or implementation [1]. Moreover, traceability is recognized as essential for efficient project and quality management, as its significance to process improvement frameworks such as CMMI bears testament.

In theory, the ability to link artifacts (and parts of artifacts for finer grained traceability) is simple. What complicates matters is the fact that engineers use a range of (often poorly integrated) CASE tools to express and store these artifacts. This normally causes 'breaks' in the traceability chain, especially traceability to and from source code.

To counter the tool integration problem, some vendors have taken to producing integrated suites of tools, normally supporting a particular software development process. Examples include IBM's Rational software suite (tailored to the Rational Unified Process) which, while offering lifecycle traceability across artifacts expressed in UML, linking and navigating to notations expressed in other tools – including compilers - is far from straightforward. This is particularly significant for developers of dependable systems who must model properties such as real-time and failure behavior of a system, aspects not easily represented or beyond the scope of the UML. For example, engineers may wish to link results of a vulnerability analysis to all source code arrays in support of security claims that all potential sources of buffer overflow have been checked.

This paper describes the MAST framework (Model-based Approach to System Traceability) which provides 'seamless' traceability between heterogeneous CASE tools (potentially, any commercial or bespoke tools). We concentrate here on traceability of Java source code for reasons outlined above.

The rest of the paper is organized as follows. Section Two provides an overview of MAST, while Section Three introduces means of structuring Java source code (or more generally any language with a formal foundation) to enable traceability. This is demonstrated by example in Section Four. Section Five has some conclusions and pointers to future work.

II. MODEL-BASED APPROACH TO SYSTEM TRACEABILITY

The premise of this work is that poor integration prevents practitioners from tracing across disparate tools (Figure 1), with lack of traceability to source code a particular concern.

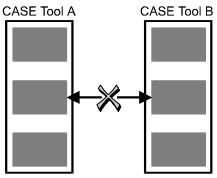

Figure1. Inter-Tool Traceability Problem

Our solution to this problem is a framework known as MAST which is realised by exporting information from the internal data structures of tools to a Workspace of notation dependent '*traceability structures*' (meta-models), represented here in UML (with constraints expressed in the Object-Constraint Language, OCL [2]). How information is structured has long been recognised as a core traceability issue [3]. By expressing the traceability structures in a common language, links (expressed in the same language as the structures) can be inserted that capture dependencies among data in CASE tools, within the Workspace.

To maintain consistency, the structures are verified against a system model – the Product Data Synthesis (PDS). PDS is similar to a data dictionary, capturing architectural and behavioral elements of the emerging system (and their inter-relationships), e.g., Module *hasInterface* Interface, Module *hasFunction*, etc. Where a 'clean' mapping of elements to the Workspace is not achieved, *tool2mast* creates an error-log. The likely cause is 'bad data' detected by PDS cross-checks. For more information on the PDS, readers are referred to [4].

The mechanics of mappings across the CASE tool/mast interface are described here by a function, *tool2mast* that takes as its input parameters, a populated CASE tool (internal) data structure (pCDS), with a corresponding un-populated notation dependent structure (uNDS) and the PDS, and returns a populated notation dependent structure (pNDS). This is expressed as follows:-

pNDS *tool2mast* (pCDS, uNDS, PDS)

The resulting Workspace provides an integrated environment

(Figure 2) allowing traceability between otherwise disjoint data, e.g. from a requirement in DOORS or low-level specification stated in RTN-SL (see Section 4), to a Java class declaration.

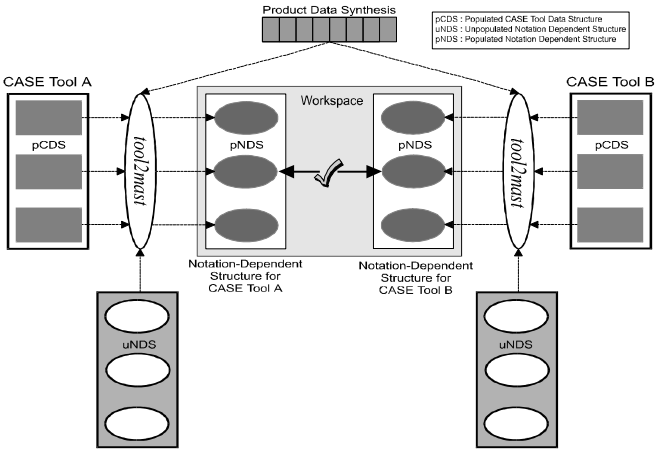

Figure2. Realising Inter-Tool Traceability

III. STRUCTURING JAVA CODE FOR TRACEABILITY

This section introduces a structure - capturing a subset of the concrete syntax for the Java programming language – based on a modeling philosophy developed previously in parallel with a SPARK Ada meta-model [5]. The philosophy (discussed in section 3*A*) provides a set of guidelines by which the structure may be extended to include the complete Java syntax, or indeed used to structure *any* other language with a formal foundation. Here we concentrate on representation of a single Java construct - the class_declaration.

Java class declarations include the following (in order):

- Modifiers such as public, private, protected, etc.
- The class name, with the initial letter capitalized.
- The name of the class's parent (superclass), if any, preceded by the keyword extends.
- A comma-separated list of interfaces implemented by the class, preceded by the keyword implements.
- The class body, surrounded by braces, {}.

The following illustrates use of class_declaration statements:-

```
public class MyClass extends MyPackage.MySuperClass
implements YourInterface {//field, constructor, and
    method declarations}
```

A. A Modeling Philosophy for Structuring String Grammars

Representation of the nominated construct takes as its starting point the concrete Java grammar stated in Backus Naur Form (BNF). In BNF, categories (i.e., entities) are defined in terms of other categories using productions consisting of the name being defined, followed by the ::= symbol and a defining sequence (which may include punctuation and reserved word 'tokens'); categories that cannot be further decomposed are known as terminals. Other symbols of note are **[ ]** square brackets enclosing optional items, **{ }** braces enclosing optional items that may appear zero to *n* times and the **|** vertical bar separating alternatives.

Our philosophy provides a series of principles allowing object-based representation of language constructs stated as BNF categories, and to do so at a level of abstraction which is sufficient to identify traceability primitives. The guidelines are deliberately general allowing their application to any language with a concrete BNF syntax (see section 5).

Further MAST modeling concepts referenced are StructureElement and SystemsEngineeringEntity [4]. The former ensures a common basis for all notation dependent structures, while the latter is a generalisation of all elements of notation dependent structures that simplifies definition. A further concept is ArtifactProperty which subsumes all built-in and abstract data types. With these considerations in minds, the guidelines are as follows:-

1. Each BNF category is represented as a class (both an instance of the StructureElement meta-class and a specialisation of SystemsEngineeringEntity).
2. Categories forming the defining sequence of a category are themselves represented as classes (related to the subject class through aggregation), except where rule 3 applies.
3. Where nothing is gained traceability-wise by mirroring definition of a category in terms of other categories (and hence the corresponding class in terms of other classes) - that is, no constituent categories can be represented by classes that map to PDS elements (nor trace to elements of other notations) - it is treated as atomic and represented through specialisation of the String type (as well as an instance of StructureElement and a specialisation of SystemsEngineeringEntity).
4. All tokens (i.e., reserved words - such as class, extends, final, etc. - together with punctuation marks - such as commas, semicolons, parentheses and ampersands) are represented as specialisations of the standard String class (and also as instances of ArtifactProperty).
5. Categories of a defining sequence that exist exactly once are modeled with a multiplicity of one (1) for aggregate component classes; attributes representing tokens have an implicit multiplicity of one.
6. Optional items from a defining sequence (expressed in BNF using square brackets) are modeled as follows:-

a) Categories are represented by applying a zero-or-one multiplicity constraint (0..1) on the component side of associations between the class representing the category being described (aggregate) and each class representing an optional defining category (component).

b) Tokens are promoted from attributes to classes (linked to their host using composition) to allow for expression of optionality.

7. Categories of a defining sequence that may be omitted, appear once, or be repeated several times (expressed in BNF using the braces formalism) are modeled using a zero-to-many multiplicity constraint (0..*) on the component side of associations between the class representing the category being described (aggregate) and each class representing an optional, singular or repeated defining category (component).
8. Categories decomposed into alternatives (expressed in BNF using the vertical bar separator) are modeled differently depending on what form their defining sequence takes. See [5] for more information.
9. The modeling of a defining sequence in which an item type appears at least once, but which may be repeated (as a comma or semicolon delimited list) - i.e., category ::= item {, item} - features a subtle variation from the BNF syntax; we represent the mandatory single item as a class (corresponding to a 'list head')

and the optional repeated part (enclosed between braces in BNF) as a separate 'list-item' class containing an appropriate delimiter attribute, together with an aggregation association (multiplicity of one) to the afore-mentioned item class.

B. Java Class_Declaration: Meta-model Definitions

We now present a brace of schemas for a partial Java structure capturing the above class declaration statement. Each constituent element is systematically expressed in terms of its BNF syntax and corresponding UML representation. To give a flavor of tool support, the UML classes are implemented in O-Telos using ConceptBase [6]. We further highlight the influence of our modeling philosophy in deriving these structures. We begin by describing the class_declaration syntax which marks the origin for our modeling.

- **class_declaration** : consists of an optional modifier, followed by the class_token reserved word, then the class identifier; this can be followed by an optional parent class (identified by its class_name and preceded by the extends_token reserved word); an optional comma-separated list of interfaces implemented by the class may follow (each identified by their interface_name, and preceded by the implements_token reserved word). Note, the UML and O-Telos representations introduce an additional class (in accordance with rule 9) - interface_name_list_item - to represent optional interface_name elements following the single mandatory instance. Finally, the class declaration includes zero or more instances of a field_declaration enclosed within braces (see Figure 3).

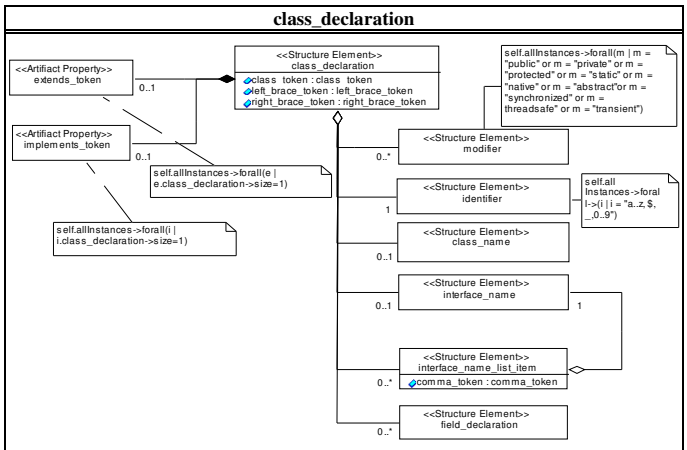

BNF Syntax

```
class_declaration ::=
    { modifier } "class" identifier
    [ "extends" class_name ]
    [ "implements" interface_name {
    "," interface_name } ]
    "{" { field_declaration } "}"
```

O-Telos

```
class_declaration in StructureElement,
SimpleClass isA
SystemsEngineeringEntity with
has_property
     class_token : class_token;
     left_brace_token :
left_brace_token; right_brace_token :
right_brace_token end
has_part
     modifier : modifier; identifier :
     identifier; class_name class_name;
     interface_name : interface_name;
interface_name_list_item :
interface_name_list_item;
field_declaration : field_declaration
end
```

Figure3. class_declaration schema

- **class_name** : comprises either an identifier, or package_name and identifier separated by a period_token (see Figure 4). Note interface_name is similarly defined.

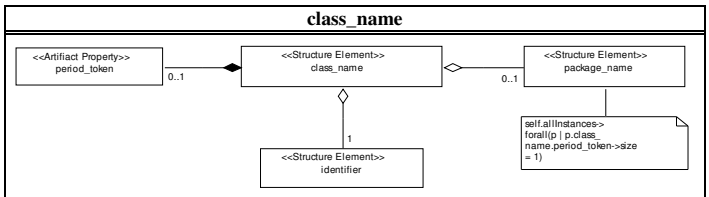

BNF Syntax

```
class_name ::=
    identifier | package_name "." identifier
```

O-Telos

```
class_name in StructureElement,
SimpleClass isA
SystemsEngineeringEntity with
has_property
     period_token : period_token
has_part
identifier : identifier;
     package_name : package_name end

period_token in ArtifactProperty,
SimpleClass isA String with constraint
period_Is_period: $ forall p/
period token p = "." $ end
```

Figure 4. class_declaration schema

- **field_declaration** is defined in BNF in terms of a method_declaration, constructor_declaration or variable_ declaration; space limitations prevent inclusion of this schema.

C. Java Meta-model: Class Declaration Worked Example

The code fragment for **MyClass** introduced in section 3 will be used as the subject of this example.

Instantiation of class_declaration schema (Figure 3)

```
myClassDeclaration in class_declaration, Token with
modifier _modifier : "public"
class_token classToken : "class"
identifier _identifier : "MyClass"
extends_token extendsToken : "extends"
class_name className : mySuperClass
implements_token implementsToken : "implements"
interface_name interfaceName : yourInterface
left_brace_token leftBraceToken : "{"
field_declaration fieldDeclaration : myClassFieldDeclaration
right_brace_token rightBraceToken : "}"end
```

Instantiation of class_name/interface_name schema (Figure 4)

```
mySuperClass in class_name, Token with
package_name packageName : "MyPackage"
period_token periodToken : "."
identifier _identifier : "MySuperClass" end

yourInterface in interface_name, Token with
identifier _identifier : "YourInterface" end
```

This example, combined with the Java meta-model and modeling philosophy illustrates our approach to representing (in this case formal textual) notations as meta-models capable of receiving data from CASE tools via *tool2mast*.

IV. REALISING TRACEABILITY FROM REQUIREMENTS TO CODE

In MAST, traceability associations are modeled as classes (Figure 5). TraceabilityAssociation is an abstract class whose subtypes – such as ImplementedBy featured in this example - realize traceability between two SystemsEngineeringEntity subtypes (as described in section 3*A*).

ImplementedBy relations link specifications to their implementation. We now demonstrate this using the Java code fragment from section 3 and a partial specification expressed in the Real-Time Network Specification Language (RTN-SL) [7].

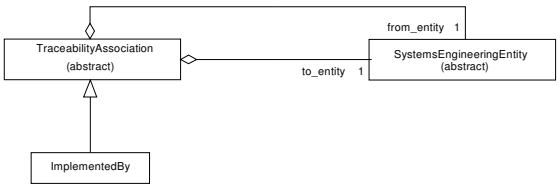

Figure 5. Traceability Association

RTN-SL is a language for defining both the functions - termed *activities* - and behavior of Real-Time systems. Activities are concurrent processes that exchange information and synchronize through shared data in their connections; they are represented in RTN-SL as circles, with behavior depicted as an abstract state machine inside each activity. Abstract data types (ADTs) - denoted as diamonds (with extension shown by dotted lines) - may be defined to support definition of a Real-Time Network. Figure 6 illustrates RTN-SL's graphical syntax, as well as traceability between the MyClass ADT and the Java code fragment (from section 3) that implements it.

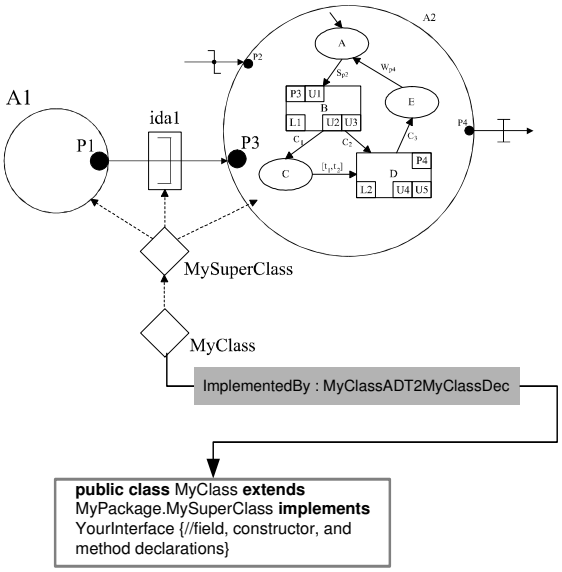

Figure 6. RTN-SL Fragment

Of course, to realize traceability between the two representations in the figure we require an RTN-SL meta-model instantiated with the network fragment shown (see Figure 7).

Finally, we populate an O-Telos instance of ImplementedBy (from Figure 5) to achieve traceability between the RTN-SL and Java fragments featured in this paper. Its source is the MyClass ADT (from Figure 6), and its target, the myClassDeclaration object from section 3*C*.

```
MyClassAdt2MyClassDec in ImplementedBy, Token with
from_entity fromEntity : MyClass
to_entity toEntity : myClassDeclaration end
```

V. CONCLUSIONS & FUTURE WORK

This paper proposed a framework called MAST to enable

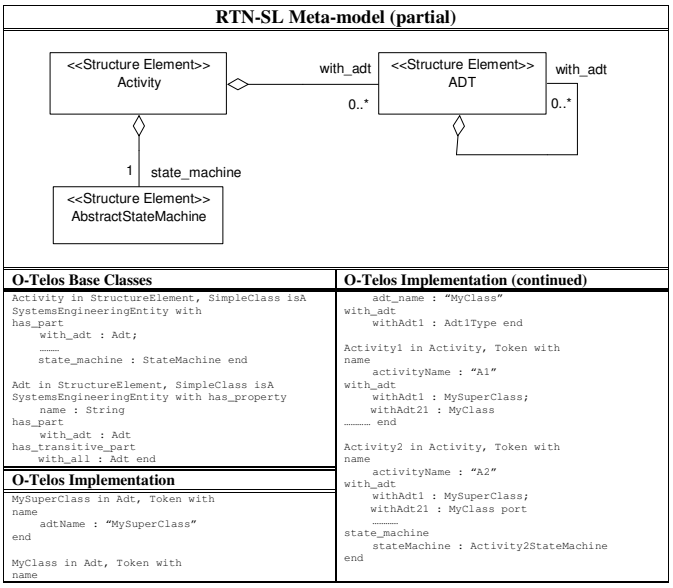

Figure 7. RTN-SL Fragment

traceability across disjoint CASE tools. MAST is achieved by exporting data from the internal models of these tools to structures (meta-models) expressed in a common modeling language. Traceability associations (expressed in the same language as the structures) may then be established between the models and their elements.

The paper concentrated on a meta-model for representing Java source code (based on the concrete BNF syntax). The structure was developed using guidelines for developing meta-models for BNF supported languages generally.

The novelty of work presented here lies in the following:-

- A framework (based on meta-modeling) enabling traceability between tools, across artifacts represented using different notations.
- A (partial) meta-model for the Java language, together with a generic modeling philosophy applicable to any BNF supported language.
- Means of creating associations among the meta-models, in this case demonstrated using the RTN-SL.

We are currently experimenting with applying the concepts discussed here to other languages with a formal grammar, including VDM and C++, which in turn will test the robustness of the modeling philosophy.

REFERENCES

[1] Spanoudakis et al., "Rule-based Generation of Requirements Traceability Relations", *Journal of Systems & Software*, 72(2), pp. 105-127, 2004
[2] J. Warmer & A. Kleppe, *The Object Constraint Language*, AW, 2003
[3] K. Pohl, *Process Centered Requirements Engineering*, RS Press, 1996
[4] P. Mason, "A Conceptual Traceability Framework for Complex ICT Systems Development", *Procs. 2nd Int. Conf. on ICT*, Bangkok, 2004
[5] P. Mason, A. Saeed & S. Riddle, On the Role of Traceability for Standards Compliance, Procs. SafeComp, 2003
[6] M. Jarke et al., "ConceptBase: - A Deductive Object Base for Meta Data", *Journal of Intelligent Info. Sys*., Mar., pp.167-192, 1995.
[7] S. Paynter et al., "ADL: An Activity Description Language for Real-Time Networks", *Formal Aspects of Computing*, 12(2), pp 120-144, 2000

CELLULAR WIRELESS NETWORK DESIGN WITH GENETIC ALGORITHM

Pakorn Leesutthipornchai[+], Naruemon Wattanapongsakorn[+] and Chalermpol Charnsripinyo*
[+]Department of Computer Engineering, King Mongkut's University of Technology Thonburi
126 Pracha-Utid, Tung-Kru, Bangkok 10140 Thailand. E-mail : *naruemon@cpe.kmutt.ac.th*
*National Electronics and Computer Technology Center, Pathumthani, Thailand

***Abstract*– This paper presents a cellular wireless backhaul network design using a genetic algorithm to minimize the cost of the design process including the cost of network equipment and their installation. The problem is to find a minimum-cost network topology which includes selecting the location and type of base station controllers and mobile switching controllers as well as their link types. In this research, a genetic algorithm (GA) is used as a meta-heuristic technique for obtaining good solution for the design problem. Various sizes of network design problem are considered and discussed. The GA results are evaluated with those from a brute force search algorithm, showing that our approach gives optimal or near optimal solutions for small-size problems and can solve large-size problems within a reasonable computational time.**

***Keywords:* Cellular Network Design, Optimization Technique, Genetic Algorithm**

I. INTRODUCTION

Cellular wireless networks have become essential to mobile users that need communication services regardless of time, location, and mobility pattern. A typical architecture of a cellular wireless network is illustrated in Figure 1. A base transceiver station (BTS) serves as a fixed access point for all mobile terminals within its coverage area. The network includes base station controllers (BSC), which manage a group of base stations and perform radio level channel management and call handoff. The BTS and BSC are connected to backbone networks via mobile switching centers (MSC). The MSC is then connected to the public switched telephone network (PSTN) or other transmission networks. The network is generally organized into a tree-like structure. Each BTS is connected to a BSC and the BSC is then connected to a MSC.

The network service providers have to dedicate a substantial amount of their resources to do the network planning, install, and maintain the network equipments, such as BTS, BSC and MSC, network link and link interface. Thus cost effective network design becomes a necessity.

In this paper, we propose a design of cellular wireless network with a heuristic approach called Genetic Algorithm. We consider a proposed network design model [1] which finds the network topology, the location of the BSCs and MSCs, the type of BSCs and MSCs, and the type of links. We consider tree network topology. The design objective is to minimize the cost of the design, network equipments and their installation.

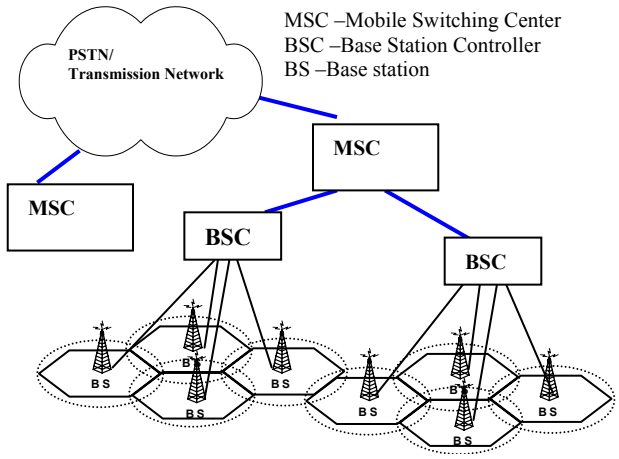

Figure 1. Typical wireless network architecture.

Previously, the model was proposed as a constraint programming model for cellular network design and solved with a local search heuristic called Constraint Programming Local Search (CPLS) [1]. Many research papers presented network design models and techniques to solve the network design problem. In 1993, an early research group [2] proposed an enumerative and branch&bound algorithm for reliable network design considering tree, ring, and chordal ring topologies. Later, Kumar et al [3, 4] proposed a genetic algorithm to solve distributed system topology design problems and optimize reliability for computer network expansion. We also use a genetic algorithm to optimize communication network design by finding network component allocation and network topology with cost constraint in our previous work [5]. Genetic Algorithm (GA) is usually used to solve many difficult engineering problems, and it is particularly effective for the combinatorial optimization problems. GA can also be used to solve optimization problems when the problem space is huge and trying all possibilities is not an option. An example of problem solving with GA is the component redundancy allocation in series- parallel systems [6].

The remainder of this paper is organized as follows. In the next section, we describe the cellular wireless network design problem and the network design model based on the constraint

programming model proposed in [1]. Section III gives a genetic algorithm concept and presents our parameter settings used for obtaining good solutions in the cellular wireless network design problem. Section IV presents our numerical results and analysis. Lastly, section V concludes our research work and contribution.

II. NETWORK DESIGN PROBLEM AND MODEL

We consider a cellular wireless backhaul network design problem to determine the network topology including the location of the BSCs and MSCs, the type of BSCs and MSCs, and the type of links. The network design problem can be formulated as an optimization-based model. In this paper, we adopt the constraint programming model from Reference [1]. The network design objective is to minimize the total network cost as shown in Equation 1 consisting of the cost of the links and interface cards and the cost of the BSCs and MSCs which include the installation cost.

Objective:

$$\min_{v,w,x,y,z} C_L(v,w,z)+C_N(x,y) \tag{1}$$

where C_L is the cost of the link and interface cards, and C_N is the cost of the allocated BSCs and MSCs. Their descriptions are represented as following

$$C_L(v,w,z)=\sum_{i\in I} a_{iv_i}+\sum_{j\in J}\sum_{i\in L} b^l_{jw_j} z^l_j \tag{2}$$

$$C_N(x,y)=\sum_{j\in J} c^{x_j}_j+\sum_{k\in K} d^{y_k}_k \tag{3}$$

where I is the set of BTSs, J is the set of BSCs, and K is the set of MSCs. The cost parameters consist of a_{ij}, b^l_{jk}, c^s_j and d^t_k where a_{ij} is the link and interface card costs including the installation cost for connecting BTS $i\in I$ to a BSC at site $j\in J$, b^l_{jk} is the link and interface card costs including installation cost for connecting a BSC at site $j\in J$ to an MSC at site $k\in K$ through a link and interface type $l\in L$, c^s_j is the cost of a BSC of type $s\in S$ and installed at site $j\in J$ and lastly is the cost of an MSC of type $t\in T$ and installed at site $k\in K$.

The decisions variables v, w, x, y and z are defined as the following. v_i is the value of the BSC site assigned to the BTS $i\in I$. w_j is the value of the MSC site assigned to site $j\in J$. x_j is the value of the BSC type installed at site $j\in J$. y_k is the value of the MSC type installed at site $k\in K$. z^l_j is the number of links of type $l\in L$ installed from the BSC site $j\in J$ to a MSC.

This network design problem has the following constraints.

*1) **BSC Capacity Constraints***: the number of BTS interfaces that can be installed at a BSC of type x can not exceed the maximum number of interfaces that the BSC can obtain. In addition, the capacity (in circuit) of all BTSs connecting to the BSC must not exceed the capacity that the BSC can obtain.

*2) **MSC Capacity Constraints***: the number of BSC interfaces that can be installed at a MSC of type x can not exceed the maximum interface cards that the MSC can obtain. In addition, the capacity (in circuit) of all BSCs connecting to the MSC must not exceed the capacity that the MSC can obtain.

*3) **Link Capacity Constraints***: the type of each BTS-BSC interface must support the capacity requirement from the connecting BTS, and the type of each BSC-MSC interface must support the capacity requirement from the connecting BSC.

*4) **BTS Type***: the type of each BTS is chosen so that the BTS can support all the traffic (in erlang) from the BTS to a BSC. The traffic (in erlang) from BTS_i to a selected BSC is

$$t_i=\sum_{i'\in I}\left(g_{ii'}+g_{i'i}\right)+\left(g_{ip}+g_{pi}\right) \quad ,i\in I \tag{4}$$

where $g_{ii'}$ is the average number of communications per hour from BTS_i to $BTS_{i'}$, g_{ip} is the average number of communications per hour from BTS_i to the public network, and g_{pi} is the average number of communications per hour from the public network to the BTS_i.

*5) **BSC Type***: the type of each selected BSC is chosen so that the BSC can support all the traffic (in erlang) from all BTS pairs (i and i') that communicate via the BSC and another BSC, and the traffic from its own BTSs and the public network (via a MSC) defined as follows.

$$t_j=\sum_{i\in I}\left[\left(v_i=j\right)\sum_{i'\in I}\left(v_{i'}\neq j\right)\left(g_{ii'}+g_{i'i}\right)\right]+\sum_{i\in I}\left(v_i=j\right)\left(g_{ip}+g_{pi}\right) \quad ;(j\in J) \tag{5}$$

where v_i is a decision variable, which is equal to 1 if BTS_i is connecting to the BSC (i.e. $(v_i=j)=1$). Otherwise it is zero. $v_{i'}$ is equal to 1 if the $BTS_{i'}$ is connecting to a different BSC (i.e. $(v_{i'}\neq j)=1$).

*6) **MSC Type***: the type of each selected MSC is chosen so that the MSC can support all the capacity (in circuit) from all the connecting BSCs and can handle all the interfaces (not exceeding the limit) as discussed in constraint (2).

III. GENETIC ALGORITHM APPROACH

Genetic Algorithm (GA) is a stochastic optimization technique that uses the biological paradigm of evolution. It has a concept where good chromosome has a better potential of being carried to the next generation than the bad chromosome.

It uses mathematical principle to indicate which chromosome is better or worse than the others.

Firstly, to use GA we must encode the solution of problem into string called "chromosome" and each string has its unique characteristic inherited by "gene". Each chromosome is evaluated by a fitness function to indicate its potentiality toward the final solutions. The desirable fitness function value is depended on the problem (maximization/minimization).

After that we must generate an initial population (a set of chromosomes), and use the three main operators to find the best solution, as described next.

Step 1: Selection operator: The process of selecting potentially good chromosomes from the current population generation to the next generation.

Step 2: Crossover operator: The process of shuffling any two randomly selected chromosomes to generate the new offspring (like breeding).

Step 3: Mutation operator: The process that randomly selects one chromosome to change one or more genes into random value for generating the new offspring.

Step 4: Repeat these 3 steps until the goal is reached.

A. Encoding

The string encoding is a set of integers that indicates the relation of the BTS, BSC, and MSC. Suppose in the network design problem, we have 8 BTSs, 4 possible BSCs, and 2 possible MSCs. The corresponding string encoding is displayed in Figure 2. The first 8 integer positions, each with position i ($i \in I$) having the value a_i represents the connection from BTS_i to BSC_{ai}. The next 4 integer positions each represents the MSC identifier number, b_j, which the BSC is connected to. The value $b_j = -1$ if the BSC is not selected for the network design problem.

Let x be the number of BTS, y be the number of BSC, z be the number of MSC. We can encode the string as shown in equation (6).

$$a_0 a_1 \cdots a_{I-1}\ b_0 b_1 \cdots b_{J-1} \tag{6}$$

where
$I = \{0, 1, 2, \ldots, I\text{-}1\}$
$J = \{0, 1, 2, \ldots., J\text{-}1\}$
$K = \{0, 1, 2, \ldots., K\text{-}1\}$
$i \in I, \quad j \in J;$
$a_i \in J;$
$b_j \in K$ or $\{-1\};$

1	1	1	1	3	3	3	4	1	-1	1	1

Figure 2. An example of string encoding.

B. Initial Population

We set the initial population by randomly generating a set of chromosomes consisting of genes with uniform random number, and calculate their fitness value according to the fitness function presented in section 3A.

C. Selection

The chromosomes or population are sorted by their fitness values. The top 10 % of population with best fitness values (low total cost) are preserved to the next generation, 80 % of population are selected for the crossover process, and the remaining 10 % of population are new chromosomes which are randomly generated.

D. Crossover

We select a pair of chromosomes from the current population for a crossover, to produce two new offspring chromosomes. One parent chromosome comes from the top 10% and another parent chromosome can be any chromosome. In each crossover, 10% of the genes are exchanged between the two parent chromosomes. The exchanged genes are randomly selected.

Example : 1 1 1 1 3 3 3 4 | 1 -1 1 1 Parents1
2 2 3 1 2 2 1 3 | 1 0 0 1 Parents2

10 % of the genes in each chromosome are 1.2. We ceil to 2.

Randomly finding 2 genes to exchange between the parents, we obtain a pair of offsprings.

For example, suppose the crossover point is at gene positions 3 and 5, the results are

1 1 **3** 1 **2** 3 3 4 | 1 -1 1 1 Offspring1
2 2 **1** 1 **3** 2 1 3 | 1 0 0 1 Offspring2

The next population generation consists of the best 10 % of the current population generation with the minimum cost values, 80 % from the crossover process, and the rest 10 % comes from randomly generated population (alien).

E. Mutation

The offsprings from the crossover process are mutated with 25% rate. Only 1-2 genes in a chromosome are mutated at a time. The resulted chromosomes are combined and considered as the chromosomes in the current population generation.

IV. COMPUTATION RESULTS

In our experiments, we consider the network design with 3 BTS types, 3 BSC types and 3 MSC types which are similar to the previous research paper [1]. Their descriptions are presented in Tables 1-3. Also we consider DS-1 links for the connection from the BTS layer to the BSC layer. DS-1 and DS-3 link types are considered for the connection from the BSC layer to the MSC layer. The interface costs and link costs are presented in Tables 4-6.

We generate various test problems with a number of BTS, BSC and MSC. Their locations are randomly generated with a uniform distribution in a square region of 100 kilometers. The type of each BTS is randomly selected. The demand between each pair of BTSs and between the BTSs and the public network was generated randomly in the interval [0,0.2] erlang with a uniform distribution. The call blocking rate is 2%.

Our GA approach is implemented in JAVA and runs on a Pentium 4 PC (1.73 GHz and 512MB of RAM). For each

problem size, three random network sites and communication demands (between 0-0.2 Erlang) are investigated. Each result is an average from the 3 networks, each with 10 simulation runs.

Table 1. Feature of the BTS types

	Type A	Type B	Type C
Capacity (circuits)	96	288	576
Number of BTS DS-1 interfaces	1	3	6

Table 2. Costs of the BSC types (including the installation costs)

	Type A	Type B	Type C
Switch fabric capacity (circuits)	5,000	10,000	15,000
Maximum number of BTS interfaces	15	30	60
Maximum number of MSC interfaces	15	30	60
Cost ($)	50,000	90,000	120,000

Table 3 Costs of the BSC types (including the installation costs)

	Type A	Type B	Type C
Switch fabric capacity (circuits)	100,000	200,000	300,000
Maximum number of BSC interfaces	50	100	150
Cost ($)	200,000	350,000	500,000

Table 4. Costs of the interface types (including the installation costs)

Interface type	Capacity (circuits)	Cost ($)
DS-1	96	500
DS-3	2,688	2,500

Table 5. Costs of the BTS-BSC links (including the installation costs)

BTS type	Number of the DS-1	Capacity (circuits)	Cost ($/km)
A	1	96	2,000
B	3	288	3,000
C	6	576	4,000

Table 6. Costs of the BSC-MSC links (including the installation costs)

Link type	Capacity (circuits)	Cost ($/km)
DS-1	96	2,000
DS-3	2,688	4,000

At first, we attempt in solving 5 small to moderate network problems with the GA and a Brute Force Search approach where the results are compared as presented in Table 7. The results show that the GA can give the optimal network costs as guarantee by the Brute Force Search approach. Moreover, the GA requires significantly less CPU time than the traditional approach.

Table 7 The result comparisons between Brute Force approach and Genetic Algorithm

Problem Size	Brute Force Search		Genetic Algorithm	
(bts_bsc_msc)	Cost	CPU Time (sec)	Cost	CPU Time (sec)
5_3_2	683,206.4	1.0	683,206.4	1.0
8_4_2	989,271.5	9.0	989,271.5	3.5
10_4_2	1,066,101.6	206.2	1,066,101.6	3.0
12_4_2	1,211,395.8	5,016.2	1,211,395.8	4.2
22_9_5	1,664,949.6	84,387.0	1,664,949.6	63.0

For larger network problem, we apply the GA and compare its results to those from the Constraint Programming Local Search (CPLS), proposed by Pomerleau et al. [1]. Since the network input data set is randomly generated, we cannot precisely compare the network costs but the simulation time. We use a comparable Pentium4 PC. In addition, the CPLS is a heuristic approach so that it cannot guarantee the optimal solutions. Therefore, we use a Brute Force Search approach to verify our GA results for small-size problems. From Table 8, we present average and best network costs and CPU time obtained from the GA. The results show that the GA approach outperforms the previous CPLS with a marginal simulation time difference.

Table 8 Number of generations, simulation time, and total network cost obtained from the Genetic Algorithm

Problem Size	Best Cost	Average Cost	GA CPU Time (sec)	CPLS CPU Time (sec)
50-20-10	2,730,402.9	2,904,218.7	207.1	1,794.0
100-20-10	5,164,524.4	5,619,468.7	1,766.0	3,875.0
100-20-20	5,111,400.3	5,464,075.7	2,116.4	4,050.0

V. CONCLUSION

From our experiments, Genetic Algorithm is effective in solving cellular wireless network design problem, as verified by a brute force search approach where all possible solutions are considered. The CPU time consumed by the GA is significantly less than those consumed by traditional searching algorithms or previous heuristic approaches such as a brute force search technique or a constraint programming approach.

REFERENCES

[1] Yanick Pomerleau and Steven Chamberland and Gilles Pesant, "A constraint programming approach for the design problem of cellular wireless networks," *Canadian Conference on IEEE*, Vol. 2, pp. 881-884, 2003.

[2] R.H. Jan, "Design of Reliable of Network," *Computer and Operation research*, Vol. 20, pp.25-43, 1993.

[3] A.Kumar, R.M. Pathark, Y.P. Gupta, H.R. Parsaei , "A genetic algorithm for distributed system topology design," *Computer and Industrial Engineering*, Vol 28, pp. 659-670,1995.

[4] A. Kumar, R.M. Pathark, Y.P. Gupta, "Genetic- algorithm base reliability optimization for computer network expansion," *IEEE Trans on Reliability*, Vol.44, pp. 63-72, 1995.

[5] Kititouch Suteeca and Naruemon Wattanapongsakorn, "Reliability optimization of communication network design using genetic algorithm," *International Technical Conference on Circuit/System, Computer and Communication* (ITC-CSCC), 2006.

[6] D.W. Coit, A.E. Smith, "Reliability Optimization of Series-parallel System Using Genetic Algorithm," *IEEE Trans on Reliability,* Vol.5, pp. 4676-4681, 1996.

Performance Analysis of IEEE 802.11g Access Point under Heavy-Loaded Condition

Roungsan Chaisricharoen and Thitiporn Pramoun
School of Information Technology, Mae Fah Luang University
333 Moo 1, Thasud
Muang, Chiang Rai 57100 Thailand

***Abstract*-The famous IEEE 802.11g wireless LAN (WLAN) provides services in contention manner utilizing the access point (AP). As the amount of clients increases, the performance of AP may be dropped due to collision avoiding. The vendor-specific maximum clients of an AP, based on an AP's capacity to keep record of the MAC address, are the upmost limit that should not blindly follow because there is no guarantee that an AP is able to service at the required quality. Therefore, full-factorial experiment is conducted under heavy-loaded conditions to examine and model the goodput of an AP based on the number of concurrent TCP streamed sessions and maximum transmission rate. The obtained regression model presents the high correlation with the experimental results based on the adjusted R^2 of 92.2%. Carefully utilizes this model, the practical limit of maximum clients that an AP can support can be systematically predicted.**

I. INTRODUCTION

Since its introduction, the IEEE 802.11g wireless LAN (WLAN) has grown rapidly to hold its place as fundamental infrastructures that organizations of any size should have. As an extension to IEEE 802.11b, IEEE 802.11g standard can support transmission rate in data link layer up to 54Mbps. This quite-high data rate attracts the consumers who prefer flexibility/mobility over transmission ability. In providing the WLAN access to clients, no matter what entire network configurations are; the access point (AP) must be utilized to serve clients as a wireless hub in the service area. It can be said that the AP is one of the most importance parts in providing WLAN because the WLAN services cannot be supplied without an AP.

Due to its roles, the quality of WLAN in a particular service area has significantly depended on the performance of the operated AP, which has been studied in many perspectives. Most of the literature concerns MAC throughput [1 – 5] and area coverage [2 – 4]. MAC throughput analyses are conducted in saturated [1, 5] and non-saturated conditions [2 – 4]. The saturation analyses are conducted in ideal operating conditions at maximum or specified signal strength while the non-saturation analyses count the quality of signal that is related to the service area as part of the throughput estimation. Though these analyses can provide framed design issues for WLAN installer, the analyzed data is based on one or few clients. As IEEE 802.11g provides contention service based on CSMA/CA, the performance of an AP may be reduced as the amount of clients increases. Usually, the number of supported clients identified by an AP is based on its capacity to keep record of the MAC address. Therefore, this specification only states the upmost limit of client's quantity without any transmissible guarantee. To install a useable WLAN practically, the amount of clients that is the practical limit, which reflects the actual ability in data transmission of an AP should be able to estimate based on the required minimum throughput. In addition, any install networks are suppose to carry the user data such as message, voice, video, etc., which resides in application layer and usually measured in byte. If the minimum required AP's throughput could be specified in byte/sec at the portal of application layer, it may be more preferable especially to non-specialist installers that are increasing rapidly as the price of WLAN products are reduced daily. In this literature, the model for predicting the goodput (the application level throughput) of an AP is presented based on the full-factorial experiment that simulates the heavy-loaded condition, which is the worst situation of an AP that all clients are connected at full possible data link capacity and simultaneously transfer TCP stream. The factors are the number of concurrent TCP sessions and the provided data link capacity of an AP. Because there is no such operating condition worse than this, an obtained model can be utilized to estimate the practical limit of the amount of clients related to the required goodput.

II. EXPERIMENTAL ENVIRONMENT

A. Network Configuration

All clients are paired while connecting to the only serviced AP at maximum transmission rate and signal strength. Each pair is composed of one server and client to establish one TCP session as illustrated in fig.1.

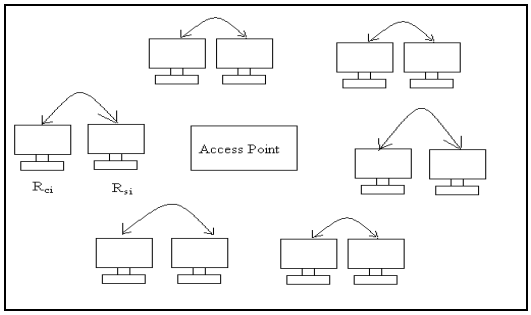

Figure 1. WLAN configuration of the experiment

The dedication of each pair to only one session is for avoiding the bottleneck situation that might happen if there is only one server. The server and client are both running the data-rate measurement program summarized in fig. 2.

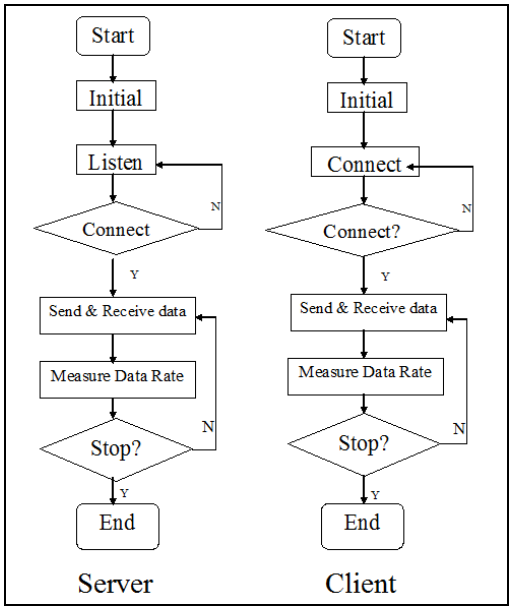

Figure 2. Flowchart of measured program

To simulate heavy-loaded condition, each side continuously transmits block of data immediately after received from a partner. In this fashion, only one pair of measured program can utilize 100% of AP's capacity. As both sides exchange data in half-duplex style and the measured data-rate on each side is the amount of receiving data divided by specified interval, the total data-rate of each pair is the summing of data-rate measured in server and client.

B. *The Access Point*

The AP in this experiment is the LINKSYS Wireless-G Access Point model WAP54G, which is configured with default value for MAC properties as illustrated in fig. 3 [6].

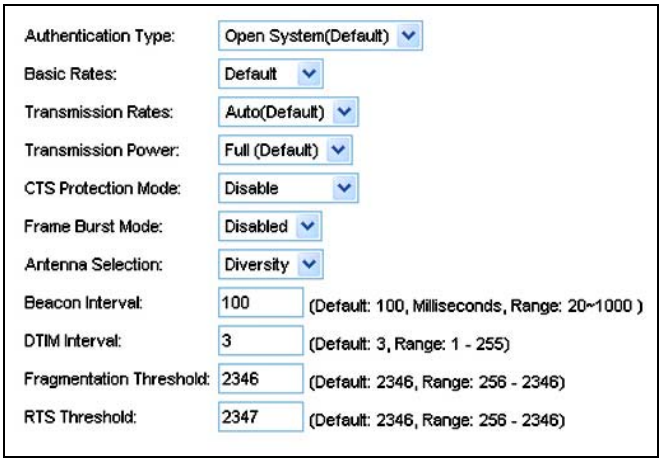

Figure 3. Advance wireless settings screen [6]

C. *The Clients*

All clients are PCs of similar configuration (P4 630, 256MB RAM, WinXP) equipped with LINKSYS Wireless-G PCI Adapter model WMP54G.

III. DESIGN OF EXPERIMENT

A. *The Factors*

The factors which we are interested in are the amount of concurrent TCP streams and the maximum transmission rate in M bit/sec at data link layer limited by the AP. To aid in presentation, the amount of streams will be designated by "S" symbol, and the transmission rate will be designated by "R" symbol.

B. *The Response*

To provide an exploitable model that can be easily interpreted by non-specialists, the response is the goodput of an AP in K byte/sec. Based on the experiment the response can be formulated as (1).

$$T_{S,R} = \sum_{i=1}^{S} (DRs_{i,R} + DRc_{i,R}) \qquad (1)$$

$T_{S,R}$ is the AP's goodput employing S stream sessions and R Mbps, $DRs_{i,R}$ and $DRc_{i,R}$ are the data rate measured at server and client of the i^{th} pair based on R Mbps.

C. *The Design*

To study the main effects and interaction between factors, the experiment is designed to be 2-factor full factorial experiment. The test is run on each combination of factors three times (three replicates).

S factor is designed to have six levels; R factor is designed to have three levels. This yields a 6×3 factorial design with the factor description in table I. With three replicates, there are 54 runs, which are assigned at random.

TABLE I
FACTORS DESCRIPTION

Factor	Level value
S	1 2 3 4 5 6
R (Mbps)	24 36 48

Though the maximum value of stream session is only six, it requires twelve PCs to produce. Incidentally, the transmission rates are specified in three values with the equal space of 12Mbps.

IV. RESULTS AND ANALYSIS

The raw results of the experiment are displayed in table II, which are checked for model adequacy at first sight for the normality and constant variance assumption.

TABLE II
EXPERIMENTAL RESULTS

TCP streamed sessions	Transmission Rate (Mbps)		
	24	36	48
1	1044	1206	1280
	1040	1204	1290
	1044	1205	1292

TCP streamed sessions	Transmission Rate (Mbps)		
	24	36	48
2	1073	1250	1310
	1085	1262	1247
	1078	1228	1288
3	1027	1258	1242
	1000	1216	1277
	1015	1183	1205
4	1006	1299	1231
	991	1132	1211
	985	1129	1246
5	1008	1218	1258
	972	1171	1268
	970	1171	1259
6	950	1111	1184
	984	1107	1220
	949	1121	1206

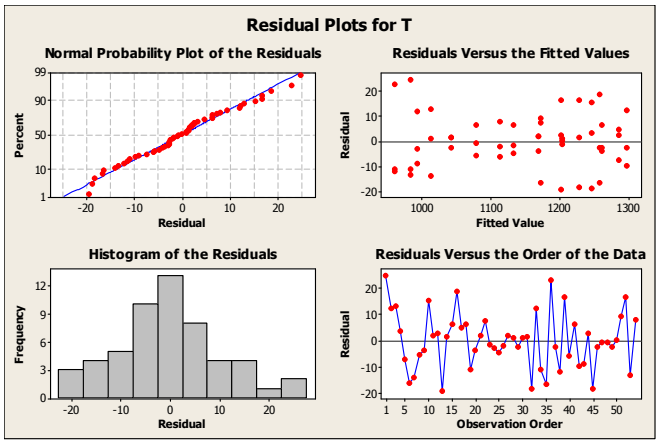

Figure 4. Residual Plots for normality checking

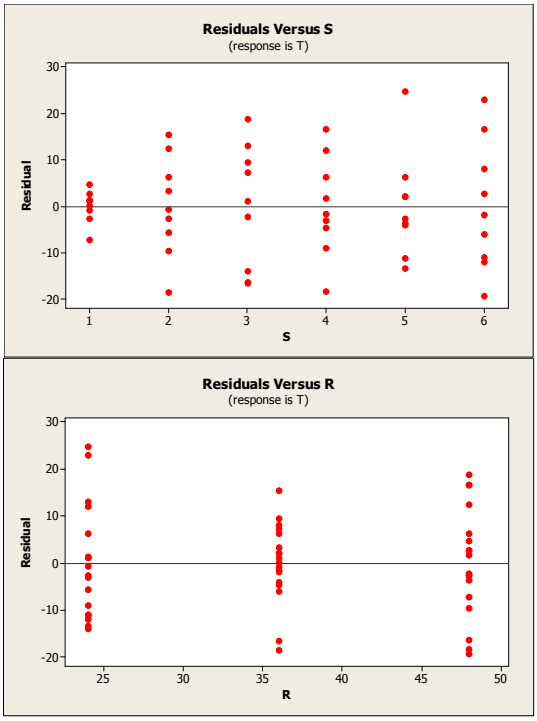

Figure 5. Residuals plot for constant variance checking

From these graphs, there is no severe indication of any problems with the validity of normality and constant-variance assumption.

To determine whether the factors affect the response or not, we use ANOVA tables with $\alpha = 0.05$.

TABLE III
ANOVA FOR THROUGHPUT, USING ADJUSTED SS FOR TESTS

Source	DF	Seq SS	Adj SS	Adj MS	F	P
R	2	554285	554285	277142	1693.33	0.000
S	5	76550	76550	15310	93.54	0.000
R*S	10	4414	4414	441	2.70	0.014
Error	36	5892	5892	164		
Total	53	641140				

From ANOVA, there are strong indications of significant effects of S and R on AP's goodput. In addition, the interaction between S and R is also significance. To intensely analyze these effects and interaction, main effects and interactions of the response are separately plotted.

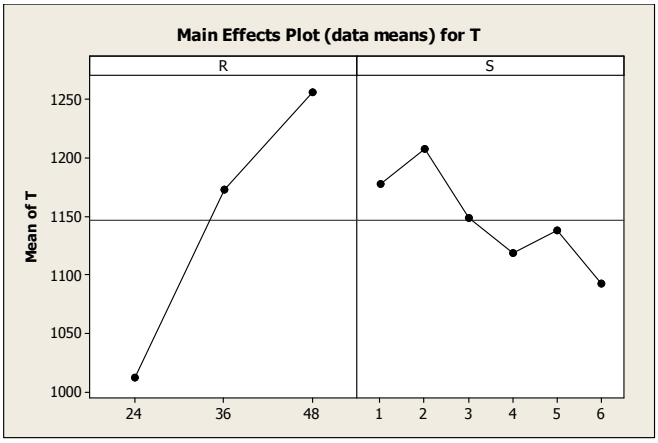

Figure 6. Main effects Plot

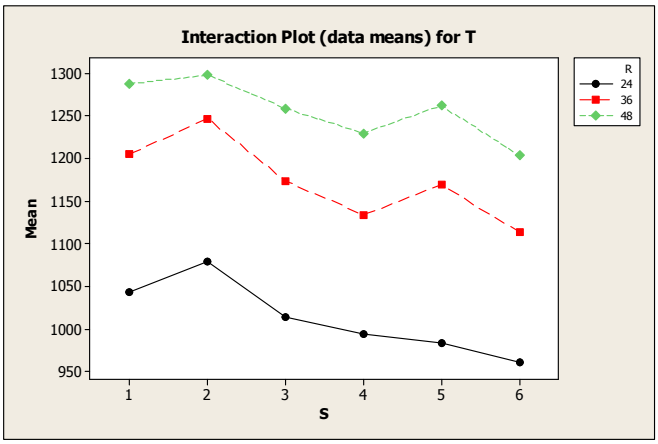

Figure 7. Interaction Plot

The main effect plots in fig.6 show the effect of each factor on the AP goodput. The interesting point is the effect of concurrent TCP stream sessions that significantly reduce the goodput of an AP. Based on fig. 7, the interaction of the transmission rate and sessions are not of serious concern because the goodput obtained at a higher transmission rate is

more than a lower one no matter how much concurrent TCP streamed sessions.

To obtain a model for predicting the goodput of an AP, the regression analysis is carried out and results in (2) with adjusted R^2 of 92.2%.

$$T(S,R) = 872 - 25.8S + 9.51R + 0.187SR \quad (2)$$

Substitute R of a configured AP in (2), results in one variable formula *T(S)*. To predict the number of clients based on the required AP's goodput, set an equation as in (3) and solve it to estimate the practical limit of maximum clients connected to particular APs.

$$T(S) = K \quad (3)$$

K denotes the minimum required goodput of an AP when carrying user data. For example; if the installer wants to guarantee that the installed AP can transfer user data at least 800k byte/sec based on the maximum data-link transmission rate of 54Mbps, (2) incorporated with (3) becomes:

$$800 = 1385.54 - 15.702s \quad (4)$$

As s = 37.2908, the amount of clients should not exceed 37 in order to guarantee the service of an AP under any situations.

However, being strict to the practical limit can cause an un-optimized installation because the worst situation as in an experiment is hardly to occur. Therefore, the maximum amount of supported clients can be dwelled reasonably between the practical limit and halfway to the upmost limit if the traffic is generally not too dense.

V. CONCLUSION

The conducted experiment shows strong evidences of the AP's goodput deterioration as the concurrent sessions are increasing. Based on the amount of clients and maximum transmission rate, the model is drafted for predicting the goodput of an AP. This model can be utilized to estimate the practical limit of maximum supported clients while vendors specify the upmost limit based on the AP's ability to keep track of MAC addresses. As the model is crafted based on worst-case simulation, any operating condition are guaranteed to function validly if the practical limit is not exceeded.

ACKNOWLEDGMENT

The authors would like to convey special thanks to Mr. Charles Lichtenberger JR. whom kindly reviewed this manuscript and provided precious comments on grammatical issues. We also like to express gratitude to the staffs of MFU's IT service center whom kindly provides technical information of AP's configurations and operations.

REFERENCES

[1] M. J. Ho, J. Wand, K. Shelby, and H. Haisch, "IEEE 802.11g OFDM WLAN Throughput Performance," Proc. IEEE VTC 2003, vol. 4, pp. 2252 – 2256, Oct 2003.

[2] A. Doefexi, S. Armour, L. Beng-Sin, A. Nix, and D. Bull, "An Evaluation of the Performance of IEEE 802.11a and 802.11g Wireless Local Area Network in a Corporate Office Environment," Proc. IEEE conf. ICC'03, vol. 2, pp. 1196 – 1200, May 2003.

[3] P. Pechac, M. Klepal, and A. Martinez, "Modeling and Optimization of Heterogeneous Wireless LAN," Proc. IEEE VTC 2004, vol 6, pp. 4442 – 4445, Sept 2004.

[4] B. Drilo and L. Flatz, "Measured Throughput and SNR of IEEE 802.11g in a Small Enterprise Environment," Proc. IEEE VTC 2005, vol. 2, pp. 1333 – 1337, May 2005.

[5] E. Palletta and H. Velayos, "Performance Measurements of the Saturation Throughput in IEEE 802.11 Access Points," Proc. WIOPT 2005, pp. 129 – 138, Apr 2005.

[6] LINKSYS Division, "Wireless- G Access Point User Guide Model No. WAP54G," Cisco System, Inc., p. 49, 2005.

Time-Optimal Graph Algorithms for Finding Adjacent and Non-Adjacent Nodes on a Completely Overlapping Network

Rasika Winit[*], Sanpawat Kantabutra[+], and Saowaluk Rattanaudomsawat[++]
Schools of Physics and Biological Earth and Environmental Science[*],
Faculty of Science, the University of New South Wales, Sydney, AUSTRALIA
The Theory of Computation Group[+],
Computer Science Department, Chiang Mai University,
Chiang Mai, 50202, THAILAND
School of Information Technology, Mae Fah Luang University[++],
Chiang Rai, 57100, THAILAND
Correspondent: sanpawat@alumni.tufts.edu

***Abstract*-A completely overlapping network (CON) is an extension of LANs with several overlapping communication lines. Given a graph $G = (V, E)$ where V is a set of vertices and E is a set of edges, and a set of vertices $V' \subseteq V$, we show that finding adjacent and non-adjacent nodes in V' on CON can be done optimally and has a significant speedup over the sequential machine.**

I. Introduction

Graph problems have many interesting applications. Applications vary, depending upon how one defines the relationship between nodes and edges of a particular graph. In this paper we discuss non-optimized and relaxed versions of two classical graph problems called *maximum clique* and *maximum independent set* problems [1]. Given a graph $G = (V, E)$ where V is a set of vertices and E is a set of edges, and a set of vertices $V' \subseteq V$, we want to find all adjacent nodes in V' and all non-adjacent nodes in V'. Sequential algorithms for these two graph problems have the running times of $O(|V'|^2)$ and this bound appears to be the lower bound for these problems. If the size $|V'|$ is proportional to $|V|$, the running times become $O(|V|^2)$. When the problem size is large, these algorithms will become impractical due to their high time complexities. Parallel computation will be useful in this case.

The concept of parallel computation has been around for decades. However, parallel architectures such as hypercube and mesh are generally expensive [2] and, hence, their use is limited to only those who can afford them. In this paper we use one alternative to these expensive parallel machines called a *completely overlapping network* or CON for short [3] to compute the solutions to our graph problems.

In the following sections we first give a review of CON. Secondly, the algorithm for finding adjacent nodes and its properties are given. Thirdly, the non-adjacent nodes finding algorithm and its properties are shown. Finally, we conclude with some comments and practical use of our algorithms on CON.

II. Completely Overlapping Network

A completely overlapping network is a generalized version of an overlapping network [4-6] and is composed of several overlapped communication lines that connect among several nodes (or processors) to provide parallelism. There are vertical communication lines and horizontal communication lines. These lines constitute a grid-like network for parallel communication as shown in Fig. 1 below.

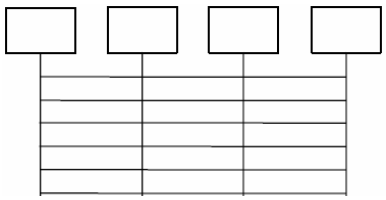

Figure 1. Four-node completely overlapping network

The number of vertical lines is equal to the number of nodes N and the number of horizontal lines is equal to $N(N-1)/2$. One straight line *segment* equates one step horizontally and vertically. (Note that a line in CON comprises several line segments.) For instance, Fig. 2 shows a communication of 9 steps between the leftmost node and the rightmost node.

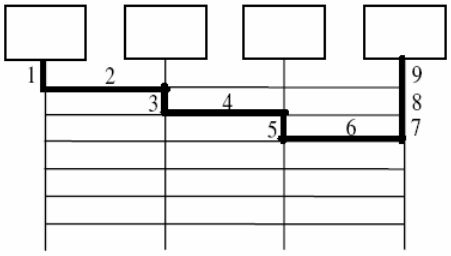

Figure 2. Nine-step communication between nodes

Like any other networks, there are rules of operations. These rules are reasonable and can certainly be implemented. The rules are as follows.

- Horizontal and vertical line segments cannot be shared. That is, any line segment can be used only one at a time.
- Each line segment is bidirectional.
- A same message can be concurrently sent from one node to several destination nodes as long as there is no collision of messages.
- If contention exists in a communication line segment, some kind of priority can be applied.

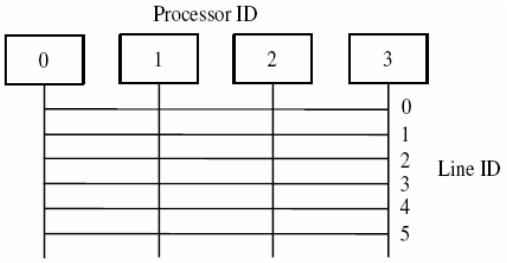

Figure 3. Numbering scheme for a four-node CON

In order to enable readers to understand our communication method, a numbering of both nodes and communication lines is necessary. Our numbering scheme is illustrated in Fig. 3. This figure shows a four-node CON with node and line identification numbers. It is easy to generalize this numbering scheme for a *N*-node CON. Hereafter, we will refer to this numbering scheme when explaining our algorithms.

III. ADJACENT NODES FINDING ALGORITHM ON CON

Given a graph $G = (V, E)$ where V is a set of vertices and E is a set of edges, and a set of vertices $V' \subseteq V$, we want to find all adjacent nodes in V' using CON. The algorithmic definition for such work is given below. Variables *dataset* and *knownPts* are V' and the set of all nodes adjacent to node *k* respectively.

It is assumed that $N > 2$ and each processor (or node) in the CON has its identification number stored in it initially. We also assume one process per processor and constant *myID* is its own process identification number. The subroutine **length**(*A*) returns the number of elements in the array *A*. There are two communication subroutines in the algorithm: **send**(*data*, *destination process*, *communication line number*) and **recv**(*data*, *source process*). These subroutines require identification numbers for both lines and nodes. Also note that **append**(*A*, *n*, *x*) is a subroutine that appends *n x*'s to the array *A*. The subroutine **pack**(*item1*, *item2*, …, *itemN*) is a subroutine that packs all stated items together as one larger item and the subroutine **unpack**(*packed items*, *item1*, *item2*, …, *itemN*) does just the opposite. It is also assumed that an amount of time spends on pack and unpack items is the same for any number of items. Subroutine **matching**(*senderID*, *adjacent nodes*) organizes the process identification number and their adjacent nodes into the form {{*senderID*, *Pts1*}, {*SenderID*, *Pts2*}, …, {*senderID*, *Ptsj*}}, where *Ptsi* is in the set of adjacent nodes and the size of this set is *j*.

INPUT: *dataset* and *knownPts*
OUTPUT: a set of adjacent nodes in V'
Adjacent Nodes Finding Algorithm for Process P_*k*
1 *mySize* = **length**(*knownPts*)
2 *maxSize* = *mySize*
3 **for** $i = 0$ to N-1 and $i \neq myID$
4 **send**(*mySize*, *P_i*, *myID*)
5 **for** $i = 0$ to $N - 1$ and $i \neq myID$
6 **recv**(*size*, *P_any*)
7 **if** *maxSize* < *size*
8 *maxSize* = *size*
9 *extralength* = *maxSize* – *mySize*
10 *newPts* = **append**(*knownPts*, *extraLength*, -1)
11 **if** *myID* ∈ *dataset*
12 *matchPts* = *newPts* ∩ *dataset*
13 *IDandPts* = **pack**(*myID*, *matchPts*)
14 **send**(*IDandPts*, *P_0*, *myID*)
15 *result* = ∅
16 **if** *myID* = 0
17 **while recv**(*IDandPts*, *P_any*) ≠ NULL
18 **unpack**(*IDandPts*, *senderID*, *Pts*)
19 *result* = *result* ∪ **matching**(*senderID*, *Pts*)
20 return *result*

One of the arguments in subroutine **send**() indicates the communication line to use. (There is no such argument in **recv**().) Fig. 4 shows how the lines are used in this algorithm in lines 3 and 5. Four different sources of communication are denoted by four different arrow patterns. There are a total of 11 communication steps. This communication scheme can be easily generalized for a *N*-node CON.

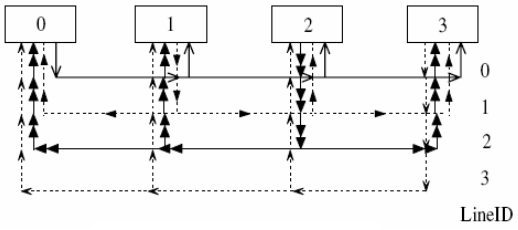

Figure 4. Overall steps

Like any communication scheme, it is vital that there be no collision of messages on any of these communication lines (or any line segment) at any point in the algorithm. Kantabutra et al [3] showed that this communication scheme produces no collision and takes O(*N*) time steps.

Theorem 3.1 (Time Complexity) *The Adjacent Nodes Finding Algorithm on CON has O(N) time complexity, where N = |V|.*

Proof: Assume one communication step is equal to one computation step. Without loss of generality, we only consider communication time. Lines 4 and 6, and lines 14 and 17 dominate the running time. Hence, the time complexity is O(*N*). The theorem holds. ■

Theorem 3.2 (Lower Bound) *The adjacent nodes finding problem on CON has Ω(N) time complexity, where N = |V|.*

Proof: In order to solve *any* instance of the adjacent nodes finding problem on CON, some *global* information is needed since each node only knows its adjacent nodes (i.e., *knownPts*) and does not have complete knowledge of graph G (i.e., does not know E). Therefore, in order to produce a solution, at least one of the nodes must gather necessary information from the other nodes either *directly* or *through some other nodes*. In either case, the distance between such pair of nodes is *at least* $\lfloor N/2 \rfloor + 2$ steps (i.e., one node in the middle and the other nodes in either leftmost or rightmost positions where N is odd). Thus, this establishes the lower bound. The theorem holds. ■

Theorem 3.3 (Optimality) *The Adjacent Nodes Finding Algorithm is time-optimal on CON.*

Proof: Theorems 3.1 and 3.2 directly imply the optimality of the algorithm. Hence, the theorem holds. ■

IV. NON-ADJACENT NODES FINDING ALGORITHM ON CON

Given a graph $G = (V, E)$ where V is a set of vertices and E is a set of edges, and a set of vertices $V' \subseteq V$, we have shown the algorithm to optimally find all adjacent nodes in V' using CON. Given the same inputs, we now want to find all non-adjacent nodes in V' using CON. The algorithmic definition for finding non-adjacent nodes in V' is almost the same as the one for finding adjacent nodes in V'. All assumptions and subroutines in the previous section still apply to this algorithm. Following are the code and some important theorems.

INPUT: *dataset* and *knownPts*

OUTPUT: a set of non-adjacent nodes in V'

Non-Adjacent Nodes Finding Algorithm for Process P_*k*

```
1  mySize = length(knownPts)
2  maxSize = mySize
3  for i = 0 to N-1 and i ≠ myID
4      send(mySize, P_i, myID)
5  for i = 0 to N – 1 and i ≠ myID
6      recv(size, P_any)
7      if maxSize < size
8          maxSize = size
9  extralength = maxSize – mySize
10 newPts = append(knownPts, extraLength, -1)
11 if myID ∈ dataset
12     matchPts = newPts ∩ dataset
13     noCon = dataset - matchPts
14     IDandPts = pack(myID, noCon)
15     send(IDandPts, P_0, myID)
16 result = ∅
17 if myID = 0
18     while recv(IDandPts, P_any) ≠ NULL
19             unpack(IDandPts, senderID, Pts)
20             result = result ∪ matching(senderID, Pts)
21     return result
```

Theorem 4.1 (Time Complexity) *The Non-Adjacent Nodes Finding Algorithm on CON has O(N) time complexity, where N = |V|.*

Proof: Because this code differs from the code in theorem 3.1 only in line 13, the time complexity is still dominated by the communication time. Hence, the time complexity is O(N). The theorem holds. ■

Theorem 4.2 (Lower Bound) *The non-adjacent nodes finding problem on CON has Ω(N) time complexity, where N = |V|.*

Proof: This problem is a complement of the Adjacent Nodes Finding problem on CON. That is, using $G = (V, \bar{E})$ as the input graph instead of G. Thus, the lower bound is the same as the one in theorem 3.2. ■

Theorem 4.3 (Optimality) *The Non-Adjacent Nodes Finding Algorithm is time-optimal on CON.*

Proof: Theorem 4.1 and 4.2 directly imply the optimality of the algorithm. Hence, the theorem holds. ■

V. CONCLUSIONS AND OPEN PROBLEM

Graphs have many applications in the real world and, as a consequence, so do our algorithms on CON. For instance, if an edge between any pair of two nodes (i.e., persons) represents a genetic relationship (i.e., great grandmother) between them. Given a subset of nodes, we may want to know who is related to whom genetically. In this paper we have shown that, given a graph $G = (V, E)$ and $V' \subseteq V$, our algorithms find adjacent and non-adjacent nodes in V' on CON in *asymptotically minimum* time and both have a speedup factor of N over their respective sequential algorithms. However, we have so far considered the fine-grained model in which one vertex in V gets mapped to one node in CON. Taking advantage of the gap between communication and computation speeds, we may want to map more than one vertex in V onto one node in the coarse-grained model in which processors are more powerful. The interesting problem in this model is how to map these vertices optimally. This remains a challenge for us to conquer.

ACKNOWLEDGMENT

This work was partially done while Sanpawat Kantabutra was visiting the School of Computing at Armstrong Atlantic State University, Georgia, USA. He would like to thank the School of Computing for letting him use computer equipments and the Internet.

REFERENCES

[1] M. R. Garey, and D. S. Johnson, *Computers and Intractability: A Guide to the Theory of NP-Completeness.,* W. H. Freeman, New York, 1979.

[2] T. E. Anderson, D. E. Culler, and D. Patterson, "A case for NOW", *IEEE Micro.,* vol. 15, No. 1, Feb., 1995, pp.54-64.

[3] S. Kantabutra, W. Jindaluang, and P. Techa-angkoon, "It's elementary, my dear Watson: Time-optimal sorting algorithms on a completely overlapping network," *Lecture Notes in Computer Science,* vol. 3758, Springer-Verlag, Nov. 2-5, 2005, pp. 252-262.

[4] B. Wilkinson, "On crossbar switch and multiple bus interconnection networks with overlapping connectivity," *IEEE Transactions Computers*, vol. 41, 1992, pp. 738-746.

[5] B. Wilkinson, and J. M. Farmer, "Reflective interconnection networks," *Computer and Electrical Engineering,* vol. 20, 1994, pp. 289-308.

[6] K. Hoganson, B. Wilkinson, and W. H. Carlisle, "Applications of rhombic multiprocessors," *Proceedings of the International Conference on Parallel and Distributed Processing Techniques and Applications*, 1997.

On the Effects of VLAN in WLAN-based Positioning System

Chalermchai Khauphung Phongsak Keeratiwintakorn
Department of Electrical Engineering
King Mongkut's Institute of Technology North Bangkok, Thailand.
Email: ckp_mee@hotmail.com, phongsakk@kmitnb.ac.th

Kamol Kaemarungsi
National Electronics and Computer Technology Center (NECTEC), Thailand
Email: kamol.kaemarungsi@nectec.or.th

***Abstract*-This paper presents a study on the effects of using virtual local area network (VLAN) on top of wireless local area networks (WLAN) that is used for indoor positioning systems based on location fingerprinting technique. This study investigates how VLAN on WLAN can improve the positioning performance of indoor positioning systems. The approach taken by this research is based on performing measurement experiments on positions within a building. We compare the results between a system with VLAN and without VLAN. Our results indicate that the system with VLAN can determine positions with higher precision than that without VLAN. The measurement results show that precision is improved by 5% - 10% on the average within the error distance (or accuracy) of 1 - 3 meters in the hallway area. The results of the experiment in this research suggest that VLAN can help increase positioning performance without having to add or install any real access points (APs) to the WLAN-based positioning system.**

Keywords: WLAN, Geolocation, Positioning System, Location Fingerprint, VLAN

I. INTRODUCTION

Nowadays, the most popular solution for positioning system is the Global Positioning System (GPS). The GPS system can find object's position by using at least three signals from at least three different satellites around the earth's orbits. However, GPS has limitation when using for indoor positioning due to the limitation in a line-of-sight between the object in indoor and the satellites. One of the solutions is to build repeaters for GPS signal in indoor as in [1]; however, the cost of the installation and additional devices becomes higher for the GPS-based indoor positioning system.

There are other alternative techniques used to create indoor positioning systems such as infrared, ultrasound and radio frequency (RF). Thus far, one of the radio frequency techniques which use only radio frequency patterns to determine locations in [2] has gained a lot of attention. This is due to a better signal penetration of RF in indoor than the other types of signals. The basic idea of this radio frequency based positioning system is to exploit the relationship between patterns of received signal strength (RSS) from access points (APs) in wireless local area network (WLAN) and locations of objects. Without determining the angle of arrival (AOA) and the time of arrival (TOA), the system uses only the pattern of RSS to determine a location of an object, and this technique is called the *location fingerprinting technique* [2]. This technique has the advantage over the other technologies in its implementation since the system can reuse the pervasive and existing installation based of WLANs in most buildings to implement indoor positioning systems. Currently, wireless local area networks have been deployed extensively in both government sector and private companies. Moreover, there is no need in adding any special devices to enable the indoor positioning system.

The idea of using WLAN for location fingerprinting has been around for some time. The direction of most researchers in this area has been focusing on improving the performance of indoor positioning system with novel algorithms [3][4][5][6]. However, recent advances in WLAN technology itself might have impact on the performance of indoor positioning systems. The IEEE standards have created 802.11b, 802.11a, 802.11g, and soon the 802.11n [7]. However, all of them can be applied to the location fingerprinting technique since the RSS is still available for measurement.

Another improvement on WLAN is to enable the use of VLAN on top of WLAN. The technique of VLAN allows only one AP to broadcast multiple service set identifiers (SSIDs) to mobile clients [8]. This creates multiple virtual networks per AP. From the client's perspective, it is as though the system has additional access points, depending on the number of VLAN created. To the best of the authors' knowledge, there is no study in the literature that has addressed the impact of VLAN on location fingerprinting technique.

Generally, the deployment of fingerprinting based positioning systems can be divided into two phases [2]. First, in the off-line phase, the location fingerprints are collected by performing a site-survey of RSSs from multiple APs at different positions. The distance between two closest physical positions during the survey period is called *grid spacing* which is usually reported in meters or feet. The RSSs from all APs that can be received on a position is measured with enough statistics to create a database of RSS patterns called a *radio map*. The vector of RSS values at a position on the grid is called the *location fingerprint*. This off-line phase can be very time-consuming if there is no survey plan with a clear performance objective, and the size of indoor area is very large.

Second, in the on-line phase, a mobile station (MS) reports a sample measured vector of RSSs from different APs to a position location server (or a group of APs collects the RSS

sample from a MS and sends it to the server). Then, the server uses a pattern classification technique to estimate the location of the MS and reports the estimate back to the MS (or an application requesting for position information). The most common algorithm used to estimate the location is to compute the Euclidean distance between the measured RSS vector and each fingerprint in the radio map.

The study in this manuscript shows the results of the experiment of the indoor positioning system based on both prototype and our own modified version of NIST (National Institute of Standards and Technology) Location Systems [11]. We compared the positioning performance of the system with and without VLAN. The organization of this paper is as follows. First, we begin our discussion of VLAN technique and fundamental of VLAN in Section II. Next, we describe our experiment environment and setup in Section III. The results of the experiments and the analysis are reported in Section IV. Finally, we conclude our finding and suggest our plan on the future work in Section V.

II. WLAN AND VLAN

Virtual Local Area Network (VLAN) is the technology that builds a model of Local Area Network (LAN) that does not depend on a physical connection [8]. Because VLAN is a LAN model, for example, one LAN switch can create a model of five networks, or three LAN switches can be combined into one network. To create one VLAN from multiple switches, a dedicated port, called a *trunk port*, is required to connect each switch together. VLAN can only be used with devices with routing or switching capability such as routers or switches.

VLAN protocol works on Layer 2 (data link layer) of a protocol stack, which is developed to control Layer 2 broadcasting. Most Layer 2 switches now support IEEE 802.1Q VLAN standard [9]. VLAN can be divided into five categories based on its membership construction. The first category creates a Layer 1 (physical layer) VLAN membership using physical ports. The second category creates a Layer 2 VLAN membership using MAC (Medium Access Control) address in which system diverts traffic according to the MAC address, and this is the case in our experiment with WLAN. The third category creates a Layer 2 VLAN membership using protocol types. The fourth category creates a Layer 3 (network layer) VLAN membership using IP subnet address. Finally, the fifth category creates higher layer VLAN. We commonly use VLAN to mitigate network congestion due to broadcast traffic, to simplify network administration, and to add security of access control to the network.

VLAN also works on WLAN, and it employs the same principle as that of wired LAN switches [8]. Most WLAN switches or access points create multiple VLANs based on MAC addresses since they do not have physical ports. In our experiment, we used Cisco 1100 AP which divided VLAN according to MAC address or Basic Service Set Identifier (BSSID)[10].Without VLAN, each AP periodically broadcasts beacon frame of 50 bytes over the air to advertise single network information such as Service Set Identifier (SSID), supported rates, capability information, parameter sets, and traffic indication map [7]. In indoor positioning system that collects RSSs from APs, the reception of beacon is a means to measure the RSS for creating location fingerprint. Note that an alternative is to send a probe request to an AP and waiting for a probe reply to determine the RSS. However, the RSS measurement is normally performed by the wireless card without user intervention. The user can obtain the RSS information through specialized API as in NIST's code [11].

In case of a system with VLAN, the AP broadcasts more beacon signals for multiple identities depending on the number of enabled VLANs. For example, if one AP is configured to have four VLANs or SSIDs, it will broadcast four beacons during a pre-determined beacon broadcasting period. Typically, the period between the burst of beacons is set to 100 ms [7]. Since the number of beacons increases with the number of VLANs, the number RSS samples is also increased. This study attempts to determine the gain from enable VLAN on APs in indoor positioning systems.

III. SYSTEM AND SETUP

A. Testbed Environments

In this research, we chose a location on the first floor of our engineering department building at King Mongkut's Institute of Technology North Bangkok as shown in Figure 1. The area of our interest is shown inside the dash-line box which is 48 by 16 meters. The building has six floors and has 11 APs which are all Cisco Aironet 1100 Series. Four out of 11 APs are installed on the first floor as denoted by the black circles in Figure 1. In our experiments, we collected RSSs from all APs to create radio map. However, the signals from all APs cannot be measured at all locations due to obstructions inside the building. Each AP is configured to have four VLANs. Thus, logically to a wireless client, it has 16 APs on the first floor!

In our experiment, we used a Compaq Presario V2427AU laptop computer with an Orinoco Classic Gold PCMCIA wireless interface card. The laptop runs a position location software prototype from NIST [11] which has graphic user interface as shown in Figure 2. The NIST's software allows us to create our own image of map layout and radio map. The deployment of the system follows the same off-line and on-line phases as described in Section I. The program starts by letting the user create an image map. Then, the user has to train the system or collecting the fingerprints in the map. After finishing the process, user can start the location mode or testing the location determination of the system.

We modified the NIST location system so that it can recognize distinct VLANs of the same physical AP. In case of a system with VLAN, the program simply considered each broadcast SSID as a real AP and recorded each RSS in different elements inside a location fingerprint pattern. Note that in one location fingerprint pattern it consists of an array of elements of pattern from multiple APs.

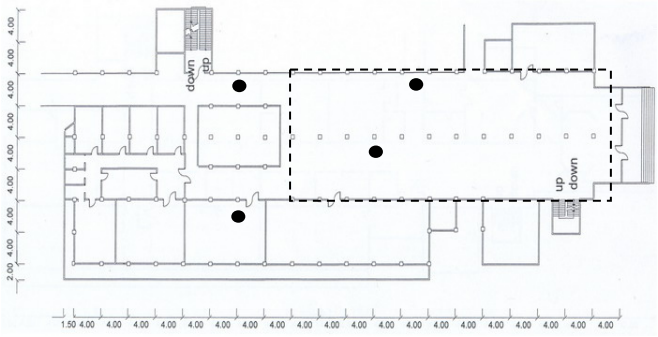

Figure 1.The first floor of our engineering building.

In case of a system without VLAN, the program combined all SSIDs of the same AP into a single element of fingerprint pattern of that AP. This in effect created a fair comparison of both systems because both use the same amount of data samples. The dimension of the radio map of the system with VLAN will be approximately four times larger than the system without VLAN. We used NetStumbler software [12] to detect beacons for the number of VLANs to verify our experiments and to identify the MAC addresses and the SSIDs of the same APs.

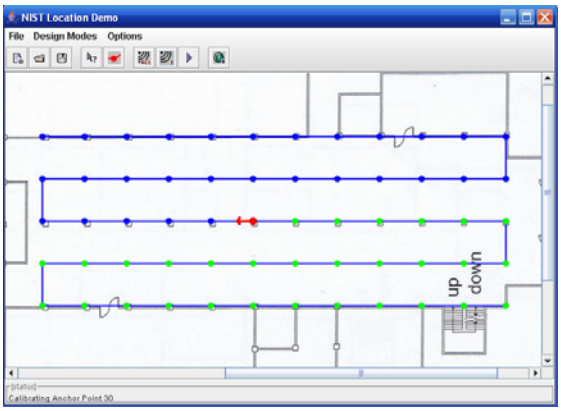

Figure 2.Example of NIST Location prototype program.

B. Experimental Setup

In our experiment, the goal is to compare the performance of the Location system with VLAN and without VLAN. We divided our setup into two phases. In the off-line phase or a training phase, we used the prototype Location System software and the modified Location System software to collect 200 samples of RSS from different APs at each grid location and to create a radio map with the grid spacing of 4 meters. Totally, we had 60 points of grid locations. The radio map is used for location finding in the localization phase. In the on-line phase, or the localization phase, we used the prototype NIST program and the modified NIST program to compare a vector of sampled RSS at a randomly selected location (100 samples from 60 points). Note that the NIST location system utilizes a Markov algorithm embedded in its program to find the most likely position according to the RSS vector [13].

We conducted two experiments of on-line phase, one with measured locations on the grid point and another with measured locations between grid points to compare the performance of the approximation algorithm. In each experiment, we sampled 100 locations and calculated the distance error between the estimated position returned by the program and the actual position. Note that the prototype NIST program and the modified NIST program do not calculated error distance for us. We performed calculation of the error distance by using Euclidean distance equation as in Equation 1. We denoted x_1 and y_1 as the coordinate of actual location while x_2 and y_2 are the coordinate of estimated location returned from the program. In each experiment, we used the same data set to calculate the performance of system with VLAN and without VLAN.

$$\text{Error distance} = \sqrt{(x_1 - x_2)^2 + (y_1 - y_2)^2} \quad (1)$$

IV. Results and Analysis

In the beginning of our investigation, we studied samples of RSSs from different VLANs that came from one of our APs. The results are shown in Figure 3. The graph indicates that the values of the RSS from different SSID are not equal. This led us to take the advantage of the variation in RSSs from different VLAN in location system.

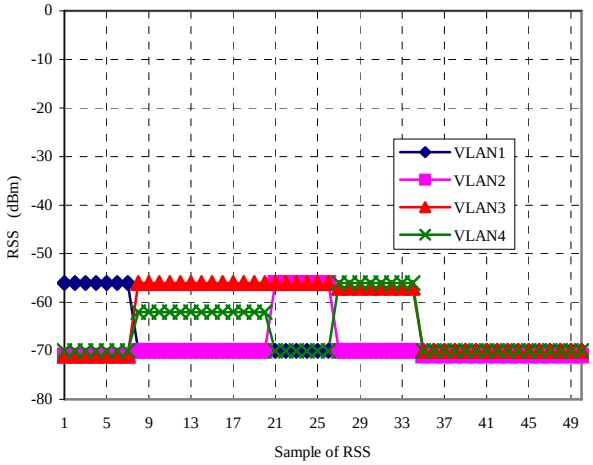

Figure 3.Comparison of the RSS of different SSID from the same AP.

The performance analysis of any positioning systems can be based on two major performance metrics: the accuracy and the precision. The location accuracy is usually reported as the error distance deviated from the actual position, while the location precision is reported in percentages of position information that are within the distance of accuracy [14]. These two performance metrics can be reported in a single plot between error distances or accuracy versus cumulative distribution function (CDF) or precision.

From the two experiments, we divide and discuss the results into two parts. Figure 4 shows the cumulative distribution function (CDF) of the error distance of the experiment that the tested locations are directly on the grid point of positions. The results compared between the system with and without VLAN.

Figure 4 shows that the system with VLAN can improve the precision by about 10% at the small distance error (accuracy)

up to 7 meters. Moreover, at the median (or CDF = 0.5), the system with VLAN can improve the accuracy by about 3 meters. However, the improvement is not significant at the large error distance.

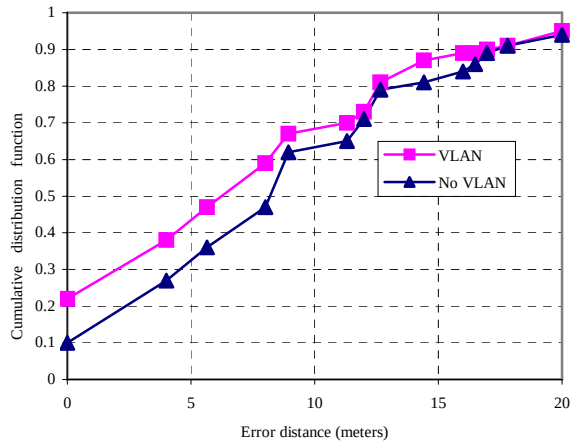

Figure 4. The error distance distribution of measurement at direct grid points.

Figure 5 shows the results of experiments that the tested locations were not directly on the grid points. This shows the similar result as the system with VLAN can improve the precision of the location system over the system without VLAN; however, the error distance is slightly more or the accuracy at the comparable precision is worst than the previous experiment with direct grid point measurement. The improvement of the precision is only about 5%. At the median, the accuracy is improved by about 1-2 meters. Note that the CDF at zero meter in this experiment is zero is because there are no measured locations that are actually in the radio map.

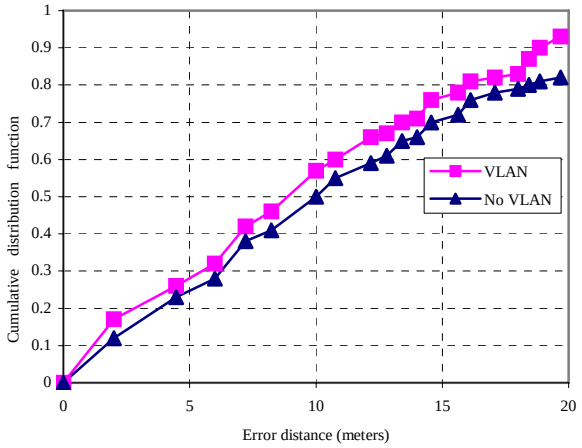

Figure 5. The error distance distribution of measurement at the location between grid points.

In [3], the authors analytically showed that the effect of increasing the number of APs in any location system could improve the overall performance of the system. The technique of using VLAN as showed above is one of efficient ways to increase number of APs to the system. The performance gain is due to a better separation of location fingerprints that have higher degree of freedom.

V. Conclusion and Future Work

Currently, most WLAN deployment employs IEEE 802.11b/g Access Points, and has been extensively used to provide indoor network access. Additionally, switches with VLAN capability become more available at the commodity price. Thus, it is easy to set up VLANs within WLANs as the testbed used in this study. We have shown that the VLAN on top of WLAN can improve the accuracy and precision of the positioning system based on the location fingerprinting technique. The accuracy can be improved by 5% to 10% on the average of 1 to 3 meters of improvement. Although, this is a small number, the improvement requires no additional hardware and can be easily set up from existing WLAN without any additional cost.

For the future work, we will take the advantage of using VLAN for indoor positioning system to track users or devices at same floor and different floors of building.

Acknowledgment

This work is supported by Thailand Graduate Institute of Science and Technology (TGIST)'s grant from the National Science and Technology Development Agency (NSTDA).

References

[1] G. M. Djuknic and R. E. Richton, "Geolocation and Assisted GPS," IEEE Computer, vol. 2, Feb.2001, pp.123-125.

[2] P. Bahl and V. N. Padmanabhan, "RADAR: an in-building RF-based user location and tracking system," in Proc. of IEEE INFOCOM'00, Tel Aviv, Israel, Mar. 2000, pp.775-784

[3] K. Kaemarungsi and P. Krishnamurthy, "Modeling of Indoor Positioning Systems Based on Location Fingerprinting", Proceedings of IEEE Infocom 2004, Hong Kong.

[4] P. Prasithsangaree, P. Krishnamurthy, P. Chrysanthis, "On Indoor Position Location with Wireless LANs," The 13th IEEE International Symposium on Personal, Indoor, and Mobile Radio Communications (PIMRC 2002), September 2002, Lisbon, Portugal

[5] M. A. Youssef, A. Agrawala, and A. U. Shankar, "WLAN location determination via clustering and probability distributions", in Proc. of IEEE PerCom 2003, Dallas-Fort Worth,TX, Mar.23-26, 2003, pp.23-26.

[6] P. Krishnan *et al*, "A System for LEASE: System for Location Estimation Assisted by Stationary Emitters for Indoor RF Wireless Networks, Proceedings of the IEEE INFOCOM 2004, Hong Kong, March 7-11, 2004

[7] IEEE standards, http://www.ieee802.org/11/[Available as of January 25, 2007]

[8] B. A. Forouzan, *Data Communications and Networking*, 3rd Edition, McGraw Hill, ISBN 007-123241-9, 2004.

[9] IEEE 802.1Q VLAN standard,http://standards.ieee.org/getieee802 /download/ 802.1Q-2005.pdf[Available as of January 25, 2007].

[10] Cisco Aironet 1100 series access point installation and configuration guide,Feb.2003,http://www.cisco.com[Available as of January 25,2007]

[11] NIST Location System, http://www.antd.nist.gov/wctg/NISTlocation/ locationdemo.htm [Available as of January 25, 2007].

[12] Netstumbler software ,http://www.netstumbler.com [Available as of January 25, 2007].

[13] C. Gentile and Luke Klein-Berndt, "Robust Location using System Dynamics and Motion Constraints", National Institute of Standards and Technology, Wireless Communication Technologies Group, March 2004.

[14] J. Hightower, and G. Borriello, "Location Systems for Ubiquitous Computing," *IEEE Computer*, vol. 34, no. 8, pp. 57—66, Aug. 2001.

On the Effect of Roadside Stations in Routing for Inter-Vehicle Communications

Phitsanu Eamsomboon and Phongsak Keeratiwintakorn
Department of Electrical Engineering
King Mongkut's Institute of Technology North Bangkok, Thailand.
Email: johnnu555@gmail.com, phongsakk@kmitnb.ac.th

Chaichana Mitrpant
National Electronics and Computer Technology Center (NECTEC), Thailand
Email: chaichana.mitrpant@nectec.or.th

***Abstract*-Inter-vehicle communications is said to be part of the next generation Internet where vehicles can communicate to other vehicles or a roadside station in ad hoc manner to realize the Intelligent Transport System (ITS) which can increase road safety and provide traffic information etc. Several existing routing protocols are extensively studied for inter-vehicle communications. In this paper, we study the effect of installing fixed roadside stations on the performance of routing protocols such as DSR, AODV and GPSR. The study has shown that by adding more roadside stations, the successful rate of transmission is increased. However, the delay is almost constant in any case. For a small city section of 1.2x1.2 km, only about 7 stations per sq. km. is needed to provide the inter-vehicle communications with the successful rate of 96%.**

Keywords: Car-to-Car communication, Inter-vehicle communication, Vehicular Ad-Hoc Network, Routing Protocols, Roadside Station

I. INTRODUCTION

Transportation is part of our daily life or business transactions. Currently, the number of vehicles on roads has constantly increased, but the expansion of road quantity is slower. This causes the traffic jam and also the increasing of road accidents. In order to provide better transportation, Intelligent Transport System (ITS) has been proposed as a solution to ease transportation problems. ITS employs information technologies to mitigate the problems. One important requirement for ITS is vehicle-to-vehicle or vehicle-to-roadside communications to acquire information or to inform vehicles in real-time. For example, a road accident in front of us can be reported from the scene by the vehicles in the accident or nearby vehicles to vehicles in the same traveling route to warn drivers to reduce car speed in real-time. Additionally, the accident is immediately reported to roadside station to inform highway police and related officers to resolve the accident quickly. The car-to-car communication can also be used to prevent serious injury such as to activate the reversible seat belt pretensioners or preconditioning of airbags when an inevitable accident is detected by sensors to prevent severe head injury [1]. The car-to-roadside communication can be used to detect accidents or traffic jams and also used to broadcast information to road users [2].

Proving car-to-car communications have been interested by car manufacturers and communications standard organizations. In 2003, an IEEE standard for car-to-car communications, Dedicated Short Range Communication (DSRC) or IEEE 802.11p, has been published to support a high speed short range communication between vehicles [3]. For example, a vehicle on-board communications system uses DSRC to detect potential accidents to provide the vehicle safety services. Additionally, many research groups have proposed several solutions to realize the vision of car-to-car communications as one of the next-generation networks. One of the problems in the area of vehicle communications is the performance of routing protocols that is not efficient enough to support inter-vehicle communications due to the frequent change of vehicle location due to the high moving speed [4]. In this research, we study the performance of car-to-car communications by adding the roadside stations as fixed wireless nodes to help vehicle communicate with each other and to improve the overall system performance. In this study, we utilize the ns-2 simulator with Restricted Random Waypoint mobility model on the city sections to evaluate the performance of AODV [5], DSR [6], and GPSR [7] routing protocols.

This paper is organized as follow. First, we overview some mobility models and the routing protocols in Section II. In Section III, we explain our simulation experiment and discuss the simulation results in Section IV. Finally, we conclude our major research findings and future research directions in Section V.

II. RELATED WORKS

A. *Mobility Model for City Sections*

Random Waypoint is a common mobility model used in many simulation studies; however, it is not appropriated for studies of inter-vehicle communications where cars are limited on roads or sections. The Random Trip model is proposed as an extension to the Random Waypoint that it restricts cars to be on roads in a city section and always follows other cars without any collision [8]. With respect to Random Trip model, the city section is a particular instance of random waypoint model on a general connected area. The domain of the model is the union of line segments defined by the edges of a given space graph.

B. *Dynamic Source Routing (DSR)*

DSR is one of popular routing protocols for ad hoc networks [6]. It uses broadcast route discovery to build a route to a particular destination. The basic operation of DSR is the hop-by-hop forwarding procedure. When a route request (RREQ) is received, a node looks at the destination address

inside the RREQ. If the address is not already in the request, it puts the address in the request, and forwards the RREQ to neighbors. If the address is already in the RREQ, it means the RREQ has already been processed, and the RREQ is discarded. If the address is its address, it keeps the incoming route and sends back the route reply (RREP) with the list of nodes transversing the route indicating that the destination is found. Due to the hop-by-hop nature, DSR has a large header when a route is long and this normally causes high delay. However, it saves up memory since it only keeps the list of nodes inside the route request.

C. Ad-hoc On Demand Distance Vector Routing (AODV)

AODV is also another popular protocol that is extensively developed and applied for ad hoc routing [5]. Similar to DSR, it broadcasts a route request to its neighbor and the request is forwarded hop-by-bop. However, to reduce the route request overhead, each node maintains a routing table keeping a list of neighbor nodes, and a request is then forwarded according to the table. Therefore, it is important for AODV nodes to keep the table up-to-date. Each node maintains the table by periodically (or on request) checking its neighbors, and broadcasts to other nodes when there is a change. This reduces the route overhead in the request. However, AODV is vulnerable high mobility, which can cause high traffic due to the table updates. To reduce the traffic, the rate of update is reduced; however, it can increase the possibility of routing failure.

D. Greedy Perimeter Stateless Routing (GPSR)

GPSR is a responsive and efficient routing protocol for mobile, wireless networks. Unlike traditional routing algorithms, which use graph-theoretic notions of shortest paths and transitive reach ability to find routes, GPSR exploits the correspondence between geographic position and connectivity in a wireless network, by using the positions of nodes to make packet forwarding decisions [7]. GPSR uses greedy forwarding to forward packets to nodes that are always progressively closer to the destination. In regions of the network where such a greedy path does not exist such as the only path requires that one move temporarily farther away from the destination. GPSR recovers by forwarding in perimeter mode, in which a packet traverses successively closer *faces* of a planar subgraph of the full radio network connectivity graph, until reaching a node closer to the destination, where greedy forwarding resumes.

III. EXPERIMENTS

In this section, we analyze and compare the results of our experiments of routing protocols for inter-vehicle communications which uses random waypoint on a city section as a mobility model. We conducted experiments using the ns-2 network simulation [9].

Our experiments use a real world map of 1200x1200m of West University area, in Houston, TX, USA. The map is extracted using the information from TIGER database [10] as shown in Figure 1. All lines represent actual roads within the plotted area. The map includes about 383 intersections and 594 road segments.

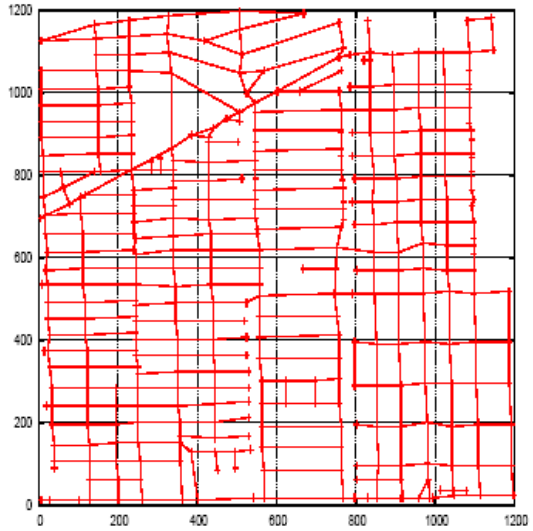

Figure 1. Realistic street scenario of size 1200m× 1200 m

To conduct a large number of experiments required in this study, each scenario was repeated with multiple mobility patterns to attain a 95% confidence interval. In this experiment we consider measuring a successful rate and end to end delay. The successful rate is a ratio of received packets at destinations divided by the number of sent packets from sources. The end to end delay is duration of a packet sent from sources and successfully received at destinations. In the experiments, we set other related routing parameters for simulation as shown in Table I.

TABLE I SIMULATION PARAMETERS

Parameter	**Value(s)**
Number of Nodes	30-300
Simulation Time	1000 sec
Routing Protocols	AODV, DSR, GPSR
NS2 Version	ns 2.29.2
Transmission Range	250m
CBR Sources	20 sources (interval 5-10 sec)
Mobility Models	Random Trip Model for a city section
Topologies	1200x1200m Grid , Real Map
Average Node Speed	5 meters/sec

IV. SIMULATION RESULTS

A. The Variation of Number of Nodes

In this section we compare the performance of different ad-hoc routing protocols as we vary the number of total nodes. The results of the successful rate and the end-to-end delay are shown in Figure 2 and Figure 3.

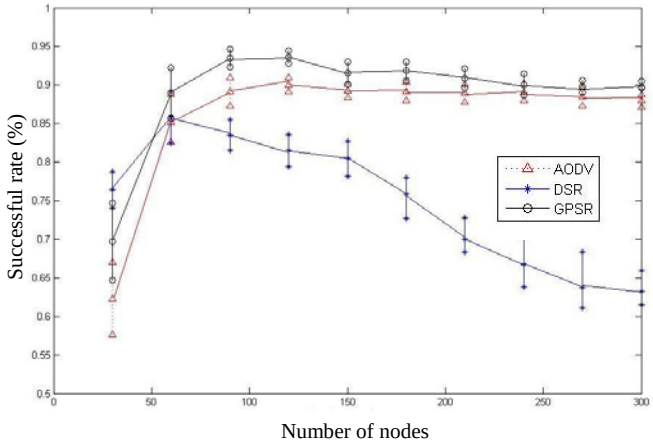

Figure 2. The successful rate with different node numbers

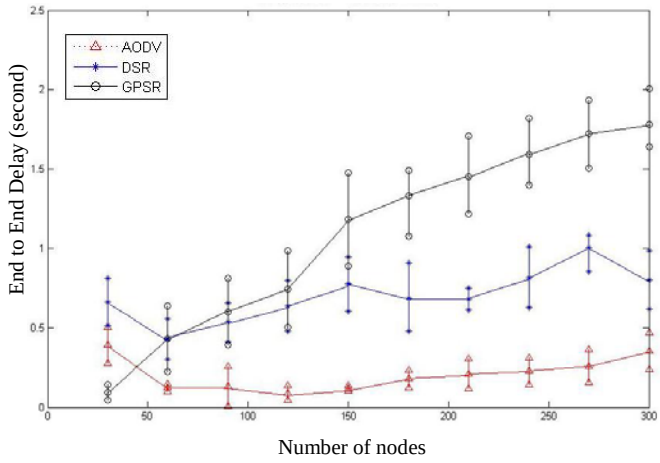

Figure 3. The end to end delay with different node numbers

In Figure 2, the results indicate that for the number of less than 50 nodes, DSR yields the highest successful rate. However, for 50 or more nodes, GPSR and AODV yield the higher successful rate. The reason is that DSR is only efficient when the network size is small, or the path length in hops is short. For GPSR, the greedy forwarding mode is activated to increase the range of packet forwarding to decrease the number of hops in a path. For AODV, each node maintains the route table locally; thus, it is more scalable than other protocols.

Figure 3 compares the end-to-end delay among all routing protocols. GPSR has increasing delay as the number of nodes increases because GPSR greedily uses perimeter forwarding to many neighbors when destination is out of range. In a large network with many neighbors, this causes the increasing delay. As AODV yields the lowest delay because each time a packet is sent, it selects the best route with the minimum number of hop. Thus, the delay tends to be stable as the number of nodes increases.

B. Roadside station into map

For this experiment, we randomly insert fixed wireless stations, called roadside stations, into the map of 1200x1200 meters to introduce vehicle-to-roadside communication to increase network connectivity. We simulate 50 vehicle nodes (the vehicle density is 34.72 nodes/km^2), with a nominal 250-meter transmission range and 10 traffic sources. The results are shown in Figures 4 and 5.

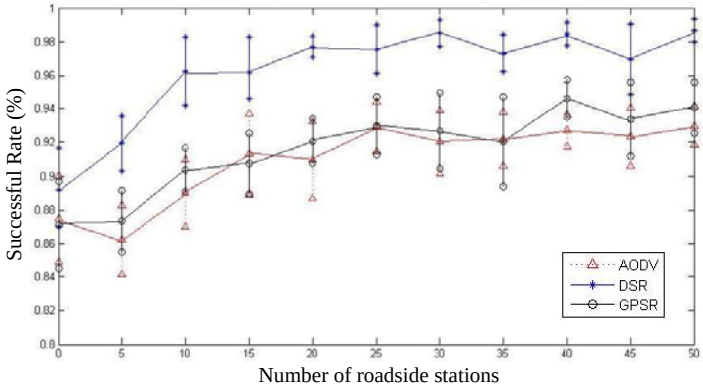

Figure4. The successful rate with different numbers of roadside stations

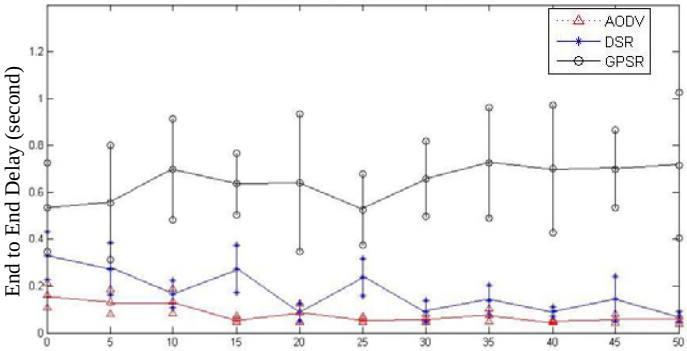

Figure 5. The end-to-end delay with different numbers of roadside stations

In Figure 4, the successful rate of all protocols increases compared to that in Figure 2 as the number of stations increases. However, DSR has the best performance as it benefits from stationary nodes or stations. We notice that the successful rate is slowly increased as the number of roadside stations is more than 10 nodes with 96% of successful transmission. Thus, this is probably the optimal number of roadside stations for this city, and the density of roadside stations for this city area is 7 nodes/km^2.

Figure 5 shows that the end-to-end delay of GPSR tends to be constant, and it is slightly longer than AODV and DSR. For GPSR, the delay depends on the number of hops in routes and the size of the network. As opposed to the delay shown in Figure 3 where adding more moving nodes increases the delay, the delay is rather constant as we add more stationary nodes. It is shown that GPSR gains benefits from having roadside stations for inter-vehicle communications.

C. The Effect of City Block Size

The city block size is also an important factor in determining the performance of the routing protocols for inter-vehicle communications. Given a larger block size, vehicles

spend a relatively longer time in traversing the distance between intersections. We perform experiments where we span the map size to be 2400x2400 meters and determine the performance as the density of vehicle nodes and roadside stations is similar as previously done. We experiment with 200 vehicle nodes ($34.72\ node/km^2$), and we vary the number of roadside stations.

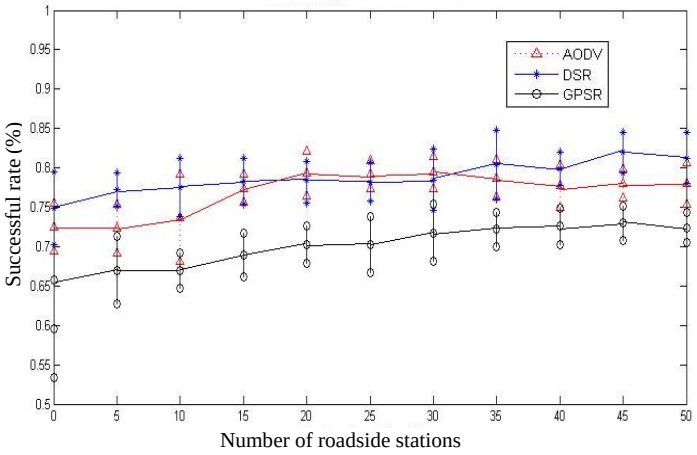

Figure6. The successful rate with different numbers of roadside stations on 2400m × 2400 m map

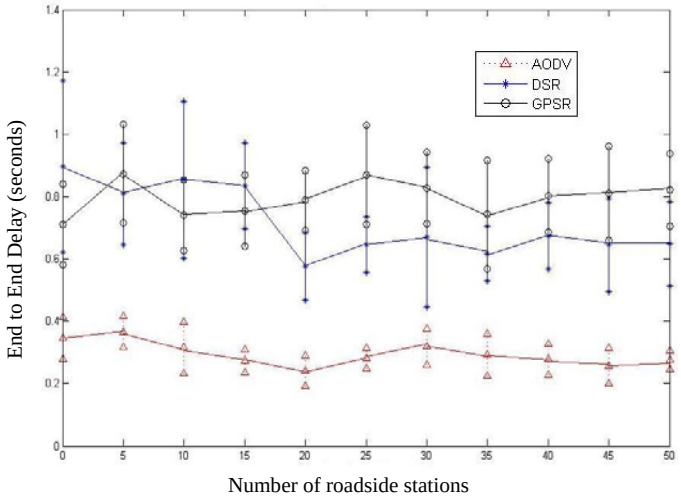

Figure 7. The delay with different numbers of roadside stations on 2400x2400m map

The results in Figure 6 indicate that for a larger map, all routing protocols tend to have constantly increasing successful rate as the number of stations increased while the vehicle density is fixed. In Figure 7, the end-to-end delay is rather stable as in previous experiments. Therefore, we can conclude that by increasing the number of roadside stations, we are able to make transmission with more successful rate in case of a larger city area network. To farther confirm our conclusion, we increase even more number of roadside stations to observe the trend. In Table II, it is shown that all routing protocols yield more successful rate when the number of roadside stations increased.

TABLE II COMPARISON OF ROUTING PROTOCOLS WITH 100 NODES

Number of roadside station	Average Successful Rate		
	AODV	DSR	GPSR
10	0.7367	0.775	0.6695
50	0.7803	0.8126	0.7238
100	0.8243	0.8699	0.7703

V. CONCLUSION

In this paper we present simulation experiments and results on the effect of the number of roadside stations for inter-vehicle communications with the use of three different routing protocols, DSR, AODV, and GPSR. First, we compare the performance of different ad hoc routing protocols as the number of vehicle nodes increase. GPSR yields the highest successful rate; however, it yields the longest delay. This is because GPSR utilizes positions of nodes to make packet forwarding decisions; thus, a packet is routed over more hops when network size is larger. Second, we evaluate the effect of the number of roadside stations, and from the experiment we conclude that the density of roadside stations for a small city section is about 7 nodes/km^2 with about 96% of successful transmission. With the larger network topology, we have the same result that the successful rate is increased if number of roadside stations increased.

ACKNOWLEDGMENT

This work is supported by Thailand Graduate Institute of Science and Technology (TGIST)'s grant from the National Science and Technology Development Agency (NSTDA).

REFERENCES

[1] M. Skutek, D. T. Linzmeier, N. Appenrodt, G. Wanielik, "A PreCash Sytem based on Sensor Data Fusion of Laser Scanner and Short Range Radars," The 7th International Conference on Information Fusion (FUSION), Philadelphia, USA, 25 - 29 July 2005.

[2] C. Hecht and K. Heinig, "Map Enabled ADAS," 5th European Congress on ITS, Hannover, Germany, June 3, 2005.

[3] Standard Specification for Telecommunications and Information Exchange Between Roadside and Vehicle Systems - 5 GHz Band Dedicated Short Range Communications (DSRC) Medium Access Control (MAC) and Physical Layer (PHY) Specifications, Sept. 2003.

[4] M. Gerla et. al. "Vehicular Grid Communications: The Role of the Internet Infrastructure," WICON'06, Boston, MA, USA.

[5] C. E. Perkins and E. M. Royer, "Ad-hoc On-demand Distance Vector Routing," in Proceedings of the 2nd IEEE Workshop on Mobile Computing Systems and Applications, New Orleans, LA, February 1999, pp. 90–100.

[6] D. B. Johnson and D. A. Maltz, "Dynamic Source Routing in Ad Hoc Wireless Networks," in Mobile Computing, vol. 353, Kluwer Academic Publishers, 1996.

[7] B. N. Karp and H. T. Kung, "GPSR: Greedy Perimeter Stateless Routing for Wireless Networks," In Proceedings of the sixth annual ACM/IEEE International Conference on Mobile computing and networking (MobiCom'00), pages 243-254, Boston, Massachusetts, August 2000.

[8] S. PalChaudhuri, Jean-Yves Le Boudec, and Milan Vojnovi´c, "Perfect Simulations for Random Trip Mobility Models," in Proceedings of IEEE Infocom 2005.

[9] The ns-2 Network Simulator, http://www.isi.-edu/nsnam/ns/.

[10] TIGER - Topologically Integrated Geographic Encoding and Referencing system, http://www.census.gov/geo/www/tiger/.

The Improvement of TCP Performance in Heterogeneous Networks

K. Kuprasert and P. Oothongsap
Department of Electrical Engineering, Faculty of Engineering,
King Mongkut's Institute of Technology North Bangkok,
Pibulsongkram Rd., Bangsue, Bangkok 10800, Thailand

***Abstract*- Currently various modified TCP congestion control algorithms have been proposed for specific network environments such as wireless or high-speed long-delay environments. However, there is no research study on a TCP congestion control algorithm in a mix environment such as high-speed long-delay and wireless environment. Thus, we study various TCP congestion control algorithms such as BIC-TCP, S-TCP, HS-TCP, TCP Westwood and TCP Hybla in the mix environment by using Network Simulator (NS-2) [1] and we propose a new TCP congestion control algorithm called NEO-TCP which can improve bandwidth utilization and fairness.**

I. INTRODUCTION

Future communication and computer networks will be characterized by requirements to carry wide varieties of network services and traffic types. Two growing technology trends, Internet and wireless technologies, are resulted in a combination network. Such environments are expected to become the norm in the future because there has been an increase in supporting data applications over networks with both wired and wireless link. Mixing wired and wireless network becomes very popular. This event creates new challenges for network designers and researchers.

This heterogeneous environment is expected to support wide ranges of applications such as high-speed data transfer, real time multimedia, multimedia web streaming, and computational grids [2]. These applications tend to use TCP [3] as a Transport control protocol because TCP supports a reliable transmission and be able to detect and resolve network congestion.

Several literatures have studied TCP performance only in a specific environment. For example, BIC-TCP [4], S-TCP [5], and HS-TCP [6] are proposed to solve the TCP performance degradation in a high-speed long-delay environment. TCP Westwood [7] and TCP Hybla [8] are proposed to solve the TCP performance degradation in a lossy environment and a satellite environment, respectively. Currently, there is no literature survey that studies and solves the problem of TCP performance in the heterogeneous environments.

As we noticed, each environment has a unique characteristic. For instance, in high-speed long-delay network, TCP congestion control algorithm prevents TCP source to fully utilize available bandwidth. Hence, the current TCP flow cannot maintain a high throughput, even though abundant network resources are available. Suppose a connection has a round-trip time (*RTT*) of 100ms, a packet size of 1500bytes and an available bandwidth of 10Gbps. With this environment, the TCP congestion window (*cwnd*) will be equal to 83333 packets. According to the AIMD in the TCP congestion control, after an immediate detection of a congestion event, the *cwnd* will be set to 41667 packets. The longest time interval that congestion avoidance phase would go through will be 4167 seconds, roughly 1.2 hours.

In the wireless environment, a wireless channel is characterized by high bit-error rates (*BER*) and random losses. Furthermore, a wireless channel may cause burst errors when the channel is in a deep fade for a significant amount of time. When random errors occur, a TCP source cannot differentiate congestion losses from random losses. A TCP source treats all packet losses as indicators of network congestion and slowdowns transmission rate unnecessarily.

In the satellite environment, TCP performance will be degraded by both long *RTT* and high bit-error rates as in [9].

To solve the above problems, this paper proposes a new congestion control mechanism called NEO-TCP. The NEO-TCP algorithm operates in two modes, each of which uses the different algorithm for changing the *cwnd* size. The first mode is for the normal network where *RTT* is equal to or less than 50ms, and the second mode is for the long-delay network where *RTT* is more than 50ms. Furthermore, it also has a special mechanism to counter with random losses in wireless environment. With these properties, the NEO-TCP algorithm promises excellent utilization, efficiency, fairness and friendliness.

The paper is organized as follows. In section II, we propose the concept and the congestion control mechanism of NEO-TCP. In section III, we present a series of NS-2 experiments. Finally, future work and conclusion can be found in section IV.

II. NEO-TCP CONGESTION CONTROL

The NEO-TCP algorithm is the modification of the congestion control algorithm of TCP Hybla. The NEO-TCP algorithm operates in two modes: a standard, and a long-delay mode. The standard mode is for the normal network where *RTT* is equal to or less than 50ms, and the long-delay mode is for the long-delay network where *RTT* is more than 50ms. To be able to acquire available bandwidth in the high-speed and long-delay environment, the congestion control algorithm of NEO-TCP is *RTT* dependent. If the *RTT* between a source and destination is large, the *cwnd* grows quickly. If the *RTT* between a source and destination is small, the *cwnd* grows

slowly. The *cwnd* increment depends on a normalized *RTT* (*k*) which is calculated as follows.

$$k = MAX\left(1\ ,\ \frac{RTT}{RTT_{ref.}}\right) \quad (1)$$

We separate the NEO-TCP operation mode by using the $RTT_{ref.}$ value which is equal to 50ms. This value is chosen because most long-delay networks have the *RTT* more than 50ms [10]. The congestion control mechanism of NEO-TCP is proposed as follows.

On the arrival of an acknowledge (*ACK*):

Slow Start Phase

Standard mode (k=1): $cwnd \leftarrow cwnd + 1$ (2)

Long-delay mode (k>1): $cwnd \leftarrow cwnd + (4^k - 1)$ (3)

Congestion Avoidance Phase

Standard mode (k=1): $cwnd \leftarrow cwnd + \frac{1}{cwnd}$ (4)

Long-delay mode (k>1): $cwnd \leftarrow cwnd + \frac{4k^2}{cwnd}$ (5)

On a packet loss :

3 DUPACKs

Standard mode (k=1): $cwnd \leftarrow \frac{cwnd}{2}$ (6)

Long-delay mode (k>1): $cwnd \leftarrow cwnd - \frac{1}{cwnd}$ (7)

Timeout

Standard mode (k=1): $cwnd = 1$ (8)

Long-delay mode (k>1): $cwnd = 2 \times k$ (9)

In the beginning of the connection, a NEO-TCP source measures the *RTT* between itself and a receiver and calculates the *k* value. Then, the NEO-TCP source will perform according to the operation mode, which concurrent with the *k* value.

If *k* is equal to 1, the NEO-TCP congestion control algorithm will operate in the standard mode, and it will perform like the standard TCP (TCP Reno).

If *k* is greater than 1, the NEO-TCP congestion control algorithm will operate in the long-delay mode. The NEO-TCP algorithm increases *cwnd* more aggressively than standard TCP does. The increased rate of *cwnd* depends on the *RTT* value in the network. If the *RTT* is so long, the *cwnd* will increase so fast. In the slow start phase, the NEO-TCP algorithm will increase the *cwnd* as in (3). In the congestion avoidance phase, it will increase the congestion window size as in (5). Equation (3) and (5) are derived from the TCP Hybla algorithm, because the congestion window update mechanism of TCP Hybla is satisfied conditions of high-speed long-delay network [8].

If the NEO-TCP sender receives triple duplicate acknowledgments, the NEO-TCP sender will not decrease the *cwnd* by half like the TCP Reno sender, but it will decrease *cwnd* as in (7). This is to prevent the NEO-TCP algorithm from decreasing *cwnd* drastically. In the high-speed long-delay and wireless environment, the loss rate is high, so the TCP sender decreases *cwnd* frequently. If the sender decreases *cwnd* by half frequently, the sender cannot send more data. This will lead to low bandwidth utilization. The NEO-TCP algorithm can improve bandwidth utilization by decrease the *cwnd* gradually as in (7).

In case of timeout, the NEO-TCP algorithm will decrease the *cwnd* as in (9).

The NEO-TCP algorithm also adopts the selective acknowledgement (*SACK*) option [8] because it allows the TCP sender to recover more than one packet per *RTT*. This option is currently widely spread and available in most TCP implementations and is also often turned on by default in most operating systems.

III. TCP PERFORMANCES

In this section, we will study the TCP performance in this heterogeneous network. All of the simulations are performed with network simulator (NS-2) and TCP performance metrics are throughput, intra-protocol fairness, TCP friendliness and round-trip time fairness (*RTT* fairness).

A. Throughput

In this section, we study the bandwidth utilization of NEO-TCP and other TCP variants in the heterogeneous network at 20ms, 100ms and 200ms *RTT*, respectively. The topology is shown in Fig. 1. S1 is the source node, R1 is the access point, and D1 is the destination node. The bandwidth between S1 and R1 is 1Gbps with the one way delay varied from 10ms, 50ms, and 100ms, respectively. The bottleneck link is the wireless link between R1 and D1. The bottleneck bandwidth is 11Mbps with 64 μs one way delay as the 802.11b standard. We choose 802.11b standard because it is popular in today wireless networks and public hotspots as well as business and home environments. The random loss rate in the wireless link is 0.001 [5]. Each TCP variant connection is established from a fix host sender (S1) to a mobile host receiver (D1). The data are transferred via FTP flow from the sender to the receiver. The FTP packet size is 1000 bytes. The queue size at the access point is 50 packets. The simulations are run for 500 seconds to eliminate transient behaviors.

The simulation results present that NEO-TCP can provide higher throughput than other TCP variants when it operates in long-delay network. Because it increases the *cwnd* aggressively depend on the *RTT* in the network. Moreover, when triple DUPACKs are received, NEO-TCP will decrease *cwnd* gradually and it uses *SACK* option for loss recovery mechanism.

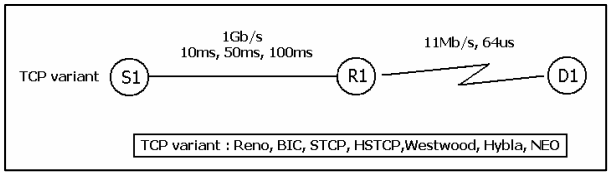

Figure 1. Topology of throughput simulation.

TABLE I
AVERAGE TCP THROUGHPUT VALUE

Protocol	Average throughput (Mbps)		
	RTT 20ms	RTT 100ms	RTT 200ms
HS-TCP	3.131	1.376	0.733
S-TCP	3.902	2.534	1.923
BIC-TCP	3.830	2.549	1.879
TCP Reno	3.256	1.604	0.789
TCP Westwood	4.048	1.444	0.669
TCP Hybla	3.490	2.904	2.689
NEO-TCP	**3.416**	**3.830**	**3.695**

B. *Intra-protocol Fairness*

Intra-protocol fairness is the fair share of bandwidth utilization when different flows use the same protocol. In this section, we study the fairness of NEO-TCP in the heterogeneous network at 100ms *RTT*. Six NEO-TCP flows are studied.

Fig. 2 shows the network topology for intra-protocol fairness simulation. The bandwidth between each source node and R1 is 150Mbps with the one way delay 10ms. The high-speed long-delay link between R1 and R2 has bandwidth 1Gbps with the one way delay 40ms. The wireless link between R2 and each destination node is bottleneck link, which has the specification follows the 802.11b standard.

The simulation result shows that NEO-TCP flows get a fair share of bandwidth, because every flow of NEO-TCP increases *cwnd* in equal rate. The reason of this result is every flow of NEO-TCP has the same *RTT*, so they operate in the same manner. If the network has so many competing flows, the throughput of each flow tends to be lower because the bandwidth in the network is saturated. Then the throughput is limited by the bottleneck link in the network.

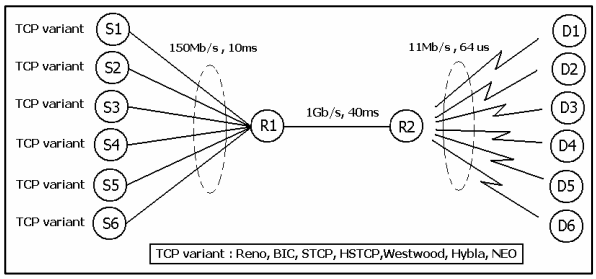

Figure 2. Topology of intra-protocol fairness simulation.

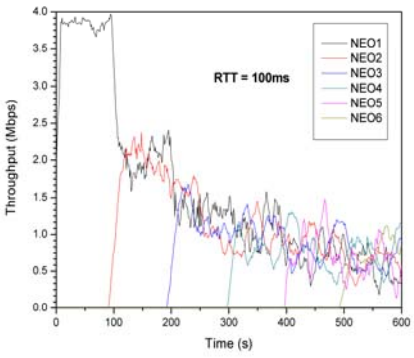

Figure 3. NEO-TCP fairness.

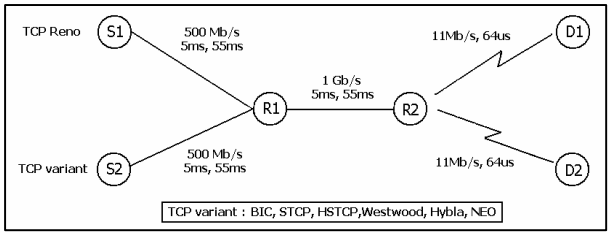

Figure 4. Topology of TCP friendliness simulation.

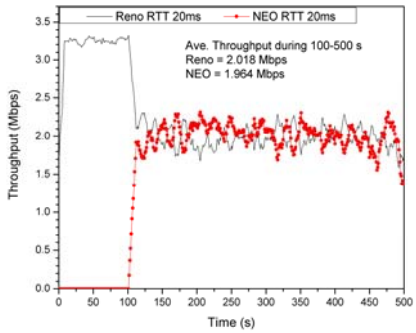

Figure 5. NEO-TCP friendliness.

C. *TCP Friendliness*

The friendliness means the connections with different TCP variants does not prevent unmodified TCP from consuming available bandwidth. In this section, we study the TCP friendliness of NEO-TCP in this environment. Two TCP flows are studied. One flow uses a TCP Reno algorithm and the other one uses a NEO-TCP algorithm.

Fig. 4 shows the network topology for TCP friendliness simulation. The bandwidth between each source nodes and R1 is 500Mbps with the one way delay varied 5ms and 55ms. The link between R1 and R2 has bandwidth 1Gbps with the one way delay varied 5ms and 55ms. The wireless link between R2 and each destination node is bottleneck link, which has the specification follows the 802.11b standard.

TCP Reno connection is established between the source node, S1 and the destination node, D1 and NEO-TCP is established on another connection from the source node, S2 to the destination node, D2. The data are transferred via two FTP flows from the senders to the receivers.

The simulation results in Fig. 5 show that NEO-TCP is friendly to standard TCP because NEO-TCP operates in a standard mode. In this mode, when the NEO-TCP sender receives the acknowledge signal from the receiver, it will increase and decrease the *cwnd* size as same as the standard TCP.

D. *RTT Fairness*

Round-trip time fairness is the fairness of two flows with different *RTT*. In this section, we study the *RTT* fairness of NEO-TCP in this environment.

Fig. 6 shows the network topology for *RTT* fairness simulation. The bandwidth between the source node, S1 and the access point, R1 is 500Mbps with the one way delay 15ms. The bandwidth between the source node, S2 and the access

point, R2 is 500Mbps with the one way delay varied from 15ms, 45ms and 105ms, respectively. The link between R1 and R2 has bandwidth 1Gbps with the one way delay 15ms. The wireless link between R2 and each destination node is a bottleneck link, which has the specification follows the 802.11b standard.

There are three cases for the simulation. For case A, the *RTT* of the first flow and the second flow is 60ms. For case B, the *RTT* of the first flow is 60ms and the *RTT* of the second flow is 120ms. For case C, the *RTT* of the first flow is 60ms and the *RTT* of the second flow is 240ms.

In case of *RTT* fairness, the simulation results show that if both flows of NEO-TCP operate in the same mode, it provides a bounded fair share, NEO-TCP with large *RTT* does not starve NEO-TCP with small *RTT*. When one flow suffers from random loss and cannot take up for more bandwidth, another flow will consume the unused bandwidth immediately.

The interested reader can find more result of NEO-TCP when compare with other TCP variants in [11].

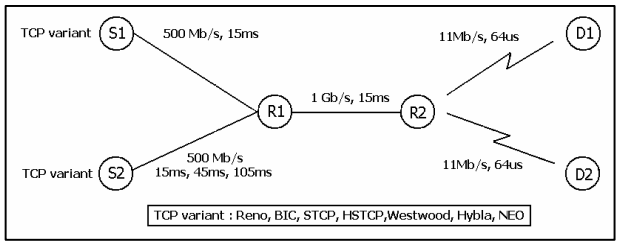

Figure 6. Topology of *RTT* fairness simulation.

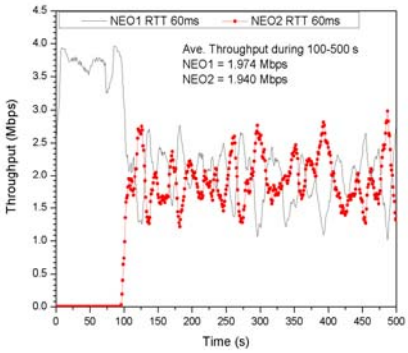

Figure 7. NEO-TCP *RTT* fairness case A.

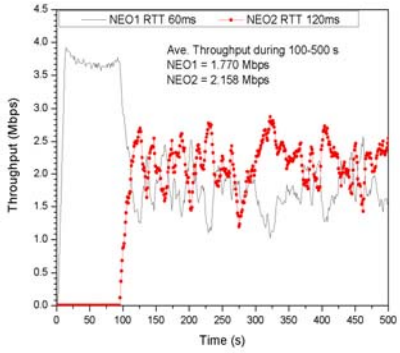

Figure 8. NEO-TCP *RTT* fairness case B.

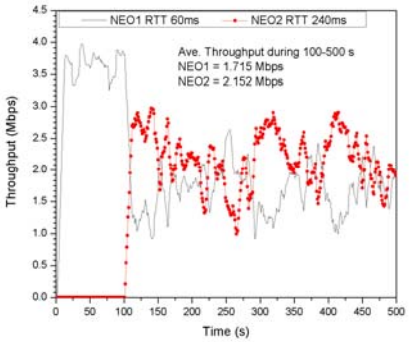

Figure 9. NEO-TCP *RTT* fairness case C.

IV. Conclusion and Future Work

In this paper, we present the simulation results evaluating the performance of TCP Reno, HS-TCP, S-TCP, BIC-TCP, TCP Westwood, TCP Hybla and NEO-TCP in the heterogeneous networks. The new congestion control algorithm, NEO-TCP can outperform the traditional in term of throughput and fairness. The major advantage of NEO-TCP is that it provides the high bandwidth utilization in the proposed environment.

Current NEO-TCP uses a constant *RTT*, which is measured only in the beginning of the connection. However, the *RTT* value should not be a constant since it reflects the network condition. Then for NEO-TCP to adopt to the current network condition, *RTT* must be measured more frequent. Thus, the normalized *RTT* parameter (k) should be changed dynamically. Moreover, the mathematical model of NEO-TCP should be researched, and it should be implemented and tested over real networks. This would reveal any implementation problems that are not foreseen during the initial design.

References

[1] Network simulator ns-2, Available from http://www.isi.edu/nsnam/ns.

[2] T. Phan, L. Huang and C. Dulan, "Challenge: Integrating mobile wireless devices into the computational Grid," *ACM Mobicom2002, Georgia, USA*, September 2002.

[3] V. Jacobson, "Congestion avoidance and control," *ACM Computer Communications Review*, vol. 18, pp. 314 –329, Aug 1988.

[4] L. Xu, K. Harfoush and I. Rhee, "Binary increase congestion control for fast long-distance networks," *IEEE INFOCOM*, 2004.

[5] T. Kelly, "Scalable TCP: Improving performance in high speed wide area networks," *Computer Communications Review*, vol. 32, April 2003.

[6] S. Floyd, S. Ratnasamy and S. Shenker, "Modifying TCP's congestion control for high speeds,"Available from http://www.icir.org/floyd/hstcps, May 2002.

[7] S. Mascolo, C. Casetti, M. Gerla, M. Sanadidi, and R. Wang, "TCP westwood: Bandwidth estimation for enhanced transport over wireless links," *ACM Mobicom 2001, Rome, Italy*, July 2001.

[8] C. Caini and R. Firrincieli, "TCP Hybla: a TCP enhancement for heterogeneous networks," *International Journal of Satellite Communication and Networking*, vol. 2, pp. 547-566, Sep.-Oct. 2004.

[9] K. Kuprasert and P. Oothongsap, "Simulation studies of TCP performance over mix environments: high-speed long-delay and wireless networks", *ECTI-CON, UbonRatchatani, Thailand*, May 2006.

[10] Martin, D. H., *Communication Satellites*. 4th ed. California : The Aerospace Press, c2000.

[11] K. Kuprasert, "The improvement of TCP performance in heterogeneous networks: high-speed long-delay and wireless environments", *Master Thesis, TGGS Department, KMIT'NB*, Jan 2007.

Early Warning of Internet Worms by ICMP Scan Data Visualization

Pitichai Pitimaneeyakul, Saroj K. Biswas
Department of Electrical and Computer Engineering
Temple University, Philadelphia, PA19122

***Abstract*—This paper investigates early detection of Internet worms using ICMP port scan data. The ICMP port scan data is plotted as a scatter plot in the plane of port scan vs. scan rate, which is referred to as 'port-scan plane'. It is observed that the normal port scan activity remains within a small boundary in the port-scan plane, and exits the normal activity boundary when a computer worm starts to infect the Internet. The normal port scan boundary is determined using historical port scan data at a monitoring station. A worm attack warning is issued when the port scan activity exceeds the threshold boundary of the port scan plane. Simulation results are presented using worm data generated by the well known epidemic model. Port scan data collected during Code Red attack was also used to validate the proposed method. Additional port scan data collected at Temple University firewall during a worm attack in the Spring of 2004 is also used to validate the results.**

I. INTRODUCTION

Security threat of the Internet dates back to 1988 when Morris worm [1] infected a large number of computers connected to the network. Since then computer viruses and worms continued their attack with the grim reminder that no computer is safe on the Internet. More recently, in 2001 a number of worms such as, Code-Red, Code Red V2, Code-Red II and Nimda, spread over the Internet, and infected hundreds of thousands of computers in a few hours. Two years later, January 25th 2003, SQL Slammer [2] appeared, and infected 90 percent of vulnerable computers in 10 minutes without any warning. Many networks around the world had to be shut down because of a lack of an appropriate defense against this worm. Moreover every new generation of worm seems to be faster and more intelligent than its predecessor, and infected more and more hosts on the Internet. Stanford et.al. [2, 3, 4] showed that, if a worm uses a better algorithm in scanning its target, then it can occupy all computers on the Internet in less than an hour.

Damage to hosts on the Internet due to a worm varies with its payload, which depends on the imagination of the worm author. Even without the payload a worm can generate a lot of traffic, which can lead to denial of service on the network. If worms can be detected early, one can develop strategies to slow down or halt attacks, and keep the system running as normal. Given the fast speed of infection, it is necessary to set up a nation-wide worm detection system for early warning.

An unknown (zero-day) worm is difficult to detect using worm signature since it is not available until the worm infects many computers. However, when the worm attacks, the network traffic is altered compared to the traffic in a normal state. Thus by monitoring the network traffic, one should be able to detect the changes in traffic, which can in turn be used to predict worm attacks.

This paper investigates detection of a worm by monitoring the network traffic. The ICMP port scan data is plotted on the *port-scan plane*, which is the plane of port scan per unit time versus scan rate. It is observed that for normal network traffic, the ICMP scanning activity remains within a small boundary in the port-scan plane, however, it grows very fast whenever a worm attacks the Internet. The normal port scan boundary may be determined using historical port scan data at a monitoring station. Simulation results are presented using worm data generated by the well known epidemic model. Port scan data collected during Code Red [5,6] attack was also used to validate the proposed method. Additional port scan data collected at Temple University firewall during a worm attack in the Spring of 2004 was also used to validate the results.

The paper is organized as follows: Section II introduces the basics of a computer worms and viruses. Section III discusses the methods that are commonly used to detect worms. Section IV presents the main result of this research, a phase-plane method for detection of appearance of a new computer worm, which is followed by concluding remarks in Section V.

II. WHAT IS A WORM

A worm is a computer program [4] that attempts to find the vulnerability on other computers, and gain access into those computers across the network. A worm typically copies itself to a target computer after it exploits the security hole of the target. When the target computer becomes infected, it starts the process to conquer new targets. Clearly, the worm's infection rate increases exponentially, and has the characteristics similar to that of human or animal diseases. Zou et.al. [6,7] modeled the Code Red worm by using a classical simple one-species epidemic model:

$$\frac{dx(t)}{dt} = \alpha x(t)[N - x(t)] \qquad (1)$$

where $x(t)$ is the number of infected hosts at time t, N is the total number of computers, and α is the infection rate. A more realistic model [9] of worm uses the classical general epidemic model, the Kermack-McKendrick Model that classifies hosts in three basic categories:

susceptible → infected → removed

A Virus is a computer program, containing malicious code that can replicate itself by human interactions, such as copying the program, running the program, sharing the diskette or open the document file. A *Worm* is a malicious computer program, which can replicate itself across network without human interaction. However, there are some worms that require user interaction, such as, opening of email or document. Thus, a worm can spread and infect vulnerable computers a lot faster than a virus.

III. Detection of Worm

Worm detection methods can be classified into two categories: 1) *detection of known worm*, 2) *detection of unknown worm.*

Known worms are detected using their signature or known pattern of network attack. The antivirus software is an example of signature-based detection, which detects worms only when its signature is available. Thus if there is a new virus/worm that spreads on the Internet, it is likely to spread quickly over the Internet because of lack of a signature. For example, if a worm uses ICMP sweep scan to the network, the anti-virus will detect the sweep scan, and will alert the network manager. Note that these signatures would not have been known when the worms first attacked the Internet.

There are a number of methods that have been proposed in recent years for detection of unknown worms. The following is a brief summary.

Monitoring Border Gateway Protocol (BGP):
When Code Red/Nimda attacked the Internet, the behavior of the BGP in the routing table of the gateway router had changed from the time before the worm attack [7]. The number of BGP update messages increased because the worm inside a local area network tried to propagate across to other networks (egress scan) so that the gateway router had to update information in the routing table to find destinations for the worm. Michael Liljenstam [10] has shown the correlation between CodeRed worm propagation and BGP instability by the SSFNET software simulation.

Monitoring ICMP:
Before breaking in, the worm sends ICMP packages to the target to check whether the target is still active and ready to receive a warhead. The destination IP addresses are often chosen randomly so that many ICMP packages are actually sent to non-existent IP addresses. Thus the ICMP "unreachable" will be returned to the source host. Gorge Bakos [11, 12] presented a method of detecting active worms by monitoring ICMP unreachable message, which can increase exponentially when the worm spreads. However, some worms use other types of the packages such as, SYN, HTTP, etc to probe the target, or do not probe the target at all. Thus monitoring of ICMP unreachable message is not suitable to detect many worms.

Kalman Filter:
Another method by Zou et.al. [7] shows how to use the Kalman filter to estimate a worm propagation on the network. Since a worm's propagation follows the epidemic model, the Kalman filter can be used to estimate the worm propagation growth rate. As the worm grows exponentially, the Kalman filter estimates the growth rate, and the worm attack is detected. Convergence of Kalman filter requires that the network traffic be monitored for many IP addresses over a long time, which might be too late for taking any actions to halt the attack.

The three methods discussed above require a considerable amount of time and a substantial amount of network traffic data before a worm is detected. Thus, although the system administrator will know that a new worm has attacked the network, it may be too late to make any defense plan.

IV. Detection Based on ICMP Traffic Visualization

In this study, we examine the relationship between the number of scans in the networks, called "scans", and difference between the number of the scans at a current time point, and the previous time point, called "delta scans". We assume that the worm uses ICMP as the scanning engine. The hypothesis is that there will be a difference between plots of scans versus delta scans under normal conditions, and those during the worm attacks. The concept is based on the phase-plane plot of a second order system, which shows a clear and significant difference between a stable and an unstable system. Our analysis is based on network ICMP scan data collected during a worm attack as well as simulated worm attack data.

1) Code RED Worm

The phase plane method of worm detection was tested using the network traffic data collected by Goldsmith [5] during the CodeRed worm attack on July 18 and 19, 2001. Figure 1A shows the normal Internet activity when there is no virus or worm attack, whereas Figure 1B representing worm attack clearly shows a significant increase in the scan activity. In fact the small dark region near the origin of Figure 1B represents data points of Figure 1A.

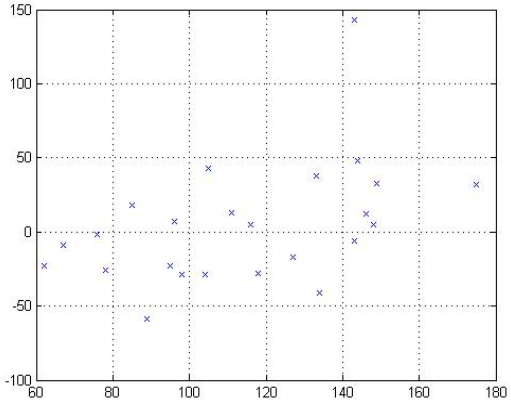

Figure 1A: Scan versus Delta Scan on 07-18-2001 before codeRed attacked the network.

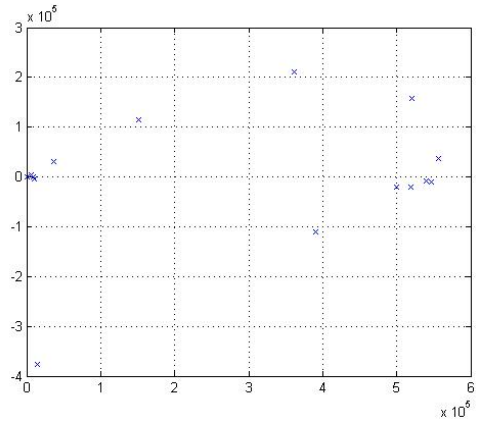

Figure 1B: Scan versus Delta Scan on 07-19-2001 when CodeRed peak attacked.

It is noticed that the network always has some ICMP activity even when there is no worm attack. Thus, the boundary of the scatter plot between scans/delta scan remains confined in a small region around the origin. However, when the worm attacks the network, the boundary of scatter plot of ICMP scan/delta scan grows substantially big.

2) Nimda worm simulation:

Propagation of Core Red worm was successfully analyzed using a simulated network [3] of 360,000 IP addresses. The simulation experiment was setup under two conditions: 1) the initial number of infected computer taken as 0 to simulate the normal condition without any worm attacks, and 2) the initial number of infected computers taken as 10 to simulate the worm attack condition. Figure 2 shows the normal ICMP activity, (i.e., no worm attack) represented as a scatter plot of scan vs. delta scan.

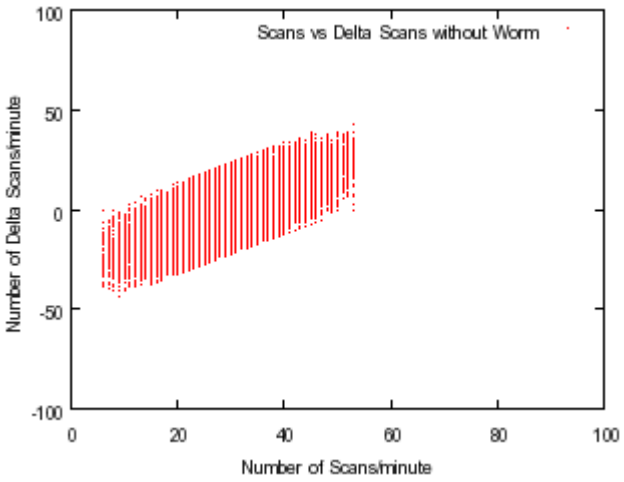

Figure 2. Scan versus Delta Scan without Worm

Figure 3 shows the simulated Code Red attack as a function of time. The figure shows that after a small incubation period, the number of infected computers increased exponentially.

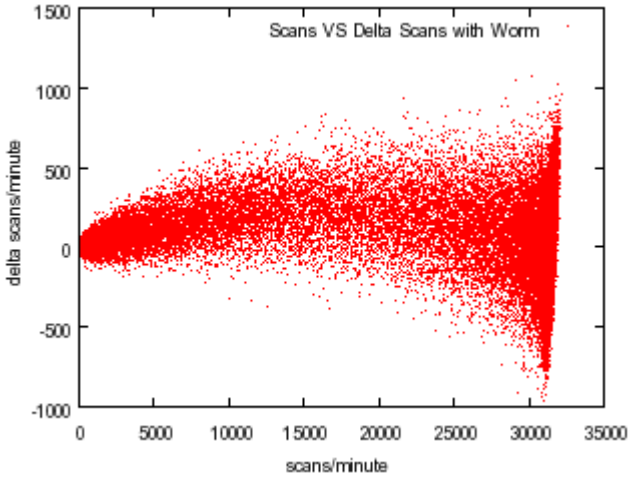

Figure 4. Scan versus Delta Scan with Worm Attacks.

Figure 4 shows the scatter plot of ICMP traffic following a simulated attack of Code Red worm. Clearly, compared to the normal network condition, the ICMP activity expressed as scan vs. delta scan grows by many orders of magnitude when there is a virus attack. In normal conditions, the boundary of the ICMP traffic scan plot would have been around the origin.

3) Data collected at Temple University Firewall

Network traffic data was collected using TCPDUMP at the Tempe University Firewall, which is the connection between the university Network and the Internet. Two sets of data were captured in the Spring of 2004: the first data set was captured inside the firewall to represent egress scan, and the second set at the external interface to represent ingress scan.

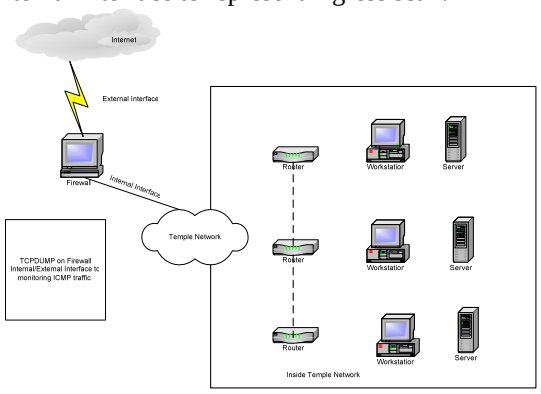

Figure 5.Topology of Capture Configuration on university Network.

On April 17, 2004, ICMP traffic data was collected from inside the university Network, which is represented in Figure 6 as a scatter plot of scan vs. delta scan. This figure shows that someone from inside the university network was sending ICMP sweeps, which was also confirmed by the university Computer Services. Periodic nature of the ICMP sweep was clear from the scatter plot of scan and delta scan which grows and loops back on a regular basis.

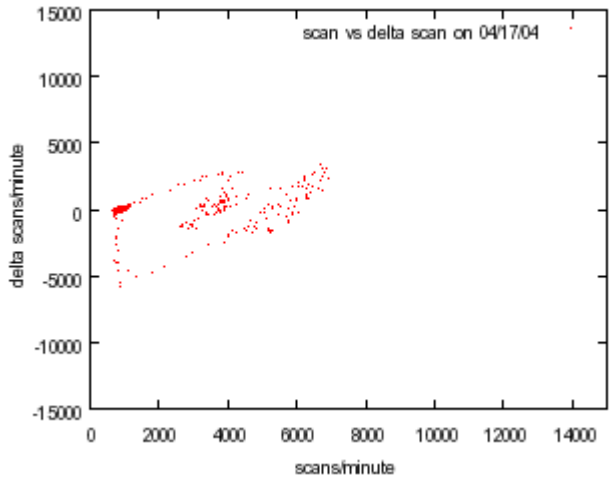

Figure 6 Delta scans versus scan on 04-17-2004

Temple University Computer Services noticed unusual network traffic from April 29th to May 7th. The scatter plot of May 1st ICMP data at the external interface is shown in Figure 7, which signifies a worm attack.

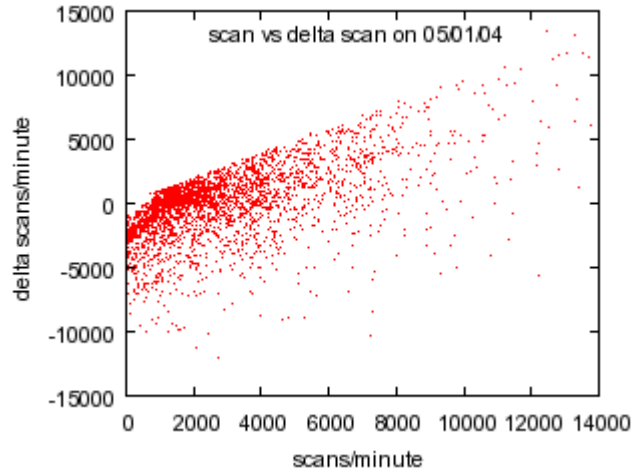

Figure 7. Plot of Scans and Delta Scan Outside university Network on May 1th 2004.

V. Conclusion

In this research, scatter plot of ICMP scan and delta scan was used to detect worm attacks on the Internet. We used three types of data: worm data from simulation of an epidemic model, simulated data of Code Red worm, and ICMP traffic data collected at Temple University firewall. In all three cases, it was observed that under normal network traffic condition, scatter plot of scan and delta scan remained confined in a small region near the origin, whereas when a worm attacks the network, the scatter plot grows by many orders of magnitude. This method presents a simple and effect way of designing an early warning system for worm attacks on the Internet. For worm detection, the network manager monitors the ICMP port scan data in real time, and plots in the port-scan plane on the computer monitor screen.

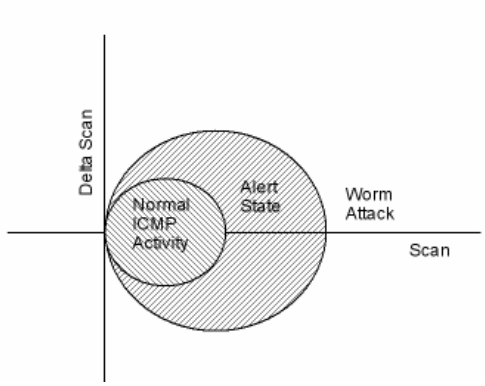

Fig 8 ICMP Port Scan Monitoring System for Worm Detection

The boundary of the normal port scan activity is determined from historical network data; an alert zone is set which could be about double the size of the normal zone. When the ICMP activity exceeds the alert zone, the network manager declares a worm attack. The size of the alert zone should not be too small or too big; a too small alert zone will cause many false alarms whereas a too large alert zone will miss actual worm attacks.

VI. References

[1] Charles Schmidt, Tom Darby "The What, Why, and How of the 1988 Internet Worm" Available: http://www.snowplow.org/tom/worm/worm.html

[2] David Moore, Vern Paxson, Stefan Savage, Collen Shannon, Stuart Stanford, Nicholas Weaver, "The Spread of the Sapphire/Slammer Worm" Available: http://www.cs.berkeley.edu/~nweaver/sapphire/

[3] Stuart Stanford, Gary Grim, Rolf Junkman, Flash Worms: Thirty Seconds to Infect the Internet, August 16th 2001 Available: http://richie.idc.ul.ie/eoin/SILICON%20DEFENSE%20-%20Flash%20Worm%20Analysis.htm

[4] S. Stanford, V. Paxson and N. Weaver, "How to 0wn the Internet in Your Spare Time", Proc. USENIX Security Symposium 2002.

[5] D. Goldsmith, Possible CodeRed Connection Attempts Available: http://lists.jammed.com/incidents/2001/07/0149.htm

[6] Cliff Changchun Zou, Weibo Gong, Don Towsley. "Code Red Worm Propagation Modeling and Analysis", 9th ACM Conference on Computer and Communication Security (CCS'02)), Nov. 18-22, Washington DC, USA, 2002.

[7] Cliff Changchun Zou, Lixin Gao, Weibo Gong, Don Towsley, "Monitoring and early warning for internet worms", Proceedings of the 10th ACM conference on Computer and communication security, pp. 190 – 199.

[8] D. J. Daley, J. Gani, J. M. Gani "Simple Epidemic model", December 1998 ISBN: 0-521-01467-0

[9] Real Secure Network Intruder Detection Software: http://www.iss.net

[10] M. Liljenstam, Y. Yuan, B. J. Premore, D. Nicol, "A Mixed Abstraction Level Simulation Model of Large-Scale Internet Worm Infestations", Proceedings of the 10th IEEE International Symposium on Modeling, Analysis, and Simulation of Computer and Telecommunications Systems, pp 109

[11] G. Bakos and V. Berk, "Early Detection of Internet Worm Activity by Metering ICMP Destination Unreachable Activity", In Proceedings of the SPIE conference on Sensors, and Command, Control, Communications and Intelligence, April 2002.

[12] G. Vincent H. Berk, Robert S. Gray, and George Bakos "Using Sensor Networks and Data Fusion for Early Detection of Active Worms", in Proceedings of the SPIE Aerosense conference, April 2003.

[13] N. Weaver Warhol Worms: The Potential for Very fast Internet Plagues Available: http://www.cs.berkerley.edu/~nweaver/warhol.html

[14] The Worm FAQ Available: http://www.networm.org/faq

A Cost-Efficient Algorithm for Arbitrary CRCW PRAM Simulation

Martti Forsell
Platform Architectures Team, VTT Technical Research Center of Finland,
Box 1100, FI 90571 Oulu, Finland

***Abstract*—The arbitrary concurrent read concurrent write (CRCW) parallel random access machine (PRAM) is a very strong model of parallel computing. Direct realization of the model is not feasible with current silicon technologies but there exists a well-known indirect realization on a top of a physically distributed memory machine via simulation known as Ranade's algorithm. Unfortunately it requires expensive sorting networks prior to a combining network and takes at least two steps per reference. In this paper we propose a novel single step algorithm for arbitrary CRCW PRAM simulation based on processor-level filtering and combining. We apply the algorithm to our scalable MP-SOC framework and give early simulation results.**

I. Introduction

As the CMOS technology is approaching the nanometer domain computer architects and chip designers are facing hard challenges: Superscalar processor architectures relying on aggressive *instruction-level parallelism* (ILP) exploitation do not scale to future technologies due to quadratic increase of the area of the forwarding network and issue logic [1], increasing complexity of future chips is invalidating current single chip system design methodologies due to raising costs and longer time-to-market delay [2], clock frequency does not any more increase in pace with shrinking feature size due to raising power consumption per silicon area ratio [3], and power saving possibilities in single processor designs are limited due to small number of independent units. To overcome these problems major processor manufacturers, e.g. Intel, IBM, AMD, Sun, ARM, have made a radical change of paradigm from sequential computing exploiting ILP towards *thread-level parallel* (TLP) computing in which multiple threads are executed in multiple processor cores [4]. Unfortunately, foreseeable TLP designs rely on *symmetrical multiprocessing* (SMP), asynchronous *coarse-grained message passing* (CMP), or locality-aware *non-uniform memory access* (NUMA) that are either hard to program or provide poor performance in fine-grained communication intensive computations utilized e.g. in general purpose applications. This is because there is no support for fine-grained interprocess communication in SMP, a programmer has to explicitly take care of data and program partitioning, subtask synchronization, and communication in the CMP model, and cache coherency maintenance generates extensive traffic that slows down radically the communication channels in the NUMA model. The best candidate to eliminate these problems is an architecture providing explicit TLP computing and realizing a strong model of computing, e.g. the *parallel random access machine* (PRAM) model [5] since it guarantees synchronous operation at the model level, makes partitioning easy allowing a programmer to allocate shared variables from shared memory and map the subtasks to threads in an arbitrary way [6]. Unfortunately PRAM has turned out to be very difficult to implement [7, 8, 6]. Therefore it is now used mostly for exploring and analyzing the intrinsic parallelism of computational problems [9]. However, in our earlier investigations, we have described a way to implement the *exclusive read exclusive write* (EREW) PRAM model on a scalable *multiprocessor system on chip* (MP-SOC) architecture [10]. In EREW PRAM all threads can refer to the shared memory in parallel but at most one reference per a single memory location is allowed. The arbitrary *concurrent read concurrent write* (CRCW) PRAM is a variant of the PRAM model in which this limitation is lifted so that in the case of multiple writes to a location an arbitrary thread succeeds. It provides up to a logarithmic factor faster execution than EREW PRAM [11, 6]. Direct realization of the model is not feasible with current silicon technologies [8] but there is a well-known indirect realization on a top of a physically distributed memory machine via simulation known as Ranade's algorithm [12]. Unfortunately it requires expensive sorting networks prior to a combining network, assumes non-scalable network topology, and takes at least two steps per operation. In this paper we propose a novel single step algorithm for arbitrary CRCW PRAM simulation based on processor-level filtering and combining. We apply the algorithm to our scalable MP-SOC framework and give early simulation results.

The rest of the paper is organized so that in section 2 existing CRCW PRAM simulation algorithms are described. In section 3, we introduce our novel single step CRCW PRAM simulation algorithm. Evaluation of the algorithm on our MP-SOC framework is given in section 4. Finally in section 5, we give our conclusions.

II. Related work

Attempts to realize CRCW PRAM include Ranade's fluent machine [Ranade88], SB-PRAM [6], and still on-going investigations of the XMT framework [13] and Eclipse MP-SOC architecture [10, 14]. All these are based on simulation of a PRAM model on top of a physically distributed memory machine since the direct implementation of the PRAM model requiring P-ported memories has turned out to be infeasible since the area of the memories would be P^2 times larger than that of a single port memory of the same number of cells [8]. The central part of PRAM realization is the simulation algorithm requiring efficient latency hiding and congestion avoiding. So far the only known technique is to exploit parallel slackness in a form of multithreading to hide the latency: Assume that a parallel machine consists of P T_p-threaded

processors and P memory modules. Let a *step* of execution be a period of time during which all T_p threads of a processor execute a single instruction. Now, the latency of the network can be hidden if the memory system can process references before their reply results are used by subsequent instructions. Congestion of messages can avoided with a high probability by using a randomized hashing of memory locations [15].

The two ongoing projects do not present full realization of the CRCW PRAM model: Vishkin does not implement fully synchronous model but assumes that synchronizations happen less frequently [13]. In our previous work we describe a partial and limited CRCW PRAM realization for our MP-SOC framework [14]. It provides only a very limited number CRCW locations (e.g. eight per thread) and full concurrent access takes three steps. Ranade has presented an algorithm for randomized simulation of CRCW PRAM requiring only constant sized queues to store memory requests [12]. The algorithm is originally targeted for priority CRCW model selecting the data of the thread with a lowest ID in the case of concurrent write but implements also the arbitrary CRCW model if the secondary sorting based on thread numbering is dropped. The algorithm is based on a butterfly network and thus executes in O(log P) time. The algorithm describes routing of a reference targeted to address x and consists of six consecutive phases:

1. Inject and sort. All processors of each row, which want to access the shared memory, insert a request into the network. All requests within a row are forwarded towards the end of the row and thereby sorted according to their destination, which is the concatenation of hashed address *h(x)* and address x.
2. Route. All requests are routed to the row in which module $h(x)$ lies. During the routing, the sorted order is maintained, because each routing switch selects from its input buffers always the request with smaller destination if two requests are destined for the same output.
3. Find and access memory. Each request moves along the row until it reaches module *h(x)*, where the memory access takes place, and then moves to the end of the row.
4-6. Reply. These phases are only necessary for read and multiprefix operations and they reverse the movements of requests in phases 1 to 3. Thus, no routing decisions are made here.

A straightforward realization of Ranade's algorithm consisting of set of processing elements connected to each other via a bidirectional butterfly network has been proposed in [16]. Each processing element emulates a single PRAM processor and switch. An optimized version of Ranade's algorithm has been developed in the University of Saarbrücken [6]. It eliminates phases 3 and 4, replaces the networked sorting of phases 1 and 6 with hardware sorting arrays, and uses a latency hiding technique in which a processor emulates multiple virtual processors or threads. The algorithm has been realized as SB-PRAM prototype computer [6]. Unfortunately the butterfly topology that does not scale in the 3D physical word. It is however quite easy to implement these algorithms on scalable topologies like coated mesh or sparse mesh [17]. Another problem is related to the utilization of the resources, which is potentially low due to two-phase (sort-route) approach relying on combining of sorted references requiring at least two steps per operation. There exists no workaround for this since two-phase execution is a fundamental property of the algorithm. Finally, an implementation of a combining network with sorting networks is potentially expensive in terms of silicon area.

III. Proposed algorithm

Consider a baseline parallel machine for which there exists an EREW PRAM simulation algorithm. Such a machine consists of P T_p threaded processors and P memory modules interconnect by a high-bandwidth network, e.g. coated mesh, sparse mesh, butterfly, or hybercube [17]. We propose an algorithm for randomized arbitrary CRCW simulation on the machine executing always in single step with a help of a special hardware called step caches in which cache lines remain valid only until the end of ongoing step of multithreaded execution [18]. The principle of the algorithm is simple: Each time a processor refers the memory a step cache search is performed. In the case of a hit, a write is just ignored and a read is just completed by accessing the data from the cache. If the access address in memory is currently being accessed by an earlier reference, the thread waits until the data becomes available. This waiting does not normally degrade the performance since the processor is T_p-threaded and will execute other threads wile one is accessing memory. In the case of a miss, the reference is stored into the cache and set into pending state (for reads). At the same time with writing information to the cache line, the reference is sent to the memory system. When a reply arrives from the memory, the data is put into the cache and the pending state is cleared. Step caches avoid cache coherency problems since the references within a single step of multithreaded execution are independent by definition. Similarly, there is no need to write any data from a step cache to the memory since its content is always coherent. During a step a thread either refers to an internal step cache of the processor or to the external shared memory. An external memory reference is processed in seven parts:

1. Inject. This part injects the reference to a randomly selected switch of the processor superswitch of the reference network.
2. Route. This part routes the reference with a greedy algorithm to a randomly selected destination switch of the memory module superswitch in the reference network.
3. Eject. This part inputs the reference from the switch to the memory module.
4. Memory access. This part accesses the target memory module.
5. Inject reply. This part injects the possible reply to a randomly selected switch of the memory module superswitch of the reply network.
6. Route reply. This part routes the reply with a greedy algorithm to a randomly selected switch of the processor superswitch in the reply network.
7. Eject reply. This part inputs the reply from the switch to the processor.

The proposed algorithm will simulate arbitrary CRCW PRAM efficiently with a high probability assuming $T_p \geq O(P \log P)$ and memory banks are as fast as processors. Given the limited space, we will not present a mathematical proof of that but refer to simulation results of section 4.

IV. Evaluation

We evaluated the proposed algorithm by measuring the key properties of parallel execution of three two-component programs (see Table 1) mixing the CRCW and EREW memory access components in 0%-100% (ea), 50%-50% (ea+ca), 100%-0% (ca) ratio on three step cached systems (see Table 2) based on our sparse mesh Eclipse MP-SOC framework [10] modified to implement the algorithm with 4-way set associative step caches with step aware FIFO replacement policy (see Figure 1). For reference purposes we made similar measurements on similarly configured non-step cached systems and ideal shared memory systems.

ca	A parallel program component that reads and writes concurrently a given sequence of locations in the shared memory
ea	A parallel program component issuing a memory pattern extracted from random SPEC CPU 2000 data reference trace on Alpha architecture [20] for each thread.

Table 1. The program components that are mixed in 0%-100%, 50%-50%, and 100%-0% ratios to form three benchmark programs.

	E4	E16	E64	C4	C16	C64
Processors	4	16	64	4	16	64
Functional units	5	5	5	5	5	5
Bank access time	1	1	1	1	1	1
Model	EREW	EREW	EREW	CRCW	CRCW	CRCW

Table 2. The configurations of machines used in evaluation.

The benchmark program components were written in assembler. The concurrent component performs a series of concurrent reads and writes for each thread and the exclusive component performs memory patterns extracted from random SPEC CPU 2000 memory access traces on Alpha processor and shifted by a random constant for each thread. The two-component trace-based benchmarking approach was used to be able to determine the effect of concurrent memory access in various use cases and to overcome the practical limitations of the application development system. This kind of an evaluation method gives quite reliable on results on performance and usability of the proposed solution for a wide range of applications utilizing different degree of concurrent memory access. Since the actual SPEC programs are not likely to refer memory as often as the traces executed at the rate of one reference per step, the obtained results may be a bit too pessimistic for EREW-intensive cases. The measurements were made with a modified Eclipse simulator. For each evaluated benchmark-configuration pair we measured the execution time, step cache hit rate, and maximum latency of memory references. The results of measurements are shown in Figure 2. We can make the following observations from the results:

- The overhead of PRAM simulation in concurrent access is very low (even lower than in exclusive access) if there is enough threads while the overhead explodes close to the number of processors without the algorithm
- The step cache hit rates comes close to the fraction of ca benchmark component if the number of threads is high enough

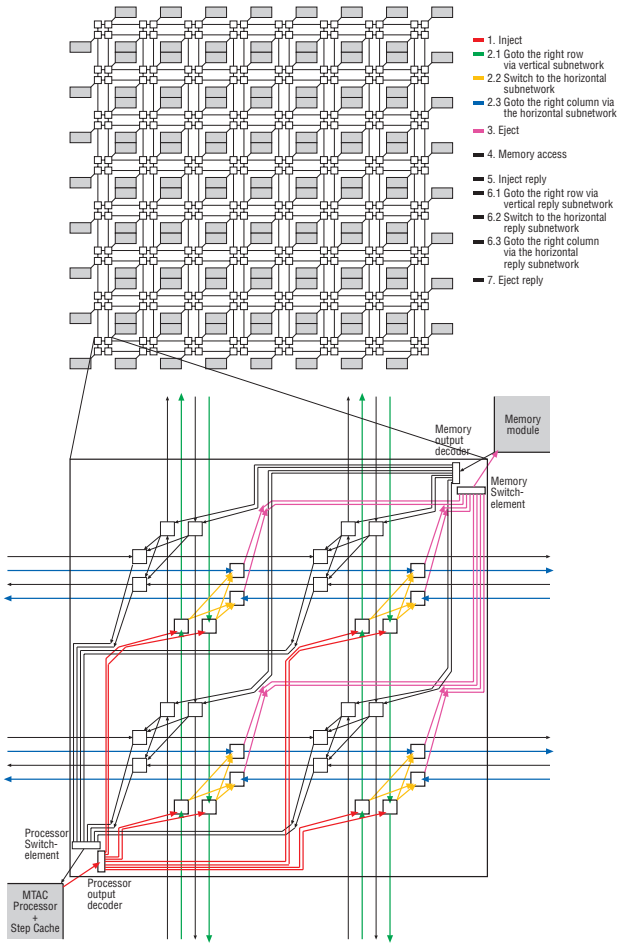

Figure 1. Algorithm applied to our MP-SOC framework with 64-processor architecture and routings.

- The maximum latency of memory references increases as the fraction of concurrent access increases for without the algorithm but decreases with the algorithm
- Changing the length of queues between 6 and 16 did not show notable effect on performance

We estimated the silicon area of the evaluated machines using our performance-area-power model for the family of MP-SOC architecture [19]. According to it the area overhead with respect to the baseline in typical MP-SOC configurations is less than 1%. Finally, we did not measure the execution times using the SB-PRAM variant of Ranade's algorithm but based on investigations about 30% of memory reads in general purpose code, like c-compiler, are dependent on the other instructions so that it is not possible to hide the delay by instruction scheduling 1]. Assuming that 2/3 of the memory references are reads, we estimate that a machine with the SB-PRAM variant runs about 20% (100%) slower than the proposed machine with (without) delayed load, respectively.

V. Conclusions

We have proposed a novel algorithm to simulate arbitrary CRCW PRAM with single step operations based on processor-level filtering and combining with a help of step caches. We applied the algorithm to our scalable MP-SOC framework and

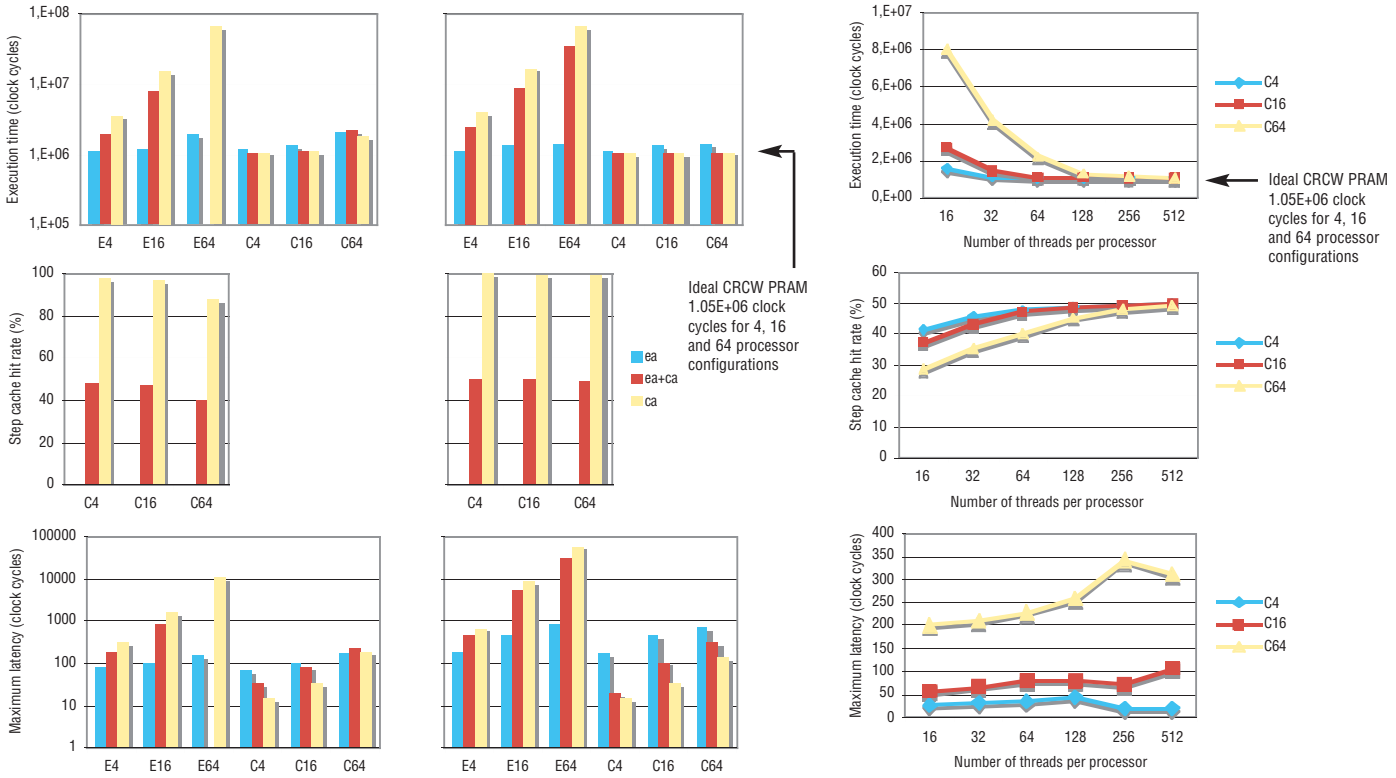

Figure 2. Execution time, step cache hit rate, and maximum latency for the baseline EREW architecture (E4, E16, E64) and modified architecture employing the proposed algorithm (C4, C16, C64) for 64 thread (left) and 512 thread configurations (middle) and in the ea+ca case (right).

performed early simulations. The results are encouraging: The proposed algorithm indeed implements the arbitrary CRCW PRAM model and the overhead of PRAM simulation for code employing concurrent access is even lower than for exclusive parallel access. Our future work includes extension of the proposed algorithm to slow memories and realization of priority CRCW PRAM using a modified version of the proposed algorithm.

Acknowledgments

This work was partially supported by the grant 107177 of Academy of Finland.

References

[1] J. Hennessy and D. Patterson, *Computer Architecture: A Quantitative Approach*, Morgan Kaufmann Publishers Inc., Palo Alto, 1990.

[[2] M. Flynn, "Microprocessor Design Issues: Thoughts on the Road Ahead", *IEEE Micro*, Vol. 25, 3 (2005), pp. 16-31.

[3] *International Technology Roadmap for Semiconductors*, Semiconductor Industry Assoc., 2005; http://public.itrs.net/.

[4] *Research at Intel From a Few Cores to Many: A Tera-scale Computing Research Overview*, White Paper, Intel, 2006.

[5] S. Fortune and J. Wyllie, "Parallelism in Random Access Machines", In the *Proc. of the 10th ACM STOC*, 1978, pp. 114-118.

[6] J. Keller, C. Keßler, and J. Träff, *Practical PRAM Programming*, Wiley, New York, 2001.

[7] J. T. Schwarz, "Ultracomputers", *ACM Transactions on Programming Languages and Systems*, Vol. 2, 4 (1980) pp. 484-521.

[8] M. Forsell, "Are Multiport Memories Physically Feasible?", *Computer Architecture News*, Vol. 22, 4 (1994), pp. 47-54.

[9] D. Culler and J. Singh, *Parallel Computer Architecture—A Hardware/Software Approach*, Morgan Kaufmann Publishers, San Francisco, 1999.

[10] M. Forsell, "A Scalable High-Performance Computing Solution for Network on Chips", *IEEE Micro*, Vol. 22, 5 (2002),pp. 46-55.

[11] J. Jaja, *Introduction to Parallel Algorithms*, Addison-Wesley, Reading, 1992.

[12] A. Ranade, "How to Emulate Shared Memory", *Journal of Computer and System Sciences*, Vol. 42, (1991), pp. 307-326.

[13] U. Vishkin, S. Dascal, E. Berkovich and J. Nuzman, "Explicit Multi-Threading (XMT) Bridging Models for Instruction Parallelism (Extended Abstract)", In the Proc. *SPAA'88*, 1998.

[14] M. Forsell, "Realizing constant time parallel algorithms with active memory modules", *International Journal of Electronic Business*, Vol. 3, 3-4 (2005), pp. 255-263.

[15] A. Karlin and E. Upfal, "Parallel Hashing—an Efficient Implementation of Shared Memory", *Journal of the ACM*, Vol. 35, 4 (1988), pp. 876-892.

[16] A. Ranade, S. Bhatt and S. Johnson, "The Fluent Abstract Machine", In the Proc. of the *5th MIT Conference on Advanced Research in VLSI*, 1988, pp. 71-93.

[17] V. Leppänen, Studies on the realization of PRAM, *Dissertation* 3, Turku Centre for Computer Science, University of Turku, Turku, 1996.

[18] M. Forsell, "Step Caches—a Novel Approach to Concurrent Memory Access on Shared Memory MP-SOCs", In the Proc. *IEEE NORCHIP'05*, November 21-22, 2005, Oulu, Finland, pp. 74-77.

[19] M. Forsell, "Performance, Area, and Power model for MP-SOCs", unpublished.

[20] A. Milenkovic and M. Milenkovic, "Exploiting Streams in Instruction and Data Address Trace Compression", In the Proc. *WWC'03*, October 27, 2003, Austin, USA, pp. 99-107.

Development of Low-cost Parachute Training Simulation System

Sombat Hathairattananon and Thavida Maneewarn
Institute of Field Robotics (FIBO)
King Mongkut's University of Technology Thonburi
126 Pracha-utid Road, Bangmod ,Thungkru, Bangkok, 10140, THAILAND

***Abstract*- This research was inspired by the problem in parachute training program in the Thai military training curriculum. The normal training routine consists of a physical training unit which suspends the body of the trainee while the trainer rotates the training set according to the given instruction routine. The current training system does not sufficiently provide the trainee the realistic perception of parachute flight operation. The parachute training simulation system is proposed to be the low-cost interactive training platform that enhances user's perception of motion and control of the parachute. The simulation system consists of the graphical user interface module that displays and updates the 3D scene according to the physical model of the parachute and the control of the steering line by the user. The parachute training simulation system is designed for parachute control practice for ground descending mission in windy situation.**

Keywords : Parachute Simulation , Parachute Training

I. INTRODUCTION

Currently, the parachute training curriculum for military training are classified into 4 steps.

Step 1: The theory of parachute control.

Step 2: Training and testing of trainee physical performance.

Step 3: Ground-based training of parachute control skill which includes.

3.1 Jumping from 34 feet tower.

3.2 Jumping 2 and 4 feet stage .

3.3 Ground-based parachute control skill training

Step 4: Air-based parachute training.

In the current training curriculum, the problem usually occurred on step 3.3 as shown in Fig. 1 ,when the trainee is unable to perceive the realistic motion of the parachute which is controlled by the trainer e.g. the trainee will control the direction of parachute by pulling the steering line and the trainer will rotate the training stage accordingly.

(A) (B)

Figure 1. (A) Training Style ,(B) Tools for Training

The lack of realistic perception of motion and control in the existing training system caused the trainee to have insufficient experience in controlling the parachute and could lead to accident in the real air-based parachute training step.

II. CONCEPTUAL FRAMEWORK

A. The interative parachute training simulation system

Parachute training system in virtual environment have been developed and improved over years for the use in military [1][2][3][6] and for sport and entertainment applications [4] [6]. Hi-speed computer, Hi-definition sensors and Head Mounted Display (HMD) have been used extensively in these research. These equipment usage results in the high cost of these existing simulation systems. The interactive parachute training simulation system consists of two majors elements: the graphical user-interface technology (software) and the steering input system (hardware). The 3D graphical scene is created by an environment simulation engine based on the real-time physical based simulation of the parachute motion in the air and the head motion of the user. The motion of the parachute is controlled by the user from the steering input system. Therefore, we propose the low-cost alternative of the parachute simulation system which is much cheaper and only required commodity equipment such as LCD projector as shown in Fig. 2. The graphical viewing system have the structure as shown Fig. 3.

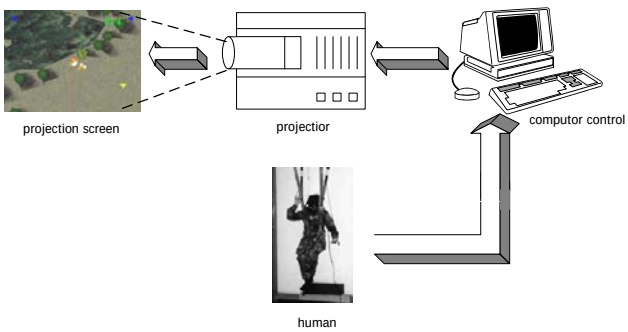

Figure 2. Design of Parachute Simulation System

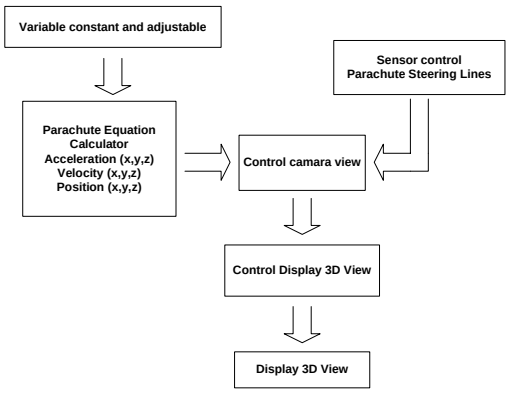

Figure 3. The design of a graphical viewing system

III. THEORY

A. Parachute physical based simulation

The motion of the parachute can be explained as 5 states as shown in Table 1 [8]. Parachute jump starts from the beginning of the jump until the point where the parachute is fully inflate and finally descend to the ground as shown Fig. 4 .

Table 1.
Function of Parachute Full Inflates [8]

	Time	Body	Status of Situation	Remark
1	$t \leq t_0$	Horizontal position	Freefall	
2	$t_0 < t \leq t_1$		Lines Extend	$t_1 - t_0 = 0.5$ sec
3	$t_1 < t \leq t_2$	Vertical position	Parachute Inflates	$t_2 - t_1 = 1.0$ sec
4	$t_2 < t \leq t_3$		Parachute Over Inflates	$t_3 - t_2 = 1.7$ sec
5	$t > t_3$		Final Descent	

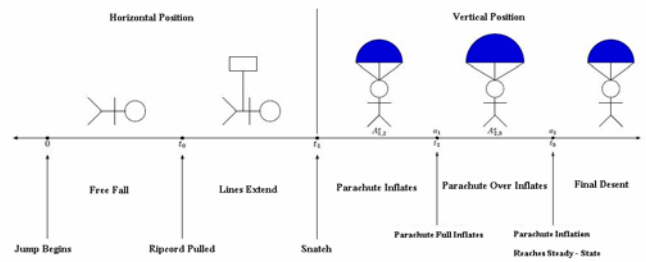

Figure 4. The 5 states of parachute jump cycle

Motion of parachute is affected by the gravity force: F_g. and the drag force: F_d. The sum of these forces are shown in (1).

$$\sum F = F_g + F_d \tag{1}$$

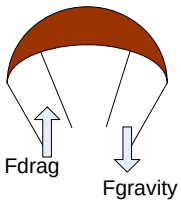

Figure 5. Forces affecting on the parachute

From these states of parachute jump cycle, the drag force is defined in (2). However, base on the condition of parachute jump, there are other factors that affects the forces acting to the body and the equipment which is given in (3).

F = total force, F_g = gravitational force, F_d = drag force, C_d = coefficient of drag, C_d^b = drag coefficient of skydiver body, C_d^e = drag coefficient of skydiver equipment, ρ = density of air flow, A^b = area of skydiver body, A^e = area of equipment ; $A_{1,2}^e$ on (t_1,t_2); $A_{2,3}^e$ on (t_2,t_3), h = height of jumper, H = height of jumping, a_1 = area of parachute, L = length of parachute lines, b_0 = area of body in horizontal position, b_1 = area of body in vertical position, m= weight of jumper include weight of parachute body, *v* and *a* are velocity and acceleration of the body.

$$F_d = \frac{1}{2}\left[C_d A \rho v^2\right] \tag{2}$$

Acceleration is given by the equation derived from sum of the force on the parachute body as in (4). Value of k in (4) derived from value of resistant force occurred from parachute body in (5).

$$F_d = F_d^b + F_d^e = \frac{1}{2}\rho\left[C_d^b A^b + C_d^e A^e\right]v^2 \tag{3}$$

$$a = \left[-g + \frac{kv^2}{m}\right] \tag{4}$$

$$k = \frac{1}{2}\rho\left[C_d^b A^b + C_d^e A^e\right] \tag{5}$$

The value of k is different at each state of the process of each as shown in (6). The velocity of the parachute in (4) can be calculated by (7).

$$k = \frac{1}{2}\rho\begin{cases} 1.95b_0 & , t \leq t_0 \\ 1.95b_0 + 0.35b_1 l\dfrac{t - t_0}{t_1 - t_0} & , t_0 < t \leq t_1 \\ 0.35b_1 h + 1.33A_{1,2}^e(t) & , t_1 < t \leq t_2 \\ 0.35b_1 h + 1.33A_{2,3}^e(t) & , t_2 < t \leq t_3 \\ 0.35b_1 h + 1.33a_1 & , t > t_3 \end{cases} \tag{6}$$

$$v(t) = \eta\left[\frac{1-e^{-\sigma t}}{1+e^{-\sigma t}}\right] \quad ,v(0) = 0 \tag{7}$$

when, $\eta = \sqrt{\frac{gm}{k}}$ $\quad ;\sigma = \frac{2\eta k}{m}$

B. 3D graphical viewing system & steering and head motion input system

3D graphical view rendering system is developed in C language using OpenGL library. The scene is updated from the viewpoint generated from the parachute equation of motion as shown in the previous section. The 3D graphical scene when the parachute descending is tested by rendering a 3D cone on the ground plane at various positions as shown Fig. 6. Steering and head motion input system is the electronic device that senses the motion of the steering line when the user pulls the steering line of the parachute in order to control the parachute and sense the head motion of the user . For the low-cost version of the parachute simulation system, potentiometers are mounted at the pulleys connected to the steering lines and the body-head suspension support. The potentiometer senses the motion of the left and right steering line then the data is used to update the physical based simulation of the parachute. The design of the low-cost parachute training simulation system is shown in Fig. 7.

Figure 6. Test of the 3D viewing System together with the steering and head motion input systems

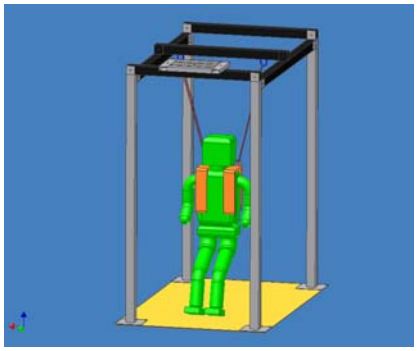

Figure 7. The model of low-cost parachute training simulation system

When the user pulls the steering line, it will cause the rotation motion of the parachute toward the pulling direction. The force equation of the parachute in (2) is modified by the angle of rotation caused by pulling the steering line(ϕ) and the turning radius (R) as described by (8) and (9) as show Fig.8 v and ω is the linear and rotational velocity of the parachute body.

$$\omega = \frac{g \times \tan\phi}{v} \tag{8}$$

$$R = \frac{v}{\omega} \tag{9}$$

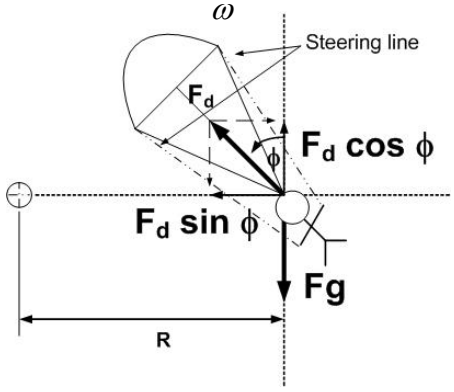

Figure 8. Parachute turning with the steering line control

IV. SIMULATION RESULT

The parachute model MC1-1C is used in this simulation. The MC1-1C model has the area of parachute (a_1) = 43.8 m^2 , length of parachute lines (L) = 8.96 m , area of body in horizontal position (b_0) = 0.5 m^2 , area of body in vertical position (b_1) = 0.1 m^2 , height of jumper (h) = 1.78 m , weight of jumper include weight of parachute body (m) = 97.2 kg , height of jumping (H) = 1,500 m (≈ 4922 ft). The simulated jump begins from time t_0 until the final decent at time t_3 as shown in figure 3.2. Different states of jump is defined by time: t_0 to t_1 = 0.5 second (Lines Extend) , time: t_1 to t_2 = 1.05 second (Parachute Inflates) , time: t_2 to t_3 = 1.7 second (Parachute Over Inflates). Take these values into parachute equations (4), (7) which can find the answer by using mathematical analysis program (MATLAB) as below Fig. 9.

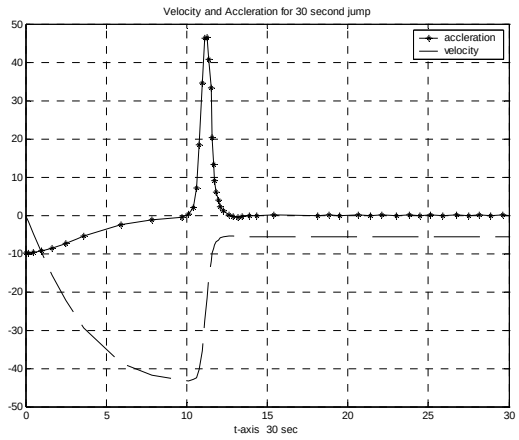

(a)

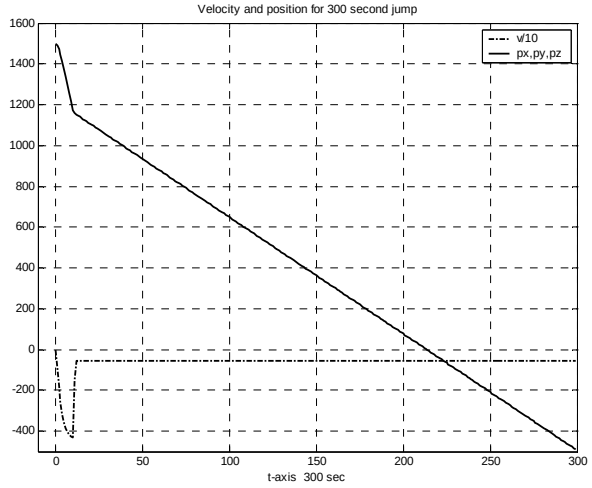

(b)

Figure 9. (a) Acceleration and velocity of parachute movement
(b) Position and velocity of parachute without external wind forces

In order to simulate windy situation necessary in parachute training exercise, the wind force is added into the parachute equation of motion. The wind force is added in axis X and Y. We can observe that when the wind force is added, the wind force directly affects the velocity and the position of parachute as shown in Fig. 10.

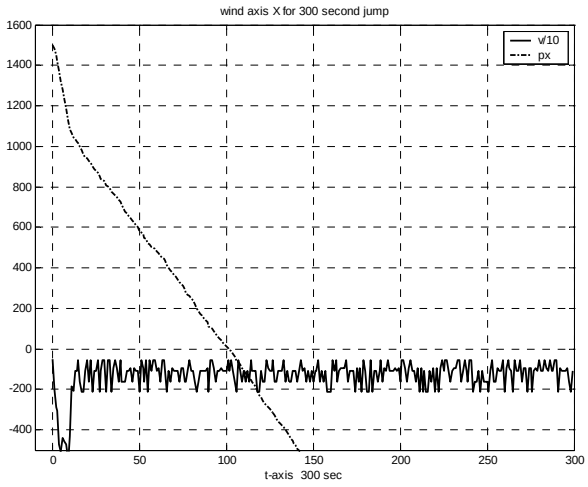

(a)

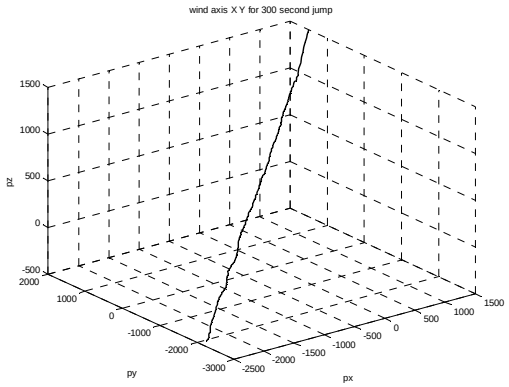

(b)

Figure 10. (a) Position and Velocity of parachute when the wind force is added in X axis (b) Position of parachute when the wind force is added in both X and Y axis

V. CONCLUSION

The low-cost parachute training simulation system consists of the physical based simulation of the parachute motion and the user interface subsystem including a 3D graphical viewing system and the steering & head motion input system. The physical based simulation of the parachute is tested with and without external wind force. The next step of this research is to test the overall performance of the low-cost parachute training system whether it can improve the skill of the trainee for ground descending mission in windy situation.

REFERENCES

[1] Hogue, Jeffrey R., Henry R. Jex, Applying Parachute Canopy Control andGuidance Methodology to Advanced Precision Airborne Delivery Systems, AIAA-95-1537, May 15-18, 1995, Clearwater Beach, Florida.

[2] Hogue, Jeffrey R., Frederick G. Anderson, Cecy A. Pelz, R. Wade Allen, Steve Markham, Arvid Harmsen, Parachute Simulation Enhancements for Post-Ejection/Egress Training, September 14-16, 1998, Phoenix, AZ.

[3] Hogue, Jeffrey R., Frederick G. Anderson, Cecy A. Pelz, R. Wade Allen, Steve Markham, Arvid Harmsen, Enhanced Parachute Simulation Training and Planning, June 8-11, 1999, Toulouse, France.

[4] Hogue, Jeffrey R., R. Wade Allen, Cecy A. Pelz, Steve Markham, Arvid Harmsen, Methodology and Improvements in Aircrew Parachute Descent Virtual Reality Simulation Training, STI-P573, October 9th-11th, 2000,Reno, Nevada.

[5] Hogue, Jeffrey R., Jerry MacDonald, Steve Markham, Arvid Harmsen, Expanding the Role of Virtual Reality Parachute Simulation, STI P-601, January 26-31, 2003, Jacksonville, Florida.

[6] Hogue, Jeffrey R., R. Wade Allen, Jerry MacDonald, Cliff Schmucker, Steve Markham, Arvid Harmsen, Virtual Reality Parachute Simulation for Training and Mission Rehearsal, AIAA2001-2061, May 21-24, 2001, Boston, Massachusetts.

[7] Hogue, Jeffrey R., R. Wade Allen, Jerry MacDonald, Cliff Schmucker, Steve Markham, Arvid Harmsen, Virtual Reality Parachute Simulation for Training and Mission Rehearsal, AIAA2001-2060, May 21-24, 2001, Boston, Massachusetts.

[8] Douglas B. Meade , Allan A. Struthers , Differential Equations in the New Millennium: the Parachute Problem ,IJEE 1097 ,2 July 1999.

Separation of Concerns in Modeling System Software for Automate Code Generation

Paniti Netinant
Computer Sceince Departmnet
Bangkok University
Bangkok, Thailand
paniti.n@bu.ac.th

Abstract

Aspect-oriented programming is a new paradigm that complements the object-oriented technology. The premise of aspect-oriented technology is the separation of concerns. Certain system properties tend to cut across group of functional components such as concurrency, security, and fault tolerance are examples of these crosscutting concerns. Aspect orientation attempts to modularize these crosscutting properties in order to avoid the code-tangling phenomena. Objects are independent entities that cooperate together t0achieve a certain task, how can we mange object interaction without violating basic object orientation principles like abstraction, what triggers an object to perform its functionality, what constraints that an object must consider before performing its task(s) are, how an object behavior impacts other object(s) behavior, how we can model our aspect oriented system with all the above questions in mind using existing CASE tools and guarantee separation of concerns at the implementation (automatic code generation).

In this position paper presents a formal methodology that addresses the above questions and supports separation of concerns for system software. The paper demonstrates aspect-oriented framework applying at the design and implementation phase with separation of system properties. Our approach uses CASE tools supporting UML without any extensions to it. Rhapsody CASE tool has been used to model and automatically generate code since it supports UML diagrams which enable us to present different views using different UML diagrams (OMD, SD, Statecharts, and Use Case diagrams).

1. Introduction

Recent advances in the software technology have reaffirmed the need for building component-oriented software systems. Object-oriented technology has delivered sound results regard supporting code reuse, and design patterns have demonstrated that large-scale software systems can benefit the most from the best documented design structures. Despite the tremendous success of object-oriented technology and design patterns to support code reusability and design reusability, little has been said regard the separation of concerns within the context of these technologies. Recent research in the separation of concerns has demonstrated the need for the separation of the functional requirements from the non-functional requirements in order to maximize code reuse and design reuse; non-functional requirements tend to cut-across the functional components. Till now aspect-oriented technology has offered very little to support the system engineer with a formal modeling technique in order to verify and validate the system design against its requirements. Experience shows that verification and validation of concurrent software systems is the most time consuming process in the software lifecycle. Modeling the behavior of concurrent software system based on aspect-orientation attempts to shorten this interval and improve software quality. The UML [1, 2] is a graphical language for specifying, visualizing, constructing, and documenting the artifacts of software systems. UML is a standard modeling language endorsed by Object Management Group (OMG) in 1997 as UML 1.1. UML is the graphical notation that defines the semantics of the object meta-model (model of UML itself), and defines a Notation for capturing and communicating object structure and behavior. UML relied heavily on (and support) Finite State Machines, UML state machine model is based on David Harels Statecharts.

Our research is bout bringing a formal methodology to automate the implementation of concurrent software systems based on aspect-orientation. In our modeling approach we distinguish between static, dynamic, inter, and intra object behavioral modeling. We believe that automatic code generation is only possible with intra object behavioral modeling, we use statecharts to describe the behavior of each object in the system, we also address inter object communication via both awareness of object state changes and message passing. An important element of a sound behavioral modeling approach is a rigorous methodology that ensures the semantics of the constructed model based on requirements. These models can be used to automatically generate code and guaranteeing that the generated code confirms to Aspect oriented principles, by that we mean separating aspectual components from main functional components at the generated code. Concurrent software systems are composed of functional requirements and concurrency requirements, like synchronization constraints, and scheduling policies. Aspect-oriented technology is an ideal solution for modeling such systems, since the distinguishing between aspects and functional requirements is at the heart of such technology.

What motivated our work is the need for a complete end-to-end requirement modeling technique that will guide the designer in the design of concurrent software systems and automate their implementations. Behavioral modeling based on requirements is the first step toward formal design methodology based on aspect-orientation.

2. UML

The UML [1, 2] is a graphical language for specifying, visualizing, constructing, and documenting the artifacts of software systems. UML is a standard modeling language endorsed by Object Management Group (OMG) in 1997 as UML 1.1. UML is the graphical

notation that defines the semantics of the object meta-model (model of UML itself), and defines a Notation for capturing and communicating object structure and behavior. UML is suited for modeling real-time and embedded systems. UML relied heavily on (and support) Finite State Machines, UML state machine model is based on David Harels Statecharts.

In UML objects have both structure and behavior, objects work together to implement higher-order behaviors defined in Use cases. UML allows software engineers to analyze and design software systems using standard object-oriented techniques, the main UML tools for analyzing the system are: Use case diagrams show general interactions between the system and external objects/actors who may want to interact with it. Sequence Diagrams show sequences of steps and messages passed between objects when executing a particular instance of a use case. Object model diagrams show the static structure of the system in terms of classes and objects, and define relationships between these objects. Statecharts [2, 9, 10, 11] define the behavior of objects, including the various states that an object can enter into over its lifetime and the messages or events that cause it to transition from one state to another. A state in a state chart is an abstraction of the model in which the object finds itself [2, 3]. A message (such as an event) can trigger a transition from one state to another. A message can be either an event or a triggered operation.

The benefits of modeling have been outlined in the literature [1, 2]. Why do we model? UML introduction [1] outlines the following benefits: Provide structure for problem solving, Experiment to explore multiple solutions, Furnish abstractions to manage complexity, reduce time-to-market for business problem solutions, Decrease development costs, and manage the risk of mistakes. Benefits of modeling Aspect oriented systems also been examined by the researchers, [3] stresses that capturing aspects at the design phase streamlines the process of aspect orientation development; it helps learning and documenting aspects. [4, 5] also outlines that capturing aspects at the design phase makes round trip development possible of aspect orientation systems, and helps to maintain consistency of requirements, design, and implementation. We in this paper also argue that when aspects are identified at an early stage of the development life cycle it makes there design components more Reusable, and it makes automatic code generation possible for AO systems with higher levels of separation of concerns at the generated code.

3. Our Approach

Modeling concurrent software systems with sequence diagrams and class diagrams will not be enough to achieve a full implementation of the system behavior. Sequence diagrams will describe the inter object behavior, it will help in describing scenarios for the system, how objects will interact with each other, but will not allow zooming into the object itself to describe its behavior, for that we need statecharts. Statecharts provide the behavior of a particular object including various states that an object can enter into over its life cycle. As stated in [7, 9, 11] statecharts are mainly used to describe intra-object behavior versus inter object behavior which can be specified using MSCs or Sequence Diagrams. Avery distinguishable characteristic of Statecharts from MSCs or Sequence Diagrams is the fact that Statecharts are part of the system model, which means they can be used to generate code.

Statecharts show the states of an object within a given context, the events that causes an object to go from one state to another, and the actions that can occur as a result of a state transition. Events could be guarded by conditions, which must evaluate to true before a transition takes place. During the object's life cycle an object move from one state to another, and produce some actions as a result of this transition, this is how the behavior of an object should be described and Statecharts does that. Modeling concurrent systems based on aspect-orientation is a new approach that has many benefits: reusability, verification and validation, and automate implementation. UML/Statecharts are used mainly to model the internal behavior of concurrent objects, though this formalism of modeling needs to support aspect orientation. In this paper we outline a modeling standard for concurrent systems based on Aspect-orientation.

Within concurrent objects, state transitions may occur if a method is invoked or a timer expired. Associating aspects that are evaluated when an object method is invoked is a troublesome for system modeler and developer, since the specification and constrains of these aspects are state dependents. For example, in the case where we have a bounded buffer with certain capacity and two methods put and get, we shall allow only put method to proceed when the buffer is an empty state and allow either put or get when we are in a partial state. Synchronization constraints and Scheduling specifications are the main aspects that influence the execution of the invoked methods based on object states. Being able to express the concurrent object behavior as StateChart and augment that by notation that allows the modeler to express aspects explicitly within the models is a step forward to automate the implementation of such systems.

3.1. Aspect Oriented Framework

The Aspect Moderator [13, 14, 15] is a framework-based solution for building concurrent software systems. In this framework, a concurrent system is represented as a cluster of co-operating objects that handle the creation of aspects as well as the interaction between components and aspects. Both analysis and design phases can be studied during two stages of operation: initialization and method invocation. A number of design principles have been taken into account while designing this framework, the first of which is to separate functional from non-functional requirements, and identify cross-cutting concerns (aspects). A functional component provides services. Those services that are associated with some aspectual behavior are referred to as participating services. Each aspectual behavior for each service of each method is extracted from the main functionality and it is treated as a separate concept in the conceptual model of the system.

In a concurrent system, a number of services (methods) in a concurrent class will be associated with synchronization constraints. During initialization, the proxy to the functional component will request from the aspect_factory the creation of aspect instances that capture the synchronization constraints associated with services (methods) of the class. Aspect instances implement the aspect-interface which is defined by two methods: precondition( ) and postcondition( ). During design, it is important to identify possible design patterns that might meet any architectural needs. During initialization the Factory Method pattern [16] can be used to create the required aspects for the participating methods of the functionality class. All aspect objects implement the AspectIF interface. The overall class diagram of the Aspect Moderator framework is shown below.

Our work is needed To complete the AM Framework and makes it acceptable by automatic code generators, we will address in this paper issues that are essential to automatic code generation, we need to describe the dynamic behavior of the AM framework objects, we will use statecharts to capture the behavior of the objects in the AM Framework. And we will use state notification mechanisms [6] to describe the coordination and interaction among these objects. [Harel, Executable object modeling, IEEE 1997] states that statecharts can be used to describe both objects communication and objects internal behavior.

3.2 Applying Our Approach

Our solution relies on the statechart semantics where object state changes are detected by other objects (state notification). When objects behavior is dependent on other objects states, it is essential that objects share their state to other object since this will impose a certain behavior on these objects. State notification [6] allows an object to monitor and synchronize with state changes of other objects. Our approach will not dedicate an object to coordinate object interaction, instead all objects will participate to achieve the coal at hand and to manage the coordination of each other states. Our approach supports the aspectual behavioral modeling for concurrent software systems, we will apply Aspect Oriented at the design phase with object coordination in mind, we guarantees separation of concerns at the implementation. We will apply our approach to the Aspect Moderator Framework described in section 3. We will try to build a complete behavioral model for the AMF using statecharts. We will use advanced features of staecharts to 1st assist in modeling complex dynamic behavior, 2nd describe communications between AM Framework classes, 3rd isolate control from functionality. We will feed the model in any existing CASE tool (Rhapsody) and the output will be classes and interfaces that observe the architecture of the AM Framework.

In this paper we present the Bounded Buffer as a case study. In modeling the behavior of the Functional Bounded Buffer we can control the states of the Synchronization Aspect from the Bounded Buffer state machine, for instance when the Buffer transits from FULL to PARTIAL state as a result of get event we set the Synchronization Aspect state to Writeable-Readable as follows: *Get / [set Synchronization Aspect to Writeable-Readable]*, the buffer state machine is outlined below:

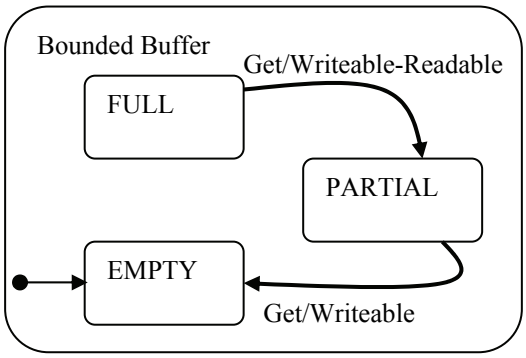

In the AM Framework requests comes in (i.e. from Producers and consumers) to the system and get intercepted by the Aspect Moderator which has a state machine that is dependent on the Synchronization Aspect states described below:

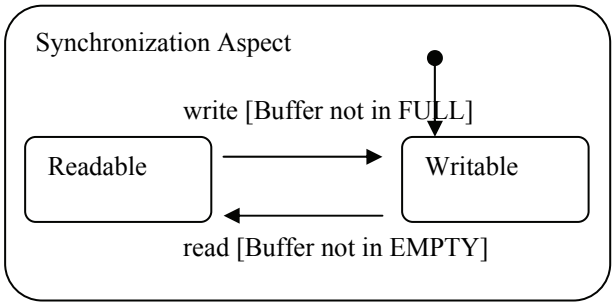

We will use message between the AM and the Synchronization Aspect, and the Buffer regions, by default the message addressed by the synchronization Aspect.

4. Future Work

The next step in our project to start applying the constructed model into existing CASE tools like Rhapsody. Also more work is needed to apply our approach to other Aspect oriented techniques other than the Aspect Moderator Framework.

5. Related Work

Behavioral modeling is getting more attention from researchers as well as practitioners since system engineers and designers describe the system requirements based on the expected system behavior. Modeling concurrent system behavior based on statecharts [7] is the first to address the issue of verification and validation of concurrent object-oriented systems. Though the approach suffers from code-tangling phenomenon where concurrency code is intermixed with the functionality code. UMLAUT is a recent approach based on aspect-oriented modeling that addresses the separation of concerns early in the design phase, though this approach didn't address the intra-object interactions. Our approach addresses aspect-oriented modeling for concurrent systems based on extension to statecharts in order to automate the implementation for such systems. [3] outlines the benefits of capturing aspects in the design phase rather than the implementation phase,

these benefits includes: streamlining the process of aspect orientation development, reuse of aspects, and round-trip development. [4] also stresses on the importance of supporting aspects throughout the development life cycle. In [5] extends the UML metamodel to support subject-oriented and focuses on extensions to UML metamodel to support AO. In [6] Stresses that UML has to be extended to support multi-dimension separation of concerns other than the object dimension. In [7] From Play in Scenarios To Code, argue that automatic code generation only possible with intra object behavioral modeling, inter object behavioral modeling allows us to capture the requirements and are not part of the system model and can't be used to generate code. This approach didn't address AO or SoC. Most of these approaches didn't address behavioral modeling and Automatic code generation, some require developing new tool other require extending UML metamodel to support aspects. We think neither extending UML nor developing a new translation tool is needed to support aspects in the design phase.

6. Conclusion

Aspect-oriented approach is the next wave of development for software systems. This paradigm stresses the separation of the ascpetual code from the functionality code in order to maximize code reusability and minimize changes that are due to code-tangling. Behavioral modeling based on statecharts are getting more popular since it addresses modeling the system behavior early in the design stage and automate the implementation of such systems. Our approach is an aspect-oriented modeling technique that uses statechart constructs like and/or states to describe the coordination between objects in concurrent software systems. We applied our modeling technique to the Aspect Moderator Framework. Our approach supports the aspectual behavioral modeling for concurrent software systems, by applying aspect-oriented techniques at the design phase with object coordination in mind. We present an approach that guarantees separation of concerns at the design and implementation phase.

REFERENCES

[1] UML Summery V1.1, OMG, ad/97-08-03, www.rational.com/UML.

[2] UML Syntax and Semantics Guide V1.1, OMG, ad/97-08-03, www.rational.com/UML.

[3] Junichi Suzuki, Yoshikazu Yamamotto, "Extending UML with Aspects:Aspect support in the design phase"3rd AOP Workshop at ECOOP 1999.

[4] Siobhan Clarket, William Harison, Ossher, Tarr, "Separation Concerns throughout the Development lifecycle" 3rd AOP Workshop at ECOOP 1999

[5] Siobhan Clarket "Extending UML Metamodel for Design Composition", 3rd AOP Workshop at ECOOP 1999

[6] Juan, Papathomas, Murillo, Sanchez, "Coordinating Concurrent Objects: How to deal with the coordination aspect?" 1st AOP Workshop at ECOOP 1997.

[7] David Harel "From Play-In Scenarios To Code: An Achievable Dream. IEEE Computer, to appear. Preliminary version in Proc. Fundamental Approaches to Software Engineering (FASE), Lecture Notes in Computer Science, Vol. 1783, Springer-Verlag, March 2000, pp. 22{34.

[8] W. Ho, F. Pennaneac'h , J. Jezequel, and N. Plouzeau, "Aspect-Oriented Design with the UML*,"

[9] D Harel and M. Politi, Modeling Reactive systems with StateCharts. McGraw-Hill, New York, 1994.

[10] UML Statecharts by Bruce Powel Dpouglass, ESP Jan-1999. "I-Logix

[11] Harel, Daveid "Statecharts": a visual formalism for complex systems, "Science of Computer Programming. Vol. 8 (1987),P. 231

[12] Lodewijk Bergmans and Mehmet Aksit. Composing Software from Multiple Concerns: A Model and Composition Anomalies. ICSE 2000 2nd Workshop on Multidimensional Separation of Concerns.

[13] A.Bader, C. A. Constantinides, T. Elrad, T. Fuller, P. Netinant. Building Reusable Concurrent Software Systems. International Conference on Parallel and Distributed Techniques and Applications (PDPTA'2000) special session on Distributed Objects in Computational Science. June 26 - 29, 2000. Las Vegas, Nevada, USA.

[14] Constantinos A. Constantinides and Tzilla Elrad. On the Requirements for Concurrent Software Architectures to Support Advanced Separation of Concerns. Object-Oriented Programming, Systems, Languages and Applications (OOPSLA 2000) Workshop on Advanced Separation of Concerns in Object-Oriented Systems. Minneapolis, Minnesota, USA. October 16, 2000.

[15] Constantinos A. Constantinides, Atef Bader and Tzilla Elrad. Separation of Concerns in the Design of Concurrent Software Systems. The 14th European Conference on Object-Oriented Programming (ECOOP 2000) Workshop on Aspects and Dimensions of Concerns. Sophia Antipolis and Cannes, France, June 11-12, 2000.

[16] Gamma, E., Helm, R., Johnson, R. and Vlissides, J. Design Patterns: Elements of Reusable Object-Oriented Software. Addison-Wesley, Reading, MA,1995.

[17] Ralph E. Johnson. Frameworks = (Components + Patterns). In Communications of the ACM. Vol. 40. No. 10. October 1997, pp. 39-42.

[18] Gregor Kiczales, John Lamping, Anurag Mendhekar, Chris Maeda, Cristina Lopes, Jean-Marc Loingtier, and John Irwin. Aspect-Oriented Programming. In Proceedings of ECOOP '97. LNCS 1241. Springer-Verlag, pp. 220-242.

[19] Kim Mens, Cristina Lopes, Badir Tekinerdogan, and Gregor Kiczales. Aspect-Oriented Programming. Report of the ECOOP '97 Workshop for Aspect-Oriented Programming.

[20] Sinan Si Alhir "Extending UML"

[21] Sinan Si Alhir "What is UML"

[22] Sinan Si Alhir "UML Extension Mechanisms"

[23] Rhapsody from I-Logix www.ilogix.com, Rhapsody Guid.

Multidimensional Binary Clustering Tree for Surface Simplification of Point-Sampled Surface

Thanet Suphan, Chakrit Watcharopas
Department of Computer Science, Faculty of Science,
Kasetsart University, Bangkok, Thailand
Email: {g4864196, fscickw}@ku.ac.th

***Abstract*-Multidimensional Binary Clustering Tree (MBC Tree) is an algorithm that adapts the Multidimensional Binary Search Tree (Kd-tree), which is generally used in nearest neighbor search problem for the use of surface simplification whereas a surface is generated from a cloud of points in 3D space. MBC Tree is an algorithm for data clustering. The algorithm separates data along chosen axis and splits them with their centroid. This paper aims to compare the effectiveness of divisive hierarchical clustering (DHC) and MBC Tree for point cloud simplification. The experimental results show that MBC Tree is faster than DHC and its algorithm is easy to implement. MBC Tree is also capable of producing high-quality surface approximations.**

I. INTRODUCTION

Surface simplification is used to reduce a geometric description of point-sampled surface in order to produce a new description that is similar in appearance to the original and that has fewer geometric primitives [1] helping to speed up the rendering process, especially for real-time rendering. Surface simplification algorithm can be broadly categorized into 3 classes: Vertex Decimation, Vertex Clustering, and Edge Contraction [2], which each class has its own quality and different disadvantages.

From their research [3], Pauly et al. present various algorithms for surface simplification and also show their efficiency. The algorithms, such as, Incremental, Divisive Hierarchical Clustering (DHC), Iterative Simplification, and Particle Simulation are listed in their paper. From this research, the surface simplification with the DHC algorithm takes the least amount of time in processing, while the iterative simplification algorithm can produce higher quality surfaces.

In our paper, we present our surface simplification algorithm, which we call our algorithm the Multidimensional Binary Clustering Tree (MBC Tree). The algorithm is categorized as a data clustering algorithm and is adapted from the Multidimensional Binary Search Tree (Kd-tree), which is generally used in nearest neighbor search problem. It works directly on sampled-point cloud and no filtering preprocess is required on the input sample points. In our paper, we also compare the efficiency of the MBC Tree algorithm with of the DHC algorithm. We find that the MBC Tree algorithm is faster than DHC algorithm, and can also procduce a good quality surfaces.

II. MULTIDIMENSIONAL BINARY CLUSTERING TREE

Multidimensional Binary Clustering Tree (MBC Tree) is adapted from Kd-tree [4], and MBC Tree algorithm is to separate sampled-point data along the chosen axis and splits them with their centroid.

1) (Initial step) Put all points into a single cluster. A user-specifies cluster size n and split axis k and $k \in \{0, 1, 2\}$ where a value of 0, 1, and 2 means the aligned axis X, Y and Z respectively.
2) Create parent node of the tree by using a centroid of cluster as the node value.
3) Create child nodes by dividing points in parent node into two subcluster along axis k.
   3.1) Left child node is a subcluster that contains points of which have value of axis k less than or equal to value of axis k of parent node.
   3.2) Right child node is subcluster that contains points of which have value of axis k more than value of axis k of parent node.
4) Increment k (k = (k+1) mod 3)
5) Repeat step 2-4 until size of the cluster less than or equal to the user-specified cluster size n.
6) For each cluster, compute its centroid and use the centroid as a new simplified point.

Figure 1. MBC Tree Algorithm

As shown in Figure 1, our algorithm starts by taking a user-specified cluster size and a split axis and then creates a tree with two major differences from Kd-tree as follows:

1) Parent node of Kd-tree is come from a median of sorted data, while MBC Tree uses data centroid as a value of the parent node.

2) Kd-tree repeatedly subdivides point data until each data point becomes a leaf node in the tree, while MBC Tree repeatedly subdivides point data until the leaf node has the number of points less than or equal to the user-specified cluster size.

III. METHODOLOGY

As data input, we use 3D points sampled from a real surface using a modern 3D scanning device. We then compare efficiencies between of the MBC Tree and of the DHC algorithm by measuring the time spent for point simplification process and surface quality. We measure the quality of surfaces by using Metro [5] which can measure distances between two surfaces. We perform MBC Tree and DHC algorithms on point clouds of different sizes as well as different cluster sizes. We conduct our experiment as follows:

For the first part of our experiment, we use point clouds of difference sizes as input into both MBC Tree and DHC in order to run these two algorithms with fixed cluster size of 10 points to produce new simplified point clouds.

For the second part, as an algorithm input, we use the fixed size point cloud of Buddha that has 543,652 points and variable cluster sizes of 5, 10, 15, 20, and 25 points. We also run both algorithms on these data sets to produce simplified point clouds.

For the last part of our experiment, we use Tight Cocone algorithm [6] to produce surfaces from original point sets as well as simplified point sets obtained from the first part and second part of our experiment. By using Metro, we measure distance between these surfaces: one created from an original point set and another created from a simplified point set.

IV. EXPERIMENTAL RESULT

Figure 2 (a) shows time spent in point simplification process using MBC Tree and DHC algorithms; the input data are point clouds of various sizes of sample points. The cluster size for these algorithms is a size of 10 points. The experimental results show that MBC Tree outperforms DHC on all input data.

Figure 2 (b) also shows time taken for MBC Tree and DHC algorithms to simplify points where the point set is a Buddha point cloud containing 543,652 points. We use various cluster sizes of 5, 10, 15, 20, and 25 points on the algorithms as the results are shown in the figure. The results also show that MBC Tree outruns DHC on all cluster sizes.

In the last part of our experiment, we use Metro to measure distance between a surface created from an original point set and a surface created from a simplified point set. The measurements are shown in Table I. The table shows values of maximum distance (Max.) and average distance (Avg.) between original point-sampled surface and point-simplified surface. The table also shows that maximum distance and average distance measured from surfaces simplified by MBC Tree algorithm are slightly different from ones simplified by DHC algorithm.

Figure 3, 4, and 5 shows a visual measurement of quantitative error for Bunny, Armadillo and Dragon point clouds, where the magenta highlights on the point-simplified surface indicate the areas of differences from the original point-sampled surface.

V. CONCLUSION

The MBC Tree is algorithm for point simplification which can be used for an unstructured point cloud sampled from a real surface using a 3D scanning device. The algorithm is easy to implement. Our experimental results show that the MBC Tree is faster than DHC and capable of producing good quality surfaces.

ACKNOWLEDGMENT

This work is supported by the Department of Computer Science at Kasetsart University. Input data sets, used in this project, come from various sources. The bunny, Buddha, dragon, and armadillo point sets are courtesy of the Stanford Graphics Lab. The horse, skeleton hand, and blade point sets are courtesy of Georgia Institute of Technology. We would like to thank Tamal K. Dey for providing us his Cocone software to be used for surface reconstruction.

TABLE I
DISTANCE BETWEEN AN ORGINAL POINT-SAMPLED SURFACE AND A POINT-SIMPLIFIED SURFACE.

model	DHC		MBC Tree	
	Max.	Avg.	Max.	Avg.
Bunny	0.00666	0.00016	0.00651	0.00015
Horse	0.00491	0.00096	0.00503	0.00009
Armadillo	1.88302	0.01684	1.79176	0.05806
S. Hand	0.05286	0.00097	0.04321	0.00090
Dragon	0.00555	0.00003	0.00550	0.00003
Buddha	0.00452	0.00003	0.00128	0.00002
Blade	13.34191	0.12480	13.36789	0.16656

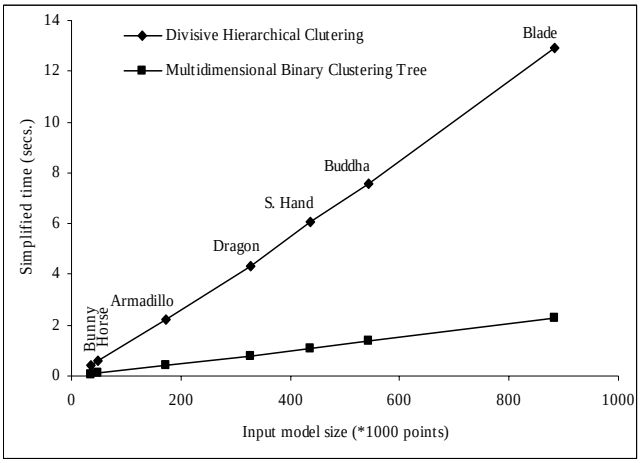

(a)

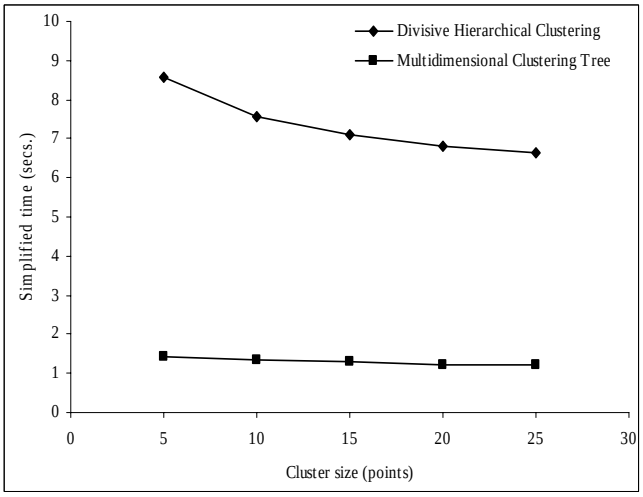

(b)

Figure 2. Execution times for simplification, measured on a Intel Core Duo processor T2300 (1.66 GHz) with 1 Gb of main memory: (a) as a function of input model point size with a cluster size of 10 points, (b) as a function of a cluster size for the Buddha model (543,652 points).

REFERENCES

[1] P. Lindstrom, and T. Greg, "Fast and memory efficient polygonal simplification," in *The conference on Visualization '98*, IEEE Computer Society Press, Los Alamitos, CA, USA, 1998, pp.279-286.

[2] M. Garland, and P.S. Heckbert, "Surface Simplification Using Quadric Error Metrics," in *International Conference on Computer Graphics and Interactive Techniques 24*, ACM Press/Addison-Wesley Publishing Co, 1997, pp.209-216.

[3] M. Pauly, G. Markus, and L.P. Kobbelt,"Efficient Simplification of Point-Sampled Surfaces," in *The conference on Visualization '02*, IEEE Computer Society, Washington, DC, USA, 2002.
[4] J.L. Bentley, "Multidimensional binary search trees used for associative searching," in *Communications of the ACM*, Vol.18, Issue 9, ACM Press, New York, NY, USA, 1975, pp.509-517.
[5] P. Cignoni, C. Rocchini, and R. Scopigno, "Metro: Measuring error on simplified surfaces," in *Computer Graphics Forum*, vol. 17 (2), Blackwell Publishers, 1998, pp.167-174.
[6] T. K. Dey and S. Goswami. "Tight Cocone: A water-tight surface reconstructor," in *Journal of Computing and Information Science in Engineering*, Vol. 3 (2003), pp. 302-307.

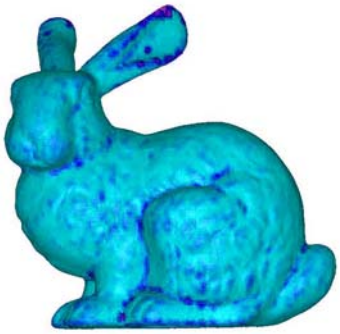

Max. Distance = 0.0067, Avg. Distance = 0.0002
(a) Divisive Hierarchical Clustering

Max. Distance = 0.0065, Avg. Distance = 0.0002
(b) Multidimensional Binary Clustering Tree

Figure 3. Surface Error for Bunny simplified with a cluster size of 10.

Max. Distance = 1.8830, Avg. Distance = 0.0168
(a) Divisive Hierarchical Clustering

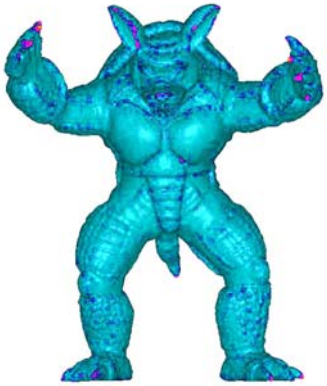

Max. Distance = 1.7918, Avg. Distance = 0.0581
(b) Multidimensional Binary Clustering Tree

Figure 4. Surface Error for Armadillo simplified with a cluster size of 10.

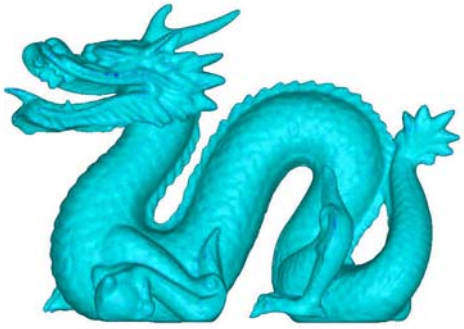

Max. Distance = 0.0555, Avg. Distance = 3.10E-05
(a) Divisive Hierarchical Clustering

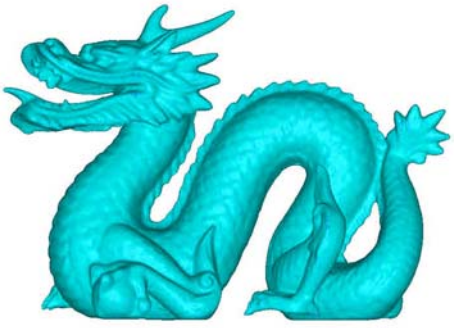

Max. Distance = 0.0555, Avg. Distance = 2.70E-05
(b) Multidimensional Binary Clustering Tree

Figure 5. Surface Error for Dragon simplified with a cluster size of 10.

Data Prediction by Support Vector Regression with a Decomposition Method

Phayung Meesad[(1)] and Tong Srikhacha[(2)]
[(1)]*Department of Teacher Training in Electrical Engineering, Faculty of Technical Education*
[(2)]*Department of Information Technology, Faculty of Information Technology*
King Mongkut's Institute of Technology North Bangkok, Bangkok, Thailand
pym@kmitnb.ac.th, tongs@tot.co.th

***Abstract*—Traditional forecasting methodologies use historical data for predicting future values. However, using only historical data does not guarantee accurate prediction results. It results in incomplete matching between historical and real target space due to the effect of pattern shifting. In this paper we propose a way to lessen this problem by analyzing the output component base applying support vector regression model (SVR). This applied method can give more general accurate prediction than traditional SVR model.**

I. INTRODUCTION

Solving a prediction problem is a critical task in those real-world applications where accuracy is strictly related to the management of economic resources. The price to pay in this case is usually an increased complexity of the computing system. Thus, the trade-off between cost and benefits must always be taken into account. [1]

A prominent time series model like Autoregressive Integrated Moving Average (ARIMA) model was introduced by G. Box and G. Jenkins in the early 1970s [2]. This time series analysis is attractive because it can capture complex arrival patterns, including those that are stationary, non-stationary, and seasonal (periodic) ones [3]. This elaborate and nice crafted technique requires an advanced level of knowledge, labor-intensive tasks, and sophistication only available from specialists [4]-[6]. However, it is more suitable if one who does not familiar with complex forecasting models can use a simple equation like applied exponential smoothing model for forecasting. [7]

In case of advance methods, artificial intelligences are alternative good techniques that can be applied in forecasting by using of prior distributed data learning. The main methods are Bayesian, fuzzy models, and neural networks.

Bayesian method assumes that past data follows a particular probability distribution [8] with simple formula can provide a good prediction. However, it requires a substantially larger inventory investment. This is much more complex and expensive [4] and impacts the risk averse pattern is not good enough [9]. Fuzzy models are particularly well suited for human decision making. Most fuzzy applications are popular in control and engineering, and even larger potential exist in business and finance [10]. Neural networks are very efficient adaptive forecasting models and superior to time series because of their excellent performances of treating non-linear data with self learning capability. However, with the effects of "black box," slow convergence, local optimal solution, it occasionally produces some very wild forecasting values [5] which strongly limited its applications in practice [11]. If the training dataset does not cover the full range of operating conditions, the model may perform badly when deployed [12]. Hybrid systems can be applied to overcome these drawbacks. The result gives better than any single algorithm, or sometimes very similar to the best prediction method [19].

Studying the historical background of abnormal behaviors of patterns is effective in prediction. Dealing with unusual, there are some effects when data are not applicable to an entire range of applications. Special neural networks and prediction systems need to have an individual standard as well [13].

Windowing is a method to discover optimal local patterns, which concisely describe the main trends in a time series at multiple time scales. It can capture meaningful patterns in a variety of settings [14]. Also, an internal structure within the time series data can be used to improve the performance [15]. In some cases, a large fraction of the training data can be discarded to improve the performance while maintaining high accuracy [16].

Some forecasting methods, such as neural networks and ARIMA model, which are based on historical data, cannot find out the hidden remarkable features or signal decomposition behind the data. Forecasting is not based on only historical data but also the understanding of the significant factors hidden in the data; thereby it greatly improves the forecast accuracy [17].

Some disadvantages of NNs, such as the ease over training or the lack of training data, the ease of relapse into local minimization, have not been solved until 1995, when Cortes and Vapnik [18] introduced a new theory named Support Vector Machine (SVM). This concept is applied to a regression model for approximate prediction, and it was named Support Vector Regression (SVR).

The successful impact of forecasting is tied directly to the one's need, understanding, and involvement for forecasts. In this paper, we propose Output Component-Based Support Vector Regression (OCB-SVR) model, applied-SVR model with, a technique for mapping better prediction in jittering domain between the historical space and target space.

The remains of this paper are organized as follows. In Section II describes the OCB-SVR model. Finally, concluding remark discussions and further studies are given in Section III. Finally, Section IV concludes the study.

II. OCB-SVR MODEL

The OCB-SVR model proposed herein is derived from the fact that the time series data with the pattern $trnX_i$ in Historical space (H-space) may be different both shape and size even providing similar patterns. In this case, if we try to train SVR, the resulting minimum error of the SVR does not always guarantee to provide accurate output prediction. This also occurs in most kinds of prediction models.

Fig. 1 shows SVR model in training mode which input of both mapping vector sets come from the same train data. If $\phi()$ is a Gaussian function for training, the user needs to define the constant σ. Another two pre-defined parameters required are C and ε for SVR's risk optimized solution in (1) and (2).

$$R = \frac{1}{2}\|\boldsymbol{w}\|^2 + C\left(\sum_{i=1}^{n}\phi\left(y_i - f\left(\boldsymbol{x}_i, \boldsymbol{w}\right)\right)\right) \quad (1)$$

$$\left|y - f\left(\boldsymbol{x}, \boldsymbol{w}\right)\right|_{\varepsilon} = \begin{cases} 0 & ; \left|y - f\left(\boldsymbol{x}, \boldsymbol{w}\right)\right| \le \varepsilon, \\ \left|y - f\left(\boldsymbol{x}, \boldsymbol{w}\right)\right| - \varepsilon & otherwise \end{cases} \quad (2)$$

where w is weighting parameter and equivalent optimizing to β in fig. 1, constant C for balancing value between maximized margin and minimized empirical risk, and ε insensitive error found in (2).

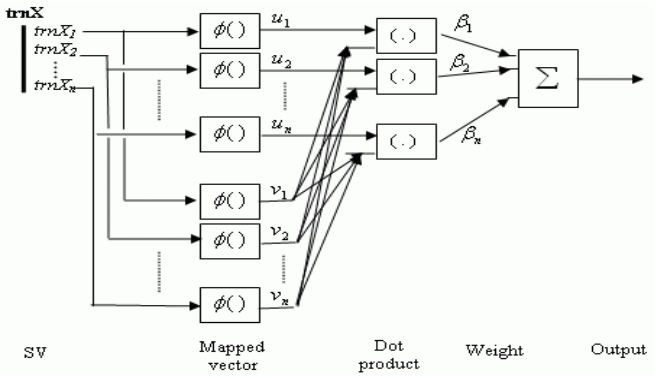

Figure 1. SVR structure model in training mode.

In testing mode, the SVR output is based on suitable weighting factors of training data in H-space, $trn = \left\{\left(X_1, Y_1\right), \left(X_2, Y_2\right), \ldots, \left(X_n, Y_n\right) \in \Re^l \times \Re\right\}$. The adjustment depends on appropriate parameters: C, ε, and σ. However, when it is evaluated with test data ($tstX$), the results may not provide good accuracy. Fortunately, the enveloped output is similar to real patterns in the Target space (T-space). The major effect comes from partial matching between H-space and T-space domain. Another factor is an optimized effect that it gives approximate outputs, which tend to be delay outputs. Another disadvantage is that it is most critical in prediction focused.

Optimizing parameters of the SVR model is depended on support vector points selected from representative multivariate in H-space. By a constraint when solving the quadratic equation, there are some dimensions of input variables scattering nearby root values.

The analysis decomposition of based inputs on output components explores significant hidden patterns. The jittering effect can be selected to final output as representative mapping from H- to T-space. We name this new method as Output Component Based–SVR (OCB-SVR). Fig. 2 shows network diagram of the proposed model.

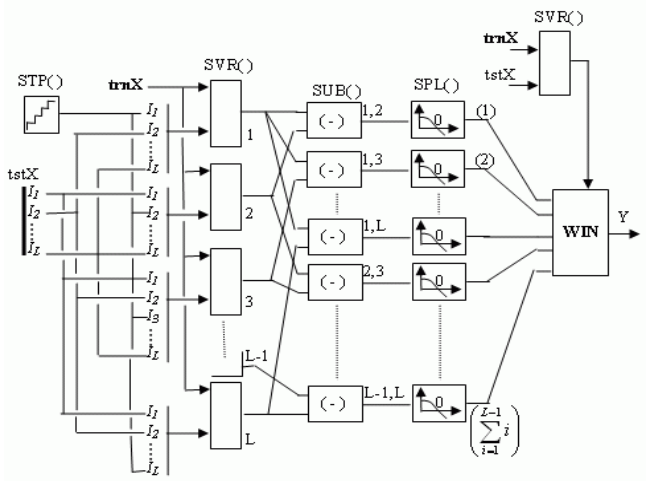

Figure 2. OCB-SVR structure model.

In Fig. 2, SVR is a standard ε-SVR module; STP stands for a stepping function; SUB stands for a subtractive function; SPL represents a spline function used to evaluate approximate root values; and WIN function represents a selector, which selects an appropriate winner output.

Train data $trnX$ has n records with L dimensions. Both $trnX_i$ and $tstX_j$ have $\{I_1, I_2, \ldots, I_L\}$ format. The evaluations of each input component are performed for curve fitting function in SPL. The expected values of each compared dimension will close to 0. The SVR function is defined as ε-SVR in (3).

$$SVR_i = \beta \cdot k(trnX \cdot vtstX_i) + b \quad (3)$$

$$vtstX_i = \begin{Bmatrix} tstX_j & : i \ne j \\ 0..1 & : i = j \end{Bmatrix} \quad (4)$$

where $\beta = \alpha - \alpha^*$, α_i, α_i^* are Largrange multiplier pairs, and b is a constant. As we use Gaussian for $k()$ function, b is closed to 0 by constraint of $1 \le i < j \le L$.

The result of stepping of each input component in (4) gives output SVR_i in (3), which is a directly related value. In case of complete mapping, all output graph lines of each component input will have the same intersection point as shown in Fig. 3. This point can represent the most suitable evaluated output value of $tstX_j$.

To compare the results of each input vector dimension, each output pair is compared using SUB function in (5). Fig. 4 shows example result of SUB function.

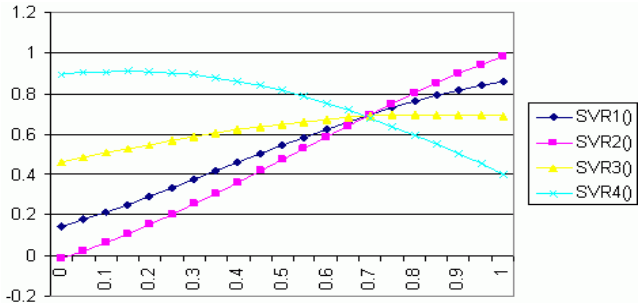

Figure 3. Example of completed intersection graph of stepping value of SVR function

$$SUB_k = SVR_i - SVR_j \tag{5}$$

where $k = \left\{ \begin{array}{c} j-i : i=1 \\ j-i+\sum_{m=1}^{L-1}(L-m) : i>1 \end{array} \right\}$ and the number of SUB value is equal to $\sum_{i=1}^{L-1} i$.

Fig. 4 illustrates a case example of SUB functions. The case example in Fig. 4 uses input vector dimension $L = 4$. This number resulting of compared value is 6, more compared dimensions.

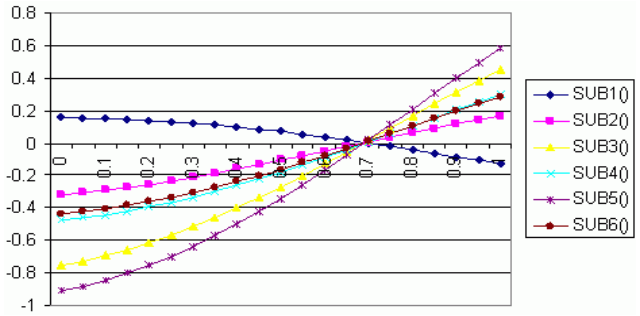

Figure 4. Example of SUB function graph lines

However, in practice, all of graph lines are not a properly intersection. This effect comes from optimizing results that $tstX_j$ is incompletely represented by $trnX$. In general case, incomplete matching between T- and H-space is resulted from the uncontrolled effect of instant environment variables.

If high accuracy is needed, an increase of precision of stepping in (4) is required. However, this leads to a large consumption of the processing time. To reduce this effect we use cubic spline interpolation technique by defining knot point (x, y) with x = SUB, y = input step values and evaluate the result at point $x = 0$. The example interpolation points near $x = 0$ of each line are shown in Fig. 5. All outputs of SPL function are candidate values. The final output is processed and selected by WIN function shown in Fig. 6.

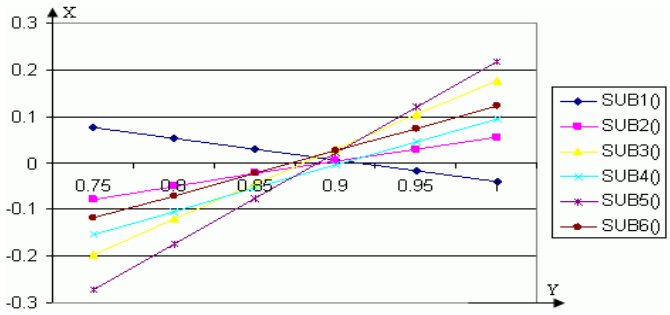

Figure 5. Example of uncompleted result of SUB function graph lines.

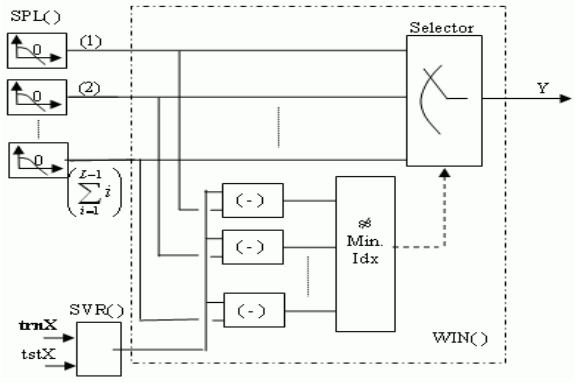

Figure 6. Structure of WIN function.

During prediction processes in T-space the system is not know the actual value. So, all outputs from SPL function can represented of OCB-SVR output. At this state, the suitable value may refer to standard SVR output for comparisons in WIN function. The closest output of SPL to SVR reference is select to final output of OCB-SVR model. Fig. 6 is equivalent to (6).

$$WIN = SPL_{(idx \min(|SUB_i - SVR(tstX, \boldsymbol{trnX})|))} \tag{6}$$

where idx is index at lowest comparison between SUB and SVR. The description of OCB-SVR algorithm in (6) assumes that all SVR models are already training with $trnX$ as standard SVR for pre-defined β parameter.

III. Experiment Case and Discussion

To evaluate OCB-SVR, we tested with a real stock data from Thailand stock market. The "PTT" stock was collected in 2 data sets: 65 records for training data and 34 records for test data. We use ε-SVR model for the same data sets as for comparison purposes. In addition, to demonstrate how OCB-SVR insists with space shifting; we separate 1 year of these two data sets. Training data were collected from 04/01/2005 to 01/04/2005, and test data were collected from 03/07/2006 to 22/08/2006. Both data sets have the same format i.e., {*close*, *high*, *low*, *open*}. The data were transformed to unit values by dividing with the maximum value equal to 302.4. Defining initial SVR's parameters: C = 100, ε = 0.001, and σ = 1, the

system was trained with *trnX* . Learning results are shown in Fig. 7. The mean square error (mse) of SVR is 32.4297 whereas OCB-SVR equals to 13.0087. Both models have similar learning result because both models used training and testing data in the same H-space.

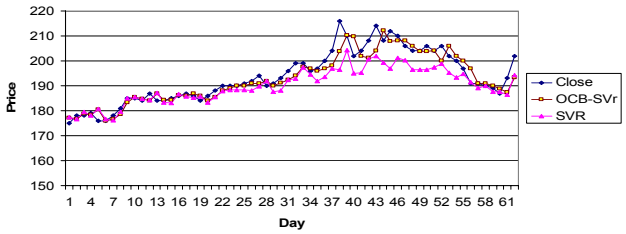

Figure 7. Learning comparison of SVR and OCB-SVR to actual PTT's closing stock price.

The trained system was tested with *tstX* as the results shown in Fig. 8. There are significant different comparisons in Fig. 8. The SVR has an optimal MSE value equal to 22.9887, while OCB-SVR has an MSE equal to 18.593. Both models have similar enveloped patterns which are related to actual patterns.

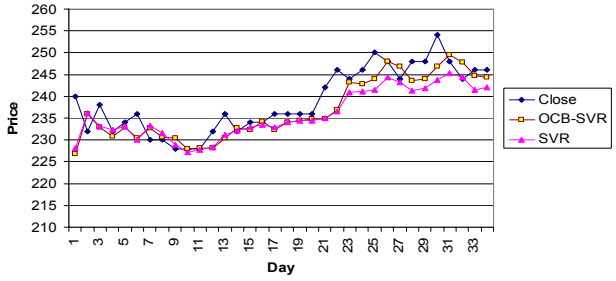

Figure 8. Testing comparison of SVR and OCB-SVR to actual PTT's closing stock price.

This is confirmed that the decomposition technique of output component base can support SVR model resulting in a better accuracy prediction mode for unmatched mapping space between training sets and test sets.

OCB-SVR still has SVRs' limitation effects: initial parameters, pattern delay prediction, and non re-trainable high dynamic input-output pair of training data because of SVR core model usage.

IV. Conclusion and Further Study

In this paper, we propose Output Component-Based Support Vector Regression (OCB-SVR) model for time series data prediction. The local optimized limitation in NNs can be eliminated by SVR's optimizing method which combines both maximize margin and minimize empirical error. Because of incomplete matching of train sets and test sets, SVR solution does not guarantee accuracy prediction result. However the enveloped pattern is similar. An appropriate target output based on historical datasets by decomposition of closest candidate value of optimizing output can improve the standard SVR prediction. Because OCB-SVR uses SVR core model, the limitation effects from SVR still exist and need to improve.

Our further study shall focus on applying hybrid fuzzy networks. Data prediction by support vector regression with decomposition method may provide a better improvement to most kinds of uncompleted matching to T-space.

References

[1] Panella, M., Rizzi, A. "Baseband Filter Banks for Neural Prediction," *CIMCA & AIWTIC '06*, Nov 2006.

[2] Pankratz, A. *Forecasting with Univariate Box-Jenkins Models: Concepts and Cases*, John Wiley & Sons. New York. 1983.

[3] Tran, N., Reed, D. A. "ARIMA Time Series Modeling and Forecasting for Adaptive I/O Prefetching," *The 15th International Conference on Supercomputing*, Jun 2001.

[4] Harrison, H. C., Qizhong, G. "An Intelligent Business Forecasting System," *The 1993 ACM Conference on Computer Science*, Mar 1993.

[5] Wu, S., Lu, R. "Combining Artificial Neural Networks and Statistics for Stock-Market Forecasting," *ACM Conference on Computer Science*, Mar 1993.

[6] Robinson, L. "Exploring time series analysis using APL," *ACM SIGAPL APL Quote Quad*, Vol. 27, No. 3, Mar 1997.

[7] Meesad, P., Srikhacha, T. "Universal Data Forecasting with an Adaptive Approach and Seasonal Technique," *CIMCA & AIWTIC '06*, Nov 2006, pp. 66.

[8] Clay, G. R., Grange, F. "Evaluating Forecasting Algorithms and Stocking Level Strategies using Discrete-Event Simulation," *The 1997 Winter Simulation Conference*. 1997.

[9] Dangelmaier, W., *et al.*, "Risk Averse Shortest Path Planning in Uncertain Domains," *CIMCA & AIWTIC '06*, Nov 2006, pp. v-xxii.

[10] Negnevitsky, M. *Artificial Intelligence: a Guide to Intelligent System*, 1st edit. Addison Wesley. 2002. pp. 315-316.

[11] Rongjun, L., Zhibin, X. "A Modified Genetic Fuzzy Neural Network with Application to Financial Distress Analysis", CIMCA, Nov 2006, pp. 120.

[12] Liu, F., *et al.*, "A Neural Network Based Short Term Electric Load Forecasting in Ontario Canada", *CIMCA & AIWTIC '06*, Nov 2006, pp. 119.

[13] Insung, J., *et al.*, "Two Phase Reverse Neural Network Based Human Vital Sign Prediction System", *CIMCA & AIWTIC '06*, Nov 2006, pp. 135.

[14] Papadimitriou S., Yu P. "Optimal Multi-Scale Patterns in Time Series Streams," *Proceedings of the 2006 ACM SIGMOD International Conference on Management of Data*, 2006.

[15] Huanmei W., *et al.* "Subsequence Matching on Structured Time Series Data," *Proceedings of the 2005 ACM SIGMOD International Conference on Management of Data*, 2005.

[16] Xiaopeng X., *et al.* "Fast time series classification using numerosity reduction," *Proceedings of the 23rd International Conference on Machine Learning ICML '06*, 2006.

[17] Huang, L., Zhong, J. "ICA-based Potential Significant Feature Extraction for Market Forecast," *CIMCA & AIWTIC '06*, Nov 2006.

[18] Mao, X., Yang, J., "Time Series Prediction Using Nonlinear Support Vector Regression Based on Classification," *CIMCA & AIWTIC '06*, Nov 2006, pp. 13.

[19] Wang, Y., Shen, Y. "Stock Predictor Algorithm: A Control Method Dealing With Distributed Control Systems," *CIMCA & AIWTIC '06*, Nov. 2006, pp. 49.

Knowledge Management System with Root Cause Analysis for IT Service Desk in Banking Business

Padej Phomasakha Na Sakolnakorn
Department of Information Technology
Faculty of Information Technology
King Mongkut's Institute of Technology North Bangkok,
Bangkok, Thailand

Phayung Meesad
Department of Teacher Training in Electrical Engineering
Faculty of Technical Education
King Mongkut's Institute of Technology North Bangkok,
Bangkok, Thailand

***Abstract*- The Knowledge Management in terms of business recommended that knowledge is the organizational asset that enables sustainable competitive advantage. Besides, an increasing demand of IT outsourcing to deliver quality services, ITIL Best practice framework is an essential key success factor for IT outsourcing quality service approach. IT Service Desk is a crucial function to the whole concept of IT service management. In this paper, we propose an enhanced model called Knowledge Management system with Root Cause Analysis, or KMRCA, IT Service Desk applied to improve the IT Service Desk. The performance of the KMRCA IT Service Desk are evaluated using a simulation study with actual data from IT Service Desk in banking business, and the experimental results indicate the KMRCA IT Service Desk approach would significantly enhance the performance and quality of the throughput of the traditional IT Service Desk, reduce times in resolving the problems, and eliminate the recurring problems.**

I. INTRODUCTION

Knowledge Management is the process of managing the organization's knowledge by means of systematic and organizational specific processes for acquiring, organizing, sustaining, applying, sharing, and renewing both tacit knowledge and explicit knowledge by employees to enhance the organizational performance and create value. [1], [2], [3].

The problem is that in today's business environment employee turnover is very high, especially for technical employees [4]. Help desk agents store significant knowledge concerning the systems, business processes, and technologies and if they leave their knowledge often goes with them [5].

An increasing in demands of customers and the delivery of a world class service are becoming a major competitive advantage. According to Gartner [6], spending on outsourcing is set for steady growth 7.2 percent from 2003 to 2008 [6]. A key success driver for efficiency and effectiveness of IT outsourcing over the next three years will be aligned on an ITIL Best practice. In addition, an IT service desk is probably the most significant in the organizational outsourcing.

The primary objective of the IT Service Desk is to resolve problems related to IT operations. Furthermore, the agents in the service desk must be very knowledgeable of their service supports, applications, and support teams. Most efforts at improving service desk performance have been to make the current system more efficient through applications of information technologies [7] and to conduct the way to eliminate the recurring problems.

Computer Telephony Integration (CTI), one of technologies is available to assist the Service desk to blend of technology, process and service desk staff will meet the needs of both the business and the users [8], [9].

In this research, we propose a new model approach called *KMRCA IT Service Desk*, Knowledge Management System (KMS) with root cause analysis (RCA) adapted to IT Service Desk. The KMRCA IT Service Desk attracts diverse knowledge and root cause sources in the service desk databases, files, domain experts, and knowledge bases. With the RCA is used to eliminate the recurring incidents and its result provides a resolution plan. However, the resolution plan has been kept tracking until its activities completed and updated the result into the KMS Database. The KMRCA IT Service Desk is designed for daily operations of service desk to ensure high utilization and maintenance of the knowledge stores.

II. KNOWLEDGE MANAGEMENT

The study of knowledge management has begun on Polanyi's Tacit Dimension. His analysis emphasized several key concepts. Firstly, the ability to identify the outside objects, and hence to know, is learned through a process of personal experience. Secondly, tacitness and explicitness are distinct dimensions; the increase of one does not come at the decrease of the other. Thirdly, since tacit knowing is an essential element of any kind of knowledge and is acquired through personal experience called indwelling, any effort to achieve absolute detachment, the objective of knowledge is mis-directed and self-defeating. Polanyi's work is situated in a philosophical context, and focuses on the definition of knowledge but not on the systematic effort of managing it [10].

The conceptualization of knowledge management did not develop; however, until knowledge became central to production and innovation in the 1990s. Peter Drucker [11] is among the first who advocated the advent of a knowledge society. In the Post-Capitalist Society [11], Drucker documented the transformation from a capitalist to a Knowledge Society, which began shortly after World War II, noting that the foremost economic resource is no longer capital, land, or labor. Rather, it is and will be knowledge [11]. The field of knowledge management has also been developed by the experience and philosophy of Eastern society.

Nonaka and Takeuchi's Knowledge-Creating Company [12], based on experience in Japanese companies, is a pioneer

work in mapping explicit and implicit knowledge, as well as individual, group, and organizational knowledge into one matrix describing called the dynamics of knowledge creation.

Stenmark [13] discovered how tacit knowledge in the form of professional interests could be shared among the organisational members in an unobtrusive way. Based on these empirical findings, and informed by Polanyi's theory of tacit knowledge, He claimed that agent-based retrieval systems could be used to capture and visualize the professional interests, thus making otherwise elusive tacit knowledge tangible so that it can benefit others.

Knowledge Management is the process of managing the organization's knowledge by means of systematic and organizational processes conducted by employees to enhance the organizational performance and create value. [1], [2], [12].

The development of knowledge management, on the other hand, has been driven by practices and development in information and data management [14]. Organizations should therefore seek and share a combination of tacit and explicit knowledge with suppliers and other parties in the value chain to satisfy customer needs in a highly competitive environment.

The Knowledge Management System (KMS) composes of five processes, knowledge capturing or knowledge discovery, knowledge creation, knowledge inventory, knowledge sharing, and knowledge transfer, applied to the community of practice. IT is related to just knowledge creation and knowledge inventory that are becoming an organisational memory (OM) and enable to competitive advantage sources.

III. Root Cause Analysis

A root cause analysis (RCA) is the process to identify the action or condition that, when eliminated or changed, will prevent the recurrence of the specific or similar problems, and therefore the benefits of the RCA are to improve the service level agreement (SLA) attainment and to enhance quality services as well as customer satisfaction.

The knowledge-based library of RCA models could be in the form of hierarchically structured and interconnected failure trees, the abnormalities in process operations and output quality can originate from abnormalities in equipment or in process conditions possibly due to basic failures [15].

IV. KMRCA IT Service Desk

A. IT Service Desk of IT Outsourcing

The first level support bank owner provides a vital day-to-day contact point between Customers, Users, IT services and third-party support organisations using the Tivoli CTI system and assigns if the particular IT incidents to IT Service Desk of IT strategic outsourcing as the second level support (SLS) to find out the proper resolution according to the service level agreement (SLA) between the Bank and its IT outsourcer. Strategically, for the Bank the IT Service Desk of IT outsourcing is the most important function in the organization that required to be improved. Hence, we propose the KMRCA IT Service Desk Concept to enhance the IT Service Desk of the IT outsourcing who is not the Tivoli software owner.

The KMRCA IT Service Desk Outsourcing concept is shown in Fig. 1.

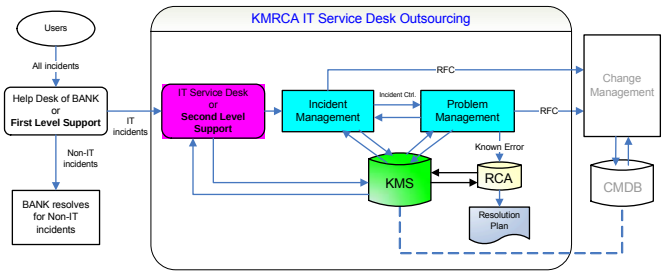

Figure 1. KMRCA IT Service Desk Outsourcing Concept.

The KMRCA IT Service Desk Outsourcing Concept embraces not just IT Service Desk and Incident Management interfacing Problem Management, but also KMS database communicating with RCA database that called *KMRCA*.

B. Conceptual Simulation Model for IT Service Desk

When Users call to the first level support with diverse incidents, the Bank staff clarify and try to resolve those incidents meanwhile the problem tickets are being opened for monitoring and tracking by Tivoli CTI. We met that more than 87% of the incidents are IT related. Consequently the first level support staff will assign severity for each IT incident and pass it on the SLS to resolve within the SLA.

Fig. 2 shows the conceptual model of IT service desk operation as the modeled simulation.

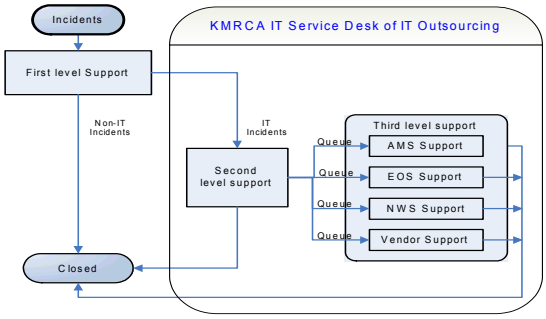

Figure 2. Conceptual model of IT Service Desk operations.

Likewise, the agents of SLS will clarify and attempt to resolve IT incidents. If there are some incidents are still not resolved, they will be escalated to Third Level Support teams, composing of AMS Support, EOS Support, NWS Support, and Vendors Support. Consequently, the details of the KMRCA IT Service Desk concept could be explained by its process shown in Fig. 3.

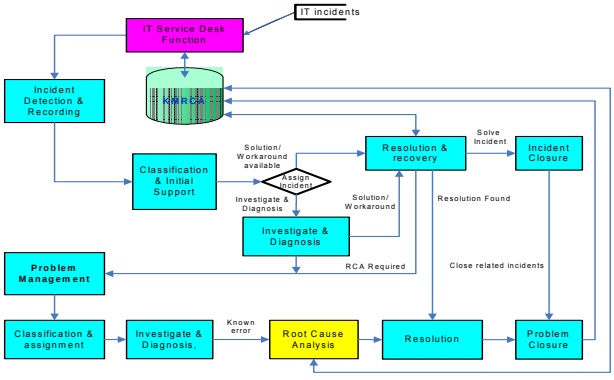

Figure 3. KMRCA IT Service Desk Process.

The IT Service Desk team is also responsible for monitoring and tracking of the assigned IT incidents until those incidents are closed. They are able to find out the resolution by searching from the KMRCA database. If the incident cannot be resolved immediately, it will be escalated to the specific specialist groups [16] or the third level support teams to handle the incident by the incident management process, including classification, investigation, and diagnosis to resolve the incident until incident closure. If the diagnosis required knowing a known error identified by means of the root cause analysis. After resolution of the cause of the incident and restoration of the agreed service, the incident is closed.

C. The Comparison of IT Service Desk with against without KMRCA

The comparison of a Typical IT Service Desk versus the KMRCA IT Service Desk is shown in Fig. 4.

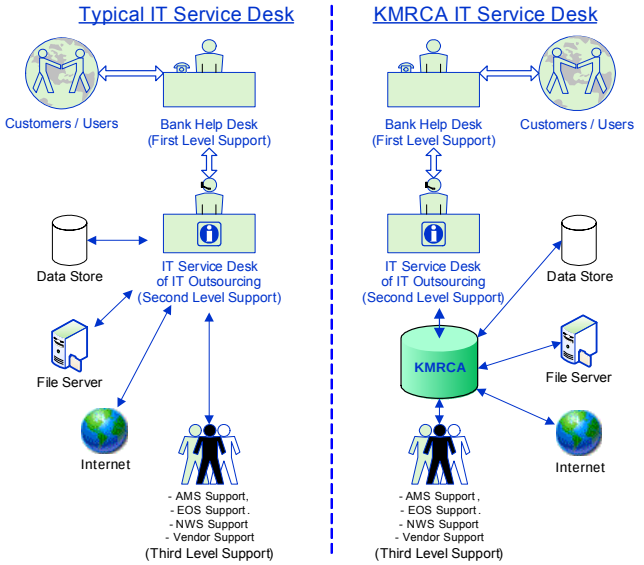

Figure 4. IT Service Desk with against without KMRCA

The KMRCA IT Service Desk, IT Service Desk of IT outsourcing communicates just KMRCA instead of several getting data sources such as data store, file server, and third level support domains.

There are at least three problems within the Service Desk without KMS and RCA. Firstly, service desk personnel report about 70% of their time is spent on solving repeat problem [17]. Secondly, in business environment today employee turnover is very high, especially for technical employees [17]. Finally, some incidents may have the same causes and they may occur again because their root causes are not eliminated.

V. Performance Evaluation

To demonstrate the concept of KMRCA IT Service Desk, we evaluate the system performance using a simulation method. The research hypothesis is that the system will have a shorter problem resolution time and will enable to eliminate the recurring problems.

A. Hypothesis

The time in system for all incidents calls except for critical severity calls will be lower in KMRCA IT Service Desk system than the previous one. The developed simulation model is to test the hypothesis that describes both systems. A simulation enables service desks to perform analysis that captures the entire interrelationship between callers, agents, skills, and technology [4].

In this case, the simulation model approach is adopted so that it can be conducted by experiments and evaluated the KMS without interrupting the IT service desk's daily operations.

B. Data Collection

The data was collected from the Tivoli, CTI for everyday from a six-month period starting from May to October 2006. The collected data in spreadsheet form was for a total of 36,981 assigned calls and consisted of problem ticket no., calling date, arrival time, resolved time, assigned resources, defined severity, identified system problem. The frequency of each severity is shown in Table I. The service times for each problem category were analyzed and determined.

TABLE I
CLASSIFICATION OF CALL BY SEVERITY

Severity	Number of Calls	Percentage (%)
1	458	1.239
2	1533	4.145
3, 4	34990	94.616
Total	36,981	100.00

C. Simulation Model

A discrete event simulation package called *Arena*™ [18] is used to imitate the conceptual models of IT Service Desk agents both with and without KMRCA. A full exposition of the simulation model is available in Simulation with Arena. The simulation model was verified to ensure that it works properly in terms of Arena functionalities and the entities of the problem calls follow the same path as described in the conceptual model shown in Fig. 2. The verification was done using the TRACE element which is used within a discrete model to generate a detailed trace report of entity processing. The TRACE was run for one replication for 6 weeks of operation time. The TRACE output allows following the sequence of an entity as it flows through the system, from entity creation until entity disposal.

The entity process flow was intended design and verifying the Trace output, the model run with different replication numbers to verify that it works properly under the different conditions. After verifying operation of the simulation model it was validated. In order to reduce variation, four replications were conducted with different random number streams on the simulation model. A t-test with a 95% confidence level was conducted to compare the results of the simulation model with the results recorded for the actual system based on the data collected from Tivoli CTI system. For each variable the null hypothesis of no difference between the systems was rejected with a 95% confidence level which indicates the simulation model adequately represents the actual system's behaviours.

D. Design of Experimental Design and Analysis

Experiments include the study of more than one factor. They are often used to study the performance of the process and the system [19]. The objective of this experiment is to determine the variables are most influential on the response of the system. By using the experimental 2^3 factorial design

which is to identify the effects of three different interesting factors, A, B and C for each at two levels of the factors and eight treatment combinations run in the 2^3 design.

In this research, three factors, time in minutes, are:

Factor A: Time to type problem information and search the relevant knowledge from the KMS.
Factor B: Time to resolve a problem using the KMS.
Factor C: Time to add new information into the KMS.

In addition, the dependent output variables are:

O1: Throughput, total no. of calls resolved in time period
O2: Time in the system of Severity 1
O3: Time in the system of Severity 2
O4: Time in the system of Severity 3 and Severity 4
O5: Number of problem calls in AMS queue.
O6: Number of problem calls in EOS queue.
O7: Number of problem calls in NWS queue.
O8: Number of problem calls in Vendors queue.

According to Gonza´lez [7] these dependent variables are performance variables tracked by the service desk which are common performance measurement.

TABLE II
INDEPENDENT VARIABLE FACTORS AND THEIRS VALUES IN TWO LEVELS

Factor	Low (min.)	High (min.)
A	1	3
B Triangular	(1,3,6)	(2,5,8)
C	2	4

Table II shows the factors and their respective levels. A different output variable is needed for each problem severity since they follow different paths through the service desk. The factors are analyzed with two levels (low and high) and their values were determined by expert opinion obtained during the interviews and by observing the service desk operations.

Replications of each experiment were run for one month (43,200 minutes) in a random order and the results were recorded for further statistical analysis.

TABLE III
STATISTICAL T-TEST FOR COMPARISON OF THE PREVIOUS IT SERVICE DESK AND THE KMRCA IT SERVICE DESK

($\alpha/2 = 0.025$ and degree of freedom = 7)

Variables	Observed *t*-value	Critical *t*-value
1) Throughput	85.139	2.365
2) Time System for Severity 1	1.318	2.365
3) Time System for Severity 2	0.702	2.365
4) Time System for Severity 3, 4	29.560	2.365

The same random number seed was used for the normal agent service desk and the KMRCA IT Service Desk conceptual models.

E. Experimental Results

The summarized results are shown in Table IV. The analysis of variance (ANOVA) for full factorial design is done to test that the main effects or interaction parameters are equal to zero. In statistical analysis, the factors with a *p*-value lower than 0.05 are considered as important factors that significantly influence the results. The ANOVA analysis shows that only the dependent variable Throughput (O1) and Time system for Severities 3, and 4 are significantly influenced by Factors A, B, and C. The other dependent variables do not have any factors that affect them significantly.

TABLE IV
SUMMARY OF KMRCA IT SERVICE DESK VERSUS IT SERVICE DESK IN AVERAGE

Variables	IT Service Desk	KMRCA IT Service Desk
Throughput (calls/time period)	12904	15185
Time System for Severity 1 (min.)	82	76
Time System for Severity 2 (min.)	140	128
Time System for Severity 3, 4 (min.)	341	293

VI. CONCLUSIONS

In the study, we conducted a computer simulation to quantitatively compare the typical IT Service Desk against a new proposed KMRCA IT Service Desk. The simulation study result showed 17.4 % increase in throughput, greater than 7.3%, around 8.5%, and 15.4% decrease in average time to resolve assigned problem of Severities 1, 2, 3 and 4, respectively. The improvements are significant and provide justification for implementing the knowledge management system with root cause analysis. Furthermore, the advantage of the simulation is that we can perform a study without disrupting the day-to-day IT Service Desk operations.

REFERENCES

[1] V. Allee, *The Knowledge Evolution: Expanding Organizational Intelligence*, Butterworth-Heinemann, New York. 1997.

[2] M. Alavi, D. E. Leidner, "Knowledge Management Systems: Emerging Views And Practices From The Field," *Proceedings of the 32nd Hawaii International Conference on System Science*, 1999.

[3] L. Hsiangchu, C. Tsai-hsib, "Knowledge Management: A Review of Theoretical Frameworks and Industrial Cases," *33rd Hawaii International Conference on System Sciences*, Vol. 3, 2000.

[4] K. Miller, V. Bapat, "Case study: simulation of the call center environment for comparing competing call routing technologies for business case Roi projection," *IEEE Winter Simulation Conference Proceedings*, Washington DC, USA, 1999, pp 1694–1700.

[5] P. Meso, R. Smith, "A resource-based view of organizational knowledge management systems," *Journal of Knowledge Management* 4 (3), 2000, pp. 224–234.

[6] B. Caldwell, R. DeSouza, A. Young, R. Silliman and Eric Goodness, "Continued Growth Forecast for IT Outsourcing Segments," Gartner's October 5, 2004 report.

[7] L. M. Gonza´lez, R. E. Giachetti, G. Ramirez, "Knowledge management-centric help desk: specification and performance evaluation," *Elsevier Decision Support Systems*, 40, 2005, pp 389– 405.

[8] K. Dawson, *The Complete Guide to Starting, Running, and Improving Your Call Center*, CMP Books, New York, 1999.

[9] S. Sandborn, "Structuring the service desk," *Information World*, 23(52), 2001, pp 28

[10] Jing Zhang, Sue R. Faerman, "Divergent Approaches and Converging Views: Drawing Sensible Linkages between Knowledge Management and Organizational Learning," *Hawaii International Conference on System Sciences 23rd*, IEEE Computer Society, 2002.

[11] P. F. Drucker, "The Post-Capitalist Executive," *Managing in a Time of Great Change*, New York, NY: Penguin, 1995.

[12] I. Nonaka, H. Takeuchi, *The Knowledge-Creating Company*, Oxford Press, New York, 1995.

[13] Dick Stenmark, "Turning Tacit Knowledge Tangible," *Hawaii International Conference on System Sciences*, 2000

[14] Thomas H. Davenport and Laurence Prusak, *Working Knowledge: How Organizations Manage What They Know*, Harvard Business School Publishing, 2000.

[15] G. Weidl , A.L. Madsenb, S. Israelson, "Applications of object-oriented Bayesian networks for condition monitoring, root cause analysis and decision support on operation of complex continuous processes," *Computers and Chemical Engineering*, Vol. 29, 2005.

[16] Jan C. Linder, Martin I. Cole, Alvin L. Jacobson, "Business transformation through outsourcing," *Emerald Strategy and Leadership*, Vol. 30, No. 4, 2002, pp. 23-28.

[17] J. Anton, D. Gusting, *Call Center Benchmarking: How Good Is Good Enough*, Purdue Univ. Press: Indiana, 2000.

[18] W. D. Kelton, R. P. Sadowski, D. T. Sturrock, "Simulation with Arena," *McGraw Hill Series in Industrial Engineering and Management Science, 3rd Edit*. 2003.

[19] D. C. Montgomery, *Design ans Analysis of Experiments*, 6th Edition, Wiley, 2005.

Web Metadata Design for Web Content Management

Natthaphon Sueb-Am, Mayuree Lertwatechakul

Department of Information Engineering

Faculty of Engineering, King Mongkut's Institute of Technology, Ladkrabang

Bangkok, Thailand 10520

Email: s7061122@kmitl.ac.th , klmayure@kmitl.ac.th

***Abstract*— Nowadays, there are many tools have been offered to webmasters to build their websites. Therefore, Web administrators still have to cope with many problems, such as ensuring validity of available documents or changing many content and restoring data. To resolve this problem, we need Web Metadata which could be used by Web Content Management (WCM) to maintenance web structure and its content and representing schedule. In this paper, we propose a temporal database design for Web Metadata by using NIAM model, which can be used for solving problems in monitoring, designing and retrieval efficiency of the website structure and its contents.**

Keywords. Web Metadata ,Web Content Management, Temporal web database, NIAM.

1. INTRODUCTION

Since the invention of websites, this technology has affected to most people's daily life. At the beginning, it was used by government and large business sectors only. However, the popularity of this technology spreads to small business and also private sectors.

There are varieties of contents, for instance: texts, images, audio clips, videos etc. Moreover, these contents have some changes regularly. The best example is portal websites, which have varieties of information, e.g. News, petrol rates, stock exchange rates, movie and music hits charts, etc. As can be seen from examples above, website management is not easy. There are so many information and data that needed to be monitored and updated very frequently. Thus, webmasters need powerful tools that can help them to manage and organize their works.

A website can be conceptually divided in the following four basic parts, like in [1]

- Content
- Structure
- Functionality
- Presentation

According to our studies, we founded that there are 2 parts of website components that are very important:

- Content
- Structure

Firstly, content is basic information that can be seen and heard from the website. In other words, all visual and audio information appeared on the website. Secondly, structure is the directions of how information is represented on the websites. Basically, the most common standard of structure is written by using HTML specifications [2]. As we have studied the HTML structure carefully, we can design the relationship of web metadata. Moreover, daily website contents and structures can also be tracked and traced. As a result, we chose NIAM model to represent database structure, which could handle temporal data for web content management.

This paper will focus on relationship of web metadata, especially in design, management and maintenance. To gain more understanding towards this research, it is needed to understand basic concepts, overview and implementation methods. The guide below described our methodology we applied on this research.

2. OVERVIEW AND RELATE WORK.

2.1 HTML Structure

HTML is a popular and powerful of computer language devised to allow website creation. These websites can then be viewed by anyone else connected to the Internet. It is constantly undergoing revision and evolution to meet the demands and requirements of the growing Internet audience under the direction of the World Wide Web Consortium (W3C), the organization charged with designing and maintaining the language.

New HTML version supports more multimedia options, scripting languages, style sheets, better printing facilities, and documents that are more accessible to users with disabilities. HTML also takes great strides towards the internationalization of documents, with the goal of making the Web truly World Wide.

HTML structure consists of elements and attributes. Elements are a part of HTML structure. They include 2 important properties, which are attributes and content. To make HTML document, these properties are used for parameter defining and follow HTML structure. An element usually has a start tag (<tag>) and an end tag (</tag>), such as <Font color="black">Content</Font>.

Attribute are used to define Element's parameter and contain 2 parts. First part is attribute name for define property's element. Another part is attribute value. Attributes are placed in the start tag (<TD width=300>) and content is located between the tags (<tag>Content</tag>). And some elements don't have any content and do not need closing tags, such as <HR>.

We can study all details of HTML structure in HTML specifications in WC3's website for this paper.

```
<!DOCTYPE HTML PUBLIC "-//W3C//DTD HTML
4.01//EN"
"http://www.w3.org/TR/html4/strict.dtd">
<HTML>
<HEAD>
<TITLE>My first HTML document</TITLE>
</HEAD>
<BODY>
<P>Hello world!
</BODY>
</HTML>
```

Figure 1. Example source code for basic web structure.

2.2. Concept of Temporal database by NIAM

In temporal relational databases [3], it consists of several types of time include this.

- Lifespan time
- Valid time
- Transaction time

Lifespan Time, Valid Time and Transaction Time are vital factors of time components in temporal databases.

Lifespan time is the period of time between the Entity type starts until its end. Any Entity type that is measured by time, will be collected in database. The components of Lifespan Time are Life Span Start (LSs), and Life Span End (LSe). The symbol for represent in NIAM model is shown below in Figure 2(a)

Valid time is the period of time, it consists of Valid Time start (VTs) and Valid Time end (VTe) are attached to each temporal fact so that the state of the fact is shown with the valid time. This enables historical facts to be manipulated as well as current facts. The symbol for represent in NIAM model is shown below in Figure 2(b)

Transaction time is simply the time that the fact is recorded into the database, which consists of Transaction Time Start (TTs) and Transaction Time End (TTe).

In temporal relational databases, lifespan, valid and transaction time are attached to each tuple.

3. IMPLEMENTATION

After carefully analyzed HTML Structure, it is very flexible and may hand to design a concrete database model for. We tried to make the most appropriate data model to handle all possible relations of HTML structure and content, e.g. retrieval speed, indexes and data constraints. Relational structure that would satisfy our common structure is shown in Figure. 3. After that we will Transformation from NIAM to Object Database Schema and mapping in tables for implement in web content management system. We will develop a tool to transform HTML code of webpages into tuples of these tables.

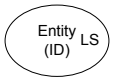

Figure 2(a). Symbol for Life span time [4].

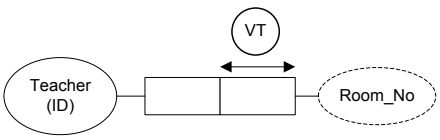

Figure 2(b). Symbol for Valid time [4].

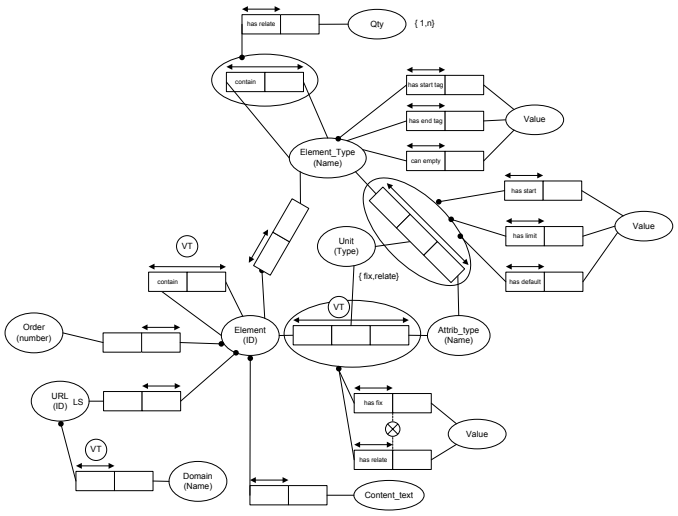

Figure 3. A NIAM conceptual schema of the Web metadata database.

From NIAM conceptual schema in Fig 3 we can map to relational schema as shown below.

URL

URL_ID	Domain_Name	LSs	LSe

CONTENT

Element_ID	VTs	Element_type_Name	URL_ID	Order_Number	Content_text	VTe

ELEMENT_ATTRIBUTE_PROPERTIES

Element_type_Name	Attrib_type_Name	Unit_Type	Start_Value	Limit_Value	Default_Value

ELEMENT_ATTRIBUTE_VALUE

Element_ID	VTs	Attrib_type_Name	Unit_Type	Value	VTe

ELEMENT_RELATION

Element_ID	Sub_Element_ID	VTs	VTe

ELEMENT_TYPE_RELATION

Element_Type_Name	Sub_Element_Type_Name	Qty

ELEMENT_PROPERTIES

Element_type_Name	Start_tag	End_tag	Empty

Figure 4. Web metadata relational schemas.

URL TABLE

URL_ID	DOMAIN_NAME	LSs	LSe
1	www.google.co.th	2006-06-15	9999-12-31

CONTENT TABLE

ELEMENT_ID	URL_ID	ELEMENT_TYPE_NAME	ORDER_NUMBER	CONTENT_TEXT	VTs	VTe
1	1	HTML	1		2006-06-15	9999-12-31
2	1	HEAD	2		2006-06-15	9999-12-31
3	1	META	3		2006-06-15	9999-12-31
4	1	TITLE	4	Google	2006-06-15	9999-12-31
...	...	...	...	...	...	...
9	1	DIV	9		2006-06-15	9999-12-31

ELEMENT_ATTRIBUTE_VALUE TABLE

ELEMENT_ID	ATTRIB_TYPE_NAME	UNIT_TYPE	VALUE	VTs	VTe	
3	content	F	text/html; charset=UTF-8	2006-06-15	9999-12-31	
3	http-equiv	F	content-type	2006-06-15	9999-12-31	
7	bgcolor	F	#ffffff	2006-06-15	9999-12-31	
...	...	...	...	...	...	
9	9	F	background:url(/intl/en_com/images/logo_plain.png) no-repeat; height:110px;width:276px	2006-06-15	9999-12-31	1
9	9	F	background:url(/intl/en_com/images/mothers_day06.png) no-repeat; height:110px;width:276px	2006-08-12	9999-12-31	2
9	9	F	background:url(/intl/en_com/images/newyear07.png) no-repeat; height:110px;width:276px	2007-01-01	9999-12-31	3
9	9	F	background:url(/intl/en_com/images/logo_plain.png) no-repeat; height:110px;width:276px	2007-01-20	9999-12-31	1

ELEMENT_RELATION TABLE

ELEMENT_ID	SUB_ELEMENT_ID	VTs	VTe
8	9	2006-06-15	9999-12-31
9	10	2006-06-15	9999-12-31
11	12	2006-06-15	9999-12-31

ELEMENT_TYPE_RELATION TABLE

ELEMENT_TYPE_NAME	SUB_ELEMENT_TYPE_NAME	QTY
ADDRESS	BODY	1
APPLET	BODY	1
BODY	ADDRESS	N

ELEMENT_ATTRIBUTE_PROPERTIES TABLE

ELEMENT_TYPE_NAME	ATTRIB_TYPE_NAME	UNIT_TYPE	START_VALUE	LIMIT_VALUE	DEFAULT_VALUE
BODY	bgcolor	F	#000000	#ffffff	#ffffff
TABLE	high	R	1%	100%	100%
TABLE	width	R	1%	100%	100%

ELEMENT_RELATION TABLE

ELEMENT_TYPE_NAME	START_TAG	END_TAG	EMPTY
BODY	O	O	N
AREA	Y	F	E
TABLE	Y	Y	N

Figure 5. A part of sample database for storing content structures.

We have proved that the designed schema could store various arbitrary styles of HTML structure by analyzing many webpages of popular websites such as index.html of www.google.co.th [5], www.cnn.com, www.msn.com. We found that all analyzed structures, can be filled in the database schema. As to show some of the success experiment, we present structure include page of www.google.co.th as relational data in the Figure 5.

In Figure 5 in ELEMENT_ATTRIBUTE_VALUE Table and other tables show example records set from www.google.co.th in different time. As can be seen from set ①, it is represented the google webpage at 15/6/2006, by using Google's logo, which collected as logo_pain.png (in Figure 6(a)). In set ②, on Mother Day: 12/6/2006, the logo of the webpage has changed to mothers_day06.png (in Figure 6(b)). According to record ③ (in Figure 6(c)), on 1/1/2007 (New Year 2007), the logo has changed for celebration of New Year. The logo file became newyear07.png. After the new year's celebrations ended, the logo has changed to default logo. The file became "logo_pain.png" as it was on 20/1/2007 (in Figure 6(a)).

Figure 6. (a). Webpage of www.google.co.th in 15-06-2006 and current date.

Figure 6(b). Retrieved Webpage of www.google.co.th in 12-08-2006.

Figure 6(c). Retrieved Webpage of www.google.co.th in 1-01-2007.

4. CONCLUSIONS AND FURTHER WORK.

In this paper, we have presented the Web Metadata model that useful for Web Content Management. By adding temporal feature, In the near future we will develop Web Content Management System (WCMS). The database model can maintain HTML Structure, Content and retrieval features. These may be changed time by time.

REFERENCES

[1] Mihaela Sokic , Viktor Matic and Alen Bazant , "*Web Content Manangement System Based on XML Native Database*"",25th Int.Conf IEEE Internet Computing , July - August 1998 , pp. 30-37.

[2] HTML 4.01 Specification, http://www.w3.org/TR/1999/REC-html401-19991224.

[3] Bundit Pasaya and Suphamit Chittayasothorn, *"A Temporal Object Oriented Conceptual Schema Modele," IEEE Transl. J. Magn. Japan*, vol. 2, pp. 740-741, August 1987 [*Digests 9th Annual Conf. Magnetics Japan*, p. 301, 2001,pp 724 -727.

[4] K Putsadee Poraphol, *"The Design and Development of a temporal database using TNIAM"*, KMTTL ,Science, 2006 .

[5] "*Source code of www.google.co.th/index.html"*,www.google.co.th.

Towards Intelligent and Adaptive Digital Library Services: Associating Contents with User Profile and Usage Pattern in Digital Libraries

Yenruedee Chanwirawong, Md Maruf Hasan
School of Technology, Shinawatra University
Shinawatra Tower III, 1010 Viphavadi-Rangsit Road, Chatuchak, Bangkok, Thailand
yoyomimi_yen@hotmail.com, maruf@shinawatra.ac.th

Abstract- **The availability of contents, user profile and usage pattern in a digital library in machine understandable formats paves the way of processing these information further using state-of-the-art technologies to introduce intelligent digital library services. Annotating, organizing and analyzing contents based on a domain-ontology give us the ability to make topic inference through content relationships. User's inaccurate and incomplete profile can also be augmented with the help of a domain-ontology and usage pattern analysis using collaborative-filtering algorithms. Nevertheless, we can also use sophisticated mathematical models to process usage-pattern data for making content recommendations that reflects user's interest-drift. In this research, we integrate DL contents with a domain-ontology, user-profile and usage-pattern data by means of intelligent algorithms and techniques. On top of an open-source digital library system, we developed required modules to capture and manipulate necessary data with the help of efficient techniques such as ontology-driven topic inference, collaborative filtering, single exponential smoothing, etc. Our prototype can demonstrate that the retrieval results for the same query by a particular user, but on different time, may yield different result-sets (in terms of ranking) since the query, profile and contents are treated in a unified manner. We also verified that the same query from different users may yield different result sets as justified by differences in user profile and usage history. Our prototype can also recommend digital library items to users by using collaborative-filtering based usage-pattern analysis that takes user's interest-drift in consideration.**

I. INTRODUCTION

A digital library (DL) is a collection of documents in organized electronic form and accessible via search and browsing interfaces. The availability of contents, user profile and usage pattern in a digital library in machine understandable formats paves the way of processing these information further using state-of-the-art technologies to introduce intelligent services in digital library. Annotating, organizing and analyzing contents based on a domain-ontology [1] give us the ability to make topic inference through content relationships. User's inaccurate or incomplete profile can also be augmented with the help of a domain-ontology and usage pattern analysis using collaborative-filtering algorithms. Nevertheless, we can also use sophisticated mathematical models to *process* usage-pattern data for making content recommendations that reflect user's interest-drift [2]. Serving DL users with the right information which best reflect their query, profile, usage history and content relationships is only possible when we process heterogeneous information in a unified manner. In this research, we try to present such a unified approach towards developing adaptive and intelligent digital library services.

On top of an open-source digital library system, we developed required modules to capture and manipulate necessary data with the help of efficient techniques and algorithms such as ontology-driven topic inference, collaborative-filtering, single exponential smoothing, etc. Our prototype can demonstrate that the retrieval results for the same query by a particular user, but on different time, may yield different result-sets (in terms of ranking) since the query, profile and contents are treated in a unified manner. We also verified that the same query from different users may yield different result sets as justified by differences in user profile and usage history. Our prototype can also recommend digital library items to users by using collaborative-filtering based usage-pattern analysis that takes user's interest-drift in consideration.

II. MATERIAL AND METHODOLOGY

A. Digital Library Services

Being organized and focused collections of information, digital libraries concentrate on a particular topic or theme; and good digital libraries will articulate the principles governing what is included there and how are they organized. Typical DL Systems provide searching and browsing interfaces. Searching implies that the user knows exactly what to look for, while browsing should assist users navigating among correlated searchable terms to look for something new or interesting. Searching interface may range from basic keyword search to field-specific advanced search, etc. Browsing interface includes categorical navigation based on certain taxonomy and meta-data such as browse by author, category and the like [3][4].

Most digital libraries provide basic search and navigation functions which maybe adequate in WWW context but are merely sufficient in the context of a digital library. In DL context, we have been continuously failing to take advantage of electronic contents using advanced content processing techniques, and also

failing to make use of user profile and usage history, etc. We argue that what makes a digital library unique is the availability of content in electronic form (which can be processed automatically and inferences can be made), and the availability of user profile and usage patterns. Unlike the WWW, Google-like Keyword Search or Yahoo-like Directory Hierarchy is certainly not adequate for harnessing information in the context of a digital library. Therefore, we tried to make use of DL content, domain-ontology, user-profile and usage patterns; and developed necessary algorithms to facilitate intelligent and adaptive services for digital library.

In a digital library, keyword search and navigation may only facilitate and entry-level access to the content. Efficient access to DL contents is only possible when we succeed to make use of heterogeneous information and facets under a unified framework. For example, (1) keyword-based search often produces enormous amount of irrelevant hits. Different users may target different information when using the same keyword to search. (2) When a DL users signs up, they may inadvertently provide incomplete or inaccurate profile information about themselves. Moreover, (3) user's profile, information-seeking behavior and information-needs, etc. change over time (a.k.a. user interest-drift). In our research, we try to augment user profile adaptively using domain-ontology and usage history. We also analyze DL contents and usage-pattern to make ontology-driven topic inference through content and usage associations. Interest-drift modeling using single exponential smoothing techniques tries to capture interest-drift in DL users adaptively.

B. The Domain Ontology

The domain-ontology helps us organizing the DL contents and representing the user profile. We used a modified version of *ACM Computing Classification System* (ACM-CCS) Ontology [5][6] in our work. The schema of the ontology is presented in Fig. 1, where each node represents a topic. It should be noted that the `hasKeyword` attribute is very useful in making topic-inference from usage-patterns and through full-text analysis. DL user's search history and bookshelf items are analyzed to extract keywords and those keywords are associated against related nodes in the domain ontology.

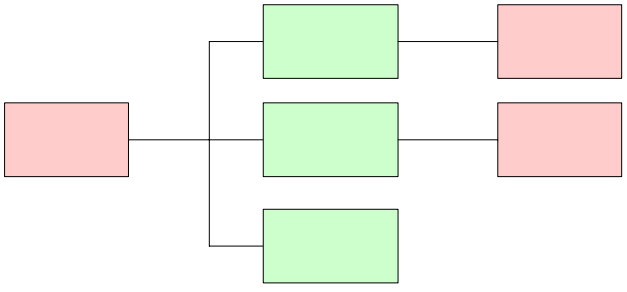

Figure 1. Schema for ACM-CCS Ontology based on CCS Taxonomy

C. Dynamic User Profile

The classes (topic nodes) defined in the ACM-CCS ontology is used to represent user profile. In the DL context, typically a user will specify their interests as they sign-up. However, such a raw profile is usually incomplete or inaccurate [7]; and requires further refinements and enhancement. We used a weight-based topic vector to represent user profile. The initial weights for each selected topic can be assigned rudimentarily. The subsequent augmented profile consists of topics and their weights as normalized and adjusted via the domain ontology by considering topic interrelationships and temporal usage history. Such a dynamic user-profile may be computed off-line in batch mode; and may more accurately reflect a user's interest and context. By keeping extra information such as user access logs including user's keyword-sets and bookshelf-items along with timestamps, we can capture user's interest-drift over time and re-weight the user-profile dynamically [2]. The mathematical formalism of interest-drift is explained below.

D. Interest-Drift Modeling

In a digital library, the user interests, information needs and information seeking behavior change over time. We adopt a policy on assigning higher weights on recent usages since topics related to recent usages reflect user's present context. We also assign exponentially weighted weights on older usage to reflect a user's general context. We use *Single Exponential Smoothing* technique (a well-known smoothing technique used in financial forecasting and engineering applications) to assign *exponentially adjusted weights* to estimate adaptive weights for each topic [8].

The smoothing is done as follows:

$$S_t = \alpha y_{t-1} + (1 - \alpha) S_{t-1} \qquad 0 < \alpha \leq 1$$

where t = any time period

S_t = the smoothed value

A = smoothing constant

y_{t-1} = the current observation

In the DL context, the frequency of a user login and user activities are directly related to the choice of the smoothing constant, α. The α values can be different for each user; and are estimated using a normalized frequency measure, fi as derived in Table 1.

$$f_i = N_i \;/\; Max_N$$

where N_i = # of transactions for $user_i$

Max_N = # of transactions for the most active user

TABLE 1
ESTIMATION OF SMOOTHING CONSTANT , α

Frequency (f_i)	Alpha (α)
frequency = 0	0
frequency < 0.3	0.05
0.3 <=frequency<0.5	0.1
0.5 <=frequency<0.7	0.2
0.7 <=frequency<0.9	0.3
frequency > = 0.9	0.4

E. Usage-Pattern Analysis using Collaborative Filtering

Collaborative Filtering (CF) is one of the key techniques for implementing a recommender system that recommends to a user a set of candidate items, which may be preferable or useful to the user based on similarity analysis with other users [9]. Collaborative Filtering techniques have been intensively used in E-commerce. The idea is easily extendable in the context of digital library. In the DL context, we can take advantage of both usage-pattern based and content-based collaborative filtering algorithms. It is interesting to note that in DL context, CF can be *bidirectional* – that is, it is not only possible to recommend new DL items for a user by analyzing profile similarity and looking at their bookshelves; but also it is possible to analyze bookshelf-item similarity and augment user-profile. We use a time-sensitive CF algorithm (similar to [2] for our purpose) to achieve adaptive effects on recommendations made.

F. Intelligent and Adaptive Digital Library Services

As a DL user undertakes new tasks or switches to new projects, an intelligent digital library should be able to adapt to such changes in the context and preference of that user. In another word, a user searching for information with the *same keyword but on different point of time* should not be served with the same retrieval results (at least the ranking of item should vary). Similarly, *two different users* searching the DL using the *same keyword at the same time* may not be served with the retrieval results. At least the ranking of the retrieval result should take into account of their profiles. We illustrated such adaptive digital library scenario in Fig. 2.

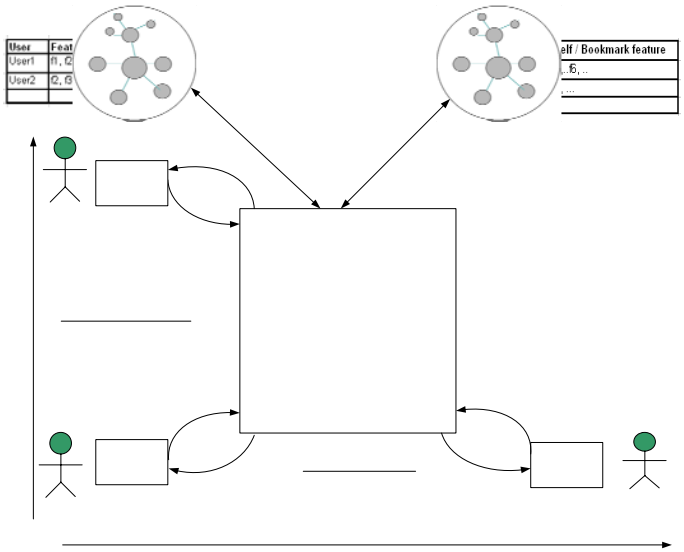

Figure 2. Intelligent and Adaptive Features in Digital Library Services
(a) Horizontal Axis illustrates that search results for a particular user using the same keyword at different time yield different retrieval results.
(b) Vertical Axis illustrates that search results for different users based on the same keyword may yield different retrieval results.

Using our prototype we try to verify that the retrieval results for the same query by a particular user, but on different time, may yield different result-sets (in terms of *ranking*) since the query; profile and contents are dynamically enhanced using intelligent algorithms based on ontology-driven topic inference, time-weighted user profile adjustment, CF-based similarity analysis and the like. We also verify that the same query from different users may yield different result sets as justified by the differences in their profiles and content relationships. Our prototype can also recommend digital library items to users by using collaborative filtering–based usage pattern analysis that reflects user's interest-drift. We test our approach using a partially synthetic datasets and analyzed the results through human judgments.

III. EXPERIMENTAL SETUP AND RESULT ANALYSIS

In order to demonstrate our proposed approach, we conducted experiments with semi-synthetic data. In this section, we will highlight some observations from those experiments.

A. User Similarity

To start with we generated random profiles for 10 users. These profiles are augmented though ontology-driven topic inference and usage pattern analysis. We use this information to find the similarity among users. Fig. 3, shows an example raw profile of users. The value '1' means a user is interested in that topic (category). The value "0" means that a user is not interested in that topic. We calculate vector similarity to find similarity among users. Fig. 4, shows user similarity. It should be noted that the profiles are continuously augmented using ontology-driven topic inference module and usage pattern analysis modules. Therefore, our CF-based recommendations reflect dynamic usage pattern of DL users and the topic associations in the DL domain.

	Category															
User	1	2	3	4	5	6	7	8	9	10	11	12	13	14	15	16
1	0.25	0.5	1	1	0	0	0	0	0	0.5	1	1	0	0	0	0
2	0.25	0	0	0	0	0.5	1	1	0	0	0	0	0.5	1	0	0
3	0	0	0	0	0	0	0	0	0	0	0	0	0	0	0	0
4	0	0	0	0	0	0	0	0	0	0	0	0	0	0	0	0
5	0.25	0.5	0	0	1	0.5	0	0	1	0.5	0	1	0.5	0	1	1
6	0	0	0	0	0	0	0	0	0	0	0	0	0	0	0	0
7	0	0	0	0	0	0	0	0	0	0	0	0	0	0	0	0
8	0.25	0.5	0	0	1	0.5	0	0	1	0.5	0	1	0.5	0	1	1
9	0.25	0.5	1	1	0	0	0	0	0	0.5	1	1	0	0	0	0
10	0.25	0	0	0	0	0.5	1	1	0	0	0	0	0.5	1	0	0

Figure 3. Examples of initial user profiles (raw-profile)

user	1	2	3	4	5	6	7	8	9	10
1	1	0.447	0.408	0.447	0.5	0.144	0.533	0.559	0.474	0.354
2	0.447	1	0.548	0.5	0.335	0.516	0.477	0.6	0.424	0.422
3	0.408	0.548	1	0.639	0.306	0.354	0.609	0.548	0.387	0.577
4	0.447	0.5	0.639	1	0.224	0.387	0.572	0.6	0.424	0.527
5	0.5	0.335	0.306	0.224	1	0.144	0.426	0.447	0.158	0.354
6	0.144	0.516	0.354	0.387	0.144	1	0.492	0.258	0.365	0.272
7	0.533	0.477	0.609	0.572	0.426	0.492	1	0.477	0.405	0.503
8	0.559	0.6	0.548	0.6	0.447	0.258	0.477	1	0.424	0.422
9	0.474	0.424	0.387	0.424	0.158	0.365	0.405	0.424	1	0.447
10	0.354	0.422	0.577	0.527	0.354	0.272	0.503	0.422	0.447	1

Figure 4. Similarity among user s

B. Time-weight Smoothing

From DL user's access-log, we calculate α value for each user to continuously augment user's raw-profile that reflects user's context and interest-drift. If α value is small, the weight changes

faster than a bigger α value. From Fig. 5, we see that the weights are changed sharply for more active DL users (with smaller α).

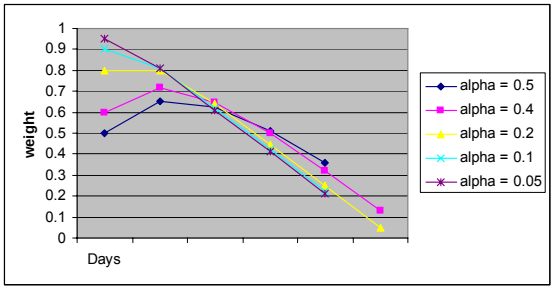

Figure 5. Graphical representations the relation between topic weight and α

In Fig. 6, we illustrate how topic-weight changes when a user starts searching the DL with new items (originally not reflected in his or her profile and usage).

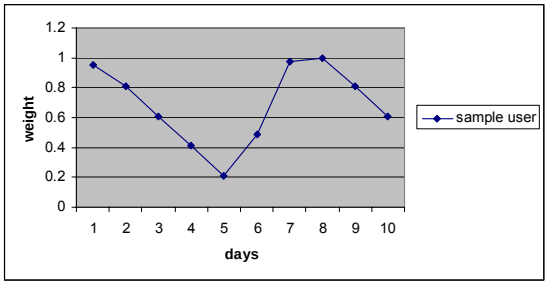

Figure 6. Weight of a topic for a particular user changing over time

IV. Conclusions and Future Work

In this paper, we presented a novel approach to associate contents with user profile and usage pattern and modeling interest-drift in Digital Libraries. Our prototype is based on a *3-Layer Architecture* as shown in Fig. 7. The core of the 3-Layer architecture is an open-source DL system surrounded by series of Add-on Modules to capture further information about contents, users and usages in Layer 2. The outer-most layer (Layer 3) consists of services developed by making intelligent use of those information with the help of efficient techniques and algorithms.

We validated our approach with preliminary experiments using synthetic data and prototype algorithms. At the moment, we are setting up a digital library with sizeable amount of contents and real users; and planning to put our prototype into practical operation. Our present experimental setup and analysis using synthetic dataset showed that our approach integrates several facets of DL information seeking scenario; and is capable of providing personalized services for digital library users. Two different users searching with the same query yield different hits. The same user searching with the same query but at different point of time, may get different hits depending on his or her recent context. For the future work, we will include systematic evaluation based on real digital library usage data.

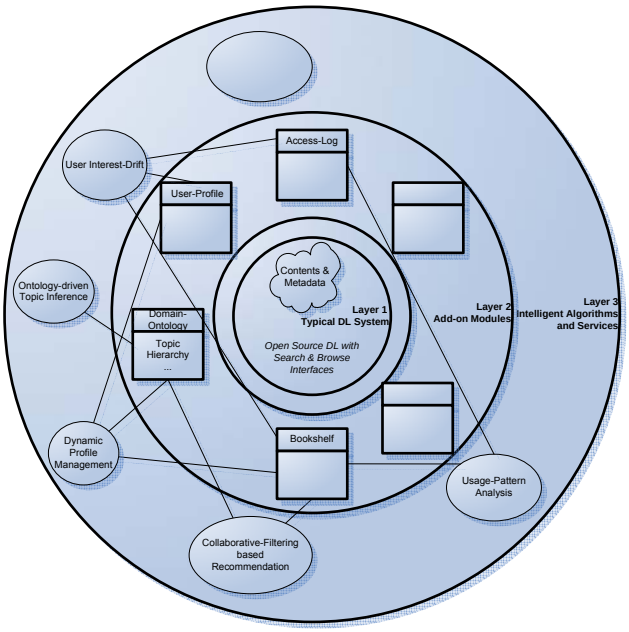

Figure 7. 3-Layer DL Architecture for Intelligent and Adaptive Digital Library Services

Acknowledgment

We would like to thank Assoc.Prof. Dr. Ekawit Nantajeewarawat and Asst.Prof. Dr. Chutiporn Anutariya for their supports and valuable comments. This research has been supported by Thailand Research Fund in terms of a TRF grant (MRG4880112) awarded to Dr. M.M. Hasan.

References

[1] S. E. Middleton, D. C. De Roure, and N. R. Shadbolt, "Capturing Knowledge of User Preferences: Ontologies on recommender systems," In Proceedings of the First International Conference on Knowledge Capture (K-CAP2001), 2001, pp. 100-107.

[2] Y. Ding and X. Li, "Time weight collaborative filtering," In Proceedings of the 14th ACM international conference on Information and knowledge management, 2005, pp. 485-492.

[3] G. G. Chowdhury and S. Chowdhury, Introduction to digital libraries, London: Facet Publishing, 2003.

[4] I. H. Witten and D. Bainbridge, How To Build a Digital Library, San Francisco, CA: Morgan Kaufman Publishers, 2003.

[5] ACM-CCS, "The ACM Computing Classification System [1998 Version]," [online]
Available: http://www.acm.org/class/1998/. [Accessed: Jan. 12, 2007]

[6] ACM-CCS Add-on Ontology, "DSpace Dev @ University of Minho," April 2003, [Online].
http://dspace-dev.dsi.uminho.pt:8080/en/research_about.jsp
[Accessed Mar. 12, 2006]

[7] I. E. Liao, S. C. Liao, K. F. Kao, and I. F. Harn, "A Personal Ontology Model for Library Recommendation System," in The 9th International Conference on Asian Digital Libraries (ICADL 2006), 2006, pp. 173-182.

[8] NIST Handbook, "NIST/SEMATECH e-Handbook of Statistical Methods," [Online]
http://www.itl.nist.gov/div898/handbook/. [Accessed: Mar. 17, 2007]

[9] B. Sarwar, G. Karypis, J. Konstan, and J. Riedl, "Item-based Collaborative Filtering Recommendation Algorithms," In Proceedings of the Tenth International World Wide Web Conference (WWW10), 2001, pp. 285-295.

Improve XML Web Services' Performance By Compressing XML Schema tag

Tanakorn Wichaiwong and Chuleerat Jaruskulchai
Department Of Computer Science, Faculty of Science, Kasetsart University, Bangkok Thailand

Abstract **The standard of data transfer and exchange between organizations through web services has become exceedingly popular, especially in electronic commerce. Data transferred through web services is in the form of XML (Extensible Markup Language). Even though XML tag can be beneficial, it can be spaced and time consuming as well and also influences the effectiveness of the system as a whole.**

In this paper presents algorithm in improving the effectiveness of XML data transferring through the network by compression under the service of Web Services which supports compression and decompress of data. The mechanism composes of 3 steps: 1) data structure analyzes 2) data compression and 3) decompress of data after compression. It has been discovered that these steps reduces the size of the data down to 35 – 47 % and uses less data exchange time when compared to before the compression. In addition, it can also send data through web services with efficiency without losing standards of data transfer.

Keywords: Compression, Web Services, XML, Data exchange

I. INTRODUCTION

A web service is a collection of protocols and standards used for exchanging data between applications or systems uses a standardized XML messaging system. Its objective is to enable interoperability by using the central technique standard which causes data exchange. As a result, web services is widely used at present and is expected to become even more popular in the future. Web services composes of UDDI (Universal Description Discovery and Integration) [1] which informs about the organization's products and services, it is composed of 3 main parts: 1) information on how to contact service provider 2) the group of service provider 3) technical data on communication, SOAP (Simple Object Access Protocol) [1] is a form of XML data reception and transfer with web services. Application will send a SOAP request to the web services and the web service will send the result back in SOAP response, WSDL (Web Services Description Schema) [1] is a manual on web services usage which includes the location of the web services, list of functions in service, list of each function's parameter, as well as the structures of SOAP Message, XML [2] the basic layers of web services as show in "Fig.1".

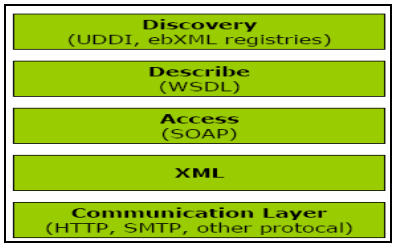

Figure 1. Basic layers of web services

```
<?xml version="1.0" encoding="utf-8" ?>
<Book>
  <Author>
    <Name>Pissamai</Name>
  </Author>
</Book>
```

Figure 2. Example of XML document

XML plays a role and is a standard in exchanging data as it is a schema that can explain the definition of the data and its usage is also very flexible by having tag as a director. Also naming the tag that defines the data makes the documents that have been created easy to understand. This is a crucial part which makes data access and the automatic compilation of such structured data an easy and fast process.

Although XML'tag describes meaningful structure and semantics for humans understanding, it requires extra space to store the XML'tag. As a result, the size of the data is big and uses up a lot of space and time in data transfer when it is necessary to exchange data between organizations though network system. From the problem of data size, the methods to solve the problem is the compression of data which can be done in two ways: lossless, is when the data remains exactly the same before compression and after the decompress and lossly, is when the data before the compression and after the decompress does not need to be the same but can still be used. XML data compression is a lossless compression. It reduces the size of the data. If it is specifically XML data compression, it can increase the effectiveness of the compression when compared to general data compression.

Details of data structure mostly uses the DTD (Document Type Definition) or XML Schema. This makes the data exchange simple as it's been specified which tag to have and how the relationships between data should be. But the construction of DTD is very complicated and detailed which unable DTD to examine the type and boundary of the data. Therefore, XML Schema has been designed to solve these problems as it is written by the grammar of XML schema. It can also specify the type of data by using Namespace and specify the attribute and element values.

```
<!ELEMENT Book (Author+)>
<!ELEMENT Author (Name)>
<!ELEMENT Name (#PCDATA)>
```

Figure 3. DTD of XML document from Figure 2

From the "Fig.2" shows XML and "Fig.3", we can see that <Book> is an element that has at least one Author and the Author element has a reference of the Name element which keeps the data with the contents of PCDATA (Parsed Character Data)

The second part of this report is a presentation on XML compression at present time which are XMill [3], XGrind [4], XPRESS [5], XPACK [6], Web services compression by SharpZipLib library [7], XBrevity [8]. Part three of this report shows the development of a new way of compression. Part four contains the results of experiments and part five is the summary.

II. Related Works

At present, researches on XML data compression stress the reduction of XML data size. Each method has its own techniques. XML data compression can be divided into 3 types: 1) data compression 2) tag compression and 3) data and tag compression

XMill [3] is a technique which compresses both data and tag in order to reduce the size by starting with separating the tag, which is composed of elements and attributes, from the data which is a character. After that, the data groups' relationships will be organized. The same data will be in the same group. The next step is the data compression by using gzip [9] so that the data will come out in the same file since grouping requires understanding of the data definitions which depends on the application type. XMill allows user check the data definition. The disvantage of XMill that data cannot be search through the compressed data. However, XMill is the first research that made researchers realizes the importance of the problem and how to solve it in XML data compression. Data that has been compressed is not in the form of XML schema structure.

XGrind [4] is a technique which compressed data and tag but the user can still search for data after the compression. This qualification results from the fact that the compressed data still maintain the structure of the old data. However, XGrind will compress only XML data that has DTD structure so some data set that does not have DTD will result in having the user waste time in creating DTD for XML data set that they wanted to compress.

XPRESS [5] uses the technique in compressing both the data and the tag. Its advantages are the same as XGrind: it can search for the data after the compression. But XPRESS does not use DTD. In addition, XPRESS presented a new idea which uses reverse arithmetic encoding which is a method in organizing data so that the search for XPath expressions can be done effectively. Also, XPRESS has developed the search of data type without having to use the information from users. However, the use of XPRESS is limited because XPRESS cannot understand documents that use ID and IDREF. It also does not have a way to decompress data back into normal XML.

XPACK [6] is a way to compress XML data which uses grammatical approaches in XML data compression and decompress. The main component of XPACK is the Grammar Generator which creates grammar. The second component is the Compressor which compresses the data. The last component is the Decompressor which decompresses the compressed data by using the old structure of the data. However, XPACK cannot manage XML data that has mixed content element (which is an element composed of element and characters), limiting users to search for data in compressed XML.

Web services compression by SharpZipLib library [7] is a technique that compresses both data and tag so that the sizes can be reduced before data. However, the process in compression and decompress is time consuming. It also requires resources from units that use high efficiency web service as well. This reduces the web services' function's effectiveness.

XBrevity [8] is a technique that compresses tag. The quality comes from compressed data which has the old data structure. However, with XBrevity, data after the compression is still quite big and there was no usage of Schema tag in data compilation.

III. XML Schema Tag Compression Technique

This research stresses the compression of tag because in electronic commerce application, most data sent through web services has many complicated elements. XML compression by using XML Schema tag compression has main components as follow 1) Schema tag Scanner which reads the data structure 2) Compressor, which compresses data and 3) Decompressor, which decompress the compression

3.1 Schema tag Scanner reads the XML data structure by analyzing all structure of all XML data.

3.2 Compressor compresses the data by compressing the data at the structure of XML Schema. The result of compression is a data that resulted from compression that can be used on web services in the future.

*3.3 Decompressor w*hen it is needed to use the data that has been compressed from the web services, it is necessary to first decompress the data by using Decompressor which will read the structure of the XML schema and decompress it back to the same data that was received from the web services by lossless compression.

This research focuses on compression of XML schema. In "Fig.5" shows an example of XML schema and their corresponding XML data in "Fig.6". It can be seen that it is using the same tag but the data inside is different. This makes the schema looks complicated and data too large.

Before sending this data over on the internet, the compressor is processed to remapping XML'tag to shorter one. In "Fig. 7 and 8" are the results of compressing the XML schema and their XML data. The redesign XML schema maintains the XML standard properties and can be exchanged through web servers. When client receives this data, Decompressor will remap back to the original.

Figure 4. Structure of XML Schema tag

```
<name="CustomerID"type="xs:string"/>
<name="CompanyName"type="xs:string"/>
<name="ContactName"type="xs:string"/>
<name="ContactTitle" type="xs:string" />
<name="Address" type="xs:string" />
<name="City" type="xs:string" />
```

Figure 5. XML Schema

```
<CustomerID>ALFKI</CustomerID>
<CompanyName>Alfreds
Futterkiste</CompanyName>
<ContactName>Maria Anders</ContactName>
<ContactTitle>Sales
Representative</ContactTitle>
<Address>Obere Str. 57</Address>
<City>Berlin</City>
```

Figure 6. XML Data

```
<name="a" type="xs:string" ms:caption="
CustomerID"/>
< name="b" type="xs:string" ms:caption="
CompanyName"/>
< name="c" type="xs:string" ms:caption="
ContactName"/>
<name="d" type="xs:string"
ms:caption="ContactTitle"/>
<name="e" type="xs:string" ms:caption="Address"/>
<name="f" type="xs:string" ms:caption="City"/>
```

Figure 7. Compressed XML schema data

```
<a>ALFKI</a>
<b>Alfreds Futterkiste</b>
<c>Maria Anders</c>
<d>Sales Representative</d>
<e>Obere Str. 57</e>
<f>Berlin</f>
```

Figure 8. Compressed XML data

IV. EXPERIMENT

In the experiment of data compression, there was development in the web services system in which there were methods of compression and non-compression. This experiment was done on 1) the database SQL Server on Intel Xeon 2.33 GHz Dual with the memory of 3.5 GB, Windows Server 2003 with Service Pack 1 2) The web services was on Intel Xeon 3.00 GHz with the memory of 2.5 GB, Windows Server 2003 with Service Pack 1 and 3) the application was on Intel Pentium M 1.70 GHz with the memory of 512 MB, Windows XP Professional with Service Pack 2 and developing all 2 systems by Microsoft Visual C#.NET 2005. This experiment was not tested with XMill, XGrind, XPRESS, XPACK, and XBrevity since there wasn't a system that support working on web services. So, there was an effectiveness test by developing XML compression and non-XML compression methods for XML on the same web services.

4.1 Effectiveness Measurement The data used in experimenting is AdventureWorks database on Microsoft SQL Server 2005 and the characteristics of example document as show in TABLE I. The effectiveness in data compression is the proportion of compression which can be found by using:

Size Proportion = [1 - (size of compressed data / size of actual data)]

As shown in TABLE II or "Fig.9", the use of XML Schema tag compression technique with web services reduces the data size down to 35 - 47 % and the effectiveness of data exchange is the proportion in data exchange which can be found by using:

Proportion = [1 – (the time used in exchanging compressed data / the actual time used in data exchange)]

As shown in TABLE III or "Fig.10", usage of XML schema tag compression technique with web services reduces the length of time in data exchange when compared to the data before compression.

4.2 Affecting Factors

To get benefit of this algorithm, the XML data should have the following characteristics:

1. The XML data should compose of many elements and few attributes of elements.
2. The XML data should have few dependent on elements.

TABLE I
CHARACTERISTICS OF EXAMPLE DOCUMENT

File Name	Size (KB)	Attribute	Record
Products	387	25	504
Contact	10,767	15	19,972
SaleOrderHeader	31,958	27	31,465
SaleOrderDetail	57,670	11	121,317
Customer	5,528	6	19,185

TABLE II
COMPARE THE SIZE AFTER COMPRESSION

File Name	Size(KB)		%
	WS	WS + XML Schema tag	
Products	387	206	47
Contact	10,767	6,773	37
SaleOrderHeader	31,958	17,378	46
SaleOrderDetail	57,670	30,648	47
Customer	5,528	3,317	40

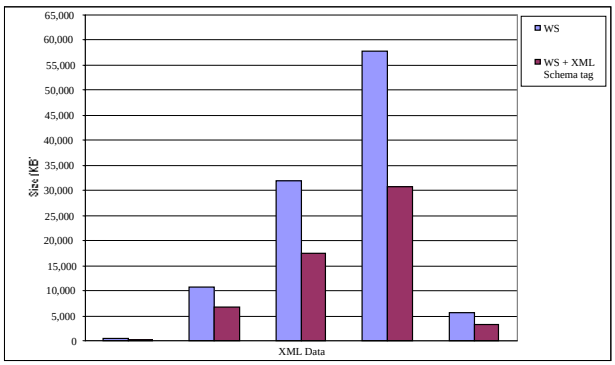

Figure 9. Graph showing the size of data

TABLE III
COMPARE THE TIME OF DATA EXCHANGE

File Name	Response Time(ms)		%
	WS	WS + Schema tag	
Products	67,790	65,342	4
Contact	290,024	269,744	7
SaleOrderHeader	594,704	523,740	12
SaleOrderDetail	1,102,036	971,187	12
Customer	189,420	179,064	5

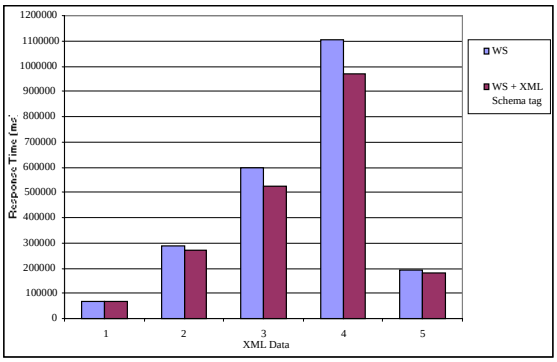

Figure 10. Graph showing data exchange time

TABLE IV
SHOW THE LENGTH OF TIME USED IN COMPRESS AND DECOMPRESS

File Name	Time (ms)	
	Compress	Decompress
Products	1,001	1,001
Contact	2,001	1,000
SaleOrderHeader	2,002	2,002
SaleOrderDetail	9,012	8,011
Customer	1,001	1,001

V. CONCLUSION

XML data compression is important because XML is a schema that has several advantages and it is used widely in the present days. But there are also limits of XML. Normally, data in the form of XML has a bigger size than text files since XML data usually uses tag to direct the data definitions. Data transfer by XML schema results in the need of large Network Bandwidth because of the data size. Web services is a service that is widely used at present and is expected to become more popular in the future that uses XML schema to transfer data. A way to increase the effectiveness of web services is to reduce the data by compression. Past researches on XML data compression, prove that the size can be reduced but it's difficult to use with web services.

The techniques presented in this paper is on XML data compression by using XML schema tag compression to reduce the data size, but still enables the easy understanding of documents because the data is already in the form of XML schema so it can maintain the advantages of being in XML schema. It is also easy to use. This research stresses the importance of tag structure compression but the characters which are inside the tag have not been compressed. Therefore, the effectiveness of compression technique can still be more and more developed because character data compression within the tag will result in the reduction of data size in the web services.

REFERENCES

[1] Solutions Architect, IBM jStart Emerging Technologies "Web services architect: Part 1," April 01, 2001

[2] D. Hunter, C. Cagle, D. Gibbons, N. Ozu, J. Pinnock and P. Spencer. "Beginning XML," *Wrox Press*, 2002.

[3] H. Liefke and D. Suciu. "XMill: an Efficient Compressor for XML Data.," *In Proceeding of the 2000 ACM SIGMOD International Conference on Management of Data*, pages 153-164, May 2000.

[4] P. M. Tolani and J. R. Haritsa. "XGRIND: A Query-friendly XML Compressor.," *In Proceedings of 18th International Conference on Databases Engineering*, February 2002.

[5] J.-K. Min, M.-J. Park, and C.-W. Chung. "XPRESS: A Queriable Compression for XML Data.," *In Proceeding of the 2003 ACM SIGMOD International Conference on Management of Data*, pages 122-133, June 9-12, 2003.

[6] K. Maireang and C. Pleurmpitiwiriyavach. "XPACK: A Grammar-based XML Document Compression," *In Proceeding of NCSEC2003 the7th National Computer Science and Engineering Conference*, October 28-30, 2003.

[7] M. Tian, T. Voigt, T. Naumowicz, H. Ritter, J. Schiller "Performance Impact Of Web Services On Internet Servers," *Freie University Berlin*

[8] P. Lekasapon and K. Runapongsa, "XML Data Compression using Brevity Encoding," *The 21st International Technical Conference on Circuits/Systems, Computers and Communications, Chiang Mai, Thailand*, July 10-13, 2006

[9] J.L. Gailly and M. Adler, "gzip: The compressor data," Available at http://www.gzip.org/

[10]SharpZipLib, http://www.icsharpcode.net/OpenSource/SharpZipLib/default.asp

[11] Solutions Architect, IBM jStart Emerging Technologies "Web services architect: Part 1," April 01, 2001

[12] Solutions Architect, IBM jStart Emerging Technologies "Best practices for Web services: Part 1, Back to the basics," October 01, 2002

[13] BEA Systems, IBM, Microsoft, SAP AG and Siebel Systems. "Business Process Execution Schema for Web Services," Available at http://www-128.ibm.com/developerworks/library/specification/ws-bpel/

An Incremental Learning Algorithm Based-On Mahalanobis Distance for Breast Cancer Diagnosis

Sunantha Sodsee[1], Maytiyanin Komkhao[1] , Phayung Meesad[2]

[1]Department of Information Technology Faculty of Information Technology
[2]Department of Teacher Training in Electrical Engineering Faculty of Technical Education
King Mongkut's Institute of Technology North Bangkok
1518 Pibulsongkarm Rd., Bangsue, Bangkok 10800 Thailand
sunantha_s@hotmail.com, maytiyanin9@hotmail.com, pym@kmitnb.ac.th

***Abstract*-We propose a new reliable and precise classification classifier for breast cancer diagnosis. The proposed classifier, which is called an Incremental Learning algorithm based-on Mahalanobis distance (ILM), employs a Mahalanobis Radial Basis Function Network to be an activation function in order to classify cancer data. The ILM uses the Mahalanobis distance to measure a similarity and dissimilarity among data, and identifies a threshold distance. An efficient covariance computation is used for avoiding a singular covariance matrix. It is also an incremental learning utilizing recurrent computation of covariance matrix based on a Simplified Fuzzy ARTMAP Network (SFAM) [1]. For evaluation, the proposed classifier is tested with the Winconsin Diagnosis Breast Cancer datasets and compared the performance with other existing classifiers.**

***Keywords*-Classification, Mahalanobis Radial Basis Function Network, Mahalanobis Distance, Similarity, Incremental Learning, Recurrent Computation**

I. INTRODUCTION

Cancer is a group of disease that occurs when any cells in the body changing or growing out of control. Most of abnormal cells are a tumor, which is called in different cancer name based on the part of body [2]. Breast cancer is the most common type of cancer in women in the United States. In Thailand, the ratio of breast cancer is 16.3:100,000 women and Bangkok has the highest number of patients [3]. "During 1998-2002, 97% of breast cancer deaths occur in women aged 40 and older"[2]. According to the problem of breast cancer, we try to develop the classification algorithm from the experiment dataset; Wisconsin diagnosis breast cancer database obtained from the University of Wisconsin Hospital by Dr. William H. Wolberg [4]. Breast cancer is classified into benign and malignancy, which is composed of 699 patterns. Each pattern consists of 10 attributes: *sample code number*, *clump thickness*, *uniformity of cell size*, *uniformity of cell shape*, *marginal adhesion*, *single epithelial cell size*, *bare nuclei*, *bland chromatin*, *normal nucleoli*, and *mitoses*.

At present, many researchers focus on the breast cancer diagnosis by using difference techniques combined several existing classifiers to generate the new one such as Hybrid Fuzzy-Genetic methodology [5], Fuzzy-ARTMAP [6], and ILFN [7] etc. to improve the reliable and accuracy.

In this research, we propose a new incremental supervised learning based on the correlation measurement between patterns that is an Incremental Learning algorithm based-on Mahalanobis distance (ILM). The details are described in Section III.

The remains of this paper are organized as follows. Section II shows the literature reviews of the related works. Section III describes the details of the proposed algorithm. Experimental results are shown in Section IV. Finally, Section V concludes the study.

II. LITERATURE REVIEWS

A. Pattern Classification

Pattern classification is a well-known technique in machine learning and data mining. It is to classify datasets into related set of class. It is divided into two types: supervised and unsupervised learning [8]. For supervised learning, the aim is to teach the network to predict an unknown input by using training data both input patterns and target group to create the prototype of system. In contrast, the unsupervised learning uses only input patterns and similarity measures to build the trained network. This is a natural way to find classes of datasets.

B. Similarity Measure

The similarity is quantity that reflects the strength of relationship between two objects or two features. This quantity is usually having range of either -1 to +1 or normalized into 0 to 1[8-9]. The similarity between feature i and feature j is denoted by $\mathbf{S}_{ij}$. On the other hand, dissimilarity is viewed as measure of disorder between two objects. Dissimilarity between object i and object j is denoted by $\boldsymbol{\delta}_{ij}$. The relationship between dissimilarity and similarity is given by

$$\mathbf{S}_{ij} = 1 - \boldsymbol{\delta}_{ij} \quad (1)$$

Where $\mathbf{S}_{ij}$ is a similarity between features i and j and $\boldsymbol{\delta}_{ij}$ is a dissimilarity between features i and j.

Distance is used for representing the similarity and dissimilarity between objects. If the objects are most similar then the distance between them is minimized; the objects are

most dissimilarity when the distance between them is maximized.

$d_{ij} \geq 0$ distance is always positive or zero
$d_{ij} = 0$ distance is zero if it measured to itself
$d_{ij} = d_{ji}$ distance is symmetry
d_{ij} : Distance between features *i* and *j*
d_{ji} : Distance between features *j* and *i* ($d_{ji} = d_{ij}$)
d_{ii} : Distance between itself (always = 0)

There are many ways to measure the similarity and dissimilarity between objects based on the types of features or variables such as quantitative variable, ordinal variable, binary variable, and nominal variable [9]. In this paper, we focus on the quantitative variable for instance: Euclidean Distance, Manhattan Distance, and Mahalanobis distance.

Mahalanobis distance is different from the Euclidean distance, which is the most popular similarity measure. It considers the orientation of data in the sample space grouping them by mean and covariance matrixes. The shape of a cluster is hyper-ellipsoids rather than hyper-spheres as Euclidean distance. The difference of them is described in mathematic function as follow [1, 9]:

Input pattern denotes by $p_n = (p^1, p^2, ..., p^d)$, while the sample set of input pattern belong to the cluster j will be denoted as: $P_j = \{p_j^{(1)}, p_j^{(2)}, ..., p_j^{(n)}\}$ by P_j is called cluster *j*, and p is an unknown pattern.

For Euclidean Distance:

$$\min_j R(p, P_j) = \min_j (p - W_j)^T (p - W_j) \qquad (2)$$

where W_j is the center of the cluster *j*.

$$W_j = \frac{1}{n} \sum_{k=1}^{n} P_j^{(k)} \qquad (3)$$

For Mahalanobis Distance:

$$\min_j R(p, P_j) = \min_j (p - W_j)^T S^{-1} (p - W_j) \qquad (4)$$

where S_j is the covariance matrix of cluster *j*.

$$S_j = \frac{1}{n-1} \sum_{k=1}^{n} (p_j^{(k)} - W_i)(p_j^{(k)} - W_j)^T \qquad (5)$$

The Mahalanobis distance calculation is more complicated than the Euclidean distance because the covariance matrix has to be as follow [8]:

1. The determinant of S is positive
2. The S^{-1} is positive
3. The determinant of S^{-1} is positive
4. All of the main diagonal elements of S is positive
5. All of the eigenvalues of S are positive
6. S is nonsingular and has S^{-1}

C. Incremental Learning

There two well-known techniques for parameter estimation: off-line learning and on-line learning [7-8]. The off-line learning sometimes is called block-wise or batch learning**.** It requires the total learning set to be available and compute the statistical moments by summation over all elements of the learning set. On the other hand, on-line learning, there are many names such as iterative learning, recursive learning, and incremental learning [7-8]. This technique differs from the previous one. It learns continuously without forgetting the previous learned knowledge. It means when training is done, new instances can be inserted to the training data at any time. This technique closes to the human learning concept because it is "the capability of continuously improving one's skills by being taught or simply by doing" [9].

The updated parameter estimation of Euclidean and Mahalanobis distance are as follow:

For Euclidean Distance:
From (2) the recurrent computation (update function) of W_j is

$$W_j = (1 - \beta) W_j + \beta\, p \qquad (6)$$

where β is the learning rate.

For Mahalanobis Distance:
From (4) the updated function of W_j and S_j are:

$$W_j = (1 - \beta) W_j + \beta\, p \qquad (7)$$

$$S_j = (1 - \beta) S_j + \beta(1 - \beta^2)(p - W_j)(p - W_j)^T \qquad (8)$$

where β is the learning rate.

From (6) to (8) [1], they can reduce the processing time of both training and classification. The success rate of Euclidean and Mahalanobis distance comparing with the off-line learning also improved one percent and 8 to 17 %, respectively.

III. Development of an Incremental Learning Algorithm Based-on Mahalanobis Distance

ILM has three different modes: Training mode, Prediction mode and Incremental learning mode shown in Fig. 1.

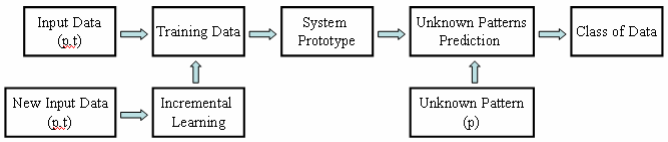

Figure 1. Architecture of ILM.

In supervised learning mode, ILM requires both input data and target data. When the algorithm learns the data, it uses the Mahalanobis distance to create the prototype of each cluster according to the degree of similarity and based on the defined threshold distance. In prediction mode, ILM will classify the unknown pattern arriving to the system to one of known classes. While predicting the unknown pattern, if it is very different from existing prototypes, the new input data can be learned to include into the system as new knowledge at anytime using the concept of the incremental learning. The output of this algorithm is the target class of each testing pattern (unknown pattern).

According to the concept of similarity measure in section B, we define the threshold distance to compare with the measured distance between data. This is to create the prototype of each cluster using the most similar data. The measured distance between data is d_m, and the defined threshold distance is d_h, where $0 < d_h < 1$. If $d_m > d_h$ then the data are less similar, in contrast if $d_m \leq d_h$ then the data are most similar.

For example, if there are three existing prototypes of clusters. If the winner cluster is the Cluster 1, and the distance between the input pattern and the Cluster 1 is less than or equal to the defined threshold distance then update the parameters in Cluster 1 (see Fig 2(a)). It means that the input pattern is most similar to the prototype of Cluster1. On the other hand, if the winner node is Cluster 1 but the distance is higher than the defined threshold distance. It shows that the input pattern is less similar to Cluster1 then a prototype of new cluster is created showing in Fig 2(b).

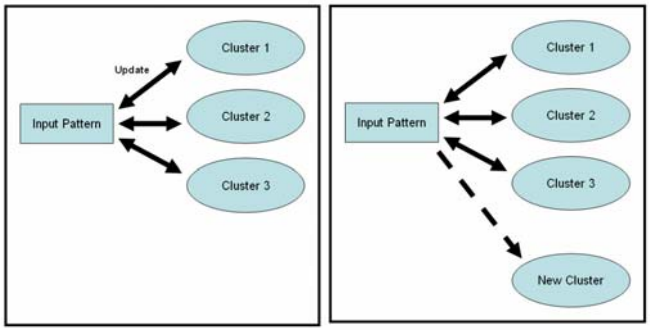

(a) (b)

Figure 2. The Threshold Distance Identification Concept.

A. Details of the Proposed Algorithm

ILM is divided into a learning phase, and a testing phase. Firstly, the system will create the system prototype using the learning phase after that classify the unknown pattern by the testing phase. The detail of each phase is described as follow:

Learning Phase

Step 1: Set up the initial value: the threshold distance (d_h), where $0 < d_h < 1$, and the covariance matrix ($S_{j,initial}$) as follow:

$$S_{j,initial} = \text{x.}(I_n) \tag{9}$$

where $I_n = \begin{bmatrix} 1 & 0 & \dots & 0 \\ 0 & 1 & \dots & 0 \\ \vdots & \vdots & \ddots & \vdots \\ 0 & 0 & \dots & 1 \end{bmatrix}$, and $0 < x < 1$

$$\text{x.}(I_n) = \text{x.}\begin{bmatrix} 1 & 0 & \dots & 0 \\ 0 & 1 & \dots & 0 \\ \vdots & \vdots & \ddots & \vdots \\ 0 & 0 & \dots & 1 \end{bmatrix} = \begin{bmatrix} x & 0 & \dots & 0 \\ 0 & x & \dots & 0 \\ \vdots & \vdots & \ddots & \vdots \\ 0 & 0 & \dots & x \end{bmatrix}$$

Step 2: Read the first input (p) and target (t) pattern to be the mean (W_j), and target of the cluster, then set up count.

$$C_{j,initial} = 1 \tag{10}$$

Step 3: Read next input pattern

Step 4: Similarity measure between p and W_j using the nonsingular covariance matrix to calculate the Mahalanobis distance (d)

$$S_{j,new} = S_{j,old} + \text{x.}(I_n) \tag{11}$$

$$\text{d} = (p - W_j)^T S^{-1} (p - W_j) \tag{12}$$

Step 5: Calculate the membership value of each cluster using Mahalanobis RBF

$$mem(p, W_j) = \exp\left(- \frac{(p - W_j)^T S^{-1} (p - W_j)}{2} \right) \tag{13}$$

Step 6: find the winner cluster that has the maximum membership value identified by fuzzy OR operator

$$winner = \arg\max(mem) = mem_1 \vee mem_2 \vee \dots \vee mem_n$$

Step 7: Update parameters: count, mean, and covariance matrix, at the winner cluster:

- if the distance between the input pattern and the winner cluster is less than or equal to the defined threshold distance

$$C_{j,new} = C_{j,old} + 1 \tag{14}$$

$$W_{j,new} = (1 - \beta) W_{j,old} + \beta p \tag{15}$$

Where: $\beta = 1 / C_{j,new}$

$$S_{j,new} = (1-\beta) S_{j,old} + \beta(1-\beta^2)(p - W_{j,new})(p - W_{j,new})^T \tag{16}$$

- if the distance between the input pattern and the winner cluster is higher than the defined threshold distance, then new cluster is created

Testing Phase

Step 1: Read the testing pattern

Step 2: Similarity measure between the testing pattern and the prototype of each cluster

$$d = (p - W_j)^T S^{-1} (p - W_j) \quad (17)$$

Step 3: Assign the membership value in each cluster using Mahalanobis RBF

$$mem(p, W_j) = \exp\left(- \frac{(p - W_j)^T S^{-1} (p - W_j)}{2} \right) \quad (18)$$

Step 4: Find the winner cluster using fuzzy OR operator

$$winner = \arg\max(mem) = mem_1 \vee mem_2 \vee \ldots \vee mem_n$$

Step 5: Assign the target class to the testing pattern

Target Class = Target of Winner Cluster

IV. EXPERIMENTAL RESULTS

In this section we show two experiments: threshold distance identification and efficiency comparison between ILM and existing classifiers.

For the threshold distance identification, we found the threshold distance that suitable for the breast cancer diagnosis. We tested it ten times to vary from 0 to 1. The result showed that 0.001 can illustrate the high performance of algorithm in the breast cancer diagnosis. Before using the threshold distance identification concept, the classification correctness is 97.633 after that the efficiency is improved to be 98.71 that shown in Table 1.

Table II

Effect of Threshold Distance Identification.

ILM	Classification Correctness (%)
Without Threshold Distance Identification	97.633
With Threshold Distance Identification	98.71

To demonstrate the performance of ILM in breast cancer diagnosis the well-known benchmark data Winsconsis Breast Cancer Database (WBCD) is used to compare our performance with other existing classifiers such as SVM [10], LVQ [10-11], Naïve Bayes [10], SOM [10-11], and SOM-RBF [10-11]. The comparison results are illustrated in Table 2.

In table 2, we try to compare ILM with the varieties types of classifiers based on different methods such as the Euclidean RBF, statistical method, fuzzy, and genetic algorithm. The results show that the classification correctness of most classifiers is more than 95. The efficiency performance of ILM is the highest correctness, it is 98.71.

Table II

The Comparison of Performance between ILM and Existing Classifiers.

Classifiers	Classification Correctness (%)
Hybrid Fuzzy-Genetic	97.8
FAM	94.29
SVM	97.20
LVQ	96.60
Naïve Bayes	96.40
SOM	97.4
SOM-RBF	97.5
ILM	**98.71**

V. CONCLUSIONS

This algorithm is a new classifier for elliptical cluster shape using Mahalanobis RBF to create the prototype of each cluster. It also supports the supervised and incremental learning to improve the success rate of performance. It uses the efficient covariance computation to avoid the singular covariance matrix. Experimental results demonstrate that this proposed algorithm is powerful and effective tool to diagnose the breast cancer with performance of over 98 and it also is the highest accuracy classification.

REFERENCES

[1] T. Kasuba, "Simplified fuzzy ARTMAP," *AI Expert*, pp. 18-25, November 1993.

[2] *National Cancer Institute*. Available online at http://www.cancer.gov [2006, December 10].

[3] W. Putthasri. et al. "Cost of screening for breast cancer with mammography in Thailand." *Journal of Health Science.* 13 (2004) : 268-276.

[4] W. H. Wolberg and O. L. Manggsarian, "Multi-surface method of pattern separation for medical diagnosis applied to breast cytology," in Proc. *National Academy of Science*, U.S.A., 2000, pp. 1917-1922.

[5] C. A. Pena-Reyes and M. Sipper, "Designing breast cancer Diagnotic system via a hybrid fuzzy-genetic methodology," in Proc. *Fuzzy Systems*, 1999, pp. 135-139.

[6] T. Ivancevic, L. Jain and M. Bottema, "A new two-feature FAM matrix classifier for breast cancer diagnosis." in Proc. *Knowledge-Based Intelligent Information Engineering Systems*, 1999, pp. 305-308.

[7] G. Yen and P. Meesad, "Pattern classification by an incremental learning fuzzy neural network," in Proc. *IJCNN*, 1999, pp. 3230-3235.

[8] J. Schurmann. *Pattern Classification*. Singapore : John Wiley & Sons, Inc

[9] S. Sodsee and P. Meesad, "Similarity measurement for multi-objective genetic algorithm clustering data: a review," in Proc. *NCCIT*, 2006, NCCIT06-061

[10] N. Jankowski, "Discrete feature weighting & selection algorithm," in Proc. *IJCNN*, 2003, pp. 636-641.

[11] T. Kohonen, *Self-Organizing Maps*, Springer-Verlag: New York, 2nd, 1995.

[12] T. Mu and A. K. Nandi, "Detection of breast cancer using v-SVM and RBF network for self organized selection of center." in Proc. *Medical Applications of Signal Processing*, 2005, pp. 47-52

Thalassaemia Classification by a Neural Network and a C4.5 Decision Tree

P. Aksornpan [1], A. Assawamakin [2], N. Chaiyaratana [1] and C. Limwongse [2]
[1] Research and Development Centre for Intelligent Systems, Department of Electrical Engineering, King Mongkut's Institute of Technology North Bangkok, Bangkok 10800, Thailand
[2] Division of Molecular Genetics, Department of Research and Development, Faculty of Medicine Siriraj Hospital, Mahidol University, Bangkok 10700, Thailand

***Abstract*-This paper presents the use of a neural network and a decision tree in thalassaemia classification. The aim is to differentiate between thalassaemic patients, persons with thalassaemia trait and normal subjects by inspecting types of haemoglobin. C4.5 is the chosen architecture for decision tree implementation. For comparison, multilayer perceptrons are explored in classification via a neural network. The classification results indicate that the performance of the C4.5 decision tree is significantly higher than that of the multilayer perceptrons. Detailed analysis of the classification errors of the C4.5 decision tree is also included. The analysis reveals that the false-positive and false-negative errors are the main cause of classification errors. These results suggest that a combination of a C4.5 decision tree with haemoglobin typing may give rise to a guideline for further investigation of thalassaemia classification.**

I. Introduction

Thalassaemia is a genetic disease that causes a reduction in the life span of a red blood cell [1]. The disease is a result of an abnormality in the genes that regulate the formation of haemoglobin (Hb)–a core component of the red blood cell. In order to make the diagnosis, the blood characteristics must be analysed. A complete blood count (CBC) and haemoglobin typing is the primary screening test for a laboratory diagnosis of thalassaemia. However, there is still a limitation in the analysis of data due to a large number of possible candidate characteristics. In addition, there are various types of thalassaemia and thalassaemia trait. (Persons with thalassaemia trait do not have the disease but inherit genes that cause the disease.) As a result, a manual diagnostic process can only be carried out by specialists [2, 3].

Early attempts to formulate an automated diagnostic tool employed image analysis [4], statistical [5] and clustering techniques [6]. Later, the implementation protocol has shifted to the expert systems, in which both rule-based [7, 8, 9] and hybrid neural network/rule-based systems [10] have been successfully tested in clinical trials. Nonetheless, these tools broadly differentiate between a wide range of blood-related diseases including various types of anaemia. In order to narrow the diagnostic target down to the differentiation between thalassaemic patients, persons with thalassaemia trait and normal subjects, an alternative automated diagnostic tool is required. Recently, a successful implementation of a neural network [11, 12], a *k*-nearest neighbour technique [12] and a support vector machine [12] as a thalassaemic diagnostic tool has been reported. However, the tool can only differentiate between two types of thalassaemic gene carriers and normal subjects. Further works are required in order to expand the tool capability to cover all major types of thalassaemic patients and persons with thalassaemia trait that are commonly found in Thailand where the total number of types is much larger [13].

The thalassaemia classification can generally be formulated into a pattern recognition problem. The input patterns or samples in this case would be blood-related data covering the blood characteristics. These characteristics can be directly obtained from haemoglobin typing. On the other hand, the target classification output would be either the disease/trait type or a normal-subject flag. The use of a neural network and a C4.5 decision tree as the classifiers is proposed. This will provide direct evidence on the suitability of both parametric and non-parametric approaches to the task.

This paper is organised as follows. The thalassaemia data and classification techniques are explained in section 2. Next, the classification results are discussed in section 3. Finally, the conclusions are drawn in section 4.

II. Materials and Methods

In this section, the thalassaemia data set and the classification techniques will be explained; the details about the data set will be covered in section 2.A while a brief explanation about the classifiers will be given in section 2.B.

A. Data Set

Thalassaemia is a form of chronic anaemia that reduces the life span of red blood cells [1]. The disease stems from an abnormality in the genes that regulate the formation of a protein called globin, which is a major component of haemoglobin. Each red blood cell contains approximately 300 million molecules of haemoglobin. Hence, a change in the structure of globin affects the structure and functionality of a red blood cell. A globin molecule contains two parts: α-globin and β-globin. The α-globin contains 141 amino acids, which are regulated by genes on chromosome 16. The β-globin consists of 146 amino acids, which are governed by genes on chromosome 11. Since the regulatory genes reside on two autosomes, the transmission mode of abnormal genes is autosomal recessive. Hence, a person must have two copies of a recessive gene on the same chromosome in order to have the disease. The types of thalassaemic patient and person with

TABLE I
THALASSAEMIA DATA THAT ARE USED TO TRAIN AND TEST THE CLASSIFIERS

Class	Description	Category	# Samples
1	α-Thalassaemia 1 trait + Hb E trait	Trait	15
2	Hb Constant Spring trait	Trait	9
3	Hb H disease	Disease	12
4	Hb H disease with Constant Spring	Disease	12
5	EA Bart's disease	Disease	9
6	HPFH disease	Disease	10
7	Hb E trait	Trait	15
8	Homozygous Hb E	Trait	15
9	β-Thalassaemia trait	Trait	15
10	Homozygous β-Thalassaemia	Disease	5
11	β^0-Thalassaemia/Hb E	Disease	6
12	β^+-Thalassaemia/Hb E	Disease	6
13	Abnormal Hb	N/A	6
14	Normal subject	Normal	15
	Total		150

TABLE II
HAEMOGLOBIN ATTRIBUTES FOR THE THALASSAEMIA CLASSIFICATION

Attribute	Type of Haemoglobin	Retention Time (sec)
1	Bart's	0-68
2	A1C/F/Unknown	69-159
3	Unknown	160-199
4	A0	200-220
5	Unknown	221-249
6	E	250-276
7	A2	277-289
8	D/S/CS/C/Unknown	290-300

thalassaemia trait summarised in Table 1 are commonly found in Thailand and will be covered in this investigation. From Table 1, it can be clearly seen that there are many types of abnormality. The most reliable method for the diagnosis is to determine the genetic makeup of the person in question. However, this process is costly and time-consuming. An alternative approach is to make a diagnosis based on the characteristics of human blood.

In this study, the data set for thalassaemia diagnosis consists of blood characteristics obtained through haemoglobin typing. Each type of haemoglobin, expressed in terms of percentage of total haemoglobin in the sample, is identified based on its chromatographic retention time. The resulting characteristics or attributes that can be extracted from the blood samples are summarised in Table 2.

B. Classifiers

Two candidate classifiers are considered in this investigation: a neural network and a C4.5 decision tree. A neural network is an interconnected group of artificial neurons that uses a mathematical or computational model for information processing based on a connectionist approach. The neural network that is selected for this implementation is a multilayer perceptron [14]. In the implementation, the number of network inputs is equal to the number of input attributes while the number of network outputs is equal to the number of output classes. Specifically, the aimed network output for each target class takes the form of a unit vector where the vector aligns with a principal axis of the output vector space. The network can have one or two hidden layers in which the number of nodes in each hidden layer can vary. As a result, the observation displays the effect of network non-linearity on the classification performance. The multilayer perceptron will be trained by a back-propagation algorithm.

C4.5 decision tree is one of the most widely used and practiced tools for inductive inference [15]. A decision tree is generally constructed in a top-down manner. The tree construction begins at the root node where each input feature or attribute is evaluated using a statistical test to determine how well it alone classifies the training samples. The best attribute is selected and used as the test at the root node of the tree. A descendant of the root node is then created for either each possible value of this attribute if the attribute value is discrete or each possible discretised range of this attribute if the attribute value is continuous. Next, the training samples are sorted to the appropriate descendant node. The entire process is subsequently repeated using the training samples associated with each descendant node to select the best attribute to test at that point in the tree. This forms a greedy search for an acceptable decision tree, in which the algorithm never backtracks to reconsider earlier choices. In this paper, the continuous attribute value is partitioned into a discrete set of intervals using an information-theoretic technique proposed by Fayyad and Irani [16].

III. RESULTS AND DISCUSSIONS

The results from the experiment using the thalassaemia classifiers will be presented in section 3.A. Furthermore, a detailed classification accuracy analysis emphasising on the classification errors will be given in section 3.B.

A. Classification Experiment and Results

The data presented in section 2.A are used to train and test a neural network and a C4.5 decision tree. The performance comparison will be carried out by a *k*-fold cross-validation technique [17]. In this investigation, *k* is set to 10, which indicates that for each fold the numbers of training and testing samples are 135 and 15, respectively. The classification performance of the multilayer perceptron (MLP) and C4.5 decision tree is summarised in Table 3. From Table 3, the results reveal that the most suitable classifier for the current scenario is the C4.5 decision tree as the classification accuracy is higher than both multilayer perceptrons with one and two hidden layers. In addition, the classification performances of the best multilayer perceptrons with one and two hidden layers are approximately the same. These results can be interpreted as follows.

Firstly, consider the results received from multilayer perceptrons with different numbers of hidden layers and hidden nodes. By increasing the number of hidden nodes, the level of non-linearity within the network will increase, implying that the network would be capable of capturing a more complex input-output relationship. However, this also means that there

is an increase in the number of connection weights, which require an adjustment via the back-propagation algorithm. For this study, it is observable that poor accuracy can be observed when the number of hidden nodes is either too low or too high. Further, both multilayer perceptrons with one and two hidden layers appear to have an adequate memory capacity to capture the required input-output characteristics. As a result, the use of two hidden layers appears unnecessary since no further improvement is observed with increasing number of hidden layers.

TABLE III
CLASSIFICATION ACCURACY OF THE MULTILAYER PERCEPTRON AND C4.5 DECISION TREE

Classifier	Accuracy	Classifier	Accuracy
MLP (in-hid-out)		MLP (in-hid-out)	
8-5-14	67.33%	8-5-5-14	62.00%
8-10-14	77.33%	8-10-10-14	70.00%
8-15-14	76.67%	8-15-15-14	80.00%
8-20-14	75.33%	8-20-20-14	80.67%
8-25-14	80.67%	8-25-25-14	80.00%
8-30-14	78.67%	8-30-30-14	78.67%
8-35-14	76.67%	8-35-35-14	80.00%
8-40-14	80.67%	8-40-40-14	82.00%
C4.5	95.33%		

TABLE IV
DISCRETISED INTERVAL OF INPUT ATTRIBUTE

Attribute	Type of Haemoglobin	Interval	Haemoglobin (%)
1	Bart's	1	Hb ≤ 1.8
		2	1.8 < Hb ≤ 4.6
		3	4.6 < Hb ≤ 7.9
		4	7.9 < Hb ≤ 9.9
		5	9.9 < Hb ≤ 22.5
		6	Hb > 22.5
2	A1C/F/Unknown	1	Hb ≤ 0.6
		2	0.6 < Hb ≤ 3.7
		3	3.7 < Hb ≤ 4.6
		4	4.6 < Hb ≤ 22.8
		5	22.8 < Hb ≤ 24.2
		6	24.2 < Hb ≤ 52.3
		7	Hb > 52.3
3	Unknown	1	Hb ≤ 3.1
		2	Hb > 3.1
4	A0	1	Hb ≤ 6.5
		2	6.5 < Hb ≤ 49.9
		3	49.9 < Hb ≤ 72.8
		4	Hb > 72.8
5	Unknown	1	Hb ≤ 0.9
		2	Hb > 0.9
6	E	1	Hb ≤ 13.1
		2	13.1 < Hb ≤ 18.8
		3	18.8 < Hb ≤ 24.6
		4	24.6 < Hb ≤ 78.7
		5	Hb > 78.7
7	A2	1	Hb ≤ 0.7
		2	0.7 < Hb ≤ 2.8
		3	2.8 < Hb ≤ 3.6
		4	3.6 < Hb ≤ 4.5
		5	Hb > 4.5
8	D/S/CS/C/Unknown	1	Hb = 0.0
		2	0.0 < Hb ≤ 2.2
		3	Hb > 2.2

```
A6 = I1
|   A2 = I1
|   |   A1 = I1: C3
|   |   A1 = I2: C3
|   |   A1 = I3: C4
|   |   A1 = I4: C4
|   |   A1 = I5: C3
|   |   A1 = I6: C4
|   A2 = I2
|   |   A4 = I1: C13
|   |   A4 = I2: C13
|   |   A4 = I3: C13
|   |   A4 = I4: C2
|   A2 = I3: C9
|   A2 = I4
|   |   A8 = I1
|   |   |   A7 = I1: C14
|   |   |   A7 = I2: C14
|   |   |   A7 = I3: C14
|   |   |   A7 = I4: C9
|   |   |   A7 = I5: C9
|   |   A8 = I2: C2
|   |   A8 = I3: C13
|   A2 = I5: C14
|   A2 = I6: C6
|   A2 = I7: C10
A6 = I2: C5
A6 = I3: C1
A6 = I4
|   A4 = I1: C11
|   A4 = I2: C12
|   A4 = I3: C7
|   A4 = I4: C7
A6 = I5: C8
```

Figure 1. C4.5 decision tree. A_i, I_i and C_i denote the ith attribute, the ith interval and the ith output class, respectively.

The result from the C4.5 decision tree is now analysed. Table 4 illustrates the discrete interval of each input attribute, which is obtained after the application of the attribute discretisation technique [16] to the data. From Table 4, the number of discrete intervals varies from two to seven. The C4.5 decision tree that utilises these discrete attributes is given in Figure 1. It is noticeable that the tree does not cover all attributes; the missing attributes are attributes 3 and 5. Recall from Table 2 that these two attributes are unknown types of haemoglobin. The absence of these attributes from the decision tree signifies that these attributes have no effects on the diagnosis capability of the decision tree. It may be possible to increase the classification performance of the multilayer perceptron after removing these attributes from the network input. In addition, the use of CBC data as additional input may also improve the performances of both classifiers [18]. These speculations will be investigated in the future work.

B. Classification Accuracy Analysis

In the previous sub-section, the classification performance of the multilayer perceptron and C4.5 decision tree has been obtained from the cross-validation analysis. The classification accuracy of the C4.5 decision tree is 95.33%. On the other hand, the accuracy of the best multilayer perceptron with one hidden layer is 80.67%. The classification errors from both classifiers can be divided into four main categories: a rejection, a misclassification within the same super-group, a false-positive error and a false-negative error. These classification errors can be explained as follows.

The classification rejection occurs when the classifier output is ambiguous. This can be either no output response or more than one output class being reported from the classifier. In contrast, the misclassification within the same super-group occurs when either a person with thalassaemia trait is identified as being a person with another type of thalassaemia trait, or a thalassaemic patient is misdiagnosed as being another type of patient. In this study, the persons with thalassaemia trait, thalassaemic patients and normal subjects are clustered into three super-groups based upon the severity of the exhibited blood characteristics. The details of all three super-groups are given in Table 5. From Table 5, the super-groups are made up from the minor trait/normal super-group, the major trait super-group and the disease super-group.

The last two types of classification error are the false-positive and false-negative errors. In this study, the false-positive error refers to the situation when a sample is misidentified as belonging to a super-group with a higher severity of thalassaemic characteristics. On the other hand, the false-negative error refers to the case when a sample is misclassified as being a member of a super-group with a lower severity of thalassaemic characteristics.

The summary of classification errors from the multilayer perceptron with 25 hidden nodes reveals that the majority of errors come from sample rejections and misclassification within the same super-group. In contrast, the majority of decision tree's classification errors come from false-positive and false-negative errors. However, the combined false-positive and false-negative error is less than 3%. This confirms the suitability of the C4.5 decision tree for this task.

IV. Conclusions

In this paper, a thalassaemia classification problem is investigated. The objective is to automatically identify whether the human subject is a person with thalassaemia trait, a thalassaemic patient, or a normal person using blood data from haemoglobin typing. The collected blood samples are divided into 14 groups where the significant blood characteristics are based on attributes of haemoglobin's types. The classification results indicate that the accuracy of the C4.5 decision tree is significantly higher than that of the multilayer perceptron. This helps emphasise the reliability of a C4.5 decision tree as an automated thalassaemic classification tool.

TABLE V
Clustering of Persons with Thalassaemia Trait, Thalassaemic Patients and Normal Subjects into Three Super-group

Super-group	Class
Minor trait/normal	2, 7, 14
Major	1, 8, 9, 13
Disease	3, 4, 5, 6, 10, 11, 12

Acknowledgement

This work was supported by the Thailand Research Fund and the Commission on Higher Education.

References

[1] D.J. Weatherall and J.B. Clegg, *The Thalassemia Syndromes*, 4th ed. Malden, MA: Blackwell Science, 2001.

[2] C.V. Jimenez, J. Minchinela, and J. Ros, "New indices from the H*2 analyser improve differentiation between heterozygous beta or delta beta thalassaemia and iron-deficency anaemia," *Clinical and Laboratory Haematology*, vol. 17, pp. 151-155, 1995.

[3] A. Demir, N. Yarali, T. Fisgin, F. Duru, and A. Kara, "Most reliable indices in differentiation between thalassemia trait and iron deficiency anemia," *Pediatrics International*, vol. 44, pp. 612-616, 2002.

[4] P.R. Lund and R.D. Barnes, "Automated classification of anaemia using image analysis," *The Lancet*, vol. 300, pp. 463-464, 1972.

[5] R.L. Engle, B.J. Flehinger, S. Allen, R. Friedman, M. Lipkin, B.J. Davis, and L.L. Leveridge, "HEME: A computer aid to diagnosis of hematologic disease," *Bulletin of the New York Academy of Medicine*, vol. 52, pp. 584-600, 1976.

[6] G. Barosi, M. Cazzola, C. Berzuini, S. Quaglini, and M. Stefanelli, "Classification of anemia on the basis of ferrokinetic parameters," *British Journal of Haematology*, vol. 61, pp. 357-370, 1985.

[7] S. Quaglini, M. Stefanelli, G. Barosi, and A. Berzuini, "ANEMIA: An expert consultation system," *Computers and Biomedical Research*, vol. 19, pp. 13-27, 1986.

[8] S. Quaglini, M. Stefanelli, G. Barosi, and A. Berzuini, "A performance evaluation of the expert system ANEMIA," *Computers and Biomedical Research*, vol. 21, pp. 307-323, 1988.

[9] G. Lanzola, M. Stefanelli, G. Barosi, and L. Magnani, "NEOANEMIA: A knowledge-based system emulating diagnostic reasoning," *Computers and Biomedical Research*, vol. 23, pp. 560-582, 1990.

[10] N.I. Birndorf, J.O. Pentecost, J.R. Coakley, and K.A. Spackman, "An expert system to diagnose anemia and report results directly on hematology forms," *Computers and Biomedical Research*, vol. 29, pp. 16-26, 1996.

[11] S.R. Amendolia, A. Brunetti, P. Carta, G. Cossu, M.L. Ganadu, B. Golosio, G.M. Mura, and M.G. Pirastru, "A real-time classification system of thalassemic pathologies based on artificial neural networks," *Medical Decision Making*, vol. 22, pp. 18-26, 2002.

[12] S.R. Amendolia, G. Cossu, M.L. Ganadu, B. Golosio, G.L. Masala, and G.M. Mura, "A comparative study of *k*-nearest neighbour, support vector machine and multi-layer perceptron for thalassemia screening," *Chemometrics and Intelligent Laboratory Systems*, vol. 69, pp. 13-20, 2003.

[13] S. Fucharoen and P. Winichagoon, "Hemoglobinopathies in Southeast Asia: Molecular biology and clinical medicine," *Hemoglobin*, vol. 21, pp. 299-319, 1997.

[14] D.E. Rumelhart and J.L. McClelland, Eds., *Parallel Distributed Processing: Explorations in the Microstructure of Cognition*, vol. 1. Cambridge, MA: MIT Press, 1986.

[15] J.R. Quinlan, *C4.5: Programs for Machine Learning*. San Mateo, CA: Morgan Kaufmann, 1993.

[16] U.M. Fayyad and K.B. Irani, "Multi-interval discretization of continuous-valued attributes for classification learning," in *Proceedings of the 13th International Joint Conference on Artificial Intelligence*, R. Bajcsy, Ed. San Mateo, CA: Morgan Kaufmann, 1993, pp. 1022-1027.

[17] T.M. Mitchell, *Machine Learning*. Singapore: McGraw-Hill, 1997.

[18] W. Wongseree, N. Chaiyaratana, K. Vichittumaros, P. Winichagoon, and S. Fucharoen, "Thalassaemia classification by neural networks and genetic programming," *Information Sciences*, vol. 177, pp. 771-786, 2007.

A Numerical Model of Magnetic Fluid Flow in Blood Vessel with Nail-like Permanent Magnet using Finite Element Method

M. Lohakan [†,††], C. Seetao [††], S. Boonsang [†] and C. Pintavirooj [†]

[†] Research Center for Communication and Information Technology (ReCCIT) and
Department of Electronics, Faculty of Engineering
King Mongkut's Institute of Technology Ladkrabang, Bangkok 10520 Thailand

[††] Department of Teacher Training in Electrical Engineering
Faculty of Technical Education
King Mongkut's Institute of Technology North Bangkok, Bangkok 10800 Thailand

***Abstract*- This paper purposes a numerical model of magnetic fluid flow using nail-like magnetic device. The magnetic liquids play an important role as drug carriers in the human body. The nail-like magnetic is also utilized to focus magnetic liquids. The Finite Element Method, FEM, is developed to solve two important sets of partial differential equation. Electromagnetic field is governed by Maxwell equation and velocity field is obtained by Navier-Stoke equation. The result shows the potential to target drug in the tumor cell locally.**

I. INTRODUCTION

In the recent years, the area of Finite Element Method (FEM) has been widely interest in biomedical engineering. Some researchers use FEM as a tool to design polymer-coated targeted drug delivery systems [1]. Based on Laplace-Beltrami operator, the geometry model of human brain is analyzed [2]. In drug delivery system, an integrated system use superparamagnetic, biocompatible nano drug carriers for targeted but non-invasive delivery [3]. Additionally, drug deliver is based on nanotechnology using magnetic guidance of drug loaded magnetic carriers to the targeted site and thereafter released by external ultrasound energy [4]. There are many alternative methods for the treatment of cancer or tumor in human body such as tumor ablation [5] and chemotherapy [6]. To avoid side effect on healthy human cells, which are made by chemotherapy, physician always face with an upper limit in the treatment dose. This limit obstructs the chance of successful treatment of the tumor cells. The objective of modern cancer researches is to focus chemotherapy drugs locally to tumor tissue and to stop the global exposure to the organism. This computational model investigates an external magnetic field that interacts with blood flow with ferrofluids. The magnetic field is described by Maxwell's equation and the dynamic flow is illustrated by Navier-Stoke equations.

In this paper, the velocity field of magnetic fluid is purposed. Based on Partial Differential Equation (PDE), the development of this algorithm comprises with equation of conservation of mass in fluid dynamic, Navier-Stokes equations, and Maxwell's equations. These nonlinear equations are analyzed by FEM. The simulated system is numerically computed to investigate the effect of nail–like magnetic potential with magnetic fluid flow in time dependent model.

II. NAVIER-STOKES EQUATIONS

A dynamic equation describing fluid motion [7] is a momentum equation that can be solved to incompressible Newtonian flow. The most famous equations in fluid dynamics are Navier-Stokes equations. A set of equations composes of three velocity equations in the rectangular coordinates (1-3) and the continuity in (4).

$$\rho\left[\frac{\partial u}{\partial t}+u\frac{\partial u}{\partial x}+v\frac{\partial u}{\partial y}+w\frac{\partial u}{\partial z}\right]=\rho g_x-\frac{\partial p}{\partial x}+\eta\left[\frac{\partial^2 u}{\partial x^2}+\frac{\partial^2 u}{\partial y^2}+\frac{\partial^2 u}{\partial z^2}\right] \quad (1)$$

$$\rho\left[\frac{\partial v}{\partial t}+u\frac{\partial v}{\partial x}+v\frac{\partial v}{\partial y}+w\frac{\partial v}{\partial z}\right]=\rho g_y-\frac{\partial p}{\partial y}+\eta\left[\frac{\partial^2 v}{\partial x^2}+\frac{\partial^2 v}{\partial y^2}+\frac{\partial^2 v}{\partial z^2}\right] \quad (2)$$

$$\rho\left[\frac{\partial w}{\partial t}+u\frac{\partial w}{\partial x}+v\frac{\partial w}{\partial y}+w\frac{\partial w}{\partial z}\right]=\rho g_z-\frac{\partial p}{\partial z}+\eta\left[\frac{\partial^2 w}{\partial x^2}+\frac{\partial^2 w}{\partial y^2}+\frac{\partial^2 w}{\partial z^2}\right] \quad (3)$$

$$\frac{\partial \rho u}{\partial x}+\frac{\partial \rho v}{\partial y}+\frac{\partial \rho w}{\partial z}=\nabla\cdot\rho\,\mathbf{u}=0 \quad (4)$$

The equations are nonlinear partial differential equations where *u, v, w,* are velocity in *x,* y, *z* direction respectively. ρ is density of material. g_x, g_y, g_z are gravitational force field in *x,* y, *z* as well. *t* is time. To observe fluid motion in blood vessel model, Navier-Stokes equation can be resolved and reduced to time dependent as shown in (5).

$$\rho\frac{\partial \mathbf{u}}{\partial t}=\mathbf{F}+\eta\nabla^2\mathbf{u}-\rho(\mathbf{u}\cdot\nabla)\mathbf{u}-\nabla p \quad (5)$$

Equation (5) is used to compute a fluid flow direction in the model assumed that the fluid is an incompressible flow. The significant parameter, $\mathbf{F}=(F_x,F_y)$, of this section is a volume force field. The relation between **F** and Maxwell's equation is described in (9) and (10).

III. MAXWELL'S EQUATIONS

The magnetic vector potential generated by magnet is calculated. The magnetic volume force created by magnetic field is affected the flow field in the blood vessel as shown in (6). A magnetic potential vector is **A** and the magnetization vector is **M**. Equation (7) and (8) [9] describe magnetization in x and y direction that is used in (9) and (10)[10]. To simulate blood flow in model, the x direction, *v*, follows a sinusoidal expression in time as illustrated in (11).

$$\nabla \times (\frac{1}{\mu_0 \mu_r} \nabla \times \mathbf{A}\text{-}\mathbf{M}) = 0 \tag{6}$$

$$M_x = \alpha \tan^{-1}(\frac{\beta}{\mu_r \mu_0} \frac{\partial A_Z}{\partial y}) \tag{7}$$

$$M_y = \alpha \tan^{-1}(\frac{\beta}{\mu_r \mu_0} \frac{\partial A_Z}{\partial x}) \tag{8}$$

$$F_x = \frac{M_x}{\mu_r} \frac{\partial^2 A_Z}{\partial x \partial y} \tag{9}$$

$$F_y = -\frac{M_y}{\mu_r} \frac{\partial^2 A_Z}{\partial y \partial x} \tag{10}$$

$$v = \sin(\omega t) + \sqrt{\sin^2(\omega t)} \tag{11}$$

The magnetic field, magnetic vector potential, generated by magnet is calculated. The computed magnetic field generates a magnetic volume force that affects the flow field in the blood vessel.

IV. PHYSICAL CONSTANTS

The important physical constants are shown in Table I for Navier-Stokes equation and Table II for Maxwell's equations.

TABLE I
Fluid Physical Constants [7], [8]

Fluid Physical Constants	Value
Density (ρ)	1,000 kg/m^3
Dynamic Viscosity (η)	5.0×10^{-3} Ns/m^2

TABLE II
Magnetic Constants

Magnetic Constants	Value
Magnetic fluid parameter (α)	1×10^{-4}
Magnetic fluid parameter (β)	3×10^{-5}
Magnet magnetization	0.5e-5 A/m
Magnet relative permeability	5e3
Tissue relative permeability	0.9998

V. FINITE ELEMENT METHOD

A. Geometry Model and Assumption

To observe magnetic potential and fluid velocity field, the model of blood vessel is created in 3D. The model consists of blood vessel, tissue and magnetic device as shown in Figure 1. The inflow of fluid comes from left side and outflow is to the right side. The magnetic device is placed on the tissue to distribute magnetic potential interacting with ferrofluids carrier in blood vessel. To reduce calculating time, 2D model is created in Figure 2 and magnetic device is assumed to be permanent magnet. The 2D geometry model is approximated by many triangles called a mesh model as shown in Figure 3. A model represents the fluid velocity field computed by mesh model. Because the Navier-Stokes equations are computationally arduous, it is considerable to utilize an appropriate mesh. If the mesh is too rough, the solution might not coverage at all or errors might be large. Contrastly, if the mesh is too fine, the solution time for the nonlinear system of equations might be unnecessarily long.

B. Boundary Condition, Initial Condition

Boundary conditions are most described by considering the magnetostatic and fluid dynamics shown in Table III-IV. For time dependent analysis, a set of initial conditions is necessary for the dependent variable. The calculation process comprise with two steps. Firstly, magnetic potential is computed. Secondly, the result of magnetic potential is used as initial condition to calculate fluid velocity field. The wall applies no-slip condition. The out flow is set to pressure condition, $p = 0$.

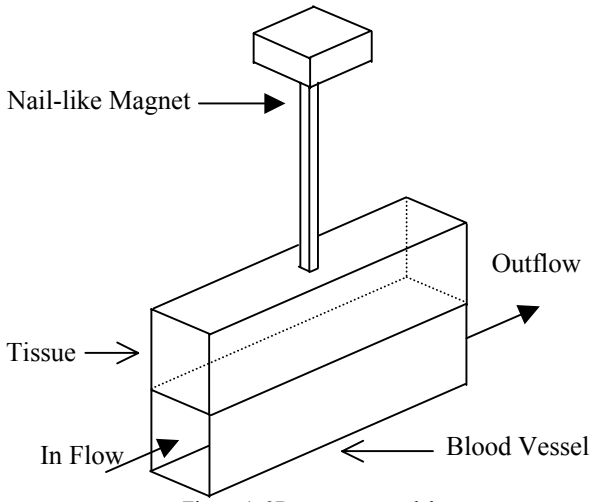

Figure 1. 3D geometry model

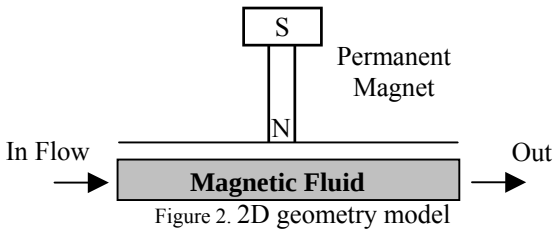

Figure 2. 2D geometry model

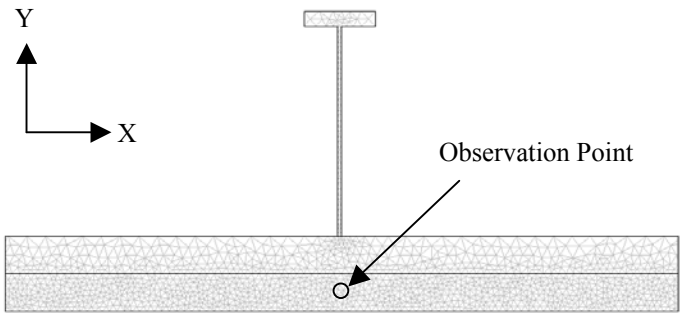

Figure 3. Mesh model

The mesh model is computed with Pentium® IV 3.2 GHz, DDR RAM 1.5 GB. The calculation time of time-dependent is around 1.5 hours per model.

TABLE III
Boundary condition of magnetostatic

Magnetostatic Equations	Boundary Condition
Magnetic Insulation	$A_Z = 0$
Constitutive Relation	$B_0=\mu_0\mu_r H+B_r$
Relative Permeability	Isotropic

TABLE IV
Boundary condition of fluid dynamics

Fluid Dynamics	Boundary Condition
Inflow	u = Heart Beat Equation
Outflow	$P_0=0$
Wall	u=0

VI. Experimental Results

Based on the FEM given in previous section, the observation point is created as shown in Figure 3. That point places on center of blood vessel model. The fluid velocity at observation point is shown in Figure 6 and 7.

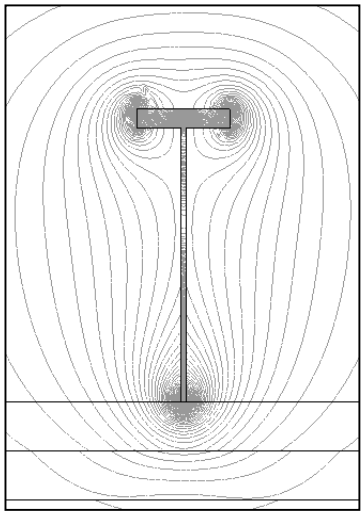

Figure 4 Magnetic flux density

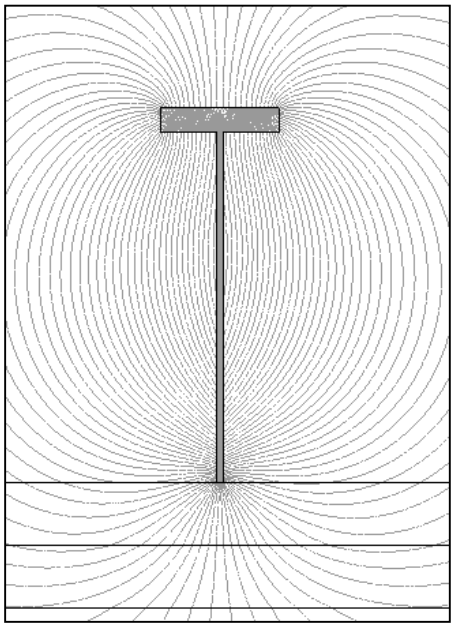

Figure 5 Magnetic potential

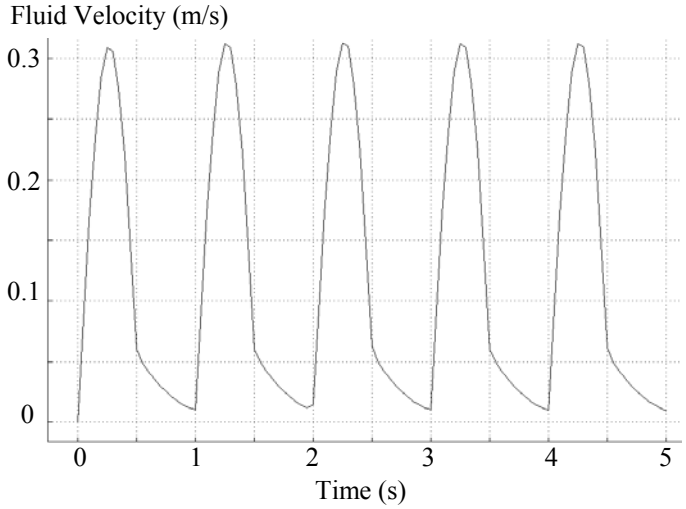

Figure 6 Fluid velocity without magnetic flux density

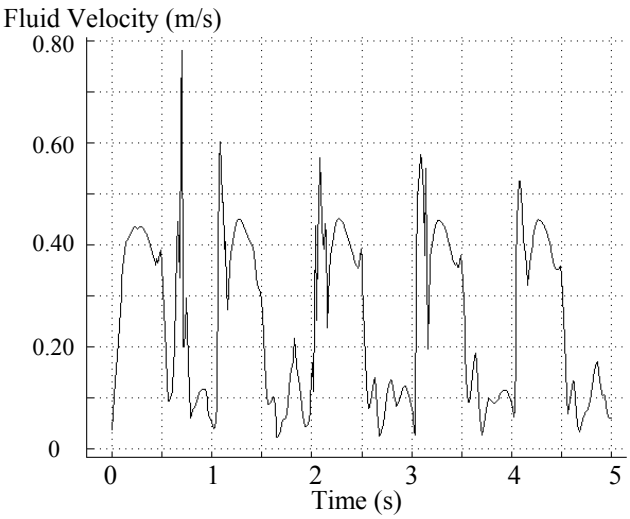

Figure 7 Fluid velocity with magnetic flux density

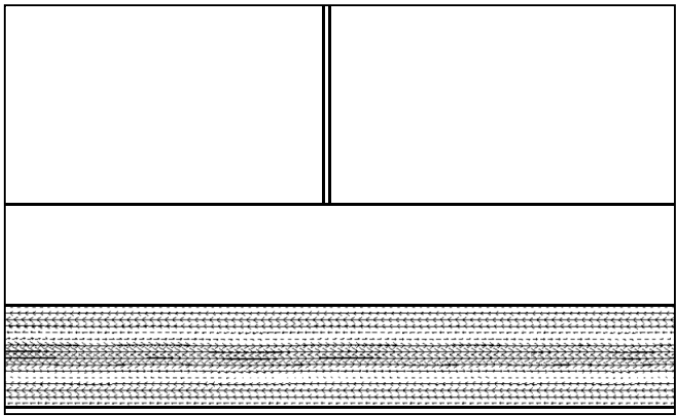

Figure 8 Fluid velocity field without magnetic flux density

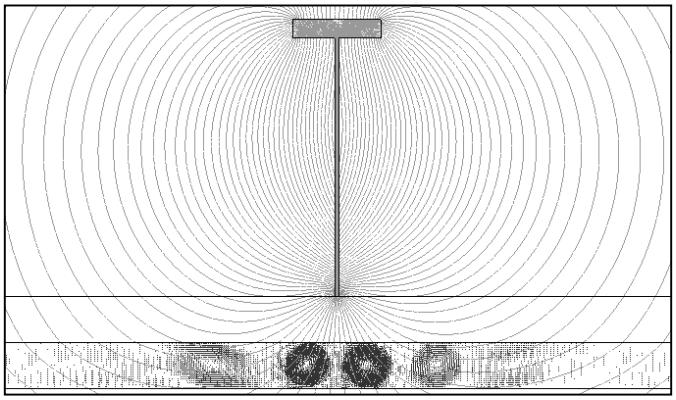

Figure 9 Fluid velocity field with magnetic potential

The experimentation is divided in two important parts. Firstly, only magnetic potential is computed with time independent, stationary state. The magnetic flux density is shown in Figure 4 and magnetic potential is shown in Figure 5. Secondly, the results of first step are applied to calculate velocity field by Navier-Stokes equations in time dependent. In Figure 6, only fluid field velocity is computed without external magnetic field. Because inflow boundary use heart beat equation, fluid velocity field is nearly sinusoidal wave at observation point. The peak velocity of fluid velocity is around 0.31 m/s and not turbulent flow as shown in Figure 8. Then, the magnetic potential field is applied to monitor fluid velocity field. The results show that peak velocity field increases from 0.31 to 0.80 m/s and decrease to 0.6 m/s at time=2 sec. The fluid velocity field after applying magnetic potential field is eddy flow. The area of eddy flow is focused only in the area that magnet is place as shown in Figure 9. The nail-like model improves resolution of focal area compared with two magnets model [11].

VII. CONCLUSION

In this model, two famous types of PDE equation are coupled together to approximate ferro-hydro-dynamic behavior. A computational algorithm of FEM is applied to compute fluid velocity field with interacted magnetic field. To reduce computational time, 2D model of blood vessel is created. The heart beat equation is created at inlet boundary. Pressure condition boundary is also used at the outlet. To improve focal resolution, the nail-like magnet is designed. The experimental results show the difference of fluid field velocity and fluid flow pattern when apply magnetic potential field. The fluid velocity field is eddied flow from magnetic potential field. This method shows the potential to target chemotherapy drug in the human body locally.

ACKNOWLEDGEMENT

This research was sponsored by TRF contract no. MRG4980072 and NSTDA contract no. F-31-206-22-02.

REFERENCES

[1] Nahor Haddish-Berhane, Chell Nyquist, Kamyar Haghighi, Carlos Corvalan, Ali Keshavarzian, Osvaldo Campanella, Jenna Rickus, Ashkan Farhadi (2005) "A multi-scale stochastic drug release model for polymer-coated targeted drug delivery systems," *ELSEVIER, Journal of Controlled Release 110*, pp. 314 – 322, 2006.

[2] Moo K. Chung, Jonathan Taylor, "Diffusion Smoothing on Brain Surface via Finite Element Method," *IEEE International Symposium on Biomedical Imaging: Macro to Nano*, Vol. 1, pp. 432 – 435, April 2004.

[3] Haitao Chen, Michael D. Kaminski, Armin D. Ebners, James A. Ritter,Axel J. Rosengart "Magnetizable Intravascular Stents for Sequestration of Systemically Circulating Magnetic Nano- and Microspheres," *Proceedings of the 3rd Annual International IEEE EMBS Special Topic Conference on Microtechnologies in Medicine and BiologyKahuku*, Oahu, May 2005.

[4] Y. Xie, M. D. Kaminski, C. J. Mertz, M. R. Finck, S. G. Guy, H. Chen, A. J. Rosengart, "Protein Encapsulated Magnetic Carriers for Micro/Nanoscale Drug Delivery Systems," *Proceedings of the 3rd Annual International IEEE EMBS Special Topic Conference on Microtechnologies in Medicine and Biology Kahuku*, Hawaii, 12 – 15, May 2005.

[5] S. Tungjitkusolmun, S. T. Staelin, D. Haemmerich, J. Tsai, H. Cao, J. H. Webster, F. T. Lee, Jr., D. M. Mahvi, V. R. Vorperian, "Three-Dimensional Finite-Element Analyses for Radio-Frequency Hepatic Tumor Ablation," *IEEE Transactions on Biomedical Engineering*, Vol. 49, No. 1, pp. 3-9, January 2002.

[6] Siddhartha P. Chakrabarty, Floyd B. Hanson, "Optimal control of drug delivery to brain tumors for a test of PDE driven models using the Galerkin finite element method," *Proceedings of the 44th IEEE Conference on Decision and Control, and the European Control Conference 2005 Seville*, Spain, December 2005.

[7] Robert W. F., Alan T. M., Philip J. P., "Introduction to fluid mechanics," John Wiley & Sons, New York, pp. 187-215, 2004.

[8] G.W.C. Kaye, T.H. Laby., "Tables of physical and chemical constants and some mathematical functions," Longman, 1973.

[9] C. M. Odenburg, S. E. Borglin, and G. J. Moridis, "Numerical Simulation of Ferrofluid Flow for Subsurface Environmental Engineering Applications", *Transport in Porous Media*, 38:319-344, 2000.

[10] R. E. Rosensweig, Ferrohydrodynamics, Dover Publications, New York, 1997.

[11] M. Lohakan , C. Seetao , S. Boonsang and C. Pintavirooj, "Simulation of Magnetic Fluid Flow based on Maxwell's Equations and Navier-Stokes Equations", *IEEE ISCIT2006 Conference*, Thailand, October 2006.

Reversal Transform for Prokaryotic Organisms

Noppadon Khiripet and Jutarat Maneewattanapluk

National Electronics and Computer Technology Center
112 Paholyothin Rd, Klong Luang
Pathumthani, 12120 Thailand

***Abstract*- For decades, evolution studies focus on the mutations of molecular clock genes, such as 16s rRNA. This is partly due to the relatively expensive to obtain any segment of DNA sequence. However, modern sequencing techniques have been rapidly advanced and give rise not only to the ability to decipher a larger block of DNA sequences but also to the availability of numerous complete genomic sequences. This new information is changing the way how biologists look at the evolution. This paper investigated the problem of how to transform one genome into another based on a reversal distance approach. The method was tested with 200+ complete bacterial genomic sequences and was found that it efficiently captured the evolution between and within bacterial phylums.**

I. INTRODUCTION

Evolution can be considered at many different scales: sequences, genes, gene families, genomes and species. Recently, there has been a rapid progress in this area, with models and methods becoming more powerful and complex. The flood of data demands the development and use of mathematical and computational tools to handle the analysis of evolution more efficiently.

Although the traditional study of 16s rRNA [1] suggests a model for the evolution, phylogenetic analysis of other genes and gene families has revealed that evolution is probably more complex and that a more appropriate evolutionary model might exist.

The availability of many whole genome sequences provides a promising new kind of data for evolution study [2]. This gene-order data, where the location of the gene sequence can also be integrated in the analysis, give rise to a modern day of phylogeny. In particular, whole genome alignment methods have recently been developed and applied to the comparison of the human and mouse genome [3]. Other methods have been used to detect regions of conserved synteny and orthologous genes between two genomes [4]. These methods formally represent chromosome as a linear order of genes.

This paper investigated the genomes of prokaryotic organisms (bacteria), all of which are known to be linear, by a sorting by reversal approach. It is organized as follows, in Section II, the method for orthologous gene detection is briefly introduced, followed by the synteny block construction. Then, the mathematical model of genome rearrangement is discussed. The method is tested with bacterial genome data in Section III. Finally, discussion and conclusions are drawn in Section IV.

II. METHOD

A. Orthologous gene matching

Two genes are to be orthologous if they diverged after a speciation event. To computationally detect orthologous genes, a pair of genes from two different genomes is aligned together with a program called NCBI BLASTP [8]. Reciprocal best hits of the pair implied that they are orthologous.

B. Synteny Blocks

Besides the gene content that is considered as the basis of evolution distance. Evidence from the study of human and mouse genome [4] shows that, in some ways, the human genome is just the mouse genome cut into about 300 large genomic fragments, called synteny blocks, which have been pasted together in a different order. These synteny blocks have been shuffled through evolution. The different order of genes is the result of genome rearrangement and a series of these rearrangements can alter the genomic architecture of one specie into another specie.

C. Genome Rearrangement

Analyzing the rearrangement history is a challenging problem and can be thought of as a reversal sorting problem. As shown in Figure 1, a rearrangement scenario depicted that there are three steps in transforming the mouse X chromosome into the human X chromosome.

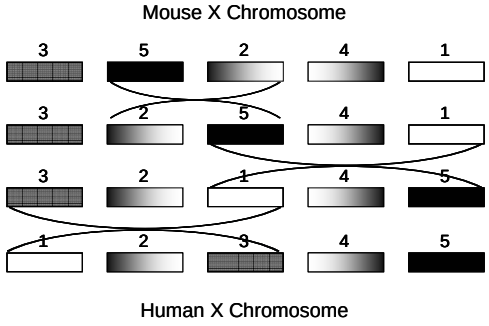

Figure 1. Transforming Mouse X chromosome to Human X chromosome (only five synteny blocks are shown).

The formal definition of a reversal can be stated as follows.

Definition 1: A reversal $\rho(i, j)$ has the effect of reversing the order synteny blocks

$$\pi_i \pi_{i+1} \pi_{i+2} \ldots \pi_{j-1} \pi_j$$

In effect, this transforms

$$\pi = \pi_1 \ldots \pi_{i-1} \pi_i \pi_{i+1} \ldots \pi_{j-1} \pi_j \pi_{j+1} \ldots \pi_n$$

into

$$\pi \cdot \rho(i, j) = \pi_1 \ldots \pi_{i-1} \pi_j \pi_{j-1} \ldots \pi_{i+1} \pi_i \pi_{j+1} \ldots \pi_n$$

For example, if $\pi = 1243756$, then $\pi \cdot \rho(3,6) = 1257346$.

We can extend the idea of reversal steps in sorting to represent the distance between a pair of genomes. However, the distance between two permutation sequences is not so straight forward. This problem can be formulated as:

Definition 2: Reversal Distance Problem

Given two permutations, find a shortest series of reversals that transforms one permutation into another

Input: Permutations π and δ.

Output: A series of reversals $\rho_1, \rho_2, \ldots \rho_t$ transforming π into δ (i.e., $\pi \cdot \rho_1 \cdot \rho_2 \cdots \rho_t = \delta$), such that t is minimum.

The distance t is called *reversal distance* or *inversion distance*. For unsigned permutation, in fact, the problem is very difficult to compute (NP-hard). For signed permutations, it can be computed in linear time [5], using the deep theoretical results of Hannenhalli and Pevzner [6]. The inversion distance between two signed permutations of *n* genes is given by

n - #cycle + #hurdles + (fortress) (1)

In our case of reversal transform from one genome into another, using the above theory, we obtained results illustrated as follows. When comparing two genomes and considering the orthologous genes, the order of these genes of one genome can be rearranged into the order of genes of another genome by repeatly reversing fragments of its DNA, e.g.

D0: 1,-7,6,-10,9,-8,2,-11,[-3,5],4
D1: 1,-7,6,-10,9,-8,2,-11,-5,[3,4]
D2: 1,-7,6,-10,9,-8,2,[-11,-5,-4,-3]
D3: 1,-7,6,[-10,9,-8,2,3,4,5],11
D4: 1,[-7,6,-5,-4,-3,-2],8,-9,10,11
D5: 1,2,3,4,5,[-6],7,8,-9,10,11
D6: 1,2,3,4,5,6,7,8,[-9],10,11
D7: 1,2,3,4,5,6,7,8,9,10,11

The minimum number of reversing steps is call optimal reversal distance. In the above example, the optimal reversal distance is 7.

III. RESULTS

Public bacterial sequences were downloaded from NCBI [8]. The complete sequences of 228 bacterial genomes are classified into 10 phylums. The results of average reversal distance for every pair of genomes within a phylum, is presented in Figure 2 and 3.

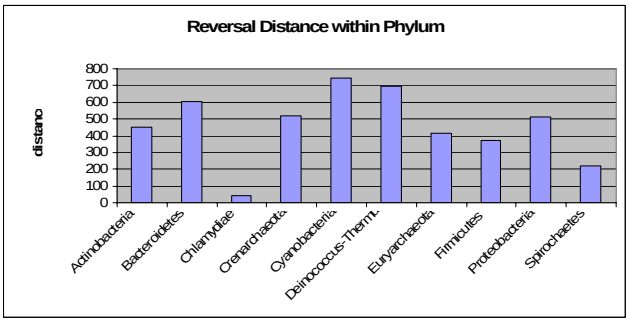

Figure 2 Average reversal distance within phylum.

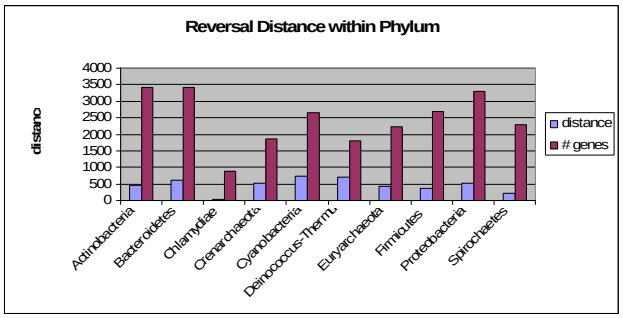

Figure 3 Average reversal distance compared to number of genes.

Applying the Neighbor-Joining [7] method to the adjacency matrix of reversal distance of the 228 baterial genomes yielded the resulting whole genome phylogenetic tree. Due to space limitation, only a subset of the tree is shown as in Figure 4.

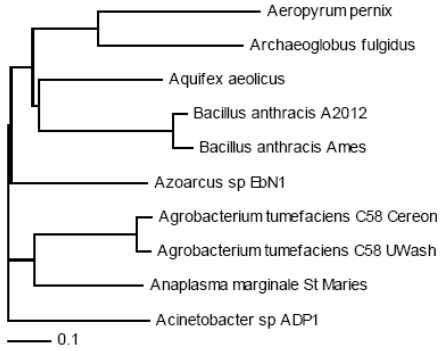

Figure 4.Whole genome phylogeny by reversal transform

IV. DISCUSSION AND FUTURE DIRECTION

The reversal transform revealed that the rates of genome rearrangement of bacterial families are various, some have it higher than the rest, i.e. the Cyanobacteria. The higher value indicates that the organisms within the family are more diverse. This implies that the family may already evolve for a very long time, longer than the family with less genome rearrangement. This finding along with the phylogeny result is consistent with the standard taxonomy [8], indicating that reversal transform is a promising approach in bacterial phylogenetic studies.

Interesting research directions related to present method is how to extend it to discover ancestral genomes, to locate the origin of replications and how to realistically present the transformation scenarios using meaningful biological constraints.

ACKNOWLEDGMENT

This work is fully supported by the National Electronics and Computer Technology Center, Thailand, Bioinformatics Project, Grant #C24803.

REFERENCES

[1] D.W. Mount, Bioinformatics: Sequence and Genome Analysis, CSHL Press, second edition, 2004

[2] M.E. Bernard, J. Tang and T. Warnow, Reconstructing phylogenies from gene-content and gene-order data, Mathematics of evolution & phylogeny, edited by O. Gascuel, Oxford University Press, 2005, p321-352

[3] A.L. Delcher, A. Phillippy, J. Carton and S.L. Salzberg, Fast algorithms for large-scale genome alignment and comparison, Nucleic Acid Research, 30(11) 2478-2483, 2002

[4] P. Pevzner and G. Tesler, Genome rearrangements in mammalian evolution: Lessons from human and mouse genomic sequences, Genome Research, 13(1), 37-45, 2003

[5] D.A. Bader, B.M.E Moret, and M. Yan, A linear-time algorithm for computing inversion distance between signed permutations with an experimental study. Journal of Computational Biology, 8(5), 483-491, 2001

[6] S. Hannenhalli, and P.A. Pevzner, P.A. Transforming cabbage into turnip: polynomial algorithm for sorting signed permutations by reversals. J. ACM 46(1), 1-27, 1999

[7] N. Saitou and M. Nei, The Neighbor-joining Method: A New Method for Reconstructing Phylogenetic Trees, Mol Biol Evol 4(4), 406-25, 1987

[8] National Center for Biotechnology Information http://www.ncbi.nlm.nih.gov/

Computing the Diameter of a Point Set on a Completely Overlapping Network

Saowaluk Rattanaudomsawat
School of Information Technology,
Mae Fah Luang University,
Chiang Rai, 57100, Thailand,
E-mail: saowalukr@mfu.ac.th

Prapaporn Techa-angkoon
The Theory of Computation Group,
Computer Science Department,
Chiang Mai University,
Chiang Mai, 50200, Thailand,
E-mail: prapapon@chiangmai.ac.th

***Abstract*- Given a finite set *P* of *n* points in *d*-dimensional Euclidean space, the diameter is defined as the maximum Euclidean distance between any two points in the set *P*. In this paper we propose an efficient algorithm, which works in any dimension, to compute the diameter of a point set on a theoretical network called a *completely overlapping network (CON)*. This network model has an applicable potential in real-life applications because it is an extension of LANs that are widely used at present. We also show that the running time of this algorithm is O(*n*) where *n* is the number of points in the input set.**

I. INTRODUCTION

Computing the diameter of a point set is one of the classical problems in high dimension computational geometry [1, 5-8]. This problem (Given a finite set *P* of *n* points in *d*-dimensional Euclidean space, the diameter of *P* is defined as the maximum Euclidean distance between any two points of *P*) is actually known as the *diameter problem* or the *farthest pair problem*. There are several interesting applications of the computation of the diameter such as image databases, visualization, clustering, and data mining [4]. Additionally, the diameter is quite useful as it provides a reliable estimate of the point-set extent, it can be used in computing a tight fitting bounding box for the point set.

Computing the diameter of a point set has a long history. Computing the diameter of *n* points in *d* dimensions requires $\Omega(n \log n)$ operations [7] while a trivial $O(n^2)$ upper bound is provided by the brute force algorithm that compares the distance between all pairs of points. In the dimensions 2 and 3, this problem can be solved optimally in $O(n \log n)$ [4] but in the higher dimensions it becomes non-trivial. Note that in such applications the number of dimensions is very high, the complexity due to the dimension must be taken into consideration in the design of efficient algorithms. Thus, this paper presents an algorithm which works in any dimensions for computing the diameter of a point set on a completely overlapping network and provides the concept of parallel computation that can solve this problem efficiently.

Parallel computation has been around for decades. Several parallel applications and architectures are available for use. However, parallel architectures such as hypercube and mesh are generally expensive and hence their use is limited to only those who can afford them. Some attempts have been made to find an alternative to these expensive parallel machines. One alternative is called a cluster of workstations and personal computers. A typical cluster of workstations is essentially a group of numerous workstations and personal computers connected through a single communication line. Each computer can send a message, bit by bit, when the communication line is free. If the communication line is currently occupied, the computer must wait before it is allowed to send its message.

One significant problem with this model of communication via a single communication line is the line can only serve one computer at any time. To lessen this problem, during the recent decade or so, a group of computer scientists in the United States has developed an experimental network called *an overlapping network* [2]. They have worked on the concept of using multiple Ethernet lines in some certain configurations. These configurations are in the general classification of overlapping connectivity networks. Overlapping connectivity networks have the characteristic that regions of connectivity are provided and the regions overlap so as to provide parallelism.

Recently, Kantabutra et al [9-10] extended the network model of Wilkinson one step further to provide complete overlapping of communication. This theoretical network model is more general than but similar to the experimental overlapping network. Henceforth, we will refer to this network as *a completely overlapping network (CON)* and in this paper we use it for computing the diameter of a point set.

In following sections the definition and rules of operations of our completely overlapping network is firstly given. Secondly, the algorithm for computing the diameter of a point set on a completely overlapping network is presented. Also, the proofs of our algorithm are shown. Finally, we conclude our paper and propose a transformation method of our fine-grained model into a course-grain model.

II. COMPLETELY OVERLAPPING NETWORK

In this section we give a review of a completely overlapping network as shown in [9-10]. A completely overlapping network is composed of several overlapped communication lines that connect among several nodes (or processors) to

provide parallelism. There are vertical and horizontal communication lines as shown in Fig. 1.

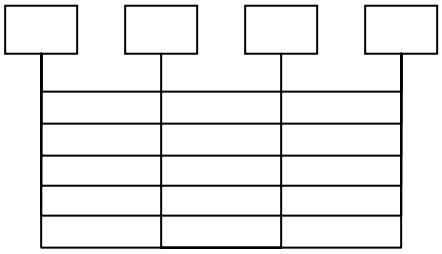

Figure 1. Four-node completely overlapping network.

The number of vertical lines is equal to the number of nodes n and the number of horizontal lines is equal to $\frac{n(n-1)}{2}$. Additionally, one straight line segment equates one step horizontally and vertically. For instance, Fig. 2 shows a communication of 5 steps between the leftmost node and the rightmost node.

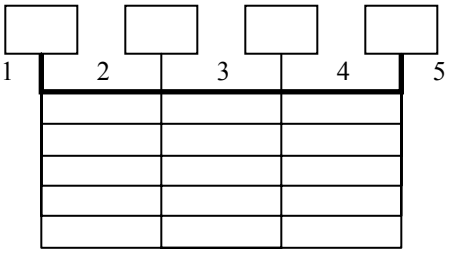

Figure 2. Five-step communication between nodes.

Like any other networks, there are rules of operations which our proposed algorithm runs follow them. The rules are as follows.

- Horizontal and vertical line segments cannot be shared. That is, any line segment can be used only one at a time.
- Each line segment is bidirectional.
- Each node has a constant memory size.
- A same message can be concurrently sent from one source node to several destination nodes as long as there is no collision of messages.
- If there exists contention for a communication line segment, some kind of priority can be applied.

In order to enable readers to understand our communication method, a numbering of both nodes and communication lines is necessary. Our numbering scheme is illustrated in Fig. 3. This figure shows a four-node completely overlapping network with node and line identification numbers, *myID* and *lineID*, respectively. It is easy to generalize this numbering scheme for a *n*-node completely overlapping network. Hereafter, we will regularly refer to this numbering scheme when explaining our algorithm.

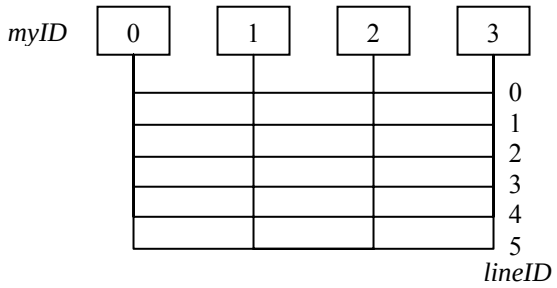

Figure 3. Numbering scheme for a four-node completely overlapping network.

III. ALGORITHM FOR COMPUTING THE DIAMETER OF A POINT SET ON A COMPLETELY OVERLAPPING NETWORK

In this section we will describe an efficient algorithm that solves the diameter problem of a point set on a completely overlapping network. The definition of this problem and our algorithm are given respectively. Then proofs of its correctness and time complexity follow.

Definition 1 (Diameter Problem) Given a finite set P of n distinct points p_i in d dimensions where $n \geq 2$, $0 \leq i \leq n$-1. Let $d(p_i,p_j)$ be a Euclidean distance between two points $p_i(x_1,x_2,\ldots,x_d)$ and $p_j(y_1,y_2,\ldots,y_d)$ when $i \neq j$, and

$$d(p_i,p_j) = \sqrt{\sum_{m=1}^{d} (x_m - y_m)^2}$$

The diameter of the set P is the maximum Euclidean distance between any two points in the set P, or that is, any pair of points of the set P that is farthest away from each other.

Our Diameter Computing Algorithm is specifically designed to suit the completely overlapping network. The following are our assumptions and the description of some variables in the algorithm.

- Each processor (or node) has a point stored in it initially.
- There is a total of $n \geq 2$ processors in the completely overlapping network where n is the number of points to be computed the diameter.
- One point per one processor and *myID* is its own point identification number.
- All processors are fine-grained.
- A variable *S* is a finite set of any pair of points that represents the diameter of the ser *P*.
- A variable *max* is the diameter of the set *P*.

There are two communication subroutines in the algorithm: **send**(*data*, *destination process*, *communication line number*) and **recv**(*data*, *source process*). One of the arguments in subroutine send() indicates the communication lines to use. (There is no such argument in recv().) These subroutines require identification numbers for both lines and nodes. These identification numbers, *myID* and *lineID*, were described in the previous section. Also note that **pack**(*item1*, *item2*,…, *itemN*) is a subroutine that packs all stated items together as one larger

item and the subroutine **unpack**(*packedItems*, *item1*, *item2*,…, *itemN*) does just the opposite.

The definition of our algorithm called *Diameter Computing Algorithm* is given as follows. Some of pseudocode conventions are borrowed from [3].

Diameter Computing Algorithm for Processor Pr_i

1. $S = \emptyset$, $max = -\infty$
2. **for** i = 0 to n-1 and $i \neq myID$
3. **send**(*myPoint*, Pr_i, *myID*)
4. **for** i = 0 to n-2
5. **recv**(*point*, Pr_{ANY})
6. *dist* = **d**(*myPoint*, *point*)
7. **if** (*dist* > *max*)
8. $S = \emptyset$
9. *max* = *dist*
10. $S = \{(myPoint, point)\}$
11. **else if** (*dist* = *max*)
12. $S = S \cup \{(myPoint, point)\}$
13. *twoItems* = **pack**(*max*, *S*)
14. **for** i = 0 to n-1 and $i \neq myID$
15. **send**(*twoItems*, Pr_i, *myID*)
16. **for** i = 0 to n-2
17. **recv**(*packedItems*, Pr_{ANY})
18. **unpack**(*packedItems*, *max_dist*, *SS*)
19. **if** (*max_dist* > *max*)
20. $S = \emptyset$
21. *max* = *max_dist*
22. $S = SS$
23. **else if** *(max_dist = max)*
24. $S = S \cup SS$

Like any communication scheme, it is essential that there be no collision of messages on any of these communication lines (or any line segment) at any point in the algorithm. Kantabutra et al [9-10] showed that this communication scheme produces no collision.

As a computer scientist, after designing the algorithm we would like to know whether this algorithm is provably correct. Theorem 1 shows that our algorithm works correctly.

Theorem 1 (Algorithm's Correctness). *The Diameter Computing Algorithm is correct.*

Proof. Let Pr_i be an arbitrary processor i, $0 \leq i \leq n$-1, in the completely overlapping network. In the algorithm two variables, *S* and *max*, are initially set to ∅ and -∞, respectively (line 1). Then, each processor Pr_i sends out its own point *myPoint* to the other processors Pr_j, $j \neq i$ (lines 2-3). Upon receiving these numbers, each processor Pr_i computes the Euclidean distance between its own point *myPoint* and the just-received point *point*, and then keeps this distance in *dist*. Each processor Pr_i compares *dist* and *max* that if *dist* is greater than *max* then it replaces *max* with the new maximum distance *dist* and also replaces any pair of points in the set *S* with the new pair of points, *myPoint* and *point*, that is just computed. If *dist* is equal to *max*, each processor Pr_i collects that pair of points which also has the maximum distance in the set *S* (lines 4-12). Presently, each processor Pr_i knows that which point is farthest away from its own point and also their corresponding distance. However, it still does not know the exact pair(s) of points which is farthest away from each other. It therefore sends the set of pairs of points *S* and the maximum distance *max* between its own point and the other points as a variable *twoItems* to the other processors Pr_j, $j \neq i$ (lines 13-15). Upon receiving the set *S* and the maximum distance *max* as *SS* and *max_dist*, respectively, each processor Pr_i compares *max_dist* to *max*, if max_dist is greater than *max* then the processor Pr_i replaces *max* with the new maximum distance *max_dist* and also replaces any pair of points in the set *S* with any pair of points in the set *SS*. If *max_dist* is equal to *max*, the processor Pr_i includes the set *SS* in the set *S* (lines 16-24). Eventually, each processor Pr_i knows the maximum distance of the set *P*, that is the diameter, and any pair of points that gives the diameter. Thus, the Diameter Computing Algorithm on completely overlapping network is correct. □

In addition, the algorithm should be also efficient in terms of time complexity. The following theorem shows that our algorithm has a running time of O(*n*).

Theorem 2 (Time Complexity). *The Diameter Computing Algorithm on a completely overlapping network has a running time of O(n) where n is the number of the distinct points in the set P.*

Proof. In parallel algorithm, running time is divided into communication time T^{comm} and computation time T^{comp}. For simplicity, assume that one step in communication is equal to one step in computation. There are four phases in our algorithm.

Phase 1 (Communication): Each processor sends its own point *myPoint* to the other processors (lines 2-3). Since this sending is done in parallel, the time of the longest communication path dominates the whole communication.

$$T_1^{comm} = 3n - 1$$

Phase 2 (Computation): Each processor computes the Euclidean distances between its own point *myPoint* and the other points *point* that receives from the other processors. By comparing, the maximum distance is eventually kept in *max*, and any pair of points corresponding to the maximum distance is also kept in the set *S*. (lines 6-12).

$$T_1^{comp} = n - 1$$

Phase 3 (Communication): Each processor sends a variable *twoItems* consisting of the set *S* and the maximum distance *max* between its own point and the other points to the other processors (lines 14-15) for finding other pairs of points that have the distance greater than or equal to *max*. For simplicity, assuming that time of sending one item and two items are the same, we therefore have

$$T_2^{comm} = 3n - 1$$

Phase 4 (Computation): Each processor checks for whether the distance that receives from the other processors *max_dist* is greater than or equal to the maximum distance *max* that it keeps (lines 19-24). There are in the worst case *n*-1 times to check. Therefore, we have

$$T_2^{comp} = n - 1$$

Hence, the total time complexity T_{total} is

$$T_{total} = T_1^{comm} + T_2^{comm} + T_1^{comp} + T_2^{comp} = O(n). \square$$

IV. CONCLUSION

In this paper we have presented an efficient algorithm called *Diameter Computing Algorithm* for computing the diameter of a finite set of *n* points in any dimension *d* on a completely overlapping network. Our algorithm not only gives the diameter of the point set but also outputs the set of pair(s) of points that represent(s) the diameter. In addition, this algorithm works in O(*n*) time. In the 2 and 3 dimensions, our algorithm has a speed up of O(log *n*) over the fastest sequential algorithm of this problem.

A theoretical network CON is an extension of Wilkinson's model. One may ask about practicality of our theoretical CON network. Even though we are not engineers (and, therefore, admittedly, are probably not a good judge on this matter!), we believe that CON can be implemented cost-effectively since it is similar to Wilkinson's experimental networks that are known to be cheaper than most parallel machines.

Throughout this paper we have only discussed the case in which all processors are fine-grained. However, like the multiple bus network with overlapping connectivity model, the concept of our theoretical network can also be applied to coarse-grained processors with larger memory. This is the case particularly worth attention because it can be applied to existing, widely-used local area networks. Fig. 4 shows an example of embedding a 16-node CON into a 8-node CON. This is certainly our further research.

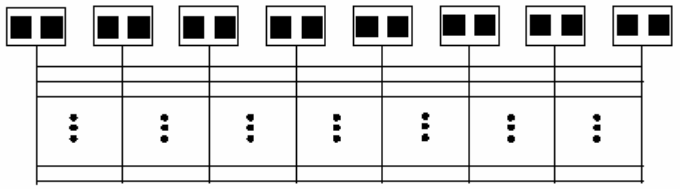

Figure 4. 16-node CON embedded in a 8-node CON

ACKNOWLEDGMENT

The authors would like to thank Assistant Professor Dr. Sanpawat Kantabutra for his suggestions and significant comments on this paper.

REFERENCES

[1] B. Chazelle, H. Edelsbrunner, L. J. Guibas, and M. Sharir, "Diameter, Width, Closest Line Pair, and Parametric Searching," *Proceeding of the Eighth Annual Symposium on Computational Geometry*, Berlin, Germany, ACM Press, June 1992, pp. 120-129.

[2] B. Wilkinson, "On Crossbar Switch and Multiple Bus Interconnection Networks with Overlapping Connectivity," *IEEE Trans. Computers*, vol. 41, 1992, pp. 738-746.

[3] Cormen T.H., Leiserson C.E., and Rivest R.L., *Introduction to Algorithms*. New York: McGraw-Hill Book Company, 1992.

[4] D. V. Finocchiaro and M. Pellegrini, "On Computing the Diameter of a Point Set in High Dimension Euclidean Space," *Theoretical Computer Science*, vol. 287 (2), pp. 501-514, September 2000.

[5] E. A. Ramos, "An Optimal Deterministic Algorithm for Computing the Diameter of a Three-Dimensional Point Set," *Discrete and Computational Geometry*, vol. 26 (2), Springer New York, pp. 233-244, May 2001.

[6] F. P. Preparata and M. I. Shamos, *Computational Geometry: An Introduction*, Springer Verlag, October 1990, 3rd edition.

[7] G. Maladian and J.-D. Boissonnat, "Computing the Diameter of a Point Set," *DGCI: Lecture Notes in Computer Science*, vol. 2301, Springer Berlin/Heidelberg, pp. 197-208, 2002.

[8] M.I. Shamos, "Geometry complexity," *Proceedings 7th Annual ACM Symposium on the Theory of Computing*, 1975, pp.224-233.

[9] P. Techa-angkoon, "The Closest Pair of Points Finding Algorithm on a Completely overlapping Network," Proceeding of JCSSE, November 2005.

[10] S. Kantabutra, W. Jindaluang, and P. Techa-angkoon, "It's Elementary, My Dear Watson: Time-optimal Sorting Algorithms on a Completely Overlapping Network," *Lecture Notes in Computer Science*, vol. 3758, Springer Berlin/Heidelberg, pp. 252-262, 2005.

Classification Using Semi-Lazy Learned First Order Rules

Sarawut Lueangampol, Sukree Sinthupinyo
Department of Computer Science, Faculty of Science and Technology,
Thammasat University THAILAND
woon115@gmail.com, sukree@cs.tu.ac.th

Two major problems of ILP learning are: very long learning process that takes very long time and unclassifiable examples in multi-class problems. Some previous works have been done using weighted partial rules which can solve the latter problem. These works can improve the accuracy of ILP on classifying multi-class data but they need to completely train ILP classifier. So that they still take long training process. Hence, this paper proposes a new method of ILP learning by using semi-lazy learning concept. The semi-lazy learned rules are created from incomplete learning of ILP in order to reduce learning time. The obtained rules are shorter and more general, so that they can cover data easier. These rules are used with some weighting information to classify unseen examples.

I. INTRODUCTION

Inductive Logic programming (ILP) is a well known machine learning that has been applied to many real world applications. The concept of ILP is to search for the best rules that cover only positive examples but not cover negative examples by using additional background knowledge. However limitations of ILP are (1) its training process takes very long time and depends on the size of background knowledge and examples; (2) ILP will give the poor accurate rules if the training set contains noisy data. Some works using the idea of partial rules have been proposed. Reference [1] and [2], the partial rules are some parts of rule obtained from the completely trained ILP rules. These partial rules are shorter and more general than the original ones. So that they can cover examples easier than the original. The covering information is then weighted by using Backpropagation Neural Networks. The weighted partial rules method shows that it can give the better result than the original rules, especially on multi-class datasets.

The weighted partial rules method needs the complete training process of ILP. This training process may take very long time. Hence, in this paper, we shorten the training process and use the idea that the rules which are not completely trained may be useful.

In machine learning studies, there are two kinds of learning, i.e. *eager* and *lazy learning*. The *eager learning* is a kind of learning in which the training examples are used to construct the hypotheses as soon as they appear to the learners. While in the *lazy learning*, the training examples are not used until we actually want to classify new examples.

As described above, we will use the rules which are not completely trained. Thus we are located at some point between eager and lazy learning. So that the kind of rules proposed in this research is called *semi-lazy learned rules.* Our proposed method can solve the problem of the weighted partial rules in which the partial rules may take very long time to be accomplished. We instead use the incompletely trained rules, so that the time spent on the training process of ILP can be reduced.

[10] Thus, another algorithm must be applied to attack this new problem. In this research, we select the Backpropagation Neural Network to assign weights to each semi-lazy learned rule and then they are combined with the weights from the networks to classify new examples.

After we obtain the incompletely trained rules or our semi-lazy learned rules, the problem is now transformed into the problem of using many shorter rules to classify new examples, like the field of using the mined association rules in classification problems.

II. RELATED WORKS

A. Inductive Logic Programming

The data components that used for ILP learning are Background knowledge, positive and negative examples.

ILP's search strategy is aimed to find the hypotheses that cover only the positive examples but not the negatives. The result would be more than one hypothesis described in the form of first order which can be use to explain the examples effecia.

Equation of ILP learning condition

$$\forall e \text{ in } E^{+} \; ((B \wedge H) \models e). \quad (1)$$

$$\forall e \text{ in } E^{-} \; ((B \wedge H) \not\models e). \quad (2)$$

One disadvantage of ILP is that the learning process takes very long time. This is caused by that the searching process of ILP try to find the best hypothesis in a large hypothesis space.

Another disadvantage of ILP learning is that the hypotheses or the rules are often too specific. When we apply these too specific rules to classify an example, the likelihood of the situation that the example is not covered by any rule may arise. This disadvantage can cause a class selection problem when we use ILP's rules to classify the examples. Because the ordinary ILP method have no information to help ILP when no rule from the rule set can be applied to the example.

For example, below is a rule from complete ILP training on

Finite-element dataset in the third fold of five-fold cross validation experiments

```
    mesh(A, 8) :- neighbour_xy_l(B, A),
neighbour_xy_l(C, B),neighbour_zx_r(C, D),
    neighbour_xy_r(A, E),not_loaded(C),
neighbour_xy_r(B, A),neighbour_yz_r(B, F),
        fixed(E),half_circuit(A).
```

According to the rule example, we have found that it covers only nine examples from 43 examples of class8. This means that in case of having only one rule for learning, then the use of ILP in classification problems may have some incorrect classification because there are 34 examples are not covered.

B. Weighted Partial Rules

A problem of ILP learning is that the rules which are the result from training process may not cover some examples or may undecidedly cover examples. Weighted Partial Rules [2] are a set of some part of rules which are weighted by using some machine learning algorithms. This method is used to attack the problem in which the class of an example cannot be determined. Unclassifiable examples are categorized into two groups; the examples which are not covered by any rule and the examples which are covered by multiple rules from different classes. This method is based on the idea when the original rules cannot exactly match the examples, some part of rules may match such examples. The partial rules are extracted from the original rules. Most of them are shorter and more general than the original rules. Hence, in case of the examples which are not covered by any original rule, the partial rules may cover these examples. By this reason, we can now have some coverage information to classify them. The coverage information can also be used in case of the examples which are covered by multiple rules from different classes. The more important partial rules which are represented in the form of the higher weight assigned to those partial rules should have more influence on the decision. The weight is given by machine learning algorithm, i.e. Backpropagation Neural Network, Winow based algorithm, or probability in Naïve Bayes algorithm. However the weighted partial rule method needs the complete process of rules learning by ILP. The problem of long time learning process is still remained.

Reference [3] studied the method that combines ILP's rules learned from multi-relational data mining. Main problem mentioned in the research is how to combine the rules from ILP to construct an accurate classifier. ILP system can still give some useful rules and each rule will show the relation to each parts of sample even though there are some errors and missing data in relational database. The research presented process of selection and combination of the rule. Using voting and Bayesian classifier to find the rule that can classify data. The research is similar to the works presented before in the way that the whole rule cannot fit to an example, but some parts of rule can apply to the example. The difference of this research from the others is that it does not have the completed rules from which the partial rules are extracted but it chooses many specific rules to be combined using voting method and Bayesian classifier. By using this way the result is more accurate.

C. Lazy Learning

Lazy learning is a class of learning techniques that spend small or on learning effort on training process and delay the computation to the classification time. There are some lazy learning concepts applied to other machine learning algorithms such as Instance Base Learning, Bayesian and Decision Tree.

Reference [7] presented the Lazy Learning of Bayesian rules. The proposed method is aimed to reduce the attribute inter-dependence problem by generating a most appropriate rule with a conjunction of attribute-value pairs as its antecedent. Hence, the local naïve Bayesian classifier is built by some part of training examples.

Reference [9] proposed the Lazy Decision tree which creates decision rules at the classification time. The procedure of LazyDT is first selecting a subset of training examples and then performing majority vote. The LazyDT differs from the common lazy algorithms which are based on the nearest-neighbor algorithm.

III. SEMI-LAZY RULES LEARNING

As mentioned in the previous section, some part of rules may be useful for selecting the class of an example. We attack the problem of particularly long training process of ILP, also Weighted Partial Rules, by trying to stop the process before it completes. The incompletely learned rules are used with the weights from a Neural Network to classify the examples. We can see that our incomplete learned rules are located at some point between the complete learned rules in eager learning style and the empty set of rules in lazy learning style. Thus we call our rules as *semi-lazy learned rules.*

Steps of using the semi-lazy learned rules to classify examples are:

1) Generate the semi-lazy rules.

This is the first step to generate the semi-lazy rules from background knowledge, positive and negative examples. This research is implemented with Aleph using a searching mode for inducing association rules by "WARMR" algorithm [11]. This mode will generate all possible rules that cover the specific numbers of positive examples. We use the negative examples as well as the positive examples to guide the learner to construct the rules for both classes. The process to generate the semi-lazy rules compared with the process to generate the partial rules is shown in Figure 1a and 1b.

Figure 1a and 1b show the difference between the creations of the partial rules (Figure 1a) and the process of the semi-lazy learned rules (Figure 1b).

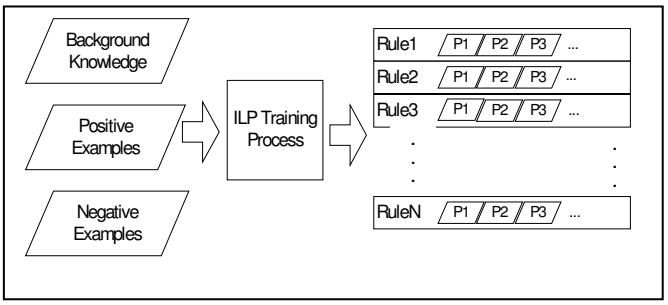

Figure 1a. Complete ILP Learning Step

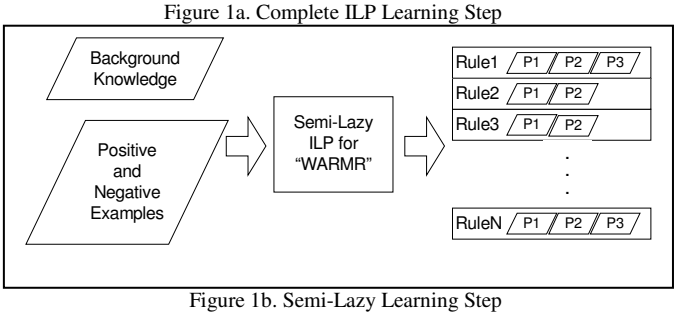

Figure 1b. Semi-Lazy Learning Step

2) Select the Rules.

We can see that our semi-lazy rules which come from the learning method presented in step 1 are different from the partial rules which come from the complete learning process. The partial rules are extracted from the obtained rules after the training process is completed. Hence the number of the partial rules is limited by the number of the original rules. The number of the semi-lazy learned rules is not bound by any number because they are constructed from the induction of the association rules which is often enormous. The number of the rules from the ordinary ILP, the partial rules, and the semi-lazy rules are shown in Table I.

Table I

Show the length of the number of the rules from each method

Dataset	Average amount of Rule after Training			
	ILP	Partial Rule	Semi-lazy	Selected Semi-lazy
Mesh	77-85	700-1200	4000-5223	270-350
Mutagenesis	7-12	65-92	850-920	35-52
Casinogenesis	28-35	305-436	3670-4280	75-103

The table shows that the number of the semi-lazy rules is much greater than the number of the rules from other methods. This huge number of the semi-lazy rules could cause the problem in classification. Thus they need to be filtered.

In order to select the influence rules which have ability for selecting the class of examples. Two methods separated by type of the problem are used, two-class and multi-class problems. In two-class problem, for each example, we choose the covering rule with maximum and minimum coverage on entire training set. The maximum coverage rule is most general rule which describes many examples while the minimum coverage rule is most specific rule which describes only that example. In multi-class problem, two more conditions are added. The maximum and minimum coverage rules of each class are selected. The reason of choosing the rules with maximum coverage of each class is that they are the best rules that describe that class. While the minimum coverage rules of each class are the rules which are very specific to that class. The step of selecting the rules shows in Figure 2b.

These selected semi-lazy rules will be used to determine the input vector of the Backpropagation neural network in next process.

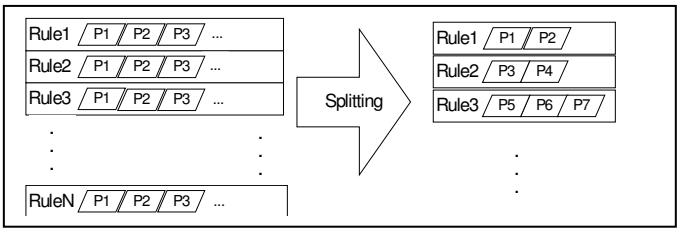

Figure 2a. Step of splitting general rules to partial rules

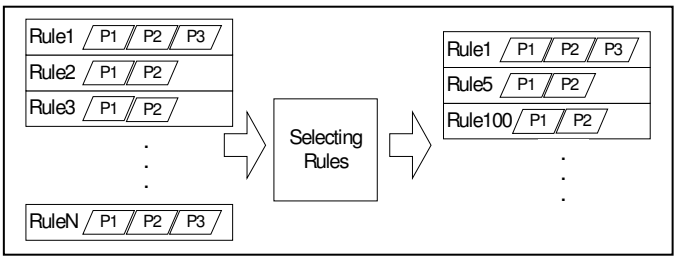

Figure 2b. Step of selecting semi-lazy rules to train neural network

3) Construct a Neural Network.

After obtaining the semi-lazy rules, the covering information of them on each example is used as the input value for each input node of the Backpropagation neural network. If the rule corresponding to each input node covers the example, the input value of that input node is set to '1' otherwise is set to '-1'.

Our network contains three layers, namely *input*, *hidden*, and *output* layer. The number of input nodes is equal to the number of the semi-lazy rules while the number of hidden nodes is simply equal to the number of input nodes. Output nodes represent the class of examples. So that he number of output nodes is equal to the number of the class of examples. The structure of our network is shown in Figure 3.

Figure 3. Show structure of Backpropagation Neural Network.

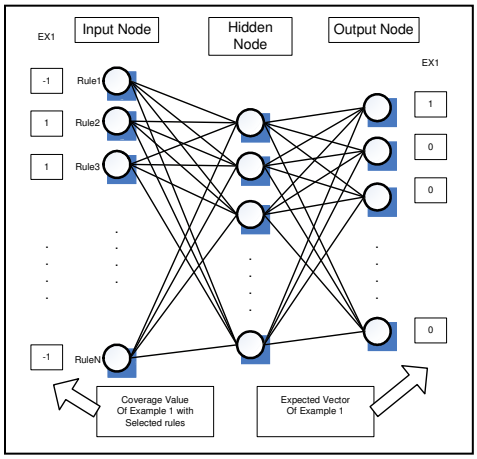

IV. EXPERIMENTAL RESULTS

We conducted the experiments on three data sets, namely Finite Element Mesh Design (FEM), Mutagenecity of molecules (MUTA), and Carcinogenesis (CARCIO).

As mentioned earlier, we said that the partial rules and our rules (semi-lazy rules) are more general. To show the coverage of each kind of rules, we select some rules obtained from each kind and illustrate their coverage in Table II.

A. *ILP with Majority Vote Classification*

Classical ILP rules alone cannot classify multi-class data well. An example which is not covered by any rule or is covered by the rules from different classes cannot be classified. To fairly compare ILP to our method, we use the Majority vote method in such cases. The example which is not covered by any rule is classified as the class with the highest number of training examples. On the other hand, the example which is covered by the rules from different classes is classified as the class having higher number of training examples.

Table II

Show partial rules' coverage comparing with the original rule's coverage.

Partial No.	Rule contents	Covered /All examples
*	mesh(A, 8) :-neighbour_xy_l(B, A), neighbour_xy_l(C, B), neighbour_zx_r(C, D), neighbour_xy_r(A, E),not_loaded(C), neighbour_xy_r(B, A), neighbour_yz_r(B, F), fixed(E),half_circuit(A).	9/43
1	mesh(A, _) :-neighbour_xy_l(B, A), neighbour_xy_l(C, B).	31/43
2	mesh(A, _) :-neighbour_xy_l(B, A), neighbour_xy_l(C, B), not_loaded(C).	23/43
3	mesh(A, _) :-neighbour_xy_r(B, A), neighbour_xy_l(C, B).	31/43
4	mesh(A, _) :-neighbour_xy_r(B, A), neighbour_yz_r(B, C).	17/43

B. *Experimental Results*

We implemented a semi-lazy learning based on the method explained in the previous section. In the following experiments, we ran five-fold cross validation and averaged the results in all experiments. The experimental results are shown in Table III.

Tables III

Show accuracy and training time of experimental result.

Dataset	ILP		Weighted Partial Rules		Semi-Lazy Rules	
	Accuracy	Time	Accuracy	Time	Accuracy	Time
Mesh	52.13±3.01	12673	56.7±2.6**	14673	62.20±2.28***	7832
Muta	79.20±3.5	1507	84.65±4.2**	1880	87.78±3.61**	990
Carcio	46.86±3.88	3710	55.24±5.51**	4130	57.22±6.77**	1630

*, **, *** AND **** DENOTE THE SIGNIFICANT LEVEL UNDER .10, AT .10, AT .05, AND .01, RESPECTIVELY. Training time in second.

The results show that the accuracy of semi-lazy rules is better than the Weighted Partial rules and ordinary ILP on all datasets. Moreover the learning time of Weighted Partial Rule and ILP are more than semi-lazy rule, as shown in the table.

V. CONCLUSION

Using the complete ILP learning to learn rules for classifying examples is a cause of two problems. The complete ILP learning is a particular long time process that gives some specific rules as results. These specific rules lead to the other problem, especially in the multi-class problems, in which an example may not be covered by any rule or may be covered by multiple rules from different classes. In this paper, we have proposed an improvement of ILP learning which combine semi-lazy learning with Backpropagation Neural Network. The experimental results show that our method can reduce the learning time and yield better results. The semi-lazy learning method can avoid full searching for the best rule so that it can reduce learning time. The results of semi-lazy learning are not specific rules, hence they can easily cover examples and give another covering information which cannot be obtained from the complete rules.

REFERENCES

[1] Boonserm Kijsirikul , Sukree Sinthupinyo, "Approximate ILP Rule by Backpropagation Neural Network: A Result on Thai Character Recognition", in *Proceedings of the 9th International Workshop on Inductive Logic Programming*, 1999 Pages: 162 – 173.

[2] Sukree Sinthupinyo , Cholwich Nattee, Masayuki Numao, Takashi Okada, Boonserm Kijsirikul ,"Improving Multiclass ILP by Com-bining Partial Rules with Winnow Algorithm: Results on Classifi-cation of Dopamine Antagonist Molecules ", in *The Third Interna-tional Workshop on Active Mining*, 2004 Pages: 183 – 195.

[3] Jesse Davis, Vitor Santos Costa, Irene M. Ong, David Page, Ines Dutra,"Using Bayesian Classifiers to Combine Rules"., in *3rd SIGKDD Workshop on Multi-Relational Data Mining conjunction with KDD-2004*, 2004.

[4] Ashwin Srinivasan, "Aleph Manual",2001

[5] Stephen Muggleton, Raedt Luc De, "Inductive Logic Programming (Theory and Methods)" , *Journal of Logic Programming 1994*,1994,

[6] Kai Ming Ting, Zijian Zheng & Geoffery Webb, "Learning Lazy Rules to Improve the Performance of Classifiers", SGES 1999, pp 122-131

[7] Zijian Zheng, Geoffrey I. Webb, "Lazy Learning of Bayesian Rules", *Machine Learning 2000 volume 41Issuse1,* pages 53-84, 2000

[8] Aha, D.W.(ed.), "Lazy Learning" , *DordrechKluwer Academic* ,1997.

[9] Jerome H. Friedman, Ron Kohavi, Yeogirl Yun, "Lazy Decision Trees", *13th National Conference in Artificial Intelligence*, 1996

[10] Stefan Mutter, "Classification using Association Rules", PhD Thesis, University of Freiburg, 2004

[11] Luc Dehaspe, "Frequent Pattern Discovery in First-Order Logic", PhD Thesis, KATHOLIEKE University, 1998

Object-Oriented Design for Thai Herbal Taxonomy

Surangkana Rawungyot
IEEE Conference Publishing
School of Information and Communication Technology
Naresuan University, Phayao, Thailand.

***Abstract*-This paper represents the model of classification algorithms for medicinal plants taxonomy and systematic classification system (MPTSCS) with object-oriented design method. The core of this design is a use case driven and class diagram with the unified modeling language (UML). Our approach to optimization of declarative data store and queries in object-oriented design that allows to exploit the specification semantic characteristic of data types occurring in science application similar to botany data. This model can implement to an intelligent application for medicinal plants taxonomy classification and retrieval in web-based application. This approach provides a UML model of an application for the MPTSCS in a large medicinal plant database, that are collected, retrieved and expected a classification for those data. The proposed models concretely classify the medicinal plants taxonomy possible. Also, this method proved by implement with object-oriented programming and botanists testing that results are sufficient. Those methods were implemented phase, which produced via web-based application, thus achieving greater portability for botanist and other users. Thai herbal database especially presented in only Thai version. In order to testify the model, both instance of the model and its implementation in a simulation are shown. In the future, this research will be implementing other models for other plants and using an image processing to find other contents for high performance in this field.**

I . INTRODUCTION

There are millions of different kinds of plants in the world. Therefore, the botanists intended to survey several plants in the natural and collected with dry or fresh process for study. The problems were many special names for one plant, that non standard name and they have a lot of name in another location. So the scientist thought of an order system for classifying a lot of plants and assigned name for plants. Botanist was invented to binomial system, that specific plant name laws or taxonomy system, used sophisticate and experience [1-2]. This paper is developing the application for Thai herbs which are especially some flower plants (angiosperms)[1][3]. The raw data, input to this system, are the common plant characteristic. They were received by survey in the forest or observation from their plant, such as shown in Fig1. In addition, the input data came from plant with dry process, that example shown in Fig2.

Figure.1: Characteristic of plants in natural.

Figure.2: Examples of plants with dry process.

After that, there were compared with type specimens from plants database system. The more you give details, the more you earn actually metadata of plant from plant databases. Therefore, each user can get coarse details, a family level, or fine details, a genus or species, which are dependent on information from them. The details are attribute for instance scientific name, morphology, anatomy, medicinal and photograph of their plants. In other words, the algorithm for plant classification was used to modifying theory of a dichotomous key [1-2]. In summary, this process was shown in Fig3, which is descriptive of over all process in this approach.

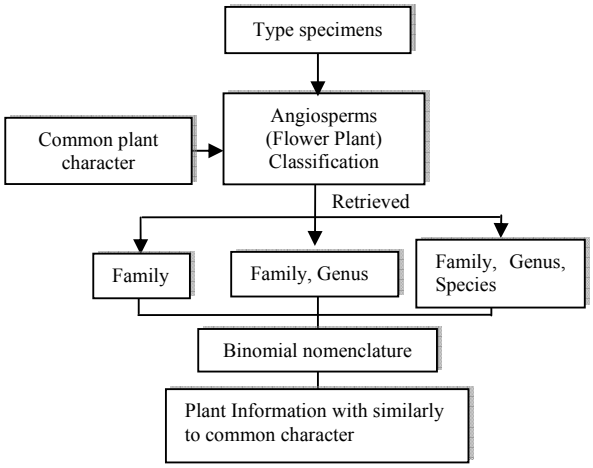

Figure.3: Examples of plants with dry process.

This paper was organized in the following way. Section 2 briefly presents the basic concept of classification in botany system. Section 3 reviews the concept of the object-oriented design. Section 4 discusses the analysis method of medicinal plant taxonomy classification with UML, and finally, section 5 gives conclusion and trends to the future of this paper.

II. CLASSIFICATION OF BOTANY SYSTEM

Plants were classified in several different ways, and further away from observation in the forest [1-3]. Also, there are more difficult for classification, because this field must be special to identify a particular plant. Classification of plants is starting from the highest category, which is class. After that, plants are classified as follows [3]. Each group has the characteristics of the level above it, but that has some distinguishing features. The further down the scale you go, the more minor the differences become, until you end up with a classification which applies to only one plant. Firstly, we distinguish plants which produce flowers (Angiosperms) or which don't produce plant flowers (Gymnosperms).In this paper is classified only the former. Secondly, several plants are separate to Dicotyledonae subclass, that is two leaves, or Monocotyledonae subclass, that is one seed leaf. After that, a group of related plant families, classified in the order in which they are thought to have developed their differences from a common ancestor. There are six Superorders in the Dicotyledonae(Magnoliidae, Hamamelidae, Caryophyllidae, Dilleniidae, Rosidae, Aateridae), and four Superorders in the Monocotyledonae(Alismatidae, Commenlinidae, Areciae, Liliidae). The names of the Superorders end in -idea. Later, each Superorder is further divided into several Orders. The names of the Orders end in –ales. Each Order is divided into Families. These are plants with many botanical features in common, and is the highest classification normally used. At this level, the similarity between plants is often easily recognizable by the layman. Modern botanical classification assigns a type plant to each Family, which has the particular characteristics which separate this group of plants from others, and names the Family after these plants. The names of the Families end in –aceae. Afterwards, the family may be further divided into a number of sub-families, which group together plants with in the Family that have some significantly botanical differences. Next, Genus is the part of the plant name, the normal name that you give a plant such as Papaver(poppy), Aquilegia(Columbine), and so on. The plants in a Genus are often easily recognizable as belonging to the same group. The name of the Genus should be written with a capital letter. Finally, Species is the level that defines an individual plant. Often, the name will describe some aspect of the plant for example, the color of the flowers, size or shape of the leaves, or it may be named after the place where it was found. Together, the Genus and Species name refer to only one plant, and they are used to identify that particular plant. Sometimes, the species is divided into sub-species that contain plants not quite so distinct that they are classified as Varieties. However, this paper can classify at the species, after that it can show about all attribute in Fig.5 for each plants, that similarly to input criteria and to retrieve plant data.

III. OBJECT-ORIENTED DESIGN

Nowadays, the software developments are including a dealing complex social process. Many software systems are embedded in an abstract, that are difficult to design overall these requirement with antiquate software design, program size grows large. Programming technologies are also change to support real-word and complexity system. Those programs must be designed to work perfectly in many areas, and business functionality is not the only one function but also many core functions in the system. Of course a well-designed architecture benefits any program, and not just the largest ones. Another consideration of structure is enable code reuse, that the design time is the simplest time to structure an application of modules or components. Eventually, enterprises build up a directory of component models, each representation are implemented and stored in a directory of code modules. When another application needs the same procedures, the designer can quickly import its module from the directory. At implementing time, the programmer can quickly import the code module into the program. So modelling, that is the designing of software applications before coding, is an essential part of the large software, and helpful to another size project as well. A model shows the analogous role in software development those blueprints or other plans. Using a model, those responsible for software development project's success can make sure the business functionality which is complete and correct, end-user needs are met, and program support business requirements before implements code and rebuild that more expensive and more difficult to perform. The models are visualizing your view, user requirement, specific program, and check again before you code of program.

Object-oriented concept is induced the unified modelling language (UML)[5-6], that has capable in mention above. UML defines a set of basic diagrams that provide multiple perspectives such as structural/static and behavioural/dynamic of system under analysis or development. UML diagram include use case diagrams, class diagrams, interaction (sequence and collaboration) diagrams, activity diagrams, state transition diagrams, deployment diagrams, etc. This paper only a subset of these diagrams will be addressed. The UML is a graphical language for visualizing, specifying, implementing, and documenting the artefacts of a software-intensive system. As such, the UML has found widespread use: it has been applied successfully to build systems for diverse tasks as information retrieval, accounting software, e-commerce, telecommunication and other information system. UML is primarily a description of a unified notation and semantics together with the definition of a metamodel. However, their application is certainly no easier than that of the old methods. Relationship between class, activity, collaboration, sequence, and state diagrams can become totally confusing to view. Hence, consistency and completeness of model can be considered only by appropriate software. Overall, the UML are more advantage than structure concept. First, manual modelling is out of the puzzle. Second, the class concept is used to work with units of data and operations. Third, object-oriented methods focus of model from the abstract problem and solution. The last, evolutionary development, a complex system is not built in one go and all complex systems in nature have developed step by step, each intermediate step had to stabilize first and prove its functional and survival capabilities. More information about UML can be found in [5].In addition,

many researches such as [7-8] were used UML concept to design their system, that results are very excellence performance. Therefore, this paper selected designing with UML for model medicinal plant taxonomy classification. These model are coding with object-oriented program for plant classify and in the same algorithm application. The third main diagram developed in the UML model for the representation of the different aspects of a MPTSCS development. These are use cases diagram, class diagram, and sequence diagrams. There are generated by using rational rose software in enterprise edition version 2002.

IV. The analysis method of medicinal plant taxonomy classification with UML

This approach is use case driven with the following steps : first, creating a use case diagram that specified the expectant user of a MPTSCS and their desired behaviour of using the system under preferable environments; second, modelling a class diagram that describes any internal objects that cooperated to support this system, which compound their attribute and their behaviour operated all entities; third, modelling some sequence diagram that show a series of messages exchanged by a selected set of object in a temporally limited situation, with an emphasis on the chronological course of events and the last, creating an activity diagram that presents how such behaviours proceed interactively to satisfy the expectations of all user. As mention above, these diagrams are UML based with desired extensions for the analysis of a MPTSCS.

A. Use case diagram

The use case diagram is compounded: the botanist is one actor, which can manipulate many Thai herbal features into a database. Everybody can be the botanist, if they must register to a botanist and pass a placement test in the system. This placement test is divided people become a botanist in this system, that has a lot of updatable people, so a large Thai herbal database was occurred. Another actor is other users, who can search, retrieve and classify the data from botany database system.

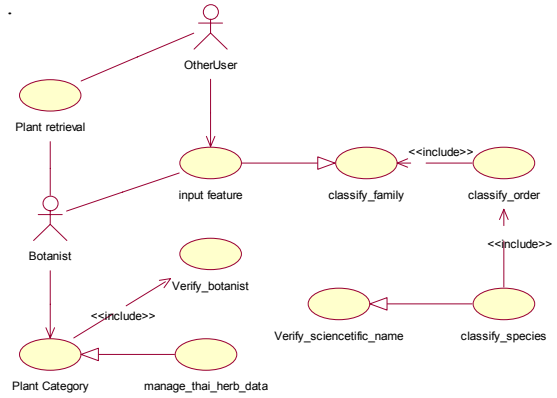

Figure.4: Use case diagram representation of the MPTSCS.

B. Class diagram

The class diagram composes of classes, which contains data and performs methods, and represents many relationships that indicate and resource sharing between classes. In this case, class represent real-word about plant classification system such as characteristic, plant morphology, medicinal properties, class in plant description, order of plant, family details, genius and species details of flower plant in Thai herbs. This model is a template for plant classification system. Classes composed of attributes and methods. Attributes are the data, which are input the databases. In addition, methods in that class are represent their functions that need for manipulate data, such as retrieve data from database, check characteristic of fruit data with specimen. This model can modify and reuse for similar to another system. Furthermore, the model used to implement by programming language. Fig.5 shows the structure of all class in MPTSCS and relationship between them

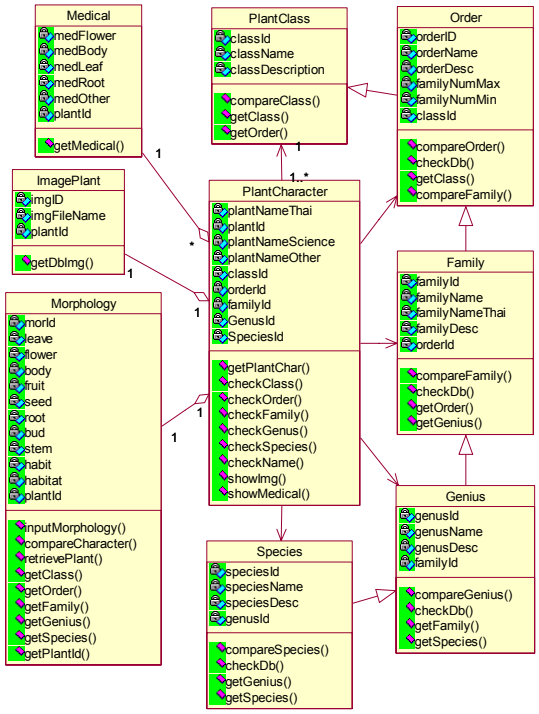

Figure.5: The attribute and method of each element involved in MPTSCS, class diagram generated by Rational Rose .

. C. Sequence diagram

Sequence diagrams were provided a dynamic high level representation of the system. They were captured and represented the interactions required to implement each use case that should have least one related sequence diagram. Fig. 6 depicts part of sequence diagrams from this approach, which illustrated a relationship between other user and MPTSCS. In this figure, relationship between PlantCharacter class and Morphology class is represented though the “input_feature”

use case. In this case, this use case requires that another use case such as classify_family use case.

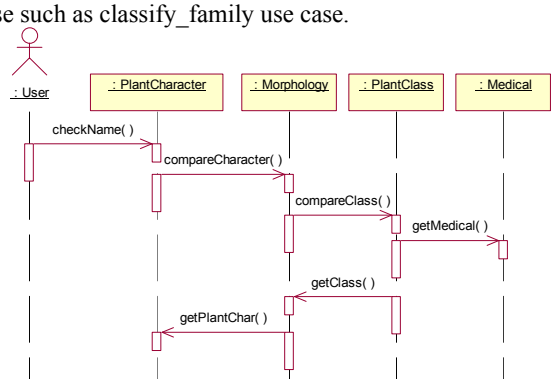

Figure.6: Sequence diagram illustrating a relationship between other users and MPTSCS.

D. Example for plants classification system

Figure.7: Capturing user interface for input all common plant characters via web browser.

Figure.8: Final process illustrating about all details similar to type specimen in MPTSCS.

In testify the UML model of MPTSCS, the application was implemented as part of a simulator. The simulator is used in some medicinal plants. Because Thai herb are a lot of species, this testify use some type of Thai herb for simulation. The simulators were depicted in Fig. 7 and Fig. 8. Fig.7 shows an input operator via web site. Fig. 8 shows an output process that shows classification in similar group from this system.

V. CONCLUSION AND THE FUTURE

This paper has presented a software development approach for MPTSCS that combines the use of the UML notation, so with this methodological approach for well-found methods. These are prepare lists of the variable plant data, which the program are find a matching record in plant database on the basis of the criteria outlined above. Not only, this data are very complexity but also this design needs some skilful botanist for classification. In addition, this paper can modify UML and mix Thai herbal botany knowledge with object-oriented technology together, as a result, this has developed to a worthy software application such a result from testify.

This approach leads to content-base retrieval concepts, which were described by text or looked for image content. Certainly, there have some mistake, which depend on attitude of everybody. In the order to control some error input process with human or some sight from person are sufficient. In the future, this application will have introduced an image processing [9-10], that help to retrieve automatic content from botany data such as shape of leaf. As a result, the plant data can usually find a match for each of these records very simplify and very actual plant classification system.

ACKNOWLEDGMENT

This research was partially supported by school of information and communication technology in Naresuan University at Phayao province, Thailand. Furthermore, The author is grateful to A.Den Keasan for his helpful guidance in plant system and my staffs for providing computing facilities and agreeable environment. In addition, the author thanks to the forest herbarium officers and the botanical garden organization ministry of natural resources and environment officers for a lot of information.

REFERENCES

[1] K. Chayamarit, *Mannual Keys to some plant families*, Pachacon Ltd, Thailand, 2002.
[2] Hsuan Keng, *Orders and Families of Malayan Seed Plants*, Singapore University Press, 2003.
[3] S.Putiyanan, *Identification of Medicinal Plants Special vol*, Text book development project the nation institute of Thai traditional medicine,1999.
[4] Nidsiri Reungrungsri and Thawutchai Mungkakrup, *Thai herbs 1*, Be healthy, Thailand, 2004.
[5] Booch , Jacobson , Rumbaugh , *Developing software with UML object-oreinted analysis and design in practice*, Addison-wesley, 2001.
[6] G.Booch,J. Rumbaugh,I.Javobson, *The Unified Modelling Language User Guide*, Addison-wesley, Longman, Reading,MA, 1999.
[7] T.Tsai, R.Sato, "A UML model of agile production planning and control system", computers in industry, vol.53, 2004, pp.133-152.
[8] C.A. Costa, J.A. Harding, and R.I.M. Young, "The application of UML and an open distributed process framework to information system design", Computers in industry, vol. 46, 2001, pp. 33-48.
[9] R.Surangkana, Color Image Retrieval by Using Spatial Relationship, 26th Electrical Engineering Conference , Vol. 2, 2003, pp. 998-1003.
[10] J.R. Smith and S.F. Chang. "Tools and techniques for color image retrieval." Storage and Retrieval for Image and Video Database IV. SPIE Processing Vol.2670, 1996.

Computer Viruses Metadata

Chittanond Pheunphiphop, Mayuree Lertwatechakul
Department of Information Engineering
Faculty of Engineering, King Mongkut's Institute of Technology, Ladkrabang
Bangkok, Thailand 10520
Email: s47061137@yahoo.com, klmayure@kmitl.ac.th

***Abstract*-As to enable a variety of the Internet users to easily achieve and share virus description, a convenient platform and well defined general terms are required. In this paper, various virus techniques, behaviors and damages have been analyzed to design the virus metaschema. We defined a set of general terms to represent virus description words for several conflict terms. This could help people to easily understand and make it comfortable to exchange to the public.**

I. INTRODUCTION

At the moment, the outbreak of virus has spread increasingly than ever while virus information source or description of each virus limited only in the websites of antivirus companies or organizations. Description of each virus has been provided as individual without distinct data exchange or sharing with other company or organization.

In this paper, analytical study has been done on technique and behavior of the viruses in order to design the structure of database by using NIAM model which is easy to be applied by illustrated presentation. This metadata presentation is provided with simple description and definition for easy access and meant to publicize this knowledge to anyone interests in virus, for better understanding and gain more viruses data exchange among people, communities & organization.

II. THE STUDY OF VIRUSES

Computer virus [1] is a type of computer program designed to rapidly replicate itself into targeted computer's files without user notice or permission. But virus unable to replicate itself across the other computer except that the user manages himself as a carrier, for instance, virus can be distributed only when infected user attaches file or document via email. Exchanging diskette, CD-ROM and Flash drive with virus infected are the other ways that allow virus to spread into other computers. That's it, the virus keep replicate itself over and over again.

Computer virus can be divided into two categories. Based on infected environment or infected methods [2]. In this paper, we have designed the concept virus metadata which is mainly concern on infected environment type.

Most viruses can be found in one of the following environments:

- **File**
- **Boot sector**
- **Macro command**
- **Script host**

A. Virus behavior

Among the various types of virus we confront with, there are always common traits which can be divided into three phases as following:

Installation phase: The phase that virus writer intends to install virus code into user's computer.

Infection phase: The phase after virus installation, virus will spread itself into targeted file as it designed by writer.

Damaged phase: This phase is meant to cause damage to user directly from virus or its side effect. The damage also includes the effect that occurred during the infection phase.

B. Virus technique

We can categorize virus technique as following [3, 4, 5]:

- **Stealth:** Stealth virus can conceal their presence from antivirus program. It can also inhibit in computer without user's awareness.
- **Polymorphic or Encrypted:** This type of virus got many appearances in order to hide their signature by scrambling virus body to avoid a detection of antivirus programs. Moreover its encrypted virus body always be changed.
- **Metamorphic:** This technique is similar to polymorphic but it has additional part which calls "Mutation Engine" which can change both of decryption routine and encryption virus body.
- **Memory Resident:** Viruses use this technique to load itself in to computer memory and to infect the next loaded program file.
- **Multipartite Viruses:** This virus infects both in file and boot sector. It can also spread itself across infected program file to boot sector.
- **Overwriting Viruses:** This virus type replaces itself to a target file.
- **Companion Viruses:** This virus is similar to overwriting virus, moreover it rename the original file to the new one. For instance PROGRAM.EXE to PROGRAM.EXD, when computer run PROGRAM.EXE virus code will activate first and execute original afterwards.
- **Prepending Viruses:** These viruses write itself to the beginning of the file.

- **Appending Viruses**: These viruses write itself to the end of the file.

C. Damages of viruses

In this paper, we define damage as an action caused by virus means harm that occurs to user no matter what it came from virus writer's intention or side effect. Damages occurred to user can categorized as following:

- **Interface damaged:** Annoying user's interface such as display monitor, mouse, speaker etc. For example, virus distorts displayed font on user monitor.
- **Data damaged:** Damage to user's documents or files by erasing or modifying user's data, for example, some virus searched text in user's document and replaced it with the virus text.
- **System file damaged:** Damage to operational system, boot sector and CMOS, for example, when virus erases or modifies system file of the operational system or boot sector of hard disk or CMOS. So that user could not run computer as usual.
- **Accessible damaged:** Virus may changes or create password access mode that's used to access a file or document. So user cannot open document or file.
- **Program damaged:** Damage to programs, virus would erase or hide significant menu, sometimes virus make program unable to run normally.
- **Security damaged:** Damage to security system, virus would erase antivirus program files or modify security menu to allow virus intrusion.
- **Overall data damaged:** Damage to all storage data, virus would erase or destroy all data in the computer, for example, virus may using command such as Format C:/, DEL *.* etc.
- **Performance damaged:** Damage which is caused by existence of virus in computer memory which mean computer has wasted its resource. This category includes computer halt, shutdown or restart itself unexpected.

III. NIAM CONCEPTUAL SCHEMA MODEL

After we have analyzed the detail of viruses' behaviors, viruses' techniques and viruses' damages from various information sources. We could design a computer virus conceptual schema as shown in Figure 1. The schema was designed on purpose that virus description has to cover all important data that useful for user and represent it in the way that is easy to understand.

According to our design, virus description has been grouped into two groups, first group is mandatory data to user such as virus name, OS, technique of virus, infected environment of virus, virus's routine, damage of virus and virus infected file type. The second group consists of supplementary data such as alias name of virus, in the wild, risk rate, reporter's name, reporting date and virus's message.

NIAM conceptual schema in Figure 1. could be mapped by optimal algorithm to relational schema as shown in Figure 2.

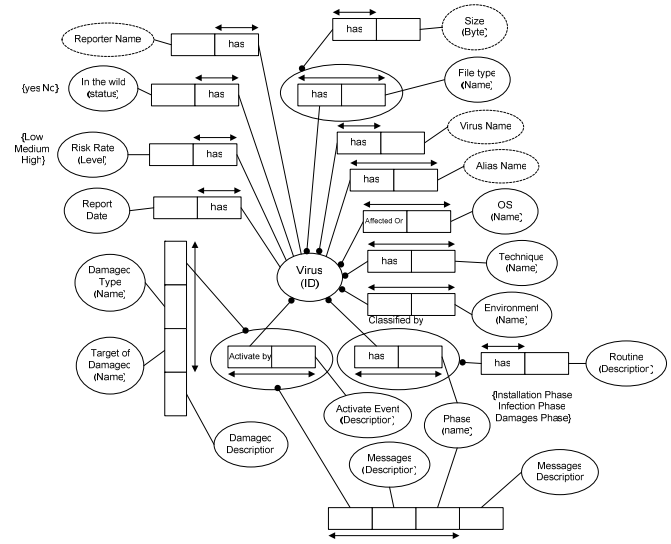

Figure 1. NIAM conceptual schema model of computer virus

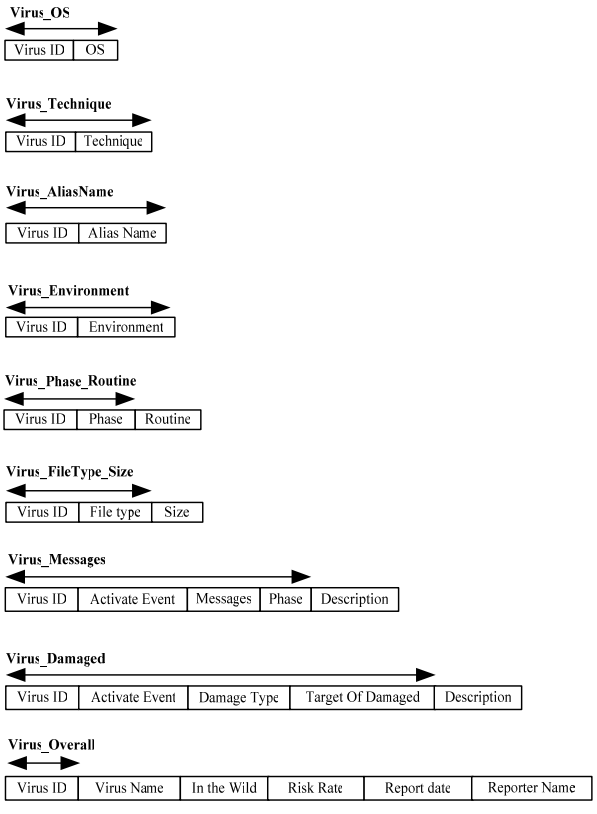

Figure 2. Corresponding relational computer virus database schemas mapped from Figure 1.

TABLE 1

Computer virus metadata

Entity \ Label name	Description	Example
Virus (ID)	Identity of virus	ID0001
Virus Name	Name of virus	Jerusalem
Alias Name	Virus alias name	Israel
OS (Name)	Operation System	Windows XP
Technique (Name)	Virus technique	Stealth
Environment (Name)	Type of virus	File virus
Phase (Name)	Phase of virus procedure	Installation
Activate Event (Description)	Event that activate virus.	Friday 13th, July 18th.
Messages (Description)	Messages that virus display to user.	"!Hola yo soy Ruperto y….."
Damaged Type (Name)	Virus damaged type.	Interface Damaged
Target of Damaged (Name)	Target of virus damage.	Monitor, Keyboards
Damaged description	Description of virus damaged.	"The systems slow down…"
Messages Description	Messages description.	"The messa..."
Report date	Date of reporting	13/10/2006
Risk Rate (Level)	Risk rate of virus.	Low.
In the wild (Status)	Show that virus is in the wild or not.	Yes, No.
Routine (Description)	Virus routine.	"Virus infec..."
File Type (Name)	Target file that virus intend to infect.	.COM .EXE
Size (Byte)	Size of virus.	1,080 bytes.
Reporter name (Name)	Name of description reporter	"MR. Smith", "MR. Neo".

Table 1 is virus metadata that describes entities name, descriptions and examples of corresponding label of NIAM schema computer viruses.

IV. EXPERIMENT

As to prove the consistency of the designed schema, we tried to populate existing data of viruses from various information sources as following:

- F-Secure Corporation [6]
- Sophos Plc [7]
- Trend Micro Incorporated [8]
- Symantec Corporation [9]

Because of limitation in this paper, we could show only some parts of some tables that are populated by existing data of Jerusalem virus. Table 2-9 is created in order to show that each virus information sources is concerning on different set of virus description attributes.

TABLE 2

Example of data in Virus_Overall table from F-Secure Corporation

Virus_ID	Virus_Name	Risk_Rate	In_the_wild	
ID0001	Jerusalem	-	-	

("-" = Not mention to.)

TABLE 3

Example of data in Virus_Overall table from Sophos Plc

Virus_ID	Virus_Name	Risk_Rate	In_the_wild	
ID0001	Jerusalem	-	-	

("-" = Not mention to.)

TABLE 4

Example of data in Virus_Overall table from Trend Micro Incorporated

Virus_ID	Virus_Name	Risk_Rate	In_the_wild	
ID0001	Jerusalem	Low	Yes	

TABLE 5

Example of data in Virus_Overall table from Symantec Corporation

Virus_ID	Virus_Name	Risk_Rate	In_the_wild	
ID0001	Jerusalem.1808	Low	Yes	

(Jerusalem.1808 in Symantec Corporation is similar to Jerusalem on other virus information source.)

TABLE 6

Example of data in Virus_Phase_Routine table from F-Secure Corporation

Virus_ID	Phase	Routine
ID0001	Installation	-
ID0001	Infection	Virus infects .exe over and over.
ID0001	Damaged	When virus is activates on Friday 13 th, it deleting programs that run on that day. Thirty minutes after an infected program is run virus will slows the computer down and make a part of the screen scroll up two lines. Virus continues infects the same file over and over in order to wastes computer resource.

("-" = Not mention to.)

TABLE 7

Example of data in Virus_Phase_Routine table from Sophos Plc

Virus_ID	Phase	Routine
ID0001	Installation	-
ID0001	Infection	Virus infected exe file over and over again and increased they size. But .com files it infected only once
ID0001	Damaged	After infected thirty minutes, virus scrolled screen up two lines, then it slows the system down. On Friday 13th it deletes every program run.

("-" = Not mention to.)

TABLE 8

Example of data in Virus_Phase_Routine table from Trend Micro

Virus_ID	Phase	Routine
ID0001	Installation	When user run infected file virus load itself in memory
ID0001	Infection	Virus stay in memory then infect program files as they are accessed
ID0001	Damaged	Virus increased infected files in order to wastes computer resource. Thirty minutes after an infected program is run virus will slows the computer down and will delete any program started on Friday the 13th of any year.

TABLE 9

Example of data in Virus_Phase_Routine table from Symantec Corporation

Virus_ID	Phase	Routine
ID0001	Installation	-
ID0001	Infection	-
ID0001	Damaged	Virus active every Friday 13th, it deletes any running program. Thirty minutes after first deletion, the computer slows down and the screen scrolls up two lines.

("-" = Not mention to.)

Each information sources got their technical terms that might be incommon and this may difficult for users to understand. As to solve this problem, we have to choose the most popular terms or defined more meaningful names to be used as general virus technical terms. The well defined general terms will be stored in Technical to general terms mapping table as shown Table 10.

TABLE 10

Technical to general terms mapping table

Entity\Company	F	S	T	Sy
OS	Platform	Affected Operating Systems	Platform	Systems Affected
Damaged	-	-	-	Damage
File Type	-	-	-	Target Of Infection
Alias Name	Alias	Aliases	Aliases	Also Known As
Reporter name	-	-	-	Writeup By
In the wild	-	-	In the Wild	Wild
Risk rate	-	-	Overall Risk Rating	Risk Level

F= F-Secure Corporation, S= Sophos Plc, T= Trend Micro Incorporated, Sy= Symantec Corporation

V. RESULT

After we have populated existing data of Jerusalem virus from various information sources into virus metadata tables. We found that each virus information source describes viruses in arbitrary way, some provides sufficient details and some doesn't. Table 11 is created to show what kind of mandatory virus description data that we found in each virus information source.

Table 11 shows that Trend Micro Incorporated reveals virus description covers almost all mandatory data except for OS information. Whereas Symantec Corporation is less mention on mandatory data which is required on each virus description such as virus's technique, infected environment of virus and routine process.

TABLE 11

Mandatory virus description table

Entity\Company	F	S	T	Sy	A
Virus Name	Yes	Yes	Yes	Yes	Yes
OS	No	No	No	Yes	Yes
Technique	Yes	No	Yes	No	Yes
Environment	No	No	Yes	No	Yes
Damaged description	Yes	Yes	Yes	Yes	Yes
Routine*	No	No	Yes	No	Yes
File type	Yes	Yes	Yes	Yes	Yes

F= F-Secure Corporation, S= Sophos Plc, T= Trend Micro Incorporated, Sy= Symantec Corporation, A= Our metadata, Routine* = Description has to covers all phase of the routine process.

VI. CONCLUSION

In this paper, we present metadata for computer viruses that and the well defined general virus technical terms for easily understand. The content of technical to general terms mapping table is intended to solve the conflict terms problems of various information sources. Furthermore this metadata can be used as exchangeable format among interested people or viruses' community.

REFERENCES

[1] Sanya Klongnaivai, "Malware on IT equipment", http://pclab.nectec.or.th/Documents/Support/Article/Malware.pdf.

[2] Kaspersky LabIndustry, "Classic Viruses.", http://www.viruslist.com/en/virusesdescribed?chapter=152540474

[3] Subramanya, S.R., Lakshminarasimhan, N., "Computer viruses", in *Potentials IEEE*, Volume 20, Issue 4, Oct-Nov 2001, pp. 16 – 19.

[4] Sanya Klongnaivai and Thanawit Chewaprapanon, "Polymorphic and Metamorphic Viruses: The formidable adversaries", http://www.thaicert.nectec.or.th/paper/virus/polymorphic.php.

[5] Peter Szor, "The art of computer virus research and defense", Addison Wesley Professional, 2005.

[6] F-Secure Corporation, http://www.f-secure.com.

[7] Sophos Plc., http://www.sophos.com.

[8] Trend Micro Incorporated, http://www.trendmicro.com.

[9] Symantec Corporation, http://www.symantec.com.

Consensus of Decision Trees

Suwimon Thawornchaoensukho, Sukree Sinthupinyo
Department of Computer Science, Faculty of Science and Technology,
Thammasat University THAILAND
suwimon_t@yahoo.com, sukree@cs.tu.ac.th

***Abstract*- This paper proposes a novel method which employs the idea of using differently weighted pieces of knowledge from individual learner in ensemble of decision trees. Ordinary ensemble methods use the class decided from each learner to collaboratively determine the class of an unseen example. On the other hand, our method, called Consensus of Decision Trees (CDT),uses newly defined *support values* of leaf nodes to identify theclass of the example. Experimental results using the CDT method on ten data sets selected from the UCI repository show an improvement over classical ensemble methods.**

I. INTRODUCTION

Decision Tree Learning [1] is one of classical machine learning methods. It is a well-known algorithm which is used in many classification problems. Many approaches have been proposed in order to improve the accuracy of the decision trees. One method which is often employed to improve the accuracy is to use more than one decision tree in ensemble. Popular ensemble methods are Bagging [3] and Boosting [5], both of which can increase the accuracy of the decision tree method.

The ensemble of classifier approach commonly focuses on methods of using multiple decision trees rather than using single decision tree. The ordinary ensemble method can be done as follows: training examples are first divided into a number of training subsets; the decision tree learning algorithm is then applied to each subset to construct the trees; finally, the results from each tree are collaboratively used to classify unseen examples by some simple voting schemes. In this paper, we thus present a new voting method which employs the idea of consensus theory to assign the different level of importance to each learned tree. Our method can determine the level of importance in the form of weight of each leaf node.

This paper is organized as follows. In the next part, we review the current ensemble methods as well as works related to methods on the consensus theory. We then present our methodology, followed by an experiment. Finally, we discuss the experimental results and conclude our work.

II. RELATED WORKS

In this part, we describe the general idea of ensemble methods which will be used to construct the decision trees and the idea of consensus method from which we will utilize the concept to combine the results from the trees.

A. Ensemble of Classifiers

In this paper, we focus on the ensemble of decision tree learning algorithms. Two popular decision tree ensemble methods which have been investigated for long time are Bagging and Boosting. Both share the idea of using several classifiers to classify an unseen example but different in each learner's training examples organizing. We can see in more detail from below.

Bagging [3] is a bootstrapping method [4] which randomly selects the training examples from the original training set and collects them in several subsets. So that, by using this method, one training example could be stored in multiple subsets or could be left out from being collected in any subset. The number of training example in each subset is equal to the number of the examples in the original training set. After the learning process of each decision tree, all trees are assigned the same weight. To classify an unseen example, a predicted class was determined by a plurality weight voting of all trees.

In the other popular ensemble method, Boosting [5], the trees are trained by using an ordered list of training sets. Each training set is constructed based on the performance of the previous tree. In other words, the Boosting algorithm attempts to construct new classifiers that can better predict the class of examples based on the current ensemble's performance. The organization of training set starts by randomly selecting training examples for the first tree. For the subsequent trees, the training examples are obtained from the previous trees based on weights of the training examples, which indicate the performance of the trees. There are two popular forms of Boosting, Arcing-x4 [6] and AdaBoost [5]. The Arcing-x4 (*A*daptively *R*esample and *C*ombine) chooses n examples from the original training set to construct the next classifier, where n is the size of the original training set. In the Arcing-x4 algorithm, the training examples are selected according to the probability each training example will be selected; whereas, in the Bagging algorithm, the probability each training example to be selected is all equal. We can see that in Arcing-x4, the probability of an example being selected is based on the number of misclassified examples from the previous classifier. This probability will increase if the number of misclassified examples rises.

The other popular method of the Boosting algorithm which we mention in this paper is AdaBoost method (came from Adaptive Boosting) [5].which consist of two forms of example selection. The first form is based on the probability of training examples being selected. In the second form, all examples are

used but they are assigned different weights so that the highly weighted examples can be selected more often.

Both Arcing-x4 and AdaBoost set the probability of each example to *1/n*. After recalculating the probabilities of training examples of each trained classifier, the AdaBoost determines the class of an example from the classifier.

$C_1,\ldots,C_k$ (where C_i is the i^{th} decision tree) using weighted vote. The algorithm calculates the weight of C_k from $log(B_k)$ where B_k is $(1- E_k)/E_k$ and E_k is sum of the probabilities of misclassified examples of the current classifier C_k. So that, the summation probabilities of the example to be selected of all examples is equal to one. On the other hand, the Arcing-x4 method computes the probability of the $(k+1)th$ decision tree as follow. Let p is probability, $p(k+1)(n) = (1+m(n)4)/ \Sigma(1+m(n)4)$, and $m(n)$ is the number of misclassifying classifier in $C_1 ,\ldots,C_k$ of case n.

B. Consensus methods

We can see from the previous section that the problem arises when we use multiple learners in ensemble. In Bagging and Boosting methods, when learners decide on different classes, we must use some simple voting method. However, in social science studies, when voters have different answers, *consensus* is used.

In this paper, we employ the idea of consensus to help the ensemble in making decisions, especially when examples are classified differently by multiple learners. Hence, we describe the concept and methods of reaching consensus in this section and explain how to utilize the idea of consensus in ensemble in the next section.

Concept of consensus is *"the group continues deliberation until all members of group find an acceptable solution"* [7]. Generally, the consensus theoretic method is applied either in statistical manner or mathematical manner. The statistical approach of consensus, which applied to multi-source data, such as forest map, radar data, and slope of topology, is a probabilistic method based on Bayesian decision theory. The study of this method is called the Consensus Theory. French [8] proposed three situations where the concluded opinion might be needed.

(1) The expert problem: A decision maker which is outside the group asks for advice from the group of experts or data sources.

(2) The group decision problem: The group may be jointly responsible for a decision.

(3) The text book problem: Members of the group might propose their opinions to one another at some time in the future.

Jon and Kolbeinn [9] and Jon and Philip [10] were interested in the expert problem. They used information from each data source to make decision outside the group of experts and used weighting as the mechanism to separate data sources. Jon and Kolbeinn [9] proposed two selected weight structures. The first structure is based on the idea of classical consensus theory which assigns weights to each data source but not to each group of data sources. While the other structure assigns the weights to both the data sources and the groups of data sources. Jon and Philip [10] suggested weight assessment methods as follows:

a) Equal weights. The decision maker does not have the knowledge on whether one example is more reliable than another. Therefore, all examples are equal weighted, $w_i = 1/n$; $i = 1,2,3,\ldots,n$

b) Weight proportional to ranking. The decision maker can rank each example. The weights are then assigned according to the rank. The ranking starts from 1 to n where n is the best assessment.

c) Weight proportional to a self-rating. The decision maker assigns weights to sources proportionally to the self-rating given by the sources themselves.

d) Weights based on some comparison of previously assessed distributions with actual outcomes. This weight uses *scoring rule* function which is applied using the method described in Jon and Kolbeinn [9]. The scoring rule, which can be thought in the sense of assessor to give his maximum expected score, is proposed to lead the assessor to reveal his knowledge

Mathematical approach of consensus is a form of arbitration. The expert systems provide the input and output in the first round of decision making. Keung-chi and Bruce [11] proposed the Multi-expert system (MKBs) which uses multiple experts to solve a single problem. After experts have their own opinions, all opinions are combined using the procedure below:

a) Assess the probability of each hypothesis

b) Assess the credibility of each probability, and then each expert system creates its own weight from the source

c) Create a combination rule from the probabilities and weights given by the expert systems

d) Give the final result to the user.

III. METHODOLOGY

In this paper, we integrate the idea of consensus theory into decision tree learning and propose an alternative method of ensemble learning. We name this new approach *Consensus of Decision Trees (CDT)* with the methodology described as follows.

CDT consists of two main processes: 1) learning of each tree and 2) determining the class of the example.

A. The learning of each tree

The training set of each tree is generated by using bootstrapping method, similar to the Bagging algorithm [3]. In this method, n examples are randomly selected from the original training set. The selection process is repeated n times, resulting in n subsets, each containing n examples. With this process, an example may be selected to multiple subsets or may not be selected to any subset at all. Each subset is then assigned one-to-one to a decision tree as the training set (Figure 1).

Figure 1
The learning of each tree; DTn is the nth decision tree; Rn is the class decided by the nth decision tree

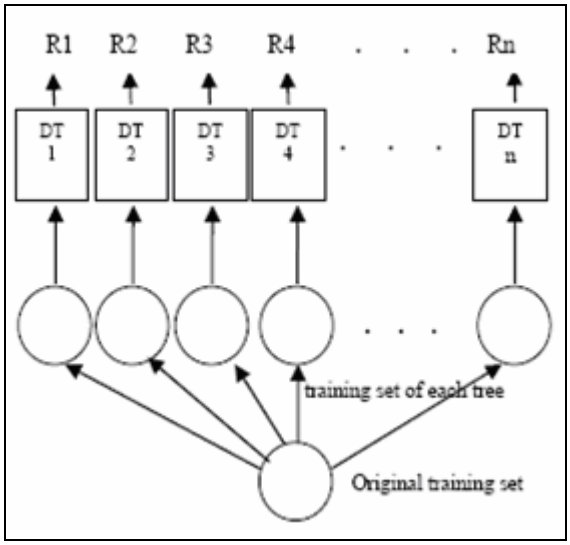

After all trees are trained, we determine a *Support Value* for each leaf in the trees, described in more detail in the next section.

B. Determining the class of the example

After all trees are trained, in order to classify a new example, we apply that example to all n trees. Thus, we will get a total of *n* answers each of which is denoted as R_n as shown in Figure 1. Unlike the classical ensemble method where the class of an example is determined by simple voting of answers from the trees, our method does not consider the answered class from the tree. Albeit, we determine the class of the example from a function of *Support value* of the leaves.

The *Support value* comes from the idea that when learners give different answers, the learner with higher confidence degree should have more influence in voting. And this confidence value should be different in each answer of the same tree.

We utilize the idea of the text book problem of French [8] to make the decision in stead of the simple voting method. Leaf nodes of the tree are similar to the member of the group in the text book problem. Each leaf node has its own answer with some confidence degree which is represented in the form of the *Support value.*

Hence, the compromising method is that the learner with less confidence or less support value should have less weight in voting.

After we present the concept of *Support value*, we can now explain how to determine this value.

First, the leaves in the trees are assigned *Support Value* which is initialized as 1. Then, the support values are adjusted using the entire original training set, each example of which is applied to all trees. The class determined by the algorithm shown in Figure 3 is selected as the class of the example. In case of wrong prediction, the *Support value* of leaf node in the tree which answers the wrong class is decreased by one while the *Support value* of the leaf node with correct answer is increased by one.

The detail of the algorithm of determining the class of the example and the algorithm of adjusting the *Support value* are shown in Figure 2 and 3, respectively.

Figure 2
Algorithm for the classifier

To classify an example *e,* we use the following procedure:

- Let P be the problem which an example is classified into class $V=\{v_1,v_2,\ldots,v_n\}$.
- $R_1,R_2,\ldots,R_m$ are the answer of decision tree $T_1,T_2,\ldots,T_m$, respectively.
- s_{iv_k} is the support value of node i which answers class v_k
- Let $L=\{l_1,l_2,\ldots,l_m\}$ is a set of leaf nodes which match the example *e*

The final result (v_{voted}) constructed by consensus method can be determined from:

$$v_{voted}=\underset{v_j\in V}{argmax}\sum_{i=1}^{m}s_{iv_j}$$

Figure 3
Algorithm for determining the Support Value

The method of determining support values of decision trees:

Let c be *Support value* of leaf node *i* and E be training set of examples

Initialize all s_{iv_k} to 1

For each learning example $e\in E$ which is class v

Classify the example e by using the approach shown in Figure 2

IF e is incorrectly classify

For each tree T_k whose answer is v_k

Increase support value s_{iv_k} of the leaf node in T_k of which node i is the answer, if $v_k=v_t$

Decrease support value s_{iv_k} of the leaf node in T_k of which node i is the answer, if $v_k\neq v_t$

V. EXPERIMENTS

To evaluate the accuracy of our method, the results were compared to results obtained from the C4.5 [2], the Bagging [3] and the Boosting [5] algorithm. In this experiment, we used the WEKA [13] tool to test the C4.5, the Bagging and the Boosting method. We constructed ten trees in ensemble style in Bagging and Boosting, similarly to our method.

The data sets come from the UCI [12] data set repository. These data sets are benchmark in machine learning studies. Our selected data sets are *balance, balloons, car, contact-lenses, mushroom, dermatology, soybean, hepatitis, Pittsburgh bridge,* and *breast cancer*. The results shown in Table I were averaged from 10- fold cross validation.

VI. CONCLUSION

We have presented the new voting method which can be used in ensemble learning of decision trees. Our method is different from classical ensemble methods such as Bagging and Boosting method in which the class of an example comes from combining of the result from each tree. The simple voting method of each tree given equal weight is used in both algorithms. On the other hand, we propose a different method in which each tree is given those unequal weights. The weights of each tree are not only unequal to another tree but also unequal to another leaf in the same tree. The experimental results also show the improvement of our method over the combining method used in classical ensemble algorithm. From our method, we obtained more accuracy than other methods run in this experiment.

REFERENCES

[1] Quinlan, J.R.(1986). "Induction of Decision Trees". In Readings in Machine Learning. Morgan Kaufmann. Orginally published in Machine Learning 1:81-106, 1986.

[2] Quinlan, J.R.(1993). "C4.5: Programs for Machine Learning". Mogra Kaufmann.

[3] Breiman, L.(1996a). "Bagging predictors". Machine Learning ,pages 123-140.

[4] Efron, B. and Tabshirani,T.(1993) "An Introduction to Bootstrap" Chapman and Hall ,New York.

[5] Freund, Y. and Schapire, R. (1996) "Experiments with a new bootsting algorithm". In Proceeding of Thirteenth International Conference on Machine Learning, pages 148-156, Bari Italy.

[6] Breiman, L. (1998). "Arcing classifiers". The Annals of Statistics, 26(3), pages 801--849.

[7] Rudolph F.V. and Kathleen S.V., The Challenge of Effective Speaking , 12thed., 2003

[8] French, S. "Group Consensus Probability Distribution: A critical Survey" in Bayesian Statistics 2, pages 183-202 J.M. Bernardo,M.H. DeGroot,D.V.Lindley, A.F.M. Smitch(eds.), New York:North Holland,1985.

[9] Jon, B. and Kolbeinn, A. "Fusion And Classification of Multitype Data" March 31, 1999.

[10] Jon, B. and Philip, S. "Consensus Theoretic Classification Method" IEEE Transaction on System, Man, and Cybernetic, VOL. 22,No 4 pages 688-704 July/August 1992.

[11] Keung-chi Ng and Bruce Abramson "Consensus in Multi-Expert System" ,1990.

[12] Murphy,P. and Aha, D.(1994). "UCI repository of machine learning database". http://www.ics.uci.edu/~mlearn/MLRepository.htm

[13] I.H. Witten and E. Frank, "Data Mining: Practical machine learning tools and techniques", 2nd Edition, Morgan Kaufmann, San Francisco, 2005.

Table I
Experimental results: means and standard derivations

Data set	CDT	DT	Bagging	AdaBoostM1
Balance	**80.98±6.06**	66.56± 4.24***	76.65± 5.86	68.33±6.70***
Balloons	78.57±12.85	68.21±15.88*	65.42±17.26**	**78.93±19.21**
Car	**95.89±1.82**	91.15± 2.24***	90.86±1.95***	70.02±3.35***
Contact-lenses	**93.33±14.05**	83.33±22.22*	83.33±22.22*	71.67±20.86***
Mushroom	**100.00±0.00**	100.00± 0.00	100.00± 0.00	96.20±0.50***
Dermatology	94.00±3.10	**94.01± 3.06**	93.20± 5.73	50.29±11.11***
Soybean	**91.76±4.96**	**91.76± 2.52**	86.18± 5.42***	24.53±5.62***
Hepatitis	81.75±12.71	77.96± 8.47	**83.08±10.11**	82.50±9.93
Pittsburgh bridges	**64.91±19.97**	62.36±20.35	64.09±16.81	56.55±13.41
Breast-cancer	95.14± 3.38	94.85± 1.93	**95.99±2.00**	95.28±2.44

*, ** AND *** DENOTE THE SIGNIFICANT LEVEL AT .10, AT .05, AND .01, RESPECTIVELY.

Combining Learned Rules in Ensembles of ILP

Yutthasit Pukdeeboon, Sukree Sinthupinyo
Department of Computer Science, Faculty of Science and Technology,
Thammasat University THAILAND
yuta.nui@gmail.com, sukree@cs.tu.ac.th

Inductive Logic Programming or ILP is aimed to construct rules which explain positive examples and exclude negative example. The learning process of ILP often takes very long time, especially in large datasets. Since the search space of the clause grows exponentially. Many works have been done using the idea of parallel learning and multiple learners to reduce the learning time. Mostly, the methodology of such methods is selecting the rules rather than combining them. There is no real combination of the rules. This paper thus proposes a new multi-learner method which can better combine results from several learners. Differently from other researches, the knowledge learned from individual learner will be used to improve the learned rules as well as to create the new rules. The results of our experiment show an improvement over other rules combining methods.

I. INTRODUCTION

Inductive Logic Programming (ILP) is a well-known machine learning algorithm. It has been used in many areas of either machine learning or data mining. ILP has advantages that background knowledge can be included and output is represented in the form of first-order rules. This makes ILP rich in expressiveness and comprehensiveness.

However, to apply the ILP algorithm to real world datasets it may take very long time to search for the rules which explain positive examples, but not negative examples, especially for the large datasets. Many approaches have been done to reduce the time spent on constructing complete and correct rules, e.g. parallel processing and multi-learner. Both employ the idea of dividing training set into smaller groups and construct the rules of each group. Finally, the rules from each dataset are selected to explain the positive examples. By using this approach, we can reduce the time for constructing the rules. Since the rules are constructed from learning in the smaller dataset, they may not cover the positive examples which are not included in their training set or they may cover the negative examples which are not included in their training set. Consequently, simply combining all rules from each group may decrease the correctness of the rule set.

This paper proposes the method which can be used to reduce the time for constructing the rules and maintain the correctness of the rule set. Our method employs multi- learner scheme by splitting the dataset into a number of smaller datasets. Then, each smaller dataset will be used as training examples for ILP algorithm to find the set of rules. All rules are then combined by selecting the set of rules from the best learner evaluated on its own training set and the clauses from other learner is finally used to improve the selected rule set. By using our method, the obtained rules are more accurate and the set of rules will better cover the entire dataset as well.

II. RELATED WORKS

A. *Inductive Logic Programming*

The basic idea of ILP consists of four parts. First, a set of positive examples which are represented the target concept, denoted as E^+. Second, a set of negative examples which are not belong to the desired concept denote as E^-. Third, a set of Horn clauses which provides background knowledge of the domain denoted as B. and the last past is the logic program representing the learned hypothesis and denoted as H.

B. *Learning Inductive Logic Programming with multi-learner*

Learning of ILP is aimed to create the rules from the background knowledge, positive and negative examples. These rules must describe the concept or pattern commonly found in the positive examples, but not the negative examples. Since the learning process of ILP takes very long time. Many researches have been done by using the idea of the multi-learner and parallel processing to solve this problem. In addition, there are some researches about the rules combining and examples selecting to get the better results. The detail is described as follows:

Reference [4] studied and compared their approach which learned by using Inductive Logic Programming in the form of parallel processing to find the best solution. They compared and evaluated three methods on the memory usage and memory type (shared memory or distributed memory) to learned the rules with the shortest processing time. The best method in their research is shown below.

Algorithm A is used to construct the rules from training set T which is divided into $\{T_1, T_2, ..., T_n\}$. The hypothesis H is obtained from applying algorithm A to T_i where $\forall i \in 1...n$. The final hypothesis can be constructed by $\cup_{i=1}^{n} H_i$ from each hypothesis H_i obtained from applying the algorithm A to T_i. By using this method, it is easy to get the final rules.

Reference [5] proposed the method which applies an ensemble method, namely Bagging, to Inductive Logic Programming. They compared two data selection methods, i.e. randomly select from dataset and select as in Bagging

selection. After that, they used Aleph [9] to construct the rules for each selected examples. The experimental results show that the simple random method is more accurate than the ensemble with Bagging selection. Because some examples in the Bagging selection are not in included in the training set, the learned rules are less complete.

Prati and Flach proposed a rule selection algorithm called ROCCER [6] which selects classification rules from a larger set of rules obtained from the rules found by Apriori [12]. Their approach relies on using ROC analysis to select rules instead of using a classical covering algorithm. A ROC graph is a plot of the fraction of misclassified positive examples (fpr) on the x axis against the fraction of correctly classified positive examples (tpr) on the y axis. A threshold-based classifier can obtain several pairs of point (fpr_i, tpr_i) by varying the threshold. If we trace a line connecting those points, we obtain a curve in the ROC space which represents the behavior of the classifier over all possible choices of their respective threshold. In a rule learning context, Furnkranz and Flach [10] showed that the rules learned by using a set covering approach can be seen as tracing of a curve in ROC space. The basic idea of ROCCER is to insert the rule into the rules list only if the insertion leads to a point outside the current ROC convex hull (the current ROC convex hull is the upper convex hull of the rules that are already in the rule list). Otherwise the rules are discarded.

Comparison with rules induction algorithms showed that ROCCER tends to produce considerably smaller rules set with compatible area under the ROC Curve (AUC). However, computational time is more expensive than other algorithms. In the worst case, the complexity is $O(n^2)$, where n is the number of rules used as the input.

Cohen and Singer proposed a rule learner called, SLIPPER [7] which uses confidence-rated boosting to learn an ensemble of rules. For the concept of SLIPPER, the rule-builder begins by randomly splitting the dataset into two disjoint subsets, i.e. GrowSet and PruneSet. The split is constrained so that the total weight of examples in GrowSet is about 2/3. The rule-builder then invokes the GrowRule routine. The GrowRule begins with empty conjunction of conditions and considers adding to this conjunction any condition~ which has the maximal values for Z_t on GrowSet where Z_t is an objective function to select the good rule. This process is repeated until the rule covers no negative examples from GrowSet, or no further improvement. However, this rule is often too specific and overfit the training data thus the resulting rule is immediately pruned using the PruneRule routine. PruneRule considers deleting any final sequence of conditions from the rule. Each sequence of deletions defines a new rule whose goodness is evaluated on PruneSet. Moreover, it is possible for a weak-leaner to generate the same rule several times. Therefore, after the last round of boosting, the final strong-hypothesis is compressed by removing duplicate rules. Experimentally, SLIPPER scales no worse than $O(n \log n)$, where n is the number of examples.

Reference [8] proposed the method to reduce the error in example data before taking it to be learned by filtering the data. There are two ways of filtering data, by giving the score and by weighting using boosting method. The principle of giving score is to divide the examples into *n* groups equally. Then, the examples are learned *n* times and each time of learning will skip one group. After that, the examples in the skipped dataset are tested for the correctness then the learned rules are given the score according to the correctness on each dataset. This approach is called cross-validated committees filter.

To weight the examples by Boosting method, the concept is that if the dataset with high error rate is learned, it has likelihood to be highly weighted. This helps us to find the high error rate dataset. Experimental results showed that the given score by their proposed methods can better reduce the error rate than weighting method of Boosting approach.

III. KNOWLEDGE EXCHANGEABLE ILP LEARNERS

Earlier in previous section, we demonstrated many works have been proposed, but none of them has paid special attention on the learned rules from each learner. Hence, this paper proposes the method which can integrate the learned rules from different learners. Our proposed method is called Knowledge Exchangeable ILP Learners (KEIL).

The ILP learners are fed by training sets which have the same distribution as the original training set. After each learner learns its own hypotheses, it exchanges its hypotheses with other learner's.

Before we explain the procedure of knowledge exchanging between the learners, we must define the basic element of the hypotheses which are represented in the form of first-order rules as follows:

Definition 1: Literal chain is the set of literals $\{l_1, l_2, ..., l_n\}$ in the body of a rule.The input variables of literal l_j must be the output of literal l_i with $i > j$ and in the last literal l_n , there must be no output variable occurring in other literals in the rule which are not included in this chain.

The idea of the literal chain is close to the idea of open chain and closed chain proposed in [11] but our definition is looser. For more details about the literal chains please refer [11]. To illustrate the concept of literal chain, we show an example of the literal chains in Fig. 1.

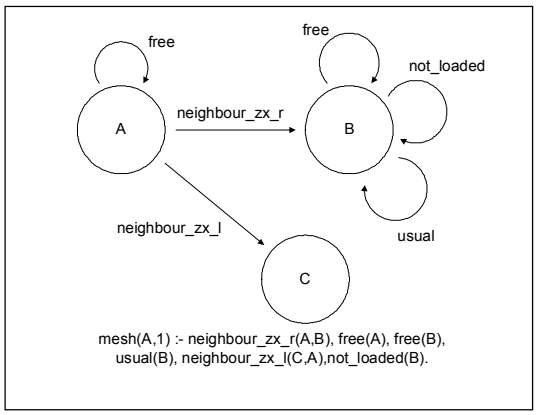

Fig. 1. An example of literal chain.

After defining the definition of literal chain, we can explain learning procedure as follows:

- Randomly divide the training set E which consists of positive examples and negative examples into $E_1, E_2, ..., E_n$.
- Use the learners $L_1, L_2, ..., L_n$ to create the hypotheses set $H_1, H_2, ..., H_n$ from $E_1, E_2, ..., E_n$, respectively. Each hypotheses set must obey the condition $H_i \cup B \models E_i^+$ and $H_i \cup B \not\models E_i^-$ where B denotes the background knowledge.
- Select hypotheses set H_i which is most accurate on its own training set E_i to be the base hypotheses set. Then adjust the hypotheses set H_i by
    - For each positive example e^+ in E_i which is not covered by H_i.
        - Insert a hypothesis h from H_j where $i \neq j$ and $\{h\} \cup B \models e^+$ into H_i. If $\{h\} \cup B \models E_k^-$ where $k \neq j$, it is required to adjust h to be more specific by adding one or more literal chains having common structure with h from H_k to h as h' whose accuracy is higher than the accuracy of h on training set E.
    - For each positive example e^+ in E_j which is not covered by H_i.
        - Insert a hypothesis h fro H_j where $i \neq j$ and $\{h\} \cup B \models e^+$ into H_i. If $\{h\} \cup B \models E_k^-$ where $k \neq j$, it is required to specialize h by adding one or more literal chains having common structure with h from H_k to h as h' whose accuracy is higher than the accuracy of h on learning dataset E.
- Use the modified hypotheses set H_i to classify test examples.

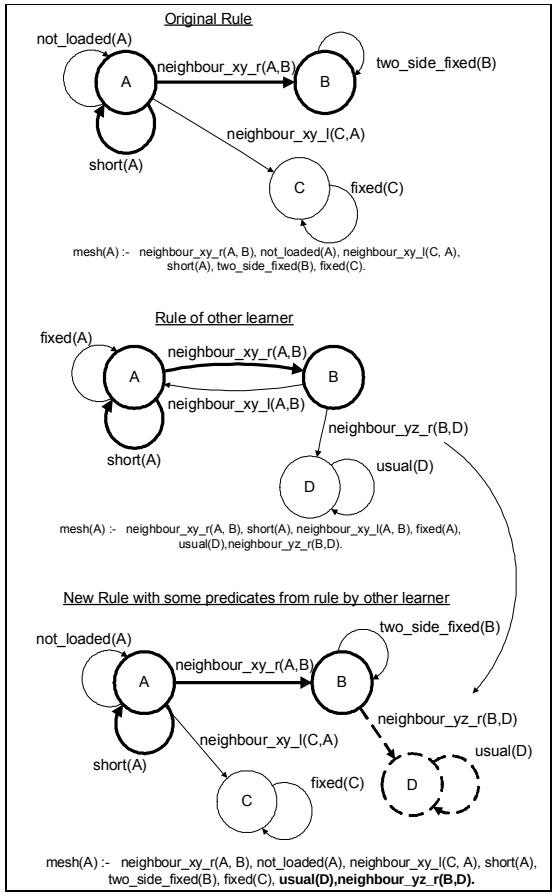

Fig. 2. Example of rule adjustment by adding literal chains from other learners

Fig. 2 illustrates how to improve the accuracy of the hypotheses set discovered by the best learner. The original hypothesis is represented in the form of first-order rule. From the figure, we assume that the original rule is too general (It means that this original rule covers some negative examples of other learners' training set), therefore we want to specialize this rule. The literal chain from the middle graph has some common structures so that we can combine these two chains. The result of combination is shown in the bottom graph. Furthermore, an example of the entire process is shown in Fig. 3.

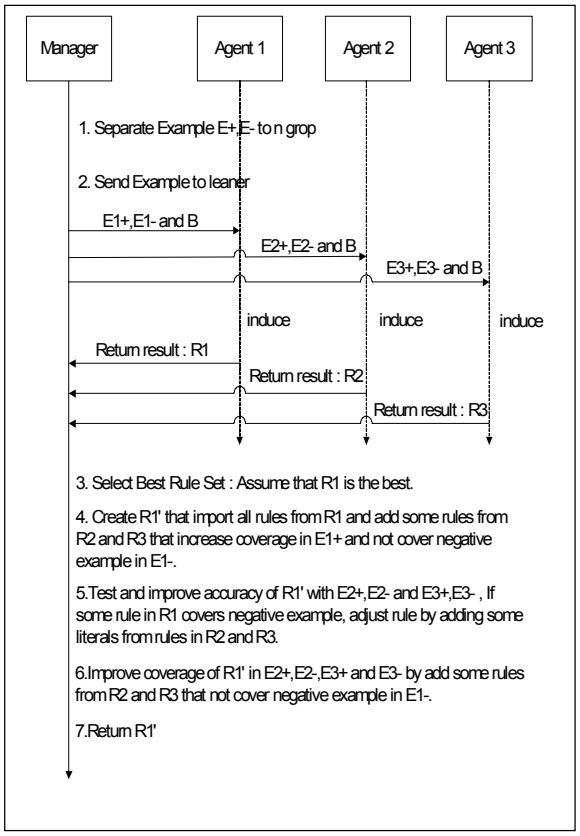

Fig. 3. shows learning process with separated dataset and how to combine result from each learner

IV. Experimental Results

We ran the experiments on three benchmarks, namely Mutagenesis, Carcinogenesis and finding the number of Finite-Element Mesh. In the last dataset, the original problem is to find the number of finite element in given structures. This problem is multi-class and it is too complicated to handle examples in multi-class fashion. We hence relax this problem by transforming it into two two-class problems which are distinguishing class one from the others (Mesh1) and distinguishing class two from the others (Mesh2).We compared our method (KEIL) to two other simple rules combining methods, i.e. All Rules (AR) and Best Learner (BL), by running 5-fold cross validation. The ILP learner used in this experiment was Aleph [9]. The results with statistical significance tested by the one-tail paired t-test are shown in Table 1.

We can see from the table that our method performed well on all datasets and better than two simple rule combining methods compared in our experiment.

TABLE I
ILLUSTRATES THE RESULTS THAT EVALUATE OUR METHOD (KEIL) COMPARING TO ALL RULES (AR) WHICH UNIONS ALL RULES FROM ALL LEARNERS AND BEST LEARNER (BL) WHICH USES THE RULES OF THE BEST LEARNER. *, **, *** AND **** DENOTE THE SIGNIFICANT LEVEL UNDER .10, AT .10, AT .05, AND .01, RESPECTIVELY.

Dataset	KEIL	AR	BL
Mesh1	90.36±1.78	84.92±2.44****	87.10±2.34****
Mesh2	84.29±2.30	79.32+4.02****	81.03±2.09**
Muta	89.36±4.25	81.38±6.77***	82.50±5.64**
Carcino	59.02±5.36	55.99±5.78**	49.66±2.51****

V. Summary

This paper has illustrated the way to use multi-learner to collaboratively construct the hypotheses by Inductive Logic Programming algorithm. Each learner creates the different hypotheses from disjoint training sets. By using this training scheme, the learner cannot see the others' training sets. We thus propose the idea of Knowledge Exchangeable ILP Learners which can import the knowledge represented in the form of the rules from other learners. To evaluate the efficiency of our method on combining rules, we conducted experiments by comparing to two simple rules combining methods, i.e. AR and BL. The results showed that our method can better combine the rules and obtain the higher accuracy than the other methods.

References

[1] S. Muggleton, editor, "Inductive Logic Programming," *Academic Press*, 1992.

[2] S. Muggleton, L. De Raedt, "Inductive Logic Programming: Theory and Methods," *Journal of Logic Programming*, 19,20, 1994, pp. 629-679.

[3] S. Muggleton and C. Feng, "Efficient Induction of Logic program," *Proceedings of the 1st Conference on Algorithmic Learning Theory*, 1990, pp. 368-381.

[4] Nuno A. Fonseca, Fernando Silva, and Rui Camacho, "Strategies to Parallelize ILP Systems," *In the Proceeding of 15th International Conference on Inductive Logic Programming (ILP 2005)*, August 12, 2005.

[5] Ines de Castro Dutra, David Page, Vitor Santos Costa and Jude Shavlik. ,"An Empirical Evaluation of Bagging in Inductive Logic Programming.," *In Proceeding Of the International Conference. on Inductive Logic Programming,* July 2002, Sydney, Australia.

[6] Ronaldo C. Prati, and Peter A. Flach.,"Roccer: an Algorithm for Rule Learning Based on ROC Analysis," *In: Proceedings of the 19th International Joint Conference on Artificial Intelligence (IJCAI'05)*, pages 823--828. IJCAI, August 2005.

[7] W. Cohen and Y. Singer, "A Simple, Fast, and Effective Rule Learner," *Proc. of 16th National Conference on Artificial Intelligence*, 1999.

[8] S. Verbaeten and A. V. Assche.,"Ensemble methods for noise elimination in classification problems," *In Proceedings of 4th International Workshop on Multiple Classifier Systems*, 2003

[9] A. Srinivasan. The Aleph Manual, 2001.

[10] J. Furnkranz and P. Flach, "ROC'n'rule learning – toward a better understanding of rule covering algorithms," *Machine Learning*, 58(1):39-77,2005.

[11] Boonserm Kijsirikul, Sukree Sinthupinyo, and Kongsak Chongkasemwongse, "Approximate Match of Rules Using Backpropagation Neural Networks," *Machine Learning Journal*, Volume 44, Issue 3, September, 2001.

[12] F. Bodon, "A fast apriori implementation," In *Proceedings of the IEEE ICDM Workshop on Frequent Itemset Mining Implementations*, 2003.

Bottom-Up Hierarchical Clustering in *CC*-Complete

Raymond Greenlaw
Department of Computer Science
Armstrong Atlantic State University
11935 Abercorn Street
Savannah, Georgia 31419-1997
Email: greenlaw@armstrong.edu

Sanpawat Kantabutra
The Theory of Computation Group
Computer Science Department
Chiang Mai University
Chiang Mai, 50200, Thailand
Email: sanpawat@alumni.tufts.edu

***Abstract*— Complex data sets are often unmanageable unless they can be subdivided and simplified in an intelligent manner. *Clustering* is a technique that is used in data mining and scientific analysis for partitioning a data set into groups of similar or nearby items. *Hierarchical clustering* is an important and well-studied clustering method involving both top-down and bottom-up subdivisions of data. In this paper we address the parallel complexity of bottom-up hierarchical clustering. We describe a sequential algorithm for bottom-up hierarchical clustering. We then define a natural decision problem based on this algorithm, and add this** HIERARCHICAL CLUSTERING PROBLEM **(HCP) to the list of *CC*-complete problems, thereby showing that HCP is one of the computationally most-difficult problems in the** COMPARATOR CIRCUIT VALUE PROBLEM **(CCVP) class. This class contains a variety of interesting problems, and now for the first time a problem from data mining as well.**

I. INTRODUCTION

Clustering is a division of data into groups of 'similar' objects, where each group is given a more-compact representation. When researchers represent data by using fewer clusters, they necessarily lose certain finer details, but achieve a simplification of sorts. Researchers use clusters to model very large data sets. It is worth presenting an example of some clusters to get an intuitive feel for this topic. Figure 1 shows a set of points in the plane which have been partitioned into four clusters. All points within the same cluster are somewhat closer or more similar to points in their own cluster than they are to points in the other clusters.

Clustering has its roots in mathematics, statistics, and numerical analysis; clustering is the subject of active research in several fields including pattern recognition and machine learning. In particular, clustering is a useful tool in data mining, where immense data sets which are difficult to store and to manipulate are involved. In this paper we study the parallel complexity of the (bottom-up) *hierarchical clustering problem*. This problem is one of the most-popular ones in the clustering literature, and in what follows we review some of the related work.

Hierarchical clustering builds a *tree of clusters*. Sibling clusters in this tree partition the points associated with their parent, thereby producing a further refinement of the data. From the opposite viewpoint, parents remove structure from the representation of the data by grouping together the data corresponding to their children. This approach permits one to explore data using various levels of granularity. There are two widely studied methods for hierarchical clustering: *bottom-up* and *top-down* [9], [11]. As the name suggests, a bottom-up approach starts with single-point clusters and then recursively merges two or more of the most-'appropriate' clusters. A top-down approach starts with one large cluster consisting of all of the data points and then recursively splits the most-'appropriate' cluster. In each of these two clustering methods, the process continues until a desired stopping condition is met. The stopping conditions can be one of several things such as a required number of clusters or a bound on the diameter of the 'largest' cluster.

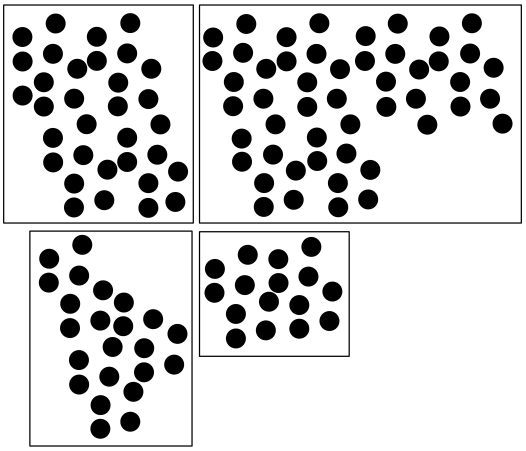

Fig. 1. A set of points partitioned into four clusters.

A variety of sequential versions of hierarchical clustering methods have been studied. We now mention a few of them. Guha et al. introduced the bottom-up hierarchical clustering algorithm CURE. Empirical evidence indicates this algorithm is good for clusters having arbitrary shapes and/or *outliers*, that is, points which do not fit into any appropriate cluster [8]. Another bottom-up hierarchical clustering algorithm called CHAMELEON was introduced by Karypis et al.; their algorithm relies heavily on graph partitioning [10]. Boley introduced the PRINCIPAL DIRECTION DIVISIVE PARTITIONING ALGORITHM; his algorithm is a top-down hierarchical approach for clustering document collections [2]. Steinbach et al. proposed another top-down hierarchical approach called

HIERARCHICAL DIVISIVE BISECTING k-MEANS [18].

A number of papers have also been written on the topic of parallel hierarchical clustering for various models of computing. When there are n input points, Olson described $O(n)$-time algorithms for hierarchical clustering using various linkage metrics on an n-processor Concurrent-Read Concurrent-Write Parallel Random Access Machine (CRCW PRAM). He also gave $O(n \log n)$-time algorithms for these metrics on butterfly networks and trees, where $n/\log n$ processors were required [15]. Li and Fang presented a single-link hierarchical clustering algorithm with an $O(n \log n)$ running time on a Simultaneous Instruction Multiple Data (SIMD) hypercube multiprocessor having *mn* processors, where n is the number of points and m is the number of dimensions [13]. In another paper by Li, he gave $O(n^2)$-time parallel algorithms on an n-processor SIMD shuffle-exchange network for n-point hierarchical clustering and cluster-validity computation [12]. When there are n input points, an $O(\log^2 n)$-time algorithm was given by Tsai et al. that uses an n^3-processor array with a reconfigurable-bus system [19]. Wu et al. discussed an $O(\log n)$-time hierarchical clustering algorithm which uses n^3 processors on a model with reconfigurable optical buses, where there are n points [20]. Let c denote the number of partitioned cells. Dash et al. provided an $O((n^2 \log n/c)/p)$-time parallel hierarchical clustering algorithm on a shared-memory multiprocessor architecture that uses p processors [5]. More recently, Rajasekaran presented an $O(\log n)$-time randomized hierarchical clustering algorithm which uses $n^2/\log n$ processors on the CRCW PRAM [16].

The outline of this paper is as follows: §II covers preliminaries and notation; §III describes a bottom-up sequential algorithm for hierarchical clustering; in §IV we state our main results; and §V contains conclusions and open problems.

II. NOTATION AND PRELIMINARIES

Let $\mathbb{N} = \{1, 2, 3, \ldots\}$ denote the set of natural numbers. Let $\mathbb{R}$ denote the set of real numbers, $\mathbb{R}^+$ the positive real numbers, and $\mathbb{R}^d$ the d-fold Cartesian product of $\mathbb{R}$. Let x and y denote two distinct points. When we choose two points from a set, we always assume that the points are distinct. We use $d(x, y)$ to denote the distance between x and y with respect to a distance measure d. If $x, y \in S$, we subscript the notation with S to $d_S(x, y)$ to denote the distance between x and y in S with respect to the distance measure d. Let S and T be sets of points. We use the notation $d_{\min}(S, T)$ ($d_{\max}(S, T)$) to denote the minimum (respectively, maximum) distance between *any* pair of points, where one point comes from S and the other point comes from T.

We are interested in relating the complexity of hierarchical clustering to that of a problem involving Boolean circuits containing a special type of gate. A *comparator* gate has two output wires and outputs the minimum of its two inputs on its first output wire and outputs the maximum of its two inputs on its second output wire. Furthermore, comparator gates are restricted so that each output has fanout at most one. We next define an important problem in complexity theory that is based on the comparator gate, and shortly define an entire complexity class based on this problem.

COMPARATOR CIRCUIT VALUE PROBLEM (CCVP)
GIVEN: An encoding $\overline{\alpha}$ of a Boolean circuit α composed of comparator gates, inputs $x_1, \ldots, x_n$, and a designated output y.
PROBLEM: Is output y of α TRUE on input $x_1, \ldots, x_n$?

We discuss a number of fundamental complexity classes in this work. Let *P* denote the class of all languages decidable in polynomial time. Let *NC* denote the class of all languages decidable in poly-logarithmic time using a polynomial number of processors on a PRAM. Let *CC* denote the class of all problems that are *NC* many-one reducible to CCVP (see Mayr and Subramanian [14]). We will use the notation $\leq_m^{NC}$ to denote *NC* many-one reducibility. For more background the reader is referred to Greenlaw, Hoover, and Ruzzo [6].

The *P*-complete problems are believed to be inherently sequential. Problems that are *CC*-complete are considered unlikely to be *P*-complete, but no fast parallel algorithms are known for them, with the exception of some $\sqrt{n}(\log n)^{O(1)}$ time algorithms that use $\sqrt{n}$ processors. So far, there are only nine known *CC*-complete problems, and they include CCVP plus the following: STABLE MARRIAGE PROBLEM, and LEXICOGRAPHICALLY FIRST MAXIMAL MATCHING PROBLEM, among others. It is known that $CC \subseteq P$, but *NC* and *CC* are incomparable using the subset relation. We should point out that if a problem is *CC*-complete, then that problem is very unlikely to have an *NC* algorithm. When we prove the equivalence of the HCP and the CCVP in §IV, we demonstrate that hierarchical clustering of this type is unlikely to have a feasible highly parallel algorithm. This result shows that the HCP is *CC*-complete.

III. BOTTOM-UP HIERARCHICAL CLUSTERING ALGORITHM

We describe the bottom-up hierarchical clustering algorithm. As input, the algorithm takes a set of points, a distance function, and the desired number of clusters k. The algorithm first pairs up all points starting with the two closest ones, then the next remaining two closest ones, and so on, until all points are paired. Next the sets of points X and Y minimizing $d_{\min}(X, Y)$ over all remaining sets are merged, until only k sets remain.

SEQUENTIAL (BOTTOM-UP) HIERARCHICAL CLUSTERING ALGORITHM

{ Input: A set S of points $p_1, \ldots, p_n$ in $\mathbb{R}^d$, where n is even, a distance function $d_S : S \times S \mapsto \mathbb{R}^+$, a distance bound B, and $k \leq n/2 \in \mathbb{N}$. }
{ Output: A partition of S into k groups. }
begin
  $S \leftarrow \{ p_1, \ldots, p_n \}$;
  for $i \leftarrow 1$ to $n/2$ do
    $C_i \leftarrow \emptyset$;

```
  // initialize leftover
  leftover ← n/2 + 1;
  T ← ∅;
{ Comment: First-phase. }
  for i ← 1 to n/2 do {
    choose x, y ∈ S such that d_S(x, y) is a
      minimum;
    if d_S(x, y) > B then {
      let T be the set of singleton sets of all
        remaining points including x and y;
      leftover ← i;
      break;
    }
    C_i ← { x, y };
    S ← S − C_i;
  } // end of for loop
  partition-set ← { C_1, ..., C_(leftover − 1) }
    ∪ T;
  number-partitions ← ( leftover − 1 )
    + |T|;
{ Comment: Second-phase. }
  while (number-partitions > k) do {
    choose C_a and C_b so that d_min(C_a, C_b)
      is a minimum over partition-set;
    partition-set ← partition-set ∪
      { C_a ∪ C_b } − { C_a } − { C_b };
    number-partitions−−;
  }
  output partition-set;
end.
```

The algorithm operates in a bottom-up fashion. Without loss of generality, we have assumed that the number of input points is even. Depending on the distribution of the initial points, the algorithm may, for example, form $k-1$ clusters having two points and one cluster containing the remaining points. If, for example, the points are distributed uniformly in the Cartesian plane and d_S is the Euclidean distance, then the clusters are expected to be balanced in terms of size. Note that there are no restrictions placed on the distance function d_S. For technical reasons in the first-phase of the algorithm we only cluster points whose distance is less than or equal to B. This version of the hierarchical clustering algorithm is equivalent to the standard version if B is greater than $d_{\max}(S,S)$. The algorithm clearly operates in polynomial time. In §IV we will focus on the complexity of the first-half of this algorithm.

IV. The Complexity of Hierarchical Clustering

A. Decision Problems

We begin here by defining a natural decision problem based on the Sequential (Bottom-Up) Hierarchical Clustering Algorithm.

> Hierarchical Clustering Problem (HCP)
> Given: A set S of n points in $\mathbb{R}^d$, a distance function $d_S : S \times S \mapsto \mathbb{N}$, number of clusters $k \leq n/2 \in \mathbb{N}$, a distance bound B, and two points $x, y \in S$.
> Problem: Are x and y with $d_S(x,y) \leq B$ in the same cluster C after the first-phase of the Sequential (Bottom-Up) Hierarchical Clustering Algorithm?

Note that in the definition of the HCP there are no restrictions placed on the properties that the distance function must satisfy. Obviously, this version of the problem easily reduces to the version of the problem where the weights come from $\mathbb{R}^+$. When we define distance functions, we are not concerned with the distance between a point and itself. The k specified in the instance of the problem refers to the number of clusters to be formed. Observe that the definition also requires that x and y be no further apart than the distance bound B.

In the statement of the HCP we were careful about the restrictions placed on the distance function since the complexity of the Distance Geometry Problem (*DGP*) is interesting in and of itself [1]. That is, given $n, d \in \mathbb{N}$ and $n(n-1)/2$ distances $d_{ij} \in \mathbb{R}$, where $1 \leq i, j \leq n$, and zeros on the diagonal, can it be determined whether or not there are n points $x_1, \ldots, x_n \in \mathbb{R}^d$ such that using the Euclidean distance between points, we have $|x_i - x_j| = d_{ij}$ for $1 \leq i, j \leq n$? The DGP can be solved sequentially in $O(n^{d+3})$ time (Personal Communication, Geir Agnarsson, 2006). We needed to define the HCP, so that the DGP's complexity did not dominate the complexity of the problem that we were really interested in studying.

We define the Lexicographically First Maximal Matching Problem (LFMMP), which we need in the proofs of Theorems 4.1, 4.2, and 4.3, as follows:

> Given: An undirected graph $G = (V, E)$ with an ordering from 1 to $|E|$ on its edges plus a distinguished edge $e \in E$.
> Problem: Is e in the lexicographically first maximal matching of G?

B. Main Theorems

Here we state our main results. Proofs may be found in our full paper [7]; most details are omitted here due to space limitations.

Theorem 4.1: The Hierarchical Clustering Problem is NC many-one reducible to the Lexicographically First Maximal Matching Problem, that is, HCP $\leq_m^{NC}$ LFMMP.

The next theorem shows that the HCP is *CC*-hard.

Theorem 4.2: The Lexicographically First Maximal Matching Problem is NC many-one reducible to the Hierarchical Clustering Problem, that is, LFMMP $\leq_m^{NC}$ HCP.

Proof: We perform an *NC* many-one reduction from the LFMMP to the HCP. Let $G = (V = \{1, \ldots, n\}, E)$, $\phi : E \mapsto \{1, \ldots, |E|\}$ be an ordering on E, and $e = \{u, v\} \in E$ be an instance of the LFMMP. From this instance of the LFMMP, we construct an instance of the HCP, that is, a set S of n points $p_1, \ldots, p_n$ in $\mathbb{R}^d$, a distance function $d_S : S \times S \mapsto \mathbb{N}$, the number of clusters $k \leq n/2 \in \mathbb{N}$, a distance bound B, and

two points $x, y \in S$. We now describe the reduction, which we will call f.

Let $S = \{1, \ldots, n, n+1, \ldots, 2n\}$. The first n points in S represent the vertices in V. The second n points are needed to balance out the clusters; call these values V', that is, $V' = \{n+1, \ldots, 2n\}$. We define the distance function between each pair of points in S as follows:

$$\begin{aligned} d_S(x,y) &= \phi(\{x,y\}) && \text{if } \{x,y\} \in E \\ &= 2|E| && \text{if } x \in V \text{ and } y \in V' \text{ or vice versa} \\ &= 3|E| && \text{if } x \in V', y \in V', \text{ and } x \neq y \\ &= 4|E| && \text{if } x \leq n, y \leq n, x \neq y, \\ & && \quad \text{and } \{x,y\} \notin E \end{aligned}$$

We let $B = |E|$, $k = n$, and choose u and v as our two points. It is clear that f is an *NC* many-one reduction. We next examine the correctness of f.

We claim that edge $e = \{u, v\}$ is in the lexicographically first maximal matching M of G if and only if the pair of points u and v is clustered in the first-phase of the SEQUENTIAL (BOTTOM-UP) HIERARCHICAL CLUSTERING ALGORITHM. We prove an even stronger result by showing that edge $\{u, v\}$ is the t-th edge added to the lexicographically first maximal independent set in G if and only if the set of points u and v with $d_S(u, v) \leq B$ is the t-th set of points clustered in the first-phase of the algorithm. We prove this result by induction on t.

By the values of the distances assigned by the reduction f, the base case holds since $e = \{u, v\}$ with $\phi(e) = 1$ is the first edge added to the matching if and only if $d_S(u, v) = 1 \leq B$ is the minimum distance between any pair of points in S which is if and only if u and v are put in the same cluster in the first step of the first-phase of the algorithm.

The remaining details of the proof may be found in [7] and are omitted here due to space limitations.

■

We combine Theorems 4.1 and 4.2 to obtain our main result.

Theorem 4.3: The HIERARCHICAL CLUSTERING PROBLEM is CC-complete.

Theorem 4.3 expands the list of *CC*-complete problems and places the very first clustering/data mining problem into this category. We should point out that the Euclidean version of the HCP in which the distance function is the Euclidean distance function is in *CC*. The Euclidean HCP is, of course, a special case of the HCP. It is an open problem whether or not the Euclidean HCP is *CC*-complete.

The results in this section show that it is very unlikely that there is an *NC* algorithm for the HCP. We have focused on the first-phase of the SEQUENTIAL (BOTTOM-UP) HIERARCHICAL CLUSTERING ALGORITHM. Notice that the first-phase of this algorithm can be reduced to the second-phase of the algorithm by considering each point as a singleton set, setting `number-partitions` equal to $n/2 + 1$, and taking k equal to 1. It is not clear how to reduce the second-phase of the algorithm, involving potentially large sets of points, to the singleton sets considered in the first-phase of the algorithm. These remarks indicate that there is the possibility for a decision problem based on the overall SEQUENTIAL (BOTTOM-UP) HIERARCHICAL CLUSTERING ALGORITHM to be more complex than the HCP.

V. CONCLUSIONS AND OPEN PROBLEMS

We have shown that a natural decision problem based on bottom-up hierarchical clustering is *CC*-complete, while in contrast in our full paper [7], we showed that top-down hierarchical clustering is in *NC*. It is an interesting open problem as to whether or not the Euclidean HCP is *CC*-complete. Knowing the complexity of the second-phase of the SEQUENTIAL (BOTTOM-UP) HIERARCHICAL CLUSTERING ALGORITHM would be very interesting since this result would shed additional light on the complexity of hierarchical clustering itself. Adding new problems to the class of *CC*-complete problems would also be of interest.

REFERENCES

[1] L. M. Blumenthal. *Theory and Applications of Distance Geometry*. Oxford University Press, 1953.

[2] D. L. Boley. Principal direction divisive partitioning. *Data Mining and Knowledge Discovery*, 2(4):325–344, 1998.

[3] K. W. Chong, Y. Han, and T. W. Lam. Concurrent threads and optimal parallel minimum spanning tree algorithms. *Journal of the ACM*, 48(2):297–323, 2001.

[4] R. Cole. Parallel merge sort. *SIAM Journal on Computing*, 17(4):770–785, 1988.

[5] M. Dash, S. Petrutiu, and P. Scheuermann. Efficient parallel hierarchical clustering. *Lecture Notes in Computer Science*, 3149:363–371, 2004.

[6] R. Greenlaw, H. J. Hoover, and W. L. Ruzzo. *Limits to Parallel Computation: P-Completeness Theory*. Oxford University Press, 1995.

[7] R. Greenlaw and S. Kantabutra. On the parallel complexity of hierarchical clustering and CC-complete problems. Unpublished manuscript, 19 pages, 2006.

[8] S. Guha, R. Rastogi, and K. Shim. Cure: An efficient clustering algorithm for large databases. In *ACM SIGMOD*, pages 378–385, Seattle, WA, 1998. Association for Computing Machinery.

[9] A. Jain and R. Dubes. *Algorithms for Clustering Data*. Prentice-Hall, 1988.

[10] G. Karypis, E. H. Han, and V. Kumar. CHAMELEON: A hierarchical clustering algorithm using dynamic modeling. *IEEE Computer*, 32(8):68–75, 1999.

[11] L. Kaufman and P. Rousseeuw. *Finding Groups in Data: An Introduction to Cluster Analysis*. John Wiley and Sons, 1990.

[12] X. Li. Parallel algorithms for hierarchical clustering and clustering validity. *IEEE Trans. Pattern Analysis and Machine Intelligence*, 12(11):1088–1092, 1990.

[13] X. Li and Z. Fang. Parallel clustering algorithms. *Parallel Computing*, 11(3):275–290, 1989.

[14] E. W. Mayr and A. Subramanian. The complexity of circuit value and network stability. *Journal of Computer and System Sciences*, 44(2):302–323, 1992.

[15] C. F. Olson. Parallel algorithms for hierarchical clustering. *Parallel Computing*, 21(8):1313–1325, 1995.

[16] S. Rajasekaran. Efficient parallel hierarchical clustering algorithms. *IEEE Transactions on Parallel and Distributed Systems*, 16(6):497–502, 2005.

[17] J. H. Reif, editor. *Synthesis of Parallel Algorithms*. Morgan Kaufmann, 1993.

[18] M. Steinbach, G. Karypis, and V. Kumar. A comparison of document clustering techniques. In 6^{th} *ACM SIGKDD World Text Mining Conference*, Boston, MA, 2000. Association for Computing Machinery.

[19] H. R. Tsai, S. J. Horng, S. S. Lee, S. S. Tsai, and T. W. Kao. Parallel hierarchical clustering algorithms on processor arrays with a reconfigurable bus system. *Pattern Recognition*, 30(5):801–815, 1997.

[20] C. H. Wu, S. J. Horng, and H. R. Tsai. Efficient parallel algorithms for hierarchical clustering on arrays with reconfigurable optical buses. *Journal of Parallel and Distributed Computing*, 60(9):1137–1153, 2000.

LMC: Label-based Metadata Creation

Pitsanu Lousangfa, Naiyana Sahavechaphan, Jedsada Phengsuwan, Seksit Suwan
Large Scale Simulation Lab
National Electronics and Computer Technology Center (NECTEC)
112 Thailand Science Park, Pahon Yothin Rd., Klong 1, Klong Luang, Pathumthani 12120 Thailand
Tel: 662-564-6900 Ext.2279, Fax: 662-564-6772
Email: pitsanu.lousangfa|naiyana.sahavechaphan|jedsada.phengsuwan|seksit.suwan@nectec.or.th

***Abstract*— Clustering elements defined in schemas has been recognized for reducing the number of element-to-element comparisons and hence improving the schema matching performance. A cluster of elements is typically identified by a *metadata* in which it is dominant in the match operation to further determine the match of its element members. The effectiveness of schema matching thus relies on the quality of metadata. To the best of our knowledge, the metadata created by previous approaches is dependent on either the predefined concepts which prohibits an automatic metadata creation, or inefficient inputs that results in poor metadata. In this paper, we propose a novel metadata development based on element labels using a linguistic technique. Specifically, the metadata is linguistically related to its element members. In this work, we have defined three metadata creation algorithms, namely *distinct-based* (DM), *synonym-based* (SM) and *relation-based* (RM) metadata creation algorithms. Our experiments showed that a metadata can be automatically created without predefined concepts (rules) and be a potential representative of its element members as shown by their similarity distances. In addition, RM provided a better metadata with respect to the number of tokens than SM and DM do.**

Keywords: Schema matching, Similarity distance, Difference distance, Cluster Metadata

I. INTRODUCTION

Schema matching [2], [5] has been recognized in several database application domains such as schema integration, data warehouse, e-commerce and semantic query processing. Its fundamental operation is *match* which takes two schemas as input and produces a mapping between elements of the two schemas that correspond semantically to each other. The *match* operation [1] is typically done in a pairwise fashion in which all possible pairs of elements are compared, resulting in unreasonably large tasks especially since most pairs do not represent the same information. To efficiently reduce the number of element-to-element comparisons, elements should be clustered into categories where each category is identified by *metadata*. The category metadata, instead of its element members, is in turn used in the process of match operation to further determine the match of its element members.

Today, some approaches ranging from element-based to content-based heuristics have been proposed in the literature [1], [2] to achieve this. In the absence of data instances (or content), Cupid [2] clusters elements and defines metadata based on either data types or concepts of tokens encapsulated in element names. Here, only all possible pairs of elements, e_s and e_t, in compatible categories of two schemas, S_s and S_t, are compared to find the matching pairs where compatible categories are determined by comparing all tokens in two given categories. While this approach provides appropriate metadata, the metadata itself is heavily dependent on concepts predefined by experts, prohibiting an automatic metadata creation or resulting in poor metadata with nonexistence of concepts. In addition, the application of metadata is totally discarded in the match operation. SemInt [1] trains neural networks to classify elements according to element specifications (i.e. type, length and value constraint) and data values (i.e. patterns and statistics). Each category is represented by *weight-based* metadata. The match between the source element (e_s) and weight-based metadata (the representative of target elements e_t) implies that e_s potentially matches with all e_t. While this approach infers element relationships unrecognized by programmers, it is limited to numeric convertible inputs (i.e. data type, key and value constraint), making it inapplicable for element names which contains the useful information. In addition, metadata based solely on such inputs is inefficient as they encapsulate either syntactic or ambiguous semantic information.

While these approaches take steps into the right direction, each approach individually is limited to the *quality* of metadata produced. To address the previous drawbacks, in this paper, we propose a novel metadata development based on element names (or labels) using a linguistic technique. Specifically, the metadata is linguistically related to its element members. In this work, we have defined three metadata creation algorithms, namely *distinct-based* (DM), *synonym-based* (SM) and *relation-based* (RM) metadata creation algorithms. Our experiments showed that a metadata can be automatically created without predefined concepts (rules) and be a potential representative of its element members as shown by their similarity distances. In addition, RM provided a better metadata with respect to the number of tokens than SM and DM do.

Roadmap: The rest of this paper is organized as follows: Section II describes three metadata creation methods. Experimental evaluation is given in Section III. We conclude in Section IV.

II. METHODOLOGY FOR METADATA CREATION

In this work, we consider metadata as a representative of a group of element labels (not data contents) defined in a

schema. For example, the metadata *address* refers to *street*, *city*, *state* and *zipcode* elements. To create such metadata, we have defined three methods, namely *distinct-based* (DM), *synonym-based* (SM) and *relation-based* (RM) metadata creation methods, in which the latter method is an extension to the former method. Specifically, each method creates a new metadata $M^{'}$ based on a current metadata M and an element label L to be added into a cluster. Details of each method are provided in the following sections. For simplicity, let T_M a set of normalized tokens t_m in M, T_L a set of normalized tokens t_l in L, and $T_M^{'}$ a set of normalized tokens $t_m^{'}$ in $M^{'}$.

A. Method DM: Distinct-based Metadata Creation

Definition 1: $T_M^{'} = T_M \cup T_L$

Description: A distinct-based metadata is simply a collection of *lexically different* tokens defined in T_M and T_L.

The algorithm *createDM* is shown in Figure 1. Here, *createDM* receives T_M and L as input and produces $T_M^{'}$ as output. Specifically, the label L is firstly normalized via the method *normalize()* which has similar process as defined by [5]. The method *normalize()* returns a set of normalized tokens as output wherein these tokens in turn are distinctly combined with T_M.

```
Set createDM(Set T_M, String L) {
  T_L = normalize(L);
  if T_M = ∅ then
    T_M = T_L;
  else
    T_M = T_M ∪ T_L;
  return T_M;
}
```

Fig. 1. createDM Algorithm.

Consider Table I that shows two metadata created based on: (1) the current metadata {*street,state*} and label *country*; and (2) the current metadata {*street,state*} and label *city*. With the method DM, in the first example, the new metadata {*street,state,country*} is created by combining all tokens defined in the current metadata and label. Similarly, in the second example, the new metadata {*street,state,city*} is created.

B. Method SM: Synonym-based Metadata Creation

Definition 2: $T_M^{'} = (T_M \cup T_L)$ - S

where $S = \{t_l \mid t_l \in T_L$ and t_l is synonym to $t_m \in T_M)\}$

Description: A synonym-based metadata is a collection of tokens defined in T_M and T_L where such tokens must be *lexically different* and are not *synonym* to each other. In particular, it is an extension to a distinct-based metadata with the exception that one of two lexically different but synonym tokens, t_m and t_l, is removed to reduce the number of tokens in metadata.

The algorithm *createSM*, an extension to algorithm *createDM*, is shown in Figure 2. Here, all possible token pairs, t_m and t_l, are linguistically compared via the method *lSim*(). Based on this match result, the new metadata is defined as a combination of (i) a set of t_m extracted from identical and synonym token pairs whose matches are the value of 1; and (ii) all the rest tokens via the method *addDistinct*() shown in Figure 3.

```
Set createSM(Set T_M, String L) {
  Set T_L = normalize(L);
  if T_M = ∅ then
    T_M = T_L;
  else {
    String[] arrayT_M = set2Array(T_M);
    String[] arrayT_L = set2Array(T_L);
    Double[][] similarity = lSim(T_M, T_L);
    // find synonym pairs
    Set synPairs = findPairs(similarity, 1);
    T_M = ∅;
    for each (i,j) ∈ synPairs {
      T_M = T_M ∪ arrayT_M[i];
    }
    T_M = addDistinct(T_M, arrayT_M, synPairs, 1);
    T_M = addDistinct(T_M, arrayT_L, synPairs, 2);
  }
  return T_M;
}
```

Fig. 2. createSM Algorithm.

```
Set addDistinct(Set T_M, String[] arrayT, Set pairs,
                Boolean opt) {
  set takenIdx = ∅;
  for each (i,j) ∈ pairs {
    if opt == 1 then
      takenIdx = takenIdx ∪ i;
    else
      takenIdx = takenIdx ∪ j;
  }
  set notTakenIdx = ∅;
  for i=0 to i < length(arrayT) {
    if i ∉ takenIdx
      notTakenIdx = notTakenIdx ∪ i;
  }
  for each idx ∈ notTakenIdx {
    T_M = T_M ∪ arrayT[idx];
  }
  return T_M;
}
```

Fig. 3. addDistinct Algorithm.

Again, consider Table I with the method SM. In the first example, the new metadata {*street,state*} remains the same as *country* is synonym to *state*. In the second example, the new metadata {*street,state,city*} is created as there is no identical or synonym taken pairs.

C. Method RM: Relation-based Metadata Creation

Definition 3: $T_M^{'} = ((T_M \cup T_L)$ - S - $R) \cup A$

where $S = \{t_l \mid t_l \in T_L$ and t_l is synonym to $t_m \in T_M\}$, $R = \{t_m, t_l \mid t_l \in T_L, t_m \in T_M$ and t_l is related $t_m\}$ and $A = \{t \mid t$ is the nearest ancestor of t_m and t_l where t_m is related to $t_l\}$

Description: A relation-based metadata is a collection of tokens defined in T_M and T_L where such tokens must be *lexically different* and are not *related*. Two tokens, t_m and t_l, are related if their match is above threshold. In particular, it is an extension to a synonym-based metadata with the exception that two lexically different but related tokens, t_m and t_l, are replaced with their nearest ancestor.

The algorithm *createRM*, an extension to algorithm *createSM*, is shown in Figure 4. Specifically, all possible token

TABLE I

EXAMPLE OF LINGUISTIC SIMILARITY

	street	state	DM method	SM method	RM method
Example 1: country	0.60	1.00	street_state_country	street_state	street_state
Example 2: city	0.74	0.89	street_state_city	street_state_city	street_region

pairs, t_m and t_l, are linguistically compared via the method *lSim*(). Based on this match result, the current metadata is defined as a combination of (i) a set of t_m extracted from identical or synonym token pairs; (ii) a set of nearest ancestors of token pairs whose matches are above threshold. The nearest ancestor is discovered by the method *findAncestor*(); and (iii) all the rest tokens via the method *addDistinct*() shown in Figure 3.

```
Set createHM(Set T_M, String L, Double threshold) {
  Set T_L = normalize(L);
  if T_M = ∅ then
    T_M = T_L;
  else {
    String[] arrayT_M = set2Array(T_M);
    String[] arrayT_L = set2Array(T_L);
    Double[][] similarity = lSim(T_M, T_L);
    // find synonym pairs
    Set synPairs = findPairs(similarity, 1);
    T_M = ∅;
    for each (i,j) ∈ synPairs {
      T_M = T_M ∪ arrayT_M[i];
    }
    // find related pairs
    Set relPairs = findPairs(similarity, threshold);
    for each (i,j) ∈ relPairs {
      String parent = findAncestor(arrayT_M, arrayT_L);
      T_M = T_M ∪ parent;
    }
    Set pairs = synPairs ∪ relPairs;
    T_M = addDistinct(T_M, arrayT_M, pairs, 1);
    T_M = addDistinct(T_M, arrayT_L, pairs, 2);
  }
  return T_M;
}
```

Fig. 4. createRM Algorithm.

Again, consider Table I with the the method RM. In the first example, the new metadata {*street*,*state*} is created in a similar manner to the method SM. In the second example, the new metadata {*street*,*region*} is created wherein *region* is the nearest ancestor of two related tokens, *state* and *city*.

III. PRELIMINARY EXPERIMENTAL EVALUATION

The **L**abel-based **M**etadata **C**reation system , LMC, is developed on the basis of three metadata creation algorithms defined in Section II. The goal of the LMC system is to improve the quality of metadata – a representative for a set of corresponding elements. A series of experiments were conducted to evaluate the potential benefits of the LMC system. In particular, the experiments were designed to test the following hypotheses:

Hypothesis 1: RM method provides a better metadata than DM and SM methods do with respect to the number of tokens.

Hypothesis 2: RM method has traded off the slight similarity distance for better metadata.

A. Experimental Setup

Figure 5 illustrates the overall architecture of LMC system[1]. The LMC system together with three metadata creation algorithms, *createDM*, *createSM* and *createRM*, are implemented by Java (SDK 2.0) and deployed on a standalone PC IV 3.2 GHz with 1 GB RAM running Microsoft Windows XP. LMC takes an element label and the current metadata as input, and returns the newly created metadata, that is defined based on the selected metadata creation algorithm, as output. Specifically, LMC invokes the *similarity* module that exists in WordNet::Similarity [4] through the method *lSim*() defined in Section II. The similarity module is used for measuring the linguistic similarity between two tokens. In the experiments, we use the wup measurement [6]. The WordNet::Similarity in turn connects to WordNet Dictionary [3] and WordNet QueryData to facilitate its tasks.

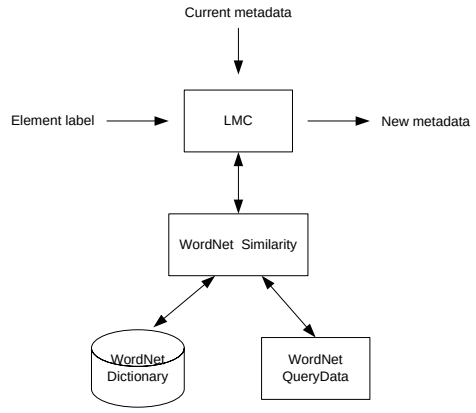

Fig. 5. The Overall Architecture of LMC.

A set of 9 element labels used for the experiments consists of *street*, *city*, *state*, *zip*, *district*, *region*, *address*, *province* and *country* wherein they are labeled with $l1$ - $l9$, respectively. In the experiments, the metadata for these elements must be created as they refer to the *address* concept and are hence related.

B. Effect of Algorithms on Metadata

The first set of experiments measured the *compactness* of metadata produced for 9 element labels by different algorithms – DM, SM and RM as well as the First-based Metadata creation algorithm (FM) that considers the first label added in a cluster as metadata. Here, the compactness of metadata was determined by the number of tokens encapsulated in metadata

[1]We assume that there is a system, responsible for clustering elements and connecting to our LMC for the corresponding metadata.

itself. Particularly, the few number of tokens indicates the few number of token comparisons and hence the better metadata. The initial metadata was set to null.

Figure 6 shows the number of tokens in the metadata produced by different algorithms while adding each of labels (from $l1$ to $l9$) in a cluster. The x-axis has the number of labels in a cluster and the y-axis is the number of metadata tokens. Here, FM performed the best with a constant of 1 token for each newly created metadata as expected. RM created fair metadata with 3 tokens. DM and SM performed the worst, providing an increasing number of tokens in metadata while accepting new element labels into a group. Their final metadata contained 9 and 7 tokens, respectively.

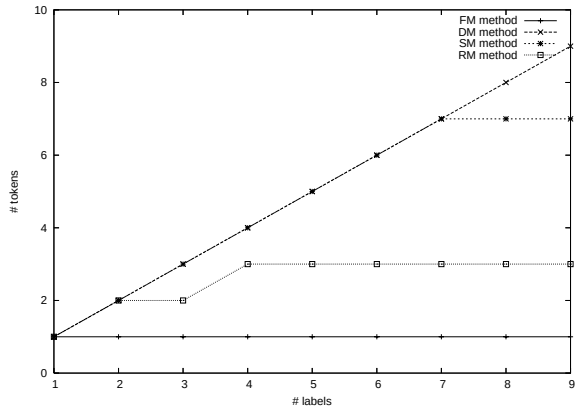

Fig. 6. The Number of Tokens in Metadata Produced by Different Methods.

C. Effect of linguistic similarity distance on LMC algorithm

The second set of experiments measured the *fitness* of metadata produced for 9 element labels by different algorithms – DM, SM, RM and FM. Here, the fitness of metadata was determined by the difference distance (compliment to similarity distance) between metadata and each individual label. Particularly, the less difference distance, the better fitness of metadata as a cluster representative.

Figures 7 shows the final metadata together with the difference distance average of metadata and all element labels as well as each individual difference distance with each label. Here, the difference distance with the value of 0 indicates that the label is either identical or synonym to the metadata, while the rest values varied by the relation of metadata and labels. In Figures 7, DM performed the best with the difference distance average of 0.22 and the individual difference distance below 0.37. SM provided the average as well as individual difference distance of 0.23 and below 0.30, respectively. RM provided an average difference distance of 0.26 as well as an individual distance below 0.34. FM performed the worst with the average of 0.33 and the individual up to 0.53.

IV. Conclusion

In this paper, we propose a novel metadata development based on element labels using the *wup* method, a linguistic similarity measurement. Particularly, a metadata, that is

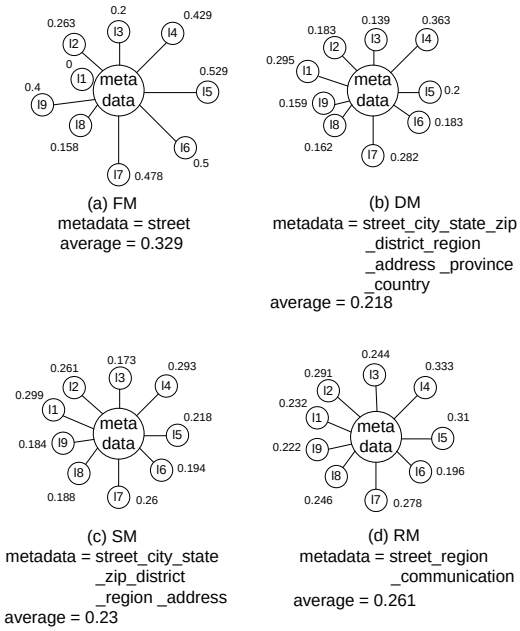

Fig. 7. The Final Metadata Produced by Different Algorithms together with The Average and Individual Difference Distances.

linguistically related to its corresponding elements, can be created using *distinct-based* (DM), *synonym-based* (SM) or *relation-based* (RM) metadata creation method. Our experiments showed that RM provided a better metadata with respect to the number of tokens than SM and DM do. However, RM has traded off the *slight* similarity distance between metadata and labels for better metadata. In addition, a metadata can be automatically created without predefined concepts (rules). While a metadata can be a potential cluster representative, the metadata itself may not be meaningful to human.

Future work focuses on (i) an extensive evaluation of our approach using information from different domains; (ii) an evaluation with existing approaches; and (iii) the application of metadata in schema matching.

References

[1] Wen-Syan Li and Chris Clifton. Semantic Integration in Heterogeneous Databases Using Neural Network. In *Proceeding of the 20th Internation Conference of Very Large Data Bases (VLDB)*, 1994.

[2] Jayant Madhavan, Philip A. Bernstein, and Erhard Rahm. Generic schema matching with cupid. In *The VLDB Journal*, pages 49–58, 2001.

[3] G.A. Miller. Wordnet: A Lexical Database for English Language. cogsci.princeton.edu/ wn/, 2002.

[4] Ted Pedersen, Siddharth Patwardhan, and Jason Michelizzi. Wordnet:: Similarity - measuring the relatedness of concepts. In *AAAI*, pages 1024–1025, 2004.

[5] Erhard Rahm and Philip A. Bernstein. A survey of approaches to automatic schema matching. *VLDB Journal: Very Large Data Bases*, 10(4):334–350, 2001.

[6] Zhibiao Wu and Martha Palmer. Verb semantics and lexical selection. In *32nd. Annual Meeting of the Association for Computational Linguistics*, pages 133 –138, New Mexico State University, Las Cruces, New Mexico, 1994.

RNET: Thailand's IT Researcher Network Collection, Analysis and Visualization

K. Maleewong and C. Anutariya
School of Technology, Shinawatra University
Shinawatra Tower III, 1010 Viphavadi-Rangsit Road, Chatuchak, Bangkok, Thailand.
47312013-7@padawan.shinawatra.ac.th, chutiporn@shinawatra.ac.th

***Abstract*-This paper proposes *RNET system* which has been developed for the collection, analysis, and visualization of Thailand's IT researcher network. The system employs Semantic Web technologies for semantically representing and manipulating researcher profiles as well as their publication collections, which are automatically and periodically retrieved from an online citation database. Such information is gathered by means of a constructed crawler and then extracted using HTMLParser. In addition, as it is founded on *RDF(S)* and *OWL* ontology language, the study extends *FOAF* (*Friend of a Friend*) schema into *RNET* vocabulary in order to semantically describe researcher profiles together with their publication details. Managing, querying and reasoning with RDF(S) and OWL data are carried out by employing *Sesame server*. Moreover, in order to enable a graphical visualization, an analysis of the researcher networks, as well as the associations among research topics and the collaborations among research institutes, *JUNG* (*Java Universal Network/Graph*) programming toolkit is adopted. Furthermore, with an emphasis on ease of use and installation, RNET system is implemented as a Web application using JAVA applets, JavaServer Pages (JSP) and JAVA servlet technologies.**

I. INTRODUCTION

Since IT is a huge research discipline, the network of IT researchers is often messy and difficult to analyze. Thus, finding answers to the following questions, for instance, is a challenging and demanding task: "Who are the experts in the Semantic Web and ontology research area in Thailand and how can they be contacted?", "Which research institutes or organizations have active collaborations with NECTEC?".

A search engine is a productive tool for resolving these questions. However, information extraction and collection by humans is tedious work, thus all electronic information on the WWW should be automatically extracted and analyzed.

This paper proposes and develops a *Semantic Web* [1] application, namely *RNET* (available online for public access at http://ict.shinawatra.ac.th/projects/rnet), which can automatically collect researcher information and publication details from an online database on the WWW. Moreover, in order to enable machine-processable semantics of the extracted information and also to allow semantic data interchange, such information is encoded in an RDF/OWL [2] metadata format and stored in an RDF/OWL database. An RDF/OWL inference engine can then reason about this semantic-enabled data, and thus derive certain implicit information. For visualization purposes, a user can browse and search for an expert in a certain area using graph and network data models. All of these functional requirements are well founded by Semantic Web and open-source technologies.

The organization of this paper is as follows: Section 2 describes the proposed system architecture and discusses the employed techniques and tools. Section 3 presents the system implementation in detail. Finally, the conclusion and direction for future research are presented.

II. SYSTEM ARCHITECTURE

RNET system is designed using a 2-tier architecture that simply demonstrates a client-to-server relationship, and can be divided into three layers: *(i) data collection*, *(ii) data analysis*, and *(iii) information visualization*, as shown in Fig.1.

A. Data Collection Layer

The system extracts researcher's publication information from an online publication database using a *crawler* [3] and a *parser* [4]. RNET ontology is developed to semantically describe such extracted data.

1) Crawler: This component browses the WWW in a systematic manner. It traverses a distributed network by following the hypertext links from a specified Web page to other pages.

2) Parser: This service is used for extracting the desired information contained in a web page. The function of a parser can be classified into two parts: *extraction* and *transformation*. The first process extracts data from text, links or other resources, while the latter transforms input data into a data structure.

3) RNET Ontology: In order to allow both machine-readable and human-representation of the extracted researcher profiles and their publications, RNET employs and extends *FOAF* (*Friend of a Friend*) [5] into RNET ontology as depicted in Fig 2.

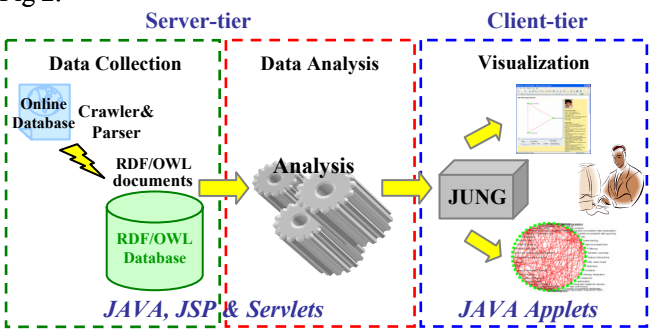

Figure 1. System Architecture of RNET.

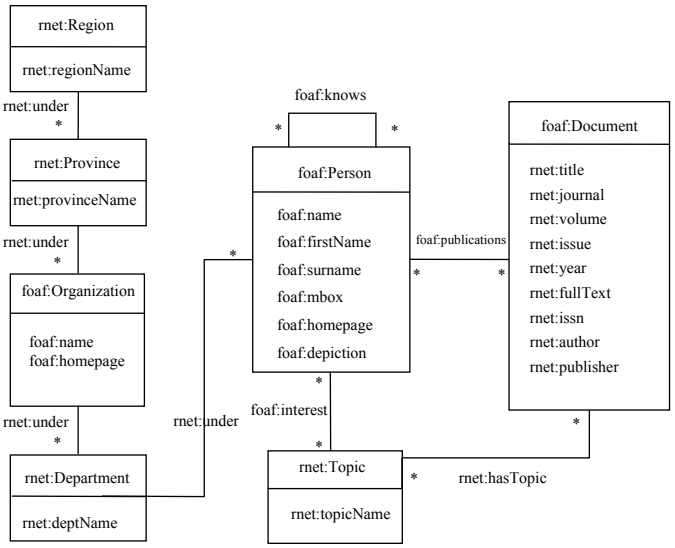

Figure 2. RNET Ontology.

In brief, FOAF is an RDF/OWL schema defining relationships between people and various attributes such as name, gender and interest. Similarly, RNET employs RDF/OWL to express relevant information about researchers including departments, organizations, provinces and regions, as well as topics of interests.

B. Data Analysis Layer

This layer obtains the RDF/OWL documents conforming to RNET ontology and generated by the Data Collection Layer, and then stores them in a database. It requires an RDF/OWL inference engine for the data analysis task as well as for the derivation of implicit information.

C. Information Visualization Layer

This layer provides graphical user interface with RNET system, which allows users to graphically explore not only IT researcher profiles and their networks, but also publication details and research topics, as well as collaboration among organizations. Such exploration and visualization can be part of a sociological study, a collaboration network investigation, and an analysis on active research topic trends.

III. SYSTEM IMPLEMENTATION

With an emphasis on ease of use and installation, RNET system is designed to be implemented as a Web application using merely standard and widely used Web technologies.

This section elaborates the implementation of the three system components corresponding to the three layers of RNET's architecture, that is: *(i) data collection*, *(ii) data analysis*, and *(iii) information visualization*.

A. Data Collection

Initially, researcher information consisting of name, email, homepage, image, and affiliation are predefined using the developed RNET ontology and stored in *Sesame* [6] – an open-source RDF/OWL database. For each of these researchers, RNET dynamically collects his/her publication details from *the Guide* [7], ACM's citation database providing a bibliographic collection from major publishers in computing with over 945,000 entries. This data collection task is accomplished by constructing an HTML crawler to automatically search and traverse the Guide's HTML result pages which indicates the specified researcher's publications. *HTMLParser* [8] is then employed to extract the desired information such as author names, title, source, year, ISBN, full text resource, publisher, and keywords. Finally, an RNET document describing a researcher's personal information and publication details and conforming to the developed RNET ontology is generated and stored in the Sesame database server. Fig. 3 illustrates an example of a generated document.

Note that apart from the Guide, other online citation databases such as *CiteSeer* [9] and *DBLP Bibliography* [10] can also be used and extracted from in the same manner.

```
<foaf:Person>
      <foaf:firstName>Chutiporn</foaf:firstName>
      <foaf:surname>Anutariya</foaf:surname>
      <foaf:mbox rdf:resource="mailto:chutiporn@shinawatra.ac.th"/>
      <rnet:under>
            <rnet:department>
                  <rnet:deptName>School of ICT</rnet:deptName>
                  <rnet:under>
                        <foaf:Organization>
                              <foaf:name>Shinawatra University</foaf:name>
                        </foaf:Organization>
                  </rnet:under>
            </rnet:department>
    </rnet:under>
    <foaf:publications>
          <rnet:title>A data model for XML databases</rnet:title>
          <rnet:journal>Journal of Intelligent Information Systems</rnet:journal>
          <rnet:volume>20</rnet:volume>
          <rnet:issue>1</rnet:issue>
          <rnet:year>2003</rnet:year>
          <rnet:issn>0925-9902</rnet:issn>
          <rnet:author>Vilas Wuwongse</rnet:author>
          <rnet:author>Kiyoshi Akama</rnet:author>
          <rnet:author>Chutiporn Anutariya</rnet:author>
          <rnet:author>Ekawit Nantajeewarawat</rnet:author>
          <rnet:publisher>Kluwer Academic Publishers Hingham</rnet:publisher>
          <rnet:hasTopic>
            <rnet:topicName>XML document</rnet:topicName>
          </rnet: hasTopic>
          <rnet: hasTopic>
            <rnet:topicName>XML expression </rnet:topicName>
          </rnet: hasTopic>
          <rnet: hasTopic>
            <rnet:topicName> data model </rnet:topicName>
          </rnet: hasTopic>
    </foaf:publications>
</foaf:Person>
```

Figure 3. RDF document using RNET Ontology.

B. Data Analysis

With a goal to enable users to explore certain knowledge about researcher networks, association of research areas and collaboration among research institutes, this component formalizes certain important axioms in order to derive implicit and hidden knowledge which is useful for analysis in the following important aspects:

1) Researcher Network Analysis: Using the collected research publication details, this analysis employs the discovered co-author relationship for the formulation of a researcher network. In other words, when a group of researchers co-author a particular paper together, one can imply that they know each other. Thus, RNET can illustrate this collaboration among them in terms of a researcher network. Fig. 4 formalizes this axiom.

2) Topic Interest Analysis: This analysis uses the axiom of Fig. 5 to derive the research topics that interest a particular researcher. Note that for the sake of simplicity and demonstration, it assumes that if a researcher has at least one publication in a certain topic, he/she is interested in that topic. However, in practice this can be implemented by specifying a threshold, where this interest relationship between a researcher and a topic can be derived only if the number of publications in that particular topic is higher than the specified threshold.

3) Organization Network Analysis: This analysis discovers the collaboration among organizations or institutes using the axiom of Fig.6. When a group of researchers from various organizations knows each other, it implies that there is some degree of collaboration between this set of organizations.

C. Information Visualization

In order to represent certain knowledge derived from the Data Analysis part, RNET provides a user-friendly interface which allows a user to explore graphical visualization. The user interface is a JAVA Web application based on the client-server model.

Description	If Publication A is co-authored by Person X and Person Y Then Person X knows Person Y.
Axiom	(foaf:Person:X foaf:puclications foaf:Document:A) AND (foaf:Person:Y foaf:puclications foaf:Document:A) => (foaf:Person:X foaf:knows foaf:Person:Y)

Figure 4. Axiom for researcher network analysis.

Description	If Person X publishes Publication A and Publication A has T as its keyword or topic Then Person X has an interest in Topic T.
Axiom	(foaf:Person:X foaf:puclications foaf:Document:A) AND (foaf:Document:A rnet:hasTopic rnet:Topic:T) => (foaf:Person:X foaf:interest rnet:Topic:T)

Figure 5. Axiom for topic interest analysis.

Description	If Person X knows Person Y and Person X under Organization A and Person Y under Organization B Then Organization A collaborates with Organization B.
Axiom	(foaf:Person:X foaf:knows foaf:Person:Y) AND (foaf:Person:X rnet:under foaf:Organization:A) AND (foaf:Person:Y rnet:under foaf:Organization:B) => (foaf:Organization:A rnet:collaborate foaf:Organization:B)

Figure 6. Axiom for organization network analysis.

The client-side employs Java Applets to create the interaction part embedded in HTML pages for users browsing. On the server-side, a Java Server Page (JSP) and servlets are used to create the system applications that hide the complexity of services.

The application exploits a variety of Semantic Web technologies to provide various network models such as the researcher networks, the associations among research areas, and the collaborations among research institutes. Once the user has submitted a search by specifying a keyword such as a researcher name, a topic interest or an organization name, the system returns a summary page of the selected domain to demonstrate a network model, which includes additional details as well as links to related information.

In order to represent a network model, the system employs the service of *JUNG* (*JAVA Universal Network/Graph*) [11] programming toolkit, a JAVA based software library developed for data manipulation, analysis, and visualization as a graph. The graph consists of vertices and edges. Vertices represent entities that are researcher, topic or organization. Edges connected to vertices represent relationships among the entities that the vertices represent.

The Web interface, as shown in Fig. 7, allows users to visualize knowledge in three domain areas including *(i) researcher network, (ii) topic interest network, and (iii) organization network*.

1) Researcher Network: This graph shows the collaboration among researchers with summarized profile information. The page's sidebar additionally gives a list of links to topics of interests and publication details. Fig. 8 illustrates such example of a researcher network.

2) Topic Interest Network: Fig. 9 depicts the associations among research topics. In brief, a relation between topics is discovered using co-occurrence analysis, i.e., if two particular topics co-occur in the same publication, they appear to have a certain relation with each other. Therefore, if they co-occur for more than a particular threshold value, their relation is considered to be significant, and hence illustrated by the visualized graph. Apart from this, the page's sidebar also provides links to researchers who are interested in such topic, as well as a list of related research topics.

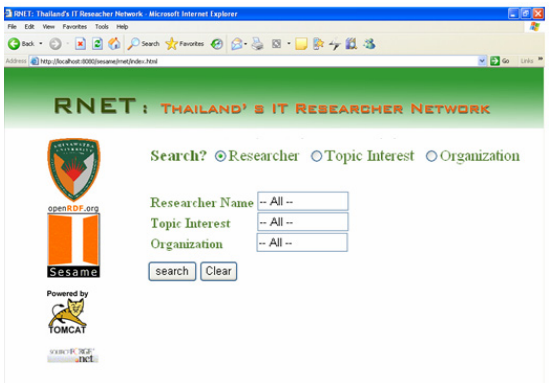

Figure 7. User Interface of RNET.

3) Organization Network: The system demonstrates collaboration networks between organizations in a graph model with all the researchers who work at certain organizations as shown in Fig. 10. This collaboration is defined from a group of researchers that know each other. Moreover, the system can show an organization network from a regional perspective.

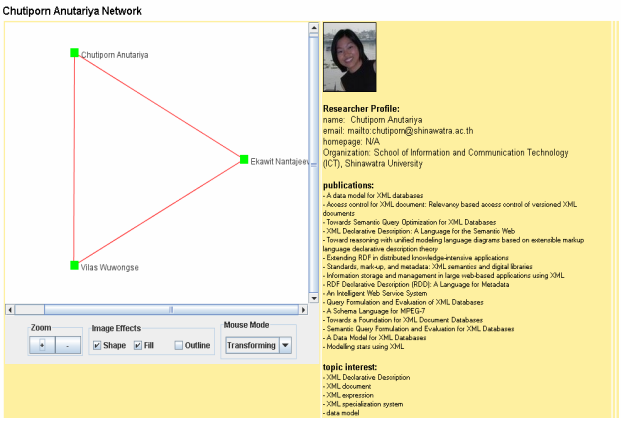

Figure 8. Example of researcher network.

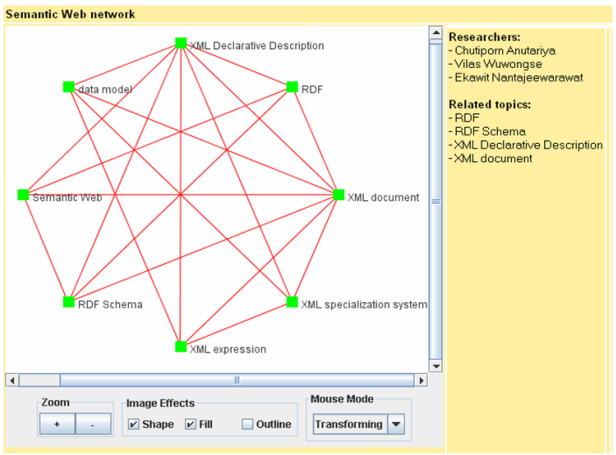

Figure 9. Example of topic interest network.

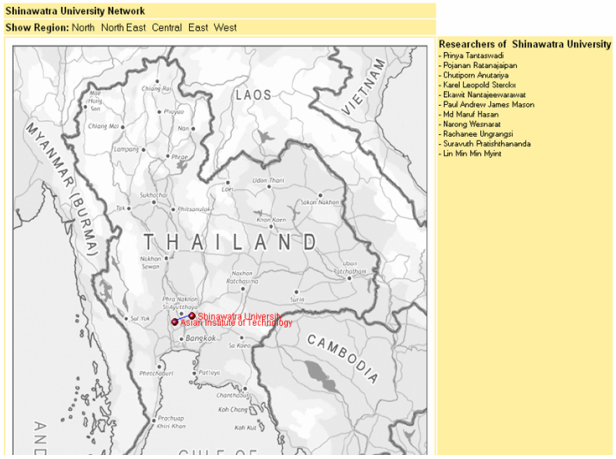

Figure 10. Example of organization network.

IV. Conclusions

The developed RNET system employs various methodologies for collection, analysis and visualization. It automatically gathers researcher's publication details from an online citation database using an implemented crawler and parser. The extracted data is represented in an RDF/OWL document using RNET Ontology and then stored in a database server. In addition, an RDF/OWL inference engine is adopted for deriving hidden and implicit data which are useful for collaboration network study and research topic analysis. The Web application is implemented using JAVA technologies to provide a Web interface, which allows visitors to explore researcher networks and the associations among research areas, as well as the collaborations among research organizations. In addition, the system also provides additional details and a list of links to related information.

Future works include various enhancements to RNET system, which are as follows: to dynamically extract researcher information from various online databases, collect more publication data with a diversity of researcher profiles from various organizations in Thailand, and extend RNET ontological schema for collecting more useful data.

Moreover, in the visualization process, some additional statistical values such as degree of centrality, betweenness, and closeness could be calculated and shown together with the visualized network in order to provide more insight into the network analysis. In a graph model, an edge could depict the strength of association among researchers by using weighted edges or colored edges. Furthermore, an optimal threshold has to be calculated to demonstrate an appropriate research area network.

References

[1] Daconta, M. C., Obrst, L. J., & Smith, K. T. (2003). The Semantic Web: *A guide to the future of XML, Web services, and knowledge management*.

[2] Brickley, D., Guha, R. V. (2000). *Resource Description Framework (RDF) Schema Specification 1.0: W3C Candidate recommendation*. Retrieved August 10, 2006, from http://www.w3.org/TR/2000/CR-rdf-schema-20000327/

[3] Blum T., Keislar D., Wheaton J., & Wold E. (1998). *Writing a Web Crawler in the Java Programming Language*. Retrieved August 8, 2006, from http://java.sun.com/developer/technicalArticles/ThirdParty/WebCrawler

[4] *Parser*. (n.d.). Retrieved August 15, 2006, from http://en.wikipedia.org/wiki/Parsing

[5] Brickley, D., & Miller, L. (2003). *FOAF Vocabulary Specification: (Tech. Rep.) RDFWeb FOAF Project.*

[6] Broekstra, J., Kampman, A., & Harmelen, F. (2002). Sesame: A Generic Architecture for Storing and Querying RDF and RDF Schema. *1st Int'l Workshop Practical and Scalable Semantic Systems*.

[7] Association for Computing Machinary (ACM). (n.d.). *The Guide.* Retrieved August 01, 2006, from ACM Portal database.

[8] SourceForge.net. (2006). *HTMLParser*. Retrieved August 01, 2006, from http://htmlparser.sourceforge.net

[9] Pennsylvania State University. (n.d.). *CiteSeer*. Retrieved August 15, 2006, from http://citeseer.ist.psu.edu/

[10] University of Trier. (n.d.). *DBLP bibilography*. Retrieved August 20, 2006, from http://www.informatik.uni-trier.de/~ley/db/

[11] SourceForge.net. (2006). *JUNG*. Retrieved August 16, 2006, from http://jung.sourceforge.net/

Object-Oriented Data Structure for Text Association Rule Mining

Alisa Kongthon
National Electronics and Computer Technology Center
112 Thailand Science Park
Pathumthani 12120, Thailand

Ralph Mueller
School of Industrial and Systems Engineering
Georgia Tech
765 Ferst Drive
Atlanta, GA 30332

Alan L. Porter
Search Technology Inc.
4960 Peachtree Ind. Blvd
Norcross, GA 30071

Abstract **- Mining association rules is being actively studied for transaction databases, but extension to text applications is relatively novel. Most of the previous studies implement an Apriori-like approach, which requires multiple passes over the database to find all frequent itemsets. However, for some type of databases such as the bibliographic database where the data are very sparse, the Apriori algorithm becomes very costly. In this paper, we propose a new algorithm called Object-Oriented Association Rule Mining (OOARM), which uses a special object-oriented data structure that holds all relevant information. The algorithm can find all frequent itemsets from a single scan through the database. Performance studies show that it is faster than the Apriori algorithm. All rules that involve a certain itemset can be generated in real time. That, in turn, opens new opportunities to organize and explore relationships in large text data sets.**

I. Introduction

Association rule algorithms were originally used for analysis of transaction data in the retail industry (market basket analysis). Agrawal et al. [1] introduced what he called the "Apriori" algorithm to analyze these data. Analyzing association rules in transaction databases has been demonstrated to be useful and technically feasible in several application areas such as retail sales [2, 3, 4]. Association rule mining (ARM) can help answer the following questions: How can the sale of a specific item be increased? What is the impact if a certain item is discontinued? Is the sale of items on shelf A related to the sale of items on shelf B?

In this paper, we propose a new algorithm for mining association rules in bibliographic databases toward the objective of enhancing research and development (R&D) management. Bibliographic databases such as INSPEC and EI Compendex contain information and abstracts of journal articles and conference papers from several thousand sources. The information provided from such databases is well structured into distinct fields such as title, author, affiliation, keywords, and abstract. This is different from the unstructured text obtained from the Internet or other full text databases (e.g., TREC).

Analyzing association rules between fields in bibliographic database can help R&D managers profile "who's doing what" on some particular research topics, for example, one can identify that 73% of the articles written by Lizhu Zhou published in PAKDD-99 Proceedings focus on Database theory, while 27% discuss about set theory.

Moreover, mining association rules within a field such as keywords can be used for building a concept hierarchy [5] or a thesaurus. In this paper, we are interested in mining association rules in bibliographic data. The word frequency distribution of a bibliographic database is very different from the item frequency distribution of a sales transaction database. Transaction data typically have a limited number of different items, but a very large number of transactions. The ratio of items/transactions therefore is typically << 1. A typical dataset for a basket analysis might have 1,000 items and more than 100,000 transactions. In contrast, the frequency of keywords often does not reach 1% of the total number of records and is usually much lower. The number of different keywords though can be relatively high. The typical ratio of items/transaction therefore is approximately 1 or larger. These differences make the existing Apriori-like algorithms ineffective in mining association rules for text databases. As a result, a new algorithm and data structure is proposed.

II. Association Rule Mining

The general statement of the association rule mining problem is as follows: Let $I = \{i_1, i_2 \ldots, i_m\}$ be a set of literals, called items. Let D be a set of transactions, where each transaction T is a set of items such that $T \subseteq I$. An association rule r is an implication of the form $X \Rightarrow Y$, where $X \subset I$, $Y \subset I$ and $X \cap Y = \varnothing$. The association rule $X \Rightarrow Y$ holds in the database D with *confidence* c if c% of transactions in D that contain X also contain Y. The rule $X \Rightarrow Y$ has *support* s if s% of transactions in D contain $X \cup Y$.

Association Rule Mining is the process of generating all association rules that have support and confidence greater than the user-specified minimum support (called *minsup*) and

minimum confidence (called *minconf*) respectively. Association rule mining is a two-step process:

1. Find all frequent itemsets. This is to find each set of items (called *itemsets*) that have a co-occurrence rate above the *minsup*. An itemset with at least the *minsup* is called a *frequent* itemset. The size of an itemset represents the number of items contained in the itemset, and an itemset containing k items will be called a *k*-itemset

2. Generate association rules from the frequent itemsets. For every frequent itemset *f*, find all non-empty subsets of *f*. For every such subset *a*, generate a rule of the form $a \Rightarrow (f - a)$, if the ratio of support *(f–a)* to support *(a)* is at least *minconf*.

A. Classic Apriori Algorithm

The literature has proposed various algorithms for discovering association rules. Most of the previous studies [2, 6, 7, 8] implement an *Apriori*-like approach, i.e., they require multiple passes over the database. The main idea of the *Apriori*-like approaches is to iteratively generate the set of *candidate itemsets* (potential *frequent itemsets*) of length *(k+1)* from the set of *frequent itemsets* of length *k* (for $k \geq 1$), and count their supports (occurrence frequencies) in the database. However, because the size of the database can be very large, it is very costly to scan the database repeatedly to count support for candidate itemsets. To reduce the combinatorial search space, all algorithms exploit the following property: if any length *k* itemset is not frequent in the database, its length *(k+1)* extension itemsets can never be frequent.

In situations with a large number of itemsets or very low minimum support thresholds, the Apriori algorithm suffers from the following costs:

• It is not reasonable to repeatedly scan the database and count supports for candidate itemsets.

• It is expensive to count the occurrences of a huge number of candidate itemsets, when only a small fraction is likely to be frequent.

To overcome these problems, we propose a new fast algorithm to generate all frequent itemsets for sparse text datasets.

III. OBJECT-ORIENTED DATA STRUCTURE FOR TEXT ASSOCIATION MINING

A. Justification for New Algorithm

The existing algorithms were developed especially for the Market Basket Data Analysis. The transaction data typically have a limited number of different items, but a potentially very large number of transactions. For the new domain of Association Rule Mining in bibliographic databases, these algorithms are not very efficient. Since the number of keywords can be relatively high, the number of 2-itemsets and larger itemsets can be also very high, depending on the minimum support that was set. The traditional Apriori-like algorithms will generate a very large number of potential candidates for which the support has to be determined. This means scanning over the database and counting the occurrences.

In order to overcome these difficulties, a special object-oriented data structure is implemented. It is specifically designed for itemsets with low support. The new data structure and algorithm has several advantages. It allows easy access and better organization of data as well as fast generation of frequent itemsets with low support and their association rules. A comparison of the performance between the proposed algorithm and the Apriori-like algorithm is presented later. The data structure can also be used for more complex tools such as graphical representation, since it contains all information needed.

B. Object-Oriented Association Rule Mining (OOARM) Algorithm

The following notation is used: Let L_k be the set of frequent *k*-itemsets (those with minimum support). Let T_k be the temporary set of itemsets used to create the new k-itemsets. The itemsets in L_k and T_k will be ordered lexicographically. Furthermore *i.records* will be used for the set of record references where itemset *i* is present, *r.itemsets* will be used for the set of itemsets associated with record *r*, *minsup* represents the minimum support. The OOARM algorithm works as follows:

1. Scan in data from file and store 1-itemsets in L_1.
2. **forall** itemsets $i \in L_1$ **do begin**
   if(|*i.records*| < *minsup*)
   delete *i* from L_1
   k=2
3. **while**($L_{k-1} > 0$)
   forall itemsets $i \in L_{k-1}$ do begin
   $T_k = \varnothing$
   forall *records* $r \in$ *i.records* **do begin**
   forall *itemsets* $c \in$ *r.itemsets* **do begin**
   if(c>i) //check if c is lexico-
   add *c* to T_k //graphically larger than *i*
   end
   end //now T_k contains all itemsets that occur //together with *i*
   forall itemsets $c \in T_k$ **do begin**
   if(|*i.records* $\cap$ *c.records*| > *minsupp*)
   create new itemset *j* with items of *i* and *c*
   j.records = *i.records* $\cap$ *c.records*
   if(*j* is *k*-itemset)
   add *j* to L_k
   end
   end
   k++
   end while

Only at the beginning the algorithm reads from the database or file. After deleting the itemsets from L_1 that do not

have minimum support, there will be no further scanning of the database. The itemsets with $k>1$ are created based on the *(k-1)* itemsets. This is similar to most other algorithms. The generation of the candidates is however entirely different. The algorithm goes through the list L_{k-1} one by one to generate the candidates T_k . Starting with an itemset *i* from L_{k-1}, potential candidates for T_k are found by following the references from *i.records* and then going back to the itemsets from *r.itemsets* for all *r i.records*. The itemsets found this way are only added if they are lexicographically larger than *i*. The itemsets of T_k are then used to create the *k*-itemset candidates. This can be done because the itemset *i* and the itemsets in T_k both occur in at least one record together. Hence the *k*-itemset candidates will have at least support 1. If the intersection of *i.records* and *c.records*, where *c* is an itemset from T_k, has at least *minsup* records, a new itemset *j* is created with the items from *i* and *c*. It can happen that this new itemset has more than *k* items. If that is the case it will be discarded, else the new itemset is added to the set of frequent items L_k.

This algorithm relies heavily on set operations. The algorithm was implemented with the JAVA collections framework which provides good support for set operations. It can easily be seen that the algorithm is not suitable for very large transactional databases, where itemsets have high support. For a database with 100,000 records and an itemset that has 50% support, this itemset would have to keep record references to 50,000 of the records. If there is a large number of such itemsets, memory will quickly become insufficient. Nevertheless for the purpose of mining bibliographic data, the algorithm works very well. The number of record references of an itemset is typically in the range of 5-50.

C. Rule Generation

Another advantage of this data structure is that all rules related to a specific itemset can easily be obtained. With this new algorithm and data structure it is possible to directly generate the desired rules. Since the number of potential association rules can be very high, it might not be reasonable to generate all rules at once but only rules that are of interest. The data structure can hold all relevant information and allows quickly extracting all association rules of interest. The researcher can pick itemsets, i.e., keywords that are of interest, and generate all rules related to it.

The usual procedure of generating rules is to take a *k*-itemset, where $k \geq 2$ and generate all subsets. The subsets then are used to calculate the rules [9]. For instance, when looking at *{ABC}*, we have the subsets *{AB}*, *{BC}* and *{AC}*. If the support is known, we can easily calculate the confidence of the rules $AB \Rightarrow C$, $BC \Rightarrow A$, $AC \Rightarrow B$. However one might be interested in all the rules that involve *{AB}*. With traditional approaches this would involve looking up all itemsets that have *{AB}* as a subset.

Using the new data structure the rule generation is greatly simplified. Now it is possible to generate all rules with a certain itemsets as antecedent or consequent. Let *R* be the set of Rules with minimum confidence *minconf* having the itemset *x* as antecedent or consequent. The algorithm to generate all rules with itemsets *x* as antecedent or consequent is as follows:

```
R= ∅
  forall records r ∈ x.records do begin
    forall itemsets c r.itemsets do begin
      generate the rules: c ⇒ x , x ⇒ c
      add the rules with
      confidence ≥ min conf  to R
    end
  end
```

The algorithm to generate the rules with itemset *c* as antecedent and *x* as consequent is:

```
create new itemset j with items of c and x
j.records= c.records ∩ x.records
  if(|c.records ∩ x.records|<minsup)
    stop, rule does not have minimum
    support
  else
```

$$confidence = \frac{\left|c.records \cap x.records\right|}{\left|c.records\right|}$$

```
  end
```

The idea behind this algorithm is similar to the itemset generation. A rule can only exist if there is a record, which has both antecedent and consequent. The algorithm works similar to the previous one. In order to generate all rules that involve itemset x the algorithm iterates through all records and finds all other possible itemsets that occur together with x. Then all rules that have x as antecedent or consequent, are generated. Rules that do not have minimum support are discarded.

D. Runtime Comparison with Apriori Algorithm

We compared our OOARM with an Apriori-like algorithm based on pseudo code provided by [9]. The two algorithms were run for different supports on two different datasets retrieved from the *INSPEC*.

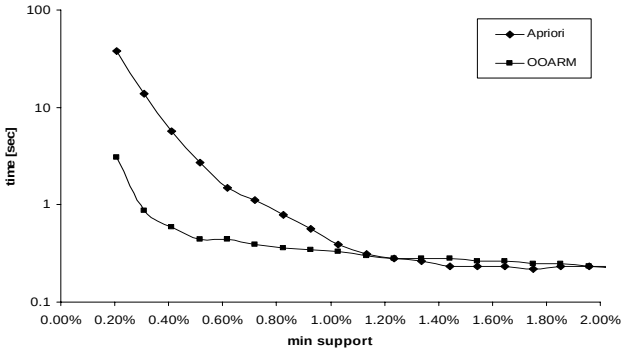

Figure 1. Runtime comparison for dataset with 971 records.

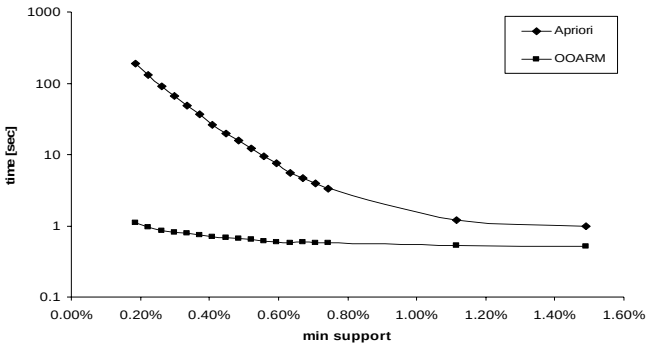

Figure 2. Runtime comparison for dataset with 2686 records.

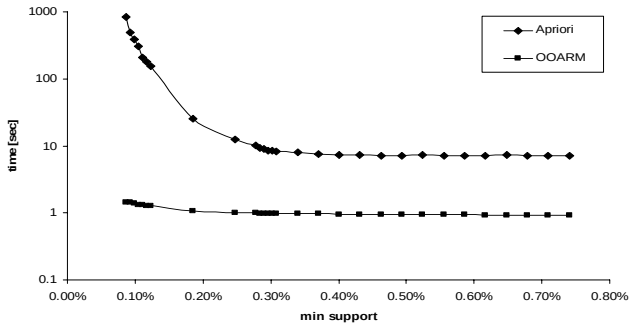

Figure 3. Runtime comparison for dataset with 16209 records.

The runtime of the OOARM algorithm is clearly smaller. For higher support values this advantage is decreasing. Note that the Y axis is in logarithmic scale. Also note the relative low support values that were used.

IV. Differences Between OOARM and Apriori Algorithm

The main difference is that for the proposed algorithm, after an initial scan, all data are held in main memory. The existing algorithms usually require several scans over the whole dataset in order to determine the support. This advantage is very substantial for itemsets with low support. However, for itemsets with high support, e.g., 20%, which can be found in retail data, the proposed algorithm requires more memory. For the domain of Association Rule Mining in bibliographic databases, this is usually not a problem, since the data are preprocessed and keywords that are too general and would have a very high support are usually not used. Keywords or phrases with very high support can also be removed easily, since their value in discovering new relations among terms is very limited.

V. Conclusion

This paper presents a new algorithm for mining association rules in bibliographic databases. The word frequency distribution of a bibliographic database makes the problem of mining association rules in text databases very different from the case of traditional sales transaction databases. Our single scan algorithm allows generating all itemsets very quickly. It is specially designed to work on itemsets with low support. The experimental results show that improvement in run time of up to 200 times can be realized compared to a traditional Apriori-like algorithm. This is due to the fact that during the candidate itemset generation the number of potential candidates is much smaller than with the traditional Apriori-algorithm.

However for higher support values the performance difference becomes smaller. Another advantage is that the data structure can hold all relevant information for association rule mining. This allows for a new way to generate rules. After the initial creation of all large itemsets, it is possible to obtain rules that involve a chosen itemset in real time. This includes all rules where the itemset is an antecedent or a consequent. The data structure can also be seen as a new way to organize and store itemsets in memory and access rules for ARM.

References

[1] R. Agrawal, T. Imielinski, and A. Swami, "Mining association rules between sets of items in large databases," *In Proceedings of ACM SIGMOD Conference on Management of Data (Washington, D.C., May 26-28, 1993)*, ACM Press, New York, NY, 1993, pp. 207-216

[2] S. Brin, R. Motwani, J. Ullman, and S. Tsur, "Dynamic Itemset Counting and Implication Rules for Market Basket Data," *In Proceedings of ACM SIGMOD Conference on Management of Data (Tucson, AZ, May 13-15, 1997)*, ACM Press, New York, NY, 1997, pp. 255-264

[3] M.S. Chen, J. Han, and P.S. Yu, "Data Mining: An Overview from a Database Perspective," *IEEE Trans. On Knowledge and Data Engineering*, Vol. 8, 6 (Dec. 1996), pp. 866-883.

[4] R. Cooley, B. Mobasher, and J. Srivastava, "Data Preparation for Mining World Wide Web Browsing Patterns," *Journal of Knowledge and Information Systems*, Vol. 1, 1, (Feb. 1999), pp. 5-32.

[5] A. Kongthon, "Deriving Tree-Structured Networks from Technical Text using Association Rule Mining: Applied to Thailand's R&D," Poster Presentation, *Arthur M. Sackler Colloquium on "Mapping Knowledge Domains"*, the National Academy of Sciences, 2003

[6] M. Houtsma, and A. Swami, "Set-oriented mining for association rules in relational databases," *Technical Report RJ 9567*, IBM Almaden Research Center, San Jose, CA, 1993.

[7] R. Agrawal and R. Srikant, "Fast algorithms for mining association rules," *In Proceedings of the 20th VLDB Conference on Very Large Data Bases (VLDB'94) (Santiago de Chile, Chile, September 12-15, 1994)*. Morgan Kaufmann, San Francisco, CA , 1994, pp. 487-499.

[8] J.D. Holt and S.M. Chung, "Mining Association Rules in Text Databases Using Multipass with Inverted Hashing and Pruning," *In 14th IEEE International Conference on Tools with Artificial Intelligence (ICTAI 2002) (Washington, D.C., 4-6 November, 2002)*. IEEE Computer Society Press, Los Alamitos, CA, pp. 49-56.

[9] R. Agrawal and R. Srikant, "Fast algorithms for mining association rules in large databases," *Research Report RJ 9839*, IBM Almaden Research Center, San Jose, CA, 1994.

Semantic Blog: An Approach to Knowledge Sharing and Knowledge Management

S. Wongwilai[1] and C. Anutariya[2]
School of Technology, Shinawatra University,
Shinawatra Tower III, 1010 Viphavadi-Rangsit Road, Chatuchak, Bangkok, Thailand
[1]sombhop@tmd.go.th, [2]chutiporn@shinawatra.ac.th

***Abstract*—By employment of the prominent *Semantic Web* technologies, recently emerging with a goal to facilitate well-defined mechanisms for representing machine-processable data, this paper enhances an ordinary *blog* system into *Semantic Blog* by enriching with semantic, machine-understandable metadata and ontology. This Semantic Blog system can be adopted as a tool in knowledge management, focusing primarily on the processes of creating, capturing, and disseminating (sharing) knowledge. In essence, it employs *RDF(S)* and *OWL* to model domain ontologies and to represent semantic-enabled blog entries, thus allowing further inference and semantic integration of blog systems. Moreover, intelligence or semantic search, which incorporates the use of ontology in order to enhance and improve a search quality, becomes possible. This can help encourage users and give a strong motivation for capturing, creating and publishing knowledge into the system.**

I. INTRODUCTION

Knowledge management (*KM*) [1] is commonly referred to processes and practices of acquiring, maintaining and managing knowledge such that it can be easily shared and reused across an organization. To accomplish this goal, there is a need to capture knowledge residing in organizational processes, members, and/or community of practices as well as to support a mechanism for precise knowledge retrieval.

Blog or *Weblog* is a recently emerging general-purpose tool for data exchange, information sharing as well as KM within organizations. It helps encourage ordinary users to publish and manage their own contents, hence becoming not only a content consumer but also a content producer. Key advantages of applying a blog system to KM come from its feature that allows employees, customers or business partners to easily and quickly annotate their work as well as to collaboratively share their experiences and expertise. Hence, its employment as part of a normal work environment can immediately facilitate knowledge creation and knowledge sharing. Each blog entry, containing any types of media, e.g., text, documents, images or videos, is therefore considered to be a knowledge resource created by an organizational member, and accompanied by its corresponding metadata, describing the title, author, posted date/time, description and categories. Thus, a metadata search which allows one to combine these various elements to express a more precise query, such as *to find entries posted in 2006 and contains the words "Semantic Web" in the tile*, is possible although this important feature is not explicitly provided by most blog systems. In general, the most common form of searching is merely a text-based one; for example, *finding entries about knowledge engineering* simply means *finding ones containing the word "knowledge engineering" in their contents*, which usually returns many non-relevant results. Therefore, intelligence or semantic-enabled search, which incorporates the use of metadata and ontology in order to enhance and improve a search quality, is increasingly demanded.

By employment of *Semantic Web* technologies [2], this paper develops a framework for *Semantic Blog* [3, 4] which extends the ordinary blogging paradigm with ontology mechanisms for modeling and representing semantic-enabled blog entries, thus enabling further inference and semantic integration of various blog systems. In particular, *OWL* (*Web Ontology Language*) [5] is employed to formalize domain conceptualization consisting of *concept taxonomy*, *axioms* and *constraints*. In addition, it can be employed to further define structure and semantics of each metadata element in order to allow a finer grained metadata search. Hence, besides annotating by a set of metadata, each blog can also be semantically related to particular concepts defined in the ontology, and thus further inference about blog entries become possible.

The remainder of this paper is organized as follows: Next section elaborates the proposed Semantic Blog framework and implementation details. Section 3 discusses its application as a tool for knowledge management and knowledge sharing. Finally, Section 4 concludes and outlines further research direction.

II. SEMANTIC BLOG SYSTEM DEVELOPMENT

This section develops a general-purpose Semantic Blog system to be used as a KM tool. First, details of the Semantic Blog framework are discussed, and followed by the implemented architecture.

A. Semantic Blog Framework

Semantic Blog [3, 4] extends the blogging paradigm with the possibility to add additional metadata to a blog entry. This metadata can cover a variety of aspects, ranging from information about the entry itself (e.g. entry's title, author, and relations to other communication sites) to metadata describing the topics mentioned in the entry.

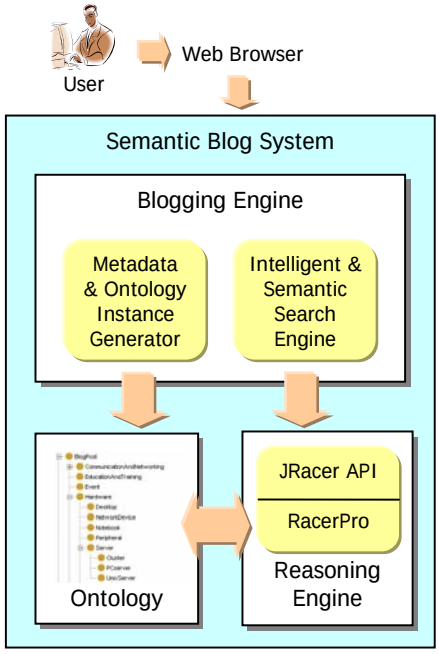

Figure 1. Semantic Blog system architecture.

Moreover, by means of the two prominent Semantic Web technologies: *Resource Description Framework* (*RDF*) [6] and *Web Ontology Language* (*OWL*) [5], which facilitate well-defined mechanisms for expressing machine-processable data in terms of *ontology* [7], each blog entry can be semantically associated with particular concepts defined in a given domain-specific ontology. Therefore, inferencing through a *concept taxonomy* (aka. *concept hierarchy*) becomes possible and thus, resulting in a capability for precise searches through the collection information.

B. Semantic Blog Implementation

Fig. 1 depicts the architecture of the developed Semantic Blog system, which consists of three important components: *domain-specific ontology*, *blogging engine* and *reasoning engine*.

1) Domain-Specific Ontology

Since ontology provides a basic infrastructure for the Semantic Blog, an *ontological schema* is first designed and constructed using OWL language and *Protégé* ontology editor [8] in order to allow semantic description and representation of knowledge in an organization. In particular, the developed ontological schema (aka. *vocabulary*) comprises important concepts such as BlogPost, Department, Member, and Position. Fig. 2, moreover, illustrates the relationships among these four concepts (using OWL's *object properties*). For instance, (i) a Member can blog a BlogPost and a BlogPost is blogged_by a Member, (ii) a Member holds a Position and affiliates_with a particular Department. Besides these object relationships, important *datatype properties* for each of these four concepts are also defined in the constructed ontology. For example, BlogPost also contains the properties title, date, link and

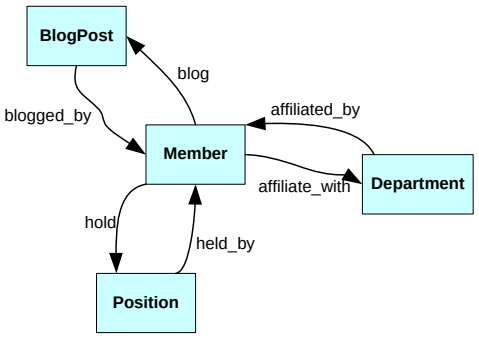

Figure 2. Semantic Blog's ontology: important concepts and relationships.

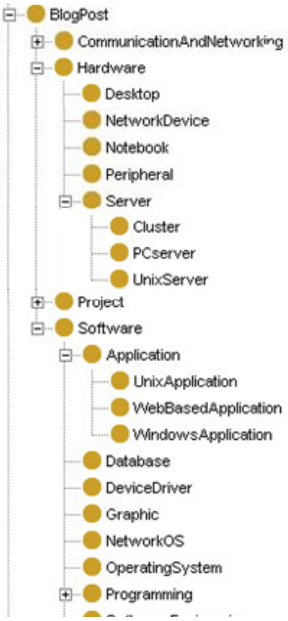

a) BlogPost concept taxonomy

b) Position concept taxonomy

c) Department concept taxonomy

Figure 3. Semantic Blog's ontology: concept taxonomy.

description, the values of which are simply textual data – rdf:literal or xsd:date; similarly, Member has the properties name, date_of_birth, email and contact-information.

Note that all of these four concepts can be further specialized to provide more precise concepts that meet the executing domain. As a sample case study of applying the developed ontology to describe knowledge in Information Technology (IT) department, the concept BlogPost can be

specialized into many IT related sub-concepts. Fig. 3-a shows the defined *concept taxonomy* (or *concept hierarchy*). In other words, it specifies that BlogPost can be classified into such categories as CommunicationAndNetworking, Hardware, Project, Software, etc. Each of these sub-concepts can also be further specialized into more specific concepts. For instance, Hardware is divided into Desktop, Notebook, Server, etc., while Server is divided into Cluster, PCServer, and UnixServer. In addition, as illustrated by Fig. 3-b, Position concept is also specialized into ManagementRelated and ITRelated, while the latter is further classified into Administration and SoftwareDeveloper, which is again specialized into ProjectManager, SystemAnalyst, etc. Department concept specialization can also be explained in a similar manner (see Fig. 3-c).

In summary, a domain-specific ontology defined using RDF/OWL language plays an important role in the system by providing explicit conceptualization of a shared understanding of a domain, and hence enabling certain inference facilities.

2) Blogging Engine

The developed system employs an open-source blog tool as an infrastructure. At present, there are several off-the-shelf blogging software publishing tools available. Since an ease of use is one of the significant features for a KM tool, the developed Semantic Blog system adopts Wordpress 2.0 (http://wordpress.org) built on PHP and MySQL, and runs on an Apache Web server. Moreover, in order to facilitate semantic capabilities, the system has been extended with two important features:

- *Metadata and Ontology Instance Generator:* This sub-component enriches each blog post with semantic, machine-readable metadata and also associates the post with an appropriate concept defined in the concept taxonomy. An ontological instance represented in terms of RDF/OWL syntax and conforming to the predefined ontological schema will then be generated and maintained by the system.
- *Intelligent and Semantic Search Engine:* This component is implemented in order to support not only simple text-based search, but also an intelligent and semantic one which allows combination of various metadata and ontology elements to express a more precise query. Moreover, it employs the defined domain ontology, and facilitates derivation of implicit information, and hence enabling a more accurate retrieval of relevant blog entries. For instance, a search for all blog posts categorized in Software category (or concept) will return not only those which are explicitly defined as Software's blog entries, but also those entries under all sub-concepts of Software. That is, the entries in the categories, Programming and Web Based Application will also be part of the results, provided that these two categories are sub-concepts of Software defined in the domain ontology.

3) Reasoning Engine

The Intelligent and Semantic Search Engine component described previously employs *RacerPro™* [9] and *JRacer API* [10], in order to support reasoning services over a given ontology. In particular, RacerPro is an OWL reasoner, which provides Java application programming interface via its JRacer API.

```
<Programming rdf:ID="NNN-60">
   <date
      rdf:datatype ="http://www.w3.org/2001/XMLSchema#dateTime">
      2006-02-16T19:03:47Z</date>
   <title rdf:datatype="http://www.w3.org/2001/XMLSchema#string">
      Alternative syntax for control structures</title>
   <link rdf:datatype="http://www.w3.org/2001/XMLSchema#string">
      http://www. ssemblog.org/wordpress/2006/02/16/1-13/</link>
   <description
      rdf:datatype="http://www.w3.org/2001/XMLSchema#string">
      PHP offers an alternative syntax for some of its control ...
   </description>
   <blogged_by rdf:resource="#Administrator"/>
</Programming>
```

Figure 4. Example of a generated RDF/OWL element, semantically describing a particular blog post.

III. Semantic Blog Approach To Knowledge Management

This section discusses as a case study how to employ the developed system to support KM processes in an IT-related organization, such as a software-development company or an IT support department.

A. Knowledge Creation and Sharing

In principle, ordinary users can freely view or search the system, while subscribed users can additionally post blog contents, which could be in various forms such as texts, documents, pictures, audio and videos, and are considered as organizational knowledge resources. Thus, by supporting users with a friendly environment to convert their tacit knowledge into codified explicit knowledge, the system can encourage them to create and share more knowledge in terms of blog posts.

In order to connect each blog post with the predefined ontology and to enable inference searches, the user who enters such a post must specify the appropriate category defined in the ontology and associate it with the post; otherwise, as default it will be assigned to "Others" category. The system will then use this specified category together with other important semantic metadata, including posted date/time, link or URL of the post, title, description and author, to automatically generate an ontology instance in RDF/OWL. Fig. 4 illustrates an example of such an element, which describes a blog post categorized in Programming category, posted at 19:03 on 2006-02-16, by the user Administrator, with the title Alternative syntax for control structures.

B. Knowledge Retrieval and Reuse

By means of semantic-enabled and inference search features, users are well-equipped with a tool to precisely retrieve required knowledge. Besides the most common form of

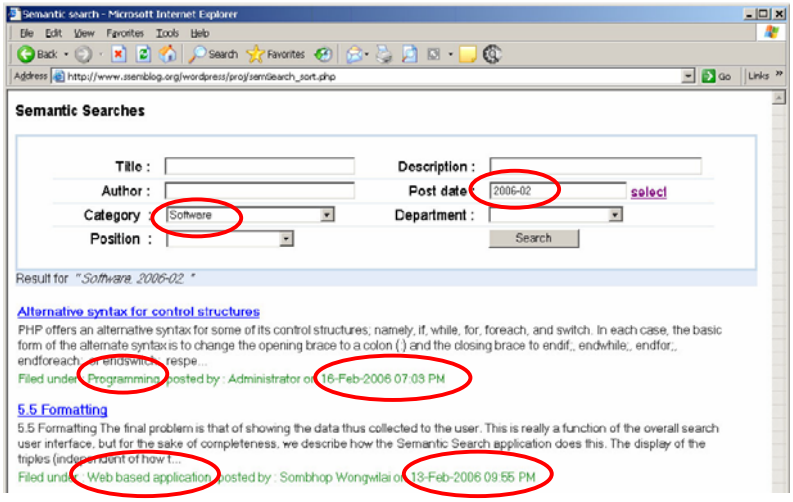

Figure 5. A sample semantic search result: a search for all blog posts created in February 2006 and categorized in Software category.

searching, which is merely text-based and usually returns many non-relevant results, the developed system supports also a semantic and intelligent search which allows combination of various ontology elements to express a more precise query. For instance:

- *To search for knowledge resources (i.e., blog posts) created in February 2006 and categorized in Software category*: Fig. 5 shows that this search will return all blog posts, which are created in the specified period, and categorized not only in the Software category, but also those in its subcategories, defined in the concept taxonomy of Fig. 3-a, such as Programming, WebBased Application, etc.
- *To find any resources in the category Hardware and created by a member working in the position of software developer*: Similar to the previous example, all blog posts returned by this search must belong to the Hardware category or any of its subcategories, defined in the concept taxonomy of Fig. 3-a, such as Desktop, NetworkDevice, etc. Moreover, the returned results must be created by those working as a SoftwareDeveloper, which includes ProjectManager, SystemAnalyst, etc. as depicted by Fig. 3-b.
- *To find knowledge resources posted by a member of IT Department*: As shown by Fig. 3-c, ITDepartment is further specialized into CustomerSupport and R-and-D-Division. Hence, this search then returns all resources posted by any members of these departments.
- *To find entries posted in 2006 and contains the words "Semantic Web" in the title.*

IV. Conclusions and Future Work

This paper has developed a Semantic Blog system and proposed its application as a tool for knowledge management, which can support users with a friendly environment to convert their tacit knowledge into codified explicit knowledge as well as to precisely retrieve required knowledge, and hence encouraging organizational members to reuse, recreate, and share in a cyclic fashion.

Future work includes an enhancement of the system by employment of efficient ontology mapping and integration techniques [11] in order to solve heterogeneity problems among semantically described data. This will allow various Semantic Blog systems using different ontologies to be easily integrated, and thus improving knowledge sharing and knowledge management processes.

References

[1] D. Schwartz, *Encyclopedia of Knowledge Management*, Idea Group Reference, ISBN 1-59140-574-2, 2005.

[2] T. Berners-Lee, J. Hendler and O. Lassila, "The Semantic Web: A new form of Web content that is meaningful to computers will unleash a revolution of new possibilities." *Scientific American*, May 2001.

[3] S. Cayzer, "Semantic blogging and Decentralized Knowledge Management," *Communications of the ACM*, Vol 47, No 12, December 2004, pp.45-47.

[4] D. R. Karger and D. Quan, "What would it mean to blog on the semantic web?," *J. Web Semantics*, Elsevier, Vol 3, 2005, pp. 147-157.

[5] M. K. Smith, C. Welty, and D. L. McGuinness, Editors, "OWL Web Ontology Language Guide," *W3C Recommendation*, 10 February 2004, Available: http://www.w3.org/TR/owl-guide/.

[6] F. Manola, E. Miller, Editors., "Resource Description Framework (RDF) Model and Syntax," *W3C Recommendation*, 10 February 2004, Available: http://www.w3.org/TR/rdf-primer/.

[7] N. F. Noy and D. L. McGuinness, "Ontology Development 101:A Guide to your first ontology," Stanford Knowledge Systems Laboratory Technical Report KSL-01-05, March 2001.

[8] M. Horridge, H. Knublauch, A. Rector, R. Stevens, C. Wroe, "A Practical Guide To Building OWL Ontologies Using The Protege-OWL Plugin and CO-ODE Tools (Edition 1.0)," Available: http://www.co-ode.org/resources/tutorials/ProtegeOWLTutorial.pdf.

[9] Racer Systems GmbH & Co. KG, "RacerPro User's Guide, Version 1.9".

[10] Racer Systems GmbH & Co. KG, "JRacer 1.8, APIs to RacerPro kernel application," 2006. Available: http://www.racer-systems.com/

[11] N. F. Noy, M. A. Musen. PROMPT: algorithm and tool for automated ontology merging and alignment. *Proc of AAAI 2000*, pp 450-455.

In-Depth Analysis of the Quicksort's Efficiency based on the Threshold and Related Factors

R. Chaisricharoen and S. Suwatthanaphiset
School of Information Technology, Mae Fah Luang University
333 Moo 1, Thasud
Muang, Chiang Rai 57100 Thailand

***Abstract*-To increase efficiency, quicksort algorithm needs to be switched from its operation characteristic to another sorting algorithm that is more efficient than the quicksort for the small set of elements. The threshold, which is the size of a small-enough subset for swapping, is believed to be around 10 for almost 30 years. In this literature, the full factorial experiment is conducted to find out whether this magic number is obsolete or not. The factors are threshold, size of unsorted set, and performance of tested computer. The results provide strong evidences of outdated assumptions of threshold of 10 elements. In addition, there is no rule of thumb for the optimal value of threshold because it is significantly related to other factors. Furthermore, the regression model for roughly predicting the optimal threshold is estimated based on the experimental results with adjusted R^2 of 88.4%.**

I. INTRODUCTION

Since the introduction of computer systems, the sorting operation has occupied itself as a significant mechanism in various applications. For example, consider a set of numbers sorted sequentially in a computer's memory. It is usually easier to find a specified element of such a set if the numbers are maintained in sorted order. Unfortunately, there are a great number of methods that can be utilized to sort a file. The programmer must be aware of several interrelated and often conflicting efficiency considerations to make an intelligent choice about which sorting method is most appropriate to a particular problem.

In general, the complexity of the algorithm is determined by examining its O notation, which is a mathematical symbol to denote "the order of". For non-particular sorting, the complexity of provided sorting algorithms range from O(nlogn) to $O(n^2)$. Obviously, the sorting algorithms with O(nlogn) are more preferred than those of $O(n^2)$. However, there are many O(nlogn) sorting algorithms with various pros and cons. Among these algorithms, the quicksort, which was originally proposed by Hoare [1, 2] in 1962, is the excellent general-purpose sorting algorithm and has many descendants [3]. Based on the principle of divide and conquer, the quicksort provides the complexity of O(nlogn) only in average cases. Despite an occasional long execution time, quicksort is still the most favorable internal sorting method because it requires less hidden constant than other O(nlogn) sorting algorithms.

Based on its attractiveness, the efficiency of quicksort is frequently studied and improved. Usually, the improvements aim at the methods to partition the set equally [4, 5] because the appearance of unbalanced subsets can significantly deteriorate the performance of quicksort especially at the root level. Though the set is partitioned equally at every level, the quicksort still faces another fatal difficulty of inefficiency at small subset. Unfortunately, as its nature is recursive, quicksort will divide the set as long as its size is greater than one. To address this problem, Hoare suggests that the divided small subset should be sorted with other more efficient methods rather than let the quicksort handle it until the end [2]. Known of its reputation of good efficiency over small file, the insertion sort which has the complexity of $O(n^2)$ is utilized to help the quicksort handle the small subset effectively. For almost 30 years, the threshold, which is the size of a small-enough subset for swap algorithm, is believed to be around ten for best practice, which is supported by the precisely modeled formula and one-factor experiment [5]. As computer technology is rapidly growing, is this magic number proposed at almost 30 years ago still provide the optimum solutions for nowadays computing power? In addition, is there really a single threshold suitable for all sorting situations? In this literature, the full factorial experiment is conducted based on three factors; original size of unsorted set, threshold, and computer's performance. Furthermore, the estimation of the new optimal threshold for all or particulars situations is expected to be modeled if the previously defined is statistically proved obsolete.

II. STANDARD ALGORITHM

The original quicksort algorithm can be simply described using two procedure calls, *pivot* and *quicksort*, which are implemented as follows [6]:

```
procedure pivot(T[i..j]; var l)
    p ← T[i]
    k ← i; l ← j +1
    repeat k ← k +1 until T[k] > p or k ≥ j
    repeat l ← l -1 until T[l] ≤ p
    while k < l do
        swap T[k] and T[l]
        repeat k ← k +1 until T[k] > p
        repeat l ← l -1 until T[l] ≤ p
    swap T[i] and T[l]

procedure quicksort(T[i..j])
```

if $(j - i) < M$ **then** *insert*($T[i..j]$)
else
pivot($T[i..j]$,l)
quicksort($T[i..l - 1]$)
quicksort($T[l + 1..j]$)

The *pivot* procedure is for permuting the elements in array $T[i..j]$ and retures a value l such that , at the end, $i \le l \le j$, $T[k] \le p$ for all $i \le k < l$, $T[l] = p$, and $T[k] > p$ for all $l < k \le j$, where p is the initial value of $T[i]$. The *quicksort* procedure utilizes the *pivot* and determines when the size of subset is less than the threshold to switch the operation to inserting sort algorithm.

III. Design of Experiment

A. The Factors

The factors that are interesting are the threshold, size of unsorted set, and the computer's performance which is the score of the famous PCMark05 from FUTUREMARK corporation. The score is increased as the configuration of system becomes better. To aid in presentation, from now on, the threshold will be stated by "M" symbol, the size will be stated by "N" symbol and the performance of computer will be stated by "P" symbol.

B. The Response

As the quicksort algorithm has the complexity of O(nlogn), the response is the normalized coefficient defined by:

$$C_{N,M,P} = \frac{10^9 t_{N,M,P}}{N \log_2 N} \qquad (1)$$

The $t_{N,M,P}$ is overall time of quicksort algorithm for sorting a set of N elements using such M threshold on the PC with P score. For convenient, t_N is multiplied by 10^9 to prevent very small value.

C. The Design

To study on three main effects and interaction between factors, the experiment is designed to be 3-factor full factorial experiment. The test is run on each combination of factors three times (three replicates).

N factor is designed to have five levels, M factor is designed to have nine levels, and the number of different configuration of PCs is three. This yields a $5 \times 9 \times 3$ factorial design with the factor description in table I. With three replicates, there are 405 runs, which are assigned randomly.

TABLE I
FACTORS DESCRIPTION

Factor	Level value
N (10^6)	1 1.5 2 2.5 3
M	0 25 50 75 100 125 150 175 200
P	913 1538 2774

The unsorted set is a randomly assign unsigned integer array of size N based on uniform distribution to prevent the unbalance subset. Then, evaluate $t_{N,M,P}$ by the average time of three serial run and use it to calculate $C_{N,M,P}$ for one replicate.

IV. Results and Analysis

As the table is large and complex, the raw data of the experiment is not displayed. Before analyzing, data is checked for model adequacy for the normality and constant variance assumption.

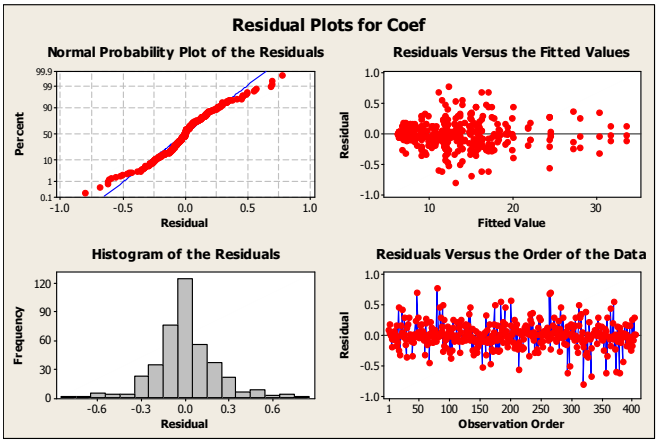

Figure 1. Residual Plots

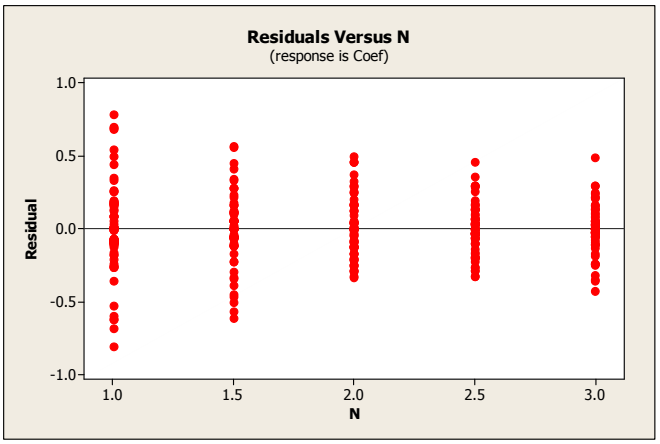

Figure 2. Residuals vs. N

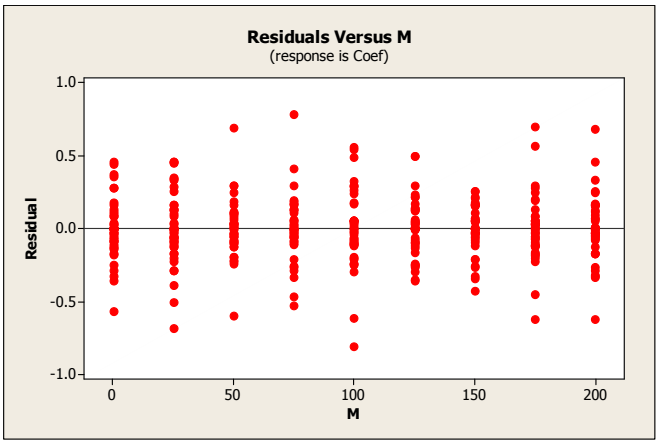

Figure 3. Residuals vs. M

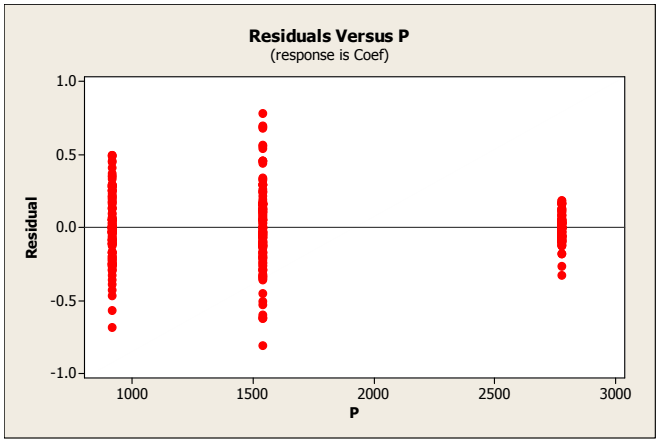

Figure 4. Residuals vs. P

From these graphs, there is no severe indication of any problems with the validity of normality and constant variance assumption.

To determine whether the factors affect the response or not, we use ANOVA tables with $\alpha = 0.05$.

Analysis of Variance for Coef, using Adjusted SS for Tests

Source	DF	Seq SS	Adj SS	Adj MS	F	P
N	4	55.81	55.81	13.95	213.06	0.000
M	8	3142.66	3142.66	392.83	5998.32	0.000
P	2	5965.65	5965.65	2982.82	45546.00	0.000
N*M	32	1458.84	1458.84	45.59	696.11	0.000
N*P	8	129.62	129.62	16.20	247.41	0.000
M*P	16	751.37	751.37	46.96	717.06	0.000
N*M*P	64	344.40	344.40	5.38	82.17	0.000
Error	270	17.68	17.68	0.07		
Total	404	11866.03				

S = 0.255911 R-Sq = 99.85% R-Sq(adj) = 99.78%

From ANOVA, there are strong indications of significant effects of N, M, and P on normalized coefficient. In addition, the interaction between N, M, and P are also significant. To analyze these effects and interaction intensely, main effects and interactions of the response are plotted separately.

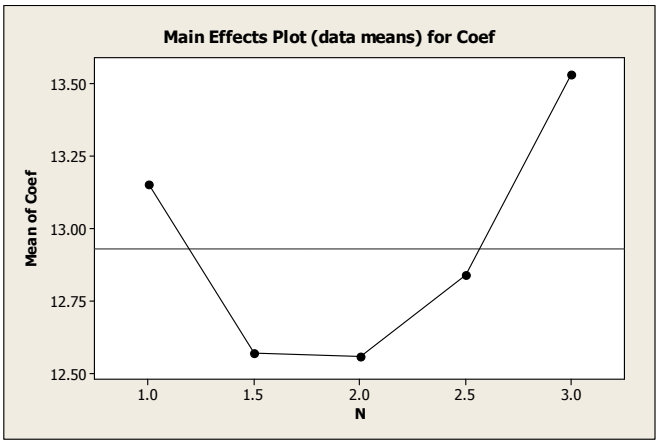

Figure 5. Main effect of N

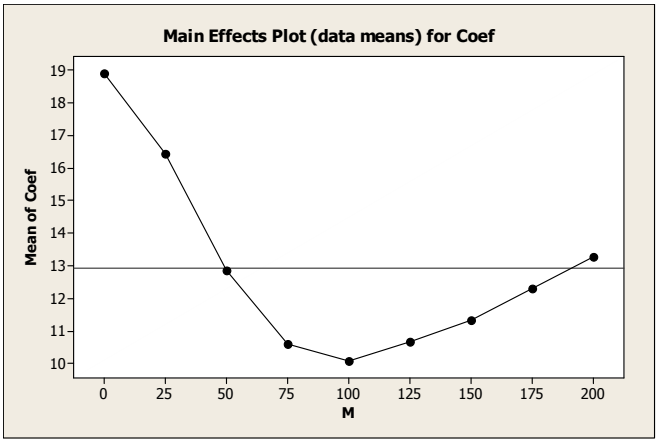

Figure 6. Main effect of M

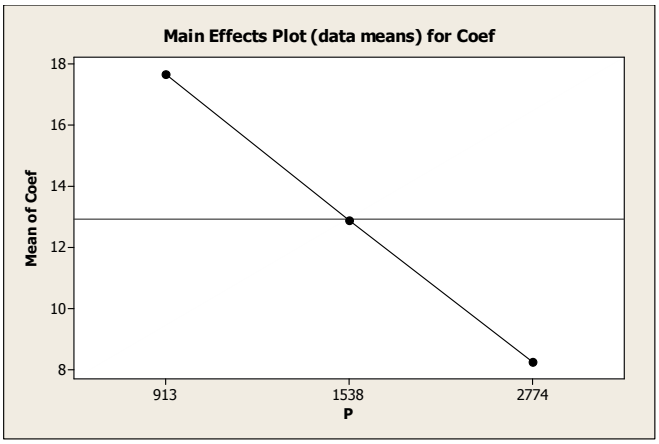

Figure 7. Main effect of P

These main effect plots show the effect of each factor on the normalized coefficient. Though the purpose is to keep it as small as possible, the conclusion of the most suitable threshold of 100 cannot be stated before the interaction plots are examined. However, these main effects plots show strong evidences that the optimal threshold will not be around 10.

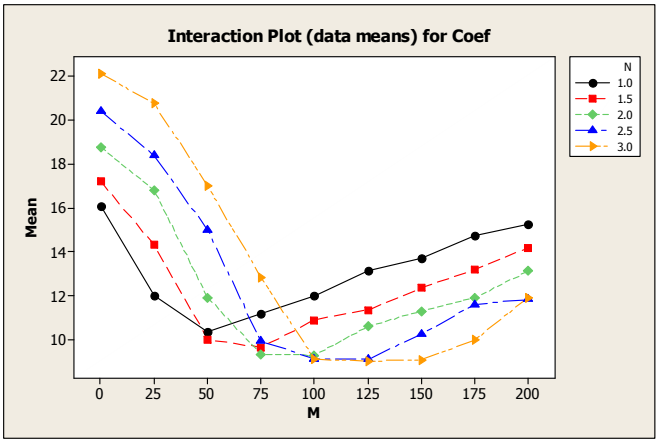

Figure 8. Interaction of N and M

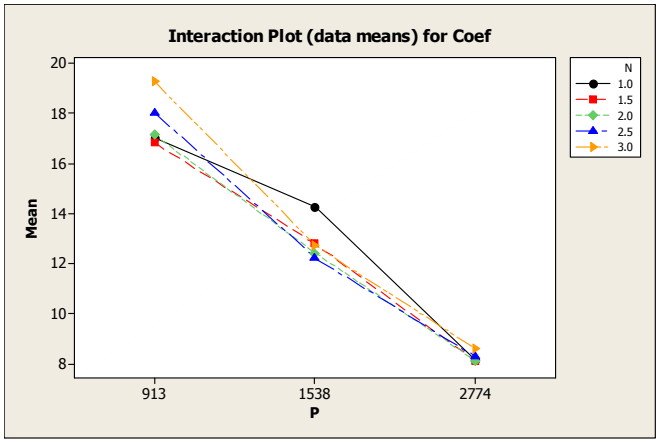

Figure 9. Interaction of N and P

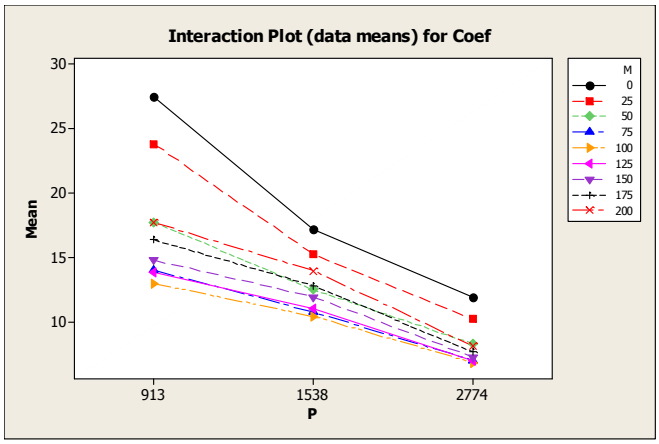

Figure 10. Interaction of M and P

Fig. 8 indicates that there is no one magic threshold that is suitable for all situations as optimal threshold tends to increase as size of unsorted set increases. Though their interactions are statistically significant, the interaction of the computer's performance with threshold and size are not to be seriously considered because the coefficient obtained at a better-performance computer is less than a lower one in all interactions.

To obtain a model for predicting the behavior of such a particular system, the regression analysis is carried out and results in (2) with adjusted R^2 of 88.4%.

$$C(N,M,P) = 22.7 + 4.73N - 0.0231M - 0.00922P - 0.0721NM - 0.00241NP - 0.000029MP + 0.000021NMP + 0.813N^2 + 0.000598M^2 + 0.000002P^2 \quad (2)$$

Substitute N and P of particular systems in (2) results in one variable formula *C(M)*. To estimate the suitable threshold for such systems, set an equation as in (3) and solve it to obtain such optimal threshold.

$$\frac{\partial C(M)}{\partial M} = 0 \quad (3)$$

V. Conclusion

The conducted experiment shows strong evidences, which lead to the proving that the assumption of one single threshold at around 10 is expired. As there is, no magic number suited for all situations, the threshold can be carefully estimated through the utilization of regression model. Nevertheless, as the size of unsorted set is increase, the optimal threshold is likely to be increase as well.

Acknowledgment

The authors would like to convey special thank to the FUTUREMARK corp. whom kindly provides the free evaluation copy of PCMark05.

References

[1] C. A. R. Hoare, "Partition; Quicksort; Find," Comm. ACM, vol. 4, pp. 321 – 322, 1961.
[2] C. A. R. Hoare, "Quicksort," Computer Journal, vol. 5, no. 1, pp. 10 – 15, 1962.
[3] J. Jaja, "A Perspective on Quicksort," Computing in Science & Engineering, vol.2, issue 1, pp. 43 – 49, 2000.
[4] M. H. V. Emden, "Increasing the Efficiency of Quicksort," Communications of the ACM, vol. 13, no. 9, pp. 563 – 567, 1970.
[5] R. Sedgewick, "The Analysis of Quicksort Program," Acta Informatica, vol. 7, pp. 327 – 355, 1977.
[6] G. Brassard and P. Bratley, *Fundamentals of Algorithmics*, Prentice-Hall, pp. 231 – 237, 1996.

Author Index

Volume.1

A

Abapour,M. 305
Adsoongnoen,C. 430
Afzulpurkar,N. 549
Airphaiboon,S. 569
Almaleki,M. 374
Amorndechaphon,D. 245
Angkeaw,K. 129,145
Aorpimai,M. 597
Apiratikul,P. 269
Artitthang,P. 597
Arunsawatwong,S. 462
Atiwongsangthong,N. 478
Aunchaleevarapan,K. 172
Aupayagoson,C. 537
Aurairatch,A. 265
Auttawaitkul,Y. 213

B

Bargmann,B. 549
Benjanarasuth,T. 209,233,237
Bhanthumnavin,W. 180
Boonchiam,P. 269,390
Boonkham,C. 402
Boonsang,S. 81,161
Boonwern,T. 261
Boonyaroonate,I. 422
Bunjongpru,W. 29
Buntem,R. 180
Bunyagul,T. 418,426
Bursri,P. 341

C

Chaichana,S. 172
Chaichana,T. 533
Chaisaengsukkul,A. 349,353
Chaisayun,I. 77,157
Chakpitak,N. 458
Chalermyanont,K. 285
Chamnongthai,K. 245,537
Chankaipol,W. 293
Chanmontree,P. 273
Chantngarm,P. 194
Chanwimalueang,T. 573
Chanwutitum,J. 129,145
Charbkeaw,N. 426
Charoen,B. 509
Chatratana,S. 414
Chatrattanawuth,W. 209
Chat-uthai,C. 406,410
Chayakulkheeree,K. 293
Chernklang,Y. 442
Chino,F. 325
Chiracharit,W. 537,577
Chivapreecha,S. 557
Chotigo,S. 261,345,357
Chuchart,P. 533
Chudjuarjeen,S. 378
Chunkag,V. 289

D,E,F

Dangkham,P. 172
Daroj,K. 450
Daungjak Na Ayutthaya,P. 180
Dejhan,K. 1,41,57,129,145,157,165
Deleroi,W. 414
Dumawipata,T. 53
Eguchi,K. 317
Eua-Arporn,B. 450,462,466
Faidz,A.R. 21
Forsell,M. 581

G,H,I

Grantham,C. 394
Greesuradej,P. 581
Hagh,M.T. 305
Hagiwara,T. 225

Hajipoor,A. 382
Hamamoto,K. 569
Harnsoongnoen,S. 497
Higuchi,K. 321,325
Hintamai,S. 293
Hirunporm,J. 113
Hosseini,S. H. 305
Hruanan,C. 29,137
Hungsasutra,S. 470
Iida,M. 105
Inkiew,W. 121

J,K

Jaikla,W. 61,65,69,89
Janchaichanakun,P. 202
Janyavilas,S. 153
Jaruwongrungsee,K. 176,184
Jasungnuen,N. 29,202
Jeamsaksiri,W. 29
Jitkreeyarn,P. 398
Jomphoak,A. 184
Jongchanachavawat,W. 165
Junnapiya,S. 121
Kaewdang,K. 49
Kaewrawang,A. 341
Kajikawa,T. 325
Kampeerawat,W. 434,438
Kando,M. 93
Kangsajian,C. 329
Kanjanachuchai,S. 141,149
Kasemsuwan,K. 493
Kasirawat,T. 458
Kerdcharoen,T. 180,482,485,493,497,505
Ketsakoon,S. 370
Khaehintung,N. 329,333
Khan-ngern,W. 93,97
Khummanee,S. 366
Khumsat,P. 85,501
Khun,C. 93
Khunkhao,S. 489
Kiatgamjorn,K. 97
Kiatwarin,N. 17
Kikuchi,K. 21
Kiranon,W. 17
Kitjaidure,Y. 529,565
Kittiratsatcha,S. 402
Klappong,K. 121
Kleesuwan,S. 265
Klongpramong,P. 109
Komine,N. 233,237
Korchareon,S. 489
Koseepaporn,P. 257
Koseeyaporn,J. 525
Koseeyaporn,P. 202,561
Krairiksh,M. 153
Krongsuk,S. 482
Krueasuk,W. 293
Kumngern,M. 1,41,57,165
Kumpai,C. 378
Kusalanukhun,T. 513

L,M,N

Laoopugsin,N. 573
Leelarasamee,E. 5,9
Limwongse,T. 149
Limyingcharoen,S. 434
Liou,C. 38
Lohakan,M. 81,161
Lomas,T. 176,184,187
Mahattanakul,J. 13
Maio,P.D. 593
Manmek,T. 394
Martinez,J.I.M. 217
Masuchun,R. 585
Matsushita,K. 325
Matsuura,T. 521
Maturos,T. 187
Meesapawong,P. 137
Meesomboon,A. 434,438
Mithulananthan,N. 390

Mongkolwai,P. 117
Monyakul,V. 213
Moungnoul,P. 121
Muanghlua,R. 137
Mudannayake,C. P. 394
Mungkung,N. 422
Naetiladdanon,S. 474
Nakano,K. 217,321,325
Nakmahachalasint,P. 398
Neammanee,B. 241,249
Ngamwiwit,J. 233,237
Nidhiritdhikrai,R. 462
Niemcharoen,S. 137,478,489
Noppanakeepong,S. 553
Nuanloy,S. 489
Nundrakwang,S. 209,233,237
Nunsuk,P. 529

O,P

Okazaki,R. 325
Oota,I. 317
Opasjumruskit,K. 9
Osaklang,S. 133
Panprayoon,K. 501
Panya,S. 237
Pathoumvahn,S. 569
Pattanadech,N. 349,353
Pattanavijit,P. 233
Pattara-Atikom,W. 589
Patthanasettakul,V. 191
Payakkawan,P. 229
Pengwon,K. 5
Phongphanchantra,N. 137
Phophongviwat,T. 410
Phumiphak,T. 406
Piluck,E. 153
Pimpao,W. 505
Pintavirooj,C. 81,161,533,573,581
Pisitchalermpong,S. 32
Piyatat,T. 32
Plangklang,B. 269
Polmai,S. 277,366,370
Pongsriwat,C. 458
Pothiya,S. 229,441
Potivejkul,S. 353
Poyai,A. 29
prasertsit,A. 285
Prasertsom,D. 32
Prathombutr,P. 589
Pratontep,S. 180
Pratoomthip,A. 545
Premrudeepreechacharn,S. 245
Promjuntuk,C. 191
Prommee,P. 41,57,129,145
Puangdownreong,D. 221
Pueiam,N. 81,161
Puengsiri,B. 345
Pukkalanun,T. 117
Pulsub,D. 45
Puttarach,A. 458

R,S

Rakbanjong,S. 565
Raphiphan,P. 589
Ratsame,C. 422
Rerkpreedapong,D. 446
Ruangphanit,A. 137
Saengsuwan,T. 281,313
Saitou,Y. 337
Sakphrom,S. 85
Sangampai,P. 285
Sa-ngiamsak,C. 545
Sangpratheep,R. 168
Sangswang,A. 297
Sa-nguanpuag,Y. 133
Sangworasil,M. 505,533,569,581
San-Um,W. 36
Sappat,A. 505
Sarasook,J. 345
Satiramatekul,T. 301

Sato,T. 21
Satoh,K. 337,478
Sawangarom,V. 53
Sawigun,C. 13
Sawut,U. 217
Seesanga,S. 357
Seewattanapon,S. 485
Senapukdee,S. 309
Shandiz,H.T. 198,382
Shimizu,Y. 225
Singhaudom,W. 553
Sinthanayothin,C. 513
Sirichai,T. 533
Siripruchyanun,M. 61,65,69,89
Sirisuk,P. 153,329,333
Sirisukprasert,S. 281
Sirisumrannukul,S. 241,386,414,454
Siritaratiwat,A. 341,541,545,549
Siwaprapakorn,W. 509
Somdetsakun,S. 489
Somdunyakanok,M. 41,57,145
Somsamai,W. 442
Songsiri,S. 386
Sookpotharom,S. 533
Sooksood,K. 125
Soorapanth,T. 73
Sowsuwan,K. 29
Sripimanwat,K. 557
Srisuchinwong,B. 36,38
Sritakaew,P. 297
Sudeng,S. 25
Sudmee,W. 249
Sueaseenak,D. 573
Sugprajun,E. 277
Sujintanarat,P. 172
Sukprong,C. 541
Sukserm,P. 221
Suksri,A. 341,253,470
Supnithi,P. 553,557
Surachet,D. 313
Surakampontorn,W. 32,45,49,53,113
Suthithummathat,N. 521
Sutthaphol,N. 541
Suwanasri,T. 269,430,426
Swatdiponphallop,S. 341
Syahlooei,K. 198

T

Takegami,E. 321
Takenaga,H. 337
Taksana,R. 454
Tangamchit,P. 229
Tangsrirat,W. 32,53,113,117
Tanitteeapan,T. 422
Tarateeraseth,V. 93,97
Teekaput,P. 172
Teera-achariyakul,N. 446
Terada,S. 317
Thainimit,S. 517
Thainoi,S. 141,149
Thammarat,C. 221
Thanachayanont,A. 85,493
Thanapong,C. 533
Thanitakul,P. 442
Tharanon,W. 513
Thaworn,A. 489
Theinmontri,S. 285
Thepa,S. 422
Therdyothin,A. 213
Thongtak,A. 25
Thoongsangngam,P. 517
Thudsalingkarnsakul,N. 141
Thumwarin,P. 521
Titiroongruang,W. 105,478
Tomioka,S. 321
Tongsomporn,D. 549
Tonmitr,K. 341
Traiphol,R. 493
Trithaveesak,O. 29
Triyangkulsri,J. 470
Tuantranont,A. 176,184,187,191,497,505

Tungpimolrut,K. 398
Tunyasrirut,S. 205

U,V,W

Udomvech,A. 485
Ueno,F. 317
Ungvichian,V. 361
Unhavanich,S. 113
Uthitsunthorn,D. 418
Uttiya,S. 180
Vasanasong,E. 273,308
Vichienchom,K. 168,
Vonglokham,M. 470
Wangnipparnto,S. 205,253
Wangsathitwong,S. 414
Wanna,Y. 176
Waranuch,N. 497
Wardkein,P. 525
Watanabe,K. 321
Wattanasophon,S. 466
Wijitpornchai,T. 525
Wisitsora-at,A. 176,184,187,191,505
Wongchoosuk,C. 482
Wongsuttitum,W. 105
Worapishet,A. 9
Worasawate,D. 109

Y,Z

Yamada,K. 225,337
Yoothanom,N. 101
Zaslavsky,A. 589
Zhu,H. 317

Author Index

Volume.2

A,B

Abbou,F. 623
Abdulahman 702
Akatimagool,S. 761
Akkaraekthalin,P. 612,643,730,734,761,813 845,825,849,931,927
Aksornpan,P. 1229
Anantarasirichai,N. 9,671,722,773,829,943,947
Anutariya,C. 1272,1280
Apiromvorakarn,M. 1147
Asdornwised,W. 1011
Asoodeh,S. 907
Assawamakin,A. 1229
Attaviriyasuwon 967
Auethavekiat,S. 995
Banjangkaprasert,C. 773,892,899,947,1110
Benjapolakul,W. 793,959
Bholsithi,W. 1117
Biswas,S. K. 1186
Boonpiam,V. 1038
Boonpramuk,P. 1050
Boonsang,S. 1233
Boonsongkusoljit,N. 853
Boonsrimuang,Pi. 745
Boonsrimuang,Po. 745,864
Boonsuk,S. 1054
Boonyanan,P. 691
Bounnady,K. 1022
Budsayaplakorn,N. 1114
Bunluechokchai,S. 979

C,D

Chaimool,S. 643 , 734 , 813 , 849 , 931
Chaisaowong,K. 687,679
Chaisricharoen,R. 1167,1284
Chaitavon,K. 1062
Chaiyaratana,N. 1229
Chamchoy,M. 884,903,915
Chamnanphrai,V. 663
Chamnongthai,K. 841,1081,1085
Chanakarn,S. 773
Chanfuangfoo,T. 1121
Chanwirawong,Y. 1217
Charnsripinyo,C. 1163
Charoenlarpnopparut,C. 691
Charoenviriyaphap,J. 987
Chawanonphithak,K. 837
Chintanasinton,A. 639
Chirathamjaree,C. 1019
Chitsobhuk,O. 1077
Choe,S. 860
Choeysakul,C. 931
Chomtong,P. 612
Chongcheawchamnan,M. 608,663,675,769
Chongstitvatana,P. 1135,1139
Chontong,T. 659
Choona,E. 1106
Chotikakamthorn,N. 991,1089
Chotjit,S. 849
Chou,P.Y. 765
Chudjuarjeen,S. 857
Chutchavong,V. 687,1110
Deeka,B. 809
Dejhan,K. 857,896
Demeechai,T. 1132
Direkpoke,P. 679,687
Duangdeun,W. 884

E,F,G

Eamsomboon,P. 1178
Elfadil,N. 702
Faidz,A.R. 623
Forsell,M. 1190
Fukase,M. 1128
Greenlaw,R. 1264

H,I,J

Haruechaiyasak,C. 1034
Hasan,M.A. 1217
Hasanayeen,M.A. 623
Hathairattananon,S. 1194
Hemmakorn,N. 963,967,975
Honghirun,M. 1151
Hossain,N. 623
Inkiew,W. 741
Intajag,S. 1102
Ishii,H. 805
Jaikla,W. 1058,1065
Jamal,M. 702
Janchitrapongvej,K. 1015,1110

Jantaworn,T. 915
Jantree,J. 813,825
Jaruskulchai,C. 1221
Jaruwanawat,A. 991
Jeeranantasin,N. 1003
Jirasakulporn,P. 734
Jiraseriamorkul,K. 841
Jitapunkul,S. 995,1011
Junnapiya,S. 896

K,L

Kaemarungsi,K. 1174
Kaewsupan,S. 943
Kaewtrakulpong,P. 1106,1121
Kakoee,M.R. 1143
Kamkleing,S. 761
Kantabutra,S. 1171,1264
Katamma,A. 635
Katanyukunanon,K. 1069
Kawdungta,S. 955
Keawon,R. 927
Keeratiwintakorn,P. 1174,1178
Ketprom,U. 789
Khan-ngern,W. 821
Khauphung,C. 1174
Khem,S. 1015
Khiripet,N. 1237
Khummanee,S. 718
Kiatkittisorn,D. 817
KIM,D.N. 1094
Kim,H. 860
Kittiamornkul,N. 841
Kittitornkun,S. 987
Kobayashi,H. 745,864
Komkhao,M. 1225
Kongsin,W. 1030
Kongthon,A. 1276
Koseeyaporn,J. 868,1046
Kositsakul,P. 935
Kosulvit,S. 837
Kovavisaruch,L. 785
Krachodnok,P. 604
Krairiksh,M. 631,643,726,841,951
Kruatrachue,B. 1022,1038
Kulsiri,J. 714
Kumar,P. 601
Kumngern,M. 857,896
Kuprasert,K. 1182
Kwanmetakun,W. 710
Lakanchanh,D. 975
Lamun,P. 857
Leelaruji,N. 975
Leesutthipornchai,P. 1163
Lekcharoen,S. 706
Lertprasert,P. 983
Lertwatechakul,M. 1213,1252
Limpiti,T. 951
Limwongse,C. 1229
Loetwassana,W. 1046
Lohakan,M. 1233
Lousangfa,P. 1268
Lueangampol,S. 1244

M,N

Madarasmi,S. 1098
Mahakittikun,S. 801
Mahapakulchai,S. 655
Mahaprom,A. 619
Mahatthanajatuphat,C. 730
Maleewong,K. 1272
Maneerat,N. 659
Maneewarn,T. 1194
Maneewattanapluk,J. 1237
Maneewongvatana,S. 1151
Manositthichai,N. 923
Marukatat,S. 1011,1038
Mason,P. A. J. 1155,1159
Matsuura,T. 1015,1022
Mattayom,C. 1155
Meelarpkit,K. 675
Meesad,P. 1205,1209,1225
Mekloi,N. 695
Mishra,V. 623
Mitrepant,C. 785,789,1178
Mitsuyama,Y. 647
Mongkolsripattana,S. 1026
Moodleah,S. 899
Moongflangklang,N. 999
Mori,K. 745,864
Moungnoul,P. 741,749,857
Mueller,R. 1276
Mustika,W. 805

Nabi,M. 1143
Nadir,Z. 702
Naji,A. 623
Nakasuwan,J. 829,939
Nakpeerayuth,S. 683
Namsang,A. 825
Navabi,Z. 1143
Netinant,P. 1198
Noymai,A. 789
Nukfron,E. 963

O,P

Onemanisone,T.J. 1073
Onoye,T. 647
Oothongsap,P. 1182
Puangpronpitag,S. 718
Pukdeeboon,Y. 1260
Punchalard,R. 1046
Puntsri,K. 627,781
Punyabukkana,P. 1054
Pakdeechard,E. 903
Panyakeow,S. 1114
Paungma,T. 745,864
Payommai,T. 919
Permpoontanalarp,Y. 1147
Phanprasit,T. 1081,1085
Phasukkit,P. 635,639,817
Phengsuwan,J. 1268
Pheunphiphop,C. 1252
Phongcharoenpanich,C. 675,726,833,837,955
Phoopattanakul,T. 691
Phromloungsri,R. 608,663,769
Piboonwattanakit,K. 821
Pichaichanlert,P. 1089
Pimpol,S. 667
Pintavirooj,C. 979,983,1073,1233
Pirak,C. 797
Pitimaneeyakul,P. 1186
Pommas,P. 722
Pongpadpinit,S. 971
Porter,A.L. 1276
Pramoun,T. 1167
Prommak,C. 809
Prommasuksakul,P. 880
Promprathom,S. 813
Promwong,S. 757,872,876,880,884,888
Promwong,S. 903 , 915 , 919, 923, 935

R,S

Rakbanjong,S. 671
Rakluea,P. 722,943
Rao,K.R. 1094
Rattanakanokkan,O. 777
Rattanasakornchai,P. 1003,1007
Rattanaudomsawat,S. 1171,1240
Rawungyot,S. 1248
Rerksngaem,T. 983
Rezazade,A. 907
Roeksabutr,A. 616
Roongruangsorakarn,S. 679
Roumsamug,P. 737
Ruangsa-ad,K. 691
Rugchatjaroen,A. 1042
Rungsubsin,T. 971
Saenghiranwattana,W. 691
Sahavechaphan,N. 1268
Saiyod,S. 911
Sakolnakorn,P.N. 1209
Sangaroon,O. 1110
Sangkeettrakarn,C. 1034
Sa-nguanpuag,Y. 1050
Sangworasil,M. 817,979,983,1081,1085
Sangworasilp,M. 1073
Sangworn,W. 769
Sanpechuda,T. 785
Sanpote,N. 892
Satayavibul,C. 1135
Sato,T. 1128
Saychum,S. 1042
Seangsae,P. 829,939
Seetao,C. 1233
Seewattanapon,S. 845
Sermwuthisarn,P. 1011
Setthawong,P. 710
Shahzad,M.A. 631
Shirakawa,I. 647
Shojaei,H. 1143
Siddhichai,S. 1121
Sinthanayothin,C. 1117
Sinthupinyo,S. 1244,1256,1260
Siripongwutikorn,P. 801
Sipruchyanun,M. 1058,1065

Sirisanyalak,B. 698
Sitichepak,S. 963
Sittichivapak,S. 714,737,777,781
Sittiwatjana,P. 737
Sodsee,S. 1225
Somboonkaew,A. 1125
Sombutkaew,R. 1077
Somwong,T. 845
Sookkaew,P. 896
Sooksomsatarn,K. 892
Sornil,O. 698
Srichavengsup,W. 683
Srikhacha,T. 1205
Srikhirin,T. 1069
Srimoon,D. 726
Sripimanwat,K. 899
Sripornprasert,J. 1139
Sritongkam,P. 1106
Srivihok,A. 1026
Suchato,A. 1054
Sueb-Am,N. 1213
Suhail,B. 702
Sukutamtanti,N. 915,919
Sumriddetchkajorn,S. 1062,1069,1125
Supanakoon,P. 872,876,880,888,919
Suphan,T. 1202
Supnithi,P. 853,967
Surareungchai,W. 1106
Sutthaphol,N. 749
Suwalak,R. 833
Suwan,S. 1268
Suwanbunyaporn,R. 608,769
Suwanchatree,S. 1007
Suwatthanaphiset,S. 1284

T,U

Tae-o-sot,S. 995
Takada,J. 753,757,872,876,880,919
Takeda,H. 1128
Tangamchit,P. 1030
Tanterdtid,S. 710
Taplee,K. 872
Tarateeraseth,V. 821
Teawchim,S. 757
Techa-angkoon,P. 1240
Thainoi,S. 1114
Thaiwattanaporn,P. 876
Thangthai,A. 1042
Tharanon,W. 1117
Thatphithakkul,N. 1038,1042
Thaworncharoensukho,S. 1256
Thipchaksurat,S. 805,911
Thummakerd,N. 781
Thumwarin,P. 1015
Tipwai,P. 1098
Tongtar,K. 999
Torrungrueng,D. 765,955
Tosranon,P. 979
Touati,F. 702
Tungjitkusolmun,S. 635,639,817
Tuntoolavest,U. 651
Udomareyasap,P. 975
Udomsripaiboon,T. 892

V,W

Varakulsiripunth,R. 659,805,911
Verma,N. 601
Vinh,N.I. 959
Visavateeranon,K. 959
Vivek,V. 927
Vonglodjanaporn,K. 714,777
Vongsack,S. 837
Wakabayashi,T. 722,829,837,939,943,947
Wangsotorn,A. 679,687
Wardkein,P. 868,1046
Watcharopas,C. 1202
Wattanapongsakorn,N. 1163
Wichaipanich,N. 967
Wichaiwong,T. 1221
Winit,R. 1171
Wiriyacosol,P. 947
Wisanmongkol,J. 785
Wisartpong,P. 868
Wong-ek,K. 1073
Wongsan,R. 604,667
Wongwilai,S. 1280
Worasawate,D. 631
Wounchoum,P. 955
Wutiwiwatchai,C. 1038,1042
Wuttisittikulkij,L. 683

Y

Yampri,P.	983
Yingkajohn,N.	888
Yofy,A.	793
Yongyat,S.	706